CODEN: JASMAN 4966

THE JOURNAL of the Acoustical Society of America

Vol. 103, No. 6 June 1998

SOUNDINGS SECTION

(Continued)

CONTENTS—*Continued from preceding page*

UNDERWATER SOUND [30]

ULTRASONICS, QUANTUM ACOUSTICS, AND PHYSICAL EFFECTS OF SOUND [35]

TRANSDUCTION [38]

STRUCTURAL ACOUSTICS AND VIBRATION [40]

ACOUSTICAL MEASUREMENTS AND INSTRUMENTATION [58]

PHYSIOLOGICAL ACOUSTICS [64]

(Continued)

CONTENTS—*Continued from preceding page*

PSYCHOLOGICAL ACOUSTICS [66]

SPEECH PRODUCTION [70]

SPEECH PERCEPTION [71]

(Continued)

CONTENTS—*Continued from preceding page*

NOTES CONCERNING ARTICLE ABSTRACTS

1. The number following the abstract copyright notice is a Publisher Item Identifier (PII) code that provides a unique and concise identification of each individual published document. This PII number should be included in all document delivery requests for copies of the article.
2. PACS numbers are for subject classification and indexing. See June and December issues for detailed listing of acoustical classes and subclasses.
3. The initials in brackets following the PACS numbers are the initials of the JASA Associate Editor who accepted the paper for publication.

SOUNDINGS

This front section of the *Journal* includes acoustical news, views, reviews, and general tutorial or selected research artcles chosen for wide acoustical interest and written for broad acoustical readership.

ACOUSTICAL NEWS—USA

Elaine Moran
Acoustical Society of America, 500 Sunnyside Boulevard, Woodbury, New York 11797

Editor's Note: *Deadline dates for news items and notices are 2 months prior to publication.*

Preliminary notice: 136th meeting of the Acoustical Society of America

The 136th meeting of the Acoustical Society of America (ASA) will be held Monday through Friday, 12–16 October 1998 at the Norfolk Waterside Marriott Hotel in Norfolk, Virginia. Registration will begin Monday, 12 October, at 7:30 a.m.

For information about the technical program refer to the ''Meetings Section'' on the ASA Home Page at ⟨http://asa.aip.org/meetings.html⟩. A special symposium and a short course on Sonic Boom is part of the technical program.

The following special sessions have been planned for the meeting:

ACOUSTICAL OCEANOGRAPHY (AO)

- **Sediment geoacoustic measurements and models**
- **Shallow-water geoacoustic inversions**

ANIMAL BIOACOUSTICS (AB)

- **Acoustics of terrestrial animals**
- **Shallow water bioacoustics** (joint with Underwater Acoustics)

ARCHITECTURAL ACOUSTICS (AA)

- **Acoustics for office spaces**
- **Acoustics of organ in performance spaces** (joint with Musical Acoustics)
- **Characterization of scattering**
- **Evaluation, selection, and application of microphones for music ensemble recording**

BIORESPONSE TO VIBRATION/BIOMEDICAL ULTRASOUND (BV)

- **Models for tissue–ultrasound interaction**

EDUCATION IN ACOUSTICS (ED)

- **''Demos 2000''**

ENGINEERING ACOUSTICS (EA)

- **In-air actuators**
- **Noise reduction in headsets**
- **Nondestructive evaluation of materials using acoustic techniques**

NOISE (NS)

- **Airbag deployment and auditory risk**
- **Acoustics and the law**
- **Measurement errors, calibration precision, and accuracy**
- **Product noise labeling**
- **Susceptibility to NIPTS and age**

PHYSICAL ACOUSTICS (PA)

- **Sonic boom Symposium**
- **Sonic boom propagation: Theoretical**
- **Sonic boom propagation: Experimental** (joint with Noise)
- **Sonic boom acceptability studies: Human and animal** (joint with Noise and Animal Bioacoustics)
- **Ultrasonic sensors, motors and other devices** (joint with Engineering Acoustics)

SIGNAL PROCESSING IN ACOUSTICS (SP)

- **Acoustics in multimedia: Content issues** (joint with Musical Acoustics)
- **Performance of active noise control systems in active real-world applications** (joint with Structural Acoustics and Vibration and Engineering Acoustics)
- **Time-frequency techniques in acoustic applications**

STRUCTURAL ACOUSTICS AND VIBRATION (SA)

- **Interior cabin noise**
- **Machinery silencing R&D in Annapolis—An historical perspective**
- **Structure-borne noise**

UNDERWATER ACOUSTICS (UW)

- **Acoustic detection and imaging of buried objects**
- **Robert J. Urick memorial session**

WOMEN IN ACOUSTICS

(joint with Education in Acoustics)

- **Diversity in science and engineering**

GALLERY OF ACOUSTICS

The Interdisciplinary Technical Group on Signal Processing in Acoustics will sponsor its third Gallery of Acoustics at the Norfolk meeting. The objective of the Gallery is to enhance ASA meetings by providing a compact and free-format setting for researchers to display their work to all meeting attendees in a forum emphasizing the diversity and interdisciplinary nature of acoustics. The Gallery of Acoustics provides a means by which we can all share and appreciate the natural beauty and aesthetic appeal of acoustical phenomena.

The Gallery will consist of posters and video displays of images generated by acoustic processes or resulting from signal processing of acoustic data. Images and videos can consist of actual visualizations of acoustic processes, or of aesthetically and technically interesting images resulting from various signal processing techniques.

A panel of referees will judge entries on the basis of aesthetic/artistic appeal, ability to convey and exchange information, and originality. A cash prize of $350 will be awarded to the winning entry. The top three entries will, with the authors' permission and cooperation, be posted on the Gallery web site.

The relevant deadlines are as follows:

1 Sept. —deadline for notice of intent to submit plus brief description of entry.

14 Sept. —deadline for receipt of all video entries and brief abstracts for all video and still entries

—deadline for receipt of still entries whose authors request that their entries be shipped to the meeting by the Gallery Committee Chair. Otherwise, contributors are responsible for shipping or carrying their entries to the meeting.

12 Oct. —deadline for receipt in Norfolk of entries whose authors have made their own arrangements for shipment to the meeting.

Entries and all other communications regarding the Gallery should be sent to: Randy Smith, Northrop Grumman Corporation, Oceanic Systems, Mail Stop 9105, P.O. Box 1488, Annapolis, MD 21404; Tel: 410-260-5478; Fax: 410-260-5454; E-mail: randall_w._smith@postal.essd.northgrum.com; Web:www.arlut.utexas.edu/asapweb/ (Click on Gallery)

 0001-4966/98/103(6)/3121/5/$10.00

SONIC BOOM SYMPOSIUM

A special event taking place in conjunction with the Norfolk meeting is the 1998 Sonic Boom Symposium. In the tradition of previous sonic boom workshops and symposia sponsored by either NASA or the ASA, the purpose of this Symposium is to provide a forum for government, industry, and university participants to present and discuss the current state of the art in sonic boom technology issues as well as new research results. The Symposium is co-sponsored by the ASA Technical Committees on Physical Acoustics, Noise, and Animal Bioacoustics.

Participants will be strongly encouraged to submit manuscripts to the *Journal of the Acoustical Society of America* for possible publication based on their oral presentations. Although the papers will be peer reviewed individually, those papers accepted by the *Journal* will be published as a group of papers representing the Symposium. The goal is to provide a set of peer-reviewed legacy papers for the next generation of sonic boom researchers, documenting the 1998 state of the art in our understanding of sonic booms including their generation, propagation, and effects on humans and animals. Details including a schedule for these submittals will be provided later.

For additional information please contact: Dr. Victor W. Sparrow, Penn State University, Graduate Program in Acoustics, 157 Hammond Building, University Park, PA 16802; Tel.: 814-865-3162; Fax: 814-863-7222; E-mail: sparrow@helmholtz.acs.psu.edu

SHORT COURSE ON SONIC BOOM

This course is intended for planners, engineers, and scientists who are interested in understanding and predicting sonic boom. The course will begin with basic descriptions of why supersonic aircraft generate booms and a review of the history of the understanding of them. Methods for prediction and analysis are presented, including a brief review of the underlying theory. Understanding of real-world sonic boom phenomena, gained from years of measurement projects, will be discussed. Use of the computer program ''PCBoom'' will be demonstrated, particularly its use as a planning tool and its ability to graphically illustrate boom footprints. The effects of sonic booms on people and structures will also be presented.

The course instructors are: Kenneth J. Plotkin, Chief Scientist of the acoustic research division of Wyle Laboratories. He first became involved with sonic boom as a graduate student at Cornell University. He has been involved with sonic boom ever since, and is the author of the PCBoom sonic boom computer model. Domenic J. Maglieri, of Eagle Aeronautics, retired several years ago from a long and distinguished career with the National Aeronautics and Space Administration (NASA). He was responsible for virtually all of the sonic boom flight test measurements conducted by NASA from the 1950s onward. Louis C. Sutherland, Consultant in Acoustics, retired several years ago as Chief Scientist at Wyle Laboratories. He conducted extensive research in environmental acoustics, especially aviation oriented, and a wide range of areas in physical acoustics and vibration.

The course will be conducted on Friday and Saturday, 15 and 16 October.

For further information about the course program contact: Kenneth J. Plotkin, kplotkin@access.digex.net or fax (703-415-4556).

Each participant will receive a copy of course notes/viewgraphs prepared by the instructors.

The registration fee is $250 and covers attendance, instructional materials, and coffee breaks. Only those who have registered by 21 September will be guaranteed receipt of instructional materials at the course. There will be a $50 discount for reservations made prior to 24 August. Full refunds will be made for cancellations prior to 21 September. Any cancellation after 21 September will be charged a $25 processing fee. To register send your name, address, and registration fee to: Acoustical Society of America, Attn: Sonic Boom Course, 500 Sunnyside Blvd., Woodbury, NY 11797; Fax: 516-576-2377.

SHORT COURSE ON AURALIZATION

Auralization is defined as an acoustic ''visualization'' process, or acoustic rendering, analogous to the visual rendering process used by architects and interior designers. Auralization is the process of rendering audible, by physical or mathematical modeling, the sound field of a source, or sources, in a hall or space, in such a way as to simulate the binaural listening experience at a given position in the modeled hall. Acousticians have been at a disadvantage in their ability to render their suggestions in such a way or form that they are comprehensible to both the client, the architect, and the public in general. Up until recently, advance acoustic information regarding the properties of a room or an outdoor environment has been limited to physical models and numerical data. Auralization now gives the acoustician and others the ability to preview a sketch of the acoustical characteristics of a space. Auralization also forms the basis of, for example, the audio side of virtual reality. The course is intended for consultants and engineers who are interested in the background, techniques, and applications of auralization. The course will help in the decision process of selecting a suitable system for a particular need. The course will include audible samples using auralization of various auditoria, concert halls, etc., as well as simplified cases. It will also be possible for the course attendants to judge the audibility of various approximations needed to make auralization feasible on today's personal computers. This course is a repeat of the very successful course held at the fall 1996 meeting.

The course instructors are: Dr. Mendel Kleiner, who has worked at the Department of Applied Acoustics, Chalmers University of Technology, since 1970. He is now professor in charge of the Chalmers Room Acoustics Group, which has been very active in the field of auralization. His review article in J. Audio Eng. Soc. **41**(11), 861–875 (1993) offers a short description of the topics which will be covered at the course. Dr. Peter Svensson is a senior researcher in Chalmers Room Acoustics Group and has worked particularly with auralization of rooms with active control of acoustics.

For more information about course program contact Mendel Kleiner at mendel@ta.chalmers.se

The course will be held Friday and Saturday, 15 and 16 October.

Each participant will receive a copy of the course notes/viewgraphs prepared by the instructors as well as a CD containing sound samples.

The registration fee is $300 and covers attendance, instructional materials, and coffee breaks. Only those who have registered by 21 September will be guaranteed receipt of instructional materials at the course. There will be a $50 discount for reservations made prior to 24 August. Full refunds will be made for cancellations prior to 21 September. Any cancellation after 21 September will be charged a $25.00 processing fee. To register send your name, address, and registration fee to: Acoustical Society of America, Attn: Auralization Short Course, 500 Sunnyside Blvd., Woodbury, NY 11797; Fax: 516-576-2377.

TUTORIAL LECTURE

A Tutorial Lecture on Probing the Unknowns of Sonoluminescence will be presented by Seth Putterman, Physics Department, UCLA, Los Angeles, CA, at 7:00 p.m. on Monday, 12 October.

ABSTRACT

Probing the unknowns of sonoluminescence. Seth Putterman (UCLA, Physics Department, Los Angeles, CA 90095)

The passage of sound through a fluid with a trapped bubble leads to the clock-like emission of picosecond flashes of ultraviolet light. In this phenomenon, sonoluminescence (or SL), acoustic energy spontaneously focuses by over 12 order of magnitude. SL is just one example of energy focusing in bubbly flows. Researchers studying cavitation from a fluid accelerating through a venturi tube in the 1960s observed subnanosecond flashes of light and had in fact at that time discovered the world's fastest man-made source of light! As with many avenues of research on cavitation luminescence, not the least of which is described in Exodus 20:18 [''And all the people saw the sounds''] these wonderful insights were abandoned. SL is extremely sensitive to ambient temperature, strength of the acoustic drive, and doping with noble gases. Despite a plethora of theoretical publications the most basic aspects of SL remain unexplained. Neither the light emitting mechanism, nor the size of the bubble, nor the range of acoustic drives at which SL can be achieved are understood. It is also a mystery as to why water is the friendliest fluid for SL and it would be most valuable to understand why pure diatomic gas bubbles are very weak, unstable sources of SL. A reasonable picture of the energy concentrating mechanism starts from Rayleigh's 1917 work on the high pressure developed in a collapsing bubble. Femtosecond light scattering from an SL bubble indicates that the collapse is strongly supersonic and suggests the formation of an imploding shock wave that further focuses the acoustic field. Measurements find that the flash of SL is emitted at the minimum radius where the acceleration exceeds 10^{11} g. The flash width is independent of wavelength from the ultraviolet to the infrared suggesting that the light is emitted when the gas is so stressed that it is in a new phase—perhaps a cold dense plasma. Methods of astronomy are being used to beat the diffraction limit and measure the

size of the sonoluminescing ''hot-spot.'' The upper limit of energy focusing that can be achieved with this ''star-in-a-jar'' has not yet been determined.

Notes summarizing the lecture will be available at the meeting. Those who register by 21 September are guaranteed receipt of a set of notes.

To partially defray the cost of the lecture a registration fee is charged. The fee is $15 for registration received by 21 September and $25 thereafter including on-site registration at the meeting. The fee for students with current ID's is $7.00 for registration received by 21 September and $12.00 thereafter, including on-site registration at the meeting. To register send your name, address, and registration fee to: Acoustical Society of America, Attn: Tutorial Registration, 500 Sunnyside Blvd., Woodbury, NY 11797; Fax: 516-576-2377.

Student transportation subsidies

A student transportation subsidies fund has been established to provide limited funds to students to partially defray transportation expenses to meetings. Students presenting papers who propose to travel in groups using economical ground transportation will be given first priority to receive subsidies, although these conditions are not mandatory. No reimbursement is intended for the cost of food or housing. The amount granted each student depends on the number of requests received. To apply for a subsidy, submit a written proposal to be received by 1 September to: Elaine Moran, ASA, 500 Sunnyside Blvd., Woodbury, NY 11797, 516-576-2360, FAX: 516-576-2377, E-mail: asa@aip.org. The proposal should indicate your status as a student, whether you have submitted an abstract, whether you are a member of ASA, method of travel, whether you will travel alone or with other students, names of those traveling with you, and approximate cost of transportation.

Students meet members for lunch

The Education Committee has established a program for students to meet with members of the ASA over lunch. Students are strongly encouraged to contact Scott Sommerfeldt, N241 ESC, P.O. Box 24673, Brigham Young Univ., Provo UT 84602-4673, USA; Tel: 801-378-2205; E-mail: s_sommerfeldt@byu.edu prior to the meeting. There will also be a sign up sheet available at the registration desk for those students who have not responded prior to the meeting.

Members who wish to participate are also encouraged to contact Scott Sommerfeldt. Participants are responsible for the cost of their own meal.

Plenary session, awards, Fellows' luncheon, and social events

Complimentary buffet socials with cash bar will be held early on Tuesday and Thursday evenings. The Tuesday Social Hour will be held at Nauticus, the National Maritime Center and will include a virtual reality display and a big-screen showing of *The Living Sea*. The Plenary session will be held on Wednesday afternoon where Society awards will be presented and recognition of Fellows will be announced. A Fellows' Luncheon will be held on Thursday; ASA Fellows may purchase tickets at the meeting.

Paper copying service

Authors are requested to provide one paper copy of their projection material and/or paper(s) to the Paper Copies Desk upon arrival. The copy should contain material on one side only on $8\frac{1}{2}\times11$ inch or A4 paper suitable for photocopy reproduction. Copies of available papers will be made for a nominal charge.

Technical tours

Technical tours have been arranged to National Aeronautics and Space Administration (NASA) Langley Research Center, Hampton, Virginia. The tours will take place Tuesday and Thursday afternoon (13 and 15 October). The tours will include many of the unique NASA facilities including wind tunnels and acoustic test facilities. Bus transportation will be provided. A schedule of tours and sign-up sheets will be available at the meeting.

Registration

The registration desk at the meeting will open on Monday morning, 12 October, at 7:30 a.m. at the Norfolk Waterside Marriott Hotel.

Registration fees are as follows:

- Acoustical Society Members: $225 [one-day: $115]
- Nonmembers: $270 [one-day $135]
- Nonmember Invited Speakers: One-day—fee waived; $225 for more than one-day participation
- Students (with ID cards): Fee waived
- Emeritus members of ASA (Emeritus status pre-approved by ASA): $35
- Accompanying Persons: $35

Nonmembers who simultaneously apply for Associate Membership in the Acoustical Society of America will be given a $50 discount off their dues payment for the first year of membership. (Full price for dues: $100).

Invited speakers who are members of the Acoustical Society of America are expected to pay the registration fee, but **nonmember invited speakers** who participate in the meeting for one day only may register without charge. Nonmember invited speakers who wish to participate in the meeting for more than one day will be charged the member registration fee of $225, which will include a one-year membership in the ASA upon completion of an application form at the meeting.

Assistive listening devices

Anyone planning to attend the meeting who will require the use of an assistive listening device, is requested to advise the Society in advance of the meeting by writing to: Acoustical Society of America, 500 Sunnyside Blvd., Woodbury, NY 11797.

Accompanying persons program

Accompanying persons are welcome. A Hospitality Room will be open from 8:00 a.m. to 11:00 a.m. daily, Monday through Friday. Information will be available on local activities including: Historical Williamsburg; The Spirit of Norfolk and American Rover Tall Ship Boat tours; Nauticus—The National Maritime Center; The MacArthur Memorial; The Chrysler Museum of Art, and many other local attractions. Information on attractions is available on the WWW at ⟨www.vgnet.com⟩.

Air transportation

The Norfolk International Airport is served by all major airlines. The airport designation is ORF.

Ground transportation

The Norfolk Waterside Marriott and Omni hotels are located eight miles from the Norfolk airport. Transportation from the airport to the hotel may be by car, taxi, or limousine service. The taxi fare is approximately $14 and the limousine fare is $18 round trip with Groome Transportation (mention ASA at reservation desk). The Omni offers complimentary shuttle service based on availability. A car is not necessary for conference participants staying at downtown hotels. Services and attractions are located within convenient walking distance from the conference hotels.

Hotel accommodations

The Norfolk Waterside Marriott Hotel is the site for the meeting where all meeting functions will be held. Rooms are also available at the Omni Waterside Hotel, across Waterside Drive from the Marriott Hotel. Blocks of rooms have been reserved at both the Marriott and Omni Hotels. Please make your reservations directly with the hotel of your choice and ask for one of the rooms being held for the Acoustical Society of America. The reservation cut-off date for the special discounted ASA rates is 12 September 1998; after this date the conference rate will not be available.

Norfolk Waterside Marriott Hotel

(All technical sessions and other meeting functions will be held at the Marriott Hotel.)

The hotel adjoins the Waterside Convention Center and offers a first-class 23-story hotel and a four-story convention center within the same complex. It is ideally located in the heart of the city across the street from the popular Waterside Festival Marketplace and a short distance from many other attractions. The hotel features 405 stylishly appointed guest rooms, most with dramatic waterviews. Stormy's Pub offers a variety of light meals. The hotel has a 140-seat dining room, a plush piano lounge, and an executive health club. Valet and self-service parking is available ($10/$8 per day).

Norfolk Waterside Marriott Hotel
235 East Main Street
Norfolk, VA 23510
Tel.: 757-627-4200 or 800-831-4004
Fax: 757-628-6452
Room rate: $109, plus 11.5% tax. Single or Double
$15 for each additional person
Reservation cut-off date: 12 September 1998

Omni Waterside Hotel

The hotel offers 446 meticulously appointed guest rooms, many of which offer balconies overlooking the waterfront. The hotel is across the street and connected by covered walkway to the Convention Center. The waterfront hotel is next to Norfolk's Waterside Festival Marketplace. The hotel offers the upscale bar, ''Alexander's,'' overlooking the working harbor, and the Riverwalk Restaurant. The Omni features the exclusive Omni Club floor, as well as nonsmoking floors. Valet and self-service parking is available ($9.50/$3 per day).

Omni Waterside Hotel
777 Waterside Drive
Norfolk, VA 23510
Tel.: 757-622-6664 or 800-The-Omni (800-843-6664)
Fax: 757-625-8271
Room Rate: $107, plus 11.5% tax. Single or double
$15 for each additional person.
Reservation cut-off date: 12 September 1998

Room sharing

ASA will compile a list of those who wish to share a hotel room and its cost. To be listed, send your name, telephone number, gender, smoker or nonsmoker, by 17 August 1998 to the Acoustical Society of America, Attn.: Room Sharing, 500 Sunnyside Blvd., Woodbury, NY 11797, e-mail: asa@aip.org. The responsibility for completing any arrangements for room sharing rests solely with the participating individuals.

Weather

Norfolk's weather is ranked among the most desirable in the U.S. by the National Weather Service. Changeable mid-October temperatures will range from 60 to 80 degrees F, with a light coat required on some evenings. There is always a possibility of rain.

CHARLES E. SCHMID
Executive Director

ASA Fellows elected to National Academy of Engineering

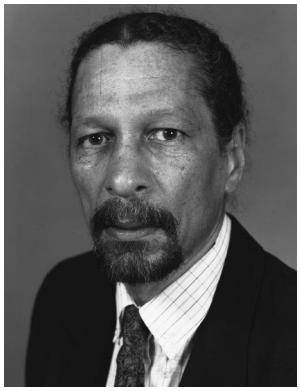

James E. West

George C. Maling

James E. West and George C. Maling were elected to the National Academy of Engineering in 1998. Academy membership honors those who have made ''important contributions to engineering theory and practice, including significant contributions to the literature of engineering theory and practice,'' and those who have demonstrated ''unusual accomplishment in the pioneering of new and developing fields of technology.'' The NAE's U.S. membership totals 1941 and foreign associates total 155.

James West, distinguished member of the technical staff, Bell Laboratories Lucent Technologies, Murray Hill, NJ, was cited ''for electret transducers and their applications to microphones.'' Jim West is the current ASA President-Elect and was awarded the ASA Silver Medal in Engineering Acoustics in 1995.

George Maling, managing director of the Institute of Noise Control Engineering of the USA, Inc., Poughkeepsie, NY was cited ''for noise-control engineering and the development of international and national noise standards.'' George Maling was awarded the ASA Silver Medal in Noise in 1992.

ASA members elected Fellows of ASME International

ASA member Robert L. Hershey, executive engineer at O'Donnell Consulting Engineers, Washington, DC, and Clark J. Radcliffe, professor of mechanical engineering at Michigan State University, East Lansing, MI, were named Fellows of ASME International (The American Society of Mechanical Engineers).

The ASME International Fellow grade is conferred upon a member with at least 10 years of active engineering practice who has made significant contributions to the field.

USA Meetings Calendar

Listed below is a summary of meetings related to acoustics to be held in the U.S. in the near future. The month/year notation refers to the issue in which a complete meeting announcement appeared.

1998

4–7 June	7th Symposium on Cochlear Implants in Children, Iowa City, IA [Center for Conferences and Institutes, The University of Iowa, 249 Iowa Memorial Union, Iowa City, IA 52242-1317; Tel.: 800-551-9029; Fax: 319-335-3533].
20–26 June	135th meeting of the Acoustical Society of America/ 16th International Congress on Acoustics, Seattle, WA [ASA, 500 Sunnyside Blvd., Woodbury, NY 11797; Tel.: 516-576-2360; Fax: 516-576-2377; E-mail: asa@aip.org, WWW: http://asa.aip.org].
26 Jun.–1 Jul.	International Symposium on Musical Acoustics, ISMA 98, Leavenworth, WA [Maurits Hudig, Catgut Acoustical Society, 112 Essex Ave., Montclair, NJ 07042; Fax: 201-744-9197; E-mail: catgutas@msn.com, WWW: www.boystown.org/isma98].
7–12 July	Vienna and the Clarinet, Ohio State Univ., Columbus, OH [Keith Koons, Music Dept., Univ. of Central Florida, P.O. Box 161354, Orlando, FL 32816-1354; Tel.: 407-823-5116; E-mail: kkons@pegasus.cc.ucf.edu].
12–15 July	Transportation Research Board A1F04 Summer Meeting on Transportation Related Noise and Vibration, Tallahassee, FL [Win Lindeman, Florida Department of Transportation, 605 Suwannee St., M.S. 37, Tallahassee, FL 32399-0450; Tel.: 850-488-2914; Fax: 850-922-7217; E-mail: win.lindeman@dot.state.fl.us].
9–14 Aug.	International Acoustic Emission Conference, Hawaii [Karyn S. Downs, Lockheed Martin Astronautics, PO Box 179, M.S. DC3005, Denver, CO 80201; Tel.: 303-977-1769; Fax: 303-971-7698; E-mail: karyn.s.downs@lmco.com].
13–17 Sept.	American Academy of Otolaryngology—Head and Neck Surgery, San Francisco, CA [American Academy of Otolaryngology—Head and Neck Surgery, One Prince St., Alexandria, VA 22314; Tel.: 703-836-4444; Fax: 703-683-5100].
18–19 Sept.	6th Annual Conference on Management of the Tinnitus

Patient, Iowa City, IA [Richard Tyler, Univ. of Iowa, Dept. of Otolaryngology—Head & Neck Surgery, 200 Hawkins Dr., C21GH, Iowa City, IA 52242; Tel: 319-356-2471; Fax: 319-353-6739; E-mail: rich-tyler@uiowa.edu].

12–16 Oct. 136th meeting of the Acoustical Society of America, Norfolk, VA [ASA, 500 Sunnyside Blvd., Woodbury, NY 11797; Tel.: 516-576-2360; Fax: 516-576-2377; E-mail: asa@aip.org, WWW:http://asa.aip.org].

15–19 March Joint meeting: 137th meeting of the Acoustical Society of America/Forum Acusticum [Acoustical Society of America, 500 Sunnyside Blvd., Woodbury, NY 11797; Tel.: 516-576-2360; Fax: 516-576-2377; E-mail: asa@aip.org; WWW: asa.aip.org].

27–30 June ASME Mechanics and Materials Conference, Blacksburg, VA [Mrs. Norma Guynn, Dept. of Engineering Science and Mechanics, Virginia Tech, Blacksburg, VA 24061-0219; Fax: 540-231-4574; E-mail: nguynn@vt.edu; WWW: http://www.esm.vt.edu/mmconf/]. Deadline for receipt of abstracts: 15 January 1999.

ACOUSTICAL NEWS—INTERNATIONAL

Walter G. Mayer
Physics Department, Georgetown University, Washington, DC 20057

Papers published in JASJ(E)

A listing of Invited Papers and Regular Papers appearing in the latest issue of the English language version of the *Journal of the Acoustical Society of Japan*, JASJ(E), was published for the first time in the January 1995 issue of the Journal. This listing is continued below.

The March issue of JASJ(E), Vol. 19, No. 2 (1998) contains the following papers:

E. Ozimek, J. Konieczny, Y. Suzuki, and T. Sone ''Random changes in envelope of AM tones and their detection''
M. Akiho, M. Haseyama, and H. Kitajima ''Virtual reference signals for active noise cancellation system''
S. Asghar and T. Hayat ''Scattering by a screen with fluid flow''
N. Nakasako and M. Ohta ''Identification and probabilistic response prediction methods for actual sound insulation systems contaminated by background noise''
M. Yamada and T. Tsumura ''Do piano lessons improve basic temporal controllability by maintaining a uniform tempo?''
S. Saito, N. Akashi, and J. Kushibiki ''Second harmonic component of nonlinearly distorted wave in a 20-MHz focused sound field''
H. Behnam, S. Ohtsuki, and M. Tanaka ''Phase correction on ultrasound speed measurements''

International Meetings Calendar

Below are announcements of meetings to be held abroad. Entries preceded by an * are new or updated listings with contact addresses given in parentheses. Month/year listings following other entries refer to issues of the *Journal* which contain full calendar listings or meeting announcements.

June 1998

8–10 **EAA/EEAA Symposium ''Transport Noise and Vibration,''** Tallinn. *10/96*

9–12 **8th International Conference on Hand-Arm Vibration**, Umea. *6/97*

11–12 **Swiss Acoustical Society Spring Meeting**, Lausanne, Switzerland. *4/98*

20–28 **Joint Meeting of the 16th International Congress on Acoustics and 135th Meeting of the Acoustical Society of America**, Seattle. *6/97*

July 1998

1–12 **NATO ASI ''Computational Hearing,''** Il Ciocco (Tuscany). *12/97*

September 1998

7–9 **Nordic Acoustical Meeting 98**, Stockholm. *10/97*

14–16 **Biot Conference on Poromechanics**, Louvain-la-Neuve. *10/97*

14–16 **ACUSTICA 98**, Lisbon. *10/97*

14–18 **35th International Conference on Ultrasonics and Acoustic Emission**, Chateau of Třešt'. *10/97*

16–18 ***International Conference on Noise and Vibration Engineering**, Leuven, Belgium. (Ms. L. Notré, K. U. Leuven, Division PMA, 3001 Leuven, Belgium; Fax: +32 16 32 29 87; e-mail: lieve.notre@mech.kuleuven.ac.be)

17–18 ***Annual Meeting of INCE/Japan**, Tokyo, Japan. (Fax: +81 423 27 3847)

17–18 ***5th Mexican Congress on Acoustics**, Querétaro, Qro., Mexico. (S. Beristáin, P.O. Box 75805, Lindavista 07300 Mexico, D.F., Mexico; Fax: +52 5 523 4742; e-mail: sberista@maxwell.esimez.ipn.mex)

21–25 **4th European Conference on Underwater Acoustics**, Rome. *4/98*

24–26 ***Autumn Meeting of the Acoustical Society of Japan**, Yamagata, Japan. (ASJ, Ikeda-Building, 2-7-7, Yoyogi, Shibuya-ku, Tokyo, 151 Japan; Fax: +81 3 3379 1456)

October 1998

4–7 **euro-noise 98**, Munich. *4/98*

12–16 ***International Conference on Signal Processing (ICSP'98)**, Beijing, China. (Yuan Baozong, Institute of Information Science, Northern Jiaotong University, Beijing 100044, China; Fax: +86 10 6828 3458; e-mail: yuanbz@sun.ihep.ac.cn; www.cie-china.org)

14–16 ***16th Yugoslav Conference on Noise and Vibration**, Nis, Yugoslavia. (e-mail: noise@znrfak.znrfak.ni.ac.yu)

31–2 ***(New date and contacts) AES International Conference ''Audio, Acoustics and Small Spaces,''** Copenhagen, Denmark. (J. Voetmann, DELTA Acoustics & Vibration, Building 356, Akademivey, 2800 Lyngby, Denmark; Fax: +45 45 93 19 90; e-mail: jv@delta.dk)

November 1998

11–13 ***1st Asia Pacific Conference on Acoustics and Vibration (APAV 98)**, Singapore, Singapore. (APAV 98 Secretariat, 1 Selegie Road #09-01, Paradiz Centre, Singapore 188308, Singapore; Fax: +65 334 7891; e-mail: apavcon@singnet.com.sg)

12–15 **Institute of Acoustics (UK) Autumn Conference: Speech and Hearing**, Windermere. *4/98*

16–18 **Inter-Noise 98**, Christchurch. *4/96*

20 **Recreational Noise**, Queenstown. *10/97*

23–27 ***(New contacts) ICBEN 98: Biological Effects of Noise**, Sydney. (Fax: +61 2 9262 3135; e-mail: noise98@tourhosts.com.au; www.acay.com.au/~dstuckey/noise-effects98) *12/96*

30–4 **5th International Conference on Spoken Language Processing**, Sydney. *6/97*

December 1998

15–16 **Sonar Signal Processing**, Loughborough. *4/98*

March 1999

15–19 **Joint Meeting of DAGA, EAA Forum Acusticum, and 137th Meeting of the Acoustical Society of America**, Berlin. *6/97*

May 1999

10–14 ***4th International Conference on Theoretical and Computational Acoustics**, Trieste, Italy. (A. Marchetto, ICTCA'99, Osservatorio Geofisico Sperimentale, P.O. Box 2011—Opicina, 34016 Trieste, Italy; Fax: +39 40 327040; e-mail: ictca99@ogs.trieste.it)

June 1999

28–30 **1st International Congress of the East European Acoustical Association**, St. Petersburg. *10/97*

28–1 ***Joint Conference of Ultrasonics International '99 and World Congress on Ultrasonics '99 (UI99/WCU99)**, Lyngby, Denmark. (L. Bjørnø, Department of Industrial Acoustics, Denmark's Technical

 0001-4966/98/103(6)/3129/2/$10.00

University, Building 425, 2800 Lyngby, Denmark; Fax: +45 45 93 01 90; e-mail: lb@ipt.dtu.dk; www.msc.cornell.edu/~ui99/)

July 1999

4–9 **10th British Academic Conference in Otolaryngology**, London. *10/97*

5–8 **6th International Congress on Sound and Vibrations**, Copenhagen. *2/98*

September 1999

1–4 **15th International Symposium on Nonlinear Acoustics (ISNA-15)**, Göttingen. *10/97*

October 2000

3–5 *__WESPRAC VII__, Kumamoto, Japan. (Computer Science Department, Kumamoto University, 2-39-1, Kurokami, Kumamoto, Japan 860-0862; Fax: +81 96 342 3630; e-mail: wesprac7@cogni.eecs.kumamoto-u.ac.jp)

BOOK REVIEWS

James F. Bartram
94 Kane Avenue, Middletown, Rhode Island 02842

These reviews of books and other forms of information express the opinions of the individual reviewers and are not necessarily endorsed by the Editorial Board of this Journal.

Editorial Policy: *If there is a negative review, the author of the book will be given a chance to respond to the review in this section of the Journal and the reviewer will be allowed to respond to the author's comments. [See ''Book Reviews Editor's Note,'' J. Acoust. Soc. Am.* ***81****, 1651 (May 1987).]*

Neural Networks and Fuzzy Systems

Bart Kosko

Prentice-Hall, Englewood Cliffs, NJ, 1992.
xxvii + 449 pp. + 2 diskettes. Price $89.33.

Neural Networks for Signal Processing

Bart Kosko, Editor

Prentice-Hall, Englewood Cliffs, NJ, 1992.
xv + 399 pp. (Out of print).

Technical texts are usually dry. Kosko breaks the mold. His writing is not only clear and concise; his explanatory anecdotes are illuminating, down-to-earth, and often amusing. The influence of his background, with degrees in philosophy, economics, math, and a doctorate in electrical engineering, lifts these books from being valuable to also being enjoyable. [See ''Bart Kosko,'' IEEE Spectrum, pp. 58–62 (February 1996), for more about Kosko the person.]

These books are for those who want a comprehensive introduction to neural networks, fuzzy systems, and their applications. As Lotfi Zadeh states in a Foreword to ''Neural Networks and Fuzzy Systems'' (NNFS). ''It is hard to overestimate the importance of this textbook. Bart Kosko has broken new ground with an outstanding work on a subject, adaptive fuzzy systems, certain to play an increasingly central role in our understanding of human cognition and our ability to build machines that simulate human decision making in uncertain and imprecise environments.''

How does the human brain function in the real world, where perception and reality are not the same, where most situations are not binary (right or wrong), and where ambiguity and uncertainty are norms? Anyone who has listened to the ''truth'' as asserted by opposing politicians knows that ''truth'' is multi-valued and vague.

Artificial neural networks and fuzzy systems are two distinct but overlapping attempts to approximate real-world human brain functionality in dealing with multi-valued and vague situations. While artificial intelligence (AI) is mostly committed to rule-based symbol manipulation and first-order logic (e.g., ''expert systems''), neural networks and fuzzy systems are numerical and model-free. They work directly with and learn from numerical data, and do not require mathematical functions as input–output models. ''Neural and fuzzy systems differ in how they estimate sampled functions. The neural approach requires the specification of a nonlinear dynamical system, usually feedforward, the acquisition of a sufficiently representative set of numerical training samples, and the encoding of those training samples in the dynamical system by repeated learning cycles. The fuzzy system requires only that we partially fill in a linguistic 'rule matrix'. This task is markedly simpler than designing and training a neural network.'' (NNFS, pp. 302–306).

Applications for neural networks and fuzzy systems are many and significant. They have been used to design high-speed modems, long-distance telephone systems, and airport bomb detectors. They ''run subways, tune televisions and computer disc heads, focus and stabilize camcorders, adjust air conditioners and washing machines and vacuum sweepers'' and more. Neural networks lead naturally to massively parallel processing (e.g., VLSI). For acousticians, the primary applications of interest may be to signal processing. This is the focus of ''Neural Networks for Signal Processing'' (NNSP).

''The basic theory uses only elementary calculus, linear algebra and probability, as found in upper-division undergraduate curricula in engineering and science. Some applications use more advanced techniques from digital signal processing, random processes, and estimation and control theory. The text and homework problems introduce and develop these techniques.'' But a nontechnical reader can glean much from chapter introductory material and conclusions, particularly chapters devoted to definitions and applications.

NNFS consists of 11 chapters that present the basic theory, with some applications, in two sections. The first develops neural network theory; the second examines fuzziness and adaptive fuzzy systems. NNFS has an Appendix with instructions on using the included software (on two $5\frac{1}{4}$-in. diskettes; MS-DOS). References and problems, including software problems using C-software on the diskettes, are arranged by chapters. The software includes executable files that nicely illustrate sample applications with default conditions. Illustrations are ample and instructive. The book includes a good Index, but lacks a glossary of the many acronyms that are scattered throughout the book. While a solutions manual was originally published, it is now out of print.

NNSP consists of 9 chapters by a variety of authors. It ''explores non-linear signal processing with neural networks. Chapters 1–5 apply neural networks to speech recognition, image processing, spectral estimation, and vision. Chapters 6 and 7 apply neural networks to robotics and control. Chapters 8 and 9 discuss new ways to implement neural networks in analog [VLSI] circuitry in optical devices.''

Both of these books should interest graduate students, researchers, and engineers who want to explore and apply neural networks and fuzzy systems. NNFS is essential as a starting point. The signal processing material in NNSP Chapters 1–5 should interest acousticians, particularly those working in speech recognition.

JOHN C. BURGESS
Department of Mechanical Engineering
University of Hawaii
2540 Dole Street
Honolulu, Hawaii 96822

 0001-4966/98/103(6)/3131/1/$10.00

REVIEWS OF ACOUSTICAL PATENTS

Daniel W. Martin
7349 Clough Pike, Cincinnati, Ohio 45244

The purpose of these acoustical patent reviews is to provide enough information for a Journal reader to decide whether to seek more information from the patent itself. Any opinions expressed here are those of reviewers as individuals and are not legal opinions. Printed copies of United States Patents may be ordered at $3.00 each from the Commissioner of Patents and Trademarks, Washington, DC 20231.

Reviewers for this issue:

GEORGE L. AUGSPURGER, *Perception Incorporated, Box 39536, Los Angeles, California 90039*
D. LLOYD RICE, *11222 Flatiron Drive, Lafayette, Colorado 80026*
CARL J. ROSENBERG, *Acentech Incorporated, 33 Moulton Street, Cambridge, Massachusetts 02138*
WILLIAM THOMPSON, JR., *The Pennsylvania State University, University Park, Pennsylvania 16802*

5,504,720

43.30.Yj FIBER OPTIC PLANAR HYDROPHONE

A. D. Meyer *et al.*, assignors to Litton Systems, Incorporated
2 April 1996 (Class 367/149); filed 20 March 1995

The sensor consists of a number of air-filled cylindrical mandrels having axes that are parallel and coplanar. The optical fibers wound on one set of these mandrels are configured to be in phase opposition to those wound on the rest of the mandrels for a sound wave impinging upon the sensor. The output signals from the two fibers then compose a Mach–Zehnder interferometer.—WT

5,572,487

43.30.Yj HIGH PRESSURE, HIGH FREQUENCY RECIPROCAL TRANSDUCER

J. A. Tims, assignor to the United States of America
5 November 1996 (Class 367/157); filed 24 January 1995

A high-frequency (100-kHz to 2-MHz) sonar transducer that can be used as either source or receiver, and at high hydrostatic pressures up to 3000 psi, is realized using a thin disc of lead titanate with no passive pressure release material, i.e., both faces of the disc are exposed to the acoustic medium. The edge of the disc is epoxied into a butyl rubber grommet to help damp out the effects of radial mode resonances. The grommet is then cast in polyurethane to form a thick disc transducer element which is supported within a mounting assembly by means of a crossed pair of annealed iron wires. The resonances of these wires are well below the frequency range of interest. Finally this mounting assembly is positioned in an oil-filled cylindrical cavity of a suitable housing. This cavity is sealed, front and back, by a pair of acoustically transparent gum rubber windows. Suitable electronics and waterproof electrical connectors reside in an adjacent, detachable, housing.—WT

5,694,477

43.35.Ud PHOTOTHERMAL ACOUSTIC DEVICE

Stephen G. Kole, Port Jervis, NY
2 December 1997 (Class 381/111); filed 8 December 1995

According to the patent, ''the photothermal device may be used to generate a three-dimensional sound shield around a noise source in order to prevent the propagation of sound waves from the noise source.'' This is said to be accomplished by directing toward the noise source three orthogonally directed laser beams of infrared radiation, each modulated at an audio frequency signal controlled in phase amplitude and frequency. ''A sound barrier may be created in accordance with the present invention by surrounding the noise source with high pressure zones which sufficiently impede the propagation of sound waves emanating from the sound source.''—DWM

5,691,475

43.35.Yb METHOD FOR MEASURING THE PROPAGATION VELOCITY OF ULTRASONIC ACOUSTIC WAVES THROUGH ROCK FRAGMENTS

Alberto Marsala *et al.*, assignors to Agip S.p.A.
25 November 1997 (Class 73/597); filed in Italy 15 December 1994

The propagation velocity of ultrasonic waves through rock samples is measured by placing the sample in a fluid between a pair of piezoelectric transducers, transmitting highly damped ultrasonic waves through the sample, observing the transmitted signals on the oscilloscope, and measuring the transit time. The pulses transmitted have widths ranging from 0.1 to 20 μs. The waves may be compressional or shear type.—DWM

5,696,326

43.35.Zc METHOD AND APPARATUS FOR ACOUSTIC TESTING OF ARMATURES

Antonio Becherucci and Dalibor Kirov, assignors to Axis USA, Incorporated
9 December 1997 (Class 73/600); filed 7 June 1995

''The armature is immersed in an acoustic coupling medium. Acoustic pulses, preferably ultrasonic pulses, are beamed onto the commutator tang/wire interface region of a commutator tang/bar fused joint or the fused joint itself and an acoustic signature is measured. The quality of the joint can be determined by comparing the acoustic signature to a predetermined acoustic signature of known quality.''—DWM

5,698,787

43.35.Zc PORTABLE LASER/ULTRASONIC METHOD FOR NONDESTRUCTIVE INSPECTION OF COMPLEX STRUCTURES

Halina M. Parzuchowski *et al.*, assignors to McDonnell Douglas Corporation
16 December 1997 (Class 73/643); filed 12 April 1995

The apparatus of this patent is for nondestructive inspection of complex structures such as airplane wings. It employs a fiber optic ultrasonic delivery system and a thermoelastic medium, producing mechanical stresses that initiate detectable sound waves regardless of the angle of the ultrasonic transducer output with respect to the test piece.—DWM

 0001-4966/98/103(6)/3132/7/$10.00

5,381,385

43.38.Fx ELECTRICAL INTERCONNECT FOR MULTILAYER TRANSDUCER ELEMENTS OF A TWO-DIMENSIONAL TRANSDUCER ARRAY

M. Greenstein, assignor to Hewlett-Packard Company
10 January 1995 (Class 367/140); filed 4 August 1993

In a two-dimensional array of transducers, each of which comprises multiple piezoelectric layers, the electrical connections to the various layers are accomplished by means of conducting via segments located at the four corners of the nominally square-faced transducer elements. One pair of diagonally opposed vias connects to the high sides of the various piezoelectric layers while the other diagonally opposed pair of vias connects the ground sides. In a two-dimensional grid array, any one via will make connection to the four transducer elements that share a point of the grid. With this arrangement, there is also redundant electrical connection to any one transducer element.—WT

5,673,329

43.38.Ja OMNI-DIRECTIONAL LOUDSPEAKER SYSTEM

David Wiener, Park City, UT
30 September 1997 (Class 381/160); filed 23 March 1995

A flexible, compressible tube is used as a loudspeaker enclosure. In one version two tubes are coupled end-to-end to form a stereophonic system. ''A fabric sleeve having a graphic display which may include an advertisement fits over the tubes.''—GLA

5,689,573

43.38.Ja FREQUENCY-DEPENDENT AMPLITUDE MODIFICATION DEVICES FOR ACOUSTIC SOURCES

P. K. G. Jones, assignor to Boston Acoustics, Incorporated
18 November 1997 (Class 381/154); filed 7 January 1992

An array of little tubes or slots is mounted on a bridge across the front of a loudspeaker. Alternatively, a necklace of little tubes surrounds the loudspeaker cone. These pipes or slots are intended to function as quarter-wave or half-wave stubs, attenuating specific frequencies at which response peaks occur. So far, so good. They are oriented at approximately 90 degrees to the axis of sound propagation because, ''...as the pipe approaches a parallel position to the axis, it will lose its correcting effect.'' Moreover, since the array partially shadows the cone, the upper frequency range of the loudspeaker is extended. ''By constricting the driver's output, the constricting object increases the output level in the upper range of the driver.'' Some interesting new acoustical principles are at work here.—GLA

5,693,916

43.38.Ja METHOD FOR DESIGNING LOUD SPEAKER ENCLOSURES

Richard F. von Sprecken, Clinton, MS
2 December 1997 (Class 181/156); filed 12 April 1996

The patent shows a simplified method for designing vented loudspeaker enclosures. It starts out by establishing the ideal vent area in relation to peak displacement volume and baffle thickness. In other words, a given loudspeaker mounted on a $\frac{1}{2}$ -in.-thick baffle requires twice the vent area as the same loudspeaker on a 1-in. baffle, according to the patent.—GLA

5,668,885

43.38.Lc LOW FREQUENCY AUDIO CONVERSION CIRCUIT

Mikio Oda, assignor to Matsushita Electric Industrial Company
16 September 1997 (Class 381/98); filed in Japan 27 February 1995

Vacuum tube circuits to generate synthetic bass were known in the 1940s. These relied on nonlinear amplifiers to produce additional harmonics. The patent describes circuitry to generate even harmonics by full-wave rectification and filtering.—GLA

5,673,326

43.38.Lc AUDIO BASS SPEAKER DRIVER CIRCUIT

Barry S. Goldfarb, assignor to BSG Laboratories
30 September 1997 (Class 381/99); filed 27 March 1995

The circuit shown functions as a bandpass filter, providing a relatively steep cutoff at subsonic frequencies. This seemingly complicated arrangement is justified on the basis that it is easily tuned to achieve optimum results with a particular loudspeaker system.—GLA

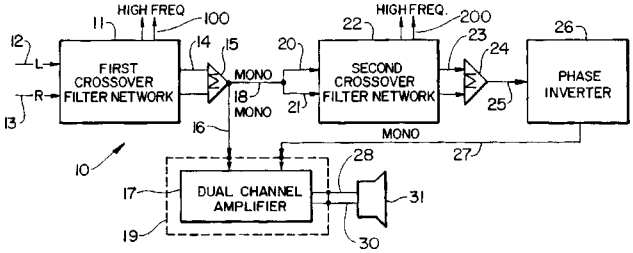

5,668,871

43.38.Si AUDIO SIGNAL PROCESSOR AND METHOD THEREFOR FOR SUBSTANTIALLY REDUCING AUDIO FEEDBACK IN A COMMUNICATION UNIT

Steven Adam Urbanski, assignor to Motorola, Incorporated
16 September 1997 (Class 379/406); filed 29 April 1994

This patent and its companion 5,696,821 (see below) describe a fairly elaborate arrangement for suppressing acoustic feedback in hands-free telephone sets. Circuitry includes an echo canceller, reverse path attenuator, forward path attenuator, forward and reverse voice detectors and processors, a noise estimator, and much, much more. Adaptive filters are not employed.—GLA

5,668,883

43.38.Si HEADPHONE APPARATUS INCLUDING AN EQUALIZER SYSTEM HAVING AN OPEN LOOP CHARACTERISTIC WITH A RISING SLOPE OUTSIDE THE CANCELLATION BAND

Kensaku Abe and Takahiro Muraguchi, assignors to Sony Corporation
16 September 1997 (Class 381/72); filed in Japan 5 September 1994

The apparatus is an active noise-cancellation in-the-ear headphone in which the frequency and dynamic ranges of cancellation are relatively improved.—GLA

5,696,821

43.38.Si RADIOTELEPHONE AND METHOD THEREFOR FOR SUBSTANTIALLY REDUCING AUDIO FEEDBACK

Steven Adam Urbanski, assignor to Motorola, Incorporated
9 December 1997 (Class 379/406); filed 28 February 1996

This patent and its companion 5,668,871 (reviewed above) describe a fairly elaborate arrangement for suppressing acoustic feedback in hands-free telephone sets.—GLA

5,661,812

43.38.Vk HEAD MOUNTED SURROUND SOUND SYSTEM

William Clayton Scofield and Stevan Otha Saunders, assignors to Sonics Associates, Incorporated
26 August 1997 (Class 381/25); filed 21 November 1996

A head-mounted assembly positions small left and right loudspeakers slightly forward of the listener's ears. With appropriate signal processing, these can provide additional phantom sources for center and surround channels. Low frequencies are reproduced by a separate subwoofer, which can serve a number of headset listeners. According to the patent, the problem of head movement is not really a problem: ''Since the localized speakers are fixed to the listener's head, visual cues on the screen provide the listener with additional information to assist in localizing the sound.''—GLA

5,666,424

43.38.Vk SIX-AXIS SURROUND SOUND PROCESSOR WITH AUTOMATIC BALANCING AND CALIBRATION

James W. Fosgate and Samuel John Wolfe, assignors to Harman International Industries, Incorporated
8 September 1997 (Class 381/18); filed 24 April 1996

The patent is a continuation in part of four earlier filings, dating back to June 1990. Fosgate surround sound processing has now been brought into the digital age, complete with video screen menus and microprocessor-controlled calibration.—GLA

5,677,957

43.38.Vk AUDIO CIRCUIT PRODUCING ENHANCED AMBIENCE

Alan Hulsebus, Excelsior, MN
14 October 1997 (Class 381/1); filed 13 November 1995

Ambience is enhanced electronically by processing a difference signal through a shelving filter and then mixing it in opposed phase to left and right sound outputs. This somehow leads to seventeen patent claims.—GLA

5,379,269

43.40.Dx POSITION DETERMINING APPARATUS

S. J. Sindeband and T. L. Stone, assignors to Science Accessories Corporation
3 January 1995 (Class 367/127); filed 13 January 1993

An apparatus for generating graphical coordinate information is discussed. Ultrasonic energy, which is input into the solid medium **105** in the form of shear waves by the movable transducer assembly **150**, is received by similar transducers **121** and **122** which are mounted in housing **110** in such

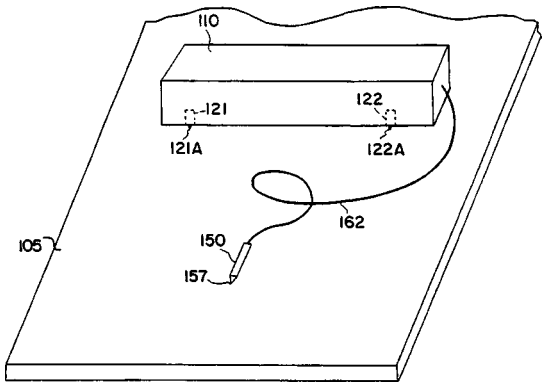

a fashion as to be always in contact with the medium **105** (which may be a sheet of glass or plastic). Simple time-of-flight calculations locate the position of **150** relative to **121** and **122**.—WT

5,703,338

43.50.Gf SOUND ABSORBER

Herman Liese, Unterhaching, Germany
30 December 1997 (Class 181/264); filed in Germany 21 October 1993

This patent is for a jet-engine-type muffler. Air is drawn through the device past sound-absorbing elements. The elements are arrayed in two rows that are spaced apart and parallel. The elements in these rows are U shaped, V shaped, or semicircular in cross section. The rows themselves are offset and the elements arranged such that the open cross-sectional areas of each row face each other in overlapping fashion. In this manner, the exhaust gas winds its way through the sound absorber on its way to the exit plane.—CJR

5,677,992

43.72.Ar METHOD AND ARRANGEMENT IN AUTOMATIC EXTRACTION OF PROSODIC INFORMATION

Bertil Lyberg, assignor to Telia AB
14 October 1997 (Class 395/2.66); filed in Sweden 3 November 1993

This is a system for performing prosody analysis on input speech signals, in particular, for assigning word stress patterns. A pitch analysis of the input is used to build a model of the intonation pattern. Minimal detail is given of how that model is to be constructed. Comparison of the input pitch profile to the intonation model consists of range normalization, declination, and ratio of pitch to declination. These are used to construct the output stress pattern.—DLR

5,684,925

43.72.Ar SPEECH REPRESENTATION BY FEATURE-BASED WORD PROTOTYPES COMPRISING PHONEME TARGETS HAVING RELIABLE HIGH SIMILARITY

Philippe R. Morin and Ted H. Applebaum, assignors to Matsushita Electric Industrial Company
4 November 1997 (Class 395/2.63); filed 8 September 1995

The patent describes an alternate representation of phonetic information for use by a speech recognition system. Using a normal frame-by-frame analysis, multiple utterances of a phrase are overlaid to determine regions of

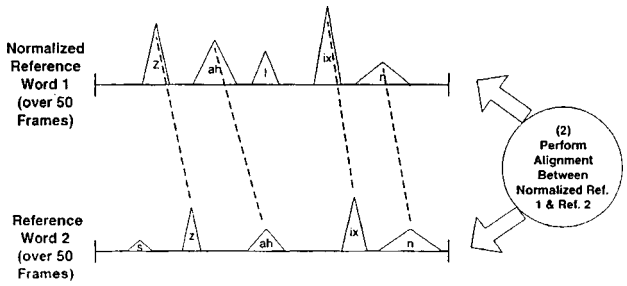

high phonetic similarity. Pruning schemes assure that only robust, reliable similar regions are maintained. Each such region is tagged with a phonetic ID and its location in a phrase. Speech to be recognized is compared with the set of phonetic regions.—DLR

5,687,280

43.72.Ar SPEECH INPUT DEVICE INCLUDING DISPLAY OF SPATIAL DISPLACEMENT OF LIP POSITION RELATIVE TO PREDETERMINED POSITION

Kenji Matsui, assignor to Matsushita Electric Industrial Company
11 November 1997 (Class 395/2.4); filed in Japan 2 November 1992

This is a speech recognizer with a built-in lip reader. A mirror and photocell are arranged to record the position of an edge, such as the lower boundary of the upper lip. From this one reading and geometrical consider-

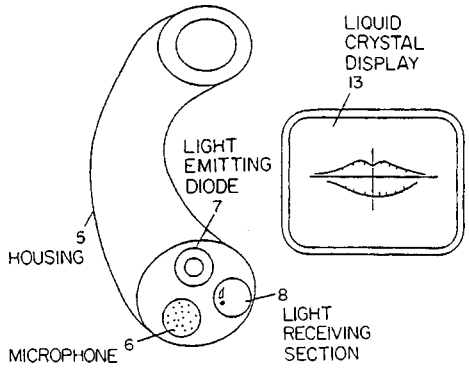

ations, the lip position is reconstructed. Various simplified lip position displays are discussed. The issue of lip position recognition and its relationship to speech is not considered.—DLR

5,680,508

43.72.Gy ENHANCEMENT OF SPEECH CODING IN BACKGROUND NOISE FOR LOW-RATE SPEECH CODER

Yu-Jih Liu, assignor to ITT Corporation
21 October 1997 (Class 395/2.36); filed 3 May 1991

This patent describes improved noise reduction for a low-rate speech coder by maintaining two excitation codebooks. Speech obtained from a noisy environment is analyzed and the best fitting excitation is chosen from a noisy-speech codebook. The corresponding entry from a clean-speech codebook is then transmitted to the receiver for reproduction. The noise codebook is adapted using an excitation recovered from the noisy input speech.—DLR

5,682,463

43.72.Gy PERCEPTUAL AUDIO COMPRESSION BASED ON LOUDNESS UNCERTAINTY

Jonathan Brandon Allen *et al.*, assignors to Lucent Technologies, Incorporated
28 October 1997 (Class 395/2.39); filed 6 February 1995

This speech coder system measures the ''tonality'' of input speech segments to determine masking threshold levels for use in the compression process. Tonality is a measure of whether the segment is perceived as tone-like (voiced) or noiselike (voiceless). The tonality measure is based on a computation of the loudness uncertainty of the speech segment.—DLR

5,684,920

43.72.Gy ACOUSTIC SIGNAL TRANSFORM CODING METHOD AND DECODING METHOD HAVING A HIGH EFFICIENCY ENVELOPE FLATTENING METHOD THEREIN

Naoki Iwakami *et al.*, assignors to Nippon Telegraph and Telephone
4 November 1997 (Class 395/2.12); filed in Japan 17 March 1994

In this speech coder, input frames are analyzed by discrete cosine transform (DCT) and linear prediction (LP). A Fourier transform of the LP coefficients gives a spectral envelope. Comparing the DCT spectrum with the envelope yields a residual signal. The residual coefficients are normalized by an envelope calculation to obtain fine structure coefficients. The fine structure coefficients are vector quantized, codebook entries from which are transmitted to the receiver.—DLR

5,684,921

43.72.Gy METHOD AND SYSTEM FOR IDENTIFYING A CORRUPTED SPEECH MESSAGE SIGNAL

Aruna Bayya *et al.*, assignors to U S West Technologies, Incorporated
4 November 1997 (Class 395/2.35); filed 13 July 1995

This speech coder includes a feedback pathway by which the transmitting side user is informed of the received signal quality. Several methods such as SNR and spectral flatness are described for computing noise levels in the received signal. The resulting signal quality measures are sent back to the transmitter and also used for selective playback to improve the quality of the reproduced speech.—DLR

5,684,922

43.72.Gy ENCODING AND DECODING APPARATUS CAUSING NO DETERIORATION OF SOUND QUALITY EVEN WHEN SINE-WAVE SIGNAL IS ENCODED

Haramitsu Miyakawa and Shuichi Kawama, assignors to Sharp Kabushiki Kaisha
4 November 1997 (Class 395/2.38); filed in Japan 25 November 1993

This speech coding system divides the incoming speech signal into variable-length blocks according to a rate of change criterion. The power in each band of a filter bank is used to determine a noise-dependent masking

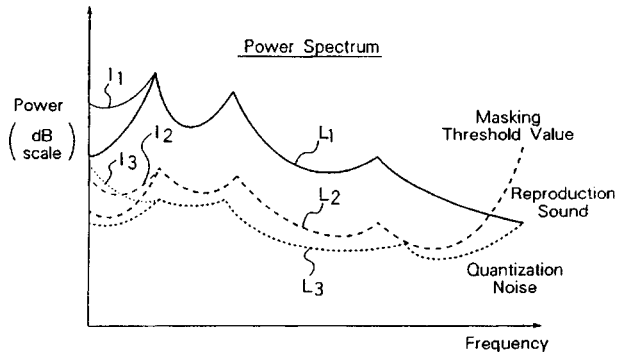

level for that band. A fixed number of bits per block is allocated for band quantization according to the masking levels.—DLR

5,684,926

43.72.Gy MBE SYNTHESIZER FOR VERY LOW BIT RATE VOICE MESSAGING SYSTEMS

Jian-Cheng Huang *et al.*, assignors to Motorola, Incorporated
4 November 1997 (Class 395/2.77); filed 26 January 1996

In a multiband excitation (MBE) vocoder, an independent voiced/unvoiced analysis is done for each frequency band. Previous MBE systems would transmit voicing and harmonic phase for each band. This low bit rate synthesis system is based on a MBE model, but uses a type of vector quantization for the harmonic indices, rather than transmitting band voicing information *per se*. The receiver includes a multiband excitation generator driven by the received indices.—DLR

5,687,283

43.72.Gy PAUSE COMPRESSING SPEECH CODING/DECODING APPARATUS

Yasuhiro Wake, assignor to NEC Corporation
11 November 1997 (Class 395/2.24); filed in Japan 23 May 1995

This speech coder detects speech presence at the transmitter and sends a silence code following a holdover period at the end of the speech signal. During the holdover period, the receiver characterizes the nonspeech signal,

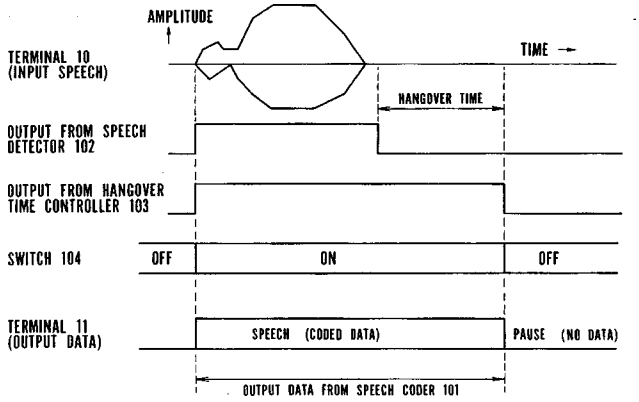

determining at least the noise signal level, and generates a corresponding noise filler as long as silence codes are received.—DLR

5,682,501

43.72.Ja SPEECH SYNTHESIS SYSTEM

Richard Anthony Sharman, assignor to International Business Machines
28 October 1997 (Class 395/2.69); filed in the United Kingdom 22 June 1994

This text-to-speech synthesis system uses hidden Markov models (HMMs) to assign durations to phonemes. Any known method is first used to derive a phonetic transcription from the input text. The sequence of phonetic units then governs the HMM state transitions, producing a duration

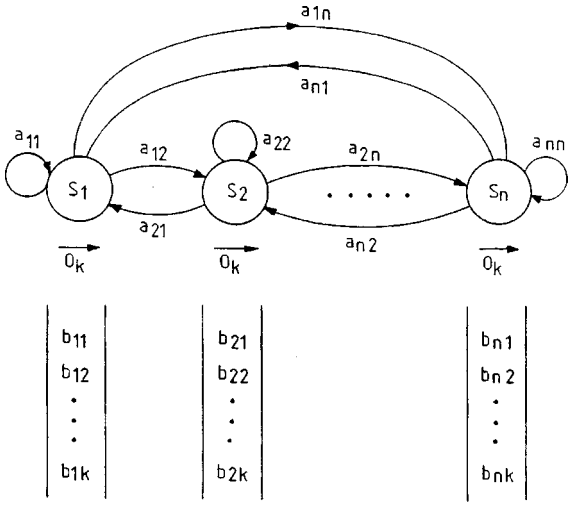

value from the state sequence. The phonetic transcription with duration annotation is used in a previous synthesis system to generate the speech output.—DLR

5,682,502

43.72.Ja SYLLABLE-BEAT-POINT SYNCHRONIZED RULE-BASED SPEECH SYNTHESIS FROM CODED UTTERANCE-SPEED-INDEPENDENT PHONEME COMBINATION PARAMETERS

Mitsuru Ohtsuka *et al.*, assignors to Canon Kabushiki Kaisha
28 October 1997 (Class 395/2.76); filed in Japan 16 June 1994

This text-to-speech synthesis system generates phonetic segment durations based on a model of speech consisting of a series of equally timed ''beat points.'' Certain phonetic patterns, such as consonant–vowel transi-

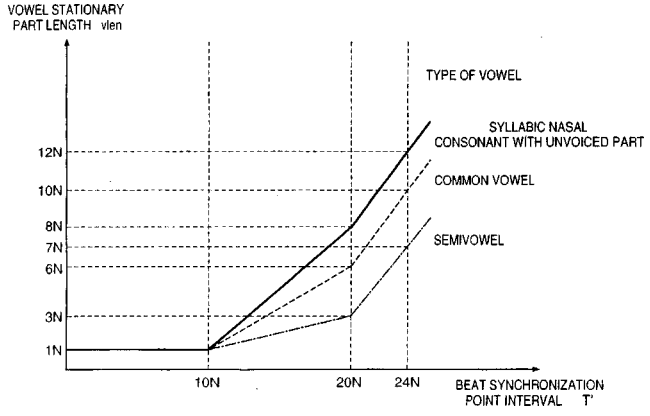

tions, have relatively fixed duration parameters. Allowing for these exceptions, the number of output frames between beat points is adjusted for the desired speaking rate.—DLR

5,677,988

43.72.Ne METHOD OF GENERATING A SUBWORD MODEL FOR SPEECH RECOGNITION

Jun-ichi Takami and Shigeki Sagayama, assignors to ATR Interpreting Telephony Research Laboratories
14 October 1997 (Class 395/2.65); filed in Japan 21 March 1992

This method grows a hidden Markov model network by splitting existing states into multiple new states, each better suited for a subset of the training speech data. The process is started with a single state representing all of the training speech. Splitting is based on maximum likelihood measures and may split in time, identifying different sequential states, or split in the available paths, adding branches to the network as needed.—DLR

5,677,990

43.72.Ne SYSTEM AND METHOD USING *N*-BEST STRATEGY FOR REAL TIME RECOGNITION OF CONTINUOUSLY SPELLED NAMES

Jean-Claude Junqua, assignor to Panasonic Technologies, Incorporated
14 October 1997 (Class 395/2.64); filed 5 May 1995

This speech recognizer is configured for the task of locating an entry in a directory based on a spoken or spelled utterance of the person's name. Rather than doing a full search with a complete grammar of all possible names, it starts with a simplified (fast) search, saving a list of best potential

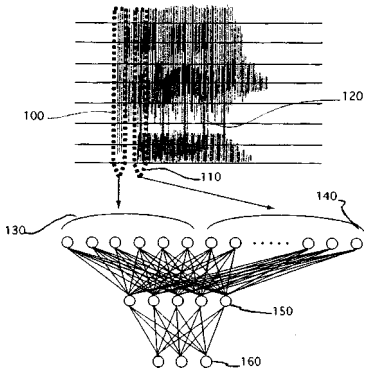

matches. This list is used to build a new grammar, much smaller than the initial full grammar. The process is repeated several times, resulting in a compact grammar. A more detailed (costly) search is then done with the small grammar.—DLR

5,677,991

43.72.Ne SPEECH RECOGNITION SYSTEM USING ARBITRATION BETWEEN CONTINUOUS SPEECH AND ISOLATED WORD MODULES

Dong Hsu *et al.*, assignors to Kurzweil Applied Intelligence, Incorporated
14 October 1997 (Class 395/2.64); filed 30 June 1995

This speech recognition strategy attempts to improve overall performance by simultaneous operation of discrete word and continuous speech methods. The discrete word method includes a large vocabulary of word models. Sequences of word candidates are compared with the continuous speech output and an arbitration system produces the highest outputs when common items are included in both.—DLR

5,680,509

43.72.Ne METHOD AND APPARATUS FOR ESTIMATING PHONE CLASS PROBABILITIES *A-POSTERIORI* USING A DECISION TREE

Ponani S. Gopalakrishnan *et al.*, assignors to International Business Machines Corporation
21 October 1997 (Class 395/2.49); filed 27 September 1994

This speech recognition decoder system converts codebook entries from vector-quantized input speech into probability classes using a decision tree classifier. The patent describes how a binary tree of decision nodes is built up by successive node splits based on the maximum likelihood correct classification of codebook entries from the training data.—DLR

5,680,510

43.72.Ne SYSTEM AND METHOD FOR GENERATING AND USING CONTEXT DEPENDENT SUB-SYLLABLE MODELS TO RECOGNIZE A TONAL LANGUAGE

Hsiao-Wuen Hon and Bao-Sheng Yuan, assignors to Apple Computer, Incorporated
21 October 1997 (Class 395/2.64); filed 26 January 1995

This tonal language recognizer contains hidden Markov models for initial and final subsyllables for the Mandarin Chinese vocabulary. The subsyllables are used together with pitch information to determine the most likely input syllable and its tone. Recognition of lone finals is improved by the use of a pseudo-initial representing a glottal stop.—DLR

5,682,464

43.72.Ne WORD MODEL CANDIDATE PRESELECTION FOR SPEECH RECOGNITION USING PRECOMPUTED MATRIX OF THRESHOLDED DISTANCE VALUES

Vladimir Sejnoha, assignor to Kurzweil Applied Intelligence, Incorporated
28 October 1997 (Class 395/2.47); filed 27 May 1994

This large vocabulary word recognizer is able to search a large dictionary by the use of a coarse distance measure matrix computed from the input speech before starting the search. A corresponding coarse form of the dictionary words can be quickly searched to find a shorter list of likely candidates.—DLR

5,684,924

43.72.Ne USER ADAPTABLE SPEECH RECOGNITION SYSTEM

Barbara Ann Stanley *et al.*, assignors to Kurzweil Applied Intelligence, Incorporated
4 November 1997 (Class 395/2.42); filed 19 May 1995

The patent describes the application of a speech recognition system in controlling itself. The architecture includes various control modules connected to signal gain, sensitivity, model selection, and the like. In addition to controlling external programs, voice commands may also be used to control voice operations.—DLR

5,677,989

43.72.Pf SPEAKER VERIFICATION SYSTEM AND PROCESS

Michael D. Rabin and Max S. Schoeffler, assignors to Lucent Technologies, Incorporated
14 October 1997 (Class 395/2.55); filed 30 April 1993

This is an application of a typical (unspecified) speaker verification system. The patent notes that a person's voice pattern cannot be ''replaced'' as can a PIN or password in the event it becomes compromised. The novel aspect is the use of encryption in storing the speaker ID templates such that unauthorized access to the speech reference database will not compromise the voice patterns of authorized users.—DLR

5,703,311

43.75.Rs ELECTRONIC MUSICAL APPARATUS FOR SYNTHESIZING VOCAL SOUNDS USING FORMANT SOUND SYNTHESIS TECHNIQUES

Shinichi Ohta, assignor to Yamaha Corporation
30 December 1997 (Class 84/622); filed in Japan 3 August 1995

The synthesizer of this patent is a computer system designed to sing a song based on stored phoneme data, performance data, and melody data. The song is automatically sung by sequentially generating the appropriate

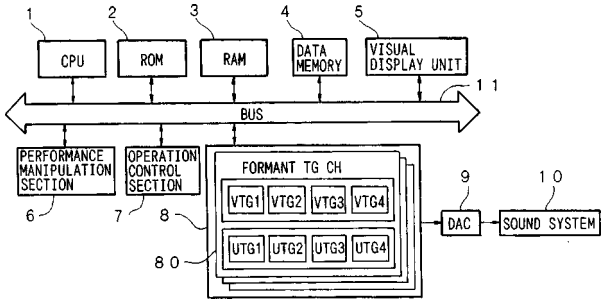

phonemes at fundamental frequencies corresponding to the melody data. Voice generation temporarily stops for breath timings. The formant tone generator can gradually shift from one phoneme to a succeeding phoneme.—DWM

5,698,807

43.75.Wx DIGITAL SAMPLING INSTRUMENT

Dana C. Massie and David P. Rossum, assignors to Creative Technology Limited
16 December 1997 (Class 84/661); originally filed 20 March 1992

It is well known that a substantial change (transposition) in the fundamental frequency of a complex tone wave of a musical instrument sounds quite unlike the tones of that instrument at the equivalent frequency in the musical scale. The reviewer has often demonstrated this for piano tones. The computer music system of this patent compensates during transposition by the following sequence of steps: (a) analysis of the original sound to extract the formant spectrum, (b) application of inverse spectrum filtering to produce an equalized tone signal, (c) transposition of the fundamental frequency of the equalized tone, and (d) application of the formant filter to give the frequency-shifted tone the original formant characteristics.—DWM

Physiological studies of the precedence effect in the inferior colliculus of the kitten[a),b)]

Ruth Y. Litovsky[c),d)]
Department of Neurophysiology, University of Wisconsin, Madison, Wisconsin 53706

(Received 9 July 1997; revised 13 January 1998; accepted 15 January 1998)

The precedence effect (PE) is a perceptual phenomenon that reflects listeners' ability to suppress echoes in reverberant environments. The PE is not present at birth and appears only several months postnatal. Recent physiological studies have demonstrated correlates of the PE in the central nucleus of the inferior colliculus (ICC) of adult animals. The present study extended the same techniques to search for similar correlates in the ICC of kittens during the first postnatal month. Stimuli consisted of pairs of clicks or noise bursts presented from different locations in free field or with different inter-aural differences in time (ITD) under headphones, with an inter-stimulus-delay (ISD) between their onsets. Results suggest that a physiological correlate of the PE, i.e. suppression of responses to the second source, is present as early as 8 days postnatal, and occurs at similar ISDs to those recorded in adult cats. Suppression in kitten neurons varies with stimulus level, duration, and azimuthal position, in a similar manner to that in adult neurons. The age at which correlates of the PE in the kitten can be found precedes the age at which kittens can localize sound sources effectively, and presumably before the age at which they would demonstrate the PE behaviorally. Thus, the neural mechanisms that might be involved in the first stages of processing PE stimuli may be in place well before the behavioral correlate develops. © *1998 Acoustical Society of America.* [S0001-4966(98)04604-9]

PACS numbers: 43.10.Ln, 43.64.Qh, 43.72.Bs [RDF]

INTRODUCTION

When a sound is produced in a reverberant environment it propagates in many directions and is subsequently reflected from nearby surfaces, hence a listener receives both the direct sound and multiple reflections of that sound. One can think of this scenario as involving competition between the first sound and its reflections for perception and localization. Despite this clutter of information two-eared animals are remarkably accurate at identifying the location and content of sound sources. This reduction in interference from reflections is thought to be related to the precedence effect (PE). Perceptual studies on the PE generally involve a simplified version of the multiple-source scenario that occurs in real rooms. That is, one source (lead) and one echo (lag) are simulated, with a variable inter-stimulus-delay (ISD). Psychophysical studies have shown that when the ISD is short (<10 ms for clicks) listeners perceive one fused auditory event whose apparent location is dominated by the lead (Blauert, 1997; Litovsky *et al.*, 1997; Wallach *et al.*, 1949; Zurek, 1980, 1987).

Developmental studies suggest that the PE is not exhibited behaviorally by newborn human infants (Clifton *et al.*, 1981; Muir *et al.*, 1989; Burnham *et al.*, 1993) or dogs (Ashmead *et al.*, 1987). Although newborn infants and dogs are able to localize the hemifield containing a single-source sound (one sound emitted from a single location), under conditions of the PE the leading source does not seem to dominate perception and localization in the same way that it does for adults (for review see Litovsky and Ashmead, 1997). The PE is first manifested behaviorally in humans at around 4–5 months of age, however at this age it is still not fully mature (Clifton, 1985; Muir *et al.*, 1989). In fact, some aspects of the PE are not fully mature in children as old as 5 years (Litovsky, 1997; Litovsky and Ashmead, 1997).

Physiological substrates of the PE are not well understood. In recent years there has been increasing interest in measuring the responses of neurons in the brainstem to PE stimuli. Several studies have shown that the central nucleus of the inferior colliculus (ICC) may be involved in mediating some basic physiological aspects of the PE. The ICC is an obligatory synaptic stage in the lemniscal pathways which transmit information to the cortex. In the adult cat, ICC neurons are known to be sensitive to wide ranges of acoustic signals, and in particular, to interaural differences in time (ITD) and intensity (IID), which are the primary cues used in azimuthal sound localization (Hind *et al.*, 1963; Kuwada and Yin, 1983; Rose *et al.*, 1966; Semple and Aitkin, 1979; Yin and Kuwada, 1983). Studies on correlates of the PE in the ICC have been made in anaesthetized cats (Yin, 1994; Yin and Litovsky, 1995; Litovsky *et al.*, 1997; Litovsky and Yin, 1998a, b) as well as in the awake rabbit (Fitzpatrick *et al.*, 1995) and awake owl (Keller and Takahashi, 1996). In these studies the PE is simulated by presenting pairs of clicks or noise bursts with variable ISDs. In all three species it has been shown that most neurons exhibit a physiological corre-

[a)] "Selected research articles" are ones chosen occasionally by the Editor-in-Chief that are judged (a) to have a subject of wide acoustical interest, and (b) to be written for understanding by broad acoustical readership.

[b)] Portions of these data were presented at the 127th Meeting of the Acoustical Society of America in June 1994.

[c)] Currently at: Boston University Department of Biomedical Engineering, 44 Cummington St., Boston, MA 02215 (where reprint requests should be sent), and Eaton Peabody Laboratory, Massachusetts Eye and Ear Infirmary.

[d)] Electronic mail: litovsky@enga.bu.edu

 0001-4966/98/103(6)/3139/14/$10.00

late of the PE. That is, responses to the lagging stimulus are suppressed at short ISDs at a similar time course to those observed in the psychophysics. More important, ICC neurons exhibit several direct correlates of the PE, such as variation of suppression with stimulus level, duration and location or ITD of the lead. Finally, at ISDs ± 2 ms neuronal responses are consistent with an aspect of the PE known as ''summing localization'' (Yin, 1994; Yin and Litovsky, 1995), whereby both humans (Blauert, 1997) and cats (Populin and Yin, 1998) perceive a phantom sound source and localize it between the lead and lag locations.

The present study describes similar physiological recordings made in the ICC of kittens during the first month of life. Kittens are known to orient towards a *single* sound source in a similar fashion to human infants and dogs, and they do so by the third postnatal week (Clements and Kelly, 1978; Norton, 1974; Olmstead and Villiblanca, 1980), suggesting that they may be utilizing binaural cues during those early postnatal days. In fact, kittens as young as 2 weeks old receive binaural excitatory and inhibitory input in about the same proportion as in the adult cat (Aitkin and Reynolds, 1975; Moore and Irvine, 1980, 1981). In addition, binaural sensitivity to IID has been reported at one month (Moore and Irvine, 1981), and as early as 8 days postnatal (Blatchley and Brugge, 1990); sensitivity to phase differences and ITDs has been reported as early as 12 days (Blatchley and Brugge, 1990). To the author's knowledge, kittens' behavioral responses to PE stimuli have not been measured. However, given the similarity in the onset of responses to single source stimuli by kittens, dogs and humans, it is reasonable to suspect that kittens probably do not show the PE during the first month or two of postnatal life. Behavioral studies must be conducted before a firm conclusion can be made.

The results presented here suggest that neural sensitivity to PE stimuli is remarkably similar in kittens to that observed in adult cats. Thus, the neural mechanisms that might be involved in the first stages of processing PE stimuli may be in place well before the behavioral correlate is expected to develop.

I. MATERIALS AND METHODS

Recordings were made from 57 neurons isolated in the ICC of 16 barbiturate/ketamine-anesthetized kittens 8–29 days old. Methods are similar to those described previously (Yin, 1994; Litovsky and Yin, 1993, 1994, 1998a, b) for measurements made in the ICC of adult cats.

A. Surgery

Preparation of the animal has been described in detail elsewhere (Brugge *et al.*, 1978; Kettner *et al.*, 1985). In short, after anesthesia was induced using ketamine (35 mg/kg), a venous cannula was inserted into the femoral vein to administer pentobarbital as needed throughout the experiment and a tracheal cannula was inserted. Body temperature was maintained at 37 °C. The dorsal surface of the inferior colliculus (IC) was exposed with a craniotomy on the right side. The overlying cortex was aspirated and in some animals the tentorium was partially removed to expose a more posterior area of the IC.

Extracellular recordings were made from the IC using commercial tungsten microelectrodes (Microprobe) with tip exposures of 8–12 μm. A motor-driven hydraulic microdrive was used to move the electrode remotely from outside the room. Single spikes were discriminated using either a level detector or a peak-detector circuit. During the experiment physiological criteria were used to locate cells within the ICC (Carney and Yin, 1989). At the end of the experiment the animals were overdosed with anesthetic and the brains immersed in 10% formalin in saline. After fixation the brainstem was removed and cut in the coronal plane with frozen sections at 50 μm thickness and stained with cresyl violet. Confirmation of the penetrations through the ICC was made from anatomical examination of these sections.

B. Stimuli

Stimuli were either 100 μsec clicks or noise stimuli usually delivered every 300 ms and repeated 20 or 50 times. Noise stimuli were either broadband or narrow bandpass noise bursts, usually 0.2 kHz wide, digitally filtered with sharp slopes (100 dB/octave) and centered at the characteristic frequency (CF) of the cell. CFs were determined by tonal tuning curves in response to contralateral or binaural stimulation.

C. Free field setup and stimuli

Experiments were conducted in a sound-insulated room (IAC) (2.25×2.15 and 2 m) (Fig. 1A). To reduce acoustic reflections all surfaces were lined with 4-in. reticulated wedged foam (Sonex). The skin overlying the skull was dissected, and a stainless steel rod was secured to the skull on the side opposite to the recording site with dental acrylic and/or screws, depending on the thickness of the skull. The rod was attached to an animal holder which maintained the head in a secure position for the duration of the experiment. After exposure of the IC, the skin was sutured back so that the ears assumed a natural position while still allowing access to the brain. The electrode manipulator was also attached to the head holder to increase stability during recording. The animal holder was anchored to the floor of the room such that the head was positioned in the center of a circle with a 90 cm radius defined by the loudspeaker array. Thirteen loudspeakers (Realistic 3-in. midrange tweeter) were positioned along the horizontal axis in the frontal hemifield at 0° elevation with loudspeakers every 15° (see Fig. 1A). Positive angles refer to sounds in the contralateral hemifield. The loudspeakers were carefully matched for frequency response by monitoring their outputs to clicks and to tone bursts delivered from 100 to 25 000 Hz in steps of 100 Hz. All speakers were matched to within 2 dB at octaves spanning 250–8000 Hz.

Auditory stimuli were digitally stored in a general waveform buffer for delivery by a digital stimulus system. The CF of each cell was defined as the frequency with the lowest threshold to tonal stimuli at $+45°$ on the horizontal axis. In a small proportion of cells that preferred the ipsilateral hemifield, CF was obtained at $-45°$. Thresholds for clicks and noise bursts were also obtained at $+45°$. Azimuthal response

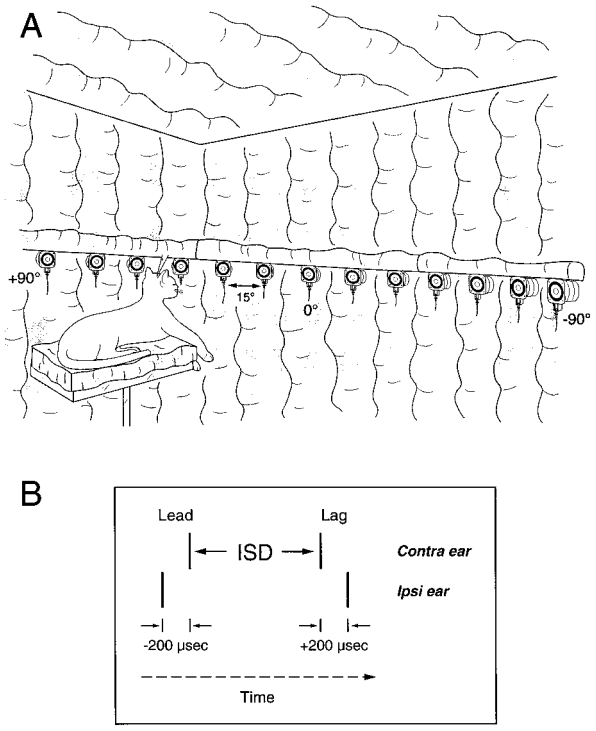

FIG. 1. Stimulus configuration in free field (A) and under dichotic conditions (B). A: A cat is placed in an anechoic chamber in the center of a semicircular array of loudspeakers positioned every 15° along the horizontal axis from +90° on the right (contralateral) to −90° on the left. B: Two pairs of clicks are delivered dichotically, separated by an inter-stimulus-delay (ISD); each click pair contains an interaural time delay, e.g., −200 and +200 msec as diagrammed. Positive ITDs refer to the convention of the contralateral stimulus presented first.

area curves were obtained by presenting 50 repetitions of either clicks or noise bursts from each loudspeaker at 5–20 dB above threshold. Finally, the PE was simulated by presenting two sounds from different loudspeakers with one sound delayed relative to the other by a variable ISD.

D. Dichotic experiments

The animal was placed in a double-walled, sound insulated chamber (IAC). Both pinnae were dissected away and the external ear canals were transected so that the tympanic membrane was visible. Acoustic stimuli were delivered independently to each ear through hollow ear-pieces which were connected to the earphones (Telex 140) and tightly sealed into the ear canals with Audalin ear impression compound. A small hole was drilled in each bulla and polyethylene tubes (0.9 mm internal diameter and 30 cm in length) were inserted into the hole to equalize middle ear pressure during the experiment. Acoustic stimuli were generated by a digital stimulus system which was calibrated in amplitude and phase for each animal. A 0.5-in. Bruel and Kjaer condenser microphone was coupled to a probe tube which was positioned inside the ear canal 1–2 mm away from the tympanic membrane, and 50 ms tone bursts were delivered from 100 to 42 000 Hz in 50-Hz steps. The CF of each cell was defined as the frequency with the lowest threshold for the contralateral ear. By convention positive ITDs refer to the contralateral ear leading. As in the free field experiments, thresholds were estimated for clicks and noise, but they were obtained either for the contralateral ear alone or for binaural stimuli with an ITD of zero. Stimuli with a PE configuration were simulated by presenting two dichotic pairs of clicks or noise separated by an ISD of several ms; ITDs were imposed separately for each stimulus pair (Fig. 1B). The ISD was defined as the time difference between the onset of the two stimuli delivered to the contralateral ear.

E. Normalizing the lagging responses in recovery curves

Data were analyzed by comparing the lagging response in the presence of the leading stimulus with the lagging response in absence of the leading stimulus. For each neuron, the number of spikes in response to the leading and lagging stimuli at each ISD was counted during discrete time windows (chosen to accommodate the latency and duration of each neuron's response). In cases where the leading and lagging stimuli were identical, such as under dichotic conditions with the same ITDs imposed, at each ISD the lagging responses were divided by the leading responses within the discrete time windows. In free field the leading and lagging stimuli never occurred at the same location and were thus never identical. The lagging responses were therefore normalized in one of two ways: (a) by the response to the lagging stimulus presented in isolation; or (b) by the lagging response at a large ISD where there was no apparent effect of the leading stimulus. When the analysis time windows for the leading and lagging response overlapped, such as when ISD was very short (see Fig. 5), we assumed that there was no variation in the response to the leading stimulus as a function of ISD and subtracted the mean leading responses at the five longest ISDs from the total number of spikes at the ISDs with overlap. In the resulting normalization recovery to 1.0 represents a lagging response that equals the response obtained in the absence of a leading stimulus.

II. RESULTS

Results from recordings made in kitten ICC are compared with those reported by Litovsky and Yin (1998a, b) in the ICC of adult cats. Results were obtained from 57 neurons recorded from the ICC of 16 kittens, ages 8–29 days. Table I shows the distribution of units recorded from animals at various ages, under free field or dichotic conditions. Once encountered and isolated, each neuron was studied for 1–6 hours. Since the survival time of most kittens was 12–18 hours, each animal yielded data from a small number of neurons.

A. Sensitivity to stimulus location in free field

Free field experiments always began by measuring a neuron's receptive field, i.e., sensitivity to clicks or noise varying in azimuth. Sensitivity is defined by the neuron's response to stimuli presented 5–10 dB above threshold; if measurements were obtained at more than one level, sensitivity was defined at the lowest level. Threshold is defined as the neuron's response to clicks at 45 deg to the left or right,

TABLE I. List of animals according to the age at which measurements were made, and the number of neurons that were studied in each animal (D =dichotic; F=free field). A total of 16 animals participated, with a mean age of 16 days.

Expt. #	Age (days)	#Neurons
049 F	8	5
164 F	9	9
089 F	10	2
099 D	10	4
008 D	11	3
039 F	12	5
109 D	13	1
103 F	14	4
165 F	15	5
018 F	15	5
105 D	20	2
009 D	20	2
056 F	22	2
096 D	24	2
086 F	27	7
030 F	29	4

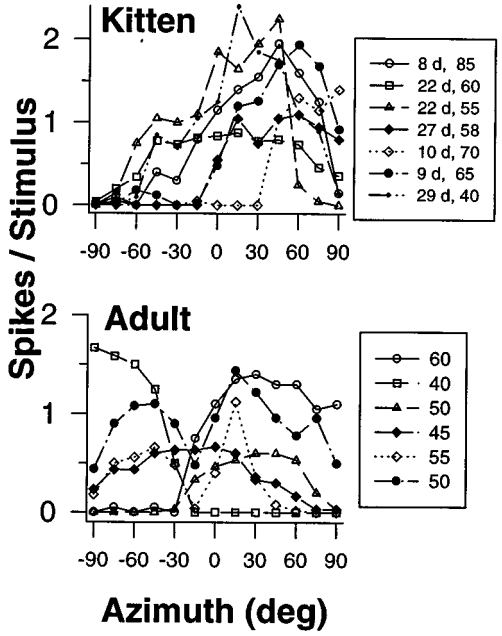

FIG. 2. Effect of varying the location of single clicks along the azimuthal plane in free field. Top: 7 representative neurons studied in kittens; Bottom: 6 representative neurons studied in cats. Each curve represents the response (number of spikes per stimulus) of one neuron to 50 repetitions of the stimuli. The legends contain the ages of the kittens and the threshold of each neuron.

whichever is lower. There does not seem to be any differences in azimuthal sensitivity to noise or clicks, thus measurements with those two stimuli are shown together.

At 5–10 dB above threshold, most neurons show sensitivity to locations along the horizontal dimension, defined by a modulated response with a difference >0.5 in spike rate (number of spikes per stimulus) between the azimuthal locations that results in the maximal and minimal spike rates. For the population of kitten neurons studied, ranging in age from 8 to 29 days, 85% (29/34) of neurons exhibit maximal responses to stimuli presented in the contralateral hemifield. A minority of neurons (15%; 5/34) are omni-directional, i.e. show no preference for either hemifield; these neurons are found in animals aged 14 and 27 days. No neurons respond maximally to stimuli presented in the ipsilateral hemifield. Figure 2 shows the azimuthal receptive field for several representative neurons studied in kittens (top) and cats (bottom). In cats 60% of neurons prefer the contralateral hemifield, 35% are omni-directional, and 5% prefer the ipsilateral hemifield.

The receptive field profiles of many ICC neurons depend on the level of presentation. In all neurons but one there is increased discharge rate with increased level. In addition, most neurons show a widened receptive field at higher levels, extending into the opposite hemifield. Responses from four neurons at several levels are shown in Fig. 3, at 8 days, 10 days, 29 days, and adult age. The lowest levels at which neurons were tested were usually near or at threshold. In all four cases the receptive fields at the lowest levels are restricted to the contralateral hemifield, and in three cases the receptive fields extend out to the ipsilateral hemifield at the higher levels, thereby reducing the neuron's spatial sensitivity. In the omni-directional neurons higher stimulus levels result in increased discharge rate, but no changes in receptive field sensitivity are observed. In summary, a neuron that showed an omni-directional response at 5 dB above threshold is not likely to gain receptive field sensitivity at higher levels; a neuron that shows sensitivity at low levels is likely to lose that sensitivity at higher levels.

Of the 15 neurons studied with the level manipulation, nine (60%) show decreased azimuthal sensitivity at higher levels, and 5/15 neurons (36%) show no azimuthal selectivity at any level. The 8-day-old neuron shown in Fig. 3 is the only one that does not lose azimuthal sensitivity at higher levels. The corresponding values in the adult data are: 31/60 (52%) of neurons show decreased spatial sensitivity with level, 8/60 (13%) of neurons show no shift into the ipsilateral

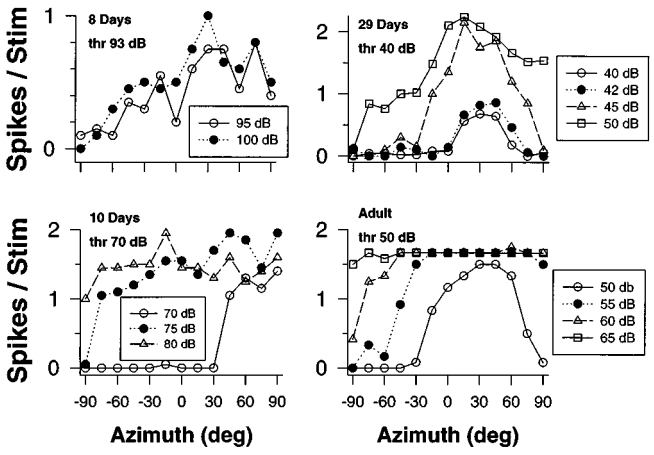

FIG. 3. Effect of varying overall stimulus level on receptive fields. Neurons from four animals are shown, at ages 8-days (CF 3 kHz), 10-days (CF 3 kHz), 29-days (CF 2.5 kHz), and adult (CF 6 kHz). Each panel shows the responses of one neuron to 50 clicks presented at $\pm 90°$ in 15° steps, and at several levels. The threshold for responding to the stimulus at 45° is shown below the age.

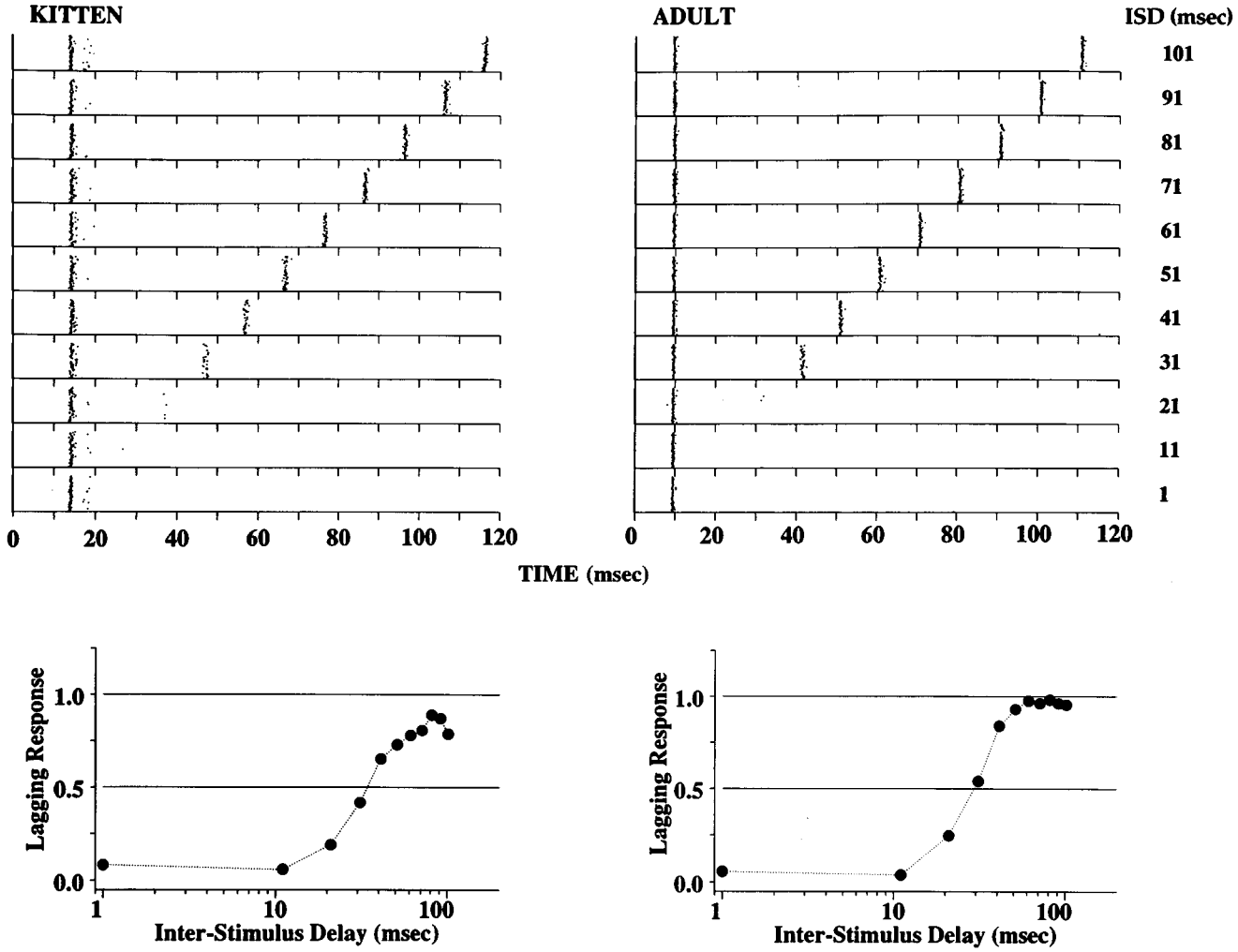

FIG. 4. Echo suppression for two neurons studied in free field, one in a 12-day-old kitten (left; CF=2.3 kHz) and one under in an adult cat (right; CF=2.4 kHz) conditions. Top: Dot rasters showing the responses to the leading and lagging stimuli, with ISDs ranging from 1 (bottom) to 101 (top) ms. The leading and lagging stimuli were placed at locations along the horizontal plane that elicited robust responses by each neuron, +30° and 0°, respectively. Each row of dots represents responses to 50 repetitions of the stimuli. The leading response occurs in each row at a latency of 14 ms, and the lagging response occurs with greater latency which depends on the ISD. For example, at ISDs of 91 and 101 ms, the lagging responses occurs at 105 and 115 msec, respectively. Bottom: Recovery curves for the dot rasters shown above. The normalized (see Sec. I) response to the lagging stimulus is plotted as a function of ISD. The delay at which the horizontal lines at 0.5 meets the function represents the *half-maximal ISD*, which is 35 ms and 29 ms, for the kitten and adult neurons, respectively.

hemifield with level, and 21/60 (35%) show no directional selectivity at any level tested.

From the kitten data it is difficult to determine whether all response types exist at 8 days of age, since only one neuron was studied at that age. The next youngest neuron, studied at 10 days, does show a decrease in azimuthal sensitivity with increased level. It is important to note that both response types can be found in the adult data.

B. Precedence and neural echo thresholds (half-maximal ISD)

Results presented below describe responses of ICC neurons to PE stimuli. Figure 4 shows examples from a 12-day-old kitten (left) and a cat (right), with the ISDs varied from 1 to 101 ms. In both cases the leading and lagging stimuli, when presented in isolation, elicit robust neural discharges. When the ISDs are long (41–101 ms), each neuron responds vigorously to both the leading and the lagging stimuli. As the ISDs are decreased, the delayed response is diminished, almost disappearing completely by 21 ms. The bottom panels in the figure show recovery functions for the lagging responses of each neuron. The neural correlates of echo threshold, or *half-maximal ISDs* (delays at which recovery functions reach 50% of the un-suppressed response) are 33 ms and 30 ms, for the kitten and cat, respectively. These particular examples were chosen to reflect the similarity between recovery functions observed in kitten and cat.

Figure 5 shows responses from populations of neurons in kittens (top) and adult cats (bottom). Since no differences were observed between free field and dichotic data, Fig. 5 contains results from both procedures. Each neuron was studied at a level 5–10 dB above threshold. Leading and lagging stimuli were both selected so that each produced a robust response when presented in isolation, i.e. within the neuron's receptive field in free field or at an ITD that produced a robust response under headphones. The left panels (A and C) each contain recovery functions from 20 neurons, demonstrating that within each population there is tremen-

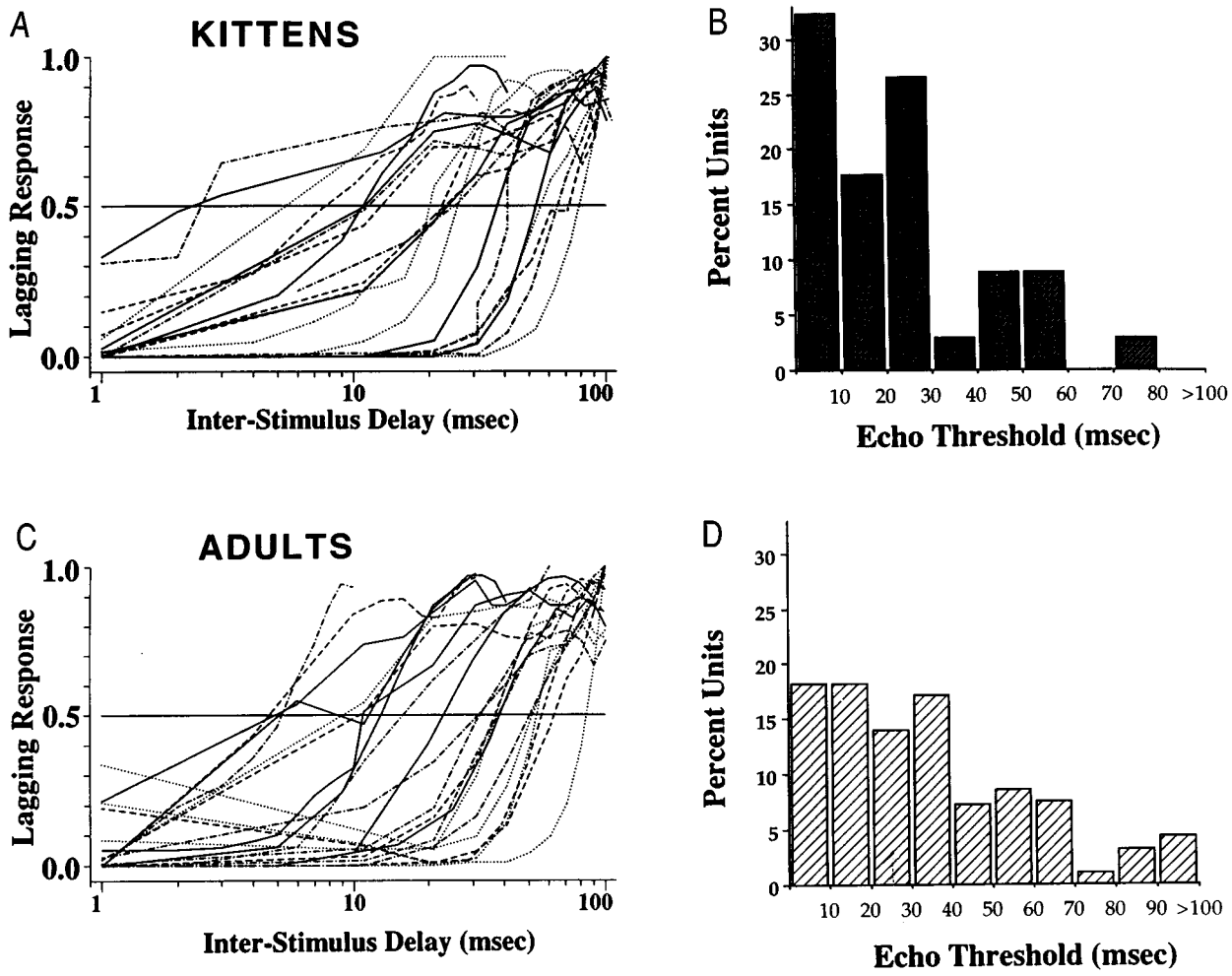

FIG. 5. Exemplary recovery functions (left) and population histograms (right) of neural echo thresholds, or *half-maximal ISDs*, plotted for kittens (top) and adults (bottom). For all neurons, both leading and lagging stimuli were at locations or ITDs which elicited robust responses with single stimuli. The recovery functions (left) represent the normalized lagging responses as a function of ISD. Although the recovery functions only include 22 sample neurons from each population, the histograms on the right are based on the entire populations of neurons studied ($N=94$ for adults and $N=34$ for kittens). Adult data are from Litovsky and Yin (1998a).

dous variability in the delays at which the *half-maximal ISD* is reached. The right panels (B and D) compare histogram distributions for *half-maximal ISDs* of 34 kitten neurons (20 free field and 14 dichotic), and 94 cat neurons (49 in free field and 45 dichotically). In both populations these values have wide ranges (2–80 ms for kittens and 2 to over 100 for adults); means and standard deviations are 21 ± 18 ms and 36 ± 32 ms for kittens and cats respectively. In addition, for the entire population the proportion of neurons with echo thresholds less than 10 ms, which approximates the range for perceptual echo thresholds in humans (Blauert, 1997; Freyman *et al.*, 1991) and cats (Cranford, 1982), is 32% (11/34) in kittens and 24% (23/94) in cats. Statistically, *half-maximal ISDs* are significantly lower in the kitten population than in the cat population ($p=0.02$).

A closer look at the data suggests that in the adult population many of the neurons with high *half-maximal ISDs* had either very low CFs (<1 kHz) or very high CFs (>16 kHz). Since the CFs of neurons in the kitten population were restricted to 1–16 kHz (perhaps due to a sampling bias), a further *t* test between all the kitten neurons and only cat neurons with CFs between 1 and 16 kHz ($N=67$) revealed a lack of significant difference ($p=0.08$).

Figure 6 shows a correlation plot between *half-maximal ISDs* and age for the kitten data; the low correlation value ($r=0.058$) suggests that, within the kitten group, the distribution of neural echo thresholds is not age-dependent. Finally, Fig. 7 shows a scatter plot of neural echo thresholds as a function of CF for the kitten (top) and adult (bottom) populations. There is no apparent relationship between these variables for either the adult group ($r=0.06$) or the kitten group ($r=-0.12$). Within the adult population, if the analysis is restricted to the 67 neurons with CF 1–16 kHz the correlation is higher (0.2488), but still not significant.

C. Effects of varying level and duration

In addition to investigating a mechanism for suppression of responses to a lagging source, this study investigated additional correlates of psychophysical effects. In everyday listening environments various stimulus parameters associated with the original source (lead) and its echo (lag) change dy-

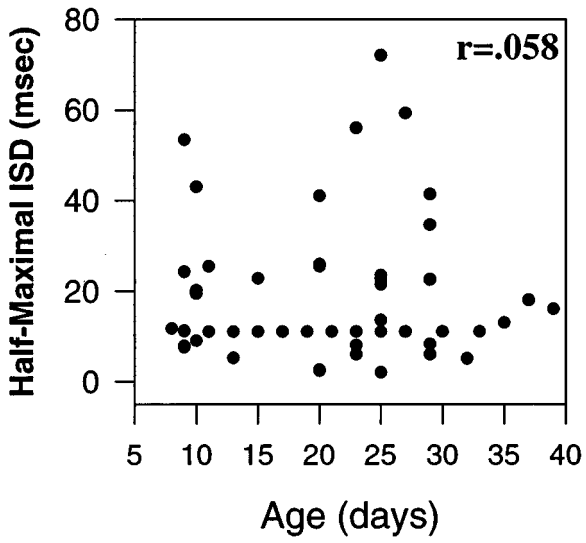

FIG. 6. Correlation plot of neural echo thresholds, or *half-maximal ISDs,* and number of days postnatal for the population of kittens neurons studied.

namically. Some examples are the level and duration of the stimuli, which are modulated in cases of ongoing dynamic stimuli such as speech or music. One approach to studying effects of level and duration is to co-vary the lead and lag, i.e., to change the overall level or duration of a stimulus, which is congruent with realistic changes that occur in a reverberant environment. In fact, the PE is reportedly weaker at higher overall stimulus levels (e.g., Shinn-Cunningham *et al.*, 1993), and stronger when the overall stimulus duration is longer (Damaske, 1971). A second approach is to vary only the level or duration of the leading source, while holding constant that of the lag. Although such stimulus manipulations may not reflect phenomena that occur in real listening environments, they are geared towards understanding the neural mechanisms that might be involved in mediating the

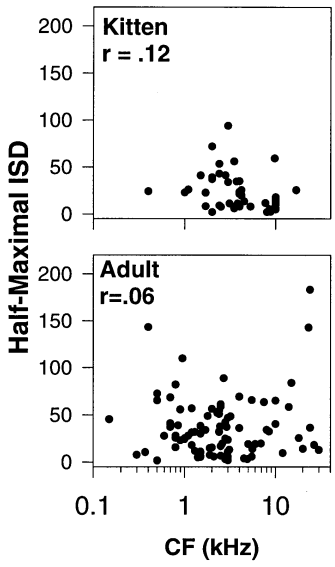

FIG. 7. Correlation plots of *half-maximal ISD* and CF for kittens (top) and adults (bottom).

PE (Yin, 1994; Litovsky and Yin, 1998b). Psychophysical data using this approach have shown that the PE is significantly stronger when the level of the lead alone is increased (Blodgett *et al.*, 1956; Thurlow and Parks, 1961; Babkoff and Sutton, 1966). Similar studies on duration have not been conducted. Comparisons made below between kitten and adult cat refers to adult data reported by Litovsky and Yin (1998a, b).

While one can expect leading stimuli of increasing level to generate more suppression, it is not obvious what to expect when the lagging stimulus level is raised concomitantly. Plotted in Fig. 8 are results from six neurons, all studied with click stimuli. The four neurons at the top show an effect of increased suppression at lower overall stimulus level at ages 10 days, 13 days, 20 days, and adult. The majority of kitten neurons (87%; 13/15) show this effect, which is consistent with findings in adult neurons (72.5%; 29/40). The two neurons at the bottom show the opposite effect, of decreased suppression at lower levels, an effect that is observed in 13% (2/15) of kitten neurons and 10% (4/40) of adult neurons.

The effect of varying the level of the leading stimulus alone was also measured. Although only 8 kitten neurons were studied, they all show a strong effect of increased suppression with increased lead level. The same effect was also seen by Litovsky and Yin (1998b) in all neurons studied ($N=17$). Figure 9 shows examples from a 12-day-old kitten neuron (9A and 9B) and from an adult neuron (9C). There is an interesting interaction between delay and lead level: In 9A at a delay of 20 ms the lead at 40 dB produces a very weak response, but the lagging response is completely suppressed. At a longer delay of 40 ms the lead at 40 dB produces weaker suppression, and finally, at a 60 ms delay the lead at 40 dB produces almost no suppression. Hence, increasing the delay compensates for the suppressive effect of the lead. Note that once the lead is above threshold the neuron only responds to the lagging sound at 60 ms, but even at that long delay the lag response is suppressed when the lead level reaches 50 dB.

The effect of stimulus duration was tested using short noise bursts rather than clicks, which allows changes in duration that do not compromise the frequency bandwidth of the stimulus. Figure 10 shows data from one 27-day old neuron (left) and one adult neuron (right), each tested under conditions in which either the overall duration (top) or lead duration alone (bottom) were varied. In the overall duration cases shown here, increasing the stimulus duration results in increased suppression in both kitten and adult neurons. In kittens this trend was observed in all neurons studied (8/8), although in adult cats the effect had been reported for only 56% of neurons (Litovsky and Yin, 1998a). In the bottom plots the lag was held constant at 10 ms (kitten) or 5 ms (adult), while the lead duration was varied. In both examples shown here the suppression increases as the durations are increased. This trend was observed in 75% (6/8) neurons studied in kittens, with no effect of duration in 25% (2/8) neurons. In adult cats longer duration produced stronger suppression in 86% (12/14) of neurons, with no effect in 14% (2/14).

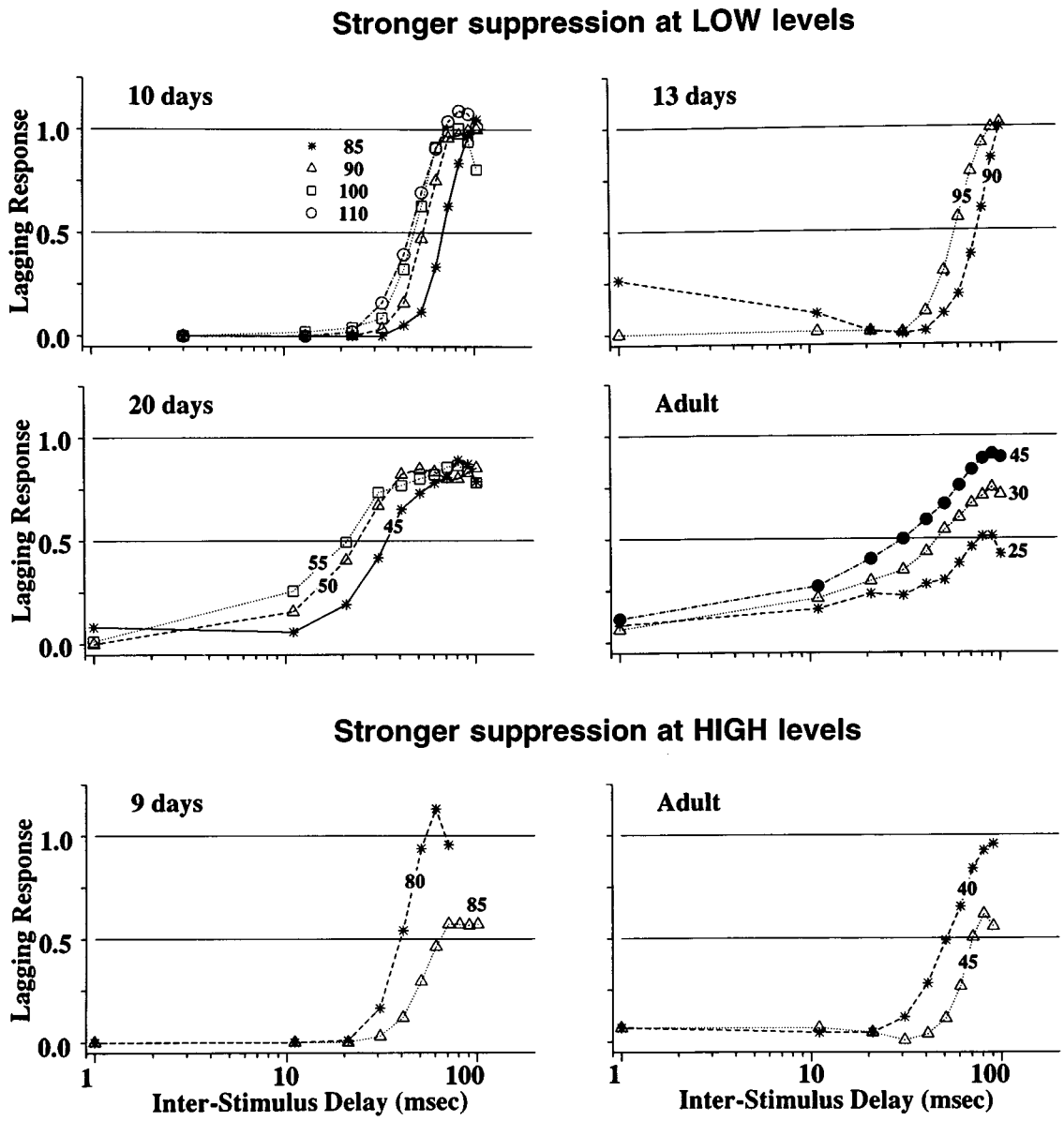

FIG. 8. Effect of overall level is shown for 6 neurons. The stimulus level of both leading and lagging sounds was always equal and co-varied between conditions. In each plot, *half-maximal ISDs* are marked by the ISD at which the normalized lagging response recovers to 0.5. The top four neurons, at 10 days (CF 2.4 kHz; threshold 80 dB), 13 days (CF 8.6 kHz; threshold 90 dB), 20 days (CF 3.7 kHz; threshold 40 dB), and adult (CF 5.5 kHz; threshold 25 dB) are examples in which lower levels resulted in *stronger* suppression. The bottom two neurons, at 9 days (CF 2.4 kHz; threshold 60 dB) and adult (CF 3.0 kHz; threshold 35 dB), are examples in which lower levels resulted in *weaker* suppression.

D. Effect of lead stimulus position on suppression

Echoes occurring in a normal listening environment naturally appear from many different locations. Since a well known feature of ICC neurons is their sensitivity to stimulus direction along the azimuth, a natural question is whether the location of the leading sound influences the degree of echo suppression. In the experimental setup the locations of the leading or lagging source could be independently varied in free field. The paradigm in this experiment consisted of varying the location of the leading stimulus while holding constant that of the lagging stimulus. Hence one can compare the amount of suppression that each leading stimulus exerts on the same lagging response. Figure 11A and B show responses to click stimuli in the form of dot rasters of a representative ICC cell in a 27-day-old kitten, in which the ISDs were 10 ms and 20 ms, respectively. In both cases, the leading stimulus was varied along the azimuth from $-90°$ to $+90°$ while the lagging stimulus was held constant at $+45°$ (black arrow in Fig. 11B). At both 10 and 20 ms delays the response to the leading sound, which occurs at a latency of about 10–13 ms, is strongest on the contralateral side between 0° and 30°; responses is weaker at negative azimuth values on the side ipsilateral to the recording site.

These data are summarized by plotting the responses to the leading (Fig. 11C) and lagging (Fig. 11D) stimuli separately. Figure 11C shows the neuron's response to the leading sound when presented as a single click in isolation, i.e., with no lagging stimulus (dark circles), and when followed

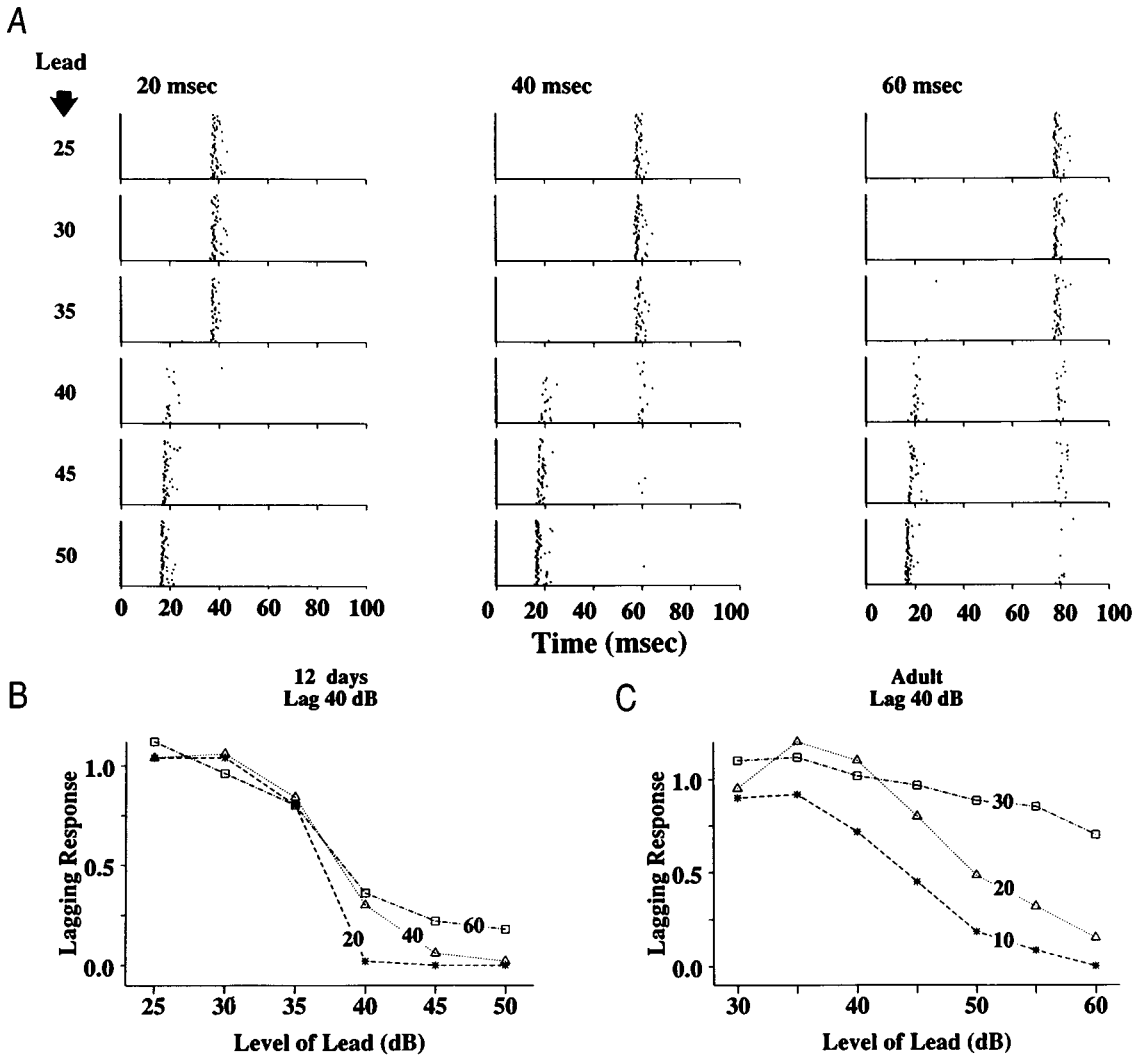

FIG. 9. Effect of the SPL of the lead. A: Data from one neuron in a 12-day-old kitten studied in free field (CF=9.8 kHz; threshold 40 dB). Both lead and lag locations were chosen such that when presented in isolation they elicited a robust response; the lagging response is slightly more robust than the leading response at 40 dB. Leading click SPL was varied from 25 to 50 dB in steps of 5 dB, while the SPL of lagging click was held constant at 40 dB. Results are shown at ISDs of 20, 40, and 60 ms (from left to right). B: Data from A are summarized, showing normalized lagging response as a function of lead level. C: Data from one neuron in an adult cat studied in free field (CF=2.65; threshold 40 dB). Lag level was held constant at 40 dB, lead level varied from 30 to 60 dB in steps of 5 dB, and measurements were conducted at ISDs of 10, 20, and 30 ms.

by a lagging stimulus at 5, 10, and 20 ms delays (stars, triangles and squares, respectively). Under all conditions the lead response shows a peak in the contralateral hemifield. In the single click condition the neuron also responds to a stimulus at $-90°$, but for unknown reasons that response does not occur in the other conditions. Figure 11D shows the response to the lagging stimulus at 5, 10, and 20 ms, as a function of the location of the leading stimulus, as well as the response to single clicks (filled circles). For all delay conditions the lagging sound was placed at $+45°$, which elicited maximal response to the lead. If the leading source has no suppressive effect then all lagging responses should approximate the neuron's response to a single click at $+45°$; any reductions in responses reflect a suppressive effect. At positive angles suppression is maximal when response to the lead is maximal, at $0°$ to $+60°$. Suppression is also strongest at the shortest delays (5 and 10 ms) and weak at the long delay (20 ms). At negative angles, where the neuron does not respond to the leading source, there is no suppression (11C).

The effect of lead location on suppression was observed in kittens as young as 9 days and as old as 29 days. Figure 12A and B shows an effect of lead location in 9-day-old and 27-day-old neurons, respectively. In 12B suppression is strongest at the shortest delays, as well as when the leading source exerts maximal responses. In 12A, the youngest animal for which these data were obtained, the effect of lead location is quite strong, although the effect of delay is somewhat weak. No examples with strong effects of both delay and location are available at the youngest ages studied. Figure 12D shows an effect of both delay and lead location in an adult neuron. The response types shown in Figs. 11, 12A, B, and D are termed SMAX (Litovsky and Yin, 1998, b), since suppression is strongest when the lead response is maximal. These responses were seen at all ages studied and represent 73% (11/15) of neurons; this proportion is consistent with proportions found in the adult data (62%; 24/39).

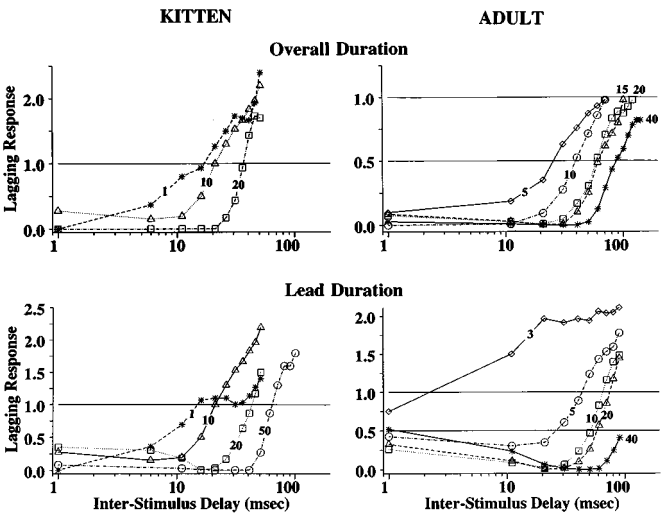

FIG. 10. Effect of stimulus duration. Top: Effects of co-varying the lead and lag durations. Responses of one kitten neuron (27 days, CF=4 kHz) and one adult neuron (CF=10 kHz), each tested using narrow-band noise bursts at CF. Bottom: Effects of varying lead duration for a constant lag duration. Responses of the same two neurons shown above; lag duration were 10 ms and 5 ms, for the kitten and adult neurons, respectively. Both lead and lag locations were chosen such that when presented in isolation they elicited a robust response.

In the adult data there exist an additional, much smaller (13%; 5/39), category of neurons termed SMIN, in which suppression is minimal when the lead response is maximal. In the kitten data 13% (2/15) of neurons exhibited a similar response type as well. For example, in Fig. 12C when the lead produces maximal excitation (+30° to +90°) the lag response is high; the lag response is weaker when the lead response is weaker at −15° to −45°. However, this neuron is not completely SMIN, since at the locations which produce minimal lead excitation (−90° to −60°), suppression of the lag at 5 ms is weak. Finally, the proportion of neurons with no effect of lead location on suppression is 13% (2/15) in kitten neurons, compared with 25% (10/39) in adult cats.

III. DISCUSSION

The principal finding is that cells in the ICC exhibit an adult-like physiological correlate of the PE. This occurs as early as 8–9 days of age, before the full maturation of the structure or function of the auditory system and before the time that a kitten functions behaviorally in its auditory environment.

A. Azimuthal sensitivity

The data presented here suggest that azimuthal sensitivity is well developed early in life. One difference between kitten and adult neurons is the lack of kitten neurons that prefer stimuli presented in the ipsilateral hemifield. However, given that ipsilateral neurons only represent 5% of the adult population (Litovsky and Yin, 1998a), this difference could be due to a sampling bias; adult data were based on almost 70 neurons, whereas kitten data were based on 34 neurons. A second difference is that the youngest neurons studied (8 days) did not show changes in azimuthal sensitivity with increased levels. The effect of level was studied in several other very young neurons (9, 10, 15, and 20 days of age), all of which did show decreased azimuthal sensitivity at higher levels (i.e., Fig. 3, 10 day neuron). Any developmental effects would thus have to occur between 8 and 10 days. A more likely explanation is that, given the small number of neurons studied for this effect ($N=15$) the difference may be attributed to a sampling bias.

B. Physiological correlates of precedence

The general finding that most cells in the IC show a suppressed response to the lagging stimulus is consistent with previous reports using stimuli that mimic the PE (Yin, 1994; Yin and Litovsky, 1995; Fitzpatrick *et al.*, 1995; Keller and Takahashi, 1996; Litovsky *et al.*, 1997; Litovsky and Yin, 1998a, b). The results presented here also show that many perceptual phenomena related to the PE exhibit correlates in responses of IC neurons. It is notable that, whereas neural echo thresholds range from 2 to 100 ms, the PE is psychophysically strongest at delays that are below 10 ms (Wallach *et al.*, 1949; Blauert, 1997; Zurek, 1987; Freyman *et al.*, 1991). However, the physiological results are consistent with the idea that perceptual thresholds are generated by those neurons with the lowest thresholds, rather than by mean behavior of the population (Elliot *et al.*, 1960; Liberman, 1978; Yin, 1994). The proportion of neurons with *half-maximal ISDs* (neural correlate of echo thresholds) less than 10 ms is quite substantial: 32% (11/34) and 24% (23/94) in kittens and adults, respectively. Fitzpatrick *et al.* (1995) have also argued that several aspects of the PE, such as accurate localization of the lag at its respective position, and equal-loudness perception of the lead and lag, are not fully in place until the delays are in the tens of milliseconds, which may account for the neurons whose *half-maximal ISDs* are long.

Responses in kitten neurons showed further correlates of psychophysical findings. First, using noise stimuli, half-maximal ISDs were longer (i.e., suppression stronger) with more excitable stimuli having longer durations, which is consistent with findings in adult cats (Litovsky and Yin, 1998a), and with human behavior (Damaske, 1971). Second, *half-maximal ISDs* varied with stimulus level, however, in this case a more excitatory stimulus at higher levels resulted in reduced suppression in most neurons, which is consistent with psychophysical reports (Shinn-Cunningham *et al.*, 1993). These findings suggest that the strength of suppression is not always predictable from the amount of excitation that a stimulus produces when presented in isolation. Rather, there seems to be a more refined interaction between the excitability of the lag and the suppression produced by the lead, which may be independent of spike rate (Yin, 1994). Third, our findings on the effect of varying the leading source level are consonant with psychophysical results in humans: an increase in the level of the lagging stimulus reduces echo thresholds, and an opposite effect occurs when the lag level is decreased (Blodgett *et al.*, 1956; Thurlow and Parks, 1961; Babkoff and Sutton, 1966). Yin (1994) has previously reported similar results in the ICC of adult cats.

Finally, the ICC is thought to be an important structure for encoding auditory cues that are used in sound localization (Yin and Kuwada, 1983; Yin and Chan, 1988). Most neurons

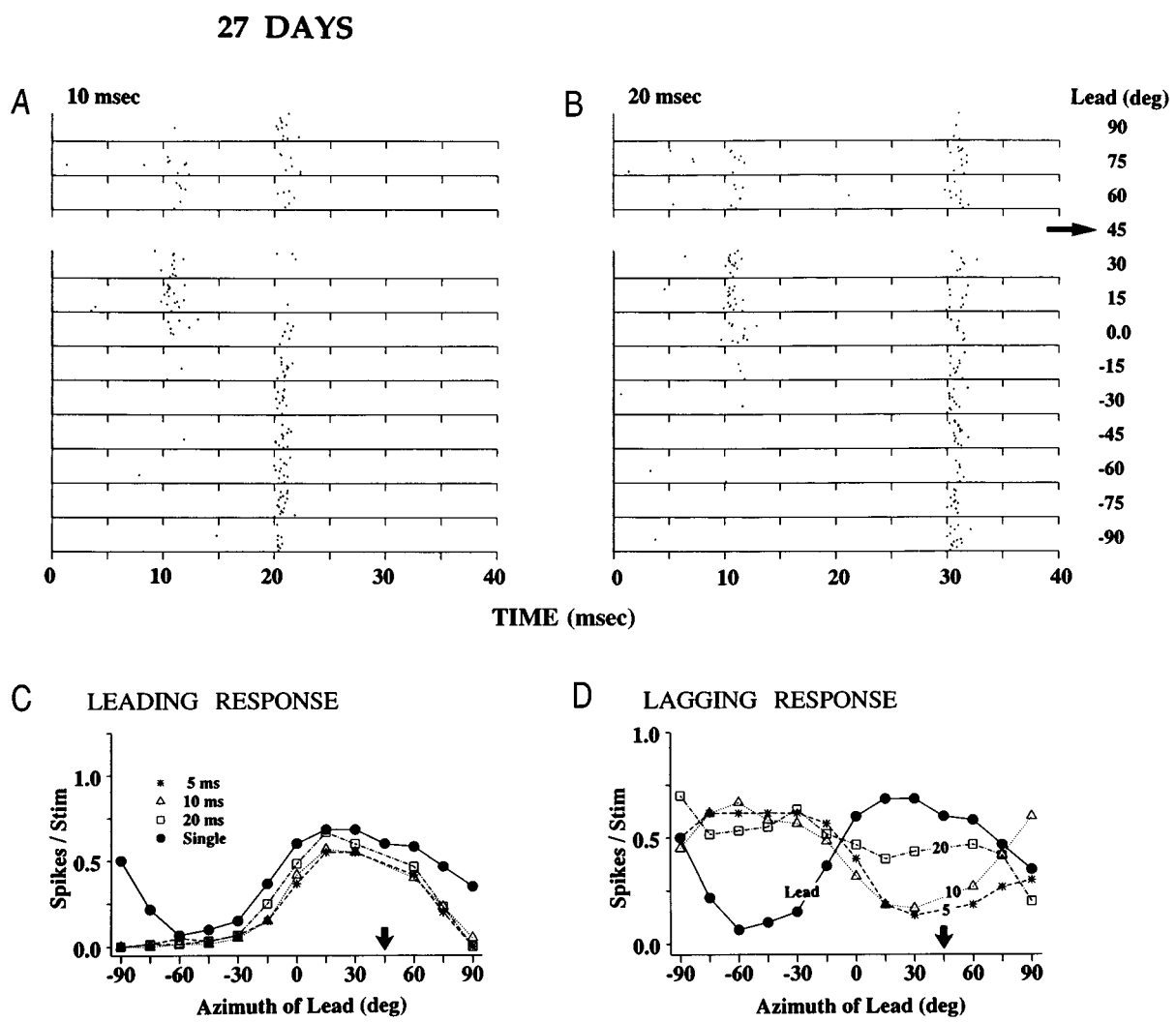

FIG. 11. Modulation of echo suppression by azimuthal location of the leading stimulus in response to clicks in one 12-day neuron (CF=3 kHz). A and B: Dot rasters with an ISD of 10 ms (A) and 20 ms (B). Responses to the leading stimuli occur at a latency of 10–14 ms, and varies with location from +90° (top) to −90° (bottom). The responses to the lagging responses occur later in time with the stimulus always at +45°. These responses are summarized in C and D. C: Responses to the leading stimulus from A and B (triangles and squares), to the lead at 5 ms (not shown above) and to single clicks (closed circles). The maximum lead/single response occurs at +15° to +60°, in the contralateral hemifield. D: Responses to the lagging stimuli from A and B, as a function of the azimuthal location of the leading stimulus. Responses to single clicks from panel C are shown again in dark circles for comparison. If no suppression occurs then the lagging response should approximately equal the response of the neuron to a single click at 45°. Open symbols represent responses to the lagging clicks at ISDs of 5, 10, and 20 ms.

in the ICC are sensitive to stimulus locations along the azimuth (Semple *et al.*, 1983; Aitkin *et al.*, 1985, 1984; Litovsky and Yin, 1994; Delgutte *et al.*, 1995), hence the importance of stimulus location for physiological correlates of the PE was studied. For most neurons, suppression of response to the lagging source occurred when the leading stimulus was presented from the same locations as the lagging source. Since those locations were most excitatory for the neurons, it may seem that these results are related to the phenomenon of forward masking, whereby the excitability of a signal is reduced by a stimulus that precedes it in time. However, in several neurons suppression of the lagging response could occur even when the response to the leading source is weak (see Fig. 12C). The SMAX neurons might be related to the auditory system's ability to separate the signal from its echo; an echo that arrives from a nearby location is potentially less confusing than one arriving from further locations, hence the further echo is less likely to be suppressed. Our results are insufficient for resolving this issue; however, it should be noted that psychophysically, the PE and forward masking are considered to reflect different mechanisms in the auditory system (Zurek, 1987).

C. Developmental issues

During the first few weeks after birth the central auditory pathway of mammals undergoes remarkable structural changes, hence it is quite surprising to find that many basic elements of responses to auditory stimuli emerge very early in postnatal life (Brugge, 1992). In the kitten, the pattern of innervation of hair cells stabilizes at around three weeks after birth (Pujol *et al.*, 1978), but myelenation of the auditory nerve is not completed until 3–6 months postpartum (Romand *et al.*, 1976; Walsh *et al.*, 1985). During the neonatal

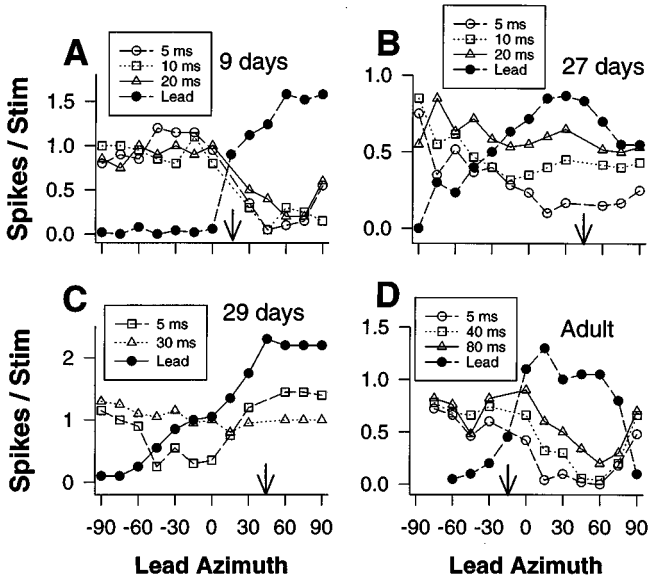

FIG. 12. Responses from four neurons whose echo suppression is modulated by the leading stimulus location. Responses to the leading stimulus by itself (filled circles) and to the lagging stimulus at various ISDs (unfilled symbols) are plotted as a function of the location of the leading stimulus. The arrows in each panel point to the azimuthal location of the lagging stimulus, which was held constant. Neurons in panels A–C are examples from kitten neurons, at 9 days (CF=11 kHz), 27 days (CF=4 kHz) and 29 days (CF=3.7 kHz), respectively. The fourth example in D is from an adult neuron (CF=0.85 kHz).

period significant structural changes also occur in the superior olivary complex (Schwartz, 1972, 1977), which is the first site of binaural interaction in the auditory pathway.

Physiological changes in stimulus coding also undergo significant changes during development. The response latency to sound sources appears to decrease with age at all levels of the auditory pathway (Moore, 1983). In the lateral superior olive (LSO), where neurons encode interaural differences in level, the resolution of single cells is poor in young gerbils tested immediately after ear canal opening (Sanes and Rubel, 1988). This functional immaturity is also found in the IC of kittens (Moore and Irvine, 1981; Blatchley and Brugge, 1990). As Sanes (1992) points out, decreased resolution in single cells at higher levels in the system cannot be accounted for simply by changes at the level of the cochlea.

In spite of all the changes that occur in the auditory system of developing animals, our data show that neurons in the ICC of kittens display a physiological correlate of the PE that is remarkably similar to effects found in the ICC of adult animals (Fitzpatrick *et al.*, 1995; Yin, 1994; Litovsky and Yin, 1998a, b). In fact, the only potential difference in the data was that of lower *half-maximal ISDs* in the kitten population than adult population, a difference which disappeared once the neurons being compared had the same range of CFs. Other than *half-maximal ISDs* (neural correlate of echo threshold), quantitative comparisons between kittens and adults are difficult to make due to the small number of kitten neurons studied. However, our results show that for every effect studied, i.e., varying stimulus level, duration, or lead location, kitten neurons responded in a similar fashion to adult neurons. Thus, the qualitative similarity between kitten and adult neurons appears to be strong.

Although the site of generation of the PE in the auditory pathway is not known, there is strong evidence to suggest that the IC is an important station in the initial stages of the pathway (Yin, 1994; Fitzpatrick *et al.*, 1995). Studies conducted on kittens in the IC have shown that the neural circuitry involved in sensitivity to ITD and IID (Blatchely and Brugge, 1990) as well as amplitude-modulation (Brugge *et al.*, 1993) is well-developed before the binaural system is matured, and before the cochlea is even capable of responding to those stimuli. Thus, it is not surprising that the responses of ICC neurons to PE stimuli is also fully matured at birth.

How do these findings relate to the behavioral data which suggest that newborn mammals do not experience the PE in a similar fashion to adult mammals (Clifton *et al.*, 1981; Muir *et al.*, 1989; Burnham *et al.*, 1993)? The auditory cortex has been implicated as an important structure in the behavioral manifestation of the PE. Cats with lesions in their auditory cortex are impaired in their ability to localize PE stimuli at the leading source, however, their localization of a single sound remains intact (Cranford *et al.*, 1971; Cranford and Oberholtzer, 1976; Whitfield *et al.*, 1972). In addition, children with temporal lobe epilepsy (Hochster and Kelly, 1981) and adults with cerebrovascular damage (Cornelisse and Kelly, 1987), whose localization of single sounds is nearly perfect, show marked decrease in their ability to localize PE stimuli. It has been suggested (Clifton, 1985) that the auditory cortex provides sensory inhibition of the lagging source, which produces the perception of a fused auditory event at the leading source location. This inhibition presumably unfolds during the first few months of life when the auditory cortex is undergoing significant changes (Dekaban, 1970; Yakovlev and Lecours, 1967). Further research is needed in order to link developmental changes in the cortex with the late onset of the PE in mammals. In particular, behavioral studies in kittens demonstrating a similar time course to that observed in dogs and humans are important.

In summary, this study provides the first measurement of physiological correlates of the PE in the IC of kittens. Our finding that most single-unit physiological observations made in adult cats can be replicated in young kittens is consistent with the notion that the behavioral manifestation of the PE is mediated at higher levels in the auditory pathway than the IC (e.g., Clifton *et al.*, 1994; Clifton and Freyman, 1997). Thus, the neurons in the brainstem are ready to carry relevant information concerning sounds and their echoes at a very young age, much before higher centers are capable of processing that information and using it effectively for behavioral purposes.

ACKNOWLEDGMENTS

The author is grateful to Dr. J. Brugge, Dr. R. Reale, and Dr. T. Yin for helpful suggestions on experimental procedures. Many thanks to R. Kochhar for computer programming, Inge Siggelkow and Jo Ann Ekleberry for histological preparation, and Terry Stewart and Carol Dizack for help in preparation of figures. The author is also grateful to Marsha

Clarkson for helpful comments during the review process. The work was supported by NIH Training grant to Ruth Litovsky (5F32 DC00078) and NIH P01 grant to U. Wisconsin (DC00116).

The care and use of animals reported on in this study were approved by the National Institutes of Health (Grant No. [53F2]DC00078, entitled *Binaural Mechanisms Involved in Spatial Hearing*).

Aitkin, L. M., and Reynolds, A. (**1975**). ''Development of binaural responses in the kitten inferior colliculus,'' Neurosci. Lett. **1**, 315–319.

Aitkin, L. M., Gates, G. R., and Phillips, S. C. (**1984**). ''Responses of neurons in inferior colliculus to variations in sound-source azimuth,'' J. Neurophysiol. **52**, 1–17.

Aitkin, L. M., Pettigrew, J. D., Calford, M. B., Phillips, S. C., and Wise, L. Z. (**1985**). ''Representation of stimulus azimuth by low-frequency neurons in the inferior colliculus of the cat,'' J. Neurophysiol. **53**, 43–59.

Ashmead, D. H., Clifton, R. K., and Perris, E. E. (**1987**). ''Precision of auditory localization in human infants,'' Dev. Psych. **23**, 641–647.

Babkoff, H., and Sutton, S. (**1966**). ''End point of lateralization for dichotic clicks,'' J. Acoust. Soc. Am. **39**, 87–102.

Blauert, J. (**1997**). *Spatial Hearing* (MIT, Cambridge, MA).

Blatchley, B., and Brugge, J. F. (**1990**). ''Sensitivity to binaural intensity and phase difference cues in kitten inferior colliculus,'' J. Neurophysiol. **64**, 582–595.

Blodgett, H. C., Wilbanks, W. A., and Jeffress, L. A. (**1956**). ''Effect of large interaural time differences upon the judgment of sideness,'' J. Acoust. Soc. Am. **28**, 639–643.

Brugge, J. F. (**1992**). ''Development of the lower auditory brainstem of the cat,'' *Development of Auditory and Vestibular Systems 2*, edited by R. Romand (Elsevier, New York), pp. 273–295.

Brugge, J. F., Blatchley, B., and Kudoh, M. (**1993**). ''Encoding of amplitude-modulated tones by neurons of the inferior colliculus of the kitten,'' Brain Res. **615**, 199–217.

Brugge, J. F., Javel, R., and Kitzes, L. M. (**1978**). ''Signs of functional maturation of peripheral auditory system in discharge patterns of neurons in anteroventral cochlear nucleus of kitten,'' J. Neurophysiol. **41**, 1557–1579.

Burnham, D., Taplin, J., Henderson-Smart, D., Earnshaw-Brown, L., and O'Grady, B. (**1993**). ''Maturation of precedence effect thresholds: Full- and Pre-Term infants, Inf. Behav. Develop. **16**, 213–232.

Carney, L. H., and Yin, T. C. T. (**1989**). ''Responses of low-frequency cells in the inferior colliculus to interaural time differences of clicks: excitatory and inhibitory components,'' J. Neurophysiol. **62**, 144–161.

Clements, M., and Kelly, J. B. (**1978**). ''Directional responses by kittens to an auditory stimulus,'' Dev. Psychobiol. **11**, 505–511.

Clifton, R. K. (**1985**). ''The precedence effect: Its implications for developmental questions,'' in *Auditory Development in Infancy*, edited by S. E. Trehub and B. Schneider (Plenum, New York).

Clifton, R. K., and Freyman, R. L. (**1997**). ''The precedence effect: Beyond echo suppression,'' in *Binaural and Spatial Hearing in Real and Virtual Environments,* edited by R. H. Gilkey and T. R. Anderson (Earlbaum, Hillsdale, NJ).

Clifton, R. K., Freyman, R. L., Litovsky, R. Y., and McCall, D. M. (**1994**). ''Listeners' expectations about echoes can raise or lower echo thresholds,'' J. Acoust. Soc. Am. **95**, 1525–1533.

Clifton, R. K., Morrongiello, B. A., Kulig, J., and Dowd, J. (**1981**). ''Newborns' orientation toward sound: Possible implications for cortical development,'' Child Dev. **52**, 833–838.

Cornelisse, L., and Kelly, J. B. (**1987**). ''The effects of cerebrovascular accident on the ability to localize sounds under conditions of the precedence effect,'' Neuropsychologica **25**, 449–452.

Cranford, J. L. (**1982**). ''Localization of paired sound sources in cats: Effects of variable arrival times,'' J. Acoust. Soc. Am. **72**, 1309–1311.

Cranford, J. L., and Oberholtzer, M. (**1976**). ''Role of neocortex in binaural hearing in the cat, II: The precedence effect in sound localization,'' Brain Res. **111**, 225–239.

Cranford, J. L., Ravizza, R., Diamond, I. T., and Whitfield, I. C. (**1971**). ''Unilateral ablation of the auditory cortex in the cat impairs complex sound localization,'' Science **172**, 286–288.

Damaske, P. (**1971**). ''Head-related two-channel stereophony with loudspeaker reproduction,'' J. Acoust. Soc. Am. **50**, 1109–1115.

Dekaban, A. (**1970**). *Neurology of Early Childhood* (William and Wilkins, Baltimore).

Delgutte, B., Joris, P., Litovsky, R., and Yin, T. C. T. (**1995**). ''Relative importance of different acoustic cues to the directional sensitivity of inferior-colliculus neurons,'' in *Advances in Hearing Research: Proceedings of the 10th International Symposium on Hearing,* edited by G. A. Manley, G. M. Klump, C. Koppl, H. Fastl, and H. Oeckinghaus (World Scientific, Singapore).

Elliott, D. N., Stein, L., and Harrison, M. J. (**1960**). ''Discrimination of absolute-intensity thresholds and frequency-difference thresholds in cats,'' J. Acoust. Soc. Am. **32**, 380–384.

Fitzpatrick, D. C.,, Kuwada, S., Batra, R., and Trahiotis, C. (**1995**). ''Neural responses to simple, simulated echoes in the auditory brainstem of the unanesthetized rabbit,'' J. Neurophysiol. **74**, 2469–2486.

Freyman, R. L., Clifton, R. K., and Litovsky, R. Y. (**1991**). ''Dynamic processes in the precedence effect,'' J. Acoust. Soc. Am. **90**, 874–884.

Hind, J. E., Goldberg, J. E., Greenwood, D. D., and Rose, J. E. (**1963**). ''Some discharge characteristics of single neurons in the inferior colliculus of the cat. II. Timing of the discharges and observations on binaural stimulation,'' J. Neurophysiol. **26**, 321–341.

Hochster, M., and Kelly, J. (**1981**). ''The precedence effect and sound localization by children with temporal lobe epilepsy,'' Neuropsychologia **19**, 49–55.

Keller, C. H., and Takahashi, T. T. (**1996**). ''Responses to simulated echoes by neurons in the barn owl's auditory space map,'' J. Comput. Phys. **178**, 499–512.

Kettner, R. E., Feng, J. Z., and Brugge, J. F. (**1985**). ''Postnatal development of the phase-locked response to low frequency tones of auditory nerve fibers in the cat,'' J. Neurosci. **5**, 275–283.

Kuwada, S., and Yin, T. C. T. (**1983**). ''Binaural interaction in low-frequency neurons in inferior colliculus of the cat. I. Effects of long interaural delays, intensity, and repetition rate on interaural delay function,'' J. Neurophysiol. **50**, 981–999.

Liberman, M. C. (**1978**). ''Auditory-nerve responses from cats raised in a low-noise chamber,'' J. Acoust. Soc. Am. **63**, 442–455.

Litovsky, R. Y. (**1997**). ''Developmental changes in the precedence effect: Estimates of minimum audible angle,'' J. Acoust. Soc. Am. **102**, 1739–1745.

Litovsky, R. Y., and Ashmead, D. M. (**1997**). ''Developmental aspects of binaural and spatial hearing,'' in *Binaural and Spatial Hearing in Real and Virtual Environments*, edited by R. H. Gilkey and T. R. Anderson (Erlbaum, Hillsdale, NJ).

Litovsky, R. Y., and Yin, T. C. T. (**1993**). ''Single-unit responses to stimuli that mimic the precedence effect in the inferior colliculus of the cat,'' Assoc. Res. Otolaryngol.

Litovsky, R. Y., and Yin, T. C. T. (**1994**). ''Physiological correlates of the precedence effect: Free-field recordings in the inferior colliculus of the cat,'' Assoc. Res. Otolaryngol.

Litovsky, R. Y., and Yin, T. C. T. (**1998a**). ''Physiological studies of the precedence effect in the inferior colliculus of the cat: I. Correlates of psychophysics,'' J. Neurophysiol. (in press).

Litovsky, R. Y., and Yin, T. C. T. (**1998b**). ''Physiological studies of the precedence effect in the inferior colliculus of the cat: II. Neural mechanisms,'' J. Neurophysiol. (in press).

Litovsky, R. Y., Rakerd, B., Yin, T. C. T., and Hartmann, W. M. (**1997**). ''Evidence for psychophysical and physiological correlates of the precedence effect in the sagittal plane,'' J. Neurophysiol. **77**, 2223–2226.

Moore, D. R. (**1983**). ''Development of inferior colliculus and binaural auditory,'' in *Development of Auditory and Vestibular Systems*, edited by R. Romand (Academic, New York).

Moore, D. R., and Irvine, D. R. F. (**1979**). ''A developmental study of the sound pressure transformation by the head of the cat,'' Acta Oto-Laryngol. **87**, 434–440.

Moore, D. R., and Irvine, D. R. F. (**1980**). ''Development of binaural input, response patterns, and discharge rate in single units of the cat inferior colliculus,'' Exp. Brain Res. **38**, 103–108.

Moore, D. R., and Irvine, D. R. F. (**1981**). ''Development of responses to acoustic interaural intensity differences in the cat inferior colliculus,'' Exp. Brain Res. **41**, 301–309.

Muir, W. D., Clifton, R. K., and Clarkson, M. G. (**1989**). ''The development of a human auditory localization response: A U-shaped function,'' Can. J. Psychol. **43**, 199–216.

Norton, T. T. (**1974**). ''Receptive-field properties of superior colliculus cells

and development of visual behavior in kittens,'' J. Neurophysiol. **37**, 674–690.
Olmstead, C. E., and Villiblanca, J. R. (**1980**). ''Development of behavioral audition in the kitten,'' Physiol. Behav. **24**, 705–712.
Populin, L. C., and Yin, T. C. T. (**1998**). ''Behavioral studies of the precedence effect: The summing localization period,'' J. Neurosci. (March).
Pujol, R., Carlier, E., and Devigne, C. (**1978**). ''Different patterns of cochlear innervation during development of the kitten,'' J. Comp. Neurol. **177**, 529–536.
Romand, R., Sans, A., Romand, M. R., and Marty, R. (**1976**). ''The structural maturation of the stato-acoustic nerve in the cat,'' J. Comp. Neurol. **170**, 1–16.
Rose, J. E., Gross, N. B., Geisler, C. D., and Hind, J. E. (**1966**). ''Some neural mechanisms in the inferior colliculus of the cat which may be relevant to localization of a sound source,'' J. Neurophysiol. **29**, 288–314.
Sanes, D. H. (**1992**). ''The refinement of central auditory form and function during development,'' in *Developmental Psychoacoustics*, edited by L. A. Werner and E. W. Rubel (American Psychological Association, Washington, DC), pp. 257–280.
Sanes, D. H., and Rubel, E. W. (**1988**). ''The ontogeny of inhibition and excitation in the gerbil lateral superior olive,'' J. Neurosci. **8**, 682–700.
Schwartz, I. R. (**1972**). ''The development of terminals in the cat medial superior olive,'' Anat. Rec. **172**, 401.
Schwartz, I. R. (**1977**). ''Dendritic arrangements in the cat medial superior olive,'' Neuroscience (NY) **2**, 81–101.
Semple, M. N., and Aitkin, L. M. (**1979**). ''Representation of sound frequency and laterality in units in central nucleus of the cat inferior colliculus,'' J. Neurophysiol. **42**, 1626–1639.
Semple, M. N., Aitkin, L. M., Calford, M. B., Pettigrew, J. D., and Phillips, D. P. (**1983**). ''Spatial receptive fields in the cat inferior colliculus,'' Hearing Res. **10**, 203–215.
Shinn-Cunningham, B. G., Zurek, P. M., and Durlach, N. I. (**1993**). ''Adjustment and discrimination measurements of the precedence effect,'' J. Acoust. Soc. Am. **93**, 2923–2932.
Thurlow, W. R., and Parks, T. E. (**1961**). ''Precedence-suppression effects for two click sources,'' Percept. Motor Skills **13**, 7–12.
Wallach, H., Newman, E. B., and Rosenzweig, M. R. (**1949**). ''The precedence effect in sound localization,'' J. Am. Psychol. **57**, 315–336.
Walsh, E. J., McGee, J., Wagahoff, D., and Scott, V. (**1985**). ''Myelination of auditory nerve, trapezoidal, and brachium of the inferior colliculus in the cat,'' *Assoc. Res. Otolaryngol. Abst.*
Whitfield, I. C., Cranford, J., Ravizza, R., and Diamond, I. T. (**1972**). ''Effects of unilateral ablation of auditory cortex in cat on complex sound localization,'' J. Neurophysiol. **35**, 718–731.
Yakovlev, P., and Lecours, A. (**1967**). ''The myelogenetic cycles of regional maturation of the brain,'' in *Regional Development of the Brain in Early Life*, edited by A. Minkowski (F.A. Davis, Philadelphia).
Yin, T. C. T. (**1994**). ''Physiological correlates of the precedence effect and summing localization in the inferior colliculus of the cat,'' J. Neurosci. **14**, 5170–5186.
Yin, T. C. T., and Chan, J. C. K. (**1988**). ''Neural mechanisms underlying interaural time sensitivity to tones and noise,'' in: *Auditory Function: Neurobiological Bases of Hearing*, edited by G. M. Edelman, W. E. Gall, and W. M. Cowan (Wiley, New York), pp. 385–430.
Yin, T. C. T., and Kuwada, S. (**1983**). ''Binaural interaction in low-frequency neurons in inferior colliculus of the cat. II. Effects of changing rate and direction of interaural phase,'' J. Neurophysiol. **50**, 1000–1019.
Yin, T. C. T., and Litovsky, R. (**1995**). ''Physiological studies of the precedence effect in the inferior colliculus of the cat,'' in *Advances in Hearing Research: Proceedings of the 10th International Symposium on Hearing*, edited by G. A. Manley, G. M. Klump, C. Koppl, H. Fastl, and H. Oeckinghaus (World Scientific, Singapore).
Zurek, P. M. (**1987**). ''The precedence effect,'' in *Directional Hearing*, edited by W. A. Yost and G. Gourevitch (Springer-Verglag, Berlin).
Zurek, P. M. (**1980**). ''The precedence effect and its possible role in the avoidance of interaural ambiguities,'' J. Acoust. Soc. Am. **67**, 952–964.

Voice *F*0 responses to manipulations in pitch feedback[a)]

Theresa A. Burnett, Marcia B. Freedland, and Charles R. Larson[b)]
Department of Communication Sciences and Disorders, Northwestern University, Evanston, Illinois 60208

Timothy C. Hain
Department of Otolaryngology Head and Neck Surgery, Northwestern University Medical School, Chicago, Illinois 60611

(Received 14 July 1997; accepted for publication 21 January 1998)

Recent studies have shown that when phonating subjects hear their voice pitch feedback shift upward or downward, they respond with a change in voice fundamental frequency ($F0$) output. Three experiments were performed to improve our understanding of this response and to explore the effects of different stimulus variables on voice $F0$ responses to pitch-shift stimuli. In experiment 1, it was found that neither the absolute level of feedback intensity nor the presence of pink masking noise significantly affect magnitude or latency of the voice $F0$ response. In experiment 2, changes in stimulus magnitude led to no systematic differences in response magnitudes or latencies. However, as stimulus magnitude was increased from 25 to 300 cents, the proportion of responses that changed in the direction opposite that of the stimulus (''opposing'' response) decreased. A corresponding increase was observed in the proportion of same direction responses (''following'' response). In experiment 3, increases in pitch-shift stimulus durations from 20 to 100 ms led to no differences in the $F0$ response. Durations between 100 and 500 ms led to longer duration voice $F0$ responses with greater response magnitude, and suggested the existence of a second $F0$ response with a longer latency than the first.
[S0001-4966(98)05204-7]

PACS numbers: 43.10.Ln, 43.70.Aj, 43.66.Hg [AL]

GENERAL INTRODUCTION

Numerous studies have demonstrated that certain aspects of speech motor control are heavily dependent on sensory feedback (Abbs and Gracco, 1984; Fairbanks, 1955; Folkins and Abbs, 1975; Gammon *et al.*, 1971; Gracco and Abbs, 1985; Shaiman, 1989). Audition is recognized as one of the most important avenues of sensory feedback for speech (Binnie *et al.*, 1982; Fairbanks, 1955; Siegel and Pick, Jr., 1974; Siegel and Kennard, 1984). Indeed, since the function of speech is to enable communication between people, the auditory signal may be the most important variable controlled by the speech motor system. Accordingly, speakers monitor their own auditory feedback to assure its clarity and agreement with the intended message. Thus if the vocal characteristics of a speaker do not match those expected, people will attempt to correct or modify pitch or loudness (Fairbanks, 1954; Howell *et al.*, 1987; Siegel and Pick, Jr., 1974). Recent studies have demonstrated that when the pitch of a subject's voice is either raised or lowered as it is fed back over headphones, the subject responds by reciprocally lowering or raising the voice $F0$. This experimental paradigm has been termed ''Transformed Auditory Feedback'' (Kawahara, 1994, 1995; Kawahara *et al.*, 1993), ''Frequency Altered Feedback'' (Kalinowski *et al.*, 1993), ''Frequency-Shifted Feedback'' (Elman, 1981; Howell *et al.*, 1987) and ''Pitch-Shifted Feedback'' (Burnett *et al.*, 1997). Here, we will use the term pitch-shifted feedback.

This technique is reliable, easy to perform, may decrease disfluency in stutterers (Kalinowski *et al.*, 1993), and has potential for enhancing the study of voice $F0$ control. Thus far, results from this technique have suggested an important connection between neural mechanisms of auditory feedback and those for voice $F0$ control. However, Elman (Elman, 1981) suggested not all subjects respond uniformly, and there is recent evidence of considerable inter-subject variability (Burnett *et al.*, 1997). One unexplained aspect of response variability reported by Burnett *et al.* (Burnett *et al.*, 1997), is that some subjects respond to pitch-shift stimuli by changing their voice $F0$ in the opposite direction of the stimulus, while other subjects change their $F0$ in the same direction as the stimulus. The value of the pitch-shift feedback technique to learning about the interaction of auditory feedback and voice control may be limited unless factors contributing to response variability can be determined. Such factors may be related to the stimulus or to the individual subject. In this paper, we address stimulus-related factors that bear on subjects' responses to pitch-shift stimuli.

I. EXPERIMENT 1. VOICE *F*0 RESPONSES TO PITCH-SHIFTED AUDITORY FEEDBACK SIGNALS: EFFECTS OF INTENSITY AND SIDE TONE MASKING

A. Introduction

This study addressed the role of stimulus intensity with and without the addition of masking noise to the feedback signal. In previous studies (Burnett *et al.*, 1997; Larson

[a)]''Selected research articles'' are ones chosen occasionally by the Editor-in-Chief, that are judged (a) to have a subject of wide acoustical interest, and (b) to be written for understanding by broad acoustical readership.
[b)]Electronic mail: clarson@casbah.acns.nwu.edu

et al., 1995), subjects' responses may have been influenced by their hearing of both the pitch-shifted signal and the non-shifted bone-conducted signal. Three ways of reducing the likelihood that subjects perceive the unaltered bone-conducted voice signal are to increase the intensity of the fed-back voice signal, present the signal with masking noise, or to combine them (Kawahara, 1994). In the first study, we manipulated the intensity of the voice presented through the earphones separately and in combination with accompanying pink masking noise.

B. Methods

1. Subjects

Twenty normal young adults (ages 18–22), 19 females and 1 male, served as subjects. All had passed a hearing screening at 20 dB (500–8 kHz), reported no neurological deficits, had no speech or voice disorder, and were not trained as professional singers.

2. Apparatus and procedures

Subjects were seated in a sound-treated room, their voices recorded with a Shure Beta 87 microphone (6-cm mouth to mike distance), amplified with a Mackie mixer (model 1202) and processed for auditory feedback pitch-shifting through an Eventide (SE 3000) Ultraharmonizer. Depending on the experimental condition, the output of the harmonizer was mixed with pink masking noise (Goldline noise generator model PN2), then amplified with a Crown D75 amplifier and presented to the subject over Sennheiser earphones (model HD 430). Subjects maintained their vocal intensity close to 70 dB SPL aided by observing a Dorrough loudness monitor (model 40-A). Adjustment of the voice feedback intensity and noise intensity were made with 2 Hewlett-Packard dB attenuators (model 350D). All acoustical equipment was calibrated with a Brüel & Kjaer 2203 sound level meter (weighting A). Voice intensity was not tightly controlled in this study since a previous study showed no systematic relationship between voice $F0$ response and intensity (Burnett *et al.*, 1997).

Subjects were instructed to phonate /a/ for 5 s, pause, then repeat for a total of 30 vocalizations (trials) in each block. They were told to ignore any change in their voice feedback over the earphones and maintain the same vocal intensity and pitch output as before the change. At the onset of each vocalization, the experimenter activated a computer program that caused the harmonizer to increase voice pitch feedback by 100 cents. This disparity between the subject's vocal output and their auditory feedback began at a random time between 500 and 1500 ms after experimenter activation, and was maintained for a duration of 500 ms.

During the experiment, the subject's voice, the harmonizer trigger signal, and a 150-Hz sine wave signal from a function generator (shifted identically and simultaneously with the subject's voice through the second channel of the harmonizer) were recorded on DAT tape with a Cygnus DAT recorder (model CDAT 16) at a sampling frequency of 2.5 kHz. The sine wave was used to indicate the precise onset time and direction of the pitch-shift stimulus for data analysis. This control signal allowed for the correction of the variable 8–20 ms delay between the trigger pulse and the actual change in feedback pitch caused by processing time related to the serial line connection to the harmonizer.

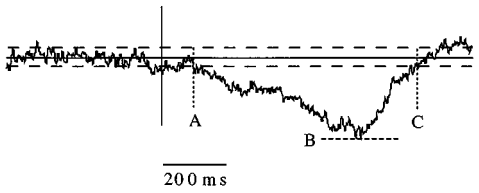

FIG. 1. Averaged $F0$ response of a subject exhibiting ''opposing'' (downward) response to upward pitch-shift stimuli. Solid vertical line is time of onset of pitch-shift stimulus. Solid horizontal line=mean of response before pitch-shift stimulus onset. Dashed lines=±2 standard deviations of the mean voice $F0$ before pitch-shift stimulus onset. A=time of response onset. B=peak response. C=time of response offset.

These pitch-shift stimuli were presented to the subjects under different listening conditions. The intensity of the subjects' processed voice signal, the masking noise, or both were altered during separate blocks of 30 vocalizations. Three different levels of vocal intensity were investigated: 65, 75, and 85 dB SPL. These vocal intensity levels were combined with four possible pink noise masking levels: none, 50, 60, or 70 dB SPL. Each of these conditions was presented for an entire block, resulting in a total of 12 different stimulus conditions (360 vocalizations) for each subject. Between each block, subjects were allowed to rest and drink water.

After the experiment, a dc signal proportional to voice $F0$ was generated by a pulse former circuit and a locally fabricated device (Larson *et al.*, 1987). The $F0$ of the sine wave signal was extracted with a Kay Visi-Pitch (model 6095-6097), which had similar timing characteristics to that of the locally fabricated device. The two methods of $F0$ extraction are generally quite reliable, although the locally fabricated technique is more accurate than the Visi-Pitch. Nevertheless, there were problems with $F0$ extraction resulting in some data being discarded.

Data were digitized at 1 kHz and analyzed on a laboratory computer. Analysis began by first averaging the voice $F0$ signals corresponding to all 30 trials by each subject in each given experimental condition. This resulted in one averaged trial for each subject in each condition. The averaging was done by time aligning the dc signal representing voice $F0$ for each vocalization to the onset of the pitch-shift stimulus. Averaged responses were then smoothed with a 10 point binomial (Gaussian) smoothing function (Igor Pro). The resulting averaged responses were considered valid if they deviated by more than 2 s.d.s from the prestimulus mean for at least 50 ms, with a latency of at least 60 ms. Onset and offset times as well as the peak (or trough) magnitude of the response were calculated from cursor positions (see Fig. 1). Response duration measures were truncated at 1000 ms in those cases where the response failed to return to baseline levels before the end of the analysis window. Measurements were then placed in spreadsheets, and the voltage corresponding to the averaged dc voice $F0$ signal was converted to Hertz according to a formula derived from calibration sig-

nals and then converted to cents according to the formula:

$$\text{Cents} = 100 \times \left(\frac{12 \times \log(R/B)}{\log(2)} \right)$$

R = response peak $F0$ in Hz

B = baseline (pre-shift) mean $F0$ in Hz.

These calculations as well as the latency measures were charted in Data Desk, Excel and Statistica and submitted to significance testing using a MANOVA in Data Desk. A Chi Square test was used to test the significance of nominal data.

C. Results

All 20 subjects responded to the pitch-shift stimulus with a valid change in average voice $F0$ under some of the 12 experimental conditions, although 6 subjects had at least one instance in which no valid averaged response could be measured. Two of these six produced more invalid responses than valid responses. There was no systematic difference in the number of valid responses across each condition. From the 20 subjects, each condition contained valid responses from 10 to 14 subjects. Out of 240 averaged responses, a total of 141 were analyzed. Nineteen averaged trials were not analyzed because they failed to meet our response validity criteria (no response). The remaining 80 averaged trials were discarded for technical reasons, the most prominent being problems with $F0$ extraction. Valid responses were categorized according to whether they changed in the same direction as the pitch-shift stimulus (''following'' response) or in the opposite direction (''opposing'' response) (Burnett *et al.*, 1997). Seven subjects opposed and one subject followed the pitch-shift stimulus direction with every response, but most subjects produced a mixture of ''following'' and ''opposing'' responses. The magnitude of responses to the 100 cent pitch-shift stimuli ranged from 8.2 to 82.6 cents (mean 27.5 s.d.=13.2), corresponding to a range of 0.8 Hz–10.8 Hz (mean=3.6 Hz, s.d.=2.0 Hz). There was no significant difference in magnitude between measures for upwardly or downwardly directed responses.

The overall mean of the response latencies across all conditions was 228 ms (range: 60–830 ms). ''Opposing'' response latencies were significantly shorter (mean 192 ms) than ''following'' responses (mean=327 ms; $F=20$, df $=106$, $p<0.05$).

Variations in voice feedback intensity, whether alone or combined with pink masking noise, had no effect on group means of response latency or magnitude. Similarly, no changes for latency or magnitude were found as a function of the difference between the voice feedback and noise intensity. In part, the failure to find significant differences in the measures between the experimental conditions may be attributed to high inter-subject variability. However, no systematic changes were observed when data for each individual subject were plotted across all experimental conditions.

In an attempt to learn why some responses oppose and others follow the pitch-shift stimulus, percentages of ''opposing'' and ''following'' responses were calculated and plotted against intensity (Fig. 2A), and the feedback intensity–noise masking level difference (Fig. 2B). No one condition led to a single direction of response but in all cases, ''opposing'' responses outnumbered ''following'' responses.

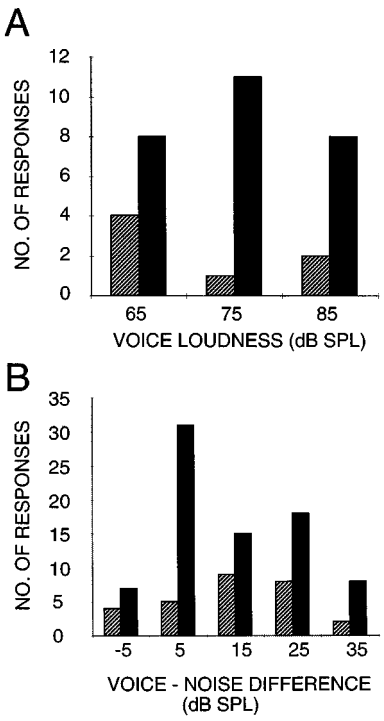

FIG. 2. A=Plot of number of ''opposing'' (solid bars) and ''following'' (hatched bars) responses by voice feedback intensity. B=Plot of number of ''opposing'' and ''following'' responses by difference in voice feedback and masking noise intensity.

II. EXPERIMENT 2. VOICE *F0* RESPONSES TO PITCH-SHIFTED AUDITORY FEEDBACK SIGNALS: EFFECTS OF STIMULUS MAGNITUDE

A. Introduction

Using the pitch-shifted feedback technique, previous investigators have presented pitch shifts of an octave (Howell *et al.*, 1987), one half an octave (Kalinowski *et al.*, 1993), 10% or 20% of an octave (Elman, 1981), 50–300 cents (Burnett *et al.*, 1997), or 25 cents (Kawahara, 1994). Here we studied the effect of stimulus magnitude systematically.

B. Methods

1. Subjects

Ten normal young adults (ages 18–22), nine females and one male, served as subjects. These subjects did not participate in the first study; however, the inclusion criteria were the same.

2. Apparatus

The methodology varied from that of the previous experiment in the following ways: The pitch-shift stimuli varied in magnitude (25, 50, 100, 150, 200, 250, or 300 cents) while the duration was held constant at 500 ms. The feedback signal at the earphones was held constant at 75 dB SPL with subjects vocalizing at an intensity level of 70 dB SPL.

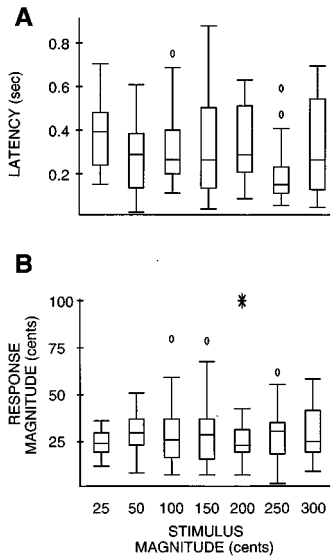

FIG. 3. A=Boxplots (mean, ±s.e., ±s.d.) of latency. B=response magnitude as a function of pitch-shift stimulus magnitude in cents.

Pink noise was presented over the earphones at 60 dB SPL. Each block of 30 vocalizations consisted of 15 upward and 15 downward pitch-shift stimuli presented in random sequence but averaged and measured separately. There was no significant difference in response magnitude as a result of pitch-shift stimulus direction. Therefore, the absolute values of measures were combined for the statistical analyses.

C. Results

All subjects responded to the pitch-shift stimulus by changing their voice *F*0 to follow or oppose it. Only one subject produced ''opposing'' responses under all experimental conditions. All other subjects opposed in most conditions but produced at least one ''following'' response. Eight averaged trials failed to meet our valid response criteria. Six responses were not analyzed due to technical difficulties, leaving a total of 124 valid responses out of 140 which were analyzed. There were no systematic differences in the number of valid responses across the experimental conditions.

Response latencies ranged from 60 to 530 ms (mean =266) but there were no significant differences between ''opposing'' and ''following'' responses or between downward and upward stimulus directions. Response magnitudes ranged from 2.6 to 100.3 cents (mean=29.2, s.d.=16.6), corresponding to a range from 0.17 to 4.8 Hz (mean =1.9 Hz, s.d.=.86). There were no significant differences in response magnitude for stimulus direction or for ''opposing'' or ''following'' responses.

The boxplots in Fig. 3 display latency (A) and response magnitude (B) measures as a function of the pitch-shift stimulus magnitudes. For this plot, measures for ''opposing'' and ''following'' responses have been collapsed together. There were no large systematic changes in latency or response magnitude as pitch-shift stimulus magnitude varied between 25 and 300 cents. As in the previous experiment, data for individual subjects were examined, but again, no systematic trends in the data could be found.

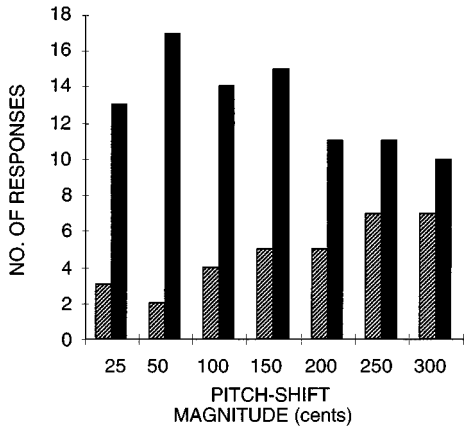

FIG. 4. Plot of number of ''opposing'' (solid bars) and ''following'' (hatched bars) responses by stimulus magnitude.

Figure 4 is the frequency distribution of ''opposing'' and ''following'' responses (collapsed across pitch-shift direction) for the various stimulus magnitude conditions. ''Opposing'' responses were most prevalent and ''following'' responses least prevalent for pitch-shift magnitudes near 50 cents. As the stimulus magnitude was increased from 50 to 300 cents, there was a progressive decrease in the number of ''opposing'' responses and an increase in the number of ''following'' responses. Due to the relatively few number of subjects, a Chi Square test failed to show significant differences in the numbers of ''opposing'' or ''following'' responses as a function of pitch-shift magnitude.

III. EXPERIMENT 3. VOICE *F*0 RESPONSES TO PITCH-SHIFTED AUDITORY FEEDBACK SIGNALS: EFFECTS OF STIMULUS DURATION

A. Introduction

In the two previous experiments, the pitch-shift stimulus duration was held constant at 500 ms, a duration easily perceived by the subject. It is important to know whether shorter duration pitch-shift stimuli, which may not be as clearly perceived, would elicit responses of the same magnitude as the longer ones. In the third experiment we examined the results of manipulating pitch-shift stimulus duration on voice *F*0 responses.

B. Methods

Twenty nine normal young adults (ages 18–20), 21 females and 8 males, participated in this experiment. None had participated in either of the previous experiments, although inclusion criteria were the same.

The experimental paradigm was identical to that of the second experiment with the exception that the pitch-shift stimulus duration of each block was varied between 20, 50, 100, 300, or 500 ms, while the pitch-shift magnitude was fixed at 100 cents. For the analysis, response duration was measured in addition to response magnitude and latency.

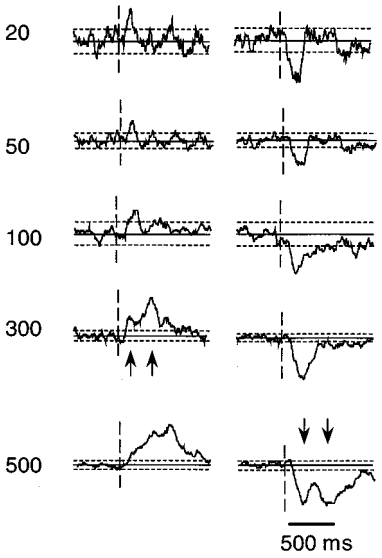

FIG. 5. Examples of averaged voice $F0$ responses from decreasing (left column) and increasing (right column) pitch-shift stimuli of 20-, 50-, 100-, 300-, and 500-ms duration. The solid horizontal line in each segment represents the mean $F0$ prior to the onset of the pitch-shift stimulus, which is indicated by the dotted vertical line. Dashed horizontal lines represent ± 2 s.d.s of the mean. Y axis is frequency in relative units. Numbers at left indicate duration of pitch-shift stimuli. Arrows highlight examples where complex responses appeared.

C. Results

All subjects responded to the pitch-shift stimulus with either an ''opposing'' or a ''following'' response, although valid responses were not observed on every condition for some subjects. A total of 132 valid responses were analyzed out of 290. Thirty-six invalid responses were discarded because they did not reach our validity criteria, while 122 responses had to be discarded because of technical problems with $F0$ extraction. For the valid responses, there were comparatively few for the short stimulus durations, e.g., 20 for 20-ms durations, versus 34 and 29 for the 300- and 500-ms durations, respectively. Thus longer duration stimuli were more likely to elicit valid responses than shorter duration stimuli. Figure 5 illustrates averaged data for the ten stimulus conditions for one subject, and shows two findings common to all subjects. As the duration of the pitch-shift stimulus increased, response magnitude and duration both increased. This subject opposed the pitch-shift stimulus on every trial. Also, for the long duration stimuli, complex responses consisting of multiple peaks were frequently observed. These complex responses were identified by visual inspection but were not quantitatively measured.

The tendency for increased response duration and magnitude with increased stimulus duration may be seen in Fig. 6, which shows boxplot data for all subjects. There are no changes in response duration to pitch-shift stimuli between 20 and 100 ms, but clear increases may be seen for the 300- and 500-ms stimulus durations. Response magnitude also appeared to increase for the 300- and 500-ms pitch-shift stimuli. Increases in response duration and magnitude were statistically significant ($F=7.7$, df$=4$, $p<0.05$ and $F=6.4$, df$=4$, $p<0.05$). *Post hoc* Scheffé tests showed that the response durations for both the 300- and 500-ms conditions were significantly greater than those for either the 20- or 50-ms pitch-shift stimulus and that response magnitudes for the 500-ms pitch-shift stimulus condition was significantly greater than those for the 20- and 50-ms pitch-shift stimulus conditions. Latency of the response was not affected by stimulus duration, as might be expected.

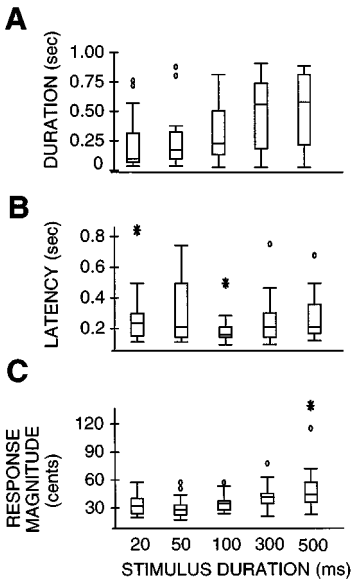

FIG. 6. Boxplots of response duration (A), latency (B), and magnitude (C) plotted as a function of stimulus duration.

It is technically difficult to measure the durations of each of the two putative responses reported here. Nor is it possible to say that in some cases there is only a first response, since two responses may have been merged together. Also, measuring the duration of the second response was not always possible since it often appeared to extend beyond the 1000-ms analysis period. Nevertheless, if it is assumed that the shortest stimuli generally produced only a first response, then measures of responses to the 20- and 50-ms pitch-shift stimuli yielding durations of 209 and 226 ms, respectively, may reflect the duration of the first response (see Fig. 6).

Because the stimulus in this study was open loop, it was expected that the subjects would change their voice $F0$ with stimulus onset and maintain the change for the duration of the pitch-shift stimulus. The fact that response magnitude also increased with stimulus duration, suggests that subjects may have had a tendency to continuously change their $F0$ as

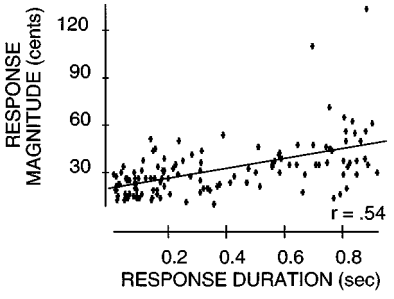

FIG. 7. Scatterplot between response magnitude and response duration. Line of linear regression was fitted to the data by the least squares method.

the pitch-shift stimulus persisted. This observation is supported by the scatterplot of response magnitude by response duration ($r=0.54$, $p<0.05$) shown in Fig. 7.

As with the previous study, the data were analyzed to determine if responses to upward and downward pitch-shift stimuli differed, and whether ''following'' responses differed from ''opposing'' responses. No differences were found between either of these.

IV. DISCUSSION

The observations from this study lead to a picture of a complex vocal control system having at least two tracking modes, ''oppose'' and ''follow,'' and at least two controllers corresponding to the early and late responses. Additionally, the high inter-subject variability suggests the presence of additional factors affecting $F0$ that were not controlled for in the present experiment. The role of feedback appears to be more that of a fine-tuning mechanism than a dominant determinant of vocal $F0$. This type of system allows cognitive and voluntary mechanisms of voice control to dominate over the influence of auditory feedback. Presumably this dominance is necessary to prevent a person's voice $F0$ from being controlled excessively by auditory signals. If voice $F0$ were exclusively controlled in this way, a person's voice $F0$ would rise and fall with nearby environmental sounds, other people's voices, etc.

Specific, relevant findings of this study bearing on the above proposition can be summarized as follows: (1) The overall intensity of the feedback signal and the presence of masking noise are not critical variables affecting the response to pitch-shift stimuli, indicating that the process of monitoring one's own voice $F0$ is not greatly disturbed by changes in absolute level of voice feedback intensity or the presence of noise. (2) Some combinations of voice and masking intensity lead to greater proportions of ''opposing'' versus ''following'' responses. (3) Variation in stimulus magnitude does not lead to parallel changes in response magnitude, suggesting vocal motor control is not rigidly bound to auditory feedback and that the system may be limited to small adjustments in voice $F0$ following pitch feedback modulations. Thus the system may be optimally suited for correction of voice errors of small magnitude, such as those due to aberrations in the neuromuscular control system, fatigue, or biomechanical changes in the cover of the vocal folds. (4) Smaller magnitude stimuli lead to greater proportions of ''opposing'' to ''following'' responses compared with larger stimulus magnitudes. (5) Response duration and magnitude vary directly with stimulus durations ranging from 100 to 500 ms. These results are unsurprising as a response should be maintained throughout a perturbation in a negative feedback system, such as we postulate for the ''opposing'' responses, and continue to build continuously for the positive feedback system inherent in the ''following'' response. (6) Longer duration stimuli may in some cases elicit a second, longer latency response.

A. Conditions affecting response type: ''Oppose'' versus ''follow''

An explanation of why subjects sometimes oppose the stimulus and at other times follow it is crucial to our understanding of the mechanisms linking the auditory and vocal systems. ''Opposing'' responses are those that compensate, at least partially, for a change in feedback and return the feedback signal closer to the value intended by the subject. They are similar to compensation responses reported in other systems, which tend to stabilize a system and correct for errors resulting from unintentional output fluctuations (Cole and Abbs, 1988; Dietz, 1992; Dietz *et al.*, 1987; Folkins and Abbs, 1975; Gracco and Abbs, 1985; Kelso *et al.*, 1984; Noth *et al.*, 1984; Sanes and Evarts, 1983; Shaiman, 1989). ''Following'' responses are those that change in the same direction as the pitch-shift stimulus. Under normal circumstances, such as while singing in a choir, this type of response would serve to bring the subject's voice into agreement with that of an external reference. However, in our experimental setup, the voice to feedback disparity maintained by the harmonizer would change the reference signal as the subject's $F0$ changed, which could stimulate additional change in $F0$. This response mode corresponds to a positive feedback loop and could lead to ''runaway,'' or a very large change in voice $F0$.

The reasons why subjects may respond in one of two control modes, ''opposing'' or ''following,'' may relate to their memory reference. When vocalizing at a particular pitch, subjects probably compare pitch memory with auditory, proprioceptive, and kinesthetic feedback (Fairbanks, 1954; Larson *et al.*, 1996; Sundberg, 1987). Subjects who oppose the direction of the pitch-shift stimulus may primarily rely on pitch memory to adjust $F0$ output, thereby bringing auditory feedback into agreement with memory. In other words, ''opposers'' use an internal $F0$ reference.

Subjects who follow the pitch-shift stimulus direction may allow an external reference to control voice $F0$. For the ''following'' responses, a comparison is probably made between the feedback signal and something representing an intentional voice $F0$, e.g., pitch, proprioceptive or muscle memory. When these comparisons result in large differences (Fig. 4), the external reference dominates the vocal control system and subjects tend to follow the stimulus direction. When the differences are small, memory dominates, and subjects oppose the stimulus. These observations suggest the system may selectively choose a compensatory strategy for small errors, and a ''following'' strategy for large errors. The ability to be flexible in choosing strategies may allow a person to learn to rely on his/her own voice feedback in conditions such as singing, and to ignore irrelevant types of feedback. We previously reported results of presenting a 100 cent pitch-shift to a trained singer as he sang a musical scale (Burnett *et al.*, 1997). Upon presentation of the pitch-shift, the singer immediately compensated for the pitch-shift stimulus and adjusted his voice $F0$ to produce the correct auditory pitch for the musical scale he was trying to sing. Thus the compensation strategy may be used to produce an $F0$ that is in accordance with an internal representation of the note. The choice of a ''following'' strategy may be ap-

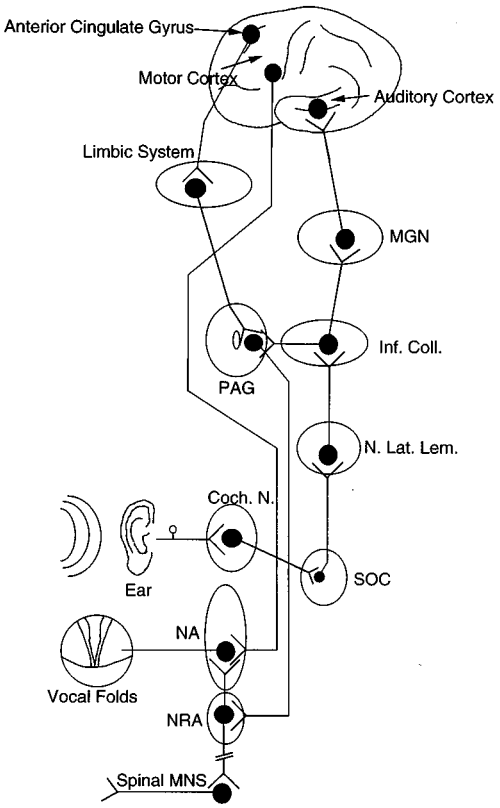

FIG. 8. Schematic illustration of vocal and auditory system pathways. Abbreviations: Coch. N.–cochlear nucleus; Inf. Col.–inferior colliculus; MGN–medial geniculate nucleus; NA–nucleus ambiguus; NRA–nucleus retroambiguus; PAG–periaqueductal gray; N. Lat. Lem.–nucleus of lateral lemniscus; SOC–superior olivary complex.

propriate for conditions where a person attempts to match their voice to an external source, such as musical accompaniment.

Nevertheless, if the only difference between the ''opposing'' and ''following'' responses is the choice of the reference signal, the two types of responses should demonstrate significant differences in response magnitude; smaller changes should be observed for ''opposing'' responses and larger changes for ''following'' responses. As we did not observe a significant difference in magnitudes produced for ''opposing'' or ''following'' responses, it follows that some other mechanism, perhaps voluntary intervention or an intrinsic limitation on the size of these responses, prevented large ''following'' responses.

B. Conditions affecting response type: First versus second vocal response

An additional aspect of the duration measures is the observation that responses to longer pitch-shift stimuli sometimes appeared to consist of two components, evidenced by an early and a late peak. Kawahara (Kawahara, 1995) also provided evidence for a short and a long latency response to pitch-shift stimuli. Different latencies for these two responses suggests they may reflect different underlying mechanisms. In the first two experiments, the pitch-shift stimuli durations were 500 ms. Although the possibility of ''double peaked'' responses was not anticipated and so it was not specifically investigated, the response magnitudes reported for these first two experiments most likely reflect a combination of a short latency and longer latency vocal $F0$ response (vocal response 1, VR1 and vocal response 2, VR2) to changes in pitch feedback.

An explanation for the origin of these two responses may be gained by considering central neural pathways of the auditory and vocal systems. Figure 8 depicts pathways of the vocal and auditory systems. One vocal pathway extends from the anterior cingulate gyrus to the midbrain periaqueductal gray (PAG), then to the nucleus retroambiguus, and finally to the motoneurons of the respiratory system in the spinal cord and of the laryngeal system in nucleus ambiguus (Holstege, 1989; Larson, 1988; Sutton *et al.*, 1974). A second vocal system may project directly from the motor cortex to the nucleus ambiguus and possibly respiratory motoneurons (Kuypers, 1958a, b). The central auditory pathways begin at the cochlear nucleus, progress through the superior olivary complex, nucleus of the lateral lemniscus, inferior colliculus (IC), medial geniculate body and terminate in the auditory (temporal) cortex (Pfingst *et al.*, 1988).

Based on latency, VR1 might be either a brainstem response or a cortical response. At the cortical level, auditory feedback could interact with vocal mechanisms in many locations including the motor cortex or the anterior cingulate gyrus (Müller-Preuss and Jürgens, 1976; Müller-Preuss *et al.*, 1980). In the brainstem, likely sites for integration of auditory feedback and vocal output include the IC and PAG. In addition to its projections to lower brainstem nuclei involved with processing auditory signals, the IC also projects to the PAG, a major site for coordinating mechanisms of vocalization in mammals, i.e., laryngeal and respiratory systems (Jürgens and Pratt, 1979; Larson, 1988). It has been suggested that both the IC and PAG are involved in the acoustic modulation of vocalization (Huffman and Henson, 1990; Jen and Suga, 1976; Suga and Yajima, 1988) and may be responsible for the VR1 reported in the present study. VR1 may also be mediated by other subcortical structures.

There are too little data available at present to decide whether VR1 and VR2 are functionally different. One possibility is that VR2 is related to a dynamic ''wobble'' in VR1, and is generated by essentially the same underlying circuitry as VR1. The main observation supporting this hypothesis is that VR1 and VR2 are usually in the same direction. A second possibility is that VR1 and VR2 are generated by two different circuits, and in particular, VR2 is generated by pathways having longer processing times or neural distances. In this case, VR2 pathways might reasonably include the cerebral cortex and may reflect cognitive processing of perceived changes in auditory feedback, which would be implemented as part of normal strategies for control of voice $F0$. Subjects could choose to follow the direction of a change in feedback, such as when matching musical accompaniment, or use the compensatory strategy to make $F0$ correspond with an internal representation of a desired $F0$. If this is the case, it should be possible to modify VR2 by instructing subjects to modulate their response to the pitch-shift stimulus. Moreover, additional modulations of the pitch-shift stimulus may further differentiate VR1 from VR2. Indeed, in

the present study VR2 only occurred in response to pitch-shift stimulus durations greater than 100 ms.

One other auditory-vocal reflex is the auditory laryngeal reflex (ALR) (Sapir *et al.*, 1983), which is demonstrated as an increase in $F0$ approximately 50 ms after the presentation of an auditory click. However, it is unlikely that VR1 is the same as the ALR. The ALR has a latency ranging from 40 to 98 ms (Sapir *et al.*, 1983) while the VR1 is generally between 100 and 150 ms. The magnitude of the ALR ranges from 0.25 to 2.4 Hz, while the VR1 ranges from less than 0.17 Hz to 10.8 Hz. Also, the ALR results in an increase in $F0$, whereas the VR1 may be increasing or decreasing, depending on the direction of the pitch-shift stimulus. Finally, the most effective stimulus for the ALR is a brief click, whereas that for the VR1 is a change in pitch feedback. Thus while the ALR appears to be a general laryngeal response to a loud auditory stimulus, the VR1 is sensitive to the direction of a change in voice feedback pitch and so may have a function in the control of voice $F0$.

The results from this and previous studies support the hypothesis that auditory feedback is important for voice $F0$ control. In the present study, the feedback mechanisms contributed a mean of about 30 cents of voice $F0$ modulation, which is less than a semitone compensation (100 cents), observed for a trained singer singing a musical scale (Burnett *et al.*, 1997). Moreover, considerable between- and within-subject variability was observed in the present study. The variability and lack of complete compensation may be due to voice training and the nature of the experimental task in the present study. It is unlikely that all inconsistency is due to stimulus parameters since stimulus intensity was more highly controlled than previously (Burnett *et al.*, 1997; Larson *et al.*, 1995), and masking noise was employed to help reduce any sidetone contributions to the feedback signal. We conclude that the primary source for the variability relates to how a subject controls his/her voice $F0$ or attends to the pitch-shift stimulus. The use of trained singers and tasks requiring precise $F0$ control would probably help us to more precisely determine which factors contribute most to $F0$ response variability, and may reveal tighter links between feedback modulations and voice $F0$.

ACKNOWLEDGMENTS

This research was supported by NIH Grant No. DC02764-01. Portions of this study have been reported in abstract form and at the First International Conference on Voice Physiology and Biomechanics (Burnett *et al.*, 1996; Freedland *et al.*, 1996; Larson *et al.*, 1997).

Abbs, J. H., and Gracco, V. L. (**1984**). ''Control of complex motor gestures: Orofacial muscle responses to load perturbations of lip during speech,'' J. Neurophysiol. **51**, 705–723.

Binnie, C. A., Daniloff, R. G., and Buckingham, H. W. (**1982**). ''Phonetic disintegration in a five-year-old following sudden hearing loss,'' J. Speech Hear. Dis. **47**, 181–189.

Burnett, T. A., Larson, C. R., Freedland, M. B., and White, J. P. (**1996**). ''Differential effects of pitch shift duration on voice $F0$ control,'' Speech Motor Control, Amelia Island, Florida.

Burnett, T. A., Senner, J. E., and Larson, C. R. (**1997**). ''Voice $F0$ responses to pitch-shifted auditory feedback; A preliminary study,'' J. Voice **11**, 202–211.

Cole, K. J., and Abbs, J. H. (**1988**). ''Grip force adjustments evoked by load force perturbations of a grasped object,'' J. Neurophysiol. **60**, 1513–1522.

Dietz, V. (**1992**). ''Human neuronal control of automatic functional movements: Interaction between central programs and afferent input,'' Physiol. Rev. **72**, 33–69.

Dietz, V., Quintern, J., and Sillem, M. (**1987**). ''Stumbling reactions in man: Significance of proprioceptive and pre-programmed mechanisms,'' J. Physiol. (London) **386**, 149–163.

Elman, J. L. (**1981**). ''Effects of frequency-shifted feedback on the pitch of vocal productions,'' J. Acoust. Soc. Am. **70**, 45–50.

Fairbanks, G. (**1954**). ''Systematic research in experimental phonetics. 1. A theory of the speech mechanism as a servosystem,'' J. Speech Hear. Dis. **19**, 133–140.

Fairbanks, G. (**1955**). ''Selective vocal effects on delayed auditory feedback,'' J. Speech Hear. Dis. **20**, 333–346.

Folkins, J., and Abbs, J. (**1975**). ''Lip and jaw motor control during speech: responses to resistive loading of the jaw,'' J. Speech Hear. Res. **18**, 207–220.

Freedland, M. B., Larson, C. R., Burnett, T. A., and White, J. P. (**1996**). ''The effects of loudness and noise on voice control in response to pitch shift stimuli,'' Speech Motor Control, Amelia Island, Florida.

Gammon, S. A., Smith, P. J., Daniloff, R. G., and Kim, C. W. (**1971**). ''Articulation and stress/juncture production under oral anesthetization and masking,'' J. Speech Hear. Res. **14**, 271–282.

Gracco, V. L., and Abbs, J. H. (**1985**). ''Dynamic control of the perioral system during speech: Kinematic analyses of autogenic and nonautogenic sensorimotor processes,'' J. Neurophysiol. **54**, 418–432.

Holstege, G. (**1989**). ''An anatomical study on the final common pathway for vocalization in the cat,'' J. Comp. Neurol. **284**, 242–252.

Howell, P., El-Yaniv., and Powell, D. J. (**1987**). ''Factors affecting fluency in stutterers,'' in *Speech Motor Dynamics in Stuttering*, edited by H. F. M. Peters and W. Hulstijin (Springer-Verlag, New York), pp. 361–369.

Huffman, R. F., and Henson, O. W. (**1990**). ''The descending auditory pathway and acousticomotor systems: Connections with the inferior colliculus,'' Brain Res. Rev. **15**, 295–323.

Jen, P. H.-S., and Suga, N. (**1976**). ''Coordinated activities of middle-ear and laryngeal muscles in echolocating bats,'' Science **191**, 950–952.

Jürgens, U., and Pratt, R. (**1979**). ''Role of the periaqueductal grey in vocal expression of emotion,'' Brain Res. **167**, 367–378.

Kalinowski, H., Armson, J., Roland-Mieszkowski, M., and Stuart, A. (**1993**). ''Effects of alterations in auditory feedback and speech rate on stuttering frequency,'' Lang. and Speech **36**, 1–16.

Kawahara, H. (**1994**). ''Interactions between speech production and perception under auditory feedback perturbations on fundamental frequencies,'' J. Acoust. Soc. Jpn. **15**, 201.

Kawahara, H. (**1995**). ''Hearing Voice: Transformed auditory feedback effects on voice pitch control,'' Computational Auditory Scene Analysis and International Joint Conference on Artificial Intelligence, Montreal.

Kawahara, H., Hirai, T., and Honda, K. (**1993**). ''Laryngeal muscular control under transformed auditory feedback with pitch perturbation'' (SP93-39). The Institute of Electronics, Information and Communication Engineers.

Kelso, J. A. S., Tuller, B., Vatikiotis-Bateson, E., and Fowler, C. A. (**1984**). ''Functionally specific articulatory cooperation following jaw perturbations during speech: Evidence for coordinative structures,'' J. Exp. Psychol.: Hum. Percept. Perform. **10**, 812–832.

Kuypers, H. G. H. M. (**1958a**). ''Corticobulbar connexions to the pons and lower brain-stem in man,'' Brain **81**, 364–388.

Kuypers, H. G. H. M. (**1958b**). ''Some projections from the peri-central cortex to the pons and lower brain stem in monkey and Chimpanzee,'' J. Comp. Neurol. **110**, 221–255.

Larson, C. R. (**1988**). ''Brain mechanisms involved in the control of vocalization,'' J. Voice **2**, 301–311.

Larson, C. R., Burnett, T. A., Freedland, M. B., and Hain, T. C. (**1997**). ''Voice $F0$ responses to manipulations in pitch feedback stimuli,'' First International Conference on Voice Physiology and Biomechanics, Evanston, IL.

Larson, C. R., Carrell, T. D., Senner, J. E., Burnett, T. A., and Nichols, L. L. (**1995**). ''A proposal for the study of voice $F0$ control using the pitch shifting technique,'' in *Vocal Fold Physiology: Voice Quality Control*, edited by O. Fujimura and M. Hirano (Singular, San Diego), pp. 321–331.

Larson, C. R., Kempster, G. B., and Kistler, M. K. (**1987**). ''Changes in voice fundamental frequency following discharge of single motor units in

cricothyroid and thyroarytenoid muscles,'' J. Speech Hear. Res. **30**, 552–558.

Larson, C. R., White, J. P., Freedland, M. B., and Burnett, T. A. (**1996**). ''Interactions Between Voluntary Modulations and Pitch-Shifted Feedback Signals: Implications for Neural Control of Voice Pitch,'' in *Vocal Fold Physiology: Controlling Complexity and Chaos*, edited by P. J. Davis and N. H. Fletcher (Singular, San Diego), pp. 279–289.

Müller-Preuss, P., and Jürgens, U. (**1976**). ''Projections from the 'cingular' vocalization area in the squirrel monkey,'' Brain Res. **103**, 29–43.

Müller-Preuss, P., Newman, J. D., and Jürgens, U. (**1980**). ''Anatomical and physiological evidence for a relationship between the 'cingular' vocalization area and the auditory cortex in the squirrel monkey,'' Brain Res. **202**, 307–315.

Noth, J., Matthews, H. R., and Friedemann, H.-H. (**1984**). ''Long latency reflex force of human finger muscles in response to imposed sinusoidal movements,'' Exp. Brain Res. **55**, 317–324.

Pfingst, B. E., Altschuler, R. A., Watkin, K. L., and Larson, C. R. (**1988**). ''Neuroanatomic bases of hearing and speech,'' in *Handbook of Speech-Language Pathology and Audiology*, edited by N. J. Lass (Decker, Toronto), pp. 77–127.

Sanes, J. N., and Evarts, E. E. (**1983**). ''Effects of perturbation on accuracy of arm movements,'' J. Neurosci. **3**, 977–986.

Sapir, S., McClean, M. D., and Larson, C. R. (**1983**). ''Human laryngeal responses to auditory stimulation,'' J. Acoust. Soc. Am. **73**, 315–321.

Shaiman, S. (**1989**). ''Kinematic and electromyographic responses to perturbation of the jaw,'' J. Acoust. Soc. Am. **86**, 78–88.

Siegel, G., and Pick, Jr., H. L. (**1974**). ''Auditory feedback in the regulation of voice,'' J. Acoust. Soc. Am. **56**, 1618–1624.

Siegel, G. M., and Kennard, K. L. (**1984**). ''Lombard and sidetone amplification effects in normal and misarticulating children,'' J. Speech Hear. Res. **27**, 56–62.

Suga, N., and Yajima, Y. (**1988**). ''Auditory-vocal integration in the midbrain of the mustached bat: Periaqueductal gray and reticular formation,'' in *The Physiological Control of Mammalian Vocalization*, edited by J. D. Newman (Plenum, New York), pp. 87–107.

Sundberg, J. (**1987**). *The Science of the Singing Voice* (Northern Illinois U.P., Dekalb, IL).

Sutton, D., Larson, C., and Lindeman, R. C. (**1974**). ''Neocortical and limbic lesion effects on primate phonation,'' Brain Res. **71**, 61–75.

Inversion of source-time functions using borehole array sonic waveforms

Chung Chang
Schlumberger-Doll Research, Ridgefield, Connecticut 06877

Qing-Huo Liu[a)]
New Mexico State University, Klipsch School of Electrical and Computer Engineering, Las Cruces, New Mexico 88003

(Received 30 September 1997; accepted for publication 25 February 1998)

Many geophysical applications of the array sonic measurements require the knowledge of the true source-time function. Recovery of the source-time function from the borehole sonic P head waves is different from the source inversion problem in exploration seismology. The difficulty in the inversion of borehole sonic measurements arises due to the inexact knowledge of the impulse response, e.g., the inability to model the whole problem including the tool body and transducers. The random noise often encountered in seismic signals is not the key obstacle here. The inverse source problem is ill posed due to the interference of P head-wave multiples. Using waveforms from a laboratory scale model we have applied two deconvolution methods, one using a Wiener filter and the other the time-domain least-squares method. As expected, without constraints on the solutions, one cannot recover a satisfactory source-time function. An unconventional smoothness constraint is applied in the source spectrum (instead of the usual smoothness in the time-domain signals), which corresponds to a finite-duration pulse in the time domain (instead of the usual band-limited spectrum). This technique is thus called the ''duration-limited'' inversion. The inverted results, obtained by Wiener filtering combined with this ''duration limiting'' process and multichannel stacking, agree well with an independent free-field measurement. Furthermore, reconstructed receiver waveforms using the inverted source function match the measured ones. The inversion procedure is robust and potentially useful for field measurements. © *1998 Acoustical Society of America.* [S0001-4966(98)03206-8]

PACS numbers: 43.20.Fn, 43.40.Ph [ANN]

INTRODUCTION

Acoustic measurement systems involve a source, a system response, and a receiver. The detected signal is in general a convolution of the source function, the system impulse response, and the receiver transfer function. The inversion of the source-time function attempts to recover the source-time function from the measured signal by removing the system response and the receiver transfer function through the deconvolution process.

In exploration seismology the inverse source problem is also known as the wavelet estimation problem. There are numerous articles concerned with wavelet estimation. Some examples include predictive deconvolution,[1] Wiener–Hop filters,[2] the least-squares method,[3] homomorphic filters,[4] minimum-entropy deconvolution,[5] adaptive maximum entropy deconvolution,[6] and the maximum-likelihood deconvolution method.[7] There is no universal procedure for deconvolution. Each method can be successfully demonstrated for certain cases, but fails in others. They all involve different assumptions either about the reflectivity distribution in the earth or the random nature of the noise. Numerous publications have explained the associated difficulties, but the inverse source problem is by no means a trivial one.

Source deconvolution has also been used for ultrasonic applications. Examples include source characterization for acoustic emissions,[8–10] source deconvolution of an ultrasonic transducer response,[11,12] and measurement of the impact force on a composite plate.[13] The deconvolution methods used are the same as the seismic deconvolution methods except that most ultrasonic measurement systems consist of only a single channel.

Although deconvolution has found its importance in exploration seismology as well as ultrasonic applications, it has not been reported yet for borehole sonic measurements, in spite of the many applications requiring the knowledge of the true source-time function. Among these applications, the amplitude information of the array sonic waveforms is becoming increasingly important. There is a growing need to match the measurements to the simulated results. It is not possible to do so unless one knows about the source-time function.

In borehole sonic measurements, the propagation of elastic waves is complicated by the presence of the fluid-filled borehole in an elastic medium.[14–16] To recover the source-time function from the P head waves of an array sonic measurement, however, is different from the source inversion problem in exploration seismology. In seismic processing neither the source wavelet nor the reflectivity function are known, and the goal is to recover both of them from the multichannel data. Generally the recovered source wavelet is assumed to be a zero-phase or minimum-phase wavelet which is not necessarily the true source-time function of the

[a)]Electronic mail: qhliu@nmsu.edu

 0001-4966/98/103(6)/3163/6/$10.00

firing. Our objective is to recover the true source-time function from the borehole-array sonic waveforms. It is preferable to choose the P head waves to recover the source function since it is expected that the P head waves will be less affected by the presence of the tool body.

One difficulty associated with the inversion arises from inexact knowledge of the impulse response (e.g., inability to model the real problem which includes the tool body and the transducers). The random noise often encountered in seismic signals is not the key obstacle here, since most borehole sonic waveforms have a very high signal-to-noise ratio because of the short T–R (transmitter–receiver) spacing and borehole waveguide. Furthermore, the random noise can be easily suppressed by signal averaging techniques. The inverse source problem is ill posed mainly due to (i) the interference of P head wave multiples, and (ii) the mismatch between the idealized model (point source and point receiver) used in calculating the impulse responses and the actual problem where the tool body is present.

I. THE FORWARD PROBLEM

Borehole sonic measurements involve one or several acoustic sources and receivers inside a fluid-filled borehole surrounded by an elastic medium. Forward modeling for sonic measurements simulates the recorded acoustic waveforms at a receiver due to the excitation of a source in the elastic medium. This problem by itself is hardly a trivial one, and has been studied by many researchers (for example, Refs. 14–16).

Even though there are different solution methods for the forward problem, the elastodynamic response of a sonic source in an elastic medium can be written as

$$w(t)=\int_{-\infty}^{\infty} r(t-T)\int_{-\infty}^{\infty} g(\tau)s(T-\tau)\,d\tau\,dT, \tag{1}$$

where $g(t)$ is the impulse response of a point source measured at a receiver, $s(t)$ is the source-time function, and $r(t)$ is the receiver transfer function. Since it is not difficult to build a wide band receiver for sonic logging, we assume that the receiver transfer function is a delta function and we only have to deal with the source and the impulse response. This assumes an ideal coupling of the receiver to the medium.

The above integration can then be approximated by a summation:

$$w(n)=\sum_{m=-\infty}^{\infty} g(m)s(n-m), \tag{2}$$

where the time interval Δt has been omitted and each function can now be regarded as a discrete vector. Equation (2) can be symbolically written as

$$w(n)=g(n)*s(n), \tag{3}$$

where the sign * denotes a convolution operation. The matrix representation of the discrete equation is:

$$\begin{bmatrix} g(0) & 0 & 0 & \dots \\ g(1) & g(0) & 0 & \dots \\ g(2) & g(1) & g(0) & \dots \\ \vdots & \vdots & \vdots & \vdots \end{bmatrix}\begin{bmatrix} s(0) \\ s(1) \\ s(2) \\ \vdots \end{bmatrix}=\begin{bmatrix} w(0) \\ w(1) \\ w(2) \\ \vdots \end{bmatrix}. \tag{4}$$

Here, we have assumed a monopole source at the center of a circular cylindrical borehole surrounded by a homogeneous elastic solid. The borehole is assumed infinitely long, and therefore the simulation of elastic waves can be obtained by the real-axis integration (RAI) method.[14,16] A more complicated situation where the solid is a cylindrically layered medium can be treated by Ref. 15. For the inverse problem discussed below, the forward solution for $w(n)$ in Eq. (3) is needed. To this end, the physical parameters for the borehole (i.e., borehole radius, sound speed in fluid) and surrounding solid (i.e., compressional and shear speeds) as well as the source/receivers are assumed to be known. With this assumed model, the RAI method[14] is used to compute the impulse response $G(\omega)$ in the frequency domain. Then the forward solution $w(n)$ can be easily obtained by either the time-domain convolution of $s(t)$ and $g(t)$ or the frequency-domain multiplication of $S(\omega)$ and $G(\omega)$.

II. THE INVERSION METHOD

The inverse problem is to recover the source-time function $s(t)$ given the measurements of acoustic waveforms $w(t)$ in the borehole at an array of receivers. In principle this can be done by the deconvolution of Eq. (3). However, the major complication in practice is that the assumed physical model for the borehole and solid is not entirely accurate. As discussed below, we propose an unconventional smoothing technique in the spectral domain to reduce the effect of this mismatch. Incidentally, electronic and environmental noises are usually negligible for sonic logging.

Let us first discuss the straightforward least-squares solution for the deconvolution. Assuming the source-time function has a finite time duration, with an array of measured signals $w(n)$, the problem of determining $s(n)$ in Eq. (3) is actually overdetermined. Therefore, the solution can be solved by any of the least-squares methods.

The time-domain least-squares solution can be found by the following equation:

$$s=(g^T g)^{-1}g^T w, \tag{5}$$

where T denotes the transpose of a matrix. The inverse of the autocorrelation matrix $g^T g$ can be ill conditioned. White noise can be added to the diagonal elements of the matrix to stabilize the solution, which is equivalent to adding a constant in the denominator of Wiener inversion formula.

Alternatively, we can solve the deconvolution problem in the frequency domain to save computation time. In the frequency domain, the signal at receiver location $z=z_k$ can be represented as

$$W(z_k,\omega)=G(z_k,\omega)S(\omega), \tag{6}$$

where $W(z_k,\omega)$ and $G(z_k,\omega)$ are respectively the Fourier transforms of $w(z_k,t)$ and $g(z_k,t)$, and $S(\omega)$ is the Fourier transform of the source-time function $s(t)$.

The inversion for Eq. (6) for $S(\omega)$ can be ill conditioned because of the zeros in the impulse response $G(z_k,\omega)$. To avoid infinite gains at these blind frequencies, we use the Wiener filter formulation to stabilize the inversion:

$$S(\omega)=\frac{G^{\star}(\omega)P_s(\omega)}{|G(\omega)|^2P_s(\omega)+P_n(\omega)}W(\omega), \tag{7}$$

where P_s and P_n are the power spectra for the signal $w(z_k,t)$ and the measurement noise, respectively. The purpose of introducing P_n is to prevent the zero division at those frequencies where the signal strengths are weak. However, since borehole sonic waveforms generally have high signal-to-noise ratios, P_n is usually chosen to be small which will cause minimum distortion to the spectrum of the source-time function. Hence, one will observe a spiky spectrum in the recovered source-time function because of the mismatch between the actual physical model (which is implicitly included in the measured W) and the one used for the simulated impulse response. Therefore, the zeros in the denominator of (7) do not cancel out those in the numerator. (If there was a perfect match between these two models, the zeros in the numerator and denominator of the inversion formula would have theoretically canceled out.) This model mismatch causes a serious ringing in the inverted result. As illustrated below, we propose a smoothness constraint in the spectrum to reduce the effect of the model mismatch.

III. INVERSION OF LABORATORY DATA

A. Laboratory setup

A laboratory scaled model experiment was done with an external ultrasonic transducer emitting on a Lucite block with a borehole of diameter 1.91 cm. The array responses were measured with a homemade broadband hydrophone scanned along the borehole. The experimental setup is shown in Fig. 1. An independent free-field direct measurement of the source-time function was done for later comparison. Note that there is an important difference between this laboratory measurement and the actual field model in that a plane-wave-like source outside the Lucite block is used in the experiment, while the source in the field can be regarded as a point source inside the wellbore.

Figure 2 shows the borehole array responses measured with the hydrophone receiver scanning along the borehole axis with a stepping size of 0.5 cm. The P head wave arrival and its multiples are clearly seen in the waveforms. Following the P head wave the larger amplitude arrival is the leaky waveguide mode which has an apparent speed slightly faster than the fluid speed v_f. Since the lucite block represents a soft formation (i.e., $v_s<v_f$), the shear head wave cannot be excited.

B. Impulse response

The impulse response at each receiver location was calculated by the RAI method[14,15] assuming an ideal point source and point receiver at the center of the borehole. The corresponding impulse responses are shown in Fig. 3. As one can see, the impulse responses are not minimum-delay signals.[17] A minimum-delay signal should have its maximum at the beginning of the signal rather than at the middle or the end of the signal. Therefore, the simple direct substitution method[8] will be unstable.

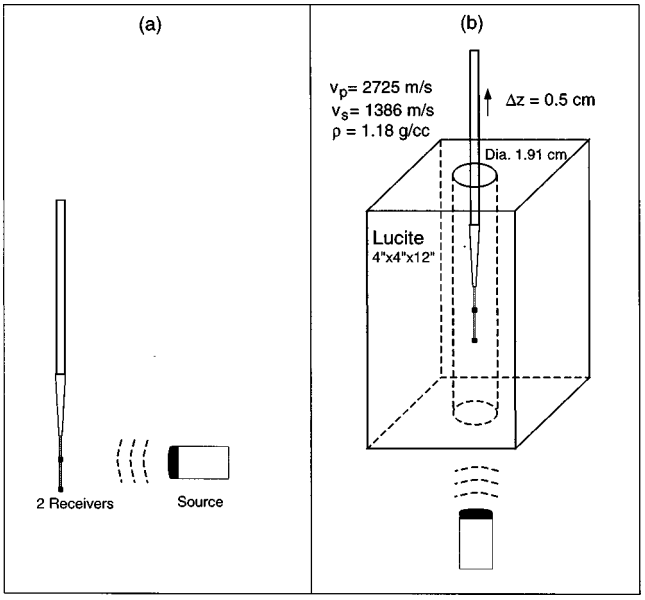

FIG. 1. Experimental configurations: (a) free-field measurement and (b) scaled borehole measurement.

As mentioned above, there is an intrinsic difference between the experiment and the field measurement (same as the simulation model) in the source excitation. The impulse responses in Fig. 3 were simulated assuming a point source and a point receiver at the center of the borehole, while the experiment used a plane-wave-like source generated by a planar transducer outside the borehole and received by a point probe at the center of the borehole. The plane wave outside the borehole goes through the borehole axis (focal point) and then acts as a point source. This focusing procedure is effectively a Hilbert transform (see Ref. 16). Therefore, the recovered source using the point source model will

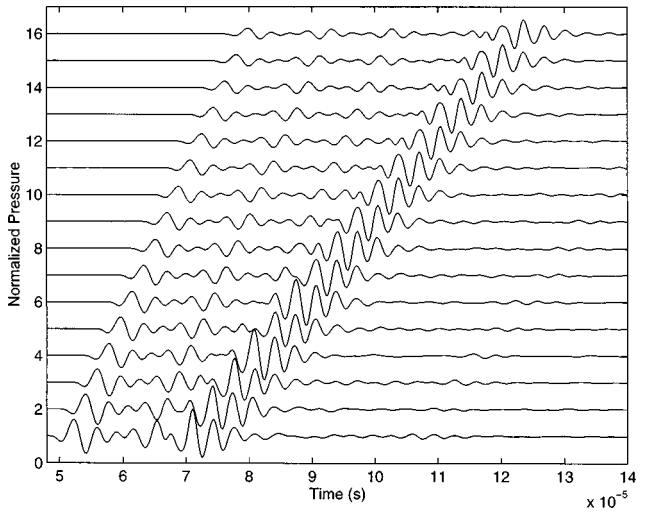

FIG. 2. Measured array hydrophone responses.

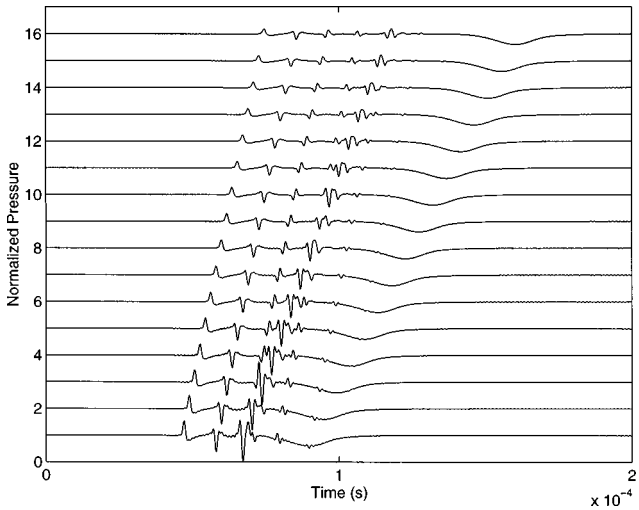

FIG. 3. Simulated impulse responses for an ideal point source and point receivers.

be different from the measured source-time function due to the plane wave by a Hilbert transform. In order to compare our inverted result with the free-field measurement we have to Hilbert transform either the recovered source-time function result or the measured source-time function result.

C. The least-squares solution

Using the impulse responses together with the measured waveforms we applied a simple least-squares deconvolution method to solve the matrix equation (4). We added a constant that is equal to 1% of the diagonal value of the autocorrelation matrix to each of the diagonal elements to improve the condition number of the matrix. The accuracy of the least-squares solution depends on the filter length as well as the delay[3] introduced into the output. Since we are interested only in finding the source-time function from the P head wave and its multiples, a proper window has to be applied to both the impulse responses and the measured receiver signals. Figure 4 shows the comparison of the least-squares solution using the last received waveform with the free-field measurement. We chose the length of the solution to be half of the windowed waveform. The optimized delay length could be found through iterations. The solution matches well at the beginning and does not match well where the signal is expected to die out at the end. Similar solutions can be obtained at other receiver locations. To solve Eq. (4) other techniques such as the singular value decomposition can be used as well. The result will not be very different unless additional constraints are imposed.

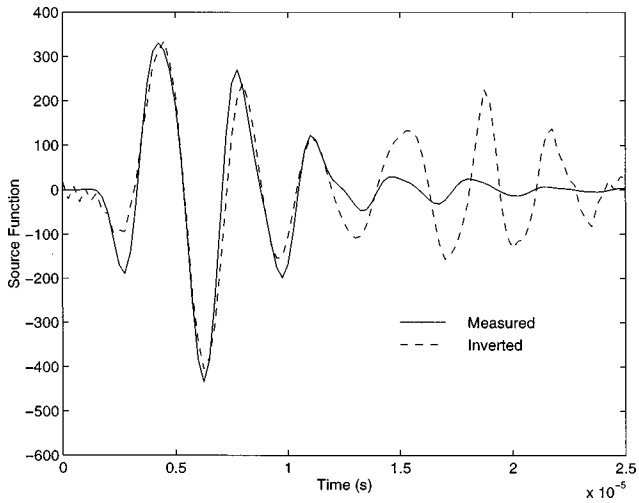

FIG. 4. A time domain comparison of the least-squares solution to the measured source-time function.

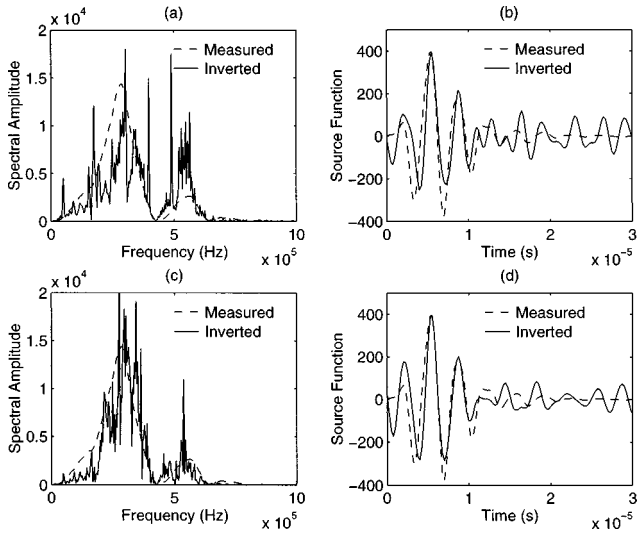

FIG. 5. Comparison of a measured source-time function with inversion using a straightforward Wiener filter. (a) Spectral amplitude from receiver 16. (b) Source-time function from receiver 16. (c) Spectral amplitude from all channels. (d) Source-time function from all channels.

D. Constrained Wiener filtering

As an alternative procedure we use a straightforward Wiener filter to invert the source-time function. For simplicity we used the whole waveform instead of using only the P head wave for the inversion. Again 1% of random noise P_n (normalized to P_s) was added to the denominator of Eq. (7) even though the noise level in the experiment is much lower because of stacking. Figure 5(a) shows the comparison of the spectrum of the recovered source-time function using the waveform at the last receiver and that of the measured source-time function. Figure 5(b) is the comparison in the time domain. As one can see the spectrum of the recovered source has many spikes corresponding to different resonant frequencies which cause the ringing in the time domain signal. The two sets of time-domain results do not agree both at the very beginning due to aliasing and at later time due to ringing that arises because of the model mismatch, similar to the problem of the least-squares solution. Figure 5(c) and (d) is the multichannel result using all the received waveforms. Although stacking of multiple receivers does help to produce a better solution, the early- and late-time errors are still substantial, and the recovered source spectrum is spiky.

To reduce the errors mentioned above, it is necessary to introduce further constraints into the problem. Two procedures are adopted in this work. First, to reduce the early time error, we band limit the inversion result to within the bandwidth of the received waveforms. In addition, a cosine taper

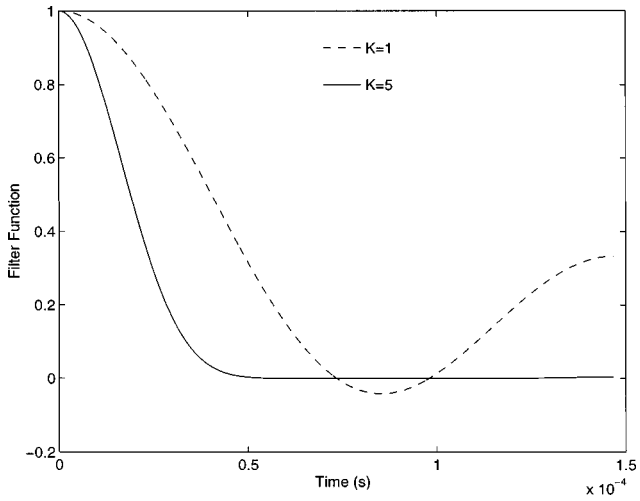

FIG. 6. The time functions corresponding to the frequency domain smoothing operation applied once ($K=1$) and applied five times ($K=5$).

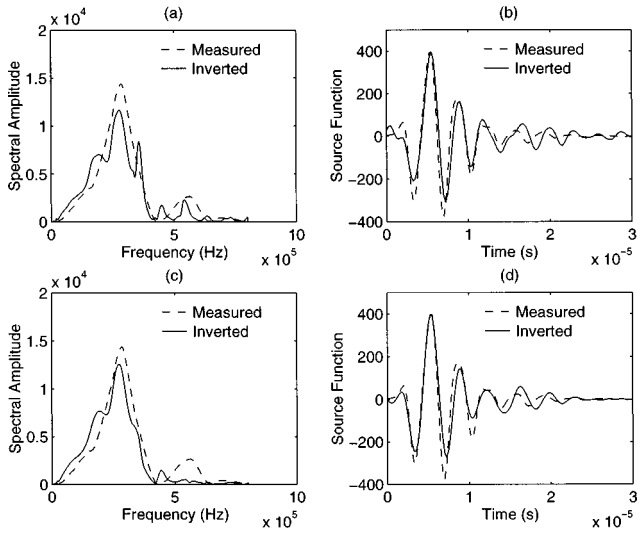

FIG. 7. Comparison of a measured source-time function with inversion using an improved Wiener filter. (a) Spectral amplitude from receiver 16. (b) Source-time function from receiver 16. (c) Spectral amplitude from all channels. (d) Source-time function from all channels.

window function is used to increase the weight of the P head waves. This window function is applied to both the received signals and simulated impulse response to decrease the effect of the model mismatch. It effectively windows out other borehole arrivals such as the Stoneley mode and other normal modes. Second, a novel smoothness constraint is used to further reduce the effect of the model mismatch, and thus the spikes in the inverted spectrum. This smoothness constraint is applied to the inverted spectrum, instead of the time-domain signals. It is achieved by filtering the complex inverted source spectrum with a five-point (1/6,1/6,1/3,1/6,1/6) smoothing operator, and repeating this procedure several times until the residual errors between the reconstructed waveforms and experimental waveforms became small. Figure 6 depicts the corresponding time domain function of the five-point smoothing operator in the frequency domain. The dashed curve represents the response using smoothing once and the solid curve is the result of applying the smoothing operator five times. As one can see, after the smoothing operation is applied five times, the ringing at late times can be suppressed substantially. This operation is equivalent to limiting the duration of the source-time function. It is worthwhile to point out that such multiple convolution produces effectively a Gaussian window function whose variance is the sum of the variance of the fundamental (five-point) window. Therefore, the above procedures can be alternatively replaced by the use of the convolution with a Gaussian function.

The result after these two procedures matches very well against the free field measured result. Figure 7(a) and (b) is the recovered source spectrum and the time domain solution using single-channel data. Figure 7(c) and (d) is the multichannel result. There is an overall better match between the measured source-time function and the recovered source-time function. Using this recovered source-time function we can reconstruct the array responses and compare to the measured responses. Figure 8 shows a very good agreement between them. In contrast, the reconstructed waveforms using the unconstrained deconvolution show substantial ringing after the first peak of the head wave, and do not give satisfactory agreement with the measured waveforms.

The spectral smoothing proposed above is an effective method for source-time functions that do not ring at late times, as one would expect for most practical downhole sonic tools. On the other hand, if the actual source does have long ringing at late times, this spectral smoothing is no longer appropriate.

It is expected that the above inversion procedures will work on field data if one can find a simple way to incorporate the full three-dimensional sonic tool body in the impulse response. Presently, however, the simulation of the large-scale full 3-D problem is still a challenge even with the modern supercomputers. A practical way of achieving this may be to approximate the effect of the tool by using an equivalent axisymmetric model, if one can find reasonably accurate parameters for such a model.

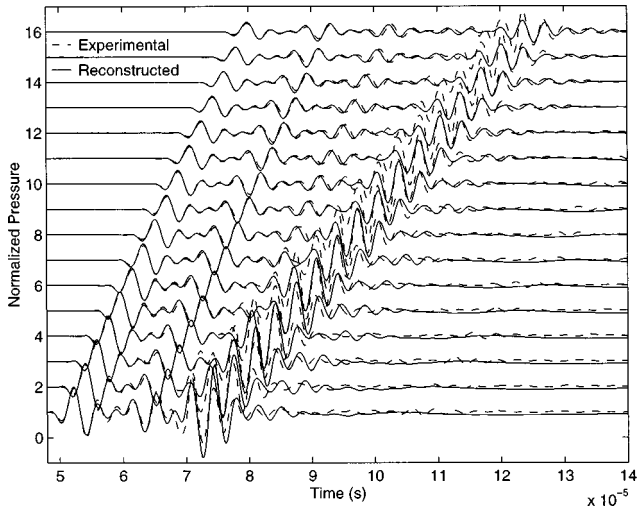

FIG. 8. Comparison of the reconstructed array responses using an inverted source-time function with the measured array responses.

IV. CONCLUSION

We report an unconventional but simple procedure to invert for the source-time function in borehole sonic measurements. It is apparently the first time that the reconstructed borehole waveforms using an inverted source-time function have been demonstrated to match well with the measured waveforms. The example shows the importance of knowing the source-time function in order to match the prediction and experiments. A spectral smoothing operation reduces the effect of the model mismatch and therefore produces a satisfactory result. This frequency domain smoothing operation corresponds to multiplying a taper-down window in the time domain, although other windows may also work. Through the inversion of a laboratory measurement, we demonstrate that our straightforward inversion method is robust. It seems feasible to recover the source-time function from the borehole measurement itself. Future study will focus on source inversion from field data.

ACKNOWLEDGMENTS

The authors would like to thank Dr. Jerry Schuster and two other anonymous reviewers for valuable suggestions to improve the manuscript. The second author would also like to thank the Environmental Protection Agency and the National Science Foundation for their support through a PECASE Grant No. CR-825-225-010 and CAREER Grant No. ECS-9702195, respectively.

[1] E. A. Robinson, ''Predictive decomposition of seismic traces,'' Geophysics **22**, 767–778 (1957).
[2] N. Wiener, *The Extrapolation, Interpolation, and Smoothing of Stationary Time Series with Engineering Applications*, MIT DIC Contract, No. 6037, Cambridge, MA, National Research Council, Section D2 (1942) (reprinted Wiley, New York, 1942).
[3] J. E. Claerbout and E. A. Robinson, ''The error in least-squares inverse filtering,'' Geophysics **29**, 118–120 (1964).
[4] T. J. Ulrych, ''Application of homomorphic deconvolution to seismology,'' Geophysics **36**, 650–660 (1971).
[5] R. A. Wiggins, ''Minimum entropy deconvolution,'' presented at the 1977 Int. Symp. on Computer Aided Seismic Analysis and Discrimination, Falmouth, MA, June 9, 1977.
[6] D. Riley and J. P. Burg, ''Time and space deconvolution filters,'' presented at the 1972 Conv. of SEG, Anaheim, CA (1972).
[7] J. M. Mendal, *Optimal Seismic Deconvolution: An Estimation Based Approach* (Academic, New York, 1983).
[8] N. N. Hsu, J. S. Simmons, and S. C. Hardy, ''An approach to acoustic emission signal analysis-theory and experiment,'' Mater. Eval. **35**, 100–106 (1977).
[9] J. E. Michaels, T. E. Michaels, and W. Sachse, ''Applications of deconvolution to acoustic emission signal analysis,'' Mater. Eval. **39**, 1032–1026 (1981).
[10] J. E. Michaels and Y. H. Pao, ''The inverse source problem for an oblique force on an elastic plate,'' J. Acoust. Soc. Am. **77**, 2005–2011 (1985).
[11] J. E. Michaels, ''Fundamentals of deconvolution with applications to ultrasonics and acoustic emission,'' MS thesis, Department of T&AM, Cornell Univ., 1982.
[12] C. Chang and W. Sachse, ''Analysis of elastic wave signals from an extended source in a plate,'' J. Acoust. Soc. Am. **77**, 1335–1341 (1985).
[13] C. Chang and C. T. Sun, ''Determination of transverse impact force on composite laminate by signal deconvolution,'' Exp. Mech. **29**, 414–419 (1989).
[14] A. L. Kurkjian and S. K. Chang, ''Acoustic multipole sources in a fluid-filled borehole,'' Geophysics **51**, 148–163 (1986).
[15] C. C. Lu and Q.-H. Liu, ''A three-dimensional dyadic Green's function for elastic waves in multilayer cylindrical structures,'' J. Acoust. Soc. Am. **98**, 2825–2835 (1995).
[16] W. L. Roever, J. H. Rosenbaum, and T. F. Vining, ''Acoustic waves from an impulsive source in a fluid-filled borehole,'' J. Acoust. Soc. Am. **55**, 1144–1157 (1974).
[17] E. A. Robinson and M. T. Silvia, *Digital Signal Processing and Time Series Analysis* (Holden-Day, San Francisco, 1978), Chap. 3, pp. 156–158.

Measurements of differential scattering cross section using a ring transducer

Tomas T. Jansson[a)]
Department of Electrical Measurements, Lund University, P.O. Box 118, 221 00 Lund, Sweden

T. Douglas Mast[a)]
Applied Research Laboratory, The Pennsylvania State University, University Park, Pennsylvania 16802

Robert C. Waag
Departments of Electrical Engineering and Radiology, University of Rochester, Rochester, New York 14627

(Received 20 June 1997; accepted for publication 10 February 1998)

A procedure for the measurement of intrinsic scattering object properties is presented and used to obtain illustrative results. The procedure is based on the measurement of the scattered acoustic field as a function of scattering angle and frequency. Measurements are normalized using analytically determined expressions for emitter and detector beams resulting from a combination of unfocused linear elements arranged in a circular configuration. The spatial effects of finite emitter pulse length and detector gate length are represented by a convolution formula valid for narrow-band transmitted signals and long receiver gates. The normalization includes correction for target absorption as well as measurement of the directly transmitted acoustic power in the free field and yields the average differential scattering cross section per unit volume. Under the Born approximation, this quantity is directly proportional to the spatial-frequency spectrum of the scattering medium inhomogeneities. Measured results are reported for two phantoms consisting of glass microspheres embedded in a weakly absorbing agar background medium. For the phantoms employed, scattering effects, rather than increased absorption, are shown to account for most of the difference in transmission loss between pure agar and agar with glass spheres. The measured differential scattering cross sections are compared with theoretical cross sections for distributions of glass spheres measured experimentally. The measured values show good relative agreement with theory for varying angle, frequency, and phantom properties. The results are interpreted in terms of wave space resolution and the potential for tissue characterization using similar fixed transducer configurations. [S0001-4966(98)00306-3]

PACS numbers: 43.20.Fn, 43.20.Ye, 43.80.Ev [JEG]

INTRODUCTION

Normal and diseased tissues have been shown to have different ultrasonic scattering properties under some circumstances.[1–5] These differences arise because varying tissue morphology results in different spatial-frequency spectra, which in turn, can be directly correlated to the average differential scattering cross section per unit volume, i.e., the average power scattered from a unit volume of tissue into some angle relative to the incident beam direction, per unit incident intensity and unit solid angle. The apparent relationship between tissue morphology and ultrasonic scattering properties has led many investigators to measure ultrasonic scattering properties of different tissue types.

Studies concerned with measurements of scattering cross section have mainly been concentrated on the backscatter case[6–19] since this is the most commonly used configuration in clinical practice. However, backscatter measurements are inherently limited in the range of spatial frequencies that can be investigated, since the only parameter that can be varied is the temporal frequency. To increase the range of possible spatial frequencies examined, the angle between emitter and detector can also be varied.[20–25] Such measurements have previously been undertaken using time-consuming physical translation of single-element transducers and have also been limited by the beam patterns produced by the transducers that were utilized.

In our experiments, a transducer array with narrow elements arranged in a circle has been used to overcome these limitations for *in vitro* measurements of scattering cross section. The ring array conveniently allows scanning at arbitrary angles between emitter and detector as well as beamforming using multi-element apertures. The fixed nature of this array allows scattering cross sections to be measured through ensemble averaging of many medium realizations, resulting in measurements with low bias and variance.

A commonly used identity in measurements and analysis of weak scattering is that the spatial-frequency spectrum of the medium variations is proportional to the average differential scattering cross section; that is, that

$$\bar{\sigma}_d(\mathbf{K}) = \frac{k_0^4 \pi}{2} S_\gamma(\mathbf{K}), \tag{1}$$

where $\bar{\sigma}_d(\mathbf{K})$ is the differential scattering cross section per unit volume for the scattering vector $\mathbf{K}$, k_0 is the wave number, and $S_\gamma(\mathbf{K})$ is a spatial-frequency spectrum of the me-

[a)]Work performed while at the Ultrasound Research Laboratory, University of Rochester, Rochester, NY.

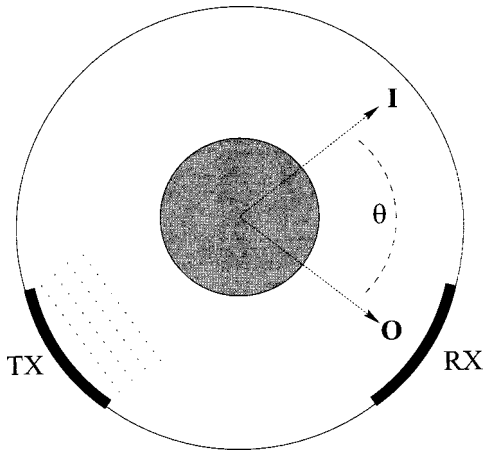

FIG. 1. Scattering configuration. A transmitting aperture (TX) emits a pulse. The scattered wave is then received by a receive aperture (RX). The scattering angle θ is defined as the angle between the corresponding vectors **I** and **O**.

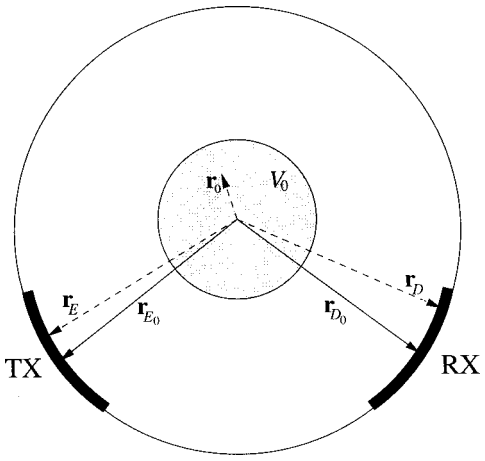

FIG. 2. Geometry for evaluation of scattering integrals. The fixed vectors $\mathbf{r}_{E_0}$ and $\mathbf{r}_{D_0}$, which are directed from the origin to the centers of the emitter and detector, respectively, are indicated by solid lines. The vector $\mathbf{r}_0$, indicated by a dashed line, corresponds to an arbitrary point within the scattering volume V_0, indicated by shading. The vectors $\mathbf{r}_E$ and $\mathbf{r}_D$, indicated by dashed lines, are directed from the origin to arbitrary points on the emitter surface and the detector surface, respectively.

dium variations.[26] However, the differential scattering cross section can only be determined approximately in a practical measurement situation employing finite apertures and time gates. Earlier work has shown that these effects can be removed by normalization of the measured data,[20–23] although the accuracy of the normalization is fundamentally limited by blurring effects associated with the finite measurement system.[25]

In the present study, a normalization procedure applicable to unfocused linear arrays and phased arrays is developed. The procedure analytically incorporates beam patterns of apertures composed of multiple line sources, spatial effects of the emitter pulse and detector gate lengths, and compensation for absorption in the scattering medium. This procedure is specifically applied to the ring transducer system used in our experiments.

In Sec. I, an overview of the normalization theory is given. To verify the validity of the method, measurements were performed on two glass sphere-agar phantoms. The production of these and the method for data collection is presented in Sec. II. Experimental results are presented and compared with theory in Sec. III, and a discussion of the applicability of the present methods to practical tissue characterization is presented in Sec. IV.

I. THEORY

The scattering configuration of our ring transducer system is sketched in Fig. 1. A transmitting aperture emits a wave that propagates in the direction corresponding to the vector **I**, and a receiving aperture records the scattered wave that propagates in the direction corresponding to the vector **O**. Both the vectors **I** and **O** have magnitudes equal to the wave number k_0. The vector $\mathbf{K}=\mathbf{I}-\mathbf{O}$ describes the spatial-frequency content of the scattered wave at the scattering angle θ, which is equal to the angle between **I** and **O**.

The inhomogeneous scattering medium is represented below as a continuous fluid with compressibility and density variations γ_κ and γ_ρ as defined in Ref. 26. For such a fluid, when the scattered amplitude is sufficiently small that the Born approximation is applicable, the scattered acoustic pressure is given by the integral equation[27]

$$p_s(\mathbf{r},t)=-\frac{1}{4\pi}\int\int\int_{V_0}\frac{1}{R}\left\{\frac{\gamma_\kappa(\mathbf{r_0})}{c^2}\frac{\partial^2 p_i(\mathbf{r}_0,t-R/c)}{\partial t^2}+\boldsymbol{\nabla}_0[\gamma_\rho(\mathbf{r}_0)\boldsymbol{\nabla}_0 p_i(\mathbf{r}_0,t-R/c)]\right\}d^3r_0, \tag{2}$$

where c is the background speed of sound, $R=|\mathbf{r}-\mathbf{r}_0|$, and p_s is the scattered pressure observed at a position $\mathbf{r}$. The integration volume V_0 includes the entire support of γ_κ and γ_ρ.

The incident pressure p_i associated with a portion of an ultrasonic array can be approximated as the radiated pressure associated with a vibrating surface in a rigid baffle.[28] For a surface A_E with a normal velocity component having spatial dependence a_E and temporal dependence W_E, such that $\dot{v}(\mathbf{r},t)=a_E(\mathbf{r})W_E(t)e^{-i\omega_0 t}$, where the envelope W_E is slowly varying, the incident pressure is given by

$$p_i(\mathbf{r}_0,t)=\frac{\rho e^{-i\omega_0 t}}{2\pi}W_E(t-|\mathbf{r}_0-\mathbf{r}_{E_0}|/c)\times\left[\int\int_{A_E}\frac{a_E(\mathbf{r}_E)e^{ik_0|\mathbf{r}_0-\mathbf{r}_E|}}{|\mathbf{r}_0-\mathbf{r}_E|}d^2r_E\right], \tag{3}$$

where $\mathbf{r_E}$ is a vector from the origin to an arbitrary point on the emitter surface, and k_0 is the wave number ω_0/c. Expression of the emitter time gate effect is simplified in Eq. (3) by the approximation $|\mathbf{r}_0-\mathbf{r}_E|\approx|\mathbf{r}_0-\mathbf{r}_{E_0}|$, where $\mathbf{r}_{E_0}$ is the vector from the origin to the center of the transducer surface. The integral term in Eq. (3) (i.e., the spatial dependence of the incident pressure) will be denoted $I_E(\mathbf{r}_0)$. The vectors employed in Eq. (3), as well as corresponding vectors defined for the detector, are sketched in Fig. 2.

Substituting Eq. (3) into Eq. (2), integrating by parts, and making use of Green's theorem yields an expression for the scattered pressure valid for slowly varying W_E:

$$p_s(\mathbf{r},t)=\frac{\rho k_0^2 e^{-i\omega_0 t}}{8\pi^2}\int\int\int_{V_0}\frac{e^{ik_0R}}{R}\times W_E(t-R/c-|\mathbf{r}_0-\mathbf{r}_{E_0}|/c)\times(\gamma_\kappa+\mathbf{i}\cdot\mathbf{o}\,\gamma_\rho)I_E(\mathbf{r}_0)d^3r_0. \quad (4)$$

This expression has employed the approximations $|\mathbf{r}_0-\mathbf{r}_E|\approx|\mathbf{r}_E|-\mathbf{i}\cdot\mathbf{r}_0$ for $|\mathbf{r}_E|\gg|\mathbf{r}_0|$ and $|\mathbf{r}-\mathbf{r}_0|\approx|\mathbf{r}|-\mathbf{o}\cdot\mathbf{r}_0$ for $|\mathbf{r}|\gg|\mathbf{r}_0|$, where $\mathbf{i}$ is a unit vector in the propagation direction of the incident wave and $\mathbf{o}$ is a unit vector in the direction of the field point $\mathbf{r}$. The length R is equal to $|\mathbf{r}-\mathbf{r}_0|$.

The received signal is now defined as the Fourier transform of the time dependent scattered wave integrated over the surface A_D of a pressure-sensitive detector with a gate function $W_D(t)$ and a sensitivity function $a_D(\mathbf{r})$. This integration can be written:

$$N(\omega)=\int_{-\infty}^{\infty}e^{i\omega t}\,W_D(t)\times\left[\int\int_{A_D}p_s(\mathbf{r}_D,t)a_D(\mathbf{r}_D)\,d^2r_D\right]dt, \quad (5)$$

where $p_s(\mathbf{r}_E)$ is given by Eq. (4).

Evaluation of Eq. (5) at the frequency $\omega=\omega_0$ yields the result

$$N(\omega_0)=\frac{\rho k_0^2}{8\pi^2}\int\int\int_{V_0}I_D(\mathbf{r}_0)\tau(\mathbf{r_0})\gamma(\mathbf{r}_0)I_E(\mathbf{r}_0)d^3r_0. \quad (6)$$

Here, the function τ represents the spatial effect of emitter and detector time gates defined by the windows W_E and W_D, each of which is nominally centered at $t=0$. This function, which expresses a spatially dependent weighting of effective scattering sources caused by the combination of emitter and detector gates, is given by the convolution integral

$$\tau(\mathbf{r_0})=\int_{-\infty}^{\infty}W_E(t)W_D(t+|\mathbf{r}_{D_0}-\mathbf{r}_0|/c+|\mathbf{r}_0-\mathbf{r}_{E_0}|/c-|\mathbf{r}_{D_0}|/c-|\mathbf{r}_{E_0}|/c)\,dt. \quad (7)$$

In Eq. (7), the delay $|\mathbf{r}_{D_0}|/c+|\mathbf{r}_{E_0}|/c$ in the argument of the detector gate accounts for the two-way propagation time of a wave traveling from the emitter center to the origin and back to the detector center.

In Eqs. (6) and (7), the scattered pressure from Eq. (4) has been used. The inhomogeneity of the medium is represented by $\gamma=\gamma_\kappa+\mathbf{i}\cdot\mathbf{o}\,\gamma_\rho$. The radius R_D is equal to $|\mathbf{r}_D-\mathbf{r}_0|$, the (dimensionless) detector sensitivity function is given by a_D, and the quantities W_D and $\mathbf{r}_D$ are defined in analogy to the emitter case. The detector integral I_D is also defined analogously to the emitter integral I_E, that is:

$$I_D(\mathbf{r}_0)=\int\int_{A_D}\frac{a_D(\mathbf{r}_D)e^{ik_0|\mathbf{r}_0-\mathbf{r}_D|}}{|\mathbf{r}_0-\mathbf{r}_D|}d^2r_D. \quad (8)$$

Next, the emitter and detector beams are each written in a quasi-plane-wave form,[23] $I_E=p_E(\mathbf{I},\mathbf{r}_0)e^{ik_0(\mathbf{i}\cdot\mathbf{r}_0)}$ and $I_D=p_D(\mathbf{O},\mathbf{r}_0)e^{-ik_0(\mathbf{o}\cdot\mathbf{r}_0)}$, so that Eq. (6) can be expressed

$$N=\frac{k_0^2}{4\pi}\int_{V_0}\Lambda(\mathbf{I},\mathbf{O},\mathbf{r}_0)\;\gamma(\mathbf{r}_0)\;e^{ik_0(\mathbf{i}-\mathbf{o})\cdot\mathbf{r}_0}\,d^3r_0, \quad (9)$$

where the integral is performed over a three-dimensional volume V_0 that contains the entire inhomogeneity γ. Here the measurement system beam function given by

$$\Lambda(\mathbf{I},\mathbf{O},\mathbf{r}_0)=\frac{\rho}{2\pi}\tau(\mathbf{r}_0)p_E(\mathbf{I},\mathbf{r}_0)p_D(\mathbf{O},\mathbf{r}_0) \quad (10)$$

has been introduced. Thus, the measured signal N is a spatial Fourier transform of the medium inhomogeneity function γ weighted by the beam function Λ.

From the mean square magnitude of Eq. (9), the average measured scattered power is expressed

$$\langle|N|^2\rangle=\frac{k_0^4}{16\pi^2}\int_{V_0}\int_{V_1}\Lambda(\mathbf{I},\mathbf{O},\mathbf{r}_0)\Lambda^*(\mathbf{I},\mathbf{O},\mathbf{r}_1)\times\langle\gamma(\mathbf{r}_0)\gamma^*(\mathbf{r}_1)\rangle\;e^{i\mathbf{K}\cdot(\mathbf{r}_0-\mathbf{r}_1)}\,d^3r_1\,d^3r_0, \quad (11)$$

where $\mathbf{K}=k_0(\mathbf{i}-\mathbf{o})$ is the scattering vector.[20,22] The magnitude of the scattering vector corresponding to the principal spatial-frequency content of a given measurement is

$$K=2k_0\,\sin(\theta/2), \quad (12)$$

where θ is the scattering angle.

For random media that are statistically homogeneous, $\langle\gamma(\mathbf{r}_0)\gamma^*(\mathbf{r}_1)\rangle$ is dependent only on the difference between $\mathbf{r}_0$ and $\mathbf{r}_1$, so that the autocorrelation function of the inhomogeneity γ can be written

$$B_\gamma(\mathbf{r}_0-\mathbf{r}_1)=\langle\gamma(\mathbf{r}_0)\gamma^*(\mathbf{r}_1)\rangle.$$

If the autocorrelation function B_γ decays to zero much more rapidly than the beam function $\Lambda(\mathbf{I},\mathbf{O},\mathbf{r}_0)\Lambda^*(\mathbf{I},\mathbf{O},\mathbf{r}_1)$, i.e., if the transducer beam patterns are constant over many correlation volumes of the scattering medium, the average scattered power is given by the expression

$$\langle|N|^2\rangle=\frac{k_0^4}{16\pi^2}\int_{V'}e^{i\mathbf{K}\cdot\mathbf{r}'}\,B_\gamma(\mathbf{r}')d^3r'\times\int_{V_0}|\Lambda(\mathbf{I},\mathbf{O},\mathbf{r}_0)|^2\,d^3r_0, \quad (13)$$

where $\mathbf{r}'=\mathbf{r}_0-\mathbf{r}_1$. The first integral can be interpreted as the power spectrum of the medium variations, $S_\gamma(\mathbf{K})$, as defined in Ref. 25.

Equation (13) can thus be rewritten

$$\frac{k_0^4\pi}{2}S_\gamma(\mathbf{K})=\langle|N|^2\rangle\Big/\int_{V_0}|\Lambda(\mathbf{I},\mathbf{O},\mathbf{r}_0)|^2\,d^3r_0. \quad (14)$$

From Eq. (1), under the Born approximation, the left hand side of Eq. (14) is equal to the differential scattering cross section per unit volume $\overline{\sigma_D}$. Therefore, under the conditions specified in the derivation above, this cross section can be obtained as the power spectrum of the measured signal evaluated at the center frequency, divided by a normalization

factor that describes measurement system effects. This normalization factor can be written

$$J_\Lambda(\mathbf{I},\mathbf{O}) = \int_{V_0} |\Lambda(\mathbf{I},\mathbf{O},\mathbf{r}_0)|^2 \, d^3 r_0 . \tag{15}$$

In the remainder of this section, the details of the evaluation of the system function Λ are presented for the specific case applicable to experiments in which the emitter and detector apertures are composed of unfocused linear elements and the scattering medium is a cylindrical inhomogeneity with tissue-mimicking ultrasonic scattering properties. Since each linear element in the system used for measurements reported here is smaller than a half-wavelength at the system center frequency, the elements are modelled as line sources. Thus, for an aperture consisting of M elements, a_E and a_D in the expressions for I_E and I_D are approximately written as

$$a_{(\cdot)} = \sum_{i=1}^{M} \delta(\sqrt{(y-y_i)^2+(z-z_i)^2}) \; q_i \; u(a-|x|), \tag{16}$$

where $(\cdot)$ is either E or D, and x, y and z represents a three dimensional coordinate system with its origin in the center of the ring transducer, with the z-y plane defining the plane of the ring and x the elevation direction. The coordinates for the ith element in the z-y plane are z_i and y_i. The constants q_i represent the system-dependent amplitude including any apodization, u is the Heaviside step function (defined to be zero for negative arguments and unity for positive arguments), and a is half the element height.

Using Eq. (16), the emitter and detector beams are written as a summation of finite line sources:

$$I_{(\cdot)} = \sum_{i=1}^{M} q_i \int_{-a}^{a} \frac{e^{ik_0\sqrt{(x-x_0)^2+(y-y_i)^2+(z-z_i)^2}}}{\sqrt{(x-x_0)^2+(y-y_i)^2+(z-z_i)^2}} \, dx_0 . \tag{17}$$

The integral in Eq. (17) can be analytically evaluated under a form of the Fresnel approximation valid for $(x-x_0)^2 \ll (y-y_i)^2+(z-z_i)^2$. In this limit, Eq. (17) takes the form

$$I_{(\cdot)} = -\frac{1}{\beta}\sum_{i=1}^{M} q_i \left[\frac{e^{ik_0 R_i}}{R_i} \{C[\beta(x-a)] - C[\beta(x+a)]\} + i\{S[\beta(x-a)] - S[\beta(x+a)]\} \right], \tag{18}$$

where $R_i = \sqrt{(y-y_i)^2+(z-z_i)^2}$ and $\beta = \sqrt{k_0/(\pi R_i)}$. The functions C and S are the Fresnel cosine and sine integrals, defined as

$$C(\xi) = \int_0^{\xi} \cos\left(\frac{\pi}{2}\mu^2\right) \, d\mu \tag{19}$$

and

$$S(\xi) = \int_0^{\xi} \sin\left(\frac{\pi}{2}\mu^2\right) \, d\mu . \tag{20}$$

While Eq. (18) can also be expressed in terms of complex Fresnel integrals or complex error functions, the form used above is amenable to computation using available subroutines for evaluation of $C(\xi)$ and $S(\xi)$.

Absorption in the scattering object is included by making the substitutions

$$p_E \rightarrow p_E \times 10^{-\alpha l_E/20}, \quad p_D \rightarrow p_D \times 10^{-\alpha l_D/20}, \tag{21}$$

where α is the ultrasonic absorption in dB/cm and l_E and l_D are distances (in cm) from emitter/detector center to $\mathbf{r}_0$ through the scattering object. The distances were calculated using trigonometric identities and the assumption of a cylindrical scattering volume. Analogous results could also be obtained by use of a complex wave number, with the imaginary part for each frequency employed determined from the absorption at that frequency.

The above derivation includes assumed forms of the emitter amplitude function a_E and the detector sensitivity function a_D. In practice, for an ultrasonic array transducer, these functions are specified electronically as a set of amplitudes and delays, so that the true amplitude and sensitivity are scaled by unknown multiplicative constants dependent on the electromechanical transfer functions of the electronics and transducer elements employed. For absolute measurement of differential scattering cross section per unit volume, these unknown constants can be removed by the calibration technique noted below.

This calibration technique is based on calculation and measurement of the acoustic power transmitted across the ring transducer with the emitter and detector apertures facing one another. The theoretical value for the transmitted power integrated over the detector surface, with all quantities defined analogously to those in the above derivation, is

$$N_T = \frac{\rho}{2\pi} \, \tau(0) \int_{A_D} I_E(\mathbf{r}_D) \; a_D(\mathbf{r}_D) \; d^2 r_D . \tag{22}$$

The differential scattering cross section per unit volume is then written

$$\overline{\sigma}_d(\mathbf{K}) = \frac{|f_s(\omega_0,\mathbf{K})|^2}{|f_T(\omega_0)|^2} \frac{|N_T(\omega_0)|^2}{J_\Lambda(\mathbf{I},\mathbf{O})}, \tag{23}$$

where f_s is the measured scattering amplitude and f_T is the measured amplitude for a directly transmitted wave.

To obtain the normalization functions employed here, the computational method outlined above was implemented as follows. The beam functions from Eq. (18) were numerically computed and spatially weighted by the absorption correction of Eq. (21) for a cylindrical volume that spanned 50 mm in diameter and 30 mm in the axial direction. The resulting beam cross section was then numerically integrated to obtain the normalization factor J_Λ. Equation (22) was also numerically evaluated for a medium without any absorption so that the normalization factor $J_\Lambda/|N_T|^2$, given by Eq. (23), could be obtained.

II. METHODS

Various phantoms consisting of glass spheres in solidified agar were made for the experiments. The phantoms had a cylindrical shape with a diameter of 48 mm and a length of

about 100 mm. Each was molded on a holder that fit a stepper motor fixture so that different circular cross sections along the axis could be scanned.

The production of agar phantoms has been described previously,[29] and a similar method was employed here. A solution consisting of 40 grams of agar (Bacto-Agar, Difco Laboratories, Detroit, MI) per liter water was heated to 90 °C. After the solution had clarified, 4 grams of glass spheres (type A2429 glass, Potters Industries, Valley Forge, PA) per liter were added. The spheres were sieved to have diameters between 75 and 90 μm. The solution was allowed to cool down to 60 °C. Prior to pouring the solution into a mold, 13.4 ml 37% formaldehyde solution (for preservation) was added for each liter of agar solution. To avoid settling of the glass beads, the mold was rotated while the agar was solidifying. ''Sparse'' phantoms were also constructed in an analogous manner except for the use of 0.4 grams of glass spheres per liter. All phantoms were imaged with a commercial ultrasound scanner and a 7 MHz probe to check for flaws and for a uniform sphere distribution.

The density of the phantom was determined by direct measurements of the weight and the volume of a cylindrical sample, and was found to be 1.015 ($\pm$0.005) g/cm^3. The average number density of spheres in the phantoms was 5.37/mm^3 for the dense phantom and 0.537/mm^3 for the sparse phantom. These number densities were calculated from the weight of glass spheres added to the total volume, an assumed mean diameter of 83 μm, and the density of the glass, 2.489 g/cm^3.

The attenuation coefficient for the dense phantom was measured by radiation force at frequencies 0.5 MHz, 1.0 MHz, 2.25 MHz, 3.5 MHz, 5.0 MHz, and 7.5 MHz. The exponential attenuation of best fit was found by a least-squares technique to be $0.032f^{1.84}$ dB/(MHz$^{1.84}\cdot$cm) (f in MHz, at 17 °C). To investigate the influence of the glass beads on the attenuation, an analogous measurement was also made for a sample without glass beads. The exponential fit yielded $0.045f^{1.31}$ dB/(MHz$^{1.31}\cdot$cm) in this case. The calculated exponential attenuation curves gave attenuation values at 2.5 MHz of 0.173 dB/cm for the glass sphere medium and 0.149 dB/cm for the background material. Plots of the measured attenuation values and exponential fits are shown in Fig. 3. The sound speed, measured using a pulse-echo configuration, was 1516 ($\pm$5) m/s at 30.0 °C. For comparison, the corresponding values for pure water are 1510 m/s and 0.9956 g/cm^3 at 30.0 °C. Attenuation was not measured for the sparse phantom.

Using these parameters for speed and density, the plane-wave, normal-incidence, pressure reflection coefficient for the dense phantom is estimated as

$$\Re_p=\frac{\rho_p c_p-\rho_0 c_0}{\rho_p c_p+\rho_0 c_0}\approx 0.0116, \tag{24}$$

where ρ_p and c_p are the measured density and sound speed for the dense phantom and ρ_0 and c_0 are the corresponding values for water at 30.0 °C. Since, therefore, only a small fraction of the incident pressure was reflected from the phantoms, the calculated internal pressure fields used in the normalization were not corrected for these reflection effects.

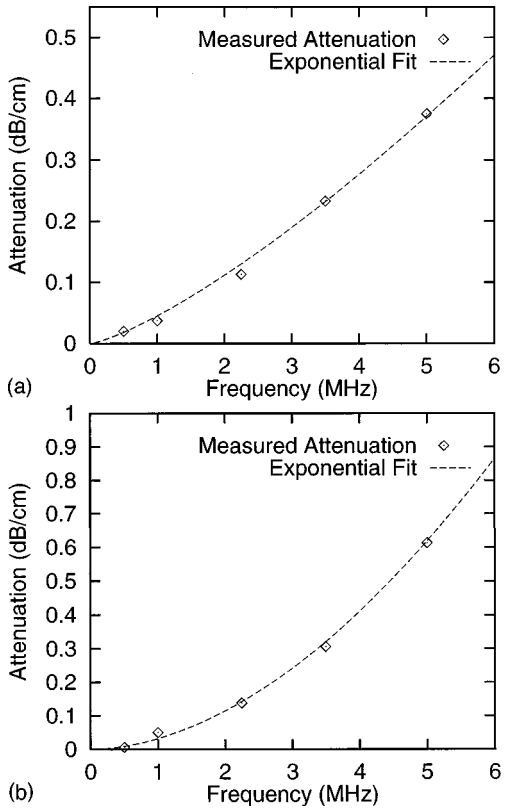

FIG. 3. Measured attenuation and exponential fits. Attenuation values are plotted as points and the corresponding power-law curve fits are plotted as dashed curves. (a) Pure agar. (b) Agar with 5.34 glass spheres per cubic millimeter.

The measured scattered intensity from a distribution of small spheres can be considered to be the sum of the scattered intensity from each sphere if the mean distance between scatterers is sufficiently large that spatial correlation effects are negligible. The theoretical scattered pressure from a single small elastic sphere was calculated using the analytic formula derived by Faran.[30] To obtain a theoretical prediction of the average differential scattering cross section per unit volume for the phantom, the size distribution of the spheres was determined with a Coulter Counter® and the theoretical scattered pressure amplitude was calculated for 28 sphere diameters linearly spaced between 41 μm and 122 μm. The radii measured by this counter are accurate to within error bounds of about 10%. Glass parameters employed in this calculation included a compressional wave speed of 5.572 mm/μs, a shear wave speed of 3.376 mm/μs, and a density of 2.489 g/cm^3. A weighted average amplitude was then found using the measured distribution of sizes. The diameter distribution employed in this calculation is plotted in Fig. 4 as a histogram with 28 bins having centers between 41 μm and 122 μm. The shape of this histogram is consistent with the 75 μm and 90 μm sieve sizes used to sort the spheres, given the limited precision of the counter employed.

The differential scattering cross section per unit volume for the distribution was obtained using the relation

$$\overline{\sigma_D}=\frac{|p_s|^2}{|p_i|^2}R^2 n, \tag{25}$$

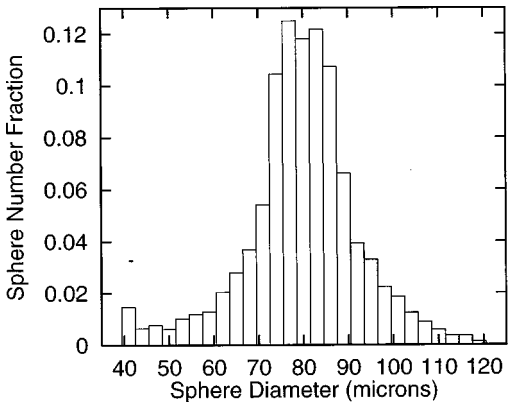

FIG. 4. Histogram of glass sphere diameters measured with Coulter Counter.

where $|p_s|$ is the weighted average scattered pressure amplitude for the sphere distribution, n is the number density of glass spheres, and R is the measurement radius. Plots of the theoretical values for $\overline{\sigma}_D$ are shown in Fig. 5. The corresponding total scattering cross section, defined as the total scattered power for unit incident intensity and unit scatterer volume, is

$$\overline{\sigma} = 2\pi \int_0^{\pi} \overline{\sigma}_D(\theta) \sin(\theta)\, d\theta. \tag{26}$$

The effect of scattering on transmission loss was calculated using the assumption that no power is scattered in the forward direction by the glass sphere distribution. Inspection of Fig. 5 confirms that this assumption is reasonable. Since the fractional power loss due to scattering per unit propagation length is simply $1-\overline{\sigma}$, the contribution of scattering to the measured attenuation per unit length is given in dB by the formula

$$\alpha_{\text{scat}} = 10 \log_{10}(1-\overline{\sigma}), \tag{27}$$

where $\overline{\sigma}$ is the total scattering cross section. Addition of theoretical values of α_{scat} to measured attenuation for the agar medium resulted in transmission loss values very close to those measured for the dense phantom, as shown in Fig. 6. Since this result implies that the increased transmission loss in the phantom is primarily due to scattering rather than to

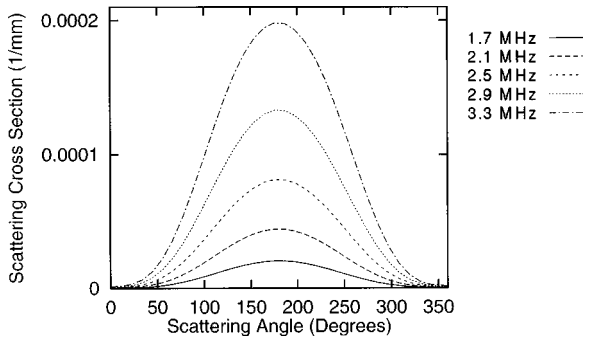

FIG. 5. Theoretical differential scattering cross sections per unit volume for the dense phantom, based on the measured sphere distribution. Cross sections are shown for five incident-wave frequencies between 1.7 MHz and 3.3 MHz.

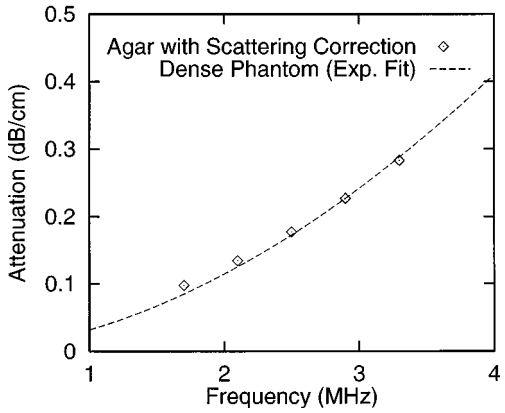

FIG. 6. Effect of scattering on transmission loss. The curve shows the power law of best fit for the dense phantom composed of agar and glass spheres. The data points show calculated values obtained by adding theoretical scattering-induced attenuation to the agar-medium attenuation.

increased absorption, attenuation values measured for the agar background medium were subsequently used for absorption correction in the data analysis.

A transducer array consisting of 2048 elements arranged in a ring with a mean diameter of 150 mm[31] was used for the scattering experiments. Each element in the ring array has an active surface that is 0.23 mm in azimuth and 25 mm in the elevation direction. Transmit signals were synthesized at a rate of 40 MHz with 8-bit resolution and transmitted on 128 contiguous elements, while received signals were sampled at 20 MHz with 12-bit resolution on 16 contiguous elements. The 128-element receiver apertures were synthesized using signals from eight sub-apertures.

Channel-to-channel variations in time delay were compensated using data from a calibration test that employed single-element, broadband, pulse-echo signals recorded from a wire reflector. Variations in channel-to-channel time delay were measured using cross correlation of adjacent signals and were compensated with a channel-to-channel correction of the effective ring radius. All signals measured in the scattering experiments were time shifted according to the delay variations measured in this calibration test.

In the scattering experiments, a plane wavefront was synthesized at the chord of an 128-element wide aperture for both transmit and receive. Thus the wavefront was approximately 29 mm wide. Gaussian apodizations were used so that the transmit and receive beams were smoothly tapered in space. Since the wave space resolution limit, which corresponds to the minimum spatial-frequency scale characterized by a given measurement, is inversely proportional to the second central moment of the beam intersection function,[25] the wide beams and smooth apodizations employed ensured that high wave space resolution was achieved.[25] The standard deviation of the Gaussian apodization functions used was 21.333 elements, or one-sixth the aperture length in azimuth, so that the amplitude at the edge elements was 1.19% of the peak amplitude.

Directly transmitted waves were measured for a water path. At each frequency, the directly transmitted wave (scattering angle 0°) was measured for 64 equally spaced positions around the ring. For each of these transmit positions,

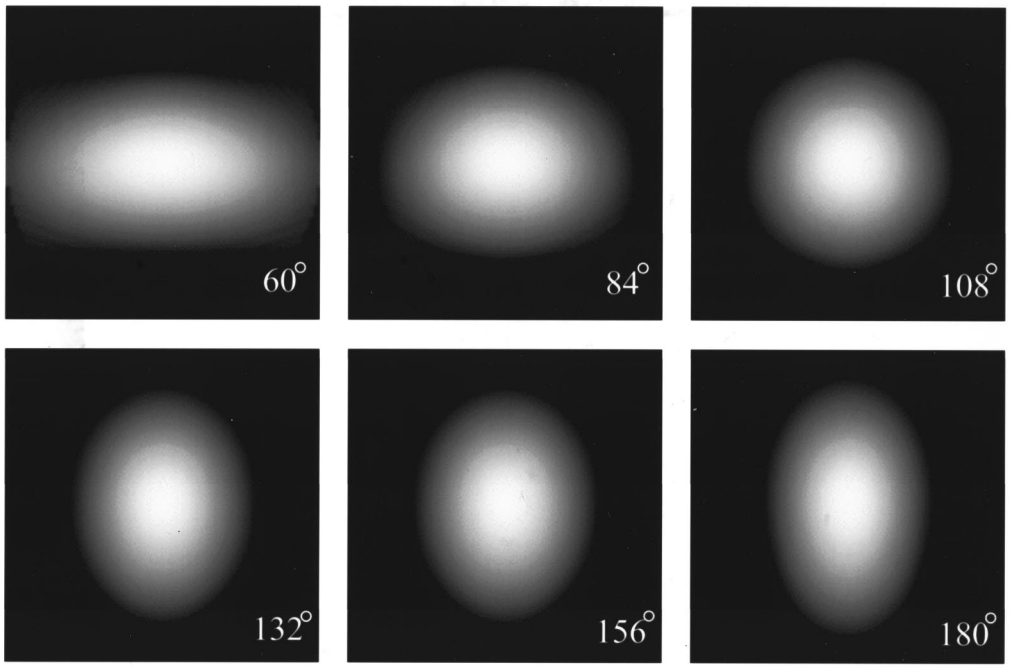

FIG. 7. Beam cross sections. Cross sections of the beam intersection function amplitude in the x-y plane are shown on a logarithmic scale with a 60 dB dynamic range. Beams were calculated for Gaussian apertures, 2.5 MHz center frequency, Gaussian time gates of duration 30 ms and standard deviation 5 ms, and absorption of the agar background medium. Six scattering angles between $\theta = 60°$ (120° between transmitter and receiver) and $\theta = 180°$ (backscatter) are shown. Each plot spans a distance of 50 mm, or one phantom diameter, in height and in width.

scattering data were collected at 49 different receive positions, starting at backscatter and using an angular increment of 2.11° or eight elements. In addition, five phantom elevations separated by about 1 cm were scanned for each temporal elevation, so that $64 \times 5 = 320$ independent measurements were obtained for each scattering angle at each frequency.

Signals from direct-transmission measurements and scattering measurements were gated using Gaussian temporal windows of length 30 μs and standard deviation 5 μs. This signal length corresponds to 75 cycles of a sinusoidal wave at the ring transducer center frequency of 2.5 MHz. The convolution of emitter and detector gates resulted in a spatial window of about 40 mm for scattering angles close to the backscatter direction.

To calculate the differential scattering cross section $\overline{\sigma}_D$, power values for the scattered and transmitted signals were calculated by integrating the signal spectra over a small band around each center frequency. All power values corresponding to equal scattering angles were averaged, so that a single average result was obtained for the transmitted power at each frequency and for scattering measurements at each of 49 scattering angles for each frequency. The scattered signal power was then normalized using Eq. (23) to obtain the differential scattering cross section for each frequency and scattering angle.

For comparison between theoretical and experimental differential scattering cross sections, the experimental cross sections were further normalized by a constant factor determined to match (in the least-square sense) the experimental and theoretical cross sections for the sparse phantom at the center frequency of 2.5 MHz, for scattering angles within $\pm 17°$ of the backscatter direction. The factor, which had a magnitude of 0.5230, was multiplied by the normalized experimental cross sections for both the dense and sparse phantoms. This approach, which is equivalent to the ''reference phantom method'' described in Ref. 32, removed any discrepancies due to inaccuracies in the measured sphere size distribution and in the measured absorption of the agar background medium.

III. RESULTS

Calculated beam pattern cross sections for the center frequency of 2.5 MHz are plotted in Fig. 7 for six scattering angles between 60° (an angle of 120° between emitter and detector) and 180° (backscatter). The beam patterns are seen to have significant support only within the scattering object so that edge effects are minimized. The large apertures, defocused beams, long time gates, and smooth apodization result in slowly varying beams of large spatial extent, so that high wave space resolution is achieved.

A comparison between theoretical and measured beam profiles is shown in Fig. 8 for a center frequency of 2.44 MHz. This figure shows the rms amplitude of the Gaussian transmit beam after direct transmission ($\mathbf{i} = \mathbf{o}$) through a water path. The theoretical transmit beam profile shown was computed using Eqs. (17) and (18) with the weights q_i specified by the plane-wave phase and Gaussian apodization described above; this profile is equivalent to the magnitude of the function $I_E(\mathbf{r}_D)$ that is integrated in Eq. (22) to obtain the transmitted power N_T.

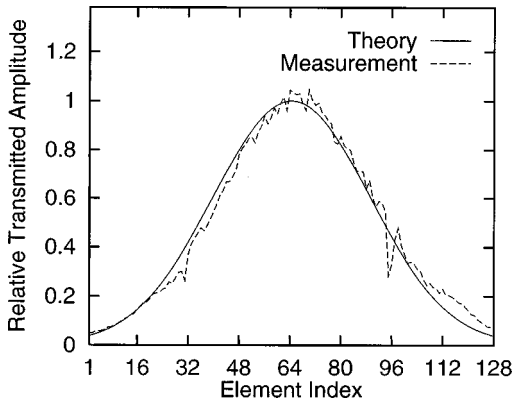

FIG. 8. Computed and measured beam profiles $|I_E(\mathbf{r}_D)|$ for a beam center frequency of 2.44 MHz. These profiles were computed and measured for direct transmission of Gaussian-apodized transmit beams through a water path.

The wave space resolution in each of the directions K_x, K_y, K_z was quantified using the method of Ref. 25 based on the calculated second central moments of the beam intersection function. The angular-dependent 3 dB wave space resolution limits for the center frequency of 2.5 MHz are plotted in Fig. 9. Limits for the other frequencies employed are very close to those for the center frequency, since the beam characteristics depend only weakly on frequency. These results indicate that spatial-frequency features having dimensions on the order of 0.4–1.0 mm^{-1} can be resolved in the present experiments. The spatial-frequency content of each measurement was determined from Eq. (12).

The central spatial frequency interrogated ranged from 1.1 to 4.4 mm^{-1} for the frequencies and scattering angles investigated. The result for the 2.5 MHz measurements is plotted in Fig. 9 together with the corresponding wave space resolution limits. Comparison of these curves indicates that the wave space resolution limit is substantially smaller than the overall spatial-frequency range measured, so that results are not substantially blurred by measurement system effects.

Normalization factors $J_\Lambda/|N_T|^2$ for the agar background medium, determined using Eqs. (15) and (22), are plotted in Fig. 10 for the five frequencies employed. Since the beam

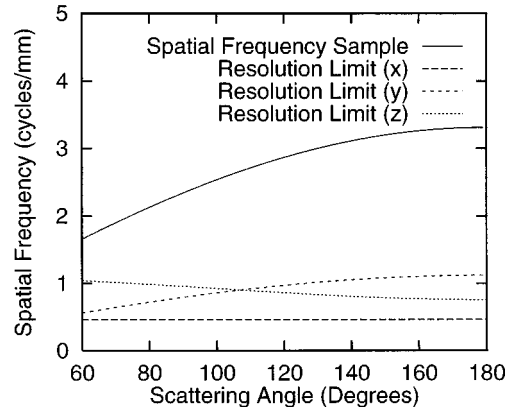

FIG. 9. Spatial-frequency content and wave space resolution limits for scattering measurements using the agar medium. Computed magnitude of the spatial-frequency vector and 3 dB resolution limits in the directions K_x, K_y, and K_z are plotted versus scattering angle for a center frequency of 2.5 MHz.

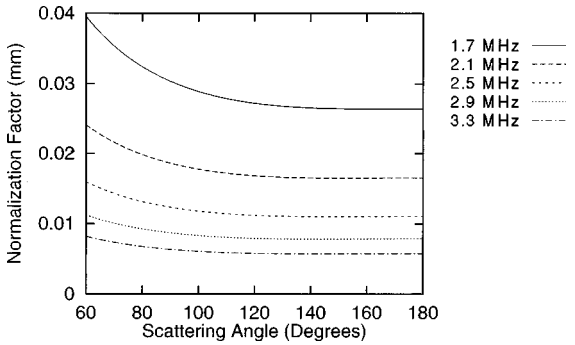

FIG. 10. Computed normalization factors $J_\Lambda/|N_T|^2$ for the agar medium and center frequencies between 1.7 MHz and 3.3 MHz. Beam and time gate parameters are as in Fig. 9.

intersection sizes were comparable for each of the frequencies used, the decrease in the normalization factor with frequency chiefly reflects the increase in ultrasonic absorption with frequency.

Experimentally determined average differential scattering cross sections $\overline{\sigma_D}$ for the dense phantom are plotted in Fig. 11 together with the corresponding theoretical values for the measured distribution of spheres. The measured and theoretical cross sections for the sparse phantom are plotted in Fig. 12. Each plot is shown over the range of scattering angles for which the scattered field was not noticeably influenced by the directly transmitted beam. The angular range is smaller for the sparse phantom because of the smaller scattered power in this case. The experimental values for the dense phantom agree well with theory. Those for the sparse phantom agree fairly well, although some disagreement is evident at the lowest and highest frequencies used as well as at scattering angles furthest from the backscatter direction (180°).

IV. DISCUSSION

The ring transducer configuration employed here is well-suited to *in vitro* characterization of biological tissues, and may be applicable to *in vivo* tissue characterization for organs such as the breast that are accessible for angular scattering measurements. Other organs, such as the liver and kidney, are accessible for a limited range of angles for *in vivo* measurements. Such organs could be directly character-

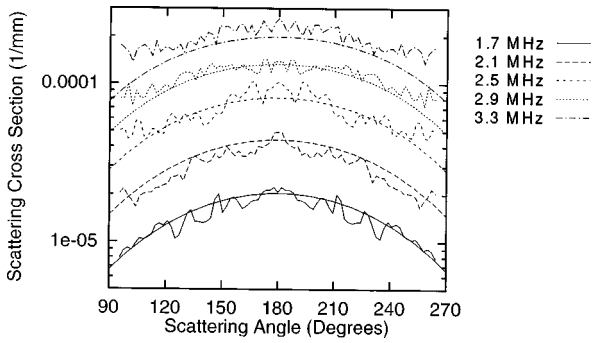

FIG. 11. Measured average differential scattering cross sections for dense glass sphere phantom with theoretical values for random glass sphere distribution.

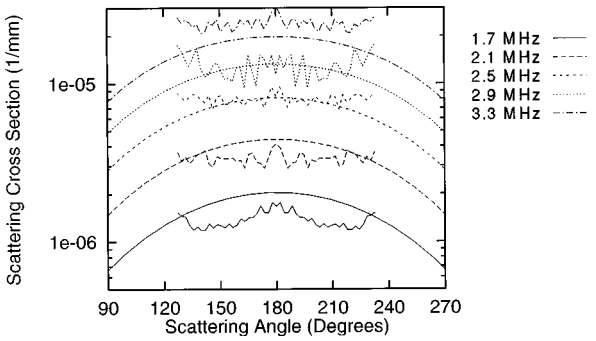

FIG. 12. Measured average differential scattering cross sections for sparse glass sphere phantom with theoretical values for random glass sphere distribution.

ized *in vitro* by the present methods, or could be characterized *in vivo* by a modified measurement configuration employing only backscatter measurements. The methods presented here are fully applicable to backscatter measurements, with the exception that a directly transmitted beam can no longer be employed as a reference. Instead, plane reflectors or reference phantoms of known properties can be employed.[32–34]

The scattering and absorption properties of the phantoms employed here may be compared to measured characteristics of liver tissue.[35] The total scattering cross section for the dense phantom is comparable to the total scattering cross section measured in Ref. 35 for calf liver tissue; however, the absorption of the agar background medium is considerably less than that for calf liver. Thus, for liver tissue, the relative contribution of scattering to attenuation is apparently smaller than that for the dense phantom employed in the present study.

The sparse phantom, which contained one tenth the glass-sphere concentration of the dense phantom, produced much smaller total scattering cross sections than calf liver tissue. Near the backscatter direction, however, the differential scattering cross section for the sparse phantom is comparable to that for calf liver as measured in Ref. 35. For this phantom, greater disagreement between theoretical and experimental cross sections occurs for scattering angles far from backscatter, where the scattered fields are very small. Although system noise may be a factor in these errors, the tendency of disagreement shown in Fig. 12 is for the scattering cross section to be overestimated, indicating that the true scattering signals are obscured by sidelobes of the main beam. These observations imply that the tissue characterization methods presented here may encounter difficulty for characterization of very weakly scattering (hypoechoic) tissue, but that these difficulties may be less important for scattering angles near the backscatter direction.

Broad, unfocused beams and long time gates were used here to achieve maximal wave space resolution. In tissue characterization studies, limiting the spatial extent of insonification may be desirable so that tissue properties can be measured with greater spatial resolution. This trade-off between wave space resolution and spatial resolution is discussed in Ref. 25.

The normalization method employed in this study accounts for the frequency-dependent absorption of the medium. Although the experiments reported here were performed using a weakly absorbing background medium, the employed method of compensation for absorption is also valid for more strongly absorbing media such as tissue.[20] Application of the employed methods to tissue characterization requires estimates of tissue absorption for quantitative accuracy to be achieved. However, since measured data for attenuation in human tissue[36–38] as well as direct methods of attenuation measurement[39,40] are available, this requirement should not greatly limit applicability of the method.

Some error in measurements of scattering cross section can result from inaccurate specification of emitter and detector beams. For instance, the true directivity of the elements employed is not precisely described by the present model of finite line sources in an infinite baffle. However, the agreement of the results obtained with theory suggests that the technique presented here is insensitive to the deviation of element characteristics from this ideal. Other possible sources of error in the measurements include uncertainty in the measured absorption of the agar background medium, neglect of element-response waveform variations in the transducer calibration, and neglect of reflection effects at the agar-water boundary. The most important of these factors is the estimated background absorption, since errors in the absorption contribute exponentially to errors in the measured cross sections.

Although theoretically exact expressions for scattering from glass spheres were employed, the scattering cross sections computed for the measured sphere distributions are still subject to uncertainty. Errors may arise from uncertainties in the electronically counted sphere distribution, which may be suspected because the measured sphere distribution does not precisely match that expected for the sieves employed. Also, the density, longitudinal sound speed, and shear wave speed of the glass spheres were estimated from nominal properties for glass that may not precisely match the spheres employed. Any error in the estimated density of the glass spheres would cause a corresponding error in the estimated number of spheres per unit volume within the phantoms.

The Born approximation was used in the present paper to relate the spatial-frequency properties of the scattering medium to the measured differential scattering cross section. This approximation is based on the assumption that the incident beam is unperturbed by the scattering medium, so that strong scattering, refraction, and diffraction effects are all neglected. Since human soft tissues have been shown to possess ultrasonic scattering properties not fully described by weak scattering approximations,[41] worthy of special note is that measurement of scattering properties employing the techniques developed here is not fundamentally dependent on the Born approximation. Although the present normalization method was derived using the Born approximation, Eq. (23), which expresses a ratio of the total scattered energy to the incident energy, is still valid in the presence of multiple scattering, diffraction, or refraction. However, in situations where the Born approximation does not apply, the relationship between the average differential scattering cross section per unit volume and the spatial-frequency spectra of medium

properties is no longer linear. Furthermore, perturbation of transmit and receive beams by tissue will cause inaccuracy in the estimated beam cross sections required for the normalization method. For scattering by human tissues, therefore, Eq. (14) and similar equations that linearly relate scattered energy to tissue spatial-frequency properties should be regarded as approximations. The utility of these approximations for tissue characterization in strongly inhomogeneous media, such as the human breast, requires further study.

V. CONCLUSION

A method has been presented for the accurate measurement of the angle- and frequency-dependent differential scattering cross sections of random media. General normalization expressions presented were evaluated for the particular case of ultrasonic beams associated with unfocused linear array or phased array transducers, narrow-band emitter signals, and long detector gates. Medium absorption was incorporated explicitly in the normalization.

The method has been applied to an experimental configuration that uses a fixed ring transducer. Beams and time gates were designed for the ring transducer to maximize the achieved wave space resolution of the scattering measurements and to ensure that scattered fields were sampled with high wave space resolution. Normalization expressions were evaluated for the ring transducer configuration using analytic expressions for field patterns of individual elements and numerical inclusion of background medium absorption.

Attenuation measurements for a pure agar medium and for an agar-glass sphere phantom indicate that increased transmission loss in the agar-glass phantom is due to scattering effects rather than to increased absorption. Experimental scattering results for two agar-glass sphere phantoms show good relative agreement with theoretical calculations for measured glass-sphere distributions, although precise comparison between theory and experiment was limited by uncertainties in the background medium absorption, sphere distribution, and the mechanical properties of the glass spheres.

The results show the feasibility for accurate *in vitro* measurements of scattering cross sections using a fixed ring transducer configuration, and suggest that tissue characterization using this method is also feasible.

ACKNOWLEDGMENTS

The authors wish to thank Daofa Zhang, who initially implemented a different method for normalization of the ring transducer scattering measurements, Timothy Heywood and DongLai Liu, whose work on calibration and testing of the ring transducer system was important for this study, Ernest Madsen, who provided valuable advice on phantom construction, and Peter Keng, who helped with use of the Coulter Counter. Helpful discussions with Laura Hinkelman are acknowledged with pleasure. Funding for this work was provided by the University of Rochester Diagnostic Ultrasound Research Laboratory Industrial Associates, NIH Grants Nos. DK 45533 and HL 150855, US Army Grant No. DAMD 17-94-J-4384, the F. V. Hunt Fellowship of the Acoustical Society of America, and the University of Rochester Exchange Visitor Program.

[1] R. Gramiak, R. C. Waag, E. A. Schenk, P. P. K. Lee, K. Thomson, and P. Macintosh, ''Ultrasonic detection of myocardial infarction by amplitude analysis,'' Radiology **130**, 713–720 (1979).
[2] S. A. Wickline, L. J. Thomas III, J. G. Miller, B. E. Sobel, and J. E. Perez, ''A relationship between ultrasonic integrated backscatter and myocardial contractile function,'' J. Clin. Invest. **76**, 2151–2160 (1985).
[3] K. A. Wear, M. R. Milunski, S. A. Wickline, J. E. Perez, B. E. Sobel, and J. G. Miller, ''Differentiation between acutely ischemic myocardium and zones of completed infarction in dogs on the basis of frequency-dependent backscatter,'' J. Acoust. Soc. Am. **85**, 2634–2641 (1989).
[4] J. C. Bamber and C. R. Hill, ''Acoustic properties of normal and cancerous human liver—I. Dependence of pathological conditions,'' Ultrasound Med. Biol. **7**, 121–133 (1981).
[5] R. Momenan, R. F. Wagner, B. S. Garra, M. H. Loew, and M. F. Insana, ''Image staining and differential diagnosis of ultrasound scans based on the Mahalanobis distance,'' IEEE Trans. Med. Imaging **13**, 37–47 (1994).
[6] R. C. Waag and R. M. Lerner, ''Tissue macrostructure determination with swept-frequency ultrasound,'' *IEEE Ultrasonics Symposium Proceedings*, IEEE Cat. No. 73CHO 807-8SU, pp. 63–66 (1973).
[7] R. C. Chivers, R. R. Hill, and D. Nicholas, ''Frequency dependence of ultrasonic backscattering cross-section: An indicator of tissue structure characteristics,'' *Proceedings of the Second World Congress on Ultrasonics in Medicine* (Amsterdam, The Netherlands: Excerpta Medica, 1973), pp. 300–303.
[8] R. A. Sigelmann and J. M. Reid, ''Analysis and measurement of ultrasound backscattering from an ensemble of scatterers excited by sine-wave bursts,'' J. Acoust. Soc. Am. **53**, 1351–1355 (1973).
[9] R. C. Chivers and C. R. Hill, ''A spectral approach to ultrasonic scattering from human tissue: methods, objectives, and backscattering measurements,'' Phys. Med. Biol. **20**, 799–815 (1975).
[10] D. Nicholas, ''Orientation and frequency dependence of backscattered energy and its clinical application,'' in *Recent Advances in Ultrasound in Biomedicine*, edited by D. N. White (Research Studies, Forest Grove, OR, 1977), pp. 29–54.
[11] R. C. Waag, R. M. Lerner, P. P. K. Lee, and R. Gramiak, ''Ultrasonic Diffraction Characterization of Tissue,'' in *Recent Advances in Ultrasound in Biomedicine*, Vol. 1, edited by D. N. White (Research Studies, Forest Grove, OR, 1977), pp. 87–116.
[12] M. O'Donnell and J. G. Miller, ''Quantitative broadband ultrasonic backscatter: An approach to nondestructive evaluation in acoustically inhomogeneous materials,'' J. Appl. Phys. **52**, 1056–1065 (1981).
[13] D. Nicholas, C. R. Hill, and D. K. Nassiri, ''Evaluation of backscattering coefficients for excised human tissues: Principles and techniques,'' Ultrasound Med. Biol. **8**, 7–15 (1982).
[14] F. L. Lizzi, M. Greenebaum, E. J. Feleppa, M. Elbaum, and D. J. Coleman, ''Theoretical framework for spectrum analysis in ultrasonic tissue characterization,'' J. Acoust. Soc. Am. **73**, 1366–1373 (1983).
[15] M. A. Fink and J. F. Cardoso, ''Diffraction effects in pulse-echo measurements,'' IEEE Trans. Sonics Ultrason. **SU-31**, 313–329 (1984).
[16] E. L. Madsen, M. F. Insana, and J. A. Zagzebski, ''Method of data reduction for accurate determination of acoustic backscatter coefficients,'' J. Acoust. Soc. Am. **76**, 913–923 (1984).
[17] M. F. Insana, R. F. Wagner, D. G. Brown, and T. J. Hall, ''Describing small-scale structure in random media using pulse-echo ultrasound,'' J. Acoust. Soc. Am. **87**, 179–192 (1990).
[18] M. F. Insana, T. J. Hall, and L. T. Cook, ''Backscatter coefficient estimation using array transducers,'' IEEE Trans. Ultrason. Ferroelectr. Freq. Control **41**, 714–723 (1994).
[19] J. Meunier and M. Bertrand, ''Echographic image mean gray level changes with tissue dynamics: A system-based model study,'' IEEE Trans. Biomed. Eng. **42**, 403–410 (1995).
[20] J. A. Campbell and R. C. Waag, ''Normalization of ultrasonic scattering measurements to obtain average differential scattering cross sections for tissues,'' J. Acoust. Soc. Am. **74**, 393–399 (1983).
[21] D. K. Nassiri and C. R. Hill, ''The differential and total bulk acoustic scattering cross sections of some human and animal tissues,'' J. Acoust. Soc. Am. **79**, 2034–2047 (1986).
[22] R. C. Waag and J. P. Astheimer, ''Characterization of measurement sys-

tem effects in ultrasonic scattering experiments,'' J. Acoust. Soc. Am. **88**, 2418–2436 (1990).
[23] R. C. Waag, J. P. Astheimer, and J. F. Smith III, ''Analysis and computations of measurement system effects in ultrasonic scattering experiments,'' J. Acoust. Soc. Am. **91**, 1284–1297 (1992).
[24] K. Chandra and C. Thompson, ''Ultrasonic characterization of fractal media,'' Proc. IEEE **81**, 1523–1533 (1993).
[25] T. D. Mast and R. C. Waag, ''Wave space resolution in ultrasonic scattering measurements,'' J. Acoust. Soc. Am. **98**, 3050–3058 (1995).
[26] P. M. Morse and K. U. Ingard, *Theoretical Acoustics* (McGraw-Hill, New York, 1968), Chap. 8.
[27] P. M. Morse and H. Feshbach, *Methods of Theoretical Physics*, *Part I* (McGraw-Hill, New York, 1953), pp. 834–838.
[28] A. D. Pierce, *Acoustics* (McGraw-Hill, New York, 1981), p. 214.
[29] M. M. Burlew, E. L. Madsen, J. A. Zagzebski, R. A. Banjavic, and S. W. Sum, ''A new ultrasound tissue-equivalent material,'' Radiology **134**, 517–520 (1980).
[30] J. J. Faran, ''Sound scattering by solid cylinders and spheres,'' J. Acoust. Soc. Am. **23**, 405–418 (1951).
[31] R. C. Waag, D.-L. Liu, T. D. Mast, A. I. Nachman, P. Jaeger, and T. Kojima, ''An ultrasonic ring transducer system for studies of scattering and imaging,'' J. Acoust. Soc. Am. **100**, 2795 (1996).
[32] J. A. Zagzebski, L. X. Xao, E. J. Boote, and Z. F. Lu, ''Quantitative backscatter imaging,'' in *Ultrasonic Scattering in Biological Tissues*, edited by K. K. Shung and G. A. Thieme (CRC, Boca Raton, 1993), pp. 451–486.
[33] K. J. Peters and R. C. Waag, ''Compensation for receiver bandpass effects on backscatter power spectra using a random medium model,'' J. Acoust. Soc. Am. **84**, 392–399 (1988).
[34] J. M. Reid, ''Standard substitution methods for measuring ultrasonic scattering in tissues,'' in *Ultrasonic Scattering in Biological Tissues*, edited by K. K. Shung and G. A. Thieme (CRC, Boca Raton, 1993), pp. 171–204.
[35] J. A. Campbell and R. C. Waag, ''Measurements of calf liver ultrasonic differential and total scattering cross sections,'' J. Acoust. Soc. Am. **75**, 603–611 (1984).
[36] S. A. Goss, R. L. Johnston, and F. Dunn, ''Comprehensive compilation of empirical ultrasonic properties of mammalian tissues,'' J. Acoust. Soc. Am. **64**, 423–457 (1978).
[37] S. A. Goss, R. L. Johnston, and F. Dunn, ''Compilation of empirical ultrasonic properties of mammalian tissues II,'' J. Acoust. Soc. Am. **68**, 93–108 (1980).
[38] F. A. Duck, *Physical Properties of Tissue: a Comprehensive Reference Book* (Academic, New York, 1990).
[39] K. J. Parker, R. M. Lerner, and R. C. Waag, ''Comparison of techniques for *in vivo* attenuation measurements,'' IEEE Trans. Biomed. Eng. **35**, 1064–1068 (1988).
[40] E. L. Madsen, ''Method of determination of acoustic backscatter and attenuation coefficients independent of depth and instrumentation,'' in *Ultrasonic Scattering in Biological Tissues*, edited by K. K. Shung and G. A. Thieme (CRC, Boca Raton, 1993), pp. 205–250.
[41] T. D. Mast, L. M. Hinkelman, M. J. Orr, V. W. Sparrow, and R. C. Waag, ''Simulation of ultrasonic pulse propagation through the abdominal wall,'' J. Acoust. Soc. Am. **102**, 1177–1190 (1997).

The evolution of phase fronts and the method of strained coordinates

Roel Snieder
Department of Geophysics, Utrecht University, P.O. Box 80.021, 3508 TA Utrecht, The Netherlands and Center for Wave Phenomena, Colorado School of Mines, Golden, Colorado 80401

(Received 18 July 1997; accepted for publication 19 February 1998)

When waves propagate through a medium with smooth velocity perturbations the propagation of wavefronts is determined by the eikonal equation. Here the propagation of wavefronts through a medium with small-scale velocity perturbations is analyzed using the method of strained coordinates. A partial differential equation for the first-order perturbation of wavefronts is derived that includes frequency-dependent wave propagation effects. It is shown that for the special case of the scalar Helmholtz equation with a homogeneous reference medium this leads to the same perturbation of wavefronts as obtained from the Rytov approximation. However, the method presented here can possibly be generalized to more complex wave propagation problems where the Rytov approximation cannot be used, such as the propagation of vector waves. [S0001-4966(98)00706-1]

PACS numbers: 43.20.Fn [ANN]

INTRODUCTION

Ray theory is a powerful tool for modeling wave propagation in inhomogeneous media. However, ray theory is only applicable when the length scale of the velocity perturbations is much larger than a wavelength and much larger than the width of the first Fresnel zone.[1] Snieder and Lomax[2] investigated the behavior of the phase and amplitude of a transmitted wave field when the velocity perturbations are so rough that the requirements for the validity of ray theory are violated. They analyzed the Helmholtz equation

$$\nabla^2 u + k_0^2(1+\varepsilon n(\mathbf{r}))u = 0, \tag{1}$$

so that the analysis is carried out in the frequency domain. In (1) $\varepsilon n(\mathbf{r})$ denotes the relative perturbation in $1/c^2$ where $c(\mathbf{r})$ is the velocity of the medium. The term ε is introduced to facilitate a systematic perturbation approach.

A key result of Snieder and Lomax[2] was that for a reference medium with constant velocity the phase perturbation $\delta\varphi$ induced by the perturbation $\varepsilon n(\mathbf{r})$ is to first order given by

$$\delta\varphi(\mathbf{r}) = \Re\left\{ \frac{\varepsilon k_0}{2} \int_0^z \frac{\int_{-\infty}^{\infty} n(\mathbf{r}') e^{ik_0 D(\mathbf{r}')}\, dx'}{\int_{-\infty}^{\infty} e^{ik_0 D(\mathbf{r}')}\, dx'} dz' \right\}, \tag{2}$$

where $\Re$ denotes the real part. Throughout this paper it is assumed that the perturbation is only nonzero for $z>0$. The geometry of the problem is given in Fig. 1. The function $D(\mathbf{r}')$ in (2) is the detour of a wave scattered at $\mathbf{r}'$ compared to the path taken by the unperturbed wave. The important point to note is that the phase perturbation is expressed as a weighted average of the velocity perturbation and that the weight function $\exp ik_0 D(\mathbf{r}')$ follows from theory. Expression (2) is for two spatial dimensions. For three dimensions and for an inhomogeneous reference model a similar expression can be derived.[2,3]

The analysis leading to (2) was based on the Rytov approximation. The goal of this work is to derive the same result without invoking the Rytov approximation. This is achieved by applying the method of strained coordinates[4] to the Helmholtz equation (1). The method of strained coordinates has been applied earlier to the high-frequency solutions of the Helmholtz equation.[5] In this work, the effects of a finite frequency on the propagation of wavefronts is investigated. It should be noted that nowhere in the subsequent analysis is it assumed that the perturbation $n(\mathbf{r})$ satisfies any smoothness conditions.

I. A BORN–WKB SOLUTION FOR THE 1-D WAVE EQUATION

In this section the 1-D wave equation is considered

$$u_{zz} + k_0^2(1+\varepsilon n(z))u = 0. \tag{3}$$

A plane wave $\exp ik_0 z$ impinges on the perturbation $n(z)$ from the left. The main effect of the perturbation is to delay or advance the wave field as it propagates through the perturbation. Such a perturbation of the phase of the wave field can be accounted for by writing the wave field as $\exp ik_0 Z$, where the new coordinate Z is a function of the old coordinate z:

$$Z = f(z). \tag{4}$$

At this point the function $f(z)$ is still arbitrary (as long as the mapping from z to Z is one-to-one). However, ultimately this function is chosen in such a way that $k_0 Z$ corresponds to the phase of the perturbed transmitted wave. Under the coordinate transformation (4) the differential equation (3) transforms to

$$\frac{d^2u}{dZ^2} + \frac{f''}{f'^2}\frac{du}{dZ} + k_0^2 \frac{(1+\varepsilon n)}{f'^2} u = 0. \tag{5}$$

In this expression and subsequent expressions the prime denotes the differentiation with respect to z.

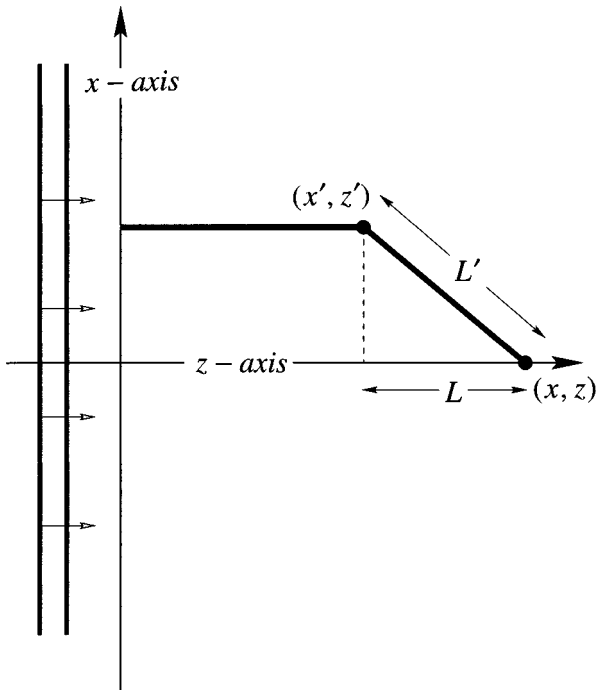

FIG. 1. Definition of the geometric variables.

The relation between the new coordinate Z and the old coordinate z is expressed as a perturbation series:

$$Z=f(z)=z+\varepsilon f_1(z)+\cdots . \tag{6}$$

The zeroth-order term in this expansion is equal to z because for the unperturbed problem there is no need to perturb the coordinate system. The wave field (as a function of Z) is also written as a perturbation series:

$$u=e^{ik_0Z}(v_0(z)+\varepsilon v_1(z)+\cdots) . \tag{7}$$

The term $\exp ik_0Z$ is introduced to make the presence of the transmitted wave explicit, but the analysis could just as well be carried out without introducing this term. Inserting expansions (6) and (7) into (5) and collecting the terms of zeroth and first order in ε leads to the equations:

$$\frac{d^2v_0}{dZ^2}+2ik_0\frac{dv_0}{dZ}=0, \tag{8}$$

$$\frac{d^2v_1}{dZ^2}+2ik_0\frac{dv_1}{dZ}=-f_1''\left(\frac{dv_0}{dZ}+ik_0v_0\right)+k_0^2(2f_1'-n)v_0. \tag{9}$$

The first expression has the solution

$$v_0=1, \tag{10}$$

which reflects the fact that to leading order the wave field is a wave of constant amplitude moving to the right. Inserting (10) into (9) yields

$$\frac{d^2v_1}{dZ^2}+2ik_0\frac{dv_1}{dZ}=-ik_0f_1''+k_0^2(2f_1'-n). \tag{11}$$

At this point the leading order solution $v_0\exp(ik_0Z)$ is known, but it is a function of a new coordinate Z that is not known yet. This coordinate follows from the requirement that Eq. (11) does not lead to secular terms in the solution v_1; see Ref. 4. The f_1''-term in (11) does not lead to secular terms but the terms $(2f_1'-n)$ lead to secular terms in the solution v_1. These secular terms are avoided when f_1 is chosen to satisfy the requirement

$$2f_1'-n=0, \tag{12}$$

which can be integrated to give

$$f_1(z)=\frac{1}{2}\int_0^z n(z')dz'. \tag{13}$$

Using this and (10) leads to the following expression for the leading order term in the expansion (7):

$$u(z)=\exp\left\{ik_0\left(z+\frac{\varepsilon}{2}\int_0^z n(z')dz'\right)\right\}+O(\varepsilon). \tag{14}$$

It is interesting to compare this result with the WKB solution of (1); see Ref. 4:

$$u_{\mathrm{WKB}}(z)=\frac{1}{(1+\varepsilon n(z))^{1/4}}\exp\left\{ik_0\int_0^z\sqrt{1+\varepsilon n(z')}dz'\right\}. \tag{15}$$

There are two differences with solution (14). First, the phase of the solutions agree only to first order. The reason for this is that in (14) only the first-order term of expansion (6) for the strained coordinate has been used. Second, the amplitude factor $(1+\varepsilon n(z))^{-1/4}$ is not accounted for in approximation (14). This is due to the fact that only the v_0-term of expansion (7) is accounted for. It is now verified to what extent the amplitude factor $(1+\varepsilon n(z))^{-1/4}$ is to first order reproduced by the v_1 term of expansion (7).

Inserting (13) into (9) gives the following differential equation for v_1:

$$\frac{d^2v_1}{dZ^2}+2ik_0\frac{dv_1}{dZ}=-ik_0\frac{dn_1}{dz}, \tag{16}$$

which can be integrated to give

$$v_1(z)=-\frac{ik_0}{2}\int_0^z n(z')e^{2ik_0Z'}\,dz'\;e^{-2ik_0Z}+Ce^{-2ik_0Z}+A, \tag{17}$$

with A and C integration constants. Using integration by parts the integral on the right-hand side can be written as

$$\int_0^z n(z')\exp(2ik_0Z')dz'$$

$$=(n(z)\exp(2ik_0Z)-n(0))/2ik_0-(1/2ik_0)\times\int_0^z dn(z')/dz'\exp(2ik_0Z')dz'. \tag{18}$$

Using this, solution (17) can be written as

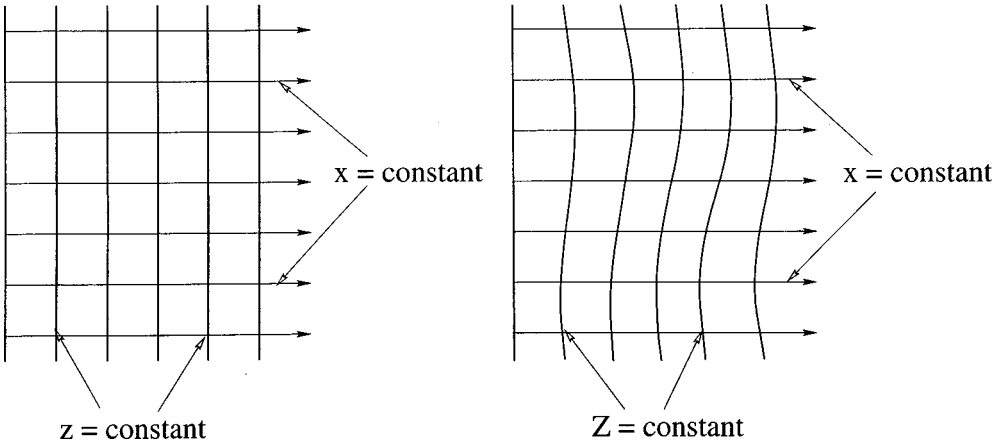

FIG. 2. Original Cartesian coordinate system (x,y,z) (left panel) and the new strained coordinate system (x,y,Z) (right panel) where the surface $Z=$const. coincide with the location of wavefronts.

$$v_1(z)=(A-\tfrac{1}{4}n(z)) + \left(B+\frac{1}{4}\int_0^z e^{2ik_0Z'}\frac{dn(z')}{dz'}dz' \right) e^{-2ik_0Z}, \quad (19)$$

with B a new integration constant. The first term in this expression accounts for right-going waves while the last term describes left-going waves. The constant A follows from the requirement that for $z<0$ the right-going waves have a unit amplitude [because $n(z)=0$ for $z<0$]. With the solution $v_0=1$ this implies that $A=0$. The requirement that for $z\to\infty$ there are no left-going waves gives

$$B=-\frac{1}{4}\int_0^\infty e^{2ik_0Z'}\frac{dn(z')}{dz'}dz'. \quad (20)$$

Inserting these results in (19) and using (10) and (7) gives

$$u(z)=\left(1-\frac{\varepsilon n(z)}{4}\right)e^{ik_0Z} - \frac{\varepsilon}{4}\int_z^\infty e^{2ik_0Z'}\frac{dn(z')}{dz'}dz'\ e^{-ik_0Z}+O(\varepsilon^2), \quad (21)$$

with $Z=z+(\varepsilon/2)\int_0^z n(z')dz'$. The amplitude factor $(1+\varepsilon n(z))^{-1/4}$ in the WKB approximation is to first order accounted for by the term $(1-\varepsilon n/4)$ in the right hand side. In addition, the second term describes the waves that are reflected to the right of z by the gradient in the heterogeneity. Note that this term is not identical to the normal Born approximation because the integral contains the propagator $\exp 2ik_0Z'$ rather than the unperturbed Green's function. This term therefore consists of a distorted-wave Born approximation.

II. DERIVATION OF THE EQUATION FOR THE PERTURBATION OF WAVE FRONTS

In this section the derivation of the previous section is generalized to the Helmholtz equation (1) in 2 or 3 spatial dimensions. It is assumed that the incoming wave is a plane wave propagating in the direction of the positive z axis and that the perturbation is only nonzero for $z\geqslant 0$. A coordinate transformation is used to transform the Cartesian coordinate system (x,y,z) to a new coordinate system (x,y,Z). The new Z coordinate is chosen in such a way that the lines of constant value of Z coincide with the wave fronts of the wave field; see Fig. 2. The new coordinate Z is related to the old coordinates by a perturbation expansion:

$$Z=z+\varepsilon f_1(x,y,z)+\cdots. \quad (22)$$

The wave field is again expanded in the perturbation series (7).

It is convenient to decompose the Laplacian in a z derivative and derivatives perpendicular to the z axis:

$$\nabla^2=\nabla_\perp^2+\frac{\partial^2}{\partial z^2}. \quad (23)$$

Using this decomposition and expansions (7) (generalized to higher dimensions) and (22) gives for the $O(1)$ and $O(\varepsilon)$ terms of the Helmholtz equation (1):

$$\frac{d^2v_0}{dZ^2}+2ik_0\frac{dv_0}{dZ}+\nabla_\perp^2 v_0=0, \quad (24)$$

$$\frac{d^2v_1}{dZ^2}+2ik_0\frac{dv_1}{dZ}+\nabla_\perp^2 v_1 = -f_1''\left(\frac{\partial v_0}{\partial z}+ikv_0\right)-2ik_0(\nabla_\perp f_1\cdot\nabla_\perp v_0) - ik_0(2ik_0f_1'-ik_0n+\nabla_\perp^2 f_1)v_0. \quad (25)$$

In these expression the prime denotes the z derivative: $f'=\partial f/\partial z$. The unperturbed solution is given by (10): $v_0=1$. For this solution (25) reduces to

$$\frac{d^2v_1}{dZ^2}+2ik_0\frac{dv_1}{dZ}+\nabla_\perp^2 v_1 = -ik_0(f_1''+2ik_0f_1'-ik_0n+\nabla_\perp^2 f_1). \quad (26)$$

The first-order solution v_1 has no secular terms when

$$\boxed{2ik_0f_1'-ik_0n+\nabla_\perp^2 f_1=0.} \quad (27)$$

Equation (27) is an equation that describes the (first-order) propagation of wavefronts. The term $\nabla_\perp^2 f_1$ ensures that the wavefronts remain smooth while they propagate. Note that if this term were absent, the wavefronts would not depend on frequency because in the absence of the term $\nabla_\perp^2 f_1$ the wave number k_0 can be divided out of expression (27). Equation (27) can thus be considered as a generalization of the (linearized) eikonal equation that includes frequency-dependent wave-propagation effects. Note the close resemblance of equation (27) with the parabolic approximation to the wave equation; see, e.g., Ref. 6. There are, however, two differences. First, (27) is a differential for the *wavefronts* rather than for the *wave field* itself. Second, the term accounting for the inhomogeneity is multiplied in the parabolic wave equation with the wave field, whereas in (27) the term $ik_0 n$ is not multiplied with the solution f_1. The analysis can be extended by constructing the solution v_1 from equation (26). In this way the contribution of first-order scattered waves can be included in the analysis in a way that is similar to the generalized Born scattering formulated by Chapman and Coates.[7]

III. RELATION WITH THE AVERAGING INTEGRAL OF SNIEDER AND LOMAX

The differential equation (27) for the propagation of phase fronts does not yet establish the connection with the averaging integrals of Snieder and Lomax.[2] This connection can be made by integrating (27). Using a standard Green's function technique the solution can be written as

$$f_1(x,z)=\Re\left\{-ik_0\int_0^z dz'\,\frac{1}{\sqrt{8\pi k_0|z-z'|}}\times\int_{-\infty}^{\infty}\exp\left(\frac{ik_0(x-x')^2}{2|z-z'|}+\frac{i\pi}{4}\right)n(x',z')dx'\right\}. \tag{28}$$

This expression can be simplified with the identity

$$\int_{-\infty}^{\infty}\exp\left(\frac{ik_0(x-x')^2}{2|z-z'|}\right)dx'=\sqrt{\frac{2\pi|z-z'|}{k_0}}e^{i\pi/4}. \tag{29}$$

Dividing (28) by the left-hand side of (29) and multiplying (28) with the right-hand side of (29) gives

$$k_0 f_1(x,z)=\Re\left\{\frac{k_0}{2}\int_0^z dz'\times\frac{\int_{-\infty}^{\infty}\exp[ik_0(x-x')^2/(2|z-z'|)]n(x',z')dx'}{\int_{-\infty}^{\infty}\exp[ik_0(x-x')^2/(2|z-z'|)]dx'}\right\}. \tag{30}$$

In this form, the phase shift $k_0 f_1(x,z)$ is expressed as a weighted average of the perturbation $n(x,z)$. The averaging integral is carried out in the direction perpendicular to the unperturbed direction of propagation. The weight function $\exp(ik_0(x-x')^2/2|z-z'|)$ follows from the theory. Expression (30) can directly be compared with the averaging integral (3.14) of Snieder and Lomax[2] which is of the same form. The averaging function of Snieder and Lomax is $\exp(ikD)$ rather than $\exp(ik_0(x-x')^2/2|z-z'|)$ in expression (30). The detour D of Ref. 6 is the path traversed by the single scattered waves compared to the path traversed by the unperturbed wave, this quantity is given by $L-L'$ in the geometry of Fig. 1. Using a Taylor expansion in the quantity $(x-x')/(z-z')$ the detour D is to first order given by

$$D=L-L'=\sqrt{(x-x')^2+(z-z')^2}-(x-x')\approx\frac{(x-x')^2}{2(z-z')}. \tag{31}$$

The quantity $(x-x')/(z-z')$ is small for small scattering angles. This implies that the averaging function in (30) is for small scattering angles identical to the averaging function derived by Snieder and Lomax.[2] For transient arrivals one only needs to consider small scattering angles, because waves scattered over large scattering angles arrive too late to interfere with the direct arriving waves and thus have no influence on the phase perturbation of the direct wave.

IV. DISCUSSION

It has been shown here that the method of strained coordinates can be used to compute the first-order perturbation of wavefronts for waves that propagate through a medium that has velocity perturbations on a scale that are so small that the conditions for geometric ray theory are violated. Although the results agree to first order with the solutions obtained from the Rytov approximation, the approach presented here has several advantages. First, there is no known generalization of the Rytov approximation to vector waves such as elastic waves. The method presented here could potentially be generalized to vector waves. Second, the method leads directly to a partial differential equation for the propagation of wavefronts that generalizes the eikonal equation to include finite-frequency effects. Such an equation could provide a starting point for new methods for describing forward and inverse problems in wave propagation for media that violate the requirements for the validity of ray theory.

[1] Ya. A. Kravtsov, ''Rays and caustics as physical objects,'' in *Progress in Optics*, XXVI, edited by E. Wolf (Elsevier, Amsterdam, 1988), pp. 227–348.

[2] R. Snieder and A. Lomax, ''Wave field smoothing and the effect of rough velocity perturbations on arrival times and amplitudes,'' Geophys. J. Int. **125**, 796–812 (1996).

[3] R. Snieder and C. Chapman, ''The reciprocity properties of geometrical spreading,'' Geophys. J. Int. **132**, 89–95 (1998).

[4] C. M. Bender and S. A. Orszag, *Advanced Mathematical Methods for Scientists and Engineers* (McGraw-Hill, New York, 1978), pp. 545.

[5] N. D. Fowkes, ''A singular perturbation method, Part II,'' Q. Appl. Math. **26**, 71–85 (1968).

[6] S. M. Rytov, Yu. A. Kravtsov, and V. I. Tatarskii, *Principles of Statistical Radiophysics 4; Wave Propagation through Random Media* (Springer-Verlag, Berlin, 1989).

[7] C. H. Chapman and R. T. Coates, ''Generalized Born scattering in anisotropic media,'' Wave Motion **19**, 309–341 (1994).

Various loss factors of a master harmonic oscillator coupled to a number of satellite harmonic oscillators

G. Maidanik and K. J. Becker
DTMB, NSWC/CD, 9500 MacArthur Boulevard, West Bethesda, Maryland 20817-5700

(Received 24 August 1997; accepted for publication 24 February 1998)

Three loss factors are defined for a master harmonic oscillator (HO); the I-loss factor, the U-loss factor, and the effective loss factor. A conductance (β) is conventionally defined as the ratio of the power imparted to a dynamic system by an external drive to the stored energy that this input power generates. The conductance (β) is related to the loss factor (η) by the frequency (ω); $\beta=(\omega\eta)$. In light of this definition, it is shown that all three loss factors are identical for an isolated master HO at resonance. Differences arise among these loss factors when the master HO is coupled to satellite harmonic oscillators (HO's). The first two loss factors retain their definitive format in the sense that the stored energy is reckoned only in the master HO; the energy stored in the coupled satellite HO's and in the couplings is discounted. The effective loss factor, on the other hand, is defined by accounting for the total stored energy that the external drive applied to the master HO generates in the complex. The complex here is composed of the master HO, the satellite HO's, and the *in situ* couplings. In those situations in which the portion of the total energy stored in the satellite HO's and in the couplings substantially exceeds the stored energy in the master HO, the I-loss factor and the U-loss factor may substantially exaggerate the true loss factor of the coupled master HO. Situations of this type are illustrated by data obtained in computational experiments, and it is argued that the true loss factor of the master HO in the complex as a whole is the effective loss factor. [S0001-4966(98)03906-X]

PACS numbers: 43.20.Ks, 43.20.Wd, 43.40.At [JEG]

INTRODUCTION

A number of questions seem to arise regarding the simplest of interactions, particularly those among harmonic oscillators (HO's). The significance of these questions lies in the fact that they bear directly on questions relating to the statistical energy analysis (SEA) and structural fuzzies. SEA and, to some extent, structural fuzzies are based on analogous interactions.[1–5] In this paper these interactions are investigated for their own sake; SEA and structural fuzzies are only obliquely involved. Any relationship of SEA and structural fuzzies to this paper lies with the definition and the deployment of loss factors. Loss factors are often cavalierly quoted and loosely interpreted. Nonetheless, it is not the intention of this paper to challenge a specific abuse of loss factors, but rather to show that vast differences can be encountered in the definitions of a loss factor and that a careful interpretation is needed, in conjunction, if the loss factor is to remain a useful parameter in noise control engineering.[6] The paper intentionally deals with a relatively simple structural complex. Accordingly, and in particular, three loss factors are defined for a complex composed of a number of HO's. In this complex, one of the HO's is designated as the master and the others are designated as satellites. The loss factors pertain to the master harmonic oscillator (HO) which is the only one to be externally driven; the responses of the satellite HO's result only from their direct and/or indirect couplings to the master HO. It is argued that a I-loss factor η_{p1} can be defined as the real part of the appropriately normalized *in situ* impedance of the master HO. An equivalent definition of the I-loss factor is proposed; this definition is more in line with the conventional definition of a loss factor. The I-loss factor is here defined as the ratio of the appropriately normalized external input power to twice the stored kinetic energy in the master HO. A close relative of the I-loss factor is the U-loss factor η_{b1}. The U-loss factor is defined as the ratio of the appropriately normalized external input power to the stored energy in the master HO. Since the stored kinetic and potential energies are equal at the resonance of a HO, at and in the vicinity of the resonance frequency, the I-loss factor and the U-loss factor are equal. If the stored energy in the complex exceeds the energy stored solely in the master HO, the I-loss factor and the U-loss factor are apparent loss factors in the sense that they raise the eternal question as to where the energy went. In a real loss factor, this question is moot. With this in mind, an *effective* loss factor η_{e1} is defined as the ratio of the appropriately normalized input power imparted into the master HO by the external drive to the stored energy in the complex. This stored energy includes not only the stored energies in all the HO's, but also the stored energies in all the couplings among these HO's. Unlike the I- and U-loss factors, this effective loss factor is a real loss factor, notwithstanding the obvious identity of the three loss factors for an isolated master HO at resonance.

In this paper the theoretical background is established and a few questions are analytically posed and answered. The questions and answers pertain, however, only to the three loss factors just discussed and the discourse is illustrated with a few chosen computational examples. In order to simplify the illustrations, the analytical generality is curtailed in that the satellite HO's are allowed to be coupled only to the master HO, but not to each other. Moreover, mass and gyroscopic coupling parameters are also removed, at this

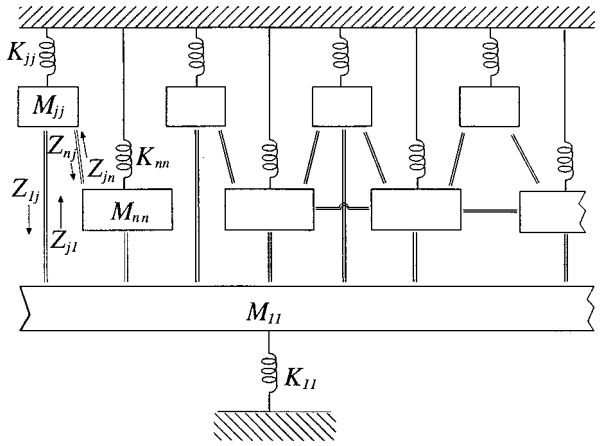

FIG. 1. A complex composed of a number of coupled harmonic oscillators. The first harmonic oscillators is designated as the master and the others are designated as the satellites. = couplings between harmonic oscillators; $\{K_{jj}, M_{jj}\}$ defines the (j)th harmonic oscillator.

stage, in order to further simplify the analytical descriptions. A cell of satellite HO's is defined and used. A cell hosts a number of satellite HO's that are identified by their resonance frequencies; the resonance frequencies of the satellite HO's in a cell reside within this cell. Cells hosting a single and multiple satellite HO's are investigated in this paper. Detailed investigations, beyond the determinations of the three loss factors; the I-, the U-, and the effective loss factors, as performed in this paper, are deferred.

I. EQUATION OF MOTION OF A COMPLEX COMPOSED OF A NUMBER OF COUPLED HARMONIC OSCILLATORS

The equation of motion may be stated in the matrix form

$$\begin{aligned} &\underset{\approx}{Z}(\omega)\underset{\sim}{V}(\omega)=\underset{\sim}{P}_e(\omega), \quad \underset{\sim}{V}(\omega)=\{V_j(\omega)\},\\ &\underset{\sim}{P}_e(\omega)=\{P_{ej}(\omega)\}, \quad \underset{\approx}{Z}(\omega)=(Z_{jn}(\omega)), \end{aligned} \tag{1a}$$

where $V_j(\omega)$ is the response and $P_{ej}(\omega)$ is the external drive that is applied to the (j)th HO and the element $Z_{jn}(\omega)$ in the *impedance matrix* describes the coupling between the (n)th and the (j)th HO's; the self-impedance element $Z_{jj}(\omega)$ describes the *in situ* impedance of the (j)th HO and, finally, $\underset{\approx}{Z}(\omega)$ is a square matrix of rank (N), (N) being the number of HO's in the complex.[7] The elements in the impedance matrix and, therefore, the impedance matrix itself is a proper functional of the complex. As such it is defined in terms of the parametric specification of the complex only; it is independent of the elements in the response vector $\underset{\sim}{V}(\omega)$ and the external drive vector $\underset{\sim}{P}_e(\omega)$. A model of the complex is sketched in Fig. 1.[1,8] The elements in the impedance matrix can be explicitly stated in the form

$$\begin{aligned} &\underset{\approx}{Z}(\omega)=(Z_{jn}(\omega)\,\delta_{jn}+Z_{jn}(\omega)(1-\delta_{jn})),\\ &Z_{jj}(\omega)=\sum_{n=1}^{N} Z_{nj}^{-}(\omega),\\ &Z_{nj}^{-}(\omega)=[i\omega M_{jn}+(i\omega)^{-1}K_{jn}]=Z_{jn}^{-}(\omega),\\ &M_{jn}=M_{nj}, \quad K_{jn}=K_{nj}, \quad K_{jn}=K_{jn}^{0}(1+i\eta_{jn}), \end{aligned} \tag{2a}$$

$$\begin{aligned} &Z_{jn}(\omega)=[Z_{jn}^{+}(\omega)-G_{jn}],\\ &Z_{jn}^{+}(\omega)=[(i\omega)M_{jn}-(i\omega)^{-1}K_{jn}],\\ &G_{jn}=-G_{nj}, \quad Z_{jn}^{+}(\omega)=Z_{jn}(\omega)|_{G=0}=Z_{nj}^{+}(\omega). \end{aligned} \tag{2b}$$

Since only passive members are defined in these elements they are required to satisfy the conditions

$$\mathrm{Re}\{Z_{jn}^{\mp}(\omega)+Z_{nj}^{\mp}(\omega)\}\begin{cases}\leqslant 0\\ \geqslant 0\end{cases}, \quad \mathrm{Im}\{Z_{jn}^{\mp}-Z_{nj}^{\mp}\}=0, \tag{2c}$$

where Re $\{\}$ and Im $\{\}$ are the real and imaginary parts of the enclosed quantities.[1] In Eq. (2), K_{jj} and M_{jj} describe the stiffness and the mass parameters of the (j)th HO, respectively, whereas K_{jn}, M_{jn}, and G_{jn} describe, respectively, the stiffness, the mass, and the gyroscopic coupling parameters that are associated with the coupling between the (n)th and the (j)th HO's, and the equality sign in the first of Eq. (2c) implies that the coupling is a *conservative coupling*.[1] In this connection, from the last of Eq. (2a) the dampings are attributed to the stiffness parameters and the degree of damping in a stiffness parameter is assessed in terms of an inherent loss factor; (η_{jj}) for the (j)th HO and (η_{jn}) for the coupling between the (n)th and the (j)th HO's. It is convenient to designate one of the HO's as the master and the remaining HO's in the complex as satellites (cf. Fig. 1). In addition, it is convenient to place the master HO (1)st and then to normalize Eq. (1a) in the form

$$\begin{aligned} &\overline{\underset{\approx}{Z}}(\omega)\overline{\underset{\sim}{V}}(\omega)=\overline{\underset{\sim}{P}}_e(\omega), \quad \overline{\underset{\sim}{V}}(\omega)=\{\overline{V}_j(\omega)\},\\ &\overline{\underset{\sim}{P}}_e(\omega)=\{\overline{P}_{ej}(\omega)\}, \quad \overline{\underset{\approx}{Z}}(\omega)=(\overline{Z}_{jn}(\omega)), \end{aligned} \tag{1b}$$

where

$$\begin{aligned} &\overline{V}_j(\omega)=\left[\frac{V_j(\omega)}{V_0}\right], \quad \overline{P}_{ej}(\omega)=\left[\frac{P_{ej}(\omega)}{P_{e1}(\omega)}\right],\\ &V_0(\omega)=\left[\frac{P_{e1}(\omega)}{(\omega M_{11})}\right], \quad \overline{Z}_{jn}(\omega)=\left[\frac{Z_{jn}(\omega)}{(\omega M_{11})}\right], \end{aligned} \tag{3}$$

and, from Eq. (2), it follows that

$$\begin{aligned} &\overline{Z}_{jj}(\omega)=\sum_{n=1}^{N}\overline{Z}_{nj}^{-}(\omega),\\ &\overline{Z}_{nj}^{-}(\omega)=i\left[\overline{M}_{nj}-\left(\frac{\omega_{nj}}{\omega}\right)^2(1+i\eta_{nj})\right],\\ &\omega_{jj}^2=\left(\frac{K_{jj}^0}{M_{11}}\right), \quad \omega_{jn}^2=\left(\frac{K_{jn}^0}{M_{11}}\right),\\ &\omega_j^2=\left(\frac{K_{jj}^0}{M_{jj}}\right), \quad \overline{M}_{nj}=\left(\frac{M_{nj}}{M_{11}}\right), \end{aligned} \tag{4a}$$

$$\begin{aligned} &\overline{Z}_{jn}(\omega)=[\overline{Z}_{jn}^{+}(\omega)-\overline{G}_{jn}(\omega)], \quad \overline{G}_{jn}(\omega)=-\overline{G}_{nj}(\omega),\\ &\overline{Z}_{jn}^{+}(\omega)=i\left[\overline{M}_{jn}+\left(\frac{\omega_{jn}}{\omega}\right)^2(1+i\eta_{jn})\right],\\ &\overline{G}_{jn}(\omega)=\left[\frac{G_{jn}}{(\omega M_1)}\right]. \end{aligned} \tag{4b}$$

The resonance frequency (ω_j) is the resonance frequency of the (j)th HO in isolation and in particular $\omega_{11}=\omega_1$.

Returning to Eq. (1b), it is recognized that this equation can be inverted in a straightforward manner to yield

$$\underset{\sim}{\overline{V}}(\omega)=\underset{\approx}{\overline{Y}}(\omega)\underset{\sim}{\overline{P}}_e(\omega), \quad \underset{\approx}{\overline{Y}}(\omega)=(\overline{Y}_{jn}(\omega))=[\underset{\approx}{\overline{Z}}(\omega)]^{-1}, \tag{5}$$

where $\underset{\approx}{\overline{Y}}(\omega)$ is the normalized *admittance matrix*. Most significantly, since the elements in the impedance matrix $\underset{\approx}{\overline{Z}}(\omega)$ are proper functionals of the complex, the elements in the admittance matrix $\underset{\approx}{\overline{Y}}(\omega)$ follow suit.

An investigative interest in Eq. (5) involves the definition of three significant loss factors; the first is dubbed a I-loss factor, the second a U-loss factor, and the third an *effective* loss factor. These three loss factors are defined in conjunction to emphasize the relationship and contrast between them; the relationship and contrast are instructive. A bonafide loss factor necessarily qualifies as such only if it is a proper functional of the complex to which it is attributed. The I-loss factor, the U-loss factor, and the effective loss factor, defined in this paper, are universally qualified loss factors. A straightforward investigation of the analytical descriptions of these loss factors readily evidences, in all cases, their functional propriety. In this paper, this functional propriety is implicitly implied in most subsequent developments.

II. DEFINITION OF THE I-, THE U-, AND THE EFFECTIVE LOSS FACTORS

Although a loss factor is often used to prescribe a degree of damping, there are several ways to define it. Unfortunately, these loss factors may be neither consistent nor simply related to each other. Thus in Eqs. (2) and (4), the inherent loss factors (η_{jj}) and (η_{jn}) are defined to be associated with the stiffness parameters of the individual HO's and the couplings among them, respectively. Although this definition is commonly used, it is seldom scrutinized. Nor is this scrutiny pursued in this paper. These inherent *stiffness controlled* loss factors, in Eqs. (2) and (4), are accepted, as such, *a priori*. It stands to reason that these loss factors govern the loss factors that are associated with the complex as a whole.

Using Eq. (5), the equation of motion for the master HO is

$$\overline{V}_1(\omega)=\overline{Y}_{11}(\omega)\overline{P}_{e1}(\omega), \quad \overline{Y}_{11}(\omega)=[\overline{Z}_1(\omega)]^{-1},$$
$$[\overline{Y}_{11}(\omega)]^{-1}\overline{V}_1(\omega)=\overline{P}_{e1}(\omega)=1. \tag{6}$$

An I-loss factor $\eta_{p1}(\omega)$ may be defined, using Eq. (6), in the form

$$\eta_{p1}(\omega)=\mathrm{Re}\{[\overline{Y}_{11}(\omega)]^{-1}\}=\mathrm{Re}\{\overline{Z}_1(\omega)\}. \tag{7}$$

In this definition the resistance controlled part in the normalized *in situ* impedance of the master HO is depicted as the loss factor. An alternative definition for the I-loss factor $\eta_{p1}(\omega)$ may be proposed. The I-loss factor, as defined in Eq. (7), may be equivalently defined by multiplying Eq. (6) by the complex conjugate of $\overline{V}_1(\omega)$ and taking the real part of the resulting equation; namely,

$$\eta_{p1}(\omega)=[\overline{\pi}_{e1}(\omega)/2\overline{\epsilon}_{k1}(\omega)]=\mathrm{Re}\{[\overline{Y}_{11}(\omega)]^{-1}\}, \tag{8}$$

where

$$\overline{\pi}_{e1}(\omega)=\mathrm{Re}\{[\overline{V}_1(\omega)]^*\overline{P}_{e1}(\omega)]\}, \tag{9a}$$

$$\overline{\epsilon}_{k1}(\omega)=(1/2)|\overline{V}_1(\omega)|^2, \tag{9b}$$

are the normalized input power imparted to the master HO by the *external drive* and the normalized stored kinetic energy in the master HO, respectively. [The normalization of the input power and stored energy are effected in this paper by $\pi_0(\omega)$ and $\epsilon_0(\omega)$, respectively, where $\pi_0(\omega)=\omega\epsilon_0(\omega)$ and $\epsilon_0(\omega)=M_{11}|V_0(\omega)|^2$, M_{11} is the mass of the master HO, and $V_0(\omega)$ is defined in Eq. (3).] Thus if factor (2), in $2\overline{\epsilon}_{k1}(\omega)$, is intended to account for the normalized potential energy $\overline{\epsilon}_{p1}(\omega)$ that is stored in the master HO, then one may claim that Eq. (8) is a conventional attempt to give credence to the I-loss factor. With that in mind, a U-loss factor $\eta_{b1}(\omega)$ may be defined in the form

$$\eta_{b1}(\omega)=\left[\frac{\overline{\pi}_{e1}(\omega)}{\overline{\epsilon}_1(\omega)}\right], \quad \eta_{b1}(\omega)=\eta_{p1}(\omega)\left[\frac{2\overline{\epsilon}_{k1}(\omega)}{\overline{\epsilon}_1(\omega)}\right],$$
$$\overline{\epsilon}_1(\omega)=(1/2)|\overline{V}_1(\omega)|^2\left[1+\left(\frac{\omega_{11}}{\omega}\right)^2\right], \tag{10}$$

where $\overline{\epsilon}_1(\omega)$ is the normalized stored energy in the master HO in response to the normalized external input power $\overline{\pi}_{e1}(\omega)$. Equation (10) states that the U-loss factor $\eta_{b1}(\omega)$ is closely related to the I-loss factor $\eta_{p1}(\omega)$, as defined in Eq. (8).

A question arises: Are either of the loss factors, $\eta_{p1}(\omega)$ or $\eta_{b1}(\omega)$, the appropriate loss factor for the coupled master HO? The loss factors $\eta_{p1}(\omega)$ and $\eta_{b1}(\omega)$ are defined under the assumption that the external normalized input power $\overline{\pi}_{e1}(\omega)$ that is imparted to the master HO is fully dissipated in this HO. Clearly this is not the case when couplings are present. Although it is assumed that only the master HO is driven externally, the satellite HO's, as well as the couplings, store energies by virtue of their direct and/or indirect couplings to the master HO. These stored energies contribute to local dissipations in these constituents of the complex. The externally imparted normalized power $\overline{\pi}_{e1}$ is, therefore, only partially dissipated in the master HO, which is contrary to the statements made in Eqs. (8) and (10). In this sense, the I-loss factor $\eta_{p1}(\omega)$ and the U-loss factor $\eta_{b1}(\omega)$ are apparent rather than real. A real loss factor of the master HO needs to account for the stored energies throughout the complex; it is the dissipation of the normalized input power $\overline{\pi}_{e1}(\omega)$ by the total normalized stored energy $\overline{\epsilon}_{e1}(\omega)$ generated that yields the effective loss factor $\eta_{e1}(\omega)$ of the master HO in the complex. Then, the effective loss factor $\eta_{e1}(\omega)$ is properly and conventionally defined in the form

$$\eta_{e1}(\omega)=\left[\frac{\overline{\pi}_{e1}(\omega)}{\overline{\epsilon}_{t1}(\omega)}\right]. \tag{11}$$

Therefore, to estimate the effective loss factor, it becomes necessary to estimate the total normalized energy $\overline{\epsilon}_{t1}(\omega)$ that is stored in the complex as a result of imparting the normalized external input power $\overline{\pi}_{e1}(\omega)$ into the master HO.

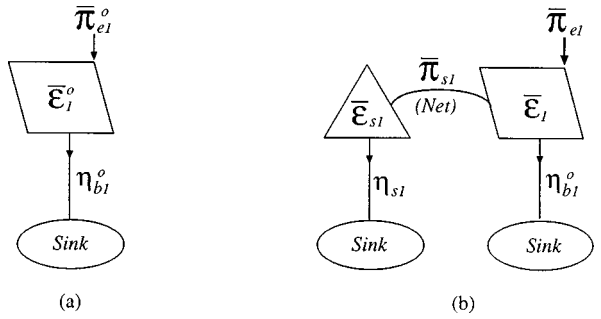

FIG. 2. Energetics in harmonic oscillators. (a) An isolated master harmonic oscillator. (b) A master harmonic oscillator coupled to an adjunct complex composed of satellite harmonic oscillators and the couplings.

Were the master HO isolated one would find from Eq. (5) that

$$\overline{V}_1^0 = \overline{Y}_{11}^0(\omega)\overline{P}_{e1}(\omega), \quad \overline{Y}_{11}^0(\omega) = \{\overline{Z}_{11}^-(\omega)\}^{-1}, \tag{12}$$

where the superscript (0) designates quantities and parameters in reference to an isolated master HO. The energetics in the master HO in isolation is depicted in Fig. 2(a). (The role that a sink plays in the determination of a loss factor is clarified in this figure; a sink is a dynamic system of zero stored energy.[1]) It follows that in the case of an externally driven master HO in isolation

$$\eta_{p1}^0(\omega) = \mathrm{Re}\{\overline{Z}_{11}^-(\omega)\} = \left[\frac{\overline{\pi}_{e1}^0(\omega)}{2\overline{\epsilon}_{k1}^0(\omega)}\right],$$

$$\eta_{b1}^0(\omega) = \left[\frac{\overline{\pi}_{e1}^0(\omega)}{\overline{\epsilon}_1^0(\omega)}\right], \quad \left[\frac{2\overline{\epsilon}_{k1}^0(\omega)}{\overline{\epsilon}_1^0(\omega)}\right] = 2\left[1+\left(\frac{\omega_{11}}{\omega}\right)^2\right]^{-1},$$

$$\overline{\epsilon}_1^0(\omega) = \left(\frac{1}{2}\right)|\overline{V}_1^0(\omega)|^2\left[1+\left(\frac{\omega_{11}}{\omega}\right)^2\right], \tag{13a}$$

$$\eta_{e1}^0(\omega) = \left[\frac{\overline{\pi}_{e1}^0(\omega)}{\overline{\epsilon}_{t1}^0(\omega)}\right], \quad \overline{\epsilon}_{t1}^0 = \overline{\epsilon}_1^0(\omega). \tag{13b}$$

One then finds that at and in the vicinity of the resonance frequency (ω_{11}) of the isolated master HO; the I-, the U-, and the effective loss factors are substantially identical and equal to the inherent loss factor (η_{11}) of the master HO; namely,

$$\eta_{e1}^0(\omega) \simeq \eta_{b1}^0(\omega) \simeq \eta_{p1}^0(\omega) \simeq \eta_{11}, \quad \left(\frac{\omega_{11}}{\omega}\right)^2 \simeq 1, \tag{14}$$

and, again, the superscript (0) designates parameters that pertain to an isolated master HO. Since, in general, only at and in the vicinity of the resonance frequency does a loss factor assume and appropriate significance, a consistency in the four loss factors, as stated in Eq. (14), is established for the case of an isolated master HO.

When the couplings are present, however, $\overline{\epsilon}_{t1}(\omega)$ accounts not only for the normalized stored energy $\overline{\epsilon}_1(\omega)$ in the master HO, but also for the normalized stored energy $\overline{\epsilon}_{s1}(\omega)$ that resides in the couplings and in the satellite HO's. To reflect the multiplicity of the stored energies, the estimate of the normalized stored energy in the complex is formally stated in the form

$$\overline{\epsilon}_{t1}(\omega) = \overline{\epsilon}_1(\omega) + \overline{\epsilon}_{s1}(\omega), \quad \overline{\epsilon}_{t1}(\omega) = |\overline{V}_1(\omega)|^2 \bar{\bar{\epsilon}}_{t1}(\omega),$$

$$\overline{\epsilon}_1(\omega) = |\overline{V}_1(\omega)|^2 \bar{\bar{\epsilon}}_1(\omega), \quad \overline{\epsilon}_{s1}(\omega) = |\overline{V}_1(\omega)|^2 \bar{\bar{\epsilon}}_{s1}(\omega),$$

$$\bar{\bar{\epsilon}}_{s1}(\omega) = \sum_{j=2}^{N} \bar{\bar{\epsilon}}_j(\omega) + \sum_{j=1}^{N}\sum_{n=1}^{N} \bar{\bar{\epsilon}}_{nj}(\omega)(1-\delta_{nj}), \tag{15}$$

where $|\overline{V}_1(\omega)|^2\ \bar{\bar{\epsilon}}_j(\omega)$ is the normalized stored energy in the (j)th HO and $|V_1(\omega)|^2 \bar{\bar{\epsilon}}_{nj}(\omega)\ (1-\delta_{nj})$ is the normalized stored energy residing in the coupling between the (j)th and the (n)th HO's and doubly normalized quantities; e.g., $\bar{\bar{\epsilon}}_j(\omega)$ and $\bar{\bar{\epsilon}}_{nj}(\omega)$, are introduced. A doubly normalized quantity; e.g., $\bar{\bar{\epsilon}}(\omega)$, is related to a corresponding singly normalized quantity; e.g., $\overline{\epsilon}(\omega)$, by the absolute square of the normalized response $|V_1(\omega)|^2$ of the master HO; i.e., $\overline{\epsilon}(\omega) = |\overline{V}_1(\omega)|^2\ \bar{\bar{\epsilon}}(\omega)$. It follows from Eq. (15) that the normalized stored energy $\overline{\epsilon}_{s1}(\omega)$ is that of the complex as a whole excepting the normalized stored energy $\overline{\epsilon}_1(\omega)$ in the master HO. It is convenient to designate the satellite HO's plus the couplings as the *adjunct complex*; the complex as a whole is synthesized of the master HO and this adjunct complex.[9] The normalized stored energy in the adjunct complex is then $\overline{\epsilon}_{s1}(\omega)$. Using Eqs. (3)–(5), the components in Eq. (15) may be more explicitly stated in the form

$$\bar{\bar{\epsilon}}_j(\omega) = \left(\frac{1}{2}\right)|C_{1j}(\omega)|^2\left[\overline{M}_{jj} + \left(\frac{\omega_{jj}}{\omega}\right)^2\right],$$

$$(\omega_{jj})^2 = \left(\frac{K_{jj}^0}{M_{11}}\right), \quad \overline{M}_{jj} = \left(\frac{M_{jj}}{M_{11}}\right), \tag{16a}$$

$$\bar{\bar{\epsilon}}_{nj}(\omega) = \left(\frac{1}{2}\right)|C_{1n}(\omega)|^2\left[\overline{M}_{nj}|1+C_{nj}(\omega)|^2 + \left(\frac{\omega_{nj}}{\omega}\right)^2|1-C_{nj}(\omega)|^2\right], \tag{16b}$$

where

$$\overline{V}_j(\omega) = \overline{Y}_{j1}(\omega), \quad C_{nj}(\omega) = \left[\frac{\overline{Y}_{j1}(\omega)}{\overline{Y}_{n1}(\omega)}\right], \tag{17}$$

and it is noted that the first of Eq. (6) is a specific case of the first of Eq. (17). Referring to Fig. 2(b), in which are sketched the distributions of the normalized input powers and the normalized stored energies between the master HO and the adjunct complex, one finds that

$$[\overline{\pi}_{e1}(\omega) - \overline{\pi}_{s1}(\omega)] = \eta_{b1}^0\overline{\epsilon}_1(\omega), \tag{18a}$$

$$\overline{\pi}_{s1}(\omega) = \eta_{s1}(\omega)\overline{\epsilon}_{s1}(\omega), \tag{18b}$$

where $\overline{\pi}_{s1}(\omega)$ is the normalized (net) input power that is dissipated in the adjunct complex and $\eta_{s1}(\omega)$ is the loss factor associated with this dissipation. This loss factor is dubbed the A-loss factor. The U-loss factor $\eta_{b1}^0(\omega)$ is the loss factor of the master HO in isolation, as stated in Eq. (13) and depicted in Fig. 2(a). Using Eqs. (3)–(5), the expression for the dissipation of the input power $\overline{\pi}_{s1}(\omega)$ may be cast in the form

$$\overline{\pi}_{s1}(\omega)=|\overline{V}_1(\omega)|^2\eta_{s1}(\omega)\bar{\bar{\epsilon}}_{s1}(\omega);$$

$$\eta_{s1}(\omega)\bar{\bar{\epsilon}}_{s1}(\omega)=\sum_{j=1}^{N}|C_{1j}(\omega)|^2\left[\left(\frac{\omega_{jj}}{\omega}\right)^2\eta_{jj}(1-\delta_{1j})+\sum_{n=1}^{N}\left(\frac{\omega_{nj}}{\omega}\right)^2|1-C_{nj}(\omega)|^2\eta_{nj}(1-\delta_{nj})\right]. \tag{19}$$

Employing the definition of the effective loss factor, stated in Eq. (11) and using Eqs. (8), (10), and (15), one further derives

$$\eta_{e1}(\omega)=\left[\frac{\eta_{p1}(\omega)}{\bar{\bar{\epsilon}}_{t1}(\omega)}\right],\quad \eta_{e1}(\omega)=\eta_{b1}(\omega)[1+\zeta(\omega)]^{-1}, \tag{20a}$$

and using Eq. (18), one finally obtains

$$\begin{aligned}&\eta_{p1}(\omega)=\eta_{b1}(\omega)\bar{\bar{\epsilon}}_1(\omega),\\ &\eta_{b1}(\omega)=[\eta^0_{b1}(\omega)+\eta_{s1}(\omega)\zeta(\omega)],\\ &\eta_{e1}(\omega)=[\eta^0_{b1}(\omega)+\eta_{s1}(\omega)\zeta(\omega)][1+\zeta(\omega)]^{-1},\end{aligned} \tag{20b}$$

where

$$\zeta(\omega)=\left[\frac{\bar{\bar{\epsilon}}_{s1}(\omega)}{\bar{\bar{\epsilon}}_1(\omega)}\right]\geqslant 0,\quad \bar{\bar{\epsilon}}_1(\omega)=\left(\frac{1}{2}\right)\left[\frac{1+\omega_{11}}{(\omega)}\right]^2. \tag{21a}$$

Equations (18)–(20) and (21a) are convincing evidence that both the stored energy ratio $\zeta(\omega)$ and the A-loss factor $\eta_{s1}(\omega)$ are proper functionals of the complex; they are completely specified by the parametric specification of the complex. Then, as Eq. (20) clarifies, the propriety of these quantities as well as that of $\eta^0_{b1}(\omega)$ essentially guarantee the propriety of $\eta_{e1}(\omega)$ to be a bonafide loss factor.

Equation (20b) is reminiscent of a expression for the effective loss factor of a structural fuzzy derived via SEA.[9] Therefore, many of the discussions, interpretations, and conclusions presented in Ref. 9 are relevant to Eq. (20b). For example, provided the stored energy ratio $\zeta(\omega)$ can be rendered to substantially exceed unity, Eq. (20b) indicates that the effective loss factor $\eta_{e1}(\omega)$ can be increased or decreased from the value of $\eta^0_{b1}(\omega)$ according to whether $\eta_{s1}(\omega)$ can be rendered to exceed or to recede, respectively, that value of $\eta^0_{b1}(\omega)$. There is, however, no one-to-one correspondence between Eq. (20b) and that expression in Ref. 9. In the former the situation may be singular whereas in the latter the statistical averaging mitigates such a singular situation.

Focusing on Eqs. (14) and (21a), it is noted that the equality sign in Eq. (21a) occurs only when the master HO is rendered onto isolation. Equations (20a) and (21a) lead, in turn, to the inequality

$$\eta_{e1}(\omega)\leqslant\eta_{b1}(\omega),\quad \eta_{b1}(\omega)\simeq\eta_{p1}(\omega),\quad \left(\frac{\omega_{11}}{\omega}\right)^2\simeq 1. \tag{21b}$$

Equations (20) and (21) state that, in the presence of couplings among the master HO and the satellite HO's, the I-loss factor $\eta_{p1}(\omega)$, and the U-loss factor $\eta_{b1}(\omega)$ tend to exaggerate the effective loss factor $\eta_{e1}(\omega)$ of the master HO in the complex, at least, in the vicinity of the resonance frequency (ω_1) of the master HO. Moreover, the exaggeration is most severe when most of the stored energy in the complex resides in the adjunct complex—in the couplings and in the satellite HO's—so that the stored energy ratio $\zeta(\omega)$, stated in Eq. (21a), substantially exceeds unity. This statement is not surprising. Comparing Eq. (8) with Eq. (15) indicates that in the definition of $\eta_{p1}(\omega)$ only the normalized stored kinetic energy in the master HO is accounted for among the stored energies in the complex. Doubling the stored kinetic energy in the definition of $\eta_{p1}(\omega)$, in an effort to account for the stored potential energy in the master HO, does not alleviate this accounting deficiency. Accounting only for the stored energy in the master HO is unsatisfactory in a complex in which the couplings drive satellite HO's, notwithstanding that the master HO alone is externally driven. The exception occurs only when the master HO is in isolation. It emerges, therefore, that with this exception acknowledged in Eq. (21), the use of the I-loss factor $\eta_{p1}(\omega)$ as a bonafide loss factor may often raise the question: Where did the energy go? This issue becomes particularly relevant in those situations for which the stored energy ratio $\zeta(\omega)$ $[=\bar{\bar{\epsilon}}_{s1}(\omega)/\bar{\bar{\epsilon}}_1(\omega)]$ is large compared with unity. It is explained herein that the energy did not go anywhere, it is merely and mistakenly discounted. In this sense and although they appear related, the I-loss factor $\eta_{p1}(\omega)$ and the effective loss factor $\eta_{e1}(\omega)$ are not, in general, consistent; the latter loss factor being the real one. Nonetheless, a number of publications, dealing with structural fuzzies, employ the I-loss factor for real.[10–13]

To further analyze the relationship and the contrast between the I-I and the effective loss factors, and to bring into view a number of computational illustrations, a more explicit definition of the quantities and parameters that describe the complex is required. Naturally, the illustrations are selected to emphasize the disparity between the I-loss factor $\eta_{p1}(\omega)$ and the effective loss factor $\eta_{e1}(\omega)$; i.e., the computational experiments are performed on complexes in which the stored energy ratio $\zeta(\omega)$ exceeds unity over an exposed range in the frequency domain. To render the experiments simple to perform and data simple to interpret it may also be useful to sacrifice a little in generality to gain much simplicity in the analytical descriptions and their manipulations. For this purpose subsequent consideration is focused on a complex in which the satellite HO's are not coupled to each other. In this complex, couplings, if any, are only between the master HO and the individual satellite HO's.

III. A COMPLEX IN WHICH THE SATELLITE HARMONIC OSCILLATORS ARE UNCOUPLED TO EACH OTHER

For this complex certain elements in the impedance matrix are equal to zero. Indeed, these zero elements, as well as those that survive, can be identified by multiplying all elements by the factor $[\delta_{jn}+(\delta_{j1}+\delta_{n1})(1-\delta_{jn})]$; e.g., in Eq. (4) a replacement needs to be implemented in the form

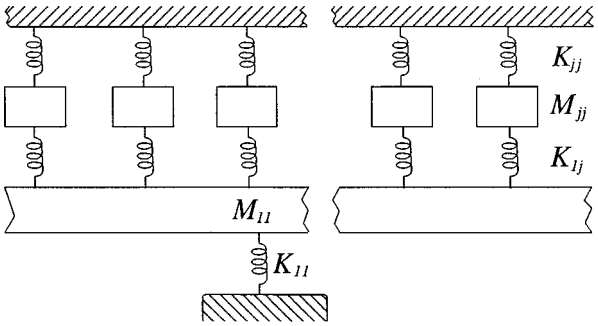

FIG. 3. A complex in which the satellite harmonic oscillators are uncoupled to each other and the couplings are restricted to stiffness controlled elements only.

$$\left.\begin{matrix}\bar{Z}_{jn}^{-}(\omega)\\ \bar{Z}_{jn}^{+}(\omega)\\ \bar{Z}_{jn}(\omega)\end{matrix}\right\}\rightarrow\left\{\begin{matrix}\bar{Z}_{jn}^{-}(\omega)\\ \bar{Z}_{jn}^{+}(\omega)\\ \bar{Z}_{jn}(\omega)\end{matrix}\right\}[(\delta_{jn}+(\delta_{j1}+\delta_{1n})(1-\delta_{jn})]. \tag{22}$$

This reduced complex is sketched in Fig. 3 (cf. Fig. 1). Substituting Eq. (22) in Eq. (1b) and then deriving Eq. (5), one finds a highly simplified form for the insitu normalized admittance $\bar{Y}_{11}(\omega)$ for the master HO

$$\bar{Y}_{11}(\omega)=\left[\bar{Z}_{11}(\omega)+\sum_{j=2}\bar{Z}_{1j}(\omega)C_{1j}(\omega)\right]^{-1}, \tag{23}$$

where

$$C_{1j}(\omega)=\left[\frac{\bar{Y}_{j1}(\omega)}{\bar{Y}_{11}(\omega)}\right]=-\left[\frac{\bar{Z}_{j1}(\omega)}{\bar{Z}_{jj}(\omega)}\right]. \tag{24}$$

Again, clarity can be gained, without too much loss in generality, by suppressing the mass and gyroscopic coupling parameters. Accordingly, the parameters $\bar{M}_{jn}(1-\delta_{jn})$ and $\bar{G}_{jn}(\omega)(1-\delta_{jn})$ are set equal to zero in Eq. (4). With this suppression

$$\bar{Z}_{jn}(\omega)=\bar{Z}_{jn}^{+}(\omega)=-\bar{Z}_{jn}^{-}(\omega),\quad \bar{Z}_{jn}(\omega)=\bar{Z}_{nj}(\omega),$$
$$j\neq n. \tag{25}$$

Substituting Eq. (25) in Eq. (23) and rearranging terms and factors, one derives

$$\bar{Z}_{1}(\omega)=[\bar{Z}_{11}^{-}(\omega)+\bar{Z}_{c1}(\omega)],\quad \bar{Z}_{1}(\omega)=[\bar{Y}_{11}(\omega)]^{-1},$$
$$\bar{Z}_{c1}(\omega)=\sum_{j=2}^{N}\bar{Z}_{cj}(\omega), \tag{26}$$
$$\bar{Z}_{cj}(\omega)=\bar{Z}_{jj}^{-}(\omega)\bar{Z}_{1j}^{-}(\omega)[\bar{Z}_{jj}^{-}(\omega)+\bar{Z}_{1j}^{-}(\omega)]^{-1},$$

where $\bar{Z}_{cj}(\omega)$ is the normalized impedance contributed to the master HO by the coupled (j)th satellite HO and its coupling to that master HO. It is remarkable that $\bar{Z}_{cj}$ is constructed of merely the parallel combination of the normalized impedance $\bar{Z}_{jj}^{-}(\omega)$ of the (j)th satellite HO in isolation with its normalized coupling impedance $\bar{Z}_{1j}^{-}(\omega)$ to the master HO. Also remarkable is that the first term in the normalized impedance $\bar{Z}_{1}(\omega)$ is the normalized impedance $\bar{Z}_{11}^{-}(\omega)$ of the master HO in isolation. The thorough investigation of this structure of $\bar{Z}_{1}(\omega)$ is deferred; in this paper the concern is with investigating the loss factors that this normalized impedance and some of its terms may be the defining elements. Substituting Eqs. (23)–(26) in Eqs. (7), (10), and (15)–(19) one obtains after nimble algebraic manipulations

$$\eta_{p1}(\omega)=[\eta_{p1}^{0}(\omega)+\eta_{c1}(\omega)],\quad \eta_{c1}(\omega)=\sum_{j=2}\eta_{pj}(\omega),$$
$$\eta_{pj}(\omega)=[|\bar{Z}_{jj}^{-}(\omega)|^{2}\ \mathrm{Re}\{\bar{Z}_{1j}^{-}(\omega)\}+|\bar{Z}_{1j}^{-}(\omega)|^{2}\ \mathrm{Re}\{\bar{Z}_{jj}^{-}(\omega)\}][|\bar{Z}_{jj}(\omega)|^{2}]^{-1}, \tag{27}$$
$$\eta_{pj}(\omega)=\left[|\bar{Z}_{1j}^{-}(\omega)|^{2}\left(\frac{\omega_{jj}}{\omega}\right)^{2}\eta_{jj}+|\bar{Z}_{jj}^{-}(\omega)|^{2}\left(\frac{\omega_{1j}}{\omega}\right)^{2}\eta_{1j}\right]\times[|\bar{Z}_{jj}(\omega)|^{2}]^{-1}, \tag{28a}$$

$$\eta_{b1}(\omega)=[\eta_{b1}^{0}(\omega)+\eta_{d1}(\omega)],\quad \eta_{d1}(\omega)=\sum_{j=2}\eta_{bj}(\omega),$$
$$\eta_{bj}(\omega)=\left[\frac{\eta_{pj}(\omega)}{\bar{\bar{\epsilon}}_{1}(\omega)}\right],\quad \bar{\bar{\epsilon}}_{1}(\omega)=\left(\frac{1}{2}\right)\left[\frac{1+\omega_{11}}{\omega}\right]^{2}, \tag{28b}$$
$$\eta_{e1}(\omega)=\left[\frac{\eta_{p1}(\omega)}{\bar{\bar{\epsilon}}_{t1}(\omega)}\right],\quad \bar{\bar{\epsilon}}_{t1}(\omega)=\bar{\bar{\epsilon}}_{1}(\omega)+\bar{\bar{\epsilon}}_{s1}(\omega),$$
$$\bar{\bar{\epsilon}}_{s1}(\omega)=\sum_{j=2}\bar{\bar{\epsilon}}_{sj}(\omega),\quad \bar{\bar{\epsilon}}_{sj}(\omega)=[\bar{\bar{\epsilon}}_{j}(\omega)+\bar{\bar{\epsilon}}_{1j}(\omega)], \tag{28c}$$

$$\eta_{s1}(\omega)=\sum_{j=2}\eta_{sj}(\omega),\quad \eta_{sj}(\omega)=\left[\frac{\eta_{pj}(\omega)}{\bar{\bar{\epsilon}}_{s1}(\omega)}\right], \tag{28d}$$

where

$$\bar{\bar{\epsilon}}_{j}(\omega)=\left(\frac{1}{2}\right)\left|\frac{\bar{Z}_{1j}^{-}(\omega)}{\bar{Z}_{jj}(\omega)}\right|^{2}\left[\bar{M}_{jj}+\left(\frac{\omega_{jj}}{\omega}\right)^{2}\right],$$
$$\bar{\bar{\epsilon}}_{1j}(\omega)=\left(\frac{1}{2}\right)\left|\frac{\bar{Z}_{jj}^{-}(\omega)}{\bar{Z}_{jj}(\omega)}\right|^{2}\left(\frac{\omega_{1j}}{\omega}\right)^{2}, \tag{29a}$$
$$\bar{\bar{\epsilon}}_{sj}(\omega)=\left(\frac{1}{2}\right)\left\{|\bar{Z}_{1j}^{-}(\omega)|^{2}\left[\bar{M}_{jj}+\left(\frac{\omega_{jj}}{\omega}\right)^{2}\right]+|\bar{Z}_{jj}^{-}(\omega)|^{2}\left(\frac{\omega_{1j}}{\omega}\right)^{2}\right\}[|\bar{Z}_{jj}(\omega)|^{2}]^{-1},\quad j\geqslant 2,$$

$$\zeta(\omega)=\sum_{j=2}^{N}\zeta_{j}(\omega),\quad \zeta_{j}(\omega)=\left[\frac{\bar{\bar{\epsilon}}_{sj}(\omega)}{\bar{\bar{\epsilon}}_{1}(\omega)}\right]. \tag{29b}$$

Equations (28a) and (28b) state that the contributions of the master HO to its own I-loss factor and the U-loss factor are, as expected, $\eta_{p1}^{0}(\omega)$ and $\eta_{b1}^{0}(\omega)$, respectively. The terms $\eta_{pj}(\omega)$ and $\eta_{bj}(\omega)$ are the contributions to the I-loss factor and to the U-loss factor, respectively, of the coupled (j)th satellite HO and its coupling to the master HO. Since both $\eta_{pj}(\omega)$ and $\eta_{bj}(\omega)$ are positive definite, the attachment of each satellite HO to the master HO always increases the I-loss factor $\eta_{p1}(\omega)$ and the U-loss factor $\eta_{b1}(\omega)$, initially from their thresholds at $\eta_{p1}^{0}(\omega)$ and $\eta_{b1}^{0}(\omega)$, respectively. Investigating, Eqs. (28) and (29) in particular, one recognizes immediately that provided the inherent loss factors (η_{jj}) and

(η_{1j}) are reasonably small compared with unity, the contributions $\eta_{pj}(\omega)$, $\eta_{bj}(\omega)$, and $\bar{\bar{\epsilon}}_{sj}(\omega)$ or equivalently $\zeta_j(\omega)$ to the I-loss factor to $\eta_{p1}(\omega)$, to the U-loss factor $\eta_{b1}(\omega)$, and to the doubly normalized stored energy $\bar{\bar{\epsilon}}_{s1}(\omega)$ or equivalently the stored energy ratio $\zeta(\omega)$, respectively, by the attached (j)th satellite HO is significant in a frequency band that is $(\omega_{0j}\eta_{0j})$ wide and is centered about the *resonance frequency* (ω_{0j}). The resonance frequency (ω_{0j}) and the *resonance frequency span* $(\omega_{0j}\eta_{0j})$ of the (j)th HO are defined by the *in situ* normalized impedance $Z_{jj}(\omega)$. This normalized impedance is that of the (j)th satellite HO with the master HO blocked. In contrast to the normalized impedance $\bar{Z}_{cj}(\omega)$, stated in Eq. (26), the normalized impedance $\bar{Z}_{jj}(\omega)$ is constructed of merely the series combination of the normalized impedance $\bar{Z}_{jj}(\omega)$ of the satellite HO in isolation with its normalized coupling impedance $\bar{Z}_{1j}(\omega)$ to the master HO, notwithstanding that $\bar{Z}_{jj}(\omega)$ is an inverse factor in $\bar{Z}_{cj}(\omega)$. At and in the vicinity of the resonance in this (j)th HO, the following relationship needs to be satisfied:

$$\mathrm{Im}\{Z_{jj}(\omega)\}\simeq 0 \quad \text{and} \quad \mathrm{Re}\{Z_{jj}(\omega)\}\ll 1, \quad j\geqslant 2. \tag{30}$$

Equation (30), as Eqs. (4) and (25) attest, defines in turn the resonance frequency (ω_{0j}) and the associated loss factor (η_{0j}) in the form

$$(\bar{M}_{jj}\eta_{0j})=\left[\left(\frac{\omega_{jj}}{\omega_{0j}}\right)^2\eta_{jj}+\left(\frac{\omega_{1j}}{\omega_{0j}}\right)^2\eta_{1j}\right],$$

$$\bar{M}_{jj}=\left(\frac{M_{jj}}{M_{11}}\right), \quad \omega_{jj}^2=\left(\frac{K_{jj}^0}{M_{11}}\right), \quad \omega_{1j}=\left(\frac{K_{1j}^0}{M_{11}}\right), \tag{31a}$$

$$\bar{M}_{jj}\simeq\left[\left(\frac{\omega_{jj}}{\omega_{0j}}\right)^2+\left(\frac{\omega_{1j}}{\omega_{0j}}\right)^2\right]. \tag{31b}$$

A point of interest emerges in Eqs. (28) and (29). The singularity at the resonance in the factor $|\bar{Z}_{jj}(\omega)|^{-2}$, as defined in Eq. (30), is common to $\eta_{pj}(\omega)$, $\eta_{bj}(\omega)$, and $\bar{\bar{\epsilon}}_{sj}(\omega)$ [or $\zeta_j(\omega)$]. This commonality ensures that this singularity is mitigated in the effective loss factor $\eta_{e1}(\omega)$ as well as in the A-loss factor $\eta_{s1}(\omega)$. This is born by the computational experiments that follow.

IV. COMPUTATIONAL ILLUSTRATIONS

A few computational experiments are conducted mostly to illustrate the commonality and disparity between the two loss factors $\eta_{p1}(\omega)$ and $\eta_{e1}(\omega)$. Also illustrated are the A-loss factor $\eta_{s1}(\omega)$ and the stored energy ratio $\zeta(\omega)$ which, as Eq. (20) states, are involved in the relationships between these loss factors. It is convenient to define a standard master HO, a standard satellite HO, and a standard coupling. Then only deviations in the HO's and the couplings, from these standards, need be indicated. The standard master HO is specified by

$$\bar{M}_{11}=1, \quad \left(\frac{\omega_{11}}{\omega_1}\right)^2=1, \quad \eta_{11}=10^{-3}, \tag{32a}$$

the standard satellite HO is specified by

$$\bar{M}_{jj}=\left[\frac{0.1}{(N-1)}\right], \quad \left(\frac{\omega_{jj}}{\omega_{11}}\right)^2=\left[\frac{0.2}{3(N-1)}\right], \quad \eta_{jj}=10^{-3}, \tag{32b}$$

and the standard coupling between the master HO and a satellite HO is specified by

$$\left(\frac{\omega_{1j}}{\omega_{11}}\right)^2=\left[\frac{0.1}{3(N-1)}\right], \quad \eta_{1j}=10^{-3}, \tag{32c}$$

where N is the number of HO's in the complex. The total mass of the satellite HO's, as Eq. (32b) states, is one-tenth of the mass of the master HO. For a complex composed of standard elements, Eqs. (30) and (31) show that

$$\left(\frac{\omega_{0j}}{\omega_{11}}\right)^2=1, \quad \eta_{0j}=10^{-3}, \tag{33}$$

and, thus, a standard cell hosts $(N-1)$ satellite HO's all possessing the same resonance frequencies. The data of an analytical experiment are exhibited in a figure that contains four graphs. Exhibited are the I-loss factor $\eta_{p1}(\omega)$, the stored energy ratio $\zeta(\omega)$, the effective loss factor $\eta_{e1}(\omega)$, and the A-loss factor $\eta_{s1}(\omega)$, respectively, as functions of the normalized frequency (ω/ω_{11}) which extends from 0.5 to 2.0. These quantities for the standard complex with $N=2$ are depicted by the light curves in Fig. 4. The unreasonable high value for a loss factor that $\eta_{p1}(\omega)$ assumes, at and in the vicinity of the resonance frequency (ω_{0j}), is clearly demonstrated in Fig. 4(a). The stored energy ratio $\zeta(\omega)$ also assumes a high value in the same frequency band indicating that in this band the stored energy in the standard adjunct complex substantially exceeds that stored in the master HO; see the light curve in Fig. 4(b). The high values of these two quantities conspire to mitigate the value that is assumed by the effective loss factor $\eta_{e1}(\omega)$. As the light curve in Fig. 4(c) shows, the effective loss factor $\eta_{e1}(\omega)$ assumes, at and in the vicinity of the resonance frequency (ω_{0j}), a value that is more commensurate with those of the inherent loss factors. Finally, the light curve in Fig. 4(d) exhibits the value of the A-loss factor $\eta_{s1}(\omega)$.

Variations on the theme are depicted in Fig. 4 by the darker and the darkest curves; these variations are specified by changing the inherent loss factor (η_{jj}) of the standard satellite HO from the standard value of 10^{-3} to 10^{-2} and onto 10^{-1}, respectively. At and in the vicinity of the resonance frequency (ω_{0j}), whereas the I-loss factor $\eta_{p1}(\omega)$ appropriately decreases, the effective loss factor $\eta_{e1}(\omega)$ increases with each successive change, as predicted by Eq. (20). Thus as the inherent loss factor (η_{jj}) of the satellite HO increases, the I-loss factor $\eta_{p1}(\omega)$ and the effective loss factor $\eta_{e1}(\omega)$ tend to converge toward a common value. In Fig. 5, the inherent loss factor (η_{11}) of the master HO is changed from the standard value of 10^{-3} to 10^{-2}. A ''dip'' in the effective loss factor is discernible in Fig. 5. At and in the vicinity of the resonance frequency (ω_{0j}) the effective loss factor $\eta_{e1}(\omega)$ decreases with this change, again, as predicted by Eq. (20). At the dip, it is noted that the portion of energy stored in the adjunct complex substantially exceeds that stored in the master HO and the adjunct complex pos-

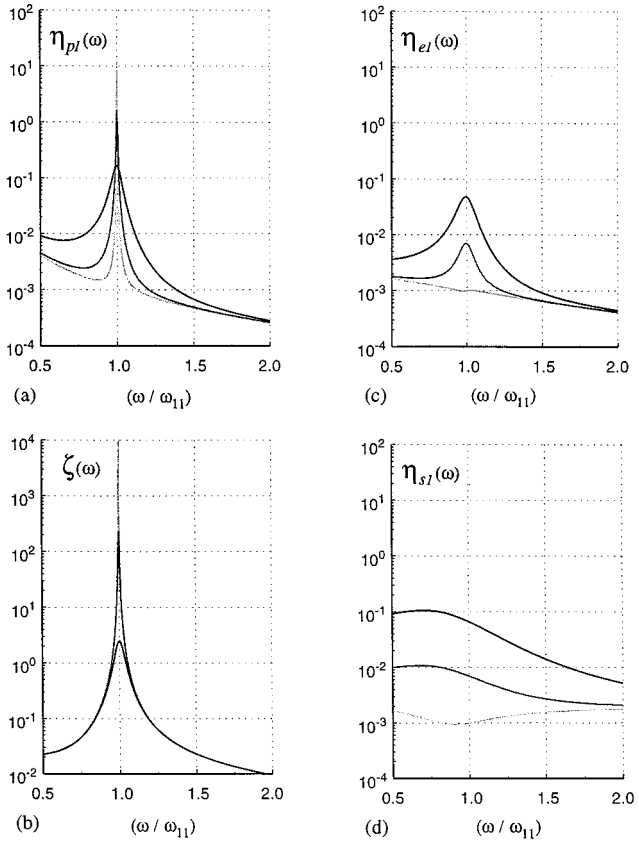

FIG. 4. The I-loss factor $\eta_{p1}(\omega)$, the stored energy ratio $\zeta(\omega)$, the effective loss factor $\eta_{e1}(\omega)$, and the A-loss factor $\eta_{s1}(\omega)$ as functions of the normalized frequency (ω/ω_{11}). The light curves are for a standard complex [specified in Eqs. (32)], the dark curves are for $\eta_{jj}=10^{-2}$ and the darkest curves are for $\eta_{jj}=10^{-1}$. (a) $\eta_{p1}(\omega)$, (b) $\zeta(\omega)$, (c) $\eta_{e1}(\omega)$, (d) $\eta_{s1}(\omega)$.

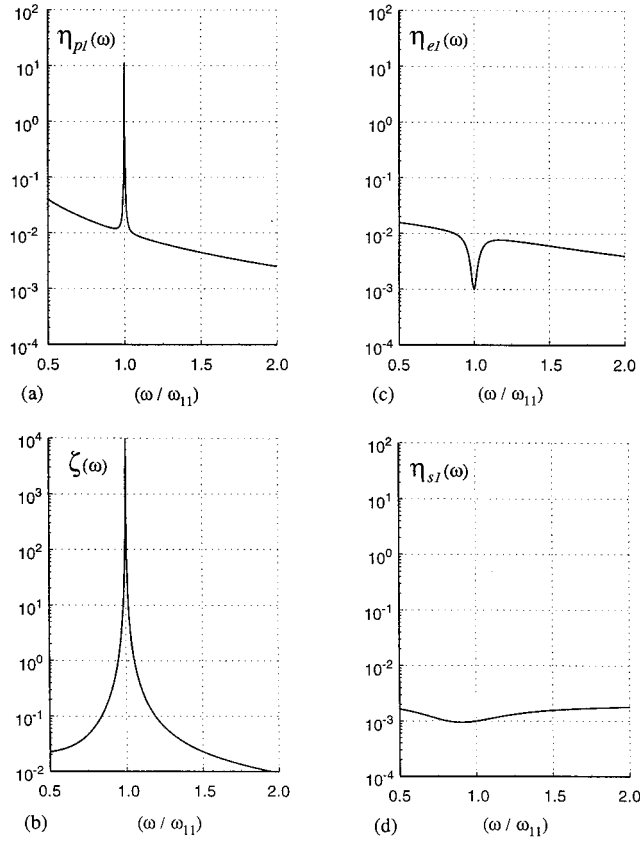

FIG. 5. As the light curves in Fig. 4, except that $\eta_{11}=10^{-2}$.

sesses a loss factor, the A-loss factor $\eta_{s1}(\omega)$, that is less than the U-loss factor $\eta^0_{b1}(\omega)$ of the master HO in isolation.[9,13]

The complex used in Figs. 4 and 5 is augmented by coupling to it eight more satellite HO's. The augmented standard complex, specified in Eq. (32), yield, in a computational experiment, data that are commensurate with the data depicted in Figs. 4 and 5. An A1-complex is defined in terms of a standard master HO, as specified in Eq. (32a), and an adjunct complex. This adjunct complex, in turn, is composed of a set of standard satellite HO's specified by

$$\overline{M}_{jj}=\left(\frac{0.1}{9}\right), \quad \left(\frac{\omega_{jj}}{\omega_{11}}\right)^2=\left(\frac{0.2}{3a_j}\right),$$

$$\eta_{jj}=10^{-3}, \quad a_j=9, \tag{34a}$$

and a set of couplings specified by

$$\left(\frac{\omega_{1j}}{\omega_{11}}\right)^2=\left(\frac{0.1}{3b_j}\right), \quad \eta_{1j}=10^{-3},$$

$$\{b_j\}=\{7.4,7.8,8.2,8.6,9.0,9.4,9.8,10.2,10.6\}. \tag{34b}$$

The quantities $\eta_{p1}(\omega)$, $\zeta(\omega)$, $\eta_{e1}(\omega)$, and $\eta_{s1}(\omega)$ for the A1-complex, in the format of the light curves in Fig. 4(a)–(d), are depicted by the light curves in Fig. 6(a)–(d), respectively. The individual contribution of each satellite HO is discernible in this figure since the loss factor η_{0j}, as defined in Eq. (31), lies below the *modal overlap* mark.[1] The distinctions among the satellite HO's arise from the differences in the couplings; the satellite HO's in the A1-complex are all standard. The high values, at and in the vicinity of the resonance frequencies (ω_{0j}), of the I-loss factor $\eta_{p1}(\omega)$ coincide with the high values of the stored energy ratio $\zeta(\omega)$ thereby mitigating the values of the effective loss factor $\eta_{e1}(\omega)$. The values of the effective loss factor are rendered commensurate with those of the inherent loss factors in the constituents of the complex.

Variations on the theme are specified by changes in the inherent loss factor (η_{jj}) of the standard satellite HO's. The changes are from the standard value of 10^{-3} to 10^{-2} and onto 10^{-1}, respectively. The data pertaining to these variations are depicted in Fig. 6 by the darker and the darkest curves, respectively. The effective loss factor $\eta_{e1}(\omega)$, at and in the vicinity of the resonance frequencies (ω_{0j}), increases with each successive change, as predicted by Eq. (20). The on-set of modal overlap in Fig. 6 is apparent in the darker curves and the strong modal overlap in Fig. 6 is obvious in the darkest curves. [It is noted, in passing, that Fig. 6 represents data for which the inherent loss factors pairs $\{\eta_{jj},\eta_{1j}\}$ are $\{10^{-3},10^{-3}\}$, $\{10^{-2},10^{-3}\}$, and $\{10^{-1},10^{-3}\}$. Figure 6 is substantially replicated if the values of the inherent loss factors pairs $\{\eta_{jj},\eta_{1j}\}$ are cast as $\{5\times10^{-4},2\times10^{-3}\}$, $\{5\times10^{-4},2\times10^{-2}\}$, and $\{5\times10^{-4},2\times10^{-1}\}$, respectively.] In Fig. 7 the inherent loss factor (η_{11}) of the master HO is changed from the standard value of 10^{-3} to 10^{-2}. The dip in the effective loss factor previously discussed with respect to

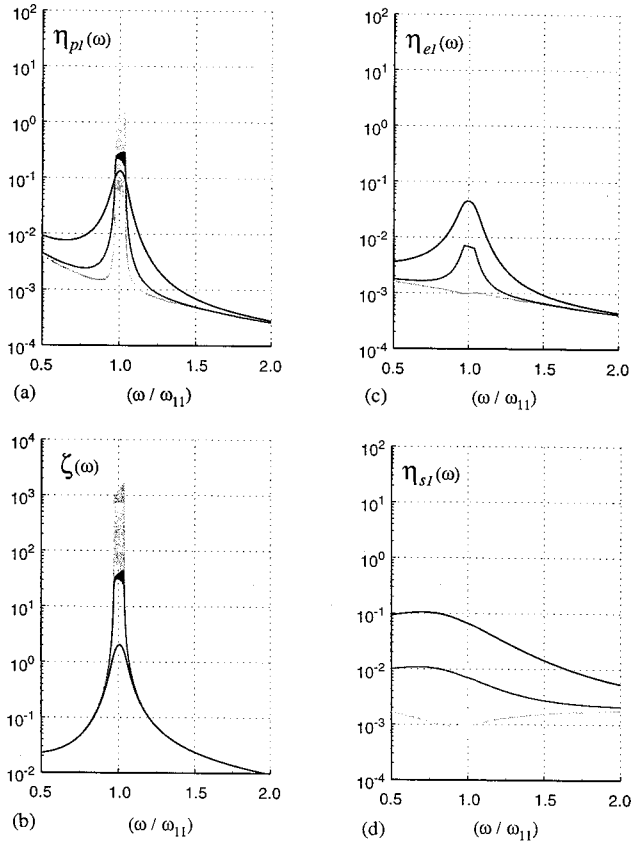

FIG. 6. The format of Fig. 4 is repeated for an A1-complex, as specified in Eqs. (32a) and (34). The dark curves are for $\eta_{jj}=10^{-2}$ and the darkest are for $\eta_{jj}=10^{-1}$.

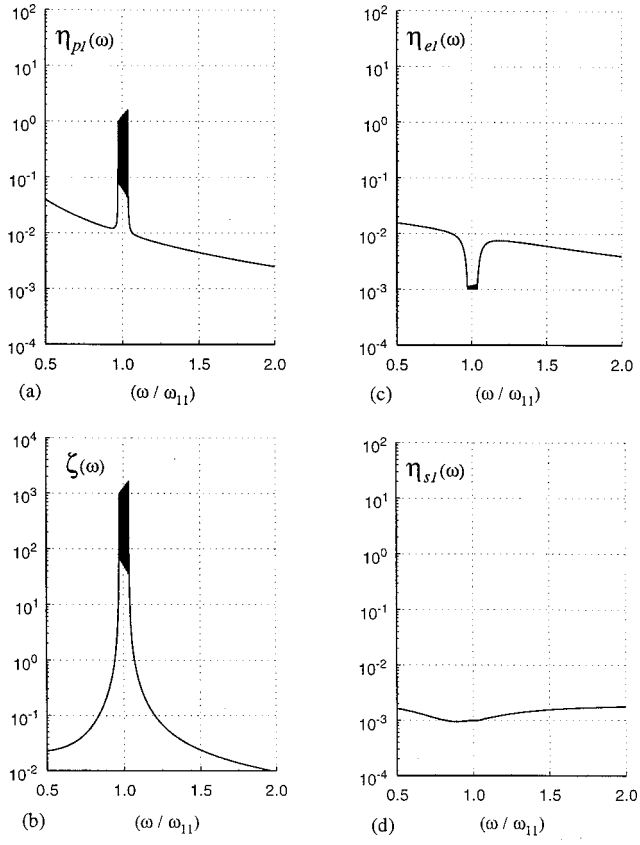

FIG. 7. As the light curves in Fig. 6, except that $\eta_{11}=10^{-2}$.

Fig. 5, is apparent in Fig. 7. Again, the reason for that ''loss of a loss factor'' is that the larger portion of stored energy resides, at and in the vicinity of the resonance frequencies (ω_{0j}), in the adjunct complex and not in the master HO. This larger portion of stored energy is, by specification, subjected to a loss factor that is smaller than the inherent loss factor of the master HO[9,13] [cf. Eq. (20)].

A companion complex to the A1-complex is defined in terms of a standard master HO, as specified in Eq. (32a), and an adjunct complex composed of a set of satellite HO's specified by

$$\overline{M}_{jj}=\left(\frac{0.1}{9}\right), \quad \left(\frac{\omega_{jj}}{\omega_{11}}\right)^2=\left(\frac{0.2}{3a_j}\right), \quad \eta_{jj}=10^{-3},$$

$$\{a_j\}=\{7.4,7.8,8.2,8.6,9.0,9.4,9.8,10.2,10.6\}, \tag{35a}$$

and a set of standard couplings specified by

$$\left(\frac{\omega_{1j}}{\omega_{11}}\right)^2=\left(\frac{0.1}{3b_j}\right), \quad \eta_{1j}=10^{-3}, \quad b_j=9. \tag{35b}$$

The companion complex is designated the A2-complex. The quantities $\eta_{p1}(\omega)$, $\zeta(\omega)$, $\eta_{e1}(\omega)$, and $\eta_{s1}(\omega)$ for the A2-complex, in the format of Fig. 4(a)–(d), are depicted in Fig. 8(a)–(d), respectively. The *modal density* $n_2(\omega)$ in the cell hosting the nine satellite HO's in the A2-complex, is approximately half the modal density $n_1(\omega)$ in the cell hosting the nine satellite HO's in the A1-complex; $n_1(\omega)\approx 2n_2(\omega)$.[1] Therefore, the individual contributions to the I-loss factor $\eta_{p1}(\omega)$ and to the stored energy ratio $\zeta(\omega)$ by a satellite HO is more readily deciphered in Fig. 8 than in Fig. 6. As expected then, in Fig. 8 the on-set and the strong modal overlaps are mollified compared with the corresponding features in Fig. 6, respectively. Taking such differences into consideration, the dip in the effective loss factor, observed in Figs. 5 and 7, is found also in Fig. 9 and for the same reasons.

Next, Figs. 10 and 11 are included to show the influence that increasing the spacings between the resonance frequencies and the normalized masses of the satellite HO's, respectively, have, separately, on the quantities depicted in Fig. 8. The first influence is implemented by changing, in Eq. (35a), the vector $\{a_j\}$ into

$$\{a_j\}=\{5.8,6.6,7.4,8.2,9.0,9.8,10.6,11.4,12.2\}. \tag{36a}$$

The second is implemented by changing, in Eq. (35a), the normalized mass $\overline{M}_{jj}$, and the normalized frequency $(\omega_{jj}/\omega_{11})$ into

$$\overline{M}_{jj}=\left(\frac{0.2}{9}\right), \quad \left(\frac{\omega_{jj}}{\omega_{11}}\right)^2=(0.4/3a_j), \tag{36b}$$

as well as changing, in Eq. (35b), the normalized frequency $(\omega_{1j}/\omega_{11})$ into

$$\left(\frac{\omega_{1j}}{\omega_{11}}\right)^2=\left(\frac{0.2}{3b_j}\right). \tag{36c}$$

In each of these changes, all other specifications in the A2-complex remain intact. The differences in Figs. 10 and 11 from Fig. 8 are within expectation and can, therefore, be readily accounted for.

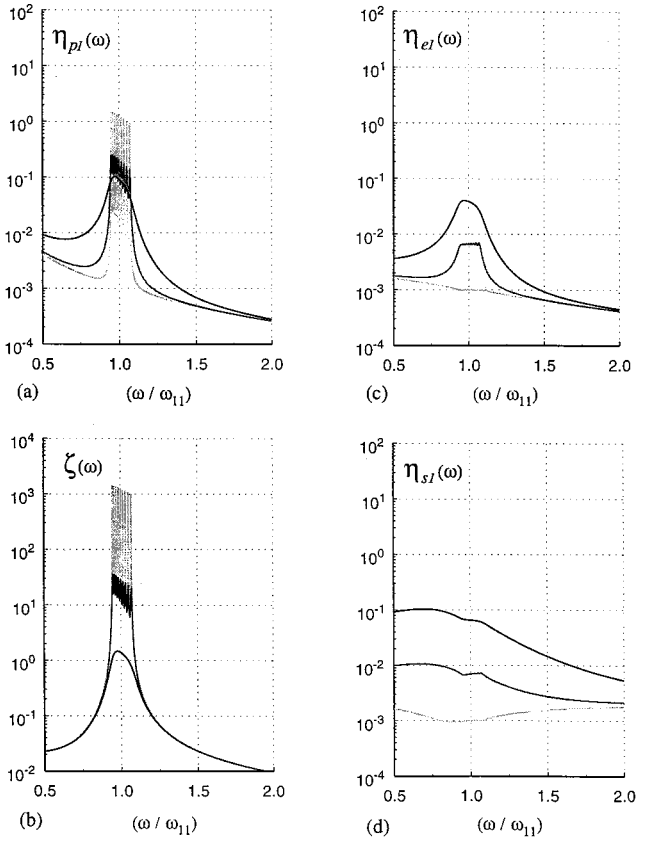

FIG. 8. The format of Fig. 4 is repeated for an A2-complex, as specified in Eqs. (32a) and (35). The dark curves are for $\eta_{jj}=10^{-2}$ and the darkest are for $\eta_{jj}=10^{-1}$.

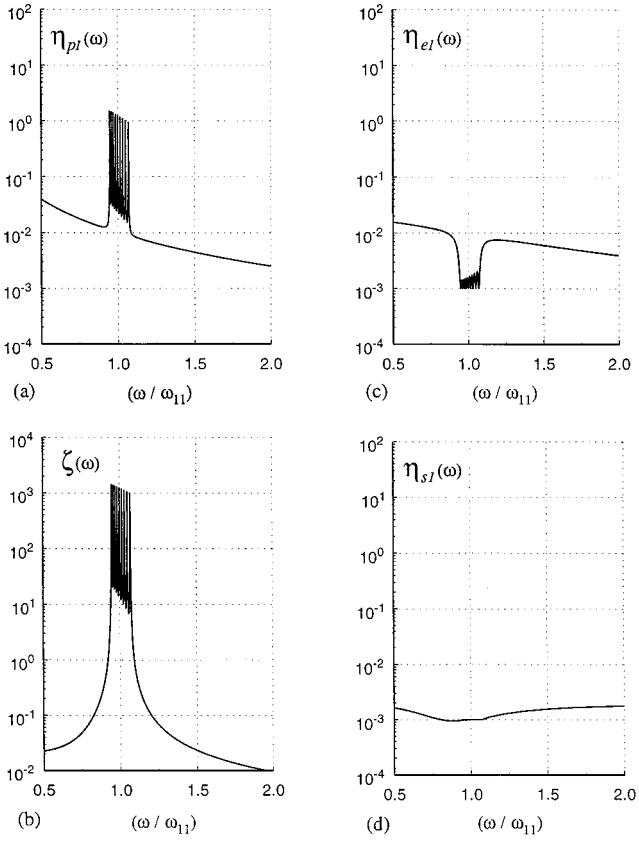

FIG. 9. As the light curves in Fig. 8, except that $\eta_{11}=10^{-2}$.

Finally, situations in which the master HO and the satellite HO's are merely masses are computationally experimented upon; the coupling between the master HO and an individual satellite HO renders the satellite HO a sprung mass.[11,13] In the specification for a complex that carries these situations, the K^0_{jj}'s are zero but not the K^0_{1j}'s. The complex, designated the A3-complex, is then specified by a master HO

$$\overline{M}_{11}=1, \tag{37a}$$

by a set of $(N-1)$ satellite HO's

$$\overline{M}_{jj}=\left[\frac{0.1}{(N-1)}\right], \tag{37b}$$

and by a set of $(N-1)$ couplings

$$\left(\frac{\omega_{1j}}{\omega_{11}}\right)^2=\left(\frac{0.1}{N_{1j}}\right), \quad \eta_{1j}=10^{-3};$$

$$N_{1j}=(N-1)+[j-(N+2)/2]\Delta, \tag{37c}$$

where Δ is a numerical increment [cf. Eqs. (34)–(36)]. The quantities $\eta_{p1}(\omega)$, $\zeta(\omega)$, and $\eta_{e1}(\omega)$ for the A3-complex with $N=10$ and Δ of 0.8, in the format of Fig. 4(a)–(c), are depicted in Fig. 12(a)–(c), respectively. The conspiracy between the I-loss factor $\eta_{p1}(\omega)$ and the stored energy ratio $\zeta(\omega)$ to yield reasonable values for the effective loss factor $\eta_{e1}(\omega)$ once again emerges in Fig. 12. In Fig. 13(a) and (b) the I-loss factor $\eta_{p1}(\omega)$ and the effective loss factor $\eta_{e1}(\omega)$,

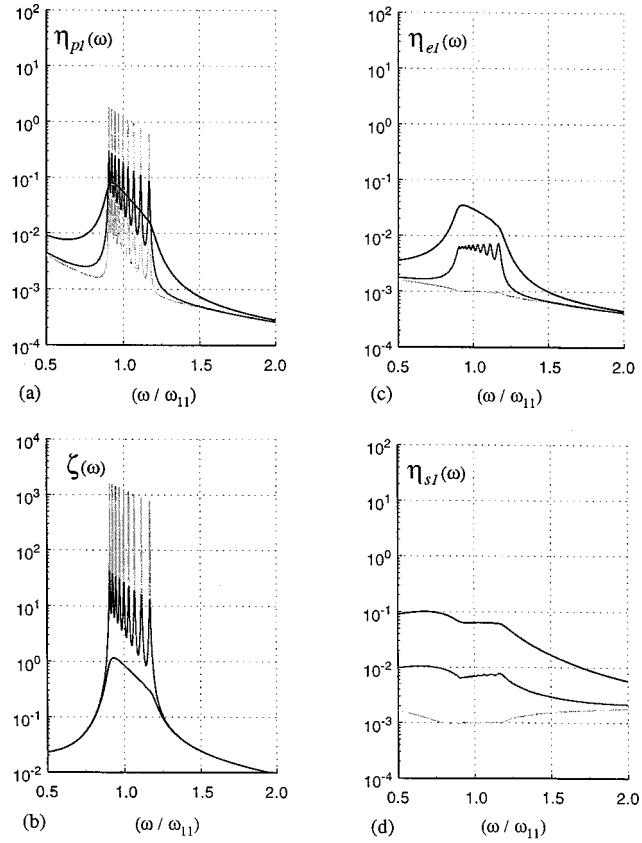

FIG. 10. Repeats Fig. 8, except that Eq. (36a) supersedes Eq. (35a).

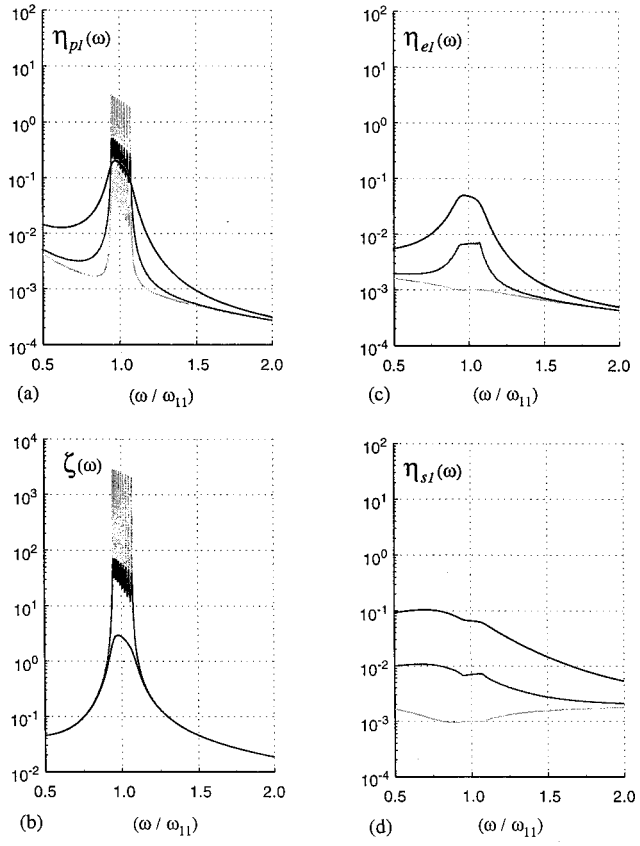

FIG. 11. Repeats Fig. 8, except that Eqs. (36b) and (36c) supersede Eqs. (35a) and (35b), respectively.

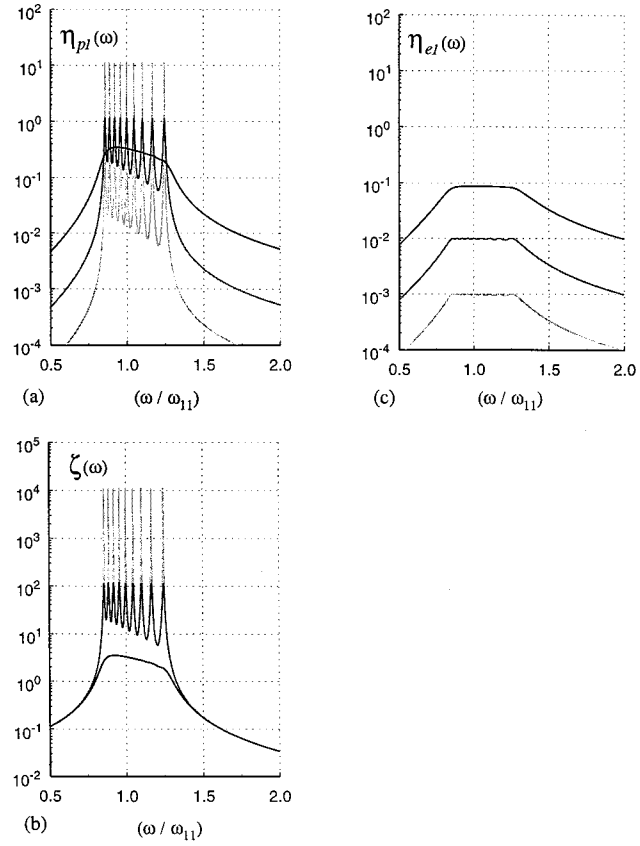

FIG. 12. The format of Fig. 4(a)–(c) are repeated for an A3-complex, as specified in Eq. (37), with $N=10$ and Δ of 0.8.

respectively, are depicted for the A3-complex with $N=10$ and Δ of 0.8. To that extent Fig. 12(a) and (c) and Fig. 13(a) and (b) present identical data. The three graphs that are superimposed in Fig. 13 depict variations on the theme that involve changing the inherent loss factor (η_{ij}) in the couplings. The changes are from the standard value of 10^{-3} to 10^{-2} and onto 10^{-1}, respectively. Figure 13(c) and (d) repeats Fig. 13(a) and (b), respectively, except that the number of HO's is changed from 10 to 22. Figure 14 repeats Fig. 13 except that the increment Δ is changed from the value of 0.8 to 1.6. The on-set of the modal overlap phenomenon is advantageously observed, in Figs. 13 and 14, from the right to the left of the frequency band spanning the resonance frequencies of the satellite HO's.[1] Especially in Fig. 14, the modal density on the right n_r and on the left n_l of that frequency band are substantially different; $n_r \gg n_l$. Indeed, the contributions by the individual satellite HO's are distinguishable on the right in Fig. 14 even in the darkest curves for which the inherent loss factor η_{1j} is as high as 10^{-1} and even when the number N of the HO's in the complex is increased from 10, in Fig. 14(a) and (b), to 22, in Fig. 14(c) and (d). Provided that the quantities plotted and the normalization used are properly identified and related, the data exhibited in Figs. 13(a), (c), 14(a), and (c) are in general agreement with similar data previously reported.[11,13] The data exhibited in Figs. 13(b), (c), 14(b), and (d) are discussed, for a simpler complex, in Ref. 13.

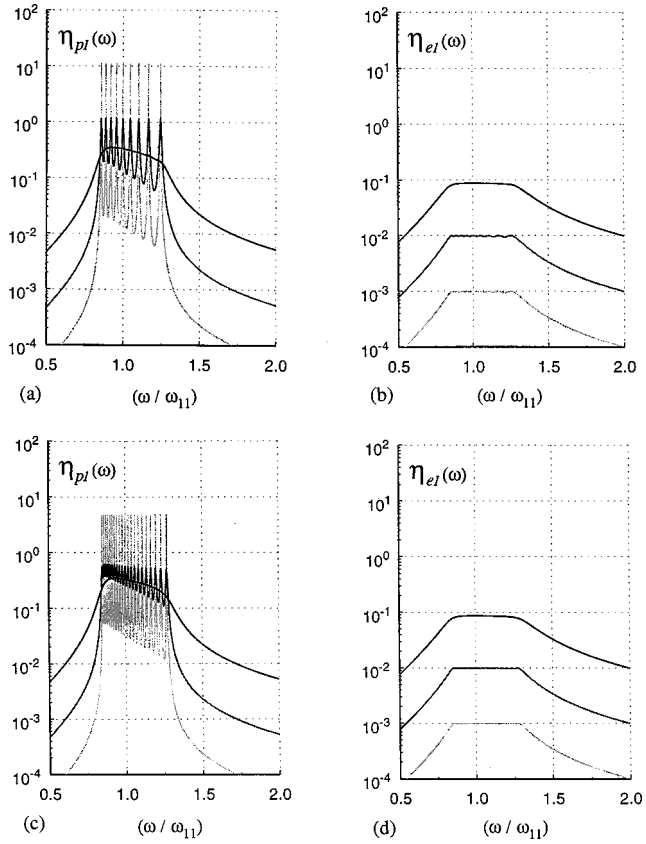

FIG. 13. The I-loss factor $\eta_{p1}(\omega)$ and the effective loss factor $\eta_{e1}(\omega)$ for an A3-complex, as specified in Eq. (37), and Δ of 0.8. The light curves are for $\eta_{1j}=10^{-3}$, the dark curves are for $\eta_{1j}=10^{-2}$ and the darkest curves are for $\eta_{1j}=10^{-1}$. (a) $\eta_{p1}(\omega)$, with $N=10$; (b) $\eta_{e1}(\omega)$, with $N=10$; (c) $\eta_{p1}(\omega)$, with $N=22$; (d) $\eta_{e1}(\omega)$, with $N=22$.

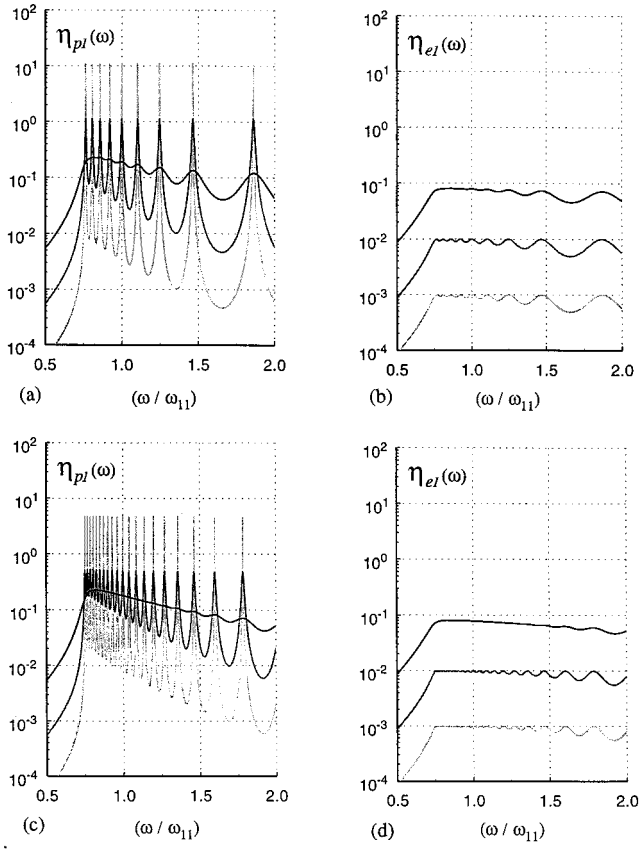

FIG. 14. Repeats Fig. 13 except that ''Δ of 0.8'' is changed to Δ of 1.6.

V. CONCLUDING REMARKS

Deferred in the computational experiments are the evaluations of the actual stored energies and the input powers pertaining to the master HO and to the satellite HO's under various specifications for the complex. The loss factors in the various forms are ratios of quantities that relate to these stored energies and input powers and, as such, they cover a number of sins that eventually need to be confessed to and atoned for. In subsequent publications the intention is to address these issues directly. Nonetheless, a few remarks may be relevantly made here.

In a complex composed of HO's with like and nearly like resonance frequencies, the couplings bring about a removal of degeneracies among such resonance frequencies; this removal yields a multiplicity of resonance frequencies for the complex as a whole. (The ''resonance frequencies'' in this context include ''anti-resonance frequencies'' as well.[1]) The distribution of the resonance frequencies are determined by the poles in the determinants of the impedance matrix $\underset{\approx}{Z}(\omega)$ and the admittance matrix $\overline{\underset{\approx}{Y}}(\omega)$. In this vein, and after a cursory investigation, one finds that the higher contribution of the couplings to $\eta_{p1}(\omega)$ occurs at frequencies at which the satellite HO's in a cell are at resonance under the condition that the master HO is essentially blocked. These frequencies are precisely those at which the stored energy ratio $\zeta(\omega)$, stated in Eq. (21a), attains values that substantially exceed unity. The I-loss factor $\eta_{p1}(\omega)$, then, hardly addresses the efficiency with which the normalized external input power is dissipated once it entered the complex. Indeed, it emerges that the higher value for the I-loss factor $\eta_{p1}(\omega)$ is more reflective of the inhibition of the stored energy in the master HO, as a fraction of the stored energy in the complex as a whole, than it is reflective of the efficiency by which the external input power is dissipated. It is the effective loss factor $\eta_{e1}(\omega)$ that addresses the efficiency of this dissipation; $\eta_{e1}(\omega)$ is, therefore, the real loss factor.

In the formalism of the loss factors pursued in this paper, it becomes clear that in seeking to establish design criteria for the loss factors of a complex, it is not merely the maximization of the values of the loss factors that is of significance. The placement of these maximal loss factors at frequencies where they are most useful is also a subject for consideration. Often these frequencies are commensurate with the *in situ* resonance frequencies of the complex as a whole and these frequencies are not necessarily located where the highest values for the I-loss factor and/or the effective loss factors reside. These considerations will be prominent features in subsequent publications.

[1] R. H. Lyon, *Statistical Energy Analysis of Dynamic Systems*: Theory and Applications (MIT, Cambridge, 1975); R. H. Lyon and R. G. DeJong, *Theory and Application of Statistical Energy Analysis* (Butterworth-Heinemann, Boston, 1995).

[2] C. Soize, ''Probabilistic structural modeling in linear dynamic analysis of complex mechanical systems,'' Rech. Aerosp. **1986-3**, 23–48 (1986); ''A model and numerical method in the medium frequency range for vibroacoustic predictions using the theory of structural fuzzy,'' J. Acoust. Soc. Am. **94**, 849–865 (1993).

[3] P. W. Smith, Jr. and R. H. Lyon, *Sound and Structural Vibration*, NASA CR-160 (U.S. Department of Commerce, Washington, DC, 1965).

[4] R. H. Lyon, ''Statistical energy analysis and structural fuzzy,'' J. Acoust. Soc. Am. **97**, 2878–2881 (1995).

[5] P. W. Smith, Jr., ''Statistical models of coupled dynamic systems and transition from weak to strong coupling,'' J. Acoust. Soc. Am. **65**, 695–698 (1979); K. L. Chandiramani, ''Some simple models describing the transition from weak to strong coupling in statistical energy analysis,'' J. Acoust. Soc. Am. **63**, 1081–1083 (1978).

[6] J. Dickey and G. Maidanik, ''Mechanical and radiated dissipations in external driven panels,'' Proceedings of Internoise 89, 397–402 (1989).

[7] L. Meirovitch, *Computational Methods in Structural Dynamics* (Sijthoff and Noordhoff, Alphen aan den Rijn, 1980).

[8] C. Lesuer, *Rayonnement Acoustique des Structures* (Editions Eyrolles, Paris, 1988).

[9] G. Maidanik and J. Dickey, ''Design criteria for the damping effectiveness of structural fuzzies,'' J. Acoust. Soc. Am. **100**, 2029–2033 (1996); and ''On the fuzz in a structural fuzzy,'' Proceedings of Internoise 96, Vol. **3**, 1297–1302 (1996).

[10] A. D. Pierce, V. W. Sparrow, and D. A. Russell, ''Fundamental structural acoustics idealizations for structures with fuzzy internals,'' Am. Soc. Mech. Eng. J. Vib. Acoust. **117**, 1–10 (1995).

[11] M. Strasberg and D. Feit, ''Vibration damping of large structures induced by attached small resonant substructures,'' J. Acoust. Soc. Am. **99**, 335–344 (1996).

[12] M. Strasberg, ''Continuous structures as 'fuzzy' substructures,'' J. Acoust. Soc. Am. **100**, 3456–3459 (1996).

[13] G. Maidanik, ''Power dissipation in a sprung mass attached to a master structure,'' J. Acoust. Soc. Am. **98**, 3527–3533 (1995).

On the problem of source identification from far-field observations in hysteretic materials

Abraham Kadish
Los Alamos National Laboratory, Los Alamos, New Mexico 87545

(Received 10 June 1997; accepted for publication 22 February 1998)

Propagation resulting from finite pulselength stresses applied at one end of a hysteretic material is analyzed using a propagation model containing a double modulus, or two-signal-speed, approximation of the stress-strain relation. The local signal speed is determined at any instant by both the value of stress and the sign of its time derivative (i.e., time-local history). It is shown that far-field waveforms do not determine unique source profiles. The propagation mechanism responsible for the ambiguity in source identification is common to broad classes of both local and global hysteretic stress-strain operators. Consequently, one may expect that it is typical of hysteretic materials that remote sources are not uniquely determined by observed waveforms. © *1998 Acoustical Society of America.* [S0001-4966(98)01706-8]

PACS numbers: 43.25.−x [MAB]

INTRODUCTION

In this article, a local hysteretic stress-strain relation is used to study one-dimensional pulse propagation in hysteretic materials. It is found that different sources applied at the same location generate identical remote far fields in hysteretic transmitting media, thereby compromising remote source identification. The underlying physical mechanism responsible for the nonuniqueness of the source is shown to be the generation of weak shocks. These are predicted by most local and nonlocal hysteresis operators. Consequently, while the nonuniqueness of solutions to the inverse problem treated here is proved for a specific state relation, the responsible physical mechanism strongly suggests that the result is shared by more complete hysteretic descriptions.

The model employed is motivated by nonlinear propagation experiments conducted at Los Alamos and the Institut du Petrole Francaise.[1,2] These experiments revealed that ideal elastic models of nonlinear resonant systems do not predict the empirical behavior of the harmonic spectrum and resonant frequency alteration for earth materials.[3,4] Similar conclusions have been reached from pulse-mode wave experiments.[5,6] Attempts to obtain more complete descriptions of the experiments have included hysteresis in the modeling of signal speeds (elastic modulii). The importance of hysteresis in describing nonideal materials has long been recognized, and propagation in hysteretic materials has been analyzed in some detail.[7] However, the effects of hysteresis on inverse problems (e.g., source identification from propagated signals) does not seem to have received much attention.

The most complete mathematical hysteretic operators are nonlocal in time, and express relations between state variables (e.g., stress and strain) as integrals over past history. When these are used in wave equations to model signal speeds, systems of differential equations describing dynamics become integrodifferential. More tractible mathematical systems containing hysteretic effects in a less complete way are obtained using local hysteretic operators. These operators specify differential relations between state variables in terms of the values of the variables and their time derivatives. The local operator used in this article is a double-modulus, or two-signal-speed, stress-strain relation in which the choice of modulus depends on the stress and its first time derivitive.

The mathematical model is described in the next section. In Sec. II, a qualitative description is given of the space-time evolution of pulses generated by simple sources applied to a hysteretic material. (Exact solutions are obtained for special sources in Appendix A.) In Sec. III, it is shown that a remote observer cannot determine the source temporal profile uniquely from passing waveforms even if the source location and hysteretic state relation for the transmitting medium are provided. (For an observed field generated by one of the sources treated in Appendix A, infinitely many sources of the same type generate the same observed field.) The results are discussed in Sec. IV.

I. MATHEMATICAL MODEL

One-dimensional compressional nonlinear pulse propagation in ideal and nonideal elastic materials can be described using the equations for conservation of mass and force balance. In Lagrangian (i.e., material) coordinates, if thermal, viscous, and drag effects are neglected, these equations are

$$\frac{\partial \sigma}{\partial t} - C^2 \frac{\partial v}{\partial z} = 0, \tag{1a}$$

$$\frac{\partial v}{\partial t} - \frac{\partial \sigma}{\partial z} = 0, \tag{1b}$$

$$C = \sqrt{\frac{d\sigma}{d\epsilon}}. \tag{1c}$$

In these equations, σ is the stress divided by the the unstressed mass density of the material (i.e., a stress per unit mass), v is the displacement (or particle) velocity, and C is the signal speed of the material. In the remainder of this article σ and v will referred to more simply as ''stress'' and ''velocity,'' respectively.

 0001-4966/98/103(6)/3196/7/$10.00

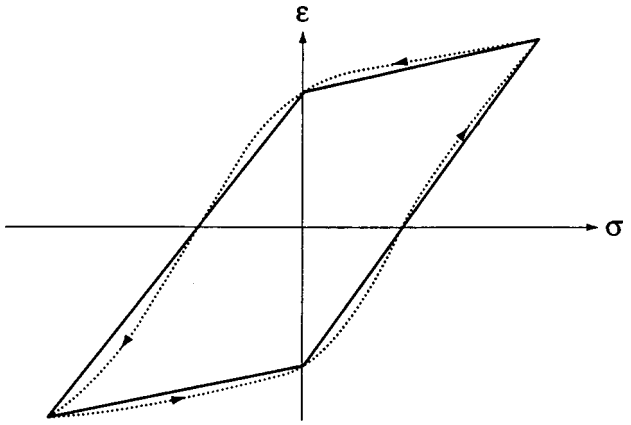

FIG. 1. A curvilinear hysteresis loop and the parallelogram approximation using a double-modulus stress-strain relation. The arrowheads indicate path direction with increasing time. The modulii for both are discontinuous at maxima and minima of stress.

In nonideal (e.g., hysteretic) materials, the stress-strain relation is not one-to-one. An example is illustrated in Fig. 1. The curvilinear loop in the figure is representative of empirical periodic hysteretic stress-strain loops. The arrowheads on the loop indicate direction with increasing time. The counterclockwise direction corresponds to hysteresis being dissipative. The parallelogram in the figure is a convenient approximation to the loop for analytical purposes. This approximation has been used in a lumped parameter model to describe hysteretic phenomena in resonant bar experiments.[8] It preserves an essential feature of many hysteretic state relations: the modulus, or signal speed changes abruptly at local maxima and minima of stress. Since the sides of the parallelogram have one of two slopes, the parallelogram corresponds to a double-modulus, or two-signal-speed stress-strain relation [see Eq. (1c)]. A two-signal-speed approximation to the hysteretic material will be assumed in the remainder of this paper. The two signal speeds will be indicated by C_{fast} and C_{slow}: $C_{\text{fast}} > C_{\text{slow}}$. As illustrated in Fig. 1, the local signal speed is then determined by the temporal monotonicity of the magnitude of stress: it is C_{slow} if $|\sigma|$ (or σ^2) is increasing in time and C_{fast} if it is decreasing.

Abrupt changes in signal speed at local extreme values of stress induce discontinuities in derivatives of stress and velocity. The onset of these discontinuities from an initially smooth pulseform is illustrated in Fig. 2 for a propagating

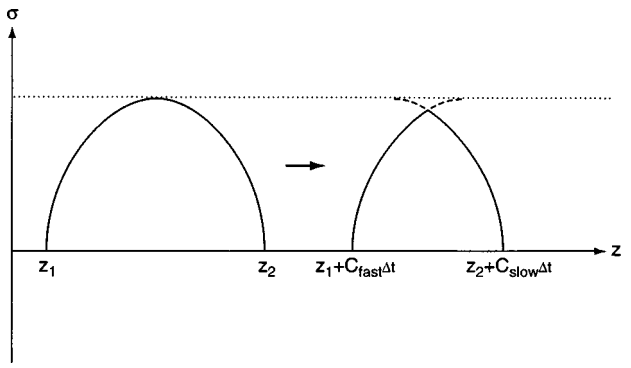

FIG. 2. Illustrating weak shock onset due to discontinuities in hysteretic modulii (i.e., signal speed) at temporal maxima of stress.

positive stress pulse. In the figure, the pulse is propagating in the direction of increasing z. The pulseform to the right of the instantaneous maximum is associated with a temporally increasing $|\sigma|$ (i.e., $C = C_{\text{slow}}$), while the portion to the left is associated with a temporally decreasing $|\sigma|$ (i.e., $C = C_{\text{fast}}$). Consequently, the discontinuity in the signal speed results in the trailing portion of the wave attempting to pass through the leading portion at the position of maximum stress (see Fig. 2). A discontinuous derivative results: i.e., a weak shock forms. The determination of the paths of these shocks is central to any analysis of hysteretic pulse propagation, since they are free boundaries between space-time regions of different stress-strain relations. Evidently, the presence of these shocks is predicted by any hysteretic state relation featuring discontinuities in the differential relation between stress and strain.

With the double modulus approximation, hysteresis is the only nonlinear and dissipative effect in Eqs. (1a)–(1c). Analytically, all of the nonlinearity of the system resides in the self-consistent determination of the interfaces between space-time regions in which $C = C_{\text{fast}}$ and $C = C_{\text{slow}}$. (For brevity, space-time regions in which $C = C_{\text{fast}}$ or $C = C_{\text{slow}}$ will be referred to as fast signal speed and slow signal speed regions, or more simply fast or slow regions, respectively.) In each separate fast or slow region, the material response is linear. Collectively, however, the response is nonlinear, since the weak shock paths, or free boundaries, separating fast and slow regions are pulse dependent.

II. CONTINUOUS PULSE PROPAGATION

We now consider the pulse generated by applying a continuous source stress at one end, $z = 0$, of the initially unstressed hysteretic material occupying $z > 0$. For $t < 0$ and $t > t^*$, the stress at $z = 0$ is zero. For $0 < t < t^*$, $\sigma(0,t) > 0$ and takes its only local maximum at t_0. The space-time evolution of the resulting continuous pulse is discussed below, assuming that at every position, z, the time evolution consists of a piecewise monotonic stress whose minimum on each time interval of monotonicity is zero. [Exact solutions to Eqs. (1a)–(1c) for piecewise-linear source stresses are compatible with these assumptions. They are given in Appendix A.]

The earlier time evolution of the pulse is illustrated in Fig. 3(a). In the figure, the region below the line $t(z) = z/C_{\text{slow}}$ is not affected by the applied stress: for $t < t(z)$, the points (z,t) are in the region of initial constant state. In the regions adjacent to the line, labeled I and I', the stress and velocity are simple waves,[9] and $C = C_{\text{slow}}$. In these simple wave regions both the stress and velocity are constant on the paths $dz/dt = +C_{\text{slow}}$.

The maximum of the source stress at $(0,t_0)$ results in a curvilinear boundary on which stress is a local maximum in time, between the simple wave region, region I, and a region II in which $C = C_{\text{fast}}$. The curve describes a weak shock path (see Fig. 2). In region II, the time derivative of the stress is negative. Consequently, region II is partially bounded by a curve on which stress vanishes. If the velocity is not a constant on this curve, the stress increases with time in a neigh-

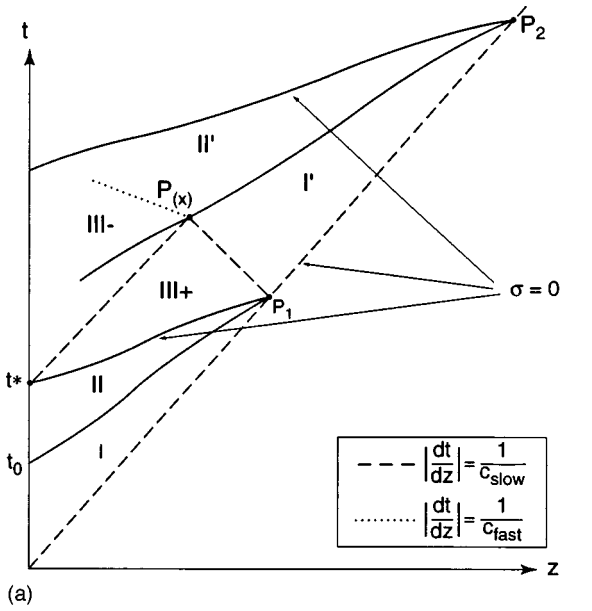

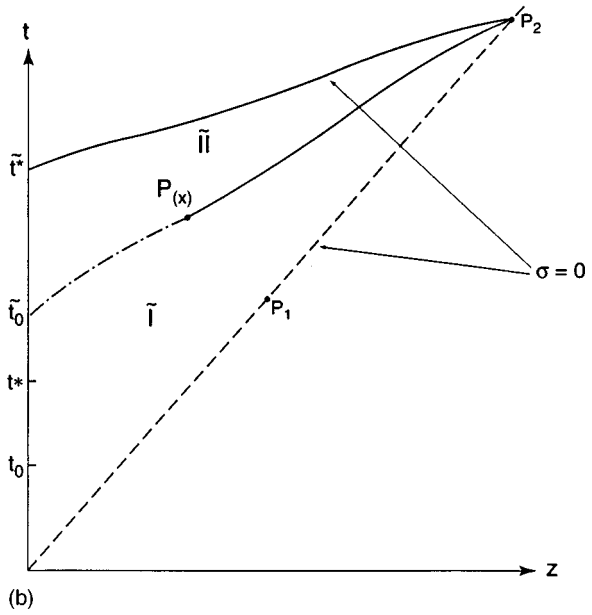

FIG. 3. (a) Illustrating the space-time evolution of propagating pulses generated by the source stresses having a single maximum [see Eq. (2)]. (b) An alternate space-time evolution inferred from waveforms detected at $z_{\text{observer}} > z(P_1)$ in (a).

boring slow region above this curve, region III_+. The two curvilinear boundaries of region II intersect the straight line $t(z)=z/C_{\text{slow}}$ at the point P_1.

The signal speed path with speed $-C_{\text{slow}}$ originating at P_1 is a partial boundary for the slow simple wave region, region I′ and region III_+, across which derivatives of the continuous stress and velocity are discontinuous. Values of stress and velocity on this boundary are propagated as constants into region I′ on paths $dz/dt=+C_{\text{slow}}$.

Since stress achieves a local maximum in time, there is a curve in space-time separating region I′ from another region, region II′, in which $C=C_{\text{fast}}$. Similarly, there is a curve in space-time separating region III_+ from another region, region III_-, in which $C=C_{\text{fast}}$. Derivatives of stress and strain are discontinuous at the boundaries between regions I′ and II′ and regions III_+ and III_-. The two fast regions, regions II′ and III_-, are separated by a signal speed path on which $dz/dt=-C_{\text{fast}}$, across which derivatives of the continuous stress and velocity are discontinuous. This curve originates at the X-like point, $P_{(X)}$.

As was the case for region II, the union of the fast region II′ and III_-, region II*, is also bounded by a curve on which stress vanishes. This curve and the boundary between regions I′ and II′ intersect the straight line $t(z)=z/C_{\text{slow}}$ at the point P_2.

The further development of the space-time evolution of the pulse proceeds as before, with the roles of P_1 and the zero stress boundary of region II, taken by P_2 and the zero stress boundaries of region II*.

The mathematical construction of the propagating pulse beyond the zero stress boundary of region II* proceeds exactly as was done in extending the pulse beyond that of region II. The description of the complete pulse in a semi-infinite medium is obtained by repeating this construction process *ad infinitum*.

We note that these heuristic arguments may be extended in a straightforward way to state relations with two stress-dependent modulii, $C^2_{\text{fast}}(\sigma)$ and $C^2_{\text{slow}}(\sigma)$, where the faster and slower signal speeds correspond to temporally decreasing and increasing σ^2 (i.e., as on a curvilinear hysteresis loop).

III. SOURCE IDENTIFICATION

With a source at $z=0$ as in the preceeding section, suppose the resulting pulse is detected downstream by an observer at $z=z_{\text{observer}}$, and for simplicity of exposition, assume the pulse is first detected at $t_{\text{observer}}=z_{\text{observer}}/C_{\text{slow}}$.

We pose the question: If the observer knows the source location, $z=0$, can the temporal profile of the source be determined? Knowing the source location allows the observer to determine the initiation time, $t=0$, of the source. However, using the construction of the preceeding section, we show that it is not possible, in general, for the observer to determine a unique source profile without additional information. We then show, using the examples in Appendix A, that many sources can generate the same detected pulseform.

A. General case

Assume that it is possible to find a simple wave slow signal speed extrapolation of the expressions for the stress and strain in region I′ to $z=0$ and a fast signal speed extrapolation of the stress and strain in region II′ to $z=0$ together with a space-time curve across which stress and strain are continuous. The extrapolated regions are illustrated in Fig. 3(b), where they are labeled regions $\tilde{\text{I}}$ and $\tilde{\text{II}}$. The extrapolated stresses and velocities of this simpler space-time evolution will not agree with those generated by the original applied stress at $z=0$. However, the extrapolated source stress at $z=0$ will have a temporal profile of the same type as that of the original source: finite support, $0<t<\tilde{t}^*$, and a single maximum, which occurs at a time $\tilde{t}_0$.

Since this new source generates stress and velocity waves which have the same values of stress ($\sigma=0$) and velocity on the boundary curve for region $\widetilde{\text{II}}$ joining $(0,\widetilde{t^*})$ and P_2 as those of the true source, both the original and extrapolated source stress generate continuous stresses and velocities which are equal for all space-time coordinates outside regions $\widetilde{\text{I}}$ and $\widetilde{\text{II}}$. They also agree in the subsets, regions I′ and II′. As a result, complete knowledge of the pulse at $z_{\text{observer}}\geqslant z(P_1)$ is insufficient to uniquely determine the source stress profile at $z=0$.

B. Piecewise-linear sources

The pulses generated by piecewise-linear source stresses

$$\sigma(0,t)=\left(\begin{array}{ll}\dfrac{t}{t_0}, & \text{if } 0\leqslant t\leqslant t_0\\ \dfrac{t^*-t}{t^*-t_0}, & \text{if } t_0\leqslant t\leqslant t^*\end{array}\right)\overline{\sigma} \tag{2}$$

(the source stress vanishes for $t<0$ and $t>t^*$) are given by Eqs. (A9)–(A14) of Appendix A using the dimensionless variables of Eq. (A1). Since the expressions for the pulse are sectionally linear in (z,t), the appropriate extrapolations of the simple waves in region I′ and the stress and strain in region II′ to $z=0$ are obvious. Moreover, the interface of the extrapolated interface is the continuation of the straight line though $P_{(X)}$ of Fig. 4(a) to $(0,\widetilde{\tau_0})$. The analogue of Fig. 3(b) for these special sources is Fig. 4(b).

In terms of physical variables, the support for the source obtained by extrapolation is the interval $0<t<\widetilde{t^*}$, and the maximum of the extrapolated source stress, $\overline{\sigma'}$, is taken at time $\widetilde{t_0}$, where

$$\widetilde{t^*}(t_0,t^*)=t^*\widetilde{\tau^*}(\tau_0)=\left(\tau_{(X)}(\tau_0)+\frac{\xi_{(X)}(\tau_0)}{c_{\text{fast}}}\right)t^*, \tag{3a}$$

$$\widetilde{t_0}(t_0,t^*)=t^*\widetilde{\tau_0}(\tau_0)=\left(\tau_{(X)}(\tau_0)-\frac{\xi_{(X)}(\tau_0)}{V'(\tau_0)}\right)t^*, \tag{3b}$$

$$\tilde{\bar{\sigma}}(t_0,t^*)=\overline{\sigma}s_{\text{I}'}(0,\widetilde{\tau_0}(\tau_0))=\overline{\sigma}s_{\text{II}''}(0,\widetilde{\tau_0}(\tau_0)). \tag{3c}$$

$\widetilde{\tau^*}$ and $\widetilde{\tau_0}$ are the dimensionless times illustrated in Fig. 4(a) at $\xi=0$. In the same figure $P_{(X)}=(\xi_{(X)},\tau_{(X)})$. These quantities all depend on the applied source profile parameter $\tau_0=t_0/t^*$. $s_{\text{I}'}(\xi,\tau)$ and $s_{\text{II}'}(\xi,\tau)$ are the expressions for the dimensionless stress in regions I′ and II′ of the figure [see Eqs. (A13) and (A14) of Appendix A]. It is shown in Appendix B that $\widetilde{t^*}>t^*$, $\widetilde{t_0}>t_0$, and $\tilde{\bar{\sigma}}<\overline{\sigma}$, and useful bounds for various quantities are derived.

C. Infinitely many piecewise-linear sources

It is possible to view the piecewise-linear applied source stresses as stresses obtained by extrapolating to $z=0$ the pulse generated by an applied stress of lesser support

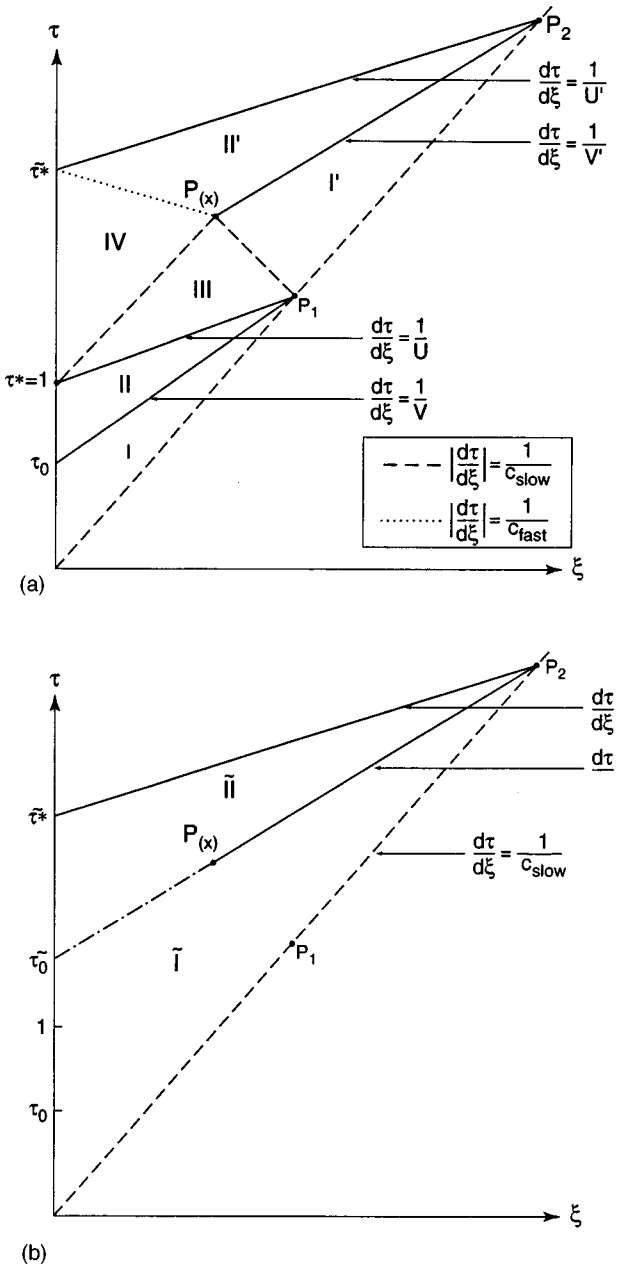

FIG. 4. (a) The space-time evolution of the exact solutions obtained for piecewise-linear sources in Appendix A (dimensionless variables are used). (b) An alternate space-time evolution inferred from waveforms detected at $\xi_{\text{observer}}>\xi(P_1)$ in (a).

$$\sigma(0,t)=\left(\begin{array}{ll}\dfrac{t}{t_0'}, & \text{if } 0\leqslant t\leqslant t_0'\\ \dfrac{t^{*\prime}-t}{t^{*\prime}-t_0'}, & \text{if } t_0'\leqslant t\leqslant t^{*\prime}\end{array}\right)\overline{\sigma'}, \tag{4}$$

where $t^{*\prime}<t^*$, and where this new source stress vanishes for all other values of t.

To show this, one introduces dimensionless variables as in Appendix A using the source parameters to be determined (e.g., $\tau'=t/t^{*\prime}$). One then obtains the same functional relationships between the true source parameters and t_0', $t^{*\prime}$, and $\overline{\sigma'}$ as those found between the extrapolated source parameters and t_0, t^*, and $\overline{\sigma}$.

The procedure may be repeated ad infinitum to obtain a sequence of source stresses of increasing amplitude and decreasing support, each of which generates the same pulse at $z=z_{\text{observer}}$. The nth procedure produces a maximum in stress whose ratio to that of the true applied stress is greater than $1/(1-\beta)^n$ [see Eq. (B5) of Appendix B] where $1-\beta=1-C_{\text{slow}}/C_{\text{fast}}$ is a hysteresis strength parameter. (If $1-\beta=0$, hysteresis is not present.) The ratio of the pulse length to that of the applied source in less than $[(1-\beta)/(1+\beta^2)]^n$ [see Eq. (B4) of Appendix B].

IV. SUMMARY AND DISCUSSION

A model for one-dimensional wave propagation with a double modulus local hysteretic relation between stress and strain was used to study properties of propagation in semi-infinite hysteretic materials. The evolution of pulses resulting from a stress applied at a boundary was analysed. It was proved that different stresses applied at the same location can generate exactly the same continuous far-field wave form in a hysteretic material. As a result, source identification from far-field data is not unique when the transmitting medium is hysteretic.

The nonuniqueness of the source in hysteretic materials results from discontinuities in derivatives of stress and velocity (i.e., weak shocks) which are generated by discontinuities in the modulii of hysteretic stress-strain relations. These discontinuities produce a downstream sequence of disjoint slow wave regions [e.g., regions I and I′ of Fig. 3(a)]. Each of these offers the potential of a backward extrapolation to a different inferred source at the same location. Since discontinuous modulii on paths in the stress-strain plane are typical of hysteresis operators, it is to be expected that remote sources are not uniquely determined by detected waveforms in hysteretic materials.

For ideal materials (i.e., those with single valued stress relations), source determination is unique. (In the absence of damping, this follows immediately from the simple wave nature of the propagating pulse. Both stress and velocity are constant on a signal speed path, and on each path the signal speed is a constant which is determined by the observed stress.) Real materials may exhibit increasingly ''narrow'' hysteresis loops (i.e., ''almost'' ideal state relations) as amplitudes decrease. For these, if the source is weak, the ratios of the support for different possible sources become large [e.g., see Eq. (B4) with $\beta\sim 1$], and for practical purposes, source identification may be unique. However, even if an observed far-field signal is weak, the nonuniqueness predicted here is important for large amplitude sources, since discontinuities in modulii will then be significant over some range of propagation.

ACKNOWLEDGMENTS

The author wishes to thank J. N. Albright and C. W. Myers for their encouragement and P. A. Johnson and J. Ten Cate for helpful technical discussions. This work was supported by the U.S. Department of Energy Office of Basic Energy Research: Scientific Computing.

APPENDIX A: PULSE PROPAGATION DUE TO A PIECEWISE-LINEAR SOURCE

Exact solutions can be obtained to Eqs. (1a)–(1c) which describe continuous propagating pulses of stress and velocity generated by piecewise-linear source stresses given by Eq. (4). In this Appendix, the development of the pulses is presented through the determination of region II′ of Fig. 3. In order to simplify the mathematical expressions for the pulses, dimensionless variables and parameters are introduced:

$$
\begin{aligned}
&t=t^*\tau,\\
&z\equiv t^*(C_{\text{slow}}+C_{\text{fast}})\xi,\\
&\sigma\equiv\bar{\sigma}s,\\
&v\equiv\frac{\bar{\sigma}}{(C_{\text{slow}}+C_{\text{fast}})}\,u,\\
&c_{\text{slow,fast}}\equiv\frac{C_{\text{slow,fast}}}{(C_{\text{slow}}+C_{\text{fast}})},\\
&\beta\equiv\frac{c_{\text{slow}}}{c_{\text{fast}}}<1.
\end{aligned}
\tag{A1}
$$

For simplicity of exposition, the dimensionless quantities s, u, c_{fast}, and c_{slow}, ξ, and τ will be referred to as the stress, velocity, fast and slow signal speeds, space, and time, respectively.

The support for the source stresses is the time interval $0<\tau<\tau^*=1$. The piecewise-linear source stress at $\xi=0$ vanishes outside the time interval $0<\tau<1$ where it is given by

$$
\begin{aligned}
&s(0,\tau)=\left(\begin{array}{ll}\dfrac{\tau}{\tau_0}, & \text{if } 0\leqslant\tau\leqslant\tau_0\\[2ex] \dfrac{1-\tau}{1-\tau_0}, & \text{if } \tau_0\leqslant\tau\leqslant 1\end{array}\right),\\
&\tau_0=t_0/t^*.
\end{aligned}
\tag{A2}
$$

The maximum of the source stress, taken at $\tau=\tau_0$, is one. The velocity at $\xi=0$ takes nonvanishing values in $\tau>1$.

In terms of the dimensionless variables, Eqs. (1a) and (1b) become

$$
\frac{\partial s}{\partial\tau}=c^2\frac{\partial u}{\partial\xi},\quad \frac{\partial u}{\partial\tau}=\frac{\partial s}{\partial\xi},
\tag{A3}
$$

where c is either c_{fast} or c_{slow}.

For piecewise-linear sources, the interfaces between all fast and slow regions are straight lines. The regions referred to in this Appendix are illustrated in Fig. 4(a). The functional dependence of a dependent variable in a region is indicated by a subscript on the variable identifying the region [e.g., $s_{\text{III}}(\xi,\tau)$ is the functional form of the stress in region III]. Regions I, I′, and III are fast regions. Regions II and II′ are slow regions. Region IV is both a fast and a slow region [see Eq. (A12)]. Expressions for the velocity parameters U, V, U', and V' for interfaces shown in Fig. 4 are given in Eqs. (A4) and (A6).

Parameters appearing in the expressions for stress and strain in Regions I, II, III, and IV are U, V, and A, where

$$\frac{c_{\text{slow}}}{V}=\sqrt{(1-\tau_0)+\tau_0\beta^2},$$

$$\frac{c_{\text{slow}}}{U}=\frac{\sqrt{(1-\tau_0)+\tau_0\beta^2}-(1-\tau_0)}{\tau_0}, \tag{A4}$$

$$A=\frac{1}{1-\tau_0}\left(\frac{1/U^2-1/c_{\text{fast}}^2}{1/c_{\text{slow}}^2-1/U^2}\right)=\frac{(1-c_{\text{slow}}/U)}{(1+c_{\text{slow}}/U)}.$$

The expressions for U and V may be used to show that

$$c_{\text{slow}}<V<U<c_{\text{fast}}. \tag{A5}$$

Note that A is positive.

Parameters appearing in the expressions for stress and strain in regions I′ and II′ are U', V', and α, where

$$\frac{c_{\text{slow}}}{U'}=\frac{1}{2}\left[\left(1-\frac{c_{\text{slow}}}{U}\right)\beta+\left(1+\frac{c_{\text{slow}}}{U}\right)\left(\frac{1+\beta^2}{2}\right)\right]$$
$$=\left(\frac{1+\beta}{2}\right)^2+\frac{c_{\text{slow}}}{U}\left(\frac{1-\beta}{2}\right)^2,$$

$$\frac{c_{\text{slow}}}{V'}=\frac{c_{\text{slow}}/U'-\beta^2}{1-c_{\text{slow}}/U'}, \tag{A6}$$

$$\alpha=-\frac{(1-c_{\text{slow}}/U)^2}{(1+c_{\text{slow}}/U)(\beta+c_{\text{slow}}/U')}.$$

The expressions for U' and V' may be used to show that

$$c_{\text{slow}}<V'<U'<c_{\text{fast}}. \tag{A7}$$

Note that α is negative. The points P_1, P_2, and $P_{(X)}$ are given by

$$P_1\equiv(\xi_1,\tau_1)=\frac{\tau_0}{1-\sqrt{(1-\tau_0)+\tau_0\beta^2}}\,(c_{\text{slow}},1)$$
$$=\frac{1}{(1-c_{\text{slow}}/U)}\,(c_{\text{slow}},1),$$

$$P_{(X)}=(\xi_{(X)},\tau_{(X)})$$
$$=\left(\frac{c_{\text{slow}}}{2}\left(\frac{1+c_{\text{slow}}/U}{1-c_{\text{slow}}/U}\right),\left(\frac{1}{2}+\frac{1}{1-c_{\text{slow}}/U}\right)\right), \tag{A8}$$

$$P_2=(\xi_2,\tau_2)=\frac{\tau^{*\prime}}{(1-c_{\text{slow}}/U')}\,(c_{\text{slow}},1),$$

$$\tau^{*\prime}=\tau_{(X)}+\frac{\xi_{(X)}}{c_{\text{fast}}}.$$

[The ''(X)'' subscript is used because the point is a corner for four regions.]

The expressions for the parameters and points given in Eqs. (A4) to (A6) are determined requiring continuity of stress and velocity in space and time. They are all functions of the dimensionless source stress parameter τ_0. For simplicity, the dependence on the parameter is suppressed in this Appendix [e.g., $V(\tau_0)$ is written more simply as V].

In region I, a simple wave region, the stress and strain are given by

$$s_{\text{I}}(\xi,\tau)=\frac{1}{\tau_0}\left(\tau-\frac{\xi}{c_{\text{slow}}}\right),$$
$$u_{\text{I}}(\xi,\tau)=-\frac{1}{\tau_0 c_{\text{slow}}}\left(\tau-\frac{\xi}{c_{\text{slow}}}\right). \tag{A9}$$

In region II, the stress and strain are given by

$$s_{\text{II}}(\xi,\tau)=\frac{1}{1-\tau_0}\left[(1-\tau)+\frac{\xi}{U}\right],$$
$$u_{\text{II}}(\xi,\tau)=-\frac{1}{c_{\text{slow}}}-\frac{1}{1-\tau_0}\left[\frac{\xi}{c_{\text{fast}}^2}-\frac{(\tau-\tau_0)}{U}\right]. \tag{A10}$$

In region III, the stress and strain are given by

$$s_{\text{III}}(\xi,\tau)=A\left[(\tau-1)-\frac{\xi}{U}\right],$$
$$u_{\text{III}}(\xi,\tau)=-\left(\frac{1}{c_{\text{slow}}}-\frac{1}{U}\right)+A\left[\frac{\xi}{c_{\text{slow}}^2}-\frac{(\tau-1)}{U}\right]. \tag{A11}$$

In region IV, the stress and strain are given by

$$s_{\text{IV}}(\xi,\tau)=\left(\frac{1}{c_{\text{slow}}}-\frac{1}{U}\right)A\xi,$$
$$u_{\text{IV}}(\xi,\tau)=\left(\frac{1}{c_{\text{slow}}}-\frac{1}{U}\right)[-1+A(\tau-1)]. \tag{A12}$$

The absence of time dependence in s and space dependence in u imply that Eqs. (A3) are satisfied for all values of c. Therefore, region IV is both a fast and a slow region.

In region I′, a simple wave region, the stress and strain are given by

$$s_{\text{I}}(\xi,\tau)=\frac{c_{\text{slow}}}{2}\left(\frac{1}{c_{\text{slow}}}-\frac{1}{U}\right)\left(\tau-\frac{\xi}{c_{\text{slow}}}\right),$$
$$u_{\text{I}'}(\xi,\tau)=-\frac{1}{2}\left(\frac{1}{c_{\text{slow}}}-\frac{1}{U}\right)\left(\tau-\frac{\xi}{c_{\text{slow}}}\right). \tag{A13}$$

In region II′, the stress and strain are given by

$$s_{\text{II}'}(\xi,\tau)=\left(\frac{1}{c_{\text{slow}}}-\frac{1}{U}\right)A\xi_{(X)}$$
$$+\alpha\left[(\tau-\tau_{(X)})-\frac{(\xi-\xi_{(X)})}{U'}\right],$$
$$u_{\text{II}'}(\xi,\tau)=\left(\frac{1}{c_{\text{slow}}}-\frac{1}{U}\right)[-1+A(\tau_{(X)}-1)] \tag{A14}$$
$$+\alpha\left[\frac{(\xi-\xi_{(X)})}{c_{\text{fast}}^2}-\frac{(\tau-\tau_{(X)})}{U'}\right].$$

This completes the description of the pulse through region II′ as described for more general pulses in Sec. II.

APPENDIX B: BOUNDS FOR EXTRAPOLATED SOURCE STRESS PARAMETERS

Bounds are derived for the parameters $t^{*\prime}$, t_0', and $\overline{\sigma'}$ of Eqs. (3a)–(3c):

$$\frac{\tilde{t}_0(t_0,t^*)}{t^*}=\tilde{\tau}_0(\tau_0)=\left(\tau_{(X)}(\tau_0)-\frac{\xi_{(X)}(\tau_0)}{V'(\tau_0)}\right), \tag{B1a}$$

$$\frac{\tilde{t^*}(t_0,t^*)}{t^*}=\tilde{\tau^*}=\left(\tau_{(X)}(\tau_0)+\frac{\xi_{(X)}(\tau_0)}{c_{\text{fast}}}\right), \tag{B1b}$$

$$\frac{\tilde{\bar{\sigma}}(t_0,t^*)}{\bar{\sigma}}=s_{I'}(0,\tilde{\tau}_0(\tau_0)). \tag{B1c}$$

Using Eq. (A8) of Appendix A,

$$\tilde{\tau}_0=\frac{(3-c_{\text{slow}}/U)-(c_{\text{slow}}/V')(1+c_{\text{slow}}/U)}{2(1-c_{\text{slow}}/U)}$$

$$>\frac{(3-c_{\text{slow}}/U)-(1+c_{\text{slow}}/U)}{2(1-c_{\text{slow}}/U)}=1, \tag{B2}$$

$$\begin{aligned}\tilde{\tau^*}-\tilde{\tau}_0&=\left(\frac{1}{V'}+\frac{1}{c_{\text{fast}}}\right)\xi_{(X)}\\&=\frac{(1+c_{\text{slow}}/U)}{2(1-c_{\text{slow}}/U)}\left(\beta+\frac{c_{\text{slow}}}{V'}\right)\\&=\frac{(1+c_{\text{slow}}/U)}{2(1-c_{\text{slow}}/U)}\left(\frac{\beta+c_{\text{slow}}/U'}{1-c_{\text{slow}}/U'}\right)(1-\beta)\\&=\frac{(1+c_{\text{slow}}/U)}{2(1-c_{\text{slow}}/U)}\\&\quad\times\left[\frac{(4\beta+(1+\beta)^2)+(1-\beta)^2\ c_{\text{slow}}/U}{(3+\beta)-(1-\beta)c_{\text{slow}}/U}\right]\\&>\frac{1}{2}\left(\frac{1+\beta}{1-\beta}\right)\frac{(1+7\beta-\beta^2+\beta^3)}{(3+\beta^2)}\\&>\frac{\beta}{2}\left(\frac{1+\beta}{1-\beta}\right)\left(\frac{7+\beta^2}{3+\beta^2}\right)>\left(\frac{1+\beta}{1-\beta}\right)\beta.\end{aligned} \tag{B3}$$

The first inequality in Eq. (B3) is obtained using $c_{\text{slow}}/U>\beta$. Using Eq. (B2) in Eq. (B3) yields

$$\tilde{\tau^*}>\frac{1+\beta^2}{1-\beta}. \tag{B4}$$

Using Eqs. (A13) and (B2)

$$\begin{aligned}\tilde{\bar{s}}&=\frac{1}{2}\left(1-\frac{c_{\text{slow}}}{U}\right)\tilde{\tau}_0\\&=\frac{1}{4}\left[\left(3-\frac{c_{\text{slow}}}{U}\right)-\frac{c_{\text{slow}}}{V'}\left(1+\frac{c_{\text{slow}}}{U}\right)\right]\\&<\frac{1}{4}\left[\left(3-\frac{c_{\text{slow}}}{U}\right)-\beta\left(1+\frac{c_{\text{slow}}}{U}\right)\right]\\&<\tfrac{1}{4}\left[3-\beta-(1+\beta)\beta\right]\\&=(1-\beta)\ \frac{(3+\beta)}{4}<1-\beta.\end{aligned} \tag{B5}$$

The first and second inequalities in Eq. (B5) are obtained using $c_{\text{slow}}/V'>\beta$ and $c_{\text{slow}}/U>\beta$, respectively.

[1] G. D. Meegan, P. A. Johnson, R. G. Guyer, and K. R. McCall, ''Observations of nonlinear elastic wave behavior in sandstone,'' J. Acoust. Soc. Am. **94**, 3387–3391 (1993).

[2] P. A. Johnson and P. N. J. Rasolofosoan, ''Manifestation of nonlinearity in rock; Convincing evidence over large frequency and strain levels from laboratory studies,'' Nonlinear Processes in Geophysics **3**, 77–88 (1996).

[3] R. A. Guyer, K. R. McCall, and G. N. Boitnott, ''Hysteresis, discrete memory and nonlinear wave propagation in rock,'' Phys. Rev. Lett. **74**, 3491–3494 (1995).

[4] P. A. Johnson, B. Zinszner, and P. N. J. Rasolofosoan, ''Resonance and nonlinear elastic phenomena in rock,'' J. Geophys. Res. **101**, 11553–11564 (1996).

[5] J. Ten Cate, K. E-A. Van Den Abeele, T. J. Shankland, and P. A. Johnson, ''Laboratory study of linear and nonlinear elastic pulse propagation in sandstone,'' J. Acoust. Soc. Am. **100**, 1383–1391 (1996).

[6] A. Kadish, J. Ten Cate, and P. A. Johnson, ''Frequency spectra of nonlinear pulse-mode waves,'' J. Acoust. Soc. Am. **100**, 1375–1382 (1996).

[7] M. Brokate and J. Sprekels, *Hysteresis and Phase Transitions* (Springer-Verlag, New York, 1996).

[8] A. Kadish, P. A. Johnson, and B. Zinszner, ''Evaluating hysteresis in earth materials under dynamic resonance,'' J. Geophys. Res. **101**, 25139–25147 (1996).

[9] P. Garabedian, *Partial Differential Equations* (Wiley, New York, 1964), Chap. 14.

New evolution equations for the nonlinear surface acoustic waves on an elastic solid of general anisotropy

Vitalyi E. Gusev,[a] Walter Lauriks, and Jan Thoen
Laboratorium voor Akoestiek en Thermische Fysica, Departement Natuurkunde, Katholieke Universiteit Leuven, Celestijnenlaan 200 D, B-3001 Leuven, Belgium

(Received 15 January 1997; revised 5 September 1997; accepted 30 January 1998)

New evolution equations for the nonlinear surface acoustic waves in anisotropic media are derived in the frame of the second-order elasticity theory. The proposed theory explicitly accounts for the possible significant difference of the depth structure of the nonlinear surface acoustic waves with the depth structure of the linear surface acoustic waves. The derived equations reduce to the form, recently obtained for the nonlinear Rayleigh surface acoustic waves in isotropic solids, when two partial waves (contributing to the surface acoustic wave propagating along a crystal axis in the basal plane of a cubic crystal) exhibit purely exponential decay in depth. © *1998 Acoustical Society of America.* [S0001-4966(98)03505-X]

PACS numbers: 43.25.Fe [MAB]

INTRODUCTION

The continuous interest in the investigation of the nonlinear effects in finite-amplitude surface acoustic waves (SAWs) is stimulated by the goals to apply the results for the description of seismic phenomena and SAW-based signal processing devices.[1] Beyond practical applications, the analysis of SAWs' time evolution in the presence of the elastic nonlinearity is a challenging physical and mathematical problem.[1] The solution of this problem could definitely contribute to the progress in the physics of nonlinear wave phenomena in general, especially in the fields of interface waves and of propagating wave guide modes.

The mathematical complexity of the nonlinear SAWs' description is clear already from the physical definition of these waves. A surface acoustic wave on an elastic half-space is a mechanical disturbance propagating along the traction-free surface (bounding the half-space), with an amplitude diminishing with increasing distance from the surface (i.e., the wave is localized near the surface). Thus the SAW is essentially a multidimensional disturbance. Moreover, with the exception of the pure shear surface waves,[2] the elastic displacement associated with a SAW is a vector field. Consequently, the nonlinear SAW should be found, in general, from the solution of the vector multidimensional nonlinear equations of elasticity subjected to the nonlinear boundary conditions at the surface.[1] The detailed overview of the theoretical activity in this field was presented recently by others.[1] Due to this we refer here only to a few typical publications sufficient to clarify both the different stages in the development of the theory and its current status. Though the number of publications on the nonlinear Rayleigh waves in isotropic solids is larger (see, for example, Refs. 3–10 and in addition the references therein), there are also some investigations of the nonlinear SAWs in anisotropic media,[11–14] which is the topic of our investigation presented here.

The first theoretical achievements for nonlinear surface acoustic waves in anisotropic substrates are related to the application of a perturbative method for the analysis.[11,12] As a first step of this step-wise-successive approximation method the solutions of the linearized problem are found. It is assumed that these solutions provide a leading-order contribution to nonlinear SAW. As usual in acoustics, the variations of the physical parameters of the media in the SAW are small in comparison with the characteristic values of the parameters (for example, particle velocity in the acoustic wave is much less than the acoustic wave velocity). Similar to the nonlinear acoustics of bulk waves,[15] it is useful to take this into account by introducing some small positive nondimensional parameter $\gamma \ll 1$. With this assumption, the leading terms in the SAW are of the order of γ (or, in other words, of the first order of smallness). Then, as a second step of the successive approximations, the solution of linearized problem is substituted in the nonlinear equations and boundary conditions of the elasticity theory and its perturbation due to the presence of the nonlinear terms is found. It is commonly sufficient to account for the so-called quadratic approximation in the equations, i.e., to keep in the equations only the nonlinear terms which have a form of the products of two linear terms (second-order elastic theory).[1] Then, clearly, the perturbation to the leading term, which is found at the second step of successive approximations, is on the order of γ^2. Along with the expected results such as the description of a possible frequency mixing (and, in particular, harmonic generation and parametric amplification), the theories[11,12] revealed a very important feature of the nonlinear phenomena in SAWs. One of the fundamental properties of the linear SAWs is the prescribed relation between the spatial distribution of the acoustic disturbance along the surface and in depth.[16–18] In the case of harmonic waves, for example, it is sufficient to fix the frequency in order to define simultaneously in a unique manner both the wavelength and the depth profile of the SAW. Theories[11,12] revealed that the γ^2-perturbation of the linear surface wave, which satisfies both the wave equations and the boundary conditions, has a depth structure which is different from that in a linear SAW.

[a]On leave from the International Laser Center, Moscow State University, 119899 Moscow, Russia.

 0001-4966/98/103(6)/3203/13/$10.00

In particular, the γ^2-perturbation can contain depth profile contributions in the form of products of the depth coordinate and the depth profile typical of the linear SAW (the so-called ''secular terms'' [3,5,14]). In other words, the SAWs generated in the process of the SAW self-action cannot be represented as a superposition of the linear SAWs. So the γ^2 perturbation is not a linear SAW itself, but it can accompany a linear SAW in a nonlinear medium.

Surely, the validity of the theoretical predictions extracted from the perturbative approach is limited as the perturbative approach itself. As a third step of successive approximations it is necessary to take into account the interaction between the first-order ($\propto\gamma$) leading wave and second-order ($\propto\gamma^2$) perturbations, which provides additional corrections of the order γ^3, etc. However, for the nondispersive waves, as SAWs are,[16–18] further extension of the successive perturbative steps is not expected to be fruitful. The reason for this is well known from the theories of nonlinear bulk acoustic waves:[15] the effect of accumulation of the disturbances. It is well established that in nondispersive nonlinear waves the combined contributions of the infinite number of perturbations of increasing order ($\propto\gamma^2+\propto\gamma^3+\propto\gamma^4+\cdots$) could be of the order γ. So, it appears that for a sufficiently precise description of the leading-order term in the nonlinear SAW, too, many successive steps have to be taken in a perturbative method (for example, in the case of shock formation). In order to overcome these complications the so-called nonlinear evolution equation for the SAW should be derived by choosing appropriate scaled coordinates.

The nonlinear evolution equation for the bulk acoustic wave[15] describes the slow variation (with time or with propagation distance) of the leading term ($\propto\gamma$) of the finite-amplitude acoustic wave due to its nonlinear selfaction. These slow changes occur in the coordinate system accompanying the wave. It is important that, though the accumulation of the nonlinear disturbances is a slow process which develops at the time scale significantly longer ($\gamma^{-1}\gg 1$ times) than the acoustic pulse duration (or the harmonic wave period), nevertheless the final action on the wave profile can be substantial. It can be of the order of the initial wave amplitude (i.e., $\propto\gamma$). Numerous attempts to derive the evolution equations for the nonlinear SAWs were undertaken (see, for example, Refs. 3–7, 13, and 14, and references therein). Unfortunately, many of the theories (for example, Refs. 6, 7, and 13), in our opinion, do not properly take into account the peculiar features of the finite-amplitude SAWs, which were revealed already in the perturbative theories.[11,12] It is explicitly assumed in the theories in Refs. 6, 7, and 13 that the leading terms $\propto\gamma$ in the nonlinear SAW have the same depth structure as in a linear SAW. This assumption has not been proven[6,7,13] and, in our opinion, this assumption cannot be made *a priori*. In fact, it follows from the perturbative approach that the finite-amplitude SAW can, in principle, support the propagation of an acoustic disturbance with a depth structure different from that of linear SAWs. Then it should be expected that, in a nondispersive medium, the accumulation of these disturbances, as well as their interaction with the leading terms of the wave, should lead to the depth structure of the leading term in the nonlinear SAW, which is different from that of a linear SAW. At least there are no reasons to neglect this possibility *a priori*. We would like to point out once more that the theories in Refs. 4, 6, and 13 allow, in principle, for the deviation of the depth structure of the nonlinear SAW from that of a linear SAW but not in the leading order, i.e., only in the second-order ($\propto\gamma^2$) terms (similar to the perturbative approach[11,12]).

The possibility for the nonlinear surface wave to have depth structure different from that of a linear SAW was taken into account in the theories Refs. 3, 5, and 14. Formally this has been achieved by assuming that in the nonlinear SAW the depth distribution, prescribed for the linear SAW, exhibits additional slow modulation in depth. Though this modulation is slow and has a characteristic spatial scale significantly ($\propto\gamma^{-1}\ll 1$ times) exceeding the penetration depth of the SAW, nevertheless this modulation could in principle lead to a significant difference between the depth profiles of nonlinear and linear SAWs (i.e., the difference can be of the order of γ). Most important, however, is not the possibility of this significant difference between the depth profiles, but rather the fact that the derivatives of the leading terms in the nonlinear SAW over this slow depth coordinate are of the same order ($\propto\gamma^2$) as the nonlinear terms in the equations. Consequently, these derivatives are contributing to the evolution equations in the interior of the medium[5] and are essential for the derivation of the evolution equation for the surface motion as well.[3,5,14] Unfortunately, the evolution equations for the nonlinear SAWs were derived in Refs. 3, 5, and 14 at the expense of introducing additional artificial constraints on the possible forms of the nonlinear SAW depth profiles. The method applied in the theories in Refs. 3, 5, and 14 was a construction of the asymptotic solution in the form of a power series in γ, similar to the general perturbative approach, but with all the terms (i.e., leading term $\propto\gamma$, γ^2 perturbation, etc.) depending both on the usual fast variables as in a linear SAW and also on slow variables (slow time and slow coordinates). The evolution equation for the leading term in the nonlinear SAW appears in these theories as a condition of the absence (cancellation) of the secular terms in the γ^2 perturbation. The cancellation of the secular terms is, in accordance with Refs. 3, 5, and 14, sufficient to make the proposed asymptotic expansions valid at all depths. It is clear that the assumption of the secular terms' cancellation is not physical in its origin, but rather a mathematical condition for the validity of the chosen mathematical approach. This point of view as well as the comparison of the assumption of the secular terms' cancellation with the results of the perturbative treatment of the problem (where this term cannot be canceled) leads to the conclusion that it would be highly desirable to avoid this assumption in the derivation of the evolution equations.

We demonstrated only recently[19,20] that the slowly varying wave profile method (well known in the nonlinear acoustics of bulk waves[15]) becomes, with proper modification, an extremely powerful tool for the derivation of the evolution equations for the nonlinear surface and interface elastic waves. The nonlinear evolution equations for the Scholte[19] and Rayleigh[20] waves in isotropic media were derived without any other assumptions than a physical one: the cumula-

tive effect of weak nonlinear interactions leads to slow variation of the SAW both in time and space. In the present publication this formal approach is extended to the analysis of nonlinear SAWs on anisotropic solids. New evolution equations are derived.

In Sec. II the basic results of the linear SAW theory are reviewed. The equations of the first order in the derivatives over the depth coordinate are derived for the linear SAWs. These equations appear to be very useful for the nonlinear generalization of the theory. In Sec. III the evolution equations for the nonlinear SAWs are derived by the slowly varying wave profile method. In Sec. III we give a few simple first steps in the physical analysis of the derived equations.

I. REDUCED-ORDER INTEGRO-DIFFERENTIAL RELATIONS FOR THE LINEAR SAWS

In the overview of the linear theory of the SAWs on anisotropic solids, which is presented in the first part of this section and which is necessary to facilitate the nonlinear generalization in Sec. II, we are very closely following some of the definitions from the treatment in Ref. 16. The equations of motion for the anisotropic solid in Lagrangian coordinates are

$$\rho \frac{\partial^2 u_i}{\partial t^2} = \frac{\partial T_{ij}}{\partial x_j}, \tag{1}$$

wherein u_i $(i=1,2,3)$ are the displacement components of a point along the corresponding Cartesian axes x_i, ρ is the uniform (reference) mass density, T_{ij} is a stress tensor, and the summation convention has been introduced in that a repeated subscript in a term implies that the term is summed over the values of the repeated index. The boundary condition at the mechanically free surface $x_3=0$ of the anisotropic half-space $x_3 \leqslant 0$ is

$$T_{3j}=0 \quad \text{at} \quad x_3=0. \tag{2}$$

In the linear elasticity Hooke's law holds, i.e.,

$$T_{ij}=c_{ijkm}\partial u_k/x_m, \tag{3}$$

where c_{ijkm} is the tensor of the first-order elastic constants. Note that the influence of piezoelectricity[1,16–18] is neglected everywhere in this publication. The substitution of Eq. (3) into Eqs. (1) and (2) leads to the following representation of the wave equations and the boundary conditions in linear elasticity theory

$$\rho \frac{\partial^2 u_i}{\partial t^2} - c_{ijkm} \frac{\partial^2 u_k}{\partial x_j \partial x_m} = 0, \tag{4}$$

$$c_{i3km}\partial u_k/x_m = 0 \quad \text{at} \quad x_3=0. \tag{5}$$

The fundamental solutions of interest here are the surface waves which propagate parallel to the surface with a phase velocity s and whose displacement amplitudes decay away from the surface (i.e., along the x_3 axis, which is the inward normal to the surface). Without loss of generality the direction of propagation can be taken along the x_1 axis, thus defining the (x_1,x_3) plane as the sagittal plane. The surface waves are assumed to be straight crested in that there is no dependence of the displacement amplitudes on the x_2 coordinate. In the linear problem it is sufficient to find the solution for the harmonic wave of frequency ω because the generalization for the wide-frequency-band signals is straightforward. The solution, satisfying these assumptions, is assumed to be a linear superposition of partial waves each of the form

$$u_j=\alpha_j \exp(i\omega b x_3/s)\exp[-i\omega(t-x_1/s)], \tag{6}$$

which propagate along the x_1 axis with a phase velocity $s>0$ and decay in depth with a decay constant $\omega b/s$. The imaginary part of the decay constant must be positive so that the amplitude vanishes for $x_3 \to +\infty$, a necessary condition for a SAW. As the cyclic frequencies ω are assumed to have real values here, then for the wave localization near the surface the sign of the imaginary part of b should coincide with the sign of the frequency ω. Thus the constant b in the partial wave of Eq. (6) should have the form

$$b=\mathrm{Re}\ b+i\ \mathrm{sgn}(\omega)|\mathrm{Im}\ b|, \quad |\mathrm{Im}\ b|>0. \tag{7}$$

Substituting Eq. (6) into Eq. (4) gives a homogeneous set

$$\rho s^2 \alpha_i - [c_{i1k1}+(c_{i1k3}+c_{i3k1})b+c_{i3k3}b^2]\alpha_k = 0. \tag{8}$$

For a nontrivial solution the principal determinant of this set should be equal to zero. This requirement provides an algebraic equation of the sixth order in b with real coefficients for a specified value of s. The roots b_n of this equation are real or occur in complex pairs. Thus in general it is possible to choose roots satisfying the condition of Eq. (7) for the confinement, and the number of the partial waves contributing to the SAW does not exceed three. It should be pointed out that each constant b, satisfying Eq. (7), is in practice composed of two roots: if a root satisfies the condition (7) for positive frequencies, for example, then the complex conjugated root satisfies the condition (7) for negative frequencies. Note that choosing only the roots satisfying Eq. (7) we are disregarding at least half of the possible solutions of the wave equations (i.e., all the waves with the amplitudes growing or oscillating along the x_3 coordinate).

In accordance with the summation convention a linear combination of the partial waves of Eq. (6) can be represented as

$$u_j=C_n\alpha_{jn} \exp(i\omega b_n x_3/s)\exp[-i\omega(t-x_1/s)], \tag{9}$$

where in general there are three partial waves (summation is over the values $n=1,2,3$) and α_{jn} are the eigenvectors or partial wave amplitudes[16] defined for the chosen b_n by Eq. (8). The weighting coefficients C_n should be selected to make the assumed solution (9) satisfy the boundary conditions of Eq. (5). Substituting Eq. (9) into Eq. (5) gives

$$(c_{j3k1}+c_{j3k3}b_n)\alpha_{kn}C_n \equiv d_{jn}C_n = 0. \tag{10}$$

For a nontrivial solution the principal determinant of the set of Eq. (10) should be equal to zero ($\det|d_{jn}|=0$). This condition can be considered as an implicit equation in phase velocity s, because the coefficients in Eq. (10) are functions of s. Once the value of s satisfying this equation has been found, the b_n and α_{jn} are then known, and the weighting coefficients C_n can be found from Eq. (10). Thus the parameters of the harmonic SAW [Eq. (9)] satisfying both the wave equations and the boundary conditions are then all

known. Unfortunately, in general, because of algebraic complexity, numerical techniques must be used to determine the actual phase velocity and the corresponding particle displacements.

In the following theoretical analysis all the parameters of the linear SAW [Eq. (9)], i.e., s, b_n, α_{jn}, and C_n can be considered now to be known. Then it is fruitful to reveal two properties of the solution (9), which are important for the nonlinear generalization in Sec. II. From Eq. (8) it is clear that Re b_n and Im b_n do not depend on the frequency ω. Thus the dependence of b_n on frequency is associated solely with a factor sgn (ω) in Eq. (7). In determining α_{jn} and C_n it can be assumed, without loss of generality, that, for example, $\alpha_{1n}=1$ and $C_1=1$ (in practice it is sufficient to consider them to be real values). Then from the form of b_n [Eq. (7)] and Eq. (8) it follows that α_{jn} has the form

$$\alpha_{jn}=\mathrm{Re}\ \alpha_{jn}+i\ \mathrm{sgn}(\omega)\mathrm{Im}\ \alpha_{jn}, \tag{11}$$

where Im α_{jn} denotes the imaginary part of α_{jn} for $\omega>0$, and Re α_{jn} and Im α_{jn} do not depend on frequency. Similarly from Eqs. (7), (10), and (11) it follows that C_n has the form

$$C_n=\mathrm{Re}\ C_n+i\ \mathrm{sgn}(\omega)\mathrm{Im}\ C_n, \tag{12}$$

where Im C_n denotes the imaginary part of C_n for $\omega>0$, and Re C_n and Im C_n do not depend on frequency. Importantly b_n, α_{jn}, and C_n, defined by Eqs. (7), (11), and (12) correspondingly, satisfy the condition $\varphi(-\omega)=\mathrm{c.c.}\varphi(\omega)$, where φ stands for a typical function and c.c. denotes the operation of complex conjugation. Consequently, direct superposition of the harmonic partial waves of Eq. (9) gives the general description of the real-valued wide-frequency-band linear SAW

$$\begin{aligned} u_j&=\frac{1}{2\pi}\int_{-\infty}^{+\infty}d\omega\ f(\omega)C_n\alpha_{jn}\exp(i\omega b_n x_3/s)\\ &\quad\times\exp[-i\omega(t-x_1/s)]\\ &\equiv\frac{1}{2\pi}\int_{-\infty}^{+\infty}d\omega\ \tilde{u}_j(\omega)\exp(-i\omega t), \end{aligned} \tag{13}$$

where $\tau=t-x_1/s$ denotes the retarded time and $\tilde{u}_j(\omega)$ denotes the frequency spectrum of the displacement component. The Fourier transform inverse to Eq. (13) is

$$\tilde{u}_j(\omega)=\int_{-\infty}^{+\infty}d\tau\ u_j(\tau)\exp(i\omega\tau). \tag{14}$$

The only additional condition on the otherwise arbitrary function $f(\omega)$ [to insure a real value for the displacement u_j in Eq. (13)] is $f(-\omega)=\mathrm{c.c.}f(\omega)$.

The easiest to derive are the relations between the displacement components at the surface $x_3=0$. From Eq. (13) it follows that at the surface the displacement components are linearly interdependent in the frequency domain. They can be related to only one of them, $\tilde{u}_i$, for example

$$\tilde{u}_j=C_n\alpha_{jn}f(\omega)\equiv\gamma_j f(\omega)=(\gamma_j/\gamma_i)\tilde{u}_i \quad \text{at } x_3=0. \tag{15}$$

Note that the summation convention is not applied in Eq. (15) to the reference index ''i,'' i.e., there is no summation over repeated index ''i.'' Equation (15) provides a relation between two particular components $\tilde{u}_j$ and $\tilde{u}_i$. In the following everywhere, where we are using γ_j/γ_i, the first index (''i'') can participate in summation, while the second (''i'') cannot. As a consequence of Eqs. (11) and (12) the relation Eq. (15) can be represented as

$$\tilde{u}_j=[\mathrm{Re}(\gamma_j/\gamma_i)+i\ \mathrm{sgn}(\omega)\mathrm{Im}(\gamma_j/\gamma_i)]\tilde{u}_i \quad \text{at } x_3=0. \tag{16}$$

As it was already the case before in Eqs. (11) and (12), we use here and further on the symbol Im to define the imaginary part of the function for the positive frequencies. The Fourier transform of Eq. (16) leads to the relation between the displacement components in the time domain:

$$\begin{aligned} u_j&=\mathrm{Re}(\gamma_j/\gamma_i)u_i-\mathrm{Im}(\gamma_j/\gamma_i)\mathrm{H}[u_i]\\ &\equiv[\mathrm{Re}(\gamma_j/\gamma_i)-\mathrm{Im}(\gamma_j/\gamma_i)\mathrm{H}]u_i \quad \text{at } x_3=0. \end{aligned} \tag{17}$$

Here H denotes the Hilbert transform operator over the retarded time,

$$\begin{aligned} \mathrm{H}[\varphi]&=-\frac{1}{2\pi}\int_{-\infty}^{+\infty}d\omega[i\ \mathrm{sgn}(\omega)]\tilde{\varphi}(\omega)\exp(-i\omega\tau)\\ &=\frac{1}{\pi}\ \mathrm{p.v.}\int_{-\infty}^{+\infty}\frac{d\tau'}{\tau'-\tau}\ \varphi(\tau'), \end{aligned}$$

where p.v. stands for the principal value of the integral.

Physical and mathematical intuition leads to the prediction that there should exist equations for the linear SAW [i.e., for the wave described by Eq. (13)], which are of a lower order in the derivatives over the depth coordinate x_3 than the original equation (4). In fact, we know that, if, for example, in the case of bulk longitudinal one-dimensional acoustic waves, it is sufficient to describe only the wave propagating in the positive direction (i.e., neglecting possible counter propagating wave), then the order of the differential equations for this unidirectional wave can be reduced. We have seen earlier that the general solution of the problem in Eqs. (4) and (5) contains both: disturbances localized near the surface $x_3=0$ (i.e., SAWs) and the disturbances infinitely growing or oscillating along the x_3 coordinate [associated with those roots b_n, which do not contribute to the solution Eq. (13)]. As the original equation (4) contains second-order derivatives over the x_3 coordinate, it looks favorable that there should exist equations of the first order in the derivatives over the x_3 coordinate, which permit only localized solutions. To derive these equations we first rewrite the spectrum of the displacement components from Eq. (13) in the form

$$\tilde{u}_j=C_n\alpha_{jn}f(\omega)\exp(i\omega b_n x_3/s)\equiv\alpha_{jn}\tilde{\phi}_n. \tag{18}$$

Then from Eq. (13) we find the following representation for the spectrum of displacement derivatives over the retarded time $\partial\tilde{u}_j/\partial\tau=\alpha_{jn}(-i\omega)\tilde{\phi}_n$. Consequently, $(-i\omega)\tilde{\phi}_n=(\alpha^{-1})_{nj}\partial\tilde{u}_j/\partial\tau$, where the notation $(\alpha^{-1})_{nj}$ is introduced for the inverse matrix. Then, starting from Eq. (18), we derive in the frequency domain

$$\frac{\partial \tilde{u}_j}{\partial x_3} = -\frac{b_n}{s}\alpha_{jn}(-i\omega)\tilde{\phi}_n = -\frac{1}{s}\, b_n \alpha_{jn}(\alpha^{-1})_{nk}\frac{\partial \tilde{u}_k}{\partial \tau}$$

$$\equiv -\frac{1}{s}\,\beta_{jk}\frac{\partial \tilde{u}_k}{\partial \tau}. \tag{19}$$

It is clear that the tensor β_{jk} (as well as all the other coefficients, which appeared before and will appear further on) has the form $\beta_{jk} = \mathrm{Re}\,\beta_{jk} + i\,\mathrm{sgn}\,(\omega)\,\mathrm{Im}\,\beta_{jk}$ with frequency-independent $\mathrm{Re}\,\beta_{jk}$ and $\mathrm{Im}\,\beta_{jk}$. Thus the time-domain version of the relations (19) is

$$\frac{\partial u_j}{\partial x_3} + \frac{1}{s}\,[\mathrm{Re}\,\beta_{jk} - \mathrm{Im}\,\beta_{jk}\mathrm{H}]\,\frac{\partial u_k}{\partial \tau} = 0. \tag{20}$$

The derived integro-differential equations (20) are valid only for the waves propagating in the positive direction of the x_1 axis. That is why they contain only the operations over the retarded time but not the operations over the time t and coordinate x_1 separately. The derived wave equations [Eq. (20)] are of the first order in the derivatives over the x_3 coordinate because they are valid only in the half-space $x_3 \geqslant 0$ and only for the acoustic waves localized near the surface $x_3 = 0$. For the nonlinear theory of Sec. II it is important that Eq. (20) provides the opportunity to relate differentiation over the x_3 coordinate to the operations over the retarded time τ at all depths. Moreover, the derivative over the x_3 coordinate of any order can be related only to the operations over the retarded time. For example, applying the rules of Eq. (20) twice successively and using the identity $\mathrm{H}[\mathrm{H}[\varphi]] = -\varphi$, we obtain

$$\frac{\partial^2 u_j}{\partial x_3^2} = \frac{1}{s^2}\,[\mathrm{Re}\,\beta_{jk}\,\mathrm{Re}\,\beta_{ki} - \mathrm{Im}\,\beta_{jk}\,\mathrm{Im}\,\beta_{ki}$$

$$-(\mathrm{Re}\,\beta_{jk}\,\mathrm{Im}\,\beta_{ki} + \mathrm{Im}\,\beta_{jk}\,\mathrm{Re}\,\beta_{ki})\mathrm{H}]\,\frac{\partial^2 u_i}{\partial \tau^2}$$

$$\equiv \frac{1}{s^2}\,[\mathrm{Re}\,\zeta_{jk} - \mathrm{Im}\,\zeta_{jk}\mathrm{H}]\,\frac{\partial^2 u_k}{\partial \tau^2}. \tag{21}$$

It should also be mentioned that the relation of the second-order derivatives over the x_3 coordinate to the operations over the retarded time can also be obtained by substituting the first-order derivative [Eq. (20)] into the original equation (4), which contains both $\partial u_j/\partial x_3$ and $\partial^2 u_j/\partial x_3^2$.

II. SLOWLY VARYING WAVE PROFILE METHOD FOR THE NONLINEAR SAWS

In the second-order elasticity theory the Piola–Kirchhoff stress tensor T_{ij} can be represented as[1]

$$T_{ij} = s_{ijkm}\,\frac{\partial u_k}{\partial x_m} + \frac{1}{2}\,s_{ijkmpr}\,\frac{\partial u_k}{\partial x_m}\,\frac{\partial u_p}{\partial x_r} \equiv s_{ijkm}\,\frac{\partial u_k}{\partial x_m} + N_{ij}, \tag{22}$$

where linear and nonlinear (N_{ij}) parts are split. Note that the coefficients s_{ijkmpr} involve both the first-order ($s_{ijkm} = c_{ijkm}$) and the second-order (c_{ijkmpr}) elastic constants.[1] Substituting Eq. (22) into Eqs. (1) and (3) gives

$$\rho\,\frac{\partial^2 u_i}{\partial t^2} - c_{ijkm}\,\frac{\partial^2 u_k}{\partial x_j \partial x_m} = \frac{\partial N_{ij}}{\partial x_j},$$

$$c_{i3km}\,\frac{\partial u_k}{\partial x_m} = -N_{i3} \quad \text{at } x_3 = 0. \tag{23}$$

For the straight-crested SAWs the wave equations and boundary conditions of Eq. (23) simplify to

$$\rho\,\frac{\partial^2 u_i}{\partial t^2} - \left[c_{i1k1}\,\frac{\partial^2}{\partial x_1^2} + (c_{i1k3} + c_{i3k1})\,\frac{\partial^2}{\partial x_1 \partial x_3} + c_{i3k3}\,\frac{\partial^2}{\partial x_3^2}\right]u_k$$

$$= \frac{\partial N_{i1}}{\partial x_1} + \frac{\partial N_{i3}}{\partial x_3} \equiv F_i, \tag{24}$$

$$\left(c_{i3k1}\,\frac{\partial}{\partial x_1} + c_{i3k3}\,\frac{\partial}{\partial x_3}\right)u_k = -N_{i3} \quad \text{at } x_3 = 0. \tag{25}$$

The possible simplification of nonlinear parts F_i and N_{i3} for the straight-crested SAWs will be taken explicitly into account only at the final stage of the nonlinear terms evaluation in the evolution equations.

Following the physical guidelines discussed in the Introduction and the principles of the slowly varying wave profile method we assume that properly normalized displacement components u_j in the SAW are of the first order of smallness, or, in other words, are the small quantities of the order of γ ($\gamma \ll 1$ small scaling parameter). We assume that u_j depends on the fast variable $\tau = t - x_1/s$, i.e., on retarded time, and has also the prescribed dependence on the fast variable x_3. The dependence of u_j on x_3 is assumed to be the same as in a linear SAW with the same profile in retarded time. So, in principle, where necessary, it can be considered as known in advance from the solution (Sec. I) of the linearized problem, i.e., from the solution [Eq. (13)] of the equations (24) and (25) in the absence of the nonlinear stresses ($N_{ij} = 0$). In practice, for the derivation of the evolution equation only the relations between the operations on linear SAWs over the different fast variables, Eqs. (19) and (20), and the relations between different displacement components in linear SAWs at the surface [Eqs. (16) and (17)] are useful, but not the precise form of the linear SAW depthprofile. We assume that, in addition to the dependence of u_j on the fast variables τ and x_3, the cumulative effect of weak nonlinear interactions causes a slow variation of u_j both in time t and depth coordinate x_3. These assumptions can be symbolically represented as

$$u_j = \gamma u_j(\theta = \gamma t, \eta = \gamma x_3, \tau = t - x_1/s, x_3). \tag{26}$$

We would like to make the following comments here. (1) Instead of two independent variables t and x_1, it is always possible to introduce two other ones. If one of these new variables is $\tau = t - x_1/s$ (as we have defined the retarded time for the SAW propagation in the positive direction of the x_1 axis), then the other should differ from it in order to be independent. It follows from the theory of the nonlinear bulk acoustic waves[15] and also from some papers on nonlinear SAWs (see Refs. 3 and 14, for example) that though it is equivalent to introduce any of the linear combinations of t and x_1 (which differs from τ) as a slow variable, the most popular variables are $\theta = \gamma t$ and $\zeta = \gamma x_1$. We preferred the

former. (2) It is possible to introduce the slow variable $\eta = \gamma x_3$ in addition to the fast variable x_3 (i.e., to use two linearly dependent variables instead of one original) only because the dependence on the fast variable x_3 is prescribed.

In the following we will not write the scaling parameter γ explicitly in the equations, keeping in mind that each multiplication by u_j or its derivatives over fast time τ, or each differentiation over a slow variable θ or η, increases the order of smallness of the particular term by one. In accordance with Eq. (26) the rules of differentiation of the slowly varying profile are

$$\frac{\partial u_j}{\partial t} = \frac{\partial u_j}{\partial \tau} + \frac{\partial u_j}{\partial \theta}, \quad \frac{\partial u_j}{\partial x_3} = \frac{\partial u_j}{\partial x_3} + \frac{\partial u_j}{\partial \eta}, \quad \frac{\partial u_j}{\partial x_1} = -\frac{1}{s}\frac{\partial u_j}{\partial \tau}. \tag{27}$$

The left-hand sides (lhs) in Eqs. (27) are the full derivatives, while in the right-hand sides (rhs) the derivatives over fast and slow variables are separated. Using the rules of Eqs. (27) on the lhs of Eqs. (24) and (25), we then retain only the terms of the order of γ and γ^2:

$$\rho\frac{\partial^2 u_i}{\partial \tau^2} - \left[\frac{c_{i1k1}}{s^2}\frac{\partial^2}{\partial \tau^2} - \frac{(c_{i1k3}+c_{i3k1})}{s}\frac{\partial^2}{\partial \tau\,\partial x_3} + c_{i3k3}\frac{\partial^2}{\partial x_3^2}\right]u_k = -2\rho\frac{\partial^2 u_i}{\partial \tau\,\partial \theta} - \left[\frac{(c_{i1k3}+c_{i3k1})}{s}\frac{\partial^2}{\partial \tau\,\partial \eta} - 2c_{i3k3}\frac{\partial^2}{\partial x_3\,\partial \eta}\right]u_k + F_i, \tag{28}$$

$$\left(\frac{c_{i3k1}}{s}\frac{\partial}{\partial \tau} - c_{i3k3}\frac{\partial}{\partial x_3}\right)u_k = c_{i3k3}\frac{\partial u_k}{\partial \eta} + N_{i3} \equiv R_i \quad \text{at } x_3 = \eta = 0. \tag{29}$$

Here the terms of the order of γ are grouped on the lhs, while the terms of the order γ^2 are all on the rhs. Note that, as the nonlinear terms in the equations are initially of the second order of smallness, the derivatives over the slow variables do not contribute to them. The lhs of the wave equation (28) coincides with the lhs of the corresponding wave equations for the linear SAW. Consequently, our assumption, that the dependence of u_j on the fast variable x_3 is the same as in linear SAW, leads to the mutual cancellation of the first-order terms in Eq. (28). As a result, Eq. (28) takes the form of the evolution equation

$$2\rho\frac{\partial^2 u_i}{\partial \tau\,\partial \theta} + \left[\frac{(c_{i1k3}+c_{i3k1})}{s}\frac{\partial^2}{\partial \tau\,\partial \eta} - 2c_{i3k3}\frac{\partial^2}{\partial x_3\,\partial \eta}\right]u_k = F_i. \tag{30}$$

With the help of Eqs. (20) and (21) and the last rule in Eq. (27), Eq. (30) can be expressed in a form which contains only the first derivatives over the slow variables θ and η, and linear and nonlinear operations over the retarded time

$$\frac{\partial}{\partial \tau}\left\{2\rho\frac{\partial u_i}{\partial \theta} + \frac{1}{s}\frac{\partial}{\partial \eta}[c_{i1k3} + c_{i3k1} + 2c_{i3j3}(\mathrm{Re}\,\beta_{jk} - \mathrm{Im}\,\beta_{jk}\mathrm{H})]u_k\right\} = F_i. \tag{31}$$

Equation (31) holds for $x_3 \geqslant 0$ (i.e., $\eta \geqslant 0$). We would like to emphasize here that F_i contains operations over the retarded time only.

It is clear that the lhs of the boundary conditions in Eq. (29) coincide with the lhs of the boundary conditions for the linear SAWs. Then, from the theory of the linear SAWs, it follows that these (in general three) lhs's are linearly interdependent in the frequency domain. Thus the lhs (i.e., all the terms of the first order of smallness) can be expelled from the boundary conditions, leading to a single relation between the second-order terms only. To derive this relation we apply the direct Fourier transform of Eq. (14) to Eq. (29):

$$\left(\frac{c_{i3k1}}{s}\frac{\partial}{\partial \tau} - c_{i3k3}\frac{\partial}{\partial x_3}\right)\tilde{u}_k = \tilde{R}_i \quad \text{at } x_3 = \eta = 0. \tag{32}$$

Then substituting Eq. (19) into Eq. (32), we rewrite

$$\frac{1}{s}(c_{j3i1} + c_{j3k3}\beta_{ki})\frac{\partial \tilde{u}_i}{\partial \tau} = \frac{1}{s}d_{jn}(\alpha^{-1})_{ni}\frac{\partial \tilde{u}_i}{\partial \tau} = \tilde{R}_j \quad \text{at } x_3 = \eta = 0. \tag{33}$$

Equation (33) can be considered as an inhomogeneous set for the unknowns $(\alpha^{-1})_{ni}\partial \tilde{u}_i/\partial \tau$. The matrix of the coefficients of this set coincides with the coefficients of Eq. (10). Then, due to the fact that the principal determinant of this system is equal to zero ($\det|d_{jn}| = 0$), the bounded solutions exist only when all the particular determinants are equal to zero. Thus the relation between the rhs of Eq. (33) can be obtained by equating any of the particular determinants to zero. For example, from

$$\det\begin{vmatrix} d_{11} & \tilde{R}_1 & d_{13} \\ d_{21} & \tilde{R}_2 & d_{23} \\ d_{31} & \tilde{R}_3 & d_{33} \end{vmatrix} = 0,$$

this relation can be represented as

$$\sigma_j\tilde{R}_j = \sigma_j\left(c_{j3k3}\frac{\partial \tilde{u}_k}{\partial \eta} + \tilde{N}_{j3}\right) = 0 \quad \text{at } \eta = 0, \tag{34}$$

with $\sigma_1 = d_{23}d_{31} - d_{21}d_{33}$, $\sigma_2 = d_{11}d_{33} - d_{13}d_{31}$, and $\sigma_3 = d_{21}d_{13} - d_{11}d_{23}$. The corresponding boundary condition in the time domain is

$$(\mathrm{Re}\,\sigma_j - \mathrm{Im}\,\sigma_j\mathrm{H})\left(c_{j3k3}\frac{\partial u_k}{\partial \eta} + N_{j3}\right) = 0 \quad \text{at } \eta = 0. \tag{35}$$

The set of Eq. (31) with the boundary condition (35) provides a complete description in the time domain for the problem of the finite-amplitude SAW time evolution in the frame of the second-order elasticity theory. All the terms in Eqs. (31) and (35) are of the same order of smallness ($\propto \gamma^2$). Due to this, it is correct to use in Eqs. (31) and (35) the expression for the particle vibrational velocity v_i, which holds in

the linear (first-order) approximation $\nu_i = \partial u_i/\partial t = \partial u_i/\partial \tau + \partial u_i/\partial \theta \approx \partial u_i/\partial \tau$. Thus Eqs. (31) and (35) can be rewritten in the form

$$2\rho \frac{\partial \nu_i}{\partial \theta} + \frac{1}{s}\frac{\partial}{\partial \eta}[c_{i1k3} + c_{i3k1} + 2c_{i3j3}(\mathrm{Re}\ \beta_{jk} - \mathrm{Im}\ \beta_{jk}\mathrm{H})]\nu_k = F_i, \tag{36}$$

$$(\mathrm{Re}\ \sigma_j - \mathrm{Im}\ \sigma_j \mathrm{H})\left(c_{j3k3}\frac{\partial \nu_k}{\partial \eta} + \frac{\partial N_{j3}}{\partial \tau}\right) = 0 \quad \text{at} \quad \eta = 0. \tag{37}$$

It should be noticed that with the help of Eqs. (20), (21), and (27) the nonlinear terms F_i and $\partial N_{j3}/\partial \tau$ can also be represented in a form containing only the operations on vibrational velocities ν_j.

It is possible, in principle, to proceed further in the solution of the problem in Eqs. (36) and (37) operating exclusively in the time domain (compare with Refs. 19 and 20). For this purpose it is necessary to combine three equations (36) and three Hilbert transformed equations (36) into a set for six unknowns $\partial \nu_k/\partial \eta$ and $\mathrm{H}[\partial \nu_k/\partial \eta]$ $(k = 1,2,3)$. The solution of this set provides the relation of the unknowns to $\partial \nu_k/\partial \theta$ and to nonlinear terms. Substituting $\partial \nu_k/\partial \eta$ and $\mathrm{H}[\partial \nu_k/\partial \eta]$ into the boundary condition (37) gives the evolution equation for the surface motion. Then using at the surface the relationships

$$\nu_j = [\mathrm{Re}(\gamma_j/\gamma_i) - \mathrm{Im}(\gamma_j/\gamma_i)\mathrm{H}]\nu_i, \tag{38}$$

which follows from Eq. (17) (valid at the surface), it is possible to derive the evolution equation containing a single unknown vibrational velocity component ν_i. As the next step the evolution equations for the components of the surface vibrational velocity should be solved. Finally, the obtained solutions should be used as the boundary conditions for the set of equations (36) of the evolution equations in the interior of the medium. However, the majority of this program is beyond the scope of the present publication. We will describe here only the first part of the program, i.e., the derivation of the evolution equations for the surface motion, and discuss in Sec. III a few properties of these equations.

To derive the evolution equation for the surface motion we operate with the linear terms of Eqs. (36) and (37) in the frequency domain. However, in contrast to previous approaches[3–5,7,21] we will evaluate nonlinear terms after returning from frequency domain to time domain. From the frequency-domain version of Eq. (36),

$$\frac{1}{s}(c_{i1k3} + c_{i3k1} + 2c_{i3j3}\beta_{jk})\frac{\partial \tilde{\nu}_k}{\partial \eta} \equiv \chi_{ik}\frac{\partial \tilde{\nu}_k}{\partial \eta} = -2\rho \frac{\partial \tilde{\nu}_i}{\partial \theta} + \tilde{F}_i,$$

we find

$$\frac{\partial \tilde{\nu}_k}{\partial \eta} = (\chi^{-1})_{ki}\left(\tilde{F}_i - 2\rho \frac{\partial \tilde{\nu}_i}{\partial \theta}\right). \tag{39}$$

Equation (39) should be substituted into the frequency-domain version of Eq. (37):

$$\sigma_j\left(c_{j3k3}\frac{\partial \tilde{\nu}_k}{\partial \eta} + \frac{\partial \tilde{N}_{j3}}{\partial \tau}\right) = 0 \quad \text{at} \quad \eta = 0.$$

This substitution gives

$$2\rho\sigma_j c_{j3k3}(\chi^{-1})_{ki}\frac{\partial \tilde{\nu}_i}{\partial \theta} = \sigma_j c_{j3k3}(\chi^{-1})_{ki}\tilde{F}_i + \sigma_i \frac{\partial \tilde{N}_{i3}}{\partial \tau}. \tag{40}$$

Then on the lhs of Eq. (40) we use the frequency-domain version of Eq. (38) [i.e., $\tilde{\nu}_i = (\gamma_i/\gamma_m)\tilde{\nu}_m$] to have in the linear terms of the evolution equation the single unknown—the component ν_m of the surface vibrational velocity

$$2\rho\sigma_j c_{j3k3}(\chi^{-1})_{ki}\left(\frac{\gamma_i}{\gamma_m}\right)\frac{\partial \tilde{\nu}_m}{\partial \theta} = \sigma_j c_{j3k3}(\chi^{-1})_{ki}\tilde{F}_i + \sigma_i \frac{\partial \tilde{N}_{i3}}{\partial \tau}. \tag{41}$$

We rewrite Eq. (41) as

$$A_m \frac{\partial \tilde{\nu}_m}{\partial \theta} = B_i \tilde{F}_i + \sigma_i \frac{\partial \tilde{N}_{i3}}{\partial \tau}, \tag{42}$$

introducing notations which are clear from the comparison of Eqs. (41) and (42). We further introduce notations $g_{mi} \equiv B_i/A_m$ and $h_{mi} = s(\sigma_i/A_m)$. Then, the inverse Fourier transform of Eq. (42), first divided by A_m, gives the evolution equation for the surface motion in the time domain:

$$\frac{\partial \nu_m}{\partial \theta} = (\mathrm{Re}\ g_{mj} - \mathrm{Im}\ g_{mj}\mathrm{H})F_j + \frac{1}{s}(\mathrm{Re}\ h_{mj} - \mathrm{Im}\ h_{mj}\mathrm{H})\frac{\partial N_{j3}}{\partial \tau}. \tag{43}$$

As was described earlier, the nonlinear terms on the rhs of Eq. (43) can be expressed in the form of operations only over the retarded time τ and only on the same component ν_m, which stands on the lhs.

We want to emphasize that, even without a solution of the problem in Eqs. (36) and (37), we demonstrated that, assuming the possibility of the slow changes of the nonlinear SAW depth structure in addition to those in the linear SAW (contrary to Refs. 4, 6, 7, and 13), we obtained terms in the wave equations (36) and boundary conditions (37) which are proportional to the derivatives over the slow coordinate η. Thus, the derived evolution equations for the surface motion, Eq. (43), takes into account that the dependence on the slow variable η is not negligible.

III. NONLINEAR EVOLUTION EQUATION FOR THE SURFACE MOTION

It is possible to describe the form of all the different terms in the evolution equation (43) for the arbitrary surface of the solid of general anisotropy. Our experience[19,20] demonstrates that it is fruitful to evaluate the nonlinear terms of Eq. (43) directly in the time domain (contrary to all the previous research[3–10,13,14]).

For the simplification of the rhs in Eq. (43) the description of the displacement spatial derivatives at the surface $x_3 = 0$, which follows from Eqs. (17), (20), (21), and (27), is very useful:

$$
\begin{aligned}
\frac{\partial u_j}{\partial x_1} &= -\left(\frac{1}{s}\right)\frac{\partial u_j}{\partial \tau} \approx -\frac{1}{s}\,\nu_j \\
&= -\frac{1}{s}\left[\mathrm{Re}\left(\frac{\gamma_j}{\gamma_i}\right) - \mathrm{Im}\left(\frac{\gamma_j}{\gamma_i}\right)\mathrm{H}\right]\nu_i, \\
\frac{\partial^2 u_j}{\partial x_1^2} &= -\left(\frac{1}{s}\right)\frac{\partial(\partial u_j/\partial x_i)}{\partial \tau} \\
&\approx \frac{1}{s^2}\left[\mathrm{Re}\left(\frac{\gamma_j}{\gamma_i}\right) - \mathrm{Im}\left(\frac{\gamma_j}{\gamma_i}\right)\mathrm{H}\right]\frac{\partial \nu_i}{\partial \tau}, \\
\frac{\partial u_j}{\partial x_3} &\approx -\frac{1}{s}\left[\mathrm{Re}\left(\frac{\beta_{jk}\gamma_k}{\gamma_i}\right) - \mathrm{Im}\left(\frac{\beta_{jk}\gamma_k}{\gamma_i}\right)\mathrm{H}\right]\nu_i, \\
\frac{\partial^2 u_j}{\partial x_3^2} &\approx \frac{1}{s^2}\left[\mathrm{Re}\left(\frac{\zeta_{jk}\gamma_k}{\gamma_i}\right) - \mathrm{Im}\left(\frac{\zeta_{jk}\gamma_k}{\gamma_i}\right)\mathrm{H}\right]\frac{\partial \nu_i}{\partial \tau}.
\end{aligned}
\tag{44}
$$

It is then clear that all the possible forms of the terms contributing to each of F_j (which contains only the various byproducts of the first and the second spatial derivatives of the displacement components) are

$$
\propto \nu_i \frac{\partial \nu_i}{\partial \tau}, \quad \propto \mathrm{H}[\nu_i]\mathrm{H}\left[\frac{\partial \nu_i}{\partial \tau}\right], \quad \propto \nu_i \mathrm{H}\left[\frac{\partial \nu_i}{\partial \tau}\right], \quad \propto \mathrm{H}[\nu_i]\frac{\partial \nu_i}{\partial \tau}, \tag{45}
$$

and only the same terms can contribute to each of $\partial N_{j3}/\partial \tau$. Surely, there is no summation over the values of the index in Eq. (45). Using the identity $2\varphi \mathrm{H}[\varphi] = \mathrm{H}[(\mathrm{H}[\varphi])^2] + \mathrm{H}[\varphi^2]$, the terms in Eq. (45) can be rewritten as

$$
\begin{aligned}
&\propto \frac{\partial}{\partial \tau}\nu_i^2, \quad \propto \frac{\partial}{\partial \tau}(\mathrm{H}[\nu_i])^2, \quad \propto \nu_i \mathrm{H}\left[\frac{\partial \nu_i}{\partial \tau}\right], \\
&\propto \mathrm{H}\left[\frac{\partial}{\partial \tau}\nu_i^2\right], \quad \propto \mathrm{H}\left[\frac{\partial}{\partial \tau}(\mathrm{H}[\nu_i])^2\right].
\end{aligned}
\tag{46}
$$

Consequently, the rhs of Eq. (43) can be represented as a superposition of the terms of Eq. (46) and their Hilbert transforms. However, the Hilbert transform adds only one additional term $\mathrm{H}[\nu_i \mathrm{H}[\partial \nu_i/\partial \tau]]$ to Eq. (46). So there are only six different nonlinear terms in the evolution equation for the surface motion. Finally, following the rules of terms grouping, proposed in Refs. 19 and 20, the evolution equation for the surface motion accompanying the propagation of the nonlinear SAW in an elastic solid of general anisotropy can be represented in the form

$$
\begin{aligned}
s\frac{\partial \nu_i}{\partial \theta} &= \varepsilon_1^{(i)}\nu_i\frac{\partial \nu_i}{\partial \tau} + \frac{\varepsilon_2^{(i)}}{2}\frac{\partial}{\partial \tau}\{\nu_i^2 + (\mathrm{H}[\nu_i])^2\} \\
&\quad + \varepsilon_3^{(i)}\left\{\nu_i\frac{\partial \nu_i}{\partial \tau} + \mathrm{H}\left[\nu_i \mathrm{H}\left[\frac{\partial \nu_i}{\partial \tau}\right]\right]\right\} \\
&\quad + \mathrm{H}\left[\varepsilon_4^{(i)}\nu_i\frac{\partial \nu_i}{\partial \tau} + \frac{\varepsilon_5^{(i)}}{2}\frac{\partial}{\partial \tau}\{\nu_i^2 + (\mathrm{H}[\nu_i])^2\}\right. \\
&\quad \left. + \varepsilon_6^{(i)}\left\{\nu_i\frac{\partial \nu_i}{\partial \tau} + \mathrm{H}\left[\nu_i \mathrm{H}\left[\frac{\partial \nu_i}{\partial \tau}\right]\right]\right\}\right].
\end{aligned}
\tag{47}
$$

Here $\varepsilon_j^{(i)}$ $(j=1,2,3,4,5,6)$ are the effective nondimensional nonlinear parameters for the evolution of the ith component of the surface vibrational velocity. The reason for this particular grouping of the nonlinear terms can be appreciated by noticing that the following simple rule for the Hilbert transform of the harmonic signals is valid: $\mathrm{H}[\exp(-i\omega\tau)] = -i\,\mathrm{sgn}(\omega)\exp(-i\omega\tau)$. Using this rule it is straightforward to check that the nonlinear operators associated in Eq. (47) with coefficients $\varepsilon_2^{(i)}$ and $\varepsilon_3^{(i)}$ (and, consequently, their Hilbert transformed pairs associated with coefficients $\varepsilon_5^{(i)}$ and $\varepsilon_6^{(i)}$) do not introduce a distortion in harmonic signals. In particular, only the operator associated with coefficient $\varepsilon_1^{(i)}$ (which is a common operator for hyperbolic waves[15]) and its Hilbert transformed pair associated with coefficient $\varepsilon_4^{(i)}$ contribute to the initial stage of the second harmonic generation.

Deeper insight in the role of the nonlinear operators associated with coefficients $\varepsilon_2^{(i)}, \varepsilon_3^{(i)}$ (and $\varepsilon_5^{(i)}, \varepsilon_6^{(i)}$) can be obtained by examining the frequency-domain version of Eq. (47):

$$
\begin{aligned}
s\frac{\partial \tilde{\nu}_i(\omega)}{\partial \theta} &= \frac{1}{4\pi}\int_{-\infty}^{\infty} d\omega'\, \tilde{\nu}_i(\omega')\tilde{\nu}_i(\omega-\omega')\langle(-i\omega) \\
&\quad \times\{\varepsilon_1^{(i)} + \varepsilon_2^{(i)}[1-\mathrm{sgn}(\omega')\mathrm{sgn}(\omega-\omega')]\} \\
&\quad - 2i(\omega-\omega')\varepsilon_3^{(i)}[1-\mathrm{sgn}(\omega)\mathrm{sgn}(\omega-\omega')] \\
&\quad - |\omega|\{\varepsilon_4^{(i)} + \varepsilon_5^{(i)}[1-\mathrm{sgn}(\omega')\mathrm{sgn}(\omega-\omega')]\} \\
&\quad - 2\,\mathrm{sgn}(\omega)(\omega-\omega')\varepsilon_6^{(i)}[1-\mathrm{sgn}(\omega) \\
&\quad \times \mathrm{sgn}(\omega-\omega')]\}\rangle.
\end{aligned}
\tag{48}
$$

In accordance with Eq. (48) the nonlinear operators associated with coefficients $\varepsilon_2^{(i)}$, $\varepsilon_3^{(i)}$, $\varepsilon_5^{(i)}$, and $\varepsilon_6^{(i)}$ can contribute to the evolution of the spectral component at frequency ω only if the component of higher frequency is already in the spectrum $\tilde{\nu}_i(\theta,\omega)$, i.e., if $|\omega'|>|\omega|$ and/or $|\omega-\omega'|>|\omega|$. These operators themselves (i.e., in the absence of the operators associated with coefficients $\varepsilon_1^{(i)}$ and $\varepsilon_4^{(i)}$) cannot broaden the spectrum of any periodic signal. Thus the nonlinear integro-differential operators associated with coefficients $\varepsilon_2^{(i)}$, $\varepsilon_3^{(i)}$, $\varepsilon_5^{(i)}$, and $\varepsilon_6^{(i)}$ are active only in the frequency down-conversion processes. From Eq. (47) it follows that the changes of the quantity $\int_{-\infty}^{\infty}\nu_i\, d\tau$ are governed by the equation

$$
\begin{aligned}
s\frac{\partial}{\partial \theta}\int_{-\infty}^{\infty}\nu_i\, d\tau &= -\varepsilon_6^{(i)}\int_{-\infty}^{\infty}\nu_i \mathrm{H}\left[\frac{\partial \nu_i}{\partial \tau}\right]d\tau \\
&= \frac{1}{\pi}\varepsilon_6^{(i)}\int_0^{\infty} d\omega|\omega||\tilde{\nu}_i(\omega)|^2.
\end{aligned}
$$

Thus the quantity $\int_{-\infty}^{\infty}\nu_i\, d\tau$ is conserved only if $\varepsilon_6^{(i)}=0$.

Before discussing the possibilities of the simplifications of the derived general evolution equation (47) in highly symmetric crystals and geometries we would like to mention that, using the identity

$$
2\mathrm{H}\left[\varphi \mathrm{H}\left[\frac{\partial \varphi}{\partial \tau}\right]\right] = \frac{\partial(\mathrm{H}[\varphi])^2}{\partial \tau} - \frac{\partial \varphi^2}{\partial \tau} - 2\mathrm{H}\left[\left(\frac{\partial \varphi}{\partial \tau}\right)\mathrm{H}[\varphi]\right],
$$

the evolution equation (47) can be represented in a slightly different mathematical form with the same physical content:

$$
\begin{aligned}
s\,\frac{\partial \nu_i}{\partial \theta} &= \varepsilon_1^{(i)} \nu_i\,\frac{\partial \nu_i}{\partial \tau} + \frac{\varepsilon_2^{(i)}+\varepsilon_3^{(i)}}{2}\,\frac{\partial}{\partial \tau}\{\nu_i^2+(\mathrm{H}[\nu_i])^2\} \\
&\quad - \varepsilon_3^{(i)}\left\{\frac{\partial \nu_i}{\partial \tau}\,\nu_i + \mathrm{H}\left[\frac{\partial \nu_i}{\partial \tau}\,\mathrm{H}[\nu_i]\right]\right\} \\
&\quad + \mathrm{H}\left[\varepsilon_4^{(i)} \nu_i\,\frac{\partial \nu_i}{\partial \tau} + \frac{\varepsilon_5^{(i)}+\varepsilon_6^{(i)}}{2}\,\frac{\partial}{\partial \tau}\{\nu_i^2+(\mathrm{H}[\nu_i])^2\}\right. \\
&\quad \left. - \varepsilon_6^{(i)}\left\{\frac{\partial \nu_i}{\partial \tau}\,\nu_i + \mathrm{H}\left[\frac{\partial \nu_i}{\partial \tau}\,\mathrm{H}[\nu_i]\right]\right\}\right].
\end{aligned}
$$

The most significant simplification of the derived evolution equation for the surface motion equation (47) could be expected if the crystal-propagation configuration is of type 5 symmetry,[18] i.e., there is a twofold crystal axis perpendicular to the sagittal plane or the sagittal plane is a crystal plane of mirror symmetry. In this case the sagittal plane displacement components u_1 and u_3 are interrelated but independent of the transverse component u_2. Thus only two components contribute to the SAW. For definiteness we evaluate the propagation of the nonlinear SAW in a basal plane ((001) plane) of a cubic crystal, when the propagation vector is along a cubic axis ([100] direction). As the basal plane of cubic crystals is a crystal plane of mirror symmetry itself, then the roots b_n for the SAW propagation have inversion symmetry in the origin of the complex plane.[17] In combination with the fact that the roots b_n occur in complex pairs, this provides an opportunity to choose two constants satisfying Eq. (7) in the form

$$
\begin{aligned}
b_1 &= \mathrm{Re}\; b + i\;\mathrm{sgn}(\omega)|\mathrm{Im}\; b|, \\
b_3 &= -\mathrm{Re}\; b + i\;\mathrm{sgn}(\omega)|\mathrm{Im}\; b|.
\end{aligned}
\tag{49}
$$

In the following qualitative analysis we explicitly account for the fact that two partial waves contributing to the SAW have in depth the same period of oscillations and the same exponential decay. We reveal that the absence ($\mathrm{Re}\, b=0$) or the presence ($\mathrm{Re}\, b\neq 0$) of oscillations along the x_3 coordinate in the partial waves is of crucial importance for the simplification of the evolution equation.

Defining $\alpha_{11}=\alpha_{13}=1$, we derive from Eq. (8) with the use of Eq. (49) the representation for the tensor α_{jn} of the partial wave amplitudes:

$$
\begin{aligned}
\alpha_{jn} &= \begin{vmatrix} 1 & 1 \\ \mathrm{Re}\;\alpha + i\;\mathrm{sgn}(\omega)\mathrm{Im}\;\alpha & -\mathrm{Re}\;\alpha + i\;\mathrm{sgn}(\omega)\mathrm{Im}\;\alpha \end{vmatrix} \\
&\propto \begin{vmatrix} \mathrm{Re} & \mathrm{Re} \\ \mathrm{Re}+i\;\mathrm{Im} & \mathrm{Re}+i\;\mathrm{Im} \end{vmatrix},
\end{aligned}
\tag{50}
$$

with

$$
\begin{aligned}
\mathrm{Re}\;\alpha &= \frac{[\rho s^2 - c_{11} - c_{44}(\mathrm{Re}\; b)^2]}{(c_{12}+c_{44})[(\mathrm{Re}\; b)^2+(\mathrm{Im}\; b)^2]}\,\mathrm{Re}\; b, \\
\mathrm{Im}\;\alpha &= \frac{[c_{11}+c_{44}(\mathrm{Im}\; b)^2 - \rho s^2]}{(c_{12}+c_{44})[(\mathrm{Re}\; b)^2+(\mathrm{Im}\; b)^2]}\,|\mathrm{Im}\; b|.
\end{aligned}
$$

In Eq. (50) and in the following formulas we will use a symbolic notation $\mathrm{Re}+i\,\mathrm{Im}$ for arbitrary complex number in order to present a qualitative description of the matrix structure. In Eq. (50) and everywhere in the following analysis we explicitly account for the particular structure of the elastic constant tensors c_{ijkm} and c_{ijkmpr} in cubic crystals and the specified crystal-propagation configuration. An elastic medium of cubic symmetry has three independent elastic moduli of second order[1,22] and six (or eight) of third order.[1,23] Starting with Eq. (50) and further we are using contracted (Voigt) indices to introduce abbreviated notations for the elastic moduli.[1,23] It should also be mentioned that starting from Eq. (50) it is assumed that the indices of the matrix coefficients [i.e., ''j'' and ''n'' in Eq. (50), for example] take only the values 1 or 3.

With the help of Eqs. (49) and (50) we find the form of the tensors β_{jk} in Eq. (19) and d_{in} in Eq. (10):

$$
\beta_{jk} \propto \begin{vmatrix} i\;\mathrm{Im} & \mathrm{Re} \\ \mathrm{Re} & i\;\mathrm{Im} \end{vmatrix},
\tag{51}
$$

$$
\begin{aligned}
d_{in} &= \begin{vmatrix} \mathrm{Re}\; d + i\;\mathrm{sgn}(\omega)\mathrm{Im}\; d & -\mathrm{Re}\; d + i\;\mathrm{sgn}(\omega)\mathrm{Im}\; d \\ \mathrm{Re}\;\overline{d} + i\;\mathrm{sgn}(\omega)\mathrm{Im}\;\overline{d} & -[-\mathrm{Re}\;\overline{d} + i\;\mathrm{sgn}(\omega)\mathrm{Im}\;\overline{d}] \end{vmatrix} \\
&\propto \begin{vmatrix} \mathrm{Re}+i\;\mathrm{Im} & \mathrm{Re}+i\;\mathrm{Im} \\ \mathrm{Re}+i\;\mathrm{Im} & \mathrm{Re}+i\;\mathrm{Im} \end{vmatrix},
\end{aligned}
\tag{52}
$$

where

$$
\begin{aligned}
&\mathrm{Re}\; d = c_{44}(\mathrm{Re}\; b + \mathrm{Re}\;\alpha), \quad \mathrm{Im}\; d = c_{44}(|\mathrm{Im}\; b| + \mathrm{Im}\;\alpha), \\
&\mathrm{Re}\;\overline{d} = c_{12} + c_{11}(\mathrm{Re}\; b\;\mathrm{Re}\;\alpha - |\mathrm{Im}\; b|\mathrm{Im}\;\alpha), \\
&\mathrm{Im}\;\overline{d} = c_{11}(\mathrm{Re}\; b\;\mathrm{Im}\;\alpha + |\mathrm{Im}\; b|\mathrm{Re}\;\alpha).
\end{aligned}
$$

Then, defining $C_1=1$, we find from Eq. (10) that the weighting coefficient C_3 is complex:

$$
\begin{aligned}
C_3 &= -\frac{d_{11}}{d_{13}}\,C_1 \\
&= \frac{(\mathrm{Re}\; d)^2 - (\mathrm{Im}\; d)^2 + 2i\;\mathrm{sgn}(\omega)\mathrm{Re}\; d\;\mathrm{Im}\; d}{(\mathrm{Re}\; d)^2 + (\mathrm{Im}\; d)^2} \\
&\propto \mathrm{Re} + i\;\mathrm{Im}.
\end{aligned}
\tag{53}
$$

With the help of Eqs. (51) and (53) we can reveal the structure of all the tensors contributing to the relationships (17) and (44):

$$
\begin{aligned}
&\frac{\gamma_j}{\gamma_i} \propto \begin{vmatrix} \mathrm{Re} & \mathrm{Re}+i\;\mathrm{Im} \\ \mathrm{Re}+i\;\mathrm{Im} & \mathrm{Re} \end{vmatrix}, \\
&\frac{\beta_{jk}\gamma_k}{\gamma_i} \propto \begin{vmatrix} \mathrm{Re}+i\;\mathrm{Im} & \mathrm{Re}+i\;\mathrm{Im} \\ \mathrm{Re}+i\;\mathrm{Im} & \mathrm{Re}+i\;\mathrm{Im} \end{vmatrix}, \\
&\zeta_{jk} \propto \begin{vmatrix} \mathrm{Re} & i\;\mathrm{Im} \\ i\;\mathrm{Im} & \mathrm{Re} \end{vmatrix}, \quad \frac{\zeta_{jk}\gamma_k}{\gamma_i} \propto \begin{vmatrix} \mathrm{Re}+i\;\mathrm{Im} & \mathrm{Re}+i\;\mathrm{Im} \\ \mathrm{Re}+i\;\mathrm{Im} & \mathrm{Re}+i\;\mathrm{Im} \end{vmatrix}.
\end{aligned}
\tag{54}
$$

For the two-component SAW analyzed here the description of the coefficients σ_j in Eqs. (34) and (35) can be reduced to

$$
\sigma_1 = d_{33} \propto \mathrm{Re} + i\;\mathrm{Im}, \quad \sigma_3 = -d_{13} \propto \mathrm{Re} + i\;\mathrm{Im}.
\tag{55}
$$

The matrix $(\chi^{-1})_{ki}$ in Eq. (39) can be also found with the help of β_{jk} in Eq. (51):

$$(\chi^{-1})_{ki} \propto \begin{vmatrix} i\ \mathrm{Im} & \mathrm{Re} \\ \mathrm{Re} & i\ \mathrm{Im} \end{vmatrix}. \tag{56}$$

Finally, using Eqs. (54), (55), and (56), we derive the coefficients and matrices in Eqs. (42) and (43)

$$A_m \propto \mathrm{Re} + i\ \mathrm{Im}, \quad B_i \propto \mathrm{Re} + i\ \mathrm{Im},$$

$$g_{mj} \propto \begin{vmatrix} \mathrm{Re}+i\ \mathrm{Im} & \mathrm{Re}+i\ \mathrm{Im} \\ \mathrm{Re}+i\ \mathrm{Im} & \mathrm{Re}+i\ \mathrm{Im} \end{vmatrix}, \tag{57}$$

$$h_{mj} \propto \begin{vmatrix} \mathrm{Re}+i\ \mathrm{Im} & \mathrm{Re}+i\ \mathrm{Im} \\ \mathrm{Re}+i\ \mathrm{Im} & \mathrm{Re}+i\ \mathrm{Im} \end{vmatrix}.$$

From Eqs. (54) and (57) it follows that the matrices contributing to the evolution equations [Eq. (43)] and to the relationships of Eqs. (17) and (44) [which are used for the evaluation of the nonlinear terms in the rhs of Eq. (43)] have the most general form. Thus no simplification was found in this part of the problem even by choosing the crystal-propagation configuration of very high symmetry. Surely in the case of only two partial waves for the specified configuration (i.e., SAWs in the basal plane of cubic crystal, propagating along a crystal axis) the nonlinear part N_{ij} $(i,j=1,3)$ of the stress tensor contains less terms than in the general case. It can be checked that, for example, in the cubic crystals of symmetry 432, $43m$ or $m3m$ (which have only six independent third-order elastic constants[23]) the only components of the tensor S_{ijkmpr} contributing to N_{ij} are

$$s_{111111} = s_{333333} = c_{111} + 3c_{11}, \quad s_{111133} = s_{113333} = c_{112} + c_{12},$$

$$s_{111331} = s_{331331} = c_{155} + c_{44},$$

$$s_{113131} = s_{331313} = c_{155} + c_{11}, \tag{58}$$

$$s_{111313} = s_{333131} = c_{155} + c_{12} + 2c_{44},$$

and those which can be obtained from the lhs of Eq. (58) by permutations of index pairs and are equal to them.[1] However, we have checked that, though the simplification of the tensor N_{ij} is significant, nevertheless the nonlinear terms of all various forms in the general equation (47) still contribute to SAW distortion (i.e., none of the six nonlinear parameters $\varepsilon_j^{(i)}$ vanishes, in principle).

The situation drastically changes in the case where $\mathrm{Re}\, b=0$ and partial waves exhibit no oscillations in the depth direction. In accordance with Refs. 16 and 17 the structure of the partial waves in the basal plane of cubic crystals strongly depends on the value of the anisotropy ratio $r=2c_{44}/(c_{11}-c_{12})$. If the anisotropy ratio appreciably exceeds unity (like in Ni, where $r=2.38$), then $\mathrm{Re}\, b \neq 0$. For cubic crystals of the other category, with r appreciably less than unity, of which KCl ($r=0.375$) is an example, $\mathrm{Re}\, b=0$. As soon as $\mathrm{Re}\, b=0$ a ''chain reaction'' of important changes in the derived formulas (50)–(57) is initiated with the following results:

$$\alpha_{jn} \propto \begin{vmatrix} \mathrm{Re} & \mathrm{Re} \\ i\ \mathrm{Im} & i\ \mathrm{Im} \end{vmatrix}, \quad d_{jn} \propto \begin{vmatrix} i\ \mathrm{Im} & i\ \mathrm{Im} \\ \mathrm{Re} & \mathrm{Re} \end{vmatrix},$$

$$\gamma_j/\gamma_i \propto \begin{vmatrix} \mathrm{Re} & i\ \mathrm{Im} \\ i\ \mathrm{Im} & \mathrm{Re} \end{vmatrix},$$

$$\beta_{jk}\gamma_k/\gamma_i \propto \begin{vmatrix} i\ \mathrm{Im} & \mathrm{Re} \\ \mathrm{Re} & i\ \mathrm{Im} \end{vmatrix}, \quad \zeta_{jk}\gamma_k/\gamma_i \propto \begin{vmatrix} \mathrm{Re} & i\ \mathrm{Im} \\ i\ \mathrm{Im} & \mathrm{Re} \end{vmatrix}, \tag{59}$$

$$\sigma_1 \propto \mathrm{Re}, \quad \sigma_3 \propto i\ \mathrm{Im}, \quad A_1 \propto i\ \mathrm{Im}, \quad A_3 \propto \mathrm{Re},$$

$$B_1 \propto i\ \mathrm{Im}, \quad B_3 \propto \mathrm{Re},$$

$$g_{mj} \propto \begin{vmatrix} \mathrm{Re} & i\ \mathrm{Im} \\ i\ \mathrm{Im} & \mathrm{Re} \end{vmatrix}, \quad h_{mj} \propto \begin{vmatrix} i\ \mathrm{Im} & \mathrm{Re} \\ \mathrm{Re} & i\ \mathrm{Im} \end{vmatrix}.$$

The first of the important results in Eqs. (59) is the fact that with $\mathrm{Re}\, b=0$ the ratio γ_3/γ_1 becomes purely imaginary: $\gamma_3/\gamma_1 = i\ \mathrm{sgn}(\omega)\mathrm{Im}\ \alpha$. Consequently the relations (38) between the components of the vibrational velocity at the surface take the form

$$\nu_3 = -\mathrm{Im}\ \alpha \mathrm{H}[\nu_1], \quad \nu_1 = (1/\mathrm{Im}\ \alpha)\mathrm{H}[\nu_3], \tag{60}$$

which is the same as in the linear Rayleigh SAWs in isotropic solids (see, for example, Refs. 10 and 20). Due to Eqs. (60) we concentrate in the following on the derivation of the evolution equation for the ''horizontal'' component ν_1 of the surface velocity. The corresponding evolution equation for the ''vertical'' component ν_3 can then be derived straightforwardly with the help of the rules in Eqs. (60). In accordance with Eqs. (59), in the case $\mathrm{Re}\, b=0$, both the form of the evolution equation and the description of the spatial derivatives (which are necessary for the evaluation of the nonlinear terms) are appreciably simplified in comparison with the general representation given by Eqs. (43) and (44). They become

$$\frac{\partial \nu_1}{\partial \theta} = \mathrm{Re}\ g_{11}F_1 - \mathrm{Im}\ g_{13}\mathrm{H}[F_3] + \frac{1}{s}\,\mathrm{Re}\ h_{13}\,\frac{\partial N_{33}}{\partial \tau} - \frac{1}{s}\,\mathrm{Im}\ h_{11}\mathrm{H}\left[\frac{\partial N_{13}}{\partial \tau}\right], \tag{61}$$

and

$$\frac{\partial u_1}{\partial x_1} = -\frac{1}{s}\,\nu_1, \quad \frac{\partial u_3}{\partial x_1} = \frac{1}{s}\,\mathrm{Im}\ \alpha \mathrm{H}[\nu_1],$$

$$\frac{\partial^2 u_1}{\partial x_1^2} = \frac{1}{s^2}\frac{\partial}{\partial \tau}\,\nu_1, \quad \frac{\partial^2 u_3}{\partial x_1^2} = -\frac{1}{s^2}\,\mathrm{Im}\ \alpha\,\frac{\partial}{\partial \tau}\,\mathrm{H}[\nu_1],$$

$$\frac{\partial u_1}{\partial x_3} = \frac{1}{s}\,\mathrm{Im}\left(\beta_{1k}\,\frac{\gamma_k}{\gamma_1}\right)\mathrm{H}[\nu_1],$$

$$\frac{\partial u_3}{\partial x_3} = -\frac{1}{s}\,\mathrm{Re}\left(\beta_{3k}\,\frac{\gamma_k}{\gamma_1}\right)\nu_1, \tag{62}$$

$$\frac{\partial^2 u_1}{\partial x_3^2} = \frac{1}{s^2}\,\mathrm{Re}\left(\zeta_{1k}\,\frac{\gamma_k}{\gamma_1}\right)\frac{\partial}{\partial \tau}\,\nu_1,$$

$$\frac{\partial^2 u_3}{\partial x_3^2} = -\frac{1}{s^2}\,\mathrm{Im}\left(\zeta_{3k}\,\frac{\gamma_k}{\gamma_1}\right)\frac{\partial}{\partial \tau}\,\mathrm{H}[\nu_1].$$

It is clear that the most important simplification consists in the fact that ν_3 and each of the spatial derivatives in Eqs. (62) are related only to ν_1 or $\mathrm{H}[\nu_1]$, but not to both simultaneously. Using Eqs. (61), (62), and (58) we have checked that only nonlinear operators associated with the coefficients $\varepsilon_1^{(1)}$, $\varepsilon_2^{(1)}$, and $\varepsilon_3^{(1)}$ contribute to the evolution equation for the horizontal component of the vibrational velocity

$$s\,\frac{\partial \nu_1}{\partial \theta}=\varepsilon_1^{(1)}\nu_1\,\frac{\partial \nu_1}{\partial \tau}+\frac{\varepsilon_2^{(1)}}{2}\,\frac{\partial}{\partial \tau}\{\nu_1^2+(\mathrm{H}[\nu_1])^2\}+\varepsilon_3^{(1)}\left\{\nu_1\,\frac{\partial \nu_1}{\partial \tau}+\mathrm{H}\left[\nu_1\mathrm{H}\left[\frac{\partial \nu_1}{\partial \tau}\right]\right]\right\}. \tag{63}$$

Equation (63) has precisely the same form as the corresponding evolution equation for the nonlinear Rayleigh SAW in isotropic solid derived recently.[20] Note that in accordance with Eq. (63) the quantity $\int_{-\infty}^{\infty}\nu_1\,d\tau$ is conserved in the nonlinear wave process. The explicit formulas for the nonlinear parameters $\varepsilon_1^{(1)}$, $\varepsilon_2^{(1)}$, and $\varepsilon_3^{(1)}$ in isotropic solids are presented in the Appendix.

With the help of Eq. (60) and some of the identities for the Hilbert transform mentioned above, the evolution equation (63) can be transformed into the evolution equation for the vertical component of the surface velocity,

$$s\,\frac{\partial \nu_3}{\partial \theta}=\mathrm{H}\left[\varepsilon_4^{(3)}\nu_3\,\frac{\partial \nu_3}{\partial \tau}+\frac{\varepsilon_5^{(3)}}{2}\,\frac{\partial}{\partial \tau}\{\nu_3^2+(\mathrm{H}[\nu_3])^2\}+\varepsilon_6^{(3)}\left\{\nu_3\,\frac{\partial \nu_3}{\partial \tau}+\mathrm{H}\left[\nu_3\mathrm{H}\left[\frac{\nu_3}{\partial \tau}\right]\right]\right\}\right], \tag{64}$$

where $\varepsilon_4^{(3)}=(\varepsilon_1^{(1)}+2\varepsilon_3^{(1)})/\mathrm{Im}\,\alpha$, $\varepsilon_5^{(3)}=-(\varepsilon_1^{(1)}+\varepsilon_2^{(1)}+2\varepsilon_3^{(1)})/\mathrm{Im}\,\alpha$, and $\varepsilon_6^{(3)}=-\varepsilon_3^{(1)}/\mathrm{Im}\,\alpha$. In accordance with Eq. (64) only the nonlinear operators associated with the coefficients $\varepsilon_4^{(3)}$, $\varepsilon_5^{(3)}$, and $\varepsilon_6^{(3)}$ contribute to the evolution of the vertical component of the surface velocity. The quantity $\int_{-\infty}^{\infty}\nu_3\,d\tau$ is conserved only if $\varepsilon_6^{(3)}$ is equal to zero.

In our opinion the derived equations (63) and (64) are reasonable from a physical point of view. As far as the two partial waves contributing to linear SAW exhibit a purely exponential depth decay (similar to scalar and vector potentials contributing to Rayleigh SAW in isotropic solids[20,24]), the evolution of the horizontal velocity ν_1 is affected only by the quadratic operators containing none or two Hilbert transforms $\nu_1\partial\nu_1/\partial\tau$, $\mathrm{H}[\nu_1]\mathrm{H}[\partial\nu_1/\partial\tau]$ and $\mathrm{H}[\nu_1\mathrm{H}[\partial\nu_1/\partial\tau]]$. At the same time the Hilbert transformed pairs of these operators influence the evolution of the Hilbert transform of ν_1 (i.e., they influence the vertical velocity ν_3). As soon as $\mathrm{Re}\,b\neq 0$ and there appear oscillations in the depth distribution of partial waves, ν_1 starts to be intercoupled not only with $\mathrm{H}[\nu_3]$ but with ν_3 as well, and all six different nonlinear operators contribute to the evolution of the horizontal (and vertical) velocity. The time-domain evolution equation for the surface motion takes then its most general form [Eq. (47)].

IV. DISCUSSION

(1) The linear SAWs propagating along the crystal axis in a basal plane of cubic crystals as well as the SAWs in many other instances, described by the solutions of the similar form (that is, having only two damped terms contributing to the particle displacements, having displacements in the sagittal plane only, having a principal axis of the surface-displacement ellipse perpendicular to the free surface, and having the power flux collinear with the propagation vector) are referred commonly[17] as ''Rayleigh-type.'' In Refs. 21 and 25 the systematic search for the crystal-propagation configurations where the SAW displacement has only two components (both in the sagittal plane) was undertaken. Sixteen possible cases have been listed in crystals belonging to the orthorhombic, tetragonal, hexagonal, and cubic systems. For some crystals the decrease versus depth of these components is similar to that in isotropic solids; however, for others it can be noticeably different, i.e., much slower and/or characterized by oscillations. The difference comes from anisotropy of the solid in the sagittal plane. The role of the anisotropy ratio has been emphasized for crystals belonging to cubic and hexagonal systems in Refs. 16 and 17, and for cubic and tetragonal systems in Refs. 21 and 25. It should be noticed that both categories of SAWs analyzed above (i.e., with $\mathrm{Re}\,b=0$ and $\mathrm{Re}\,b\neq 0$) satisfy the definition of ''Rayleigh-type SAW.'' However, our theoretical investigations (Sec. III) demonstrate that in the second-order elasticity theory only the nonlinear SAWs based on the pure exponentially damped ($\mathrm{Re}\,b=0$) partial waves are described by the equations similar to those for the nonlinear Rayleigh SAWs. When the decay constants b have real parts ($\mathrm{Re}\,b\neq 0$), and thus the depth dependence of the partial waves consists of exponentially damped sinusoids rather than real exponentials,[16] the number of the nonlinear processes contributing to the evolution on the nonlinear SAWs in anisotropic solids appreciably increases in comparison with the case of nonlinear Rayleigh waves in isotropic solids.

(2) From a methodological point of view our approach to the derivation of the evolution equations in the time domain looks to be closest to the approach proposed for the frequency-domain analysis in Ref. 26. In Ref. 26 the same multiple scale perturbation method as in Refs. 3, 5, and 14 was applied, but, importantly, no artificial constraints on the depth structure of the nonlinear SAWs were imposed. It was additionally assumed in Ref. 26 that the amplitudes of the partial wave harmonics did not slowly depend on the depth coordinate and the coordinate along the propagation direction separately, but only on their linear combinations $x_1+\alpha_n^{(r)}x_3$ [where the indices n and (r) in the parameters $\alpha_n^{(r)}$ denote particular harmonic ($n=1,2,...,\infty$) and partial wave ($r=1,2,3$) correspondingly]. In our opinion, this is not a strong constraint, especially if we allow the possibility for $\alpha_n^{(r)}$ to be complex and depend on the sign of frequency. But unfortunately, no prescription of how to find the unknown coefficients $\alpha_n^{(r)}$ was proposed in Ref. 26 and the evolution equations (derived in the frequency domain) contain, in our opinion, undetermined parameters. Contrary to that, in the evolution equations (47) and (48) derived in the theory presented here, all the parameters are known.

(3) In comparison with model time-domain equations proposed for the hyperbolic surface waves[6] our derived evolution equations appear to be more general. It was assumed

in Ref. 6 that the third and the forth operators in Eq. (45) (i.e., $\nu_i H[\partial\nu_i/\partial\tau]$ and $H[\nu_i]\partial\nu_i/\partial\tau$) can act in the equations only in the combination $\partial(\nu_i H[\nu_i])/\partial\tau$. Both the theory presented here and the theory of the nonlinear Rayleigh waves in isotropic solids demonstrate that this assumption is not valid in reality.

(4) It should be mentioned that the evolution equations for the vertical displacement in the nonlinear surface acoustic waves in anisotropic solids, derived in the frequency domain in Ref. 13, were transformed into the time domain.[27,28] It follows both from the analysis in the frequency domain[13] and in the time domain[27,28] that the evolution equations could always have purely antisymmetric (i.e., odd over retarded time) solutions. Our equation (47) for the solids of general anisotropy does not support pure antisymmetric and pure symmetric solutions, because the nonlinear terms with coefficients $\varepsilon_1^{(i)}$, $\varepsilon_2^{(i)}$, and $\varepsilon_3^{(i)}$ (in the case when the vibrational velocity component is symmetric or antisymmetric) always have opposite symmetry to that of the nonlinear terms with coefficients $\varepsilon_4^{(i)}$, $\varepsilon_5^{(i)}$, and $\varepsilon_6^{(i)}$. Only in the case of purely exponential partial waves could our equations have purely odd solutions for the horizontal velocity and purely even solutions for the vertical velocity (the latter correspond to the purely antisymmetric solutions for vertical displacement as predicted in Ref. 13).

(5) In order to get better insight in the physics of the nonlinear surface elastic phenomena, it was proposed in Ref. 9 to separate in the time-domain evolution equations the terms associated with local and nonlocal nonlinearity. In our opinion the grouping of the nonlinear terms, which is based on their different role in spectrum transformations and is represented terms,which is based on their different role in spectrum transformations and is represented in Eq. (47), could also be fruitful. The further progress in the understanding of the nonlinear SAW phenomena could be then related to the detailed investigation of the properties of the nonlinear operators introduced in Eq. (47). In addition to the properties described in Sec. III, it is known[6] that the operator $\partial(\nu_i^2+(H[\nu_i])^2)/\partial\tau$ associated with the coefficient $\varepsilon_2^{(i)}$ (and, consequently, Hilbert transformed operator associated with the coefficient $\varepsilon_5^{(i)}$) alone (i.e., when $\varepsilon_1^{(i)}=\varepsilon_3^{(i)}=\varepsilon_4^{(i)}=\varepsilon_6^{(i)}=0$) supports propagation of a Lorentzian solitary wave. Thus, the proposed grouping of the nonlinear terms directly addresses the problem of the nonlinear SAWs of permanent form (i.e., stationary nonlinear SAWs).[4,8,13]

V. CONCLUSIONS

New evolution equations for the nonlinear SAWs in anisotropic media are derived by the slowly varying wave profile method. No additional assumptions concerning the depth structure of the nonlinear SAWs was used except a physical one: cumulative effect of weak nonlinear processes leads to slow changes of SAW profiles both in time and in space. The proposed theory explicitly accounts for a possible significant deviation of the nonlinear SAW depth structure from that of linear SAW. The explicit form of the nonlinear terms in the evolution equation was found both in the time domain and in the frequency domain. The derived equations in the case of general anisotropy and arbitrary crystal-propagation configuration are very complicated, containing different nonlinear integro-differential operators. No significant simplification in the description was found even for the general nonlinear SAWs propagating in the basal plane of cubic crystal in the direction along the crystal axis. However, if two partial waves contributing to SAW in this case exhibit pure exponential decay in depth (i.e., without any superimposed oscillations), the derived equations degenerate to the form of the evolution equations for the nonlinear Rayleigh SAWs in isotropic solids.

ACKNOWLEDGMENTS

This work was supported by the Belgian National Science Fund (NFWO) through FKFO project No. G.0115.95. Support from the Research Council of the Katholieke Universiteit Leuven in the form of a Fellowship to one of us (VG) is gratefully acknowledged.

APPENDIX: NONLINEAR SAWS IN ISOTROPIC SOLIDS

In order to achieve transformation to the isotropic limit, it was convenient for us to introduce two linear Lamé constants λ and μ instead of second-order elastic constants: $c_{11}=\lambda+2\mu$, $c_{12}=\lambda$, and $c_{44}=\mu$. We represented the third-order elastic constants contributing to Eq. (58) using Landau and Lifshitz constants A, B, and C[1,24] as follows: $c_{111}=2(A+3B+C)$, $c_{112}=2(B+C)$, and $c_{155}=(c_{111}-c_{112})/4$. We also introduced the notations $\delta_{L,T}\equiv(c_{L,T}^2/s^2-1)$ for the deviation of the propagation velocity s from the longitudinal velocity $c_L=[(\lambda+2\mu)/\rho]^{1/2}$ and shear velocity $c_T=(\mu/\rho)^{1/2}$ of bulk waves.[20] Then we derived

$$\text{Re } g_{11}=b_1/2\rho, \quad \text{Im } g_{13}=-b_2/2\rho,$$

$$\text{Re } h_{13}=b_3/2\rho, \quad \text{Im } h_{11}=-b_4/2\rho,$$

where b_1, b_2, b_3, and b_4 are the coefficients introduced in Ref. 20. One explicitly finds

$$b_1=a_5/a_9, \quad b_2=a_6/a_9, \quad b_3=a_7/a_9, \quad b_4=a_8/a_9,$$

with

$$a_1=c_Lc_T/s^2-\delta_L^{1/2}\delta_T^{1/2}, \quad a_2=\delta_L^{1/2}\delta_T^{1/2}-(\delta_L+\delta_T)a_1/2,$$

$$a_3=2a_1c_T/c_L-1, \quad a_4=(2\delta_T+1)s/2c_T\delta_T^{1/2},$$

$$a_5=a_2a_3c_L/c_T-\delta_T, \quad a_6=a_3c_L\delta_L^{1/2}/s-a_2s\delta_T^{1/2}/c_L,$$

$$a_7=2a_3(c_Tc_L\delta_L^{1/2}\delta_T^{1/2}-s^2a_2^2)/a_1c_Tc_L,$$

$$a_8=a_7s\delta_T^{1/2}/a_3c_T, \quad a_9=a_5-a_4a_6.$$

Note that the coefficient a_1 provides a compact description of the matrix β_{ij} in the reduced-order equations (20) for the linear Rayleigh SAW in isotropic solid

$$\beta_{ij}=\begin{vmatrix} i\ \mathrm{sgn}(\omega)s\delta_t^{1/2}/c_Ta_1 & 1-c_L/c_Ta_1 \\ -(1-c_T/c_La_1) & i\ \mathrm{sgn}(\omega)s\delta_T^{1/2}/c_La_1 \end{vmatrix}.$$

Coefficient a_4 gives the expression for Im α in the isotropic case (Im $\alpha=-a_4$), while the coefficients σ_j in Eq. (37) are

related to a_3: $\sigma_1 \propto \delta_T^{1/2}$, $\sigma_3 \propto i\ \mathrm{sgn}(\omega)(c_T/s)a_3$. Then the coefficients in Eq. (62) are

$$\mathrm{Im}(\beta_{1k}\gamma_k/\gamma_1)=a_4,$$

$$\mathrm{Re}(\beta_{3k}\gamma_k/\gamma_1)=2(c_T^2/c_L^2)-1\equiv -d_1,$$

$$\mathrm{Re}(\zeta_{1k}\gamma_k/\gamma_1)=(s^2/c_T^2)-2-d_1\equiv d_2,$$

$$\mathrm{Im}(\zeta_{3k}\gamma_k/\gamma_1)=-a_4[(s^2/c_L^2)+d_1]\equiv -d_3.$$

Finally, the three effective nonlinear coefficients are

$$\varepsilon_1=b_1(e_2-e_3-e_5+e_6)-b_2(2e_1+2e_7+e_8/2)+b_3(e_4-e_2)-2b_4e_1,$$

$$\varepsilon_2=b_1(e_5-e_2)+b_2(e_7+e_1)+b_3e_2+b_4e_1,$$

$$e_3=b_2e_8/2,$$

where

$$e_1=a_4(d_1-1)(K+\mu/3)/2\rho s^2,\quad e_2=a_4^2(K+\mu/3)/\rho s^2,$$

$$e_3=[(3K/2+2\mu+A+3B+C)-d_1(K-2\mu/3+2B+2C)+d_1^2(K/2-\mu/3+B+C)]/\rho s^2,$$

$$e_4=[d_1^2(3K/2+2\mu+A+3B+C)-d_1(K-2\mu/3+2B+2C)+(K/2-\mu/3+B+C)]/\rho s^2,$$

$$e_5=a_4(d_3-a_4)(K+\mu/3)/2\rho s^2,$$

$$e_6=(d_1-1)[d_2(K+4\mu/3+A/2+B)-d_1(\mu+A/2+B)]/2\rho s^2,$$

$$e_7=a_4(d_1+d_2)(K+\mu/3)/2\rho s^2,$$

$$e_8=[d_1d_3(3K+4\mu+2A+6B+2C)-(d_3-a_4+a_4d_1)(K-2\mu/3+2B+2C)-a_4(d_1+d_2)(K+\mu/3)]/\rho s^2.$$

It should be noticed that we omitted the subscripts in nonlinear parameters, because in isotropic media the coefficients ε_1, ε_2, and ε_3 are nonzero only for the horizontal component as it was demonstrated in Sec. III. The estimates of the nonlinear parameters ε_1, ε_2, and ε_3 for some isotropic solids (obtained with the formulas presented here) can be found in Ref. 20.

[1] A. P. Mayer, ''Surface acoustic waves in nonlinear elastic media,'' Phys. Rep. **256**, 237–366 (1995).

[2] V. G. Mozhaev, ''A new type of surface acoustic waves in solids due to nonlinear elasticity,'' Phys. Lett. A **139**, 333–337 (1989).

[3] R. W. Lardner, ''Nonlinear surface waves on an elastic solid,'' Int. J. Eng. Sci. **21**, 1331–1342 (1983).

[4] D. F. Parker and F. M. Talbot, ''Analysis and computation for nonlinear elastic surface waves of permanent form,'' J. Elast. **15**, 389–426 (1985).

[5] E. A. David, ''A uniform asymptotic solution for the nonlinear surface acoustic waves,'' Int. J. Eng. Sci. **7**, 699–708 (1985).

[6] J. K. Hunter, ''Nonlinear surface waves,'' Contemporary Math. **100**, 185–202 (1989).

[7] E. A. Zabolotskaya, ''Nonlinear propagation of plane and circular Rayleigh waves in isotropic solids,'' J. Acoust. Soc. Am. **91**, 2569–2575 (1992).

[8] M. F. Hamilton, Yu. A. Il'insky, and E. A. Zabolotskaya, ''On the existence of stationary nonlinear Rayleigh waves,'' J. Acoust. Soc. Am. **93**, 3089–3095 (1993).

[9] M. F. Hamilton, Yu. A. Il'insky, and E. A. Zabolotskaya, ''Local and nonlocal nonlinearity in Rayleigh waves,'' J. Acoust. Soc. Am. **97**, 882–890 (1995).

[10] M. F. Hamilton, Yu. A. Il'insky, and E. A. Zabolotskaya, ''Evolution equation for the nonlinear Rayleigh waves,'' J. Acoust. Soc. Am. **97**, 891–897 (1995).

[11] P. J. Vella, T. C. Padmore, and G. I. Stegeman, ''Nonlinear surface-wave interactions: Parametric mixing and harmonic generation,'' J. Appl. Phys. **45**, 1993–2006 (1974).

[12] V. I. Pavlov and I. Yu. Solodov, ''Nonlinear properties of elastic surface waves in solids,'' Fiz. Tverd. Tela (Leningrad) **19**, 2948–2954 (1977) [Sov. Phys. Solid State **19**, 1727–1730 (1977)].

[13] D. F. Parker, ''Waveform evolution for the nonlinear surface acoustic waves,'' Int. J. Eng. Sci. **26**, 59–75 (1988).

[14] R. W. Lardner, ''Nonlinear surface acoustic waves on an elastic solid of general anisotropy,'' J. Elast. **16**, 63–73 (1986).

[15] O. V. Rudenko and S. I. Soluyan, *Theoretical Foundations of Nonlinear Acoustics* (Consultants Bureau, New York, 1977).

[16] G. W. Farnell, ''Types and properties of surface waves,'' in *Acoustic Surface Waves*, edited by A. A. Oliner (Springer-Verlag, Berlin, 1978), pp. 13–60.

[17] G. W. Farnell, ''Properties of elastic surface waves,'' in *Physical Acoustics, Principles and Methods*, edited by W. P. Mason and R. N. Thurston (Academic, New York, 1970), Vol. VI, pp. 109–166.

[18] G. W. Farnell and E. L. Adler, ''Elastic wave propagation in thin layers,'' in *Physical Acoustics, Principles and Methods*, edited by W. P. Mason and R. N. Thurston (Academic, New York, 1972), Vol. IX, pp. 35–127.

[19] V. Gusev, W. Lauriks, and J. Thoen, ''Evolution equation for the nonlinear Scholte waves,'' IEEE Trans. Ultrason. Ferroelectr. Freq. Control **45**, 170–178 (1998).

[20] V. Gusev, W. Lauriks, and J. Thoen, ''New theory for the time-evolution of the nonlinear Rayleigh waves in an isotropic solid,'' Phys. Rev. B **55**, 9344–9347 (1997).

[21] D. Royer and E. Dieulesaint, ''Rayleigh wave velocity and displacement in orthorhombic, tetragonal, hexagonal, and cubic crystals,'' J. Acoust. Soc. Am. **76**, 1438–1444 (1984).

[22] B. A. Auld, *Acoustic Fields and Waves in Solids* (Wiley, New York, 1973) Vol. I.

[23] LANDOLT-BÖRNSTEIN, Numerical Data and Functional Relationships in Science and Technology, New Series, Editor in Chief: K.-H. Hellwege (Springer-Verlag, Berlin, 1969), Group III, Vol. 2, pp. 102–125.

[24] L. D. Landau and E. M. Lifshitz, *Theory of Elasticity* (Pergamon, London, 1959).

[25] E. Dieulesaint and D. Royer, ''The relationship between surface wave displacement and anisotropy on selected crystal structures,'' in *Rayleigh-Wave Theory and Application*, edited by E. A. Ash and E. G. S. Paige (Springer-Verlag, Berlin, 1985), pp. 29–36.

[26] M. Planat, ''Multiple scale analysis of the nonlinear surface acoustic wave propagation in anisotropic crystals,'' J. Appl. Phys. **57**, 4911–4915 (1985).

[27] A. M. Ionov, ''A space-time evolution equation for Rayleigh waves in a nonlinear dissipative medium: basic relations,'' Akust. Zh. **40**, 262–269 (1994) [Acoust. Phys. **40**, 237–243 (1994)].

[28] A. M. Ionov, ''Space-time evolution equation for Rayleigh wave in a nonlinear dissipative medium: analysis of results,'' Akust. Zh. **40**, 405–412 (1994) [Acoust. Phys. **40**, 363–368 (1994)].

Dispersion of nonlinearity, nonlinear dispersion, and absorption of sound in micro-inhomogeneous materials

Vitalyi E. Gusev,[a] Walter Lauriks, and Jan Thoen
Laboratorium voor Akoestiek en Thermische Fysica, Departement Natuurkunde, Katholieke Universiteit Leuven, Celestijnenlaan 200 D, B-3001 Leuven, Belgium

(Received 24 March 1997; accepted for publication 15 February 1998)

New evolution equations for nonlinear acoustic waves in micro-inhomogeneous media, which take into account relaxation processes, are derived. The proposed theory provides the description of such physical effects as frequency-dependent nonlinear absorption of sound, nonlinearity of its velocity dispersion, and dispersion of the nonlinear acoustic parameters of micro-inhomogeneous materials. The theory predicts that, depending on the ratio of the characteristic relaxation time to the wave period, nonlinearity can grow or diminish with increasing frequency, while an increase in wave amplitude can lead to a rise or fall of the propagation velocity. In the limiting cases where the relaxation processes are instantaneous or quasi-frozen, analytical solutions of the nonlinear equations are found and analyzed.
[S0001-4966(98)06105-0]

PACS numbers: 43.25.Dc [MAB]

INTRODUCTION

The last decade was marked by rapid growth of research activity in the area of nonlinear acoustics of micro-inhomogeneous materials.[1–11] A significant part of this activity was recently reviewed in Refs. 12 and 13. In the present paper we (following the authors of Ref. 2) are using the term ''micro-inhomogeneous materials'' for a medium that contains mechanical elements, such as grains, grain joints, cracks, pores, dislocations, etc., with a characteristic spatial scale significantly exceeding the inter-atomic spacing, but significantly less than the acoustic wavelengths considered. Interest for nonlinear acoustic phenomena in such materials, for example, rocks, polycrystalline metals and ceramics, is motivated by the following two main factors. First, the acoustic nonlinearity of the micro-inhomogeneous materials can be up to four orders of magnitude higher than that of perfect monocrystals or liquids free of gas bubbles.[2,3,7,8,12] Second, the nonlinear acoustic parameters are much more sensitive to the nature and the state of the micro-inhomogeneities than linear acoustic parameters.[9,14–17] Strong nonlinearity of inhomogeneous materials is not due to the anharmonicity of the inter-atomic potential, but due to the nonlinear motion of the mechanical elements responsible for the inhomogeneity. Consequently, nonlinear acoustics becomes an extremely promising tool for nondestructive characterization of micro-inhomogeneous materials. It is important to note that, in parallel with the expansion of the experimental research,[1–17] significant progress in the theoretical description of the nonlinear acoustic phenomena in micro-inhomogeneous media was achieved quite recently.[18,19] Its success is related to the emerged understanding[2,3,18,19] that the nonlinear evolution of the longitudinal acoustic wave in micro-inhomogeneous materials cannot be properly described by the simple wave equation[20] $v_x-(\epsilon/2c^2)vv_\tau=0$ (where v is the vibrational velocity of the material in the acoustic wave, c is the velocity of the linear sound, and $\tau=t-(x/c)$ is the retarded time, with t and x denoting temporal and spacial variables) even with extremely high values of the nonlinear parameter ϵ. Also adding higher order nonlinear terms to the simple equation does not lead to a proper description.[21–23] It was proposed[18] that the wave equation should take into account hysteretic and endpoint memory in the stress/strain relationship, which are typical for micro-inhomogeneous materials.[24,25] This results in the following evolution equation for weakly nonlinear sound waves:

$$v_x-(\epsilon/2c^2)vv_\tau+(h/2c^2)(v^Av_\tau+v|v_\tau|)=0, \tag{1}$$

where h is the parameter of hysteretic nonlinearity, and v^A denotes the amplitude of a periodic wave with a single minimum and a single maximum during a period. Parameters ϵ and h are related to parameters β and ρ_B of Ref. 26 for the description of the dependence of the quasi-static elastic modulus on strain via $\epsilon=-\beta$ and $h=\rho_B$. In comparison with the simple wave equation the evolution equation (1) for the sound in micro-inhomogeneous media contains an additional quadratic nonlinearity [described by the operator between parentheses in Eq. (1)[26,27]] which leads to the generation of only odd harmonics in the initially monochromatic wave, and to hysteretic attenuation, and causes dependence of the wave propagation velocity on the wave amplitude. The presence of this additional quadratic nonlinearity in micro-inhomogeneous materials provides an explanation for such observations as the proportionality of the shift in the resonance frequency of a vibrating bar to the amplitude of the oscillations[2,3] and to the quadratic dependence of the third harmonic amplitude on the excitation amplitude in some experiments.[6]

Although the evolution equation (1) describes hysteretic attenuation of sound waves, it does not explicitly account for

[a]On leave from the International Laser Center, Moscow State University, 119899 Moscow, Russia.

any relaxation processes in the material that may occur at the time scale of excitation. Indeed, the derivation of Eq. (1) incorporates the main features of the quasi-static stress/strain relationship for the case of cyclic loading[18,19,24,25] rather than a dynamic relationship that should be more appropriate. The mathematical formalism that derives the nonlinear terms in Eq. (1) from the superposition of the individual response to stress (or strain) of mechanical elements responsible for the inhomogeneity incorporates a static model for the dependence of the parameters of the elements on stress (or strain). However, there is experimental evidence for the possible importance of relaxation in nonlinear acoustic phenomena in inhomogeneous media. In polycrystalline metals the time relaxation of the parametric generation threshold was discovered quite long time ago.[28] Recently, observation of slow dynamics in nonlinear elastic response of rocks[10,29] and the frequency dispersion of the nonlinear parameter ϵ in lead zirconate–titanate (PZT) ceramics[9] were reported. For this reason we address in the present paper the theoretical generalization of the evolution equation (1) to the case of the micro-inhomogeneous media with relaxation. The derived new generalized equation predicts effects as dispersion of the nonlinearity, nonlinear dispersion, and frequency-dependent nonlinear attenuation for the propagation of the finite-amplitude sound in micro-inhomogeneous media such. Some exact analytical solutions of the derived nonlinear equations have also been found and analyzed.

I. THEORY

The theory presented here is a combination of the formalism leading to Eq. (1) with the phenomenological approach to the description of relaxation processes by Mandelshtam and Leontovich.[20,30] In accordance with this phenomenological approach we assume that mechanical stress σ in a micro-inhomogeneous material is a single-valued function of the strain s and of some internal nondimensional parameters p_i $(i=1,2,...)$, which characterize the mechanical elements responsible for the inhomogeneity. Importantly, the dynamics of the parameters depend on strain. Under the assumptions to be adopted in this paper, the contributions of different internal parameters to the dynamic stress/strain relationship and, consequently, to the wave evolution equation, will be additive. That is why we omit the subscript ''i'' in the course of the following analysis and recover it only at the stage of the final discussion.

For the description of the periodic wave propagation it is sufficient to use the expansion of the stress/strain relationship around the values of the functions averaged over the acoustic period (i.e., around $\langle\sigma\rangle$, $\langle s\rangle$, and $\langle p\rangle$). The form of this expansion (which includes terms up to the second order in the deviations $\sigma'\equiv\sigma-\langle\sigma\rangle$ and $p'\equiv p-\langle p\rangle$) is

$$\sigma'\equiv\sigma-\langle\sigma\rangle\cong\sigma_s s'+\sigma_p p'+\sigma_{ss}(s')^2/2+\sigma_{sp}s'p' +\sigma_{pp}(p')^2/2, \tag{2}$$

where the derivatives of stress over s and p are evaluated at the average values $\sigma=\langle\sigma\rangle$ and $p=\langle p\rangle$.

Constructing a realistic model, we note that the second term in the right-hand side of Eq. (2) should be much smaller than the first one in order to describe the weak influence of the inhomogeneity on the linear acoustic properties of the material. If we assume $\sigma_s\propto\mu^0$, $s'\propto p'\propto\mu^1$ (where $\mu\ll 1$ is a small scaling parameter), the above condition can be formulated as $\sigma_p\propto\mu^{\beta_1}(\beta_1>0)$. Then in the frame of the adopted accuracy (i.e., retaining only the terms not smaller than $\propto\mu^2$ in the stress/strain relation) the approach of the parameter p to its equilibrium value p_0 can be described by a linear equation[30]

$$p_t=-(p-p_0)/\tau_R. \tag{3}$$

Here τ_R is a characteristic relaxation time. It should be noted that the mathematical condition for the validity of the approximate equation (3) can be formulated as $(\tau_R)_p/\tau_R\propto\mu^{-\beta_2}$, $\beta_2<\beta_1$. Taking into account that $\langle p\rangle_t=0$, the solution of Eq. (3) leads to the following description of the dynamics of the parameter deviation

$$p'=R[p_0-\langle p\rangle], \tag{4}$$

where we introduced the notation

$$R[\psi(t)]\equiv\frac{1}{\tau_R}\int_{-\infty}^{t}\psi(t')e^{(t-t')/\tau_R}\,dt' \cong\frac{1}{\tau_R}\int_{t}^{t+T}\psi(t')e^{(t-t')/\tau_R}\,dt'/[e^{T/\tau_R}-1] \tag{5}$$

for the relaxation integral operator acting on the arbitrary function $\psi(t)$. Note that the second form of the relaxation operator in Eq. (5) holds for periodic processes with period T in time. It is important to note that in Eq. (4) the deviation $p_0-\langle p\rangle$ of the equilibrium value of the parameter from its average value depends explicitly on the acoustic strain $s'(t)$ but not on time. Consequently, the dynamic stress/strain relationship is completely determined by Eq. (2) and Eq. (4) as soon as the static (i.e., equilibrium) dependence of the internal parameter on strain is specified.

Following the physical ideas formulated in Refs. 31, 24, and 18, we assume that the equilibrium internal parameter $p_0(s)$ can be described as a linear superposition of the corresponding parameters $p_0(s,s_1,s_2)$ of the individual mechanical elements responsible for the inhomogeneity

$$p_0(s)=\int_{-\infty}^{s_2}ds_1\int_{s_1}^{\infty}ds_2\;p_0(s,s_1,s_2)f_{12}(s_1,s_2). \tag{6}$$

In the integral superposition of Eq. (6) it is assumed[31,24,18] that the specific dependence of the parameter $p_0(s,s_1,s_2)$ of the individual mechanical elements on strain can be characterized by two parameters (characteristic strains s_1 and s_2). The adopted dependence of $p_0(s,s_1,s_2)$ on the strain is presented in Fig. 1. As shown in Fig. 1, the dependence of the parameter $p_0(s,s_1,s_2)$ of an individual mechanical element on strain s contains hysteretic. An individual mechanical element can only be in the two possible states characterized by the values p_2 and p_1 of the internal parameter. Transition from the first to the second state with increasing strain occurs when $s=s_2$; the inverse transition occurs when $s=s_1\leqslant s_2$. The fact that $s_1\leqslant s_2$ is taken into account mathematically by imposing corresponding limits for the integration in Eq. (6). Although the values of parameters p_2 and p_1 can vary from

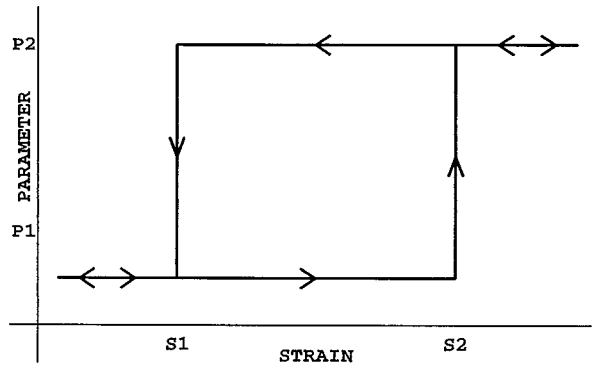

FIG. 1. The dependence of an internal parameter $p_0(s,s_1,s_2)$ of the individual hysteretic mechanical element on strain s. The arrows indicate the direction of the strain variation.

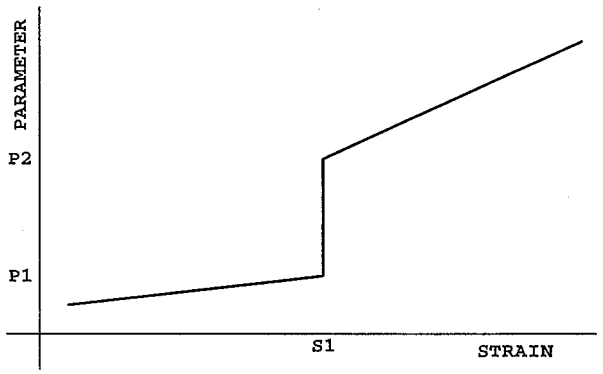

FIG. 2. The dependence of an internal parameter $p_0(s,s_1)$ of the individual nonhysteretic mechanical element on strain s.

one individual mechanical element to another, we assume that $p_2-p_1\equiv\Delta p\equiv$const, while the possible variation of this difference among the elements is incorporated in the magnitude of the distribution function $f_{12}(s_1,s_2)$ of the mechanical elements in the (s_1,s_2)-space (Preiscach–Mayergoyz space[18,19,31]). The most important feature of this model is that it describes memory effects.[31] In fact, the contribution to the total $p_0(s)$ from the mechanical elements with $s_1<s<s_2$ depends on whether the strain $s=s(t)$ is increasing or decreasing.

For the case of a simple cyclic strain history (when the strain varies with an amplitude s^A around its average value $\langle s\rangle$ with a single maximum and single minimum during a period), the mechanical elements with $s_1<\langle s\rangle-s^A$ and $s_2>\langle s\rangle+s^A$ do not change their state and, consequently, do not contribute to the variation of the parameter $p_0(s)$. When the strain increases ($s_t>0$) the variation of $p_0(s)$ is due to the transition of the elements from the state p_1 to the state p_2 when $s(t)=s_2$, and is given by

$$\begin{aligned}\frac{\partial p_0}{\partial s}&=\int_{\langle s\rangle-s^A}^{s_2}ds_1\int_{s_1}^{\langle s\rangle+s^A}ds_2\,\frac{\partial p_0(s,s_1,s_2)}{\partial s}\,f_{12}(s_1,s_2)\\&=\Delta p\int_{\langle s\rangle-s^A}^{s_2}ds_1\int_{s_1}^{\langle s\rangle+s^A}ds_2\;\delta(s-s_2)f_{12}(s_1,s_2)\\&=\Delta p\int_{\langle s\rangle-s^A}^{s}ds_1\;f_{12}(s_1,s)\\&\cong\Delta p\langle f_{12}\rangle[s-\langle s\rangle+s^A]\\&\equiv\Delta p\langle f_{12}\rangle[s^A+s'].\end{aligned}\tag{7}$$

When the strain diminishes ($s_t<0$), the variation of $p_0(s)$ is due to the transition of the elements from the state p_2 to the state p_1 when $s(t)=s_1$. An evaluation similar to the one in Eq. (7) leads to

$$\frac{\partial p_0}{\partial s}\cong\Delta p\langle f_{12}\rangle[s^A-s'].\tag{8}$$

Thus from Eqs. (7) and (8) it follows that

$$\frac{\partial p_0}{\partial s}\cong\Delta p\langle f_{12}\rangle[s^A+s'\ \mathrm{sign}(s_t')].\tag{9}$$

Note that, when doing the integrals in Eq. (7), we only accounted for the leading term $\langle f_{12}\rangle\equiv f_{12}(\langle s_1\rangle,\langle s_2\rangle)$ of the distribution function expansion near its average value. Accounting for the next terms in the expansion $(f_{12}(s_1,s_2)\cong\langle f_{12}\rangle+\langle\partial f_{12}/\partial s_1\rangle(s_1-\langle s\rangle)+\langle\partial f_{12}/\partial s_2\rangle(s_2-\langle s\rangle)+\cdots)$ contributes only to the quadratic dependence of $\partial p_0/\partial s$ on acoustic strain and thus only to the contributions in the stress/strain relationship to the order in strain higher than the second. It is important to note that possible modifications of the individual mechanical element model in Fig. 1 (for example, by taking into consideration the dependence of the parameters p_2 and p_1 on strain; see Fig. 2, for comparison) only lead to higher than second order terms in strain in the stress/strain relationship. Consequently, it seems that Eq. (9) provides the only important contribution to the σ'/s' relationship. However, this is only so if the distribution function $f_{12}(s_1,s_2)$ contains no anomalies at the scale of the acoustic strain variation (i.e., for $\langle s\rangle-s^A\leqslant s\leqslant\langle s\rangle+s^A$).

In Ref. 18 it was demonstrated that the density of mechanical elements in the (s_1,s_2)-space can significantly increase near the space diagonal $s_1=s_2$. Thus an anomalous contribution to the parameter p_0 from the mechanical elements with $s_1=s_2$ (i.e., nonhysteretic) is expected. This can be incorporated in the theory assuming that $f_{12}(s_1,s_2)\cong\langle f_{12}\rangle+f_1(s_1)\delta(s_1-s_2)$, where the function $f_1(s_1)$ describes the distribution of the nonhysteretic mechanical elements. The contribution of nonhysteretic mechanical elements to the parameter p_0 is found from Eq. (6) to be

$$p_0(s)=\int_{-\infty}^{\infty}ds_1\;p_0(s,s_1)f_1(s_1).\tag{10}$$

Note that in Eq. (10) the notation $p_0(s,s_1)$ for the parameter of the individual mechanical element is *not* just a short hand for $p_0(s,s_1,s_2=s_1)$. A more general description of the nonhysteretic elements than that provided by $p_0(s,s_1,s_2=s_1)$ is necessary in Eq. (10) to account for all the important contributions to the σ'/s' relationship. This generalization (presented in Fig. 2) includes the linear dependence of the parameters p_2 and p_1 on strain ($\partial p_2/\partial s\equiv r_2\equiv$const, $\partial p_1/\partial s\equiv r_1\equiv$const, $r_2-r_1\equiv\Delta r$). In evaluating $\partial p_0/\partial s$ with the help of Eq. (10) and the model in Fig. 2, we should also account for the changes of the distribution function $f_1(s_1)$ of the elements at the scale of the acoustic strain variation $[f_1(s_1)\cong\langle f_1\rangle+\langle\partial f_1/\partial s_1\rangle(s_1-\langle s\rangle)]$

$$\frac{\partial p_0}{\partial s}=\Delta p\int_{-\infty}^{\infty}ds_1\ \delta(s-s_1)f_1(s_1)+\int_{s}^{\infty}ds_1\ r_1f_1(s_1)$$
$$+\int_{-\infty}^{s}ds_1\ r_2f_1(s_1)$$
$$=\Delta pf_1(s)+\int_{\langle s\rangle}^{\infty}ds_1\ r_1f_1(s_1)+\int_{-\infty}^{\langle s\rangle}ds_1\ r_2f_1(s_1)$$
$$+r_1\int_{s}^{\langle s\rangle}ds_1\ f_1(s_1)+r_2\int_{\langle s\rangle}^{s}ds_1\ f_1(s_1)$$
$$\cong\Delta p\langle f_1\rangle+\int_{\langle s\rangle}^{\infty}ds_1\ r_1f_1(s_1)+\int_{-\infty}^{\langle s\rangle}ds_1\ r_2f_1(s_1)$$
$$+[\Delta p\langle\partial f_1/\partial s_1\rangle+\Delta r\langle f_1\rangle]s'. \tag{11}$$

In accordance with Eqs. (9) and (11) the general description of the derivative of the internal parameter p_0 over the acoustic strain has the form

$$\frac{\partial p_0}{\partial s}=a_1+a_2s'+a_3[s^A+s'\ \mathrm{sign}(s_t')], \tag{12}$$

where the formulas for the coefficients a_1, a_2, and a_3 can be recovered by comparison with Eqs. (9) and (11). Consequently, the deviation of the parameter p_0 from its equilibrium value $\langle p\rangle$ is described by

$$p_0-\langle p\rangle=a_1s'+\tfrac{1}{2}a_2(s')^2$$
$$+a_3\{s^As'+\tfrac{1}{2}[(s')^2-(s^A)^2]\mathrm{sign}(s_t')\}. \tag{13}$$

When substituting Eqs. (13) and Eq. (14) into the stress/strain relationship (2) we also take into account the kinematic nonlinearity of longitudinal strain[32] $s'=s_1'+(1/2)(s_1')^2$ (where $s_1'\equiv\partial u/\partial x\propto\mu$ is a linear strain and u denotes the mechanical displacement). Then, retaining only the terms that can in principle not be smaller than $\propto\mu^2$, we derive

$$\sigma'\cong\sigma_ss_1'+\sigma_pa_1R[s_1']+\tfrac{1}{2}(\sigma_s+\sigma_{ss})(s_1')^2$$
$$+\tfrac{1}{2}\sigma_pa_2R[(s_1')^2]+\sigma_pa_3R[s_1^As_1'+\tfrac{1}{2}((s_1')^2$$
$$-(s_1^A)^2)\mathrm{sign}((s_1')_t)]+\sigma_{sp}a_1s_1'R[s_1']$$
$$+\tfrac{1}{2}\sigma_{pp}a_1^2(R[s_1'])^2. \tag{14}$$

However, additional simplification of Eq. (14) is possible due to the following physical arguments. For Eq. (14) the condition of the weak influence of relaxation on linear acoustic waves can be formulated as $\sigma_pa_1\propto\mu^{\beta_1}\sigma_s$ (or $\partial/\partial p\propto(\mu^{\beta_1}/a_1)\partial/\partial s$), with $\mu\ll1$, $\beta_1>0$. Then it is possible to estimate that

$$|\sigma_{sp}a_1s_1'R[s_1']|\leqslant\mu^{\beta_1}|\sigma_{ss}|(s_1')^2\ll|\sigma_{ss}|(s_1')^2,$$
$$|(1/2)\sigma_pa_2R[(s_1')^2]|\leqslant\mu^{\beta_1}|\sigma_s(a_2/2a_1)|(s_1')^2$$
$$\ll|\sigma_s|(s_1')^2. \tag{15}$$

In inequalities Eq. (15) we used $|R[\psi]|\leqslant|\psi|$ and $|a_2|\leqslant|a_1|$, the latter is valid in the case when the distribution function of nonhysteretic elements f_1 does not change abruptly at the scale of the acoustic strain variation [precisely, if $(f_1)_s/f_1\propto\mu^{\beta_3-1}$, $\beta_3>0$]. Due to inequalities (15), the estimated contributions can be neglected in Eq. (14) in comparison with the usual quadratic nonlinearity [associated with the third term on the right-hand side of Eq. (14)]

$$\sigma'\cong\sigma_ss_1'+\sigma_pa_1R[s_1']+\tfrac{1}{2}(\sigma_s+\sigma_{ss})(s_1')^2$$
$$+\sigma_pa_3R[s_1^As_1'+\tfrac{1}{2}((s_1')^2-(s_1^A)^2)\mathrm{sign}((s_1')_t)]$$
$$+\tfrac{1}{2}\sigma_{pp}a_1^2(R[s_1'])^2. \tag{16}$$

Finally, substituting the dynamic equation of state Eq. (16) in the wave equation ($\rho u_{tt}=\sigma_x$), with ρ the density of the material, and applying the method of slowly varying wave profile,[20] we derived the evolution equation for the nonlinear acoustic waves in inhomogeneous materials with hysteretic, endpoint memory and linear relaxation

$$v_x+(1/2c_\infty^2)[1+(\sigma_{ss}/\sigma_s)]vv_\tau-(1/2c_\infty)(\sigma_p/\sigma_s)a_1R[v_\tau]$$
$$-(1/2c_\infty^2)(\sigma_{pp}/\sigma_s)a_1^2R[v]R[v_\tau]$$
$$+(1/2c_\infty^2)(\sigma_p/\sigma_s)a_3R[v^Av_\tau+v|v_\tau|]=0. \tag{17}$$

In Eq. (17) $c_\infty\equiv c(\tau_R=\infty)=\sqrt{\sigma_s/\rho}$ is the velocity of the linear sound in the medium with frozen relaxation processes and $\tau=t-(x/c_\infty)$ is the retarded time.

In the limit $\tau_R=\infty$, and when none of the mechanical elements responsible for the inhomogeneity contribute to stress, Eq. (17) reduces to a simple wave equation with the sound velocity c_∞ and with a nonlinear parameter $\epsilon=\epsilon(\tau_R=\infty)\equiv\epsilon_\infty=-[1+(\sigma_{ss}/\sigma_s)]$ corresponding to an homogeneous medium.

In the opposite limiting case $\tau_R=0$ when the relaxation of the parameter to its equilibrium value is instantaneous, Eq. (17) reduces to Eq. (1), where

$$\epsilon=\epsilon(\tau_R=0)\equiv\epsilon_0=\epsilon_\infty+(\sigma_{pp}/\sigma_s)a_1^2,$$
$$h=h(\tau_R=0)\equiv h_0=(\sigma_p/\sigma_s)a_3, \tag{18}$$

with the retarded time $\tau=t-(x/c_0)$ defined via the equilibrium sound velocity $c_0\equiv c(\tau_R=0)$. Note that the transformation from Eq. (17) to Eq. (1) reveals the relationship between the maximum variation of the linear sound velocity $c_\infty-c_0$ and the parameter a_1 $[(\sigma_p/\sigma_s)a_1=-2(c_\infty-c_0)/c_0]$. Thus the condition $(\sigma_p/\sigma_s)a_1\propto\mu^{\beta_1}$ used before for the derivation of Eq. (16) has a clear physical meaning $|c_\infty-c_0|/c_0\ll1$. As follows from Eqs. (17) and (18) the micro-inhomogeneous medium could have anomalously high nonlinearity in comparison with the homogeneous medium if $|\epsilon_0-\epsilon_\infty|\gg\epsilon_\infty|$ and/or $|h_0|\gg|\epsilon_\infty|$. Note that the experimental observations of the softening of the material with increasing wave amplitude at sufficiently low frequencies can be formulated as the condition $h_0>0$. All of these inequalities are in fact conditions on the values of the parameters and on the distribution functions of the mechanical elements responsible for the inhomogeneity.

One important result of our theory should also be mentioned here. In accordance with Eq. (18) and the derived form for the parameter a_1 $[a_1\equiv\Delta p\langle f_1\rangle+\int_{\langle s\rangle}^{\infty}ds_1\ r_1f_1(s_1)+\int_{-\infty}^{\langle s\rangle}ds_1\ r_2f_1(s_1)]$ to the nonlinear parameter ϵ contribute not only the mechanical elements exhibiting a discontinuity in the internal parameter (i.e., with $\Delta p\neq0$), as postulated in

Ref. 18, but also elements exhibiting a discontinuity in the derivative of the parameter over strain (i.e., with $\Delta r \neq 0$) in addition to the elements with perfectly linear response [with $\Delta p = 0$, $\Delta r = 0$, i.e., $\partial p_0(s, s_1, s_2)/\partial s \equiv \text{const}$].

A. Equilibrium micro-inhomogeneous medium

For the analysis of Eq. (1) it is suitable to use the following nondimensional functions and variables $V = v/v_0$, $\theta = \omega\tau$, and $\zeta = x/x_{NL}$, where $v_0 = v^A(x=0)$ is the wave amplitude at the boundary, $\omega = 2\pi/T$ is the characteristic cyclic frequency of the wave, and $x_{NL} = 2c_0^2/(h_0 \omega v_0)$ is the characteristic length of wave transformation caused by hysteretic nonlinearity (which was introduced in Ref. 27 in the case of the analysis of nonlinear shear waves). Hysteretic nonlinearity causes wave propagation velocity changes, hysteretic (nonlinear) absorption and wave spectrum transformation.[27] In these notations evolution equation (1) takes the form

$$V_\zeta - H^{-1} V V_\theta + V^A V_\theta + V|V_\theta| = 0. \tag{19}$$

The nondimensional parameter $H \equiv h_0/\epsilon_0$ in Eq. (19) characterizes the relative strength of the hysteretic quadratic nonlinearity and nonhysteretic quadratic nonlinearity. The third term in Eq. (19) describes the change in the sound propagation velocity proportionally to the local wave amplitude $V^A = V^A(\zeta)$.[27] This term can be eliminated in the equation by introducing a modified nondimensional retarded time

$$\theta' = \theta - \varphi(\zeta) = \theta - \int_0^\zeta V^A(\zeta')\, d\zeta', \tag{20}$$

where $\varphi(\zeta)$ is the wave phase shift. By changing variables in accordance with Eq. (20) we transform Eq. (19) into

$$V_\zeta - H^{-1} V V_{\theta'} + V|V_{\theta'}| = 0. \tag{21}$$

The solution of this equation in the case $H \ll 1$ [when the hysteretic nonlinearity is negligible and Eq. (21) reduces to a simple wave equation] is well known.[20] The analytical solutions in the case $H \gg 1$ were derived in Ref. 27. The general solution of Eq. (21) for arbitrary values of the parameter H and periodic boundary condition $V(\zeta = 0) = \Phi(\theta)$ in implicit form is

$$V = \Phi\{\theta' + [H^{-1} - \text{sign}(V_{\theta'})] V \zeta\}, \tag{22}$$

with Φ an arbitrary function. This solution describes independent and different transformations of the parts of the initial wave profile $\Phi(\theta)$ which have a different sign of the slope with respect to the θ-axis [i.e., with a different sign $(V_{\theta'})$].

Solution Eq. (22) can be graphically analyzed by any of the well-known methods.[20,33] This analysis demonstrates that at the distances $0 \leqslant \zeta < \zeta_0 \equiv (\pi/2) H/\sin[(\pi/2)(1-H)]$ the initially sinusoidal profile $V = \sin\theta$ splits into two branches characterized by a different sign of $V_{\theta'}$ (curves a–a and b–b in Fig. 3, which presents a period of the wave). Note, that we consider for definiteness that $\epsilon_0 > 0$ and adopt that $h_0 > 0$ in accordance with softening of the elastic modulus observed experimentally in low-frequency experiments.[24,25] The physical solution consists of the parts of this branches that are closest to the θ' axis. Thus it consists of the a–a branch in the region between the intersection points of the a–a and b–b curves and of the b–b branch elsewhere. Due to this choice the physical solution has the lowest acoustic energy in comparison with the other (mathematical) solutions which can be constructed by connecting a–a and b–b branches by vertical fronts. From the physical point of view, solutions with shock fronts are impossible at this stage of wave evolution [precisely at the distances $0 \leqslant \zeta < \zeta_F \equiv H/(1-H)$], because a wave with a shock front exhibits higher absorption than a wave without a shock front[20] and, consequently, it cannot conserve more energy in the process of evolution than a wave without a shock front.

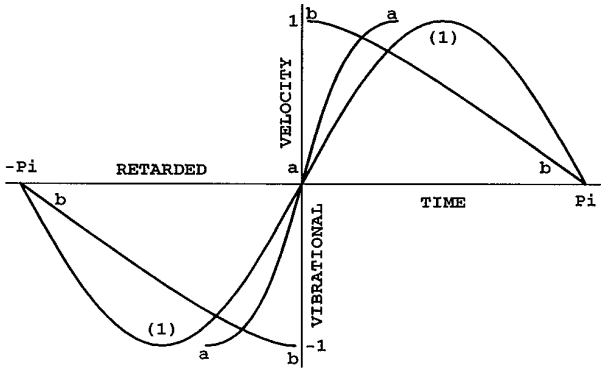

FIG. 3. To the choice of the physical solution of the evolution equation [Eq. (21)]. The curves a-a and b-b present the mathematical prediction [Eq. (22)] for the initially sinusoidal wave (1) at the distance $\zeta = 1$ in the case $H = 0.5$. The physical solution consists of those parts of the mathematical solution which are the closest to the retarded time axis.

The solution Eq. (22) predicts the formation of a weak shock front in the wave profile with minimal acoustic energy at the distance $\zeta = \zeta_F \equiv H/(1-H)$. The physics of this process is similar to the well-known process in the absence of hysteretic nonlinearity (i.e., when $h_0 = 0$).[20] The position of the shock front in the profile with minimal acoustic energy can be found from the same physical principles as in the case $h_0 = 0$.[20] The transformation of an initially sinusoidal wave with increasing propagation distance is presented in Fig. 4. Note that in this case the position of the shock front easily follows from symmetry considerations.

In accordance with the obtained solution, hysteretic nonlinearity increases the distance of shock front formation. In the general case a weak shock front develops in the process of harmonic wave evolution if $h_0 > |\epsilon_0|$ $(|H| < 1)$. The physical reason for this is the hysteretic absorption[27] that diminishes the wave amplitude and, consequently, suppresses shock formation. In Fig. 4 we present the profiles of the initially sinusoidal wave at different propagation distances in the case when the formation of the shock front takes place [$H < 1$, Fig. 4(a)] and when it is not realized [$H > 1$, Fig. 4(b)]. We remark that for definiteness we consider that $\epsilon_0 > 0$. In the case $\epsilon_0 < 0$ the formation of the shock front will not be in the points $\theta' = 2\pi n$, but in the points $\theta' = (2n+1)\pi$ $(n = 0, \pm 1, \pm 2, \ldots)$.

For the evaluation of the local propagation velocity and the prediction of the wave phase shift it is important that the solution Eq. (22), in the case of sinusoidal excitation, provides an analytical description of the wave amplitude. Analysis of the solution demonstrates that if the formation of the

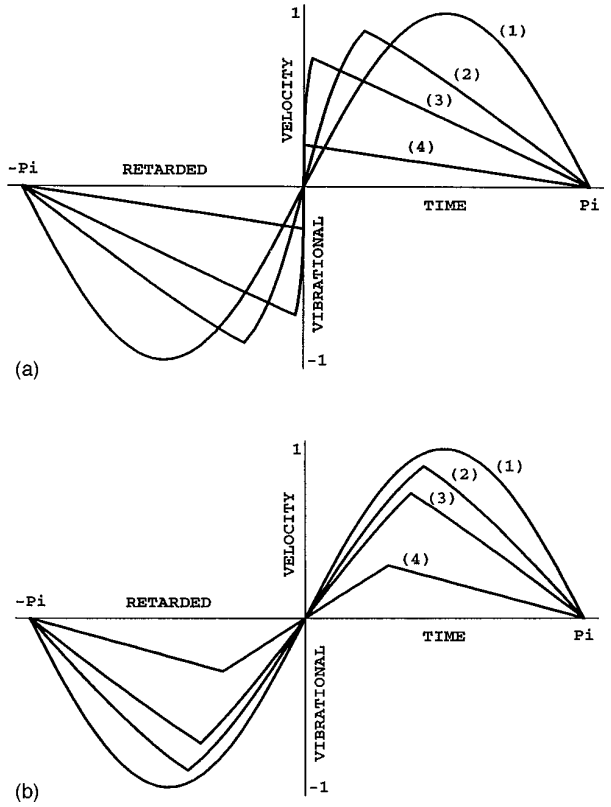

FIG. 4. Transformation of the initially sinusoidal wave with increasing propagation distance in the case $H=0.5$ (a) and $H=2$ (b). The wave profiles are presented at the distances $\zeta=0$ (1), $\zeta=0.5$ (2), $\zeta=1$ (3), $\zeta=4$ (4).

shock front is suppressed (i.e., in the case $H>1$) then the dependence of the wave amplitude on propagation distance is implicitly described by

$$\zeta=[(\pi/2)-\arcsin V^A]/V^A \tag{23}$$

at all distances. The reduction of the wave amplitude in this case is due to hysteretic nonlinearity.[27] In the case when $0 \leqslant H \leqslant 1$ and, consequently, a shock front emerges in $\theta'=0$ at the distance $\zeta=\zeta_F \equiv H/(1-H)$, the description of Eq. (23) is valid only until the peaks of the wave profile reach $\theta'=0$ at the distance $\zeta=\zeta_0 \equiv (\pi/2)H/\sin[(\pi/2)(1-H)]$. (Note that $\zeta_0 \geqslant \zeta_F$.) At larger distances (i.e., at $\zeta \geqslant \zeta_0$) the amplitude of the wave is equal to half the shock front amplitude and is implicitly described by

$$\zeta=[H/(H+1)](\pi-\arcsin V^A)/V^A. \tag{24}$$

The reduction of the wave amplitude at the distances $\zeta \geqslant \zeta_0$ is due both to hysteretic absorption and to the energy absorption at the shock front.[20] The dependence of the wave amplitude on the propagation distance for different values of the parameter H is presented in Fig. 5.

The solution given by Eq. (22) also provides an analytical description of the shock front amplitude. After its formation at the distance $\zeta=\zeta_F$, the amplitude $V_F \equiv |V(\theta'+0) - V(\theta'-0)|$ of the shock front grows at the distances $\zeta_F \leqslant \zeta \leqslant \zeta_0$ in accordance with the implicit law $\zeta=[H/(1-H)]\arcsin(V_F/2)/(V_F/2)$. At the distances $\zeta \geqslant \zeta_0$ the diminishing of the shock amplitude is described by $V_F=2V^A$, where $V^A(\zeta)$ is determined by Eq. (24). The dependence of the shock front amplitude on the wave propagation distance

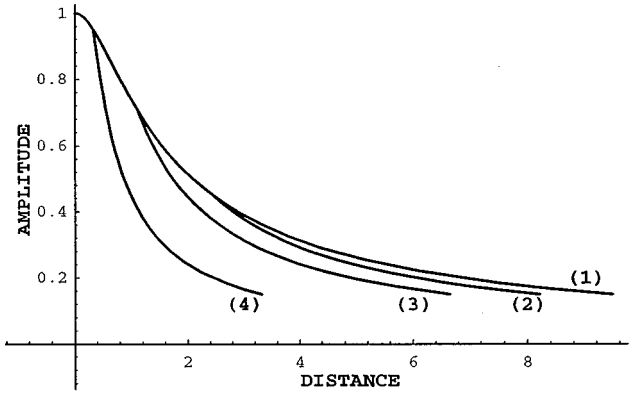

FIG. 5. The dependence of the normalized wave amplitude on the nondimensional propagation distance for different values of the parameter H, that characterizes the relative importance of hysteretic and usual quadratic nonlinearities [(1): $H \geqslant 1$, (2): $H=0.7$, (3): $H=0.5$, (4): $H=0.2$].

for the different values of the parameter H is presented in Fig. 6. It is also important that with analytical solution (22) and the formulated rules for choosing the physical solution, the frequency spectrum of the wave can be found at all distances by numerical Fourier transform if necessary (see, for example, Ref. 27).

Finally, both the discontinuities in the profile derivatives over time (near its extrema) and the discontinuities of the profile at the shock front can be eliminated by taking into account extra terms in the evolution equation, which are proportional to the second derivative of the vibrational velocity over retarded time (i.e., $\propto V_{\theta\theta}$). These terms appear if in the expansion of Eq. (17) in the limit $(\omega\tau_R) \to 0$, we retain not only the leading terms $[\propto(\omega\tau_R)^0]$ but also the terms proportional to the first power of $(\omega\tau_R)$. Even though these terms contain an additional small parameter $(\omega\tau_R) \ll 1$ [in comparison with the terms of Eq. (1)] they play an important role in defining the structure of the wave in the vicinity of its extrema[27] and in determining the structure of the shock front.[20]

B. Quasi-frozen micro-inhomogeneous medium

For the derivation from Eq. (17) of an asymptotic equation for the case of quasi-frozen relaxation processes [i.e., when $(\omega\tau_R) \gg 1$ but $(\omega\tau_R) \neq \infty$] the following expansion of the relaxation operator [Eq. (5)] is useful;

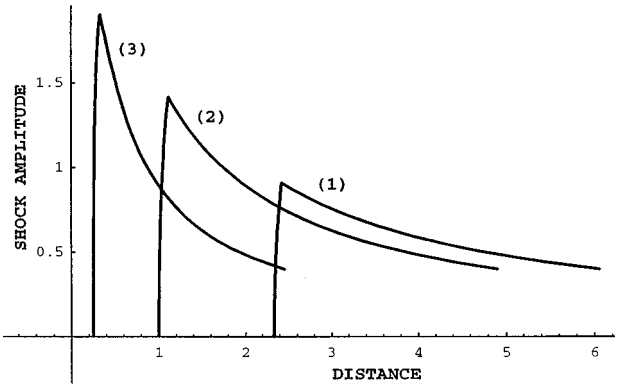

FIG. 6. The dependence of the normalized shock wave amplitude on the propagation distance for the different values of the parameter H [(1): $H=0.7$, (2): $H=0.5$, (3): $H=0.2$].

$$R[\psi] \cong \frac{1}{\tau_R}\left[\Psi - \frac{1}{T}\int_t^{t+T}\Psi(t')dt'\right]. \tag{25}$$

Here $\Psi_t \equiv \psi$, i.e., Ψ is the indefinite integral function of ψ, and the neglected terms are proportional to τ_R^{-2}. In accordance with Eq. (25) the nonlinear operator $R[v]R[v_\tau]$ in Eq. (17) can be neglected in the regime under consideration, because the corresponding contribution to the evolution equation will be proportional to $(\omega\tau_R)^{-2} \ll 1$ (in comparison with the term $\epsilon_\infty v v_\tau$). Retaining in Eq. (17) only the terms of the zero and first order in the small parameter $(\omega\tau_R)^{-1} \ll 1$ we derive

$$v_x + \left(\frac{1}{2c_\infty^2}\right)\epsilon_\infty v v_\tau + \left[\left(\frac{1}{c_0}\right) - \left(\frac{1}{c_\infty}\right)\right]\left(\frac{1}{\tau_R}\right)v + \left(\frac{1}{2c_\infty^2}\right)\left(\frac{h_0}{\tau_R}\right)\left\{v^A v + \left(\frac{1}{2}\right)[v^2 - (v^A)^2]\,\mathrm{sign}(v_\tau)\right\} = 0. \tag{26}$$

In the derivation of Eq. (26) it was assumed that the second term in the right-hand side of Eq. (25) is equal to zero as it is in the case of harmonic excitation, for example. In the limit $|\epsilon_\infty| \gg (h_0/\omega\tau_R)$ the hysteretic nonlinearity can be neglected in Eq. (26). In this case, Eq. (26) provides the description of the wave evolution in an homogeneous nonlinear medium with relaxation and its solution is well-known.[20] Thus we are interested here in the opposite limiting situation $|\epsilon_\infty| \ll (h_0/\omega\tau_R)$, when the hysteretic nonlinearity due to the inhomogeneity of the medium is dominant. In this case we neglect the operator $v v_\tau$ in Eq. (26). Then, by transforming to the nondimensional functions and variables $V = v/v_0$, $\theta = \omega\tau$ and $\zeta = x/x_{NL}$ with $x_{NL} = 2c_\infty^2\tau_R/h_0 v_0$, we obtain the evolution equation (26) in the form

$$V_\zeta + (\Gamma + V^A)V + \tfrac{1}{2}[V^2 - (V^A)^2]\,\mathrm{sign}(V_\tau) = 0. \tag{27}$$

In Eq. (27) the nondimensional parameter Γ characterizes the relative importance of the hysteretic nonlinear processes[27] and the frequency-independent absorption caused by linear relaxation[20]

$$\Gamma \equiv [(1/c_0) - (1/c_\infty)](2c_\infty^2/h_0 v_0) \cong (c_\infty - c_0)/(h_0 v_0/2). \tag{28}$$

To simplify Eq. (28) we used $(c_\infty - c_0)/c_0 \ll 1$. In accordance with Eq. (28) the nondimensional parameter Γ is equal to the ratio of the changes in sound velocity due to relaxation and due to hysteretic nonlinearity. It is interesting that, even though we assume that the same relaxation time τ_R controls both the hysteretic mechanical elements (which contribute to hysteretic nonlinearity) and the nonhysteretic mechanical elements (which are responsible in particular for the linear absorption and dispersion of sound), the characteristic parameter Γ does not depend on the relaxation time. In this situation the relaxation influences only the characteristic spatial scale x_{NL} of wave transformation. Equations (26) and (27) are equations of a new type for nonlinear acoustics. Fortunately some analytical results can be obtained from their analysis.

The exact analytical solution of Eq. (27) [in case of a sinusoidal boundary condition $V(\zeta = 0) = \sin\theta$] is

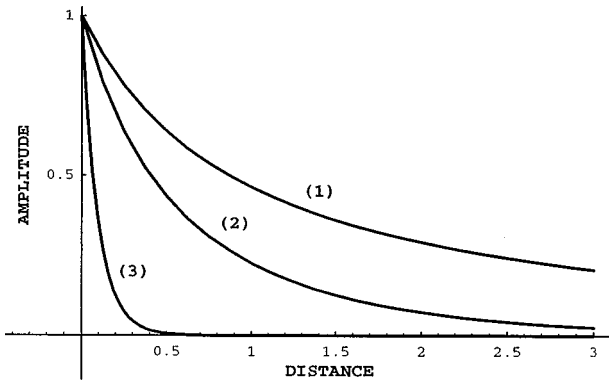

FIG. 7. The dependence of the normalized amplitude of the wave on the propagation distance for different values of the nondimensional parameter Γ, which characterizes the relative importance of the linear absorption of sound and the processes caused by hysteretic nonlinearity [(1): $\Gamma = 0.1$, (2): $\Gamma = 1$, (3): $\Gamma = 10$].

$$\begin{aligned} V(-\pi/2 \leqslant \theta \leqslant \pi/2) &\equiv V_1(\theta) \\ &= \left\{\frac{\exp(-\Gamma\zeta)}{1 + [1 - \exp(-\Gamma\zeta)]/\Gamma}\right\} \\ &\quad \times \left\{\frac{2\sin\theta + (1 + \sin\theta)[1 - \exp(-\Gamma\zeta)]/\Gamma}{2 + (1 + \sin\theta)[1 - \exp(-\Gamma\zeta)]/\Gamma}\right\}, \\ V(\pi/2 \leqslant \theta \leqslant 3\pi/2) &= -V_1(\theta - \pi), \\ V(-\pi \leqslant \theta \leqslant -\pi/2) &= -V_1(\theta + \pi). \end{aligned} \tag{29}$$

The first factor in Eq. (29) describes the dependence of the wave amplitude on the propagation distance. In particular, $V^A \cong (1 - \Gamma\zeta)/(1 + \zeta)$ when $\Gamma\zeta \ll 1$ and $V^A \cong [\Gamma/(\Gamma + 1)]\exp(-\Gamma\zeta)$ when $\Gamma\zeta \geqslant 3$ [and, consequently, $\exp(-\Gamma\zeta) \ll 1$]. Thus the diminishing of the wave amplitude at small distances $\zeta \ll 1/\Gamma$ is caused by linear and nonlinear attenuation. At large propagation distances $\zeta \geqslant 3/\Gamma$, where the amplitude becomes small, the linear absorption dominates. Nonlinear attenuation can dominate at small distances $\zeta \ll 1/\Gamma$ if $\Gamma \ll 1$ [then $V^A \cong 1/(1 + \zeta)$]. In Fig. 7 we illustrate the dependence of the normalized wave amplitude on the scaled propagation distance for a few values of the parameter Γ.

The second factor in Eq. (29) describes the transformation of the wave shape. It is interesting to note that the nonlinear processes in combination with frequency-independent absorption cause a stabilization of the wave shape at the distances $\zeta \geqslant 3/\Gamma$:

$$\frac{V_1(\theta, \zeta \geqslant 3/\Gamma)}{V^A(\zeta)} \cong \frac{2\sin\theta + (1 + \sin\theta)/\Gamma}{2 + (1 + \sin\theta)/\Gamma}. \tag{30}$$

In accordance with Eq. (30) in the case $\Gamma \gg 1$ the asymptotic profile is $V_1/V^A \equiv \sin\theta$, because in this limit the role of the nonlinearity in Eq. (27) is negligible. When the parameter Γ diminishes, the asymptotic profile in Eq. (30) deviates more and more from the harmonic shape (see Fig. 8). The transformation of the wave profile with increasing propagation distance is shown in Fig. 9.

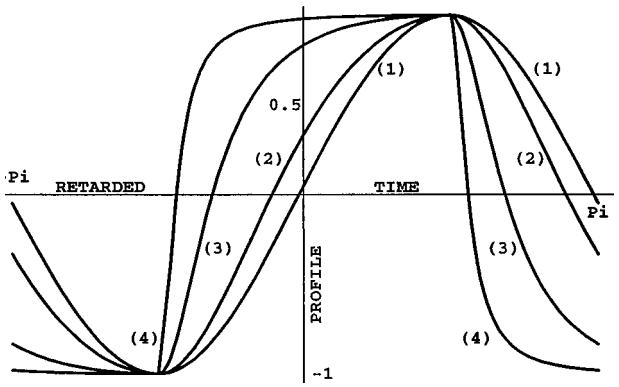

FIG. 8. Asymptotic profiles of the wave at large propagation distances ($\zeta \geqslant 3/\Gamma$) for the different values of the parameter Γ [(1): $\Gamma=10$, (2): $\Gamma=1$, (3): $\Gamma=0.1$, (4): $\Gamma=0.01$].

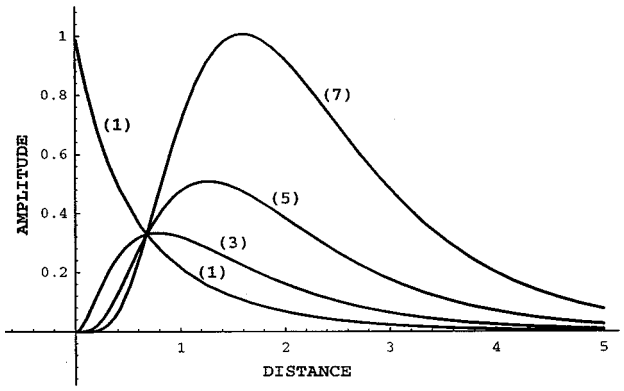

FIG. 10. Dependence of the normalized amplitudes $10^{n-1}|\overline{v_n}|$ of the harmonics on the propagation distance in the case $\Gamma=1$ [(1): $n=1$, (3): $n=3$, (5): $n=5$, (7): $n=7$].

The transformation of the wave frequency spectrum (which contains only the odd harmonics) in the propagation process also can be described analytically

$$\overline{V}_{2n+1} \cong \frac{1}{\pi}\int_{-\pi}^{\pi} V(\theta)\sin[(2n+1)\theta]d\theta$$

$$=(-1)^n \frac{2(1-b)[1-(2\Gamma+1)b]}{b} \times\left(\frac{1-\sqrt{1-b^2}}{b}\right)^{2n+1},$$

$$b\equiv b(\zeta)=[1-\exp(-\Gamma\zeta)]/\{2\Gamma +[1-\exp(-\Gamma\zeta)]\}, \quad n=0,1,2,\ldots . \tag{31}$$

The dependence of the amplitudes $|\overline{V}_{2n+1}|$ of the first few spectral components on the propagation distance is presented in Fig. 10.

C. Initial stage of the wave transformation

In order to clarify the physical meaning of the different terms in evolution equation (17) in the general case (i.e., when the medium is not in equilibrium and is not quasi-frozen) it is useful to analyze its solution at such a short propagation distance that there is not yet mutual influence of the various physical processes affecting the wave transformation. At sufficiently short propagation distances linear and nonlinear processes act independently on the acoustic wave and, for example, the influence of the linear absorption on the process of nonlinear interaction of the spectral components can be neglected. From the formal mathematical point of view this physical stage of the wave evolution can be described by solving Eq. (17) by an iterative procedure (stepwise successive approximations) and taking into account the first iterative step.

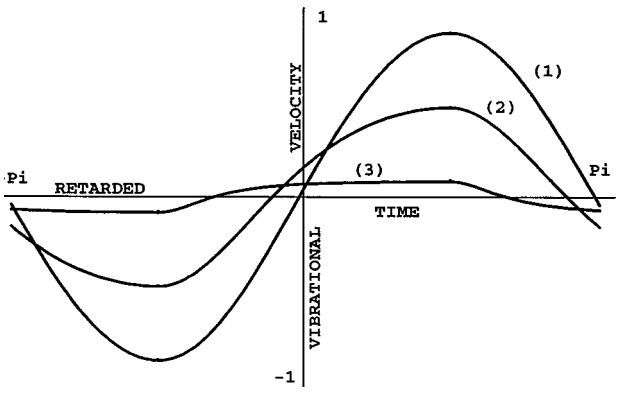

FIG. 9. Transformation of the wave profile with increasing propagation distance in the case when $\Gamma=0.01$ [(1): $\zeta=0.1$, (2): $\zeta=1$, (3): $\zeta=10$].

For convenience we first rewrite Eq. (17) using the notation introduced before

$$v_x=-[(1/c_0)-(1/c_\infty)]R[v_\tau] +(1/2c_\infty^2)\{\epsilon_\infty v v_\tau+(\epsilon_0-\epsilon_\infty)R[v]R[v_\tau]\} -(1/2c_\infty^2)h_0\{v^A R[v_\tau]+R[v|v_\tau|]\}. \tag{32}$$

In order to find the attenuation and dispersion of an initially harmonic acoustic wave at short distances it is sufficient to substitute $v(x)=v_0\exp(-\alpha x)\sin\{\omega[\tau+((1/c_\infty)-(1/c))_x]\}$ in Eq. (32) and retain only the terms at the fundamental frequency. It then follows that the coefficient α, which controls the initial rate of the diminishing of the fundamental harmonic amplitude, is

$$\alpha=\left[\frac{1}{c_0}-\frac{1}{c_\infty}+\frac{h_0 v_0}{2c_\infty^2}\left(1+\frac{5}{3\pi(\omega\tau_R)}\right)\right]\frac{\omega^2\tau_R}{1+(\omega\tau_R)^2} \cong \frac{c_\infty-c_0}{c_\infty^2}\left[1+\frac{1}{\Gamma}\left(1+\frac{5}{3\pi(\omega\tau_R)}\right)\right]\frac{\omega^2\tau_R}{1+(\omega\tau_R)^2}. \tag{33}$$

In accordance with Eq. (33) in addition to the ordinary relaxation attenuation[20] in the micro-inhomogeneous media there is a nonlinear frequency-dependent damping of sound proportional to the parameter of hysteretic nonlinearity $h_0=h(\tau_R=0)$. This additional contribution to the reduction of the amplitude of the fundamental harmonic is caused by hysteretic nonlinearity, and is due to both hysteretic absorption and energy conversion into higher harmonics. Note that at sufficiently low frequencies the nonlinear attenuation dominates over the linear, because for $(\omega\tau_R)\ll 1$ the coefficient of linear absorption is proportional to ω^2, while the nonlinear attenuation is proportional to ω.

The velocity c of the harmonic wave propagation at the initial stage is described by

$$\frac{1}{c}=\frac{1}{c_\infty}+\left[\frac{1}{c_0}-\frac{1}{c_\infty}+\frac{h_0 v_0}{2c_\infty^2}\left(1-\frac{5(\omega\tau_R)}{3\pi}\right)\right]\frac{1}{1+(\omega\tau_R)^2},$$

or

$$c\cong c_\infty-(c_\infty-c_0)\left[1+\frac{1}{\Gamma}\left(1-\frac{5(\omega\tau_R)}{3\pi}\right)\right]\frac{1}{1+(\omega\tau_R)^2}. \tag{34}$$

The approximate formulas in Eq. (33) and Eq. (34) are approximations derived under the usual assumption $(c_\infty - c_0)/c_0 \ll 1$. In accordance with Eq. (34), there is a nonlinear dispersion of the propagation velocity that is described by the term containing the nonlinear parameter Γ introduced in Eq. (27) in addition to the well-known linear dispersion due to relaxation[20] in a micro-inhomogeneous medium. It is interesting that the sign of the amplitude-dependent changes in the wave velocity depends on the nondimensional parameter $(\omega\tau_R)$. Thus in accordance with the presented theory an increase of the wave amplitude can cause dynamic softening or stiffening of an inhomogeneous material depending on whether $(\omega\tau_R)<3\pi/5$ ($\tau_R<0.3$ T) or $(\omega\tau_R)>3\pi/5$ ($\tau_R>0.3$ T). Summarizing the results presented in Eqs. (33) and (34): the amplitude-dependent attenuation and amplitude-dependent changes in the wave velocity caused by hysteretic nonlinearity[27] become also frequency dependent in a medium with relaxation. Or, in other words, in inhomogeneous media with relaxation, both frequency-dependent attenuation and velocity dispersion are nonlinear.

Hysteretic nonlinearity described by the term proportional to h_0 in the right-hand side of Eq. (32) contributes not only to dispersion and absorption, but also causes the generation of the odd harmonics.[26,27] At the initial stage the amplitudes of the odd harmonics grow proportionally to the wave propagation distance $|\overline{v_{2n+1}}|\cong(v_0/c_\infty)^2[\pi(2n-1)(2n+3)]^{-1}|h(\omega)|\omega x$ $(n=1,2,3,...)$, where the function

$$|h(\omega)|\equiv|h_0|/\sqrt{1+(\omega\tau_R)^2} \tag{35}$$

describes the dispersion of the parameter which is responsible for the harmonics generation by hysteretic nonlinearity. Note that the phases of the generated harmonics also depend on $(\omega\tau_R)$. In accordance with Eqs. (33)–(35), relaxation suppresses hysteretic nonlinearity.

The second term in the right-hand side of Eq. (32) describes the second harmonic generation at short distances. At the initial stage the second harmonic amplitude grows proportionally to the wave propagation distance $|\overline{v_2}| \cong (v_0/c_\infty)^2(1/2)|\epsilon(\omega)|\omega x$, where

$$|\epsilon(\omega)/\epsilon_\infty|\equiv\frac{\sqrt{(\epsilon_0/\epsilon_\infty)^2+2[2-(\epsilon_0/\epsilon_\infty)](\omega\tau_R)^2+(\omega\tau_R)^4}}{[1+(\omega\tau_R)^2]}. \tag{36}$$

Equation (36) describes the dispersion of the nonlinearity responsible for the second harmonic generation in a micro-inhomogeneous medium with relaxation. It should be noted that the phase of the excited second harmonic also depends on the nondimensional parameters $E_0\equiv\epsilon_0/\epsilon_\infty$ and $F\equiv\omega\tau_R$. It is interesting to note that the dependence of the nonlinear parameter on frequency is nonmonotonous if $E_0 > -2$ (and $E_0\neq 1$). The extremum in the value of the nonlinear parameter is reached when $F=\sqrt{E_0+2}$. The dependence of the normalized nonlinear parameter $|E| \equiv|\epsilon(\omega)/\epsilon_\infty|$ on the normalized frequency F is presented in Fig. 11 for several characteristic values of the parameter $E_0\equiv\epsilon_0/\epsilon_\infty$. We remark here that ϵ_∞ denotes the high-frequency value of the nonlinear parameter (i.e. in the absence of the influence from micro-inhomogeneities) while the low-frequency value ϵ_0 includes the contribution from the mechanical elements responsible for the inhomogeneity when their relaxation is instantaneous.

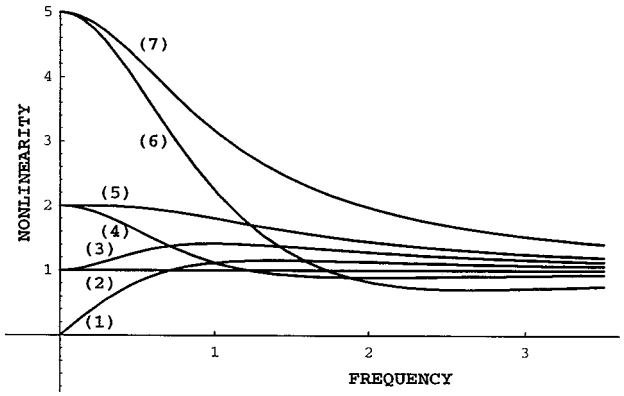

FIG. 11. Dependence of the normalized nonlinear parameter $E\equiv E(F)$, which is responsible for the second harmonic generation, on the normalized wave frequency $F\equiv\omega\tau_R$ for different static values $E_0\equiv E(0)$ of the nonlinear parameter [(1): $E_0=0$, (2): $E_0=1$, (3): $E_0=-1$, (4): $E_0=2$, (5): $E_0=-2$, (6): $E_0=5$, (7): $E_0=-5$].

II. DISCUSSION

In our opinion the theory presented in this paper is a necessary step toward the development of a general theory of nonlinear acoustic waves in micro-inhomogeneous materials. The theory developed in this paper takes into account the process of linear relaxation of the nonlinear parameters describing the mechanical elements, that are responsible for the micro-inhomogeneity of the medium. It does not, however, take into consideration the possible nonlinearity of the relaxation process itself (although we have formulated the conditions when this additional nonlinearity is negligible). In other words, we described relaxation of nonlinearity rather than nonlinearity of the relaxation. It should also be noted that, by postulating linear superposition of the parameters of the individual mechanical elements, we deliberately choose not to treat the problem of interaction between elements responsible for the inhomogeneity,[19] although it can be expected that relaxation implicitly accounts for at least a part of these interactions. So, our theory is a generalization of the existing theories rather than a general theory.

However, it is very important, in our opinion, that even this first step toward a general theory (which is the step from a static model to the simplest dynamic model of the stress/strain relationship in micro-inhomogeneous media) results in a variety of possible frequency-dependent effects. Moreover, the developed theory could provide insight in the interpretation of some intriguing experimental observations. We

would like to mention here only one of those. It was experimentally observed[9] that the nonlinear parameter responsible for the second harmonic generation in PZT ceramics can be an increasing or decreasing function of the wave frequency, depending on the content ratio of $PbTiO_3$ and $PbZrO_3$ in the samples. The theory presented provides at least a few ways for the explanation of these observations. It should be noted, of course, that due to the additivity of the contributions to nonlinearity from different types of internal parameters p_i $(i=1,2,3,...)$ practically any dependence of nonlinearity on frequency can be modeled by combining a sufficient number of different elements with different relaxation times $\tau_R^{(i)}$. Still, it is very promising that, even with a single parameter characterizing mechanical elements and a single relaxation time, the decreasing or increasing dependence of the nonlinearity on frequency can be attributed to the dependence of the quasi-static nonlinearity E_0 and/or relaxation time τ_R on the composition of the ceramics (see Fig. 11). Perhaps the variation of the relaxation time with temperature could explain at least a part of the strong temperature dependence of the nonlinear parameters near a phase transition in PZT.[9] But, of course, the change in the structure of the mechanical elements responsible for the inhomogeneity in the vicinity of the phase transition can also play an important role.

In Ref. 34 the dispersion of the nonlinear parameter responsible for the second harmonic generation was modeled by introducing an additional differential term in the wave equation. In line with the mathematical formalism adopted in our theory here the corresponding additional term in the evolution equation (in comparison with a simple wave equation) is $\propto v v_{\tau\tau\tau}$. Although the authors[34] succeeded in fitting the experimental curves of Ref. 9 by introducing this term with a huge coefficient, we would like to point out here that any modeling of dispersion effects by differential terms has a limited range of validity. This statement is correct both for the dispersion due to the existence of an internal characteristic time in the medium (addressed in our present paper) and for the dispersion which can be attributed to the existence of an internal characteristic spatial scale (grain size, for example). So, we consider the present theory to be more general than one proposed in Ref. 34. The differential term $\propto v v_{\tau\tau\tau}$ explicitly appears in our equations if we use an expansion of the relaxation operators in Eq. (17) in the parameter $(\omega\tau_R)<1$. However, the term $\propto v v_{\tau\tau\tau}$ is not the only term of the order of $(\omega\tau_R)^2$ in this expansion. The expansion of the relaxation operators in Eq. (17) also gives some other terms of the same order in the parameter $(\omega\tau_R)$ [i.e., $\propto(\omega\tau_R)^2$]. Among them the term $\propto v_\tau v_{\tau\tau}$ also contributes to the dispersion of the nonlinear parameter responsible for the second harmonic generation.

It is clear that more experiments, in a wider frequency range and with wider variation in the sample composition are necessary to determine the correct explanation. We are sure that such experiments will be done, because applying nonlinear acoustics methods for material characterization is very attractive and promising.

III. CONCLUSIONS

New evolution equations for nonlinear acoustic waves in micro-inhomogeneous media, which take into account relaxation processes, are derived. The proposed theory provides the description of several physical effects such as frequency-dependent nonlinear absorption of sound, nonlinearity of velocity dispersion, and dispersion of the nonlinear acoustic parameters of micro-inhomogeneous materials. The theory predicts that, depending on the ratio of the characteristic relaxation time and the wave period, the nonlinearity can grow or diminish with increasing frequency, while an increase in wave amplitude can lead to an increase or decrease of the propagation velocity. In the limiting cases where the relaxation processes are instantaneous or quasi-frozen, analytical solutions of the nonlinear equations were found and analyzed. We hope that our theory will be useful for experimentalists in providing physical insight in the nonlinear acoustic phenomena observed in micro-inhomogeneous materials.

ACKNOWLEDGMENTS

This work was supported by the Belgian National Science Fund (NFWO) through FKFO project (G.0115.95). Support from the Research Council of the Katholieke Universiteit Leuven in the form of a Fellowship to one of us (V.G.) is gratefully acknowledged.

[1] P. A. Johnson, T. J. Shankland, R. J. O'Connell, and J. N. Albright, ''Nonlinear generation of elastic waves in crystalline rock,'' J. Geophys. Res. **92**, 3597–3602 (1987).
[2] V. E. Nazarov, L. A. Ostrovsky, I. A. Soustova, and A. M. Sutin, ''Nonlinear acoustics of micro-inhomogeneous media,'' Phys. Earth Planet. Inter. **50**, 65–73 (1988).
[3] V. E. Nazarov, L. A. Ostrovskii, I. A. Soustova, and A. M. Sutin, ''Anomalous acoustic nonlinearity in metals,'' Akust. Zh. **34**, 491–499 (1988) [English transl.: Sov. Phys. Acoust. **34**, 284–289 (1988)].
[4] P. A. Johnson and T. J. Shankland, ''Nonlinear generation of elastic waves in granite and sandstone: Continuous wave and travel time observations,'' J. Geophys. Res. **94**, 17729–17733 (1989).
[5] V. E. Nazarov and L. A. Ostrovksii, ''Elastic waves in media with strong acoustic nonlinearity,'' Akust. Zh. **36**, 106–110 (1990) [English transl.: Sov. Phys. Acoust. **36**, 57–60 (1990)].
[6] V. E. Nazarov, ''Nonlinear acoustic effects in annealed copper,'' Akust. Zh. **37**, 150–156 (1991) [English transl.: Sov. Phys. Acoust. **37**, 75–78 (1991)].
[7] G. D. Meegan, Jr., P. A. Johnson, R. A. Guyer, and K. R. McCall, ''Observations of nonlinear elastic wave behavior in sandstone,'' J. Acoust. Soc. Am. **94**, 3387–3391 (1993).
[8] P. A. Johnson and K. R. McCall, ''Observation and implications of nonlinear elastic wave response in rock,'' Geophys. Res. Lett. **21**, 165–168 (1994).
[9] J. K. Na and M. A. Breazeale, ''Ultrasonic nonlinear properties of lead zirconate-titanate ceramics,'' J. Acoust. Soc. Am. **95**, 3213–3221 (1994).
[10] P. A. Johnson, B. Zinszner, and P. N. J. Rasolofosaon, ''Resonance and elastic nonlinear phenomena in rock,'' J. Geophys. Res. **101**, 11553–11564 (1996).
[11] J. A. Ten Cate, K. E. A. Van Den Abeele, T. J. Shankland, and P. A. Johnson, ''Laboratory study of linear and nonlinear elastic pulse propagation in sandstone,'' J. Acoust. Soc. Am. **100**, 1–9 (1996).
[12] P. A. Johnson and P. N. J. Rasolofosaon, ''Manifestation of nonlinear elasticity in rock: Convincing evidence over large frequency and strain intervals from laboratory studies,'' Nonlinear Processes in Geophysics, **3**, 77–88 (1996).
[13] K. R. McCall and R. A. Guyer, ''A new theoretical paradigm to describe hysteretic, discrete memory and nonlinear elastic wave propagation in rock,'' Nonlinear Processes in Geophysics **3**, 89–101 (1996).
[14] B. P. Bonner and B. J. Wanamaker, ''Nonlinear acoustic effects in rocks

and soils,'' in *Review of Progress in Quantitative Nondestructive Evaluation*, edited by D. O. Thompson and D. E. Chimenti (Plenum, New York, 1990), Vol. 9, pp. 1709–1713.
[15] I. Shkolnik, L. Zarembo, and V. Krasilnikov, ''On structural non-linear diagnostics of solids and estimation of their strength,'' in *Frontiers in Nonlinear Acoustics: Proceedings of the 12th ISNA*, edited by M. F. Hamilton and D. T. Blackstock (Elsevier Science, London, 1990), pp. 589–594.
[16] V. E. Nazarov, ''Sound damping by sound in metals,'' Acoust. Lett. **15**, 22–25 (1991).
[17] B. Zinszner, P. A. Johnson, and P. N. J. Rasolofosaon, ''Influence of change in physical state on elastic nonlinear response in rock: Significance of effective pressure and water saturation,'' J. Geophys. Res. **102**, 8105–8120 (1997).
[18] K. R. McCall and R. A. Guyer, ''Equation of state and wave propagation in hysteretic nonlinear elastic materials,'' J. Geophys. Res. **99**, 23887–23897 (1994).
[19] R. A. Guyer, K. P. McCall, and G. N. Boitnott, ''Hysteretic, discrete memory, and nonlinear wave propagation in rock: A new paradigm,'' Phys. Rev. Lett. **74**, 3491–3494 (1995).
[20] O. V. Rudenko and S. I. Soluyan, *Theoretical Foundations of Nonlinear Acoustics* (Consultants Bureau, New York, 1977).
[21] K. E-A. Van Den Abeele, ''Elastic pulsed wave propagation in media with second or higher order nonlinearity. Part I. Theoretical framework,'' J. Acoust. Soc. Am. **99**, 3334–3345 (1996).
[22] K. E-A. Van Den Abeele and P. A. Johnson, ''Elastic pulsed wave propagation in media with second or higher order nonlinearity. Part II. Simulation of experimental measurements on Berea sandstone,'' J. Acoust. Soc. Am. **99**, 3346–3352 (1996).
[23] A. Kadish, J. A. Ten Cate, and P. A. Johnson, ''Frequency spectra of nonlinear elastic pulse-mode waves,'' J. Acoust. Soc. Am. **100**, 1375–1382 (1996).
[24] D. J. Holcomb, ''Memory, relaxation, and microfracturing in dilatant rock,'' J. Geophys. Res. **86**, 6235–6248 (1981).
[25] G. N. Boitnott, ''Nonlinear rheology of rock at moderate strains: Fundamental observations of hysteretic in the deformation of rock,'' in the Proceedings of 15th Annual Seismic Research Symposium, Vail, Colorado, edited by J. F. Lewkowicz and J. M. McPhetres (Philips Laboratory of the Air Force Material Command. Handsom Air Force Base, MA, 1993), Environmental Research Papers no. 125, pp. 121–133.
[26] K. E-A. Van Den Abeele, P. A. Johnson, R. A. Guyer, and K. R. McCall, ''On the quasi-analytic treatment of hysteretic nonlinear response in elastic wave propagation,'' J. Acoust. Soc. Am. **101**, 1885–1898 (1997).
[27] V. Gusev, C. Glorieux, W. Lauriks, and J. Thoen, ''Nonlinear bulk and surface shear acoustic waves in materials with hysteretic and endpoint memory,'' Phys. Lett. A **232**, 77–86 (1997).
[28] L. A. Ostrovsky, I. A. Soustova, and A. M. Sutin, ''Nonlinear and parametric phenomena in dispersive acoustic systems,'' Acustica **39**, 298–306 (1978).
[29] J. A. Ten Cate and T. J. Shankland, ''Slow dynamics in the nonlinear elastic response of Berea sandstone,'' Geophys. Res. Lett. **23**, 3019–3022 (1996).
[30] L. D. Landau and E. M. Lifshitz, *Fluid Mechanics* (Pergamon, London, 1959), pp. 305–309.
[31] I. D. Mayergoyz, ''Hysteretic models from mathematical and control theory point of view,'' J. Appl. Phys. **57**, 3803–3805 (1985).
[32] L. D. Landau and E. M. Lifshitz, *Theory of Elasticity* (Pergamon, London, 1959), pp. 1–3.
[33] V. E. Gusev and A. A. Karabutov, *Laser Optoacoustics* (American Institute of Physics, New York, 1993), pp. 173–233.
[34] K. Van Den Abeele and M. A. Breazeale, ''Theoretical model to describe dispersive nonlinear properties of lead zirconate–titanate ceramics,'' J. Acoust. Soc. Am. **99**, 1430–1437 (1996).

Experimental detection of a subharmonic route to chaos in acoustic cavitation through the tuning of a piezoelectric cavity

C. Cabeza, A. C. Sicardi-Schifino, C. Negreira, and G. Montaldo
Instituto de Física, Facultad de Ciencias, Universidad de la República Oriental del Uruguay, CC 10773, CP 11200, Uruguay

(Received 4 November 1996; revised 22 January 1998; accepted 7 February 1998)

Experimental observation is reported of a subharmonic route to chaos through the tuning of a piezoelectric cavity. The emission spectrum of bubbles generated in a liquid contained in the cavity through the application of a pressure ultrasonic field of constant frequency is analyzed. The cavity height is used as control parameter to vary the resonance frequency of the cavity. In the emission spectrum of the bubbles subharmonics of the excitation frequency are observed. This phenomenon is identified as a period-doubling bifurcation and is explained on the basis of a simple model of resonance in the cavity. The appearance of subharmonics is highly sensitive to changes in the cavity height. © *1998 Acoustical Society of America.* [S0001-4966(98)05005-X]

PACS numbers: 43.25.Rq [MAB]

INTRODUCTION

The phenomenon of acoustic cavitation generated by an ultrasonic field has been extensively studied in the last few years[1,2] since it leads to important applications in various domains such as medicine and biology. In this domain Lauterborn *et al.*[3] have made several experiments showing that a period-doubling route to chaos occurs when the acoustic pressure is increased.

In the experiment we report in this paper, the fluid is confined in a piezoelectric-tuned resonant cavity, and the cavity height is used as a control parameter to tune the system. Varying the cavity height and keeping constant the pressure and the frequency a period-doubling bifurcation takes place. For some particular cavity heights, the appearance of a second subharmonic of the excitation frequency is observed. The system is highly sensitive to the variation of the cavity size: Under a variation of only 2% of the total water amount, the system undergoes a bifurcation.

In this work we propose a simple model to explain the observed resonance phenomena. However, greater emphasis is placed in the experimental measurements that show the sensitivity in the generation of subharmonics when the geometry of the cavity varies.

I. THEORY

When a liquid is irradiated with sound of sufficient intensity, gas and vapor cavities are formed, which are called cavitation bubbles. These bubbles start to oscillate in the sound field and begin to radiate sound by themselves, which is called acoustic cavitation noise. Nonlinear phenomena may be observed and subharmonics appear for certain values of the parameters.[3] Experimentally, if the pressure amplitude is used as a control parameter, subharmonics appear above a certain threshold.

The following equation, developed by Keller and Miksis,[4] describes the dynamic behavior of the bubbles:

$$\left(1-\frac{R}{c}\right)RR+\frac{3}{2}R^2\left(1-\frac{R}{3c}\right)=\left(1+\frac{R}{c}\right)\frac{P}{\rho}+\frac{R}{\rho c}\frac{dP}{dt}, \tag{1}$$

$$P(R,R,t)=\left(P_{\text{stas}}-P_v+\frac{2\sigma}{R_n}\right)\left(\frac{R_n}{R}\right)^{3\kappa}-\frac{2\sigma}{R}-4\mu\frac{R}{R}-P_{\text{stas}}+P_v-P(t),$$

where R is the radius of the bubbles, R_n is the equilibrium radius, c is the sound velocity, ρ is the density of liquid, σ is the surface tension, μ is the viscosity, P_{stas} is the static pressure, P_v is the vapor pressure, κ is the polytropic exponent, and $P(t)$ is the external pressure with which the fluid is excited. On the basis of this equation, Lauterborn *et al.* showed[5] that the dynamic evolution of a bubble undergoes a period-doubling route to chaos, i.e., a subharmonic cascade.

In the following we consider a cylindrical hollow cavity filled with a fluid (here water), which is excited by an ultrasonic field in order to produce gas bubbles. We assume that the walls oscillate harmonically with frequency ω_0, producing an acoustic field that propagates in the fluid. That leads to a pressure distribution in the fluid, which depends on position and time. If, at a given instant, the pressure on the bubble exceeds a critical value, a flip bifurcation occurs; and subharmonics appear in the emission spectrum. Varying the height of the column of water inside the cavity, we modify the characteristic frequency of oscillation and thus tune the system. When the characteristic frequency is in resonance with the excitation frequency, a significant increase in the pressure inside the cavity is produced, though modulated by a geometric factor associated with the cavity (cylinder plus water column). Then, there are some zones in which the pressure overpasses the threshold or critical value, leading to subharmonics in the emission spectrum.

In order to link the nonlinear oscillations of the bubble with the effective pressure that is generated for an ultrasonic field in the cavity, we propose a simple model that allows a first qualitative approach in order to elucidate the phenomena

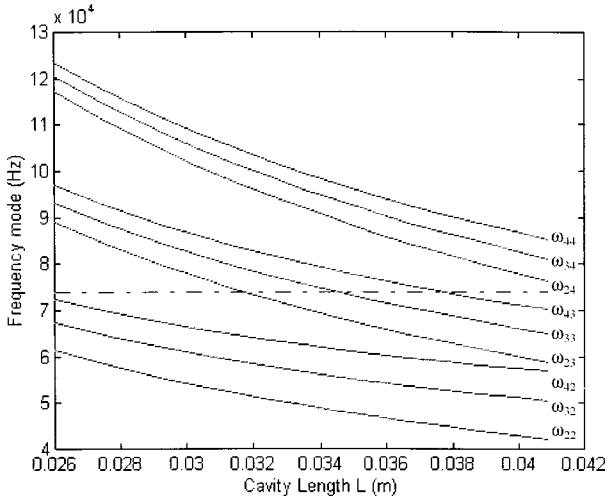

FIG. 1. Mode frequency as a function of cavity length. The dot-dashed line correspond to the drive frequency, 73.6 kHz.

that we observe experimentally. Adding a forcing and a damping term to the wave equation we obtain

$$\nabla^2 P = \frac{1}{c^2}\frac{\partial^2 P}{\partial t^2} + P_0 \exp(i\omega t) + \beta\frac{\partial P}{\partial t}. \tag{2}$$

Solving this equation with cylindrical boundary conditions by standard techniques, the following pressure distribution is obtained:

$$P(r,t) = \exp(ik_l z)\exp(ik_m \theta) J_m(k_n \rho)(P_1 \exp(i\omega_{\ln} t - \beta c^2 t) + \tilde{P}_0 \exp(i\omega t)), \tag{3}$$

where β is a damping factor, P_0 is the amplitude pressure of excitation, c is the sound velocity, $\omega_{\ln}$ is the characteristic frequency of the cavity, and $\tilde{P}_0 = P_0/[c^2(\omega^2 - \omega_{\ln}^2) - ic^2\beta\omega]$ is a resonant factor.

Obviously for a time $t \gg 1/(\beta c^2)$, the only term that survives in the Eq. (3) is proportional to P_0. We observe that this factor depends on the driving frequency as well as on the characteristic frequency of the cavity, and that it increases significantly near a resonance. At a resonance, when the relative growth of the factor with respect to the pressure threshold is high enough, a zone appears in which the pressure of the fluid $P(r,t)$ overpasses the aforementioned threshold and the first period-doubling bifurcation occurs.

From Eq. (3), we obtain the characteristical frequencies $\omega_{\ln}$ of the cavity:

$$\omega_{\ln}^2 = c^2\left(\frac{\pi^2 l^2}{L^2} + \frac{\pi^2 X_{mn}^2}{a^2}\right), \tag{4}$$

where L is the length and a the radius of the cavity, l is the wave number associated with the axial coordinate of the cavity, and X_{mn} is a root of a Bessel function and satisfies $J'_m(aX_{mn}) = 0$. Equation (4) shows the dependence of the characteristic frequency $\omega_{\ln}$ on the radius and the height of the cavity. As the cavity height varies, there is always a mode which becomes resonant.

Figure 1 shows the dependence of the modes on the cavity height. It can be seen that for certain lengths there is a mode whose frequency is close to the driving frequency, and then resonance takes place. This plot, based on the simple model considered in Eq. (2), should be interpreted only qualitatively. However, it has the importance to show that in the region of work there is at least one resonant mode.

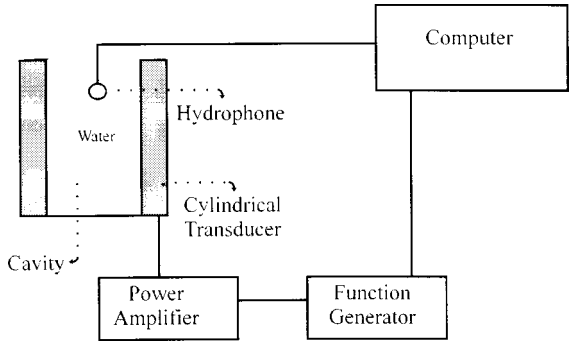

FIG. 2. Experimental setup.

II. EXPERIMENTAL SETUP

Figure 2 shows the experimental setup. The high acoustic intensity which is required to observe the nonlinear phenomena is obtained with a cylindrical transducer of piezoceramic material (PZ-26), and the resonant cavity is defined by the transducer containing distilled water. The cavity height is varied by increasing or diminishing the water column. The inner diameter of the cavity is of $R = 2.5$ cm.

This is a fully computer-controlled experiment, containing a function generator which produces the sinusoidal frequency $f_0 = 73.6$ kHz of the driving sound field and a power amplifier which gives the necessary amplitude. Both parameters are kept constant during the experiment. The amount of water which is added in the cavity is our control parameter. The variation is 2% on the initial volume.

The sound field radiation is measured with a Brüel & Kjaer hydrophone (model 8101), with a frequency range of 1 Hz–125 kHz, and with a sensitivity of 184 dB per 1 V/μPa. The acquisitions were carried out with an oscilloscope HP 54520A, and we worked with 32k points.

III. RESULTS

Figure 3 shows the power spectrum obtained for four values of the cavity height L. The spectra are carried out with 32k points. Figure 4 shows the reconstructed trajectories in a phase space through time-delayed pressure values $p(t)$. A point in this phase space is given by the set of three variables $\{P(t),\ P(t+\tau),\ P(t+2\tau)\}$. The time-delay τ is kept constant and corresponds to approximately 1/20 of the excitation period. It can be proved[6] that this reconstruction of the attractor in the phase space is topologically equivalent to the corresponding representation in the phase space of the dynamic variables appearing in Eq. (1).

For a certain value of the cavity height L [Fig. 3(a)] we can clearly see that there is only one frequency present in the spectrum, i.e., the driving frequency, f_0. The same phenomenon appears in Fig. 4(a), where a limit cycle is obtained whose frequency is equal to the driving one. When we increase the cavity size, the limit cycle is destabilized and a flip

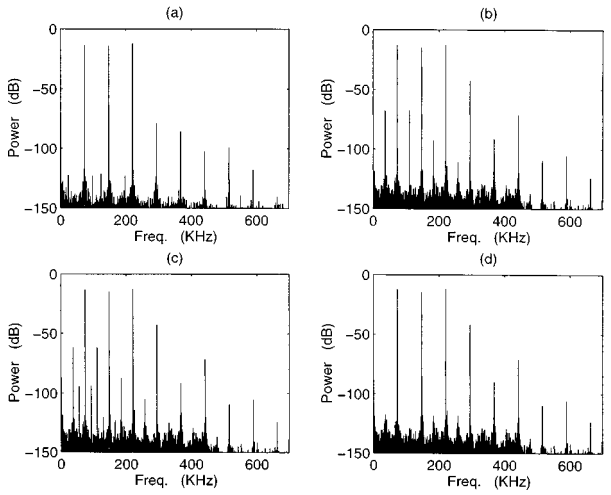

FIG. 3. Power spectrum of the received signal. Drive frequency is 73.6 kHz. The control parameter is the cavity length L. (a) $L=2.60$ cm. (b) $L=3.14$ cm. (c) $L=3.35$ cm. (d) $L=3.88$ cm.

bifurcation takes place [Fig. 4(b)]. The same behavior occurs with the spectrum obtained in the Fig. 3(b), where the appearance of the first subharmonic is observed, i.e., a $f_0/2$ peak is found. If we continue to increase the control parameter L, we observe a new flip bifurcation, that corresponds to the appearance of the second subharmonic $f_0/4$ in the spectrum [see Fig. 3(c) and Fig. 4(c)]. Figure 4(d) shows that, for a greater value of L, the system returns to a regime of a limited cycle whose frequency is equal to the excitation frequency, thus undergoing an inverse cascade process. Similarly, Fig. 3(d) shows that the subharmonics have disappeared and that only one line corresponding to the driving frequency is present.

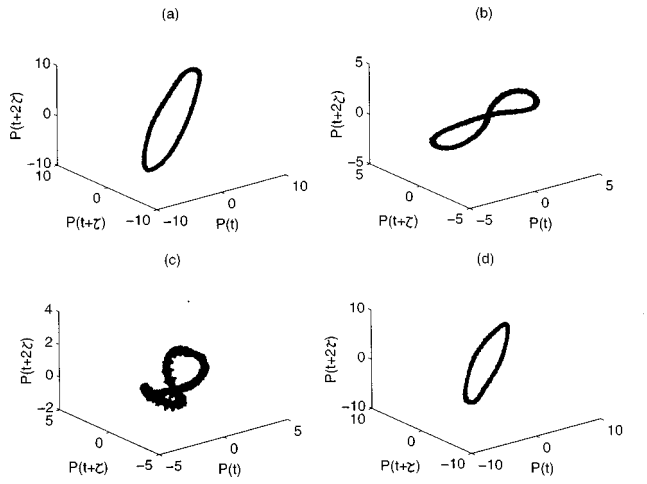

FIG. 4. Phase space reconstruction from the drive frequency 73.6 kHz. The control parameter is the cavity length L. (a) $L=2.60$ cm. (b) $L=3.14$ cm. (c) $L=3.35$ cm. (d) $L=3.88$ cm.

IV. SUMMARY

In this work we have shown the appearance of subharmonics in a resonant cavity. Taking the cavity height as a control parameter, we obtain a subharmonic cascade. First, when we increase the cavity size, the nonlinear effects are greater and the period-doubling bifurcation occurs, following a direct cascade. However, the system behavior is recurrent with the cavity height L. For each resonance, there is an optimum cavity height L_c, for which the nonlinear effects are maximized. When L overpasses this optimum length, the system returns again to a limit cycle regime of frequency f_0 following an inverse cascade. A further increase in L leads to a period-doubling zone again, with a new optimum cavity height (corresponding to a new resonance).

From these results we can also conclude that the appearance of subharmonics is very sensitive to the tuning of the cavity; just a 2% variation on the amount of total water in the cavity leads to the subharmonic emission.

Although the model that we have developed to elucidate this resonance phenomenon is very simple, it allows qualitative explanation of the experimental results. In a future, we will determine experimentally the spatial distribution of the pressure in order to improve the quantitative understanding of the cavitation phenomenon produced in a resonant cavity.

ACKNOWLEDGMENTS

That work was supported by the Project 47 and 221 of the BID-CONICYT Program of the Consejo Nacional de Ciencia y Tecnologia (CONICYT) of Uruguay, the Comision Sectorial de Investigacion Cientifica (CSIC) and the PEDECIBA (Proyecto URU/84/002/UNDP).

[1] T. G. Leighton, *The Acoustic Bubble* (Academic, San Diego, 1994).
[2] W. Lauterborn and J. Holzfuss, ''Acoustic chaos,'' Int. J. Bifurcation Chaos Appl. Sci. Eng. **1**, 13–26 (1991).
[3] W. Lauterborn and U. Parlitz, ''Methods of chaos physics and their application to acoustics,'' J. Acoust. Soc. Am. **84**, 1975–1993 (1988).
[4] J. B. Keller and M. Miksis, ''Bubble oscillations of large amplitude,'' J. Acoust. Soc. Am. **68**, 628–633 (1980).
[5] U. Parlitz, V. Englisch, C. Scheffczyk, and W. Lauterborn, ''Bifurcation structure of bubble oscillators,'' J. Acoust. Soc. Am. **88**, 1061–1077 (1990).
[6] D. S. Broomhead and G. P. King, ''Extracting qualitative dynamics from experimental data,'' in *Analysis of Chaotic Data and The Exploitation of Chaotic Systems. Coping with Chaos* (Wiley, New York, 1994).

Transporting objects without contact using flexural traveling waves

Yoshiki Hashimoto
Kaijo Corporation, 3-1-5 Sakae-cho, Hamura, Tokyo, 205 Japan

Yoshikazu Koike and Sadayuki Ueha
Precision and Intelligence Laboratory, Tokyo Institute of Technology, 4259 Nagatsuta, Midori-ku, Yokohama, 226 Japan

(Received 30 September 1996; accepted for publication 2 March 1998)

Near-field acoustic levitation is successfully applied to transport objects without contact. Planar objects having a weight greater than 10 kgf can be stably levitated near a vibrating plate. An experimental apparatus has been fabricated to measure the transportation speed and transient characteristics. © *1998 Acoustical Society of America.* [S0001-4966(98)04206-4]

PACS numbers: 43.25.Uv [MAB]

INTRODUCTION

In conventional acoustic levitation, very small objects of a few grams have been levitated at the nodal points of a standing wave acoustic field.[1] In contrast, the authors have determined that planar heavy objects (as heavy as 10 kg)[2,3] can be levitated. In this case, the heavy objects can be levitated at a distance of several micrometers above the acoustic wave radiation surface. We have studied experimentally the relationship among levitation distance, vibration amplitude, and weight per unit area for several kinds of vibration modes: (1) an in-phase longitudinal vibration mode which is similar to piston motion, and (2) several kinds of flexural vibration of a thin plate.[2] By using the acoustic levitation phenomenon, the following four methods can be utilized to transportation of objects:

(1) tilting the vibration plate and harnessing,
(2) radiating air, gas, or acoustic waves to an object to be levitated,
(3) transporting the levitated object together with the sound source, and
(4) using traveling waves.

The last method, using traveling waves, was chosen for this study because of the potential benefits, and the feasibility of construction. A method of transporting an object by exciting traveling waves of a flexural vibration along a vibration plate was devised. As a result, it was confirmed that levitated objects could be transported without contact. This paper describes the principle, structure, and design of the vibrating plate necessary for stable transportation of levitated objects, and gives data measured for various characteristics.

I. PRINCIPLE OF THE TRANSPORTATION MECHANISM

Figure 1 shows the configuration of the noncontact transporting system. Flexural vibration is excited in a rectangular thin plate. The vibration amplitude along the length is distributed like a thin beam flexural vibration mode. Across the orthogonal direction it is constant. In order to obtain a flexural traveling wave, two longitudinal transducers are attached near the ends of the plate, at right angles to the plate. One of these transducers generates the wave while the other absorbs it. This requires a mechanical impedance match between the plate and the receiving transducer. A planar object above the vibrating plate is levitated at a distance of several hundred micrometers.

A planar object must be levitated by an acoustic radiation pressure. Therefore, the levitation force in the flexural traveling wave is equal to that generated by compressional motion, the same equation in the vibration mode of a flexural standing wave mode or of an in-phase vibration mode like piston motion. Considering the nonlinearity of the acoustics, the levitation force can be calculated by[4–6]

$$W = \frac{1+\gamma}{4}\,\rho c^2\,\frac{\xi^2(x,y)}{h^2}, \tag{1}$$

where W is the weight of levitated object, γ is the specific heat ratio, ρ is the density of medium, c is the sound velocity of medium, $\xi(x,y)$ is the vibration amplitude on vibration plate, and h is the levitation distance.

Equation (1) indicates that the levitation distance is proportional to the vibration amplitude of the radiation surface, and to the $-\frac{1}{2}$ power of the levitated object's weight unit per area. In order to calculate the levitation force, it is necessary that Eq. (1) be integrated over the bottom surface of the levitation object since the vibration displacement is distributed on the vibration plate. It is confirmed experimentally that a levitated object moves away from the generating transducer to the absorbing one. On the other hand, an object in contact with the flexural vibrating plate in an ultrasonic linear motor is transported from the absorbing transducer to the generating one.[7] The transporting direction in the acoustic levitation appears to be opposite to that of the ultrasonic motor. Thus, it is considered that a transporting force is provided by acoustic viscous force.[8,9] The levitated object is gradually accelerated in the same direction as the traveling wave. The steady transporting velocity is obtained when the acoustic viscous force is equal to the resistance force of air.

The transporting system is quite new as an application although the driving setup of the flexural traveling wave is

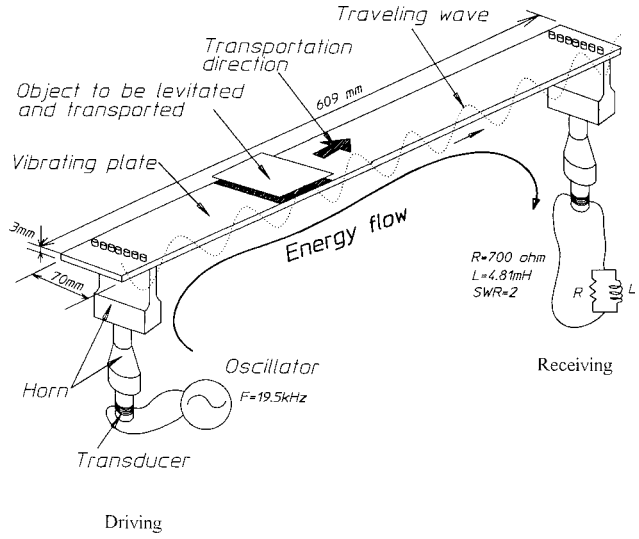

FIG. 1. Experimental levitation and transportation setup.

the same as that of the ultrasonic linear motor.[6] The differences between the proposed system and an ultrasonic linear motor are described briefly as follows:

(1) The object is not in contact with the vibrating plate, while a slider or a rotor is in contact with the vibrating plate for linear traveling-wave motors.
(2) The direction of the transportation of the object for this is opposite to that for the ultrasonic linear motor. In a system using the flexural mode, a levitated object is transported away from the sound source, while a slider for the linear motor moves towards the sound source.

II. EXPERIMENTAL SETUP OF THE TRANSPORTATION SYSTEM

Figure 1 shows the configuration of the experimental setup and Fig. 2 is a photograph of the setup. A duralumin plate with thickness of 3 mm is employed. The driving frequency is 19.5 kHz, and the wavelength of flexural mode is 38.1 mm. The plate length is 609 mm, which corresponds to 15.5 wavelengths. It has been observed that the width of the vibration plate must be less than one-third of longitudinal wavelength for flexural traveling waves to vibrate uniformly across the width of the vibration plate. Therefore, the width

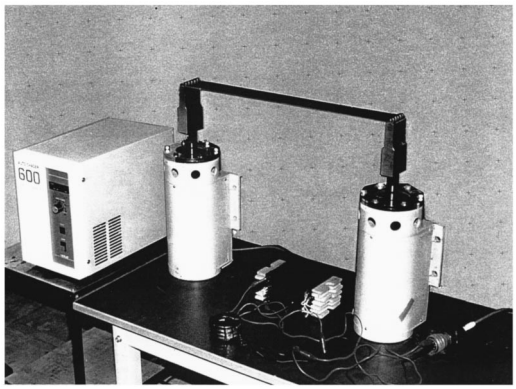

FIG. 2. Photograph of the experimental setup.

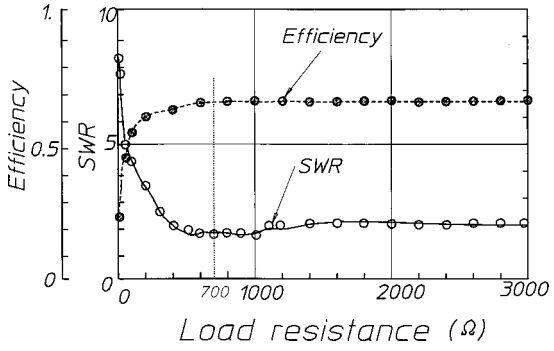

FIG. 3. The SWR and efficiency versus the load resistance value.

of the vibration plate is 70 mm. Two longitudinal vibration systems consisting of a bolted Langevin transducer (D5520, NTK, Co., Ltd.), a stepped plate horn, and a stepped cone are attached to the plate at a distance of $\lambda/4$ from the end. The motional admittance of the two transducers is almost the same. The generating transducer is connected to a self-induced oscillator (6271, Kaijo Corp.); the absorber transducer is connected to a matching load consisting of a resister and an inductance.[7] The direction of transportation of the levitated object can be changed by reversing the oscillator and the matching load. The vibrating plate is leveled precisely with a digital level meter so that the same transportation speed is obtained if the driving side and the receiving side are exchanged.

The standing wave ratio (SWR) approaches 1 as the degree of excitation of the pure traveling wave increases. The mechanical losses in the system, however, make it impossible to attain a perfect traveling wave. Therefore, to obtain the maximum excitation of traveling wave, (to minimize the standing wave ratio), the resistance connected to the absorbing transducer is adjusted. The result is shown in Fig. 3, where the SWR is calculated by

$$\mathrm{SWR}=\frac{\text{The maximum amplitude}}{\text{The minimum amplitude}}. \tag{2}$$

The maximum and minimum amplitudes were measured in the middle of the vibrating plate. The efficiency is also plotted in Fig. 3 as a function of the load resistance, where the efficiency is defined by

$$\text{Efficiency}=\frac{\text{Output power(resistance consumption)}}{\text{Input power}}. \tag{3}$$

A resistance of $R=700\,\Omega$ for SWR$=1.7$ and an efficiency of 68% are used throughout the following experiment. The matching inductance to cancel the clamped capacity C_d of the bolted Langevin transducer is calculated from the equation $L=1/\omega^2 C_d$. An inductance of 4.81 mH is used.

III. SHAPING THE VIBRATION PLATE TO PREVENT DROPPING THE TRANSPORTED OBJECTS

Since there is no sustaining force across the width of the vibrating plate, the levitation object is not stable and slides off easily during transportation. It is necessary to make appropriate vibration distributions across the plate in order to

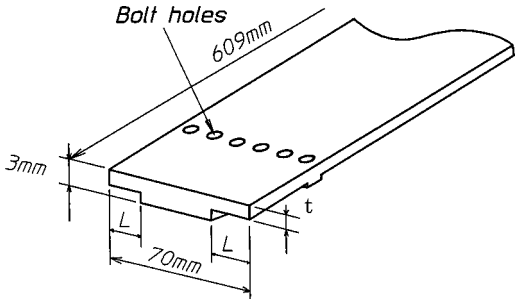

FIG. 4. Shape of the nonuniform vibration plate.

transport a levitated object stably. Thinning of both ends in the cross section seems to obtain the desirable vibration distribution.

To optimize the dimension of the cross section of the vibration plate, the number of times the transportation of the object succeeded was counted while transporting a bakelite plate repeatedly. The bakelite plate is a square 70 mm on a side, 2 mm thick, and 7.6 g in weight. The vibration plates is diagrammed in Fig. 4 and the dimensions are listed in Table I.

A plate with the dimensions of $L=20$ mm and $t=2.7$ mm provides the most stable levitation. The measured distribution of the vibration amplitude across the plate is shown in the lower part of Fig. 5. The vibration displacement is measured by using a high-frequency displacement meter (model JEQ-102, JRC). As a reference, a vibration distribution of a plate with a uniform thickness is shown in the upper part of Fig. 5. The vibration amplitude increases at the edges for the shaped plate, while the vibration amplitude of the uniform plate is essentially constant. The object fell off the uniform plate in one-third of the transportation experiments. In contrast, the nonuniform plate with cutouts never dropped the transported object. The shaping of the plate greatly improves the stability of the transportation.

IV. TRANSPORTATION CHARACTERISTICS OF THE EXPERIMENTAL SYSTEM

Using the system shown in Fig. 1, the levitated object's transportation characteristics are measured as a function of the vibration amplitude of the plate. A typical transient curve of the transportation speed is shown in Fig. 6. After the onset of vibration, the levitated object is gradually accelerated to a steady speed. The transition time is defined in Fig. 6. The steady transportation speed was measured as a function of vibration by using a Laser displacement sensor (LB-040 and LB-1000 systems, Keyence Corp.). The vibration amplitude was measured at the head of the screw at the horn end. The

TABLE I. The dimensions of the vibration plates.

Plate No.	Width L (mm)	Thickness t (mm)
1	5	2.7
2	10	2.7
3	20	2.7
4	20	2.9
5	20	2.8
6	20	2.6

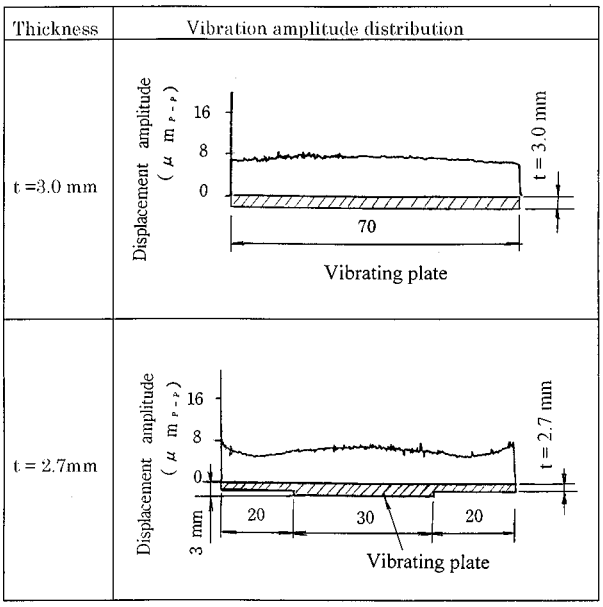

FIG. 5. Shape of the uniform and nonuniform vibration plates and the resulting transverse vibration distributions.

result is shown in Fig. 7. As can be seen from Fig. 7, the steady transportation speed is proportional to the vibration amplitude. This indicates that the transportation speed can be controlled easily by the vibration amplitude of the plate. The bakelite plate with a planar bottom surface of 90 mm long and 65 mm wide and a weight of 8.6 g is transported with a vibration amplitude of 20 μm_{pp}. A steady transportation speed of 0.7 m/s is achieved.

Figure 8 shows the steady transportation speed, the acceleration, and the transition time as a function of weight per unit area of the levitated object. The transportation speed is calculated by differentiating the measured displacement with respect to time. It is clear from Fig. 8 that both the steady transportation speed and the acceleration decrease as the weight is increased. Thus, the weight of an object limits the possibility of transportation by using flexural traveling waves.

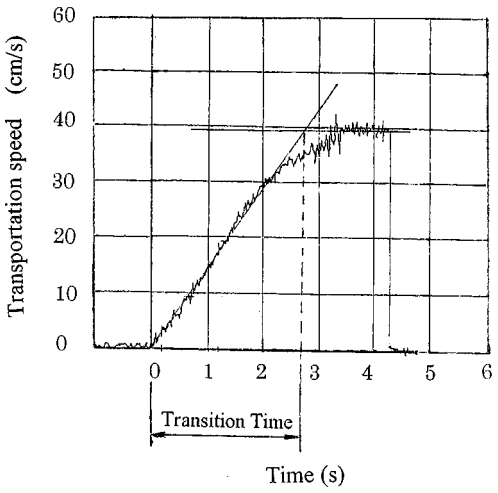

FIG. 6. The transportation speed as a function of time.

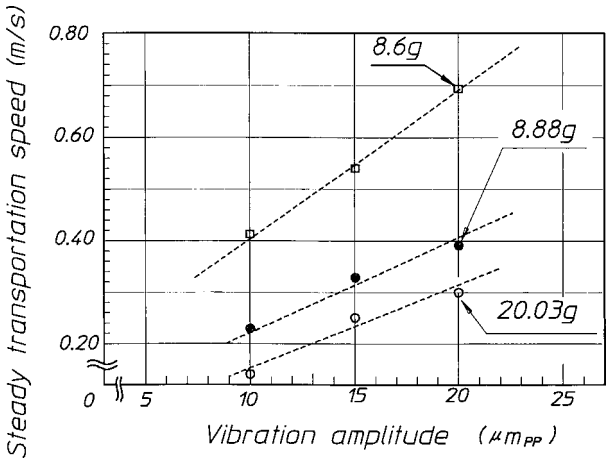

FIG. 7. Steady transportation speed versus the vibration amplitude of the plate.

V. CONCLUSIONS

A transportation system of planar objects by using acoustic levitation and flexural traveling waves is proposed. An experiment was devised and was performed to test the technique.

From this investigation, the following points have been clarified:

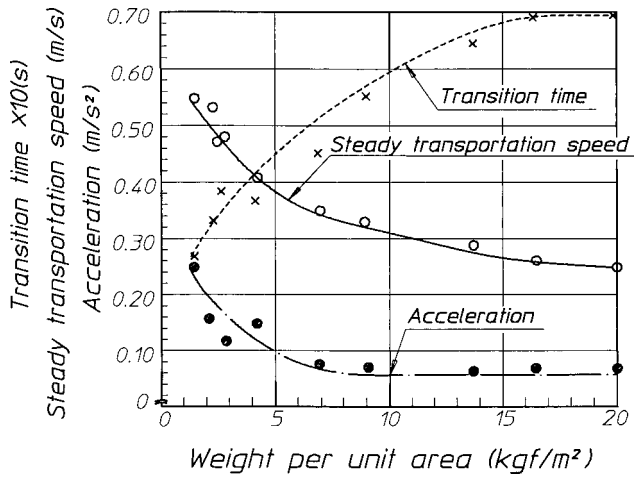

FIG. 8. Transportation speed, acceleration, and transition time as a function of weight per unit area of the levitated object.

(1) An object can be levitated and transported by using traveling waves.
(2) The transportation speed is proportional to the vibration amplitude of the vibrating plate and inversely proportional to the weight of the levitated object.
(3) The levitated object can be prevented from dropping from the vibration plate by shaping the vibrating plate with cutouts to obtain nonuniform vibrations across the plate's cross section so that the amplitude of the acoustic waves increases at the sides.

This technique can transport objects regardless of their material properties or their size.

In the near future, the authors expect to apply this technique to transport 12-in. silicone wafers and large-sized glass liquid crystal boards 650 mm by 550 mm by 0.7 mm. Important future research topics in this area will be the ability to control the stopping and the merging of levitated objects.

ACKNOWLEDGMENTS

The authors would like to express their sincere gratitude to Hisashi Fujita, the managing director of Kaijo Corporation and the head of the Industrial System Division, for his generous support of this research.

[1] H. Hatano, Y. Kanai, Y. Ikegami *et al.*, ''Ultrasonic levitation and positioning of samples,'' Jpn. J. Appl. Phys., Part 1 **21**, Suppl. 21-3, 202–204 (1982).
[2] Y. Hashimoto, Y. Koike, and S. Ueha, ''Near-field acoustic levitation of planar specimens using flexural vibration,'' Ultrasonics World Congress 1995 Proc. (1995), pp. 835–838.
[3] Y. Hashimoto, Y. Koike, and S. Ueha, ''Near-field acoustic levitation of planar specimens using flexural vibration,'' J. Acoust. Soc. Am. **100**, 2057–2061 (1996).
[4] Y. Koike, S. Ueha, and Y. Hashimoto, ''A theoretical study of near-field acoustic levitation of planar objects,'' in Ultrasonics World Congress 1995 Proc. (1995), pp. 839–842.
[5] H. Pan, N. Torii, S. Ueha, and Y. Hashimoto, ''Study on near-field acoustic levitation produced by a practical vibration source,'' J. Acoust. Soc. Am. (to be submitted).
[6] B. Chu and R. E. Apfel, ''Acoustic radiation pressure produced by a beam of sound,'' J. Acoust. Soc. Am. **72**, 1673–1687 (1982).
[7] M. Kuribayashi, S. Ueha, and E. Mori, ''Excitation conditions of flexural traveling waves for a reversible ultrasonic linear motor,'' J. Acoust. Soc. Am. **77**, 1431–1435 (1985).
[8] J. H. Hu, K. Nakamura, and S. Ueha, ''Characteristics of a Noncontact Ultrasonic Motor Using Acoustic Levitation,'' Proc. 1996 Ultrasonics Symp. (1996), pp. 373–376.
[9] W. L. Nyborg, ''Near-boundary streaming near a boundary,'' J. Acoust. Soc. Am. **30**, 329–339 (1958).

A time-reversal mirror with variable range focusing

Hee Chun Song,[a] W. A. Kuperman, and W. S. Hodgkiss
Marine Physical Laboratory, Scripps Institution of Oceanography, University of California, San Diego, La Jolla, California 92093-0701

(Received 16 June 1997; accepted for publication 24 February 1998)

Recently a time-reversal mirror (or phase-conjugate array) was demonstrated experimentally in the ocean that spatially and temporally refocused an incident acoustic field back to the original position of the probe source [Kuperman *et al.*, J. Acoust. Soc. Am. **103**, 25–40 (1998)]. Here this waveguide time-reversal mirror technique is extended to refocus at ranges other than that of the probe source. This procedure is based on the acoustic-field invariant property in the coordinates of frequency and range in an oceanic waveguide [Brekhovskikh and Lysanov, *Fundamentals of Ocean Acoustics*, 2nd ed. (Springer-Verlag, Berlin, 1991), pp. 139–145]. Simulations are combined with experimental data to verify this technique. © *1998 Acoustical Society of America.* [S0001-4966(98)03106-3]

PACS numbers: 43.30.Bp, 43.30.Hw, 43.60.Gk [DLB]

INTRODUCTION

Recently a time-reversal mirror (TRM) was demonstrated experimentally in the ocean which spatially and temporally refocused an incident acoustic field back to the original position of the probe source.[1] This result confirmed previous theoretical ocean acoustics work[2] and extended ultrasonic laboratory studies in this area.[3,4] The time-reversal process has been introduced as an approach to compensate for distortion due to various inhomogeneous media.[4] For acoustic imaging in an unbounded geometry, the ultrasonic TRM has been extended recently by Dorme and Fink[5] to focus not only on the reflector, but also on areas surrounding the reflector in the presence of an aberrating layer. Their method combines conventional beam steering in a homogeneous medium with synthesized data banks obtained from numerical computation for each steering point. In more complex waveguide environments, we also are interested in focusing the received field back to a new location. In this paper, we develop a variable focal range TRM that works in a waveguide geometry.

The sound field in the ocean is characterized by the interference pattern of different modes. It has been shown[6] that the slope, β, of lines of constant sound intensity, constant rate of change of the phase along the waveguide, and constant envelope group delay, is invariant in the frequency-range (ωr) plane, such that

$$(\Delta\omega/\omega)=\beta(\Delta r/r). \tag{1}$$

For example, β can be determined by evaluating the total derivative of intensity with respect to range and frequency for constant intensity. We apply this invariant property to move the focal range in the time-reversal technique in the ocean by appropriately shifting the spectral components of the data used to construct the TRM. To demonstrate the proposed method, we use the experimental data collected from the TRM experiment carried out in the Mediterranean Sea in April 1996.[1]

[a]Electronic mail: hcsong@mpl.ucsd.edu

In the Sec. I, we briefly review the TRM experiment and relevant basic issues of phase conjugation (the frequency domain process corresponding to time reversal). Section II addresses the acoustic invariant properties of a waveguide which subsequently are applied to shifting the focal range in Sec. III. Simulations combined with experimental data then are presented in Sec. III to verify the procedure.

I. PHASE CONJUGATION

The theory of phase conjugation *vis-a-vis* ocean acoustics already has been presented.[1,2] Here we briefly review the basics of phase conjugation using the geometry of the TRM experiment as shown schematically in Fig. 1. More details on the theory and experiment are given in Ref. 1.

A. TRM experiment

The April 1996 TRM experiment utilized a vertical source–receive array (SRA) spanning 77 m of a 125-m water column with 20 sources and receivers and a probe source (PS) co-located in range with another vertical receive array (VRA) of 46 elements spanning 90 m of a 145-m water column located 6.3 km away from the SRA. Phase conjugation was implemented by transmitting a 50-ms pulse with center frequency of 445 Hz from the PS to the SRA, digitizing the received signal, and retransmitting the time-reversed signal from all sources of the SRA. The retransmitted signal then was received at the VRA.

Figure 2 shows the pulse and its spectrum as received on the SRA and VRA for a PS at 75-m depth. It should be noted that all of the various acoustic field and simulated data plots are self-normalized throughout this paper. The data at the SRA are combinations of the signal centered on 445 Hz and noise components at 410, 460, and 510 Hz. A 233-ms segment of data was digitized and time reversed for transmission to the VRA. When the VRA and PS have the same range to the SRA (within 40 m for the data shown in Fig. 2), we observe focusing. In the simulations of focal range shift presented in Sec. III, we will backpropagate numerically the pulse received at the SRA as shown in Fig. 2(a).

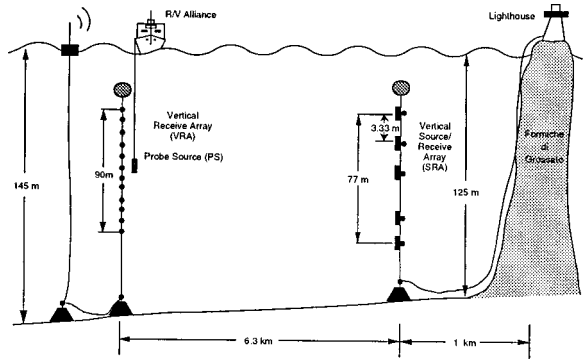

FIG. 1. Experimental setup of April 1996 phase conjugation experiment.

B. Overview of theory

For simplicity in this section, we briefly review the basics of phase conjugation in a range-independent waveguide following the conventions used in Ref. 1 (here we use ϕ_n for the modal eigenfunctions). The probe source, PS, is located a horizontal distance R from the source–receive array, SRA.

Let the acoustic field at frequency ω at the jth receiving element of the SRA (depth z_j) from the probe source PS (depth z_{ps}) be $G_\omega(R;z_j,z_{ps})$. The phase-conjugation process consists of exciting the SRA sources by the complex conjugate of the received field, $G^*_\omega(R;z_j)$. For a vertical line of discrete sources, the phase-conjugate field reduces to a sum over the source positions,

$$P_{pc}(r,z;\omega)=\sum_{j=1}^{J} G_\omega(r;z,z_j)G^*_\omega(R;z_j,z_{ps}), \tag{2}$$

where R is the horizontal distance of the SRA from PS, r is the horizontal distance from the SRA to a field point of depth z, and J denotes the number of sources in SRA. The azimuthally symmetric normal mode solution $G_\omega(r;z_j,z_{ps})$ is given by

$$G_\omega(r;z_j,z_{ps})=\frac{i}{\rho(z_{ps})(8\pi r)^{1/2}}\exp\left(-\frac{i\pi}{4}\right)\times\sum_n \frac{\phi_n(z_{ps})\phi_n(z)}{k_n^{1/2}}\exp(ik_n r), \tag{3}$$

where ϕ_n, k_n are the normal mode eigenfunctions and modal wave numbers obtained by solving the depth-dependent Helmholtz equation with boundary conditions.[7]

We notice that the intensity of the phase-conjugate field, i.e., the magnitude squared of the right hand side of Eq. (2), corresponds to the ambiguity function of the Bartlett matched-field processor (MFP)[8] with an appropriate normal-

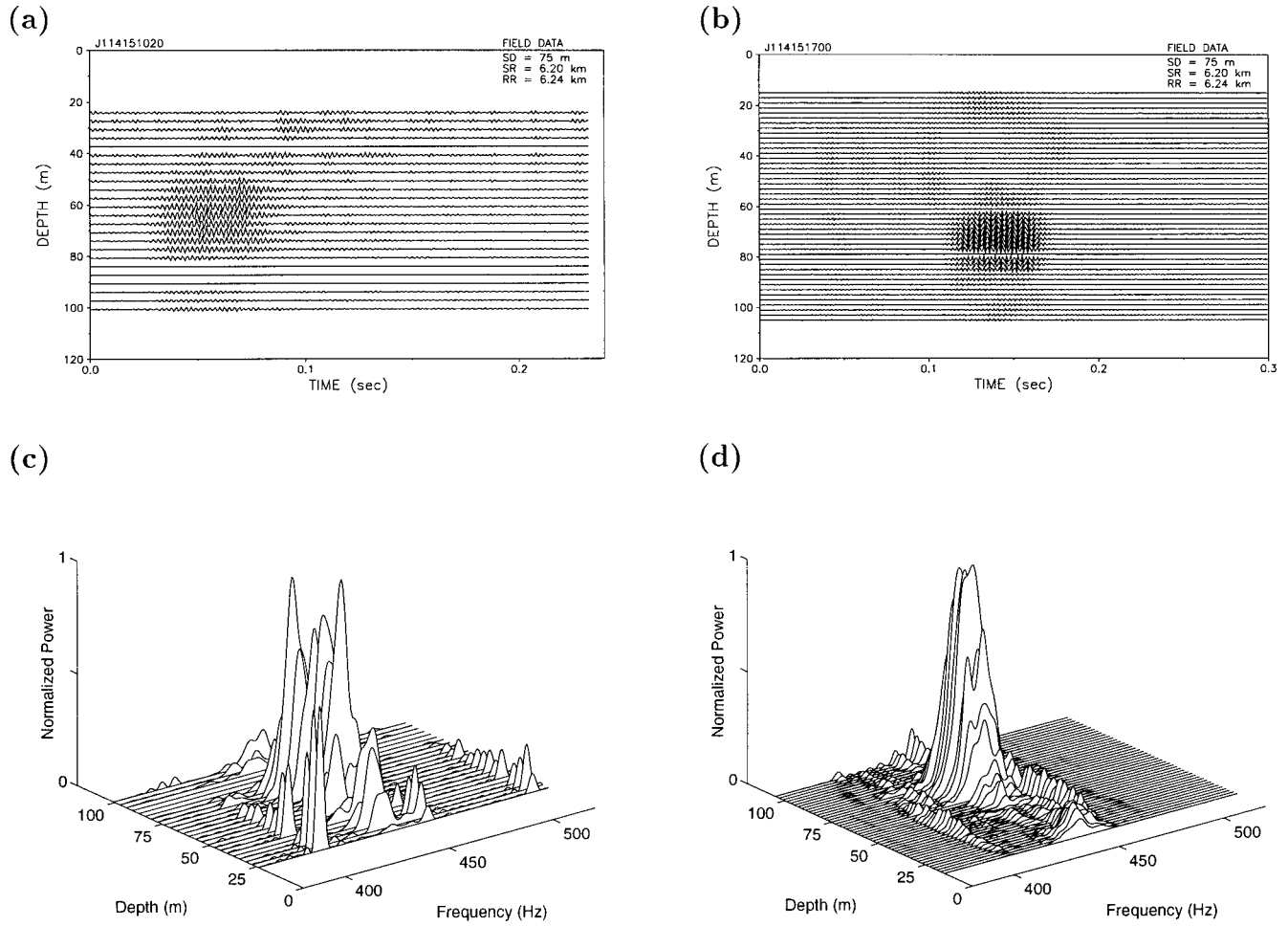

FIG. 2. Experimental results for PS and VRA at the same (focal) range. (a) The pulse data received on the SRA for PS at depth of 75 m. (b) The data received on the VRA from the time-reversed transmission of the pulse shown in (a). (c) and (d) are the spectra of (a) and (b), respectively. Note three spectral noise components at 410, 460, and 510 Hz in (c).

ization factor where the data is given by $G_\omega(R;z_j,z_{ps})$ and the replica field by $G_\omega(r;z,z_j)$. In effect, the process of phase conjugation is an implementation of matched-field processing where the ocean itself is used to construct the replica field. Or, alternatively, matched-field processing simulates the experimental implementation of phase conjugation in which a source–receive array is used.

For an array which spans most of the water column and adequately samples most of the modes so that the orthonormality condition is satisfied, Eq. (2) simplifies to

$$P_{pc}(r,z,\omega)\approx\sum_m \frac{\phi_m(z)\phi_m(z_{ps})}{\rho(z_{ps})k_m\sqrt{rR}}\exp\left[ik_m(r-R)\right]. \quad (4)$$

In general, the individual terms change sign rapidly with mode number. However, for the field at PS, $r=R$, the closure relation $\Sigma_m\phi_m(z)\phi_m(z_{ps})/\rho(z_{ps})\approx\delta(z-z_{ps})$ can be applied approximately with the result that $P_{pc}(r,z)\approx\delta(z-z_{ps})$.[1] Figure 3(a) is a single frequency simulation of the phase conjugation process for a probe source at 74-m depth and 6.24-km range from a 20 element SRA. The source frequency is 445 Hz. Range-dependent bathymetry was used as an input to an adiabatic mode model[9] for the specific sound-speed structure shown in Fig. 4. Notice the focusing in the vertical is indicative of the closure property of the modes. We will return to Fig. 3(b) and (c) when demonstrating focal range shift in the next section.

II. ACOUSTIC FIELD INVARIANT

The horizontal variability of the sound field in the ocean is due to the mutual interference of different normal modes. The interference pattern in the coordinates of range and frequency is of considerable importance since it has been observed in experiments to be stable.[10]

Results of numerical calculations of the sound field for the environment shown in Fig. 4 at different source frequencies are plotted in Fig. 5. Each curve shows the range r dependence (in the 5–7 km interval) of the sound intensity at a fixed frequency. For convenience, adjacent curves are displaced relative to one another by 2 dB. The lower curve corresponds to 445 Hz, the upper curve corresponds to 465 Hz, and there are 2-Hz increments between adjacent curves. Note that the lines of maximum intensity are straight and their slopes are constant in the frequency-range plane.

It has been shown previously in Refs. 10 and 11 that the interference structure in oceanic waveguides is characterized by the existence of lines of maximum intensity $I(\omega,r)$ having a slope β and this slope is an invariant for a particular group of modes:

$$\beta=\frac{r}{\omega}\left(\frac{\Delta\omega}{\Delta r}\right)=-\frac{d(1/v)}{d(1/u)}, \quad (5)$$

where v and u are the phase and group velocities characterizing the given mode group. It is stated in Refs. 10 and 11 that β is an invariant since it does not depend on the frequency f, the range r (in a range-independent waveguide), the source depth z_s, or the receiver depth z_r for a particular group of modes, but is determined by the properties of the medium and the derivative in Eq. (5) averaged over this group. Aspects of sound interference in a range-dependent waveguide in conjunction with β are addressed in Refs. 12 and 13. The invariant property applies not only to the sound intensity, which is of primary interest for practical applications, but also to the phase velocity and envelope (group) delay.[6] Thus this invariance extends to broadband pulse propagation as discussed in Sec. III.

Typically, β is equal to 1 in an ideal or Pekeris wave-

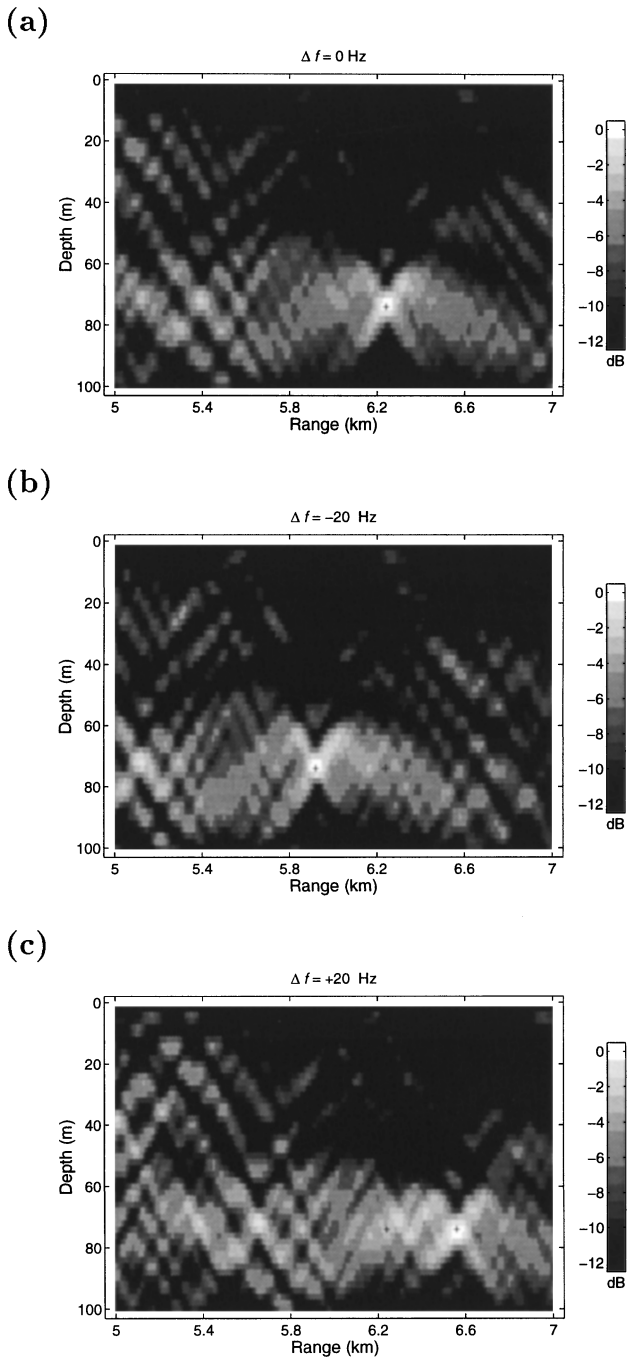

FIG. 3. Single frequency phase conjugation simulation for the geometry of Fig. 1 and probe source located at 74-m depth and 6.24-km range. The true source frequency is 445 Hz. (a) Simulation without frequency shift. The peak occurs at the correct range and depth of the source. (b) Simulation with a −20-Hz frequency shift at the SRA. The focal range is moved about 300 m toward the SRA. (c) Simulation with +20-Hz frequency shift at the SRA. As opposed to (b), the focal range is moved about 300 m away from the SRA.

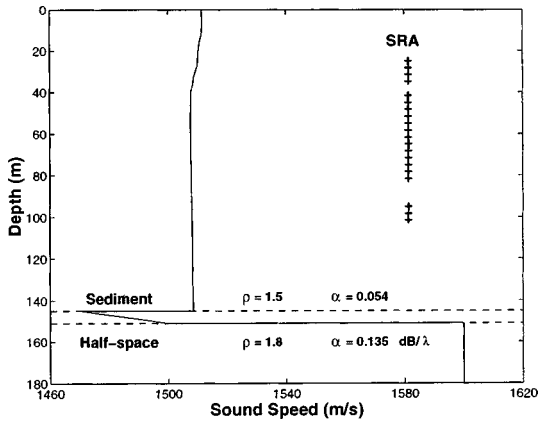

FIG. 4. Sound-speed profile used in the simulations along with the bottom geoacoustic parameters. The depths of the SRA elements also are included.

guide. In our example of Fig. 5, β is about 0.9 at the range of 6.24 km (note that range-dependent bathymetry was incorporated in the model). On the other hand, $\beta \approx -3$ for a surface sound channel or in a waveguide with a deeply submerged channel axis.[14] The minus sign indicates that if there is an interference maximum at range r and frequency ω, then an increase of the frequency by $\Delta\omega$ will displace this maximum by Δr toward the sound source. Dependence of β on various ocean environments is reported in Refs. 6 and 10.

In the next section, it is demonstrated that the above relationship carries over to the phase-conjugation procedure. The result is that we can change the focal range by retransmitting the conjugate of the complex amplitude received by the SRA on a different carrier frequency $\omega+\Delta\omega$. Figure 3(b) and (c) show the resulting backpropagated fields with ± 20-Hz shifts in source frequency as compared to Fig. 3(a) where no frequency shift is applied. As expected for $\beta \approx 0.9$, the focal range has moved 300 m toward the SRA with a -20-Hz shift and 300 m away from the SRA with a $+20$-Hz shift. We also notice that the field structure remains the same in the vicinity of the new focus.

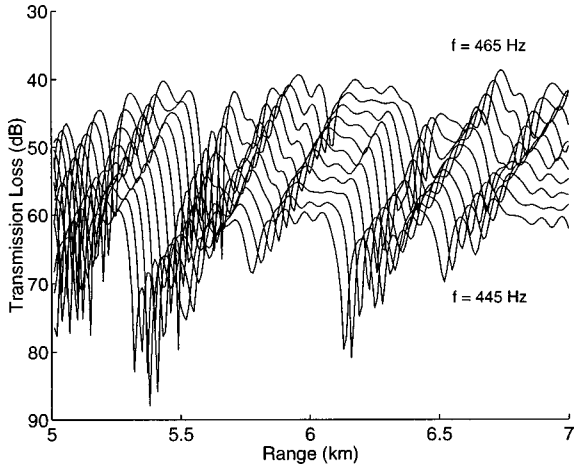

FIG. 5. Interference structure of the sound field computed for the environment shown in Fig. 4. For convenience, adjacent curves are displaced relative to one another by 2 dB. The lower curve corresponds to 445 Hz, the upper curve corresponds to 465 Hz, and there are 2-Hz increments between adjacent curves. The depths of source and receiver are 40 m and 50 m, respectively.

III. FOCAL RANGE SHIFT

A. Theoretical analysis

When we have a shift in source frequency, the replica field (using MFP terminology) becomes $G_{\omega+\Delta\omega}(r;z,z_j)$, i.e., the SRA retransmits the complex conjugate of the received data at a different carrier frequency. The phase-conjugate field around the true probe source range R then is given by

$$P_{pc}(r,z;\omega,\Delta\omega)=\sum_{j=1}^{J} G_{\omega+\Delta\omega}(r;z,z_j)G^{*}_{\omega}(R;z_j,z_{ps}). \tag{6}$$

Ignoring the weak dependence of mode amplitudes $\phi_m(z)$ on frequency in the vicinity of frequency ω and exploiting the orthonormality condition, we obtain the following equation similar to Eq. (4):

$$P_{pc}(r,z,\omega,\Delta\omega)=\sum_{m} B_m \exp\,[i(k'_m r-k_m R)], \tag{7}$$

with

$$B_m=\frac{\phi_m(z)\phi_m(z_{ps})}{\rho(z_{ps})\sqrt{k'_m k_m}\sqrt{rR}}, \tag{8}$$

where k'_m denotes the modal wave number at a shifted frequency $\omega+\Delta\omega$, i.e., $k'_m=k_m(\omega+\Delta\omega)$. In practice, k'_m in the denominator of B_m can be treated as k_m.

Then a measure of the sound intensity I at range r around the probe source PS can be written as

$$I(r,z,\omega,\Delta\omega)=|P_{pc}|^2=\sum_{m}\sum_{n} B_m B_n \times \exp\, i[(k'_m-k'_n)r-(k_m-k_n)R]. \tag{9}$$

The new focal range due to the shift in source frequency is determined by

$$(k'_m-k'_n)r-(k_m-k_n)R=0. \tag{10}$$

If there is no shift in frequency, we have a focal point back at $r=R$.

Here we expand k'_m in the vicinity of k_m such that

$$k'_m=k_m(\omega+\Delta\omega)\simeq k_m(\omega)+\frac{dk_m}{d\omega}\Delta\omega. \tag{11}$$

Substituting Eq. (11) into Eq. (10) and using $k_m=\omega/v_m$, $dk_m/d\omega=1/u_m$, where v_m, u_m are the phase and group velocities, respectively, we obtain

$$\left(\frac{1}{v_m}-\frac{1}{v_n}\right)\frac{r-R}{r}+\left(\frac{1}{u_m}-\frac{1}{u_n}\right)\frac{\Delta\omega}{\omega}=0. \tag{12}$$

In the following, we simply follow the derivation given in Ref. 14. The sound field at a fixed range in a stratified ocean is formed by a group of modes with phase and group velocities v_m, u_m close to some average values which we designate as v and u, respectively. Moreover, the phase and group velocities are related by a functional dependence, $u=u(v)$. In the WKB approximation and sometimes also in exact solutions, this relationship depends neither on the

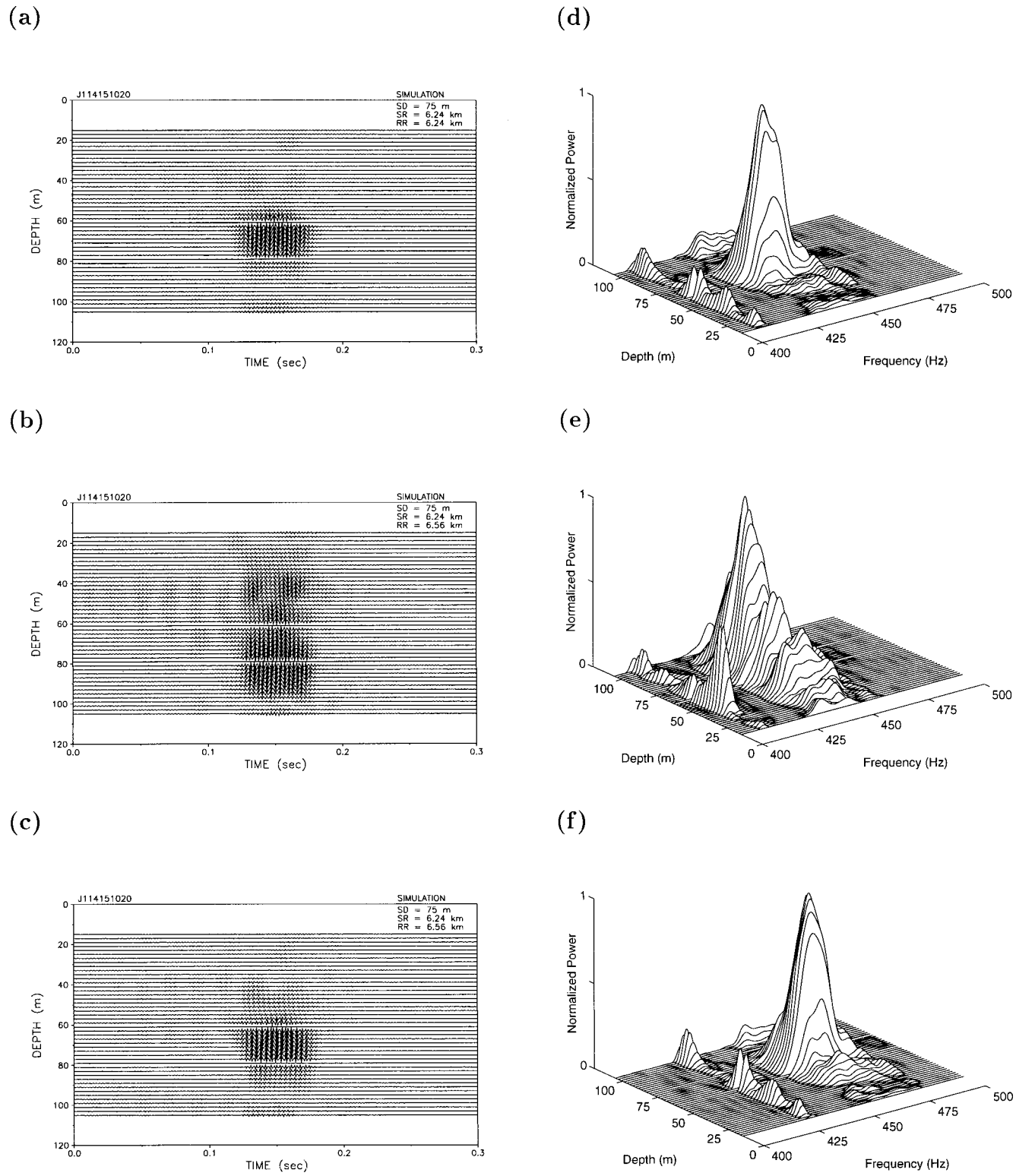

FIG. 6. Simulated backpropagation and corresponding spectra using real received data from the SRA shown in Fig. 2(a) for the PS at a depth of 75 m. (a) Focused results on the VRA at the same range as the PS, which is similar to the experimental data in Fig. 2(b). (b) Out-of-focus results on the VRA when the VRA is 300-m offset in range from the PS. (c) Same as (b) except a +20-Hz frequency shift has been applied to the real data before backpropagation. We note that the focus is brought back on the VRA and looks similar to (a).

mode number nor on the sound frequency. For example, $uv=c^2$ for an ideal waveguide with a perfectly reflecting bottom, and $u=3v/[2+(v/c_0)^2]$ for a surface sound channel.[14]

We expand $1/u_m$ in the vicinity of $1/u$ in a power series of $(1/v_m-1/v)$, and retain only the first two terms

$$\frac{1}{u_m}=\frac{1}{u}+\frac{d(1/u)}{d(1/v)}\left(\frac{1}{v_m}-\frac{1}{v}\right). \tag{13}$$

Substituting this relationship into Eq. (12), we finally obtain

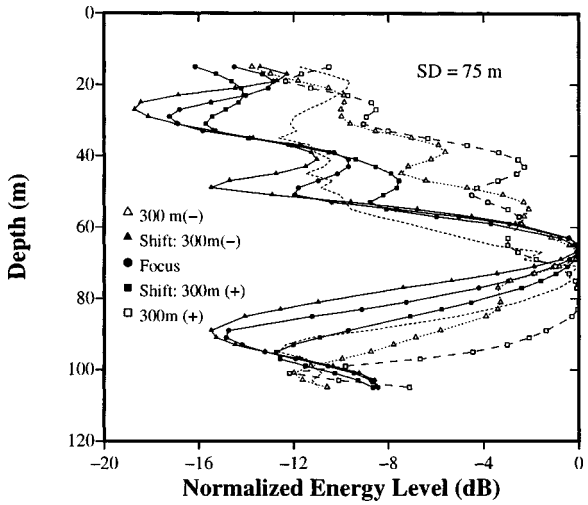

FIG. 7. Energy over a 0.3-s time window of the simulated backpropagation as a function of depth for various ranges from the focal region. The depth of the probe source was 75 m. ''+'' means the VRA is outbound from the focus (PS). ''Shift'' indicates frequency shifting has been applied to the real data as shown in Fig. 2(a) before backpropagation for variable range focusing.

$$\left(\frac{r-R}{r}\right)=\left(\frac{1}{\beta}\right)\left(\frac{\Delta\omega}{\omega}\right);\quad \beta\equiv-\frac{d(1/v)}{d(1/u)}=-\left(\frac{u}{v}\right)^2\frac{dv}{du}, \tag{14}$$

where β is an invariant of the interference pattern within a group of modes determining the sound intensity at the point (r,z) and frequency ω. First introduced in Ref. 10, the invariant β is related only to the average value of the derivative $d(1/v)/d(1/u)$ for a given group of modes. In a slowly varying, range-dependent waveguide, the value of β varies with range r and a detailed discussion is given in Refs. 12 and 13.

We note that the above equation is equivalent to Eq. (5) except that the PS range R is replaced by the field point r in the denominator (a negligible difference around the PS). The new focal range R' is then determined by the expression

$$R'=R\left(1-\frac{1}{\beta}\frac{\Delta\omega}{\omega}\right)^{-1}\simeq R\left(1+\frac{1}{\beta}\frac{\Delta\omega}{\omega}\right). \tag{15}$$

This equation along with Eq. (9) shows that the relative shift in focal range is proportional to the relative shift in source frequency for a given β. In addition, the structure of phase-conjugate field remains unchanged around the new focal range as shown in Fig. 3. For instance, in a Pekeris waveguide with β equal to 1, a 5% increase in frequency results in a 5% increase in focal range. It should be mentioned that the above equation also enables us to determine the value of β from the shift in the peak of a matched-field processing ambiguity surface induced by a shift in the frequency of the replica field.

Note that the above equation is approximate in three respects. In the derivation, we have neglected the dependence of mode amplitudes upon frequency, and we have used an expansion valid only for a bounded group of modes for a given R and ω. If R and ω change, the sound field will be determined by another group of modes for which the function $u_m(v_m)$ may have a different form. For example, Ref. 11 shows that β varies over successive convergence zones in underwater sound channel due to different group of modes contributing to each convergence zone. Finally, multimode propagation involving many modes is assumed implicitly in the derivation of Eqs. (13) and (14), so that β is invariant for frequencies far from the mode critical frequencies. It is shown in Ref. 15 that in few-mode propagation, β depends explicitly on the frequency and mode order, and there exist singularities where $\beta^{-1}(f)=0$ for a certain frequency interval in a shallow water waveguide.

B. Data/simulations for the TRM

Since the invariant property applies not only to the intensity, but also to the phase velocity and group delay,[6] shifting of the focal range can be implemented for broadband pulse propagation. We demonstrate this with a combination of simulation and real data.

Since the invariant β is not a function of frequency, we can generalize the single frequency case to pulse propagation as long as the ratio of the frequency shift to the signal bandwidth around the carrier frequency is small enough such that $\Delta\omega/\omega_{\min}\approx\Delta\omega/\omega_{\max}$. Then we can apply a constant shift to all spectral components over the bandwidth. This can be implemented easily in near real time by an FFT bin shift at the TRM before retransmission.

To demonstrate shifting of the focal range for the TRM, we first simulate backpropagation using the real data received on the SRA as shown in Fig. 2(a). The sound speed profile for the simulation is displayed in Fig. 4. Figure 6(a) is in a good agreement with the focused real data in Fig. 2(b), which permits us to use Fig. 6(a) as a reference solution at the focal point for comparison purposes.

Figure 6(b) and (c) both show simulated backpropagation results on the VRA which has been placed 300-m offset in range from the PS. As expected, the results in Fig. 6(b) are out-of-focus since the VRA and PS are not co-located. In Fig. 6(c), a +20-Hz frequency shift has been applied to the real data before backpropagation which brings the field back into focus with results that look similar to Fig. 6(a). The corresponding spectrum in Fig. 6(f) clearly indicates that the spectral components have been shifted by +20 Hz.

As the VRA moves in range away from the focal region, the vertical sidelobe structure typically looks as shown in Fig. 6(b). An alternative way to present these results which provides a more quantitative display of the main peak and sidelobe structure is shown in Fig. 7. Here, the energy received by the VRA from the simulated backpropagation over a 0.3-s time window is plotted as a function of depth when the VRA and PS are co-located as well as when they are offset by ±300 m. The solid lines represent focusing (VRA and PS co-located) or variable range focusing through frequency shifting while the dashed lines represent out-of-focus results.

IV. CONCLUSIONS

We have extended the time-reversal mirror (TRM) procedure in the ocean to refocus at ranges other than that of the probe source. To accomplish this, we applied the acoustic-

field invariant property in the frequency-range plane of an oceanic waveguide characterized by the interference structure between different modes. The basic idea of this approach is that we can shift the sound field maxima to different ranges by increasing or decreasing the source frequency appropriately for a specific propagation environment. Since the invariant property applies not only to sound intensity, but also to phase velocity and group delay, focal range shifts can be applied to pulse propagation incident on a TRM as long as the bandwidth of the signal is relatively small compared to the carrier frequency. The advantage of this approach is that it can be implemented easily in near real time by an FFT bin shift. Simulations combined with experimental data demonstrated that shifting of the focal range can be achieved by an appropriate shift of the carrier frequency prior to retransmission.

ACKNOWLEDGMENT

This research was supported by the Office of Naval Research Code 321US, Contract No. N00014-96-D-0065.

[1] W. A. Kuperman, W. S. Hodgkiss, H. C. Song, T. Akal, C. Ferla, and D. R. Jackson, ''Phase conjugation in the ocean: Experimental demonstration of an acoustic time reversal mirror,'' J. Acoust. Soc. Am. **103**, 25–40 (1998).

[2] D. R. Jackson and D. R. Dowling, ''Phase conjugation in underwater acoustics,'' J. Acoust. Soc. Am. **89**, 171–181 (1991).

[3] M. Fink, ''Time Reversal Mirrors,'' in *Acoustical Imaging*, Vol. 21, edited by B. F. Jones (Plenum, New York, 1995), pp. 1–15.

[4] M. Fink, ''Time reversed acoustics,'' Phys. Today , 34–40 (March 1997).

[5] C. Dorme and M. A. Fink, ''Ultrasonic beam steering through inhomogeneous layers with a time reversal mirror,'' IEEE Trans. Ultrason. Ferroelectr. Freq. Control **43**, 167–175 (1996).

[6] G. A. Grachev, ''Theory of acoustic field invariants in layered waveguide,'' Acoust. Phys. **39**, 33–35 (1993).

[7] F. B. Jensen, W. A. Kuperman, M. B. Porter, and H. Schmidt, *Computational Ocean Acoustics* (American Institute of Physics, New York, 1994).

[8] A. B. Baggeroer, W. A. Kuperman, and P. N. Mikhalevsky, ''An overview of matched field methods in ocean acoustics,'' IEEE J. Ocean Eng. **18**, 401–424 (1993).

[9] M. B. Porter, ''The KRAKEN normal mode program,'' SACLANTCEN Memorandum, SM-245, La Spezia, Italy (1991).

[10] S. D. Chuprov and N. E. Mal'tsev, Dokl. Akad. Nauk SSSR **257**, 475–479 (1981).

[11] S. D. Chuprov, ''Interference structure of a sound field in a layered ocean,'' *Acoustics of the Ocean: Current Status* (in Russian), edited by L. M. Brekhovskikh and I. B. Andreevoi (Nauka, Moscow, 1982), pp. 71–91.

[12] S. V. Burenkov, ''Distinctive features of the interference structure of a sound field in a two-dimensionally inhomogeneous waveguide,'' Sov. Phys. Acoust. **35**, 465–467 (1989).

[13] V. M. Kuzkin, ''The effect of variability of ocean stratification on a sound field interference structure,'' Acoust. Phys. **41**, 300–301 (1995).

[14] L. M. Brekhovskikh and Yu. Lysanov, *Fundamentals of Ocean Acoustics* (Springer Verlag, Berlin, 1991), pp. 139–145.

[15] V. N. Lobanov and Yu V. Petukhov, ''Space-frequency distribution of the intensity of wideband sound in a shallow sea,'' Acoust. Phys. **39**, 574–581 (1993).

Laboratory measurements of forward and bistatic scattering of fish at multiple frequencies

Li Ding,[a] Y. Takao, K. Sawada, T. Okumura, and Y. Miyanohana
National Research Institute of Fisheries Engineering, Hasaki, Ibaraki, Japan 314-04

M. Furusawa
Tokyo University of Fisheries, Tokyo, Japan

D. M. Farmer
Institute of Ocean Sciences, Sidney, BC, Canada

(Received 7 August 1997; accepted for publication 6 February 1998)

Forward and bistatic scattering of sound by individual fish at frequencies of 120 and 200 kHz have recently been measured in the laboratory following an earlier experiment conducted at acoustic frequency of 38 kHz by Ding [J. Acoust. Soc. Am. **101**, 3398–3404 (1997)]. The results of forward-scattering strength obtained here, combined with those obtained in Ding, provide an empirical dependence of forward-scattering strength on acoustic frequency. It is observed that the forward-scattering strength increases rapidly with frequency and is much stronger than the backscattering strength. Scattering patterns, or scattering strength as a function of receiving angle, have also been measured for the first time in this new experiment. These results are currently being examined using theoretical models taking appropriate account of effects of both fish flesh and swimbladder. © *1998 Acoustical Society of America.* [S0001-4966(98)05405-8]

PACS numbers: 43.30.Gv, 43.30.Sf, 43.30.Xm [DLB]

INTRODUCTION

Forward scattering of fish has drawn significant attention since it was demonstrated that migrating salmon in the Fraser river of B.C., Canada could be discerned with an acoustic scintillation flowmeter (based on forward scattering by inhomogeneities in the water) deployed across the river (Curran *et al.*, 1994; Ye *et al.*, 1996). While effective techniques based on the forward-scattering principle are still yet to be developed for practical application in estimating fish population, fundamental knowledge of more general scattering characteristics of fish is essential for such a development. Ding (1997) carried out a novel laboratory experiment to measure directly forward scattering (at 38 kHz) by single fish with simultaneous measurements of backscattering, and it was found that the forward scattering is much stronger and varies with the angle of incidence less significantly, than the backscattering. In the meantime, Ding and Ye (1997) used a sound scattering model developed in Ye *et al.* (1997) to model the data of Ding (1997), and found that the fish body tends to be a more important factor than the swimbladder in determining forward-scattering strength. The results support an earlier model study by Ye and Farmer (1996).

Given the interesting results obtained in the first experiment, we carried out a second experiment at higher frequencies (120 and 200 kHz). Of more general interest, measurements of scattering patterns of fish (i.e., scattering strength versus scattering angle) have also been obtained. This paper describes the second experiment and reports the results, while a more careful analysis of the data will be the subject of subsequent papers.

[a]Now at VITECH Innovative Research & Consulting, Victoria, BC V8P 3M3, Canada.

I. LABORATORY EXPERIMENTS

Both the first and second experiments were carried out in the water tank (15 m long, 10 m wide, and 10 m deep, filled with fresh water) of the National Research Institute of Fisheries Engineering (NRIFE) of Japan. The primary purpose of the first experiment was to measure the dependence of forward scattering of individual fish on the incident angle of sound. Details and results of the experiment are referred to Ding (1997). The second experiment was aimed at measuring bistatic scattering of fish at much higher frequencies (120 and 200 kHz), and will be described here in detail.

A. Setup

In this experiment, the transducers were mounted on a steel plate which can be moved by a motor to a desired position (Fig. 1). They were placed near one end-wall of the tank and in the middle of the water body, looking horizontally towards the other end-wall (with sound absorbers) near which hydrophones were placed. As pointed out by Ding (1997), it is essential to keep the positions of the hydrophones stable relative to the transducers. Therefore three broadband hydrophones were suspended within thin steel-string frames connected to rigid bars, and positioned to the same depth as the transducers. A target was then positioned between the transducers and the hydrophones at the same depth, and near the center of the tank.

A fourth broadband hydrophone was also mounted on the plate very close to the 200-kHz transducer for measurement of backscattering, as we intended to use a simple receiving system for multiple frequencies. This setup resulted in more noise in the backscattered signal since the hydrophone is nearly omnidirectional. We found that the measurements were 1 to 2 dB higher than the theoretical value for a

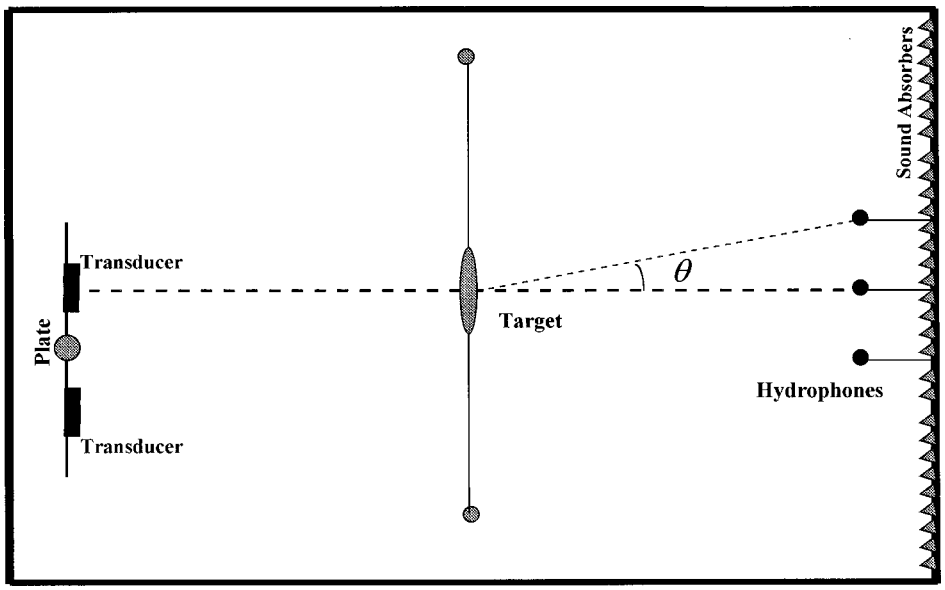

FIG. 1. Experimental setup.

copper sphere of 60-mm diameter. However, the measured backscatter merely served as a reference for forward scatter, rather than for a precise measurement.

Signal transmission was through a function generator and a power amplifier. The function generator produces a prescribed pulse length and carrier frequency; pulsed sinusoidal signals were sent to the power amplifier and applied to the transducers. The pulse repetition rate was controlled by a trigger signal generator, which was also used to synchronize the transmission and reception.

B. Procedure

For each measurement, the transducers were positioned so that the target was located on the beam axis. The hydrophones were positioned in such a way that desired scattering angles relative to the target (θ in Fig. 1) were formed. For measurement of forward scattering (i.e., scattering angle equal to the incident angle), special care was taken to align one of the hydrophones and the target on a common axis of the transmitted beam. For each measurement, received signals were recorded first in the absence of the target (reference direct-path signal) and then with the target in place. The difference of the received signals thus obtained is the scattered signal (Ding, 1997). After each measurement, the hydrophones were moved to new positions and the same procedure was repeated. Note that in this experiment, the incidence of sound was always normal and only the scattering angle is changed by moving the hydrophones.

Let P_d and P_s be the received amplitude of direct-path waves and scattered waves. Following Ding (1997), the amplitude of the scattering function at the scattering angle θ (Fig. 1), is given by

$$|F| = \frac{P_s}{P_d}\frac{r_i r_s}{r_d}, \tag{1}$$

where r_i and r_d are the distance from the transmitter to the target and to the receiver at $\theta=0$, respectively. The distance from the target to the receiver at $\theta=0$ is given by $r_s = r_f/\cos\theta$, where $r_f = r_d - r_i$.

C. The first Fresnel zone

When a target is large relative to the wavelength, and close to the transmitter, the Fresnel (phase) zones have to be considered. The radius of the first Fresnel zone in the case of forward scattering can be expressed as [extended from Clay and Medwin (1977)]

$$a_1 = \sqrt{\lambda r_i r_f / r_d}, \tag{2}$$

where λ is the wavelength. If a target is not entirely within the first Fresnel zone, the scattered waves from the first and second zone tend to interfere destructively. In this experiment, $r_i = 5.23$ m, $r_f = 6.36$ m, and $r_d = r_i + r_f = 11.60$ m. Thus $a_1 = 19$ cm at frequency 120 kHz, and 15 cm at 200 kHz. The fish length ranges from 31 to 35 cm. That is, at 120 kHz the fish are entirely within the first Fresnel zone, whereas at 200 kHz the main body of the fish is still in the zone with only 0.5–2.5 cm of the head and tail outside the zone.

II. RESULTS

In this experiment we have measured several immobile (dead) Japanese mackerel (*Scomber Japonicus*) in similar conditions (directly sent from a nearby fishing port). The fork lengths (fork length is defined as the distance from the tip of the snout to the end of the rays in the center of the caudal fin) of these fish ranged from 31.0 to 35.5 cm. Of particular interest here is the measured forward- and backscattering target strengths (TS) at normal incidence versus frequencies, which are shown in Fig. 2(a) for a number of Japanese mackerel [including those used in the earlier experiment (Ding, 1997)]. It is seen that the forward-scattering TS increases from about -19 dB at 38 kHz to about 4 dB at 200 kHz. The backscattering TS, however, varies within a much smaller range (from -36 to -31 dB), with one excep-

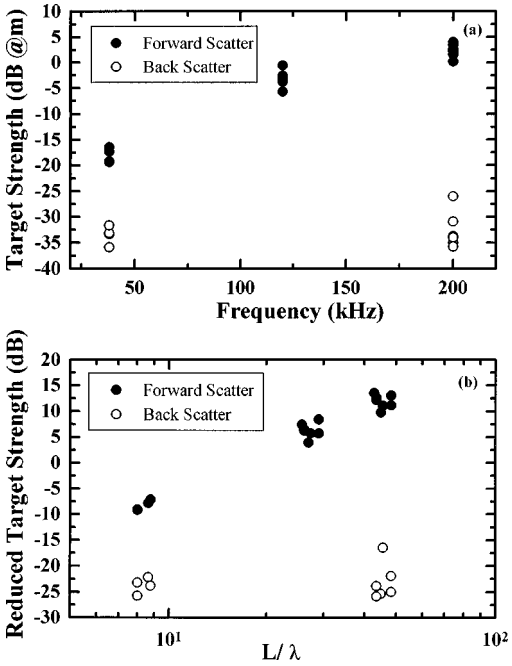

FIG. 2. Forward- and backscattering strength at three frequencies (38, 120, and 200 kHz). (a) Target strength, (b) reduced target strength. Backscattering at 120 kHz was not measured in the experiment.

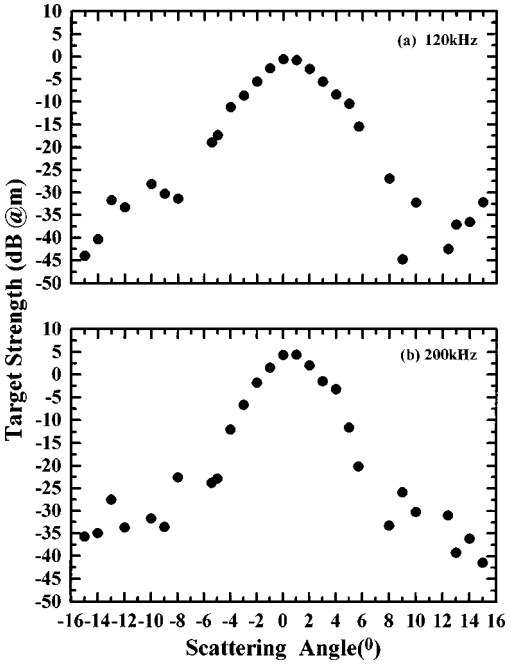

FIG. 3. Bistatic scattering pattern of a Japanese Mackerel, for a length of 35 cm and a weight of 546 g. (a) 120 kHz, (b) 200 kHz.

tional point near -25 dB due to a fish with an exceptionally large swimbladder. Note that the backscattering at 120 kHz was not measured in this experiment.

As the data were collected for fish of various fork lengths, which also affect target strength, it is useful to choose dimensionless or normalized parameters. By a similarity analysis, it is reasonable to normalize scattering amplitude $|F|$ by fork length L, and investigate its dependence on L/λ, where λ is the wavelength. Therefore we define normalized, or reduced target strength, either forward or backscatter, as

$$\mathrm{TS}_n = 20 \log_{10}\left(\frac{|F|}{L}\right). \tag{3}$$

Figure 2(b) shows the reduced target strength for the data in Fig. 2(a). Two important features can be observed immediately from Fig. 2. First, the forward-scattering TS increases rapidly with frequency. This result qualitatively supports earlier theoretical modeling of forward scatter by Ye and Farmer (1996) who show that forward scatter of fish increases monotonically with frequency while backscatter oscillates with frequency. Second, the forward-scattering TS is much stronger than the backscattering TS, and the difference increases dramatically with frequency. For example, in Fig. 2(b), the forward scatter is 13 dB higher than the backscatter at 38 kHz and becomes 36 dB stronger at 200 kHz.

Another interesting aspect of the measured acoustic scattering by fish, never obtained before, is scattering pattern. Figure 3 shows the measured scattering pattern, i.e., target strength versus the scattering angle θ in Fig. 1, for a single fish with a fork length of 35.0 cm and a weight of 546 g. It was measured at frequencies of 120 and 200 kHz, and at scattering angles ranging from $-15°$ to 15°. At $\theta = 0$, the result corresponds to the forward-scattering strength. It is seen that with a 20-dB threshold, the scattering pattern at 120 kHz has a well-defined mainlobe between $-6°$ and 6°. The mainlobe narrows to $\pm 5°$ at 200 kHz. Beyond the mainlobe, the scattering pattern fluctuates.

Preliminary analysis of the data using the model of Ye *et al.* (1997) indicates that the model overestimates the forward-scattering strength by a few dB. It is speculated that this may be due to lack of a coupling mechanism between fish body and swimbladder in the model (Ding and Ye, 1997). An improved model taking appropriate account of the coupling is under development.

Both forward and bistatic scatter could be used for the purpose of detecting fish. For example, consider a situation where a receiver is spatially separated from a transmitter as in Fig. 1. When fish pass across the acoustic beam, their forward-scattered signals can interfere strongly with the direct-path signal, thus inducing signal fluctuation. This can be analyzed using scintillation techniques to detect the passage of the fish (Ye *et al.*, 1996), if the contribution from the fish is well above the background signal variability. On the other hand, in the case of low fish density or strong background variability, bistatic scatter could be used. Figure 3 shows that for a single fish of 35 cm and at 200 kHz, the bistatic scattering strength at scattering angle $\pm 5°$ is still approximately 20 dB stronger than the backscattering strength. If the fish is still in the acoustic beam but the receiver is displaced far from the beam, then the bistatic scatter can be separated from the direct-path signal when a sufficiently short pulse is used. In both cases, the fish can be well within the first Fresnel zone as long as they are not too close to the transmitter or the receiver. Although practical techniques have yet to be developed, we believe that this laboratory study provides a more complete understanding of sound scattering by fish, and lays the foundations for future development of related technology.

ACKNOWLEDGMENTS

This work received support from the Science and Technology Agency of Japan and the Department of Fisheries and Oceans of Canada. We thank Dr. Zhen Ye of National Central University, Taiwan, Dr. Tim Mulligan and Dr. Robert Kieser of the Pacific Biological Station, Canada, and Dr. Richard Dewey of the University of Victoria, Canada, for useful discussions.

Clay, C. S., and Medwin, H. (**1977**). *Acoustical Oceanography* (Wiley, New York).

Curran, T., Lemon, D., and Ye, Z. (**1994**). ''The acoustic scintillation flowmeter: Applications for a new environmental tool,'' J. Association Canadian Hydrographic Service, Spring, 24–29.

Ding, L. (**1997**). ''Direct laboratory measurement of forward scattering by individual fish,'' J. Acoust. Soc. Am. **101**, 3398–3404.

Ding, L., and Ye, Z. (**1997**). ''A method for acoustic scattering by slender bodies. II. Comparison with laboratory measurements,'' J. Acoust. Soc. Am. **102**, 1977–1981.

Ye, Z., and Farmer, D. M. (**1996**). ''Acoustic scattering by fish in forward direction,'' ICES Journal of Marine Science **53**, 249–252.

Ye, Z., Curran, T., and Lemon, D. (**1996**). ''Fish detection by the acoustic scintillation technique,'' ICES Journal of Marine Science **53**, 317–321.

Ye, Z., Hoskinson, E., Dewey, R., Ding, L., and Farmer, D. M. (**1997**). ''A method for acoustic scattering by slender bodies. I. Theory and verification,'' J. Acoust. Soc. Am. **102**, 1964–1976.

A viscous-elastic swimbladder model for describing enhanced-frequency resonance scattering from fish

C. Feuillade and R. W. Nero
Naval Research Laboratory, Stennis Space Center, Mississippi 39529-5004

(Received 12 February 1997; accepted for publication 25 February 1998)

Acoustic scattering from many species of fish is strongly increased by the resonance response of the swimbladder. This gas-filled, elastic-walled internal sac may have several functions, including hearing and buoyancy. A complete physical description of the response must include the swimbladder wall, the surrounding flesh, and the gas enclosed. This work presents a new mathematical/physical model to describe resonance scattering from swimbladder fish. The model consists of a spherical air bubble enclosed, first, by an elastic shell (representing the swimbladder wall), and then by a viscous shell (representing the surrounding fish flesh). The rigidity of the inner shell increases the monopole resonance frequency of the bubble. The viscosity of the outer shell causes the resonance to be damped. By allowing these factors to vary within physically reasonable bounds, the new model has been used to explain the experimentally measured resonance frequencies and damping of swimbladder resonances in Atlantic cod. The model provides insights into the physiological mechanisms by which fish may actively control the resonance frequencies of their swimbladders to improve hearing, and how this control can be lost under varying water pressure conditions. The impact of this issue on fisheries survey procedures is discussed.
[S0001-4966(98)05106-6]

PACS numbers: 43.30.Gv, 43.30.Sf, 43.20.Ks, 43.30.Ft [DLB]

INTRODUCTION

Scattering from an individual fish may be significantly increased by the acoustic resonance response of the swimbladder. This gas-filled saccate internal organ is found in many species, and may have several functions, including hearing and buoyancy. A swimbladder is similar to an air bubble within a fish; and this fact led Marshall[1] to examine the possibility that scattering from fish with air-filled swimbladders was the cause of high levels of acoustic volume reverberation within deep scattering layers. The primary mechanism was considered to be swimbladders vibrating in the volume pulsation (i.e., ''monopole'' or ''breathing'') mode when ensonified at the appropriate resonance frequency. It is now generally accepted that resonance scattering by swimbladder-bearing fish is the major cause of volume reverberation in the ocean at frequencies up to at least 10 kHz.[2]

Since the monopole resonance characteristics of fish swimbladders and air bubbles in water are physically similar, ''bubblelike'' models have been a popular method for describing resonance scattering from swimbladder bearing fish. One clear difference between bubbles and swimbladders, however, is in their respective shapes. Although the interspecific, and even intraspecific, variability of swimbladder shapes is high,[3] they are usually elongated and, unlike bubbles, not typically spherical (a swimbladder example, for Atlantic cod, is shown in Fig. 1). However, the assumption has usually been made in swimbladder scattering models that, since the acoustic wavelength at the monopole resonance frequency is much greater than the dimensions of the object, the detailed shape of the swimbladder is relatively unimportant. The monopole term dominates the scattering response, suggesting that the physical parameters determining the behavior of the system may be incorporated within a spherically symmetric model to produce a mean value approximation. This assumption has received support recently from scattering studies of deformed air bubbles,[4,5] which have indicated that the monopole mode is indeed the predominant factor determining the resonance response of highly nonspherical bubbles, and that the azimuthal scattering distribution remains principally isotropic even for very elongated bubbles. In accordance with this ''dominant monopole'' assumption (which is adopted in this present work also), swimbladder models have typically consisted of spherical air bubbles entrained in various media, either infinite or bounded, whose physical properties are adapted to represent the observed action of the surrounding fish body, which strongly influences and modifies the resonance response. The elongated shape of the swimbladder is believed to have no significant physical effect, other than to produce a small upward shift in the resonance frequency, which can be easily incorporated in the modeling by means of a simple geometrical factor described by Strasberg[6] and Weston.[7]

The first widely used model of this type was developed by Andreeva,[8] who considered a swimbladder as a spherical air bubble in an infinite elastic medium (i.e., with the properties of fish flesh). Extensive analysis of fisheries data has shown that, in general, the resonance frequency of a fish swimbladder is practically equivalent to that of an air bubble containing the same mass of gas,[9] apart from the known geometrical corrections due to the nonspherical shape of the bladder.[6,7] This is corroborated by other experimental data which shows that the physical action of fish flesh surrounding the swimbladder does not itself appear to produce a systematic bias of the resonance frequency.[10] In relation to this fact, a characteristic discrepancy arises from Andreeva's

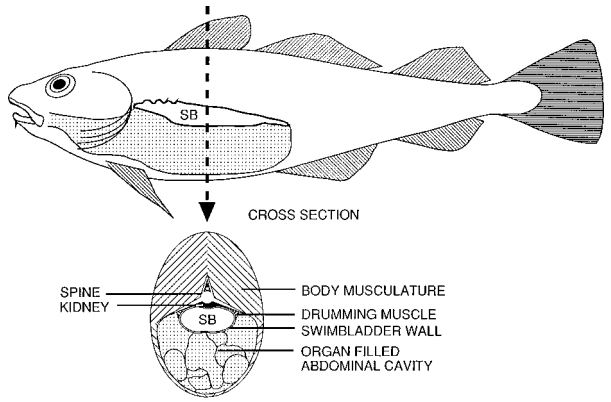

FIG. 1. Stylized drawing of a cod. This drawing, showing the side aspect of a cod, and a cross section, is based upon photographs and figures in Ref. 3. The elastic-walled swimbladder is labeled ''SB.''

model[8] when it is used to fit data. While the elastic parameters in the infinite medium external to the air bubble may be readily adjusted within bounds compatible with the known properties of fish flesh, in order to reproduce the low values of Q typically observed in experimental measurements, an attendant and unwarranted upward bias in the resonance frequency is also produced, which is not indicated by the same data. Similar remarks can be made about subsequent modifications of Andreeva's model, which attempt to take the thickness of the tissues into account.[11,12] The contradictions inherent in Andreeva's approach led Love[13] to consider fish flesh as a viscous (rather than an elastic) medium. He solved a multilayer boundary value problem for an air bubble enclosed by a viscous shell, entrained in water, to produce a spherical swimbladder model which correctly emulates the generally observed experimental behavior. The viscous shell causes the resonance response of the air bubble to be damped, thus reproducing low values of Q, but has a negligible effect on the resonance frequency. Love's model has been successfully used to correlate fisheries data with acoustic measurements of volume reverberation.[9]

Love's model has proved adequate for many experimental applications (see, for example, citations in Ref. 9), but one set of measurements, those made by Sand and Hawkins on depth-adapted Atlantic cod,[14] have found resonance frequencies much higher than can be realistically explained by means of a viscous shell approach alone. Sand and Hawkins,[14] and Hawkins,[15] suggested that the enhanced resonance frequencies they measured may be actively controlled by the fish through a change in tonus of the musculature immediately surrounding the swimbladder and imparting a stress to it. Observing that cod maintain the resonance frequency well above their normal hearing range, they suggested that the swimbladder is used as a displacement amplifier, and that the purpose for the shift in resonance frequency by the fish is to maintain a stable hearing capability during extensive vertical movements.

This issue is of considerable importance, since active control of the swimbladder implies that determination of the resonance frequency alone may not be sufficient for fish assessment exercises. Extreme bias could be introduced in the results of studies where measured resonance frequencies have been used to determine swimbladder volume and, deductively, fish size and abundance.[9,16] These studies usually assume a simple resonant bladder with no active change in resonance frequency by the fish. Typically, swimbladder models used to evaluate fisheries data have treated the physical properties of the fish body as fixed quantities (which are sometimes formulated as lump constant terms in a ''mass-spring'' equation for the bubble resonance). This approach allows no realistic rationale for describing the acoustic phenomenon reported by Sand and Hawkins, which is evidently due to a physiological mechanism controlled by the fish, which causes the properties of fish flesh to vary. There is a clear need for a new modeling approach, to incorporate and formalize the changes in physical action resulting from the actual fish behavior.

Recently, Clay and Horne introduced a new swimbladder model for Atlantic cod.[17] This model, which uses the Kirchhoff approximation to describe scattering from the faces of the swimbladder, is primarily intended to be used for frequencies well above the swimbladder resonance. In this high-frequency region, it characteristically predicts no change in scattering as a function of water depth. The swimbladder resonance region is ignored.

The work described here stemmed from the recognition that a satisfactory explanation of the results of Sand and Hawkins (and, therefore, an improved understanding of the swimbladder resonance response) appears to require the incorporation of changes in the acoustic parameters of the swimbladder due to the physiological behavior of the fish. Swimbladder models, to be simple and useful, inevitably involve some degree of mathematical abstraction. Realistically, however, a swimbladder is not equivalent to an air bubble in an infinite (or even bounded) elastic or viscous medium with uniform constant properties. This is indicated in Fig. 1, which presents a stylized drawing of the side aspect, and a cross section, of a cod. The swimbladder (labeled ''SB'') is a gas-filled, elastic-walled sac, which lies below the spine and kidney, and is enclosed on the bottom by the abdominal cavity, which contains other organs, such as the stomach, liver, gonads, etc. In cod, the swimbladder is attached to the vertebrae, and also to the drumming muscles.[18] If, as we assume here, Sand and Hawkins are correct in their suggestion that the cod uses its musculature to impart stress to the swimbladder, the question arises as to which changes in the acoustic properties of the swimbladder, initiated by the physiological control of the fish, and mediated through its anatomical features, can be advanced to explain the enhancement of the observed resonance frequency, and incorporated within a not overly complex model.

In this paper a new mathematical/physical model for a swimbladder is presented, which couples acoustical signals with both viscous *and* elastic properties to describe the scattering (see Fig. 2). The model consists of a spherical air bubble enclosed, first, by an elastic shell (representing the swimbladder wall), and then, as in Love's model, by a viscous shell (representing the surrounding fish flesh). It is used to interpret the experimental data of Sand and Hawkins,[14] and shows that the enhanced resonance frequency phenomenon can be explained by varying the elastic properties of the

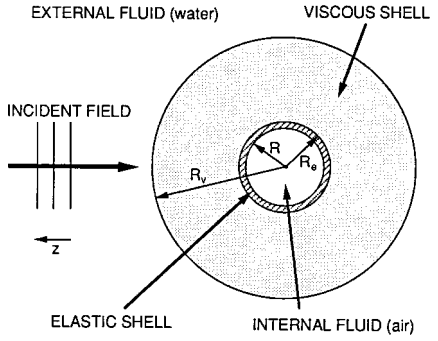

FIG. 2. The double shell swimbladder model. The external fluid (medium 1) is water with density ρ_1, and sound speed c_1. The viscous outer shell (medium 2) has density ρ_2, sound speed c_2, and viscosity ξ_2. The elastic inner shell (medium 3) has density ρ_3, and Lamé constants λ_3 and μ_3. The internal fluid (medium 4) is air with density ρ_4, and sound speed c_4.

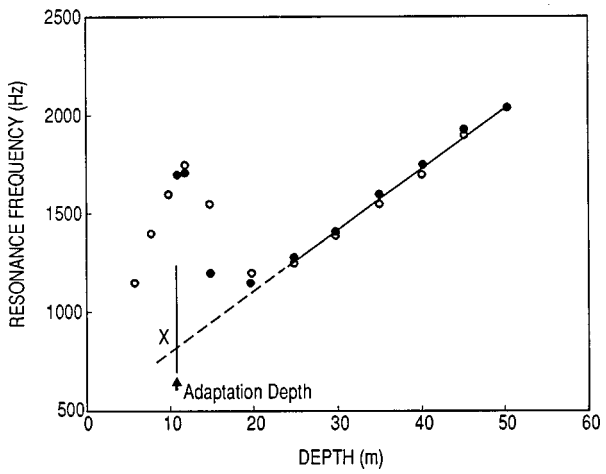

FIG. 3. Experimental data for cod. The data points indicate some of the experimental measurements made by Sand and Hawkins (Ref. 14) on Atlantic cod. A 16-cm cod was kept at 11 m for 48 h, and then lowered rapidly in stages from 11 m to 50 m, and then raised again to 6 m. The filled symbols indicate resonance frequency measurements made as the fish was lowered, the open symbols indicate measurements made as the fish was raised. The solid line shows the fit to the data for depths 25 m and lower, assuming the frequency variation is determined by Boyle's law. The dashed line is an extrapolation downward from the solid line. The predicted resonance frequency due to compression effects alone, at the 11-m adaptation depth (see the point ''×'') is about 800 Hz. The measured frequency, however, is much greater, about 1700 Hz.

inner shell; while the viscous properties of the outer shell may be adjusted practically independently to describe the damping of the resonance, as in Love's model. Since cod are believed to adjust the configuration of their swimbladders by changing muscle tonus in the surrounding flesh, we suggest that it is collateral changes in the rigidity of the swimbladder wall and its immediately attached tissues (represented by the inner shell) that provide the mechanism by which the fish controls the resonance frequency and, thereby, stabilizes its hearing capability. We believe this to be a very reasonable hypothesis. Sand and Hawkins recognized (and, through an ingenious sequence of experiments, demonstrated) that the phenomenon they observed was due to the muscular action of the fish, and to physiological reflex action under quickly varying depth conditions. The model we have presented here proposes a framework for understanding this physiological behavior, and for representing the physical changes which accompany it. It also provides a point of departure for determining which species of fish may or may not be reliably surveyed using simple swimbladder models.

In Sec. I of this paper the enhanced resonance frequency phenomenon observed by Sand and Hawkins is discussed. In Sec. II we introduce the viscous-elastic double shell swimbladder model, and develop the theoretical formalism for describing scattering from it. In Sec. III we apply the formalism to study the behavior of air bubbles enclosed by elastic and viscous shells, and to model experimental data for Atlantic cod. Section IV gives a discussion of some questions raised by the work, and this is followed by a summary of conclusions.

I. THE SAND AND HAWKINS DATA

The measurements of Sand and Hawkins are unique in the literature on the scattering of sound by fish in the low-frequency resonance region. The phenomenon observed by Sand and Hawkins is indicated in Fig. 3, which shows some of their experimental measurements. Cod tend to regulate the amount of gas in their swimbladders in order to maintain constant volume at different depths, and thereby ensure that the contribution to buoyancy remains the same. The data in Fig. 3 were taken from a 16-cm juvenile cod, which was initially kept at a depth of 11 m for about 48 h. During this period the fish slowly adapted to the ambient pressure by secreting gas to, or absorbing gas from, its swimbladder (cod have closed swimbladders with no orifices to allow rapid gas exchange) until the latter became *regularly* inflated (i.e., probably rather fully extended, but not overstretched). The fish was then lowered quickly in stages from 11 m to 50 m, and subsequently raised again to 6 m. At each stage, the resonance frequency of the swimbladder response was measured. The filled symbols in Fig. 3 indicate measurements made as the fish was lowered, the open symbols indicate measurements made as the fish was raised. The total time for the whole sequence of measurements (about 30 min) was too short for gas to be added or removed from the swimbladder, so that the data observations must be related to the behavior of a constant *mass* of gas.

Consider first the data points for depths 25 m and greater in Fig. 3, which noticeably fall on a straight line. In this region, changes in the swimbladder volume with depth are inversely related to variations in the water pressure, as prescribed by Boyle's law. The solid line drawn through the data points for depths 25 m and greater was calculated by assuming that, as the fish is lowered in depth, the swimbladder is compressed by the higher external water pressure, and the consequent reduction in size causes the resonance frequency to increase. The additional Strasberg–Weston upward shift of the resonance frequency due to the nonspherical shape of the swimbladder,[6,7] which also increases with depth, is also incorporated in the calculation. The swimbladder model of Love[13] (which implicitly contains this compression mechanism), together with the Strasberg–Weston shift, accurately predicts the data points of Sand and Hawkins for depths in this region. Furthermore, the shell viscosity in

Love's model may be adjusted to achieve the low values of Q also measured in the experiment.

What is surprising about Fig. 3 is the behavior observed at depths *less* than 25 m. The dashed line extending beyond the solid line in the figure indicates the expected decrease in the resonance frequency at shallower depths prescribed by Boyle's law. At the adaptation depth (see the point denoted ''X'') the resonance frequency should be about 800 Hz. However, the recorded data clearly diverge markedly from the Boyle's law predictions. At the adaptation depth, the observed resonance frequency was about 1700 Hz, i.e., more than double the expected value. This remarkable feature of the Sand and Hawkins data cannot be realistically explained by standard swimbladder modeling approaches.

Careful examination of Fig. 3 shows that there are, in fact, two aspects of the Sand and Hawkins data that require explanation: (a) the anomalously high values of the resonance frequency close to the adaptation depth; (b) the abrupt fall in resonance frequency as the fish was moved a few meters to deeper *or* shallower depths. Like (a), the second aspect (b) is very significant. In another set of measurements during the same experiment, Sand and Hawkins showed (see Fig. 7 of Ref. 14) that rapid transfers of a depth-adapted cod to a new depth, either deeper or shallower, resulted in an immediate and large decrease in the swimbladder resonance frequency. However, regardless of whether the fish was lowered or raised, it was observed to be capable of quickly (i.e., within 28 min) and autonomously restoring the resonance frequency to the original value. Sand and Hawkins believed this to be strong evidence of the muscular control of the fish on the swimbladder and the consequent physiological origin of the enhanced frequency phenomenon.

Before using the swimbladder model presented in this paper to fit the data, let us consider other physical mechanisms which might provide alternative explanations. One possible explanation for this phenomenon is that an excess static gas pressure ΔP is present in the bladder at the adaptation depth. If this is the case, P in Eq. (1) could be replaced by $P+\Delta P$, and this would increase the resonance frequency. However, Sand and Hawkins remark that internal excess pressures of several atmospheres would be required to explain the enhanced resonance frequencies they observed, and experimental evidence has not indicated that cod are able to maintain excess pressures greater than about 6-cm H_2O.[19] There is another objection to this explanation. Inspection of Fig. 3 shows that when the cod was lowered from 11 m to 20 m, the resonance frequency fell quickly from 1700 Hz to about 1100 Hz. However, since the external water pressure would increase by about 1 atmosphere for this downward vertical excursion, and thereby cause the internal pressure to increase by the same amount, this should lead, by Eq. (1), to an increase in the resonance frequency, not a decrease as observed.

Another possible alternative is the presence of surface tension in the swimbladder wall. A formalism for introducing surface tension, and thereby increasing the resonance frequency, is provided in Love's swimbladder model.[13] Very high values of surface tension are needed, however, to explain the Sand and Hawkins observations and these values, in turn, necessitate the postulation of large internal excess pressures to oppose the resulting physical contraction of the swimbladder induced by the surface tension. Also, while a reduction in surface tension as the cod was lowered from 11 m to 20 m, due to size reduction of the swimbladder, might possibly be advanced to explain the fall in resonance frequency in that region, it certainly cannot be used to explain the corresponding fall in resonance frequency as the fish was *raised* from 11 m to shallower depths. In this case the swimbladder would expand, and the surface tension should therefore increase.

A third possibility is offered by changes in the shape of the swimbladder as the cod was moved up and down in the water column. For example, as the fish was lowered, the swimbladder volume would decrease as the external water pressure increased. The length of the swimbladder probably remained quite constant, so that the volume decrease was effected primarily by reductions in the width and, possibly, by asymmetric buckling. Could these variations in shape lead to changes in the resonance frequency of the correct tendency, and of sufficient magnitude, to explain the Sand and Hawkins data shown in Fig. 3?

Let us first consider reductions in the width of the swimbladder and assume, for the moment, that they are prolate spheroidal in form. In this case an upward frequency shift will occur which is prescribed exactly by the Strasberg–Weston geometrical correction.[6,7] Sand and Hawkins note that the typical aspect ratio of a cod swimbladder is between 5 and 6, which gives rise to a frequency shift of about 13% over a sphere of the same volume.[7] When the cod was lowered through the water column from 11 m to 20 m (see again Fig. 3), the water pressure increased from about 2 atmospheres to 3 atmospheres. By Boyle's law, the swimbladder volume would decrease in inverse proportion from V to about $2V/3$. The width reduction corresponding to this volume change should, in turn, cause the aspect ratio to increase from (say) 6 to only 7.35, which gives rise to a frequency shift of about 18%.[7] We see that this effect clearly cannot explain the sudden decrease in resonance frequency as the fish was lowered from 11 m to 20 m: (a) because the tendency is wrong, i.e., the reduction in width predicts an *increase*, not a decrease in frequency as observed; and (b) because the magnitude is insufficient, i.e., the small increase in the frequency shift from 13% to 18% is much smaller than the order of magnitude effect seen in the data.

What is the effect of asymmetric buckling of the swimbladder? The resonance action of swimbladders (like that of bubbles) is predominantly determined by the monopole mode. Sand and Hawkins point out that the resonance frequency of a bubble of constant volume increases with any deformation of its spherical shape. A similar phenomenon was observed by Feuillade and Werby for prolate spheroidal bubbles.[4] They found that the resonance frequencies of bubbles in the shape of cylinders with hemispherical endcaps were slightly but consistently higher than prolate spheroidal bubbles of the same volume and aspect ratio. While we are not aware of any comparable studies for general arbitrarily shaped asymmetric swimbladders, it seems very probable that increasingly irregular deformations would cause the

resonance frequency to shift upward, rather than downward. In this case, buckling of the swimbladder as the cod was lowered from 11 m to 20 m cannot explain the abrupt *fall* in resonance frequency that was observed. In any event, the degree of buckling (and frequency shifting) would likely be too small to explain the observations. The decrease in volume from V to $2V/3$ corresponds to a reduction in the typical dimensions of the swimbladder of only about 13%, which does not seem to allow much room for extreme irregularities in shape.

Having eliminated other possibilities, the only factor that remains to explain the increased resonance frequency is the effect on the swimbladder response of the fish tissues themselves. Now, Andreeva's model[8] (and its modifications[11,12]), which treats the fish surrounding the swimbladder as an elastic medium of uniform elastic shear modulus, does predict a frequency shift. However, as discussed in the Introduction, this shift is invariably linked to the degree of resonance damping and, in the great majority of data sets, no general shift in the frequency due to the presence of the fish body is indicated, even though the swimbladder resonance is typically very highly damped. Also, as Andreeva states,[8] her theory predicts a persistent frequency bias which should remain detectable as the fish moves vertically through the water column, at least for depths above 200 m. Her model, therefore, offers no explanation for the sudden drop in the resonance frequency observed in Fig. 3 as the cod was moved below the adaptation depth of 11 m.

The idea that the large and sudden variations in resonance frequency seen in the Sand and Hawkins data should be due to changes in the physical properties of fish tissues, as a result of the physiological behavior of the fish, was suggested by Sand and Hawkins themselves. They proposed varying the shear modulus of fish flesh, as entered in Andreeva's model, to correspond to the changing degrees of muscular tonus (and therefore stiffness) as stress is applied to the swimbladder. In an attempt to overcome the discrepancies arising from Andreeva's model when the residual shear modulus of relaxed tissue (e.g., as measured by Lebedeva[20]) is entered, they adopted the scheme, suggested by McCartney and Stubbs,[11] of incorporating a term to represent the effective thickness of the surrounding tissues. By this means they were able to more successfully explain the observed frequency variations. However, the required alterations in elasticity also gave rise unavoidably to rapid changes in the Q of the resonance, which were not seen in the data.

It seems clear that neither the elasticity of fish flesh (as analyzed by Sand and Hawkins) nor the viscous effect of fish flesh (which gives rise to a generally negligible frequency shift, as detailed in Love's work) offers a consistent explanation of the Sand and Hawkins resonance frequency data. A much more sensible explanation seems to be that the rapid variations in resonance frequency with water depth must be due to some alteration in the swimbladder itself, since this is the internal organ most responsive to changes in water pressure. However, we have seen before that the effect cannot be due to changes in the physical size or shape of the swimbladder, or to the presence of excess pressure or surface tension. After these elements are eliminated, the only factor that remains to explain the effect is a change in the effective physical characteristics of the *swimbladder wall*, and possibly also in the tissues immediately attached to it.

In this present work, we suggest that the Sand and Hawkins data may be simply, realistically, and consistently explained by modeling: (a) the *elastic rigidity* properties of the swimbladder wall; (b) the *viscous* properties of the surrounding fish flesh. By implementing these two independent factors, a number of difficult issues are resolved. First, adjusting the shear rigidity of the swimbladder wall allows the enhanced resonance frequency phenomenon to be explained. The mechanism is similar to that of Andreeva's model, but with a critical difference. Since the swimbladder wall is thin, and the tissue of which it is made is normally soft and pliable, the residual shear modulus of relaxed swimbladder tissue is very small, and the wall then gives rise to a negligible frequency shift. The range of rigidity values needed to explain the data is practically equivalent to the shear modulus measurements made by Lebedeva on fish flesh.[20] Second, adjusting the viscosity of the surrounding fish flesh changes the damping and allows the values of Q also measured in the Sand and Hawkins experiment to be explained. The range of viscosity values needed is comparable with those used by Love to model the same data.[13]

II. THEORY

The great difference between the acoustic impedances of air and water causes air bubbles to be highly effective scatterers of sound. The acoustical properties of an ideal spherical air bubble were first treated by Minnaert[21] who showed that the frequency of the monopole resonance (where the bubble pulsates in and out without changing its spherical shape) is given by the following expression:

$$k_0 R = \frac{1}{c}\sqrt{\frac{3\gamma P}{\rho}}, \tag{1}$$

where k_0 is the wave number at the resonance frequency, R is the bubble radius, γ is the ratio of gas specific heats; and P, ρ, and c are the pressure, density, and sound speed, respectively, of the surrounding liquid. Clay and Medwin[22] give a full description of this method. They point out that for an air bubble at atmospheric pressure in water ($c=1500$ m/s) the value of $k_0 R \cong 0.0136$.

An alternative method of investigating the acoustical resonances of a bubble is to examine the scattering of sound from its surface. For a spherical bubble, Anderson' s fluid sphere model[23] may be used, which characterizes a bubble as an air-filled inclusion in water. Scattering occurs because of the abrupt change of acoustical impedance at the spherical interface between the two media. Using appropriate values for the density and sound speed of air and water at atmospheric pressure, it predicts a monopole resonance frequency identical to the Minnaert result.

The problem of scattering from an elastic spherical shell was treated by Goodman and Stern.[24] Their approach was later adopted to describe scattering from an air bubble enclosed by a viscous spherical shell by Feuillade *et al.*[25] In the present work, we will extend this method to study scattering

from a swimbladder, which is modeled using the double shell scheme depicted in Fig. 2. An air (medium 4) bubble of radius R is enclosed by two concentric spherical shells. The innermost shell consists of a thin elastic (medium 3) layer of outer radius R_e, whose physical properties may be adjusted to represent the behavior of swimbladder wall tissue.[26] The outer shell consists of a viscous (medium 2) fluid layer of outer radius R_v, which replicates the acoustic properties of fish flesh.[13] The whole object is entrained in water (medium 1).

In the viscous shell the displacement $\mathbf{u}_2$ is represented in terms of a scalar potential Φ_2 and a vector potential Ψ_2 by the equation

$$\mathbf{u}_2 = \text{grad } \Phi_2 + \text{curl } \Psi_2, \tag{2}$$

where Φ_2 and Ψ_2 satisfy the equations:

$$\frac{\partial^2 \Phi_2}{\partial t^2} = \left\{ (c_2)^2 + \frac{(\eta_2 + 4\mu_2/3)}{\rho_2} \frac{\partial}{\partial t} \right\} \nabla^2 \Phi_2; \tag{3}$$

$$\rho_2 \frac{\partial \Psi_2}{\partial t} = -\mu_2 \text{ curl curl } \Psi_2. \tag{4}$$

In these equations η_2 and μ_2 are the coefficients of bulk and shear viscosity, respectively. In fish flesh they may be conveniently combined into a single viscosity parameter given by[13]

$$\xi_2 = \eta_2 + \frac{4\mu_2}{3}. \tag{5}$$

The quantities c_2 and ρ_2 are the sound speed and density, respectively, of fish flesh. If we assume harmonic solutions for Eqs. (3) and (4) of the form $\Phi_2 = \phi_2 e^{-i\omega t}$ and $\Psi_2 = \psi_2 e^{-i\omega t}$, where ω represents the frequency of the incident field, then effective wavenumbers for compressional propagation (k_{L2}) and shear propagation (k_{T2}) in fish flesh may be derived, and are given by

$$k_{L2} = \frac{\omega}{c_2} \left\{ 1 - \frac{i\omega\xi_2}{\rho_2 c_2^2} \right\}^{-1/2}, \tag{6}$$

$$k_{T2} = (1+i) \left(\frac{\omega \rho_2}{2\mu_2} \right)^{1/2}. \tag{7}$$

Likewise, in the elastic shell the displacement $\mathbf{u}_3$ is represented in terms of a scalar potential Φ_3 and a vector potential Ψ_3, which satisfy the following equations:

$$\frac{\partial^2 \Phi_3}{\partial t^2} = \left\{ \frac{\lambda_3 + 2\mu_3}{\rho_3} \right\} \nabla^2 \Phi_3; \tag{8}$$

$$\frac{\partial^2 \Psi_3}{\partial t^2} = \left\{ \frac{\mu_3}{\rho_3} \right\} \nabla^2 \Psi_3. \tag{9}$$

In these equations ρ_3 is the density of the elastic medium, and λ_3 and μ_3 are the Lamé constants (μ_3, of particular importance, is the shear rigidity modulus). Again, assuming harmonic solutions for Eqs. (8) and (9) yields wave numbers for compressional propagation (k_{L3}) and shear propagation (k_{T3}) as follows:

$$k_{L3} = \omega \left(\frac{\rho_3}{\lambda_3 + 2\mu_3} \right)^{1/2}; \tag{10}$$

$$k_{T3} = \omega \left(\frac{\rho_3}{\mu_3} \right)^{1/2}. \tag{11}$$

We will consider the case in which a plane wave is incident on the multiple spherical shell as shown in Fig. 2. For simplicity, and with no loss of generality, the z-axis is chosen for the direction of incidence. The origin of coordinates is placed at the center of the spheres. The scattering behavior is calculated by expanding the acoustic field in each of the four media in terms of normal modes (i.e., products of Legendre polynomials and spherical Bessel functions) and applying appropriate boundary conditions at the three spherical interfaces between the media. We write the compressional field in the water as

$$\phi_1 = \sum_{m=0}^{\infty} P_m(\cos\theta) A_m^1 h_m(k_1 r). \tag{12}$$

The compressional field in the viscous shell is written

$$\phi_2 = \sum_{m=0}^{\infty} P_m(\cos\theta) \{ A_m^2 j_m(k_{L2} r) + B_m^2 n_m(k_{L2} r) \}, \tag{13}$$

and the corresponding shear field is

$$\psi_2 = \sum_{m=0}^{\infty} \frac{\partial}{\partial \theta} P_m(\cos\theta) \{ C_m^2 j_m(k_{T2} r) + D_m^2 n_m(k_{T2} r) \}. \tag{14}$$

In the elastic shell the compressional field is

$$\phi_3 = \sum_{m=0}^{\infty} P_m(\cos\theta) \{ A_m^3 j_m(k_{L3} r) + B_m^3 n_m(k_{L3} r) \}, \tag{15}$$

and the shear field is

$$\psi_3 = \sum_{m=0}^{\infty} \frac{\partial}{\partial \theta} P_m(\cos\theta) \{ C_m^3 j_m(k_{T3} r) + D_m^3 n_m(k_{T3} r) \}. \tag{16}$$

In the air bubble the compressional field is

$$\phi_4 = \sum_{m=0}^{\infty} P_m(\cos\theta) A_m^4 j_m(k_4 r). \tag{17}$$

The incident plane wave is described by

$$\phi_i = e^{ikr\cos\theta} = \sum_{m=0}^{\infty} i^m (2m+1) P_m(\cos\theta) j_m(k_1 r). \tag{18}$$

In Eqs. (12) and (18), $k_1 = \omega/c_1$; in Eq. (17), $k_4 = \omega/c_4$.

At the outermost interface between the water and the viscous shell, and at the innermost interface between the air and the elastic shell, three boundary conditions are applicable. The normal displacement and normal stress must be continuous, and the tangential stress must be zero. The boundary conditions for viscous fluids are given by Epstein and Carhart.[27] Letting $x = k_1 R_v$, $x_L = k_{L2} R_v$, and $x_T = k_{T2} R_v$, the following equations are obtained for the outermost interface. First, by the continuity of normal displacement,

$$A_m^1 x h_m'(x) + i^m(2m+1)x j_m'(x)$$
$$= A_m^2 x_L j_m'(x_L) + B_m^2 x_L n_m'(x_L) - m(m+1)C_m^2 j_m(x_T)$$
$$- m(m+1)D_m^2 n_m(x_T). \quad (19)$$

Then, by the continuity of normal stress,

$$\{-i\omega\rho_1 A_m^1 h_m(x) - i\omega\rho_1 i^m(2m+1)j_m(x)\}R_v^2$$
$$= \mu_2(2x_L^2 - x_T^2)\{A_m^2 j_m(x_L) + B_m^2 n_m(x_L)\}$$
$$+ 2\mu_2 x_L^2\{A_m^2 j_m''(x_L) + B_m^2 n_m''(x_L)\}$$
$$+ 2m(m+1)\mu_2 C_m^2\{j_m(x_T) - x_T j_m'(x_T)\}$$
$$+ 2m(m+1)\mu_2 D_m^2\{n_m(x_T) - x_T n_m'(x_T)\}. \quad (20)$$

Finally, since the tangential stress must be zero, we find

$$-2A_m^2\{x_L j_m'(x_L) - j_m(x_L)\} - 2B_m^2\{x_L n_m'(x_L) - n_m(x_L)\}$$
$$+ C_m^2\{(m+2)(m-1)j_m(x_T) + x_T^2 j_m''(x_T)\} + D_m^2\{(m+2)$$
$$\times(m-1)n_m(x_T) + x_T^2 n_m''(x_T)\} = 0 \quad (m \geqslant 1). \quad (21)$$

As described by Goodman and Stern,[24] a corresponding set of equations (with variables $y = k_4 R$, $y_L = k_{L3} R$, and $y_T = k_{T3} R$) is obtained when these boundary conditions are applied at the innermost interface. The same boundary conditions (with the slight difference that the tangential stress must be continuous, rather than zero) are also applicable at the intermediate interface between the viscous and elastic shells. However, while the stress in an elastic medium is a function of displacement, in a viscous medium it is a function of velocity. This leads to the appearance of an additional factor $-i\omega$ (due to the harmonic time derivative) premultiplying A_m^2, B_m^2, C_m^2, and D_m^2 in those equations resulting from the continuity of normal and tangential stress. Also, since both viscous and elastic media support shear waves, a further boundary condition applies at the intermediate interface, arising from the continuity of tangential displacement. This yields

$$A_m^2 j_m(z_{L2}) + B_m^2 n_m(z_{L2}) - C_m^2\{z_{T2} j_m'(z_{T2}) + j_m(z_{T2})\}$$
$$- D_m^2\{z_{T2} n_m'(z_{T2}) + n_m(z_{T2})\}$$
$$= A_m^3 j_m(z_{L3}) + B_m^3 n_m(z_{L3}) - C_m^3\{z_{T3} j_m'(z_{T3}) + j_m(z_{T3})\}$$
$$- D_m^3\{z_{T3} n_m'(z_{T3}) + n_m(z_{T3})\} \quad (m \geqslant 1), \quad (22)$$

where $z_{L2} = k_{L2} R_e$, $z_{T2} = k_{T2} R_e$, $z_{L3} = k_{L3} R_e$, and $z_{T3} = k_{T3} R_e$.

In all, ten equations are obtained by applying the boundary conditions at the various interfaces. If the monopole ($m = 0$) term only is considered, the number of equations reduces to six. Goodman and Stern[24] describe a method of tabulating the equations in matrix form, and then solving for the scattered field A_m^1 using Kramer's rule. This proves to be a convenient and accurate procedure for investigating the resonance behavior of the present swimbladder model, and has been adopted for this study. Calculating the elements of the matrix and evaluating the determinant are also readily vectorizable operations, and an efficient algorithm has been implemented in MATLAB to determine the scattering as a function of frequency.

III. RESULTS

In the first three cases studied here the excitation frequencies $k_1 R$ are scaled to the radius R of the innermost boundary of the composite spherical shell. The fourth case models experimental data, and the frequency is given in Hz. The sound speed and density of air are 330 m/s and 0.001 26 g/cc, respectively. The sound speed and density of water are 1500 m/s and 1 g/cc respectively. According to Love,[13] the sound speed and density of fish flesh (represented by the outer of the two shells) are similar to water, and we have used values of 1500 m/s and 1.05 g/cc for fish flesh in this study. The viscosity ξ_2 is allowed to vary within a range of values, with an upper limit of 1200 poise. This appears quite reasonable from the studies of fish tissue data available (see Table II in Ref. 13). We have assumed that the density of swimbladder wall tissue (represented by the inner of the two shells) is the same as fish flesh, i.e., 1.05 g/cc. Measurements made on excised swimbladder tissue from cod show that it has elastic properties similar to soft rubber.[26] However, when stress is applied to a fully inflated swimbladder by the internal musculature within a living fish, we suggest that collateral changes in the rigidity of the swimbladder wall, and the tissues immediately attached to it, also occur. To model the elastic properties of swimbladders, we have assumed that the tissues involved may be represented by an isotropic elastic shell and have adopted values for the elastic moduli λ_3, μ_3 which represent a range of rubber types of varying hardness.[28] As it turns out, the scattering effect of the elastic shell is practically independent of the values of λ_3 applicable to rubbers within the range used, but is strongly determined by the shear rigidity modulus μ_3.

In all of the examples considered in this work, the scattering response is dominated by the monopole term. Careful comparisons showed that the effects of terms higher than $m = 0$ was very small, and could safely be neglected. This is consistent with the ''dominant monopole'' rationale of the spherical swimbladder approach, and also reduced the size of the matrices to be evaluated and, therefore, greatly simplified the calculations.

A. The effect of an elastic shell

Figure 4(a) shows the monopole resonance response of an air bubble enclosed by an elastic shell only (i.e., the viscous shell is absent), at atmospheric pressure. The value of $\lambda_3 = 1149.3 \times 10^6$ N/m^2 (Newtons per square meter), while $\mu_3 = 1.06 \times 10^6$ N/m^2. These values represent a rubber of medium hardness.[28] The leftmost curve in the figure shows the resonance response for an air bubble without a shell. Moving to the right, the second curve shows the response for a bubble enclosed by an elastic shell whose thickness is 1% of the bubble radius. The presence of the shell has three effects on the scattering response. First, the resonance is shifted to a higher frequency. Second, the peak scattered field amplitude is reduced. Third, the Q of the resonance is also reduced. All of these effects show a progressive increase

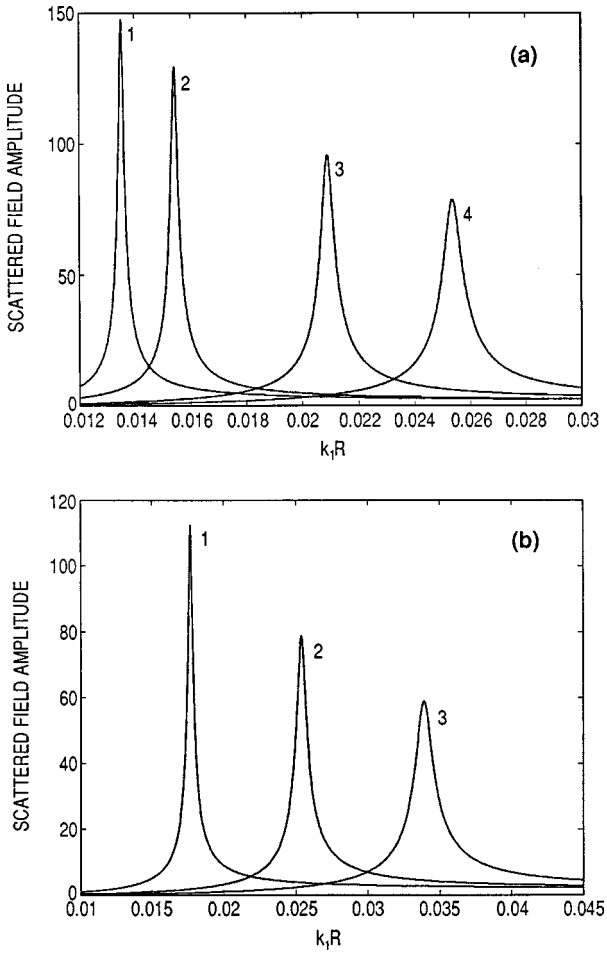

FIG. 4. The effect of an elastic shell. These figures show the monopole resonance of an air bubble enclosed by an elastic shell only. (a) The value of $\lambda_3 = 1149.3 \times 10^6$ N/m^2, and $\mu_3 = 1.06 \times 10^6$ N/m^2. Curve 1 shows the resonance response for an air bubble without a shell. Curve 2 shows the response for a bubble enclosed by an elastic shell whose thickness is 1% of the bubble radius. Curve 3 shows the response for a bubble enclosed by a 5% shell, while curve 4 shows the response for a bubble enclosed by a 10% shell. (b) The thickness of the elastic shell is kept at 10% of the bubble radius. Maintaining $\lambda_3 = 1149.3 \times 10^6$ N/m^2, the shear rigidity μ_3 is increased from 0.3×10^6 N/m^2 (curve 1)$\rightarrow 1.06 \times 10^6$ N/m^2 (curve 2)$\rightarrow 2.22 \times 10^6$ N/m^2 (curve 3).

as the elastic shell becomes thicker. This is indicated by the remaining curves in Fig. 4(a), which represent the resonance responses for air bubbles with 5% and 10% shells. Figure 4(b) shows the response for an air bubble enclosed by an elastic shell of 10% thickness, but of variable rigidity. Maintaining $\lambda_3 = 1149.3 \times 10^6$ N/m^2; μ_3 is increased from 0.3×10^6 N/m^2 (soft rubber)$\rightarrow 1.06 \times 10^6$ N/m$^2 \rightarrow$(medium rubber) 2.22×10^6 N/m^2 (hard rubber). The effects of increasing the shear rigidity are similar to those produced by increasing the shell thickness. Analogous results due to increasing shear rigidity have been reported within a different context by Ye.[29] As mentioned earlier, the effects produced by varying λ_3 within a corresponding range are negligible, and they are not shown here.

B. The effect of a viscous shell

Figure 5 shows the monopole resonance response of an air bubble of 2-cm radius enclosed by a viscous shell only

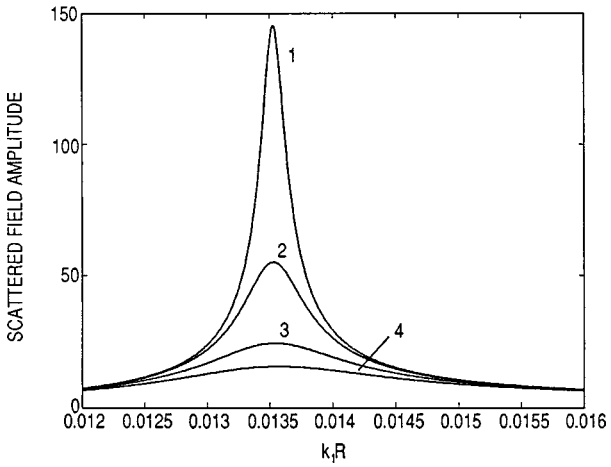

FIG. 5. The effect of a viscous shell. These figures show the monopole resonance of an air bubble enclosed by a viscous shell only. The viscosity ξ_2 is increased progressively from a value of 1 poise (curve 1), to 100 (curve 2), 300 (curve 3), and 500 poise (curve 4).

(i.e., the elastic shell is absent). The radius of the viscous shell is six times the bubble radius, which was shown to produce a damping effect asymptotically close to the largest achievable value. In the figure, the viscosity ξ_2 is increased progressively from a value of 1 poise, to 100, 300, and 500 poise. Again, there are three points to note. First, increasing the viscosity reduces the peak scattered field amplitude of the resonance; and, second, the value of Q is also reduced. Third, and in contrast with the effect of the elastic shell discussed above, the increase in viscosity leads to a minimal and generally negligible increase in the resonance frequency.

C. The combined effect of a viscous shell and an elastic shell

Figure 6 shows the monopole resonance response of an air bubble of 2-cm radius which is enclosed: (i) by an elastic shell (10% thickness; $\lambda_3 = 1149.3 \times 10^6$ N/m^2); and (ii) by a

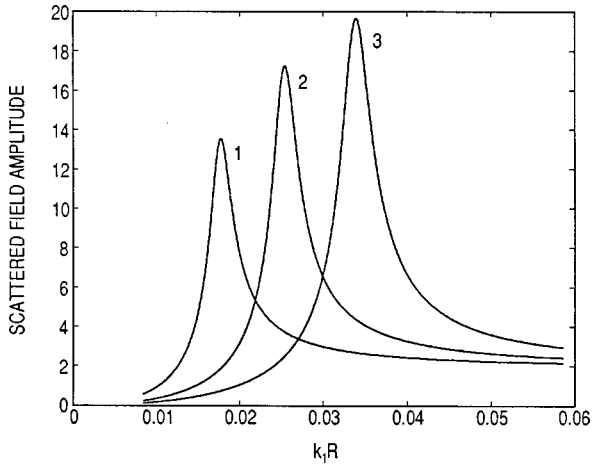

FIG. 6. The effect of concentric viscous and elastic shells. These curves show the monopole resonance response of an air bubble enclosed: (i) by an elastic shell (10% thickness; $\lambda_3 = 1149.3 \times 10^6$ N/m^2); and (ii) by a viscous shell ($\xi_2 = 500$ poise). The shear rigidity μ_3 of the elastic shell is increased from 0.3×10^6 N/m^2 (curve 1)$\rightarrow 1.06 \times 10^6$ N/m^2 (curve 2)$\rightarrow 2.22 \times 10^6$ N/m^2 (curve 3).

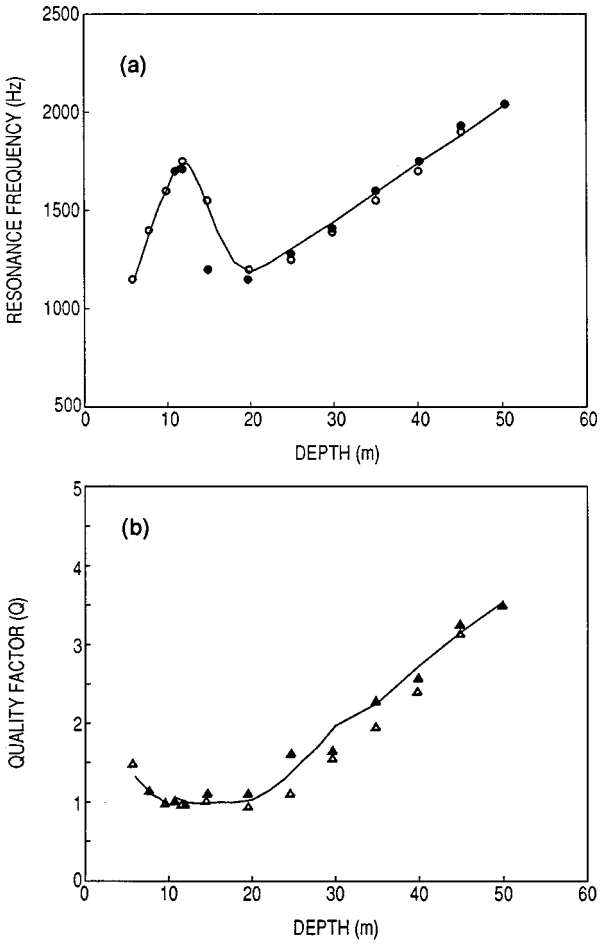

FIG. 7. Result of fitting experimental data for cod. The new viscous-elastic swimbladder model has been used to fit both the resonance frequency data of Sand and Hawkins (Fig. 3), and their corresponding data for the quality factor Q (see Fig. 4 of Ref. 14). (a) The fit to the resonance frequency measurements. (b) The fit to Q.

viscous shell ($\xi_2 = 500$ poise), whose radius is again six times the bubble radius. The three curves indicate the effects of increasing the shear rigidity μ_3 of the elastic shell from 0.3×10^6 N/m$^2 \rightarrow 1.06\times10^6$ N/m$^2 \rightarrow 2.22\times10^6$ N/m^2. These were the same values used to produce Fig. 4(b), but the effects produced are quite different in this case. Again we see the upward shift in the resonance frequency, which takes the same values as in Fig. 4(b). However, the peak value of the scattered field amplitude shows a progressive increase, rather than a decrease. Similarly, the value of Q also shows an increase. In Fig. 4(b), the dominant mechanism affecting the response of the air bubble was the elastic shell, which caused the resonance peak to be both broadened and reduced in magnitude. In Fig. 6, however, the dominant mechanism is the viscosity of the outer shell. In this case, increasing the shear rigidity of the inner elastic shell (which represents a stiffening of the elastic material) appears to introduce a barrier which insulates the air bubble from the damping influence of the viscous medium, thus allowing the bubble to resonate more freely and scatter more sound.

D. Fitting experimental data for cod

The solid lines fitted to the data points in Fig. 7(a) and (b) were obtained by using the composite viscous-elastic swimbladder model presented here. In the modeling, the appropriate radius R of the air bubble at the adaptation depth was determined from other data reported by Sand and Hawkins.[14] The thickness of the elastic shell was 1 mm, and $\lambda_3 = 10^9$ N/m^2. The values of μ_3 and ξ_2 needed to achieve the fits are shown in Fig. 8. At the 11-m adaptation depth, the shear rigidity modulus used was $\mu_3 = 2.15\times10^6$ N/m^2, which achieved enhanced values for the resonance frequency, as indicated in Fig. 4. At depths greater than 11 m the rigidity was rapidly reduced until, at 22 m and below, $\mu_3 = 0.05\times10^6$ N/m^2. At depths less than 11 m, the rigidity was also reduced until, at 6 m, $\mu_3 = 1.2\times10^6$ N/m^2. The frequency increase due to compression, and to the Strasberg–Weston correction, were also incorporated in the modeling.

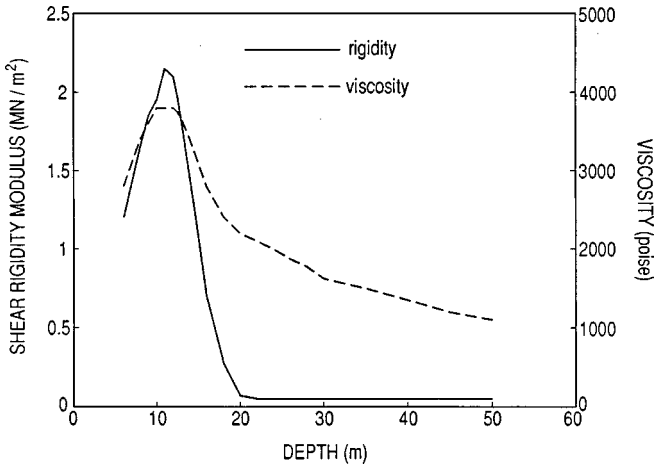

FIG. 8. Variation of shear rigidity modulus and viscosity with depth. The values of μ_3 (solid line, and see lhs vertical scale) and ξ_2 (dashed line, and see rhs vertical scale) needed to fit the resonance frequency and Q data, respectively, for Atlantic cod [Fig. 7(a), (b)] are shown. Note the sharp increase in both μ_3 and ξ_2 at the adaptation depth.

The range of μ_3 values shown in Fig. 8 is quite reasonable, and almost exactly coincides with the range of fish flesh measurements made by Lebedeva,[20] who determined experimental values for the shear modulus lying between 0.01×10^6 N/m^2 and 1.0×10^6 N/m^2. The largest value of μ_3 used, i.e., 2.15×10^6 N/m^2, is an order of magnitude less than the maximum 2.0×10^7 N/m^2 shear modulus value proposed by Sand and Hawkins to fit some of their data (see discussion on pages 811, 812 of Ref. 14). Similarly, the range of values for ξ_2 shown in Fig. 8 falls well within the 1–5000 poise range proposed by Love for use with his model (see Table I in Ref. 13).

What is the physical justification for using a high value of the shear rigidity modulus for an adapted fish, and then reducing μ_3 as the fish is moved deeper or shallower, to fit the data? At the adaptation depth, the swimbladder is regularly inflated. We suggest that, as proposed by Sand and Hawkins, the cod is able to enhance the resonance frequency in this state (probably to stabilize hearing) by creating a tonus in the musculature surrounding the swimbladder, which imparts a stress to the swimbladder wall. To explain the frequency enhancement, we also postulate that, as a result of this stress, there is an associated increase in the rigidity of the swimbladder wall (perhaps by contraction of the attached

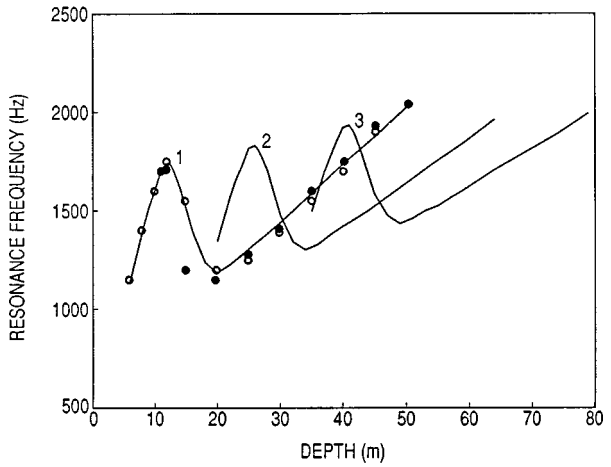

FIG. 9. The effect of increasing adaptation depth. The variation in resonance frequency predicted for the 16-cm cod of Fig. 7 is shown, but now it is initially adapted to three different depths: 11 m (curve 1), 25 m (curve 2), and 40 m (curve 3). Identical values of λ_3, μ_3, and ξ_2 are used in each case. The data points of Fig. 3 are again shown.

drumming muscles[18]). Now, when the water depth is increased below the adaptation depth, the swimbladder is compressed and reduced in size within the body of the cod, and we suggest that the ability of the musculature to sustain the tonus is quickly lost. The consequent reduction in the rigidity of the swimbladder wall leads to a rapid fall in the resonance frequency. Below 26 m, the swimbladder is quite flaccid and the resonance frequency is predominantly determined by compression effects. What happens, however, when the fish is moved to shallower depths? In this case, as the external pressure decreases, the swimbladder tends to expand, and thereby imparts strain to the stiffly toned musculature. As a result, we suggest, the fish is induced to relax the muscular tonus and allow the swimbladder to expand unimpeded within the body cavity. Again, there is a reduction in the rigidity of the swimbladder wall leading to a fall in the resonance frequency.

Sand and Hawkins also performed a sequence of measurements in which the same individual fish was allowed different periods of time to adapt to a number of interim depth locations in the water column, and was then moved up and down from these interim locations to determine the change in resonance frequency produced. The data obtained showed that the resonance frequency varied with depth in basically the same way for each case (i.e., as shown in Fig. 7), except that the peak value of the measured resonance frequency (i.e., at the adaptation depth) increased as the adaptation depth increased. Figure 9 shows the variation in resonance frequency predicted for the same 16-cm cod used for Fig. 7, but now it is initially adapted to three different depths: 11 m, 25 m, and 40 m. In each case, identical values of λ_3, μ_3, and ξ_2 are used (i.e., the same as for Fig. 7). The only difference in the three curves presented in Fig. 9 is the initial adaptation depth, and the range of depths over which the resonance frequency is calculated. The increase in the predicted peak value of the resonance frequency as the adaptation depth is increased, together with the overall shape of the curves, reproduces the behavior observed by Sand and Hawkins.

IV. DISCUSSION

Active control of the swimbladder resonance frequency by fish would seriously impact low-frequency assessments of fish size and abundance by, for example, leading us to believe that they are much smaller and perhaps more numerous than is actually the case. Fortunately, however, there is currently little reason to believe this phenomenon is widespread. Although representatives of many widely different families of fish (see the review by Jones and Marshall[30]) have muscles associated with the swimbladder wall, enhanced resonance frequencies have, so far, only been observed in experimentally held Atlantic cod, *Gadus morhua*.[14,31] Experiments on coalfish, *Pollachius virens*, sprat, *Sprattus sprattus*, herring, *Clupea harengus*, and arctic char, *Salvelinus alpinus*, indicate that the swimbladders of these fish exhibit ''normal'' swimbladder behavior.[31,32] In addition, measurements of the low-frequency resonances of commercial-size fish, in conjunction with fisheries survey estimates of fish type and size, have not indicated any disparity between measured resonance frequencies and those predicted using models which assume a simple resonant bladder (see Table I). Nothing remotely approaching the doubling of the resonance frequency, as Sand and Hawkins observed for Atlantic cod, has so far been reported for any species of fish in the natural environment. Measurements that have been made include those on two members of the cod family Gadidae (blue whiting and Pacific hake), but not the genus *Gadus*. Clearly, measurements on Atlantic cod *in situ* are required if we are to determine whether they exhibit enhanced swimbladder resonance frequencies in their natural state.

Also, from a bioacoustic point of view, it is important to consider whether cod may tension their bladders in order to stabilize hearing ability during periods of stress, such as when placed in an unfamiliar environment or when exposed to unusual sounds (both occurred during the experiments of Sand and Hawkins[14]). Such a phenomenon could explain why measurements on cod in a laboratory setting exhibited enhanced resonance frequencies, and suggests that measurements on undisturbed fish *in situ* probably would not.

V. CONCLUSIONS

A new mathematical/physical model for a fish swimbladder has been developed. The model consists of a spherical air bubble enclosed, first, by an elastic shell (which represents the swimbladder wall), and then by a viscous shell (which represents the surrounding fish flesh). The shear rigidity properties of the inner elastic shell cause the monopole resonance frequency of the bubble to increase. The viscosity of the outer shell causes the resonance to be damped. By introducing physically realistic values for these factors (i.e., values which correspond to those found in actual fish), and allowing reasonable variations, the new model has been used to explain the experimentally measured resonance frequencies and damping rates of acoustic swimbladder resonances in Atlantic cod. The model provides insights into the physi-

TABLE I. Species of fish where measurements of swimbladder resonance *in situ* match predictions from models which assume a simple resonant bladder.

Order Family Species	Common name	Author
Clupeiformes		
Engraulidae		
Engraulis mordax	northern anchovy	Holliday (Ref. 33)
Salmoniformes		
Salmonidae		
Oncorhynchus spp.	Pacific salmon	Nero and Huster (Ref. 34)
Gadiformes		
Gadidae		
Merluccius productus	Pacific hake	Nero *et al.* (Ref. 35)
Micromesistius poutassou	blue whiting	Love (Ref. 9)
Macrouridae		
Coryphaenoides spp.	grenadiers	Nero *et al.* (Ref. 36)
Scorpaeniformes		
Scorpaenidae		
Sebastes spp.	rockfish	Holliday (Ref. 33)
Sebastes mentella	deepwater redfish	Love (Ref. 9)
Perciformes		
Carangidae		
Trachurus symmetricus	jack mackerel	Holliday (Ref. 33)

ological mechanisms by which fish may actively control and enhance the resonance frequencies of their swimbladders to improve hearing, and how this control can be lost under increased water pressure as the fish is moved to greater depths.

ACKNOWLEDGMENTS

The authors would like to thank C. S. Clay and R. H. Love for helpful discussions. This work was supported by the U.S. Office of Naval Research.

[1] N. B. Marshall, ''Bathypelagic Fishes as sound scatterers in the ocean,'' J. Mar. Res. **10**, 1–17 (1951).
[2] G. B. Farquhar, ''Biological sound scattering in the oceans: a review,'' in *Oceanic Sound Scattering Prediction*, edited by N. R. Andersen and B. J. Zahuranec (Plenum, New York, 1977), pp. 493–527.
[3] E. Ona, ''Physiological factors causing natural variations in acoustic target strength of fish,'' J. Mar. Biol. Ass. U.K. **70**, 107–127 (1990).
[4] C. Feuillade and M. F. Werby, ''Resonances of deformed gas bubbles in liquids,'' J. Acoust. Soc. Am. **96**, 3684–3692 (1994).
[5] Z. Ye and E. Hoskinson, ''Low-frequency acoustic scattering from gas-filled prolate spheroids in liquids. II. Comparison with the exact solution,'' J. Acoust. Soc. Am. **103**, 822–826 (1998).
[6] M. Strasberg, ''The pulsation frequency of nonspherical gas bubbles in liquids,'' J. Acoust. Soc. Am. **25**, 536–537 (1953).
[7] D. E. Weston, ''Sound propagation in the presence of bladder fish,'' in *Underwater Acoustics*, edited by V. M. Albers (Plenum, New York, 1967), Vol. 2, Chap. 5, p. 59, Eq. (13). Please note that this equation contains a typographical error. It is correctly quoted in Ref. 13, Eq. (8).
[8] I. B. Andreeva, ''Scattering of sound by air bladders of fish in deep sound-scattering ocean layers,'' Sov. Phys. Acoust. **10**, 17–20 (1964).
[9] R. H. Love, ''A comparison of volume scattering strength data with model calculations based on quasi-synoptically collected fisheries data,'' J. Acoust. Soc. Am. **94**, 2255–2268 (1993).
[10] W. E. Batzler and G. V. Pickwell, ''Resonant acoustic scattering from gas-bladder fishes,'' in *Proceedings of an International Symposium on Biological Sound Scattering in the Ocean*, edited by G. B. Farquhar (Maury Center for Ocean Science, Rep. 005, Washington, DC, 1970), pp. 168–179.
[11] B. S. McCartney and A. R. Stubbs, ''Measurements of the acoustic target strengths of fish in dorsal aspect, including swimbladder resonance,'' J. Sound Vib. **15**, 397–420 (1971).
[12] Z. Ye and D. M. Farmer, ''Acoustic scattering from swim-bladder fish at low frequencies,'' J. Acoust. Soc. Am. **96**, 951–956 (1994).
[13] R. H. Love, ''Resonant acoustic scattering by swimbladder-bearing fish,'' J. Acoust. Soc. Am. **64**, 571–580 (1978).
[14] O. Sand and A. D. Hawkins, ''Acoustic properties of the cod swimbladder,'' J. Exp. Biol. **58**, 797–820 (1973).
[15] A. D. Hawkins, ''Fish sizing by means of swimbladder resonance,'' Rapp. P.-v. Réun. Cons. int. Explor. Mer. **170**, 122–129 (1977).
[16] C. H. Thompson and R. H. Love, ''Determination of fish size distributions and areal densities using broadband low-frequency measurements,'' ICES J. Mar. Sci. **53**, 197–201 (1996).
[17] C. S. Clay and J. K. Horne, ''Acoustic models of fish: The Atlantic cod (*Gadus morhua*),'' J. Acoust. Soc. Am. **96**, 1661–1668 (1994).
[18] A. D. Hawkins, ''Underwater sound and fish behaviour,'' in *Behaviour of Teleost Fishes*, edited by T. J. Pitcher (Chapman and Hall, London, 1993), 2nd ed., pp. 136–141.
[19] O. Sand and A. D. Hawkins, ''Measurements of swimbladder volume and pressure in the cod,'' Norw. J. Zool. **22**, 31–34 (1974).
[20] L. P. Lebedeva, ''Measurement of the dynamic complex shear modulus of animal tissues,'' Sov. Phys. Acoust. **11**, 163–165 (1965).
[21] M. Minnaert, ''On musical air-bubbles and the sounds of running water,'' Philos. Mag. **16**, 235–248 (1933).
[22] C. S. Clay and H. Medwin, *Acoustical Oceanography* (Wiley, New York, 1976), pp. 194–203 and pp. 461–465.
[23] V. C. Anderson, ''Sound scattering from a fluid sphere,'' J. Acoust. Soc. Am. **22**, 426–431 (1950).
[24] R. R. Goodman and R. Stern, ''Reflection and transmission of sound by elastic spherical shells,'' J. Acoust. Soc. Am. **34**, 338–344 (1962).
[25] C. Feuillade, R. H. Love, and M. F. Werby, ''Characteristic resonance signatures for acoustical scattering from fish,'' in *Automatic Object Recognition IV*, edited by Firooz A. Sadjadi, Proc. SPIE **2234**, 120–126 (1994).
[26] V. Mohr, ''On the constitution and physical-chemical properties of the connective tissue of mammalian and fish skeletal muscle,'' PhD. thesis, University of Aberdeen, 1971.
[27] P. S. Epstein and R. R. Carhart, ''The absorption of sound in suspensions and emulsions. I. Water fog in air,'' J. Acoust. Soc. Am. **25**, 553–565 (1953).
[28] R. J. Crawford, *Plastics and Rubbers Engineering Design and Applications* (Mechanical Engineering, London, 1985), pp. 21–23.
[29] Z. Ye, ''On sound scattering and attenuation of Albunex® bubbles,'' J. Acoust. Soc. Am. **100**, 2011–2028 (1996).
[30] F. R. H. Jones and N. B. Marshall, ''The structure and functions of the teleostean swimbladder,'' Biological Reviews of the Cambridge Philosophical Society, **28**, 16–83 (1953).
[31] A. Lovik and J. M. Hovem, ''An experimental investigation of swimbladder resonance in fishes,'' J. Acoust. Soc. Am. **66**, 850–854 (1979).
[32] G. Sundnes and O. Sand, ''Studies of a physostome swimbladder by resonance frequency analyses,'' J. Cons. Int. Explor. Mer. **36**, 176–182 (1975).
[33] D. V. Holliday, ''Resonance structure in schooled pelagic fish,'' J. Acoust. Soc. Am. **51**, 1322–1332 (1972).
[34] R. W. Nero and M. E. Huster, ''Low frequency acoustic imaging of Pacific salmon on the high seas,'' Can. J. Fish. Aquat. Sci. **53**, 2513–2523 (1996).
[35] R. W. Nero, C. H. Thompson, and R. H. Love, ''Low-frequency acoustic measurements of Pacific hake, *Merluccius productus*, off the west coast of the United States,'' Fishery Bulletin **96**, 329–343 (1998).
[36] R. W. Nero, C. H. Thompson, and R. H. Love, ''Abyssopelagic grenadiers: The probable cause of low frequency sound scattering at great depths off the Oregon and California coasts,'' Deep-Sea Res. **44**, 627–645 (1997).

Modeling the propagation from a horizontally directed high-frequency source in shallow water in the presence of bubble clouds and sea surface roughness

Guy V. Norton
Naval Research Laboratory, Stennis Space Center, Mississippi 39529-5004

Jorge C. Novarini
Planning Systems, Inc., 21294 Johnson Road, Long Beach, Mississippi 39560-9702

Richard S. Keiffer
Naval Research Laboratory, Stennis Space Center, Mississippi 39529-5004

(Received 30 April 1997; accepted for publication 20 February 1998)

Among the many factors affecting the propagation of sound in shallow water, surface-generated microbubbles have remained virtually unexplored. The collection of microbubbles, bubbles which usually do not result in a uniform layer, presents a complex structure that varies not only in depth but also in range, and can be characterized as a collage of bubble clouds. A numerical procedure is developed in which the bubble clouds are modeled following a classification scheme proposed by Monahan [*Natural Physical Sources of Underwater Sound*, edited by B. V. R. Kerman (Kluwer Academic, Dordrecht, 1993), pp. 503–517]. An effective complex index of refraction of the bubble mixture is calculated for each point of the resulting range-dependent environment. The combined effect that the sea surface roughness and the bubbly environment have on forward propagation is then modeled through a high fidelity model [Norton *et al.*, J. Acoust. Soc. Am. **97**, 2173–2180 (1995)] which combines a finite element Parabolic Equation model with conformal mapping to handle surface roughness. The case of a horizontally directed source, operating at 20 kHz for a single realization of a shallow water environment is analyzed in detail. The presence of the bubble clouds severely affects the amplitude near the surface, but their influence rapidly diminishes in depth. For the case considered, the surface roughness, which has little effect on the transmission loss of the propagating field, is, however, responsible for interference effects of the forward field observed throughout the water column, while ignoring the rough surface and bubble clouds leads to a 12–15 dB error in the acoustic field near the surface, at a range of 150 m. To assume a uniformly stratified (range independent) bubble layer results in large errors near the surface at the location of the high void fraction packets, but is an acceptable approximation away from these features. [S0001-4966(98)01906-7]

PACS numbers: 43.30.Hw, 43.30.Re, 43.30.Es, 43.30.Dr [DLB]

INTRODUCTION

This paper is concerned with a procedure to model the combined effects that a near-surface bubbly environment and a rough air/sea interface have on high-frequency propagation in shallow water. Here we use ''high-frequency,'' sometimes ''moderate-to-high-frequency,'' to refer to the band between 4.0 and 200.0 kHz. We use ''shallow water'' to indicate that the propagation distances are large compared to the water depth. It is well known that, for wind speeds exceeding a few meters per second, microbubbles are introduced into the underwater environment as the result of waves breaking at the sea surface. The collection of microbubbles due to a single breaking wave evolves in shape and composition (i.e., the bubble spectrum) in a complex manner, eventually becoming indistinguishable from the bubbles that are due to temporally and spatially nearby breaking waves. The aim of this paper is to investigate the possible effects that a combination of surface roughness and bubble clouds have on transmission loss in high-frequency shallow water propagation, under conditions where the interactions with the boundaries are intended to be minimized.

One of the earliest comprehensive sets of bubble data measured at sea (Johnson and Cook, 1979) provided long time averages (10–20 min) for the bubble population density as a function of bubble radius at a few points in depth. Eventually these measurements led to empirical models for the bubble spectrum (Wu, 1981; Novarini and Bruno, 1982; Hall, 1989) that were wind speed and depth dependent but range independent. Taken together with standard approximate theories for acoustic propagation in a tenuous bubbly medium (Clay and Medwin, 1977), the bubble spectrum and the acoustic frequency allow for the specification of an ''effective fluid'' for the water bubble mixture. In this approximation, the impact of the bubbles on acoustic propagation is modeled by introducing a complex sound speed. The chief advantage of the effective fluid is that it can be readily used by standard ocean acoustic propagation models. Hall (1989) gives a good synopsis of those efforts published prior to 1989 aimed at investigating the acoustic implications of a range independent bubble layer on high-frequency propagation.

In the early 80s, high-frequency upward looking sonar

(Thorpe, 1982) began producing images confirming that the bubble populated region near the sea surface was spatially nonuniform, consisting of assemblages of microbubbles from current and previous breaking activity. Since then, numerous measurements of the bubbles have been made. Generally speaking, these more recent data continue to point to a bubble spectrum that varies in space and time. While almost all of these measurements have been in deep water, where the surface waves do not ''sense'' the sea floor, more recently there has also been a strong interest in the acoustic impact of bubbles in shallower water. Unfortunately, there is at this time a significant lack of information about bubbles in shallow water.

There are three main modeling aspects to the work presented in this paper. First, a model is described for the simulation of a spatially varying, temporally ''frozen'' bubbly environment. Because there is a lack of ready-to-use models quantifying the bubble population in general and in particular within the bubble clouds, we have coupled a variety of measurements with a description offered by Monahan (1993) for the stages of evolution of the bubble clouds in deep water. Because of the lack of information on bubbles in shallow water we adopted this model for the bubbly environment in shallower water [intermediate depth water according to Kinsman (1965)] but away from the surf zone. The surf zone is excluded because in that region the dynamics of the water mass is extremely complex and bubble generation and transport are greatly affected by the surf. At this time, no reliable information is available to model such an environment. This interim model allows bubbles to enter into the modeling in a comprehensive manner and will be updated when a more suitable bubble distribution becomes available.

Once the bubbly environment is simulated, another model based on standard approximate theory for propagation through tenuous bubbly media (Clay and Medwin, 1977), is used to replace the bubbly environment with an acoustically equivalent fluid medium. Finally, the combined parabolic equation and conformal mapping model (Norton *et al.*, 1995) is used to calculate the combined propagation loss and energy redistribution that results when this effective fluid is below a rough sea surface. While the modeling presented in this study is for single realizations of a bubbly environment and rough air/sea interface, the modeling technique allows for the calculation of the statistical moments of the acoustic field through ensemble averages. However, statistical analysis will not be pursued here. The effect of introducing sea surface roughness and bubble clouds together within a propagation model in a mathematically consistent manner, represents a first step toward the understanding of the magnitude of their contributions in forward propagation, and the error incurred when resorting to strong approximations.

With this modeling approach the rough surface, or the bubbles, or both, can be added or removed from the environment and the changes in the acoustic field noted. In the frequency range of interest, the presence of the microbubbles effectively changes the sound speed, which perturbs the surface ensonification, and introduces additional attenuating phenomena. A realistic analysis of the impact that the sea surface roughness has on sound propagation cannot be made without including them. The current lack in the literature of a complete modeling approach for such an analysis is the main motivation for this paper.

Since the papers' aim is to elucidate the role of a range-dependent bubble layer in conjunction with the sea surface roughness, the bottom will be assumed flat. To include bottom roughness posses no problem when propagating via a PE method, since the roughness can be included in a trivial manner as changes in bathymetry. A formal approach to the high-frequency, shallow water problem has been recently outlined by Uscinski (1995). In this approach, based also on the parabolic approximation, the propagating field interacting with two rough boundaries is obtained by solving two coupled integral equations. However, the method is limited to a linear velocity gradient in the water column, and only qualitative results are shown in the paper. In a recent study, Rouseff and Ewart (1995) have verified that at high wind speeds the surface and bottom scattering should be considered coupled mechanisms, where the sea surface roughness randomizes the deterministic nature of the bottom, even at bottom roughness smaller than the acoustic wavelength.

I. SIMULATION OF A SPATIALLY VARYING BUBBLE SPECTRUM

A. Background

Models that describe a horizontally averaged subsurface bubble layer have been available to acousticians for over a decade. They provide a dependence of the bubble size spectrum (i.e., the number of bubbles per unit volume that have radii within a unit increment in radius) on basic parameters (wind speed and depth). Hall (1989), utilizing published ocean measurements and previous parameterizations (Crowther, 1980; Wu, 1981; Novarini and Bruno, 1982), set forth a comprehensive bubble spectrum for a horizontally averaged bubble layer, suitable for use in acoustic modeling. Most recently, Novarini and Norton (1994) updated Hall's model by modifying the small radii part of the spectrum to include more recent findings on bubble spectra.

To better simulate a real ocean environment, a tentative model for a range- and depth-dependent bubble environment must be adopted. The development of such a model involves describing the bubble spectrum inside and outside the bubble clouds, modeling the shape of the bubble clouds, and modeling the spatial distribution of breaking events that give rise to the bubble clouds. Since there is no single set of measurements from which to draw all the information necessary to develop this model, the observations, parameterizations, and (in some cases) speculations from a number of oceanographic papers have been used. On the other hand, as an overall framework for the different stages of evolution of bubble clouds, we have followed the description proposed by Monahan (1988, 1993) and Monahan and Lu (1990). To our knowledge it is the only comprehensive model available in the literature describing the various stages of development of a bubble cloud, from its genesis under a breaking wave to its dissipation into the weak background.

In Thorpe's 1982 paper revealing the range dependence of the bubble layer, the bubble clouds were identified as one

TABLE I. Estimated properties of the bubble formations (Monahan, 1993).

	α-plume	β-plume	γ-plume	Background
Horizontal area (m^2)	0.2–1	8–50	1–500	⋯
Time scale (s)	1.0	3.5–4.3	100–1000	⋯
Void fraction	4×10^{-2}–8×10^{-2}	10^{-4}–10^{-3}	10^{-7}–10^{-6}	10^{-9}–10^{-8}
Bubble density (m^{-3},μ^{-1}) at 100 μ	10^{7}–10^{8}	10^{5}–10^{6}	10^{2}–10^{4}	10

of two types: columnar clouds and billow clouds. The columnar type, also referred to as plumes, appear to be roughly v-shaped, decreasing in width with depth (Crawford and Farmer, 1987). These are the type described by Monahan and modeled here. Henceforth, to make the distinction clear and more compact, we shall drop the term ''columnar clouds'' and refer to them as plumes.

B. Stages of a bubble plumes life

Monahan (1988, 1993) discretized the time evolution of a bubble plume into three stages, which he labeled α, β, γ, and associated two of them with two stages of white caps (type A: crest of the spilling breaker; type B: foam patch). The α-plumes are the subsurface extension of the spilling crest and therefore are associated with type A whitecaps. These plumes have the highest void fractions (order of 10^{-1}–10^{-2}), but are very small in size and have a very short lifetime (less than 1 s). The whitecap type A evolves into a foam patch (whitecap type B) and associated with them are the β-plumes (void fraction about 10^{-3}–10^{-4}). The β-plumes that are attached to the foam patch, are much bigger than the α-plumes and have a longer lifetime (about 4 s). The β-plume then detaches from the foam patch and evolves into a γ-plume. The γ-plume has a lower void fraction, much larger dimension, and a longer lifetime (about 15 min). The γ-plume drifts freely and may be affected by circulation processes (such as Langmuir cells). The γ-plumes then decay into a weak, quasi-uniform background layer. Both the β-plumes and the γ-plumes are modeled as conical intrusions with the cross section decreasing exponentially with depth. At any given time, under a conditions were braking waves occur, there is always a collection of plumes in different stages of development.

C. Bubble spectra

Monahan (1988) assigned a tentative spectral shape to the different stages of the plumes evolution, but does not provide an explicit functional form for the different stages. Those spectral shapes are essentially identical to each other, resembling a Johnson and Cooke spectrum, but the bubble concentration (and consequently the void fraction) changes. Although the different stages are described by Monahan, they were not fully parameterized to the extent needed for acoustic modeling. However, Monahan (1993) tabulated the main characteristics of the different clouds, which serves as a classification scheme. Based on Monahan's ideas, the different stages of the bubble clouds will be parameterized in a manner similar to the work done earlier for a horizontally stratified bubble layer. This parameterization may serve in the interim. However, it should be mentioned that some of the more recent data (Medwin and Breitz, 1989; Cartmill and Su, 1993) indicate that the spectral slope changes over the life span of a bubble plume. More precisely, measurement directly under breaking waves show shallower spectral slopes for the larger bubbles.

Besides the lack of functional form for the specific stages of the plumes, another shortcoming of Monahan's model for bubble population for use in acoustic propagation modeling is the lack of depth dependence of the bubble spectra. Away from the surface the bubble concentration not only decreases for all radii but also the spectral slope changes (Hall, 1989). Based on the fact that near the surface Monahan's prediction for the bubble concentration agrees with Johnson and Cooke's data at large radii, we have adopted a scheme similar to that proposed by Hall for the ''average bubble layer'' in order to parameterize Monahan's plumes, since it fits the same data for large bubbles and prescribes a dependence with depth that satisfies the dependence shown by those data sets.

Hall's model is modified to include a -4 power for the spectral slope for small bubbles (smaller than about 50 μm). The plateau in Hall's model is removed because it represents the peak in Johnson and Cooke's data set (1979), which seems to be an artifact of the photographic technique. The bubble density within the different structures (β-plumes, γ-plumes, and background layer) will be modeled by changing the constants so as to fit Monahan's reference points for the corresponding structure (bubble density at a radius of 100 μm and void fraction; see Table I).

The generic functional form for the bubble density spectra of the different structures can be written as (Hall, 1989)

$$n(a,z,u_{10}) = N_0 G(a,z) Y(z) U(u_{10}), \tag{1}$$

where u_{10} is the wind speed measured 10 m above the surface. The function $G(a,z)$ has the form (Novarini and Norton, 1994)

$$G(a,z) = \begin{cases} 0, & a < 10 \ \ \mu\text{m}, \\ (a_{\text{ref}}/a)^{4.0}, & 10 \ \ \mu\text{m} \leqslant a \leqslant a_{\text{ref}}, \\ (a_{\text{ref}}/a)^{p(z)}, & a > a_{\text{ref}}, \end{cases} \tag{2}$$

where a is the bubble radius in μm. The reference radius (a_{ref}) and the spectral slope $p(z)$ are obtained from Hall (1989),

$$a_{\text{ref}} = 54.4 + (1.98)z, \tag{2a}$$

$$p(z) = 4.37 + (z/2.55)^2, \tag{2b}$$

where z is the depth in meters and the radius is in μm. In this work, a_{ref} is the radius at which the spectral slope changes

from -4 to $-p(z)$ (identified as radius a_2 in Hall's paper). The spectrum truncates at 10 μm because of the uncertainty of its functional form for smaller radii.

The constant N_0 is the value of $n(a,z,u_{10})$ at the surface, for the reference radius and the reference wind speed (13 m/s). For the γ-plume, we chose the value used by Hall to fit Johnson and Cooke's data which, as explained before, are long time averages and should be close to the value representing the γ-plumes (since they have the longest lifetime). Thus $N_{0\gamma}=1.6\times10^4$ m$^{-3}(\mu\text{m})^{-1}$. For a radius of 100 μm and a wind speed of 13 m/s, this results in a bubble population density of $n=1.1\times10^3$ m$^{-3}(\mu\text{m})^{-1}$, and void fraction, $V=2.0\times10^{-6}$ at the surface (1000 μm was the maximum bubble radius used in the integration). For the β-plume, a larger concentration and void fraction are required to satisfy Monahan's classification. We chose $N_{0\beta}=1.6\times10^6$ m$^{-3}(\mu\text{m})^{-1}$ which, under the same conditions, leads to $n=1.0\times10^5$ m$^{-3}(\mu\text{m})^{-1}$, and $V=2.0\times10^{-4}$. In Monahan's scheme the resident background bubble layer is assumed to be very weak and uniform. In this case we adopted $N_{0\mathbf{bk}}=1.6\times10^2$ m$^{-3}(\mu\text{m})^{-1}$, which leads to $n=1.0\times10^1$ m$^{-3}(\mu\text{m})^{-1}$, and $V=2.0\times10^{-8}$. These values are within the limits suggested by Monahan (see Table I).

In Monahan's description, the β-plume should be uniformly populated. Therefore, the function $Y(z)$ is set equal to unity and the values of a_{ref} and $p(z)$ correspond to $z=0$ m. The maximum depth allowed for the β-plume is wind speed dependent and is set to one-half of the significant wave height assuming a fully developed sea described by a Pierson–Moskowitz spectrum (Pierson and Moskowitz, 1964). For the γ-plume and the background layer, the function, $Y(z)$ is assumed to have the form given by Hall which resulted from fitting the depth dependence of Johnson and Cooke's and Thorpe's data:

$$Y(z,u_{10})=\exp\left(\frac{-z}{LW(u_{10})}\right), \tag{3}$$

with

$$LW(u_{10})=\begin{cases}0.4, & u_{10}<7.5 \text{ m/s},\\ 0.4+0.115(u_{10}-7.5), & u_{10}\geqslant 7.5 \text{ m/s}.\end{cases} \tag{4}$$

The factor $U(u_{10})$ in Eq. (1) is given by (Hall, 1989),

$$U(u_{10})=(u_{10}/13.0)^3. \tag{5}$$

Figure 1 shows the predicted bubble concentration for a γ-plume as prescribed by the present model for a 13-m/s wind at $z=0.25$ m. Also shown is Monahan's prediction [Monahan, 1993, Eq. (5)] for the average bubble population ''just underneath the surface'' for a 13-m/s wind speed assuming dirty bubbles in the calculation of their rise velocities and three jet-droplets per bursting. Monahan's spectrum is plotted only over its approximate range of validity (25 μm $<a<$ 300 μm). Also shown in the figure are the spectra for the corresponding β-plume and the background layer.

Note that the α-plumes are not included in the modeling. Although they present the highest void fraction, their life span is very short (less than 1 s). In addition they are very small in size (less than 1 m^2 in area and a few centimeters in depth) and are attached to the breaking crest. Thus the α-plumes and breaking crest constitute a single entity. Since the numerical surfaces do not include breaking waves, the α-plumes are not included in the model. They constitute isolated scatters embedded (buried) in the surface roughness that, because of the size, will not affect the index of refraction below the troughs of the surface. Although they might play a role in some direct path scattering problems, they are not expected to play any significant role in high-frequency waveguide propagation.

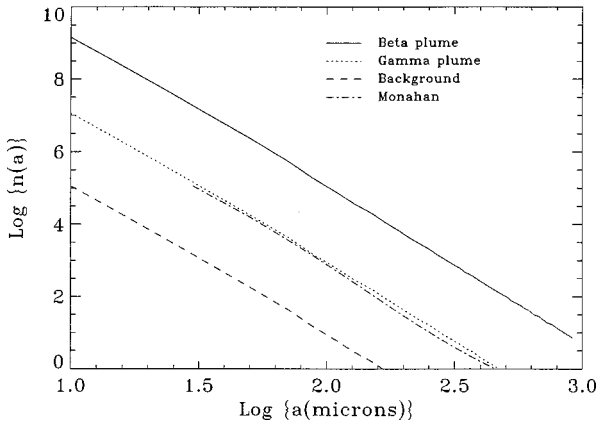

FIG. 1. Predicted bubble concentration for a γ-plume with a 13.0 m/s wind at $z=0.25$ m.

D. Spatial distribution of the plumes

To complete the picture we have been synthesizing we need to specify the relative location of the plumes, their size, and geometrical aspect. In this work, we will limit ourselves to the one-dimensional (1-D) problem. Staying within the framework of Monahan's description, where the β-plumes are attached to the type B whitecap (foam patch), the average spacing between β-plumes (S_β) can be obtained from the average spacing between foam patches, which is given by (Wu, 1992),

$$S_\beta=237.0(u_{10})^{-1.07}. \tag{6}$$

The area of the of the foam patch determines the size (or equivalent length in this 1-D case) of the β-plume at the surface. From Bondur and Sharkov (1982) the area (m^2) of the foam patch can be estimated from:

$$A_p=17.0+0.0307(u_{10}-5.0)^2, \tag{7}$$

and so the equivalent length (m) of the β-plume at the surface is given by $L_\beta(0)=(A_p)^{1/2}$.

Monahan hypothesized that the β-plume has a cross section that decays exponentially with depth, with an e-folding depth of approximately 0.5 m. Therefore, the equivalent length of the β-plume as a function of depth is given by

$$L_\beta(z)=[A_p]^{1/2}\exp(-z/0.5). \tag{8}$$

The γ-plumes have a lifetime much longer than the originating breaking wave; they drift around and can be found almost everywhere. For practical purposes it can be assumed that close to the surface they are contiguous to each other. From Monahan's parameterization, the area of the γ-

plume at the surface, can be estimated to be about nine times that of the β-plume; hence, its equivalent length at the surface is three times that of the 1-D β-plume. Concerning their shape, Monahan described them as having a cross section decaying exponentially with depth. Since for the γ-plume the concentration changes with depth, he adopted an e-folding depth based on Thorpe's measurements of the average acoustic scattering cross section versus depth. Along the same line, and based on the same arguments involved in getting the spectral form of the γ-plumes, we adopt as the e-folding depth for the area that of the bubble population (LW). Thus the equivalent length for the 1-D γ-plume is assumed to decay with depth as:

$$L_\gamma(z) = 3.0[A_p]^{1/2} \exp[-z/LW(u_{10})]. \tag{9}$$

Since no statistical analysis of the acoustic field is pursued here, the deterministic environment used in the propagation model will consist of a single realization of a stochastic environment. Therefore, it is necessary to introduce statistical variations in the description of the clouds. These fluctuations in spacing, size, and concentration also avoid spurious effects that may be introduced by a strict periodicity that should not occur in a natural environment. For example, within each bubble plume category (γ-plume, β-plume) the bubble concentration will change from plume to plume, the e-folding depth will fluctuate, the size of the foam patch will change and the spacing between plumes will also be randomly distributed. This was done adopting Gaussian and uniform deviates with different variances. However, since no statistical analysis is pursued in this paper, the chosen statistics are irrelevant.

II. SPECIFICATION OF AN EFFECTIVE FLUID MEDIUM

The sound speed in a bubbly media can be characterized by a complex number the real part of which provides the phase velocity and the imaginary part leads to the attenuation. The effective complex sound speed in a bubbly mixture (c_{eff}) can be calculated as (Hall, 1989)

$$c_{\text{eff}}^{-2} = [(1-V)\rho_w + V\rho_{\text{gas}}][(1-V)K_W + \Delta K], \tag{10}$$

where K_W is the compressibility of the water; ρ_w and ρ_g are the densities of water and air, respectively; V is the fractional volume occupied by bubbles; and ΔK is the complex compressibility introduced by the bubbles. From Clay and Medwin (1977), ΔK is given by

$$\Delta K(f,z) = \frac{1}{f^2 \boldsymbol{\rho}_w \boldsymbol{\pi}} \int_{a_{\min}}^{a_{\max}} \frac{n(a)a(Y^2 - 1 - i\boldsymbol{\delta})}{(Y^2-1)^2 + \boldsymbol{\delta}^2}\, da \tag{11}$$

with $Y = f_r/f$.

The resonant frequency f_r of the bubbles and the damping constant δ are calculated with due regard to thermal and viscous effects. The reader is referred to Clay and Medwin for details and numerical values of the parameters involved.

We will refer to the phase velocity that occurs in the presence of the bubbles as the perturbed sound speed c_b which is given

$$c_b = \text{Re}\{c_{\text{eff}}\}, \tag{12}$$

where Re denotes the real part, and the attenuation coefficient (in dB/m) is given by

$$\alpha_b = \left(\frac{20.0}{\ln(10.0)}\right) \text{Im}\left\{\frac{1.0}{c_{\text{eff}}}\right\}, \tag{13}$$

where Im denotes the imaginary part.

For low void fractions ($V \ll \rho_{\text{gas}}/\rho_w$), say for void fractions smaller than 10^{-6}, Eq. (10) can be simplified to

$$c_{\text{eff}}^{-2} = {c_0}^{-2} + \Delta K. \tag{14}$$

This approximation has been widely used for the ''uniform background bubble layer.'' However, when dealing with void fractions typical of the beta β-plume Eq. (10) should be used instead of Eq. (14).

In the calculation of c_{eff}, the maximum bubble radius at the surface is set to 1000 μm. We have assumed that the maximum bubble radius decreases with depth in the manner specified by Wu (1981),

$$a_{\max}(z) = a_{\max}(0)\exp\left(\frac{-z}{4.1}\right). \tag{15}$$

The calculation of c_{eff} includes the contribution from bubbles of all radii (not just the resonate bubbles), with due regard to viscous and thermal effects. Multiple scattering between bubbles is ignored because, at the void fractions involved in the simulation (less than 10^{-4}), it has been shown they have no significant effect on the complex sound speed (Feuillade, 1995).

III. MODELING PROPAGATION IN A OCEAN WAVEGUIDE WITH A ROUGH SEA SURFACE

For details on the conformal mapping (CM) technique the reader is referred to Dozier (1984) for the original implementation and to Norton *et al.* (1995) concerning its current implementation in the split-step Pade solution for the parabolic equation method (EFEPE) (Collins, 1993). The technique for propagating in an ocean waveguide with sea surface roughness has been validated by Norton *et al.* (1995) through comparisons with a full wave scattering model for the case of periodic surfaces, as well as for single realizations of randomly rough surfaces having a power spectrum characteristic of a sea surface. The method has also been applied to study the effect of sea surface roughness on low-frequency (400 Hz, 800 Hz) propagation, for a point source in a realistic shallow water environment (Norton and Novarini, 1996). In that study it was found that when using a point source where strong upper refracting conditions exist (which will be the case when plumes are present), coherence effects and energy redistribution cannot be ignored. From this it was noted that the results from a simple procedure which attempts to incorporate the effect of the surface roughness through a loss mechanism will be in error.

Although the paper focuses on the combined effect of surface roughness and bubble plumes, it should be made clear that in this simulation the bubble plumes are uncoupled from the rough surface. In reality, a young bubble plume (α- and β-plumes in this paper) is originally attached to a breaking wave. However, as explained elsewhere, the numerical

surfaces do not actually include breaking waves, since they are created through a linear filtering technique. Therefore, in the present modeling effort, the β-plumes are positioned under an arbitrary feature of the surface relief, since the sharp breaking crest is missing. The lack of breaking waves should not affect the forward scattered field, which is mainly controlled by the rms surface height and by the long surface waves, which are adequately included in the surface spectrum. However, it should be pointed out that the plumes (β or γ) are attached to the surface profile and not to an imaginary average flat plane.

The rough surface was generated by a standard linear filtering technique, where a set of random numbers (1-D white surface) is passed through a filter whose transfer function (in the wave number domain) is given by the square root of the desired power density spectrum of the output surface. Since the authors are not aware of a wave spectrum for shallow water fully parameterized to use in acoustics a deep water spectrum is adopted, with the safeguard of modeling a moderate wind speed such that the resulting rms height is just a small fraction of the water depth. In this case we chose the Pierson–Moskowitz spectrum (Pierson and Moskowitz, 1964) for a fully developed wind driven sea surface

$$E(\omega)=\frac{\alpha g^2}{\omega^5}\exp\left[-\frac{\beta g^4}{\omega^4 u^4}\right], \tag{16}$$

where ω is the angular frequency (rad/s) of the surface waves, α is the so called Phillips' constant (8×10^{-3}), and $\beta=0.74$. The frequency (scalar) spectrum was converted to the (scalar) wave number domain by imposing the conditions of equal variance (total energy) symmetry on the wave number spectrum, and invoking the dispersion relationship for deep water ($\omega^2=gK$). The latter was adopted for simplicity. The use of the dispersion relationship for deep water, although consistent with the chosen spectrum, is a poor approximation for the dispersion that occurs in shallow water (the use of which makes the spectral transformation cumbersome). The approximation in the dispersion relationship, although crude, is of secondary importance for the present application. In forward propagation the role of the surface roughness is mainly through the rms height of the surface elevations, which is control by the total energy in the spectrum. The use of the dispersion relationship for shallow water would lead to a different distribution of spectral energy among wave numbers. This could have a larger impact in modeling backscattering, where resonant scattering is dominant, but it is not critical to forward propagation. Thus the main approximation is the adoption of a deep water spectrum, since, for the same wind speed, the total energy in a spectrum suitable for shallow water could be significantly different. The resulting spectrum is given by

$$S(K)=\frac{\alpha}{4|K|^3}\exp\left[-\frac{\beta g^2}{|K|^2 u^4}\right]. \tag{17}$$

It is a 1-D spectrum, suitable for the adopted 1-D propagation model. Note that when converting a nondirectional frequency spectrum to a 1-D wave number spectrum, all the energy of the wave system is contained in the plane of modeling (which is different from taking a slice of a 2-D surface).

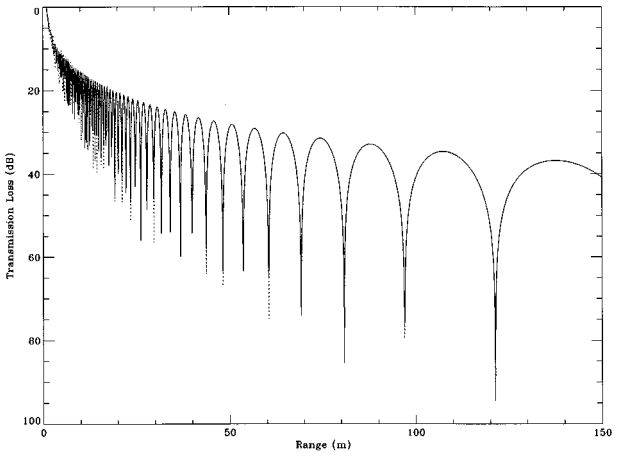

FIG. 2. Comparison of transmission loss versus range for the Lloyd's mirror problem at 20 kHz. The solid line is the analytic solution and the dotted line is EFEPE-CM.

The range step adopted for generating the surface realization was $\Delta x=0.05$ m, and the total length of the surface is 150 m. For a 10-m/s wind speed (at 10 m above the surface) the standard deviation of the surface realization is 0.59 m.

IV. APPLICATION OF THE MODELS TO SHALLOW WATER

For the numerical experiments that follow the EFEPE acoustic propagation model is used in conjunction with a conformal mapping technique to handle the sea surface roughness. As with any model applied in an unfamiliar regime, some demonstration of the validity of the model is in order. In the present case, the EFEPE model is being employed at rather high frequencies whereas most of the benchmarking has occurred at low to moderate frequencies. The Lloyd's mirror problem at 20 kHz can serve as an adequate test. Shown in Fig. 2 is a comparison between the analytic solution for the transmission loss versus range and the EFEPE prediction. In this test the source-and-receiver depth were 4.27 m. This comparison is overall quite good and excellent at the longer ranges.

In order to gain a more thorough understanding of the combined impact that near-surface microbubbles and a rough sea surface have on high-frequency sound propagation in shallow water, we have developed a series of numerical experiments in which the transmission loss predicted for the unperturbed environment (i.e., the one without sea surface roughness or microbubbles) is compared with predictions made when one or both of these features of the underwater environment (bubbles and rough seas) are included. In all cases, an acoustic frequency of 20 kHz is assumed. The unperturbed environment, which is tabulated in Table II, is 8 m deep at the source and slopes gently over a range of 150 m to a depth of 9 m. The sea surface is flat for this environment.

The perturbed environments have either a rough one-dimensional (fully developed) sea surface [see Fig. 3(a)], a

TABLE II. Initial environmental and model parameters used by EFEPE-CM for the numerical experiments.

Depth (m)	Sound speed (m/s)	Density (g/cc)	Attenuation (dB/λ)
0.0	1500.0	1.0	3.5×10^{-6}
8.0	1500.0	1.0	3.5×10^{-6}
8.25	1700.00	2.0	3.5×10^{-6}
100.0	1700.0	2.0	10.0

Attenuation gradient specified by endpoints given above.

Bathymetry	
Range (m)	Depth (m)
0.0	8.0
150.0	9.0

Bathymetry gradient specified by endpoints given above.

Pade	Range step (m)	Depth step (m)
6	0.05	0.005

bubble-induced range and depth varying complex index of refraction [see Fig. 3(b) and (c)] or both. In either case, the rough sea surface and the bubble induced sound-speed changes are assumed to be due to a constant 10-m/s wind speed. The impact of the bubbles throughout the shallow water environment can be seen in Fig. 3(b) and (c) which shows contours of the sound-speed defect (the surface is flat). The sound speed defect is the difference between the real parts of the sound speed for the unperturbed and perturbed environments. In Fig. 3(b), contour levels of 1 and 5 m/s are shown. In Fig. 3(c), a single contour at 500 m/s is drawn. In these figures the outlines of the β-plumes and γ-plumes are easily recognizable. The highest values of sound speed defect are controlled by the β-plumes. Note that in this figure the horizontal scale is highly compressed relative to the vertical scale. To further illustrate the changes in sound speed introduced by the bubble plumes, Fig. 4 shows the sound-speed profile at a range of 8 m (axis of the first β-plume) and at a range of 14 m (axis of the first γ-plume), respectively. For reference the unperturbed sound-speed profile (isovelocity) is also shown.

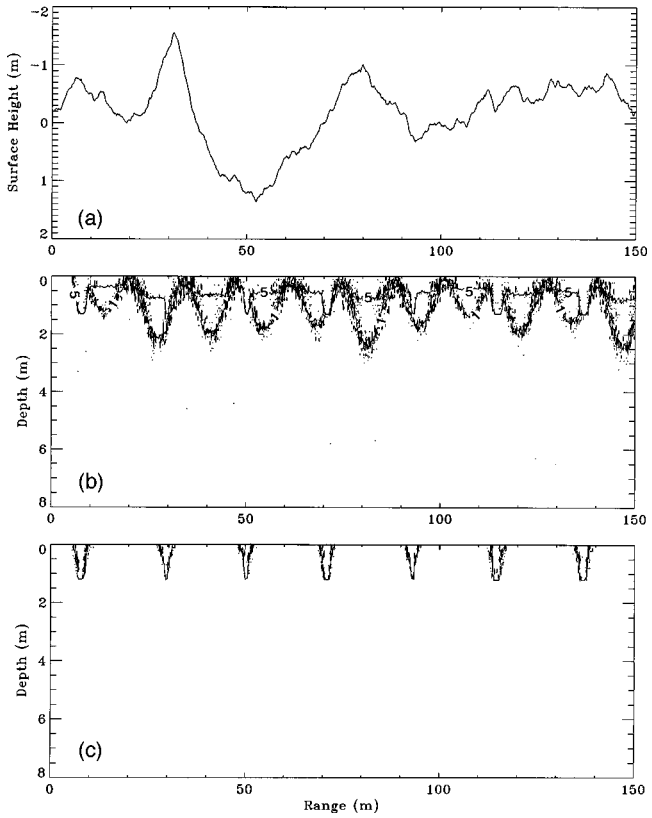

FIG. 3. (a) Sea surface profile. Sound-speed defect due to the presence of bubbles; (b) contour levels 0.1 and 5.0 m/s; (c) contour level 500 m/s.

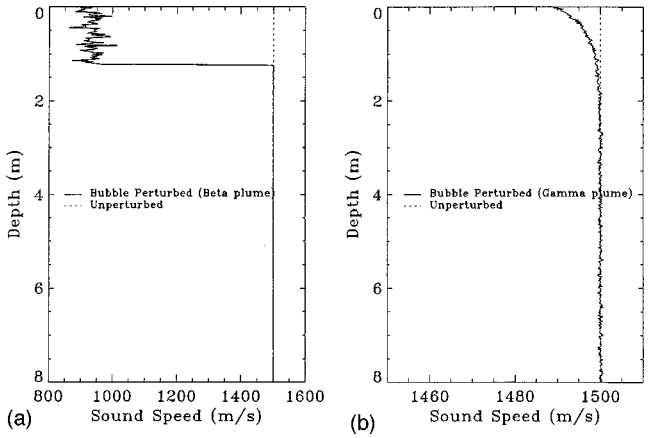

FIG. 4. Sound-speed profile at a range of (a) 8 m (axis of the first β-plume); (b) 14 m (axis of the first γ-plume). For both cases, the unperturbed sound speed profile is shown by the dotted line.

To make the acoustic calculations, the environment was discretized 0.005 m in depth (Δz) and 0.05 m in range (Δr); a total of six Pade terms were used. As a check for convergence, a finer range increment ($\lambda/10$) was used for the environment containing both a rough surface and bubbles. The results indicated that the environment was adequately sampled using the coarser Δr. These are the same parameters used to achieve good agreement with the analytic expression for the Lloyd's mirror problem (see Fig. 2). Also it should be noted that the standard application of EFEPE does not include attenuation in the water column. Since both chemical and, in particular, bubble-induced attenuation are significant at 20 kHz, the EFEPE code was modified to accept complex sound speeds in the water column (EFEPE already does this in the bottom). Chemical attenuation was calculated using Schulkin and Marsh's (1963) equation, assuming a water temperature of 15 °C, and 35-ppm salinity and is included in all transmission loss predictions.

In all of the model predictions that follow, the source is a vertical line array consisting of 512 elements spaced at 0.005-m intervals. The source array is Hamming weighted to reduce side lobes. This yields a main lobe that has an angular beam width (defined by the 3-dB down point of the source intensity) of 2 degrees. The center of the source array is at a depth of 4.27 m. This particular source was chosen to simulate the case in which interaction with the boundaries is to be minimized. The intent of this numerical experiment is not to highlight the effects of either the surface or bottom but to investigate what effect the rough surface and bubble plumes

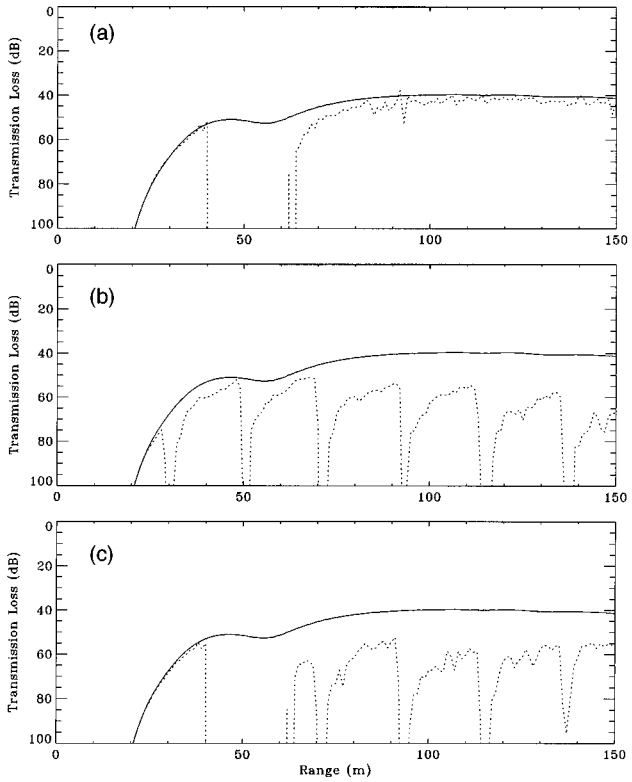

FIG. 5. Transmission loss versus range at a depth of 0.5 m. In each plot the solid line is the transmission loss predicted for the unperturbed environment (flat surface, no bubbles). (a) Predicted transmission loss when the surface is rough and bubbles not included; (b) predicted transmission loss when the surface is flat and bubbles included; (c) predicted transmission loss when the surface is rough and bubbles included. (Center of the source array is 4.27 m.)

have on transmission loss under conditions where such interaction is to be avoided.

Since this is a computer simulation, it is easy to include or remove the rough surface or the change in the complex index of refraction. Figure 5 contains a set of three transmission loss versus range predictions for a receiver at a depth of 0.5 m. In each plot, the solid line is the transmission loss predicted for the unperturbed environment (flat surface, no bubbles). Notice that the plots show a large amount of transmission loss prior to a range of 20 m. The reason being, for this horizontally focused source no appreciable energy arrives at the receiver depth until approximately 20 m in range. The dashed line in Fig. 5(a) is the predicted transmission loss when the surface is rough but bubbles are ignored. The pronounced notch in the transmission loss curve at a range of approximately 60 m is due to the presence of a deep trough in the surface wave shape. This trough occupies about 1/8 of the waveguide's depth [see Fig. 3(a)]. Note that starting at a range of approximately 40 m up to a range of 65 m, the receiver is technically in the air medium above the water. Farther in range, the field mimics the structure shown in the unperturbed case but with an additional 3–5 dB or so of loss. Since the source is highly focused in the horizontal direction, the impact of the rough surface is minimized except where a deep trough plunges down into the water column.

In Fig. 5(b), the transmission loss for the unperturbed situation is compared to a prediction for an environment that has a flat surface but the bubble-induced range- and depth-dependent complex index of refraction [see Fig. 3(b) and (c)]. Clearly, for this receiver depth, the bubbles have changed the overall level and structure of the transmission loss. The location of the β-plumes are clearly identified by the strong dropouts in the predicted transmission loss. These dropouts are mostly due to the high attenuation (approx. 20 dB/m) in the β-plumes.

Figure 5(c) shows the transmission loss when both surface roughness and bubbles are included (dashed line). At this receiver depth and for this particular example, we find that the effect of the rough surface is to perturb the ''bubble-only'' transmission loss result. There are still, however, some features of the transmission loss prediction shown in Fig. 5(c) that are due primarily to the presence of the rough surface. For example, the strong dropout between the ranges 40 and 66 m, which was associated with a deep trough in the sea surface, shows up clearly. It can be noted that at a range of 150 m, the combination of rough surface with bubble clouds yields slightly less loss than the case with a flat surface with bubble clouds [Fig. 5(b)]. This result is due in part to the enhanced upward refraction that occurs inside of the bubble clouds which redirects more acoustic energy from the source beam toward the surface when the bubble cloud depths are modulated by the presence of the rough surface. Finally, at a range of 150 m there is approximately 15 dB more transmission loss associated with the rough surface and bubble plume environment than for the flat surface and no bubble environment. It should be emphasized that this result is for the particular deterministic case at hand. If results from many realizations are averaged together results can be very different. Nevertheless, this example shows that modeling propagation with a deterministic model which includes the surface roughness and bubble clouds in a consistent manner leads to significant differences from those obtained from the standard procedure of using a flat surface and ignoring bubbles.

Although the perturbed environment is highly dependent on both range and depth, the bubble plumes extend only a few meters in depth. Therefore, it is of interest to see how the perturbed environment affects the transmission loss away from the surface for this waveguide. Figure 6 compares transmission loss versus range at four depths: 0.5 m, 0.75 m, 4.27 m, and 8.0 m. The solid line in each case is the prediction for the transmission loss in the unperturbed environment. The dashed line in each case is the prediction for the transmission loss when both the rough surface and bubble plumes are included. Notice that Fig. 6(a), (b), and (d) shows a large amount of transmission loss prior to a range of 20 m. The explanation is the same as for Fig. 5. The transmission loss differs by approximately 10–15 dB between the two environments near the surface [Fig. 6(a) and (b)]. In comparison, at deeper receiver depths [Fig. 6(c) and (d)] we see that the combined effect of the bubble plumes and the rough surface on the amplitude of the acoustic field is very small.

In order to gauge the impact of the range dependence of the bubbly environment we compared the transmission loss predicted for a range-dependent and an ''effective'' range independent bubbly environment. To define the range inde-

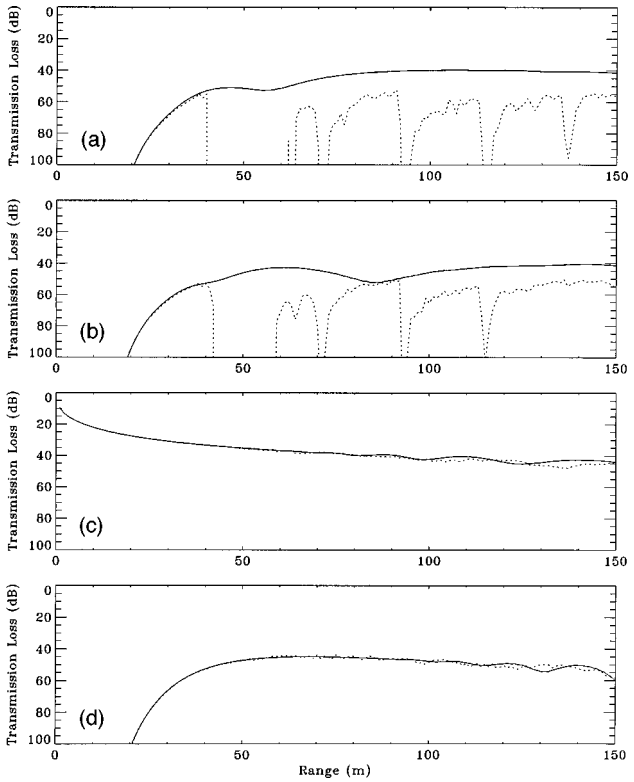

FIG. 6. Comparison of the transmission loss versus range at four depths when the rough surface with range- and depth-dependent bubble layer are included (dashed line) and when the unperturbed environment (flat surface, no bubble plumes) is used (solid line). (a) 0.5 m; (b) 0.75 m; (c) 4.27 m; (d) 8 m. (Center of the source array is 4.27 m.)

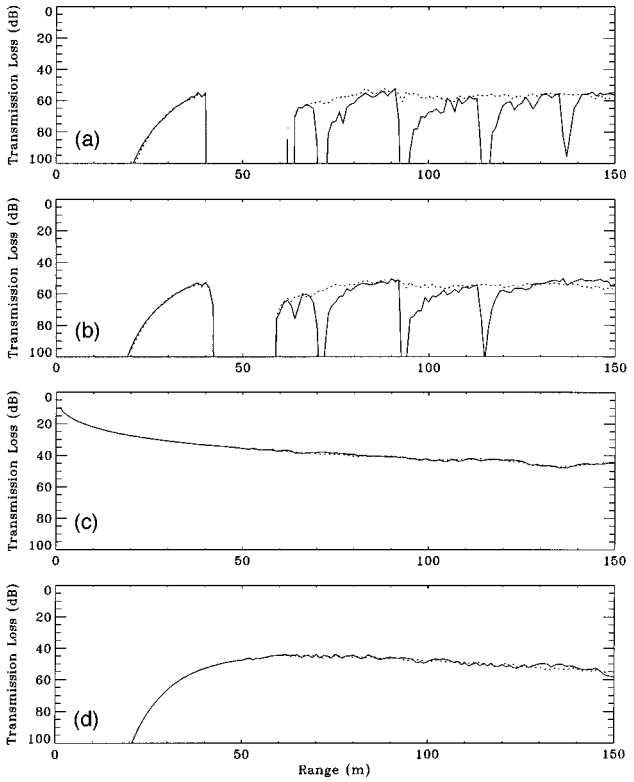

FIG. 7. Comparison of the transmission loss versus range at four depths when both the rough surface and range-independent bubble layer are included (dashed line) and when the rough surface and range- and depth-dependent bubble layer is used (solid line). (a) 0.5 m; (b) 0.75 m; (c) 4.27 m; (d) 8 m. (Center of the source array is 4.27 m.)

pendent situation, both the β- and γ-plumes were removed, leaving only the range independent, background bubble layer. Next, the numerical constant $N_{0\mathbf{bk}}$ for the background bubble layer was increased to match that of the γ-plume ($N_{0\mathbf{bk}}=1.6\times10^4\ \mathrm{m}^{-3}\,\mu\mathrm{m}^{-1}$). Incidentally, this value for $N_{0\mathbf{bk}}$ equals the one obtained by Hall when matching Johnson and Cooke's data for the time averaged bubble density. In replacing the plumes by an effective uniform bubble layer with a concentration equal to that of a γ-plume, we have removed not only the high void fraction β-plumes, but also the patchiness of the γ-plumes that form effective obstacles/scatters (modeled through the index of refraction). Figure 7 depicts transmission loss versus range for the same four depths considered earlier. The rough surface was present in all cases. The solid line in each plot is the prediction for the range-dependent bubble environment. The dashed line corresponds to the prediction for the ''effective'' range-independent bubble environment. Notice that Fig. 7(a), (b), and (d) does not show any transmission loss prior to a range of 20 m. The explanation is the same as for Figs. 5 and 6.

Considering first the shallow receivers [Fig. 7(a) and (b)], it can be noted that except for the absence of notches created by the highly attenuating β-plumes, the overall agreement in level elsewhere is remarkable. This indicates that, in spite of their high void fraction, the effect of β-plumes on forward propagation is very localized. Furthermore, the patchiness of the γ-plumes has virtually no consequence on the transmission loss. These observations are essentially confirmed by the results for receivers deeper and consequently further from the bubble plumes [Fig. 7(c) and (d)]. In both of these cases, the transmission loss predictions for the two environments are essentially identical. Hence, although the presence of the bubble plumes and rough surface affects the propagation at all depths, the patchiness of the layer and the presence of pockets of high void fraction play a very localized role. Therefore, the use of a range independent bubble layer when modeling propagation away from the sea surface and its associated bubble clouds may suffice.

In order to visualize the different effects on the propagating field, contour plots of the transmission loss are shown in Fig. 8. Figure 8(a) is the result using the unperturbed environment. It shows the source beam directed horizontally at mid-depth. Penetration into the bottom is minimal. Figure 8(b) shows transmission loss contours for an environment that has only the rough surface (no bubbles). Due to the source beam, the effect of the rough surface only manifests itself in the neighborhood of the deep surface trough (approx. range 35–70 m). The field is perturbed in both depth and range. The field penetrates into the bottom more than when the unperturbed environment is used, due to energy being transferred to steep angles upon interaction with the rough surface. At approximately 90 m there is another much smaller trough. The interference patterns associated with acoustic energy scattering from the trough can be seen. Figure 8(c) is the result of introducing the bubble plumes only. The effect that the bubble plumes have on the field is quite

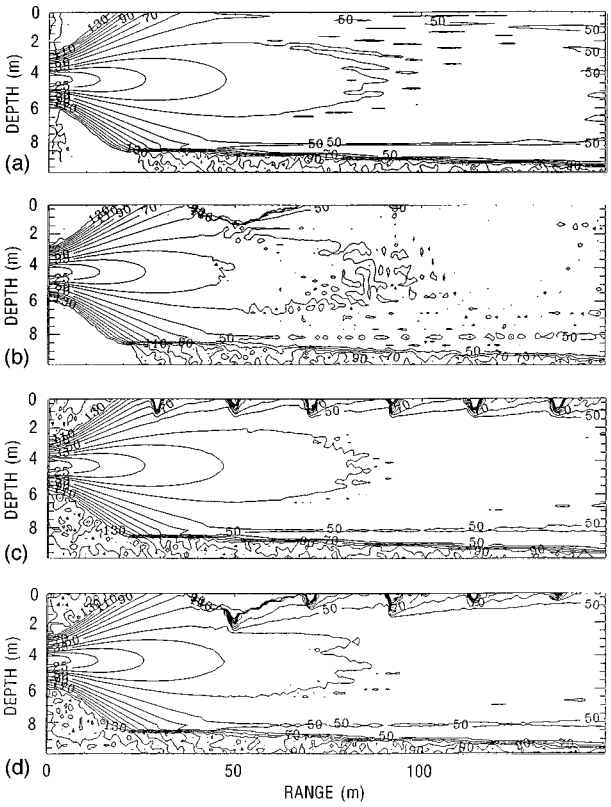

FIG. 8. Depth versus range contour plots of transmission loss; (a) unperturbed environment (flat surface, no bubble plumes); (b) rough surface and no bubble plumes; (c) flat surface and bubble plumes; (d) rough surface and bubble plumes. (Center of the source array is 4.27 m.)

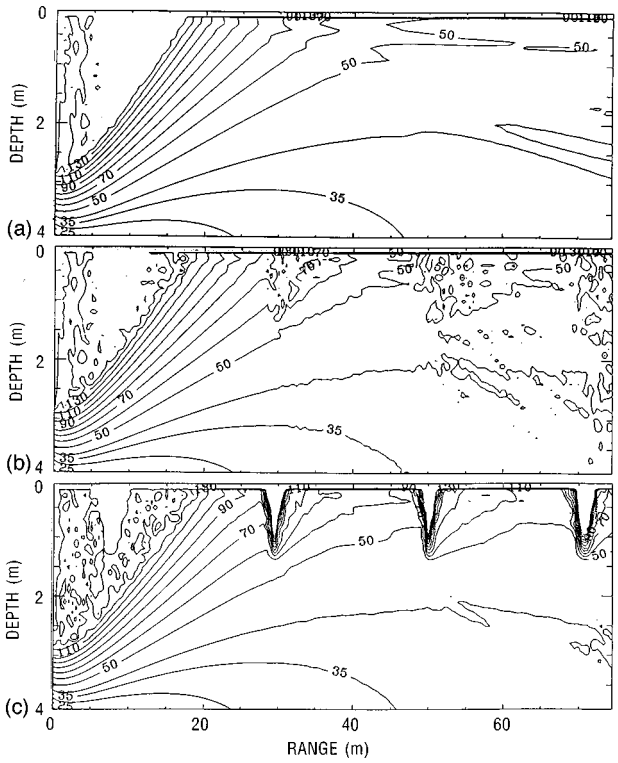

FIG. 9. Depth versus range contour plots of transmission loss; (a) unperturbed environment (flat surface, no bubble plumes); (b) flat surface and real part of sound speed due to bubble plumes; (c) flat surface and complex sound speed due to bubble plumes. (Center of the source array is 4.27 m.)

dramatic. The acoustic energy is drawn toward the surface at a closer range (steeper angles) resulting in energy striking the bottom at steeper angles when compared to the results using the unperturbed environment. In addition the field diminishes quite rapidly near the surface, a direct consequence of the attenuation. Finally, the rough surface and the bubble plumes are both included [Fig. 8(d)]. The resulting field is greatly different from the unperturbed environment result [Fig. 8(a)]. The field below the depth of the γ-plumes resemble the unperturbed environment response. The effect that the bubble plumes has on the field in the presence of the rough surface is to act as a shield preventing the acoustic field to interact as strongly with the surface as it does when the bubble plumes are absent.

In order to visualize the impact that the bubble-induced attenuation has on the acoustic field, contour plots of the propagated field are shown in Figs. 9 and 10. The three plots shown in Fig. 9 are depth versus range contour plots of transmission loss. Only the first 4 m in depth and the first 75 m in range are shown. Figure 9(a) is the result of using the unperturbed environment. It shows the field spreading uniformly in range and depth. Figure 9(b) is the result of introducing only the real part of the effective sound speed (not including attenuation). The field is perturbed at the locations of the β-plumes due to refractive effects caused by the change in sound speed. Figure 9(c) is the result when the imaginary part of the effective sound speed is included. The attenuation has a dramatic effect on the field. The attenuation in the β-plume is approximately 20 dB/m. The refractive effects are clearly shown. The three plots in Fig. 10 are similar to those of Fig. 9 except that now the rough surface is included. Figure 10(a) is the result using the rough surface with out bubbles. The surface trough is located from approximately 35 to 70 m. The acoustic field scattering off this trough is clearly shown. Now only the real part of the sound speed associated with the bubble plumes is included and the results are shown in Fig. 10(b). The β-plumes at approximately 50 and 70 m have the same effect as shown in Fig. 9(b), namely, that they have a refractive effect on the propagating field resulting in a complex interference pattern. Finally Fig. 10(c) depicts the effects with the rough surface and the complex sound speed resulting from the presence of the bubble plumes. It has already been noted that the β-plumes, and thus the entire bubble plume environment, have been properly introduced into the waveguide with a rough surface. Again note that the effect that the bubble plumes have on the field in the presence of the rough surface is namely to act as a shield preventing the acoustic field to interact as strongly with the surface as it does when the bubbles are absent. Thus the field below the depth of the γ-plumes resembles the unperturbed environment response.

V. CONCLUSIONS

The combined effect that a near-surface bubbly environment and a rough air/sea interface has on moderate high-frequency shallow water forward propagation from a directional source has been investigated through numerical modeling for a single realization of a stochastic environment.

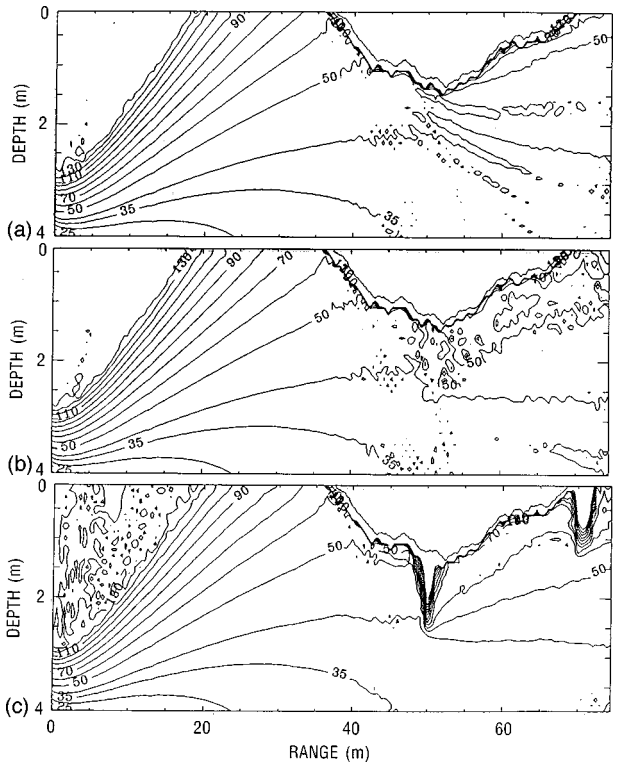

FIG. 10. Depth versus range contour plots of transmission loss; (a) rough surface and no bubble plumes; (b) rough surface and real part of sound speed due to bubble plumes; (c) rough surface and complex sound speed due to bubble plumes. (Center of the source array is 4.27 m.)

By turning on and off the different constituent parts of the environment, their separate contributions were examined. One of the main findings is that, in spite of using a horizontally directed source placed below the bubbly region, the presence of the plumes manifest itself in the acoustic field close to the surface.

For this specific deterministic environment and experimental configuration the modeling has shown that, near the surface at a range of 150 m, differences up to approximately 15 dB exist between the transmission loss for the unperturbed environment and for the environment which includes both a rough surface and bubble plumes. Ignoring the bubble plumes and using a uniform (range-independent) bubble layer underneath the rough surface will result in large errors near the surface and near the location of the strongest plumes (β). Everywhere else the patchiness of the layer has no significant impact in transmission loss calculations. On the other hand, the study also shows that (in spite of the waveguide propagation characteristic of the chosen scenario) for this specific case of a horizontally directed source, transmission loss away from the bubbly region is insensitive to both, the surface roughness and to the presence of the bubble plumes. The rough surface, which for this environment has little effect on the transmission loss of the propagating field, is, however, responsible for interference effects of the forward field observed throughout the water column. Thus any processing of a vertical array will not only be severely affected by the distorted field near the surface, but will also suffer from the interference effects everywhere in the water column.

ACKNOWLEDGMENTS

This work has been supported by the Office of Naval Research. This work has also been supported by a grant of HPC time from the DoD HPC Shared Resource Center, CEWES Cray YMP, and NAVO Cray C90. Finally the authors would like to thank the reviewers for their useful comments and suggestions and especially the reviewer who was so thorough on the environmental aspect of the work.

Bondur, V. G., and Sharkov, E. A. (**1982**). ''Statistical properties of whitecaps on a rough sea,'' Oceanology **22**, 274–279.

Cartmill, J. W., and Su, M. Y. (**1993**). ''Bubble size distribution under saltwater and freshwater breaking waves,'' Dyn. Atmos. Oceans **20**, 25–30.

Clay, C. S., and Medwin, H. (**1977**). *Acoustical Oceanography* (Wiley, New York).

Collins, M. D. (**1993**). ''A split-step Pade solution for the parabolic equation method,'' J. Acoust. Soc. Am. **93**, 1736–1742.

Crawford, G. B., and Farmer, D. M. (**1987**). ''On the spatial distribution of Ocean Bubbles,'' J. Geophys. Res. **92**, 8231–8243.

Crowther, P. A. (**1980**). ''Acoustic scattering from near-surface bubble layers,'' in *Cavitation and Inhomogeneities in Underwater Acoustics*, edited by W. Luterborn (Springer-Verlag, Berlin).

Dozier, L. B. (**1984**). ''PERUSE: A numerical treatment of rough surface scattering for the parabolic wave equation,'' J. Acoust. Soc. Am. **75**, 1415–1432.

Feuillade, C. (**1995**). ''The collective acoustic properties of water containing resonating air bubbles, and its effect on the propagation of sound,'' J. Acoust. Soc. Am. **98**, 2937(A).

Hall, M. V. (**1989**). ''A comprehensive model of wind generated bubbles in the ocean and predictions of the effects on sound propagation at frequencies up to 40 kHz,'' J. Acoust. Soc. Am. **86**, 1103–1116.

Johnson, R. C., and Cook, B. D. (**1979**). ''Bubble population and spectra in coastal waters: A photographic approach,'' J. Geophys. Res. **84**, 3761–3766.

Kinsman, B. (**1965**). *Wind Waves: Their Generation and Propagation in the Ocean* (Prentice-Hall, Englewood Cliffs, NJ).

Medwin, H., and Breitz, N. (**1989**). ''Ambient and transient bubble spectral densities in quiescent seas and under spilling breakers,'' J. Geophys. Res. **94**, 12751–12759.

Monahan, E. C. (**1988**). ''Whitecap coverage as a fully monitor able indication of the rate of bubble injection into the oceanic mixed layer,'' in *Sea Surface Sound*, edited by B. R. Kerman (Academic, New York), pp. 85–96.

Monahan, E. C., and Lu, M. (**1990**). ''Acoustically relevant bubble assemblages and their dependence on meteorological parameters,'' IEEE J. Ocean Eng. **15**, 340–349.

Monahan, E. C. (**1993**). ''Occurrence and evolution of acoustically relevant sub-surface bubble plumes and their associated, remote monitorable, surface whitecaps,'' in *Natural Physical Sources of Underwater Sound*, edited by B. V. R. Kerman (Kluwer Academic, Dordrecht), pp. 503–517.

Novarini, J. C., and Bruno, D. R. (**1982**). ''Effects of the sub-surface bubble layer on sound propagation,'' J. Acoust. Soc. Am. **72**, 510–514.

Novarini, J. C., and Norton, G. V. (**1994**). ''Acoustic index of refraction in the background bubble layer of the ocean: An up-dated bubble spectrum and computer program CBUBBLY,'' NRL Tech. Rept. Ref NRL/FR/7181–93-9432.

Norton, G. V., Novarini, J. C., and Keiffer, R. S. (**1995**). ''Coupling scattering from the sea surface to a one-way marching propagation model via conformal mapping: Validation,'' J. Acoust. Soc. Am. **97**, 2173–2180.

Norton, G. V., and Novarini, J. C. (**1996**). ''The effect of sea surface roughness on waveguide propagation: A coherent approach,'' J. Acoust. Soc. Am. **99**, 2013–2021.

Pierson, W. J., and Moskowitz, L. (**1964**). ''A proposed spectral form for fully developed wind seas based on the similarity theory of S. Kitaigorodskii,'' J. Geophys. Res. **69**, 5181–5190.

Rouseff, D., and Ewart, T. E. (**1995**). ''Effect of random sea surface and bottom roughness on propagation in shallow water,'' J. Acoust. Soc. Am. **98**, 3397–3404.

Schulkin, M., and Marsh, H. W. (**1963**). ''Sound absorption in seawater,'' J. Acoust. Soc. Am. **34**, 864.

Thorpe, S. A. (**1982**). ''On the clouds of bubbles formed by breaking waves in deep water and their role in the air-sea gas transfer,'' Philos. Trans. R. Soc. London, Ser. A **304**, 155–210.
Uscinski, B. J. (**1995**). ''High frequency propagation in shallow water. The rough waveguide problem,'' J. Acoust. Soc. Am. **98**, 2702–2707.
Wu, J. (**1981**). ''Bubble population and spectra in near-surface ocean: Summary and review,'' J. Geophys. Res. **86**, 453–463.
Wu, J. (**1988**). ''Bubbles in the near-surface ocean: A general description,'' J. Geophys. Res. **93**, 587–590.
Wu, J. (**1992**). ''Individual characteristics of white caps and volumetric description of bubbles,'' IEEE J. Ocean Eng. **17**, 150–158.

Laboratory target strength measurements of free-swimming Antarctic krill (*Euphausia superba*)

Timothy Pauly
Australian Antarctic Division, Channel Hwy, Kingston 7050, Tasmania

John D. Penrose
Centre for Marine Science and Technology, Curtin University of Technology, Kent St., Bentley 6102, Western Australia

(Received 17 February 1996; revised 1 March 1997; accepted 31 December 1997)

Target strength measurements of free-swimming krill at 120 kHz were made using a single-beam monostatic system in a 10-m^3 laboratory tank. Krill (grouped according to length classes) swam freely in the tank triggering a data acquisition system when generating a backscattered signal larger than a threshold, determined by the system noise level. Dorsal and ventral target strength estimates were calculated indirectly by deconvolution of the cumulative probability function of echo ensembles of single-animal insonifications. For mean length classes in the range [29.6 to 36.2] mm the median single-animal target strengths are in the range [−76.7 to −71.8] dB. Monte Carlo computer simulations were used to evaluate the effects of varying the ratio of largest to smallest echo amplitudes for a given ensemble, thus enabling the estimation of threshold induced bias in the target strength estimates. The threshold induced bias was then determined for each ensemble of experimental data and used to determine corrections which were in the range of [−0.84 to −0.33] dB. An error analysis of the target strength estimates detailing the components due to measurement accuracy and precision, and the indirect signal processing techniques used is also presented.
 [S0001-4966(98)02804-5]

PACS numbers: 43.30.Sf [JHM]

INTRODUCTION

Biological acoustic scatterers in the ocean usually constitute point targets, such that individual acoustic cross sections are small compared with the cross-sectional area of an interrogating sound beam. Aggregated scatterers of various types, including air bubbles (Medwin *et al.*, 1975), ice crystals (Penrose *et al.*, 1994), and biological scatterers, represent the major source of marine volume reverberation.

Volume reverberation intensity depends on both the target strengths (TS) and the spatial distribution of the scatterers involved. Here

$$\overline{\mathrm{TS}} = 10\log \overline{\sigma}_{bs} = 20 \log \overline{l}_{bs}, \tag{1}$$

where $\overline{\sigma}_{bs}$ = average acoustic backscatter cross section in m^2 and l_{bs} = average scattering length in m. Assessment of marine biomass using echo integration techniques is now widespread (MacLennan and Simmonds, 1992). These methods depend on the accurate assessment of the TS of the scatterers involved.

Early experiments to determine such TS values used tethered specimens in laboratory test tanks. Nakken and Olsen (1977) used this technique in a substantial series of measurements on fish. Later work used free swimming targets in either tank or caged field locations (Foote *et al.*, 1990) and *in-situ* measurements at sea (Hewitt and Demer, 1991). Foote (1991) recently reviewed target strength measurements. The present paper reports a suite of measurements made on free-swimming Antarctic krill, *Euphausia superba*, in a laboratory test tank.

Antarctic krill are recognized as a major component of the Antarctic food chain. The distribution and abundance of krill has been a subject of continued interest over the last two decades, and a research focus for the BIOMASS (Biological Investigations of Marine Antarctic Systems and Stocks) program and the Commission for the Conservation of Antarctic Marine Living Resources (CCAMLR). Managing the harvesting of krill has been a key issue for CCAMLR.

Extracting TS values from measurements of freely swimming krill requires a method of dealing with the uncertainties arising from the unknown angular position of a scatterer in the sound beam. In addition, for scatterers large enough to enter the geometric scattering regime, the detailed morphology and attitude of the scatterer provides a further source of fluctuation in instantaneous TS values. Two general approaches have been developed to enable the TS of single-point targets to be estimated from signals subject to such stochastic processes.

One approach, termed by Foote (1991) the ''Indirect'' approach, can be traced to Craig and Forbes (1969) and was later applied by Peterson *et al.* (1976) and Ehrenberg *et al.* (1981). This approach uses a statistical treatment of an ensemble of echoes to yield TS estimates. It enables data derived from a single-beam transducer, operating in monostatic mode, to be processed for TS estimates, provided a set of assumptions relating to the scattering regime are applicable.

The second ''Direct'' approach requires a modified beam structure; various forms involve dual or split beam geometries (Ehrenberg, 1974). Such techniques offset one of the uncertainties inherent in the Indirect approach, that is, the location of the target with respect to the axis of the beam

pattern. This is achieved at the cost of a more complex transducer configuration.

The work reported here utilized the Indirect approach, where a simple piston transducer was used for tank measurements and the set of assumptions defined by Peterson *et al.* (1976) were invoked as a basis for a signal processing methodology. This methodology has been the subject of a detailed performance analysis (Palumbo *et al.*, 1993) and evaluation (Penrose and Pauly, 1993). Simulated data (generated using Monte Carlo techniques) were used to assess signal processing performance under a number of nonideal operating conditions likely to be experienced in tank or field TS measurement programs. TS estimates were evaluated for the influence of variations in the size distribution of scatterers, the spatial density of scatterers, the target attitude effects on scattering statistics, and beam shape uncertainties.

The present paper adds to this work by using Monte Carlo simulations to assess the influence of backscatter signal-to-noise ratio and by providing a thorough assessment of the error budget for the TS estimates reported here. The signal-to-noise ratio is of key importance in dealing with small targets such as krill, leading to the concept of threshold bias discussed below. A series of TS estimates and uncertainties corrected for threshold bias (including ventral and dorsal measurements for a single group of krill, and the effects of controlled behavior modification using light) are presented below.

I. EXPERIMENT

A series of experiments was conducted in a purpose built tank at the Australian Antarctic Division Laboratories in Tasmania. The krill swam freely in the tank, triggering a data acquisition system on entering the acoustic beam when a backscattered signal exceeded the system noise level threshold. The digitized echo-traces (received transducer voltage as a function of time) were stored for later processing. Data were collected from five groups of krill. Observations of the swimming attitude and behavior of the krill were made through viewing ports built into the side of the tank. Simultaneous stereo photographic and acoustic data were collected to determine the attitude and location of the target within the beam, and will be reported separately.

A. Tank systems

The $\sim$10-m^3 stainless steel tank, 2 m in diameter and 3.2-m deep, was filled with seawater and maintained within a temperature range of -0.5 to 1.0 °C [Fig. 1(a)]. The water was continuously circulated to prevent formation of a structured temperature profile and ice development on the inner surface of the tank.

B. Acoustics and data acquisition

The 120-kHz monostatic acoustic system used [Fig. 1(b)], consisted of an ITC-3003 transducer, Hewlett–Packard Function Generator and Timer Counter, purpose built amplifier, transmit/receive (T/R) unit and software, Hameg Digital Storage Oscilloscope, and an IBM compatible personal computer (PC). For all but one experiment the transducer was mounted at the top of the tank $\sim$200 mm below the surface of the water, thus providing dorsal measurements. To collect data for a ventral TS estimate the transducer was mounted $\sim$200 mm above the tank bottom in an upward looking configuration.

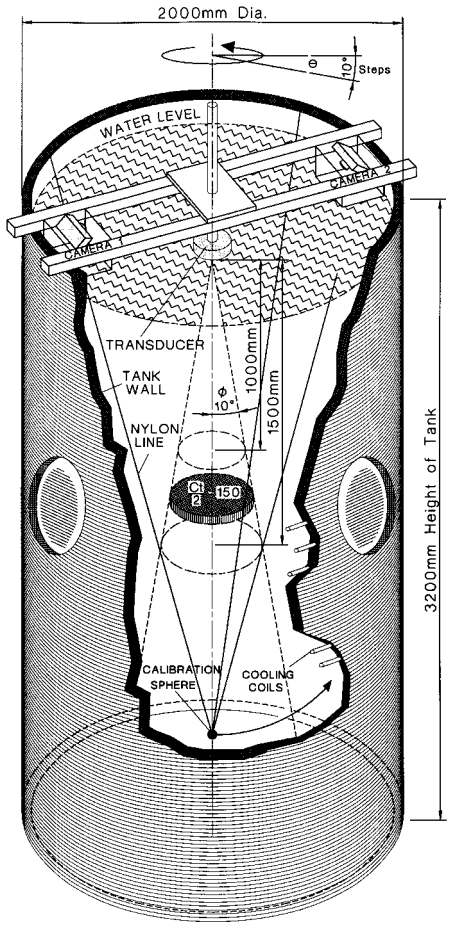

FIG. 1. (a) The configuration of the experimental tank and systems. (b) A schematic showing the configuration of the electronic components of the acoustics and data acquisition system.

The received signal was gated from ~0.0014 to ~0.002 s giving a sampling volume starting at a range of ~1 m and extending out to ~1.5 m from the face of the transducer. To achieve maximum signal-to-noise ratio the range window for data acquisition, or time gate, was determined after balancing far-field requirements, transmitter output level, pulse length, and transducer ring down, against signal reduction due to transmission effects. The ring down of the transducer was minimized by temporarily switching in a matched load to the transducer terminals after transmission. This was switched out before the gated component of the signal was received. The pulse length ($\tau = 0.14$ ms) was chosen as the minimum required to effect a steady-state return in target signals, ensuring that the bandwidths of the signal and transceiver were appropriately matched.

The data acquisition system was controlled by the PC through IEEE 488 interface connections with the function generator and storage oscilloscope. The function generator, triggered by the PC, provided signal input to the amplifier T/R unit and simultaneously triggered the timer counter, which was used to generate the time base delay on the oscilloscope. The T/R unit directed the amplifier output to the transducer, and the received signal to the oscilloscope. The oscilloscope captured the required component of the digitized voltage signal time series, which was down-loaded to the PC, and stored or discarded subject to the result of the thresholding routine. Initial thresholding, formed from a cosine filter convolved with a subset of the signal squared was applied to each time series. The thresholding algorithm consisted of a window within which a given percentage of data must exceed the threshold level for a positive target identification. This process was developed for the speed required when operating with the stereo photographic system.

Upon detection of a target, the cameras were triggered immediately with a second acoustic pulse so that simultaneous acoustic and photogrammetric data could be recorded. If the time between a target detection and the following photogrammetric data acquisition cycle was too great, then generally the krill were no longer within a detectable region of the beam. The two echo traces were then stored on hard disk and the system continued sounding at the pulse repetition frequency (~0.8 Hz), until another target was detected.

C. Electronics

The electronics consisted of a timing circuit (triggered from the 120-kHz input burst from the function generator); a MOSFET amplifier; diode switching network for transmission, reception, and load switching (driven by the timing circuit); and a transducer impedance matching circuit. The diode switching network directed the power signal to the transducer, the received signal to the oscilloscope, and switched an ideal load across the transducer as described above.

D. Photogrammetrics

The photogrammetric system [Fig. 1(a) and (b)] consisted of a pair of Pentax SFX cameras used with manual focus SMC Pentax-A 1:1.4 50-mm lenses and data backs. These cameras were chosen for automatic film advance and electronic remote triggering features. The standard remote triggering switches were modified and paralleled into a high-speed micro relay circuit, driven from the digital-to-analog output of a PC interface card. The data acquisition software triggered the camera.

E. Calibration

From a set of voltage time series the effective scattering length of the target can be calculated. This requires an absolute calibration of the data acquisition and data processing systems. Target spheres are used for calibration of hydroacoustic systems over a range of operating frequencies and hydrographic parameters (Foote, 1983). They are optimized, by choice of diameter and material, for minimal target strength variation at a given frequency as a function of hydrographic parameters (Welsby and Hudson, 1972) and Foote (1982).

The backscatter pressure amplitude p_e, arising from an acoustic system operated monostatically, may be written as

$$p_e = \frac{p_0 r_0}{r^2}\, e^{-2ar} D^2(\phi) l_{bs}, \tag{2}$$

where p_0 is the source-pressure level measured at reference distance r_0 from the projector, a is the absorption coefficient (Np/m), $D^2(\phi)$ is the pressure directional response for both transmission and reception (given D is the transducer directional response), and l_{bs} is the instantaneous value of the scattering length, such that $l_{bs} = \sigma_{bs}^{1/2}$.

A target sphere was suspended on the acoustic axis ($\phi = 0$) at a known range r from the transducer; thus from Eq. (2):

$$p_s = \frac{r_0 p_0}{r^2}\, e^{-2ar} l_{\mathrm{Cu}\,30} \quad \text{since } D(0) = 1, \tag{3}$$

where p_s is the backscattered pressure amplitude from the target sphere and $l_{\mathrm{Cu}\,30}$ is the scattering length of the 30.05-mm diameter copper target sphere used.

For linear transducer elements Eq. (3) can be rewritten as follows:

$$V_s = \frac{V_0 r_0}{r^2}\, e^{-2ar} l_{\mathrm{Cu}\,30}, \tag{4}$$

where V_s is the received voltage corresponding to p_s, and V_0 is the voltage response to p_0.

Taking natural logs of both sides and regrouping the terms gives:

$$\ln V_s = -2 \ln(r e^{ar}) + \{\ln(V_0 r_0) + \ln(l_{\mathrm{Cu}\,30})\}. \tag{5}$$

Measurement of V_s at different ranges (r) enables the use of linear regression to determine the constant term and hence $V_0 r_0$, while also providing a measure of the quality of the fit. The term $V_0 r_0$ contains all corrections for system amplification or attenuation, and the transmit and receive sensitivities of the transducer/amplifier combination. If $D(\phi)$ is known, then the system can measure instantaneous effective scattering lengths l_{bs} from an instantaneous value V_s:

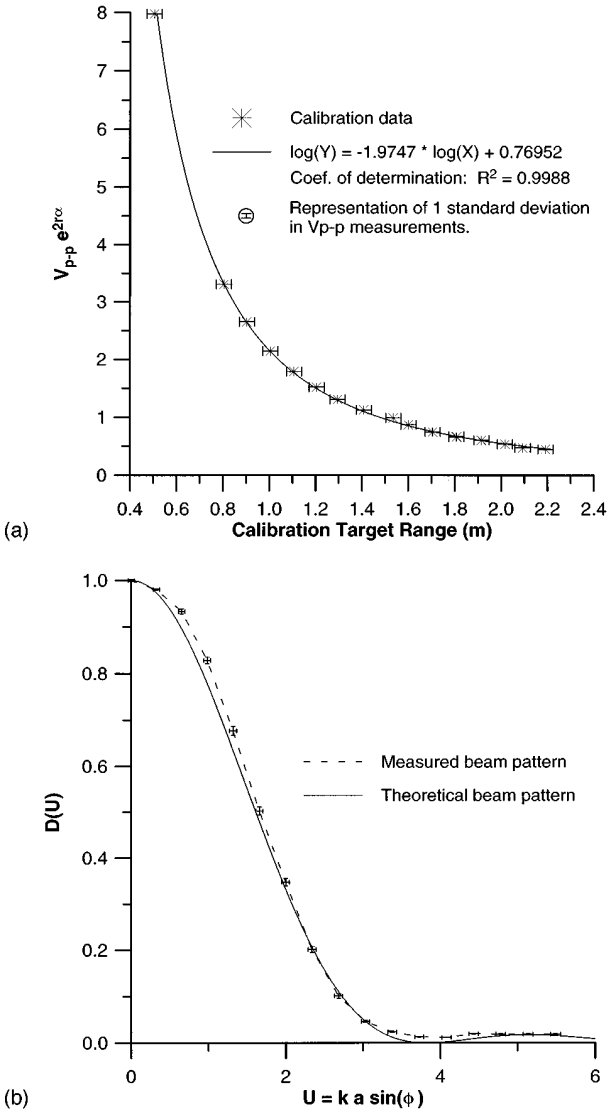

FIG. 2. (a) The on-axis calibration data corrected for absorption as a function of calibration target range from the transducer. (b) The theoretical and experimental beam patterns. The experimental beam pattern is constructed from averages of measurements at 10° increments in θ for constant ϕ [see Fig. 1(a)].

$$l_{bs}=\frac{V_s r^2 e^{2ar}}{V_0 r_0 D^2(\phi)}. \tag{6}$$

On-axis output levels were recorded for several ranges of the calibration sphere from the transducer and combined with temperature and salinity measurements to determine the value of the product $V_0 r_0$. Figure 2(a) shows the calibration data for experiment 4 where the calibration target range was varied approximately 0.5 m above and below the krill data range acquisition window to check how well far-field operating conditions were met.

F. Beam pattern

The beam pattern was measured by moving the sphere through the beam at $\sim 1°$ steps in ϕ. The angle and range were calculated for each position of the sphere. A set of measurements were taken for each 10° of rotation (θ) of the transducer. This process was conducted at two ranges from the transducer and repeated at the beginning and end of each series of experiments. Figure 2(b) shows the collated results of the beam pattern (expressed as a function of U where $U = ka \sin(\phi)$, where k is the wave number and a is the transducer radius) calculated from range corrected amplitudes for each measurement at a particular value of ϕ. Figure 2(b) also shows the appropriate theoretical beam pattern for a baffled piston transducer.

G. Krill

Krill were selected and grouped according to length for the TS experiments, initially by $S1$ length (Mauchline, 1980) measurements made with vernier callipers. After the acoustic experiments, moults were collected from each krill for final size determination. The uropod $S7$ lengths (Mauchline, 1980) were converted to $S1$ lengths using the regression relation $S1(S7) = 6.342.S7 + 2.255$ (F ratio $= 450$, $P > F$: < 0.0005). This was determined from a series of measurements on the group of krill, from which the krill for these experiments were selected. There were instances when one or two of the animals died during the experiment and hence a final measurement was not available.

H. First series of experiments conducted in 1988 (experiments 1–3 in Table I)

An aim of the first series of experiments was to develop effective operating configurations and methodologies for both the calibration and krill experiments. Care was taken to maintain the condition of the animals throughout the duration of this and subsequent experiments. The mortality rate ranged from $\sim 0\%$ to $\sim 5\%$ for all experiments, not significantly different to that of other animals kept at the laboratory.

To obtain highly accurate stereo images required significant effort to obtain a workable configuration for the photogrammetry system, and calibration and operating techniques. During the first series of experiments only a small number of stereo pairs containing a krill were obtained. These were used to determine the accuracy with which a krill head and tail could be located in three-space relative to the acoustic beam geometry. The results of this component of the work are to be presented separately as they included a detailed assessment of the effects of orientation on single TS values, and the subsequent implications for the choice of probability density function (PDF) used in describing orientation effects.

Three series of data were collected for three different sized groups of krill. System calibrations and beam pattern measurements were conducted before and after each experiment.

I. Second series of experiments conducted in 1989 (experiments 4 and 5 in Table I)

A second series of calibration and krill experiments were conducted after modifications to improve the signal-to-noise ratio of the amplifier and T/R unit, and initial photogrammetry analysis indicated the establishment of a viable photogrammetric system. A single sized group of krill were

TABLE I. Summary of results for each experiment.

Exp.	No. of krill	Kril length Avg. mm	Kril length Std. mm	No. of data acquired	e_n range	TS threshold bias correction dB	Ranked array TS Median dB	Ranked array TS Min. dB	Ranked array TS Max. dB	Ranked array TS Range of TS dB	Corrected TS Median dB	Combined corrections and uncertainties Min. dB	Combined corrections and uncertainties Max. dB
1	22	36.17	2.57	244	2.59	−0.84	−71.82	−72.90	−71.66	1.24	−72.66	−73.87	−72.37
2	38	29.57	3.03	644	3.01	−0.69	−74.86	−76.57	−74.40	2.17	−75.55	−77.39	−74.96
3	57	34.11	2.02	716	3.72	−0.52	−72.97	−74.06	−72.56	1.50	−73.49	−74.71	−72.95
4	48	32.86	1.46	2254	4.75	−0.37	−76.74	−78.04	−76.54	1.50	−77.11	−78.54	−76.78
5	48	32.86	1.46	680	4.91	−0.36	−76.57	−76.78	−75.87	0.91	−76.93	−77.27	−76.10
6	44	34.46	1.99	111	4.32	−0.42	−75.76	−77.13	−75.28	1.85	−76.18	−77.69	−75.57
7	44	34.46	1.99	154	4.36	−0.42	−75.87	−77.38	−75.36	2.02	−76.29	−77.93	−75.65
8	44	34.46	1.99	179	4.33	−0.42	−75.53	−77.49	−74.84	2.65	−75.95	−78.04	−75.13
9[a]	44	34.46	1.99	213	5.19	−0.33	−75.99	−76.78	−75.70	1.08	−76.32	−77.24	−75.90

[a]All measurements are at 120 kHz except experiment 9 which was at 118 kHz.

used for the joint acoustic and photogrammetric experiment. The experiment ran for several weeks in order to collect sufficient photogrammetric data; consequently a large acoustic data set was also acquired. Then data were collected from the same krill with the transducer mounted near the bottom of the tank for a ventral TS estimate.

J. Third series of experiments conducted in 1990 (experiments 6–9 in Table I)

A third series of tank experiments was conducted on a single size group of krill under varied light conditions. The first two experiments were run under the same conditions with tank lighting being continuously cycled on for 15 min then off for 1 h. This achieved a higher rate of data acquisition, thus it is assumed that krill behavior modification occurred. The first of this series of experiments was immediately followed by a second run with the same operating conditions. A third run was conducted with exactly the same conditions except the tank was kept continuously dark. With the tank kept dark, a fourth experiment (experiment 9, Table I) was conducted with the center frequency shifted from 120 to 118 kHz, the resonant frequency of the transducer, for which the system was recalibrated. While a small increase in the signal-to-noise level was observed no change in TS could be discerned with this small change in frequency.

K. Krill behavior observations

During the experiments regular observations of the krill showed that they generally swam near the sides of the tank out of the transducer main beam, often ascending and descending at this boundary. At any instant a small number of krill swam through the rest of the volume of the tank. While clear from the sides of the tank the krill swam at a constant velocity, horizontally, or at a very modest rate of ascent or descent, with a head-up orientation just off the horizontal. Occasionally krill were seen to ascend or descend at nearer vertical velocities and during such movements their orientation was more vertical. Under these conditions the backscattering cross section presented would be expected to vary considerably from that of the horizontal orientation, as indicated by Greenlaw (1977).

II. SIMULATIONS

A. Background

Peterson *et al.* (1976) derived a PDF for the envelope of the echoes. This enables the extraction of the average backscattering cross section $\overline{\sigma_{bs}}$ and number of fish per cubic meter from a measured echo ensemble. The derivation of the PDF is based on the following assumptions: (1) A uniform population of a single species is measured, such that all targets have the same $\overline{\sigma_{bs}}$. (2) Targets are randomly located throughout the acoustic sampling volume. (3) Only single targets are present in any one range slice of thickness $c\tau/2$ (where c is the sound speed). (4) Scattering is geometric, which leads to the assumption that backscattered instantaneous pressure amplitudes are Rayleigh distributed. (5) The transducer beam pattern $D^2(\phi)$ is accurately known.

Given Eq. (2) and following Clay and Medwin (1977), a normalized backscatter pressure amplitude e for a target may be written as

$$e=\frac{p_e r^2 e^{2ar}}{p_0 r_0} \quad \text{or} \quad e=\frac{V_e r^2 e^{2ar}}{V_0 r_0}, \tag{7}$$

where V_e is the voltage response to p_e so that

$$e=l_{bs}D^2(\phi). \tag{8}$$

Thus e is the product of two statistically varying parameters l_{bs} and $D^2(\phi)$ of the target in the beam, which are functions of the random orientation and location, respectively. The joint PDF for the envelope of the echoes is formed from the product of distributions for l_{bs} and $D^2(\phi)$. Palumbo *et al.* (1993) have established a processing technique, entitled the Ranked Array method, to treat ensembles of e values from experimental measurements. In the present work, this method has been extended to deal with the threshold bias. This is the effect of a noise threshold, masking small amplitude echoes, which induces a bias in the estimates produced from the experimental distributions.

This extended method of the Ranked Array processing technique consists of the following steps: (1) The e's are ranked smallest to largest giving e_n, where $n=1,2,3,...,m$ and m is the number of e data points; (2) the range of the e_n values is determined (i.e., e_m/e_1); (3) the cumulative prob-

ability distribution function (CDF) of the theoretical distribution $C(e/l_{bs})$ is then calculated over the range of e_n values determined above; (4) the experimental CDF is determined for each value of $e_n(C'(e_n))$, then for each value of $C(e/l_{bs})$ the corresponding e_n value is determined such that $C(e/l_{bs})=C'(e_n)$; (5) letting $n=e/l_{bs}$ leads to $l_{bs}=e_n/n$ and hence, TS can be determined for each e_n; (6) TS is then calculated and corrected for the e_n range, i.e., threshold bias.

B. Methods

A series of Monte Carlo simulations were used to check the processing and analysis software. The simulations were also used to assess the effects of a reduced range of e_n values on the accuracy of the Ranked Array technique presented in Palumbo *et al.* (1993).

The model had the following inputs:

TS_{in}	input target strength {dB}
ka	{wave number}×{effective transducer radius}
c	sound speed {m/s}
t_s, t_e	start and end times for the gated region of interest in the signal time series {s}
ϕ_{max}	maximum value of the beam angle ϕ for a target location defined as the angle of the first minimum in the directivity pattern {deg}
$V_0 r_0$	system calibration parameter {V m}
a	absorption coefficient {Np/m}

The following parameters were simulated:

$t_{T/R}$ the transmit/receive (T/R) time for a pressure signal to travel to and from a target, located at range r, where the $t_{T/R}$ values are distributed linearly increasing with r^2 and $t_s \leqslant t_{T/R} \leqslant t_e$ is

$$t_{T/R}=(t_s^3+u(t_e^3-t_s^3))^{1/3}, \tag{9}$$

where u is a random number on the interval [0,1].

ϕ simulated beam angle ϕ for the target location, where values of ϕ are distributed linearly and increasing with ϕ, and $0 \leqslant \phi \leqslant \phi_{max}$

$$\phi=\phi_{max}\sqrt{u} \tag{10}$$

l_{bs} scattering length for an instantaneous target orientation, assuming a Rayleigh PDF for l_{bs}

$$l_{bs}=(-2(10^{TS_{in}/10})\ln(1-u))^{1/2} \tag{11}$$

$V_{p\text{-}p}$ simulated target voltage signal for $t_{T/R}$, ϕ, and l_{bs}

$$V_{p\text{-}p}=\frac{V_0 r_0 D^2(\phi) l_{bs}}{r^2 e^{2ar}} \quad \text{where} \quad r=\frac{c t_{T/R}}{2}. \tag{12}$$

1. Target signal T/R time

The parameter $t_{T/R}$ was simulated to compare data and simulation plots of signal $V_{p\text{-}p}$ as a function of $t_{T/R}$ and to provide simulated data for postprocessing routines in the same form as the experimental data.

2. Range of echo amplitude values

Antarctic krill are weak scatterers, thus krill TS measurements result in a small range of e_n values. Peterson *et al.* (1976) in experimental work with swim bladder bearing fish were able to use e_n values with a range of 30 fold (i.e., $e_m/e_1=30$). In this experimental program the variation in range of e_n values was approximately 2.5 to 6 fold. This variation resulted from the different sized krill groups, and variation in signal-to-noise ratios for different versions of the electronic systems.

A series of simulations of varying e_n ranges were conducted. Each simulation consisted of generating a set of 500 echoes exceeding a given threshold level, which were processed as an echo ensemble for a TS estimate. A set of 50 TS estimates for each e_n range was produced for analysis. The mean, standard deviation, maximum, and minimum of the l_{bs} values were calculated for each e_n range.

C. Results

1. Comparison with Palumbo et al. (1993)

For results of a simulation series ($TS_{in}=-40.8$ dB, range of e_n values=30, $\overline{TS}_{out}=-40.89$ dB with a standard deviation $s=0.440$ dB), good agreement was found with Palumbo *et al.* (1993) (where $\overline{TS}_{out}=-40.85$ dB and $s=0.605$ dB). The reduction in s for this work is due to a modification of the Ranked Array method.

Using analysis of variance, Palumbo *et al.* (1993) showed that it was sufficient to compute a single TS estimate for each simulated echo ensemble, using the point $e/l_{bs}=1$. While this is true if the theoretical PDF for the envelope of the echoes is an exact representation of the experimental PDF, as in the simulations here and in Palumbo *et al.*'s (1993) work, it may not be the case for experimental work.

For example, if the experimental PDF varies even slightly from the theoretical PDF, then the use of a single-point determination will introduce a systematic error, dependant on the choice of e/l_{bs} value for a TS computation. Hence the processing presented here for the experimental work computed a TS estimate for each point on the theoretical distribution as outlined in background above under the Ranked Array steps (4)–(6). This modification to the Ranked Array method reduces the spread of TS estimates.

2. e_n range and TS correction for threshold bias

The range of e_n values can be expected to modify the performance of the Ranked Array or similar ensemble processing techniques. As the range of e_n decreases due to an increase in the threshold level, then the time required collecting a given number of samples increases. Thus the likelihood of populating the larger e_n valued region of the distribution increases. That is, a larger sample is required to obtain a given number of e_n values above the threshold, increasing the likelihood of obtaining larger values and hence biasing a TS estimate. This effect was identified by Weimer and Ehrenberg (1975) as threshold bias.

The $\overline{TS}$ output for the two different simulated TS_{in} values was compared as a function of e_n range for each series of simulations. Figure 3 shows the difference $TS_{out}-TS_{in}$ as a function of e_n range demonstrating the independence of the e_n range effects for two different TS regimes. As expected, the same e_n range results in the same signal-to-noise ratio. Hence the systems simulated are effectively identical, and

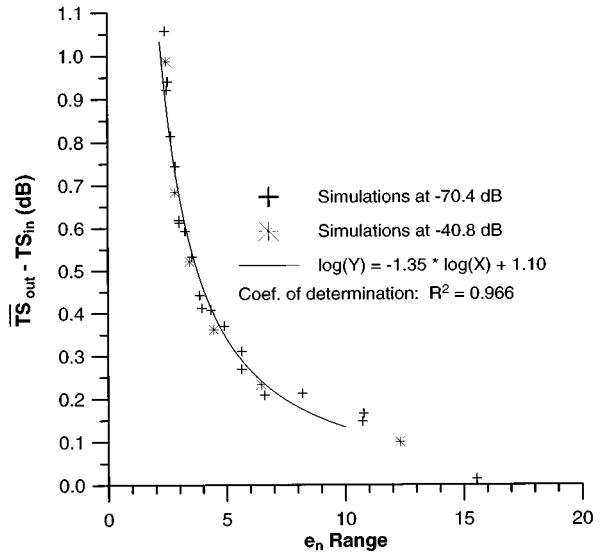

FIG. 3. The difference between the mean target strength estimates $\overline{\mathrm{TS}}_{\mathrm{out}}$ computed for a simulated echo ensemble of $\mathrm{TS}_{\mathrm{in}}$ as a function of varied e_n range (i.e., e_m/e_1). The parametrized curve fit was used for the calculation of threshold induced bias.

result in no change in threshold bias. For a real experimental system, an increase in the target size would be accompanied by an increase in the e_n range and hence a decrease in the threshold bias observed.

A curve fit to TS as a function of e_n range was computed (Fig. 3) and used to calculate the threshold bias for correcting the krill TS estimates. Table I shows this correction computed for each of the krill experiments.

III. ANALYSIS

A. Data processing

1. Echo analysis

Individual digitized pings, stored by the data acquisition system, were screened for noise and multiple targets. The echo-traces were bandpass filtered in the frequency domain to reduce the noise signal. A polynomial curve fit was determined for both the maximum and minimum peak values of the carrier frequency about the target signal defining the modulated envelope, for which the maximum peak-to-peak voltage V_e and $t_{\mathrm{T/R}}$ were determined. Finally the data were screened for multiple targets. This filter was based on signal phase coherency and amplitude structure of the target signal. A data ensemble of range and amplitude values for accepted echos was thus formed for each experiment. Then an echo ensemble was calculated according to Eq. (7), which includes corrections for transmission effects and system calibrations.

2. TS computation

As outlined in Sec. II A, the TS estimates were calculated using a modified version of the Ranked Array method described by Palumbo *et al.* (1993). Figure 4 presents the theoretical and experimental CDF's and point TS estimates for four of the nine experiments conducted. These four figures present echo ensembles illustrating best and worst experimental and theoretical CDF's of dorsal measurements [Fig. 4(a) and (b)], as well as dorsal and ventral results for a single group of krill [Fig. 4(c) and (d)]. The point TS estimates were computed for each datum on the experimental curve. Given the systematic differences between the experimental and theoretical distributions, best illustrated in Fig. 4(a), an arithmetic mean is inappropriate, thus the median TS value was chosen as a representative ''$\overline{\mathrm{TS}}$'' estimate.

Table I lists the number of krill in each size group; the mean and standard deviation of the length measurements; the number of data points in each ensemble (after processing as outlined above); the range of e_n values and the estimated correction for threshold bias; the median TS and extreme values $\mathrm{TS}_{\mathrm{min}}$ and $\mathrm{TS}_{\mathrm{max}}$; and finally the TS values corrected for threshold bias and their associated uncertainties.

The threshold bias correction was determined from the results outlined in Sec. II C using the range of the e_n values for each experiment and added to the TS estimates.

B. Error analysis

A major emphasis of this work was to determine uncertainties in the TS estimates. The uncertainty includes the accuracy of each measurement, the measured variation in parameters monitored for the duration of each experiment, and the precision of the processing techniques.

1. Methods

Figure 5 presents the uncertainties for the calibration and TS experiments, broken down into categories of experimental measurements, computations, and results, followed by the post-processing and analysis of data. The section labeled ''Calibration Experiments'' (Fig. 5) includes uncertainties arising from beam pattern measurements and data acquisition system calibrations. The section labeled ''Krill TS Experiments'' deals with factors involved in the acquisition of echo ensembles from krill. The resulting uncertainties then combine in postprocessing for the TS determination.

The independent parameters directly measured are salinity, water temperature, signal level and receive time, signal trace, and transmitter frequency. Figure 5 shows the uncertainty associated with each parameter which includes the measurement accuracy and range of variation for the duration of each experiment. For example, the temporal variation is reflected in the temperature uncertainty, while the acquisition of krill echo ensembles continued for days, the calibrations took only hours and hence the temperature uncertainties varied accordingly.

For the calibration work, the target signal level and receive time were measured directly using a digital oscilloscope with built in measurement facilities of known accuracy. Simultaneously, the digitized signal time series were recorded by the data acquisition system. The signal level and receive time (determined by the data processing algorithm) were then compared with the directly measured values to determine the accuracy of this processing. The precision of this processing was measured independently by repeatedly processing a range of randomly varied known signals. These results were combined to form the uncertainties of the data

processing routines for target signal level and receive time measurements, which are specified in Fig. 5 in terms of one standard deviation for the measurements. The accuracy of the TS estimate for the calibration sphere (± 0.1 dB, MacLennan, 1981, 1982; Foote, 1983) was combined with the uncertainties of the sound velocity estimates used in the sphere TS determination.

The sound velocity and absorption were calculated using computations after Del Grosso (1974) and Fisher and Simmons (1977), respectively. In both cases, the uncertainties were formed by combining the measurement accuracy and the range of variation computed using the appropriate extremes of the uncertainties as specified in the measurements of their respective independent variables.

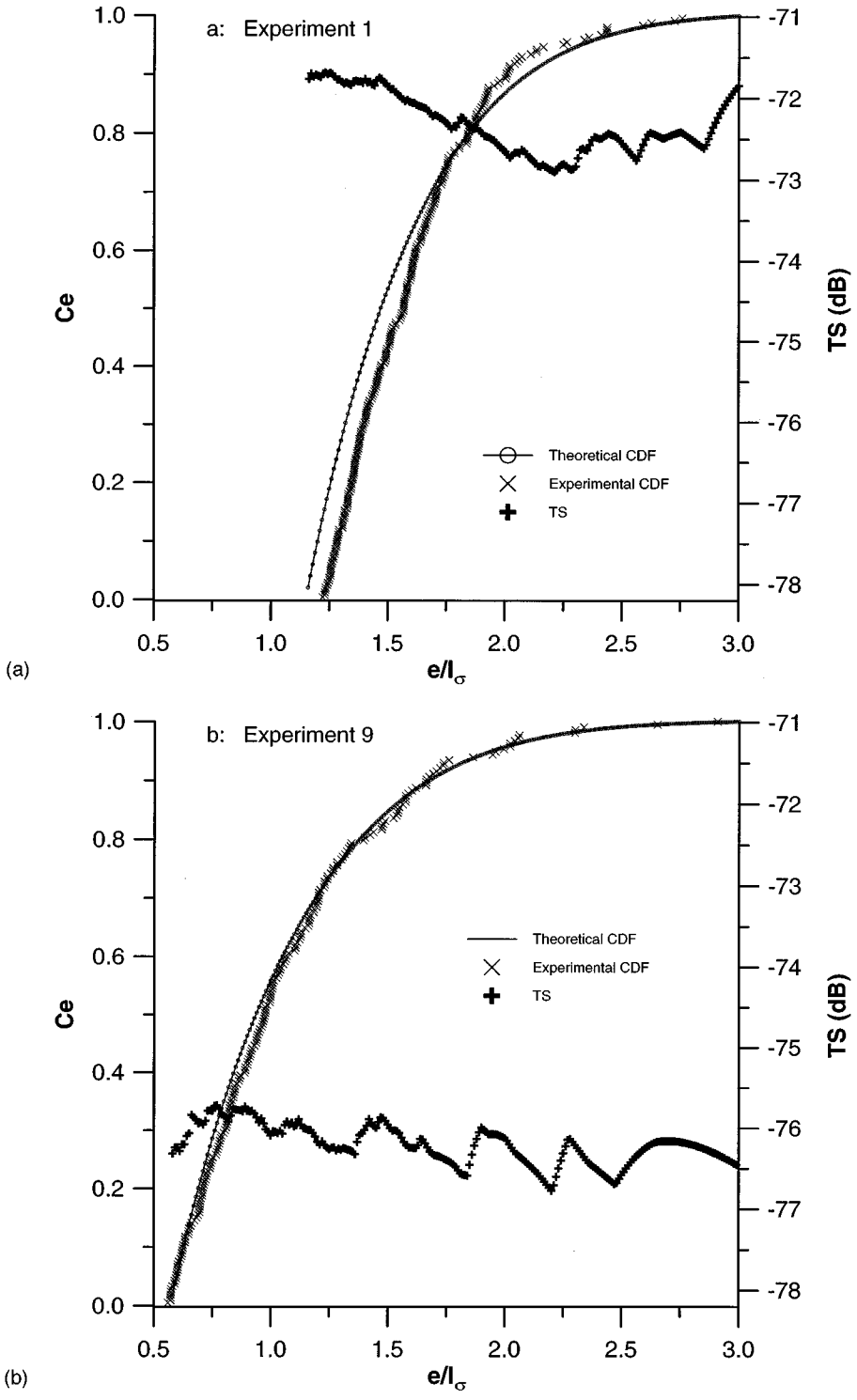

FIG. 4. The theoretical and experimental cumulative probability functions and target strengths computed at each experimental data point. (a) Showing the largest systematic difference between theoretical and experimental results. (b) Showing best agreement between theoretical and experimental dorsal results. (c) Dorsal results from the same krill group used for ventral measurements. (d) Results from ventral experiment.

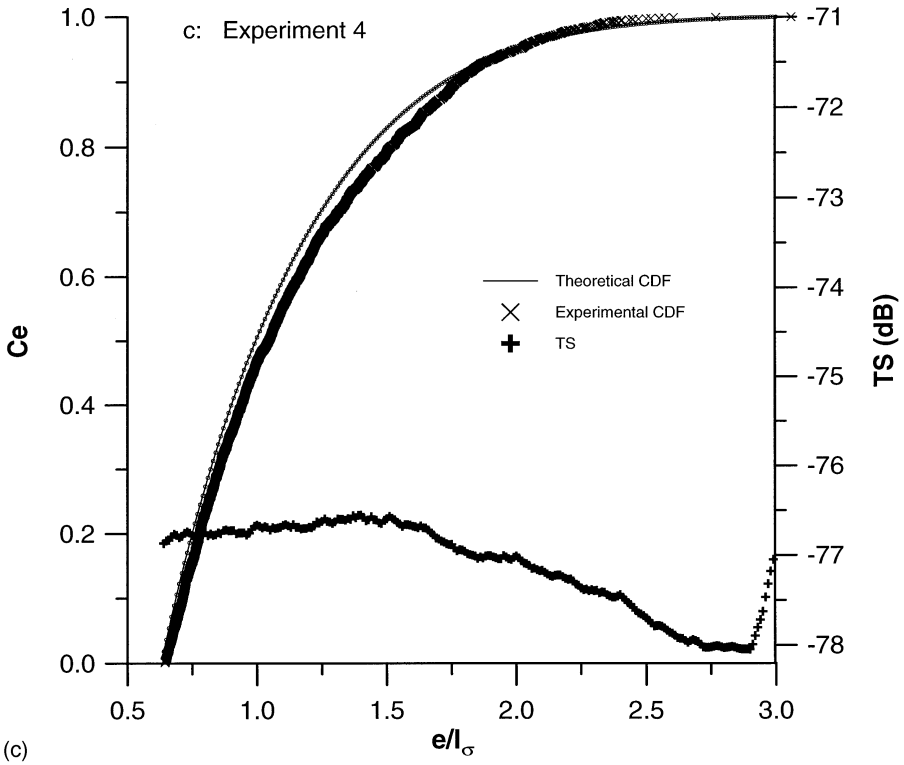

(c)

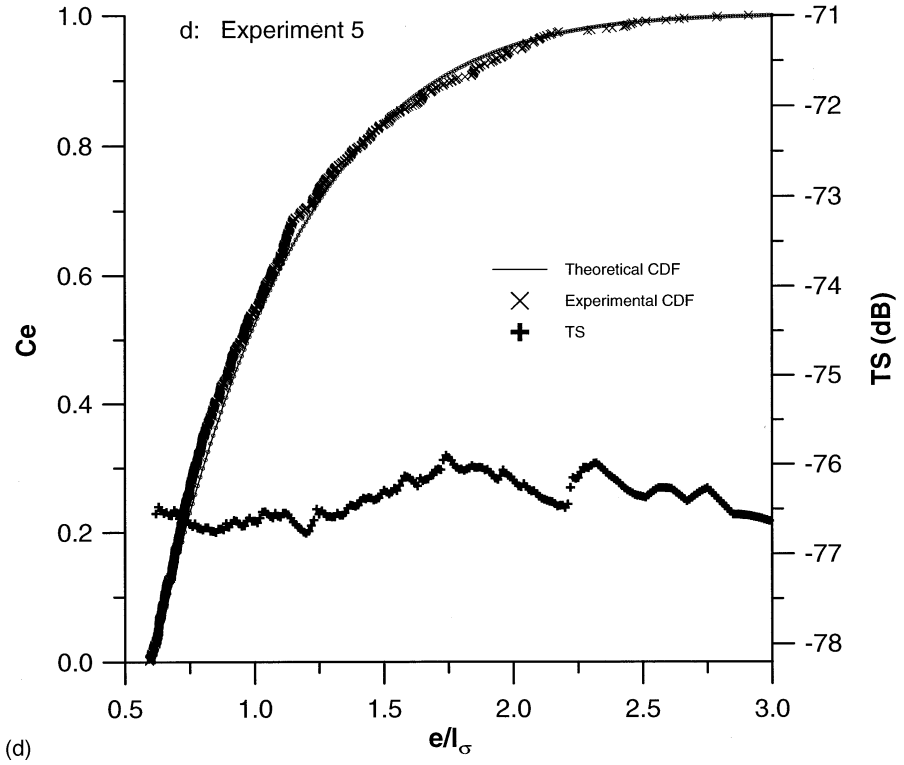

(d)

FIG. 4. (*Continued.*)

2. Combining uncertainties

The determination of the normalized echo ensemble e_n depends both on the experimental computations and the calibration determination $V_0 r_0$, as seen in Eq. (4). The combination of uncertainties for this computation was as follows: The uncertainties were converted to equivalent standard deviations, using the approximation that the range of uncertainty is equivalent to 2σ's. These values were then combined using regular techniques for standard deviations of products, quotients, powers, and functions (Brown, 1968). The final standard deviation was then converted into an uncertainty range which was combined with the uncertainties determined through simulations, and the maximum and minimum computed values for the TS from the Ranked Array analysis.

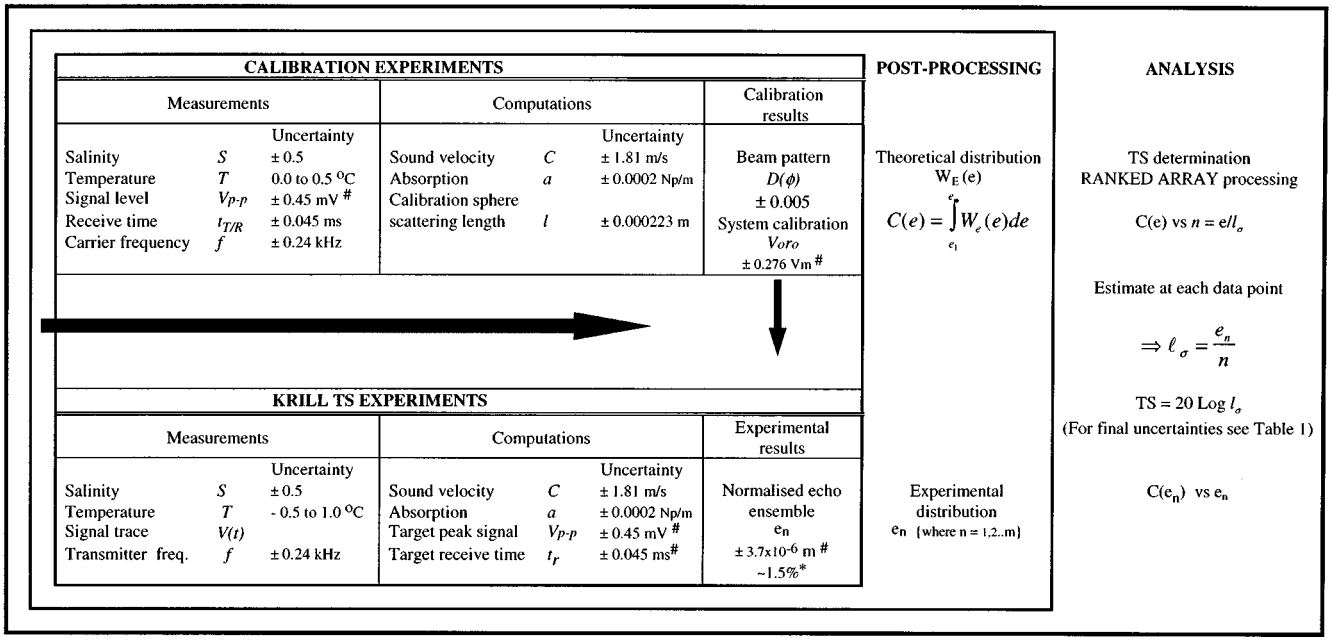

Values expressed as single standard deviations, all other uncertainties are expressed as range limits which include both measurement precision and accuracy.
* Approximate percentage based on a minimum e_n value.

FIG. 5. Flow of uncertainty estimates through measurement and analysis procedures.

IV. DISCUSSION

The results presented here corroborate those of Foote *et al.* (1990) and Hewitt and Demer (1991) which emerged from different methodologies. Foote *et al.* (1990) used caged aggregations of krill while Hewitt and Demer (1991) related field split beam sounder results to net hauls. The work reported here used echoes from single targets in an experimental tank. Both tank and cage enclosures may modify krill behavior, whereas field measurements linked with net hauls make it difficult to establish coincident acoustics and morphometrics. Vessel and net haul effects may also influence behavior, species composition, and morphometrics.

Each of the methods is subject to concerns about the influence of the measuring process on krill behavior and, in some cases, morphology. It is therefore significant that the TS values from these disparate techniques yield comparable results, particularly in view of the need expressed by CCAMLR for a revision to the operational TS versus length expression used in Antarctic krill biomass estimation.

In the past results have generally been reported as estimates of $\overline{\text{TS}}$ with little or no indication of the measurement uncertainty. The application of such estimates in biomass determination for use in stock assessment and management must be greatly improved with reliable estimates of the TS uncertainties involved. Given well parametrized TS estimates, the application of such estimates to survey analysis should only depend on the sampling statistics of the survey process.

The uncertainties in the TS estimates presented are produced by the combination of: the measurement of krill length, calibration, beam pattern, and krill echo measurements, Ranked Array processing, and deviations from the assumptions underlying the formulation of the techniques used. Uncertainties also arise in parametrizing krill dimensions.

A. Calibration and echo ensemble measurements

The calibration and echo ensemble determinations have four contributing components: the calibration constant for the system ($V_0 r_0$), absorption losses, range, and echo level determination (V_{pp}). The dominant components are $V_0 r_0$ and V_{pp} which both have $\sim 1\%$ uncertainties, while the range determination and absorption loss uncertainties are, respectively, one and two orders of magnitude smaller.

B. Beam pattern measurements

Shown with the beam pattern in Fig. 2(b) is the measurement uncertainty as two standard deviations in both U and D. The uncertainty in D is calculated from the standard deviation of the 36 measurements in 10° steps of θ for each value of ϕ [see Fig. 1(a)]. To estimate the sensitivity of the TS estimates to the uncertainty in the beam pattern measurements, two alternative PDF's were constructed using variations of one and two standard deviations in D. The data sets were then reprocessed using these two alternative PDF's and compared with the original processing. A single standard deviation modification results in a 0.6% shift in the results and two standard deviations 1.3% shift ($\sim$0.05 and 0.11 dB, respectively). When compared with the other experimental uncertainties, the TS estimates are comparatively sensitive to the beam pattern measurements. The uncertainty of the beam pattern measurement is equivalent to $\sim 50\%$ of the combined uncertainties of all the other experimental components.

C. Animals length weight (volume) relationship

TS has typically been related to krill body length. The animals used for this work were grouped into length classes for each set of experiments. Wiebe *et al.* (1990) suggest that TS is dependent on target volume rather than cross-section area for the given target type and frequency (where $ka \gg 1$). The modeling work of Stanton *et al.* (1993) shows that the average TS is strongly dependent on both the standard deviation of angle of orientation and the target size, which includes terms for both cylindrical radius and length.

There are numerous length–weight relationships in the literature, many of which are listed and assessed in Morris *et al.* (1988). The ability of krill to shrink in length and weight if starved (Ikeda and Dixon, 1982; Nicol *et al.*, 1991) raises the issue of whether or not a specific allometric relationship between length and weight is conserved after shrinking. The animals available for laboratory work have shrunk after capture in the field. For a given length measurement within one sample set, the variation of sample weights can be considerable (Fig. 7). Assuming a density of unity, for a given length the weight variation translates to a volume variation of up to ~30%. This represents a TS variation of ~1.2 dB. Weights were not measured for the animals used in these experiments, due to the limited number of animals available in the laboratory at the time, and because accurate weight measurements are destructive. These effects offer in part a possible explanation for the difference in TS estimates for the 1988 experiments 1–3 as compared with the following experiments 4–9.

D. Ranked array method

Palumbo *et al.* (1993) reported on the effects of modification of a number of the assumptions on which the Ranked Array method is based. To understand the implications of these results on the work presented here, a significant difference in the processing approach must be considered. Palumbo *et al.* (1993) chose a single point on the cumulative distribution for the TS estimate. The results presented here are based on a TS estimate derived at each point on the $C(e/l_\sigma)$ distribution. The TS uncertainty is then computed using the maximum and minimum of these estimates. Therefore included in the range of the uncertainty of these results is any deviation due to experimental effects which might represent modifications to the fundamental assumptions and hence the form of the experimental distribution. Also, given a knowledge of the smallest and largest e_n values of a sample and the beam pattern, this work presents a method for threshold bias correction using the results of the simulation work. This correction process leads to a further refinement in the performance of techniques such as the Ranked Array method.

E. Distributions

The difference between the theoretical and experimental cumulative distributions, seen particularly in Fig. 4(a) and to a lesser extent in Fig. 4(c), are characteristic of the systematic differences seen in the majority of the other experiments [Fig. 4(b) and (d) are the main two exceptions to this observation]. Two possible sources of this difference are threshold bias and the initial assumption of Rayleigh distributed instantaneous backscatter cross-section values due to target orientation. The alternative more general Rice distribution (Clay and Heist, 1984) may well be more appropriate. Further work underway incorporates simultaneous acoustic and stereo photographic results of target orientation and location within the acoustic beam for experiment 4. A reduction of up to ±1 dB in the uncertainty of these TS estimates may be obtained by further refinement of the theoretical distribution.

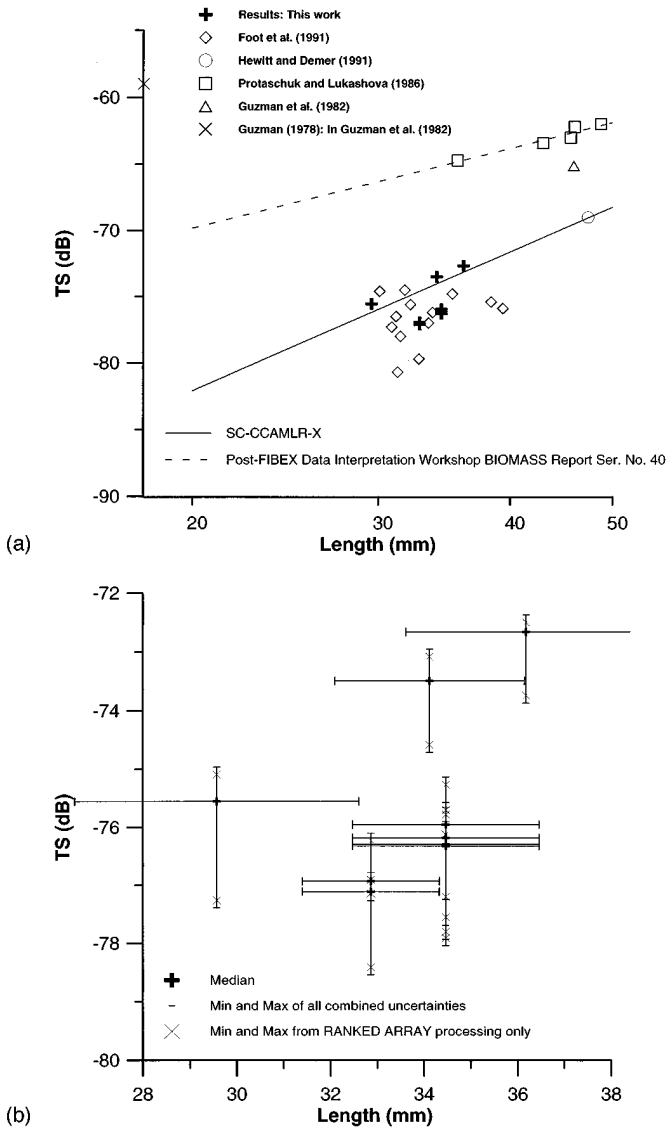

FIG. 6. Target strength estimates as a function of krill overall length. (a) Results from this work and previous measurements (Foote *et al.*, 1991; Hewitt and Demer, 1991; Protashuk and Lakashova, 1986; Guzman, 1978; Guzman *et al.*, 1982) on Antarctic krill at 120 kHz. (b) Uncertainties in target strength and length measurements, with the TS component due to the deviation in the theoretical and experimental cumulative distributions also indicated.

F. Regressions used by CCAMLR

In 1991 the Scientific Committee for CCAMLR adopted a change for the relationship used to derive TS from krill length (SC-CCAMLR-X, 1991, p. 11, 3.34). Figure 6(a) shows the current and previous relationship used to deter-

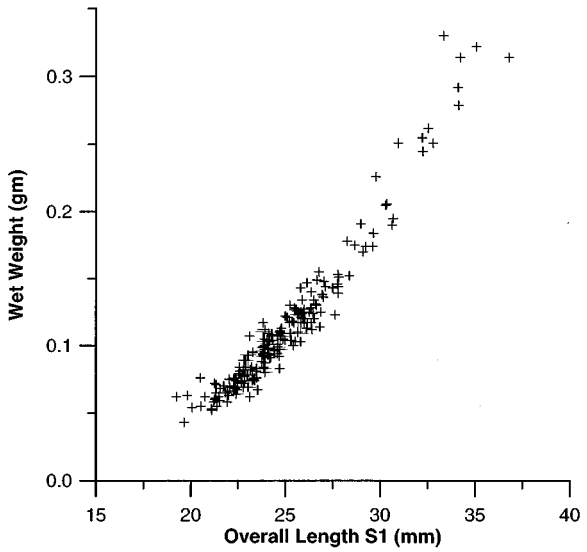

FIG. 7. Spread of wet weights as a function overall length indicating a spread of up to approximately 30% for a given length.

mine the TS and hence biomass estimates. These results and those of Foote *et al.* (1990) were in part the reason for the recommendation and indicate that the current relationship may still overestimate TS.

G. Possible tank effects

A fundamental problem with laboratory in situ experiments is the evaluation of possible behavioral effects of the experimental configuration. Greenlaw (1977) reported a possible variation of up to -20 dB for zooplankton in a vertical orientation compared to a horizontal orientation. The modeling work Stanton *et al.* (1993) demonstrates the dependence of average TS on the standard deviation of angle of orientation. This modeling work also shows that average TS is largely independent of the degree of bend of the cylindrical target over a wide range of orientations. Thus if the experimental conditions modified behavior, specifically animal orientation, then potential exists for generating results significantly different for those that might be expected for *in situ* field measurements. This is one of the fundamental problems with experiments which use tethered targets. The last series of experiments involved apparent behavior modification.

The behavior of the animals was modified by turning an underwater light on for 15 min in every 75 min. This varied the rate of data acquired, compared to experiments run in continued darkness, indicating a behavior modification. The data acquisition rate increased from 1 or less samples per hour up to 10 samples per hour. Though the activity of the animals was thus increased by this modification, no significant variation occurred in the TS estimates (experiments 6–9, Table I). This increased activity may or may not have involved changes in animal orientation.

H. Ventral measurement

TS estimates for ventral measurements are relevant to the use of upward acoustic systems such as towed bodies used for surveying surface layers not visible to hull mounted transducers. The two sample Kolmogorov Smirnov test was used to test the likelihood that the distributions for experiments 4 and 5 were equivalent. The maximum difference of $D=0.043$ was found where the critical value of $D_{\max}=0.059$ at $\alpha=0.05$ and thus sustains the null hypothesis that the distributions are equivalent, i.e., that no significant differences were observed between dorsal and ventral target strength estimates for the same group of krill.

I. Further work

Uncertainty in the TS estimates presented is dominated by two factors: the PDF used for modeling the effects of target orientation and the measurements of krill size. Figure 6(b) shows the TS estimates as a function of $S1$ length and includes the uncertainties for each experiment broken down into two components. The dominant component represented by the crosses in Fig. 6(b) indicates the minimum and maximum TS values determined from the Ranked Array processing. Added to this component is the smaller uncertainty due to measurements for determining e_n's and the beam pattern.

Little gain can be expected from improvements to the careful measurement procedures used in this work. Thus to significantly reduce the uncertainty of these estimates, the theoretical distribution requires further refinement. An investigation of the PDF due to target orientation, using the photogrammetric results combined with the acoustic results of this work, will give further insight. Also required is an improvement in the measurement of krill dimensions, giving a reduced range in weight and length variations. However, the nature of further TS estimates should be determined by the requirements for the estimates.

ACKNOWLEDGMENTS

The assistance of the Australian Antarctic Division, Hobart, Tasmania, in providing funding, krill, and tank facilities is gratefully acknowledged. In particular the authors wish to thank S. Nicol, M. Stolp, and I. Higginbottom for their assistance with the experimental work, and S. Wright for his editorial assistance.

Brown, A. F. (**1968**). *Statistical Physics* (Edinburgh U. P., Edinburgh), Chap. 7, pp. 178–210.

Clay, C. S., and Heist, B. G. (**1984**). ''Acoustic scattering by fish—Acoustic models and a two parameter fit,'' J. Acoust. Soc. Am. **75**, 1077–1083.

Clay, C. S., and Medwin, H. (**1977**). *Acoustical Oceanography, Principles and Applications* (Wiley, New York), Chap. 7, pp. 216–252, Appendix A7, pp. 477–485.

Craig, R. E., and Forbes, S. T. (**1969**). ''Design of a sonar for fish counting,'' FiskDir. Skr. Ser. Havaunders. **15**, 210–219.

Del Grosso, V. A. (**1974**). ''New equation for the speed of sound in natural waters (with comparisons to other equations),'' J. Acoust. Soc. Am. **56**, 1084–1091.

Ehrenberg, J. E. (**1974**). ''Two applications for a dual-beam transducer in hydroacoustic fish assessment systems,'' Proc. IEEE Conf. Eng. Ocean Environ. **1**, 152–155.

Ehrenberg, J. E., Carlson, J. J., Traynor, J. J., and Williamson, N. J. (**1981**). ''Indirect measurement of the mean acoustic scattering cross section of fish,'' J. Acoust. Soc. Am. **69**, 955–962.

Fisher, F. H., and Simmons, V. P. (**1977**). ''Sound absorption in sea water,'' J. Acoust. Soc. Am. **6**, 558–564.

Foote, K. G. (**1982**). ''Optimizing copper spheres for precision calibration of hydroacoustic equipment,'' J. Acoust. Soc. Am. **71**, 742–747.
Foote, K. G. (**1983**). ''Maintaining precision calibrations with optimal copper spheres,'' J. Acoust. Soc. Am. **73**, 1054–1063.
Foote, K. G., Everson, I., Watkins, J. L., and Bone, D. G. (**1990**). ''Target strength of Antarctic krill (*Euphausia superba*) at 38 and 120 kHz,'' J. Acoust. Soc. Am. **87**, 16–24.
Foote, K. G. (**1991**). ''Summary of methods for determining fish target strength at ultrasonic frequencies,'' ICES J. Mar. Sci. **48**, 211–217.
Greenlaw, C. F. (**1977**). ''Backscatter spectra of preserved zooplankton,'' J. Acoust. Soc. Am. **62**, 44–52.
Guzman, O. F. (**1978**). ''Investigaciones biologicas-pesqueras del krill. Analisis comparativo de metodos estadisticos y calculo de una constante de ecointegracion,'' in *Serie Investigacion Pesquera* (IFOP), p. 37.
Guzman, O. F., Lillo, S. V., and Marin, B. I. (**1982**). ''Calibration of the echointegration constant of krill (*Euphausia superba*),'' INACH, Scientific Series **28**, 47–71.
Hewitt, R. P., and Demer, D. A. (**1991**). ''Target strength of Antarctic Krill,'' Nature (London) **353**, 310.
Ikeda, T., and Dixon, P. (**1982**). ''Body shrinkage as a possible overwintering mechanism of the Antarctic krill, *Euphausia superba Dana*,'' J. Exp. Mar. Biol. Ecol. **62**, 143–151.
MacLennan, D. N. (**1981**). ''The theory of solid spheres as sonar calibration targets,'' Scott. Fish. Res. Rep. (22), pp. 1–17.
MacLennan, D. N. (**1982**). ''Target strength measurements on metal spheres,'' Scott. Fish. Res. Rep. (25), pp. 1–20.
MacLennan, D. N., and Simmonds, E. J. (**1992**). *Fisheries Acoustics* (Chapman and Hall, London), Chap. 5, pp. 124–162.
Mauchline, J. (**1980**). ''The biology of mysids and euphausiids,'' Adv. Mar. Biol. **18**, 681.
Medwin, H., Fitzgerald, J., and Rautmann, G. (**1975**). ''Acoustic miniprobing for ocean microstructure and bubbles,'' J. Geophys. Res. **80**, 405–413.
Morris, D. J., Watkins, J. L., Ricketts, C., Buchholz, F., and Priddle, J. (**1988**). ''An assessment of the merits of the length and weight measurements of Antarctic krill *Euphausia superba*,'' Br. Antarct. Surv. Bull. No 79, pp. 27–50.
Nakken, O., and Olsen, K. (**1977**). ''Target strength measurements of fish'', Rapp. P.-V. Reun. Cons. Int. Explor. Mer. **170**, 52–69.
Nicol, S., Stolp, M., and Hosie, G. W. (**1991**). ''Accumulation of fluorescent age pigments in a laboratory population of Antarctic krill *Euphausia superba Dana*,'' J. Exp. Mar. Biol. Ecol. **146**, 153–161.
Palumbo, D., Penrose, J. D., and White, B. A. (**1993**). ''Target strength estimation from echo ensembles,'' J. Acoust. Soc. Am. **94**, 2766–2775.
Penrose, J. D., and Pauly, T. J. (**1993**). ''An evaluation of target strength estimations from echo ensembles,'' edited by J. M. F. Moura and I. M. G. Lourtie, *Acoustic signal processing for ocean exploration, funchal, Madeira, Portugal*, NATO ASI Series C: Mathematical and Physical Sciences **388**, 433–440.
Penrose, J. D., Conde, M., and Pauly, T. J. (**1994**). ''Acoustic detection of ice crystals in Antarctic waters,'' J. Geophys. Res. **99**, 12573–12580.
Peterson, M. L., Clay, C. S., and Brandt, S. B. (**1976**). ''Acoustic estimates of fish density and scattering function,'' J. Acoust. Soc. Am. **60**, 618–622.
Protaschuk, V. A., and Lukashova, T. A. (**1986**). ''Determination of Antarctic krill acoustic back-scattering cross-section,'' Selected Scientific Papers (SC-CAMLR-SSP/3). CCAMLR, Hobart, Australia, 141–151.
Stanton, T. K., Wiebe, P. H., and Clay, C. S. (**1993**). ''Average echoes from randomly oriented random-length finite cylinders: Zooplankton models,'' J. Acoust. Soc. Am. **94**, 3464–3472.
SC-CCAMLR. (**1991**). Report of the Tenth Meeting of the Scientific Committee (SC-CCAMLR-X). CCAMLR, Hobart, Australia, p. 11.
Weimer, R. T., and Ehrenberg, J. E. (**1975**). ''Analysis of threshold-induced bias inherent in acoustic scattering cross-section estimates of individual fish,'' J. Fish. Res. Bd. Can. **32**, 2547–2551.
Welsby, V. G., and Hudson, J. E. (**1972**). ''Standard small targets for calibrating underwater sonars,'' J. Sound Vib. **20**, 399–406.
Wiebe, P. H., Greene, C. H., Stanton, T. K., and Burczynski, J. (**1990**). ''Sound scattering by live zooplankton and micronekton: Empirical studies with dual-beam acoustical system,'' J. Acoust. Soc. Am. **88**, 2346–2359.

Source signature measurements of underwater explosives at very high ambient pressures

John A. Collins and James E. Broda
Dept. of Geology and Geophysics, Woods Hole Oceanographic Institution, Woods Hole, Massachusetts 02543

G. M. Purdy
Division of Ocean Sciences, National Science Foundation, Washington, DC

Joel Gaspin, Tom Griffin, Carl Peletski, Len Lipton, and Bryan Baudler
Naval Surface Warfare Center, Indian Head Division, White Oak, Silver Spring, Maryland 20903-5000

(Received 26 April 1996; revised 22 April 1997; accepted 1 September 1997)

The interpretation of seismic refraction experiments carried out on the deep-ocean floor has been hampered by lack of knowledge of the source signatures of explosives at these high ambient pressures. In order to fully exploit the data from such experiments, the source signatures of four explosives detonated at deep water depths have been measured. The explosives were commercially available Pentolite and three U.S. Navy explosives: PBXN-103, PBXN-111, and PBXW-127. A total of 75 ~10 lb (4.54 kg) charges were detonated at depths of 2350–4593 m, and the source signatures were recorded at offset ranges of 160–230 m. For all four explosives, the period of the first oscillation follows the theoretically established relationship $T=K^*M^{1/3}(Z+10)^{-5/6}$, where T is the period (s), M is the charge mass (kg), and Z is the detonation depth (m). The optimum value of K for Pentolite (2.07 ± 0.01 s m$^{5/6}$ kg^{-1}) is identical to the value previously reported from the analysis of explosives detonated at depths of less than a few hundred meters. The optimum values for PBXN-103, PBXN-111, and PBXW-127 are 2.67 ± 0.01 s m$^{5/6}$ kg^{-1}, 2.64 ± 0.01 s m$^{5/6}$ kg^{-1}, and 2.73 ± 0.01 s m$^{5/6}$ kg^{-1}, respectively. The greater bubble pulse period of the PBX-based explosives means that they are richer in low-frequency energy than Pentolite. The total energy flux in the frequency band 30–100 Hz is ~6 dB greater for the PBX-based explosives than that for Pentolite at all detonation depths.
[S0001-4966(98)02301-7]

PACS numbers: 43.30.Xm, 43.30.Lz, 43.30.Ma, 43.30.Qd [JHM]

INTRODUCTION

The scientific use of underwater explosives as artificial seismic sources dates back to 1935. Ewing *et al.* (1937) describe the first marine seismic refraction experiment, carried out off the east coast of the U.S. The gelatin explosives, ranging up to 30 lbs (13.6 kg) in mass, were detonated on the seafloor in water depths of less than 200 m. Ewing *et al.* (1950) carried out the first deep-water refraction profile in 1949, in water depths of about 5000 m off Bermuda. Charge sizes ranged up to 300 lb (136 kg) of TNT, and the charges were detonated at shallow depths. By 1960, many hundreds of such refraction profiles had been collected throughout the deep-ocean basins (e.g., Raitt, 1956). The early refraction data sets were typically interpreted by inverting the travel times of refracted phases for velocity structure as a function of depth below the seafloor. Modern seismological techniques allow the complete seismic waveform, i.e., amplitude and phase, to be inverted for each structure. Such inversions are more complete if the source waveform is known.

Our knowledge of the source waveforms generated by underwater explosions comes primarily from military-funded research during and after World War II (e.g., Cole, 1948; Arons, 1948, 1954; Weston, 1960). Underwater explosions are characterized by an initial shock wave that is followed by a number of ''bubble pulses'' caused by oscillations of the gas bubble released by the explosion. Based on experiment, Arons (1948, 1954) expressed the pressure-time function as a function of charge mass and detonation depth. The validity of the pressure-time function developed by Arons and Weston was established for detonation depths of less than a few hundred meters only. These empirical functions have proved very useful to marine seismologists analyzing refraction data sets shot with explosives. An outstanding example of waveform analysis of a marine seismic refraction data set is presented by Spudich and Orcutt (1980). The great majority of these studies, both military and academic, have focused on the use of explosives detonated at shallow (less than a few hundred meters) depths. However, some modern geophysical research requires explosives to be detonated at depths of many thousands of meters.

As our knowledge of the structure of the deep-ocean floor increases, it is becoming clear that many widely contrasting structural characteristics exhibit important variability on scales of as little as a few hundred meters. It is necessary to develop seismic techniques that will allow sub-seafloor structures to be mapped on these lateral scales in water depths of 3000 m and greater. For example, at slow spreading mid-ocean ridges, the predominant mode of emplacement of the surface volcanic layer appears to be via large numbers of small volcanoes (Smith and Cann, 1993) each a

few hundreds meters in extent. The structure of these features and the depth at which their magma source lies remains unknown. On fast spreading ridges, a uniform volcanic layer less than 100 m in thickness at the rise crest more than doubles in thickness within 1–2 km of the rise crest (Christeson *et al.*, 1992, 1994a; Harding *et al.*, 1993). The geological nature of the boundary marking the base of this layer remains in doubt, and the processes that control the thickness of this layer—a key to understanding temporal variability in the crustal accretion process itself—are unknown.

Although conventional seismic techniques, primarily based on source and receiver systems located at or near the sea surface, have made substantial progress in tackling these (and many other comparable) problems in marine earth sciences, the need for testing of more rigorous process-oriented models requires increasingly precise structural determinations. One approach to this is to place the complete seismic experiment—both source and receiver systems—actually on the seafloor, and to use higher frequency energy. The optimal wavelengths to use are strongly dependent on the characteristics of the particular structure being studied, of course. For example, in the case of studies of the oceanic volcanic layer the highly attenuative characteristics of this strata ($Q \sim 15-20$; Christeson *et al.*, 1994b) restrict most practical experiments to frequencies below 100 Hz.

The use of ocean floor receiver systems is commonplace in modern marine seismology, but the design and operation of an effective near-bottom source system, that generates sufficient energy in the appropriate seismic band, presents a substantial technical challenge. One successful solution to this problem is the NOBEL (Near Ocean Bottom Explosives Launcher) system that has been operated by Woods Hole Oceanographic Institution for the past several years (Koelsch *et al.*, 1991), and has been successfully used in studies of the structure of the East Pacific Rise crest (Christeson *et al.*, 1992, 1994a, b). NOBEL is towed within a few tens of meters of the ocean floor in water depths up to 6000 m on a conventional oceanographic 0.68-in. (1.73 cm) coaxial cable. It carries 47 5–15 lb (2.3–6.8 kg) explosive charges that can be deployed and detonated on command from the research vessel. The time of detonation is known to better than a millisecond, and the height of the charge above the seafloor can be measured from 12-kHz pinger data to within 1–2 m. This system allows unusually precise small-scale experiments to be carried out actually on the seafloor, even in areas of rough terrain. It allows a relatively large number of charges to be positioned according to some predetermined plan and detonated at intervals of anything greater than ~ 2.5 min.

Other approaches have also been used to fire explosives in a controlled manner at deep-ocean depths. Sauter *et al.* (1986) and Schreiner *et al.* (1991) describe an experimental procedure whereby charges of up to 5 kg are detonated, by a timer, inside a pressure case that has been lowered to the seafloor on the research vessel's wire. Much larger amounts of explosive (up to 45 kg) have been detonated at deep-ocean depths by lowering one or more charges to the seafloor on a coaxial cable and detonating the charge via a signal sent down the cable from the research vessel. This approach has been used successfully to determine the internal structure of a 12-Ma seamount in the eastern Pacific (Hildebrand *et al.*, 1989), and the seismic structure of the shallow igneous crust at Hess Deep in the eastern Pacific (Wiggins *et al.*, 1993, 1996).

Until the work described in this paper, the on-bottom experimental procedures described above suffered from one important shortcoming—a lack of reliable knowledge of the characteristics of the source spectrum at these extreme depths, and it was to the solution of this problem that many of the observations presented here were directed. However, these are not the first-measurements of deep explosions. Blaik and Christian (1965), and Christian and Blaik (1965) measured the source waveform of explosives detonated at depths of up to 6700 m. These earlier studies recorded the explosion source signatures on a hydrophone deployed at a depth of less than 61 m below the sea surface. Consequently, these workers were not able to separate the effects of two important variables, propagation distance and detonation depth. Moreover, these studies focused on the high frequency portion (above the bubble-oscillation frequency) of the source spectra. This portion of the source spectrum is of limited use in the kinds of studies described above.

In this paper we present the observations, with some interpretation, of the source characteristics of approximately 75 $\sim$10 lb (4.54 kg) explosive charges detonated at depths between 2350 m and 4593 m below the sea surface. The source signatures were recorded at offsets ranges of 160–230 m. Important comparisons are made of the signatures of four different explosives. The custom-designed experimental system used to collect these data is described briefly in the following paragraphs.

I. EXPERIMENTAL TECHNIQUE

The only feasible way to record far-field interference-free signatures of explosive charges of this magnitude ($\sim$10 lb, 4.54 kg) at pressures corresponding to depths below the sea surface of 2500–4500 m is in the deep ocean. Water depths must be approximately $\sim$500 m greater than the test depth so that adequate time is available to record the full signature before contamination by the seafloor reflection occurs. The measurements presented here were recorded during a ten-day cruise on the R/V CAPE HATTERAS in April, 1995 working near 31 °N 73 °W in the western Central Atlantic where water depths exceeded 5000 m. The experimental configuration is illustrated in Fig. 1.

From the research vessel, a conventional oceanographic 4700-m-long, 0.68-in. (1.73 cm) coaxial cable was used both to transfer data from the monitoring hydrophones to the shipboard recording system and to control the charge detonation. At the end of the coaxial cable, the main instrumentation package housed three primary systems: a telemetry package that permitted both 9600 baud and broadband FM telemetry along the coaxial cable; a microprocessor-based firing control system (one module from the NOBEL system); and two independent monitoring hydrophones each with controllable gain and attenuation settings. To provide the requisite safe stand-off distance between the explosives and the electronics, a 150-m-long multiconductor Kevlar strength member

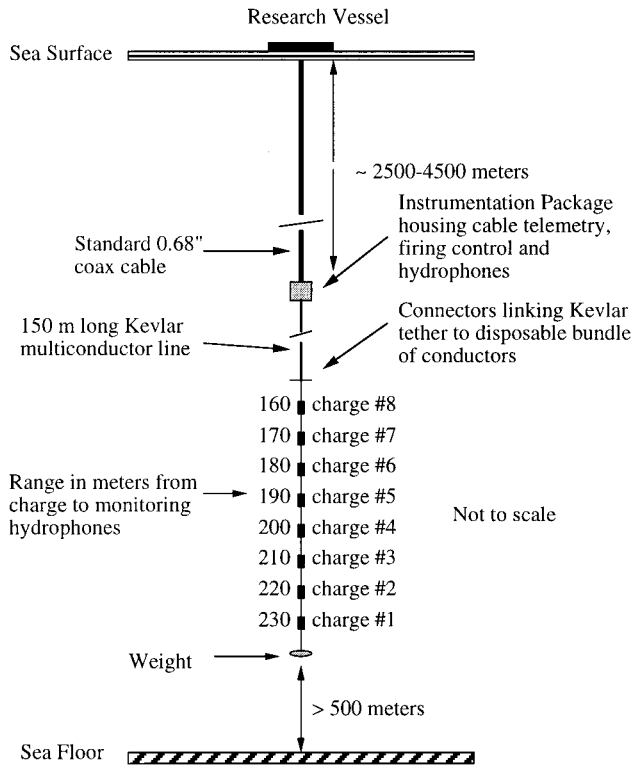

FIG. 1. Cartoon depicting the primary components of the underwater instrumentation used to measure the explosive source signatures. See text for further explanation.

extended beneath the main instrumentation package. On the end of this strength member were connectors for the attachment of the disposable firing lines on which the firing detonators and up to eight individual charges were attached at 10-m intervals. Of the 101 attempts made during the ten-day cruise to fire detonators using this system, all but six were successful. Five failures occurred on the second of the 15 lowerings and were determined to be due to an improperly seated connector between the firing lines and the Kevlar cable; the sixth was caused most probably by a detonator malfunction. Rigorous procedures were adopted to insure safety during loading, lowering, operation, and recovery of this system.

The detonation of the charges was controlled from the research vessel, each charge being fired in turn, starting with the lowermost. The signature of each charge was inspected in order to check proper operation of the hydrophones and data recording systems before the next charge was detonated. The time required for each lowering was dependent primarily upon the depth at which the measurements were to be taken, but the typical duration was 5–6 h.

TABLE I. Number of measurements of each explosive at each depth.

Explosive/ nominal shot depth (m)	Pentolite	PBXN-103	PBXN-111	PBXW-127
2500	4	5	5	5
3000	3	3	3	3
3500	8	4	4	3
4000	3	4	4	3
4500	2	2		1

TABLE II. Statistics of charge masses for each explosive.

Explosive mass (g)	Pentolite	PBXN-103	PBXN-111	PBXW-127
Mean total mass,	4038	4800	4650	5274
standard deviation	50	31	35	116
Mean booster mass,	0	480	466	472
standard deviation	0	25	29	19
Mean mass of PETN Detonating cord,	0	54	0	137
standard deviation	0	6	0	115

Knowledge of the depth below the sea surface of each charge at the time of detonation is essential to the interpretation of the data collected during this experiment. Detonation depths were determined using two methods. In one approach, depths were calculated by measuring the travel times of (i) the direct arrival from shot to receiver, (ii) the arrival that traveled via the path: shot to seafloor to hydrophone, and (iii) the arrival that travelled via the path: shot to sea surface to hydrophone. This method assumed that the horizontal offset between source and hydrophone was negligible. The validity of this assumption was verified by comparing the difference in the measured depths of the shot and hydrophone to their known offset. The other approach used to calculate shot depths made use of the measured travel times of (i) the direct arrival from the shot to the research vessel, and (ii) the arrival that travelled via the path: shot to seafloor to ship. The arrival time at the ship was measured by digitizing the output of the ship's 3.5-kHz transducer. Note that this second approach to determining shot depth remained valid even if the shot and hydrophone trailed well behind the ship.

Two independent approaches were used for data acquisition and recording. In order to provide the maximum possible data fidelity, one system used a 12 bit analog-to-digital converter (A/D), located in the deep-towed instrumentation package, that recorded one second of data from each hydrophone at a sampling rate of 3000 samples per second with 12 bit resolution. These data were stored temporarily in memory and retrieved along the digital telemetry link on the coaxial cable following each detonation. To maximize the bandwidth of the data recording, an FM analog system was also used, one channel for each hydrophone, that provided on the coaxial cable a bandwidth from 20 Hz to 10 kHz and a dynamic range of 42 dB. These two analog channels were digitized on board ship at sampling rates of 50 kHz with a resolution of 12 bits. The ability to adjust the hydrophone preamplifier gains from the research vessel meant that the limited dynamic range of these recording systems was not a handicap.

Comparisons were made of the signatures of four explosives as well as the variation of these with depth (Tables I and II). The four explosives were conventional, commercially available Pentolite (50% TNT, 50% PETN), two U.S. Navy qualified underwater explosives PBXN-103 and PBXN-111, and a relatively new formulation currently being

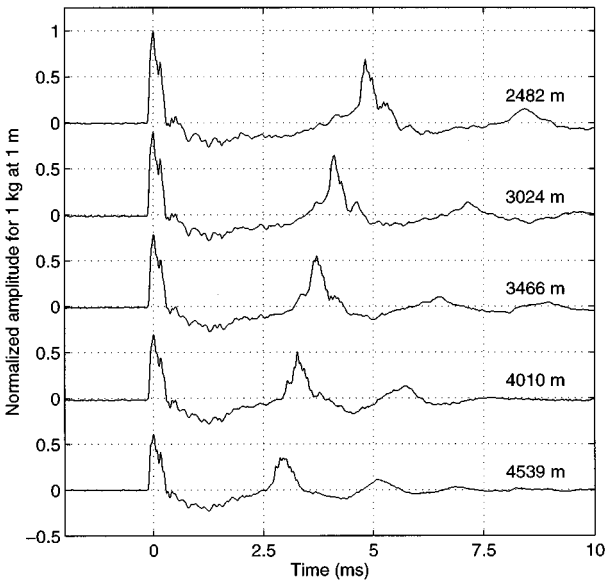

FIG. 2. Representative examples of the source signature of Pentolite. The charges were detonated at the indicated depths. The time series are offset vertically from each other by one unit. The measured amplitudes (volts) were scaled by dividing by the factor $(M^{1/3}/R)^{1.13}$, where M is the charge mass in kilograms and R is the distance between source and receiver in meters. The resulting amplitudes were then normalized relative to the maximum amplitude of the source signature recorded for the charge detonated at 2482 m. Peak pressures of the shockwave range from 43 to 79 MPa.

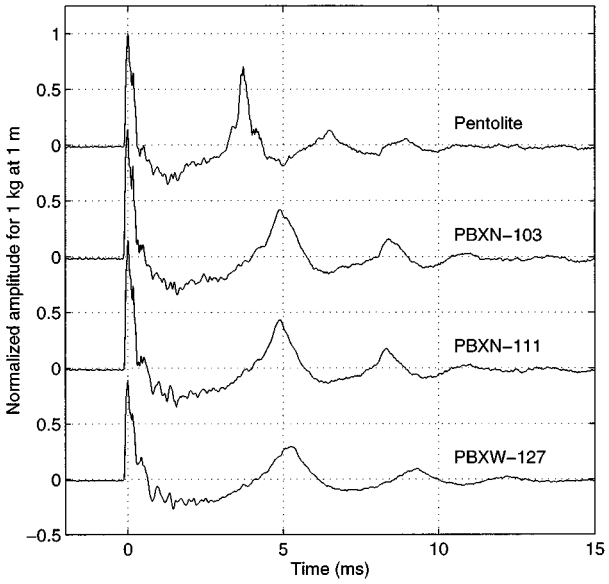

FIG. 3. Representative examples of the source signature of Pentolite, PBXN-103, PBXN-111, and PBXW-127; detonation depths were 3466, 3430, 3401, and 3370 m, respectively. The time series are offset vertically from each other by one unit. The measured amplitudes (volts) were scaled by dividing by the factor $(M^{1/3}/R)^{1.13}$, where M is the charge mass in kilograms, and R is the distance between source and receiver in meters. The resulting amplitudes were then normalized relative to the maximum amplitude of the Pentolite source signature.

reviewed by the U.S. Navy, PBXW-127. A Pentolite booster charge was used to ensure detonation of the PBXN-103, PBXN-111, and PBXW-127 explosives.

The data shown in the figures have been corrected for geometrical spreading losses by multiplying the raw data by the offset in meters between the source and receiver. The data have also been corrected for the variation in charge size. A simple scaling argument shows that, for a given explosive, the peak amplitude of the shockwave generated by an underwater explosion is proportional to the cube root of the charge mass (e.g., Cole, 1948). The energy flux density spectrum of the source signatures is proportional to the mass to the four-thirds power (Weston, 1960). These scaling factors have been applied as appropriate to the data presented here.

II. RESULTS

Representative examples of the explosive source signatures are presented in Figs. 2 and 3. These data were recorded using the shipboard acquisition system, i.e., were digitized at a sampling rate of 50 kHz. The data have not been deconvolved by the impulse response of the recording system. The transfer function is flat (<1 dB ripple) between 30 and 6000 Hz. All of the waveforms shown in Figs. 2 and 3 were recorded at identical acquisition parameters, i.e., gain and filter settings, etc. The most striking features of Figs. 2 and 3 are (i) the decrease in bubble pulse period with increased detonation depth (Fig. 2), and (ii) the substantially greater bubble pulse period of the PBX-based explosives relative to Pentolite (Fig. 3). A key aspect in establishing an empirical pressure-time function for explosives detonated at deep-ocean depths is determining a relationship between detonation depth and bubble oscillation period for a given explosive. A theoretical argument (Freidman, 1947) shows the the following relationship between the bubble oscillation period, charge mass, and shot depth:

$$T = K^* M^{1/3} (Z+10)^{-5/6}, \tag{1}$$

where T = period (s), K = constant (s $m^{5/6} kg^{-1}$), M = charge mass (kg), and Z = shot depth (m). Based on observations of TNT detonated at shallow depths (<100 m), Arons (1948) determined a value of K equal to 2.11 s $m^{5/6}$ kg^{-1} for the first bubble pulse. Blaik and Christian (1965) determined a similar value from their deep explosion data.

Figure 4 shows the observed period of the first bubble oscillation for Pentolite, PBXN-103, PBXN-111, and PBXW-127 as a function of shot depth. At a given detonation depth, the bubble oscillation periods of the PBX-based explosives are greater than the period for Pentolite. The solid curves represent the predicted periods calculated for values of the constant K in Eq. (1) that result in the minimum misfit (in the least squares sense) between the observed and predicted values. The estimated values of K for Pentolite, PBXN-103, PBXN-111, and PBXW-127 are 2.07 ± 0.01 s $m^{5/6}$ kg^{-1}, 2.62 ± 0.01 s $m^{5/6}$ kg^{-1}, 2.59 ± 0.01 s $m^{5/6}$ kg^{-1}, and 2.67 ± 0.01 s $m^{5/6}$ kg^{-1}, respectively. The curves were calculated for the mean mass of each explosive, and hence exaggerate the difference between the observed and predicted values. For the PBX explosives, the values of K obtained via the least-squares analysis must be corrected for the mass of the Pentolite booster (Price, 1979). The corrected values for PBXN-103, PBXN-111, and PBXW-127 are 2.67 ± 0.01 s $m^{5/6}$ kg^{-1}, 2.64 ± 0.01s $m^{5/6}$ kg^{-1}, and 2.73 ± 0.01 s $m^{5/6}$ kg^{-1}, respectively.

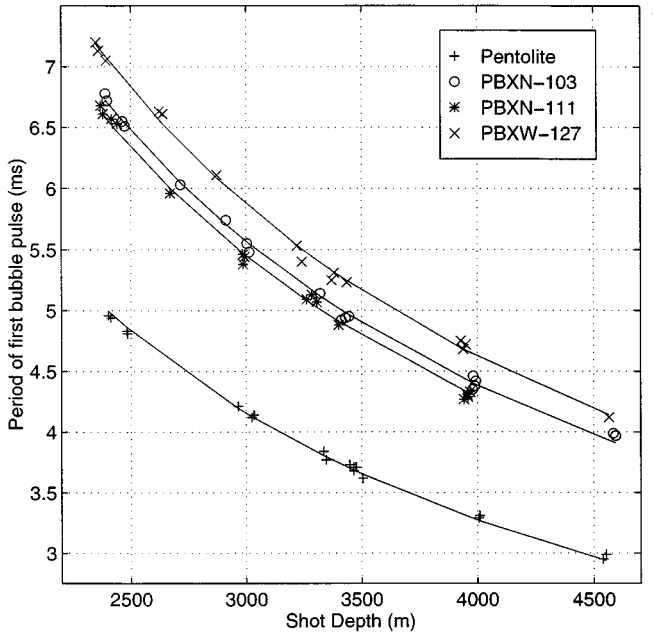

FIG. 4. Symbols show the observed periods of the first bubble pulse for Pentolite, PBXN-103, PBXN-111, and PBXW-127 as a function of detonation depth. The solid curves represent the predicted periods calculated for values of the constant K in Eq. (1) that result in the minimum misfit (in the least squares sense) between the observed and predicted values. The estimated values of K for Pentolite, PBXN-103, PBXN-111, and PBXW-127 are 2.07 ± 0.01 s m$^{5/6}$ kg^{-1}, 2.62 ± 0.01 s m$^{5/6}$ kg^{-1}, 2.59 ± 0.01 s m$^{5/6}$ kg^{-1}, and 2.67 ± 0.01 s m$^{5/6}$ kg^{-1}, respectively. The curves were calculated for the mean mass of each explosive, and hence exaggerate the difference between the observed and predicted values.

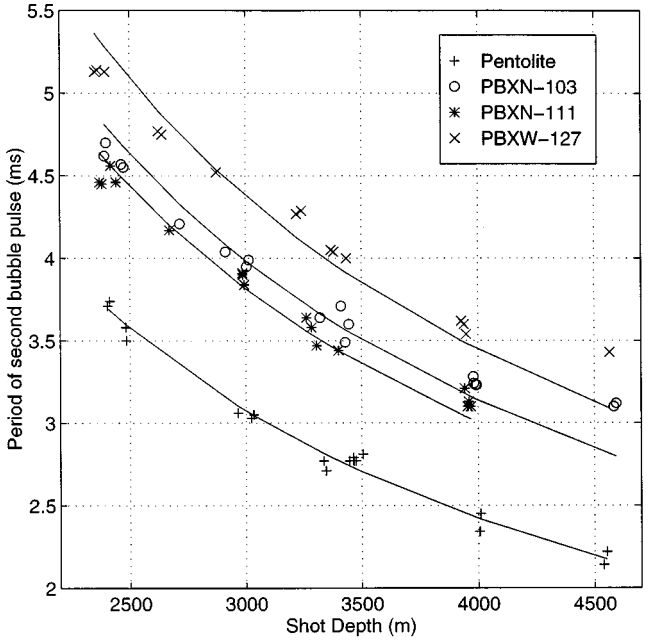

FIG. 5. Symbols show the observed periods of the second bubble pulse for Pentolite, PBXN-103, PBXN-111, and PBXW-127 as a function of detonation depth. The solid curves represent the predicted periods calculated for values of the constant K in Eq. (1) that result in the minimum misfit (in the least squares sense) between the observed and predicted values. The curve for Pentolite matches the observed data satisfactorily; the chi-square statistic is 15. The estimated value of K for Pentolite is 1.53 ± 0.01 s m$^{5/6}$ kg^{-1}. The predicted curves for PBXN-103, PBXN-111, and PBXW-127 are a poor fit to the observed data; the chi-square statistics are 94, 42, and 96, respectively. By fitting for the depth exponent as well as the constant K in equation 1, the chi-square statistics are reduced to 15, 23, 14, and 12, respectively. The estimated values of the depth exponent for PBXN-103, PBXN-111, and PBXW-127 are 0.66, 0.72, and 0.66, respectively. The estimated values of K are 0.48 ± 0.01 s m$^{5/6}$ kg^{-1}, 0.72 ± 0.01 s m$^{5/6}$ kg^{-1}, and 0.51 ± 0.01 s m$^{5/6}$ kg^{-1}, respectively. The curves were calculated for the mean mass of each explosive, and hence exaggerate the difference between the observed and predicted values.

The periods of the second bubble oscillation for the four explosives are shown in Fig. 5. The solid curves were calculated as described earlier, i.e., assuming a depth dependence of $Z^{-5/6}$. The curve for Pentolite matches the observed data satisfactorily; the chi-square statistic is 15. The estimated value of K for Pentolite is 1.53 ± 0.01 s m$^{5/6}$ kg^{-1}. Again, this value is within 1% of the value reported by Arons (1948) for shallow-water detonations. The predicted curves for PBXN-103, PBXN-111, and PBXW-127 are a poor fit to the observed data; the chi-square statistics are 94, 42, and 96, respectively. By fitting for the depth exponent as well as the constant K in Eq. (1), the chi-square statistics are reduced to 23, 14, and 12, respectively. The estimated values of the depth exponent for PBXN-103, PBXN-111, and PBXW-127 are 0.66, 0.72, and 0.66, respectively. The estimated values of K are 0.48 ± 0.01 s m$^{5/6}$ kg^{-1}, 0.72 ± 0.01 s m$^{5/6}$ kg^{-1}, and 0.51 ± 0.01 s m$^{5/6}$ kg^{-1}, respectively. The cause of the different behavior of Pentolite and the PBX-based explosives must be due to the rate of energy release on detonation. This is discussed below in more detail.

Inspection of Fig. 2 suggests that the peak amplitude of the shock wave decreases as a function of detonation depth. This is verified by the data shown in Fig. 6. The measured amplitudes are, of course, relative to the ambient hydrostatic pressure. The observed decrease in the amplitude of the shock wave is consistent with the hypothesis that the absolute peak pressure of the shock wave is independent of detonation depth. Under this assumption, slopes (a) of the best-fit straight lines through the data shown in Fig. 6 should equal the negative of the intercepts (b) plus one, i.e., $a=1-b$. The observed values of the slopes of the best-fit straight lines for the Pentolite, PBXN-103, PBXN-111, and PBXW-127 data are -0.46 ± 0.04, -0.41 ± 0.02, -0.38 ± 0.02, and -0.43 ± 0.02, respectively. The corresponding values of $1-b$ are -0.45 ± 0.05, -0.39 ± 0.03, -0.37 ± 0.03, and -0.41 ± 0.03, respectively. Thus the data are consistent with this hypothesis.

For each shot, the energy flux spectral density (J/m^2/Hz at 1 m) over the frequency interval 0–1500 Hz was calculated. All of the spectra shown here were calculated using channel 1 of the data digitized in the deep-towed instrumentation package because the transfer function of this acquisition system is better known than that of the shipboard system. The energy spectra were calculated as described by Fricke *et al.* (1985) and Johnston *et al.* (1988), assuming values for the density and sound velocity of seawater equal to 1026 kg/m^3 and 1500 m/s, respectively:

$$E(m)=\frac{1}{\rho c}\,|X(m)|^2, \quad m=0,1,...,N-1,$$

where

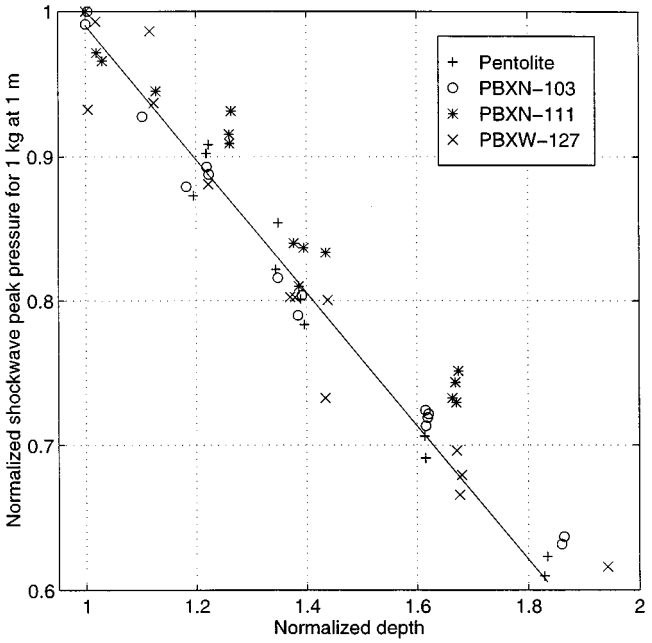

FIG. 6. Variation in the peak pressure of the shock wave for Pentolite, PBXN-103, PBXN-111, and PBXW-127 as a function of normalized detonation depth. The measured amplitudes (volts) were scaled by dividing by the factor $(M^{1/3}/R)^{1.13}$, where M is the charge mass in kilograms, and R is the distance between source and receiver in meters. The exponent value of 1.13 is from Arons (1954), and is based on measurements made, in shallow water, of the change in the shock wave peak pressure with distance. The detonations depths are normalized relative to 2482 m, 2464 m, 2370 m, and 2350 m, for Pentolite, PBXN-103, PBXN-111, and PBXW-127, respectively. The solid curve is the best-fit straight line through the Pentolite data. The slope of the line is -0.46. The slopes of the best-fit straight lines for PBXN-103, PBXN-111, and PBXW-127 are -0.41, -0.38, and -0.43, respectively.

$$X(m)=\Delta t\sum_{n=0}^{N-1}x(n)\exp[-i(2\pi mn/N)],$$

$$m=0,1,...,N-1,$$

and E = energy flux spectral density, X = Fourier coefficients, x = digital samples of time series, N = number of samples in the time series, ρ = density of seawater, c = speed of sound in seawater, and Δt = sampling interval. The raw energy spectra were corrected for the frequency-dependent transfer function of the analog section of the deep-towed instrumentation package. (The system transfer function was measured for each combination of attenuation and gain used during the experiment. We estimate the error in the transfer function to be approximately 1 dB.) Finally, the spectra were corrected for the frequency-independent but depth-dependent sensitivity of the hydrophone.

Energy flux density spectra for Pentolite detonated at depths of 2482–4539 m are shown in Fig. 7. The spectrum maximum moves to higher frequencies with detonation depth. As discussed above, this is due to the decrease in the bubble pulse period as the detonation depth increases. A similar shift in energy is seen for all explosives. Figure 8 compares the energy spectra for all four explosives, at a detonation depth of ~3500 m. The frequencies at which the spectra of PBXN-103, PBXN-111, and PBXW-127 are

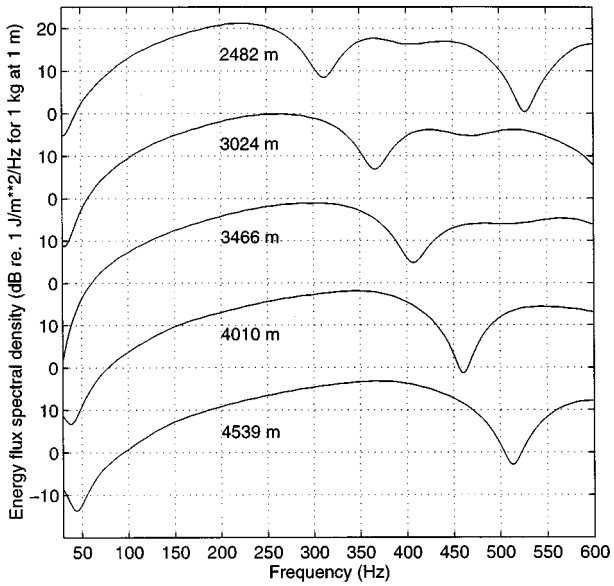

FIG. 7. Representative energy flux density spectra for Pentolite detonated at the indicated depths. The spectra are offset vertically from each other by 20 dB. The maximum spectral value occurs at approximately the inverse of the first bubble pulse period. The increase in the frequency value of the spectral maximum as a function of detonation depth correlates with the decrease in the period of the first bubble oscillation with depth (see Fig. 4).

greatest are 50–100 Hz less than the frequency where the spectrum for Pentolite is a maximum. This variation in the location of the spectrum maximum is consistent with the observation that the bubble oscillation periods of the Navy explosives are up to 2 ms greater than the bubble period for Pentolite.

For on-bottom seismic experiments carried out on the very attenuative shallow igneous crust exposed along mid-

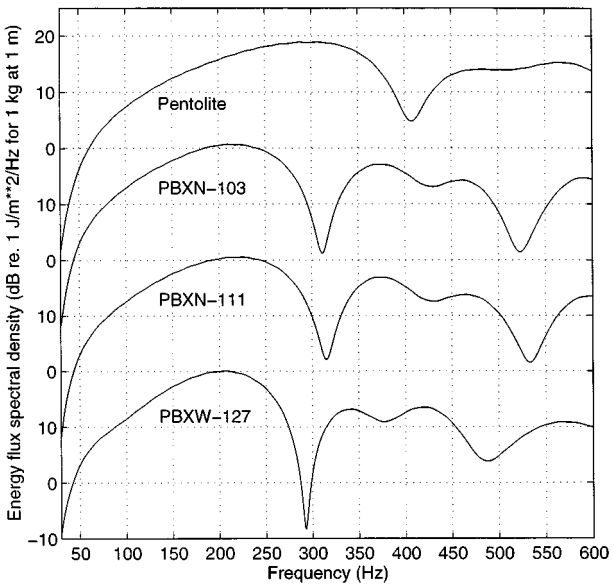

FIG. 8. Representative energy flux density spectra for Pentolite, PBXN-103, PBXN-111, and PBXW-127; the detonation depths were 3466 m, 3430 m, 3401 m, and 3370 m. The spectra are offset vertically from each other by 20 dB. The lower frequency value of the spectral maxima of the PBX-based explosives correlates with the greater oscillation periods of these explosives (see Fig. 4).

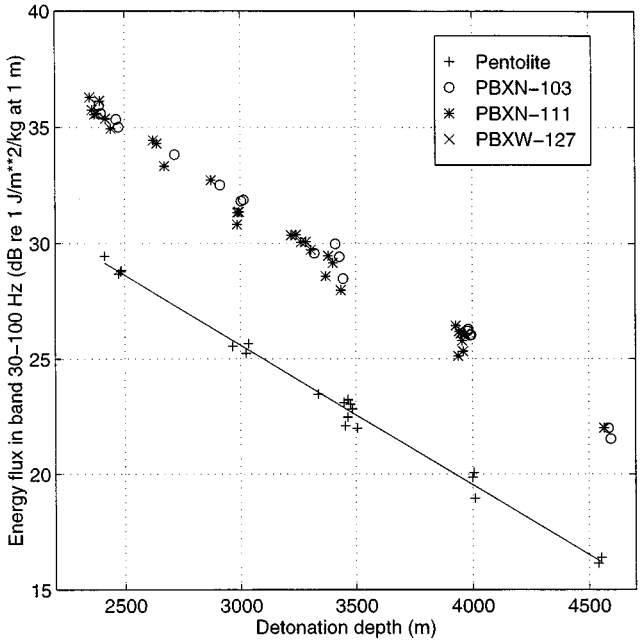

FIG. 9. Total energy flux in the frequency band 30–100 Hz for Pentolite, PBXN-103, PBXN-111, and PBXW-127, as a function of detonation depth. The energy flux has been normalized by the total charge mass. The energy fluxes of the PBX-based explosives are ~6 dB greater than that of Pentolite at all depths. The solid curve is the best-fit straight line through the Pentolite data. The slope of the line is -6 dB km^{-1}. The slopes of the best-fit straight lines for PBXN-103, PBXN-111, and PBXW-127 are of identical value.

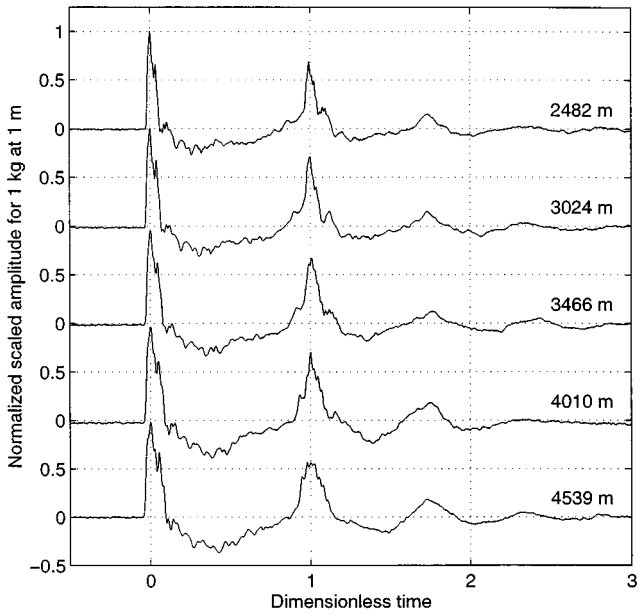

FIG. 10. Representative examples of the scaled source signatures of Pentolite at the detonation depths indicated. The time series are offset vertically from each other by one unit. The amplitudes are corrected for the observed variation of shockwave peak-pressure with detonation depth using the empirical function determined from the observations illustrated in Fig. 6. The horizontal axis is time divided by the predicted bubble pulse period (see Fig. 4), i.e., scaled such that the bubble pulse period of each signature is 1 unit.

ocean ridges, the frequency band greater than ~100 Hz contains little useful energy. The total energy flux (J/m^2) in the frequency band 30–100 Hz for each explosive is plotted in Fig. 9 as a function of depth. The energy flux is calculated as follows:

$$U = \Delta f \sum_{k=k0}^{k=k1} E(k),$$

where U = cumulative energy flux from $(k_0 \Delta f)$ Hz to $(k_1 \Delta f)$ Hz, Δf = frequency sampling interval, and E = energy flux spectral density. Inspection of Fig. 9 shows that the energy flux of the Navy explosives is ~6 dB greater than that of Pentolite at all depths.

The slope of the energy flux density spectra for Pentolite in the frequency band up to the bubble oscillation frequency varies as a function of detonation depth. At a frequency of 100 Hz, the slope of the spectrum increases with increased detonation depth. In the band 40–100 Hz, the spectral density is approximately proportional to the frequency raised to the fourth power, irrespective of detonation depth.

The different behavior of the PBX-based explosives relative to Pentolite can be explained by their different chemistry. Pentolite and TNT are considered ''ideal'' explosives because the energy release occurs nearly instantaneously, and is all available to drive the detonation front. Ideal explosives are characterized by relatively high detonation velocities and pressures. Over the past several decades, the U.S. Navy has developed a class of nonideal explosives tailored for underwater use. Underwater explosives obtain a large percentage of their energy (about 50%) from the reaction of a fuel-oxidizer system (typically aluminium and ammonium perchlorate) included in the explosive. The total energy density of these explosives may be twice that of ideal explosives (9600 vs 4600 J/g). The energy from this reaction is developed too slowly to drive the detonation, but serves to keep the pressure and temperature of the detonation products higher for a longer time. These explosives have lower detonation pressures than ideal explosives, leading to an underwater shock wave which dissipates less energy at the shock front as it moves through the water. The bubble of gaseous explosion products formed by nonideal explosives is considerably hotter than that from an ideal explosive. This drives the bubble expansion to a greater maximum size, and consequently, a longer bubble pulse period (as much as 30%–40%). This is reflected in the lower fundamental frequency of underwater explosives relative to conventional explosives, and a shifting of the acoustic energy to lower frequencies.

It is of interest to determine whether the data described above can be used to predict the source signature at depths other than those where the measurements described here were made. That is, do the source signatures and spectra for each explosive scale simply with detonation depth? Figure 10 shows examples of scaled source signatures of Pentolite. The data have been corrected for the observed variation of shockwave peak-pressure with detonation depth using the empirical function determined from the observations illustrated in Fig. 6. The time axis is scaled by the predicted bubble oscillation period. The time series show a fair degree of similarity. However, the scaled data differ in the width of the positive pulses, and in the magnitude of the first negative pulse. The source spectra may be scaled in a similar manner. The spectra shown in Fig. 7 show a decrease in the magni-

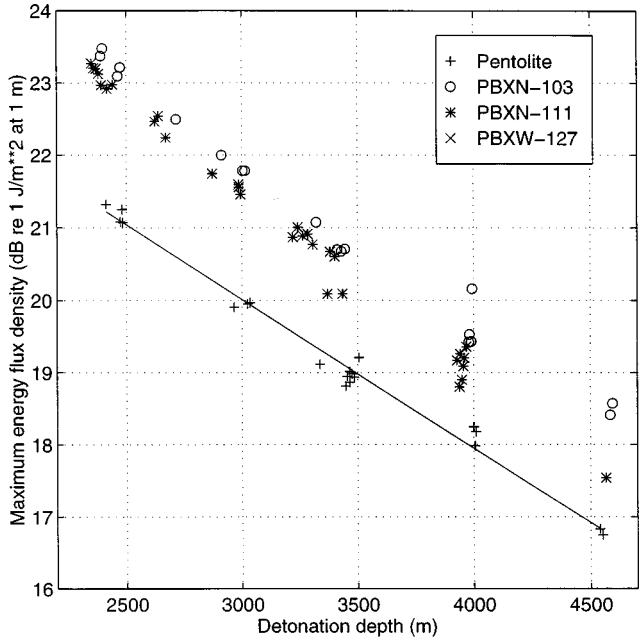

FIG. 11. Variation in the magnitude of the maximum energy flux density as a function of detonation depth for Pentolite, PBXN-103, PBXN-111, and PBXW-127. The solid curve is the best-fit straight line through the Pentolite data. The slope of the line is -2.1 dB km^{-1}. The slopes of the best-fit straight lines for PBXN-103, PBXN-111, and PBXW-127 are -2.3 dB km^{-1}, -2.5 dB km^{-1}, and -2.6 dB km^{-1}, respectively.

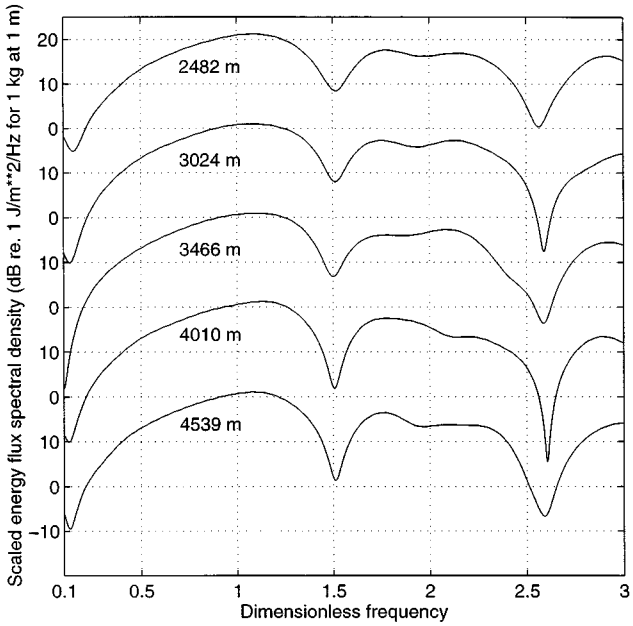

FIG. 12. Scaled energy flux density spectra for Pentolite as a function of dimensionless frequency. The detonation depths are indicated. The magnitude of the spectra were corrected for the observed variation with detonation depth using the empirical function determined from the observations illustrated in Fig. 11. The frequency values were scaled by the predicted bubble pulse periods (see Fig. 4), i.e., scaled such that the inverse of the bubble pulse period is one unit.

tude of the maximum energy flux density with increased detonation depth. Figure 11 shows that this maximum value varies linearly with depth. The observed decrease in magnitude can be used to correct the spectral density values of the spectra shown in Fig. 7. The scaled spectra are shown in Fig. 12. The spectra are similar in magnitude and shape up to frequencies one and a half times the bubble oscillation frequency.

III. CONCLUSIONS

We have measured the source signatures of Pentolite, PBXN-103, PBXN-111, and PBXW-127 at deep-ocean depths. A total of 75 ~10 lb (4.54 kg) explosive charges were detonated at depths of 2350–4539 m. Comparison of the different explosives shows that the bubble pulse periods of the PBX-based explosives are up to 2 ms greater than the bubble period of Pentolite. For all four explosives, the period of the first oscillation follows the theoretically established relationship $T=K^*M^{1/3}(Z+10)^{-5/6}$, where T is the period (s), M is the charge mass (kg), and Z is the detonation depth (m). The optimum value of K for Pentolite (2.07 ± 0.01 s m$^{5/6}$ kg^{-1}) is identical to the value previously reported from the analysis of explosives detonated at depths of less than a few hundred meters. The optimum values for PBXN-103, PBXN-111, and PBXW-127 are 2.67 ± 0.01 s m$^{5/6}$ kg^{-1}, 2.64 ± 0.01 s m$^{5/6}$ kg^{-1}, and 2.73 ± 0.01 s m$^{5/6}$ kg^{-1}, respectively, i.e., for a given charge mass and detonation depth, these explosives have a greater bubble pulse period than Pentolite. For Pentolite, the period of the second bubble oscillation obeys the above relationship with a K value of 1.53 ± 0.01 s m$^{5/6}$ kg^{-1}. In contrast, for the PBX-based explosives, the period of the second oscillation does not obey the above relationship; the period decreases less rapidly with depth than predicted. Relative to ambient hydrostatic pressure, the peak pressure of the shock wave is observed to decrease linearly with detonation depth. The absolute peak pressure of the shock wave is approximately constant as a function of detonation depth. The greater bubble pulse period of the PBX-based explosives means that they are richer in low-frequency energy than Pentolite. The total energy flux in the frequency band 30–100 Hz is ~6 dB greater for the PBX-based explosives than that for Pentolite at all detonation depths. The greater energy content in this frequency band means that the PBX explosives are more useful for on-bottom seismic refraction experiments. The spectra for each explosive scale simply with depth. Thus the data presented here can be used to predict the source spectrum at any water depth.

ACKNOWLEDGMENTS

Funding for this project was provided by the Naval Sea Systems Command, Insensitive Munitions Advanced Development Office, SEA-91WM, and the Office of Naval Research. We thank the Captain and crew of the R/V CAPE HATTERAS who participated in cruise CH 2-95 for their outstanding cooperation.

Arons, A. B. (**1948**). ''Secondary pressure pulses due to gas globe oscillation in underwater explosions, II, selection of adiabatic parameters in the theory of oscillation,'' J. Acoust. Soc. Am. **20**, 277–282.

Arons, A. B. (**1954**). ''Underwater explosion shock wave parameters at large distances from the charge,'' J. Acoust. Soc. Am. **26**, 343–346.

Blaik, M., and Christian, E. A. (**1965**). ''Near-surface measurements of deep explosions. I: Pressure pulses from small charges,'' J. Acoust. Soc. Am. **38**, 50–56.

Christian, E. A., and Blaik, M. (**1965**). ''Near-surface measurements of deep explosions. II: energy spectra of small charges,'' J. Acoust. Soc. Am. **38**, 50–56.

Christeson, G. L., Purdy, G. M., and Fryer, G. J. (**1992**). ''Structure of young upper crust at the East Pacific Rise Near 9°30′N,'' Geophys. Res. Lett. **19**, 1045–1048.

Christeson, G. L., Purdy, G. M., and Fryer, G. J. (**1994a**). ''Seismic constraints on shallow crustal emplacement processes at the fast-spreading east Pacific rise,'' J. Geophys. Res. **99**, 17 957–17 973.

Christeson, G. L., Wilcock, W. S. D., and Purdy, G. M. (**1994b**). ''The shallow attenuation structure of the fast spreading east Pacific rise near 9 30′N,'' Geophys. Res. Lett. **21**, 321–324.

Cole, R. H. (**1948**). *Underwater Explosions* (Princeton U. P., Princeton, NJ).

Ewing, M., Crary, A. O., and Rutherford, M. H. (**1937**). ''Geophysical investigations in the emerged and submerged Atlantic coastal plain. I. Methods and results,'' Geol. Soc. Am. Bull. **48**, 753–802.

Ewing, M., Worzel, J. L., Hersey, J. B., Press, F., and Hamilton, G. R. (**1950**). ''Seismic refraction measurements in the Atlantic Ocean basin,'' Bull. Seismol. Soc. Am. **40**, 233–242.

Fricke, J. R., Davis, J. M., and Reed, D. H. (**1985**). ''A standard quantitative calibration procedure for marine seismic sources,'' Geophysics **50**, 1525–1532.

Friedman, B. (**1947**). ''Theory of underwater explosion bubbles,'' Report IMM-NYU 166, Institute for Mathematics and Mechanics, New York University.

Gaspin, J., Griffin, T., Peletski, C., Baudler, B., Lipton, L., Collins, J. A., Broda, J., and Purdy, G. M. (**1995**). Source Signatures of Explosives Under Very High Ambient Pressures: Data Acquisition and Analysis, NSWC Technical Report (unpublished).

Harding, A. J., Kent, G. M., and Orcutt, J. A. (**1993**). ''A multichannel seismic investigation of upper crustal structure at 9°N on the East Pacific Rise: Implications for crustal accretion,'' J. Geophys. Res. **98**, 13 925–13 944.

Hildebrand, J. A., Dorman, L. M., Hammer, P. T. C., Schreiner, A. E., and Cornuelle, B. D. (**1989**). ''Seismic tomography of Jasper Seamount,'' Geophys. Res. Lett. **16**, 1355–1358.

Johnston, R. C., Reed, D. H., and Desler, J. F. (**1988**). ''Special report of the SEG Technical Standards Committee, SEG standards for specifying marine seismic energy sources,'' Geophysics **53**, 566–575.

Koelsch, D. E., Purdy, G. M., and Broda, J. E. (**1991**). ''A Multiple Charge Deep Deployed Explosive Source for High Resolution seismic Refraction Experiments in the Deep Ocean,'' paper presented at Fall MTS Conference, Mar. Technol. Soc., New Orleans, LA.

Price, R. S. (**1979**). ''Similitude equations for explosives fired underwater,'' Naval Surface Warfare Center, Dahlgren, VA, NSWC TR 80-299.

Raitt, R. W. (**1956**). ''Seismic refraction studies of the Pacific Ocean basin,'' Geol. Soc. Am. Bull. **67**, 1623–1640.

Sauter, A. W., Dorman, L. M., and Schreiner, A. E. (**1986**). ''A study of sea floor structure using ocean bottom shots,'' in *Ocean Seismo-Acoustics Low-Frequency Underwater Acoustics*, edited by T. Akal and J. M. Berkson, NATO Conference Series 4 (Plenum, New York), Vol. 16, pp. 673–681.

Schreiner, A. E., Dorman, L. M., and Bibee, L. D. (**1991**). ''Shear wave velocity structure from interface waves at two deep water sites in the Pacific Ocean,'' in *Shear Waves in Marine Sediments*, edited by J. M. Hovem, M. D. Richardson, and R. D. Stoll (Kluwer Academic, Boston, MA), pp. 231–238.

Smith, D. K., and Cann, J. R. (**1993**). ''Building the crust at the Mid-Atlantic Ridge,'' Nature (London) **365**, 707–715.

Spudich, P., and Orcutt, J. (**1980**). ''Petrology and porosity of an oceanic crustal site: Results from wave form modeling of seismic refraction data,'' J. Geophys. Res. **85**, 1409–1433.

Weston, D. E. (**1960**). ''Underwater explosions as acoustic sources,'' Proc. Phys. Soc. **76**, 233–249.

Wiggins, S. M., Canuteson, E. L., Dorman, L. M., Hildebrand, J. A., Cornuelle, B. D., Sauter, A. W., and Schreiner, A. E. (**1993**). ''Crustal Structure at the Hess Deep: Seismic Studies Show High Velocities in the Intra-Rift Ridge and Low Velocity in the Deep,'' Eos, Fall Meeting Supplement, p. 666.

Wiggins, S. M., Dorman, L. M., Cornuelle, B. D., and Hildebrand, J. A. (**1996**). ''Hess deep rift valley structure from seismic tomography,'' J. Geophys. Res. **101**, 22335–22353.

Resonator frequency shift due to ultrasonically induced microparticle migration in an aqueous suspension: Observations and model for the maximum frequency shift

Christopher S. Kwiatkowski[a] and Philip L. Marston
Department of Physics, Washington State University, Pullman, Washington 99164-2814

(Received 22 October 1997; accepted for publication 23 February 1998)

Aqueous suspensions of plastic and hollow-glass microspheres are subjected to the radiation pressure of an ultrasonic standing wave. It is well known that the particles are attracted to the pressure nodes of the standing wave for the particle and host properties considered. We demonstrated that the radiation pressure induced migration of particles leads to a significant shift in the resonant frequency of a suitably designed chamber. This shift is easily resolved with a phase-locked loop even if the particle volume fraction is as small as 0.001. For sufficient ultrasonic amplitudes, the shift is found to saturate at a limiting value. To approximate the limiting frequency shift, the principle of adiabatic invariance is first applied to the case of a single compressible sphere in a standing wave and then superposition is used to give the collective shift for the suspension. The measured limiting shifts are typically within 25% of the calculated value and this method may have application to the characterization of dilute suspensions since the shift is proportional to the volume fraction and to a material contrast factor. The applicability of adiabatic invariance is confirmed by comparing frequency shifts for certain cases of idealized particle spatial distributions with results based on transfer matrix eigenvalues combined with an effective-medium approximation. [S0001-4966(98)02806-9]

PACS numbers: 43.35.Bf, 43,25.Qp, 43.35.Ty [HEB]

INTRODUCTION

The acoustic characterization of spatially confined single microparticles has been demonstrated even for situations where the scattering cross sections can be quite small.[1] For particles uniformly distributed in a suspension, the speed of sound and the attenuation in the effective medium are means of characterization,[2] however, in the limit of a very dilute suspensions, resolving those effects which are due to particles from experimental artifacts may be difficult. Another approach for dilute suspensions which has been analyzed[3] and experimentally demonstrated[4,5] is to ultrasonically scatter sound at the Bragg condition from the particle layers induced by the radiation pressure of a standing ''pump'' wave. The approach investigated in the present study is similar except that instead of using the Bragg scattering of a probe wave, the direct effect of particle migration on the standing pump wave is investigated.[5] The particles are initially uniformly distributed within an acoustic resonator and the natural frequency of the resonator is determined at low acoustic amplitude for a prominent mode. For a sufficiently large increase in the acoustic amplitude, the radiation pressure of the standing wave enhances the particle concentrations near the pressure nodes of the standing wave and because of this migration, the natural frequency of the resonator is shifted. We demonstrate here that this shift can be detected with good resolution for particle volume fractions as small as 0.001. While it is not the central thrust of the present investigation, it is appropriate to note that radiation pressure induced migration of suspended particles has been investigated by others because of potential applications (see, e.g., Refs. 6–8). The present authors are not aware of any prior investigations of the frequency shift for particle suspensions considered here.

The present research concerns situations where the dimensions of the suspended microparticles are very much less than the acoustic wavelength. The experimental cases considered were spheres such that for a typical measurement the mean particle radius $\bar{a}$ is 5 μm and $k\bar{a}\approx 0.017 \ll 1$ where k is the acoustic wave number. The analysis given here is for the case of small *spheres*, although it is anticipated that the frequency shift calculated should be only weakly affected by shape except for cases where the particles aspect ratio is appreciable (see Sec. V). For the dilute suspensions considered, the frequency shift is found to be proportional to the uniform particle volume fraction X_p and a material contrast factor B which depends on the ratio of the particle and host compressibilities, β_p and β_0, and on their densities ρ_p and ρ_0. In the experiments the complications of sedimentation or buoyancy were avoided by raising the density of the host water with sugar or salt so that $\rho_0 = \rho_p$.

Both the frequency-shift method of ultrasonically characterizing a dilute suspension and the Bragg scattering method[3–5] are associated with an evolution of the scattering properties of the suspension. When the particles have a homogenous spatial distribution the local number density n_p (particles/m^3) is uniform and the scattering of sound is effectively incoherent.[9] With the spatially periodic enhancement of n_p introduced by the acoustic radiation pressure, the sound may be coherently scattered when certain conditions are met. In the limiting case of highly localized particles in

[a]Present address: Institute for Shock Physics, Washington State University, Pullman, WA 99164-2814.

periodic layers, the scattering from each particle can be of the same phase (modulo 2π). With the local enhancement of n_p there is a local variation in the effective speed of sound. Since n_p is enhanced each half-wavelength of the pump wave, the pump frequency lies within the stop band[10–12] of the periodic grating induced by the particles. Nevertheless, the acoustic standing wave can be maintained for the situation of very small equilibrium volume fraction X_p since the attenuation associated with the stop band is small.

The paper is organized as follows: Section I introduces the experimental method and shows a representative experimental result for the case of a dilute suspension of plastic microspheres. The experiment is summarized so as to better motivate the approximations in Sec. II for the change in frequency of a one-dimensional resonant chamber due to the redistribution of microparticles inside the resonant cavity. Section II begins with a phenomenological argument for the frequency shift based on the location of the volume excluded by a rigid sphere in a resonant chamber. A scattering correction is included and an approximate value for the frequency shift due to migration of a distribution of suspended dense-rigid microspheres is obtained for the dilute situation where the effects of each microsphere are additive. Second, an approximation based on adiabatic invariance is used to extend the predictions to compressible spheres. Section III gives a more detailed description of the experimental method used to measure the frequency shift. Section IV gives results obtained using plastic and hollow glass microspheres. Section V gives additional discussion of the results. The Appendix shows a transfer matrix approach for calculating the frequency shifts exactly with *idealized models* for the position dependence of n_p. That method shows good agreement with the adiabatic invariance technique and gives additional support for the analysis given in Sec. II.

I. FREQUENCY SHIFT MEASUREMENT PRINCIPLES AND PHENOMENOLOGY

In the course of ultrasonic Bragg scattering experiments,[5] it was noticed that during a measurement the resonant frequency of a standing wave cell containing a suspension should be monitored and manually tuned in order for the ultrasound to maintain a maximum resonant response. It was originally thought that the major factor in this detuning was a temperature drift in the cell over the course of the experiments. The technique originally used to tune the cell consisted of determining the maximum received pump amplitude from a set of measurements at three frequencies around the last known amplitude peak. The frequency that gave the maximum amplitude was estimated and selected as the new drive frequency. For a typical operating frequency of 833 kHz, this technique had a resolution of 20 Hz, and was limited by the quality factor of the chamber. (The sample frequencies had to be chosen sufficiently away from each other for the measured pump amplitudes to be appreciably different at the different frequencies.) To increase the resolution of the frequency shift, the experimental setup shown in Fig. 1 was introduced and this is the system used to obtain the results of the present paper. This system monitored the resonant frequency of the chamber with higher precision. A

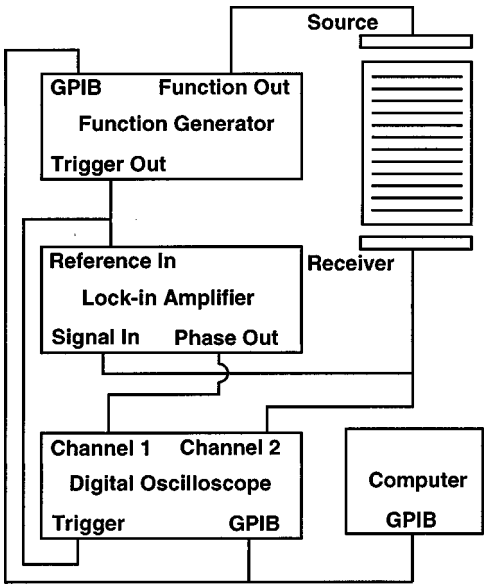

FIG. 1. The experimental setup used in the frequency shift measurements. The pump wave is produced by a PZT disk at one end of a sealed cylindrical chamber. To maintain resonance of the chamber, the received pump phase is held constant. This phase is measured by a lock-in amplifier, and used (by way of a computer) to control the frequency of the sine wave applied to the source transducer. The chamber is placed in a bath of water to stabilize its temperature.

phase measurement was made using a lock-in amplifier and high resolution frequency synthesizer under computer control. Since the phase of the received pump wave changes most rapidly at resonance, this allowed for the determination of the resonator frequency within a few Hz. A representative result is shown in Fig 2.

Initially, the particles are uniformly distributed along the axis and across the diameter of the cylindrical resonator. With the application of a pump ultrasonic standing wave of sufficient amplitude, the particles migrate to the pressure nodes inside the cell, forming a periodic variation. As in the analysis of Simpson and Marston,[3] the acoustic wave within the resonator is modeled as a plane standing wave which completely fills the chamber. (See Sec. V for additional discussion.) Following Gor'kov,[13] in the presence of a standing wave the equilibrium number density is taken to be proportional to a thermal Boltzman factor. If buoyancy and all particle–particle interactions are neglected, the equilibrium number density along the axis of the cylinder a distance z along the axis can be shown to be[3]

$$n_p(z) = \frac{n_0 \exp[q \cos(2kz)]}{I_0(q)}, \tag{1}$$

where the standing wave acoustic pressure is $p_0 \sin kz \sin \omega t$. In Eq. (1), $n_0 = X_p / V_p$ is the initial number of particles/volume, k is the wave number of the pump wave, I_0 is the modified Bessel function required for normalization, and q is a ratio of the depth of the particle's effective potential energy to the thermal energy of a suspended particle. The value of q is given by[3,13]

$$q = \frac{V_p \beta_0 p_0^2}{8 k_B T} B(\beta_p/\beta_0, \rho_p/\rho_0), \tag{2}$$

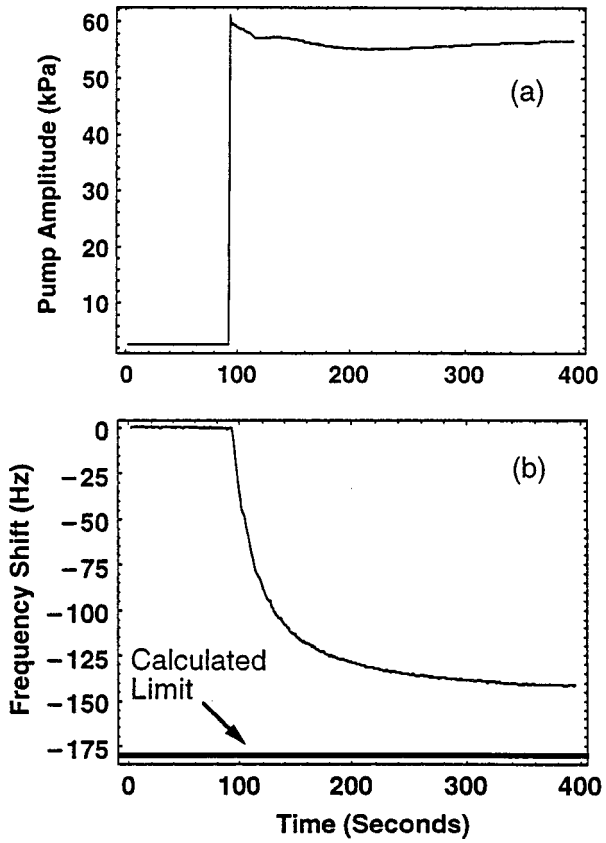

FIG. 2. Plotted as a function of time are the pump wave amplitude (a) and the corresponding frequency shift (b) for polystyrene microspheres in a 1.05-g/cm^3 sugar solution. The volume fraction is 0.0010. The initial pump amplitude is small enough that banding of particles does not occur until the pump is gated on to a high value. The maximum frequency shift measured is -140 Hz, compared to a calculated limiting value of -180 Hz from Eq. (16).

where B is a dimensionless factor given by Eq. (9b) in Sec. II, p_0 is the pump standing wave pressure amplitude, β_0 is the host solution compressibility, β_p is the particle compressibility, and V_p is the volume of the particle, ρ_p and ρ_0 are the densities of the particle and the host fluid, k_B is Boltzmann's constant and T is the absolute temperature. The normalization in Eq. (1) is such that the total number of particles in the standing wave is conserved,[3] consequently it is assumed that particles can not be drawn into the resonator from an external reservoir. In this parameterization of the response to the standing wave it is assumed that the particles are spherical and all of the same size. (For the dilute solutions under consideration the final result for the frequency shift depends on the initial volume fraction instead of the particle size so that the detailed size distribution is unimportant.) For the experiments $\rho_p=\rho_0$, $\beta_p<\beta_0$, and the frequency shift is measured with pump pressure amplitudes giving $q\gg 1$. This leads to the equilibrium configuration of thin parallel layers of particles, much thinner than a wavelength, that are at the pressure nodes of the pump standing wave. The effect of the migration to the nodes is shown by the time dependence of the resonant frequency of the cell in Fig. 2. The slow response of the particles to the applied pump wave can be readily resolved. The analysis given in Sec. II concerns the frequency shift after the particle layers have completely formed. The problem of the time evolution of the local density n_p is considered elsewhere[4,14] and a theoretical estimate for the time for particle migration is reviewed in Sec. V.

II. THEORY FOR THE FREQUENCY SHIFT

A. Rigid small sphere approximations

To understand the effects of the spatial distribution of a large number of compressible particles on the resonant frequency of the chamber, consider a single rigid spherical particle whose size is small compared to a wavelength. The resonance frequency shift of a rigid chamber due to shifting the position of the sphere can be found by solving the Helmholtz equation for the velocity potential ϕ, having Neumann boundary conditions. The frequency $\nu=kc/2\pi$ and wave number k are given from the integrals

$$k^2=\int |\nabla\phi|^2 dV \Big/ \int |\phi|^2 dV, \tag{3}$$

where the integration excludes the volume occupied by the sphere. It can be seen from this equation that the numerator is proportional to the kinetic energy of the standing wave, and that the denominator is proportional to the potential energy. A phenomenological approximation for the position dependence is given by replacing ϕ in (3) by an approximate value ϕ_a for the empty chamber.[15] For axial modes ϕ_a is proportional to $\sin kz$ where k is evaluated for the unperturbed fundamental frequency ν_0 in the absence of a sphere. The frequency shift resulting from the excluded volume of a single sphere with particle volume V_p at a position z in a resonant cavity of volume V_{ch} becomes[15]

$$\frac{\Delta\nu}{\nu_0}=\frac{-V_p}{V_{ch}}\cos(2kz), \tag{4}$$

where $-L/2<z<L/2$, L is the length of the chamber, $k=\pi/L$, and pressure antinodes are located at $z=\pm L/2$. Consider the two following cases to illustrate the predictions of Eq. (4). For a rigid particle close to the pressure antinode at the end wall of the container, the chamber is seen to have an effectively smaller length and therefore a larger resonant frequency. This can be seen from Eq. (3) as resulting from the excluded volume of the sphere diminishing the magnitude of the denominator; however, the excluded volume does not have a large contribution to the numerator, since the term proportional, $|\nabla\phi_a|^2$ vanishes at the wall. The ratio of integrals gives an increase in the frequency of the mode. Similarly, if the particle is near the center of the chamber at $z=0$, which is a pressure node, then the numerator is seen to decrease while the denominator stays nearly constant, resulting in a lowering in the resonant frequency. A more detailed analysis based on Green's functions gives corrections to Eq. (4) which survive even for small k_0a and the limit for vanishing k_0a is[15]

$$\frac{\Delta\nu}{\nu_0}=-\frac{V_p}{V_{ch}}\left(\frac{5}{4}\cos 2kz+\frac{1}{4}\right). \tag{5}$$

B. Compressible particles: Frequency shift from adiabatic invariance

To extend the predictions to the case of the compressible particles used in the experiment, the principle of adiabatic invariance was used.[5] As reviewed by Beyer,[16] this principle may be used to relate changes in length and energy E to changes in the natural frequency ω_0 of an oscillating system such as pendulum. For slow changes in any parameter of the system that lead to changes in both E and ω, the action (the ratio E/ω) is invariant.[17] This leads to the following equation relating the change in the frequency of the system to the change in energy, with initial energy E_0 and initial frequency ω_0 as

$$d\omega = \frac{\omega_0}{E_0}\, dE. \tag{6}$$

This can be applied to the particle system. By knowing how the acoustic energy of the system changes as a function of particle position, the change in the resonant frequency can be approximated. Furthermore, as shown by Putterman *et al.*,[18] adiabatic invariance may be used to relate the acoustic radiation force on a rigid object to the natural acoustic frequency of chamber-object system. In the discussion which follows these arguments are generalized (without a formal proof) to the case of the frequency shift associated with a compressible sphere of finite density. In addition to the experimental tests of this generalization for the case where the spheres have the same density as the sounding water, a theoretical check for a specific spatial distribution of particles is given in the Appendix.

Following Putterman *et al.*,[18] the radiation force in the z direction on a small spherical particle from a planar acoustical standing wavefield using Eq. (6) becomes:

$$F_z = -\frac{\partial U}{\partial z} = -\frac{E_0}{\omega_0}\frac{\partial \omega}{\partial z}, \tag{7}$$

where changes in the acoustic mode energy E_0 correspond to changes in the effective acoustic potential energy U used to express the radiation force. Following Gor'kov,[13] for a small compressible sphere in a standing wave U becomes

$$U(z) = \frac{V_p \beta_0 p_0^2}{8}\,[A - B\,\cos(2kz)] \tag{8}$$

with the coefficients A and B given by

$$A = -\left[\frac{\beta_p}{\beta_0} - \frac{4\rho_0 - \rho_p}{2\rho_p + \rho_0}\right], \tag{9a}$$

$$B = -\left[\frac{\beta_p}{\beta_0} - \frac{5\rho_p - 2\rho_0}{2\rho_p + \rho_0}\right], \tag{9b}$$

and $-\partial U/\partial z$ reproduces radiation force on a compressible sphere in a standing wave in the inviscid analysis of Yosioka and Kawasima.[19] Integration of the right hand expression of Eq. (7) gives

$$\omega(z) - \omega_1 = \frac{\omega_0}{E_0}\,[U(z) - U(z_1)], \tag{10}$$

where $\omega_1 = \omega(z_1)$ and z_1 is a reference position within the resonator for the center of the sphere. The total acoustic energy E_0 is evaluated with the sphere removed and may be related to the peak pressure amplitude p_0 of the standing wave as follows. The fluid velocity within the standing wave is $v_z = v_0 \cos kz \sin \omega t$ where $v_0 = p_0/\rho_0 c$. During the standing wave oscillations while the total acoustic energy within the resonator E_0 remains constant, the energy is oscillating in form such that at $t = \pi/2\omega$, E_0 is given by the kinetic energy of the fluid. Integration of the kinetic energy density $(\rho_0 v^2)/2$ over the volume of the chamber gives

$$E_0 = V_{ch}\,\frac{\beta_0 p_0^2}{4}. \tag{11}$$

Combining Eqs. (8)–(11) gives the fractional frequency shift

$$\frac{\nu(z) - \nu_1}{\nu_0} = -\frac{B}{2}\,\frac{V_p}{V_{ch}}\,[\cos(2kz) - \cos(2kz_1)], \tag{12}$$

where $\nu_1 = \omega_1/2\pi$. In the limit of a rigid-massive sphere, $\beta_p/\beta_0 = 0$ and $\rho_p/\rho_0 = \infty$ so that $A = -1/2$ and $B = 5/2$. The derivative of the frequency $d\nu/dz$ from Eq. (12) is seen to go over to the correct value for that limiting case given by Eq. (5).

While it is not essential for the purpose of this paper, the reference frequency ν_1 and position z_1 in Eq. (12) may be eliminated so that the shift is relative to the frequency ν_0 in the absence of a sphere:

$$\frac{\nu(z) - \nu_0}{\nu_0} = -\frac{1}{2}\,\frac{V_p}{V_{ch}}\,[B\,\cos(2kz) - A], \tag{13}$$

where the constant term goes over to the result in Eq. (5) in the appropriate limit. The frequency shift associated with constant term A is consistent with Eq. (6) and the corresponding energy contribution to Eq. (8). As explained below, the introduction of this term facilitates an approximation for the resonance frequency for a dilute spatially uniform suspension.

C. Application to dilute suspensions

Equation (12) will now be used to give the frequency shift within a chamber *relative to* the frequency ν_u when the particles are uniformly distributed throughout the chamber. In this application the reference location z_1 is found to be irrelevant. Initially the case where the chamber is only a half-wavelength long is considered. For the sparse particle limit the frequency shifts for each particle are additive, being proportional to the particle volume. The superposition of frequency shifts from Eq. (12) may be compared for uniform and nonuniform spatial distributions giving

$$\frac{\nu - \nu_u}{\nu_0} = -\frac{B}{2L}\int_{-L/2}^{L/2} [V_p n_p(z)] \cos\left(\frac{2\pi z}{L}\right) dz, \tag{14}$$

where $[V_p n_p(z)]$ is the local volume fraction of particles. For a *uniform* spatial distribution n_p is constant and $(\nu - \nu_u)$ vanishes. If all of the particles are attracted to the pressure node, the integral may be approximated by taking $n_p(z) = n_0 L\,\delta(z)$ where $\delta(z)$ is a Dirac δ function giving

$$\frac{(\Delta\nu)_{\text{limit}}}{\nu_0} = -\frac{B}{2} X_p, \tag{15}$$

where $X_p = n_0 V_p$ is the global volume fraction of particles.

The actual resonator is several wavelengths in length. Since the initial particle distribution is uniform throughout the length, the particle enhancement within each half-wavelength interval is modeled in the same way. It follows that if a rigid wall were placed along each pressure antinodal plane, the limiting value of the frequency shift for each subchamber may be modeled independently of the others. Each shift is approximated by Eq. (14) and this gives the frequency shift for the entire system.

To leading order in X_p, ν_0 may be replaced by ν_u in the denominator in Eqs. (14) and (15). This result for $(\nu - \nu_u)$ expressed in terms of ν_u is convenient since ν_u is measured in the experiment prior to raising the acoustic amplitude. For the situation where $\rho_p = \rho_0$, Eq. (15) reduces to the limiting value

$$\frac{(\Delta\nu)_{\text{limit}}}{\nu_u} \approx -\frac{X_p}{2}\left(1 - \frac{\beta_p}{\beta_0}\right). \tag{16}$$

The more general limit given by Eqs. (9b) and (15) should be applicable to situations where even though $\rho_p \neq \rho_0$, the pressure amplitude p_0 is sufficiently large that the buoyancy induced displacement from the pressure node is small.

For the uniform dilute suspension, the frequency ν_u may be related to the frequency ν_0 for a pure host by simply modifying the sound speed of the mixture as reviewed in the Appendix. (It is assumed that the walls of the resonator satisfy either perfectly rigid or perfectly soft boundary conditions.) Elementary considerations give $(\nu_u - \nu_0) = (m_u^{-1} - 1)\nu_0$ where $m_u = c_0/c_u$ and c_u is the speed of sound for the uniform mixture. For small X_p the approximation of the acoustical refractive index m_u gives

$$(\nu_u - \nu_0) \approx \frac{\nu_0}{2} X_p\left(2 - \frac{\beta_p}{\beta_0} - \frac{\rho_p}{\rho_0}\right). \tag{17}$$

This may be compared with the result of superposing the frequency shifts from Eq. (13) for a spatially uniform distribution which gives

$$(\nu_u - \nu_0) = \frac{\nu_0}{2} X_p A \approx \frac{\nu_0}{2} X_p\left(2 - \frac{\beta_p}{\beta_0} - \frac{\rho_p}{\rho_0}\right), \tag{18}$$

where the expression on the right follows by approximating A from Eq. (9a) for particles having $|\rho_p - \rho_0| \ll \rho_0$. Comparison of Eqs. (17) and (18) shows that the expression based on adiabatic invariance and superposition recovers the correct linear dependence on X_p when $|\rho_p - \rho_0| \ll \rho_0$.

An approximation for frequency shifts away from the limiting value is given by evaluating Eq. (14) with $n_p(z)$ thermally weighted as in Eq. (1). The integral is proportional to a modified Bessel function $I_1(q)$ and Eq. (14) gives[20]

$$\Delta\nu = (\Delta\nu)_{\text{limit}} I_1(q)/I_0(q), \tag{19}$$

where q is given by Eq. (2) and $(\Delta\nu)_{\text{limit}}$ by Eq. (15). For large positive values of q the ratio $I_1(q)/I_0(q)$ saturates and approaches unity so that $\Delta\nu$ goes over to $(\Delta\nu)_{\text{limit}}$ as expected.

III. APPARATUS AND EXPERIMENTAL PROCEDURE

The resonant chamber shown in Fig. 1 was an acrylic tube having an outside diameter of 9.5 cm, a wall thickness of 0.63 cm, and a length of 10 cm. A shoulder was cut on the inside of both ends of the tube as a holder for circular ceramic PZT transducers, making sure the inserted PZT transducer was parallel with the transducer on the opposite end. Thin wires were soldered onto both sides of the PZT, which allowed electrical contact to be made to the transducers without the need for fairly massive mounts. One PZT was used as a pump source, and one as the receiver. The ends of the tube were sealed to allow for the entire assembly to be submerged in a large water bath to lessen the effects of temperature variations on the frequency of the resonant chamber. To further increase the reflectivity of the ends, the sealed PZT transducers were air backed.

The typical pump frequency used was 833 kHz. This operating mode was selected to be the lowest mode of a group of modes within the chamber associated with a fixed number of pressure antinodes along the axis of the chamber. The quality factor of this mode (measured from the width of the resonance peak) was estimated to be 4500.

The amplified output of a Stanford Research Systems SRS 345 digitally synthesized function generator was used to drive the source PZT transducer. The synchronization output from the function generator was used as the reference signal for a high-frequency lock-in amplifier (PAR model 5202). The phase-difference output from the lock-in was monitored. Using a linear model of the phase difference between the reference and received signal as a function of frequency, the computer adjusted the frequency of the SRS function generator to compensate for changes in the frequency of the acoustic mode. This setup allowed for automated recording of the mode frequency with independent control of the drive amplitude. A background frequency drift rate was determined for each measurement and a drift linear in time was subtracted from the measured frequency shift when the drifts were significant. The typical background drift rate was less than 10 mHz/s and the drift was always a small fraction of the limiting frequency shift.

A source of polystyrene-DVB (divinylbenzene) microspheres was found, manufactured by Duke Scientific (Palo Alto, CA), which allowed large volume fractions of these particles to be made at a low cost. These particles have a uniform compressibility[1,3] ($\beta_p = 2.35 \times 10^{-10}$ s^2/mkg) and density ($\rho_p = 1.05$ g/cm^3) though they have a range of sizes. The range of sizes of a batch of polystyrene particles used was 1–35 μm diameter, with an average diameter of 10 μm. Ordinary sugar was added to the water until the density of the host liquid matched those of the particles to give a measured sound speed of $c = 1516$ m/s and $\beta_0 = 4.14 \times 10^{-10}$ s^2/mkg. A typical experiment was initiated by mixing the contents of the cell by gentle shaking. It was found that the orientation of the cell underwater, either with the axis vertical or horizontal for the plastic microsphere solutions didn't seem to have any effect on the experimental results over the short times that the experiment was performed, on the order of 10 mins. However, all the data displayed here was taken with the cell's axis vertical. After a

few minutes, to wait for the motion of the particles inside the cell to cease, a low amplitude pump beam was gated on. This amplitude was such that it was low enough not to cause banding of the particles, but high enough for the lock-in amplifier to register a signal and be able to track the resonance of the chamber. In the experiments, the received pump amplitude, the phase, and the frequency of the function generator were recorded as functions of time. The volume fractions X_p for the mixture was determined from the dry weight of the particles put into solution and from the combined volume of the host liquid-particle mixture. A small hole in the side of the resonant chamber was opened to fill the chamber and was sealed during measurements.

The voltage output of the receiver transducer was monitored and used to estimate the pump pressure amplitude by the following calibration procedure. A few particles were acoustically levitated in pure water with the axis of the cylinder vertical. The drive amplitude was reduced until the threshold for trapping the particles in the vertical standing wave was reached. The associated standing wave pressure amplitude at threshold may be determined by balancing the acoustic radiation force[13,19] and the buoyancy of the particles. The reported pressure amplitudes are based on a linear extrapolation from this receiver calibration. The actual value for the pressure amplitude is not needed for the interpretation of the limiting frequency shift measurement. The frequency shift was driven to saturation where the typical predicted $q \geqslant 500$ from Eq. (2) and $n_p(z)$ is predicted to be narrowly peaked after the particles have migrated. Additional measurements at saturation taken with hollow-glass microspheres will be noted at the end of the next section.

IV. RESULTS

Figure 2 shows the measured resonant frequency shift and received pump amplitude for a gated pump. The temporal response of the feedback system is less than a second, so the data is assumed to be a good representation of the actual resonant frequency.

The effect of linearly ramping the pump amplitude instead of gating it can be seen in Fig. 3. For lower pump amplitudes, the system takes longer to reach a steady state. This is seen in the difference of the frequency as the pump is ramped up to that of it being ramped down. As the pump is ramping up, the frequency shift should be smaller than the steady state value (for a given amplitude) since the particles haven't had enough time to reach their equilibrium position. As the pump is decreased however, the resonant frequency of the chamber should be nearer the steady state value, since the time required for the particles to spread apart is relatively small. The graphs show the difference between the pump ramping up and down. The smaller frequency shift is the situation where the pump is ramping up. Note that at high and low pump amplitude extremes, the frequencies are similar and that Fig. 3 clearly shows the expected saturation of $\Delta\nu$ for increasing pump amplitude.

Figures 2 and 3 show that the frequency shifts achieved, while having the correct sign, are smaller in magnitude than the limiting value predicted by Eq. (16). Notice, however, that the shift is easily resolved though the volume fraction

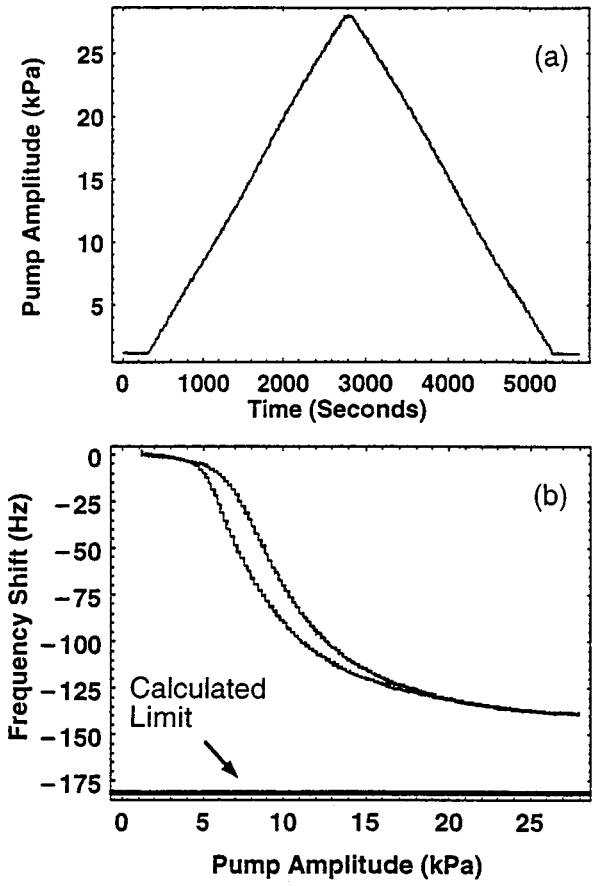

FIG. 3. The effect of ramping the pump amplitude while tracking the resonance of the cell, as opposed to an abrupt gated pump as in Fig. 2 for the same solution. (a) The pump amplitude history. (b) Frequency shift for the up-down ramp shown in (a). The slow response of the particles to low pump amplitudes is seen as the difference in the frequencies in (b) at the same pump amplitude depending on whether the pump is ramping up (upper curve) or down (lower curve).

X_p is small. It was also demonstrated that $|\Delta\nu|$ at saturation increases with increasing X_p as is evident by comparing these results in Figs. 2 and 3 with the next example.

Figure 4 illustrates some of the difficulties which can

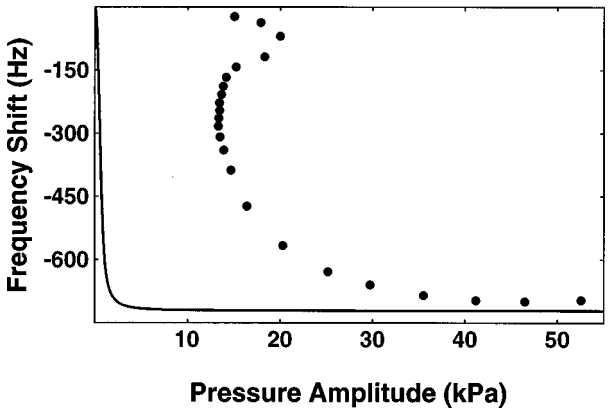

FIG. 4. The solid curve shows the equilibrium frequency shift plotted as a function of pressure from Eq. (19) for a 0.0040 volume fraction solution. The points are a sequence of measurements taken at the end of a 600-s gated pump. Between successive measurements the solution was allowed to disperse and the drive voltage amplitude in the gated region was incremented by a fixed amount. The saturation value for the frequency shift of -700 Hz is close to the -721 Hz prediction of Eq. (16).

occur when attempting to measure equilibrium frequency shifts below the saturation value. The equilibrium volume fraction X_p was 0.0040. The measurement procedure was to gate the pump transducer drive amplitude to a constant elevated value for 600 s. The plotted circles show the frequency shift and pump wave amplitude at the end of that time interval, just prior to decreasing the amplitude so as to recover a uniform distribution. The drive voltage amplitude was incremented a fixed value between measurements. The measured saturation value of the frequency shift lies close to the limiting value from Eq. (16) while at low amplitudes there are significant discrepancies with Eqs. (16) and (19). The points in Fig. 4 are ordered sequentially with the smaller values of $\Delta\nu$ corresponding to smaller values of drive voltage. Inspection of Fig. 4 shows that for measurements in the region near $\Delta\nu \approx -150$ Hz that $|\Delta\nu|$ decreases with increasing measured pressure amplitude p_0 and p_0 decreases with increasing drive voltage. The cause of this anomalous response was not determined though the time required for the particle to migrate and approach equilibrium for low drive voltages and pressure amplitudes (discussed in Sec. V) increases the difficulty in interpreting pressure and frequency shift measurements well below saturation conditions. Measurements show that for a range of drive voltages including those in the anomalous region between $\Delta\nu \approx -300$ Hz and -150 Hz the received amplitude varies with time during the applied 600-s duration tone burst in a pattern significantly different from the minor variations evident in Fig. 2(a). The anomalous behavior is characterized by an initial amplitude overshoot followed by a relaxation toward the reported value of pressure amplitude. The overshoot in certain cases exceeds the final value by as much as three times having a width as short as 40 s.

Experiments with hollow-glass microspheres: The saturation frequency shift was also measured for empty hollow-glass microspheres in a salt water solution. The average density (mass/V_p) for each glass microsphere was not as uniform as for the plastic spheres though the population could be made more uniform by allowing the denser spheres to sink and the lighter ones to rise and using only the suspended remainder in the experiment. The sphere outer radius and wall thickness were typically 5 μm and 1 μm, respectively. In this case the volume fraction $X_p = 0.0010$ and the measured limiting value of $\Delta\nu$ was -225 Hz and the calculated value from Eq. (16) is -267 Hz. The material properties used in this calculation give $\beta_p/\beta_0 = 0.36$ where β_p was approximated from the quasi-static effective compressibility of a hollow thick shell[5] and β_0 is found from the density (1.1 g/cm^3) and sound speed of the salt solution.

V. DISCUSSION

Equation (15) predicts the limiting frequency shift $\Delta\nu$ of the resonator due to the banding of small particles at pressure nodes when the final frequency is compared to the value for the same mode with a uniform spatial distribution of the same of small particles. The predicted frequency shift $\Delta\nu$ is proportional to the volume fraction $X_p \ll 1$ and to an acoustical contrast factor B from Eq. (9b). Experimentally, the sign and general magnitude of the saturation frequency shift were in agreement with the predictions. Additional support for the dependence of frequency shift on the spatial distribution predicted from adiabatic invariance by Eq. (14) is given by the comparison with exact transfer matrix calculations given in the Appendix for certain idealized spatial distributions of particles. The measurements in the regions away from the saturation conditions in Figs. 3 and 4 are generally poorly described by an approximation based on a Boltzmann weighting factor for $n_p(z)$ and it is recommended that such measurements not be used in applications pertaining to the characterization of suspensions.

The discrepancies between the predicted and measured limiting $\Delta\nu$ evident from Figs. 2, 3, and 4 ranges between 3% and 28%. These discrepancies may be attributable in part to assumptions of the theory that may not be fully applicable to our experimental apparatus. The analysis neglected to explicitly allow for any lateral dependence of the excited mode within the cylindrical resonator. Such dependence produces lateral variations of the potential function U and of the equilibrium spatial distribution of particles and a lateral contribution to the radiation force. To minimize this dependence, the lowest frequency mode of the family having a given axial wave number for the resonator was used. Visual inspection of the resonator failed to show any clear lateral dependence of banded particles, however, such a dependence would have been difficult to resolve because of the opacity of the suspension. It is plausible that for a weak lateral dependence of the equilibrium particle distribution, that the coupling to the limiting mode frequency is at least partially canceled in the superposition of the $\Delta\nu$ associated with each particle. It is noteworthy in this context that if the phase-locked loop was deliberately initially locked onto a laterally dependent mode at a low pump amplitude, following a subsequent increase in the pump amplitude and the associated migration of particles, it was not uncommon for the mode to hop to a lower lying mode which was presumably more spatially uniform.[5]

Another assumption made in the analysis leading to Eq. (15) is that all of the mechanical energy lies in the particle–liquid suspension. That assumption is not exactly true because of the chamber boundaries, however, those boundaries should only weakly affect the limiting frequency shift for the following reasons. (i) Because of the high quality factor of the chamber, the vibrations of the cylindrical chamber wall must have been small; otherwise, there would have been significant radiation losses into the surrounding water bath. (ii) The transducers entirely covered the ends of the chamber and were selected so as to have a much higher characteristic impedance than that of the suspension.

For the purposes of evaluating this method as a means of acoustically characterizing dilute suspensions, some comments on the limitations are appropriate. The analysis given in Sec. II was for the case of spherical particles so that $(\Delta\nu)_{\text{limit}}$ was determined by the volume fraction. As reviewed by Putterman *et al.*,[18] nonspherical objects in standing waves are generally subjected to an acoustic radiation torque proportional to p_0^2 where p_0 is the standing wave amplitude. Furthermore, adiabatic invariance shows that with the rotation of such objects, there is a shift of the natural frequency of the enclosing acoustic resonator.[18] For a sus-

pension of particles initially having random orientations, it is anticipated that a large amplitude standing wave will introduce angular as well as spatial regularity.[21] Consequently, if the aspect ratio of the particles is sufficiently large, there is expected to be a rotational contribution to $\Delta\nu$. An additional practical limitation to this characterization method is the assumption that the global volume fraction X_p is small. One geometric consequence of violating this assumption is that for sufficiently large X_p, the spatial overlap between particles would make it impossible for all of the particles within a layer to be situated on the pressure node. This geometric overlap is expected to be significant for spherical monodisperse particles of radius a if X_p is similar in magnitude to ka where k is the pump wave number.[4,5] It is anticipated that the secondary Bjerknes force between particles[6] may significantly alter the equilibrium spatial distribution prior to this geometric limiting value for X_p. (For our typical experiment, $k\bar{a}\approx 0.017$.) It is also appropriate to note that to avoid the complications of the time scale for particle migration to the pressure node, it is necessary for the ratio of the depth of the radiation-force energy well from Eq. (9) to be large in comparison to the thermal energy k_BT and for the viscosity of the host fluid to not be abnormally large. For situations where Stokes viscous drag inhibits the formation of the grating, the general magnitude of the formation time is estimated to be[3,4]

$$\tau_f \approx 9\eta\lambda^2/(8\pi\beta_0 B a^2 p_0^2), \tag{20}$$

where η is the shear viscosity of the host liquid and λ denotes the pump acoustic wavelength. For the experiments described here, the saturation measurements were taken over intervals significantly in excess of τ_f. For low drive amplitudes, the duration of the excitation and τ_f were similar in magnitude; for example, at $p_0=15$ kPa and $a=5$ μm, Eq. (20) gives $\tau_f\approx 550$ s. Since the dispersions were not monodisperse the actual relaxation process is not determined by a single time scale.

Equations (19), (15), and (2) may be combined to give a prediction for the frequency shift $\Delta\nu$ when the acoustic pressure amplitude p_0 is significantly below the values required to saturate $\Delta\nu$. The subsaturation predictions are based on Gor'kov's assumption[13] that it is only the thermal energy which counteracts the complete migration of the particles to the pressure nodes of the standing wave which yields the spatial distribution given by Eqs. (1) and (2). As shown by the curve in Fig. 4, for the case of a monodisperse distribution with radius $a=5$ μm the predicted $|\Delta\nu|$ is within 95% of $|(\Delta\nu)_{\text{Limit}}|$ when p_0 reaches 2 kPa. The observed dependences in Figs. 3 and 4 are quite different from Eq. (19) so that it is clear that the assumptions of the model are not applicable to the conditions of our observations. In addition to complications due to the relaxation process associated with particle migration, the equilibrium value of $n_p(z)$ may differ from Eq. (1) if the force on each particle due to the sound wave is not given by $-\nabla U$ with the effective potential U given by Eqs. (8) and (9). For a plane standing wave in a viscous fluid, Doinikov has analyzed the radiation forces on small rigid[22] and viscous[23] spheres. It was found that the viscous effects are weak if the oscillating viscous boundary layer near the surface of the particle has a width δ such at $\delta/a \ll 1$ and $k\delta \ll 1$. This prediction may be argued on physical grounds since the radial pressure change across the oscillating boundary layer should be negligible and any tangential radiation stresses on the sphere's surface (which are associated with dissipation[24]) should cancel because of the symmetry of the counterpropagating waves in the standing wave. For the conditions of our experiment we estimate that $\delta \approx 0.6$ μm so that for a typical sphere $\delta/a\approx 0.12\ll 1$. While a detailed analysis does not seem to be available for an elastic sphere in a viscous fluid, the similarity of Doinikov's results for viscous and rigid spheres suggests that the viscous effects on the radiation force should be small in plane standing waves for the case of our elastic spheres. Recent measurements of the migration velocity (and by inference the radiation force) for polystyrene spheres in a 500-kHz standing wave have the predicted dependence on a near $a=5$ μm.[25] The complications on the radiation force resulting from the elasticity of the sphere[26] are avoided because $ka\ll 1$ with $\delta \ll a$ so that (as experimentally verified by Roy and Apfel[1]) the scattering (and hence the associated radiation pressure) may be approximated by replacing the sphere by a fluid sphere having a compressibility $\beta_p=\rho_p^{-1}[c_l^2-(4/3)c_t^2]^{-1}$ where c_l and c_t are the longitudinal and transverse wave speeds of the elastic particle. The conditions appropriate for approximating the radiation force by $-\nabla U$ [with U from Eq. (8)] breakdown, however, if the counter propagating components of the pump wave are no longer equal in amplitude. In addition the presence of an appreciable traveling wave component may be associated with a steady acoustic streaming which could lead to drag forces on the particles. The anomalously low values for the received amplitude noted in the discussion of Fig. 4 is suggestive of an imbalance in the counterpropagating pump wave components over a range of pump amplitudes below the saturation of $\Delta\nu$. These complications and the ones associated with the time required for the grating to form indicated that for the diagnostics of particle suspensions it is appropriate to use a sufficiently large amplitude pump wave to saturate the frequency shift.

It is instructive to compare the limiting frequency $\nu_{\text{limit}}=\nu_u+(\Delta\nu)_{\text{limit}}$ from Eq. (16) with the mixture theory result from Eq. (17). Inspection of Eq. (9b) shows that when $|\rho_p-\rho_0|/\rho_0$ is small, ν_{limit} is closely approximated by ν_0, the resonator frequency in the absence of a suspension. Consequently the migration of particles to the pressure node approximately *suppresses* the shift in mode frequency introduced by the suspended particles. The limiting frequency shift and the aforementioned result for ν_{limit} are easily generalized to the case where B is negative in Eq. (8) so that the particles are attracted to pressure antinodes. In Eq. (14) the integration is now from 0 to L and the limiting distribution becomes $n_p=n_0L\,\delta(z-L/2)$ which gives

$$\frac{(\Delta\nu)_{\text{limit}}}{\nu_0}=\frac{B}{2}X_p. \tag{21}$$

As in the case where B is positive, the frequency is predicted to decrease in response to particle migration.

ACKNOWLEDGMENT

This research was supported by the Office of Naval Research.

APPENDIX: TRANSFER MATRIX CALCULATION OF FREQUENCY AND COMPARISON WITH ADIABATIC INVARIANCE

This Appendix gives a theoretical comparison of the shift predicted by Eq. (14) from adiabatic invariance with an exact calculation of the frequency based on a transfer matrix method. To facilitate this comparison the spatial distribution of particles $n_p(z)$ is taken to be uniform within a specified layer and zero outside that layer. It is convenient to define an acoustical refractive index function $m(z)=c_0/c(z)$, where $c(z)$ is the local speed of sound and c_0 is the speed of sound in the host liquid. It follows from the theory of mixtures[27] that $m(z)$ is uniform within the layer and unchanged outside the layer as illustrated in Fig. A1. The transfer matrix approach facilitates the exact calculation of the frequency and may be formulated to allow both the density and $c(z)$ to differ within the layer from the host, however, for brevity, we consider only examples where $\rho_p=\rho_0$. The present application closely resembles the computation of quantum mechanical eigenvalues by the transfer matrix[28] though a related approach is widely used to compute ultrasonic transmission and reflection by layers.[29]

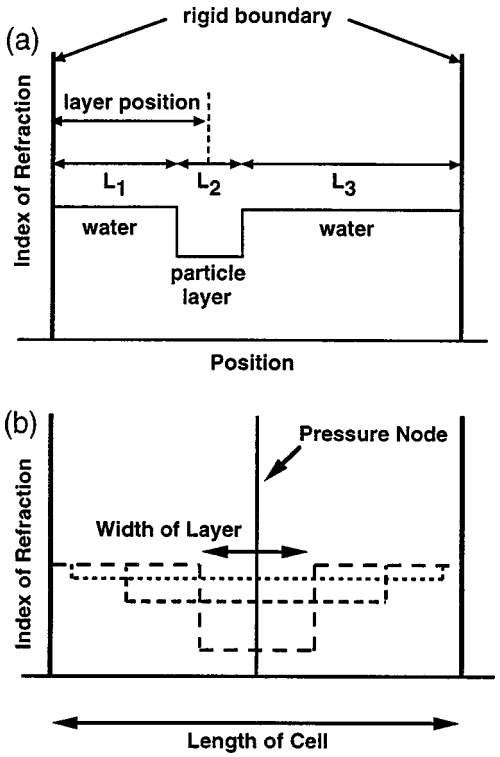

FIG. A1. Models used in comparisons between the adiabatic invariance and transfer matrix methods. The total length of the cell is $L=L_1+L_2+L_3$, with rigid boundary conditions on each end. In each case pure water is outside the particle layer and the relative acoustical refractive index is reduced in the layer according to Eq. (A1). In (a) the center of the layer is varied while in (b) the number of particles is held fixed as the width of the layer is varied. The refractive index changes are exaggerated for clarity. Only the lowest frequency modes are investigated. The layer width L_2 is much smaller than a wavelength. All the particles are confined to the middle region, with water ($n=1$) bordering them.

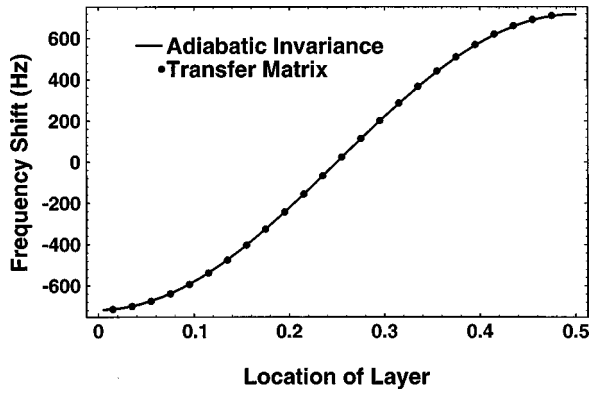

FIG. A2. For the situation shown in Fig. A1 (a) with $L_2/L=0.05$ and $X_p=0.004$, the curve shows the adiabatic invariance prediction, Eq. (A6). The points are from the transfer matrix method. The location is shown relative to the total length of the cell.

To facilitate the comparison given below, it is convenient to relate the particle number density n_{pL} within the layer and the relative acoustical refractive index m_L within the layer by using Urick's formulation of the speed of sound in mixtures which gives[4,27]

$$m_L=\left[1-X_L\left(1-\frac{\beta_p}{\beta_0}\right)-X_L\left(1-\frac{\rho_p}{\rho_0}\right)+X_L^2\left(1-\frac{\beta_p}{\beta_0}\right)\left(1-\frac{\rho_p}{\rho_0}\right)\right]^{1/2}, \tag{A1}$$

where $X_L=n_{pL}V_p$ is the volume fraction within the layer. If w denotes the width of the layer (L_2 for the example shown in Fig. A1(a) and L the length of the resonator, it follows that $X_L=X_pL/w$ where X_p is the global volume fraction. Consequently, the volume per particle does not directly enter into the calculation of frequency as is also the case in Eq. (14).

The present application of the transfer matrix[5,28] may be summarized as follows. In the physical region of interest the medium is partitioned into layers specified by an index j where j increases from left to right beginning with $j=1$ on the left. The velocity potentials in the respective layers are designated by

$$\phi_j(z')=f_je^{ik_jz'}+g_je^{-ik_jz'}, \tag{A2}$$

where $k_j=\omega m_j/c_0$, m_j is the acoustical refractive index in the jth layer and the choice of the origin for the coordinate z' is discussed below. For the situation shown in Fig. A1, $m_1=m_3=1$ and $m_2=m_L$. The boundary conditions are that the fluid velocity and acoustic pressure are continuous across the interface. If the coordinate origin is selected to lie on the interface, the coefficients f_{j+1} and g_{j+1} for the waves on the right side are related to f_j and g_j for the waves on the left side by the discontinuity matrix

$$d_{j,j+1}=\begin{pmatrix}1+r_{j,j+1} & 1-r_{j,j+1}\\ 1-r_{j,j+1} & 1+r_{j,j+1}\end{pmatrix}, \tag{A3}$$

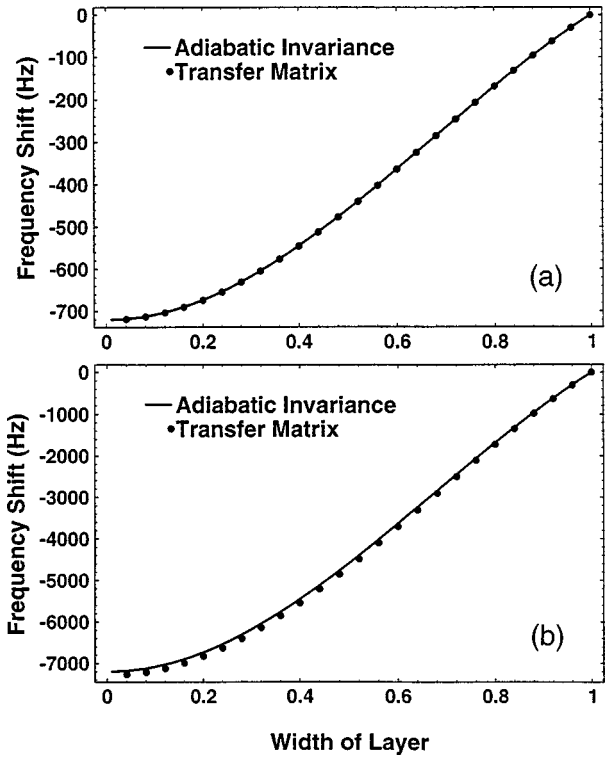

FIG. A3. For the situation shown in Fig. A1 (b) with X_p of (a) 0.004 and (b) 0.04, the curve shows the adiabatic invariance prediction, Eq. (A6). The width is shown relative to the total length of the cell. The points are from the transfer matrix method. In qualitative agreement with the observations, as the layer becomes narrow, the mode frequency is reduced.

where $r_{j,j+1}=m_j/m_{j+1}$ and it has been assumed that the mass density is uniform. The transposes $(f_j,g_j)^T$ and $(f_{j+1},g_{j+1})^T$ define column matrices which are related by the boundary conditions which give $(f_{j+1},g_{j+1})^T = d_{j,j+1}(f_j,g_j)^T$. It is desirable to relate $(f_{j+1},g_{j+1})^T$ to counter-propagating waves expressed in terms of a new coordinate system for which the origin vanishes at the right-hand interface of medium $j+1$. This is facilitated by introducing a propagation matrix[5,28]

$$p_{j+1}=\begin{pmatrix} \exp(ik_{j+1}L_{j+1}) & 0 \\ 0 & \exp(-ik_{j+1}L_{j+1}) \end{pmatrix}, \quad \text{(A4)}$$

where L_{j+1} denotes the width of the $(j+1)$st layer. Propagation across the three-layer system is described by the matrix product

$$t(\omega)=p_3 d_{2,3} p_2 d_{1,2} p_1, \quad \text{(A5)}$$

which is a function of the frequency ω. For rigid boundary conditions on the outside boundaries of the first and third layers, the natural frequencies of the sandwich are the roots of the expression $(1,1)^T=t(\omega)(1,1)^T$ which may be also written as $(1,-1)t(1,1)^T=0$. This gives the condition $t_{11}+t_{12}-t_{21}-t_{22}=0$ where the subscripts denote the row and column of the matrix product in Eq. (A5).

The natural frequency was calculated for the situation shown in Fig. A1 (a) for different positions of the center of the layer. The width to length ratio was $w/L=0.05$ where $L=L_1+L_2+L_3$ and the global volume fraction $X_p=0.004$ with $\beta_p/\beta_0=0.568$. The roots gives the points in Fig. A2 while the solid curve is given by evaluating the approximate expression given by the integral in Eq. (14) which gives:

$$(\nu-\nu_u)=-\nu_0\left(1-\frac{\beta_p}{\beta_0}\right)\frac{X_p}{2}\,\mathrm{sinc}(\alpha)\cos\left(\frac{2\pi z_c}{L}\right), \quad \text{(A6)}$$

where $\mathrm{sinc}(\alpha)=(\sin\alpha)/\alpha$, $\alpha=\pi w/L$, and z_c is the location of the mid-point of layer 2. In this example and in the others given here, ν_0 is taken to be 833 kHz. Inspection of Fig. A2 shows that Eq. (A6) from adiabatic invariance is in good agreement with the frequency shift given by numerical solution of the transfer matrix condition.

Additional computational support for Eq. (14) was provided by considering the idealized model of an evolving spatial distribution shown in Fig. A1 (b) where the distribution is taken to be initially uniform. Figure A3 shows the frequency shift as a function of the width of the particle layer for (a) $X_p=0.004$ and (b) $X_p=0.04$. The curve is given by Eq. (A6) with $z_c=0$. The difference between the methods is again found to be negligible when X_p is small.

[1] R. A. Roy and R. E. Apfel, ''Mechanical characterization of microparticles by scattered ultrasound,'' J. Acoust. Soc. Am. **87**, 2332–2341 (1990).

[2] J. R. Allegra and S. A. Hawley, ''Attenuation of sound in suspensions and emulsions: Theory and experiments,'' J. Acoust. Soc. Am. **51**, 1545–1564 (1972); G. Horváth-Szabó and H. Hóila, ''Compressibility determination of Silica particles by ultrasound velocity and density measurements on their suspensions,'' J. Colloid Interface Sci. **177**, 568–578 (1996).

[3] H. J. Simpson and P. L. Marston, ''Ultrasonic four-wave mixing mediated by an aqueous suspension of microspheres: Theoretical steady-state properties,'' J. Acoust. Soc. Am. **98**, 1731–1741 (1995).

[4] H. J. Simpson, ''Interaction of sound with sound by novel mechanisms: Ultrasonic four-wave mixing mediated by a suspension and ultrasonic three-wave mixing at a free surface,'' Ph.D. dissertation, Department of Physics, Washington State University, Pullman, WA, 1992. For abstract see: J. Acoust. Soc. Am. **94**, 1167 (1993). See also: H. J. Simpson and P. L. Marston, ''Parametric layers, four-wave mixing, and wave-front reversal,'' in *Nonlinear Acoustics*, edited by M. F. Hamilton and D. T. Blackstock (Academic, San Diego, 1998), pp. 399–420.

[5] C. S. Kwiatkowski, ''Ultrasonic probes of aqueous particle suspensions: collinear four-wave mixing and resonator detuning,'' Doctoral dissertation, Washington State University, 1997.

[6] M. H. Weiser, R. E. Apfel, and E. A. Neppiras, ''Interparticle forces on red cells in a standing wave field,'' Acustica **56**, 144–119 (1984); M. H. Weiser and R. E. Apfel, ''Extension of acoustic levitation to include the study of micron-size particles in a more compressible host liquid,'' J. Acoust. Soc. Am. **71**, 1261–1268 (1982).

[7] G. Whitworth and W. T. Coakley, ''Particle column formation in a stationary ultrasonic field,'' J. Acoust. Soc. Am. **91**, 79–85 (1992).

[8] G. Whitworth, M. A. Grundy, and W. T. Coakley, ''Transport and harvesting of suspended particles using modulated ultrasound,'' Ultrasonics **29**, 439–444 (1991).

[9] P. M. Morse and K. U. Ingard, *Theoretical Acoustic* (McGraw Hill, New York, 1968), pp. 436–441.

[10] L. Brillouin, *Wave Propagation in Periodic Structures* (Dover, New York, 1953).

[11] D. Bai and J. B. Keller, ''Sound waves in a periodic medium containing rigid spheres,'' J. Acoust. Soc. Am. **82**, 1436–1441 (1987).

[12] C. E. Bradley, ''Time harmonic acoustic Bloch wave propagation in periodic waveguides Part I. Theory,'' J. Acoust. Soc. Am. **96**, 1844–1853 (1994).

[13] L. P. Gor'kov, ''On the forces acting on a small particle in an acoustical field in an ideal fluid,'' Sov. Phys. Dokl. **6**, 773–775 (1962).

[14] K. Higashitani, M. Fukushima, and Y. Matsuno, ''Migration of suspended particles in plane stationary ultrasonic field,'' Chem. Eng. Sci. **36**, 1877–1882 (1981).

[15] E. Leung, C. P. Lee, N. Jacobi, and T. G. Wang, ''Resonance frequency shift of an acoustic chamber containing a rigid sphere,'' J. Acoust. Soc. Am. **72**, 615–620 (1982).

[16] R. T. Beyer, ''Radiation pressure—The history of a mislabeled tensor,'' J. Acoust. Soc. Am. **63**, 1025–1030 (1978).
[17] I. Percival and D. Richards, *Introduction to Dynamics* (Cambridge U.P., Cambridge, 1989).
[18] S. Putterman, J. Rudnick, and M. Barmatz, ''Acoustic Levitation and the Boltzmann-Ehrenfest principle,'' J. Acoust. Soc. Am. **85**, 68–71 (1989).
[19] K. Yosioka and Y. Kawasima, ''Acoustic radiation pressure on a compressible sphere,'' Acustica **5**, 167–173 (1955).
[20] M. Abramowitz and I. A. Stegun, *Handbook of Mathematical Functions* (Dover, New York, 1965), Eq. (9.6.19).
[21] P. Brodeur, ''Motion of fluid-suspended fibers in a standing wave field,'' Ultrasonics **29**, 302–307 (1991).
[22] A. A. Doinikov, ''Acoustic radiation pressure on a rigid sphere in a viscous fluid,'' Proc. R. Soc. London, Ser. A **447**, 447–466 (1994).
[23] A. A. Doinikov, ''Acoustic radiation pressure on a compressible sphere in a viscous fluid,'' J. Fluid Mech. **267**, 1–21 (1994).
[24] P. L. Marston, S. G. Goosby, D. S. Langley, and S. E. LoPorto-Arione, ''Resonances, radiation pressure, and optical scattering phenomena of drops and bubbles,'' in *Proceedings of the Second International Colloquium on Drops and Bubbles*, edited by D. H. LeCroissette (Jet Propulsion Laboratory, Pasadena, 1982), pp. 166–174.
[25] K. Yasuda and T. Kamakura, ''Acoustic radiation force on micrometer-size particles,'' Appl. Phys. Lett. **71**, 1771–1773 (1997).
[26] T. Hasegawa, ''Comparison of two solutions for acoustic radiation pressure on a sphere,'' J. Acoust. Soc. Am. **61**, 1445–1446 (1977).
[27] E. J. Urick, ''A sound velocity method for determining the compressibility of finely divided substances,'' J. Appl. Phys. **18**, 983–987 (1947).
[28] J. S. Walker and J. Gathright, ''A transfer-matrix approach to one-dimensional quantum mechanics using Mathematica,'' Comput. Phys. **6**, 393–399 (1992).
[29] D. L. Folds and C. D. Loggins, ''Transmission and reflection of ultrasonic waves in layered media,'' J. Acoust. Soc. Am. **62**, 1102–1109 (1977); D. Lévesque and L. Piché, ''A robust transfer matrix formulation for the ultrasonic response of multilayered absorbing media,'' J. Acoust. Soc. Am. **92**, 452–467 (1992).

The natural frequency of oscillation of gas bubbles in tubes

H. N. Oğuz and A. Prosperetti
Department of Mechanical Engineering, The Johns Hopkins University, Baltimore, Maryland 21218

(Received 28 July 1997; accepted for publication 27 February 1998)

A numerical study is presented of the natural frequency of the volume oscillations of gas bubbles in a liquid contained in a finite-length tube, when the bubble is not small with respect to the tube diameter. Tubes rigidly terminated at one end, or open at both ends, are considered. The open ends may be open to the atmosphere or in contact with a large mass of liquid. The numerical results are compared with a simple approximation in which the bubble consists of a cylindrical mass of gas filling up the cross section of the tube. It is found that this approximation is very good except when the bubble radius is much smaller than that of the tube. An alternative approximate solution is developed for this case. The viscous energy dissipation in the tube is also estimated and found generally small compared with the thermal damping of the bubble. This work is motivated by the possibility of using gas bubbles as actuators in fluid-handling microdevices. © *1998 Acoustical Society of America.* [S0001-4966(98)02606-X]

PACS numbers: 43.35.Pt [HEB]

INTRODUCTION

An extensive literature exists on the small-amplitude volume oscillations of gas bubbles in unbounded liquids, near rigid plane boundaries and free surfaces (see, e.g., Strasberg, 1953; Howkins, 1965; Blue, 1966; Plesset and Prosperetti, 1977; Apfel, 1981; Scott, 1981; Prosperetti *et al.*, 1988; Oğuz and Prosperetti, 1990; Prosperetti, 1991). The case of bubbles confined in channels and tubes, however, does not seem to have been considered before except in a brief unpublished report by Devin (1961). Of course, when the radius of the tube is much larger than the bubble—as would be the case, for example, for bubbles entrained in ordinary macroscopic flows—the results for bubbles in unbounded liquids can be used to a good approximation. In the situations of concern here, however, the size of the bubble is not small and the effect of the proximity of the boundary very significant.

The situations considered in this paper are all axisymmetric and are sketched in Fig. 1. The bubble is inside a liquid-filled, finite-length, rigid-walled tube that may be open at both ends [Fig. 1(a), (a′), and (b)], or rigidly terminated at one end and open at the other [Fig. 1(c) and (d)]. The open end(s) of the tube may be in contact with the atmosphere [Fig. 1(b) and (d)], or with a large mass of the same liquid [Fig. 1(a), (a′), and (c)].

Our interest in these problems is motivated by the possibility to use gas bubbles as actuators in the small fluid-handling systems that advances in silicon manufacturing technology are rendering possible (see, e.g., Fujita and Gabriel, 1991; Lin *et al.*, 1991; Gravesen *et al.*, 1993). These include bioassay chips, integrated micro-dosing systems, miniaturized chemical analysis systems, and others. The advantage of bubbles in this setting would be the possibility to power them remotely by ultrasonic beams with no need for direct contact between the actuator and the power supply. A particularly intriguing possibility in this regard may be offered by the ability of ultrasound to propagate through living tissue.

While the scale that we envisage is of the order of one millimeter or less and the flow velocities relatively small, so that viscous effects would not be negligible, it seems natural for a first analysis of this problem to start from a consideration of the inviscid case, treating viscous effects in an approximate way (see Sec. IV). The attending simplification enables us to focus with greater clarity on the inertial aspects of the bubble–fluid interaction, which are one of the dominant aspects of the system. Second, it will be easier to establish a connection with the available results for the unbounded case. Third, one can envisage situations in which viscosity is indeed negligible, such as an oscillation frequency so large that the viscous boundary layer is much thinner than the tube.

Since, in order to maximize the effectiveness of the actuator, it is desirable to operate near resonance conditions, the natural frequency of the bubble is the most significant quantity to be determined. This is the objective of this paper. In the future we shall consider forced oscillations, damping mechanisms, and nonlinear effects.

I. FORMULATION

As shown by Strasberg (1953; see also Oğuz and Prosperetti, 1990), it is possible to obtain a relation for the natural frequency directly by using the analogy with the capacitance problem of electrostatics. To this end we start from the condition expressing the balance of normal forces at the bubble surface:

$$p_i = p_L + \sigma \mathscr{C}. \tag{1}$$

Here, p_i is the pressure in the bubble, assumed spatially uniform, p_L the pressure in the liquid at the bubble surface, σ the surface tension coefficient, and $\mathscr{C}$ the local curvature of the interface. Upon using the (linearized) Bernoulli integral to express p_L in terms of the velocity potential ϕ and the

 0001-4966/98/103(6)/3301/8/$10.00

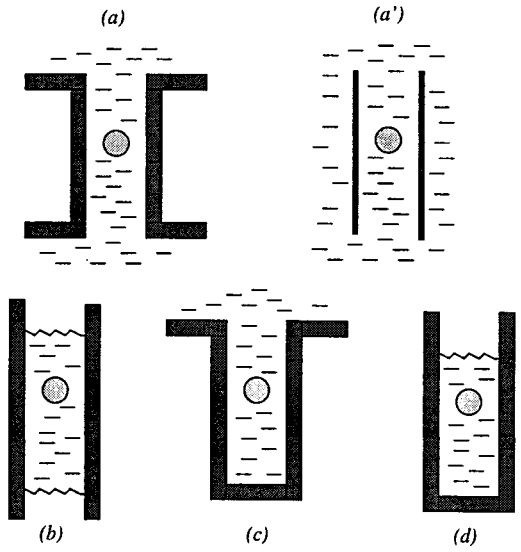

FIG. 1. The various configurations of a bubble in a tube considered in this paper: (a) open tube with infinite thickness immersed in an unbounded liquid; (a) open tube with negligible thickness immersed in an unbounded liquid; (b) partially filled tube with liquid surfaces exposed to the atmosphere; (c) rigidly terminated tube in the bottom of a large container; (d) partially filled tube closed at one end.

static pressure p_∞, the previous relation becomes

$$p_i = -\rho \frac{\partial \phi}{\partial t} + p_\infty + \sigma \mathscr{C}, \tag{2}$$

where ρ is the liquid density. The bubble internal pressure p_i can be assumed to remain spatially uniform at all times. Since p_∞ is a constant, this equation implies then that ϕ will remain essentially uniform over the bubble surface provided it is uniform (e.g., equal to zero) at the initial time, and provided the surface curvature is either uniform or small. The former possibility prevails in the case of small bubbles, which tend to remain spherical, while the latter one is encountered for large bubbles for which the surface tension contribution is negligible. Upon balancing variations in curvature and variations in internal pressure, it is found that the appropriate scale to judge whether a bubble is to be considered ''small'' or ''large'' is of the order of σ/p_∞ which, for the case of water at atmospheric pressure, is a few micrometers.

With the assumption of a uniform internal pressure, averaging Eq. (2) over the bubble surface, we have

$$p_i = -\rho \left\langle \frac{\partial \phi}{\partial t} \right\rangle + p_\infty + \sigma \langle \mathscr{C} \rangle, \tag{3}$$

where $\langle ... \rangle$ denotes the surface average. In the linear approximation, to which we confine ourselves, the surface average of any first-order quantity can consistently be calculated on the unperturbed equilibrium surface, rather than on the moving one. As a consequence, time differentiation and surface averaging commute and therefore, upon differentiating once more with respect to time, we find

$$\rho \frac{d^2}{dt^2} \langle \phi \rangle = -\frac{dp_i}{dt} + \sigma \frac{d}{dt} \langle \mathscr{C} \rangle. \tag{4}$$

For linear oscillations at a single frequency ω, any variable is proportional to any other so that we may write

$$\frac{dp_i}{dt} = \frac{dp_i}{dV} \frac{dV}{dt}, \tag{5}$$

where V is the instantaneous bubble volume and dp_i/dV a possibly complex constant. Furthermore,

$$\frac{dV}{dt} = \int_S \mathbf{u} \cdot \mathbf{n} \, dS \equiv S \left\langle \frac{\partial \phi}{\partial n} \right\rangle, \tag{6}$$

where $\mathbf{n}$ is the outward directed unit normal to the bubble surface S. With the neglect of gravity, the equilibrium configuration of the bubble is necessarily spherical, although the instantaneous shape during volume oscillations is not necessarily so. However, again in the linear approximation, it is easy to show that

$$\frac{d}{dt} \langle \mathscr{C} \rangle = \langle \mathscr{C}_0 \rangle \left\langle \frac{\partial \phi}{\partial n} \right\rangle, \tag{7}$$

where $\langle \mathscr{C}_0 \rangle = 2/a$ is the curvature of a spherical bubble of radius a. Upon substituting these results into Eq. (4), and further writing $i\omega$ for d/dt, we find

$$\omega^2 = -\frac{1}{\rho} \left(S \frac{dp_i}{dV} + \frac{2\sigma}{a^2} \right) \frac{1}{\langle \phi \rangle} \left\langle \frac{\partial \phi}{\partial n} \right\rangle. \tag{8}$$

For a spherical bubble in an infinite liquid $\phi = (a^2/r) \times (da/dt)$ (where r is the distance from the bubble center and da/dt the radial velocity) and this expression reduces to

$$\omega_0^2 = -\frac{1}{a\rho} \left(S \frac{dp_i}{dV} + \frac{2\sigma}{a^2} \right), \tag{9}$$

where ω_0 denotes the bubble angular frequency in this case. Upon taking the ratio with Eq. (8) and introducing the frequencies $f = \omega/2\pi$, $f_0 = \omega_0/2\pi$, we thus have

$$\left(\frac{f}{f_0} \right)^2 = \frac{a}{\langle \phi \rangle} \left\langle \frac{\partial \phi}{\partial n} \right\rangle, \tag{10}$$

which expresses in a compact form the change in the natural frequency of the bubble due to the presence of boundaries. The validity of this result presupposes of course that dp_i/dV in Eq. (8) has the same value as for a bubble in an infinite fluid. This assumption may be justified as follows. The rate of change of the internal pressure with volume is determined essentially by the thermal processes in the bubble. It is well known that, to an excellent approximation, these can be evaluated assuming the bubble surface temperature to remain undisturbed (see, e.g., Kamath *et al.*, 1993), which effectively decouples the thermal problem from the environment surrounding the bubble.

If the length of the tube were infinite, volume changes of the bubble would only be possible in a compressible fluid. However, if the length of the tube is much smaller than the wavelength of sound in the liquid, we may use the incompressible approximation so that the velocity potential satisfies Laplace's equation $\nabla^2 \phi = 0$. For simplicity we only consider axisymmetric situations. The boundary condition on the surrounding solid boundaries is of course $\mathbf{n} \cdot \nabla \phi = 0$. If the liquid mass in the tube is bounded by a free surface in con-

tact with the atmosphere, as in Fig. 1(b) and (d), $\phi=0$ is the appropriate boundary condition there. Furthermore, unless the bubble is very close to this surface, there will be little error in assuming it to be plane. If, on the other hand, the tube is part of an extended (infinite) mass of liquid, as in Fig. 1(a), (a′), and (c), ϕ is required to vanish at infinity.

As noted before, provided the bubble is either relatively small or relatively large, one may assume that ϕ remains uniform over the bubble surface. Since the problem for ϕ is linear and, aside from the boundary condition on the bubble surface, it is homogeneous, it follows that $\langle \partial\phi/\partial n \rangle$ will also be proportional to the average value of ϕ evaluated on the bubble surface. It is therefore sufficient to calculate the surface averages appearing in Eq. (10) by solving Laplace's equation subject to the boundary condition $\phi=1$ on the undisturbed spherical bubble.

The solution of the potential problem formulated before can readily be obtained by using the boundary integral method (see, e.g., Pozrikidis, 1992). Our version of this method is already well documented in the literature, to which the reader is referred (see, e.g., Oğuz and Prosperetti, 1990).

The derivation of the numerical results shown below, the accuracy of which was verified by the standard convergence and grid-independence tests, did not require a very high degree of discretization. The line representing the bubble surface in the meridian plane was approximated by cubic splines with 10 nodal points. Up to 70 points were used on the tube's wall, depending on its length. In situations where the solid boundary extends to infinity [Fig. 1(a) and (c)], the integration over its surface must be stopped at some large distance from the axis of symmetry. Ten tube radii proved sufficient for convergence.

II. APPROXIMATIONS

The numerical calculation of the natural frequency according to the method described before is a matter of some complexity and it is useful therefore to obtain approximate expressions. We consider separately the case of large and small bubbles.

A. Large bubbles

When the radius a of the bubble is not small compared with the radius R of the tube, an obvious approximation to the situation envisaged here is that of a one-dimensional ''slice'' of gas filling the entire cross section of the tube and with a thickness h adjusted to give the same volume as the real bubble:

$$Ah=\tfrac{4}{3}\pi a^3, \tag{11}$$

where A is the tube's cross sectional area. Since the considerations that follow are applicable to tubes of general cross section, we do not specialize the formulae to circular tubes in this subsection.

Let the bubble center be at a distance L_1 from one end of the tube and $L_2=L-L_1$ from the other. For greater accuracy, these geometrical parameters can be adjusted to reflect more closely the physical situation. In the first place, in order to preserve the total volume, an amount

$$l=\frac{1}{2}\,h=\frac{2}{3}\,\pi\,\frac{a^3}{A} \tag{12}$$

must be subtracted from both L_1 and L_2. If the tube's ends are in contact with the atmosphere [Fig. 1(b) and (d)], this is the only adjustment to the lengths of the liquid columns. If an end is immersed in an unbounded liquid [Fig. 1(a), (a′), and (c)], however, there is an added mass effect that can be accounted for by augmenting the geometrical length by an amount ΔL. For the situation of Fig. 1(a) one can simply estimate this end correction by noting that, from the point of view of the fluid outside the tube, the effect of the liquid entering and exiting the tube opening is similar to the pulsations of a ''half-bubble'' with diameter equal to the hydraulic diameter D_h of the tube. (The hydraulic diameter is four times the ratio of the cross-sectional area A to the perimeter P of the tube.) Since such a bubble in an unbounded liquid would have an added, or virtual, mass $4\pi(D_h/2)^3\rho$, the added mass for the half-bubble is $2\pi(D_h/2)^3\rho$, which can be accounted for by extending the tube by an amount ΔL chosen so that $A\Delta L$ contains an equal mass of liquid. The result is

$$\Delta L=16\pi\,\frac{A^2}{P^3}, \tag{13}$$

and equals $2R$ for a circular tube. This result can also be derived in an alternative, more rigorous way (Oğuz and Zeng, 1995, 1997). The same procedure applied to the thin-walled tube of Fig. 1(a′) is inaccurate, however, as shown by Levine and Schwinger (1948). In this case, for a circular tube, one finds $\Delta L\simeq 1.22R$.

On the basis of these arguments we define equivalent lengths of the liquid columns on the two sides of the bubble by

$$L_i^e=L_i-l+\Delta L, \quad i=1,2. \tag{14}$$

If the system is regarded as an oscillator, its equivalent mass is [see Eq. (33) in Sec. IV]:

$$M_{\rm eq}=\rho A\left(\frac{1}{L_1^e}+\frac{1}{L_2^e}\right)^{-1}, \tag{15}$$

while the ''spring constant'' is

$$K=-A^2\,\frac{dp_i}{dV}. \tag{16}$$

The natural frequency of the system is therefore

$$\omega_a^2=\frac{K}{M_{\rm eq}}=-\left(\frac{1}{L_1^e}+\frac{1}{L_2^e}\right)\frac{A}{\rho}\,\frac{dp_i}{dV}. \tag{17}$$

With $f_a=\omega_a/2\pi$, upon taking the ratio of this expression to the natural frequency of a bubble of equal radius in an unbounded liquid (neglecting surface tension effects), we find

$$\left(\frac{f_a}{f_0}\right)^2=\frac{A}{4\pi a}\left(\frac{1}{L_1^e}+\frac{1}{L_2^e}\right). \tag{18}$$

If one of the ends is rigidly terminated, we assume that the liquid on that side does not partake of the motion in this one-dimensional approximation. This limit is contained in

the previous formulae by taking the corresponding effective length to be infinite. It will be seen in the next section that this is a good approximation.

B. Small bubbles

The model just described is evidently a poor approximation when the bubble is small compared with the tube radius. We now turn to this case considering explicitly a tube open at the two ends. The adjustment (14) to the length of the liquid columns permits one to adapt the results to the other cases depicted in Fig. 1.

It is particularly convenient to use the following special representation of the velocity potential:

$$\phi=\sum_{n=0}^{\infty} A_n \frac{a^{n+1}}{\rho^{n+1}} P_n(\cos\,\theta)+\sum_{n=1}^{\infty} B_n I_0\left(\frac{n\pi r}{L}\right)\sin\frac{n\pi z}{L} + C_0\frac{z}{L}+D_0\frac{L-z}{L}+\sum_{n=1}^{\infty}\left[C_n\frac{\sinh\,\alpha_n(z/R)}{\sinh\,\alpha_n(L/R)} + D_n\frac{\sinh\,\alpha_n(L-z)/R}{\sinh\,\alpha_n(L/R)}\right]J_0\left(\alpha_n\frac{r}{R}\right). \tag{19}$$

Here the P_n's are Legendre polynomials, and ρ and θ are polar coordinates centered at the bubble center; r and z are cylindrical coordinates with the two free surfaces of the liquid at $z=0$ and $z=L$. The modified and ordinary Bessel functions of order 0 are denoted by I_0 and J_0, the α_n's are the zeros of J_1, and the coefficients A_n, B_n, C_n, D_n are to be determined from the boundary conditions. This particular form for ϕ is constructed in such a way that the first summation describes the flow near the bubble, the second one in the tube away from the bubble, the next two terms the bulk translation of the liquid away from the bubble, and the last summation the end effects. The proof that Eq. (19) gives an accurate representation of the potential follows from the fact that, as will be seen shortly, all the coefficients are uniquely determined and all the boundary conditions are satisfied.

On the tube wall the velocity must vanish, which requires

$$\frac{\partial}{\partial r}\sum_{n=0}^{\infty} A_n\frac{a^{n+1}}{\rho^{n+1}}P_n(\cos\,\theta) + \sum_{n=1}^{\infty} B_n\frac{n\pi}{L}I_1\left(\frac{n\pi R}{L}\right)\sin\frac{n\pi z}{L}=0. \tag{20}$$

At the lower and upper free surfaces of the tube, $z=0$ and $z=L$, the condition of vanishing pressure perturbation simply requires $\phi=0$, i.e.,

$$\sum_{n=0}^{\infty} A_n\frac{a^{n+1}}{\rho^{n+1}}P_n(\cos\,\theta)+\sum_{n=1}^{\infty} D_n J_0\left(\alpha_n\frac{r}{R}\right)+D_0=0, \tag{21}$$

$$\sum_{n=0}^{\infty} A_n\frac{a^{n+1}}{\rho^{n+1}}P_n(\cos\,\theta)\sum_{n=1}^{\infty} C_n J_0\left(\alpha_n\frac{r}{R}\right)+C_0=0. \tag{22}$$

A consideration of these boundary conditions furnishes a rationale for the representation (19) of the potential. Indeed, from these three homogeneous boundary conditions one can conceptually think of expressing B_n, C_n, and D_n in terms of the A_n, which are in turn determined by the pressure condition on the bubble surface.

If the bubble radius is small, the magnitude of the higher-order terms of the Legendre polynomial expansion is rapidly decreasing and therefore we truncate this infinite sum to just the first term which, in the cylindrical coordinate system used to express the other terms, is

$$A_0\frac{a}{\rho}P_0=A_0\frac{a}{[r^2+(z-d)^2]^{1/2}}, \tag{23}$$

where d is the position of the bubble center. Using well-known orthogonality properties we then have from Eqs. (20) to (22):

$$\frac{B_n}{A_0}=\frac{2}{n\pi}\frac{1}{I_1(n\pi R/L)}\int_0^L\frac{R}{[R^2+(z-d)^2]^{3/2}}\sin\left(\frac{n\pi z}{L}\right)dz, \tag{24}$$

$$\frac{D_0}{A_0}=-\frac{2}{R^2}\int_0^R\frac{r}{\sqrt{r^2+d^2}}\,dr, \tag{25}$$

$$\frac{D_n}{A_0}=-\frac{2}{R^2J_0^2(\alpha_n)}\int_0^R\frac{r}{\sqrt{r^2+d^2}}J_0\left(\alpha_n\frac{r}{R}\right)dr, \tag{26}$$

$$\frac{C_0}{A_0}=-\frac{2}{R^2}\int_0^R\frac{r}{\sqrt{r^2+(L-d)^2}}\,dr, \tag{27}$$

$$\frac{C_n}{A_0}=-\frac{2}{R^2J_0^2(\alpha_n)}\int_0^R\frac{r}{\sqrt{r^2+(L-d)^2}}J_0\left(\alpha_n\frac{r}{R}\right)dr. \tag{28}$$

In principle, A_0 should now be determined by imposing a condition on $\langle\phi\rangle$ at the bubble surface. As is evident from the previous relations, however, all the coefficients are proportional to A_0 and it will be recalled from Eq. (10) that we are only interested in the ratio $(1/\langle\phi\rangle)\langle\partial\phi/\partial n\rangle$ that is obviously independent of A_0. It is therefore unnecessary to impose the last boundary condition explicitly and A_0 can simply be taken as 1.

Of course, it is not necessary to truncate the spherical harmonic expansion in Eq. (19) at the first term. In principle, one can retain any number of terms in the sums. Upon taking scalar products, one is then reduced to a linear system for the coefficients. As discussed in the next section, we have found that the truncation used here is sufficient for the present purposes of approximation. Solution (19), however, is in principle exact and represents a valid alternative to the boundary integral calculation, at least for situations of the type shown in Fig. 1(b) and (d). It is interesting to note that this procedure can be extended to deal with bubbles off-axis, and tubes of noncircular cross section, more simply than the boundary integral method.

Devin (1961) calculated the natural frequency for the situation of Fig. 1(a′) in terms of the potential and kinetic energies of the system. The former is simply expressed in terms of the relation between the pressure and volume of the bubble, which he assumed to be adiabatic. To estimate the kinetic energy, he used the solution for a point source in an

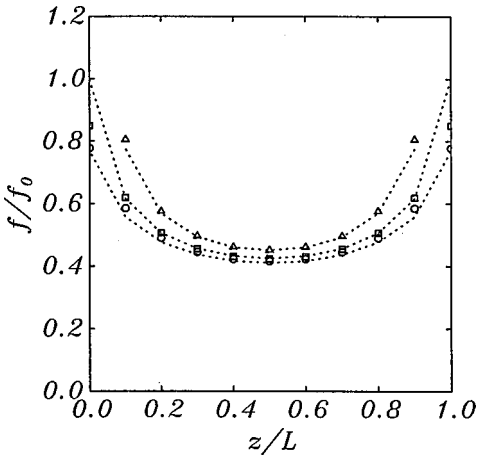

FIG. 2. The natural frequency of a bubble of radius a in a tube of radius R and length L as a function of the axial distance of the bubble center from the tube bottom for $L/R=10$, $a/R=0.5$. The dotted lines show the result given by the approximate formula (18) and the symbols show the boundary integral results; ○ case of Fig. 1(a); □ case of Fig. 1(a′); △ case of Fig. 1(b).

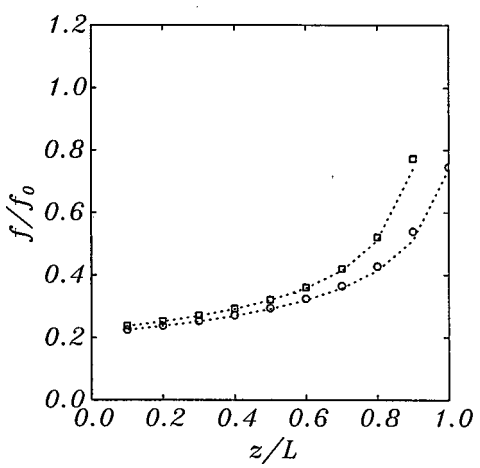

FIG. 3. The natural frequency of a bubble of radius a in a tube of radius R and length L as a function of the axial distance of the bubble center from the tube bottom for $L/R=10$, $a/R=0.5$. The dotted lines show the result given by the approximate formula (18) and the symbols show the boundary integral results; ○ case of Fig. 1(c); □ case of Fig. 1(d).

infinite tube up to a distance of 1.108 R from the bubble center (at which point the potential along the axis vanishes) combined with that of solid-body motion of the liquid in the remainder of the tube. His argument for chosing the particular value 1.108 is that, in this way, ''the decrease in the tube potential from the surface of the bubble... is exactly equal to the decrease in the free field potential from the surface of an identical bubble to a point at infinity.'' His final result is

$$\left(\frac{f_D}{f_0}\right)^2=\left[1+\frac{2a}{R}\left(\frac{\frac{1}{2}L+\Delta L}{R}-1.108\right)\right]^{-1}. \tag{29}$$

Here the bubble is assumed to be located at the midpoint of the tube and $\Delta L\simeq 1.22R$. It is evident from the manner of its derivation that the result is only applicable provided the bubble radius is much smaller than that of the tube, and that the term in brackets is greater than 1.

III. RESULTS

Any one of the situations shown in Fig. 1 is characterized by four dimensional lengths: the bubble radius a, the tube radius R, the tube length L, and the distance of the bubble center from the lower end of the tube (as sketched in Fig. 1), z. [In the case of Fig. 1(a′), the tube thickness would also appear, but we take it as negligibly small in the following.] One can thus form three dimensionless ratios that fully characterize each case. The presentation of a sufficient number of results to cover the entire parameter space is impractical. Thus we limit ourselves to a few examples which also serve to illustrate the excellent performance of the approximations described in the previous section. It may be noted that, by symmetry, a bubble placed at the tube's midpoint in the situations of Fig. 1(a) and (b) is equivalent to a ''half-bubble'' resting on the rigid bottom of Fig. 1(c) and (d) for a tube of half the length.

Figures 2 to 5 show a few representative results. In all these figures the open symbols are the (numerically) exact results obtained with the boundary integral method, the dotted lines are the large-bubble approximation of Sec. II A, and the solid lines the small-bubble approximations of Sec. II B.

Figures 2 and 3 give the ratio f/f_0 as a function of the position of the bubble center along the tube for the five situations depicted in Fig. 1. Here the tube's radius is twice that of the bubble. Figures 4 and 5 are graphs of f/f_0 as a function of a/R for $L/R=10$, again for four of the situations of Fig. 1. Here the bubble center is at the midpoint of the tube axis. The small-bubble approximation of Sec. II B (solid lines) has been evaluated retaining only B_1, C_0, C_1, D_0, and D_1.

The first obvious feature shown by these figures is that the effect of the tube can be large. For example, from Fig. 3, we see that a bubble in a tube closed at one end [Fig. 1(c) and (d)] has a 50% reduction in the natural frequency when the tube radius is twice the bubble radius and the depth of

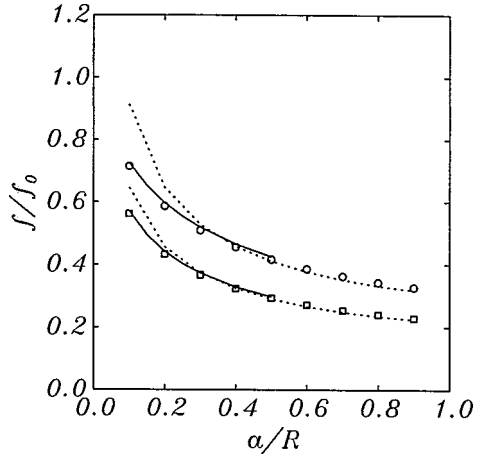

FIG. 4. The natural frequency of a bubble centered at the midpoint of the axis of a tube of radius R and length L as a function of the normalized bubble radius a/R for $L/R=10$. The dotted lines show the result given by the approximate formula (18), the solid lines those given by the small-bubble approximation, and the symbols show the boundary integral results; ○ case of Fig. 1(a); □ case of Fig. 1(c).

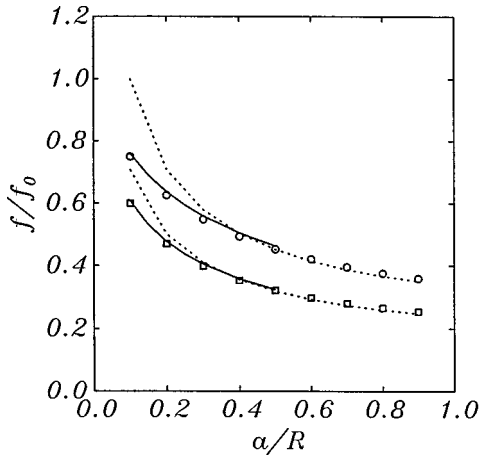

FIG. 5. The natural frequency of a bubble centered at the midpoint of the axis of a tube of radius R and length L as a function of the normalized bubble radius a/R for $L/R=10$. The dotted lines show the result given by the approximate formula (18), the solid lines those given by the small-bubble approximation, and the symbols show the boundary integral results; ○ case of Fig. 1(b); □ case of Fig. 1(d).

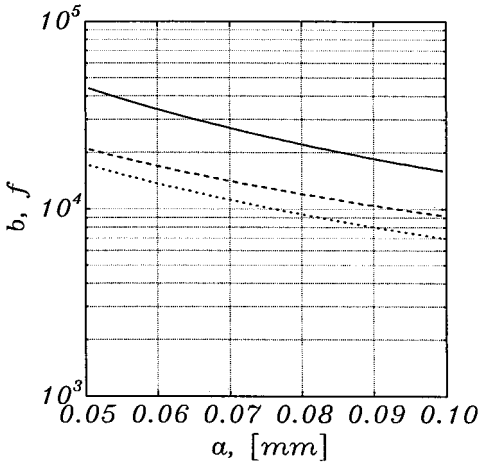

FIG. 7. Natural frequency f in Hz (solid line) and total damping parameter b in s^{-1} [Eq. (40), dashed line] as a function of bubble radius in a tube of radius 0.1 mm and length 1 mm for an air bubble in water. The bubble is positioned at the bottom of the tube. The dotted line is the thermal contribution to the damping. This figure refers to case (d) of Fig. 1 but, with the adjustment to the tube length described in Sec. II A, the results can be adapted to the case of Fig. 1(c) as well.

submergence below the tube mouth is of the order of twice the tube radius.

Another obvious remark suggested by the numerical results is the surprising degree to which the approximations of the previous section are able to reproduce the exact results. In particular, the adjustments to the liquid column length described in Sec. II A are seen to work very well. The large-bubble approximation breaks down around $a/R\simeq 0.2$, while the small bubble model works relatively well at least up to $a/R\simeq 0.5$. It is therefore found that there is a domain in which both approximations are reasonably accurate.

We have examined the effect of retaining more terms in the summations of representation (19) of the velocity potential. The effect of adding two terms to each of the sums is small, and any more terms give differences that are indistinguishable in a graph such as those of Figs. 4 to 7.

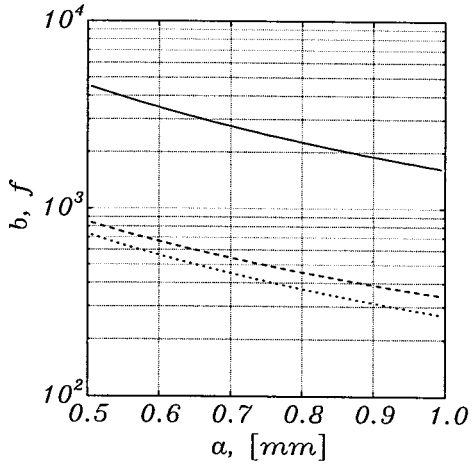

FIG. 6. Natural frequency f in Hz (solid line) and total damping parameter b in s^{-1} [Eq. (40), dashed line] as a function of bubble radius in a tube of radius 1 mm and length 10 mm for an air bubble in water. The bubble is positioned at the bottom of the tube. The dotted line is the thermal contribution to the damping. This figure refers to case (d) of Fig. 1 but, with the adjustment to the tube length described in Sec. II A, the results can be adapted to the case of Fig. 1(c) as well.

In addition to the theoretical development leading to Eq. (29) quoted before, Devin's report contains a few data taken in an experimental setup similar to that of our Fig. 1(a′). The bubbles were generated by a needle placed at the midpoint of the axis of vertical brass cylinders with a diameter of 30 mm, a wall thickness of 3.2 mm, and a length of 120 or 240 mm. In order to investigate the effect of static pressure, two depths of submergence of the tube below the surface of a large water tank were used, 5 and 15 ft. A hydrophone placed at a distance of 0.1 m recorded the sound emitted by the bubbles pinching off the needle and a few graphs of the acoustic power spectral density are shown in the report. By digitizing these figures, we have read off the position of the maximum of these spectra which, in view of the small damping, give a good estimate of the natural frequency. Values of the bubble radius are not given but, in his graphs, Devin shows the natural frequency of the bubble generated by the same method in an unbounded liquid from which the radius can be deduced according to the results of Prosperetti (1991). Table I shows all of Devin's data together with the result given by the first four terms of the series solution of Sec. II B and two estimates obtained from Devin's report. The first one is found from his approximate formula (29), while the second one is the theoretical value read from his graph. These two numbers should agree but, for the first case, we find a 2% discrepancy the origin of which is not clear. This data point also exhibits a greater difference with the theory, about 5%. For the second and third data points agreement with theory is within about 3% and 1%, respectively, and seems to be slightly better for the present theory than for Devin's although, on the basis of the information provided, it is not possible to estimate accurately the error in his data.

TABLE I. Comparison between Devin's data, the present series solution of Sec. II B, and Devin's theory. The tube was brass with a radius of 15 mm.

a (mm)	L (cm)	Exp.	Present theory	Devin, Eq. (29)	Devin, graph
1.51	24	0.67	0.636	0.638	0.653
1.52	12	0.74	0.762	0.777	0.779
1.50	12	0.76	0.764	0.780	0.777

IV. DAMPING RATE

In reality, the oscillations executed by the bubbles shown in Fig. 1 are, of course, damped. In the previous developments we have disregarded dissipative effects which, as is well known, affect the natural frequency only to second order. The decay rate is however a first-order effect, that we now consider.

A bubble oscillating in an unbounded liquid loses energy by thermal conduction across the gas–liquid interface, acoustic radiation, and the action of viscous stresses at the interface. In water, acoustic losses only dominate for bubble radii larger than several millimeters, while viscous losses are significant only for bubbles smaller than about 10 μm. The dominant energy loss for intermediate values of the radius is of thermal origin, and this can be assumed to happen also in the cases of Fig. 1. Indeed, in the underlying process, the significant aspects are the gas volume expansion and contraction and the fact that the bubble surface remains essentially at the undisturbed liquid temperature during the oscillations due to the large thermal capacity of the liquid. Both circumstances occur also in the situations of present concern, as already noted in connection with Eq. (10). In the case of a bubble in a tube, however, a new energy loss mechanism is present, namely viscous dissipation due to liquid flow along the surface of the tube surrounding the bubble. An estimate of the rate of damping due to this effect can be found on the basis of the simple one-dimensional model of Sec. II A as follows.

Consider the bubble as occupying a ''slice'' of the tube extending between $z_1(t)$ and $z_2(t)$. If m_1 and m_2 are the (effective) masses of the two liquid columns, and β_1, β_2 the damping rates due to viscous dissipation, the equations of motion of the two interfaces are

$$m_1\ddot{z}_1+2\beta_1\dot{z}_1+K(z_1-z_2)=0, \tag{30}$$

$$m_2\ddot{z}_2+2\beta_2\dot{z}_2-K(z_1-z_2)=0, \tag{31}$$

with the ''spring constant'' K given by Eq. (16). The equation for the (complex) frequencies of oscillation Ω of this system is readily written down and is

$$\begin{vmatrix} m_1\Omega^2-K-2i\beta_1\Omega & K \\ K & m_2\Omega^2-K-2i\beta_2\Omega \end{vmatrix}=0. \tag{32}$$

Upon setting $\Omega=\omega+ib_t$, up to terms of the first order in β_i, one readily finds

$$\omega^2=K\left(\frac{1}{m_1}+\frac{1}{m_2}\right), \tag{33}$$

which is the same as Eq. (17), and

$$b_t=\frac{1}{m_1+m_2}\left(\beta_1\frac{m_2}{m_1}+\beta_2\frac{m_1}{m_2}\right). \tag{34}$$

In the spirit of Sec. II A, the masses appearing here are given by $m_j=\rho L_j^e A$, $j=1,2$.

To estimate the damping parameters β_i we proceed approximately as follows (disregarding the index i for the moment). The energy dissipated during one cycle by each oscillator is

$$\mathscr{E}_d=2\beta\int_0^{2\pi/\omega}\dot{z}^2\,dt, \tag{35}$$

which furnishes an estimate of β if the other two quantities can be evaluated. Since, to leading order, z oscillates sinusoidally with a frequency ω and velocity amplitude V, the integral has the value $(\pi/\omega)V^2$. The energy loss can be estimated by integrating the dissipation function over the volume occupied by the fluid. With the approximation of periodic, parallel flow, we have

$$\mathscr{E}_d=\mu L\int_0^{2\pi/\omega}dt\int_A dA\left(\frac{\partial u}{\partial r}\right)^2, \tag{36}$$

where μ is the liquid viscosity, the integral is over the cross section of the tube, and u is the axial velocity. Since, in fully developed parallel flow, the problem for u is linear, we have $u\propto V$ and therefore

$$\beta=\frac{\omega}{2\pi}\,\mu L\int_0^{2\pi/\omega}dt\int_A dA\left[\frac{\partial}{\partial r}\left(\frac{u}{V}\right)\right]^2. \tag{37}$$

The velocity field required here is readily calculated from the Navier–Stokes equations (see, e.g., Leal, 1992), but the answer is in terms of Bessel functions with complex argument and it does not appear possible to obtain closed-form expressions for this integral at arbitrary frequency. Approximations for $\sqrt{\mu/\omega\rho}\gg R$ and $\sqrt{\mu/\omega\rho}\ll R$ are, however, readily found. In the first case we have

$$\beta=4m\,\frac{\mu}{\rho R^2}, \tag{38}$$

which can also be obtained from the Poiseuille flow solution, while, in the latter one,

$$\beta=m\sqrt{\frac{\mu\omega}{2\rho R^2}} \tag{39}$$

which, in the spirit of a boundary layer approximation, can also be obtained from the known form of the velocity field over an infinite oscillating flat plate. This latter result is therefore valid for tubes of arbitrary cross section.

The preceding arguments provide an approximation to the viscous damping in the tube b_t. As already mentioned, the gas–liquid heat exchange gives rise to another dissipation mechanism. If the corresponding damping rate is much less than ω, the two damping mechanisms are additive and the total damping of the oscillations is therefore

$$b = b_t + b_b, \tag{40}$$

where b_b is the bubble damping constant that has been exhaustively studied in the literature (see, e.g., Prosperetti *et al.*, 1988; Prosperetti, 1991).

To illustrate the magnitude of the effect, we consider two particular cases in Figs. 6 and 7. These figures refer to the situation of Fig. 1(d) for an air bubble in water at 1 atm but, with the adjustment to the tube length described in Sec. II A, the results are also representative of case 1(c). In Fig. 6 the tube has a length of 10 mm and a radius of 1 mm, while in Fig. 7 the corresponding values are 1 and 0.1 mm, respectively. The bubble is positioned at the bottom of the tube (in the sense of the approximate conceptual model of Sec. II A; strictly speaking, therefore, the radius shown is an equivalent spherical radius). The horizontal axis shows the bubble radius, the solid line the natural frequency, the dotted line the thermal damping, and the dashed line the total damping. The viscous contribution is just the difference between the two lines, and is therefore seen to be small in both cases. Just as in the case of a bubble in an unbounded fluid, we thus see that thermal damping is the dominant mechanism of energy dissipation.

ACKNOWLEDGMENTS

The authors are grateful to Dr. Murray Strasberg for calling their attention to Devin's work on this problem. Thanks are also due to X. M. Chen for her help with the calculations of Sec. IV. This study has been supported by the Air Force Office of Scientific Research under Grant No. F49620-96-1-0386.

Apfel, R. E. (**1981**). *Acoustic Cavitation,* in *Methods of Experimental Physics—Vol. 19 Ultrasonics*, edited by P. D. Edmonds (Academic, New York), pp. 355–411.

Blue, J. E. (**1966**). ''Resonance of a bubble on an infinite rigid boundary,'' J. Acoust. Soc. Am. **41**, 369–372.

Devin, C. (**1961**). ''Resonant frequencies of pulsating air bubbles generated in short, open-ended pipes,'' Technical Report 1522, David Taylor Model Basin, Hydromechanics Laboratory.

Fujita, H., and Gabriel, K. J. (**1991**). ''New opportunities for micro actuators,'' in *Transducers '91* (IEEE, New York), pp. 14–20.

Gravesen, P., Branebjerg, J., and Jensen, O. S. (**1993**). ''Microfluidics—A review,'' J. Micromech. Microeng. **3**, 168–182.

Howkins, S. D. (**1965**). ''Measurements of the resonant frequency of a bubble near a rigid boundary,'' J. Acoust. Soc. Am. **37**, 504–508.

Kamath, V., Prosperetti, A., and Egolfopoulos, F. (**1993**). ''A theoretical study of sonoluminescence,'' J. Acoust. Soc. Am. **93**, 248–260.

Lin, L., Pisano, A. P., and Lee, A. P. (**1991**). ''Microbubble powered actuator,'' in *Transducers '91* (IEEE, New York), pp. 1041–1044.

Leal, L. Gary (**1992**). *Laminar Flow and Convective Transport Processes, Scaling Principles and Asymptotic Analysis* (Butterworth-Heinemann, Boston).

Levine, H., and Schwinger, J. (**1948**). ''On the radiation of sound from an unflanged circular pipe,'' Phys. Rev. **73**, 383–405.

Oğuz, H. N., and Zeng, J. (**1995**). ''Boundary integral simulations of bubble growth and detachment in a tube,'' in *Boundary Elements XVII* (Computational Mechanics Publications, Madison, WI), pp. 645–652.

Oğuz, H. N., and Zeng, J. (**1997**). ''Axisymmetric and three-dimensional boundary integral simulations of bubble growth from an underwater orifice,'' Engineering Analysis with Boundary Elements **19**, 313–330.

Oğuz, H. N., and Prosperetti, A. (**1990**). ''Bubble entrainment by the impact of drops on liquid surfaces,'' J. Fluid Mech. **219**, 143–179.

Plesset, M. S., and Prosperetti, A. (**1977**). ''Bubble dynamics and cavitation,'' Annu. Rev. Fluid Mech. **9**, 145–185.

Pozrikidis, C. (**1992**). *Boundary Integral and Singularity Methods for Linearized Viscous Flow* (Cambridge U.P., Cambridge).

Prosperetti, A., Crum, L. A., and Commander, K. W. (**1988**). ''Nonlinear bubble dynamics,'' J. Acoust. Soc. Am. **83**, 502–514.

Prosperetti, A. (**1991**). ''The thermal behaviour of oscillating gas bubbles,'' J. Fluid Mech. **222**, 587–616.

Scott, J. F. (**1981**). ''Singular perturbation theory applied to the collective oscillation of gas bubbles in a liquid,'' J. Fluid Mech. **113**, 487–511.

Strasberg, M. (**1953**). ''The pulsation frequency of nonspherical gas bubbles in liquids,'' J. Acoust. Soc. Am. **25**, 536–537.

Linear thermoacoustic instability in the time domain

S. Karpov and A. Prosperetti
Department of Mechanical Engineering, The Johns Hopkins University, Baltimore, Maryland 21218

(Received 30 April 1997; accepted for publication 17 February 1998)

An approximate time-domain description of the development of the thermoacoustic instability in gas-filled tubes is developed by exploiting the difference between the instability time scale and the period of standing waves. The perturbation results compare very favorably with the exact frequency-domain theory of Rott. The perturbation results are further simplified by introducing a short-stack approximation which is numerically much simpler and only slightly less accurate. An approximate expression for the critical temperature gradient accounting for viscous effects and other design features is also derived. In addition to the fundamental mode of a tube closed at both ends, the theory includes higher modes as well as open-end boundary conditions. © *1998 Acoustical Society of America.* [S0001-4966(98)00606-7]

PACS numbers: 43.35.Ud [HEB]

INTRODUCTION

The linear theory of thermoacoustic effects as developed in the well-known series of papers by Rott[1–4] (good reviews are provided by Wheatley[5] and Swift[6]) is based on a formulation in the frequency domain. In the present paper we develop an approximate time-domain approach that is valid when the period of standing waves is much shorter than the growth rate of the instability. Since this condition is commonly met in practice, we expect the present formulation to furnish a realistic description of the time evolution of the instability in a wide variety of situations.

One of the main results of the present work is an expression for the linear growth rate of the thermoacoustic instability or, below threshold, for the decay rate of standing waves. This latter result can also be viewed as expressing the power requirement for the operation of a thermoacoustic refrigerator. In the past these results have been approached by estimating the so-called work flux (see, e.g., Ref. 6) or Q-value of the device.[7–9] Our method may therefore be interpreted as a different approach to the evaluation of these quantities. Its advantage is a greater flexibility that enables us to considerably simplify their quantitative evaluation with respect to the exact theory of Rott while at the same time maintaining a greater accuracy than existing approximations.

A second result of the paper is an unambiguous definition of the concept of critical temperature gradient when viscous and thermal effects are both important and an accurate approximate expression for this quantity.

I. MATHEMATICAL MODEL

In Watanabe *et al.*[10] it was shown that a model of thermoacoustic devices that, in the frequency domain, is exactly equivalent to Rott's, may be written in the form

$$\frac{\partial \rho}{\partial t}+\frac{1}{S}\frac{\partial}{\partial x}(S\rho_0 u)=0, \tag{1}$$

$$\rho_0\frac{\partial u}{\partial t}+\frac{\partial p}{\partial x}=-\rho_0\mathscr{D}(u), \tag{2}$$

$$\frac{\partial p}{\partial t}+\frac{\gamma p_0}{S}\frac{\partial (Su)}{\partial x}=(\gamma-1)\left[\mathscr{H}(T_w-T)-\frac{dT_w}{dx}\mathscr{Q}(u)\right]. \tag{3}$$

The system of equations is closed by assuming the validity of the perfect gas law. Here ρ, p, T, and u are the density, pressure, temperature, and velocity fields. The spatial coordinate x is directed along the axis of the device, $S(x)$ is the (possibly variable) cross-sectional area, and γ the ratio of specific heats. The subscript zero denotes undisturbed quantities. The temperature $T_w(x)$ of the solid surfaces in contact with the gas (i.e., the tube walls and the stack plates) is assumed to be only a function of x and is taken to be prescribed in the following. It should be noted that, even when this quantity evolves with time, it does so only slowly (compared with the period of the oscillations) and therefore the present method can be extended to deal with this case as well as noted below.

The drag operator $\mathscr{D}$ and the heat transfer operators $\mathscr{H}$ and $\mathscr{Q}$ are given, in the frequency domain, by

$$\tilde{\mathscr{D}}(u)=i\omega\frac{f_V}{1-f_V}\tilde{u}, \tag{4}$$

$$\tilde{\mathscr{H}}(T_w-T)=-i\omega\rho_0 c_p\frac{f_K}{1-f_K}\tilde{T}', \tag{5}$$

$$\tilde{\mathscr{Q}}(u)=\rho_0 c_p\left[\frac{1}{1-\sigma}\left(\frac{1}{1-f_V}-\frac{\sigma}{1-f_K}\right)-1\right]\tilde{u}. \tag{6}$$

Here $T'=T-T_w$ and tildes denote frequency-domain quantities. The parameters $f_{V,K}$ depend on the ratio of the diffusion lengths $\delta_{V,K}$ to the plate spacing l and, for disturbances proportional to $\exp i\omega\hat{t}$, are given by[6]

$$f=(1-i)\frac{\delta}{l}\tanh(1+i)\frac{l}{2\delta}, \tag{7}$$

where the index can be V or K. The viscous and thermal penetration lengths $\delta_{V,K}$ are given by

 0001-4966/98/103(6)/3309/9/$10.00

$$\delta_V=\sqrt{\frac{2\nu}{\hat{\omega}}},\quad \delta_K=\sqrt{\frac{2\alpha}{\hat{\omega}}}=\frac{\delta_V}{\sqrt{\sigma}},\tag{8}$$

with ν the kinematic viscosity, σ the Prandtl number, and $\alpha=\nu/\sigma$ the thermal diffusivity. For a circular cross section with radius r_0 one has instead[1]

$$f=\frac{2J_1((i-1)(r_0/\delta))}{(i-1)(r_0/\delta)J_0((i-1)(r_0/\delta))},\tag{9}$$

again valid for both f_V and f_K. When the diffusion penetration depths are small compared with either l or r_0, f given by either (7) or (9) admits the asymptotic approximation

$$f\simeq(1-i)\,\frac{\delta}{l},\quad f\simeq(1-i)\,\frac{\delta}{r_0}.\tag{10}$$

More generally, for other cross section shapes, in this limit one may set $f\simeq 2(1-i)\delta/d_h$, where $d_h=4S(x)/s(x)$ is the hydraulic diameter defined in terms of the cross-sectional area S and the ''wetted'' perimeter s.

If Eqs. (1)–(3) are written in the frequency domain, after reduction to a single equation by differentiation and elimination, one recovers Rott's equation:

$$\frac{1}{S}\frac{d}{dx}\left[(1-f_V)S\,\frac{d\tilde{p}}{dx}\right]+\frac{1}{T_w}\frac{dT_w}{dx}\left(1+\frac{\sigma f_V-f_K}{1-\sigma}\right)\frac{d\tilde{p}}{dx}+\frac{\hat{\omega}^2}{c^2}\,[1+(\gamma-1)f_K]\tilde{p}=0.\tag{11}$$

The local adiabatic speed of sound $c(x)$ equals $\sqrt{\gamma RT_w(x)}$, with R the universal gas constant divided by the gas molecular mass, and is therefore also variable in general along the axis of the system.

II. THE STABILITY CALCULATION

Experiment (see, e.g., Refs. 5, 8) shows that the initial build-up of the thermoacoustic instability has the character of a modulated standing wave the frequency of which is essentially dictated by the resonator, while the amplitude is slowly varying in time. This observations suggests the possibility of setting up a perturbation scheme based on the smallness of the ratio of the characteristic period of oscillation to the characteristic time for the development of the instability.

In the framework of the previous model, the terms in the left-hand side of Eqs. (1)–(3) describe linear acoustic waves in a gas column with variable cross-sectional area and temperature stratification and are therefore responsible for the ''carrier'' frequency of the wave. The heart of the thermoacoustic effect is in the terms in the right-hand sides and, more specifically, in the right-hand side of the energy equation (3). The observed slowness of the modulation implies that these terms are small or, since $\mathscr{D}$, $\mathscr{H}$, and $\mathscr{Q}$ all vanish with $f_{V,K}$, that the f's are small. In order to set up a perturbation scheme, we take therefore $f_{V,K}$ to be of order $\epsilon\ll 1$ and we will treat the ratio $f_{V,K}/\epsilon$ as a quantity of order 1. While a formal definition of ϵ is not necessary as the final results do not explicitly depend on this parameter, according to (10), one may think of it as the ratio δ/l.

To proceed with a formal development of the previous observation, we introduce the scaled times

$$\hat{t}=t,\quad \tau=\epsilon t,\tag{12}$$

and, according to the method of multiple time scales, we treat $\hat{t}$ and τ as independent variables. The original variable t is recovered at the end of the calculation by using (12) (see, e.g., Refs. 11, 12). As a consequence of these definitions we have, correct to order ϵ,

$$\frac{\partial}{\partial t}=\frac{\partial}{\partial\hat{t}}+\epsilon\,\frac{\partial}{\partial\tau}.\tag{13}$$

We also expand the dependent variables p, u, etc., in a power series in ϵ; for example,

$$p=p_1+\epsilon p_2+\cdots,\tag{14}$$

with a similar notation for u, etc. Now these expansions are substituted into (1) to (3) where (13) is used to express the time derivative. Upon separating orders, to zero order in ϵ, we have

$$\frac{\partial\rho_1}{\partial\hat{t}}+\frac{1}{S}\frac{\partial}{\partial x}\,(S\rho_0u_1)=0,\tag{15}$$

$$\rho_0\,\frac{\partial u_1}{\partial\hat{t}}+\frac{\partial p_1}{\partial x}=0,\tag{16}$$

$$\frac{\partial p_1}{\partial\hat{t}}+\frac{\gamma p_0}{S}\,\frac{\partial(Su_1)}{\partial x}=0,\tag{17}$$

and, at the next order,

$$\frac{\partial\rho_2}{\partial\hat{t}}+\frac{1}{S}\frac{\partial}{\partial x}\,(S\rho_0u_2)=-\frac{\partial\rho_1}{\partial\tau},\tag{18}$$

$$\rho_0\,\frac{\partial u_2}{\partial\hat{t}}+\frac{\partial p_2}{\partial x}=-\frac{\partial u_1}{\partial\tau}-\frac{1}{\epsilon}\,\rho_0\mathscr{D}(u_1),\tag{19}$$

$$\frac{\partial p_2}{\partial\hat{t}}+\frac{\gamma p_0}{S}\,\frac{\partial(Su_2)}{\partial x}=-\frac{\partial p_1}{\partial\tau}-(\gamma-1)\times\left[\frac{1}{\epsilon}\,\mathscr{H}(T_1')+\frac{1}{\epsilon}\,\mathscr{Q}(u_1)\,\frac{dT_w}{dx}\right].\tag{20}$$

A. Zero order

The three equations (15) to (17) can be combined to give

$$\frac{1}{S}\frac{\partial}{\partial x}\left(c^2S\,\frac{\partial p_1}{\partial x}\right)-\frac{\partial^2p_1}{\partial\hat{t}^2}=0.\tag{21}$$

The solution of this equation may be taken in the form

$$p_1(x,\hat{t},\tau)=A(\tau)P_1(x)\exp(i\omega\hat{t})+\text{c.c.},\tag{22}$$

where c.c. denotes the complex conjugate, and the eigenfunction $P_1(x)$ and eigenfrequency ω are determined by solving the eigenvalue problem

$$\frac{1}{S}\frac{d}{dx}\left(c^2 S\frac{dP_1}{dx}\right)+\omega^2 P_1=0, \tag{23}$$

subject to appropriate boundary conditions. In this paper we only consider rigid or open terminations at the ends of the tube and therefore

$$\frac{dP_1}{dx}=0 \quad \text{or} \quad P_1=0 \quad \text{at} \quad x=0,\ x=L. \tag{24}$$

With these conditions, it can readily be shown by standard techniques that the eigenvalue ω is real (see, e.g., Refs. 14, 15). The eigenfunction P_1 can therefore also be taken real and, for later convenience, we normalize it so that

$$\int_0^L S(x)P_1^2(x)dx=Vp_0^2, \tag{25}$$

where V is the volume of the device and p_0 is the undisturbed static pressure. Since the total acoustic energy in the device, to the present approximation, is given by (see, e.g., Ref. 16 section 63)

$$\mathscr{E}=\int_0^L S(x)\frac{\langle p_1^2\rangle}{\rho_0 c^2}\,dx=\frac{A^2}{2\gamma p_0}\int_0^L S(x)P_1^2 dx=A^2\mathscr{E}_0, \tag{26}$$

we see that normalization (25) is equivalent to normalizing the energy by

$$\mathscr{E}_0=\frac{Vp_0}{2\gamma}. \tag{27}$$

It is readily found that u_1, ρ_1, and T_1' also satisfy Eq. (21) and therefore they can also be written in the form (22) with the same ω and proportionality to the same function $A(\tau)$. In particular, from (16),

$$U_1(x)=\frac{i}{\omega\rho_0}\frac{dP_1}{dx}. \tag{28}$$

B. First order

To order ϵ, the drag and heat transfer operators $\mathscr{D}$, $\mathscr{H}$, and $\mathscr{Q}$ operate on the variable $\hat{t}$ and, since the dependence on this variable is only through the exponential factor $\exp i\omega\hat{t}$, one can use the Fourier-space representation of these operators given in (4)–(6). Upon substitution of solution (22) for p_1 and similar expressions for the other first-order fields into (18)–(20), we thus find

$$\begin{aligned}\frac{1}{S}\frac{\partial}{\partial x}\left(c^2 S\frac{\partial p_2}{\partial x}\right)-\frac{\partial^2 p_2}{\partial\hat{t}^2}&=\left\{2i\omega\frac{dA}{d\tau}P_1-\frac{A}{\epsilon}\left[\frac{1}{S}\frac{\partial}{\partial x}\left(\frac{if_V}{1-f_V}\omega\rho_0 Sc^2U_1\right)\right.\right.\\&\quad+(\gamma-1)\omega^2 f_K P_1(x)\\&\quad\left.\left.-i\frac{f_V-f_K}{(1-\sigma)(1-f_V)}\gamma\frac{\omega p_0 U_1}{T_w}\frac{dT_w}{dx}\right]\right\}\exp i\omega\hat{t}+\text{c.c.}\end{aligned} \tag{29}$$

The forcing at frequencies $\pm\omega$ in the right-hand side will generate resonant terms proportional to $\hat{t}\exp i\omega\hat{t}$ in the solution for p_2 which lead to a breakdown of the approximation over times of order $(\epsilon\omega)^{-1}$. To avoid this resonance, as in the standard procedure,[11–13] we impose the solvability condition that the right-hand side of the equation be orthogonal to the solution of the (adjoint) homogeneous equation, namely $\exp(-i\omega\hat{t})P_1$:

$$\int_0^L S[\exp(-i\omega\hat{t})P_1]\left(2i\omega\frac{dA}{d\tau}P_1-\frac{A}{\epsilon}\{\cdots\}\right)\exp(i\omega\hat{t})dx=0, \tag{30}$$

where, for brevity, we write $\{\cdots\}$ to denote the coefficient of A in (29). Multiplication by $S(x)$ before integration is necessary so that the x-operator in the left hand side of (29) be self-adjoint with the boundary conditions (24). In this way we find

$$\frac{dA}{d\tau}+\frac{\Omega}{\epsilon}A=0, \tag{31}$$

where

$$\Omega=\tfrac{1}{2}(M_D+iN_D+M_H+iN_H) \tag{32}$$

with, after an integration by parts,

$$M_D+iN_D=\frac{i}{Vp_0^2\omega}\int_0^L Sc^2\frac{f_V}{1-f_V}\left(\frac{dP_1}{dx}\right)^2 dx, \tag{33}$$

$$M_H+iN_H=i\frac{\gamma-1}{Vp_0^2\omega}\int_0^L dx\,SP_1\left[f_K\omega^2P_1-\frac{f_K-f_V}{(1-\sigma)(1-f_V)}c_p\frac{dT_w}{dx}\frac{dP_1}{dx}\right], \tag{34}$$

where c_p is the specific heat at constant pressure.

Since the f's are essentially the small parameter ϵ, and since these results have an accuracy of first order in ϵ, one might be tempted to replace $1-f_V$ simply by 1 in the denominators. While justified in principle in the limit $\epsilon\to 0$, we have found that the numerical accuracy of these results extends to significantly larger values of δ/l if the forms given above are retained.

Clearly (34) is also applicable when T_w depends slowly (i.e., on the time scale τ) on time. Integration of the amplitude equation (31) in this case is however somewhat more complicated and therefore, as already mentioned before, we limit ourselves to the simpler situation in which T_w is independent of time. In this case the solution of (31) is

$$A(\tau)=A_0\exp\left(-\Omega\frac{\tau}{\epsilon}\right)=A_0\exp(-\Omega t), \tag{35}$$

with A_0 dependent on the initial conditions, and therefore grows or decays according to the sign of M_D+M_H. The second form of solution (35) demonstrates explicitly the independence of the result from the definition of ϵ. The previous results imply the following approximation for the exact eigenfrequency $\hat{\omega}$ in Rott's equation (11):

$$\hat{\omega}\simeq\omega+i\Omega. \tag{36}$$

It is interesting to verify that (35) reduces to the standard expressions for the viscous and thermal damping of a standing wave in a hollow isothermal cylindrical tube. If we consider the case of rigid terminations at both ends, by the normalization (25), we may write

$$P_1 = \sqrt{2} p_0 \cos \frac{n\pi x}{L}. \tag{37}$$

With this expression, noting that $\omega = n\pi c/L$, and using approximation (10) for $f_{V,K}$, it is immediate to verify that, to lowest order in these quantities,

$$M_D + iN_D \simeq (1+i)\,\frac{\sqrt{2\nu\omega}}{r_0}, \tag{38}$$

$$M_H + iN_H \simeq (1+i)(\gamma-1)\,\frac{\sqrt{2\alpha\omega}}{r_0}, \tag{39}$$

in agreement with well-known results (see, e.g., Ref. 17, p. 534).

In view of the proportionality of $\mathscr{E}$ to the A^2 shown by (26), we also see that (31) implies

$$\frac{d\mathscr{E}}{dt} = -(M_D + M_H)\mathscr{E}. \tag{40}$$

In the unstable case $M_D + M_H < 0$ and this relation gives the growth rate of the disturbance energy. In the stable case $M_D + M_H > 0$ and, in order to maintain the oscillations, one needs to supply energy externally at the rate dictated by the right hand side of (40). In this case the energy lost is in part dissipated by viscosity and thermal conduction, but in part is also the work needed to transport heat from the colder to the warmer regions as, in this case, the device behaves as a heat pump, or acoustic refrigerator.

Swift[6] defines the work flux $\dot{W}_2$ in a thermoacoustic engine. This is equivalent to the rate of growth (or decay) of the total acoustic energy in the device and, in the present notation, is therefore given by

$$\dot{W}_2 = -(M_D + M_H)\mathscr{E}. \tag{41}$$

The connection between Swift's expression for $\dot{W}_2$ and our result is best explained after the considerations of Subsection III A.

The quality factor Q is defined by

$$Q = -\frac{\omega\mathscr{E}}{\dot{W}_2}, \tag{42}$$

which, with (32) and (41), becomes

$$Q = \frac{\omega}{2\,\mathrm{Re}\,\Omega}. \tag{43}$$

This relation establishes a connection between the present study and the work of Atchley[7–9] who estimated the growth rate of the instability using an approximate calculation of $\mathscr{E}$ and $\dot{W}_2$. The present approach has the advantage of greater generality which, as will be seen in the following sections, leads to very accurate results.

III. SHORT-STACK APPROXIMATION

The asymptotic results of Sec. I can be approximated by adopting the so-called ''short-stack approximation'' (see, e.g., Ref. 6). We thus assume that the stack occupies a length much smaller than the wavelength of the standing waves so that the pressure field in the stack can be considered as constant. We take $f_{V,K} \simeq 0$ outside the stack region.

We thus write (33), approximately, as

$$M_D + iN_D \simeq \frac{i\overline{f_V}}{1-\overline{f_V}}\,\frac{V_S}{V}\,\frac{\overline{c^2}}{\omega p_0^2}\left(\frac{dP_{1S}}{dx}\right)^2. \tag{44}$$

Here $\overline{f_V}$ and $\overline{c^2}$ (or, equivalently, $\overline{T_w}$) are evaluated at the mean temperature in the stack, $T_w = \frac{1}{2}(T_C + T_H)$. It is difficult on the basis of *a priori* considerations to formulate the kind of averaging that is most effective for the present purposes. We have tried several definitions, such as averaging computed by integration along the stack, but found insignificant differences. Furthermore,

$$V_S = \int_{x_{S-(1/2)L_S}}^{x_{S+(1/2)L_S}} dx\; S(x) \tag{45}$$

is the volume of the gas in the stack region extending from $x_S - \frac{1}{2}L_S$ to $x_S + \frac{1}{2}L_S$. The index S appended to P_1 denotes evaluation at the stack's midpoint x_S. In a similar way, from (34),

$$M_H + iN_H \simeq i\,\frac{V_S}{V}\,\frac{\omega}{p_0^2}\left[(\gamma-1)\overline{f_K}(P_{1S})^2 - \frac{\overline{f_K}-\overline{f_V}}{(1-\sigma)(1-\overline{f_V})}\,\frac{1}{\omega^2}\,\overline{\frac{dc^2}{dx}}\,P_{1S}\,\frac{dP_{1S}}{dx}\right], \tag{46}$$

and, upon combining results (44) and (46),

$$M_D + M_H \simeq \frac{V_S}{V}\,\frac{\omega}{p_0^2}\left[Z_1\,\frac{\overline{c^2}}{\omega^2}\left(\frac{dP_{1S}}{dx}\right)^2 + (\gamma-1)Z_2(P_{1S})^2 - Z_3\,\frac{1}{\omega^2}\,\overline{\frac{dc^2}{dx}}\,P_{1S}\,\frac{dP_{1S}}{dx}\right], \tag{47}$$

where we have set for brevity

$$Z_1 = -\,\mathrm{Im}\left(\frac{\overline{f_V}}{1-\overline{f_V}}\right),\quad Z_2 = -\,\mathrm{Im}(\overline{f_K}),\quad Z_3 = \frac{1}{1-\sigma}\,\mathrm{Im}\left(\frac{\overline{f_V}-\overline{f_K}}{1-\overline{f_V}}\right). \tag{48}$$

For small diffusion penetration depths, from (10), these quantities are given by

$$Z_1 \simeq \frac{\overline{\delta_V}}{l},\quad Z_2 \simeq \frac{1}{\sqrt{\sigma}}\,\frac{\overline{\delta_V}}{l},\quad Z_3 \simeq \frac{1}{\sqrt{\sigma}(1+\sqrt{\sigma})}\,\frac{\overline{\delta_V}}{l}. \tag{49}$$

Use of these approximations in actual numerical calculations is not recommended. We show them to stress the dependence of the quantities Z_j on the Prandtl number and the ratio of the viscous boundary layer thicknesses to the the plate spacing.

From definitions (41) of $\dot{W}_2$ and (22) of p_1, and relation (26) we have

$$\dot{W}_2 = -\frac{V_S \omega}{\gamma p_0}\left[Z_1 \frac{\overline{c^2}}{\omega^2}\left\langle \left(\frac{\partial p_{1S}}{\partial x}\right)^2 \right\rangle + (\gamma-1) Z_2 \times \langle (p_{1S})^2 \rangle - Z_3 \frac{1}{\omega^2}\frac{\overline{dc^2}}{dx}\left\langle p_{1S}\frac{\partial p_{1S}}{\partial x}\right\rangle \right], \tag{50}$$

where the angle brackets denote time average over one cycle. In his Eq. (80) Swift[6] gives an expression for the work flux $\dot{W}_2$. It can be shown that his expression is the same as ours provided that $f_{V,K}$ in (48) are approximated by (10) and $\overline{dT_w/dx}$ is much larger than $\overline{T_w}/L$. Since usually $T_H - T_C$ is not very much smaller than T_w, while $L_S \ll L$, this latter approximation is often satisfied.

By equating (47) to zero we find a critical value of the temperature gradient that, if exceeded, leads to instability:

$$\left.\frac{dT_w}{dx}\right|_{\text{crit}} = \frac{1}{Z_3}\left[Z_2 \frac{\omega^2}{c_p}\frac{P_{1S}}{dP_{1S}/dx} + Z_1 \overline{T_w}\frac{dP_{1S}/dx}{P_{1S}}\right]. \tag{51}$$

If viscous effects are neglected, $\overline{f_V}=0$, $\sigma=0$ and this expression is readily shown to coincide with the critical temperature gradient defined in the elementary theory of thermoacoustic processes (see, e.g., Ref. 6). The minimum of $dT_w/dx|_{\text{crit}}$ occurs for

$$\frac{P_{1S}}{dP_{1S}/dx} = \frac{1}{\omega}\left[\frac{Z_1}{Z_2} c_p \overline{T_w}\right]^{1/2}, \tag{52}$$

where it has the value

$$\left.\frac{dT_w}{dx}\right|_{\text{min}} = 2\omega \frac{\sqrt{Z_1 Z_2}}{Z_3}\left(\frac{\overline{T_w}}{c_p}\right)^{1/2}. \tag{53}$$

In particular, in the inviscid case, any nonzero value of the temperature gradient will give rise to an instability if the stack is positioned at a pressure node.

To obtain further explicit results, we distinguish several types of boundary conditions.

A. Closed tube

Use of the previous formulae requires the approximate knowledge of ω and P_1 in the stack region. We calculate ω from

$$\omega^2 \simeq \left(\zeta \frac{n\pi}{L}\right)^2 \gamma R T_e, \tag{54}$$

where T_e is an effective temperature and ζ is a factor accounting for the difference between the actual and the ''effective'' length of the tube (see, e.g., Ref. 18 art. 265). We have used Rayleigh's method to estimate ζ, but found a negligible difference and therefore we set this quantity to 1 in the following. We take T_e to be the average temperature of the system

$$T_e = \frac{1}{L}\int_0^L T_w(x)\,dx. \tag{55}$$

We approximate the nth pressure eigenmode P_1 in the stack region by

$$P_1 = \sqrt{2} p_0 \cos\frac{\omega}{c_H}(L-x), \tag{56}$$

where $c_H = \sqrt{\gamma R T_H}$ and the factor $\sqrt{2}$ is suggested by the form of (37). Taking the wave number as ω/c_H rather than $n\pi/L$ is motivated by the result shown later that the optimal stack position for instability is near the hot end of the tube. We find that this choice indeed improves agreement with the exact solution as expected.

With these approximations we find from (47)

$$M_D + M_H \simeq 2\frac{V_S}{V}\omega\left\{ Z_1 \frac{\overline{T_w}}{T_H}\sin^2\left[\frac{\omega}{c_H}(L-x_S)\right] + (\gamma-1) Z_2 \cos^2\left[\frac{\omega}{c_H}(L-x_S)\right] - \frac{1}{2} Z_3 \frac{c_H}{\omega T_H}\frac{\overline{dT_w}}{dx}\sin\left[\frac{2\omega}{c_H}(L-x_S)\right]\right\}. \tag{57}$$

The first two terms are positive definite—and hence stabilizing—and correspond to viscous and thermal dissipation, respectively. The only potentially destabilizing term is the last one. If, as we assume, $dT_w/dx \geqslant 0$, it is therefore evident that, for instability to be possible, the stack must be positioned in a region where $\sin 2(\omega/c_H)(L-x_S) > 0$. In particular, for the fundamental mode for which $n=1$, the stack must be placed to the right of the tube's midpoint. In this case it is easy to see that $\overline{T_w} > T_e$.

With expression (54) for ω, the smallest critical temperature gradient (53) becomes

$$\left.\frac{dT_w}{dx}\right|_{\text{crit}} = 2\frac{n\pi T_e}{L}\frac{\sqrt{Z_1 Z_2}}{Z_3}\sqrt{(\gamma-1)\frac{\overline{T_w}}{T_e}}. \tag{58}$$

This relation shows that, for a given mean temperature gradient, only a finite number of modes can be unstable.

Expression (57) can be identically rewritten as

$$M_D + M_H \simeq \frac{V_S}{V}\omega Z_2\left[\frac{Z_1 \overline{T_w}}{Z_2 T_H} + \gamma - 1 + B\cos\left(2\frac{\omega}{c_H}(L-x_S) + \phi\right)\right], \tag{59}$$

where

$$B = \left[\left(\gamma - 1 - \frac{Z_1 \overline{T_w}}{Z_2 T_H}\right)^2 + \left(\frac{Z_3 c_H}{Z_2 \omega T_H}\frac{\overline{dT_w}}{dx}\right)^2\right]^{1/2}, \tag{60}$$

$$\sin\phi = \frac{1}{B}\frac{Z_3}{Z_2}\frac{c_H}{\omega T_H}\frac{\overline{dT_w}}{dx}. \tag{61}$$

Upon ignoring the small effect of the dependence of ω on x_S, it is evident from (59) that the instability will be greatest at the position where the cosine equals -1, from which

$$\sin\left[2\frac{\omega}{c_H}(L-x_S)\right] = \sin\phi. \tag{62}$$

It is readily verified that, if the mean pressure gradient is very small, this relation requires that the stack be positioned near a pressure node, as found before. However, in typical

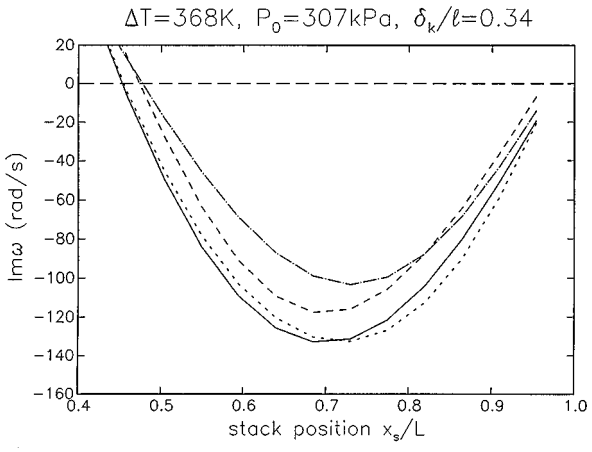

FIG. 1. Imaginary part of the eigenfrequency Im $\hat{\omega}$ as a function of the stack position x_S/L along the resonant tube. The temperature difference between the two ends of the stack is 368 K and the gas pressure 307 kPa. When the stack is positioned at the midpoint of the tube the ratio of the thermal penetration length to the spacing of the stack plates is 0.34. The solid line is the exact result from (11), the dotted line the two-time-scales result (32), the dashed line the short-stack approximation (57), and the dash-dot line Swift's result. Instability corresponds to Im $\hat{\omega}<0$.

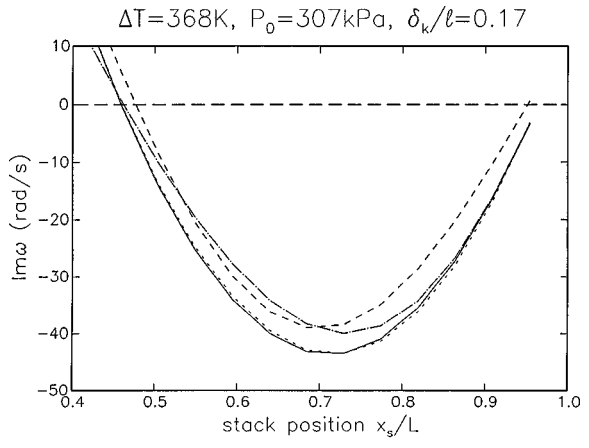

FIG. 2. Imaginary part of the eigenfrequency Im $\hat{\omega}$ as a function of the stack position x_S/L along the resonant tube. The temperature difference between the two ends of the stack is 368 K and the gas pressure 307 kPa. When the stack is positioned at the midpoint of the tube the ratio of the thermal penetration length to the spacing of the stack plates is 0.17. The solid line is the exact result from (11), the dotted line the two-time-scales result (32), the dashed line the short-stack approximation (57), and the dash-dot line Swift's result. Instability corresponds to Im $\hat{\omega}<0$.

conditions of operation of thermoacoustic devices, the stack length is much smaller than the tube length, while the temperature difference along the stack is of the order of the cold-end absolute temperature.[6] As a consequence, $\overline{dT_w/dx}$ is usually much larger than T_e/L so that, for moderate mode number n, we may approximate B and ϕ by

$$B \simeq \frac{Z_3}{Z_2}\frac{c_H}{\omega T_H}\overline{\frac{dT_w}{dx}}, \quad \sin\phi \simeq 1. \tag{63}$$

With these approximations, the optimal position of the stack to destabilize the nth mode is very nearly $\sin 2(\omega/c_H)(L-x_S)=1$, i.e., $x_S/L=1-(k+1/4)c_H/(nc_e)$, with k an integer subject to the only restrictions that $0\leqslant x_S/L\leqslant 1$. In particular, for the fundamental mode $n=1$, k must be taken as 0, so that

$$\frac{x_S}{L}=1-\frac{1}{4}\sqrt{\frac{T_H}{T_e}}. \tag{64}$$

In the elementary theory of the thermoacoustic instability, the optimal stack position is found to be at the three-quarter point $x_S=\frac{3}{4}L$, i.e., one-eighth of a wavelength from the hot end (Ref. 6; recall that here distances are measured from the cold-end of the tube). Since $T_H>T_e$, our result (64) shows that the optimal stack position is actually slightly displaced further away from the hot end of the tube, in agreement with the exact results shown in Figs. 1 and 2. It should be remarked that this conclusion only applies under the condition that $|dT_w/dx| \gg T_e/L$ and therefore it can lead to erroneous conclusions when $|dT_w/dx|$ is small.

As the order n of the mode increases, ω also increases and the constant B given by (63) accordingly decreases. Thus higher-order modes are found to be always less unstable than the fundamental one.

B. Tube open at one end

For a tube open at the cold end $x=0$ and rigidly terminated at $x=L$, we approximate the nth eigenfrequency by

$$\omega^2 \simeq \left[\left(n+\frac{1}{2}\right)\frac{\pi}{L}\right]^2 \gamma R T_e, \tag{65}$$

where the average temperature T_e is defined as before by (55). The corresponding eigenmode P_1 is taken as

$$P_1=\sqrt{2}p_0 \sin\frac{\omega}{c_C}x, \tag{66}$$

where $c_C=\sqrt{\gamma R T_C}$. Unlike the previous case, here we use ω/c_C for the wave number since the optimal stack position for instability will be found to be close to the cold end. Proceeding as before, we find

$$M_D+M_H \simeq 2\frac{V_S}{V}\omega\left[Z_1\frac{\overline{T_w}}{T_C}\sin^2\left(\frac{\omega}{c_C}x_S\right) + (\gamma-1)Z_2\cos^2\left(\frac{\omega}{c_C}x_S\right) - \frac{1}{2}Z_3\frac{c_C}{\omega T_C}\overline{\frac{dT_w}{dx}}\sin^2\left(\frac{\omega}{c_C}x_S\right)\right]. \tag{67}$$

With (65), the critical gradient (53) is

$$\left.\frac{dT_w}{dx}\right|_{\text{crit}} = 2\left(n+\frac{1}{2}\right)\frac{\pi T_e}{L}\frac{\sqrt{Z_1 Z_2}}{Z_3}\sqrt{(\gamma-1)\frac{\overline{T_w}}{T_e}}. \tag{68}$$

When $|\overline{dT_w/dx}| \gg T_e/L$ the maximum instability occurs approximately at $x_S/L=\frac{1}{2}[(4k+1)/(2n+1)](c_C/c_e)$, where $c_e=\sqrt{\gamma R T_e}$. For the lowest mode $n=0$, $k=0$ and $x_S=\frac{1}{2}L(c_C/c_e)$. This result is easily understood on the basis of the previous one as the present situation is similar to a tube of length $2L$ closed at both ends.

The case of a tube closed at the cold end and open at the other one is contained in the preceding formulae if dT_w/dx is taken to be negative. The critical gradient is the negative of (68). Again with the hypothesis that $|dT_w/dx| \gg T_e/L$, the maximum instability occurs approximately at $x_S/L = \frac{1}{2}(4k+3)/(2n+1)$. For the lowest mode $n=0$, there is no integer k such that $x_S/L \leqslant 1$. The instability condition cannot be therefore satisfied for the lowest mode of a tube open at the hot end.

C. Both ends open

For a tube open at both ends, with the cold end at $x=0$, the nth eigenfrequency is approximately given by (54). The same relations (67) and (68) of the previous case apply. The condition for instability is again given by (58). When $|\overline{dT_w/dx}| \gg T_e/L$ the maximum instability occurs for $x_S/L = \frac{1}{4}[(4k+1)/n](c_C/c_e)$, approximately. For the fundamental mode $n=1$ we thus have $k=0$ and $x_S = \frac{1}{4}(c_C/c_e)L$.

IV. COMPARISON WITH EXACT THEORY

We compare here the results of the multiple-time-scales calculation and the short stack approximation with those obtained from the exact equation (11) for some typical parameter values.

The geometry that we simulate is that of the experiments of Atchley[7,8] in which the tube length was 99.87 cm, its radius 3.82 cm, and the stack length $L_S = 3.5$ cm. The combined cross-sectional area of the stack plates was 3.1 cm^2, i.e., 27% of the entire cross section. We have calculated the exact eigenvalue $\hat{\omega}$ both accounting for, and neglecting, the blockage effect of the plates. As the differences between the two cases are very small, in the results shown below we neglect blockage for simplicity.

Of course, our purpose here is not to compare Rott's theory or our approximations with the data, a task that has already been carried out, e.g., by Atchley himself and others,[7–9,19,10] but to validate the asymptotic results against the exact ones.

The gas used in the experiment was helium and accordingly we take $\gamma = 5/3$, $\sigma = 0.71$, $c_p = 5.2$ kJ/kg K. Over the temperature range of interest here, from 300 K to 700 K, we fit thermal conductivity data[20] by a linear function of temperature as $k = 0.151 + 3.228 \times 10^{-4}(T-300)$, with k in W/m K and T in K, which provides a better fit than a power law. We have included this effect in our calculation as the value of k determines the boundary layer thickness, and therefore the heat transfer parameters. The measured temperature was approximately constant and equal to its cold and hot values to the left and right of the stack respectively, and linear in the stack and therefore we take $T = T_C$ for $0 \leqslant x \leqslant x_S - \frac{1}{2}L_S$, $T = T_H$ for $x_S + \frac{1}{2}L_S \leqslant x \leqslant L$, and

$$T = T_C + \frac{x - (x_S - \frac{1}{2}L_S)}{L_S}(T_H - T_C), \tag{69}$$

for $x_S - \frac{1}{2}L_S < x < x_S + \frac{1}{2}L_S$. Here x_S denotes the position of the midpoint of the stack.

To solve Eq. (11) numerically we multiply by S and discretize by centered differences on an equispaced grid. This procedure requires the values of $(1-f_V)S$ at the half-integer nodes which are calculated as simple arithmetic averages. Typically 2000 cells were used along the tube length, with approximately 100 in the stack region. The eigenvalues were searched by the inverse iteration method.[21] The same method was used to calculate the eigenvalues and eigenfunctions of the first-order approximation (21). The integrations necessary to calculate Ω in Eqs. (33) and (34) were effected by the trapezoidal rule. In order to avoid introducing an additional parameter—the radius of the tube—we have taken f_V and f_K to vanish outside the stack region.

As the operation of a thermoacoustic prime mover is critically dependent on the imaginary part of the eigenfrequency, we focus on this quantity. In Figs. 1 and 2 we show Im $\hat{\omega}$ as a function of the stack position x_S/L normalized by the tube length. These figures are for an undisturbed pressure of 307 kPa, with a temperature difference of 368 K along the stack. The choice of this particular case is suggested by the experimental conditions of Atchley *et al.*[9,22] The frequency Re $\hat{\omega}/2\pi$ of the fundamental mode changes from about 505 Hz to 590 Hz as the stack is moved from the hot to the middle of the tube. Within about 10%, these values are well predicted by the formula (54) with $n=1$, $\zeta=1$. Since the thermal penetration depth depends on frequency, the ratio $\overline{\delta_K}/l$ is also a function of the stack's position. When the stack is in the middle of the tube this ratio has the value 0.34 in Fig. 1 and 0.17 in Fig. 2. As the stack is moved toward the hot end, the frequency decreases and the penetration depth correspondingly increases to 0.37 for Fig. 1 and 0.19 for Fig. 2.

In Figs. 1 and 2 the solid lines mark the results from the solution of the exact Rott equation (11), the dotted lines are the two-time-scales approximation (32), the dashed lines are the short-stack approximation (57), and the dash-dot lines are the results obtained from Eq. (80) in Swift[6] according to (41). The zero is marked by the horizontal line; a negative value of Im $\hat{\omega}$ implies instability, and a positive one stability. Agreement between the two-times approximation (32) and the exact solution is excellent even at the relatively large value of $\overline{\delta_K}/l$ of Fig. 1. The difference is hardly noticeable at the smaller value of Fig. 2, and practically disappears for even larger gaps. The short-stack approximation (57) is not as accurate, but the error is less than about 15% even in the worst case. Swift's result is good for the wider gap case of Fig. 2 but, as Fig. 1 shows, it rapidly deteriorates as the gap width decreases. It should be noted that, in plotting Swift's result, the values of pressure and velocity appearing in Swift's formula have been obtained from the exact solution of Rott's equation.

Another important quantity is the critical temperature gradient, which is shown in Figs. 3 to 5 as a function of $\overline{\delta_K}/l$ for stack positions at $x_S/L = 0.594$, 0.729, 0.864, respectively. Here the geometry and conditions are as in the previous figures except for the hot temperature T_H which is evaluated as follows. In the case of the exact Rott solution T_H is adjusted so as to achieve marginal stability conditions (i.e., Im $\hat{\omega}=0$) with a fixed stack length L_S, after which the critical temperature gradient is calculated as $(T_H - T_C)/L_S$. (Recall that the stack temperature is prescribed to be linear in

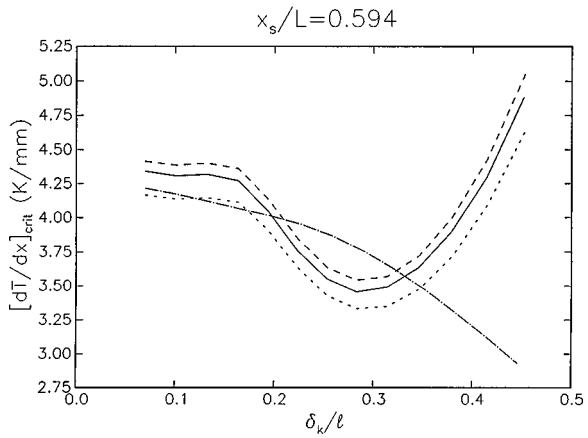

FIG. 3. Critical temperature gradient as a function of the ratio of the thermal penetration length δ_K to the gap width l for a stack positioned at $x_S/L = 0.594$, i.e., near the midpoint of the tube. The solid line is the exact Rott result, the dotted line the short-stack approximation (51) with P_1 approximated by the hot-temperature wave function (56), and the dashed line by the cold-temperature wave function (66). The dash-dot line is the result found by setting Swift's (Ref. 6) Eq. (80) to 0. The large discrepancy is principally due to the use of the approximation (10) for the $f_{V,K}$'s in (48).

this work.) These results are shown by the solid lines in the figures. The short-stack approximation to the critical temperature gradient has been calculated from (51) which, with $dT_w/dx=(T_H-T_C)/L_S$, can be regarded as an equation for T_H. The dotted line shows this result with P_1 approximated by (56), while the dashed line is found from a corresponding approximation, (66), based on the cold-temperature wave number. For the two positions closest to the hot end of the tube (Figs. 4 and 5) most of the tube is occupied by gas at the cold temperature and use of the second form of the eigenfunction gives a somewhat better result. When the stack is positioned near the midpoint of the tube (Fig. 3), on the other hand, both alternatives give a comparable error that can be reduced by using the average of the two approximations to P_1 (not shown). We have repeated these calculations using

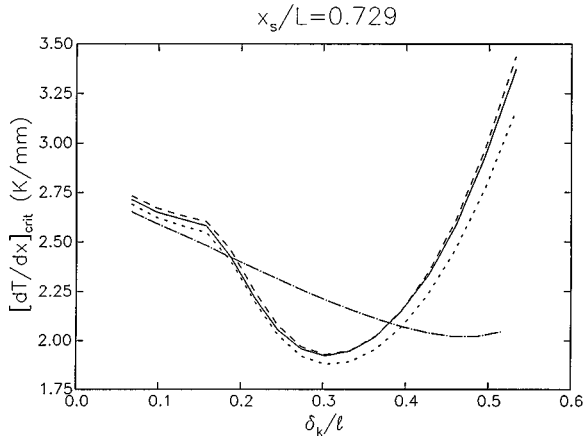

FIG. 4. Critical temperature gradient as a function of the ratio of the thermal penetration length δ_K to the gap width l for a stack positioned at $x_S/L = 0.729$. The solid line is the exact Rott result, the dotted line the short-stack approximation (51) with P_1 approximated by the hot-temperature wave function (56), and the dashed line by the cold-temperature wave function (66). The dash-dot line is the result found by setting Swift's (Ref. 6) Eq. (80) to 0. The large discrepancy is principally due to the use of the approximation (10) for the $f_{V,K}$'s in (48).

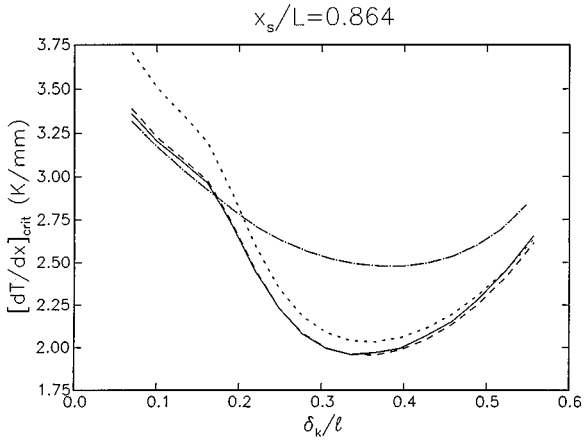

FIG. 5. Critical temperature gradient as a function of the ratio of the thermal penetration length δ_K to the gap width l for a stack positioned at $x_S/L = 0.864$. The solid line is the exact Rott result, the dotted line the short-stack approximation (51) with P_1 approximated by the hot-temperature wave function (56), and the dashed line by the cold-temperature wave function (66). The dash-dot line is the result found by setting Swift's (Ref. 6) Eq. (80) to 0. The large discrepancy is principally due to the use of the approximation (10) for the $f_{V,K}$'s in (48).

the exact two-time-scale expression (51) with P_1 found numerically from (23). When the stack is positioned near the tube's midpoint the error is about 1%. When however the stack is moved toward the hot end, this result is comparable to that obtained by the short-stack approximation with the cold-temperature wave number.

In Figs. 3 to 5 the dash-dot lines show the result obtained by setting Swift's expression for $\dot{W}_2$ to 0. The error incurred in the approximation of $f_{V,K}$ by (10) is seen to lead to a substantial discrepancy with the exact results. Our result would show a comparable error if the same approximations for $f_{V,K}$ were used.

V. CONCLUSIONS

By exploiting the difference between the time scale for the development of the thermoacoustic instability and the period of standing waves in a resonant tube, we have developed a time-domain description of the instability and approximate formulae for its growth rate. We have carried out a multiple-time-scales expansion to first order and we have given simplified formulae exploiting the short-stack approximation. In addition to closed tubes, we have also considered tubes open at either or both ends. Results for modes higher than the fundamental one have also been presented.

The exact perturbation results are very close to the theoretical prediction of the full Rott equation. In practice, their evaluation requires the solution of the eigenvalue problem (21) that is self-adjoint and has therefore real eigenvalues. Accordingly, numerically the problem is more tractable than Rott's equation. Even this rather modest computational task can be avoided—at the price of an error of a few percent—by adopting the short-stack approximation discussed in Sec. III.

Another significant result of the present study is an accurate (and numerically manageable) approximation for the critical temperature gradient including viscosity, heat trans-

fer, and cross-sectional area changes. As Figs. 3 to 5 show, the present expression is significantly more accurate than others available in the literature.

As a final point, the approximate result (40) for the rate of energy loss of a thermoacoustic device below the instability threshold enables one to readily calculate the minimum power required to maintain a certain temperature difference across the stack, i.e., to operate the device as a refrigerator.

Although we have only considered a particular type of thermoacoustic devices, in which the heated region contains the so-called stack, the same method can be applied to other configurations. The present results imply that good accuracy may be expected as a result of this approach.

ACKNOWLEDGMENTS

The authors would like to express their gratitude to one of the referees useful suggestions. They are also grateful to the Office of Naval Research for the support of this work.

[1] N. Rott, ''Damped and thermally driven acoustic oscillations in wide and narrow tubes,'' Z. Angew. Math. Phys. **20**, 230–243 (1969).
[2] N. Rott, ''Thermally driven acoustic oscillations, Part IV: Tubes with variable cross section,'' Z. Angew. Math. Phys. **27**, 197–224 (1976).
[3] N. Rott, ''Thermoacoustics,'' Adv. Appl. Mech. **20**, 135–175 (1980).
[4] N. Rott, ''Thermally driven acoustic oscillations, Part VI: Excitation and power,'' Z. Angew. Math. Phys. **34**, 609–626 (1983).
[5] J. Wheatley, ''Intrinsically irreversible or natural heat engines,'' in *Frontiers in Physical Acoustics*, edited by D. Sette (North-Holland, New York, 1986), pp. 35–475.
[6] G. W. Swift, ''Thermoacoustic engines,'' J. Acoust. Soc. Am. **84**, 1145–1180 (1988).
[7] A. A. Atchley, ''Standing wave analysis of a thermoacoustic prime mover below onset of self-oscillation,'' J. Acoust. Soc. Am. **92**, 2907–2914 (1992).
[8] A. A. Atchley, ''Analysis of the initial build-up of oscillations in a thermoacoustic prime mover,'' J. Acoust. Soc. Am. **95**, 1661–1664 (1994).
[9] A. A. Atchley, H. E. Bass, T. J. Hofler, and H.-T. Lin, ''Study of a thermoacoustic prime mover below onset of self-oscillation,'' J. Acoust. Soc. Am. **91**, 734–743 (1992).
[10] M. Watanabe, A. Prosperetti, and H. Yuan, ''A simplified model for linear and nonlinear processes in thermoacoustic prime movers. Part I. model and linear theory,'' J. Acoust. Soc. Am. **102**, 3484–3496 (1997).
[11] J. Kevorkian and J. D. Cole, *Perturbation Methods in Applied Mathematics* (Springer-Verlag, New York, 1996), 2nd ed., Sec. 3.2.
[12] J. A. Murdock, *Perturbations* (Wiley, New York, 1991), pp. 227–233.
[13] E. J. Hinch, *Perturbation Methods* (Cambridge U.P., Cambridge, 1991), pp. 116–126.
[14] P. M. Morse and H. Feshbach, *Methods of Theoretical Physics* (McGraw-Hill, New York, 1953).
[15] A. W. Naylor and G. R. Sell, *Linear Operator Theory in Engineering and Science* (Springer-Verlag, New York, 1982), 2nd ed.
[16] L. Landau and E. M. Lifshitz, *Fluid Mechanics* (Pergamon, Oxford, 1959).
[17] A. D. Pierce, *Acoustics* (American Institute of Physics, Woodbury, NY, 1989), 2nd ed.
[18] Lord Rayleigh, *The Theory of Sound* (Macmillan, London, 1896, Reprinted by Dover, 1945).
[19] A. A. Atchley and F. M. Kuo, ''Stability curves for a thermoacoustic prime mover,'' J. Acoust. Soc. Am. **95**, 1401–1404 (1994).
[20] N. B. Vargaftik, *Handbook of Physical Properties of Liquids and Gases* (Wiley, New York, 1975).
[21] W. H. Press, W. T. Vetterling, S. A. Teukolsky, and B. P. Flannery, *Numerical Recipes in FORTRAN* (Cambridge U.P., Cambridge, 1992), 2nd ed.
[22] A. A. Atchley, H. E. Bass, and T. J. Hofler, ''Development of nonlinear waves in a thermoacoustic prime mover,'' in *Frontiers in Nonlinear Acoustics*, edited by M. F. Hamilton and D. T. Blackstock (Elsevier, New York, 1990), pp. 603–608.

A model for transverse heat transfer in thermoacoustics

George Mozurkewich
Ford Motor Company Research Laboratory, Mail Drop 3028, P.O. Box 2053, Dearborn, Michigan 48121-2053

(Received 14 April 1997; revised 24 November 1997; accepted 27 February 1998)

A model for transverse heat transfer in parallel thermoacoustic pores is developed. The model is one-dimensional, in the sense that the temperatures in the gas, T_g, and in the solid walls, T_w, are assumed to be fully represented by their dependences on the pore's axial coordinate, z. All effects of transverse variation across the cross section of the pore are subsumed into a transverse heat-transfer coefficient, h_1, that couples the temperatures according to $q(z)=h_1[T_g(z)-T_w(z)]$, where q is the transverse heat transfer per unit area. First the model is applied to thermally isolated pores, and results are compared to a recent three-dimensional analysis of this case [G. Mozurkewich, J. Acoust. Soc. Am. **103**, 380–388 (1998)]. Then it is extended to the case of heat-exchanger pores immediately adjacent to the end of a long stack. The heat-transfer results are cast in nondimensional form as the product of two factors. One factor depends on gas properties and the geometry of the heat exchanger, the other on the length of the stack and on a parameter related to the relative total heat pumping capacity of heat exchanger and stack. Plots of both factors are given for the special case of planar pores. The results may be applied to the design of heat exchangers for practical thermoacoustic devices. © *1998 Acoustical Society of America.* [S0001-4966(98)02906-3]

PACS numbers: 43.35.Ud [HEB]

LIST OF SYMBOLS

F_V	transverse function (Ref. 6); see Fig. 2
h_0, h_1	transverse heat-transfer coefficients
h_z	time-average axial energy-flux density
H_z	total time-average axial energy flux
k	thermal conductivity
L	pore length
q	transverse heat-flux density
Q	total heat passing through exchanger
R	prefactor in h_z, Eq. (3)
s	decay length
S	cross-sectional area
T	temperature
w,w'	transverse functions (Ref. 6); see Fig. 2
y_0	half-thickness of pore
X	temperature gradient for $H_z=0$, Eq. (15)
z	axial coordinate
z_1	acoustic displacement amplitude
α	conductivity parameter, Eq. (11)
δ_k,δ_v	thermal and viscous penetration depths
Φ	geometry parameter, Eq. (21)
Π	pore perimeter
	Subscripts
g	gas
h	heat exchanger
s	stack
w	wall
1	oscillatory quantity
	Other
overbar	section average
∇T_c	critical temperature gradient (traditionally defined)

INTRODUCTION

In practical thermoacoustic refrigerators, heat pumps, and prime movers, the internal heat exchangers are among the most critical elements. Whereas they are introduced to effect time-average heat transfer into or out of the thermoacoustic fluid, they necessarily involve time-average temperature differences between the fluid and adjacent solid surfaces. Such heat transfer may be described as ''transverse,'' as distinguished from the axial energy flux that plays a central role in thermoacoustic phenomena. Yet the standard theory of thermoacoustics[1–3] explicitly assumes that the time-average temperature of the fluid is the same as that of the adjacent walls. The early work of Merkli and Thomann[4] did not make this assumption, and recent analyses[5–7] have begun to treat transverse heat transfer explicitly.

The literature contains very little experimental or analytical guidance for the design of heat exchangers for thermoacoustic devices. On heuristic grounds, Swift originally argued that the optimum length of a heat-exchanger pore should be of the order of the peak-to-peak acoustic displacement amplitude,[1] although appreciably shorter lengths have been advocated by Hofler.[8] Several investigators have conjectured that the transverse heat transfer can be characterized by a transverse heat-transfer coefficient of order k_g/δ_k, where k_g is the thermal conductivity of the gas and δ_k is the thermal penetration depth in the gas.[9–12]

The goal of the present investigation is to develop a simple, one-dimensional model for transverse heat transfer in thermoacoustic devices consisting of parallel pores. The development is based on a recent analytical calculation of the

three-dimensional time-average temperature distribution in a thermally isolated pore, applicable within the acoustic and short-pore approximations.[6] The transverse heat-flux density deduced from that distribution, q, varies with axial coordinate in the pore, z, and can be written in the form $q(z) = h_0(z)[T_g(z) - T_w(z)]$, where T_w is the wall temperature and T_g is the gas temperature along the center line of the pore. Moreover, $h_0(z)$ was shown to attain a z-independent value, h_1, except very near the pore ends, with h_1 having the conjectured form. This observation suggests the construction of a one-dimensional model, in which the time-average gas temperature is regarded as a function of axial coordinate only, and the gas and wall temperatures are coupled through h_1.

The one-dimensional differential equations for gas and wall temperatures are formulated in Sec. I within the acoustic and short-pore approximations. While the transverse heat-exchange problem may seem intuitively to require a finite amplitude treatment, Ref. 6 has shown that the acoustic (small amplitude) approximation adequately reproduces the dramatic transverse heat-transfer effects near pore ends displayed in a recent full-blown numerical computation.[13] Therefore the acoustic approximation seems to be a worthwhile starting point for the analysis of heat exchangers, although future experiments may reveal a role for large amplitude effects. The short-pore approximation could also be relaxed, but only at the cost of substantially increased complexity and reduced instructive value. The treatment applies for straight pores of general cross section, although numerical values will be given only for planar pores.

Section I also presents the general solution to the simultaneous equations in terms of four coefficients to be determined from boundary conditions. These solutions apply equally to pores in a stack or a heat exchanger, the practical distinction between them being only the magnitude of the thermal conductivity of the walls. Several quantities, defined in Ref. 6 and required for evaluating the solutions, are given graphically.

In the next two sections we illustrate applications of the model. A thermally isolated stack is one for which no heat is allowed to enter or leave either transversely or axially through the ends. The straightforward solution for this geometry, sketched in Fig. 1(a), is given at the beginning of Sec. II. The remainder of the section compares that solution to both the full and approximate three-dimensional treatments given in Ref. 6.

In Sec. III we treat the geometry shown in Fig. 1(b), where a heat exchanger ($0<z<L_h$) is located immediately adjacent to a very long stack ($z<0$). For simplicity, it is assumed that the walls of a heat-exchanger pore have essentially infinite thermal conductivity and that there is no direct heat transfer between the adjacent solid materials of stack and heat exchanger. The resulting complicated expressions for T_g and T_w are plotted for a particular, illustrative situation. Then the heat transfer through the heat exchanger to the external world is computed for the general case and is displayed in nondimensional form. In Sec. IV we summarize our results.

I. FORMULATION

Consider a straight pore of cross-sectional area S_g and perimeter Π. (For the special case of planar pores, $S_g/\Pi = y_0$, half the spacing between plates.) Let z be the coordinate axis lying along the pore axis. The working fluid is taken to be an ideal gas with density ρ_0, specific heat c_p, thermal conductivity k_g, and Prandtl number σ. The gas is excited at angular frequency ω by a standing acoustic wave, with local pressure, velocity, and displacement amplitudes p_1, u_1^s, and z_1, respectively. The thermal and viscous penetration depths are $\delta_k = \sqrt{2k_g/\rho_0 c_p \omega}$ and $\delta_v = \delta_k \sqrt{\sigma}$. Overbars will indicate averages over pore section. Upon solving for harmonically oscillating quantities in such a pore, one finds that u_1 and the oscillatory temperature, T_1, vary across the section. These transverse variations are expressed by dimensionless functions F_V and F_T of the transverse coordinates $\boldsymbol{\rho}$, defined in Ref. 6 and related there to f_v, f_k of Ref. 1 and F of Ref. 3.

A central thermoacoustic phenomenon is the existence of a time-average axial energy-flux density h_z (power per unit area) that can be deduced from suitable products of the oscillatory solutions. Whereas the time-average transverse thermal diffusion of interest in this investigation occurs only in response to time-average temperature differences, it is unnecessary to go into detail here about the oscillatory temperature, and attention will be directed immediately to analysis of time-average temperatures.

The standard theory of thermoacoustics expresses h_z as a sum of a thermoacoustic part and a thermal-diffusion term. The thermoacoustic part itself has two terms, one proportional to the axial temperature gradient, the other proportional to the critical temperature gradient, ∇T_c. Specifically,[6]

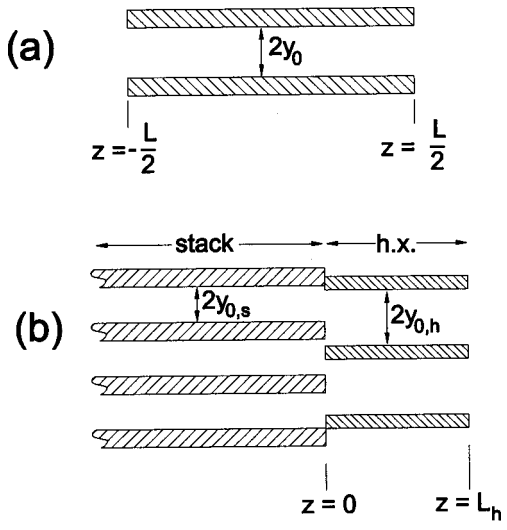

FIG. 1. Geometry of (a) an isolated pore and (b) a heat exchanger (''h.x.'') adjacent to a long stack.

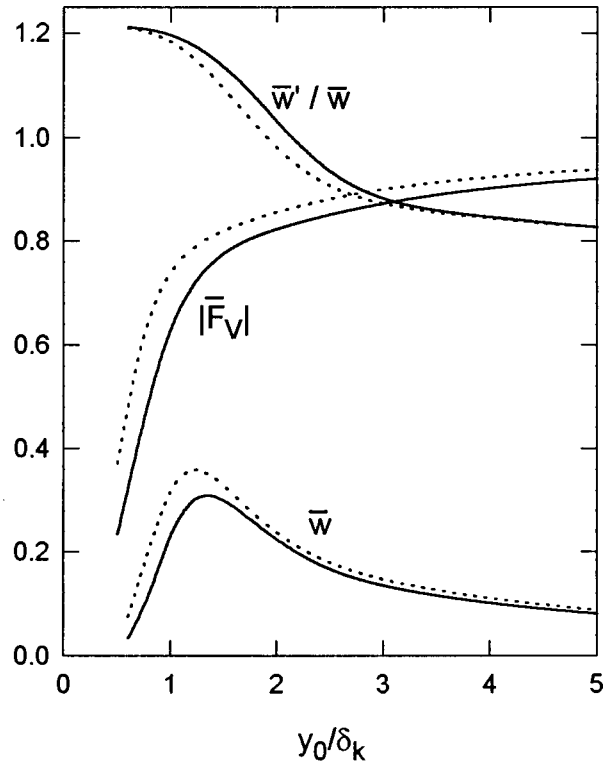

FIG. 2. Variation of $\bar{w}$, $\bar{w}'/\bar{w}$, and $|\bar{F}_V|$ with y_0/δ_k for Prandtl numbers $\sigma=0.68$ (solid lines) and 0.40 (broken lines). Planar pores.

$$h_z(z,\boldsymbol{\rho})=R\left[w'(\boldsymbol{\rho})\nabla T_c-w(\boldsymbol{\rho})\,\frac{\partial T_g(z,\boldsymbol{\rho})}{\partial z}\right]-k_g\,\frac{\partial T_g(z,\boldsymbol{\rho})}{\partial z},\tag{1}$$

where T_g is the time-average temperature of the gas. The transverse components contain only the diffusive term: $h_x=-k_g\partial T_g/\partial x$, etc. The dimensionless functions w and w' vary with transverse coordinates only and account for the transverse variations of acoustic velocity and oscillatory temperature. The critical temperature gradient and prefactor are defined by

$$\nabla T_c=\frac{\omega p_1}{\rho_0 c_p \bar{u}_1^s},\tag{2}$$

$$R=\frac{k_g}{\delta_k}\,\frac{|\bar{z}_1|^2}{|\bar{F}_V|^2},\tag{3}$$

with $|\bar{F}_V|$ given in Fig. 2. The magnitude of R is determined principally by the acoustic displacement amplitude, z_1. It has units of thermal conductivity, and the term containing RdT_g/dz, which is usually much larger than $k_g dT_g/dz$, can be thought of as an acoustically enhanced thermal flux.[14]

By applying conservation of energy ($\nabla\cdot\mathbf{h}=0$), Ref. 6 shows that the time-average temperature obeys

$$Rw(\boldsymbol{\rho})\,\frac{\partial^2 T_g}{\partial z^2}+k_g\nabla_\tau^2 T_g=0\tag{4}$$

in the short-pore approximation. Here ∇_τ^2 is the transverse part of the Laplacian operator; the axial part is omitted because $k_g \ll R$. Following Watanabe *et al.*,[15] this equation can be reduced to a one-dimensional form by integrating over the cross-sectional area of the pore and applying Gauss's theorem, yielding

$$S_g R\bar{w}\,\frac{d^2 T_g}{dz^2}+k_g\oint\frac{\partial T_g}{\partial n}\,d\Pi=0.\tag{5}$$

In the spirit of a one-dimensional approximation, the left-hand side has been evaluated under the assumption that the temperature derivative is independent of transverse coordinates. The three-dimensional treatment in Ref. 6 has shown that this is a very good approximation in the central region of the pore and has discussed the degree to which it is applicable near a thermally isolated end of the pore.

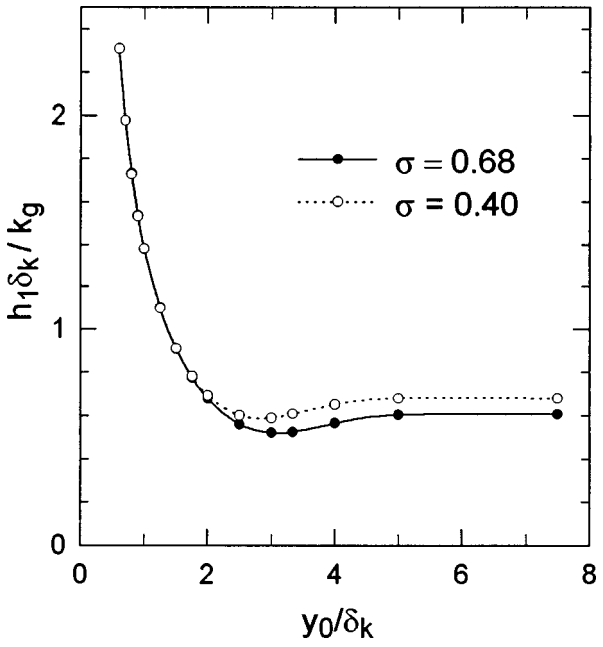

FIG. 3. Normalized h_1 vs y_0/δ_k for two values of Prandtl number, computed following Ref. 6. Planar pores.

The second term in Eq. (5) represents heat conducted transversely through the pore wall. Except very near the pore ends, the transverse heat flux per unit area may be represented by

$$q(z)=h_1[T_g(z)-T_w(z)].\tag{6}$$

The constant h_1 may be evaluated from the transverse eigenvalue problem,[6] and its variation with y_0/δ_k is given in Fig. 3 for the case of planar pores. Substituting into Eq. (5), one finds

$$S_g R\bar{w}\,\frac{d^2 T_g}{dz^2}-\Pi h_1[T_g(z)-T_w(z)]=0.\tag{7}$$

Likewise, the temperature in the wall, assumed independent of transverse coordinates in the wall, obeys

$$S_w k_w\,\frac{d^2 T_w}{dz^2}-\Pi h_1[T_w(z)-T_g(z)]=0,\tag{8}$$

where S_w is the cross-sectional area of wall, per pore, and k_w is its thermal conductivity.

Equations (7) and (8) are a pair of simultaneous, ordinary differential equations between which T_w can be eliminated, yielding

$$\frac{d^4T_g}{dz^4}-s^2\,\frac{d^2T_g}{dz^2}=0. \tag{9}$$

Here

$$s^2=h_1\Pi\left[\frac{1}{R\overline{w}S_g}+\frac{1}{k_wS_w}\right]=s_\infty^2(1+\alpha^{-1}), \tag{10}$$

where

$$\alpha=\frac{S_wk_w}{S_gR\overline{w}}, \tag{11}$$

$$s_\infty^2=\frac{h_1\Pi}{R\overline{w}S_g}. \tag{12}$$

The last expression is the $k_w\to\infty$ limit of s. Thus the general solution of Eqs. (7) and (8) is

$$T_g(z)=A+Bz+Ce^{sz}+De^{-sz}, \tag{13a}$$

$$T_w(z)=A+Bz-\alpha^{-1}(Ce^{sz}+De^{-sz}). \tag{13b}$$

This general solution features a characteristic length s^{-1}. For large k_w (large α), the solid wall's ability to distribute heat is essentially unrestricted, and, according to Eq. (12), s^{-1} is determined by a tradeoff between the transverse heat exchange and the axial thermoacoustic pumping, respectively proportional to $h_1\Pi$ and $R\overline{w}S_g$. Such behavior characterizes heat exchangers. In the opposite limit, the solid's ability to redistribute heat is limited, and the heat tends to build up or be depleted locally, wherever the transverse heat flux is greatest. This is the common case in stacks.

The unknown coefficients must be evaluated from boundary conditions. There are two kinds: conditions on the temperature and conditions on the energy flux. For example, at the interface between the stack and the heat exchanger, such as at $z=0$ in Fig. 1(b), one would expect that both the gas temperature and the axial energy flux through the gas are continuous. Similarly, one would expect the energy flux to vanish at an isolated end of a pore, as at $z=L_h$. By integrating Eq. (1) over the entire gas-occupied section of a stack containing N pores, the total energy flux is

$$H_z=NS_gR\overline{w}\left(X-\frac{dT_g}{dz}\right), \tag{14}$$

assuming that $k_g\ll R$ and that the temperature gradient is uniform across the pore section. Here X is the temperature gradient corresponding to zero energy flux:

$$X=\nabla T_c\overline{w'}/\overline{w}. \tag{15}$$

It differs from the traditionally (albeit approximately) defined ''critical temperature gradient,'' ∇T_c (Ref. 1, p. 1160) by the factor $\overline{w'}/\overline{w}$, also plotted in Fig. 2.

The temperature profiles may be plotted from Eq. (13). Assuming that the pore and wall geometry and the thermophysical properties of the gas and solid are specified, the explicit parameters in that solution, α and s, are determined by the acoustic displacement amplitude, z_1, which enters via R and is the only parameter that is freely variable experimentally. Through the boundary conditions, the solution also depends implicitly on X, which, through Eqs. (15) and (2), depends on p_1/u_1^s, a ratio set by overall resonator geometry but not excitation amplitude. In Sec. III, the boundary conditions also introduce B_s, the temperature gradient in the stack, which is also freely variable experimentally. The expressions for R and s contain the four geometry- and gas-dependent quantities $\overline{w}$, $\overline{w'}/\overline{w}$, $|\overline{F_V}|$, and h_1. Their dependences on y_0/δ_k and Prandtl number are presented in Figs. 2 and 3 for planar pores, in which $S_g/\Pi=y_0$ is half the spacing between plates. In terms of the plotted quantities, a convenient form for s_∞ is

$$s_\infty^2=\left(h_1\,\frac{\delta_k}{k_g}\right)\left(\frac{\delta_k}{S_g/\Pi}\right)\frac{|\overline{F_V}|^2}{\overline{w}}\,\frac{1}{|\overline{z_1}|^2}. \tag{16}$$

II. THERMALLY ISOLATED PORE

A thermally isolated pore may be defined as one that cannot exchange heat with the external world. It does, however, exchange work with the acoustic field, which creates a temperature gradient of such magnitude that the energy pumped thermoacoustically towards the velocity node is balanced by the heat conducted away from the node through the walls (and gas, if k_g is not neglected). In the short-pore approximation, to which this treatment is limited, the work consumed in the stack is relatively small (Ref. 1, p. 1158). Therefore it will be assumed that $H_z=0$ at pore ends, neglecting any work flux that simply passes through the pore. By Eq. (14), the boundary condition becomes simply $dT_g/dz=X$. Likewise, if no heat passes through the end of the pore wall, $dT_w/dz=0$.

To evaluate the constants in Eq. (13), these two boundary conditions may be applied at each end of the pore; that is, at $z=\pm L/2$ in Fig. 1(a). Because only three of the resulting equations are independent, the constant A may be freely varied; this makes sense because no reference temperature has been specified. Taking $A=0$, the one-dimensional solution is

$$T_g(z)=X\left[\frac{1}{1+\alpha}\,z+\frac{\alpha}{1+\alpha}\,\frac{1}{s}\,\frac{\sinh(sz)}{\cosh(sL/2)}\right], \tag{17a}$$

$$T_w(z)=X\,\frac{1}{1+\alpha}\left[z-\frac{1}{s}\,\frac{\sinh(sz)}{\cosh(sL/2)}\right], \tag{17b}$$

$$q(z)=\frac{S_g}{\Pi}\,R\overline{w}X\,\frac{\alpha}{1+\alpha}\,s\,\frac{\sinh(sz)}{\cosh(sL/2)}. \tag{17c}$$

For a pore that is long compared to the acoustic displacement amplitude, $sL\gg1$, and the hyperbolic sines describe exponential decays inward from each end of the pore. The temperatures also contain a linearly sloping term.

The limits $\alpha\gg1$ and $\alpha\ll1$ are representative of heat exchangers and stacks, respectively. For copper or aluminum $k_w\geqslant150$ W/mK, while for typical stack materials $k_w<1$ W/mK. Typically $S_w/S_g\approx0.25$, $|\overline{F_V}|\approx0.5$, $\overline{w}\approx0.3$, and $k_g\approx0.1$ W/mK. Taking a typical acoustic displacement to be one order of magnitude larger than δ_k (e.g., a few millimeters compared to a few tenths of millimeter), Eqs. (3) and

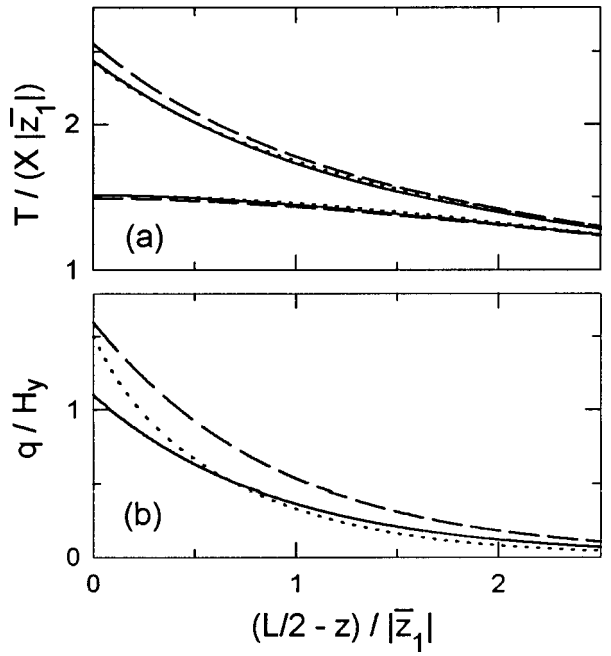

FIG. 4. Profiles of (a) normalized temperatures and (b) normalized transverse heat-flux density near the end of a thermally isolated pore, for $\alpha=5$. The one-dimensional results from Eq. (17) (solid lines) are compared to the full three-dimensional results [Eqs. (10), (13), and (17) of Ref. 6] (dotted lines), and the approximate three-dimensional results from Eq. (18) (dashed lines). In (a), the upper set of three lines represents T_g and the lower set T_w.

(11) give $\alpha>3$ for a heat exchanger and $\alpha\leqslant 0.02$ for a stack. The solid lines in Figs. 4 and 5 illustrate the behaviors of Eqs. (17) in the two limits.

The remainder of this section compares these forms with the previous, more exact analysis;[6] the reader interested in applications may skip to Sec. III without loss of continuity. Equations (34), (30), and (37) of Ref. 6 give approximate three-dimensional results in terms of infinite sums. Retaining only the leading term in each sum, the gas center-line temperature, wall temperature, and transverse heat-flux density are

$$T_g(z)\approx X\left[\frac{1}{1+\alpha}\,z+\frac{\alpha}{1+\alpha}\,\frac{\langle\Theta_1\rangle_w\Theta_1(0)}{s_1}\,\frac{\sinh(s_1z)}{\cosh(s_1L/2)}\right], \tag{18a}$$

$$T_w(z)\approx X\,\frac{1}{1+\alpha}\left[z-\frac{1}{s_w}\,\frac{\sinh(s_wz)}{\cosh(s_wL/2)}\right], \tag{18b}$$

$$q(z)\approx\frac{S_g}{\Pi}\,RX\left[\frac{\alpha}{1+\alpha}\,s_1\langle\Theta_1\rangle_w^2\,\frac{\sinh(s_1z)}{\cosh(s_1L/2)}+\frac{1}{1+\alpha}\,\frac{s_1^2\Sigma}{s_w}\,\frac{\sinh(s_wz)}{\cosh(s_wL/2)}\right]. \tag{18c}$$

In these expressions the Θ_m are transverse eigenfunctions and $\langle\ \rangle_w$ represents a weighted average over pore section. Also $s_w^{-1}=\delta_k\sqrt{R/k_g}\sqrt{\alpha/(1+\alpha)}$, $\Sigma=\Sigma_m(s_m/s_1)^2\langle\Theta_m\rangle_w^2$, and s_m is defined in Ref. 6. It can be shown that $s_1\approx s_\infty$ and $s_w\approx s\approx s_\infty\sqrt{(1+\alpha)/\alpha}$.

For $\alpha\gg 1$, $s\approx s_1\approx s_w$, and Eq. (18c) is dominated by its first term. In this limit, the one-dimensional and approximate three-dimensional expressions for T_g, T_w, and q differ only by factors of order unity. For $\alpha\ll 1$, $s_w\approx s\approx\alpha^{-1/2}s_1$, and Eq. (18c) is dominated by its second term. In this case, the two forms for T_w and q again agree except for factors of order unity. The second terms in the expressions for T_g differ substantially with respect to the argument of the hyperbolic functions, but the factor containing α lessens the importance of this difference.

Computed behaviors near a pore end are plotted in Figs. 4 and 5, assuming planar pores. All temperatures are normalized by $X|\bar{z}_1|$ and all q's by $H_y=(S_g/\Pi)R\bar{w}X\alpha(1+\alpha)^{-1}$, deduced from Eq. (17) by the procedure of Cao *et al.*[13] All plotted quantities are antisymmetric about the pore center at $z=0$, where they pass through zero. For $\alpha=5$ (Fig. 4), the one-dimensional, approximate three-dimensional, and full three-dimensional expressions show generally good agreement, while for $\alpha=0.02$ (Fig. 6), significant differences exist. The discrepancies are partly traceable to truncating the second sum in the full three-dimensional solution at $n=7$. For small α, the variations near pore ends occur on a much shorter spatial scale; representing the correspondingly increased curvature would require many more terms in the sum. Thus the approximate three-dimensional expressions may be more appropriate than the full ones when α is small. The remaining discrepancy, between the one-dimensional and approximate three-dimensional calculations of q, is due to the factor Σ in Eq. (18c), which was taken to be 2 based on some results in Sec. III D of Ref. 6. Clearly the agreement would be better with $\Sigma=1$, which would correspond to using only the $m=1$ term in the sum.

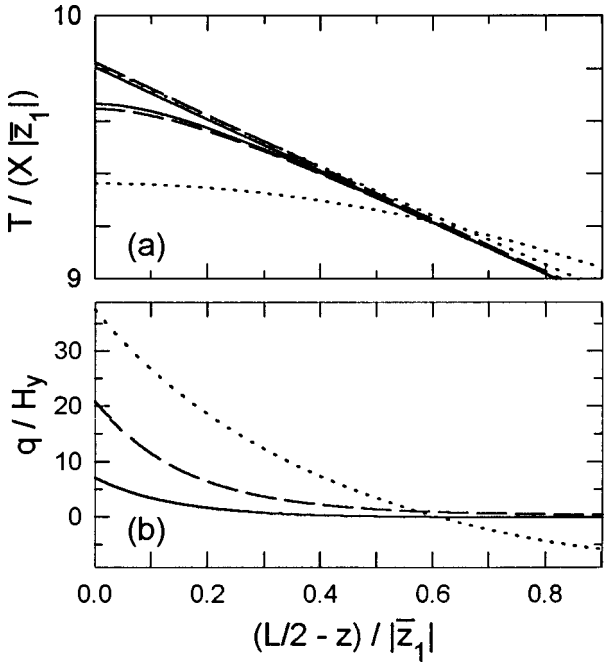

FIG. 5. Same as Fig. 4, except $\alpha=0.02$.

III. HEAT EXCHANGER ADJACENT TO STACK

In a practical thermoacoustic device, each end of the stack has an adjacent heat exchanger. Unlike the situation in Sec. II, the heat exchanger involves intentional heat transfer, both with the stack, axially through the gas, and with the

external world, by unspecified means that may, for example, involve conduction to liquid-bearing tubes. The physical arrangement is sketched in Fig. 1(b). The heat exchanger extends along z between 0 and L_h; the stack extends from 0 in the negative direction for an unspecified distance, long compared to all characteristic lengths. Both entities are assumed to consist of parallel pores. Quantities which differ between the stack and the heat exchanger will be identified by subscripts s or h, respectively. It will also be assumed that there is no direct thermal conduction between the stack walls and heat-exchanger walls.

The solid material of the stack is taken to have finite thermal conductivity $k_{w,s}$, while, to simplify the analysis, that of the heat exchanger will be approximated by infinite conductivity because heat exchangers are generally constructed from highly conducting metals. Thus A and B in Eq. (13) will be equated to zero in the exchanger; cf. Eq. (17) with $\alpha \to \infty$. In the stack, $z<0$,

$$T_{g,s}(z)=A_s+B_s z+C_s e^{s_s z}+D_s e^{-s_s z}, \tag{19a}$$

$$T_{w,s}(z)=A_s+B_s z-\alpha_s^{-1}C_s e^{s_s z}-\alpha_s^{-1}D_s e^{-s_s z}, \tag{19b}$$

and in the heat exchanger, $0<z<L_h$,

$$T_{g,h}(z)=C_h e^{s_h z}+D_h e^{-s_h z}, \tag{19c}$$

$$T_{w,h}(z)=0. \tag{19d}$$

Here B_s may be treated as an independent variable, quantifying the measured or imposed temperature gradient in the stack. The stack will be assumed long enough that its far end has no influence: $D_s=0$. This is easily satisfied, because typically the stack is long compared to z_1, which is in turn long compared to s_s^{-1}. Four more boundary conditions are required. First, because the gas at the end of the heat exchanger away from the stack is isolated, $dT_{g,h}/dz=X_h$ at $z=L_h$, exactly as in Sec. II. Second, T_g is continuous at $z=0$. Third, $dT_{w,s}/dz=0$ at $z=0$ because the walls of the stack are assumed to be isolated from those of the heat exchanger. This approximation is made merely to simplify the analysis; it is likely more accurate than an alternative simplification, $T_{w,s}=T_{w,h}$, which implies a large heat transfer directly between the walls of stack and heat exchanger. Fourth, the total energy flux in the gas is constant across the interface. In terms of the coefficients, these four conditions become, respectively,

$$s_h C_h e^{s_h L_h}-s_h D_h e^{-s_h L_h}-X_h=0, \tag{20a}$$

$$C_h+D_h=A_s+C_s, \tag{20b}$$

$$B_s-s_s C_s/\alpha_s=0, \tag{20c}$$

$$\Phi(s_h C_h-s_h D_h-X_h)=B_s+s_s C_s-X_s, \tag{20d}$$

where

$$\Phi=\frac{N_h S_{g,h} R_h \overline{w}_h}{N_s S_{g,s} R_s \overline{w}_s}. \tag{21}$$

The solution is

$$C_h=\frac{\Phi X_h-[(1+\alpha_s)B_s-X_s+\Phi X_h]e^{-s_h L_h}}{2\Phi s_h \sinh(s_h L_h)}, \tag{22a}$$

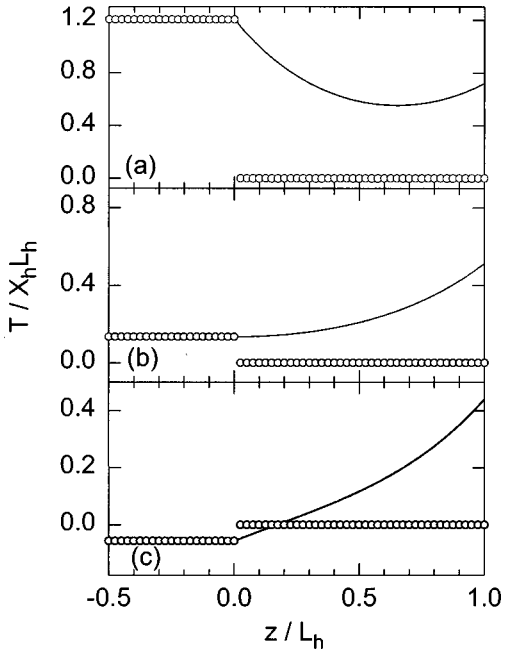

FIG. 6. Normalized temperature profiles in gas (lines) and walls (circles) for $L_h=2|\overline{z_1}|$ and $y_{0,s}/\delta_k=2$. In all panels $B_s=0$, while $y_{0,h}/\delta_k=4$ in (a), 2 in (b), and 1.6 in (c). Other parameters are $\sigma=0.68$ and $\alpha_s=0.1$. The heat exchanger location is $0\leqslant z/L_h\leqslant 1$; the stack occupies $z<0$. Note changes in vertical scales.

$$D_h=\frac{\Phi X_h-[(1+\alpha_s)B_s-X_s+\Phi X_h]e^{+s_h L_h}}{2\Phi s_h \sinh(s_h L_h)}, \tag{22b}$$

$$C_s=\frac{\alpha_s}{s_s}B_s, \tag{22c}$$

$$A_s-\frac{C_s}{\alpha_s}=\frac{\Phi X_h-[(1+\alpha_s)B_s-X_s+\Phi X_h]\cosh(s_h L_h)}{\Phi s_h \sinh(s_h L_h)}-\frac{(1+\alpha_s)}{s_s}B_s. \tag{22d}$$

The last quantity is given instead of A_s because of its physical significance as the temperature difference $\Delta T=T_{w,s}(0)-T_{w,h}(0)$ between the heat-exchanger wall and the immediately adjacent stack wall.

Explicit temperature profiles are obtained by substituting Eqs. (22) into Eqs. (19). Figures 6 and 7 illustrate some features of the results for a hot-end heat exchanger, $X_s>0$. Here L_h is chosen to be twice the peak acoustic displacement. The local transverse heat transfer corresponding to these profiles is proportional to the temperature difference between gas and exchanger.

In Fig. 6, the temperature gradient in the stack is $B_s=0$. The panels compare different pore widths in the heat exchanger. Beginning with Fig. 6(b), the pores in the stack and the heat exchanger have equal hydraulic radii so that there is no discontinuity in thermoacoustically transported energy at the interface between the stack and the heat exchanger: the transition is ''transparent.'' Decreasing H_z towards the end of the heat exchanger away from the stack deposits heat there, causing a monotonically increasing temperature gradient in the gas exactly like the one for an iso-

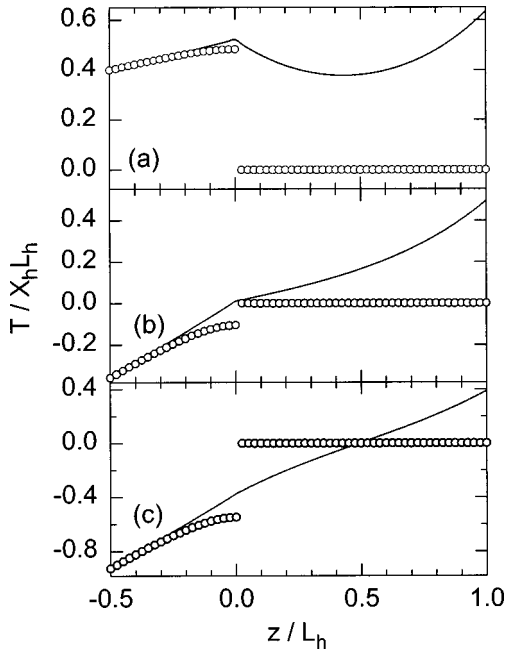

FIG. 7. Same as Fig. 6, except $y_{0,h}/\delta_k = 3$ in all panels, and $B_s/X_s = 0.2$ in (a), 0.6 in (b), and 0.9 in (c).

lated pore. The deposited heat diffuses back axially through the gas and transversely into the heat exchanger, and then to the external world. In Fig. 6(a), the heat exchanger's pores are much wider, they pump much less energy than the stack's, and the difference is deposited in the gas near the interface. None of that heat can be conducted through the stack walls, because $B_s = 0$. Therefore it all diffuses away from the stack, through the gas to the heat exchanger, resulting in a temperature gradient of opposite sign to the one in Fig. 6(b); the remaining energy flux, pumped by thermoacoustic processes in the heat-exchanger pores, causes the positive gradient towards $z = L_h$. In Fig. 6(c), because the heat exchanger's pores are slightly narrower than in Fig. 6(b), the heat exchanger is capable of pumping somewhat more energy than the stack. Consequently the gas draws heat out of the $z = 0$ end of the heat exchanger, reversing the sign of the gradient there. All three panels show a temperature discontinuity or ''jump,'' ΔT, between stack walls and exchanger walls at $z = 0$, due to the assumption that the walls are thermally isolated from each other.

Although the stack pumps the same amount of energy in all three panels (because $B_s = 0$), the average temperature difference in the heat exchanger diminishes with decreasing y_0. This is caused by increasing exchanger surface area and increasing h_1 (Fig. 3).

In Fig. 7, the pore width is fixed at a value intermediate between those of Fig. 6(a) and (b), and the temperature gradient is varied. Recall that H_z, the energy pumped thermoacoustically along the stack axis, decreases as the gradient increases. In Fig. 6(a), B_s is small, H_z is large, and the heat transferred to the heat exchanger is large. Note that the heat is deposited fairly uniformly over the length. In Fig. 6(b), where B_s has roughly half its critical value, less energy is pumped and less heat is deposited into the exchanger. A positive quantity of heat is removed from the gas even though the heat-exchanger walls reside at a slightly higher temperature than the end of the stack. This is possible, of course, because the direction of heat conduction is determined by the temperature, relative to the exchanger walls, of the gas, not the stack. In Fig. 6(c), B_s is nearly as large as X_s, H_z is small, and the *net* heat transferred into the exchanger is nearly zero. In this situation, the heat exchanger is acting principally like a stack. Some heat is extracted from its left end, transported thermoacoustically from left to right, then returned to the walls. For $B_s > X_s$ (not shown), net heat is extracted from the exchanger, and the device becomes a prime mover.

In all three panels of Fig. 7, a temperature difference exists between the gas and the wall just inside the stack, in response to which some heat diffuses transversely into the stack. That heat is conducted through the wall material back down the temperature gradient to the left. In Fig. 7(c), the amount of heat so conducted is nearly equal to the amount of energy thermoacoustically transported from left to right in the stack.

Both plots apply equally well to a cold-end heat exchanger, for which $X_s \leqslant 0$; because of the factor X_h in the temperature normalization, the plots look identical, while descriptions of directions in the preceeding paragraphs must be reversed in sense.

The reason for the existence of heat exchangers is, of course, to provide means for transferring heat between the gas and the external world. In this respect, they differ in an essential way from the thermally isolated pores treated in Sec. II, in which any heat transported into the walls at one end of the stack was conducted through the solid to the other end, where it was ''recycled'' into the gas. The total heat transported from the gas to the heat exchanger (and then to the external world) is

$$Q = h_{1,h} N_h \Pi_h \int_0^{L_h} [T_g(z) - T_w]\, dz$$

$$= \frac{h_{1,h} N_h \Pi_h}{s_h^2 \Phi} [X_s - (1+\alpha_s) B_s], \tag{23}$$

where $N_h \Pi_h$ is the *total* pore perimeter in the heat exchanger. (The same result may be obtained by calculating the *net* axial energy flux through the center of the stack.) This form is convenient for determining Q when B_s, the gradient in the stack, is given. For experiments focusing on the heat exchangers themselves, however, it may be more suitable to examine how Q depends on the temperature jump, $\Delta T = A_s - C_s/\alpha_s$, between heat exchanger walls and stack walls. Upon inverting Eq. (22d) to obtain B_s in terms of ΔT and substituting back into Eq. (23), one finds

$$Q = Q_0 + Q_1 \Delta T, \tag{24a}$$

$$Q_0 = \frac{h_{1,h} N_h \Pi_h}{s_h^2} \cdot \frac{X_h[\cosh(s_h L_h) - 1] + (s_h/s_s) X_s \sinh(s_h L_h)}{\cosh(s_h L_h) + (s_h/s_s)\Phi \sinh(s_h L_h)}, \tag{24b}$$

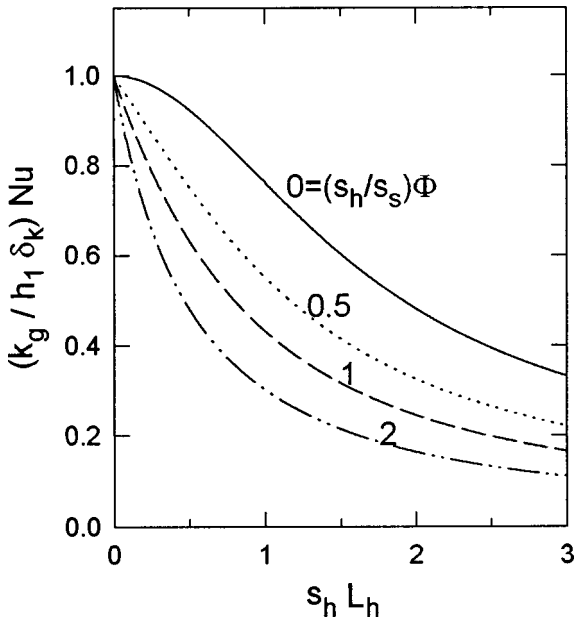

FIG. 8. Variation of Nu with heat-exchanger length for four values of $(s_h/s_s)\Phi$.

$$Q_1 = \frac{h_{1,h} N_h \Pi_h}{s_h} \cdot \frac{\sinh(s_h L_h)}{\cosh(s_h L_h) + (s_h/s_s)\Phi \sinh(s_h L_h)}, \tag{24c}$$

which demonstrates that Q is a linear function of the temperature jump, with nonzero intercept.

For the purpose of heat-exchanger design, the slope, Q_1, is of greatest interest. It is convenient to recast Q_1 as a dimensionless Nusselt number:

$$\begin{aligned} \mathrm{Nu} &\equiv \frac{Q_1}{N_h \Pi_h L_h} \cdot \frac{\delta_k}{k_g} \\ &= \left(\frac{h_{1,h} \delta_k}{k_g} \right) \\ &\quad \times \left[\frac{1}{s_h L_h} \cdot \frac{\sinh(s_h L_h)}{\cosh(s_h L_h) + (s_h/s_s)\Phi \sinh(s_h L_h)} \right]. \end{aligned} \tag{25}$$

Because $h_{l,h} \propto k_g/\delta_k$, δ_k was chosen as the characteristic spatial dimension in the definition of Nu; the alternative choice, $y_{0,h}$ for the planar case, would have introduced an additional strong, but trivial, dependence on $y_{0,h}/\delta_k$. Here Nu is expressed as the product of two factors. The first has been given in Fig. 3, and the second, which depends on the two dimensionless groups $s_h L_h$ and $(s_h/s_s)\Phi$, is plotted in Fig. 8. Clearly, the optimal length, from the perspective of materials usage, is of order $s_h^{-1} \approx |\overline{z_1}|_h$, in general agreement with expectations.[1,8] Of course, because longer heat exchangers cause more dissipation, the optimum length from the perspective of energy efficiency may be less.[8] Large Nu is favored by small values of the parameter, which can be written for planar pores, using Eqs. (21), (3), and (10), as

$$\frac{s_h}{s_s}\Phi = \frac{|\overline{F_V}|_s}{|\overline{F_V}|_h} \left(\frac{\overline{w}_h h_{1,h} y_{0,s}}{\overline{w}_s h_{1,s} y_{0,h}} \frac{\alpha_s}{1+\alpha_s} \right)^{1/2}. \tag{26}$$

Small values correspond to relatively wide heat-exchanger pores. An initial, small increase of $(s_h/s_s)\Phi$ causes a large reduction in Nu, but successive doublings of that parameter are required for roughly equal incremental effect.

This analysis may be used in practical heat-exchanger design as follows. Suppose that the design specification involves quantity of heat and allowable temperature difference, fixing Q_1. Initially one may assume boundary-layer conditions in the exchanger, such that h_1 is obtained from the large-y_0 limit in Fig. 3. One may also choose a representative value (1/2, say) for the ordinate in Fig. 8. From these inputs, Eq. (25) determines the required surface area, $N_h \Pi_h L_h$. Some combination of $y_{0,h}$ and L_h must be chosen to achieve this area. Finally the process may be iterated using improved values from Figs. 3 and 8.

This procedure assumes proportionality between Q and ΔT. If Q_0 is not negligible, the temperature difference that produces zero heat transfer through the exchanger is, from Eq. (24),

$$\Delta T_{Q=0} = -\frac{X_s}{s_s} - \frac{X_h}{s_h} \frac{\cosh(s_h L_h) - 1}{\sinh(s_h L_h)}. \tag{27}$$

Typically X_s and X_h have similar magnitudes, while $s_s \gg s_h$. The order of magnitude of the first term is $X_s |\overline{z_1}|_s \sqrt{\alpha_s}$, assuming small α_s, which may typically be one degree or less. The factor containing hyperbolic functions varies smoothly from 0 to 1 with increasing L_h, but its prefactor may be several times as large, amounting to perhaps several degrees. Thus proportionality between Q and ΔT may not hold at large acoustic amplitude and for long exchangers.

This procedure also assumes linear processes. Nonlinear processes fall beyond the scope of this investigation. However, in the writer's opinion, nonlinear processes are likely to increase the rate of heat transfer. Thus the procedure described should produce a conservative design.

IV. SUMMARY

A one-dimensional model for transverse heat exchange in thermoacoustic pores has been developed. Applied to a thermally isolated pore, the model produces results similar to those of a recent three-dimensional analysis; agreement is best for highly conducting walls. Applied to a parallel-pore heat exchanger immediately adjacent to the end of a stack, several new features are found that may productively be subjected to experimental test. The gas temperature within the heat exchanger can be quite nonuniform. Net heat transfer can occur into a hot-end heat exchanger (or out of a cold-end one) even when there is no temperature difference between the walls of the heat exchanger and the adjacent end of the stack. Optimum heat exchanger length (disregarding dissipation) is roughly equal to the acoustic displacement amplitude, as anticipated, and wide pores are mildly favored. The heat transfer through the exchanger can be expressed as the product of two factors, one dependent only on gas properties and exchanger geometry, and the other only on exchanger length and the parameter $(s_h/s_s)\Phi$. Figure 8 may assist in the sizing of practical heat exchangers.

The model is based on a recent three-dimensional analysis of the temperature distribution in a thermally isolated pore.[6] Like its parent theory, it is restricted to the acoustic and short-pore approximations, and its accuracy cannot be assured at distances from pore ends substantially less than one acoustic displacement amplitude. Furthermore, in an actual thermoacoustic device, the conditions existing between the stack and the heat exchanger are more complicated than has been acknowledged in this treatment. No consideration has been given to details of the relative arrangements of pore ends at the interface; only the overall average properties, as expressed for example in the parameter Φ, are taken into account. Such details, as well as the neglect of nonlinear effects, may introduce substantial inaccuracies when comparison with experiments is attempted.

Furthermore, perfect thermal isolation of the end of the stack is unlikely to hold. This situation could be treated straightforwardly within the model by including a series thermal resistance. The case of an ''integral'' stack-exchanger combination, in which direct thermal conductance between them is maximized, may prove particularly interesting. On the other hand, a physical gap may exist between the heat exchanger and the stack. One may expect that a gap much shorter than the acoustic displacement amplitude would have little effect, but the model cannot presently treat this case because the spatial variation of the axial energy flux H_z outside a pore is not known.

[1] G. W. Swift, ''Thermoacoustic engines,'' J. Acoust. Soc. Am. **84**, 1145–1180 (1988).

[2] N. Rott, ''Thermoacoustics,'' Adv. Appl. Mech. **20**, 135–175 (1980), and references therein.

[3] W. P. Arnott, H. E. Bass, and R. Raspet, ''General formulation of thermoacoustics for stacks having arbitrarily shaped pore cross sections,'' J. Acoust. Soc. Am. **90**, 3228–3237 (1991).

[4] P. Merkli and H. Thomann, ''Thermoacoustic effects in a resonance tube,'' J. Fluid Mech. **70**, 161–177 (1975).

[5] L. Bauwens, ''Oscillating flow of a heat-conducting fluid in a narrow tube,'' J. Fluid Mech. **324**, 135–161 (1996).

[6] G. Mozurkewich, ''Time-average temperature distribution in a thermoacoustic stack,'' J. Acoust. Soc. Am. **103**, 380–388 (1998).

[7] A. Gopinath, N. L. Tait, and S. L. Garrett, ''Thermoacoustic streaming in a resonant channel: the time-averaged temperature distribution'' J. Acoust. Soc. Am. **103**, 1388–1405 (1998).

[8] T. J. Hofler, ''Effective heat transfer between a thermoacoustic heat exchanger and stack,'' J. Acoust. Soc. Am. **94**, 1772 (1993).

[9] G. W. Swift, ''Analysis and performance of a large thermoacoustic engine,'' J. Acoust. Soc. Am. **92**, 1551–1563 (1992).

[10] W. C. Ward and G. W. Swift, ''Design environment for low-amplitude thermoacoustic engines,'' J. Acoust. Soc. Am. **95**, 3671–3672 (1994).

[11] S. L. Garrett, D. K. Perkins, and A. Gopinath, ''Thermoacoustic refrigerator heat exchangers: design, analysis, and fabrication,'' in *Heat Transfer 1994*, Proceedings of the Tenth International Heat Transfer Conference (1994), Vol. IV, pp. 375–380.

[12] B. L. Minner, J. E. Braun, and L. Mongeau, ''Theoretical Evaluation of the Optimal Performance of a Thermoacoustic Refrigerator,'' ASHRAE Trans. **103**, 873–887 (1997).

[13] N. Cao, J. R. Olson, G. W. Swift, and S. Chen, ''Energy flux density in a thermoacoustic couple,'' J. Acoust. Soc. Am. **99**, 3456–3464 (1996).

[14] U. H. Kurzweg, ''Enhanced heat conduction in oscillating viscous flows within parallel-plate channels,'' J. Fluid Mech. **156**, 291–300 (1985).

[15] M. Watanabe, A. Prosperetti, and H. Yuan, ''A simplified model for linear and nonlinear processes in thermoacoustic prime movers. Part I. Model and linear theory,'' J. Acoust. Soc. Am. **102**, 3484–3496 (1997).

Laser-modulated phase-stepping digital shearography for quantitative full-field imaging of ultrasonic waves

Benjamin A. Bard, Grant A. Gordon, and Shudong Wu
Applied Research Laboratory, The Pennsylvania State University, P.O. Box 30, State College, Pennsylvania 16804

(Received 26 August 1997; accepted for publication 17 February 1998)

Measurement of surface displacements due to ultrasonic wave propagation in elastic solids has traditionally been studied using single-point measurement techniques such as ultrasonic transducers or interferometers. Full-field methods, excluding scanning techniques, are uncommon; examples include holographic interferometry and Schlieren imaging. In many cases, these techniques have been used to yield qualitative results due to inherent difficulties in processing the data. Laser-modulated phase-stepping digital shearography is a full-field, common-path, interferometric method which can be used to quickly visualize ultrasonic wave fields. A shearography system will be described that provides not only whole-field images of ultrasonic waves, but quantitative displacement data within these fields. Images are shown of propagating plate and bar waves, and mathematics relating the calculated optical phase to the ultrasonic wave parameters are presented. [S0001-4966(98)00506-2]

PACS numbers: 43.35.Yb, 43.35.Sx, 43.35.Pt [HEB]

INTRODUCTION

Whole-field images of ultrasonic wave fields in elastic solids are helpful for understanding the physics of wave propagation as well as the interaction of sound fields with defects. Few experimental methods are available for generating these images. Several types of point sensors (piezoelectric, capacitive, magnetic, and single-point interferometric techniques) can be scanned over the surface of a wave-supporting solid and the collected data later reconstructed to form a two-dimensional representation of the wave field.[1] Schlieren imaging[2] has the benefit of capturing the entire wave field simultaneously; it is a full-field as opposed to a scanning technique. Regardless of the acoustic source, however, the field measured by Schlieren must be supported by an optically transparent medium such as water. Another full-field approach is double-pulsed holography.[1,3] This noncontact optical method captures and compares the entire displacement field at two different states of vibration via illumination from two high-energy laser pulses. The high quality fringes formed on a holographic plate represent the difference in surface displacement between the two states ''frozen'' by the laser pulses. Although the wave field is clearly seen, surface displacement is not easily quantified—fringe centers must be located and orders (sequential numbering) determined. In addition, pulsed holography requires a special pulsed laser as well as hologram filtering and reconstruction.

This paper introduces laser-modulated phase-stepping digital shearography—an optical technique similar in design to holography, while overcoming some of its inherent limitations—for full-field, quantitative imaging of ultrasonic waves on the surfaces of elastic solids.

I. SHEAROGRAPHY BACKGROUND

Speckle-shearing interferometry, more commonly known as shearography, is an offspring of holographic interferometry and was first introduced by Hung and Taylor[4] and Leendertz and Butters[5] over 20 years ago. Although originally designed for full-field strain analysis, shearography has recently started to become accepted in the NDE community for detection of delaminations and disbonds in composite structures.[6–9] It is commonly used, much like holography, in a qualitative fashion: Comparison of two object states produces a fringe pattern, then familiar patterns are interpreted as acceptable object deformation and anomalies in the fringes as evidence of a flaw. In its electronic form, using a CCD camera and framestore rather than film or thermoplastic plates, fringes can be displayed in real-time on a video monitor, updating 30 times per second. Electronic shearography falls into the Electronic Speckle Pattern Interferometry (ESPI)[10] family along with electronic, or TV, holography. While the fringes produced by both systems have a noisy character due to speckle, those of shearography are not as prone to environmental disturbances as those of its holographic counterpart due to shearography's common-path nature.

To locate flaws with shearography, an appropriate excitation method must be chosen that has the best chance of revealing subsurface flaws at the surface. Thermal stressing or vacuum loading are often used. When vibration is chosen as the excitation source (usually less than 100 kHz), time-averaged fringes are often utilized to locate flaws. These fringes are commonly formed by comparing a reference image of the object at rest with an image of the time-averaged motion of the object during vibration. Compared to the fringes formed by static loading, these time-averaged fringes have contrast which decreases with increasing fringe order, making higher vibration amplitudes difficult to analyze.[11,12] When producing either static or time-averaged fringes, shearography not only has the limitations of low contrast fringes and their need for interpretation, but its general use is usually limited to displacements large enough to produce at

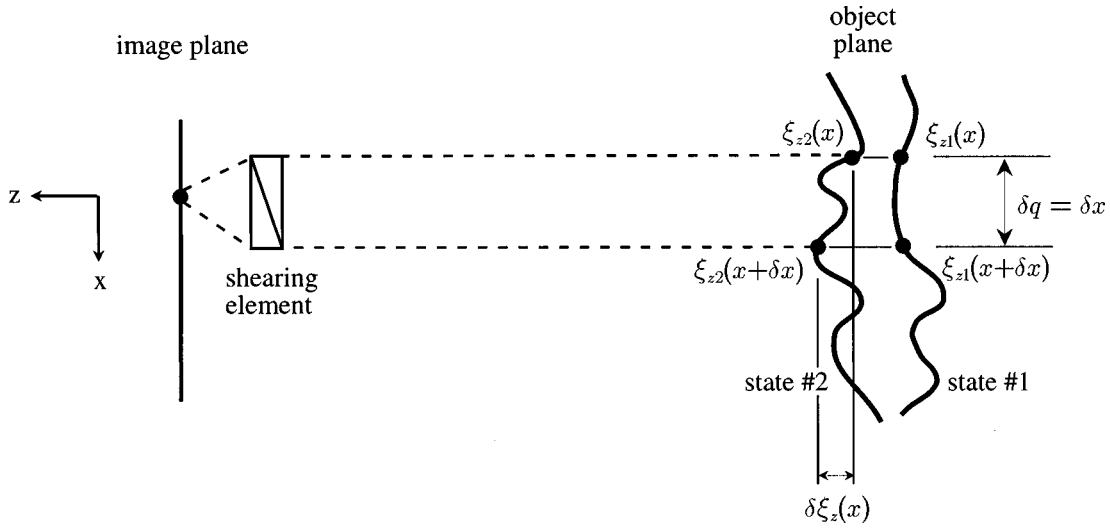

FIG. 1. For each of the two object states, two points on the object separated by the shearing distance, δq (completely in the x direction for this example, hence $\delta q = \delta x$), are combined into a single point in the image. When the two states are later compared, the result reflects the out-of-plane differential displacement, $\delta\xi_z$.

least one entire fringe. Furthermore, the sign, or direction, of these displacements is lost. Regardless of these shortcomings, shearography has proven to be a useful technique for fast and easy location of flaws on the order of a centimeter across.

The displacement of ultrasonic waves is commonly on the order of nanometers, a fraction of that necessary to produce a time-averaged fringe. Shearography systems commonly used in NDE hence do not have the out-of-plane sensitivity to measure ultrasonic wave displacement amplitudes. For higher frequencies, their spatial resolution, without sacrificing a large field of view, is also insufficient to satisfy the sampling criteria when measuring ultrasonic wavelengths. These systems are unable to image ultrasonic wave fields, hence missing out on the opportunity to utilize their guided wave and small wavelength characteristics for flushing out small but critical flaws. These shortcomings are overcome in the current work via several methods: (1) a high resolution digital camera provides a lower noise floor and greatly enhanced spatial resolution without decreasing the field of view; (2) phase-stepping interferometry removes the speckle phase term responsible for noisy fringes, produces *quantitative* displacement amplitude results that retain the sign of deformation (equivalent to vibration phase for single frequencies), and allows sub-fringe displacements to be easily detected; and, (3) synchronized laser modulation freezes the wave motion at two different instants in time, eliminating the drawbacks of time-averaged fringes, and allowing phase stepping to be utilized for vibration analysis.

II. THEORY

An elementary setup for electronic, or TV, shearography, begins with the illumination of a sample by coherent laser light. The reflection of laser light from a surface whose roughness is on the order of, or greater than, the optical wavelength produces the random interference phenomenon known as speckle.[13] In shearography, this speckle pattern serves as the carrier of information regarding motion of the sample's surface. In front of the CCD camera used to image the speckle pattern is the shearing element, a birefringent prism in the current work. The purpose of the shearing element is to image two points on the object, separated by the shearing distance, δq, as a single point in the image plane. This shearing is responsible for the name ''shearography,'' as well as the wave interference of the system. The coherent combination of light from the two sheared images results in an optical interference pattern that defines the current state of the object's surface. The sheared speckle pattern has intensity[13]

$$I_1 = I' + I'' \cos(\phi), \tag{1}$$

where I' is the object, or background,[14] intensity, I'' the fringe contrast, and ϕ the phase difference between light scattering from two object points separated by the shearing distance. All variables are functions of x and y, the coordinates defining the plane of the object's surface. The sample is now slightly deformed, due to static or dynamic excitation, and a second sheared speckle pattern is captured,[13]

$$I_2 = I' + I'' \cos(\phi + \Delta). \tag{2}$$

Upon deformation, each of the two points sheared together will travel a different distance in the out-of-plane (z) direction. This difference, $\delta\xi_z$, will be called the *differential displacement* and is shown in Fig. 1; it will be described mathematically in Sec. V.

For normal illumination and viewing of the object,[4]

$$\Delta = \frac{4\pi}{\lambda}\,\delta\xi_z, \tag{3}$$

where λ is the wavelength of the laser light. In electronic shearography, images representing the two object states are subtracted, resulting in the intensity, after rectification:

$$I_{\text{sub}} = \left| 2I'' \sin\left(\phi + \frac{\Delta}{2}\right) \sin\left(\frac{\Delta}{2}\right) \right|. \tag{4}$$

The surface is optically rough, and ϕ is the phase difference between two points on the resulting speckle pattern; hence, ϕ is essentially random across the entire image. Dark speckle correlation fringes occur when the $\sin(\phi+\Delta/2)$ term is nullified by the $\sin(\Delta/2)$ term. Each dark fringe appears at the locus of points whose displacement is an integer multiple of $\lambda/2$ relative to that of the points δq away in the shearing direction. Fringe centers can be assigned quantitative displacement values if their locations and orders are correctly identified. The fringe pattern is of low quality since it is encoded in a speckle carrier, making quantitative analysis complicated. For $\delta\xi_z<\lambda/2$ everywhere, no fringes are formed from the subtraction, and useful information is even more difficult to attain without further image processing.

Upon further examination of Eq. (3), it is seen that if the differential displacement, $\delta\xi_z$, is divided by the shearing distance, δq, then the fringe pattern (or in a following section, the phase profile) represents the change in slope between the two object states: $\Delta/2=(2\pi/\lambda)(\delta\xi_z/\delta q)\delta q$. This represents slope in the familiar ''rise over run'' form. For small shear, this is often taken as a first-order approximation to the displacement derivative. It should be pointed out that, in general, the information directly calculated from shearography is *not* slope *nor* displacement derivative, but differential displacement, as previously described. As shown in Fig. 1, when deformation of spatial periodicity smaller than the shearing distance is studied, this differential displacement is no longer proportional to slope since the ''run'' now exceeds the curvature being examined.

III. LASER MODULATION

Laser modulation is simply the method of stroboscopic illumination of a vibrating object by laser light. The beam from a continuous wave (cw) laser is passed through an external acousto-optic modulator, the input to which is synchronized with the excitation signal driving the vibration of the object. The laser light is hence switched on and off, illuminating the object for a short segment of its vibration period. Each ''burst'' of light is called a *stroke* (the term *pulse* being avoided so it is not confused with the output of a pulsed laser). The laser stroke can be shifted so as to occur during vibration minima or maxima, effectively ''freezing'' two different states of the object within its vibration period. The two instantaneous object states captured in this manner can be used to produce subtraction fringes, avoiding problems associated with time-averaged fringes. They can also be used in conjunction with phase stepping, as described in the following section.

In practical situations, the stroke duration can be anywhere from 20 to 90 degrees of the vibration period. Longer strokes provide more energy and allow shorter overall exposure times; however, more averaging of the object's motion occurs during the time interval of the laser stroke. Conversely, a negligible degree of averaging occurs during short strokes, but a long exposure time is required and 70%–80% of the available laser power is sacrificed. Regardless of averaging, longer stroke durations are usually favored since the effect of environmental instabilities (e.g., thermal drifts) are reduced due to decreased exposure times.

Since a cw laser is being used, a single short stroke does not provide sufficient energy for quality exposure of an image. For most frequencies of interest, however, the camera exposure time is much greater than the vibration period; hence, many cycles of vibration, and many laser strokes, can occur during the exposure of a single image. During this time, all of the laser strokes illuminate the object in the same position, but their integration on the CCD array allows proper exposure. For this to succeed, it is assumed that the object is undergoing either steady-state vibration or a repeatable transient phenomenon.

IV. PHASE STEPPING

Phase-stepping (or phase-shifting) interferometry (PSI), first introduced by Carré in 1966,[15] involves the introduction of a series of known, or at least equal, phase shifts between the reference and object arms of an interferometer.[16] PSI refers more to an analysis method than an optical configuration, as it allows the direct point-by-point calculation of optical phase change rather than necessitating the extraction of limited phase information from fringe patterns. PSI was extended in 1985 both to holography[17] and shearography.[17,18] When implementing phase stepping with shearography, the common-path nature of the system—responsible for its environmental stability—creates a difficult situation: There are no separate reference and object beams between which to introduce the phase step. The step has to be introduced between every pair of sheared points comprising a sheared image, the shearing often taking place inside a solid glass wedge. Numerous phase-stepping schemes have been presented to overcome this difficulty.[18–22]

A four-bucket phase-step algorithm[16] is used in this work, the phase step introduced via a lateral translation of the shearing wedge by means of a computer-controlled motorized translation stage. Rather than a single image, four images are captured for each of the two object states, eight in all. The first four images capture the object in one position, the second four in another. In between each of the four images of a given object state, an optical phase step is introduced by laterally shifting the shearing wedge. This step adds a $\pi/2$ radian optical path difference between the two sheared images.

Phase stepping is normally used to calculate the optical phase change between two static positions of an object's surface. It cannot be used directly to study time-averaged vibration, as previously described for time-averaged subtraction fringes. In the present work, phase stepping is combined with laser modulation to compare two instantaneous states of the object captured during vibration. A timing diagram for the laser modulation and phase stepping process is shown in Fig. 2. This diagram shows only a few cycles of vibration for each of the eight captured images; in reality, for ultrasonic frequencies, thousands of cycles and laser strokes occur during the exposure time of a single frame.

The first object state, when laser modulation is synchronized to the acoustic maxima, is described by Eq. (1). Now, four phase-stepped images, I_1 through I_4, are captured:

$$I_i=I'+I''\cos(\phi+\delta_i),$$

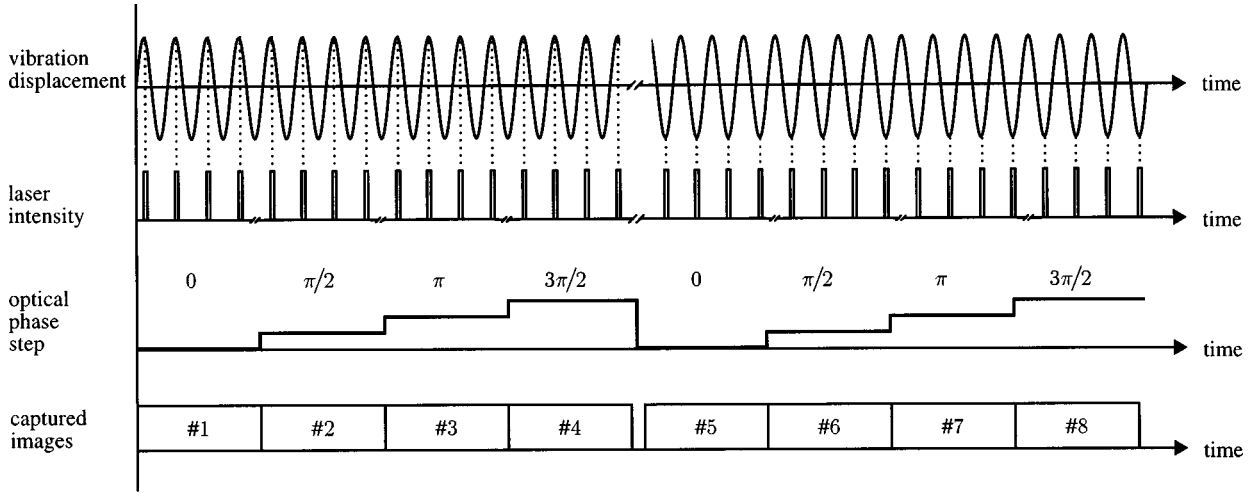

FIG. 2. Timing diagram depicting signals used for laser-modulated phase-stepping shearography. Note that the laser modulation for the first four images is synchronized to the acoustic maxima, while for the second four images to the minima.

where

$$\delta_i = (i-1)\,\pi/2 \tag{5}$$

and

$$i = 1,2,3,4.$$

The second object state, when laser modulation is synchronized to the acoustic minima, is described by Eq. (2). Four additional phase-stepped images, with identical phase steps to the first four, are captured:

$$I_i = I' + I''\,\cos(\phi + \Delta + \delta_i),$$

where

$$\delta_i = (i-5)\,\pi/2 \tag{6}$$

and

$$i = 5,6,7,8.$$

Here, Δ represents the optical phase change due to the object's shift from maximum to minimum displacement during vibration. From these eight images, Δ, which is directly related to the differential displacement by Eq. (3), can be calculated on a point-by-point basis:[16]

$$\Delta = \tan^{-1}\left(\frac{I_8 - I_6}{I_5 - I_7}\right) - \tan^{-1}\left(\frac{I_4 - I_2}{I_1 - I_3}\right). \tag{7}$$

The random phase component, ϕ, has been completely removed, and differential displacement is obtained at every pixel. Due to the inverse tangent operation, Δ is calculated modulo 2π, and a two-dimensional unwrapping algorithm may be needed to reconstruct continuous phase data.

V. EFFECT OF SHEARING DISTANCE AND DIRECTION

To illustrate the effect of shearing distance and direction, first consider a plane elastic wave traveling along the object's surface in the same direction as the optical shearing. At one instant in time, the first object state is captured by laser modulation and the out-of-plane surface displacement in this direction is sinusoidal:

$$\xi_{z1}(\mathbf{x}) = A\,\sin(\mathbf{k}\cdot\mathbf{x} + \alpha), \tag{8}$$

where A is the wave amplitude, $\mathbf{k}$ the acoustic wave number vector, $\mathbf{x}$ the position vector of the evaluation point, and α an appropriate acoustical phase value. Boldface text denotes a vector quantity.

At another instant in time, when the laser modulation has been shifted by 180 degrees relative to the acoustic signal, the surface displacement for the second object state is flipped:

$$\xi_{z2}(\mathbf{x}) = A\,\sin(\mathbf{k}\cdot\mathbf{x} + \alpha + \pi). \tag{9}$$

A 180 degree shift in laser modulation is chosen to provide the maximum difference in displacement between the two compared object states.

As discussed previously, the quantity $\delta\xi_z$ represents the difference in out-of-plane displacement between two points separated by the shearing distance. When applied to ultrasonic waves, this concept is crucial for optimal adjustment of the optical shearing distance for a given acoustic frequency. As shown in Fig. 1, $\xi_{z1}(\mathbf{x})$ and $\xi_{z1}(\mathbf{x}+\delta\mathbf{q})$ are the positions (or displacements from the reference axis) of two points separated by the shearing distance for the first object state. Likewise, $\xi_{z2}(\mathbf{x})$ and $\xi_{z2}(\mathbf{x}+\delta\mathbf{q})$ are the positions of the same two points for the second object state. The differential displacement, $\delta\xi_z$, can then be defined as

$$\delta\xi_z(\mathbf{x}) = [\xi_{z2}(\mathbf{x}) - \xi_{z1}(\mathbf{x})] - [\xi_{z2}(\mathbf{x}+\delta\mathbf{q}) - \xi_{z1}(\mathbf{x}+\delta\mathbf{q})]. \tag{10}$$

The differential displacement due to the comparison of the two plane wave object states is found by substituting Eqs. (8) and (9) into Eq. (10). After application of suitable vector and trigonometric identities, this substitution yields

$$\delta\xi_z(\mathbf{x}) = 4A\,\sin\left(\frac{\mathbf{k}\cdot\delta\mathbf{q}}{2}\right)\cos\left(\mathbf{k}\cdot\mathbf{x} + \alpha + \frac{\mathbf{k}\cdot\delta\mathbf{q}}{2}\right), \tag{11}$$

where $\delta\mathbf{q}$ is the shearing vector.

For the plane wave under discussion, $\delta\xi_z$ is sinusoidal, its spatial period equal to the wavelength of the acoustic

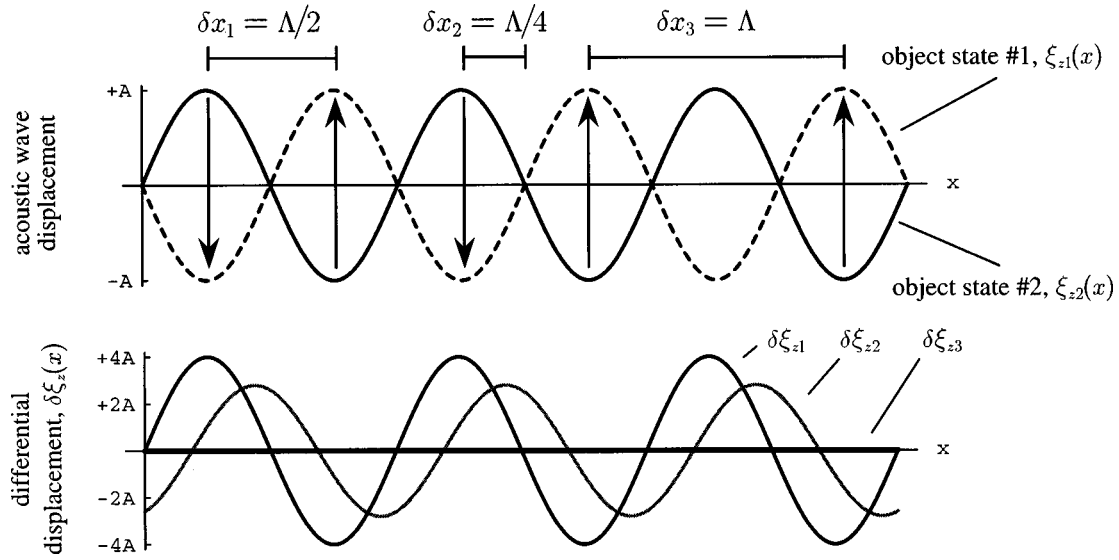

FIG. 3. The upper plot shows the ultrasonic wave displacement at the two instants of time captured by laser modulation. Three examples of shearing distance ($\delta x_1, \delta x_2, \delta x_3$) are shown. Arrows denote the direction of travel of acoustic extrema between the two object states. The lower plot shows the resulting differential displacements ($\delta\xi_{z1}, \delta\xi_{z2}, \delta\xi_{z3}$) for the corresponding shear values. As long as $\delta\xi_z$ is not zero everywhere, it will have the same spatial periodicity as the acoustic wave (in the shearing direction), but an amplitude dependent upon the shearing distance.

wave, Λ. If the shearing distance is exactly $\Lambda/2$, or any odd integer multiple, $\delta\xi_z$ is maximized. In this case, one point on the object that travels from a valley at the first object state to a peak at the second object state (a displacement of $+2A$) is compared to a point that travels from a peak at the first object state to a valley at the second (a displacement of $-2A$), a difference of $4A$. If the shear is Λ (or any integer multiple), $\delta\xi_z$ will be zero everywhere; the two points compared travel the same distance, in the same direction, the difference being zero everywhere along the surface. These relationships are diagrammed in Fig. 3. It is clearly desirable to adjust the shearing distance for optimum sensitivity to the acoustic disturbance by *a priori* knowledge of the resulting acoustic wavelength. For a given frequency, this is only possible if the resulting wavetype (and its phase speed) can be predicted.

If the plane wave is traveling at an angle to the shearing direction, then the critical relationship is that between the shearing distance and the trace wavelength in the shearing direction. This geometry is shown in Fig. 4. The trace wavelength in the shearing direction, Λ_q, is seen in Fig. 4 to be $\Lambda_q = \Lambda/\cos(\theta-\sigma)$. In terms of the wave number and shearing vectors, this can be described as

$$\Lambda_q = \Lambda \frac{k\,\delta q}{\mathbf{k}\cdot\delta\mathbf{q}}. \tag{12}$$

Substitution of Eq. (12) into Eq. (11) gives

$$\delta\xi_z(\mathbf{x}) = 4A \sin\left(\pi \frac{\delta q}{\Lambda_q}\right)\cos\left(\mathbf{k}\cdot\mathbf{x} + \alpha + \pi \frac{\delta q}{\Lambda_q}\right). \tag{13}$$

Here, the relationship between the shearing distance and trace wavelength is seen to be both an amplitude scaling factor and an additional phase angle of the cosinusoidally varying differential displacement. For the extreme case where the shearing direction is perpendicular to the wavenumber vector, $\delta\xi_z$ is seen to be zero everywhere.

From the previous discussion, it can be seen that it is useful to have a shearing mechanism allowing adjustable direction and magnitude of the optical shear. First, the zero-sensitivity situation can be avoided. Second, the sensitivity can be continuously adjusted, a feature not available in holography. For the optimized shearing distance of $\delta q = n(\Lambda_q/2)$, where n is an odd integer, Eq. (13) shows the differential displacement amplitude to be $4A$. A similar derivation for holography results in the displacement at each point (not differential, as with shearography) having an optimal amplitude of $2A$. Since the calculated phase from either system is proportional to this value, it is seen that shearography can be twice as sensitive to the same disturbance as holography.

VI. EXPERIMENTAL RESULTS AND ANALYSIS

The experimental setup is shown schematically in Fig. 5. Two aluminum samples were used, a bar measuring 46 by

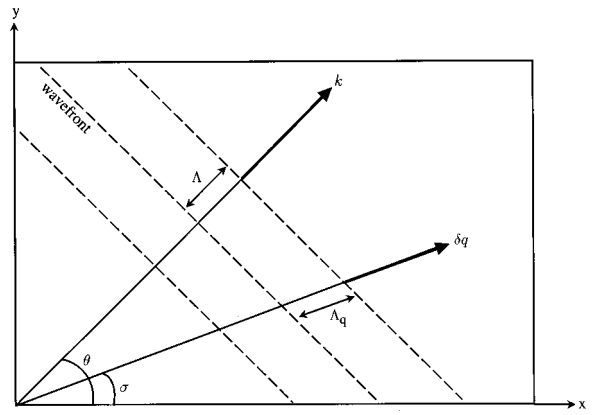

FIG. 4. Geometry of an ultrasonic plane wave of wavelength Λ traveling in the xy-plane that defines the object's surface. The optical shearing is at angle $\theta-\sigma$ to the wave number vector of the acoustic wave, and sees a periodicity of the trace wavelength in that direction, Λ_q.

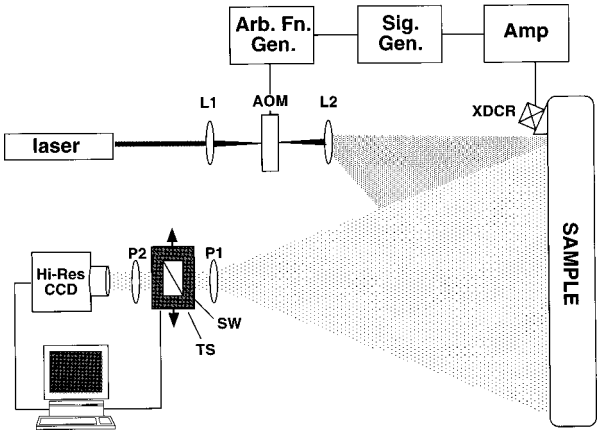

FIG. 5. Schematic of the shearography system. L1, L2: lenses for focusing and diverging the beam. SW: polarization shearing wedge. P1, P2: polarizers for evenly splitting the light between the two polarization modes sheared by SW. TS: computer-controlled translation stage for phase stepping. XDCR: ultrasonic transducer. AOM: acousto-optic modulator for laser modulation. The arbitrary function and signal generators are used to synchronize the laser modulation and acoustic signals.

2.5 by 2.5 cm, and a plate measuring 66 by 46 by 0.3 cm. A piezoelectric transducer was mounted on an acrylic wedge with a fixed angle of approximately 60 degrees. In all tests, the transducer and wedge were clamped to the sample and continuous wave excitation was used to generate ultrasonic waves. To properly sample the small ultrasonic wavelengths, imaging was performed with a Princeton Instruments high resolution digital camera, its CCD array comprised of 1317 by 1035 pixels. (Note that, with proper lenses and distances, a CCD camera of lower spatial resolution has the ability to image small features, but ends up with a greatly reduced field of view; this defeats the primary advantage of this being a full-field method.) An exposure time of between 2 and 4 s was used for each of the eight images necessary to form one phase map. An argon-ion laser provided illumination, operating at approximately 3 W, and laser strokes ranged from 35 to 90 degrees of the vibration period.

Figure 6 shows wavefronts along the entire 46-cm length of the aluminum bar for 200, 300, 400, and 500 kHz. The transducer is on the left end of the bar. Figure 7 shows a 25 by 16 cm section and Fig. 8 a 31 by 16 cm section of the aluminum plate for 580 and 330 kHz, respectively. Discolored ovular regions show the transducer position in the plate images. The value plotted in each of these figures is $\Delta(x,y)$, calculated from Eq. (7) and scaled to 256 gray levels.

Knowledge of the shearing distance and direction allows application of Eqs. (11) and (3) to the shearograms. Displacement amplitudes calculated from these equations can then be adjusted for the slight degree of time averaging that occurred due to sinusoidal motion during the laser stroke. On the aluminum bar, calculations show that the 200-kHz wave was of 2.9-nm displacement amplitude. The remaining bar wave trials reduced in amplitude as frequency increased, from 5.1 nm for 300 kHz down to 0.6 nm for 500 kHz. On the plate, the displacement amplitudes were 0.7 and 1.6 nm for Figs. 7 and 8, respectively.

Equation (13) shows that calculated phase can also be used to evaluate the wavelength of the traveling ultrasonic wave. Each shearogram was broken into a set of strips parallel to the wavenumber vector and an ensemble-averaged Fourier transform was applied to the set. The dominant spatial frequency in the resulting wave number spectrum (in 1/pixels) was converted to wavelength using the magnification factor of the optical system.

Phase speeds of the imaged waves were found by multiplying measured wavelengths by the known driving signal frequencies. These values are plotted in Fig. 9 as a function of $f \cdot d$, where f is the driving frequency and d the thickness of the plate or the width of the square bar, as appropriate.

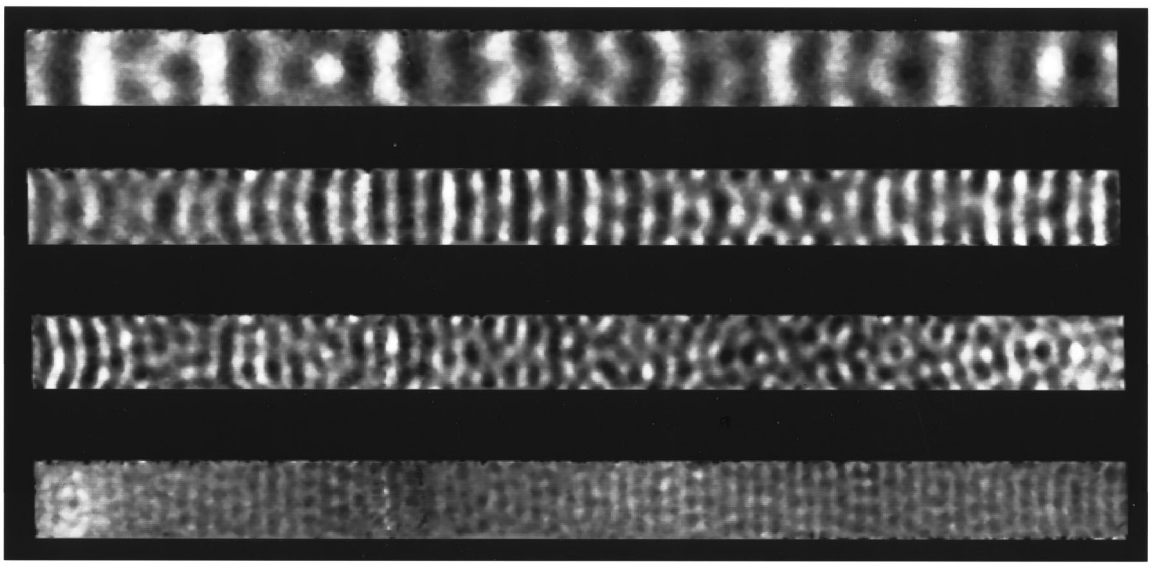

FIG. 6. Waves on a 46 by 2.5 by 2.5 cm aluminum bar. The ultrasonic transducer is at the left end. Frequencies, from top to bottom, are 200, 300, 400, and 500 kHz.

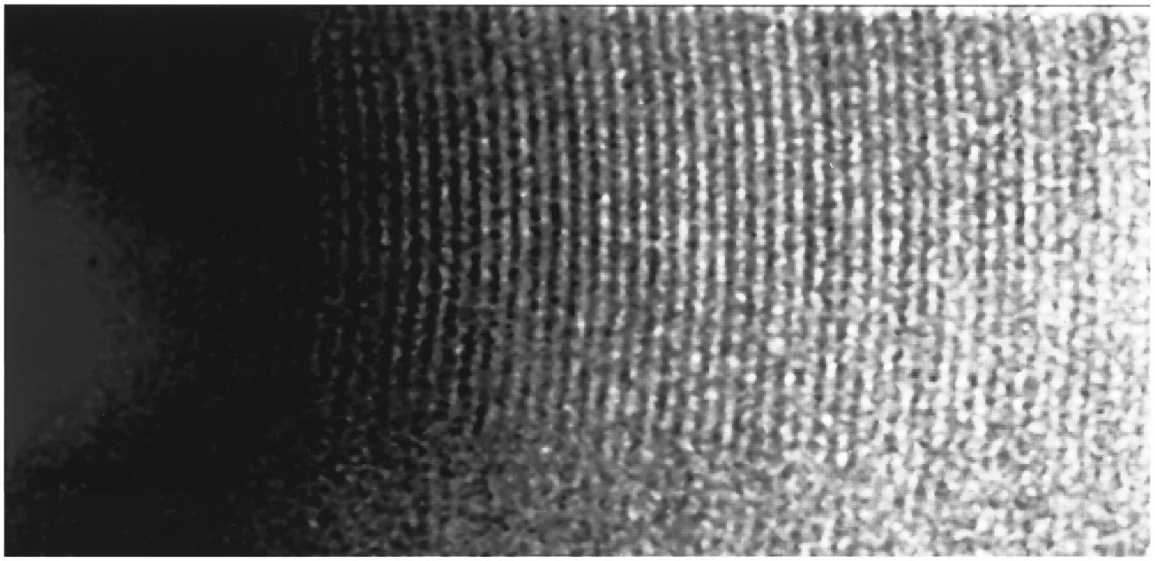

FIG. 7. A 25 by 16 cm section of the 0.3 cm thick aluminum plate. The location of the transducer can be seen at the left edge of the image.

The full-width half-max (FWHM) values of the spatial frequency estimates determined the extent of the phase speed error bars.

Also shown in Fig. 9 are five theoretical dispersion curves. Rayleigh–Lamb equations were used to obtain plate wave dispersion curves (S_0,A_0,A_1) and Pochhammer–Chree equations were used to obtain the first two longitudinal bar wave dispersion curves (L_1,L_2). (See, for example, Ref. 23.) In bars, an exact analytical solution for elastic wave propagation is only possible for cases of circular cross section.[24] In 1948, Morse[25] observed experimentally that the first longitudinal mode of a square bar gives a dispersion curve indistinguishable from that of a circular bar if the diameter of the latter is 1.13 times the square bar width. Dispersion curves for a circular bar of equivalent cross-sectional area to the square bar used are hence plotted in Fig. 9. Note that Morse only showed this equivalence to hold true for the fundamental mode, and that this relationship was not proven for higher-order modes in a square bar.

From Fig. 9, it can be seen that the phase speed estimates taken from the plate shearograms are in good agreement with the fundamental antisymmetric Lamb wave (A_0)

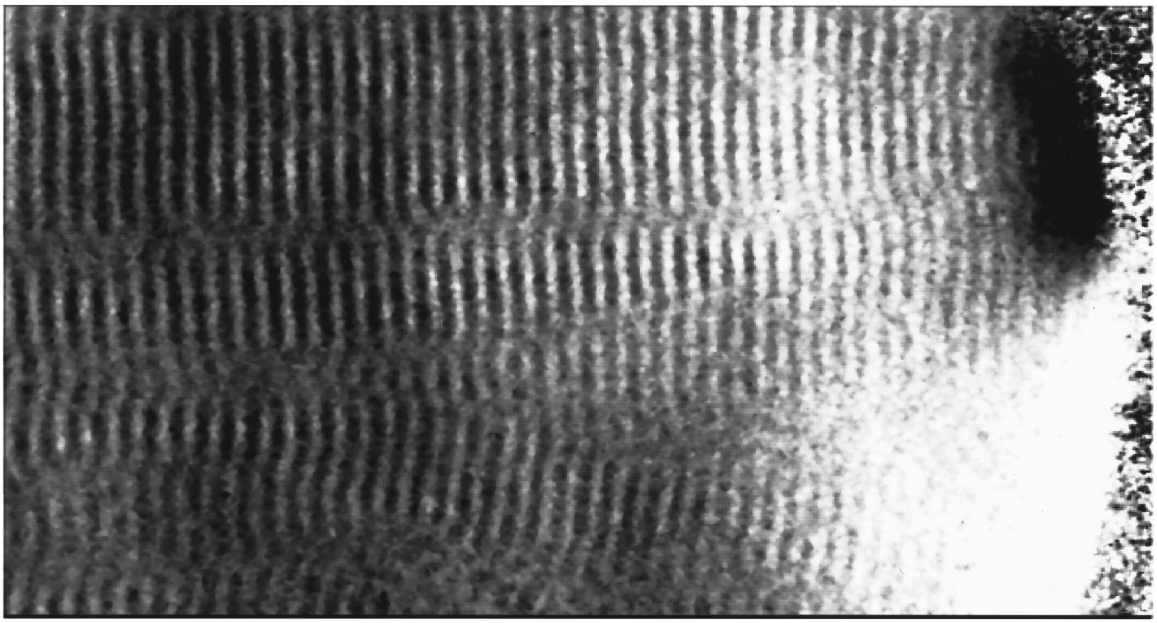

FIG. 8. A 31 by 16 cm section of the 0.3 cm thick aluminum plate. The transducer is now at the top right of the image, and left-going waves are angled slightly downward. Reflection off of the left edge causes interference throughout the image; the right-going wave can be seen at the bottom center of the image.

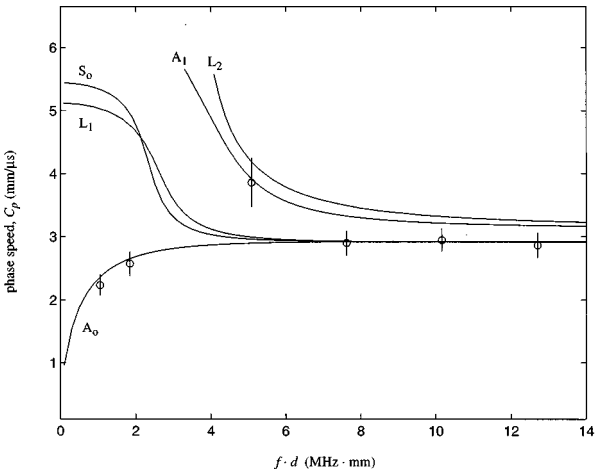

FIG. 9. Theoretical dispersion curves for aluminum, based on wavespeeds $c_l = 6320$ m/s and $c_s = 3130$ m/s. Points are calculated from estimates of the dominant spatial frequency component as determined via Fourier transforms of shearograms (the smallest two $f \cdot d$ values from the plate, the next four from the bar).

dispersion curve prediction. Likewise, the upper three bar wave phase speeds agree well with the first-order longitudinal bar mode. The lowest bar phase speed (for 200 kHz) is of particular interest, seemingly agreeing better with the theoretical dispersion curve of an A_1 Lamb wave than that of the second-order longitudinal bar mode. The equivalence of this second-order square bar mode to that of a bar of circular cross section, as implied by this plot, is suspicious. It is also noted that five other modes in addition to the longitudinal mode can exist on a square bar. A conclusive statement about the exact mode type for this datum would require a more detailed study of particle motion in addition to the phase speed analysis.

VII. SUMMARY AND FUTURE RESEARCH

A full-field, noncontact, quantitative method for the visualization of ultrasonic waves has been presented. The combination of shearography with laser modulation, phase stepping, and a high resolution digital camera has shown to provide many benefits. The high spatial resolution of the digital camera allows imaging of very small characteristics such as ultrasonic wavelengths without sacrificing the large field of view so appealing to shearography. Synchronized laser modulation captures wave motion at two instantaneous states during vibration, providing not only higher contrast fringes, but the ability to utilize the phase-stepping technique.

Exact displacement is independently calculated at every point via a series of phase-stepped images. Results have much higher contrast than fringe patterns, and unlike the discrete data points extracted from fringes, the sign, or direction, of displacement is retained. The detection of displacements a small fraction of an optical wavelength is possible, permitting ultrasonic wave displacements to be measured. If properly optimized, this system can be of higher sensitivity than the equivalent holography system.

This method provides the opportunity for wavelength and phase speed calculations, as well as potential measurement of attenuation due to interaction with flaws. A real-time system currently under development displays optical phase at high resolution once per second, rather than as the result of post-processing; this will provide even greater user interaction and flexibility during parameter adjustment.

ACKNOWLEDGMENTS

This work was supported by the Penn State University Applied Research Laboratory under its Exploratory and Foundational Program, and the Navy Manufacturing Technology LINC program. The authors wish to thank the reviewers for their many helpful comments and suggestions.

[1] J. W. Wagner, ''Heterodyne holography for visualization of surface acoustic waves,'' Nondestr. Test. Commun. **2**, 77–99 (1985).
[2] D. R. Andrews, ''Study of wavefronts in acoustic diffraction patterns using a stroboscopic schlieren technique,'' Proc. Soc. Photo-Opt. Instrum. Eng. **348**, 565–575 (1983).
[3] K.-J. Pohl, H.-A. Crostack, and H. Meyer, ''Holographic visualization of laser generated ultrasound for the detection and description of subsurface flaws,'' Proc. Soc. Photo-Opt. Instrum. Eng. **1756**, 258–269 (1992).
[4] Y. Y. Hung and C. E. Taylor, ''Measurement of slopes of structural deflections by speckle-shearing interferometry,'' Exp. Mech. **14**, 281–285 (1974).
[5] J. A. Leendertz and J. N. Butters, ''An image-shearing speckle-pattern interferometer for measuring bending moments,'' J. Phys. E **6**, 1107–1110 (1973).
[6] Y. Y. Hung, ''Shearography for nondestructive evaluation of composite structures,'' Opt. Lasers Eng. **24**, 161–182 (1996).
[7] J. W. Newman, ''Shearographic inspection of aircraft structure,'' Mater. Eval. **49**, 1106–1109 (1991).
[8] T. C. Chatters and S. Krishnaswamy, ''Nondestructive evaluation using shearing interferometry,'' Rev. Prog. Quant. Nondestr. Eval. **11**, 479–486 (1992).
[9] S. L. Toh, H. M. Shang, F. S. Chau, and C. J. Tay, ''Flaw detection in composites using time-average shearography,'' Opt. Laser Technol. **23**, 25–30 (1991).
[10] O. J. Løkberg, ''ESPI—The ultimate holographic tool for vibration analysis?'' J. Acoust. Soc. Am. **75**, 1783–1791 (1984).
[11] T. W. Ng and F. S. Chau, ''A digital shearing speckle interferometry technique for modal analysis,'' Appl. Acoust. **42**, 175–185 (1994).
[12] K. J. Gåsvik, ''Optical techniques,'' in *Interferogram Analysis: Digital Fringe Pattern Measurement Techniques*, edited by D. W. Robinson and G. T. Reid (Institute of Physics, Bristol, 1993), Chap. 2, pp. 23–46.
[13] R. Jones and C. Wykes, *Holographic and Speckle Interferometry* (Cambridge U.P., Cambridge, 1989), 2nd ed., Chaps. 1–4.
[14] G. O. Rosvold, ''Fast measurements of phase using a PC-based frame grabber and phase stepping technique,'' Appl. Opt. **29**, 237–241 (1990).
[15] P. Carrè, ''Installation et Utilisation du Compateur Photoelectrique et Interferential du Bureau International des Poids et Mesures,'' Metrologia **2**, 13–23 (1966).
[16] J. E. Greivenkamp and J. H. Bruning, ''Phase shifting interferometry,'' in *Optical Shop Testing*, edited by D. Malacara (Wiley, New York, 1992), 2nd ed., pp. 501–598.
[17] S. Nakadate and H. Saito, ''Fringe scanning speckle-pattern interferometry,'' Appl. Opt. **24**, 2172–2180 (1985).
[18] M. P. Kothiyal and C. Delisle, ''Shearing interferometer for phase shifting interferometry with polarization phase shifter,'' Appl. Opt. **24**, 4439–4442 (1985).
[19] M. Owner-Petersen, ''Digital speckle pattern shearing interferometry: Limitations and prospects,'' Appl. Opt. **30**, 2730–2738 (1991).
[20] H. Kadono, S. Toyooka, and Y. Iwasaki, ''Speckle-shearing interferometry using a liquid-crystal cell as a phase modulator,'' J. Opt. Soc. Am. A **8**, 2001–2008 (1991).

[21] B. A. Bard, S. Wu, and B. R. Tittmann, ''A compact digital phase-stepping shearography system,'' Rev. Prog. Quant. Nondestr. Eval. **15**, 673–677 (1996).
[22] J. D. Valera and J. D. C. Jones, ''Phase stepping in fiber-based speckle shearing interferometry,'' Opt. Lett. **19**, 1161–1163 (1994).
[23] T. R. Meeker and A. H. Meitzler, ''Guided wave propagation in elongated cylinders and plates,'' in *Physical Acoustics*, edited by W. P. Mason (Academic, New York, 1964), Vol. 1, Part A, pp. 111–167.
[24] W. B. Fraser, ''Stress wave propagation in rectangular bars,'' Int. J. Solids Struct. **5**, 379–397 (1969).
[25] R. W. Morse, ''Dispersion of compressional waves in isotropic rods of rectangular cross section,'' J. Acoust. Soc. Am. **20**, 833–838 (1948).

Finite element modeling of lead magnesium niobate electrostrictive materials: Static analysis

Jean-Claude Debus, Bertrand Dubus, and Jocelyne Coutte
Institut d'Electronique et de Microélectronique du Nord, U.M.R. C.N.R.S. 9929, Département I.S.E.N., 41 Bd Vauban, 59046 Lille Cedex, France

(Received 16 May 1997; accepted for publication 29 January 1998)

New lead magnesium niobate (PMN) ceramics, which can generate large strains at moderate electric fields, are good candidates for future actuators or sonar projectors. In this paper, two finite element models are proposed to describe static analysis of electrostrictive materials. Both models include quadratic dependence of strain with electrical displacement, assume constant temperature, and exclude hysteresis. One of the models includes the saturation of the polarization. The theoretical formulation is justified by the method of the weighted residuals. The numerical implementation is presented. The validation is performed by comparing numerical results with measurements for a PMN bar subjected to mechanical prestress and dc electric field. © *1998 Acoustical Society of America.* [S0001-4966(98)03405-5]

PACS numbers: 43.38.Ar, 43.38.Fx, 43.30.Yj [SLE]

INTRODUCTION

New electrostrictive lead magnesium niobate ceramics (PMN)[1–5] are promising materials for applications in the design of actuator devices[6] and of new underwater acoustic projectors.[7] These materials have strains roughly an order of magnitude larger than those of the lead zirconate titanate (PZT) ceramics. This is due to the large dielectric permittivities of PMN materials which are a factor of 10 or more, larger than those of the PZT materials.

However, the use of PMN materials for acoustic projectors presents some difficulties: highly nonlinear properties, temperature dependence of dielectric permittivity, dc bias field needed. To help in the design of underwater acoustic applications with PMN materials, progress is needed in the development of constitutive laws and modeling tools. A general transducer perturbation model including electrostriction as a special case has been proposed recently[8] to describe one-dimensional vibrators.

The scope of this paper is to present the development of a two-dimensional electrostrictive finite element in the ATILA code[9,10] to enable nonlinear static analysis of PMN materials. The constitutive laws currently available to describe PMN ceramics are reviewed in Sec. I. The theoretical formulation of the electrostrictive finite element and its numerical implementation are presented in Sec. II. The validity of the new model is discussed in Sec. III where numerical, analytical, and measured results are compared for a PMN bar at various electric dc fields and mechanical prestresses.

I. CONSTITUTIVE LAWS FOR ELECTROSTRICTORS

Three different models have been proposed to describe the mechanical and dielectric behavior of electrostrictive ceramics:

(i) the first one is an extension of Voight's model,[11]
(ii) the second one is a phenomenological model initially formulated by Devonshire[12] and applied to PMN materials by Hom *et al.*,[13,14]
(iii) the third model has been proposed recently by Piquette *et al.*[15]

All models describe the quadratic dependence of strain with electrical displacement at zero stress, assume constant temperature, and exclude hysteresis. The last two models include the phenomenon of the polarization saturation. Due to the very recent publication of the third model, it has not been included in our finite element formulation. This paper discusses only the first two models.

A. Model 1

The constitutive equations for the classical theory of linear piezoelectricity are generally attributed to Voight.[11] Assuming stress and electric field as independent state variables, the equations are

$$\mathbf{S}=[s^E]\mathbf{T}+[d]^t\mathbf{E}, \quad \mathbf{D}=[d]\mathbf{T}+[\varepsilon^T]\mathbf{E}, \tag{1}$$

where $[s^E]$ is the elastic compliance tensor at constant electric field, $[d]$ is the piezoelectric constants tensor, $[\varepsilon^T]$ is the dielectric permittivity matrix at constant stress. **D** is the electric displacement vector, **E** is the electric field vector, **T** is the condensed stress tensor, and **S** is the condensed strain tensor. ^{t} is used to denote matrix transposition. The relations between strain and electric field (converse piezoelectricity) and between electric displacement and stress (direct piezoelectricity) are developed assuming a linear dependence of strain on electric field and electric displacement on stress.

Considering that the relative dielectric permittivity of electrostrictive ceramics is very large, it can be assumed that $\mathbf{P}\approx\mathbf{D}$, where **P** is the polarization. The constitutive equations of electrostriction are written[17]

$$\begin{aligned} S_{ij}&=s^D_{ijkl}T_{kl}+Q_{ijlm}D_1D_m, \\ E_i&=-2Q_{klji}D_jT_{kl}+\beta^T_{ij}D_j, \end{aligned} \tag{2}$$

where $[s^D]$ is the elastic compliance tensor at constant excitation and $[\beta^T]$ is the dielectric impermeability matrix at

 0001-4966/98/103(6)/3336/8/$10.00

constant stress. Here $[Q]$ is the fourth rank tensor of the electrostrictive constants defined as

$$2Q_{ijkl}=\frac{\partial^2 S_{ij}}{\partial D_k\,\partial D_1}=-\frac{\partial^2 E_1}{\partial T_{ij}\,\partial D_k}. \tag{3}$$

In a condensed notation, Eq. (2) is written

$$\mathbf{S}=[s^D]\mathbf{T}+[g([Q],\mathbf{D})]^t\mathbf{D}, \tag{4}$$

$$\mathbf{E}=-2[g([Q],\mathbf{D})]\mathbf{T}+[\beta^T]\mathbf{D}.$$

When comparing Eq. (4) with the constitutive equations of piezoelectricity (using stress and electrical displacement as independent state variables), two differences are noted: the factor 2 in the second line due to the quadratic nature of electrostriction, and the nonlinearity of the ''piezoelectric strain constant'' tensor $[g]$, defined as

$$[g]=\begin{bmatrix} Q_{11}D_1 & Q_{12}D_1 & Q_{12}D_1 & 0 & (Q_{11}-Q_{12})D_3 & (Q_{11}-Q_{12})D_2 \\ Q_{12}D_2 & Q_{11}D_2 & Q_{12}D_2 & (Q_{11}-Q_{12})D_3 & 0 & (Q_{11}-Q_{12})D_1 \\ Q_{12}D_3 & Q_{12}D_3 & Q_{11}D_3 & (Q_{11}-Q_{12})D_2 & (Q_{11}-Q_{12})D_1 & 0 \end{bmatrix}, \tag{5}$$

where Q_{ij} are the electrostrictive constants of the condensed tensor. Equation (4) assumes that the dielectric impermeability matrix is constant, i.e., that the strain exhibits a quadratic dependence on the electric field. As shown in Fig. 1, this assumption is verified in PMN ceramics when $E<E_0$ ($E_0\approx 0.6$ MV/m).

B. Model 2

For an electric field larger than E_0, the induced polarization begins to saturate (Fig. 1) and higher-order terms must be added to the previous model. Hom's model[13,14] was inspired by the Devonshire theory[12] and the Suo adaptation[18] for an isotropic relaxor-ferroelectric. It was written using a set of empirical assumptions:

(1) the electrically induced strain only depends on second-order polarization terms,
(2) the elastic modulus of the crystal is independent of polarization and temperature, and
(3) the stress-free dielectric behavior can be expressed by the hyperbolic tangent function[19] (originally proposed to describe the dielectric behavior of piezoelectric materials with hysteresis):

$$|\mathbf{P}|=P_s\,\tanh(k|\mathbf{E}|), \tag{6}$$

where P_s is the spontaneous polarization (the saturation value of polarization at very high electric fields) and k is a new material constant. Here P_s and k depend on the temperature; $|\mathbf{P}|$ is the magnitude of the polarization and $|\mathbf{E}|$ is the magnitude of the electric field.

Considering again that $\mathbf{P}\approx\mathbf{D}$ and, choosing the electric displacement and the stress as the independent state variables, the constitutive equations may be written

$$\mathbf{S}=[s^D]\mathbf{T}+[g([Q],\mathbf{D})]^t\mathbf{D},\quad \mathbf{E}=-2[g([Q],\mathbf{D})]\mathbf{T}+[\beta^T(k,P_s,\mathbf{D})]\mathbf{D}, \tag{7}$$

with

$$[\beta^T]=\begin{bmatrix} \frac{1}{k|\mathbf{D}|}\operatorname{arctanh}\left(\frac{|\mathbf{D}|}{P_s}\right) & 0 & 0 \\ 0 & \frac{1}{k|\mathbf{D}|}\operatorname{arctanh}\left(\frac{|\mathbf{D}|}{P_s}\right) & 0 \\ 0 & 0 & \frac{1}{k|\mathbf{D}|}\operatorname{arctanh}\left(\frac{|\mathbf{D}|}{P_s}\right) \end{bmatrix}, \tag{8}$$

assuming that

$$k=\frac{1}{P_s(\beta_{33}^T)_{\mathbf{D}=\mathbf{0}}}. \tag{9}$$

II. FINITE ELEMENT MODEL OF ELECTROSTRICTIVE MATERIALS

A. Theoretical formulation for static analysis

A linear piezoelectric transducer design can be formulated in variational form by the finite element method. The mathematical formulation of a variational principle usually involves finding the nodal parameters that yield a stationary value of a specific integral relation known as a functional. This quantity was first found using a trial and error procedure by Lewis[20] and by Holland *et al.*[21] It was then justified using the virtual work principle by Allik *et al.*[22] A full demonstration and a discussion of this quantity are given in the book by Holland and Eer Nisse.[23] If the behavioral law of the material is nonlinear, this quantity does not exist and another approach must be used.

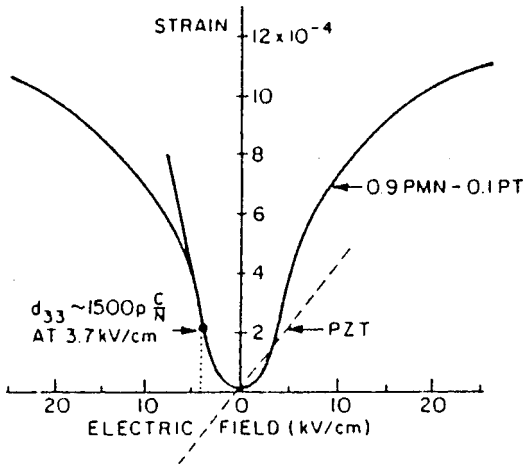

FIG. 1. Typical strain-electric field curve for electrostrictive (PMN-PT) and piezoelectric ceramics from Ref. 16.

Let us consider an electrostrictive domain Ω limited by a closed surface Γ pointing outwards. The equilibrium equation of an elementary volume can be written in terms of the components of the symmetric Cartesian stress tensor as

$$\frac{\partial \overline{T_{ij}}}{\partial x_j}=0. \tag{10}$$

The superscript is used on T to denote the (noncondensed) second rank stress tensor. Gauss's theorem is written as

$$\frac{\partial D_i}{\partial x_i}=0. \tag{11}$$

For an electrostrictive material, the stress and the electrical displacement can be obtained by inverting the set of equations (4) for model 1 or (7) for model 2. Let us consider model 2. The first line of Eq. (7) is written as

$$\mathbf{T}=[s^D]^{-1}\mathbf{S}-[s^D]^{-1}[g([Q],\mathbf{D})]^t\mathbf{D} \tag{12}$$

and combined with the second line of Eq. (7):

$$\mathbf{E}=-2[g([Q],\mathbf{D})][s^D]^{-1}\mathbf{S}+(2[g([Q],\mathbf{D})]\times[s^D]^{-1}[g([Q],\mathbf{D})]^t+[\beta^T(k,P_s,\mathbf{D})])\mathbf{D}. \tag{13}$$

Therefore, we obtain

$$\begin{aligned}\mathbf{T}&=[c^E(k,P_s,[Q],\mathbf{D})]\mathbf{S}-[e(k,P_s,[Q],\mathbf{D})]^t\mathbf{E}\\ \mathbf{D}&=2[e(k,P_s,[Q],\mathbf{D})]\mathbf{S}+[\varepsilon^S(k,P_s,[Q],\mathbf{D})]\mathbf{E},\end{aligned} \tag{14}$$

with

$$[\varepsilon^S(k,P_s,[Q],\mathbf{D})]=([\beta^T(k,P_s,\mathbf{D})]+2[g([Q],\mathbf{D})]\times[s^D]^{-1}[g([Q],\mathbf{D})]^t)^{-1}, \tag{15}$$

$$[e(k,P_s,[Q],\mathbf{D})]=[\varepsilon^S(k,P_s,[Q],\mathbf{D})]\times[g([Q],\mathbf{D})][s^D]^{-1}, \tag{16}$$

$$[c^E(k,P_s,[Q],\mathbf{D})]=[s^D]^{-1}-2[s^D]^{-1}[g([Q],\mathbf{D})]^t\times[\varepsilon^S(k,P_s,[Q],\mathbf{D})][g([Q],\mathbf{D})]\times[s^D]^{-1}. \tag{17}$$

It can be noted that Eqs. (15)–(17) are similar to usual relations between tensors in piezoelectricity.

Equations (10) and (11) can be written as a differential equation set:

$$\mathbf{A}(\boldsymbol{\Theta})=\mathbf{0}, \tag{18}$$

where

$$\boldsymbol{\Theta}=\begin{Bmatrix}\mathbf{T}\\ \mathbf{D}\end{Bmatrix}. \tag{19}$$

is the generalized stress vector. The solution of Eq. (18) can be obtained applying the method of weighted residuals.[24] An arbitrary weighting function vector $\delta\mathbf{w}$ called elementary generalized displacement vector is defined as

$$\delta\mathbf{w}=\begin{Bmatrix}\delta\mathbf{u}\\ \delta\varphi\end{Bmatrix}, \tag{20}$$

where $\delta\mathbf{u}$ and $\delta\varphi$ are arbitrary variations of the displacement field and of the electrical potential, respectively. The method of the weighted residuals is applied by writing for any $\delta\mathbf{w}$:

$$\int\int\int_\Omega \delta\mathbf{w}^t\ \mathbf{A}(\boldsymbol{\Theta})\ d\Omega = \int\int\int_\Omega\left(\delta u_i\ \frac{\partial \overline{T_{ij}}}{\partial x_j}+\delta\varphi\ \frac{\partial D_i}{\partial x_i}\right)\ d\Omega=0, \tag{21}$$

where Ω is the electrostrictive domain. After integrating each term of the integral by parts and rearranging, Eq. (21) can be written as

$$-\int\int\int_\Omega(\overline{T_{ij}}\ \delta\overline{S_{ij}}-D_i\ \delta E_i)\ d\Omega+\int\int_\Gamma(\delta u_i\ \overline{T_{ij}}n_j+\delta\varphi\ D_in_i)\ d\Gamma=0 \tag{22}$$

or, in a condensed notation,

$$\int\int\int_\Omega\delta\boldsymbol{\Sigma}^t\boldsymbol{\Theta}\ d\Omega-\int\int_\Gamma\delta\mathbf{w}^t\ \boldsymbol{\theta}\ d\Gamma=0, \tag{23}$$

where $\mathbf{n}$ is the unitary vector normal to Γ pointing outwards. The superscript on S denotes the (noncondensed) second rank strain tensor. Here $\boldsymbol{\Sigma}$ is the generalized strain vector written as

$$\boldsymbol{\Sigma}=\begin{Bmatrix}\mathbf{S}\\ -\mathbf{E}\end{Bmatrix}, \tag{24}$$

and $\boldsymbol{\theta}$ is the generalized force vector acting per unit area of the surface Γ,

$$\boldsymbol{\theta}=\begin{Bmatrix}\mathbf{f}\\ -q\end{Bmatrix}, \tag{25}$$

where $\mathbf{f}$ is the surface force acting on Γ,

$$f_i=\overline{T_{ij}}n_j; \tag{26}$$

and q is the charge density on Γ,

$$q=-D_in_i. \tag{27}$$

Equation (23) is similar to the virtual work theorem. The virtual work statement is precisely the weak form of the equilibrium equations and is valid for nonlinear as well as linear stress–strain relations.[24]

B. Finite element discretization

When using the finite element method, the domain Ω (and the surface Γ) are divided into subdomains called elements interconnected at some points called nodes. Inside an element e, the physical variables (displacement, electrical potential) are related to their nodal values by means of interpolation (or shape) functions[10,25] $[N_u^{(e)}]$ and $[N_\varphi^{(e)}]$:

$$\mathbf{u}^{(e)}=[N_u^{(e)}]\mathbf{U}^{(e)}, \tag{28}$$

$$\varphi^{(e)}=[N_\varphi^{(e)}]\mathbf{\Phi}^{(e)}. \tag{29}$$

Here $\mathbf{U}^{(e)}$ is the vector of the nodal values of the displacement for element e and $\mathbf{\Phi}^{(e)}$ is the vector of the nodal values of the electric potential. The strain and the electrical field in each element are expressed as

$$\mathbf{S}^{(e)}=[B_u^{(e)}]\mathbf{U}^{(e)}, \tag{30}$$

$$\mathbf{E}^{(e)}=-[B_\varphi^{(e)}]\mathbf{\Phi}^{(e)}, \tag{31}$$

where $[B_u^{(e)}]$ and $[B_\varphi^{(e)}]$ are matrices obtained from derivatives of the shape functions with respect to space coordinates. Inside element e, the generalized stress vector is expressed using Eq. (14) as

$$\mathbf{\Theta}^{(e)}=\begin{Bmatrix}\mathbf{T}^{(e)}\\ \mathbf{D}^{(e)}\end{Bmatrix}=\begin{bmatrix}[c^{E(e)}] & -[e^{(e)}]^t\\ [2e^{(e)}] & [\varepsilon^{S(e)}]\end{bmatrix}\begin{bmatrix}[B_u^{(e)}] & 0\\ 0 & -[B_\varphi^{(e)}]\end{bmatrix}\times\begin{Bmatrix}\mathbf{U}^{(e)}\\ \mathbf{\Phi}^{(e)}\end{Bmatrix}. \tag{32}$$

After applying the finite element discretization, Eq. (23) becomes

$$\sum_{e=1}^{m}\int\int\int_{\Omega^{(e)}}\delta\mathbf{\Sigma}^{(e)^t}\,\mathbf{\Theta}^{(e)}\,d\Omega^{(e)} - \sum_{e=1}^{n}\int\int_{\Gamma^{(e)}}\delta\mathbf{w}^{(e)^t}\boldsymbol{\theta}^{(e)}\,d\Gamma^{(e)}=0, \tag{33}$$

where m is the number of elements in the domain Ω and n is the number of elements on the boundary Γ. Combining Eqs. (28)–(32) with Eq. (33), we obtain

$$\sum_{e=1}^{m}\int\int\int_{\Omega^{(e)}}\{\delta\mathbf{U}^{(e)^t},\delta\mathbf{\Phi}^{(e)^t}\}\begin{bmatrix}[B_u^{(e)}]^t & 0\\ 0 & [B_\varphi^{(e)}]^t\end{bmatrix}\times\begin{bmatrix}[c^{E(e)}] & -[e^{(e)}]^t\\ [2e^{(e)}] & [\varepsilon^{S(e)}]\end{bmatrix}\begin{bmatrix}[B_u^{(e)}] & 0\\ 0 & -[B_\varphi^{(e)}]\end{bmatrix}\begin{Bmatrix}\mathbf{U}^{(e)}\\ \mathbf{\Phi}^{(e)}\end{Bmatrix}d\Omega^{(e)} - \sum_{e=1}^{n}\int\int_{\Gamma^{(e)}}\{\delta\mathbf{U}^{(e)^t},\delta\mathbf{\Phi}^{(e)^t}\}\begin{Bmatrix}[N_u^{(e)}]^t\mathbf{f}\\ -[N_\varphi^{(e)}]^t q\end{Bmatrix}d\Gamma^{(e)}=0. \tag{34}$$

We define the elastic stiffness matrix $[K_{uu}]$, the electromechanical coupling matrix $[K_{u\varphi}]$, and the dielectric stiffness matrix $[K_{\varphi\varphi}]$ of the finite element model as the result of the assembling of the elementary matrices:

$$[K_{uu}]=\sum_{e=1}^{m}\int_{\Omega^{(e)}}[B_u^{(e)}]^t[c^{E(e)}][B_u^{(e)}]\,d\Omega^{(e)}, \tag{35}$$

$$[K_{u\varphi}]=\sum_{e=1}^{m}\int_{\Omega^{(e)}}[B_u^{(e)}]^t[e^{(e)}]^t[B_\varphi^{(e)}]\,d\Omega^{(e)}, \tag{36}$$

$$[K_{\varphi\varphi}]=-\sum_{e=1}^{m}\int_{\Omega^{(e)}}[B_\varphi^{(e)}]^t[\varepsilon^{S(e)}][B_\varphi^{(e)}]\,d\Omega^{(e)}. \tag{37}$$

We define the vectors of the nodal values of the external force $\mathbf{F}$ and the electric charge $\mathbf{Q}$ as

$$\mathbf{F}=\sum_{e=1}^{n}\int\int_{\Gamma^{(e)}}[N_u^{(e)}]^t\mathbf{f}\,d\Gamma^{(e)}, \tag{38}$$

$$\mathbf{Q}=\sum_{e=1}^{n}\int\int_{\Gamma^{(e)}}[N_\varphi^{(e)}]^t q\,d\Gamma^{(e)}. \tag{39}$$

Equation (34) becomes

$$\{\delta\mathbf{U}^t,\delta\mathbf{\Phi}^t\}\left(\begin{bmatrix}[K_{uu}] & [K_{u\varphi}]\\ 2[K_{u\varphi}]^t & [K_{\varphi\varphi}]\end{bmatrix}\begin{Bmatrix}\mathbf{U}\\ \mathbf{\Phi}\end{Bmatrix}-\begin{Bmatrix}\mathbf{F}\\ -\mathbf{Q}\end{Bmatrix}\right)=0. \tag{40}$$

Here $\mathbf{U}$ and $\mathbf{\Phi}$ are the vectors of the nodal values of the displacement and the electric potential, respectively. They result from the assembling of the associated elementary vectors defined previously. As Eq. (40) is valid for any value of the arbitrary displacement, we obtain

$$\begin{bmatrix}[K_{uu}] & [K_{u\varphi}]\\ 2[K_{u\varphi}]^t & [K_{\varphi\varphi}]\end{bmatrix}\begin{Bmatrix}\mathbf{U}\\ \mathbf{\Phi}\end{Bmatrix}=\begin{Bmatrix}\mathbf{F}\\ -\mathbf{Q}\end{Bmatrix}. \tag{41}$$

Equation (41) constitutes the finite element set of equations of an electrostrictive material for static analysis. The physical tensors appearing in Eqs. (35)–(37) are functions of the electrical displacement [Eq. (14)] which is expressed in each element using $\mathbf{U}^{(e)}$ and $\mathbf{\Phi}^{(e)}$ [second line of Eq. (32)]. Therefore, Eq. (41) is nonlinear and must be solved using a specific numerical process.

C. Numerical implementation

The static calculation for an electrostrictive structure is obtained using a numerical procedure. The electrostrictive finite elements developed in this work are an eight-node quadrilateral and a six-node triangle for axisymmetrical analysis. These elements are isoparametric and therefore displacement and electrical potential are described by functions with quadratic spatial variations in each element. The element data for an electrostrictive ceramic are the matrices $[s^D]$, $[Q]$ and $[\varepsilon^T]$ (or P_s and k for model 2) which are assumed as being constant values. The nonlinear equation to solve [Eq. (41)] can be written in a condensed form:

$$[K(\mathbf{D})]\mathbf{W}=\mathbf{R}. \tag{42}$$

The nonlinear equation is solved using direct method[24] which can be described as (i is the iteration number)

(1) initialization of $\mathbf{D}_i(i=0)$,
(2) assembling of the stiffness matrix $[K(\mathbf{D}_i)]$,

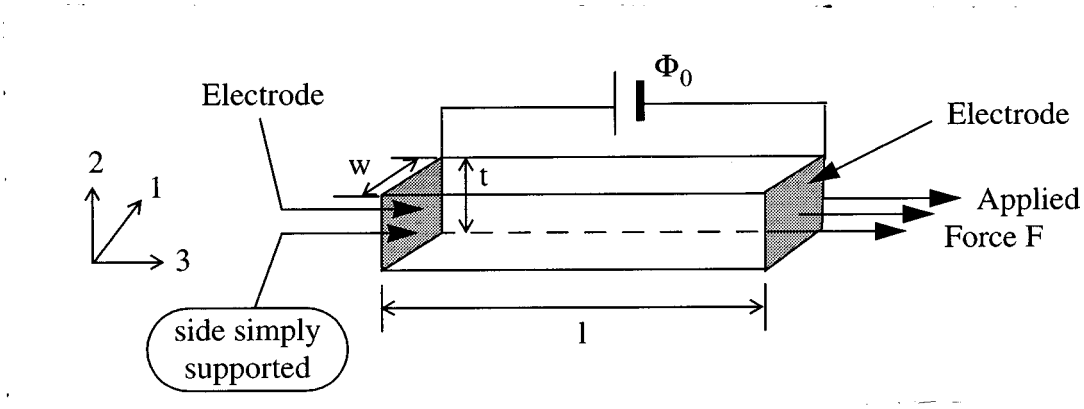

FIG. 2. Geometry of the electrostrictive PMN bar submitted to a static mechanical prestress and a quasi-static electric field.

(3) linear solving of $[K(\mathbf{D}_i)]\mathbf{W}_{i+1}=\mathbf{R}$,
(4) computation of $\mathbf{D}_{i+1}$,
(5) convergence test $(|\mathbf{D}_{i+1}-\mathbf{D}_i|)/|\mathbf{D}_{i+1}|<\varepsilon$. If the test is not verified, return to (2).

Integration of the stiffness matrix [Eqs. (35)–(37)] is done by the Gauss integration method.[24] Initialization of **D**, computation of **D**, and convergence test are performed at each Gauss point used for the numerical integration of the matrices. Linear solving is performed using the Gauss method. In the numerical process, step (4) is critical because it determines the convergence of the solution. After solving Eq. (41), the strain and the electric field can be evaluated exactly in the element e using Eqs. (30) and (31). The computation of the electric displacement is approximate because the equation (32) is nonlinear:

$$\mathbf{D}_{i+1}^{(e)}=2[e^{(e)}(\mathbf{D}_i^{(e)})]\mathbf{S}_i^{(e)}+[\varepsilon^{S(e)}(\mathbf{D}_i^{(e)})]\mathbf{E}_i^{(e)}. \tag{43}$$

For model 2, another technique is used to obtain $\mathbf{D}_{i+1}$ starting from Eq. (7). It consists of the following operations:

$$\mathbf{T}_i^{(e)}=[s^D]^{-1}\mathbf{S}_i^{(e)}-[s^D]^{-1}[g^{(e)}([Q],\mathbf{D}_i^{(e)})]^t\mathbf{D}_i^{(e)}, \tag{44}$$

$$\mathbf{E}_i'^{(e)}=\mathbf{E}_i^{(e)}+2[g^{(e)}([Q],\mathbf{D}_i^{(e)})]\mathbf{T}_i^{(e)}, \tag{45}$$

$$\mathbf{D}_{i+1}^{(e)}=\frac{\mathbf{E}_i'^{(e)}}{|\mathbf{E}_i'^{(e)}|}P_s\tanh(k|\mathbf{E}_i'^{(e)}|). \tag{46}$$

The main advantage of this technique comes from Eq. (46) which exactly inverts the electric displacement-electric field relationship. The use of Eq. (43) together with model 2 in the computation of $\mathbf{D}_{i+1}$ can lead to values of $\mathbf{D}_{i+1}$ exceeding P_s. The computation of the physical tensors in the next iteration becomes impossible.

III. VALIDATION: ANALYSIS OF AN ELECTROSTRICTIVE BAR

To validate the previous developments, a long electrostrictive bar with electrodes located at both ends is analyzed (Fig. 2). A static mechanical force F is applied at both ends and a quasi-static (10 Hz) electric voltage Φ_0 is prescribed between the electrodes. An analytical model can be written at low electric field using model 1. It is described in Sec. III A. Numerical and analytical results are compared to measurements made on a PMN-PT-La bar at NUWC New London[26,27] in Sec. III B for low ($E<E_0$) and high ($E>E_0$) applied electric fields.

A. Analytical model

It is assumed that the width w and the thickness t of the bar are small compared to its length l. Mechanical and electrical boundary conditions on lateral faces give[28]

$$T_1=T_2=T_4=T_5=T_6=0, \tag{47}$$

$$D_1=D_2=0. \tag{48}$$

Here, **D** and **T** are chosen as independent variables. The electrostrictive set of equations is (model 1)

$$\begin{aligned} S_3&=s_{33}^D T_3+Q_{11}D_3^2,\\ E_3&=-2Q_{11}D_3T_3+\beta_{33}^T D_3. \end{aligned} \tag{49}$$

Using Newton's law,

$$\frac{\partial T_3}{\partial z}=0, \tag{50}$$

it is found that T_3 is constant along the bar:

$$T_3=\frac{F}{wt}. \tag{51}$$

Using Gauss's theorem,

$$\frac{\partial D_3}{\partial z}=0, \tag{52}$$

it is found that D_3 is constant along the bar. From the second line of Eq. (49), E_3 is constant and is equal to

$$E_3=-\frac{\Phi_0}{l}. \tag{53}$$

After combining Eqs. (49), (51), and (53), we obtain

$$D_3=-\frac{\Phi_0}{l(\beta_{33}^T-2Q_{11}F/wt)}, \tag{54}$$

$$S_3=s_{33}^D\frac{F}{wt}+\frac{Q_{11}\Phi_0^2}{l^2(\beta_{33}^T-2Q_{11}F/wt)^2}. \tag{55}$$

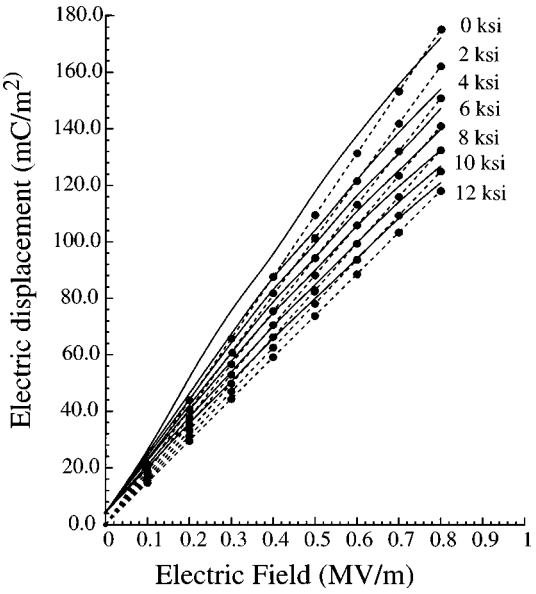

FIG. 3. Quasi-static electric displacement versus quasi-static electric field curves for the PMN bar submitted to various static mechanical prestresses. Full line: measurements from Ref. 26; dashed line: analytical; dark dots: finite element (model 1).

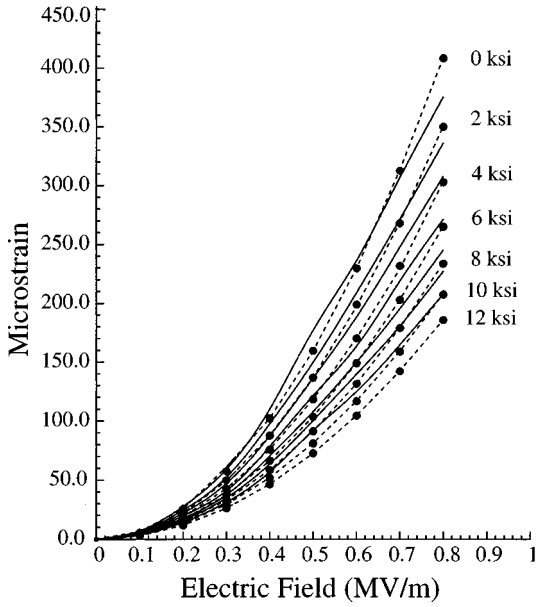

FIG. 4. Quasi-static strain versus quasi-static electric field curves for the PMN bar submitted to various static mechanical prestresses. The static strain due to mechanical prestress is not included. Full line: measurements from Ref. 26; dashed line: analytical; dark dots: finite element (model 1).

B. Comparison of analytical, numerical, and experimental results

1. Results at low electric field

The applied potential ranges from 0–8 kV, corresponding to $0<E<0.8$ MV/m. The bar is modeled assuming axisymmetry. Half of the bar is described using four elements based on model 1. The material properties are obtained from Refs. 26 and 27,

$$\begin{aligned} &s_{11}^D=s_{22}^D=s_{33}^D=0.890\times10^{-11}\ \text{m}^2/\text{N},\\ &s_{12}^D=s_{13}^D=s_{23}^D=-0.311\times10^{-11}\ \text{m}^2/\text{N},\\ &s_{44}^D=s_{55}^D=s_{66}^D=2.4\times10^{-11}\ \text{m}^2/\text{N}, \end{aligned} \tag{56}$$

$$\varepsilon_{33}^T=2.1928\times10^{-7}\ \text{C}/(\text{V}\cdot\text{m}), \tag{57}$$

and the electrostrictive constants from Ref. 14,

$$\begin{aligned} &Q_{11}=0.133\times10^{-1}\ \text{m}^4/\text{C}^2,\\ &Q_{12}=-0.606\times10^{-2}\ \text{m}^4/\text{C}^2. \end{aligned} \tag{58}$$

These values were obtained on a PMN-PT-BT sample at 5 °C and therefore can only be considered as approximate values for the PMN-PT-La sample used in the experiment at room temperature.

Figure 3 presents the charge density on the electrodes (equal to the electrical displacement) versus the quasi-static applied electric field for various static prestresses. The analytical and numerical models agree very well. Measurements[26] are slightly different from theoretical results due to a small nonlinearity of the dielectric permittivity. A remanent electric displacement is measured at zero-electric field. Figure 4 presents the quasi-static strain versus the quasi-static applied electric field for various prestresses. The static strain is not measured. The quadratic behavior is perfectly described by both numerical and analytical models. The deviation observed on measurements is due to the nonlinearity on the dielectric permittivity which is not taken into account in the model. From a numerical point of view, the convergence of the result is obtained with 2, 4, 5, 7, 8, 9, and 12 iterations for prestresses of 0, 2, 4, 6, 8, 10, and 12 ksi, respectively. The number of iterations is independent of the applied electric field except at zero-field. At zero-electric field, the problem is linear and the result is obtained with one iteration for any prestress.

2. Results at high electric field

The applied potential ranges from 0–20 kV, corresponding to $0<E<2$ MV/m. Half of the bar is meshed using four axisymmetrical elements (model 1 or model 2). The $[s^D]$ tensor and the electrostrictive constant Q_{12} are unchanged. The electrostrictive constant Q_{11} and dielectric parameters are determined by fitting the constitutive law with experiment[27] at zero prestress:

$$\begin{aligned} &Q_{11}=0.121\times10^{-1}\ \text{m}^4/\text{C}^2,\quad P_s=0.262\ \text{C}/\text{m}^2,\\ &k=9.2\times10^{-7}\ \text{m}/\text{V},\quad \varepsilon_{33}^T=kP_s. \end{aligned} \tag{59}$$

Figures 5 and 6 compare the measured variations of the electric displacement and strain with electric field at zero prestress with numerical results obtained with both models. Model 1 is clearly unable to describe PMN material behavior for an electric field larger than 0.6 MV/m. Figures 7 and 8 display the quasi-static electric displacement (or charge density) and the quasi-static strain versus the quasi-static applied electric field for prestresses of 0, 4, 8, and 12 ksi, respectively. Agreement between numerical results and measurements shows that model 2 is valid up to 2 MV/m. From a numerical point of view, the convergence of the result depends upon the applied mechanical prestress and the electric field. For the larger applied electric field, the number of it-

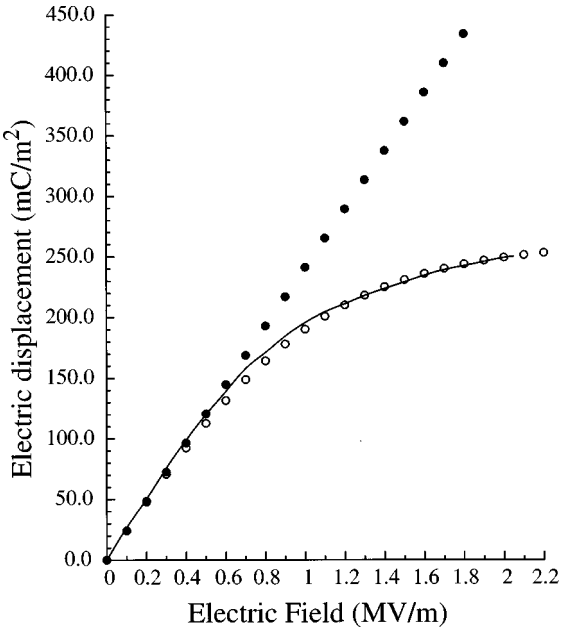

FIG. 5. Quasi-static electric displacement versus quasi-static electric field curves for the PMN bar at zero prestress. Full line: measurements from Ref. 27; dark dots: finite element (model 1); white dots: finite element (model 2).

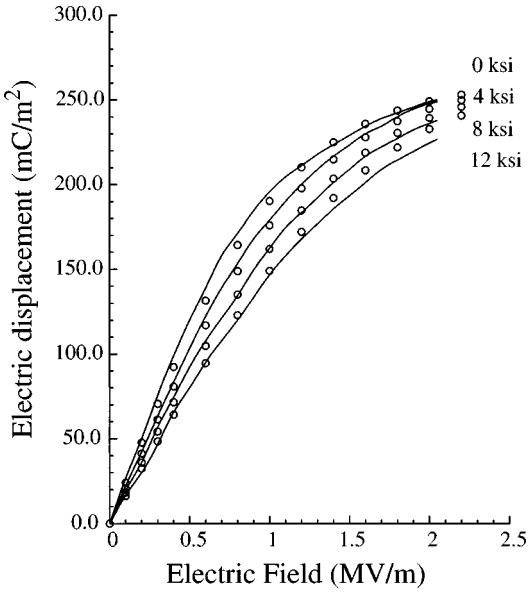

FIG. 7. Quasi-static electric displacement versus quasi-static electric field curves for the PMN bar submitted to various static mechanical prestresses. Full line: measurements from Ref. 27; white dots: finite element (model 2).

erations is 2, 6, 8, and 13 for prestresses of 0, 4, 8, and 12 ksi, respectively.

IV. CONCLUSION

The electrostrictive finite element described in this paper is based on constitutive laws which assume quadratic variation of the induced strain with the electric displacement and constant temperature, and neglects hysteretic effects. Two models are proposed taking or not taking the polarization saturation into account. The theoretical formulation of the electrostrictive finite element is justified by the weighted residuals method and leads to a nonlinear set of equations. The solution is obtained by solving iteratively a linear set of equations until convergence. The validation is performed by analyzing a PMN bar submitted to a static prestress and a quasi-static voltage. Numerical results are in very good agreement with experiments both at low electric field (models 1 and 2) and at high electric field (model 2). For simple geometries, model 1 can give closed form solutions. However, it is limited to applied electric fields lower than 0.6 MV/m. Model 2 is valid on the whole range of applied electric field, but it is more difficult to handle analytically. Further validation of the model requires comparison with mea-

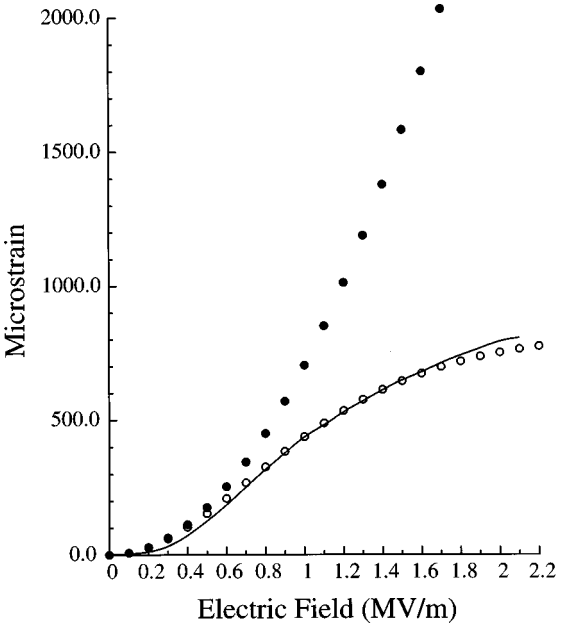

FIG. 6. Quasi-static strain versus quasi-static electric field curves for the PMN bar at zero prestress. Full line: measurements from Ref. 27; dark dots: finite element (model 1); white dots: finite element (model 2).

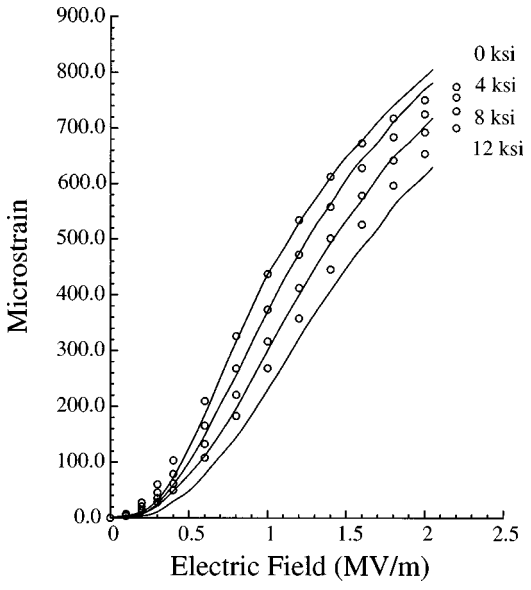

FIG. 8. Quasi-static strain versus quasi-static electric field curves for the PMN bar submitted to various static mechanical prestresses. The static strain due to mechanical prestress is not included. Full line: measurements from Ref. 27; white dots: finite element (model 2).

surements for tridimensionnal problems, i.e., for PMN samples of other shapes submitted to arbitrary mechanical or electrical loads.

ACKNOWLEDGMENTS

This work was supported by ONR under Contract No. 68171-95-M-6064 and by a DRET/DCN grant. The authors wish to thank Dr. R. Bossut of IEMN/ISEN for his help in developing the numerical procedure and Dr. M. D. McCollum and Dr. S. Black of NUWC/USRD for stimulating discussions.

[1] J. Kuwata, K. Uchino, and S. Nomura, ''Electrostrictive coefficients of $Pb(Mg1/3Nb2/3)O_3$ ceramics,'' Jpn. J. Appl. Phys. **19**, 2099–2103 (1980).
[2] L. E. Cross, ''Relaxor ferroelectrics,'' Ferroelectrics **76**, 241–267 (1987).
[3] W. Y. Pan, W. Y. Gu, D. J. Taylor, and L. E. Cross, ''Large piezoelectric effect induced by direct current bias in PMN: PT relaxor ferroelectric ceramics,'' Jpn. J. Appl. Phys. **28**, 653–661 (1989).
[4] S. M. Pilgrim, M. Massuda, J. D. Prodey, and A. P. Ritter, ''Electromechanical properties of some $Pb(Mg1/3Nb2/3)O_3$–$PbTiO_3$–(Ba, Sr)TiO_3 ceramics: I,'' J. Am. Ceram. Soc. **75**, 1964–1969 (1992).
[5] K. M. Rittenmyer, ''Electrostrictive ceramics for underwater transducer application,'' J. Acoust. Soc. Am. **95**, 849–856 (1994).
[6] K. Uchino, ''Electrostrictive actuators: materials and applications,'' Ceram. Bull. **65**, 647–652 (1986).
[7] S. M. Pilgrim, M. Massuda, J. D. Prodey, J. M. Hock, and A. P. Ritter, ''Electrostrictive sonar drivers for flextensional transducers,'' in *Transducers for Sonics and Ultrasonics*, edited by M. D. McCollum, B. F. Hamonic, and O. B. Wilson (Technomic, Lancaster, PA, 1993), pp. 95–102.
[8] C. H. Sherman and J. L. Butler, ''Analysis of harmonic distortion in electroacoustic transducers,'' J. Acoust. Soc. Am. **98**, 1596–1611 (1995).
[9] ATILA Finite-Element code for Piezoelectric and Magnetostrictive Transducer Modeling Version 5.1.1, User's Manual, Institut Supérieur d'Electronique du Nord, Acoustics Laboratory (1997).
[10] J.-N. Decarpigny, ''Application de la méthode des éléments finis à l'étude de transducteurs piézoélectriques'' (Application of the finite element method to the modeling of piezoelectric transducers), Doctoral thesis, Université des Sciences et Techniques de Lille, 1984.
[11] W. Voight, *Lehrbuch der Kristallphysik* (Leipzig, 1910).
[12] A. F. Devonshire, ''Theory of ferroelectrics,'' Philos. Mag. **3**, 85–130 (1954).
[13] C. L. Hom and N. Shankar, ''A fully coupled constitutive model for electrostrictive ceramic materials,'' J. Intell. Mater. Syst. Struct. **5**, 795–801 (1994).
[14] C. L. Hom, S. M. Pilgrim, N. Shankar, K. Bridger, M. Massuda, and S. R. Winzer, ''Calculation of quasi-static electromechanical coupling coefficients for electrostrictive ceramic materials,'' IEEE Trans. Ultrason. Ferroelectr. Freq. Control **41**, 542–551 (1994).
[15] J. C. Piquette and S. E. Forsythe, ''A nonlinear material model of lead magnesium niobate (PMN),'' J. Acoust. Soc. Am. **101**, 289–296 (1997).
[16] D. Damajanovic and R. E. Newhnam, ''Electrostrictive and piezoelectric materials for actuator applications,'' J. Intell. Mater. Syst. Struct. **3**, 190–208 (1992).
[17] W. P. Mason, *Piezoelectric Crystals and their Application to Ultrasonics* (Van Nostrand Princeton, 1950), Chap. XII.
[18] Z. Suo, ''Mechanical concepts for failure in ferroelectric ceramics,'' in *Smart Structures and Materials* (American Society of Mechanical Engineers, New York, 1991), AD-Vol. 24/AMD-Vol. 123, pp. 1–6.
[19] X. D. Zhang and C. A. Rodgers, ''A macroscopic phenomenological formulation for coupled electromechanical effects in piezoelectricity,'' J. Intell. Mater. Syst. Struct. **4**, 307–316 (1993).
[20] J. A. Lewis, Bell Syst. Tech. J. **60**, 1259 (1961).
[21] R. Holland and E. P. Eer Nisse, IEEE Trans. Sonics Ultrason. **15**, 119 (1968).
[22] H. Allik and T. J. R. Hughes, ''Finite element method for piezoelectric vibration,'' Int. J. Numer. Methods Eng. **2**, 151–157 (1970).
[23] R. Holland and E. P. Eer Nisse, *Design of Resonant Piezoelectric Devices*, Research monograph No. 56 (MIT, Cambridge, 1959).
[24] O. C. Zienkiewicz and R. L. Taylor, *The Finite Element Method* (McGraw–Hill, New York, 1989), 4th ed.
[25] J.-N. Decarpigny, J.-C. Debus, B. Tocquet, and D. Boucher, ''In-air analysis of piezoelectric Tonpilz tranducers in a wide frequency band using a mixed finite element-plane wave method,'' J. Acoust. Soc. Am. **78**, 1499–1507 (1985).
[26] J. M. Powers, E. A. McLaughlin, and M. B. Moffett, ''PMN measurements at NUWC,'' NUWC Report (1996).
[27] E. A. McLaughlin, J. M. Powers, M. B. Moffett, and R. S. Janus, ''Characterization of PMN-PT-La for use in high-power electrostrictive projectors,'' J. Acoust. Soc. Am. **100**, 2729 (1996).
[28] O. B. Wilson, *Introduction to Theory and Design of Sonar Transducers* (Peninsula, Los Altos, 1988).

Improving the bandwidth of 1-3 connectivity composite receivers using mode coupling

Anthony Gachagan and Gordon Hayward
Ultrasonics Research Group, University of Strathclyde, Glasgow G1 1XW, United Kingdom

(Received 18 August 1997; accepted for publication 29 January 1998)

Temporal resolution in an ultrasonic system may be enhanced by the application of mechanical damping to the transducer rear face, thereby reducing internal reverberation and increasing effective bandwidth. However, for thickness drive transducers, this is accompanied inevitably by a reduction in sensitivity and, moreover, manufacture of suitable damping blocks can be difficult, particularly for lower frequency, small signal applications such as the detection of gas coupled ultrasound. This work describes an interesting alternative approach that utilizes the relatively strong coupling between the fundamental thickness mode and first lateral mode in 1-3 connectivity piezocomposite transducers. Finite element modeling is used to evaluate the influence of mode interaction on electromechanical coupling efficiency, surface displacement, sensitivity, and bandwidth as functions of the ceramic pillar dimensions for operation into both water and air load media. A range of composite devices was constructed and close agreement between theory and experiment is demonstrated, with a measured device bandwidth of 130% centered at 1.15 MHz. An example of using such a device within a gas-coupled ultrasonic system is presented and the response is shown to compare favorably with alternative transducer configurations. © *1998 Acoustical Society of America.* [S0001-4966(98)03305-0]

PACS numbers: 43.38.Ar, 43.38.Fx [SLE]

INTRODUCTION

The resonance modes of vibration within 1-3 connectivity composite transducers are of significant interest for the transducer design engineer. As a result of the regular periodicity of the piezoelectric ceramic pillars within this structure, a number of mechanisms exist to support both thickness and lateral modes and hence the design process becomes quite complex.[1–5] The three classifications of lateral vibrational mechanisms are width-dilational, interpillar, and intrapillar modes, where the inter- and intrapillar modes are of most significance for the design of high-frequency ultrasonic transducers. Interpillar resonances arise due to the periodic spacing of the piezoelectric ceramic pillars within the structure and are influenced by the ceramic pillar separation, shape, and the shear velocity in the passive phase. These vibrational modes present design problems for low ceramic volume fraction composites, where the lateral activity may degrade the desired thickness mode. Intrapillar resonances arise as a consequence of the finite dimensions of the ceramic pillars and can create difficulties in the manufacture of high ceramic volume fraction devices

Considerable data has been reported on the resonances generated within the 1-3 composite structure. For example, Gururaja *et al.* described the mechanism for each resonance mode observed within a composite transducer and discussed their implication for optimization of transducer designs.[1] This was further extended by Smith[2] and Auld,[3] with the work being supported subsequently by various finite element investigations of the microstructural behaviour.[4–7] The essential output has been a set of design guidelines to promote homogeneous behavior by ensuring that both the interpillar and intrapillar resonances are sufficiently decoupled from the fundamental thickness mode resonance. For example, Smith *et al.* reported that these resonance modes should occur at a frequency at least twice that of the desired thickness mode.[2] Auld and Wang used a theory based on Bragg scattering to predict the resonance frequency of the interpillar vibrational mode.[3] Chan *et al.* have described the mode coupling between the lateral and thickness resonances, as the thickness of the transducer was varied.[8] In this case it was concluded that as the aspect ratio (the ratio of pillar width to height) increased, there was a frequency band where strong mode coupling occurred and, consequently, the transducer should operate such that the fundamental thickness mode resonance lies outwith this region.

The present work describes an alternative design methodology which utilizes maximum mode coupling to enhance the bandwidth of piezoelectric composite devices operating as receivers of ultrasound. For a given composite device, as the ceramic pillar aspect ratio is increased, the coupling between the fundamental thickness mode and the first lateral resonance also increases. When the two resonances are in close proximity, it is shown that they combine to produce a single broadband peak in the transducer frequency spectrum. The stimulus for the investigation was to develop a broadband air-coupled piezoelectric receiver to complement the high resolution afforded by laser generation of ultrasound[9] and hence experimental validation is presented for the detection situation. A PZT5A/CIBA-GEIGY CY1301-HY1300 (Shore 80) epoxy 1-3 connectivity piezoelectric composite receiver, with a ceramic volume fraction of 20%, was used throughout, in accordance with the design guidelines described in Refs. 5 and 10. This composite transducer configuration, comprising a regular array of square piezoelectric ceramic pillars embedded within an epoxy matrix, will be referred to as a 20% composite throughout the text. The ini-

 0001-4966/98/103(6)/3344/9/$10.00

tial design assessment in terms of electromechanical coupling efficiency and surface displacement characteristics was performed via finite element modelling using the ANSYS[11] code. The fractional bandwidth was then evaluated for a range of 20% composite receivers, with aspect ratios ranging from 0.1–0.37, under both undamped and damped conditions. Favorable correlation with experimental data was obtained. First experiments were conducted under water loading conditions and a piezoelectric polymer (PVDF) transmitter was used to generate a wideband ultrasonic signal for evaluation of reception performance. The modeling was then extended to analyze the bandwidth improvement for composite receivers operating in the air environment. Subsequently, a mode-coupled composite receiver was manufactured and observed to perform according to theoretical expectations as a wideband detector of through-air generated ultrasound.

I. METHODOLOGY

To quantify the bandwidth characteristic for the new piezoelectric composite receivers, a broadband polyvinylidene fluoride (PVDF) ultrasonic source was employed. The use of PVDF was considered appropriate, as a consequence of its wide potential bandwidth, and reasonable specific acoustic impedance match to both air and water. In addition, PVDF transducers can be constructed to minimize edge diffraction, thus approximating well to an ultrasonic plane wave source.[12] Earlier work by the authors utilized a PVDF transmitter to deliver a wideband pressure pulse for the characterisation of air-coupled transducers, operating between 500 kHz and 1 MHz.[13] Using simulation data, the impulse response of an air-coupled 25-μm PVDF transmitter was shown to comprise a unipolar pressure wavelet, bandlimited due to attenuation in the propagation medium, which acts as an effective low pass filter. For the present work, unidimensional modeling[14] was used to predict the pressure profile from a 25-μm PVDF transmitter, driven by a Panametrics 5052 PR pulser/receiver unit, in both air and water loads. Figure 1(a) and (b) illustrates the predicted pressure temporal and spectral characteristics, at a propagation distance of 20 mm, where each has been normalized (factor of 48) to assist interpretation. For an air propagation distance of 20 mm, the resultant unipolar pressure profile has a center frequency of 1.3 MHz, while the corresponding impulse response in water is centred at approximately 20 MHz. As indicated in Ref. 13, these pressure profiles are considered adequate to obtain the frequency response characteristics for the range of transducers under investigation.

The experimental configuration is shown in Fig. 2, where the PVDF transmitter is fixed and the receiving transducer attached to a manipulator. In all experiments, the PVDF transducer was driven by a Panametrics 5052 PR pulser/receiver unit, which produces a unipolar voltage function, characterized by a 30-ns triangular spike delivered through a 50 Ω source resistance. For the air-coupled experiments, the receiving transducer was interfaced to a high-gain preamplifier (90 dB) with an input resistance of 1 MΩ and a -3-dB bandwidth of 6 MHz. All coaxial cabling connections between the transducers and electronic equipment were

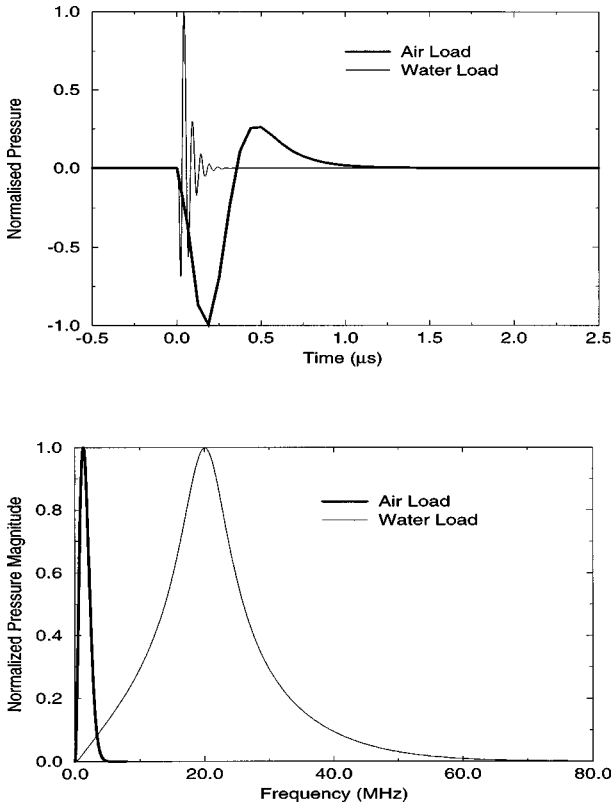

FIG. 1. Predicted pressure response from a PVDF transmitter, operating into both air and water loads, at a propagating distance of 20 mm. (a) Temporal response. (b) Spectral response.

1.2 m in length. A glass water tank was used throughout, providing a convenient enclosure to minimize the influence of air currents in the final experimental phase.

A unidimensional, linear systems model[14] was used to illustrate the conventional situation, whereby reception bandwidth and sensitivity may be controlled by means of mechanical damping at the transducer rear face. Using the air-coupled PVDF transmitter described previously, the open circuit receive voltage response for a 20% piezoelectric composite receiver with three different loading conditions are shown in Fig. 3, corresponding to low damping (air backing), medium damping (backing impedance is 50% of composite impedance), and high damping (backing impedance is 100% of composite impedance). The receiver, comprising an array of PZT5A pillars embedded within a CIBA-GEIGY CY1301/HY130 epoxy matrix, was designed to operate at 1

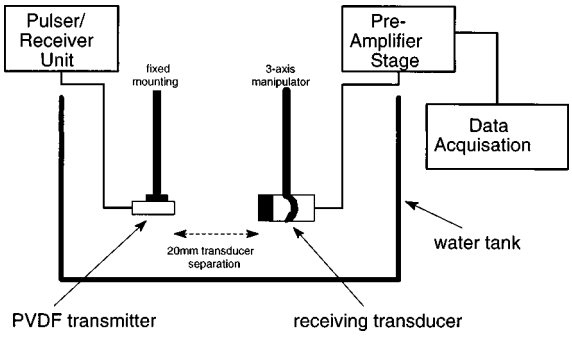

FIG. 2. Experimental arrangement.

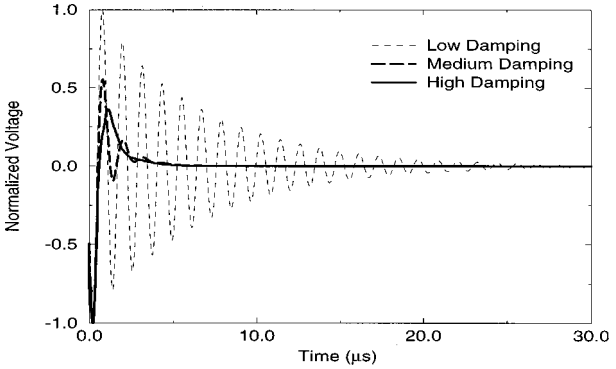

FIG. 3. Predicted temporal receive responses for a 20% composite under various damping conditions.

MHz, which for the 20% composite corresponds to a thickness of 1.75 mm and a specific acoustic impedance of 8.6 MPa·s/m. This figure demonstrates the influence of the increased damping conditions on the pulse length, where a short single cycle pulse has been predicted for high damping compared to over 25 cycles under no damping conditions. As anticipated, a reduced peak-to-peak receive sensitivity for the 100% damped transducer (-9.4 dB) has been predicted compared to the undamped case. The medium damping conditions are a compromise between these two conditions, where a five-cycle pulse is predicted with a 4.1 dB reduction in receive sensitivity. The corresponding fractional bandwidths, expressed as a percentage of the 1-MHz center frequency, are 8%, 34%, and 107% for low, medium, and high damping, respectively.

Although the linear systems approach is useful for the prediction of design trends, it is not appropriate for investigation of composite behavior where mode coupling is involved. The commercial finite element package used for this work was ANSYS v5.0A and, within the code, a multifield solid element and a standard isotropic solid element are employed to model the active piezoelectric ceramic and inactive polymer phases, respectively. These are both eight-node brick elements in which three-dimensional nodal displacements are the degrees of freedom for the system. Additionally, each node of the multifield element has voltage as the degree of freedom. The constructed model utilized a full-height quarter-symmetry, harmonic analysis model for the 1-3 connectivity piezoelectric composite element, attached to a backing block at the rear face. Within the ANSYS code it is assumed that the device operates into a vacuum. Therefore no additional loading mechanism is required for air-coupled simulations because the specific acoustic impedance of air is close to that of a vacuum, when compared to the relatively high specific acoustic impedance of a composite transducer. Fluid-loaded simulations require the introduction of a fluid column, at the transducer front face, to enable analysis under realistic loading conditions. Here the open end of the fluid column was forced to have zero pressure and includes an absorbing boundary to simulate a medium extending to infinity.[15]

The analysis produces the complex charge, $\hat{Q}(\omega)$, as a reaction to the input voltage, $\hat{V}(\omega)$, allowing the electrical impedance, $\hat{Z}_T(\omega)$, to be calculated as

$$\hat{Z}_T(\omega)=\frac{\hat{V}(\omega)A_{\text{cell}}}{j\omega\hat{Q}(\omega)A_{\text{total}}}, \tag{1}$$

where A_{cell} and A_{total} are the surface areas of the unit cell and physical transducer, respectively.

With 1-3 piezoelectric composites, the displacement across the surface is not constant as the ceramic pillars may demonstrate different displacements from the passive regions of the transducer. An indicator of surface displacement uniformity is the dilation quality factor, Q_{dil}, which is defined as

$$Q_{\text{dil}}=\frac{\Sigma_{i=1}^{N} d_i A_i}{A_{\text{cell}} d_{\max}}, \tag{2}$$

where A_i is the area surrounding node i, N is the number of surface nodes, $d_{\max}$ is the maximum nodal displacement of the cell, and d_i is the nodal displacement in the thickness direction of the ith surface node.

Under open circuit receive conditions, $\hat{V}_{\text{out}}(\omega)$ is the complex output voltage generated by the complex pressure, $\hat{p}_{\text{ln}}(\omega)$, impinging on the whole front surface of the transducer, giving the receive sensitivity, $S_{RX}(\omega)$, as

$$S_{RX}(\omega)=\left|\frac{\hat{V}_{\text{out}}(\omega)}{\hat{p}_{\text{in}}(\omega)}\right|. \tag{3}$$

It should be noted that the finite element code implements the mechanical stimulation under ideal voltage drive conditions (zero source impedance), as the ANSYS code cannot readily incorporate accurately the actual electrical stimulation circuitry.

Previous work by the authors indicates that a 20% PZT5A/CIBA-GEIGY CY1301-HY1300 epoxy composite transducer will operate well as an air-coupled receiver, without recourse to mechanical matching.[10] A selection of the relevant material properties for both the active and passive phases are presented in Table I. For the present work, the ceramic pillar width (0.22 mm) and kerf width (0.32 mm) were maintained constant and the transducer thickness varied between 0.6 and 2.2 mm, resulting in a spread of aspect ratios from 0.37 to 0.1, respectively. The manufacturing specifications were chosen to support the first diagonal interpillar mode at approximately 2 MHz. Table II describes the thickness, fundamental mechanical resonance (f_n), and electromechanical coupling efficiency (k_t) for the range of transducers constructed. The composite receivers were evaluated under both low and medium damping conditions, with the latter achieved by bonding a 40-mm-thick Plexiglas block, conically shaped to minimize internal reflections, to the transducer rear faces. Each device was then housed in a water-proofed aluminum casing.

II. COMPARISONS BETWEEN THEORY AND EXPERIMENT

A. Impedance profiles

In order to validate the resonance positions and the trends in mode shifting as the transducer dimensions vary, the finite element method was used to predict electrical im-

TABLE I. Constituent material properties for both PZT5A and CIBA-GEIGY CY1300-HY1301.

	Dielectric constant, ϵ_{33}/ϵ_0	Young's modulus, Y	Poisson ratio, σ	Density, ρ
CY1300/HY1301	4.0	4.10×10^9 N/m^2	0.37	1132 kg/m^3
	Stiffness matrix (10^{10} Pa^{-1})			
	c_{11}^E	c_{12}^E	c_{13}^E	c_{33}^E	c_{44}^E
PZT5A	12.0	7.52	7.51	11.1	2.11
Density	Piezoelectric coefficients (C·m^{-1})			Dielectric constants	
ρ	e_{13}	e_{33}	e_{15}	$\epsilon_{11}^s/\epsilon_0$	$\epsilon_{33}^s/\epsilon_0$
7750 kg/m^3	−5.4	15.8	12.3	916	830

pedance as a function of frequency. For example, Fig. 4(a) illustrates the impedance magnitude profile (in air) for the undamped composite with a pillar aspect ratio of 0.196, while Fig. 4(b) depicts the corresponding data for a device possessing an aspect ratio of 0.234 and loaded by a Plexiglas backing block. In each case the impedance data, presented in logarithmic format and referenced to 1 Ω (Z_{ref}), was measured in air and demonstrates reasonable correlation with theory. It should be noted that the finite element code permits only one damping parameter to be associated with each material. Consequently, analysis of both thickness and lateral modal behavior requires a compromise in the value chosen for the longitudinal and shear damping coefficients. Notwithstanding, these figures serve to illustrate mode coupling, where the close proximity of both the fundamental thickness and interpillar resonance is clearly evident.

B. Coupling between the fundamental thickness and interpillar resonances

One of the authors[4] has used finite element methods to investigate coupling between the fundamental resonance and the interpillar resonances and hence evaluate the maximum pillar aspect ratio (MPAR) conditions which will permit the composite to behave as a homogeneous medium. For a 20% composite device, the MPAR criteria ensure that the first lateral resonance is at least double the frequency of the fundamental thickness mode when the aspect ratio is less than 0.17. Using the modeling methods described in Ref. 4, the influence of mode coupling on the first two resonance frequencies (measured at the impedance maxima—the mechanical resonance), electromechanical coupling coefficient, and surface dilation quality (also measured at the mechanical resonance) were predicted and compared with experimental data. The mechanical resonance was selected because the present work is primarily concerned with reception characteristics and, under open circuit conditions, the composite receivers are expected to demonstrate maximum fundamental thickness mode voltage response at this frequency. The results are shown in Figs. 5 and 6, in which good correlation is evident.

Figure 5(a) illustrates the relative positions of the fundamental thickness and first lateral resonances. As anticipated, the frequency of the fundamental thickness mode increases almost linearly as the aspect ratio is increased. When these modes are well separated, i.e., for aspect ratios less than 0.2, the lateral resonance remains relatively constant. As the aspect ratio is increased, mode coupling then forces the first

TABLE II. Properties of manufactured 20% composite transducers.

Aspect ratio	0.1	0.126	0.141	0.177	0.196
Thickness (mm)	2.17	1.74	1.56	1.24	1.12
f_n(MHz)	0.77	0.96	1.13	1.28	1.48
k_t	0.541	0.532	0.534	0.514	0.473
Aspect ratio	0.216	0.234	0.262	0.301	0.367
Thickness (mm)	1.02	0.94	0.84	0.73	0.61
f_n(MHz)	1.68	1.77	1.82	2.06	2.38
k_t	0.441	0.386	0.375	0.356	0.287

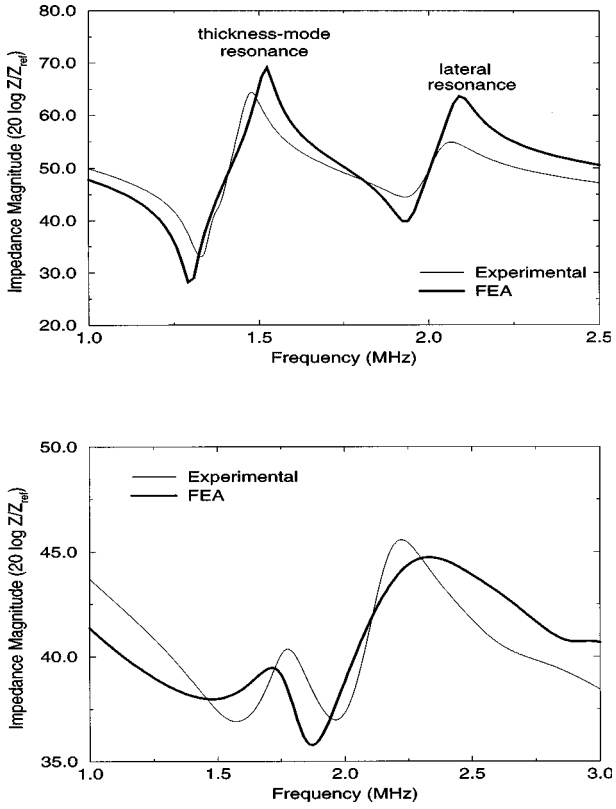

FIG. 4. (a) Impedance profile for an undamped 20% composite transducer, with aspect ratio 0.196. (b) Impedance profile for a damped 20% composite transducer, with aspect ratio 0.234.

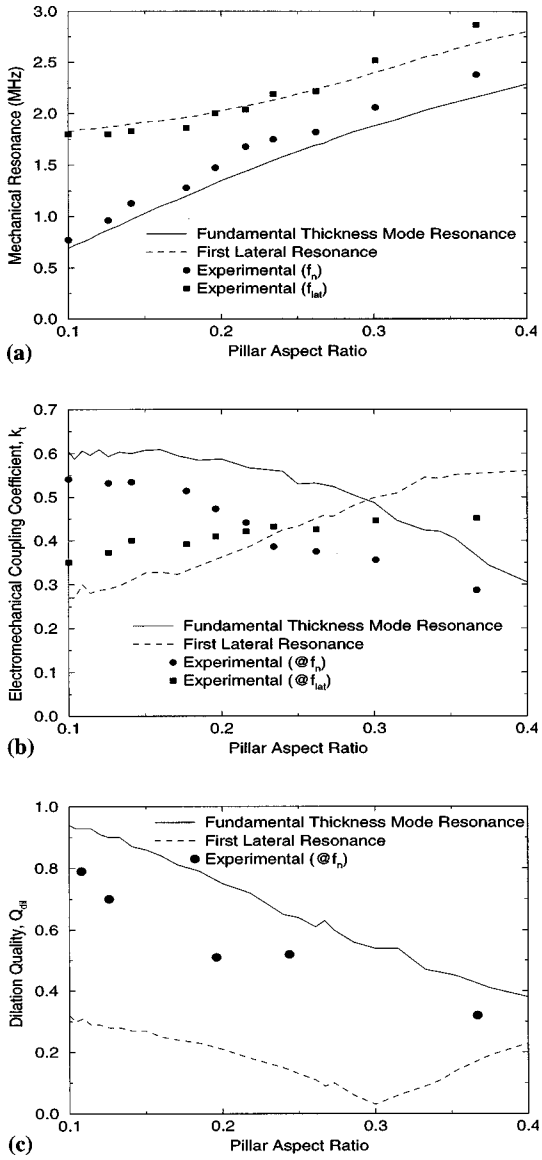

FIG. 5. Transducer characteristics as a function of aspect ratio for a 20% PZT5A/CIBA-GEIGY CY 1301-HY 1300 composite transducer: (a) mechanical resonance frequencies, (b) electromechanical coupling efficient, and (c) dilation quality at the mechanical resonance.

lateral mode to a higher frequency. The influence of mode coupling on the electromechanical coupling coefficient is shown in Fig. 5(b). Estimated values of k_t for the fundamental thickness resonance are observed to decrease with increasing pillar aspect ratio. In contrast, the coupling of the lateral mode increases until this resonance is dominant. There is an observable difference between the experimentally measured and theoretical crossover points, as the experimentally acquired values are lower than those predicted. This is believed to arise as a consequence of some ceramic depolarization during the slicing process and practical difficulties in extrapolating the exact resonance positions from experimental impedance characteristics. Corresponding data for surface dilation quality is outlined in Fig. 5(c), where Q_{dil} is shown to decrease generally as a function of aspect ratio, although the lateral mode does demonstrate some improvement after the crossover point. Experimental data, measured using a scanning laser vibrometer (Polytec single point interferometer, OFV-302, and displacement decoder, OVD-30), is in good agreement, although somewhat lower than that predicted by the finite element theory.

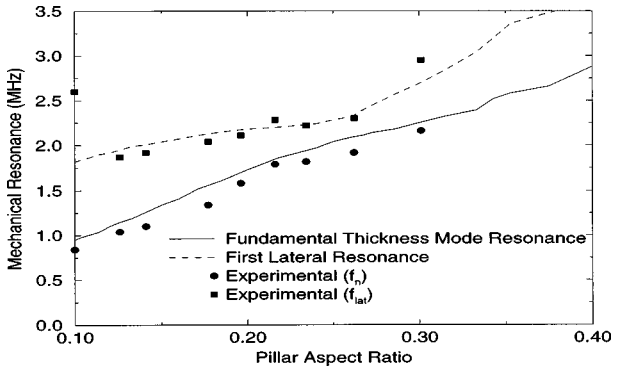

FIG. 6. Mechanical resonance frequencies as a function of aspect ratio for a 20% PZT5A/CIBA-GEIGY CY 1301-HY-1300 composite transducer, under medium damping conditions.

The application of mechanical damping to the rear face of the composite transducer results in a slightly different relationship between the thickness and lateral resonance mechanisms, when compared to the undamped case illustrated in Fig. 5(a). The mechanical resonances for the range of medium damped composite devices are shown in Fig. 6, where good correlation between theory and experiment has again been achieved. For an aspect ratio of 0.234, the predicted values for the fundamental thickness and first lateral resonances are separated by only 25 kHz, compared to approximately 50 kHz for the undamped case. Therefore, the application of mechanical damping to the rear face of the composite may be considered to increase the effective coupling between the two modes. There are no experimental entries for the composite transducer with an aspect ratio of 0.37 in Fig. 6, due to difficulty in positive identification of the relevant modes.

C. Lateral coupling under fluid loading

The peak-to-peak receive voltage sensitivity and bandwidth for the range of undamped transducers were measured experimentally under water load. Reasonable correlation may be observed between the experimental and the corresponding theoretical results shown in Fig. 7. Although not shown, it is interesting to note that the unidimensional linear

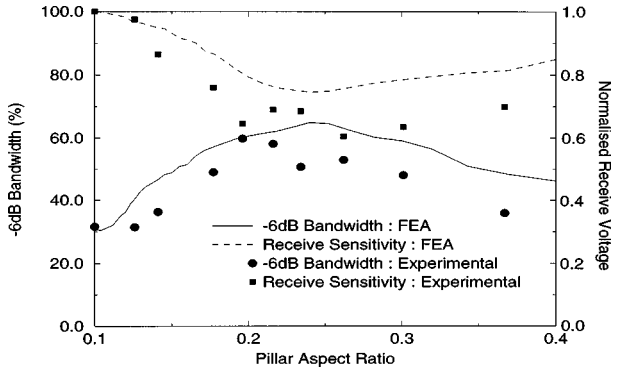

FIG. 7. Bandwidth and sensitivity characteristics for 20% composite transducers under water loading.

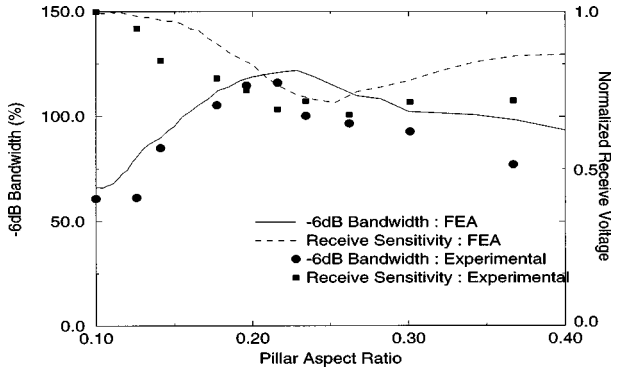

FIG. 8. Bandwidth and sensitivity characteristics for 20% damped composite transducers under water loading.

systems model predicts a fractional bandwidth of 27%, which is close to both the FEA and experimental results for an aspect ratio of 0.1, which is approximately 31%. It is to be expected, as the results from the previous section indicate, that the transducer is effectively unimodal at this geometry. As the aspect ratio is increased, the experimental transducer bandwidth peaks at a maximum value of 60% corresponding to an aspect ratio of 0.196. The corresponding receive sensitivity is 3.75 dB down compared to the maximum under unimodal conditions.

The receive sensitivities and bandwidths for those situations where the composite transducers were subject to mechanical damping at the rear face are compared in Fig. 8 and this again illustrates good agreement between theory and experiment. However, as expected, the bandwidth for the lowest aspect ratio composite has increased to 66% compared with 31% for the unbacked case. The experimental transducer bandwidth peaks at a value of 116% for an aspect ratio of 0.216 and the subsequent receive sensitivity is reduced by 3.25 dB over a device with an aspect ratio of 0.1. As was the case for the undamped transducer, maximum device bandwidth appears to occur in the vicinity of the aspect ratio that generates maximum mode coupling and these trends are also supported by the theoretical modeling. To illustrate what this implies in terms of received signal quality, the experimental time and frequency domain characteristics of the 0.1 and 0.216 aspect ratio devices are shown in Fig. 9(a) and (b), respectively. In Fig. 9(a), the lower operating frequency of the thicker transducer (0.1) is clearly evident and the measured -6-dB bandwidth from Fig. 9(b) is approximately 66%, centered around 780 kHz, the expected fundamental thickness mode mechanical resonance frequency. The 0.216 aspect ratio composite has a shorter pulse length, as a consequence of both its slightly higher operating frequency and increased mode coupling. In this case the device has a -6-dB bandwidth of 116%, centered around 2.15 MHz.

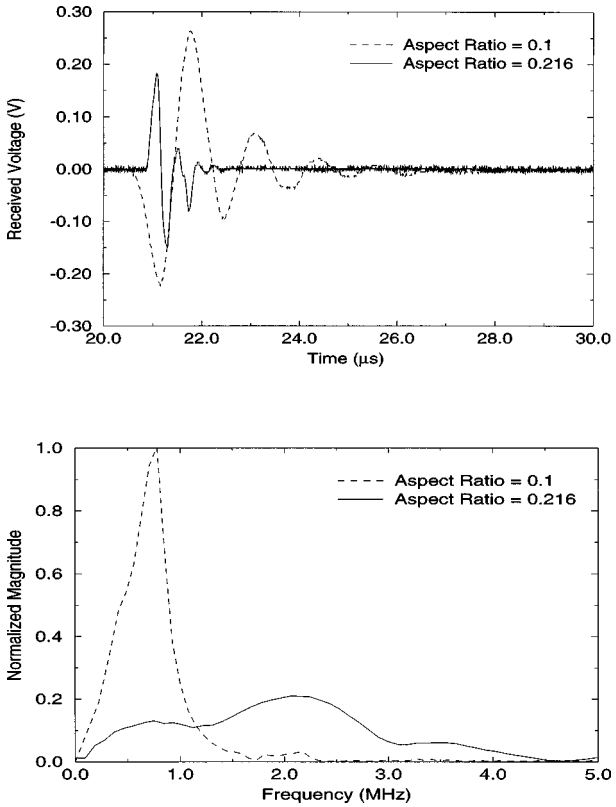

FIG. 9. (a) Experimentally acquired temporal response for transducers, with different aspect ratio, under water load conditions. (b) Corresponding spectral response for temporal responses shown in (a).

tively small amount of damping at the rear face could be beneficial in promotion of mode coupling and hence extending device bandwidth. The subsequent bandwidth and sensitivity variation as a function of pillar aspect ratio are shown in Fig. 10, from which the fractional bandwidth is observed to peak at 86%, for an aspect ratio of approximately 0.24. This corresponds to a -6 dB bandwidth of 1.65 MHz, centered around 1.92 MHz. The open circuit receive sensitivity has been reduced by 3.7 dB when compared with the theoretical maximum (at 0.1 aspect ratio) on the graph. Interestingly, these values compare favorably with the 9.4-dB reduction in sensitivity and 107% bandwidth that would be expected by means of conventional 100% damping as described in Sec. I.

III. EVALUATION OF RECEIVER PERFORMANCE IN AIR

A. Simulation of bandwidth improvement

The FEA analysis was used to investigate the composite receivers, under medium damping conditions, for operation in the air environment. As suggested previously, the rela-

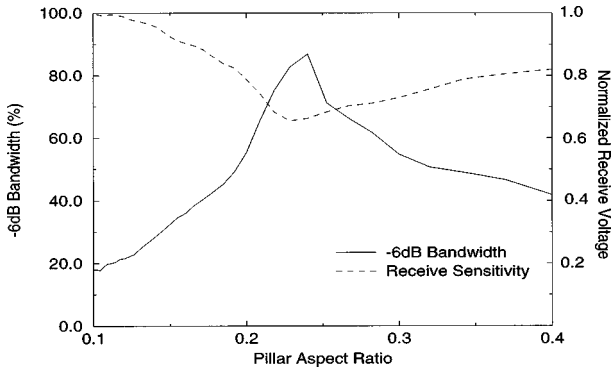

FIG. 10. Bandwidth and sensitivity characteristics for 20% composite transducers, with varying aspect ratios, under ideal impulsive conditions.

TABLE III. Properties for manufactured air-coupled composite transduers.

Composite	Thickness (mm)	Aspect ratio	Resonance	Mechanical resonance (MHz)	k_t
Thickness mode	0.9	0.108	thickness	1.97	0.525
Laterally coupled	0.9	0.244	thickness lateral	1.63 2.11	0.386

B. Construction of air-coupled composite receivers

A 20% composite receiver, with an aspect ratio of 0.24, was constructed using the FEA prediction for maximum bandwidth, as observed in Fig. 10. To complement the evaluation of this device, a corresponding 'thickness-mode' composite, possessing an aspect ratio of 0.1, was also manufactured and lapped to an identical thickness. Both transducers were cut from a common block of PZT5A and potted from the same mix of CIBA-GEIGY CY1300/HY1301 epoxy resin. The electromechanical coupling efficiency, k_t, mechanical resonances, f_n and f_{lat}, and the device dilation quality, Q_{dil}, were all measured prior to the application of a Plexiglas backing block to the rear face of the transducers. These details are presented in Table III. Although the thickness of each device has been maintained constant, the fundamental thickness mechanical resonances are different, as a consequence of the enhanced coupling with the lateral mode in the higher aspect ratio device. As anticipated, the fundamental thickness electromechanical coupling coefficient for the laterally coupled composite is lower than that of the ''unimodal'' transducer.

It is interesting to compare the surface displacement profiles for the two composite transducers described in Table III. A Polytec single point interferometer (OFV-302) and displacement decoder (OVD-30) were used to acquire out-of-plane displacement from the surface of the transducers. The focused spot size from the interferometer was 25 μm. A precision manipulator, capable of 1-μm resolution, was utilized to scan the transducer in front of the laser interferometer. Each transducer was driven by a ten-cycle tone burst centered at its mechanical resonance frequency. The composite transducer with an aspect ratio of 0.108 has a 97-μm pillar width, and a step size of 30-μm was considered adequate to scan the transducer microstructure. Corresponding data sections are illustrated in Fig. 11(a) and (b) for the 0.108 and 0.244 aspect ratio devices, respectively, where the lighter shading indicates a higher surface displacement. In Fig. 11(a), the attachment to the front face electrode can be seen in the top right-hand corner. There are also some localized low intensity areas to the left of this point. However, the transducer has a reasonable overall uniformity, which is apparent in the measured dilation quality of 0.79. In fact, it is difficult to differentiate between the piezoelectric ceramic pillars and the epoxy filler material. For the higher aspect ratio composite, shown in Fig. 11(b), a quite different response has been acquired. Here, the matrix of square pillars is clearly evident, although adjacent pillars have different displacement values. In addition, the polymer filler material has a lower displacement value, indicated by the darker shading, compared to the ceramic pillars. Clearly, the device is not acting as a homogeneous medium and, consequently, the measured dilation quality for this transducer was 0.52.

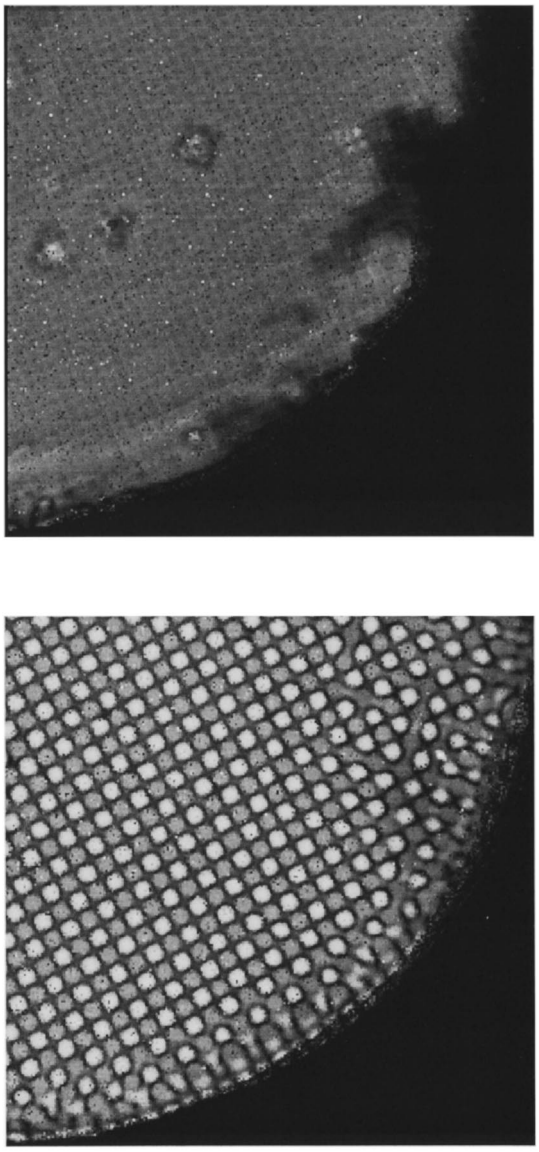

FIG. 11. (a) Laser vibrometer scan for the 20% composite transducer (aspect ratio of 0.108). (b) Laser vibrometer scan for the 20% composite transducer (aspect ratio of 0.244).

C. Experimental results

The receive performance of the laterally coupled composite was evaluated in conjunction with the 'thickness-mode' composite, described in Table III, and an electrostatic transducer. Comparison between the two composite transducers permitted measurement of the bandwidth improvement of the laterally coupled receiver, whereas the electrostatic device was used to facilitate evaluation with a conventional wideband air-coupled transducer. The electrostatic transducer was constructed from 2.5 μm Mylar film stretched across a polished steel backplate, with an average roughness of 3 μm.[13] A 120-V bias voltage was applied to the device in order to tension the film onto the backplate. A shaped Plexiglas backing block was bonded onto the rear

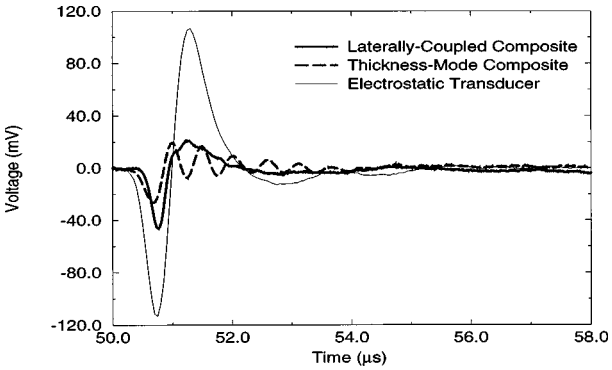

FIG. 12. Experimentally acquired signals detected by three different air-coupled wideband receivers.

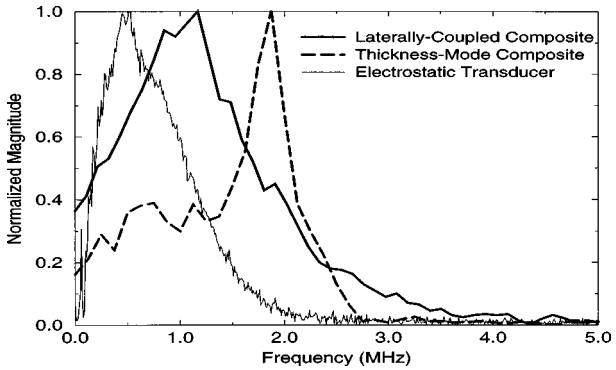

FIG. 13. Comparison of the spectral characteristics for the air-coupled detectors under investigation.

face of the two composite transducers, thus the 0.244 aspect ratio composite construction corresponds to the FEA prediction from Sec. III A. As described in Sec. II, a PVDF transmitter was utilized to provide a ''unipolar'' pressure wavelet at the front face of the air-coupled receivers. The receive sensitivity and bandwidth of the transducers were acquired at an air separation distance of 20 mm.

The receive temporal responses acquired by the three transducers are illustrated in Fig. 12. The laterally coupled composite has realized an excellent bandwidth in the form of an almost unipolar response. This signal is in excellent agreement with the predicted incident pressure wavelet, illustrated in Fig. 1(a), confirming the wideband nature of this composite transducer. In addition, the signal acquired by the 'thickness-mode' composite reveals good correlation with the unidimensional model prediction for a 20% composite under medium damping conditions, as presented in Fig. 3. Moreover, the 'thickness-mode' composite demonstrates a reduced bandwidth, compared to the laterally coupled composite, as evidenced by the increasing ringing in the received signal. It is also apparent that the peak-to-peak received signal level from the 'thickness-mode' composite is lower than that produced by the laterally coupled composite. This is a consequence of the realizable bandwidth of the incident pressure wavelet, where the influence of airborne attenuation has reduced the magnitude of frequency components above approximately 1.3 MHz. In fact, the 1.8 MHz spectral component is 1.94 dB down on the peak spectral component, at 1.3 MHz. Interestingly, the receive sensitivity for the electrostatic transducer has outperformed both composite transducers. This is to be expected, as no mechanical matching layers were attached to the composite transducers for these experiments. Reasonable bandwidth is demonstrated, but the acquired pulse is not as compact as the laterally coupled response.

In order to appreciate fully the bandwidth for each of these detectors, Fig. 13 presents a comparison of the receive spectral characteristics calculated from the signals shown in Fig. 12. The results shown in this figure have been normalized in order to facilitate logical comparison of the bandwidth characteristics. The influence of airborne attenuation is evident in the lack of high-frequency components above 2.5 MHz. The laterally coupled composite transducer has a better -6-dB bandwidth characteristic of 1.5 MHz, centered around 1.15 MHz, compared to 825 kHz, centered around 500 kHz, for the electrostatic transducer. The resonant behavior of the thickness drive composite is illustrated in the spectral peak at approximately 1.8 MHz. It is interesting to note that the finite element modeling predicted an absolute frequency bandwidth of 1.65 MHz for a laterally coupled composite with an aspect ratio of 0.24, which is in good agreement with the experimentally measured value.

IV. CONCLUSIONS

This paper has demonstrated a novel technique to improve the bandwidth for 1-3 connectivity piezoelectric composite transducers, operating in reception. Strong coupling between the fundamental thickness and first lateral resonances, in a damped composite device, may be used to extend the transducer bandwidth characteristic. Finite element analysis has been utilized to investigate this effect, where reasonable correlation was demonstrated with experimentally acquired data, under water load conditions. It is important to note that the maximum bandwidth was obtained in the region of maximum coupling between the fundamental thickness and first lateral resonances and when the electromechanical coupling coefficients of both resonance modes are equally strong. In addition, damping applied to the rear face of the transducer enhances the coupling between these two resonance modes. The modeling techniques were then extended to evaluate air-coupled performance and, subsequently, design for a wideband air-coupled composite receiver was proposed.

In order to attain a high bandwidth performance from a piezoelectric composite transducer, reverberation within the device must be minimized. Conventionally, this is achieved by attaching an appropriate damping medium to the rear face of the device. For the transducers employed in this study, a Plexiglas backing medium was utilized and shown to increase the coupling between the fundamental thickness and first lateral modes. Although, the acoustic mismatch between the piezoelectric composite transducer and the Plexiglas block will only partially reduce the reverberation and, consequently, the characteristic time response should reverberate for several cycles. In order to achieve the bandwidth response demonstrated by the laterally coupled composite transducer, a secondary effect must take place. As stated earlier, the point of maximum bandwidth corresponds to the

region where both resonance modes are equally strong. Consequently, at this point the charge generated by the lateral mode could cancel out the charge due to the thickness-drive reverberation. This hypothesis holds true for the results presented in this paper for the range of 20% 1-3 connectivity piezoelectric composite transducer that were evaluated. This concept requires a more rigorous investigation to fully evaluate the physical interaction between the thickness and lateral resonances. It is envisaged that this further analysis, using an upgraded version of the ANSYS finite element package, will be reported in the near future.

The proposed design for a wideband air-coupled composite receiver was constructed and the bandwidth improvement verified experimentally. This device exhibits an enhanced -6-dB bandwidth when compared with both a 'thickness-mode' composite and an electrostatic of comparable ''center'' frequency. For the stated application, adequate sensitivity was maintained, albeit with a lower efficiency than demonstrated by the electrostatic transducer. The air-coupled signal acquired using the wideband composite transducer compares very favorably with the predicted pressure wavelet incident on the front face of the device.

Finally, because of the specific application, this paper has concentrated on the composite transducer performance in reception. Further work would provide an insight into the influence of mode coupling on piezoelectric composite transmitter operation. An initial investigation, using the same range of 20% composite transducers, was not successful as a consequence of the low transmit sensitivity associated with a 20% composite operating in air.[10] For transmission, higher volume fractions are to be preferred (60%–80%). A similar analysis to that performed here would indicate if bandwidth enhancements via mode coupling is possible over this range.

[1] T. R. Gururaja, W. A. Schulze, L. E. Cross, R. E. Newham, B. A. Auld, and Y. J. Wang, ''Piezoelectric composite materials for ultrasonic transducer applications. Part I: Resonant modes of vibration of PZT rod-polymer composites,'' IEEE Trans. Sonics Ultrason. **SU-32**(4), 481–498 (1985).

[2] W. A. Smith, A. Shaulov, and B. A. Auld, ''Tailoring the properties of composite piezoelectric materials for medical ultrasonic transducers,'' Proceedings of IEEE Ultrasonics Symposium, Chicago, IL (1988), pp. 617–622.

[3] B. A. Auld and Y. J. Wang, ''Acoustic wave vibrations in periodic composite plates,'' Proceedings of IEEE Ultrasonics Symposium, Dallas, TX, (1984), pp. 528–532.

[4] G. Hayward and J. Bennett, ''Assessing the influence of pillar aspect ratio on the behaviour of 1–3 connectivity composite transducer,'' IEEE Trans. Ultrason. Ferroelectr. Freq. Control **43**(1), 98–108 (1996).

[5] G. Hayward, J. Bennett, and R. Hamilton, ''A theoretical study on the influence of some constituent material properties on the behaviour of 1–3 connectivity composite transducers,'' J. Acoust. Soc. Am. **98**, 2187–2196 (1995).

[6] J. A. Hossack and G. Hayward, ''Finite-element analysis of 1–3 composite transducers,'' IEEE Trans. Ultrason. Ferroelectr. Freq. Control **38**(6), 618–629 (1991).

[7] R. Lerch, ''Simulations of piezoelectric devices by two- and three-dimensional elements,'' IEEE Trans. Ultrason. Ferroelectr. Freq. Control **37**(3), 233–247 (1990).

[8] H. L. W. Chan, J. Unsworth, and T. Bui, ''Mode coupling in modified lead titanate/polymer 1–3 composites,'' J. Appl. Phys. **65**(4), 1754–1758 (1989).

[9] W. M. D. Wright, D. A. Hutchins, G. Hayward, and A. Gachagan, ''Polymer composite material characterisation using a laser/air-transducer system,'' Ultrasonics **34**(8), 825–833 (1996).

[10] G. Hayward and A. Gachagan, ''An evaluation of 1-3 connectivity composite transducers for air coupled applications,'' J. Acoust. Soc. Am. **99**, 2148–2157 (1996).

[11] Swanson Analysis Systems, ''ANSYS User's Manual for Revision 5.0 Vol III: Elements,'' DN-R300:50-3 (Dec 1992).

[12] D. A. Hutchins and G. Hayward, ''Radiated fields of ultrasonic transducers,'' in *Physical Acoustics*, Vol. XIX (Academic, New York, 1990), pp. 1–80.

[13] A. Gachagan, G. Hayward, S. P. Kelly, W. Galbraith, ''Characterisation of air coupled transducers,'' IEEE Trans. Ultrason. Ferroelectr. Freq. Control **43**(4), 678–689 (1996).

[14] G. Hayward and J. Hossack, ''Unidimensional modelling of 1-3 composite transducers,'' J. Acoust. Soc. Am. **88**, 599–608 (1990).

[15] C. Rajakumar, A. Ali, and S. M. Yunus, ''A new acoustic interface element for fluid-structure interaction problems,'' Int. J. Numer. Methods Eng. **33**(2), 369–386 (1992).

A tonpilz projector for use in an underwater horn

Mark B. Moffett, James M. Powers, and Michael D. Jevnager
Code 2131, Naval Undersea Warfare Center, Newport, Rhode Island 02841

(Received 25 October 1997; accepted for publication 23 February 1998)

Tonpilz transducer head piston diameters are usually about one-half wavelength in diameter, so that ''ρ-c'' radiation loading will be approximately achieved. However, for this underwater tracking application, the transducer is required to fit inside the throat of a 360-degree horn. The piston diameter is limited to 1 in. (25 mm), or about 0.22 wavelength at the resonance frequency, 13 kHz. The design is based on a lumped-element model. The lead zironate-titanate (PZT-8) ring stack is 2.1 in. (53 mm) long with an outer diameter of 0.49 in. (12.5 mm) and an inner diameter of 0.24 in. (6.0 mm). The head mass is 0.25-in. (0.635-mm)-thick aluminum, and the tail mass is wolfram (tungsten), with a mass of 93 g. The transducer is isolated from its cylindrical housing with a syntactic foam spring. An O-ring piston seal is used, and a similar O-ring provides support for the tail mass. The results of free-field measurements are used to determine the parameters of a lumped-parameter equivalent circuit model, which is then used to predict the performance after installation in the horn. [S0001-4966(98)01006-6]

PACS numbers: 43.38.Ar, 43.38.Fx, 43.30.Yj [SLE]

LIST OF SYMBOLS

A	piezoelectric ring-stack cross-sectional area [m^2]
A_1	horn sector area at throat [m^2], Eq. (16)
a	piston radius [m]
C_a	adhesive bond compliance [m/N]
C_b	blocked capacitance [F], Fig. 3, Eqs. (1), (33)
C_c	cable capacitance [F]
C_f	free capacitance [F], Eq. (26)
C_m	mechanical compliance [m/N], Fig. 3, Eqs. (3), (35)
C_{mot}	motional capacitance [F], Eq. (22)
C_t	tie-rod compliance [m/N]
c	seawater sound speed [m/s]
D	diameter of horn at mouth [m]
DI	directivity index [dB], Eqs. (38), (39)
d_{33}	piezoelectric strain coefficient [m/V]
E	drive voltage amplitude [V], Fig. 3
f	frequency [Hz]
f_c	horn cutoff frequency [Hz], Eq. (13)
f_0	resonance frequency [Hz], Eq. (28)
G	transducer conductance [S], Eq. (37)
G_b	blocked conductance [S], Fig. 3
$G_{\max}$	maximum conductance [S], Eq. (27)
H	height of horn waveguide [m]
H_1	height of horn at throat [m]
H_2	height of horn at mouth [m]
j	$=(-1)^{1/2}$
k_{eff}	effective coupling factor, [dimensionless], Eq. (25)
k_{33}	electromechanical coupling factor, [dimensionless], Eq. (5)
L	length of piezoelectric ceramic ring stack [m]
L_{mot}	motional inductance [H], Eq. (23)
M	dynamic mass [kg], Fig. 3, Eq. (4)
M_b	back mass [kg], Eq. (8)
M_f	front mass [kg], Eq. (6)
M_h	head mass [kg]
M_r	radiation mass [kg], Eq. (9)
M_t	tail mass [kg]
M_x	one-third of the piezoelectric ring-stack mass [kg], Eq. (7)
N	electromechanical turns ratio [N/V], Fig. 3, Eqs. (2), (34)
n	number of piezoelectric ceramic rings in stack
Q_m	mechanical quality factor, [dimensionless], Eq. (29)
R_m	mechanical loss resistance [kg/s], Fig. 3
R_{mot}	motional resistance [Ω], Eq. (24)
R_r	modal radiation resistance [kg/s], Fig. 3, Eq. (10)
R_0	radiation resistance [kg/s], Eqs. (11), (19)
R_1	radiation resistance at throat of horn sector [kg/s], Eq. (15)
R_2	radiation resistance at mouth of horn sector [kg/s], Eq. (14)
r	radius from center of horn [m]
r_1	radius of horn center post baffle [m]
s_{33}^E	short-circuit compliance coefficient [m^2/N]
T	axial stress amplitude [Pa], Eq. (40)
$T_{\max}$	maximum axial stress amplitude [Pa], Eq. (41)
TVR	transmitting voltage response [dB *re*: 1 μPa·m/V], Eq. (36)
$\mathrm{TVR}_{\max}$	maximum value of TVR [dB *re*: 1 μPa·m/V]
V	modal (head+tail) velocity amplitude [m/s], Fig. 3
V_0	piston velocity amplitude [m/s]
V_1	particle velocity amplitude at throat of horn sector [m/s]
x_0	horn flaring parameter [m]
Z_{mot}	motional impedance [Ω], Eq. (20)
ϵ_{33}^T	free permittivity [F/m]
η_{ea}	electroacoustic efficiency, [dimensionless], Eq. (30)
η_{em}	electromechanical efficiency, [dimensionless], Eq. (31)
η_{ma}	mechanoacoustic efficiency, [dimensionless], Eq. (32)
ρ	piezoceramic material mass density [kg/m^3]
ρ_0	seawater mass density [kg/m^3]
ω	angular frequency [rad/s], Eq. (21)

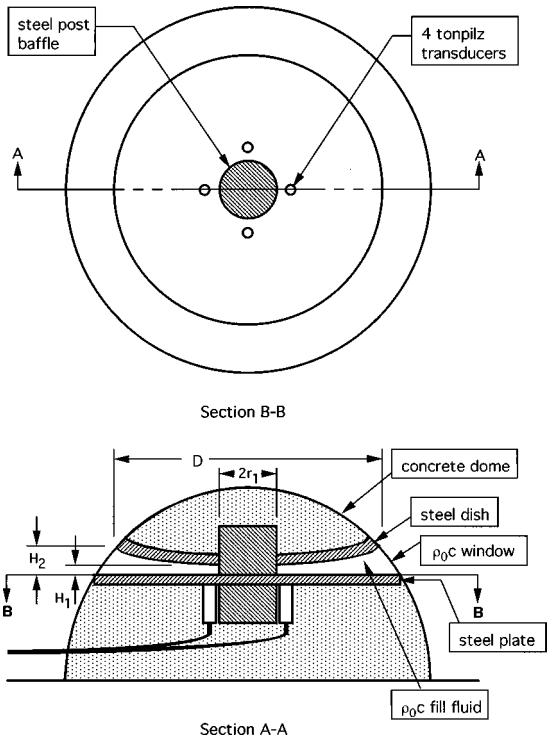

FIG. 1. Cross-sectional views of underwater, tracking-range bunker containing 360-degree, fluid-filled horn.

INTRODUCTION

Underwater acoustic tracking ranges in shallow water must be designed to withstand the onslaughts of fishing trawlers, in addition to the natural vicissitudes of the seawater environment. To protect the transducers at such a site, one proposed installation utilizes concrete dome-shaped bunkers. The transducers, which must be capable of generating a source level of 179 dB *re*: 1μPa·m over a frequency band of 8–16 kHz, are coupled to the seawater via a 360-degree, fluid-filled horn contained within the bunker (see Fig. 1). The horn provides a controlled acoustic environment for resistive loading of the transducers, with a larger radiation resistance than could be achieved in the free field. The horn diameter is roughly 1.1 m, and the vertical aperture at the mouth is about 2.6 in. (67 mm). At the center of the bunker (i.e., the throat of the horn) is a steel support post, 6 in. (0.15 m) in diameter, that also serves as a cylindrical baffle. The height at the throat is 0.5 in. (12.7 mm). Four projector elements are to be located near the post, with their acoustic centers well within one-quarter wavelength (to avoid destructive interference caused by reflection from the post), or 0.9 in. (23 mm), of its surface. Therefore, we have limited the outer diameter of each element to 1.5 in. (38 mm) and the radiating piston diameter to 1.0 in. (25 mm). The horn has a small amount of vertical directivity, but the azimuthal beam pattern is expected to be omnidirectional. The system must be capable of withstanding hydrostatic pressures as large as 900 psi (6.2 MPa). We have designed and built tonpilz[1] elements (see Fig. 2) to meet these requirements.

I. THEORY

The canonical, lumped-element equivalent circuit,[2,3] valid for low-frequency piezoelectric transducers, is depicted in Fig. 3, where C_b is the blocked capacitance, G_b is the blocked conductance, N is the electromechanical turns ratio, C_m is the short-circuit mechanical compliance, R_m is the mechanical loss resistance, R_r is the radiation resistance, and M is the dynamic mass. The transducer is driven by a voltage of amplitude, E, to which it responds with the modal velocity, V, shown in the mechanical part of the equivalent circuit.

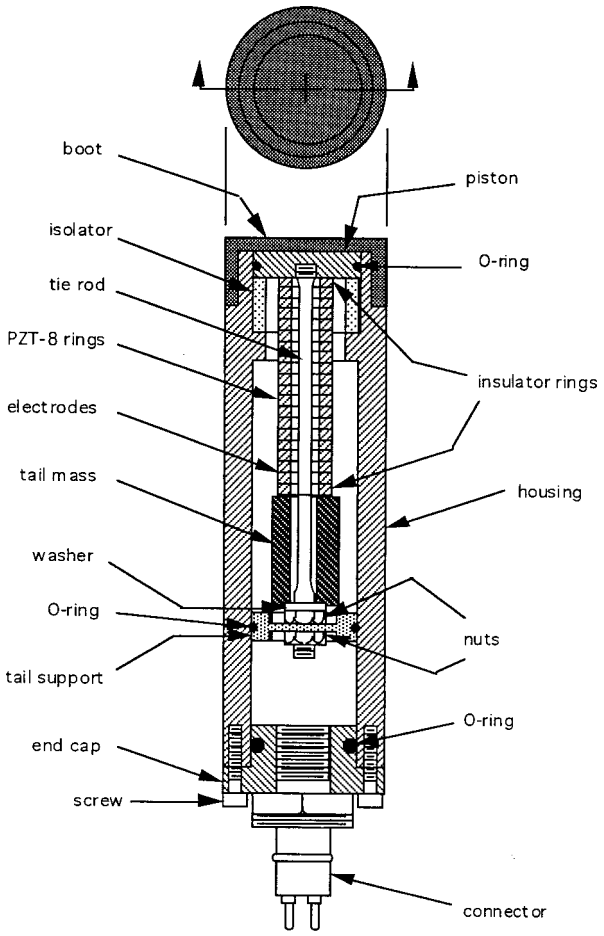

FIG. 2. Cross-sectional view of tonpilz transducer for installation within underwater horn.

For a tonpilz transducer having a stack of n rings of cross-sectional area, A, and total length, L, we have[4]

$$C_b = n^2 \epsilon_{33}^T (1 - k_{33}^2) A/L, \tag{1}$$

$$N = n d_{33} A/(s_{33}^E L), \tag{2}$$

$$C_m = s_{33}^E L/A, \tag{3}$$

and

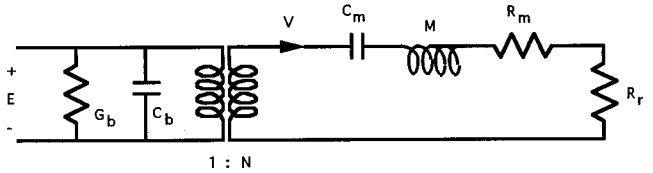

FIG. 3. Canonical, lumped-element equivalent circuit for low-frequency piezoelectric transducer.

$$M = M_f M_b / (M_f + M_b), \tag{4}$$

where ϵ_{33}^T is the free permittivity, s_{33}^E is the short-circuit compliance coefficient, d_{33} is the piezoelectric strain coefficient, and k_{33} is the electromechanical coupling factor of the piezoelectric ceramic material,

$$k_{33} = d_{33} / (\epsilon_{33}^T s_{33}^E)^{1/2}. \tag{5}$$

In order to determine the electromechanical and mechanical quantities in Eqs. (2)–(4), we have taken the modal velocity, V, to be the sum of the head and tail velocities, i.e., the relative velocity of the ends of the piezoelectric ceramic ring stack.

In Eq. (4), we have the front mass,[5]

$$M_f = M_h + M_r + [(M_t + M_x)/(M_t + M_h + M_r + 2M_x)]M_x, \tag{6}$$

consisting of the head mass, M_h, the radiation mass, M_r, and a portion of the piezoelectric ceramic stack mass,[6]

$$M_x = \rho AL/3, \tag{7}$$

where ρ is the piezoelectric ceramic material density, and the back mass,[5]

$$M_b = M_t + [(M_h + M_r + M_x)/(M_t + M_h + M_r + 2M_x)]M_x, \tag{8}$$

involving the tail mass, M_t, and a smaller portion of the stack mass.[6] The radiation mass, M_r, depends, of course, on the manner in which the transducer is loaded. In a free-field, underwater situation, we expect[7]

$$M_r = 1.927 \rho_0 a^3, \tag{9}$$

where ρ_0 is the density of the water medium and a is the radius of the vibrating piston. For the transducer in air, or mounted in the horn, we assume that the radiation mass is negligible.

Because the modal velocity, V, is the sum of the head and tail velocities, and not just that of the head, the radiation resistance, R_r, to be used in the equivalent circuit of Fig. 3, depends on the front and back masses, i.e.,

$$R_r = R_0 [M_b / (M_f + M_b)]^2, \tag{10}$$

where R_0 is the radiation resistance relative to the piston (i.e., head) velocity. For the transducer in air, R_0 is negligible, and in the free field underwater, we expect[7]

$$R_0 = \pi \rho_0 (\pi a^2 f)^2 / c, \tag{11}$$

where f is the frequency and c is the sound speed.

We now proceed to determine the radiation resistance, R_0, for operation of the transducers near the throat of the horn, as shown in Fig. 1. Because the four transducer elements in the horn will be driven in phase, symmetry considerations allow us to consider each 90-degree sector as a separate horn with rigid vertical walls, with one of the projector elements located near the throat of the horn sector. The mouth of the horn sector is then rectangular with height, H_2, and width, $\pi D/4$, where D is the horn diameter. The impedance at the mouth of the horn sector will be resistive as long as[8] the circumference of the mouth is greater than one wavelength, c/f. In our case, because the height is smaller than the width, this condition will be assured if $H_2 > c/4f$. (For simplicity, we are assuming that the horn fill fluid has the density and sound speed of seawater.)

The vertical dimension of the horn sector, H, is given by[9]

$$H = H_1 \cosh[(r - r_1)/x_0], \tag{12}$$

where H_1 is the height at the throat, r is the radial distance from the axis of the bunker, r_1 is the radius of the central cylindrical baffle, and x_0 is a flaring parameter. (We assume that the assymetric shape of the horn, i.e., curved above and flat below, does not greatly affect the impedances or the cutoff frequency, but we might expect the beam pattern to be directed slightly upward.) Well above the cutoff frequency,[10]

$$f_c = c/(2\pi x_0), \tag{13}$$

the mechanical impedance at the mouth is purely resistive, i.e.,

$$R_2 = \rho_0 c H_2 \pi D/4, \tag{14}$$

and that at the throat is also purely resistive, with[10]

$$R_1 = \rho_0 c A_1, \tag{15}$$

where

$$A_1 = \pi r_1 H_1/2, \tag{16}$$

the throat sector area. However, R_1 is not the radiation impedance seen by the projector element, because the radiating area of the element, πa^2, is smaller than A_1. We estimate the mechanical radiation impedance, R_0, by equating the power at the throat to that produced by the source element, i.e.,

$$R_1 V_1^2 = R_0 V_0^2, \tag{17}$$

where V_1 and V_0 are the particle velocities at the throat and at the radiating piston head of the projector element, respectively. In addition, we assume that the fluid flow between the source and the throat is incompressible,[11] i.e.,

$$V_1 A_1 = V_0 \pi a^2. \tag{18}$$

Combination of Eqs. (15), (17), and (18) yields

$$R_0 = \rho_0 c (\pi a^2)^2 / A_1 \tag{19}$$

for use in Eq. (10) when the transducer is placed within the horn sector.

From the equivalent circuit of Fig. 3, we can determine the motional impedance,

$$Z_{\text{mot}} = R_{\text{mot}} + j\omega L_{\text{mot}} + 1/j\omega C_{\text{mot}}, \tag{20}$$

where

$$\omega = 2\pi f, \tag{21}$$

and where

$$C_{\text{mot}} = N^2 C_m, \tag{22}$$

is the motional capacitance,

$$L_{\text{mot}} = M/N^2, \tag{23}$$

is the motional inductance, and

$$R_{\mathrm{mot}}=(R_m+R_r)/N^2, \tag{24}$$

is the motional resistance. The effective coupling factor,[2]

$$k_{\mathrm{eff}}=(C_{\mathrm{mot}}/C_f)^{1/2}, \tag{25}$$

is related to the free capacitance,

$$C_f=C_b+N^2C_m. \tag{26}$$

The conductance has a maximum value,

$$G_{\max}=G_b+1/R_{\mathrm{mot}}. \tag{27}$$

at the (short-circuit) resonance frequency,

$$f_0=[2\pi(MC_m)^{1/2}]^{-1}. \tag{28}$$

A measure of the width of the conductance peak near resonance is the mechanical quality factor,

$$Q_m=2\pi f_0M/(R_m+R_r). \tag{29}$$

The electroacoustic efficiency is given by

$$\eta_{\mathrm{ea}}=\eta_{\mathrm{em}}\eta_{\mathrm{ma}}, \tag{30}$$

where

$$\eta_{\mathrm{em}}=(1+G_b|Z_{\mathrm{mot}}|^2/R_{\mathrm{mot}})^{-1}, \tag{31}$$

is the electromechanical efficiency, and

$$\eta_{\mathrm{ma}}=R_r/(R_m+R_r), \tag{32}$$

is the mechanoacoustic efficiency.

In practice, the simple relations of Eqs. (1)–(3) must be modified to account for the capacitance of the cable, C_c, the compliance of the adhesive bonds between the rings, C_a, and the compliance of the tie rod, C_t, that applies compressive prestress to the ring stack.[5] We obtain

$$C_b=C_c+[1-k_{33}^2+k_{33}^2/(1+s_{33}^EL/C_aA)]n^2\varepsilon_{33}^TA/L, \tag{33}$$

$$N=nd_{33}A/[(s_{33}^EL)(1+C_aA/s_{33}^EL)], \tag{34}$$

and

$$C_m=(s_{33}^EL/A)/[(s_{33}^EL/AC_t)+(1+C_aA/s_{33}^EL)^{-1}]. \tag{35}$$

All three parasitic quantities act to reduce the coupling factor from the ideal value, k_{33}. The cable capacitance, C_c, adds to the blocked capacitance, C_b, as indicated in Eq. (33). The tie-rod compliance, C_t, reduces the short-circuit mechanical compliance, C_m, as can be seen in Eq. (35). The compliance of the adhesive joints, C_a, reduces the electromechanical turns ratio, N, while increasing both C_b and C_m.

The transmitting voltage response, TVR, of the transducer element can be expressed in terms of the equivalent circuit parameters and the directivity index, DI, as

$$\mathrm{TVR}=10\log(\rho_0c\,\eta_{ea}G/4\pi)+\mathrm{DI}+120, \tag{36}$$

where

$$G=G_b+\mathrm{Re}(1/Z_{\mathrm{mot}}), \tag{37}$$

is the conductance. For free-field operation, the directivity index is approximately

$$\mathrm{DI}=10\log[1+(\omega a/c)^2], \tag{38}$$

and for operation in the horn,

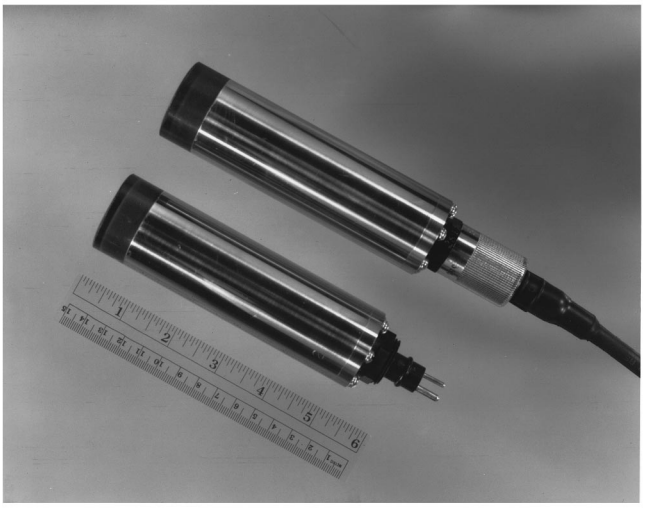

FIG. 4. Photograph of two tonpilz transducers.

$$\mathrm{DI}=10\log[4\{1+(2H_2f/c)^3\}^{1/3}]. \tag{39}$$

Equations (38) and (39) are the results of curve fits to plots in Refs. 12 and 13, respectively. They can be seen to have the correct high- and low-frequency asymptotic limits. [In Eq. (39), the factor 4, appears, because each transducer radiates into a 90-degree sector.]

The amplitude of the axial stress in the ring stack can be calculated from the equivalent circuit of Fig. 3 as

$$T=(NE/A)|(R_{\mathrm{mot}}+j\omega L_{\mathrm{mot}})/Z_{\mathrm{mot}}|. \tag{40}$$

In order to prevent tension within the ring stack, the compressive stress bias should be made to exceed the maximum stress amplitude, occurring at resonance, namely,

$$T_{\max}=(NE/A)[1+Q_m^2]^{1/2}. \tag{41}$$

II. DESIGN AND CONSTRUCTION

Figure 2 is a schematic drawing of the tonpilz transducer. Two transducer elements, shown in the photographs of Figs. 4–6, were constructed. Each element was enclosed in a watertight, stainless steel, 1.5 in.-diam. (38-mm) housing to allow free-field testing of the individual units. The 1 in.-diameter (25-mm) piston head mass was machined from 6061-T6 aluminum alloy. The piezoelectric ceramic material was Edo EC-69, a PZT-8, i.e., Navy Type III, lead zirconate-titanate. The tail mass material was a machinable wolfram (tungsten) alloy, CMW 1000.

In order to minimize losses at the piston-housing interface, an O-ring piston seal was used, but with a reduced amount of squeeze, 18%, compared to that for conventional, static O-ring seals, which is 27% for 0.070-in. (1.8-mm) cross-section O-rings.[14] Because O-rings are not recommended for contact against an anodized surface,[15] a polyurethane boot was used to protect the aluminum piston against sea water corrosion. One of the transducer elements, unit no. 1, utilized a partially cured polyurethane dam to prevent flow into the 0.003-in. (0.08-mm) annular, piston-housing gap

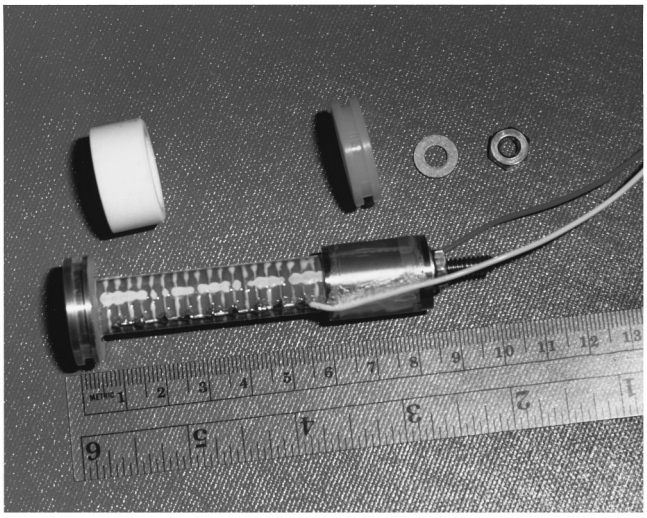

FIG. 5. Photograph of assembled driver, consisting of ring stack, head and tail masses, and tie rod. Also shown as separate parts are (from left) the syntactic foam isolator, the nylon tail support, and the washer and nut that secure the tail support.

during the potting process. No dam was used on unit no. 2; the annular gap is presumed to be filled with the primer used to prepare the piston surface for potting.

The tail mass was supported by a nylon support and a loose-fitting (i.e., no squeeze) O-ring. To withstand the thrust force on the piston due to hydrostatic pressure and to isolate the stack assembly from hydrostatic pressure variations, a syntactic foam spring isolator was placed between the back of the piston and a circumferential step in the housing wall. The isolator mounting resonance (with the static mass of the suspended transducer assembly) was estimated to be about 2 kHz. Hydrostatic pressure of 900 psi (6.2 MPa) will apply a uniaxial compressive stress to the syntactic foam of approximately 2 kpsi (14 MPa). According to the manufacturer,[16] the uniaxial compressive strength of the foam is 2.7 kpsi (19 MPa).

The stack consisted of 18 active rings of dimensions

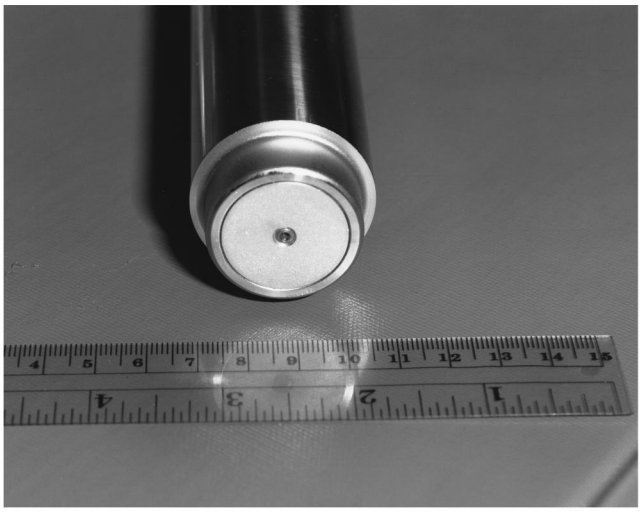

FIG. 6. Photograph of transducer front end showing piston, tie-rod end, and front of housing.

TABLE I. Transducer masses.

Mass (g)	Free field	Inside horn
M_h, head+tie-rod end	8.4	
M_t, tail assembly	93.4	
ρAL, ring stack	40.9	
M_r, radiation mass	3.9	0.0
M_f, front mass	23.3	19.7
M_b, back mass	96.1	95.7
M, effective mass	18.7	16.3

0.49-in. (12.5-mm) outer diameter by 0.24-in. (6.0-mm) inner diameter by 0.10 in. (2.5 mm) thick. Two additional rings were depolarized (by heating them above the Curie temperature) and used as insulator rings at each end of the stack. Perforated nickel foil electrodes of 0.003-in. (0.08-mm) thickness were used between the rings and at the stack-end mass interfaces. The perforations consisted of 16 0.047-in. (1.2-mm)-diam holes, and so the electrode coverage was about 80% of the ring-stack cross-sectional area. The electrodes provided a controlled spacing of the adhesive bond joints, and they helped to stiffen the stack assembly. The length of the assembled stack, L, was 2.1 in. (53 mm).

The tie rod for applying the compressive prestress to the ring stack was machined from a beryllium–copper alloy, C17300, which was supplied in a hard drawn temper. The uniform (i.e., nonthreaded) portion of the tie rod was 2.88 in. (73.0 mm) in length and 0.125 in. (3.18 mm) in diameter. The ring stack was calibrated as a force gage by placing and then removing a weight from the end of the stack and using a charge meter to measure the response. For the initial testing described here, the prestress magnitude was approximately 2000 psi (14 MPa). Masses of the various pieces are listed in Table I.

III. MEASUREMENTS AND TRANSDUCER CHARACTERIZATION

Measurements were made of the admittance at each stage of construction of the two transducer elements in order to ensure that the assembly was proceeding satisfactorily. The effective coupling factor, k_{eff}, was approximately 0.52 for both units throughout the manufacturing process. Connection of the 50-ft length cable to either transducer lowered k_{eff} to about 0.42, however. The mechanical quality factor, Q_m, decreased as construction proceeded, from initial values of 160 and 130 for the ring stacks of units 1 and 2, respectively, to final values of 41 and 19 when the assemblies were completed. The latter, significant difference in Q_m, appearing after installation of the polyurethane boot, is thought to be a result of the difference in potting methods. The annular gap between the piston and the housing on unit 1, which utilized the dam, was supposedly air filled, whereas the unit 2 gap was probably filled with primer material that introduced a mechanical loss mechanism. The stiffer, filled gap of unit 2 is thought to have been the cause of the increased resonance frequency in air, 14.3 kHz, as compared to 13.2 kHz for unit 1.

There was no significant difference for the resonance frequencies measured in water, however. Figure 7 shows the

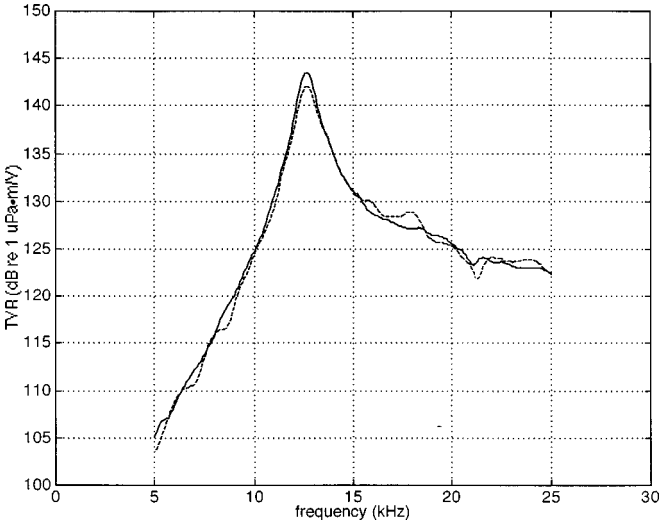

FIG. 7. Transmitting voltage response measured for two tonpilz transducer elements. Unit No. 1: solid curve; Unit No. 2: dashed curve.

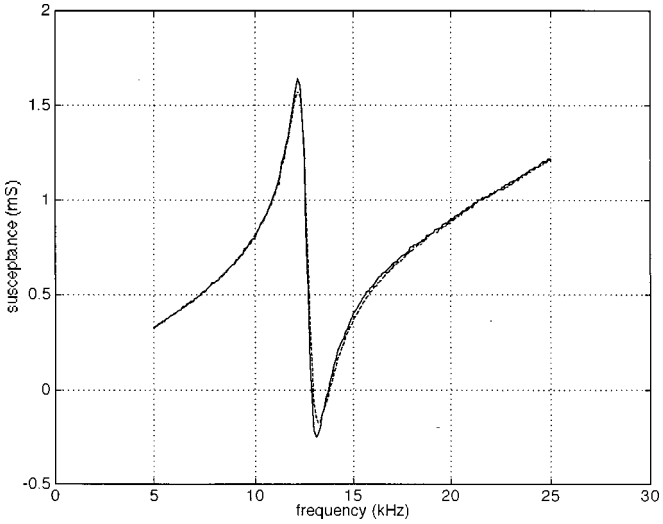

FIG. 9. Susceptance measured for two tonpilz transducer elements. Unit No. 1: solid curve; Unit No. 2: dashed curve.

transmitting voltage response (TVR) of the two elements, with the unit 1 response as a solid curve and that of unit 2 shown dashed. Figures 8 and 9 provide similar comparisons of the underwater conductances and susceptances, respectively. Table II is a summary of the measured transducer parameters. Although the resonance frequencies are in close agreement, the maximum TVR of unit 1 was 1.5 dB higher than that of unit 2. Higher values of $G_{\max}$ and of Q_m for unit 1 are also apparent. Unit 2 is obviously lossier than unit 1.

Table III presents the transducer parameters that can be inferred from the experimental data of Table II. The motional resistance is higher for unit 2, whose motional reactance is lower than that of unit 1. The effective coupling factors are roughly equal, as are the blocked capacitances.

To obtain values for the equivalent circuit mechanical elements of Fig. 3, we first calculated the effective mass, M, from Eqs. (4) and (6)–(9) and the masses listed in Table I. Then the electromechanical turns ratio, N, and the remaining mechanical parameters could be determined with the aid of Eqs. (22)–(24) and (32). From Table III, it can be seen that the compliances of the two units are not much different.

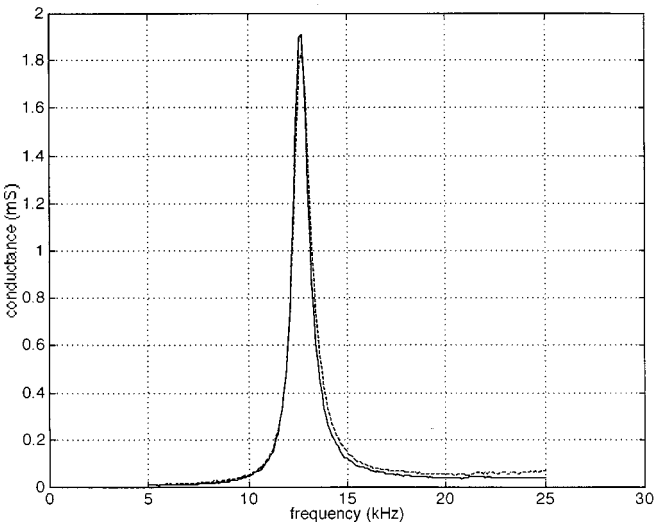

FIG. 8. Conductance measured for two tonpilz transducer elements. Unit No. 1: solid curve; Unit No. 2: dashed curve.

Figure 10 compares the beam patterns at 12.6 kHz of the two units (the 0-degree direction corresponds to the piston axis). The 3-dB beamwidth, in each case, is about 140 degrees. Computation of the directivity index from the solid curve of Fig. 10 yielded a directivity index of approximately 3.2 dB. Theoretically, from Eq. (38), a 25-mm-diam piston beam pattern should be nearly omnidirectional, with a directivity index of 1.7 dB. A directivity of 3.2 dB would be expected if the piston diameter were 39 mm, i.e., approximately equal to the outer diameter of the housing. It is unlikely that the entire frontal area would move with the piston, but it is not unreasonable to suppose that the effective area is slightly larger than that of the piston alone. Most of the increase in directivity is probably due to the mounting clamp for the transducer. The clamp was about 3.5 in. (90 mm) behind the front surface and presented a flat, bafflelike, 2.6-in. (67-mm)-wide frontal area.

The electrical losses were almost negligible, as indicated by the high electromechanical efficiencies, 0.98, for the two units. To determine the other efficiencies, which depend on the directivity index, we used both values, 1.7 dB and 3.2 dB, for the DI to get some appreciation for the magnitude of its effect. Then the maximum values of TVR and G were substituted into Eq. (36) to obtain the electroacoustic efficiencies of Table III. The mechanoacoustic efficiency, η_{ma}, was then obtained via Eq. (30). It is clear that, for both units, most of the losses are mechanical in nature.

TABLE II. Measured free-field transducer performance.

	Unit 1	Unit 2
f_0 (kHz)	12.65	12.71
$G_{\max}$ (μS)	1920	1840
G_b (μS)	30	37
Q_m	13.3	12.0
$\mathrm{TVR}_{\max}$ (dB *re*: 1 μPa·m/V)	142.9	141.4
C_f (nF)	10.1	10.3

TABLE III. Transducer parameters inferred from data of Table II. Two DI values are used: 1.7 dB (theoretical) and 3.2 dB (measured).

	Unit 1		Unit 2	
R_{mot} (Ω)	530		550	
L_{mot} (mH)	89		83	
C_{mot} (nF)	1.8		1.9	
k_{eff}	0.42		0.43	
C_b (nF)	8.3		8.4	
η_{em}	0.98		0.98	
M (g)		18.7		
N (N/V)	0.46		0.47	
C_m (nm/N)	8.5		8.4	
DI (dB)	1.7	3.2	1.7	3.2
η_{ea}	0.58	0.41	0.43	0.30
η_{ma}	0.59	0.42	0.44	0.31
R_r (kg/s)	66	47	55	39
R_m (kg/s)	46	65	70	86

It is interesting to compare the radiation resistances of Table III with the expected value, calculated from Eqs. (10) and (11). At the resonance frequency of 12.7 kHz, and for the sound speed of 1485 m/s, we obtain $R_r = 57$ kg/s. This value falls between those computed for the two directivity indices, 1.7 dB and 3.2 dB, of Table III, suggesting that the correct DI lies between those two values, perhaps about 2.0 dB. Assuming an effective piston diameter much larger than 1 in. quickly leads one to values for R_r that are much larger than those of Table III. Therefore, we conclude that the effective piston diameter is very close to the actual value, viz., 1 in. (25.4 mm).

The mechanical loss resistances are greater for unit 2 than for unit 1. Because the only significant difference in their construction was in allowing the primer to penetrate the annular gap region of unit 2, we believe that filling the gap with solid material introduced a loss mechanism not present in unit 1, in which the dam prevented incursion into the gap.

We can estimate the adhesive joint compliance by comparing the measured electromechanical turns ratio, N, with that calculated from Eq. (34). With book values[17] for d_{33} and s_{33}^E of 225 pm/V and 13.5 pm^2/N, respectively, Eq. (2) yields an ideal value for the turns ratio of 0.535 N/V. The measured values, 0.46–0.47 N/V, are presumed to be reduced by the nonzero adhesive compliance, C_a, as indicated in Eq. (34), which yields $C_a = 1.1$ nm/N. This is a remarkably small compliance, corresponding to an adhesive bond thickness of about 0.0008 in. (20 μm). In designing this transducer, we assumed that the adhesive joint compliance would be considerably larger, about 5 nm/N, because we failed to account for the stiffening effect of the perforated nickel electrodes. As a result the resonance frequency was higher than we expected. Stiff adhesive joints are good, because the coupling factor is not degraded as much as it would have been with softer bonds. However, in order to arrive at a specified resonance frequency, the designer needs to allow realistically for the joint compliance.

There was a substantial reduction of the effective coupling factor due to the large cable capacitance, C_c, of 3.9 nF. The cable was a shielded, two-conductor type that was operated with the low-voltage side connected to the shield at the amplifier with a resultant capacitance of about 80 pF/ft (260 pF/m). A lower capacitance cable, such as a coaxial type, would result in a higher coupling factor and would require less reactive amplifier power.

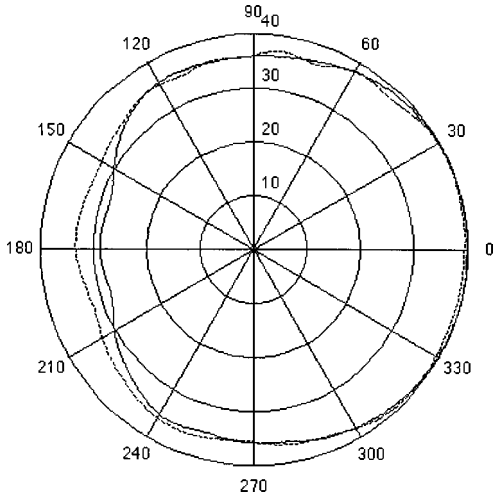

FIG. 10. Beam patterns measured at 12.6 kHz for two tonpilz transducer elements. Unit No. 1: solid curve; Unit No. 2: dashed curve.

IV. PERFORMANCE PREDICTIONS

Having obtained all the equivalent circuit parameters for the tonpilz transducer, we can now predict the performance of four of them placed at the throat of the horn. Because the radiation loading presented by the horn is unlike that in the free field, however, we must adjust the radiation impedance accordingly. The horn dimensions are given in Table IV. The cutoff frequency, calculated from Eq. (13) and the flaring parameter, x_0, from Table IV, is expected to be about 1.2 kHz. For operation well above cutoff, we assume that the radiation mass, M_r, is negligible, and so the effective transducer mass, M, becomes 16.3 g, as indicated in Table I. We use Eqs. (10) and (19) to calculate the radiation resistance, $R_r = 170$ kg/s.

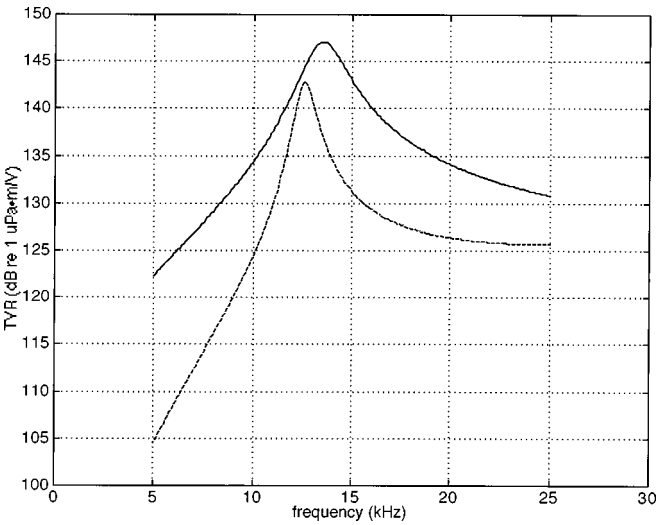

FIG. 11. Transmitting voltage response predicted for single tonpilz transducer element in free field (dashed curve) and four elements in horn having dimensions of Table IV (solid curve).

TABLE IV. Horn dimensions.

radius at throat, r_1	3.0 in.	76 mm
radius at mouth, $D/2$	21.8 in.	554 mm
flaring parameter, x_0	8.0 in.	203 mm
height at throat, H_1	0.5 in.	12.7 mm
height at mouth, H_2	2.64 in.	67 mm

The predicted TVR is shown in Fig. 11 as the solid curve. Also shown, as the dashed curve, is the free-field TVR for a single element. (The dashed curve is quite similar to the curves of Fig. 7, because it amounts to a curve fit to the data for unit 1.) The more favorable horn loading is expected to reduce Q_m from 13.3 to 6.3. We also expect an increase in the resonance frequency, from 12.7 kHz to 13.5 kHz, because of the reduction in the effective mass.

At the low-frequency end of our band, 8 kHz, the expected TVR is approximately 129 dB *re*: 1 μPa·m/V, and so the required 179 dB *re*: 1 μPa·m source level should be achievable with a drive voltage of 310-V rms. At this drive level, the peak stress predicted by Eq. (40) at resonance is 2.0 kpsi (13.5 MPa), i.e., just equal to the stress bias, and so, to provide a safety factor, we plan to increase the prestress magnitude to about 3 kpsi.

In Fig. 12 is shown the magnitude of the admittance for the two different situations. The solid curve is for one of the four elements in the horn. The dashed curve is for a single element in the free field. Again, the more favorable acoustic loading in the horn environment is apparent.

V. CONCLUSIONS

We conclude that our tonpilz transducers will perform satisfactorily in the horn environment, producing 179 dB *re*: 1 μPa·m over the 8–16 kHz band when driven with 310-V rms. The resonance frequency will be higher than we intended it to be, however, because we did not realize how good (i.e., stiff) the adhesive bonds would be with the use of perforated nickel electrodes. Thanks to the stiff bonds, the effective coupling factor of the transducer itself (without cable attached) was approximately 0.52, or about 80% of the material coupling factor, $k_{33}=0.65$, for PZT-8. The coupling factor was degraded considerably, to 0.42, by our choice of cable, which had a capacitance of about 80 pF/ft (260 pF/m) with the low-voltage conductor connected to the shield.

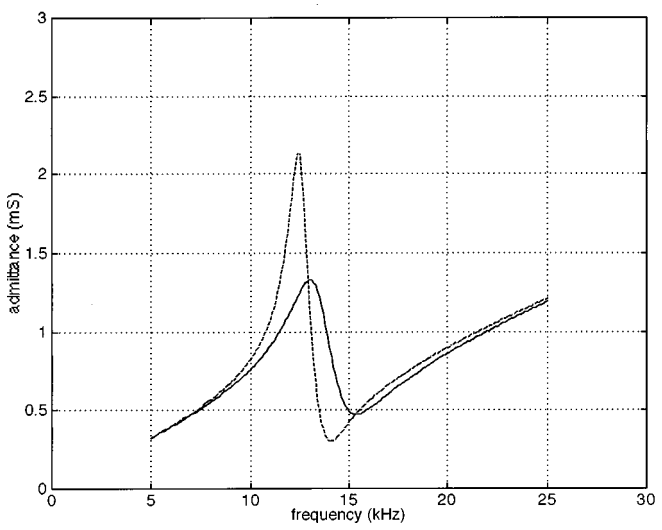

FIG. 12. Admittance magnitude predicted for single tonpilz transducer element in free field (dashed curve) and each of four elements in horn having dimensions of Table IV (solid curve).

One of the two units we built had excessive mechanical losses that we attribute to the entry of solid primer material into the annular gap between the piston and the transducer housing. Frictional losses incurred from the O-rings and the syntactic foam isolator that support the driver were deemed acceptable.

The transducer performance will be improved by the more favorable loading provided by the horn, but the resonance frequency will increase as a result of the reduced radiation mass.

The tonpilz transducer design and analysis were based on a lumped-parameter treatment that was made possible by the inclusion of a distributed mass contribution from the piezoelectric ceramic ring-stack and by the smallness of the other tranducer parts (compared to their appropriate wavelengths).

ACKNOWLEDGMENTS

The authors wish to acknowledge the contributions of A. Mark Young and Stephen C. Butler for useful design suggestions, William A. Bunker (International Transducer Corp.) for a design review, William A. Clay, Jr. and Michael E. Werbicki for drafting assistance, Bruce A. Dyer for coordinating the machining of parts, Patrick J. Monahan for developing the encapsulation procedure, and Walter H. Boober, Gorham G. Lau, and Hugo F. Mendoza (OASIS, Inc.) for underwater testing. Peter J. Stein (Scientific Solutions, Inc.) provided the horn design. The authors are indebted to Richard K. Menoche for his continuing support and encouragement. This work was sponsored by the Naval Air Systems Command, Code PMA 248.

[1] D. Stansfield, *Underwater Electroacoustic Transducers: A Handbook for Users and Designers* (Bath U.P. and Institute of Acoustics, Bath, UK, 1990), p. 180.
[2] R. S. Woollett, ''Effective coupling factor of single-degree-of-freedom transducers,'' J. Acoust. Soc. Am. **40**, 1112–1123 (1966).
[3] K. S. Van Dyke, ''The piezoelectric resonator and its equivalent network,'' Proc. IRE **16**, 742–764 (1928).
[4] D. A. Berlincourt, D. R. Curran, and H. Jaffe, ''Piezoelectric and piezomagnetic materials and their function in transducers,'' in *Physical Acoustics: Principles and Methods*, Vol. I–Part A, edited by W. P. Mason (Academic, New York, 1964), p. 247.
[5] D. Stansfield, *Underwater Electroacoustic Transducers: A Handbook for Users and Designers* (Bath University Press and Institute of Acoustics, Bath, UK, 1990), p. 199.
[6] R. S. Woollett, Sec. II, ''The longitudinal vibrator,'' in *Sonar Transducer Fundamentals*, edited by D. T. Porter (Naval Underwater Systems Center, New London, CT, 1990), pp. 101–102.
[7] L. L. Beranek, *Acoustics* (McGraw-Hill, New York, 1954), p. 125.
[8] L. L. Beranek, *Acoustics* (McGraw-Hill, New York, 1954), p. 268.
[9] P. J. Stein, private communication to one of the authors (MBM).
[10] L. L. Beranek, *Acoustics* (McGraw-Hill, New York, 1954), pp. 277–278.

[11] R. S. Woollett, *The Flexural Bar Transducer*, edited by L. C. Maples (Naval Underwater Systems Center, New London, CT, 1986), p. 67.
[12] L. L. Beranek, *Acoustics* (McGraw-Hill, New York, 1954), p. 112.
[13] J. W. Horton, *Fundamentals of SONAR* (U.S. Naval Institute, Annapolis, MD, 1957), p. 196.
[14] Parker Hannifin Corp., ''O-Ring Reference Guide'' (Parker Seal Group, Lexington, KY, 1995), p. 22.
[15] C. E. Conover and Co., ''Seal Design Manual'' (C. E. Conover and Co., Inc., Fairfield, NJ, 1967), p. 3-3.
[16] Grace Syntactics Technical Bulletin, ''Eccofloat TG-24A'' (Emerson and Cuming, Inc., Canton, MA, 1991), p. 1.
[17] D. Berlincourt, ''Piezoelectric crystals and ceramics,'' in *Ultrasonic Transducer Materials*, edited by O. E. Mattiat (Plenum, New York, 1971), p. 103.

Coupling between dissimilar modes in an asymmetrically forced string

P. V. Bayly
Department of Mechanical Engineering, Washington University, St. Louis, Missouri 63130-4899

K. D. Murphy
Department of Mechanical Engineering, University of Connecticut, Storrs, Connecticut 06269-3139

(Received 10 November 1997; accepted for publication 10 February 1998)

It is well known that a stretched string subjected to symmetric harmonic excitation in a single plane may exhibit large amplitude, coupled motion between the nth in-plane mode and the nth out-of-plane mode (n:n coupling). Significant coupling between modes of different indices (n:m coupling) is not expected in the steady state; if the nth in-plane mode is directly excited, it can be shown that the amplitude of the mth mode ($m \neq n$), both in-plane and out-of-plane, will decay monotonically, for any m. The present study illustrates that steady-state n:m coupled motion of the string may exist, provided that a constant in-plane bias force is superimposed on the harmonic excitation, thereby breaking the symmetry of the problem. In particular, the case of 2:1 coupling between in-plane and out-of-plane modes is examined using a perturbation approach. Results are confirmed by numerical simulations and physical experiments. © *1998 Acoustical Society of America.* [S0001-4966(98)05705-1]

PACS numbers: 43.40.Cw [CBB]

INTRODUCTION

The vibrating string is one of the most common and accessible examples of a vibratory system. The classical linear model of the string, fixed at each end, is characterized by sinusoidal mode shapes and harmonics which are integer multiples of the fundamental frequency. To obtain such results, it is assumed that the tension in the string is uniform and that only transverse, planar motion takes place. In fact, finite transverse displacements of the string necessarily produce longitudinal displacements and variations in the internal tension of the string. To incorporate the effect of longitudinal displacements Narasimha[1] developed a consistent set of nonlinear equations describing the full three-dimensional displacement field of the string. Subsequently, this model has been used by Bajaj and Johnson,[2] Feng,[3] and others to investigate the nonlinear response of the string. Miles,[4] and O'Reilly and Holmes[5] examined a model which to first order yields the same averaged equations as those studied by Bajaj and Johnson.[2] These efforts have revealed that the nonlinear string is susceptible to various bifurcations and may undergo chaotic motion. O'Reilly and Holmes[5] and Molteno and Tufillaro[6] have conducted experimental studies confirming chaotic behavior of the string.

One of the most important consequences of nonlinearity in the string is that harmonic excitation in one plane may lead to coupled in-plane and out-of-plane motion, so that the string describes a ''tubular'' or ''balloon'' shape. This response of the string was first observed in a series of experiments by Harrison.[7] These experiments preceded any detailed analysis on the behavior of the nonlinear string.

Bajaj and Johnson[2] showed that if weak excitation is added to the Narasimha string model near one of its resonant frequencies, only the modes corresponding to that frequency (either in-plane or out-of-plane) will exhibit large-amplitude motion. For example, if the string experiences light, in-plane forcing near its first resonant frequency, only the first in-plane mode and the first out-of-plane mode may be excited. Similarly, if light, in-plane forcing is applied near the second resonance, only the second in-plane mode and the second out-of-plane mode may exhibit large amplitude motion. In other words, only n:n coupling will produce large in-plane and out-of-plane oscillations of the stretched string.

The present authors observed experimentally that 2:1 coupling exists in the stretched string lightly excited by a tensioned wire stinger, apparently contradicting the assertion that only n:n coupling is significant. This observation is reconciled with the theory by showing that if a static load is added to the lateral harmonic excitation, coupling between the (directly excited) second in-plane mode and the first out-of-plane mode can be found. It is also shown that the 2:1 response evolves into a coupled 2:1,2 response as the excitation frequency is increased. In other words, the second in-plane mode is coupled to both the first and second out-of-plane modes. These results are demonstrated using a multiple scales perturbation approach and confirmed by simulation and experiment.

I. THEORETICAL STUDY

A. Equations of motion

The fundamental equations describing the nonlinear motion of the string were developed by Narasimha.[1] These equations account for finite transverse deformations of the string as well as longitudinal deformations of the string. In the derivation of these equations, it is assumed that the longitudinal displacement $u(x,t)$ changes quasi-statically as a function of the in-plane and out-of-plane transverse displacement fields given by $v(x,t)$ and $w(x,t)$, respectively; see

Narasimha.[1] In this case the string may be described by the two following nonlinear, coupled partial differential equations:

$$v_{,tt}+2\zeta\omega_1 v_{,t}-\left(c_0^2+\frac{c_1^2}{2L}\int_0^L (v_{,x}^2+w_{,x}^2)dx\right)v_{,xx} = \frac{1}{M}F^{\text{in}}(x,t), \tag{1}$$

$$w_{,tt}+2\zeta\omega_1 w_{,t}-\left(c_0^2+\frac{c_1^2}{2L}\int_0^L (v_{,x}^2+w_{,x}^2)dx\right)w_{,xx} = \frac{1}{M}F^{\text{out}}(x,t), \tag{2}$$

where $c_0=\sqrt{T/\rho A}$ is the transverse wave speed; $c_1=\sqrt{EA_c/(\rho A)}$ is the longitudinal wave speed; T is the nominal tension; ρ is the string density; E is the Young's modulus; L is the length of the string; ζ is the damping ratio; $\omega_1=c_0\pi/L$ is the first mode natural frequency; M is the mass per unit length; and A is the total cross sectional area. The string under consideration is a wound guitar string which consists of a central wire with additional wire wrapped around it. The central wire (the core) has cross sectional area A_c and is the only portion of the string which is capable of sustaining any substantial axial load. Hence, the longitudinal stiffness is EA_c rather than EA.

The in-plane and out-of-plane excitation are described by the terms $F^{\text{in}}(x,t)$ and $F^{\text{out}}(x,t)$, respectively. The excitation will be restricted to the in-plane direction and will consist of a constant load and an harmonic component which are both applied at the same point on the string, namely L_0. In this case

$$\begin{aligned} &F^{\text{out}}(x,t)=0,\\ &F^{\text{in}}(x,t)=[f_0+f\cos(2\pi\omega t)]\delta(x-L_0), \end{aligned} \tag{3}$$

where $\delta(x)$ is the Dirac delta function and ω is given in Hertz.

The nonlinear partial differential equations of motion may be transformed into a set of ordinary differential equations (ODEs) by a Galerkin projection. The displacement field is expressed as the following series expansions:

$$v(x,t)=v_0(x)+\sum_{n=1}^{\infty} v_n(t)\sin\left(\frac{n\pi x}{L}\right), \tag{4}$$

$$w(x,t)=\sum_{n=1}^{\infty} w_n(t)\sin\left(\frac{n\pi x}{L}\right), \tag{5}$$

where $v_0(x)$ is a time-independent, initial deformation of the string arising from the constant bias force f_0 applied at $x=L_0$. The initial deflection $v_0(x)$ is assumed to take on the ''V-shape'' shown in Fig. 1. In this case,

$$v_0(x)=\begin{cases} \dfrac{v_0}{L_0}x, & 0<x<L_0,\\ \left(\dfrac{-v_0}{L-L_0}\right)x+\dfrac{v_0 L}{L-L_0}, & L_0<x<L. \end{cases} \tag{6}$$

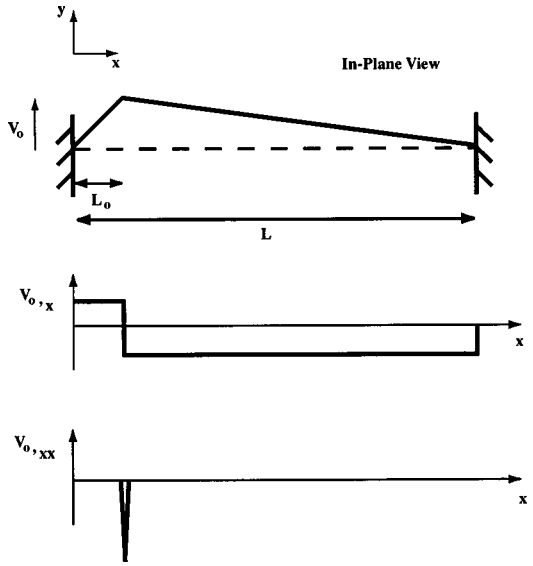

FIG. 1. A schematic diagram of the initial string shape (V_0) and its first two spatial derivatives.

In order to examine coupling between the first two modes, the displacement field, Eqs. (4) and (5), are truncated to two terms. These truncated expansions are substituted into Eqs. (1) and (2), and Galerkin's method is applied. Four nonlinear, coupled ordinary differential equations result.

To investigate the existence of a 2:1 internal resonance, the harmonic component of the excitation is assumed small and near the second linear natural frequency. Applying the scaling procedure of Bajaj and Johnson,[2] a small parameter ϵ is defined in terms of the small excitation level f:

$$\epsilon=\frac{2^{3/2}\pi f}{L^2\omega_1^2 M}\sin\left(\frac{2\pi L_0}{L}\right). \tag{7}$$

To ensure that both quadratic and cubic nonlinearities appear at the first nonlinear order an augmented small parameter is defined as

$$\hat{\epsilon}=\frac{1}{4}\left(\frac{\epsilon^2}{s}\right)^{1/3}, \tag{8}$$

where $s=(c_0/c_1)^2$ is usually much less than one. The excitation frequency is written in terms of its detuning from the second linear natural frequency

$$\frac{\omega^2}{(2\omega_1)^2}=1+\sigma\hat{\epsilon}, \tag{9}$$

where σ is the external detuning parameter. Time is also nondimensionalized: $\tau=(2\pi\omega)t/2$. Using these expressions, along with the definitions given in the Appendix, the four ODEs may be expressed in the nondimensional in-plane and out-of-plane modal coefficients $V_n(t)$ and $W_n(t)$ for $n=1,2$:

$$(1+\sigma\hat{\epsilon})V_n''+2\hat{\epsilon}\alpha V_n'+A_{n1}V_0+A_{n2}V_n$$
$$=-\hat{\epsilon}[A_{n3}V_0^3+A_{n4}V_0^2V_n+A_{n5}V_0^2V_1+A_{n6}V_0^2V_2$$
$$+A_{n7}V_0W_1^2+A_{n8}V_0W_2^2+A_{n9}V_0V_1V_n+A_{n10}V_0V_2V_n$$
$$+A_{n11}(V_nV_1^2+V_nW_1^2)$$
$$+A_{n12}(V_nV_2^2+V_nW_2^2)-\Gamma_{on}-\sqrt{2}n^{3/2}\cos(2\tau)], \quad (10)$$

$$(1+\sigma\hat{\epsilon})W_n''+2\hat{\epsilon}\alpha W_n'+B_{n1}W_n$$
$$=-\hat{\epsilon}[B_{n2}V_0^2W_n+B_{n3}V_0V_1W_n+B_{n4}V_0V_2W_n$$
$$+B_{n5}(W_nV_1^2+W_nW_1^2)+B_{n6}(W_nV_2^2+W_nW_2^2)], \quad (11)$$

where $\alpha=4\zeta(s/\epsilon^2)^{1/3}(\omega/(2\omega_1))$. The coefficients $A_{n1}\rightarrow A_{n12}$, $B_{n1}\rightarrow B_{n6}$, and Γ_{on} are obtained by a straightforward but algebraically cumbersome manipulation.

B. Perturbation analysis

Before searching for periodic solutions, the magnitude of the initial deflection V_0 must be determined. This is accomplished by considering the static terms of Eqs. (10):

$$A_{n1}V_0+\hat{\epsilon}(A_{n3}V_0^3-\Gamma_{on})=0. \quad (12)$$

For a prescribed bias force f_0 (which specifies Γ_{on}), this equation may be used to determine the resulting offset V_0. It should be noted that Eq. (12) is the same whether $n=1$ or 2. Hence, the value of V_0 is unique and does not depend on the choice of n.

To identify periodic solutions to Eqs. (10) and (11), two different time scales are defined:

$$T_n=\hat{\epsilon}^n(2\tau), \quad n=0,1, \quad (13)$$

where T_0 is the fast time scale and T_1 is a *slow* time scale which captures the effects of structural nonlinearities, damping, and the harmonic excitation.

The modal amplitudes are expressed as uniform expansions in the new time scales

$$V_m=\sum_{n=1}^{2}\hat{\epsilon}^{(n-1)}\alpha_{mn}(T_0,T_1), \quad (14)$$

$$W_m=\sum_{n=1}^{2}\hat{\epsilon}^{(n-1)}\beta_{mn}(T_0,T_1). \quad (15)$$

Temporal derivatives may be expressed in terms of the new time scales as

$$\frac{d}{d\tau}=2[D_0+\hat{\epsilon}D_1+\hat{\epsilon}^2D_2+\cdots],$$
$$\frac{d^2}{d\tau^2}=4[D_0^2+2\hat{\epsilon}D_0D_1+\hat{\epsilon}^2D_1^2+2\hat{\epsilon}^2D_0D_2+\cdots]. \quad (16)$$

Because of the scaling procedure employed in the previous section, neither the excitation nor the damping need to be expanded in $\hat{\epsilon}$. The squared linear natural frequencies are $A_{n2}=(n\pi/L)^2(c_0/\omega_1)^2=n^2$ and $B_{n1}=(n\pi/L)^2(c_0/\omega_1)^2=n^2$. Thus the linear natural frequency of the second V mode and the linear natural frequency of the first W mode remain exactly in a 2:1 ratio and there is *no internal detuning* away from this condition.

Substituting Eqs. (13)–(16) into the discretized equations of motion, Eqs. (10) and (11), the resulting equations may be grouped in like powers of $\hat{\epsilon}$. The $\mathcal{O}(\hat{\epsilon}^0)$ equations are

$$D_0^2\alpha_{11}+\tfrac{1}{4}\alpha_{11}=0, \quad (17)$$

$$D_0^2\alpha_{21}+\alpha_{21}=0, \quad (18)$$

$$D_0^2\beta_{11}+\tfrac{1}{4}\beta_{11}=0, \quad (19)$$

$$D_0^2\beta_{21}+\beta_{21}=0, \quad (20)$$

and their solutions are

$$\alpha_{11}=C_{A1}(T_1)e^{i(T_0/2)}+\overline{C}_{A1}(T_1)e^{-i(T_0/2)}, \quad (21)$$

$$\alpha_{21}=C_{A2}(T_1)e^{i(T_0)}+\overline{C}_{A2}(T_1)e^{-i(T_0)}, \quad (22)$$

$$\beta_{11}=C_{B1}(T_1)e^{i(T_0/2)}+\overline{C}_{B1}(T_1)e^{-i(T_0/2)}, \quad (23)$$

$$\beta_{21}=C_{B2}(T_1)e^{i(T_0)}+\overline{C}_{B2}(T_1)e^{-i(T_0)}. \quad (24)$$

Note that the amplitude coefficients are complex quantities which are slowly varying, i.e., changes occur on the T_1 time scale. They are determined by substituting Eqs. (21)–(24) into the $\mathcal{O}(\hat{\epsilon}^1)$ equations and eliminating secular terms. These secular terms are then used to express the modulations of the complex amplitudes on the original time scale, i.e., $\dot{C}_i=\epsilon D_1C_i$, $i=A1, A2, B1, B2$. This procedure leads to the following state equations:

$$\dot{C}_{A1}=\frac{i\hat{\epsilon}}{4}[3A_{111}C_{A1}^2\overline{C}_{A1}+2A_{112}C_{A1}C_{A2}\overline{C}_{A2}$$
$$+A_{111}(\overline{C}_{A1}C_{B1}^2+2C_{A1}C_{B1}\overline{C}_{B1})$$
$$+2A_{112}C_{A1}C_{B2}\overline{C}_{B2}+i\mu C_{A1}-\sigma C_{A1}$$
$$+A_{110}V_o\overline{C}_{A1}C_{A2}+(A_{14}+A_{15})V_o^2C_{A1}], \quad (25)$$

$$\dot{C}_{A2}=\frac{i\hat{\epsilon}}{8}[2A_{211}C_{A1}\overline{C}_{A1}C_{A2}+3A_{212}C_{A2}^2\overline{C}_{A2}$$
$$+2A_{211}C_{A2}C_{B1}\overline{C}_{B1}+A_{212}(\overline{C}_{A2}C_{B2}^2$$
$$+2C_{A2}C_{B2}\overline{C}_{B2})+2i\mu C_{A2}-4\sigma C_{A2}+A_{27}V_oC_{A2}^2$$
$$+A_{27}V_oC_{B1}^2+(A_{24}+A_{26})V_o^2C_{A2}-2], \quad (26)$$

$$\dot{C}_{B1}=\frac{i\hat{\epsilon}}{4}[B_{15}(2C_{A1}\overline{C}_{A1}C_{B1}+C_{A1}^2\overline{C}_{B1})+3B_{15}C_{B1}^2\overline{C}_{B1}$$
$$+2B_{16}C_{A2}\overline{C}_{A2}C_{B1}+2B_{16}C_{B1}C_{B2}\overline{C}_{B2}+i\mu C_{B1}$$
$$-\sigma C_{B1}+B_{14}V_oC_{A2}\overline{C}_{B1}+B_{12}V_o^2C_{B1}], \quad (27)$$

$$\dot{C}_{B2}=\frac{i\hat{\epsilon}}{8}[2B_{25}C_{A1}\overline{C}_{A1}C_{B2}+2B_{25}C_{B1}\overline{C}_{B1}C_{B2}$$
$$+B_{26}(2C_{A2}\overline{C}_{A2}C_{B2}+C_{A2}^2\overline{C}_{B2})+3B_{26}C_{B2}^2\overline{C}_{B2}$$
$$+2i\mu C_{B2}-4\sigma C_{B2}+B_{22}V_o^2C_{B2}], \quad (28)$$

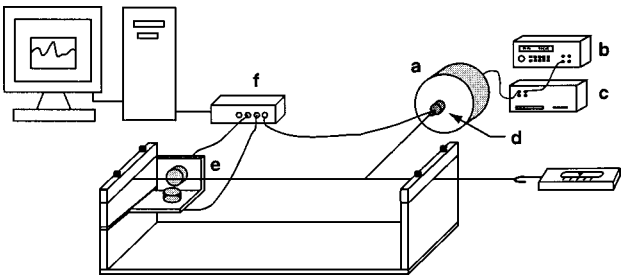

FIG. 2. A schematic diagram of the experimental system.

where $\mu = 2\alpha$. Since there is no internal detuning, steady-state solutions correspond to the condition: $\dot{C}_i = 0$, $i = A1$, $A2$, $B1$, $B2$. The resulting set of nonlinear algebraic equations may be solved using a multi-dimensional complex root-finding algorithm.

II. NUMERICAL SIMULATION

Analytical results were checked by direct numerical integration of the Galerkin-projected equations of motion [Eqs. (10) and (11)]. Integration was performed over exactly two excitation periods using a Runge–Kutta method of order 4–5 with automatic step size adjustment. Periodic solutions, both stable and unstable, were found by iteratively choosing initial conditions via a Newton–Raphson method until the initial state of the system converged to the final state.

III. EXPERIMENTAL STUDY

A. Experimental system

A schematic diagram of the experiment is shown in Fig. 2. An electric bass guitar string, 0.965 m long, was mounted between two fixed supports separated by 0.635 m. The guitar string consisted of a steel wire core (diameter 0.61 mm) plus wire windings which provided an overall diameter of 2.0 mm. The core wire was assumed to carry the bulk of the tensile load. To produce the desired tension, one end of the wire was clamped while the other end was connected to a spring scale and stretched until a tension of approximately 22 N was obtained. When the desired tension was reached the second end was clamped.

Periodic in-plane excitation was provided by an MB Dynamics FA1250 shaker (a) driven by an HP 3311A signal generator (b), and an MB Dynamics MB 2120 power amplifier (c). To deliver the load, a lightweight nylon thread ''stinger'' (0.3 m long) was stretched from the wire to the shaker armature. The stinger was attached close to one end of the wire at $x = L_0 = 0.019$ m. The stinger was attached to the shaker armature via a PCB 208-B01 force sensor (d). A miniature accelerometer (PCB 309A) was also mounted on the armature. The cumulative mass of the armature and the sensors was 0.118 kg.

The in-plane and out-of-plane displacements of a point 22 mm from the unforced end of the wire ($x = L_1 = 0.613$ m) were monitored using two Keyence EX-110 inductive displacement sensors (e) oriented horizontally and vertically in the plane perpendicular to the wire. These non-contacting sensors produced a voltage which was proportional to the proximity of the wire. When in use, the face of the sensor was placed 1.0 mm from the wire. The output was fed to a DSP Siglab 20-22 signal analysis system (f) interfaced to a 133-MHz Pentium PC. Signals were anti-alias filtered at 200 Hz and sampled with 18-bit precision at 400 Hz. The amplitude of each harmonic component of the sensor output was computed from the FFT of a 2048-sample time series.

The voltage output of the sensors was calibrated to the modal displacements. This procedure was warranted even though the modal amplitude is, in theory, related to the local amplitude by Eqs. (4) and (5). Because the wire has nonzero bending stiffness and behaves like a beam close to its clamped ends, the theoretical relationship between local displacement and modal amplitude are inaccurate at the measurement site.

The oscillatory force delivered to the wire by the shaker was estimated by comparing the rms acceleration of the free shaker armature to its rms acceleration when connected to the string. The observed difference in acceleration, multiplied by the armature mass (0.118 kg) approximates the force of the string on the shaker, and vice versa. Force estimates obtained by this method, which rely on the assumption that inertial forces are much larger than suspension forces (because of the shaker's soft suspension and small displacement), were confirmed by checking the small-amplitude displacement of the string at frequencies away from resonance. The output of the force transducer was not used because the signal included significant inertial effects due to the mass of the sensor.

B. Experimental procedure

The goal of the experiment was to capture the 2:1 behavior of the in-plane and out-of-plane modal amplitudes as a function of the excitation frequency. To obtain these results the following procedure was developed.

First, the in-plane sensor was activated while the out-of-plane sensor was deactivated and moved away from the wire. The purpose was to prevent magnetic and mechanical interference between the sensors. A prescribed static offset of 2.5 mm (0.10 in.) was applied to the wire. The offset displacement was measured by a micrometer. Fine adjustment of the offset was achieved by turning the screw which attached the stinger thread to the shaker. The static force produced by this offset was expected to be approximately 5.8 N. Because of nonzero bending stiffness in the wire, the maximum displacement offset was observed several millimeters from the point of attachment of the stinger.

The excitation frequency was set at $\omega = 60$ Hz, which was just below the range in which the second in-plane mode was expected to be excited. The rms amplitude of the input to the shaker was fixed at 0.081 V. This amplitude was chosen to provide an oscillatory force with an amplitude of approximately 0.2 N (0.05 lbs) to the wire. In the frequency range from 60 to 72 Hz, the actual force amplitudes were estimated from acceleration data and varied from 0.18 N to 0.27 N. The force transmitted to the wire appeared to increase significantly when large-amplitude out-of-plane motions occurred, up to a maximum of 0.66 N (0.165 lbs) at the

upper limit of the frequency range. However, the force amplitude remained approximately constant at frequencies up to and through the range of the observed bifurcations. Maintenance of a fixed input amplitude to the shaker ensured that measurements from sequential frequency sweeps were consistent. Attempts to maintain a fixed output force from the shaker would have required approximate and sensitive (and hence difficult to duplicate) adjustments of the manual control for every parameter combination.

Beginning at a frequency of 60 Hz, the wire was forced harmonically until all transients decayed. The excitation frequency was increased slowly until the pure in-plane motion became unstable and the wire exhibited steady, coupled motion between in-plane and out-of-plane modes. The frequency was then increased further to approximately 80 Hz, and measurements of the in-plane modal amplitude were taken. Measurements were then repeated at frequencies from 80 Hz to approximately 60 Hz in decrements of approximately 1 Hz. The in-plane sensor was then deactivated and the out-of-plane sensor was activated. The frequency was increased again to 80 Hz. The amplitudes of the out-of-plane displacement components at $\omega/2$ (first mode) and at ω (second mode) were measured at 1-Hz frequency steps from 80 Hz down to the frequency at which out-of-plane motion disappeared.

Time series of vertical and horizontal motion, as well as y-z displacement trajectories, were also obtained and stored at several frequencies (67 Hz, 70 Hz, 72 Hz, and 75 Hz). Although the in-plane and out-of-plane motion could not be recorded simultaneously, time series of y and z displacements from different periods were acquired at a fixed phase by triggering the data acquisition with the force transducer signal. Periodic y-z trajectories were reconstructed from these phase-aligned time series.

The clearest difference between the experiment and the mathematical model is that the force delivered to the wire was not constant, but depended on the frequency response of the entire system including the shaker. The problem of accurately maintaining a very light force input with this equipment was difficult. However, the variation in the force output obtained with a constant-amplitude voltage input was small over the frequency range which included the bifurcation frequencies. Hence, the simplifying assumption of a constant force amplitude was retained in the analysis.

IV. RESULTS

A. Existence of coupled 2:1 motion

An important general result may be obtained without solving the autonomous form of the state equations. A measure of the *energy* in the first mode is provided by the sum of the squared first mode amplitudes, i.e.,

$$E_1 = |C_{A1}|^2 + |C_{B1}|^2 = C_{A1}\overline{C}_{A1} + C_{B1}\overline{C}_{B1}. \tag{29}$$

To examine the behavior of this *energy*, the derivative of E_1 is taken with respect to the T_0 time scale and the expressions for $\dot{C}_{k1} = \hat{\epsilon} D_1 C_{k1}$, $k = A, B$ are used from the state equations. Doing this, Bajaj and Johnson[2] showed for the symmetric case ($V_0 = 0$) that

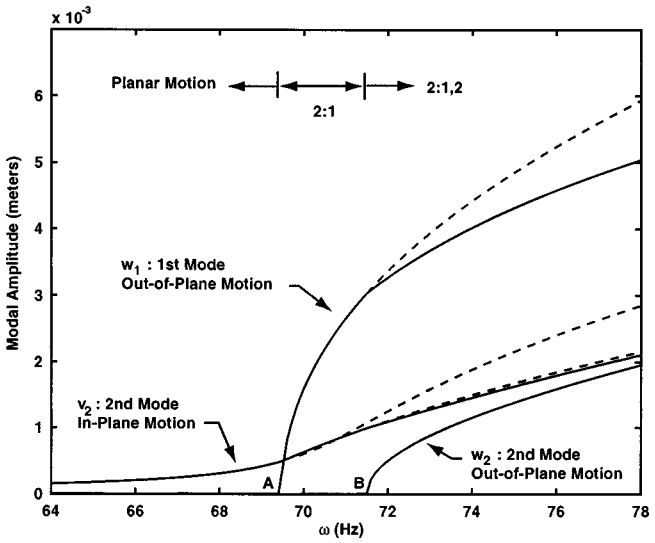

FIG. 3. The modal amplitude response diagram computed from the perturbation solution. Solid (dashed) lines indicate stable (unstable) solutions.

$$\frac{dE_1}{dT_0} = -\frac{1}{2}\,\hat{\epsilon}\mu E_1. \tag{30}$$

This result requires that E_1 exponentially decay toward zero. In other words, if the second in-plane mode is directly excited, there can be no large-amplitude steady-state, first mode response in either direction; only the second in-plane and the second out-of-plane modes may be excited.

However, if a nonzero static force is applied (resulting in $V_0 \neq 0$) the corresponding equation becomes

$$\frac{dE_1}{dT_0} = -\frac{1}{2}\,\hat{\epsilon}\mu E_1 + \frac{i\hat{\epsilon}}{4} A_{110} V_0 [-C_{A1}^2 \overline{C}_{A2} + \overline{C}_{A1}^2 C_{A2} + C_{A2}\overline{C}_{B1}^2 - \overline{C}_{A2} C_{B1}^2]. \tag{31}$$

This relationship implies that if the static offset and the amplitude of the directly excited, second in-plane mode are large enough, then dE_1/dT_0 is not necessarily negative. Hence, the amplitude of the first mode may remain large in steady state.

B. Typical amplitude response characteristics

For the experimental system under consideration, the string has an unstretched length of $L = 0.635$ m. The point load is applied at $L_0 = 0.019$ m. The string has modulus $E = 205 \times 10^3$ MPa, density $\rho = 6.67$ g/cm^3, total diameter $d = 2$ mm, inner core diameter $d_c = 0.61$ mm, and damping $\zeta = 0.0005$. The applied static axial load is $T = 22$ N. Under these conditions $\omega_1 = 27.25$ Hz. A static offset of $v_0 = 2.5$ mm is then imposed. This static offset stiffens the system, and so resonances occur at frequencies higher than the linear natural frequencies of the simple stretched string.

Figure 3 shows the modal amplitudes as a function of the excitation frequency based on the multiple-scales perturbation solution. Starting at 64 Hz, only the directly excited second in-plane mode (V_2) responds and its amplitude is small. As the excitation frequency is gradually increased the V_2 amplitude grows but the motion remains planar. At point

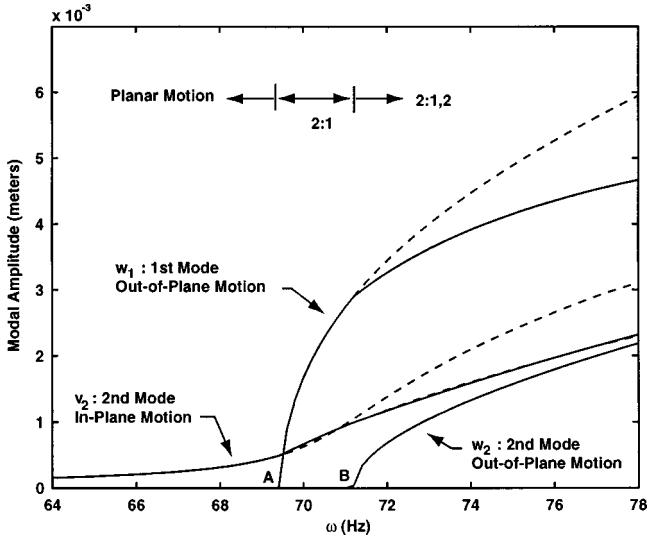

FIG. 4. The modal amplitude response diagram computed by numerical integration of the equations of motion (with Newton–Raphson iteration to find periodic solutions). Solid (dashed) lines indicate stable (unstable) solutions.

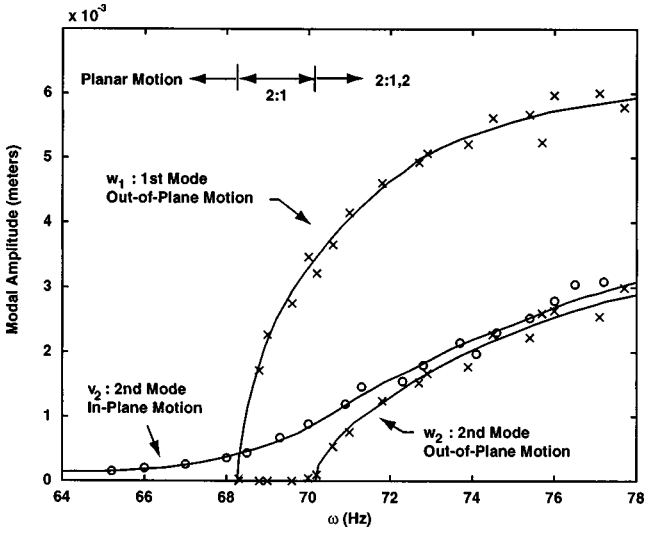

FIG. 5. The modal amplitude response diagram measured from the experimental system. Markers indicate data points and solid lines correspond to best fit curves through the data.

$A(\omega \approx 69.5\ \text{Hz})$, the system undergoes a supercritical pitchfork bifurcation and the first out-of-plane mode (W_1) takes on a nonzero amplitude. Because the second in-plane mode (V_2) remains nonzero above this frequency, this corresponds to the initiation of the 2:1 response. Also, above point A, the unstable planar motion, consisting of only the second in-plane (directly excited) mode, is shown with the dashed line.

As the excitation frequency is increased still further, the out-of-plane amplitude (W_1) grows quickly while the in-plane amplitude (V_2) increases more gradually. At $\omega \approx 71.45$ Hz, the system encounters another pitchfork bifurcation. Here, the second out-of-plane mode (W_2) is activated. The resulting motion is a combination of the second in-plane mode with the first *and* second out-of-plane modes. In other words, this is a 2:1,2 response. Beyond point B, all of the (stable) active response amplitudes continue to increase with increased ω. Also, above point B, the unstable 2:1 amplitudes are also shown in dashed lines.

In Fig. 4 the modal response amplitudes predicted from numerical simulations are given as a function of the excitation frequency. These amplitudes were computed from the numerical integration of the four discretized equations of motion given by Eqs. (10) and (11). As before, the response at the low-frequency end is restricted to the second in-plane mode, V_2. A pitchfork bifurcation occurs at point $A(\omega \approx 69.5$ Hz) and the 2:1 motion is initiated. As the frequency is increased still further, another pitchfork bifurcation occurs at point $B(\omega \approx 71.45$ Hz). This corresponds to the onset of the 2:1,2 motion in which V_2, W_1, and W_2 all have nonzero amplitudes.

Experimental results are shown in Fig. 5. Again, in the low-frequency range, the motion is confined to planar motion in V_2. At point A, $\omega \approx 68.25$ Hz, the system undergoes a pitchfork bifurcation which results in the 2:1 response. This response continues with growing amplitudes V_2 and W_1 until point B is encountered at $\omega \approx 70$ Hz. At this point, another pitchfork bifurcation occurs and the 2:1,2 response is initiated.

The experimental response diagram shows the same trends depicted by the numerical simulation and perturbation analysis. Two noticeable differences exist, however. First, the points of bifurcation (A and B), occur at slightly lower frequencies in the experiment than are predicted in Figs. 3 and 4. Second, the experimental modal amplitudes, V_2, W_1, and W_2, are larger than those found in the simulation or the analysis. Both of these differences may be explained in part by nonideal variations in the excitation force.

C. Typical spatial patterns

Four photos showing the spatial behavior of the experimental response are given in Fig. 6. Here, Fig. 6(A) and (B) shows the directly excited, in-plane motion at $\omega = 72$ Hz and $\omega = 78$ Hz, respectively. Figure 6(C) and (D) shows the out-of-plane responses corresponding to 6(A) and (B), respectively. At $\omega = 72$ Hz, the second mode in-plane [6(A)] is evident and the out-of-plane motion [6(C)] is dominated by the first mode with an imperceptible contribution from the second mode. At $\omega = 78$ Hz, the second mode, in-plane response [6(B)] persists and has a larger amplitude. However, the out-of-plane response now has a visible contribution from both the first and second mode [6(D)]. This is a clear indication of the coupled 2:1,2 response predicted in the previous section.

D. Typical time series and trajectories in the *y-z* plane

Figure 7 shows the response of the system at four distinct excitation frequencies as found using the analytical model. The first two columns correspond to the in-plane (directly excited) and out-of-plane displacements of the string at the measurement site. The third column shows the response in the y-z plane. Each row is associated with a spe-

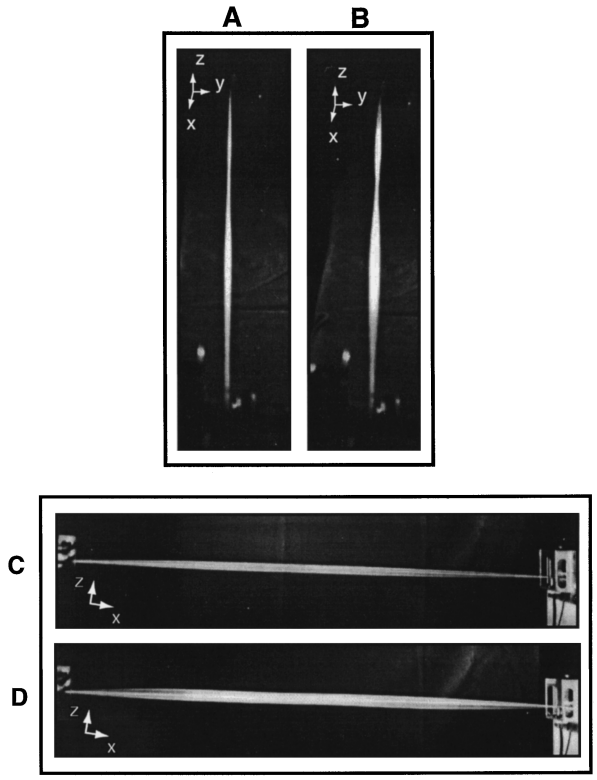

FIG. 6. Photographs of the string motion. (A) and (C) correspond to V and W, respectively, at $\omega=72$ Hz. (B) and (D) show V and W, respectively, at $\omega=78$ Hz. (D) clearly shows the growing influence of the second W mode.

cific excitation frequency, namely: $(A,\omega=67\ \text{Hz})$, $(B,\omega=70\ \text{Hz})$, $(C,\omega=72\ \text{Hz})$, $(D,\omega=75\ \text{Hz})$. The units of displacement in these figures are millimeters.

Figure 7(A) shows the response is confined to the in-plane direction. All of the out-of-plane amplitudes are zero. In Fig. 7(B), the in-plane amplitude has increased and the out-of-plane amplitude is nonzero. Furthermore, the out-of-plane response frequency is approximately half of the (directly excited) in-plane frequency. This is the 2:1 response. Figure 7(C) shows a second frequency component arising from the activation of the W_2 mode; this is the 2:1,2 response. The 2:1,2 motion is even more clearly shown in Fig. 7(D) where both out-of-plane frequencies are evident and the motion in the y-z plane has two distinct loops.

Figures 8 and 9 contain the time and y-z plane trajectories based on numerical simulations and experiments, respectively. Each subplot (A, B, C, D) corresponds to the same excitation frequencies as given in Fig. 7. Again, 8(A) and 9(A) show motion confined to the in-plane direction with a

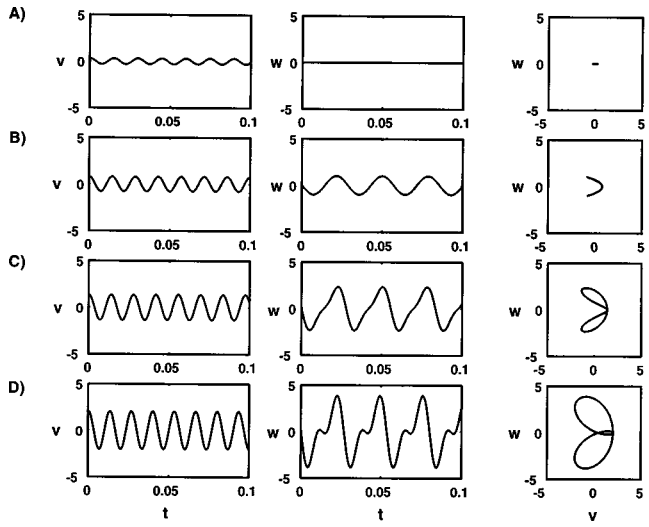

FIG. 7. Analytical trajectories. Column 1 and 2 are time series (V and W, respectively) corresponding to the in-plane and out-of-plane displacements of the string at the measurement site ($x=L_1$). Column 3 shows the trajectory in the V-W plane. All displacements are in millimeters and time is in seconds. Results are shown for four different excitation frequencies: (A) 67 Hz, (B) 70 Hz, (C) 72 Hz, (D) 75 Hz.

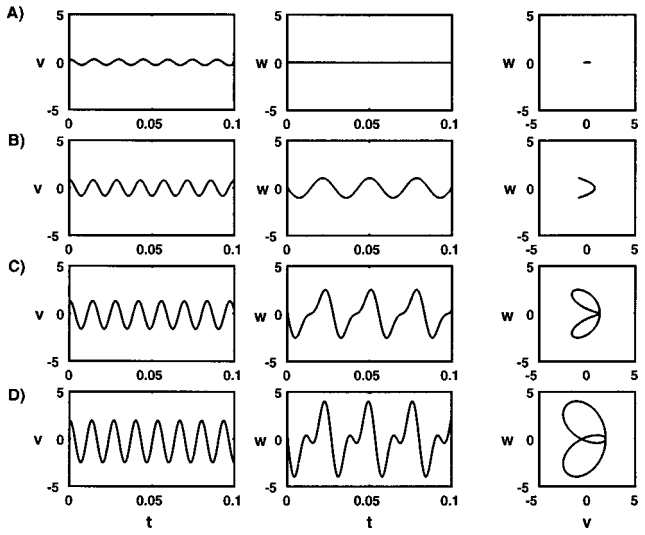

FIG. 8. Numerical trajectories. Column 1 and 2 are time series (V and W, respectively) corresponding to the in-plane and out-of-plane displacements of the string at the measurement site ($x=L_1$). Column 3 shows the trajectory in the V-W plane. All displacements are in millimeters and time is in seconds. Results are shown for four different excitation frequencies: (A) 67 Hz, (B) 70 Hz, (C) 72 Hz, (D) 75 Hz.

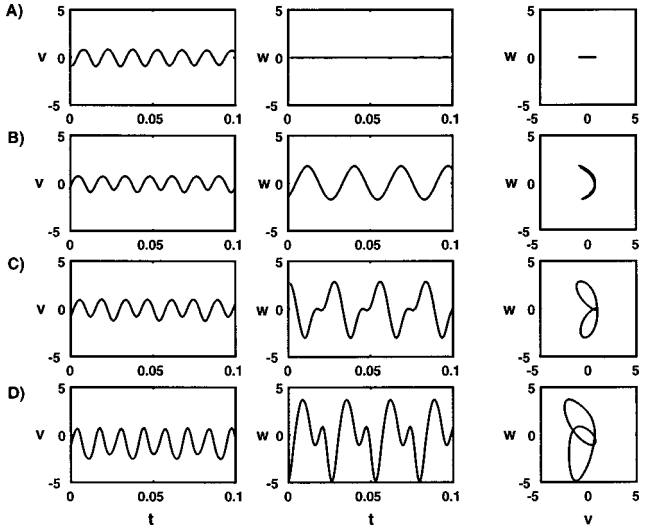

FIG. 9. Experimental trajectories. Column 1 and 2 are time series (V and W, respectively) corresponding to the in-plane and out-of-plane displacements of the string at the measurement site ($x=L_1$). Column 3 shows the trajectory in the V-W plane. All displacements are in millimeters and time is in seconds. Results are shown for four different excitation frequencies: (A) 67 Hz, (B) 70 Hz, (C) 72 Hz, (D) 75 Hz.

frequency near the excitation frequency. Figures 8(B) and 9(B) show the out-of-plane response is nonzero with a frequency of approximately half the excitation frequency. Figures 8(C) and 9(C) reveal the contributions of a second out-of-plane frequency. The time series of Figs. 8(D) and 9(D) illustrate the growing influence of the second frequency. This is also evident in the y-z trajectories which undergo a double loop. Overall, agreement between the perturbation solution, the numerical simulation, and the experimental data is very good.

V. CONCLUSIONS

Previous studies on the large-amplitude oscillations of periodically excited strings have demonstrated that in-plane (directly excited) motion may initiate out-of-plane motion. This coupled, nonplanar motion corresponds to a ''tubular'' shape of the displacement field. Previous studies have also shown that only n:n coupling leads to large-amplitude oscillations in a symmetrically forced string. For example, a first mode motion in-plane may *only* initiate a first mode motion in the out-of-plane direction.

The present work shows that the possible motions are not restricted to n:n coupling provided a static lateral load is applied in the direction of the excitation. This work focuses specifically on the 2:1 case. In particular, if the second in-plane mode is excited with a sufficiently large amplitude, a general result is developed which indicates that the amplitude of the first mode out-of-plane does not necessarily decay to zero.

A specific case of asymmetric excitation was investigated to illustrate 2:1 behavior in the string. The modal response for both in-plane and out-of-plane motion was determined in three ways: (1) by perturbation analysis (the method of multiple time scales); (2) by numerical integration of the discretized equations of motion; and (3) by physical experiment. The results of each method show that, in a frequency range just below the second resonance, motion is confined to the directly excited second in-plane mode, V_2. As the excitation frequency is increased, a supercritical pitchfork bifurcation is responsible for the activation of the first out-of-plane mode W_1. As the excitation frequency is increased still further, another pitchfork bifurcation occurs and the second out-of-plane mode, W_2, becomes active; the motion evolves into a coupled 2:1,2 motion.

This behavior is illustrated by plots of amplitude response as a function of frequency, by photos of the wire motion, as well as by time series and displacement trajectories in the y-z plane. Very good qualitative and quantitative agreement is observed between the perturbation analysis, simulation, and experiment.

ACKNOWLEDGMENTS

Both authors gratefully acknowledge the support of the National Science Foundation. NSF Grant Nos. CMS-9625161 (PVB) and CMS-9625319 (KDM).

APPENDIX

$$\epsilon = f\,\frac{\pi 2^{3/2}}{L^2\omega_1^2 M}\,\sin\left(\frac{2\pi L_0}{L}\right),$$

$$v_n = \frac{2L(\epsilon s)^{1/3}}{\pi n^{3/2}}\,V_n,$$

$$v_o = \frac{2L(\epsilon s)^{1/3}}{\pi}\,V_o,$$

$$w_n = \frac{2L(\epsilon s)^{1/3}}{\pi n^{3/2}}\,W_n,$$

$$\Gamma_{on} = \frac{\pi n^{3/2} f_o}{\omega_1^2 L^2 M(\epsilon s)^{1/3}}\,\sin\left(\frac{n\pi L_0}{L}\right),$$

$$\beta = 4\left(\frac{s}{\epsilon^2}\right)^{1/3}\left[\frac{\omega^2}{4\omega_1^2} - 1\right],$$

$$\hat{\epsilon} = \frac{1}{4}\left(\frac{\epsilon^2}{s}\right)^{1/3},$$

$$\tau = \left(\frac{2\pi\omega}{2}\right)t.$$

[1] R. Narasimha, ''Nonlinear vibration of an elastic string,'' J. Sound Vib. **8(1)**, 134–146 (1968).

[2] A. K. Bajaj and J. M. Johnson, ''On the amplitude dynamics and crisis in resonant motion of stretched strings,'' Philos. Trans. R. Soc. London, Ser. A **338**, 1–41 (1992).

[3] Z. C. Feng, ''Does nonlinear intermodal coupling occur in a vibrating stretched string?'' J. Sound Vib. **182(5)**, 809–812 (1995).

[4] J. W. Miles, ''Resonant nonplanar motion of a stretched string,'' J. Acoust. Soc. Am. **75**, 1505–1510 (1984).

[5] O. O'Reilly and P. J. Holmes, ''Nonlinear, nonplanar, and nonperiodic vibration of string,'' J. Sound Vib. **153(3)**, 413–435 (1992).

[6] T. C. A. Molteno and N. B. Tufillaro, ''Torus doubling and chaotic string vibrations: Experimental results,'' J. Sound Vib. **137(2)**, 237–330 (1990).

[7] H. Harrison, ''Plane and circular motion of a string,'' J. Acoust. Soc. Am. **20**, 874–875 (1948).

Effects of tensile loading on the properties of elastic-wave propagation in a strand

Hegeon Kwun, Keith A. Bartels, and John J. Hanley
Southwest Research Institute, 6220 Culebra Road, San Antonio, Texas 78228-0510

(Received 23 July 1997; accepted for publication 10 February 1998)

Effects of tensile loading on the properties of longitudinal-mode elastic-wave propagation in a 1.52-cm-diam, seven-wire strand used for prestressed concrete structures were investigated experimentally. In an unloaded state, the wave propagation properties in strand matched those seen in individual wires comprising the strand, namely, straight center wire and helical outer wires. In the strand, however, extraneous signals were found to be produced from the propagating wave due to physical interactions between the adjacent wires. Under tensile loading, it was observed that a certain portion of the frequency components of the wave became highly attenuative and, thus, absent in the frequency spectrum of the wave. The center frequency of this missing portion, called notch frequency, was found to increase linearly with $\log N$, where N is the applied tensile load. In addition, on both sides of the notch frequency, the wave exhibited a large dispersion in a manner similar to the behavior near a cutoff frequency. Possible causes of the observed behavior under tensile loading are discussed. [S0001-4966(98)02106-7]

PACS numbers: 43.40.Cw [PJR]

INTRODUCTION

Steel strands and cables are widely used in highway bridges, including pre-stressed and post-tensioned concrete, suspension, and cable-stayed bridges, as the primary load-carrying members. As such, their physical condition (for example, presence of any corrosion material loss, fractured wires, and loss of preloading) has a direct impact on the overall integrity and safety of the bridge. To assess the integrity and load-bearing capability of a bridge, knowledge of the physical condition of the steel members in the bridge is essential.

In the United States alone, there are about 500 000 highway bridges, the majority of which were built before 1950. Because of aging and the ever-increasing highway traffic loads, extensive numbers of highway bridges are now in distressed conditions, and more than 20% of them are known to be structurally deficient. To effectively manage the vast number of highway bridges undergoing degradation using the limited budget allocated for maintenance, rehabilitation, and construction, accurate assessment of the structural integrity of bridges is indispensable. Therefore, a great need exists for nondestructive evaluation (NDE) methods for determining the extent of degradation, in particular, the condition of steel members in bridges.

Under an initiative of the Federal Highway Administration, efforts are ongoing for developing NDE methods for application to bridge structures. As a part of this effort, NDE techniques for evaluating the condition of steel members in highway bridges, particularly those constructed of prestressed and post-tensioned concrete beams, using a technology termed ''magnetostrictive sensor (MsS)'' are under development. With this technology,[1,2] elastic waves in acoustic and ultrasonic frequency ranges are launched along a length of strand in all wires comprising the strand. Signals produced from the interaction of the propagating wave with the particular strand geometry are detected and analyzed. The transmission and detection of elastic waves are achieved using sensors that utilize the magnetostrictive effect in the steel strand material.

The experimental work presented in this paper was aimed at understanding the fundamental properties of elastic-wave propagation in prestressed steel strands for use in NDE technique development. In Sec. I, the experimental arrangement used in this study is described, including the strand sample, experimental setup, and data acquisition and processing procedures. In Sec. II, experimental data acquired from an unloaded strand and a strand under various values of tensile load are presented and discussed, together with the data acquired from individual wires (straight and helical) comprising the strand. Finally, conclusions and potential extension of the work to other areas are summarized in Sec. III.

I. EXPERIMENTAL ARRANGEMENT

Approximately 3-m-long specimens of a seven-wire, 1863-MPa, low-relaxation, pre-stressing strand (ASTM A-416-74) with a 12.7-mm nominal diameter were used in this study. The strand consisted of a straight center wire wrapped with six helical outer wires at an approximately 22-cm pitch. The nominal diameter of each wire was 4.23 mm, and each wire in the strand was in physical contact with its adjacent wires.

A schematic diagram of the MsS and associated instrumentation used in this study is illustrated in Fig. 1. This illustration, together with the physical principles and operation of the MsS, was reported before,[3,4] but for completeness, a short description of them is repeated here.

The MsS consists of an encircling coil in a biasing dc magnetic field. The transmitting MsS operates under the magnetostrictive effect, in which the changing magnetic field deforms the steel strand material. The local deformation of the material results in an elastic wave that travels in both directions from the sensor. The receiving MsS operates un-

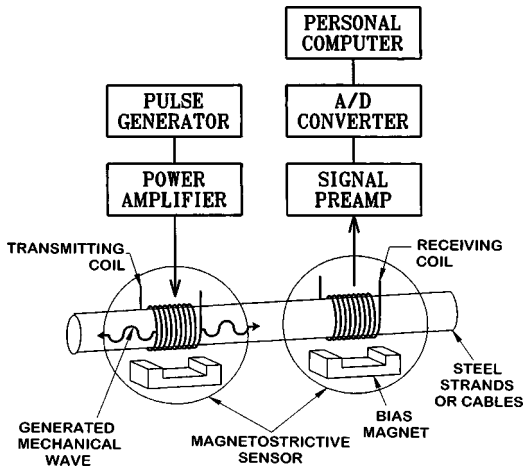

FIG. 1. Schematic diagram of magnetostrictive sensors and associated instrumentation.

der the reciprocal effect, called the inverse magnetostrictive effect, in which the strain (or stress) associated with the elastic wave changes the magnetic induction of the strand material. This changing magnetic induction induces an electric voltage that is detected and processed electronically.

In this study, the transmitting and receiving MsSs were placed at 1/4 and 1/2 of the specimen length, respectively. Due to the reflection of the wave at the ends, this sensor placement allows the detection of waveforms at every traveling distance of $nL/4$, where L is the length of the sample and n is an odd integer.[3,4] This arrangement thus provides a very convenient way to study the properties of wave propagation over a long period of traveling time without requiring a long specimen and multiple sensors.

Also, high-bandwidth elastic waves were transmitted into the specimens to allow an investigation of their properties over a wide frequency range.[3] Wave propagation properties were then determined by performing a time-frequency analysis of the signals[3,4] detected as the transmitted wave traveled up and down the length of the specimen.

Data from an unloaded specimen were acquired with the specimen laid horizontally on a floor. Data under various levels of tensile loading were acquired from a specimen positioned vertically in a loading machine. Mechanical chucks with serrated teeth were used to grip the ends of the strand specimen during the loading.

II. RESULTS AND DISCUSSION

A. With no applied load

Figure 2(a) shows the MsS signals taken from a 3-m-long specimen at zero applied load. The first signal in the figure is the initial electrical pulse applied to the transmitting MsS that leaked electrically to the receiver side of the instrumentation. The subsequent signals are from the transmitted elastic-wave pulse after it traveled approximately 0.76, 2.28, 3.79, 5.30,... m, respectively, as illustrated in Sec. I. After the first detected signals, there were low-amplitude random signals in the background whose origin will be discussed later in this section.

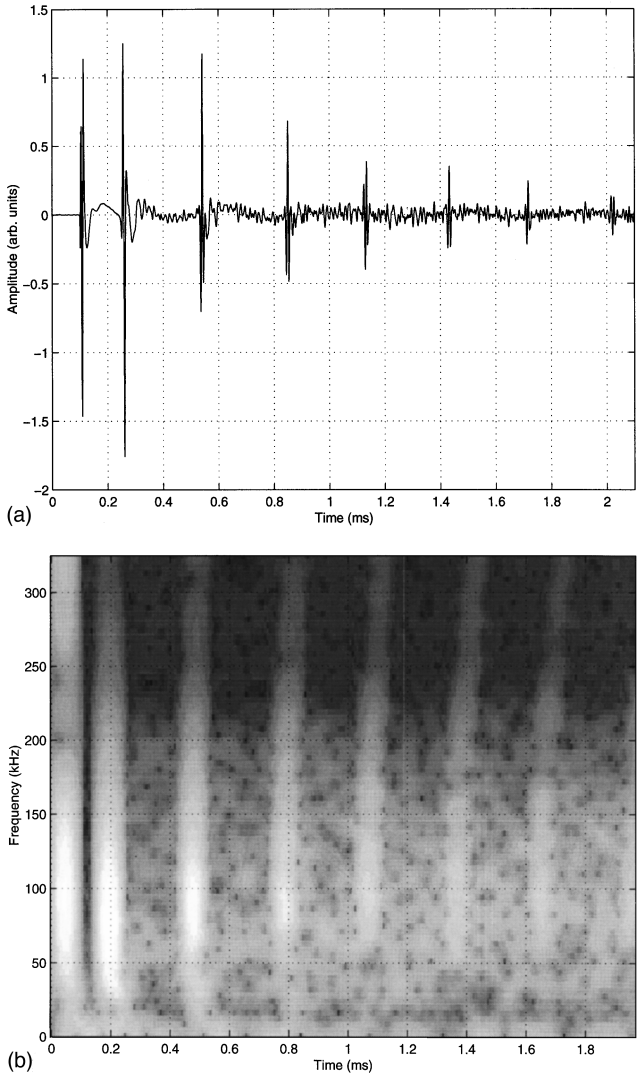

FIG. 2. Data acquired from a 3-m-long, seven-wire prestressing strand with a 12.7-mm nominal diameter: (a) detected signals and (b) a time-frequency representation of the detected signals via the STFT. The gray scale is in dB.

Figure 2(b) shows a time-frequency representation of the data in Fig. 2(a) obtained by performing a short-time Fourier transform (STFT) on the data.[3] As shown, the time evolution of the frequency components of the detected signals over a more than 350-kHz frequency range can be clearly observed, together with the dispersive characteristics of the wave. Based on the known theories on the elastic-wave propagation in a solid rod,[5,6] the mode of the wave in Fig. 2(b) is identified as the lowest order, first longitudinal mode [designated as $L1$, which is the same as the mode designated as $L(0,1)$ in Ref. 5]. The velocity of this mode at low frequencies is called the rod or bar velocity and is given as $v_0 = (E/\rho)1/2$, where E and ρ are Young's modulus and the density of the material, respectively. The group velocity then decreases with increasing frequency until it reaches a minimum, which occurs when v_0/af is approximately equal to 3.2, where a is the radius of the rod, and f is the wave frequency.[6,7] The velocity increases with further increase in wave frequency and approaches the value of the Rayleigh surface wave velocity at very high frequencies.

The time-frequency patterns of the detected signals in

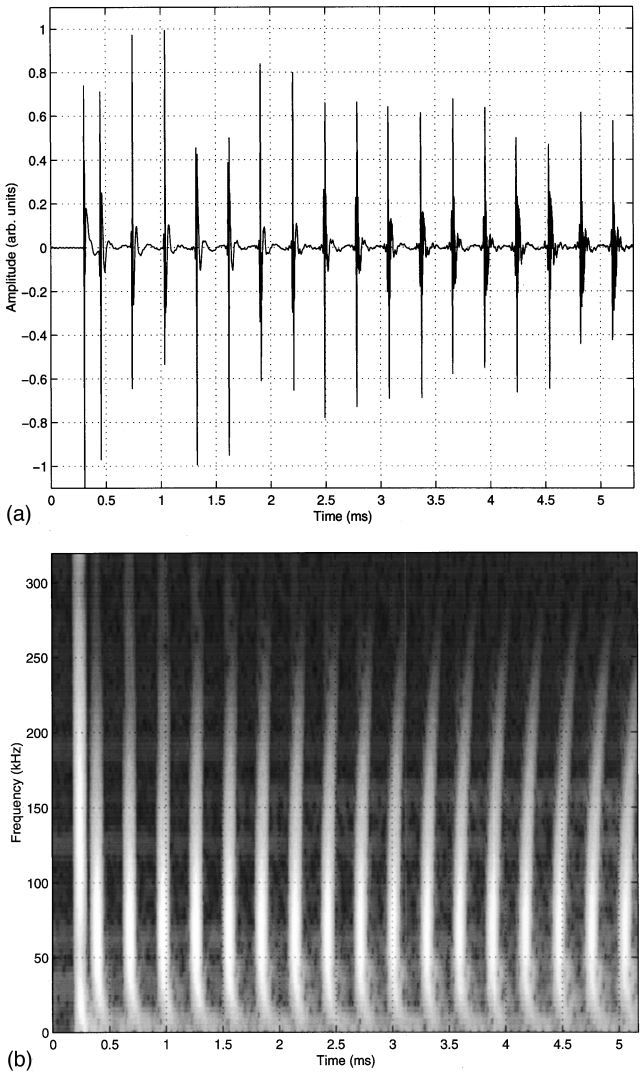

FIG. 3. MsS signals from a straight center wire of a seven-wire, pre-stressing strand (a) and the processed data using the short-time Fourier transform (b).

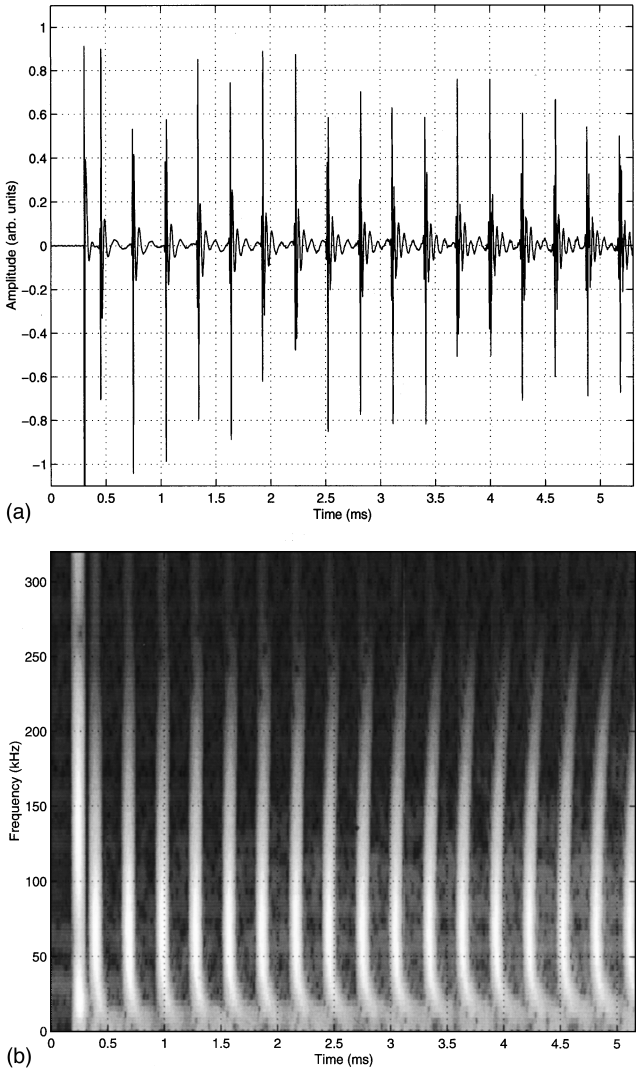

FIG. 4. MsS signals from a helical wire of a seven-wire, pre-stressing strand (a) and the processed data using the short-time Fourier transform (b).

Fig. 2(b) show a gentle curving toward the right at higher frequencies, indicating the gradual decrease in the group velocity of the wave with increasing frequency, which is the expected behavior of the $L1$ mode. From the time difference between the two signals and their known traveling distances, the group velocity was determined to be approximately 5.21×10^5 cm/s at 100 kHz (which can be treated as v_0 in the wire comprising the strand). The velocity was then decreased to approximately 4.88×10^5 cm/s at 350 kHz. In the wire comprising the strand, the minimum velocity would have occurred at about 770 kHz, which was beyond the frequency range covered in this study.

The data in Fig. 2(b) also show that the random signals in the background contain observable components up to 220 kHz. To identify the cause of these background signals, data were acquired individually from the center wire and a helical outer wire after extracting them from the strand. The pitch of the helical wires changed from 22 cm to 18 cm when extracted from the strand. The resulting data are given in Figs. 3 and 4 for the center and the helical wires, respectively. In these figures, the detected signals are shown in (a) and the STFT of the signals are shown in (b).

Contrary to the data taken from the strand given in Fig. 2(a), the data in Figs. 3(a) and 4(a) exhibited no random signals in the background. The absence of these random signals in individual wires indicates that the signals observed in the strand were a result of physical contact between the adjacent wires in the strand. In addition, the signals in Figs. 3(a) and 4(a) showed a negligible attenuation, whereas those shown in Fig. 2(a) exhibited a relatively large attenuation (about 2.4 dB/m). From these two observations, it can be deduced that a wave propagating in an individual wire of a strand generates secondary waves through physical contact with the adjacent wires. These secondary waves result in the random background signals in Fig. 2(a) and the energy loss in the primary signals. This gives rise to the high attenuation of the primary signals.

Additionally, the data in Figs. 3(a) and 4(a) show a reversal in the phase of the signal each time the wave reflected from an end of the wire. Also, the detected signals in the helical outer wire occurred slightly later in time (by approximately 1%) than the corresponding signals in the straight

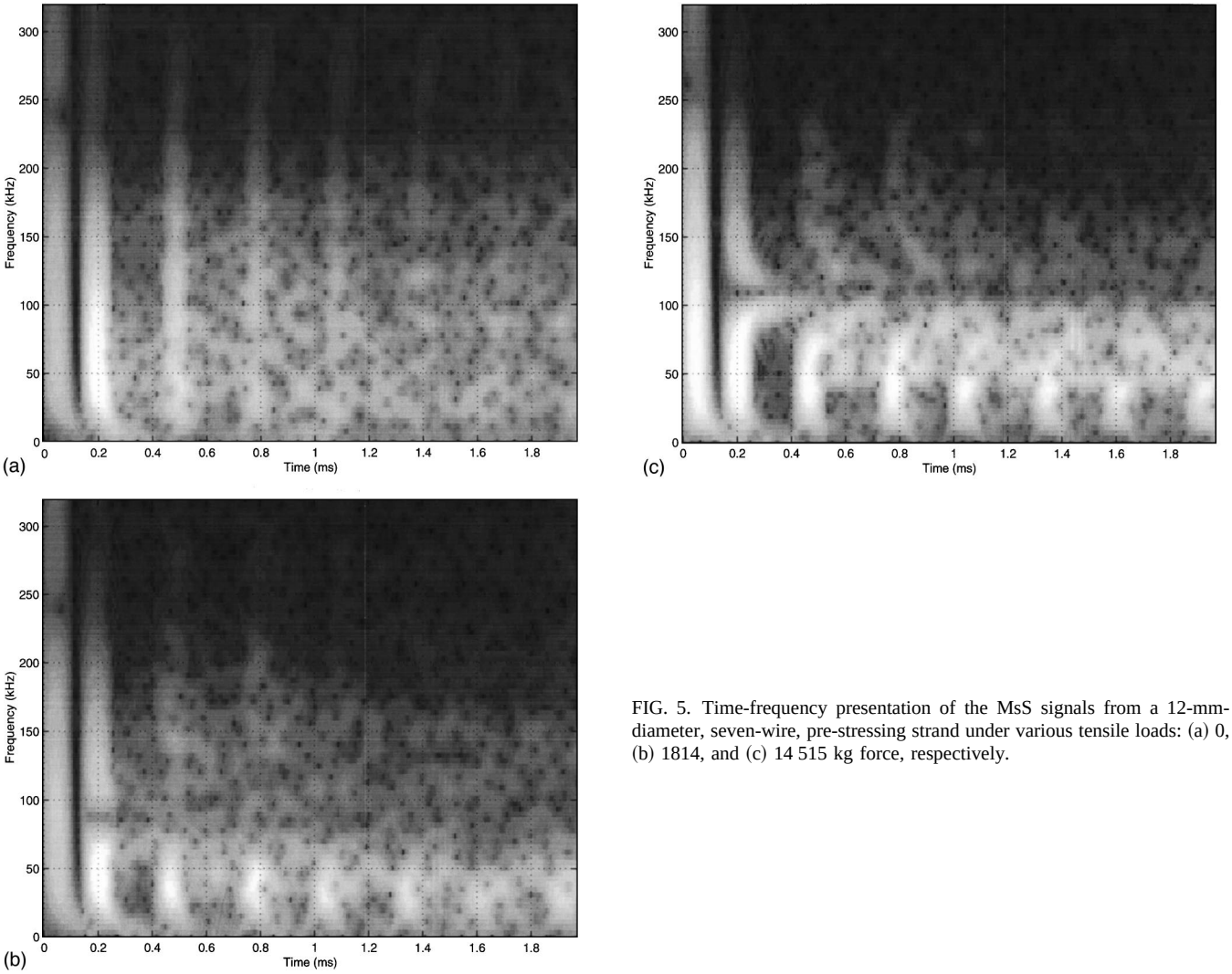

FIG. 5. Time-frequency presentation of the MsS signals from a 12-mm-diameter, seven-wire, pre-stressing strand under various tensile loads: (a) 0, (b) 1814, and (c) 14 515 kg force, respectively.

center wire. This is expected because the actual length of the helical wire is greater (by approximately 1%) than that of the straight wire.

The time-frequency representations in Figs. 3(b) and 4(b) showed that the dispersion characteristics of the wave in the straight and the helical wires were very similar. For frequencies larger than 40 kHz, they were identical to those shown in Fig. 2(b). For frequencies less than 40 kHz, however, the wave velocity in the helical wire decreased with decreasing frequency (from approximately 5.22×10^5 cm/s at 40 kHz to approximately 5.15 and 5.09×10^5 cm/s at 20 and 10 kHz, respectively) instead of remaining constant at the rod velocity as in the straight wire. Although no detailed investigation of the wave dispersion characteristics in these low frequencies was conducted (partly due to instrument limitations), the above was similar to the behavior near a cutoff frequency. It appears that, as the wavelength approaches the pitch of the helical wire, the mode of wave propagation undergoes a change. A further detailed study of this phenomenon, including modeling, is recommended.

B. Under tensile loading

Detected signals obtained from a strand specimen under various values of tensile load (up to 14515-kg force that corresponded to approximately 1449-MPa stress in the strand) are shown in the time-frequency domain in Fig. 5.

Compared with the data shown in Fig. 2, the corresponding data acquired at zero applied load, shown in Fig. 5(a), exhibited a greater attenuation in the signal amplitude, particularly in the frequencies below about 200 kHz. The cause of this difference is the interaction of the wave with the serrated teeth of the chucks that gripped the strand at its ends. This interaction caused energy loss from the main wave, contributing to the apparently greater attenuation in the signal amplitude. As can be seen in Fig. 5(a), the apparent attenuation was greater for lower frequency components, indicating that the interaction with the serrated teeth is stronger at lower frequencies.

When approximately 1814-kg force of tensile load (which was equivalent to 10% of the nominal yield strength of the strand) was applied, the resulting data, shown in Fig. 5(b), exhibited observable changes. One of the changes is the absence of spectral content in the second detected signal between about 75 and 140 kHz. Another change is the appearance of a shaded area, representing an amplitude decrease, in the time-frequency representation of the first detected signal near 90 kHz. Also, spectral components of frequencies lower than about 75 kHz exhibited less attenuation.

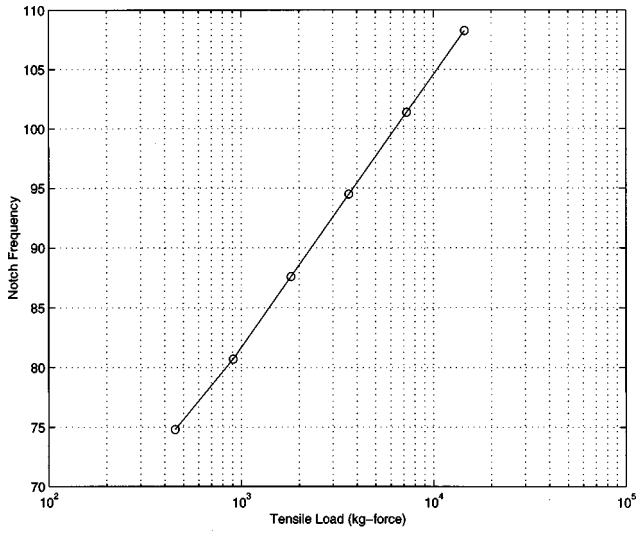

FIG. 6. A plot of notch frequency versus applied tensile load to a seven-wire prestressing strand with a 12.7-mm nominal diameter.

When the tensile load was further increased, the above changes became more pronounced, as can be seen in Fig. 5(c), in which the tensile load was approximately 14 515 kg. The following general trends occurred as the tensile load was increased—a shifting of the missing portion of the spectral content to a higher frequency and a further reduction in the wave attenuation at lower frequencies. In addition to the breakage in the spectrum of the first detected signal, dispersion of the signals was observed around this missing portion of the spectrum at higher loads, as shown in Fig. 5(c). The wave dispersion was more pronounced at higher tensile loads and exhibited a behavior similar to that near a cutoff frequency.

When the center frequency of the missing portion of the spectrum, called the notch frequency, was plotted as a function of the applied tensile load, N, the notch frequency was found to increase linearly with $\log N$, as illustrated in Fig. 6.

Of the several detected signals shown in Fig. 5(a)–(c), the first detected signal is the wave traveled directly from the transmitting MsS to the receiving MsS. The first detected signal, therefore, is the only wave which was not reflected at the ends of the specimen. Consequently, it is safe to conclude that the occurrence of a notch in the spectrum and the wave dispersion around the notch in the time-frequency plane in Fig. 5(b) and (c) are a direct result of the tensile loading effect on the wave propagation properties. The same may not be said of the other loading effects seen in the subsequent signals, including a reduced attenuation in the lower frequency side of the notch and an increased attenuation in the higher-frequency side of the notch. This is because these subsequently detected signals were reflected from the gripped ends of the specimen. It is likely that the condition of the physical contacts at the serrated teeth varied with the load level, and this then altered the wave interaction at the gripped end and influenced the reflected wave. Separating the effects of the end from the direct loading effects on the wave propagation properties was beyond the scope of work reported in this paper. It is recommended for further study.

As far as the authors are aware, the occurrence of the notch frequency and associated wave dispersion in a strand due to tensile loading has not been previously reported. Although there is no direct reference known to the authors which would suggest the causes for the observed tensile loading effects, some of the past work on wave propagation in rods and on the mechanical response of a strand under loading are discussed below to shed some light on the possible mechanisms for the observed phenomenon.

When a tensile load is applied to a strand, contact forces are exerted between neighboring wires that deform the individual wires and constrain their displacement.[8] Under loading, therefore, the original circular cross section of wires becomes somewhat distorted. In a rod, a wave mode called ''screw,'' that is neither a longitudinal nor torsional mode and has unsymmetric displacements around the longitudinal axis of the rod, was theoretically shown to exist.[6,9] According to the theory,[9] the dispersion curve for this screw mode intersects the curve for $L1$ mode. When the cross-sectional shape of the rod is distorted, the two modes separate from each other and cease to intersect. This means that up to a certain amount of distortion, the frequency of the intersection would increase with tensile loading. Since the expected effect of loading on the intersection frequency is in the same direction as the effect of loading on the notch frequency, the explanation of the observed tensile loading effects using this theory was examined. According to the theory, the intersection where a coupling of the two modes is possible occurs when $\rho c^2/\mu = 2$ and $k^2K^2 = 2.7$, where ρ is the density, c is the phase velocity, μ is the shear modulus, k is the wave number, and K is the radius of gyration of the cross section about the longitudinal axis of the rod. Utilizing a typical value for the shear wave velocity V_s in steel (that is approximately 3×10^5 cm/s) and $V_s^2 = \mu/\rho$, the intersection is calculated to occur at about 740 kHz in the wires comprising the strand specimen. As the notch frequencies observed from the strand were much lower than the above calculated value, it was deemed very unlikely that the coupling of the screw and $L1$ modes caused the observed tensile loading effects.

In a single rod, a short-duration pulse of $L1$ mode was reported to undergo a large elongation of its waveform when the frequency of the wave was adjusted to a certain specific value. Meitzler, who reported the above phenomenon, attributed it to a coupling of the flexural and longitudinal modes because, at these frequencies, the phase velocities of the two wave modes were the same. For the $L1$ mode, the first of such frequencies occurs due to the coupling with $F(2,1)$ mode—a second order flexural mode—when $2\pi fa/V_s$ is approximately 2.4, where f is the frequency and a is the radius of the rod. In the wires constituting the strand specimen, this frequency is about 540 kHz. Like the intersection frequency for the screw mode discussed above, this frequency is much higher than the observed notch frequencies, indicating that this particular mode coupling cannot explain the observed tensile loading effects.

It might be argued that under tensile loading, the strand may effectively behave like a single rod to an increasing degree as the load increases. If the strand is treated like a single rod, the above mode coupling would occur at about 180 kHz, which is still far higher than the notch frequencies.

Furthermore, if the above hypothesis were correct, the behavior of the strand would gradually change from an assembly of individual wires to an effectively single rod with an increasing level of tensile load. This means that the mode-coupling frequencies would gradually decrease with increasing level of tensile load. Since the notch frequencies actually increased with increasing tensile load, this particular mode coupling cannot explain the observed tensile loading effect.

In the discussions by Meitzler,[10] no consideration was given to a possible coupling between $L1$ and $F(1,1)$—the lowest flexural mode—because the dispersion curves of both modes in his plots of dimensionless frequency versus wave number meet only at zero. When a static tension N is applied to a rod, the velocity of the $F(1,1)$ mode approaches $(N/\rho)^{1/2}$ (the velocity of transverse waves in a stretched string at low frequencies) instead of approaching zero.[11] This means that the dispersion curve of the $F(1,1)$ mode changes with tension, with its change extending to a higher frequency with increasing stress level because of the higher wave velocity. It might be possible, therefore, that the altered dispersion curve for $F(1,1)$ mode intersects the curve for $L1$, and the resulting mode coupling produces the observed spectral notch and associated dispersion of $L1$ mode. If this is the case, the frequency at which this coupling occurs would increase with the applied tensile load that is consistent with the observed behavior of the notch frequency with the tensile load. There is, however, one crucial problem with the above argument. The problem is that the argument should also apply to a single rod, and test results from a straight wire subjected to tension failed to show the notch. In fact, no observable changes were found in the wave propagation properties, even though the straight wire was subjected to the same range of tension applied to the strand specimen.

Although the reasons for the observed tensile loading effects on the $L1$ mode propagation are unclear, it is certain that they are related to physical contacts between the neighboring wires in a strand. In a previous publication,[3] the authors reported an occurrence of a missing portion in the spectrum of the $L1$ mode propagating in a somewhat corroded 1.52-cm-diam, seven-wire strand. The missing portion was much like that observed at low values of tension and was centered around about 60 kHz. Since no stress was applied to that sample, the missing portion was believed to be caused by the physical contacts effected by corrosion, which is generally expansive.

III. SUMMARY

This paper described experimentally observed tensile loading effects on the properties of $L1$ wave mode propagation in a 1.52-cm-diam, seven-wire strand used for prestressed concrete structures. In an unloaded state, the wave propagation properties in strand were the same as those seen in individual wires comprising the strand, namely, straight center wire and helical outer wires. In the strand, however, extraneous signals were found to be produced from the propagating wave due to physical interactions between the adjacent wires. Under tensile loading, it was observed that a certain portion of the frequency components of the wave became highly attenuative and, thus, absent in the frequency spectrum of the wave. The center frequency of this missing portion, called notch frequency, was found to increase linearly to log N, where N is the applied tensile load. In addition, on both sides of the notch frequency, the wave exhibited a large dispersion in a manner similar to the behavior near a cutoff frequency. Causes of the observed tensile loading effects are unclear presently, and further studies are recommended to understand the phenomenon. Although the underlying physics of the observed phenomenon is not yet understood, it could be used for measurements of tension in a strand, cable, or wire rope for NDE of their conditions. The results also are helpful in selecting suitable wave frequencies for detection of defects in strands or cables by, for example, avoiding the frequencies near the spectral notch.

Additionally, the same approach used in this investigation could be extended to studying the effects of physical contacts on the wave propagation. Such a study would be useful for devising NDE techniques for determining structural conditions of strands or cables in areas under physical contacts, such as at terminations, clamps, and saddles, and in concrete.

ACKNOWLEDGMENTS

This work was funded by the Federal Highway Administration (FHWA) under Grant Agreements Nos. DTFH 61-93-X-00036 and DTFH 61-95-X00044. Technical supports from Drs. Steve Chase and Richard Livingston in the Office of Engineering and Highway Operations R&D of FHWA are greatly appreciated.

[1] H. Kwun and C. M. Teller, ''Detection of fractured wires in steel cables using magnetostrictive sensors,'' Mater. Eval. **52**, 503–507 (1994).
[2] H. Kwun and C. M. Teller, ''Nondestructive evaluation of steel cables and ropes using magnetostrictively induced ultrasonic waves and magnetostrictively detected acoustic emissions,'' U.S. Patent No. 5,456,113 (October 1995).
[3] H. Kwun and K. A. Bartels, ''Experimental observation of elastic-wave dispersion in bounded solids of various configurations,'' J. Acoust. Soc. Am. **99**, 962–968 (1996).
[4] H. Kwun, J. J. Hanley, and K. A. Bartels, ''Recent developments in nondestructive evaluation of steel strands and cables using magnetostrictive sensors,'' Oceans'96 MTS/IEEE Conference Proceedings, pp. 144–148 (Sept. 1996).
[5] J. Zimanek, ''An experimental and theoretical investigation of elastic wave propagation in a cylinder,'' J. Acoust. Soc. Am. **51**, 265–283 (1972).
[6] M. Redwood, *Mechanical Waveguides, The Propagation of Acoustic and Ultrasonic Waves in Fluids and Solids with Boundaries* (Pergamon, New York, 1960), Chap. 6.
[7] E. A. Flinn, ''Dispersion curves for longitudinal and flexural waves in solid circular cylinders,'' J. Appl. Phys. **29**, 1261–1262 (1958).
[8] S. Machida and A. J. Durelli, ''Response of a strand to axial and torsional displacements,'' Inst. Mech. Eng. Proc. Part C: J. Mech. Eng. Sci. **15**, 241–251 (1973).
[9] G. J. Kynch, ''The fundamental modes of vibration of uniform beams for medium wavelengths,'' Br. J. Appl. Phys. **8**, 64–73 (1957).
[10] A. H. Meitzler, ''Mode coupling occurring in the propagation of elastic pulses in wires,'' J. Acoust. Soc. Am. **33**, 435–445 (1961).
[11] G. Mott, ''Elastic waveguide propagation in an infinite isotropic solid cylinder that is subjected to a static axial stress and strain,'' J. Acoust. Soc. Am. **53**, 1129–1133 (1973).

Vibration analysis of line-coupled structures using a coupling load decomposition technique

M. Hatam, L. Cheng, and D. Rancourt
Mechanical Engineering Department, Laval University, Quebec G1K 7P4, Canada

(Received 4 February 1997; revised 28 October 1997; accepted 5 February 1998)

A new substructuring technique is proposed to perform vibration analysis of line-coupled structures. In dividing the whole structure into a master structure and several auxiliary structures, a variational formulation is used to model the master structure, enabling one to introduce the effects of all auxiliary structures by using their compliance characteristics at several observation points along the junction. Continuous functions of the compliance are obtained via a regression analysis. Given the problem of using the compliance inverse to attain a straightforward formulation, a ''Coupling Load Decomposition'' technique is proposed since a direct formulation using the compliance inverse is not feasible. By decomposing the interactive load between substructures, relations with displacement decomposition of the master structure can be found. This new formulation permits the direct use of the compliance of the junction, which may be obtained analytically, numerically, or experimentally. Numerical examples using both calculated and experimentally measured compliance data are given. Simulation results are also compared to those obtained experimentally, showing good agreement in low- and medium-frequency ranges. © *1998 Acoustical Society of America.* [S0001-4966(98)04205-2]

PACS numbers: 43.40.Dx, 43.40.At [CBB]

INTRODUCTION

Mechanical systems may be composed of different elements coupled together through points, lines, or surfaces. The complexity of such systems requires efficient simulation techniques. Moreover, some elements may be already complex so that any attempt to model all elements in the same manner becomes too demanding for most of the existing simulation techniques. From this point of view, the development of hybrid approaches that can make use of different simulation techniques becomes extremely attractive. Such a hybrid approach is proposed in this paper. The method is illustrated by analyzing the forced vibration of a plate coupled to different structures along continuous lines. Plate assemblies and stiffened plates are typical applications of such systems.

A number of techniques have been developed over the past few decades to study complex systems involving coupled structures. A good summary of the techniques is given by Min.[1] As far as planar structures are concerned, apart from some well-known techniques like the finite element methods, the statistical energy analysis method,[2] and the mobility power flow approaches,[3,4] many other investigations have been conducted to analyze particular configurations composed of coupled structures through continuous lines. Shen and Gibbs[5] have proposed a deterministic solution to study different configurations of rectangular plates at low frequencies. Guyader *et al.*[6] have used a technique based on analytical calculations of the eigenmodes of connected rectangular plates. The approach has been applied to platelike structures with a single junction. Other techniques have also been presented for platelike structures.[7,8] A semianalytical approach was also proposed using artificial springs to characterize the junction between substructures.[9] However, the technique becomes cumbersome when the number of substructures increases, since all substructures must be modeled with the same technique. Beam-stiffened plates is another category of coupled structures which has been investigated by some authors.[10,11] In an effort to develop a more general approach, Jezequel and Seito[12] have presented an extension of the classical component modal synthesis technique. The modal synthesis methods were reformulated to make them compatible with the finite element method.

In a real-life coupled system, there may exist some substructures with complex effects that can hardly be theoretically modeled. In such cases, experimental data are necessary to represent such substructures. However, very few methods allow structures identified by tests to be coupled through continuous interfaces. Some substructural or modal synthesis techniques are potentially capable of achieving the same task.[12–14] However, modal identification of complex structures may be a very difficult task, since it requires a detailed description of each substructure. Even if one is capable of obtaining the modal characteristics, they may be difficult to work with computationally.[15] On the contrary, compliance (or impedance, mobility) functions which carry the dynamic information of substructures are much easier to work with since measurements can only be conducted along the junction with other structures. Although some impedance or mobility model found in the literature[7,8] would be eventually modified to fit the hybrid requirement, methods should still be developed to incorporate measured data with the simulation model since they depend very much on the way in which the measured data are used in the whole formulation.

In this paper, a method using a regression approach to model the compliance distribution along continuous lines is presented. Complex systems are divided into a main structure and auxiliary structures. The main structure is analyzed using a variational formulation while the effects of all sub-

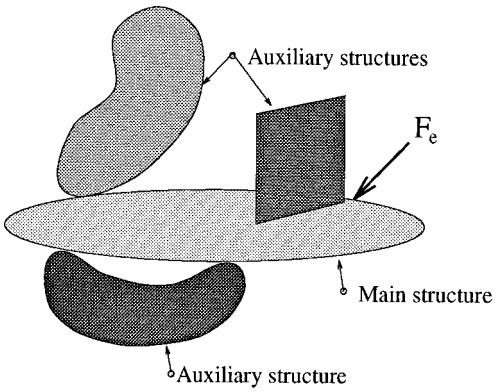

FIG. 1. A typical complex system.

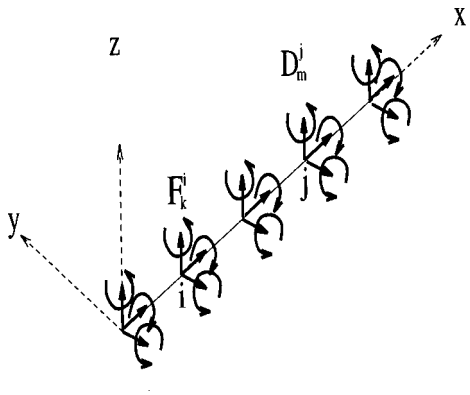

FIG. 2. Distribution of forces and moments due to coupling along a line.

structures are introduced using their compliances at the contact line with the main structure. Using a plate as the master structure, it is first demonstrated that direct use of compliance inverse data, which could have led to a straightforward formulation, results in an unstable solution. To address this problem, a new technique, named the ''Coupling Load Decomposition'' technique (CLD) is proposed. By decomposing the coupling load between substructures into a polynomial series, relations with the displacement of the master structure are found. Based on this new formulation, compliance data can be directly used with the help of a regression analysis.

Several examples are treated to numerically and experimentally assess the technique. A real-life structure demanding both numerical and experimental treatments is also presented to illustrate the hybrid aspect of the method. Whenever possible, simulated results are compared either to finite element simulations or to experimental data. The results are restricted to low- and middle-frequency ranges, since a semianalytical formulation is used to model the main structure. However, the proposed methodology is quite general and may be used in conjunction with any other energy-based formulations.

I. METHODOLOGY AND COUPLING REPRESENTATION

Consider a structure composed of different elements connected along continuous lines, or as a special case, through specific points. The whole structure is divided into two parts: a master structure and several auxiliary structures as shown in Fig. 1. The dynamic behavior of the master structure may be formulated using any energy-based approach which involves the effects of the auxiliary structures via their energy terms. In this paper, the formulation is based on a semianalytical approach using artificial springs inspired by our previous work.[9] The effects of all auxiliary structures are represented by their compliance characteristics. At each contact zone, compliance data may be obtained by treating each auxiliary substructure separately via any available approach: analytical, numerical, or experimental. Interfaces should then be developed to incorporate the effects of auxiliary structures.

In the case of a multipoint contact between two structures, the compliance $\beta^{ij}_{k'm'}$ is defined by the following relation

$$\beta^{ij}_{k'm'}=\frac{D^j_{k'}}{F^i_{m'}}, \tag{1}$$

where $D^j_{k'}$ is the displacement at point ''j'' in direction ''k''' due to a load $F^i_{m'}$, applied at point ''i'' in direction ''m'.'' If more than one contact point is involved, a compliance matrix should be used. When the contact zone between two coupled structures has dimensions comparable to the wavelength of the vibrating system, the point coupling representation is no more valid. In this case, each component of the compliance matrix is a continuous function of the excitation and response point coordinates.

The compliance variation along the junction may be obtained by first considering the line of contact as a combination of a finite number of contact points as shown in Fig. 2. A regression analysis leads to continuous functions representing the compliance components and ensures a continuous variation along the junction. Each component of the compliance matrix $\beta^{ij}_{k'm'}$ is replaced by a continuous function $\beta_{k'm'}(x,\xi)$. Here x and ξ indicate the local coordinate of the excitation and response points, respectively, along the contact line.

Consider a system composed of a thin rectangular plate as the master structure shown in Fig. 3, with $-b\leqslant x\leqslant b$,

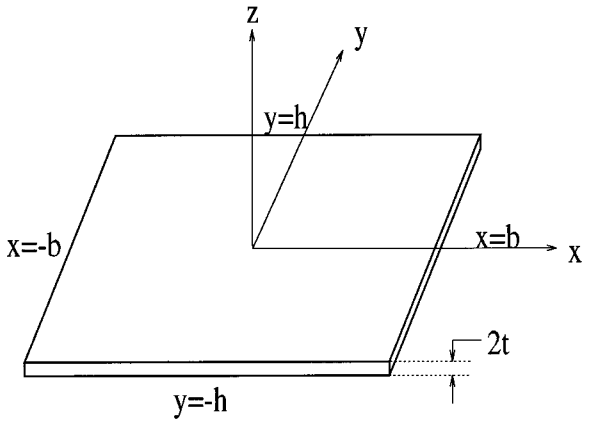

FIG. 3. A thin plate used as the main structure.

$-h \leqslant y \leqslant h$, and $-t \leqslant z \leqslant t$. The boundary conditions of the plate are modeled using artificial springs. Both translational and rotational springs are supposed to be uniformly distributed at each edge. Use of artificial springs enables one to simulate various boundary conditions. In the present work, small deformations are assumed and classical linear thin plate theory (Love–Kirchhoff) is used.

In order to achieve a general solution of the plate with arbitrary boundary conditions, an approximative solution can be obtained using the Rayleigh–Ritz method. The transverse displacement of the rectangular plate is approximated by a series:

$$w(x,y,t)=\sum_{i}^{\infty}\sum_{j}^{\infty} a_{ij} f_i(x) g_j(y), \tag{2}$$

where functions $f_i(x)$ and $g_j(y)$ are linearly independent. Assuming polynomial functions for $f_i(x)$ and $g_j(y)$ yields

$$w(x,y,t)=\sum_{i=0}^{m}\sum_{j=0}^{n} a_{ij}\left(\frac{x}{b}\right)^i\left(\frac{y}{h}\right)^j, \tag{3}$$

where the series is truncated to m and n terms, in the x and y directions, respectively. Appropriate values of m and n depend on the configuration of the plate and the desired frequency range.

Using the Rayleigh–Ritz method, the coefficients of the polynomial decomposition a_{ij} may be obtained by minimizing Lagrangian of the system L:

$$\frac{d}{dt}\left(\frac{\partial L}{\partial \dot{a}_{pq}}\right)-\left(\frac{\partial L}{\partial a_{pq}}\right)=0, \tag{4}$$

$$L=E_c-E_p^T+W, \tag{5}$$

with E_c and E_p^T being, respectively, the kinetic and total potential energies of the system. The term W represents the contribution of (or the work done by) surface loads or body forces. The total potential energy can be written as

$$E_p^T=E_p+E_p^b+E_p^{cp}, \tag{6}$$

where E_p is the total strain energy of the main structure, E_p^b is the potential energy stored at the boundary springs, and E_p^{cp} is the substructure contribution to the total energy of the coupled system. The energy approach and a double series of admissible functions for the field variable leads to the following forms of the energy terms

$$E_c=\frac{1}{2}\sum_{p}\sum_{q}\sum_{r}\sum_{s} M_{pqrs}\dot{a}_{pq}(t)\dot{a}_{rs}(t), \tag{7}$$

$$E_p+E_p^b+E_p^{cp}=\frac{1}{2}\sum_{p}\sum_{q}\sum_{r}\sum_{s} K_{pqrs}a_{pq}(t)a_{rs}(t), \tag{8}$$

where M_{pqrs} and K_{pqrs} are the general mass and stiffness of the system, respectively. The procedure for deriving the generalized mass and stiffness matrices of the plate (i.e., the main structure) with boundary springs and generalized force are explained in Ref. 16. It should be noted that the effect of the auxiliary structures are modeled through the term E_p^{cp}, which should be further analyzed.

II. CHARACTERIZATION OF AUXILIARY SUBSTRUCTURES

A. Direct formulation using compliance inverse matrix

Using the compliance inverse leads to a quite straightforward formulation. Assuming a junction parallel to the x axis, the coupling load vector between the main plate and an arbitrary substructure may be written as

$$F_{m'}(x)=\int_{-b}^{b}\sum_{k'}^{N} \eta_{k'm'}(x,\xi)D_{k'}(\xi)d\xi, \tag{9}$$

where $F_{m'}(x)$ and $D_{m'}(\xi)$ denote the functions representing the coupling load and the corresponding deformation variations, respectively, along the junction. It should be mentioned that the so-called ''coupling load'' represents the interacting effects between the connected substructures, which may be in the form of forces or moments. Consequently the corresponding deformations are translation and rotation, respectively. In the above equation, $\eta_{k'm'}(x,\xi)$ is the inverse of the compliance matrix of a substructure. Each component is a continuous function of x and ξ. The terms ''k''' and ''m''' vary from 1 to N and N denotes the number of coupling load components along the junction and depends on the configuration. In a general problem where all degrees of freedom are present, N is equal to 6. The energy term stored in the substructure, in its general form, can be written as

$$E_{cp}=\frac{1}{2}\int_{-b}^{b}\sum_{m'}^{N} F_{m'}(x)D_{m'}(x)dx. \tag{10}$$

Applying Eq. (9) yields

$$E_{cp}=\frac{1}{2}\int_{-b}^{b}\int_{-b}^{b}\sum_{k'}^{N}\sum_{m'}^{N} \eta_{k'm'}(x,\xi)D_{k'}(\xi)D_{m'}(x)d\xi\, dx. \tag{11}$$

In order to derive the compliance matrix, the junction line is discretized into a series of observation points as illustrated in Fig. 2. By applying a unit excitation at point i while measuring the response at point j, the compliance matrix $\beta_{ij}^{k'm'}$ can be constructed. The inverse of this matrix gives $\eta_{ij}^{k'm'}$. A polynomial regression analysis can then be performed on η, and a continuous function $\eta_{k'm'}(x,\xi)$ can be found as follows:

$$\eta_{k'm'}(x,\xi)=\sum_{k=0}^{n1}\sum_{l=0}^{n2} c_{kl}^{k'm'}x^k\xi^l, \tag{12}$$

where $c_{kl}^{k'm'}$ denotes the regression coefficients and ''$n1$'' and ''$n2$'' are the degree of regression for independent variables x and ξ, respectively. The regression technique is briefly explained in the Appendix. Notice that the procedure is, in principle, applicable to the analysis of both the compliance and its inverse. For special cases when there is only one compliance function $F_{m'}(x)$ at the junction or in any special case where the substructure compliance inverse $\eta_{m'm'}(x,\xi)$ is decoupled from other components, the energy contribution

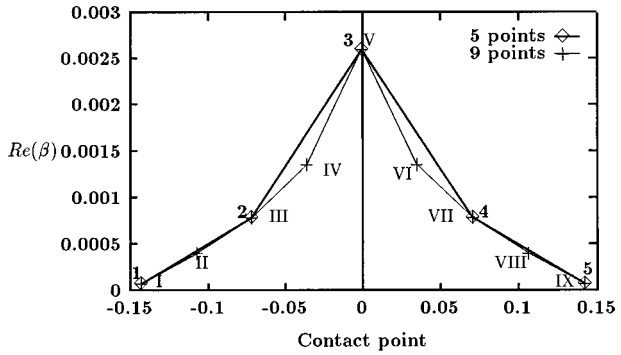

FIG. 4. Variation of the real part of β along the line of contact.

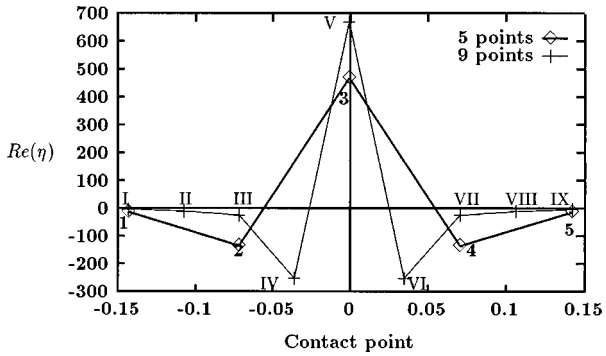

FIG. 5. Variation of the real part of η along the line of contact.

of the substructure, given by Eq. (11), can be written as

$$E_{cp}=\frac{1}{2}\int_{-b}^{b}\int_{-b}^{b}\eta_{m'm'}(x,\xi)D_{m'}(\xi)D_{m'}(x)d\xi\,dx. \quad (13)$$

This equation may then be used to obtain the generalized stiffness matrix representing the contribution of substructures on the vibration of the coupled system. As we can notice, this formulation is quite straightforward and is based, however, on a successful regression analysis on the η matrix. This issue is addressed below.

The formulation developed previously uses the compliance inverse function (or matrix) η. The direct measurement of this quantity is not feasible, since there is no practical way of introducing a unit displacement at one location, while keeping the other locations fixed. On the contrary, the compliance matrix β is much easier to obtain. In this case, the compliance matrix must be inverted to obtain the η matrix. However, this inversion process becomes difficult when the number of contact points is increased. This phenomenon has been explained by Fung[17] for the flexibility matrix which is a special case of the compliance matrix in the static case. It turns out that when the number of observation points approaches infinity, the distance between adjacent points approaches zero and the components of the η matrix approach infinity. As a result, by increasing the number of contact points, the compliance matrix becomes hardly invertible.

Apart from the problem mentioned above, inherent to the characteristics of the η function, an additional problem emerges when a regression analysis should be further performed on the η matrix. To illustrate this problem, let us consider how the compliance function β and the compliance inverse function η vary with the number of observation points. A simply supported rectangular thin plate (Fig. 3) is taken as an example, whose rotational compliance β_{44}^{ij} and its inverse along one edge ($y=-h$) are studied. The plate used is made of aluminum with dimensions $b=15$ cm, $h=22.5$ cm, and $t=15.875$ mm. Figure 4 shows the variation of the β matrix when a unit torque is applied at the midpoint of the junction ($x=0$) and the rotational responses are measured at different contact points along the junction. Two curves using, respectively, five and nine contact points are presented. In the case of nine observation points, points I, III, V, VII, and IX have the same coordinates as points 1, 2, 3, 4, and 5, in the five observation point case. Points II, IV, VI, and VIII are four new observation points added to form the nine contact points case. It can be observed, in Fig. 4, that in both cases, the compliance values are the same for each common observation point. Obviously, the nine point configuration defines the compliance characteristics of the plate more precisely than the five point configuration does. The smoothness of the compliance variation makes it possible to perform a stable regression analysis.

Under the same conditions, Fig. 5 shows the variation of η. Again, two curves denote the η variations for the five and nine contact point cases, respectively. It can be seen that the value of η at an arbitrary point strongly depends on the number of contact points. For example, although points 2, 3, and 4 have the same coordinates as points III, V, and VII, values of η considerably vary from one case to another for these common points. This strong dependency on the number of contact points is such that the regression analysis on the η matrix should be avoided. Therefore a new formulation is required to directly use the compliance matrix.

B. Formulation via coupling load decomposition

A new formulation is proposed to avoid the use of the η matrix in the computation of the energy contributed by the substructures. A load distribution along the junction is considered and efforts are made to find a relation between the coefficients of the load distribution and coefficients of previously defined displacement fields. The formulation is developed for an arbitrary load distribution which can either be forces or moments. At this point, for the sake of briefness, it is supposed that there is no coupling between coupling loads of different natures (forces and moments corresponding to a different degree of freedom, for example) and, accordingly, the summation term in Eq. (9) can be removed. It should be noted that in cases where this simplification does not apply, the formalism that will be developed still remains valid, although the mathematical description will be different. Equation (9) can be rewritten in the following form to relate the displacement of the junction $D_{m'}(x)$ to the load function $F_{m'}(x)$ using the compliance function $\beta_{m'm'}(x,\xi)$

$$D_{m'}(x,y_0)=\int_{-b}^{b}\beta_{m'm'}(x,\xi,y_0)F_{m'}(\xi,y_0)d\xi. \quad (14)$$

In the above expression, the junction is obviously assumed to be parallel to the x axis with y_0 as its y coordinate. A regression analysis over the compliance matrix gives

$$\beta_{m'm'}(x,\xi,y_0)=\sum_{k=0}^{n1}\sum_{l=0}^{n2} c_{kl}^{m'm'}x^k\xi^l. \tag{15}$$

Inserting Eq. (15) into Eq. (14) yields

$$D_{m'}(x,y_0)=\int_{-b}^{b}\sum_{k=0}^{n1}\sum_{l=0}^{n2} c_{kl}^{m'm'}x^k\xi^l F_{m'}(\xi,y_0)d\xi. \tag{16}$$

In the above expression, the load distribution $F_{m'}(\xi,y_0)$ is an unknown function which constitutes the major obstacle when using the compliance matrix. To tackle this problem, the load distribution along the junction is decomposed over a polynomial base as

$$F_{m'}(\xi,y_0)=\sum_{i}^{m}\sum_{j}^{n} b_{ij}\left(\frac{\xi}{b}\right)^i\left(\frac{y_0}{h}\right)^j, \tag{17}$$

with b_{ij} being unknown coefficients to be determined. Hence Eq. (16) may be written as

$$D_{m'}(x,y_0)=\int_{-b}^{b}\sum_{k=0}^{n1}\sum_{l=0}^{n2}\sum_{i}^{m}\sum_{j}^{n} c_{kl}^{m'm'}b_{ij}x^k\xi^l \times\left(\frac{\xi}{b}\right)^i\left(\frac{y_0}{h}\right)^j d\xi. \tag{18}$$

The polynomial decomposition for transverse displacements of a rectangular thin plate given by Eq. (3) may be written in a more general form for $D_{m'}(x,y)$ as

$$D_{m'}(x,y)=\sum_{i=0}^{m}\sum_{j=0}^{n} B_{ij}\left(\frac{x}{b}\right)^i\left(\frac{y}{h}\right)^j. \tag{19}$$

Inserting this polynomial decomposition in Eq. (18) yields

$$\sum_{i}^{m}\sum_{j}^{n} B_{ij}\left(\frac{x}{b}\right)^i\left(\frac{y_0}{h}\right)^j=\int_{-b}^{b}\sum_{k=0}^{n1}\sum_{l=0}^{n2}\sum_{i}^{m}\sum_{j}^{n} c_{kl}^{m'm'}b_{ij}x^k\xi^l \times\left(\frac{\xi}{b}\right)^i\left(\frac{y_0}{h}\right)^j d\xi. \tag{20}$$

After integrating with respect to ξ, the following relation is obtained

$$\sum_{i}^{m}\sum_{j}^{n} B_{ij}\left(\frac{x}{b}\right)^i\left(\frac{y_0}{h}\right)^j =\sum_{k=0}^{n1}\sum_{l=0}^{n2}\sum_{i}^{m}\sum_{j}^{n} c_{kl}^{m'm'}b_{ij} \times\left(\frac{y_0}{h}\right)^j\frac{b^{l+1}}{i+l+1}(1+(-1)^{i+l})x^k. \tag{21}$$

In order to find the relation between two series of coefficients B_{ij} and b_{ij}, the two sides of the above equation are multiplied by x^τ, where $\tau=0,...,m$. Integrating the resulting equation with respect to x along the junction yields

$$\sum_{i}^{m}\sum_{j}^{n} B_{ij}\frac{b^{\tau+1}}{i+\tau+1}\left(\frac{y_0}{h}\right)^j(1+(-1)^{\tau+i}) =\sum_{i}^{m}\sum_{j}^{n}\sum_{k=0}^{n1}\sum_{l=0}^{n2} c_{kl}^{m'm'}b_{ij}\left(\frac{y_0}{h}\right)^j \times\frac{b^{k+l+\tau+2}}{(i+l+1)(k+\tau+1)} \times(1+(-1)^{i+l})(1+(-1)^{k+\tau}). \tag{22}$$

Two series of coefficients are defined as

$$\Gamma_i=\sum_{j} b_{ij}\left(\frac{y_0}{h}\right)^j, \tag{23}$$

$$\Omega_i=\sum_{j} b_{ij}\left(\frac{y_0}{h}\right)^j. \tag{24}$$

The above procedure is only valid at the junction, and accordingly, a complete relation between the series of coefficients B_{ij} and b_{ij} is not available. Fortunately, only the global relation between two series of new coefficients Γ_i and Ω_i is needed in the formulation. This relation can be found by inserting Eqs. (23) and (24) in Eq. (22) as

$$\sum_{i}^{m}\Gamma_i\frac{b^{\tau+1}}{i+\tau+1}(1+(-1)^{\tau+i}) =\sum_{i}^{m}\sum_{k=0}^{n1}\sum_{l=0}^{n2} c_{kl}^{m'm'}\Omega_i\frac{b^{k+l+\tau+2}}{(i+l+1)(k+\tau+1)} \times(1+(-1)^{i+l})(1+(-1)^{k+\tau}). \tag{25}$$

Note that the above equation is valid for each value of $\tau=0,...,m$ so that the whole set of equations can be written in matrix form as

$$\underset{(\hat{m}\times\hat{m})(\hat{m}\times 1)}{[\Delta]}\ \{\Gamma\}=\underset{(\hat{m}\times\hat{m})(\hat{m}\times 1)}{[\Lambda]}\ \{\Omega\}, \tag{26}$$

where $\hat{m}=m+1$,

$$\Delta(i,j)=\frac{b^{i+1}}{i+j+1}(1+(-1)^{i+j}) \tag{27}$$

and

$$\Lambda(i,j)=\sum_{k=0}^{n1}\sum_{l=0}^{n2} c_{kl}^{m'm'}\frac{b^{k+l+i+2}}{(i+l+1)(k+i+1)} \times(1+(-1)^{i+k})(1+(-1)^{j+l}). \tag{28}$$

Consequently,

$$\underset{(\hat{m}\times 1)}{\{\Omega\}}=\underset{(\hat{m}\times\hat{m})}{[\Lambda]^{-1}}\ \underset{(\hat{m}\times\hat{m})(\hat{m}\times 1)}{[\Delta]}\ \{\Gamma\}. \tag{29}$$

Finally, the following relation between the two series of coefficients Γ_i and Ω_i is obtained

$$\{\Omega\}=[H]\{\Gamma\} \tag{30}$$

where

$$[H]=[\Lambda]^{-1}[\Delta]. \tag{31}$$

The substructural energy term, resulting from the presence of the coupling load $F_{m'}(\xi,y_0)$ on the main plate, is then calculated as

$$E_{cp}=\frac{1}{2}\int_{-b}^{b}F_{m'}(x,y_0)D_{m'}(x,y_0)dx$$

$$=\frac{1}{2}\int_{-b}^{b}\sum_i\sum_j\sum_r B_{ij}\Omega_r\left(\frac{y_0}{h}\right)^j\left(\frac{x}{b}\right)^{i+r}, \tag{32}$$

where

$$F_{m'}(x,y_0)=\sum_r \Omega_r\left(\frac{x}{b}\right)^r, \tag{33}$$

$$\Omega_r=\sum_j b_{rj}\left(\frac{y_0}{h}\right)^j. \tag{34}$$

After integrating along the junction, Eq. (32) becomes

$$E_{cp}=\frac{1}{2}\sum_i\sum_j\sum_r B_{ij}\Omega_r\left(\frac{y_0}{h}\right)^j$$

$$\times\frac{b}{(i+r+1)}\,(1+(-1)^{i+r}). \tag{35}$$

One may write Eq. (30) in the following form

$$\Omega_r=\sum_s H_{rs}\Gamma_s. \tag{36}$$

Hence Eq. (35) is given as

$$E_{cp}=\frac{1}{2}\sum_i\sum_j\sum_r\sum_s B_{ij}\Gamma_s H_{rs}\left(\frac{y_0}{h}\right)^j$$

$$\times\frac{b}{(i+r+1)}\,(1+(-1)^{i+r}), \tag{37}$$

where

$$\Gamma_s=\sum_t B_{st}\left(\frac{y_0}{h}\right)^t. \tag{38}$$

The final form of the substructure energy is obtained by replacing the above equation in Eq. (37)

$$E_{cp}=\frac{1}{2h^2}\sum_i\sum_j\sum_p\sum_q\sum_r jqB_{ij}B_{pq}H_{rp}\left(\frac{y_0}{h}\right)^{q+j-2}$$

$$\times\frac{b}{(i+r+1)}\,(1+(-1)^{i+r}), \tag{39}$$

where $i,p,r=0,...,m$ and $j,q=0,...,n$. Differentiation must be conducted to obtain the substructural stiffness matrix

$$\frac{\partial E_{cp}}{\partial B_{ij}}=\frac{1}{2}\sum_p\sum_q\sum_k B_{pq}b\left(\frac{y_0}{h}\right)^{q+j}$$

$$\times\left\{\frac{H_{kp}}{(i+k+1)}\,(1+(-1)^{i+k})+\frac{H_{ki}}{(p+k+1)}\right.$$

$$\left.\times(1+(-1)^{p+k})\right\}. \tag{40}$$

Finally, the generalized stiffness matrix due to the mth component of the coupling loads is obtained.

$$k_{pqrs}^{cp}=\frac{1}{2}\sum_k b\left(\frac{y_0}{h}\right)^{q+s}\left\{\frac{H_{kp}}{(r+k+1)}\,(1+(-1)^{r+k})\right.$$

$$\left.+\frac{H_{kr}}{(p+k+1)}\,(1+(-1)^{p+k})\right\}. \tag{41}$$

It is a complex frequency-dependent matrix which must be added to the previously developed stiffness matrices of the main structure.

Several factors affect the accuracy of the present formulation. Limiting the infinite series in Eq. (2) to a finite series is a computational restriction. The general criteria for truncating the series is to ensure sufficient accuracy in the resulting solutions. The number of terms in the series is therefore increased until no significant variations are noticed in the frequency range of interest. This problem, related to the Rayleigh–Ritz method, has been fully discussed.[9]

The determination of the degree of the polynomial series in the regression analysis is also an important factor. In general, the maximum degree of the polynomial should be chosen in such a way that the number of coefficients does not exceed the number of samples so that

$$(n1+1)\times(n2+1)\leqslant(np)^2, \tag{42}$$

where ''$n1$'' and ''$n2$'' are the degree of regression for independent variables x and ξ, respectively, and np is the number of observation points. The proposed regression technique permits minimizing errors when more contact points are used.

The choice of the appropriate number of observation points plays an important role in determining the accuracy of this hybrid approach. During our simulations, it was noted that the discretization distance should be at least four or five times smaller than the minimum wavelength in the frequency range of interest. This ensured an acceptable representation of the compliance variation along the junction. The same criteria is used in finite element analysis to estimate a sufficient number of elements for modal analysis of structures.

III. NUMERICAL APPLICATIONS

The developed technique has been applied to a series of platelike structures and beam-stiffened plates. In the forthcoming examples, the components of the coupled system are made of aluminum with modulus of elasticity $E=0.7E+11$ N/m^2, mass density $\rho=2700$ kg/m^3, and Poisson's ratio $\nu=0.3$. A damping factor $\xi=0.01$ is used in all cases. The main plate is 30-cm wide ($2b$), 45-cm long ($2h$) and 3.175-mm thick ($2t$). In all cases, nine observation points are considered with $n1=n2=8$, where ''$n1$'' and ''$n2$'' are the degree of regression for the two independent variables, respectively.

The first example considers two plates connected together along one edge to form an L-shaped plate. Both plates are simply supported along their edges and, consequently, only a rotational moment distribution along the junction is

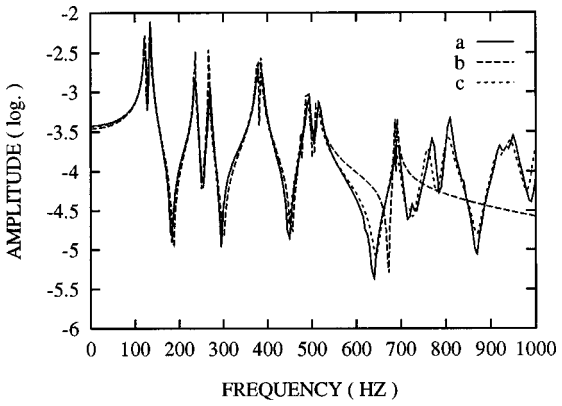

FIG. 6. Response of an L-shaped plate, (a) CLD technique, (b) FE method using the first 12 modes, (c) FE method using the first 24 modes.

present. A transverse force excitation of 100 N is applied at point $x=y=7.5$ cm of the main plate and the transversal response is calculated at the same point.

A finite element simulation using the IDEAS package is conducted to validate the CLD technique. Linear quadrilateral thin shell elements have been used and mode superposition is applied to derive the response of the coupled system up to 1000 Hz. Figure 6 shows the comparison between the two methods. The response of the coupled system is shown when 12 or 24 modes of vibration are superimposed. Good agreement is observed between the CLD technique and the finite element method using 24 modes over the frequency band of interest.

Another example is presented in Fig. 7 using a ribbed plate. The previously used plate is stiffened by three identical stiffeners with cross section 1.5×0.9 cm along lines $y=0.125$ m, $y=0$ m, and $Y=-0.125$ m. The presence of the stiffeners introduces two kinds of coupling with the plate. The first one is related to the torsional effect of the beam which includes a distribution of torsional moment along the junction, and the second one is due to its flexural stiffness, which includes a transverse force distribution. Assuming small deformations,the torsional and flexural behavior of the beam are decoupled and may be treated separately to form two generalized stiffness matrices related to the torsional and transverse vibrations of the stiffener. The compliances were derived semianalytically in this case. Again, comparisons

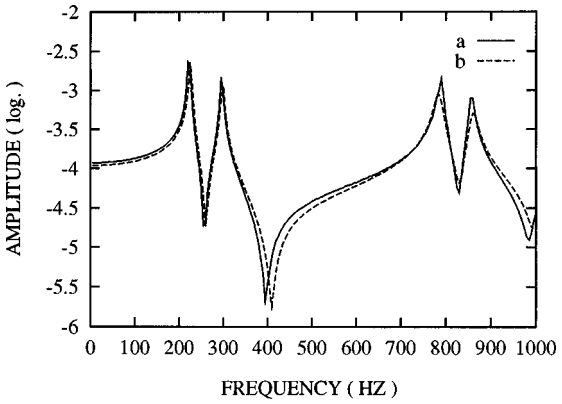

FIG. 7. Responses of the plate stiffened by three identical beams: (a) CLD technique, (b) finite element model.

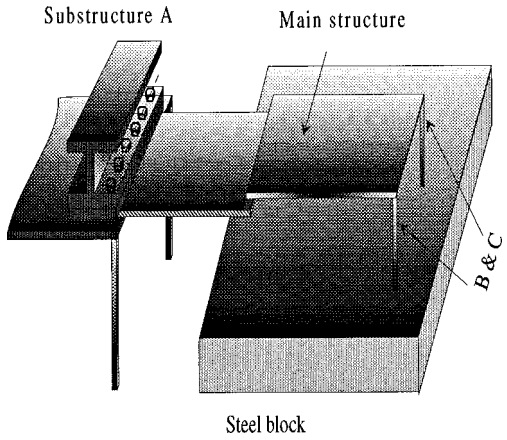

FIG. 8. Schematic view of the complex structure under study.

with FE simulation validates the CLD technique.

The advantage of the proposed technique in dealing with structures with identical elements is quite obvious. The generalized stiffness matrix of a substructure may be obtained as a function of the global coordinates of the connection line. When the number of contact points and the degree of regression for different substructures remain unchanged, the dynamic stiffness matrix related to a series of identical substructures can be simply obtained. A typical indication of the computation efficiency of the approach can be shown using a previously treated L-shaped plate by increasing the number of auxiliary plates. It was shown that there is typically an increase of 140% in processing time when six other plates are added to the original configuration.

IV. EXPERIMENTAL APPLICATIONS

As an example to show the hybrid aspect of the method, a system composed of simple and complex elements is investigated. Figure 8 shows a schematic view of the system that was studied. The whole structure consists of a thin steel plate (45.7-cm long, 30.5-cm wide, and 2.3-mm thick) as the main structure. The coordinate system is located at the center of the plate. Two steel circular rods with a radius of 3.2 mm and a length of 15.6 cm were coupled to the plate at the two corners. The main structure was supported by a more complex substructure along the line $y=-22.9$ cm. This support substructure was composed of a plate (30.5-cm wide, 45.7-cm long, 5.1-mm thick) which is connected to a steel table. Notice that the supporting plate has similar dimensions and properties to the main plate to ensure an effective coupling between both. The main plate is held by the supporting plate and caught between two symmetrical notches. The bolts were tightened so that both the main structure and the supporting plate underwent the same translational movement along the line of junction. At the same time, no moment was transmitted across the plates.

Different procedures were used to get the compliance characteristics of the subsystems. For each of the steel rods (substructures B and C), the translational compliance in the axial direction of the rod, as well as two bending compliance terms were calculated using a classical approach. Since only the flexural vibration of the main structure is considered,

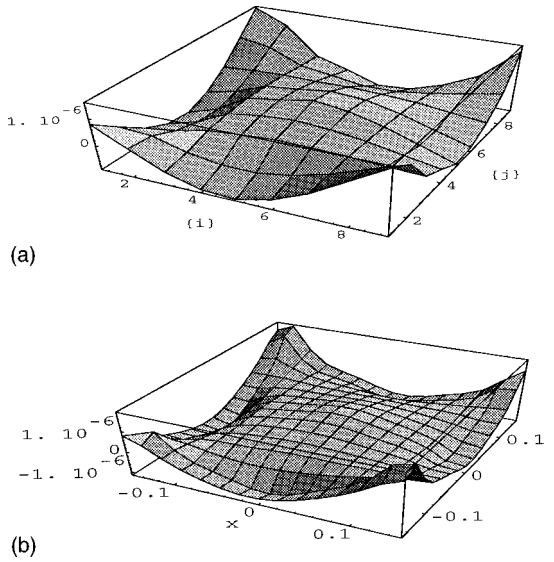

FIG. 9. Variation of the real part of the compliance function of substructure A at a frequency of 420 H. (a) Measured values, (b) result of the regression analysis.

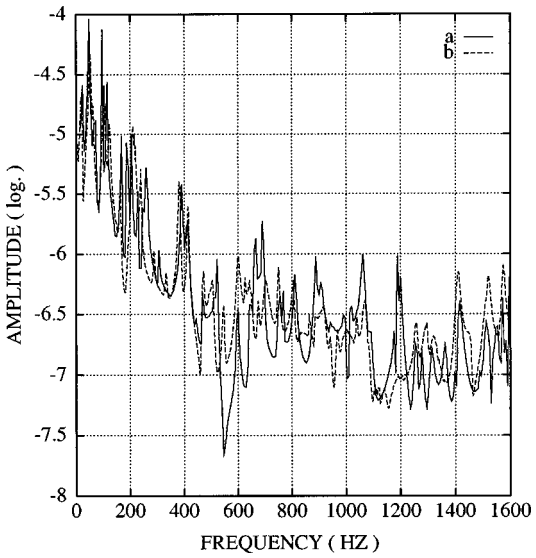

FIG. 10. Frequency response function of the complex structure. (a) Hybrid method and (b) experimental measurements.

other components of interactive forces and moments related to the in-plane vibration of the main structure were neglected. Substructure A (supporting plate with the steel table) is, by itself, a complex system composed of different elements. Experimental measurements were conducted at nine observation points along the line of contact to obtain the compliance matrix. A regression analysis was then performed on the measured data. At each observation point along the contact line, the supporting plate was excited by a shaker driven by a broadband random signal produced by an analyzer. Transverse responses were measured at all observation points using an accelerometer. The two measured signals, the acceleration and the force, were then captured by the analyzer to compute the compliance function. In order to enhance the quality of the measurements, a mass correction procedure was used to compensate for the effect of the added mass due to the exciter and the force transducer.[19]

Figure 9 shows the variation of the real component of the compliance function of the supporting structure at 420 Hz. Both measured data and the results of the regression analysis with $n1=n2=7$ are compared. In this figure, ''i'' denotes the excitation point and ''j,'' the response point. It can be seen that the regression model adequately represents the compliance variation as a continuous function.

Using these compliance data, the response of the whole system is calculated using the hybrid approach. Experimental measurements were also carried out to validate the simulation results. In both cases, the excitation is a unit transverse harmonic force applied at point (8.35, 7.0). The displacement response of the structure was obtained using an average over three points (12.25, 3.0), (−12.25, 3.0), and (3.25, 14.3), with all coordinates in centimeters.

Simulated results and experimental data are compared up to 1600 Hz in Fig. 10. Generally speaking, results suggest that the hybrid model works reasonably well to predict the general trend of the structure in the whole frequency range of interest. Considering the fact that a large number of structural modes are involved, one gets a good appreciation of the hybrid method's ability to handle complex structures. Agreement between the two sets of results is excellent up to about 600 Hz, where 16 modes of vibration are involved. The deviation at higher frequencies indicates that there is still room for improvement in both experimental and numerical aspects. One of the plausible factors may be the fact that the condition of line coupling (which is supposed to transmit only transverse forces) becomes doubtful at higher frequencies. Also, the variational formulation with polynomial decomposition has been shown to be reliable mainly at low frequencies. The developed method permits the use of any other energy based formulations involving the effects of the auxiliary structures via their energy terms. As a result, alternative formulations on the main structure may improve the precision of the technique at higher frequencies.

V. CONCLUSIONS

Vibrations of coupled structures along a continuous line have been investigated. Difficulties inherent to the inversion of the β matrix and the feasibility of a regression analysis on the η matrix has been illustrated. It was shown that the value of η at a fixed point significantly varies with the number of contact points and, accordingly, the regression analysis does not converge toward a correct estimation of the η function. This point prevents the use of a direct formulation. To tackle the problem, a new approach, based on the direct use of the compliance matrix via a coupling load decomposition technique was proposed. The approach was illustrated for systems composed of a thin plate as the main structure. The approach is versatile enough to include both calculated and experimentally measured compliance data of the substructures. This hybrid feature may allow one to go beyond the limit of the most commonly used approaches to handle more complex structures. Vibrations of typical coupled structures along a continuous line were investigated. Numerical results were compared to finite element models and good agreement was observed. The proposed approach was also applied to a

real-life configuration which required different treatment for each substructure. Comparisons with experimental data showed good agreement in a frequency range involving a large number of structural modes.

Further improvement of the approach should focus on its extension to higher frequency applications. Extension of the method to cases where all possible degree of freedoms exist along the junction requires the development of reliable compliance measurement techniques (especially rotational terms).

APPENDIX: REGRESSION ANALYSIS ON THE COMPLIANCE MATRIX OR ITS INVERSE

The linear model for relating a dependent variable Y to p-independent variables is

$$Y_i = \alpha_0 + \alpha_1 x_{i1} + \alpha_2 x_{i2} + \cdots + \alpha_p x_{ip}, \tag{A1}$$

where subscript i, varying from one to n, indicates the observation unit from which data Y and p-independent variables are taken. The second subscript designates the independent variable. Hence there are $(p+1)$ coefficients α to be estimated. For convenience, let us assume that $p' = p+1$. In matrix form, one has

$$\mathbf{Y} = \mathbf{X}\alpha, \tag{A2}$$

where Y is a $n \times 1$ column vector observation on the dependent variables Y_i; X a $n \times p'$ matrix consisting of a column of ones, followed by the p column vectors of the observations on the independent variables; A least-squares estimate on the optimal values of coefficients α_i can be obtained by

$$\hat{\alpha} = (\mathbf{X^T X})^{-1}(\mathbf{X^T Y}), \tag{A3}$$

where $\mathbf{X^T}$ is the transpose of matrix $\mathbf{X}$.

The most frequently used curvilinear response model, in practice, is a polynomial regression model. As a special case of the general linear regression model,[18] it is easy to handle. This model can contain, one, two, or more independent variables. In the case where two variables are used, the $\mathbf{X}$ matrix can be written as

$$\mathbf{X} = \begin{bmatrix} 1 & X_{11} & X_{12} & X_{11}^2 & X_{12}^2 & X_{11}X_{12} & \cdots \\ 1 & X_{21} & X_{22} & X_{21}^2 & X_{22}^2 & X_{21}X_{22} & \cdots \\ \vdots & \vdots & \vdots & \vdots & \vdots & \vdots & \\ 1 & X_{n1} & X_{n2} & X_{n1}^2 & X_{n2}^2 & X_{n1}X_{n2} & \cdots \end{bmatrix}. \tag{A4}$$

This regression analysis technique may be applied to the compliance function β which is approximated by a polynomial of two variables. For example the rotational term β_{44}^{ij} can be defined as

$$\beta_{44}^{ij}(x,\xi) = \sum_{k=0}^{n1} \sum_{l=0}^{n2} c_{kl}^{44} x^k \xi^l. \tag{A5}$$

Using the above definition, Eq. (A2) may be written in the following form

$$\begin{Bmatrix} \beta_{44}^{11} \\ \beta_{44}^{12} \\ \vdots \\ \beta_{44}^{1z} \\ \beta_{44}^{21} \\ \beta_{44}^{22} \\ \vdots \\ \beta_{44}^{2z} \\ \vdots \\ \beta_{44}^{zz} \end{Bmatrix} = \begin{bmatrix} 1 & x_1^0\xi_1^1 & \cdots & x_1^0\xi_1^{n2} & x_1^1\xi_1^1 & \cdots & x_1^1\xi_1^{n2} & \cdots & x_1^{n1}\xi_1^{n2} \\ 1 & x_1^0\xi_2^1 & \cdots & x_1^0\xi_2^{n2} & x_1^1\xi_2^1 & \cdots & x_1^1\xi_2^{n2} & \cdots & x_1^{n1}\xi_2^{n2} \\ \vdots & \vdots & & \vdots & \vdots & & \vdots & & \vdots \\ 1 & x_1^0\xi_z^1 & \cdots & x_1^0\xi_z^{n2} & x_1^1\xi_z^1 & \cdots & x_1^1\xi_z^{n2} & \cdots & x_1^{n1}\xi_z^{n2} \\ 1 & x_2^0\xi_1^1 & \cdots & x_2^0\xi_1^{n2} & x_2^1\xi_1^1 & \cdots & x_2^1\xi_1^{n2} & \cdots & x_2^{n1}\xi_1^{n2} \\ 1 & x_2^0\xi_2^1 & \cdots & x_2^0\xi_2^{n2} & x_2^1\xi_2^1 & \cdots & x_2^1\xi_2^{n2} & \cdots & x_2^{n1}\xi_2^{n2} \\ \vdots & \vdots & & \vdots & \vdots & & \vdots & & \vdots \\ 1 & x_2^0\xi_z^1 & \cdots & x_2^0\xi_z^{n2} & x_2^1\xi_z^1 & \cdots & x_2^1\xi_z^{n2} & \cdots & x_2^{n1}\xi_z^{n2} \\ \vdots & \vdots & & \vdots & \vdots & & \vdots & & \vdots \\ 1 & x_z^0\xi_z^1 & \cdots & x_z^0\xi_z^{n2} & x_z^1\xi_z^1 & \cdots & x_z^1\xi_z^{n2} & \cdots & x_z^{n1}\xi_z^{n2} \end{bmatrix} \begin{Bmatrix} c_{0\ 0}^{44} \\ c_{0\ 1}^{44} \\ \vdots \\ c_{0\ n2}^{44} \\ c_{1\ 0}^{44} \\ c_{1\ 1}^{44} \\ \vdots \\ c_{1\ n2}^{44} \\ \vdots \\ c_{n1\ n2}^{44} \end{Bmatrix}, \tag{A6}$$

where $\mathbf{Y}$, a column vector $(n \times 1)$, is a vector representation of β as stated above. $z = 1,...,np$, $n = np \times np$ where np is the number of selected contact points or observation points. The $\mathbf{X}$ matrix is a $(n \times \hat{n})$ matrix where $\hat{n} = (n1+1) \times (n2+1)$ with $n1$ and $n2$ being the maximum degree of x and ξ in the response surface function, respectively. Hence the vector of parameters, consisting of the elements of c_{kl}^{44}, is a column vector with dimension $(\hat{n} \times 1)$. In a regression analysis, the number of observations must be equal or greater than the number of parameters.

The dependent variable vector $\mathbf{Y}$ is a frequency-dependent vector. It means that the above process must be repeated for each frequency. It seems to be a relatively tedious approach. Fortunately, as long as the observation points remain unchanged for different frequencies, the $\mathbf{X}$ matrix remains the same. Therefore at each frequency, parameters α are obtained by the following relation

$$\hat{\alpha}(\omega) = \overline{\mathbf{X}}\mathbf{Y}, \tag{A7}$$

where $\overline{X}$ can be calculated by

$$\overline{\mathbf{X}} = (\mathbf{X^T X})^{-1}\mathbf{X^T}. \tag{A8}$$

As explained before, matrix $\overline{\mathbf{X}}$ depends only on independent variables and, accordingly, does not change with frequency

if the number and location of observation points remain unchanged. It is clear that at higher frequencies, the shape of the compliance curve along the junction line becomes more complicated and more observation points are required. Matrix $\overline{\mathbf{X}}$ must be recalculated after each change in the number of contact points. This constitutes the major part of the regression analysis and takes more than 80% of the total required time for the analysis. Therefore it is recommended to choose a sufficient number of observation points for a relatively large band of frequency to avoid recalculation of $\overline{\mathbf{X}}$ too frequently.

The whole procedure gives an analytical expression for estimating the variation of the compliance between an excitation point ξ and the response point x in the form of $\beta(x,\xi)$ along the junction. It is written as

$$\beta(x,\xi)=\psi^{\mathbf{T}}\alpha, \tag{A9}$$

where

$$\psi^{\mathbf{T}}=[1 \quad x^0\xi^1 \quad \cdots \quad x^0\xi^{n2} \quad x^1\xi^1 \quad \cdots \quad x^1\xi^{n2} \quad \cdots \quad x^{n1}\xi^{n2}], \tag{A10}$$

$$\alpha=\{c_{0\,0} \quad c_{0\,1} \quad \cdots \quad c_{0\,n2} \quad c_{1\,0} \quad c_{1\,1} \quad \cdots \quad c_{1\,n2} \quad \cdots \quad c_{n1\,n2}\}. \tag{A11}$$

[1] K. W. Min, T. Igusa, and J. D. Achenbach, ''Frequency window method for forced vibration of structures with connected substructures,'' J. Acoust. Soc. Am. **92**, 2726–2733 (1992).

[2] R. H. Lyon, *Statistical Energy Analysis of Dynamical Systems, Theory and Applications* (MIT, Cambridge, MA, 1975).

[3] H. G. D. Goyder and R. G. White, ''Vibrational power flow from machines into built up structures, Part I: Introduction and approximate analysis of beam and plate-like foundations,'' J. Sound Vib. **68**, 59–75 (1980).

[4] R. J. Pinnington and R. G. White, ''Power flow through machine isolators to resonant and non-resonant beams,'' J. Sound Vib. **75**, 179–197 (1981).

[5] Y. Shen and B. M. Gibbs, ''An approximate solution for the bending vibration of a combination of rectangular thin plates,'' J. Sound Vib. **105**, 73–90 (1986).

[6] J. L. Guyader, C. Boisson, P. Millot, and C. Lesueur, ''Energy transmission in finite coupled plates, part I: Theory,'' J. Sound Vib. **81**, 81–92 (1982).

[7] J. M. Cushieri, ''Structural power-flow analysis using a mobility approach of an *L*-shaped plate,'' J. Acoust. Soc. Am. **87**, 1159–1165 (1990).

[8] B. Petersson, ''A thin-plate model for the moment mobility at the intersection of two perpendicular plates,'' J. Sound Vib. **108**, 471–485 (1986).

[9] L. Cheng and J. Nicolas, ''Free vibration analysis of a cylindrical shell-circular plate system with general coupling and various boundary conditions,'' J. Sound Vib. **155**, 231–247 (1992).

[10] E. Goldfracht and G. Rosenhouse, ''Use of Lagrange multipliers with polynomial series for dynamic analysis of constrained plates, Part I: Polynomial series,'' J. Sound Vib. **92**, 83–93 (1984).

[11] L. J. Hu, I. Smith, and Y. H. Chui, ''Vibration analysis of ribbed plates with a rigid intermediate line support,'' J. Sound. Vib. **178**, 163–175 (1994).

[12] L. Jezequel and H. D. Seito, ''Component modal synthesis methods based on hybrid models, Part I: Theory of hybrid models and modal truncation methods,'' Trans. ASME, J. Appl. Mech. **61**, 100–108 (1994).

[13] W. C. Hurty, ''Dynamic analysis of structural systems using component modes,'' AIAA J. **3**, 678–685 (1965).

[14] L. E. Suarez and M. P. Singh, ''Modal synthesis method for general dynamic systems,'' Trans. ASCE, J. Eng. Mech. **118**, 1488–1503 (1992).

[15] G. M. L. Gladwell, ''Branch mode analysis of vibrating systems,'' J. Sound Vib. **1**, 41–59 (1964).

[16] L. Cheng and R. Lapointe, ''Vibration Attenuation of panel structures by optimally shaped viscoelastic coating with added weight consideration,'' Thin-Walled Struct. **21**, 307–326 (1995).

[17] Y. C. Fung, *An Introduction to the Theory of Aeroelasticity* (Wiley, New York, 1955), Chap. 1, pp. 19–27.

[18] J. Neter and W. Wasserman, *Applied Linear Statistical Models* (Irwin, Homewood, IL, 1974).

[19] Y. C. Qu, L. Cheng, and D. Rancourt, ''Rotational compliance measurement of a flexible plane structure using an attached beam-like tip. Part II: Experimental study,'' Trans. ASME, J. Vib. Acoust. **119**, 603–608 (1997).

Power flow to a cylindrical shell with an attached structure

J. Gregory McDaniel
Department of Aerospace and Mechanical Engineering, Boston University, 110 Cummington Street, Boston, Massachusetts 02215

(Received 27 August 1997; revised 29 January 1998; accepted 25 February 1998)

This paper presents an analytical framework for understanding and controlling the physical mechanisms which govern power flow to infinitely long cylindrical shells from applied point forces. It has been observed by others that the power flow to an empty shell peaks dramatically when the excitation frequency is near the cutoff frequency of a wave in the shell. In this paper, these observations are explained and generalized by a new analytical expression for power flow based on classic analyses of a shell's response to an applied point force. This expression quantifies the partition of power among propagating waves excited by an applied force. Furthermore, the expression confirms that power flow increases dramatically as a propagating wave is excited in the vicinity of its cutoff frequency. In the context of this understanding, the attachment of a passive structure to the shell is explored as a means of controlling power flow. The nonlinear problem of designing a structure which satisfies practical constraints and minimizes power flow is formulated in such a way as to be solvable by a variety of optimization techniques. The formulation, which can be extended to other structures, is based on an expression for power flow in which the impedance of the attached structure acts in mechanical parallel with the shell's impedance at the points of attachment. An example indicates that a significant reduction in power flow can be achieved by the attachment of a passive structure whose parameters have been optimized by a genetic algorithm.
 [S0001-4966(98)03006-9]

PACS numbers: 43.40.Ey, 43.20.Gp [CBB]

INTRODUCTION

Power flow from mechanical excitations to cylindrical shells is of practical concern because it often leaves the shell as unwanted sound or degrades the performance of equipment attached to the shell. In order to understand the fundamental mechanisms governing power flow from an applied point force, this paper presents a new analytical framework which expresses power flow in terms of the propagating waves excited by the force. A technique of controlling power flow is proposed in which a structure attached to the shell is designed to constrain the shell at the drive point. In the latter half of this paper, a new formulation is proposed for finding the relevant design parameters of a structure which satisfies practical constraints and minimizes power.

Although there has been very little work on understanding the physical mechanisms of power flow to shells, a vast amount of work exists on the related problem of predicting the vibrational response of a shell to an applied point force. Solution of the shell's differential equations of motion by Fourier analysis dates back to the work of Yuan[1] in 1946. Similar analyses have been used to study the input impedance of cylindrical shells[2,3] and the transfer impedance of cylindrical shells.[4–6] Grigolyuk and Tolkachev[7] list 88 related works published prior to the early 1970's. In recent years, Guo[8] has extended these methods to investigate the radiation characteristics of fluid-loaded cylindrical shells excited by point forces.

Most analyses contained in the works cited above begin with a coupled system of partial differential equations governing the motion of the shell's midsurface with applied point forces represented by Dirac delta distributions. For infinitely long shells, one proceeds by expressing the shell response variables in terms of Fourier series expansions in the circumferential coordinate and Fourier transforms in the axial coordinate. Axial symmetry of the shell leads to an uncoupling of circumferential harmonics. For each circumferential harmonic, residue theory is used to perform the Fourier inversion to the axial coordinate. The final result for each circumferential harmonic consists of four exponential terms which describe the axial dependence of the shell's response. Each of these terms represents either a propagating wave or an evanescent field.

Generally speaking, propagating waves are described by complex wave numbers having small imaginary parts due to whatever intrinsic damping mechanisms are present. Dispersions and polarizations of the propagating waves in a thin cylindrical shell have been described by Smith.[9] At sufficiently high frequencies, the three propagating waves resemble the flexural, shear, and longitudinal waves which propagate in a flat plate.[10] Each propagating wave has an associated cutoff frequency, below which it becomes highly attenuated. In contrast, evanescent fields are described by complex wavenumbers with large imaginary parts over the entire frequency range. These fields exhibit substantial exponential decays of response as one moves axially away from the force. Most of the average power flow over a cycle of harmonic forcing goes to the propagating waves, which carry energy from the drive point. In contrast, evanescent waves mostly store energy.

A significant clue to understanding the physical mechanisms which govern power flow was provided by Borgiotti and Rosen,[11] who used the state vector approach to study

power flow in a cylindrical shell excited by an applied point force. The state vector approach introduces additional variables, leading to a larger set of equations which is often more amenable to numerical calculations of wave dispersion, vibrational response, and power flow. In a discussion of their numerical results, Borgiotti and Rosen noted that when the shell was excited by a radial point force of varying frequency, the power flow into the shell spiked at the cutoff frequencies of flexural waves associated with various circumferential harmonics. They associated the effect with a type of resonance, however, detailed study of this phenomenon was beyond the scope of their paper. The present work explains and generalizes this observation based on an analytical expression for power flow from a point force to a cylindrical shell.

The analysis is also used to explore the potential of reducing power flow by attaching passive structures to several points on the shell. Analysis of the coupled system involves a nonlinear relationship between the impedance of the attached structure and the power flow. Given practical constraints on the structure, nonlinear optimization techniques are proposed for finding parameters which describe the attached structure. Although previous research by others has addressed the forced response of cylindrical shells with attached structures and inhomogeneities (see, for example, Refs. 12–15), the present work is apparently the first to address the constrained optimization of an attached structure to limit power flow to a shell.

In the analysis and numerical examples presented here, the shell is assumed to be of infinite length so that waves generated by the force propagate away and never return. Power flow to finite length shells is qualitatively similar to the infinite case when damping limits reflections from the shell's terminations. For lightly damped shells of finite length, the power flow is generally controlled by the shell's resonances, which depend on the boundary conditions at the terminations[16] and on material damping in the shell. For either case, power flow can be most effectively reduced by constraining the shell from vibrating in the circumferential harmonics which absorb the most power. In this sense, the methodology developed here for constraining harmonics of an infinite shell may be extended to finite shells.

I. ANALYSIS OF POWER FLOW TO AN EMPTY SHELL

The essential physics which govern the injection of power into a cylindrical shell from forces oriented in the radial, circumferential, and longitudinal directions can be inferred from the shell's admittance matrix $[Y_{\mathrm{sh}}]$, which is defined in Eq. (A11) of the Appendix. A brief derivation of the admittance matrix used here is included in the appendix for convenience of referral. Similar admittance matrices can be found in many references and may differ from the one used here depending on the choice of shell theory. This matrix is sometimes more generally referred to as the Green's matrix of the shell, however, the more traditional term *admittance matrix* will be used here to precisely indicate a relation between velocity and force.

As defined here, elements of the admittance matrix are the ratio of the complex velocity amplitude at a location (ϕ_v, z_v) to the complex amplitude of a point force applied at a location (ϕ_f, z_f) when there is only one such force applied. Physically, the admittance matrix represents the contributions of propagating waves and evanescent fields to the velocity measured at a point on the shell. Only the diagonal elements of $[Y_{sh}]$, which relate velocities to forces in the same direction, enter into calculations of power flow.

For harmonic excitation of mechanical systems, input power P averaged over a cycle can be computed from the complex amplitudes of force F and velocity V measured in the same direction according to $P=(1/2)\Re\{FV^{\star}\}$, where $V^{\star}$ is the complex conjugate of V. Given an admittance defined by $Y=V/F$ and a specified force F, the power is then $P=(1/2)\Re\{Y\}|F|^2$. Power flow to the shell can therefore be calculated from the expression for the shell's admittance given in Eq. (A11) of the Appendix. The resulting flow from a force with complex amplitude F_α oriented in a cylindrical coordinate indicated by α (where α can be z, ϕ, or r) is

$$P_\alpha=(1/2)\frac{\Omega}{2\pi a h\rho c_p m_\nu \beta^2}\times\Re\left\{\sum_{n=-\infty}^{\infty}\sum_{m=1}^{4}\frac{C_\alpha(x_{mn})}{2x_{mn}\prod_{\substack{p=1\\p\neq m}}^{4}(x_{mn}^2-x_{pm}^2)}\right\}|F_\alpha|^2, \tag{1}$$

where

$$C_z(x_{mn})=(1-i\eta)\{(mx_{mn}^2+n^2-\hat{\Omega}^2)\times[1+\beta^2(x_{mn}^2+n^2)^2-\hat{\Omega}^2]-n^2\}, \tag{2}$$

$$C_\phi(x_{mn})=(1-i\eta)\{(x_{mn}^2+m_\nu n^2-\hat{\Omega}^2)\times[1+\beta^2(x_i^2+n^2)^2-\hat{\Omega}^2]-\nu x_{mn}^2\}, \tag{3}$$

and

$$C_r(x_{mn})=(1-i\eta)\{(x_{mn}^2+m_\nu n^2-\hat{\Omega}^2)\times(m_\nu x_{mn}^2+n^2-\hat{\Omega}^2)-np_\nu x_{mn}^2\}. \tag{4}$$

The shell is described by its mass density ρ, Young's modulus E, material loss factor η, thickness h, and nominal radius a. The quantity $c_p=\sqrt{E/[\rho(1-\nu^2)]}$ is the low-frequency phase speed of an longitudinal waves in an equivalent flat plate with no damping. The nondimensional parameters $\beta=h/(a\sqrt{(12)})$, $m_\nu=(1-\nu)/2$, $p_\nu=(1+\nu)/2$, $\Omega=\omega a/c_p$, and $\hat{\Omega}^2=\Omega^2/(1-i\eta)$ have been introduced for convenience.

Each term in the double summation of Eq. (1) represents power flow to either a propagating wave or an evanescent field described by the nondimensional wave number x_{mn}. The m subscript on x_{mn} specifies one of the four roots to the determinental equation $|[Z_n]|=0$, where $[Z_n]$ is an impedance matrix of the shell defined in Eq. (A8). Physically, x_{mn} is a nondimensional wave number of either a propagating wave or an evanescent field which naturally exists on the shell in the absence of distributed forces. While the amplitude of each wave depends on the frequency, amplitude, and orientation of excitation, wave number x_{mn} depends only the frequency of excitation and the shell parameters.

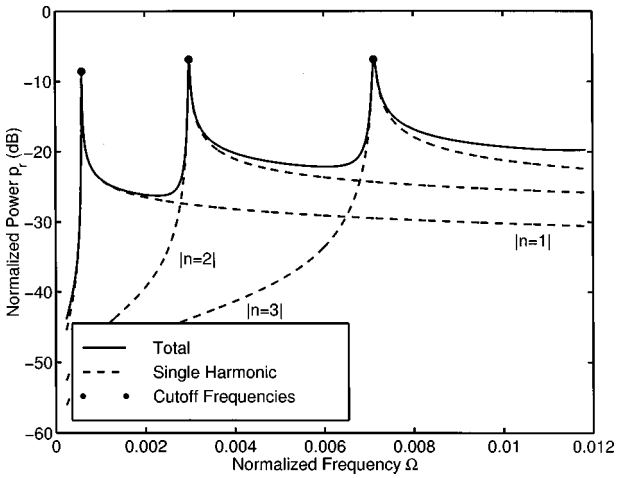

FIG. 1. Plot of normalized power injected by a radial point force applied to a cylindrical shell. The dashed lines represent contributions of the $|n|=1,2,3$ harmonics to the summation in Eq. (1). The solid circles indicate cutoff frequencies of flexural waves with $|n|=1,2,3$ harmonics.

Power flow approaches infinity whenever any normalized wave number x_{mn} approaches zero due to uncancelled factors of each x_{mn} in the denominator of the expression for P_α. In reality, intrinsic damping within the shell would prevent x_{mn} from ever being equal to zero. Nevertheless, as frequency is varied the idealized result given above indicates that one would observe peaks in P_α whenever the excitation frequency is near the cutoff frequency of any wave. This conjecture will be supported by numerical results presented below.

For generality in the numerical results, power is normalized so as to depend on the fewest number of nondimensional quantities. In addition, the normalization should not alter the frequency dependence of power flow. Therefore, power will be normalized by the power flow from a normal force acting on an undamped flat plate of infinite extent having the same material and thickness as the shell. The expression for this quantity, which is independent of frequency, is[17]

$$P_p=(1/2)\frac{1}{4h^2}\sqrt{\frac{3(1-\nu^2)}{E\rho}}|F_\alpha|^2. \tag{5}$$

The normalized power $p_\alpha=P_\alpha/P_p$, which only depends on the nondimensional parameters Ω, β, ν, and η, is then

$$p_\alpha=\frac{4\Omega}{m_\nu\beta}\Re\left\{\sum_{n=-\infty}^{\infty}\sum_{m=1}^{4}\frac{C_\alpha(x_{mn})}{2x_{mn}\Pi_{\substack{p=1\\p\neq m}}^{4}(x_{mn}^2-x_{pm}^2)}\right\}|F_\alpha|^2. \tag{6}$$

Plots of the normalized power injected by axial, circumferential, and radial point forces are shown in Figs. 1–3 for the parameter values $h/a=0.01$, $\nu=0.3$, and $\eta=0.01$. In each of these figures, the relevant cutoff frequencies of various waves are indicated with solid circles. The vertical locations of these circles have been chosen to coincide with the peaks in power from the circumferential harmonic of associated with the wave.

The power flow from a radial force is illustrated in Fig. 1. Three peaks in the total power appear, each in the vicinity of a cutoff frequency of a flexural wave with the indicated circumferential harmonic. For example, consider the contribution of the $|n|=1$ harmonic which peaks at $\Omega\approx0.0005$ and is responsible for the majority of power flow from $\Omega\approx0.0005$ to 0.006. This peak is due to the excitation of a $|n=1|$ flexural wave whose cutoff frequency falls in this frequency range.

Figures 2 and 3 show similar characteristics for longitudinally and circumferentially oriented forces. The shell's curvature causes strong coupling between these forces and radial motion, so that the majority of power flow is to flexural waves excited near cutoff. The frequency ranges shown in these two figures span the cutoff frequencies of many flexural waves, which explains the rapid oscillations in total power flow. Contributions from the $|n|=1,2,3$ harmonics exhibit peaks which correlate with peaks in the total power and correspond to cutoff frequencies of longitudinal waves in Fig. 2 and shear waves in Fig. 3. These frequencies are indicated by solid circles. Increasing the material loss factor within reasonable bounds has a relatively small effect. When the material loss factor was increased to $\eta=0.05$ the basic character of the plots in Figs. 1–3 remained, however the peaks became broader in frequency.

Equation (1) and the supporting numerical calculations shown in Figs. 1–3 explain and generalize the observations made by Borgiotti and Rosen.[11] The power flow to a particular wave peaks dramatically at excitation frequencies near its cutoff frequency because the wave number, which is in the denominator of the power flow expression, becomes very small. This phenomenon is not limited to wave generation in cylindrical shells; it has been observed in classic analyses of wave propagation in ducts[18] and in horns.[19]

II. ANALYSIS OF POWER FLOW TO A SHELL WITH AN ATTACHED STRUCTURE

The expression for power flow, $P=(1/2)\Re\{Y\}|F|^2$, indicates that power can be reduced by decreasing the real part of the structural admittance at the drive point. In the next two sections, we consider ways of decreasing $\Re\{Y\}$ by attaching a structure which dynamically constrains the motion at the

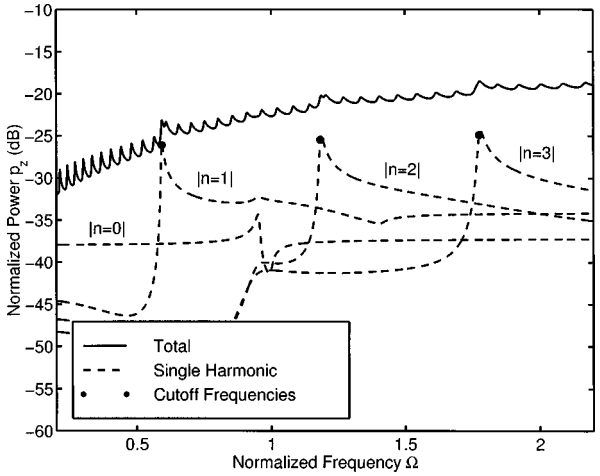

FIG. 2. Plot of normalized power injected by an axial point force applied to a cylindrical shell. The dashed lines represent contributions of the $|n|=1,2,3$ harmonics to the summation in Eq. (1). The solid circles indicate cutoff frequencies of longitudinal waves with $|n|=1,2,3$ harmonics.

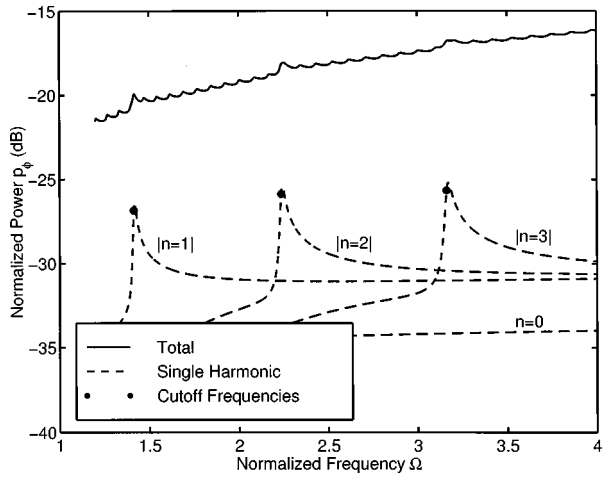

FIG. 3. Plot of normalized power injected by a circumferential point force applied to a cylindrical shell. The dashed lines represent contributions of the $|n|=1,2,3$ harmonics to the summation in Eq. (1). The solid circles indicate cutoff frequencies of shear waves with $|n|=1,2,3$ harmonics.

drive point. However, this does not automatically imply that the structure should be attached to the drive point. Indeed, numerical results presented in the following section will indicate the advantages of attaching a structure at several other locations.

In order to analyze power flow to a shell with a structure attached at more than one location, it is expedient to identify locations on the shell, hereafter referred to as *ports*, where the structure attaches to the shell or where the shell is excited by an externally applied force. Combining the force and velocity vectors from all ports into vectors $\{F_p\}$ and $\{V_p\}$, the unconstrained shell response can be expressed as $\{F_p\}=[Z_{\mathrm{sh}}]\{V_p\}$, where the impedance matrix $[Z_{\mathrm{sh}}]$ is found by inverting a partitioned admittance matrix developed from Eq. (A11).

The force vector $\{F_p\}$ applied to the shell is the algebraic sum of forces applied by the attached structure and externally applied forces, or $\{F_p\}=\{F_{\mathrm{st}}\}+\{F_e\}$. The attached structures considered here are assumed linear and can therefore be represented by an impedance matrix $[Z_{\mathrm{st}}]$ relating constraint forces and velocities at all ports by $\{F_{\mathrm{st}}\}=-[Z_{\mathrm{st}}]\{V_p\}$. The diagonal elements of $[Z_{\mathrm{st}}]$ and $[Z_{\mathrm{sh}}]$ are often referred to as *drive point impedances* and the off-diagonal elements as *transfer impedances*. The assumption of a point-reacting structure, which will be invoked in the numerical examples, implies that the off-diagonal elements of $[Z_{\mathrm{st}}]$ are zero.

Recognizing that the velocities of the shell and attached structure must be identical at the attachment points, algebraic combination of the impedance relations yields the following result for the velocity of the constrained shell at the ports:

$$\{V_p\}=([Z_{\mathrm{sh}}]+[Z_{\mathrm{st}}])^{-1}\{F_e\}. \tag{7}$$

This equation expresses the fact that the attached structure's impedance acts in mechanical parallel with the shell's impedance. This result is a dynamic analogue to the ''direct stiffness method'' used in finite element analysis.[20] Power flow to the shell with the attached structure is given as

$$P_\alpha=(1/2)\Re\{\{F_e\}^T([Z_{\mathrm{sh}}]+[Z_{\mathrm{st}}])^{-1}\{F_e\}\}, \tag{8}$$

where the T superscript indicates the hermitian transpose of the force vector.

Equation (8) can be applied to other structures by interpreting $[Z_{\mathrm{sh}}]$ as the impedance matrix of a master structure. Although the present work utilizes an analytical solution for $[Z_{\mathrm{sh}}]$, the impedance matrices of more complex structures can be computed from finite element models or obtained experimentally. Once $[Z_{\mathrm{sh}}]$ is known, Eq. (8) can be efficiently evaluated for choices of $[Z_{\mathrm{st}}]$. Efficient evaluation time is critical in the example presented below because nonlinear optimizations are used to determine a $[Z_{\mathrm{st}}]$ which satisfies practical constraints and minimizes power. This approach is discussed in the following section.

III. OPTIMAL PARAMETERS OF AN ATTACHED STRUCTURE

The design of an attached structure to reduce power flow and satisfy practical constraints is an iterative process. Practical constraints often limit the choice of attachment locations as well as the impedance which the structure can present to the shell. For example, weight limitations typically limit the total mass of the structure and flexibility of any structure limits its ability to dynamically constrain the shell. In addition to these practical limitations, Eq. (8) indicates a nonlinear relationship between the attached structure's impedance $[Z_{\mathrm{sh}}]$ and power flow P_α. This precludes a direct solution for an optimal $[Z_{\mathrm{st}}]$. Therefore, the results presented below will illustrate the use of a nonlinear optimization technique to minimize power flow by iteratively adjusting the impedance matrix of the attached structure. To this end, Eq. (8) will be used to compute power flow.

As an example, consider the optimal design of an attached structure to limit the power flow illustrated in Fig. 1. Recall that results in this figure correspond to a radial point force acting on a thin cylindrical shell. In this example, 16 structures are attached at equally spaced locations about the circumference of the shell and at the same axial location as the applied radial point force, as shown in Fig. 4. The number of attached structures has been chosen so that the spacing between attachment points is less than a quarter of the circumferential harmonic wavelengths which contribute most to the power flow over the frequency range $0<\Omega<0.012$.

The structure is assumed to be radially point-reacting, so that it applies a radial point force in reaction to a radial velocity at the same location. Therefore, the impedance matrix of the attached structure is diagonal. Furthermore, the magnitude of the structure's impedance at each location is taken to be $|Z_i|=10|Z_p|$, where $Z_p=4\rho c_p h^2/\sqrt{3}$ is the impedance of an infinite flat plate with the same thickness and material properties as the shell. In this example, the phases of the impedances presented at each attachment location will be chosen so as to minimize power flow. Because our interest lies in steady-state response, the phase of each attached impedance is allowed to vary arbitrarily with frequency without regard to causality in the time domain.

Figure 5 shows the normalized power flowing to a shell with attached structure whose impedance matrix has been optimized in two ways. In all cases, the real part of the attached structure's impedance is constrained to be greater

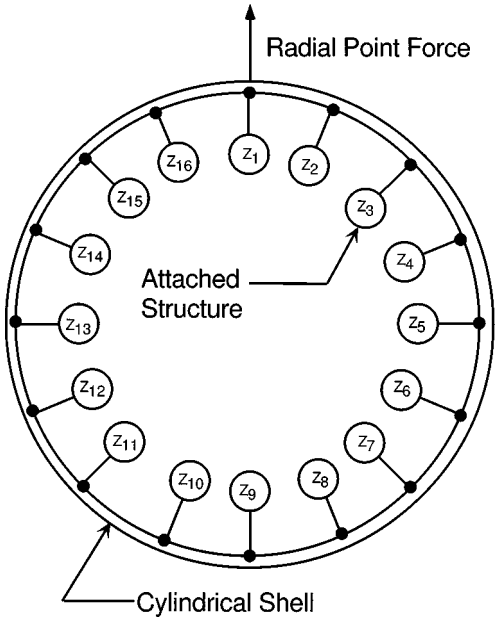

FIG. 4. Schematic showing a cross-section of the shell at the axial location where a radial force is applied and 16 passive structures are attached to the shell.

than zero in keeping with the assumption of a passive structure. For the curve labeled ''Uniform Optimization,'' the phases of all constraint impedances are required to be identical. At each frequency, the phase has been varied and the minimum power has been plotted. For the curve labeled ''Independent Optimization,'' the phase of the impedance at each attachment location has been allowed to be independent of the others. At each frequency, a genetic algorithm[21] has been used to find the 16 impedance phases which minimize the power flow. Without further study there is no guarantee that the algorithm has found a global minimum, however the result serves to demonstrate the dramatic effect of optimizing the individual impedance phases. On average, the optimized attachments produce a 6.5 dB reduction in power flow whereas the uniform attachments hardly produce any reduction at all.

A question remains regarding the distribution of structural impedance. Is distributing the impedance better than simply attaching all impedances at the drive point? From the discussion in the previous section, the latter alternative is desirable if placing all impedances at the drive point would more effectively lower the admittance at the drive point. To answer this question, Fig. 6 shows a plot of power flow for the two cases. The plot labeled ''Drive-Point Impedance'' represents an impedance with magnitude $160|Z_p|$ at the drive point, which is equivalent to attaching all 16 impedances at the drive point. At each frequency, the phase has been varied and the minimum power has been plotted. For this example, distributed impedances result in a power flow which is lower than that resulting from a single drive-point impedance. A probable explanation is that distributed impedances more effectively limit the generation of waves associated with the $|n|=1,2,3$ harmonics by constraining these harmonics.

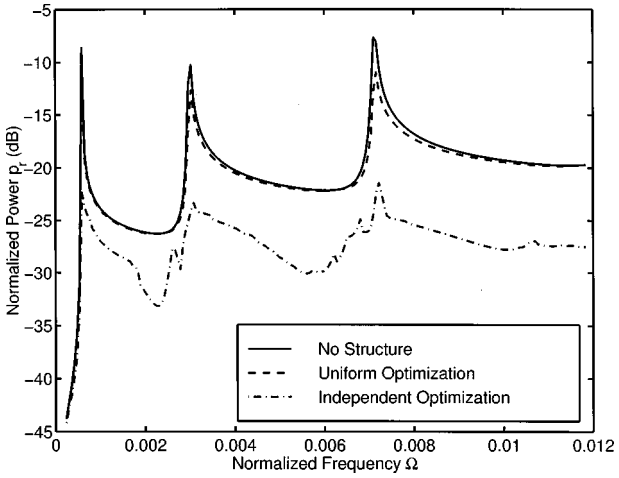

FIG. 5. Plot of normalized power injected by a radial point force applied to a cylindrical shell with 16 attached structures.

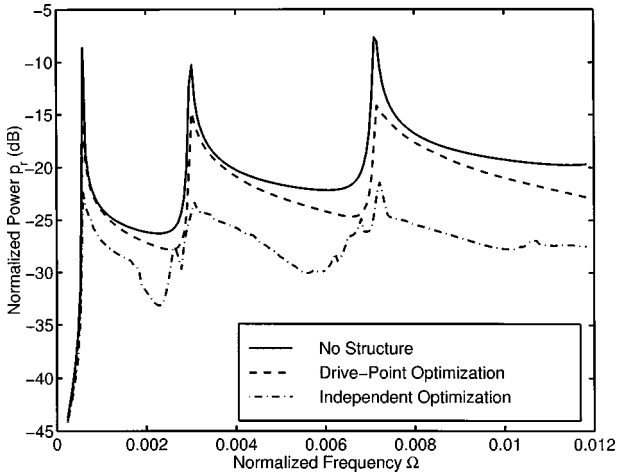

FIG. 6. Plot of normalized power injected by a radial point force applied to a cylindrical shell with 16 attached structures.

IV. CONCLUSIONS

The physical mechanisms governing power flow to cylindrical shells have been inferred from an analytical expression which quantifies the partitioning of power among the shell's propagating waves. In particular, analysis and numerical examples have shown that large fractions of power flow are associated with propagating waves excited at frequencies near their cutoff frequencies. A formulation for investigating the reductions in power flow achieved by the attachment of a passive structure was developed in which the power flow is nonlinearly related to the impedance of the attached structure.

The examples presented here illustrate that dramatic reduction in power flow which can be achieved by employing nonlinear optimization algorithms to adjust parameters of the attached structure. Furthermore, the examples demonstrate that a shell might be more effectively constrained from accepting power by attaching structures at locations other than the drive point. If this result applies to other wave-bearing structures, then the formulation presented here could provide an analytical means of improving the passive control of power flow and subsequent noise radiation.

ACKNOWLEDGMENTS

The author would like to thank Drs. Allan Pierce, P.W. Smith, Jr., and Kevin LePage for providing many helpful comments.

APPENDIX: POINT-FORCE EXCITATION OF WAVES IN A CYLINDRICAL SHELL

This Appendix summarizes the derivation of an admittance matrix for the shell which relates the velocity vector at a location (ϕ_v, z_v) caused by a point force vector applied at a location (ϕ_f, z_f). The derivation is similar to that presented by Averbukh and Grigolyuk,[7] but uses complex Fourier series expansions which do not require the assumption of circumferential symmetry. This derivation begins with the following differential equations of motion based on Donnell's theory (see Ref. 22, pp. 31–33):

$$-\frac{Eh}{(1-\nu^2)a^2}\left(a^2\frac{\partial^2 u}{\partial z^2}+m_\nu\frac{\partial^2 u}{\partial \phi^2}+p_\nu a\frac{\partial^2 v}{\partial z\ \partial \phi}+\nu a\frac{\partial w}{\partial z}\right)+\rho h\ddot{u}=q_z, \tag{A1}$$

$$-\frac{Eh}{(1-\nu^2)a^2}\left(p_\nu a\frac{\partial^2 u}{\partial z\ \partial \phi}+m_\nu a^2\frac{\partial^2 v}{\partial z^2}+\frac{\partial^2 v}{\partial \phi^2}+\frac{\partial w}{\partial \phi}\right)+\rho h\ddot{v}=q_\phi, \tag{A2}$$

$$\frac{Eh}{(1-\nu^2)a^2}\left(a^2\frac{\partial^2 u}{\partial z^2}+m_\nu\frac{\partial^2 u}{\partial \phi^2}+p_\nu a\frac{\partial^2 v}{\partial z\ \partial \phi}+\nu a\frac{\partial w}{\partial z}\right)+\rho h\ddot{w}=q_r, \tag{A3}$$

where ρ is the shell's mass density, h is its thickness, and a is the radius of its midsurface. The longitudinal, circumferential, and radial displacements are denoted by u, v, and w, respectively. Subscripts on the applied tractions q_z, q_ϕ, and q_r indicate they direction in which they act. The following nondimensional parameters $\beta=h/(a\sqrt{12})$, $m_\nu=(1-\nu)/2$, and $p_\nu=(1+\nu)/2$ have been introduced for convenience.

Considering only steady-state responses to time harmonic excitations, the time dependences of the force and velocity vectors are

$$\begin{Bmatrix}\dot{q}_z\\ \dot{q}_\phi\\ \dot{q}_r\end{Bmatrix}=\Re\{Qe^{-i\omega t}\}\ \text{and}\ \begin{Bmatrix}\dot{u}\\ \dot{v}\\ \dot{w}\end{Bmatrix}=\Re\{Ve^{-i\omega t}\}. \tag{A4}$$

Consistent with this time dependence, hysteretic damping in the shell is introduced by allowing the Young's modulus to become complex, $E\rightarrow E(1-i\eta)$, in Eqs. (A1)–(A3).

Equations (A1)–(A3) are transformed from the (ϕ,z) domain to the (n,k) domain by the following two-dimensional Fourier transforms:

$$\begin{Bmatrix}\{\hat{Q}_n\}\\ \{\hat{V}_n\}\end{Bmatrix}=\frac{1}{(2\pi)^2}\int_0^{2\pi}\int_{-\infty}^{\infty}\begin{Bmatrix}\{Q\}\\ \{V\}\end{Bmatrix}\times\exp[-i(kz+n\phi)]dz\ d\phi. \tag{A5}$$

The associated inversion formulas are

$$\begin{Bmatrix}\{Q\}\\ \{V\}\end{Bmatrix}=\sum_{n=-\infty}^{\infty}\int_{-\infty}^{\infty}\begin{Bmatrix}\{\hat{Q}_n\}\\ \{\hat{V}_n\}\end{Bmatrix}\exp[i(kz+n\phi)]dk. \tag{A6}$$

The derivation proceeds by substituting Eqs. (A4) and (A6) into Eqs. (A1)–(A3) and performing the two-dimensional transform indicated in Eq. (A5). This yields the following algebraic relationship between the transformed variables:

$$\{\hat{Q}_n\}=\rho c_p[Z_n]\{\hat{V}_n\}, \tag{A7}$$

where the nondimensional impedance matrix $[Z_n]$ is given by

$$[Z_n]=(1-i\eta)\left(\frac{i}{\Omega}\right)\left(\frac{h}{a}\right)\begin{bmatrix}(x^2+mn^2-\hat{\Omega}^2) & npx & -i\nu x\\ npx & (mx^2+n^2-\hat{\Omega}^2) & -in\\ i\nu x & in & [1+\beta^2(x^2+n^2)^2-\hat{\Omega}^2]\end{bmatrix} \tag{A8}$$

and $c_p=\sqrt{E/[\rho(1-\nu^2)]}$ is the low-frequency phase speed of a longitudinal wave in an equivalent flat plate with no damping. Nondimensional frequency and wave number are defined by $\Omega=\omega a/c_p$ and $x=ka$ and the complex parameter $\hat{\Omega}^2$ is defined as $\hat{\Omega}^2=\Omega^2/(1-i\eta)$.

To find the response to a point force with amplitude vector $\{F\}$ applied at (ϕ_f,z_f), this force is expressed in terms of Dirac delta distributions as

$$\{Q\}=\delta(a\phi-a\phi_f)\delta(z-z_f)\{F\}. \tag{A9}$$

This distribution is transformed in accordance with Eq. (A5) and the resulting expression for $\{\hat{Q}_n\}$ is substituted into Eq. (A7). For each circumferential harmonic, the transformed velocity $\{\hat{V}_n\}$ is found by inverting the impedance matrix. Subsequent algebraic manipulation is facilitated by expressing this inversion as the ratio of the adjoint of $[Z_n]$ to the determinant of $[Z_n]$ or $[Z_n]^{-1}=\text{adj}([Z_n])/|[Z_n]|$.

Transformation of the velocity vector back to the (ϕ,z) domain, as indicated in Eq. (A6), involves an integral over wave number which can be analytically evaluated using residue integration. Evaluating the velocity amplitude vector $\{V\}$ at a location (ϕ_v,z_v) yields

$$\{V\}=[Y_{\text{sh}}]\{F\}, \tag{A10}$$

where the admittance matrix is

$$[Y_{\mathrm{sh}}]=\frac{\Omega}{2\pi a h\rho c_p m\beta^2}\sum_{n=-\infty}^{\infty}\sum_{i=1}^{4}\frac{\mathrm{adj}([Z_n])\exp[i(x_{mn}/a)(z_v-z_f)+in(\phi_v-\phi_f)]}{2x_{mn}\prod_{\substack{p=1\\p\neq m}}^{4}(x_{mn}^2-x_{pm}^2)} \tag{A11}$$

for $z_v \geqslant z_f$. Each x_{mn} is a root of the determinental equation $|[Z_n]|=0$ and is chosen to lie in the upper half of the complex plane, $\Im\{x_{mn}\}>0$. There are always four such roots to the determinental equation, which is fourth-order in x^2. The m subscript of x_{mn} refers to one of the four roots while the n subscript designates the circumferential harmonic number.

[1] S. W. Yuan, ''Thin cylindrical shells subjected to concentrated loads,'' Q. Appl. Math. **4**, 13–26 (1946).

[2] P. A. Franken, ''Input impedances of simple cylindrical structures,'' J. Acoust. Soc. Am. **32**, 473–477 (1960).

[3] M. Heckl, ''Vibrations of point-driven cylindrical shells,'' J. Acoust. Soc. Am. **34**, 1553–1557 (1962).

[4] J. L. Palladino and V. H. Neubert, ''Mobility of a long cylindrical shells,'' J. Acoust. Soc. Am. **42**, 403–411 (1967).

[5] D. Feit, ''High-frequency response of a point-excited cylindrical shell,'' J. Acoust. Soc. Am. **49**, 1499–1504 (1971).

[6] Y. P. Lu and Y. F. Wang, ''Dynamic responses of elastic cylindrical shells to a concentrated radial load,'' J. Acoust. Soc. Am. **52**, 441–444 (1972).

[7] E. I. Grigolyuk and V. M. Tolkachev, *Contact Problems in the Theory of Plates and Shells* (Mir, Moscow, 1987), Chap. 6. Translated from Russian by Alexander Repyev.

[8] Y. P. Guo, ''Radiation from cylindrical shells driven by on-surface forces,'' J. Acoust. Soc. Am. **95**, 2014–2021 (1994).

[9] P. W. Smith, Jr., ''Phase velocities and displacement characteristics of free waves in a thin cylindrical shell,'' J. Acoust. Soc. Am. **27**, 1065–1072 (1955).

[10] K. F. Graff, *Wave Motion in Elastic Solids* (Dover, New York, 1975), Chap. 8.

[11] G. V. Borgiotti and E. M. Rosen, ''The state vector approach to the wave and power flow analysis of the forced vibrations of a cylindrical shell. Part I: Infinite cylinders in vacuum,'' J. Acoust. Soc. Am. **91**, 911–925 (1992).

[12] Yu P. Zhigalko and Z. V. Skvortsova, ''Transfer of local dynamic load through a strut to a hollow cylindrical shell,'' Sov. Appl. Mech. **21**, 940–944 (1985).

[13] E. A. Fiyaksel, R. A. Dudnik, and E. V. Cherneeva, ''Influence of the driving technique on the radiation from an inhomogeneous cylindrical shell,'' Sov. Phys. Acoust. **34**, 597–600 (1988).

[14] L. Cheng and J. Nicolas, ''Free vibration analysis of a cylindrical shell-circular plate system with general coupling and various boundary conditions,'' J. Sound Vib. **155**, 231–247 (1992).

[15] Y. P. Guo, ''Acoustic radiation from cylindrical shells due to internal forcing,'' J. Acoust. Soc. Am. **99**, 1495–1505 (1996).

[16] A. Leissa, *Vibration of Shells* (Acoustical Society of America, New York, 1993), Chap. 2.

[17] M. C. Junger and D. Feit, *Sound, Structures, and Their Interaction* (MIT, Cambridge, MA, 1986), 2nd ed.

[18] P. M. Morse and K. Uno Ingard, *Theoretical Acoustics* (Princeton U. P., Princeton, NJ, 1968), pp. 501–503.

[19] A. D. Pierce, *Acoustics, An Introduction to Its Physical Principles and Applications* (The Acoustical Society of America, New York, 1989), pp. 357–365.

[20] R. H. Gallagher, *Finite Element Analysis Fundamentals* (Prentice-Hall, Englewood Cliffs, NJ, 1975), pp. 54–60.

[21] D. E. Goldberg, *Genetic Algorithms in Search, Optimization, and Machine Learning* (Addison-Wiley, New York, 1989).

[22] A. Leissa, *Vibration of Shells* (Acoustical Society of America, New York, 1993).

Reduced models in the medium-frequency range for general external structural-acoustic systems

Christian Soize
Structures Department, ONERA, BP 72, F-92322 Chatillon Cedex, France

(Received 6 June 1997; revised 1 February 1998; accepted 23 February 1998)

This paper presents a theoretical approach for constructing a reduced model in the medium-frequency range in the area of structural acoustics for a general three-dimensional dissipative structure made of an anisotropic, inhomogeneous, viscoelastic bounded medium coupled with an external acoustic fluid. All the results presented can be used if the structure is made of beams, plates, and shells. The boundary value problem in the frequency domain and its variational formulation are presented. For a fixed medium-frequency band, an energy operator related to the structural-acoustic system is introduced. This operator is symmetric positive definite and has a countable set of positive eigenvalues. Its dominant eigensubspace allows a reduced model to be constructed using the Ritz–Galerkin method. A finite dimension approximation of the three-dimensional continuous case is presented and an effective construction of the dominant subspace using the subspace iteration method is developed. As an example, the reduced model is used for constructing the time-stationary random response of the structural-acoustic system submitted to a random wall pressure field. Finally, the theory is validated for a finite length circular cylindrical shell coupled with several dashpots and springs and immersed in a gas (air) and in a liquid (water). © *1998 Acoustical Society of America.* [S0001-4966(98)02006-2]

PACS numbers: 43.40.Hb, 43.40.Rj [CBB]

INTRODUCTION

This paper is the continuation of initial papers published by the author[1,2] in the area of modeling and associated solving methods for linear dissipative structural-acoustic systems in the medium-frequency (MF) range. It is known[3–6] that for low-frequency (LF) dynamic analysis in structural dynamics, reduced models are a very efficient tool for constructing the solution. These techniques correspond to a Ritz–Galerkin reduction of the structural-dynamics model using, for instance, the normal modes corresponding to the lowest eigenfrequencies of the associated conservative structure and called modal reduction. The efficiency of this kind of reduced model is due to the small number of generalized dynamical degrees of freedom used in the representation and, in addition, is obtained by solving a well-stated generalized symmetric eigenvalue problem for which only the first eigenvalues and the corresponding eigenfunctions have to be calculated. In addition, when such a reduced model is obtained, responses to deterministic or random excitations can be calculated for no significant additional numerical cost, and the reduced model can be used directly for solving various structural-acoustic problems in the LF range.[7,8] The fundamental problem related to the construction of a reduced model in the MF range for general dissipative structural-acoustic systems has not yet been solved. The author[9] recently proposed an efficient solution for constructing such a reduced model for general structural-dynamics systems (structures in a vacuum). Here, we present an extension of this theory to the case of general structural-acoustic systems consisting of a structure coupled with an external acoustic fluid (gas or liquid). Concerning the structure, these theoretical developments are presented in the context of three-dimensional viscoelasticity for an arbitrary domain geometry and for an anisotropic, inhomogeneous material. Extension of the results presented to beams, plates, and shells is straightforward. Concerning the external acoustic fluid, the geometry of the fluid–structure interface is arbitrary. In Sec. I, we present the boundary value problem to be solved in the frequency domain and we establish its variational formulation. In Sec. II, we construct a functional basis adapted to the MF range. To do so, we introduce an energy operator related to the dynamics of the structural-acoustic system in an MF band. This operator is symmetric positive definite and has a countable set of positive eigenvalues. The corresponding eigenfunctions form a complete family in the set of admissible displacement fields of the structure. In Sec. III, the reduced model is introduced using the Ritz–Galerkin projection of the variational formulation on the dominant eigensubspace of the energy operator, spanned by the eigenfunctions which correspond to the highest eigenvalues. In Sec. IV, we present the finite dimension approximation of the three-dimensional continuous case allowing the effective calculation to be carried out for the general case. In Sec. V, we give an efficient procedure for constructing the dominant subspace using the subspace iteration method. To illustrate the interest of such a reduced model, Sec. VI deals with the construction of the time-stationary random response of structural-acoustic systems submitted to a random wall pressure field. Finally, the theory is validated for a finite length circular cylindrical shell coupled with several dashpots and springs and immersed in a gas (Sec. VII) and in a liquid (Sec. VIII). The method proposed can also be used in the low-frequency range, but in this case there is no additional gain with respect to the usual modal reduction method. Nevertheless, it should be noted that, for a structure

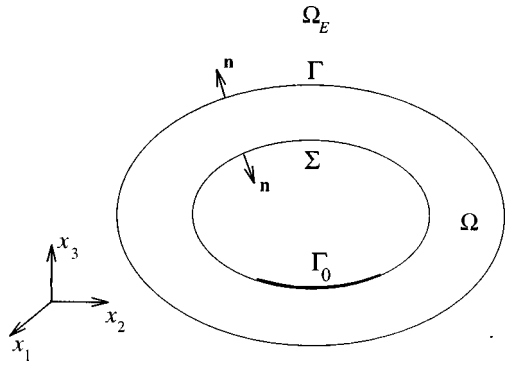

FIG. 1. Geometrical configuration of the structural-acoustic system.

in a vacuum, if the structural damping tends to zero, then it can be proved that the present MF method and the usual modal BF method give the same reduced model in the low-frequency range.

I. BOUNDARY VALUE PROBLEM AND ITS SOLUTION

A. Definition of the boundary value problem

We consider linear vibrations (formulated in the frequency domain ω) of a three-dimensional structural-acoustic system around a static equilibrium configuration considered as a natural state at rest (see Fig. 1). Let Ω be a bounded domain of $\mathbb{R}^3$, occupied by the structure at static equilibrium and made of viscoelastic material. Let $\partial\Omega=\Gamma_0\cup\Sigma\cup\Gamma$ be the boundary which is assumed to be sufficiently smooth and such that $\Gamma_0\cap\Sigma\cap\Gamma=\varnothing$. Let $\mathbf{n}$ be its outward unit normal. Let $\mathbf{u}(\mathbf{x},\omega)=(u_1(\mathbf{x},\omega),u_2(\mathbf{x},\omega),u_3(\mathbf{x},\omega))$ be the displacement field in each point $\mathbf{x}=(x_1,x_2,x_3)$ in Cartesian coordinates and at frequency ω. On part Γ_0 of the boundary, the structure is fixed ($\mathbf{u}=\mathbf{0}$) whereas on part $\Sigma\cup\Gamma$ it is free. The structure is surrounded by an external inviscid acoustic fluid (gas or liquid) occupying the unbounded three-dimensional domain Ω_E whose boundary $\partial\Omega_E$ is Γ. Let c_E be the constant speed of sound and ρ_E be the constant mass density of the external fluid at equilibrium. The pressure field and the velocity potential in each point $\mathbf{x}$ in Ω_E and at frequency ω are denoted as $p(\mathbf{x},\omega)$ and $\psi(\mathbf{x},\omega)$, respectively. We introduce a narrow MF band B such that $B=[\omega_B-\Delta\omega/2,\omega_B+\Delta\omega/2]$ in which ω_B is the center frequency and $\Delta\omega$ is the bandwidth such that $\Delta\omega/\omega_B\ll 1$ and $\omega_B>\Delta\omega/2$. With B we associate interval $\widetilde{B}=[-\omega_B-\Delta\omega/2,-\omega_B+\Delta\omega/2]$. The structure is submitted to a square integrable body force field $\mathbf{x}\mapsto\eta(\omega)\mathbf{f}(\mathbf{x},\omega)$ from Ω into $\mathbb{C}^3$ and a square integrable surface force field $\mathbf{x}\mapsto\eta(\omega)\mathbf{f}_\Sigma(\mathbf{x},\omega)$ from Σ into $\mathbb{C}^3$, in which $\eta(\omega)$ is a function from $\mathbb{R}$ into $\mathbb{C}$, such that $\eta(\omega)=0$ if ω is not in $B\cup\widetilde{B}$, continuous on B, verifying $|\eta(-\omega)|=|\eta(\omega)|$ and such that $|\eta(\omega)|\neq 0$ for all ω in B. Introducing components (f_1,f_2,f_3) and $(f_{\Sigma,1},f_{\Sigma,2},f_{\Sigma,3})$ of $\mathbf{f}$ and $\mathbf{f}_\Sigma$, respectively, the boundary value problem is written as follows in terms of $\mathbf{u}$ and ψ (the convention for the Fourier transform being $v(\omega)=\int_{\mathbb{R}}e^{-i\omega t}v(t)dt$);

$$-\omega^2\rho u_i-\sigma_{ij,j}=\eta f_i \text{ in } \Omega, \tag{1}$$

$$\sigma_{ij}n_j=\eta f_{\Sigma,i} \text{ on } \Sigma, \tag{2}$$

$$\sigma_{ij}n_j=-pn_i \text{ on } \Gamma, \tag{3}$$

$$u_i=0 \text{ on } \Gamma_0, \tag{4}$$

in which $i=1,2,3$ and where the summation over index j is used. Concerning the external acoustic fluid, we have

$$p=-i\omega\rho_E\psi \text{ in } \Omega_E\cup\Gamma, \tag{5}$$

$$\boldsymbol{\nabla}^2\psi+\frac{\omega^2}{c_E^2}\psi=0 \text{ in } \Omega_E, \tag{6}$$

$$\frac{\partial\psi}{\partial\mathbf{n}}=i\omega\mathbf{u}\cdot\mathbf{n} \text{ on } \Gamma, \tag{7}$$

$$|\psi|=O\left(\frac{1}{R}\right),$$

$$\left|\frac{\partial\psi}{\partial R}+i\frac{\omega}{c_E}\psi\right|=O\left(\frac{1}{R^2}\right) \text{ as } R=\|\mathbf{x}\|\to+\infty. \tag{8}$$

In Eq. (1), $\rho(\mathbf{x})>0$ is the mass density of the structure and $\sigma_{ij,j}=\Sigma_{j=1}^3\partial\sigma_{ij}/\partial x_j$. For a linear viscoelastic material, stress tensor σ_{ij} is written as,

$$\sigma_{ij}=\mathbb{a}_{ijkh}(\mathbf{x},\omega)\epsilon_{kh}(\mathbf{u})+\mathbb{b}_{ijkh}(\mathbf{x},\omega)\epsilon_{kh}(i\omega\mathbf{u}), \tag{9}$$

in which the summation over indices k and h is used and where $\epsilon_{kh}(\mathbf{u})=(\partial u_k/\partial x_h+\partial u_h/\partial x_k)/2$ is the linearized strain tensor. Coefficients $\mathbb{a}_{ijkh}(\mathbf{x},\omega)$ and $\mathbb{b}_{ijkh}(\mathbf{x},\omega)$ are real, depend on $\mathbf{x}$ and ω, verify the usual properties of symmetry and positiveness,[10–12] and are such that $\mathbb{a}_{ijkh}(\mathbf{x},-\omega)=\mathbb{a}_{ijkh}(\mathbf{x},\omega)$ and $\mathbb{b}_{ijkh}(\mathbf{x},-\omega)=\mathbb{b}_{ijkh}(\mathbf{x},\omega)$. Equation (8) is the outward Sommerfeld radiation condition at infinity and $\partial/\partial R$ denotes the derivative in the radial direction from the origin.

B. Acoustic impedance boundary operator and radiation impedance operator

For all real $\omega\neq 0$ and for a normal velocity field $v=i\omega\mathbf{u}\cdot\mathbf{n}$ given on Γ, the exterior Neumann problem related to the Helmholtz equation defined by Eqs. (6)–(8) has a unique solution[13] ψ. Denoting the values of ψ on surface Γ as ψ_Γ, the corresponding pressure field $p_\Gamma=-i\omega\rho_E\psi_\Gamma$ on Γ can be written as

$$p_\Gamma=\mathbf{Z}_\Gamma(\omega)\{i\omega\mathbf{u}\cdot\mathbf{n}\}, \tag{10}$$

in which $\mathbf{Z}_\Gamma(\omega)$ is the acoustic impedance boundary operator related to surface Γ. At any point $\mathbf{x}$ in unbounded domain Ω_E, pressure $p(\mathbf{x},\omega)$ can be written as

$$p(\mathbf{x},\omega)=\mathbf{Z}_{\text{rad}}(\mathbf{x},\omega)\{i\omega\mathbf{u}\cdot\mathbf{n}\}, \tag{11}$$

in which $\mathbf{Z}_{\text{rad}}(\mathbf{x},\omega)$ is the radiation impedance operator. For simply shaped geometries of Γ such as baffled rectangular or circular plates, baffled circular cylinder, etc., analytical methods[14] can be used for constructing operators $\mathbf{Z}_\Gamma(\omega)$ and $\mathbf{Z}_{\text{rad}}(\mathbf{x},\omega)$. For an arbitrary shaped surface Γ, boundary element methods can be used. This numerical method must be based on the use of integral equation techniques overcoming the mathematical difficulty induced by the problem of spurious or irregular frequencies.[8,15–17]

C. Variational formulation

For the general methodology concerning the construction of a variational formulation of a boundary value problem, we refer the reader to Refs. 13, 18, and 19. Let H be the space of all the square integrable functions on Ω with values in $\mathbb{C}^3$, equipped with the inner product $(\mathbf{u},\mathbf{v})_H = \int_\Omega \mathbf{u}(\mathbf{x})\cdot\overline{\mathbf{v}(\mathbf{x})}d\mathbf{x}$ and the associated norm $\|\mathbf{v}\|_H = (\mathbf{u},\mathbf{u})_H^{1/2}$, in which $\overline{z}$ denotes the conjugate of the complex number z. Let $V \subset H$ be the space of admissible displacement fields $\mathbf{u}$ defined on Ω with values in $\mathbb{C}^3$ such that $\mathbf{u}=\mathbf{0}$ on Γ_0 and such that $\nabla u_k \in H$ for $k=1,2,3$. The variational formulation of the boundary value problem in $\mathbf{u}$ defined by Eqs. (1)–(9) can be expressed as follows. For all ω in $B\cup\widetilde{B}$, find $\mathbf{u}(\omega)$ in V such that

$$a(\mathbf{u},\mathbf{v};\omega) = f(\mathbf{v};\omega), \quad \forall \mathbf{v}\in V, \tag{12}$$

in which $f(\mathbf{v};\omega)$ is defined by

$$f(\mathbf{v};\omega) = \eta(\omega)\left\{ \int_\Sigma \mathbf{f}_\Sigma(\mathbf{x},\omega)\cdot\overline{\mathbf{v}(\mathbf{x})}ds(\mathbf{x}) + \int_\Omega \mathbf{f}(\mathbf{x},\omega)\cdot\overline{\mathbf{v}(\mathbf{x})}d\mathbf{x}\right\}, \tag{13}$$

and where $a(\mathbf{u},\mathbf{v};\omega)$ is written as

$$\begin{aligned} a(\mathbf{u},\mathbf{v};\omega) &= -\omega^2(m(\mathbf{u},\mathbf{v}) + b_\Gamma(\mathbf{u},\mathbf{v};\omega)) \\ &\quad + i\omega d(\mathbf{u},\mathbf{v};\omega) + k(\mathbf{u},\mathbf{v};\omega), \\ m(\mathbf{u},\mathbf{v}) &= \int_\Omega \rho(\mathbf{x})\mathbf{u}(\mathbf{x})\cdot\overline{\mathbf{v}(\mathbf{x})}d\mathbf{x}, \\ d(\mathbf{u},\mathbf{v};\omega) &= \int_\Omega \mathbb{b}_{ijkh}(\mathbf{x},\omega)\epsilon_{kh}(\mathbf{u})\epsilon_{ij}(\overline{\mathbf{v}})d\mathbf{x}, \\ k(\mathbf{u},\mathbf{v};\omega) &= \int_\Omega \mathbb{a}_{ijkh}(\mathbf{x},\omega)\epsilon_{kh}(\mathbf{u})\epsilon_{ij}(\overline{\mathbf{v}})d\mathbf{x}, \end{aligned} \tag{14}$$

in which the summation over indices i, j, k and h is used. It is assumed that $d(\mathbf{u},\mathbf{v};\omega)$ and $k(\mathbf{u},\mathbf{v};\omega)$ are continuous functions on band B with respect to ω. Finally, $b_\Gamma(\mathbf{u},\mathbf{v};\omega)$ is such that

$$-\omega^2 b_\Gamma(\mathbf{u},\mathbf{v};\omega) = i\omega\int_\Gamma (\overline{\mathbf{v}}\cdot\mathbf{n})\mathbf{Z}_\Gamma(\omega)\{\mathbf{u}\cdot\mathbf{n}\}ds.$$

For all ω in $B\cup\widetilde{B}$, Eq. (12) has a unique solution $\mathbf{u}(\omega)$ in V.

II. CONSTRUCTION OF A FUNCTIONAL BASIS FOR THE REDUCED MODEL

In order to construct a functional basis adapted to MF band B and useful for the Ritz–Galerkin method, we begin by introducing the operator-valued frequency response function defined for a special class of mechanical excitations. In a second step, we define the energy operator and we construct the functional basis as its eigenfunctions.

A. Operator-valued frequency response function

Let us assumed that $\mathbf{f}_\Sigma = \mathbf{0}$ and that $\mathbf{f}$ is independent of ω. This assumption is only used for constructing the functional basis. As soon as the reduced model is obtained, the response of the mechanical system can be calculated for any deterministic and random excitations which do not use this restrictive assumption [see Eq. (13), Secs. III and IV]. Then Eq. (13) yields $f(\mathbf{v};\omega) = \eta(\omega)(\mathbf{f},\mathbf{v})_H$. It is proved[1,2,9] that for all ω fixed in $B\cup\widetilde{B}$, Eq. (12) has a unique solution $\mathbf{u}^\mathbf{f}(\omega)$ belonging to $V\subset H$ which can be written as

$$\mathbf{u}^\mathbf{f}(\omega) = \eta(\omega)\mathbf{T}_H(\omega)\mathbf{f}, \tag{15}$$

where $\mathbf{T}_H(\omega)$ is an operator in H. Solution $\mathbf{u}^\mathbf{f}(\omega)$ corresponds to the vibration induced by excitation $\eta(\omega)\mathbf{f}$ and $\mathbf{T}_H(\omega)$ is the operator-valued frequency response function.

B. Definition of an energy operator

The energy $\epsilon_B(\mathbf{u}^\mathbf{f})$ of a structural vibration corresponding to $\mathbf{u}^\mathbf{f}$ given by Eq. (15) is defined as twice the value of the total kinetic energy of the structure, i.e., using the Plancherel formula,

$$\epsilon_B(\mathbf{u}^\mathbf{f}) = \frac{1}{2\pi}\int_{B\cup\widetilde{B}} \omega^2(\mathbf{M}\mathbf{u}^\mathbf{f}(\omega),\mathbf{u}^\mathbf{f}(\omega))_H\, d\omega, \tag{16}$$

in which $\mathbf{M}$ is the mass operator in H such that $(\mathbf{M}\mathbf{u},\mathbf{v})_H = m(\mathbf{u},\mathbf{v})$. Let $\mathbf{u}^\mathbf{f}(\omega) = \eta(\omega)\mathbf{T}_H(\omega)\mathbf{f}$ and $\mathbf{u}^\mathbf{g}(\omega) = \eta(\omega)\mathbf{T}_H(\omega)\mathbf{g}$ be the solutions corresponding to the vibrations induced by excitations $\eta(\omega)\mathbf{f}$ and $\eta(\omega)\mathbf{g}$, respectively, where $\mathbf{f}$ and $\mathbf{g}$ are in H and are independent of ω. The energy operator $\mathbf{E}_B$ relative to band B is defined by

$$(\mathbf{E}_B\mathbf{f},\mathbf{g})_H = \frac{1}{2\pi}\int_{B\cup\widetilde{B}} \omega^2(\mathbf{M}\mathbf{u}^\mathbf{f}(\omega),\mathbf{u}^\mathbf{g}(\omega))_H\, d\omega. \tag{17}$$

We then deduce that $\epsilon_B(\mathbf{u}^\mathbf{f}) = (\mathbf{E}_B\mathbf{f},\mathbf{f})_H$. It should be noted that operator $\mathbf{E}_B$ depends on B and η but does not depend on spatial parts $\mathbf{f}$ and $\mathbf{g}$ of the excitations. In addition, this operator depends on the external acoustic fluid due to the coupling operator. In the present context, operator $\mathbf{E}_B$ is only used to calculate a functional basis for constructing a reduced model of the structure coupled with the external acoustic fluid. In Sec. VII which is devoted to the coupling with an external liquid, we will see that the coupling operator must be kept for the calculation of $\mathbf{E}_B$. *A contrario*, the coupling operator can be omitted for the calculation of $\mathbf{E}_B$ in the case of a coupling with a gas as shown in Sec. VIII.

C. Properties of the energy operator

Energy operator $\mathbf{E}_B$ is a positive-definite symmetric operator in H whose range space is a subspace of V and which can be written as

$$\mathbf{E}_B = \frac{1}{\pi}\int_B \omega^2|\eta(\omega)|^2\ \mathrm{Re}\{\mathbf{T}_H(\omega)^*\mathbf{M}\mathbf{T}_H(\omega)\}d\omega, \tag{18}$$

in which Re denotes the real part and where $\mathbf{T}_H(\omega)^*$ is the adjoint of $\mathbf{T}_H(\omega)$. Consequently, operator $\mathbf{E}_B$ has a countable set of decreasing positive eigenvalues with finite multiplicity, possibly excepting zero, $\lambda_1 \geqslant \lambda_2 \geqslant \ldots \to 0$, in which the λ_ν terms are the repeated eigenvalues of $\mathbf{E}_B$. The corresponding eigenfunctions $\{\mathbf{e}_\nu\}_{\nu\geqslant 1}$ such that

$$\mathbf{E}_B\mathbf{e}_\nu = \lambda_\nu\mathbf{e}_\nu \tag{19}$$

are functions $\mathbf{e}_\nu(\mathbf{x})$ from Ω into $\mathbb{R}^3$ and form a complete family in admissible space $V \subset H$, orthonormal for the inner product of H. This fundamental result allows a reduced model to be constructed in the MF range. We then have $(\mathbf{e}_\nu, \mathbf{e}_{\nu'})_H = \delta_{\nu\nu'}$. Finally, the eigenvalues are such that $\sum_{\nu=1}^{+\infty} \lambda_\nu < +\infty$ (one says that $\mathbf{E}_B$ is a trace operator[20,21]) and its trace norm denoted as tr $\mathbf{E}_B$ is written as

$$\text{tr } \mathbf{E}_B = \sum_{\nu=1}^{+\infty} \lambda_\nu < +\infty. \tag{20}$$

The proof of these results is a straightforward extension of the proof established by the author[9] for the case of a three-dimensional viscoelastic structure in a vacuum.

III. CONSTRUCTION OF A REDUCED MODEL IN THE MF RANGE

The reduced model adapted to MF band B is obtained using the Ritz–Galerkin projection of the variational formulation defined by Eq. (12) on the subspace V^N of V spanned by the eigenfunctions $\{\mathbf{e}_1, \ldots, \mathbf{e}_N\}$ corresponding to the N highest eigenvalues $\{\lambda_1, \ldots, \lambda_N\}$ of energy operator $\mathbf{E}_B$. Let $\mathbf{u}(\omega) \in V$ be the solution of Eq. (12) and let $\mathbf{u}^N(\omega)$ be its projection on V^N,

$$\mathbf{u}^N(\mathbf{x}, \omega) = \sum_{\nu=1}^{N} \theta_\nu(\omega) \mathbf{e}_\nu(\mathbf{x}), \tag{21}$$

in which $\theta_\nu(\omega) \in \mathbb{C}$. From Eq. (12), we deduce that, for all ω in $B \cup \tilde{B}$, $\boldsymbol{\theta}(\omega) = (\theta_1(\omega), \ldots, \theta_N(\omega)) \in \mathbb{C}^N$ is the unique solution of the linear equation

$$[\mathscr{A}_N(\omega)] \boldsymbol{\theta}(\omega) = \eta(\omega) \mathscr{F}(\omega), \tag{22}$$

in which $[\mathscr{A}_N(\omega)]$ is the symmetric $(N \times N)$ complex matrix defined by $[\mathscr{A}_N(\omega)]_{\nu\nu'} = a(\mathbf{e}_{\nu'}, \mathbf{e}_\nu; \omega)$ and where $\mathscr{F}(\omega) = (\mathscr{F}_1(\omega), \ldots, \mathscr{F}_N(\omega)) \in \mathbb{C}^N$ is such that $\eta(\omega) \mathscr{F}_\nu(\omega) = f(\mathbf{e}_\nu; \omega)$. Equations (21) and (22) constitute the reduced model in MF band B of the structural-acoustic dynamical system described by Eqs. (1)–(9). For all ω in $B \cup \tilde{B}$, matrix $[\mathscr{A}_N(\omega)]$ is invertible and the solution of Eq. (22) is written as $\boldsymbol{\theta}(\omega) = \eta(\omega) [\mathscr{T}_N(\omega)] \mathscr{F}(\omega)$ in which $[\mathscr{T}_N(\omega)] = [\mathscr{A}_N(\omega)]^{-1}$. For all ω in $B \cup \tilde{B}$, $\mathbf{u}^N(\omega) \to \mathbf{u}(\omega)$ in V as $N \to +\infty$.

IV. FINITE DIMENSION APPROXIMATION

An explicit construction of eigenfunctions $\{\mathbf{e}_1, \ldots, \mathbf{e}_N\}$ of energy operator $\mathbf{E}_B$ cannot be obtained in the general case. A finite dimension approximation $\mathbf{E}_{B,n}$ of $\mathbf{E}_B$ must be introduced and the eigenfunctions $\{\mathbf{e}_1^n, \ldots, \mathbf{e}_N^n\}$ of $\mathbf{E}_{B,n}$ associated with the N highest eigenvalues $\lambda_1^n \geqslant \ldots \geqslant \lambda_N^n$, are the approximation of $\{\mathbf{e}_1, \ldots, \mathbf{e}_N\}$. This finite approximation is obtained by using the Ritz–Galerkin method. We then consider a subspace $V_n \subset V$ of finite dimension $n \geqslant 1$, spanned by a family $\{\psi_1, \ldots, \psi_n\}$ of independent $\mathbb{R}^3$-valued functions $\{\psi_\alpha\}_\alpha$ in V. In practice, this family can be either a finite element basis[13,22,23] associated with a finite element mesh of domain Ω or, for a particular case, any functional basis constructed in the context of an analytical approach, for instance the sequence of the structural normal modes of a homogeneous, simply supported rectangular plate with a constant thickness. Let $\mathbf{u}(\omega) \in V$ be the solution of Eq. (12). Its projection on V_n is written as

$$\mathbf{u}_n(\mathbf{x}, \omega) = \sum_{\alpha=1}^{n} q_\alpha(\omega) \boldsymbol{\psi}_\alpha(\mathbf{x}). \tag{23}$$

From Eq. (12), we deduce that $\mathbf{q}(\omega) = (q_1(\omega), \ldots, q_n(\omega)) \in \mathbb{C}^n$ is the unique solution of the linear equation

$$[A_n(\omega)] \mathbf{q}(\omega) = \eta(\omega) \mathbf{F}(\omega), \tag{24}$$

in which symmetric $(n \times n)$ complex matrix $[A_n(\omega)]$ is such that $[A_n(\omega)]_{\alpha\beta} = a(\boldsymbol{\psi}_\beta, \boldsymbol{\psi}_\alpha; \omega)$ and can be written as

$$[A_n(\omega)] = -\omega^2([M] + [B_\Gamma(\omega)]) + i\omega[D(\omega)] + [K(\omega)], \tag{25}$$

in which $[M]$, $[D(\omega)]$ and $[K(\omega)]$ are positive-definite symmetric $(n \times n)$ real matrices such that $[M]_{\alpha\beta} = m(\boldsymbol{\psi}_\beta, \boldsymbol{\psi}_\alpha)$, $[D(\omega)]_{\alpha\beta} = d(\psi_\beta, \psi_\alpha; \omega)$ and $[K(\omega)]_{\alpha\beta} = k(\boldsymbol{\psi}_\beta, \boldsymbol{\psi}_\alpha; \omega)$, and $[B_\Gamma(\omega)]$ is a symmetric $(n \times n)$ complex matrix such that $[B_\Gamma(\omega)]_{\alpha\beta} = b_\Gamma(\boldsymbol{\psi}_\beta, \boldsymbol{\psi}_\alpha; \omega)$. Vector $\mathbf{F}(\omega) = (F_1(\omega), \ldots, F_n(\omega)) \in \mathbb{C}^n$ is such that

$$\eta(\omega) F_\alpha(\omega) = f(\boldsymbol{\psi}_\alpha; \omega). \tag{26}$$

The pressure field radiated by the structure is written as

$$p_n(\mathbf{x}, \omega) = i\omega \sum_{\alpha=1}^{n} Z_\alpha^n(\mathbf{x}, \omega) q_\alpha(\omega), \tag{27}$$

in which $Z_\alpha^n(\mathbf{x}, \omega) = \mathbf{Z}_{\text{rad}}(\mathbf{x}, \omega)\{\boldsymbol{\psi}_\alpha \cdot \mathbf{n}\}$. Concerning the far field radiated by the structure, we introduce the spherical coordinates

$$\mathbf{x} = \mathbf{x}(R, \theta, \varphi) = (R \sin\varphi \cos\theta, R \sin\varphi \sin\theta, R \cos\varphi), \tag{28}$$

with $\varphi \in [0, \pi]$ and $\theta \in [0, 2\pi]$. The far field can then be characterized by the pressure coefficient $c^n(\theta, \varphi, \omega)$ defined by

$$c^n(\theta, \varphi, \omega) = \lim_{R \to +\infty} \left\{ \frac{R e^{i\omega R/c_E}}{\rho_E c_E^2} p_n(\mathbf{x}(R, \theta, \varphi), \omega) \right\}. \tag{29}$$

Substituting Eq. (27) in Eq. (29) yields

$$c^n(\theta, \varphi, \omega) = i\omega \mathbf{r}^n(\theta, \varphi, \omega)^T \mathbf{q}(\omega) = i\omega \sum_{\alpha=1}^{n} r_\alpha^n(\theta, \varphi, \omega) q_\alpha(\omega), \tag{30}$$

in which $\mathbf{r}^n(\theta, \varphi, \omega) = (r_1^n(\theta, \varphi, \omega), \ldots, r_n^n(\theta, \varphi, \omega)) \in \mathbb{C}^n$ and where $r_\alpha(\theta, \varphi, \omega)$ is such that

$$r_\alpha^n(\theta, \varphi, \omega) = \lim_{R \to +\infty} \left\{ \frac{R e^{i\omega R/c_E}}{\rho_E c_E^2} Z_\alpha^n(\mathbf{x}(R, \theta, \varphi), \omega) \right\}. \tag{31}$$

A. Projection of the energy operator

Projection $\mathbf{E}_{B,n}$ of operator $\mathbf{E}_B$ on $V_n \subset H$ is written as

$$\mathbf{E}_{B,n} = \sum_{\alpha,\beta=1}^{n} [E_n]_{\alpha\beta} (., \boldsymbol{\psi}_\beta)_H \boldsymbol{\psi}_\alpha, \tag{32}$$

in which $[E_n]$ is a positive-definite symmetric $(n\times n)$ real matrix such that

$$[E_n]=\int_B [e_n(\omega)]d\omega, \tag{33}$$

$$[e_n(\omega)]=\frac{1}{\pi}\,\omega^2|\,\eta(\omega)|^2\ \mathrm{Re}\{[T_n(\omega)]^*[M][T_n(\omega)]\}, \tag{34}$$

where $[T_n(\omega)]$ is the symmetric $(n\times n)$ complex matrix such that

$$[T_n(\omega)]=[A_n(\omega)]^{-1},\quad [T_n(\omega)]^*=\overline{[T_n(\omega)]}. \tag{35}$$

B. Generalized symmetric eigenvalue problem

Each eigenfunction $\mathbf{e}_\nu^n$ such that $\mathbf{E}_{B,n}\mathbf{e}_\nu^n=\lambda_\nu^n\mathbf{e}_\nu^n$ can be written as

$$\mathbf{e}_\nu^n=\sum_{\alpha=1}^{n} P_\alpha^\nu\boldsymbol{\psi}_\alpha. \tag{36}$$

Introducing vector $\mathbf{P}^\nu=(P_1^\nu,\ldots,P_n^\nu)$, it can easily be seen that eigenvalues $\{\lambda_1^n,\ldots,\lambda_n^n\}$ and the corresponding eigenvectors $\{\mathbf{P}^1,\ldots,\mathbf{P}^n\}$ are the solutions of the generalized symmetric eigenvalue problem

$$[H]\mathbf{P}=\lambda^n[G]\mathbf{P}, \tag{37}$$

in which $[G]$ and $[H]$ are positive-definite symmetric $(n\times n)$ real matrices such that $[G]_{\beta\alpha}=(\psi_\alpha,\psi_\beta)_H$ and $[H]=[G][E_n][G]$. Eigenvectors $\{\mathbf{P}^1,\ldots,\mathbf{P}^n\}$ form a basis of $\mathbb{R}^n$ and verify the usual orthogonality conditions with respect to $[G]$ and $[H]$ and consequently, we have $(\mathbf{e}_\nu^n,\mathbf{e}_{\nu'}^n)_H=([G]\mathbf{P}^\nu,\mathbf{P}^{\nu'})_{\mathbb{R}^n}=\delta_{\nu\nu'}$.

C. Reduced model adapted to MF band *B*

Let $N<n$ (generally $N\ll n$). Let $\mathbf{u}(\omega)\in V$ be the solution of Eq. (12). The reduced model adapted to MF band B is defined as the projection $\mathbf{u}_n^N(\omega)$ of $\mathbf{u}(\omega)$ on the subspace $V_n^N\subset V_n\subset V$ spanned by the eigenfunctions $\{\mathbf{e}_1^n,\ldots,\mathbf{e}_N^n\}$ which correspond to the N highest eigenvalues $\lambda_1^n\geqslant\lambda_2^n\geqslant\ldots\geqslant\lambda_N^n$ of operator $\mathbf{E}_{B,n}$. Projection $\mathbf{u}_n^N(\omega)$ can be written as

$$\mathbf{u}_n^N(\mathbf{x},\omega)=\sum_{\nu=1}^{N}\theta_\nu^n(\omega)\mathbf{e}_\nu^n(\mathbf{x}), \tag{38}$$

in which $\boldsymbol{\theta}^n(\omega)=(\theta_1^n(\omega),\ldots,\theta_N^n(\omega))\in\mathbb{C}^N$ is the solution of the linear equation

$$[\mathscr{A}_N^n(\omega)]\boldsymbol{\theta}^n(\omega)=\eta(\omega).\mathscr{F}^n(\omega), \tag{39}$$

where $[\mathscr{A}_N^n(\omega)]$ is the symmetric $(N\times N)$ complex matrix defined by $[\mathscr{A}_N^n(\omega)]_{\nu\nu'}=a(\mathbf{e}_{\nu'}^n,\mathbf{e}_\nu^n;\omega)$ and where $\mathscr{F}^n(\omega)=(\mathscr{F}_1^n(\omega),\ldots,\mathscr{F}_N^n(\omega))\in\mathbb{C}^N$ is such that $\eta(\omega).\mathscr{F}_\nu^n(\omega)=f(\mathbf{e}_\nu^n;\omega)$. Matrix $[\mathscr{A}_N^n(\omega)]$ is invertible and we have

$$\begin{aligned}&\boldsymbol{\theta}^n(\omega)=\eta(\omega)[\mathscr{T}_N^n(\omega)].\mathscr{F}^n(\omega);\\ &[\mathscr{T}_N^n(\omega)]=[\mathscr{A}_N^n(\omega)]^{-1}.\end{aligned} \tag{40}$$

The pressure field radiated by the structure is written as

$$p_n^N(\mathbf{x},\omega)=i\omega\sum_{\nu=1}^{N} Z_{N,\nu}^n(\mathbf{x},\omega)\,\theta_\nu^n(\omega), \tag{41}$$

in which $Z_{N,\nu}^n(\mathbf{x},\omega)=\mathbf{Z}_{\mathrm{rad}}(\mathbf{x},\omega)\{\mathbf{e}_\nu^n\cdot\mathbf{n}\}$. For this reduced model, the pressure coefficient defined by Eq. (29) and given by Eq. (30) is written as

$$c_N^n(\theta,\varphi,\omega)=i\omega\mathbf{r}_N^n(\theta,\varphi,\omega)^T\boldsymbol{\theta}^n(\omega), \tag{42}$$

in which complex vector $\mathbf{r}_N^n(\theta,\varphi,\omega)\in\mathbb{C}^N$ is such that

$$r_{N,\nu}^n(\theta,\varphi,\omega)=\lim_{R\to+\infty}\left\{\frac{Re^{i\omega R/c_E}}{\rho_E c_E^2}\,Z_{N,\nu}^n(\mathbf{x}(R,\theta,\varphi),\omega)\right\}. \tag{43}$$

Let $[P]$ be the $(n\times N)$ real matrix whose columns are the N eigenvectors $\{\mathbf{P}_1,\ldots,\mathbf{P}_N\}$ corresponding to the N highest eigenvalues $\lambda_1^n\geqslant\ldots\geqslant\lambda_N^n$. We then deduce that

$$\mathbf{q}(\omega)=[P]\boldsymbol{\theta}^n(\omega), \tag{44}$$

$$[\mathscr{A}_N^n(\omega)]=[P]^T[A_n(\omega)][P], \tag{45}$$

$$\mathscr{F}^n(\omega)=[P]^T\mathbf{F}(\omega), \tag{46}$$

$$\mathbf{r}_N^n(\theta,\varphi,\omega)=[P]^T\mathbf{r}^n(\theta,\varphi,\omega), \tag{47}$$

in which matrix $[A_n(\omega)]$ is given by Eq. (25), vector $\mathbf{F}(\omega)$ by Eq. (26) and vector $\mathbf{r}^n(\theta,\varphi,\omega)$ by Eq. (31). Matrix $[E_n^N]$ corresponding to $[E_n]$ for the reduced model is a positive-semidefinite symmetric $(n\times n)$ real matrix such that

$$[E_n^N]=\int_B [e_n^N(\omega)]d\omega, \tag{48}$$

$$[e_n^N(\omega)]=[P][\boldsymbol{\epsilon}_n^N(\omega)][P]^T, \tag{49}$$

in which $[\boldsymbol{\epsilon}_n^N(\omega)]$ is a positive-definite symmetric $(N\times N)$ real matrix such that

$$[\boldsymbol{\epsilon}_n^N(\omega)]=\frac{1}{\pi}\,\omega^2|\,\eta(\omega)|^2\ \mathrm{Re}\{[\mathscr{T}_N^n(\omega)]^*[\mathscr{M}]\times[\mathscr{T}_N^n(\omega)]\}, \tag{50}$$

where $[\mathscr{M}]=[P]^T[M][P]$.

D. Dominant eigensubspace and order of the reduced model

In this subsection, we assume that $\mathbf{F}(\omega)=\mathbf{F}$ is independent of ω and consequently, $\mathscr{F}^n$ is also independent of ω. Let $\mathbf{u}(\omega)$ be the solution of Eq. (12), $\mathbf{u}_n(\omega)$ its projection on V_n and $\mathbf{u}_n^N(\omega)$ its projection on $V_n^N\subset V_n$. The energy of $\mathbf{u}_n$ is such that $\boldsymbol{\epsilon}_B(\mathbf{u}_n)=\Sigma_{\nu=1}^n\lambda_\nu^n|\mathscr{F}_\nu^n|^2$ and the energy of $\mathbf{u}_n^N$ is $\boldsymbol{\epsilon}_B(\mathbf{u}_n^N)=\Sigma_{\nu=1}^N\lambda_\nu^n|\mathscr{F}_\nu^n|^2$. We then have $\boldsymbol{\epsilon}_B(\mathbf{u}_n)\leqslant\lambda_1^n\|\mathscr{F}^n\|^2$ and since the upper bound is effectively reached, the maximum $\boldsymbol{\epsilon}_{\max}$ of $\boldsymbol{\epsilon}_B(\mathbf{u}_n)$ is such that $\boldsymbol{\epsilon}_{\max}=\max_{\mathscr{F}^n\in\mathbb{C}^n}\boldsymbol{\epsilon}_B(\mathbf{u}_n)=\lambda_1^n\|\mathscr{F}^n\|^2$. We then deduce that $[\boldsymbol{\epsilon}_B(\mathbf{u}_n)-\boldsymbol{\epsilon}_B(\mathbf{u}_n^N)]/\boldsymbol{\epsilon}_{\max}\leqslant\lambda_{N+1}^n/\lambda_1^n$. Since $\{\lambda_\nu\}_\nu$ is a decreasing sequence of positive numbers as $\nu\to+\infty$, if n is sufficiently large, then there exists $N<n$ such that $\lambda_{N+1}^n/\lambda_1^n\ll 1$. Subspace V_n^N is called the dominant eigensubspace of operator $\mathbf{E}_{B,n}$ corresponding to the N highest eigenvalues $\lambda_1^n\geqslant\ldots\geqslant\lambda_N^n$ and N is called the order of the reduced model. In Secs. VII and VIII, we present

the graphs of the distribution of eigenvalues λ_ν^n for two examples which clearly show how N must be chosen.

V. CONSTRUCTION OF THE DOMINANT EIGENSUBSPACE

All the developments and details concerning the effective construction of the dominant eigensubspace are given in Ref. 9. In order to facilitate the understanding of Secs. VII and VIII and illustrate the extension necessary to take into account the presence of an external acoustic fluid, we summarize below the main results of the method. The reduced model defined by Eqs. (38)–(50) requires calculation of eigenvectors $\mathbf{P}^1,\ldots,\mathbf{P}^N$ in $\mathbb{R}^n$ corresponding to the N highest eigenvalues $\lambda_1^n \geqslant \ldots \geqslant \lambda_N^n$ of the generalized symmetric eigenvalue problem defined by Eq. (37). Since n is large and $N \ll n$, the Lanczos method or the subspace iteration method[22,24–26] can *a priori* be used. The algebraic structure of matrix $[E_n]$ defined by Eq. (33) shows that the use of the subspace iteration method allows a very efficient solving method to be constructed, avoiding the explicit calculation of matrix $[E_n]$. Let m be the dimension of the subspace used for the iterations such that $N<m\ll n$ (in practice,[22] $m=\min\{2N,N+8\}$). Since the usual formulation of the subspace iteration method is adapted to calculating the lowest eigenvalues, Eq. (37) is transformed as follows. We have to calculate the N lowest eigenvalues and associated eigenvectors of the symmetric eigenvalue problem defined by

$$[G][S]=[H][S][\Gamma], \tag{51}$$

in which $[S]$ is an $(n\times m)$ real matrix and $[\Gamma]$ a diagonal $(m\times m)$ real matrix such that $[S]^T[H][S]=[I]$ and $[S]^T[G][S]=[\Gamma]$ in which matrices $[\Gamma]$ and $[S]$ are such that $[\Lambda]=[\Gamma]^{-1}$ and $[\tilde{P}]=[S][\Gamma]^{-1/2}$, where $[\Lambda]$ is the $(m\times m)$ real diagonal matrix such that the N highest eigenvalues are $\lambda_1^n=[\Lambda]_{11}\geqslant\ldots\geqslant\lambda_N^n=[\Lambda]_{NN}$ and where $[\tilde{P}]$ is the $(n\times m)$ real matrix whose first N columns are eigenvectors $\mathbf{P}^1,\ldots,\mathbf{P}^N$ defining matrix $[P]$. If we examine the subspace iteration algorithm, it would seem that calculation of matrix $[E_n]$ is necessary. In fact, for each iteration of the algorithm, we only need to calculate an $(n\times m)$ real matrix $[W]$ such that $[W]=[E_n][X]$, in which $[X]$ is a given $(n\times m)$ real matrix.

A. Direct procedure in the frequency domain

The direct procedure in the frequency domain consists in calculating $[E_n]$ using Eqs. (33) and (34), then calculating $[W]$ each iteration.[9] This method is inefficient because matrix $[E_n]$ has to be constructed explicitly. Two other solutions are presented below.

B. Indirect procedure in the frequency domain

Since $[X]$ is a real matrix, it can easily be verified that $[W]$ can be written as $[W]=\int_B \mathrm{Re}\{[\hat{Z}(\omega)]\}d\omega$ where $[\hat{Z}(\omega)]$ is an $(n\times m)$ complex matrix which is the solution of

$$[A_n(\omega)][\hat{Y}(\omega)]=\hat{\chi}(\omega)[X], \tag{52}$$

$$[A_n(\omega)][\hat{Z}(\omega)]=[M]\overline{[\hat{Y}(\omega)]}, \tag{53}$$

in which $\hat{\chi}(\omega)$ is a function defined on $\mathbb{R}$ such that,

$$\hat{\chi}(\omega)=\frac{1}{\pi}\,\omega^2|\,\eta(\omega)|^2\mathbf{1}_B(\omega). \tag{54}$$

It is proved[9] that this procedure is much more efficient than the previous one defined in Sec. V A.

C. Procedure based on the use of the MF solving method in the time domain

This method is based on the use of the MF solving method[2,27] and requires factorization of only one symmetric $(n\times n)$ complex matrix. Consequently, much less core memory is necessary for this procedure than for the indirect procedure in the frequency domain (Sec. V B) for which N_{freq} factorizations are simultaneously present in the memory, where N_{freq} is the number of frequency points required for calculation of the integral in Eq. (33). A detailed analysis of this procedure is given in Ref. 9 and cannot be reproduced here. Let $\chi_0(t)$ be a function such that $\chi_0(t)=e^{-i\omega_B t}\chi(t)$ in which $\chi(t)=(1/2\pi)\int_B e^{i\omega t}\hat{\chi}(\omega)d\omega$ is the inverse Fourier transform of function $\hat{\chi}(\omega)$ defined by Eq. (54). Therefore, the Fourier transform $\hat{\chi}_0(\omega)=\int_{\mathbb{R}} e^{-i\omega t}\chi_0(t)dt$ is a square integrable function on $\mathbb{R}$ such that $\hat{\chi}_0(\omega)=0$ if $\omega\notin B_0$ where B_0 denotes the LF band $B_0=[-\Delta\omega/2,\Delta\omega/2]$. Function $\chi_0(t)$ is the LF signal associated with the MF narrow-band signal $\chi(t)$. Let $[M_B]$, $[D_B]$, and $[K_B]$ be the symmetric $(n\times n)$ matrices independent of the frequency such that $[M_B]=[M]+[B_\Gamma(\omega_B)]$, $[D_B]=[D(\omega_B)]$, and $[K_B]=[K(\omega_B)]$. It can be proved[9] that $[W]=[E_n][X]$ can be calculated by $[W]=2\pi\ \mathrm{Re}\{[Z_0(0)]\}$ in which $[Z_0(t)]$ is the solution of the following LF equations in the time domain associated with the MF equations,

$$[M_B][\ddot{Y}_0(t)]+[\tilde{D}_B][\dot{Y}_0(t)]+[\tilde{K}_B][Y_0(t)]=\chi_0(t)[X], \tag{55}$$

$$[M_B][\ddot{Z}_0(t)]+[\tilde{D}_B][\dot{Z}_0(t)]+[\tilde{K}_B][Z_0(t)]=[M]\overline{[Y_0(-t)]}, \tag{56}$$

in which the symmetric $(n\times n)$ complex matrices $[\tilde{D}_B]$ and $[\tilde{K}_B]$ are written as $[\tilde{D}_B]=[D_B]+2i\omega_B[M]$ and $[\tilde{K}_B]=-\omega_B^2[M]+i\omega_B[D_B]+[K_B]$. It should be noted that the Fourier transforms $[\hat{Y}_0(\omega)]$ and $[\hat{Z}_0(\omega)]$ of $[Y_0(t)]$ and $[Z_0(t)]$, respectively, are such that $[\hat{Y}_0(\omega)]=[\hat{Z}_0(\omega)]=[0]$ if $\omega\notin B_0$. That is why Eqs. (55) and (56) are called the LF equations in the time domain associated with the MF equations related to MF band B. The associated LF Eqs. (55) and (56) are solved using an unconditionally stable implicit step-by-step integration method such as the Newmark method or the Wilson θ method.[22] Since Eqs. (55) and (56) have the same differential operator $[M_B]d^2/dt^2+[\tilde{D}_B]d/dt+[\tilde{K}_B]$, only one symmetric $(n\times n)$ complex matrix has to be factorized. The basic sampling time step denoted as τ is given by Shannon's theorem and consequently, $\tau=2\pi/\Delta\omega$. The integration time step of the step-by-step integration method is then written as $\Delta t=\tau/\mu$ where $\mu>1$ is an integer. Since χ_0 and $[Y_0]$ are square integrable functions, for any $\epsilon>0$, there exists an initial time $t_I=-I_0\times\tau$ where $I_0>1$ is an integer

and a final time $t_F = J_0 \times \tau$ where $J_0 > 1$ is another integer, such that

$$\int_{-\infty}^{t_I} |\chi_0(t)|^2 \, dt \leq \epsilon \|\chi_0\|_{L^2}^2,$$
$$\int_{t_F}^{+\infty} \|[Y_0(t)]\|^2 \, dt \leq \epsilon \int_{t_I}^{t_F} \|[Y_0(t)]\|^2 \, dt, \tag{57}$$

in which $\|[Y_0(t)]\|^2 = \mathrm{tr}\{[Y_0(t)]^*[Y_0(t)]\}$. We have the following procedure.

Step 1. Construction of the sequence $[Y_0(i \times \Delta t)]$ for $i = -I, \ldots, J$ with $I = I_0 \times \mu$ and $J = J_0 \times \mu$ by solving Eq. (55) for $t \in]t_I, t_F]$ with the initial conditions $[Y_0(t_I)] = [\dot{Y}_0(t_I)] = [0]$.

Step 2. Construction of the sequence $[Z_0(j \times \Delta t)]$ for $j = -J, \ldots, 0$ by solving Eq. (56) for $t \in]-t_F, 0]$ with the initial conditions $[Z_0(-t_F)] = [\dot{Z}_0(-t_F)] = [0]$.

As explained in Ref. 9, this procedure can be much more efficient than the previous one.

VI. TIME-STATIONARY RANDOM RESPONSE USING THE REDUCED MODEL

In this section, the structural-acoustic system is submitted to a time-stationary second-order centered random wall pressure field $\{p(\mathbf{x},t), \mathbf{x} \in \Gamma, t \in \mathbb{R}\}$ with values in $\mathbb{R}$ and we are interested in the stationary response of the structural-acoustic system. The cross-correlation function of random field p is denoted as $R_p(\mathbf{x},\mathbf{y},\tau) = \mathbb{E}\{p(\mathbf{x},t+\tau)p(\mathbf{y},t)\}$ in which $\mathbb{E}$ is the mathematical expectation and is such that

$$R_p(\mathbf{x},\mathbf{y},\tau) = \int_{\mathbb{R}} e^{i\omega\tau} S_p(\mathbf{x},\mathbf{y},\omega) d\omega, \tag{58}$$

in which $S_p(\mathbf{x},\mathbf{y},\omega)$ is the cross-spectral density function which is written as

$$S_p(\mathbf{x},\mathbf{y},\omega) = |\eta(\omega)|^2 s_p(\mathbf{x},\mathbf{y},\omega). \tag{59}$$

A. Finite dimension approximation

Let $\{\mathbb{F}_\alpha(t), t \in \mathbb{R}\}$ be the stochastic process defined by

$$\mathbb{F}_\alpha(t) = -\int_\Gamma p(\mathbf{x},\mathbf{t}) \mathbf{n}_\mathbf{x} \cdot \boldsymbol{\psi}_\alpha(\mathbf{x}) ds_\mathbf{x}. \tag{60}$$

Therefore the $(n \times n)$ matrix-valued spectral density function $[S_\mathbb{F}(\omega)]$ of stationary stochastic process $\mathbb{F} = (\mathbb{F}_1, \ldots, \mathbb{F}_n)$ indexed by $\mathbb{R}$ with values in $\mathbb{R}^n$ is such that

$$[S_\mathbb{F}(\omega)]_{\alpha\beta} = \int_\Gamma \int_\Gamma |\eta(\omega)|^2 s_p(\mathbf{x},\mathbf{y},\omega) \mathbf{n}_\mathbf{x} \cdot \boldsymbol{\psi}_\alpha(\mathbf{x}) \times \mathbf{n}_\mathbf{y} \cdot \boldsymbol{\psi}_\alpha(\mathbf{y}) ds_\mathbf{x} \, ds_\mathbf{y}. \tag{61}$$

From Eq. (24), we deduce that the $(n \times n)$ matrix-valued spectral density function $[S_\mathbf{q}(\omega)]$ of the second-order stationary stochastic process $\{\mathbf{q}(t), t \in \mathbb{R}\}$ with values in $\mathbb{R}^n$ is such that[28–30]

$$[S_\mathbf{q}(\omega)] = [T_n(\omega)][S_\mathbb{F}(\omega)]\overline{[T_n(\omega)]}^T. \tag{62}$$

Below, we assume that θ and φ are fixed in $[0, 2\pi]$ and $[0, \pi]$, respectively. The autocorrelation function $R_{c^n}(\theta,\varphi;\tau) = \mathbb{E}\{c^n(\theta,\varphi,t+\tau)c^n(\theta,\varphi,t)\}$ of the second-order stationary stochastic process $\{c^n(\theta,\varphi,t), t \in \mathbb{R}\}$ with values in $\mathbb{R}$, corresponding to the quantity $c^n(\theta,\varphi,\omega)$ defined by Eq. (30), is written as

$$R_{c^n}(\theta,\varphi;\tau) = \int_\mathbb{R} e^{i\omega\tau} S_{c^n}(\theta,\varphi;\omega) d\omega. \tag{63}$$

Its power spectral density function $S_{c^n}(\theta,\varphi;\omega) \geq 0$ is given by[28–30]

$$S_{c^n}(\theta,\varphi;\omega) = \omega^2 ([T_n(\omega)]\mathbf{r}^n(\theta,\varphi,\omega))^T [S_\mathbb{F}(\omega)] \times \overline{[T_n(\omega)]\mathbf{r}^n(\theta,\varphi,\omega)}. \tag{64}$$

B. Reduced model

Using the reduced model defined in Sec. IV C, the $(n \times n)$ matrix-valued spectral density function $[S_\mathbf{q}(\omega)]$ of the stationary stochastic process $\mathbf{q}(t) = [P]\boldsymbol{\theta}^n(t)$ is written as

$$[S_\mathbf{q}(\omega)] = [P][S_{\boldsymbol{\theta}^n}(\omega)][P]^T, \tag{65}$$

in which the $(N \times N)$ matrix-valued spectral density function $[S_{\boldsymbol{\theta}^n}(\omega)]$ of the reduced model is written as[28–30]

$$[S_{\boldsymbol{\theta}^n}(\omega)] = [\mathscr{T}_N^n(\omega)][S_N(\omega)]\overline{[\mathscr{T}_N^n(\omega)]}^T, \tag{66}$$

in which the $(N \times N)$ matrix $[S_N(\omega)]$ is such that

$$[S_N(\omega)] = [P]^T [S_\mathbb{F}(\omega)][P]. \tag{67}$$

The autocorrelation function $R_{c_N^n}(\theta,\varphi;\tau) = \mathbb{E}\{c_N^n(\theta,\varphi,t+\tau)c_N^n(\theta,\varphi,t)\}$ of the second-order stationary stochastic process $\{c_N^n(\theta,\varphi,t), t \in \mathbb{R}\}$ with values in $\mathbb{R}$, corresponding to the quantity $c_N^n(\theta,\varphi,\omega)$ defined by Eq. (42), is written as

$$R_{c_N^n}(\theta,\varphi;\tau) = \int_\mathbb{R} e^{i\omega\tau} S_{c_N^n}(\theta,\varphi;\omega) d\omega. \tag{68}$$

Its power spectral density function $S_{c_N^n}(\theta,\varphi;\omega) \geq 0$ is given by[28–30]

$$S_{c_N^n}(\theta,\varphi;\omega) = \omega^2 ([\mathscr{T}_N^n(\omega)]\mathbf{r}_N^n(\theta,\varphi,\omega))^T [S_N(\omega)] \times \overline{[\mathscr{T}_N^n(\omega)]\mathbf{r}_N^n(\theta,\varphi,\omega)}. \tag{69}$$

VII. VALIDATION FOR A STRUCTURE COUPLED WITH A LIQUID

This first example concerns an inhomogeneous continuous structure immersed in a liquid (water).

A. Description of the structural-acoustic system

The structure is a thin circular cylindrical shell referred to an r, θ, x_3 coordinate system and coupled with springs and dashpots as shown in Fig. 2. The shell is homogeneous and isotropic, with length $L = 1.7$ m, constant thickness $h = 0.025$ m, radius $a = 0.5$ m, simply supported at its ends located at $x_3 = 0$ and $x_3 = L$, mass density $\rho = 7850$ kg/m^3, Young's modulus $E = 2.1 \times 10^{11}$ N/m^2, Poisson's coefficient $\nu = 0.3$, constant damping rate $\xi = 0.001$. The area S of the shell surface Γ is $S = 2\pi aL$. The ring frequency of the shell is 1726 Hz. This cylindrical shell is coupled with 16 dashpots and 16 springs acting radially direction to the shell and

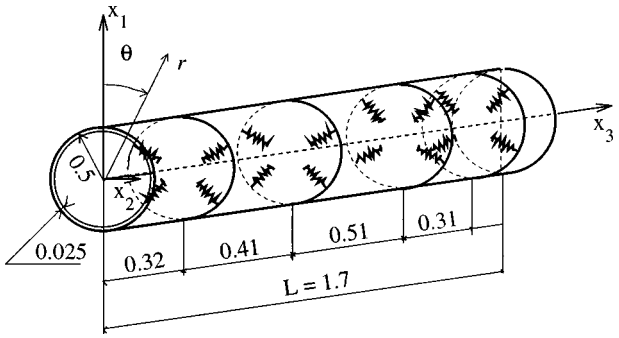

FIG. 2. Finite length circular cylindrical shell coupled with springs and dashpots and immersed in an acoustic fluid.

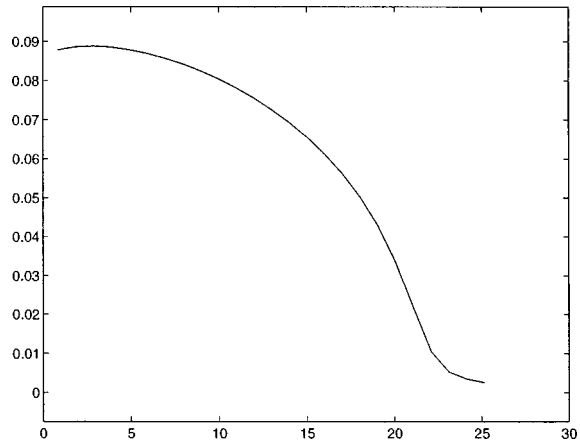

FIG. 3. Graph of function $ka \mapsto \mu_\Gamma(ka)$ defined by Eq. (72) for the structure coupled with a liquid.

located at points $\{a,\theta_j,x_{3,j}\}$ on surface Γ. The jth dashpot has a damping coefficient $d_j=2\epsilon_j^D\mu\xi_{\rm ref}\omega_{\rm ref}$ and the jth spring has a stiffness coefficient $k_j=2\epsilon_j^K\mu\omega_{\rm ref}^2$ in which $\mu=\rho hS$ is the total mass of the shell, $\xi_{\rm ref}=0.001$, $\omega_{\rm ref}=2\pi\times3750$ rad/s, and where ϵ_j^D and ϵ_j^K are dimensionless coefficients whose values are defined in Table I. We assume that the cylindrical shell is extended by two semi-infinite, rigid cylindrical baffles and is immersed in an unbounded liquid with a constant mass density $\rho_E=1000$ kg/m^3 and speed of sound $c_E=1500$ m/s. The coincidence frequency of the shell is 9152 Hz (i.e., $ka=19.2$ with $k=\omega/c_E$). We consider the MF response of this structural-acoustic system on the narrow MF band $B=2\pi\times[4300,4800]$ rad/s corresponding to the [9.00, 10.05] ka-band and we assume that for all ω in B, $|\eta(\omega)|=1$. We are only interested in calculation of the symmetric predominantly radial response of the shell. The excitation is the time-stationary random wall pressure $\{p(\mathbf{x},t),\mathbf{x}\in\Gamma,t\in\mathbb{R}\}$ introduced in Sec. VI, for which the cross-spectral density function defined by Eq. (59) is such that $s_p(\theta,x_3,\theta',x_3';\omega)=(aS)^{-1}\delta(\theta-\theta')\delta(x_3-x_3')$ where δ is the Dirac delta function.

B. Description of the finite dimension approximation

The family $\boldsymbol{\psi}_1,\ldots,\boldsymbol{\psi}_n$ introduced in Sec. IV is chosen as the first n symmetric predominantly radial modes of the associated conservative uncoupled shell whose corresponding eigenfrequencies are $f_1<f_2<\ldots<f_n$. Using Donnel–Mushtani's theory,[31] the value chosen for n is 409. It was deduced from the convergence study of the structural-acoustic response over the [500, 7000] Hz frequency band corresponding to the [1.0, 14.7] ka band. We have $f_1=268$ Hz and $f_n=11979$ Hz. The inner product $(\mathbf{u},\mathbf{v})_H$ introduced in Sec. I C is defined by

$$(\mathbf{u},\mathbf{v})_H=\int_0^{2\pi}\int_0^L \mathbf{u}(\theta,x_3)\cdot\overline{\mathbf{v}(\theta,x_3)}a\,d\theta dx_3. \tag{70}$$

The normalization of the shell modes is such that, for all α, we have $(\psi_\alpha,\psi_\beta)_H=S\delta_{\alpha\beta}$. Concerning the finite dimension approximation introduced in Sec. IV, matrices $[M]=\mu[I]$ and $[G]=S[I]$ are diagonal, $[I]$ being the $(n\times n)$ unity matrix, and matrices $[D]$ and $[K]$ are independent of the frequency and are dense due to the presence of the dashpots and springs. The lowest eigenfrequency of the associated conservative structure (shell coupled with the springs) is $f_1^S=352$ Hz (to be compared with $f_1=268$ Hz). Complex matrix $[B_\Gamma(\omega)]$ associated with the acoustic impedance boundary operator (see Sec. I C) is constructed explicitly using the methodology developed by Junger and Feit.[14] The intermodal fluid couplings are neglected and consequently, $[B_\Gamma(\omega)]$ is a diagonal complex matrix which can be written as

$$-\omega^2[B_\Gamma(\omega)]=-\omega^2[M_\Gamma(\omega)]+i\omega[D_\Gamma(\omega)], \tag{71}$$

in which $[M_\Gamma(\omega)]=\mathrm{Re}[B_\Gamma(\omega)]$ and $[D_\Gamma(\omega)]=-\omega\Im m[B_\Gamma(\omega)]$. Figure 3 shows the graph of function

$$\mu_\Gamma(\omega)=\frac{1}{a\rho_E S}\,\frac{1}{n}\,\mathrm{tr}[M_\Gamma(\omega)], \tag{72}$$

and Fig. 4 shows the graph of function

$$\sigma_\Gamma(\omega)\;\frac{1}{\rho_E c_E S}\,\frac{1}{n}\,\mathrm{tr}[D_\Gamma(\omega)], \tag{73}$$

over the [400, 12 000] Hz frequency band corresponding to the [0.8, 25.1] ka band (in Figs. 3 and 4, the abscissas are expressed in ka). Complex vector $\mathbf{r}^n(\theta,\varphi,\omega)$ associated with the calculation of the far field radiated by the structure [see

TABLE I. Values of ϵ_j^D and ϵ_j^K.

θ_j (deg)	$x_{3,j}$ (m)	ϵ_j^D	ϵ_j^K
81.81	0.32	0	0.1
−81.81	0.32	0	0.1
138.33	0.32	0.1	0.15
−138.33	0.32	0.1	0.15
81.81	0.73	0	0.1
−81.81	0.73	0	0.1
138.33	0.73	0.1	0.15
−138.33	0.73	0.1	0.15
52	1.24	0.1	0.11
−52	1.24	0.1	0.11
118	1.24	0.1	0.14
−118	1.24	0.1	0.14
52	1.55	0.1	0.11
−52	1.55	0.1	0.11
118	1.55	0.1	0.14
−118	1.55	0.1	0.14

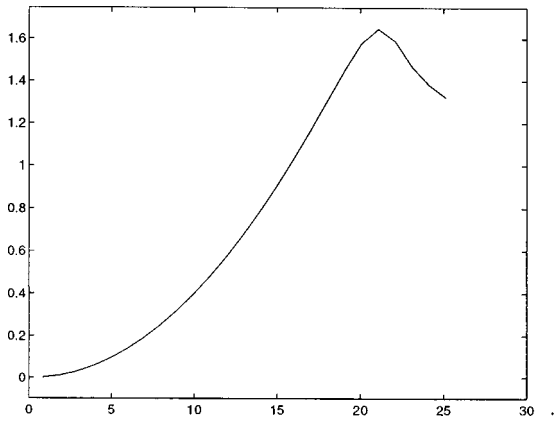

FIG. 4. Graph of function $ka \mapsto \sigma_{\mathrm{I}}(ka)$ defined by Eq. (73) for the structure coupled with a liquid.

Eq. (30)] is obtained using a stationary-phase approximation.[14]

C. Constructing the reference solution on a broad frequency band

Concerning the vibration of the shell coupled with dashpots, springs and external liquid, the reference solution on the [500, 7000] Hz broad frequency band is obtained by constructing the mapping $\omega \mapsto \mathrm{tr}[e_n(\omega)]$ using Eq. (34), with a sampling frequency step $\delta\omega = 2\pi \times 4.33$ rad/s. In Eq. (34), $[T_n(\omega)]$ is calculated using Eq. (35) in which matrix $[A_n(\omega)]$ is calculated by Eq. (25). Figure 5 shows the mapping $\omega \mapsto 10 \times \log_{10}(\mathrm{tr}[e_n(\omega)])$ over the $2\pi \times [500,7000]$ rad/s broad frequency band corresponding to the [1.0, 14.7] ka-band. Concerning the far field radiated by the structure in the external liquid, Figs. 6 and 7 show the mapping $\omega \mapsto 10 \times \log_{10}(L^{-2} S_{c^n}(\theta,\varphi;\omega))$ over the [1.0, 14.7] ka-band, calculated by using Eq. (64), for the normal and the oblique directions with respect to the shell defined by $\theta = 0$, $\varphi = \pi/2$ and $\theta = 0$, $\varphi = \pi/4$, respectively.

D. Constructing the reference solution on the narrow MF band

The reference solution on narrow MF band $B = 2\pi \times [4300,4800]$ rad/s is constructed as explained in Sec. VII C but using the frequency resolution $\delta\omega = \Delta\omega / N_{\mathrm{freq}}$ in which $\Delta\omega = 2\pi \times 500$ rad/s and $N_{\mathrm{freq}} = 300$. The graphs of functions $10 \times \log_{10}(\mathrm{tr}[e_n(\omega)])$, $10 \times \log_{10}(L^{-2} S_{c^n}(0,\pi/2;\omega))$ and $10 \times \log_{10}(L^{-2} S_{c^n}(0,\pi/4;\omega))$ (corresponding to Figs. 5, 6, and 7) of this reference solution on the [9.00, 10.05] narrow MF ka band are used below (see Figs. 9, 10, and 11) to evaluate the accuracy of the response using the reduced model.

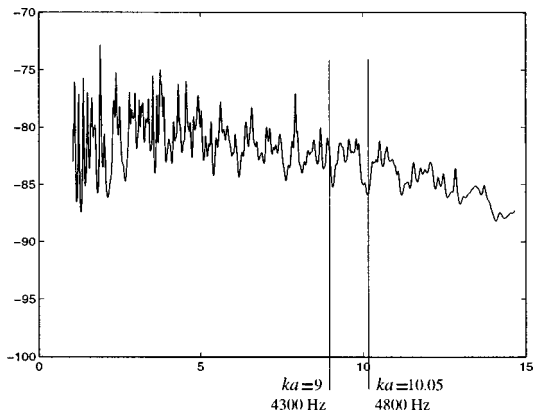

FIG. 5. Reference solution of the dynamical response of the structure coupled with a liquid: graph of function $ka \mapsto 10 \times \log_{10}(\mathrm{tr}[e_n(ka)])$.

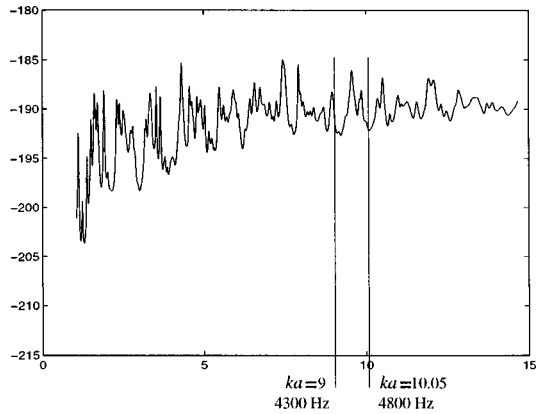

FIG. 6. Reference solution of the far field radiated in the normal direction by the structure coupled with a liquid: graph of function $ka \mapsto 10 \times \log_{10}(L^{-2} S_c n(0,\pi/2;\omega))$.

E. Constructing the dominant eigensubspace

In order to validate the reduced model procedure for a structure coupled with an external liquid, the direct procedure in the frequency domain described in Sec. V A is used to construct the dominant eigensubspace of matrix $[E_n]$ defined by Eq. (33). The approximation $[E_n] \simeq \delta\omega \Sigma_{j=1}^{N_{\mathrm{freq}}} [e_n(\omega_j)]$ is used, in which the ω_j terms are the sampling frequencies of band B. The eigenvalues $\lambda_1^n \geqslant \lambda_2^n \geqslant \ldots > 0$ and the corresponding eigenfunctions $\{\mathbf{e}_1^n, \mathbf{e}_2^n, \ldots\}$ of energy operator $\mathbf{E}_{B,n}$ are calculated using Eqs. (36)–(37). It should be noted that the procedure based on the use of the MF solving method in the time domain, which avoids the explicit calculation of matrix $[E_n]$ as explained in Sec. V C, has also been used to construct the dominant eigensubspace of matrix $[E_n]$. The results obtained are quite similar but we

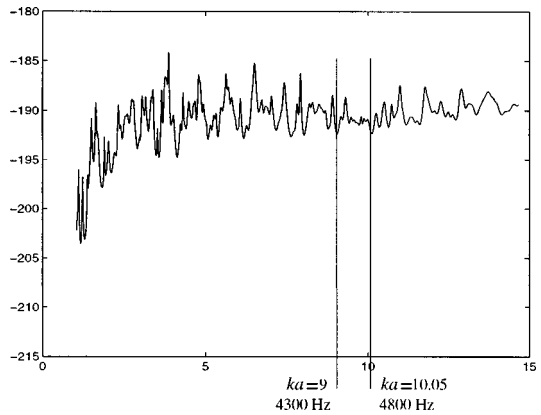

FIG. 7. Reference solution of the far field radiated in an oblique direction by the structure coupled with a liquid: graph of function $ka \mapsto 10 \times \log_{10}(L^{-2} S_c n(0,\pi/4;\omega))$.

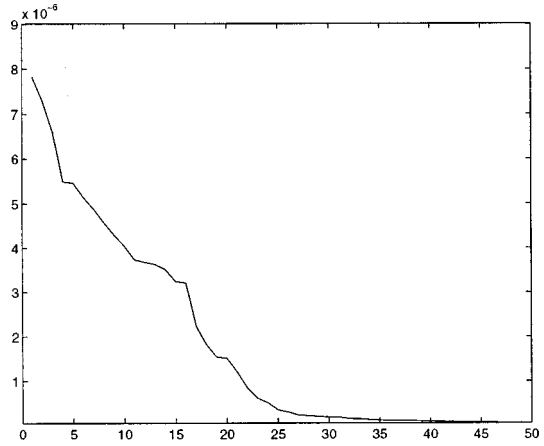

FIG. 8. Reference solution: graph of function $\nu \mapsto \lambda_\nu^n$ showing the distribution of eigenvalues λ_ν^n of energy operator $\mathbf{E}_{B,n}$ of the structure coupled with a liquid.

must limit the length of the present paper. We show the use of such a procedure in Sec. VIII. Figure 8 shows the graph of the function $\nu \mapsto \lambda_\nu^n$ for $\nu \in \{1,2,...,50\}$. There is a strong decrease in the eigenvalues which means there exists the possibility of constructing an efficient reduced model independent of the spatial excitation of the structural-acoustic system. Figure 8 shows that the order N of the reduced model is about 25 for band B.

F. Reduced model adapted to the narrow MF band

In this section, we present a comparison of the reference solution constructed in Sec. VII D with the solution obtained by the reduced model constructed using the results of Sec. IV C in which eigenfunctions $\{\mathbf{e}_1^n,\ldots,\mathbf{e}_N^n\}$ are those calculated in Sec. VII E. For the three values 25, 30, and 40 of N, Figs. 9, 10, and 11 show the comparison of functions $10\times\log_{10}(\mathrm{tr}[e_n(\omega)])$, $10\times\log_{10}(L^{-2}S_{c^n}(0,\pi/2;\omega))$ and $10\times\log_{10}(L^{-2}S_{c^n}(0,\pi/4;\omega))$ (reference solution) with functions $10\times\log_{10}(\mathrm{tr}[e_n^N(\omega)])$, $10\times\log_{10}(L^{-2}S_{c_N^n}(0,\pi/2;\omega))$ and $10\times\log_{10}[L^{-2}S_{c_N^n}(0,\pi/4;\omega)]$ (reduced model) calculated for each value of order N using Eqs. (49)–(50) and (66), versus dimensionless wave number ka. It can be seen that the reduced model of order $N=25$ yields a good approximation.

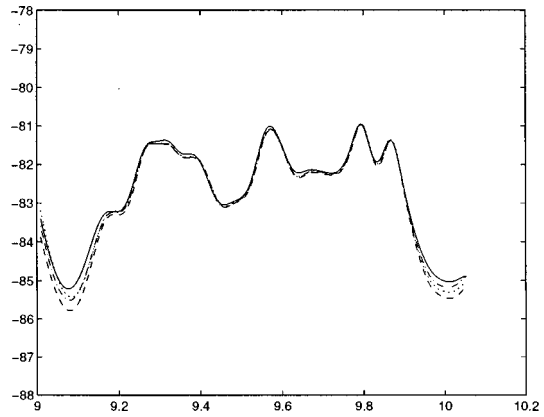

FIG. 9. Reduced model of the dynamical response of the structure coupled with a liquid: comparison between function $ka \mapsto 10\times\log_{10}(\mathrm{tr}[e_n(ka)])$ [reference solution (solid line)] and function $ka \mapsto 10\times\log_{10}(\mathrm{tr}[e_n^N(ka)])$ [reduced model for $N=25$ (dashed line), for $N=30$ (dotted line), and for $N=40$ (dashdot line)].

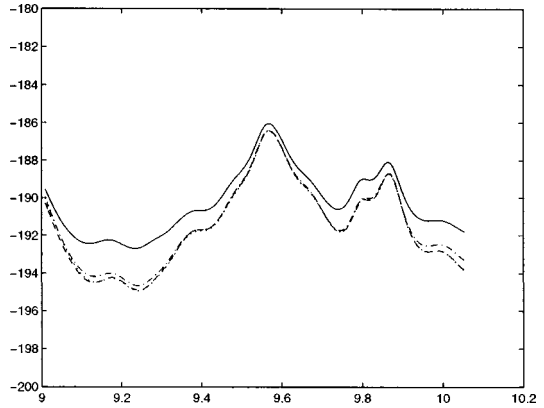

FIG. 10. Reduced model of the far field radiated in the normal direction by the structure coupled with a liquid: comparison between function $ka \mapsto 10\times\log_{10}(L^{-2}S_{c^n}(0,\pi/2;\omega))$ [reference solution (solid line)] and function $ka \mapsto 10\times\log_{10}(L^{-2}S_{c_N^n}(0,\pi/2;\omega))$ [reduced model for $N=25$ (dashed line), for $N=30$ (dotted line), and for $N=40$ (dashdot line)].

VIII. VALIDATION FOR A STRUCTURE COUPLED WITH A GAS

This second example concerns an inhomogeneous continuous structure immersed in a gas (air).

A. Description of the structural-acoustic system

The structure is the thin circular cylindrical shell coupled with springs and dashpots defined in Sec. VII A (see Fig. 2) with only two differences related to the constant thickness which is $h=0.004$ m instead of $h=0.025$ m, and reference frequency ω_{ref} which is $\omega_{\mathrm{ref}}=2\pi\times1000$ rad/s instead of $\omega_{\mathrm{ref}}=2\pi\times3750$ rad/s. We assume that the cylindrical shell is extended by two semi-infinite, rigid cylindrical baffles and is immersed in an unbounded liquid with a constant mass density $\rho_E=1\ \mathrm{kg/m^3}$ and speed of sound $c_E=300$ m/s. The coincidence frequency of the shell is 2034 Hz (i.e., $ka=21.3$ with $k=\omega/c_E$). We consider the MF re-

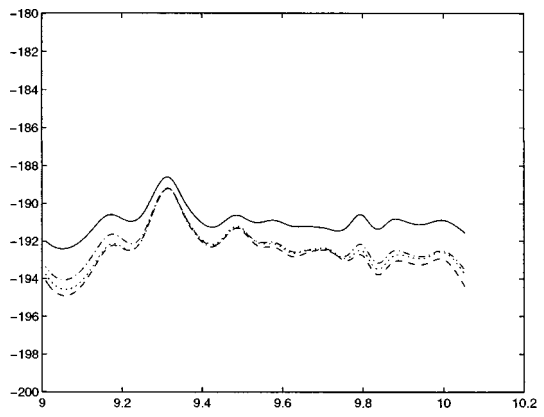

FIG. 11. Reduced model of the far field radiated in an oblique direction by the structure coupled with a liquid: comparison between function $ka \mapsto 10\times\log_{10}(L^{-2}S_{c^n}(0,\pi/4;\omega))$ [reference solution (solid line)] and function $ka \mapsto 10\times\log_{10}(L^{-2}S_{c_N^n}(0,\pi/4;\omega))$ [reduced model for $N=25$ (dashed line), for $N=30$ (dotted line), and for $N=40$ (dashdot line)].

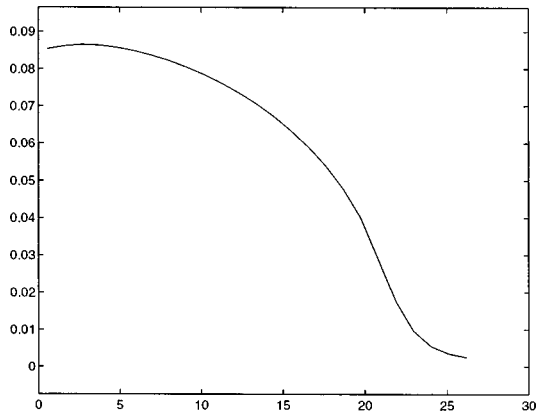

FIG. 12. Graph of function $ka \mapsto \mu_\Gamma(ka)$ defined by Eq. (72) for the structure coupled with a gas.

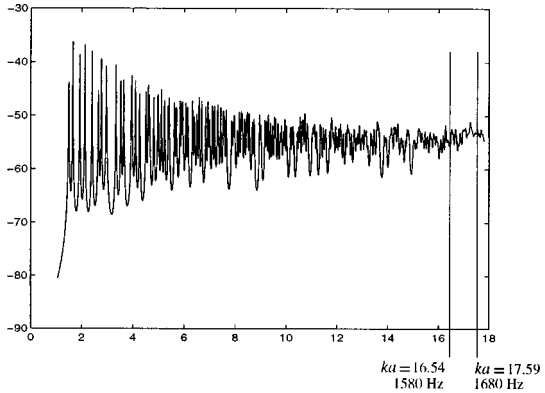

FIG. 14. Reference solution of the dynamical response of the structure coupled with a gas: graph of function $ka \mapsto 10 \times \log_{10}(\mathrm{tr}[e_n(ka)])$.

sponse of this structural-acoustic system on the narrow MF band $B = 2\pi \times [1580,1680]$ rad/s corresponding to the [16.54, 17.59] ka-band and we assume that for all ω in B, $|\eta(\omega)| = 1$. As in Sec. VII, we are only interested in the calculation of the symmetric predominantly radial response of the shell. The excitation is the time-stationary random wall pressure $\{p(\mathbf{x},t), \mathbf{x} \in \Gamma, t \in \mathbb{R}\}$ introduced in Sec. VII.

B. Description of the finite dimension approximation

The finite dimension approximation is constructed as explained in Sec. VII B. The value chosen for n is 432. It was deduced from the convergence study of the structural-acoustic response over the [100, 1700] Hz frequency band corresponding to the [1.0, 17.8] ka band. We have $f_1 = 109$ Hz and $f_n = 2499$ Hz. The lowest eigenfrequency of the associated conservative structure (shell coupled with the springs) is $f_1^S = 142$ Hz (to be compared with $f_1 = 109$ Hz). Figures 12 and 13 show the graphs of functions defined by Eqs. (72) and (73) respectively, over the [50, 2500] Hz frequency band corresponding to the [0.5, 26.2] ka-band (in Figs. 12 and 13, the abscissas are expressed in ka).

C. Constructing the reference solution on a broad frequency band

This construction is performed as explained in Sec. VII C. Concerning the vibration of the shell coupled with dashpots, springs and external liquid, the reference solution on the [100, 1700] Hz broad frequency band is obtained by constructing the mapping $\omega \mapsto \mathrm{tr}[e_n(\omega)]$ using Eq. (34), with a sampling frequency step $\delta\omega = 2\pi \times 1.06$ rad/s. In Eq. (34), $[T_n(\omega)]$ is calculated using Eq. (35) in which matrix $[A_n(\omega)]$ is calculated by Eq. (25). Figure 14 shows the mapping $\omega \mapsto 10 \times \log_{10}(\mathrm{tr}[e_n(\omega)])$ over the $2\pi \times [100,1700]$ rad/s broad frequency band corresponding to the [1.0, 17.8] ka-band. Concerning the far field radiated by the structure in the external liquid, Figs. 15 and 16 show the mapping $\omega \mapsto 10 \times \log_{10}(L^{-2} S_{c^n}(\theta, \varphi; \omega))$ over the [1.0, 17.8] ka band, calculated by using Eq. (64), for the normal and the oblique directions with respect to the shell defined by $\theta = 0$, $\varphi = \pi/2$ and $\theta = 0$, $\varphi = \pi/4$, respectively.

D. Constructing the reference solution on the narrow MF band

The reference solution on narrow MF band $B = 2\pi \times [1580,1680]$ rad/s is constructed as explained in Sec. VIII C but using the frequency resolution $\delta\omega = \Delta\omega / N_{\mathrm{freq}}$ in which $\Delta\omega = 2\pi \times 100$ rad/s and $N_{\mathrm{freq}} = 300$. The graphs of functions $10 \times \log_{10}(\mathrm{tr}[e_n(\omega)])$, $10 \times \log_{10}(L^{-2} S_{c^n}(0, \pi/2; \omega))$, and $10 \times \log_{10}(L^{-2} S_{c^n}(0, \pi/4; \omega))$ (corresponding to Figs. 14, 15, and 16) of this reference solution on the [16.54, 17.59]

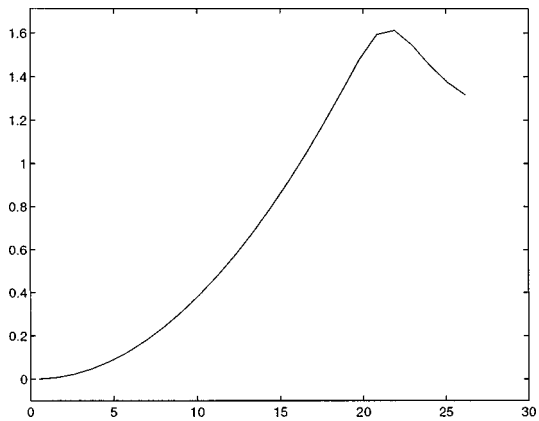

FIG. 13. Graph of function $ka \mapsto \sigma_\Gamma(ka)$ defined by Eq. (73) for the structure coupled with a gas.

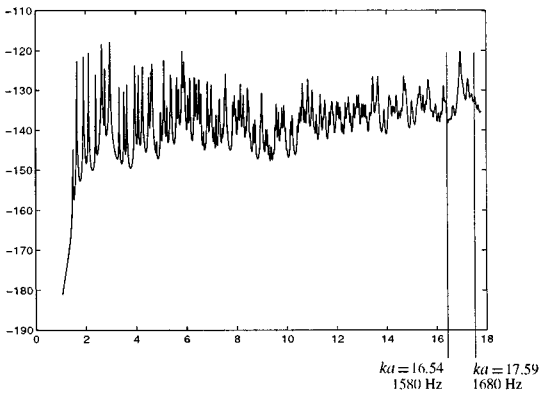

FIG. 15. Reference solution of the far field radiated in the normal direction by the structure coupled with a gas: graph of function $ka \mapsto 10 \times \log_{10}(L^{-2} S_{c^n}(0, \pi/2; \omega))$.

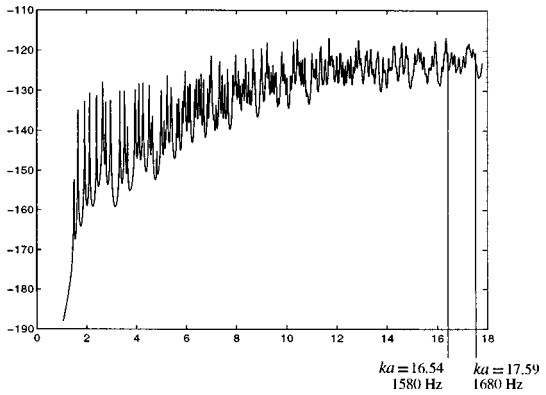

FIG. 16. Reference solution of the far field radiated in an oblique direction by the structure coupled with a gas: graph of function $ka \mapsto 10 \times \log_{10}(L^{-2} S_{c^n}(0,\pi/4;\omega))$.

narrow MF ka band are used below (see Figs. 20, 21, and 22) to evaluate the accuracy of the response constructed using the reduced model.

E. Constructing the dominant eigensubspace

Since the structure is coupled with a gas, two possibilities can be examined for constructing the dominant eigensubspace of the energy operator related to band B. The first one consists in using the ''exact'' approach as was done in the first example presented in Sec. VII. In this case, the construction of matrix $[E_n]$ is based on Eqs. (33)–(35) in which matrix $[A_n(\omega)]$ is defined by Eq. (25). This means that eigenfunctions $\{\mathbf{e}_1^n \ldots, \mathbf{e}_N^n\}$ of $\mathbf{E}_{B,n}$ are constructed for the energy operator of the structure coupled with the external fluid. Since the external fluid is a gas, a second possibility is to construct $\{\mathbf{e}_1^n \ldots, \mathbf{e}_N^n\}$ as the dominant eigensubspace of the energy operator of the structure in a vacuum (not coupled with the gas). In this case, the procedure is exactly the same, except that matrix $[A_n(\omega)]$ is not defined by Eq. (25) but is written as

$$[A_n(\omega)] \simeq -\omega^2[M] + i\omega[D(\omega)] + [K(\omega)]. \tag{74}$$

It should be noted that Eq. (74) is only used to construct $\{\mathbf{e}_1^n \ldots, \mathbf{e}_N^n\}$ but obviously not to construct the reference solution (see Secs. VIII C and VIII D) and the reduced model (see Sec. VIII F) for which Eq. (25) is used. For the present example, we analyzed the two above possibilities and we obtained quite similar results for the reduced model. We present the results corresponding to the second approach, i.e., using Eq. (74) instead of Eq. (25) to calculate $\{\mathbf{e}_1^n \ldots, \mathbf{e}_N^n\}$. We also compared the procedures described in Sec. V A with the procedure described in Sec. V C which avoids the explicit construction of matrix $[E_n]$. Below we present the results corresponding to the procedure based on the use of the MF solving method in the time domain (see Sec. V C). Figure 17 shows the graph of function $\nu \mapsto \lambda_\nu^n$ corresponding to $[E_n]$ calculated using Eq. (74). There is a strong decrease in the eigenvalues which means there exists the possibility of constructing an efficient reduced model independent of the spatial excitation of the structural-acoustic

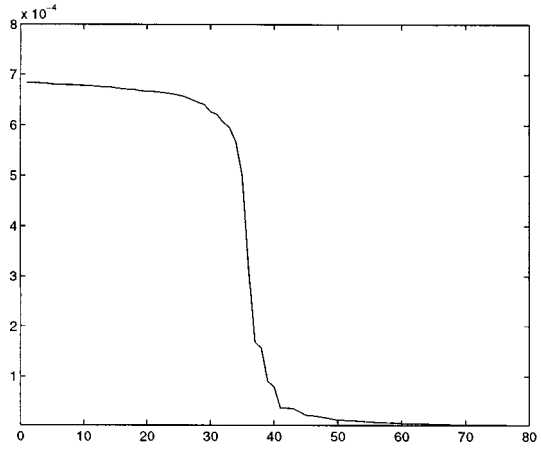

FIG. 17. Reference solution: graph of function $\nu \mapsto \lambda_\nu^n$ showing the distribution of eigenvalues λ_ν^n of energy operator $\mathbf{E}_{B,n}$ of the structure in a vacuum (not coupled with the fluid).

system. Figure 17 shows that the order N of the reduced model is about 40 for band B. The values of the parameters of the procedure described in Sec. V C are as follows. The subspace iteration algorithm (see Sec. V) is used with $m = 48$. Each iteration, matrix $[W] = [E_n][X]$ defined in Sec. V is calculated using the MF solving method in the time domain described in Sec. V C, with the approximation $[M_B] \simeq [M]$ instead of $[M_B] = [M] + [B_\Gamma(\omega_B)]$ for this particular example of a structure coupled with a gas. The Newmark step-by-step integration method is used[22] with scheme parameters $\alpha = 1/4$ and $\delta = 1/2$. Function $\chi_0(t)$ is deduced from Eq. (54) in which $|\eta(\omega)| = 1$ if $\omega \in B$. The parameters introduced in Step 1 and Step 2 of Sec. V C for the time-solving procedure are $\mu = 6$, $I_0 = 4$ and $J_0 = 18$, i.e. $I = 24$ and $J = 108$. Figure 18 shows the graph of function $i \mapsto \|[Y_0(i \times \Delta t)]\|^2$ for $i = -I, \ldots, J$ and Fig. 19 shows the graph of function $j \mapsto \|[Z_0(j \times \Delta t)]\|^2$ for $j = -J, \ldots, 0$, corresponding to the last iteration of the subspace iteration algorithm (see Step 1 and Step 2 described in Sec. V C). These two figures show that the values of parameters I_0 and J_0 are correctly chosen (a similar result is obtained for each iteration, and not only for the last one).

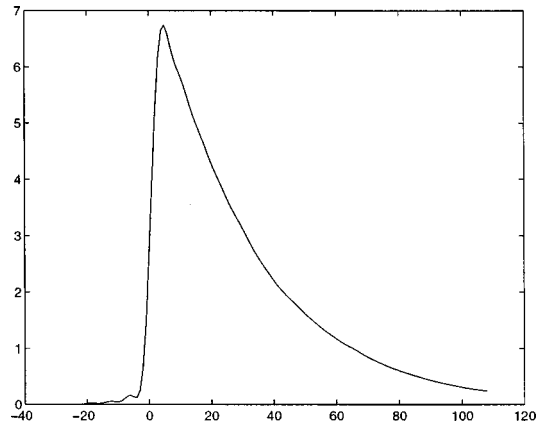

FIG. 18. Graph of function $i \mapsto \|[Y_0(i \times \Delta t)]\|^2$ corresponding to the last iteration of the subspace iteration algorithm.

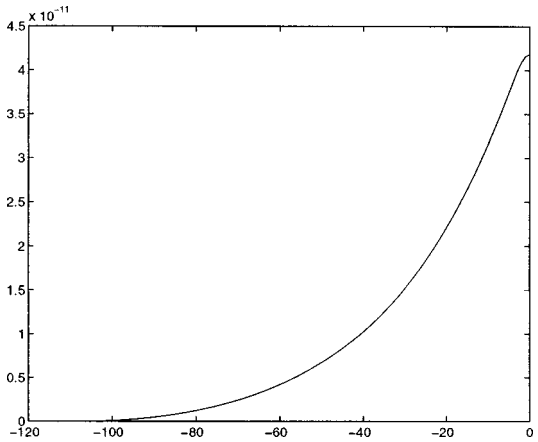

FIG. 19. Graph of function $j \mapsto \|[Z_0(j\times\Delta t)]\|^2$ corresponding to the last iteration of the subspace iteration algorithm.

F. Reduced model adapted to the narrow MF band

In this section, we compare the reference solution constructed in Sec. VIII D with the solution obtained by the reduced model constructed using the results of Sec. IV C in which eigenfunctions $\{\mathbf{e}_1^n,\ldots,\mathbf{e}_{NJ}^n\}$ are those calculated in Sec. VIII E. For the two values 35 and 40 of N, Figs. 20, 21, and 22 show the comparison of functions $10\times\log_{10}(\mathrm{tr}[e_n(\omega)])$, $10\times\log_{10}[L^{-2}S_{c^n}(0,\pi/2;\omega)]$, and $10\times\log_{10}[L^{-2}S_{c^n}(0,\pi/4;\omega)]$ (reference solution) with functions $10\times\log_{10}(\mathrm{tr}[e_n^N(\omega)])$, $10\times\log_{10}[L^{-2}S_{c_N^n}(0,\pi/2;\omega)]$, and $10\times\log_{10}[L^{-2}S_{c_N^n}(0,\pi/4;\omega)]$ (reduced model) calculated for each value of order N using Eqs. (49)–(50) and (66), versus dimensionless wave number ka. It can be seen that the reduced model of order $N=40$ yields a very good approximation.

IX. CONCLUSIONS

A theoretical approach is presented for constructing a reduced model in the MF range in the area of structural acoustic for a general three-dimensional anisotropic, inhomogeneous, viscoelastic bounded medium with an arbitrary geometry coupled with an external acoustic fluid (gas or liquid). The boundary value problem formulated in the frequency domain and its variational formulation are presented. For a given MF band, the energy operator of the structure coupled or not with the acoustic fluid is a positive-definite symmetric operator which has a countable set of decreasing positive eigenvalues. The eigenfunctions corresponding to the highest eigenvalues (dominant eigensubspace) of the energy operator are an appropriate functional basis of the admissible function space of the displacement field of the structure coupled with the external acoustic fluid. This functional basis allows a reduced model of the structural-acoustic system to be constructed using the Ritz–Galerkin method. A finite dimension approximation of the continuous case is introduced in a general context (using the finite element method or not). For construction of the dominant eigensubspace of the energy operator, an efficient procedure based on the use of the subspace iteration method is proposed. It does not require explicit calculation of the energy operator. We then obtain an efficient method for constructing a reduced model in the MF range. In addition, it can easily be seen that all the results presented can be extended straightforwardly to

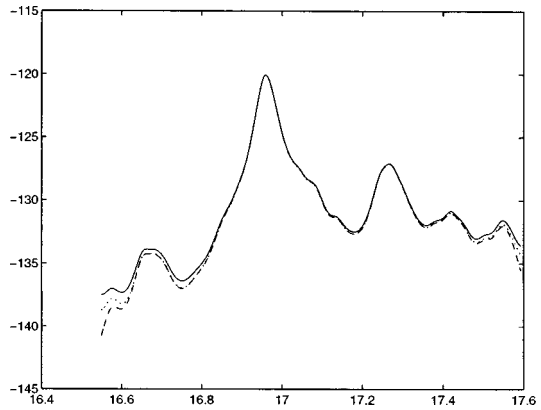

FIG. 21. Reduced model of the far field radiated in the normal direction by the structure coupled with a gas: comparison between function $ka\mapsto 10\times\log_{10}(L^{-2}S_{c^n}(0,\pi/2;\omega))$ [reference solution (solid line)] and function $ka\mapsto 10\times\log_{10}(L^{-2}S_{c_N^n}(0,\pi/2;\omega))$ [reduced model for $N=25$ (dashed line), for $N=30$ (dotted line), and for $N=40$ (dashdot line)].

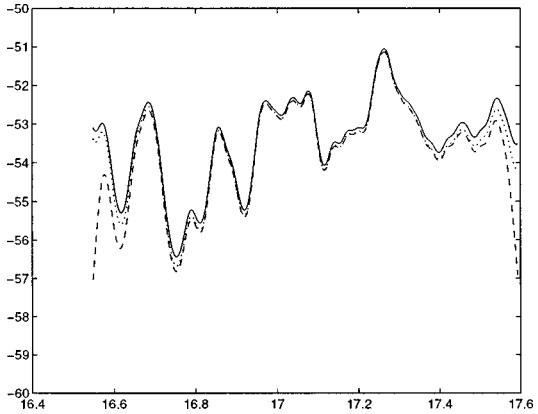

FIG. 20. Reduced model of the dynamical response of the structure coupled with a gas: comparison between function $ka\mapsto 10\times\log_{10}(\mathrm{tr}[e_n(ka)])$ [reference solution (solid line)] and function $ka\mapsto 10\times\log_{10}(\mathrm{tr}[e_n^N(ka)])$ [reduced model for $N=25$ (dashed line), for $N=30$ (dotted line), and for $N=40$ (dashdot line)].

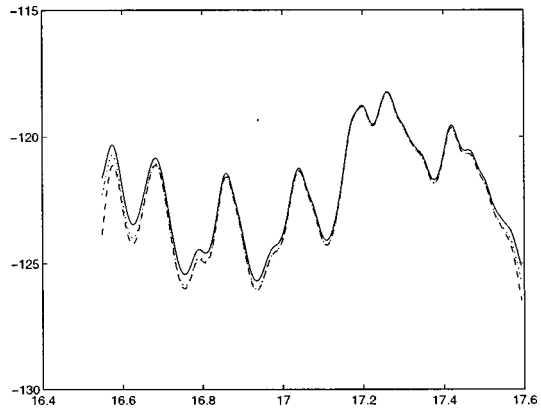

FIG. 22. Reduced model of the far field radiated in an oblique direction by the structure coupled with a gas: comparison between function $ka\mapsto 10\times\log_{10}(L^{-2}S_{c^n}(0,\pi/4;\omega))$ [reference solution (solid line)] and function $ka\mapsto 10\times\log_{10}(L^{-2}S_{c_N^n}(0,\pi/4;\omega))$ [reduced model for $N=25$ (dashed line), for $N=30$ (dotted line), and for $N=40$ (dashdot line)].

a structure made of beams, plates and shells. Analysis of the first example devoted to coupling with an external acoustic liquid (the complete analysis cannot be presented herein) shows that if the energy operator of the structure in a vacuum is used to construct the functional basis adapted to the MF band, then the order of the reduced model is much larger than if the energy operator of the structure coupled with the liquid is considered. This is due to the ''added mass effect'' of the fluid (this phenomenon is also encountered for the low-frequency range for which the normal modes of the structure in a vacuum are used). Consequently, it is more efficient to use the energy operator of the structure coupled with the external acoustic fluid when the fluid is a liquid. Conversely, if the external acoustic fluid is a gas, the second example presented shows that the energy operator of the structure in a vacuum can be used to construct the functional basis adapted to the MF band. Finally, the two examples presented show that the reduced model constructed yields good results.

[1] C. Soize, ''Vibrations linéaires moyennes fréquences des structures élastiques anisotropes,'' C. R. Acad. Sci., Ser. II: Mec., Phys., Chim., Sci. Terre Univers **294**, 895–898 (1982).
[2] C. Soize, ''Medium-frequency linear vibrations of anisotropic elastic structures,'' Res. Aerosp. (English edition) 5, 65–87 (1982).
[3] J. Argyris and H. P. Mlejnek, *Dynamics of Structures* (North-Holland, Amsterdam, 1991).
[4] R. W. Clough and J. Penzien, *Dynamics of Structures* (McGraw-Hill, New York, 1975).
[5] A. Y. T. Leung, *Dynamic Stiffness and Substructures* (Springer-Verlag, New York, 1993).
[6] L. Meirovitch, *Computational Methods in Structural Dynamics* (Sijthoff and Noordhoff, Groningen, The Netherlands, 1980).
[7] H. J. P. Morand and R. Ohayon, *Fluid-Structure Interaction* (Wiley, New York, 1995).
[8] R. Ohayon and C. Soize, *Structural Acoustics and Vibration* (Academic, San Diego, 1998).
[9] C. Soize, ''Reduced models in the medium-frequency range for general dissipative structural-dynamics systems,'' Eur. J. Mech. A/Solids **17** (in press) (1998).
[10] Y. C. Fung, *Foundations of Solid Mechanics* (Prentice-Hall, Englewood Cliffs, 1968).
[11] C. Truesdell, *Mechanics of Solids, Vol. III, Theory of Viscoelasticity, Plasticity, Elastic Waves and Elastic Stability* (Springer-Verlag, Berlin, 1984).
[12] P. G. Ciarlet, *Mathematical Elasticity, Vol. I: Three-Dimensional Elasticity* (North-Holland, Amsterdam, 1988).
[13] R. Dautray and J.-L. Lions, *Mathematical Analysis and Numerical Methods for Science and Technology* (Springer-Verlag, Berlin, 1992).
[14] M. C. Junger and D. Feit, *Sound, Structures and Their Interaction* (Acoustical Society of America Publications on Acoustics, Woodbury, 1993). Originally published by MIT, Cambridge, 1972.
[15] A. J. Burton and G. F. Miller, ''The application of integral equation methods to the numerical solution of some exterior boundary value problems,'' Proc. R. Soc. London, Ser. A **323**, 201–210 (1971).
[16] D. L. Colton and R. Kress, *Integral Equation Methods in Scattering Theory* (Krieger, Malabar, FL, 1992).
[17] J. J. Angelini and P. M. Hutin, ''Exterior Neumann problem for Helmholtz equation. Problem of irregular frequencies,'' La Recherche Aérospatiale (English edition) **3**, 43–52 (1981).
[18] J. T. Oden and J. N. Reddy, *Variational Methods in Theoretical Mechanics* (Springer-Verlag, New York, 1983).
[19] G. Duvaut and J.-L. Lions, *Inequalities in Mechanics and Physics* (Springer-Verlag, Berlin, 1976).
[20] T. Kato, *Perturbation Theory for Linear Operators* (Springer-Verlag, New York, 1966).
[21] M. Reed and B. Simon, *Methods of Modern Mathematical Physics. I. Functional Analysis* (Academic, New York, 1980).
[22] K. J. Bathe and E. L. Wilson, *Numerical Methods in Finite Element Analysis* (Prentice-Hall, New York, 1976).
[23] O. C. Zienkiewicz and R. L. Taylor, *The Finite Element Method* (McGraw-Hill, New York, 1989).
[24] B. N. Parlett, *The Symmetric Eigenvalue Problem* (Prentice-Hall, Englewood Cliffs, NJ, 1980).
[25] G. H. Golub and C. F. Van Loan, *Matrix Computations* (The Johns Hopkins University Press, Baltimore, 1989), 2nd ed.
[26] F. Chatelin, *Eigenvalues of Matrices* (Wiley, New York, 1993).
[27] C. Soize, P. M. Hutin, A. Desanti, J. M. David, and F. Chabas, ''Linear dynamic analysis of mechanical systems in the medium frequency range,'' Comput. Struct. **23**, 605–637 (1986).
[28] C. Soize, *The Fokker-Planck Equation for Stochastic Dynamical Systems and its Explicit Steady State Solutions* (World Scientific, Singapore, 1994).
[29] P. Kree and C. Soize, *Mathematics of Random Phenomena* (Reidel, Dordrecht, 1986).
[30] Y. K. Lin, *Probabilistic Theory of Structural Dynamics* (McGraw-Hill, New York, 1967).
[31] A. Leissa, *Vibration of Shells* (Acoustical Society of America Publications on Acoustics, Woodbury, 1993). Originally published by NASA, 1973.

Predicting hearing aid response in real ears

Per-Eric Sanborn
Department of Ear, Eye and Skin, Unit of Technical Audiology, Karolinska institutet, Box 70025, S-100 44 Stockholm, Sweden

(Received 8 December 1994; revised 21 February 1998; accepted 3 March 1998)

A hearing aid fitted to different ears will produce very different sound pressure spectra in the ear canal. In addition, this variation in response is different among hearing aids. A description in terms of an electrical analog model of the ear and hearing aid system is given. The applicability of this model is tested through series of measurements. The measurement and prediction procedure was first verified on a coupler (ear simulator) with good results from 300 to 8000 Hz. Three types of hearing aids were then measured and used on five different human ears. Where the measured and predicted response was compared a fairly good agreement was obtained from 300 Hz to approximately 6000 Hz. A major source of error is probe misalignment. The theoretical description given in the present work is likely to be valid from low frequencies to at least 10 kHz. Although solutions for related problems have been given for low frequencies, a solution of the hearing aid fitting problem at high frequencies has not been published earlier. [S0001-4966(98)04106-X]

PACS numbers: 43.58.Bh, 43.58.Ta, 43.58.Vb, 43.66.Ts [SLE]

LIST OF SYMBOLS

k	Wave number
L_i	Length of calibration tube i
M	Number of known impedances (calibration tubes) in impedance probe calibration
n	Frequency number
n_1, n_2	Frequency number limits
$N(n)$	Nondimensional error function
N_T	Average normalized error
P	Sound pressure
P_0	Thevenin pressure of impedance probe
P_{EM}	Measured complex sound pressure in prediction check measurement
P_H	Thevenin pressure of hearing aid
P_i	Sound pressure measured in impedance probe calibration tube i
P_x	Sound pressure in impedance measurement
SPL(max)	Maximum sound pressure level in one measurement
Xfer_{PH}	Transfer function representing impedance probe Thevenin pressure
Z	Acoustic impedance
Z_0	Thevenin impedance of impedance probe
Z_{Ci}	Characteristic impedance of tube i
Z_E	Ear input impedance
Z_H	Thevenin impedance of hearing aid
Z_i	Input impedance of calibration tube i
Z_x	Impedance to be determined
Γ_i	Propagation wave number of tube i
Δ	Determinant in LMS solution
ε	Error function

INTRODUCTION

The response from a hearing aid may show great variations when used on different ears. The variation may reach 20 dB at high frequencies (Olsson, 1985). This is a major problem when fitting hearing aids. The basis for selecting hearing aids is measurement of the hearing aid response on a coupler (ear simulator), which does not give enough information about the final response on an individual ear. When fitting hearing aids the hearing aid response is compared to the individual hearing loss. The fact that the hearing aid response is not unique makes the hearing aid fitting time consuming.

In order to estimate the variations a study was carried out at three hospitals in Stockholm (Berninger *et al.*, 1992). The results from these tests in the frequency range 500 Hz to 4 kHz with one aid on 16 ears were large variations throughout the entire range. One explanation for these large variations is the fact that the output impedances of various hearing aids are different, and that the input impedances of the human ears also vary between individuals.

Egolf *et al.* presented a model for predicting response of *in situ* hearing aids (Egolf *et al.*, 1977). The different parts of the hearing aid are modeled with four-pole parameters which are determined from measurements. The result on an ear simulator was good up to 5000 Hz and on real ears up to 1000 Hz.

In the present work a description in terms of an electrical analog model of the ear and hearing aid system is given. To predict the sound pressure developed in a real canal, two measurement steps are required. First, the electroacoustic behavior of the hearing aid must be characterized in terms of its Thevenin equivalent impedance Z_H and sound pressure P_H. Second, the input impedance of the ear canal Z_E must be measured. The sound pressure that will be predicted will then be $P_{EM}=P_H Z_E/(Z_E+Z_H)$ (see Fig. 1). The ear canal input impedance and the hearing aid equivalent impedance

 0001-4966/98/103(6)/3407/11/$10.00

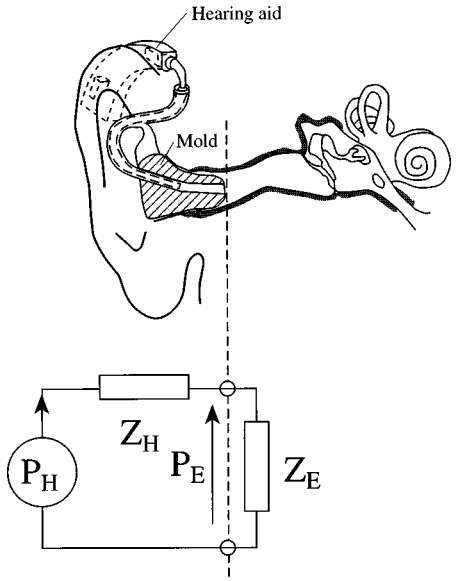

FIG. 1. Theoretical model of the acoustical system ''hearing aid and ear.''

are measured using an impedance probe consisting of an insert earphone and a probe microphone, as shown in Fig. 2. The electroacoustic properties of the probe are characterized via Thevenin equivalents (P_0, Z_0) and determined ahead of time using the Allen procedure (Allen, 1985).

The proposed method will give the predicted sound pressure level at a point slightly outside the mold. All comparisons between measured and predicted sound pressure levels are carried out at this point.

The proposed measurement procedure is expected to be useful when fitting hearing aids. With P_H and Z_H from the large amount of hearing aids available stored in a data base, measurement of Z_E on the patient ear in combination with some calculations will give the predicted sound level. Fitting hearing aids can therefore be carried out by predicting the result without the need of hearing aids at hand.

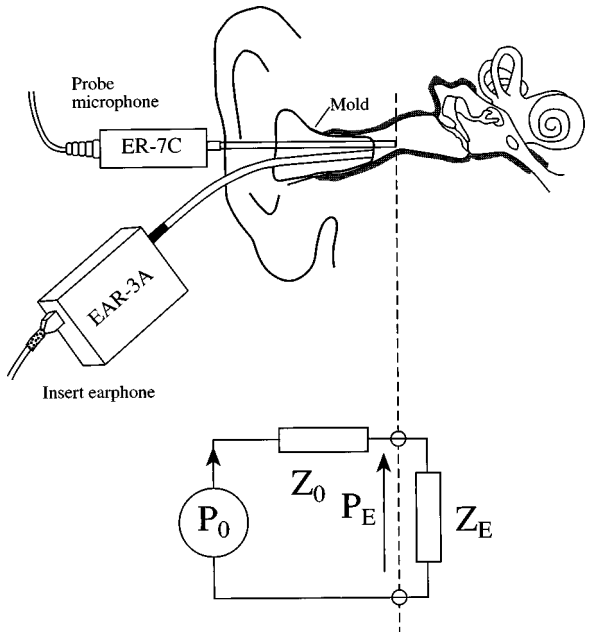

FIG. 2. Theoretical model of the ''impedance probe and ear.''

I. THEORETICAL DESCRIPTION

The aim of the present work was to give a description of the acoustical system ''hearing aid and ear.'' It should be accurate enough to describe the acoustical parameters involved with sufficient accuracy and yet simple enough for easy applications at the clinics. The frequency range of interest is that of hearing aids today with some margin for further developments. The theoretical model used in this work is shown in Fig. 1. This electrical analogy is a low-frequency model expected to be valid for plane waves (below the first cut-on frequency). However, it may also include the effects of near-field modes. Acoustic impedance defined as sound pressure divided by volume velocity (1 acoustic ohm$=1$ Pa$\cdot$s/m^3) is used throughout this paper and the time factor is

$$e^{+j\omega t}.$$

The model describes the hearing aid (including tube and form-fitted hard plastic mold) as a sound pressure generator and an output impedance (Thevenin parameters). The ear is described with an input acoustic impedance. This model has no geometrical spread. The parameters involved are valid only at the point of connection between the hearing aid and the ear.

In order to determine the impedances for the system ''hearing aid and ear'' an ''impedance probe'' is used. This impedance probe is also modeled by an electrical analog circuit as described in Sec. II.

Measurements and calculations for verification of the model have been carried out in the frequency range 100 Hz to 10 kHz. Verification of the model consists of determining the pressure generator and impedances, calculating the sound pressure in the ear canal, and measuring the sound pressure for comparison (see Figs. 12–14).

II. IMPEDANCE MEASUREMENT METHOD

The impedance probe consists of an insert earphone (EAR-3A by Etymotic Research) and a probe microphone (ER-7C by Etymotic Research) (Fig. 2). The earphone is emitting sound into the ear canal through the hard plastic mold and the microphone is measuring the sound pressure at a position remote to the mold. The earphone and microphone together are calibrated and used as an impedance probe. With the Thevenin parameters (P_0, Z_0) of the impedance probe known, the impedance of an object can be calculated from measurement data.

With the assumption that the earphone is giving (approximately) constant volume velocity this configuration of impedance probe has been in use since the 1950s [see ''two tube method'' in Sanborn (1990)]. In the present work a more nearly complete description of the probe is used. The impedance probe is modeled as an electrical analog with complex-valued Thevenin parameters consisting of a pressure generator (P_0) and an internal impedance (Z_0) as given in Fig. 2. For determining the two Thevenin parameters two

measurements on two known impedances are required. However, the accuracy of such a calibration is limited near antiresonance dips.

A calibration procedure useful for a wider frequency range has been presented by Allen (1985). Allen's procedure makes use of calibration measurements on four known impedances. This will give an overdetermined system for determination of the Thevenin parameters [solved with a least mean square (LMS) method] leading to a more robust calibration. Keefe *et al.* (1992) has been using this method with some changes, and their version of it is used in the present work.

The known impedances are in this investigation those of circular uniform brass tubes with rigid ends. Kirchhoff's solution for sound in a tube with rigid walls includes the effects of both viscosity and heath conduction on acoustic propagation through a rigid cylindrical tube. It assumes that the oscillatory flow is laminar, nonlinear terms in the equation of motion are negligible, and that the inner wall is isothermal. For use in the present work the input impedance and propagation wave number of these tubes are calculated with a high-frequency (small acoustic boundary layer) approximation of Kirchhoff's exact solution given by Keefe (1984).

With characteristic acoustic impedance Z_{Ci}, propagation wave number Γ_i, and tube length L_i, the input acoustic impedance of brass tube No. i is given by (Keefe *et al.*, 1992)

$$Z_i(k) = Z_{ci}(k)\coth(\Gamma_i(k)L_i). \tag{1}$$

When the impedance probe is connected to the impedance to be measured, Z_x, the relation between P_x (the sound pressure measured by the microphone), Z_x, and the Thevenin parameters of the probe is

$$P_x = P_0 \frac{Z_x}{Z_0 + Z_x}. \tag{2}$$

Suppose the calibration is carried out with M known impedances (in the present work $M=10$). Equation (2) used for each of the M measurements in the calibration gives the system

$$\begin{bmatrix} Z_1 & -P_1 \\ Z_2 & -P_2 \\ \vdots & \vdots \\ Z_M & -P_M \end{bmatrix} \begin{bmatrix} P_0 \\ Z_0 \end{bmatrix} = \begin{bmatrix} P_1 Z_1 \\ P_2 Z_2 \\ \vdots \\ P_M Z_M \end{bmatrix}. \tag{3}$$

Explicit reference to frequency is suppressed in the system equations, and it is understood that they must be solved separately for each frequency. For optimization of this system the error function $\varepsilon(n)$ is first calculated for each frequency n as

$$\varepsilon(n) = \sum_{i=1}^{M} |Z_i P_0 - P_i Z_0 - P_i Z_i|^2. \tag{4}$$

Whatever values are chosen for the lengths, they must be applied for all frequencies when computing the Thevenin parameters. For visualizing the error, it is convenient to define a nondimensional error function $N(n)$,

$$N(n) = \frac{\varepsilon(n)}{\sum_{i=1}^{M} |P_i Z_i|^2}. \tag{5}$$

The average normalized error N_T quantifies the error across the optimization bandwidth and is defined to be

$$N_T = \frac{1}{n_2 - n_1 + 1} \sum_{n=n_1}^{n_2} N(n). \tag{6}$$

The error function N_T is a function of the M closed tube lengths, and the lengths L_i are chosen such that N_T is minimized. This may be regarded as a weighted least-squares method where the weighting coefficient is the denominator of Eq. (5).

The minimization method used in the M-dimensional space is the modified Powell's method. In each dimension the minimization technique of Brent is used (Press *et al.*, 1986).

When the optimization is through, P_0 and Z_0 are given by the LMS solution (Allen, 1985):

$$\begin{bmatrix} P_0 \\ Z_0 \end{bmatrix} = \frac{1}{\Delta} \begin{bmatrix} \sum_{i=1}^{M} |P_i|^2 & -\sum_{i=1}^{M} \overline{Z_i} P_i \\ \sum_{i=1}^{M} \overline{P_i} Z_i & -\sum_{i=1}^{M} |Z_i|^2 \end{bmatrix} \begin{bmatrix} \sum_{i=1}^{M} |Z_i|^2 P_i \\ \sum_{i=1}^{M} |P_i|^2 Z_i \end{bmatrix} \tag{7a}$$

with

$$\Delta = \left(\sum_{i=1}^{M} |Z_i|^2 \right) \left(\sum_{i=1}^{M} |P_i|^2 \right) - \left(\sum_{i=1}^{M} \overline{P_i} Z_i \right) \left(\sum_{i=1}^{M} \overline{Z_i} P_i \right). \tag{7b}$$

The tip of the probe microphone extends 5 mm past the flush surface of the plastic insert (see Fig. 2) in order to reduce the contribution of the evanescent mode coupling between the earphone source and the probe tip. This leaves a cavity between the probe tip and the surface of the earphone source. This cavity will have a volume depending on the tube diameter. The calibration will therefore give different results in terms of P_0 and Z_0, depending on the tube diameter. The impedance probe is used without modification with the calibration carried out for diameters 7.5 mm, corresponding approximately to the outer part of the ear canal, and 3 mm, corresponding to the canal in the mold (see Fig. 1). This gives two sets of Thevenin parameters to be used with the two tube diameters.

With the two sets of Thevenin parameters P_0 and Z_0 determined by the procedure above, the impedance probe is used for measuring input impedance in tubes of diameters 7.5 and 3 mm. This will give Z_E through measurements in the ear canal and Z_H from measurement on the hearing aid through the mold and calculations according to the model in Fig. 2.

III. THE MEASUREMENT PROCEDURE IN BRIEF

In order to check the validity of the model in Fig. 1, P_H, Z_H, and Z_E were calculated from measurements, the pre-

dicted pressure calculated, and the real pressure measured for comparison. All parameters in the comparison are valid in the point of comparison only.

With the impedance probe calibrated according to Sec. II, the ear input impedance Z_E is measured according to Fig. 2. P_{EM} is the measurement variable, P_0 and Z_0 are known from the calibration procedure, and Z_E is given by $Z_E = Z_0(P_{EM}/(P_0 - P_{EM}))$ according to the model in Fig. 2.

Here Z_H is measured the same way as Z_E with the ear replaced by hearing aid plus mold. Z_H is measured into the mold canal entrance towards the hearing aid.

Also, P_H was calculated from the response obtained with the hearing aid connected to an IEC 711 coupler. With an electrical analog as in Fig. 1 but with the ear replaced by the coupler, P_{EM} was measured with the coupler built-in microphone and P_H calculated from this model ($P_H = P_{EM}(Z_H + Z_C)/Z_C$). This requires knowledge of the coupler input impedance Z_C, which is determined the same way as Z_E and Z_H.

Here P_H and Z_H are measured at the mold end, and Z_E is measured 5 mm in front of the mold according to Fig. 2. In order to make a correct prediction, P_H and Z_H are translated to the remote point of Z_E measurement. This is carried out with a T matrix formulation according to Sec. 7-7 of Pierce (1981). The ear canal does not reveal constant cross section but for a short distance it is considered sufficiently constant.

After this translation the predicted sound pressure P_{EM} is calculated according to Fig. 1 (with the exact point of comparison 5 mm from the mold end according to Fig. 2). For comparison the real sound pressure from the hearing aid is then measured at the same point with a probe microphone positioned according to Fig. 2.

This point of measurement is remote from the eardrum and is not directly related to the sensation of hearing. However, the difference in sound pressure along the ear canal is a problem not directly related to the prediction problem addressed by this work.

The measurement system used was Tektronix 2630 spectrum analyzer in swept sine mode. All measurements were carried out at 397 frequency points (100 Hz to 10 kHz in 25-Hz steps). Usually a bandwidth of 100 Hz was used with the tracking filter and an average of five measurements. For the calculation of complex-valued parameters the transfer function is needed. However, the reference in this case is the output signal of the analyzer. In order to get a sound pressure level with 20×10^{-6} Pa as a reference the autospectrum from the calibrated probe microphone was used, 5 mm from the mold end as shown in Fig. 2. Although not able to detect all measurement errors, the coherence function is a useful parameter. In measurements like those used in the present work it will detect nonlinearities such as amplitude distortion and noise. The minimum coherence requirement was set to be 0.99, giving a maximum error in level of 0.1 dB for each measurement (Bendat and Piersol, 1986). This requirement was nearly always met.

IV. PROBLEMS AND LIMITATIONS OF THE METHOD

Different sources of error may distort the results. Those expected to dominate were checked and are discussed below.

A. Stapedius contraction

At high sound pressure levels the stapedius muscle is contracted. The muscle will pull the ossicle chain in such a way that the eardrum is pulled inwards and becomes stiff. This will in turn increase the input impedance of the middle ear. For sinusoidal stimulus the threshold of contraction is 90–95 dB SPL (Margolis, 1993). The stapedius reflex is bilateral, that is, a sufficiently high sound level into one ear will cause a contraction in both ears. It has been shown that the sound pressure level in the ear canal is increased approximately 2.5 dB when the stimulus tone was increased from 85 to 110 dB hearing level in the contralateral ear (Anderson, 1969).

The stapedius reflex is active throughout long-term exposure to an industrial noise which is variable with respect to frequency and amplitude (Borg *et al.*, 1979). In the present work the stimulus signal was a sine wave stepped in frequency over the measurement range. It has not been found in the literature whether or not a change in frequency only will reactivate the stapedius muscle. If the stapedius was not reactivated from a frequency shift only, it may have caused problems turning on and off during our measurements.

In order to check the reactivation from frequency shifts, measurements were therefore carried out on two persons with normal audiograms. The stimulus was emitted into the left ear, from the generator via amplifier, attenuators, and earphone. The stimulus level was monitored through a probe microphone and a measurement amplifier. On the right side the same type of equipment for monitoring the change in impedance was connected. The impedance itself was not measured, but the change in sound pressure due to the change in impedance was.

In the first experiment the stimulus tone was 500 Hz, 110 dB SPL for 10 s. The probe tone was 800 Hz, 65 dB. Over the 10-s period the probe tone level decreased approximately 0.5 dB. This indicates that the stapedius is contracted at the onset of the stimulus tone and is released over the measurement time.

In the second experiment the stimulus tone was 300 Hz to 1 kHz in 25-Hz steps, 3 s for each frequency, 110 dB SPL. The frequency step and time are those of most measurements in the main investigations in this project. The probe tone was the same as in the first experiment. In this case there was no significant change in the level of the probe tone. This indicates that the stapedius is reactivated by the change in frequency only. Although not found in the literature, this result was expected.

B. Probe location in the ear canal

While making measurements in the ear canal it is important to know the position of the probe end. As will be shown below, it is important to measure the input impedance of the ear and the sound pressure (for comparison) at the same

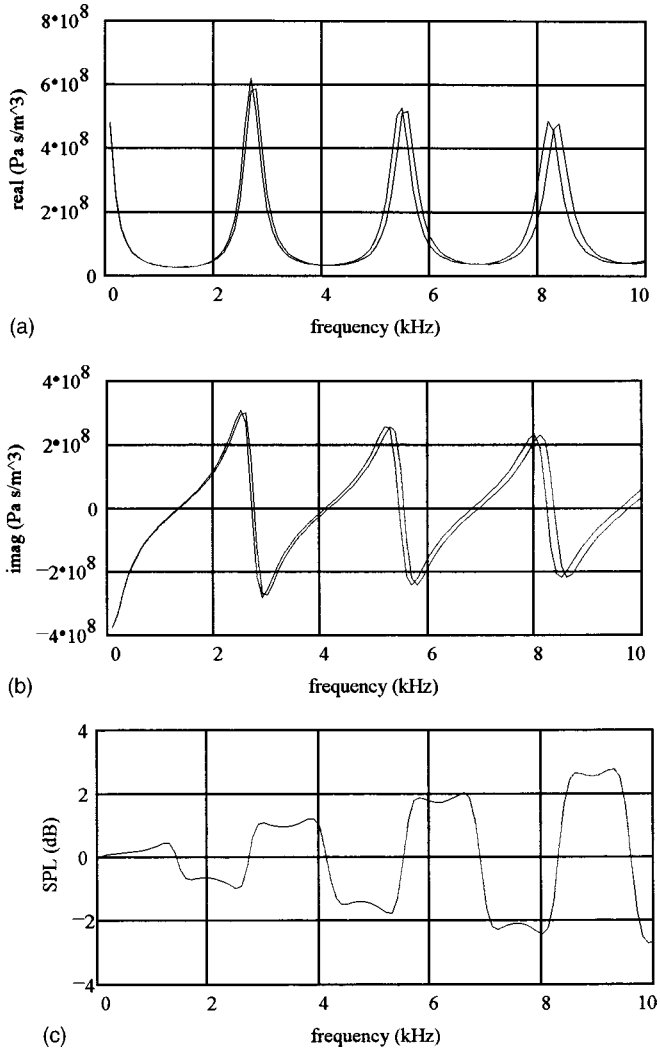

FIG. 3. (a) and (b) Probe positioning error in the impedance measurement of the hearing aid. Real part (upper) and imaginary part of the hearing aid Thevenin impedance. Left-most curves are valid for correct probe position; right-most curves are valid for a probe position 1 mm closer to the hearing aid. (c) Probe positioning error in the impedance measurement of the hearing aid. Resulting error in predicted sound pressure level is from the 1-mm probe position error.

point. This problem was to a large degree solved by making identical molds for the hearing aid and impedance probe on each ear.

A simulation model using MathCAD was made for checking the dependence of probe position in the hearing aid Thevenin impedance measurement on the predicted sound pressure level. The hearing aid receiver is modeled as a resistor (10^9 acoustic ohms), and the middle ear is modeled with Shaw's electrical analog (Shaw and Stinson, 1981). The tube (diameter: 2 mm, length: 60 mm) and ear canal (diameter: 7 mm, length: 15 mm) are modeled as loss-free straight tubes of constant cross section. An impedance translation procedure, Chap. 3-7 in Pierce (1981), was used for sound propagation in the tubes.

In Fig. 3 the real part [Fig. 3(a)] and the imaginary part [Fig. 3(b)] of the hearing aid Thevenin impedance are given. The left-most curves are valid for the correct position of the impedance probe. The right-most curves are valid for a probe position 1 mm closer to the hearing aid. In Fig. 3(c) the

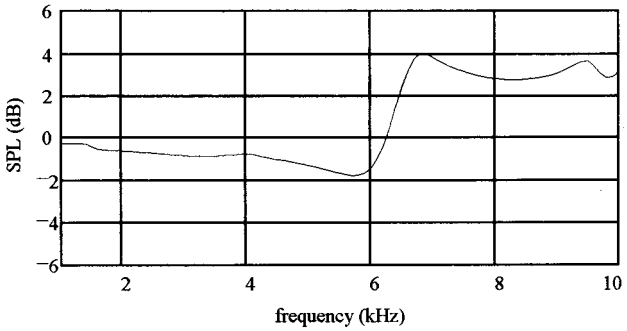

FIG. 4. Probe positioning error in the impedance measurement of the hearing aid. Resulting error in predicted sound pressure level is from the 1-mm probe position error.

differences in predicted sound pressure level in the ear canal of these two cases are given.

The corresponding error caused by an impedance probe misalignment in the ear canal is given in Fig. 4. The same situation as in Fig. 3 is assumed. The difference in predicted sound pressure level between a correct measurement and a measurement with the impedance probe 1 mm closer to the ear is shown.

All measurements on the ear were carried out with hard plastic molds for probe mounting and tightening of the ear canal. The age of the mold may have an impact on the results of this project. The ear canal of the hearing aid user will change in size and shape over time. Therefore a fresh cast giving a mold that fits tightly is essential.

C. Near-field modes

Propagating higher modes in the human ear canal are not present below the first cut-on frequency. This is expected to be approximately 18 kHz for adults (Rabbitt, 1988). For children this frequency limit is even higher. Higher modes in the sense of near-field modes (primarily near the ear canal entrance and the eardrum) may be found above 2.5 kHz (Rabinowitz, 1981). According to Hudde (1989), the near-field modes may exist as low as $\frac{1}{10}$ of the first cut-on frequency but there is no distinct limit.

The step in cross-sectional area between the sound canal of the mold and the ear canal will also produce near-field modes. These modes are commonly described as a mass loading of the mold canal or as an extension of the mold canal. From an impedance point of view this can easily be taken into account (Karal, 1953). Measurements in these near fields will, however, give nonpredictable results and, therefore, measurements are taken some distance from these area steps.

V. COMPARISON WITH CALCULATED TUBE IMPEDANCE

In order to evaluate the errors in the impedance measurements, a comparison between measured and calculated input impedance of two tubes was carried out. Tube dimensions not used in the calibration measurements were used.

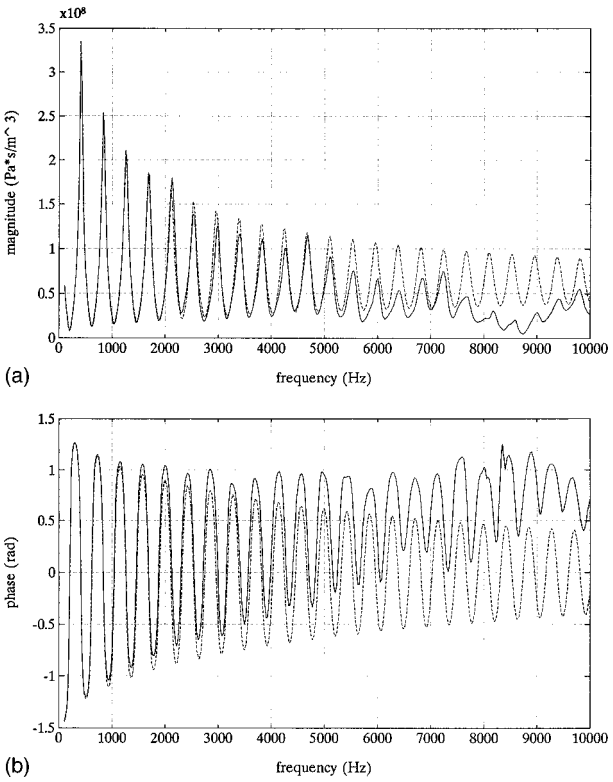

FIG. 5. (a) Magnitude of measured (solid) and calculated (dashed) input impedance of the small diameter tube. (b) Phase of measured (solid) and calculated (dashed) input impedance of the small diameter tube.

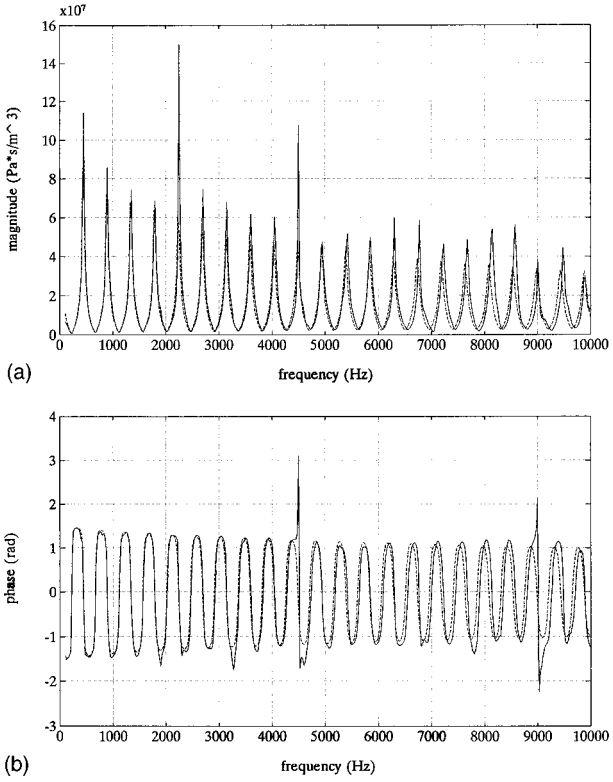

FIG. 6. (a) Magnitude of measured (solid) and calculated (dashed) input impedance of the large diameter tube. (b) Phase of measured (solid) and calculated (dashed) input impedance of the large diameter tube.

Measured and calculated tube impedance is given in Fig. 5 for a small diameter tube ($\varnothing = 3$ mm, length$=403$ mm). At low frequencies the difference is small and increasing toward high frequencies, and it is large in the range 7.5–9.5 kHz. In this range the EAR-3A earphone gives a low output level. The coherence is more than 0.999 throughout the frequency range for the tube measurement and all calibration measurements involved. However, the earphone response makes the autospectrum fall from approximately 3 kHz and is 30 dB down at 8 kHz. The damping in the tube is also increasing with frequency.

In Fig. 6 measured and calculated impedance is given for a large diameter tube ($\varnothing = 7.5$ mm, length$=380$ mm). The damping is less in this tube and the result is better. The phase plot does reveal sharp peaks at 4.5 and 9 kHz in addition to other minor errors. These peaks may be due to the fact that some of the calibration tubes have impedance dips very close to the tube length determined by the calibration program.

VI. PREDICTION ON A COUPLER

The measurement and prediction procedure was first carried out with the IEC 711 coupler (ear simulator) used instead of the human ear. In order to check the reproducibility four measurements of each parameter were carried out. The Philips M49 hearing aid was used.

Figures 7 and 8 show measured and predicted sound pressure levels in coupler for best and worst result, respectively. From 230 Hz to 8 kHz the error is within ± 5 dB. Above this frequency range large errors occurs.

VII. PREDICTION ON REAL EARS

For verification of the model on real ears three behind-the-ear hearing aids and five ears where used. The following hearing aids where used:

(i) Widex ES1,
(ii) Philips M49,
(iii) Phonak Pico SC.

A. Hearing aid Thevenin impedance

The Thevenin impedance of the Widex ES1 hearing aids is given in Fig. 9 for three measurements. The coherence is very good in these measurements except for the very lowest

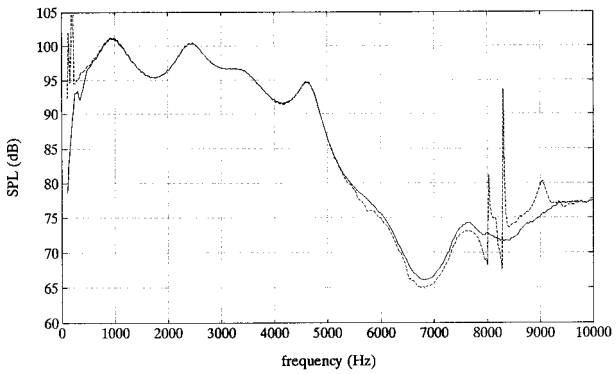

FIG. 7. Measured (solid) and predicted (dashed) sound pressure levels from the second measurement in the prediction-in-coupler experiment.

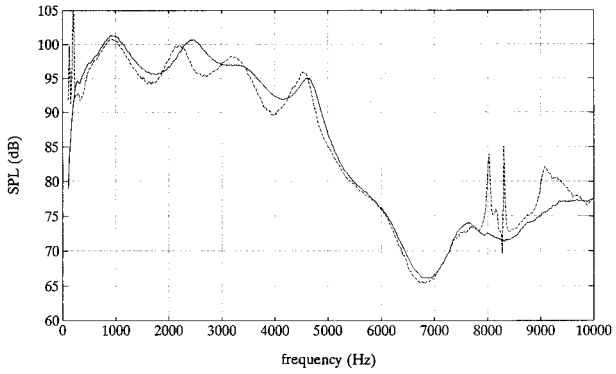

FIG. 8. Measured (solid) and predicted (dashed) sound pressure levels from the third measurement in the prediction-in-coupler experiment.

frequencies. The Thevenin impedance is dependent not only on the receiver, tube, and mold, but also on the output impedance of the hearing aid amplifier.

B. Hearing aid Thevenin pressure

These measurements were carried out with the same hearing aid input signal as in the prediction check in Sec. VII D.

The result is depending not only on the same parameters as the Thevenin impedance, but also on the signal processing of the hearing aid and the microphone characteristics if used.

The coherence function was in excess of 0.999 in these measurements, except in the frequency range where the hearing aid output level is low. The transfer function for hearing aid+coupler, XferP_H, representing P_H as translated to the end of the mold (see Sec. III), is given for the Widex ES1 hearing aid in Fig. 10.

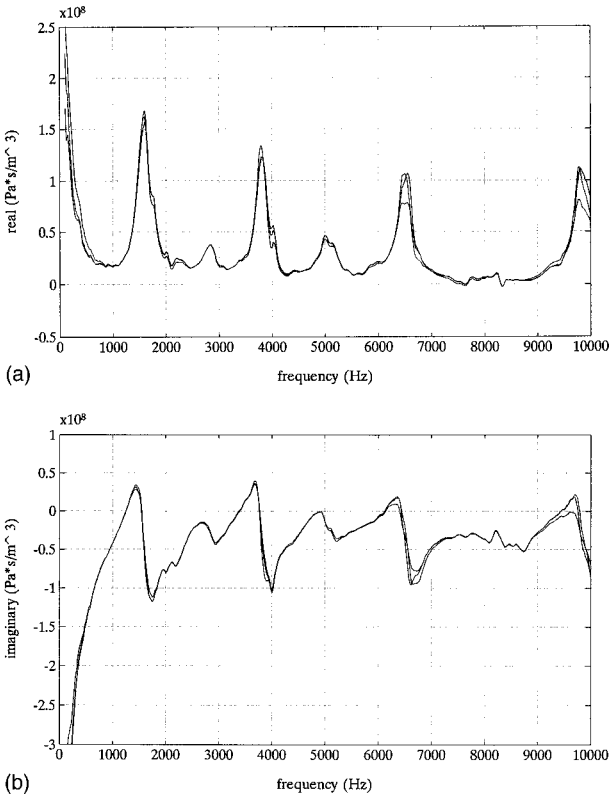

FIG. 9. (a) Example of a hearing aid Thevenin impedance on Widex ES1, real part. Three measurements. (b) Example of a hearing aid Thevenin impedance on Widex ES1, imaginary part. Three measurements.

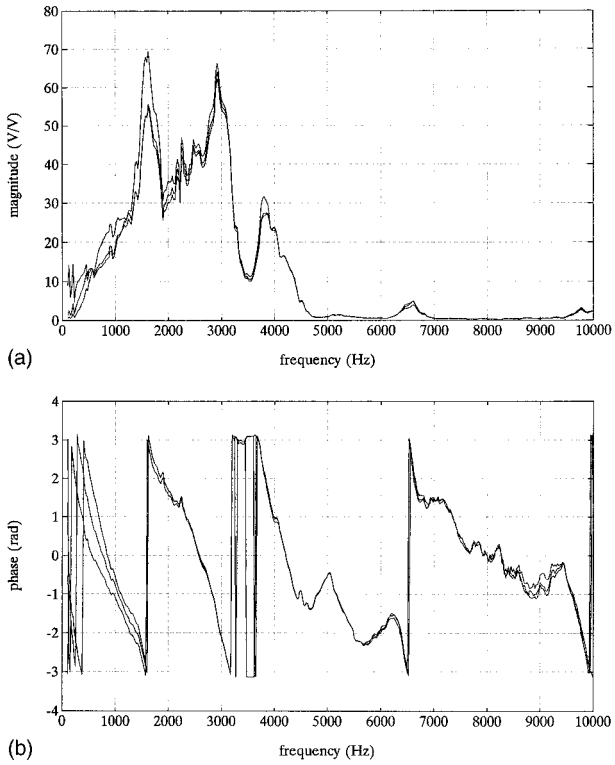

FIG. 10. (a) Example of a hearing aid Thevenin pressure transfer function on Widex ES1, magnitude. Three measurements. (b) Example of a hearing aid Thevenin pressure transfer function on Widex ES1, phase. Three measurements.

C. Ear impedance

All real ears used in the main investigations of this project are pathological. Results from the impedance audiometry gives an idea of whether or not the ear input impedance is normal. Of the five real ears used, only one subject (A) has a documented normal result from the impedance audiometry.

Due to the stapedius contraction the human ear is expected to have an input impedance varying with sound level. Impedance measurements on the ear were therefore carried out at two different sound pressure levels. SPL(max) denotes the maximum sound pressure level in one measurement. In Fig. 11 mean, max, and min from three measurements at 100–105 dB SPL(max) are given for subject E. The measurements at 80–85 dB SPL(max) show very little difference from these results.

In some of the results the reactance differs substantially from the expected cavity shape. This occurs for the high- and low-level measurements in case E. The reason for this is likely to be leakage, although Vaseline was used in an attempt to get an airtight seal. In the frequency range 4000–7000 Hz the result is very different between measurements. The six impedance measurements on each ear were carried out in pairs, one measurement at each level without remounting the probe.

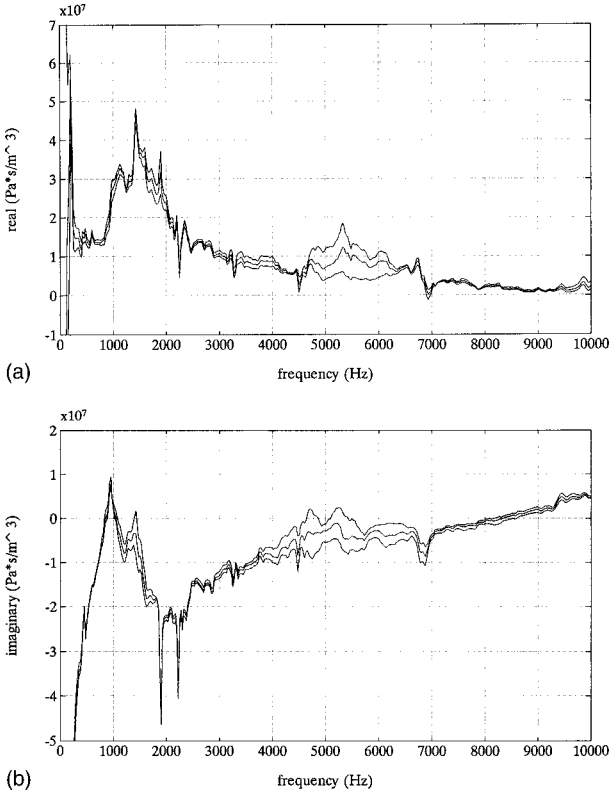

FIG. 11. (a) Real part of ear input impedance at 100–105 dB(max), subject E. (b) Imaginary part of ear input impedance at 100–105 dB(max), subject E.

The coherence function from these measurements exceeds 0.99 except for the frequency range 7–9 kHz, where it sometimes was as low as 0.7.

D. Prediction check

In Figs. 12–14 examples of measured and predicted (from measured parameters in Fig. 1) response are given for the three hearing aids on subject A. The measurements were carried out over a wider frequency range than the hearing aids are expected to reproduce. Noise problems were experienced at the low levels in the high-frequency dips.

As all parameters above were calculated from three different measurements, the prediction check was also carried out three times. The error ''predicted sound pressure level minus measured sound pressure level'' is given for all hearing aids on subject E in Figs. 15–17. Maximum, minimum, and average (in dB values) out of three measurements and calculations of each parameter are given. Subjects D and E show better reproducibility than the others; this may be due to molds of a later date than in the other cases. For these two subjects a good mold fit was noted.

In general, there is a low-frequency region and a high-frequency region with large spread. A mid-frequency region, 1–6 kHz, usually reveals better accuracy (approximately ± 5 dB in most cases). The frequency range 3–4 kHz is very important when fitting hearing aids. The error in this range is in general within ± 3 dB.

Average (in dB values), maximum, and minimum were also calculated for each hearing aid over all subjects. Results are given in Fig. 18 for Widex ES1, in Fig. 19 for Philips M49, and in Fig. 20 for Phonak Pico SC.

The hearing aids are expected to have Thevenin parameters independent of sound pressure level as mentioned earlier. The human ear is expected to have an input impedance varying with sound pressure level. The prediction check was therefore carried out in two cases, with ear impedance measured at 80–85 dB(max) and 100–105 dB(max). The difference between averages over all hearing aids and subjects measured at 100–105 dB(max) and 80–85 dB(max) are given in Fig. 21. There is no significant difference between

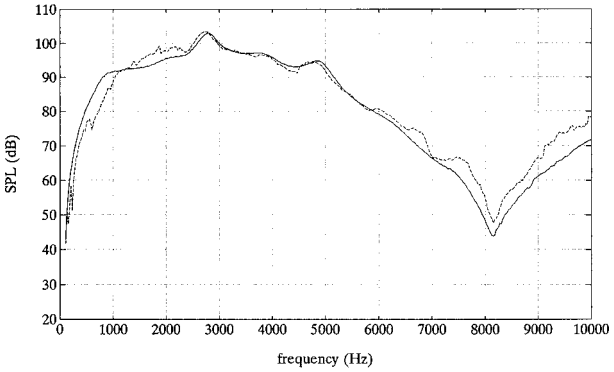

FIG. 13. Measured (solid) and predicted (dashed) sound pressure level from Philips M49 on subject A.

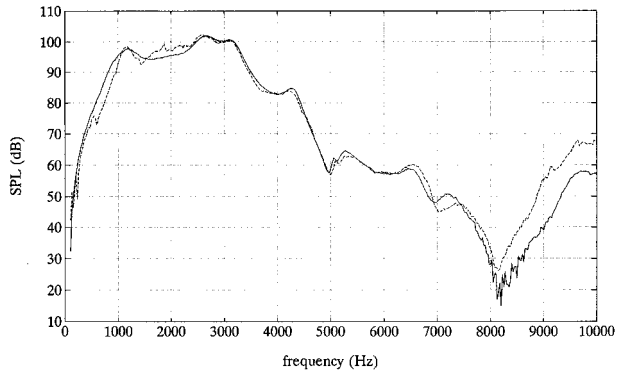

FIG. 12. Measured (solid) and predicted (dashed) sound pressure level from Widex ES1 on subject A.

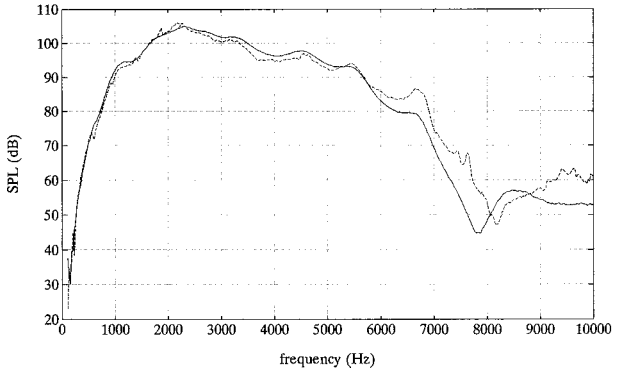

FIG. 14. Measured (solid) and predicted (dashed) sound pressure level from Phonak Pico SC on subject A.

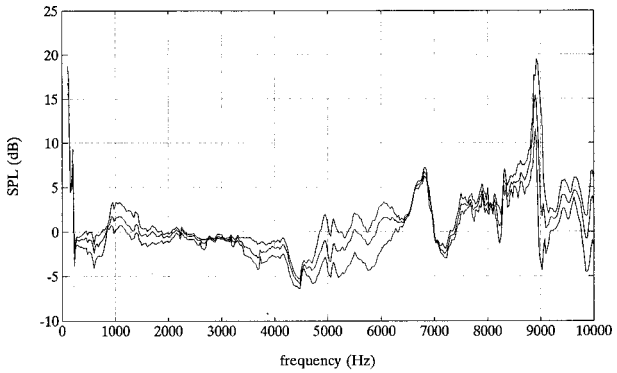

FIG. 15. Predicted minus measured sound pressure level of Widex ES1 on subject E. Maximum, average, and minimum of three measurements.

the results at the two levels. The peak at 8.4 kHz is due to measurement errors.

VIII. DISCUSSION AND CONCLUSIONS

An electrical analog model (Fig. 1) has been given as a theoretical description of the acoustical system ''hearing aid and ear.'' This model has been tested in the frequency range 100 Hz to 10 kHz.

The comparison between predicted and measured sound pressure level on coupler is clearly showing the influence of probe misalignment in Fig. 8. The error is on the order of 4 dB up to 8 kHz. Apart from this type of error the result is good from 300 Hz up to 8 kHz. Large errors occur at 8–9 kHz. These are due to calibration errors in this frequency range of the impedance probe at small tube diameters (see Fig. 5) and low hearing aid response at these frequencies.

The prediction check on real ears shows larger errors as expected. Below 250 Hz large errors occur in all measurements. A common problem at low frequencies (<1 kHz) is leakage. This seems to be present for some subjects but not all. A good mold fit, and thus a tight mold, was noted on subjects D and E.

In the frequency range 1–6 kHz the average predicted sound pressure level is usually within approximately ± 5 dB of the measured level. The coherence functions from the Z_H measurements are exceeding 0.999. In the Xfer_{PH} measurements it exceeds 0.999, except for the frequency range where

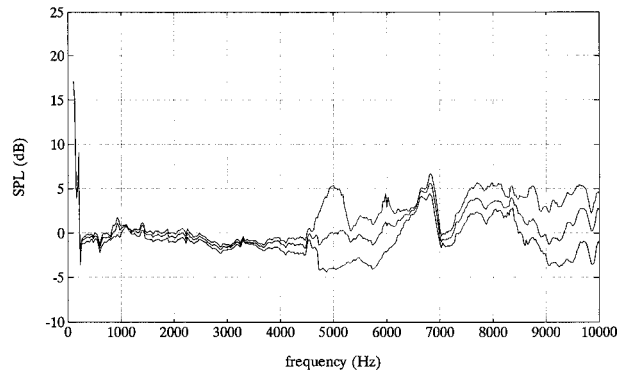

FIG. 16. Predicted minus measured sound pressure level of Philips M49 on subject E. Maximum, average, and minimum of three measurements.

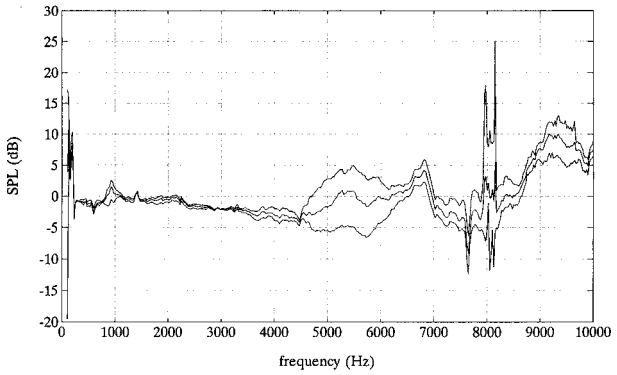

FIG. 17. Predicted minus measured sound pressure level of Phonak Pico SC on subject E. Maximum, average, and minimum of three measurements.

the hearing aid output is low (7–9 kHz). The coherence functions from Z_E measurements exceeded 0.999, except for frequencies above 7 kHz where it was sometimes as low as 0.7. The reproducibility of Z_H (Fig. 9), Xfer_{PH} (Fig. 10), and Z_E (Fig. 11) is not excellent. However, the influence in detail of each parameter on the prediction error is not always easily detected, since all parameters involved are varying between different prediction results. An alternative way of comparison would be to study the variation of one parameter at a time with the other parameters fixed. Since the fixed parameters would be estimates of the real ones, the results of such a comparison would be uncertain. The comparison used in the present work simulates the results obtained in a measurement situation at a clinic.

The large variations in the frequency range 6–9 kHz are caused partly by the low sound pressure levels in the Xfer_{PH}, Z_E and P_{EM} measurements. This causes problems since the noise level of the probe microphone is rather high (55 dB SPL equivalent, 20 Hz to 20 kHz bandwidth). The variations are caused partly by the error in impedance probe calibration mentioned in Sec. V and shown in Fig. 5. It is also important to keep in mind that all measurements, including prediction check, also include errors from probe misalignment. In Figs. 18–20 the prediction errors for all subjects on each hearing aid are given. In general the reproducibility is bad at high frequencies but is somewhat better on subjects D and E. As these two subjects revealed a

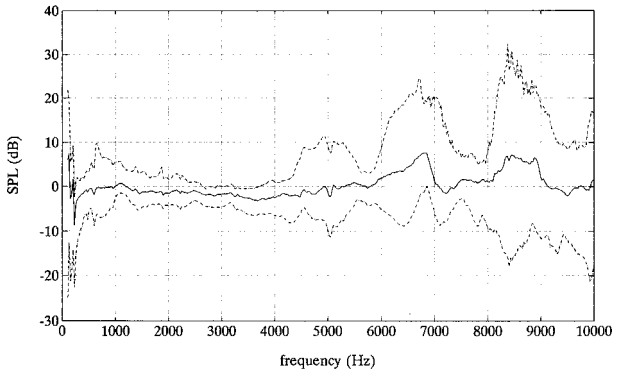

FIG. 18. Maximum, average, and minimum of prediction error with Widex ES1 over all subjects.

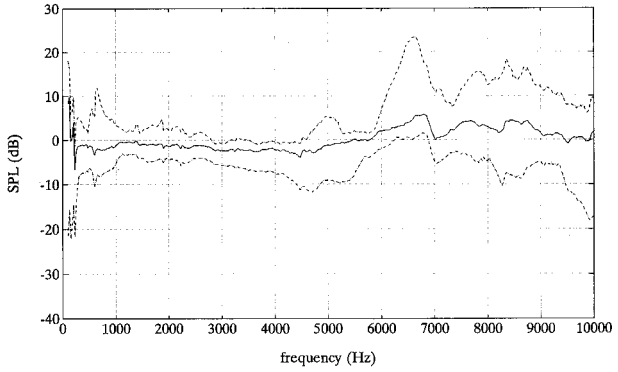

FIG. 19. Maximum, average, and minimum of prediction error with Philips M49 over all subjects.

better mold fit than the others, this indicates the importance of a good mold fit and thus a more nearly accurate probe alignment.

The overall shape of the averaged prediction error curves, negative at low frequencies and positive at high frequencies, may be caused by probe misalignments. However, this would mean that this type of error is systematic. The example in Fig. 14 shows dips at different frequencies for measured and predicted result. This error is probably caused by probe misalignment. These errors are simulated for the case of Z_H and Z_E measurements as described in Sec. IV B and shown in Figs. 3 and 4.

Measurements of Z_E and P_{EM} reveal errors in the frequency range 7–9 kHz. This is due to the frequency response of the insert earphone and the hearing aids. The tube earphone model ER-3A has the response of the TDH-39 supra-aural earphone. This means low levels at high frequencies. The EAR-3A was chosen for its high-level capabilities. As the sound pressure level used is not critical in the prediction of hearing aid response, insert earphones for use at lower levels may be used. In that case earphone models with a more nearly flat frequency response are available.

A main reason for the bad result at high frequencies is the low hearing aid response. The hearing aids used in this project were chosen from their ''deviation in response on different ears'' (Svärd, 1995) as this is of primary importance. The development in hearing aid technology is directed towards better high-frequency response. The measurement

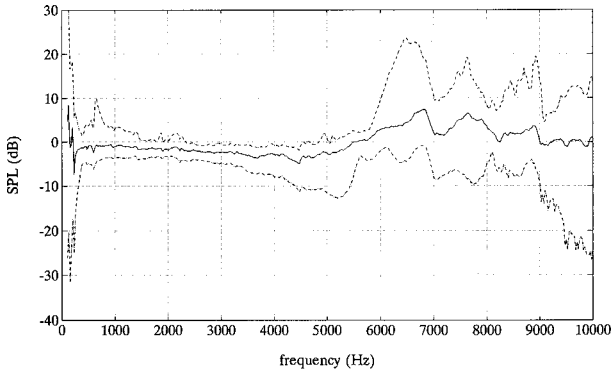

FIG. 20. Maximum, average, and minimum of prediction error with Phonak Pico SC over all subjects.

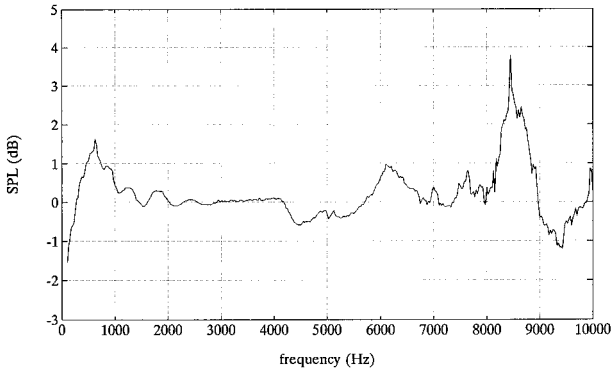

FIG. 21. Average over hearing aids and subjects of prediction error with ear impedance measured at 100–105 dB(max) minus average over hearing aids and subjects of prediction error with ear impedance measured at 80–85 dB(max).

and calculation procedure given in this report is thus expected to give a better result as development goes on.

Summing up sources of errors, we have the following.

(i) Calibration errors, shown as deviations from expected results in Figs. 5 and 6. In the present work the calibration tube lengths were measured with a rule. The acoustical measurement of calibration tube lengths in Keefe *et al.* (1992) should be used.

(ii) Response of EAR-3A earphone. Measurements can be carried out at lower sound pressure levels. This means that an earphone with a more flat response can be used.

(iii) Noise level of ER-7C probe microphone. The noise from the probe microphone causes errors in the frequency ranges were the sound pressure level is low.

(iv) Response of hearing aids. At high frequencies the output level is low. In combination with a rather high microphone noise this causes problem.

(v) Probe misalignments. Misalignments cause errors increasing with frequency. Molds made from not too old individual casts of the ear canal are necessary.

To conclude, the described measurement and calculation procedure appears to be useful between approximately 300 Hz and 6 kHz. In this frequency range probe positioning errors dominate. At higher frequencies large errors occur, mainly due to the response of the hearing aids and insert earphone used.

ACKNOWLEDGMENTS

The author owes many thanks to Dr. Mats Åbom at Technical Acoustics, Department of Vehicle Technology/ Royal Institute of Technology, Stockholm. Thanks also for the use of the Tektronix 2630 measurement system, at Technical Acoustics. Thanks to the five patients for their participation. Thanks to Ingmar Svärd/Karolinska Sjukhuset for providing contact with these nice people and also for supplying the project with hearing aids for the main investigations. Many thanks to Göran Lundberg at the Department of Tech-

nical Audiology/Karolinska Institutet for support with the Turbo Pascal-programming. Thanks also to Åke Svanberg/ Philips försäljning AB for providing a Philips M46 hearing aid for the preliminary investigations of this project. This work was supported by the Swedish National Board for Industrial and Technical Development (NUTEK).

Allen, J. B. (**1985**). ''Measurement for eardrum acoustic impedance,'' in *Peripheral Auditory Mechanisms*, edited by J. B. Allen, J. L. Hall, A. Hubbard, S. T. Neely, and A. Tubis (Springer-Verlag, New York).

Anderson, H. (**1969**). ''Acoustic intra-aural reflexes in clinical diagnoses,'' Doctoral thesis, Department of Audiology and Otolaryngology, The Karolinska Hospital, Stockholm.

Bendat, J. S., and Piersol, A. G. (**1986**). *Random Data* (Wiley–Interscience, New York), p. 137.

Berninger, E., Overgård, A., and Svärd, I. (**1992**). ''Coupler-related real ear gain,'' Scand. Audiol. **21**, 15–22.

Borg, E., Nilsson, R., and Lidén, G. (**1979**). ''Fatigue and recovery of the human acoustic stapedius reflex in industrial noise,'' J. Acoust. Soc. Am. **65**, 846–848.

Egolf, D. P., and Leonard, R. G. (**1977**). ''Experimental scheme for analyzing the dynamic behavior of electro-acoustic transducers,'' J. Acoust. Soc. Am. **62**, 1013–1023.

Hudde, H. (**1989**). ''Acoustical higher-order mode scattering matrix of circular nonuniform lossy tubes without flow,'' J. Acoust. Soc. Am. **85**, 2316–2330.

Karal, F. C. (**1953**). ''The analogous acoustical impedance for discontinuities and constrictions of circular cross section,'' J. Acoust. Soc. Am. **25**, 327–334.

Keefe, D. H. (**1984**). ''Acoustical wave propagation in cylindrical ducts: Transmission line parameter approximations for isothermal and nonisothermal boundary conditions,'' J. Acoust. Soc. Am. **75**, 58–62.

Keefe, D. H., Ling, R., and Bulen, J. C. (**1992**). ''Method to measure acoustic impedance and reflection coefficient,'' J. Acoust. Soc. Am. **91**, 470–485.

Margolis, R. H. (**1993**). ''Detection of Hearing Impairment with the Acoustic Reflex,'' Ear and Hearing **14(1)**, 3–10.

Olsson, U. (**1985**). ''Hearing aid measurements on occluded-ear simulator compared to simulated in-situ and in-situ measurements,'' Report No. 111, Department of Technical Audiology, Karolinska Institutet, Stockholm.

Pierce, A. D. (**1981**). *Acoustics, An Introduction to Its Physical Principles and Applications* (McGraw-Hill, New York).

Press, W. H., Flannery, B. P., Teukolsky, S. A., and Vetterling, W. T. (**1986**). *Numerical Recipes* (Cambridge U. P., Cambridge).

Rabbitt, R. D. (**1988**). ''High-frequency plane waves in the ear canal: Application of a simple asymptotic theory,'' J. Acoust. Soc. Am. **84**, 2070–2080.

Rabinowitz, W. M. (**1981**). ''Measurement of the acoustic input immittance of the human ear,'' J. Acoust. Soc. Am. **70**, 1025–1035.

Sanborn, P-E. (**1990**). ''Hearing-aid to ear impedance-matching: A literature survey,'' Report No. 118, Department of Technical Audiology, Karolinska Institutet, Stockholm.

Shaw, E. A. G., and Stinson, M. R. (**1981**). ''Network concepts and energy flow in the human middle-ear,'' J. Acoust. Soc. Am. **69**, S43(A).

Svärd, I. (**1995**). ''Coupler-related real ear gain, part 2,'' Scand. Audiol. (to be published).

Growth behavior of the $2f1-f2$ distortion product otoacoustic emission in tinnitus

Thomas Janssen,[a] Peter Kummer, and Wolfgang Arnold
Hals-Nasen-Ohren-Klinik, Technische Universität, Ismaningerstr. 22, 81675 München, Germany

(Received 20 August 1997; revised 20 January 1998; accepted 23 February 1998)

High-resolution hearing threshold and $2f1-f2$ distortion product otoacoustic emission (DP) were measured with the same in-the-ear sound probe and same calibration at 51 frequencies between 500 and 8000 Hz in 39 sensorineural hearing loss ears associated with tinnitus. Using a primary tone setting $L1=0.4L2+39$ that accounts for the nonlinear interaction of the two primary tones at the DP generation site at $f2$, DPs were elicited in a wide range from $L2=65$ to 20 dB SPL. We failed to find a uniform DP behavior in the 39 tinnitus ears tested. Seventeen of them behaved like impaired ears without tinnitus. In these ears a linearized DP growth was observed where the DP level decreased and the slope of the DP I/O functions steepened with increasing hearing loss and as a result both the DP level and the DP slope strongly correlated with hearing threshold. The other population, 22 tinnitus ears, exhibited a poor or even inverse relationship between DP level and hearing threshold, i.e., displayed an increase of DP level with increasing hearing loss. Despite the severe hearing loss but due to the high level, DPs could be recorded well in the frequency range that corresponded to the appearance of the tinnitus. The DP slope, however, increased with increasing hearing loss and, therefore, did still correlate with hearing threshold revealing pathological alteration. The data suggest that the DP level alone is hardly capable of assessing hearing impairment in tinnitus ears and may even be misleading. Thus just the DP slope seems to be the only reliable indicator of cochlear malfunction around the tinnitus frequency. The observed nonuniform DP behavior suggests different cochlear impairments in tinnitus ears. In those ears where the DP level decreases and the slope of the I/O functions increases with hearing loss, cochlear sensitivity and tuning are supposed to be diminished. In those ears where the DP level increases with increasing hearing loss, a reinforced mechanical distortion is hypothetized to be generated by cochlear hyperactivity that can be the source of both the abnormally high DP level and the tinnitus. [S0001-4966(98)01306-X]

PACS numbers: 43.64.Jb, 43.64.Kc, 43.64.Ri [BLM]

INTRODUCTION

Until recently, no correlation between tinnitus and neither spontaneous nor evoked otoacoustic emissions has been detected and there has been a lack of its objective proof (Norton *et al.*, 1990; Wilson, 1987; Zwicker, 1987). However, some evidence exists that otoacoustic emissions do reflect specific changes in cochlear micromechanics being related to tinnitus. Transiently evoked otoacoustic emissions (TEOAEs) in acoustic trauma ears with tinnitus have been found to be less suppressible or even increased by contralateral stimulation compared to those of similar hearing loss but without tinnitus (Attias *et al.*, 1996). This observation was interpreted as a hyperactivity of outer hair cells (OHCs) due to an improper function of the cochlear efferents. Enhancement of TEOAE was also reported in temporary noise-induced tinnitus after exposure of a loud low-frequency tone, but interpreted as a mechanical instability and self-sustained oscillation within the cochlea (Kemp, 1982, 1986). It was further speculated that localized oscillations of isolated cochlear elements could induce a mild tinnitus without producing a detectable sound (Kemp, 1981). Similarly, the impedance alteration of cochlear micromechanics caused by OHC impairments was supposed to be responsible for the generation of inner-ear standing waves (Allen *et al.*, 1995; Zweig and Shera, 1995), which can result in both spontaneous otoacoustic emission (SOAE) and tinnitus.

Clues to a hyperactivity of cochlear micromechanics as a potential correlate of tinnitus can also be found in animal models and isolated OHCs. Neural tuning curves were shown to reflect a hypersensitivity of the cochlea due to a specific lesion of OHCs (Liberman and Dodds, 1984). Impairment of isolated OHCs was reported to result in a greater elongation and distortion indicating a hypermotility of OHCs which was speculated to be the motor arm of cochlear tinnitus (Zenner and Ernst, 1993). Recently, the swelling of OHCs has been shown to result in an increase in magnitude and gain of OHC electromotility that might have crucial significance in hearing disorders associated with tinnitus (Sziklai and Dallos, 1997).

Distortion product otoacoustic emissions (DPs) are thought to arise from the nonlinear OHC amplification process (Dallos, 1992) and should therefore reflect even minute alterations in OHC function. Although the efficacy of DP has recently been increasing for diagnosing cochlear impairment (Gorga *et al.*, 1993; Harris, 1990; Kummer *et al.*, 1998; Lonsbury-Martin *et al.*, 1991; Martin *et al.*, 1990; Nelson and Kimberly, 1992; Popelka *et al.*, 1995; Smurzynski,

[a]Electronic mail: T.Janssen@lrz.tu-muenchen.de

1994; Stover *et al.*, 1996; Stover and Norton, 1993), there are only little, partly controversial reports on the DP behavior in tinnitus. DP levels in tinnitus patients with normal audiograms were reported to be lower or higher than those in healthy individuals (Mitchell *et al.*, 1995; Norton *et al.*, 1990; Shiomi *et al.*, 1997). In tinnitus patients with sensorineural hearing loss both decrease and increase in DP amplitude has been observed (Janssen and Arnold, 1995).

The aim of this study was to further investigate to what extent DPs behave differently in cochlear disorders with tinnitus. By applying a stimulus paradigm of divergent primary tone levels $L1 = 0.4L2 + 39$, which accounts for unequal primary tone responses at the DP generation site in the cochlea, DPs could be measured over a range from high to close-to-threshold stimulus intensities. It was found that DP growth functions obtained with that special stimulus paradigm provide a powerful tool for assessing subtle cochlear pathology.

I. METHODS

A. Subjects

Thirty-nine ears in 31 patients suffering from sensorineural hearing loss associated with chronic tinnitus were measured in this study. Hearing losses ranged from 20 to 90 dB HL. In three ears the hearing loss was due to acoustic trauma, in four ears Ménière disease, and in four ears head trauma. In the remainder 28 ears (15 sudden and 13 progressive hearing loss) the etiology of the complaint has not been reached. Thirty-four ears had a tone and five a noiselike tinnitus. Pitch and loudness matching of the tinnitus were performed by means of a clinical audiometer (see Vernon, 1987). As a rule, the patients estimated the loudness of the tinnitus somewhat above the audiometric threshold around the tinnitus frequency. Auditory brainstem responses (ABRs) were recorded and the I–V interpeak interval was measured in an attempt to exclude a retrocochlear pathology (see Stockard *et al.*, 1980). In severe hearing-loss cases, where ABR wave I could not be detected and, correspondingly, the I–V interpeak interval was not available, computer tomography (CT) was performed. In all cases neither ABR nor CT revealed a retrocochlear process. SOAE could be registered in two ears only, their frequencies being within the range of the preserved hearing but not of the hearing loss and, respectively, of the tinnitus.

Apart from the 39 chronic tinnitus ears an in-depth description of the DP behavior in an acute acoustic trauma ear associated with tinnitus during trauma and after recovery is presented. This case has been chosen in order to demonstrate, in the same ear, the different DP growth behavior during the two cochlear states, one with and another without tinnitus. The case concerns a 21-year-old female, who suffered from acoustic trauma and tinnitus, that appeared when visiting a discotheque. DP measurements and audiometrical investigations were obtained 36 h (referred to as the trauma state) and 3 days after the trauma (recovery state).

B. DP and pure-tone threshold measurements

The measurements of $2f1 - f2$ DP and high-resolution pure-tone threshold were performed at 51 frequencies between $f2 = 488$ and 8008 Hz with a constant $f2/f1$ ratio of 1.2 using Cub^{e}dis™/Etymotic Research (ER-10C) instrumentation (Mimosa Acoustics, NJ). Ten stimulus levels from $L2 = 65$ to 20 dB SPL have been applied, whereby $L1 - L2$ increased with decreasing primary tone level according to equation $L1 = 0.4L2 + 39$ dB (for details see Kummer *et al.*, 1998). DPs were accepted as valid for signal-to-noise ratios exceeding 6 dB. From the numerical data obtained, DP grams $[L_{dp}(f2)]$ and DP I/O functions $[L_{dp}(L2)]$ were reconstructed. In order to quantify the DP growth, the slope s of the I/O functions was calculated between $L2 = 40$ and 60 dB SPL, where normal and pathological DP behavior did differ most: in the lower stimulus level region both in normal and pathological ears the I/O functions had similar steep slope, while just in the 40–60 dB SPL stimulus level region in normally hearing ears the I/O functions considerably flattened but in pathological ears the steep slope was generally preserved (see also Sec. II). The slope s was calculated if there were at least three data points in the range between $L2 = 40$ and 60 dB SPL. For a reliable comparison, the pure-tone threshold L_t was assessed immediately after the DP recording at all $f2$ frequencies using a computer controlled method of adjustment. By button press or release the sound-pressure level was decreased or increased by 5 dB/s. At each frequency, the tone was presented for 30 s and the threshold level L_t was estimated from an average of the points within the flat run of the adjustment (usually from the fifth second). DP and threshold levels were recorded with the same in-the-ear probe (ER-10C) without changing the probe fit. Threshold measurements were done immediately after DP testing using the previously obtained frequency response of the transducers for stimulus calibration. To avoid artificial distortion maximum tone level was restricted to 65 dB SPL. Measurements were performed in a double-walled soundproof room. The patients were instructed to remain quiet during the measurements. DP measurement took up to 35, threshold measurement up to 25 min. Before the actual experimental runs in each case the patient's pure-tone threshold was obtained by means of a conventional clinical audiometer.

DP and high-resolution pure-tone threshold data from 20 normally hearing ears obtained in the same manner were used as reference data (for details see Kummer *et al.*, 1998). The range of one standard deviation of the DP level L_{dp} and the slope s of the DP I/O function of this ears served in particular to distinguish the pathological DP pattern.

II. RESULTS

A. DP level and growth behavior in a case of acoustic trauma with tinnitus and during recovery

Apart from the 39 chronic tinnitus ears, we will first report on the case example of the acute acoustic trauma with rapid subsequent hearing restoration and tinnitus abolishment. The clinical audiogram, carried out during the acoustic trauma, revealed in the right ear a 30-dB notch at 4 kHz and a tonelike tinnitus of a loudness of 25 dB HL around 6 kHz [Fig. 1(a)]. With respect to this notch, the DP did show a

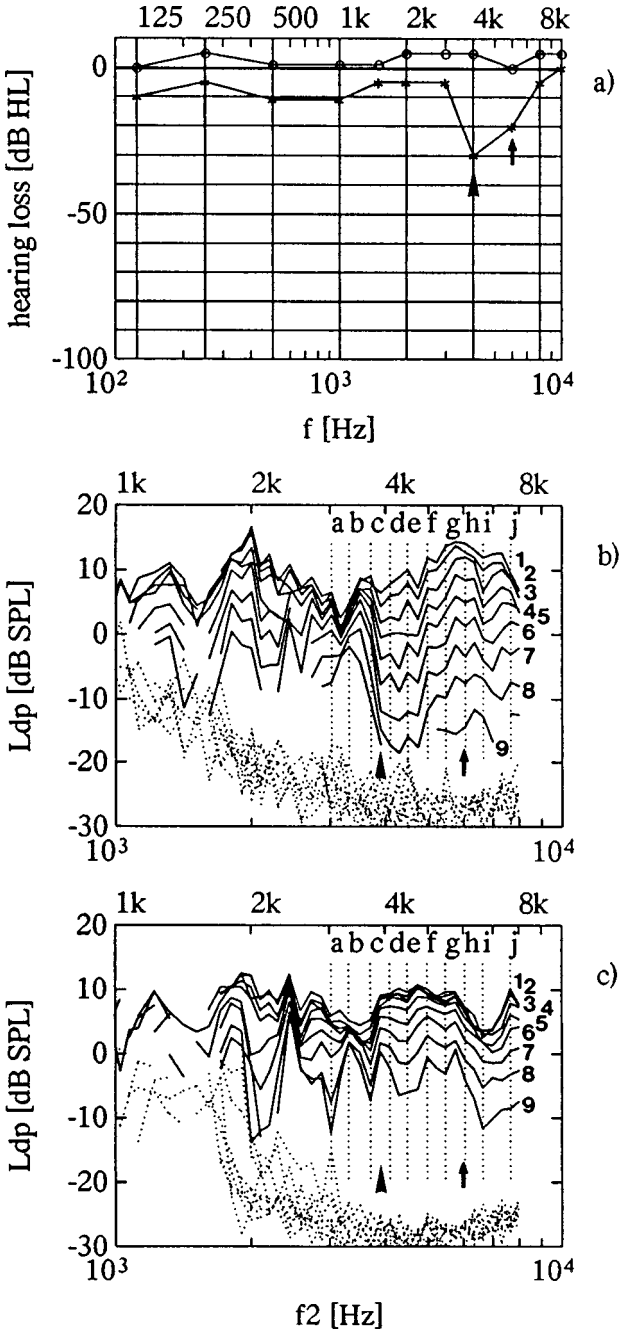

FIG. 1. Audiograms (a) and DP grams (S/N>6 dB) in one ear during (b) acute acoustic trauma and tinnitus and (c) following recovery at different primary tone levels from $L2=60$ to 20 dB SPL, in 5-dB steps, with $L1=0.4L2+39$ dB (1–9). Arrows indicate the frequency range of maximum hearing loss and tinnitus, respectively.

differential sensitivity. Specifically, at high primary tone levels, the DP level did not drop, but rather increase. Around the tinnitus [g through i in Fig. 1(b)] the DP levels were up to 10 dB higher than at the maximum hearing loss (d). Only with lowering primary tone level does the DP gram reflect the audiogram notch, which decreases by about 20 dB. Due to this, there was an obvious change in the DP growth behavior. In the region of normal hearing below 3 kHz, the DP grams are widely spaced at lower primary tone levels, but lay close together at the higher ones indicating compressive growth [Fig. 1(b)]. In the notch region and around the tinnitus, the DP grams are widely spaced and actually equidistant, revealing linearized growth. The difference between the highest and lowest DP levels equaled 30 dB. Three days after the acoustic trauma, the hearing had been completely restored and the tinnitus had disappeared [see audiogram in Fig. 1(a)]. In this state, the DP grams were found to be close together at higher primary tone levels and separated only at the lower ones within the entire frequency range, demonstrating normal nonlinear compressive growth with strong saturation at moderate primary tone levels [Fig. 1(c)]. The DP response now covered less than 20 dB. It should be emphasized that in this state the DP level was considerably lower around the tinnitus frequency (g through i) as compared to the pathological state.

The different DP growth behavior during acoustic trauma and after recovery could most clearly be seen in the I/O functions, plotting the DP level against $L2$ (Fig. 2). In the region of normal hearing (a through c and j) in both states the I/O functions were alike, having a steep slope (up to 1 dB/dB) in the lower primary tone level region and a flat run (as low as 0.1 dB/dB) in the upper one that is characteristic for normal hearing. This can be seen when comparing the individual data with the shaded area which indicate the range of $\pm$ standard deviation of the DP level of the normally hearing control group at the corresponding frequencies. In the notch region (d through f), the I/O functions during trauma (* symbols) and after recovery (o symbols) differed considerably. The DP losses during trauma occurred predominantly at the lowest stimulus levels. At $L2=25$ dB SPL, the DP level difference amounted to almost 20 dB (d). At the highest stimulus levels, at $L2=60$ dB SPL, however, the difference was minimum and amounted a tenth of that found at $L2=25$ dB SPL. Thus the DP growth became linearized during acoustic trauma revealing loss of compression. Note that the DP growth predominantly changed at primary tone levels above $L2=40$ dB SPL, where there was a steep slope during trauma and a shallow slope after recovery. Below $L2=40$ dB SPL, the respective I/O functions run almost parallel, the slopes of both being about 1 dB/dB [e.g., (e) in Fig. 2]. In the tinnitus region (g through i), the DP did behave differently. Above $L2=40$ dB SPL, the DP level were higher during trauma, the difference amounting to almost 10 dB. At lower primary tone levels, the DP level were either equal (i) or lower (h). Taking into account the amount of hearing loss around the tinnitus, these high DP levels are quite surprising and could result in incorrect conclusions about cochlear integrity. However, the steep I/O function unambiguously indicates the pathological state.

In order to quantify the DP growth, the slope s was calculated between $L2=40$ and $L2=60$ dB SPL, where there was a flat course in the normally hearing state and a steep one in the pathological state. Calculation of the slope s between 40 and 60 dB SPL was chosen because in that range normal and pathological DP growth did differ most. In Fig. 3 s is plotted as a function of $f2$ during trauma (a) and after recovery (b). Corresponding to the threshold run, the slope s increased rapidly on the low-frequency side of the notch, but gradually decreased on the high-frequency side. The DP level yields an ambiguous pattern at different primary tone

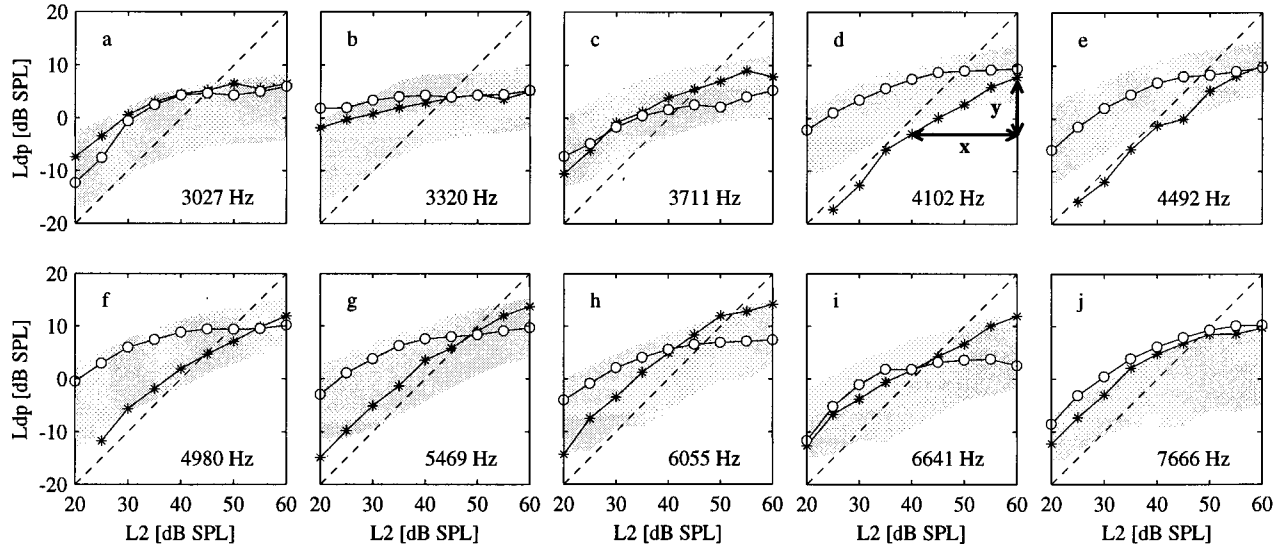

FIG. 2. DP I/O functions, plotting the DP level L_{dp} (S/N>6 dB) against the $L2$ primary tone level from the data in Fig. 1 at the specified frequencies. Different symbols identify the acoustic trauma condition (*) and the recovery state (○). In panel (d), y and x illustrate the calculation of the slope $s=y/x$ between $L2=40$ and 60 dB SPL. For comparison, the dashed line indicates 1-dB/dB slope. Shaded area in each panel indicates ranges of mean ± one standard deviation of the normally hearing subject sample at the corresponding frequencies.

levels. Thus the slope s reflected the threshold better than the DP level. Also, high slopes were found between 2 and 3 kHz, possibly revealing a disturbance that was not reflected in the behavioral audiogram. After recovery, the slope of all I/O functions became shallow [on average below 0.2 dB/dB, see Fig. 3(b)], demonstrating the conventional compressive growth of normal hearing function in the entire frequency range (compare also range of mean ± one standard deviation of the slope s across $f2$ in the normally hearing subject sample in Fig. 4, bottom most panel).

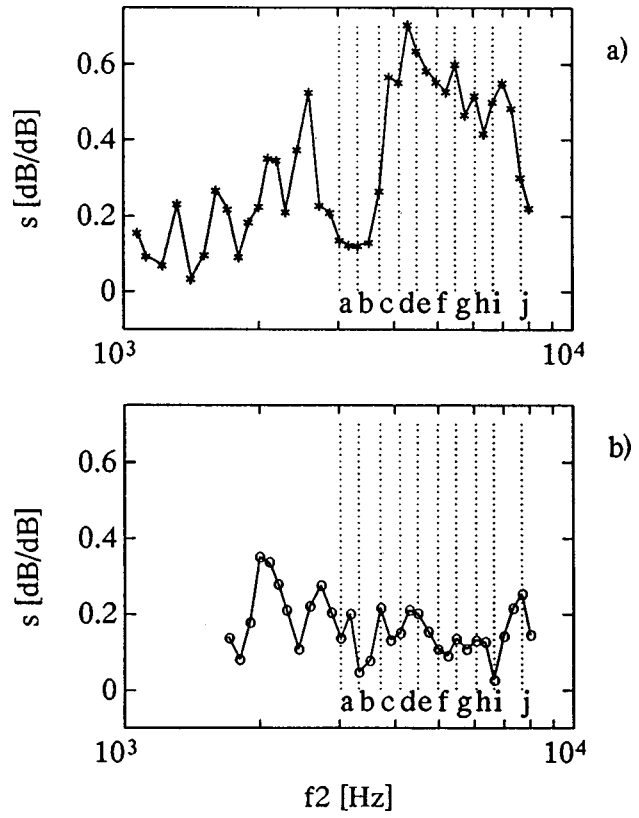

FIG. 3. The slope s of the DP I/O functions from the data of Fig. 2 across $f2$ frequency, (a) during acute acoustic trauma and tinnitus and (b) following recovery. Vertical dotted lines identify frequencies (a)–(j) in Figs. 1 and 2.

B. DP behavior in hearing loss ears with chronic tinnitus

The peculiar DP behavior observed around the tinnitus in the described case was found in 22 of the 39 chronic tinnitus ears as well. In the following, these are designated as high-DP-level tinnitus ears. In 17/39 ears, a decrease of the DP level with increasing hearing loss was evidenced similarly to the hearing loss ears without tinnitus (see Kummer *et al.*, 1998). These are further designated as low-DP-level tinnitus ears. The examples below give details on the DP growth behavior around the tinnitus in these two subgroups. Figure 4 summarizes the pure-tone threshold L_t, the DP grams at the different primary tone levels (from $L2=65$ dB SPL to $L2=20$ dB SPL), and the slope s in the selected patients (A through C). The shaded area represents the range of ± one standard deviation of the hearing threshold level L_t, the DP level L_{dp} at $L2=65$ dB SPL, and the slope s calculated from the 20 normally hearing ears.

1. High-DP-level tinnitus ears

Patient A has been suffering from tinnitus for two years, following a sudden hearing loss. He classified his tinnitus as being high pitched with a frequency around 6 kHz and a loudness of about 45 dB HL. Between 1 and 3 kHz, where the hearing threshold level L_t was within normal limits, the DP levels were unusually low. The DP grams at high primary tone levels, however, lay close together indicating normal compressive growth behavior. Above 3 kHz, where the threshold continuously increased up to 45 dB, the DP level rose by more than 10 dB, demonstrating a run that was actually inverse to that of the hearing threshold. That is, there

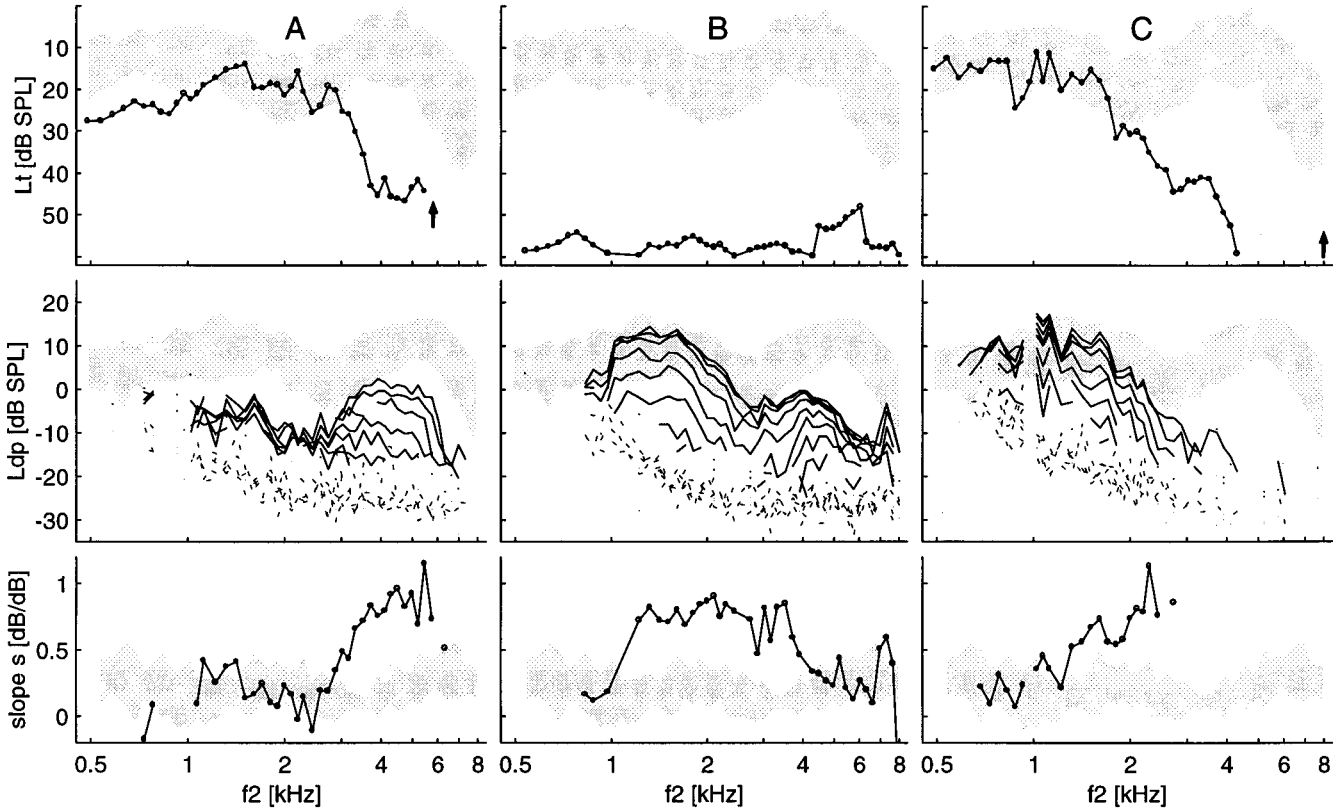

FIG. 4. Data from three ears (A–C) with cochlear hearing impairment and tinnitus, comparing the pure-tone threshold level L_t measured at $f2$ (upper panels) to the DP level L_{dp} (middle panels) at primary tone levels decreasing from $L2=65$ to 20 dB SPL and the slope s (lower panels). Shaded areas indicate ranges of mean ± one s.d. of the corresponding measures calculated from the normally hearing subject sample (for the DP level at $L2=65$ dB SPL only). A and B are examples from the high-DP-level tinnitus ears, C from the low-DP-level ears. Arrows indicate the frequency range of tonal tinnitus.

was an increase of the DP level with increasing hearing loss. Even at lower primary tone levels, the DP level did not decrease with increasing hearing loss. Only the growth behavior of the DP did correlate to the hearing threshold. With increasing hearing loss, the distance of the DP grams increased, demonstrating a linearized, i.e., pathological growth behavior. The slope s, which was within the normal ranges up to 3 kHz, rose considerably above where the hearing threshold started to increase and reached values of 1 dB/dB.

In patient B, suffering from Ménière's disease with a noiselike tinnitus and a flat hearing loss, the described peculiar DP behavior appeared almost over the entire frequency range. Despite the severe hearing loss of about 60 dB, DP could be recorded over the whole frequency range even at lower primary tone levels, down to $L2=40$ dB SPL. However, in contrast to normal, the DP grams were widely spaced manifesting the pathologically altered growth behavior. Correspondingly, the differences between the highest and lowest DP levels (up to 30 dB) significantly exceeded those found in the normally hearing ears [cf. Fig. 1(c)]. Between 1 and 4 kHz, the slope s considerably exceeded the normal limits and reached 1 dB/dB, while above 4 kHz and below 1 kHz, it remained within normal limits.

2. Low-DP-level tinnitus ears

Patient C was suffering from Ménière's disease with tinnitus and a high-frequency steep-sloping hearing loss up to 80 dB HL at 8 kHz (as revealed by the clinical audiogram, not shown here). The patient identified the tinnitus with a pitch of around 6 kHz and a loudness of 70 dB HL. In this case, the DP level decrease between 1 and 3 kHz corresponded to the increase of the hearing threshold, resembling the situation in the nontinnitus ears (see Kummer *et al.*, 1998). Most distinctly, the DP level decreased at lower primary levels, as indicated by the spread of the DP grams, turning the DP growth linearized. The slope s, which was within or slightly above the normal range below 1 kHz considerably rose with increasing hearing loss up to about 1 dB/dB.

3. DP behavior versus hearing loss

In the majority of low-DP-level tinnitus ears, the tinnitus appeared in frequency regions where the hearing loss exceeded 60 dB (as in case C in Fig. 4). In a minority of ears with hearing losses below 60 dB, it appeared in the frequency region where hearing was almost normal. Much more consistently, in the high-DP-level ears the tinnitus was mostly associated to frequency regions with hearing losses below 60 dB HL, although greater hearing losses appeared. Here, the observed uncommon DP behavior concerned the frequency range of the tinnitus, being noisy-like (case B in Fig. 4) or tonal (case A in Fig. 4). For hearing losses below 60 dB HL, the tinnitus mostly appeared at the frequency of

the maximum hearing loss (cf. case A in Fig. 4) or at the high-frequency side of the notch [cf. Fig. 1(a)].

C. The correlation of DP level and DP slope to the hearing threshold

1. Pooled data

To demonstrate the scatter and the trends, the DP level L_{dp} and the DP slope s were pooled and plotted against the pure-tone threshold level L_t in Fig. 5, divided into (a) the high- and (b) the low-DP-level ears. The curves (with the exception of those in the bottom most panel) represent 101-point moving averages derived from the data. The DP level and its moving average for $L2=60$ dB SPL are plotted in the upper most panel. The panel below illustrates the moving averages at all primary tone levels from $L2=65$ dB SPL to $L2=20$ dB SPL. The third and the fourth panel from top demonstrate the DP growth. The third panel shows the scatter and the moving average of the slope s of the DP I/O functions calculated between $L2=40$ and 60 dB SPL, the forth panel the moving averages of the instantaneous slopes of the DP I/O functions, calculated between $L2=20$ and 25 (indicated as $L2=20$), 30 and 35, 40 and 45, 50 and 55, and 60 and 65 dB SPL (indicated as 60), respectively, following from top to bottom. The bottom most panel shows the DP I/O functions at different pure-tone threshold levels from $L_t=10$ to 50 dB SPL in 10-dB steps derived from the moving averages of the DP level at the different primary tone levels (second panel from top).

Despite the wide scatter, the characteristics found in the reported individual data sets do reappear in the pooled data. In the high-DP-level ears, the weak correspondence or even inverse relationship of the DP and pure-tone threshold level is manifested in the nonmonotonic course of the moving averages. Although first decreasing, the DP level increased at threshold levels around 30 dB SPL and decreased only with threshold levels above 40 dB SPL. This is in contrast to the low-DP-level ears, where a monotonic decrease of the DP level with increasing threshold level was found at pure-tone threshold levels above $L_t=30$ dB SPL. Despite this different behavior of the DP level the growth behavior was much more uniform. In both high- and low-DP-level ears, the slope s calculated between $L2=40$ and 60 dB SPL almost continuously increased with increasing pure-tone threshold level from about 0.2 to 0.7 dB/dB. In more detail, the instantaneous slopes of the I/O functions reflected the DP growth behavior. The instantaneous slope calculated between $L2=60$ and 65 dB SPL remained constant for pure-tone threshold levels below $L_t=40$ dB SPL being low (about 0.15 dB/dB) and thus reflecting saturation of the DP growth as found in the normally hearing ears. However, the instantaneous slopes calculated in the lower primary tone level regions continuously increased with increasing L_t indicating linearization of the DP growth with increasing hearing loss. With decreasing $L2$ the rate of increase of the instantaneous slopes became smaller (apart from the instantaneous slope calculated between $L2=40$ and 45 dB SPL in the low-DP-level ears). This demonstrates that the DP growth at low primary tone levels is hardly affected by the hearing loss. Largest rates, however, were achieved in the upper primary tone

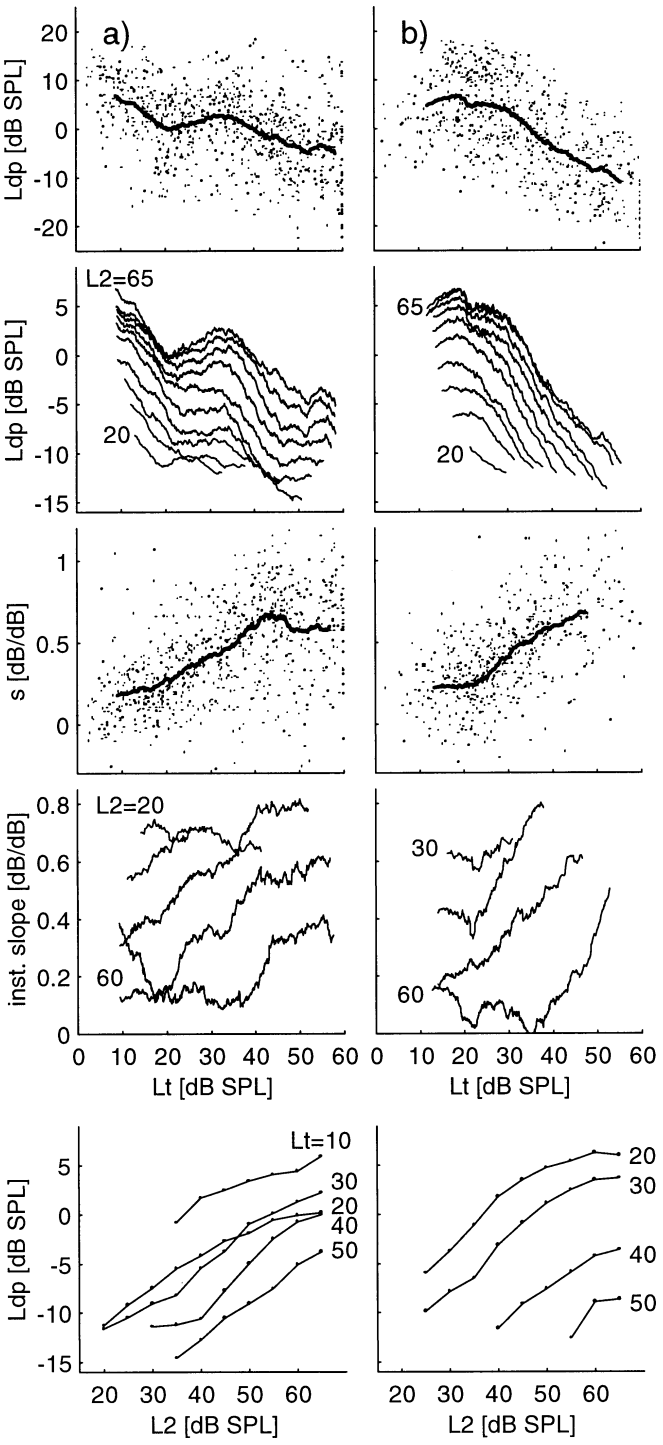

FIG. 5. Pooled data from (a) 22 high-DP-level and (b) 17 low-DP-level tinnitus ears. The top panel plots the DP level L_{dp} (S/N>6 dB) against threshold level L_t for $L2=60$ dB SPL. The bold line is the moving average. Below are shown corresponding moving averages at primary tone levels from $L2=65$ to 20 dB SPL, following from top to bottom in 5-dB steps. The third panel from top shows the slope s of the I/O functions calculated between $L2=40$ and 60 dB SPL and its moving average. The fourth panel from top shows the moving averages of the instantaneous slope of the DP I/O functions, calculated in a 5-dB ranges above $L2=20$, 30, 40, 50, and 60 dB SPL, respectively (from top to bottom). The moving averages were constructed by averaging the DP level or slope of 101 data points neighboring along the L_t scale, and stepwise moving this window along L_t. The bottom most panel shows the DP level L_{dp} as a function of $L2$ calculated from the moving averages (second panel from top) at different pure-tone threshold levels from $L_t=10$ to 50 dB SPL in 10-dB steps termed as derived DP I/O functions.

level regions, where the normal and the pathological DP growth differ most. The calculation of the slope s of the DP I/O functions between $L2=40$ and 60 dB SPL therefore appears to be a good compromise for assessing essential features of the DP growth.

The decrease of the DP level L_{dp} and the increase of the slope s of the DP I/O functions with increasing pure-tone threshold level L_t observed in the individual data in the nontinnitus region are also manifested in the pooled data [bottom most panel (b)]. The I/O function derived from the moving average of the DP level at $L_t=20$ dB SPL demonstrates nonlinear compressive growth with strong saturation in the upper primary tone level region that is typical for normal hearing as shown in the acoustic trauma ear after recovery (see Fig. 2). With increasing L_t the DP level decreased and the DP slope increased similar to that found in the individual cases [e.g., Fig. 2(d) and case C in Fig. 4]. In contrast, there is an inconsistency of the derived I/O functions in the high-DP-level ears [bottom most panel (a)] reflecting the uncommon growth behavior around the tinnitus frequency as observed in the individual cases (see Fig. 2, g–i and case A in Fig. 4). The I/O functions derived at $L_t=10$ and 20 dB SPL showed nonlinear compressive growth with a flat course at high $L2$. However, at $L_t=30$ dB SPL there was a steep I/O function without saturation and the DP levels in the upper primary tone level region were much higher than those at $L_t=20$ dB SPL (note crossing curves at $L_t=20$ and 30 dB SPL). This behavior is just the same observed in the individual case when comparing the I/O functions of normal hearing with those around the tinnitus frequency during acute trauma (see Fig. 2, g–i). The I/O functions at $L_t=40$ and 50 dB SPL were also steep but their DP levels were much higher compared to those found in the low-DP-level ears. Once more, this makes clear the different DP behavior in tinnitus and nontinnitus ears.

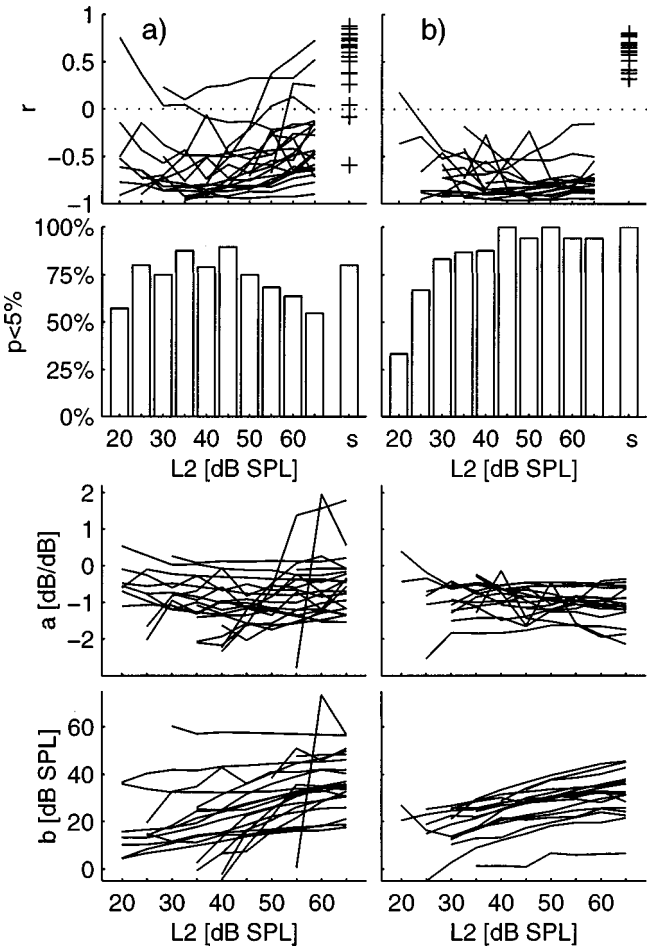

FIG. 6. Results of linear regression analysis of individual data sets from (a) 22 high-DP-level and (b) 17 low-DP-level tinnitus ears. Upper panels show the correlation coefficients r of the DP level L_{dp} at the different $L2$ levels and the slope s of the I/O functions to the pure-tone threshold L_t. The bar plots indicate the percentage significant correlations ($p<0.05$) and the lower panels the coefficients a,b of regression lines $L_t=aL_{dp}+b$, at the different $L2$ levels.

2. Linear regression analysis of individual data sets

Figure 6 and Tables I and II summarize the results of linear regression analysis performed on the individual data sets from the 22 high-DP-level [Fig. 6(a), Table II] and 17 low-DP-level tinnitus ears [Fig. 6(b), Table II], providing the correlation coefficients r at the different $L2$ levels and for the slope s, the percentage significant correlations ($p<0.05$) and the coefficients a, b of the regression lines $L_t=aL_{dp}+b$, $L_t=as+b$ and a', b' of the regression lines $L_{dp}=a'L_t+b'$, $s=a'L_t+b'$, respectively.

The correlation of the DP level strongly depended on the primary tone level in the high-DP-level ears [Fig. 6(a), Table I]. At high primary tone levels, the correlation was relatively weak and even positive coefficients of the regression lines occurred, as may be expected from the weak correspondence or even inverse course of the DP and the threshold level in individual cases (e.g., case A in Fig. 4) and the nonmonotonic run of the averaged DP-to-threshold relationship [Fig. 5(a)]. With decreasing $L2$ to 40 dB SPL, however, the average correlation coefficients r doubled and the number of significant correlations correspondingly increased from about 50% to about 85%, reflecting the greater sensitivity of the DP at lower primary tone levels. The coefficients a' of regressions lines $L_{dp}=a'L_t+b'$, that allow to infer what drop in DP level may be expected for a given threshold elevation, grow from about 0.2 dB/dB to 0.55 dB/dB with decreasing $L2$ from 65 to 35 dB SPL. Obviously, this reflects the nonmonotonic DP-to-threshold relationship at high primary tone levels and the disappearance of this bump with lowering primary tone level. In the low-DP-level ears [Fig. 5(b) and Table Ib], there was a negative correlation of the DP level to the hearing threshold, which was less dependent on the primary tone level. The correlations were maximum over a range of high-to-medium primary tone levels down to $L2=45$ dB SPL, where virtually all ears had significant correlations ($p<0.05$). The considerable scatter of the regression coefficients b reflects the great inter-individual variability of the DP level, that is maximal in the high-DP-level ears.

The correlation of the slope s to the hearing threshold was positive apart from one exception in the high-DP-level ears. It was best in the low-DP-level ears, where all ears showed significant correlations. In the high-DP-level ears, only 75% showed significant correlations. When comparing to the correlation of the DP level at $L2=40$ and 60 dB SPL, however, the slope s did better correlate in 5 and 10/22

TABLE I. The correlation of the DP level L_{dp} at the different stimulus intensities and the slope s to the pure-tone threshold level L_t in 22 high-DP-level ears. The table gives the average correlation coefficient $r(\pm$s.d.), the number n of correlation coefficients calculated (on a basis of at least 10 data points), the number of positive and negative correlation coefficients at a significance level of $p<5\%$ and $p>5\%$, respectively and the average ($\pm$s.d.) coefficients a, b and a', b' of regression lines $L_t=aL_{dp}+b$, $L_t=as+b$, and $L_{dp}=a'L_t+b'$, $s=a'L_t+b'$, respectively.

$L1,L2$ [dB SPL]	$r\pm$s.d.	n	$p<0.05$ $r<0/r>0$	$p>0.05$ $r<0/r>0$	$a\pm$s.d.	$b\pm$s.d.	$a'\pm$s.d.	$b'\pm$s.d.
65, 65	-0.321 ± 0.42	22	12/2	7/1	-0.54 ± 0.75	36.8 ± 11.2	-0.19 ± 0.40	4.1 ± 20.1
63, 60	-0.378 ± 0.40	22	14/2	4/2	-0.56 ± 0.92	36.5 ± 13.2	-0.23 ± 0.34	5.1 ± 16.2
61, 55	-0.470 ± 0.36	22	15/2	4/1	-0.80 ± 0.84	32.1 ± 13.1	-0.30 ± 0.34	5.8 ± 16.2
59, 50	-0.571 ± 0.32	20	15/1	4/0	-0.95 ± 0.52	29.3 ± 11.1	-0.37 ± 0.35	6.7 ± 15.9
57, 45	-0.624 ± 0.30	19	17/0	1/1	-1.05 ± 0.55	25.0 ± 12.5	-0.42 ± 0.34	6.4 ± 14.8
55, 40	-0.656 ± 0.34	19	15/0	3/1	-1.09 ± 0.74	21.3 ± 15.7	-0.46 ± 0.35	5.1 ± 14.0
53, 35	-0.660 ± 0.33	16	14/0	0/2	-0.94 ± 0.65	22.0 ± 14.7	-0.54 ± 0.34	6.5 ± 11.5
51, 30	-0.554 ± 0.36	12	19/0	1/2	-0.65 ± 0.47	23.2 ± 15.6	-0.53 ± 0.43	3.3 ± 12.7
49, 25	-0.548 ± 0.39	10	8/0	1/1	-0.79 ± 0.69	17.8 ± 10.9	-0.46 ± 0.42	3.0 ± 7.8
47, 20	-0.388 ± 0.56	7	4/1	2/0	-0.43 ± 0.52	17.3 ± 13.6	-0.37 ± 0.71	-4.6 ± 17
slope s	0.501 ± 0.36	20	1/16	1/2	19.9 ± 13.7	24.9 ± 15.1	0.01 ± 0.01	0.06 ± 0.7

cases, respectively. In the low-DP-level ears, better correlations occurred in 2 and 4/17 ears, respectively. This indicates that the slope s generally may contribute to the assessment of cochlear function. Especially in the high-DP-level ears, where no clear relationship of the DP level to the threshold was found, the slope s may greatly contribute.

III. DISCUSSION

A. DP growth reveals different cochlear signal processing in impaired hearing with and without tinnitus

1. Assessment of OHC function in a wide dynamic range

Otoacoustic emissions were the first experimental indicators of amplification processes in the cochlea (Kemp, 1979). DPs are thought to arise due to the compressive nonlinearity of cochlear micromechanics, which has been described as a frequency selective process near the characteristic frequency of a particular place (Johnstone *et al.*, 1986; Ruggero and Rich, 1991a; Ruggero *et al.*, 1997). It is based on the precise functioning of OHCs and has been termed the cochlear amplifier (Davis, 1983). Characteristically, its gain is greatest at low, but strongly saturates starting at moderate stimulus levels. At low-to-moderate stimulus levels, DPs are thought to originate from OHCs, sharing their vulnerability to various interferences that reduce or destroy OHC function, as has been noted during administration of loop diuretics (Mills and Rubel, 1994, 1996; Whitehead *et al.*, 1992), chronic gentamicin poisoning (Brown *et al.*, 1989), acoustic overstimulation (Wiederhold *et al.*, 1986), and asphyxia and post-mortem (Lonsbury-Martin *et al.*, 1987; Norton and Rubel, 1990).

In the present study, DP growth functions were measured from close-to-threshold to moderate stimulus intensities ($20\leqslant L2\leqslant 65$ dB SPL). A stimulus paradigm, $L1=0.4L2+39$ dB, has been used that increases the primary tone level difference from high-to-low stimulus intensities. As discussed elsewhere (Kummer *et al.*, 1998), this paradigm accounts for unequal primary tone responses at the DP generation site, most probably at the $f2$ place (Kummer *et al.*, 1995). Basilar membrane data (Johnstone *et al.*, 1986; Robles *et al.*, 1986a, b; Robles *et al.*, 1991; Ruggero *et al.*, 1991a, b; Sellick *et al.*, 1982) indicate a higher threshold and less compressive growth of the amplification process for the $f1$ primary tone at the $f2$ site, compared to the $f2$ primary tone, which will have the lowest threshold and most compressive growth, being CF at this site. Accounting for these

TABLE II. The correlation of the DP level L_{dp} at the different stimulus intensities and the slope s to the pure-tone threshold level L_t in 17 low-DP-level tinnitus ears. The table gives the average correlation coefficient $r(\pm$s.d.), the number n of correlation coefficients calculated (on a basis of at least 10 data points), the number of positive and negative correlation coefficients at a significance level of $p<5\%$ and $p>5\%$, respectively and the average ($\pm$s.d.) coefficients a, b and a', b' of regression lines $L_t=aL_{dp}+b$, $L_t=as+b$, and $L_{dp}=a'L_t+b'$, $s=a'L_t+b'$, respectively.

$L1,L2$ [dB SPL]	$r\pm$s.d.	n	$p<0.05$ $r<0/r>0$	$p>0.05$ $r<0/r>0$	$a\pm$s.d.	$b\pm$s.d.	$a'\pm$s.d.	$b'\pm$s.d.
65, 65	-0.744 ± 0.19	17	16/0	1/0	-1.07 ± 0.50	31.6 ± 9.8	-0.62 ± 0.36	20.5 ± 14.5
63, 60	-0.757 ± 0.18	17	16/0	1/0	-1.07 ± 0.45	30.9 ± 9.1	-0.63 ± 0.32	20.4 ± 13.7
61, 55	-0.791 ± 0.15	17	17/0	0/0	-1.02 ± 0.35	29.4 ± 8.7	-0.71 ± 0.35	21.8 ± 14.6
59, 50	-0.783 ± 0.19	17	16/0	1/0	-0.98 ± 0.35	28.0 ± 8.3	-0.72 ± 0.38	21.1 ± 14.6
57, 45	-0.781 ± 0.14	17	17/0	0/0	-1.02 ± 0.43	25.5 ± 8.7	-0.71 ± 0.35	19.0 ± 13.6
55, 40	-0.748 ± 0.21	16	14/0	2/0	-0.88 ± 0.42	23.0 ± 8.3	-0.73 ± 0.35	17.5 ± 13.9
53, 35	-0.693 ± 0.22	15	13/0	2/0	-0.86 ± 0.45	19.8 ± 7.9	-0.64 ± 0.34	12.4 ± 12.2
51, 30	-0.714 ± 0.18	12	10/0	2/0	-0.96 ± 0.45	18.2 ± 7.5	-0.62 ± 0.33	9.6 ± 11.8
49, 25	-0.632 ± 0.34	6	4/0	2/0	-0.94 ± 0.84	15.6 ± 11.1	-0.50 ± 0.35	4.5 ± 12.5
47, 20	-0.318 ± 0.47	3	1/0	1/1	-0.45 ± 0.84	16.4 ± 13.4	-0.23 ± 0.27	-7.7 ± 8.2
slope s	0.625 ± 0.14	17	0/17	0/0	24.2 ± 6.8	19.7 ± 7.4	0.02 ± 0.01	-0.12 ± 0.3

differences, the offered paradigm is expected to result in equal primary tone responses locally at the $f2$ site. We suggest that this allows to better examine the cochlear amplification process. Thus considering the DP growth behavior one can infer the OHC function at the $f2$ place.

Indeed, the strongly compressive DP growth in normal hearing closely reflects saturation of the active cochlear processes starting from moderate stimulus levels. This is in contrast to the mostly linear DP growth that appears when using equal primary tone levels which showed saturation, if ever, at high stimulus levels above 60 dB SPL (Gaskill and Brown, 1990; Lonsbury-Martin *et al.*, 1991; Popelka *et al.*, 1993). The novel paradigm offers obvious advantages over the conventional $L1=L2$ paradigm for assessing OHC impairments, considerably extending the potential stimulus level range toward hearing threshold. Higher DP levels allow detection of DP changes in the low primary tone level region than may be observed with the equilevel paradigm, where DP level and correspondingly signal-to-noise ratio much more rapidly decreases with decreasing primary tone level. For a more gradual assessment of OHC dysfunction, and the detection of minute changes, the presented paradigm seems to be of particular benefit. The significance of an appropriate stimulus paradigm for a more sensitive detection of subtle cochlear pathology has already been emphasized in animal DP studies (Whitehead *et al.*, 1995).

The DP growth behavior in the low-DP-level tinnitus ears reflects physiological characteristics and pathological changes attributed to the cochlear amplifier as has already been observed in animal DP data documenting that the cochlear mechanical response becomes linear with significant pathology (e.g., Mills *et al.*, 1993).

2. Nonuniform DP behavior in tinnitus

The findings in this study, which look at the OHC function in tinnitus ears across a wide stimulus intensity range appear to contribute to the understanding of the pathophysiology of tinnitus. We failed to find a uniform DP behavior in the tinnitus ears tested. One group of them, the low-DP-level ears, did behave like the nontinnitus ears (see Kummer *et al.*, 1998). In this subgroup, there was a congruent relationship between DP and hearing threshold, i.e., a decrease of DP level and an increase of the slope of the DP I/O functions with increasing hearing loss. This points to a OHC malfunction as a potential cause of the observed hearing loss, decreasing the gain of the cochlear amplifier and thus diminishing low-level responses and hearing sensitivity. Thus we speculate that in the low-DP-level ears the underlying cochlear impairment is similar to that in nontinnitus ears, and suggest the tinnitus not to be generated on the OHC level.

The other group of the tinnitus ears, the high-DP-level ears, did show an opposite DP behavior. Here, despite severe hearing loss, high DP levels were found, especially at high primary tone levels. In these ears, there was a much poorer or even inverse relationship of the DP to the hearing threshold level around the tinnitus frequency. The divergent relationship between DP and hearing threshold appears to indicate a more complex cochlear impairment pattern, making a general interpretation difficult. From high emission levels, OHCs are obviously functioning. Despite the high DP levels, however, the linearized DP growth indicates OHC malfunction. Apparently, impaired OHCs seem to produce unusually high mechanical distortion when stimulated by high-level stimuli as happens in overmodulated technical systems during signal clipping. In the acoustic trauma ear described (Fig. 2) the speculated overmodulation probably happened in the acute period, where the DP level was 10 dB higher as compared to that after recovery. Also, in the chronic tinnitus ear, despite the 40-dB hearing loss, the DP level was 15 dB higher in the tinnitus frequency region than in the normal hearing region (case A in Fig. 4). The uncommon DP behavior around the tinnitus frequency is also reflected in the inconsistency of the I/O functions derived from the pooled data [Fig. 5(a), bottom most panel].

Thus OHC hyperactivity may be postulated in the high-DP-level tinnitus ears. Whereas in the low-DP-level tinnitus ears OHC dysfunction may decrease mechanical sensitivity, resulting in hearing loss, in the high-DP-level tinnitus ears partial OHC impairments may cause abnormal mechanical distortion obstructing the perception of sound. Hence, just discrimination but not sensitivity might be affected in these ears. If the proposed OHC hyperactivity results in an improper excitation of the inner hair cells, then impaired OHCs might be the immediate cause of the tinnitus.

The tinnitus associated DP features have distinctly been manifested in the acoustic trauma ear reported (Figs. 1–3), where DPs have been measured in acute acoustic trauma and after recovery, the latter condition serving as an intraindividual ''control.'' Corresponding to the audiogram, the hearing loss was most obvious and quantitatively reflected in the decrease of DP level at the lower but not at the higher stimulus levels. At higher primary tone levels the DP level was only slightly affected in the region of maximum hearing loss, while noticeably increased in the tinnitus region. Thus in both cochlear regions a loss of compression of the cochlear amplifier is suggested. The compressive DP growth, observed in normal hearing regions and in all regions after recovery, we interpret as evidence of the physiological OHC function with nonlinear gain of cochlear active processes. Decreases of the DP level, which occurred predominantly at low stimulus levels and linearized DP growth, could correspondingly be explained as a result of disturbances of OHC function, leading to a loss of gain and causing the elevation of the hearing threshold. In the tinnitus frequency region, smaller DP losses at low stimulus levels appear to indicate minor violation of OHC function, corresponding to the smaller hearing loss and consistent with the commonly observed behavior. However, at high primary tone levels the DP level exceeded the normal limits, possibly revealing reinforced distortion within cochlear micromechanics. High emission levels and steep I/O functions can be interpreted as a reflection of missing saturation of the active processes, due to an immediate structural OHC damage or improper function of the mechanisms controlling OHCs.

The threshold-uncorrelated behavior of the DP level at high primary tone levels was observed in 22/39 tinnitus ears in regions of hearing loss with associated tinnitus. There was no consistent relationship between the DP level and the hear-

ing threshold at either the high or low primary tone levels. Despite increasing hearing losses, the DP level at high primary tone levels could increase (e.g., case A in Fig. 4) or not being correlated with the pure-tone threshold at all (e.g., case B in Fig. 4). Even at lower stimulus intensities the DP level course followed the hearing threshold only in single cases, but often did not (cases A, B in Fig. 4). This also appeared in the pooled data in the form of the nonmonotonic run of the DP level across hearing threshold and the crossing I/O functions derived from the moving averages of the DP level [Fig. 5(a)]. Compared to the DP level, the DP growth does more consistently indicate cochlear pathology, matching the course of the hearing threshold (e.g., case A in Fig. 4).

The frequency range of the threshold-uncorrelated DP behavior appeared to be related to the pitch of the tinnitus. It was narrow and matched to the pitch of the tinnitus in cases of tonelike tinnitus (case A in Fig. 4), but being broadband in cases of noisy tinnitus (case B in Fig. 4). This favors the idea of a peripheral involvement of the tinnitus producing mechanisms and supports the concept that just the extent of cochlear impairment defines the pitch of the tinnitus (Tonndorf, 1980). Abnormal high DP levels and steep I/O functions mostly appeared in tinnitus ears where the tinnitus appeared in regions of low-to-moderate hearing losses. This is clearly documented in the bump of the moving averaging curves around 30–40 dB pure-tone threshold levels and the inconsistency of the derived I/O functions [Fig. 5(a)]. Since OHCs are essential just for low-level signal processing this observation supports the idea of the involvement of OHCs in tinnitus generation.

3. Tinnitus correlates

The mechanisms underlying the assumed cochlear hyperactivity as a potential source of tinnitus may be both structural or functional and should be reversible. Structural changes may relate to partial OHC impairments. The effects of partial OHC dysfunction on basilar membrane and neural tuning are well documented in animal studies (Murugasu and Russell, 1995; Liberman and Dodds, 1984). Isolated OHCs perfused with salicylate solution have shown a reversible reduction in the turgidity (Shehata *et al.*, 1991) and an altered axial stiffness and electromotile force generation (Russell and Schauz, 1995). Administration of salicylate is reported to either decrease or increase cochlear microphonics, DPs and spontaneous discharging rate of eighth nerve fibers (Brown *et al.*, 1993; Evans and Borerwe, 1982; Fitzgerald *et al.*, 1993; Kössl, 1992; Stypulkowsky, 1990) and to induce tinnitus in human (Boetcher and Salvi, 1991). Hyposmotic induced swelling of OHCs has been shown to result in an increase in magnitude and gain of their electromotility (Sziklai and Dallos, 1997) and may be derived from alteration in the turgor of OHCs and their hydraulic skeleton (Brownell, 1990). Swelling of OHCs might have pathological consequences in cochlear hearing impairment. Since no chemical agents are necessary to induce these functional and structural changes, swelling-induced alterations in the electromotile performance of OHCs might be a pathological correlate of the tinnitus in acoustic trauma ears. Thus disturbances in the electromechanical feedback might enhance mechanical distortions that can generate both abnormal DP and tinnitus.

Abnormal functioning of the cochlear efferents could also be related to tinnitus generation (Jastreboff and Hazell, 1993). Interestingly, in noise-induced tinnitus ears, compared to nontinnitus ears, TEOAEs were less suppressible by contralateral white noise or even increased, what was interpreted as efferent dysfunction and hyperactivity of OHCs (Attias *et al.*, 1996). Supposing the efferent system controls OHC function, a pathological dysfunction of the efferents could lead to mechanical overstimulation of OHCs resulting in tinnitus.

The efferent improper control and OHC dysfunction may also arise as secondary change following a non-OHC cochlear lesion, when assuming that OHC function is efferently modulated in a feedback loop. It was shown in DP studies on cats that just with the presentation of the primary tones the efferents are strongly activated resulting in complex changes of the DP level with both suppression and enhancement at different primary tone levels (Liberman *et al.*, 1996). Given a primary lesion at a processing stage central of the OHC, e.g., at the inner hair cells, a change of OHC function may arise from deafferentiation. In this sense, high DP levels despite considerable hearing loss and linearized DP growth as observed in this study might as well be interpreted that the hearing loss arises from a lesion central from the OHC, e.g., the inner hair cells and OHC function is only functionally changed through opening of the afferent part of the feedback loop that control OHC function and saturation of the active cochlear processes.

B. Relation of DP to hearing threshold

Earlier, only a weak correlation between DP level and pure-tone threshold has been reported in humans, apparently limiting the clinical application of DPs for the prediction of the hearing threshold (Avan and Bonfils, 1993; Gorga *et al.*, 1993; Kimberly and Nelson, 1989; Lonsbury-Martin and Martin, 1990; Lonsbury-Martin *et al.*, 1993; Martin *et al.*, 1990; Nelson and Kimberly, 1992). The findings of the present study contribute to the understanding of this weak correlation, measuring high-resolution DP and pure-tone threshold with the same into-the-ear probe and applying a stimulus paradigm, which is basically different from those in the literature, where equilevel primary tones or a constant $L1-L2$ difference were used. Stimulus level settings that account for the nonlinear interaction of the primary tone on the DP generation site by continuously increasing $L1-L2$ with decreasing stimulus intensity as used in this study, allow recording of DPs at considerably lower primary tone levels. Focusing on the behavior of the DP in tinnitus ears, which represents a majority of ears undergoing DP testing in a clinical setting, it was found that in individual ears both strong correlations occur but as well weak correlations need to be expected. Strong correlations were found in 17/39 of the ears tested, refered to as the low-DP-level tinnitus ears. In these ears, the DP level monotonically decreased with increasing threshold level and significant negative correlations occurred virtually in all ears at medium to high primary tone levels ($45 \leqslant L2 \leqslant 65$ dB SPL), similar to the behavior in

nontinnitus ears in which DP and hearing threshold were recorded in the same manner (Kummer *et al.*, 1998). With lowering primary tone levels, the sensitivity of the DP to hearing loss distinctly increased. These observations thus confirm previous findings indicating that low-level DPs are more sensitive than high-level DPs to subtle cochlear pathology (Wiederhold *et al.*, 1986; Brown *et al.*, 1989; Norton and Rubel, 1990; Whitehead *et al.*, 1992; Mills *et al.*, 1993; Mills and Rubel, 1994). Most obviously, this appeared in the relationship of the hearing threshold and slope s of the I/O functions, calculated between $L2=40$ and 60 dB SPL, which quantifies the growth behavior and differential sensitivity of the DP. With the increasing hearing threshold from 20 to 50 dB SPL, the average slope s increased by 0.5 dB/dB, from about 0.2 to 0.7 dB/dB [Fig. 5(b)]. Since s was calculated over a 20-dB primary tone level range between $L2=40$ and 60 dB SPL, this 0.5-dB/dB increase indicates that the DP level at $L2=40$ dB SPL decreased on average by some 10 dB more than at $L2=60$ dB SPL. Considering that the DP level at $L2=60$ dB SPL decreased by on average 18 dB in this 30-dB range ($a'=0.6$ dB/dB, Table I), lowering primary tone levels from $L2=60$ dB SPL by 20 dB thus may be expected to considerably increase changes in DP level with hearing loss, by more than 50%. The sensitivity of DP testing thus may be considerably improved. Limitations of any threshold prediction, however, arise from the interindividual variability of the DP level, which is expressed in the great scatter of the regression coefficients b, b' (Table I).

In a second group of ears (22/39), that were referred to as high-DP level ears, high DP levels occurred despite considerable hearing losses and poor or even inverse correlations of the DP level and the hearing threshold were found, especially at high primary tone levels. The average relationship between DP level and hearing threshold was clearly nonmonotonic at high primary tone levels, with an increase of the DP level at moderate hearing losses around 35 dB SPL [Fig. 5(a)]. In this region, the DP level thus is ambiguous: Sharing two threshold levels, the DP level alone may clearly be an even misleading measure. Besides the great interindividual variability of the DP level, this ambiguity compromises the prediction of the hearing threshold from the sole DP level. Only with decreasing primary tone levels did a better correlation to the hearing threshold appeared. With lowering $L2$ from 65 to 35 dB SPL, the DP-to-threshold correlation distinctly improved. Significant correlations increased from about 50% to about 85% and the average regression coefficients a' ($Ldp=a'L_t+b'$) and the correlation coefficients r about doubled.

Much more uniform, however, was the relationship of the DP growth behavior to the hearing threshold. In both groups, the DP growth linearized with increasing hearing loss. Significant correlations of the slope s to the hearing threshold were found in all low-DP-level ears and about three-fourths of the high-DP-level ears. Compared to the correlation of the DP level at $L2=40$ and 60 dB SPL, respectively, the slope s correlated better in 5 and 10/22 of the high-DP-level ears and in 2 and 4/17 of the low-DP-level ears. Thus a relative measure as the slope of the DP I/O functions may become a valuable additional parameter contributing to the prediction of the hearing threshold, especially in tinnitus ears where the DP level weakly correlates.

C. Conclusions

Accepting the OHC to be the source of DPs, our findings suggest that at least in a particular subgroup of the tinnitus patients the tinnitus may involve basic changes in signal processing on the OHC level.

The observed dual DP growth behavior in tinnitus ears proposes two different cochlear impairment patterns. In those ears, where the DP level decreases and the slope of the DP I/O function increases with increasing hearing loss, sensitivity and tuning of the cochlear amplifier seem to be diminished. It is assumed that in this cases mechanical distortion of OHCs is not involved in tinnitus generation. In those ears where despite growing hearing loss the DP level increases, predominantly when elicited at high primary tone levels, a peculiar impairment in OHC micromechanics appears to generate reinforced distortion that gives rise to the tinnitus. The abnormal mechanical distortion in the organ of Corti micromechanics manifested in the DP growth behavior seems to obstruct the perception of sound. Thus discrimination but not sensitivity is affected. In these ears, partial OHC impairment is assumed to violate the amplification process and thus initiate an abnormal sensory transduction in the inner hair cells. Mechanical mismatch of outer and inner hair cells is therefore supposed to be one potential correlate of tinnitus of cochlear origin.

Since the sensitivity of the DP considerably increases with lowering $L2$, DP measurement should routinely be performed both at high and at low primary tone levels. With the stimulus paradigm $L1=0.4L2+39$ dB used, which accounts for the nonlinear interaction of the two primaries at the DP generation site, DPs can be recorded over a wide primary tone level range. For assessment of OHC function, not only the DP level but also the DP growth behavior should be taken into account. In cases where the DP level may be assessed as normal due to the great scatter of the reference range, cochlear pathology can much more accurately be determined by the DP I/O functions.

ACKNOWLEDGMENTS

We greatly appreciate the discussions and valuable comments on the manuscript of S. Kevanishvili and M. Kössl. The critical remarks of the anonymous reviewers of this article are also greatly acknowledged. This work was supported by the Deutsche Forschungsgemeinschaft within the SFB 204 ''Gehör.''

Allen, J. B., Shaw, G., and Kimberley, B. P. (**1995**). ''Characterization of the nonlinear ear canal impedance at low sound levels,'' Abstract No. 757 of the Eighteenth Annual Mid-Winter Research Meeting of the Association for Research in Otolaryngology.

Attias, J., Bresloff, I., and Furman, V. (**1996**). ''The influence of the efferent auditory system on otoacoustic emission in noise induced tinnitus: Clinical relevance,'' Acta Oto-Laryngol. **116**, 534–539.

Avan, P., and Bonfils, P. (**1993**). ''Frequency specificity of human distortion product otoacoustic emissions,'' Audiology **32**, 12–26.

Boetcher, F. A., and Salvi, R. J. (**1991**). ''Salicylate ototoxicity: Review and synthesis,'' Am. J. Otolaryngol. **12**, 33–47.

Brown, A. M., McDowell, B., and Forge, A. (**1989**). ''Acoustic distortion products can be used to monitor the effects of chronic gentamycin treatment,'' Hearing Res. **42**, 143–156.
Brown, A. M., Williams, D. M., and Gaskill, S. A. (**1993**). ''The effects of aspirin on cochlear mechanical tuning,'' J. Acoust. Soc. Am. **93**, 3298–3307.
Brownell, W. E. (**1990**). ''Outer hair cell electromotility and otoacoustic emissions,'' Ear Hear. **11**, 82–92.
Dallos, P. (**1992**). ''The active cochlea,'' J. Neurosci. **12**, 4575–4585.
Davis, H. (**1983**). ''An active process in cochlear mechanics,'' Hearing Res. **9**, 79–90.
Evans, E. F., and Borerwe (**1982**). ''Ototoxic effects of salycilates on the responses of single cochlear nerve fibers and cochlear potentials,'' Br. J. Audiol. **16**, 101–108.
Fitzgerald, J. J., Robertson, D., and Johnstone, B. M. (**1993**). ''Effects of intra-cochlear perfusion of salycilates on cochlear microphonic and other auditory responses in the guinea pig,'' Hearing Res. **67**, 147–156.
Gaskill, S. A., and Brown, A. M. (**1990**). ''The behaviour of the acoustic distortion product, $2f_1-f_2$, from the human ear and its relation to auditory sensitivity,'' J. Acoust. Soc. Am. **88**, 821–839.
Gorga, M. P., Neely, S. T., Bergmann, B., Beauchaine, K. L., Kaminski, J. K., Peters, J., and Jestead, W. (**1993**). ''Otoacoustic emissions from normal hearing-hearing and hearing-impaired subjects: Distortion product responses,'' J. Acoust. Soc. Am. **93**, 2050–2060.
Harris, F. P. (**1990**). ''Distortion-product otoacoustic emissions in humans with high frequency sensorineural hearing loss,'' J. Speech Hear. Res. **33**, 594–600.
Janssen, T., and Arnold, W. (**1995**). ''Growth functions of distortion product otoacoustic emissions in cochlear tinnitus,'' Otorhinolaryngol. Nova **5**, 127–144.
Jastreboff, P. J., and Hazell, J. W. P. (**1993**). ''A neurophysiological approach to tinnitus: Clinical applications,'' Br. J. Audiol. **27**, 7–17.
Johnstone, B. M., Patuzzi, R., and Yates, G. K. (**1986**). ''Basilar membrane measurements and the travelling wave,'' Hearing Res. **22**, 147–153.
Kemp, D. T. (**1979**). ''Evidence of mechanical nonlinearity and frequency selective wave amplification in the cochlea,'' Arch. Otorhinolaryngol. **22**, 437–455.
Kemp, D. T. (**1981**). ''Physiologically active cochlear micromechanics—One source of tinnitus,'' in *Tinnitus*, edited by D. Evered and G. Lawrenson (Pitman, London), pp. 54–81.
Kemp, D. T. (**1982**). ''Cochlear echoes: Implications for noise-induced hearing loss,'' in *New Perspectives on Noise Induced Hearing Loss*, edited by R. P. Hamerik, D. Henderson, and R. Salvi (Raven, New York), pp. 189–207.
Kemp, D. T. (**1986**). ''Otoacoustic emissions, travelling waves, and cochlear mechanisms,'' Hearing Res. **21**, 95–104.
Kimberley, B. P., and Nelson, D. A. (**1989**). ''Distortion product emissions and sensorineural hearing loss,'' J. Otorhinolaryngol. **18**, 365–369.
Kössl, M. (**1992**). ''High frequency distortion products from the ears of two bat species, *Megaderma Lyra and Carollia Perspicillata*,'' Hearing Res. **56**, 156–164.
Kummer, P., Janssen, T., and Arnold, W. (**1995**). ''Suppression tuning characteristics of the $2f_1-f_2$ distortion-product otoacoustic emission in humans,'' J. Acoust. Soc. Am. **98**, 197–210.
Kummer, P., Janssen, T., and Arnold, W. (**1998**). ''The level and growth behavior of the $2f_1-f_2$ distortion product otoacoustic emission and its relationship to auditory sensitivity in normal hearing and cochlear hearing loss,'' J. Acoust. Soc. Am. **103**, 3431–3444.
Liberman, M. C., and Dodds, L. W. (**1984**). ''Single-neuron labeling and chronic cochlear pathology. III. Stereocilia damage and alterations of threshold tuning curves,'' Hearing Res. **16**, 55–74.
Liberman, M. C., Puria, S., and Guinan, Jr., J. J. (**1996**). ''The ipsilaterally evoked olivocochlear reflex causes rapid adaptation of the $2f_1-f_2$ distortion product otoacoustic emission,'' J. Acoust. Soc. Am. **99**, 3572–3584.
Lonsbury-Martin, B. L., Cutler, W. M., and Martin, G. K. (**1991**). ''Evidence for the influence of aging on distortion-product otoacoustic emissions in humans,'' J. Acoust. Soc. Am. **89**, 1749–1759.
Lonsbury-Martin, B. L., and Martin, G. K. (**1990**). ''The clinical utility of distortion-product otoacoustic emissions,'' Ear Hear. **11**, 144–154.
Lonsbury-Martin, B. L., McCoy, M. J., Whitehead, M. L., and Martin, G. K. (**1993**). ''Clinical testing of distortion-product otoacoustic emissions,'' Ear Hear. **1**, 11–22.
Lonsbury-Martin, B. L., Probst, R., Coats, A. C., and Martin, G. K. (**1987**). ''Acoustic distortion products in rabbits. I: Basic features and physiological vulnerability,'' Hearing Res. **28**, 173–189.
Martin, G. K., Ohlms, L. A., Franklin, D. J., Harris, F. P., and Lonsbury-Martin, B. L. (**1990**). ''Distortion product otoacoustic emissions: III. Influence of sensorineural hearing loss,'' Ann. Otol. Rhinol. Laryngol. **99**, 30–42.
Mills, D. M., and Rubel, E. D. (**1994**). ''Variation of distortion product otoacoustic emissions with furosemide injection,'' Hearing Res. **77**, 183–199.
Mills, D. M., and Rubel, E. D. (**1996**). ''Development of the cochlear amplifier,'' J. Acoust. Soc. Am. **100**, 428–441.
Mills, D. M., Norton, S. J., and Rubel, E. D. (**1993**). ''Vulnerability and adaption of distortion product otoacoustic emissions to endocochlear potential variation,'' J. Acoust. Soc. Am. **94**, 2108–2122.
Mitchell, C., Lilly, D. J., and Henry, J. (**1995**). ''Otoacoustic emissions in subjects with tinnitus and normal hearing,'' in *Proceedings of the 5th International Tinnitus Seminar*, edited by G. Reich and J. Vernon (Am. Tinnitus Association, Portland), pp. 180–185.
Murugasu, E., and Russell, I. J. (**1995**). ''Salicylate ototoxicity: The effects on basilar membrane displacement, cochlear microphonics, and neural responses in the basal turn of the guinea pig cochlea,'' Aud. Neurosci. **1**, 139–150.
Nelson, D. A., and Kimberley, B. P. (**1992**). ''Distortion-product emissions and auditory sensitivity in human ears with normal hearing and cochlear hearing loss,'' J. Speech Hear. Res. **35**, 1142–1159.
Norton, S. J., and Rubel, E. R. (**1990**). ''Active and passive ADP components in mammalian and avian ears,'' in *The Mechanics and Biophysics of Hearing*, edited by P. Dallos, C. D. Geisler, J. W. Matthews, M. A. Ruggero, and C. R. Steele (Springer-Verlag, Berlin), pp. 219–227.
Norton, S. J., Schmidt, A. R., and Stover, L. J. (**1990**). ''Tinnitus and otoacoustic emissions: Is there a link?'' Ear Hear. **11**, 159–166.
Popelka, G. R., Karzon, R. K., and Arjmand, E. M. (**1995**). ''Growth of the $2f_1-f_2$ distortion product otoacoustic emission for low level stimuli in human neonates,'' Ear Hear. **16**, 159–165.
Popelka, G. R., Osterhammel, P. A., Nielsen, L. H., and Rasmussen, A. N. (**1993**). ''Growth of distortion product otoacoustic emissions with primary-tone level in humans,'' Hearing Res. **71**, 12–22.
Robles, L., Ruggero, M. A., and Rich, N. C. (**1986a**). ''Basilar membrane mechanics at the base of the chinchilla cochlea. I. Input–output functions, tuning curves, and response phases,'' J. Acoust. Soc. Am. **80**, 1364–1374.
Robles, L., Ruggero, M. A., and Rich, N. C. (**1986b**). ''Mössbauer measurements of the mechanical response to single-tone and two-tone stimuli at the base of the chinchilla cochlea,'' in *Peripheral Auditory Mechanisms*, edited by J. B. Allen, J. L. Hall, A. Hubbard, S. T. Neely, and A. Tubis (Springer-Verlag, Berlin), pp. 121–128.
Robles, L., Ruggero, M. A., and Rich, N. C. (**1991**). ''Two-tone distortion in the basilar membrane of the cochlea,'' Nature (London) **349**, 413–414.
Ruggero, M. A., and Rich, N. C. (**1991a**). ''Application of a commercially-manufactured Doppler-shift laser velocimeter to the measurement of the basilar-membrane vibration,'' Hearing Res. **51**, 215–230.
Ruggero, M. A., and Rich, N. C. (**1991b**). ''Furosemide alters organ of Corti mechanics: Evidence for feedback of outer hair cells upon the basilar membrane,'' J. Neurosci. **11**, 1057–1067.
Ruggero, M. A., Rich, N. C., Recio, A., and Narayan, S. S. (**1997**). ''Basilar-membrane responses to tones at the base of the chinchilla cochlea,'' J. Acoust. Soc. Am. **101**, 2151–2163.
Russell, I., and Schauz, C. (**1995**). ''Salicylate ototoxicity: Effects on the stiffness and electromotility of outer hair cells isolated from the guinea pig cochlea,'' Aud. Neurosci. **1**, 309–319.
Sellick, P. M., Patuzzi, R., and Johnstone, B. M. (**1982**). ''Measurement of basilar membrane motion in the guinea pig using the Mössbauer technique,'' J. Acoust. Soc. Am. **72**, 131–141.
Shehata, W. E., Brownell, W. E., and Dieler, R. (**1991**). ''Effects of salicylate on shape, electromotility and membrane characteristics of isolated outer hair cells from guinea pig cochlea,'' Acta Oto-Laryngol. **111**, 707–718.
Shiomi, Y., Tsuji, J., Naito, Y., Fujiki, N., and Yamamoto, N. (**1997**). ''Characteristics of DPOAE audiogram in tinnitus patients,'' Hearing Res. **108**, 83–88.
Smurzynsky, J. (**1994**). ''Longitudinal measurements of distortion-product and click evoked otoacoustic emissions of preterm infants: Preliminary results,'' Ear Hear. **15**, 210–223.
Stockard, J. J., Stockard, J. E., and Sharbrough, F. W. (**1980**). ''Brainstem auditory evoked potentials in neurology: Methodology, interpretation,

clinical application,'' in *Electrodiagnosis in Clinical Neurology*, edited by M. Aminoff (Churchill Livingstone, New York), pp. 370–413.
Stover, L., Gorga, M. P., Neels, S. T., and Montoya, D. (**1996**). ''Toward optimizing the clinical utility of distortion product otoacoustic emission measurements,'' J. Acoust. Soc. Am. **100**, 956–967.
Stover, L., and Norton, S. J. (**1993**). ''The effects of aging on otoacoustic emissions,'' J. Acoust. Soc. Am. **94**, 2670–2681.
Stypulkowski, P. H. (**1990**). ''Mechanisms of salicylate ototoxicity,'' Hearing Res. **46**, 113–146.
Sziklai, I., and Dallos, P. (**1997**). ''Hyposmotic induces magnitude and gain change in the electromotile performance of isolated outer hair cells,'' Acta Oto-Laryngol. **117**, 222–225.
Tonndorf, J. (**1980**). ''Acute cochlear disorder: The combination of hearing loss, recruitment, poor speech discrimination, and tinnitus,'' Ann. Otol. Rhinol. Laryngol. **89**, 353–358.
Vernon, J. (**1987**). ''Assessment of the tinnitus patient,'' in *Tinnitus*, edited by J. W. P. Hazell (Churchill Livingstone, Edinburgh), pp. 71–95.
Whitehead, M. L., Lonsbury-Martin, B. L., and Martin, G. K. (**1992**). ''Evidence for two discrete sources of $2f_1-f_2$ distortion-product otoacoustic emissions in rabbit. II: Differential physiological vulnerability,'' J. Acoust. Soc. Am. **92**, 2662–2682.
Whitehead, M. L., Stagner, B. B., McCoy, M. J., Lonsbury-Martin, B. L., and Martin, G. K. (**1995**). ''Dependence of distortion-product otoacoustic emissions on primary levels in normal and impaired ears. II. Asymmetry in L_1,L_2 space,'' J. Acoust. Soc. Am. **97**, 2359–2377.
Wiederhold, M. L., Mahoney, J. W., and Kellog, D. L. (**1986**). ''Acoustic overstimulation reduces $2f_1-f_2$ cochlear emissions at all levels in the cat,'' in *Peripheral Auditory Mechanisms*, edited by J. B. Allen, J. L. Hall, A. Hubbard, and A. Tubis (Springer-Verlag, New York), pp. 322–329.
Wilson, J. P. (**1987**). ''Theory of tinnitus generation,'' in *Tinnitus*, edited by J. W. P. Hazell (Churchill Livingstone, Edinburgh), pp. 20–45.
Zenner, H. P., and Ernst, A. (**1993**). ''Cochlear-motor, transduction, and signal-transfer tinnitus: Models for three types of cochlear tinnitus,'' Eur. Arch. Otorhinolaryngol. **249**, 447–454.
Zweig, G., and Shera, C. A. (**1995**). ''The origin of periodicity in the spectrum of evoked otoacoustic emissions,'' J. Acoust. Soc. Am. **98**, 2018–2047.
Zwicker, E. (**1987**). ''Objective otoacoustic emissions and their uncorrelation to tinnitus,'' in *Third International Tinnitus Seminar Munster*, edited by H. Feldmann (Harsch, Karlsruhe), pp. 75–81.

The level and growth behavior of the $2f1-f2$ distortion product otoacoustic emission and its relationship to auditory sensitivity in normal hearing and cochlear hearing loss

Peter Kummer, Thomas Janssen, and Wolfgang Arnold
Hals-Nasen-Ohren Klinik, Technische Universität München, Ismaninger Str. 22, 81675 Munich, Germany

(Received 20 August 1997; revised 20 January 1998; accepted 23 February 1998)

The $2f1-f2$ distortion product otoacoustic emission (DP) was measured in 20 normal hearing subjects and 15 patients with moderate cochlear hearing loss and compared to the pure-tone hearing threshold, measured with the same probe system at the $f2$ frequencies. DPs were elicited over a wide primary tone level range between $L2=20$ and 65 dB SPL. With decreasing $L2$, the $L1-L2$ primary tone level difference was continuously increased according to $L1=0.4L2+39$ dB, to account for differences of the primary tone responses at the $f2$ place. Above 1.5 kHz, DPs were measurable with that paradigm on average within 10 dB of the average hearing threshold in both subject groups. The growth of the DP was compressive in normal hearing subjects, with strong saturation at moderate primary tone levels. In cases of cochlear impairment, reductions of the DP level were greatest at lowest, but smallest at highest stimulus levels, such that the growth of the DP became linearized. The correlation of the DP level to the hearing threshold was found to depend on the stimulus level. Maximal correlations were found in impaired ears at moderate primary tone levels around $L2=45$ dB SPL, but at lowest stimulus levels in normal hearing ($L2=25$ dB SPL). At these levels, 17/20 impaired ears and 14/15 normally hearing ears showed statistically significant correlations. It is concluded that for a clinical application and prediction of the hearing threshold, DPs should be measured not only at high, but also at lower primary tone levels. [S0001-4966(98)01406-4]

PACS numbers: 43.64.Jb, 43.64.Kc, 43.64.Ri [BLM]

INTRODUCTION

Distortion product otoacoustic emissions (DP), which can be measured in the outer ear canal during stimulation with two primary tones $f1$ and $f2$, arise from a compressive nonlinearity in cochlear mechanics. This nonlinearity has been described as frequency selective amplification of the motion of the cochlear partition which is most pronounced at low stimulus levels and is responsible both for the high hearing sensitivity and frequency selectivity (Johnstone *et al.*, 1986; Robles *et al.*, 1986; Ruggero and Rich, 1991a; Ruggero *et al.*, 1997). Outer hair cells (OHC) act as motor of this so-called cochlear amplifier (Davis, 1983; Dallos, 1992), feeding back energy to the vibration of the cochlear partition and provide thus the appropriate stimulus to the inner hair cell receptors. Arising as a byproduct of the cochlear amplifier, the level of the DP correlates with hearing sensitivity in normal (Gaskill and Brown, 1990) and impaired hearing (e.g., Martin *et al.*, 1990; Harris, 1990; Nelson and Kimberley, 1992; Stover *et al.*, 1996). Since OHC amplification and response losses due to OHC impairment are greatest at lowest stimulus levels, it may be predicted that the efficiency of DP testing is greatest, when stimulus levels close to the hearing threshold are applied. For a stimulation at close-to-threshold levels, appropriate settings of the primary tone levels $L1$,$L2$ deserve considerable attention, as indicate both animal data of the basilar membrane vibration and DP studies in animals and humans.

Animal data of the basilar membrane vibration during single-tone stimulation (e.g., Johnstone *et al.*, 1986; Ruggero and Rich, 1991a; Ruggero *et al.*, 1997) show that both primary tone responses considerably differ at low levels at the $f2$ place, where the DP is generally thought to originate. As characteristic frequency (CF) at this site, $f2$ has the lowest threshold and most compressive growth, whereas the response to $f1$, which is about 0.25 octaves below CF ($f2/f1=1.2$), has a higher threshold and a less compressive growth. From the data of Johnstone *et al.* (1986), e.g., who examined a place with a CF at 18 kHz, it appears that between 20 and 60 dB SPL, the growth of $f1$ was about twice that of $f2$. Both responses were equal at about 60 dB SPL. Thus $L1=0.5L2+30$ dB describes stimulus conditions that result in equal primary tone responses at the $f2$ place in this preparation.

DP studies in animals (Whitehead *et al.*, 1995b; Mills and Rubel, 1994) and humans (Gaskill and Brown, 1990; Whitehead *et al.*, 1995b), that systematically varied $L1-L2$, confirmed that DP measurements may be optimized with such stimulus conditions, and demonstrated that with decreasing $L2$, maximal DP levels are generated when $L1-L2$ is continuously increased. Given the differences in method, species, frequency range, and $f2/f1$ ratios, the optimal $L1-L2$ settings empirically defined in these studies appear to be almost identical to those predictable from theoretical considerations. In animal experiments it was shown that such stimulus settings most distinctly reflect loss of OHC function (e.g., Whitehead *et al.*, 1995b; Mills *et al.*, 1993; Mills and Rubel, 1994). Human studies in clinical settings, however, did not take up such a paradigm so far, but rather

TABLE I. The levels of the primary tones ($L1 = 0.4\,L2 + 39$).

$L1$ [dB SPL]	65	63	61	59	57	55	53	51	49	47
$L2$ [dB SPL]	65	60	55	50	45	40	35	30	25	20

used either equilevel primary tones (e.g., Nelson and Kimberley, 1992) or a constant $L1 - L2$ level difference over an extended primary tone level range (e.g., Kimberley *et al.*, 1995; Stover *et al.*, 1996).

It was the aim of this study to examine the relationship of DPs to the hearing threshold that were measured over a wide stimulus intensity range down to close-to-threshold levels (20 dB SPL$\leqslant$L2$\leqslant$65 dB SPL) allowing for these considerations about appropriate stimulus conditions. As an initial step toward this aim, the stimulus level paradigm $L1 = 0.4L2 + 39$ dB was derived from human DP data available at the beginning of this study (Gaskill and Brown, 1990). In this paper we report on the relationship between DPs and the hearing threshold in normal and cochlear hearing impaired ears without tinnitus. A second paper examines DPs in cochlear hearing impaired ears with tinnitus, where distinctly different behavior was found in part of the ears (Janssen *et al.*, 1998).

I. METHODS

A. DP measurements

The DP were recorded with an Etymotic Research probe system (ER-10C) and a digital signal processing board (ARIEL DSP-16+), driven by CUB^{e}DIS™ software (Mimosa Acoustics). The system was installed on an IBM compatible PC. The two primary tones were presented on separate D/A channels. The signal from the ER-10C was amplified, sampled at 50 kHz, and averaged 200 times into a 20.48 ms (1024-point) buffer. The total sampling time for each frequency pair was thus 4.096 s. The time-averaged response was Fourier transformed, resulting in a spectrum sampled every 48.8 Hz. Because of the time-domain averaging, the equivalent bandwidth amounted to about 0.25 Hz. In that bandwidth, the minimum noise floor was about -28 dB SPL. The system distortion measured in an ear simulator cavity was below the noise floor for the primary tone levels used. Both stimulus channels were calibrated separately by exciting them with a broadband chirp. Corresponding to their frequency responses, as measured by the probe microphone, the outputs to the two transducers were corrected.

DP were measured at 51 frequencies from $f2 = 0.488$ to 8.008 kHz at 11–15 steps per octave. The primary tone frequency ratio was kept constant at $f2/f1 = 1.2$. Such DP-versus-frequency functions, that will be referred to as DP grams, were obtained at 10 different primary tone levels, over a 45-dB $L2$ stimulus level range (see Table I). Starting from $L1 = L2 = 65$ dB SPL, $L2$ was decreased in 5-dB steps down to 20 dB SPL, whereas $L1$ was decreased in 2-dB steps down to 47 dB SPL, according to $L1 = 0.4L2 + 39$ dB. The primary tone level difference $L1 - L2$ thus continuously increased up to 27 dB at $L2 = 20$ dB SPL.

Data were analyzed off-line with MATLAB. From the CUBDIS output file, the DP and the primary tone levels were read as well as an estimate of the measurements noise floor. The latter was formed of an average of six Fourier transform bins, neighboring the DP. Only DP readings with signal-to-noise ratios exceeding 6 dB were included in the data analysis.

I/O functions were constructed from the data, plotting DP level L_{dp} against the higher primary tone level $L2$. The growth of the DP was than quantified by measuring the I/O functions slope between $L2 = 40$ and 60 dB SPL,[1] further below referred to as the slope s.

B. Pure-tone threshold

For comparison with the hearing sensitivity, the pure-tone threshold was measured with the same probe system at all $f2$ frequencies, using a computer controlled method of adjustment. The subjects were instructed to press a button, as long as the continuously presented tone was audible. By button press and release, its SPL was decreased and increased by 5 dB/s, respectively. The maximum and starting SPL at the first test frequency was 60 dB SPL. For the following frequencies, the starting SPL was 20 dB above the preceding measurements mean value. At each frequency, the tone was presented 30 s and the threshold level L_t was estimated from an average of the points within the flat run of the adjustment (usually from about the fifth second). Threshold measurements were done immediately after DP testing, without changing the probe fit and using the previously measured frequency response of the transducers. In one case of sudden deafness, which did not enter data pooling, pure-tone thresholds were measured with a high resolution clinical audiometer within 50 Hz of selected $f2$-frequencies.

All measurements were performed with the subjects quietly reclined on a comfortable chair in a double-walled, sound-proof room and instructed to remain quiet during the measurements. DP measurements took up to 35 min per ear, the threshold measurements up to 25 min.

C. Subjects

Two groups of subjects were examined in this study, one with normal hearing ($n = 20$) and one diagnosed with moderate cochlear hearing impairment, but with no history of tinnitus ($n = 15$). The hearing impaired group consisted of 8 males and 7 females, aged between 16 and 76 years (mean 45.6 years) and were diagnosed with sudden deafness ($n = 6$), acoustic trauma ($n = 4$), hereditary hearing loss ($n = 2$), and hearing loss of unknown etiology ($n = 3$). In one additional patient, DP were measured on five consecutive days during recovery from sudden deafness. The normally hearing subjects, 12 females and 8 males, were aged between 18 and 32 years (mean 24.6 years) and had, according to clinical audiometry, hearing thresholds within 15 dB HL at octave frequencies from 0.125 to 8 kHz and from 0.75 to 6 kHz. None of the subjects reported any otological history such as ear infection, ototoxic drugs, or noise exposure. Data were collected only from one ear per subject.

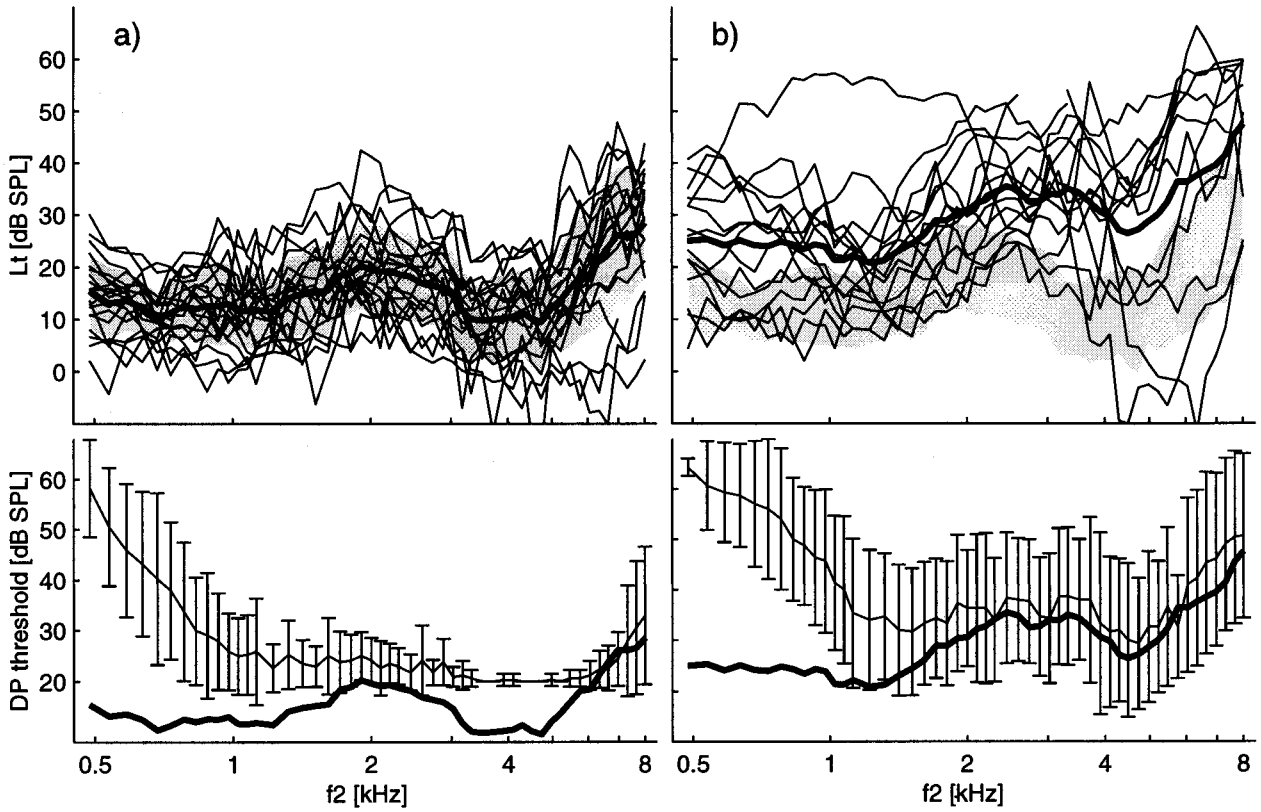

FIG. 1. The level of the hearing threshold L_t and the DP threshold in (a) 20 normal hearing and (b) 15 cochlear hearing impaired ears. The upper panels show the individual (thin lines) and average hearing threshold levels (bold line) in both subject groups. The shaded area indicate the normal range (mean ± one s.d.) calculated from the normal hearing subjects. In the lower panels, the error bars indicate ranges of mean± one s.d. of the DP threshold, i.e., the lowest $L2$ primary tone level a DP was recorded 6 dB above the noise floor. The average hearing threshold (bold line) of the respective sample is added for comparison.

II. RESULTS

A. Increasing $L1-L2$ with decreasing $L2$ according to $L1=0.4L2+39$ dB allowed to measure DPs down to hearing threshold levels

Figure 1 compares the hearing threshold L_t and the DP threshold in both subject groups with (a) normal hearing ($n=20$) and (b) moderate cochlear hearing loss ($n=15$). Both upper panels show the individual (thin lines) and average hearing threshold level (bold line) in both subject groups. The shaded area indicates the normal range, which was calculated from the normally hearing subjects, i.e., mean ± one standard deviation. With respect to normal, moderate hearing losses in the hearing impaired subject sample were up to about 40 dB and most pronounced in the mid-to-high-frequency range.

In both lower panels, the error bars indicate ranges of mean ± one s.d. of the DP threshold in both subject groups, i.e., the lowest $L2$ primary tone level a DP was recorded 6 dB above the noise floor. For comparison, the average hearing threshold (bold line) of the respective sample is added. Above about 1.5 kHz, the average DP thresholds lay within 10 dB of the average hearing thresholds, in both subject groups. In normal hearing, the DP thresholds mostly lay close to the lowest primary tone levels used, on average between 20 and 30 dB SPL. Here, the DP thresholds deviated from the average hearing threshold only just above 1 kHz and around 5 kHz, i.e., in the region of the hearing threshold minima, which were about 10 dB SPL and thus were even below the lowest $L2=20$ dB SPL. In the hearing impaired subject group, the average DP threshold follows the average hearing threshold within 5 dB above 1.5 kHz. In both groups, no close-to-threshold stimulation was possible at low frequencies due to the increased noise floor (cf. Figs. 2, 4, and 6). Below about 1 kHz, the average DP thresholds distinctly increased and substantially deviated from the average hearing threshold in both groups.

B. The relationship of the DP level to hearing sensitivity in normal hearing depends on stimulus levels

In general, there was a good correspondence of the DP to the threshold level. Figure 2 compares the DP grams at the different primary tone levels to the pure-tone threshold in four normal hearing subjects. The DP level correlates well with the hearing threshold. With decreasing stimulus level, the correlation was found to increase (for a quantitative statistical analysis, see Sec. II G).

One reason was the DP fine structure, which was mostly found to develop only at the lowest stimulus levels where peaks and troughs in the DP and the threshold level often coincided (A,B,C). At high stimulus levels, the DP grams were comparably smooth[2] and only roughly followed the hearing threshold. With decreasing primary tone levels down

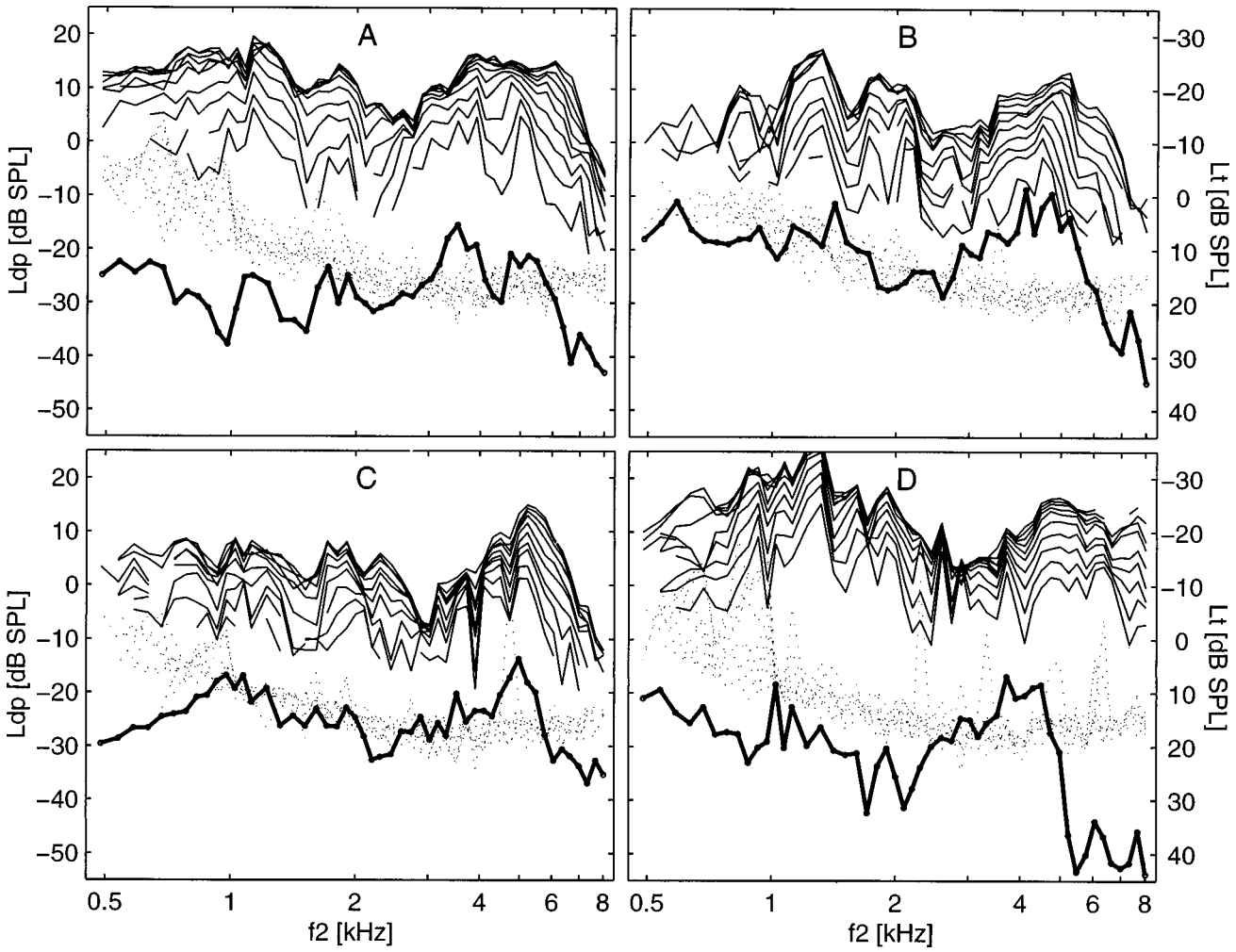

FIG. 2. Examples of data from four normally hearing subjects (A through D). Thin lines are DP grams, plotting the DP level against $f2$ frequency (left-hand ordinate) for S/N ratios >6 dB. DP grams follow with decreasing intensity from $L2=65$ to 20 dB SPL, in 5-dB steps, from top to bottom. Dotted lines indicate the noise floor. The bold line is the puretone threshold L_t at $f2$, plotted inverse with reference to the right-hand scale.

to 20 dB SPL, however, mostly a clear fine structure appeared.

By subjective assessment, a match with the threshold fine structure thus developed in 11 of the 20 ears. This can be seen in subject A slightly below 2 kHz and between 3 and 6 kHz, where a DP fine structure developed at $L2=30$ to 25 dB SPL (third and second DP gram, from bottom). A DP representation of three local threshold dips at 1.8, 4.3, and 6.6 kHz thus appeared only for lowest stimulus levels. Note the correspondence to the subjective threshold level L_t that was measured at the $f2$ frequencies, both plots sharing the same frequency scale. Indeed, $L2$ stimulus levels are as low as only 10–15 dB above threshold. Similarly, in subject B, the 3–6 kHz threshold fine structure appeared only in the lowest DP gram ($L2=20$ dB SPL), i.e., with $L2$ about 20 dB above the pure-tone threshold levels, which were between 0 and 5 dB SPL.

Over other frequency ranges, however, many of the data hardly showed a correspondence of the DP fine structure to that of the threshold or appeared being shifted one versus the other. Also, the DP fine structure partly changed with stimulus level. There were cases where the peaks and dips shifted with decreasing primary tone levels, both toward lower and higher frequencies. For example, in subject B a peak at about 5 kHz shifts downward by about 1000 Hz when $L2$ was lowered from 65 to 35 dB SPL. In subject D, the pattern shifts upward between about 1.5 and 2 kHz with decreasing primary tone levels.

Apart from the fine structure, also the gross DP run appeared to be shifted against that of the threshold in 3/4 of the data. Subject C, for example, showed a pure-tone threshold with two local minima around 1 and 5 kHz. Relative to that shape, the DP data are shifted toward higher frequencies. The rising slopes below 1 and 5 kHz more closely approached the threshold than the falling slopes above. A similar impression arises from the data of subjects B and D. Also, this shift partly appeared to increase with increasing primary tone level (e.g., subject A). More pronounced and more easily visible was this shift in the pooled data (Sec. II D).

C. The growth of the DP is compressive in normal hearing

Typically, the DP growth was quite compressive in normal hearing. Figure 3 shows I/O functions from the four subjects of Fig. 2, at $f2$ frequencies near 1, 2, 4, and 6 kHz

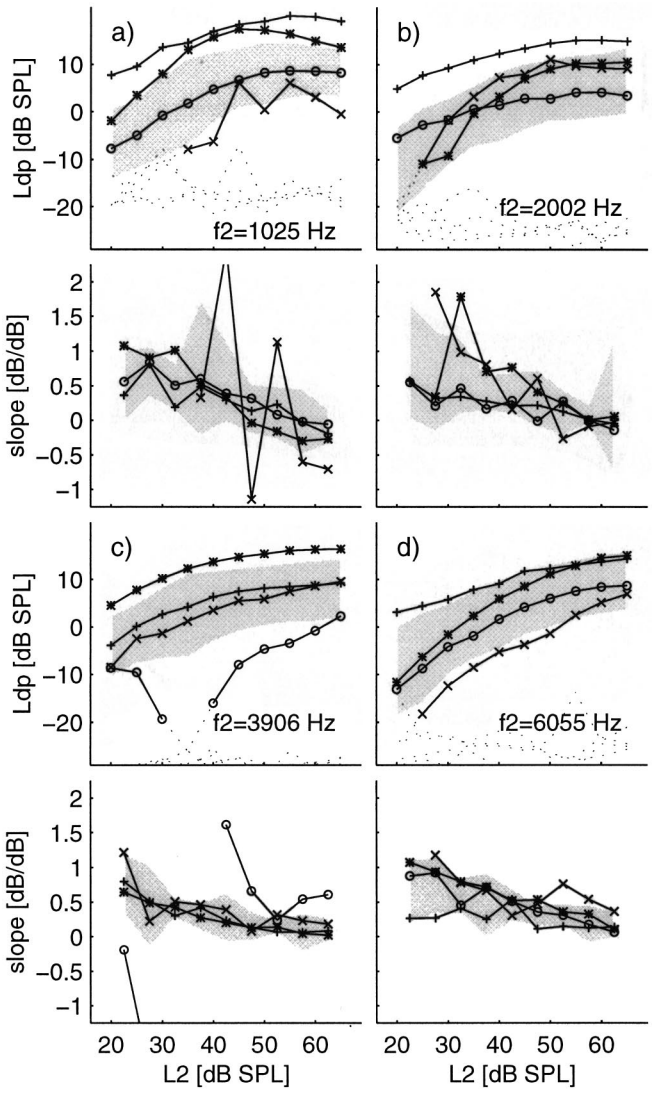

FIG. 3. I/O functions from the data in Fig. 2 with $f2$ near 1, 2, 4, and 6 kHz and the slope of these I/O functions (a through d). The DP level L_{dp} is plotted against $L2$ for S/N ratios >6 dB (noise floor: dotted lines). The slope is also plotted against $L2$, and was calculated for two consecutive DP readings (S/N$>$6 dB). Different symbols identify data from subject A (*), B ($\times$), C ($\bigcirc$), and D (+). Shaded area indicate mean $\pm$ one s.d. ranges of the normal hearing subject sample ($n=20$).

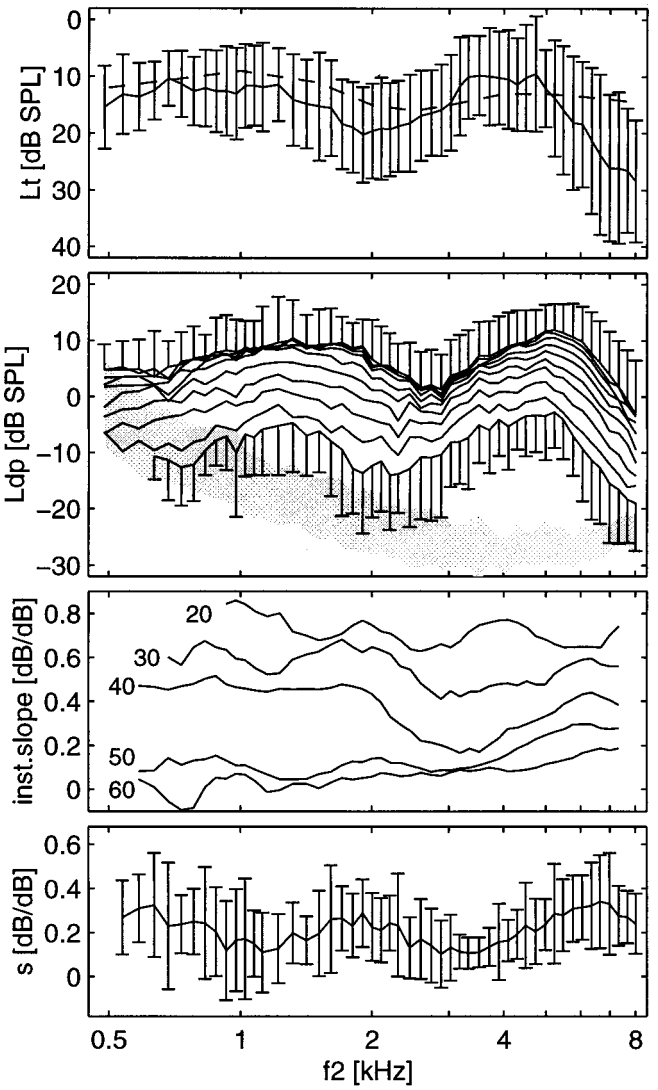

FIG. 4. Average DP and pure-tone hearing threshold data from the normally hearing subject sample ($n=20$): From top to bottom, the panels show the inverse hearing threshold level L_t, the DP level L_{dp} for $L2=65$ to 20 dB SPL (curves with decreasing primary tone levels follow from top to bottom), the growth of the DP 5 dB above $L2=20$, 30, 40, 50, and 60 dB SPL (curves with increasing primary tone levels follow from top to bottom and are smoothed with a five point moving average, for clarity), and the growth s of the DP between $L2=40$ and 60 dB SPL. Error bars indicate ranges of the mean $\pm$ one standard deviation; for the DP level L_{dp}, one s.d. ranges are given only for the lowest and highest primary tone levels. For comparison, the inverse minimum audible pressure data from Killion (1978) is added as dashed line in the upper most panel.

(a through d). The growth rates calculated from the curves are shown below each I/O function plot. The shaded areas indicate ranges of the mean $\pm$one s.d. from all normally hearing subjects ($n=20$). At the lowest stimulus levels, the DP level most rapidly increased, with average growth rates almost up to 1 dB/dB. With increasing stimulus level, generally strong saturation occurred. In 13% of the cases, also an actual decrease of the DP level was found at the highest stimulus levels [Fig. 3(a)]. Nonmonotonic growth with more or less pronounced notches (>2 dB) was observed only exceptionally in about 3% of all I/O functions (30/1020). Occurring mainly below 4 kHz [e.g., Fig. 3(c)], less than half of these I/O functions showed pronounced notches greater than 10 dB.

D. Pooled data from normally hearing ears

The average DP level L_{dp} and threshold level L_t share a characteristic bimodal shape (two upper panels in Fig. 4), with maxima in the DP level and corresponding minima in the threshold level at about 1 and 5 kHz. However, there is a shift of the DP maxima in relation to the threshold minima toward higher frequencies, which increases with increasing stimulus level. Its amount was estimated by linear regression analysis, whereby correlation coefficients were calculated as a function of the distance between ft and $f2$ (0.05 octave steps). At high stimulus levels of $L2=65$ to 55 dB SPL, maximum correlation was found for a distance of 0.3 octaves ($L2=65$ dB SPL: $r=-0.8471$, $p<0.001$).[3] Below, this distance continuously decreased to 0.1 octaves at $L2=30$ dB SPL ($r=-0.822$, $p<0.001$), remaining constant further below.

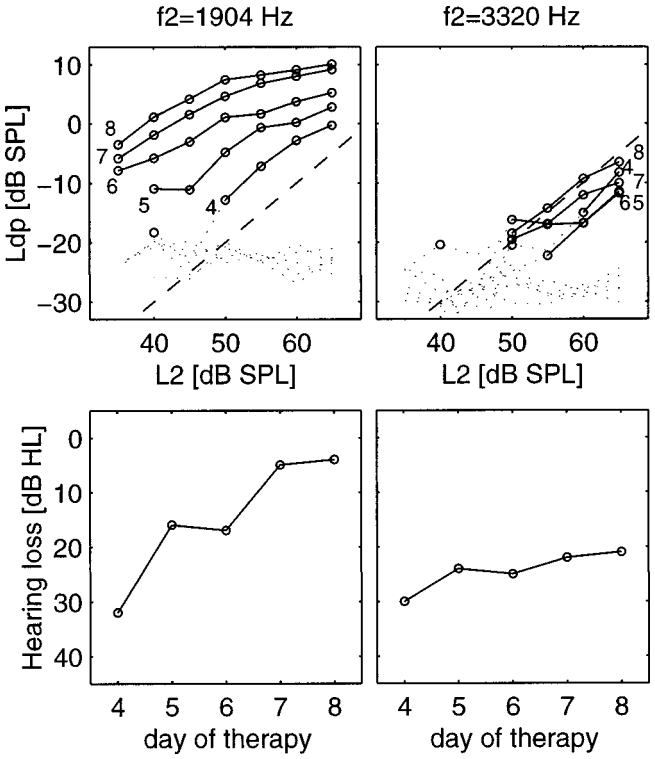

FIG. 5. Examples of DP I/O functions and hearing threshold data of a patient suffering from sudden deafness, on five consecutive days during recovery of hearing, at $f2=1.904$ kHz, where hearing completely recovered (left column) and at $f2=3.320$ kHz, where it did almost not (right column). Numbers at the individual I/O functions curves refer to the day of therapy. (○)-symbols indicate DP with S/N ratios >6 dB, the dashed lines indicate the noise floor. For comparison, the long-dashed lines indicate unity slope. The lower panels show the hearing loss, measured with an audiometer within 50 Hz of $f2$.

The compressive growth of the DP can be estimated from the distance of the average DP grams. The upper DP grams were much closer together than the lower ones. Quantitatively, the average growth of the DP is shown in the third panel from top of Fig. 4. The growth rate was calculated in a 5-dB range at five different primary tone levels, i.e., 5 dB above $L2=20$, 30, 40, 50, and 60 dB SPL. The corresponding curves follow one below the other from top to bottom: The growth rates continuously decrease with increasing stimulus level.

With regard to the identification of hearing impairment, the compression of the DP growth was quantified by measuring the I/O functions slope between $L2=40$ to 60 dB SPL,[1] referred to as the slope s. This was the range, where normal and pathological growth differed most (cf. the bottom panels of Fig. 7). The lower panel in Fig. 4 shows the mean slope s ($\pm$one s.d.) as a function of $f2$. When comparing to the threshold L_t, it can be seen that the slope s increases, i.e., the growth becomes less compressive, when the threshold increases ($r=0.4804$; $p<0.001$).

E. The growth behavior of the DP linearizes in cochlear hearing loss

Figure 5 compares I/O functions (upper panels) and hearing loss (lower panels) at two frequencies in a patient who was recovering from sudden deafness. At $f2=1.904$ kHz (left column), where hearing completely recovered by about 30 dB, the DP level distinctly increased. The amount of change, however, strongly depended on the stimulus level. The lower the stimulus level was, the greater the change in the DP level. At $L2=45$ dB SPL, the DP level increased during therapy by about 30 dB, corresponding to the amount of hearing improvement. At $L2=65$ dB SPL, however, the DP level changed only by about 12 dB. Due to this differential sensitivity, the growth pattern, which was almost linear, turned compressive. The slope of the I/O function between 45 and 65 dB SPL, which was about 1.1 dB/dB at the beginning of the therapy, continuously decreases to about 0.25 dB/dB. Conversely, from the quantified slope of the I/O functions, the differential sensitivity of the DP may be read: Over the 20-dB stimulus level range, the growth difference of 0.85 dB/dB indicates that the DP level at $L2=40$ dB SPL decreased by 17 dB more than at $L2=60$ dB SPL. Although this implies linear extrapolation to data points that actually were lost in the noise, it clearly demonstrates the differential sensitivity of the DP. At $f2=3.320$ kHz, a 30-dB hearing loss only recovered by less than 10 dB. Correspondingly, DP were measurable only at higher stimulus intensities, and changes were much smaller. At all days, the I/O functions were almost linear, having steep slopes of about 1 dB/dB.

These exemplary data demonstrate that the sensitivity of DPs to cochlear hearing impairment greatly increases with decreasing stimulus intensity. The growth of the emission, which is compressive in normal hearing, distinctly changes and becomes linearized in hearing impairment. In the next section, DP level and growth behavior will be compared to the high resolution hearing threshold, confirming these findings.

F. Low and high primary tone level DP are differentially sensitive to cochlear hearing loss

Figure 6 provides examples from six representative ears with cochlear hearing impairment. In each case, the upper most panel shows the threshold level L_t, the middle one the DP grams at $L2$ from 65 down to 20 dB SPL and the lower the slope s of the I/O functions between $L2=40$ and 60 dB SPL.

In general, the DP grams closely followed the pure-tone threshold. When comparing to data from normal hearing subjects (shaded areas for L_{dp} given only at $L2=65$ dB SPL), similar reductions can be seen for the DPs and for the hearing sensitivity, closely resembling one another with respect to their width, slopes and, as far as the DP S/N ratio allows, also their depth. DPs evoked by lower primary tone levels, however, reflect the threshold changes better than DPs at high primary tone levels. This can be seen, e.g., in A, when comparing reductions of the DP level to those of the hearing threshold. Compared to normal ranges, reductions of the DPs at $L2=65$ dB SPL are comparably small (upper most curve). With decreasing primary tone level the slopes of the DP grams much closer approach that of the threshold run. Due to that differential sensitivity, the distance between the DP grams increases around the notch. This indicates that the compressive growth of the emission becomes more linear.

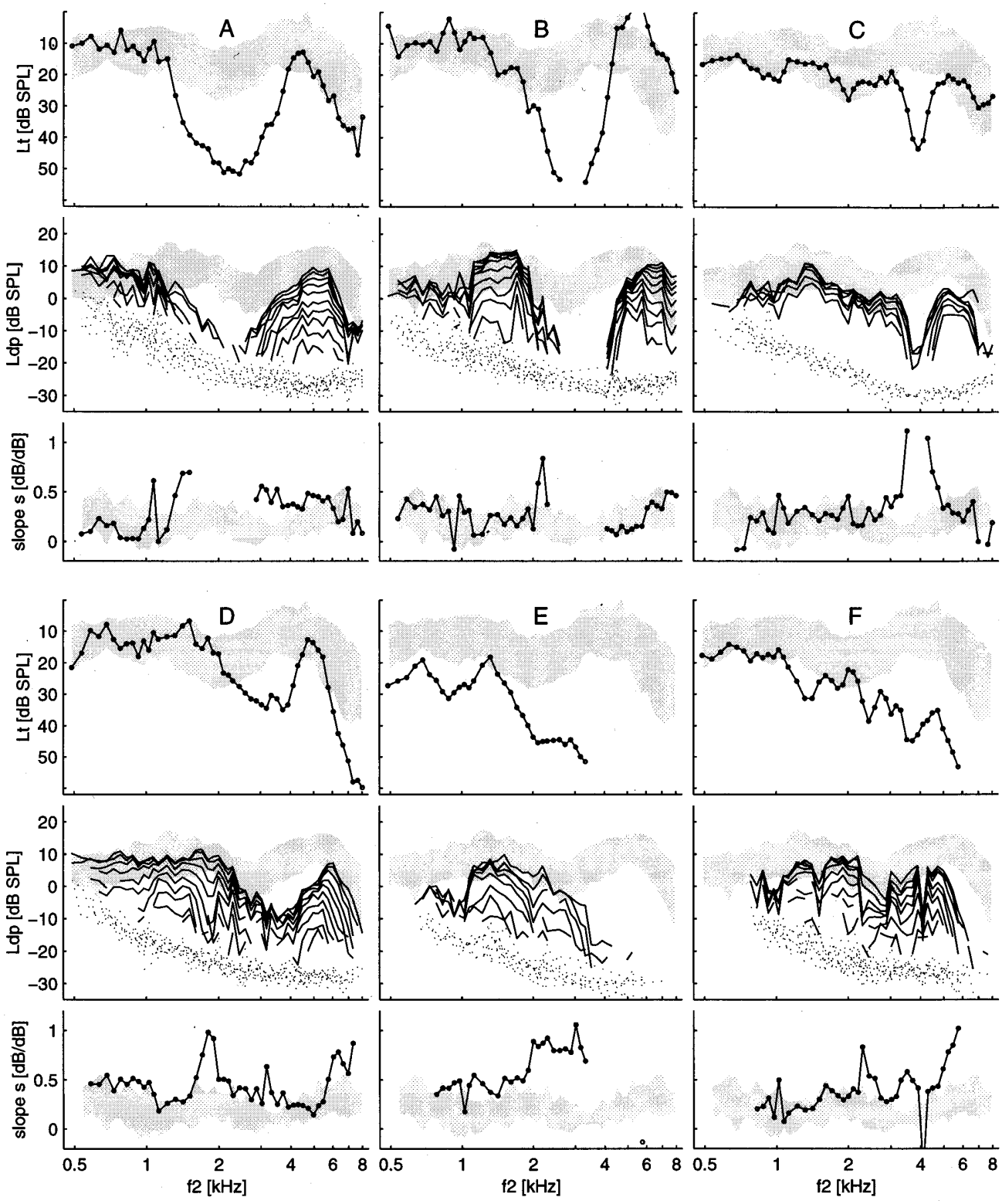

FIG. 6. Data from six ears (A through F) with cochlear hearing impairment, comparing the threshold level L_t measured at $f2$ (upper panels) to the DP level L_{dp} (middle panels) at primary tone level decreasing from $L2=65$ to 20 dB SPL (in C only down to 40 dB SPL) and the slope s of the DP I/O functions between $L2=40$ and 60 dB SPL (lower panels). The shaded area indicate ranges of mean $\pm$ one s.d. of the normally hearing subject sample (cf. Fig. 4), for the DP level given only at $L2=65$ dB SPL. Note that the hearing threshold L_t is plotted inverse.

The slope s quantifies this linearization and distinctly increases from about 0.1 dB/dB up to about 0.8 dB/dB at the low-frequency slope of the notch. Remembering that the slope s is calculated between $L2=40$ and 60 dB SPL, a growth difference of 0.7 dB/dB indicates that the DP level at $L2=40$ dB SPL decreases by about 14 dB more than the DP level at $L2=60$ dB SPL.

The same is true for cases B–D. In B, the high-

frequency slope of the notch, however, is very steep and no growth change appears. In C, the linearized growth with increasing hearing loss is most evident and the slope s sharply increases from less than 0.5 dB/dB up to 1.2 dB/dB, demonstrating that at $L2=40$ dB SPL, the DP may decrease by at least 14 dB more than at $L2=60$ dB SPL. In D, according to the small hearing loss, the growth is only slightly changed between 3 and 4 kHz. Also, there is a DP minimum with linearized growth at 2 kHz, despite normal hearing threshold in this frequency region. From I/O functions this increase was related to an exceptional nonmonotonic growth with a notch at moderate $L2$ levels, that increased the slope between $L2=40$ and 60 dB SPL.

In E, high primary tone level DP properly match the low-frequency threshold, but decrease by only 10 dB between 1.5 and up to 3 kHz, despite the fact that the hearing threshold continuously increases by 30 dB. High primary tone level DP thus stay within normal ranges, despite clear hearing loss at 3 kHz. The lower primary tone level DP, however, does follow the threshold much more closely. Due to this differential sensitivity, the DP growth becomes more linear. The slope s indicates this and increases above about 1.5 kHz from about 0.4 dB/dB to 1 dB/dB. This shows that the DP decreases by 12 dB more at $L2=40$ dB SPL than at $L2=60$ dB SPL. Similarly, in F, the DPs at high primary tone levels follow the threshold, but are unusually high and within normal ranges despite considerable hearing losses above 2 kHz. The slope s most closely indicates the higher sensitivity of lower primary level DPs, following the hearing threshold run and even its fine structure.

It can be summarized that in hearing impaired ears there is a close correspondence of the DP and the threshold level. Whereas the DP is less sensitive to cochlear hearing loss at high primary tone levels and may be even unchanged compared to normal ranges, the correspondence greatly increases with decreasing primary tone levels. Reflecting this differential sensitivity, the growth of the DP steepens with increasing hearing loss. Between $L2=40$ and 60 dB SPL, where strongly saturating growth was found in normal hearing, the greatest change occurred. Measuring the I/O functions' slope in this range thus allows to quantify the greater sensitivity of lower primary tone level DPs.

G. Pooled data and statistical analysis of the correlation between DP level, slope, and the hearing threshold

Figure 7 presents pooled DP data from the normally hearing (left column) and the hearing impaired subject sample (right column), plotted against the threshold level L_t. Dots indicate raw data to illustrate the scatter. The curves show moving averages of the data to illustrate the relationship of the DP level and slope to the hearing threshold, respectively. The moving averages were constructed by averaging the DP level or slope of 101 data points neighboring along the L_t scale, and stepwise moving this window along L_t. In the upper panels, the dots show the DP level L_{dp}, for $L2=60$ dB SPL and their moving average. The second panels from the top show corresponding curves for all $L2$ levels, from $L2=65$ dB SPL to 20 dB SPL. In the third panels from the top, the slope s between $L2=40$ and 60 dB SPL is plotted against threshold level L_t. In the bottom panel, moving averages of the instantaneous slope of the I/O functions are shown, measured in a 5-dB range above $L2=20$, 30, 40, 50, and 60 dB SPL, respectively (from top to bottom).

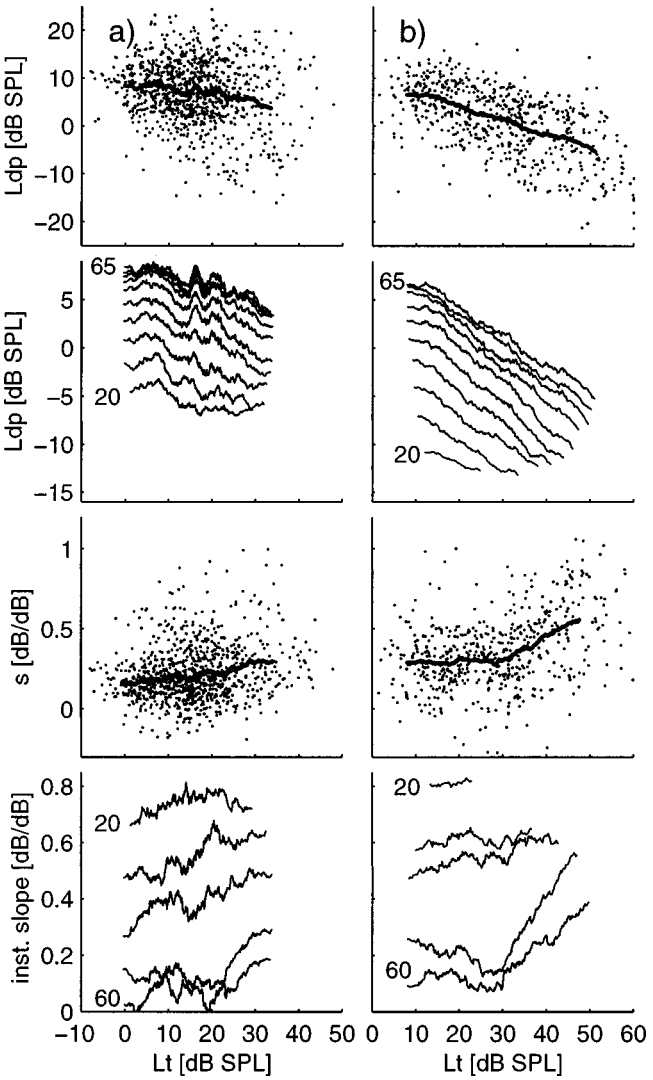

FIG. 7. Pooled DP data from (a) 20 normal hearing and (b) 15 hearing impaired ears, plotted against threshold level L_t and/or 101 point moving averages derived from the data. The upper most panels plot the DP level L_{dp}, for $L2=60$ dB SPL (S/N>6 dB). Just below are shown moving averages for all primary tone levels, decreasing from 65 to 20 dB SPL in 5-dB steps, from top to bottom. The second panels from bottom show the slope s of the I/O functions, calculated between $L2=40$ and $L2=60$ dB SPL. The bottom panels show the growth of the DP, i.e., moving averages of the instantaneous slope of the DP I/O functions, calculated 5 dB above $L2=20$, 30, 40, 50, and 60 dB SPL. With increasing primary tone level, the curves follow from top to bottom.

In normal hearing, there is a great variability of the DP level (upper panel). The average DP level only slightly decreases with increasing threshold. With increasing primary tone levels, the distance between the moving average curves for the DP level decreases, confirming the compressive DP growth in normal hearing (second panel from top). Most distinctly, this compression can be seen in the bottom panel: at the lowest thresholds, the slope of the I/O functions continuously drops from about 0.7 dB/dB to a zero slope. Even in

TABLE II. The correlation between the DP level L_{dp} at the different stimulus intensities and the slope s to the pure-tone threshold level L_t in 20 normally hearing ears. The table gives the average correlation coefficient $r(\pm$s.d.), the number n of data sets analyzed (on a basis of at least 10 data points), the number of positive and negative correlation coefficients at a significance level of $p<5\%$ and $p>5\%$, respectively and the average ($\pm$s.d.) coefficients a, b and a', b' of regression lines $L_t=aL_{dp}+b$, $L_t=as+b$, and $L_{dp}=a'L_t+b'$, $s=a'L_t+b'$, respectively.

$L1, L2$ [dB SPL]	$r\pm$s.d.	n	$p<0.05$ $r<0/r>0$	$p>0.05$ $r<0/r>0$	$a\pm$s.d.	$b\pm$s.d.	$a'\pm$s.d.	$b'\pm$s.d.
65, 65	−0.313±0.23	20	13/0	4/3	−0.42±0.33	18.0±7.3	−0.26±0.23	11.0±3.9
63, 60	−0.318±0.22	20	11/0	7/2	−0.44±0.34	17.9±7.3	−0.26±0.22	10.5±3.9
61, 55	−0.326±0.21	20	12/0	6/2	−0.45±0.34	18.1±7.4	−0.26±0.20	10.3±4.4
59, 50	−0.375±0.21	20	11/0	9/0	−0.52±0.35	18.1±7.7	−0.31±0.22	10.5±4.7
57, 45	−0.392±0.21	20	13/0	7/0	−0.52±0.32	17.5±7.5	−0.33±0.23	9.5±4.8
55, 40	−0.430±0.19	20	15/0	5/0	−0.54±0.27	16.6±7.3	-0.37±0.22	8.4±4.6
53, 35	−0.463±0.17	20	17/0	3/0	−0.61±0.28	15.6±7.3	−0.38±0.18	6.7±4.6
51, 30	−0.469±0.18	20	17/0	3/0	−0.61±0.34	14.3±7.4	−0.40±0.18	4.4±5.1
49, 25	−0.493±0.18	20	17/0	3/0	−0.61±0.32	12.4±7.6	−0.43±0.19	2.0±4.7
47, 20	−0.436±0.24	17	12/0	4/1	−0.51±0.32	11.2±8.6	−0.40±0.25	0.9±5.8
slope s	0.259±0.19	20	0/7	2/11	11.9±9.60	12.7±7.1	0.006±.005	0.1±0.1

normal hearing, the slope of the I/O functions steadily increases with increasing hearing threshold, indicating a slight linearization of the DP growth (bottom panel). Calculated between $L2=40$ and 60 dB SPL, the slope s shows again this behavior (third panel from top).

In the hearing impaired ears the DP level is generally somewhat lower, especially at the lowest primary tone levels. The different frequency distributions of the hearing losses in both subject groups certainly contribute to this. With increasing threshold level, the DP level continuously drops by about 0.3 dB/dB at high primary tone levels (second panel from top). With decreasing primary tone levels, the slope of the moving averages increases, reflecting the higher DP sensitivity at lower primary tone levels (quantitatively, the regression coefficients a' in Table III show this). Only at lowest primary tone levels do the curves become shallower again, presumably because the noise floor is approached.

The slope s, calculated between $L2=40$ and 60 dB SPL, increases with hearing loss up to about 1 dB/dB. Between $L_t=30$ and 50 dB SPL, s increases on average by 0.3 dB/dB. Over this 20-dB threshold range, this indicates a 6 dB greater drop of the DP level at $L2=40$ dB SPL compared to $L2=60$ dB SPL. This shows that lowering $L2$ by 20 dB doubles the DP sensitivity, since the average decrease of the DP in this range is only 6 dB at $L2=60$ dB SPL.

In more detail, the instantaneous slope of the I/O functions reflects the DP growth behavior (bottom panel). At all stimulus levels, the instantaneous slope increases with increasing hearing loss, indicating a linearization of the DP growth. However, even at highest threshold levels some compression can still be seen. Maximal growth rates were found above $L2=50$ dB SPL, and reached values of 1.4 dB/dB (individual data points not shown).

Tables II and III summarize the results of the linear regression analysis performed on the individual data sets from the normally (Table II) and hearing impaired (Table III) ears, i.e., the correlation coefficients r of the DP level at the different $L2$ levels and the slope s, the percentage of significant correlations ($p<0.05$) and the coefficients a,b of the regression lines $L_t=aL_{dp}+b$, $L_t=as+b$ and a',b' of the regression lines $L_{dp}=a'L_t+b'$, $s=a'L_t+b'$, respectively. The correlation coefficients r and the percentage significant correlations ($p<0.05$) are also illustrated in Fig. 8. In general, there was a negative correlation of the threshold level to the DP level and a positive correlation to the slope s. In hearing impaired ears, the correlations were distinctly higher. Here, maximal correlations were found at medium primary

TABLE III. The correlation between the DP level L_{dp} at the different stimulus intensities and the slope s to the pure-tone threshold level L_t in 15 hearing impaired ears. The table gives the average correlation coefficient $r(\pm$s.d.), the number n of data sets analyzed (on a basis of at least 10 data points), the number of positive and negative correlation coefficients at a significance level of $p<5\%$ and $p>5\%$, respectively and the average ($\pm$s.d.) coefficients a, b and a', b' of regression lines $L_t=aL_{dp}+b$, $L_t=as+b$, and $L_{dp}=a'L_t+b'$, $s=a'L_t+b'$, respectively.

$L1, L2$ [dB SPL]	$r\pm$s.d.	n	$p<0.05$ $r<0/r>0$	$p>0.05$ $r<0/r>0$	$a\pm$s.d.	$b\pm$s.d.	$a'\pm$s.d.	$b'\pm$s.d.
65, 65	−0.561±0.22	15	13/0	2/0	−1.03±0.41	30.6±7.5	−0.32±0.14	10.2±3.5
63, 60	−0.628±0.18	15	13/0	2/0	−1.12±0.32	29.5±7.2	−0.36±0.13	10.7±3.5
61, 55	−0.652±0.17	15	15/0	0/0	−1.10±0.33	27.9±7.6	−0.40±0.11	10.8±3.3
59, 50	−0.667±0.19	15	14/0	1/0	−1.10±0.37	25.8±7.4	−0.42±0.12	10.4±4.1
57, 45	−0.684±0.19	15	14/0	1/0	−1.01±0.33	23.8±7.7	−0.47±0.15	10.4±5.3
55, 40	−0.684±0.20	15	14/0	1/0	−1.04±0.36	21.3±7.7	−0.47±0.16	8.0±5.7
53, 35	−0.683±0.20	15	13/0	2/0	−0.96±0.37	19.4±8.3	−0.51±0.19	7.2±5.9
51, 30	−0.640±0.24	13	10/0	3/0	−0.85±0.34	16.9±9.4	−0.49±0.21	4.5±6.9
49, 25	−0.473±0.25	11	5/0	5/1	−0.70±0.43	14.8±9.8	−0.35±0.19	−2.7±4.8
47, 20	−0.406±0.20	7	2/0	5/0	−0.66±0.34	10.5±8.5	−0.27±0.18	−5.7±3.6
slope s	0.488±0.23	15	0/11	0/4	24.1±10.6	18.9±10	0.01±0.01	0.03±0.2

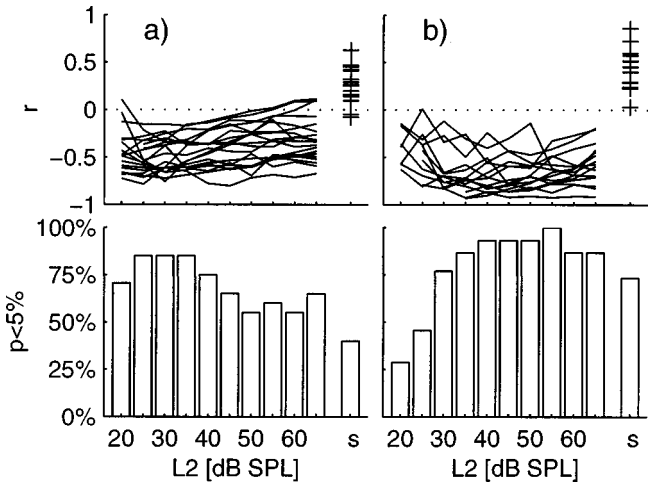

FIG. 8. Results of the linear regression analysis of individual data sets from (a) 20 normal and (b) 15 hearing impaired ears. The top panels show the correlation coefficients r of the DP level L_{dp} at the different $L2$ levels and of the slope s of the I/O functions (+) to the hearing threshold L_t. The bar plots just below indicate the percentage of significant correlations ($p < 0.05$).

tone levels, around $L2 = 40$ dB SPL, whereas in the normally hearing ears, the correlation tended to continuously increase with further decreasing $L2$ and was maximal at $L2 = 25$ dB SPL. Thus significant correlations were found in 14/15 impaired ears at moderate and high stimulus intensities, but were found in 17/20 normal ears at lowest primary tone levels. In the impaired ears, the coefficients a' of regressions lines $L_{dp} = a'L_t + b'$, which allow to infer what drop in DP level may be expected for a given threshold elevation, most distinctly reflected the differential sensitivity of the DP: whereas at $L2 = 65$ dB SPL, a' was only 0.32 dB/dB, a' increased up to 0.51 dB/dB with decreasing $L2$ to 35 dB SPL. This indicates that the DP level changes that may be expected with growing hearing loss are about 60% larger at low primary tone levels than at high levels. Similarly, slope s showed better correlations in impaired hearing, although the average correlation of slope s to L_t was worse than that of the DP level at all primary tone levels. On the other hand, in 4/15 impaired ears and 6/20 normal ears the correlations between the slope and the hearing threshold were better than those of the DP level at $L2 = 40$ or 60 dB SPL, which indicates a partial independence of the DP level and the growth behavior.

III. DISCUSSION

A. A physiologically motivated stimulus level paradigm results in compressive DP growth in normal hearing

In normal hearing, the DP showed a strongly compressive growth behavior. The growth rates decreased continuously with increasing stimulus level (Figs. 3, 4, and 7). This is quite different from the growth behavior described in the literature. With equal level primary tones, the DP growth in humans was found to be best described as a straight line with a slope of about 1 dB/dB (Popelka *et al.*, 1993), or just below (Lonsbury-Martin *et al.*, 1990; Gaskill and Brown, 1990), and showed saturation only, if at all, at high stimulus levels of about 60 dB SPL (see Sec. III B, for discussion of nonmonotonic growth behavior).

The growth behavior observed in this study obviously results from the different stimulus paradigm used. Essentially, the primary tone level difference $L1 - L2$ was systematically increased with decreasing primary tone level, according to $L1 = 0.4L2 + 39$ dB. That is, at highest stimulus levels of 65 dB SPL, $L1$ and $L2$ were set equal, whereas $L1 - L2$ was monotonically increased with decreasing $L2$, such that $L1 - L2$ was 27 dB at $L2 = 20$ dB SPL.

Such stimulus settings may be deduced from DP studies which have examined the dependence of the DP level on $L1 - L2$ primary tone level difference. While varying $L1$ at different stationary $L2$ levels, Gaskill and Brown (1990) have first shown that there is a local maximum in DP level at a $L1 - L2$ difference, which systematically increases with decreasing $L2$. Later, these findings were confirmed (Hauser and Probst, 1991; Rasmussen *et al.*, 1993) and extended by Whitehead *et al.* (1995b). Whitehead *et al.* (1995b) indicated that the optimum $L1 - L2$ difference may well be approximated by a linear equation $L1 = aL2 + (1 - a)b$, with $a \approx 0.5$ and $b \approx 90$ dB SPL for primary tones with a geometric mean frequency at 3 kHz ($f2/f1 = 1.25$). The limited data in this study suggested that a was relatively constant across frequency ($1 < f2 < 8$ kHz, $f2/f1 = 1.21$), but b may vary between 65 and 85 dB SPL. With respect to this, the stimulus paradigm chosen in this study ($a = 0.4$, $b = 65$ dB SPL) presents an initial effort to match stimulus conditions that generate maximum distortion over a wide range of $L2$ levels, based on literature data available at the beginning of this study (Gaskill and Brown, 1990). Both interindividual differences and a frequency dependence may need to be allowed for when individually optimal stimulus conditions are aimed.

The physiological significance of such a stimulus setting may be understood considering implications of mechanical excitation patterns for the DP generation process, as far as these are predictable from basilar membrane vibration data. Since the DP is most likely to be generated at the $f2$ place, i.e., the site of maximum nonlinear interaction of both primary tones, it is important to compare presumable responses of both primary tones at this site. Available basilar membrane data during single-tone stimulation (Johnstone *et al.*, 1986; Robles *et al.*, 1986; Ruggero and Rich, 1991a; Sellick *et al.*, 1982; Ruggero *et al.*, 1997) indicate that the growth and the threshold of both responses would greatly differ. Corresponding to the characteristic frequency (CF) at a given BM location, $f2$ has lowest threshold and most compressive growth, whereas the response to $f1$, which is about 0.25 octaves below the CF ($f2/f1 = 1.2$), will have a higher threshold and a less compressive growth. From the data of Johnstone *et al.* (1986), who examined a 18-kHz CF place, it appears that between 20 and 60 dB SPL, the $f1$ growth was about twice that of $f2$. At 60 dB SPL, the responses for both primary tone were equal. From this it can be derived that $L1 = 0.5L2 + 30$ dB describes stimulus conditions that most likely result in equal primary tone levels at the $f2$ place. Similar conclusions can be drawn from the other data cited.

Given the differences in method, species, frequency

range, and $f2/f1$ ratios, the optimal $L1-L2$ settings empirically defined in the above cited DP studies appear to be identical to those predictable from theoretical considerations. An attempt to approach optimal $L1-L2$ settings thus may be understood to equalize stimulus responses at the DP generation site.

B. Compressive growth of the DP reflects characteristics of the cochlear amplifier

In normal hearing, DPs were reliably measured over the whole primary tone intensity range at $f2$ frequencies above about 1.5 kHz using only a short averaging time (4 s); below 1.5 kHz, the noise floor limited measurements at low stimulus levels (Fig. 1). Above 1.5 kHz, the average DP thresholds thus lay within 10 dB of the average hearing thresholds, the minima of which around 1 and 5 kHz were about 10 dB SPL. Accounting for appropriate stimulus conditions (see Sec. III A), however, not only allowed to easily measure DP down to close-to-threshold stimulus levels, but is also suggested to provide more relevant information about the dominant nonlinearity underlying DP generation, which is thought to correspond to the nonlinear OHC transfer function, used to describe the ''cochlear amplifier'' (Davis, 1983; Dallos, 1992). Indeed, the compressive growth behavior of the DP we have observed in this study strongly reminds us of the nonlinear gain attributed to the cochlear amplifier.

Basilar membrane data show strong compression and nonlinearity at the CF of a particular place (Johnstone *et al.*, 1986; Ruggero and Rich, 1991a, 1991b; Nuttall and Dolan, 1996; Ruggero *et al.*, 1997). Mechanisms interfering with OHC function abolish low level responses and produce linear response growth, which is thought to be the passive response. The sensitivity difference between both states has been interpreted in terms of the gain of the cochlear amplifier, which predominantly boosts basilar membrane motion at low input levels, but gradually saturates at moderate levels.

Intermodulation distortion is thought to be generated as a by-product of this amplification and may be expected to reflect its fundamental properties. The compressive growth behavior, which was observed in this study, we therefore relate to nonlinear gain and saturation of the active processes.

Differing growth behavior does not contradict this interpretation. Both overbending DP growth, which was found in 13% of all I/O functions and more linear growth may be expected, since some variability in the DP growth as a function of $L1,L2$ has been reported and one fixed stimulus paradigm across frequency and subjects need not match individual optimum $L1,L2$ conditions (Gaskill and Brown, 1990; Whitehead *et al.*, 1995b). Nonmonotonic DP growth we only rarely observed in 3% of all I/O functions (30/1020). In agreement with ideas proposed to account for nonmonotonic DP growth, assuming phase cancellation between wavelets at the primary tone place (Zwicker, 1980; Matthews and Molnar, 1986) or between this primary source and a secondary SFE source stimulated by the DP propagated apically to its own characteristic place (e.g., Kemp and Brown, 1983; Kummer *et al.*, 1995; Heitmann *et al.*, 1997), we attribute the relatively rare occurrence in this study to the stimulus paradigm used.

C. Differential sensitivity of low and high primary tone level DP to cochlear impairment

In cochlear impairment DPs were reliably measured down to threshold stimulus levels above $f2=1.5$ kHz, where the average DP thresholds lay within 5 dB of the average hearing thresholds (Fig. 1). Within this stimulus level range, a differential sensitivity of low and high primary tone level DPs to cochlear impairment was found. Exemplary cases showed that at medium primary tone levels ($L2=40$ dB SPL) the DPs may change twice as much as those at high primary tone levels ($L2=60$ dB SPL, see Figs. 5 and 6). Due to this the growth of the DP linearized. The I/O functions' slope s that was calculated between $L2=40$ and 60 dB SPL increased with hearing loss up to about 1 dB/dB (Fig. 7). Conversely, this linearization allowed quantifying the differential sensitivity. An increase of the slope s from physiologically shallow growth (0.2 dB/dB), e.g., up to 1 dB/dB indicated that the DP level at $L2=40$ dB SPL dropped by 16 dB more than at $L2=60$ dB SPL. Maximal growth rates above $L2=50$ dB SPL were up to 1.4 dB/dB.

The behavior of the DP thus reflects in detail not only physiological characteristics but also pathophysiological changes attributed to the cochlear amplifier, as have been observed during loss of OHC function. In the vibration of the basilar membrane, the greatest response loss is found at the lowest stimulus levels, but few changes occur at high levels above about 70 dB SPL (e.g., Johnstone *et al.*, 1986; Ruggero and Rich, 1991b). In terms of the response growth, the physiologically compressive growth becomes more linear, approaching 1 dB/dB. Since the behavior of the DPs in this study parallels this, we conclude that DP level and growth behavior closely reflect changes to OHC function. The significance of an appropriate stimulus paradigm appears to optimize stimulus conditions such that changes of OHC function can be observed at stimulus levels where its function is greatest, i.e., close to the hearing threshold. Animal DP studies do indicate this (Whitehead *et al.*, 1995b).

Compared to DP data reported in the literature, the linearization of the DP growth observed in this study, with the average growth rate approaching 1 dB/dB in cochlear impairment, is distinctly different. In experimental animals (e.g., Mills *et al.*, 1993; Whitehead *et al.*, 1992, 1995b), the DP growth is expansive with $L1-L2=a$ constant and approaches, but generally does not attain, 3 dB/dB with loss of OHC function, as predicted by a simple power law nonlinearity. Two reasons appear to explain for this apparent difference. One is related to the stimulus paradigm. A DP growth rate of 3 dB/dB is predicted when $L1-L2=a$ constant. In our study, however, $L1$ was increased in smaller steps than $L2(L1=0.4L2)$. Thus a growth rate of only 1.8 dB/dB is predicted, when the DP growth is related to $L2$. Experimental data from animals, which were collected over a wide range of $L1,L2$ combinations, confirm this dependence on the stimulus settings (Mills *et al.*, 1993; Whitehead *et al.*, 1992, 1995b). For example, the data in Whitehead *et al.*

(1995b, their Fig. 4b) indicate that with $L1=L2$, the DP growth was 2.7 dB/dB in impaired hearing; with $L1=0.4L2+39$ dB, however, the DP grew by only 1.4 dB per dB increase in $L2$. The maximal growth rates observed in this study, i.e., up to 1.4 dB/dB above $L2=50$ dB SPL, closely approach this. The second reason why maximal growth rates were lower in this study relates to signal-to-noise ratios, which are about 20 dB smaller in humans than in experimental animals. Assuming that the DP level decreases and the DP growth rate increases by about the same amount in hearing impaired animals and humans, smaller S/N in humans certainly limit the range of growth rates that may be observable in humans. In other words, the truly passive DP growth may be hardly observable in humans because of smaller S/N ratios.

Using the same stimulus paradigm as in this study, Janssen *et al.* (1998) reported distinctly different behavior of the DP in cochlear hearing impaired ears with tinnitus. In part of these ears, the DPs were actually enhanced in the frequency region of the tinnitus and even increased with increasing hearing loss. Whereas strong, negative correlations between DP level and hearing threshold, which were dependent on the primary tone level were found in this study, tinnitus ears partly exhibited a poor or even inverse relationship between the DP level and the hearing threshold.

D. The correlation of the DP level to the hearing threshold in normal hearing

In normal hearing there was generally a negative correlation of the DP level to the threshold level, confirming previous findings of Gaskill and Brown (1990), the only comparable study measuring hearing threshold and DP level ($L2=40/45$ dB SPL) with the same probe system. Extending their findings the correlation was found to depend on the primary tone level. The average correlation coefficient increased with decreasing $L2$ to 25 dB SPL, such that 17/20 data sets showed significant correlations ($p<5\%$) versus only 11 to 13 at the highest primary tone levels ($L2=60,65$ dB SPL). Two reasons appeared to be responsible for this.

First, with decreasing primary tone levels, a fine structure appeared in the DP grams, which was often not visible at high primary tone levels and ran parallel to that of the hearing threshold. This occurred only when $L2$ was close to the threshold level and f_t was compared to $f2$. With regard to the DP generation, this strongly suggests that the same active process supposed to determine the hearing threshold at f_t also underlies the DP generation. Thus OHC function relevant for the pure-tone threshold at a given frequency is best tested with DP elicited with close-to-threshold stimuli and the DP generation site seems to be close to the $f2$ place in the cochlea. The fact that $L1$ greatly exceeded $L2$ appeared not to compromise this. A missing correspondence in the fine structure in part of the data does not necessarily contradict this, since it is suspected that, especially at low stimulus levels, a SFE component that is elicited by apical propagation of the DP may significantly contribute to the ear canal signal (Kemp and Brown, 1983; Kummer *et al.*, 1995; Heitmann *et al.*, 1997). Thus OHC activity from places about half an octave below $f2$ may contribute in a complex way to the DP generated at $f2$. It remains to be examined, however, if with suppression of this component the correspondence of the DP to the threshold level becomes more robust, as suspected by Heitmann *et al.* (1997).

Second, besides the fine structure, also the bimodal shape of the gross DP gram corresponded best to the very similar shape of the hearing threshold at lowest stimulus levels. With increasing primary tone level, the average DP grams shifted upward by 0.2 octaves (Figs. 2 and 4). In part of the data from normally hearing ears, the DP correlation to the hearing threshold thus decreased and even positive correlations resulted (Table II). As long as the origin of the bimodal shape itself is unclear, however, one can only speculate about the origin of this upward frequency shift. A first step to clarify this would be the calibration of the transducers with reference to eardrum SPL. It is known that the in-the-ear calibration method used in this study will underestimate ear drum SPLs because of standing wave minima in the outer ear canal at the probe microphone location at frequencies between 3.5 and 7 kHz (e.g., Siegel and Hirohata, 1994; Whitehead *et al.*, 1995c). Comparison of the average hearing threshold levels in this study to the human minimum audible pressure (MAP) data of Killion (1978) in Fig. 4 (upper most panel), which generally shows good agreement, may indicate some underestimation of eardrum SPLs in this frequency range: hearing threshold levels are lower between 3 and 5 kHz, but higher in all other frequency ranges. Thus eardrum SPLs of the primary tones may have been greater than ''nominal'' SPLs at the probe microphone between 3.5 and 7 kHz. Compared to the nominal $L1-L2$ difference, $L1-L2$ at the eardrum (for typical $f2/f1$ ratios in DP studies) may be expected to be both smaller and greater in the lower and upper half of this frequency range, respectively (Whitehead *et al.*, 1995c, their Fig. 1). Since the DP level depends in a complex way on $L2$ and-especially-$L1$ (Gaskill and Brown, 1990; Whitehead *et al.*, 1995b), the influence of such errors can hardly be predicted; certainly, the growth and level of the DP will be affected in a frequency specific manner and the observed upward frequency shift could emerge.

One argument which may be thought to restrict the primary tone level dependence of the DP-to-threshold correlation we report here is a frequency dependence of this correlation reported in the literature (e.g., Martin *et al.*, 1990; Kim *et al.*, 1996). In these studies, lower correlations at low primary tone frequencies compared to higher frequencies have been observed. Since with lowering primary tone level fewer low-frequency data would enter data pooling because of smaller S/N at low frequencies, a confounding influence may arise which partly underlies the level dependence we observed in this study. Although one may basically agree with this argumentation, the crucial question, i.e., whether low-frequency DPs had poorer correlations to the hearing threshold, is not clearly answered in the literature in our opinion, as it was not considered there that low-frequency DPs had distinctly lower variability because of smaller S/N ratios. Since lower variability decreases possible correlations, S/N effects apparently confounded the reported frequency effects.

Despite significant correlations in individual ears, a wide

interindividual variability of the DP level was found, which is displayed by the scatter of the DP level plotted against threshold level [upper panel, Fig. 7(a)] and quantitatively reflected in 7-dB standard deviations of the coefficients b of regression lines $L_t = aL_{dp} + b$ fitted to individual data sets (Table II). Certainly, this seems to be the major limiting factor in terms of a threshold prediction test from DP level data.

E. The correlation of the DP level and growth to the hearing threshold in impaired hearing

In hearing impaired ears there were strong negative correlations of the DP level to the hearing threshold. The correlations were maximal at low-to-moderate primary tone levels around $L2 = 35$ to 55 dB SPL (Table III). Lower correlations at lowest primary tone levels ($L2 \leqslant 30$ dB SPL) may be due to a decrease of the signal-to-noise ratio. At higher primary tone levels ($L2 \geqslant 60$ dB SPL), however, the correlations clearly decreased since the DP were less sensitive to hearing loss (Figs. 5 and 6). Linear regression analysis of the individual data sets (Table III) revealed that DP level changes may be expected to increase by on average 60% with decreasing $L2$ from 65 to 35 dB SPL and that regression coefficients a' increase from 0.3 to 0.5 dB/dB. Compared to observations in individual data sets (Fig. 6), however, the absolute values of these averaged coefficients appear to be smaller. Possibly, this indicates limitations of applying *linear* regression analysis to the data.

These observations thus confirm previous findings in animal studies that indicated a greater sensitivity of the DP at lower primary tone levels (Wiederhold *et al.*, 1986; Brown *et al.*, 1989; Norton and Rubel, 1990; Whitehead *et al.*, 1992; Mills *et al.*, 1993; Mills and Rubel, 1994). Few human studies, however, systematically examined the influence of primary tone level on the correlation of the DP level to the hearing threshold. Kimberley *et al.* (1995) found that across a primary tone level range between $L2 = 20$ and 50 dB SPL, the DP level at $L2 = 50$ dB SPL was the most important variable discriminating normal from impaired hearing ($\geqslant 30$ dB SPL). Within a wider primary tone level range ($10 \leqslant L2 \leqslant 65$ dB SPL), Stover *et al.* (1996) similarly found that a primary tone level of $L2 = 55$ dB SPL produced the best separation between normal and impaired hearing (> 20 dB HL) in terms of DP amplitudes. In both studies, however, a constant primary tone level difference of $L1 - L2 = 10$ dB was used, a condition that appears disadvantageous for $L2$ levels below about 50 dB SPL (see Sec. III A). Other studies compared equilevel with more appropriate primary tone level settings and found that compared to $L1 = L2 = 55$ dB SPL, the DP sensitivity to the effects of tonal overexposure was greatly increased with $L1 - L2 = 25$ dB, although preexposure signal-to-noise ratios were comparable (Sutton *et al.*, 1994). Very similar observations were reported by Whitehead *et al.* (1995a). The results of the present study systematically extend these findings and demonstrate that the effects of cochlear impairment on the DP level increase on average by 2/3 with lowering $L2$ from 65 to 35 dB SPL.

To detect OHC impairment, DPs thus should be measured at stimulus levels as close as possible to the hearing threshold, i.e., at levels where OHC function is maximal. In practice, this implies DP measurements not only at high but also at lower primary tone levels. With a stimulus paradigm, as the one presented in this study, which continuously increases $L1 - L2$ with decreasing $L2$ and maximizes the DP level, measurement time is not unreasonably extended with lowering primary tone levels, in contrast to other investigators' experiences with constant $L1 - L2$ (Stover *et al.*, 1996). With a constant variability of normative DP levels, independent on the primary tone level, most distinct changes of the DP level with lowering $L2$ thus may be expected to optimize the performance of DP testing of cochlear impairment.

Despite the fact that lowering $L2$ may considerably improve DP sensitivity, however, the prediction of the hearing threshold appears limited by the weak overall DP-to-threshold correlation (Fig. 7), also reflected in the 7-dB standard deviations of the regression coefficients b (Table III). For a prediction of the hearing threshold, it therefore appears potentially useful to also consider relative DP measures, i.e., the growth of the DP. In about two-thirds of the impaired ears, the slope s was significantly correlated with the hearing threshold. In 3 and 4/15 ears the slope s even better correlated to the hearing threshold than the DP level at $L2 = 40$ and 60 dB SPL, respectively. More importantly, weak or even inverse correlations between DP level and hearing threshold were found in tinnitus ears (Janssen *et al.*, 1998). In part of these ears, the DP level *per se* was found to be hardly capable to manifest hearing impairment and to be even a misleading measure. Much more consistent correlations, however, were found between the DP growth and the hearing threshold in these ears. Together with the data in this study, this indicates some independence of the absolute DP level and the DP growth. For a clinical application and the prediction of the hearing threshold, DP thus should be measured not only at high, but also at lower primary tone levels, also enabling assessment of the growth behavior of the DP.

ACKNOWLEDGMENTS

We greatly appreciate the discussions and valuable comments on earlier versions of this manuscript of M. Kössl along with the efforts of the two anonymous reviewers. This work was supported by the Deutsche Forschungsgemeinschaft within the SFB 204 ''Gehör.''

[1]With loss of lower primary tone level DPs in hearing impairment, the slope s was calculated from a smaller $L2$ range over at least 10 dB, i.e., mostly between $L2 = 50$ and 60 dB SPL. From Fig. 7 (bottom panels), which shows still compression although the DP growth generally linearized with increasing hearing loss, it can be deduced that the actual slope thus might be underestimated.

[2]At $L2 = 65$ dB SPL, the DP level changed on average by 2.4 dB from one point to the next. With lowering stimulus levels to $L2 = 20$ dB SPL, the mean point-to-point DP level change continuously increased to 4 dB.

[3]For $f2 = f_t$, this correlation was worse: $r = -0.4887$, though still significant ($p < 0.001$).

Brown, A. M., McDowell, B., and Forge, A. (**1989**). ''Acoustic distortion products can be used to monitor the effects of chronic gentamycin treatment,'' Hearing Res. **42**, 143–156.

Dallos, P. (**1992**). ''The active cochlea,'' J. Neurosci. **12**, 4575–4585.

Davis, H. (**1983**). ''An active process in cochlear mechanics,'' Hearing Res. **9**, 79–90.
Gaskill, S. A., and Brown, A. M. (**1990**). ''The behavior of the acoustic distortion product, $2f_1-f_2$, from the human ear and its relation to auditory sensitivity,'' J. Acoust. Soc. Am. **88**, 821–839.
Harris, F. P. (**1990**). ''Distortion-product otoacoustic emissions in humans with high frequency sensorineural hearing loss,'' J. Speech Hear. Res. **33**, 594–600.
Hauser, R., and Probst, R. (**1991**). ''The influence of systematic primary-tone level variation L_2-L_1 on the acoustic distortion product emission $2f_1-f_2$ in normal human ears,'' J. Acoust. Soc. Am. **89**, 280–286.
Heitmann, J., Waldmann, B., Schnitzler, H. U., Plinkert, P. K., and Zenner, H.-P. (**1997**). ''Suppression growth functions of DPOAE with a suppressor near $2f_1-f_2$ depends on DP fine structure: Evidence for two generation sites for DPOAE,'' Abstr. 20th Midwinter Mtg. Assoc. Res. Otolaryngol. 83.
Janssen, T., Kummer, P., and Arnold, W. (**1998**). ''Growth behavior of the $2f_1-f_2$ distortion product otoacoustic emission in tinnitus,'' J. Acoust. Soc. Am. **103**, 3418–3430.
Johnstone, B. M., Patuzzi, R., and Yates, G. K. (**1986**). ''Basilar membrane measurements and the traveling wave,'' Hearing Res. **22**, 147–153.
Kemp, D. T., and Brown, A. M. (**1983**). ''An integrated view of cochlear mechanical nonlinearities observable from the ear canal,'' in *Mechanics of Hearing*, edited by E. de Boer and M. A. Viergever (Martinus Nijhoff, The Hague, The Netherlands), pp. 75–82.
Killion, M. C. (**1978**). ''Revised estimate of minimum audible pressure: Where is the ''missing 6 dB''?,'' J. Acoust. Soc. Am. **63**, 1501–1508.
Kim, D. O., Paparello, J., Jung, M. D., Smurzynski, J., and Sun, X. (**1996**). ''Distortion otoacoustic emission test of sensorineural hearing loss: Performance regarding sensitivity, specificity, and receiver operating characteristics,'' Acta Oto-Laryngol. (Stockh) **116**, 3–11.
Kimberley, B. P., Hernadi, I., Lee, A. M., and Brown, D. K. (**1995**). ''Predicting pure tone threshold in normal and hearing-impaired ears with distortion product emission and age,'' Ear and Hearing **15**, 199–209.
Kummer, P., Janssen, T., and Arnold, W. (**1995**). ''Suppression tuning characteristics of the $2f_1-f_2$ distortion product otoacoustic emission in humans,'' J. Acoust. Soc. Am. **98**, 197–210.
Lonsbury-Martin, B. L., Harris, F. P., Stagner, B. B., Hawkins, M. D., and Martin, G. K. (**1990**). ''Distortion product emissions in humans. I. Basic properties in normally hearing subjects,'' Ann. Otol. Rhinol. Laryngol. (Suppl. 147) **99**, 3–14.
Martin, G. K., Ohlms, L. A., Franklin, D. J., Harris, F. P., and Lonsbury-Martin, B. L. (**1990**). ''Distortion product otoacoustic emissions: III. Influence of sensorineural hearing loss,'' Ann. Otol. Rhinol. Laryngol. **99**, 30–42.
Matthews, J. W., and Molnar, C. E. (**1986**). ''Modeling intracochlear and ear canal distortion products $2f_1-f_2$,'' in *Peripheral Auditory Mechanisms*, edited by J. B. Allen, J. L. Hall, A. Hubbard, S. T. Neely, and A. Tubis (Springer-Verlag, New York), pp. 258–265.
Mills, D. M., Norton, S. J., and Rubel, E. D. (**1993**). ''Vulnerability and adaptation of distortion product otoacoustic emissions to endocochlear potential variation,'' J. Acoust. Soc. Am. **94**, 2108–2122.
Mills, D. M., and Rubel, E. D. (**1994**). ''Variation of distortion product otoacoustic emissions with furosemide injection,'' Hearing Res. **77**, 183–199.
Nelson, D. A., and Kemberley, B. P. (**1992**). ''Distortion-product emissions and auditory sensitivity in human ears with normal hearing and cochlear hearing loss,'' J. Speech Hear. Res. **35**, 1142–1159.
Norton, S. J., and Rubel, E. R. (**1990**). ''Active and passive ADP components in mammalian and avian ears,'' in *The Mechanics and Biophysics of Hearing*, edited by P. Dallos, C. D. Geisler, J. W. Matthews, M. A. Ruggero, and C. R. Steele (Springer-Verlag, Berlin), pp. 219–226.
Nuttall, A. L., and Dolan, D. F. (**1996**). ''Steady-state sinusoidal velocity responses of the basilar membrane in the guinea pig,'' J. Acoust. Soc. Am. **99**, 1556–1565.
Popelka, G. R., Osterhammel, P. A., Nielsen, L. H., and Rasmussen, A. N. (**1993**). ''Growth of distortion product otoacoustic emissions with primary-tone level in humans,'' Hearing Res. **71**, 12–22.
Rasmussen, A. N., Popelka, G. R., Osterhammel, P. A., and Nielsen, L. H. (**1993**). ''Clinical significance of relative probe-tone levels on distortion product otoacoustic emissions,'' Scand. Audiol. **22**, 223–229.
Robles, L., Ruggero, M. A., and Rich, N. C. (**1986**). ''Basilar membrane mechanics at the base of the chinchilla cochlea. I. Input–output functions, tuning curves and response phases,'' J. Acoust. Soc. Am. **80**, 1364–1374.
Ruggero, M. A., and Rich, N. C. (**1991a**). ''Application of a commercially-manufactured Doppler-shift laser velocimeter to the measurement of the basilar-membrane vibration,'' Hearing Res. **51**, 215–230.
Ruggero, M. A., and Rich, N. C. (**1991b**). ''Furosemide alters organ of Corti Mechanics: Evidence for Feedback of outer hair cells upon the basilar membrane,'' J. Neurosci. **11**, 1057–1067.
Ruggero, M. A., Rich, N. C., Recio, A., and Narayan, S. S. (**1997**). ''Basilar-membrane responses to tones at the base of the chinchilla cochlea,'' J. Acoust. Soc. Am. **101**, 2151–2163.
Sellick, P. M., Patuzzi, R., and Johnstone, B. M. (**1982**). ''Measurement of basilar membrane motion in the guinea pig using the Mössbauer technique,'' J. Acoust. Soc. Am. **72**, 131–141.
Seigel, J. H., and Hirohata, E. T. (**1994**). ''Sound calibration and distortion product otoacoustic emissions at high frequencies,'' Hearing Res. **80**, 146–152.
Stover, L., Gorga, M. P., Neels, S. T., and Montoya, D. (**1996**). ''Towards optimizing the clinical utility of distortion product otoacoustic emission measurements,'' J. Acoust. Soc. Am. **100**, 956–967.
Sutton, L. A., Lonsbury-Martin, B. L., Martin, G. K., and Whitehead, M. L. (**1994**). ''Sensitivity of distortion-product otoacoustic emissions in humans to tonal overexposure: Time course of recovery and effects of lowering $L2$,'' Hearing Res. **75**, 161–174.
Wiederhold, M. L., Mahoney, J. W., and Kellog, D. L. (**1986**). ''Acoustic overstimulation reduces $2f_1-f_2$ cochlear emissions at all levels in the cat,'' in *Peripheral Auditory Mechanisms*, edited by J. B. Allen, J. L. Hall, A. Hubbard, and A. Tubis (Springer-Verlag, New York), pp. 322–329.
Whitehead, M. L., Lonsbury-Martin, B. L., and Martin, G. K. (**1992**). ''Evidence for two discrete sources of $2f_1-f_2$ distortion-product otoacoustic emissions in rabbit. II: Differential physiological vulnerability,'' J. Acoust. Soc. Am. **92**, 2662–2682.
Whitehead, M. L., McCoy, M. J., Lonsbury-Martin, B. L., and Martin, G. K. (**1995a**). ''Dependence of distortion-product otoacoustic emissions in primary levels in normal and impaired ears. I. Effects of decreasing $L2$ below $L1$,'' J. Acoust. Soc. Am. **97**, 2346–2358.
Whitehead, M. L., Stagner, B. B., McCoy, M. J., Lonsbury-Martin, B. L., and Martin, G. K. (**1995b**). ''Dependence of distortion-product otoacoustic emissions on primary levels in normal and impaired ears. II. Asymmetry in L_1,L_2 space,'' J. Acoust. Soc. Am. **97**, 2359–2377.
Whitehead, M. L., Stagner, B. B., Lonsbury-Martin, B. L., and Martin, G. K. (**1995c**). ''Effects of ear-canal standing waves on measurements of distortion-product otoacoustic emissions,'' J. Acoust. Soc. Am. **98**, 3200–3214.
Zwicker, E. (**1980**). ''Nonmonotonic behavior of $(2f_1-f_2)$ explained by a saturation-feedback model,'' Hearing Res. **2**, 513–518.
Zwicker, E. (**1986**). ''Suppression and $(2f_1-f_2)$ difference tones in a nonlinear cochlear model with active feedback,'' J. Acoust. Soc. Am. **80**, 163–176.

Observing middle and inner ear mechanics with novel intracochlear pressure sensors

Elizabeth S. Olson[a)]
Physics Department, Princeton University, Princeton, New Jersey 08544

(Received 16 July 1997; revised 17 February 1998; accepted 18 February 1998)

Intracochlear pressure was measured *in vivo* in the base of the gerbil cochlea. The measurements were made over a wide range of frequencies simultaneously in scalae vestibuli and tympani. Pressure was measured just adjacent to the stapes in scala vestibuli and at a number of positions spaced by tens of micrometers, including a position within several micrometers of the basilar membrane, in scala tympani. Two findings emerged from the basic results. First, the spatial variation in scala tympani pressure indicated that the pressure is composed of two modes, which can be identified with fast and slow waves. Second, at frequencies between 2 and 46 kHz (the upper frequency limit of the measurements) the scala vestibuli pressure adjacent to the stapes had a gain of approximately 30 dB with respect to the pressure in the ear canal, and a phase which decreased linearly with frequency. Thus, over these frequencies the middle ear and its termination in the cochlea operate as a frequency independent transmission line. A subset of the data was analyzed further to derive the velocity of the basilar membrane, the pressure difference across the organ of Corti complex (defined to include the tectorial and basilar membranes) and the specific acoustic impedance of the organ of Corti complex. The impedance was found to be tuned in frequency. [S0001-4966(98)00906-0]

PACS numbers: 43.64.Kc, 43.64.Ha, 43.64.Yp, 43.38.Kb [RDF]

INTRODUCTION

The cochlea is a fluid dynamic system. Of special interest is the motion of the cochlea's organ of Corti (O.C.) because it stimulates hair cells, and this motion has been the emphasis of intracochlear experimentation and models of cochlear mechanics. One force driving the motion is the fluid pressure difference across the organ of Corti. Localized measurements of pressure, and the pressure gradients that indicate fluid motion, are key to understanding the motion and mechanics of the organ of Corti, and cochlear fluid dynamics in general. On another note, scala vestibuli (S.V.) pressure near the stapes, the ''input'' pressure to the inner ear, is also the ''output'' of the middle ear, and its measurement is key to understanding the middle ear's operation.

In previous studies the pressure measured near the stapes in S.V. has been used to estimate the cochlear input impedance and to determine the gain of the middle ear (Dancer and Franke, 1980; Nedzelnitsky, 1980; Lynch *et al.*, 1982; Decory *et al.,* 1990). The current measurements extend those measurements to another species and include much higher frequencies. The frequency range extended from either 200 or 500 Hz to 46 kHz, which comprises much of the approximately 60-kHz auditory range of the gerbil (Ryan, 1976). A particularly simple relationship between the S.V. pressure just inside the stapes and the pressure in the ear canal emerged at frequencies between 2 and 46 kHz. The pressure gain was relatively flat, at approximately 30 dB, and the linear phase versus frequency relationship could be characterized as a constant 25-μs delay. The gain decreased as the frequency was reduced below 2 kHz, and was approximately 10 dB at 200 Hz.

Intracochlear pressure is fundamentally a field, and for illuminating cochlear mechanics examining the pressure's spatial variation is essential. In the current study the pressure field in scala tympani (S.T.) was mapped close to the basilar membrane (B.M.) through the round window opening. The S.T. pressures and spatial variations that were found can be economically interpreted as being a combination of two pressure modes, a ''fast wave'' mode and a ''slow wave'' mode. The fast mode was dominant at positions relatively far from the B.M. and the slow mode at positions less than 100 μm from the B.M. The fast and slow waves have been discussed in the theoretical and experimental literature. In a theoretical model Peterson and Bogart (1950) showed that the pressure in the cochlea could be mathematically separated into a component that traveled with the speed of sound (fast) and a component that traveled at the speed of the O.C. traveling wave (slow). Because it is linked to the O.C. traveling wave, the slow mode has been emphasized in most cochlear models. However, Lighthill (1981) suggested that the fast wave might be responsible for the high frequency plateaus in B.M. motion found by Rhode (1971) and subsequently in many other B.M. motion studies (Ruggero *et al.*, 1997; Nuttall and Dolan, 1996; Ulfendahl and Khanna, 1993; Cooper and Rhode, 1992a). The fast wave was implicated by Cooper and Rhode (1996) in producing artifactual O.C. motions in cochleae in an unnatural condition (open apex). Dancer and Franke (1980) discussed the two pressure waves, and the associated difficulty of using point intracochlear pressure measurements to find the pressure across the O.C. complex.

The spatial variation of the S.T. pressure and in particular the emergence of a slow wave pressure close to the B.M.

a)Electronic mail: olson@pupgg.princeton.edu

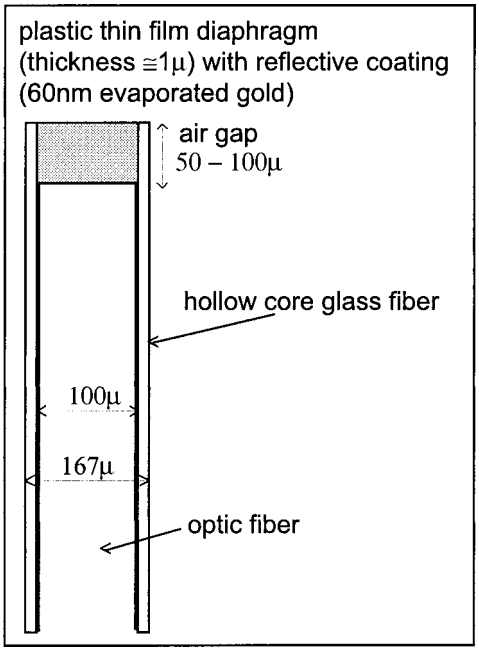

FIG. 1. Fiber optic pressure sensor tip. During measurements the pressure sensitive diaphragm was located at the measurement position within the cochlea or ear canal. The optic fiber that is shown threaded into the sensor tip is one of two output arms of a fiber coupler. The second output arm is not used. The two input arms are coupled to a LED, which delivers light to the sensor diaphragm, and a photodiode, which detects the light that reflects off the diaphragm.

underscore the intimate link between the intracochlear pressure field and the motion of the O.C. complex. The final analysis demonstrates the use of the pressure data to estimate the quantitative form of the impedance of the O.C. complex, and finds that it is tuned.

It is important to note at the outset that the condition of the cochleae, as determined from changes in compound action potential threshold, was not optimal.

I. METHODS

A. Sensor

The sensor is illustrated in Fig. 1. The sensor has been described briefly (Olson and Borawala, 1997), and its construction is detailed here.

1. Sensor tip

The sensor tip is composed of a hollow core glass fiber (inner diameter 100 μm, outer diameter 167 μm, Polymicro Technologies, Phoeniz, AZ), terminated with a pressure sensitive diaphragm made reflective with a thin layer of gold. The diaphragm is a plastic thin film, formed by floating a drop of photosensitive polymer adhesive (Norland, New Brunswick, NJ, type #68) on water. With proper surface tension, vessel and drop size, the drop expands into a thin film of submicron thickness (Zhou *et al.*, 1993). The thickness is estimated by the interference-induced coloration of the film, in a manner described in texts on electron microscopy. As the adhesive expands bands of bright interference colors become visible, and then fairly broad regions of one color. At that point, the film is probably less than one optical wavelength in thickness, some hundreds of nanometers. The floating adhesive is cured with ultraviolet light for 5 min. Following curing the film appears thicker, but bright interference colors are still present, indicating that the thickness is still on the order of a micrometer. (Films several micrometers thick appear clear, not colored.) The diaphragm is formed by scooping up the floating film with a glass hollow core fiber. The sensor tip is cured for at least 15 additional minutes. The hollow core fiber is prepared by removing sections of the outer plastic coating using the heat of a microelectrode puller and cleaving the fiber into sections 1–2 cm in length, with blunt perpendicular ends. After a batch of diaphragms was prepared, 50–60 nm of gold was evaporated on their outer surfaces to make them reflective.

2. Optical system

The position of the diaphragm is read optically, using an optic lever. Optic levers are available commercially (Opto-acoustic sensors, Raleigh, NC), although the one in use is home-made. Much larger optic-lever-based microphones have been described previously (Hu *et al.*, 1992). The LED light is delivered down one of the input fibers of an optic fiber coupler with a 50:50 splitting ratio (Gould Corp., Millersville, MD). The light that returns in the second input arm is collected by a photodiode. Only one output fiber is used (the other is optically sunk), and it is etched down from its original 125 μm diameter to slightly less than 100 μm by soaking in 6% hydrofluoric acid for 4 h. After etching, the output fiber is cleaved to a blunt 90 degree angle, which is monitored both under the microscope, and by the amount of light reflected off the blunt surface.

The output fiber is threaded into the sensor tip and glued in position (using Norland adhesive NEA 123) with the fiber end 50 to 100 μm from the diaphragm. In operation, the LED light fans out as it exits the fiber, reflects from the diaphragm, and returns to the fiber. The amount of light that reenters the fiber core for transmission back to the photodiode depends on the distance to the diaphragm. This position detection scheme, based on geometric optics, is the essence of an optic lever. In order to control the quality of the constructed sensors, in practice the fiber is threaded into different tips until a high level of reflected light is collected by the fiber. Prior to fixing the fiber in place, the response to acoustic stimuli is checked in air. The sensors are fragile, and might be used in many experiments, or be broken almost immediately. The fiber couplers can be reused. At least three sensors are on hand during an experiment. Complete sensors are made up at least a few days prior to an experiment so that their sensitivity and stability can be checked. Sensors have lasted up to 8 months.

The linear working range of an optic lever depends on the fiber size and is roughly equal to the fiber radius, at a position approximately one fiber diameter from the reflector. In operation in the pressure sensor the fiber–reflector distance is modulated by the diaphragm's pressure induced deflections, and the variation in returning light comprises the sensor's output signal. Based on the sensor stiffness (see below) the deflections we expect are at the most tens of nanometers, well within the working range.

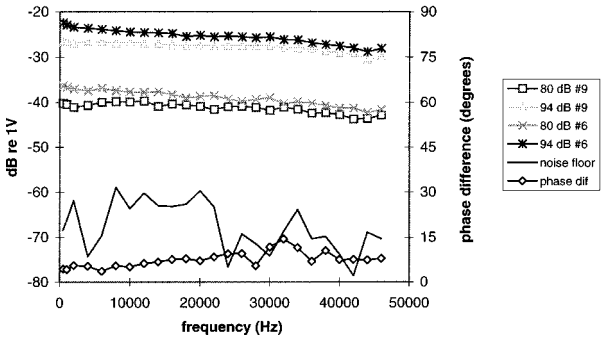

FIG. 2. Absolute sensor calibration in fluid. A vibrating fluid column was used to deliver a known pressure to the sensor over a wide range of frequencies. The stimulus level in dB SPL is indicated in the legend. The sensor responses are almost flat with frequency, and the calibrations are represented by a single value at all frequencies. Sensor #6 would be calibrated at −38 dBV/80 dB SPL, sensor #9 at −41 dBV/80 dB SPL. The noise level shown corresponds to roughly 60 dB SPL and was determined in the absence of stimulation with 6.4 s of signal averaging. During experiments signals were typically averaged for 3.2 s, and the noise floor was approximately 65 dB SPL. The phase differences between sensor #6 and its electronic system and sensor #9 and its electronic system are less than 15°. When analyzing experimental data, phase data taken with one sensor at one location (S.T. or S.V.) are referenced to phase data taken with another sensor in another location (S.V. or ear canal).

3. Sensor calibration

a. In fluid. The sensitivity, as photodetector voltage/pressure, was calibrated by delivering a known pressure to the sensor by immersing it in a vibrating column of water (Schloss and Strassberg, 1962; Nedzelnitsky, 1980). The sensor head was immersed a prescribed distance (typically 0.5 to 2 mm) under the surface of a small vial of water on a dynamic shaker with a built-in monitor accelerometer (Bruel & Kjær model 4290). The shaker was vibrated at a prescribed acceleration over 25 frequencies ranging between 0.5 and 46 kHz. The shaker produces a hydrodynamic pressure proportional to the immersion depth, the fluid density, and the acceleration amplitude. At high frequencies the effects of the acoustic standing wave set up in the vial modify the simple proportionality, and the depth of the fluid column must be accounted for (Schloss and Strassberg, 1962). Due to the small vial size, the standing wave correction is small even at the highest frequencies (less than 20%). Nevertheless, the correction is made in the calibration. In Fig. 2, the shaker amplitude was set to deliver calibration pressures of 80 and 94 dB SPL. The responses of two sensor/electronic systems are shown. The calibrations are nearly flat with frequency, indicating that the diaphragm's motion in response to pressure is dominated by the sensor/diaphragm stiffness. (See more on the sensor impedance below.) Both sensors show a slow decrease that accumulates 3 (#9) or 6 dB (#6) over the 46-kHz span, suggesting that viscous drag is not completely negligible. With 6.4 s of signal averaging the signal of 80 dB SPL is 20 dB out of the noise. Sensor linearity has been verified at levels ranging from 70 to 120 dB SPL. Figure 2 shows that the two sensor/electronic systems have nearly equal phases. This was generally true, and is essential because all of the pressure data is referenced to pressure data taken with a similar sensor.

A measure of the absolute phase of the sensor was made by referencing it to the phase of the shaker's monitor accelerometer. The pressure induced by the shaker's motion in theory is in phase with the acceleration of the shaker. If the sensor's specific acoustic impedance is dominated by acoustic stiffness, the phase of the sensor output will be in phase with pressure, and thus will be in phase with the output of the monitor accelerometer. The phase difference between the sensor and the accelerometer was found to be close to zero at the lowest frequencies, and to decrease monotonically to −30 degrees at 46 kHz. The phase departure from zero might indicate that, in deflecting the sensor diaphragm, the pressure is working not just against the stiffness of the diaphragm and air gap, but against viscosity in the fluid or diaphragm. This explanation is consistent with the small decrease in the magnitude of the sensitivity as frequency is increased.

The small decrease in the magnitude of the sensitivity with frequency was not accounted for because it is similar in size to inherent calibration uncertainties. The calibrated sensitivity of a sensor sometimes changed during the course of an experiment, introducing an uncertainty in the calibration of up to ± 6 dB. When calibration changes occurred, they included all frequencies approximately equally. Changes $\geqslant 4$ dB occurred in at least one sensor in 50% of the experiments. In order to minimize this uncertainty, sensors were recalibrated whenever it was practical in the course of an experiment. (See Sec. I E below.)

b. In air. Independent calibrations were performed using the substitution method, in air. Tones were measured with a Bruel & Kjær microphone ($\frac{1}{4}$ in. model 4135), and then with a sensor placed in the same sound field. The relative outputs of the sensor and the microphone, and the factory specified sensitivity of the microphone were used to calibrate the sensor. Sensor calibrations in air were flat with frequency, with a value within a few dB of the sensitivity in water. The phase of the sensor output relative to the microphone was close to zero at the lowest frequencies, and 10 to 20 degrees at frequencies above 40 kHz. The maximum variation, 35 degrees, occurred between 20 and 30 kHz, where the microphone sensitivity exhibits small dips and peaks. At these frequencies, it is likely that the phase difference occurs because the impedance of the microphone is not simply that of an acoustic stiffness.

4. Sensor impedance: The ratio of pressure to diaphragm velocity

The specific acoustic (S.A.) impedance of the sensor, defined as the ratio of sound pressure to the velocity of a center point on the diaphragm, is critical to gauging whether, and to what degree, the sensor loads the measurement. The sensor's S.A. impedance is expected to be dominated by S.A. stiffness, and the calibration described above supports this expectation. The S.A. stiffness has two additive components: the diaphragm's S.A. stiffness, and the S.A. stiffness of the air gap between the diaphragm and the fiber end. The Young's modulus of the diaphragm material is reported by the manufacturer as 0.14 GPa, and plate theory predicts a

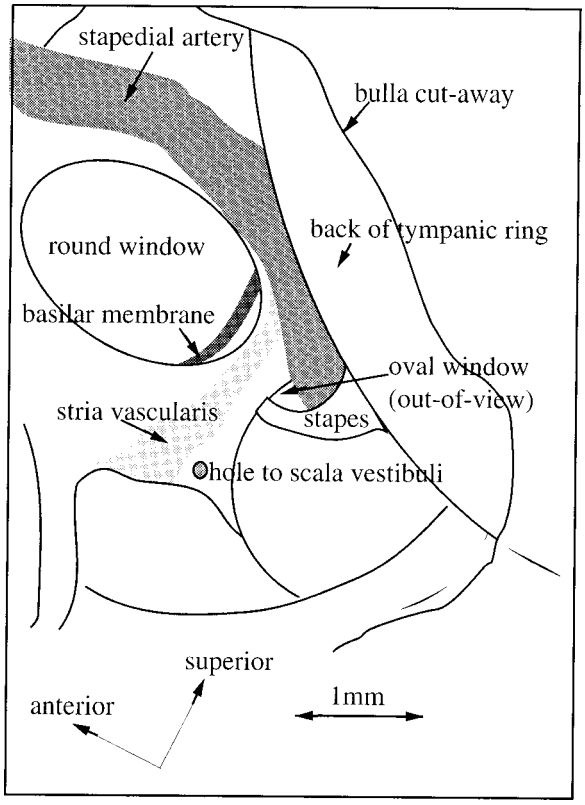

FIG. 3. The approach to the cochlea. The drawing is traced from a photomicrograph. The S.V. sensor was inserted into the hole indicated, usually to a depth between 0.25 and 1 mm. The S.T. sensor was inserted via the round window opening following removal of the round window membrane. The CAP electrode was positioned on the bone outside the round window opening.

S.A. stiffness (pressure/center deflection) slightly greater than 0.1 Pa/nm for a circular plate of 1-μm thickness and 100 μm diameter (Timoshenko and Woinowsky-Krieger, 1959). The S.A. stiffness is proportional to diaphragm thickness cubed, so small variations in thickness produce relatively large variations in stiffness. Tension in the plate will increase the stiffness, but because the adhesive is cured before being attached to the hollow core fiber, it is not expected to be under tension. The S.A. stiffness of a 100-μm-deep air gap (air gap depths vary between 50 and 100 μm) is calculated as either approximately 1 Pa/nm (isothermal compression, where PV = constant) or 1.4 Pa/nm (adiabatic compression, where PV^{γ}= constant, and γ, the specific heat ratio, has a value of 7/5 in air). Air gap stiffness scales as 1/gap depth, so a 50-μm gap has twice this stiffness. In summary, the air gap stiffness should dominate and the total S.A. stiffness should have a value of approximately 2 Pa/nm. This is best considered a lower bound due to uncertainty in the diaphragm stiffness.

The sensor S.A. stiffness should be compared with the S.A. stiffness of the organ of Corti. *In vivo* measurements of O.C. stiffness at the same longitudinal position as the current measurements found a mechanical stiffness of approximately 7 N/m [20-μm-diameter probe tip, radially centered measurements (Olson and Mountain, 1994)]. With a beam model of the O.C. this translates to a S.A. stiffness of approximately 4 Pa/nm (Olson and Mountain, 1991). Therefore, the sensor has a S.A. stiffness similar to that of the O.C. complex, and when it is close to the basilar membrane it is likely to reduce the pressure.

The sensor's acoustic impedance (pressure/volume velocity) should also be compared with the cochlear input acoustic impedance, which is primarily resistive, with a value of approximately 10^{11} Pa m^{-3}s in cat (Lynch *et al.*, 1982). (No data on gerbil are available.) The acoustic impedance of the sensor is proportional to 1/frequency, and at 40 kHz is calculated as 10^{12} Pa m^{-3}s. Therefore, the sensor's acoustic impedance is substantially larger than that of the cat cochlea even at the highest frequencies. If the gerbil cochlea is similar, the sensor is not expected to reduce the cochlear input pressure substantially.

5. Spatial resolution of the sensor

In order to resolve cochlear micromechanics, the sensor diameter should be at most half the size of the traveling wave wavelength. The wavelength varies both with frequency and with longitudinal location. At a given longitudinal location, it is expected to be smallest at the local characteristic frequency (c.f.) (Lighthill, 1981). Rhode (1971) found the c.f. wavelength to be 1.5 mm at the 7-kHz place in squirrel monkey. Cooper and Rhode (1992a) found the c.f. wavelength to be 0.6 mm in cat and 0.9 mm in guinea pig, in both cases at the 31-kHz place. Three-dimensional passive cochlear models indicate a wavelength of approximately 1 mm (Steele, 1974, 1-kHz place). Therefore, it is reasonable to believe that the sensor's 0.1-mm-diameter diaphragm is capable of resolving cochlear micromechanics.

B. Animal

1. Basic preparation

The experimental animals were young adult mongolian gerbils (*Meriones unguiculatus*) 40 to 60 g in weight. The gerbil was given a subdermal injection of the analgesic tranquilizer acepromazine (dose 1 mg/kg) followed by an intraperitoneal injection of the anesthetic sodium pentobarbital (initial dose 60 mg/kg). Supplemental 10 mg/kg doses of sodium pentobarbital were given when deemed necessary from a toe pinch response. The animal temperature was maintained at 38 °C with an animal blanket and a room heater. To maintain a clear airway, a slit was made in the trachea. The anesthetized animal was secured in a stereotaxic frame on its back and surgery was performed to expose the left cochlea. The pinna was removed and an earphone tube was positioned into the ear canal. The bulla was widely opened, as indicated in Fig. 3, during all data collection. A silver wire electrode, insulated to its tip, was placed on the bone just outside the round window opening. With it, the compound action potential (CAP) response to tone pips was measured as a monitor of cochlear condition. At or close to the end of an experiment animals were euthanized with an overdose of anesthetic.

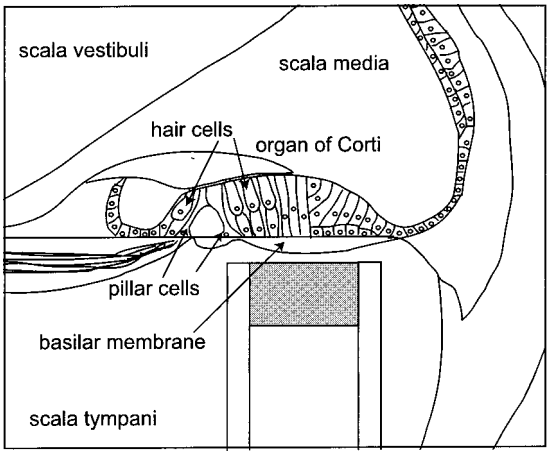

FIG. 4. Position of the S.T. sensor. This sketch shows an ideal approach to the basilar membrane: the sensor is centered radially, and approaches perpendicularly. The outer diameter of the sensor is 167 μm, and is drawn approximately to scale. The drawing of the O.C. derives from a 2 μm plastic-embedded section prepared by Dr. Martin Feldman of Boston University School of Medicine.

2. Sensor approach for intracochlear pressure measurements

Figure 3 illustrates the approach. In order to access scala vestibuli, a hole just large enough to accommodate a sensor was hand drilled through the cochlear bone adjacent to the oval window, in the region between the oval and round windows. The S.V. sensor was held in a micromanipulator attached to the stereotaxic frame. The sensor was inserted less than 1 mm into the hole unless otherwise noted. It was not sealed into the cochlea with cement or glue, but was mechanically quite well sealed in most experiments because of the precise hole size.

Scala tympani was accessed through the round window opening following removal of the round window membrane. Part of the basal turn of the basilar membrane is visible through the round window, and the S.T. sensor was angled to approach the B.M. perpendicularly, and (typically) centered radially, as indicated in Fig. 4. The c.f. at this position is close to 30 kHz (Xue *et al.*, 1995). Perilymph often wells out of the round window opening after removing the membrane. In order to control the perilymph fluid level, in later experiments a wick was positioned behind the round window opening. Sensor fibers were held in a glass micropipette glued to a stainless steel rod, with less than 2 cm emerging. A small amount of modeling clay fixed the sensor fiber where it emerged from the pipette, so that it could not move laterally within the pipette. This was necessary to reduce the influence of the forces due to surface tension, which could interfere with controlled positioning of the S.T. sensor. The S.T. sensor rod was held in a motorized micromanipulator, capable of undergoing prescribed 0.5-μm motions in three dimensions.

C. Stimulus delivery and response collection and analysis

1. Pressure measurements

Stimuli were pure tones, 32 ms in duration, with rise and fall times of 0.3 ms. The tones were generated at levels of 40, 60, and 80 dB SPL, as measured in the ear canal (see sound system calibration below), and frequencies of approximately 500 Hz, 1 kHz, 2 kHz, and then with a 2-kHz spacing to 46 kHz. The actual frequencies were adjusted from these values in order to coincide with the frequencies of the analysis FFT. In a series of S.V. pressure measurements made after the main data set the frequencies 188, 264, and 378 Hz were added. The earphone was a Radio Shack 40-1377 tweeter. Stimuli were generated and responses collected with a Tucker Davis Technologies (Gainesville, FL) DD1 using a 6.48-μs sampling rate. Typically 100 averages were taken, for total averaging times of 3.2 s. During ''simultaneous'' pressure measurements in the two scalae, actually the S.T. measurement followed the S.V. measurement, so the two occurred within approximately 7 s. The averaged data record of each response to each tone was stored for later analysis. The standard analysis was a FFT of the 4096 points of the data record beginning 5 ms into the record (point 805). The first 5 ms were truncated to exclude any transient response. The amplitude and phase at the stimulus frequency were extracted from the FFT. The complete FFT spectrum and raw data record was occasionally inspected. When plotting the phase as a function of frequency, ambiguity is handled by subtracting or adding 360 degrees or a multiple of it when the resultant phase differs from that of the adjacent lower frequency by less than ± 180 degrees.

2. CAP

Stimuli were pure tones, 3 ms in duration, with 0.3 ms rise/fall times. The polarity of alternate tones was reversed to cancel the cochlear microphonic in the averaged responses. The tones were generated at levels of 60, 80 and in later experiments also 40 and 100 dB SPL and frequencies of 2, 6, 10, 20, 30, and 40 kHz. Typically, 100 averages were taken. The averaged data records were displayed on line, and stored for later inspection. ''Threshold'' CAP is defined as the visible threshold, 5 to 10 μV peak-to-peak. The CAP was used as a monitor of cochlear condition (Johnstone *et al.*, 1979). Of particular interest are changes in the CAP after drilling the S.V. hole, after removal of the round window, and with time following opening the cochlea.

D. Sound system calibration

A 1-in. long earphone tube, coupled to the earphone via a machined housing, was inserted into the ear canal of the left ear following removal of the pinna. The bone of the bulla that overlies the tympanic ring and tapers down to form the ear canal contains natural cracks. A hole less than 1 mm in diameter was made in the skin-like tissue beneath one of the cracks, allowing access to the ear canal approximately 3 mm from the eardrum. A sensor was inserted approximately 1 mm into the hole and the hole was sealed with tissue paper reinforced by the slightly mucous fluids in the region. Tones generated with a constant voltage were delivered to the ear and the sensor's response to these tones was used to calibrate the sound system. Following calibration, 80 dB SPL tones at the standard frequencies were delivered to the ear, and recorded in order to check the magnitudes (which were 80 dB

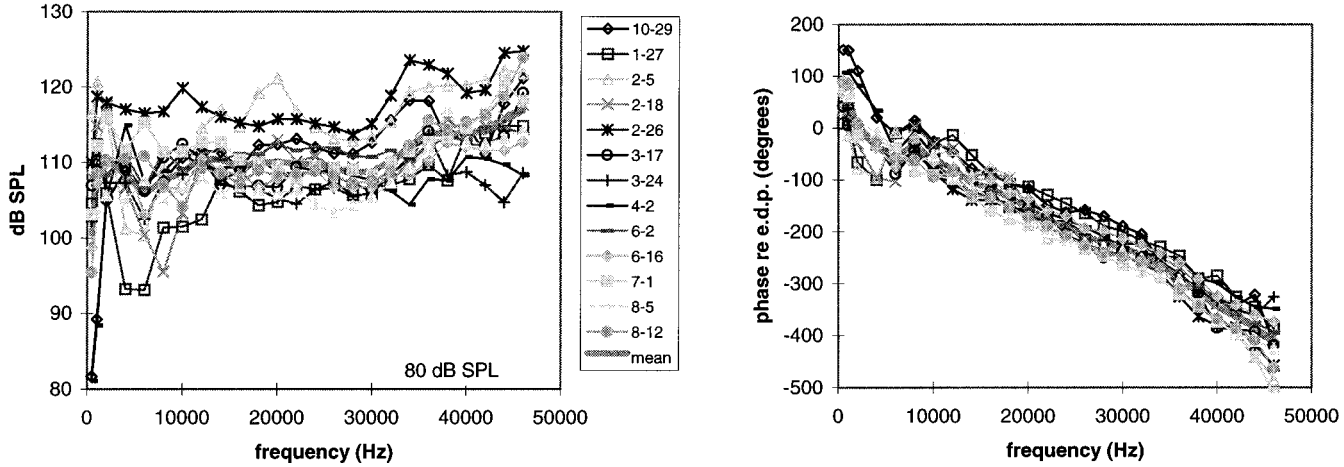

FIG. 5. The S.V. pressure with a stimulus level in the ear canal of 80 dB SPL; 500 Hz to 46 kHz. (a) Magnitude. (b) Phase relative to the pressure near the eardrum in the ear canal.

by construction) and to find the phase in the ear canal as a reference. The tissue paper was dampened to loosen it, the sensor removed, and the tissue paper replaced to cover the opening.

In two experiments following the set reported here the pressure field within the ear canal was mapped along the line between the sensor entrance and the umbo, a distance of approximately 3 mm, with a 0.5-mm resolution. The results of the two experiments were very similar. The detailed description of the results is beyond the scope of the present paper, but a brief description is relevant to the sound system calibration. At frequencies through 40 kHz the pressure close to the umbo was not more than 5 dB greater, and the phase at the umbo differed by at most -60 degrees, relative to the usual calibration position approximately 1 mm within the ear canal. At 46 kHz, the largest differences were seen. The magnitude at the umbo was 15 dB greater than at the usual calibration position and the phase differed by $-160°$.

E. Standard experimental sequence

(1) Sensors calibrated by immersion.
(2) Initial surgery, CAP electrode and earphone in place.
(3) Sensor 1 in ear canal, sound system calibration, CAP, recalibrate sensor 1.
(4) Scala vestibuli hole, CAP.
(5) Sensor 1 in scala vestibuli, pressure measurement, CAP, recalibrate sensor 1.
(6) Round window membrane removed, sensor 1 in S.V., sensor 2 in S.T., CAP, near simultaneous pressure measurements.
(7) Sensor 2 advanced towards B.M., pressure measured in both scalae after every 20- or 30-μm advance. CAP measured periodically.
(8) Sensor 2 contacted B.M., as determined by sensor 2 photodetector voltage, which undergoes abrupt increase in low frequency fluctuations.
(9) Sensor 2 retracted several micrometers, pressure measurements, CAP.
(10) Further measurements including post mortem measurements following anesthetic overdose.
(11) Sensors recalibrated.

II. RESULTS AND DISCUSSION

The results reported here are from 13 animals. The S.T. pressure data are not presented from all the experiments. In 6-16, 7-1, 8-5, and 8-12 S.T. pressure was not measured by design. In 10-29, 1-27, 2-5, and 2-18 it is not presented either because the B.M. was damaged during removal of the round window membrane, or because the S.V. and S.T. pressures were unstable. Instability was apparently caused by a changing round window fluid level or by an unvented ear canal.

A. CAP

The baseline CAP response was determined just after sound system calibration and prior to opening the cochlea, but with the bulla opened widely. The usual baseline CAP response was as follows: The CAP was visible at the lowest SPL (40 or 60 dB SPL) at 2, 6, 10, and 20 kHz. At 30 kHz the CAP was suprathreshold at 60 or 80 dB SPL, and at 40 kHz the CAP was suprathreshold at 80 or 100 dB SPL. Through 30 kHz, these results are in keeping with those of Müller (1996), who found (in his Fig. 1) a CAP threshold of 30 dB SPL at frequencies between 1 and 10 kHz, rising to 40 dB SPL at 20 kHz, and close to 60 dB SPL at 30 and 40 kHz. The 40 kHz threshold here is 20 dB higher than Müller's. The difference might be due to differences in method (electrode placement, sound system calibration, definition of ''threshold'') or to physiological changes in the extreme base related to the widely open middle ear.

Following drilling the S.V. hole, a change in sensitivity was always seen. Typically, both 30- and 40-kHz tones required one increment (20 dB) in sound level to be suprathreshold (a notable exception is experiment 2-26, in which the 30-kHz threshold was unchanged), whereas the CAP response to the 2- to 20-kHz tones was unchanged to the coarse degree measured. Following round window removal, the CAP response could be unchanged, and remain largely unchanged over hours of experimentation. A temporary threshold shift that might be due to the close proximity of the S.T. sensor to the B.M. occurred in experiment 2-26 (as described more fully below), and suggests that the sensor might indeed ''load'' the organ of Corti when positioned close to it.

B. Scala vestibuli input pressure

1. Grouped data

In Fig. 5 scala vestibuli pressure is shown when the sound level in the ear canal was set to 80 dB SPL. The measurements were made with the round window membrane intact. Figure 5(a) shows the pressure magnitude. In main, the S.V. input pressure lies between 105 and 120 dB SPL, indicating a middle ear pressure gain between 25 and 40 dB. The mean of the measurements (thick line without symbols) shows a frequency dependence which is flat at 110 dB SPL, a gain of 30 dB relative to the ear canal pressure, between 10 and 30 kHz, with a slight increase at the highest frequencies, and a slight decrease at the lowest frequencies. Some of this frequency dependence might be produced in part by experimental procedures. (i) High frequency increase: When fluid wells up in the round window, S.V. input pressure can increase by several dB, especially at high frequencies. In the data of Fig. 5, the round window membrane was intact, but the fluid level beneath the round window sometimes rose beneath the membrane when the cochlea was manipulated. Additionally, as discussed under ''sound system calibration'' above, the sound pressure in the ear canal which is used as a calibration might be underestimated at the highest frequencies. (ii) Low-frequency decrease, and structure: Sets 10-29 and 4-2 show a markedly low pressure at 0.5 and 1 kHz. The hole to S.V. was larger than optimal in the experiment of set 4-2. This is expected to reduce the pressure, especially at low frequencies. (Notes on the hole size from set 10-29 were not made.) Sets 1-27, 2-5 and 2-18 show dips in the 5- to 10-kHz region. These experiments were performed without a vent to the ear canal, an unnatural condition which can lead to buildup of static pressure. In the experiments following 2-18, a vent was purposely maintained, and the structure in the 5- to 10-kHz regions is less apparent in the later experiments. The variability from experiment to experiment is due in part to errors in sensor calibration, which might be up to 6 dB (see sensor notes above). In the mid-frequency region, where systematic errors due to calibration uncertainties, fluid level and static pressure are least apparent, the interexperiment spread is 12 dB, so calibration errors could account for much of the variability. The magnitude data indicates that the gain of the middle ear is approximately 30 dB, and is fairly flat with frequency above 2 kHz. The phase of S.V. input pressure relative to the pressure in the ear canal shows a linear decrease with frequency. The linear phase can be expressed as a delay which, in this case, accumulating one cycle between 2 and 42 kHz, is 25 μs. *Thus, both the magnitude and phase indicate that, at frequencies above 2 kHz, the middle ear and its cochlear termination have the properties of a frequency-independent transmission line.* From a signal processing standpoint, this is a good system, because the temporal qualities of the input are preserved in the output. Other investigators have noted a transmission-line-like character of the middle ear, based on measurements of middle ear impedance (Puria and Allen, 1997) and middle ear motion (Decraemer *et al.*, 1997).

In Fig. 6, results from five later experiments are shown in which the frequency range was extended down to 188 Hz.

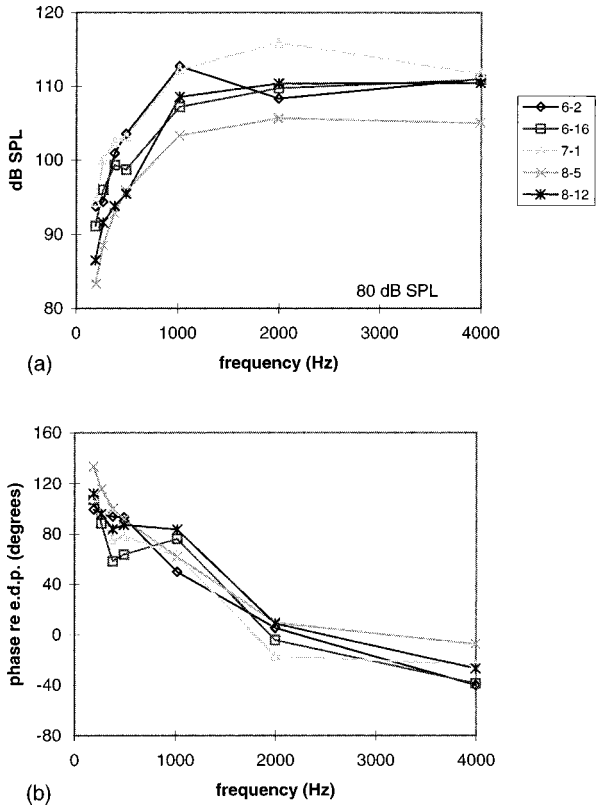

FIG. 6. The S.V. pressure with a stimulus level in the ear canal of 80 dB SPL; low-frequency extension. In these cochleae, measurements were made at the usual frequencies, and at three additional low frequencies. Here responses are only shown through 4 kHz to emphasize the low frequency behavior. (a) Magnitude. (b) Phase relative to the pressure near the eardrum in the ear canal.

The gain of the middle ear decreased as frequency decreased below 2 kHz, and was approximately 10 dB at 188 Hz. The phase relative to the pressure within the ear canal was approximately 0 degrees at 2 kHz, and increased as frequency decreased. At 188 Hz it ranged between 95 and 115 degrees in four experiments, and in the fifth was 135 degrees.

2. Comparison with previous measurements of basal S.V. pressure

Basal S.V. pressure has been measured *in vivo* by others (guinea pig, Dancer and Franke, 1980; cat, Nedzelnitsky, 1980; cat, chinchilla and guinea pig, Decory *et al.*, 1990). The variations in amplitude and phase at frequencies below 2 kHz and the maximal gain value of approximately 30 dB here adhere to the standard pattern that has been reported. However, the frequency range over which the 30 dB gain obtains is relatively large. Specifically, there is no indication that the gain comes down at high frequencies. Presumably, it comes down at high enough frequencies, but through 46 kHz (well within the hearing range of the gerbil) the gain is fairly steady, at 30 dB, at frequencies above 1 kHz. This finding *is* in agreement with Dancer and Franke's 1980 measurements in guinea pig turn 1, which showed a gain that was within a few dB of 32 dB between the frequencies of 1 and 20 kHz,

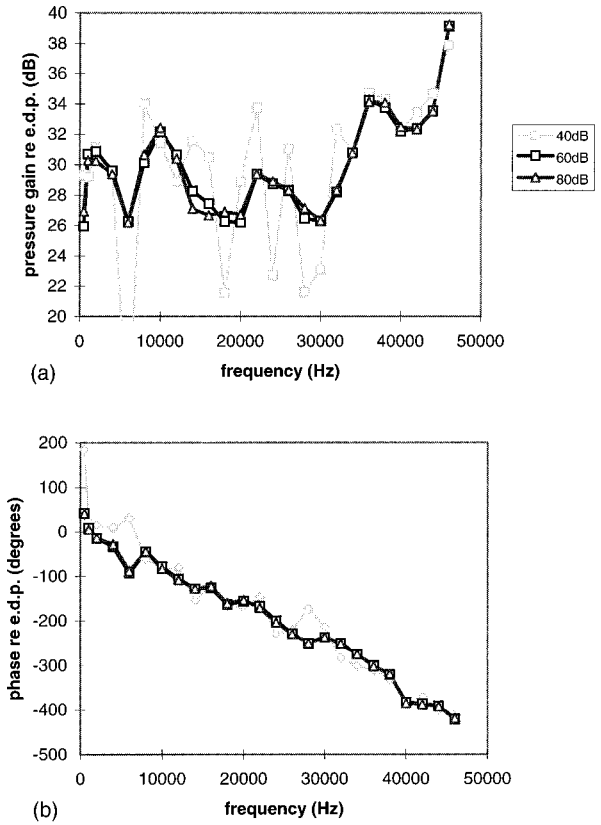

FIG. 7. Linearity in the S.V. pressure. (a) Scala vestibuli pressure gain relative to ear canal pressure at SPLs of 40, 60 and 80 dB. (b) The S.V. pressure phase relative to the pressure near the eardrum in the ear canal. One experiment is shown for clarity (3-17), but the linearity in evidence was common to all measurements of S.V. input pressure. The responses to the 40-dB stimulus were close to the noise floor.

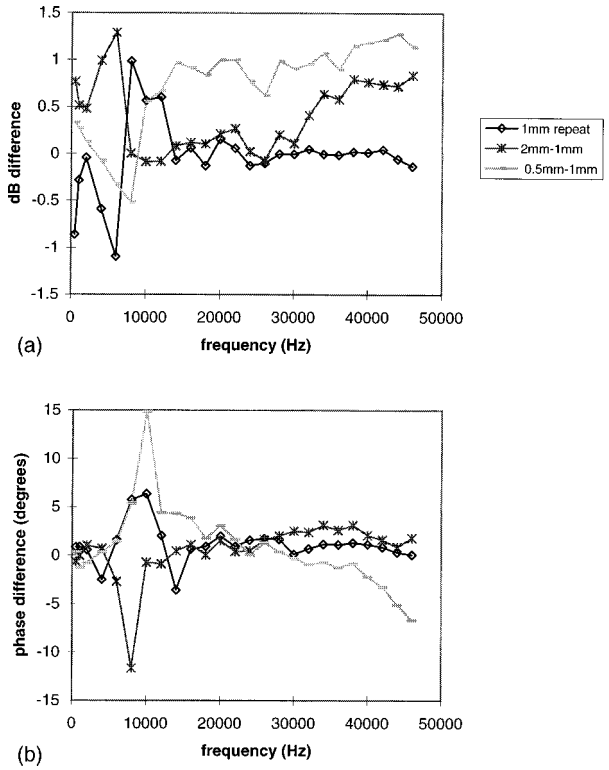

FIG. 8. Changes in S.V. pressure with changes in the insertion depth of the S.V. sensor (expt 2-18). The S.V. pressure appears relatively insensitive to millimeter-sized changes in insertion depth. As indicated in the legend, the changes are plotted (i) between two repeated measurements, both at a depth of 1 mm, (ii) between the initial 1-mm measurement and a measurement with a 2-mm insertion, and (iii) between the initial 1-mm measurement and a measurement with a 0.5-mm insertion. (a) Magnitude changes. (b) Phase changes.

the highest frequency they measured. However, most previous reports find a reduction in gain beginning at frequencies around 10 kHz. For example, the basal S.V. pressure measured by Decory *et al.* dropped off markedly at frequencies above 14 kHz (chinchilla), 12 kHz (guinea pig) and 8 kHz (cat). The measurements were made 5.5 (chinchilla), 7.2 (guinea pig) and 8 (cat) mm from the extreme base; perhaps the high-frequency S.V. pressure changes substantially over these distances. Puria *et al.* (1997) show a drop off in basal S.V. pressure at frequencies above about 8 kHz in human temporal bones, but the report states that temporal bone preparations might not be comparable with live preparations at frequencies above 5 to 10 kHz. The phase data reported here are in keeping with those of others, for example, Dancer and Franke (1980), who reported a phase of approximately +90 degrees at 1 kHz, decreasing monotonically to −200 degrees at 20 kHz.

3. Linearity

In Fig. 7 the scala vestibuli pressure gain and phase relative to the pressure in the ear canal are shown for 40, 60 and 80 dB SPL stimuli. The results from 3-17 are displayed. The gains at 60 and 80 dB lie essentially on top of each other, and at 40 dB are basically the same, but are so close to the noise floor that a strict comparison is not possible. The linearity illustrated applies to all measurements of S.V. input pressure.

4. Variations with insertion depth

The position of measurement in scala vestibuli does not allow for the sensor to be inserted much further than 1 mm without potential harm to the saccule. For this reason, generally the sensor was inserted less than 1 mm and variations in S.V. pressure due to insertion depth were not explored. One case in which the insertion depth variation *was* explored (2-18) is illustrated in Fig 8. In Fig. 8(a), the differences in measured SPL are displayed, and in Fig. 8(b), the differences in phase. The changes are small, and show no clear position dependence. The S.V. pressure appears to be relatively insensitive to millimeter-sized changes in insertion depth.

5. The effect of removing the round window membrane

Following round window membrane removal, the S.V. pressure usually changed very little, less than 2 or 3 dB. When fluid welled up in the round window opening the S.V. pressure sometimes increased, especially at the highest frequencies. The changes were typically less than 5 dB.

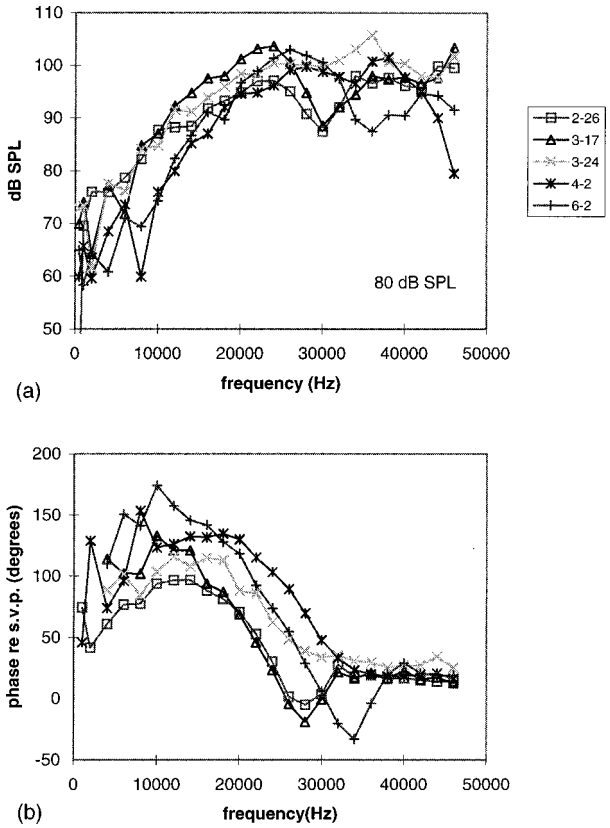

FIG. 9. The S.T. pressure with a stimulus level in the ear canal of 80 dB SPL. Shown are the initial S.T. measurements, made prior to the approach to the B.M. The distances from the B.M. are not known precisely, but are estimated as between approximately 300 and 800 μm. (a) Magnitude. (b) Phase relative to the simultaneously measured S.V. pressure.

6. Abnormal conditions

Data collected following severe manipulations to the middle ear, whether intentional or unintentional, serve as controls for systematic errors in the form of electronic cross-talk. In an early experiment the ossicles were suspected damaged during drilling of the S.V. hole and an air bubble was inadvertently introduced into S.V. The S.V. pressure gain (relative to the ear canal pressure) was 5 dB at the lowest frequency, and decreased steadily with frequency to -20 dB at 20 kHz, where the pressure went beneath the noise floor. These manipulations are known to decrease scala vestibuli pressure (Nedzelnitsky, 1980; Puria *et al.*, 1997). At the end of one experiment the annular ligament was purposely broken. The S.V. pressure gain was reduced at all frequencies to approximately 0 dB.

C. Scala tympani pressure

In the phase data in the figures below S.T. pressure is referenced to the simultaneously measured S.V. pressure.

1. Grouped data

In Fig. 9 scala tympani pressure is presented from five animals. The following conditions are of note: At the time of the presented measurements the CAP thresholds were relatively healthy in 2-26, 3-24, and 6-2, but were elevated more than 20 dB at all frequencies in 3-17 and 4-2. In 3-24 a portion of the round window membrane was covering the B.M. basal to the measurement position, and in 4-2 the round window membrane was covering all accessible regions of the B.M., including the region where measurements were made.

Figure 9(a) shows the magnitude of the S.T. pressure when the sensor was initially positioned into scala tympani. The stimulus level in the ear canal was 80 dB SPL. Recall that the c.f. in this region is thought to be in the neighborhood of 30 kHz. The distance from the B.M. is not known precisely, but in all cases is estimated as between 300 and 800 μm. The pressure increases with frequency from approximately 70 dB SPL (-10 dB *re:* ear canal pressure) at 4 kHz to approximately 100 dB SPL ($+20$ dB *re:* ear canal pressure) at 24 kHz. The pressure contains notches and peaks in the region of the c.f.

The phase relative to simultaneously measured scala vestibuli pressure is shown in Fig. 9(b). At the lowest frequencies the phase is erratic in part because the magnitudes were close to the noise floor. In general the phase lies between 50 and 100 degrees at 5 kHz, increases about 50 degrees to a maximum slightly above 10 kHz and then decreases to close to 0 degrees at the highest frequencies. In the region around 30 kHz a phase dip is evident in experiments in which pronounced structure is apparent in the magnitude data.

2. Variations in S.T. pressure as B.M. is approached

In Figs. 10–13 S.T. pressure versus position with 80 dB SPL stimuli is shown for experiments 2-26, 3-24 and 3-17 pre-mortem, and 2-26 post-mortem. In experiment 6-2 the fluid drained out of the round window opening while the B.M. was being approached, and a pressure versus position series was not possible. The magnitude and phase showed little change with position in experiment 4-2. As described above, in this experiment the round window membrane had not been successfully removed, and was between the sensor and the B.M. Based on the 4-2 results, the membrane probably prevented the sensor from making a close approach to the B.M., and might have modified the intracochlear fluid motions.

Figure 10 shows S.T. pressure versus position from 2-26 pre-mortem. The numbers in the legend indicate the distance from the B.M. in micrometers. The order of the measurements advances from top to bottom, but are not all consecutive. (Consecutive measurements were spaced by 20 to 30 μm; not all are shown.) After the measurement 28 μm from the B.M. was recorded the sensor was advanced 28 μm, where it contacted the B.M. and was retracted approximately 3 μm. Following the measurement there, the sensor was retracted 20 μm for the final measurement of this series. The similarities between the measurements 23 and 28 μm from the B.M. attests to the experimental stability. In general, the scala tympani pressure increased as the B.M. was approached, although the region of notches displays a non-monotonic increase. Below 10 kHz and above 38 kHz the pressure changes were relatively small. The pressure changes were most striking in the 30-kHz region. Figure 10(c) reinforces these points by displaying the pressure as a function of position from the B.M. for five frequencies. Figure 10(b) illustrates the 2-26 S.T. pressure phase, referenced to simul-

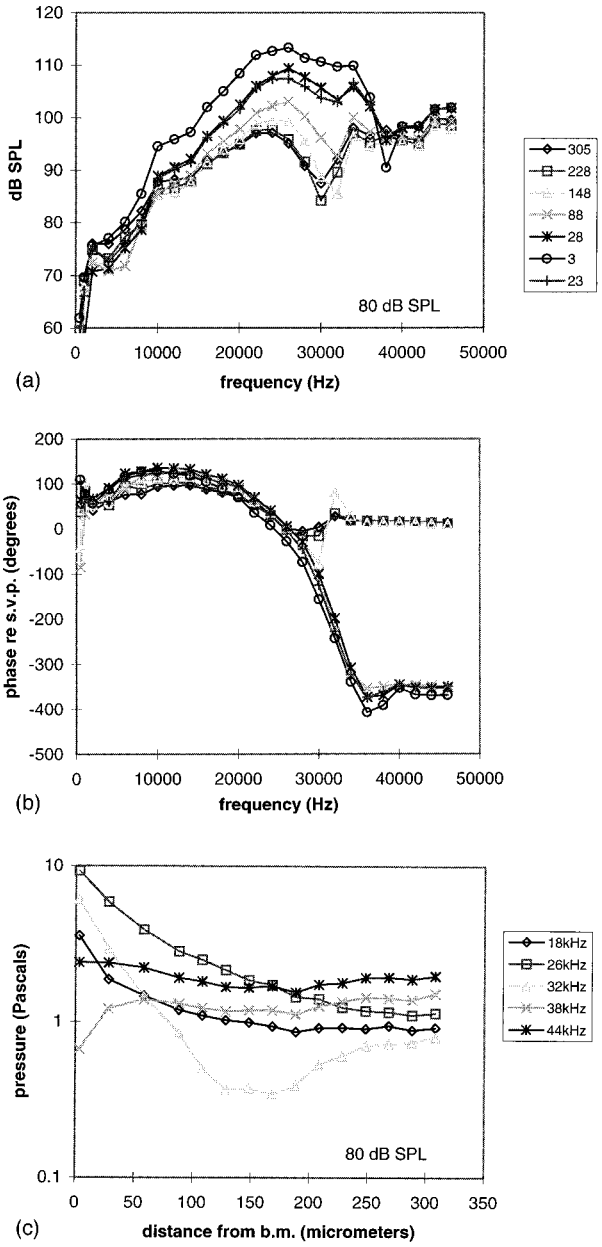

FIG. 10. The S.T. pressure, with a stimulus level in the ear canal of 80 dB SPL, as the B.M. was approached (expt. 2-26). The legend indicates the distance of the sensor from the B.M. in micrometers. The order of the measurements advances from legend top to legend bottom. (a) Magnitude. (b) Phase relative to the simultaneously measured S.V. pressure. (c) Magnitude plotted as a function of distance from the B.M. at selected frequencies.

taneous S.V. pressure. The phase dip/rise in the 30-kHz region becomes more and more pronounced until, when the distance to the B.M. is approximately 100 μm, it is appropriate to unwrap it. This reveals the phase as advancing, accumulating more than 500 degrees.

In Fig. 11 S.T. pressure versus position is shown from 3-24. The numbers in the legend indicate the distance from the B.M. in micrometers, and are from consecutive measurements beginning with the 84-μm position. A prominent notch at 22–24 kHz becomes deeper as the B.M. is approached. The phase exhibits dips and peaks in the same range of frequencies. At the position closest to the B.M. the

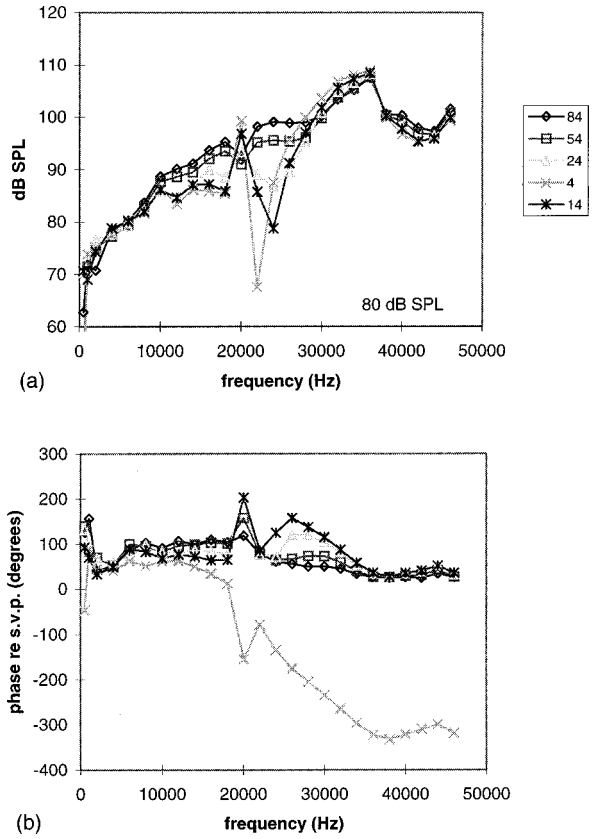

FIG. 11. The S.T. pressure, with a stimulus level in the ear canal of 80 dB SPL, as the B.M. was approached (expt. 3-24). The legend indicates the distance of the sensor from the basilar membrane in micrometers. The order of the measurements advances from legend top to legend bottom. (a) Magnitude. (b) Phase relative to the simultaneously measured S.V. pressure.

phase accumulates more than 370 degrees between 4 and 38 kHz. It is notable that at most frequencies between 10 and 24 kHz, the magnitude of the pressure decreased as the B.M. was approached.

In Fig. 12 S.T. pressures from 3-17 are shown at three different positions. Difficulties with surface tension prevented well-controlled positioning of the S.T. sensor in this experiment and the positions are only approximate, as the figure legend indicates. In general the pressure increased as the B.M. was approached. At the closest position, the phase accumulates almost 500 degrees.

Following the measurement 23 μm from the B.M. in experiment 2-26 (Fig. 10) the sensor was retracted an additional 20 μm, and the animal was administered a lethal dose of anesthetic. Just post-mortem pressure versus position was again recorded. Figure 13 shows these measurements, at distances 42, 22, and 2 μm from the B.M. The closest measurement was made after contacting the B.M., and retracting the sensor 2 μm.

In summary, as the B.M. was approached the S.T. pressure magnitude generally increased but sometimes decreased, typically in frequency regions where notches were present. The amount of phase accumulation with frequency increased as the B.M. was approached.

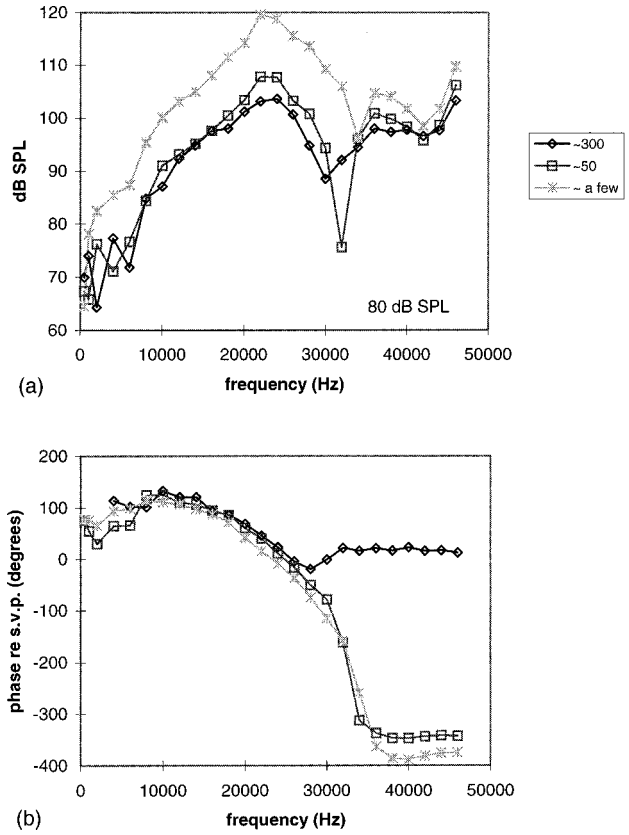

FIG. 12. The S.T. pressure, with a stimulus level in the ear canal of 80 dB SPL, as the B.M. was approached (expt. 3-17) The forces due to surface tension prevented well-controlled positioning in this experiment and the legend indicates the approximate distance from the basilar membrane in micrometers. The order of the measurements advances from legend top to legend bottom. (a) Magnitude. (b) Phase relative to the simultaneously measured S.V. pressure.

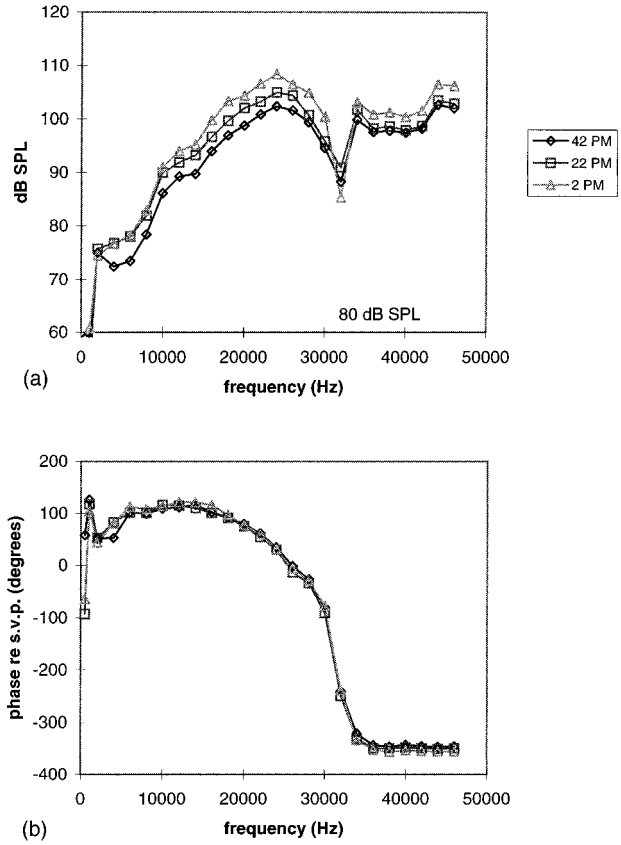

FIG. 13. The S.T. pressure, with a stimulus level in the ear canal of 80 dB SPL, as the B.M. was approached (expt. 2-26 postmortem). Following the measurement 23 μm from the B.M. in Fig. 10 the sensor was retracted an additional 20 μm, and the animal was administered a lethal dose of anesthetic. The measurements here were made immediately post-mortem. The legend indicates the distance of the sensor from the basilar membrane in micrometers. (a) Magnitude. (b) Phase relative to the simultaneously measured S.V. pressure.

3. Discussion of notches, peaks and phase accumulation

The pronounced notches in the magnitude data, and the position-dependent phases of Figs. 10–13 can be interpreted as the interaction of two pressure modes: a fast mode whose phase changes little with frequency, and a slow traveling wave mode whose accumulating phase chronicles the wave's travel. Interpreted in this framework, the notches in the magnitude data are produced by interference between the two modes. At frequencies where the modes are out of phase they sum destructively, and if their magnitudes are similar notches appear. The phase data indicate which mode is dominant: the fast mode is dominant in the data of Fig. 9(b), far from the B.M. As the B.M. is approached, the slow mode can dominate, producing a phase that accumulates smoothly with frequency. The transition region between the two modes can be quite erratic.

Fast and slow modes are explicit in mathematical models, where slow modes are associated with the traveling wave motion of the organ of Corti complex and fast modes are required to satisfy the boundary conditions. In a 1-D model, one fast and one slow mode suffices (Peterson and Bogart's P+ and P−, 1950). In 2-D and 3-D models more than one fast mode is present (Taber and Steele, 1981). Perhaps there are several slow modes as well (Taber and Steele, 1981; Hubbard, 1993). The emergence of phase accumulation as the B.M. is approached can be related to modeling predictions. At all but low frequencies, and more-so as frequency is increased, the pressure of the slow wave is predicted to be localized close to the B.M. (Lighthill, 1981; Taber and Steele, 1981). The S.T. pressure is predicted to be largest at frequencies near the peak of the traveling wave, and to penetrate the scalae a distance on the order of the traveling wave wavelength. (The penetration distance is the distance at which the traveling wave pressure is reduced from its value at the B.M. by roughly a factor of e.) This penetration distance is estimated from Taber and Steele's figure 7 (1981) as about 100 μm at 10 kHz, near the position where 10 kHz was the c.f. (Their model was based on guinea pig, and was passive with an orthotropic B.M.) In Fig. 10(b) (2-26) at distances relatively far from the B.M. substantial phase accumulation is not apparent, indicating that the fast wave is dominant. Within 88 μm of the B.M., similar to the predicted penetration depth of the slow wave, phase accumulation is apparent, indicating that the slow wave pressure has become dominant. Thus, this modeling prediction is in rough agreement with the data.

Referring to phase data where the slow mode is dominant, the phase versus frequency slope is much less steep

between 10 and 20 kHz than between 20 and 36 kHz. At the lowest frequencies, the sign of the slope is reversed. Traveling wave models predict that the phase versus frequency slope becomes steeper as frequency increases towards c.f., with details of the increase dependent on the impedance of the O.C. complex (e.g., Taber and Steele, 1981; Neely and Kim, 1986). Still, traveling wave models do not predict a low-frequency reversal in phase slope. A possible explanation for the behavior lies in the relative strengths of the fast and slow modes. At frequencies much lower than c.f. the traveling wave is expected to be small, and S.T. pressure even close to the B.M. is likely dominated by the fast mode. Then the phase is not expected to accumulate. The fast mode probably dominates at frequencies above c.f. as well, where models predict there is no longer a traveling wave. At frequencies above c.f. the measured phase-frequency slope is close to zero.

4. Interanimal variability

Although there are basic similarities in the S.T. data from different cochleae, there are some clear differences. The notches and peaks appear at different frequencies. In 2-26 (Fig. 10) the phase changes smoothly with large accumulation at positions 88 μm from the B.M. and closer, whereas in 3-24 (Fig. 11) the phase shows a *reasonably* smooth accumulation at the closest position, 4 μm from the B.M., but even 14 μm from the partition it is not appropriate to unwrap it. The reasons for the variability probably fall into two basic categories. First, the S.T. pressure probably depends on the basic condition of the cochlea. The condition is known to some degree, and based on the cochlear conditions noted when discussing Fig. 9 it is evident that the phase accumulation that signifies the dominance of the slow mode can be present post-mortem (from 2-26PM), and in experiments with elevated CAP threshold (from 3-17). When the round window membrane is unnaturally positioned on top of the B.M. it might obscure the slow mode (from 4-2) or alter it (from 3-24).

The second categorical reason for experimental variability is that S.T. pressure was not measured at identical points in different animals. Due to experimental variability in the portion of the RW membrane that was successfully removed, and the exact positioning of the animal in the stereotaxic frame and relative to the sensor apparatus, the angle of the sensor varied, its longitudinal position varied, and its radial position varied. The resulting positional variations are probably on the order of 200 μm. This distance is significant in these measurements, where S.T. pressure was found to vary by a factor of 10 over distances of 100 μm. Referring to the theoretical literature, in a 3-D model Taber and Steele (1981) predict that at a distance 100 μm from the B.M. the magnitude of the slow mode pressure at a radially centered location is more than twice that of the slow mode pressure over the pillar cells. Closer to the B.M., the predicted difference is much greater. Therefore, a pressure measurement made over the pillar cells is expected to be substantially different than one made over the pectinate zone. In short, the scala tympani measurements from different animals cannot be regarded as precisely repeated measurements.

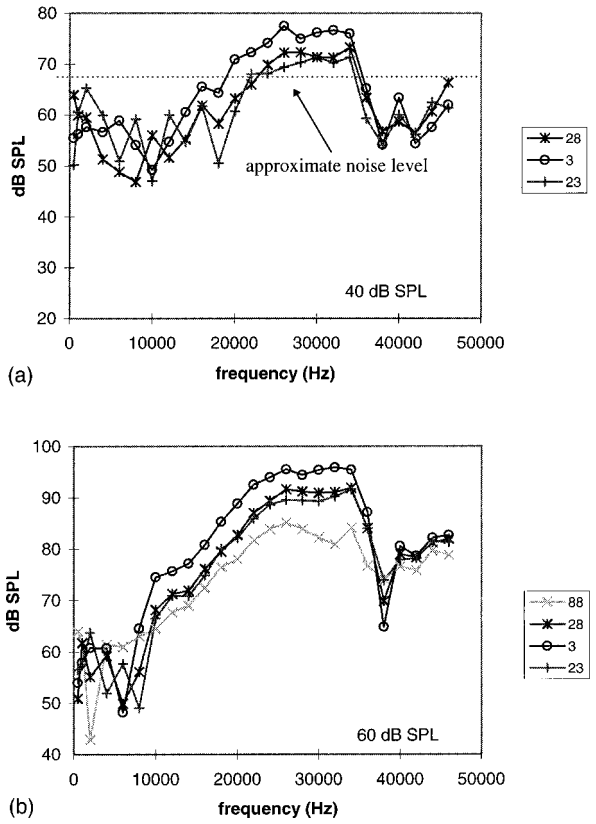

FIG. 14. Scala tympani pressure, with stimulus levels in the ear canal of 40 and 60 dB SPL, as the B.M. was approached (expt. 2-26). The data are from the same experimental run as the data in Fig. 10.

5. Comparison with previous measurements

The S.T. data can be compared with measurements of Dancer and colleagues, who have presented basal scala tympani pressure measurements from guinea pigs. Our measurements relatively far from the B.M. (Fig. 9) are similar to the recent publication in which Dancer *et al.* (1997) find the S.T. pressure to peak in the region close to the c.f. (10 kHz in their case) with a gain relative to ear canal pressure close to 20 dB. Those measurements found little phase difference between S.T. and S.V. pressures: a small lead at low frequencies, and a small lag at the highest measured frequencies, just over 10 kHz. Due to this lack of phase accumulation, Dancer *et al.* take an extreme viewpoint, and question the presence of a traveling wave pressure at all. However, an earlier publication (Dancer and Franke, 1980) reported S.T. pressure with a larger gain (up to 40 dB near 10 kHz), suggesting that it was measured closer to the B.M. than the measurements presented later. In this case, the phase of S.T. relative to S.V. did exhibit phase accumulation, from 90 to -270 degrees between 500 and 12 000 Hz. The results here include these two extremes, and illustrate the progression between them.

6. Linearity, expt. 2-26

In Fig. 14, the magnitude data recorded in the same run as that of Fig. 10 are shown for 40 and 60 dB SPL stimuli. The noise floor is at a measured pressure of approximately 65 dB SPL, restricting the frequency ranges over which the data are reliable. The S.T. pressures scale almost linearly.

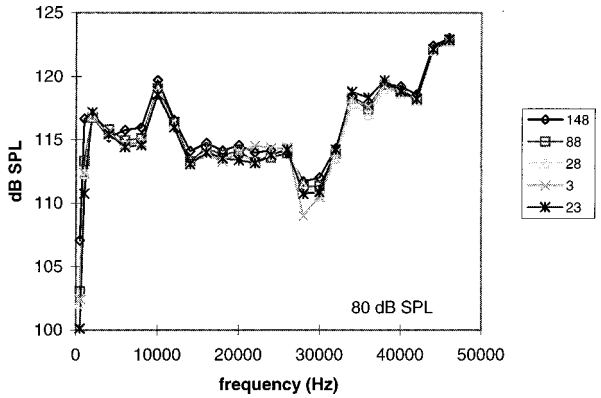

FIG. 15. Scala vestibuli pressure measured when the S.T. sensor was at distances from the B.M. indicated in the legend (expt. 2-26). The stimulus level in the ear canal was 80 dB SPL. Changes in S.V. pressure due to the proximity of the S.T. sensor to the B.M. indicate that the S.T. sensor was loading the cochlea.

However, the profiles differ from each other slightly in the c.f. region, particularly comparing the data taken with the stimulus levels at 60 and 80 dB SPL. At 32 kHz the departure from linearity is maximal, approximately 8 dB at positions close to the B.M.

7. Simultaneous scala vestibuli pressure, and pressure changes with changing position of S.T. sensor

A pressure change in S.V. due to S.T. sensor proximity to the B.M. could indicate that the S.T. sensor was ''loading'' the system. Fig. 15 displays the S.V. pressure measured as the S.T. sensor approached the B.M. Distances from the B.M. in micrometers are listed in the legend and occurred consecutively starting at the 148-μm position. A 3-dB dip in S.V. pressure occurred close to the c.f. when the sensor was closest to the B.M., suggesting that the sensor perturbed the pressure field. The S.V. pressure is measured far from the O.C.; the S.V. pressure close to the O.C. was presumably perturbed more. The change at very low frequencies is not linked to the position of the S.T. sensor but is increasing in time. It might be due to a slowly widening gap between the S.V. sensor and the hole to S.V.

III. ANALYSIS: DERIVED QUANTITIES

In this section the results are analyzed to estimate the velocity of the B.M, the pressure across the organ of Corti complex, and the specific acoustic impedance of the organ of Corti complex. The derivation was sketched previously (Olson and Borawala, 1997) and is presented here in the Appendix. The analysis is carried out for experiments 3-24 and 2-26. In both these experiments the overall CAP thresholds were relatively low (particularly in 2-26) and the scala tympani pressure measurements close to the B.M. were checked for repeatability, ruling out time-dependent changes in S.T. pressure as a source of error.

There are numerous measurements of basal B.M. velocity in the literature, and the general form of its frequency dependence has been documented under various physiological conditions (Cooper and Rhode, 1992a, 1992b; Nuttall and Dolan, 1996; Xue *et al.*, 1995; Khanna and Leonard, 1986; Ruggero *et al.*, 1996, 1997). That the derived B.M. velocity is similar to the B.M. velocity measured by direct methods serves as an important measure of the reliability of the current analysis. By this measure, the analysis of experiment 2-26 will be found to be the most credible. Because of the lack of high-quality data from more experiments, the primary purpose of the current presentation is to establish the analytical method.

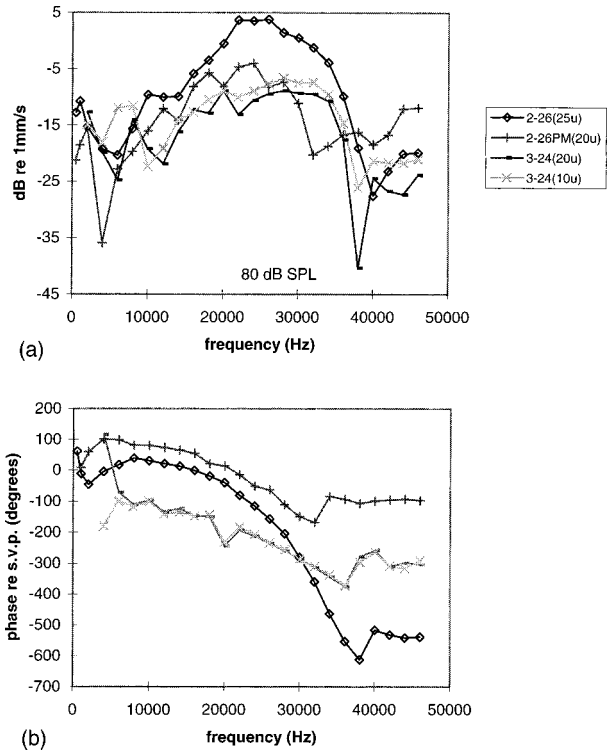

FIG. 16. Derived B.M. velocity from experiments 3-24 and 2-26. The stimulus level in the ear canal was 80 dB SPL. The velocities are derived from pairs of S.T. pressure measurements. 2-26(25u) is derived from the S.T. pressure 3 μm, and the previous measurement 28 μm, from the B.M. 2-26PM(20u) was derived from the S.T. pressure 2 μm, and the previous measurement 22 μm, from the B.M. 3-24(20u) was derived from the S.T. pressure 4 μm, and the previous measurement 24 μm, from the B.M. 3-24(10u) was derived from the S.T. pressure 4 μm, and the following measurement 14 μm, from the B.M. Phases are referenced to the S.V. pressure measured simultaneously with the S.T. pressure of closest approach. A phase of 0 degrees indicates velocity towards scala tympani.

A. Basilar membrane velocity

1. Results from two animals, discussion of derivation method

Figure 16(a) displays the magnitude of the B.M. velocity calculated from 2-26 and 3-24. Figure 16(b) shows the velocity phase relative to S.V. pressure. A phase of 0 degrees indicates velocity towards scala tympani. The stimulus level was 80 dB SPL in the ear canal. As described in the Appendix, fluid velocity is calculated from a pair of consecutive S.T. pressure measurements, where one member of the pair is the pressure closest to the B.M. The B.M. velocity is then equated to this fluid velocity, based on the argument that close to the B.M. the fluid must move with the B.M. The S.T. pressure measurements used in these calculations are in

Figs. 10 (2-26), 11 (3-24) and 13 (2-26PM). The two 3-24 velocities in the figure were derived from two such pairs, one comprised of the pressure at the closest position and the pressure at the previous position (20-μm distant), and one comprised of the pressure at the closest position and the pressure at the following position (10-μm distant). Figure 16's legend specifies the distance between the measurements within a pair. The differences between the 3-24 results with 10- or 20-μm separation are generally small, indicating that the results are not extremely sensitive to changes in this distance.

The derived velocities are similar in: (i) their broadly peaked shapes, (ii) the positions of their maxima, which vary from 24 to 28 kHz, (iii) the absolute values of their maxima, which vary from 0.3 to 1.6 mm/s, and (iv) dropping off relatively sharply at a frequency above their maxima. The phases from the different measurements all decrease with increasing frequency at a steadily increasing rate above about 8 kHz, then level off at approximately the frequency where the corresponding amplitude drops off. Although the phase shows these basic similarities, the amount of phase accumulation and the value of the phase at both low and high frequencies varies substantially. Experiments 2-26PM and 3-24 show much less phase accumulation (approximately 270 degrees in both cases) than 2-26, which accumulates more than 600 degrees. Although similar in overall phase accumulation, the 3-24 and 2-26PM phases are offset from each other by close to 180 degrees at all frequencies. Referring to the S.T. pressure data that was used to derive the velocities, the underlying reasons for the 180-degree difference can be investigated. The phase offset originates in the unusual behavior of the 3-24 pressure, which over a wide range of frequencies was smaller at the position closest to the B.M. than at the position one step back. Only in the region of the maximum, 28–36 kHz, does the pressure convincingly increase as the B.M. was approached. This observation shifts the question from ''Why are the velocities different?'' to ''Why does the pressure decrease as the B.M. is approached?'' In fact, a decrease in S.T. pressure as the B.M. was approached was evident in all experiments. The decrease occurred in association with a notch, and is thought to originate in interference between the fast and slow modes. In 3-24 the decrease is associated with a notch in the frequency range from 20–26 kHz, somewhat lower than the position of the prominent notch in the other experiments. The significance of 3-24's lower notch frequency, as well as of the unusually large frequency extent of the decrease is not known. The behavior was repeatable within this approach and in a second approach in this animal, ruling out a confounding influence of time-dependent changes. As noted previously, S.T. sensor positioning was not optimal in 3-24 because a portion of the basal B.M was covered with the remains of the round window membrane. Perhaps the S.T. pressure was perturbed by the unnatural condition of the basal B.M.

The S.T. pressure data that underlies the velocity calculation indicates the frequency regions over which the derived velocity is most reliable. Because velocity is derived from the pressure differences between two consecutive positions, its derived value is most robust at frequencies for which (i) the pressure was well above the noise level, (ii) the differences with position were substantial, and (iii) the pressure was only position dependent, and not changing over time. The first of these requirements is most restrictive at low frequencies. The second requirement is most restrictive at frequencies above those where the velocity drops off, because the pressure differences are small while the levels are relatively high. The third requirement underscores the need for measurements both before and after contacting the B.M. to ascertain repeatability. For data sets 3-24 and 2-26 the repeatability was documented. Although time-dependent changes (due to fluid level changes for example) were not noted when set 2-26PM was collected, it was not deliberately checked for repeatability.

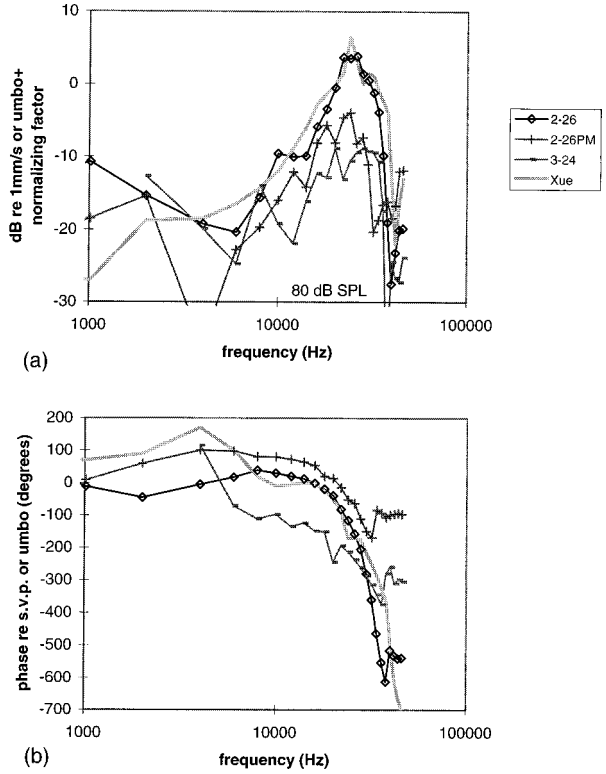

FIG. 17. Derived B.M. velocity at a stimulus level of 80 dB SPL replotted on a logarithmic scale, along with results from Xue *et al.* (1995) at 90 dB SPL. 3-24(10u) has been excluded to reduce clutter. (a) Magnitude. (Xue *et al.*'s magnitude data were referenced to umbo motion and are shifted vertically to line up with the 2-26 data.) (b) Phase. (Xue *et al.*'s phase is referenced to umbo velocity.)

2. Comparison with direct velocity measurements

In Fig. 17 the velocities are plotted on a logarithmic frequency scale to facilitate comparison with the B.M. motion literature. Included in the figure is Xue *et al.*'s (1995) direct measurement of gerbil B.M. velocity, made through the open round window, and taken with the stimulus level at 90 dB SPL. Xue *et al.*'s B.M. velocity is reported relative to umbo velocity. The derived B.M. velocity is found with a constant SPL in the ear canal, and its phase is reported relative to S.V. input pressure. Although the references are different, above 2 kHz Xue *et al.*'s data can be directly compared to the derived velocity based on the following: (i) From the S.V. pressure results here, the gain of the S.V. pressure relative to the pressure in the ear canal is approxi-

mately flat with frequency above 2 kHz. (ii) The cochlear input impedance is approximately resistive above 2 kHz (Lynch *et al.*, 1982; Puria and Allen, 1991). (iii) The umbo and stapes move in phase (Ruggero *et al.*, 1990). When these three conditions are met, the magnitude of the derived B.M. velocity (referred to pressure in the ear canal) and the magnitude of B.M. velocity (referred to umbo motion) can be plotted together, with an offset which on a log scale is an additive constant. (The constant is treated as free parameter.) When (ii) and (iii) are met the phase of the derived B.M. velocity (referred to S.V. pressure near the stapes) and the phase of the B.M. velocity (referred to umbo velocity) are equivalent, and can be plotted together with no free parameters. Actually, at high frequencies (ii) and (iii) are not known to hold. Lynch *et al.*'s measurements of cochlear input impedance only extend through about 7 kHz. With regards to (iii), although Ruggero *et al.* (1990) showed that the malleus and stapes moved almost in phase up to about 8 kHz, at higher frequencies the stapes velocity lagged malleus velocity. At approximately 20 kHz, the phase lag could be as large 130 degrees. The complexity of ossicle motion at high frequencies has been noted by others as well (e.g., Decraemer *et al.*, 1994). Therefore, the different references might sully the comparison somewhat, but a correction is not attempted. What is presented in Fig. 17 is a straight comparison with Xue *et al.*'s data, in which there is one free parameter, which is used to move Xue *et al.*'s magnitude data along the vertical axis so that the peaks line up. The form of the 2-26 derived velocity is similar to that measured by Xue *et al.* The agreement lends credibility to the general method of deriving B.M. velocity with pressure differences. The values of the derived velocity magnitudes are close to that found in basal locations of the chinchilla and guinea pig at stimulus levels of 80 dB SPL (Ruggero *et al.*, 1997; Sellick *et al.*, 1982), and the variation with frequency of both the magnitude and phase of the derived velocity 2-26 is in keeping with what has been reported in many studies in addition to that of Xue *et al.* (e.g., Cooper and Rhode, 1992a; Nuttall and Dolan, 1996). The phases of 2-26PM and 3-24 do not possess the multiple cycles of phase accumulation that is characteristic of B.M. motion. However, similarly small accumulations can be found in the B.M. motion literature. For example, Cooper and Rhode found less than one cycle of phase accumulation between 10 and 40 kHz, measuring at the 30-kHz place in guinea pig (1992a) and in linear cat cochleae (1992b).

3. Linearity, expt. 2-26

In Fig. 18 the 2-26 results at 40, 60 and 80 dB SPL are shown. The 40- and 60-dB data have been scaled by factors of 100 and 10, respectively, as indicated in the y-axis title. Results are shown within the frequency ranges for which S.T. pressure was out of the noise. At all SPLs, the maximum occurred at 26 kHz. The velocity scaled nearly linearly with sound pressure, but compression at frequencies on the high-frequency side of the peak extended the peak through relatively higher frequencies (32 kHz) at 40 and 60 dB SPL. The observation that the nonlinearity is very modest is not surprising since high-frequency CAP thresholds were elevated slightly when the cochlea was opened. Additionally, when the S.T. sensor was closest to the B.M., the CAP threshold at 30 kHz was temporarily elevated from 60 to 80 dB SPL. When the sensor was retracted 20 μm, the 60-dB response at 30 kHz recovered. The degree to which pressure measurements like those here can explore cochlear activity, and the associated nonlinearity, without interfering with it, is not yet established.

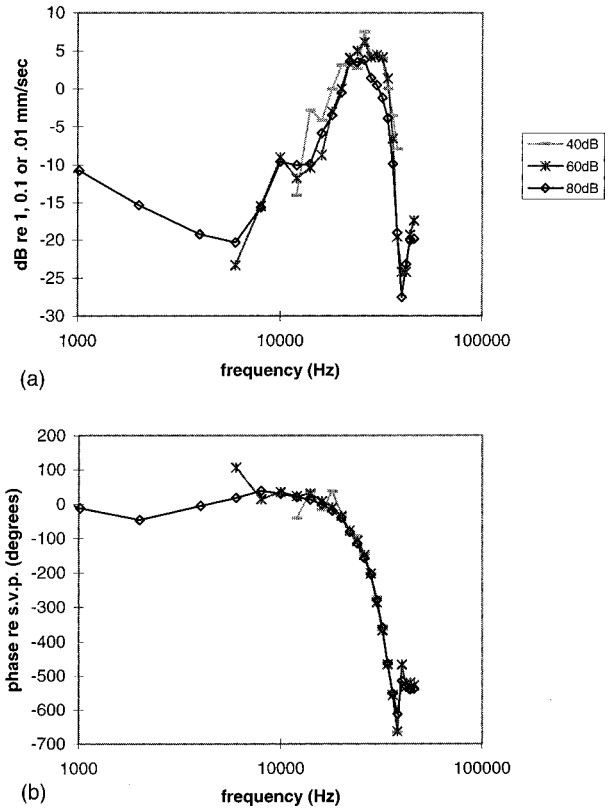

FIG. 18. Derived B.M. velocity from experiment 2-26 at stimulus levels of 40, 60 and 80 dB SPL. (a) Magnitude. The results at 40, 60 and 80 dB SPL are plotted *re*: 0.01 mm/s, 0.1 mm/s, and 1 mm/s, respectively. (b) Phase relative to S.V. pressure.

B. Localized pressure difference across the organ of Corti complex

1. Results

The derivation of the local pressure difference across the organ of Corti complex, ΔP_{oc}, is in the Appendix. In Fig. 19 ΔP_{oc} is shown. Pre-mortem, ΔP_{oc} values calculated from 2-26 (40, 60 and 80 dB SPL) and 3-24 show a mild peak in the region of c.f. A small degree of nonlinearity is in evidence in the 2-26 results. In ΔP_{oc} calculated from 2-26PM the pressure peak is absent, and a pronounced notch is apparent. Most notably, in all the results, ΔP_{oc} is not small at frequencies above c.f., where the velocity was small.

In Fig. 19(b) the phase is shown relative to the S.V. pressure. At low and high frequencies, the phase is close to 0 degrees (or 360 degrees), simply because the S.V. pressure was much greater than the S.T. pressure. Pre-mortem in experiment 2-26, between 14 and 34 kHz, the phase accumulates almost 500 degrees. The results from 2-26 PM and 3-24 show only the beginning of phase accumulation, similar to

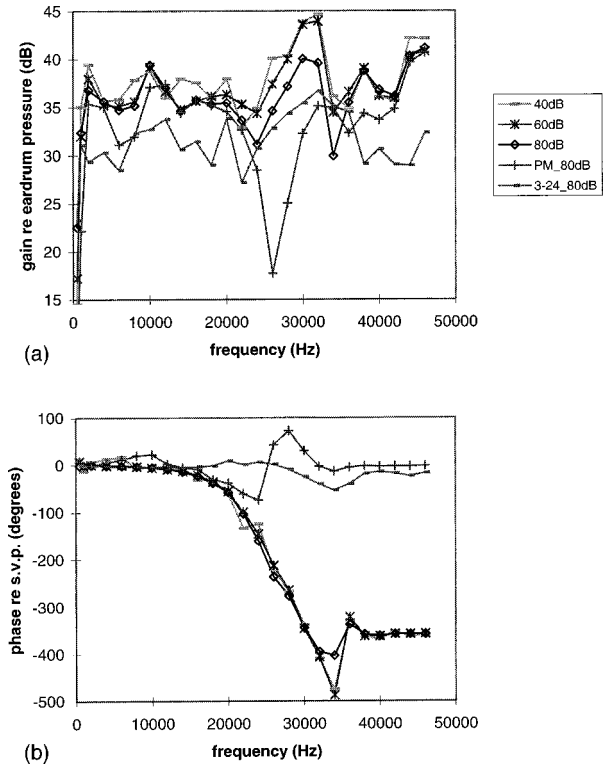

FIG. 19. Derived pressure across the O.C. complex, ΔP_{oc}, from experiments 2-26 and 3-24. The stimulus level was 40, 60 or 80 dB SPL as indicated in the legend. ΔP_{oc} is equal to the pressure on the S.V. side of the O.C. complex minus the pressure on the S.T. side of the O.C. complex. (a) Magnitude. (b) Phase relative to S.V. pressure.

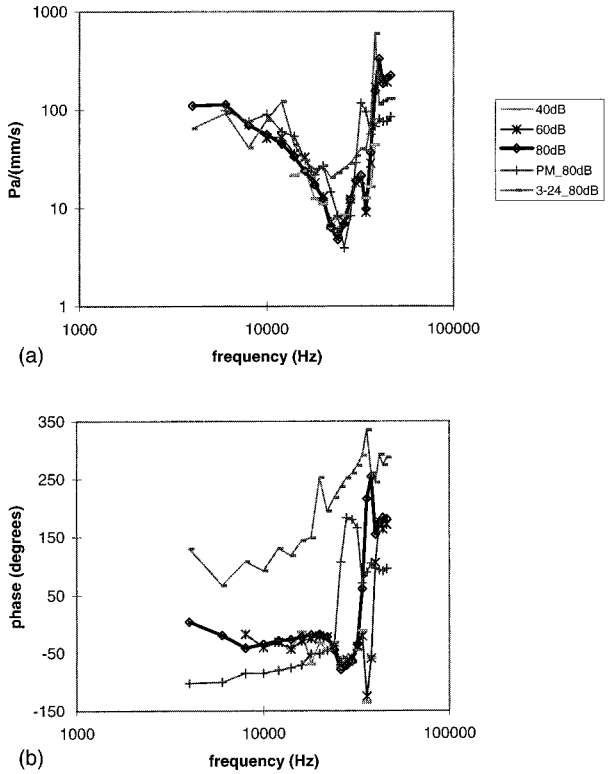

FIG. 20. The specific acoustic impedance of the organ of Corti. Results are shown at stimulus levels of 40, 60 or 80 dB SPL, as indicated in the legend. (a) Magnitude=ΔP_{oc}/B.M. velocity. (b) Phase=ΔP_{oc} phase−B.M. velocity phase.

the velocity measurements of these approaches. The basis for the difference in 2-26 ΔP_{oc} post-mortem compared to pre-mortem lies in the S.T. pressure close to the B.M. The S.T. pressure was larger pre-mortem, and the phase decreased through the c.f. region more smoothly pre-mortem than post-mortem, indicating that the slow mode was relatively dominant. The quantitative change in the relative strengths of the fast and slow pressure modes pre- versus post-mortem resulted in a qualitative change in the character of ΔP_{oc}.

2. Discussion

Similarly to S.T. pressure, ΔP_{oc} appears to be composed of the sum of a fast and a slow mode. The significance of the fast mode is undoubtedly emphasized in the current measurements, made at a position sandwiched between the stapes and round window. At longitudinal positions apical to the windows, presumably the fast mode of ΔP_{oc} is smaller. On the other hand, the significance of the fast mode of ΔP_{oc} to cochlear mechanics should not be undervalued. A sizable fraction of the O.C. complex lies in the region between the windows (Plassman *et al.*, 1987), and is close to the round window membrane; the anatomy of the cochlea does not seem to be set up to protect the O.C. complex from being effectively stimulated by the fast mode.

Based on point pressure measurements not particularly close to the B.M. Dancer *et al.* (1997) concluded that ΔP_{oc} did not have a traveling wave mode. The results here do not substantiate this view, but they do support a milder form of the contention of Dancer *et al.*: that the traveling wave pressure is not the only pressure across the O.C. complex, and, moreover, that it is not always the dominant pressure.

C. Specific acoustic impedance of the organ of Corti

1. Results

In Fig. 20 the magnitude and phase of the specific acoustic impedance is shown for experiments 3-24 and 2-26. Its derivation is in the Appendix. The impedance magnitude is tuned to frequencies between 22 and 26 kHz. Its size is approximately 100 Pa/(mm/s) at low (6 kHz) and high (approximately 40 kHz) frequencies, and at its minimum is approximately 5 Pa/(mm/s) in experiment 2-26, and 20 Pa/(mm/s) in experiment 3-24. The 2-26 pre-mortem impedances at 40, 60 and 80 dB SPL show a primary minimum at 24 kHz, with a secondary minimum close to half an octave above at 32 kHz. These impedances nearly overlie each other; the small degree of compressive nonlinearity evident in 2-26 ΔP_{oc} and 2-26 velocity cancel each other.

2. Discussion

The impedance phase of a simple mechanical resonance begins at −90 degrees at low frequencies, rises through 0 degrees at the resonance frequency, and ends up at +90 degrees. The post-mortem 2-26 data do that, except for an overshoot to +180 degrees just beyond the resonance. The pre-mortem 2-26 impedance phase is more complicated, with a low-frequency plateau at −30 degrees, a slight decrease to −70 degrees in the region of the magnitude's primary minimum, and a notch and peak at higher frequencies. Compared

to the 2-26 data, the 3-24 phase shows a large offset. This offset is produced by the phase of the 3-24 velocity, which is in turn rooted in the large frequency extent over which S.T. pressure decreased as the B.M. was approached.

In the ''low-frequency'' region from 6 to 12 kHz, the slope of the magnitude curve is nearly constant, at −6 dB/oct, both pre- and post-mortem in experiment 2-26. Experiment 3-24 decreases less smoothly. A 6-dB/oct decrease is expected for a stiffness dominated impedance. In phase, a pure stiffness is constant, at −90 degrees. Post-mortem 2-26 the impedance phase is close to −90 degrees between 6 and 12 kHz, but the pre-mortem 2-26 approach has a phase close to −30 degrees, suggesting that at these frequencies the impedance is a combination of stiffness and damping. The viscoelasticity of biological tissue is capable of producing an impedance with the low-frequency character of the pre-mortem data (Fung, 1993). The specific acoustic stiffness indicated is approximately 2 Pa/nm (pre-mortem approach), or 6 Pa/nm (post-mortem approach). These compare favorably with the point stiffness found by direct methods, 7 N/m for a 20-μm probe tip (Olson and Mountain, 1994), which translates to a specific acoustic stiffness of 4 Pa/nm (Olson and Mountain, 1991).

It is generally believed that *in vivo* the impedance is active in some sense — that the O.C. pumps energy into the traveling wave (de Boer, 1983; Diependaal *et al.*, 1986). To date, however, direct experimental probes of activity have not been able to substantiate its existence (Allen and Fahey, 1992; Cody, 1992). With respect to this important question the results here are not very helpful. A driving point impedance without negative real components must have a phase between +90 and −90 degrees; a phase beyond these limits indicates that the real part of the impedance is negative. Although the 2-26 impedance phases are somewhat interpretable in the framework of what is predicted for a resonant impedance, at frequencies near c.f. the phase is most aptly described as erratic. This undoubtedly stems in part from an oversimplified analysis; the phase is more sensitive than the magnitude to the simplifications imposed by the analytical method, particularly the assumption that the ΔP_{oc} we derive corresponds spatially exactly to the v_{bm} we derive. Further measurements and possibly more sophisticated analyses are required to address the question of activity.

Computer models (Steele and Taber, 1979; Steele, 1974) demonstrated that frequency selectivity in the cochlea could be present without a tuned O.C. impedance. In these models the O.C. complex is an acoustic stiffness whose value decreases apically. The slow mode (which propagates with the traveling wave) is essentially the only pressure across the O.C. complex in the models; the fast mode pressure across the complex is negligible except very close to the base. The models predict that the slow mode pressure peaks and then dies out at frequency-dependent longitudinal positions along the O.C. The motion of the O.C. will die out, resonant impedance or not, when its stimulus dies out. Physical models of the cochlea have demonstrated this inherent tuning (Zhou *et al.*, 1993). Most computer models incorporate a tuned O.C. impedance which enhances the peak of the traveling wave and steepens the drop off at frequencies above c.f. In

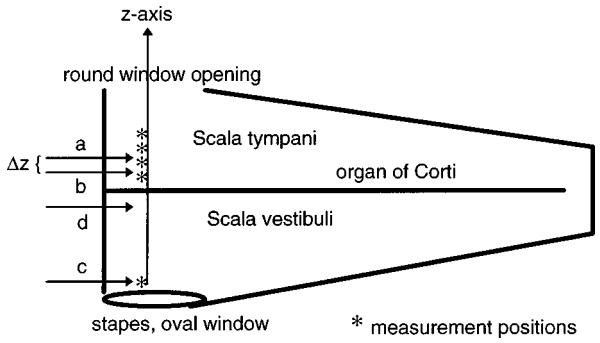

FIG. 21. Symmetric cochlear model. The asterisks indicate positions where pressure is measured. B.M. velocity is derived from measured pressures P_a and P_b . $\Delta P_{\mathrm{oc}} = P_d - P_b$ is derived from measured pressures P_b and P_c , and an assumption that the pressure at the round window is 0.

all these models the pressure difference across the O.C. complex is carried by the traveling wave and dies out at frequencies above c.f. (Peterson and Bogart, 1950; Taber and Steele, 1981; Neely and Kim, 1986; Kolston, 1988).

The results here indicate that in the base of the gerbil cochlea the pressure difference across the organ of Corti does not die out at frequencies above the characteristic frequency. The slow mode of ΔP_{oc} dies out, but the fast mode remains sizable. Therefore, the current analysis argues that in the extreme base, tuning in the impedance of the O.C. complex is doing the job, not just of enhancing the response of the O.C. complex near c.f., but of attenuating the response at frequencies above c.f. as well.

IV. CONCLUSION

The detailed form of the fluid pressure within the cochlea is governed by the motion of its boundaries. One of these boundaries is the stapes, and the cochlear pressure adjacent to the stapes is key to understanding the workings of the middle ear. In this vein, the results of the current study extend previous studies to higher frequencies and support the view that over a wide range of frequencies the middle ear operates as a transmission line. Another, more elusive cochlear boundary in motion is the organ of Corti. Because it both drives and responds to the motion of the O.C. complex, the fluid pressure encodes fundamental information about the O.C.'s mechanical properties. In this study, the signature of the O.C.'s motion was apparent in the slow wave dominated S.T. pressure close to the B.M. A simple method for extracting the specific acoustic impedance of the O.C. from the pressure field indicated that the impedance is tuned.

ACKNOWLEDGMENTS

Sejal Borawala, as a research intern at Rutgers/Newark, helped develop the first sensor tips. Shuwan Xue generously shared his basilar membrane motion data. Joe Santos-Sacchi, Dana Anderson, Reg Cook, Betsy Keithley and Mike Ravicz advised in various technical matters. Bob Austin made room for me in his lab at Princeton. Discussions with the scientists at Boston University, the Eaton Peabody Laboratory and Rockefeller University influenced the manuscript, and Dave Mountain's comments on its first version stimulated many revisions. I am very grateful to the JASA reviewers, John

Rosowski and a second reviewer who remained anonymous. This work was supported by N.I.H. Grant No. DC03130. Initial sensor development was supported by a Visiting Professorship for Women from the N.S.F.

APPENDIX: DERIVED QUANTITIES

The analysis refers to the symmetric cochlear model in Fig. 21. In the formulation, pressures and velocities are complex quantities with a harmonic time dependence, $e^{i\omega t}$.

1. B.M. velocity

The difference between two adjacent S.T. pressure measurements was used to estimate the vertical (z) component of the pressure gradient. From this the z component of fluid velocity was found. Close to the B.M. (within about 30 μm, a fraction of the width of the B.M.) the fluid is assumed to move with the B.M. because of conservation of fluid mass. Therefore, the fluid velocity just adjacent to the B.M. is an approximate measure of B.M. velocity. In the quantitative derivation below, the following are used: ρ is fluid density, assumed similar to that of water, 10^3 kg/m^3; μ is the viscosity of the fluid, taken as that of water, 10^{-3} kg/(m-s); ∇ represents the gradient operator, which is written in component form as $\nabla = \partial/\partial x i + \partial/\partial y j + \partial/\partial z k$; P_a and P_b are the pressures measured at the two positions closest to the B.M., a and b in Fig. 21; v is the fluid velocity; v_z is its vertical component, and $v_{\rm bm}$ is the velocity of the B.M. As the sketch indicates, the positive z-axis points from the stapes towards the round window.

Here, L, U, and ω are scale factors used to characterize the fluid system, with the purpose of simplifying its mathematical description. L is the extent over which fluid velocities vary appreciably (nominally, by a factor of e), and it is taken as 100 μm, half the width of the basilar membrane. U is the maximum characteristic velocity of the basilar membrane and the fluid, and is taken as 1 mm/s, while ω represents the angular frequency (2π frequency), and is taken as 10^4, which is a conservative value for frequencies above 1.5 kHz.

The Navier–Stokes equation (A1) describes the relationship between fluid pressure gradients and fluid motion in an incompressible fluid:

$$\nabla P = -\rho \frac{\partial v}{\partial t} + -\rho v \cdot \nabla v + \mu \nabla^2 v. \tag{A1}$$

The relative sizes of the three terms involving fluid velocity can be estimated using the standard tools of dimensional analysis. Using L, U and ω we write v, t and spatial derivatives as dimensionless quantities, and Eq. (A2) is rewritten in terms of dimensionless coefficients:

$$\left(\frac{L}{\mu U}\right)\nabla P = -\left\{\frac{L^2\omega\rho}{\mu}\right\}\frac{\partial \mathrm{v}}{\partial \mathrm{t}} - \left\{\frac{UL\rho}{\mu}\right\}(\mathrm{v}\cdot\nabla \mathrm{v}) + \{1\}\nabla^2 \mathrm{v}. \tag{A2}$$

In Eq. (A2) all roman quantities are dimensionless (v, t, and ∇). The bracketed coefficients are also dimensionless, and by comparing their sizes, the dominant velocity term is identified. $\{L^2\omega\rho/\mu\}=100$ and $\{UL\rho/\mu\}=0.1$. Because the first coefficient is much larger than the other two coefficients, only the first velocity term is retained in this analysis.

Therefore, (A2) is simplified as

$$\nabla P = -\rho \frac{\partial v}{\partial t}. \tag{A3}$$

We are interested in the z component:

$$\frac{\partial P}{\partial z} = -\frac{\rho \partial v_z}{\partial t} \approx \frac{(P_a - P_b)}{\Delta z}, \tag{A4}$$

$$\therefore \frac{\partial v_z}{\partial t} = -\frac{(P_a - P_b)}{(\rho \Delta z)}. \tag{A5}$$

For pressures with a harmonic time dependence

$$v_z = (i/\omega)(P_a - P_b)/(\rho \Delta z). \tag{A6}$$

Finally, just adjacent to the B.M., $v_{\rm bm} \approx v_z$, so we assume

$$\boldsymbol{v_{bm} = (i/\omega)(P_a - P_b)/(\rho \Delta z)}. \tag{A7}$$

2. Local pressure difference across the organ of Corti complex

In a symmetric cochlea [Eq. (A1)] the z components of fluid motion are the same on both sides of the organ of Corti complex. Pressure gradients in the z direction indicate the z component of the fluid motion. The total pressure difference from the round window to the B.M. will be equal to the total pressure difference from above the organ of Corti complex in scala vestibuli to the oval window:

$$P(rw) - P(b) = P(d) - P(c). \tag{A8}$$

We assume that $P(rw) = 0$, and measure $P(b)$ and $P(c)$. We want

$$\Delta P_{\rm oc} = P(d) - P(b). \tag{A9}$$

From Eqs. (A8) and (A9)

$$\boldsymbol{\Delta P_{oc} = P(c) - 2P(b)}. \tag{A10}$$

3. Specific acoustic impedance of the organ of Corti complex

The magnitude of the acoustic impedance is found as $|\mathbf{\Delta P_{oc}/v_{bm}}|$. The phase of the impedance is found

$$\boldsymbol{(\Delta P_{oc}\ \ phase) - (v_{bm}\ \ phase).} \tag{A11}$$

Allen, J., and Faley, P. (**1992**). ''Using acoustic distortion products to measure the cochlear amplifier gain on the basilar membrane,'' J. Acoust. Soc. Am. **92**, 178–188.

de Boer, E. (**1983**). ''No sharpening? A challenge for cochlear mechanics,'' J. Acoust. Soc. Am. **73**, 567–573.

Cody, A. (**1992**). ''Acoustic lesions in the mammalian cochlea: Implications for the spatial distribution of the 'active process,' '' Hearing Res. **62**, 166–172.

Cooper, N. P., and Rhode, W. S. (**1992a**). ''Basilar membrane mechanics in the hook region of cat and guinea-pig cochlea: Sharp tuning and nonlinearity in the absence of baseline position shifts,'' Hearing Res. **63**, 163–190.

Cooper, N. P., and Rhode, W. S. (**1992b**). ''Basilar membrane tonotopicity in the hook region of the cat cochlea,'' Hearing Res. **63**, 191–196.

Cooper, N. P., and Rhode, W. S. (**1996**). ''Fast travelling waves, slow travelling waves, and their interactions in experimental studies of apical cochlear mechanics,'' Aud. Neurosci. **2**, 207–212.

Dancer, A., and Franke, R. (**1980**). ''Intracochlear sound pressure measurements in guinea pigs,'' Hearing Res. **2**, 191–205.
Dancer, A., Avan, P., and Magnan, P. (**1997**). ''Can the traveling wave be challenged by direct intracochlear pressure measurements?,'' in *Diversity in Auditory Mechanics*, edited by E. R. Lewis, G. R. Long, R. F. Lyon, P. M. Narins, C. R. Steele, and E. Hecht-Poinar (World Scientific, Singapore), pp. 340–346.
Decory, L., Franke, R. B., and Dancer, A. L. (**1990**). ''Measurement of middle ear transfer function in cat, chinchilla and guinea pig,'' in *The Mechanics and Biophysics of Hearing*, edited by P. Dallos, C. D. Geisler, J. W. Matthews, M. A. Ruggero, and C. R. Steele (Springer Verlag, Berlin), pp. 270–277.
Decraemer, W. F., Khanna, S. M., and Funnell, W. R. J. (**1994**). ''A method for determining three-dimensional vibration in the ear,'' Hearing Res. **77**, 19–37.
Decraemer, W. F., Khanna, S. M., and Funnell, W. R. J. (**1997**). ''Vibrations of the cat tympanic membrane measured with high spatial resolution,'' Abstract 192 from the 20th Midwinter Research Meeting, Association for Research in Otolaryngology.
Diependaal, R. J., Viergever, M. A., and deBoer, E. (**1986**). ''Are active elements necessary in the basilar membrane impedance?,'' J. Acoust. Soc. Am. **80**, 124–132.
Fung, Y. C. (**1993**). *Biomechanics: Mechanical Properties of Living Tissues*, 2nd ed. (Springer Verlag, New York), Chap. 7.
Hu, A., Cuomo, F. W., and Zuckerwar, A. J. (**1992**). ''Theoretical and experimental study of a fiber optic microphone,'' J. Acoust. Soc. Am. **91**, 3049–3056.
Hubbard, A. (**1993**). ''A traveling-wave amplifier model of the cochlea,'' Science **259**, 68–71.
Johnstone, J. R., Alder, V. A., Johnstone, B. M., Roberstons, D., and Yates, G. K. (**1979**). ''Cochlear action potential threshold and single unit threshold,'' J. Acoust. Soc. Am. **65**, 254–257.
Khanna, S. M., and Leonard, D. G. B. (**1986**). ''Relationship between basilar membrane tuning and hair cell condition,'' Hearing Res. **23**, 55–70.
Kolston, P. J. (**1988**). ''Sharp mechanical tuning in a cochlear model without negative damping,'' J. Acoust. Soc. Am. **83**, 1481–1487.
Lighthill, J. (**1981**). ''Energy flow in the cochlea,'' J. Fluid Mech. **106**, 149–213.
Lynch, T. J., Nedzelnitsky, V., and Peake, W. T. (**1982**). ''Input impedance of the cochlea in cat,'' J. Acoust. Soc. Am. **72**, 108–123.
Müller, M. (**1996**). ''The cochlea place-frequency map of the adult and developing mongolian gerbil,'' Hearing Res. **94**, 148–156.
Nedzelnitsky, V. (**1980**). ''Sound pressures in the basal turn of the cat cochlea,'' J. Acoust. Soc. Am. **68**, 1676–1689.
Neely, S. T., and Kim, D. O. (**1986**). ''A model for active elements in cochlear biomechanics,'' J. Acoust. Soc. Am. **79**, 1472–1480.
Nuttall, A. L., and Dolan, D. F. (**1996**). ''Steady-state sinusoidal responses of the basilar membrane in guinea pig,'' J. Acoust. Soc. Am. **99**, 1556–1565.
Olson, E. S., and Borawala, S. (**1997**). ''The design and purpose of an intracochlear pressure sensor.'' in *Diversity in Auditory Mechanics*, edited by E. R. Lewis, G. R. Long, R. F. Lyon, P. M. Narins, C. R. Steele, and E. Hecht-Poinar (World Scientific, Singapore), pp. 347–353.
Olson, E. S., and Mountain, D. C. (**1991**). ''*In vivo* measurement of basilar membrane stiffness,'' J. Acoust. Soc. Am. **89**, 1262–1275.
Olson, E. S., and Mountain, D. C. (**1994**). ''Mapping the cochlea's mechanical properties to its cellular architecture,'' J. Acoust. Soc. Am. **95**, 395–400.
Peterson, L. C., and Bogart, B. P. (**1950**). ''A dynamical theory of the cochlea,'' J. Acoust. Soc. Am. **22**, 369–381.
Plassman, W., Peetz, W., and Schmidt, M. (**1987**). ''The cochlea in gerbilline rodents,'' Brain Behavior and Evolution **30**, 82–101.
Puria, S., and Allen, J. B. (**1991**). ''A parametric study of cochlear input impedance,'' J. Acoust. Soc. Am. **89**, 287–309.
Puria, S., and Allen, J. B. (**1997**). ''Cat middle-ear measurements and model: Evidence of acoustic delay in the tympanic membrane,'' Abstract 193 from the 20th Midwinter Research Meeting, Association for Research in Otolaryngology.
Puria, S., Peake, W. T., and Rosowski, J. J. (**1997**). ''Sound pressure measurements in the cochlear vestibule of human-cadaver ears,'' J. Acoust. Soc. Am. **101**.
Rhode, W. S. (**1971**). ''Observations of the vibration of the basilar membrane in squirrel monkeys using the Mossbauer technique,'' J. Acoust. Soc. Am. **49**, 1218–1231.
Ruggero, M. A., Rich, N. C., Robles, L., and Recio, A. (**1996**). ''The effects of acoustic trauma, other cochlear injury, and death on basilar-membrane responses to sound,'' in *Scientific Basis of Noise-Induced Hearing Loss*, edited by A. Axelsson *et al.* (Thieme Medical, New York), pp. 23–35.
Ruggero, M. A., Rich, N. C., Robles, L., and Shivalpuja, B. G. (**1990**). ''Middle-ear response in the chinchilla and its relationship to mechanics at the base of the cochlea,'' J. Acoust. Soc. Am. **87**, 1612–1629.
Ruggero, M. A., Rich, N. C., Recio, A., Srayan, S. S., and Robles, L. (**1997**). ''Basilar membrane responses to tones at the base of the chinchilla cochlea,'' J. Acoust. Soc. Am. **101**, 2151–2163.
Ryan, A. (**1976**). ''Hearing sensitivity of the mongolian gerbil, Meriones unguiculatus,'' J. Acoust. Soc. Am. **59**, 1222–1226.
Schloss, F., and Strasberg, M. (**1962**). ''Hydrophone calibration in a vibrating column of liquid,'' J. Acoust. Soc. Am. **34**, 958–960.
Sellick, P. M., Patuzzi, R., and Johnstone, B. M. (**1982**). ''Measurement of basilar membrane motion in the guinea pig using the Mossbauer technique,'' J. Acoust. Soc. Am. **72**, 131–141.
Steele, C. R. (**1974**). ''Behavior of the basilar membrane with pure-tone excitation,'' J. Acoust. Soc. Am. **55**, 148–162.
Steele, C. R., and Taber, L. A. (**1979**). ''Comparison of WKB calculations and experimental results for three-dimensional cochlear models,'' J. Acoust. Soc. Am. **65**, 1007–1018.
Taber, L. A., and Steele, C. R. (**1981**). ''Cochlear model including three-dimensional fluid and four modes of partition flexibility,'' J. Acoust. Soc. Am. **70**, 426–436.
Timoshenko, S. P., and Woinowsky-Krieger, S. (**1959**). *Theory of Plates and Shells* (McGraw–Hill, New York), Chap. 3.
Ulfendahl, M., and Khanna, S. M. (**1993**). ''Mechanical tuning characteristics of the hearing organ measured with the sensory cells in the gerbil temporal bone preparation,'' Pflugers Arch. Ges. Physiol. Menschen Tiere **424**, 95–104.
Xue, S., Mountain, D. C., and Hubbard, A. E. (**1995**). ''Electrically evoked basilar membrane motion,'' J. Acoust. Soc. Am. **97**, 3030–3041.
Zhou, G., Bintz, L., Anderson, D. Z., and Bright, K. E. (**1993**). ''A life-sized physical model of the human cochlea with optical holographic readout,'' J. Acoust. Soc. Am. **93**, 1516–1523.

Paradoxical relationship between frequency selectivity and threshold sensitivity during auditory-nerve fiber development

Janet L. Fitzakerley,[a] JoAnn McGee, and Edward J. Walsh[b]
Boys Town National Research Hospital and the Department of Physiology, Creighton University, 555 North 30th Street, Omaha, Nebraska 68131

(Received 1 August 1997; revised 6 February 1998; accepted 11 February 1998)

The acquisition of adultlike frequency selectivity is generally assumed to be tightly coupled to improvements in threshold sensitivity during cochlear development. In this study, frequency versus threshold (tuning) curves obtained from 1108 auditory-nerve fibers were used to investigate the relationship between tuning and threshold at characteristic frequency (CF) during postnatal development in kittens. At the earliest ages included in this study, sharpness was within the adult range, but thresholds were significantly higher than adult values. Tuning and thresholds improved along different exponential time courses that varied with CF. For units with CFs below 1 kHz, tuning curve slopes below CF matured earliest, followed by CF threshold, and then by slopes above CF. In contrast, for CFs above 1 kHz, the high-frequency slopes matured first, followed by threshold and then by slope below CF. One interpretation of these results is that tuning and thresholds *are not* tightly coupled in immature animals. Paradoxically, however, high-frequency slopes were correlated with threshold for individual units at all ages, suggesting that the relationship between tuning and threshold *is* maintained during development. This contradiction can be resolved by a developmental model that features a functional separation between cochlear nonlinearities and mechanical/electrical conversion. © *1998 Acoustical Society of America.* [S0001-4966(98)05605-7]

PACS numbers: 43.64.Pg, 43.64.Kc [RDF]

INTRODUCTION

Adult mammals possess a cochlear transduction process featuring both acute frequency selectivity and threshold sensitivity. These properties result from complex mechanical and electrical specializations within the organ of Corti, whose properties have been the focus of considerable experimental study. Examination of evidence obtained directly from measurements of basilar membrane motion (Ruggero and Rich, 1991a) or indirectly from auditory-nerve fiber recordings (Liberman, 1978), has revealed a tight correlation between the sharpness of tuning and threshold in mature animals. These two characteristics are therefore often attributed to the same underlying mechanism [for review, see Neely and Kim (1983); Dallos (1992)]. Cochlear damage has been shown to result in both decreased frequency selectivity and increased thresholds among adult auditory-nerve fibers innervating the damaged region (Kiang *et al.*, 1976; Robertson *et al.*, 1980; Liberman and Dodds, 1984), although there is qualitative evidence that threshold elevation can occur without significant degradation of tuning (Dallos and Harris, 1978; Schmiedt *et al.*, 1980).

The precise relationship between frequency selectivity and threshold has not been determined during inner ear development. It has been well established that altricial mammalian species exhibit elevated thresholds and decreased frequency selectivity during the early postnatal period [for review, see Rubel (1978); Walsh and Romand (1992)]. This similarity with the responses of traumatized adult cochleas has led to the hypothesis that one key feature of cochlear development is a shift from linear to nonlinear transduction (Romand, 1983; Walsh and McGee, 1990; Norton *et al.*, 1991; Fitzakerley *et al.*, 1994a). However, it is equally well documented that auditory-nerve fibers recorded from immature animals can exhibit elevated thresholds while tuning appears to be in the adult range (Romand, 1983; Walsh and McGee, 1990), and that thresholds continue to improve beyond the age where cochlear nonlinearities, such as two-tone suppression (Fitzakerley *et al.*, 1994b), responses to combination tones (Tubach *et al.*, 1996), and otoacoustic emissions (Norton *et al.*, 1991; Tierney *et al.*, 1994), are observed. Current models of cochlear development do not attempt to reconcile this discrepancy between the establishment of nonlinear behavior and the development of adultlike threshold sensitivity, particularly with respect to auditory-nerve data. In this report, two approaches were used to determine when the adult relationship between tuning and threshold is established. First, the time courses for the development of frequency selectivity and threshold sensitivity were established using population data. Second, tuning and threshold were explicitly compared for individual neurons throughout postnatal development. The results of these comparisons were used to develop a more complete model of the immature cochlear transduction process.

I. METHODS

Data were obtained from 1108 auditory-nerve fibers of 44 cats, which ranged in age from 72 gestational days to

[a]Current address: Departments of Pharmacology and Molecular Physiology, University of Minnesota School of Medicine, 307 Med 10 University Drive, Duluth, MN 55812.
[b]Electronic mail: walsh@novell.boystown.org

adulthood. Gestational ages are based on a 24-h breeding period. The mean gestational length was 67 ± 2 days for the 20 litters that provided animals for this study. Gestational age was used as the unit of measure in this investigation because response parameters were less variable when measured in that manner than when based on postnatal age. A complete description of the experimental methods can be found in Fitzakerley *et al.* (1994a).

A. Surgical and recording procedures

Briefly, animals were initially anesthetized via intraperitoneal (IP) injection of 25–40 mg/kg sodium pentobarbital (Nembutal), and supplemented with doses of pentobarbital (2.5–5 mg/kg IP) or ketamine (2.5–5 mg/kg IM) as needed to maintain areflexia. A tracheotomy was performed, and the animals were artificially ventilated as necessary. Body temperature was maintained at approximately 37 °C. The tympanic membrane was exposed by resecting the right pinna and external auditory canal. A speculum was sealed to the exposed external auditory meatus with ear mold material (Audalin), establishing a closed acoustic system. In older animals, a small hole was drilled in the bulla and a small diameter ventilation tube was inserted to equalize middle ear pressure. The animals were positioned in a stereotaxic apparatus, and placed within a double-walled sound attenuating chamber (Industrial Acoustics Corporation). The auditory nerve was exposed by opening the posterior fossa and aspirating the overlying cerebellum. Glass micropipettes were positioned visually over the auditory nerve and advanced from outside the recording chamber. Electrodes were filled with 2 M potassium acetate and had tip impedances between 15 and 30 MΩ. The recording electrode was coupled to a silver–silver chloride wire and referenced to a ground wire placed in the neck musculature. Recorded voltages were delivered to a preamplifier (Dagan Corporation 8100-1) and viewed on an oscilloscope. Event times for individual action potential discharges were digitized in real time with 10 μs accuracy.

B. Sound generation

Tone bursts were synthesized digitally, amplified (Crown International 150A), and shaped and gated using custom-built hardware. Stimuli were attenuated using custom-built attenuators (resolution of ± 1 dB; accuracy of 1%), and delivered to the ear via dynamic earphones (BeyerDynamic DT-48) coupled to the speculum. The stimulus generation system was computer controlled (PDP 11/83; Digital Equipment Corporation), and fully integrated with data acquisition. Before each experiment, the acoustic system was calibrated *in vivo* by measuring sound-pressure levels at the tympanic membrane using a 1/2-in. condenser microphone (Brüel & Kjær 4134) and subtracting previously calibrated values for the probe tube. Sound-pressure levels are reported in dB *re*: 20 μPa (dB SPL). Due to the high thresholds of younger animals, voltage levels at the earphones were adjusted to maximal levels for animals less than 81 days of gestational age. This resulted in a peak output of approximately 145 dB SPL between 0.8 and 2.75 kHz. The peak voltage was decreased by 20 dB in older animals to minimize the potential for delivery of damaging sounds to the cochlea.

TABLE I. CF groups used for analyses. Region refers to the cochlear place encoding each frequency range in the adult, and is not intended to imply that units within each CF group are recorded from the same cochlear location at all ages.

Group	CF range	Midfrequency	Region
1	0.190–0.307	0.245	
2	0.308–0.450	0.375	Apical
3	0.451–0.624	0.533	Turn
4	0.625–0.835	0.724	
5	0.836–1.090	0.956	
6	1.091–1.401	1.238	
7	1.402–1.778	1.580	Middle
8	1.779–2.235	1.995	Turn
9	2.236–2.790	2.499	
10	2.791–3.463	3.110	
11	3.464–4.280	3.852	
12	4.281–5.271	4.752	
13	5.272–6.473	5.843	
14	6.474–7.933	7.168	Basal
15	7.934–9.704	8.776	Turn
16	9.705–11.852	10.726	
17	11.853–14.459	13.093	
18	14.460–17.622	15.928	
19	17.623–21.461	19.449	
20	21.462–26.118	23.677	
21	26.119–31.769	28.807	Hook
22	31.769–38.626	35.032	

C. Data analysis

Tuning curves were collected using 50-ms tone bursts presented every 100 ms using an automated procedure [modified from Liberman (1978)]. This algorithm mapped a frequency span from 45 kHz to 100 Hz in steps of 24 points per octave (ppo) for frequencies greater than or equal to 2 kHz and 16 ppo for frequencies below 2 kHz. In the youngest animals, the ability to produce effective stimulus levels was limited by the maximum output of the stimulus generation system. All tuning curve data were smoothed before being analyzed, and curves that did not have a measurable Q_5 value or had a Q_5 less than 1.0 were excluded from the slope measurements. This eliminated the majority of the most broadly tuned units (obtained from the youngest animals) from the analyses (cf. Fig. 1). Characteristic frequency (CF) was defined for each unit as the frequency having the lowest threshold for producing a detectable increase in discharge rate. Slopes of the frequency-threshold curves were calculated by linear regression on a maximum of three frequency regions both above and below CF, with points of inflection being identified by eye. All slopes included in the analyses consisted of at least three points, and had statistically significant correlation coefficient (r) values ($\alpha = 0.05$). The steepest slopes above CF ($A_{\max}$) and below CF ($B_{\max}$) were determined for each tuning curve; these corre-

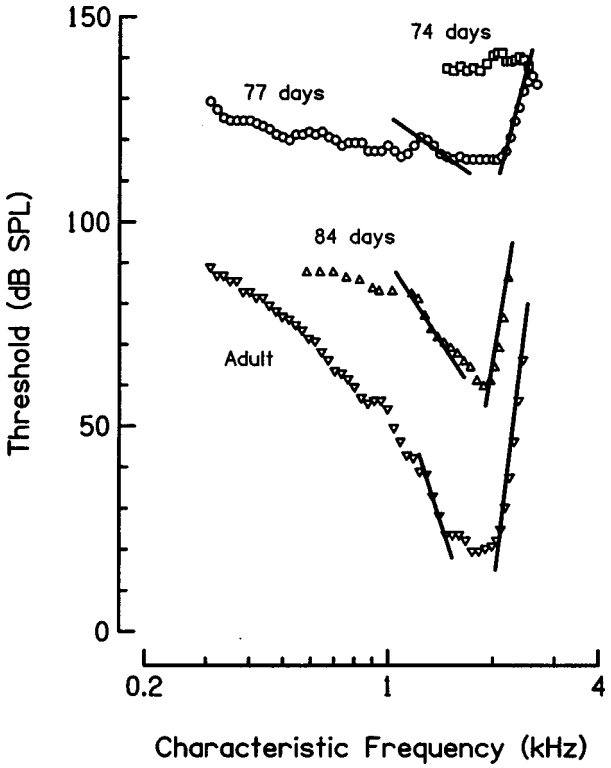

FIG. 1. Examples of auditory-nerve fiber tuning curves obtained from animals at various gestational ages. Slope values increased and thresholds decreased with increasing age. The solid lines indicate the linear regressions used to calculate the A_{max} and B_{max} values (slopes were obtained from as many as three regions on both the high- and low-frequency sides of each curve). Data from broadly tuned units recorded from the youngest animals (e.g., this 74 day example) were excluded from the slope calculations. All of these units had CFs in group 8 (1.779–2.235 kHz). 74 days (open squares): CF=2.094 kHz, threshold=138 dB SPL. 77 days (open circles): CF=2.047 kHz, threshold=115 dB SPL, A_{max}=255.0 dB/oct, B_{max} =−63.8 dB/oct. 84 days (open triangles): CF=1.877 kHz, threshold=60 dB SPL, A_{max}=521.2 dB/oct, B_{max}=−138.6 dB/oct. Adult (open inverted triangles): CF=1.823 kHz, threshold=19 dB SPL, A_{max} =711.9 dB/oct, B_{max}=−258.4 dB/oct.

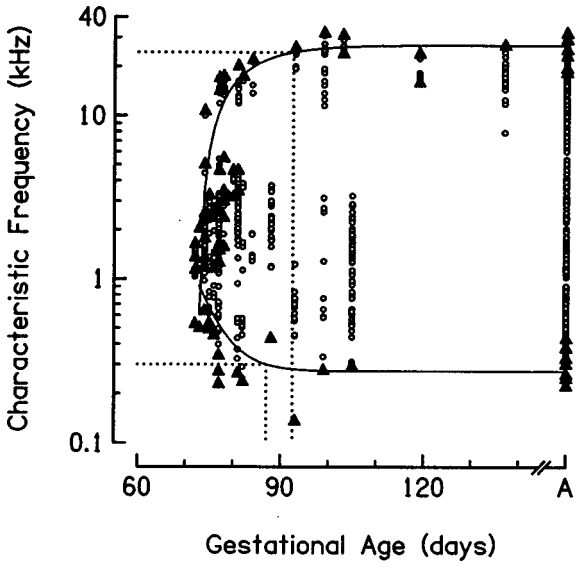

FIG. 2. Relationship between CF and age. The responsive frequency range increased during the first postnatal month. Data points represent CFs measured from individual units. Solid lines indicate saturating exponential functions fit to the minimum and maximum CF values obtained in each experiment (filled triangles). Dotted lines indicate ages where the functions reach 90% of their saturating values.

sponded to the region of the curve closest to the tip in 63% (284/451) of slopes above CF and 68% (290/425) below CF in adult animals.

To facilitate analyses, the responsive frequency range, which spans from approximately 0.1 to 45 kHz in the adult cat, was divided into 25 frequency groups (Table I). The boundaries were set at frequencies representing basilar membrane distances of 0.5 mm in the adult, as determined using the frequency/cochlear distance relationship described by Greenwood (1961, 1990) and confirmed by Liberman (1982). No neurons were observed with CFs less than 0.189 kHz or greater than 38.626 kHz, even in adult animals, resulting in the use of 22 frequency groups for most analyses.

Units were not segregated according to spontaneous rate for two reasons. First, although the correlation of threshold with spontaneous rate has been well documented in adult animals (Liberman, 1978; Robertson and Wilson, 1991), differences in threshold among classic spontaneous rate groups [low, medium, and high (Liberman, 1978)] were not statistically significant in any of the CF groups in the data obtained from adult animals in this study. Second, spontaneous rate distributions in immature animals are significantly different from those of the adult, having lower median values and unimodal distributions (Romand and Dauzat, 1981; Romand, 1984; Kettner *et al.*, 1985; Walsh and McGee, 1987).

II. RESULTS

There were several qualitative differences between tuning curves obtained from immature animals as compared to adults (Fig. 1). Curves obtained from animals less than 72 gestational days of age were very broadly tuned (i.e., had Q_5 values less than 1), with thresholds that were grossly elevated relative to adult values. Tuning curves obtained from such units have been the focus of several other investigations (Dolan *et al.*, 1985; Romand, 1987; Walsh and McGee, 1990; Fitzakerley *et al.*, 1994a). Data from these units were excluded from all but the preliminary analyses of this study (i.e., data are included only in Figs. 1 and 2), as the mechanism underlying the production of such tuning curves may complicate interpretation of the results. Among more sharply tuned units, tuning curve slopes above and below CF generally increased with age, while thresholds declined. It is the time course of these improvements among sharply tuned units that is the focus of this study.

A. Place code maturation

An estimate of the age at which the cochlear frequency/place code was mature in kittens was made by determining when the adult span of CFs was first observed. This was used to establish a framework for the description of tuning and threshold maturation. The expansion of the encoded frequency range during the postnatal period is demonstrated in Fig. 2, where CF values for individual units are plotted as a function of gestational age. The gap in the data in the 6–9-kHz region is due to limitations in transducer output in that frequency range. As has been described previously (Romand,

1983; Walsh and McGee, 1990), all units recorded from the youngest animals ($\leqslant$72 gestational days) response to low frequencies, with CFs ranging between 0.542 and 1.672 kHz. The expansion of this range toward the adult minimum and maximum was described by two saturating exponential functions having slightly different time courses. Exponential functions were fit to data pooled from the minimum and maximum CF values obtained from each animal at each age (filled triangles); fits were of the form $y=a(1-e^{-b(x-67)})+c$, where b is the time constant, c is the y intercept, and $a+c$ is the saturating value of the function. The function describing the time course of the lower CF boundary had a time constant of 0.22 days, and reached 90% of the adult value by 87 days. In contrast, the upper CF boundary changed more rapidly, with a time constant of 0.12 days, but reached saturation at an older age (93 days). These ages correspond, approximately, to the beginning and end of the third postnatal week. Clearly these boundaries represent an upper limit on the age at which the peripheral auditory system of an individual animal is capable of encoding the adult frequency range, as units with CFs outside the curves were found in both the high- and low-frequency regions in some animals. Using absolute criteria, a unit having a CF lower than 0.301 kHz (90% of the adult lower CF boundary) was first observed at 78 days, and greater than 24.413 kHz (90% of the adult upper CF boundary) at 81 days, 9–12 days earlier than ages estimated from the population data.

B. Tuning and threshold maturation

The difference between tuning and threshold values in immature and mature animals can be simply illustrated by comparing the values obtained from the youngest animals to the adult range (Fig. 3). All tuning curves in this and subsequent analyses had a Q_5 value greater than 1. In this figure, data obtained from immature animals (filled circles) represent values obtained from minimally tuned units at the youngest ages within each CF group ($n=1$ for group 20; $n=2$ for groups 15, 16; $4\leqslant n\leqslant 10$ for remaining groups). CF groups are defined in Table I. Due to the expansion of the frequency range described above (Fig. 2), the data from the immature animals were obtained at different ages for each CF group, as indicated in the lower frame of each panel. The ranges of slope and threshold values observed in adult animals are shown as boxes in the upper frames. Most of the slope values obtained from the youngest animals were within the lower boundary of the adult range, although only units within the highest CF groups ($>$21 kHz) exhibited tuning that consistently covered the entire adult range [Fig. 3(a) and (b)]. In contrast to this correspondence between immature slopes and minimum adult values, virtually all of the units recorded from immature animals had thresholds that were considerably higher than maximum adult thresholds [Fig. 3(c)]. The exceptions to these general findings were units with CFs greater than 26 kHz, where thresholds were within the adult range, and the data for one CF group (3.464–4.280 kHz) which were biased by the inclusion of data from one animal that was precocious with respect to both tuning and threshold development.

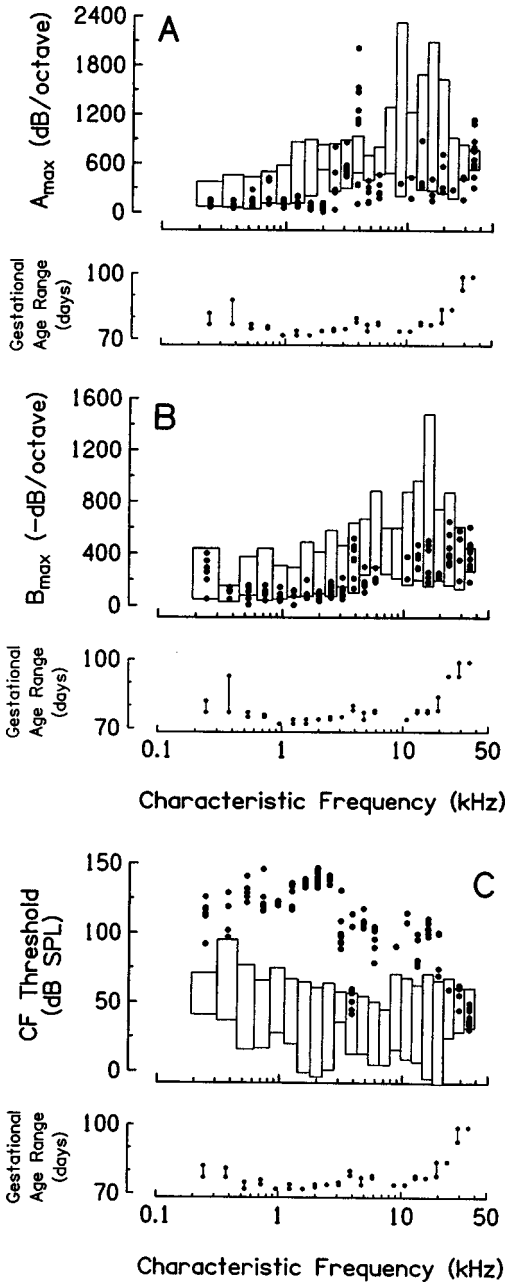

FIG. 3. Comparison of immature tuning curve properties with adult values. Slope measures were consistently within the lowest part of the adult range when first recorded. In contrast, thresholds were generally higher than the highest thresholds observed in adult animals. (a) Maximum slope above CF (A_{max}). (b) Maximum slope below CF (B_{max}). (c) Threshold. In the top frame of each panel, individual data points represent the values obtained from the youngest animals in each CF group, and rectangles indicate the adult range for each CF group. The age ranges over which the data from the minimally tuned units were obtained are plotted in the lower frame of each panel.

The time courses of the improvement in frequency selectivity and threshold sensitivity were both described by exponential functions, as illustrated for two CF groups in Fig. 4. The time course of the improvements was exponential for both tuning and threshold measures. Slope data [Fig. 4(a)–(d)] were fit with saturating exponentials of the form described previously for CF range. A term representing the peak output of the stimulus generation system was added to the equation used to fit the threshold versus age data [Fig.

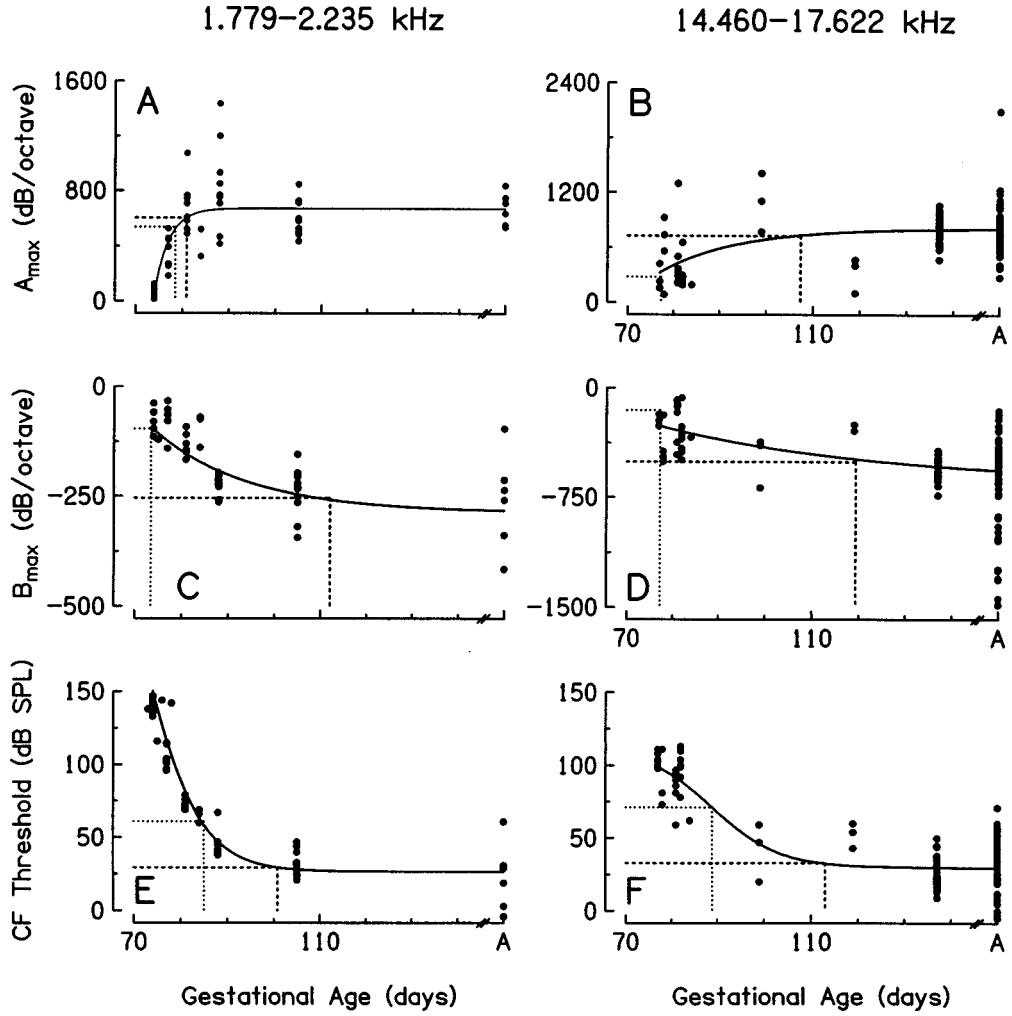

FIG. 4. Developmental changes in tuning curve properties for units with CFs in group 8 (left panels) and group 18 (right panels). The time course of the improvements was exponential for both tuning and threshold measures. (a) and (b) A_{max}. (c) and (d) B_{max}. (e) and (f) Threshold. Solid lines represent exponential fits to the data of the forms described in the text. Dotted and dashed lines indicate the ages where the data were estimated to reach the minimum adult and 90% of adult criteria, respectively. These estimates were calculated for all CF groups and used to generate the data plotted in Figs. 5 and 6.

4(e) and (f)], in order to improve the fits in cases where threshold estimates appeared to be limited by the maximum output of the stimulus generation system. Threshold versus age data were therefore fit using the equation $y=(a-d)/(1+e^{-b(x-c)})+d$, where a=the maximum available intensity (in dB SPL; different for each frequency), b=the slope of the function, c=the age of the inflection point, and d=the adult threshold value. Slope and threshold data from several CF groups could not be fit due to low sample sizes and these data were therefore excluded from subsequent analyses.

These exponential functions were then used to estimate the age when units within each CF group exhibited adultlike tuning and thresholds. To facilitate comparison with other studies and other techniques, two criteria were used to define maturity. The first criterion determined the age when the exponential function reached the minimum observed adult slopes or highest adult threshold (dotted lines, Fig. 4); this criterion varied for each CF group. This age represents a lower bound on the estimate of maturity, and is similar to that used in a previous single unit study (Walsh and McGee, 1990). The second criterion established the age when the functions reached 90% of their adult values (dashed lines, Fig. 4); this criterion also varied with CF. This standard was used to estimate the upper age limit for acquisition of adult properties. The age estimates obtained using these criteria were used to generate plots of the age of maturity as a function of CF (''criterion functions;'' Figs. 5 and 6). The estimates of the age of maturity produced using the minimum adult and 90% criteria were significantly different, as shown in Fig. 5 for slope values. Using the minimum adult values as the criterion, all CF groups exhibited adultlike A_{max} values when first recorded [Fig. 5(a)], as indicated by the overlap of the minimum criterion function with the dotted line identifying the age at which units with CFs in each group range were first observed (data replotted from Fig. 2). Using the minimum adult criterion, therefore, definition of the''first'' units to demonstrate sharp tuning was clearly dependent on the age that those frequencies were first transduced, rather than being dependent upon an overall improvement in the sharpness of tuning. In contrast, the developmental pattern defined by use of the 90% of adult criterion was significantly different. The resulting function exhibited a sharp dependence on CF and at most frequencies was shifted to older ages com-

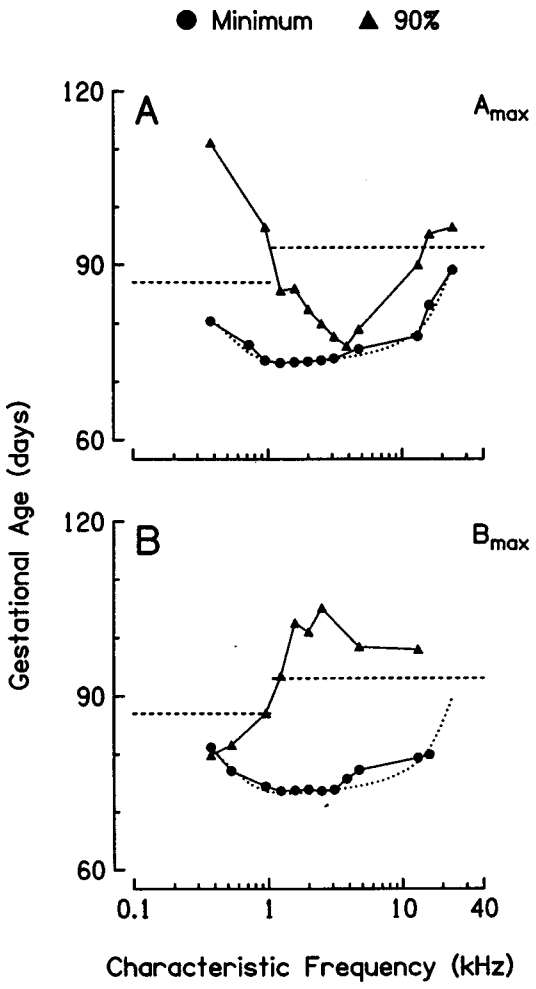

FIG. 5. Comparison of the age at which slope values reach adult criteria for different CF groups. (a) A_{max}. (b) B_{max}. The plots generated using the minimum adult criterion overlap the function describing the age at which each CF group was first observed, as calculated from the population data (dotted line; data from Fig. 2). A_{max} and B_{max} criterion plots had different forms when the 90% of adult criterion was used to estimate maturity. Data are smoothed and plotted at the center frequency for each CF group. The dashed line represents the upper estimate of the age at which the adult range of frequencies was observed.

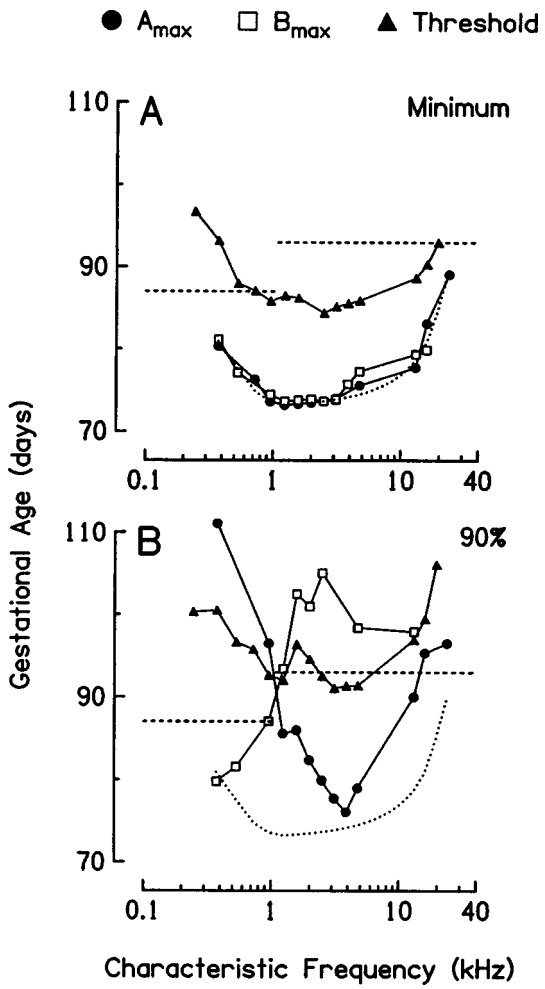

FIG. 6. Comparison of criterion functions for threshold and tuning measures. Threshold functions reached maturity at significantly older ages than slope functions for units with CFs greater than 1.090 kHz, while tuning measures were delayed relative to threshold for units with lower CFs. (a) Minimum adult criterion. (b) 90% of adult criterion. A_{max} and B_{max} data are replotted from Fig. 5. Analyses and layout are as in Fig. 5.

pared to the curve describing the age where each CF group was first observed. Using the 90% criterion, mature A_{max} values were first observed for units with CFs in the 3.464–4.280 kHz range, and those units met the 90% criterion when first observed. Units with CFs outside the 3.464–4.280 kHz range demonstrated mature tuning at increasingly older ages, as the age at which the exponential functions reached the 90% criterion increased progressively for units with both higher and lower CFs. Despite these differences in the forms of the curves, both criterion functions demonstrate that most of the improvement in A_{max} for units with CFs greater than 1 kHz occurred during the period that the responsive frequency range was expanding (i.e., before 93 gestational days; dashed line), whereas A_{max} values for units with CFs$<$1 kHz reached 90% of adult values after the acquisition of the adult low-frequency range (after 89 gestational days).

B_{max} and A_{max} criterion functions were similar when the minimum adult criterion was used [Fig. 5(b)]. However, the criterion function determined for the slopes below CF using the 90% criterion contrasted sharply with that for slopes above CF. B_{max} values exhibited an increase in the age of maturity as a function of CF for units with CFs less than 1.778 kHz, while units with higher CFs all reached 90% of adult values by approximately 100 days. These differences may have significant implications regarding the mechanism responsible for generation of sharp tuning in high- and low-CF regions of the cochlea.

Regardless of the criterion chosen to evaluate maturity, threshold maturation followed a more prolonged time course and different pattern of CF dependence from that described above for tuning curve slopes. In contrast to the tuning measures, the form of the functions describing age of maturity and CF for thresholds was similar using both criteria (Fig. 6). Thresholds matured at approximately the same age for units with CFs between 0.836 and 5.272 kHz, with units having lower and higher CFs maturing at older ages. Using the minimum adult criterion, single unit thresholds for units with CFs in the 0.836 to 5.272 kHz range were mature by approximately 85 days. Adult thresholds were reached by approximately 93 days using the 90% of maximum criterion. There was a substantial difference in the age of maturity between

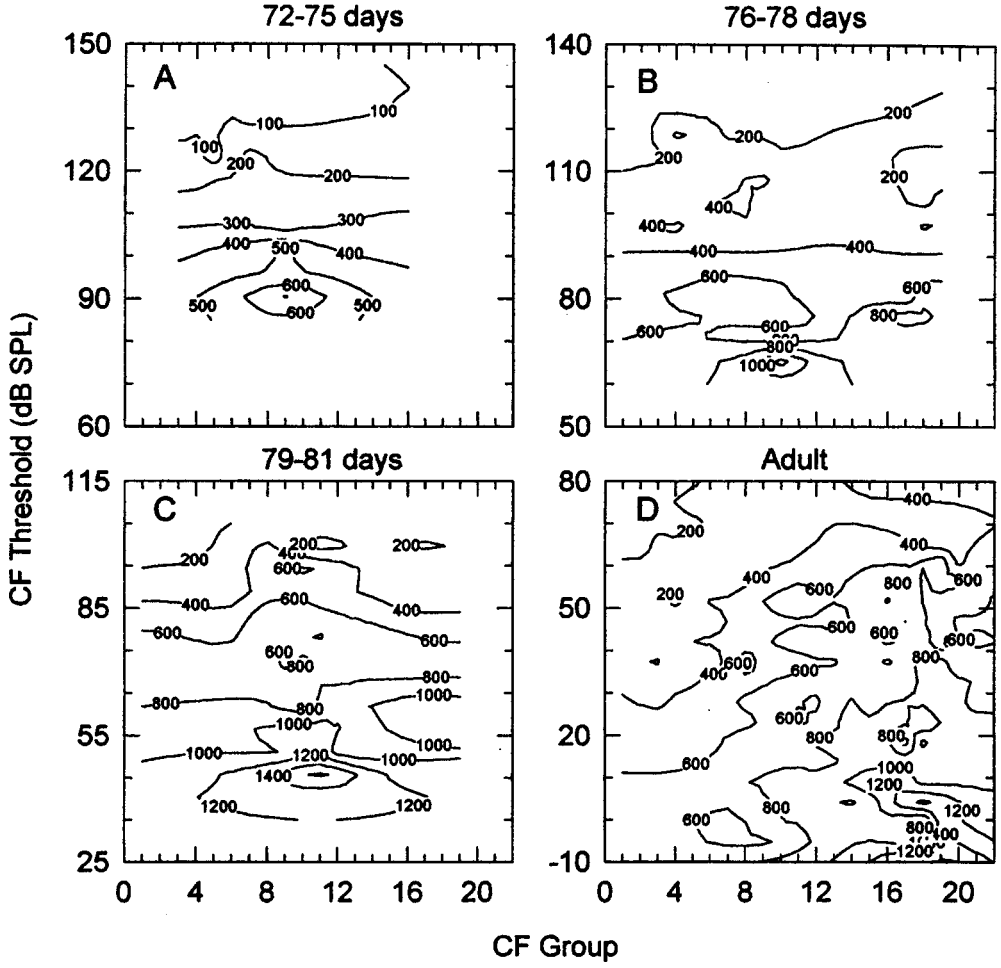

FIG. 7. Relationship between A_{max}, threshold, and CF among data from different age groups. Slope/threshold contours generally became less flat with increasing age, although thresholds within each CF group were generally correlated with slope at all ages. (a) 72–75 days. (b) 76–78 days. (c) 79–81 days. (d) Adult. Each contour represents the interpolated region corresponding to the indicated slope value. Note the different threshold scales for each age group, and the narrower slope bands in the plot for 72–75 days.

the threshold and tuning measures. Using the minimum adult criterion [Fig. 6(a)], thresholds reached minimum adult levels 6–16 days after neurons were first observed in each CF group, and therefore considerably later than tuning measures reached minimum adult values. The complicated relationship between tuning and threshold maturation was more evident when the 90% criterion was used to evaluate maturity [Fig. 6(b)]. In that instance, A_{max} values matured at older ages than thresholds for units with CFs less than 1.090 kHz, and at younger ages for all higher frequencies. The pattern was reversed for slopes below CF: thresholds matured at older ages for low CFs and at younger ages for high CF units. Using the 90% estimate, there is therefore a clear inversion in the relationship between tuning and slopes above and below CF for units with CFs above and below 1 kHz.

C. Relationship between tuning and threshold during development

The apparent dissociation between the age at which mature frequency selectivity was obtained and the age at which thresholds were in the adult range could indicate that threshold and tuning are not as tightly correlated in the immature animal as they are presumed to be in the adult. This hypothesis was tested by considering the relationship between threshold and tuning data among individual units at different ages. The first issue examined was whether the general relationship between tuning, threshold, and CF remained constant during development (i.e., whether the units with the sharpest tuning were consistently the ones with the lowest thresholds). This was analyzed by constructing contour plots that mapped A_{max} as a function of *CF group* and threshold. Contour plots were generated by interpolating a three-dimensional (3-D) mesh using inverse distance weighting of the CF group, threshold, and slope data. At the youngest ages studied [72–75 days; Fig. 7(a)], thresholds were generally inversely correlated with slopes. Threshold/slope contours were relatively flat as a function of CF, indicating that all CF groups exhibited similar tuning. Units with the sharpest tuning and lowest thresholds were not found at the highest CF, but rather in the *groups* with CFs between 1.402 and 4.280 kHz (groups 7–11), which corresponded approximately to the range of CFs that were transduced earliest. In the 76–78 day group [Fig. 7(b)], there was an obvious improvement in both threshold and tuning. The inverse A_{max}/threshold relationship and the generally uncomplicated contours were maintained at this age, although the data from this group

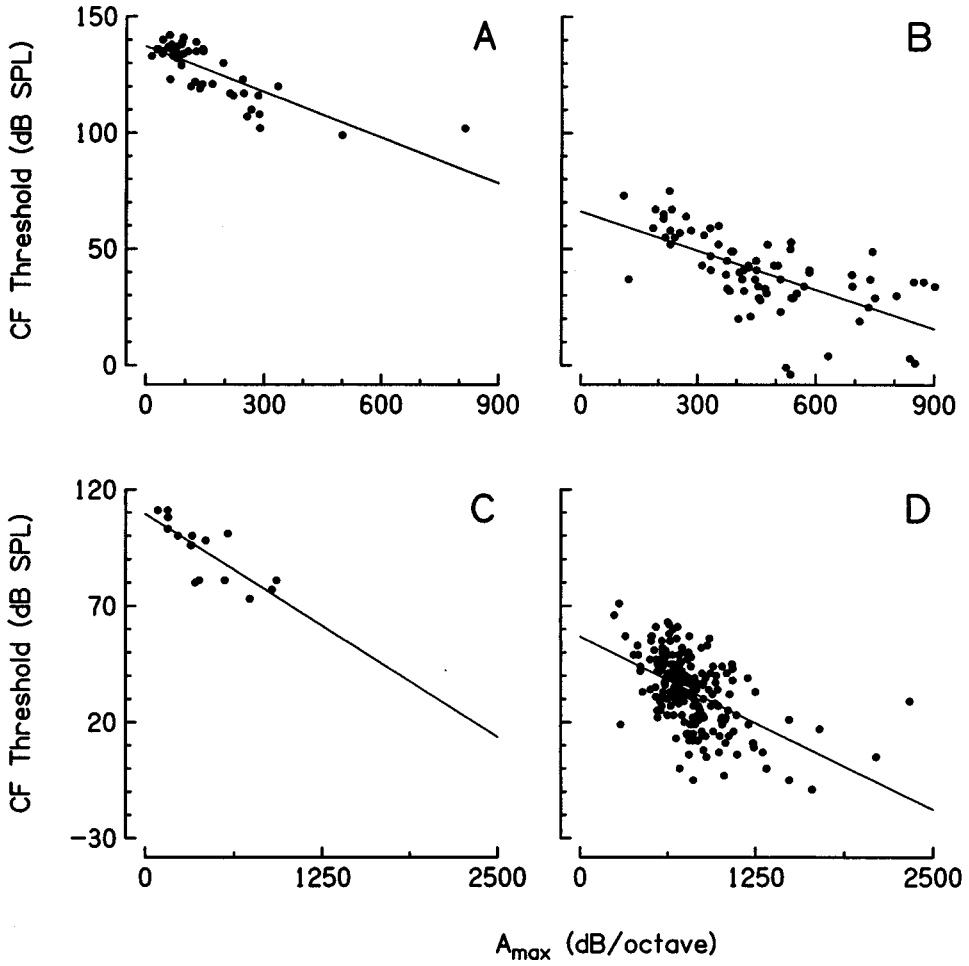

FIG. 8. Correlation of threshold and slope above CF for units with CFs between 0.836 and 2.79 kHz (top frames) and 7.934–21.461 kHz (lower frames). Although the contours were complicated, threshold and slope were linearly correlated at most ages. 0.836–2.790 kHz: (a) 72–75 days (slope=−0.655 oct, *y* intercept=137.7 dB SPL). (b) Adult (slope=−0.559 oct, *y* intercept=66.1 dB SPL). 2.934–21.461 kHz: (c) 76–78 days (slope=−0.383 oct, *y* intercept=109.4 dB SPL). (d) Adult (slope=−0.298 oct, *y* intercept=56.8 dB SPL).

diverged from a linear relationship between threshold and tuning in two ways. First, there were clear ''peaks'' and ''troughs'' of A_{max} values found embedded in the contours. Second, in the CF range with the sharpest tuning, the units with the steepest slopes were not always the ones with the lowest thresholds (the 1200 and 1000 dB/oct. contours are above the 800 dB/oct. contour). These patterns were also observed in the 79–81 day group [Fig. 7(c)]. As in the younger groups, contours were still relatively flat as a function of CF, with the largest peak occurring for units in the midfrequency range (groups 8–13; 1.779–6.473 kHz). The most sharply tuned units in this range also did not have the lowest thresholds at this age (the 1600- and 1400-dB/oct contours are inside that of 1200 dB/oct). In sharp contrast to these immature patterns that were relatively flat in the threshold/CF plane, adult contours were curved as a function of CF [Fig. 7(d)], with the largest peak occurring for units with CFs between 14.460 and 26.118 kHz, which were also the units with the lowest thresholds.

The explicit relationship between tuning and threshold was examined for the population of units by performing a linear regression to the A_{max} and threshold data. Data were collapsed across several CF groups in order to increase the sample size for the fit. Data from two CF ranges are shown as examples in Fig. 8 (0.836–2.79 kHz, top frames; 7.934–21.461 kHz, lower frames). Tuning and threshold measurements were generally well correlated in both young animals and in adults (Table II). However, there were several cases where the tuning/threshold relationship was not significantly correlated. In animals less than 84 days of age, frequency selectivity and thresholds were only weakly correlated for units with CFs less than 0.835 kHz. This may be another reflection of differences between the relationship of tuning and threshold for low-CF fibers. Tuning and threshold were also not significantly correlated among units recorded from the lower basal turn region of adult animals (CFs between 2.791 and 7.933 kHz). This was probably due to the presence of a threshold ''notch'' in this frequency region that has been attributed to localized damage in nonchamber raised animals (Liberman, 1978). The lack of correlation among other age/CF groups may reflect low sample sizes.

In CF groups where there was sufficient data to compare the regression data across age, and where there was a significant linear correlation between slope above CF and thresh-

TABLE II. Correlation between threshold and A_{max} within various CF ranges for different age groups. Asterisks indicate where the correlation coefficient values (r) were greater than the critical value ($\epsilon = 0.05$). Data were collapsed across several CF groups.

CF range (kHz)	Age (days)	N	Slope (dB/dB/oct)	Y intercept (dB SPL)	r	Sig.
0.189–0.835	72–75	5	−0.0691	131.1	0.423	···
	76–78	12	−0.0165	116.4	0.294	···
	79–81	6	−0.0435	103.0	0.816	*
	82–84	8	−0.0615	122.0	0.672	···
	93–99	15	−0.1544	85.0	0.872	*
	Adult	61	−0.0852	68.3	0.669	*
0.836–2.790	72–75	46	−0.0655	137.7	0.790	*
	76–78	40	−0.0550	128.7	0.783	*
	79–81	27	−0.0112	82.6	0.364	···
	82–84	10	−0.0670	102.5	0.451	···
	88	20	−0.0202	52.1	0.663	*
	93–99	5	−0.0605	71.1	0.902	*
	Adult	73	−0.0559	66.1	0.640	*
2.791–7.933	72–75	10	−0.0220	110.0	0.738	*
	76–78	23	−0.0550	117.2	0.755	*
	79–81	36	−0.0249	88.1	0.588	*
	82–84	4	−0.184	150.1	0.898	···
	88	8	−0.0202	52.1	0.647	*
	Adult	53	−0.0090	41.1	0.137	···
7.934–21.461	76–78	16	−0.0383	109.4	0.781	*
	79–81	18	−0.0355	101.2	0.946	*
	82–84	9	−0.0493	101.4	0.504	···
	93–99	14	−0.0297	63.6	0.584	*
	119–137	98	−0.0192	41.5	0.453	*
	Adult	203	−0.0298	56.8	0.518	*
21.462–38.626	93–99	27	−0.0200	60.9	0.535	*
	119–137	9	−0.0037	39.8	0.054	···
	Adult	60	−0.0352	68.4	0.516	*

old, there were significant developmental changes in both the slope and y-intercept values of the fits (Fig. 9). Slope values tended to increase slightly for units with CFs above 0.835 kHz and decrease for units with lower CFs. As would be expected, y-intercept values decreased for all CF groups due to improvements in threshold. In summary, tuning and threshold were as significantly correlated in young animals as in the adult, but developmental changes in the relationship

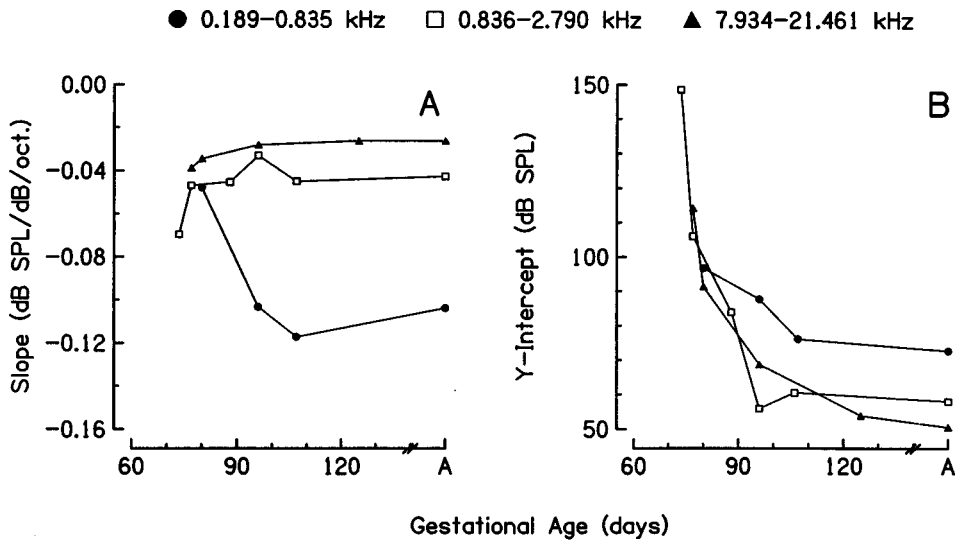

FIG. 9. Threshold versus A_{max} regression values as a function of gestational age for the three CF ranges where slope and threshold were linearly correlated across several ages (data from Table II). (a) Slope values. (b) y-intercept values. The A_{max}/threshold relationship became progressively steeper with increasing age for low-CF units, but tended to flatten during development for high-CF units. Predictably, the y-intercept of the A_{max}/threshold regressions decreased with increasing age. Only statistically significant regression values are plotted.

TABLE III. Time course of the emergence of key physiological properties and changes in cochlear anatomy for the cat. Data taken from this study are unreferenced.

Gest. age (days)	General	Midbasal turn (6.474–9.704 kHz)		Apical turn (0.308–0.624 kHz)		Post. age
		Anatomy	Physiology	Anatomy	Physiology	
61	1st cochlear microphonic response[a]					
67	onset of myelination; distinction between type I and II cells[b,c]					1st
68	1st single unit[d,e,f,g] and behavioral[h] responses	tunnel of Corti and marginal pillars present; TM extended to Hensen's cells[i]				week
71	1st auditory brainstem response[j]					
74	Adult areal ratios[k]				1st CF's	
75			1st CF's; adult tuning			2nd
77		TM fully mature (loss of marginal pillars)[i]	1st two-tone suppression,[m] combination tone responses[m] and OAE[n]	appearance of tunnel and marginal pillars; TM extended to sensory cells[l]		week
81	loss of rhythmic activity[o]			mature TM[i]	1st OAE[h]	
93	encoding of adult frequency range	mature IHC/OHC distance[i]		mature IHC/OHC distance[i]		4th
95	mature EP[p]		adult thresholds		adult thresholds	week
97+	mature distribution of SR[q,r,s,t]		adult AP amplitude[u]		adult tuning adult AP amplitude[u]	week

[a]Pujol and Hilding (1973).
[b]Lindeman (1971).
[c]Romand and Romand (1990).
[d]Carlier *et al.* (1975).
[e]Dolan *et al.* (1985).
[f]Romand (1983).
[g]Walsh and McGee (1990).
[h]Ehret and Romand (1981).
[i]Lim (1977).
[j]Walsh *et al.* (1986).
[k]Thomas and Walsh (1990).
[l]Fitzakerley *et al.* (1994a).
[m]Walsh and McGee (1987).
[n]Tierney *et al.* (1994).
[o]Walsh and McGee (1988).
[p]Fernandez and Hinojosa (1974).
[q]Kettner *et al.* (1985).
[r]Romand (1984).
[s]Romand and Dauzat (1981).
[t]Tubach *et al.* (1996).
[u]Moore (1981).

between tuning and threshold resulted in differences in the age at which threshold and tuning measures reached adult values.

III. DISCUSSION

The conversion of acoustic stimuli to auditory-nerve responses can be considered a three stage process, consisting of: (1) transmission of the signal through the external and middle ears, (2) spectral analysis at the level of the basilar membrane, and (3) transduction by the inner hair cell and generation of action potentials by the auditory nerve. Since all three components of auditory signal processing are subject to changes during development, they must all be considered when an attempt is made to explain the observed differ-

ences between tuning and threshold maturation. Relevant timing regarding anatomical and physiological changes in the kitten peripheral auditory system is summarized in Table III. For brevity, only data from studies with specifically identified ages and cochlear locations are included.

In several species, middle ear transfer functions have been shown to contribute significantly to the nature of sound transduction during development (Relkin *et al.*, 1979; Relkin and Saunders, 1980; Saunders and Summers, 1982). Among other factors, changes in lever and areal ratios, the presence of mesenchyme, and growth of the bullae are thought to alter transmission of stimuli through the middle ear during early postnatal life. In the cat, tympanic membrane:stapedial footplate areal ratios are known to mature during the first postnatal week, while expansion of bullae volume and the resorption of mesenchyme are mostly completed by the end of the second postnatal week (Thomas and Walsh, 1990). The latter changes, in particular, may be responsible for the fact that the responsive frequency range of the cat progresses towards both higher and lower frequencies during postnatal development. Our observation that the improvement in encoding of the lowest frequencies is completed during the third postnatal week is consistent with the hypothesis that this is due, at least in part, to increased middle ear compliance. Similar observations regarding the impact of changes in middle ear function on the expansion of the frequency range have been made in gerbil, mouse, and rat (Woolf and Ryan, 1988; Cohen *et al.*, 1993; Doan *et al.*, 1994, 1996; Mills *et al.*, 1994). However, based on the available estimates of the timing of external and middle ear maturity in kittens (Villablanca and Olmstead, 1979; Thomas and Walsh, 1990), it is unlikely that changes in middle ear impedance are solely responsible for the observed disparity between the age of maturation of threshold and tuning, particularly for mid-CF units.

As has been hypothesized previously (Walsh and McGee, 1990), the most likely explanation for the developmental changes in frequency selectivity is a change within the organ of Corti that influences the spectral analysis performed by the cochlea. This process has been subdivided into two components: a passive process, which is dependent upon the mass and stiffness characteristics of the cochlear partition (von Bekesy, 1960), and an active process, which requires the presence of a functional outer hair cell system (Neely and Kim, 1983). The concept that it is the interactions between these two systems that produces the changes in the relationship among frequency, tuning, and threshold during development is not new [see especially Rubel (1978); Romand (1983); Norton *et al.* (1991); Walsh and Romand (1992)]. However, several observations made in this study contribute in a novel manner to our understanding of this interaction.

It is apparent from the present study that most units recorded from immature animals have tuning curve slopes that fall in the lower portion of the adult range, and there is a general improvement in tuning that follows an exponential time course. An improvement in tuning with age is also supported by the observation that the highest CF units recorded at each age are not always the *most* sharply tuned, as indicated by the contour plots. However, it is also clear from population data that units from all CF groups meet minimal adult criteria from the time that they are first observed. Definition of whether tuning improves during development therefore clearly depends upon the criterion chosen to define maturity. Criterion choice also affects the definition of the CF range that matures ''first.'' For example, if the minimum adult criterion is used, definition of the CF group that matures ''first'' depends solely on the age at which a particular frequency is transduced (since all CF groups meet the minimum adult criterion when first observed). This interpretation of the results is consistent with recent descriptions of the development of midfrequency otoacoustic emissions (OAE) (Mills *et al.*, 1994).

It can be inferred from the data presented in this paper that there is a developmental change in the nature of the active process that contributes to the improvement of tuning and/or the ability to transduce high-frequency stimuli. However, it is not obvious how an immaturity in the active process could maintain the mature relationship between sharp tuning and low thresholds in relative terms, while producing thresholds that are elevated in absolute terms. Comparison with the anatomical data supports the hypothesis that the interaction between the tectorial membrane (TM) and the outer hair cells (OHC) is required for the expression of nonlinear behavior, a suggestion that has been made previously (Walsh and McGee, 1990; Fitzakerley *et al.*, 1994a; He *et al.*, 1994). The tectorial membrane appears to be in contact with the outer hair cells approximately two weeks before adultlike thresholds are established in the cat (Lim, 1977). In the gerbil, it is also clear that the onset of outer hair cell contractility occurs earlier than either the appearance of sharp tuning or the presence of otoacoustic emissions (He *et al.*, 1994). If it is assumed that the immaturity of the endocochlear potential (Fernandez and Hinojosa, 1974) does not produce a sufficient change in the driving force for contractility to produce a threshold shift without affecting tuning, and given the apparent structural maturity of the outer hair cell system at the relevant ages, it is not likely that immaturity in the outer hair cell system is responsible for the discrepancy between threshold and tuning maturation. The hypothesis that a developmental change in endocochlear potential is not a sufficient explanation for an improvement in tuning without a similar improvement in threshold is supported by experiments using furosemide to manipulate endocochlear potential. Such experiments have found that tuning is decreased and thresholds are simultaneously increased when the endocochlear potential is decreased (Sewell, 1984; Ruggero and Rich, 1991b). These results would argue against developmental changes in basilar membrane mechanics being the cause for the observed delay in threshold maturation relative to improvements in frequency selectivity.

Another argument against a simplistic interpretation of the relationship between tuning and threshold during development is the observation in this study that the tuning curves of low-CF fibers (particularly below 1 kHz) mature differently from those of high-CF fibers. Most significantly, the developmental relationships between $A_{\max}$, $B_{\max}$, and thresholds are reversed, with slopes below CF improving significantly before those above CF at low frequencies. Acqui-

sition of mature tuning (using A_{max} criteria) among low-CF fibers is generally coincident with that of thresholds, and divorced from both tectorial membrane maturation (Lim, 1977) and expression of otoacoustic emissions (Tierney *et al.*, 1994). A differential delay in the maturation of high- and low-CF regions of the cochlea has also been suggested by Romand (1983, 1987) and by Mills *et al.* (1994). It is possible that these high versus low CF disparities reflect the influence of changes in middle ear compliance described above. The observed differences in the maturation of low- and high-CF units in this study may also be associated with developmental expression of tuning curve asymmetry, which has been documented previously in adult animals of several species (Kiang *et al.*, 1965; Liberman, 1978; Ohlemiller and Echteler, 1990).

Another factor that must be considered is the use of fixed CF groups established from the adult frequency/place map used in these analyses. Obviously, a shift in the location of transduction of a particular CF group would significantly complicate the interpretation of these results. Most anatomical evidence supports the hypothesis that cochlear development proceeds along a base-to-apex gradient (Retzius, 1884; Pujol and Marty, 1970; Mair, 1973; Lim, 1977; Kraus and Aulbach-Kraus, 1981). In many species, clear shifts in CF have been described in structures encoding basal turn frequencies using a variety of techniques (Lippe and Rubel, 1983, 1985; Harris and Dallos, 1984; Yancey and Dallos, 1985; Arjmand *et al.*, 1988; Echteler *et al.*, 1989; Rubsamen *et al.*, 1989; Sanes *et al.*, 1989; Muller, 1991; Webster and Martin, 1991; Romand, 1997). However, this observation may not be generalized to all cochlear locations, as a similar shift in CF is not observed in the middle turn of the cochlea during the same period (Arjmand *et al.*, 1988). Of critical importance to this study is the timing of these observations. The majority of place code changes have been described within the period immediately after the onset of hearing. In the gerbil, for example, a 1.5-oct increase in CF is observed in the basal turn during the third postnatal week, ending approximately 7 days after the onset of function (Arjmand *et al.*, 1988; Echteler *et al.*, 1989). Place code shifts have also been correlated with the time of establishment of the adult frequency range in this species (Muller, 1991). Using the oldest estimate for establishment of the adult frequency range in the kitten in this study, it is possible that changes in the cochlear frequency map have a significant impact on the improvement of slopes above CF for high-frequency fibers, and on slopes below CF for low-frequency fibers. However, adultlike thresholds were obtained after the time when any place code shifts may be presumed to occur, which eliminates this as an explanation for the difference in the maturation of thresholds and tuning.

Returning to the question of mechanism, inner hair cell (IHC) transduction must also be considered as an explanation for the delayed maturation of threshold relative to tuning among auditory-nerve fibers. In adult animals, there is a clear relationship between spontaneous rate (SR) and threshold (Liberman, 1978; Ohlemiller and Echteler, 1990), which is thought to be due to the release of transmitter at the synapse between the inner hair cell and the auditory-nerve fiber (Liberman, 1978; Liberman and Dodds, 1984; Geisler *et al.*, 1985). Spontaneous rate (and, by inference, threshold) is therefore thought to be influenced by the standing potential within the inner hair cell, which is partially controlled by the endocochlear potential (Yates, 1991). The timing of the maturation of thresholds is more similar to the acquisition of adultlike spontaneous rate distributions and endocochlear potential than it is to tuning, at least for high-CF fibers. The delayed nature of threshold maturation reported in this study is consistent with a report of prolonged maturation (6–9 weeks) of compound auditory-nerve action potential (AP) amplitude in cats (Moore, 1981). On the basis of these data, it can be suggested that the factors preventing expression of the adult distribution of spontaneous rate may also be responsible for the higher thresholds among sharply tuned units in immature animals. In the adult, differences in spontaneous rate of fibers have been correlated with differences in axon diameter and the location of primary afferent terminals on the inner hair cell (Liberman and Oliver, 1984), as well as the number of olivocochlear fiber synapses per radial fiber dendrite (Liberman *et al.*, 1990). Anatomical studies have demonstrated developmental increases in radial fiber diameter (Simmons *et al.*, 1991) and changes in inner hair cell innervation (Perkins and Morest, 1975; Pujol *et al.*, 1978; Simmons *et al.*, 1991, 1996a, b) which may be relevant with respect to acquisition of mature spontaneous rate distributions, and therefore to the paradox of tuning and threshold maturation that was identified in this study. Structural changes associated with the transduction apparatus (inner hair cell/auditory nerve) are temporally correlated with the disparity between threshold and tuning described in this study. Unlike developmental changes in middle ear and basilar membrane function, changes in the transduction apparatus are in a position to affect threshold but not tuning, and therefore likely represent a major cause of the paradoxical relationship between tuning and threshold during development.

IV. SUMMARY

The principal observation of this study is that thresholds of auditory-nerve fibers mature over a more protracted time course than frequency selectivity, based on population data. However, a significant correlation between tuning and threshold was also found to be maintained on an individual unit basis at most ages. The most parsimonious explanation of these paradoxical observations is that there is a functional separation between the spectral analysis and inner hair cell transduction processes during later stages of cochlear development. One prediction of this hypothesis is that the separation of tuning and threshold development is a phenomenon that is restricted to auditory-nerve fiber recordings. Preliminary data from otoacoustic emission studies in kittens (Tiemey *et al.*, 1994) support this hypothesis, as thresholds for otoacoustic emissions are considerably below those of auditory-nerve fibers recorded in this study from animals of a similar age. Experiments designed to manipulate this aspect of auditory system development should provide considerable insight into the functioning of the cochlea.

ACKNOWLEDGMENTS

The care and use of all animals were in accordance with the guidelines of the animal welfare committee of Creighton University and BTNRH. This research was supported by NIDCD Grants No. DC01007 and No. DC00982 awarded to E.J.W. The authors would like to thank Brian Jacob, Louis Giorgi, and Dr. Ye Liu for their technical and surgical assistance.

Arjmand, E., Harris, D., and Dallos, P. (**1988**). ''Developmental changes in frequency mapping of the gerbil cochlea: Comparisons of two cochlear locations,'' Hearing Res. **32**, 93–96.

Carlier, E., Abonnenc, M., and Pujol, R. (**1975**). ''Maturation des responses unitaires a la stimulation tonale dans le nerf cochleaire du chaton,'' J. Physiol. (Paris) **70**, 129–138.

Cohen, Y. E., Doan, D. E., Rubin, D. M., and Saunders, J. C. (**1993**). ''Middle-ear development. V: Development of umbo sensitivity in the gerbil,'' Am. J. Otolaryngol. **14**, 191–198.

Dallos, P. (**1992**). ''The active cochlea,'' J. Neurosci. **12**, 4575–4585.

Dallos, P., and Harris, D. (**1978**). ''Properties of auditory nerve responses in absence of outer hair cells,'' J. Neurophysiol. **41**, 365–383.

Doan, D. E., Cohen, Y. E., and Saunders, J. C. (**1994**). ''Middle-ear development. IV. Umbo motion in neonatal mice,'' J. Comp. Physiol. A **174**, 103–110.

Doan, D. E., Igic, P. G., and Saunders, J. C. (**1996**). ''Middle-ear development.7. Umbo velocity in the neonatal rat,'' J. Acoust. Soc. Am. **99**, 1566–1572.

Dolan, D. F., Teas, D. C., and Walton, J. P. (**1985**). ''Postnatal development of physiological responses in auditory nerve fibers,'' J. Acoust. Soc. Am. **78**, 544–554.

Echteler, S. M., Arjmand, E., and Dallos, P. (**1989**). ''Developmental alterations in the frequency map of the mammalian cochlea,'' Nature (London) **341**, 147–149.

Ehret, G., and Romand, R. (**1981**). ''Postnatal development of absolute auditory thresholds in kittens,'' J. Comp. Physiol. Psychol. **95**, 304–311.

Fernandez, C., and Hinojosa, R. (**1974**). ''Postnatal development of endocochlear potential and stria vascularis in the cat,'' Acta Oto-Laryngol. **78**, 173–186.

Fitzakerley, J. L., McGee, J., and Walsh, E. J. (**1994a**). ''Responses of peripheral auditory neurons to two-tone stimuli during development. I. Correlation with frequency selectivity,'' Hearing Res. **77**, 135–149.

Fitzakerley, J. L., McGee, J., and Walsh, E. J. (**1994b**). ''Responses of peripheral auditory neurons to two-tone stimuli during development. II. Factors related to neural responsiveness,'' Hearing Res. **77**, 150–161.

Geisler, C. D., Deng, L., and Greenberg, S. R. (**1985**). ''Thresholds for primary auditory fibers using statistically defined criteria,'' J. Acoust. Soc. Am. **77**, 1102–1109.

Greenwood, D. D. (**1961**). ''Critical bandwidth and the frequency coordinates of the basilar membrane,'' J. Acoust. Soc. Am. **33**, 1344–1356.

Greenwood, D. D. (**1990**). ''A cochlear frequency-position function for several species—29 years later,'' J. Acoust. Soc. Am. **87**, 2592–2605.

Harris, D. M., and Dallos, P. (**1984**). ''Ontogenetic changes in frequency mapping of a mammalian ear,'' Science **225**, 741–743.

He, D. Z. Z., Evans, B. N., and Dallos, P. (**1994**). ''First appearance and development of electromotility in neonatal gerbil outer hair cells,'' Hearing Res. **78**, 77–90.

Kettner, R. E., Feng, J. Z., and Brugge, J. F. (**1985**). ''Postnatal development of the phase-locked response to low frequency tones of auditory nerve fibers in the cat,'' J. Neurosci. **5**, 275–283.

Kiang, N. Y.-S., Liberman, M. C., and Levine, R. A. (**1976**). ''Auditory nerve activity in cats exposed to ototoxic drugs and high-intensity sounds,'' Ann. Otol. Rhinol. Laryngol. **85**, 752–769.

Kiang, N. Y.-S., Watanabe, T., Thomas, E. C., and Clark, L. F. (**1965**). *Discharge Patterns of Single Fibers in the Cat's Auditory Nerve* (MIT, Cambridge, MA).

Kraus, H. J., and Aulbach-Kraus, K. (**1981**). ''Morphological changes in the cochlea of the mouse after the onset of hearing,'' Hearing Res. **4**, 89–102.

Liberman, M. C. (**1978**). ''Auditory nerve response from cats raised in a low-noise chamber,'' J. Acoust. Soc. Am. **63**, 442–455.

Liberman, M. C. (**1982**). ''The cochlear frequency map for the cat: Labeling auditory-nerve fibers of known characteristic frequency,'' J. Acoust. Soc. Am. **72**, 1441–1449.

Liberman, M. C., and Dodds, L. W. (**1984**). ''Single-neuron labeling and chronic cochlear pathology. III. Stereocilia damage and alterations of threshold tuning curves,'' Hearing Res. **16**, 55–74.

Liberman, M. C., Dodds, L. W., and Pierce, S. (**1990**). ''Afferent and efferent innervation of the cat cochlea: Quantitative analysis with light and electron microscopy,'' J. Comp. Neurol. **301**, 443–460.

Liberman, M. C., and Oliver, M. E. (**1984**). ''Morphometry of intracellularly labeled neurons of the auditory nerve: Correlations with functional properties,'' J. Comp. Neurol. **223**, 163–176.

Lim, D. J. (**1977**). ''Fine morphology of the tectorial membrane,'' in *Inner Ear Biology*, edited by M. Portmann and J.-M. Aran (Alnserin, Paris), pp. 47–60.

Lindeman, H. H., Ades, H. W., Bredberg, G., and Engstrom, H. (**1971**). ''The sensory hairs and the tectorial membrane in the development of the cat's organ of Corti,'' Acta Oto-Laryngol. **72**, 229–242.

Lippe, W., and Rubel, E. W. (**1983**). ''Development of the place principle: Tonotopic organization,'' Science **219**, 514–516.

Lippe, W. R., and Rubel, E. W. (**1985**). ''Ontogeny of tonotopic organization of brain stem auditory nuclei in the chicken: Implications for development of the place principle,'' J. Comp. Neurol. **237**, 273–289.

Mair, I. W. S. (**1973**). ''Hereditary deafness in the white cat,'' Acta Oto-Laryngol. Suppl. **314**, 5–48.

Mills, D., Norton, S. J., and Rubel, E. W. (**1994**). ''Development of active and passive mechanics in the mammalian cochlea,'' Aud. Neurosci. **1**, 77–99.

Moore, D. R. (**1981**). ''Development of the cat peripheral auditory system: Input-output functions of cochlear potentials,'' Brain Res. **219**, 29–44.

Muller, M. (**1991**). ''Developmental changes of frequency representation in the rat cochlea,'' Hearing Res. **56**, 1–7.

Neely, S. T., and Kim, D. O. (**1983**). ''An active cochlear model showing sharp tuning and high sensitivity,'' Hearing Res. **9**, 123–130.

Norton, S. J., Bargones, J. Y., and Rubel, E. W. (**1991**). ''Development of otoacoustic emissions in gerbil: Evidence for micromechanical changes underlying development of the place code,'' Hearing Res. **51**, 73–92.

Ohlemiller, K. K., and Echteler, S. M. (**1990**). ''Functional correlates of characteristic frequency in single cochlear nerve fibers of the Mongolian gerbil,'' J. Comp. Physiol. A **167**, 329–338.

Perkins, R. E., and Morest, D. K. (**1975**). ''A study of innervation patterns in cats and rats with Golgi method and Normarski optics,'' J. Comp. Neurol. **163**, 129–158.

Pujol, R., Carlier, E., and Devigne, C. (**1978**). ''Different patterns of cochlear innervation during the development of the kitten,'' J. Comp. Neurol. **177**, 529–536.

Pujol, R., and Hilding, D. (**1973**). ''Anatomy and physiology of the onset of auditory function,'' Acta Oto-Laryngol. **76**, 1–10.

Pujol, R., and Marty, R. (**1970**). ''Postnatal maturation in the cochlea of the cat,'' J. Comp. Neurol. **139**, 115–126.

Relkin, E. M., and Saunders, J. C. (**1980**). ''Displacement of the malleus in neonatal golden hamsters,'' Acta Oto-Laryngol. **90**, 6–15.

Relkin, E. M., Saunders, J. C., and Konkle, D. F. (**1979**). ''Development of middle-ear admittance in the hamster,'' J. Acoust. Soc. Am. **136**, 133–139.

Retzius, G. (**1884**). *Das Gehorogan der Wirbeltiere II. Das Gehorogan der Reptilien, der Vogel and Sangetiere* (Samson & Wallin, Stockholm).

Robertson, D., Cody, A. R., Bredberg, G., and Johnstone, B. M. (**1980**). ''Response properties of spiral ganglion neurons in cochleas damaged by direct mechanical trauma,'' J. Acoust. Soc. Am. **67**, 1295–1303.

Robertson, D., and Wilson, S. A. (**1991**). ''Changes in cochlear sensitivity do not alter relative thresholds of different spontaneous rate categories of primary auditory nerve fibres,'' Hearing Res. **51**, 29–32.

Romand, M.-R., and Romand, R. (**1990**). ''Development of spiral ganglion cells in mammalian cochlea,'' J. Electron Microsci. Tech. **15**, 144–154.

Romand, R. (**1983**). ''Development in the frequency selectivity of auditory nerve fibers in the kitten,'' Neurosci. Lett. **35**, 271–276.

Romand, R. (**1984**). ''Functional properties of auditory-nerve fibers during postnatal development in the kitten,'' Exp. Brain Res. **56**, 395–402.

Romand, R. (**1987**). ''Tonotopic evolution during development,'' Hearing Res. **28**, 117–123.

Romand, R. (**1997**). ''Modification of tonotopic representation in the auditory system during development,'' Progress in Neurobiology (Oxford) **51**, 1–17.

Romand, R., and Dauzat, M. (**1981**). ''Spontaneous activity and signal pro-

cessing in the cochlear nerve of kittens,'' J. Acoust. Soc. Am. **69**, 52.
Rubel, E. W. (**1978**). ''Ontogeny of structure and function in the vertebrate auditory system,'' in *Handbook of Sensory Physiology, Vol. IX. Development of Sensory Systems*, edited by M. Jacobson (Springer-Verlag, Berlin), pp. 135–237.
Rubsamen, R., Neuweiler, G., and Marimuthu, G. (**1989**). ''Ontogenesis of tonotopy in inferior colliculus of a hipposiderid bat reveals postnatal shift in frequency-place code,'' J. Comp. Physiol. A **165**, 755–769.
Ruggero, M. A., and Rich, N. (**1991a**). ''Application of a commercially-manufactured Doppler-shift laser velocimeter to the measurement of basilar-membrane motion,'' Hearing Res. **51**, 215–220.
Ruggero, M. A., and Rich, N. C. (**1991b**). ''Furosemide alters Organ of Corti mechanics: Evidence for feedback of outer hair cells upon the basilar membrane,'' J. Neurosci. **11**, 1057–1067.
Sanes, D. H., Merickel, M., and Rubel, E. W. (**1989**). ''Evidence for an alteration of the tonotopic map in the gerbil cochlea during development,'' J. Comp. Neurol. **279**, 436–444.
Saunders, J. C., and Summers, R. M. (**1982**). ''Auditory structure and function in the mouse middle ear: an evaluation by SEM and capacitive probe,'' J. Comp. Physiol. A **146**, 517–525.
Schmiedt, R. A., Zwislocki, J. J., and Hamemik, R. P. (**1980**). ''Effects of hair cell lesions on responses of cochlear nerve fibers. I. Lesions, tuning curves, two-tone inhibition, and responses to trapezoidal-wave patterns,'' J. Neurophysiol. **43**, 1367–1389.
Sewell, W. F. (**1984**). ''The effects of furosemide on the endocochlear potential and auditory-nerve fiber tuning curves in cats,'' Hearing Res. **14**, 305–314.
Simmons, D. D., Mansdorf, N. B., and Kim, J. H. (**1996a**). ''Olivocochlear innervation of inner and outer hair cells during postnatal maturation: Evidence for a waiting period,'' J. Comp. Neurol. **370**, 551–562.
Simmons, D. D., Manson-Gieseke, L., Hendrix, T. W., Morris, K., and Williams, S. J. (**1991**). ''Postnatal maturation of spiral ganglion neurons: A horseradish peroxidase study,'' Hearing Res. **55**, 81–91.
Simmons, D. D., Moulding, H. D., and Zee, D. (**1996b**). ''Olivocochlear innervation of inner and outer hair cells during postnatal maturation: An immunocytochemical study,'' Dev. Brain Res. **95**, 213–226.
Thomas, J. P., and Walsh, E. J. (**1990**). ''Postnatal development of the middle ear: Areal ratios in kittens,'' Otolaryngology—Head and Neck Surgery **103**, 427–435.
Tierney, T., McGee, J., and Walsh, E. J. (**1994**). ''Development of cubic distortion product otoacoustic emissions in the cat,'' Association for Reserach in Otolaryngology Abstracts **17**, 50.
Tubach, M., McGee, J., and Walsh, E. J. (**1996**). ''Distortion generated by the ear: Its emergence and evolution during development,'' Laryngoscope **106**, 822–830.
Villablanca, J. R., and Olmstead, C. E. (**1979**). ''Neurological development of kittens,'' Dev. Psychobiol. **12**, 101–27.
von Bekesy, G. (**1960**). *Experiments in Hearing* (McGraw-Hill, New York).
Walsh, E. J., and McGee, J. (**1987**). ''Postnatal development of auditory nerve and cochlear nucleus neuronal responses in kittens,'' Hearing Res. **28**, 97–116.
Walsh, E. J., and McGee, J. (**1988**). ''Rhythmic discharge properties of caudal cochlear nucleus neurons during postnatal development in cats,'' Hearing Res. **36**, 233–248.
Walsh, E. J., and McGee, J. (**1990**). ''Frequency selectivity in the auditory periphery: Similarities between damaged and developing ears,'' Am. J. Otolaryngol. **11**, 23–32.
Walsh, E. J., McGee, J., and Javel, E. (**1986**). ''Development of auditory-evoked potentials in the cat. I. Onset of response and development of sensitivity,'' J. Acoust. Soc. Am. **79**, 712–724.
Walsh, E. J., and Romand, R. (**1992**). ''Functional development of the cochlea and cochlear nerve,'' in *Development of Auditory and Vestibular Systems*, edited by R. Romand (Elsevier, Amsterdam), pp. 161–219.
Webster, W. R., and Martin, R. L. (**1991**). ''The development of frequency representation in the inferior colliculus of the kitten,'' Hearing Res. **55**, 70–80.
Woolf, N. K., and Ryan, A. F. (**1988**). ''Contributions of the middle ear to the development of function in the cochlea,'' Hearing Res. **35**, 131–142.
Yancey, C., and Dallos, P. (**1985**). ''Ontogenetic changes in the cochlear characteristic frequency at a basal turn location as reflected in the summating potential,'' Hearing Res. **18**, 189–195.
Yates, G. K. (**1991**). ''Auditory-nerve spontaneous rates vary predictably with threshold,'' Hearing Res. **57**, 57–62.

Interrupted noise exposures: Threshold shift dynamics and permanent effects

Roger P. Hamernik[a] and William A. Ahroon
State University of New York at Plattsburgh, 107 Beaumont Hall, Plattsburgh, New York 12901

(Received 19 August 1997; revised 20 January 1998; accepted 10 March 1998)

A parametric study of the reduction of threshold shift (toughening phenomena) that takes place during the course of an interrupted noise exposure is described. 266 chinchillas randomly assigned to one of 32 experimental groups were exposed to one of the following: a 400-Hz narrow-band impact noise having a center frequency of 0.5, 1.0, 2.0, 4.0, or 8.0 kHz and peak sound-pressure levels of 109, 115, 121, or 127 dB. The impacts were presented for 5 d, 24 h/d or for 20 d, 6 h/d. Corresponding pairs of exposures had equal energy. Group mean noise effects were estimated from pure-tone thresholds obtained from inferior colliculus evoked potentials and from surface preparation histology. The threshold shift (TS) toughening phenomena is shown to occur in response to all stimuli that produce a TS and at all audiometric test frequencies. The amount of toughening, which is limited to less than 35 dB, varies with noise frequency and intensity. Based on group mean data the auditory system is not protected from the permanent effects of an interrupted noise exposure as a result of the toughening effect but rather differences in permanent effects between the 5- and 20-d exposures are attributed to the spreading of the exposure energy over an extended period of time. [S0001-4966(98)06206-7]

PACS numbers: 43.64.Wn, 43.66.Ed, 43.50.Pn [RDF]

INTRODUCTION

The ISO-1999 (1990) document, relating levels of noise exposure to an estimated noise-induced hearing loss (NIHL) in the exposed population, uses an energy metric to organize the exposure data and an age correction (dB) that, when subtracted from hearing thresholds, yields NIHL. The energy approach to the standards document has been questioned by Bies and Hansen (1990) who showed that an alternate formulation is consistent with the demographic data base and by Kraak (1981) whose approach is consistent with that of Bies and Hansen. Similarly, there are many examples in the literature that demonstrate, on the basis of experimental evidence, the limitations of an energy metric (Lei *et al.*, 1994). The ISO approach to an age correction has also been questioned on methodological grounds by Bies and Hansen (1990) and by Humes and Jesteadt (1991) and most recently on experimental grounds by Mills *et al.* (1997). The approach to the interaction between noise and other threshold-elevating variables (e.g., age) suggested by Humes and Jesteadt is conceptually consistent with the approach of Bies and Hansen.

Experiments involving noise exposure paradigms that modulate postexposure threshold shifts (TS) (temporary or permanent) further question the suitability of an energy metric for noise exposure standards. One class of such experiments is typified by the exposure paradigms used by Canlon *et al.* (1988) and are referred to as ''conditioning'' or ''priming'' experiments. In this paradigm a continuous low-level noise, that produces little or no TS, is used to alter the susceptibility of the cochlea (i.e., usually to reduce its susceptibility to noise or to ''toughen'' it) prior to further experimental noise treatment. A second class of TS-modulating experiments is typified by the interrupted exposure paradigms used by, for example, Clark *et al.* (1987), Subramaniam *et al.* (1991a), and Hamernik *et al.* (1994). In this paradigm, a noise of sufficient intensity, presented to an experimental animal on a daily repeated cycle, produces a TS following the first day of exposure. Threshold shifts measured on subsequent days of the exposure sequence have been shown to decrease relative to the initial TS. This reduction of TS, despite a continuing daily exposure regime, has been called a cochlear toughening effect and the exposures referred to as ''toughening'' exposures.

A fundamental issue that appears throughout the toughening literature is the extent, if any, of the protection from permanent noise-induced changes afforded to the auditory system by the toughening phenomena as a result of an interrupted noise exposure. This issue has at least two different but related facets: (1) Does a population exposed to an interrupted noise that produces toughening develop less or more permanent threshold shift (PTS) than a matched population exposed to an uninterrupted noise of the same total energy? That is, is the ear that is being gradually toughened by a noise protected from that noise? In the absence of any toughening effects the interrupted paradigm would generally be expected to produce less permanent auditory system changes than the equivalent uninterrupted exposure (Ward, 1991). (2) Is the cochlea, toughened by an interrupted noise exposure and subsequently exposed to a more traumatic noise, affected less by the traumatic noise than an untoughened cochlea?

This latter question is addressed in a number of papers where the answer is arguably equivocal. The earliest reference to the issue of just such a protective effect can be found in the Miller *et al.* (1963) paper in which the noise-toughened cat cochlea was shown to be affected by a high-

[a]Electronic mail: HamernRP@SPLAVA.CC.PLATTSBURGH.EDU

level noise to the same extent as the untoughened cochlea. More recently, Subramaniam *et al.* (1993) showed that, under some conditions, the cochlea toughened by a low-frequency, interrupted noise did not provide any protection from a subsequent high-frequency [4-kHz octave band noise (OBN)] exposure, instead the 4-kHz exposure produced an exacerbation of both PTS and outer hair cell (OHC) loss. However, protection from a low-frequency noise exposure was reported by, for example, Campo *et al.* (1991) and McFadden *et al.* (1997). A confounding factor in both of these papers was that when statistically less PTS was found in the toughened ears there was no protective effect on the OHC population as measured by conventional cochleograms. With this inconsistency the standard ''escape clause,'' that more subtle sensory cell damage must be present that is not seen in the light microscopic analysis, is invoked. The effect of an impact noise exposure on the noise-toughened cochlea was explored by Roberto *et al.* (1996) and by Henselman *et al.* (1994). In the former paper, the protective effects, if any, were inconsistent, while in the latter very large protective effects were observed in both the PTS and sensory cell data. The McFadden *et al.* (1997) paper presents a good overview of most of the literature on this topic.

Since one might expect that the underlying mechanisms of these two classes of TS-modulating experiments (i.e., priming and toughening) have some processes in common, the effects produced by each should mutually interact. The extent of the interaction, however, has not been sufficiently studied. The efforts of Roberto *et al.* (1996), to first prime the cochlea with a low-level noise followed by an interrupted noise which was known to also toughen the cochlea, yielded inconsistent results. Following a similar protocol, Dagli and Canlon (1997), using otoacoustic emissions metrics, showed that a primed cochlea responds differently to an interrupted noise than does an unprimed cochlea.

The question of whether the cochlea that is gradually being toughened by an interrupted noise is in fact being protected from that same noise has had only limited attention. In the Clark *et al.* (1987) paper the interrupted exposures that produced a toughening also resulted in less hearing and sensory cell loss than an equal energy control group. However, the effect was small, the experimental conditions were limited, and the group sample sizes were small. Furthermore, whether the reduced permanent effects were the result of a toughened cochlea or just the moderating effect of the noise interruption as is often seen following interrupted exposures (e.g., Ward, 1991) that produce no toughening is not clear. The toughening phenomena produced by an interrupted noise exposure has also been shown to be manifested in physiological data (single unit and whole nerve action potential measures) (Sinex *et al.*, 1987; Boettcher *et al.*, 1992). However, the relation of the physiological data to the status of the sensory epithelium is also not clear. Boettcher *et al.* (1992), for example, show a continuing increase in OHC pathology despite a nearly complete recovery of the AP thresholds thus indicating that despite the recovered AP, the final condition of the cochlea will be altered.

The modulation of TS during an interrupted noise exposure is further complicated by the frequency and intensity parameters of the stimulating noise and the audiometric test frequency used to monitor the effects (Subramanian *et al.*, 1991a, b). The mechanisms responsible for the toughening phenomena are not known, however, the mechanical properties of the OHC system and the efferent systems have been shown to play a role (Zheng *et al.*, 1997).

In the present paper, we present data from a parametric experimental design involving 32 different exposure conditions and 266 subjects. The presentation and discussion of the group mean data address the following issues: (1) The applicability of the equal energy concept to interrupted noise exposures; (2) the relation among stimulus frequency, energy, audiometric test frequency, and the amount of toughening; and (3) the extent of the protection from permanent noise-induced changes afforded to the noise-toughened cochlea.

I. METHODS

Summary data from 135 chinchillas exposed to an uninterrupted, 5d, asymptotic threshold shift (ATS) producing impact noise and 131 chinchillas exposed to an equivalent energy, 20-d, interrupted impact noise are used to assesses the three issues identified above. Brainstem (inferior colliculus) auditory evoked potentials (AEP) collected from monaural chinchillas were used to estimate pure-tone thresholds and surface preparation histology was used to quantify sensory cell populations. A narrow-band transient (impact) noise, of varying intensity and center frequency (CF), was used to probe the extent of the toughening phenomena. Details of the experimental methods, beyond those that are presented below, can be found in Ahroon *et al.* (1993).

A. Noise exposures

Thirty-two different noise exposures were used; 16 were used to produce different ATS conditions and 16 similar exposures, having equal energy but presented on a 20d interrupted schedule, were used to induce toughening. The exposures consisted of narrow-band impacts (NBI) 400-Hz wide, having center frequencies of 0.5, 1.0, 2.0, 4.0, and 8.0 kHz. The NBIs were presented at a rate of 1/s, 24 h/d for 5 d or 6 h/d for 20 d. Peak sound-pressure levels (SPLs) were 109, 115, 121, or 127 dB. All noise stimuli were generated digitally using a virtual instrument developed using the LabView™ software package. A fixed-length pulse was fed through a 4th-order bandpass Butterworth filter. The resulting waveform was played though the computer's sound output and fed to an AB International Precedent Series 900A amplifier. The output of the amplifier was fed to either a JBL model 2445J speaker with model 2360H horn and model 2360T transition piece (1-, 2-, and 4-kHz CF impacts); Electro-Voice dual DH1Amt-16 transducers with MTA-22 transition piece and HP640 horn (8.0-kHz CF impacts), or an Electro-Voice TL550D speaker system (0.5-kHz CF impacts). Table I shows the experimental groups and the number of subjects in each group. Figure 1 shows the relative spectrum and temporal waveform of each NBI at the 121-dB peak SPL. Waveforms and spectra at other levels were qualitatively similar.

TABLE I. Experimental groups: number of animals in each group exposed to the narrow-band impacts (NBI) for 5 or 20 d having the indicated center frequencies (CF) and peak sound-pressure levels (SPL).

	5-d exposures dB peak SPL				20-d exposures dB peak SPL			
NBI CF (kHz)	109	115	121	127	109	115	121	127
0.5	···	10	5	6	···	9	9	6
1.0	10	9	9	10	9	9	9	9
2.0	···	9	9	5	···	9	9	6
4.0	···	9	9	9	···	9	9	8
8.0	9	9	8	···	6	9	6	···

During exposure, individual chinchillas were confined to cages ($10\times11\times16$ in.) with free access to food and water. A maximum of six animals was exposed at a time. Peak SPLs in the exposure field were uniform to within less than 2 dB.

B. Threshold testing procedures

Thresholds for all audiograms were measured at octave intervals from 0.5 to 16.0 kHz. The mean of three threshold determinations measured on different days defined each animal's pre-exposure audiogram. A complete audiogram was measured once daily during each of the five exposure days of the ATS exposure paradigm and the average daily TS established the mean ATS levels. For the 20-d interrupted exposure paradigm a complete audiogram was measured prior to and immediately following each daily 6 h exposure in order to establish the magnitude and time course of the toughening. The amount of toughening at each audiometric test frequency was defined as the difference between the TS measured at a given frequency following the first day exposure (TS_1) and the mean of the thresholds measured following exposure on days 16, 18, and 20 (TS_{16-20}). Following a 30-d postexposure recovery period thresholds for both sets of animals were measured again on different days and averaged for each animal to establish PTS. PTS was defined as the difference between the 30-d post- and pre-exposure audiograms.

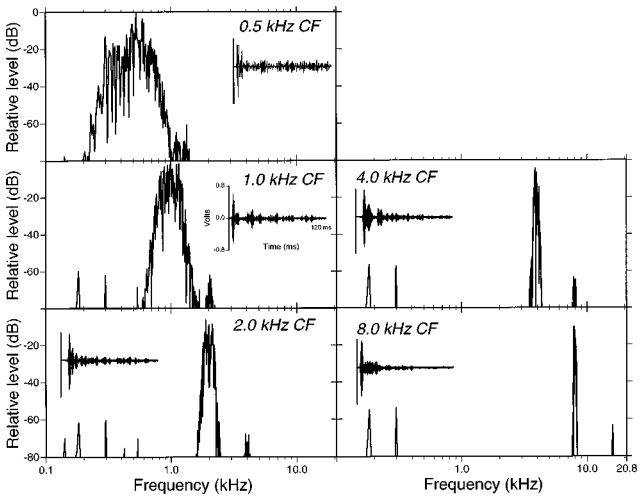

FIG. 1. The relative spectrum and waveform of each of the 400-Hz narrow-band impact stimuli. Peak SPL for each waveform shown is 121 dB. Spectra and waveforms for the other impact levels were qualitatively similar. The ordinate of the time waveform is calibrated at 1 V=125 dB.

C. Histology

Following the last AEP test protocol, each animal was euthanized under anesthesia and the right auditory bulla removed and opened to gain access to the cochlea for perfusion. Fixation solution consisting of 2.5% glutaraldehyde in veronal acetate buffer (final pH=7.3, 605 mOs) was perfused through the cochlea. After 12 h of fixation the cochlea was postfixed in 1% OsO_4 in veronal acetate buffer. Surface preparation mounts of the entire organ of Corti were prepared and inner and outer hair cell (IHC, OHC) populations were plotted as a function of frequency and location using the frequency-place map of Eldredge *et al.* (1981). For purposes of this presentation, sensory cell population data is presented as group averages taken over octave band lengths of the cochlea centered on the primary AEP test frequencies.

II. RESULTS AND DISCUSSION

A. Pre-exposure thresholds

The group mean pre-exposure thresholds are shown in Fig. 2. The large open symbols connected by the solid line in this figure represent the mean AEP thresholds of 924 non-noise-exposed monaural chinchillas from our laboratory. The dashed lines represent one standard deviation above and below the mean thresholds. The 16 group means for subjects exposed to the 5-d ATS or 20-d interrupted exposures are indicated by small points in the upper and lower panels of this figure, respectively. Only five of the 192 group means (32 groups×6 frequencies) differed from the laboratory norm by more than one standard deviation and none exceeded two standard deviations from the mean. Since the audiometric dependent variables used in this study are threshold shifts (as opposed to shifted thresholds) the small differences in group mean pre-exposure thresholds should not affect the overall conclusions drawn from this data base.

B. Threshold shifts and sensory hair cell losses

The correspondence between the group mean TS generated during the 5- and 20-d exposure paradigms for all the groups is shown in Fig. 3, where the group mean TS measured immediately following the first 6-h exposure (TS_1) of the interrupted paradigm is compared with the group mean ATS produced by the corresponding, equivalent energy, uninterrupted exposure for each of the NBIs at each AEP test frequency. [In this and in some of the subsequent figures standard error (SE) bars are indicated. When an SE bar is not

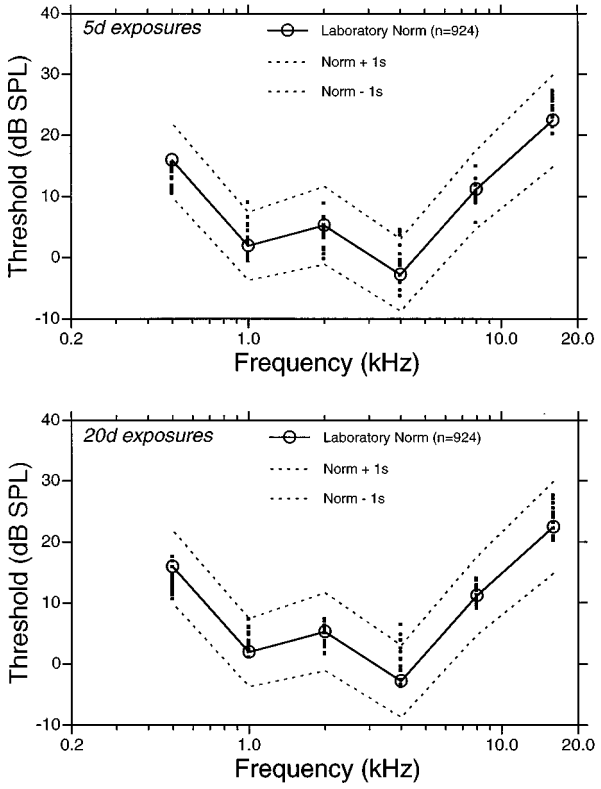

FIG. 2. Group mean pre-exposure auditory evoked potential audiograms for the 16 groups exposed to the 5-d uninterrupted noise (upper panel) and the 16 groups exposed to the 20-d interrupted noise (lower panel) compared with the laboratory norm ($n=924$). The dashed lines indicate one standard deviation above and below the laboratory norm.

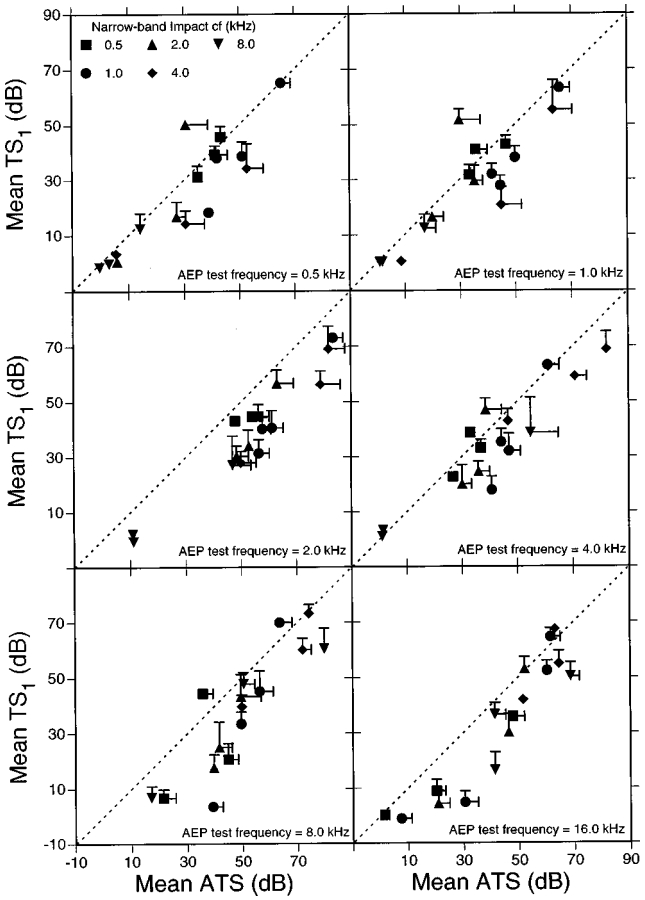

FIG. 3. The correspondence between the group mean threshold shift measured immediately following the first 6-h exposure (TS_1) of the 20-d interrupted exposure paradigm and the mean asymptotic threshold shift (ATS) produced by the equivalent energy uninterrupted 5-d exposure. Each of the six audiometric test frequencies is shown in a separate panel and symbols identify each of the five narrow-band impact stimuli. Error bars represent one standard error of the mean. If error bars are not present, the standard error was less than the width of the symbol.

present, the SE was less than or equal to the size of the symbol representing the datum point.] The mean ATS is defined as the average of the five TSs that were measured on each of the five days of the uninterrupted exposure. As expected, TS_1 is in general less than or equal to the ATS level. That is, the mean ATS level sets the upper bound for TS_1. At a number of exposure conditions and AEP test frequencies mean ATS and TS_1 are equal, reflecting the observation of Blakeslee *et al.* (1978) that the ATS level can be reached rapidly using high-level impact stimuli; often during the first hour of exposure. Both sets of exposures produced TSs consistent with stimulus parameters; group mean TS_1 and ATS increased with increasing stimulus energy and TSs occurred at audiometric test frequencies appropriate to the impact center frequency.

Figures 4, 7, and 8 provide some perspective on the nature of the data base that was reduced in order to produce the remaining figures. Figure 4(A) and (B) show the group mean TS at the 4.0- and 8.0-kHz AEP test frequency immediately prior to (open symbols) and following (closed symbols) each of the 6-h exposures to the 1.0-kHz NBI at 127-dB peak SPL. Figure 4(C) and (D) show a comparable data set from the 4.0-kHz NBI at 121-dB peak SPL. Clearly seen in these plots is the regular and generally systematic decrease in TS (toughening) with increasing repetitions of the 6-h exposure. In each panel the amount of toughening [i.e., $TS_r=(TS_1-TS_{16-20})$] is indicated, where TS_{16-20} is the mean TS measured following days 16, 18, and 20. Exposures to the higher frequency impacts (i.e., the 4.0- and 8.0-kHz NBIs), produced a TS recovery (toughening) effect that took place at a slower rate than it did for the lower frequency NBIs. In fact, it appears that after 20 d, TS is still decreasing for some exposure conditions. Thus in some limited number

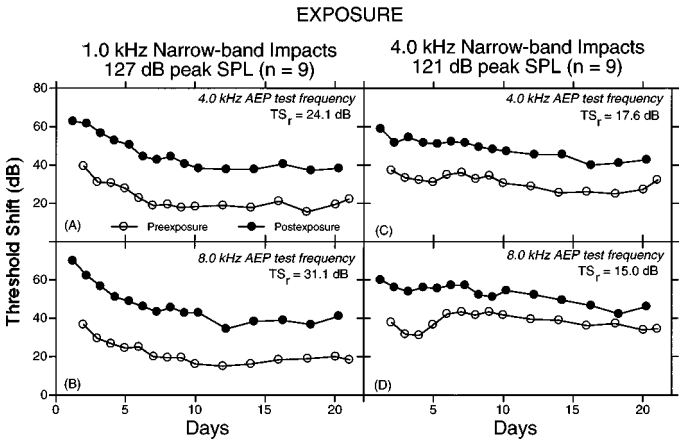

FIG. 4. Group mean threshold shifts measured immediately prior to and following the 6-h exposures on the days indicated during the 20-d exposure. Examples of data measured at the 4.0- and 8.0-kHz AEP test frequencies from two different exposure conditions are shown. The amount of toughening, TS_r, defined as TS_1-TS_{16-20} is indicated in each panel.

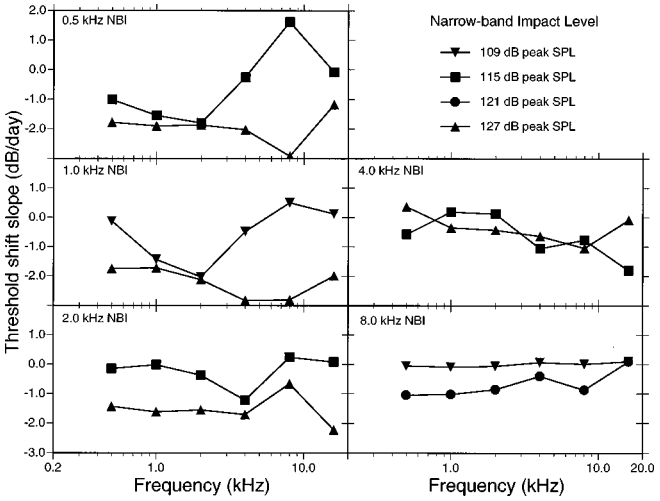

FIG. 5. Slope of the regression line drawn through the group mean threshold shifts measured following each of the 6-h exposures over the first 10-d of the exposure sequence. Slopes are plotted against AEP test frequency. Each panel presents data from one of the narrow-band impact (NBI) stimuli at the highest and lowest peak SPL used for that NBI.

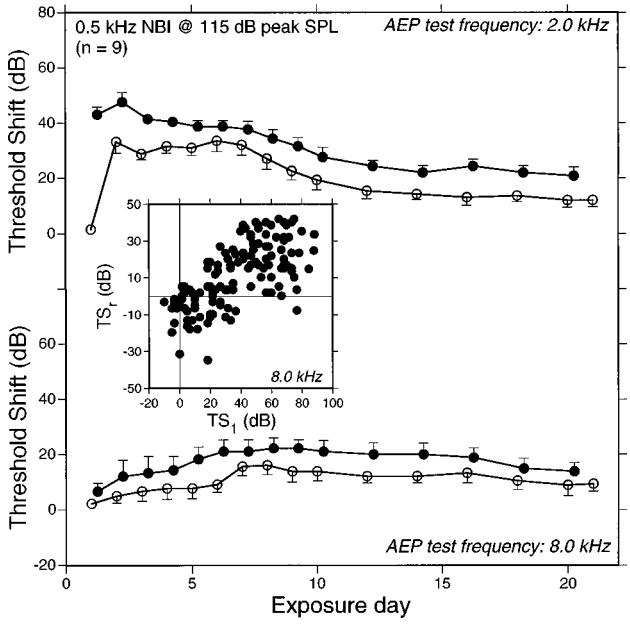

FIG. 6. Examples of group mean threshold shifts measured at the 2.0- and 8.0-kHz AEP test frequencies, prior to and following the daily 6-h exposures to the indicated narrow-band impact (NBI) stimulus. Examples were chosen to illustrate different threshold shift dynamics at different AEP frequencies within a single group. The insert shows the individual animals ($n=131$) TS_r at the 8.0-kHz test frequency as a function of TS_1 for all NBI interrupted exposures. Error bars represent one standard error of the mean. If error bars are not present, the standard error was less than the width of the symbol.

of conditions our TS_r may be underestimating the maximum TS_r that might be achieved with that particular stimulus if the exposure was allowed to continue. Subramaniam *et al.* (1991b) also indicate differences in the rate at which toughening progresses but, unlike the present results, their results using 0.5- and 4.0-kHz CF octave band Gaussian noise stimuli indicate that the TS decline takes place more rapidly for the high-frequency stimuli.

Figure 5 provides an estimate of the rate at which toughening occurs at different AEP test frequencies as the NBI stimulus frequency and intensity are varied. This figure plots the slope of the daily postexposure TS, obtained from the linear regression line on the group mean TS values over the first 10 d of the interrupted exposure. Clear from this figure is the generally reduced slopes, or slower development of toughening, as the NBI stimulus frequency is increased or peak NBI levels are decreased. Slope data for only the high and low extremes of NBI peak SPL are shown. The slope data at other intensities were generally intermediate to those shown in Fig. 5. For the lowest intensity NBIs at some AEP frequencies either there was no TS or no toughening effect (i.e., a zero slope). Interestingly, at some of the lowest intensities there were some AEP frequencies that, rather than showing toughening, showed a group mean growth of TS (a positive slope) as the exposure was repeated. In most cases for which this occurred the effect, while consistent over the 20-d exposure period, was small amounting to less than a 10-dB growth. The single exception is the group exposed to the 115-dB peak SPL, 0.5-kHz NBI, which at the 8.0-kHz AEP frequency, showed about a 20-dB growth in the group mean TS. This is shown in Fig. 6 along with the group mean TS function, measured at 2.0 kHz, that showed the typical toughening effect. This result for the 8-kHz test frequency is consistent with the findings of Sinex *et al.* (1987) and Boettcher *et al.* (1992). On the basis of the group mean data it is clear that all AEP test frequencies that are affected by the noise are not necessarily toughened by the noise. In individual subjects such frequency-specific differences in TS dynamics during an interrupted exposure can be very dramatic as seen in the inset of Fig. 6. The inset shows the TS_r versus TS_1 data measured at the 8-kHz AEP frequency for all 131 chinchillas that received one of the interrupted exposures. Data at the 8-kHz AEP test frequency were chosen for illustrative purposes since this was a frequency that was generally affected by all of the NBI stimuli. The data at the other frequencies are similar. At any given value of TS_1 there is considerable variability in TS_r. Interesting is the observation that for $TS_1<20$ dB a number of subjects show a growth of TS (i.e., a negative TS_r). Considerable variability in individual responses was also reported by Hamernik *et al.* (1994). The daily pre-exposure TS generally followed a time course during the 20-d exposure that was roughly parallel to that of the daily postexposure TS.

Figure 7(a), showing the group mean data from the 127-dB peak SPL, 1.0-kHz NBI exposures, compares the ATS level at various AEP test frequencies with TS_1, and with TS_{16-20}. Toughening, TS_r, is seen to clearly exceed 30 dB at 8.0 kHz (i.e., the distance between the open and closed circles). In this example all audiometric frequencies have been toughened 20 dB or more. Panel B of this figure shows the mean PTS for these two equal energy groups. A two-way analysis of variance with repeated measures on one factor (frequency) indicated no differences in the levels of PTS (main effect: $F=0.126$, df $=1/17$, interaction: $F=0.508$, df $=5/85$). Panel C presents the profile of the mean OHC loss averaged over octave band lengths of the basilar membrane which, as with the PTS, shows no statistical difference between the two groups (main effect: $F=0.518$, df $=1/17$; in-

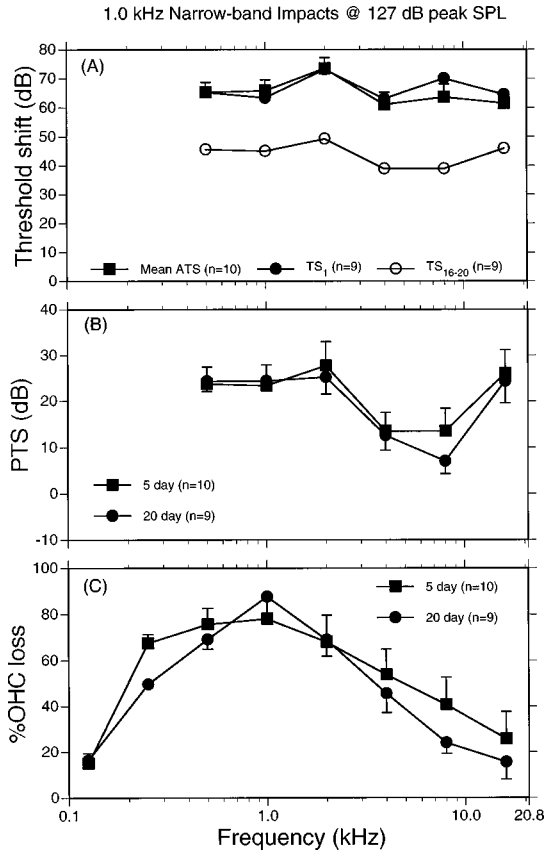

FIG. 7. A comparison of group mean audiometric and histological data from the 5-d and 20-d exposure to the indicated narrow-band impact stimuli. (A) Mean asymptotic threshold shift (ATS), the threshold shift immediately following the first 6-h exposure (TS_1) and the mean of the threshold shifts measured over days 16–20 ($TS_{16-20\,d}$) of the interrupted exposure measured at each audiometric test frequency. Toughening is identified by the dB difference between the filled and open circles. (B) Permanent threshold shifts (PTS) at each audiometric test frequency for the two groups. (C) Percent of outer hair cell (OHC) loss over octave band lengths of the basilar membrane centered on the audiometric test frequencies. Despite the toughening there is no statistically significant differences in PTS or OHC loss between these two groups. Error bars represent one standard error of the mean. If error bars are not present, the standard error was less than the width of the symbol.

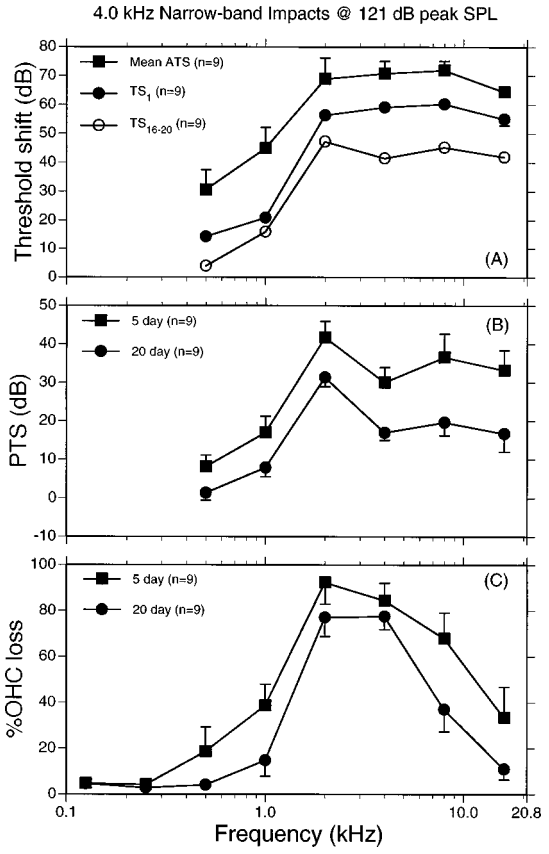

FIG. 8. A comparison of group mean audiometric and histological data from the 5- and 20-d exposure to the indicated narrow-band impact stimuli. (A) Mean asymptotic threshold shift (ATS), the threshold shift immediately following the first 6-h exposure (TS_1) and the mean of the threshold shifts measured over days 16–20 ($TS_{16-20\,d}$) of the interrupted exposure measured at each audiometric test frequency. Toughening is identified by the dB difference between the filled and open circles. (B) Permanent threshold shifts (PTS) at each audiometric test frequency for the two groups. (C) Percent of outer hair cell (OHC) loss over octave band lengths of the basilar membrane centered on the audiometric test frequencies. There is a statistically significant difference in the PTS and OHC loss between these two groups. Error bars represent one standard error of the mean. If error bars are not present, the standard error was less than the width of the symbol.

teraction: $F=1.361$, df$=7/119$). This pair of exposures produced high levels of TS, PTS, and considerable sensory cell loss. Despite these severe noise-induced changes the toughening phenomena was robust across a broad range of AEP frequencies. In this case the toughened cochlea did not gain any advantage (protection).

A somewhat different set of results is seen in Fig. 8. (These two sets of examples were chosen to illustrate the different conclusions one can draw from a limited set of experimental conditions.) Figure 8 shows a parallel set of data for the pair of 121-dB peak SPL, 4.0-kHz NBI exposures. The profile of TS_1 and ATS is consistent with the level and CF of the stimulus. For this exposure TS_1 is less than the level of ATS, by from 10 to 22 dB, across all test frequencies, and a 15- to 20-dB toughening effect is seen between 4.0 and 16.0 kHz. A striking difference between the data in Figs. 7 and 8 is seen in the PTS and OHC losses for the two groups. The 4.0-kHz NBI interrupted exposure has produced statistically significant less permanent change (PTS: $F=8.991$, df$=1/16$, $p<0.05$; OHC: $F=4.935$, df$=1/16$, $p<0.05$). [The interactions of exposure group and frequency were not statistically significant (PTS: $F=1.068$, df$=5/80$; OHC: $F=1.372$, df$=7/112$).] One might infer from the 10- to 22-dB difference between ATS and TS_1 that such differences in permanent effects might indeed turn out to be the case. However, other groups having similar TS_1 and ATS differences show no such differences in PTS or OHC losses. The results from the pair of groups shown in Fig. 8 are the only set of results showing such relatively large and consistent differences in permanent changes. The only other data in the literature that is somewhat related to the experimental conditions reflected in Fig. 8 are to be found in Subramaniam *et al.* (1992) where a 4.0-kHz OBN at 85 dB SPL was used to toughen the cochlea in an interrupted exposure paradigm. When the toughened subjects were exposed 5 d later to a 4.0-kHz OBN at 100 dB SPL for 48 h the toughened subjects showed more PTS than, and about the same sensory cell loss as, the controls. Since the opposite results were found for low-frequency exposures (Campo *et al.*, 1991) the differences were attributed to differences in the base–apex re-

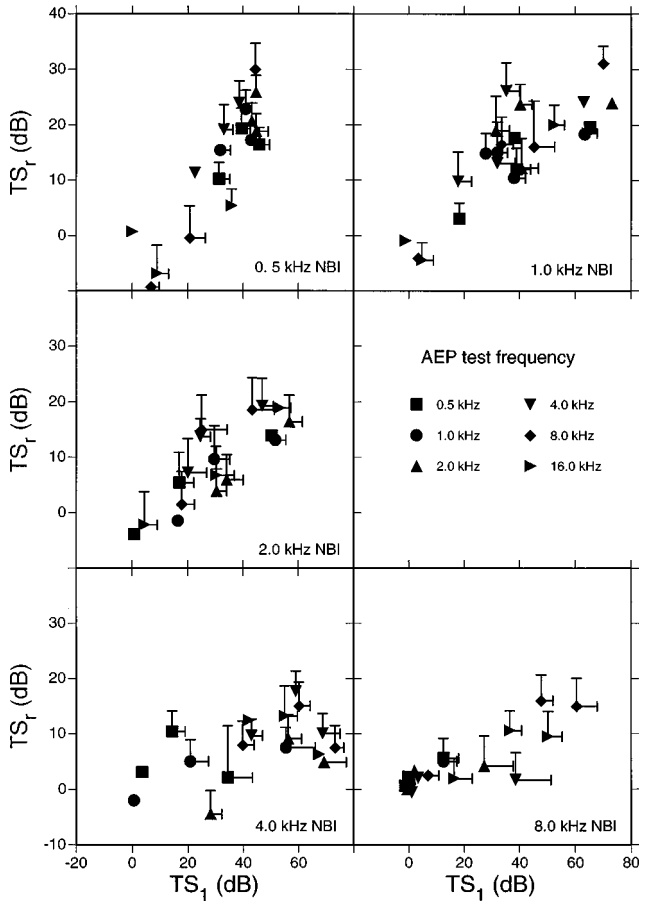

FIG. 9. The relation between the group mean amount of toughening (TS_r) and threshold shift (TS_1) measured immediately following the first 6-h interrupted narrow-band impact (NBI) exposure for each NBI exposure with audiometric (AEP) test frequency as a parameter. Error bars represent one standard error of the mean. If error bars are not present, the standard error was less than the width of the symbol.

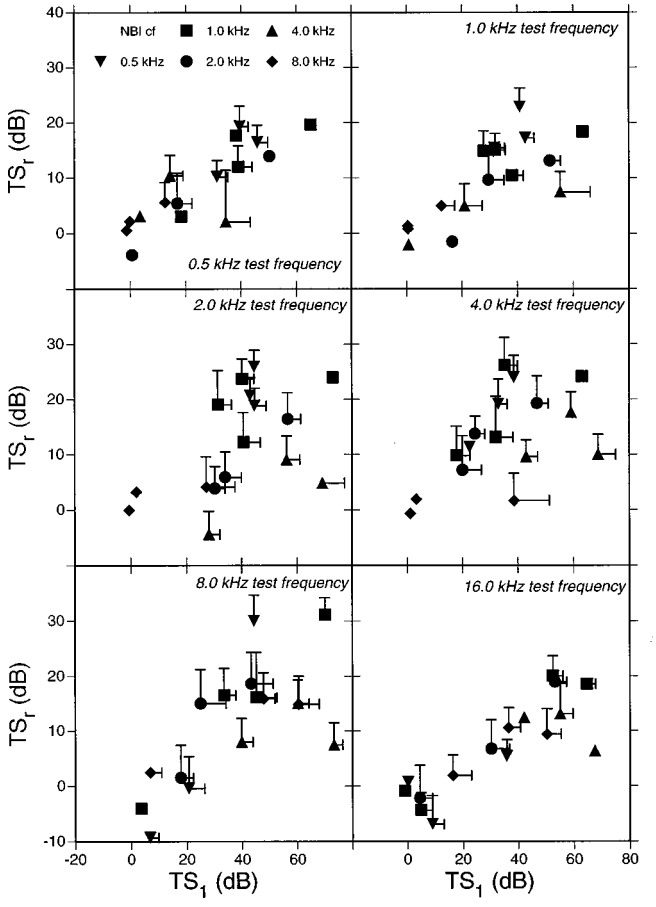

FIG. 10. The relation between the group mean amount of toughening (TS_r) and threshold shift (TS_1) measured immediately following the first 6-h interrupted narrow-band impact (NBI) exposure for each audiometric (AEP) test frequency with NBI center frequency (NBI CF) as a parameter. Error bars represent one standard error of the mean. If error bars are not present, the standard error was less than the width of the symbol.

sponses of the cochlea. However, using the same paradigm but with only an 18-h recovery between the toughening and the traumatic exposures, Subramaniam *et al.* (1992) measured about 18 dB less PTS in the toughened cochleas. This latter result is somewhat consistent with the singular results shown in Fig. 8.

C. Effects of NBI frequency and intensity on TS_r

For each experimental group, data such as that presented in Figs. 7 and 8 have been reduced in an effort to extract some of the basic trends from the large mass of available data. The effects of exposure stimulus (NBI) frequency and intensity on toughening at the various audiometric test frequencies can be estimated from Fig. 9 where TS_r is shown plotted as a function of TS_1 for each NBI with AEP test frequency as a parameter or from Fig. 10 where TS_r is shown plotted as a function of TS_1 for each AEP test frequency with NBI CF as a parameter. Although NBI intensities are not specifically coded in the symbols of Figs. 9 and 10, the effect of NBI level is well ordered with respect to TS_1 and should pose no difficulty in interpretation. The following points can be made from Figs. 9 and 10:

(1) Toughening is seen to be a general phenomena associated with all the AEP test frequencies and can be evoked by a broad spectral range of noise stimuli although much less so as the NBI CF is increased. This might be expected considering the increasingly restricted spread of excitation on the basilar membrane as NBI frequency is increased. Clark *et al.* (1987) have indicated that maximum TS_r is to be found a half-octave above the stimulating noise. Inspection of Fig. 9 or 10 indicates that AEP test frequencies as much as several octaves above the frequency of the stimulating noise may experience maximum or near maximum TS_r.

(2) Generally, as the level of the noise stimulus increases, TS_r increases although there is the suggestion in some of the intensity series and at some AEP test frequencies that TS_r begins to decrease for stimulus levels that produce a TS_1 greater than about 50 dB.

(3) For different NBIs that produce the same TS_1 at a given AEP test frequency a large difference in TS_r can be produced. Consider, for example, that both the 121-dB, 8.0-kHz NBI and the 127-dB, 0.5-kHz NBI produce a 40-dB TS_1 at 4.0 kHz. However, the former produces no TS_r while the latter produces a TS_r of more than 25 dB.

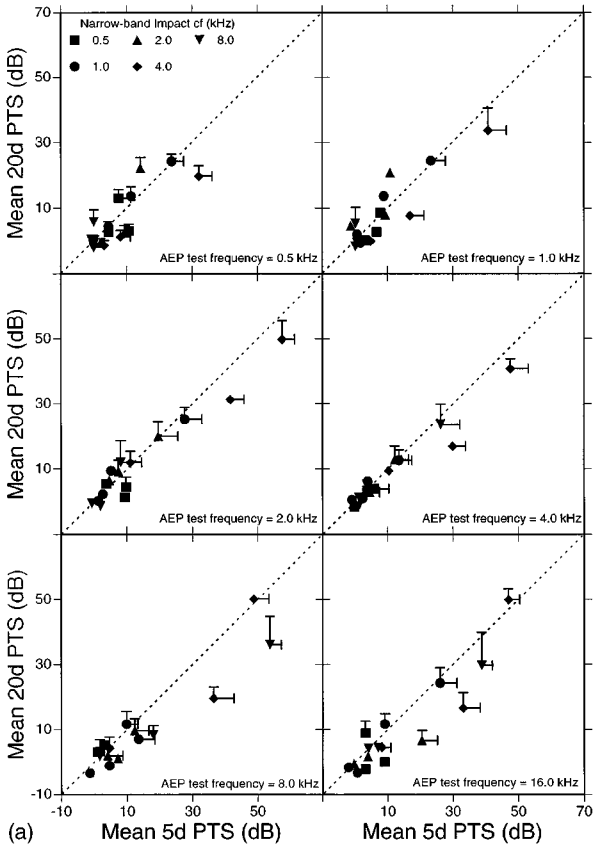

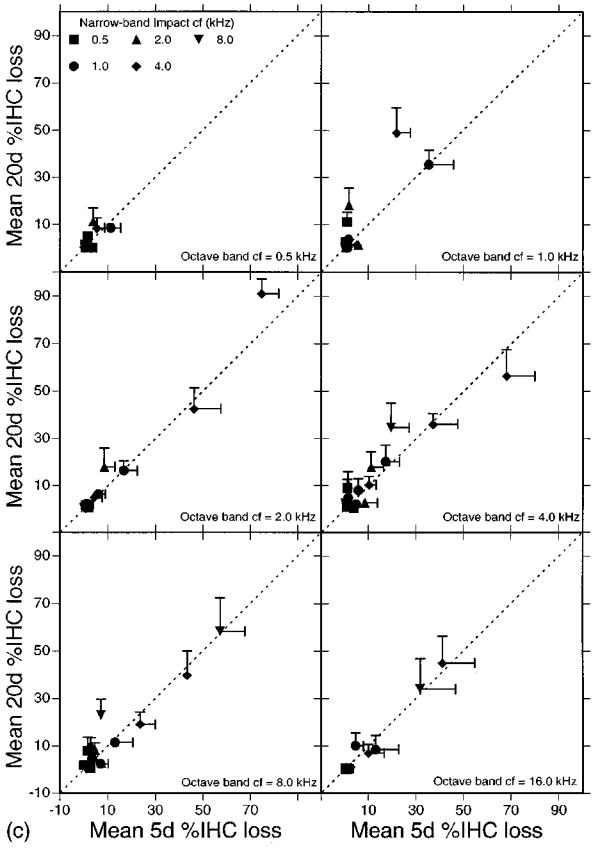

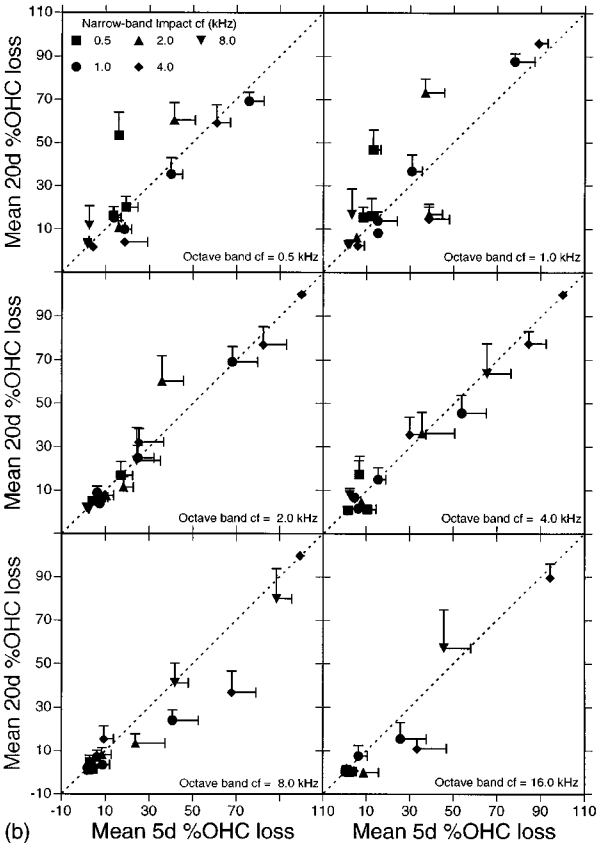

FIG. 11. A comparison of group mean PTS (panel a) and OHC and IHC loss (panels b and c) from the 5- and 20-d exposure to the indicated NBI impacts. Error bars represent one standard error of the mean. If error bars are not present, the standard error was less than the width of the symbol.

D. Evaluation of the equal energy/equal damage concept

Since corresponding pairs of groups, from the interrupted and uninterrupted exposure, received equal energy exposures an evaluation of the equal energy principal was performed. Figure 11(a)–(c) show the relation between the PTS, OHC, and IHC for corresponding pairs of equal-energy exposures (i.e., 5 versus 20 d). Symbols reflect the narrow-band

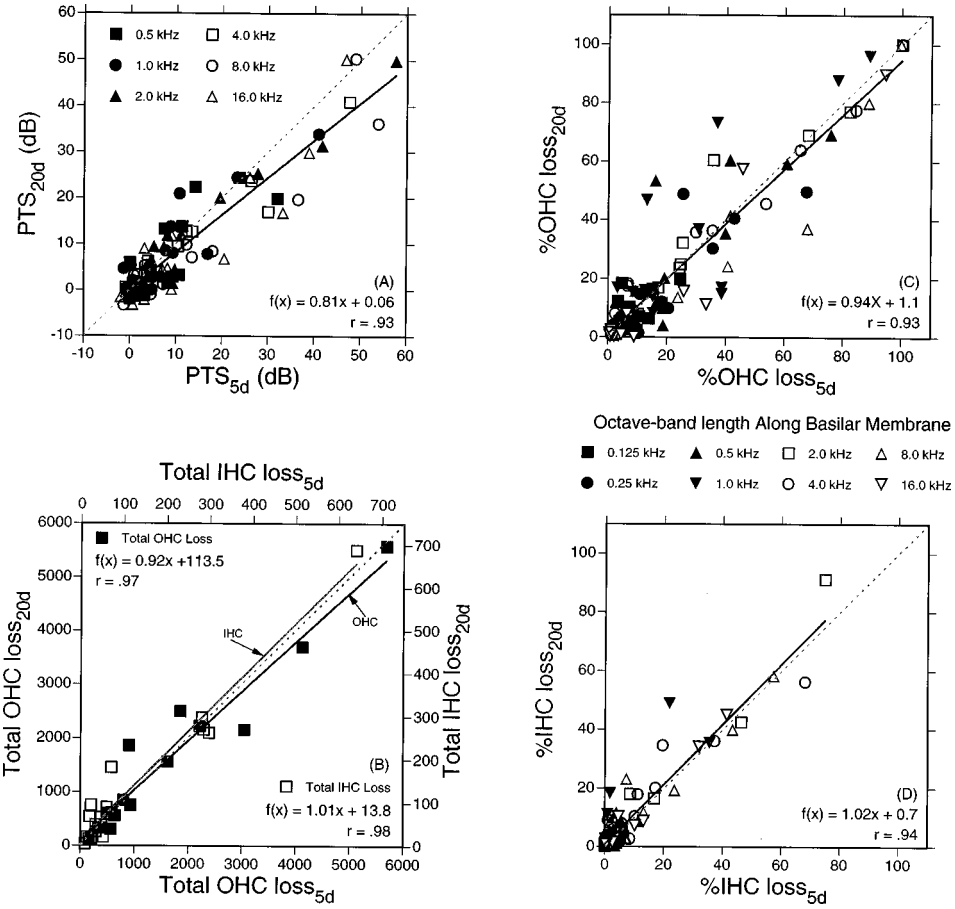

FIG. 12. A comparison of the group mean permanent audiometric and histological changes produced by each of the equal energy pairs of impact noise exposures. (A) Relation between permanent threshold shifts produced by the 20-d interrupted exposures ($PTS_{20\,d}$) and that produced by the 5-d exposures ($PTS_{5\,d}$). The symbols code for AEP test frequency. (B) The relations between total loss of outer and inner hair cells (OHC, IHC) for each of the corresponding exposures. (C) The relation between the percent OHC loss estimated over octave band lengths of the basilar membrane at the indicated center frequencies for corresponding pairs of exposures. (D) The relation between the percent IHC loss estimated over octave band lengths of the basilar membrane at the indicated center frequencies for corresponding pairs of exposures. In each of the above plots the equation for the linear regression line $f(x)$ and the correlation coefficient (r) are given.

stimulus used and each panel gives either the PTS measured at the indicated AEP test frequency or the sensory cell loss within the indicated octave band length of the cochlea. The frequency-distance translation was made using the data of Eldredge *et al.* (1981). From these figures there would appear to be very little and in many cases no difference in the permanent effects elicited by corresponding pairs of equal energy exposures. The data in Fig. 11 were replotted as shown in Fig. 12 and subjected to statistical analyses.

Figure 12(A) shows the group mean PTS, measured at each of the AEP test frequencies, for the groups exposed to the 5-d, uninterrupted and 20-d, interrupted exposures. OHC and IHC sensory cell loss data is similarly plotted either as total cochlear losses in panel (B) or as frequency-specific octave band losses in panels (C) and (D). Less PTS and sensory cell loss produced by the interrupted noise exposures should yield a linear regression line with a slope less than 1.0 describing points below the diagonal. The results of linear regression analyses of each of these data sets are indicted in the corresponding panels of Fig. 12. The analyses indicated that the predictor and criterion variables were all highly correlated. Thus, as expected, the permanent effects produced by corresponding pairs of equal energy exposures are highly correlated with correlations ranging from 0.93 (PTS) to 0.98 (total IHC loss). An analysis of the regression line slope for the comparison of PTS ($\beta_1 = 0.81$) revealed a slope significantly different from $\beta_1 = 1$ ($t = -5.559$, df$=94$, $p < 0.05$), indicating that PTS in the 5-d exposure was generally greater than for the 20-d exposures. The analyses of the slopes for each of the four sensory cell loss variables were not statistically significantly different from the diagonal (%OHC: $t = -1.879$, df$=126$; %IHC: $t = 0.719$, df$=126$; total OHC: $t = -1.258$, df$=14$; total IHC: $t = 0.083$, df$=14$). Thus the 20-d interrupted exposures resulted in slightly lower permanent threshold shifts than the 5-d exposures, and no difference in the extent of sensory cell losses.

E. Is the toughened cochlea a protected cochlea?

Figure 13 summarizes the relation between TS_r and any protective effect induced by TS_r, where protection is defined in terms of PTS as the difference, at each audiometric test frequency, between the PTS produced by the uninterrupted, 5-d exposure and that produced by the 20-d, equivalent energy interrupted exposure, that is, $[PTS_{5\,d} - PTS_{20\,d}]$. In terms of sensory cell loss protection is similarly defined as

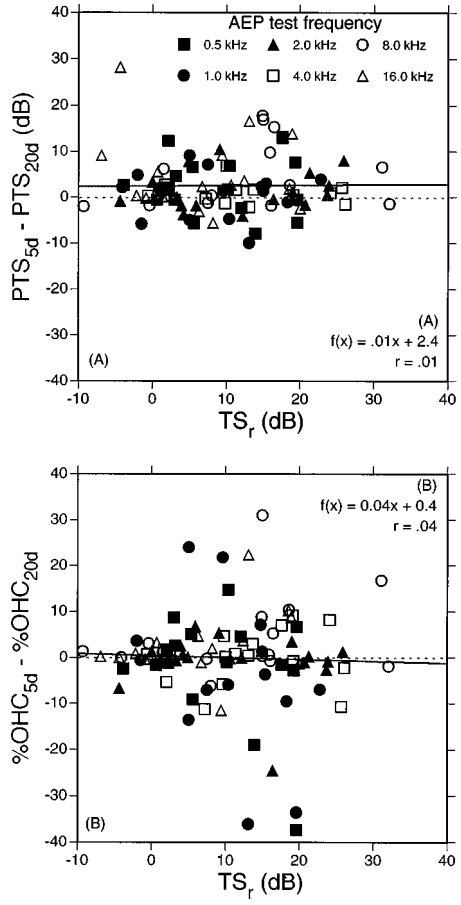

FIG. 13. The protective effect of toughening on the auditory system as a function of the amount of toughening (TS_r). Protection in terms of audiometric variables is defined as the difference between the permanent threshold shift produced by the 5-d exposure and the 20-d exposure ($PTS_{5\,d}-PTS_{20\,d}$), and in terms of histological variables as the difference between the outer hair cell loss produced by the 5- and 20-d exposures ($OHC_{5\,d}-OHC_{20\,d}$). In each of the above plots the equation for the linear regression line $f(x)$ and the correlation coefficient (r) are given.

$[\%OHC_{5\,d}-\%OHC_{20\,d}]$ computed across adjacent octave band lengths of the basilar membrane centered on the AEP test frequencies. The data points in this figure are derived from Figs. 9 and 11. Plotted in this format, a protected cochlea as a result of toughening should result in data points above the zero horizontal line. Analysis of these data using linear regression shows that there is a very low correlation between TS_r and the metrics that we have used to define protection. Neither correlation was statistically different from zero. Furthermore, a statistical analysis of the PTS regression shows that its slope is not significantly different from zero ($t=0.137$, df$=94$), but that the y intercept ($\beta_0=2.4$ dB) is statistically different from zero ($t=2.543$, df $=94$, $p<0.05$). A parallel analysis of the percent OHC data revealed that neither the slope ($t=-0.357$, df$=94$) nor the y intercept ($t=0.262$, df$=94$) were significantly different from zero.

A protective effect, as a consequence of an interrupted noise exposure, is achieved by either (1) decreasing the susceptibility of the system to permanent noise-induced effects (i.e., increasing the system's resistance to noise; toughening) or (2) delivering a given amount of energy to the system over an extended time course thus allowing recovery processes to intervene during the quiet interludes. The data in Fig. 13 indicating no correlation between TS_r and $(PTS_{5\,d}-PTS_{20\,d})$ and $(OHC_{5\,d}-OHC_{20\,d})$ suggests that the operative mechanism for any protective effect is that associated with the spreading of energy over time rather than a toughening of the cochlea. This conclusion is further strengthened by the high correlations shown in Fig. 12. Thus an auditory system toughened by noise is not necessarily a protected system.

III. CONCLUSIONS

The foregoing analysis of an extensive set of group mean data from animals exposed to a variety of interrupted noises has served to confirm and extend a number of the results that have recently appeared in the literature on the toughening phenomena. We have shown that toughening, TS_r, is a general cochlear phenomena that can be measured at all audiometric test frequencies provided that a sufficient TS_1 is produced by the noise exposure stimulus. TS_r generally increases with an increasing TS_1 (or equivalently with an increasing exposure SPL). There is, however, the suggestion that for large values of TS_1, the amount of toughening will begin to decrease. The magnitude of TS_r and the number of audiometric frequencies showing a TS_r is very dependent on the frequency content of the noise stimulus, where lower frequency stimuli are more effective in the production of TS_r.

Across the range of audiometric test frequencies, within an exposure group, the TS_r variable can take on both positive and negative values indicating that while thresholds at some audiometric test frequencies are getting better (being toughened) others are getting worse as the exposure repeats.

Perhaps the most significant aspect of these results is that, based on group mean data, there was no correlation between the amount of toughening and the extent of the permanent noise-induced changes. However, relative to the equal-energy control groups, the interrupted exposures produced slightly less PTS but no differences in sensory cell losses. Taken together these results suggest that a toughened cochlea is not necessarily a protected cochlea and that the concept of equal energy-equal damage is overly conservative for interrupted exposures that allow for recovery processes to intervene between exposures cycles.

IV. ANIMAL USE

The care and use of the animals reported on in this study were approved by the SUNY Plattsburgh Institutional Animal Care and Use Committee. In conducting the research described in this report, the investigators adhered to the *Guide for Care and Use of Laboratory Animals*, as promulgated by the Committee on Care and Use of Laboratory Animals of the Institute of Laboratory Resources Commission on Life Sciences, National Academy of Sciences-National Research Council, revised 1985.

ACKNOWLEDGMENTS

This work was supported by Grant No. 1-R01-OH02317 from the National Institute for Occupational Safety and Health. The able technical assistance of George A. Turrentine, Laurel Mitchell, Derrick P. Arquiett, Brenda M. Jock, and Ann Johnson is greatly appreciated.

Ahroon, W. A., Hamernik, R. P., and Davis, R. I. (**1993**). ''Complex noise exposures: An energy analysis,'' J. Acoust. Soc. Am. **93**, 997–1006.

Bies, D. A., and Hansen, C. H. (**1990**). ''An alternative mathematical description of the relationship between noise exposure and hearing loss,'' J. Acoust. Soc. Am. **88**, 2743–2754.

Blakeslee, E. A., Hynson, K., Hamernik, R. P., and Henderson, D. (**1978**). ''Asymptotic threshold shift in chinchillas exposed to impulse noise,'' J. Acoust. Soc. Am. **63**, 876–882.

Boettcher, F. A., Sponger, V. P., and Salvi, R. J. (**1992**). ''Physiological and histological changes associated with the reduction in the threshold shift during interrupted noise exposure,'' Hearing Res. **62**, 217–236.

Campo, P., Subramaniam, M., and Henderson, D. (**1991**). ''The effect of 'conditioning' exposures on hearing loss from traumatic exposure,'' Hearing Res. **55**, 195–200.

Canlon, B., Borg, E., and Flock, A. (**1988**). ''Protection against noise trauma by pre-exposure to a low level acoustics stimulus,'' Hearing Res. **34**, 197–200.

Clark, W. W., Bohne, B. A., and Boettcher, F. A. (**1987**). ''Effects of periodic rest on hearing loss and cochlear damage following exposure to noise,'' J. Acoust. Soc. Am. **82**, 1253–1264.

Dagli, S., and Canlon, B. (**1997**). ''The effect of repeated daily noise exposure on sound-conditioned and unconditioned guinea pigs,'' Hearing Res. **104**, 39–46.

Eldredge, D. H., Miller, J. D., and Bohne, B. A. (**1981**). ''A frequency-position map for the chinchilla cochlea,'' J. Acoust. Soc. Am. **69**, 1091–1095.

Hamernik, R. P., Ahroon, W. A., Davis, R. I., and Lei, S. F. (**1994**). ''Hearing threshold shifts from repeated 6-h daily exposure to impact noise,'' J. Acoust. Soc. Am. **95**, 444–453.

Henselman, L. W., Henderson, D., Subramaniam, M., and Sallustio, V. (**1994**). ''The effect of 'conditioning' exposures on hearing loss from impulse noise,'' Hearing Res. **78**, 1–10.

Humes, L. E., and Jesteadt, W. (**1991**). ''Modeling the interactions between noise exposure and other variables,'' J. Acoust. Soc. Am. **90**, 182–188.

ISO-1999 (**1990**). ''Acoustics: Determination of Occupational Noise Exposure and Estimation of Noise-Induced Hearing Impairment'' (International Organizaton for Standardization, Geneva).

Kraak, W. (**1981**). ''Investigations on criteria for the risk of hearing loss due to noise,'' in *Hearing Research and Theory Vol. 1*, edited by J. V. Tobias and E. D. Schubert (Academic, New York), pp. 187–303.

Lei, S. F., Ahroon, W. A., and Hamernik, R. P. (**1994**). ''The application of frequency and time domain kurtosis to the assessment of hazardous noise exposures,'' J. Acoust. Soc. Am. **96**, 1435–1444.

McFadden, S. L., Henderson, D., and Shen, Y. H. (**1997**). ''Low-frequency 'conditioning' provides long-term protection from noise-induced threshold shifts in chinchillas,'' Hearing Res. **103**, 142–150.

Miller, J. D., Watson, C. S., and Covell, W. P. (**1963**). ''Deafening effects of noise on the cat,'' Acta Oto-Laryngol. Suppl. **176**, 1–91.

Mills, J. H., Boettcher, F. A., and Dubno, J. R. (**1997**). ''Interaction of noise-induced permanent threshold shift and age-related threshold shift,'' J. Acoust. Soc. Am. **101**, 1681–1686.

Robert, M., Hamernik, R. P., Ahroon, W. A., and Case, C. J. (**1996**). ''The effects of primed and interrupted impact noise exposures on hearing loss in the chinchilla,'' in *Auditory System Plasticity and Regeneration*, edited by R. J. Salvi, D. Henderson, F. Fiorino, and V. Colletti (Thieme, New York), pp. 165–180.

Sinex, D. G., Clark, W. W., and Bohne, B. A. (**1987**). ''Effects of periodic rest on physiological measures of auditory sensitivity following exposure to noise,'' J. Acoust. Soc. Am. **82**, 1265–1273.

Subramaniam, M., Campo, P., and Henderson, D. (**1991a**). ''The effect of exposure level on the development of progressive resistance to noise,'' Hearing Res. **52**, 181–188.

Subramaniam, M., Campo, P., and Henderson, D. (**1991b**). ''Development of resistance to hearing loss from high frequency noise,'' Hearing Res. **56**, 65–68.

Subramaniam, M., Henderson, D., Campo, P., and Spongr, V. (**1992**). ''The effect of 'conditioning' on hearing loss from a high frequency traumatic exposure,'' Hearing Res. **58**, 57–62.

Subramaniam, M., Henderson, D., and Spongr, V. (**1993**). ''Effect of low-frequency 'conditioning' on hearing loss from high-frequency exposure,'' J. Acoust. Soc. Am. **93**, 952–956.

Ward, W. D. (**1991**). ''The role of intermittence in PTS,'' J. Acoust. Soc. Am. **90**, 164–169.

Zheng, X. Y., Henderson, D., McFadden, S. L., and Hu, B. H. (**1997**). ''The role of the cochlear efferent system in acquired resistance to noise-induced hearing loss,'' Hearing Res. **104**, 191–203.

Double-evoked otoacoustic emissions. I. Measurement theory and nonlinear coherence

Douglas H. Keefe
Boys Town National Research Hospital, 555 North 30th Street, Omaha, Nebraska 68131

(Received 2 May 1997; revised 27 January 1998; accepted 23 February 1998)

An evoked otoacoustic emission (OAE) measurement technique is proposed to better control for probe distortion. Each double-evoking (2E) stimulus sequence includes three, equal-duration subsequences defined as follows: $s_1(t)$ is a single chirp or click, $s_2(t)=\epsilon s_1(t-\tau)$ is a copy of s_1 with relative amplitude ϵ and delay τ, and $s_{12}(t)=s_1(t)+s_2(t)$ is the superposition of the first two stimuli. The pressure response to each subsequence is p_1, p_2, and p_{12}, respectively. The double chirp-evoked distortion product (2ChDP) and double click-evoked otoacoustic emission (2CEOAE) are defined by $p_D=p_{12}-(p_1+p_2)$. The 2ChDP response may be time compressed to analyze as an equivalent 2CEOAE response. The 2E response family provides a complementary representation between DP measurements and double click-evoked OAE measurements. A technique based on nonlinear coherence quantifies random noise in terms of a nonlinear signal-to-noise ratio. © *1998 Acoustical Society of America.* [S0001-4966(98)01106-0]

PACS numbers: 43.64.Yp, 43.64.Jb [BLM]

INTRODUCTION

The purpose of this report is to introduce evoked otoacoustic emission (OAE) measurement techniques with improved control over measurement nonlinearity and system noise, artifacts which fundamentally limit the ability to measure OAEs.[1] A companion report (Keefe and Ling, 1998) presents results obtained using the techniques described herein. Acoustic response measurements are briefly reviewed to introduce the various types of evoked OAE responses.

OAEs are classified into evoked otoacoustic emissions (EOAE), which arise in response to an acoustic stimulus delivered into the ear canal, and spontaneous otoacoustic emissions (SOAE), which refer to cochlear-based responses in the ear canal in the absence of any external stimulus. The evoked responses are categorized according to the type of stimulus. The stimulus-frequency otoacoustic emission (SFOAE) is obtained using a sinusoidal stimulus (Kemp and Chum, 1980). The SFOAE is a low-level signal measured in the ear canal at the frequency of the sine tone, and has a saturating nonlinearity as stimulus level is increased.

Kemp (1978) measured a click-evoked otoacoustic emission (CEOAE) response, which is the ear-canal pressure response to the presentation of a single click, or the differential pressure response to the presentation of two or more clicks delivered at different intensity levels. Adopting more precise terminology, a click is a wide-bandwidth, deterministic, short-duration signal. The acoustic duration of the click is limited by the impulse-response duration of the source transducer; the electrical input signal to the source transducer typically has a much shorter duration. The acoustic click duration is typically 1–4 ms, whereas the overall duration of the CEOAE response is in the range of 10–40 ms.

Click-evoked OAE measurement systems have good frequency selectivity in the sense that a response is obtained in each frequency bin. Potential difficulties include the need to extract the cochlear response from the middle-ear response, and to minimize the influence of measurement-system distortion, primarily probe distortion (sometimes called stimulus artifact). This probe distortion is produced by high peak levels in the electrical input signal, which overload the acoustic source. The time-gated response is obtained by omitting the initial few milliseconds of the CEOAE response after presentation of the click. However, time-gating eliminates the portion of the cochlear response whose latency is shorter than the duration of the time gate (2–5 ms). This limits the bandwidth of CEOAE spectra to approximately 5 kHz, depending on implementation details.

Averaging of the ear-canal response has been used with artifact rejection (Kemp *et al.*, 1986). ''Artifact rejection,'' more often called the linear-balance technique, refers to a differential subtraction of ear-canal responses to eliminate the linear response associated with the middle ear, and to eliminate probe distortion by time gating the initial 2–5 ms of the response. The linear-balance technique uses four stimuli consisting of three identical clicks and a fourth click of opposite polarity and three times the amplitude of each of the preceding clicks. The four respective responses are summed to produce a response which equals zero if the system under test is linear. Averaging reduces random noise, but does not control for any measurement-system nonlinearity except by discarding the initial portion of the response waveform.

Distortion product otoacoustic emissions (DPs) are OAEs measured in response to a stimulus comprised of two continuous, sinusoidal tones whose frequencies are denoted by f_1 and f_2 with $f_2>f_1$ (Kemp, 1979). When analyzed using a discrete Fourier transform (DFT) of sufficient length, the distortion components of DPs lie in frequency bins that are distinct from each other and from the f_1 and f_2 bins, thus simplifying the interpretation of DPs. It is customary to indirectly measure the ambient background noise by comparing the DP bin level with the levels in adjacent frequency bins that do not contain DP components. The levels in these latter bins are implicitly assumed to be representative of the

 0001-4966/98/103(6)/3489/10/$10.00

noise level in the DP bin, despite the fact, for an ideal noise distribution, that the noise in each bin is statistically independent of the noise in any other bin.

To control for probe nonlinearity in DP measurements, it is typical to use two source probes—one probe outputs the sine tone at f_1, and the other outputs the sine tone at f_2. This controls for the inter-modulation distortion that would otherwise occur at sum and difference frequencies if a single probe were used.

DP measurement systems have the advantage that the strongly evoked signals are widely separated in frequency from those in the stimulus, so that they can easily be extracted. They have the disadvantages that the response is obtained at only a single pair of stimulus frequencies, which must be varied to obtain a broad-bandwidth response. Typically, special frequencies are used for f_1 and f_2 whose periods are exact subharmonics of the number of the samples N in the window length N. This may limit frequency selectivity. Furthermore, the DP response may fluctuate significantly if the stimulus frequencies are co-varied by small amounts, for example, in the vicinity of a SOAE site.

More complex stimuli have been designed to measure EOAEs, including tone bursts created using short-duration, rectangular-windowed sinusoids. Other windows, including Gaussian, have also been used.

EOAE responses to a pair of clicks with inter-click delay times of 0–5 ms and relative amplitude levels of 10 dB were measured by Kemp and Chum (1980). The higher level click was termed the masker. The lower-level click response was measured as the masker click was presented both before and after the lower-level click. Time gating was used over the initial 6 ms after the lower-level click. The masker was switched in polarity so that its response could be cancelled at measurement times in which the click response was defined.

Advances in EOAE measurement techniques are aimed at providing more accurate, or more comprehensive, data pertinent to the understanding of the cochlear mechanisms and for clinical applications to hearing tests in neonates and adults. Current CEOAE techniques are limited at high frequencies because time gating is used. It has been difficult to compare CEOAE and DP responses, because no formal relationship has existed between the stimulus sets. It turns out that formal relationships do exist when the response to a double-click stimulus is compared to the response to a double-frequency (DP) stimulus.

The theory underlying these new types of responses are discussed below. The problem of extracting a nonlinear signal from random noise is addressed using the nonlinear coherence technique.

I. MEASUREMENT THEORY

The theory underlying the new class of OAE stimulus/response pairs is presented using a continuous-time representation. The actual implementation is in discrete time using a sample period T, and, thus, some of the discussion uses a discrete-time representation.

The first step in stimulus design is the construction of an N-sample window (of duration NT) with a deterministic waveform $s_1(t)$. The second step constructs an N-sample window with a waveform $s_2(t)$. The third step constructs an N-sample window with the superposition of these two waveforms, $s_{12}(t)=s_1(t)+s_2(t)$. The composite stimulus $s(t)$ is formed as a $3N$-sample window whose initial N samples in the first window contain $s_1(t)$, whose intermediate N samples in the second window contain $s_2(t)$, and whose final N samples in the third window contain $s_{12}(t)$. The order of the initial, intermediate, and final windows may be permuted without loss of generality.

The pressure response in the ear canal is measured to this $3N$-sample stimulus $s(t)$, and ensemble-averaged through multiple presentations of the stimulus. The response is partitioned into three N-sample windows, defined as the response $p_1(t)$ to the stimulus $s_1(t)$, the response $p_2(t)$ to the stimulus $s_2(t)$, and the response $p_{12}(t)$ to the stimulus $s_{12}(t)$.

The double-evoking (2E) stimulus set has the property that

$$0=s_{12}(t)-[s_1(t)+s_2(t)]. \tag{1}$$

The linear response of the ear or cavity is eliminated by forming the double-evoked (2E) pressure response $p_D(t)$ defined by

$$p_D(t)=p_{12}(t)-[p_1(t)+p_2(t)]. \tag{2}$$

This 2E response is a measure of the nonlinear distortion embedded in the set of responses to the 2E stimuli. This family of evoked responses depends on the specific choices of $s_1(t)$, $s_2(t)$, and $s_{12}(t)$. If $p_D(t)$ is measured in a cavity, it differs from zero only due to the presence of random noise and measurement-system distortion.

An important subfamily of stimuli is that for which $s_2(t)$ is equal to $s_1(t)$, but delayed in time and scaled in amplitude, that is, $s_1(t)$ and $s_2(t)$ take the form

$$s_1(t)=a(t), \quad s_2(t)=\epsilon a(t-\tau). \tag{3}$$

The amplitude ratio ϵ has an arbitrary positive or negative value and the relative time delay is τ. The resulting response $p_D(t)$ to this choice of stimuli is called the double-evoked otoacoustic emission (2EOAE). The waveform $a(t)$ is an arbitrary N-sample array of values. An interesting range of time delays is likely to include $\tau<2$ ms, since the transient response of the ear is largest for these smaller delays. The joint stimulus $s_{12}(t)$ takes the form

$$s_{12}(t)=a(t)+\epsilon a(t-\tau). \tag{4}$$

The distinguishing feature of this stimulus set is that a signal $a(t)$ is superposed with a delayed and attenuated (or amplified, with or without inversion) copy of itself. The evoked OAE response to $a(t)$ overlaps the evoked OAE response to $a(t-\tau)$ and the nonlinear interaction in the overlap region is controlled by the relative amplitude ϵ. The 2EOAE response $p_D(t)$ thus contains a nonlinearly evoked OAE that includes overlapping cochlear reflections to overlapping signals.

There remains arbitrariness in the choice of $a(t)$. One choice is where $a(t)$ is a click, leading to the double click-evoked otoacoustic emission (2CEOAE) discussed below. Another choice is where $a(t)$ has a duration that is long compared to the impulse response of the acoustic source,

which itself happens to be comparable to the duration of evoked OAE responses. A subset of such stimuli may be expressed as an allpass-filtered click waveform. The allpass filter influences only the phase of the signal, and not its magnitude. A particular class of allpass filters results in chirp waveforms. The 2E response to this class of chirp stimuli leads to the double-chirp distortion product (2ChDP), described below.

The $3N$-sample stimulus set $s(t)$ is output as an electrical signal by one or more digital-to-analog converters (DAC), each driving an acoustic source in the ear-canal probe assembly. Two variants are considered in the 2E technique. In the *single-source variant*, each of the N-sample subwindows is output by a single DAC driving a single acoustic source. This is typical of systems presently used for CEOAE measurements. When $s_2(t)$ is a time-delayed, rescaled copy of $s_1(t)$, the time delay between $s_1(t)$ and $s_2(t)$ in the jointly presented subwindow $s_{12}(t)$ reduces the level of probe distortion due to peak overload by temporal separation of each of the peaks.

In the *double-source variant*, $s_1(t)$ is output by a first source, and $s_2(t)$ is output by a second source. In the presentation of $s_{12}(t)$, defined as the superposition of $s_1(t)$ and $s_2(t)$, $s_1(t)$ is again output by the first source and $s_2(t)$ is output by the second source. Thus each of the acoustic sources outputs only one signal at one level, and the subtraction technique substantively eliminates the distortion of each source from the output 2EOAE response. Without loss of generality, it can be assumed that the two acoustic sources have equal output sensitivities. Their peak overloading characteristics may not be identical, although they should be similar for nominally identical transducer designs. The double-source variant eliminates probe distortion only if the inter-modulation distortion of the probe is negligible. One component of probe distortion important at low frequencies is due to nonlinear vortex shedding at the entryway of each of the source-probe capillaries into the ear canal. This vortex shedding is discussed in the Appendix, where it is shown by an order-of-magnitude argument that the inter-modulation distortion is negligible as long as the distance between the source-probe capillaries is much larger than the i.d. of each capillary.

To summarize, a single source can be used with sufficiently large τ, because the response to the joint presentation of s_1 and s_2, followed by subtraction of each of the single responses to s_1 and s_2, produces negligible distortion artifact. The double-source variant is always preferred to the single-source variant because it provides a greater reduction in probe distortion. However, the double-source variant eliminates probe distortion only if the intermodulation distortion of the probe is negligible. One component of measurement distortion is due to nonlinear vortex shedding by each of the two capillaries leading from one of the acoustic sources into the ear canal. These issues are discussed further in the Appendix.

The above 2EOAE approach is in contrast to the linear-balance technique used to measure CEOAEs, which uses only a single source and which does not maintain constant level from that source. Since the amplitude of the electrical stimulus to the probe is not maintained constant, the distortion produced by that probe is not controlled. This distortion is quantified in measurements reported in a subsequent report (Keefe and Ling, 1998).

Based on a study using a different stimulus presentation method and a time-gated response (Kemp and Chum, 1980), the cochlear reflection to a pair of clicks was sensitive to the time delay τ used, but the trade-offs in interpreting the cochlear response to variations of in time delay have not been extensively studied.

A. Double-click-evoked otoacoustic emissions

The 2E stimulus set in Eqs. (3)–(4) is constructed for the special case such that $a(t)=d(t)$ is a click. The corresponding double-click-evoked otoacoustic emission (2CEOAE) response is defined by the 2E pressure response in Eq. (2). The 2CEOAE manipulates the time delay between clicks and their relative amplitude as independent variables.

Three examples of 2CEOAE stimulus sets are illustrated in Fig. 1 with click delays τ of 1, 2, and 3 ms and relative click amplitude $\epsilon=1$. The initial third of each plot illustrates the s_1 waveform and is identical for each of the three plots. The middle third of each plot illustrates the s_2 waveform including the respective click delay. The final third of each plot illustrates the s_{12} waveform with the pair of clicks separated by their respective delay. The up-state of each click has a duration of 0.125 ms. The overall duration of each stimulus set is 128 ms, leading to a 2E duration of approximately 43 ms after combining the pressure responses according to Eq. (2). This particular choice of 2E duration is not essential and may be reduced to obtain a greater number of independent responses in a given measurement duration.

The double-source variant of the 2CEOAE measurement has a significant degenerate case when the time delay between the clicks is zero ($\tau=0$). Suppose the relative click amplitude is unity ($\epsilon=1$). The two click stimuli coalesce into a single acoustic click of twice the amplitude in the ear canal, assuming, without loss of generality, that the two output probes have identical sensitivity. By using separate transducers for s_1 and s_2, the differential subtraction eliminates measurement-system nonlinearity that is synchronous to the stimulus window (except for electrical or acoustical intermodulation). This allows measurement of a CEOAE without the need for nulling out the initial 2–5 ms of the response that contains the high-frequency portion of the CEOAE.

This is the exact analog in the time domain to the use of separate sources in DP measurements in the frequency domain. This dual relationship is further examined in the theory underlying the measurement of double-chirp distortion products.

B. Double-chirp distortion products

One potential advantage of using chirp waveforms is understood in terms of the crest factor, defined as the ratio of the peak amplitude to the root-mean-square amplitude. For constant stimulus power, higher crest factors are typically associated with larger amounts of distortion in the measurement system. For example, if a probe exhibits peak-clipping

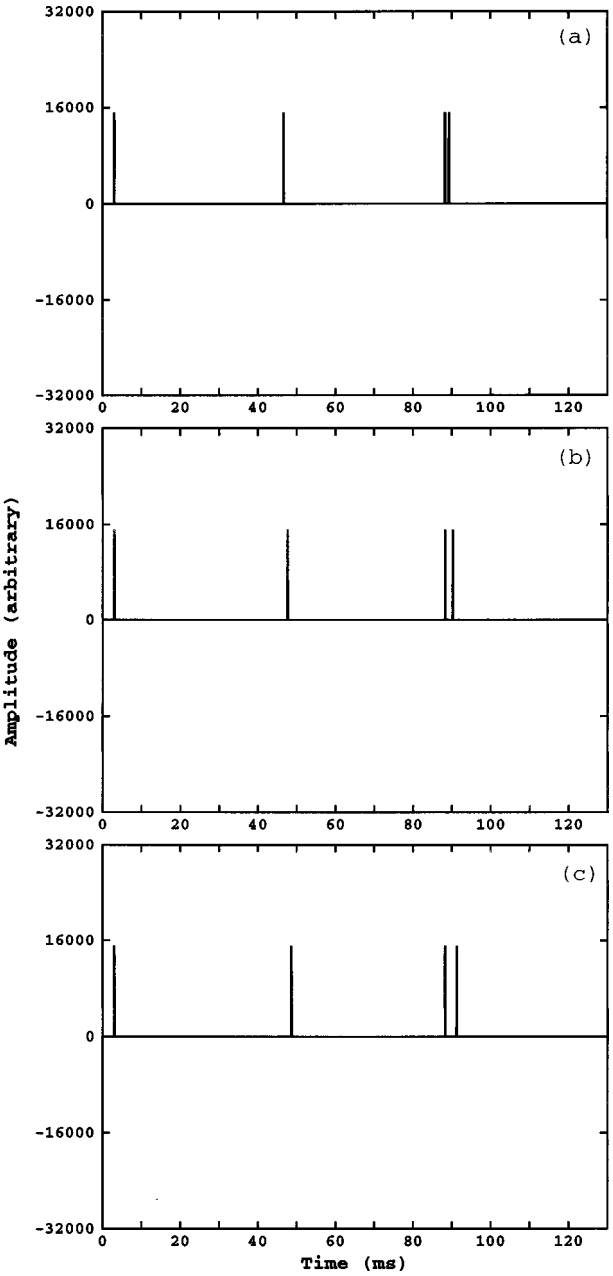

FIG. 1. The three click waveforms show the 2CEOAE stimuli for three different delays, 1 ms (top), 2 ms (middle), and 3 ms (bottom).

behavior, then the use of a chirp can significantly reduce probe distortion by reducing the peak levels associated with a given root-mean-square stimulus level.

The basic idea in the double-chirp distortion product (2ChDP) technique is to simultaneously present two chirps, $s_1(t)$ and $s_2(t)$, with a well-defined relationship between group delay and level. Intuitively, each chirp resembles a swept sine wave. If two sine waves are swept simultaneously, such that their frequency ratio $m=f_2/f_1>1$ is maintained constant, then two corresponding DP responses will be evoked.

Three stimuli are used, s_1, s_2, and their superposition, $s_{12}=s_1+s_2$, and the three corresponding ear-canal pressure responses p_1, p_2, and p_{12}, respectively, are measured. The response $p_D(t)$ is formed using Eq. (2), which in this case is called the double-chirp distortion product (2ChDP). It is the nonlinear signal that remains from the joint presentation of two chirps, after subtracting out the individual responses to each chirp.

The 2ChDP stimulus set is specified in the frequency domain, filtered by an allpass filter, and transformed to a time-domain signal using the inverse discrete Fourier transform (DFT^{-1}). Uppercase letters denote frequency-domain variables, and lowercase letters denote time-domain variables. The allpass filter is expressed in the frequency domain by $C(f)=e^{j\Theta(f)}$ where the phase response $\Theta(f)$ varies with frequency f and the unit imaginary number is j, based on a complex time dependence $e^{j2\pi ft}$.

The group delay $\tau_g(f)$ of the allpass filter is defined by

$$\tau_g(f)=-\frac{1}{2\pi}\frac{d\Theta}{df}. \tag{5}$$

In a discrete-time implementation based upon a duration of N samples at sample period T, the group delay must be in the range of $0-NT$ for window duration NT. The upper frequency desired in the stimulus is f_u, which is less than $(2T)^{-1}$ in a discrete-time implementation.

The *log chirp* is constructed using an allpass filter whose group delay is proportional to the logarithm of the frequency. Its phase function Θ is expressed using the common logarithm as

$$\Theta(f)=2\pi\alpha NTf\left[\log\left(\frac{f}{f_c}\right)-1\right]. \tag{6}$$

The center frequency f_c is the geometrical mean of the lowest $(f_l>0)$ and highest (f_u) frequencies present, $f_c=\sqrt{f_l f_u}$. The group delay at frequency f is calculated to be

$$\tau_g(f)=-\alpha NT\log\left(\frac{f}{f_c}\right), \tag{7}$$

which varies logarithmically with frequency. When the constant α is positive, the group delay at high frequencies is less than that at low frequencies; when α is negative, these relationships are reversed. The group delay is normalized for convenience to be zero at the center frequency.

The total range $\Delta\tau_g$ of group delays is

$$\Delta\tau_g=|\alpha|NT\log\left(\frac{f_u}{f_l}\right)=0.301|\alpha|NTN_{\mathrm{oct}}, \tag{8}$$

where the latter is expressed in terms of the number of octaves in the passband $[N_{\mathrm{oct}}=\log_2(f_u/f_l)]$. It follows that $|\alpha|$ should be less than $(0.301N_{\mathrm{oct}})^{-1}$ so that $\Delta\tau_g<NT$. In practice, the log chirp is designed to have a duration shorter than this limit so that the OAE response is contained within the sampling window.

After the inverse DFT, the log chirp can be arbitrarily rotated within the buffer of N samples to align its onset near the beginning of the buffer, thereby translating the time origin to any convenient value.

The spectra $S_1(f)$ and $D(f)$ are the DFTs of the stimulus waveform $s_1(t)$ and short-duration waveform $d(t)$, respectively. The stimulus spectrum is calculated as the product of the allpass filter and click spectra by $S_1(f)=C(f)D(f)$, corresponding to the convolution $s_1(t)$

$=c(t)*d(t)$ which produces the *time-stretched* stimulus. The click amplitude $D(f)$ must be of finite bandwidth and avoid the logarithmic singularity of the log chirp filter at zero frequency.

In contrast to the standard DP measured with a pair of sine tones, the 2ChDP is defined at all frequencies in the measurement bandwidth. Since $|S_2(f)|=|\epsilon S_1(f)|$, the chirps differ in level by $\Delta L=20\log|\epsilon|$. This enables the amplitude spectrum of the overall signal to be adjusted as desired, but a well-defined spectral level difference is produced that is constant across frequency. Denoting the relative time delay between the pair of chirps by τ the stimulus spectra corresponding to Eqs. (3)–(4) with the allpass phase filter $\Theta_1(f)$ are

$$\begin{aligned} S_1(f)&=D(f)e^{j\Theta_1},\\ S_2(f)&=\epsilon D(f)e^{j\Theta_2}=\epsilon D(f)e^{j\Theta_1}e^{-j2\pi f\tau},\\ S_{12}(f)&=S_1(f)+S_2(f). \end{aligned} \tag{9}$$

How does one emulate a common DP measurement paradigm, in which a fixed ratio $m=f_2/f_1$ is maintained between the stimulus frequencies, while f_1 is varied? The solution is to use a pair of chirps such that the group delay $\tau_{g1}(f_1)$ of chirp S_1 at frequency f_1 is equal to the group delay $\tau_{g2}(f_2)$ of chirp S_2 at frequency f_2. This can be constructed using a standard chirp with linear group delay by using different sweep rates, but the log chirp allows a simpler form. It follows from Eq. (7) for the log chirp that

$$\begin{aligned} \tau_{g1}(f)&=-\alpha NT\log\left(\frac{mf}{f_c}\right),\\ \tau_{g2}(f)&=-\alpha NT\log\left(\frac{f}{f_c}\right). \end{aligned} \tag{10}$$

The corresponding allpass phase functions, Θ_1 and Θ_2, are needed to construct the stimuli s_1 and s_2, respectively, and are calculated from

$$\begin{aligned} \Theta_1(f)&=2\pi\alpha NTf\left[\log\left(\frac{mf}{f_c}\right)-1\right],\\ \Theta_2(f)&=2\pi\alpha NTf\left[\log\left(\frac{f}{f_c}\right)-1\right]. \end{aligned} \tag{11}$$

It follows that

$$\begin{aligned} \tau_{g2}(f)&=\tau_{g1}(f)+\tau,\\ \Theta_2(f)&=\Theta_1(f)-2\pi f\tau,\\ \tau&=\alpha NT\log m. \end{aligned} \tag{12}$$

The relation between the chirp phase functions is in accord with Eqs. (9), which states that the time-stretched stimulus s_2 is simply a time-delayed copy of the time-stretched stimulus s_1, with a relative amplitude ϵ. The time delay τ is determined by the desired DP frequency ratio and the duration of the log chirp.

While the correspondence of the 2ChDP with the DP measurement paradigm has been stressed, it is also interesting to contrast its properties with evoked OAE responses. Evoked OAE responses typically rely on the subtracted response to a stimulus presented at different levels, whereas the 2ChDP response is a subtracted response to a set of stimuli whose levels are maintained. It has been argued that DP measurements have better signal-to-noise properties than CEOAE measurements because DPs do not rely on subtracting out the signal response at different levels. The 2ChDP measurement shares this desirable property with DPs.

The 2ChDP response can be analyzed in the frequency domain, to provide a measure of DP-evoked energy at all frequencies in the measurement bandwidth. Alternatively, it may be useful to analyze the 2ChDP response using a time-frequency representation or wavelet transform to track how the various DPs evolve with the stimulus, for example, referenced on the time axis to the group delay of f_2. This may enable the identification of trajectories of particular DPs (both relative group delay and amplitude), for example, the $2f_1-f_2$ component.

The procedure has two variants. The set of stimuli may be output by a single transducer, and measurement-system nonlinearity is partially controlled for by the 2E subtraction. This variant is suggested by the linear cancellation procedures used in the 2CEOAE technique, but is expected to have lower distortion due to the lower crest factor of the chirp stimulus. The second, and preferred, variant is to use two acoustic sources in the probe assembly. Probe 1 outputs s_1 and probe 2 outputs s_2. This controls at all values of m for intermodulation distortion created by joint presentation of both stimuli using a single probe.

A degenerate case exists for $m=0$. When two sources are used, the two electrical stimuli comprising s_{12} coalesce into a single acoustic chirp. The resulting 2ChDP response has similarities to the pulsed SEOAE (and DPOAE) method (Kemp *et al.*, 1990), although the 2E subtraction is slightly different, and the 2ChDP stimulus waveform uses wideband chirps rather than iso-frequency sinusoids.

The 2ChDP waveform response $p_D(t)$ cannot be easily interpreted in the time domain because the stimuli have been allpass filtered, and the responses share the time-stretched characteristic of the stimulus set. One solution is to remove the influence of the allpass filter by applying the inverse allpass filter $C^{-1}(f)=e^{-j\Theta(f)}$ to the response. The corresponding time-domain response is denoted as the *time-compressed* response.

If time compression (with $\Theta=\Theta_1$) is applied to the stimulus set in Eqs. (9), the 2ChDP stimulus set is transformed into the 2CEOAE stimulus set defined by $s_1(t)=d(t)$, and $s_2(t)=\epsilon d(t-\tau)$. The time-compressed, double-chirp response in the time domain is isomorphic to the double click-evoked response to a pair of short-duration pulses that vary in relative latency and level. Furthermore, this time-domain representation of the 2ChDP response allows data analysis within the framework of a response evoked by a pair of equivalent clicks. This suggests a novel relationship between DP measurements and evoked OAE measurements: The dual to the frequency-domain DP response is the time-domain, double-click response.

While the stimuli in the 2ChDP and 2CEOAE have this dual relationship, their nonlinear responses may not be simply related. By comparing both 2ChDP and 2CEOAE re-

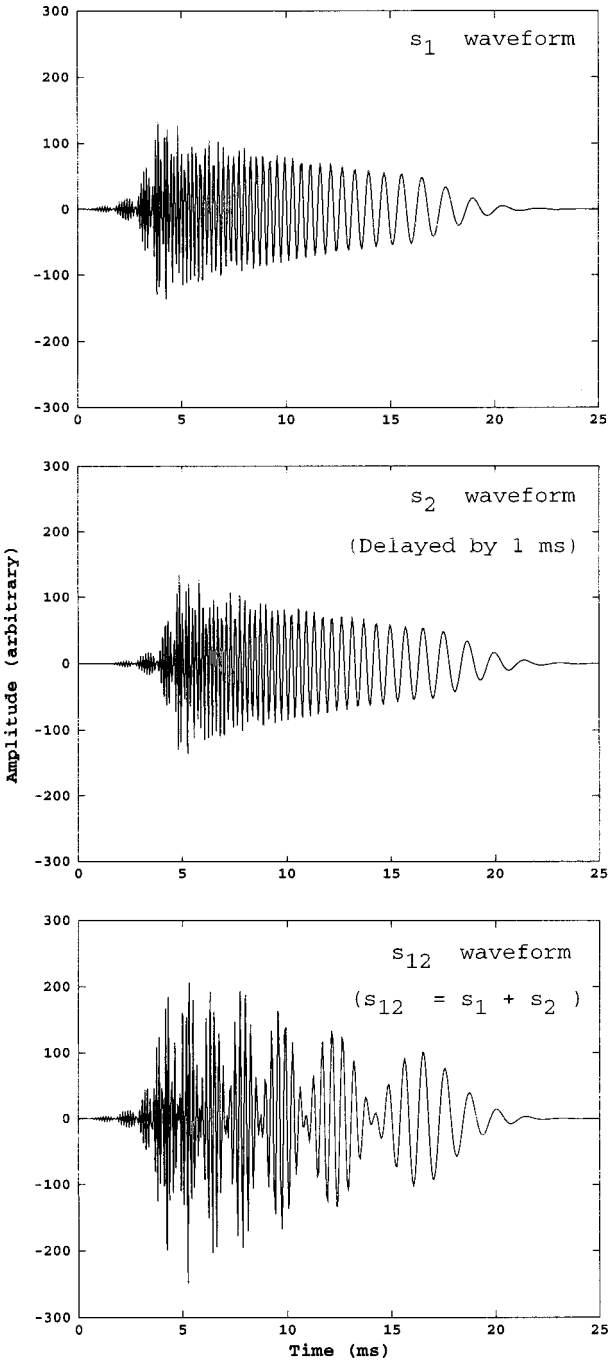

FIG. 2. Log chirp waveforms are illustrated for s_1, s_2, and $s_{12}=s_1+s_2$.

sponses under both conditions, the spectral-temporal nature of the nonlinearity can be probed.

An example of a chirp stimulus set is illustrated in Fig. 2. The amplitude spectrum $|D(f)|$ is constant from 500 to 7800 Hz, with a smooth, cosine-squared high-pass window in the spectral domain at frequencies below 500 Hz and a cosine-squared low-pass filter above 7800 Hz. This particular form of window was chosen for convenience, but such a window leads to smooth onset and decay properties in the time-domain waveform. The relative amplitude is set to unity ($\epsilon=1$), the log chirp coefficient is $\alpha=0.15$, and the total chirp duration is $D=43$ ms, for which the initial 25 ms is illustrated in the plot. A 1-ms delay is selected for s_2 relative to s_1. Some amplitude modulation effects are visible in the s_{12} waveform. The chirp delay τ is 1 ms, which corresponds to a DP frequency ratio of approximately $m=1.43$. For this example, a frequency ratio $m=1.2$ typical of DP measurements could be achieved by setting $\tau=0.51$ ms.

II. NONLINEAR COHERENCE

The signal-to-noise ratio in evoked otoacoustic emission (OAE) measurements may be rigorously measured using coherence theory (Bendat, 1990). A particular form of nonlinear coherence function is defined below in a form convenient for evoked OAE measurements. Two derivations of the nonlinear coherence function are presented, one based on cross-spectral analysis and the other based on an analysis of the nonlinear output signal alone. The relationships to other definitions of signal-to-noise ratio in the OAE literature are discussed.

At frequency f, the electrical stimulus input to the source is $X(f)$, and the electrical response output measured by the microphone is $Y(f)$. It is assumed that the microphone has linear response and negligible internal noise. The linear transfer function between stimulus and response is $H(f)$. This transfer function takes account of the frequency response of the source and microphone, and the linear response of the external, middle and inner ear to stimulus presentation at the probe tip. The signal $H(f)X(f)$ linearly contributes to the measured output $Y(f)$. There are two additional outputs that are assumed. One is the random measurement noise $R(f)$, due to source-transducer noise, physiologic, and environmental noise. The signal $R(f)$ is uncorrelated with $X(f)$. Another is a nonlinear distortion signal $D(f)$, which arises through two mechanisms: measurement-system nonlinearity and the cochlear nonlinearity (i.e., the EOAE). The total output signal is

$$Y(f)=H(f)X(f)+R(f)+D(f). \tag{13}$$

The technique of cross-spectral estimation using ensemble averaging is used, such that $G_{uv}(f)$ denotes the cross-spectrum between any pair of signals $U(f)$ and $V(f)$, and $G_{uu}(f)$ denotes the autospectrum of $U(f)$, termed the total power in the signal (this is not to be confused with acoustic power). The technique is developed for the case of transient OAEs, and the applicability of the result is discussed later for DPOAEs.

The cross-spectrum $G_{xy}(f)$ of the input and output signals is

$$G_{xy}(f)=HG_{xx}+G_{xr}+G_{xd}=H(f)G_{xx}+G_{xd}, \tag{14}$$

because $G_{xr}=0$ since $R(f)$ is uncorrelated with the input signal. G_{xd} is the cross spectrum of the input with the distortion signal. The frequency response function $\hat{H}$ of the system is conventionally defined by (Bendat, 1990)

$$\tilde{H}(f)=\frac{G_{xy}}{G_{xx}}=H+\frac{G_{xd}}{G_{xx}}. \tag{15}$$

This demonstrates that the frequency response of the system is biased by the presence of nonlinearities, since $\hat{H}(f)$ is not equal to $H(f)$.

Examples of calculations of the coherence function C^2 have been performed for the general case of system distortion excited by a deterministic stimulus (Maki, 1986). It is defined by

$$C^2(f)=\frac{|G_{xy}|^2}{G_{xx}G_{yy}}. \tag{16}$$

The remaining autospectrum needed to calculate the coherence is the output autospectrum G_{yy} given by

$$G_{yy}(f)=|H|^2G_{xx}+G_{rr}+G_{dd}+HG_{dx}+H^*G_{xd}, \tag{17}$$

where the asterisk denotes the complex conjugation operation. The coherence function is nonlinear because of the influence of the distortion signal. Its interpretation is difficult because of the complexity of the expressions for the input–output cross spectrum (G_{xy}) and the output autospectrum (G_{yy}).

In the present application to OAEs, a subtraction procedure is carried out to remove the linear response of the system, thus resulting in a newly defined output variable. This results in an alternative definition of a *nonlinear coherence function* with simpler properties than the ordinary nonlinear coherence function. The new output variable $Z(f)$ is defined by subtracting the linear system response from the output $Y(f)$ as follows:

$$Z(f)=Y(f)-H(f)X(f)=R(f)+D(f). \tag{18}$$

The variable $Z(f)$ corresponds equally well to the linearly balanced response in the approach of Kemp *et al.* (1986) or the 2E response of Eq. (2). It is an inherently nonlinear response variable.

The cross spectrum G_{xz} of $X(f)$ with $Z(f)$ is

$$G_{xz}(f)=G_{xy}-HG_{xx}=G_{xd}, \tag{19}$$

where Eq. (14) has been applied. The autospectrum of $Z(f)$ is similarly calculated to be

$$G_{zz}(f)=G_{dd}+G_{rr} \tag{20}$$

since the noise is uncorrelated with the deterministic distortion. This output autospectrum is much simpler than G_{yy} in Eq. (17): It is the sum of the distortion power and the noise power.

The nonlinear coherence function γ^2 is defined and calculated in terms of the linear input stimulus and the nonlinear output response by

$$\gamma^2(f)=\frac{|G_{xz}|^2}{G_{xx}G_{zz}} \tag{21}$$

and quantifies the ratio of the output nonlinear power G_{zz} that is correlated with the input power G_{xx}. The nonlinear coherence varies between zero and unity, and an equivalent relation is found to be

$$\gamma^2(f)=\frac{G_{dd}}{G_{dd}+G_{rr}}. \tag{22}$$

The fact that $|G_{xd}|^2=G_{xx}G_{dd}$ is used to derive this result. Thus the nonlinear coherence is the ratio of the distortion power to the sum of the distortion and the noise power. This is the nonlinear generalization of a useful linear-systems property of the ordinary coherence function.

The steps in calculating nonlinear coherence are as follows. The autospectra are calculated by a sum (i.e., ensemble average) over K independent measurements of the underlying variables X_i and Z_i, i ranging from $1,\ldots,K$. A simplification occurs because the input variable is the stimulus $X(f)=S_1(f)$, which is precisely known. The spectra are calculated using

$$\begin{aligned}
G_{xz}(f)&=\left(\frac{1}{K}\right)\sum_{i=1}^{K} X_i^*(f)Z_i(f)\\
&=\left(\frac{1}{K}\right)S_1^*(f)\textstyle\sum_{i=1}^{K} Z_i(f),\\
G_{zz}(f)&=\left(\frac{1}{K}\right)\sum_{i=1}^{K} |Z_i(f)|^2,\\
G_{xx}(f)&=\left(\frac{1}{K}\right)\sum_{i=1}^{K} X_i^*(f)X_i(f)=|S_1(f)|^2.
\end{aligned} \tag{23}$$

The random-error variance of the autospectra is proportional to G_{xx}^2/K, and the variance of the cross spectra is proportional to $|G_{xz}|^2/(\gamma^2K)$ (Bendat, 1990). Thus increasing the number of averages increases the accuracy of the spectral estimation. The nonlinear coherence, with the substitutions of the stimulus $S_1(f)=X(f)$ and the 2E response $P_{Di}(f)=Z_i(f)=P_{12}(f)-[P_1(f)+P_2(f)]$, is calculated from Eq. (21) to be

$$\gamma^2(f)=\frac{1}{K}\frac{|\Sigma_{i=1}^{K}P_{Di}(f)|^2}{\Sigma_{i=1}^{K}|P_{Di}(f)|^2}. \tag{24}$$

An advantage of the nonlinear coherence technique is that the nonlinear signal-to-noise ratio, termed the *distortion-to-noise ratio* DNR, may be rigorously defined as follows:

$$\mathrm{DNR}(f)=\frac{\gamma^2}{1-\gamma^2}. \tag{25}$$

The DNR is large when the coherence approaches unity, and small when the coherence approaches zero. Using Eq. (22), the DNR evaluates to

$$\mathrm{DNR}(f)=\frac{G_{dd}}{G_{rr}}. \tag{26}$$

This relation embodies the notion of a nonlinear signal-to-noise ratio, and cannot be obtained for the nonlinear coherence function $C^2(f)$ defined in Eq. (16). The corresponding distortion-to-noise level measured in decibels is 10 log DNR.

A typical problem in acquiring an ensemble-averaged response is to choose an objective criterion for determining the number of averages. A criterion that takes into account the signal-to-noise ratio of the nonlinear component of the OAE response may be useful in practical applications.

When the OAE signal-to-noise ratio is relatively poor, the total measured autospectrum G_{zz} may exceed the distortion autospectrum G_{dd} that should properly be taken as the OAE amplitude (assuming negligible measurement-system

distortion). The distortion and random noise autospectra are calculated in terms of the total measured autospectrum and the nonlinear coherence by

$$G_{dd}(f)=\gamma^2 G_{zz},$$
$$G_{rr}(f)=(1-\gamma^2)G_{zz}. \tag{27}$$

A sometimes useful fact is that averaging over frequency is equivalent to averaging over ensembles, since random noise is uncorrelated across frequencies. Thus the variance of estimating the autospectra and cross spectra can be reduced by averaging over adjacent frequencies. It is typical for hearing applications to average over the log frequency axis. In the ith frequency bin, the number of elements K in the sum is the product of the number of subensembles M and the number of frequency bins N_i per octave, or suboctave.

A. DPOAE and alternate derivation

The main conclusion of this section is that the particular form of the nonlinear coherence and its suitability for calculating the DNR is applicable for DPOAE experiments even though the preceding derivation is no longer valid. The main result is Eq. (24), which shows how to calculate the nonlinear coherence in terms of the ensemble of measurements of $P_D(f)$. Once this is obtained, the DNR, distortion autospectrum and noise autospectrum are calculated using Eqs. (25)–(27).

The problem is in using the cross-spectral density method to calculate $\gamma^2(f)$. The purpose of a DPOAE measurement is to use stimuli at f_1 and f_2 to measure a response at some other frequency f_d, typically at $f_d=2f_1-f_2$. In Eq. (14), the stimulus autospectrum components $G_{xx}(f_1)$ and $G_{xx}(f_2)$ are nonzero, but $G_{xx}(f_d)=0$ since there is no stimulus energy at the frequency of the distortion product. It follows that $G_{xd}(f_d)=G_{xy}(f_d)=G_{zz}(f_d)=0$, so that $\gamma^2(f_d)$ in Eq. (21) is undefined at the distortion-component frequency of interest.

An alternative, and simpler, derivation of nonlinear coherence is presented, which addresses this problem in application to DPOAEs. There exists an ensemble of K independent measurements of the distortion pressure $P_{Di}(f)$, for i varying from 1 to K. Each distortion pressure measurement is a complex phasor, i.e., with independent magnitude and phase components. Each measurement is a sum of a distortion signal and a noise signal. The distortion signal is estimated as the average $\langle P_D(f)\rangle$ over the ensemble by

$$\langle P_D(f)\rangle=\left(\frac{1}{K}\right)\sum_{i=1}^{K} P_{Di}(f). \tag{28}$$

The corresponding power of the average phasor, defined as the square of the magnitude of the average phasor, is

$$|\langle P_D(f)\rangle|^2=\left(\frac{1}{K^2}\right)\left|\sum_{i=1}^{K} P_{Di}(f)\right|^2. \tag{29}$$

The average power of the ensemble of phasor powers is defined based on their incoherent sum:

$$\langle |P_D(f)|^2\rangle=\left(\frac{1}{K}\right)\sum_{i=1}^{K} |P_{Di}(f)|^2. \tag{30}$$

The definition of nonlinear coherence in Eq. (24) is simply the ratio of $|\langle P_D(f)\rangle|^2$ to $\langle |P_D(f)|^2\rangle$, which is the ratio of a suitably normalized coherent sum to an incoherent sum of the phasors. Because $Z_i(f)=P_{Di}(f)$, the nonlinear output autospectrum $G_{zz}(f)$ is $\langle |P_D(f)|^2\rangle$. It follows that the distortion and noise autospectra are calculated from

$$G_{dd}(f)=|\langle P_D(f)\rangle|^2,$$
$$G_{rr}(f)=\langle |P_D(f)|^2\rangle-|\langle P_D(f)\rangle|^2. \tag{31}$$

This completes the alternative derivation.

What this implies for DPOAEs is that an ensemble of independent spectral measurements may be used to calculate the nonlinear coherence and the nonlinear signal-to-noise ratio. This result is applicable not only to the 2E OAE responses that are the main subject of this investigation, but also to any ensemble of evoked OAE responses.

Examples of the use of nonlinear coherence and DNR are presented in part II.

B. Discussion

Existing systems of measuring noise have used cross-correlational and cross-spectral analyses to assess reproducibility of evoked OAE waveforms, and to measure noise and a signal-to-noise function. Some DPOAE techniques have based an estimate of noise in the distortion-frequency bin on the average noise power measured in a number of adjacent frequency bins. Other techniques reported have used an ensemble a pair ($K=2$) of independent measurements. These techniques are briefly compared. One statistic used is the reproducibility, defined in terms of the cross correlation between the pair of response waveforms, which is equal to unity if the two waveforms are identical (ideal coherence) and zero if the two waveforms are statistically independent (ideal incoherence) (Kemp *et al.*, 1986). This statistic does not provide a frequency-specific measure of the signal-to-noise ratio in individual frequency bins, but subsequent systems have calculated the reproducibility in frequency bandwidths using a pair of responses.

Other statistics have used cross-spectral analyses that do provide frequency-specific information. A simpler notation is adopted in this section such that the pair of distortion OAEs are expressed as $A=P_{D1}(f)$ and $B=P_{D2}(f)$. The signal and noise powers from Eq. (31) are

$$G_{dd}(f)=(\tfrac{1}{4})|A+B|^2,$$
$$G_{rr}(f)=(\tfrac{1}{4})|A-B|^2. \tag{32}$$

The corresponding signal power $\hat{G}_{dd}(f)$ and noise power $\hat{G}_{rr}(f)$ proposed by Kemp *et al.* (1986) are

$$\hat{G}_{dd}(f)=(\tfrac{1}{2})(A^*B+AB^*),$$
$$\hat{G}_{rr}(f)=(\tfrac{1}{4})|A-B|^2. \tag{33}$$

Definitions of signal and noise powers identical to Eq. (32) have been used in studies of TEOAEs (Prieve *et al.*, 1993)

and DPOAEs (Gorga *et al.*, 1994). It is straightforward to verify that $G_{dd}(f)$ and $\hat{G}_{dd}(f)$ are approximately equal if A and B are approximately equal. In summary, there is no significant difference between the nonlinear coherence technique and prior techniques when only a pair of responses is used.

Significant differences do emerge when three or more responses are used, because the noise power cannot simply be estimated as a difference in a pair of responses. As has already been indicated, the variances in estimating the autospectra and cross-spectra, as well as the (nonlinear) coherence, are inversely proportional to K. Increasing the number of responses in the ensemble decreases the uncertainty in measuring the distortion signal-to-noise ratio as well as the distortion signal and noise powers. In this sense, time averaging into a pair of buffers (A and B) does not provide as much information as spectral averaging using the nonlinear coherence approach. This information is directly relevant to improving the ability to measure evoked OAEs the power of which is small compared to the noise power.

It must be cautioned that an evoked OAE measurement can provide both absolute reproducibility and meaningless data. If the coherence is close to unity, then the random noise power is negligible, but there remain two components to distortion—probe and cochlear distortion. In practice, measurements in a 1-cm^3 (or other) cavity provide a partial measure of the distortion power due to measurement-system nonlinearities (Gorga *et al.*, 1994) It is partial because the cavity and ear canal differ in their acoustic impedance, and thus a given electrical stimulus to each probe source delivers a differing acoustic power to the probe or ear canal. When an evoked OAE response is measured, the DNR should be high *and* the distortion power should be significantly larger than that in the cavity, in order to validate that a response has a physiologic component, subject to the exclusion that impedance effects have not been controlled. It is not sufficient to measure the ear-canal and cavity impedances, because the issue here is how distortion varies with load, and it is the influence of varying load on the generation of nonlinearities within the probe that is important. The optimum situation would be to use a cavity the impedance of which is identical to the ear being tested. This situation is approximated by use of a ear simulator for cavity comparisons with adult ear responses, but this remains a difficult problem.

III. CONCLUSIONS

A new 2E stimulus/response family of stimuli has been defined for measurements of evoked otoacoustic emissions, as has been reported earlier in a preliminary form (Keefe, 1996). New variables to explore in the 2CEOAE procedure include the time delay between the two pulses, the relative levels in the pulse amplitudes, and the relative pulse polarity (i.e., the sign of ϵ). New variables to explore in the 2ChDP procedure include the manipulation of τ and the relative levels and polarity of the two chirps.

Techniques using chirp-based distortion products share advantages with both DP and evoked OAE measurement systems. They use a repetitive, but noncontinuous, signal well-suited to ensemble averaging. A wide-band multi-chirp stimulus can be created with controllable crest factor whose strongly evoked cochlear response components are separable from those of the stimulus. Furthermore, such a stimulus may have desirable group delay properties for DP measurements. There exists formal relationships between the double-click and double-chirp-evoked OAE techniques that may be useful in comparing 2CEOAE and DPOAE measurements, and in understanding the time-frequency pattern of cochlear reflections.

Nonlinear coherence describes the relative contributions of noise and distortion power in an EOAE measurement. The use of nonlinear coherence provides a rigorous treatment of the influences of random noise and system distortion on OAE measurements that is well-suited for techniques using ensemble averaging of evoked OAE spectra. This technique is proposed as a means to address the practical difficulty of measuring weakly evoked OAE signals in the presence of background noise.

One mechanism for the production of probe distortion at low frequencies is vortex shedding associated with small-diameter sound delivery tubes used in current designs of ear-canal probe assemblies.

ACKNOWLEDGMENTS

Stephen Neely and Michael Gorga provided useful critiques of a preliminary version of this report.

APPENDIX: LOW-FREQUENCY PROBE DISTORTION

The low-frequency distortion associated with high peak levels can be understood in terms of vortex shedding from the small-diameter sound tubes of the ear-canal probe. Vortex shedding is associated with the importance of the convective nonlinearity in the aeroacoustic field. A dimensionless Strouhal number $S_0 = fD_t/V_t$ is used to assess the influence of nonlinearity due to jet formation occurring just outside the aperture of the sound delivery tube (Blake, 1986). The sound tube diameter is D_t and the linear acoustic velocity within the tube is V_t. The convective nonlinearity is negligible if $S_0 \gg 1$, and is important if S_0 is of order unity.

Suppose the tube diameter is $D_t = 0.05$ cm, which is typical for the sound delivery tube of an Etymotic ER-10C probe. For a characteristic impedance Z_c of 80 CGS ohms, which is typical of an ear-canal of diameter 0.80 cm, a peak acoustic pressure of 80 dB SPL generates a peak volume velocity of 0.025 cm^3/s. This corresponds to a peak linear velocity of $V_t = 13$ cm/s through the sound delivery tube. The resulting Strouhal number is equal to unity at a frequency of 250 Hz, which predicts that vortex shedding losses are important at this frequency and lower frequencies. Vortex shedding losses can typically be neglected when $S_0 > 10$, corresponding to a frequency of 2500 Hz. This numerical example suggests that these nonlinear losses are important for typical ear-canal probe designs at low frequencies and may be present at moderate frequencies.

Many ear-canal probes used to measure DPOAEs use two sound delivery tubes. The tube centers are separated by 0.14 cm in the ER-10C probe, which is nearly three times

larger than either of their diameters. Each diameter scales the diameter of the core of the jet. Thus the unstable jets associated with each these well-separated sound delivery tubes do not strongly interact, which implies that the nonlinearities associated with each of the sound tubes are separable and do not produce a temporal intermodulation distortion. This condition is important for the double-source variant of the 2E stimulus/response technique to eliminate low-frequency probe distortion. In general, it is preferable to use a larger diameter sound delivery tube in order to minimize overall distortion, but this also reduces the source impedance of the probe, which may be undesirable if it is not controlled by direct measurement.

Regarding stimulus design, the stimulus spectrum $A(f)$ may be carefully shaped to minimize measurement-system distortion. The clipping that characterizes the source transducer nonlinearity is mainly a low-frequency problem because of the larger acoustic particle displacements at lower frequencies for a constant volume-velocity condition. Thus $A(f)$ may be attenuated at low frequencies (below 100–500 Hz) to minimize probe distortion. There is a trade-off at low frequencies because the physiologic noise is higher in this frequency range. At higher frequencies, $A(f)$ can be increased so as to provide an adequate DNR, although other sources of measurement-system distortion may become significant.

[1]This research was undertaken in order to address measurement difficulties in otoreflectance (Keefe, 1997). The application of double-evoked stimulus sets to otoreflectance is described therein.

Bendat, J. S. (**1990**). *Nonlinear System Analysis and Identification from Random Data* (Wiley, New York).

Blake, W. K. (**1986**). *Mechanics of Flow-Induced Sound and Vibration, Volume I, General Concepts and Elementary Sources* (Academic, Orlando).

Gorga, M. P., Neely, S. T., Bergman, B. M., Beauchaine, K. L., Kaminski, J. R., and Liu, Z. (**1994**). ''Towards understanding the limits of distortion product otoacoustic emission measurements,'' J. Acoust. Soc. Am. **96**, 1494–1500.

Keefe, D. H. (**1996**). ''New evoked cochlear responses: Double chirp-evoked distortion products and double click-evoked otoacoustic emissions,'' J. Acoust. Soc. Am. Suppl. 1 **99**, S2562(A).

Keefe, D. H. (**1997**). ''Otoreflectance of the cochlea and middle ear,'' J. Acoust. Soc. Am. **102**, 2849–2859.

Keefe, D. H., and Ling, R. (**1998**). ''Double-evoked otoacoustic emissions. II. Intermittent noise rejection, calibration and ear-canal measurements,'' J. Acoust. Soc. Am. **103**, 3499–3508.

Kemp, D. T. (**1978**). ''Stimulated acoustic emissions from within the human auditory system,'' J. Acoust. Soc. Am. **64**, 1386–1391.

Kemp, D. T. (**1979**). ''Evidence of mechanical nonlinearity and frequency selective wave amplification in the cochlea,'' Arch. Otol. Rhinol. Laryngol. **224**, 37–45.

Kemp, D. T., Brass, D. N., and Souter, M. (**1990**). ''Observations on Simultaneous SFOAE and DPOAE Generation and Suppression,'' in *Mechanics and Biophysics of Hearing*, edited by P. Dallos, C. Geisler, J. Matthews, M. Ruggero, and C. Steele (Springer-Verlag, Berlin), pp. 202–209.

Kemp, D. T., Bray, P., Alexander, L., and Brown, A. M. (**1986**). ''Acoustic emission cochleography–Practical aspects,'' Scand. Audiol. Suppl. **25**, 71–95.

Kemp, D. T., and Chum, R. A. (**1980**). ''Observations on the generator mechanism of stimulus frequency acoustic emissions-two tone suppression,'' in *Psychophysical, Physiological and Behavioral Studies in Hearing*, edited by E. deBoer and M. A. Viergever (Delft U.P., Delft), pp. 34–41.

Maki, B. (**1986**). ''Interpretation of the coherence function when using pseudorandom inputs to identify nonlinear systems,'' IEEE Trans. Biomed. Eng. **BME-33**, 775–779.

Prieve, B., Gorga, M., Schmidt, A., Neely, S., and Peters, J. (**1993**). ''Analysis of transient-evoked otoacoustic emissions in normal-hearing and hearing-impaired ears,'' J. Acoust. Soc. Am. **93**, 3308–3319.

Double-evoked otoacoustic emissions. II. Intermittent noise rejection, calibration and ear-canal measurements

Douglas H. Keefe
Boys Town National Research Hospital, 555 North 30th Street, Omaha, Nebraska 68131

Robert Ling
Department of Speech and Hearing Sciences, University of Washington, Seattle, Washington 98195

(Received 2 May 1997; revised 27 January 1998; accepted 23 February 1998)

Measurements of double-click-evoked otoacoustics emissions (2CEOAEs) and double-chirp distortion products (2ChDPs) are reported for normal-hearing adults based upon theory presented in an earlier report [Keefe, J. Acoust. Soc. Am. **103**, 3489–3498 (1998)]. The nonlinear acoustic response of a probe assembly used in ear-canal measurements is tested in a calibration cavity to compare the double-evoked (2E) technique with existing OAE techniques. The 2E technique reduces the peak distortion by approximately 30 dB relative to existing click-evoked techniques. The 2E subtraction of click responses is partially analogous to current techniques in that the linear response is eliminated, but differs in that high-frequency measurements are improved by eliminating time gating of the cochlear response, and low-frequency measurements are improved by reducing probe distortion, especially when two acoustic sources are used. Because time gating is eliminated, it is straightforward to measure the onset of a click-evoked OAE. The nonlinear coherence function is used to measure the nonlinear distortion signal-to-noise ratio (DNR) for the 2ChDPs and 2CEOAEs. The DNR is typically 20–30 dB. An intermittent noise rejection technique is implemented in real time that compares a currently acquired ear-canal response with a stored response. Dissimilar responses indicate the presence of intermittent noise, and the noise-contaminated responses are thereby discarded before ensemble averaging. © *1998 Acoustical Society of America.* [S0001-4966(98)01206-5]

PACS numbers: 43.64.Jb, 43.64.Yp [BLM]

INTRODUCTION

The theory underlying a new class of double-evoked (2E) otoacoustic emission measurements was described in a companion report (Keefe, 1998) denoted herein as part I. In particular, the double-click-evoked otoacoustic emission (2CEOAE) response and the double-chirp distortion product (2ChDP) were proposed in implementations based on the use of either a single digital-to-analog channel (DAC), or a pair of DACs. A technique was proposed to calculate a form of nonlinear coherence, and thereby obtain a direct measure of nonlinear distortion signal-to-noise ratio (DNR).

This report begins by introducing a real-time intermittent noise rejection technique that is of special relevence for ear-canal measurements and by describing observations gained using the technique. A description follows of experimental measurements of 2CEOAEs and 2ChDPs in an acoustic cavity and in adult ear canals. The measurement-system distortion in the cavity measurements is compared with distortion associated with alternative OAE techniques. The ear-canal measurements demonstrate the feasibility of the 2E OAE techniques in both the single-source variants. The nonlinear coherence is measured in these ear-canal measurements and used to calculate the nonlinear distortion-to-noise ratio. Finally, click-evoked OAEs measured using the double-source variant of the 2CEOAE are reported that include the early onset of the click response generated by the cochlear reflection. Preliminary accounts of this research have been presented at conferences (Keefe, 1996, 1997).

I. REAL-TIME INTERMITTENT NOISE REJECTION

It can be difficult to obtain a meaningful acoustic response from a measurement in a human ear canal. The noise in the ear canal is much higher, and there exist transient changes in the noise that are associated with changes in the physiologic state of the individual. Moreover, the noise levels in infants tend to be higher than levels in adults, and it can be a significant challenge to obtain valid data from an intermittently noisy infant.

Ensemble averaging of responses to the multiple presentations of a given stimulus in the time or frequency domain is a useful method of noise reduction, and the theory is well understood for the case of stationary noise. Because physiologic noise is nonstationary, the short-time statistics of the noise tend to vary considerably over the duration of the measurement. Averaging may be ineffective in extracting the desired signal from the intermittent noise. This section describes a real-time intermittent-noise rejection technique designed to solve this problem.

Real-time intermittent-noise rejection is defined as the elimination of exceptionally noisy data prior to averaging, whether due to physiologic, environmental, or measurement-system sources. These exceptional events, denoted as invalid data, must be detected and excluded while data are being acquired, so that the invalid data are not included in the averaged response.

For click-evoked OAE measurements, Kemp *et al.* (1986) have described a real-time intermittent-noise rejection

technique, which they called ''noise rejection,'' based on the following criterion: The response buffer contains invalid data if the peak waveform pressure amplitude exceeds some threshold value during the portion of the response after the initial 5 ms or so. This criterion focuses on the presence of a large-amplitude component in the time-gated response. Neely and Liu (1993) have developed intermittent-noise rejection techniques for use in a system to measure CEOAEs and DPOAEs. In the CEOAE measurement, a subaverage is collected and a peak amplitude is obtained for each of the nonlinear outputs calculated using the linear-balance technique with time gating. The subaverage is discarded if the peak amplitude exceeds a threshold, as in Kemp *et al.* In the DPOAE measurement, the data are considered to be valid if the magnitude of the difference of the two subaverages over an interval of approximately 4 s is less than some threshold value (Neely, 1997).

The intermittent-noise rejection technique to be described differs in that the similarity of the currently obtained response is calculated in real time with respect to a previously measured response. The new technique is based on pattern recognition of the overall response rather than to one feature, i.e., its peak value. A sufficiently large dissimilarity in the low-amplitude components of the waveform will be sufficient to categorize the current data as invalid. This technique is similar to the DPOAE technique of Neely and Liu insofar as intermittent noise may be detected by a peak difference in two signals, which is a measure of dissimilarity, but differs in that it operates in real time and that it is intended for use in any evoked OAE measurement including CEOAEs.

The inputs are the pressure responses measured by a probe assembly in the ear canal using a microphone, and a threshold level for rejecting data as invalid. The outputs from the technique include judgments of whether each buffer of data is valid or not, and, if valid, the corresponding buffer of data.

The technique depends on the comparison of a vector of the current measured response with a vector of the stored measured response. Since the stimulus is repetitively output, the ideal response of a deterministic system in the absence of noise is assumed to be constant (this assumption does not have to be strictly satisfied for a real-time noise rejection technique to be useful). The currently measured response is compared to the stored measured response. If the two responses are sufficiently similar, then the currently measured response is considered valid data, and, as such, can be used to calculate an averaged response over valid data sets. Otherwise, the currently measured response is invalid—it is discarded and not used to calculate the averaged response. The real-time aspect of this technique is to determine the degree of similarity, and hence, whether or not the currently measured response is valid, during the process of data acquisition.

Both the stored and currently measured responses are vectors, the elements of which comprise a set of sampled responses. Any algorithm to calculate the similarity of two time series may be used in this technique. One choice of similarity is the norm of the difference of the two vectors, using any convenient norm. The smaller the norm of the difference, the more similar are the two responses.

Any algorithm to classify the relative similarities obtained into two categories, valid and invalid, may be used. One choice is to test whether the similarity is less than some threshold, and, if so, to accept the currently measured response as valid. Otherwise, it is invalid. This is the current implementation. To begin data acquisition, the stored and currently measured response in one version are the first and second data buffers acquired.

The stored measured response may be the previous response, as in the current implementation, or a previously judged valid response. Another version is where the stored measured response is a function of two or more of the previously judged valid response buffers. This might be a running average, calculated as the running sum divided by the number of valid buffers acquired, or a time-weighted average in which the most recently acquired buffers are more highly weighted than less recently acquired buffers.

A real-time refinement allows the experimenter to adjust during data acquisition the parameters governing the classification into valid or invalid responses. The experimenter sets a lower threshold of rejection for cavity measurements than for ear-canal measurements, but it may also be advantageous to set a lower threshold for measurements in adult ears than for infant ears.

Systems exist in which peak levels of the currently measured response are used with a threshold criterion to test for the presence of artifact. However, significant noise may be present, but not exceeding the threshold criterion used. The ability to calculate a real-time differential response between two responses may provide a more sensitive method of intermittent-noise rejection.

Initial experience in using this real-time intermittent-noise rejection technique in measuring otoacoustic emissions is promising. The implementation uses a norm that is the peak magnitude difference between the vector of samples in the current and previous responses. In a quiet adult subject, it is straightforward to set this threshold of similarity rejection such that valid responses are obtained during expiration by the subject, but rejected as invalid during inspiration. This real-time intermittent-noise rejection technique has potential for use in noisy subjects such as neonates. The number of time averages to achieve a given nonlinear signal-to-random noise ratio should be significantly reduced by rejecting intermittently noisy responses.

II. METHODS

The first set of experimental tests compared the distortion responses measured in a 1-cm^3 acoustic cavity for the 2CEOAE and 2ChDP techniques with responses measured using the linear-balance CEOAE technique. Data were acquired using software written for an Intel Pentium computer (MS-DOS operating system). The data acquisition board was an Ariel DSP32C with the 16-bit Ariel Proport analog-to-digital converters (ADC) and digital-to-analog converters (DAC). The sample rate was 16 kHz for these cavity measurements.

The Etymotic ER-10C probe was used to generate the acoustic stimulus and measure the acoustic response. This probe has two acoustic sources and one pressure microphone. For leak-free insertion into the ear canal or cavity, the probe assembly has a foam tip, through which three capillary tubes couple the acoustic signals to, or from, each of the transducers. 2E stimuli were generated using a single acoustic source in the single-source variant, as well as using two acoustic sources in the double-source variant (see part I). Pressure responses were measured in a 1-cm^3 cavity to compare the noise floor and probe nonlinearities.

The implementation issues are common for the 2ChDP and 2CEOAE procedures. Each stimulus and response is based on an N-sample window with sample period T and duration NT. A $3N$-sample sequence is defined by $\{s_1, s_2, s_{12}\}$, as discussed in part I. To allow time averaging of responses and ensemble averaging of nonlinear coherence (see part I), each sequence is repeated $2M$ times to form an ensemble of $K=2$ subensembles, each subensemble having a length of M sequences. Numbering each sequence in the ensemble from 1,...,$2M$, subensemble A contains sequences 1,3,...,$2M-1$, and subensemble B contains sequences 2,4,...,$2M$. Thus the sequences are interleaved within each subensemble. A typical value for the size of each subensemble was as small as $M=8$, for which the ensemble included $2M=16$ responses, and as large as $M=64$. Intermittent noise in each response was minimized using the real-time intermittent-noise rejection technique.

III. ACOUSTIC CAVITY MEASUREMENTS

A. Results

The 2E stimulus sets are illustrated for the click (Fig. 1) and log chirp (Fig. 2) stimuli in the double-source variant for the special case that the relative delay between s_2 and s_1 is zero ($\tau=0$) and the relative gain is unity ($\epsilon=1$).

The *log chirp* is defined as the convolution of the click stimulus with an allpass filter $C(f)$, whose group delay increases logarithmically with frequency (see part I). The log chirp stimuli have the same power spectrum as the corresponding click stimuli, but reduced peak amplitudes, as expected from their lower crest factor. Were time delay to be introduced ($\tau\neq 0$), the corresponding response would mimic a DPOAE experiment insofar as the instantaneous frequencies of the two signals maintain a fixed frequency ratio $m=f_2/f_1$ over the duration of the 2E transient.

For either stimulus type, the top plot shows the waveform $s_1(t)$ output by DAC1 to Acoustic Source 1 on the ER10C, and the middle plot shows the waveform $s_2(t)$ output by DAC2 to Acoustic Source 2 on the ER10C. The bottom plot shows the superposition, i.e., $s_{12}(t)=s_1(t)+s_2(t)$, of these two waveforms that would be output if only a single DAC and a single Acoustic Source were used.

1. Phase distortion

The probe is inserted into the 1-cm^3 cavity and time-averaged pressure responses are measured using both the click and chirp 2E sets (64 stimulus presentations). The acoustic levels are referenced by the peak SPL of the ear-canal response to the initial click s_1. The resulting peak

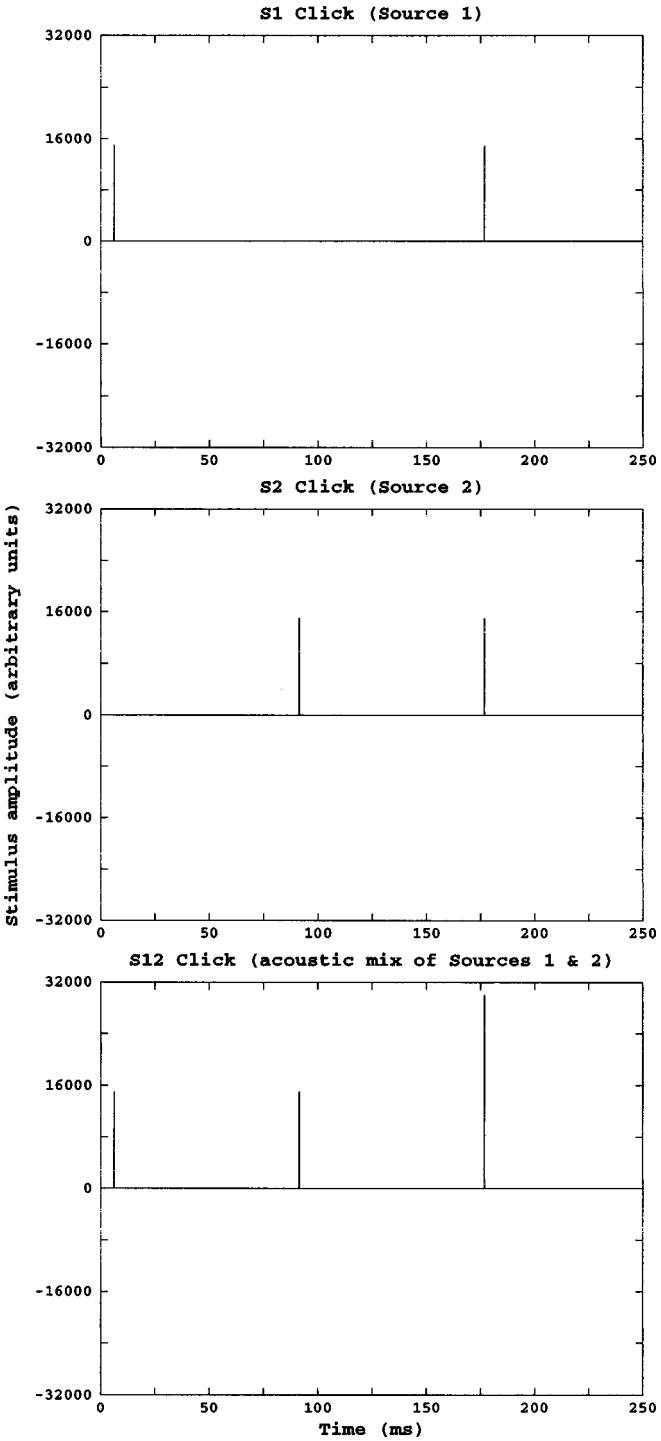

FIG. 1. 2E click stimuli for the double-source variant. Top: stimulus output by source 1. Middle: stimulus output by source 2. Bottom: sum of stimuli output by both sources.

response levels were 80, 90, and 100 dB SPL. The click and log chirp pressure responses to the initial presentation of s_1 are illustrated in the top pair of plots in Fig. 3 for the stimulus level that produces a peak cavity response to the click of 90 dB SPL [i.e., the peak amplitude of 620 mPa in Fig. 3(a)]. It is apparent that the crest factors of the equal-power click and chirp stimuli in Figs. 1–2 are more different than those of the click and chirp responses in Fig. 3.

Since the two types of stimuli have the same power, any power difference between the click and chirp responses is

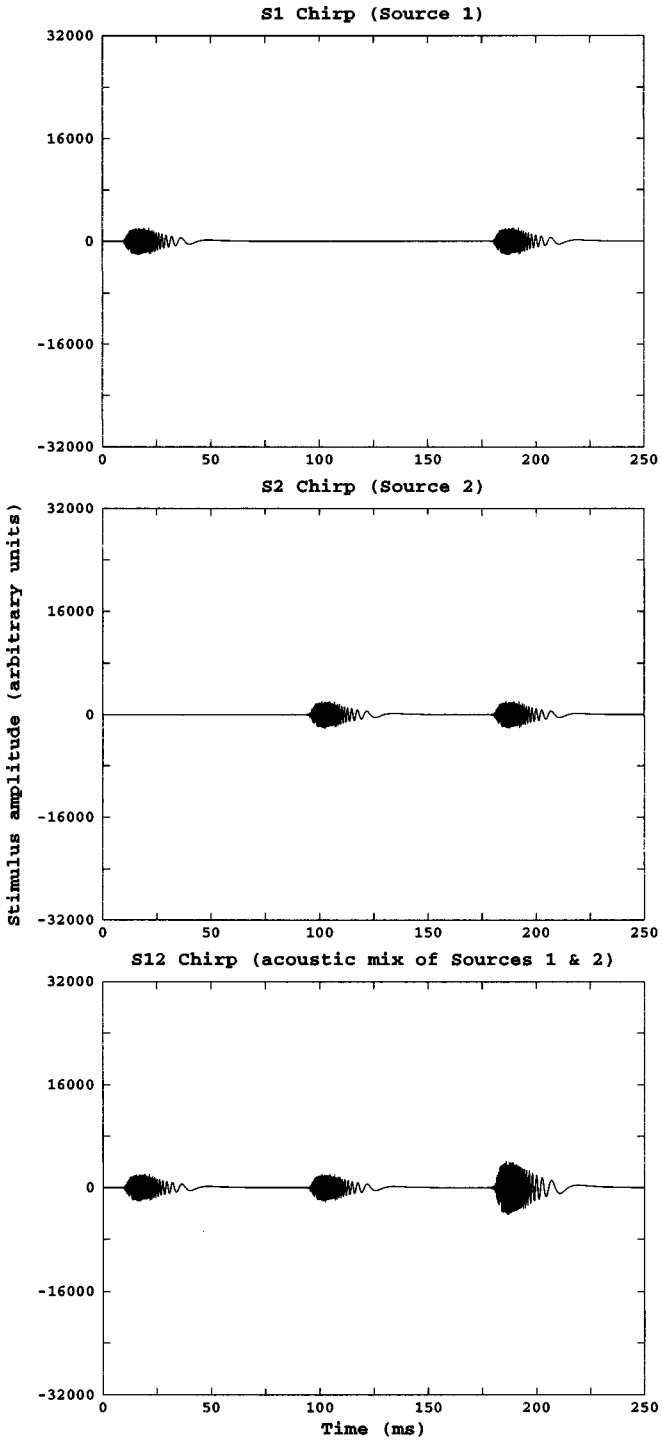

FIG. 2. 2E log chirp stimuli for the double-source variant. Top: stimulus output by source 1. Middle: stimulus output by source 2. Bottom: sum of stimuli output by both sources.

due to measurement-system distortion. Preliminary tests showed no significant distortion in the DACs and ADC, so that the observed distortion in this and other acoustic cavity tests is due to the presence of the probe. This distortion is analyzed in the time domain. The chirp response is time compressed using the inverse allpass filter $C^{-1}(f)$ of that used to design the log chirp. This is the dechirped (or time-compressed) response in Fig. 4(a). In the absence of measurement-system distortion and numerical errors in calculating the DFT, this dechirped waveform should be identical to that of the corresponding click response [Fig. 3(a)]. The numerical errors were insignificant as all calculations were performed using ANSI double-precision real numbers, but discretization errors in the ADC and DAC remain a possibility.

The relative difference in these waveforms is calculated by subtracting the dechirped response from the click response, as illustrated in Fig. 4(b). The vertical scale on this plot has been magnified ten-fold to show the fine structure of the difference response. The peak difference is 28 mPa (63 dB SPL) compared to the peak value of 620 mPa (90 dB SPL) in the click response. This amounts to a peak signal-to-distortion ratio (SDR) of (90–63) dB=27 dB. The distortion waveform has significant amplitude over the initial 10 ms after the click presentation. Measurement-system distortion is significant, as assessed using this constant-power, but variable-phase, measurement technique.

2. Magnitude distortion

A second technique to assess measurement-system distortion is the differential-click-response technique, which has been widely used in evoked OAE measurements. A pair of clicks is presented by a single acoustic source that differ in level by 10 dB. These clicks are presented in an interleaved manner so that their measurement is substantively simultaneous. The response at the lower level is boosted by 10 dB and subtracted from the response at the higher level; this difference is the differential click response. Any deviation from zero is due to measurement-system distortion.

This type of magnitude distortion affects responses measured by the linear-balanced stimulus technique (see Fig. 5) used in CEOAE systems (Kemp *et al.*, 1986). In this technique, the first click has positive polarity, while the remaining three clicks are inverted with amplitudes reduced by one-third. In both the 2E and the linear-balanced set, a linear combination of the clicks equals zero. The response at the lower level is boosted by a factor of 3 and subtracted from the response at the higher level, resulting in the differential click response illustrated below. Any deviation from zero is due to measurement-system distortion.

In contrast, in the double-source 2E technique, each acoustic source generates a click at a constant level, so that any probe distortion is cancelled out. The largest peak amplitude output by the DAC in the linear-balanced set (Fig. 5) is equal to the largest peak amplitude output by either of the DACs in the 2E set (Fig. 1). Each click stimulus in the linear-balanced and 2E stimuli has a nonzero duration of 0.125 ms.

Figure 6(a) (top left panel) shows the differential click response to a pair of clicks with s_1-induced peak cavity levels of 90 and 100 dB SPL. There are considerable amounts of distortion generated in the first 10 ms following the click presentation that exceeds the ± 25-mPa range of the plot. The same response is plotted in Fig. 6(b) (top right panel) over a ten-fold larger range to show the full range of the distortion. Figure 6(c) (left bottom panel) shows the differential click response to a pair of clicks with cavity levels of 80 and 90 dB SPL over the same ± 25-mPa range. There remains considerable distortion in these responses.

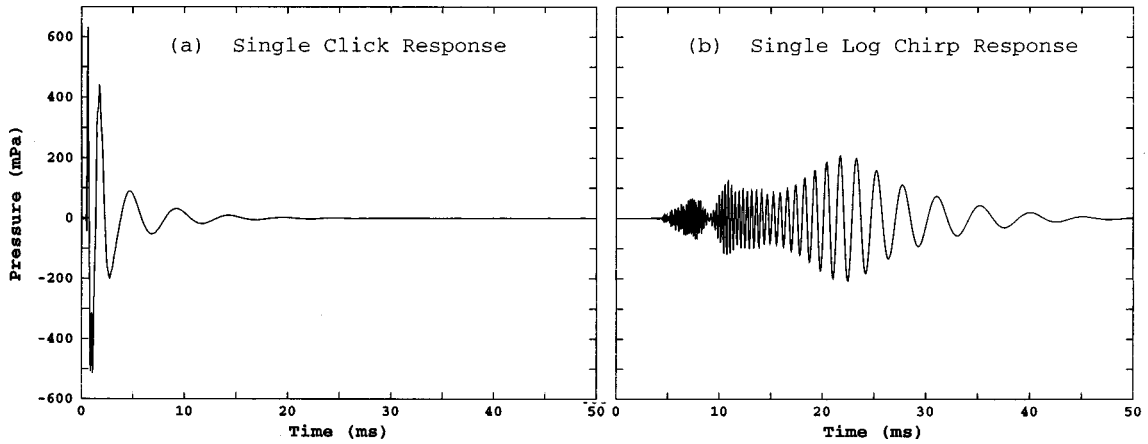

FIG. 3. Measurements in 1-cm^3 cavity. (a) Waveform response to single click. (b) Waveform response to single chirp with same energy as single click.

For the higher-level pair of clicks, the peak distortion magnitude is 100 mPa, or 74 dB SPL. The corresponding peak SDR is (90–74) dB=26 dB, and the distortion persists for approximately 15 ms after the click onset time. For the lower-level pair of clicks, the peak SDR is (80–61) dB=29 dB, and the distortion persist for approximately 7 ms after the click onset time.

This exemplifies the need to time gate the early part of (0–2.5 ms) of the CEOAE response, but suggests that significant distortion can persist (at least, for this probe at these peak cavity levels) over longer durations. In fact, one would not attempt to measure CEOAEs with this probe at 100 dB SPL peak levels, but it provides a useful baseline of comparison with the 2E technique.

The corresponding double-source 2E cavity responses $p_D(t)$ calculated using the theory in part I are illustrated in Fig. 7 for the case of the click stimulus set at three different levels. The time-compressed chirp responses were generally similar to the click responses, and are not illustrated. The 2E responses are shown for p_1 peak click levels of 100, 90, and 80 dB SPL in the top, middle, and bottom panels, respectively. The middle panel is the $p_D(t)$ response associated with the $p_1(t)$ click response discussed earlier (in Fig. 4). For the 100 dB SPL click, some temporal distortion of the response is apparent in the initial 5 ms, with a SDR of (100–44) dB=56 dB. This is approximately 30 dB larger than that obtained in the foregoing phase or magnitude distortion measurements. In the middle and bottom panels, no distortion is evident with respect to the random noise level. This means that measurement-system distortion is effectively eliminated for p_1 levels of 90 dB SPL or less, which is the range in which CEOAE responses are typically measured.

B. Discussion

Simulations have determined that the particular combination of stimuli in the linear-balance technique is essentially optimal in terms of the best signal-to-noise ratio (Kemp *et al.*, 1986; Bray, 1989). However, this analysis was concerned only with the extraction of a deterministic signal from a stationary random noise signal. Measurement-system distortion is deterministic and is not reduced by signal averaging. The differential-click technique used in the linear-balance method produces approximately 30 dB more distortion than the 2E technique. It is this magnitude distortion that necessitates the use of time gating in CEOAE technique. The performance of the 2E technique in substantively eliminating magnitude distortion means that time gating is not required in the 2CEOAE technique.

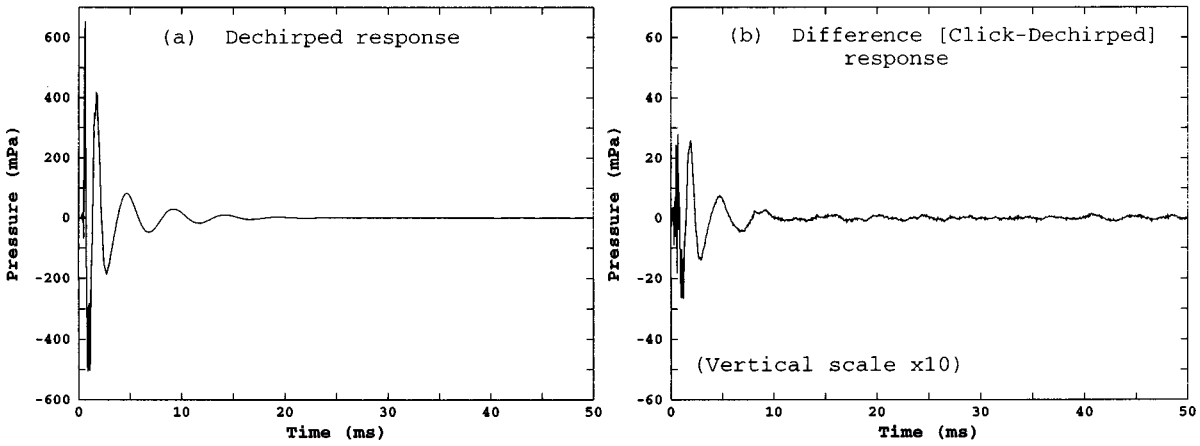

FIG. 4. Measurements in 1-cm^3 cavity. (a) Time-compressed output of waveform response to single chirp. (b) Difference between single-click response and time-compressed single-chirp responses that are individually plotted in Figs. 3(a) and 4(a), respectively.

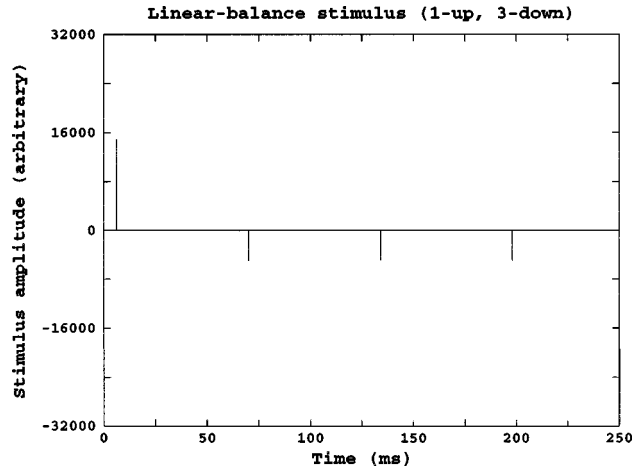

FIG. 5. The plot shows the 1-up, 3-down stimulus waveform used in the linear-balance CEOAE technique. The 1-up click is three times the amplitude of each of 3-down click.

The measurement-system distortion is mainly due to distortion by the sound source in these measurements. An alternative explanation proposed to account for result obtained using 12-bit converters is that measurement-system distortion is due to overloading of the ADC (Bray, 1989). If distortion by the ADC, or the measurement microphone and its associated electronics, were significant, it would not be eliminated by use of the 2E double-source technique. The present measurements used 16-bit converters, and identify sound-source distortion as the most significant contributor to the measured distortion.

IV. EAR-CANAL MEASUREMENTS

The subjects in all tests were two adult males with normal hearing.

A. Single-source variant

For the first pair of experiments, one subject was tested using the single-source variant, that is, the stimulus was delivered to a single acoustic source using a single DAC channel, using a stimulus/response sample rate of 16 kHz per channel.

1. 2CEOAE responses

The influence of variations in time delay τ on the 2CEOAE waveforms was tested. For $\tau = 1$ ms delay, there was a large-amplitude spike in the ear-canal response at early latencies corresponding to probe distortion (Fig. 8). This spike was also observed in cavity measurements. The probe distortion was just noticeable at a delay of $\tau = 2$ ms, and was absent at a delay of $\tau = 3$ ms.

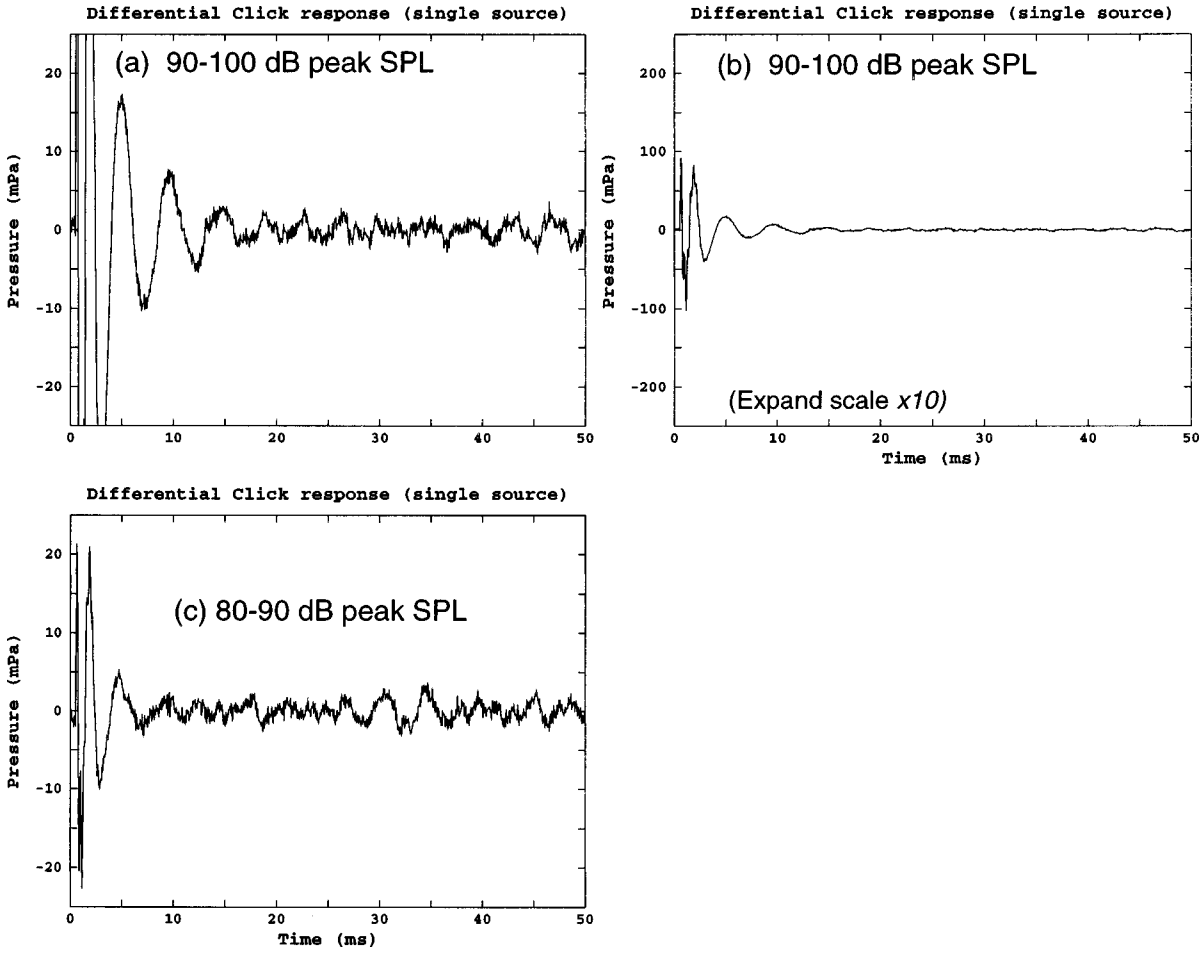

FIG. 6. Magnitude distortion in probe responses measured in the 1-cm^3 cavity. (a) Differential click response to single clicks at peak levels of 90 and 100 dB SPL. (b) Same response plotted with vertical scale expanded by a factor of 10 to show large-amplitude behavior at short times. (c) Differential click response to single clicks at peak levels of 80 and 90 dB SPL.

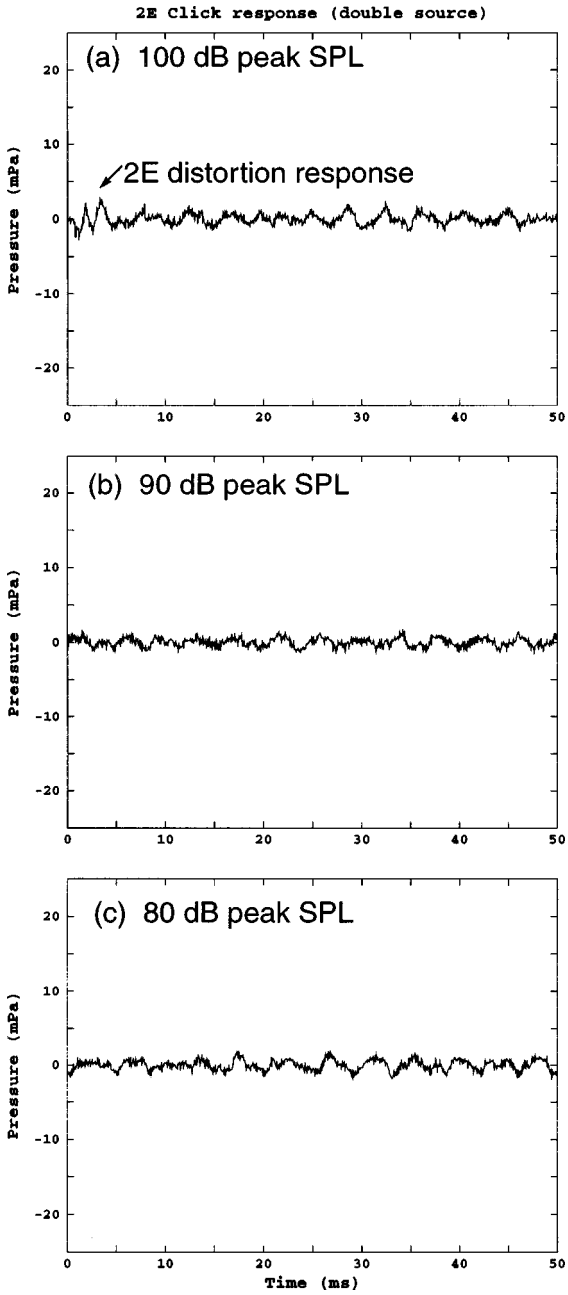

FIG. 7. 2E click responses measured in a 1-cm^3 cavity at various peak levels: (a) 100 dB SPL; (b) 90 dB SPL; (c) 80 dB SPL.

Even at the 1-ms delay, the peak 2E distortion was only 3% of the peak distortion in a CEOAE measurement using the linear-balance stimulus set with magnitude distortion characteristics similar to those shown in Fig. 6. In accordance with the discussion in part I, the temporal offset of one click stimulus from the other was helpful in controlling probe distortion, but some residual probe distortion remained.

2. 2ChDP responses

The 2ChDP responses were measured using the stimulus set shown in Fig. 2 of part I in the ear canal of the same subject for a time delay of 1 ms. The frequency ratio m of the instantaneous frequencies of each of the chirp stimuli is calculated using Eq. (12) of part I to be 1.43. Each time-

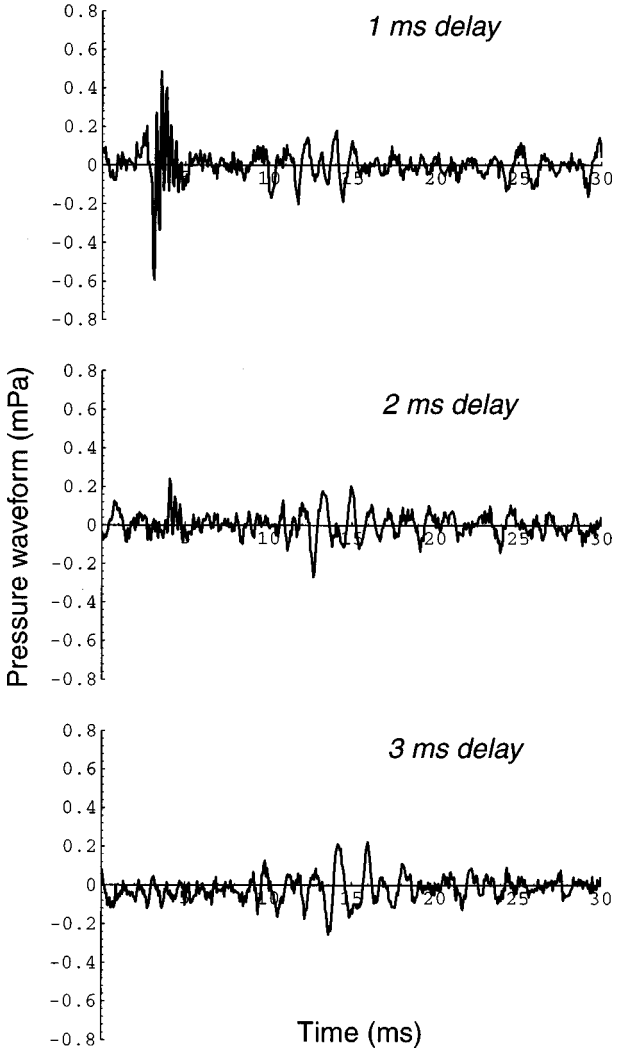

FIG. 8. 2CEOAE pressure waveforms measured in the ear at inter-click delays of 1, 2, and 3 ms. A 30-ms duration is shown with an arbitrary time origin.

averaged response was an average of 64 responses, each individual response, and thus the time-averaged response as well, comprised of two subensembles of responses for the nonlinear coherence analysis. Using an uppercase symbol to denote a frequency-domain representation, the chirp spectra $P_D(f)$ were calculated along with the nonlinear coherence and distortion signal-to-noise ratio DNR defined in part I. These DNRs were calculated in terms of the two subensembles of time-averaged responses without additional frequency averaging. Since the microphone output signal was filtered by analog high-pass filter with a cut-on frequency of 430 Hz prior to digitizing, the results are illustrated only above 500 Hz.

The nonlinear coherence (Fig. 9) exceeded 0.9 over most frequencies, but low coherence values were observed below 700 Hz, in a region near 1400 Hz, and in narrow bands near 3000 and 6700 Hz. These frequency ranges of low coherence indicate noise-contaminated responses. This nonlinear coherence function further allowed the measurement of the coherent distortion signal, as explained in part I. The total measured 2E distortion level is plotted in Fig. 10 in

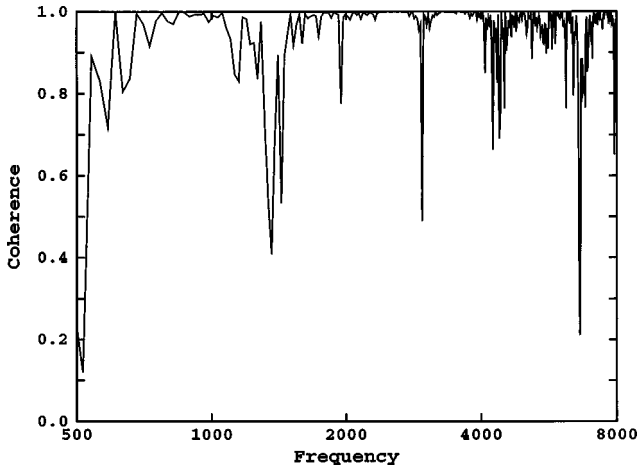

FIG. 9. Measured nonlinear coherence function for 2ChDP response in ear canal with $\tau = 1$ ms.

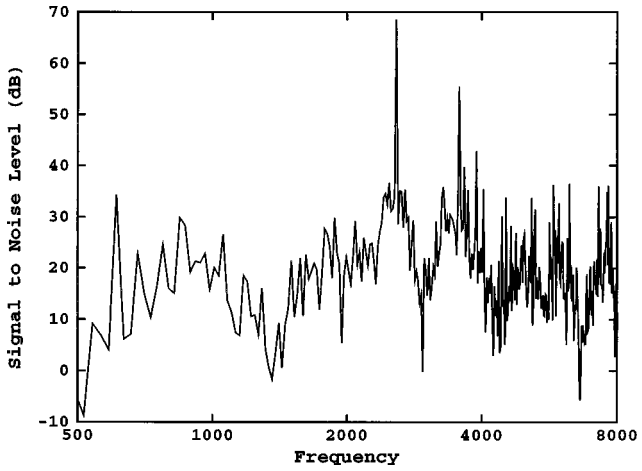

FIG. 11. Measured signal-to-noise level for 2ChDP response in ear canal with $\tau = 1$ ms.

the curve labeled $S+N$, i.e., the distortion signal plus noise. The coherent signal level corresponding to the 2ChDP was calculated and is plotted on the same figure. It is nearly equal to the total distortion level except at frequencies where the coherence is low. The random noise level is also plotted on the same figure. The total level and the coherent signal level differed by as much as 3 dB near 1400 Hz due to the presence of noise. The 2ChDP had significant energy in the 4–8 kHz octave range, limited above only by the Nyquist frequency.

The corresponding distortion signal-to-noise level was typically in the range of 20–30 dB, and could be increased by further averaging (Fig. 11). Isolated DNR levels upward of 70 dB were due to apparent notches in the noise level rather than peaks in the coherent signal level. It is possible, even likely, that these notches were due to an insufficient number of independent subensembles used to calculate the nonlinear coherence. This was a limitation of the low-level data acquisition software that will be improved in future work. Of much greater importance is to ensure that the signal-to-noise level is adequate at all frequencies of interest.

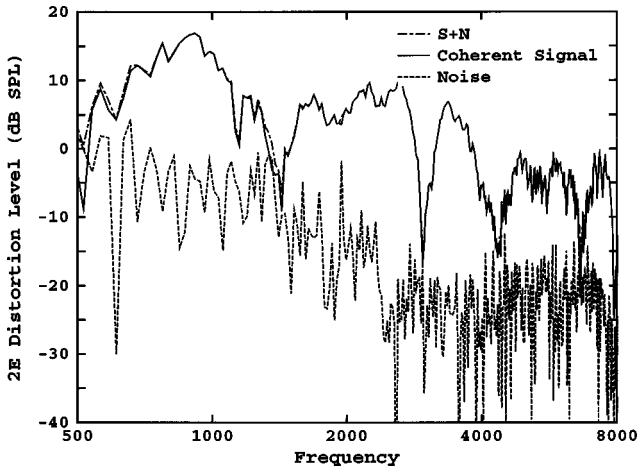

FIG. 10. Measured 2E distortion spectra for 2ChDP response in ear canal with $\tau = 1$ ms. The $S+N$ curve is the total distortion level, the coherent signal curve shows the distortion level that is coherent with the stimulus, and the Noise curve shows that random noise level.

The nonlinear coherence method decouples the separate influences of random noise from probe distortion. These results have been obtained with a single source, for which probe distortion effects were not entirely eliminated—they dominate the low-frequency response peak near 900 Hz (Fig. 10). These results are preliminary in the sense that the full power of the nonlinear coherence technique requires that a fairly large number K of independent spectral responses are used, whereas the current results are based on $K=2$ responses.

The influence of dechirping is illustrated in the next analyses. Figure 12 shows the 2ChDP chirp response in the ear for $\tau = 3$ ms, a sufficiently long delay such that the pair of responses can be well separated after time compression. It is obvious that the chirp response to the simultaneous presentation of s_1 and s_2 produced overlapping responses. The dechirped responses $d_1(t)$, $d_2(t)$ and $d_{12}(t)$ show this separation in their equivalent click response (Fig. 13). The equivalent peak amplitude of 800 mPa corresponds to a peak equivalent level of 92 dB SPL, which is larger than would ordinarily be used in a click-evoked OAE measurement.

Figure 14 illustrates the 2ChDP spectrum for $\tau = 3$ ms in

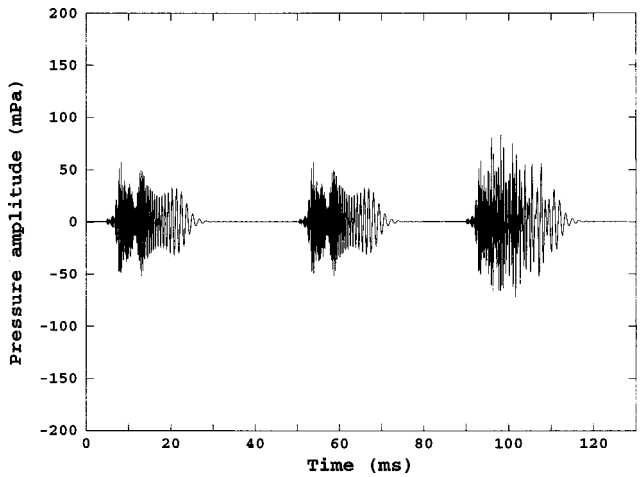

FIG. 12. This illustrates the raw ear 2ChDp waveforms, i.e., the set of chirp responses $p_1(t)$, $p_2(t)$, and $p_{12}(t)$ for the 2E stimulus sequence with $\tau = 3$ ms.

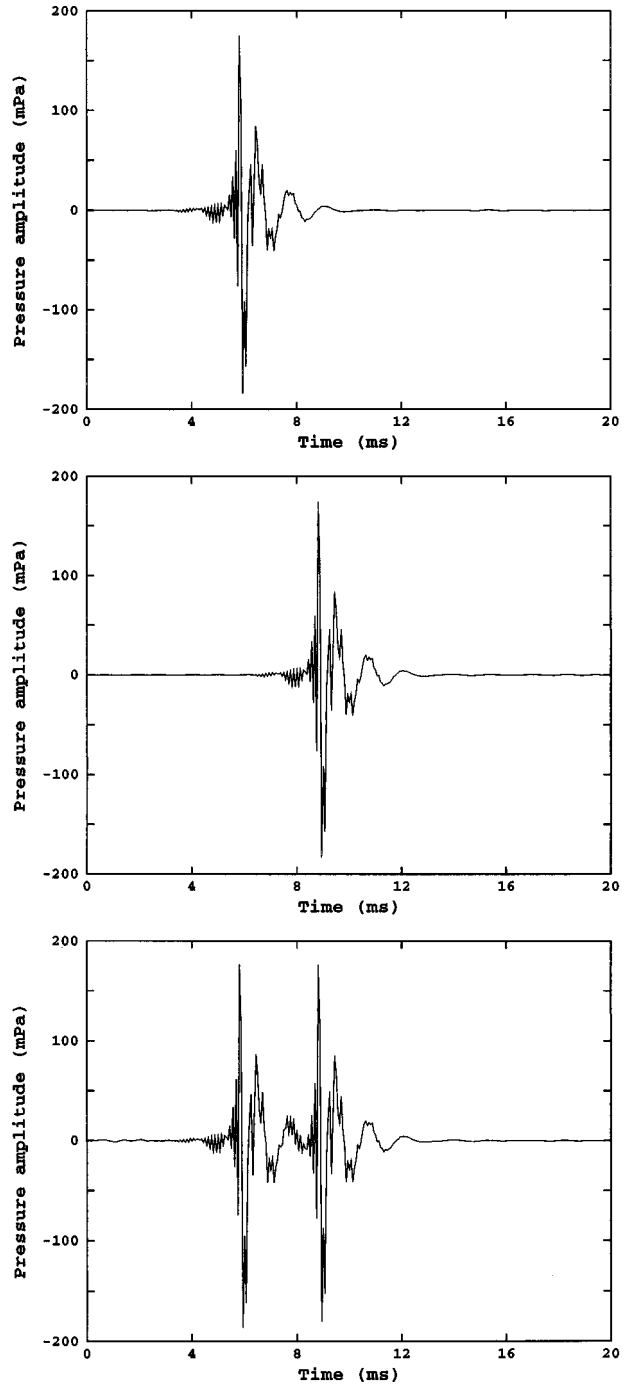

FIG. 13. These plots show the dechirped responses $d_1(t)$, $d_2(t)$, and $d_{12}(t)$ in the top, middle, and bottom panels, respectively, based on the chirp responses in the previous figure.

the frequency-domain representation, in conjunction with the spectrum of the ''$P_1(f)$ Response'' level to the presentation of $S_1(f)$ alone. There was no frequency averaging of these spectra. This delay corresponds to a frequency ratio $m = 2.92$, which is much larger than that ordinarily used in DPOAE measurements. The ear-canal pressure level was reduced near 4000 Hz due to the corresponding peak in the acoustic conductance G (not illustrated), but the absorbed power level in the ear, which is proportional to the sum of the SPL and 10 log G (Keefe *et al.*, 1993), was fairly constant and the emission level (i.e., the coherent distortion signal level in the figure) was not reduced at this frequency. The conductance in the average adult reaches a maximum near 4000 Hz, and maintaining constant SPL in the ear canal can thus inject greater amounts of power into the middle ear near 4000 Hz, which may lead to increased levels of evoked OAEs.

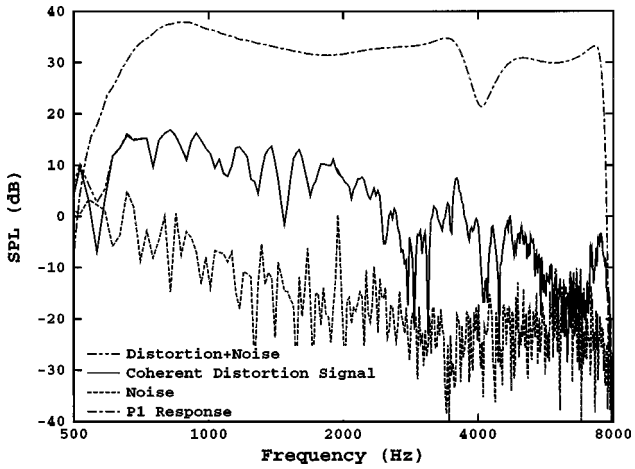

FIG. 14. This figure shows four spectral levels based on the 2ChDP response in the ear using the 2E stimulus set with $\tau = 3$ ms delay. The highest level spectrum is that of the $P_1(f)$ response to the original $S_1(f)$ stimulus (long–short line). The coherent distortion signal level (solid line), i.e., the 2ChDP, is essentially identical to the total distortion plus noise level (long-short-short line) except where the noise level (short-dashed line) is significant.

B. Double-source variant

The cavity measurements demonstrated the advantage of using the double-source variant of the 2E technique over the single-source variant by means of reducing the probe distortion. This suggested the use of the double-source variant of the 2E technique in measuring click-evoked OAE responses. The electrical signal to each DAC channel was of a form so that each acoustic source produced a short-duration acoustic click in a cylindrical tube with a diameter of 8.02 mm that was sufficiently long that the acoustic signal decayed before any reflected energy from the far end of the tube was received by the microphone. The sample rate was increased to 32 kHz for these measurements. Responses were obtained in two adults, and are presented for one of the adults.

The measured 2E response $p_D(t)$ is illustrated below for the click stimulus presented at a p_1 peak level of 90 dB SPL (Fig. 15). The time origin in this 2CEOAE waveform is arbitrary, and the time at which the peak value of the stimulus occurs is labeled on the figure. In contrast to other techniques to measure click-evoked otoacoustic emissions, there is no need to use time gating, and the early-latency portion of the 2EOAE shows large amounts of high-frequency oscillations. This onset would be even more clearly delineated if more averaging were used. These results suggest that the 2CEOAE response may be useful in studying the cochlear response to clicklike stimuli, by extending the high-frequency portion of the click-evoked OAE response.

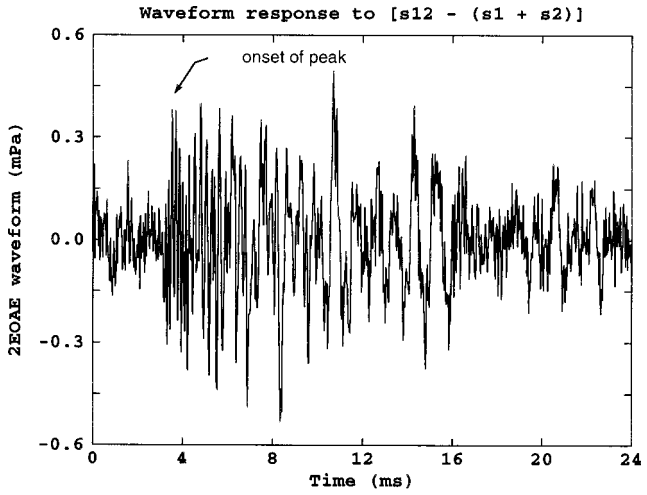

FIG. 15. 2CEOAE response waveform to double-source stimulus presentation.

V. CONCLUSIONS

Real-time intermittent-noise rejection may be effective in reducing the influence of intermittent noise, and thereby reducing total test time for a given nonlinear signal-to-noise ratio. Based on measurements in a 1-cm^3 cavity, the use of two acoustic sources in evoked OAE measurements reduces the measurement-system distortion by as much as 30 dB compared to a measurement using a single acoustic source. This makes possible the measurement of double-click-evoked, and double-click-evoked, OAEs without the use of time gating. This double-source variant of the 2CEOAE technique enables measurement of the early onset of the click-evoked OAE response, thus providing a more nearly complete representation of the cochlear reflected signal. The 2CEOAE and 2ChDP responses measured in the ear canal demonstrate the feasibility of these measurement techniques. The nonlinear coherence technique can be used to directly measure the distortion signal-to-noise ratio at the frequency at which the evoked OAE is measured, and can be used to extract an evoked OAE signal that is coherent with the stimulus.

The primary emphasis of this report was to demonstrate the feasibility of the 2E measurement methods in a small number of subjects, not to systematically compare the 2E techniques with existing evoked OAE techniques. Such a study will require a large subject population. That being said, the demonstration that the onset of a transient-evoked OAE response can be measured without the use of time gating has potentially broad significance for basic and clinical studies using evoked OAEs, because a more complete representation of the cochlear-reflected signal is obtained including the short-latency component dominated by the cochlear response at high frequencies. For example, one might compare the 2E OAE responses from a population of normal-hearing subjects with a population of subjects with a high-frequency hearing loss to test whether normal-hearing subjects have higher levels of 2E OAEs at high frequencies.

ACKNOWLEDGMENTS

Michael Gorga and Stephen Neely provided useful critiques of an earlier version of this report. This research was partially supported by NIH Grant No. P01 DC00520.

Bray, P. J. (**1989**). *Click Evoked Otoacoustic emissions and the Development of a Clinical Otoacoustic Hearing Test Instrument* (University of London, London, England).

Keefe, D. H. (**1996**). ''New evoked cochlear responses: Double chirp-evoked distortion products and double click-evoked otoacoustic emissions,'' J. Acoust. Soc. Am. **99**, S2562(A).

Keefe, D. H. (**1998**). ''Double-evoked otoacoustic emissions. I. Measurement theory and nonlinear coherence,'' J. Acoust. Soc. Am. **103**, 3489–3498.

Keefe, D. H. (**1997**). ''Nonlinear otoreflectance responses using double-evoked stimulus sets,'' in *Abstracts of the 20th Midwinter Research Meeting of the ARO* (Association for Research in Otolaryngology, Des Moines), S. 166.

Keefe, D. H., Bulen, J. C., Arehart, K. H., and Burns, E. M. (**1993**). ''Ear-canal impedance and reflection coefficient in human infants and adults,'' J. Acoust. Soc. Am. **94**, 2617–2638.

Kemp, D. T., Bray, P., Alexander, L., and Brown, A. M. (**1986**). ''Acoustic emission cochleography—Practical aspects,'' Scand. Audiol. Suppl. **25**, 71–95.

Neely, S. (**1997**). personal communication.

Neely, S., and Liu, Z. (**1993**). ''EMAV: Otoacoustic Emission Averager,'' Boys Town National Research Hospital.

Dichotic pitches as illusions of binaural unmasking. I. Huggins' pitch and the "binaural edge pitch"

John F. Culling,[a] A. Quentin Summerfield, and David H. Marshall
MRC Institute of Hearing Research, University of Nottingham, University Park, Nottingham NG7 2RD, United Kingdom

(Received 21 February 1996; revised 2 March 1998; accepted 4 March 1998)

The two most salient dichotic pitches, the Huggins pitch (HP) and the binaural edge pitch (BEP), are produced by applying interaural phase transitions of 360 and 180 degrees, respectively, to a broadband noise. This paper examines accounts of these pitches, concentrating on a ''central activity pattern'' (CAP) model and a ''modified equalization-cancellation'' (mE-C) model. The CAP model proposes that a dichotic pitch is heard at frequency f when an individual across-frequency scan in an interaural cross-correlation matrix contains a sharp peak at f. The mE-C model proposes that a dichotic pitch is heard when a plot of interaural decorrelation against frequency contains a peak at f. The predictions of the models diverge for the BEP at very narrow transition bandwidths: the mE-C model predicts that salience is sustained, while the CAP model predicts that salience declines and that the dominant percept is of the in-phase segment of the noise. Experiment 1 showed that the salience of the BEP was sustained at the narrowest bandwidths that could be generated (0.5% of the transition frequency). Experiment 2 confirmed that the pitch of a BEP produced by a 0.5% transition bandwidth was close to the frequency of the transition band. Experiment 3 showed that pairs of simultaneous narrow 180-degree transitions, whose frequencies corresponded to vowel formants, were perceived as the intended vowels. Moreover, the same vowels were perceived whether the in-phase portion of the noise lay between the two transition frequencies or on either side of them. In contrast, different patterns of identification responses were made to *diotic* band-pass and band-stop noises whose cutoff frequencies corresponded to the same formants. Thus, the vowel-identification responses made to the dichotic stimuli were not based on hearing the in-phase portions of the noise as formants. These results are not predicted by the CAP model but are consistent with the mE-C model. It is argued that the mE-C model provides a more coherent and parsimonious account of many aspects of the HP and the BEP than do alternative models. [S0001-4966(98)05906-2]

PACS numbers: 43.66.Ba, 43.66.Dc, 43.66.Pn [RHD]

INTRODUCTION

Dichotic pitches arise through processes of binaural interaction when broadband noises are presented to the two ears (i.e., the pitches cannot be heard monaurally). The present investigations of these phenomena were motivated by the observation that the dominant account of these pitches, the CAP model (Bilsen, 1977), invokes a process similar to ''across-frequency grouping by common interaural time delay (ITD).'' This is a putative process in which energy in different frequency regions originating from the same source would be grouped together by virtue of possessing the same ITD. However, several recent experiments (Culling and Summerfield, 1995; Hukin and Darwin, 1995; Darwin and Hukin, 1997) have cast doubt on the idea that auditory analysis includes the capacity to group energy in this way. Culling and Summerfield proposed instead that each frequency channel in the binaural system operates independently when recovering signals from noise. They embodied this concept in a multi-channel model of binaural unmasking (the mE-C model). This model makes acceptably accurate predictions of the clarity and frequency of dichotic pitches. In the course of the present investigations, it also emerged that, despite its intuitive appeal, the CAP model has some previously unreported shortcomings. Consequently, this article and its companion (Culling *et al.*, 1998) have two objectives. The first is to demonstrate that the CAP model, employing an across-frequency process, does not predict dichotic pitches correctly. The second is to show that the mE-C model, without such a process, can explain them well.

Four dichotic pitches have been described:[1] the Huggins pitch (Cramer and Huggins, 1958), the binaural edge pitch (Klein and Hartmann, 1981), the Fourcin pitch (Fourcin, 1970), and the dichotic repetition pitch (Bilsen and Goldstein, 1974). These four phenomena fall into two classes, which differ in their method of generation. The Fourcin pitch (FP) and the dichotic repetition pitch (DRP) are generated by applying large interaural delays (>1 ms) to broadband noise. To generate the FP, two independent noises are presented simultaneously and binaurally. The two noises have different interaural delays. If an interaural phase shift of 180 degrees is given to one of the noises, the period of the perceived pitch frequency is equal to the difference between the two interaural delays (Fourcin, 1970; Bilsen and Goldstein, 1974; Bilsen, 1977). Without the interaural phase shift, the

[a]New address: University Laboratory of Physiology, Parks Road, Oxford OX1 3PT, United Kingdom.

overall pitch is ambiguous (Bilsen, 1977). To generate the DRP, a single noise is presented binaurally with a large interaural delay (2–20 ms). The period of the perceived pitch frequency corresponds to the interaural delay (Bilsen and Goldstein, 1974). Although there are similarities between the stimuli which give rise to these two pitches, the FP is much more salient perceptually than the DRP. A companion paper (Culling *et al.*, 1998) compares explanations for the FP and the DRP. It argues that the FP is produced by the same mechanism that underpins the Huggins pitch and the binaural edge pitch, while the DRP is produced by a different mechanism.

The Huggins pitch (HP) and the binaural edge pitch (BEP) are generated by producing an interaural phase transition at a particular frequency within a broadband noise. For the HP, the noise is identical at the two ears below the transition frequency. At the transition frequency, the interaural phase relationship changes sharply with increasing frequency, shifting through 360 degrees over a narrow bandwidth (e.g., 6% of the transition frequency). Above the transition band, the noise is identical at the two ears. For the BEP, a similar transition occurs, but over a range of only 180 degrees, so that the noise is out-of-phase between the ears above the transition frequency and in-phase below, or *vice versa*. HP and BEP stimuli both evoke the perception of a pure-tone-like pitch, corresponding approximately to the transition frequency, which can be heard against the background of the noise (Guttman, 1962; Klein and Hartmann, 1981; Frijns *et al.*, 1986). The more salient percept is provided by the HP, but the BEP is also clearly audible by naive listeners. Most listeners hear the HP lateralized to one side or the other. Some listeners also hear the BEP lateralized away from the mid-line.

I. MODELING HP AND BEP

A. The central activity pattern (CAP) model

The central activity pattern (CAP) (Bilsen, 1977; Raatgever and Bilsen, 1986; Frijns *et al.*, 1986) is similar to an interaural cross-correlation matrix[2] of the kind proposed by Jeffress (1948, 1972) to account for the lateralization of sound sources. The CAP is a matrix which displays a map of interaural correlation by frequency and interaural delay. To explain the HP, Raatgever and Bilsen (1986) suggested that the matrix might be scanned across frequency at a chosen internal delay to produce a ''central spectrum,'' whose structure would determine the pitch and timbre of the perceived sound. The CAP model does not include an explicit mechanism for choosing which of the many possible across-frequency scans is selected. Rather, Raatgever and Bilsen (1986) suggested that the mechanism ''recognises and selects the frequency spectrum information by making use of cues like harmonicity and depth of modulation or *a priori* knowledge of spectral features'' (p. 431). Despite the lack of an explicit selection mechanism, there is intuitive appeal in the idea that attention can be directed selectively to an individual across-frequency scan, since in real listening situations one would expect such scans to display the spectra of sound sources which lie on different azimuths. The CAP model adheres to this principle rigorously: dichotic pitches are explained by features found in the spectrum of a single scan; evidence from several scans is not combined.

Raatgever and Bilsen illustrated the workings of the CAP model with a computational procedure in which the interaural phase relationship at each frequency was used to generate a pattern of activity which was a sinusoidal function of internal delay [Raatgever and Bilsen, 1986, Eq. (6)]. We refer to their formulation as the ''original'' version of the CAP model. The sinusoidal functions were accepted as an approximation to the corresponding cross-correlation functions. In fact, they are equivalent to cross-correlation functions produced with infinitely long time windows and infinitely narrow frequency channels. The following paragraphs demonstrate that these assumptions materially affect the predictions of the CAP model.

Figure 1(a) and (c) shows CAPs generated by the original version of the model.[3] Figure 1(a) illustrates the CAP of a HP stimulus with the transition frequency at 600 Hz and a transition bandwidth of 6%.[4] The model produces peaks at the transition frequency in some across-frequency scans. For example, the inset illustrates such a peak in the scan taken at an interaural delay of 0.83 ms. Similar peaks can also occur in across-frequency scans of BEP stimuli. Figure 1(c) shows the CAP of a BEP stimulus with the transition frequency at 600 Hz and a transition bandwidth of 6%. The inset contains the across-frequency scan taken at an interaural delay of 1.25 ms. In discussing the BEP, Frijns *et al.* (1986) drew attention to the sharp peak at 600 Hz which is found in this scan.

A difficulty in relating the predictions of the original version of the CAP model to the performance of listeners is that the model assumes unrealistically high values for the frequency resolution of the auditory system. Figure 1(b) and (d) shows the results of convolving the CAPs of Fig. 1(a) and (c) across frequency with a rounded-exponential-shaped moving-average filter which increases in bandwidth with frequency in accordance with estimates of the bandwidth of auditory filters [Moore and Glasberg, 1983, Eq. (3)]. Such an integration across frequency in order to obtain more realistic patterns was suggested, but not performed, by Raatgever and Bilsen (1986). We refer to the formulation of the CAP model that incorporates this smoothing filter as the ''smoothed'' version. After smoothing, the peaks in across-frequency scans are very much less apparent, but, in this example, remain visible.

An important prediction of the CAP model is that the strength of the BEP, like that of the HP, should be reduced or eliminated when stimuli have very narrow transition bandwidths. This prediction is tested in experiment 1. To illustrate the prediction, Fig. 2 shows scans generated by the original (dotted lines) and smoothed (solid lines) versions of the model for HP and BEP stimuli with transitions at 600 Hz. The scans were taken at a delay of 0.83 ms for the HP and 1.25 ms for the BEP (similar to the insets of Fig. 1). Scans have been plotted for transition bandwidths, w, which are 0.5%, 1%, 8%, and 64% of the transition frequency. In the limit, as w is reduced, the transition band of the HP becomes infinitesimally small and so the stimulus becomes a diotic noise. In practice, the limit is reached when w is less than or

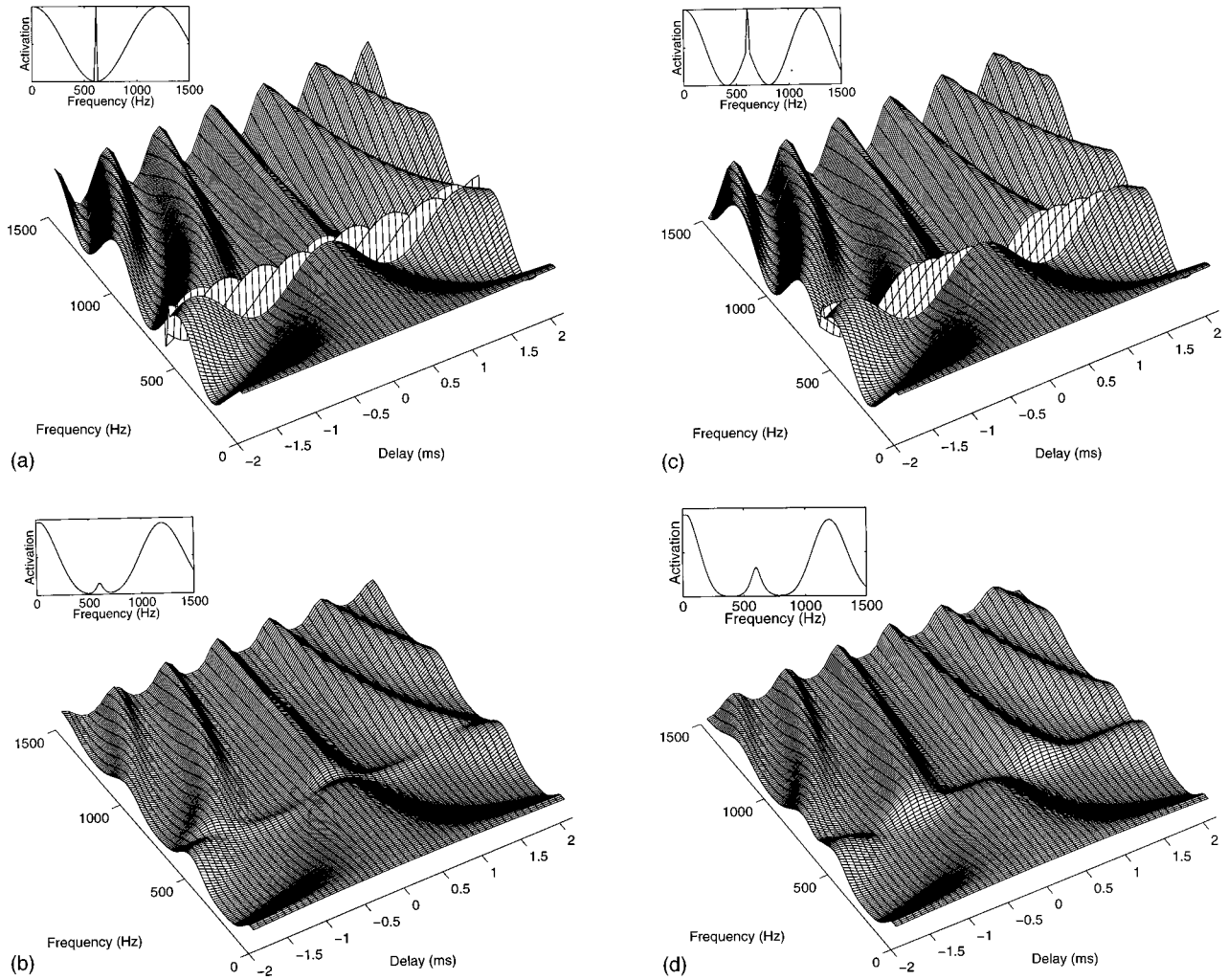

FIG. 1. The effect of the assumptions made by Raatgever and Bilsen [1986, Eq. (6)] in predicting the HP and BEP: (a) ''original'' CAP for a HP, produced from Eq. (6) of Raatgever and Bilsen (1986); (b) ''smoothed'' CAP produced by convolving the original CAP in panel (a) with a rounded-exponential-shaped, moving-average filter whose bandwidth varied with frequency according to Moore and Glasberg [1983, Eq. (3)]; (c) original CAP for a BEP; (d) smoothed CAP for the original CAP in panel (c). The insets show across-frequency scans taken at optimal internal delays for detecting peaks at the transition frequencies (0.83 ms for HP and 1.25 ms for BEP).

equal to the frequency spacing between adjacent bins in the Fourier spectrum of the stimulus. For the stimuli used to create Fig. 2, the limit is reached when w is 0.5%. For this value of w the transition bandwidth for the HP stimulus is effectively 0%. Such a limit does not exist for the BEP.

For $w=1\%$ and $w=8\%$, the scans produced by the original version of the model (dotted lines) contain spectral peaks at the 600-Hz transition frequency which are characterized by high amplitude and narrow bandwidths. According to the CAP model, these ''sharp peaks'' are responsible for the perception of the dichotic pitch. The sharp peaks are produced by the changing phase within the transition band. This phase shift compensates for the internal delay at just one frequency within the band, to produce maximal cross correlation at that frequency. Since the phase changes so abruptly with frequency, the same effect does not occur at closely adjacent frequencies, where the idealized cross correlation is consequently much lower. It is a necessary requirement of the model that peaks with broader bandwidths, such as those which occur at 1200 Hz in the panels of Fig. 2, are *not* treated as candidate pitches. Consistent with this view, when $w=64\%$ (bottom panel in each column), where the stimuli no longer give rise to tonal pitches (Cramer and Huggins, 1958), the peaks at the 600-Hz transition frequency are broader than when $w=8\%$.

In contrast to the scans produced by the original version of the model, the scans produced by the smoothed version include peaks at the transition frequency which reduce in height and width as the transition bandwidth is reduced from 8%, through 1%, to 0.5% for both the HP and BEP. Since a higher, narrower peak occurs for $w=8\%$ than for $w=0.5\%$, $w=1\%$, or $w=64\%$, the smoothed version of the model predicts that both the HP *and* the BEP should be heard most clearly at intermediate values of w. In particular, it should be harder to hear the BEP when w equals 0.5% or 1% than when w equals 8%.

In discussing the BEP, Frijns *et al.* (1986) distinguished the tonal quality of the dichotic pitch from the percept of a low-pass or high-pass noise which may also be heard, depending on whether the in-phase portion of the noise is below or above the transition frequency. The CAP account predicts that these percepts will determine the pattern of

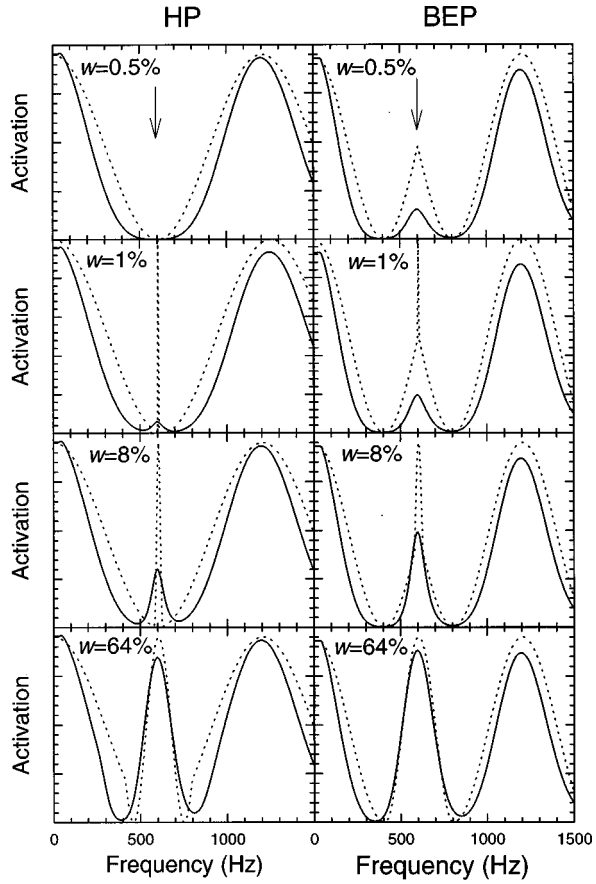

FIG. 2. Across-frequency scans from central activity patterns. The dotted lines are scans derived from the original CAP model of Raatgever and Bilsen [1986, Eq. (6)]. The solid lines are the same scans spectrally smoothed by a rounded-exponential-shaped, moving-average filter with bandwidth varying according to Moore and Glasberg [1983, Eq. (3)]. In different panels the patterns for the HP and BEP have nominal transition bandwidths, w, of 0.5%, 1%, 8%, and 64%. The vertical arrows indicate the frequency of the perceived pitch of 600 Hz. The scans are taken at internal delays which are optimal for detecting peaks at the appropriate frequencies (0.83 ms for HP and 1.25 ms for BEP). (Note that the effective bandwidth is 0% when w is set to 0.5% for the HP stimulus.)

listeners' responses when dichotic pitches cannot be heard. This prediction is tested in experiments 2 and 3.

B. The augmented equalization-cancellation (aE-C) model

Durlach (1962) pointed out that the HP can be explained by the equalization cancellation (E-C) model of binaural masking release (Durlach, 1960, 1972). In this model, the signals from each ear are equalized by any or all of a specified set of transformations (including changes in interaural delay, phase, and level), and are then cancelled by addition or subtraction. The E-C model was originally developed to account for the detection of tones in noise, and so did not include separate operations within different frequency channels. In line with this formulation of E-C, Klein and Hartmann (1981) also applied transformations to the whole signal when accounting for HP. In this case, the E-C process is particularly simple. Since the waveforms at the two ears are largely identical, they can be cancelled over most of the frequency range by subtraction without any prior equalization process, leaving a narrow band of noise centered on the transition frequency which would be heard as a warbling tone.

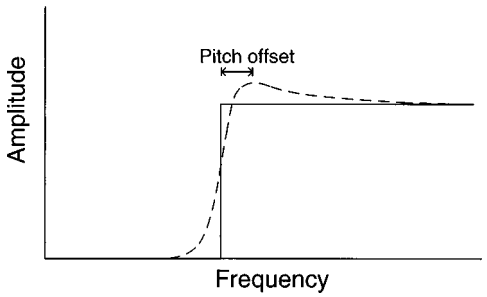

FIG. 3. Schematic illustration of the effect of lateral inhibition on the internal representation of a high-pass noise. The stimulus spectrum (after broadband interaural cancellation for a BEP) is represented by the solid line. The perceived spectrum, following lateral inhibition, is represented by the dashed line.

In the case of the BEP, broadband E-C gives rise to a low-pass or high-pass noise which would not directly be heard as a tone. When Klein and Hartmann (1981) discovered the BEP, they suggested that listeners do indeed hear a high-pass or low-pass noise, but that a process of central lateral inhibition enhances the edge of the noise, giving rise to the perceived tone (Fig. 3). Another process of lateral inhibition may be responsible for a different pitch sensation, called the ''edge pitch'', which arises monaurally when a high-pass or low-pass noise is presented (Small and Daniloff, 1967; Fastl, 1971; Fastl and Stoll, 1979; Klein and Hartmann, 1981). Consequently, Klein and Hartmann termed their phenomenon the ''binaural edge pitch'' or BEP.

Klein and Hartmann collected pitch-matching data to support their analogy between the BEP and the monaural edge pitch. Listeners were required to match monaural and binaural edge pitches to pure tones. The resulting matches were offset from the frequency of the cutoff or phase transition by a frequency difference of 3%–8%. Figure 3 shows schematically how lateral inhibition would give rise to such an offset. In the case of the monaural edge-pitch, Klein and Hartmann found that pitch matches were consistently offset into the noise, whereas for BEP stimuli, matches were offset to both higher and lower frequencies, giving rise to a bimodal distribution of matches. It was possible to account for the bimodal distribution by invoking a feature of the E-C model which states that cancellation can occur either by adding or by subtracting the waveforms at the two ears. If addition is performed, a BEP stimulus which is in-phase below the transition frequency would give rise to a low-pass residue, while if subtraction is performed, the same stimulus would produce a high-pass residue. So, depending on which cancellation operation is applied, the binaural edge pitch can be offset in either direction, compatible with the observed bimodal distribution. Thus, Klein and Hartmann concluded that a process of broadband E-C could explain the HP, and that broadband E-C augmented by lateral inhibition on the residue could explain the BEP. We refer to the latter account as the ''augmented equalization-cancellation model'' (aE-C).

Other results have not supported these conclusions consistently. Frijns *et al.* (1986) repeated Klein and Hartmann's pitch-matching experiments for the BEP and found that lis-

teners matched the dichotic pitch close to the transition frequency. The distribution of matches had a standard deviation of 1.5% with no evidence of a bimodal distribution of matches, thereby undermining one of the predictions of the aE-C model. Hartmann (1984a) sought to measure the lateral inhibition directly using the pulsation threshold method (Houtgast, 1972), but found no evidence for it. These two results imply that lateral inhibition does not underlie the BEP. However, Hartmann (1984b) has described a further dichotic pitch whose existence is difficult to explain without invoking central lateral inhibition. The binaural coherence edge pitch (BICEP) occurs when noise below a specified transition frequency is uncorrelated (i.e., statistically independent) at the two ears, while above that frequency it is correlated. A pitch is heard which corresponds to the transition frequency. The aE-C model can easily account for the BICEP. Interaural cancellation by subtraction leaves a low-pass residue. Lateral inhibition at the high-frequency edge of the residue generates the pitch. In summary, therefore, the balance of current evidence favors the existence of central lateral inhibition, but is equivocal about its role in the BEP.

This uncertainty motivates the exploration of alternative bases for the BEP. The aE-C model invokes central lateral inhibition to explain the BEP because it incorporates broadband E-C which does not itself generate a dichotic pitch. In the next section we consider a modified form of the E-C which can account for the BEP directly, without requiring central lateral inhibition as an additional process.

C. The modified equalization-cancellation (mE-C) model

A third account of the HP and BEP is provided by a modified version of the E-C model (mE-C) which was designed to account for the binaural masking release of broadband sounds, such as speech (Culling and Summerfield, 1995). Since no tone is physically present in the stimuli, the perception of the HP and BEP is, according to the mE-C model, an illusion of binaural unmasking. In this model, auditory frequency analysis is simulated by analyzing the waveforms presented to each ear with a gamma-tone filterbank (Patterson *et al.*, 1987, 1988). Mechanical to neural transduction in each of the resulting frequency channels is simulated with a model of hair cell transduction (Meddis, 1986, 1988). The time-varying excitation in corresponding frequency channels (f_L and f_R) from each ear is equalized in two steps. First, the rms levels are equated. Second, the internal delay is sought at which the residue, R, after subtraction (i.e., cancellation) of the excitation from each ear is minimized. Thus, the residue within a channel is a function of internal delay, τ, which is evaluated for $-5\ \text{ms} < \tau < 5\ \text{ms}$. The residue is weighted according to an exponentially tapering temporal window with a time constant, T, of 50 ms [Eq. (1)]:

$$R(\tau) = \int_0^{3T} (f_L(t) - f_R(t+\tau)) e^{-t/T}\, dt. \qquad (1)$$

The process is repeated in each frequency channel independently (i.e., permitting different adjustments of rms level and τ). The minimum residue in each channel is taken as a measure of the strength of the signal in that channel. Effectively, the model detects the degree of interaural decorrelation present in each channel, since excitation which correlates at internal delays within the range ± 5 ms cancels, while uncorrelated noise does not. Signals which have a different interaural phase from the masking noise are detected because they disrupt the interaural correlation of the noise. In this respect the model is similar to Colburn's model of binaural unmasking (Colburn, 1973, 1977). A key feature of the mE-C model is that it performs equalization and cancellation in each frequency channel *independently*.[5]

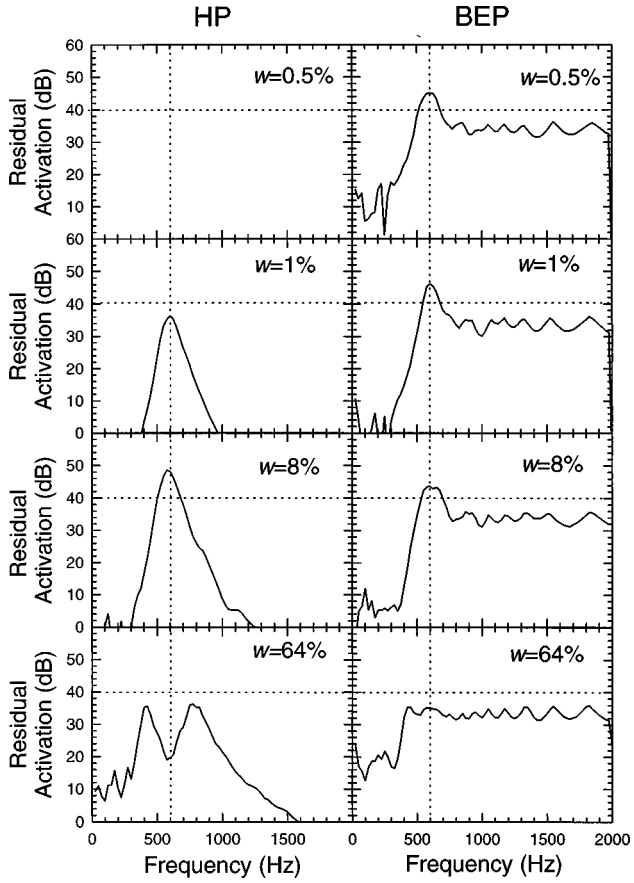

FIG. 4. The spectra recovered by the mE-C model of Culling and Summerfield (1995) for the HP and BEP for transition bandwidths, w, of 0.5%, 1%, 8%, and 64%. The vertical arrows indicate the frequency of the perceived pitch of 600 Hz. The dotted horizontal line defines an arbitrary threshold, which could predict whether or not the peaks were audible. (Note that the effective bandwidth is 0% when w is set to 0.5% for the HP stimulus.)

Figure 4 contains residual-activation spectra generated by the mE-C model for the same HP and BEP stimuli as were analysed by the CAP model in Fig. 2. In each panel, the stimulus contains an interaural phase transition at 600 Hz. For the HP, the prediction is straightforward and similar to that described in Sec. I B. The noise is in-phase both above and below the transition frequency and consequently cancels almost completely at zero internal delay. Close to the transition, however, noise with different interaural phases enters the same frequency channel and consequently cannot be cancelled completely at any internal delay, resulting in the peak in the residual-activation spectrum recovered by the model. For the BEP, the prediction is less obvious. On one side of

the transition (below 600 Hz in Fig. 4), the noise is in-phase, but on the other side it is 180 degrees out-of-phase. The in-phase noise is completely cancelled, leaving no residual activation below the transition frequency. The noise which is 180 degrees out-of-phase is partly cancelled because each channel admits only a narrow band of frequencies; a phase difference of 180 degrees at each of these frequencies is approximately equivalent to an internal delay of half the period of the center frequency of the channel. Channels close to the transition frequency itself, however, admit energy with a range of widely differing interaural delays which cannot be canceled, leaving a peak in the residual-activation spectrum. When $w \leqslant 8\%$, the peak is about 10 dB higher than the residual activation in the higher frequency channels which receive out-of-phase noise. According to the mE-C model, it is this peak which gives rise to the perception of the BEP.

In order to show how the model might predict the detection of the HP and BEP for different transition bandwidths, a dotted horizontal line has been drawn (arbitrarily) at 40 dB. If this level of residual activation were required for listeners to detect spectral features in residual-activation spectra relative to internal noise (whose effects are not simulated in the mE-C model), then the model would predict that listeners should hear the HP for a transition bandwidth of 8%, but not for 0.5%, 1%, or 64%, and that they should hear the BEP for 0.5%, 1%, and 8%, but not for a 64% transition bandwidth.[6] Thus, the mE-C model diverges from the CAP model in predicting that BEP should be heard strongly in stimuli containing very narrow transition bandwidths.

D. Empirical questions

The following experiments investigated the perceptual properties of the BEP and HP. The results are used to compare the predictions of the CAP, aE-C, and mE-C models. Experiment 1 shows that BEPs produced by narrow interaural phase transitions ($\leqslant 0.5\%$ of the transition frequency) are as perceptually prominent as BEPs produced by wider transitions. Experiment 2 confirms that the pitch evoked by BEP stimuli containing narrow transitions is matched to that of a pure tone at the transition frequency. Experiment 3 shows that two BEPs generated by narrow phase transitions at the formant frequencies of a vowel can be used in combination to evoke the perception of that vowel. These results are difficult for the aE-C model and the CAP model to explain, but receive a straightforward explanation from the mE-C model.

II. EXPERIMENT 1

Cramer and Huggins (1958) measured the ability of listeners to detect the HP as a function of the bandwidth of the interaural phase transition. Because of technical limitations, the narrowest bandwidth which they could explore was 3% of the transition frequency. They found that listeners could detect the HP reliably for transitions of 3% and 6%, but that the pitch was harder to detect when broader transitions were employed. Van Tilburg (1974) reported that the ease of detection of the HP also declines for transitions narrower than 3%. The present experiment extends these investigations by including both the HP and the BEP, each generated with a wide range of transition bandwidths.

A. Stimuli

The stimuli were triplets of 409.6-ms noises containing interaural phase transitions at three different frequencies. They were generated digitally with 16-bit amplitude quantization and a 10-kHz sampling rate and filtered in the frequency domain. To make each stimulus, three white noises of 409.6-ms duration were synthesized using the method recommended by Klatt (1980) in which 16 consecutive numbers from a pseudorandom number generator are summed to form each output sample. These noises were low-pass filtered at 2 kHz. A copy of each noise was further filtered in order to produce a linear phase transition between specified frequencies. The copy was combined with the original to form a stereo file containing an interaural phase transition. The three noises making each triplet contained transitions centered on 500, 600, and 700 Hz. In the case of the BEP, only stimuli which were in-phase below the transition frequency were generated. Each resulting sound file was shaped with 10-ms raised-cosine onset and offset ramps. Finally, the stereo sound files were concatenated to form an ascending sequence of dichotic pitches. This method was repeated to create ten stimuli based on different samples of noise in each of the following conditions. Each of the two dichotic pitches (HP and BEP) was created with eight transition bandwidths, which were 0.5%, 1%, 2%, 4%, 8%, 16%, 32%, and 64% of the transition frequency, giving 16 conditions and 160 stimuli in all. The smallest transition bandwidth, nominally 0.5%, was a single bin in the Fourier transform (2.4 Hz) for all transition frequencies. In the case of the HP, a transition from 0 to 360 degrees in a single bin is equivalent to no transition at all, so the ''0.5%'' members of the HP stimulus set were simply diotic noises. Results from these stimuli are therefore plotted at 0% in Fig. 5 but shall be refered to in the text as ''0.5%'' to preserve the symmetry of the experimental design. In addition to these stimuli, ten further diotic noises were created to form a control condition.

The digital stimuli were converted to analog using a Loughborough Sound Images delta-sigma digital-to-analog converter and presented to listeners via Sennheiser HD414 headphones in a double-walled sound attenuating chamber at 66 dB(A). Stimulus levels were measured with a B&K artificial ear type 4153, with a flat-plate adapter type DB0843, a half-inch microphone type 4134, and a sound-level meter type 2235 on its ''fast'' setting.

B. Procedure

Four listeners, including the first author, who had normal hearing at audiometric frequencies from 0.25–8 kHz inclusive and who had participated in previous psychoacoustic experiments, attended one 40-min session. The session was broken into four 10-min runs in which the 160 experimental stimuli were each presented once and the ten control stimuli were each presented eight times. The random stimulus ordering was changed for each run. Listeners were required to

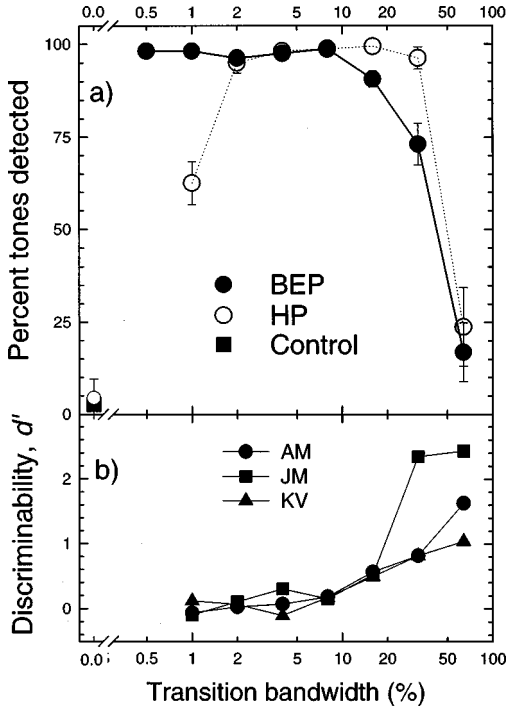

FIG. 5. Upper panel: The percentage of BEPs and HPs detected by four listeners in experiment 1 as a function of the transition bandwidth, which is expressed as a percentage of the transition frequency. Error bars mark ± 1 standard error of the mean. Note that the effective bandwidth was 0% when w was set to 0.5% for the HP stimuli, and so is plotted at 0%. Lower panel: Values of the discrimination index, d', for three listeners who attempted to discriminate the tonal prominence of BEPs with transition bandwidths of 0.5% from BEPs with the larger transition bandwidths plotted on the abscissa.

report whether or not they heard a sequence of ascending tones in the noise via a single key-press on the keyboard of a VDU. No feedback was given.

C. Results

Figure 5(a) shows the percentage of trials on which the tone sequence was detected as a function of the transition bandwidth, with data averaged over listeners. The HP was detected on nearly 100% of trials when the transition bandwidth ranged from 4% to 32% of the transition frequency. The corresponding range for the BEP was 0.5% to 8%. In accordance with van Tilberg's (1974) observations, the proportion of trials on which the HP was detected declined as the transition bandwidth of the HP was reduced. For the widest transition bandwidths, detection declined for both pitches in the way originally observed by Cramer and Huggins (1958) for the HP, although the BEP was detected less frequently than the HP for $w=32\%$.

The control stimuli (diotic noises) yielded an overall false-alarm rate of 3%. Compared to this rate, all other conditions (save the HP with $w=0.5\%$, which was also diotic noise) showed significantly higher detection rates [binomial probability, 160 trials and $p(\text{hit})=0.03$, $p<10^{-6}$ for all conditions with data pooled across listeners].

A two-way analysis of variance covering type of dichotic pitch (BEP versus HP) and transition bandwidth (0.5%, 1%, 2%, 4%, 8%, 16%, 32%, and 64%) showed significant main effects of pitch type [$F(3,1)=76.49$, $p<0.005$] and transition bandwidth [$F(3,7)=70.93$, $p<0.0001$] and a significant interaction between the two [$F(7,21)=125.66$, $p<0.0001$]. Tukey pairwise comparisons indicated that the interaction was produced by differences between detection rates for the BEP and HP at transition bandwidths of 0.5%, 1%, and 32% ($q=35.94$, 13.66, and 8.87, respectively, $p<0.01$). Comparisons among the different transition-bandwidth subconditions of the BEP condition showed that there were no significant differences among bandwidths of 0.5%, 1%, 2%, 4%, 8%, and 16%. For the HP condition, those among the 2%, 4%, 8%, 16%, and 32% subconditions did not differ significantly from one another. All other comparisons (bar 0.5% versus 64% in the HP condition) differed significantly ($p<0.05$).

D. Discussion

Experiment 1 shows that listeners can reliably detect BEP's which are produced by interaural transitions with very narrow bandwidths (0.5%, 1%, and 2% of the transition frequency). This result is consistent with the predictions of the aE-C and mE-C models. The aE-C model requires only that there should be a transition in interaural phase from in-phase to out-of-phase for a dichotic pitch to be heard. Such a transition will form an edge after broadband interaural cancellation; the perceived pitch is predicted by assuming lateral inhibition (Fig. 3). The mE-C model requires only that a frequency channel centered on the transition frequency should contain widely differing interaural phases for a peak to appear at the transition frequency in the residual activation spectrum (Fig. 4). The result is problematic, however, for the account of the BEP offered by the CAP model. As illustrated in Fig. 1(d) and in Fig. 2, the CAP model requires a progressive change in interaural phase across frequency to produce a sharp peak within the transition band. As the transition band narrows, so must the sharp peak. In the limit, the sharp peak disappears (Fig. 2), yet experiment 1 shows that, although the HP declines in this way, the salience of the BEP remains high even at the smallest transition bandwidths.

In order to underline this point, a supplementary experiment was conducted on a separate group of three listeners. These listeners were naive to the purposes of the experiment. In a two-interval forced-choice procedure, they were required to discriminate the loudness/salience of the pitches evoked by pairs of BEP stimuli with different transition bandwidths. On each trial, one stimulus had a transition bandwidth of 0.5%, while the other stimulus had one of the wider transition bandwidths (1%–64%). Listeners indicated which interval contained the stimulus with the clearer or louder pitch. The resulting values of the discriminability index, d', are plotted in Fig. 5(b). None of the listeners were able to discriminate stimuli with bandwidths in the range 1%–8% from stimuli with a bandwidth of 0.5% ($-0.2<d'<0.2$). Thus, BEP stimuli with transition bandwidths ranging from 0.5% to 8% cannot be distinguished from one another on the basis of the strength of the pitch percept. Bandwidths of 16%, 32%, and 64% gave progressively more positive values of d' which, according to the marking scheme employed, indicates that the resulting BEPs were

less salient than those produced by smaller transition bandwidths. Negative d' values, indicating that the 0.5% bandwidth was less salient than the comparison stimulus, were not observed consistently in any condition, showing that there is no perceptible loss of salience for the BEP as transition bandwidth is reduced.

A legitimate criticism of the main part of experiment 1 is that it provides no guarantee that listeners actually heard BEPs, only that they could distinguish stimuli containing a 180-degree interaural phase transition from a diotic noise. Listeners might have made the distinction by noting that the lateralization of BEP stimuli is relatively diffuse, because the noise is out-of-phase above the transition frequency, whereas the lateralization of diotic noise is compact. There are, nonetheless, two reasons for believing that listeners' detection responses were based on hearing dichotic pitches: (1) without feedback, listeners other than the first author had no guidance in their use of alternative cues; (2) for the broader transition bandwidths, which produced equally diffuse localization but a less salient dichotic pitch, detection rates dropped substantially. Nonetheless, it is important to demonstrate that listeners do hear tones of an appropriate frequency when they listen to BEP stimuli synthesized with very narrow transition bandwidths. This was the primary aim of experiment 2.

III. EXPERIMENT 2

In experiment 2, listeners compared the pitches evoked by a range of BEP and HP stimuli with different transition frequencies against that of a single pure tone. If the pitch of a BEP or HP stimulus with transition frequency f is equivalent to that of a pure tone of frequency f, then listeners should judge stimuli with higher transition frequencies to have a higher pitch than the tone, and those with lower transition frequencies to have a lower pitch. If listeners respond in this way to BEP stimuli with very narrow interaural transition bandwidths, and without feedback, it indicates that, contrary to the predictions of the CAP model, a gradual phase transition is not necessary to evoke a pitch which corresponds closely to the transition frequency. Rather, it suggests that listeners detect a narrow band of binaural excitation at the transition frequency, as predicted by the mE-C model. Thus the primary focus of experiment 2 was on the perception of BEP stimuli. The HP stimuli were included for purposes of comparison.

A. Stimuli

The stimuli were generated, presented, and calibrated in a similar manner to those of experiment 1. The HP stimuli had a fixed transition bandwidth of 6% of the transition frequency. The BEP stimuli had transition bandwidths of $\approx$0.4% (a single bin). In separate conditions, the BEP stimuli were prepared with in-phase noise either above (BEPa) or below (BEPb) the transition frequency. Figure 4 shows recovered spectra only for BEPb stimuli. The positions of spectral peaks produced by the mE-C model are determined by the CFs of interaural phase transitions, since the CFs determine the maximally decorrelated parts of the spectrum. Hence, recovered spectra for BEPa stimuli are similar to those plotted in Fig. 4, but contain residual activation below the peak, rather than above it. (Spectra for both orientations of the transition are illustrated in Fig. 7 for the stimuli of Experiment 3.) The transition frequencies of the different stimuli were distributed around 600 Hz, the frequency which Bilsen (1977) and Raatgever and Bilsen (1986) reported to produce the most potent dichotic pitches. The transition frequencies were mistuned from 600 Hz by -64, -48, -32, -16, -8, -4, -2, -1, 0, 1, 2, 4, 8, 16, 32, 48, and 64 Hz. Thus, there were 17 mistunings$\times$3 dichotic pitches$=$51 stimuli in all. Each stimulus consisted of three 409.6-ms dichotic pitches with the same transition frequency (but synthesized from separate samples of noise) alternating with three 409.6-ms, 600-Hz pure tones, beginning with the dichotic pitch. The level of the noise was 66 dB and that of the tone was 29 dB. These values were chosen so that the pure tone and dichotic pitch had approximately equal loudness when the transition bandwidth of the HP was 3%.

B. Procedure

The four listeners who participated in experiment 1 attended ten 30-min sessions. In each session, they listened to each stimulus ten times in a random sequence and classified the dichotic pitch as either higher or lower than the pitch of the pure tone via the keyboard of a VDU.

C. Results

The results for each listener are shown separately in Fig. 6. The fitted curves were derived using a logistic regression based on Eq. (2), where y is the percentage of ''lower pitch'' judgments, x is the mistuning in Hz, and b and k are free parameters, which jointly control the location and steepness of the slope of the curve. Three of the four subjects showed more accurate discrimination of the pitch of the HP stimuli than of the pitch of the BEP stimuli, as reflected in the steeper slopes in the fitted functions. Estimates of the dichotic pitch transition frequencies whose pitches correspond to that of the 600 Hz tone can be determined by evaluating the offset between 600 Hz and the fitted curves as they cross the 50% point on the y axis [Eq. (3)]:

$$y = \frac{100}{1 + ke^{bx}}, \tag{2}$$

$$\text{offset} = \frac{-\log_e k}{b}. \tag{3}$$

Table I lists the transition frequencies (with 95% confidence intervals) at the 50% point of the fitted curves for each of the three binaural conditions. For the three listeners whose fitted functions showed steeper slopes for the HP than the BEP, the confidence intervals of the offset are also smaller. For the HP, the offset in the fitted curve is within 2% of 600 Hz for each of the four listeners, and the mean offset is 0.11% of 600 Hz. For the BEP, the offsets are within 3% of 600 Hz for each listener and the mean offset is within 1%, for each condition.

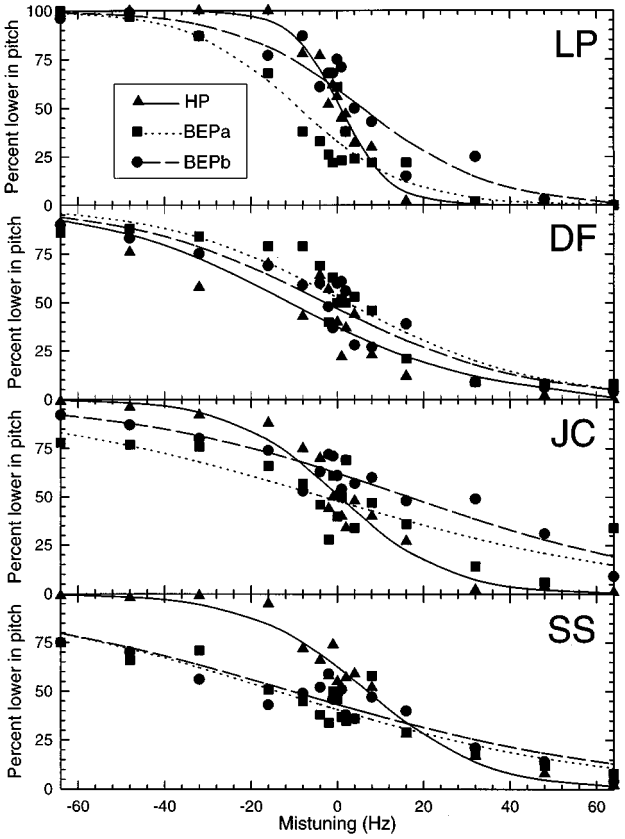

FIG. 6. The percentage of stimuli from each condition in experiment 2 (HP, triangles; BEPa, squares; BEPb, circles) which were judged lower in pitch than a 600 Hz comparison tone, as a function of the mistuning of the transition frequency from 600 Hz, for each subject. Logistic curves, fitted using two free parameters [see Eq. (1)], are also shown for each condition (HP, solid; BEPa, dotted; BEPb, dashed).

D. Discussion

Frijns *et al.* (1986) drew a distinction between the tonal percept which BEP stimuli produce and a low- or high-pass noise percept, which may also be heard. According to the CAP model, if the interaural transition is very narrow, the tonal percept should disappear, leaving only the high- or low-pass percept. The primary objective of experiment 2 was to show that the narrow transitions in the BEP condition of experiment 1 give rise to the perception of a pitch which is tonal in nature and is equivalent to the transition frequency, rather than giving rise only to the perception of a low- or high-pass noise. The important outcome of experiment 2, therefore, is that listeners perceived a tonal pitch in the BEP stimuli which they matched closely to the reference frequency. Moreover, there was only a negligible offset between the fitted logistic curve at its 50% point and 600 Hz. The tolerance of the offset was similar in size to the 1.5% tolerance of matches observed by Frijns *et al.* for BEP stimuli with wider transition bandwidths. Thus, contrary to the predictions of the CAP model, very narrow transition bandwidths do not prevent the perception of a tonal pitch in BEP stimuli.

Three of the four listeners discriminated HP stimuli more accurately than BEP stimuli. In fact, one of these three subjects (SS) showed no discrimination of the BEP during his first seven runs, while performing well with the HP. Data collection was restarted from scratch once he began to perform above chance with BEP stimuli. More accurate discrimination with the HP may reflect the lesser prominence of the peak in interaural decorrelation which is recovered from a BEP compared to that from a HP (e.g., Fig. 4, $w=8\%$).

TABLE II. Vowel percepts formed by different combinations of formant frequencies.

	*F*2	
*F*1	975 Hz	1925 Hz
225 Hz	OO	EE
625 Hz	AR	ER

IV. EXPERIMENT 3

A. Rationale

Experiment 3 provides a further test of the prediction of the mE-C model that BEP's defined by narrow interaural phase transitions give rise to dichotic pitches. The experiment exploited characteristics of a stimulus developed by Culling and Summerfield (1995). They combined two first- and two second-formant frequencies to produce sounds akin to the vowels in British-English pronunciations of the words ''hard'' (AR), ''heed'' (EE), ''haired'' (ER), and ''who'd'' (OO) (Table II). Dichotic stimuli were synthesized containing two BEPs with narrow ($<1.2\%$) interaural phase transitions at pairs of these formant frequencies in order to evoke the perception of vowels in noise. Two sets of dichotic (BEP) stimuli were generated. In one set, the noise was in-

TABLE I. Results of experiment 2. Transition frequencies (in Hz) which were matched by each listener to the 600-Hz comparison tone for each dichotic pitch, with 95% confidence intervals (conf. intvl.) and the % age mistuning which these matches represent.

	HP			BEPa			BEPb		
Listener	Frequency (Hz)	95% conf. intvl.	% age offset	Frequency (Hz)	95% conf. intvl.	% age offset	Frequency (Hz)	95% conf. intvl.	% age offset
LP	600.8	598.8–603.1	+0.13%	591.2	586.4–595.0	−1.46%	605.9	601.2–611.4	+0.98%
JC	600.5	597.9–603.3	+0.08%	596.8	583.0–609.3	−0.53%	616.5	610.6–623.8	+2.75%
DF	589.0	581.1–595.3	−1.82%	602.3	596.4–608.5	+0.38%	597.3	591.6–602.7	−0.44%
SS	607.0	604.3–610.0	+1.12%	586.0	577.6–592.9	−2.32%	589.5	581.3–596.4	−1.75%
$\bar{x}$	599.3		−0.11%	594.1		−0.98%	602.3		+0.38%

phase between the two transition frequencies (BEP1). In the other set, the noise was 180 degrees out-of-phase between the transition frequencies (BEP2).

The formants were centered on 225, 625, 975, and 1925 Hz. Table II shows that no formant on its own uniquely specifies a particular vowel; only in combination do the formants define the different vowels. A limitation in this design is that dichotic pitches are not audible for the majority of listeners above 1500 Hz (Cramer and Huggins, 1958; Yost, 1991). Thus, a formant defined by a BEP at 1925 Hz should not be detectable. However, listeners can obviate this problem. They can identify OO and AR from two audible formants below 1000 Hz (225 and 975 Hz for OO; 625 and 975 Hz for AR). They can identify EE and ER by detecting the lower formant of those vowels (225 Hz for EE and 625 Hz for ER) and determining that a second formant at 975 Hz is absent. Nonetheless, because of this complication, the predictions which follow are made more strongly for OO and AR than for EE and ER.

The CAP model predicts that stimuli containing BEPs with very narrow transition bandwidths are not heard as containing a tonal dichotic pitch. Instead, they are heard as either high- or low-pass noise. Thus, if two transitions are combined in a single stimulus, band-pass or band-stop noise percepts should result. For this reason, the experiment also included two sets of diotic control stimuli which were band-pass and band-stop noises with the cutoffs placed at the formant frequencies. The CAP model makes two predictions for the pattern of identification responses that should be given to these diotic (control) stimuli and to the dichotic (BEP) stimuli. First, the BEP1 and the diotic band-pass stimuli should receive the same pattern of responses; likewise, the BEP2 and diotic band-stop stimuli. Second, neither set of responses should correspond systematically to the intended vowels.

To the extent that the aE-C model draws a strong analogy between the detection of edge pitches by the monaural and binaural systems, it predicts that listeners will hear the intended vowels both in the dichotic (BEP) conditions and the diotic (control) conditions. In the dichotic (BEP) conditions, formants will be defined by binaural edge pitches close in frequency to the interaural phase transitions. In the diotic (control) conditions, formants will be defined by edge pitches at roughly the same frequencies. Thus, the aE-C model predicts that responses in all four conditions should correspond to the intended vowels.

The mE-C model predicts that the dichotic stimuli will elicit percepts of the intended vowels. Excitation will be largely canceled in channels with center frequencies away from the interaural phase transitions, but not in channels close to the frequencies of the transitions themselves, leaving two peaks in the residual activation spectrum which can be interpreted as formants. The model itself does not predict how the diotic (control) stimuli will be identified. However, in our experience the first-order percept of a low-, band-, or high-pass diotic noise is determined by the spectrum of the noise, rather than its edge pitch(es). Therefore, we expect the pattern of identification responses to the diotic (control) stimuli to differ from that to the dichotic (BEP) stimuli, and to be based on listeners interpreting the spectral profiles of the noise bands as if they were the spectral envelopes of vowels. In the case of some stimuli, this strategy should yield percepts that differ systematically from the intended vowels. Thus, the mE-C model predicts that listeners will identify the stimuli as the intended vowels in the dichotic conditions, and will give different, and generally less accurate, patterns of responses in the diotic conditions. Moreover, these latter patterns should differ between the band-pass and band-stop conditions.

TABLE III. Predictions of three models for the accuracy of vowel-identification responses in experiment 3. The entries ''Incorrect (pattern A)'' and ''Incorrect (pattern B)'' imply that different patterns of misidentifications would occur.

	Condition			
	Diotic		Dichotic	
Model	Band-pass	Band-stop	BEP1	BEP2
aE-C	Correct	Correct	Correct	Correct
CAP	Incorrect (pattern A)	Incorrect (pattern B)	Incorrect (pattern A)	Incorrect (pattern B)
mE-C	Incorrect (pattern A)	Incorrect (pattern B)	Correct	Correct

In summary, the CAP model predicts that the dichotic (BEP) stimuli will elicit the same pattern of identification responses as the diotic (control) stimuli (at least for AR and OO), but that neither set of responses will correspond to the intended vowels. The aE-C model also predicts that both the dichotic (BEP) and the diotic (control) stimuli will elicit the same pattern of identification responses, but that the response patterns will correspond to the intended vowels. Finally, the mE-C model predicts that the dichotic (BEP) stimuli will elicit percepts of the intended vowels, while the diotic (control) stimuli will elicit different patterns of identification responses in which the band-stop and band-pass noises are themselves interpreted as defining the spectral envelopes of vowels. These predictions are summarized in Table III.

B. Stimuli

The stimuli were generated, presented, and calibrated in a similar manner to experiments 1 and 2. White noise was synthesized and was filtered in the time domain by a 512-point linear FIR filter in order to produce a 3-dB/oct spectral roll-off. The resulting pink noise was filtered in the frequency domain in order to produce both BEP and diotic control stimuli using the formant frequencies listed in Table II. The dichotic stimuli were, in separate conditions, in-phase between the two transition frequencies (BEP1) or out-of-phase between the two transition frequencies (BEP2). The corresponding diotic control stimuli were band-pass and band-stop noises using the same transition frequencies as cut-off frequencies. Each corresponding pair of stimuli (e.g., BEP1 and band-pass) was generated using the same noise sample. The 180-degree interaural phase transitions and the diotic low-pass and high-pass cutoffs were one analysis bin wide (2.4 Hz), giving transition bandwidths of 0.13%–1.1% of the transition frequency, depending on the center fre-

quency of the transition. Eight stimuli based on different samples of noise were created for each of the four vowels in each of the four conditions, giving 128 experimental stimuli. In addition, four practice stimuli (one for each vowel) were created which incorporated HPs at the formant frequencies with 6% transition bandwidths. The stimuli were presented at 64 dB.

C. Procedure

Five listeners, including the first two authors, all of whom had previously participated in vowel identification experiments, attended a single 40-min session. Each session consisted of four runs. Each run began with 20 practice trials in which the listeners identified the HP practice stimuli five times each, in a random order without feedback. The rest of the run consisted of two blocks. In two runs, the first block contained the diotic control stimuli, while in the other two runs the first block contained the dichotic stimuli. The ordering of the blocks was counterbalanced across runs. The stimuli were presented in a random order, which changed for each run.

Pilot experiments showed that some of the control stimuli compellingly evoked percepts of the vowel in the word ''hoard'' (OR), which lay outside the nominal stimulus set. In order to accommodate this effect, listeners were permitted five response categories, including OR, but were advised that they should not necessarily expect to use all of them equally often. Listeners identified the vowel presented on each trial with a single key-press on a VDU. No feedback about the accuracy of responses was given.

D. Results

Table IV contains the confusion matrices for each of the four conditions pooled across the five listeners. These data were analyzed in three ways: first, to assess overall accuracy; second, to compare the pattern of responses between the four conditions; and third, to compare the patterns of responses with the predictions of a model of vowel identification.

In the dichotic conditions, with the data pooled over subjects, each of the four stimuli in each condition was identified as the intended vowel more often than chance (from binomial probability, $p \ll 0.01$, for each vowel). The response category corresponding to the intended vowel received the greatest proportion of the responses made to each of the eight stimuli. Individually, four of the five listeners identified the stimuli as the intended vowel significantly more often than chance according to binomial probability ($p \ll 0.01$ for 512 trials and 5 choices). The fifth listener's responses were at chance (21% correctly identified). In the diotic control conditions, listeners identified some stimuli consistently as the intended vowel, but made consistently different responses to other stimuli. In the pooled data, the response category corresponding to the intended vowel received the highest proportion of responses made to a stimulus in only five out of the eight possible cases.

The second analysis tested the prediction of the mE-C model that the same pattern of responses would be made in the BEP1 and BEP2 conditions, while two different patterns of responses would be made in the band-pass and band-stop conditions. The patterns of results in the pooled data in each pair of conditions were compared using a chi-squared (χ^2) test. The χ^2 value provides a metric for assessing the degree to which the patterns of responses differ between pairs of conditions. Table V lists the χ^2 values for all pairwise comparisons among the four conditions. The patterns of responses made in the dichotic (BEP1 and BEP2) conditions differ significantly from each other, but only at the $p<0.05$ level, while the patterns in every other pair of conditions differ significantly at the $p<0.001$ level ($\chi^2_{(19)}>43.82$). The values in parentheses are the corresponding values of $\chi^2_{(9)}$ computed from the submatrices containing responses to OO and AR (the vowels for which both formants would have been clearly audible). They show the same pattern as the overall analysis.

The third analysis tested the prediction that listeners would classify the stimuli in the dichotic conditions by locating formants at the frequencies of the interaural phase transitions, but would classify the stimuli in the diotic con-

TABLE IV. Confusion matrices for the four conditions of experiment 3, pooled across five listeners. Figures in parentheses are the numbers of responses predicted by the vowel classifier described in the Appendix.

		Target			
Condition	Response	AR	EE	ER	OO
Band-pass	AR	188 (217)	21 (93)	160 (130)	9 (58)
	EE	1 (6)	24 (18)	2 (15)	0 (11)
	ER	10 (43)	221 (171)	154 (142)	29 (27)
	OO	15 (18)	48 (21)	0 (17)	177 (57)
	OR	106 (37)	6 (17)	4 (16)	105 (168)
Band-stop	AR	3 (35)	1 (7)	1 (24)	35 (10)
	EE	4 (77)	310 (210)	21 (126)	39 (149)
	ER	262 (112)	0 (23)	9 (110)	39 (23)
	OO	16 (73)	9 (68)	9 (47)	199 (116)
	OR	35 (23)	0 (12)	280 (13)	8 (22)
BEP1	AR	178 (219)	14 (2)	36 (73)	13 (17)
	EE	36 (2)	185 (285)	43 (8)	45 (8)
	ER	66 (40)	32 (14)	194 (167)	44 (18)
	OO	15 (21)	80 (4)	25 (15)	201 (200)
	OR	25 (36)	9 (14)	22 (57)	17 (77)
BEP2	AR	171 (219)	13 (2)	33 (73)	20 (17)
	EE	21 (2)	216 (285)	62 (8)	69 (8)
	ER	84 (40)	22 (14)	182 (167)	33 (18)
	OO	27 (21)	63 (4)	25 (15)	187 (200)
	OR	17 (36)	6 (14)	18 (57)	11 (77)

TABLE V. A pairwise comparison of the patterns of data produced by the four conditions of experiment 3 (Table IV). The values given are χ^2 values which are larger the greater the differences. Values in parentheses were computed from the submatrices for the AR and OO stimuli.

	BEP1	BEP2	Band-stop
Band-pass	671.6 (238.5)	791.5 (294.9)	1686.3 (590.6)
Band-stop	905.4 (327.7)	828.7 (288.2)	
BEP2	32.4 (21.1)		

trol conditions by interpreting the spectral profiles of the band-pass and band-stop noises as the spectral envelopes of vowels. In order to evaluate both parts of this prediction on an equal footing, it was necessary to assume that listeners extracted formants not only from the dichotic stimuli but also from the diotic control stimuli. The vowel classifier described in the Appendix includes rules for extracting formants from both types of stimulus. In the dichotic (BEP) stimuli, the classifier assumes that formants are detected at the frequencies of both interaural phase transitions in OO and AR, but only at the lower-frequency transition in EE and ER. In the diotic (control) condition, the classifier assumes that formants are detected at locations within the bands of noise. The classifier includes rules for estimating the similarity of formant frequencies extracted from stimuli to stored templates, and for converting the similarities to predicted numbers of identification responses. These predictions are listed in Table IV as the numbers in parentheses.

The accuracy of predictions was assessed by computing product-moment correlation coefficients between the predicted and observed numbers of identification responses. Analyses were conducted on the pooled data from the two diotic control conditions and on the pooled data from the two dichotic conditions, with 40 identification scores to be predicted in each case. The coefficient of correlation was 0.89 for the dichotic conditions; the vowel classifier correctly predicted that the majority of identification responses made to each of the eight stimuli would correspond to the intended vowel. The coefficient of correlation was 0.61 for the diotic conditions. One way of judging the overall accuracy of this prediction is to note that 11 cells in the matrices for the diotic conditions in Table IV received 100 or more responses. The classifier correctly predicted that 8 of these 11 would receive more than 100 responses. A more critical test is to establish whether the accuracy of prediction declines when the rules for locating formants in the diotic and dichotic conditions are reversed. If it is assumed that formants are located at the band edges in the diotic conditions, the correlation between observed and predicted numbers of responses falls from 0.61 to 0.39. If it assumed that formants are located within the noise bands in the dichotic conditions, the correlation falls from 0.89 to 0.47. Overall, therefore, although the classifier does not make completely accurate predictions particularly for the diotic conditions, its performance is consistent with the prediction of the mE-C model that listeners locate formants at the frequencies of the interaural phase transitions in the dichotic conditions, but within the noise bands in the diotic conditions.

E. Discussion

1. Predictions of the CAP model

The CAP and mE-C models make divergent predictions with respect to experiment 3. The CAP model predicts that listeners should not be able to identify the intended vowels in the dichotic stimuli, primarily because the bandwidth of the interaural transitions is too narrow to generate peaks at the formant frequencies in across-frequency scans.

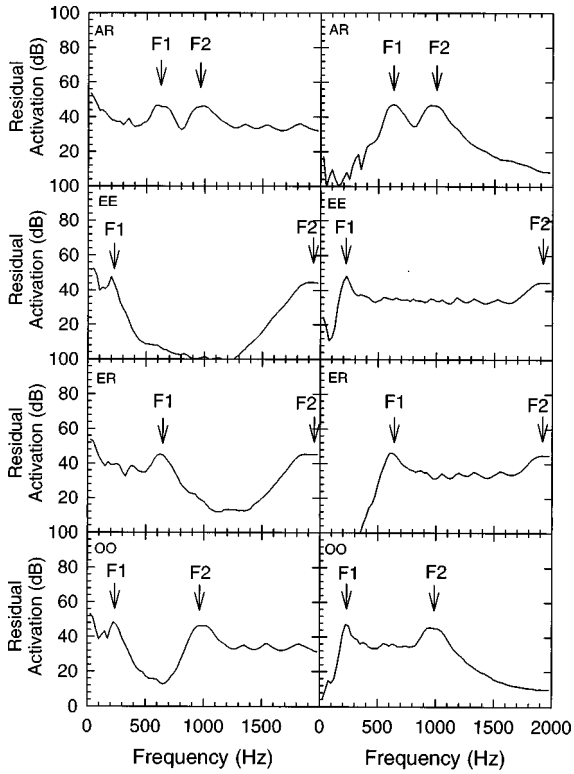

FIG. 7. Residual-activation spectra from the mE-C model for the BEP1 stimuli (left column) and BEP2 stimuli (right column) used in experiment 3, showing peaks at the two transition frequencies (marked with arrows) in each stimulus. Descending each column, stimuli are identified as exemplars of ''AR,'' ''EE,'' ''ER,'' and ''OO.''

If dichotic pitches are not heard, the CAP account predicts that listeners should hear the dichotic stimuli as band-pass and band-stop noises, in which case the dichotic stimuli should have received the same pattern of identification responses as the diotic stimuli. In fact, the patterns differed significantly from one another (Table V).

2. Predictions of the mE-C model

The results of experiment 3 are broadly consistent with the predictions of the mE-C model. Listeners gave identification responses to the dichotic stimuli that were consistent with detecting formants at the frequencies of the interaural phase transitions in OO and AR, and with detecting a low-frequency formant in EE and ER, while noting the absence of a high-frequency formant. Figure 7 shows the recovered spectra generated by the model in response to each of the stimuli. Clearly, the model performs ''too well'' at high frequencies: the recovered spectra contain two peaks at the frequencies of the interaural phase transitions of all eight stimuli. Thus, these spectra are incompatible with demonstrations that listeners are unable to detect interaural phase transitions at frequencies as high as 2000 Hz (Yost, 1991). Bernstein and Trahiotis (1996) have shown that the deterioration of binaural masking release with frequency can be modeled by incorporating the change from phase locking to the waveform to phase locking to the envelope with increasing frequency. The mE-C model uses the Meddis (1986, 1988) hair-cell model for this purpose. That model substantially overestimates the degree of phase locking at high fre-

quencies. A peripheral model which is more accurate in this respect should yield recovered spectra that reflect the information available to listeners more accurately.

V. GENERAL DISCUSSION

The Huggins pitch (HP) is produced by introducing an interaural phase transition of 360 degrees over a narrow bandwidth to a diotic noise. A closely related phenomenon, the binaural edge pitch (BEP), is generated with an interaural phase transition of 180 degrees. In each case, listeners hear a tone with a pitch which matches the center frequency of the transition, suggesting that a binaural process produces an output spectrum with a single spectral peak at the transition frequency. The experiments described in this paper demonstrate that most aspects of these phenomena do not require a special explanatory framework beyond that provided by the general principles of binaural unmasking which are embodied in the mE-C model. The model applies equalization of level and internal delay in each frequency channel independently and then cancels by interaural subtraction. This process detects the degree of interaural decorrelation in each frequency channel. It yields an output spectrum which is closely related to a plot of interaural decorrelation by frequency. That spectrum contains a single peak at the transition frequency of HP and BEP stimuli. An attraction of accounting for the HP and BEP with the mE-C model is that a satisfactory explanation can thus be achieved without invoking additional perceptual processes. This simplicity is not shared by the aE-C and CAP models.

The aE-C model incorporates a conventional model of binaural unmasking (broad-band E-C). However, in the case of the BEP the output of this process is a high- or low-pass noise, so the aE-C model needs to invoke central lateral inhibition as an additional process in order to produce a spectrum with a single peak near the transition frequency. The CAP model incorporates a conventional multi-channel cross-correlation process, typical of models of binaural sound localization, but in order to find spectra with peaks at the transition frequencies of HP and BEP stimuli the model requires an additional across-frequency scanning process.

The following paragraphs review the strengths and weakness of the three alternative models of dichotic-pitch phenomena in the light of the results reported in this paper.

A. The aE-C model

The aE-C model invokes two processes to account for the BEP: (1) broadband E-C and (2) central lateral inhibition on the residue after cancellation. Broadband E-C is equivalent to applying the same equalizing and cancelling operations in each frequency channel. This process differs from processes performed by the mE-C model where different delays can be applied in different channels. Strong evidence in favor of using different delays is that the mE-C model provides the only complete account of the Fourcin pitch (Fourcin, 1970; Culling *et al.*, 1998). Supporting evidence comes from demonstrations that the model provides a straightforward account of the HP and BEP, as shown in the present paper, and of a range of other cases of binaural masking release involving broadband signals (Culling and Summerfield, 1995). Thus the balance of evidence favors the conclusion that binaural analysis involves independent E-C in different frequency channels, rather than broadband E-C.

Released from the constraints imposed by broadband E-C, it is not necessary to invoke central lateral inhibition to account for the BEP. The involvement of central lateral inhibition was originally supported by evidence that the pitch frequency of the BEP is offset from transition frequency by 3%–8%, as are monaural edge pitches from the cutoff frequencies of low- and high-pass noises. Subsequent experiments by Hartmann (1984a) and by Frijns *et al.* (1986) failed to corroborate the involvement of central lateral inhibition and failed to replicate the offset in pitch matches. Nonetheless, the existence of the binaural coherence edge pitch (Hartmann, 1984b) provides independent evidence of the existence of central lateral inhibition. These results would be reconciled if the mE-C process generated the primary auditory representation of the BEP, and central lateral inhibition enhanced edges in that representation. In this case, the largest contribution to the BEP would derive from the primary representation with a small additional contribution from lateral inhibition which results from less effective cancellation of the N_π noise.

Further evidence against the aE-C model was provided by experiment 3. This model predicts that listeners hear low- or high-pass noise when presented with a BEP stimulus. In experiment 3, two transitions at frequencies which corresponded to vowel formant frequencies were used to produce stimuli which sounded like vowels in noise. According to the aE-C model, binaural analysis converts these stimuli into band-pass or band-stop noises, depending on whether the noise was in-phase or out-of-phase between the two transition frequencies (and on whether the binaural system adds or subtracts the signals at the two ears). Then, lateral inhibition enhances the spectrum near the transition boundary exactly as for a monaural edge-pitch. Thus, the model predicts that listeners should give similar responses to these stimuli as to diotic band-pass and band-stop noises, and that listeners should hear the appropriate vowels in both cases. In fact, listeners heard the appropriate vowels from the dichotic stimuli, but produced a systematically different pattern of responses for the band-pass and band-stop noises. The aE-C model can only be reconciled with these results if the lateral inhibition process which it uses is assumed to be much stronger than the lateral inhibition process(es) which generate the monaural edge pitch. In conclusion, we suggest that the aE-C model should be rejected as an account of the HP and BEP, but that the conditions giving rise to central lateral inhibition should be explored further.

B. The CAP model

The CAP model is based on four interrelated ideas. First, an array of interaural cross-correlation functions is computed forming a two-dimensional central activity pattern in frequency and interaural delay. Second, attention can be focused on individual across-frequency scans taken at particular interaural delays. Third, in certain respects, these across-frequency scans, or ''central spectra,'' can be interpreted like monaural spectra; in particular, sharp peaks in scans, but not

broader peaks, give rise to the perception of tones. Fourth, the interaural delay of a scan determines the lateralization of the features detected within it.

Bilsen and his colleagues have argued that the CAP model provides a basis for explaining three aspects of the HP and BEP: (1) their frequencies; (2) their masking patterns; and (3) their lateralization. In the paragraphs which follow, we argue that there are plausible alternative accounts of the first two of these aspects, though not yet of the third.

1. Detection and pitch matching of the HP and BEP

A weakness of the CAP model is that it includes no explicit mechanism for choosing which across-frequency scan receives a listener's attention and determines the sound pattern that is heard. Instead, the model relies on some scans containing features of sufficient prominence that they command attention. In this respect, the explanatory power of the model is materially reduced when it is implemented with realistic frequency and temporal resolution in place of the idealized parameters used by Raatgever and Bilsen (1986). With this revision, features that appeared as prominent peaks in scans generated by the original version of the model may be diffused to the point where they should no longer command attention.

A critical test is provided by BEP stimuli created with very narrow interaural phase transitions. The original version of the model predicts that such dichotic pitches should be harder to detect than pitches created from broader transitions. The ''smoothed'' version of the model incorporating realistic frequency resolution predicts that dichotic pitches should not be heard in such stimuli. However, experiment 1 showed that the pitch sensation produced by such stimuli is as strong as that produced by stimuli with wider transitions. Experiment 2 showed that this pitch closely matches that of a tone whose frequency is equal to the transition frequency. Experiment 3 showed that stimuli containing two such transitions at frequencies which correspond to vowel formant frequencies can be identified as vowels in noise. Thus, the results of experiments 1, 2, and 3 contradict the predictions of the CAP model.

Further evidence against the predictions of the CAP model was provided by Culling and Summerfield (1995), Hukin and Darwin (1995), and Darwin and Hukin (1997). They demonstrated that listeners are very poor at grouping energy in separate frequency regions which share the same interaural delay. An across-frequency scanning mechanism of the kind used in the CAP model would have been able to perform such across-frequency grouping.

2. Measurements of the CAP

Raatgever (1980), Raatgever and Bilsen (1986), and Frijns *et al.* (1986) used measures of binaural masking release to support the idea that listeners can attend to individual across-frequency scans in the CAP. They measured the threshold for detection of a diotic tone in the presence of a dichotic pitch stimulus, which acted as a masker. It was argued that listeners could restrict attention to a single spatial location (the center) while performing the task. The CAP was sampled at specific frequency/internal-delay coordinates

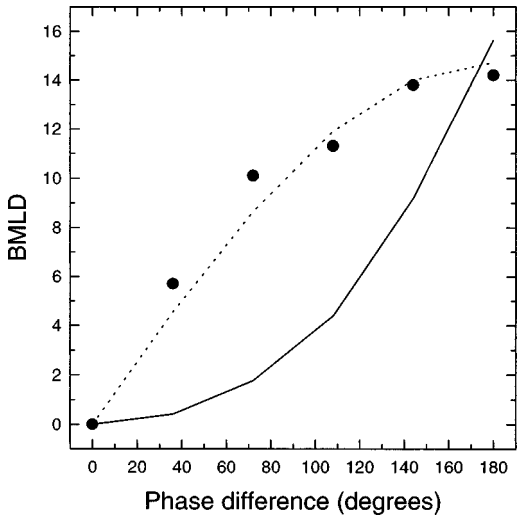

FIG. 8. The relationship between BMLDs and the relative interaural phase of masker and tone. The filled symbols are empirical data from Jeffress *et al.* (1952), the dashed line was fitted using Eq. (4), and the solid line was fitted using Eq. (7). Data from Jeffress *et al.* (1952) were digitized from a scanned image of their Fig. 1(f).

by using target tones of different frequencies and by applying interaural delays to the masker in order to place different parts of the CAP in the center of auditory space. For each interaural delay, thresholds were measured at a range of different frequencies. The BMLDs (re:NoSo) were plotted as a function of frequency and were compared with across-frequency scans generated by the CAP model. The resulting scans were qualitatively similar to thresholds predicted from the CAP [using Eq. (7) in Raatgever and Bilsen, 1986].

Potentially, these results provide powerful evidence listeners can attend to individual across-frequency scans, and thus that they are in a position to detect the features in such scans that support the perception of dichotic pitches. However, the following analysis demonstrates that the pattern of masking release across frequency reported by Raatgever (1980), Raatgever and Bilsen (1986), and Frijns *et al.* (1986) can be predicted without invoking the assumption that the listener has attended to a particular spatial location. There is an established relationship between the BMLD and the phase difference between the interaural phases of the target tone (ϕ_s) and the masking noise (ϕ_n). Durlach and Colburn (1978) pointed out that ''to a rough approximation [the BMLD] depends only on the phase difference ($\phi_n - \phi_s$) rather than on the individual values of ϕ_n and ϕ_s.'' This relationship is illustrated in Fig. 8 (filled symbols) with data from Jeffress *et al.* (1952). The interaural delays used in that study have been converted to the corresponding phases in the figure. A satisfactory fit to the data can be produced using Eq. (4) and is illustrated by the dotted line in Fig. 8:

$$\mathrm{BMLD} = \mathrm{BMLD}_{\max} |\sin(\phi/2)|. \tag{4}$$

In this equation, ϕ is the difference in interaural phase between signal and noise ($\phi_n - \phi_s$) and $\mathrm{BMLD}_{\max}$ is the BMLD in dB which is obtained with NoSπ versus NoSo. For a dichotic pitch stimulus, the interaural phase of the masker is frequency dependent. The threshold for detecting a tone of

frequency f is therefore dependent on the interaural phase of the masker at that frequency, ϕ_f. If, as in the experiments in question, an interaural delay τ_e has also been applied, Eq. (5) is required:

$$\phi_n = 2\pi f \tau_e + \phi_f. \tag{5}$$

Since $\phi_s = 0$, this is also the expression for $\phi_n - \phi_s$. Substituting Eq. (5) into Eq. (4), we obtain

$$\text{BMLD} = \text{BMLD}_{\max} |\sin([2\pi f \tau_e + \phi_f]/2)|. \tag{6}$$

For comparison, it is necessary to substitute Eq. (7) from Raatgever and Bilsen (1986) into their Eq. (6) to obtain

$$\text{BMLD} = 10 \log_{10}\left[\frac{10^{\text{BMLD}_{\max}/10}}{(10^{\text{BMLD}_{\max}/10} - 1)[\frac{1}{2} + \frac{1}{2}\cos(2\pi f \tau_i + \phi_f)] + 1}\right], \tag{7}$$

where τ_i is the internal delay. However, since this internal delay is interrogated using an interaural delay applied to the noise, $\tau_i = \tau_e$.

Although Eqs. (6) and (7) look different, each expression relates the BMLD monotonically to the difference in interaural phase ($0 < \pi < \phi$) between the tone and the masker at the frequency of the tone. The equations differ in that Eq. (6) defines a function whose slope decreases with increases in the phase difference, while Eq. (7) defines a function of increasing slope. In Fig. 8, the solid line was derived from Eq. (7). The accuracy of its fit to the data of Jeffress *et al.* (1952) can be compared with the empirical fit of Eq. (4) which is plotted as the dotted line.

Figure 9 compares the accuracy with which Eqs. (6) and (7) predict the BMLD data obtained by Frijns *et al.* (1986) using a BEP stimulus as the masker. The transition frequency was 600 Hz with a transition bandwidth of 36 Hz (6%). The open circles plot the empirical BMLDs; the predictions from Eq. (6) are shown as dotted lines, those from Eq. (7) as continuous lines. The data in the top panel were obtained with no interaural delay applied to the masker, those in the middle panel with a delay of 0.83 ms, and those in the bottom panel with a delay of 1.25 ms. This figure may be compared with Fig. 9 of Frijns *et al.* (1986, p. 449). The predictions derived in the present paper, based empirically on the relationship between BMLD and $\phi_n - \phi_s$, are as accurate as those based on the CAP model.

The foregoing analysis shows that it is not necessary to assume that listeners attended to a particular spatial location during the BMLD experiments of Raatgever (1980), Raatgever and Bilsen (1986), and Frijns *et al.* (1986). Therefore, the results of those experiments do not prove that listeners can attend to particular across-frequency scans in the CAP. Rather, they confirm that the size of the BMLD is largely determined by the relationship between the interaural phases of signal and masker within the frequency channel occupied by the signal.

3. The lateralization of the HP and BEP

It is an important feature of the original version of the CAP model that it can account for the lateralization of the HP and BEP, because the sharp peaks in across-frequency scans that are judged to be responsible for these dichotic pitches occur at the particular internal delays which correspond to the perceived lateralization(s) of the pitches. Raatgever and Bilsen (1986) demonstrated that the reported lateralizations for HP stimuli correspond closely with the predictions of the CAP model. They also demonstrated that the lateralization can be shifted in a consistent fashion by applying additional interaural delays to stimuli. Frijns *et al.* (1986) reported difficulty in collecting similar data for the BEP. Using a rather complex procedure, they confirmed that two of three listeners frequently perceived lateralizations consistent with the peak at +1.25-ms internal delay in Fig. 2(a). However, these listeners also frequently heard centrally located images. The third listener reported centrally located images almost exclusively.

The mE-C model is not intended to predict the lateralization of sounds and we have not found a satisfactory way to extend it to predict the lateralization of the HP and BEP.[7] Thus the original version of the CAP model provides the only account of the lateralization of the HP. Its predictions with respect to the lateralization of the BEP are also supported by the data, but to a more limited extent.

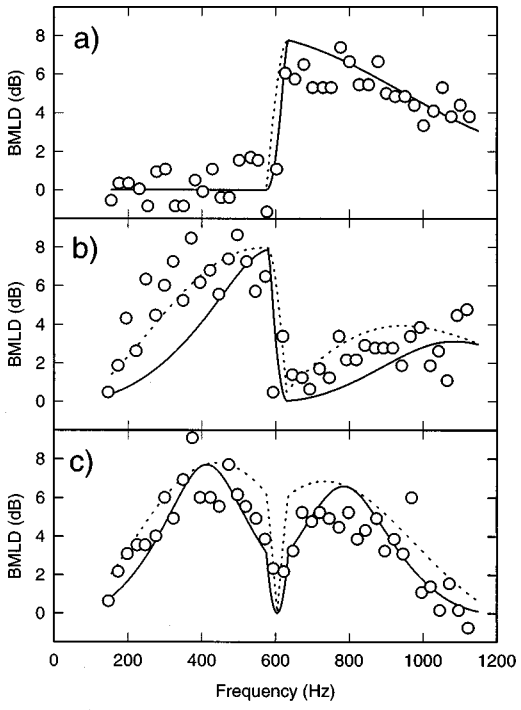

FIG. 9. The empirical and predicted BMLDs from Frijns *et al.* (1986) for a BEP masker (600-Hz transition frequency) and a diotic tone. In panels (a), (b), and (c) interaural delays of 0, 0.83, and 1.25 ms have been applied to the masker. The open symbols are the empirical data from Fig. 9 of Frijns *et al.* The solid lines are predictions based on their model [Eq. (7)]. The dotted lines are predictions based on the phase difference between tone and masker [Eq. (6)]. In each case, $\text{BMLD}_{\max}$ is a function of frequency which was derived by fitting a fourth-order polynomial function to the NπSo data of listener FB in Raatgever and Bilsen (1986, Fig. 9). The empirical data were digitized from scanned images of the published figures.

VI. CONCLUSIONS

The arguments presented in this paper reinforce the conclusion that the aE-C model is inadequate to account for the

characteristics of dichotic pitches because of the limited explanatory power of broadband E-C. However, we believe that one component of that model, central lateral inhibition, warrants further study. The relative merits of the CAP and mE-C models can be summarized as follows. The mE-C model has the weakness that it does not predict the lateralization of dichotic pitches. The CAP model, on the other hand, accurately predicts the lateralization of the HP and to a lesser extent that of the BEP. In every other respect that we have investigated, the mE-C model provides a more satisfactory account. First, it automatically produces an output spectrum which is qualitatively consistent with the spectral features perceived in dichotic pitches. In comparison, the CAP model is under-specified in that it contains no explicit mechanism for choosing which of the available array of central spectra determines what is perceived, nor for distinguishing peaks in scans which are perceived from those which are not perceived. Second, the mE-C model is more parsimonious in that it does not assume any perceptual processes beyond those which are strictly necessary to account for binaural masking release, while the CAP model incorporates an across-frequency scanning process which is not required to account for any independent findings. Indeed, Culling and Summerfield (1995) and Hukin and Darwin (1995) sought independent evidence of such a process but found no evidence for its existence. Third, the mE-C model was designed with, and operates successfully using, realistic parameters of frequency and temporal resolution, while the CAP model is not robust when implemented with realistic parameters (Figs. 1 and 2). Fourth, the mE-C model correctly predicts the range of transition bandwidths over which the HP and BEP are audible, while the CAP model fails to predict that the BEP is clearly audible with very narrow transition bandwidths (experiments 1–3; Figs. 2 and 4).

These arguments favor the explanation for the Huggins pitch and the binaural edge pitch offered by the mE-C model. However, before its account can be fully accepted, the reasons for the perceived lateralization of dichotic pitches will need to be understood.

ACKNOWLEDGMENTS

The authors thank Johann Raatgever and Steve Colburn for helpful discussions and for suggesting improvements to Experiment 3, Alain de Cheveigné for useful comments on an earlier draft of this paper, and Frans Bilsen and Bill Hartmann for their thorough and insightful reviews.

APPENDIX: VOWEL CLASSIFIER

The pooled identification responses of listeners in experiment 3 were predicted by simple template-matching models of vowel classification derived from the PEAK procedure described by Assmann and Summerfield (1989). The templates were the center frequencies of the first two formants ($F1$ and $F2$) of each of the five vowels that were available as response categories. These frequencies were averages of measures from the speech of four adult male talkers of British English, each of whom produced five tokens of each vowel in an /h/–vowel–/d/ context. These values were used directly in modeling listeners' responses to the diotic band-pass and band-stop stimuli. They are listed in Table AI as the ''diotic'' templates. When considering the dichotic (BEP) stimuli, it was necessary to accommodate the strategy which listeners were presumed to have adopted; that is, of identifying OO and AR from both interaural transitions, while identifying EE and ER from the lower transition only, while noting the absence of a higher transition (Sec. IV A). Here $F1$ and $F2$ had the same values in the ''dichotic'' templates for OO, AR, and OR as in the diotic templates for those three vowels. For EE and ER, however, the frequency of $F1$ was assigned to *both* $F1$ and $F2$. These values are listed in Table AI as the ''dichotic'' templates. Frequencies for two formants were estimated in each stimulus in the diotic (control) conditions and in the dichotic (BEP) conditions in the following ways. In the diotic (control) conditions, it was assumed that the perceived locations of the formants must be well within the noise bands. Various different schemes for placing the formants were explored, but the results of the modeling were found to be relatively insensitive to this variable. In the *band-pass* condition, $F1$ was taken as the frequency one-quarter of the way through the noise band above its low-frequency edge, while $F2$ was taken as the frequency three-quarters of the way through the noise band. In the *band-stop* condition, $F1$ was taken as the mid-frequency of the lower-noise band. Where a band started at 0 Hz, its lower edge was taken as 150 Hz for the purpose of this calculation in order to avoid estimates of $F1$ outside the range found in adult male speech. $F2$ was taken as the mid-frequency of the upper noise band. Where a band extended to the Nyquist frequency, its upper edge was taken as 2250 Hz for the purpose of this calculation in order to avoid estimates of $F2$ outside the range found in adult male speech. In the BEP1 and BEP2 conditions, the frequencies of $F1$ and $F2$ were taken as the center frequencies of the two 180-degree interaural phase transitions for OO and AR; for EE and ER, the center frequency of the lower-frequency transition was assigned to both $F1$ and $F2$. The spectral distance d_i between stimulus s and each of the templates i was calculated using Eq. (A1):

TABLE AI. Frequencies in Hz of the templates corresponding to each response category and of the formant frequencies estimated in the four classes of stimuli used in experiment 3.

	Vowels									
	AR		EE		ER		OO		OR	
	$F1$	$F2$	$F1$	$F2$	$F1$	$F2$	$F1$	$F2$	$F1$	$F2$
	Diotic templates (Hz)									
	658	1001	269	2115	540	1640	281	1140	362	695
	Dichotic templates (Hz)									
	658	1001	269	269	540	540	281	1140	362	695
Condition	Formant estimates (Hz)									
Band-pass	713	888	650	1500	950	1600	413	788	⋯	⋯
Band-stop	388	1613	188	2088	388	2088	188	1613	⋯	⋯
BEP1	625	975	225	1925	625	1925	225	975	⋯	⋯
BEP2	625	975	225	1925	625	1925	225	975	⋯	⋯

$$d_i = \sqrt{\frac{(\log_{10}(f_{1s}) - \log_{10}(f_{1i}))^2 + (\log_{10}(f_{2s}) - \log_{10}(f_{2i}))^2}{2}}, \tag{A1}$$

where f_{1s} and f_{2s}, are the frequencies in Hz of the first and second formants estimated in the stimulus, and f_{1i} and f_{2i} are the frequencies in Hz of the first and second formants for template i. The number of responses, n_i, out of a total of 320 given to response category i was calculated using Eq. (A2) which incorporates the idea that the proportion of responses given to response category i is a function not only of the similarity of the stimulus to template i but also of its similarity to the other four templates:

$$n_i = 320\left(\frac{e^{-d_i/K}}{\Sigma_{i=1}^{5} e^{-d_i/K}}\right). \tag{A2}$$

The constant K was adjusted to minimize the squared error between predicted and observed numbers of responses. The resulting value of K was 0.1. The resulting values of n_i are tabulated in parentheses in Table IV.

[1]Several taxonomies of dichotic pitches can be defined. The one which is set out in the Introduction regards the ''MPS Pitch'' described by Bilsen (1977) and Raatgever and Bilsen (1986) as a multiple Huggins pitch which inherits its properties from the component pitches; since the Huggins pitch is the most salient of the pitches in our classification, a stimulus with many Huggins pitches is proportionately more salient. On the other hand, we have preserved the distinction between the Huggins pitch and the binaural edge pitch, although the distinction may be artificial. The binaural coherence edge pitch, described in an abstract by Hartmann (1984b) and in Sec. I A, of this paper, may be more deserving of separate classification.

[2]In generating the CAP, cross correlation was employed as a simple mathematical surrogate for a process of neural coincidence detection using a range of different delays. Jeffress (1948) suggested that localization on the basis of interaural time delays was based on an array of units in the medial superior olive which are connected to the two ears by axons with varying transmission times and which respond to simultaneous action potentials arriving from the two ears. In such a network, a given neuron will selectively respond to sound of a given frequency, determined by the place in the two cochleae from which it receives innervation, and a given interaural delay, determined by the relative delays imposed by the converging axons.

[3]Raatgever (1980) and Raatgever and Bilsen (1986) applied a two-dimensional envelope to the CAP which emphasized frequencies around 600 Hz and delays around 0 ms (Raatgever, 1980, eqs. IV.1 and IV.2). However, the delay dimension of this envelope has no effect upon the peak-to-valley ratio within an individual scan, and it is this ratio which defines a scan as ''well-modulated'' in the CAP model, causing that scan to command attention. Consequently we did not include the weighing in our illustrations of the CAP model.

[4]Those previous studies, which employed analog methods of stimulus generation (Cramer and Huggins, 1958; Bilsen, 1977; Raatgever and Bilsen, 1986), reported transition bandwidths which reflected the bandwidth over which half of the phase transitions took place. This specification was used because the transitions were not linear with frequency. Rather their steepness declined away from the center of the transition, gradually asymptoting to zero. Consequently no bandwidth for the complete transition could be specified. In the present report, bandwidths for those studies will be reported in the same way, but bandwidths for the digitally generated linear phase transitions employed here will be specified as for the complete transition (i.e., 6% in the present study $\approx$3% in Cramer and Huggins).

[5]Such independence is necessary, given that the model does not perform phase equalization, to account for two related observations: (1) a large release from masking occurs when speech is presented in the NπSo condition relative to NoSo (Licklider, 1948); and (2) this amount of masking release is greater than that observed when the noise is given a fixed interaural delay with respect to the speech (i.e., NτSo relative to NoSo) (Carhart *et al.*, 1968; Levitt and Rabiner, 1967a, b). If the model were constrained to apply the same cancelling delay in all channels, it would erroneously predict that more masking release would be measured in case 2 than case 1.

[6]The split peak which occurs for the HP when $w = 64\%$ occurs whenever the transition band is approximately one octave. When the transition band is narrower, the phase transition produces interaural decorrelation, which is detected by the mE-C model as a spectral peak. However, when the transition extends over an octave the phase transition is approximately equivalent to an interaural delay within the transition region. The duration of the delay is half the period of the center frequency of the transition band. So, for a 600-Hz transition, the delay is 3.33 ms. The model can apply this delay within the transition region and largely cancel the noise. At the edges of the transition region, there are sharp changes in interaural delay (between 0 and 3.33 ms), which prevent the model from performing cancellation and so cause lateral peaks in the recovered spectrum on either side of the transition. Informal listening indicates that these peaks can sometimes be heard.

[7]One way in which the mE-C model might be extended to predict the lateralization of the HP and BEP is as follows. The binaural detection of a tone could trigger perceptual segregation mechanisms that label the frequency channels close to the transition as containing a separate auditory object from the background noise. The auditory system might lateralize the perceived tone by pooling the cross-correlation functions in the labeled channels and identifying the largest peak in the pooled function. This approach is consistent with demonstrations (1) that segregation of concurrent sources of sound occurs prior to lateralization (e.g., Hill and Darwin, 1996), and (2) that the lateralization of broad-band sounds can be predicted from the interaural delay of the largest peak in pooled cross-correlation functions (Shackleton *et al.*, 1992). However, this strategy does not predict the lateralization of the HP and BEP correctly, because the cross-correlation function in the frequency channel centered on the transition of a HP stimulus contains a peak at an interaural delay of 0 ms, whereas the tone is clearly lateralized to one side or the other.

Assmann, P. F., and Summerfield, A. Q. (**1989**). ''Modeling the perception of concurrent vowels: Vowels with the same fundamental frequency,'' J. Acoust. Soc. Am. **85**, 327–338.

Bernstein, L. R., and Trahiotis, C. (**1996**). ''The normalized correlation: Accounting for binaural detection across center frequency,'' J. Acoust. Soc. Am. **100**, 3774–3784.

Bilsen, F. A. (**1977**). ''Pitch of noise signals: Evidence for a 'central spectrum,' '' J. Acoust. Soc. Am. **61**, 150–161.

Bilsen, F. A., and Goldstein, J. L. (**1974**). ''Pitch of dichotically delayed noise and its possible spectral basis,'' J. Acoust. Soc. Am. **55**, 292–296.

Carhart, R., Tillman, T. W., and Johnson, K. R. (**1968**). ''Effects of interaural delays on masking by two competing signals,'' J. Acoust. Soc. Am. **43**, 1223–1230.

Colburn, H. S. (**1973**). ''Theory of binaural interaction based on auditory-nerve data. I. General strategy and preliminary results on interaural discrimination,'' J. Acoust. Soc. Am. **54**, 1458–1470.

Colburn, H. S. (**1977**). ''Theory of binaural interaction based on auditory-nerve data. II. Detection of tones in noise,'' J. Acoust. Soc. Am. **61**, 525–533.

Cramer, E. M., and Huggins, W. H. (**1958**). ''Creation of pitch through binaural interaction,'' J. Acoust. Soc. Am. **30**, 858–866.

Culling, J. F., and Summerfield, Q. (**1995**). ''Perceptual separation of concurrent speech sounds: Absence of across-frequency grouping by common interaural delay,'' J. Acoust. Soc. Am. **98**, 785–797.

Culling, J. F., Marshall, D. H., and Summerfield, Q. (**1998**). ''Dichotic pitches as illusions of binaural unmasking. II. the Fourcin pitch and the Dichotic Repetition Pitch,'' J. Acoust. Soc. Am. **103**, 3527–3539.

Darwin, C. J., and Hukin, R. W. (**1997**). ''Perceptual segregation of a harmonic from a vowel by interaural time difference and frequency proximity,'' J. Acoust. Soc. Am. **102**, 2316–2324.

Durlach, N. I. (**1960**). ''Note on the equalization-cancellation theory of binaural masking level differences,'' J. Acoust. Soc. Am. **32**, 1075–1076.

Durlach, N. I. (**1962**). ''Note on the creation of pitch through binaural interaction,'' J. Acoust. Soc. Am. **34**, 1096–1099.

Durlach, N. I. (**1972**). ''Binaural signal detection: Equalization and cancellation theory,'' in *Foundations of Modern Auditory Theory Vol. II*, edited by J. V. Tobias (Academic, New York).

Durlach, N. I., and Colburn, H. S. (**1978**). ''Binaural Phenomena,'' in *The Handbook of Perception,* edited by E. C. Carterette and M. P. Friedman (Academic, New York).

Fastl, H. (**1971**). ''Über Tonhöhenempfindungen bei Rauschen,'' Acustica **25**, 350–354.
Fastl, H., and Stoll, G. (**1979**). ''Scaling of pitch strength,'' Hearing Res. **1**, 293–301.
Fourcin, A. J. (**1970**). ''Central pitch and auditory lateralization,'' in *Frequency Analysis and Periodicity Detection in Hearing,* edited by R. Plomp and G. F. Smoorenburg (Sijthoff, The Netherlands).
Frijns, J. H. M., Raatgever, J., and Bilsen, F. A. (**1986**). ''A central spectrum theory of binaural processing. The binaural edge pitch revisited,'' J. Acoust. Soc. Am. **80**, 442–451.
Guttman, N. (**1962**). ''Pitch and loudness matches of a binaural subjective tone,'' J. Acoust. Soc. Am. **34**, 1996(A).
Hartmann, W. M. (**1984a**). ''A search for central lateral inhibition,'' J. Acoust. Soc. Am. **75**, 528–535.
Hartmann, W. M. (**1984b**). ''Binaural coherence edge pitch,'' J. Acoust. Soc. Am. **75**, K10.
Hill, N. I., and Darwin, C. J. (**1996**). ''Lateralization of a perturbed harmonic: Effects of onset asynchrony and mistuning,'' J. Acoust. Soc. Am. **100**, 2352–2364.
Houtgast, T. (**1972**). ''The psychophysical evidence for lateral inhibition in hearing,'' J. Acoust. Soc. Am. **51**, 1885–1894.
Hukin, R. W., and Darwin, C. J. (**1995**). ''Effects of contralateral presentation and of interaural time differences in segregating a harmonic from a vowel,'' J. Acoust. Soc. Am. **98**, 1380–1387.
Jeffress, L. A. (**1948**). ''A place theory of sound localization,'' J. Comp. Physiol. Psychol. **61**, 468–486.
Jeffress, L. A. (**1972**). ''Binaural signal detection: vector theory,'' in *Foundations of Modern Auditory Theory, Vol. II,* edited by J. V. Tobias (Academic, New York).
Jeffress, L. A., Blodgett, H. C., and Deatherage, B. H. (**1952**). ''The masking of tones by white noise as a functions of the interaural phases of both components. I. 500 cycles,'' J. Acoust. Soc. Am. **24**, 523–527.
Klatt, D. H. (**1980**). ''Software for a cascade/parallel formant synthesizer,'' J. Acoust. Soc. Am. **67**, 971–995.
Klein, M. A., and Hartmann, W. M. (**1981**). ''Binaural edge pitch,'' J. Acoust. Soc. Am. **70**, 51–61.
Levitt, H., and Rabiner, L. R. (**1967a**). ''Binaural release from masking for speech and gain in intelligibility,'' J. Acoust. Soc. Am. **42**, 601–608.
Levitt, H., and Rabiner, L. R. (**1967b**). ''Predicting binaural gain in intelligibility and release from masking for speech,'' J. Acoust. Soc. Am. **42**, 620–629.
Licklider, J. C. R. (**1948**). ''The influence of interaural phase relations upon the masking of speech by white noise,'' J. Acoust. Soc. Am. **20**, 150–159.
Meddis, R. (**1986**). ''Simulation of mechanical to neural transduction in the auditory receptor,'' J. Acoust. Soc. Am. **79**, 702–711.
Meddis, R. (**1988**). ''Simulation of auditory-neural transduction: further studies,'' J. Acoust. Soc. Am. **83**, 1056–1063.
Moore, B. C. J., and Glasberg, B. R. (**1983**). ''Suggested formulae for calculating auditory-filter bandwidths and excitation patterns,'' J. Acoust. Soc. Am. **74**, 750–753.
Patterson, R. D., Nimmo-Smith, I., Holdsworth, J., and Rice, P. (**1987**). ''An efficient auditory filterbank based on the gammatone function,'' paper presented to the I.O.C. speech group on auditory modelling at R.S.R.E, December 14–15.
Patterson, R. D., Nimmo-Smith, I., Holdsworth, J., and Rice, P. (**1988**). ''Spiral VOS final report, Part A: The auditory filter bank,'' Cambridge Electronic Design, Contract Report (A.P.U. 2341).
Raatgever, J. (**1980**). ''On the Binaural Processing of Stimuli with Different Interaural Phase Relations,'' doctoral dissertation, Delft University of Technology.
Raatgever, J., and Bilsen, F. A. (**1986**). ''A central theory of binaural processing. Evidence from dichotic pitch,'' J. Acoust. Soc. Am. **80**, 429–441.
Shackleton, T. M., Meddis, R., and Hewitt, M. J. (**1992**). ''Across-frequency integration in a model of lateralization,'' J. Acoust. Soc. Am. **91**, 2276–2279.
Small, A. M., and Daniloff, R. G. (**1967**). ''Pitch of noise bands,'' J. Acoust. Soc. Am. **41**, 506–512.
van Tilburg, J. J. (**1974**). ''Central Residu Effekt Met Behulp van de Dichotische Toonhoogtegewaarwording volgens Huggins,'' Masters thesis, Delft University of Technology (unpublished).
Yost, W. A. (**1991**). ''Thresholds for segregating a narrow-band from a broadband noise based on interaural phase and level differences,'' J. Acoust. Soc. Am. **89**, 838–845.

Dichotic pitches as illusions of binaural unmasking. II. The Fourcin pitch and the dichotic repetition pitch

John F. Culling,[a] David H. Marshall, and A. Quentin Summerfield
MRC Institute of Hearing Research, University of Nottingham, University Park, Nottingham NG7 2RD, United Kingdom

(Received 21 February 1996; revised 2 March 1998; accepted 4 March 1998)

The predictions of three models are compared with respect to existing experimental data on the perception of the Fourcin pitch (FP) and the dichotic repetition pitch (DRP). Each model generates a central spectrum (CS), which is examined for peaks at frequencies consistent with the perceived pitches. A modified equalization-cancellation (mE-C) model of binaural unmasking [Culling and Summerfield, J. Acoust. Soc. Am. **98**, 785–797 (1995)] generates a CS which reflects the degree of interaural decorrelation present in each frequency channel. This model accounts for the perceived frequencies of FPs, but produces no output for DRP stimuli. A restricted equalization-cancellation (rE-C) model [Bilsen and Goldstein, J. Acoust. Soc. Am. **55**, 292–296 (1974)] sums the time-varying excitation in corresponding frequency channels, without equalization, to form a CS. A central activity pattern (CAP) model [Raatgever and Bilsen, J. Acoust. Soc. Am. **80**, 429–441 (1986)] generates a CS by scanning an interaural cross-correlation matrix across frequency. The rE-C and CAP models yield inaccurate predictions of the perceived frequencies of FPs, but predict the occurrence of the DRP and its correct pitch. The complementary predictions of the mE-C model compared to the rE-C and CAP models, together with the evidence that the FP is clearly audible for the majority of listeners, while the DRP is faintly heard by a minority of listeners, suggest that the mE-C model provides the best available account of the FP, and that the DRP is produced by a separate mechanism. © *1998 Acoustical Society of America.* [S0001-4966(98)06006-8]

PACS numbers: 43.66.Ba, 43.66.Dc, 43.66.Pn [RHD]

INTRODUCTION

A dichotic pitch occurs when broadband noises applied to the two ears creates a pitch percept through a process of binaural interaction. Four dichotic pitches have been described. Two of them, the Huggins pitch (Cramer and Huggins, 1958) and the binaural edge pitch (Klein and Hartmann, 1981), are addressed in a companion paper (Culling *et al.*, 1998). That paper reports psychoacoustic experiments whose results suggest that a more accurate and parsimonious account of the detection and perceived frequency of these two pitches is provided by a modified equalization-cancellation (mE-C) model of binaural unmasking (Culling and Summerfield, 1995) than by models proposed previously. The present paper is concerned with the other two dichotic pitches: the Fourcin pitch (FP) (Fourcin, 1970) and the dichotic repetition pitch (DRP) (Bilsen and Goldstein, 1974).

The FP and the DRP are produced by presenting noise binaurally with large interaural delays (>1 ms). At least one of the interaural delays must be larger than those which can occur for human listeners in the free field, although the range of interaural delays which give rise to the FP and DRP overlaps the range which can produce the perception of lateralization. To produce the FP [Fig. 1(a)] two independent noises with different interaural delays are presented simultaneously (Fourcin, 1970). A noise is heard containing a sound with an identifiable pitch. The pitch is related to the difference between the interaural delays applied to the two noises. The pitch is ambiguous when the two noises are both interaurally in-phase (i.e., only delayed). An unambiguous pitch is heard if one of the noises is given an interaural phase shift of π radians. Measurements by Bilsen and Wesdorp (1974; Bilsen, 1977) showed that in this latter condition the FP is matched by listeners to a tone whose period is equal to the difference between the interaural delays used in generating the dichotic stimulus.

Fourcin (1970) reported that no pitch was heard if only one noise was presented. Later, Bilsen and Goldstein (1974) showed that a faint pitch could be heard in these circumstances. They called this pitch the ''Dichotic Repetition Pitch'' [Fig. 1(b)]. The name emphasizes a similarity in the generation of the DRP to the generation of monaural repetition pitches (Bilsen, 1966). A monaural repetition pitch is heard in a broadband noise which has been comb filtered by summation with a delayed copy of itself. Like the monaural repetition pitch, the DRP is matched by listeners to a tone whose period is equal to the interaural delay used in generating the stimulus (Bilsen and Goldstein, 1974; Bilsen, 1995).

In fact, one of Fourcin's listeners in his 1958 tests did report hearing a DRP (Fourcin, 1995). Fourcin (1970) did not report the phenomenon because he was uncertain whether this pitch was an artefact. The difficulty most listeners experience in hearing the DRP and its similarity to the monaural repetition pitch have prompted concerns that it might be produced by cross talk through air or bone conduction between the left-ear and right-ear channels, giving rise

[a]New address: University Laboratory of Physiology, Parks Road, Oxford OX1 3PT, United Kingdom.

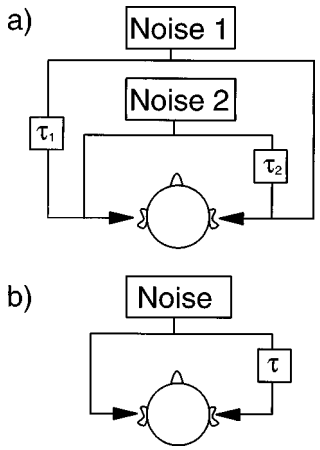

FIG. 1. Schematic illustration of the stimulus configurations which give rise to (a) the Fourcin pitch and (b) the dichotic repetition pitch.

to a repetition pitch which is detected monaurally. However, this concern now appears to be unfounded, since DRPs have been reported (a) at sensation levels as low as +5 dB (Bilsen, 1995) where such cross talk would be inaudible, and (b) using insert earphones (Culling, 1996) which generate very low levels of interaural cross talk (Killion *et al.*, 1985).

In summary, the FP [Fourcin (1970); Fig. 1(a)] is a relatively robust phenomenon. It can be heard by the majority of listeners. In contrast, the DRP [Bilsen and Goldstein (1974); Fig. 1(b)] is a weaker phenomenon. It is not heard easily by all listeners. It would be desirable, therefore, for models of the two phenomena to predict that the FP has materially greater strength than the DRP.

I. THE PRESENT INVESTIGATION

This paper describes three models which can account for the occurrence of dichotic pitches and examines the extent to which each model predicts the DRP and the FP. The principal finding is that the rE-C and CAP models account well for the DRP, but make erroneous predictions of the FP, while the mE-C model cannot predict the DRP, but gives accurate predictions of the FP. In addition, since the mE-C model's account of the FP relies on the use of independent internal delays in each frequency channel, the exitence of the FP corroborates that aspect of the model.

In the following section, Sec. II, we describe the models in qualitative terms. In Sec. III we describe how the models were implemented computationally. In Sec. IV we compare the accuracy with which the models predict examples of the FP and the DRP, explain their mechanisms, and discuss the reasons for the accuracy of their predictions.

II. THREE MODELS OF THE FP AND THE DRP

The models are essentially qualitative. They share the property of generating a spectral display of energy plotted as a function of frequency, often termed a ''central spectrum.'' Central spectra are interpreted in much the same way in each model: the presence of peaks at the frequency of the fundamental and/or its harmonics is taken as evidence of a pitch corresponding to that fundamental frequency.

A. Restricted E-C model (rE-C)

Bilsen and Goldstein (1974) described a model of the FP and the DRP which was based on aspects of Durlach's (1960, 1972) equalization-cancellation (E-C) model of binaural masking release. We call their model the ''restricted'' E-C model (rE-C). The rE-C model is distinct from the ''modified'' E-C (mE-C) model which is described below. In the rE-C model, the signals from the two ears are filtered into separate passbands, internal noise is added, and the waveforms in corresponding channels from the two ears are either summed or cancelled *without* any process of time or phase equalization. The resulting energy in each channel is plotted as a function of channel frequency to produce a central spectrum.

B. Central activity pattern (CAP) model

Bilsen (1977, 1995), Raatgever (1980), and Raatgever and Bilsen (1977, 1986) suggested a model of the DRP and the FP which shares similarities with Jeffress' (1948, 1972) account of sound localization. Their ''central activity pattern'' (CAP) model incorporates the ideas that, following peripheral frequency analysis, time-varying excitation in corresponding frequency channels from the two ears converges on coincidence detectors through internal delay lines of different lengths. Therefore, each coincidence detector is tuned to a particular interaural delay. A set of coincidence detectors covers a range of interaural delays for each center frequency. Thus, the coincidence detectors form a two-dimensional matrix in frequency and interaural delay. The CAP for a given stimulus represents the output of the coincidence detectors across this matrix. For the purposes of predicting pitch values and the lateralization of pitch images, Raatgever and Bilsen assumed that the pattern of activity across the coincidence detectors for a particular center frequency can be approximated by a cross-correlation function. They further approximated the cross-correlation function for each frequency channel with a sinusoid. This approximation is equivalent to the assumption that auditory frequency selectivity is infinitely fine at each center frequency. The resulting CAPs are interpreted by scanning across frequency at a chosen internal delay to produce a central spectrum. It is assumed that central mechanisms can inspect central spectra at all internal delays, but that attention is focused on a single spectrum which displays clear evidence of harmonicity or large amounts of modulation in spectral amplitude as a function of frequency. An ambiguous pitch occurs when more than one well-modulated spectrum is available, and the pitches derived from each are different. The model predicts that listeners hear sounds with spectral properties corresponding to the attended spectrum, which are lateralized according to the internal delay of the spectrum in which it is detected.

C. Modified equalization cancellation (mE-C) model

Culling and Summerfield (1995) described a modified version of Durlach's equalization-cancellation (E-C) model which is designed to account for the binaural masking release of complex sounds. This mE-C model simulates peripheral frequency selectivity using time-domain filters

whose shapes and bandwidths approximate those of human auditory filters (Patterson *et al.*, 1987, 1988). The time-varying excitation in corresponding channels from the two ears is equalized as far as possible by applying (i) adjustments in rms level[1] and (ii) internal delays of up to ± half the period of the center frequency of the channel (but no greater than ±5 ms), and is then cancelled (to the extent that equalization was achieved) through subtraction. The equalization process is performed independently in each frequency channel (i.e., using different adjustments of internal delay and level, if necessary). The residual energy in each channel after subtraction is plotted as a function of center frequency to generate a central spectrum [termed a ''recovered spectrum'' by Culling and Summerfield (1995)]. Culling *et al.* (1998) demonstrated that recovered spectra display spectral peaks at frequencies consistent with the Huggins pitch and the binaural edge pitch.

III. IMPLEMENTATION OF THE MODELS

The models were implemented in a common format. Their input was the digitized waveforms of the sounds presented to the left and right ears in a stimulus generating a FP or a DRP. Their outputs were displays of central spectra; that is, plots of energy as a function of frequency.

A. The E-C model

In order to simplify comparisons with the CAP and mE-C models, the rE-C model was implemented in a slightly different way from that described by Bilsen and Goldstein (1974). They made the reasonable assumption that auditory frequency channels have Gaussian-shaped passbands whose bandwidths correspond to psychophysical estimates of critical bandwidths measured by Zwicker and Feldkeller (1967). Our implementation of the rE-C model reflects more recent estimates of the shapes and bandwidths of auditory filters (Patterson, 1976; Moore and Glasberg, 1983). Auditory frequency selectivity was modeled with the Patterson *et al.* (1987, 1988) gamma-tone filterbank, whose frequency channels have passbands which approximate a rounded-exponential shape and equivalent rectangular bandwidths which vary with center frequency according to the formula provided by Moore and Glasberg [1983, Eq. (3)]. Moore and Glasberg's formula specifies somewhat narrower bandwidths in channels than those suggested by Zwicker and Feldkeller. Following frequency analysis, the waveforms in corresponding frequency channels from the two ears are both added and subtracted. For each of these operations separately, the resulting rms energy in each channel is plotted in dB as a function of channel center frequency to generate two alternative central spectra.

B. The CAP model

Three versions of the CAP model were implemented. In the first version, here called the ''original'' version, cross-correlation functions at each frequency were calculated as sinusoidal functions of internal delay using the formulas suggested by Raatgever and Bilsen [1986, Eq. 6)]. Following Raatgever (1980), the principle of superposition was assumed to hold when this version of the model was used to model the FP; the CAP for a FP stimulus was generated by summing the two CAPs for appropriate DRP configurations, producing an interference pattern. In the second (''weighted'') version of the model, the CAP from the first version was weighted according to frequency and internal delay in the manner suggested by Raatgever (1980, Eqs. IV.1 and IV.2), thereby giving greatest emphasis to frequencies around 600 Hz and to ''central'' locations (i.e., those close to the median plane). This central-weighting function was previously postulated by Colburn (1973, 1977) to account for the variation of the BMLD with frequency. The third (''smoothed'') version of the model was used to examine the effects of incorporating more realistic frequency resolution; the across-frequency scans from the first version were low-pass filtered using a rounded-exponential-shaped moving-average filter, whose bandwidth varied with frequency in accordance with Moore and Glasberg [1983, Eq. (3)]. With each version of the model, the resulting CAP could either be scanned across frequency at any fixed internal delay to generate an across-frequency scan, or analyzed for individual peaks across all scans which are particularly prominent.

C. The mE-C model

The mE-C model was implemented in the way described by Culling and Summerfield (1995) and Culling *et al.* (1998). Stimulus waveforms were filtered using the gamma-tone filterbank and peripheral transduction was simulated using the Meddis (1986, 1988) hair-cell model; the waveforms in corresponding frequency channels were equalized in rms level[1] and then internal delay using delays of up to ±5 ms; the waveforms were cancelled using subtraction over a exponentially tapering window with a 50-ms time constant; the residual rms energy was plotted in dB as a function of channel center frequency.

IV. RESULTS OF MODELING THE DRP

The ability of the models to predict DRPs was systematically examined for stimuli with a range of interaural delays. We report results obtained with a representative test stimulus which consisted of a segment of white noise, duplicated in the left-and right-ear channels, and leading at the right ear by 4 ms. Bilsen and Goldstein (1974) showed that the pitch frequencies of DRP stimuli are the reciprocals of their interaural delays, $\tau(2<\tau<12$ ms). So, a 4-ms interaural delay should generate a pitch equivalent to that of a 250-Hz tone.

A. The rE-C model

Figure 2 shows the central spectrum of the DRP test stimulus generated by the present implementation of the rE-C model for both the subtraction and addition operations. The spectrum from the addition operation contains peaks at the harmonics of the fundamental frequency corresponding to the DRP: 250, 500, 750 Hz, etc. The low-frequency peaks are well defined with a peak–valley ratio of about 5–10 dB. As observed by Bilsen and Goldstein (1974), the rE-C model

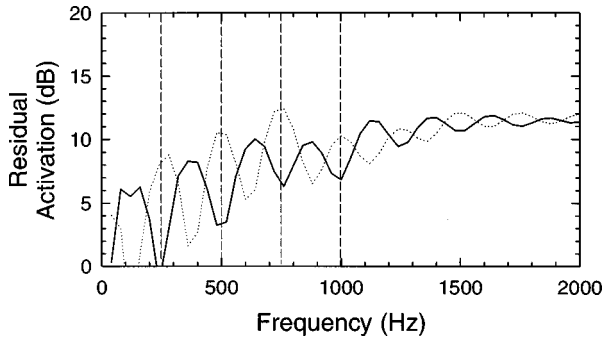

FIG. 2. Output spectra produced by the rE-C model in subtraction mode (solid line) and addition mode (dotted line) when presented with a 4-ms DRP (white noise which is interaurally delayed by 4 ms).

predicts a clear pitch at the frequency of the DRP using the addition operation. Using the subtraction operation, however, the pattern of peaks and valleys is inverted.

The model produces a central spectrum with the correct pattern using the addition operation for the following reason. The filtered waveforms in corresponding channels are approximately sinusoidal waveforms of equal frequency. When added together, the amplitude of the resulting waveform depends, therefore, on the phase difference between these sinusoids. In channels whose center frequencies are integer multiples of the reciprocal of the interaural delay, the sinusoids from the delayed ear are delayed by an integer number of cycles, and their phases are therefore similar to those at the other ear. As a result, the waveforms maximally reinforce each other when they are summed. Conversely, in channels whose center frequencies are located half-way between integer multiples of the reciprocal of the interaural delay, the phases at the two ears differ by approximately π radians, and the waveforms cancel when summed. Thus, with an interaural delay of 4 ms, reinforcement occurs at frequencies that are integer multiples of 250 Hz.

B. The CAP model

Figure 3 shows the results of analyzing the DRP test stimulus with the three versions of the CAP model described in Sec. II B. Figure 3(a)–(c) illustrates results from the original, weighted, and smoothed versions of the model, respectively. In each case, values on the (internal) delay axis indicate the cross-correlation delay of channels from the right ear. The insets contain plots of an across-frequency scan taken at 0-ms internal delay.

All three CAPs contain ridges of activation which sweep gradually down in frequency with increasing internal delay. An across-frequency scan taken at any particular internal delay displays a succession of peaks at integer multiples of a common fundamental. However, the frequency of the fundamental depends on the internal delay at which the scan is made. This result can be seen most clearly in Fig. 3(a): at -1-ms internal delay, the peaks are at multiples of 333 Hz; at 0-ms internal delay, the peaks are at multiples of 250 Hz; at $+1$-ms internal delay, the peaks are at multiples of 200 Hz. Therefore, according to the CAP model, the listener may

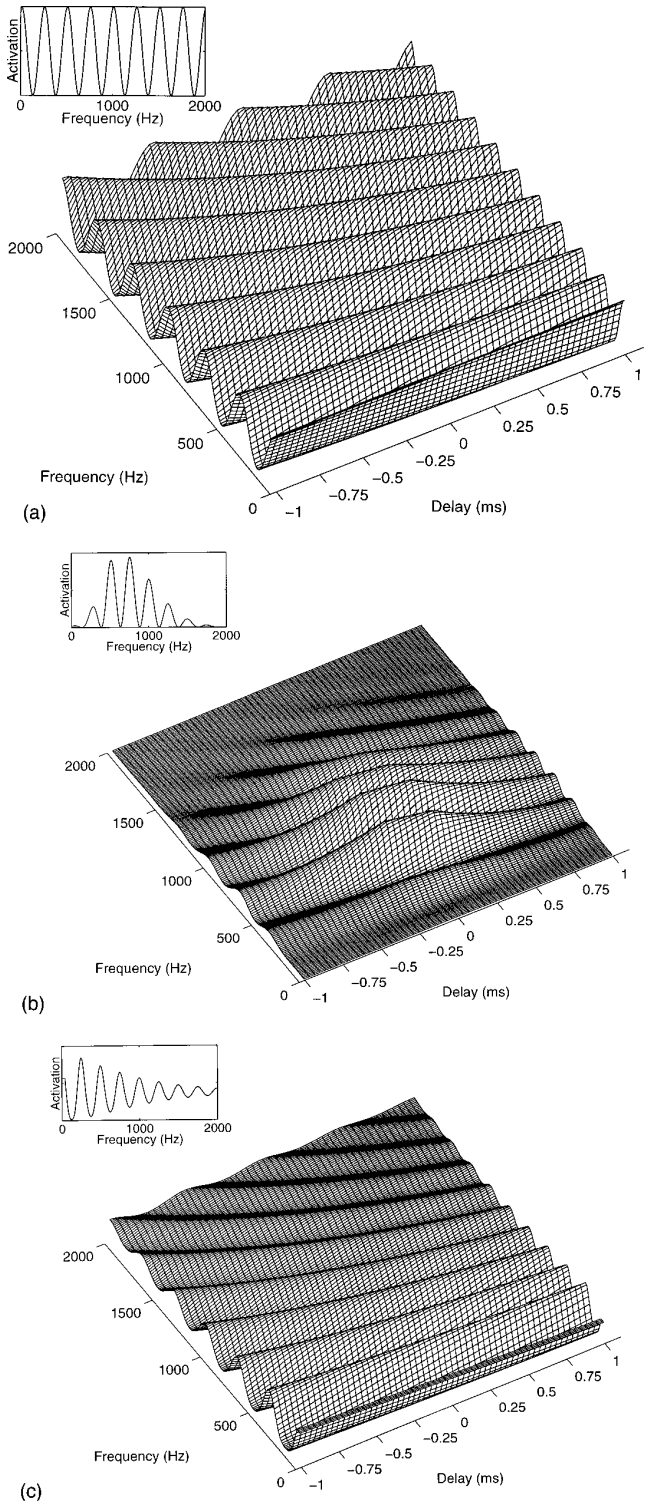

FIG. 3. Central activity patterns (CAPs) produced by the three versions of the CAP model from a 4-ms DRP (white noise which is interaurally delayed by 4 ms). (a) The CAP produced by the ''original'' version, described by Raatgever and Bilsen [1986, Eq. (6)]. (b) The CAP produced by the ''weighted'' version, using Raatgever and Bilsen [1986, Eq. (6)] with central weighting applied in accordance with Raatgever (1980, Eqs. IV.1 and IV.2). (c) The CAP produced by the ''smoothed'' version, using Raatgever and Bilsen [1986, Eq. (6)] and smoothing across frequency by a rounded-exponential-shaped, moving-average filter of varying bandwidth (Moore and Glasberg, 1983), to reflect realistic frequency resolution.

experience a continuum of pitches with different spatial locations, or possibly experience different pitches on successive presentations in accordance with the current direction of attention. When measured psychophysically using a match-

ing paradigm (Bilsen and Goldstein, 1974; Bilsen, 1995), the pitch of the DRP always corresponds to the pattern of peaks found in the central across-frequency scan (i.e., at 0-ms internal delay). One way in which the correct prediction can be made consistently is to invoke the principle of central weighting which was incorporated in the weighted version of the model [Fig. 3(b)], and might emphasize features which are located close to the median plane. However, the weighting function does not fulfill this role in the model, since the model searches for spectra which are well modulated in the sense that they have high peak-to-valley ratios (Bilsen, 1997). The central weighting cannot have any effect upon peak-to-valley ratios within a single scan, so an eccentric scan is no less likely to display high modulation in this sense than a central one.[2] The resulting ambiguity is thought responsible for the fact that the perceived pitch is ''faint'' (Bilsen, 1995).

Figure 3 shows that the three versions of the model produce CAPs which contain broadly similar cues for the DRP. The assumption of infinitely high frequency resolution, which is inherent in Raatgever and Bilsen's use of sinusoids as an approximation to cross-correlation functions in the original version of the model, is not critical for the model to predict the DRP. This assumption was also found to have little influence on predictions of the Fourcin pitch which are discussed below. In contrast, the original version of the CAP model predicts both the Huggins pitch and the binaural edge pitch while the smoothed version does not (Culling *et al.*, 1998). For simplicity, further illustrations in the present paper of the predictions of the CAP model are based on CAPs obtained from the original version of the model [as in Fig. 3(a)].

C. The mE-C model

The spectra recovered by the mE-C model in response to the DRP are irregular noise spectra with no sign of peaks at multiples of 250 Hz. There is no evidence that the mE-C model can predict the DRP. This outcome is easy to understand from the mechanism of the model. The stimulus contains identical white noise which is interaurally delayed by 4 ms. The model can apply internal delays of up to 5 ms before canceling the signals so the model applies a compensating 4-ms internal delay and then cancels the waveforms completely.

V. RESULTS OF MODELING THE FP

Before considering the responses of the three models to the Fourcin pitch it is worth considering a representative set of example stimuli on which they may be tested. There are three interesting dichotomies which divide the possible configurations of a two-noise Fourcin pitch: (1) whether or not one of the two noises is interaurally inverted, (2) whether or not the delay applied to one of the noises lies within the ecological range of delays (i.e., $\pm 600\ \mu$s), and (3) in the case of a stimulus in which one noise is inverted and one noise has a delay within the ecological range, whether those are the same noise or different noises. To explore each of these dichotomies requires a minimum of five cases (a)–(e).

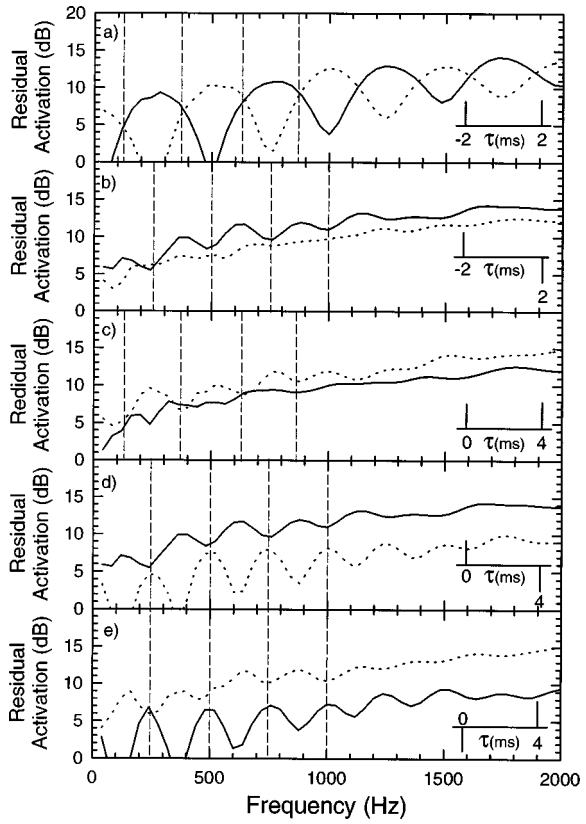

FIG. 4. Output spectra produced by the rE-C model when presented with different FP stimuli in subtraction mode (solid lines) and addition mode (dotted lines). (a) Two independent noises delayed by ± 2 ms. (b) Two independent noises delayed by ± 2 ms; one noise is also phase shifted at one ear by π radians. (c) Two independent noises delayed by 0 and 4 ms. (d) Two independent noises delayed by 0 and 4 ms; one noise is also phase shifted at one ear by π radians. (e) Two independent noises delayed by 0 and 4 ms; the first noise is also phase shifted at one ear by π radians. In each panel, the different stimuli are signified by schematic illustrations of their cross-correlation functions.

We have chosen to investigate stimuli for which $\tau_1 - \tau_2 = 4$ ms; the delays used were either ± 2 ms, or 0 and 4 ms.

A. The rE-C model

Figure 4 shows spectra recovered by the rE-C model from the five test stimuli, using the addition (dotted-line spectra) and subtraction (solid-line spectra) operations. Figure 4(a) contains the spectra recovered from a stimulus with interaural delays of ± 2 ms. Figure 4(b) contains the spectra recovered from the same stimulus, but with one noise phase shifted by π radians at one ear. Figure 4(c) contains the spectra recovered from a stimulus with interaural delays of 0 and 4 ms. Figure 4(d) contains the spectra recovered from the same stimulus, but with the 4-ms-delayed noise phase shifted by π radians at one ear. Figure 4(e) shows the spectra from the same stimulus, but with the undelayed noise inverted. Bilsen and Wesdorp (1974) found that listeners hear a clear pitch corresponding to a tone, whose frequency, f, can be predicted using Eq. (1) when one noise is phase shifted, where τ_d is the difference in interaural delay between the two noises in milliseconds ($\tau_1 - \tau_2$). In the cases shown in Fig. 4(b), (d), and (e), therefore, a pitch of 250 Hz

is heard. When neither noise is phase shifted, Bilsen and Wesdorp (1974) reported that listeners hear an ambiguous pitch which is matched to a tone whose frequency can be predicted using Eq. (2). Thus, the examples shown in Fig. 4(a) and (c) would be matched to 204 and 323 Hz:

$$f = 1000/|\tau_d|, \tag{1}$$

$$f = 1000/|\tau_d \pm 0.9|. \tag{2}$$

The rE-C model does not predict these outcomes. For reasons which will be elucidated fully in Sec. V C, an ambiguous pitch is predicted for $\tau_d = 4$ ms when the spectrum displays peaks at odd multiples of 125 Hz. An unambiguous pitch is obviously predicted when peaks occur at multiples of 250 Hz. The vertical dashed lines in Fig. 4 indicate the frequencies at which peaks should appear in order to provide these correct predictions. On this basis, none of the spectra in Fig. 4(a)–(c) reflect the pitches which should be heard, while in Fig. 4(d) and (e), one of the two spectra show the correct pattern while the other does not. Figure 4(a), which should be ambiguous, has spectra with peaks at multiples of 500 Hz and at odd multiples of 250 Hz, rather than at odd multiples of 125 Hz. Figure 4(b), which should be unambiguous, has one featureless spectrum and one with peaks at odd multiples of 125 Hz rather than multiples of 250 Hz, implying an ambiguous pitch rather then an unambiguous one. Figure 4(c), which should be ambiguous, shows a featureless pattern in the subtraction (solid) spectrum, and an inverted pattern in the addition (dotted) spectrum. Figure 4(d), which should be unambiguous, shows the appropriate pattern in the addition (dotted) spectrum, but the inverse pattern in the subtraction (solid) spectrum. Figure 4(e) shows the appropriate pattern in the subtraction (solid) spectrum, but the inverse in the addition (dotted) spectrum. Thus, although each of Fig. 4(d) and (e) is predicted correctly by one or another operation of the rE-C model (with different operations required to predict different cases), it is not clear how the model would select the appropriate operation each time. In the case of the DRP which was analyzed in Sec. IV A, one could argue that the addition spectrum should be selected because it gives a harmonic spectrum. If that rule were applied here, the pitches of Fig. 4(d) and (e) would both be unambiguous, because each stimulus generates the option of a harmonic spectrum. In summary, therefore, the rE-C model does not predict the Fourcin pitch, since none of the spectra produced in Fig. 4(a)–(c) are correct, although cases (d) and (e) can be predicted correctly by selecting different operations for different cases.

B. The CAP model

In order to properly assess the performance of the CAP model in predicting the perception of Fourcin pitches it is necessary to consider in a little more detail the mechanism by which scans and features within scans are selected. Raatgever and Bilsen (1986) nominated three cues which might be used in this process, but did not propose algorithms for evaluating the cues and combining the information which they provide. The cues are (1) depth of spectral modulation within a scan, (2) harmonicity of the peaks within a scan, and (3) other spectral patterning. We shall confine ourselves here to the first two cues, whose detection and evaluation can be implemented computationally with relative ease.

Depth of modulation is defined as peak-to-valley ratio. However, modulation cannot be calculated simply as the ratio of the largest maximum in the function to the smallest minimum; if it were so, then all scans in a Fourcin pitch stimulus would be judged to have equal modulation. Rather, peaks must be compared with adjacent valleys. Furthermore, those peaks which are close to the spectral dominance region are assumed to play a greater role in selection than those further away (Bilsen, 1997), so each ratio is weighted according to the function suggested by Raatgever (1980, Eq. IV.1). Finally, it seems reasonable that the *mean* weighted peak-to-valley ratio across all the peaks in the scan should be the relevant selection parameter.

It would be a straightforward matter to select a psychoacoustically appropriate metric for harmonicity from the literature. However, as will become clear, the peaks produced by the CAP model in response to Fourcin pitch stimuli tend either to be precisely harmonic, or quite inharmonic, so a simple dichotomous distinction will serve the current purpose. It is also unclear how information about degree-of-harmonicity and depth-of-modulation might be combined in an overall salience measure, but, again, for these particular stimuli, no conflict of interpretation turns on this issue.

As a result of these considerations, our modeling of the process of selecting scans and of selecting features within scans has the following steps. First, the CAP is generated using Eq. (3), where the magnitude of the pattern at frequency f and delay τ_i is related to the two external delays applied to the noises in the stimuli τ_1 and τ_2. Equation (3) is derived from Raatgever and Bilsen's (1986) Eq. (6), which gives the CAP for a single noise source, by following the principle of superposition (Raatgever, 1980). Addition or subtraction is used depending upon whether the noise of interaural delay τ_2 has been interaurally inverted (subtraction being employed in the inverted case). We have added a small shift parameter, s, that prevents the CAP from evaluating to zero and causing problems when calculating the peak-to-valley ratio. The results below were produced using $s = 0.01$:

$$\mathrm{CAP}(f, \tau_i) = (1 - s) \times \frac{2 + \cos(2\pi\tau_i f + 2\pi f\tau_1) \pm \cos(2\pi\tau_i f + 2\pi f\tau_2)}{4} + s. \tag{3}$$

Each scan (at internal delay τ_i) is assessed for its modulation index (mean weighted peak-to-valley ratio), M, by locating all the n peaks of height, P_j, and valleys of height, V_j, that occur in the range 0–2 kHz [Eq. (4)]. In Eq. (4) w_j is the mean weight of the jth peak and valley calculated according to Eqs. (5) and (6) from Raatgever (1980), where f is the frequency at which the peak or valley is found. The value of s scales the values of M (a quasi-power-law com-

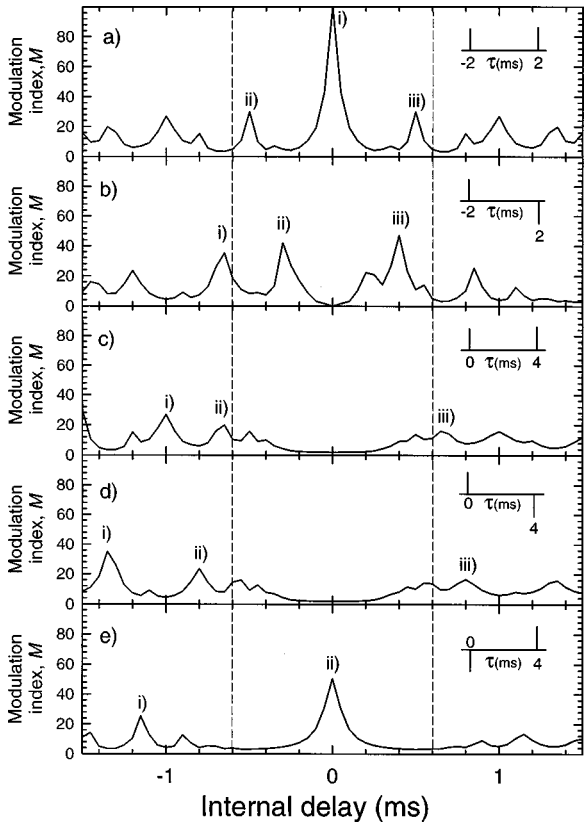

FIG. 5. The modulation index, M, as a function of internal delay of scans taken from central activity patterns (CAPs) produced according to Eq. (3) for different FP stimuli. (a) Two independent noises delayed by ± 2 ms. (b) Two independent noises delayed by ± 2 ms; one noise is also phase shifted at one ear by π radians. (c) Two independent noises delayed by 0 and 4 ms. (d) Two independent noises delayed by 0 and 4 ms; the second noise is also phase-shifted at one ear by π radians. (e) Two independent noises delayed by 0 and 4 ms, the first noise is also phase shifted at one ear by π radians. In each panel, the different stimuli are signified by schematic illustrations of their cross-correlation functions. Prominent peaks have been marked for reference by lower case numerals.

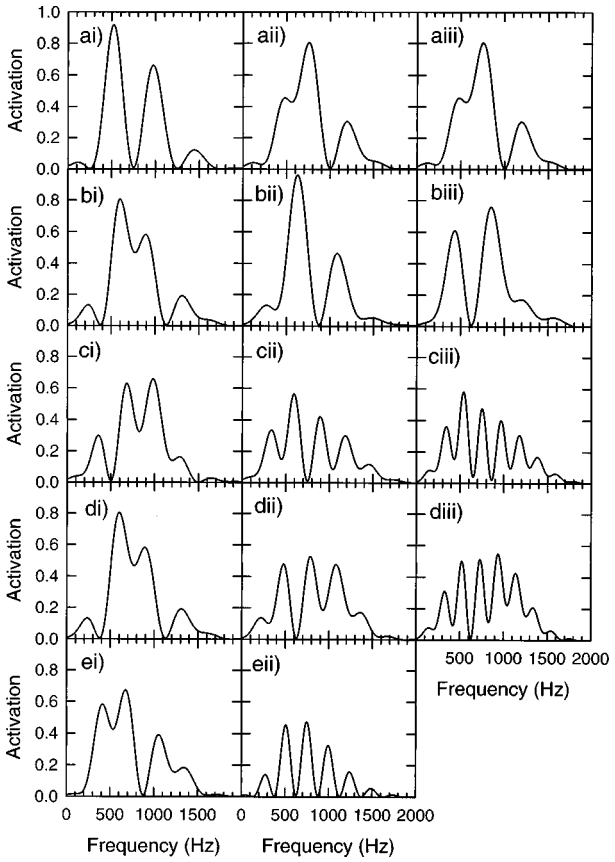

FIG. 6. Across-frequency scans from the CAP at each of the interaural delays marked in Fig. 5 (i–iii), for each of the five example stimuli (a)–(e). The scans have been weighted according to Eq. (5) in order to emphasize the features within the dominance region.

pression), but does not affect the delays at which maxima in $M(\tau_i)$ occur:

$$M(\tau_i)=\frac{\Sigma_{j=1}^{n}(P_j/V_j)w_j}{\Sigma_{j=1}^{n}w_j}, \tag{4}$$

$$w(f_j)=\exp([f_j/300-2]^2), \quad f_j<600 \text{ Hz}, \tag{5}$$

$$w(f_j)=\exp([f_j/600-1]^2), \quad f_j\geqslant 600 \text{ Hz}, \tag{6}$$

One or more well-modulated scans are then assessed for their harmonic content. Figure 5 shows the variation of M as a function of internal delay for each of the five example stimuli. A number of prominent peaks in M are evident which have been labelled (lower case numerals) for future reference. Dashed vertical lines have been drawn on the figure at ± 600 μs, which represent the approximate boundaries of the ecological range of delays. Well-modulated scans which occur at substantially larger internal delays should be regarded with some scepticism, as there is no biological reason for the auditory system to have developed a scanning mechanism which operates outside this range.[3]

Figure 6 shows the central spectra which can be found by scanning at each of the delays which were labelled as prominent peaks in M in Fig. 5. Table I gives the frequencies of the most prominent spectral peaks in each of these scans, along with the closest fitting fundamental frequency ($F0$) for each set. The $F0$'s were derived by a weighted least-squares fitting procedure in which the squared difference between each peak frequency and the matched harmonic frequency was weighted according to the peak frequency using Eqs. (5) and (6).[4] These $F0$'s are discrepant in many cases with the pitch-matching data collected by Bilsen and his colleagues, as summarized by Eqs. (1) and (2). As noted above, the expected pitch from Eq. (1) for Fig. 5(b), (d), and (e) is 250 Hz, while those from Eq. (2) for Fig. 5(a) and (c) are 204 and 323 Hz. These predictions are correct only in cases (c) and (e): in case (c) an ambiguous pitch is correctly predicted whose frequency is 336, 297, or 214 Hz, depending on which scan is selected; 336 and 214 Hz may be acceptable approximations to 323 or 204 Hz; in case (e), an unambiguous pitch of 250 Hz is correctly predicted [Fig. 6(eii)] by the scan at zero delay and it seems reasonable that the other scan should be neglected since it comes from a delay outside the range ± 600 μs. In the other cases, the CAP model's predictions are incorrect: in case (a) a pitch of 500 Hz is strongly predicted by a scan which is both the most modulated of all scans investigated and also perfectly harmonic, but the pitch should be ambiguous; in case (b) pitches of 290, 302, and 417 Hz are predicted when the pitch should be unambiguously 250 Hz; similarly in case (d), pitches of 290, 248, and

TABLE I. The frequencies at which prominent peaks occur in the best modulated scans for each of the five example Fourcin pitch stimuli. The frequencies are derived from the unweighted scans, but only those peaks which show prominently in the panels of Fig. 6 (showing the weighted scans) are listed. In the two cases indicated in the penultimate column, the frequencies of the peaks form a perfect harmonic series. For all cases, the closest fitting $F0$'s, according to a weighted least-squares metric, are given in the last column.

Panel of Fig. 6	τ_1 (μs)	τ_2 (μs)	Inverted?	τ_i (μs)	Peak 1 (Hz)	Peak 2 (Hz)	Peak 3 (Hz)	Peak 4 (Hz)	Peak 5 (Hz)	Harmonic?	Closest $F0$ (Hz)
ai)	−2000	2000	n	0	500	1000	1500			y	500
aii)				−500	432	768	1232	1568		n	396
aiii)				+500	432	768	1232	1568		n	396
bi)	−2000	2000	y	−650	158	596	912	1349		n	290
bii)				−300	630	1118				n	302
biii)				400	386	864				n	417
ci)	0	4000	n	−1000	317	683	1000			n	336
cii)				−650	290	591	900	1203		n	297
ciii)				650	425	643	862	1080	1294	n	214
di)	0	4000	y	−1350	158	596	912	1349		n	290
dii)				−800	460	790	1102			n	248
diii)				800	307	518	732	943	1149	n	178
ei)	4000	0	y	−1150	363	679	1076			n	346
eii)				0	250	500	750	1000	1250	y	250

178 Hz are predicted when the pitch should be 250 Hz. In this last case, the correct pitch is among those predicted by the model, but unlike case (e), there is no reason to believe that the 250-Hz pitch should be preferred over the alternatives, as the scans containing each pitch lie outside the ecological range. The CAP model can account for cases (c) and (e), but it is clearly in error when compared with Eqs. (1) and (2) in cases (a), (b), and (d).

In summary, the CAP model fails to predict the FP correctly in an important set of cases. Raatgever (1980) has shown that some stimulus configurations produce appropriate results and the CAP model can also predict the lateralization of the pitch for these stimuli (Raatgever and Bilsen, 1986). However, our more systematic exploration yielded clearly erroneous predictions. Interestingly, both here and in Raatgever's treatment, the model predicts the Fourcin pitch for stimulus configurations in which one of the two noises has a small delay (i.e., within the ecological range) relatively well. We have shown here that when the delays are equal and opposite, and thus both outside the ecological range, the CAP model is clearly at odds with Eqs. (1) and (2), and the extensive empirical data on which they are based (Bilsen, 1997, Fig. 5).

C. The mE-C model

Figure 7 contains spectra recovered by the mE-C model in response to the same five FP stimuli which were analyzed by the other two models. The predictions are consistent with the pitches heard in these stimuli, which were summarized by formulas suggested by Bilsen and Wesdorp (1974). Psychophysically, cases (b), (d), and (e) yield unambiguous pitches of 250 Hz. Correspondingly, Fig. 7(b), (d), and (e) contains peaks at integer multiples of 250 Hz, consistent with an unambiguous pitch of $1000/(\tau_d)$ Hz; i.e., 250 Hz in the case where the interaural delays are ± 2 ms. Psychophysically, cases (a) and (c) yields ambiguous pitches. According to Bilsen and Wesdorp the pitches should be $1000/(\tau_d \pm 0.9)$ Hz or 204 and 323 Hz, where the interaural delays are ± 2 ms. Figure 7(a) and (c) shows dips at multiples of 250 Hz. This pattern might be expected to give rise

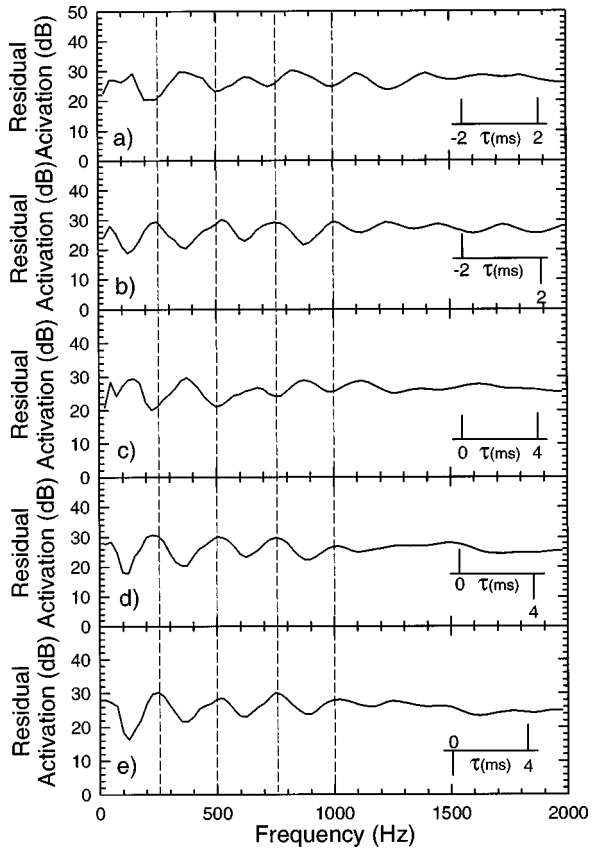

FIG. 7. Spectra recovered by the mE-C model in response to different FP stimuli. On each panel, the different stimuli are signified by schematic illustrations of their cross-correlation functions.

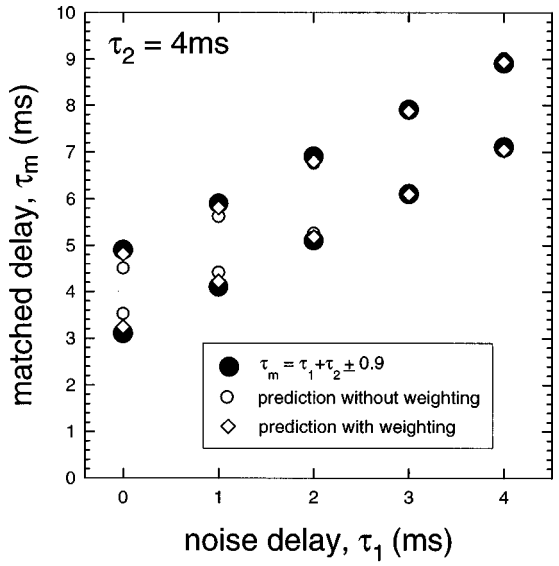

FIG. 8. Predictions of the ambiguous pitches of the FP stimuli which do not have any interaural phase inversion. The figure is designed for comparison with Bilsen (1977, Fig. 5), and consequently shows the period of the matching fundamental frequency on the ordinate. Predictions from the empirically derived Bilsen and Wesdorp formula [Eqs. (1) and (2)], which represent the observed data, are shown as filled circles. Predictions from a simple least-squares fitting procedure which matched the frequencies of the first five audible components produced by the mE-C model to the harmonics 1–5 or 2–6 of an adjustable fundamental frequency are shown as open circles. Predictions from a similar, but weighted, fit (see text) are shown as open diamonds.

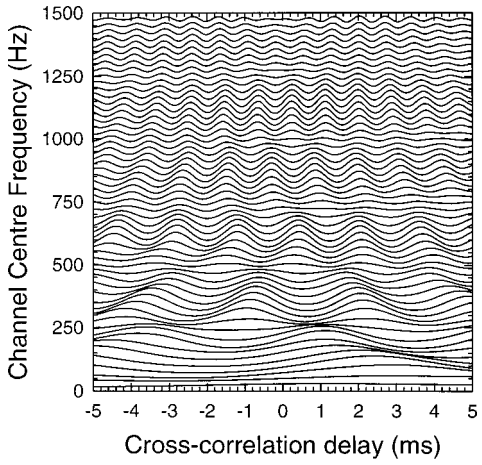

FIG. 9. Cross correlogram of a Fourcin pitch stimulus with delays of ± 2 ms and inversion of one noise at one ear. The cross correlogram was generated by passing the left- and right-channel waveforms through a pair of gammatone filterbanks, with frequency channels 25 Hz apart. The filtered waveforms were processed by the Meddis (1986, 1988) hair cell model and then waveforms from corresponding channels from left and right were cross correlated over and exponentially tapering window (time constant 50 ms).

to an unambiguous pitch with a fundamental frequency of 125 Hz, represented by odd-numbered harmonics. The ambiguity which is heard by listeners can be explained if it is assumed that the first harmonic is inaudible or is very weak and that de Boer's (1956, 1976) rule can, therefore, be applied to the remaining components. This assumption is reasonable given the weakness of binaural masking release below about 200 Hz. de Boer's rule states that the pitch of an inharmonic series will correspond to the fundamental frequency whose *consecutive* harmonic frequencies best fit the frequencies in the stimulus. Figure 8 compares the results of such a fitting process, using a weighted, least-squares procedure, with the predictions of the Bilsen and Wesdorp formula. Harmonics 1–5 and 2–6 of an adjustable fundamental frequency were fitted to the frequencies of the first five audible peaks in the CS [i.e., odd harmonics 3–11 of $1/(2\tau_d)$]. The two fits, matching to different sets of harmonics, yield two points at each value of τ_1. The ordinate of Fig. 8 is the reciprocal of the fitted fundamental, because the figure is designed for comparison with Fig. 5 of Bilsen (1977).

Bilsen's figure shows matches between various FPs and monaural repetition pitches generated with interaural delay (τ_m); that data was used to derive the Bilsen and Wesdorp formula. For simplicity, only the results of modeling a subset of the data in Bilsen's figure are shown in Fig. 8, but both the predictions of the Bilsen and Wesdorp formula and of the present fitting process can be extended to the other conditions in Bilsen's figure by horizontal translation. Two weighting functions were used in the fitting process which (1) weighted the input frequencies according to the variation in the strength of binaural masking release with frequency [Eqs. (5) and (6)] and (2) weighted the fitted harmonics according to harmonic number in order to reflect the relative dominance of low-numbered harmonics in pitch perception (Ritsma, 1967) using the formula suggested by Cohen *et al.* [1995, Eq. (9)]. Each of these weighting functions improved the quality of the fit (compare open circles and diamonds for the combined effect). The quality of fit was also poorer if fewer than five components were compared, but did not change if more components were compared.

Further evidence that the spectra produced by the mE-C model predict listeners' percepts correctly is provided by Fourcin's (1958) pitch-matching data. Fourcin asked listeners to match the FP to the pitch of a pure tone by adjusting the magnitude of one of the two delays. He found that the matching difference in delays was always related to the period of the tone by a simple-number ratio. The majority[5] of Fourcin's data can be reconciled with those from Bilsen's group if one assumes that Fourcin's listeners, cued by the use of a pure-tone comparison stimulus, listened analytically and matched the frequency of the second spectral peak in the recovered spectrum to that of the tone, while Bilsen's listeners, cued by the use of a comparison stimulus with multiple spectral peaks (the monaural repetition pitch), listened synthetically and matched the pitch of the whole recovered spectrum.

The action of the mE-C model in this context may be better understood by looking at a cross-correlogram generated (as in the mE-C model) using a gammatone filterbank and hair cell model, but then following it by cross correlation of corresponding frequency channels from the two ears. Figure 9 shows such a cross correlogram for a Fourcin pitch stimulus generated using delays of ± 2 ms with inversion of one noise at one ear. The pattern clearly shows frequency regions where the cross-correlation function is modulated and those where it is nearly flat, the latter being bands of decorrelation. These bands of decorrelation give rise to the

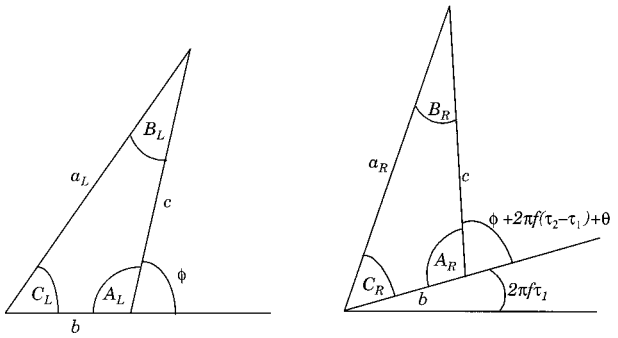

FIG. 10. Vector diagrams illustrating the vector summation of components from each of the two noises in a Fourcin pitch stimulus at the left and right ears. The amplitudes of these two components, b and c, are the same at each ear. The phases of the two components (at source) differ by ϕ. The noises are interaurally delayed by τ_1 and τ_2, and the second noise is phase shifted by θ at the right ear. The resultant amplitudes, a_L and a_R, and the resultant phase difference, $C_R+2\pi f\tau_1-C_L$, can be derived using the sine and cosine rules (see text). For completeness, the other angles have been given the usual labels for the vertices of a triangle when describing the sine and cosine rules.

perception of the frequency components which are heard, together, as the pitch. In other frequency bands, the mE-C model finds delays at which the cross correlation is at a maximum and is able, using those delays, to equalize the waveforms to some extent and so to partially cancel them. In the decorrelated bands this process is impossible, because the waveforms are dissimilar at all delays. Notice that in order for the model to cancel all the frequency bands which display correlation, different delays must be used at different frequencies. This feature of the mE-C model, originally included in order to account for the masking release of speech in the NπSo condition, is essential to the correct prediction of the Fourcin pitch.

D. Mathematical analysis

The scope of the mE-C model can be generalized to all stimulus configurations by considering the process which gives rise to these results. It should be emphasized that the analysis that follows is not a detailed mathematical analysis of the computational model described above; the analysis takes account of only the most essential features of that model, optimal delay and cancellation. This simplification can be justified on the grounds that we have found the peripheral nonlinearities of the Meddis hair cell model to be superfluous to the prediction of the Fourcin pitch using the computational model.

The stimuli are filtered by the peripheral auditory system into narrow frequency bands within which the two noises in a FP stimulus interact. Each channel admits a small group of sinusoidal components of similar frequency but widely differing amplitudes and phases. At each ear, and at each frequency, corresponding sinusoidal components from the two noises summate vectorially. The resultant components are illustrated in Fig. 10 here: τ_1 and τ_2 are the interaural delays of the two noises; ϕ is the difference in the phase of the two sources at the left ear, ranging from 0 to 2π at frequency, f; b and c are the amplitudes, from a Rayleigh distribution, of the two sources at frequency, f; and θ is 0 or π depending on whether or not one noise source has been inverted at one ear. Equations (7) and (8) specify the signal at each ear, at one frequency. Here $L(t)$ and $R(t)$ are the signals at each ear:

$$L(t)=a_L \sin(2\pi ft+C_L), \tag{7}$$

$$R(t)=a_R \sin(2\pi f(t+\tau_1)+C_R). \tag{8}$$

From Fig. 10, Eqs. (7) and (8) can be expanded, using the sine and cosine rules:

$$L(t)=\sqrt{b^2+c^2+2bc\cos(\phi)}\times\sin\left(2\pi ft+\sin^{-1}\left[\frac{c\sin(\phi)}{\sqrt{b^2+c^2+2bc\cos(\phi)}}\right]\right), \tag{9}$$

$$R(t)=\sqrt{b^2+c^2+2bc\cos(\phi+2\pi f[\tau_2-\tau_1]+\theta)}\times\sin\left(2\pi f(t+\tau_1)+\sin^{-1}\times\left[\frac{c\sin(\phi+2\pi f[\tau_2-\tau_1]+\theta)}{\sqrt{b^2+c^2+2bc\cos(\phi+2\pi f[\tau_2-\tau_1]+\theta)}}\right]\right). \tag{10}$$

The model applies an internal delay, τ_i, to these two signals in order to align the sinusoids at each ear (say delaying R relative to L) and also an amplitude compensation. Each channel will admit many such sinusoids, so for cancellation to be effective, the required internal delay, τ_i, and the interaural difference in amplitude must be relatively constant across all frequencies within the channel.

Consider first the equalization of amplitude. The interaural difference in amplitude, Δ_{amp}, at a given frequency may be calculated by subtracting the amplitude parts of Eqs. (9) and (10):

$$\Delta_{\text{amp}}=\sqrt{b^2+c^2+2bc\cos(\phi)}-\sqrt{b^2+c^2+2bc\cos(\phi+2\pi f[\tau_2-\tau_1]+\theta)}. \tag{11}$$

Since ϕ will be uniformly distributed within a given frequency band, the differences in resultant amplitudes will, in most cases, also be random across the frequencies within that channel. Thus, the interaural differences in amplitude of the component frequencies within a channel cannot be equalized simultaneously, guaranteeing that there will be some residue after cancellation. However, it may readily be seen from Eq. (11) that, for certain values of τ_1, τ_2, and f, Δ_{amp}, will evaluate to zero for all ϕ, all b, and all c. When $\theta=\pi$, $\Delta_{\text{amp}}=0$, for integers N, where

$$f=(2N+1)/(2[\tau_2-\tau_1]). \tag{12}$$

Also, when $\theta=0$, $\Delta_{\text{amp}}=0$ for all ϕ, where

$$f=N/[\tau_2-\tau_1]. \tag{13}$$

In fact, the variance of Δ_{amp}, averaged over all ϕ (0–2π), is a cyclic function of f, which is zero where Eqs. (12) and (13) are satisfied and maximal at intermediate values of f. To derive the frequencies at which Δ_{amp} is maximally

variable, therefore, the roles of Eqs. (12) and (13) may be reversed; Eq. (12) gives the frequencies of maximum variability in Δ_{amp} when neither noise is inverted and Eq. (13) gives the frequencies of maximum variability in Δ_{amp} when one noise is inverted. Near the minima of the function all components are roughly equal in amplitude at each ear and so it may be possible to cancel them without any amplitude equalization, but at the maxima, the components entering a frequency channel will have widely differing interaural amplitude ratios and so cannot be cancelled. Hence, these are the same frequencies which give peaks in the residual activation produced by the mE-C model (e.g., Fig. 7).

Next, considering the equalization of delay, a similar pattern is found. Equations (9) and (10) can be used to determine the internal delay at which cancellation takes place. This internal delay depends upon the phase of the sine terms of Eqs. (9) and (10). The optimum delay for cancellation is related to the interaural phase difference, Δ_{phase}, which is given by

$$\Delta_{phase} = \sin^{-1}\left[\frac{c\ \sin(\phi)}{\sqrt{b^2+c^2+2bc\ \cos(\phi)}}\right] - 2\pi f\tau_1 - \sin^{-1}\left[\frac{c\ \sin(\phi+2\pi f[\tau_2-\tau_1]+\theta)}{\sqrt{b^2+c^2+2bc\ \cos(\phi+2\pi f[\tau_2-\tau_1]+\theta)}}\right]. \quad (14)$$

From these equations, it can be seen that the optimum internal delay for cancellation of a single frequency depends upon the two interaural delays, τ_1 and τ_2, the amplitudes, b and c, the interaural phase difference, ϕ, and upon frequency, f. However, as with amplitude equalization, there are certain frequencies at which the values of b, c, and ϕ have no effect on Δ_{phase}. These are the same frequencies which give zero interaural amplitude differences [Eqs. (12) and (13)]. Furthermore, within an auditory frequency channel there will be limited variation in f, so the same internal delay should suffice for all frequencies within the channel. So, the same frequencies which have no interaural amplitude differences also have interaural phase differences which are independent of the random features of the two noises, and are therefore consistent across a given frequency channel.

Thus, the mE-C model always predicts that when one noise is inverted, a pitch will be heard whose period is equal to the difference in the interaural delays applied to the two noises, and that when neither noise is inverted the pitch will be related to an odd-harmonic series, whose fundamental has a period which is half the difference between the two interaural delays.

VI. DISCUSSION

This paper has considered the respects in which three models can account for the occurrence and the frequency of two dichotic pitches: the dichotic repetition pitch (Bilsen and Goldstein, 1974) and the Fourcin pitch (Fourcin, 1970) (Fig. 1). It was noted in the Introduction that the FP is heard easily by the majority of listeners, while the DRP is more difficult to hear. Accordingly, it would be desirable for a model, or models, to predict that the FP is produced by a different mechanism from the DRP, and that the FP is generally more salient.

The rE-C model makes accurate predictions of the occurrence and frequency of the DRP, but makes inaccurate predictions of the FP. Similarly, the CAP model makes accurate predictions of the DRP, but not of the FP. In contrast, the mE-C model accounts for the FP, but produces no output for a DRP stimulus. Thus, none of the models accurately predict both pitches, suggesting that the FP and DRP may depend on different mechanisms, with the mE-C mechanism accounting for the FP and either the rE-C and/or CAP mechanisms accounting for the DRP.

The mE-C model accounts for the FP, as shown in the present paper, and for two other dichotic pitches, the Huggins pitch (HP) (Cramer and Huggins, 1958) and the binaural edge pitch (BEP) (Klein and Hartmann, 1981), as shown in a companion paper (Culling *et al.*, 1997). Overall, the mE-C model provides a more accurate and straightforward account of the detection and perceived frequency of the FP, HP, and BEP than do other models.

It is less obvious whether the DRP should be attributed to the rE-C or the CAP mechanisms. There is little difference between the output spectrum generated by the rE-C model performing addition and an across-frequency scan from the CAP taken at 0-ms internal delay. The first corresponds to the addition of the waveforms in corresponding frequency channels from the two ears, and the second to their multiplication. In a compressive nonlinear system, there may be little practical difference between the two results. However, there are some grounds for favoring the CAP model. Although the rE-C model directly generates an output spectrum which displays evidence of the DRP, it is, as its name implies, only a partial implementation of equalization-cancellation, and would have no major role beyond accounting for the DRP. In comparison, an attraction of the CAP model is that it is based on well-established mechanisms of sound localization and binaural masking release (Colburn and Durlach, 1978).

Across-frequency scanning is more or less equivalent to across-frequency grouping by common interaural delay. The mE-C model was designed partly on the principle that such across-frequency grouping does not occur in binaural analysis (Culling and Summerfield, 1995; Hukin and Darwin, 1995; Darwin and Hukin, 1997). The model consequently analyzes each channel independently of all others. It is interesting to note that without this feature the mE-C model would not predict the FP correctly, so its success in this area provides an independent verification of the principle of channel independence. On the other hand, the success of the CAP model in accounting for the DRP suggests that some limited across-frequency scanning does occur. Yet, the ridges in the CAP for DRP stimuli are clear (e.g., Fig. 3) and should be easily extracted by a scanning process. The weakness of the pitch sensation which most listeners experience in a DRP stimulus is, therefore, a testament to the limited efficiency of across-frequency scanning.

ACKNOWLEDGMENTS

The authors would like to thank the following people: Alain de Cheveigné and Adrian Fourcin for helpful comments on previous versions of this manuscript; Johann Raatgever, Frans Bilsen, and Julius Goldstein for responding helpfully to our enquiries about the workings of the CAP and rE-C models; Chris Darwin for recommending the use of weighting functions to improve the fit between the model's predictions of pitch matches and those observed by Bilsen and Wesdorp; and Frans Bilsen and Bill Hartmann for their thorough and thoughtful reviews.

[1]The rms levels from left- and right-ear channels are calculated and one waveform is scaled so that the rms will be the same as that of the other. Different delays are then tested using this fixed level adjustment.

[2]There has to be a limit to the range internal delays at which scans are made. However, no explicit specification for the model has been given. Bilsen (1997) agrees with the current authors that scans well outside the ecological range ($\approx \pm 600\ \mu$s) should be neglected. The exact limit has material effects on the predictions of the model.

[3]It is an empirical fact that neural units with large characteristic delays [up to $\pm 1/(2f)$] exist in the mid-brain (e.g., McAlpine *et al.*, 1996, Fig. 6B). Possibly, the developing auditory system may have little precise control over the delays which are implemented. However, across-frequency models like the CAP model require that such units are connected in a systematic way to units in higher centers (i.e., information from units with different characteristic frequencies but the same characteristic delays must be combined). It is difficult to see how such systematic connections across large interaural delays could arise in development or evolution when the system is never exposed to broadband sounds with such large delays.

[4]The fitting procedure minimized the squared difference in frequency between all peaks in the scan and a series of consecutive harmonics by adjusting the $F0$ of the harmonic series. All peaks in the scan were used, not just those listed in Table I, but each peak was weighted according to Eqs. (5) and (6), so that the other peaks will have played a minor role in the fit. The height of the peak and the depth of the adjacent valleys were not considered in this process. The best fits were invariably obtained using harmonic series which began with the 1st harmonic.

[5]Fourcin (1958) summarized the results of his pitch matching data as giving $1/\tau_d = 2/3f$ and $1/\tau_d = 1/2\ f$, where f is the frequency of the tone for the uninverted and inverted cases, respectively. Fourcin (1970) summarized the same matches as $1/\tau_d = 2/3f$ and $1/\tau_d = 1/2\ f$. The raw data on which both these summaries were based showed a mixture of the two patterns, suggesting the occurrence of octave errors. The differences between Fourcin's summaries reflect alternative ways in which he attempted to correct the octave errors. However, the majority of matches fit the $1/\tau_d = 2/3f$ and $1/\tau_d = 1/2\ f$ lines, which are consistent with matches to the second peak in the mE-C model's recovered spectrum. The matches fitting $1/\tau_d = f$ are also consistent with the mE-C model as matches to the first peak in the recovered spectrum. Only the matches fitting $1/\tau_d = 4/3f$ must, according to the mE-C model, be interpreted as octave errors.

Bilsen, F. A. (**1966**). ''Repetition pitch: monaural interaction of a sound with the repetition of the same, but phase-shifted sound,'' Acustica **17**, 295–300.

Bilsen, F. A. (**1977**). ''Pitch of noise signals: Evidence for a central spectrum,'' J. Acoust. Soc. Am. **61**, 150–161.

Bilsen, F. A. (**1995**). ''What do dichotic pitch phenomena tell us about hearing?,'' in *Advances in Hearing Research*, edited by G. A. Manley, G. M. Klump, C. Köppl, H. Fastl, and H. Oeckinghaus (World Scientific, Singapore).

Bilsen, F. A. (**1997**). Personal communication.

Bilsen, F. A., and Goldstein, J. L. (**1974**). ''Pitch of dichotically delayed noise and its possible spectral basis,'' J. Acoust. Soc. Am. **55**, 292–296.

Bilsen, F. A., and Wesdorp, C. (**1974**). ''Dichotic pitch phenomena and their common spectral basis,'' in *Proceedings of the Eighth International Congress on Acoustics* (Goldcrest, London).

Cohen, M. A., Grossberg, S., and Wyse, L. L. (**1995**). ''A spectral network model of speech perception,'' J. Acoust. Soc. Am. **98**, 862–879.

Colburn, H. S. (**1973**). ''Theory of binaural interaction based on auditory-nerve data. I. General strategy and preliminary results on interaural discrimination,'' J. Acoust. Soc. Am. **54**, 1458–1470.

Colburn, H. S. (**1977**). ''Theory of binaural interaction based on auditory-nerve data. II. Detection of tones in noise,'' J. Acoust. Soc. Am. **61**, 525–533.

Colburn, H. S., and Durlach, N. I. (**1978**). ''Models of binaural interaction,'' in *Handbook of Perception, Vol. IV*, edited by E. C. Carterette and P. Morton (Academic, New York), pp. 467–518.

Cramer, E. M., and Huggins, W. H. (**1958**). ''Creation of pitch through binaural interaction,'' J. Acoust. Soc. Am. **30**, 858–866.

Culling, J. F. (**1996**). ''Dichotic pitches as illusions of binaural unmasking,'' J. Acoust. Soc. Am. **99**, 2515.

Culling, J. F., and Summerfield, Q. (**1995**). ''Perceptual separation of concurrent speech sounds: absence of across-frequency grouping by common interaural delay,'' J. Acoust. Soc. Am. **98**, 785–797.

Culling, J. F., Summerfield, Q., and Marshall, D. H. (**1998**). ''Dichotic pitches as illusions of binaural unmasking I: Huggins' pitch and the binaural edge pitch,'' J. Acoust. Soc. Am. **103**, 3509–3526.

Darwin, C. J., and Hukin, R. W. (**1997**). ''Perceptual segregation of a harmonic from a vowel by interaural time difference and frequency proximity,'' J. Acoust. Soc. Am. **102**, 2316–2324.

de Boer, E. (**1956**). ''On the 'Residue' in Hearing'' (doctoral dissertation, Amsterdam).

de Boer, E. (**1976**). ''On the 'Residue' in Auditory Pitch Perception,'' in *Handbook of Sensory Physiology Vol. 3*, edited by W. D. Keindel and W. D. Neff, pp. 479–584.

Durlach, N. I. (**1960**). ''Note on the equalization-cancellation theory of binaural masking level differences,'' J. Acoust. Soc. Am. **32**, 1075–1076.

Durlach, N. I. (**1972**). ''Binaural signal detection: Equalization and cancellation theory,'' in *Foundations of Modern Auditory Theory, Vol. II*, edited by J. V. Tobias (Academic, New York).

Fourcin, A. J. (**1958**). ''Speech perception and bandwidth compression,'' S.R.D.E. report #1126.

Fourcin, A. J. (**1970**). ''Central pitch and auditory lateralization,'' in *Frequency Analysis and Periodicity Detection in Hearing*, edited by R. Plomp and G. F. Smoorenburg (Sijthoff, The Netherlands).

Fourcin, A. J. (**1995**). Personal communication.

Hukin, R. W., and Darwin, C. J. (**1995**). ''Effects of contralateral presentation and of interaural time differences in segregating a harmonic from a vowel,'' J. Acoust. Soc. Am. **98**, 1380–1387.

Jeffress, L. A. (**1948**). ''A place theory of sound localization,'' J. Comp. Physiol. Psychol. **61**, 468–486.

Jeffress, L. A. (**1972**). ''Binaural signal detection: vector theory,'' in *Foundations of Modern Auditory Theory, Vol. II*, edited by J. V. Tobias (Academic, New York).

Killion, M. C., Wilber, L. A., and Gudmundsen, M. A. (**1985**). ''Insert earphones for more interaural attenuation,'' Hearing Instruments **36**, 34–36.

Klein, M. A., and Hartmann, W. M. (**1981**). ''Binaural edge pitch,'' J. Acoust. Soc. Am. **70**, 51–61.

McAlpine, D., Jiang, D., and Palmer, A. R. (**1996**). ''Interaural delay sensitivity and the classification of low best-frequency binaural responses in the inferior colliculus of the guinea pig,'' Hearing Res. **97**, 136–152.

Meddis, R. (**1986**). ''Simulation of mechanical to neural transduction in the auditory receptor,'' J. Acoust. Soc. Am. **79**, 702–711.

Meddis, R. (**1988**). ''Simulation of auditory-neural transduction: further studies,'' J. Acoust. Soc. Am. **83**, 1056–1063.

Moore, B. C. J., and Glasberg, B. R. (**1983**). ''Suggested formulae for calculating auditory-filter bandwidths and excitation patterns,'' J. Acoust. Soc. Am. **74**, 750–753.

Patterson, R. D. (**1976**). ''Auditory filter shapes derived with noise stimuli,'' J. Acoust. Soc. Am. **59**, 640–654.

Patterson, R. D., Nimmo-Smith, I., Holdsworth, J., and Rice, P. (**1987**). ''An efficient auditory filterbank based on the gammatone function,'' paper presented to the I.O.C. speech group on auditory modelling at R.S.R.E, December 14–15.

Patterson, R. D., Nimmo-Smith, I., Holdsworth, J., and Rice, P. (**1988**). ''Spiral VOS final report, Part A: The auditory filter bank,'' Cambridge Electronic Design, Contract Report (A.P.U. 2341).

Raatgever, J. (**1980**). ''On the Binaural Processing of Stimuli with Different Interaural Phase Relations,'' doctoral dissertation, Delft University.

Raatgever, J., and Bilsen, F. A. (**1977**). ''Lateralization and dichotic pitch as

a result of spectral pattern recognition,'' in *Psychophysics and Physiology of Hearing*, edited by E. F. Evans and J. P. Wilson (Academic, London).
Raatgever, J., and Bilsen, F. A. (**1986**). ''A central theory of binaural processing. Evidence from dichotic pitch,'' J. Acoust. Soc. Am. **80**, 429–441.
Ritsma, R. (**1967**). ''Frequencies dominant in the perception of the pitch of complex sounds,'' J. Acoust. Soc. Am. **42**, 191–198.
Zwicker, E., and Feldkeller, R. (**1967**). *Das Ohr als Nachrichtenempfänger* (Hirzel, Stuttart, Germany), 2nd ed.

Measurements of the binaural temporal window using a detection task

John F. Culling[a] and Quentin Summerfield
MRC Institute of Hearing Research, University Park, Nottingham NG7 2RD, United Kingdom

(Received 16 November 1996; revised 9 January 1998; accepted 2 March 1998)

Two experiments investigated the shape of the binaural temporal window using a detection task. In experiment 1, a 10-ms tone burst was presented binaurally out-of-phase during a burst of white noise, which changed from being interaurally uncorrelated, to correlated, and back to uncorrelated. The tone occurred during the correlated portion of the noise in one interval of each 2I-FC trial. Detection thresholds were recorded using a 2-down/1-up adaptive procedure. Thresholds were measured for different durations of correlated noise (0–960 ms), frequencies of tone burst (125, 250, 500, and 1000 Hz) and levels of noise [20, 30, 40, and 50 dB(SPL)/Hz]. Window shapes based on nine candidate functions were fitted to the data using the assumption that the binaural masking release was related to the overall interaural correlation of noise admitted by the window. Fitted windows included both a forward and a backward lobe. Gaussian functions tended to give closer fits than exponential and rounded-exponential functions, and simple functions gave more parsimonious fits that those which included dynamic-range-limiting terms. Using simple Gaussian fits, the shape of the window was largely independent of frequency and level, and the windows for individual listeners had equivalent rectangular durations ranging from 55 to 188 ms. The asymmetry was variable, although forward lobes were generally shorter than backward lobes. Experiment 2 ruled out the possibility that the forward lobe might be an artefact caused by distraction of the listener, when the interaural phase change in the noise closely followed the signal. In this experiment, the out-of-phase tone was presented during a burst of partially correlated noise which changed, after a variable interval, to a fully correlated noise. Thresholds for detecting the tone rose (i.e., performance worsened) as the interval was increased. Distraction would have produced the opposite effect. [S0001-4966(98)03706-0]

PACS numbers: 43.66.Ba, 43.66.Dc, 43.66.Pn [RHD]

INTRODUCTION

The binaural system assists in the localization of sound sources and in the detection and identification of sounds in noise. In both of these roles, the system has been found to react slowly to changes in the interaural pattern of stimulation. This ''sluggishness'' is widely thought to reflect the minimum integration time (i.e., maximum temporal resolution) of the binaural system. Models of binaural processing have typically incorporated temporal integration by including a leaky integrator. New events are fully incorporated into the activation state of such an integrator but, as an event recedes into the past, it contributes progressively less to that activation state. A leaky integrator can be viewed as a single-sided exponentially tapering temporal window, which applies progressively lower weight to events which occurred in the past. The primary objective of the present study was to measure the size and shape of the binaural temporal window, so that this process of integration can, if necessary, be modeled more accurately than by a simple leaky integrator.

A. Sluggishness in sound localization

In the case of sound localization, sounds coming from different azimuths display different interaural level differences (ILDs) and different interaural time differences (ITDs). Two azimuths can be finely discriminated using these cues, provided that the auditory system has time to analyze them. The minimum audible angle (MAA) is the minimum angle of arc which must separate two sources emitting sounds in succession for a listener to discriminate them from a single source emitting the same sounds. Estimates of the MAA (Mills, 1958; Perrot and Pacheco, 1989) are of the order of 1°. The sluggishness of the binaural auditory system is revealed by demonstrations that the spatial resolution which underpins the MAA depends on the interstimulus-onset-interval (ISOI). Perrot and Pacheco (1989) used 10-ms bursts of pink noise as stimuli. They observed the smallest MAAs when the ISOI was 100 ms or greater (i.e., there was at least 90 ms of silence between bursts). MAAs were significantly larger for ISOIs less than 75 ms, and rose to over 3° at ISOIs shorter than about 40 ms. Sluggishness is also evident in measurements of the minimum audible movement angle (MAMA) made by Perrot and Musicant (1977) and Chandler and Grantham (1992). The MAMA is the angle of arc which a moving sound source must traverse in order for a listener to discriminate it from a stationary sound source. The MAMA is larger than the MAA, and increases in size as the rate of movement increases, from 8.3° at 90°/s to 21.2° at 360°/s (Perrot and Musicant, 1977). The corresponding threshold durations of the moving sounds observed in measuring the MAMA (90 ms at 90°/s and 60 ms at 360°/s) are of the same

[a]Current address: University Laboratory of Physiology, Parks Rd., Oxford OX1 3PT, U.K.

order as the ISOIs which give the smallest MAA ($\geqslant$100 ms). In each case, therefore, listeners are impaired in their detection of the change in position when different source locations are presented within a duration of about 100 ms.

The temporal resolution of the two binaural cues underlying sound localization, ILDs and ITDs, has also been measured individually. Grantham and Wightman (1978) created stimuli whose ITDs were modulated. Listeners were required to discriminate these sounds from dichotic noises with the same long-term interaural correlation. Performance was at chance at modulation rates exceeding 2–5 Hz. In comparison, listeners can discriminate changing ILDs produced by amplitude modulation which is interaurally out-of-phase from stimuli without ILDs, but still amplitude modulated at the same frequency, up to a modulation rate of about 20 Hz (Grantham, 1984). A similar advantage was found by Blauert (1972) who showed that listeners can detect higher rates of modulation of the ILD of a pulse train compared with modulation of its ITD. It is generally believed that ITDs and ILDs are analyzed by different mechanisms, although the separation may not be complete at all levels and frequencies (see Grantham, 1995, for a discussion). Certainly, however, the analysis of ITDs depends on the cross correlation of phased-locked spike trains from the two ears, while that of ILDs does not. Thus the relatively poor temporal resolution of changes in ITD is compatible with the view expressed by Moore and Sek (1996) that sluggishness is a general feature of processes which exploit phase locking, rather than an exclusive property of processes which analyse binaural cues.

B. Sluggishness in signal detection

Signals are more easily detected in noise if the interaural phase of the noise differs from that of the signal (Hirsh, 1948; for a review, see Durlach and Colburn, 1978). For example, if the noise is in-phase across the ears and the signal is out-of-phase (NoSπ), or vice versa (NπSo), the signal can be detected at a lower signal-to-noise ratio than if both are in-phase (NoSo) or both out-of-phase (NπSπ). The difference between two such thresholds is called the binaural masking level difference (BMLD).

The sluggishness of the binaural system has also been studied using the BMLD as the dependent variable. Several experiments have measured the effects of changes in the interaural phase of a masking noise over time on the detection threshold of a brief signal (Bell, 1972; Grantham and Wightman, 1979; Shackleton and Bowsher, 1989; Kollmeier and Gilkey, 1990; Culling and Summerfield, 1995a). These studies have shown that detection in the NoSπ condition can be disrupted by a temporally contiguous Nπ noise which either precedes or follows the No noise. In a related study, Yama (1992) has demonstrated that a brief Sπ signal can be detected at a lower intensity than an equivalent So signal for at least 40 ms after the offset of an No masker.

In their experiment, Grantham and Wightman (1979) varied the interaural correlation of a masking noise sinusoidally between full interaural correlation (No) and full anti-correlation (Nπ). An Sπ tone pulse was presented at one or other extreme of this cycle. Thus in one case the stimulus was, instantaneously, NoSπ, and in the other NπSπ. In this way, the size of the BMLD was measured as a function of the masker-modulation rate. Grantham and Wightman found that the BMLD declined steeply in size with increasing modulation rate, and was largely abolished at a modulation rate of just 2 Hz. It is difficult, however, to derive a reliable measure of the minimum binaural integration time from these results because the very slow rate of modulation sufficient to abolish the BMLD results from the conjunction of applying continuous changes to the correlation of the masking noise together with the steep elevation of detection thresholds for only small increases in the decorrelation of a masking noise (Robinson and Jeffress, 1963; see Fig. 1).

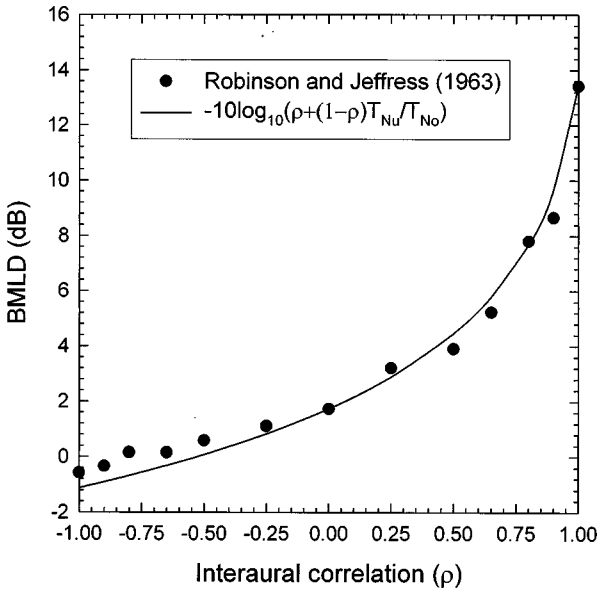

FIG. 1. The relationships between noise correlation and binaural threshold measured by Robinson and Jeffress (1963). The filled symbols are the BMLDs measured by Robinson and Jeffress using an Sπ tone, which have been measured from their figure and replotted. The solid line is a curve which has been fitted to the data using Eq. (1). Since the curve is scaled by the ratio $T_{\mathrm{Nu}}/T_{\mathrm{No}}$ the line passes through the data points at correlations of 0 and 1. The accuracy of the fit is therefore strongly influenced by these two measurements.

A stimulus configuration that allows a more mathematically tractable analysis can be created by applying instantaneous changes to the interaural phase of the masker (Bell, 1972;[1] Shackleton and Bowsher, 1989;[2] Kollmeier and Gilkey, 1990; Culling and Summerfield, 1995a[3]). In the best designed of these studies, Kollmeier and Gilkey measured the detection thresholds of Sπ tone pulses at various points in time around an instantaneous transition in a masking noise from Nπ to No, or from No to Nπ. This design thus formed a binaural analog of monaural forward and backward masking experiments. The results revealed approximately equal amounts of binaural forward and backward masking. Thresholds were still elevated some time after the noise had changed from Nπ to No, and were *also* elevated when the tone occurred *before* the noise changed from No to Nπ. Kollmeier and Gilkey (1990) explored the extent to which integration windows with five different shapes accounted for the data: rectangular, triangular, Gaussian, exponential, and rounded exponential. Both the forward and backward mask-

ing data were best fitted by exponentially tapering integration windows, although the advantage for exponential windows over rounded-exponential windows was small. The complete window was a *double-sided* exponential. The forward lobe of the window was quite extensive in time, suggesting that there is no access to information about binaural events which are close to detection threshold for as long as 50 ms after they have occurred.[4]

C. The notched-noise method

The present experiments form a logical extension of Kollmeier and Gilkey's binaural analog of forward and backward masking. A difficulty arises in interpreting data from forward and backward masking in terms of temporal resolution because the method allows listeners to exploit ''off-time'' listening (Moore *et al.*, 1988; Plack and Moore, 1990). If the listener has access to a sequence of temporal windows centered on different moments in time, then the window centered on the signal does not necessarily provide the best signal-to-noise ratio; a better signal-to-noise ratio may be found by listening to a window centered just before or just after the occurrence of the signal. If off-time listening is occurring, but is not taken into account in the window-fitting procedure, the sharpness of the window may be overestimated. The advantage for an exponential over a rounded-exponential window shape found by Kollmeier and Gilkey might have been reduced if off-time listening had either been prevented or taken fully into account in the fitting procedure.

Patterson (1976) faced the same problem when measuring frequency selectivity, where listeners may exploit off-*frequency* listening. Patterson addressed the problem by presenting tones for detection within the stop-band of a band-stop noise. With this arrangement, listeners are less advantaged by listening off-frequency because the presence of noise on both sides of the signal largely ensures that the auditory filter centered on the signal gives the best signal-to-noise ratio. Subsequently, Patterson and Nimmo-Smith (1980) refined the technique by explicitly modeling the process of off-frequency listening within the filter-shape fitting process (see also Patterson and Moore, 1986). Moore *et al.* (1988) and Plack and Moore (1990) translated the notched-noise technique into the time domain. They measured thresholds for detecting a brief tone pulse in a silent gap between two bursts of noise to derive the shape of the (monaural) auditory temporal window.

In experiment 1 of the present study, the notched-noise technique was transposed into the binaural temporal domain in order to control effects of off-time listening. The experiment took advantage of the fact that the threshold for detecting an $S\pi$ signal is about 10–12 dB lower in No noise than in an uncorrelated (Nu) noise. An $S\pi$ signal was presented against a concurrent segment of No noise which was both preceded and followed by segments of Nu noise. The primary cue for detection of an $S\pi$ signal in No noise is the interaural decorrelation of the noise that is produced by the presence of the signal (Gabriel and Colburn, 1981; Durlach *et al.*, 1986; Koehnke *et al.*, 1986; Jain *et al.*, 1991; Culling and Summerfield, 1995b). Thus if the duration of the No segment is sufficiently long, the Nu noise falls outside the window centered on the $S\pi$ signal and so does not interfere with the detection of the signal. Any relative elevation of the detection threshold as the duration of the No noise is reduced can be taken as an indication of the amount of Nu noise entering the optimally positioned binaural temporal window. One can thus derive the shape of the window by modeling the threshold data with candidate fitting functions and determining which function gives the best fit to the data (Patterson and Nimmo-Smith, 1980; Patterson and Moore, 1986; Moore *et al.*, 1988; Plack and Moore, 1990).

The window-fitting procedure differed in some important respects from that used in estimating the shape of the monaural temporal window (Plack and Moore, 1990), which assumed that the ratio of noise to signal energy entering the window was constant at threshold. A directly analogous method was used by Culling and Summerfield (1995a). However, Kollmeier and Gilkey (1990) modified the method so as to account for the ''internal noise'' of the binaural system. They calculated the correlation, ρ, of the noise entering the window and, from this value, predicted thresholds using an expression derived from Durlach's equalization-cancellation theory of binaural masking release. The present procedure is equivalent to that employed by Kollmeier and Gilkey. Nine different fitting functions were employed as candidate window shapes. These shapes were based on exponential, Gaussian, and rounded-exponential functions.

The three base functions each came in three forms. In the ''simple'' form, the base functions were used directly. In the ''floor'' form, the dynamic range of the window was explicitly constrained by assigning a common floor parameter to both sides of the shape; the shape asymptoted at large excursions from zero time with the floor value. In the ''skirt'' form, the dynamic range of the window was bounded by a second function with a larger time constant; each side of the shape was the product of two weighted component functions, with one function sitting on the top of another, so that the two functions formed the ''peak'' and ''skirt'' part of the overall shape. The functions with limited dynamic ranges were originally designed for the purpose of modeling spread of excitation at high signal levels in monaural frequency selectivity and were not employed by Kollmeier and Gilkey in their modeling of the binaural temporal window. For consistency with the notch-noise literature we modeled these windows as well as the simple exponential, Gaussian, and rounded-exponential functions used in their study.

The fitting procedures permitted all windows to be asymmetric in time.[5] Consequently, the simple functions had two parameters, representing the breadth of each side of the function; the floor shapes had three parameters, representing the breadth of each side of the function and the depth of the floor; the skirt shapes had four parameters, representing the breadth of each side (at the peak), the breadth of the skirt (assumed to share the same temporal asymmetry as the peak) and the relative weighting of peak and skirt. The fitting procedure is described in more detail in the Appendix.

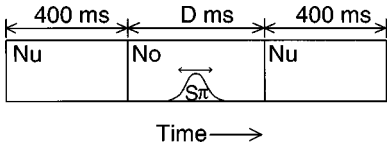

FIG. 2. Schematic illustration of the stimulus structure used in experiment 1.

I. METHODS COMMON TO BOTH EXPERIMENTS

All stimuli were generated digitally on a SUN SPARCstation 10, using a 10-kHz sampling rate and 12-bit amplitude quantization. The noise was generated using the method recommended by Klatt (1980) in which 16 numbers from a pseudo-random number generator are summed to form each output sample. In each experiment, ten maskers were generated for each masking condition and were selected at random before each presentation interval. Each masker was digitally low-pass filtered using a 512-point low-pass filter with a 2-kHz cutoff. The maskers were shaped with 10-ms raised-cosine onset and offset ramps. The signal tones to be detected were 20 ms in duration, including 10-ms raised-cosine onset and offset ramps. They were, therefore, 10 ms in duration between the -6-dB points.

The experiments were controlled by a Dell 386 PC. Signals and maskers were played simultaneously through four separate, time-locked, 12-bit, digital-to-analog converters (Cambridge Electronic Design 1401) and then through four KEMO VBF/25 filters (4.5-kHz low pass, 96 dB/octave). Each analog channel was attenuated by a purpose-built, digitally controlled attenuator. The two attenuators carrying the signal applied the attenuation determined by the adaptive algorithm. The two attenuators carrying the noise applied a fixed attenuation, which depended on the experimental condition. The two left-ear channels were then mixed, as were the two right-ear channels. Following amplification, the two signals were passed through fixed attenuators (Marconi Instruments TF2612) which balanced the levels of the two channels at the headphones (Sennheiser HD414).

II. EXPERIMENT 1

In the first experiment, masked signal detection thresholds for an $S\pi$ signal were measured as a function of the duration of an No noise which was preceded and followed by 400-ms segments of Nu noise (Fig. 2). Uncorrelated noise (Nu) was used rather than out-of-phase ($N\pi$) noise for the reasons given in footnote 3. In different conditions, measurements were made for several signal frequencies and several noise levels.

A. Stimuli and procedure

Three adult listeners, with normal hearing thresholds ($<$20 dB HL *re*: ISO 389 at audiometric frequencies between 125 Hz and 8 kHz inclusive) attended a series of 1-h sessions. Listener DF was an experienced participant in psychoacoustic experiments, while listeners NPW and IC were recruited for the present study. Masked-signal thresholds were measured using a 2-down/1-up adaptive algorithm (Levitt, 1971). The algorithm continued until three reversals had been completed using a 4-dB step-size and ten reversals using a 2-dB step-size. The mean signal level at the last ten reversals was taken as an estimate of the listener's threshold for that run. Each threshold was taken as the mean of three such runs. For each condition of tone frequency and masker level, 33 thresholds were estimated for each subject. These thresholds were for 13 different durations of correlated noise (0, 20, 30, 40, 60, 80, 120, 160, 240, 320, 480, 640, and 960 ms): for No durations of 0, 20, and 30 ms the signal tone was centered temporally within the stimulus (3 thresholds); for the ten longer No durations, the signal tone was located at one of three places within the No duration, located a quarter of the way, half-way, or three-quarters of the way through the No noise (30 thresholds). These different tone positions will be described as ''leading-tone,'' ''symmetrical,'' and ''lagging-tone.'' The No noise was preceded and followed by 400 ms of temporally contiguous uncorrelated noise (see Fig. 2). The maskers were produced by concatenating sections of noise with different interaural parameters prior to low-pass filtering. In different conditions, tones were presented at 125, 250, 500, and 1000 Hz in noise at a level of 40 dB(SPL)/Hz. Tones of 500 Hz were also presented in noise at levels of 20, 30, and 50 dB(SPL)/Hz, making seven different conditions in all. With 7 conditions of tone frequency and noise level $\times$ 33 thresholds $\times$ 3 runs, each listener completed a minimum of 693 runs in all. Where the variance of thresholds in the three runs was greater than 10 dB^2, an extra threshold was collected and the most eccentric threshold was discarded.

B. Results

Figure 3 shows average thresholds obtained for each listener in the 500-Hz tone, 40-dB/Hz noise condition. The different symbols represent thresholds for $S\pi$ tone bursts presented in the leading-tone (squares), symmetrical (filled circles), and lagging-tone (open circles) positions. The lines are the thresholds predicted by the best fitting window (see below). The listeners produced similar results. Thresholds tended to decrease with increasing No duration, improving by between 10 and 12 dB, overall. For a given No duration, thresholds tended to be higher for leading tones than for symmetrical or lagging tones, particularly for durations in the 50–200 ms range, over which thresholds vary most as a function of No duration. Aside from variations in the size of the effect of No duration on threshold (i.e., the size of the BMLD), these observations were generally true for each of the listeners in each of the conditions. The BMLD was smaller at lower noise levels, but the only substantial reduction occurred for listener NPW in the 20-dB(SPL)/Hz condition. The BMLD was substantially reduced for all listeners in the 125-Hz condition, and eliminated entirely in the case of listener NPW. Also in this condition, listener DF displayed a strongly reversed effect of tone position compared with all the other data sets; here the leading-tone tended to give lower thresholds than the symmetrical and lagging-tone conditions rather than the other way around.

Temporal window shapes were fitted to the data. The fitting procedure computed the interaural correlation of the combination of uncorrelated and correlated noise intersected

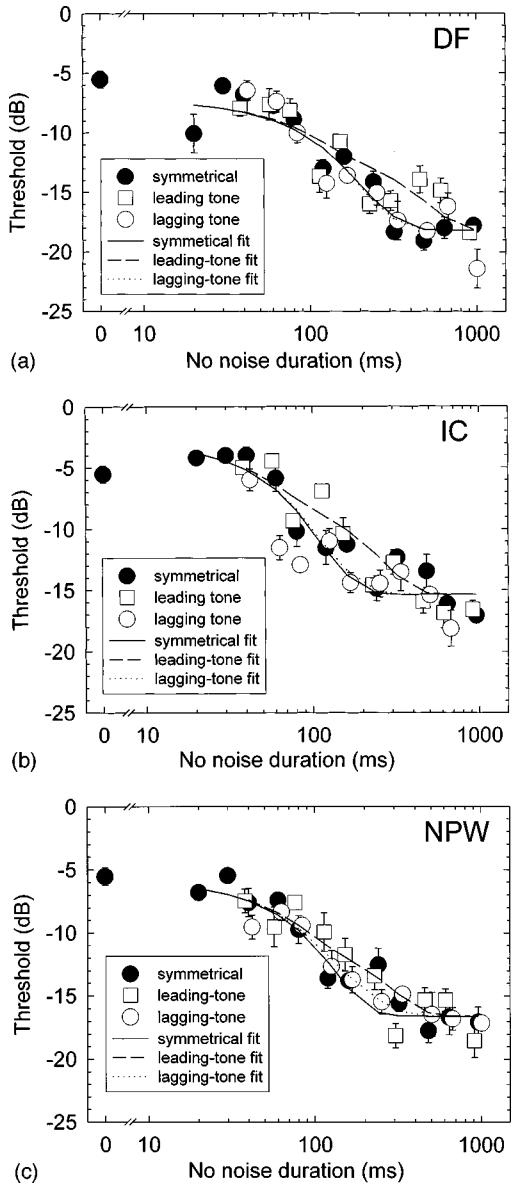

FIG. 3. Examples of the raw threshold data and the quality of the fit achieved by the window fitting algorithm. The thresholds (dB *re*: arbitrary zero) with standard error bars for each of the three subjects in the 40-dB (SPL/Hz)/500-Hz condition are shown in separate panels. The symbols show the observed threshold data. The lines show the closest match to this data achieved by the window fitting program using simple Gaussian windows. Filled circles and solid lines are for the symmetrically placed tones (50% point); open squares and dashed lines are for the leading tones (25% point); open circles and dotted lines are for the lagging tones (75% point).

by the window; it assumed that the BMLD was related to the interaural correlation by Eq. (1), which is adapted from van der Heijden and Trahiotis (1996, Eq. 4). Van der Heijden and Trahiotis showed that their equation accounts for 98% of the variance in the data from Robinson and Jeffress (1963) (Fig. 1). T_{No} is the mean threshold in linear units of intensity observed for 960 ms of No and T_{Nu} is the mean threshold in linear units for durations of No up to 30 ms. These values were calculated separately for each listener, frequency, and level. The amount of signal energy admitted by the window, when placed in a given position, was also taken into account:

$$\mathrm{BMLD} = -10 \log\left(\rho + (1-\rho)\,\frac{T_{\mathrm{Nu}}}{T_{\mathrm{No}}}\right). \qquad (1)$$

Each of the nine candidate window functions defined in the Appendix was fitted separately to the data of each of the three listeners in each of the seven conditions of noise level and tone frequency. The mean parameters, averaged across the three listeners, are listed in Table I. Figure 4 shows the nine window shapes derived by averaging the parameters fitted with the overall correlation method to the data of the three listeners in the 500-Hz/40-dB condition. Aside from the inevitable differences in shape defined by the three different base functions, the windows are always similar in width near the peak, and, as illustrated by the example in Fig. 4, only for the Gaussian-with-skirt shape is there a substantial broadening of the window away from the peak.

The fitting procedure estimates the dynamic range of the BMLD from the measured thresholds. The dynamic range of the resulting window is therefore unconstrained by the range of the data. The dynamic ranges of the windows were large and differed widely across the different fits. This outcome suggests that, except in the case of the Gaussian-with-skirt shape, other aspects of the data tend not to constrain the dynamic range of the windows in a consistent manner, and that the dynamic range is probably not an important parameter of the window.

An analysis of variance for goodness-of-fit (χ^2) covering the three listeners (random factor), the three base functions (exponential, Gaussian, and rounded exponential), the three fit-types (simple, floor and skirt), and the six conditions for which all three listeners displayed a BMLD (i.e., excluding the 125-Hz condition) showed a significant main effect of fit-type [$F(2,4)=4.7$, $p<0.02$] and a significant interaction between base function and fit-type [$F(4,8)=16.3$, $p<0.002$]. The effect of base function itself fell short of significance ($p=0.082$). These effects are illustrated in Fig. 5 where lower values of χ^2 indicate a better fit. Table II lists the χ^2 values for each of the nine window shapes in each of the seven conditions. Since the lowest values of χ^2 were achieved by the simple Gaussian function, all further illustrations of window shapes and threshold predictions will be based on this function. The thresholds predicted in the condition of 40-dB(SPL)/Hz noise and 500-Hz signal are shown as lines in Fig. 3.

Figure 6 shows the shape of the simple Gaussian window as a function of signal frequency. The parameters were averaged across all the listeners who produced a BMLD at each frequency. The shape of the window varies in duration and asymmetry across the four frequencies. If only the 250-, 500-, and 1000-Hz conditions are considered (those which produced sizeable BMLDs from each listener), the window consistently shows a larger rearward than forward lobe, and the duration decreases monotonically with increasing frequency. In other words, there was greater forward than backward masking, since it is the ''rearward'' lobe which represents ''forward'' masking. However, the duration trend was not significant in an analysis of variance of the equivalent rectangular durations (ERDs) for the three listeners across these three frequencies [$F(2,4)=3.9$, $p=0.12$].

Figure 7 shows the shape of the simple Gaussian window as a function of noise level. The window shapes vary less across level than across frequency. The asymmetry

TABLE I. Mean fitting parameters, averaged across the three listeners (only two for the 125-Hz signal frequency), for each of the seven conditions of masker level and signal frequency and each of the nine window shapes. p_r is the time constant of the rearward lobe and p_f the time constant of forward lobe of the window, s_r is the time constant of the skirt of the window, w is the weight applied to the skirt of a skirt-type window and r is the dynamic range of the floor-type window. The E.R.D. is the integral in milliseconds of the entire window.

Noise level dB(SPL)/Hz	Signal frequency (Hz)	Fitting function (simple functions) Exponential p_r(ms)	p_f(ms)	E.R.D.	Gaussian p_r(ms)	p_f(ms)	E.R.D.	Rounded exponential p_r(ms)	p_f(ms)	E.R.D.
40	1000	37.7	10.6	48.3	36.9	11.7	86.0	53.4	20.7	74.2
40	500	39.9	27.8	67.6	39.1	23.8	111.6	55.7	37.4	93.1
40	250	59.7	34.3	94.0	61.1	28.1	158.1	83.6	45.0	128.7
40	125	28.8	39.8	68.1	35.9	28.7	132.2	55.4	58.5	113.9
50	500	33.4	16.4	49.8	33.3	20.3	94.9	47.9	28.8	76.6
30	500	42.9	29.5	72.3	37.7	26.3	113.4	57.4	39.8	97.2
20	500	47.4	25.9	73.3	44.5	24.4	122.1	65.6	39.1	104.7

Noise level dB(SPL)/Hz	Signal frequency (Hz)	(floor functions) Exponential p_r(ms)	p_f(ms)	r(dB)	E.R.D.	Gaussian p_r(ms)	p_f(ms)	r(dB)	E.R.D.	Rounded exponential p_r(ms)	p_f(ms)	r(dB)	E.R.D.
40	1000	39.2	10.5	−53.0	49.6	37.9	12.7	−48.4	89.7	55.3	21.0	−51.0	76.4
40	500	39.9	27.9	−64.9	67.7	40.5	24.9	−38.8	116.0	56.0	37.6	−47.9	93.6
40	250	60.8	34.5	−55.6	95.3	61.7	30.2	−38.7	162.8	85.4	46.5	−49.0	131.9
40	125	44.2	44.5	−56.9	88.7	35.8	38.6	−53.9	131.8	55.3	58.4	−57.3	113.7
50	500	33.5	16.4	−67.3	49.9	34.0	20.9	−52.7	97.3	48.2	29.1	−55.2	77.3
30	500	42.9	29.5	−65.0	72.4	37.8	26.3	−62.3	112.6	57.4	39.8	−70.5	97.3
20	500	47.3	25.8	−61.1	73.1	44.5	24.4	−60	122.1	65.6	39.1	−63.9	104.7

Noise level dB(SPL)/Hz	Signal frequency (Hz)	(skirt functions) Exponential p_r(ms)	p_f(ms)	s_r(ms)	w(dB)	E.R.D.	Gaussian p_r(ms)	p_f(ms)	s_r(ms)	w(dB)	E.R.D.	Rounded exponential p_r(ms)	p_f(ms)	s_r(ms)	w(dB)	E.R.D.
40	1000	39.0	27.1	114	−25.3	66.1	34.0	14.5	73.8	−24.5	86.0	51.5	21.4	133.8	−33.6	72.9
40	500	60.3	33.7	731	−34.4	94.0	34.6	22.0	119.0	−13.9	100.4	63.6	35.9	181.9	−27.4	89.5
40	250	44.3	44.3	285	−51.6	88.6	60.8	29.9	477.8	−27.5	160.7	84.3	45.6	812.2	−34.9	129.9
40	125	33.1	15.9	83.3	−38.2	49.1	35.8	38.4	61.7	−33.2	131.5	34.4	48.4	167.1	−42.1	82.7
50	500	42.9	29.5	77.8	−39.7	72.4	32.8	18.5	93.1	−28.8	90.9	47.3	27.6	130.5	−36.1	74.9
30	500	47.4	25.9	80.5	−41.5	73.2	35.8	25.3	78.6	−32.2	108.4	56.6	39.3	110.0	−37.7	95.9
20	500	42.9	23.1	85.3	−34.2	117.0	42.9	23.1	85.3	−34.2	117.0	65.6	39.0	111.7	−37.7	104.5

is fairly constant and again shows a forward lobe which is half to one-third the size of the rearward lobe, reflecting greater forward than backward masking. There is a slight tendency for the window to become shorter at higher noise levels. Although the mean ERDs vary monotonically with noise level, an analysis of variance for ERD, covering the three listeners across all four noise levels showed that this effect was far from statistical significance [$F(3,6)=0.66$, $p=0.61$].

The equivalent rectangular duration (ERD) of the win-

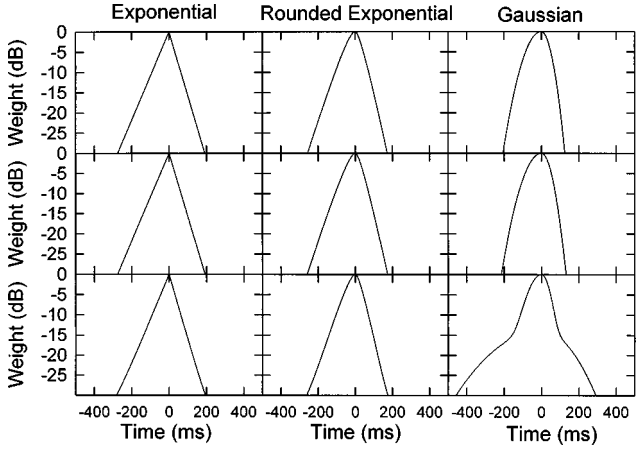

FIG. 4. Mean window shapes (i.e., the parameters have been averaged across three listeners) produced by each of the nine window shapes in the 40-dB(SPL/Hz)/500-Hz condition.

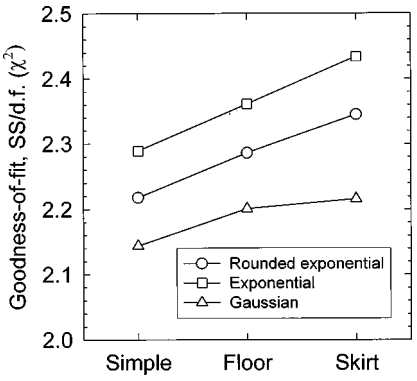

FIG. 5. Mean goodness-of-fit (χ^2) for each of the nine candidate window shapes, averaged across subjects, noise levels, and signal frequencies (excluding 125 Hz).

TABLE II. The mean goodness-of-fit achieved by the nine candidate window shapes in the seven experimental conditions, averaged across the three listeners. The goodness-of-fit is expressed as a χ^2 statistic (the sum of the squared error divided by the number of degrees of freedom; the number of degrees of freedom is the number of data points, less the number of parameters in the fit). Note that the means here include the 125-Hz condition, which has data from only two listeners and was consequently excluded from the analysis of variance and also from the means plotted in Fig. 5.

Condition		Fitting function: Simple			Floor			Skirt		
Noise level (dB(SPL)/Hz)	Signal freq. (Hz)	exp.	Gauss.	ro. exp.	exp.	Gauss.	ro. exp.	exp.	Gauss.	ro. exp.
40	1000	2.06	2.02	2.07	2.12	2.09	2.13	2.18	2.14	2.19
40	500	2.61	2.51	2.51	2.70	2.57	2.60	2.77	2.44	2.61
40	250	2.16	1.91	2.03	2.22	1.94	2.08	2.29	2.00	2.14
40	125	2.82	2.70	2.67	2.95	2.79	2.77	3.05	2.88	2.83
50	500	2.56	2.49	2.61	2.65	2.55	2.70	2.74	2.56	2.77
30	500	2.44	2.20	2.28	2.52	2.27	2.35	2.61	2.31	2.43
20	500	1.90	1.74	1.80	1.96	1.80	1.86	2.03	1.85	1.93
	$\bar{x}$	2.36	2.22	2.28	2.45	2.28	2.35	2.52	2.31	2.41

dow can be calculated by integrating the function in the time dimension. Table I lists the ERDs for each of the nine window shapes in each condition, derived for each subject separately, but then averaged across subjects. Table III gives the individual ERDs for each listener in each condition, using a simple-Gaussian fit. Averaging across the simple-Gaussian fits for each listener in each condition (20 fits), the mean duration of the window is 116 ms (s.d. 34 ms).

C. Discussion

The results of experiment 1 show that the ERD of the binaural temporal window is a little over 100 ms. The window appears to lengthen at lower frequencies. The window shape differs in some ways from the one derived by Kollmeier and Gilkey (1990).

1. The shape of the window

Significantly more efficient fits (i.e., lower χ^2) were produced by the simple versions of the window shapes, than by the floor, or skirt versions. This finding confirms the assumption made by Kollmeier and Gilkey (1990), that no advantage would accrue from using more complex, multiparameter window shapes. In fact, the sum-of-squares was, for the majority of fits, identical for the simple, floor, and skirt implementations of a given base function. Since the simple function had fewer parameters, it had more degrees of freedom and, so delivered a smaller χ^2. Only for the Gaussian-with-skirt shape did the extra parameters improve the sum-of-squares noticeably. Figure 5, and the significant interaction between fit-type and base function, show how the introduction of extra parameters has a less detrimental effect on χ^2 for the Gaussian base function, than for the other two.

The best fits were obtained using Gaussian base functions and the poorest fits using exponential base functions, with rounded-exponential base functions giving fits of intermediate goodness (Fig. 5). Put another way, the goodness-of-fit improved monotonically (although not significantly) with the roundness of the peak of the fitting function.[6] This relationship is the inverse of that reported by Kollmeier and Gilkey (1990). They estimated the shape of the binaural temporal window from detection thresholds for Sπ tones presented in noise that changed either from Nπ to No or from No to Nπ. Using this method, they found that an exponential window shape gave the best fits to the data, followed by rounded-exponential shapes, and then by Gaussian shapes. The difference between Kollmeier and Gilkey's results and the present results may stem from the effects of off-time

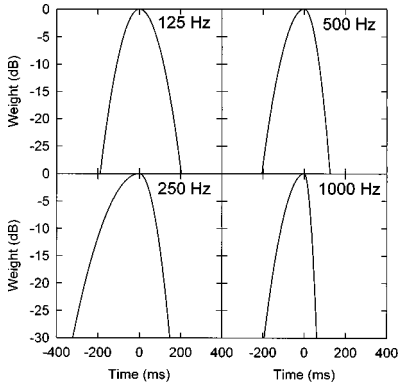

FIG. 6. Mean effect of frequency. The simple-Gaussian window shapes (parameters averaged across listeners) at each of the four signal frequencies for a noise spectrum level of 40 dB(SPL)/Hz. The different panels show windows at the indicated frequencies. The 125-Hz shape is based upon data from two of the three listeners (DF and IC) only.

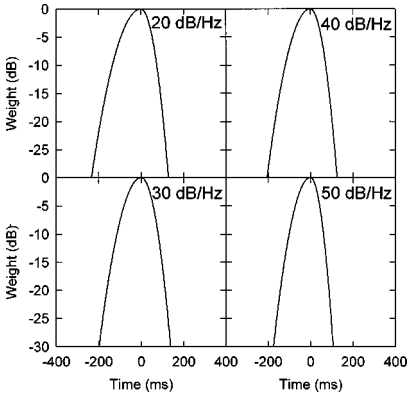

FIG. 7. Mean effect of level. The mean simple-Gaussian window shapes (parameters averaged across listeners) for each of the four noise levels for a 500-Hz signal. The different panels show windows for the indicated noise levels.

TABLE III. The equivalent rectangular duration (ERD) of the binaural temporal window for individual listeners in each of the seven conditions from experiment 1, when modeled using an asymmetric, simple-Gaussian window shape.

Noise level (dB(SPL)/Hz)	Signal frequency (Hz)	Listener		
		DF	IC	NPW
40	1000	56	84	118
40	500	153	80	102
40	250	151	156	168
40	125	188	76	⋯
50	500	87	88	109
30	500	102	110	127
20	500	135	130	100

listening which could not be taken fully into account in fitting functions to Kollmeier and Gilkey's data. Kollmeier and Gilkey assumed a fixed amount of off-time listening in most cases (see footnote 4) by placing the temporal window at the offset of the tone in the forward masking case and at its onset in the backward masking case. In each case this represents an offset of 10 ms. In the current experiments, the Gaussian windows were often more asymmetric (i.e., the ratio of rearward to forward lobe parameters differed from unity) than the other windows (Table I) and more off-time listening was assumed by the fitting algorithm in predicting thresholds from the Gaussian windows than from the rounded-exponential windows: For Gaussian windows the offset between the time of occurrence of the signal and the optimal position for the window found by the fitting algorithm had a standard deviation of 10.9 ms and ranged from -49 to $+61$ ms; for rounded exponential windows the standard deviation was 6.0 ms and ranged from -30 to $+33$ ms; for exponential windows, off-time listening makes no difference to the thresholds,[7] so the fitting algorithm automatically took an offset of 0 ms throughout.

It could be argued that the advantage for Gaussian windows observed in the present study is the product of a residual effect of distraction (see footnote 3) that remains despite the use of uncorrelated noise as the interfering stimulus. This argument is supported by the observation that some elevation of thresholds for short No durations compared to zero No duration was evident in the present data, suggesting that some distraction occurred; thresholds at 20-, 30-, and 40-ms No duration were elevated by an average of 0.7, 1.4, and 0.3 dB, respectively, compared to the 0-ms condition. If the distracting effect is limited to these short delays (where the distracting event is closest to the occurrence of the signal), it may have conferred an advantage on broad-peaked functions, like the Gaussian, because such functions predict the smallest decreases in thresholds at short No durations. In order to assess the likelihood of this possibility, we exploited the fact that the distraction, as measured by the elevation of thresholds, varied across listeners and conditions (compare, for instance, listener IC with listeners DF and NPW in Fig. 3); the size of these elevations (averaged across 20-, 30-, and 40-ms No durations) did not correlate significantly with the degree to which Gaussian functions were favoured by the fitting algorithm ($r=0.15$, $p=0.53$). The weakness of this relationship suggests that the fitting process must favor rounded peaked functions for some reason other than the elevations of threshold at short No durations. It is possible that the steeper sides of rounded functions are more important.

2. The asymmetry of the window

The asymmetry of the window varied across the three listeners; the average duration of the rearward lobe for a simple Gaussian fit was 1.3, 1.9, and 2.3 times longer than the average duration of the forward lobe for listeners DF, IC, and NPW, respectively. It did not vary much across the different fitting functions.

3. The duration of the window

The ERD of the window is about 100 ms, an order of magnitude greater than the ERD of the (monaural) temporal window measured by Moore *et al.* (1988) and by Plack and Moore (1990) using an analogous paradigm in the monaural domain (8–13 ms). This difference between the temporal integration time of the binaural and monaural auditory systems is consistent with that estimated by Grantham (1982) who also found a difference of an order of magnitude. The ERD found here is rather longer than that found by Kollmeier and Gilkey who obtained values between 33.2 and 83.2 for their four listeners using the exponential fit which they favoured. However, their Gaussian fits show quite similar values to ours, ranging from 61 to 134 ms.

The ERD and, to a lesser extent, the shape of the window should determine performance in other binaural tasks which have been used to investigate binaural sluggishness. Kollmeier and Gilkey (1990, Fig. 4) made predictions, based on their fitted window shape, for the detection thresholds of tones in noise with sinusoidally modulated interaural correlation (Grantham and Wightman, 1979). Kollmeier and Gilkey found that their window gave rather poor predictions, and calculated that it would need to be substantially longer in order to predict Grantham and Wightman's results accurately. We modeled Grantham and Wightman's data by convolving sinusoidal functions (representing the sinusoidal variation in ρ) by the mean temporal window shape derived from the four noise-level conditions in experiment 1, to give the variation in ρ at the output of the window. BMLDs were then predicted from Eq. (1) using a value for $(T_{\mathrm{Nu}}/T_{\mathrm{No}})$ derived from Grantham and Wightman's data at 0- and 4-Hz modulation rates (T_{No} and T_{Nu}, respectively). The results were quite similar to those obtained by Kollmeier and Gilkey. Thus although the windows estimated from the data of experiment 1 are about 25% longer than those estimated by Kollmeier and Gilkey, they are insufficiently long to account for Grantham and Wightman's results.

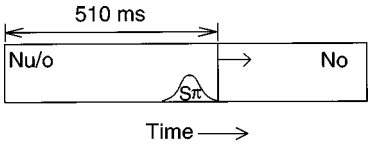

FIG. 8. Schematic illustration of the stimulus design in experiment 2.

4. The effect of noise level and signal frequency

There was no effect of noise level on the window shape (Fig. 7).

The mean window shape changes somewhat erratically with frequency, showing nonmonotonic changes in both duration and asymmetry. Grantham and Wightman (1979) also found that the effect of signal frequency on their estimate of the binaural integration time was not systematic. They found evidence of longer integration at 250 Hz than at 500 Hz. However, the apparent duration of integration was different for different listeners at 1000 Hz. Culling and Summerfield (1995a) measured a longer window at 125 Hz than at other frequencies. Taken together, these results suggest a tendency toward a longer window at lower frequencies. However, recent measurements by Akeroyd and Summerfield (1998), based on a binaural analog of gap detection show no effect of frequency. The present results support a reduction in ERD with frequency to the extent that there is weak evidence of longer windows at lower frequencies across the 250-Hz, 500-Hz, and 1000-Hz conditions. However, this trend does not extend to 125 Hz for the two listeners who produced a BMLD at this frequency.

III. EXPERIMENT 2

The results of experiment 1 indicate that the binaural temporal window contains a forward lobe in addition to a backward lobe. For most listeners and most combinations of level and frequency, the forward lobe made a smaller contribution to the ERD of the window than the backward lobe. It is possible, however, that the forward lobe measured here reflects an effect of distraction rather than of temporal integration. Thresholds might have been elevated when the switch from No to Nu noise came shortly after the presentation of the signal because of the distracting effect of the switch, rather than because its proximity allowed uncorrelated noise to enter the window. Experiment 2 was designed to distinguish this ''distraction'' hypothesis from the ''forward-lobe'' hypothesis (i.e., that the binaural window, like the monaural window, contains a genuine forward lobe). Thresholds were measured in conditions where the predictions of the distraction hypothesis are in the opposite direction to those of the forward-lobe hypothesis. Maskers were prepared which contained a single transition from partially correlated noise to fully correlated noise. The $S\pi$ signal was presented during the partially correlated noise. The time interval between the signal and the transition was varied systematically (Fig. 8). According to the distraction hypothesis, thresholds for detecting the signal should be higher, the closer the transition is to the signal. According to the forward-lobe hypothesis, thresholds should be lower, the closer the transition is to the signal. This result should follow because the signal will be detected more easily the more correlated noise that enters the window, and more correlated noise will enter the forward lobe of the window the closer the transition is to the occurrence of the signal.

A. Stimuli and procedure

Masking noises of one second duration were generated which contained a transition from partial interaural correlation to full interaural correlation at 510, 550, 600, 650, 700, 750, or 1000 ms. The partial interaural correlation was produced by taking a copy of a 1638.4-ms noise and offsetting the phases of each frequency in the frequency domain by adding a value randomly chosen from the range $\pm 60°$. One channel of a 1-s stereo sound file was filled with the original noise, while the other channel was filled with the phase-randomized copy up to the appropriate transition point; the remainder of the second channel was filled with the original noise, so that it was identical with the first channel after the transition. The same pair of noises was used to generate a set of eight stimuli with different transition times.

The $\pm 60°$ phase offsets reduced the product-moment correlation with the original noise to 0.82. According to Robinson and Jeffress (1963) the BMLD for NoSπ vs NoSo is reduced by about 6 dB if the interaural correlation of the noise falls to 0.82. Thus the thresholds had roughly equal scope to rise or fall in response to the location of the transition.

The signal was a 20-ms 500-Hz Sπ tone burst which was centered 500 ms into the stimulus. The end of the offset of the tone burst at 510 ms therefore coincided with the earliest of the eight transition times.

Three subjects with normal hearing thresholds (<20 dB HL *re*: ISO 389 at audiometric frequencies between 125 Hz and 8 kHz inclusive) attended fifteen 45-min sessions. Two listeners, DF and LP, were very experienced listeners, while listener SS was recruited at the beginning of this study. In each session, their thresholds for detecting the signal with each of the eight transition times was measured concurrently using eight interleaved, 1-up/3-down, adaptive staircases (Levitt, 1971). A more exacting, but time-consuming adaptive rule was employed in experiment 2 than in experiment 1, because the anticipated size of effect was very small and because the volume of data to be collected was more manageable. The algorithm continued until all eight staircases had undergone three reversals using a 4-dB step-size and then ten reversals using a 2-dB step-size. The mean signal level at the last eight reversals was used as an estimate of the listener's threshold for that run. The maskers were presented at a level of 40 dB(SPL)/Hz.

B. Results

Figure 9 shows the mean thresholds for each listener, and the mean data pooled across listeners, as a function of the time of the Nu-No transition with respect to the time of signal. Thresholds rose as the time between the end of the signal and the transition increased. One-way analyses of variance for each individual listener (with session as the ran-

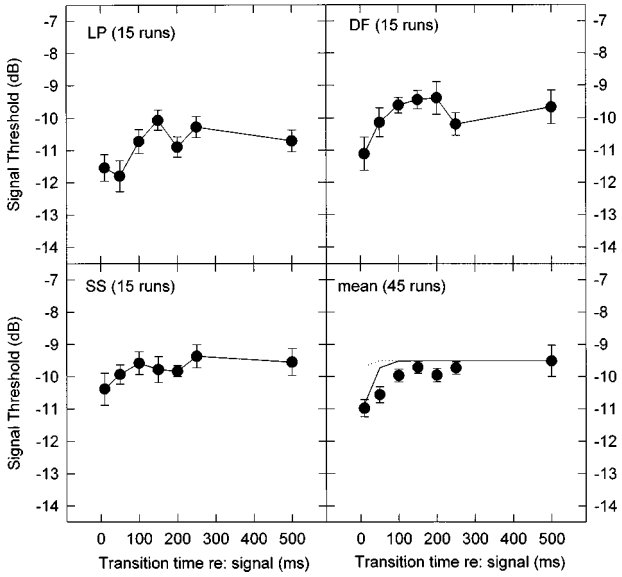

FIG. 9. Mean thresholds for each of three listeners, and thresholds pooled across the three listeners, for the detection of $S\pi$ tone pips presented during partially correlated noise (Nu/o; $\rho=0.82$) with correlated noise (No) commencing at different times following the presentation of the tone. The lines on the bottom-right panel show predictions based on the asymmetric-simple-Gaussian window shape derived from experiment 1 (solid line) and the predictions based on a similar window shape, with equal duration, but which has no forward lobe (dotted line).

dom factor) showed that the increases in threshold were significant for listeners DF and LP ($p<0.01$), but not for SS. An overall analysis of variance covering the 7 transition times and the 15 sessions (with listener as the random factor) showed a main effect of transition time [$F(6,12)=9.45$, $p<0.01$], no effect of session and no interaction between the two.

C. Discussion

If an abrupt transition between uncorrelated and correlated noise elevated detection thresholds when it occurred shortly after a signal, then thresholds would have been highest in experiment 2 when the the signal and the transition were close in time. This result did not occur. Rather, thresholds were lowest when the transition and the signal were close in time (Fig. 9). This outcome is expected if the binaural temporal window has a forward lobe. The further the transition is from the signal, the greater the proportion of Nu to No within the window, and the harder it is to detect the signal due to the background interaural decorrelation. This result is consistent with some of the data points measured by Kollmeier and Gilkey (1990, Fig. 2, panels a–d and Fig. 3), which show a reduction in threshold for signals embedded in $N\pi$ noise when a transition to No noise is approaching.

However, one further possible explanation must be considered. It is conceivable that while no substantial distraction occurred, the small effect observed in experiment 2 could be due to off-time listening, rather than to a forward lobe. If listeners could listen through a one-sided window placed just after the offset of the signal, they would reduce the amount of signal entering the window, but might gain an advantage if there were a compensating reduction in the amount of uncorrelated noise entering the window. In order to test this alternative explanation, the mean data plotted in Fig. 9 was modeled in two ways: first using the double-sided, but asymmetric Gaussian window derived from experiment 1, and second using a single-sided Gaussian window of the same ERD. Each of these windows was convolved with 1-s step functions which went from a correlation of 0.82 (the correlation of the partially decorrelated noise) to 1.0 at each of seven transition times used in the experiment (10, 50, 100, 150, 200, 250, and 500 ms after the mid-point), to give the correlation of the noise within the window at each point in time for each condition. The window was also convolved with the envelope of the $S\pi$ signal to give the signal energy within the window at each point in time. The detection threshold for each window position was then derived by adding the signal level in the window (in dB) to the expected BMLD derived from the overall interaural correlation according to Eq. (1), and subtracting these from an arbitrary constant. In order to model off-time listening, the best possible window positions for each window shape in each condition were derived from the maxima in the resulting functions and the threshold values at those positions were recorded. The arbitrary constant was adjusted in order to give the same threshold as the listeners for the 500-ms step position, and the results plotted in Fig. 9 in the panel showing the mean results (averaged across listeners). The solid line shows the results for the double-sided window and the dotted line for the single-sided window. The effect of off-time listening can be seen in the slight reduction in threshold which occurs at 10 ms compared to the other transition times for the single-sided window (dotted line). The double-sided window derived from experiment 1 produces a much more accurate fit to the data than does the single-sided window. Although the double-sided window under-estimates the amount of masking release, the discrepancy is only a fraction of a decibel, and can be tolerated.

The results of experiment 2 are further evidence that the forward lobe described by Kollmeier and Gilkey (1990), Culling and Summerfield (1995a), and in experiment 1 is a genuine feature of the window; it is unlikely to be a spurious feature produced by a distraction effect.

IV. GENERAL DISCUSSION

The results of the two experiments in this study give a consistent picture of the binaural temporal window as an integrating window of about 100-ms duration with a rounded top and a rearward lobe which is 1.5–2.5 times longer than the forward lobe. The motivation for the study was to provide an accurate summary representation of the sluggishness displayed by the binaural auditory system. It was anticipated that the resulting window shape would enable predictions of binaural phenomena for a variety of time-varying stimuli. The underlying assumptions of the study were that a window measured in this way would reflect the integration time of the binaural system at some level of analysis, and that the interaural parameters of any stimulus, convolved with such a window, would reveal the variation in these parameters which is heard by the listener. The same assumptions were made by Moore *et al.* (1988) and Plack and Moore (1990) in

measuring the monaural temporal window, and have been applied to monaural spectra to obtain a representation of the temporal variation in timbre as heard by a listener (see, for instance, Culling and Darwin, 1994).

The application of the binaural temporal window, as indicated in the Introduction, is likely to be in cross-correlation models, which are supposed to represent processing in the medial superior olive (MSO) (Jeffress, 1948). Such models currently use leaky integrators (with widely varying time constants) in order to accumulate information over time. A leaky integrator is effectively a single-sided, exponential window. Thus a straight-forward approach would be to replace the leaky integrator with the 100-ms-long asymmetric Gaussian window shape derived here. There are, however, some grounds for doubting the appropriateness of this approach. Two kinds of problem arise. One is that the window may not apply to all signals which the binaural system processes, but only to continuous signals. The other is that the window may not map onto the functioning of a particular part of the ascending auditory system in the way implied by its application to Jeffress' theory of cross correlation in the MSO.

The first problem arises from evidence that the binaural system can, in some sense, be ''reset'' (see: Hafter and Buell, 1983; Yost, 1985; Gilkey *et al.*, 1995). In particular, Yost (1985) found that the detection of short duration $S\pi$ tones with gated No maskers of the same duration was unaffected by the presence of a preceding ''fringe'' of $N\pi$ noise, which was separated from the masker and signal by a brief interval of silence; in comparison, Kollmeier and Gilkey (1990) and Gilkey *et al.* (1995) had shown that $N\pi$ noise which preceded a brief signal with no intervening silence elevated thresholds markedly (see Gilkey *et al.*, 1995, footnote 6). The phenomenon identified by Yost can be explained if the binaural integrators are zeroed whenever the input is briefly silenced. The evidence for this phenomenon is, so far, somewhat limited, but if future experiments confirm the existence of such a resetting effect then the applicability of the window derived in this paper would require revision.

The second problem in the application of the present results to models of binaural analysis stems from the results of Joris (1996). He investigated the occurrence of sluggishness in the inferior colliculus (IC), through which all innervation from the MSO passes *en route* to higher centers. Joris performed physiological experiments on single units in the IC of the cat which were analogous to those performed psychophysically by Grantham (1982) with human listeners. Grantham's study took the principal cue which is thought to mediate binaural unmasking, degree of interaural correlation, and measured the ability of listeners to detect modulation in interaural correlation over time. Grantham's results showed a rapid loss of sensitivity to modulation of interaural correlation as the modulation rate was increased from 5 Hz to 10 Hz. In comparison, Joris found that single units in the IC show modulations of response rate with interaural correlation at modulation frequencies an order of magnitude higher. These results are important for three reasons. First, if IC units can modulate their responses rapidly to changes in the interaural parameters of a stimulus then the MSO is presumably also able to do so, making it physiologically inaccurate to put sluggishness in a cross-correlation model which is supposed to represent the pattern of activity across different units of the MSO. An accurate model would place the sluggishness at some higher level of representation. In order to maintain the notion of using cross correlation with a long integration window as a psychophysical model of binaural processing, it may be necessary to redefine the relationship of the model to the physiology as including processing at higher centers which are responsible for the sluggishness. Second, it suggests that single units are capable of making a discrimination which the listener is incapable of making. This situation is unusual because it is generally assumed, in electrophysiological studies, that to show that a single unit can perform a task is to offer an explanation of how the entire system might perform it. Third, Joris' findings are problematic for Moore and Sek's hypothesis that sluggishness is a general feature of the auditory processes which require the interpretation of phase-locking information. The ability of a single unit to interpret phase locking at the two ears and rapidly modulate its firing rate in response, suggest that there is no fundamental obstacle within the auditory system to deriving the necessary information from phase-locking information without a long integration time.

Notwithstanding these two possible limitations, it seems likely that the binaural temporal window measured in the experiments reported in this paper will prove useful as a modeling tool, provided that it is remembered that it may reflect the integration times of a range of centers in the auditory pathway. Should the phenomenon of binaural resetting prove robust in future experiments, it may well be possible to incorporate the resetting process into a window model. In any case the window should provide an adequate model for uninterrupted stimuli such as those used here.

V. CONCLUSIONS

The data and modeling described in this paper point to the following conclusions about the shape of the binaural temporal window:

(1) The window has an equivalent rectangular duration of about 100 ms; this value is consistent with a number of previous estimates of the integration time of the binaural system.
(2) The window is broadly similar in shape at different frequencies and noise levels. However, we found a tendency toward shorter windows at higher frequencies.
(3) The window is best fitted by a function with a rounded peak, such as a Gaussian function.
(4) The use of parameters which limit the dynamic range of the window does not improve the goodness-of-fit to the experimental data.
(5) The window is asymmetric to varying degrees across listeners; its forward-going lobe is generally shorter than

its backward-going lobe. However, material effects of the forward lobe can be demonstrated.

ACKNOWLEDGMENTS

The authors thank the following people for their invaluable assistance in conducting this study: Chris Plack and Brian Glasberg for providing various versions of the sophisticated programs which are required to fit multi-parameter windows to threshold data produced by the notched-noise paradigm; David Marshall for advice and assistance with the window-fitting process and other aspects of the data analysis; Brian Moore for insightful comments regarding our pilot data which prompted the second experiment; Mike Akeroyd for asking incisive questions which prompted improvements to the method of window-fitting; two anonymous reviewers for their helpful suggestions and encouragement. Summaries of these findings were presented at the 1996 B.S.A. Short Papers Meeting and at the Twentieth A.R.O. Midwinter Meeting.

APPENDIX: WINDOW FITTING

The window fitting algorithm was similar to that employed by Plack and Moore (1990), but included simple versions of each function which lacked any limitation on the dynamic range. The number of free parameters varied according to the fit type (simple, floor or skirt). For the skirt function the width of the peak of the function and of the skirt were given separate parameters p and s; the latter parameter was not used for simple functions, or if the function had a floor value. The floor and skirt functions both had a weighting value which either determined the depth of the floor, r, or the relative weight, w, of the skirt. All window shapes were asymmetric in time, t, and the asymmetry of a function added another parameter, which, in the case of a skirt, scaled the width of the peak and floor parameters together (i.e., the asymmetry of the skirt was always constrained to be equal to the asymmetry of the peak of the function). Thus the functions had, two, three or four parameters.

The fitting process assumed that threshold was related to the overall correlation of noise entering the window, according to Eq. (1), plus the attenuation of the signal by the window. The ratio $T_{\mathrm{Nu}}/T_{\mathrm{No}}$ was derived separately from each set of data (a given subject in a given condition of noise level and signal frequency) such that fully correlated noise would yield the mean threshold from among the three results at 960-ms No duration (T_{No}) and fully uncorrelated noise would yield the mean threshold for 0-, 20-, and 30-ms No duration (T_{Nu}). Predicted thresholds were derived for a given window by integrating the intersection of its profile with the signal and with the interfering noise. A multi-parameter successive approximation algorithm was used to set the parameters of the window in order to predict the observed thresholds as closely as possible. For Gaussian and rounded-exponential functions, off-time listening was modeled whenever the algorithm tested a given set of parameters; a single parameter minimization method was used to optimally position the window, so as to minimize the predicted threshold (as opposed to minimising the difference between actual and predicted thresholds which was achieved purely by adjusting the shape of the window).

The following equations relate one side of each of the nine different functions (in square brackets) to their integrals:

(1) The simple exponential:

$$\int [e^{-t/p}]dt = pe^{-t/p}.$$

(2) The simple Gaussian:[8]

$$\int [e^{-(t/2p)^2}]dt = p\sqrt{\pi}\ \mathrm{erf}(t/2p).$$

(3) The simple rounded exponential:

$$\int [(1+2t/p)e^{-2t/p}]dt = (p+t)e^{-2t/p}.$$

(4) The exponential with dynamic range limitation (floor):

$$\int [(1-r)e^{-t/p}+r]dt = (r-1)pe^{-t/p}+rt.$$

(5) The Gaussian with dynamic range limitation (floor):

$$\int [(1-r)e^{-(t/2p)^2}+r]dt = (r-1)p\sqrt{\pi}\ \mathrm{erf}(t/2p)+rt.$$

(6) The rounded-exponential with dynamic range limitation (floor):

$$\int [(1-r)(1+2t/p)e^{-2t/p}+r]dt = (r-1)(p+t)e^{-2t/p}+rt.$$

(7) The weighted sum of two exponentials (peak and skirt):

$$\int [(1-w)e^{-t/p}+we^{-t/s}]dt = (w-1)pe^{-t/p}-wse^{-t/s}.$$

(8) The weighted sum of two Gaussians (peak and skirt):

$$\int [(1-w)e^{-(t/2p)^2}+we^{-(t/2s)^2}]dt = (w-1)p\sqrt{\pi}\ \mathrm{erf}(t/2p)+ws\sqrt{\pi}\ \mathrm{erf}(t/2s).$$

(9) The weighted sum of two rounded-exponential (peak and skirt):

$$\int [(1-w)(1+2t/p)e^{-2t/p}+w(1+2t/s)e^{-2t/s}]dt = (w-1)(p+t)e^{-2t/p}-w(s+t)e^{2t/s}.$$

The forward and rearward lobe of the window may be generated using separate parameters p_f and p_r, and s_f and s_r, where $s_f = s_r p_f / p_r$.

[1]Bell (1972) measured the detection threshold of a 125-ms Sπ signal in No noise of variable duration which was temporally fringed by uncorrelated noise. The stimulus configuration was, therefore, similar to that employed in the present study, except that the tone pulses were much longer. Although the Sπ signals were quite long it is clear from his results that a 100-ms fringe of correlated noise improved the detectability of the signal considerably, and that the leading fringe was more beneficial than the trailing fringe, suggesting an asymmetric temporal window with larger rearward lobe.

[2]Shackleton and Bowsher (1989) measured detection thresholds for 20-ms, 500-Hz So and Sπ tone pulses presented during a noise which changed instantaneously from Nπ to No and back to Nπ, or from No to Nπ and back to No. They concluded that the binaural integration time was approximately 100 ms. However, the design of their experiment made it difficult to interpret the results in terms of a window shape.

[3]The stimulus configuration used in the present experiment is a refinement

of one which we used in a pilot study (Culling and Summerfield, 1995a) where we measured detection thresholds for an Sπ tone in a masking noise which changed abruptly from Nπ to No and then back to Nπ, with the tone presented during the No segment. One problem which arose with this configuration was that listeners paradoxically often produced higher thresholds for brief No durations (50 or 75 ms) than in the condition where the No duration was zero and the task required the detection of an Sπ signal against an Nπ noise. Kollmeier and Gilkey (1990) encountered similar problems (see their footnote 3) which were exacerbated when using maskers containing double transitions. Consequently, they did not report data collected with that method in their paper (Gilkey, 1996). These results suggest that listeners might be distracted by abrupt transitions between No and Nπ segments. Distraction could arise from either or both of two causes: (1) the transitions result in rapid changes in the perceived location of the noise from being diffusely lateralized to each side, to being centred within the head, to being lateralized again; (2) as the transitions occur, the noise within the temporal window becomes decorrelated, because it is a mixture of Nπ and No noise. The decorrelation caused in this way is similar to the cue which the listeners use to detect the presence of the signal. Thus thresholds may rise because listeners cannot distinguish the decorrelation caused by the transition from the decorrelation caused by the signal. Irrespective of the cause of the distraction, the use of uncorrelated interfering noise in place of antiphasic noise should reduce the problem, because (1) the change in perceived location of the noise is less dramatic and (2) because the interfering noise is uncorrelated to start with, there is no burst of decorrelation at the transition, rather the noise becomes progressively more correlated as more No noise enters the window. Overall, the subjective impression produced by these Nu-No-Nu maskers is much less ''eventful'' than that produced by Nπ-No-Nπ maskers. Consequently, elevations of thresholds for a 20-ms No duration, compared to uninterrupted Nu, averaged only around 1 dB in the present experiment. A minor disadvantage of using Nu noise is that NuSπ vs NoSπ gives a smaller BMLD than NπSπ vs NoSπ (Robinson and Jeffress, 1963). Consequently, the range of thresholds measured in the present experiment (although dependent on conditions of signal frequency and noise intensity) was typically reduced in extent from 15 dB to 10–12 dB. Bearing the limitations of the pilot study in mind, it is worth recording its three principal findings. The window was found to have an equivalent rectangular duration of around 100 ms at frequencies of 250 Hz, 500 Hz, and 1000 Hz, but to be substantially longer at 125 Hz. The window was also found to have a rounded top, best fit by a Gaussian shaped function.

[4]The differences between the time of the signal, the optimal temporal placement of the temporal window and the time at which the information from that window becomes available to the listener are often confused. The time of the signal is straightforward enough. However, the optimal placement of the sliding window may place its centroid before or after the signal, the only limitation being that the window must intersect the signal sufficiently for that position to provide the best evidence of the signal's presence. The optimal position may place the centroid at a point in time when the signal is physically off. At threshold, the time at which the information from the window becomes fully available must be after the entire window has been collected, including any forward lobe that it might possess, so one must add the total duration of the forward lobe to the temporal location of the centroid in order to derive the earliest moment that detection can occur. Unfortunately, the duration of the forward lobe cannot be derived from the fitting process used here, because all the fitting functions we have employed extend infinitely forward and backward in time. Clearly, the forward lobe does not share this property or one would never hear anything. However, the approximate delay to detection can be estimated from the ERD.

[5]In Kollmeier and Gilkey's (1990) analyses, only the exponential and rounded-exponential functions were permitted to be asymmetric in time. The second parameter of their Gaussian function (τ_2) changed the location in time of a symmetrical Gaussian. This parameter moved the window to positions which permitted off-time listening. However, like other parameters of their window shapes, it was varied in order to optimize the fit with the data (i.e., to yield the lowest discrepancy with the data), rather than to model optimal off-time listening (i.e., to yield the lowest thresholds). In contrast, in the analysis of experiment 1 of the current study, parameters were varied to model off-time listening explicitly.

[6]The rank ordering is in agreement with the findings of the pilot study described in footnote 2 (Culling and Summerfield, 1995a).

[7]Off-time listening makes no difference to the thresholds predicted by an exponential window because the integral of an exponential is an exponential with the same time constant. Thus if the centroid of an exponential window is moved further from the noise the amount of signal energy entering the window is reduced by the same proportion as the amount of noise energy entering the window, giving no net effect on the signal-to-noise ratio. Of course, if in moving the window away from one band, it is moved closer to another (as would be the case in the notch-noise paradigm), then the signal-to-noise ratio worsens as a result of placing the window anywhere but directly over the signal. In the current binaural application, it is the overall correlation of the noise in the window which is linearly related to signal threshold [Eq. (1)], rather than the noise power, but the correlation is directly proportional to the amount of Nu noise in an exponential window, so the two situations are equivalent.

[8]The factor $\sqrt{\pi}$ is missing from the equations published by Moore *et al.* (1988) and Plack and Moore (1990). The function 'erf' is defined as follows:

$$\mathrm{erf}(x)=\frac{2}{\sqrt{\pi}}\int_0^x e^{-t^2}.$$

Akeroyd, M. A., and Summerfield, Q. (**1998**). ''A binaural analog of gap detection,'' J. Acoust. Soc. Am. (submitted).

Bell, D. (**1972**). ''Effect of fringe on masking-level difference when gating from uncorrelated to correlated noise,'' J. Acoust. Soc. Am. **52**, 525–529.

Blauert, J. (**1972**). ''On the lag of lateralization caused by interaural time and intensity differences,'' Audiology **11**, 265–270.

Chandler, D. W., and Grantham, D. W. (**1992**). ''Minimum audible movement angle in the horizontal plane as a function of stimulus frequency and bandwidth, source azimuth and velocity,'' J. Acoust. Soc. Am. **91**, 1624–1636.

Culling, J. F., and Darwin, C. J. (**1994**). ''Perceptual and computational separation of simultaneous vowels: cues arising from low-frequency beating,'' J. Acoust. Soc. Am. **95**, 1559–1569.

Culling, J. F., and Summerfield, Q. (**1995a**). ''The binaural temporal window,'' Br. J. Audiol. **29**, 74–75.

Culling, J. F., and Summerfield, Q. (**1995b**). ''Perceptual segregation of concurrent speech sounds: Absence of across-frequency grouping by common interaural delay,'' J. Acoust. Soc. Am. **98**, 785–797.

Durlach, N. I., and Colburn, H. S. (**1978**). ''Binaural phenomena,'' in *The Handbook of Perception*, edited by E. C. Carterette and M. P. Friedman (Academic, New York).

Durlach, N. I., Gabriel, K. J., Colburn, H. S., and Trahiotis, C. (**1986**). ''Interaural correlation discrimination II: Relation to binaural unmasking,'' J. Acoust. Soc. Am. **79**, 1548–1557.

Gabriel, K. J., and Colburn, H. S. (**1981**). ''Interaural correlation discrimination I: Bandwidth and level dependence,'' J. Acoust. Soc. Am. **69**, 1394–1401.

Gilkey, R. H., Simpson, B. D., and Weisenberger, J. M. (**1995**). ''Masker fringe and binaural detection,'' J. Acoust. Soc. Am. **88**, 1323–1332.

Gilkey, R. H. (**1996**). personal communication.

Grantham, D. W. (**1982**). ''Detection of time-varying interaural correlation in narrow band noise stimuli,'' J. Acoust. Soc. Am. **72**, 1178–1184.

Grantham, D. W. (**1984**). ''Discrimination of dynamic interaural intensity differences,'' J. Acoust. Soc. Am. **76**, 71–76.

Grantham, D. W. (**1995**). ''Spatial hearing and related phenomena,'' in, *Hearing: Handbook of Perception and Cognition*, 2nd ed., edited by B. C. J. Moore (Academic, San Diego), pp. 297–345.

Grantham, D. W., and Wightman, F. L. (**1978**). ''Detectability of varying interaural temporal differences,'' J. Acoust. Soc. Am. **63**, 511–523.

Grantham, D. W., and Wightman, F. L. (**1979**). ''Detectability of a pulsed tone in the presence of a masker with time-varying interaural correlation,'' J. Acoust. Soc. Am. **65**, 1509–1517.

van der Heijden, M., and Trahiotis, C. (**1997**). ''A new way to account for binaural detection as a function of interaural noise correlation,'' J. Acoust. Soc. Am. **101**, 1019–1022.

Hafter, E. R., and Buell, T. N. (**1983**). ''Recovery from saturation in lateralization of high frequency stimuli,'' J. Acoust. Soc. Am. **74**, S40.

Hirsh, I. J. (**1948**). ''The influence of interaural phase on interaural summation and inhibition,'' J. Acoust. Soc. Am. **20**, 536–544.

Jain, M., Gallagher, D. T., Koehnke, J., and Colburn, H. S. (**1991**). ''Fringed

correlation discrimination and binaural detection,'' J. Acoust. Soc. Am. **90**, 1918–1926.
Jeffress, L. A. (**1948**). ''A place theory of sound localization,'' J. Comp. Physiol. Psychol. **61**, 468–486.
Joris, P. X. (**1996**). ''Integration time of binaural coincidence detection,'' Society for Neurosci. Abstr. **22**, 648.
Klatt, D. H. (**1980**). ''Software for a cascade/parallel formant synthesizer,'' J. Acoust. Soc. Am. **67**, 838–844.
Koehnke, J., Colburn, H. S., and Durlach, N. I. (**1986**). ''Performance in several binaural-interaction experiments,'' J. Acoust. Soc. Am. **79**, 1558–1562.
Kollmeier, B., and Gilkey, R. H. (**1990**). ''Binaural forward and backward masking: Evidence for sluggishness in binaural detection,'' J. Acoust. Soc. Am. **87**, 1709–1719.
Levitt, H. (**1971**). ''Transformed up-down methods in psychoacoustics,'' J. Acoust. Soc. Am. **49**, 467–477.
Mills, A. W. (**1958**). ''On the minimum audible angle,'' J. Acoust. Soc. Am. **30**, 237–246.
Moore, B. C. J., Glasberg, B. R., Plack, C. J., and Biswas, A. K. (**1988**). ''The shape of the ear's temporal window,'' J. Acoust. Soc. Am. **83**, 1103–1116.
Moore, B. C. J., and Sek, A. (**1996**). ''Detection of frequency modulation at low rates: Evidence for a mechanism based on phase locking,'' J. Acoust. Soc. Am. **100**, 2320–2331.
Patterson, R. D. (**1976**). ''Auditory filter shapes derived with noise stimuli,'' J. Acoust. Soc. Am. **59**, 640–654.
Patterson, R. D., and Nimmo-Smith, I. (**1980**). ''Off-frequency listening and auditory-filter asymmetry,'' J. Acoust. Soc. Am. **67**, 229–245.
Patterson, R. D., and Moore, B. C. J. (**1986**). ''Auditory filters and excitation patterns as representations of frequency resolution'' in *Frequency Selectivity in Hearing*, edited by B. C. J. Moore (Academic, London).
Perrot, D. R., and Musicant, A. D. (**1977**). ''Dynamic minimum audible angle: Binaural localization of moving sound sources,'' J. Acoust. Soc. Am. **62**, 1463–1466.
Perrot, D. R., and Pacheco, S. (**1989**). ''Minimum audible angle thresholds for broadband noise as a function of delay between the onset of the lead and lag signals,'' J. Acoust. Soc. Am. **85**, 2669–2672.
Plack, C. J., and Moore, B. C. J. (**1990**). ''Temporal window shape as a function of frequency and level,'' J. Acoust. Soc. Am. **87**, 2178–2187.
Robinson, D. E., and Jeffress, L. A. (**1963**). ''Effect of varying the interaural noise correlation on the detectability of tonal signals,'' J. Acoust. Soc. Am. **65**, 1947–1952.
Shackleton, T. M., and Bowsher, J. M. (**1989**). ''Binaural effects of the temporal variation of a masking noise upon the detection thresholds of tone pulses,'' Acustica **69**, 218–225.
Yama, M. F. (**1992**). ''Effects of temporal separation and masker level on binaural analysis in forward masking,'' J. Acoust. Soc. Am. **91**, 327–335.
Yost, W. A. (**1985**). ''Prior stimulation and masking level difference,'' J. Acoust. Soc. Am. **78**, 901–907.

Evidence for an across-frequency, between-channel process in asymptotic monaural temporal gap detection[a)]

C. Formby, M. J. Gerber, and L. P. Sherlock
University of Maryland School of Medicine, Division of Otolaryngology—HNS, Department of Surgery, 16 South Eutaw Street, Suite 500, Baltimore, Maryland 21201

L. S. Magder
University of Maryland School of Medicine, Department of Epidemiology & Preventive Medicine, Baltimore, Maryland 21201

(Received 30 October 1997; accepted for publication 3 March 1998)

Monaurally measured temporal gap detection (TGD) thresholds characteristically increase as the frequency difference is increased over a range of about half an octave to an octave between two sinusoids that mark the onset and offset of the silent gap. For greater sinusoidal frequency separations, the TGD thresholds often become asymptotic. This pattern probably reflects two different processes. The first process likely reflects *within-channel* processing within a single auditory filter or channel. The second process is less certain, but may reflect *between-channel* processing of the silent gap stimulus across two or more independent frequency channels. To evaluate the hypothesis that asymptotic monaural gap detection can be explained by a simple *between-channel* process, TGD thresholds were measured as a function of frequency separation between a pregap sinusoid presented to the left ear (channel 1) and a postgap sinusoid, of higher frequency, presented to the right ear (channel 2). The rationale for dichotic presentation of the sinusoidal markers and gap signal followed from the fact that the gap detection task must be performed between two independent channels by combining the outputs from each channel (ear) and recovering the gap information centrally. The resulting TGD thresholds for pregap sinusoids from 250 to 4000 Hz were relatively invariant and increased only slightly with increasing marker frequency separation. The average TGD thresholds for four listeners were in the range of 30 to 40 ms, which corresponded closely with their asymptotic TGD thresholds for the same set of stimulus conditions measured monaurally. This correspondence of the two data sets supports an across-frequency, *between-channel* process for asymptotic monaural gap detection at marker frequency separations greater than about half an octave. [S0001-4966(98)04906-6]

PACS numbers: 43.66.Ba, 43.66.Mk [JWH]

INTRODUCTION

Detection of silent temporal gaps is characterized by two prominent features when measured as a function of frequency separation between two sinusoids that mark the onset and offset of a silent gap. First, over a range of about a half-octave to an octave separation, temporal gap detection (TGD) thresholds measured for monaural presentation routinely increase as the frequency of the postgap marker (F_2) is increased relative to a lower frequency pregap marker (F_1) (Neff *et al.*, 1982; Formby and Forrest, 1991; Formby *et al.*, 1996). Second, TGD thresholds tend to become asymptotic for greater sinusoidal marker frequency separations (see Formby *et al.*, 1996). This characteristic TGD pattern probably reflects two different processes. The first process almost certainly reflects a TGD cue that is based on the output of a single auditory filter or channel (Williams and Perrott, 1972; Formby and Forrest, 1991; Formby *et al.*, 1996; Phillips *et al.*, 1997). The nature of the second process is less certain, but may reflect across-frequency, *between-channel* processing of the silent gap stimulus in two or more independent frequency channels (Viemeister and Plack, 1993; Phillips *et al.*, 1997).

The aim of this study was to evaluate the idea that asymptotic TGD thresholds measured monaurally as a function of marker frequency separation can be explained parsimoniously by *between-channel* processing of the gap stimulus across two functionally independent channels. These channels presumably are uncorrelated, independent auditory filters whose outputs are combined (after peripheral filtering has been completed) at some higher level of the auditory system to recover the gap signal. A simple experiment to test this idea was to measure TGD dichotically. Operationally, the two ears of the human listener are independent and uncorrelated channels whose outputs are combined centrally at stages after peripheral filtering. Thus TGD measured dichotically as a function of frequency separation between a pregap sinusoidal marker F_1 presented by earphone to one ear (channel 1) and a postgap sinusoidal marker F_2 presented by a second earphone to the other ear (channel 2) appeared to offer an opportunity to test the idea of *between-channel* processing of the temporal gap stimulus. This opportunity ap-

[a)]A preliminary version of these results was presented at the 133rd Meeting of the Acoustical Society of America in State College, PA [J. Acoust. Soc. Am. **101**, 3150(A) (1997)].

pears further justified by evidence suggesting that TGD measured dichotically is relatively invariant to differences in the spectral properties of the markers (Penner, 1977; Phillips *et al.*, 1997). These virtues make the dichotic measurement of TGD an ideal *between-channel* task with which to compare asymptotic monaural TGD.

The hypothesis of this study was straightforward. If asymptotic detection of a silent temporal gap signal depends on an across-frequency, *between-channel* monaural process, then the resulting monotic TGD thresholds (measured between the F_1 marker presented in one frequency channel and the F_2 marker presented in a second, independent frequency channel) should correspond closely to the TGD thresholds measured dichotically, between ears (channels), over the range of marker frequency separations yielding asymptotic monaural TGD performance. A corollary to this hypothesis is that TGD performed monaurally at small marker frequency separations, *within* a single channel, should yield lower thresholds than those measured dichotically, *between* channels, for corresponding small marker frequency separations. This differential TGD performance for *within*- and *between-channel* tasks presumably can be explained by the listener's use of different cues. The cue available *within channel* is the conventional gap cue and that used *between channels* is probably a temporal offset-to-onset across-channel cue (Viemeister and Plack, 1993). That is, the offset of F_1, marking the beginning of the silent gap, occurs in one channel (or set of channels) while the onset of F_2, marking the end of the gap, occurs in a separate channel (or set of channels).

I. METHODS

A. Overview of measurement conditions

To test the simple two-channel hypothesis for asymptotic TGD, we measured and compared performance in two measurement paradigms. The idealized standard and signal intervals are shown in Fig. 1 for the two paradigms, which are identified as MONOTIC and DICHOTIC. For the MONOTIC paradigm, the pregap sinusoidal marker F_1 and the postgap sinusoidal marker F_2 in both the standard and the signal intervals (including the silent gap in the signal interval) were presented to each listener's right ear. For the DICHOTIC paradigm, F_1 and F_2 were also presented nonsimultaneously. F_1 was presented first to the left ear, and F_2 was then presented to the right ear in both the standard and signal intervals. The silent temporal gap in the signal interval followed after the offset of F_1 presented to the left ear and before the onset of F_2 presented to the right ear. In both measurement paradigms, the starting phase of each pregap and postgap marker was selected randomly and chosen anew for each presentation. A temporally continuous, broadband noise was also presented as a background masker in both paradigms. The noise background served to mask the contribution of audible gating artifacts that otherwise might have confounded the TGD tasks. These extraneous cues arose from instantaneous gating of the silent gap.

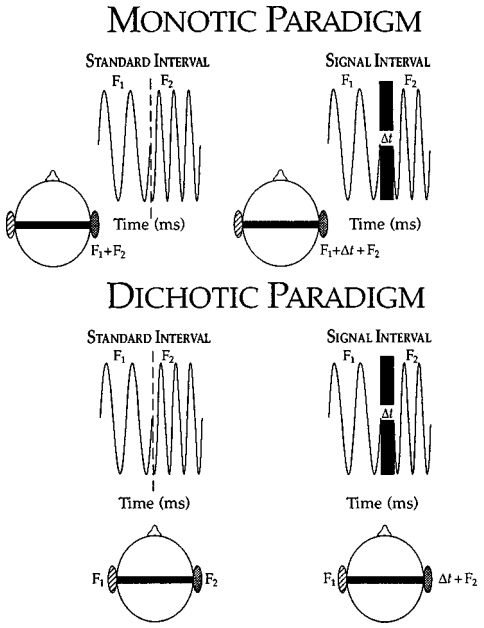

FIG. 1. Idealized pregap (F_1) and postgap (F_2) sinusoidal marker configurations are depicted for the standard and signal intervals of a trial for the MONOTIC and DICHOTIC paradigms. Markers F_1 and F_2 in the standard interval and also in the signal interval, which contained the silent gap (Δt), were presented to each listener's right ear in the MONOTIC paradigm. In the DICHOTIC paradigm, F_1 was presented to the listener's left ear and F_2 was then presented to the right ear in both the standard and signal intervals. The signal interval contained the silent gap (Δt), which followed after the offset of F_1 in the left ear and before the onset of F_2 in the right ear.

B. Subjects

Four normal-hearing adults (ages 25–45 years) participated as subjects in this study. Each subject had normal audiometric hearing sensitivity at octave intervals from 250 to 8000 Hz (ANSI, 1970). Three of the four subjects were paid. None of these subjects had previous experience as a laboratory listener. The senior investigator (CF), who was an experienced listener, served as the fourth listener. All subjects received several hours of practice on representative MONOTIC and DICHOTIC conditions prior to formal data collection. The training was adequate for all listeners to achieve asymptotic performance on the experimental conditions.

C. Stimulus and apparatus

The sinusoidal markers and silent gap signal were produced via an array processor that was programmed by a personal computer. These stimuli were presented via a 16-bit digital-to-analog converter (TDT, model DA1) (61-μs sampling period) and filtered (TDT, model FT5-9) below 7500 Hz. Silent gaps were introduced instantaneously between the sinusoidal markers by placing zeros in the buffer. The stimuli were attenuated (TDT, model PA4) and mixed (TDT, model SM3) with a temporally continuous, broadband noise masker that was low-pass filtered (TDT, model FT5-9) at 7500 Hz. The stimuli and masker were then routed to a set of headphones (Telephonics, TDH-39). Both sinusoidal markers, F_1 and F_2, and the noise masker were presented to the right earphone in the MONOTIC paradigm. In the

DICHOTIC paradigm, the noise masker was presented in phase to the two earphones, and F_1 and F_2 were delivered sequentially to the left and right earphones, respectively. The experiments were performed with each subject seated in a sound-attenuating double-wall room.

The markers were presented at a level ($10 \log E/N_0 = 40$ dB) that was clearly audible in the noise masker (spectrum level $N_0 = 30$ dB). The overall duration of F_1 was a constant value (500 ms) in all observation intervals. We randomized the overall duration of each F_2 marker over an 800-ms range from 100 to 900 ms (average marker duration $= 500$ ms). This randomization procedure was performed to neutralize overall stimulus duration differences as a possible cue for the gap signal interval. In each observation interval, we also randomized the onset phase of each marker over a range of 360° to neutralize onset phase cues that otherwise might have confounded TGD performance. The onset of each F_1 marker and the offset of each F_2 marker were ramped with 10-ms raised cosine rise and fall times, respectively.

D. Procedure

The listener's task on each two-interval, two-alternative forced-choice (2I, 2AFC) trial in both the MONOTIC and DICHOTIC measurement paradigms was to detect the observation interval that contained the silent temporal gap between markers F_1 and F_2. A second, standard observation interval on each trial contained the same pair of markers, but these were presented without the gap signal. The gap signal was presented with equal *a priori* probability in one of the two visually cued observation intervals. After each trial, the listener selected the observation interval perceived to have the silent gap. The listener then received visual feedback for the correct interval.

The frequency values of markers F_1 and F_2 were constant across a block of 50 trials. For each block, the listener adaptively tracked a 70.7% correct gap detection threshold in a one-up, two-down paradigm (Levitt, 1971). The tracking procedure was implemented with logarithmic steps. The first three reversals in each adaptive track used the equivalent of a 3-dB step size in duration, typically starting from an initial gap duration of either 50 or 100 ms. Subsequent reversals were based on the equivalent of a 1-dB step in duration. The estimate of TGD threshold for each block of trials was based on the geometric mean of the gap durations at the last even number of reversals for the small adaptive steps. TGD thresholds were measured as a function of the frequency separation between markers F_1 and F_2. A set of TGD thresholds was collected for each of five pre-gap marker frequency values, $F_1 = 250$, 500, 1000, 2000, or 4000 Hz. The postgap marker frequency values that were paired with F_1 included $F_1 = F_2$ and F_2 frequencies that were 5%, 10%, 15%, 24%, 50%, and 100% higher than each F_1 frequency. The exception was for $F_1 = 4000$ Hz for which the frequency range of marker F_2 was limited by the earphone response to frequencies $\leqslant$50% above F_1. The specific frequency values of marker F_2 presented with each F_1 marker frequency are shown in Table I. This set of F_2 marker frequencies for each F_1 marker frequency value typically spanned a range of at least three critical bandwidths (Zwicker and Feldtkeller, 1967), which made possible *between-channel* comparisons of pregap and postgap markers in independent frequency channels.

TABLE I. Pregap and postgap sinusoidal marker frequency conditions.

F_1 frequency (Hz)	F_2 frequencies (Hz)
250	250, 262.5, 275, 287.5, 310, 375, 500
500	500, 525, 550, 575, 620, 750, 1000
1000	1000, 1050, 1100, 1150, 1240, 1500, 2000
2000	2000, 2100, 2200, 2300, 2480, 3000, 4000
4000	4000, 4200, 4400, 4600, 4960, 6000

II. RESULTS

The four listeners each provided three consistent estimates of the TGD threshold for all of the marker conditions in both measurement paradigms.[1] The group average TGD thresholds (and standard error bars) are presented in Fig. 2 for the MONOTIC (unfilled circles) and DICHOTIC (filled circles) paradigms. Shown separately in each panel are the results for a different value of the F_1 marker, which is identified. The TGD thresholds for each condition of F_1 are shown as a function of relative marker frequency separation, which is expressed as a ratio index F_2/F_1. Our ratio spans a range between a value of 1.0, which corresponds to $F_1 = F_2$, and a value of 2.0, which reflects an octave separation between the markers. GRAND MEAN TGD thresholds, calculated by pooling the group TGD threshold estimates across all values of F_1 for each F_2/F_1 ratio, are also shown in the lower right panel of Fig. 2. The TGD threshold functions in each panel reflect the same general trend across the range of F_2/F_1 ratios for each value of F_1, and these group results are typical of the individual results from each listener. The TGD thresholds for the MONOTIC paradigm increased systematically from values usually less than 5 ms for the small marker frequency separations (represented by small F_2/F_1 ratios) to threshold values typically $\geqslant$30 ms for large marker frequency separations (represented by large F_2/F_1 ratios). In contrast, the TGD thresholds for the DICHOTIC paradigm were relatively invariant across the range of marker frequency separations and, except for $F_1 = 4000$ Hz, generally reflected only a slight deterioration in performance with increasing F_2/F_1 ratio. (This pattern is supported by the slope values presented subsequently in Table III.) Typical TGD thresholds across the range of marker frequency separations for $F_1 \leqslant 2000$ Hz fell between about 20 and 40 ms. Threshold values for $F_1 = 4000$ Hz varied from about 40 to 60 ms across the measurable range of marker frequency separations, which spanned 2000 Hz. The larger TGD thresholds measured for $F_1 = 4000$ Hz can be explained by the reduced effective signal-to-noise ratio expected for this measurement condition (see Formby and Forrest, 1991).

By way of comparison, the DICHOTIC TGD thresholds were from threefold to tenfold larger than the corresponding MONOTIC TGD thresholds across the various conditions of $F_1 = F_2 (F_2/F_1 = 1.0)$ shown in Fig. 2. The threshold differences between the MONOTIC and DICHOTIC functions

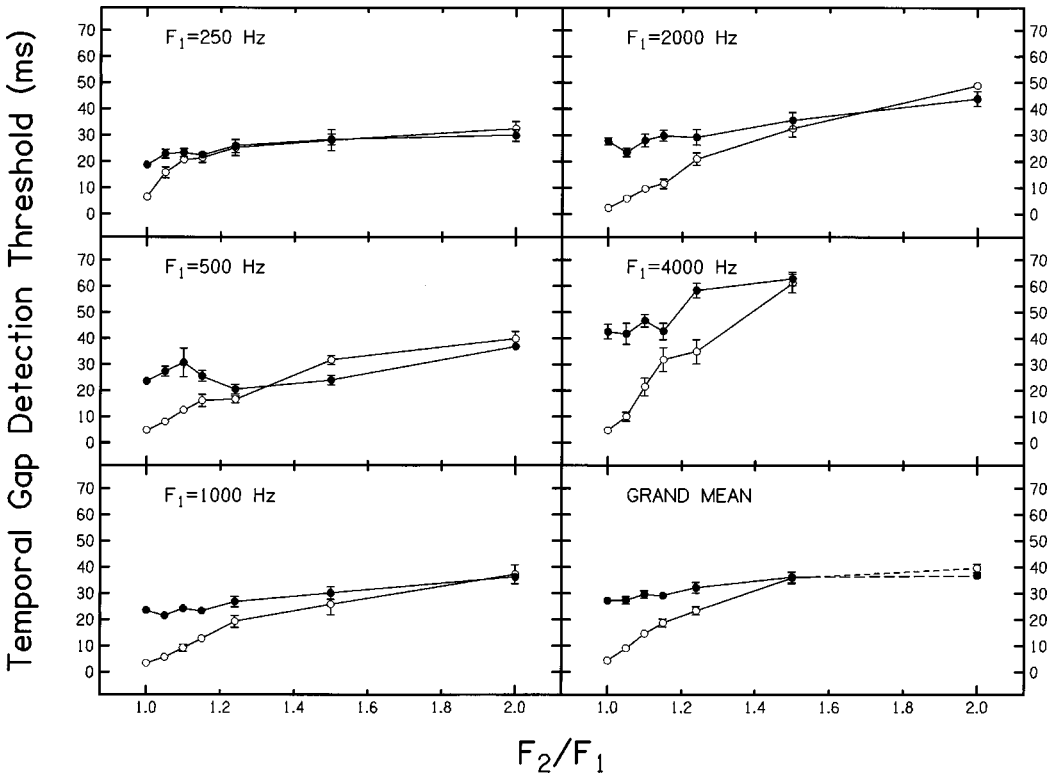

FIG. 2. TGD thresholds measured in the MONOTIC (unfilled circles) and DICHOTIC (filled circles) paradigms are compared as a function of relative marker frequency separation. TGD thresholds (and corresponding standard error bars) for both paradigms were averaged for the same four listeners, and these results are shown in individual panels for five values of the pregap marker frequency identified as $F_1 = 250$, 500, 1000, 2000, and 4000 Hz. Also shown in the lower right panel are the GRAND MEAN TGD thresholds that were pooled across F_1 frequency for the MONOTIC and DICHOTIC paradigms. The TGD thresholds in each panel are compared as a function of the relative marker frequency separation between F_1 and F_2, which is expressed in the form of a ratio index F_2/F_1. Increases in the value of the F_2/F_1 ratio correspond to systematic increases in the frequency separation between markers F_1 and F_2. The dashed lines connecting GRAND MEAN threshold estimates between F_2/F_1 ratios of 1.5 and 2.0 reflect the fact that the TGD thresholds for the $F_1 = 4000$ Hz versus $F_2 = 8000$ Hz conditions were not measured and are not represented in the GRAND MEAN panel.

were diminished systematically with increasing marker frequency separation in each panel. On average, the MONOTIC and DICHOTIC TGD threshold functions converged for marker frequency ratios $F_2/F_1 \geq 1.5$. This trend is most evident in the GRAND MEAN results shown in the lower right panel of Fig. 2. The close agreement between the two sets of GRAND MEAN results indicates that TGD is virtually the same for the MONOTIC and DICHOTIC conditions at large marker frequency separations. It is these marker conditions in this study (i.e., $F_2/F_1 \geq 1.5$) and in previous studies (e.g., Neff *et al.*, 1982; Formby and Forrest, 1991; Formby *et al.*, 1996; Phillips *et al.*, 1997) that most often reflect asymptotic TGD performance in the conventional MONOTIC paradigm.

To evaluate statistically the trends described above for the MONOTIC and DICHOTIC paradigms, we performed analyses of variance (ANOVA) on the TGD data. The TGD thresholds were analyzed separately for each F_2 marker frequency to assess the effect of the standard F_1 marker frequency and presentation mode (MONOTIC versus DICHOTIC) on TGD performance. The TGD thresholds were available for all seven F_2 marker frequency conditions for each of the standard marker frequencies $F_1 = 250-2000$ Hz. Because of equipment limitations, however, thresholds were measurable for only six of the seven F_2 marker frequency conditions for standard marker $F_1 = 4000$ Hz. The latter data set was therefore eliminated from the main statistical analysis. The results from two-way ANOVAs with repeated measures are shown in Table II for the main effect of presentation mode. The analyses revealed significant differences between the MONOTIC and DICHOTIC paradigms for F_2 marker frequencies within 15% of the standard F_1 marker frequency (i.e., $F_2/F_1 \leq 1.15$). This statistical analysis confirms the visual pattern that is evident in Fig. 2, namely, that the MONOTIC TGD thresholds were better than the corresponding DICHOTIC TGD thresholds for the conditions of the F_1 and F_2 marker frequencies presented relatively close together. As the marker frequency separation was increased further, for F_2/F_1 ratios ≥ 1.24, the presentation mode was not a significant factor in TGD performance.

TABLE II. *F* values for main effect of presentation mode (MONOTIC versus DICHOTIC).

F_2/F_1	F (1,9)	p
1.00	575.66	0.0000[a]
1.05	189.11	0.0008[a]
1.10	46.10	0.0065[a]
1.15	16.28	0.0274[a]
1.24	3.54	0.1565
1.50	0.00	0.9931
2.00	0.71	0.4602

[a]Significant at $\alpha = 0.01$.

There were no significant interactions in the analysis across F_1 frequency and presentation mode.

III. GENERAL DISCUSSION

The MONOTIC TGD thresholds measured in this study are consistent with past reports that TGD (1) deteriorates with increasing marker frequency separation and (2) may become asymptotic for marker frequency separations of an octave or greater (see Formby *et al.*, 1996). The first trend appears to reflect directly the role of peripheral auditory filtering on TGD. Indeed, statistical analysis of the TGD thresholds by presentation mode (MONOTIC versus DICHOTIC) in Table II reveals a significant overall change in performance (irrespective of F_1 frequency) between F_2/F_1 ratios of 1.15 and 1.24. This transition in performance corresponds to TGD conditions for which the F_2 marker frequencies were presented between 15% and 24% higher than the F_1 marker frequency. The transition range agrees well with many psychophysical estimates of peripheral frequency selectivity, including popular estimates of roex auditory filter shape (equivalent-rectangular) bandwidths (ERBs) measured by notched-noise methods (see Patterson and Moore, 1986). This transition range also agrees very well with our most recent and precise estimates of roex half-power bandwidths, which were derived from TGD thresholds measured with sinusoidal markers in a paradigm that controlled for confounding effects of off-frequency listening (Formby *et al.*, 1997). Moreover, this transition range is consistent with the observation that results simulated with a single-channel envelope detector model [implemented with a front-end peripheral filter (ERB=0.16 fc) having characteristic roex properties (Patterson and Moore, 1986)] become unstable when the sinusoidal markers are separated beyond about 0.25 F_1 (Forrest and Formby, 1996).

When all of the evidence above is considered together, the most direct and parsimonious explanation of TGD for small marker frequency separations (i.e., F_2/F_1 ratios $\leqslant$1.15) is that MONOTIC performance was based on a *within-channel* process, probably constrained by the bandwidth of a single local peripheral auditory filter centered between the two marker frequencies (Forrest and Formby, 1996). For marker frequency separations exceeding the bandwidth of the local peripheral auditory filter (i.e., F_2/F_1 marker frequency ratios $\geqslant$1.24 F_1), the MONOTIC and DICHOTIC TGD thresholds were not significantly different (see Table II). Indeed, the MONOTIC TGD thresholds measured at these large marker frequency separations were virtually indistinguishable from the DICHOTIC GRAND MEAN TGD thresholds (see F_2/F_1 ratios $\geqslant$1.5 in Fig. 2), which themselves were relatively invariant across the octave range of F_2 marker frequencies for each corresponding F_1 marker frequency.

Consider again the DICHOTIC TGD thresholds. These values varied from about 28 to 38 ms across the octave representation of marker frequency separations in the GRAND MEAN results (see Fig. 2). We suspect the subtle increase in the TGD thresholds with increasing marker frequency separation may reflect listener uncertainty in detecting a gap between a pair of perceptually and qualitatively different markers. On average, our results are in general agreement with related reports of TGD measured dichotically with noise stimuli (Penner, 1977; Phillips *et al.*, 1997). Penner (1977) reported TGD thresholds in the range of 30 ms for broadband noise markers, whereas Phillips *et al.* (1997) measured TGD thresholds of about 20 ms between narrow-band noise markers (for marker durations $\geqslant$50 ms). Phillips *et al.* (1997) used center frequencies of 4000 and 1000 Hz, respectively, for their pregap and postgap noise band markers. When considered together, our experimental results for sinusoidal markers and these previous TGD results for noise markers suggest that gap detection measured dichotically is relatively invariant to differences in the marker spectral properties. Accordingly, the concepts of *within-* and across-frequency, *between-channel* processing, which are relevant to MONOTIC paradigms, are probably an irrelevant distinction for TGD performed dichotically.

The important finding in this study is that MONOTIC TGD performance measured under conditions that present the pregap and postgap markers at large marker frequency separations (i.e., F_2/F_1 ratios $\geqslant$1.24 F_1), and presumably in different frequency channels, is statistically indistinguishable from DICHOTIC TGD. We know that the latter task must depend on the detection of gap information across the two ears and between two independent channels. Intuitively, it seems reasonable to conclude, therefore, that asymptotic MONOTIC TGD, like DICHOTIC TGD, is based on *between-channel* processing of the gap information in two independent channels. Asymptotic MONOTIC TGD, however, is unlike DICHOTIC TGD in that *between-channel* MONOTIC processing at large marker frequency separations is synonymous with the concept of *across-frequency* processing, which the available evidence suggests is an ambiguous concept for DICHOTIC TGD.

The experimental TGD results measured in this study provide compelling support for the idea of an across-frequency, *between-channel* process as a workable model for asymptotic TGD measured in the MONOTIC paradigm at marker frequency separations exceeding about half an octave. This general scheme appears to be viable for all values of F_1 between 250 and 4000 Hz. We are a little surprised by the apparent generality of this model in light of established trends in the estimates of peripheral auditory filter bandwidths with increasing frequency (see Patterson and Moore, 1986). There is some indication in Fig. 2 that the MONOTIC and DICHOTIC functions may converge at slightly different F_2/F_1 ratios across the various F_1 values. Close inspection of the results in each panel hints that the F_2/F_1 ratio at which the two sets of functions converge may be somewhat lower for our smaller F_1 values than for the larger F_1 values. This apparent trend is opposite to the pattern that one might predict from an ERB scale. The ERB of the auditory filter is a relatively constant value through 500 Hz and decreases slightly relative to the center frequency of the filter as signal frequency increases above 1000 Hz (Patterson and Moore, 1986). Thus the predicted convergence of the MONOTIC and DICHOTIC functions would be expected at a slightly higher F_2/F_1 ratio for $F_1\leqslant$500 Hz. A statistical analysis of our results, however, does not reveal a consistent trend in

TABLE III. Models of transition (intersection) frequencies for MONOTIC and DICHOTIC TGD functions.

F_1	Transition frequency (Hz)	Expected TGD threshold (in ms) at transition frequency	Slope for DICHOTIC function across F_2	Slope for MONOTIC function below transition frequency
250	269	20.8	0.13	1.90
500	720	30.2	0.12	0.57
1000	1360	27.0	0.14	0.68
2000	3180	38.7	0.19	0.61
4000	5560	57.8	0.40	1.36

support of either the visual pattern of the TGD data in Fig. 2 or the ERB scale. The findings from this analysis are shown in Table III and are considered below.

Our analysis was performed by fitting models for each value of F_1 to evaluate convergence of the MONOTIC and DICHOTIC TGD functions. The models assumed that the slope of the expected threshold function for each DICHOTIC condition was constant across F_2 frequency for each value of F_1. The models also assumed that up to some transition point (F_2 frequency), the slope of the function for MONOTIC presentation of the gap signal differed from that for DICHOTIC presentation. Above that transition point, performance for both modes of presentation was assumed to be the same. We fit mixed effects models with maximum likelihood for many different values of the F_2 frequency transition point to see what point resulted in the best fit of the model. A range of different transition points fit the data almost equally well. For the criteria of maximum likelihood, we came up with the following models outlined in Table III. The transition frequencies at which the MONOTIC and DICHOTIC functions intersected represented relative increases of F_2 above F_1 corresponding to 7.5%, 44%, 36%, 59%, and 39%, respectively, for values of $F_1 = 250$, 500, 1000, 2000, and 4000 Hz. Thus, as we noted in the discussion above, no consistent trend was evident across F_1 in the intersection patterns of the MONOTIC and DICHOTIC TGD functions.

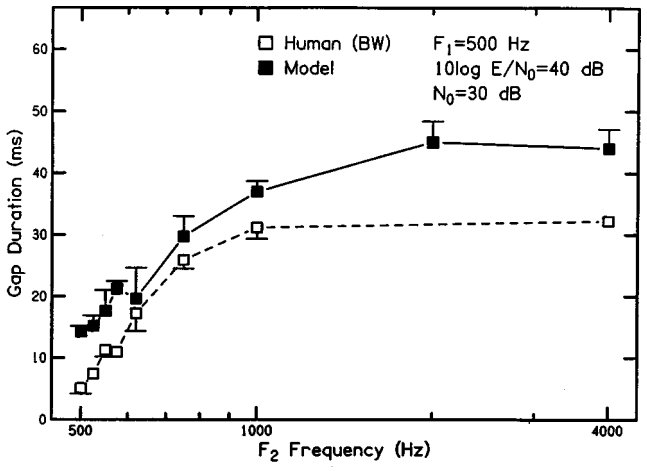

FIG. 3. Simulated and human TGD thresholds are compared as a function of F_2 frequency for a large range of marker frequency separations between pregap marker $F_1 = 500$ Hz and postgap marker F_2 frequencies presented up to 4000 Hz. Asymptotic TGD thresholds are evident in both data sets for $F_2 \geqslant 1000$ Hz. The simulated (model) TGD thresholds (filled symbols with upward standard error bars) are results from a multichannel model implemented with a within-channel decision metric reported by Heinz *et al.* (1996). Human TGD thresholds (open symbols with downward standard error bars) were measured for monaural stimulus presentation by Formby *et al.* (1996) from their listener BW. [Figure from Heinz *et al.* (1996).]

Notwithstanding the compelling evidence presented here for a *between-channel* process, our experimental findings do not necessarily prove that a *between-channel* comparison mechanism is responsible for asymptotic TGD measured in the MONOTIC paradigm at the large marker frequency separations. Heinz *et al.* (1996) have also presented convincing evidence that a multichannel model of the auditory periphery, implemented with a *within-channel* decision statistic, can simulate asymptotic TGD performance at large marker frequency separations. Their simulation results are shown in Fig. 3. [Also shown are TGD thresholds measured in a MONOTIC paradigm as a function of F_2 frequency for a human listener reported by Formby *et al.* (1996) for $F_1 = 500$ Hz.] Heinz *et al.* (1996) were successful in simulating asymptotic TGD thresholds with a majority vote scheme taken across individual channel votes (i.e., a channel vote was based on the comparison of the max/min ratios of the temporal envelopes in the signal and standard intervals). The individual channel votes were calculated with a *within-channel* decision statistic, and there was no mechanism at the output of their 29-channel model by which to perform *between-channel* comparisons of simulated neural information.

Thus our experimental findings do not resolve the controversial roles of *within-* and *between-channel* (across-frequency) comparison processes in TGD and, more generally, for temporal resolution (see Viemeister and Plack, 1993). At this time, both an across-frequency, *between-channel* process (which is supported by the empirical TGD results presented here) and a multichannel model implemented with a *within-channel* decision statistic (which precluded *between-channel* comparisons) remain viable schemes with which to account for asymptotic TGD thresholds measured by conventional monaural marker presentation at large marker frequency separations. Notwithstanding support for both schemes, the evidence for *between-channel* processes appears stronger and less likely serendipitous than that for *within-channel* processing. We therefore tend to favor the former over the latter for explaining the asymptotic TGD results.

IV. CONCLUSIONS

(1) For small marker frequency separations (i.e., F_2/F_1 ratios $\leqslant 1.15$), MONOTIC TGD thresholds were several fold smaller than DICHOTIC TGD thresholds.

(2) MONOTIC TGD thresholds deteriorated with increasing marker frequency separation for F_2/F_1 ratios $\leqslant 1.24$, whereas DICHOTIC TGD thresholds were relatively invariant with increasing marker frequency separation.

(3) For marker frequency separations greater than or equal to half an octave (i.e., $F_2/F_1 \geqslant 1.5$), the MONOTIC TGD threshold function for each condition of F_1 ($=250$, 500, 1000, 2000, or 4000 Hz) became asymptotic and converged with the corresponding DICHOTIC TGD threshold function.

(4) These findings support the hypothesis that an across-frequency, *between-channel* process can explain asymptotic TGD thresholds measured by MONOTIC stimulus presentation at marker frequency separations greater than about half an octave for F_2 marker frequencies greater than the standard F_1 marker frequency.

(5) Other modeling schemes are also viable for MONOTIC TGD and cannot be dismissed at this time. An alternative scheme is a multichannel model implemented with a *within-channel* decision statistic. This scheme precludes across-frequency, *between-channel* comparisons of neural information about the pregap marker offset and postgap marker onset for the gap signal. Heinz *et al.* (1996) have used this alternative model successfully to simulate asymptotic monaural TGD thresholds at large marker frequency separations.

ACKNOWLEDGMENTS

This research was supported by NIH award R01 DC00951. We thank A. Shutt for editorial assistance, and Peggy Nelson and Mike Heinz for reading and providing constructive comments on this manuscript. We also thank Chris Plack and an anonymous reviewer for their suggestions in revising this report. International Publishers Distributor and Harwood Academic Publishers provided permission for reprinting our Fig. 3 from Heinz *et al.* (1996).

[1]The criterion for consistency for a given listener was based on achieving a constant relative standard deviation of the mean threshold estimate (i.e., constant coefficient of variation) for each condition. We adopted this strategy because the absolute standard deviation tended to increase generally with increases in the mean threshold. Usually the coefficient of variation was somewhat smaller for TGD thresholds measured at large marker frequency separations than for thresholds measured for the smaller marker frequency separations.

ANSI (**1970**). ANSI S3.6-1969 ''Specifications for audiometers'' (American National Standards Institute, New York).

Formby, C., and Forrest, T. G. (**1991**). ''Detection of silent temporal gaps in sinusoidal markers,'' J. Acoust. Soc. Am. **89**, 830–837.

Formby, C., Sherlock, L. P., and Forrest, T. G. (**1996**). ''An asymmetric roex filter model for describing detection of silent temporal gaps in sinusoidal markers,'' Aud. Neurosci. **3**, 1–20.

Formby, C. C., Sherlock, L. P., and Forrest, T. G. (**1997**). ''Temporal gap detection thresholds measured for conditions that minimize off-frequency listening,'' J. Acoust. Soc. Am. **101**, 3150.

Forrest, T. G., and Formby, C. (**1996**). ''Temporal gap detection thresholds in sinusoidal markers simulated with a single-channel envelope detector model,'' Aud. Neurosci. **3**, 21–33.

Heinz, M. G., Goldstein, Jr., M. H., and Formby, C. (**1996**). ''Temporal gap detection thresholds in sinusoidal markers simulated with a multi-channel, multi-resolution cochlear model,'' Aud. Neurosci. **3**, 35–56.

Levitt, H. (**1971**). ''Transformed up-down methods in psychoacoustics,'' J. Acoust. Soc. Am. **49**, 467–477.

Neff, D. L., Jesteadt, W., and Brown, E. L. (**1982**). ''The relation between gap discrimination and auditory stream segregation,'' Percept. Psychophys. **31**, 493–501.

Patterson, R. D., and Moore, B. C. J. (**1986**). ''Auditory filters and excitation patterns as representations of frequency resolution,'' in *Frequency Selectivity in Hearing*, edited by B. C. J. Moore (Academic, Orlando), pp. 123–177.

Penner, M. J. (**1977**). ''Detection of temporal gaps in noise as a measure of the decay of auditory sensation,'' J. Acoust. Soc. Am. **61**, 552–557.

Phillips, D. P., Taylor, T. L., Hall, S. E., Carr, M. M., and Mossop, J. E. (**1997**). ''Detection of silent intervals between noises activating different perceptual channels: Some properties of central auditory gap detection,'' J. Acoust. Soc. Am. **101**, 3694–3705.

Viemeister, N. F., and Plack, C. J. (**1993**). ''Time analysis,'' in *Human Psychophysics*, edited by W. A. Yost, A. N. Popper, and R. R. Fay (Springer Verlag, New York), pp. 116–154.

Williams, K. N., and Perrott, D. R. (**1971**). ''Temporal resolution of tonal pulses,'' J. Acoust. Soc. Am. **51**, 644–647.

Zwicker, E., and Feldtkeller, R. (**1967**). *Das Ohr als Nachrichtenempfänger* (Hirzel Verlag, Stuttgart).

The role of auditory filters in comodulation masking release (CMR)

Emily Buss and Joseph W. Hall III
Department of Surgery, Division of Otolaryngology, University of North Carolina, Chapel Hill, North Carolina 27599-7070

(Received 8 August 1997; revised 19 January 1998; accepted 5 March 1998)

Comodulation masking release (CMR) is the detection advantage conferred by coherence of amplitude modulation across masker frequency. This phenomenon has typically been described in terms of across-frequency comparisons or in terms of cueing, where analysis of the output of an auditory filter in the region of the signal is aided by the outputs of independent auditory filters. An alternative approach is to assume a broad initial predetection filter, one which encompasses frequencies generally thought to fall into disparate auditory filters. These two basic approaches are compared. Stimuli consisted of comodulated maskers, spaced in frequency at one of three fixed intervals, with fine structure that either produced strong envelope beats in the summed waveform or did not. The signal was a pure tone of random starting phase. For the smallest masker frequency spacing detection of a high-frequency signal seemed to be improved in the presence of envelope beats, while detection of a low-frequency signal seemed to be degraded by envelope beats. These results are discussed in terms of the number of maskers assumed to sum in an auditory filter and the relative availability of within- and between-channel cues. This explanation is consistent with an initial stage of auditory filtering and is fundamentally inconsistent with a broad initial filter. Results for larger masker frequency spacings showed this trend less reliably, a finding that was further explored via data from a modulation discrimination task. © *1998 Acoustical Society of America.* [S0001-4966(98)04506-8]

PACS numbers: 43.66.Dc [RVS]

INTRODUCTION

Comodulation masking release (CMR) is the advantage associated with coherent amplitude modulation across masker frequency for detection of a masked signal. This effect can be demonstrated in a bandwidening paradigm (Hall *et al.*, 1984). For an unmodulated masker, increases in bandwidth lead to increases in threshold up to a point (the critical bandwidth), beyond which thresholds asymptote. This finding is explained in terms of an initial bank of auditory filters where only energy falling in the filter at the signal frequency affects detection of the signal (Fletcher, 1940). For an amplitude modulated (AM) masker, on the other hand, thresholds begin to fall once the bandwidth of the masker exceeds a critical bandwidth. The most common explanation for this finding also assumes an initial stage of auditory filtering, followed by some type of across-channel processing during which the temporal pattern of energy falling in channels distant from the signal is exploited in analyzing the information in the channel at the signal frequency. Several types of detection cues have been suggested to explain how this might happen, including change in envelope correlation across the outputs of different channels (Richards, 1988) and cued listening (Buus, 1985). More recently there has been some doubt cast on whether the cue underlying CMR is best characterized in terms of information separated into distinct frequency channels (Berg, 1996; Richards *et al.*, 1997), the alternative being a broader initial filter, perhaps similar to that proposed to explain temporal modulation transfer function (TMTF) data (Viemeister, 1979) and gap detection (Forrest and Green, 1987). Previous data from this lab (Buss *et al.*, 1997) suggest that a change in envelope beats in the summed waveform due to the addition of the signal, one possible cue in this type of model, is probably not responsible for CMR. The possibility remains, however, that some other aspect of the envelope of the summed stimulus falling within a relatively broad filter is responsible for CMR.

If the initial stage of processing CMR stimuli resembles a broad initial filter, then the modulation of the stimulus summed across frequency should be the characteristic most relevant for detection, as opposed to the coherence of envelopes across isolated frequency regions (e.g., the outputs of independent auditory filters). For example, a set of tones harmonically spaced in frequency and multiplied by a common low-pass noise source will all have identical envelopes when considered individually. The envelope of the summed waveform, however, will look very different depending on the relative starting phases of the component tones. If all the tones are in cosine starting phase, then the summed waveform will contain a prominent beating at the harmonic frequency (provided a sufficiently large number of tones are present). If the tones each have a randomly chosen starting phase, however, this beating pattern will be largely absent. One of the defining characteristics of a filter in the auditory system is the importance of relative phase of the stimulus components falling within that filter (e.g., Schorer, 1986); all of the energy within the region subsumed by the filter can be said to be summed, allowing interactions at the level of the fine structure. The experiment described here uses the relevance of fine structure to coarsely assess the width of the predetection filter, to determine whether it is relatively nar-

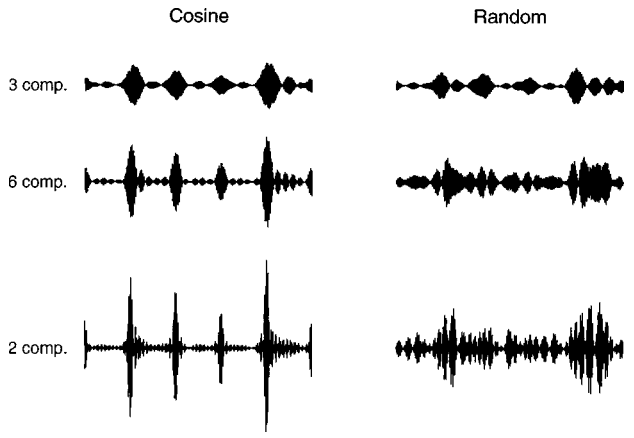

FIG. 1. Time-domain waveforms are plotted for multiple summed narrow-band maskers, generated by multiplying harmonically spaced tones by a sample of low-pass noise. The starting phase for the component tones is either uniformly cosine (left column) or randomly chosen for each tone (right column). The number of narrow bands summed is either 3, 6, or 12 (rows 1–3).

row, as an auditory filter, or relatively broad, as suggested by some models of the TMTF.

The maskers used here consist of a set of comodulated Gaussian noise bands spaced at harmonic intervals of a common fundamental, constructed such that the summed waveform is either characterized by a prominent beating pattern or by the absence of such beats. The presence or absence of beats was manipulated via the selection of starting phase of the AM tones used to construct these bands. Narrow-band maskers that are particularly ''peaky'' are associated with increased sensitivity to an added pure-tone signal (Richards, 1992; Bernstein and Trahiotis, 1994). This finding suggests that masker component starting phase assignment leading to prominent envelope beats in the summed waveform should be associated with lower thresholds. This effect would not be uniform across signal frequency, however, if auditory filters constitute the first stage of processing. The width (in Hz) of an auditory filter increases with center frequency, such that the output of an auditory filter centered in the low-frequency region of the masker passes fewer of the harmonically spaced masker bands than a filter in a high-frequency region. Figure 1 illustrates the effect of increasing the number of maskers (in this illustration pure tones multiplied by a sample of low-pass noise) that are summed together. The left column shows the result for component tones with cosine starting phase, and the right column for a random starting phase selection. These two types of starting phase assignment produce waveforms that are increasingly different for increasing numbers of summed maskers. If more maskers fall into the auditory filters at the higher frequencies, then the effect of masker fine structure, in particular starting phase of the component tones, should have more of an effect in the high- than in the low-frequency region of the masker. The difference in thresholds resulting from within-channel cues, then, should become more pronounced for detection based on the output of auditory filters tuned to higher frequencies (i.e., at high signal frequencies). On the other hand, if there is no interaction between the beating pattern of the summed masker waveform and signal frequency, then auditory filters need not be included in a model of CMR.

I. STIMULUS

Maskers were generated digitally (AP2, TDT). First, a set of harmonically spaced tones was computed, either in cosine starting phase (*cosine* condition) or with the starting phase of each tone chosen independently from a uniform distribution from 0 to 2π (*random* condition). A second set of tones was then generated, identical to the first except that a 90° phase delay was introduced to each tone in the set. These two sets of tones were then played out of separate channels of a DAC (DD1, TDT) at a sampling rate of 50 kHz, multiplied (MT3, TDT) by independent low-pass noise sources (cutoff at 10 Hz), summed (SM3, TDT), attenuated (PA4, TDT), and antialias filtered at 8.5 kHz (Kemo, 85 dB/oct). Tones were harmonics of 100, 200, or 400 Hz. When spacings of 100 or 200 Hz were used, harmonics 1–40 were present. When a spacing of 400 Hz was used, only harmonics 1–20 were present. The resulting maskers were comprised of bands of Gaussian noise, all comodulated, centered on the frequencies of the original tones. An additional condition (*on-signal-band* condition) consisted of just the masker band at the signal frequency. Each band in each masker was 50 dB SPL, and maskers were played continuously throughout a track.

The signal was a pure tone (WG1, TDT), attenuated (PA4, TDT), and added to the masker prior to antialias filtering. Each presentation of the signal had a sine starting phase and was 400 ms in duration, including 50-ms $\cos^2$ ramps. The signal frequencies tested were the 5th, 15th, and 20th harmonics for the maskers generated with harmonics of 100 or 200 Hz, and the 5th and 15th harmonics for the masker generated with harmonics of 400 Hz. All stimuli were presented diotically over headphones (HB6, TDT; Sony, MDR-V6).

II. PROCEDURES

Three observers participated in the experiment, ranging in age from 28 to 47 years. Observers had pure-tone thresholds better than 20 dB HL for frequencies between 250 and 8000 Hz, the only exception being a conductive loss in Obs 3's left ear. For Obs 3's left ear, thresholds at 250, 500, 1000, 2000, and 4000 Hz were 30, 30, 20, 15, and 25 dB, respectively; the air/bone gaps at those frequencies were 20, 20, 10, 5, and 10 dB. All observers were very experienced in psychophysical procedures and with CMR stimuli in particular.

Observers were tested in a single-walled sound-treated booth. Stimuli were presented in a three alternative forced choice paradigm, with an interstimulus interval of approximately 350 ms. Each observation interval was marked by a light on the response box and lasted 400 ms. The signal was equally likely to appear in each of the three intervals, and feedback was provided visually after each trial. A three-down one-up tracking procedure estimated the 79% correct point on the psychometric function for detection of the signal (Levitt, 1971). The initial step size of 8 dB was reduced to 4

dB after the second track reversal, and reduced again to 2 dB after the fourth reversal. Trials continued until a total of ten reversals were obtained. Threshold estimates were the average signal level at the last six track reversals.

All observers began with conditions employing multiple masker bands, the *cosine* and *random* conditions. The total of 16 such conditions (3 signal positions×2 masker component starting phases for both the 100- and 200-Hz-harmonic maskers; 2 signal positions×2 masker component starting phases for the 400-Hz-harmonic maskers) were randomly ordered for each observer. Observers completed blocks of three tracks for each condition according to this ordering, then completed another three tracks going back through the conditions in reverse order. Data were then inspected for practice effects, though no improvement that warranted retesting was ever observed.[1] Results for these conditions are reported as the mean of all six estimates. Observers then completed conditions employing a single masker at the signal frequency, the *on-signal-band* condition. The total of four conditions (signal frequencies of 0.5, 1, 2, and 4 kHz) were randomly ordered for each observer. All observers completed blocks of three tracks for each according to this ordering. Because of time constraints and the remarkable stability of thresholds within and across these conditions, as well as within and across observers, only a subset of these conditions was retested in the reverse order. As a result, some of the thresholds for the *on-signal-band* conditions are based on six estimates and others on only three estimates.

III. RESULTS AND DISCUSSION

Figure 2 shows average thresholds as a function of signal frequency, clustered by masker harmonic spacing (left to right: 100-, 200-, and 400-Hz harmonics), for the three observers and the average across observers. Data for *cosine* (open squares) and *random* (open triangles) conditions are distinguished by symbol, and data for the *on-signal-alone* condition are plotted with a line. In all cases thresholds in the *on-signal-band* condition were higher than those in the *cosine* or *random* conditions, with an average difference of 17 dB. In the data for the 100-Hz-harmonic maskers, functions for *cosine* and *random* conditions cross for all observers. Cosine starting phase appears to be associated with higher thresholds for the lower signal frequency (500 Hz) and lower thresholds for the higher signal frequency (2000 Hz). Because of individual differences, particularly for the highest signal frequency, thresholds at the three signal positions in the *cosine* condition do not differ reliably [$F(1,7)=4.39$, $p=0.074$]. The apparent increase in thresholds as a function of signal frequency for the random starting phase stimuli, however, does reach significance [$F(1,7)=9.12$, $p<0.05$]. An analysis of variance (ANOVA) was performed on all the data, using modulation condition (*cosine* and *random*) and signal position (0.5, 1, and 2 kHz) as the independent variables. Neither of the main effects reaches significance [$F(1,12)=0.88$, $p=0.37$ and $F(2,12)=0.20$, $p=0.82$, respectively], but the interaction is significant [$F(2,12)=4.38$, $p<0.05$]. In the data for the 200-Hz-harmonic maskers, only Obs 1 appears to show this pattern, the other two observers showing two different patterns. Data for the 400-Hz-harmonic maskers also lack a consistent interaction. Results for the 100-Hz-harmonic maskers will be considered first, and then those for the 200- and 400-Hz-harmonic maskers.

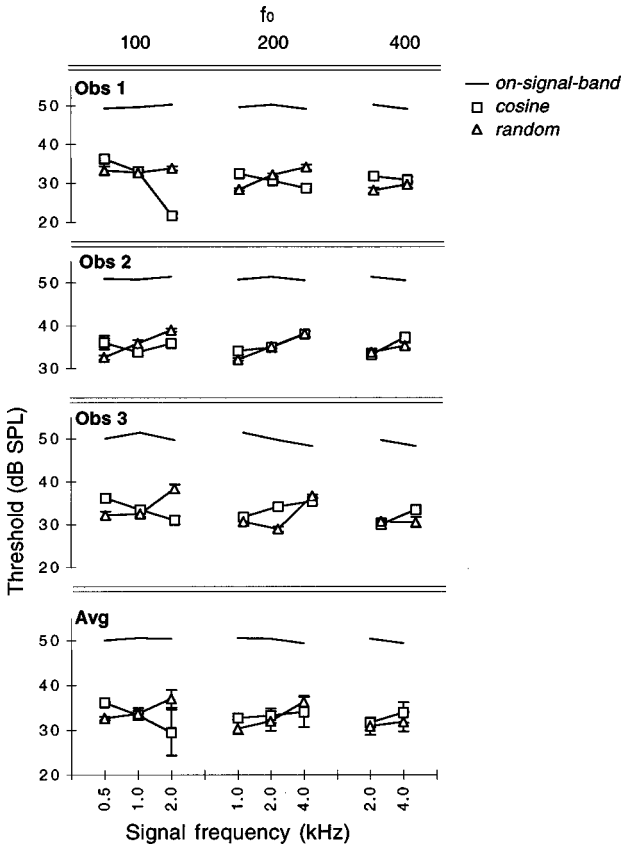

FIG. 2. Average thresholds (dB SPL) are plotted as a function of signal frequency for each masker harmonic spacing (left to right: 100, 200, and 400 Hz). Data for the *on-signal-band* (plain lines), *cosine* (squares), and *random* (triangles) conditions are plotted separately. Each observers' data are plotted separately, as well as the average across observers. Error bars are the standard error of the mean ($n=6$ for most obs' data points, $n=3$ for average data).

A. 100-Hz-harmonic maskers

We hypothesized that a broad initial predetection filter should lead to lower thresholds in the *cosine* condition, but no interaction between starting phase and signal frequency. The data, particularly those for the 100-Hz-harmonic maskers, suggest a strong interaction. Our initial hypothesis about the effect of auditory filtering was only partially supported. As expected, thresholds in the *cosine* condition were lower than those in the random condition at the high signal frequencies. The reversal of this trend at the low signal frequencies for the 100-Hz-harmonic maskers, however, was not predicted. Rather, we had expected thresholds to converge with narrower auditory filters, consistent with the increasing similarity between *cosine* and *random* stimuli for small numbers of summed components.

One *post-hoc* explanation for the observed interaction between signal frequency and component tone starting phase (*cosine* versus *random* conditions) with the 100-Hz-harmonic maskers is based on the availability of across- and within-channel cues for the *cosine* and *random* conditions.

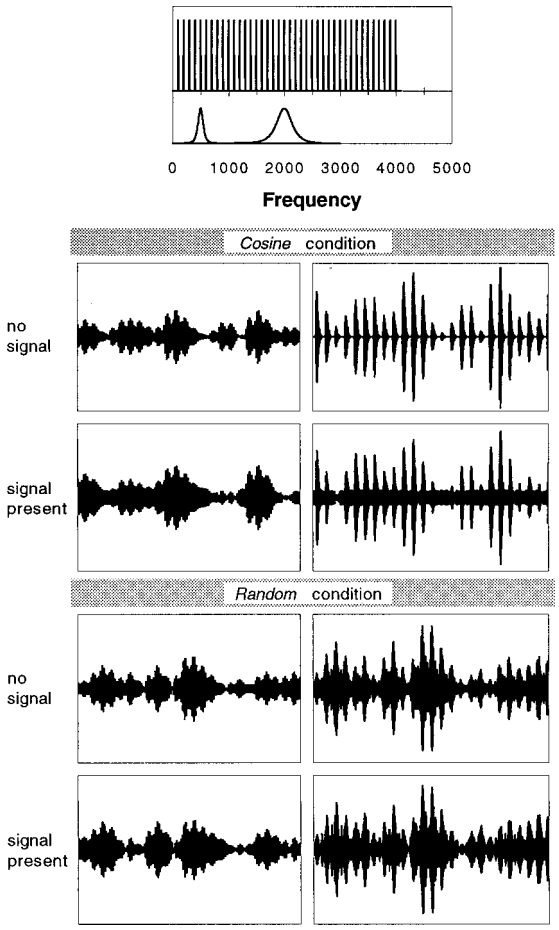

FIG. 3. The top section shows the power spectrum of a 100-Hz-harmonic masker, and below that two Gammatone filters. These filters are centered on the low signal frequency (500 Hz) and the high signal frequency (2000 Hz). The middle section shows examples of the time-domain output of these filters for the *cosine* condition, low- and high-frequency filter outputs appearing in the left and right columns. The case of no added signal and the case of an added pure-tone signal appear in the top and bottom rows. The bottom section shows analogous time-domain plots for the *random* condition. The signal level was constant in all four signal-present cases shown.

This explanation is illustrated in Fig. 3. The top section of this figure shows the power spectrum of a 100-Hz-harmonic masker and the power spectra of two Gammatone filters,[2] one centered on the low signal frequency and one centered on the high signal frequency. The middle section shows low- and high-frequency filter outputs for a *cosine* condition stimulus, and the bottom section shows analogous low- and high-frequency filter outputs for a *random* condition stimulus. In each section the no signal stimulus is in the top row and signal present stimuli in the bottom row. The signal level used was consistent across conditions and frequencies. In the *cosine* condition the outputs of auditory filters tuned to the high frequencies, where multiple tones are summed, are dominated by the 100-Hz beating. For the high-frequency signal, this prominent and deep modulation might provide a very reliable within-channel cue (middle section, right column: compare top and bottom panels to see the effect of adding a signal). For the low-frequency signal, however, envelope beats might obscure the low-pass noise envelope pattern present in the high-frequency channels that could otherwise be used to detect a signal in the lower-frequency channels (middle section, top row: compare left and right panels to see the differences in envelope across frequency even in the no-signal case). The result could be a degradation in the across-channel cue (cf. Eddins and Wright, 1994) and/or across channel masking (Moore *et al.*, 1990). In the *random* condition the higher-frequency auditory filters are not dominated by regular envelope beats, the effect of which might be less effective within-channel cues for the high-frequency signal and absence of competing envelope patterns across frequency that might interfere with across-frequency CMR in detection of the lower-frequency signal (bottom section).

This discussion makes at least two predictions regarding the effect of minimizing across-frequency processing by way of limiting the masker in frequency. If the difference in thresholds between the *cosine* and *random* conditions for the high-frequency signal is driven by the quality of the within-channel cue, then eliminating the lower-frequency masker tones which fall outside of the filter at the signal frequency should not have much effect on performance. If the difference in thresholds for the low-frequency signal is due to the degradation of across-channel cues caused by envelope beats in the high-frequency channels, then eliminating the high-frequency bands ought to eliminate the difference.

This *post-hoc* explanation of the data was tested using procedures and stimulus generation methods identical to those described above, only with a reduction in the number of comodulated noise bands comprising each masker. Thresholds for the low-frequency signal (500 Hz) were measured with masker bands centered on the 1st–6th harmonics of 100 Hz. Thresholds for the high-frequency signal (2000 Hz) were measured with masker bands centered on the 16th–40th harmonics of 100 Hz. The results are shown in Fig. 4, where average thresholds for the reduced masker in the *cosine* (filled squares) and *random* (filled triangles) conditions are plotted as a function of the signal frequency for each observer. Thresholds for the full maskers are replicated from Fig. 2 for contrast, shown as open, connected symbols. As predicted, thresholds for the limited masker and low signal frequency are the same in the *cosine* and *random* conditions ($0.58 \geqslant p \leqslant 0.97$ for the three observers, as compared to $p < 0.05$ for all observers in the original data set). This suggests that the difference observed with the full range of masker frequencies was due to the degradation of across-channel cues caused by envelope beats in the high-frequency channels. Thresholds for the limited masker and high signal frequency, however, remain different for the *cosine* and *random* conditions ($p < 0.0001$ for all observers, as compared to $p < 0.0005$ in the original data set). This suggests that the difference in the initial data was due to a within-channel process. These results could be interpreted as providing support for an initial stage of auditory filtering, as opposed to a broader predetection filter.

B. 200- and 400-Hz-harmonic maskers

Data for the maskers generated with higher-frequency harmonics, 200 and 400 Hz, are less consistent than those for the 100-Hz-harmonics maskers. For Obs 1 the functions for the 200-Hz-harmonic maskers cross, showing a pattern simi-

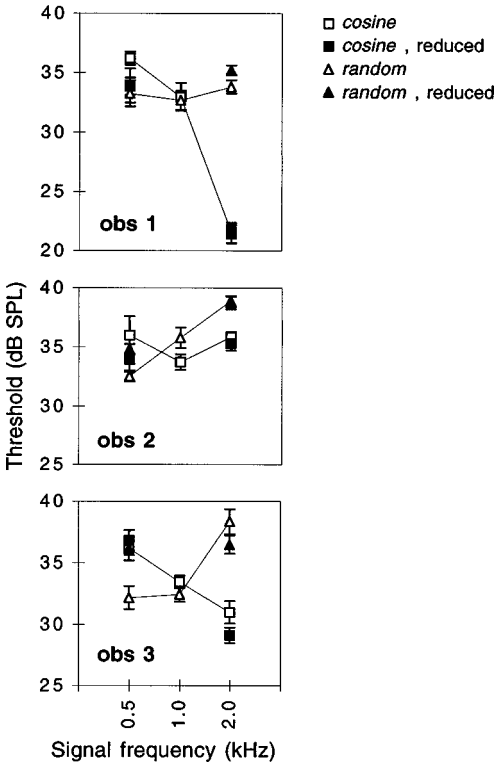

FIG. 4. Average thresholds (dB SPL) are plotted as a function of signal frequency for the 100-Hz-harmonic masker. Unfilled symbols replicate the data from Fig. 2 for the *cosine* (open squares) and *random* (open triangles) conditions. Filled symbols show data with maskers reduced in bandwidth for the *cosine* (filled squares) and *random* (filled triangles) conditions. Error bars are the standard error of the mean ($n=6$).

lar to that described above for the 100-Hz-harmonic maskers. The other two observers, however, show a different pattern, thresholds tending to rise with increasing signal frequency (with the exception of data for Obs 3, 2-kHz signal frequency, *random* condition). One possible reason for these different patterns of results is variation in the ability to take advantage of within-channel modulation at higher rates. Because Obs 1 shows a particularly large phase effect at the high signal frequency, where performance is argued (above) to be based on differences in modulation characteristics within an auditory channel, it is hypothesized that this listener is better able to exploit detection cues based on high rates of amplitude modulation as compared to the other listeners.

Data on modulation discrimination were collected on all three observers in an attempt to get an independent measure of the ability to utilize amplitude modulation as a function of modulation rate. Procedures were similar to those described above. Stimuli consisted of a band of amplitude modulated Gaussian noise, bandlimited to 1600–4000 Hz, 400 ms in duration, and presented at 65 dB. The task was to detect a reduction in modulation depth from $m=1$, tracking on 20 log(m). Three rates of AM were tested: 100, 200, and 400 Hz. Results appear in Fig. 5, where the average threshold in 20 log(m) is plotted as a function of modulation rate for each observer. As expected, Obs 1 was most sensitive to decrements from 100% modulation depth for the higher modulation rates. Observer 2 was least sensitive. This is grossly

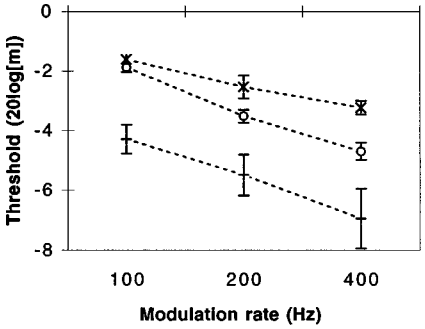

FIG. 5. Average modulation discrimination thresholds in units of 20 log(m) are plotted as a function of modulation rate for Obs 1 (asterisks), Obs 2 (pluses), and Obs 3 (circles). Error bars show the standard error of the mean across estimates ($n=6$).

consistent with the large starting phase effects at the high signal frequency observed for Obs 1 and the small (or absent) effects for Obs 2, with both 100- and 200-Hz-harmonic maskers. One aspect of the modulation discrimination data that is obviously inconsistent with the CMR data in Fig. 2 occurs for Obs 1 and Obs 3 with the 100-Hz modulation rate: based on sensitivity to decrements in modulation depth at this rate these two observers should be equally sensitive to the within-channel cues present in the CMR stimuli, though the phase effects for Obs 1 are greater than those for Obs 3 for the analogous CMR condition.

IV. CONCLUSIONS

For the CMR paradigm used here, sensitivity to an added pure tone varies in a way consistent with an initial stage of auditory filtering, as opposed to a single broader filter. At low frequencies a small number of masker bands fall within the auditory filter at the signal frequency, more bands falling within each of the filters at higher frequencies. The presence of pronounced envelope beats in the higher-frequency auditory filters for stimuli with cosine starting phase across frequency is argued to have one of two effects, depending on the frequency of the signal: (1) it can aid detection of a signal centered in that high-frequency region via a within-channel cue, or (2) it can hamper detection of a signal located in the lower-frequency region by interjecting a competing modulation pattern into the high-frequency auditory filter outputs and thus interfering with across-channel envelope processing. The relative lack of an effect of starting phase at the higher frequency masker band separations (i.e., increased rate of modulation) and the individual differences obtained are grossly consistent with individual observers' modulation discrimination data.

ACKNOWLEDGMENTS

This work was supported by Grant No. RO1 DC00418 from NIH-NIDCD. We thank John Grose, Madhu Dev, Peggy Nelson, and one anonymous reviewer for their helpful comments on earlier drafts of this manuscript.

[1]Data for Obs 3, 200-Hz-harmonic masker and signal frequency of 2 kHz, were different from those of the other observers. A second set of six threshold estimates was collected for both the *cosine* and the *random* conditions

after completion of the other conditions. This second set of data was not different from the first and so was discarded.

[2]Gammatone filters were computed as described in Patterson *et al.* (1992). Stimulus generation and filtering was carried out using MATLAB.

Berg, B. G. (**1996**). ''On the relation between comodulation masking release and temporal modulation transfer functions,'' J. Acoust. Soc. Am. **100**, 1013–1023.

Bernstein, L. R., and Trahiotis, C. (**1994**). ''The effect of nonsimultaneous on-frequency and off-frequency cues on the detection of a tonal signal masked by narrow-band noise,'' J. Acoust. Soc. Am. **95**, 920–930.

Buss, E., Hall III, J. W., and Grose, J. H. (**1997**). ''Change in envelope beats as a possible detection cue in comodulation masking release (CMR),'' J. Acoust. Soc. Am. **103**, 1592–1597.

Buus, S. (**1985**). ''Release from masking caused by envelope fluctuations,'' J. Acoust. Soc. Am. **78**, 1958–1965.

Eddins, D. A., and Wright, B. A. (**1994**). ''Comodulation masking release for single and multiple rates of envelope fluctuation,'' J. Acoust. Soc. Am. **96**, 3432–3442.

Fletcher, H. (**1940**). ''Auditory patterns,'' Rev. Mod. Phys. **12**, 47–65.

Forrest, T. G., and Green, D. M. (**1987**). ''Detection of partially filled gaps in noise and the temporal modulation transfer function,'' J. Acoust. Soc. Am. **82**, 1933–1943.

Hall, J. W., Haggard, M. P., and Fernandez, M. A. (**1984**). ''Detection in noise by spectro-temporal pattern analysis,'' J. Acoust. Soc. Am. **76**, 50–56.

Levitt, H. (**1971**). ''Transformed up-down methods in psychoacoustics,'' J. Acoust. Soc. Am. **49**, 467–477.

Moore, B. C. J., Glasberg, B. R., and Schooneveldt, G. P. (**1990**). ''Across-channel masking and comodulation masking release,'' J. Acoust. Soc. Am. **87**, 1683–1694.

Patterson, R. D., Robinson, K., Holdsworth, J., McKeown, D., Zhang, C., and Allerhand M. (**1992**). ''Complex sounds and auditory images,'' in *Auditory Physiology and Perception*, edited by Y. Cazals, L. Demany, and K. Horner (Pergamon, Oxford), pp. 429–446.

Richards, V. M. (**1988**). ''Components of monaural envelope correlation perception,'' Hearing Res. **35**, 47–58.

Richards, V. M. (**1992**). ''The detectability of a tone added to narrow bands of equal-energy noise,'' J. Acoust. Soc. Am. **91**, 3424–3435.

Richards, V. M., Buss, E., and Tian, L. (**1997**). ''Effects of modulator phase for comodulation masking release and modulation detection interference,'' J. Acoust. Soc. Am. **102**, 468–476.

Schorer, E. (**1986**). ''Critical modulation frequency based on detection of AM versus FM tones,'' J. Acoust. Soc. Am. **79**, 1054–1057.

Viemeister, N. F. (**1979**). ''Temporal modulation transfer functions based upon modulation thresholds,'' J. Acoust. Soc. Am. **66**, 1364–1380.

Auditory perception following hair cell regeneration in European starling (*Sturnus vulgaris*): Frequency and temporal resolution[a)]

G. Cameron Marean
Department of Speech and Hearing Sciences and Virginia Merrill Bloedel Hearing Research Center, University of Washington, Box 357923, Seattle, Washington 98195

John M. Burt
Department of Psychology, University of Washington, Seattle, Washington 98195

Michael D. Beecher
Department of Psychology and Virginia Merrill Bloedel Hearing Research Center, University of Washington, Box 357923, Seattle, Washington 98195

Edwin W Rubel[b)]
Virginia Merrill Bloedel Hearing Research Center and Department of Oto-HNS, University of Washington, Box 357923, Seattle, Washington 98195

(Received 7 October 1996; accepted for publication 23 February 1998)

Behavioral detection thresholds, auditory filter widths, and temporal modulation transfer functions were obtained from four starlings before, during, and after 11 days of subcutaneous injections of kanamycin, an aminoglycoside antibiotic. Birds were operantly conditioned to respond to pure tones and amplitude modulated noises ranging in frequency from 0.25 to 7 kHz using adaptive staircase procedures and were tested daily for 92 days after the first injection of aminoglycoside. All birds had threshold shifts of at least −60 dB at frequencies above 4 kHz. Lower frequencies were affected in some birds, although none of the birds had hearing loss below 3 kHz. All four birds had wider auditory filters at 5 kHz immediately after the aminoglycoside series. Any changes in frequency resolution at frequencies below 5 kHz were slight, transitory, and rarely observed. Two of the four birds had permanently wider auditory filters at 5 kHz. Temporal modulation transfer functions were briefly affected in two birds during the time of greatest threshold shift. Recovery of detection thresholds began soon after the injections ceased and continued for approximately 60 days. Recovery in frequency resolution lagged behind auditory threshold by about 10 days. Normal temporal resolution was observed in the context of impaired intensity and frequency resolution. Changes in auditory threshold and frequency resolution were closely associated for all birds at 5 kHz, but were correlated with statistical significance in only two birds. Scanning electron microscopy was performed on all four birds after 90 days of recovery and confirmed that the extent of initial damage was consistent with the pattern of observed hearing loss. [S0001-4966(98)02706-4]

PACS numbers: 43.66.Dc, 43.66.Mk, 43.64.Wn, 43.80.Lb [JWH]

INTRODUCTION

Noise or drug induced damage to hair cells in the basilar papilla of birds results in a deterioration in behavioral detection threshold and an increase in the critical ratio (Hashino and Sokabe, 1989; Marean *et al.*, 1993; Linzenbold *et al.*, 1993). The damage pattern observed by scanning electron microscopy in these studies is a good predictor of changes in the shape of the audibility curve, and visa versa. After trauma, hair cells and associated structures in the avian basilar papilla regenerate (Ryals and Rubel, 1988; Corwin and Cotanche, 1988; Lippe *et al.*, 1991). Hair cell regeneration appears to lead to partial, and, in some cases, full behavioral recovery (Hashino and Sokabe, 1989; Marean *et al.*, 1993; Linzenbold *et al.*, 1993; Saunders *et al.*, 1995).

Little is known about auditory perception in birds following hair cell regeneration beyond detection thresholds. Critical ratio measurements in budgerigars (Hashino and Sokabe, 1989) suggest that critical bands broaden substantially following aminoglycoside ototoxicity and that thresholds and critical bandwidths partially recover in a linear relationship to each other. The bandwidths calculated from critical ratios in these birds are wide enough, however, to beg the question as to whether or not budgerigars have any ''useful'' degree of frequency resolution remaining after hair cell regeneration. Moreover, changes in efficiency in extracting signal from noise which might occur with hearing loss and hair cell regeneration could not be assessed with the critical ratio method.

[a)]This article is based on a part of the first author's dissertation submitted to the Graduate School of the University of Washington in partial fulfillment of the requirements for the Doctorate. A preliminary report of these data was presented at the Nineteenth Midwinter Research Meeting of the Association for Research in Otolaryngology, St. Petersburg, FL, February, 1996.

[b)]To whom correspondence and requests for reprints should be addressed.

The only behavioral study to examine temporal resolution is Saunders *et al.* (1995). They exposed adult chickens to a 120-dB pure tone at 525 Hz for 48 h which led to a relatively flat hearing loss from 500 Hz to 5 kHz. The slope of the temporal integration function became quite shallow following the damage, but gradually recovered over 25 days as thresholds returned to normal.

The species used, the type of damage, and the degree of damage obtained were quite different in these two studies. It would be useful to obtain a set of data from the same birds on a variety of perceptual measures in order to provide a better qualitative and quantitative description of audition following hair cell trauma and regeneration. Moreover, obtaining measures of frequency and temporal resolution before, during, and after hair cell regeneration is a way of investigating relationships among auditory functions in normal and impaired vertebrate hearing.

The two experiments reported here measured frequency and temporal resolution before, during, and after aminoglycoside ototoxicity in starlings, a passerine songbird. We chose to use notched-noise masking to calculate auditory filter shapes (Patterson, 1976), and temporal modulation transfer functions (''TMTFs,'' Viemeister, 1979) to measure temporal resolution.

A previous study in our lab (Marean *et al.*, 1993) found that a 10-day dose of 200-mg/kg/day dose kanamycin results in both temporary and permanent threshold shifts, depending on frequency. Below 3 kHz, auditory threshold remained normal. We chose, therefore, to measure the auditory filter (shape, bandwidth, and efficiency), and TMTF at 1, 3, and 5 kHz, because these frequencies should be associated with differing degrees of threshold shift. Measurements obtained at 1 kHz should reflect cochlear function of presumably normal, undamaged hair cells. At 3 kHz, auditory processing should reflect both the contribution of normal, damaged, and regenerated epithelium. Finally, at 5 kHz, the response should be primarily from regions of regenerated hair cells (Marean *et al.*, 1995, 1993).

I. METHODS

A. Subjects

Four adult European starlings served as subjects. The birds were caught in the wild in West Seattle in the Spring of 1993. All birds were in juvenile plumage at the time and were thus approximately 1 3/4 years of age when training began.

Birds were acclimated to individual home cages in our aviary and given an unlimited supply of dog food kibble (*ad lib* feeding). After a month on this diet the birds were weighed. From this point on birds were weighed daily and rationed to maintain a weight equal to 90% of their weights, when allowed to feed ad libitum.

B. Stimulus and apparatus: Frequency resolution study

Noise bands were created by multiplying a low-pass filtered noise by pure tones. The noise was generated by a Tucker-Davis WG2 function generator.[1] The noise source was fed to a Frequency Devices 901 low-pass filter set to 300 Hz. The output of the FD901 was fed through a Tucker-Davis programmable filter (PF1) set to low pass at 300 Hz using a twelfth-order 32BIQUAD configuration. Double filtering increased the slope of the low-pass filter attenuation from 70 dB per octave to >120 dB per octave prior to multiplication. The output of the PF1 was then split, with each being fed into a signal multiplier (Tucker-Davis MT3). Two Tucker-Davis function generators (WG1s) were used to generate pure tones. The output of each WG1 was fed into the signal multipliers. One WG1 determined the center frequency of the high-side noise band, and the other, the low-side noise band. The noise bands created by the multiplication process were 600 Hz wide with extremely sharp skirts (>400 dB per octave).

The pure-tone probes were generated digitally at a 44-kHz sampling rate and stored on a NEC 386SX PC. During presentation, they were played through a Data Translation DT2821 AD/DA board and fed to a Tucker-Davis digital programmable attenuator (PA4). The pure tones were 500 ms in duration and ramped on and off with 20-ms rise/fall times.

The outputs of the multipliers and the attenuator were sent to a Gemini PMX-1000 preamp/mixer console and fed to a Technics SA303 amplifier. A Phillips D2223 speaker was mounted to a wire mesh assembly and hung on the side of a special test cage at 6 in. from the response key (to the bird's right). The speaker face was protected by a material which did not influence the acoustic output of the speaker below 10 kHz, and the entire cage, including portions of the response key panel, was lined with acoustic foam.

The test cage was placed in an IAC single-walled acoustic sound chamber during testing. Calibration of test signals were made weekly with a Hewlett-Packard signal analyzer through a General Radio microphone to ensure that the noise bands were flat and that the drop-off of the notches was >400 dB per octave. The combination of the IAC sound chamber and specially designed test cage provided for a low noise floor: Notch depth was greater than 50 dB SPL in the 50-dB spectrum level (dBN0) conditions.

Figure 1 (panel A) is a schematic of how the stimuli were generated and a representative power spectrum measured at the approximate location of a bird's right ear in the test chamber. In this example, the notch width is 40% of center frequency.

C. Stimuli and apparatus: Temporal resolution study

Broadband noise was generated by a Tucker-Davis WG-3 noise generator. The noise was fed to a signal multiplier (Tucker-Davis MT3) and multiplied by a dc offset (4 V) pure tone from a Tucker-Davis WG-1 waveform generator. The output was fed to a digital attenuator (Tucker-Davis PA-4) where an attenuation correction factor was applied for the increase in intensity of the modulated conditions. The degree of attenuation was determined by the formula:

$$10*\mathrm{Log}(1+m^2/2),$$

where the modulation index (m) = the amplitude of the pure-tone modulator divided by the dc offset.

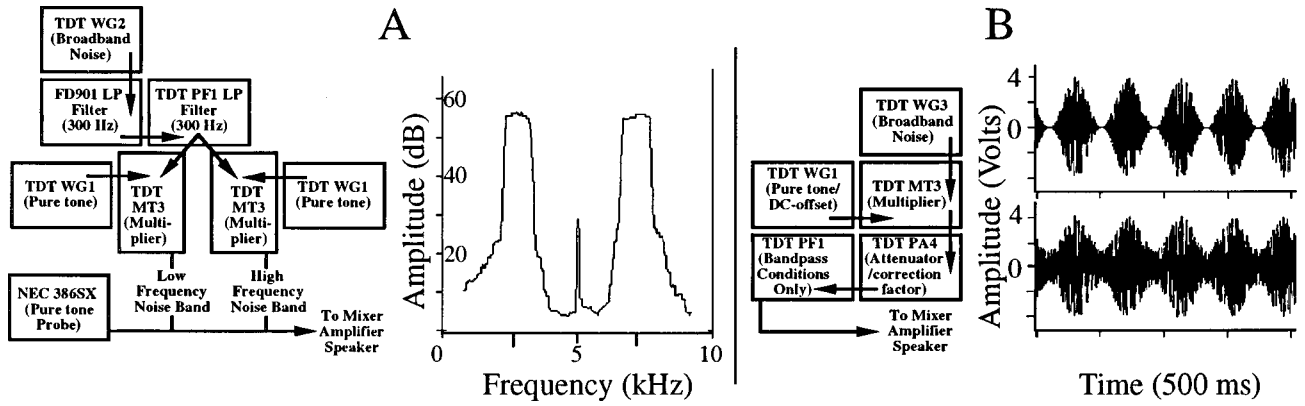

FIG. 1. Stimuli used in the current experiment. A. Schematic of how stimuli were produced and the acoustic power spectrum of a 5-kHz pure tone in a 50-dBNo notched-noise masker. Notch width is 2 kHz or 40% of center frequency. B. Schematic for temporal resolution study and amplitude modulated broadband noise at 100% modulation (upper panel) and 50% modulation (lower panel).

In this experiment, dc offset was held constant, and the voltage of the WG-1 was varied to change modulation depth. For temporal modulation transfer function (TMTF) conditions with bandpass carriers of center frequencies 1 kHz, 3 kHz and 5 kHz, the signals were sent to a Tucker-Davis PF-1 programmable filter. Filter settings were calibrated so that bandwidth in absolute Hertz remained constant at @ 2200 Hz for each frequency at the half-power point (-3 dB). The skirts of the noise bands were @70 dB/oct.

The output of the attenuator was sent to the same mixing and amplification apparatus previously described. The same speaker assembly, test cage, and response panel was used as well. Stimuli were calibrated using the same system used in the auditory filter study, plus the addition of a Hewlett-Packard digital storage oscilloscope. The stimuli were calibrated to be 30 dBNo and 50 dBNo.

Figure 1 (panel B) shows several periods of a broadband noise modulated at 10 Hz. In the upper trace, the modulation depth is nearly 100%; in the lower trace, the modulation depth has been reduced by 50%.

D. Training and testing procedure: Frequency resolution[2]

Birds were trained to peck an ''observation key'' until they detected a pure tone. During an 1100-ms interval following the tone, the computer waited for the bird to hit the response key. If the bird responded during the interval, a ''hopper'' containing dog food kibble was extended for 1000 ms. Failure to respond caused the lights in the test chamber to turn off for 500 ms.

In masking conditions, the masker was turned on at the beginning of the session and remained on throughout. On a certain percentage of the trials, the computer presented no tone but waited for a response. If the subject responded during the trial interval (a false alarm), the lights in the test chamber were turned off for 8000 ms. Correct rejections were neither rewarded or punished; the panel lights flashed to indicate that the trial was over and a new observation interval was begun.

Prior to beginning a threshold run, subjects were put through a ''warm-up period.'' During this time (a minimum of 10 trials), the probability of a signal trial was 0.5, and all signal trials were at least 60 dB (70 dB in some conditions), but varied in level up to 85 dB. When the subject attained a percent correct of at least 90%, the threshold run was begun. Masker properties and signal frequency were set at the beginning of the warm-up period to be the same as during the adaptive procedure. Masker intensity was either 30 dBNo or 50 dBNo in the final experiment. For the high intensity condition, a higher level masker would have been preferable, but birds would not tolerate noise intensities greater than 50 dBNo. In humans, the difference between 30 dBNo and 50 dBNo maskers would not be expected to lead to significant changes in auditory filter shape (Patterson, 1976; Rosen and Baker, 1994).

The adaptive procedure used a two-down, one-up rule to estimate the 70% point on the psychometric function (Levitt, 1970). The probability of a signal trial was 0.64; the probability of a no-signal trial was 0.2, and the probability of a probe trial was 0.16. Probe trials were constrained to be no lower than the lowest values used during the warm-up period. Only signal trials were used in the stepping procedure. False alarm rate and probe trial hit rate were monitored.

After each reversal, a set of rules similar to PEST (Taylor and Creelman, 1967) was used to decrease or increase step size. The adaptive staircase began at a randomly selected intensity between 60 dB and 70 dB; initial step size was 20 dB. Minimum step size was 1 dB. A minimum of six reversals was required for a complete threshold run, with the final four being averaged to obtain threshold. If the standard deviation of the last 4 reversals was greater than 10 dB, the run was continued, for up to a maximum of 16 reversals, until the standard deviation was below 10 dB.

Sessions were discounted if the false alarm rate was above 0.39, if the probe hit rate was below 0.9, or if any of the reversals were above the probe level. Sessions with an uneven number of reversals were also not used in the final sample. These exclusion criteria were selected based upon several years of observing starling psychoacoustic performance and receiver operating characteristic analysis (Green and Swets, 1966).

Thresholds in quiet were obtained at 0.5, 1, 2, 3, 4, 5, and 7 kHz. Thresholds in notched-noise were obtained at 1, 3, and 5 kHz. Quiet thresholds were used to ensure that each

bird had normal pre-exposure audiograms across the frequency range. They also served as a check on performance at the widest notch conditions, which should approximate performance in quiet. For thresholds in quiet, the order of testing frequency was randomly determined.

When noise bands were placed symmetrically about center frequency, total notch width in Hertz is described as a percentage of center frequency. For example, a total notch width of 10% at 5 kHz is a 500-Hz-wide notch, and a 10% total notch width at 1 kHz is a 100-Hz-wide notch. When noise bands were placed asymmetrically about center frequency, the distance in Hertz from probe frequency to the lower and upper noise bands are described as a proportion of probe frequency. Thus a notch configuration of 0.15–0.3 at 5 kHz describes an asymmetrical notched-noise masker with a lower noise band 750 Hz below 5 kHz and an upper noise band 1500 Hz above 5 kHz (total notch width: 45%).

At 1 and 3 kHz, birds were tested at total notch widths of 0%, 20%, 40%, 60%, and 80% of center frequency. Due to the relatively narrower filter at 5 kHz, total notch widths of 0%, 10%, 30%, 40%, and 60% were used. When birds were tested on notched-noise, they were tested on one frequency per day. Block order of different notch configurations was randomly determined.

To test for the symmetry of the auditory filter, two to four blocks were included with the upper and lower noise bands asymmetrically placed about center frequency (Stone *et al.*, 1992). At 1 kHz and 3 kHz, the asymmetrical notches were placed at 0.2–0.4 and 0.4–0.2. At 5 kHz, the asymmetrical notch conditions were 0.15–0.3 and 0.3–0.15. After dosing, more blocks were added in 5-kHz conditions. The birds were tested at total notch widths of 20% and 80%, as well as the asymmetrical notch conditions of 0.2–0.4 and 0.4–0.2. This was done so that changes in the auditory filter expected to occur at 5 kHz could be tracked more accurately.

Filter shapes were fitted to the data from a program obtained from Dr. Richard Baker (see Rosen and Baker, 1994). The procedure approximates filter shape in a manner similar to the ROEX (p,r) filter originally described by Patterson *et al.* (1982):

$$W(g)=(1-r)(1+pg)\exp(-pg)+r,$$

where g is the normalized deviation from the center of the filter, p is a parameter determining the slope of the skirts, and r is a parameter which flattens the filter at frequencies remote from the center frequency.

The Rosen and Baker (1994) polynomial fitting (PolyFit) procedure replaces each parameter with a linear function which changes with masker level. Filter shapes were also fitted to the data from a program obtained from Drs. B. C. J. Moore and B. R. Glasberg (see Glasberg and Moore, 1990). The filter shapes obtained by both methods were similar, but the results obtained from the Rosen and Baker (1994) procedure are reported here. This was done primarily because of extensions in the PolyFit procedure to the ROEX p,r model which allowed us to estimate r separately for the high- and low-frequency side, as well as taking into account absolute threshold (which we expected to change dramatically after dosing) in the fitting procedure. The PolyFit procedure allowed us to find the values of p (upper and lower) and r (upper and lower) that best fit the data. The best fitting values define the filter shape.

Data from incomplete sessions were not included in the final analysis because the sum-squared deviations of the fit from the data were routinely higher than for complete sets despite there being fewer residuals. For sessions using at least seven notch conditions, the sum-squared deviations for a fixed masker level were below 100 in all of the sessions reported here (mean=48, $\pm$1 s.e.=18). Thus the average deviation between data and fit was @ 2.7 dB.

Bandwidth estimates from fitted filters represent the passband at the -3 dB down points. Equivalent rectangular bandwidth estimates were also obtained. The -3 dB passbands are less sensitive to changes in dynamic range than equivalent rectangular bandwidth (ERB) estimates, since the ERB of an auditory filters is an area measure. On average, the -3 dB passbands were 5%–15% narrower than ERB estimates of the same auditory filters.

E. Training and testing procedure: Temporal resolution

The basic training and testing procedure did not differ between the frequency and temporal resolution studies. At the beginning of each session, the noise carrier was turned on. It remained on for the duration of the session. On some trials, the computer presented no modulation of the background noise but waited for a response. If the bird responded during this time (a false alarm), the lights in the test chamber were turned off for 8000 ms. Correct rejections were neither rewarded or punished; the panel lights flashed to indicate that the trial was over and a new observation interval was begun.

Prior to beginning a threshold run, birds were run through a warm-up period. During this time (a minimum of ten trials), the probability of a signal trial was 0.5, and all signal trials were near 100% modulation. When the bird attained a percent correct of at least 90%, the threshold run was begun. Modulation and carrier frequency were set at the beginning of the warm-up period to be the same as during the adaptive procedure.

At each carrier band, the birds were tested at five modulation rates: 10, 50, 100, 500, and 1000 Hz. The carriers were presented at 30 dBNo; the 5-kHz carrier and the broadband noise carrier were also presented at 50 dBNo.

The adaptive procedure was the same as in the frequency resolution study. The adaptive staircase began at a modulation depth at or close to 100%. The initial step size was 0.5 V; minimum step size was 0.1 V. Probe trials were near 100% modulation depth. A minimum of six reversals was required for a complete threshold run, with the final four being averaged to obtain threshold. If the standard deviation of the last 4 reversals was greater than $m=10$, the run was continued until the standard deviation was below 10 for up to a maximum of 16 reversals. All other exclusion criteria were the same.

F. Kanamycin injections, testing schedule, and scanning electron microscopy

Once baseline performance had been determined for all conditions (absolute threshold, frequency, and temporal resolution), each bird was given subcutaneous injections of 100 mg/kg/day for 2 days and 200-mg/kg/day kanamycin for 9 days. An 11-day dosing period was used instead of the standard 10-day dosing period so that the first day's dose could be spread over 2 days to reduce the shock of these high dosages of aminoglycoside.

Testing was continued during this dosing period: Birds were tested several hours after their daily injection. Food rations were provided immediately after behavioral testing.

One bird, 95–134 (identified in the results as Bird IV), was given an extra two days of injections because its threshold shift lagged behind the other three birds (see results).

After all post-injection data were collected (92 days after the first dose), the inner ears of each bird were examined by scanning electron microscopy (SEM). For SEM, birds were decapitated following administration of an overdose of pentobarbital sodium. Both cochleas from each bird were perfused via the round window with 2.5% gluteraldehyde and 2% paraformaldehyde in 0.1 molar phosphate buffered saline (PBS). The temporal bones were removed and the basilar papilla exposed using standard microdissection techniques. The specimens were then placed in 1% osmium tetroxide for 1 h, followed by several washes in PBS. Specimens were then dehydrated in a graded ethanol series, followed by final dissection. The tectorial membrane was removed under 70% ethanol. After critical point drying, specimens were mounted on aluminum stubs and coated with gold palladium prior to examination with the JEOL 63005 electron microscope.

Our previous work suggested that the extent of damage from the dosing regimen could be ascertainable from orientation patterns of stereociliary bundles even after long survival times (@90 days in the current study). We also expected that the linear extent of disorientation (measured from the base of each papillae) would be predictable from the pattern of behavioral threshold shift observed (and vice versa). However, our goal in the present study was not to provide detailed correlations between structural and functional properties as a function of frequency and place. Thus other than measuring the area of presumed damage (disoriented hair cell bundles) along the superior edge of each papilla, detailed quantitative analyses of hair cell parameters such as number, size, and bundle orientation were not undertaken.

II. RESULTS

A. Predose thresholds in quiet

Average threshold data across birds at seven frequencies agree with previously published data from our laboratory (Marean *et al.*, 1993) and other labs using similar methods (e.g., Dooling *et al.*, 1986).

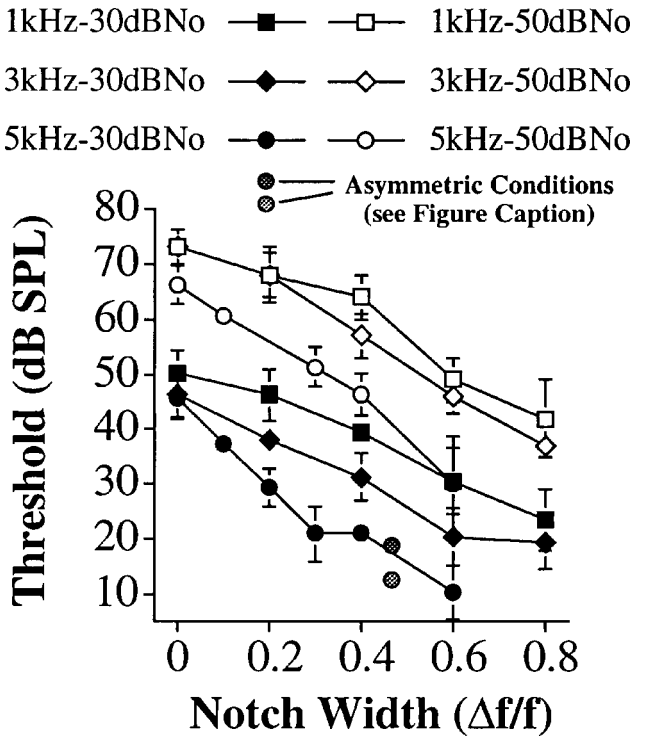

FIG. 2. Pre-dose average masked thresholds in 30-dBNo and 50-dBNo notched-noise conditions. Error bars are ±1 standard deviation of all the points used to make the figure. Dark stimpled filled circle shows data from an asymmetric notch condition at 5 kHz (0.15–0.3: Total notch width =45%). Light stimpled filled circle shows data from an asymmetric notch condition at 5 kHz (0.3–0.15: Total notch width=45%). Slope values for 30 dBNo: 1 kHz=−0.34; 3 kHz=−0.37; 5 kHz=−0.57. Slope values for 50 dBNo: 1 kHz=−0.4; 3 kHz=−0.47; 5 kHz=−0.59.

B. Auditory filters[3]

Figure 2 shows the average raw data for birds in all symmetrical notch conditions; the filled symbols are data at a masker level of 30 dBNo. The open symbols show data from 50-dBNo masker level conditions. Asymmetrical notch conditions for the 30-dBNo maskers at 5 kHz are also shown.

The data show that relative width of the auditory filter of starlings narrows as a function of frequency since the slope of the 5-kHz data is steeper than 3 kHz, which in turn is steeper than 1 kHz (see figure caption). These data also show that thresholds at the widest notch widths are comparable to thresholds obtained in quiet. Finally, since performance at 5 and 3 kHz at notch widths of 0% are better than performance at 1 kHz, these data also illustrate that efficiency improved with increasing frequency. Efficiency, the signal to noise ratio at threshold independent of filter bandwidth, was estimated from both Glasberg and Moore's (1990) and Rosen and Baker's (1994) procedures and was determined to be 10–15 dB better at 5 kHz than 1 kHz.

Masker level influenced performance in a predictable manner in that thresholds were 20 dB higher in the 50-dBNo conditions than in the 30-dBNo conditions. Unfortunately, birds found the noise level of 50 dBNo to be aversive at 1 and 3 kHz, and they were frequently unwilling to complete these sessions. Thus for both masker intensities, the predose average raw data at 5 kHz is comprised of several complete sessions from each bird, but at both 1 and 3 kHz, the predose

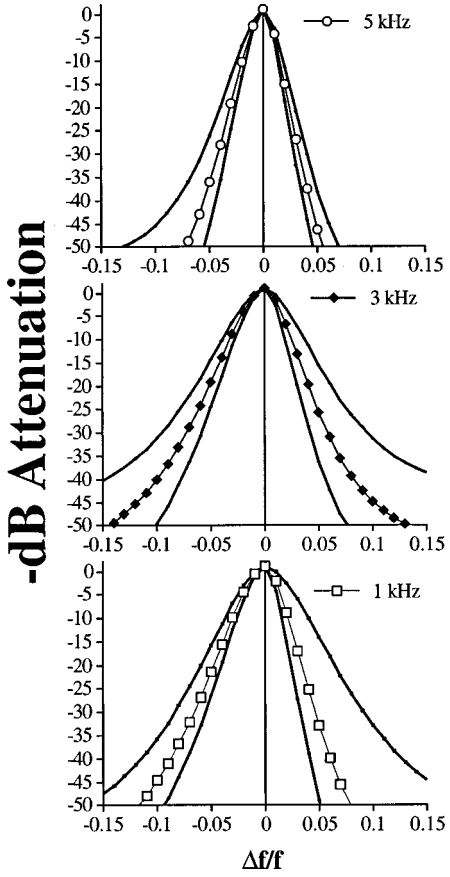

FIG. 3. Average predose auditory filters at three frequencies. Average bandwidth at 5 kHz = 480.1 Hz (s.d. 19.87); 3 kHz = 382.1 Hz (s.d. 44.84); 1 kHz = 135.5 Hz (s.d. 21.07). Unmarked lines are filters representing ±2 standard errors of predose slopes and dynamic ranges obtained from all birds predose.

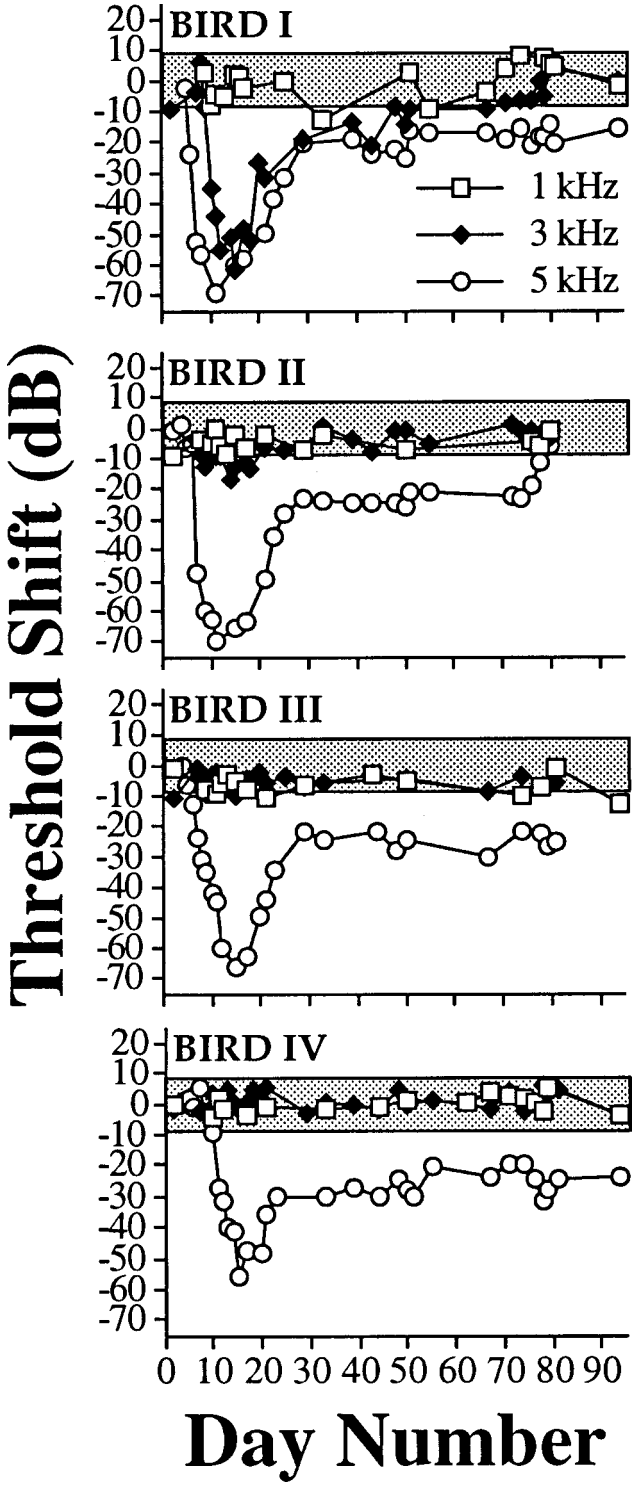

FIG. 4. Threshold shifts throughout the experiment for individual birds. Day numbers refers to the number of days from the first kanamycin injection. Shaded area represents ±2 standard errors of the mean for all pre-dose thresholds.

average raw data for the 50-dBNo masker intensities may be based upon only a single estimate per bird. Despite fewer data points, the pattern of response remained the same at all frequencies.

The raw data from the asymmetric conditions suggested a slight skewing of the auditory filter toward the low-frequency side, since thresholds were lower in the asymmetric conditions where the low-frequency masker was further from the probe frequency than the high-frequency masker (total notch width was the same). The same effect was seen at both masker intensities for all frequencies, although only the 30-dBNo data from 5 kHz are shown. The asymmetric notch conditions figure prominently in filter slope estimates; since only two asymmetric conditions are plotted in Fig. 2, only qualitative comparisons can be made between Fig. 2 and subsequent filter estimates.

Auditory filters were fitted to raw data using the PolyFit procedure of Rosen and Baker (1994). The output provided estimates of the high- and low-frequency slopes, the dynamic range, efficiency in extracting signal from noise (in dB), and the bandwidth −3 dB (in Hertz).

In Fig. 3 and all subsequent figures showing fitted auditory filters, symbols have been added to the fits for identification purposes. In the case of group data, additional filters have been plotted using slopes and dynamic ranges ±2 standard errors from the mean plotted in the figure. Group filter estimates are calculated from average individual filter estimates, and not from group means of thresholds at different notch widths (plotted in Fig. 2).

Predose group data at three frequencies are shown in Fig. 3. The −3 dB bandwidth for each frequency is given in the figure caption, and shows that especially for 1 and 5 kHz, bandwidth estimates are remarkably stable within and across

TABLE I. Bandwidths for individual birds at four time periods during the experiment. Bandwidths in boldface are outside the range of predose measures. The symbol (^) appears after data showing bandwidths narrower than obtained predose.

BIRD	Freq.	Week	BW	Freq.	Week	BW	Freq.	Week	BW
	5 kHz	Pre	454.33	3 kHz	Pre	406.5	1 kHz	Pre	163.36
Bird I		0–2	**891.4**		0–2	332.67^		0–2	**278.92**
		3–6	**677.07**		3–6	**507.66**		3–6	**218.3**
		7–10	**694.38**		7–10	425.92		7–10	108.65^
	5 kHz	Pre	499.89	3 kHz	Pre	380.21	1 kHz	Pre	127.79
Bird II		0–2	**1,821.22**		0–2	426.92		0–2	130.02
		3–6	**581.44**		3–6	**469.53**		3–6	158.56
		7–10	429.41^		7–10	352.9		7–10	110.83
	5 kHz	Pre	490.6	3 kHz	Pre	421.75	1 kHz	Pre	137.65
Bird III		0–2	**641.32**		0–2	392.53		0–2	128.84
		3–6	**552.64**		3–6	370.56		3–6	109.34
		7–10	**547.41**		7–10	371.24		7–10	125.77
	5 kHz	Pre	475.75	3 kHz	Pre	319.94	1 kHz	Pre	113.34
Bird IV		0–2	**659.44**		0–2	295.47		0–2	103.4
		3–6	**689.9**		3–6	282.95		3–6	106.29
		7–10	476.4		7–10	303.49		7–10	**141.4**

birds. Individual differences in filter shape were primarily differences in skew and did not result in highly variable filter bandwidths.

Filter shapes and bandwidths were most variable at 3 kHz, and least variable at 5 kHz. The fitted data show the slight low-side skewing of the auditory filter suggested by the raw data reviewed above and represent the first published data of auditory filter shapes in birds.

C. Aminoglycoside-induced changes in detection threshold

Figure 4 shows individual threshold shifts during and after the aminoglycoside treatment at the three primary frequencies: 1, 3, and 5 kHz. Not shown are threshold shifts at 7, 4, and 2 kHz, and frequencies below 1 kHz. In all birds, threshold shift at 7 kHz preceded threshold shift at 5 kHz by two days. Thresholds at 4 kHz shifted to the same degree as 5 kHz, but lagged behind 5 kHz by one day. No threshold shift was observed at 2 kHz or below in any of the four starlings. The pattern of results replicated our earlier findings (Marean *et al.*, 1993) in that threshold shift occurred first at higher frequencies, and proceeded toward lower frequencies.

These data were used to order subject numbers so that each subject's number would describe their relative degree of hearing loss. Thus Bird I had the greatest degree of hearing loss (severe threshold shift at all frequencies >2 kHz). Bird II had only a mild shift at 3 kHz, and severe shifts at all frequencies >3 kHz. Bird III had no hearing loss at frequencies below 4 kHz, and severe threshold shift at 4 kHz and above. Finally, Bird IV had significant hearing loss only at frequencies 5 kHz and higher.

The course of recovery in auditory threshold at 3, 4, and 5 kHz proceeded rapidly over a period of 20 days after the last dose. Thresholds recovered from a loss of approximately -70 dB to approximately -30 dB at 5 kHz. An additional 10–20 dB improvement sometimes occurred during the next 20-day period, except for at 3 kHz where the threshold returned to normal by 20 days after the aminoglycoside treatment. No additional recovery occurred after 60 days following the last dose in birds I, III, and IV, consistent with our earlier findings. Bird II had further improvement at 5 kHz beginning on day 70, but not at 4 kHz or 7 kHz.

D. Post-dose changes in auditory filter bandwidth

Changes in filter bandwidth were considered significant if they exceeded ± 2 standard deviations of predose estimates for individual data, and ± 2 standard errors for group data. Table I shows bandwidth data from auditory filters averaged for individual birds within four discrete time periods of the experiment. The first time interval was pre-dose; the second was during the first two weeks following the dose; the third was during the period of three to six weeks following the dose, and the final time interval was the average of auditory filter bandwidths seven to ten weeks after kanamycin injections. Filter bandwidths were significantly wider for all birds at 5 kHz in the first two weeks following the dosing period. Birds I and II also had wider bandwidths at 3 kHz, although the effect was not observed until at least three weeks following the dose. Finally, the bird with the broadest range of hearing loss also had a broadening of the auditory filter at 1 kHz.

In all but three cases, bandwidth recovered to within normal limits by the end of the experiment. Bird I and Bird III had permanently wider filter bandwidths at 5 kHz. Bird IV had a wider bandwidth at 1 kHz at the end of the experiment; however, given the pattern of results observed in this and other birds, this is likely due to an outlier filter estimate.

There were three instances where auditory filter bandwidths were narrower than those obtained predose: The 5-kHz auditory filters of Bird II at the end of the experiment, the 3-kHz auditory filter for Bird I immediately following the injection series, and the final auditory filters obtained for Bird I at 1 kHz were all narrower than seen prior to dosing.

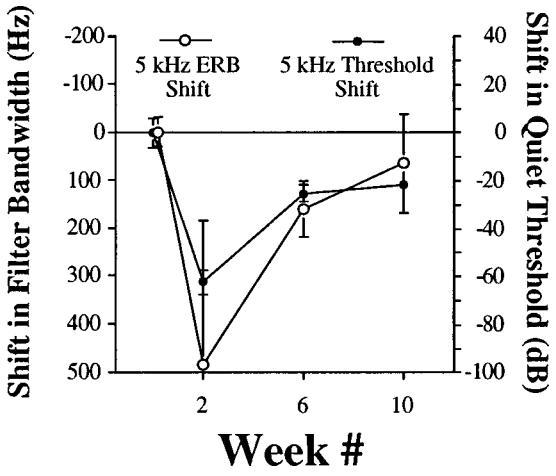

FIG. 5. Group average shift in filter bandwidth (left ordinate) plotted with shift in quiet threshold (right ordinate) for 5 kHz. ±1 standard deviation is shown.

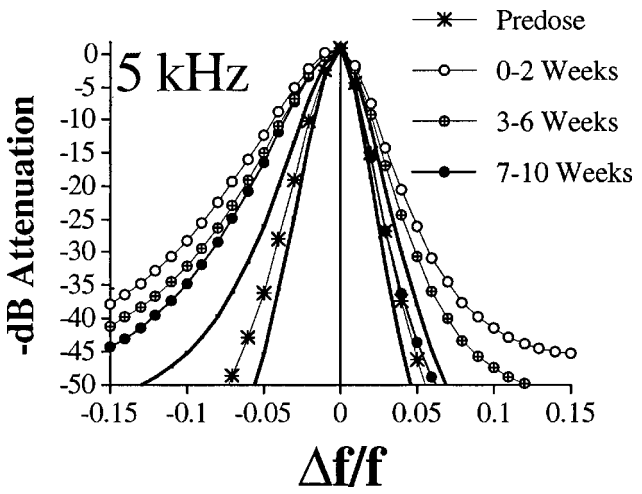

FIG. 6. Average auditory filters during four time periods of the experiment at 5 kHz.

E. The relationship between threshold shift and filter bandwidth

A correlation matrix of threshold shift and bandwidth shift was constructed for all birds at all frequencies. Out of this matrix, only two correlations were significant: Auditory threshold at 5 kHz was significantly correlated to filter bandwidth at 5 kHz for Bird I [$r=0.831$, $p<0.05$]* and Bird II [$r=0.912$, $p<0.05$]*. One other correlation approached significance: For Bird I, filter bandwidth at 5 kHz correlated with auditory threshold at 3 kHz [$r=0.808$, $p<0.06$].

Although not statistically significant, the group data at 5 kHz illustrate the close association between changes in frequency resolution and detection threshold (see Fig. 5). The open circles are estimated bandwidth shifts (left ordinate) and the filled symbols are detection threshold shifts (right ordinate). The lack of a significant correlation was likely due to the high variability in filter bandwidth immediately following the dosing period and at the very end of the experiment. Normal frequency resolution was observed in two of the four birds in the context of abnormal detection thresholds.

F. Post-dose changes in filter shape: Group Data

High- and low-frequency slopes and dynamic ranges were averaged for the four time periods displayed in Table I in order to examine general trends in the response of the auditory filter to ototoxic damage and hair cell regeneration. The resulting average filters at 5 kHz are shown in Fig. 6. Predose slope estimates of ±2 standard errors are also shown in the figure. Average filters from three other time periods are shown and correspond to the same intervals used to average individual data in Table I. Filters broadened on both sides, with nearly complete recovery on the high-frequency side by the end of the experiment. Permanently shallower slopes were observed on the low-frequency side of the filter. No significant bandwidth changes were evident in the group data at lower frequencies.

Changes to the 5-kHz filters shown in Fig. 6 do not look as austere as the ERB bandwidth changes shown in Fig. 5

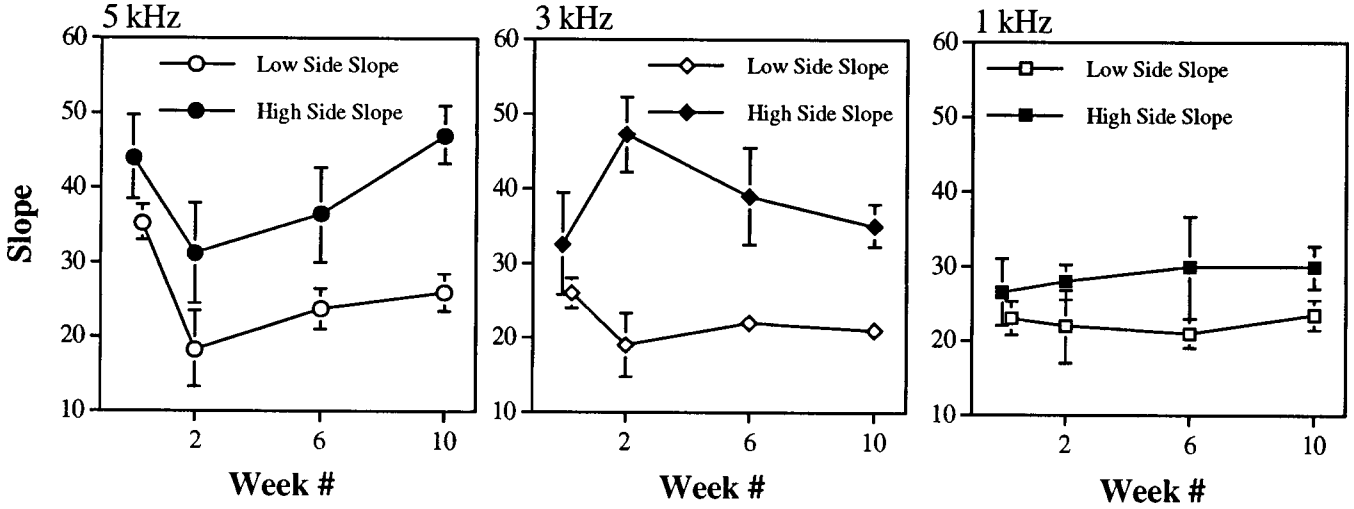

FIG. 7. Average slopes for both the high- and low-frequency side of the auditory filter during four time periods of the experiment. Error bars show ±2 standard errors.

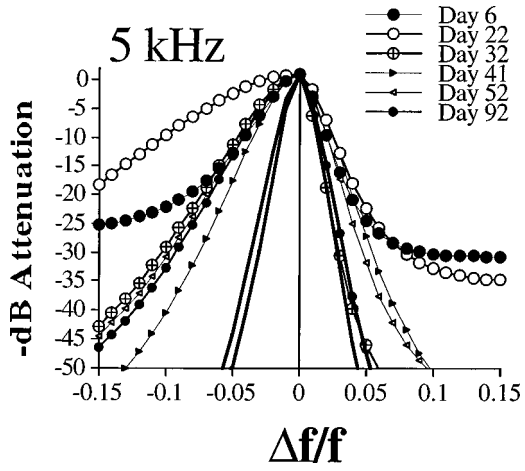

FIG. 8. Auditory filter estimates for Bird I at 5 kHz during the experiment. In this and the following three figures, thin symbol-less lines show the extent of variation predose in high- and low-frequency slopes; each estimate is independent.

because Fig. 6 shows frequency as a proportion of center frequency, whereas Fig. 5 shows frequency in absolute Hertz.

Permanent changes in slope were found at both 5 and 3 kHz. Figure 7 shows the average slope values (± 2 s.e.) at four time periods during the experiment at each frequency. At 5 kHz, both the high-frequency and low-frequency slopes become shallower after the dose period. Recovery is greater on the high-frequency side than the low-frequency side with a permanent significant change in slope occurring on the low-frequency side.

At 3 kHz, where no significant changes in bandwidth for the group occurred, the high side slope became steeper and the low side shallower, indicating that the skew of the filter was significantly shifted toward lower frequencies. The high side recovers to within normal limits, but with a higher average slope. Combined with a permanently significant shift on the low-frequency side, the filter appears to be permanently shifted in skew while retaining its normal bandwidth.

At 1 kHz, none of the changes in slope are significant for the group, although the trend mimics that of the 3-kHz filters. Although individual birds did have significant changes in slope at 1 kHz (see below), changes in skew were transitory when observed.

G. Post-dose changes in the auditory filter: Individual data

1. 5 kHz

Figure 8 shows individual auditory filters from Bird I at 5 kHz during and after kanamycin injections. The broadest and the narrowest high- and low-frequency slopes obtained prior to dosing for that bird have been drawn on the figure with lines without plot symbols. Data outside the range in these figures also fall outside ± 2 standard deviations of predose estimates for each individual bird. By day 6, both the high- and low-frequency slopes decreased, with substantially greater decreases on the low-frequency side of the filter. The dynamic range of the filter was reduced. The threshold shift at this time was -30 dB.

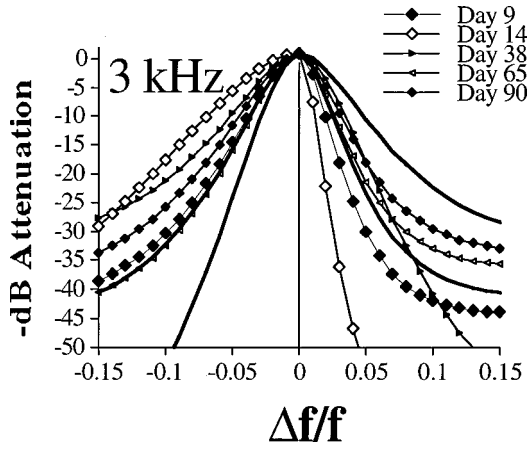

FIG. 9. Same as Fig. 5 but for Bird II at 3 kHz.

By day 22, the filter broadened further on the low-frequency side, and was only slightly broader on the high-frequency side. This pattern was observed in all birds, although filter widening was more drastic in some birds. For example, the change in filter bandwidth for Bird I (shown in Fig. 8) was from 9% predose to 27% on day 22; for bird II, the change was from 9% to 66%.

By day 32, the low- and high-frequency sides of the auditory filter recovered and stabilized. The low-frequency slope was permanently shallower; the high-frequency slope returned to normal. The overall effect in this bird was a permanently wider auditory filter at 5 kHz accompanied by a change in skew toward the low frequencies. Two of the birds had complete recovery of auditory filter bandwidth at 5 kHz, but all four birds showed the same pattern of permanent changes in skew.

Day 41 and day 52 have been plotted with smaller and different identification symbol shapes. Although there is an orderly pattern of broadening and partial recovery of the auditory filter, these data illustrate the variability in performance observed post-dose compared to pre-dose.

2. 3 kHz

Figure 9 shows individual auditory filters for Bird II at 3 kHz during kanamycin dosing (day 9), and at day 14, immediately following kanamycin dosing. Also shown is the last filter estimate from data obtained at day 90. As shown in Fig.

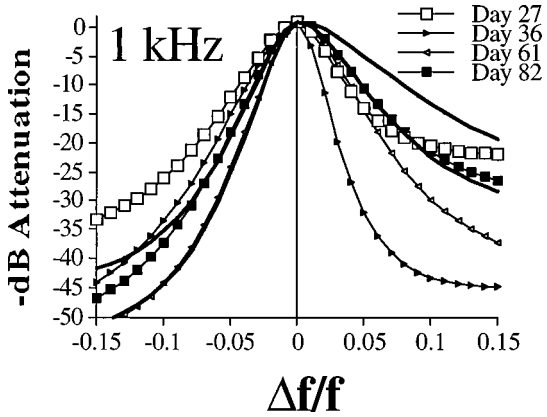

FIG. 10. Same as Fig. 5 but for Bird III at 1 kHz.

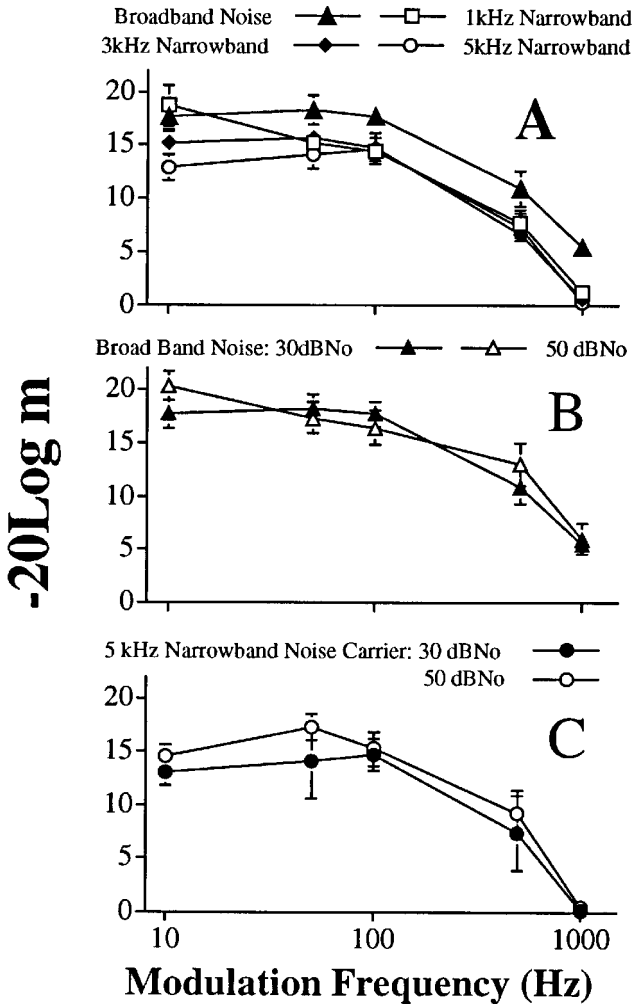

FIG. 11. A. Pre-dose average TMTFs in all conditions with 30-dBNo carriers. B. For broadband noise carriers at 30 dBNo and 50 dBNo. C. For 5-kHz narrow-band carriers at 30 dBNo and 50 dBNo. ±1 standard error of the means is shown.

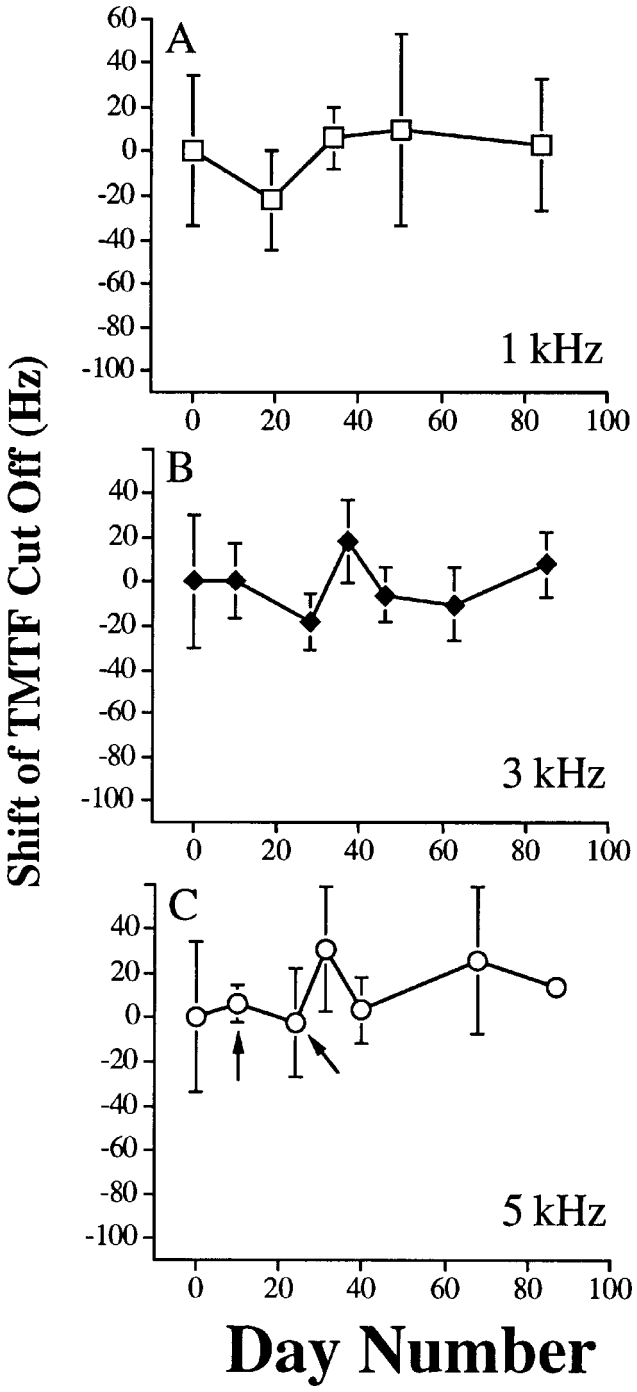

FIG. 12. A. Average shift in upper frequency cutoff (−3 dB) of TMTFs at 1 kHz; calculations were made from exponential fits to raw data. B. Same at 3 kHz. C. Same at 5 kHz. Two data points are marked with arrows to show when averages were determined from less than four birds. Representative raw data from excluded birds are shown in Fig. 13.

4, this bird had a mild threshold shift at 3 kHz by day 9. The bandwidth of the auditory filter was not significantly broader, but the filter noticeably changed in skew toward lower frequencies. By day 14, the filter was 5.3% broader, which was a significant change in bandwidth: pre-dose filters for this bird at 3 kHz did not vary by more than 2%. Bird I also had hearing loss at 3 kHz and also had a broadening of the auditory filter. Birds III and IV had no change in threshold or filter width at 3 kHz, but did show the same change in skew toward lower frequencies.

The change in skew was permanent for this bird, but not the change in bandwidth. The permanent decrease in the low-frequency slope of the filter did not result in a wider auditory filter, since the high-frequency slope increased proportionally.

3. 1 kHz

Bird III's post-injection auditory filters are shown in Fig. 10. Prior to dosing, its filters had an unusual tendency to be skewed toward high frequencies at 3 kHz and 1 kHz. The filter bandwidths for this bird at 1 kHz did not change at any time during the experiment, and yet its filters underwent changes in skew toward lower frequencies during the time of threshold loss and recovery at higher frequencies. By the end of the experiment, the skew returned to normal. Birds II and IV also had no change in filter bandwidth. Their auditory filters skewed toward lower frequencies as well, although the changes in slope were not significant, and the skew changes were also not permanent.

Bird I, the most seriously affected bird, had a nonpermanent broadening of the auditory filter at 1 kHz. The primary change was to the high-frequency slope (measured on

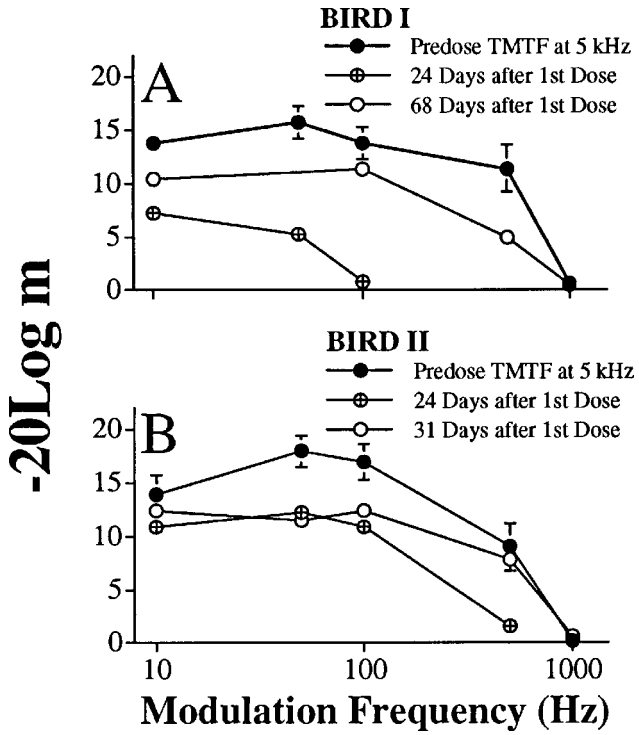

FIG. 13. A. TMTFs from bird I at 5-kHz pre-dose and at two different days after the dose. B. Same for bird II.

days 17 and 36), a pattern not observed at other frequencies. By day 61, the filter had returned to its normal shape.

H. TMTFs: Pre-dose group data[4]

Figure 11A shows group average data for TMTFs with a broadband noise carrier and narrow-band carriers at 30 dBNo. There was no difference in the TMTF as a function of level for broadband carriers or the 5-kHz narrow-band carrier (Fig. 11B and C). The broadband data are consistent with previously published data from starlings (Klump and Okanoya, 1991).

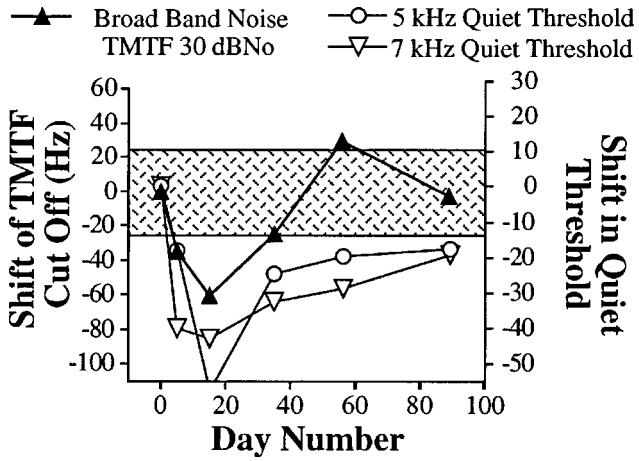

FIG. 14. Average change in the upper frequency cutoff of the TMTF with a broadband 30-dBNo carrier (left ordinate) plotted along with average shift in auditory threshold on the same days at 5 kHz and 7 kHz. The darkened area shows ±2 standard error of the mean of predose TMTFs in this condition.

TMTF bandwidth was determined by the 1/2 power points of group and individual functions, which were calculated from exponential curves fitted to raw data. Group average TMTF bandwidth was 49 Hz for the narrow-band carriers; performance in a broadband noise was about 100 Hz better (149 Hz, with individual averages ranging from 115 to 155 Hz). Although generally less sensitive than humans to low-frequency amplitude modulation, the upper cutoff of the TMTF bandwidth is higher for starlings (see also Dooling and Searcy, 1981; Klump and Okanoya, 1991).

I. Post-dose changes in the TMTF

No change in TMTF bandwidth cutoff occurred at 1 and 3 kHz for any bird (see Fig. 12A–B). No apparent change occurred in the TMTF at 5 kHz in terms of the group average bandwidth, but Bird I and Bird II had functions which showed a severe loss in sensitivity soon after the dosing period. When sensitivity was reduced to a point where data could not be obtained from at least four modulation frequencies, exponential fits could not be obtained. Thus the second and third data points in Fig. 12C (indicated by arrows) do not reflect the performance of all four birds.

Examples of some of the less sensitive functions are shown in Fig. 13A–B. The obvious changes which occurred for Birds I and II immediately following the dose period coincided with the period of maximum hearing loss at 5 kHz. Energy from the carrier band may have been available to less impaired regions of the basilar papilla in Birds III and IV which is why the performance of these birds did not change. The TMTF bandwidth quickly returned to normal in Birds I and II as soon as the stimuli became audible within the carrier band.

Figure 14 shows the shift of the upper frequency cutoff averaged for all birds for broadband TMTFs at 30 dBNo (left ordinate). Also shown are high-frequency absolute thresholds measured on the same day. The cutoff is lower when the audible portion of the stimulus is restricted to lower frequencies. As soon as threshold recovered to a point where frequencies above 4 kHz were audible at this stimulus level, TMTF bandwidth returned to normal. No significant change in TMTF bandwidth occurred in the 50-dBNo condition, indicating that sensation level was sufficiently compensated for at the higher intensity.

J. Scanning EM

The basilar papillae of all four birds were examined with SEM. Measurements were made along the superior edge from the base toward the apex to measure the extent of previous damage due to the aminoglycoside ototoxicity. This was identifiable from regions of hair cell disorientation which was limited to regenerated portions of the epithelium (Marean *et al.*, 1993, 1995). The proportion of regenerated epithelium was compared to a frequency place code map available from Manley (1990). As in our previous work, the spread of threshold shift to lower frequencies is predicted (and vice versa) by comparing previously damaged regions to the map. We used these observations simply to confirm that the association between damage patterns and threshold

shifts seen in our earlier work was true for the current group of animals. The reader is referred to Marean *et al.* (1993) for representative scanning electron micrographs.

III. DISCUSSION

A. Normal hearing in starlings

The pre-dose performance of starlings in the current study replicates and confirms recent published reports from other laboratories. In the case of frequency resolution, Langemann *et al.* (1995) measured critical bands and critical ratios in starlings and found that the critical band grew from 135 Hz at 1 kHz (13.5% of center frequency) to 233 Hz at 2 kHz (11.6% of CF), to 345 Hz at 4 kHz (8.6% of CF). In the current study, -3 dB filter bandwidth increased from 135 Hz at 1 kHz (13.5% of CF) to 382 Hz at 3 kHz (12.7% of CF) to 480 Hz at 5 kHz (9.6% of CF). Equivalent rectangular bandwidth (ERB) estimates (Glasberg and Moore, 1990) of our data are slightly wider at each frequency (16.87% at 1 kHz, 13.47% at 3 kHz, and 11% at 5 kHz). ERBs are probably a more appropriate comparison measure, since the ERB of an auditory filter is meant to estimate critical bandwidth from notched-noise data. The frequencies above 1 kHz were not the same in the two studies, but curves fitted to show the growth of bandwidth with frequency in each study show a parallel increase, with our estimates being slightly wider. Both studies show the widening of the auditory filter in absolute Hertz, but a relative narrowing of the filter as a proportion of center frequency, characteristic of most vertebrates.

The only notable difference between Langemann *et al.* (1995) and the current study was the behavior of the critical ratio. In that study, the critical ratio estimated the critical band without a correction factor. This result was also apparent in our data, but only at 1 kHz. At 3 and 5 kHz, thresholds in notch widths of 0%[5] showed that threshold improved with increasing frequency, which incorrectly indicates that the auditory filter narrowed in absolute Hertz. Our auditory filter data revealed, however, that the filter was widening in absolute Hertz with increasing frequency, as expected. The auditory filter data also revealed that birds became increasing efficient in extracting signals from noise at higher frequencies (at least up to 5 kHz). When our critical ratio data were corrected for changes in efficiency, they accurately predicted our ERB estimates. This result demonstrates the importance of using a measure which can estimate efficiency, since there are evidently differences between populations of birds in efficiency as a function of frequency.

In the case of temporal resolution, the current findings concur with previously reported TMTFs in both parakeets (Dooling and Searcy, 1981) and Starlings (Klump and Okanoya, 1991). These studies show the transfer function for modulation detection to be low pass or band pass, with the function ending at about 1.2 kHz modulation rate.

B. Effects of hearing loss on frequency and temporal resolution

In humans, hearing loss is associated with an increase in the critical ratio and a broadening of the auditory filter (see Moore, 1995 for a review). Hearing impairment in birds clearly shows the same effects (see also Hashino and Sokabe, 1989).

Tyler *et al.* (1984) measured auditory filters in hearing impaired human listeners at 2 kHz. Their results showed that similar patterns of hearing loss can lead to very different behavior of the auditory filter (assuming that the pre-hearing loss auditory filters of listeners were similar). Some listeners had an decrease in slope to the high-frequency side of the filter, while others showed the same effect on the low-frequency side. In the current study, most of the variability in the behavior of auditory filters occurred at frequencies without hearing loss. At 5 kHz, where all birds had significant threshold shifts, the auditory filter broadened on both the high- and low-frequency sides, although the low-frequency slope decreased on average more than the high-frequency slope. The only marked variability was the degree of filter broadening. One bird's filter broadened by 2800 Hz, while another broadened by only 400 Hz. At 3 and 1 kHz, on the other hand, a variety of outcomes were observed. These changes were typically changes in the skew of the filter rather than the bandwidth, although bandwidth changes did occur at 1 kHz for one bird.

Individual differences to filter shape in humans have been attributed to selective impairments to either inner hair cells or outer hair cells (see Liberman *et al.*, 1986). In the case of birds, the initial effects of ototoxicity are not selective to presumably analogous tall hair cells or short hair cells (Marean *et al.*, 1993, 1995), although selective differences in their regenerative capacity could play a role in the recovery of function.

There has been considerable debate in the human psychophysics literature regarding hearing impairment and impairments to temporal resolution. Several studies in humans have shown that when hearing impaired subjects and normal hearing subjects are tested at equal sensation levels, they can perform equivalently (Florentine and Buus, 1984; Grose *et al.*, 1989; Bacon and Viemeister, 1985; Bacon and Gleitman, 1992; Turner *et al.*, 1995). Our data were consistent with the assertion that changes in threshold have little to no effect on temporal resolution, but we did not hold sensation level constant for the 5-kHz carrier in the current study. Two of the birds could either not perform the task at all, or could only respond to low-frequency amplitude modulation during the period of greatest threshold shift at 4, 5, and 7 kHz.

In the case of the broadband noise carriers, the data were consistent with a reduced internal bandwidth of the stimulus as a result of high-frequency hearing loss. Shailer and Moore (1983) and Formby and Muir (1988) have shown that performance on temporal tasks improves with increasing bandwidth of the stimulus. The restricted range of frequencies due to hearing loss in the current study would have reduced the effective bandwidth of the broadband carrier. However, as soon as the 30-dBNo carriers became audible in the region of impaired hearing, the effective bandwidth increased and performance returned to normal. For broadband carriers, 50 dBNo sufficiently maintained effective internal bandwidth, and thus no changes in temporal resolution were observed.

C. Recovery of function

Hair cell regeneration led to functional recovery of threshold, frequency resolution, and temporal resolution. The degree of functional recovery varied based on several factors, some known and some unknown. One factor which was clearly related to functional recovery was degree of impairment. Mild to moderate impairments were not permanent, but severe to profound hearing loss resulted in some degree of permanent threshold shift. However, in both Marean *et al.* (1993) and the current study, one out of four birds had complete recovery of threshold at 5 kHz, although complete recovery of threshold was not observed at 4 or 7 kHz in both of these birds.

A similar statement can be made in the case of frequency resolution. Increases in filter bandwidth of less than a 10% were not permanent. Increases in filter bandwidth of greater than 10% may or may not be permanent. Interestingly, the bird with the greatest increase in filter bandwidth at 5 kHz had normal frequency resolution at 5 kHz by the end of the experiment. Neither resolution at CF (or adjacent frequencies) nor threshold shift predicted which would occur.

All birds show malformed and disoriented stereociliary bundles throughout the region of ototoxic damage, but some birds appear to hear normally despite these structural changes. Permanent changes in hearing may not be solely due, however, to structural changes within the basilar papilla. Temporary hearing loss may have caused changes to the central auditory system in some birds, but not in others. There are, however, a variety of changes which might occur in the avian cochlea to account for individual variation in the recovery of function (see Cotanche *et al.*, 1994, 1991).

Auditory filters at both high and low frequencies typically change their skew toward low frequencies in the regenerated cochlea. Any number of factors may contribute to this behavior, including the loss of off-frequency, high-frequency suppression regions. This explanation does not account for changes in skew without concomitant changes in bandwidth.

Salvi *et al.* (1994) showed that damage to high-frequency regions in the chicken cochlea influenced the tuned response of low-frequency regions of the auditory nerve. The skew and occasional bandwidth changes seen at low frequencies in our data with high-frequency hair cell damage is consistent with their findings.

D. Relation of auditory functions

There was no way to predict changes in frequency resolution directly from auditory threshold. There were instances where frequency resolution was normal in the context of permanent threshold shifts (and in one case, Bird II, vice versa). Auditory threshold at adjacent frequencies did not correlate with frequency resolution either. On average, filter bandwidth at 5 kHz was associated with threshold shift at 5 kHz, but there was no way to predict from threshold data which auditory filters would recover completely, and which would not.

One aspect of the relationship between recovery of threshold and recovery of frequency resolution which stands out is that frequency resolution continued to improve after auditory thresholds had stabilized. This was evident in the 5-kHz data from Birds I, III, and IV. Bird II also showed improvement in frequency resolution between week 7 and week 10, but threshold at 5 kHz also improved during this time. By the time thresholds stabilize, the permanent changes in the low-frequency slope of the auditory filter were fixed, and additional improvement tended to be the high-frequency slope.

Changes in frequency resolution appeared to have little or no effect on temporal processing as assessed by the TMTF. Changes to the TMTF bandwidth were limited to time periods when the carrier bands were at extremely low sensation levels. This made obtaining high modulation rate thresholds more difficult for Birds I and II, presumably because even the low-frequency edge of the 5-kHz carrier band was barely audible at 50 dBNo. It is probable that had we increased the intensity of the carrier band during this time, TMTFs might have appeared normal.

It is also *not* the case that wider auditory filters led to *improved* temporal resolution, an idea sometimes discussed in the literature as being hypothetically possible due to changes in the impulse response of wide filters versus narrow ones (e.g., Evans, 1985). Evidently, other than affecting stimulus audibility, regenerated hair cells did not alter the auditory system's ability to follow the temporal properties of a stimulus. Apparently, normal orientation of hair cell bundles was not functionally required for this task.

Data from the current study suggest that more complex auditory behavior could be preserved after hair cell regeneration in birds. The temporal aspects of birdsong, for example, should be well preserved in the regenerated basilar papilla based on TMTFs. Only minor changes to the spectral representation of song would be expected. In humans, frequency resolution is highly correlated to the perception of speech in noise, but not in quiet (Festen and Plomp, 1983). Thus even birds with permanent changes in frequency resolution may be able to perceive song in a controlled setting. The effects of temporary hearing loss on the neural control centers for song behavior are unknown. Thus we cannot conclude at this time that hair cell regeneration results in the restoration of all complex auditory functions, especially those involved in acoustic communication.

ACKNOWLEDGMENTS

G. C. Marean was supported for this work on a NIH predoctoral training grant (HD07391), and J. M. Burt was supported by NSF62-6746. Additional funding came from NIH DC00395, The Virginia M. Bloedel Hearing Research Center, The National Organization for Hearing Research, The Dean's Office of The Graduate School (University of Washington), and The Oberkotter Foundation. The authors would like to thank Bob and Toni Reineke for their help in obtaining birds, Ian Young and John Featherstone for running many of the test sessions, and Dale Cunningham for expert histological assistance. We are especially grateful to Ed Burns for consulting with us on numerous occaisions and for comments on earlier versions of the manuscript.

[1]The noise bands used in this study were correlated since they were generated by the same source. There is no evidence that having the noise bands generated by a common source resulted in any release from masking, which can occur when tones are presented in the presence of co-modulated noise bands.

[2]In the present experiment we fixed masker level and varied probe level to find threshold. A preferable method would have been to vary masker level and fix probe level in order to keep the overall stimulus power in the auditory filter constant across different notch width conditions. We chose not to use this method for the sake of simplicity in the trial structure which facilitated animal training. See Rosen and Baker (1994) for discussion and comparison of results obtained by these two methods.

[3]Exclusions for quiet thresholds and auditory filter study: Prior to dosing the four birds with kanamycin, a total of 157 sessions were run to obtain thresholds in quiet and in notched-noise, resulting in 835 individual threshold runs. Of these, 22 runs were incomplete, 61 had reversal values above the probe level, 100 had high false alarm rates, and 4 were excluded due to experimenter error. Each bird had approximately 162 usable threshold runs, or roughly five thresholds per condition.

[4]Exclusions for TMTF study: Prior to dosing, 48 sessions resulted in 224 threshold runs. Of these, 30 runs were incomplete, 15 had reversals above the probe levels, and 17 were excluded due to high false alarm rates. There were thus 158 usable threshold runs, a yield rate of 70%. Most of the excluded sessions were from carrier intensities of 50 dBNo. Individual birds in some cases had but one completed function at this higher level.

[5]Broadband noise data are not reported because they did not differ from data obtained at 0% notch widths.

Bacon, S. P., and Gleitman, R. M. (**1992**). ''Modulation detection in subjects with relatively flat hearing losses,'' J. Speech Hear. Res. **35**, 642–653.

Bacon, S. P., and Vemeister, N. F. (**1985**). ''Temporal modulation transfer functions in normal-hearing and hearing-impaired listeners,'' Audiology **24**, 117–134.

Corwin, J. T., and Cotanche, D. A. (**1988**). ''Regeneration of sensory hair cells after acoustic trauma,'' Science **240**, 1772–1774.

Cotanche, D. A., Lee, H. K., Stone, J. S., and Picard, D. A. (**1994**). ''Hair cell regeneration in the bird cochlea following noise damage or ototoxic drug damage,'' Anatomy and Embryology **189**, 1–18.

Cotanche, D. A., Petrell, A., and Picard, D. A. (**1991**). ''Structural reorganization of hair cells and supporting cells during noise damage, recovery, and regeneration in the chick cochlea,'' in *Regeneration of Vertebrate Sensory Cells*, edited by G. R. Bock (Wiley, New York), pp. 131–150.

Dooling, R. J., Okanoya, K., Downing, J., and Hulse, S. (**1986**). ''Hearing in the starling (Sturnus vulgaris): Absolute thresholds and critical ratios,'' Bull. Psychonom. Soc. **24**, 462–464.

Dooling, R. J., and Searcy, M. H. (**1981**). ''Amplitude modulation thresholds for the parakeet (*Melopsittacus undulatus*),'' J. Comp. Physiol. **143**, 383–388.

Evans, E. F. (**1985**). ''Aspects of the neural coding of time in the mammalian peripheral auditory system relevant to temporal resolution,'' in *Time Resolution in Auditory Systems*, edited by A. Michelson (Springer-Verlag, Berlin), pp. 74–95.

Festen, J. M., and Plomp, R. (**1983**). ''Relations between auditory functions in impaired hearing,'' J. Acoust. Soc. Am. **73**, 652–662.

Florentine, M., and Buus, S. (**1984**). ''Temporal gap detection in sensorineural and simulated hearing impairments,'' J. Speech Hear. Res. **27**, 449–455.

Formby, C., and Muir, K. (**1988**). ''Modulation and gap detection for broadband and noise signals,'' J. Acoust. Soc. Am. **84**, 545–550.

Glasberg, B. R., and Moore, B. C. J. (**1990**). ''Derivation of auditory filter shapes from notched-noise data,'' Hearing Res. **47**, 103–138.

Green, D. M., and Swets, J. A. (**1966**). *Signal Detection Theory and Psychophysics* (Peninsula, Los Altos).

Grose, J. H., Eddins, D. A., and Hall, J. W. (**1989**). ''Gap detection as a function of stimulus bandwidth with fixed high-frequency cutoff in normal-hearing and hearing-impaired listeners,'' J. Acoust. Soc. Am. **86**, 1747–1755.

Hashino, E., and Sokabe, M. (**1989**). ''Kanamycin induced low-frequency hearing loss in the budgerigar (*Melopsittacus undulatus*),'' J. Acoust. Soc. Am. **85**, 289–294.

Hawkins, J. E., and Stevens, S. S. (**1950**). ''The masking of pure tones and speech by white noise,'' J. Acoust. Soc. Am. **22**, 6–13.

Klump, G. M., and Okanoya, K. (**1991**). ''Temporal modulation transfer functions in the European starling (Sturnus vulgaris): I. Psychophysical modulation detection thresholds,'' Hearing Res. **52**, 1–11.

Langemann, U., Klump, G. M., and Dooling, R. J. (**1995**). ''Critical Bands and critical-ratio bandwidth in the European starling,'' Hearing Res. **84**, 167–176.

Levitt, H. (**1970**). ''Transformed up-down methods in psychoacoustics,'' J. Acoust. Soc. Am. **49**, 467–477.

Liberman, M. C., Dodds, L. W., and Learson, D. A. (**1986**). ''Structure-function correlation in noise-damaged ears: A light and electron-microscopic study, in *Basic and Applied Aspects of Noise-Induced Hearing Loss*, edited by R. J. Salvi, D. Henderson, R. P. Hamernik, and V. Colletti (Plenum, New York), pp. 163–176.

Linzenbold, A., Dooling, R. J., and Ryals, B. (**1993**). ''A behavioral audibility curve for a Japanese quail,'' Paper presented to the Abstracts of the 16nth Midwinter Meeting of the Association for Research in Otolaryngology, St. Petersburg Beach, FL.

Lippe, W. R., Westbrook, E. W., and Ryals, B. M. (**1991**). ''Hair cell regeneration in the chicken cochlea following aminoglycoside ototoxicity,'' Hearing Res. **56**, 203–210.

Manley, G. A. (**1990**). *Peripheral Hearing Mechanisms in Reptiles and Birds* (Springer-Verlag, New York).

Manley, G. A., Schulze, M., and Oeckinghaus, H. (**1987**). ''Otoacoustic emissions in a songbird,'' Hearing Res. **26**, 257–266.

Marean, G. C., Burt, J., Beecher, M. D., and Rubel, E. W. (**1993**). ''Hair cell regeneration in the European starling (*Sturnus vulgaris*): Recovery of pure tone detection threshold,'' Hearing Res. **71**, 125–136.

Marean, G. C., Cunningham, D., Burt, J. M., Beecher, M. D., and Rubel, E. W. (**1995**). ''Regenerated hair cells in the European starling: Are they more resistant to kanamycin ototoxicity than original hair cells?,'' Hearing Res. **82**, 267–276.

Moore, B. C. J. (**1995**). *Perceptual Consequences of Cochlear Damage* (Oxford U. P., London).

Patterson, R. D. (**1976**). ''Auditory filter shape derived with noise stimuli,'' J. Acoust. Soc. Am. **59**, 640–654.

Patterson, R. D., Nimmo-Smith, I., Weber, D. L., and Milroy, R. (**1982**). ''The deterioration of hearing with age: Frequency selectivity, the critical ratio, the audiogram, and speech threshold,'' J. Acoust. Soc. Am. **72**, 1788–1803.

Rosen, S., and Baker, R. J. (**1994**). ''Characterizing auditory filter nonlinearity,'' Hearing Res. **73**, 231–243.

Ryals, B. M., and Rubel, E. W. (**1988**). ''Hair cell regeneration after acoustic trauma in adult Coturnix quail,'' Science **240**, 1774–1776.

Salvi, R. J., Saunders, S. S., Hashino, E., and Chen, L. (**1994**). ''Discharge patterns of chicken cochlear ganglion neurons following kanamycin-induced hair cell loss and regeneration,'' J. Comp. Physiol. **174**, 351–369.

Saunders, J., and Dooling, R. J. (**1974**). ''Noise induced threshold shift in the parakeet (Melopsittacus undulatus),'' Proc. Natl. Acad. Sci. USA **71**, 1962–1965.

Saunders, S. S., Salvi, R. J., and Miller, K. M. (**1995**). ''Recovery of thresholds and temporal integration in adult chickens after high level 525-Hz pure tone exposure,'' J. Acoust. Soc. Am. **97**, 1150–1164.

Scharf, B. (**1970**). ''Critical bands,'' in *Foundations of Modern Auditory Theory*, Vol. 1, edited by J. V. Tobias (Academic, New York).

Shailer, M. J., and Moore, B. C. (**1983**). ''Gap detection as a function of frequency, bandwidth and level,'' J. Acoust. Soc. Am. **74**, 467–473.

Stone, M. A., Glasberg, B. R., and Moore, B. C. J. (**1992**). ''Simplified measurement of auditory filter shapes using the notched-noise method,'' Br. J. Audiol. **26**, 329–334.

Taylor, M. M., and Creelman, C. D. (**1967**). ''PEST: Efficient estimates on probability function,'' J. Acoust. Soc. Am. **41**, 782–787.

Turner, C. W., Souza, P. E., and Forget, L. N. (**1995**). ''Use of temporal envelope cues in speech recognition by normal and hearing-impaired listeners,'' J. Acoust. Soc. Am. **97**, 2568–2576.

Tyler, R. S., Hall, J. W., Glasberg, B. R., and Moore, B. C. J. (**1984**). ''Auditory filter asymmetry in the hearing impaired,'' J. Acoust. Soc. Am. **76**, 1363–1368.

Viemeister, N. F. (**1979**). ''Temporal modulation transfer functions based upon modulation thresholds,'' J. Acoust. Soc. Am. **66**, 1364–1380.

Auditory scene analysis by European starlings (*Sturnus vulgaris*): Perceptual segregation of tone sequences

Scott A. MacDougall-Shackleton,[a] Stewart H. Hulse,[b] Timothy Q. Gentner, and Wesley White[c]
Department of Psychology, Johns Hopkins University, Baltimore, Maryland 21218

(Received 23 July 1997; revised 14 February 1998; accepted 2 March 1998)

Like humans, animals that use acoustic stimuli to perceive their world ought to be able to parse the auditory scene into functionally significant sounds. The ability to do so ought to have significant adaptive value when, for example, an animal can identify the sounds of a predator among other natural noises. In earlier work it was shown that a species of songbird, the European starling, can identify excerpts of both its own song and songs from other avian species when the songs are mixed concurrently with other natural signals. In this experiment it is demonstrated that starlings can segregate two synthetic pure-tone sequences when the sequences differ in frequency. Taken together, the experiments show that at least one nonhuman species is capable of auditory scene analysis both for natural and for non-natural acoustic stimuli. This suggests in turn that auditory scene analysis may be a general perceptual process that occurs in many species that make use of acoustic information. © *1998 Acoustical Society of America.* [S0001-4966(98)03606-6]

PACS numbers: 43.66.Gf, 43.66.Lj [RHD]

INTRODUCTION

People readily parse concurrent overlapping sounds into separate functional auditory objects identified by a unique set of acoustic cues such as spatial location, spectral composition, and pitch (Bregman, 1990). Because one can attend to just one auditory object at a time, selective attention is important for auditory scene analysis, as in the familiar example of the ''cocktail party effect'' (Bregman, 1990; Cherry and Taylor, 1954). The processes involved in auditory scene analysis have been studied over the past 25 years or so, and the topic remains a very active area of research in human audition (Bregman, 1990; Bregman and Campbell, 1971; Darwin and Carlyon, 1995; Darwin *et al.*, 1995; Dowling *et al.*, 1987; Hartmann and Johnson, 1991; Newman and Jusczyk, 1996; Wood and Cowan, 1995). Here we report prototypical auditory stream segregation by a nonhuman animal, a songbird. European starlings (*Sturnus vulgaris*) were found, like humans, to segregate and organize perceptually a serial tone pattern into two subpatterns on the basis of differences in tone frequency.

There are few reports of auditory scene analysis by nonhuman animals. Yet the capacity to parse the auditory scene into significant objects—a predator's rustle amidst other forest sounds, for example—would surely convey significant evolutionary advantage. To our knowledge only two previous reports have appeared. First, Hulse *et al.* (1997) found that European starlings could be trained to discriminate and identify a sample of one species' bird song presented concurrently with a sample of another species' bird song. Such species identification also held when the test songs were presented amidst the added distractors provided by a recording of the dawn chorus, the cacophonous mixture of sounds of many songbirds singing early on a spring morning (e.g., Henwood and Fabrick, 1979; Kacelnik and Krebs, 1983; Staicer *et al.*, 1996). Second, Wisniewski and Hulse (1997) discovered that European starlings could not only learn to discriminate between many samples of the songs of two individual starlings, starling A and starling B, but most important, could maintain that discrimination when song samples from a third individual, starling C, were added to both A and B stimuli, and when additional songs from starlings D, E, and F were added as further background distractors. To be sure, discrimination accuracy by the test birds decreased as more and more distractors were added to the background mixture, but individual identification was still well above chance even with the target A and B songs mixed concurrently with song samples from four other starlings. The basis on which the starlings were performing the scene analysis remains to be identified, but the process appears to be robust when European starlings listen to natural sounds like bird song.

Although it seemed sensible to begin a study of auditory scene analysis in nonhuman animals by using stimuli with ecological significance, the available data do not establish the process as a general auditory capacity even within the single species studied to date. The question is whether or not the process is somehow unique to natural signals like bird song, or if scene analysis holds more generally for other acoustic events, such as non-natural arbitrary stimuli. The present experiment was directed to that latter issue.

I. THEORY

The theoretical strategy we chose to study the problem was based on a variation of the experimental procedure used

[a]Now at Department of Ecology and Evolutionary Biology, Princeton University, Princeton, NJ. Electronic mail: Shackles@princeton.edu
[b]Electronic mail: hulse@jhu.edu
[c]Now at Department of Psychiatry, Johns Hopkins University Medical School, Baltimore, MD.

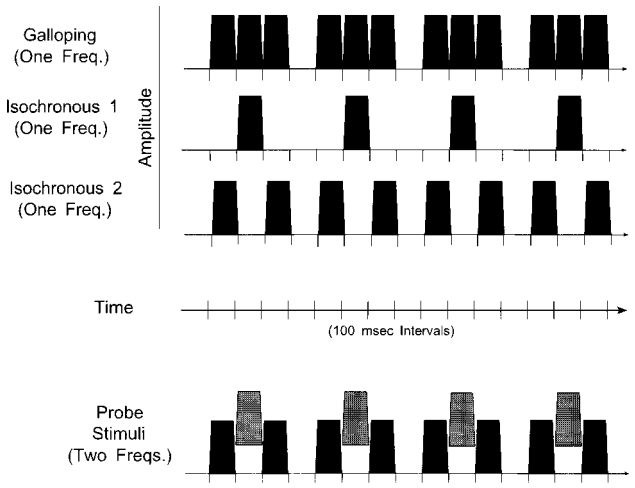

FIG. 1. Schematic diagram of the experimental plan. Each filled quadrangle at the top of the figure represents a time-amplitude plot of a single-frequency sine tone (e.g., 1000 Hz). The sine tones are arranged to form three stimulus sequences with which the starlings were trained initially, a galloping stimulus and two isochronous stimuli, isochronous 1 and isochronous 2. The sequence below the time line represents a Probe stimulus. With the probe stimuli, there are two frequencies in the sequence, one (say, 1000 Hz) represented by the filled quadrangle, and one (say, 1710 Hz) represented by the stippled quadrangle. Note that although the overall temporal structure of the probe stimulus has a galloping pattern, the use of two frequencies turns the probe stimuli into two intermixed isochronous stimuli—on the assumption that stream segregation takes place.

originally by Van Noorden to study stream segregation in humans (Van Noorden, 1975). The basics of the strategy are outlined in Fig. 1.

Subjects, European starlings in this case, are first trained to make one response (peck, say, the left key for food in an operant task) in response to a galloping stimulus. The galloping stimulus (displayed at the top of Fig. 1) is so termed because the pause introduced after every third tone adds an accent that makes the stimulus sequence seem to ''gallop'' like the hoof beats of a race horse to human listeners—especially at relatively fast tempos. At the same time, the starlings are trained to make another response (peck, say, the right key) when they hear *either* the isochronous 1 or isochronous 2 stimuli. During initial discrimination training, all stimuli are presented at a single frequency; therefore the birds learn the discrimination solely on the basis of the temporal structure of the stimuli.

Once this initial discrimination has been learned, occasional probe stimuli (displayed at the bottom of Fig. 1) are then introduced during ongoing trials with the training stimuli. Unlike the training stimuli, the probe stimuli contain *two* frequencies arranged as shown in the figure, but the temporal structure of the probe stimuli is just like that of the galloping stimuli. Note that the frequency changes in the probe stimuli provide the basis on which auditory stream segregation might take place because the frequency changes restructure the probe stimuli, potentially, into one or the other of the two isochronous stimuli. That is, if stream segregation does occur, and if selective attention holds for starlings as it does for humans in auditory scene analysis (a tenable proposition that nevertheless remains to be tested directly in future research with starlings), the birds ought to hear the probe stimuli as sometimes the isochronous 1 stimulus and sometimes the isochronous 2 stimulus. They should therefore peck the key associated with the isochronous stimuli. Presumably, furthermore, the tendency to respond as if the probe stimuli are isochronous should increase as the size of the frequency change in the probe stimuli increases. That is so because the tendency for stream segregation to occur is a function (at least for humans) of the magnitude of the frequency difference between the two streams (Van Noorden, 1975). If, however, streaming fails to occur, the birds ought to peck the key associated with the galloping stimulus because the probe stimuli have a galloping temporal structure.

We now turn to the experiment that tested these theoretical predictions.

II. METHOD

A. Subjects

The subjects were ten adult male European starlings (*Sturnus vulgaris*) of unknown age caught in the wild near Baltimore, MD. The starlings were kept in a mixed aviary containing approximately 50 starlings of both sexes, zebra finches (*Taeniopygia guttata*), and ring doves (*Streptopilia risoria*). The starlings were fed commercial poultry starter (Start and Grow, Purina, Inc., St. Louis, MO) supplemented periodically with raw spinach. None of the birds had prior experience with operant conditioning procedures. During the experiment, the birds' access to food was controlled to ensure that body weight was approximately 85% of *ad libitum* weight before each experimental session.

Three starlings failed to complete the experiment: one died and two failed to reach the criterion for initial baseline discrimination learning. Thus seven birds completed the experiment and are included in the analysis.

B. Apparatus

During experimental sessions, each starling was tested inside an IAC, Inc. (Bronx, NY) model AC-3 sound attenuation chamber (80 cm×60 cm×60 cm interior dimensions) containing a speaker, response panel, and two feeders. The response panel formed one wall of a 28 cm×20 cm×30 cm stainless steel weld-wire cage that housed the bird. Two 2.8-W light bulbs behind a translucent screen on the rear wall indirectly illuminated the chamber.

The response panel was a 26 cm×30 cm sheet of 2-mm-thick stainless steel equipped with three response keys and two 4.5 cm×6 cm openings that provided controlled access to food hoppers. The keys were 2-cm-diam plastic disks attached to microswitches; keys were spaced 6 cm apart in a horizontal row. Each food hopper opening was 4.5 cm below the left- and rightmost keys. A Bose 101 loudspeaker was mounted above and behind the response panel. A PC microcomputer generated sound stimuli from its hard disk drive through a Data Translation model 2801 D/A converter. The stimuli were then fed to a Crown model D75 amplifier and then to the speaker in the test chamber. The computer also monitored the response keys, house lights, and food hoppers, and collected data.

Stimuli for Baseline Discrimination
Between Isochronous and Galloping Tone Patterns

Isochronous Patterns	Galloping Pattern	Stimulus Frequency
(1) X - X - X - X - (2) X - - - X - - - X - - -	X X X - X X X -	1000 Hz
(1) A - A - A - A - (2) A - - - A - - - A - - -	A A A - A A A -	1050 Hz
(1) B - B - B - B - (2) B - - - B - - - B - - -	B B B - B B B -	1710 Hz
(1) C - C - C - C - (2) C - - - C - - - C - - -	C C C - C C C -	4538 Hz

Stimuli for Test Probes

Pattern	Frequency Difference
A X A - A X A - A X A -	1050 Hz and 1000 Hz = 50 Hz
B X B - B X B - B X B -	1710 Hz and 1000 Hz = 710 Hz
C X C - C X C - C X C -	4358 Hz and 1000 Hz = 3538Hz

FIG. 2. Details of the stimulus patterns used in the experiment. The birds were trained initially to discriminate between one galloping and two isochronous baseline patterns. On any trial, the tones in a given stimulus pattern were of constant frequency, but over the course of training, the birds were exposed to patterns containing four frequencies: 1000, 1050, 1710, and 4538 Hz. The stimuli for the test probes, shown at the bottom of the figure, were combinations of the 1000-Hz tone with the other three frequencies. All probe stimuli had a galloping temporal structure.

C. Stimuli

The stimuli were created from repeated sine tones with frequencies of 1000, 1050, 1710, or 4538 Hz. Each tone was 100 ms in duration and began and ended with a 10-ms linear amplitude ramp. Successive tones either followed one another immediately or were separated by intertone intervals that varied according to experimental conditions (Fig. 2). Tones and intertone intervals repeated to form a stimulus that was 10 s in total duration. Each 10-s stimulus began and ended with a 2-s linear amplitude ramp.

The tones and intertone intervals were combined to form one stimulus type that had a galloping rhythm and two other stimulus types that had an isochronous rhythm (Figs. 1 and 2). The galloping stimulus consisted of repeated sequences of a group of three consecutive 100-ms tones separated by a 100-ms intertone interval. One isochronous stimulus (isochronous 1) consisted of 100-ms tones separated by 300-ms intertone intervals. The other isochronous stimulus (isochronous 2) consisted of alternating 100-ms tones and 100-ms intertone intervals. Both the galloping stimulus and the isochronous stimuli for the initial *baseline discrimination* task contained tones of a single frequency (Fig. 2). For *probe stimuli* used for later testing, each stimulus contained 1000-Hz tones and tones of either 1050, 1710, or 4538 Hz (Figs. 1 and 2). Thus, the probe stimuli consisted of sequences containing small (5%), intermediate (71%), or large (354%) frequency changes within the sequence.

The stimuli were created with SoftSynth software (Peabody Conservatory, Baltimore, MD) on a Macintosh IIx computer, digitized with 16-bit accuracy at a 20 kHz sampling rate, and stored in PC format on computer disk for on-line retrieval. The stimuli were played through the speaker at a level of 69 dB SPL as measured by a Rion sound level meter placed at a location approximately at the level of a bird's head in the test chamber.

D. Procedure

1. Shaping

Birds were trained initially to peck the keys in the apparatus by attaching a small amount of food directly to the center key. In the first 2-h shaping session, pecks to the center key were rewarded with access to one of the food hoppers for 2 s. In the next session on the following day, pecks to the center key followed by pecks to the left or right key were rewarded with 2-s food access at the left or right hopper, respectively. In the next session, baseline discrimination began.

2. Baseline discrimination

In the baseline discrimination task, the starlings were tested in the apparatus for 2-h sessions, 6 days per week. Birds initiated a trial by pecking the center key. This resulted in playback of a 10-s tone stimulus with either the galloping ($p=0.50$) or the isochronous ($p=0.50$) stimulus structure. Within the isochronous stimuli, the isochronous 1 and 2 stimuli appeared with equal likelihood. Pecks to any of the keys during the 10 s while the stimulus played had no consequence. The first peck following the 10-s observation period led either to 2-s access to food or to a 12-s time-out period during which the house lights were turned off. Left or right pecks, counterbalanced across birds, were rewarded with food following a galloping stimulus or either of the two isochronous sound stimulus, respectively. Incorrect pecks led to the time-out period, and the trial then repeated until the bird performed correctly. If the bird did not peck any key for 10-s following the listening period, the trial ended and the stimulus was repeated on the next trial. There was a 250-ms interval between trials.

The birds were tested in two groups. In the first group ($n=2$), baseline stimuli constructed with all four frequencies were used ($p=0.25$) beginning with the first session of baseline training. In the second group ($n=5$), the four frequencies were introduced one by one in an order partially counterbalanced across birds. When a bird demonstrated statistically significant acquisition of the task with one frequency, stimuli at another frequency were added to the pool of baseline stimuli. This was repeated until birds were discriminating baseline stimuli at all four frequencies.

For the second group of birds, once a bird reached an acquisition criterion of 80% correct or better for three consecutive sessions, the reward probability for a correct response was reduced over four or five sessions so that only 80% of correct responses led to food reward. This was to prepare the birds for nonreinforced probe trials in later probe

sessions. Once a bird performed at the 80% correct criterion for three consecutive sessions at this reward probability, probe sessions began. For the first group of birds, probe sessions began without the reduction in reinforcement levels for the baseline stimuli.

3. Probe sessions

During probe sessions, some baseline discrimination trials were replaced with probe trials using the three galloping probe stimuli that varied in the size of the frequency differences between successive tones (Figs. 1 and 2). On probe trials, the three galloping probe stimuli were sampled randomly ($p=0.33$). In the first group of birds, 20% of the trials in a probe session were galloping probe trials, and the remainder were baseline trials. One hundred per cent of correct responses to baseline stimuli were rewarded. Pecks to either the left or right key in response to a probe stimulus were rewarded. In the second group of birds, 10% of the trials in a probe session were galloping probe trials, and 90% of correct responses to baseline stimuli were rewarded. Pecks to either the left or right key in response to galloping probe stimuli led neither to reward nor punishment. Probe sessions were continued in both groups until each bird had responded to at least 100 of each type of probe stimulus in the first group of two birds, and until each bird had responded to at least 20 (range 20–87) of each probe type in the second group of five birds.

E. Data analysis

The probability that a bird responded to the galloping and isochronous stimuli as if they were isochronous was determined for each daily session during initial baseline training. The data averaged over the last three sessions of baseline training were used to assess discrimination at the end of training, prior to the introduction of probe stimuli. Accurate discrimination was indicated by a high probability of a response on the key associated with isochronous stimuli when an isochronous stimulus occurred, and a corresponding low probability of a response on the isochronous key when a galloping stimulus occurred. The birds never failed to respond, and correction trials were excluded from the analysis.

For sessions that included probe trials, the mean probability that a bird responded to a probe stimulus as if it were an isochronous stimulus was calculated over all probe trials for that bird, and then averaged across birds. Also, for comparison purposes with baseline performance, mean performance with baseline stimuli across birds during probe sessions was calculated.

A preliminary analysis revealed no significant differences between the data for birds in the first and second groups that were tested with somewhat different procedures, so data from the two groups were combined for further analysis.

III. RESULTS

During baseline training, all starlings achieved a high probability of pecking the response key associated with isochronous stimuli when isochronous stimuli occurred, and a correspondingly low response probability of pecking the isochronous key when galloping stimuli occurred. As Fig. 3 shows, that was true both for mean probabilities over the last 3 days of initial baseline training and for baseline trials during probe sessions. To be sure, the initial baseline discrimination task was difficult, requiring a mean of 8296 trials (range 5368–13 459) for the birds to reach criterion. Nevertheless, once acquired, the birds maintained stable performance on the baseline task at a high level of accuracy.

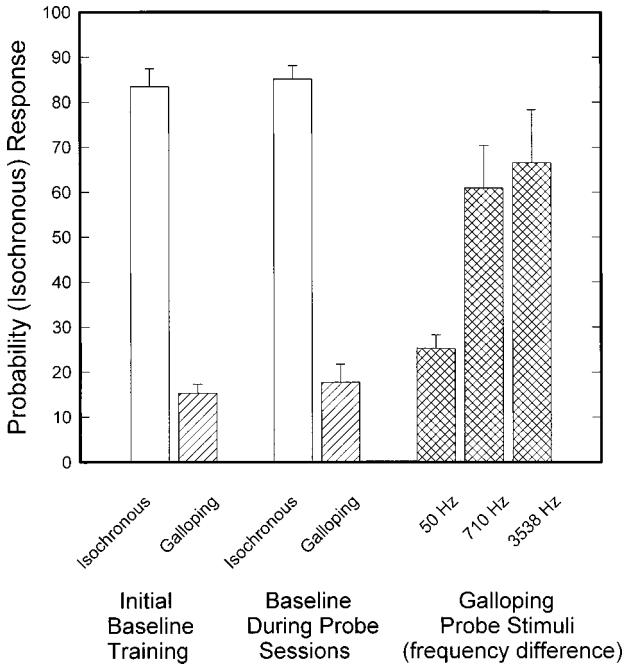

FIG. 3. The two left pairs of columns show the average probability (+SEM) that a starling pecked the key associated with the isochronous stimuli for isochronous and galloping stimuli during initial baseline training and on trials with baseline stimuli during sessions that included probe trials. The three columns at the right of the figure show the average probability (+SEM) of pecking the isochronous key when galloping probe stimuli occurred containing sine tones that differed in frequency by 50, 710, or 3538 Hz.

Most important, when frequency changes were introduced within the galloping stimuli on probe trials, there was a progressively higher probability of responding to a probe stimulus as if it were isochronous the larger the frequency change between successive tones in the probe stimuli. For a 50-Hz frequency change there was little change in the probability of a response to the isochronous key, but as the frequency difference increased from 50 to 710 Hz to 3538 Hz, the probability of pecking the isochronous key when the probe stimulus occurred approached that for the baseline isochronous stimuli. Therefore, when frequency differences between tones within the probe stimulus were sufficiently large on probe trials, the starlings apparently reorganized the galloping stimulus perceptually into one (or two) isochronous stimuli (Fig. 1), attended to one or the other, and responded accordingly—an example of auditory stream segregation at work.

Statistical analysis amply supports these conclusions. The starlings first learned accurate discrimination of the baseline stimuli and then maintained that discrimination during sessions with probe trials. A two-way within-subject

analysis of variance (ANOVA) on the probability of pecking the isochronous key for isochronous and galloping stimuli during initial baseline training and over baseline trials during probe sessions yielded a significant difference for isochronous as compared with galloping stimuli, $F(1,6)=361.70$, $p<0.001$. No other effects were significant, indicating no reliable evidence for a change in discrimination performance on baseline stimuli during sessions with probe trials.

For large frequency differences on galloping probe trials, the probability of producing responses associated with isochronous stimuli was very similar to that observed for baseline isochronous stimuli. A one-way within-subject ANOVA on the probability of pecking the isochronous key that included (a) data for baseline stimuli during probe sessions and (b) the three frequency-difference conditions yielded a significant difference among the means for conditions, $F(4,24)=24.557$, $p<0.001$. Subsequent Tukey's tests showed significantly greater ($p<0.05$) probability of pecking the isochronous key during baseline trials as compared with the galloping probe stimuli incorporating a small 50-Hz frequency difference. However, with the larger 710- and 3538-Hz frequency differences on galloping probe trials, the difference between the probability of an isochronous response on baseline trials with isochronous stimuli and on probe trials with galloping stimuli was not significantly different (p's>0.05).

Comparisons among the probe stimuli themselves showed that the probabilities of pecking the isochronous key for the 710- and 3538-Hz probe stimuli were both significantly greater by Tukey test than the probability of an isochronous response to the 50-Hz probe stimuli (p's <0.001). Interestingly, there was no significant difference between the probability of pecking the isochronous key given a 50-Hz probe stimulus, and the probability of pecking the isochronous key given a galloping baseline stimulus ($p>0.05$). This indicates that a 50-Hz frequency difference on galloping probe trials was insufficient to cause stream segregation to occur. It would be interesting to know from future research the frequency difference on galloping probe trials that would just be sufficient for stream segregation to occur.

IV. DISCUSSION

These data, to our knowledge, provide the first observation of auditory stream segregation in nonhuman animals of non-natural, arbitrary (pure tone) stimuli based on frequency differences. The interpretation of our results is straightforward (Bregman and Campbell, 1971; Bregman, 1990; Van Noorden, 1975). Gestalt principles hold that sounds of common frequency will group together. The stimulus structures we used on probe trials provided the possibility that two separate streams, marked by different temporal structures, could form on the basis of common frequencies within streams, but different frequencies between streams. The data show that grouping did indeed occur, as measured by a shift in the starlings' perception of the temporal structure of a stimulus sequence from galloping to isochronous with the introduction of frequency differences between adjacent tones in the stimuli. Furthermore, grouping tendencies should be more pronounced the larger the frequency difference between two stimulus groups. Once again, the data support this prediction. The tendency of the starlings to respond to the galloping sequence as if it were isochronous was an increasing function of the frequency disparity between the tones of the two putative isochronous streams within the galloping stimulus.

The process of selective attention is one of the hallmarks of stream segregation. Observers can attend to one or the other of two ongoing streams, but not to both at the same time. Although we have no direct evidence that selective attention was taking place between the high- and low-frequency streams on probe trials, the data are not out of line with that idea. Presumably, the starlings were hearing one of the two isochronous streams as an isochronous 1 stimulus on some probe trials, and as an isochronous 2 stimulus on others (Figs. 1 and 2)—or perhaps shifting attention between the two stimuli within a trial—but we do not know for sure. This issue could be settled by introducing a third response contingency into baseline training. Starlings would be trained to peck one key for a galloping stimulus, a second key for an isochronous 1 stimulus, and a third key for an isochronous 2 stimulus. During subsequent probe trials with galloping stimuli containing sufficiently different frequencies, the starlings should always show a low probability of responding to the key associated with galloping stimuli, but might well distribute their responses from probe trial to probe trial between both isochronous keys—on the assumption that selective attention between the two streams would vary from trial to trial (or even from time to time within a trial until the moment when a response decision was made). A bias to respond to the stimulus stream associated with one isochronous key as compared with the other could be introduced in many ways and might be interesting to explore from the point of view of selective attention, and so would the introduction of spatial location as a cue correlated with different streams.

A. Auditory scene analysis as an adaptive phenomenon

The present results join our earlier observations with natural stimuli, birdsong in particular, to support the claim that auditory stream segregation is a general process in at least one avian species and, we venture to guess, in others (Hulse *et al.*, 1997; Wisniewski and Hulse, 1997). Whether or not auditory stream segregation is a general process with boundaries extending beyond avians (and humans) remains to be determined. However, the potential significance of the process for evolutionary development in species that uses acoustic information certainly suggests that auditory scene analysis, in some form, is probably quite common.

For example, although not cast specifically in terms of scene analysis, there are suggestions that auditory object formation in the sense of scene analysis has been observed in green tree frogs (e.g., Gerhardt, 1989, 1992; Gerhardt and Klump, 1988) and in chorusing insects (e.g., Otte, 1974), among other species, where the identification of a potential mate in a ''noisy'' background is of singular importance. The problem arises not only when individuals must be identified in a chorus of other individuals of the same species, but

also when important sounds are ''degraded'' by the context (e.g., forest or city sounds) in which they occur (Dabelsteen *et al.*, 1993). McGregor and Dabelsteen (1996), in their discussion of communication networks in birds, clearly implicate scene analysis as a process in avian auditory interactions. Any circumstance in which auditory communication (or the detection of functional auditory objects) must take place in an acoustic environment that is full of ecologically relevant noise provides a likely place to look for scene analysis at work. An especially interesting comparison would be to examine auditory objects that require long as compared with short time constants for integrating functionally useful information, e.g., bird song lasting several seconds or more as compared with a single loud alarm call. The former may be more amenable to streaming and scene analysis than the latter.

1. Noise versus distraction in auditory stream segregation of functional auditory objects

In the foregoing connection, we wish to make a distinction between noise as is it usually conceived in psychoacoustics, and noise—we prefer the term *distraction*—as it is conceived in the analysis of functional, perhaps ecologically relevant, auditory stimuli. The distinction is but tangentially relevant for the simple two-stream segregation phenomenon we report here, but it has important implications for auditory scene analysis broadly construed.

In psychoacoustics, noise generally refers to a broadband spectrum of some kind, at some level, of which white noise is a prime example. Such noise has random structure through time. Psychoacoustics is replete, of course, with studies of auditory perception modulated by such noise. In auditory scene analysis, however, ''noise'' is perhaps best conceived as the auditory scene—a collection of auditory objects that have potential functional or ecological significance (Bregman, 1990). In that context, auditory objects are different from noise; that is, when parsed from the auditory scene by the auditory system, they have a location, a pitch, a spectral structure, perhaps a name, and so on, in a real world. Perhaps most important, auditory objects are usually acoustic signals that flow through time with a predictable serial or temporal structure from moment to moment, such as the syntax of speech or of bird song. That is not to say that auditory objects cannot be treated as noise in the psychoacoustic sense. One can obtain frequency spectra and their associated levels for any collection of sounds. A critical difference, however, is that a pool of auditory objects provides an opportunity for active *selective attention* among individual objects in the pool, and this is important for the perception of functional, ecologically significant auditory events in a real world.

2. Central versus peripheral factors in auditory scene analysis

Although we stress the role of central factors associated with attention in auditory scene analysis, we do not intend to say that some of the principles of basic psychoacoustics might not also play a significant role. For example, Hartmann and Johnson (1991) have stressed the potential importance of peripheral channeling, especially frequency and spatial location, in the development of stream segregation and Klump (summarized in Klump, 1996) has stressed the role of comodulation masking release in hearing signals in noise. Klump and Langemann (1995) showed that European starlings demonstrated comodulation masking release for signals in background noise for rates of amplitude modulation of the noise not unlike those found for background sounds in the birds' natural habitat (50 Hz). Also, Schwartz and Gerhardt (1989) found spatially mediated release from masking in treefrogs. We do claim, however, that selective attention, especially of functional auditory objects, implies a central process in the acoustic domain—based especially on Gestalt grouping principles or other high-level processes—that plays a significant role in auditory scene analysis. That is especially true for natural signals in the everyday world in which both human and nonhuman animals live.

B. Neurophysiology and models of auditory scene analysis

Finally, we note briefly that the demonstration of robust auditory scene analysis in a nonhuman animal provides a ready source of neurophysiological information with which to constrain models of auditory scene analysis that are currently under rapid development (e.g., Beauvois, 1996; Beauvois and Meddis, 1991; McCabe and Denham, 1997; Todd, 1996; Wang, 1996). The songbird brain has been under close scrutiny for some time, especially because of significant structural and chemical changes that take place annually in a neural song control system unique to songbirds (e.g., Ball and Hulse, 1998). Consequently we know a great deal about the neural circuitry that is involved in the learning and production of bird song, and advances are forthcoming rapidly in understanding the neural basis of song perception. Therefore, research designed to study directly the neural control of auditory scene analysis in songbirds may be especially helpful in formulating models of how auditory scene analysis takes place.

V. CONCLUSIONS

We have demonstrated that European starlings show auditory stream segregation for sequences of pure tones that differ in frequency, and that the magnitude of the segregation effect is a function of the size of the frequency difference between the streams. When combined with earlier data from starlings that have demonstrated segregation of ecologically relevant auditory signals (birdsong), the present data support the conclusion that auditory scene analysis plays a general role in the auditory perception of at least one avian species. It seems reasonable that the scene analysis process is potentially significant for many nonhuman species that must parse the world into significant auditory events. Moreover, the demonstration of robust auditory scene analysis in a nonhuman animal provides a potentially fruitful source of neurological information that should facilitate the construction of formal models of scene analysis.

ACKNOWLEDGMENTS

The research was supported by National Science Foundation Grant No. IBN 9317868 to Stewart H. Hulse.

Ball, G. F., and Hulse, S. H. (**1998**). ''Bird song,'' Am. Psychol. **53**, 37–58.

Beauvois, M. W. (**1996**). ''Computer simulation of auditory stream segregation in alternating-tone sequences,'' J. Acoust. Soc. Am. **99**, 2270–2280.

Beauvois, M. W., and Meddis, R. (**1991**). ''A computer model of auditory stream segregation,'' Quarterly Journal of Experimental Psychology **43**, 517–541.

Bregman, A. S. (**1990**). Auditory Scene Analysis. (MIT, Cambridge).

Bregman, A. S., and Campbell, J. (**1971**). ''Primary auditory stream segregation and perception of order in rapid sequences of tones,'' J. Exp. Psychol. **89**, 244–249.

Cherry, E. C., and Taylor, W. K. (**1954**). ''Some further experiments upon the recognition of speech, with one and with two ears,'' J. Acoust. Soc. Am. **26**, 554–559.

Dabelsteen, T., Larsen, O., and Pedersen, S. B. (**1993**). ''Habitat-induced degredation of sound signals: Quantifying the effects of communication sounds and bird location on blur ratio,'' J. Acoust. Soc. Am. **93**, 2206–2220.

Darwin, C. J., and Carlyon, R. P. (**1995**). ''Auditory grouping,'' in *Hearing*, edited by B. C. J. Moore (Academic, San Diego), pp. 387–424.

Darwin, C. J., Hukin, R. W., and Al-Khatib, B. Y. (**1995**). ''Grouping in pitch perception: Evidence for sequential constraints,'' J. Acoust. Soc. Am. **98**, 880–885.

Dowling, W. J., Lung, K. M-T., and Herrbold, S. (**1987**). ''Aiming attention in pitch and time in the perception of interleaved melodies,'' Percept. Psychophys. **41**, 642–656.

Gerhardt, H. C. (**1989**). ''Acoustic pattern recognition in anuran amphibians,'' in *The Comparative Psychology of Audition: Perceiving Complex Sounds*, edited by R. J. Dooling and S. H. Hulse (Erlbaum, Hillsdale, NJ), pp. 175–197.

Gerhardt, H. C. (**1992**). ''Multiple messages in acoustic signals,'' The Neurosci. **4**, 391–400.

Gerhardt, H. C., and Klump, G. M. (**1988**). ''Masking of acoustic signals by the chorus background noise in the green treefrog: a limitation on mate choice,'' Animal Beh. **36**, 1247–1249.

Hartmann, W. M., and Johnson, D. (**1991**). ''Stream segregation and peripheral channeling,'' Music Perception **9**, 155–184.

Henwood, K., and Fabrick, A. (**1979**). ''A quantitative analysis of the dawn chorus: temporal selection for communicatory optimization,'' Am. Nat. **114**, 260–274.

Hulse, S. H., MacDougall-Shackleton, S. A., and Wisniewski, A. B. (**1997**). ''Auditory scene analysis by songbirds: Stream segregation of birdsong by European starlings (*Sturnus vulgaris*),'' J. Comp. Psych. **111**, 3–13.

Kacelnik, A., and Krebs, J. R. (**1983**). ''The dawn chorus in the great tit (*Parus major*): Proximate and ultimate causes,'' Behaviour **83**, 297–309.

Klump, G. M. (**1996**). ''Bird communication in the noisy world,'' in *Ecology and Evolution of Acoustic Communication in Birds*, edited by D. E. Kroodsma and E. H. Miller (Cornell U.P., Ithaca, NY), pp. 321–338.

Klump, G. M., and Langemann, U. (**1995**). ''Comodulation masking release in a songbird,'' Hearing Res. **87**, 157–164.

McCabe, S. L., and Denham, M. J. (**1997**). ''A model of auditory streaming,'' J. Acoust. Soc. Am. **101**, 1611–1621.

McGregor, P. K., and Dabelsteen, T. (**1996**). ''Communication networks,'' in *Ecology and Evolution of Acoustic Communication in Birds*, edited by D. E. Kroodsma and E. H. Miller (Cornell U.P., Ithaca, NY), pp. 409–525.

Newman, R., and Jusczyk, P. W. (**1996**). ''The cocktail party effect in infants,'' Percept. Psychophys. **58**, 1145–1156.

Otte, D. (**1974**). ''Effects and functions in the evolution of signaling systems,'' Annu. Rev. Ecology and Systematics **5**, 385–417.

Schwartz, J. J., and Gerhardt, H. C. (**1989**). ''Spatially mediated release from auditory masking in an anuran amphibian,'' J. Comp. Physiol. A **166**, 37–41.

Staicer, C. A., Spector, D. A., and Horn, A. G. (**1996**). ''The dawn chorus and other diel patterns in acoustics signaling,'' in *Ecology and Evolution of Acoustic Communication in Birds*, edited by D. E. Kroodsma and E. H. Miller (Cornell U.P., Ithaca, NY), pp. 426–453.

Todd, N. (**1996**). ''An auditory cortical theory of primitive auditory grouping,'' Network Computation in Neural Systems **7**, 349–356.

Van Noorden, L. P. A. S. (**1975**). ''Temporal coherence in the perception of tone sequences,'' unpublished doctoral dissertation, Eindhoven University of Technology, Eindhoven, The Netherlands.

Wang, D. (**1996**). ''Primitive auditory segregation based on oscillatory correlation,'' Cogn. Sci. **20**, 409–456.

Wisniewski, A. B., and Hulse, S. H. (**1997**). ''Auditory scene analysis in European starlings (*Sturnus vulgaris*): Discrimination of starling song segments, their segregation from conspecific songs, and evidence for conspecific song categorization,'' J. Comp. Psych. **111**, 337–350.

Wood, N., and Cowan, N. (**1995**). ''The Cocktail Party phenomenon revisited: how frequent are attention shifts to one's name in an irrelevant auditory channel?,'' J. Exp. Psychol. **21**, 255–260.

Effects of spectral pattern on the perceptual salience of partials in harmonic and frequency-shifted complex tones: A performance measure

Brian Roberts[a)]
School of Psychology, University of Birmingham, Edgbaston, Birmingham B15 2TT, England

(Received 12 November 1997; revised 27 January 1998; accepted 2 March 1998)

A single even harmonic added to an odd-harmonic complex is often judged to be more salient than its odd neighbors in a clarity rating task [Roberts and Bregman, J. Acoust. Soc. Am. **90**, 3050–3060 (1991)]. This study used similar complexes in a two-interval forced-choice procedure. Each interval consisted of a complex tone followed by a pure tone, whose frequency matched that of a harmonic in one interval but was changed by $\pm 0.5\times$fundamental frequency in the other. Subjects were asked to identify the matching interval. Since the pure tone followed the complex tone, it could not cue listening to a particular frequency region. The possibility of cross-interval cuing was reduced by changing the fundamental frequency between intervals (100–150 Hz range). The procedure was designed to maximize the effects on performance of differences in immediate perceptual salience between the partials. The added even harmonic was typically judged with greater accuracy than its odd neighbors (experiment 1), though this effect was greatly reduced for harmonics above 8 (experiment 2). The even–odd difference persisted when the original stimuli were made inharmonic by applying a frequency shift of 15%, but was abolished for stimuli consisting of successive partials (experiment 3). [S0001-4966(98)04606-2]

PACS numbers: 43.66.Lj, 43.66.Fe, 43.66.Jh, 43.66.Ba [DWG]

INTRODUCTION

Roberts and his colleagues have proposed that the perceptual coherence of a complex tone is affected by the regularity of the spectral pattern defined by its partials (Roberts and Bregman, 1991; Roberts and Bailey, 1993a, 1993b, 1996a, 1996b). This proposal was originally based on the finding that a single even harmonic could be heard out more easily than its odd neighbors from a complex tone consisting otherwise only of odd harmonics, at least for fundamental ($F0$) frequencies of 100 and 200 Hz (Roberts and Bregman, 1991). Neither a harmonic sieve model (Duifhuis *et al.*, 1982) nor a time-domain equivalent (Hermes, 1988) can account for this result.

Roberts and Bregman reasoned that the regular spectral spacing of the components constituting the odd–harmonic ''base'' led to their fusion, and that the relative salience of the added even harmonic resulted from its inconsistency with this pattern. They proposed a spectro-temporal mechanism for the detection of this local inconsistency that depended on a cross-channel comparison of amplitude modulation (AM) rates at the outputs of the auditory filterbank. Their proposal assumed that intermodulations between the odd harmonics would lead to a common AM rate in the outputs of many channels, and that the addition of an even harmonic would change the AM rate locally to half this value. However, Roberts and Bailey (1993a) found no evidence that the even–odd difference could be explained in this way, as it was not affected much either by changing the relative phases of the partials to minimize the depth of AM or by adding noise to reduce the cross-channel coherence of AM.

Support for an interpretation of the even–odd difference in terms of spectral regularity has come from Roberts and Bailey (1996a), who manipulated the pattern properties of the base spectrum in order to reduce the odd-one-out status of the added even harmonic. This was achieved either by reducing the number of odd harmonics in the base or by including extra components that were inconsistent with the spectral pattern formed by the odd harmonics. Both manipulations reduced the relative ease with which the added even harmonic could be heard out from the complex. Furthermore, Roberts and Bailey (1996b) have extended this research by demonstrating a similar even–odd difference in regular but inharmonic complex tones, created by applying frequency shift and spectral stretch transformations to harmonic stimuli. Their finding that the pattern of spectral spacing can affect the relative saliences of partials in both kinds of inharmonic stimuli suggests that the auditory system has a broad definition of regularity when common spectral pattern is used as a basis for grouping.

The results of these studies of auditory fusion by common spectral pattern are based almost exclusively on subjective measures of perceptual segregation.[1] In particular, most of the experiments reported have used a clarity rating procedure, in which subjects heard on each trial a complex tone preceded by a pure tone of the same level and frequency as one of the components in the complex. Subjects were required to listen for the cued partial and to judge how clearly they could hear it on a rating scale. Interpreting data of this kind is not straightforward. The nature of the task, the response, and the design of the stimuli can all affect the validity of the procedure as a measure of perceptual segregation. These issues are considered in turn, and the basis for the design of the procedure used currently is discussed.

a)Electronic mail: b.roberts@bham.ac.uk

 0001-4966/98/103(6)/3588/9/$10.00

A. The validity of subjective methods

There is a strong tradition of using subjective methods for the study of auditory organization (see Bregman, 1990). For example, Anstis and Saida (1985) asked subjects to monitor and continuously report changes in the number of auditory streams they heard (1 or 2) when listening to an alternating sequence of pure tones of different frequency. Subjective measures have also been applied specifically to the perceptual segregation of partials from a complex tone. For example, Moore *et al.* (1986) studied the perceptual segregation of mistuned partials from an otherwise harmonic complex by explicitly asking the listeners whether or not they heard a mistuned partial as a separate perceptual entity.

A disadvantage of subjective measures is that their interpretation requires validation by indirect means. The usual approach is one of converging operations–broad agreement between results obtained using different subjective measures is taken to support a particular hypothesis (see Bregman, 1990). The original even–odd effect found for harmonic stimuli using the clarity method (Roberts and Bregman, 1991) has been validated in this way. Roberts and Bailey (1993b, experiment 2) presented subjects with complex tones, comprising the odd-harmonic base plus a single even harmonic, preceded by a pure tone matching the frequency of either the added even harmonic or one of its directly adjacent odd neighbors. Subjects were required to judge whether the harmonic that they heard out from the complex was lower, the same, or higher in pitch than the preceding pure tone. Pitch jumps towards the added even harmonic were often heard when the pure tone matched the frequency of one of its odd neighbors, despite the direct correspondence in frequency with the preceding pure tone. In contrast, ''same'' judgments were always dominant when the pure tone matched the even harmonic. This indication that the added even harmonic had a high perceptual salience, even when its odd neighbors were cued, supports the original finding of the clarity method (Roberts and Bregman, 1991). However, the need for such indirect means of validation could be avoided if a performance measure of segregation were devised that provided objectively verifiable responses.

B. The interpretation of differences in clarity ratings

The validation by other subjective methods of the clarity procedure as a measure of perceptual segregation does not solve the problem of interpreting *differences* in clarity ratings. Roberts and Bailey (1993a, 1993b, 1996a, 1996b) used a rating scale ranging from 1 (least clear) to 7 (most clear). It cannot be assumed that this scale maps linearly onto sensation. For example, a compressive nonlinearity in the use of the scale would mean that the perceptual distance between ratings of 5 and 6 was greater than that between 3 and 4. Hence, even–odd clarity differences may not be directly comparable across conditions when they derive from different parts of the rating scale. In practice, this has not proved a severe limitation in interpreting the results obtained (see, e.g., Roberts and Bailey, 1996a, experiment 1), but a measure for which it was safer to assume an approximately linear mapping between sensation and response would avoid this problem. Subject to the assumptions of signal detection theory (Green and Swets, 1974), the development of a d' measure of perceptual salience would achieve this aim. Such a measure of discriminability also has the advantage of being easy to interpret and to compare across experiments.

C. Differentiating the effects of resolution and segregation

Frequency resolution and perceptual segregation are neither synonymous nor independent processes (see, e.g., Hartmann *et al.*, 1990). Since both of these factors will affect the ability to hear out a component from a complex, the design of the stimuli and the task need careful consideration to optimize the measurement of one or other process. Studies of component resolution typically attempt to optimize the conditions for analytical listening. For example, Plomp (1964) asked subjects to judge which of two pure tones had the same frequency as one of the components in a complex tone when allowed to switch freely between the stimuli. This method repeatedly cued the frequency region in the complex that should be attended in order to make the decision. Extensive training and the use of feedback on performance can also help to optimize analytical listening. In contrast, perceptual segregation implies an immediate salience, or ''attention capturing'' quality, of a partial that should not need to be encouraged by the techniques used to study resolution.

The clarity rating method was designed to favor the measurement of segregation by restricting access to the stimuli within each trial (no repeated listening), by using subjects with limited training, and by not providing feedback on performance. However, analytical listening was still assisted by preceding the complex with a pure tone, which cued the appropriate frequency region. What is required to optimize the measurement of segregation is a task that estimates the salience of a target component when it is uncued, as the response obtained will then depend primarily on the inherent tendency of the component to ''pop out'' from the complex, and hence capture the attention of the listener. This can be achieved by reversing the order of the pure tone and the complex, so that the listener only knows the target frequency region in the complex after it has been heard.

I. EXPERIMENT 1

The purpose of this experiment was to employ a new method in a reinvestigation of differences in relative perceptual salience between a single even harmonic and its neighbors in a complex tone consisting otherwise only of odd harmonics. This method, designed in response to the issues raised in the Introduction, was a performance measure yielding d' scores for stimuli that did not cue the target components.

A. Method

1. Stimuli and conditions

A two-interval forced-choice (2IFC) procedure was employed. Each interval consisted of a complex tone followed by a pure tone, separated by a silent gap of 100 ms. The two intervals were separated by a silent interval of one second.

The standard form of the complex tone, the base, consisted of all odd harmonics of $F0$, up to and including harmonic 15. Four variants of the complex were derived from the base by adding a single even harmonic of $F0$: 2, 4, 6, or 8. There was no discernible change in the low pitch of the complex resulting from the addition of an even harmonic.

In one interval, the frequency of the pure tone was chosen to match that of one of the harmonics 1–9. In the other, the pure tone was mistuned from a match to the same harmonic number by a change in frequency of $\pm 0.5 \times F0$ frequency. There was an equal likelihood that the match to the target would occur in either of the two intervals. Hence for each harmonic number tested, there were four configurations of frequencies for the pure tones with respect to the targets in the two intervals: same-higher, same-lower, higher-same, or lower-same. When the pure tone in the matching interval corresponded to an odd harmonic, the complex tone used in each interval was the odd-harmonic base with no additional partials. When the pure tone in the matching interval corresponded to an even harmonic, the complex tone used in each interval was the base plus the appropriate even harmonic.

The order of the tones in each interval prevented within-interval cuing, but did not rule out the possibility that the pure tone in the first interval might cue the target component in the second interval. The use of a 1-s gap between the two intervals was expected to minimize this possibility, but a condition using cross-interval changes in $F0$ frequency was included as a further precaution. There were three conditions in all, and these differed in the $F0$ frequencies used to generate the complex tones. In conditions 1 and 3, the $F0$ frequencies were fixed at 100 and 150 Hz, respectively. In condition 2, the $F0$ frequency varied both across trials and also between intervals within a trial. The $F0$ frequency was chosen randomly from one of 11 values, ranging from 100 to 150 Hz in 5-Hz steps, but was constrained so that the complex tones in the two intervals within each trial always differed.

All stimuli were generated using MITSYN software (see Henke, 1990). The partials comprising the complex tones were in cosine phase and of equal amplitude (63 dB SPL), except for the $F0$ component, which was boosted in level to counteract the effects of decreased auditory sensitivity at low frequencies. These increases were 7.4 and 2.7 dB at 100 and 150 Hz, respectively.[2] The overall level of the odd-harmonic base used in condition 1 was about 74 dB SPL. The pure tones were presented at the same level as appropriate for the corresponding frequencies in the complex tones. For each interval, both the complex tone and the pure tone were presented for a duration of 440 ms, including linear onset and offset ramps of 20 ms each.

Stimuli were synthesized and played at a sampling rate of 16 kHz with a precision of 16 bits via a D/A converter (Data Translation DT2823). They were low-pass filtered (corner frequency=5.2 kHz, cutoff frequency=8.0 kHz) and presented binaurally over Sennheiser HD 480-13II earphones. The levels of the stimuli were set using a programmable attenuator (0.25-dB steps), and were calibrated with a sound-level meter (Brüel & Kjaer type 2209, linear weighting) connected to the earphones by an artificial ear (type 4153). The stimuli were presented to the listeners in a sound-attenuating chamber (Industrial Acoustics).

2. Task

Subjects were told that each trial consisted of two intervals, separated by a silence of one second, and that in each interval they would hear a sequence of two tones, separated by a brief silent gap. The first tone was described as ''rich'' in quality, and the second as ''pure'' in quality. Hidden in the rich tone was said to be a pure-sounding ''target'' tone, which had the same pitch as the subsequent pure tone in one interval, but not in the other. The subjects' task was to listen carefully to the two intervals and to identify the matching interval. They were told that the target might appear to ''stand out'' from the rich tone in some cases, making it easy to compare with the following pure tone, but that in other cases the comparison would be difficult. Subjects were also told that variations in the low pitch of the rich tone would occur in one of the conditions, but that these changes should be ignored. They were allowed to listen to each stimulus only once before choosing their response, and received no feedback of any kind. After each response, there was an interval of about 1 s before the next trial.

3. Procedure and subjects

The main experimental session was divided into three blocks of trials, corresponding to the three conditions used. Alternate subjects were run in the order of conditions 1-2-3 and 3-2-1. This was to ensure that the roving-$F0$ condition was preceded and followed by the two possible fixed-$F0$ conditions with equal likelihood. Within each block, the stimuli were presented as five repetitions. Each repetition consisted of a single presentation of 36 stimuli (9 harmonics$\times$4 configurations). The order of presentation within each of the five repetitions was randomized independently. The total number of stimuli presented to subjects during the main session was 540 (3 conditions$\times$36 stimuli$\times$5 repetitions). Subjects were free to rest at any time.

Twelve subjects participated, all of whom reported normal hearing. They were drawn, as available, from a panel of subjects who had successfully completed a screening procedure intended to ensure that they could perform the task according to the instructions given. In the first stage of the screening procedure, the $F0$ frequency of the complex tones was fixed at 100 Hz, and the order of the rich and pure tones was reversed within each interval. This made the task easier, as the pure tone could act as a cue to the frequency region of the complex that contained the target. To begin with, all 36 stimuli (9 harmonics$\times$4 configurations) were presented with repeated listening permitted before choosing a response. These stimuli were then presented again, but this time subjects were allowed to hear each stimulus only once before choosing a response. Finally, subjects were presented with three repetitions of these stimuli (108 trials), again without the option of repeated listening. An overall measure of performance was derived for this run of trials by collapsing across harmonic number. Subjects had to exceed 65% correct to enter the second stage of the screening. The second stage

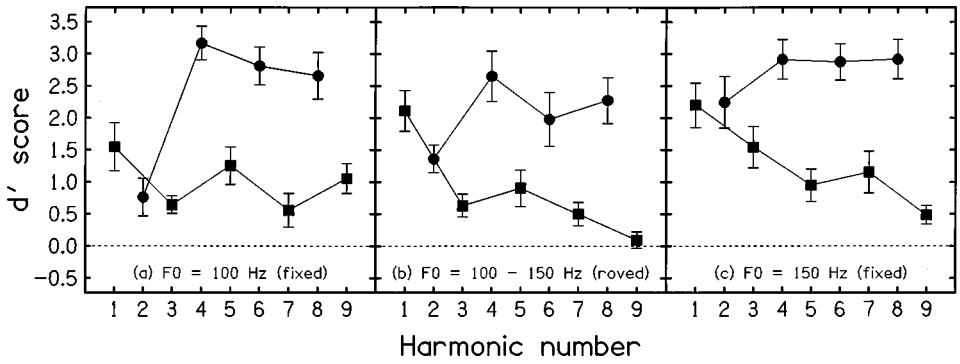

FIG. 1. Mean d' scores for 12 subjects (with between-subject standard errors). Parts (a)–(c) correspond to conditions 1–3 in experiment 1, respectively. Each part shows the scores across harmonic numbers 1–9. The scores for odd and even harmonic numbers are represented by filled squares and filled circles, respectively.

was like the first, except that the order of the rich and pure tones was returned to that used in the main session. Subjects had to exceed 60% correct to join the subject panel. This more lenient criterion reflected the greater difficulty of the task. About 70% of the subjects tested passed both stages of the screening.

Immediately before each block of trials in the main session, subjects were given a short practice run to help stabilize their performance. The practice run consisted of two repetitions of each stimulus in the experimental set. Repeated listening was permitted only during the first repetition.[3]

4. Data analysis

Each subject made a total of 20 responses per harmonic (5 repetitions×4 configurations) for each condition in the main session. These responses were used to derive d' scores as a linear, bias-free, measure of discrimination. Since d' cannot be calculated when there are no false alarms or misses, zero scores were adjusted according to the formula used by Macmillan and Creelman (1991, Appendix 6). For each harmonic in each condition, the d' scores were then averaged across subjects. Furthermore, an even–odd d' difference was computed for each condition by subtracting the mean d' score for the five odd harmonics tested from the mean d' score for the four even harmonics tested.

B. Results

The results are displayed in Fig. 1. The significance of changes in d' across harmonic number was assessed using a separate repeated-measures analysis of variance (ANOVA) for each condition. A planned comparison of d' scores for the odd (base) and the even (added) harmonics was achieved using a contrast within the harmonic number factor.

A highly significant effect of harmonic number on accuracy of performance was found for all three conditions [(1): $F(8,88)=15.13$, $p<0.0001$; (2): $F(8,88)=12.25$, $p<0.0001$; (3): $F(8,88)=12.55$, $p<0.0001$]. Moreover, the planned comparison between the odd and the even harmonics showed that the difference in d' between these two sets of partials was also highly significant in all cases [(1): $F(1,11)=35.32$, $p<0.0001$; (2): $F(1,11)=19.48$, $p=0.001$; (3): $F(1,11)=49.19$, $p<0.0001$]. These results indicate that, in all conditions, the single even harmonic was generally more salient perceptually than its odd neighbors. This outcome supports the findings of Roberts and his colleagues using clarity ratings (Roberts and Bregman, 1991; Roberts and Bailey, 1993a, 1993b, 1996a, 1996b).

The finding of an almost absent even–odd difference between harmonic 2 and its immediate odd neighbors, evident in all conditions, also confirms previous findings. Roberts and Bailey (1996b) noted that harmonic 2 was both an octave above the $F0$ component and at a frequency equal to the difference frequency between the base components, either of which might have been important factors. A difference from earlier studies using clarity ratings can be seen for the odd harmonics tested. Clarity ratings typically showed a rise in clarity with increasing odd-harmonic number, whereas the tendency here was for d' scores to fall with increasing odd-harmonic number. This was most apparent in condition 2, where the possibility of cross-interval cuing was reduced by roving the $F0$ frequency. In this condition, d' fell from 2.1 for harmonic 1 to 0.1 for harmonic 9. In contrast, d' scores for the even harmonics tended to remain relatively high and stable across harmonics 4, 6, and 8.

The mean even–odd d' differences (with between-subject standard errors) for conditions 1–3 were 1.337 (0.225), 1.218 (0.276), and 1.470 (0.210), respectively. These means were not significantly different [$F(2,22)=1.02$, $p=0.377$]. This indicates that a change in $F0$ frequency in the range 100–150 Hz, whether fixed or roving, had little effect on the magnitude of the even–odd difference.

C. Discussion

The principal finding of this experiment is that the main observation of Roberts and his colleagues using subjective measures like clarity rating (Roberts and Bregman, 1991; Roberts and Bailey, 1993a, 1993b, 1996a, 1996b) has been confirmed using the new accuracy of performance measure. Specifically, the d' difference between the even and odd harmonics supports their conclusion that an added even harmonic in an otherwise odd-harmonic complex tends to stand out from the complex, relative to its odd-harmonic neighbors. Furthermore, these data are consistent with the idea that

it is easier to segregate a harmonic from a periodic complex tone when it is not part of the regular pattern of spectral spacing defined by the other harmonics.

The fixed-$F0$ conditions (1 and 3) could have been affected by cross-interval cuing. On a given trial, the pure tone in the first interval might have been used to listen for a matching harmonic of the rich tone in the second interval. The use of this strategy would be expected to reduce the effect of uncued perceptual salience on task performance, and thereby to reduce the even–odd difference. This was not the case, as the magnitude of the even–odd difference did not increase in the roving-$F0$ condition (2), for which cross-interval cuing was a less useful strategy.[4] It seems likely that the 1-s gap between the two intervals was enough to discourage cross-interval cuing in the fixed-$F0$ conditions. The modest decline in overall performance in condition 2 may reflect the increased stimulus uncertainty for the listener introduced into the task by roving the $F0$ frequency.

Studies of frequency resolution have shown that the ability to resolve a partial from a complex tone comprising successive harmonics declines with an increase in harmonic number (Plomp, 1964, 1976). There is no abrupt transition from resolved to unresolved partials with increasing harmonic number, but the average number of harmonics resolved for an $F0$ of 100 Hz is around seven (Plomp and Mimpen, 1968). The decline in d' scores typically observed across the odd harmonics 1–9 is consistent with frequency resolution acting as one of the factors limiting performance in this task for these harmonics.[5] A related factor that may have contributed to this response profile is the reduction in the discriminability of frequencies corresponding to the matching and nonmatching pure tones as harmonic number increases. This is because the frequency separation between them ($\pm 0.5 \times F0$) was constant across harmonic number on a linear rather than a logarithmic scale. Roberts and Bailey (1993b) explained the rise typically seen for clarity ratings across the odd harmonics tested as an artifact of the change in subjective quality of the components from dull to bright with increasing frequency. Their pilot work with isolated pure tones had shown that subjects tended to report tones with a bright timbre as clearer than tones of similar loudness but with a dull timbre.

The pattern of performance for the even harmonics is not as expected if frequency resolution were the limiting factor. Rather, the high and sustained level of accuracy for even harmonics 4–8 indicates that these components were highly salient despite the absence of a preceding pure tone to cue them.[6] Furthermore, in the context of the experiment, the odd harmonics had a resolution advantage over the even harmonics, because each even harmonic was tested in the presence of its odd neighbors, but each odd harmonic was tested in the absence of its even neighbors. Clearly, the best resolved components in a complex tone need not be the most salient.

II. EXPERIMENT 2

It has already been noted that the even–odd differences in d' found in experiment 1, like those reported for clarity in earlier studies, were obtained by comparing judgments of even and odd harmonics tested in different stimulus contexts. Our interpretation of the even-odd d' difference would be in doubt if, for example, it turned out that the addition of a single even harmonic to an odd-harmonic complex increased the tendency for its odd neighbors to be heard out. A finding of Roberts and Bailey (1993b, experiment 2), discussed in Sec. A of the Introduction, suggests that this does not happen. These authors demonstrated that an added even harmonic could often perceptually capture a preceding pure tone that was equal in frequency to one of the adjacent odd harmonics. However, it is important to confirm this using a performance measure rather than a subjective one. It is also of interest to extend the range of harmonics tested in order to discover whether or not a large even–odd difference is maintained beyond harmonic 8, where the potential effects of limitations on frequency resolution become more pronounced.

A. Method

1. Stimuli and conditions

The stimuli were the same as those used in experiment 1, except where specified. In no case was the odd-harmonic base heard in isolation, rather all complex tones consisted of the base plus a single even harmonic. Hence, unlike before, both odd and even harmonics were tested using the same complex tones. Furthermore, the added even harmonic was either 2, 4, 6, 8, 10, or 12, which served to extend the range of harmonic numbers tested from 1–9 to 1–13. Harmonic 14 was not included, as the edge pitch (Kohlrausch and Houtsma, 1992) expected for harmonic 15, the highest in the complex, would have affected the apparent even–odd difference. For each of the six types of complex tone derived from the base, the added even harmonic and the two immediately neighboring odd harmonics were tested. Hence, harmonics 3, 5, 7, 9, and 11 were each judged in the context of two types of complex, depending on the component number of the added even harmonic. In all cases, the $F0$ frequency used to generate the complexes varied both within and across trials in the range 100–150 Hz, as for condition 2 in experiment 1.

2. Procedure and subjects

Twelve subjects from the panel of listeners took part, of whom five were also subjects in experiment 1. The task used was the same as before. A short practice session was given immediately prior to each block in the main session.

The main session was divided into six blocks of trials, corresponding to the six odds-plus-even complex tones used. The presentation order of these blocks was counterbalanced using a 6×6 Latin square. Within each block, the stimuli were presented as five repetitions. Each repetition consisted of a single presentation of 12 stimuli (3 harmonics$\times$4 configurations), giving a grand total of 360 trials for the experiment (6 blocks$\times$12 stimuli$\times$5 repetitions). Even–odd differences in d' were calculated separately for each block of trials (by subtracting the mean d' score for the odd-harmonic neighbors from the d' score for the even harmonic).

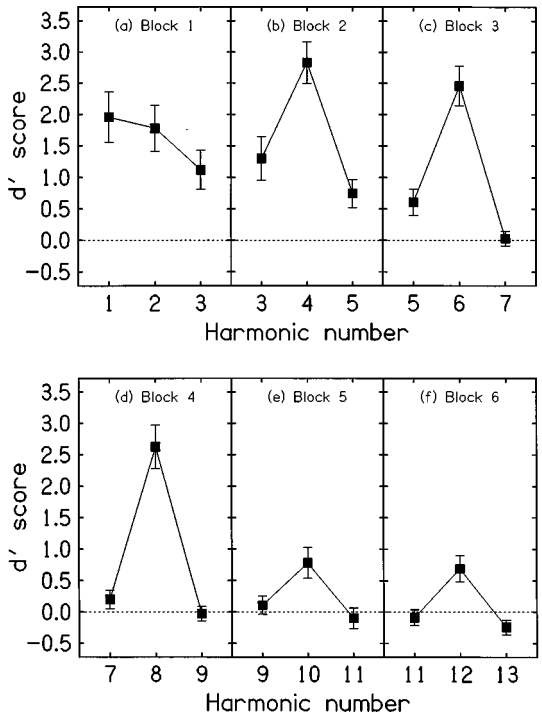

FIG. 2. Mean d' scores for 12 subjects (with between-subject standard errors). Parts (a)–(f) correspond to blocks 1–6 in experiment 2, respectively. Each part shows the scores for the appropriate added even harmonic and the immediately adjacent odd harmonics.

B. Results

The results are displayed in Fig. 2. The mean even–odd d' differences (with between-subject standard errors) for blocks 1–6 were 0.243 (0.335), 1.810 (0.293), 2.142 (0.343), 2.540 (0.406), 0.778 (0.341), and 0.859 (0.298). The added even harmonics for blocks 1–6 were 2, 4, 6, 8, 10, or 12, respectively. One-sample t tests showed that the even–odd differences were significantly different from zero, except when harmonic 2 was added to the complex [(1): $t(11)=0.73$, $p=0.480$; (2): $t(11)=6.19$, $p<0.0001$; (3): $t(11)=6.24$, $p<0.0001$; (4): $t(11)=6.26$, $p<0.0001$; (5): $t(11)=2.28$, $p=0.044$; (6): $t(11)=2.88$, $p=0.015$]. The variation in even–odd differences across blocks was examined by a repeated-measures ANOVA. A highly significant effect of block number was found [$F(5,55)=10.00$, $p<0.0001$]. Pairwise comparisons (Tukey's HSD test) between those blocks with significant even–odd differences (2–6) showed those values to be significantly different between blocks 3 and 5 [1.364, $p<0.01$], blocks 3 and 6 [1.283, $p<0.05$], blocks 4 and 5 [1.762, $p<0.01$], and blocks 4 and 6 [1.681, $p<0.01$]. None of the other comparisons made were significant.

C. Discussion

The results indicate that, except for harmonic 2, the single even harmonic was more salient perceptually than its odd neighbors when odd and even harmonics were tested in the same spectral context. While differences in the subjects used make it difficult to make detailed comparisons with experiment 1, there is certainly no evidence that the change in testing context has reduced the magnitude of the even–odd difference.

The tendency was for d' scores to fall gradually with increasing odd-harmonic number, again reflecting a decline in resolution with increasing harmonic number. The point at which d' scores fell to chance was slightly different from that seen in experiment 1, harmonic 7 here as opposed to harmonic 9 in experiment 1. This is probably also a result of differences in component resolution, since the odd harmonics were tested in the presence of a neighboring even harmonic here, but not in experiment 1. As for experiment 1, d' scores for the even harmonics remained relatively high and stable across harmonics 4, 6, and 8. However, the extension of the range of harmonic numbers tested has shown a marked decline in d' scores for even harmonics above 8, perhaps the result of resolution limitations becoming the dominant factor governing performance.

III. EXPERIMENT 3

After experiments 1 and 2 were completed, another concern arose with regard to a possible confound in the interpretation of those experiments. A subject who had taken part in both experiments, and also in some of our pilot work using similar stimuli, reported that he had become aware of a difference between the two task intervals that was correlated with which of them contained the matching pure tone. Specifically, the musical interval heard between the low pitch of the complex and the pitch of the following pure tone often sounded flatter or sharper in the task interval containing the mismatch than in the task interval containing the match. Since the even harmonics generally form simpler musical intervals with the $F0$ frequency than do the odd harmonics, the use of this cue might have resulted in more accurate performance for the even harmonics and hence led to an artifactual even–odd difference. Although an effect of this kind was not evident for clarity ratings of partials in successive-harmonic complexes (Roberts and Bailey, 1993b, experiment 1), the different nature of the tasks does not guarantee an absence of musical effects here. Therefore a listener with extensive musical experience was tested informally on the 2IFC task using successive-harmonic complexes, and some evidence was found for an even–odd difference. It was then decided to run a further experiment using new, musically inexperienced subjects whose exposure to the stimuli was restricted solely to the screening procedure, and to include a successive-harmonic condition to provide a measure of any even–odd artifact that might still occur.

Roberts and Bailey (1996b) used the clarity rating method to explore whether or not the effects of spectral pattern on auditory grouping were restricted solely to complex tones with harmonically related partials. In their first experiment, they employed a manipulation of the spectrum designed to change a complex tone from harmonic to inharmonic while preserving the equal spacing of the partials. Following de Boer (1956, 1976), this was achieved by adding a constant increment to the frequency of each component of a harmonic stimulus so as to create a frequency-shifted stimulus. Roberts and Bailey (1996b) found that an added even component could still be heard out from an odd-component complex more easily than its odd neighbors for these frequency-shifted stimuli. Hence the other aim of this

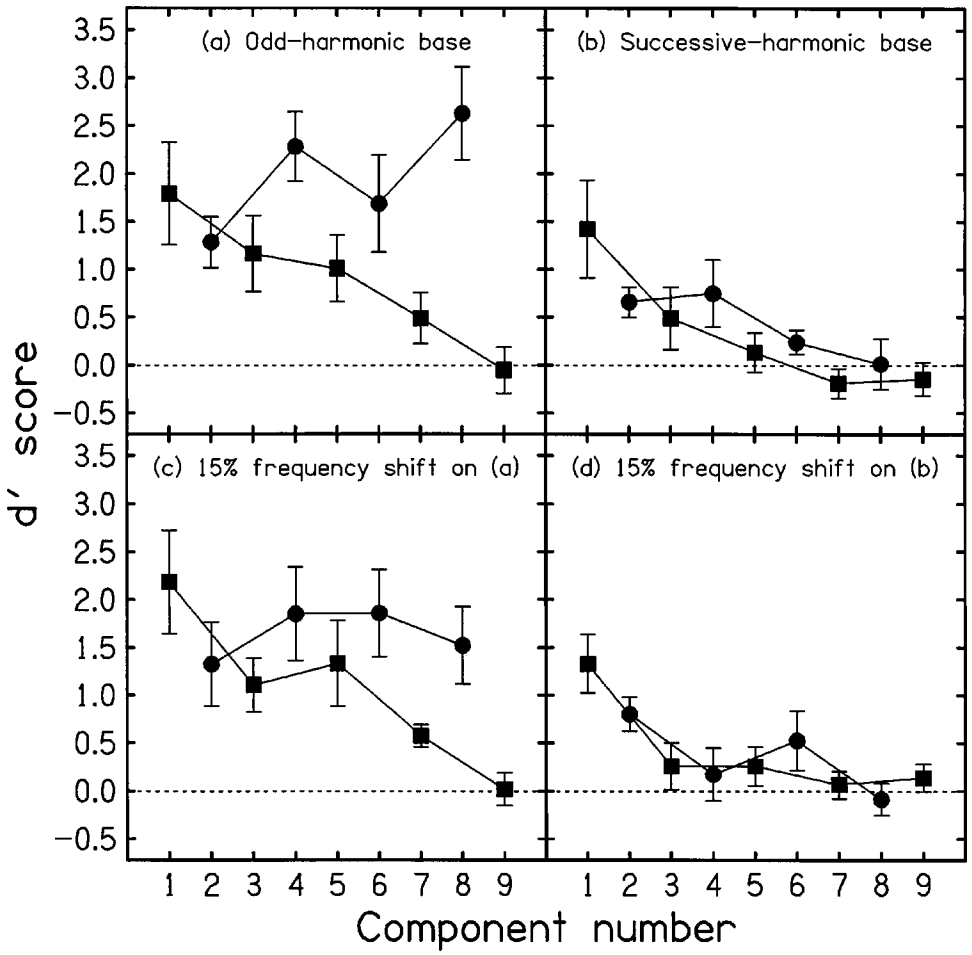

FIG. 3. Mean d' scores for 8 subjects (with between-subject standard errors). Parts (a)–(d) correspond to conditions 1–4 in experiment 3, respectively. Each part shows the scores across component numbers 1–9. The scores for odd and even component numbers are represented by filled squares and filled circles, respectively.

experiment was to confirm this effect using a performance measure. The finding of an even–odd d' difference for such stimuli would also be difficult to explain in terms of musical cues, thus providing an additional control. For completeness, a fourth condition was included that used frequency-shifted successive-component complexes.

A. Method

1. Stimuli and conditions

The stimuli were the same as those used in experiment 1, except where specified. There were four conditions, for all of which the $F0$ frequency varied between intervals and trials in the range 100–150 Hz. Condition 1 served as a reference condition, as the complex tones used were identical to those of condition 2 (roving $F0$) in experiment 1. In condition 2, the odd-harmonic base was replaced by a base consisting of all successive harmonics 1–15 of $F0$. There were no variants of the complex derived from the base, as it included all of the harmonics tested (1–9). The complex tones used in conditions 3 and 4 were frequency-shifted equivalents of those used in conditions 1 and 2, respectively. The frequency shift used was 15% of $F0$ (e.g., 15 Hz added to the frequency of each component of a complex with an $F0$ frequency of 100 Hz). The frequencies of the pure tones used, both matching and mistuned, were transformed in the same way. The use of component numbers for these stimuli is analogous to its use in the harmonic case. Similarly, the $F0$ frequencies used to describe these stimuli are nominal. Based on its transformed frequency, the level of the $F0$ component was adjusted as described in experiment 1.

2. Procedure and subjects

Eight subjects from the panel of listeners took part, none of whom had taken part in either experiment 1 or 2. The basis of this selection was to minimize the acquisition of secondary cues to the task based on judgments of the musical interval formed by the low pitch of the complex tone and the pitch of the subsequent pure tone. The main session was divided into four blocks of trials, corresponding to the four conditions. The presentation order of these blocks was counterbalanced using a 4×4 Latin square. The grand total for the main session was 720 trials (4 conditions×9 components×4 configurations×5 repetitions). As before, a short practice session was given immediately prior to each block.

B. Results

The results are displayed in Fig. 3. The analysis was the same as for experiment 1.

A significant effect of component number on accuracy of performance was found for all four conditions [(1): $F(8,56)=9.58$, $p<0.0001$; (2): $F(8,56)=4.15$, $p=0.0006$; (3): $F(8,56)=6.17$, $p<0.0001$; (4): $F(8,56)=6.00$, $p<0.0001$]. However, the planned comparison between the odd- and the even-numbered components showed that the difference in d' between these two sets was significant for conditions 1 and 3 [(1): $F(1,7)=27.52$, $p=0.0012$; (3): $F(1,7)=9.33$, $p=0.0185$], but not for conditions 2 and 4 [(2): $F(1,7)=0.09$, $p>0.5$; (4): $F(1,7)=0.22$, $p>0.5$]. The mean even–odd d' differences (with between-subject standard errors) for conditions 1–4 were 1.090 (0.208), 0.073 (0.241), 0.597 (0.195), and −0.057 (0.120), respectively. These means were significantly different [$F(3,21)=8.85$, $p=0.0005$]. Pairwise comparisons (Dunnett's test) showed significant differences between condition 1 (control mean) and two of the other conditions [condition 1 vs 2=1.017, $p<0.01$; 1 vs 3=0.493, $p>0.05$; 1 vs 4=1.147, $p<0.01$]. The results indicate that the relatively high perceptual salience of the even-numbered components was restricted to those conditions in which only one of these components was added to a regular odd-component base (conditions 1 and 3). There was no even–odd difference when the even-numbered components tested were part of a base comprising consecutive components (conditions 2 and 4). As before, d' scores tended to decline with increasing component number for the odd-numbered components, suggesting a resolution limitation on performance. Performance for the even components was generally consistent with this pattern in conditions 2 and 4.

C. Discussion

The outcome supports Roberts and Bailey's (1993b, experiment 1) finding that the even–odd clarity difference was abolished when the even harmonics were tested as part of a successive-harmonic base. Furthermore, the finding of a significant even–odd difference for the odds-plus-even complexes when they were frequency-shifted (condition 3) is consistent with Roberts and Bailey's (1996b, experiment 1) finding for clarity ratings of similar stimuli. However, the results of these experiments differ in some respects. For example, the size of the even–odd clarity difference was maintained when harmonic complexes were transformed into frequency-shifted complexes, whereas the even–odd d' difference observed here was only a little over half of that found in the equivalent harmonic condition, although this difference between the conditions was not significant statistically. Furthermore, there is no equivalent here to the general rise in clarity ratings seen for the lower components when the complexes were frequency shifted. Roberts and Bailey (1996b) interpreted their finding as a result of the greater deviation from harmonic relations for the lower components in frequency-shifted complexes leading to a reduction in their perceptual cohesion. Another difference is that the even–odd clarity difference for component 2 and its odd neighbors, almost absent in the harmonic condition, became apparent for the frequency-shifted stimuli. An equivalent change in d' was not found here. The reason for this is unclear, but it casts doubt on the suggestion earlier that the near-absent even–odd difference for harmonic 2 resulted either from its octave relation to the $F0$ component or from the equality of its frequency with the difference frequency between the partials of an odd-harmonic complex.

The significant even–odd d' difference observed in condition 3 cannot be explained in terms of cues based on musical intervals. Rather, the finding supports Roberts and Bailey's (1996b) conclusion that the pattern of spectral spacing influences auditory grouping in regular inharmonic complexes as well as in harmonic complexes. If musical cues were responsible for the greater size of the even–odd difference observed in condition 1, then one would also expect to see clear evidence of an even–odd difference for the successive-harmonic stimuli used in condition 2. However, the results for condition 2 were primarily similar to those for their frequency-shifted counterparts in condition 4. It would appear that the use of subjects with limited exposure to the stimuli employed here, and without extensive musical experience, can minimize the possible confounding effects of musical cues on the results. As a precautionary measure, it may in the future prove prudent to include successive-harmonic stimuli as a control for musical confounds in studies that require greater exposure of the subjects to stimuli of the kind used here.

IV. SUMMARY AND CONCLUDING DISCUSSION

The performance measure used in the experiments reported here has confirmed the effect of spectral pattern on the perceptual integrity of a harmonic series, demonstrated previously using a clarity rating procedure (Roberts and Bregman, 1991; Roberts and Bailey, 1993a, 1993b). Subjects were generally better able to judge the frequency of an uncued even harmonic than that of its neighbors in an otherwise odd-harmonic complex, whether they were tested in the same spectral context (experiment 2) or not (experiments 1 and 3). Experiment 2 extended the range of harmonics tested, and showed that the even–odd difference was most prominent for even harmonics 4, 6, and 8, with a marked decline in magnitude for higher or lower components. The procedure used has shown that the even–odd difference in perceptual salience can be substantial, peaking at a mean d' difference of over 2.5 for harmonic 8 and its odd neighbors in experiment 2. These differences in discriminability cannot be explained in terms of frequency resolution.

The possible confounding effects on performance of musical cues were considered in the design of experiment 3. In particular, it was thought possible that differences in the simplicity of the musical interval formed between the low pitch of the complex tone and the pitch of a pure tone corresponding either to an even- or an odd-harmonic frequency might account for the even–odd difference found for odds-plus-even harmonic complexes. However, the absence of a significant even–odd difference for successive-harmonic complexes suggested that the apparent effect of spectral spacing on harmonic fusion was not an artifact. Furthermore, experiment 3 has also confirmed the finding of Roberts and Bailey (1996b, experiment 1) that the even–odd difference persists when odds-plus-even harmonic stimuli are transformed into

regular but inharmonic stimuli using a frequency-shift manipulation (de Boer, 1956, 1976).

Roberts and Bailey (1996b) interpreted their results as evidence that the auditory system is sensitive to the spectral pattern of inharmonic complex tones as well as of harmonic ones, but noted that the possible role of such a mechanism in auditory scene analysis (Bregman, 1990) remains unclear. Roberts and Brunstrom (1998) consider further the suggestion of grouping by common spectral pattern, by exploring the perceptual effects of mistuning components in both harmonic complexes and in regular inharmonic complexes. To conclude, the experiments reported here indicate that the procedure used can provide a useful performance measure of the relative perceptual saliences of partials in a complex tone.

ACKNOWLEDGMENTS

This research was supported in part by Research Grant 6/SO4782 from the Biotechnology and Biological Sciences Research Council (UK). My thanks go to Peter Bailey, Al Bregman, Jeff Brunstrom, Rhodri Cusack, Mark Georgeson, and Mike Harris for their valuable assistance, advice, and criticism. I am grateful to Rajeev Desai, Richard Freeman, and Andrew Parton for their assistance in the recruitment and testing of subjects. My thanks also go to Alain de Cheveigné and the two anonymous reviewers for their comments on an earlier version of this manuscript.

[1]The one exception was a task tried by Roberts and Bregman (1991) in which listeners were required to judge the pitch of a harmonic in a complex tone in relation to a preceding pure tune mistuned from the corresponding frequency by ±6%. This approach was abandoned in the subsequent studies of Roberts and Bailey (1993a, 1993b, 1996a, 1996b) owing to limitations of the design, particularly an increasing ambiguity over which component number was the target for the higher harmonics tested and ceiling effects for the lower harmonics tested.

[2]The correction was based on the 70-phon equal-loudness contour, published in ISO recommendation 226: 1987 (E). It was applied to frequencies below 200 Hz, relative to 200 Hz.

[3]Since repeated listening to the stimuli might have encouraged analytical listening, the opportunity was kept as limited as possible while ensuring that it was sufficient to help stabilize the performance of subjects in the main experiment. In practice, many subjects made little use of the opportunity beyond the first few trials.

[4]Roving $F0$ frequency in the range 100–150 Hz did not entirely rule out the possibility of cross-interval cuing. While the first pure tone could no longer be compared directly with the components of the second complex tone, it may have provided some useful information about which frequency region to attend in the second complex tone for subsequent comparison with the second pure tone. The usefulness of this cue would have been greatest when the cross-interval difference in $F0$ frequencies on any trial was small, and when the low-numbered components were tested. Therefore the even–odd difference may have been underestimated in some instances.

[5]The near-chance performance for harmonic 9 in the roving-$F0$ condition indicates that frequency resolution was not the only limiting factor, because harmonic 9 in an odd-harmonic complex is better resolved than harmonic 5 in a successive-harmonic complex. This result is unsurprising given that the task was not designed to optimize analytical listening.

[6]The even harmonics were relatively novel in comparison with the odd harmonics, the full set of which were present on every trial. One of the reviewers has noted that the roving range for $F0$ was insufficient to rule out an effect of listening more often to certain spectral regions (encompassing the odd harmonics) than to other regions (encompassing the added even harmonics). Therefore it is possible that listeners tended to direct their attention to those spectral regions in the stimuli encompassing the more novel even harmonics, and that this tendency can account for their higher salience. While it is true that harmonics 3 and 4 were the lowest pair with overlapping frequency ranges, the extent of this overlap was considerable for harmonics 7–9. Given this, it is noteworthy that a comparison of the response profiles for the roving-$F0$ condition and the fixed-$F0$ conditions shows them to be as similar for the higher partials tested as for the lower ones. Moreover, the largest even–odd difference in the roving-$F0$ condition was for harmonic 8. Furthermore, the use of a greater roving range would not exclude the possibility that listeners learned something about the odd-harmonic base that generalized across $F0$ frequency. Roberts and Bailey (1993b) acknowledged this possibility for their clarity rating data, but noted that any learning of this kind would have to be rapidly acquired, because naive listeners typically showed evidence of even–odd differences after 100 trials or fewer.

Anstis, S., and Saida, S. (**1985**). ''Adaptation to auditory streaming of frequency-modulated tones,'' J. Exp. Psychol. **11**, 257–271.

Bregman, A. S. (**1990**). *Auditory Scene Analysis: The Perceptual Organization of Sound* (MIT, Cambridge, MA).

de Boer, E. (**1956**). ''On the 'Residue' in Hearing,'' Doctoral thesis, University of Amsterdam, The Netherlands.

de Boer, E. (**1976**). ''On the 'residue' and auditory pitch perception,'' in *Handbook of Sensory Physiology, Vol. 5*, edited by W. D. Keidel and W. D. Neff (Springer-Verlag, Berlin), pp. 479–583.

Duifhuis, H., Willems, L. F., and Sluyter, R. J. (**1982**). ''Measurement of pitch in speech: An implementation of Goldstein's theory of pitch perception,'' J. Acoust. Soc. Am. **71**, 1568–1580.

Green, D. M., and Swets, J. A. (**1974**). *Signal Detection Theory and Psychophysics* (Kreiger, New York).

Hartmann, W. M., McAdams, S., and Smith, B. K. (**1990**). ''Hearing a mistuned harmonic in an otherwise periodic complex tone,'' J. Acoust. Soc. Am. **88**, 1712–1724.

Henke, W. L. (**1990**). MITSYN: A coherent family of high-level languages for time signal processing [Software package] (Belmont, MA: Author).

Hermes, D. J. (**1988**). ''Measurement of pitch by subharmonic summation,'' J. Acoust. Soc. Am. **83**, 257–264.

Kohlrausch, A., and Houtsma, A. J. M. (**1992**). ''Pitch related to spectral edges of broadband signals,'' in *Processing of Complex Sounds by the Auditory System*, edited by R. P. Carlyon, C. J. Darwin, and I. J. Russell (Oxford U.P., Oxford, England), pp. 81–88.

Macmillan, N. A., and Creelman, C. D. (**1991**). *Detection Theory: A User's Guide* (Cambridge U.P., Cambridge, England).

Moore, B. C. J., Glasberg, B. R., and Peters, R. W. (**1986**). ''Thresholds for hearing mistuned partials as separate tones in harmonic complexes,'' J. Acoust. Soc. Am. **80**, 479–483.

Plomp, R. (**1964**). ''The ear as a frequency analyzer,'' J. Acoust. Soc. Am. **36**, 1628–1636.

Plomp, R. (**1976**). *Aspects of Tone Sensation* (Academic, London).

Plomp, R., and Mimpen, A. M. (**1968**). ''The ear as a frequency analyzer. II,'' J. Acoust. Soc. Am. **43**, 764–767.

Roberts, B., and Bailey, P. J. (**1993a**). ''Spectral pattern and the perceptual fusion of harmonics. I. The role of temporal factors,'' J. Acoust. Soc. Am. **94**, 3153–3164.

Roberts, B., and Bailey, P. J. (**1993b**). ''Spectral pattern and the perceptual fusion of harmonics. II. A special status for added components?'' J. Acoust. Soc. Am. **94**, 3165–3177.

Roberts, B., and Bailey, P. J. (**1996a**). ''Regularity of spectral pattern and its effects on the perceptual fusion of harmonics,'' Percept. Psychophys. **58**, 289–299.

Roberts, B., and Bailey, P. J. (**1996b**). ''Spectral regularity as a factor distinct from harmonic relations in auditory grouping,'' J. Exp. Psychol. **22**, 604–614.

Roberts, B., and Bregman, A. S. (**1991**). ''Effects of the pattern of spectral spacing on the perceptual fusion of harmonics,'' J. Acoust. Soc. Am. **90**, 3050–3060.

Roberts, B., and Brunstrom, J. M. (**1998**). ''Perceptual segregation and pitch shifts of mistuned components in harmonic complexes and in regular inharmonic complexes,'' J. Acoust. Soc. Am. (submitted).

Adaptation in the processing of interaural time differences revealed by the auditory localization aftereffect[a)]

Makio Kashino[b)] and Shin'ya Nishida
Information Science Research Laboratory, NTT Basic Research Laboratories, 3-1, Morinosato Wakamiya, Atsugi, Kanagawa 243-0198, Japan

(Received 25 February 1997; revised 10 September 1997; accepted 2 March 1998)

Two experiments were conducted involving the auditory localization aftereffect, in which the perceptual lateralization of a test sound having an interaural time difference (ITD) shifts away from that of a prior adapting sound having a different ITD. First, the frequency selectivity of the aftereffect was examined for sinusoids presented through headphones, with various combinations of adapter and test frequencies below 800 Hz, using the method of constant stimuli. The magnitude of the aftereffect was found to be largest when the frequencies of the two tones were similar, and virtually disappeared at a frequency difference of one-half octave. Second, the ITD selectivity of the aftereffect was examined for 400-Hz sinusoids. Subjects' judgments of lateralization were measured directly in terms of the perceived azimuth of the test tone for various combinations of adapter and test ITDs in the range of ± 625 μs. The magnitude of the aftereffect was found to be largest when adapter and test ITDs differed by approximately 250 μs. These results were successfully simulated by an interaural cross-correlation model having gain control. The results are consistent with the idea that the gain of ITD-selective units, located after binaural interaction but before across-frequency integration, is changed by recent input. © *1998 Acoustical Society of America.* [S0001-4966(98)03806-5]

PACS numbers: 43.66.Pn, 43.66.Qp, 43.66.Mk [RHD]

INTRODUCTION

This paper describes two experiments involving the auditory localization aftereffect, performed to investigate processing channels in the auditory system and their dynamic adaptation during auditory spatial processing. The aftereffect involves shifts in the apparent location of a test sound following prolonged exposure to an adapting sound. The aftereffect was initially reported in 1920's, but has been the subject of only a few studies (Flügel, 1920–1921; Bartlett and Mark, 1922–1923; James, 1936; Békésy, 1960; Thurlow and Jack, 1973). It has been shown that the displacement of the test sound is away from the adapter. It has also been shown that the localization aftereffect can be produced not only by an adapting sound that has only an interaural level difference (ILD), but also by an adapting sound that has only an interaural time difference (ITD) (Thurlow and Jack, 1973). However, the nature of the localization aftereffect remains largely unclear, and no effort has been made to interpret the aftereffect in relation to the mechanisms of binaural processing.

We revisited the localization aftereffect for two reasons. First, we expected that the localization aftereffect would provide useful tools to analyze perceptual processing channels and their interaction in auditory spatial processing. The usefulness of aftereffects as a psychophysical tool has been proven in the study of vision, where various aftereffects have been known for years. For instance, apparent shifts in spatial frequency or orientation provide convincing evidence for the existence of processing units (or channels) in the early stages of visual processing, each selectively tuned to a certain range of spatial frequencies and orientations (Blakemore and Sutton, 1969; Coltheart, 1971). The selectivity of aftereffects, as well as that of visual masking, has been widely used to measure the tuning of such processing channels. In hearing, on the other hand, it is primarily masking that has been used to analyze processing channels, and only a few studies have measured aftereffects (Kay and Matthews, 1972; Green and Kay, 1974; Regan and Tansley, 1979; Tansley and Suffield, 1983; Grantham, 1989; Shu *et al.*, 1993). Electrophysiological studies have shown that ITDs and ILDs are extracted separately in channels that are frequency selective at early levels of binaural interaction. Neurons selectively tuned to specific ITDs have been found in the brainstem nuclei of some animals such as the owl (Carr and Konishi, 1990) and the cat (Yin and Chan, 1990). However, direct evidence for the existence of such mechanisms in the human auditory system has been lacking, due in part to the difficulty of physiological measurements. One of our purposes is to determine if the selectivity of the auditory localization aftereffect is consistent with the idea that there are ITD-selective units in the human auditory system.

The second reason we revisited the localization aftereffect is that it represents dynamic adaptation in auditory spatial processing. Recently, there is increased interest in the perception of spatially dynamic sounds, as exemplified in the study of binaural sluggishness and the precedence effect (for review, Grantham, 1995). However, dynamic changes in the mechanisms responsible for spatial perception have been paid little attention, except for a series of studies by Hafter and his colleagues (Hafter *et al.*, 1988). They found that, in the ITD detection task for click trains, information from

[a)]Portions of this research were presented at the 131st meeting of the Acoustical Society of America.
[b)]Electronic mail: kashino@av-hp.brl.ntt.co.jp

 0001-4966/98/103(6)/3597/8/$10.00

later-arriving portions becomes progressively less effective when information is presented at high rates. At a glance, this may seem to be a loss of information, but Hafter *et al.* (1988) pointed out that ''binaural adaptation'' may prevent the perceptual system from being overloaded by redundant directional information. Also in vision, we can find many examples in which adaptation promotes efficient information processing in the real world. For instance, light adaptation improves the effective resolution of brightness using sensors which have a limited dynamic range, by shifting the operation point according to the recent brightness distribution in the environment (Werblin, 1973). Barlow (1990) argues that adaptation reduces redundancy in sensory messages and makes the system specially sensitive to new associations. We thought that dynamic adaptation in sound localization may also play an important role in efficient directional information processing, and the existence and nature of such adaptation could be revealed by the localization aftereffect. If correct, then models of auditory spatial processing should incorporate the mechanisms that underlie adaptation.

To clarify the nature of the localization aftereffect, we examined how the magnitude and direction of the aftereffect depend on the frequency relationship and the ITD relationship between the adapter and test sound in experiments 1 and 2, respectively. To best focus on the mechanisms processing ITDs, we used sinusoids presented through headphones with frequencies below 800 Hz, where ITDs of ongoing waveforms act as a major determinant of the perceptual lateralization of tones. We found that the aftereffect shows strong frequency selectivity comparable to that of auditory filters, and that the aftereffect is largest when the two tones are separated by an ITD of around 250 μs. The psychophysical results were then successfully simulated using an interaural cross-correlation model with a newly introduced gain control function. These results are consistent with the idea that there are neural channels that have selectivity both in ITD and in frequency in the human auditory system, and that changes in the sensitivity of such channels produce the localization aftereffect.

I. EXPERIMENT 1: FREQUENCY SELECTIVITY OF THE LOCALIZATION AFTEREFFECT

A. Method

We measured the magnitude of the aftereffect with various combinations of adapter and test frequencies. Psychometric functions were obtained for left–right judgment of test using the method of constant stimuli, with and without adaptation. The shift of the psychometric function between the adaptation and no-adaptation conditions corresponds to the magnitude of the aftereffect.

In each adaptation session, an initial adapter tone having an ITD (either -375 or 375 μs; Positive values indicate that the right-ear signal leads) was presented for 60 s, followed by a 0.25-s test tone. The ITD of the test tone was chosen randomly on each trial from the five values (-250, -125, 0, 125, or 250 μs). Subjects' task was to judge whether the test tone was perceived at the left or right in a two-alternative forced-choice paradigm. Following each test tone (1 s after the offset of each test tone), the adapter tone was presented again for 5 s to reinforce the adaptation. This time pattern of adaptation (60-s initial adaptation and 5-s adaptation between trials) was determined based on informal observations of conditions required to obtain a stable aftereffect throughout the session. The adapter frequency was either 200, 283, 400, 566, or 800 Hz, and the test frequency was either 283, 400, or 566 Hz. The frequency combination was fixed throughout a session. In no-adaptation sessions, the adapter tones were replaced with the same duration of silence. Twenty measurements were conducted for each data point per subject. The proportion of ''right'' responses was obtained as a function of test ITD for each frequency combination.

To ensure that the aftereffect reflects binaural processing of ongoing ITDs, other cues that may affect sound source lateralization were removed. In the previous studies, ITDs of ongoing waveforms and ITDs of onsets and envelopes (if available) were co-varied (Bartlett and Mark, 1922–1923; James, 1936; Thurlow and Jack, 1973). In the present experiment, a raised-cosine ramp (0.05 s) was applied at every onset and offset of the stimuli. The ramps were synchronous across the left and right channels, eliminating onset and envelope ITD cues. The A-weighted sound pressure level at both ears was adjusted to 55 dB.

The stimuli were synthesized digitally on a computer (Macintosh Quadra 950). The sampling rate was 48 kHz and quantization was 16 bit. The stimuli were converted to analog signals using a Digidesign Pro Tools Audio Interface, and presented through Sennheiser HDA 200 headphones in a sound-insulated booth.

Four young-adult listeners participated, all of whom had quiet thresholds within 15 dB of the ANSI, 1969 standard at all audiometric frequencies. They had experience in psychoacoustic tasks other than sound lateralization judgments, and received several hours of training on sound lateralization judgments of sinusoids used in the experiment.

B. Results and discussions

Figure 1 shows the results when both adapter and test tones were 400 Hz. With no adapter tone, a subjective center (50% response) was brought about by a test tone having an ITD near zero. With the left-leading (right-leading) adapter, the psychometric function, estimated using the maximum likelihood procedure (Bock and Jones, 1968), shifted left (right). Although there were individual differences in the absolute magnitude of the aftereffect, the overall tendency was similar for all subjects. The shift of the psychometric functions at the 50% points was 108 μs in average for the left-leading and right-leading adapters across four subjects.

Figure 2 shows the magnitude of the aftereffect (shift of psychometric functions) as a function of the adapter and test frequencies. For all test frequencies and all subjects except one case (subject: HO, test frequency: 566 Hz), the magnitude of the localization aftereffect was found to be largest when the frequencies of the adapter and test tones were identical. It decreased as the frequency difference increased, and virtually disappeared at a difference of one-half octave.

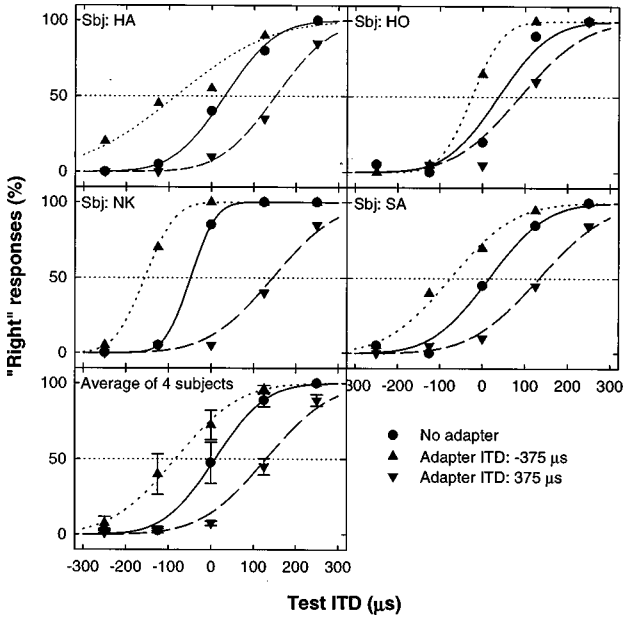

FIG. 1. Proportion of ''right'' responses as a function of test ITD when both the adapter and test sounds were 400-Hz tones (the adapter ITD was −375 or 375 μs), and when only the 400-Hz test tone was presented as a no-adapter control condition. Individual data and the average of the four subjects are shown. Dots indicate the obtained data, error bars indicate the standard error of the mean, and curved lines indicate the psychometric functions estimated using the maximum likelihood procedure.

II. EXPERIMENT 2: ITD SELECTIVITY OF THE LOCALIZATION AFTEREFFECT

A. Method

We measured the magnitude of the localization aftereffect for 400-Hz sinusoids using various combinations of adapter and test ITDs. Subjects indicated the azimuth of the intracranial image of the test tone on a half-circle arc for various combinations of adapter and test ITDs in the range of

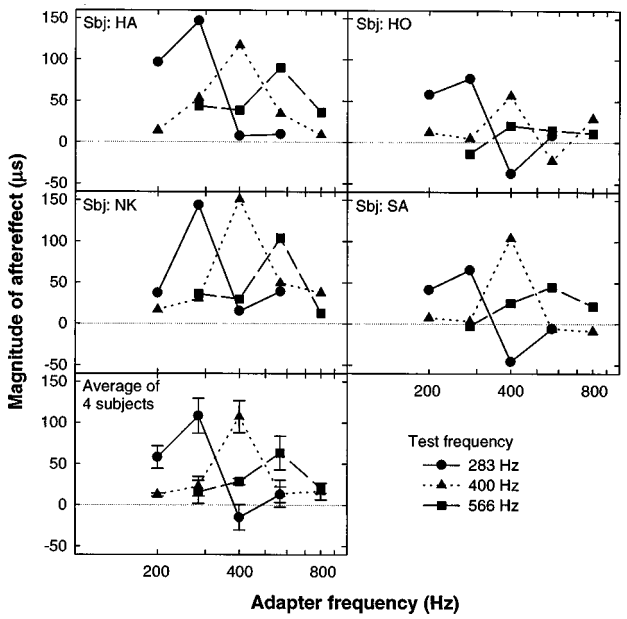

FIG. 2. Magnitude of the localization aftereffect as a function of the adapter and test frequencies. Individual data and the average of the four subjects are shown. Error bars indicate the standard error of the mean.

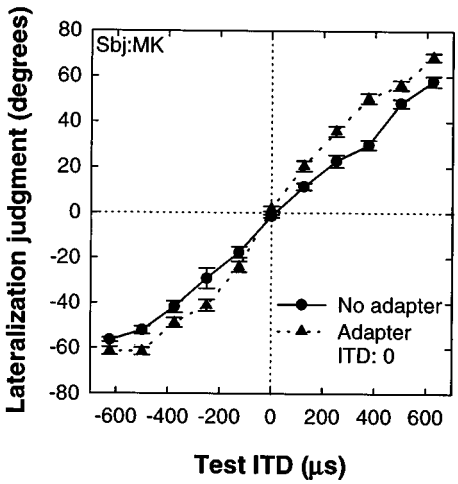

FIG. 3. Mean lateralization judgments as a function of the test ITD for a trained subject (MK) when no adapter was presented and when the adapter ITD was 0. Error bars indicate the standard error of the mean. The data for the other four subjects were similar.

± 625 μs and also for a no-adapter control condition. They were instructed to ignore the distance and elevation of the perceived image. The azimuths of the marked points from the center were measured (positive value: right of center, negative value: left of center). The difference between each adapter condition and the no-adapter condition represents the magnitude of the aftereffect.

In each adaptation session, an initial adapter tone having an ITD (either −375, −125, 0, 125, or 375 μs) was presented for 60 s, followed by a 0.25−s test tone. The ITD of the test tone was chosen randomly on each trial from the the eleven values (−625, −500, −375, −250, −125, 0, 125, 250, 375, 500, or 625 μs). Following each test tone (4 s after the offset of each test tone), the adapter tone having the same ITD as the initial adapter tone was presented again for 5 s to reinforce the adaptation. Subjects made their decision during the silent interval between the test tone and the next adapter tone. Twenty measurements were conducted for each data point per subject. In no-adaptation sessions, the adapter tones were replaced with the same duration of silence. Three subjects (HA, NK, and HO) who had participated in experiment 1 and two new subjects (MK and HM) participated in experiment 2. MK was the first author. HM was similar in experimental experience and hearing sensitivity to the three subjects who had participated in experiment 1. Three of the five subjects (HA, HM, and HO) participated in the no-adaptation condition and only one adaptation condition (adapter ITD $=0$). The other two subjects (MK and NK) completed all the conditions. The apparatus of the experiment was the same as in experiment 1.

B. Results and discussions

Figure 3 shows the lateralization judgments of a subject (MK) when no adapter tone was presented and when the adapter ITD was zero. The differences between the two conditions are shown in Fig. 4, along with the other four subjects' data. There are relatively large individual differences in the absolute size of the aftereffect, but we can still see a

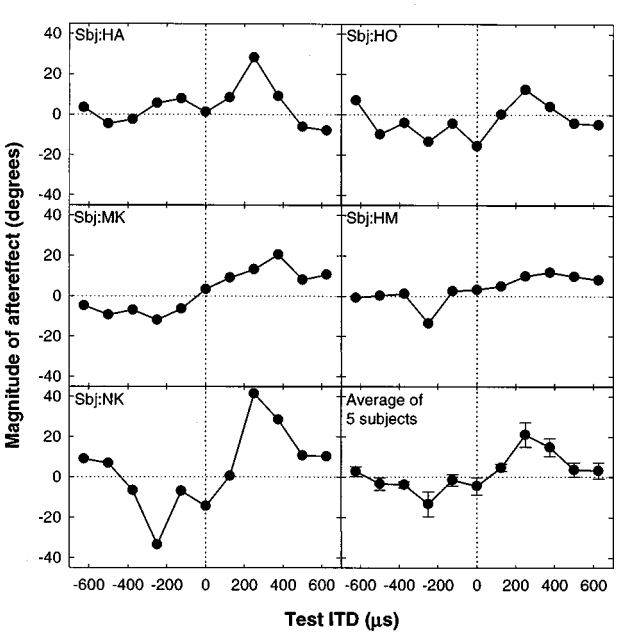

FIG. 4. Mean lateralization judgments (adapter ITD=0) relative to the no-adapter condition as a function of the test ITD for five subjects. When the test ITD is larger than zero, a positive value of the relative lateralization judgment indicates that the test tone shifted away from the adapter tone (the first quadrant). When the test ITD is smaller than zero, a negative value indicates the same repulsion effect (the third quadrant).

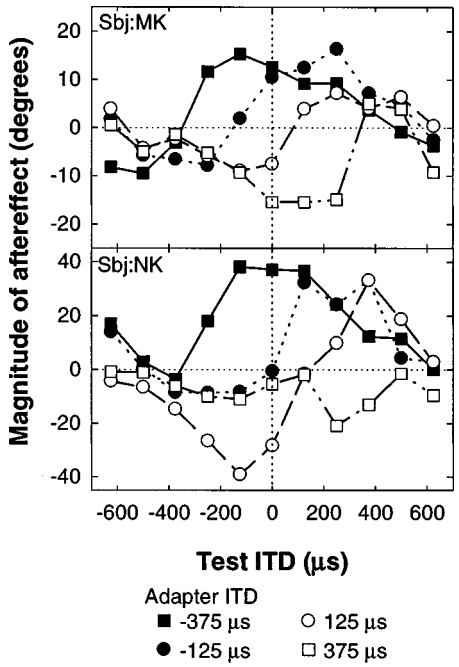

FIG. 5. Mean lateralization judgments (adapter ITD= −375, −125, 125, or 375 μs) relative to the no-adapter condition as a function of the test ITD for two subjects (MK and NK). When the test ITD is larger than the adapter ITD, a positive value of the relative lateralization judgment indicates that the test tone shifted away from the adapter tone. When the test ITD is smaller than the adapter ITD, a negative value indicates the same repulsive effect.

common tendency across subjects. First, the magnitude of the aftereffect was rather small when the ITDs of the adapter and test tones were similar, and was largest when ITDs differed by around 250 μs. Second, most of the data points fell in the first or the third quadrant, indicating that the displacement of the test tone was away from the perceived location of the adapter tone. In other words, the aftereffect enhances the spatial separation between the adapter and test tones.

The same tendency was also observed in conditions in which the adapter ITDs were not zero (Fig. 5). The magnitude of the aftereffect was largest when ITDs of the adapter and test tones differed by approximately 250 μs. These results support the earlier findings concerning the direction of the localization aftereffect (Bartlett and Mark, 1922–1923; James, 1936; Thurlow and Jack, 1973).

III. DISCUSSION

A. Summary of the results

(1) The localization aftereffect occurs for low-frequency tones that are lateralized based only on ITDs of ongoing waveforms.
(2) Following adaptation, the apparent lateralization of the test tone shifts away from that of the adapter tone, no matter where the adapter tone is lateralized.
(3) The magnitude of the localization aftereffect is, under optimal conditions, about 20 degrees in average subjects.
(4) The localization aftereffect is frequency selective, that is, the magnitude of the aftereffect is largest when the frequencies of the adapter and test tones are identical, and disappears at a frequency difference of one-half octave.
(5) The localization aftereffect is ITD-selective, that is, the magnitude of the aftereffect is smallest when the ITDs of the adapter and test tones are similar, and is largest when they differ by around 250 μs.

B. Underlying mechanism of the localization aftereffect

The current results indicate that the localization aftereffect based only on ITDs is selective both in ITD and in frequency. This suggests that processing units having selectivity both in ITD and in frequency are responsible for the aftereffect. To confirm this idea, we created a model of ITD processing which incorporates adaptation, and compared the results of our computer simulation with the psychophysical data.

Our model is based on the widely accepted idea that binaural interaction contains a process to compute the interaural cross correlation separately in each frequency region after processing by the peripheral auditory system (for review, see Stern and Trahiotis, 1995; Colburn, 1995). In such models, it is assumed that the interaural cross correlation is computed by a delay-coincidence network, originally proposed by Jeffress (1948). Each coincidence detector records coincidences of neural impulses from the two ears after a series of internal time delays. Thus the coincidence detectors can be thought of as ITD channels, each responding selectively to a certain range of ITDs. The short-term average of the set of coincidence outputs, as a function of their internal delay, approximates a short-term cross-correlation function of the neural signals arriving at the coincidence detectors. The cross-correlation functions from different frequency bands are then integrated into a summary cross correlation.

Subjective lateral position is assumed to then correspond either to the location of peaks of the summary cross-correlation function or to the location of a centroid along the internal delay axis (Stern and Colburn, 1978; Lindemann, 1986; Shackleton *et al.*, 1992).

In vision, adaptation is often thought of as a temporary change in the sensitivity of a particular population of single neurons after prolonged stimulation. The sensitivity change is assumed to occur either by fatigue of the activated neurons (Sutherland, 1961; Coltheart, 1971) or by continued lateral inhibition from adjacent neurons (Blakemore *et al.*, 1970; Barlow, 1990). Here we assumed that such a sensitivity change occurs in the coincidence detectors according to the magnitude of previous activation. We implemented the sensitivity change by using independent multiplicative gain controls affecting each frequency-selective coincidence detector.

In our model, the sounds reaching the two ears were first bandpass filtered by the ERB filter bank containing 78 frequency channels equally spaced on an ERB-rate scale between 50 and 3000 Hz (Moore and Glasberg, 1986). The outputs of the filter bank were then half-wave rectified to mimic the unidirectional response properties of the hair cells. The rectified signals from the left and right ears were then fed into the delay-coincidence network. In the simulation, the adapter and test signals used as input to the model were sampled from the 50-ms portion at the midpoint of the stationary sinusoidal signals used in experiments 1 and 2. Therefore, the shape of the temporal weighting function used to compute the running interaural cross correlation is not crucial here. The coincidence count with internal delay τ at frequency f during the time period between t_1 and t_2 is

$$\phi(f,\tau)=\sum_{t=t_1}^{t_2} X_l(f,t)X_r(f,t-\tau), \tag{1}$$

where $X_l(f,t)$ and $X_r(f,t)$ are the rectified outputs from the left and right ears, respectively, and t_2-t_1 was set to 50 ms. The variables τ and t took discrete values, with a step size of 1/96 000 s. The range of τ was between -1 ms and 1 ms, which covered the possible range of ITDs for human listeners. The coincidence count was normalized into the range between 0 and 1, by dividing $\phi(f,\tau)$ by the maximum coincidence count for the sound in the entire $f-\tau$ plane. The output from the coincidence detector is

$$\psi(f,\tau)=g(f,\tau)\cdot\bar{\phi}(f,\tau), \tag{2}$$

where $g(f,\tau)$ is a gain function and $\bar{\phi}(f,\tau)$ is a normalized coincidence count. The gain, which represents the effect of adaptation, should decrease according to the magnitude of the previous input, and keep changing during adaptation until it reaches an asymptote. However, we do not know the exact temporal course of adaptation yet. Therefore, we assumed that after long adaptation, the gain function becomes

$$g(f,\tau)=\frac{1}{1+k\cdot\bar{\phi}_{\text{adapt}}(f,\tau)}, \tag{3}$$

where k is a positive constant to control the amount of gain control, and $\bar{\phi}_{\text{adapt}}(f,\tau)$ is the normalized coincidence count for the adapter at frequency f and interaural delay τ. There is only one free parameter (k) in this model. Figure 6 illustrates how this model works in each frequency band. Before adaptation (upper panel), the outputs from the coincidence detectors $\psi(f,\tau)$ are equal to the inputs $\bar{\phi}(f,\tau)$, since the gain $g(f,\tau)=1$. The peak of the coincidence outputs $\psi(f,\tau)$ for the 400-Hz test tone having an ITD of 375 μs is located at the internal delay of 375 μs. After long exposure to an adapter tone having zero ITD, the gain $g(f,\tau)$ changes as is represented by a dotted line, making the peak of the coincidence output $\psi(f,\tau)$ shift away from the adapter ITD. The perceived lateral position is then determined by the location of the peak in the summary cross-correlation function

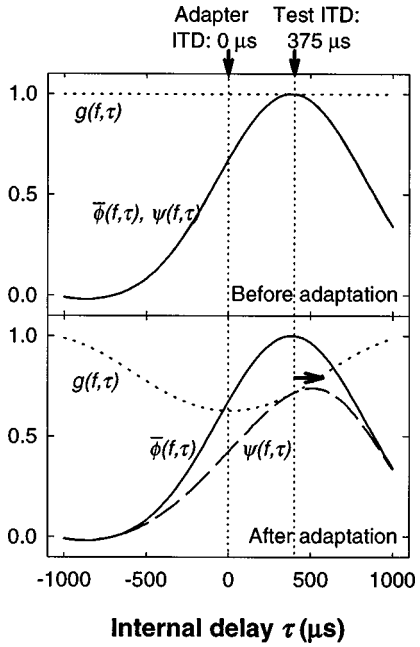

FIG. 6. Behavior of the gain control model in a frequency channel. Before adaptation, the gain function $g(f,\tau)$ is unity. As a consequence, the outputs of the coincidence detectors, $\psi(f,\tau)$, is equal to the cross correlation of the signal from the two ears, $\bar{\phi}(f,\tau)$. The peak of $\psi(f,\tau)$ for a test tone having an ITD of 375 μs is located at the internal delay of 375 μs. After long exposure to an adapter tone having zero ITD, the gain $g(f,\tau)$ changes (dotted line), resulting in the shift of the peak location of the coincidence outputs, $\psi(f,\tau)$. The shift of the peak corresponds to the localization aftereffect.

$$s(\tau)=\sum_{i=1}^{78}\psi[f(i),\tau], \tag{4}$$

where $f(i)$'s are equally spaced on an ERB-rate scale between 50 and 3000 Hz (Shackleton *et al.*, 1992). The shift of this peak corresponds to the localization aftereffect. Figure 7 represents the multi-channel outputs of the coincidence detectors and the summary cross correlation. The brightness of each cell corresponds to the magnitude of the value at the cell. The top-left panel shows the coincidence outputs for the 400-Hz adapter tone with an ITD of -375 μs, and the top-right panel shows the gain function for the adapter tone. With this adaptation, the activity pattern of the coincidence detectors for the 400-Hz test tone shifts rightward (middle-left: before adaptation, bottom-left: after adaptation). On the other hand, the coincidence activities for the 566-Hz test

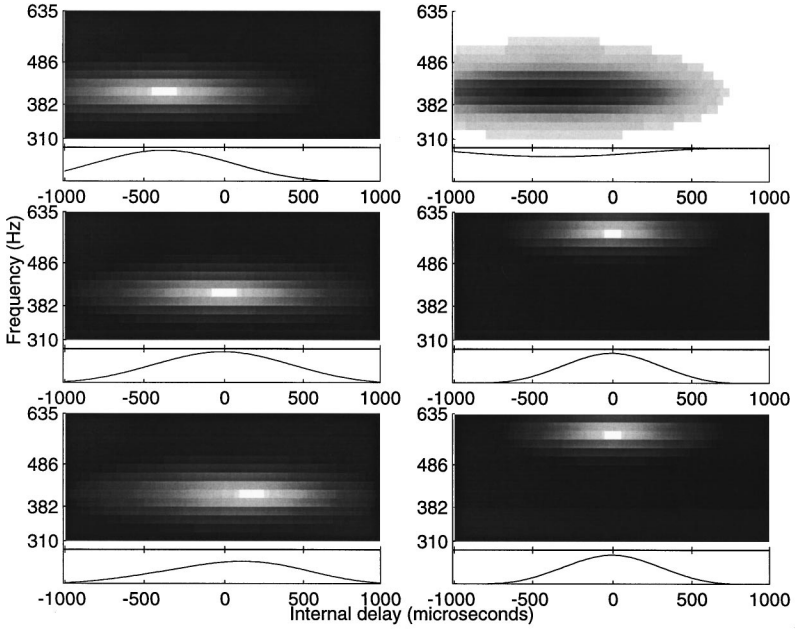

FIG. 7. Top-left: The multi-channel activities of the coincidence detectors $\psi(f,\tau)$ and the summary cross correlation $s(\tau)$ for a 400-Hz adapter tone with an ITD of -375 μs. Top-right: The gain function $g(f,\tau)$ for the adapter tone. Middle-left: $\psi(f,\tau)$ and $s(\tau)$ for a 400-Hz test tone with an ITD of 0 μs before adaptation, bottom-left: $\psi(f,\tau)$ and $s(\tau)$ for a 400-Hz test tone with an ITD of 0 μs after adaptation. Middle-right: $\psi(f,\tau)$ and $s(\tau)$ for a 566-Hz test tone with an ITD of 0 μs before adaptation, bottom-right: $\psi(f,\tau)$ and $s(\tau)$ for a 566-Hz test tone with an ITD of 0 μs after adaptation. The brightness of each cell corresponds to the magnitude of the value at the cell.

tone stay the same (middle-right: before adaptation, bottom-right: after adaptation).

We then tested how well the model predicts the aftereffect observed in experiment 2. We adjusted the parameter k to fit subject MK's data when the adapter ITD was zero, minimizing the squared deviations between the model predictions and the lateralization judgments. To convert ITD to lateralization azimuth, we used an equation

$$\text{Lateralization(deg)} = \text{ITD}(\mu\text{s}) * 0.096, \tag{5}$$

obtained from the linear regression for MK's lateralization judgment data in the no-adapter condition (Fig. 3, closed circles). The top panel of Fig. 8 shows the predicted aftereffect (solid line) when $k = 1.05$ and the experimental data (closed circles). Next, we used the same k value to predict the other four adapter conditions (Fig. 8, middle and lower panels). The predicted aftereffect captures three important features of the experimental data for all the adapter ITD conditions. First, the aftereffect is close to zero at the adapter ITD. Second, the displacement of the test tone is away from the adapter tone. Third, the aftereffect is largest when they differ by, in the case of this subject, approximately 300 μs. The parameter k does not change the overall shape of the predicted aftereffect; it changes the magnitude of the aftereffect and the location of the peak. For subjects who show a larger aftereffect (such as NK), a larger k produces a better fit.

Next, we tested if the model predicts the frequency selectivity of the aftereffect observed in experiment 1. We used the same k as the previous simulation, and ITDs of the adapter and test tones were set to -375 μs and 0 μs, respectively. The magnitude of the aftereffect was expressed in microseconds rather than degrees. The simulation represents essential features of the data from experiment 1: The predicted aftereffect disappeared at a frequency difference of one-half octave, and was smaller when the test frequency was 566 Hz (Fig. 9). This is apparently due to the independent operation of gain control in each frequency band, as is depicted in Fig. 7, rather than operating after across-frequency integration.

In the current simulation, we assumed that the delay-coincidence network contains many coincidence detectors

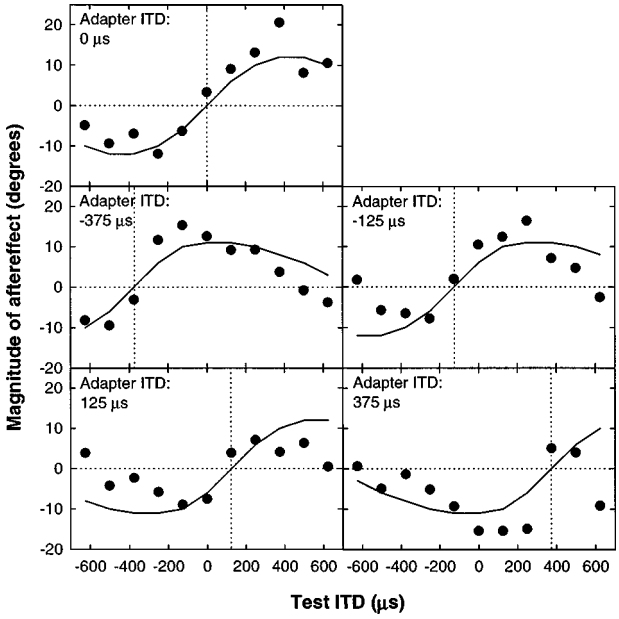

FIG. 8. The predicted localization aftereffect (solid lines) and subject MK's data (closed circles) as a function of test ITD in five adapter ITD conditions. The vertical dotted lines represent the adapter ITDs. For details, see text.

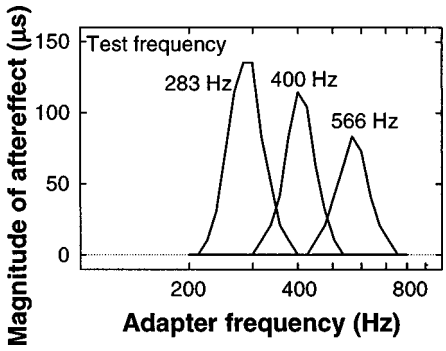

FIG. 9. The predicted localization aftereffect (solid lines) and subject MK's data (closed circles) as a function of the adapter and test frequencies. For details, see text.

with very small (1/96 000 s) steps, and that the apparent sound location was determined by the peak location of the coincidence outputs. However, these assumptions are not necessary to predict the localization aftereffect. For example, the selectivity of the aftereffect would be predicted based on the activity ratio (or centroid) of the coincidence detectors. In this case, a relatively small number of coincidence detectors are sufficient to predict the psychophysical data, as is the case for color vision (Boynton, 1979). For now, it is not possible to determine which strategy is used in sound lateralization.

Although this model can predict the localization aftereffect fairly successfully with only one free parameter, there are several limitations. First, in the simulation of ITD selectivity, the discrepancy between the prediction and the experimental data tends to get larger at the edges of the ITD axis. Second, the model cannot capture the left–right asymmetry some subjects showed. Third, and more importantly, the current model does not incorporate the temporal course of gain change. More empirical data are required to modify the model concerning these points.

In sum, both the psychophysical and computational results support the idea that the gain of ITD-selective units, which also have frequency selectivity, changes according to recent input, producing the localization aftereffect.

C. Physiological basis of the localization aftereffect

There are anatomical and physiological data supporting the idea that ITDs are extracted by a delay-coincidence network separately in each frequency region, and information from different frequency regions is integrated into a single spatial representation at later stages. It has been shown that the principal cells of the medial superior olive (MSO) perform coincidence detection between phase-locked inputs from the two ears in the cat and in the barn owl (Yin and Chan, 1990; Carr and Konishi, 1990). In the barn owl, the across-frequency integration of ITD information is shown to take place at the level of the external nucleus of the inferior colliculus (ICX).

As for human listeners, there has been no direct physiological data concerning the mechanisms of ITD detection. Our current data provides evidence that the human auditory system contains ITD-selective units, which can be modeled as a group of cross correlaters. Moreover, the frequency selectivity of the localization aftereffect observed in experiment 1 indicates that such ITD-selective units operate independently in different frequency bands. The frequency selectivity of the ITD-selective units appears comparable to that of the auditory filters.

It is premature to determine the specific neural site where the adaptation of ITD-selective units takes place in the human auditory system. For now, we can say that the adaptation occurs after binaural interaction, but before across-frequency integration.

D. Functional roles of the adaptation in ITD processing

An important task of hearing is to detect changes or differences in sound localization, which may indicate the emergence of a new acoustic event. The adaptive processing revealed by the localization aftereffect may promote the detection of changes or differences around the adapter ITD. This possibility is supported by Kashino (1998), who shows that ITD discrimination is selectively improved following adaptation if the adapter and test sounds are similar in the ITD domain and in the frequency domain. The adaptation can be thought of as a recalibration of the mechanism extracting ITDs in order to represent a small change in the recently experienced sound with maximum resolution.

ACKNOWLEDGMENTS

We thank Richard M. Warren and Willard R. Thurlow for directing our attention to relevant early studies and sending copies of those papers. We also thank Eric W. Healy, Tatsuya Hirahara, and Hisashi Uematsu for helpful discussion, and Ken'ichiro Ishii for supporting this research.

Barlow, H. B. (**1990**). ''A theory about the functional role and synaptic mechanisms of visual aftereffects,'' in *Vision: Coding and Efficiency*, edited by C. Blakemore (Cambridge U. P., Cambridge, England), pp. 363–375.

Bartlett, F. C., and Mark, H. (**1922–1923**). ''A note on local fatigue in the auditory system,'' Br. J. Psychol. **13**, 215–218.

von Békésy, G. (**1960**). *Experiments in Hearing* (McGraw-Hill, New York).

Blakemore, C., Carpenter, R. H. S., and Georgeson, M. A. (**1970**). ''Lateral inhibition between orientation detectors in the human visual system,'' Nature (London) **228**, 37–39.

Blakemore, C., and Sutton, P. (**1969**). ''Size adaptation: a new after-effect,'' Science **166**, 245–247.

Bock, R. D., and Jones, L. W. (**1968**). *The Measurement of Prediction of Judgment and Choice* (Holden Day, San Francisco).

Boynton, R. M. (**1979**). *Human Color Vision* (Holt, Rinehart, and Winston, New York).

Carr, C. E., and Konishi, M. (**1990**). ''A circuit for detection of interaural time differences in the brainstem of the barn owl,'' J. Neurosci. **10**, 3227–3246.

Colburn, H. S. (**1995**). ''Computational models of binaural processing,'' in *Auditory Computation*, edited by H. Hawkins and T. McMullin (Springer-Verlag, New York), pp. 332–400.

Coltheart, M. (**1971**). ''Visual feature analyzers and aftereffects of tilt and curvature,'' Psychol. Rev. **78**, 114–121.

Flugel, J. C. (**1920–1921**). ''On local fatigue in the auditory system,'' Br. J. Psychol. **11**, 105–134.

Grantham, D. W. (**1995**). ''Spatial hearing and related phenomena,'' in *Hearing*, edited by B. C. J. Moore (Academic, New York), pp. 297–345.

Grantham, D. W. (**1989**). ''Motion aftereffects with horizontally moving sound sources in the free field,'' Percept. Psychophys. **45**, 129–136.

Green, G. G. R., and Kay, R. H. (**1974**). ''Channels in the human auditory system concerned with the wave form of the modulation present in amplitude- and frequency-modulated tones,'' J. Physiol. (London) **241**, 29P–30P.

Hafter, E. R., Buell, T. N., and Richards, V. M. (**1988**). ''Onset-coding in lateralization: Its form, site, and function,'' in *Auditory Function: Neurological Bases of Hearing*, edited by G. M. Edelman, W. E. Gall, and W. M. Cowan (Wiley, New York), pp. 647–676.

James, H. E. O. (**1936**). *The Localisation of Sound* (Medical Research Council, Special Report Series No. 207, H. M. Stationery Office, London).

Jeffress, L. A. (**1948**). ''A place theory of sound localization,'' J. Comp. Physiol. Psychol. **41**, 35–39.

Kashino, M. (**1998**). ''Adaptation in sound localisation revealed by auditory after-effects,'' in *Psychological and Physiological Advances in Hearing*, edited by A. R. Palmer, A. Rees, Q. Summerfield, and R. Meddis (Whurr, London), pp. 322–328.

Kay, R. H., and Matthews, D. R. (**1972**). ''On the existence in human auditory pathways of channels selectively tuned to the modulation present in frequency modulated tones,'' J. Physiol. (London) **225**, 657–677.

Lindemann, W. (**1986**). ''Extension of a binaural cross-correlation model by contralateral inhibition. I. Simulation of lateralization for stationary signals,'' J. Acoust. Soc. Am. **80**, 1608–1622.

Moore, B. C. J., and Glasberg, B. R. (**1986**). ''The role of frequency selectivity in the perception of loudness, pitch and time,'' in *Frequency Selectivity in Hearing*, edited by B. C. J. Moore (Academic, London), pp. 251–308.

Regan, D., and Tansley, B. W. (**1979**). ''Selective adaptation to FM tones: Evidence for an information-processing channel selectively sensitive to frequency changes,'' J. Acoust. Soc. Am. **65**, 1249–1257.

Shackleton, T. M., Meddis, R., and Hewitt, M. J. (**1992**). ''Across frequency integration in a model of lateralization,'' J. Acoust. Soc. Am. **91**, 2276–2279(L).

Shu, Z. J., Swindale, N. V., and Cynader, M. S. (**1993**). ''Spectral motion produces an auditory after-effect,'' Nature (London) **364**, 721–723.

Stern, R. M., and Colburn, H. S. (**1978**). ''Theory of binaural interaction based on auditory-nerve data. IV. A model for subjective lateral position,'' J. Acoust. Soc. Am. **64**, 127–140.

Stern, R. M., and Trahiotis, C. (**1995**). ''Models of binaural interaction,'' in *Hearing*, edited by B. C. J. Moore (Academic, New York), pp. 347–386.

Sutherland, N. S. (**1961**). ''Figural after-effects and apparent size,'' Q. J. Exp. Psychol. **13**, 222–228.

Tansley, B. W., and Suffield, J. B. (**1983**). ''Time course of adaptation and recovery of channels selectively sensitive to frequency and amplitude modulation,'' J. Acoust. Soc. Am. **74**, 765–775.

Thurlow, W. R., and Jack, C. E. (**1973**). ''Some determinants of localization-adaptation effects for successive auditory stimuli,'' J. Acoust. Soc. Am. **53**, 1573–1577.

Werblin, F. S. (**1973**). ''The control of sensitivity in the retina,'' Sci. Am. **228**, 70–79.

Yin, T. C. T., and Chan, J. C. K. (**1990**). ''Interaural time sensitivity in medial superior olive of cat,'' J. Neurophysiol. **65**, 465–488.

Analytical expressions for the envelope correlation of narrow-band stimuli used in CMR and BMLD research

Steven van de Par and Armin Kohlrausch
IPO, Center for Research on User-System Interaction, P.O. Box 513, NL-5600 MB Eindhoven, The Netherlands

(Received 8 November 1996; revised 20 February 1998; accepted 24 February 1998)

Analytical solutions are presented for the correlation between the envelopes of certain narrow-band stimuli that are typically used in experiments on binaural unmasking and on Comodulation Masking Release (CMR). These stimuli consist of two maskers with identical envelopes and a signal that is added to one of the maskers. If the two maskers have the same center frequency and are presented to the right and left ear, the stimulus resembles a binaural MoS*m* condition. If the two maskers have different center frequencies, we have a CMR condition with one flanking band. The solutions for the envelope correlation differ depending on whether the envelope correlation is expressed as normalized cross correlation or as normalized cross covariance (Pearson product-moment correlation). The envelope correlation depends on the statistics of the masker and the signal whereas the waveform correlation depends on neither. This influence only disappears for the normalized envelope *cross correlation* provided that the masker level is much higher than the signal level. In this case the envelope cross correlation is approximately equal to the square root of the waveform correlation. It is argued that the different properties of both types of envelope correlation are of relevance for CMR research. © *1998 Acoustical Society of America.* [S0001-4966(98)02406-0]

PACS numbers: 43.66.Pn, 43.66.Ba, 43.66.Dc [JWH]

INTRODUCTION

In an earlier paper (van de Par and Kohlrausch, 1995), analytical solutions were presented for the envelope correlation between certain types of narrow-band stimuli. These solutions were restricted to the specific case where one of the stimuli was generated by adding a signal to a masker and the other by subtracting a signal from a masker (an MoSπ condition). In the present paper we present solutions for a closely related stimulus type where the signal is added to only one of the two maskers (an MoS*m* condition). This stimulus is often utilized in experiments dealing with binaural masking level differences (BMLDs) and the monaural equivalent of this stimulus is frequently used in studies on Comodulation Masking Release (CMR). In the latter case two or more maskers are used with identical envelopes, but with different center frequencies. A sinusoidal signal is added to only one of the masker bands. Because only the envelopes are used for obtaining the correlation, the center frequency of the maskers is not relevant. Therefore, all derivations in this study apply to both binaural and CMR conditions.

For the description of high-frequency BMLDs, the envelope correlation is suggested to be an important simulus property (Bernstein and Trahiotis, 1992; van de Par and Kohlrausch, 1995). More specifically, it is assumed that subjects are sensitive to changes in the interaural envelope correlation as a result of, for example, the addition of an antiphasic signal to a homophasic masker.

The envelope correlation has also been discussed in the context of CMR experiments. In many of these experiments two or more narrow bands of noise of different center frequencies are presented simultaneously. The subject has to detect the presence of a sinusoidal signal centered in one of these bands. Subjects can detect the signal at a lower level when the envelopes of the noisebands are identical (comodulated) than when the noises are uncorrelated or when only a single noise band is present. Richards (1987) proposed that CMR may be explained by the subject's sensitivity to changes in the normalized envelope cross covariance (referred to as the Pearson product-moment correlation by Richards). Several later studies, however, produced data inconsistent with this hypothesis (Hall *et al.*, 1988; Moore and Emmerich, 1990; Fantini, 1991; Eddins and Wright, 1994).

The discussion of correlation cues in the framework of CMR is, however, limited by the fact that nearly all papers dealing with this issue have made the specific choice for defining envelope correlation as the normalized cross covariance (cf. Bernstein and Trahiotis, 1996). A previous study (van de Par and Kohlrausch, 1995) and the present study show that different definitions of envelope correlation, namely the envelope cross *correlation* and the envelope cross *covariance*, can lead to very different predictions. However, no paper has explicitly addressed the question of which measure is more appropriate in the context of CMR experiments.

For binaural masking at high frequencies, there are experimental results which can only be explained by using the interaural envelope cross correlation, but not by using the cross covariance (Bernstein and Trahiotis, 1996). This indicates that, although binaural and comodulation masking release are different issues, the difference between the two forms of correlation may also be important for CMR and that the envelope cross correlation cannot be rejected a priori as a possible cue for subjects.

In order to get a better understanding of the properties of

the envelope cross correlation and the envelope cross covariance for the MoS*m* condition, analytical expressions are derived for both in Secs. I–V. From these results it will be evident that there are differences in the properties of both forms of envelope correlation. In Sec. VI of this paper, these results are related to the discussion about envelope correlation in the context of CMR conditions.

I. DEFINITIONS AND ASSUMPTIONS

The derivations that follow are all based on an MoS*m* condition for which the envelope correlation is derived as a function of the signal-to-masker ratio (SMR). In our previous paper (van de Par and Kohlrausch, 1995), several definitions and assumptions with respect to the masker, $M(t)$, and the signal, $S(t)$, were stated. These assumptions apply in the same way to the present paper and will not be repeated in full. We only mention that $M(t)$ and $S(t)$ can be written in terms of their respective Hilbert envelopes $m(t)$ and $s(t)$:

$$M(t)=m(t)\cos[\omega t+\phi_m(t)], \tag{1}$$

$$S(t)=s(t)\cos[\omega t+\phi_s(t)], \tag{2}$$

where $\phi_m(t)$, $\phi_s(t)$, $m(t)$, and $s(t)$ are random functions that vary slowly with respect to $\cos \omega t$ (Davenport and Root, 1958). We can write

$$\langle M^2\rangle=\tfrac{1}{2}\langle m^2\rangle, \tag{3}$$

$$\langle S^2\rangle=\tfrac{1}{2}\langle s^2\rangle. \tag{4}$$

In these equations, ''$\langle\ \rangle$'' is used to denote an expected value.

The two definitions of correlation between two random processes x and y that will be used are:

(1) The normalized cross correlation (in short, *cross correlation*), which is defined as

$$\rho_{xy}=\frac{\langle xy\rangle}{\sqrt{\langle x^2\rangle\langle y^2\rangle}}. \tag{5}$$

(2) The normalized cross covariance (in short, *cross covariance*), which is defined as

$$r_{xy}=\frac{\langle (x-\langle x\rangle)(y-\langle y\rangle)\rangle}{\sqrt{\langle (x-\langle x\rangle)^2\rangle\langle (y-\langle y\rangle)^2\rangle}}. \tag{6}$$

Here and in the rest of this paper only cross correlations and cross covariances with zero time lag are considered. Clearly both types of correlation are identical when x and y have zero mean, which is in general not the case for envelopes.

The two waveforms for which the envelope correlation is derived are defined as

$$L(t)=M(t)+S(t), \tag{7}$$

$$R(t)=M(t). \tag{8}$$

$L(t)$ and $R(t)$ denote waveforms that can, for instance, be presented dichotically in a binaural experiment.

Because the means of $M(t)$ and $S(t)$ are zero, the means of $L(t)$ and $R(t)$ are also equal to zero. This implies that the two definitions of correlation [Eqs. (5) and (6)] give the same value if applied to $L(t)$ and $R(t)$.

In order to derive the expression for the waveform correlation, we will use the definition of the normalized cross correlation in Eq. (5). Using the fact that M and S are uncorrelated and stationary, we get the waveform correlation:

$$r_{LR}=\rho_{LR}=\frac{\langle (M+S)(M)\rangle}{\sqrt{\langle (M+S)^2\rangle\langle (M)^2\rangle}}$$

$$=\frac{\langle M^2\rangle}{\sqrt{(\langle M^2\rangle+\langle S^2\rangle)\langle M^2\rangle}}=\frac{1}{\sqrt{1+\langle S^2\rangle/\langle M^2\rangle}}, \tag{9}$$

as was also derived by others (e.g., Durlach *et al.*, 1986). The relative power of the masker, M, and the signal, S, is the only determining factor for the correlation value; other statistical properties of M and S have no effect.

The Hilbert envelopes of L and R are derived by substituting Eqs. (1) and (2) into Eqs. (7) and (8):

$$E_L=|m(t)e^{i\phi_m(t)}+s(t)e^{i\phi_s(t)}|, \tag{10}$$

$$E_R=|m(t)e^{i\phi_m(t)}|. \tag{11}$$

The frequency ω is not present in the expressions for the envelope. Because all further calculations of the envelope correlation are based on these two expressions, the waveforms L and R may also be located at different places in the frequency domain as long as the functions $m(t)$, $s(t)$, $\phi_m(t)$, and $\phi_s(t)$ remain the same. Therefore the derivations of the envelope correlations are also applicable to stimuli used in CMR experiments.

II. NORMALIZED CROSS CORRELATION OF THE ENVELOPES

In this section, the normalized cross correlation of the envelopes of two waveforms L and R, as defined in the previous section, is calculated. The envelopes of the waveforms L and R as given by Eqs. (10) and (11) can be written as

$$E_L=|me^{i\phi_m}+se^{i\phi_s}|$$

$$=\sqrt{(m\cos\phi_m+s\cos\phi_s)^2+(m\sin\phi_m+s\sin\phi_s)^2} \tag{12}$$

and

$$E_R=|me^{i\phi_m}|=|m|. \tag{13}$$

By using the fact that $\cos^2\alpha+\sin^2\alpha=1$ and that $\cos\alpha\cos\beta+\sin\alpha\sin\beta=\cos(\beta-\alpha)$, we can write an expression for the product of the envelopes:

$$\langle E_L E_R\rangle=\left\langle |m|\sqrt{m^2+s^2}\sqrt{1+\frac{2ms}{m^2+s^2}\cos\phi}\right\rangle, \tag{14}$$

where

$$\phi=\phi_s-\phi_m. \tag{15}$$

Using the Taylor series:

$$\sqrt{1+x}=\sum_{l=0}^{\infty}c_l x^l, \tag{16}$$

with $x=(2ms/m(^2+s^2))\cos\phi$, $c_0=1$, and for $l>0$

$$c_l = \frac{1}{l!} \prod_{k=1}^{l} \left(\frac{3}{2} - k \right), \tag{17}$$

we obtain the expression:

$$\langle E_L E_R \rangle = \left\langle \sum_{l=0}^{\infty} c_l 2^l \frac{m^l |m| s^l}{(m^2+s^2)^{l-1/2}} \cos^l \phi \right\rangle. \tag{18}$$

The summation in this equation converges provided that $-1<x<1$. This requirement is always satisfied except for $|\cos\phi|=1$ and simultaneously $|m|=|s|$. However, the probability of finding this situation is vanishingly small and it will not contribute to the expected value of Eq. (18).[1]

We can now use the fact that ϕ is uniformly distributed. This means that all odd terms in the sum vanish and that we can use the following substitution: $2n=l$, where n is a nonnegative integer. This allows us to use the following substitution:

$$\int_0^{2\pi} \cos^{2n} \theta \, d\theta = \frac{(2n-1)!!}{(2n)!!} 2\pi, \tag{19}$$

where $n!!=n(n-2)(n-4)\cdots 2$ for n even and $n!!=n(n-2)(n-4)\cdots 1$ for n odd. We get:

$$\langle E_L E_R \rangle = \sum_{n=0}^{\infty} c_{2n} 4^n \frac{(2n-1)!!}{(2n)!!} \left\langle \frac{m^{2n+1} s^{2n}}{(m^2+s^2)^{2n-1/2}} \right\rangle. \tag{20}$$

Note that the absolute value signs in Eq. (20) have been omitted because m denotes the Hilbert envelope of the masker M, which implies that $m>0$.

The denominator for the normalized cross correlation of the envelopes, from Eq. (5), reduces rather straightforwardly to

$$\sqrt{\langle E_L^2 \rangle \langle E_R^2 \rangle} = \sqrt{\langle m^2 + s^2 + 2ms \cos\phi \rangle \langle m^2 \rangle}$$
$$= \langle m^2 \rangle \sqrt{1 + \frac{\langle s^2 \rangle}{\langle m^2 \rangle}}, \tag{21}$$

because ϕ is uniform. Now we can write the cross correlation of the envelope as the ratio of Eqs. (20) and (21):

$$\rho_{E_L E_R} = \frac{\langle E_L E_R \rangle}{\sqrt{\langle E_L^2 \rangle \langle E_R^2 \rangle}}$$
$$= \frac{\sum_{n=0}^{\infty} c_{2n} 4^n \frac{(2n-1)!!}{(2n)!!} \left\langle \frac{m^{2n+1} s^{2n}}{(m^2+s^2)^{2n-1/2}} \right\rangle}{\langle m^2 \rangle \sqrt{1+\langle s^2 \rangle / \langle m^2 \rangle}}. \tag{22}$$

The expected value in the sum of Eq. (22) indicates that the cross correlation of the envelopes depends on the statistics of the envelopes of the masker and the signal.

In Fig. 1, the cross correlation ρ is plotted for several MoSm conditions as a function of the SMR. The waveform correlation is shown by the solid line. Envelope correlations are shown for a noise masker and a noise signal (dotted line), a noise masker and a sinusoidal signal (short-dashed line), a sinusoidal masker and a noise signal (long-dashed line), and a sinusoidal masker and a sinusoidal signal of different frequencies (dash-dotted line). The noise in Figs. 1–4 is assumed to have a Gaussian waveform distribution. The curves are obtained by calculating Eqs. (9) and (22). The mean square values of m and s are calculated directly (e.g., Råde and Westergren, 1990). The expected value in the series of Eq. (22) is evaluated numerically,[2] using the probability distribution functions of $m(t)$ and $s(t)$. For a noise with a Gaussian waveform distribution, the distribution of the envelope is Rayleigh distributed (Davenport and Root, 1958).

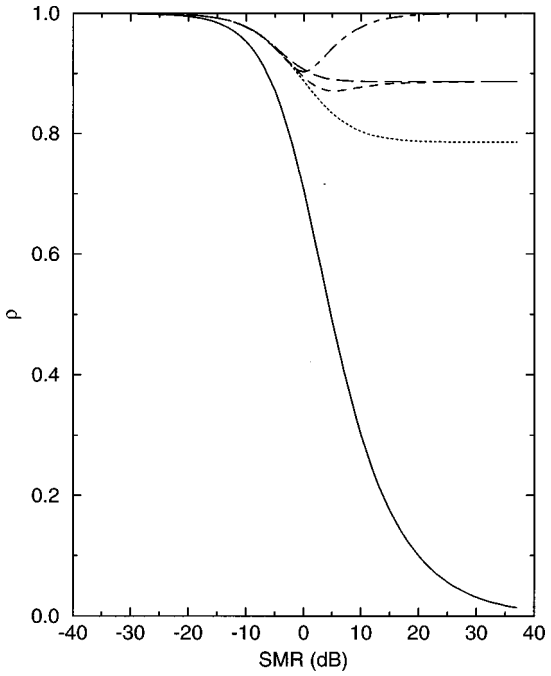

FIG. 1. The normalized cross correlation as a function of the SMR in the MoSm condition. The solid line shows the waveform cross correlation. The envelope cross correlation is shown for a noise masker and a noise signal (dotted line), for a noise masker and a sinusoidal signal (short-dashed line), for a sinusoidal masker and a noise signal (long-dashed line), and for a sinusoidal masker and a sinusoidal signal with different frequencies (dash-dotted line). Note that from Eq. (9) it follows that the *waveform* cross correlation is the same for all these masker-signal combinations.

We can see that the envelope cross correlations for the various conditions in Fig. 1 differ for SMRs around 0 dB and above. This illustrates the dependence of the MoSm envelope cross correlation on the statistics of the masker $M(t)$ and the signal $S(t)$. Such a dependence for large positive SMRs is not observed for the MoSπ envelope cross correlation (cf. van de Par and Kohlrausch, 1995).

For a noise masker and noise signal (dotted line) and for a sinusoidal masker and noise signal (long-dashed line), the envelope cross correlations decrease monotonically toward asymptotic values at large SMRs; these asymptotes differ for the two conditions. For a noise masker and a sinusoidal signal (short-dashed line), the envelope cross correlation first decreases toward a minimal value and then increases again to the same asymptotic value as the long-dashed curve. For the case that the masker and signal are sinusoids of different frequencies, the (dash-dotted) curve is symmetrical around 0-dB SMR. Because signal and masker are both sinusoidal,

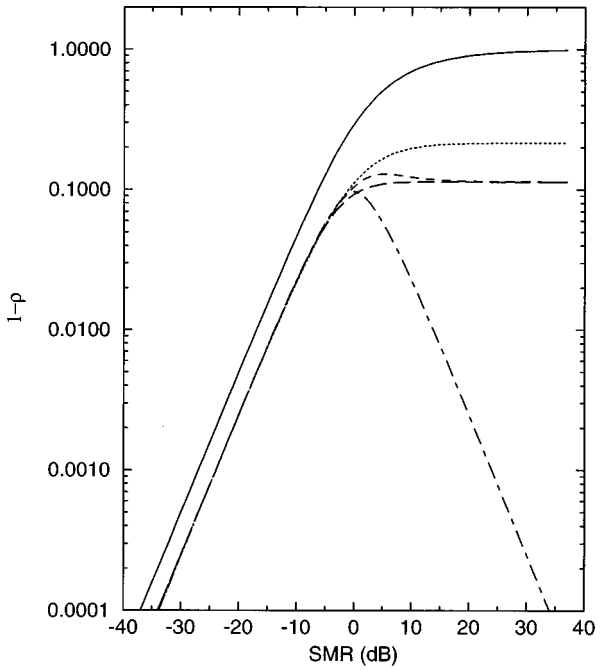

FIG. 2. Change in the normalized cross correlation as a function of the SMR in the MoS*m* condition. The solid line shows the waveform cross correlation. The envelope cross correlation is shown for a noise masker and a noise signal (dotted line), for a noise masker and a sinusoidal signal (short-dashed line), for a sinusoidal masker and a noise signal (long-dashed line), and for a sinusoidal masker and a sinusoidal signal with different frequencies (dash-dotted line).

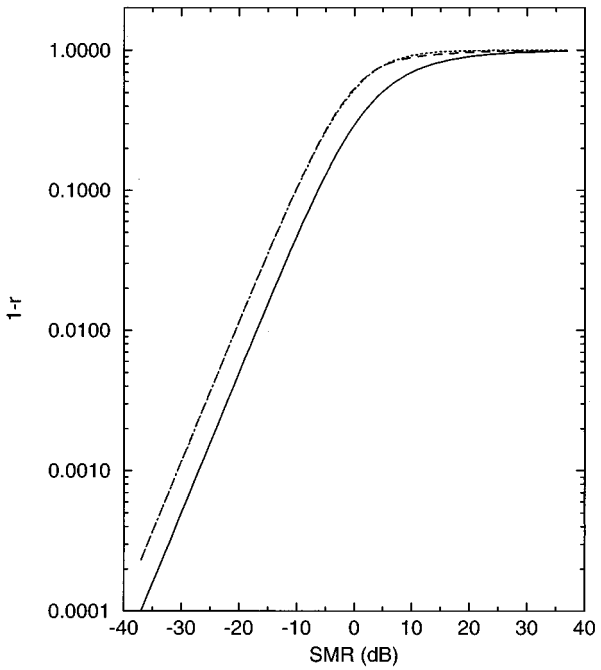

FIG. 4. Change in the normalized cross covariance as a function of the SMR in the MoS*m* condition. The solid line shows the waveform cross correlation. The envelope cross covariance is shown for a noise masker and a noise signal (dotted line), and for a noise masker and a sinusoidal signal (dashed line).

changing the sign of the SMR will affect neither the masker-plus-signal envelope statistics (E_L) nor the masker envelope statistics (E_R), which implies that the envelope cross correlation will not be affected either.

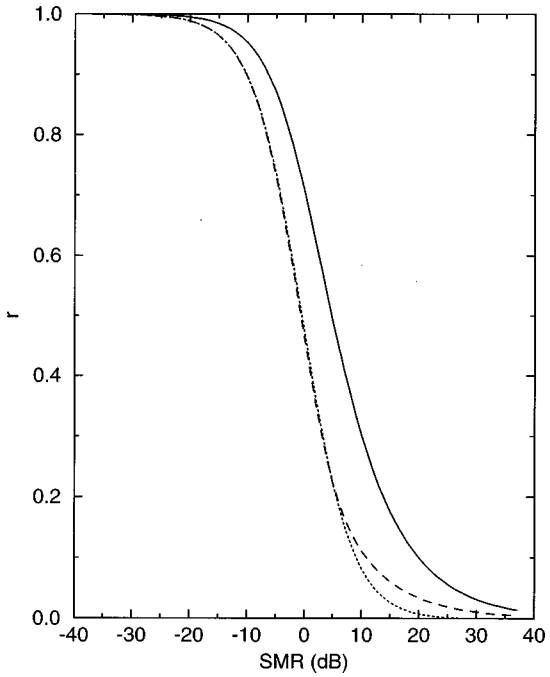

FIG. 3. The normalized cross covariance as a function of the SMR in the MoS*m* condition. The solid line shows the waveform cross correlation. The envelope cross covariance is shown for a noise masker and a noise signal (dotted line), and for a noise masker and a sinusoidal signal (dashed line).

The waveform correlation (solid line) varies from near 1 for very small SMRs, where the homophasic masker dominates, to nearly 0 for very large SMRs, where the signal dominates the masker plus signal stimulus, L, resulting in the correlation of two independent processes with zero mean.

In high-frequency binaural experiments, the relevant quantity in detecting the signal in the condition MoS*m* is the change $\Delta\rho = 1-\rho$ in the cross correlation. This quantity is plotted on a log scale in Fig. 2 as a function of the SMR for the same conditions as in Fig. 1. The curves approximate straight lines for small SMRs, in a range that is relevant in both binaural detection and CMR experiments. For this range of levels, the cross correlation can be approximated by a simpler equation as is shown in Appendix A:

$$\rho_{E_L E_R} \approx \frac{\langle M^2\rangle - \frac{1}{8}\langle S^2\rangle}{\langle M^2\rangle + \frac{1}{8}\langle S^2\rangle}. \tag{23}$$

In contrast to the exact equation [Eq. (22)], the approximation of the envelope cross correlation is dependent only on the SMR and not on the statistics of S and M. Comparing the present result for MoS*m* with the result for MoSπ [van de Par and Kohlrausch, 1995, Eq. (30)], we find that in order to obtain the same value for the envelope cross correlation, the SMR for the MoS*m* condition has to be 6 dB higher than for the MoSπ condition.

Because $\langle M^2\rangle \gg \langle S^2\rangle$, we know that $\rho_{E_L E_R}$ in Eq. (23) is nearly one. The difference from one can be approximated from Eq. (23) and is given by $\Delta\rho_{E_L E_R} \approx \frac{1}{4}\langle S^2\rangle/\langle M^2\rangle$. A similar statement can be made for the waveform correlation ρ_{LR} in Eq. (9). If the denominator of this equation is approxi-

TABLE I. Maximum SMRs for several error margins in the approximation of the normalized cross correlation of the envelope for the MoS*m* condition with a noise masker. The second column applies to the case that the signal is a sinusoid and the third column applies to the case that the signal is a noise. The noises are assumed to have Gaussian waveform statistics.

	SMR for MoS*m*	
Error in $\rho_{E_L E_R}$	*S* sinusoid	*S* noise
<1%	≤−7 dB	≤−12 dB
<5%	≤−3 dB	≤−8 dB
<10%	≤−1 dB	≤−6 dB

mated by the first two terms of a Taylor series we find $\Delta\rho_{LR} \approx \frac{1}{2}\langle S^2\rangle/\langle M^2\rangle$. This leads to the following relation:

$$2\Delta\rho_{E_L E_R} \approx \Delta\rho_{LR}. \tag{24}$$

For small $\Delta\rho_{LR}$ this is equivalent to

$$\rho_{E_L E_R} \approx \sqrt{\rho_{LR}}. \tag{25}$$

For the approximation at small SMRs, the relation between the waveform correlation and the envelope correlation is identical for the MoS*m* and the MoSπ conditions [cf. Eqs. (31) and (32) in van de Par and Kohlrausch, 1995].

In Table I the accuracy of the approximation in Eq. (23) is shown for the cases of a sinusoidal signal and a Gaussian noise signal, both in combination with a Gaussian noise masker. For an SMR of −3 dB or less the approximation of the envelope cross correlation differs 5% or less from the exact value. Thresholds obtained in a CMR condition with a sinusoidal signal and a narrow-band masker typically correspond to an SMR of −7 dB or less (cf. McFadden, 1986; Cohen and Schubert, 1987). In this case, the approximation in Eq. (23) is accurate to within 1%.

For the case that the SMR is very large, the following approximation can be made for the asymptotic value of the envelope correlation as is shown in Appendix A:

$$\rho_{E_L E_R} \approx \frac{\langle m\rangle\langle s\rangle}{\sqrt{\langle m^2\rangle\langle s^2\rangle}}. \tag{26}$$

Using the relation between the mean and the rms value of the envelopes of masker and signal we can derive the asymptotic values for $\rho_{E_L E_R}$. For the condition that both masker and signal have a flat envelope, $\rho_{E_L E_R}=1$. For the case that either the masker or the signal is a sinusoid while the other is a Gaussian noise we find $\rho_{E_L E_R}=\frac{1}{2}\sqrt{\pi}$. This can be understood by considering that for a Gaussian-noise masker, the probability distribution of the envelope, m, is Rayleigh. For this type of noise it can be shown that $\langle m\rangle/\sqrt{\langle m^2\rangle}=\frac{1}{2}\sqrt{\pi}$ (Råde and Westergren, 1990). If the envelope s results from a sinusoidal signal, it is easy to see that $\langle s\rangle/\sqrt{\langle s^2\rangle}=1$. In a similar way it can be understood that when masker and signal are both Gaussian noises, we find $\rho_{E_L E_R}=\frac{1}{4}\pi$.

III. NORMALIZED CROSS COVARIANCE OF THE ENVELOPES

In this section, the cross covariance $r_{E_L E_R}$ of the envelopes of the two waveforms L and R as defined in Sec. I is calculated using Eq. (6). This equation can be rewritten as:

$$r_{E_L E_R} = \frac{\langle (E_L-\langle E_L\rangle)(E_R-\langle E_R\rangle)\rangle}{\sqrt{\langle (E_L-\langle E_L\rangle)^2\rangle\langle (E_R-\langle E_R\rangle)^2\rangle}} = \frac{\langle E_L E_R\rangle-\langle E_L\rangle\langle E_R\rangle}{\sqrt{(\langle E_L^2\rangle-\langle E_L\rangle^2)(\langle E_R^2\rangle-\langle E_R\rangle^2)}}. \tag{27}$$

This equation indicates that in order to calculate $r_{E_L E_R}$, we need to know $\langle E_L E_R\rangle$, $\langle E_L^2\rangle$, $\langle E_R^2\rangle$, $\langle E_L\rangle$, and $\langle E_R\rangle$. The first term has been derived in the previous section [cf. Eq. (20)]. Furthermore, it is easy to see that $\langle E_L^2\rangle=\langle m^2\rangle+\langle s^2\rangle$, that $\langle E_R^2\rangle=\langle m^2\rangle$, and that $\langle E_R\rangle=\langle m\rangle$. The average value $\langle E_L\rangle$ has been calculated previously by van de Par and Kohlrausch (1995). It was found that

$$\langle E_L\rangle = \langle\sqrt{m^2+s^2}\rangle + \sum_{n=1}^{\infty} c_{2n} 4^n \left\langle \frac{m^{2n}s^{2n}}{(m^2+s^2)^{2n-1/2}}\right\rangle \frac{(2n-1)!!}{2n!!}. \tag{28}$$

With these expressions we know all terms needed for the cross covariance as defined in Eq. (27).

For certain conditions, the cross covariance is not defined. This can be seen in the middle part of Eq. (27). We see that the cross covariance $r_{E_L E_R}$ is undefined when $E_R=\langle E_R\rangle$, or in other words, when E_R is constant. This situation occurs when the masker has a flat envelope. Therefore, the derivations for the cross covariance are only valid for maskers with a fluctuating envelope. Note that it is not possible to have a situation where $E_L=\langle E_L\rangle$ under the assumptions that have been stated with respect to the masker and signal.

In Fig. 3, the cross covariance r is plotted for several MoS*m* conditions as a function of the SMR. The waveform correlation is shown by the solid line, envelope correlations are shown for a noise masker and noise signal (dotted line) and a noise masker and a sinusoidal signal (dashed line). In contrast to the observation for the cross correlation, the cross covariance of the envelopes for MoS*m* approaches zero for large positive SMRs. This can be understood if we consider that for large SMRs the signal dominates over the masker in the signal ear. Effectively, we obtain the envelope cross covariance between the envelope of the masker and the envelope of the signal. For the case that the signal has a fluctuating envelope, we can rewrite the second numerator of Eq. (27) using the fact that masker and signal result from statistically independent processes: $\langle E_L E_R\rangle-\langle E_L\rangle\langle E_R\rangle=\langle E_L\rangle\langle E_R\rangle-\langle E_L\rangle\langle E_R\rangle=0$. This relation implies that $r_{E_L E_R}=0$. When the signal has a flat envelope, it is more difficult to see what the envelope cross covariance will be for large positive SMRs because the denominator will also approach zero. Without treating the problem formally, it can be intuitively seen that adding the masker to the signal only causes minor perturbations in the otherwise flat envelope of

TABLE II. Maximum SMRs for several error margins in the approximation of the normalized cross covariance of the envelope for the MoSm condition with a noise masker. The second column applies to the case that the signal is a sinusoid and the third column applies to the case that the signal is a noise. The noises are assumed to have Gaussian waveform statistics.

	SMR for MoSm	
Error in $r_{E_L E_R}$	S sinusoid	S noise
$<1\%$	$\leqslant -11$ dB	$\leqslant -11$ dB
$<5\%$	$\leqslant -8$ dB	$\leqslant -8$ dB
$<10\%$	$\leqslant -6$ dB	$\leqslant -6$ dB

the masker-plus-signal stimulus. Depending on the phase difference ϕ with which the masker is added to the signal, an increase or a decrease in size will result. Since each perturbation for a specific phase difference ϕ and envelope m is the opposite of the perturbation for a phase difference $\phi + \pi$ and envelope m, and since ϕ has an uniform probability distribution, on average the perturbation for one value of m is zero, yielding a covariance of zero for the case of a flat signal envelope as well.

In Fig. 4, the quantity $\Delta r = 1 - r$ is plotted on a log scale as a function of the SMR for the same conditions as in Fig. 3. We can see that the curves for the envelope cross covariance are generally higher than the curves for the waveform correlation. This result is the opposite of what was found for the envelope cross correlation (cf. Fig. 2). The two curves for the envelope cross covariance are nearly identical in this plot. Again all curves approximate straight lines for small SMRs. A simple approximation is possible, just as was derived previously for the cross correlation of the envelope.

Appendix B shows that for small SMRs, assuming that $\langle m^2\rangle - \langle m\rangle^2 \gg \langle s^2\rangle$, we can write:

$$r_{E_L E_R} \approx \frac{\langle m^2\rangle - \langle m\rangle^2 - \frac{1}{4}\langle s^2\rangle}{\langle m^2\rangle - \langle m\rangle^2}. \tag{29}$$

In Table II the accuracy of the approximation in Eq. (29) is shown for the two cases of a sinusoidal signal and a Gaussian noise signal.

Because $\langle m^2\rangle - \langle m\rangle^2 \gg \langle s^2\rangle$, we find that $r_{E_L E_R}$ is close to one. From Eq. (29) is can be easily seen that

$$\Delta r_{E_L E_R} \approx \frac{\frac{1}{4}\langle s^2\rangle}{\langle m^2\rangle - \langle m\rangle^2}. \tag{30}$$

Comparing the present result for MoSm with the result that was obtained for MoSπ (van de Par and Kohlrausch, 1995) we find that in order to obtain the same value for the envelope covariance, the SMR for the MoSm condition again has to be 6 dB higher than for the MoSπ condition.

IV. MULTIPLIED NOISE

A special type of noise to which the derivations in the previous sections are not generally applicable is multiplied noise. Multiplied noise is generated by multiplying a lowpass noise by a sinusoidal carrier.

Multiplied noise is often utilized in CMR experiments because it provides an easy way of creating comodulated noise bands of different center frequencies. An important aspect of experiments employing multiplied-noise maskers is the phase relation between the signal and the fine structure of the masker. The sinusoidal signal can be added to the multiplied-noise masker without any control of the phase between carrier and the signal. This is typically done in CMR experiments where multiplied noise is used (Schooneveldt and Moore, 1987; Moore *et al.*, 1990). For this random-phase case, the phase difference between carrier and signal can be assumed to have an uniform distribution provided that the carrier and signal have different frequencies and thus the derivations in Secs. II and III can be applied. When they have identical frequencies, the phase difference is not uniform. However, averaged over many successive additions of masker and signal, the phase difference will have a uniform distribution again.

Differently, the phase ϕ between the carrier and signal can be controlled such that it has a fixed value (van de Par and Kohlrausch, 1998). This can only be achieved provided that the signal has the same frequency as the sinusoidal carrier. The derivations of Secs. II and III need to be adapted for this last case because the derivations were based on the uniformity of the distribution of ϕ.

We start by writing an expression for the multiplied-noise masker which is the product of a sinusoidal carrier $\cos(\omega t + \phi_m)$ and a low-pass noise m_{LP}. We assume that m_{LP} has a probability distribution that is symmetric around zero and note that ϕ_m is a constant:

$$M(t) = m_{LP}(t)\cos(\omega t + \phi_m). \tag{31}$$

This expression for the masker, M, is different from the definition given in Sec. I. Instead of using the masker envelope, m, which only can have non-negative values, we now use the low-pass noise, m_{LP}.

The masker envelope $m(t)$ is given by

$$m(t) = |m_{LP}(t)|. \tag{32}$$

Using the definition of Eq. (31) we can reformulate the expressions for the envelopes presented to left and right ears as defined in Eqs. (10) and (11):

$$E_L = |m_{LP}(t)e^{i\phi_m} + se^{i\phi_s}|, \tag{33}$$

$$E_R |m_{LP}(t)e^{i\phi_m}|. \tag{34}$$

Note that Eqs. (33) and (34) have identical forms as Eqs. (10) and (11) except that in the new equations the Hilbert envelope of the masker $m(t)$ is replaced by a low-pass noise $m_{LP}(t)$ which has positive as well as negative values and ϕ_m and ϕ_s are constants instead of time dependent functions.

Therefore, the derivations that were used in Secs. II and III can essentially be repeated except that some steps in the derivations will differ somewhat. The expression for $\langle E_L E_R\rangle$ in Eq. (18) cannot change into the same form as given in Eq. (20) because this step was based on the uniformity of ϕ. Instead, $\cos^l\phi$ can be rewritten as $\cos^l\vartheta$ where ϑ is a constant denoting the phase between the sinusoidal carrier and the sinusoidal signal. Since the probability distribution of m_{LP} is symmetric around zero, all factors m_{LP}^l will be zero

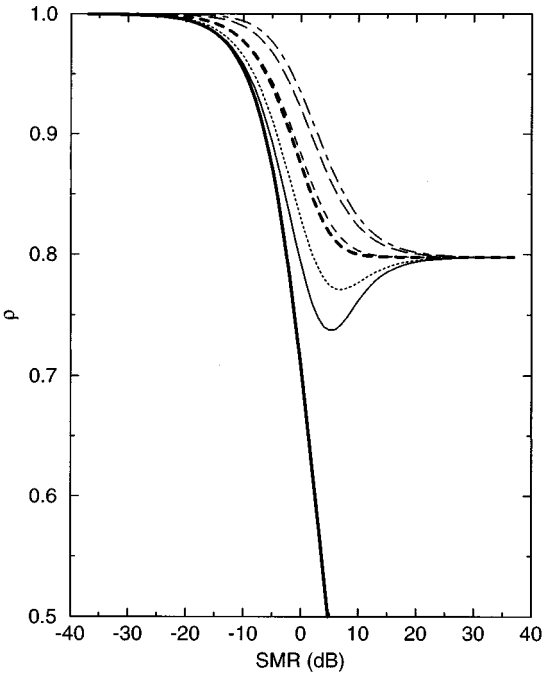

FIG. 5. The normalized cross correlation as a function of the SMR for the waveform for MoS*m* (bold line), the envelope for multiplied noise for MoS*m* with *M* a multiplied noise (low-pass Gaussian noise multiplied by a sinusoid), and *S* a sinusoid, with $\vartheta=0$ (thin continuous line), $\vartheta=\frac{1}{8}\pi$ (dotted line), $\vartheta=\frac{1}{4}\pi$ (short-dashed line), $\vartheta=\frac{3}{8}\pi$ (long-dashed line), $\vartheta=\frac{1}{2}\pi$ (dash-dotted line), and random phase (bold-dashed line).

for odd values of l and consequently all odd terms vanish in the summation in Eq. (18). For multiplied noise we therefore get the following expression:

$$\langle E_L E_R\rangle=\sum_{n=0}^{\infty} c_{2n}4^n\cos^{2n}\vartheta\left\langle\frac{m_{LP}^{2n}|m_{LP}|s^{2n}}{(m_{LP}^2+s^2)^{2n-1/2}}\right\rangle$$
$$=\sum_{n=0}^{\infty} c_{2n}4^n\cos^{2n}\vartheta\left\langle\frac{m^{2n+1}s^{2n}}{(m^2+s^2)^{2n-1/2}}\right\rangle, \qquad (35)$$

where we used Eq. (32) in order to substitute m_{LP} by m.

The normalization in Eq. (21) can be written in the same form based on the fact that $\langle m_{LP}\rangle=0$.

Combining Eqs. (35) and (21), the envelope correlation for multiplied noise is

$$\rho_{E_L E_R}=\frac{\sum_{n=0}^{\infty} c_{2n}4^n\cos^{2n}\vartheta\left\langle\frac{m^{2n+1}s^{2n}}{(m^2+s^2)^{2n-1/2}}\right\rangle}{\langle m^2\rangle\sqrt{1+\langle s^2\rangle/\langle m^2\rangle}}. \qquad (36)$$

In Fig. 5, the cross correlation for the waveform (thick continuous line) and the envelope cross correlation for a multiplied-noise masker with random phase (thick dashed line) is shown as a function of the SMR. Furthermore, the thin lines show the cross correlation of the envelope for a multiplied-noise masker and a sinusoidal signal as a function of the SMR with the phase angle ϑ as parameter. The phase angle ϑ has a marked effect on the envelope cross correlation. For $\vartheta=0$ (thin continuous line), the values for this cross correlation are smallest. They are also smaller than those for the conditions with a Gaussian-noise masker (cf. Fig. 1). This allows a test of the hypothesis that signal detection is based on envelope correlation cues, because MoS*m* thresholds should be lower for a multiplied-noise masker with $\vartheta=0$ than for a Gaussian-noise masker. The envelope correlation values for the random phase (thick dashed line) condition are very close to those for the condition with $\vartheta=\pi/4$ (thin dashed line).

For very large SMRs, the envelope cross correlation again approximates the value given in Eq. (26). Since the multiplied noise that we used here has an envelope which is Gaussian distributed, we know that if $\langle m^2\rangle=1$, $\langle m\rangle=\sqrt{2/\pi}$. This leads us to the asymptotic value of the envelope cross correlation at large SMRs of $\sqrt{2/\pi}$.

As in the previous section, it is possible to find an approximation for small SMRs. When $\langle m^2\rangle\gg\langle s^2\rangle$, the first two terms of the series in Eq. (36) are sufficient for a good approximation. The cross correlation of the envelopes can be written as

$$\rho_{E_L E_R}\approx\frac{\langle m\sqrt{m^2+s^2}\rangle-\frac{1}{2}\cos^2\vartheta\left\langle\frac{m^3s^2}{(m^2+s^2)^{3/2}}\right\rangle}{\langle m^2\rangle\sqrt{1+\langle s^2\rangle/\langle m^2\rangle}}$$
$$\approx\frac{\langle m^2\rangle+\frac{1}{2}\langle s^2\rangle-\frac{1}{2}\cos^2\vartheta\langle s^2\rangle}{\langle m^2\rangle+\frac{1}{2}\langle s^2\rangle}$$
$$\approx 1-\frac{\langle s^2\rangle}{2\langle m^2\rangle}\cos^2\vartheta, \qquad (37)$$

where only the first two terms of the series in Eq. (36) are taken into account. Furthermore, the square roots in Eq. (37) are approximated by the first terms of a Taylor series. This approximation shows that the decrease of the envelope cross correlation, $\Delta\rho_{E_L E_R}$, for small SMRs is only dependent on the SMR. The higher-order terms that have been omitted in this approximation become dominant when $\cos\vartheta=0$, and consequently, in this case, $\Delta\rho_{E_L E_R}$ can not be simply expressed in terms of the SMR. In Fig. 6, $\Delta\rho_{E_L E_R}$ is shown for the same conditions as in Fig. 5 except the random phase condition is omitted because it is very similar to the $\vartheta=\pi/4$ (short-dashed line) condition. For almost all values of ϑ, the curves approximate straight parallel lines. Only the curve for $\vartheta=\pi/2$ (dash-dotted line) is not parallel to the other curves because here the higher-order terms become dominant. Another interesting result can be found for $\vartheta=0$ (thin continuous line). When the square root in the denominator of Eq. (37) is not expanded in a Taylor series we can derive that the envelope correlation is approximately equal to the pure waveform correlation (solid line) as given in Eq. (9).

The accuracy of the approximation of Eq. (37) is given in Table III for several values of ϑ.

For the cross covariance, apart from the derivation of the expression for $\langle E_L E_R\rangle$, the derivation of the expression for $\langle E_L\rangle$ as shown in Eq. (28) is also slightly different. The reason for this is again that ϕ is not uniformly distributed. This results in an expression for $\langle E_L\rangle$ which depends on $\cos\vartheta$:

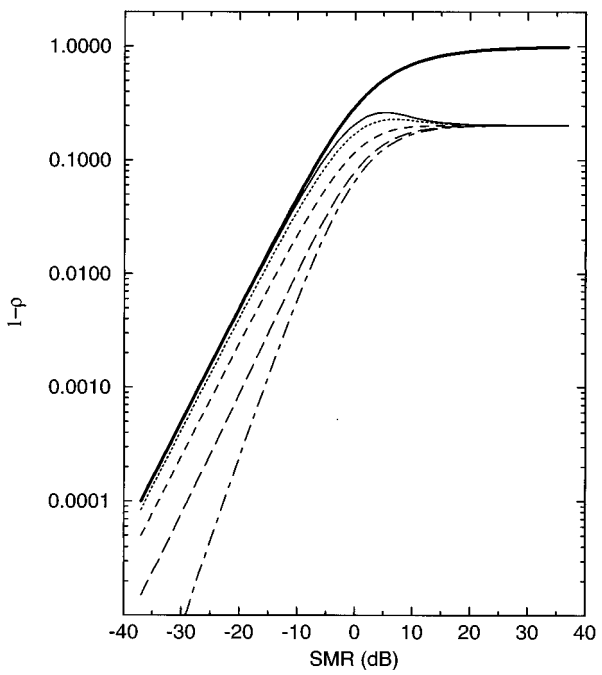

FIG. 6. Change in the normalized cross correlation as a function of the SMR for the waveform for MoSm (solid line), the envelope for multiplied noise for MoSm with M a multiplied noise (low-pass Gaussian noise multiplied by a sinusoid), and S a sinusoid, with $\vartheta=0$ (thin continuous line), $\vartheta=\frac{1}{8}\pi$ (dotted line), $\vartheta=\frac{1}{4}\pi$ (short-dashed line), $\vartheta=\frac{3}{8}\pi$ (long-dashed line), and $\vartheta=\frac{1}{2}\pi$ (dash-dotted line).

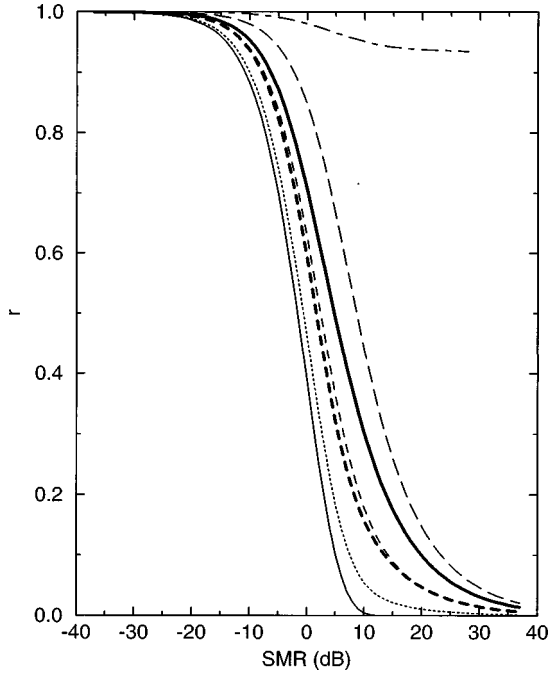

FIG. 7. The normalized cross covariance as a function of the SMR for the waveform for MoSm (bold line), the envelope for multiplied noise for MoSm with M a multiplied noise (low-pass Gaussian noise multiplied by a sinusoid), and S a sinusoid, with $\vartheta=0$ (thin continuous line), $\vartheta=\frac{1}{8}\pi$ (dotted line), $\vartheta=\frac{1}{4}\pi$ (short-dashed line), $\vartheta=\frac{3}{8}\pi$ (long-dashed line), $\vartheta=\frac{1}{2}\pi$ (dash-dotted line), and random phase (bold-dashed line).

$$\langle E_L\rangle=\langle\sqrt{m^2+s^2}\rangle + \sum_{n=1}^{\infty} c_{2n}4^n\left\langle\frac{m^{2n}s^{2n}}{(m^2+s^2)^{2n-1/2}}\right\rangle\cos^{2n}\vartheta. \tag{38}$$

In Fig. 7 the cross covariance of the envelope for multiplied noise is plotted as a function of the SMR with the phase angle ϑ as parameter (thin lines). In the range from 0 to $\frac{1}{2}\pi$, with increasing ϑ, the curves shift to the right at all SMRs. The thick dashed line shows the random-phase condition, which nearly coincides with the $\vartheta=\pi/4$ condition (thin dashed line), just as for the envelope cross correlation (cf. Fig. 5). The thick continuous line shows the waveform covariance.

When $\langle m^2\rangle-\langle m\rangle^2\gg\langle s^2\rangle$, the following approximation can be made for the cross covariance:

$$r_{E_LE_R}\approx\frac{\langle m^2\rangle-\langle m\rangle^2-\frac{1}{2}\langle s^2\rangle\cos^2\vartheta}{\langle m^2\rangle-\langle m\rangle^2}. \tag{39}$$

In Table IV the accuracy of the approximation in Eq. (39) is shown for several values of ϑ.

For large SMRs we can use the same argument as in the previous section, which leads us to the conclusion that for large SMRs the cross covariance approaches zero. For multiplied noise there is one exception, namely, when $\cos\vartheta=0$. In this case the addition of the very small masker to the large signal always leads to an increase of the magnitude of the envelope. Thus, in this case, the fluctuations in the envelope of the signal-plus-masker stimulus are correlated to the fluctuations in the masker, yielding an envelope cross covariance larger than zero.

The change in cross covariance of the envelope is shown in Fig. 8. In contrast to the outcome for the cross correlation (cf. Fig. 6), the change in cross covariance for the waveform (solid line) is not always larger than for the envelope. In

TABLE III. Maximum SMRs for several error margins in the approximation of the normalized cross correlation of the envelope for the MoSm condition with a multiplied-noise masker and a sinusoidal signal for several values of ϑ.

	SMR for MoSm			
Error in $\rho_{E_LE_R}$	$\vartheta=0$	$\vartheta=\frac{\pi}{8}$	$\vartheta=\frac{\pi}{4}$	$\vartheta=\frac{3\pi}{8}$
$<1\%$	$\leqslant-10$ dB	$\leqslant-10$ dB	$\leqslant-8$ dB	$\leqslant-5$ dB
$<5\%$	$\leqslant-6$ dB	$\leqslant-6$ dB	$\leqslant-4$ dB	$\leqslant3$ dB
$<10\%$	$\leqslant-4$ dB	$\leqslant-4$ dB	$\leqslant2$ dB	$\leqslant4$ dB

TABLE IV. Maximum SMRs for several error margins in the approximation of the normalized cross covariance of the envelope for the MoSm condition with a multiplied-noise masker and a sinusoidal signal for several values of ϑ.

	SMR for MoSm			
Error in $r_{E_LE_R}$	$\vartheta=0$	$\vartheta=\frac{\pi}{8}$	$\vartheta=\frac{\pi}{4}$	$\vartheta=\frac{3\pi}{8}$
$<1\%$	$\leqslant-13$ dB	$\leqslant-12$ dB	$\leqslant-10$ dB	$\leqslant-5$ dB
$<5\%$	$\leqslant-9$ dB	$\leqslant-8$ dB	$\leqslant-6$ dB	$\leqslant-1$ dB
$<10\%$	$\leqslant-7$ dB	$\leqslant-7$ dB	$\leqslant-4$ dB	$\leqslant1$ dB

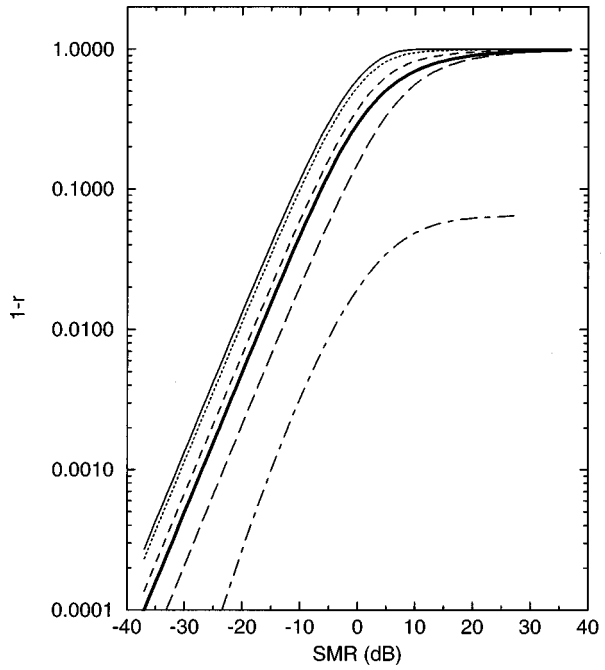

FIG. 8. Change in the normalized cross covariance as a function of the SMR for the waveform for MoS*m* (solid line), the envelope for multiplied noise for MoS*m* with *M* a multiplied noise (low-pass Gaussian noise multiplied by a sinusoid), and *S* a sinusoid, with $\vartheta=0$ (thin continuous line), $\vartheta=\frac{1}{8}\pi$ (dotted line), $\vartheta=\frac{1}{4}\pi$ (short-dashed line), $\vartheta=\frac{3}{8}\pi$ (long-dashed line), and $\vartheta=\frac{1}{2}\pi$ (dash-dotted line).

addition, we observe that for all angles ϑ, except for $\vartheta=\frac{1}{2}\pi$ (dash-dotted line), the curves approximate straight parallel lines. For $\vartheta=\frac{1}{2}\pi$, we find a deviating curve. The reason for this is identical to that given for the deviating curve in Fig. 6 for the envelope cross correlation.

In this section the particular example of a multiplied-noise masker and a sinusoidal signal was treated. Basically, the same derivations can be used when the signal is a multiplied noise.

V. THE RELATION BETWEEN THE ENVELOPE CROSS CORRELATION AND THE ENVELOPE CROSS COVARIANCE

As already mentioned in the introduction, most arguments and simulations regarding envelope correlation in the framework of CMR have been based on the cross covariance (Pearson product-moment correlation). In order to allow easy translations of these results into cross correlation values, a relation between envelope cross correlation and cross covariance for pairs of Gaussian noises is derived in this section.

For this purpose the general definition of the envelope cross covariance is used:

$$r_{E_LE_R}=\frac{\langle E_LE_R\rangle-\langle E_L\rangle\langle E_R\rangle}{\sqrt{(\langle E_L^2\rangle-\langle E_L\rangle^2)(\langle E_R^2\rangle-\langle E_R\rangle^2)}}. \tag{40}$$

Performing some simple algebraic manipulations, taking into account the definition of the envelope cross correlation [Eq. (5)], this expression can be rewritten as:

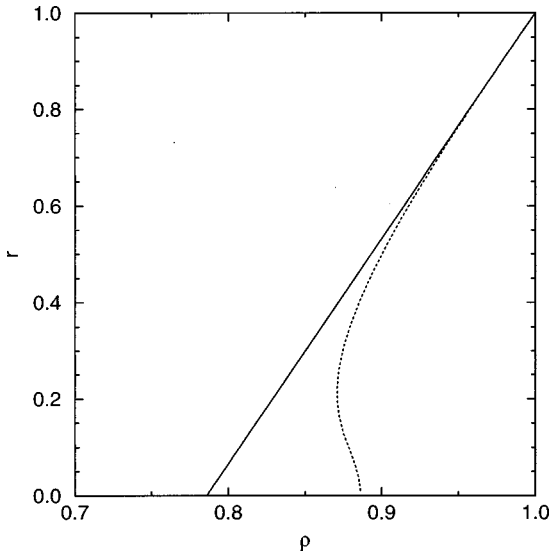

FIG. 9. Curves relating the MoS*m* envelope cross correlation to the envelope cross covariance for stimuli consisting of a Gaussian-noise masker and either a Gaussian-noise signal (solid line) or a sinusoidal signal (dotted line).

$$A_1A_2r_{E_LE_R}+B_1B_2=\frac{\langle E_LE_R\rangle}{\sqrt{\langle E_L^2\rangle\langle E_R^2\rangle}}=\rho_{E_LE_R}, \tag{41}$$

where we define:

$$A_1=\frac{\sqrt{(\langle E_L^2\rangle-\langle E_L\rangle^2)}}{\sqrt{\langle E_L^2\rangle}}, \tag{42}$$

$$A_2=\frac{\sqrt{(\langle E_R^2\rangle-\langle E_R\rangle^2)}}{\sqrt{\langle E_R^2\rangle}}, \tag{43}$$

$$B_1=\frac{\langle E_L\rangle}{\sqrt{\langle E_L^2\rangle}}, \tag{44}$$

and

$$B_2=\frac{\langle E_R\rangle}{\sqrt{\langle E_R^2\rangle}}. \tag{45}$$

In general A_1, A_2, B_1, and B_2 are dependent on the shape of the envelope distribution of E_L and E_R. Since the shapes of these distributions in general change with the SMR, it is not obvious that there is a simple relation between $\rho_{E_LE_R}$ and $r_{E_LE_R}$. However, when both the masker and the signal are Gaussian noises, the resulting stimulus will be a Gaussian noise, independent of the SMR. Therefore, A_1, A_2, B_1, and B_2 will be constants and thus, $\rho_{E_LE_R}$ and $r_{E_LE_R}$ are linearly related. For Gaussian noise the following expression can be written:

$$\rho_{E_LE_R}=\left(1-\frac{\pi}{4}\right)r_{E_LE_R}+\frac{\pi}{4}. \tag{46}$$

This relation is true for the envelope correlation and covariance of any pair of Gaussian noises (cf. van de Par and Kohlrausch, 1995).[3]

In Fig. 9 curves are plotted that show the relation between the envelope cross correlation and the envelope cross covariance. The solid curve shows the condition where the

TABLE V. An overview of approximations for the change in the cross correlation and the cross covariance of the envelope (columns 5 and 6) and of the waveforms (column 4) for the case that $\langle m^2\rangle \gg \langle s^2\rangle$. The first two columns show the properties of masker and signal envelope, the third column shows the distribution of the phase difference between masker and signal.

m	s	ϕ	$\Delta\rho_{LR}=\Delta r_{LR}$	$\Delta\rho_{E_LE_R}$	$\Delta r_{E_LE_R}$	Description
P_m	P_s	unif.	$\frac{1}{2}l$	$\frac{1}{4}l$	$\frac{\langle m^2\rangle}{4\langle m^2\rangle-4\langle m\rangle^2}\,l$	noise masker, noise signal
P_m	const.	unif.	$\frac{1}{2}l$	$\frac{1}{4}l$	$\frac{\langle m^2\rangle}{4\langle m^2\rangle-4\langle m\rangle^2}\,l$	noise masker, sinsoidal signal
const.	P_s	unif.	$\frac{1}{2}l$	$\frac{1}{4}l$	Not defined	sinusoidal masker, noise signal
const.	const.	unif.	$\frac{1}{2}l$	$\frac{1}{4}l$	Not defined	sinusoidal masker, sinusoidal signal with different freq.
Rayl.	Rayl.	unif.	$\frac{1}{2}l$	$\frac{1}{4}l$	$\frac{1}{4-\pi}\,l$	Gaussian masker and signal
Rayl.	const.	unif.	$\frac{1}{2}l$	$\frac{1}{4}l$	$\frac{1}{4-\pi}\,l$	Gaussian masker, sinusoidal signal
const.	Rayl.	unif.	$\frac{1}{2}l$	$\frac{1}{4}l$	Not defined	sinusoidal masker, Gaussian signal
P_m	P_s	const.	$\frac{1}{2}l$	$\frac{1}{2}l\cos^2\vartheta$	$\frac{\langle m^2\rangle\cos^2\vartheta}{2\langle m^2\rangle-2\langle m\rangle^2}\,l$	multiplied noise masker, and signal
P_m	const.	const.	$\frac{1}{2}l$	$\frac{1}{2}l\cos^2\vartheta$	$\frac{\langle m^2\rangle\cos^2\vartheta}{2\langle m^2\rangle-2\langle m\rangle^2}\,l$	multiplied noise masker, sinusoidal signal
const.	P_m	const.	$\frac{1}{2}l$	$\frac{1}{2}l\cos^2\vartheta$	Not defined	sinusoidal masker, multiplied noise signal

masker and the signal are both Gaussian noises and the dashed curve shows the conditions where the masker is a Gaussian noise and the signal is a sinusoid. Whereas the solid curve is a straight line, as predicted, the dashed curve shows that two values of $r_{E_LE_R}$ exist for certain values of $\rho_{E_LE_R}$.

VI. DISCUSSION

A. General aspects

In the previous sections we have derived expressions for the envelope correlation for the MoSm condition. Comparing the results for this condition with the results derived for MoSπ (van de Par and Kohlrausch, 1995) we find in nearly all cases that for small SMRs, the change in correlation due to the addition of the signal to the masker in the MoSm condition is close to one quarter of that for MoSπ. This implies that in experiments where the envelope correlation of a stimulus is a good predictor for the detectability of the signal, thresholds for the MoSπ condition should be 6 dB lower than for the comparable MoSm condition.

The only two exceptions to this rule are that for the MoSm condition the envelope cross covariance is not defined for a masker with a flat envelope and that the MoSm envelope cross correlation and cross covariance for multiplied noise with $\cos\vartheta=0$ depend on the SMR in a much more complex way than for MoSπ.

In addition, we found that the approximations for the MoSm envelope correlation for very large SMRs are very different from the approximations for very small SMRs. For the MoSπ condition, envelope correlations for very small and very large SMRs can always be related to each other by exchanging the masker and signal types.

The approximations derived in this paper are summarized in Tables V and VI showing correlation values for very small and very large signal-to-masker ratios, respectively. Table V shows Δr and $\Delta\rho$ values while Table VI shows r and ρ values. In order to present the approximations in a uniform way, some of the approximations were rewritten in a different form. In these tables the first three columns show the statistical properties of the envelopes. The probability distributions of the signal and masker envelope, P_s, and P_m in the first two columns are used to denote that the envelopes result from a random process and consequently are not constant. The following columns show the waveform correlation, the envelope cross correlation, the envelope cross covariance, and a description of the masker and signal.

The variable l is defined as the SMR: $l=\langle s^2\rangle/\langle m^2\rangle$. For

TABLE VI. An overview of approximations for the cross correlation and the cross covariance of the envelope (columns 5 and 6) and of the waveforms (column 4) for the case that $\langle m^2\rangle \ll \langle s^2\rangle$. The first two columns show the properties of masker and signal envelope, the third column show the distribution of the phase difference between masker and signal.

m	s	ϕ	$\rho_{LR} = r_{LR}$	$\rho_{E_L E_R}$	$r_{E_L E_R}$	Description
P_m	P_s	unif.	0	$\frac{\langle m\rangle\langle s\rangle}{\sqrt{\langle m^2\rangle\langle s^2\rangle}}$	0	noise masker, noise signal
P_m	const.	unif.	0	$\frac{\langle m\rangle\langle s\rangle}{\sqrt{\langle m^2\rangle\langle s^2\rangle}}$	0	noise masker, sinusoidal signal
const.	P_s	unif.	0	$\frac{\langle m\rangle\langle s\rangle}{\sqrt{\langle m^2\rangle\langle s^2\rangle}}$	Not defined	sinusoidal masker, noise signal
const.	const.	unif.	0	1	Not defined	sinusoidal masker, sinusoidal signal with different freq.
Rayl.	Rayl.	unif.	0	$\frac{1}{4}\pi$	0	Gaussian masker and signal
Rayl.	const.	unif.	0	$\frac{1}{2}\sqrt{\pi}$	0	Gaussian masker, sinusoidal signal
const.	Rayl.	unif.	0	$\frac{1}{2}\sqrt{\pi}$	Not defined	sinusoidal masker, Gaussian signal
P_m	P_s	const.	0	$\frac{\langle m\rangle\langle s\rangle}{\sqrt{\langle m^2\rangle\langle s^2\rangle}}$	0	multiplied noise masker and signal
P_m	const.	const.	0	$\frac{\langle m\rangle\langle s\rangle}{\sqrt{\langle m^2\rangle\langle s^2\rangle}}$	0	multiplied noise masker, sinusoidal signal
const.	P_m	const.	0	$\frac{\langle m\rangle\langle s\rangle}{\sqrt{\langle m^2\rangle\langle s^2\rangle}}$	Not defined	sinusoidal masker, multiplied noise signal

the case that the phase difference between the masker and the signal is constant, the variable ϑ denotes the phase difference between masker and signal. The approximations presented here are only valid for $\cos\vartheta \neq 0$.

B. The definition of envelope correlation in binaural and CMR studies[4]

From the mathematical analysis it is clear that the envelope cross correlation and the envelope cross covariance are dependent on the statistics of the masker and the signal in very different ways. This is true for both the MoSm and the MoSπ conditions. When assumptions are made about the sensitivity of the auditory system to envelope correlation, a distinction has to be made between the two definitions of correlation.

Bernstein and Trahiotis (1996) have argued that for binaural detection at high frequencies, the envelope cross correlation is a more appropriate stimulus property for describing signal detection than the envelope cross covariance. They asked subjects to discriminate between an MoSo stimulus and an MoSπ stimulus using a Gaussian noise masker and a sinusoidal signal. The signal-to-masker ratio was varied from -30 to 30 dB. The resulting psychometric function was symmetrical around an SMR of 0 dB. Bernstein and Trahiotis (1996) concluded that this was in good agreement with the assumption that the normalized cross correlation of the envelope is the stimulus property that describes the cue for this condition, and not the cross covariance.

In relation to CMR, several researchers have discussed the idea that changes in the envelope correlation between the various spectral components of a stimulus may be the basis of CMR (e.g., Richards, 1987; Buus *et al.*, 1996). Attention has been paid, however, only to the envelope cross covariance and for this measure it was often found that observed data could not be explained satisfactorily (e.g., Hall *et al.*, 1988; Fantini, 1991; Eddins and Wright, 1994). Little or no attention has been paid so far to the normalized cross correlation in relation to CMR.

In the light of our findings about the differences between the two types of envelope correlation, it is interesting to reevaluate the results of a number of CMR studies. Richards (1987) was the first author to propose that the envelope cross covariance was an important cue in CMR. This hypothesis was supported by experimental data which showed that subjects were sensitive to a change of the covariance of the envelopes of two noise bands centered at different frequencies. Moreover, an analysis of the data revealed that the discriminability of stimuli with different mean values of the

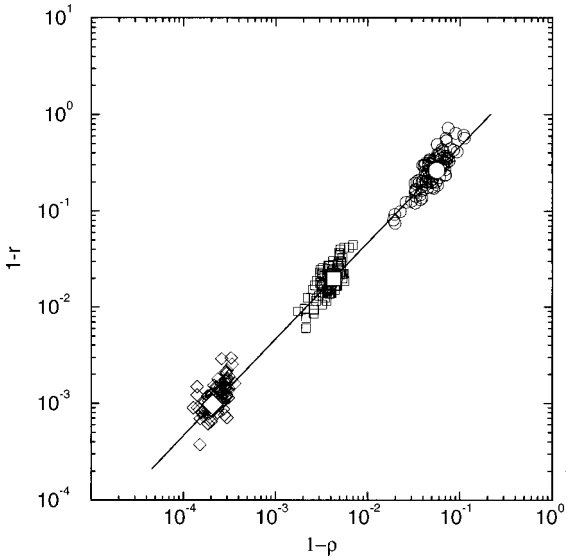

FIG. 10. Relations between the change in envelope cross correlation and the change in envelope cross covariance with respect to unity for partially correlated Gaussian noise. The solid line shows expected values. The opaque symbols show expected values for three specific values of ρ, for which the sample-to-sample values of $1-\rho$ and $1-r$, using stimuli with the same bandwidth and duration as in Richards experiment (1987), are indicated by the open symbols.

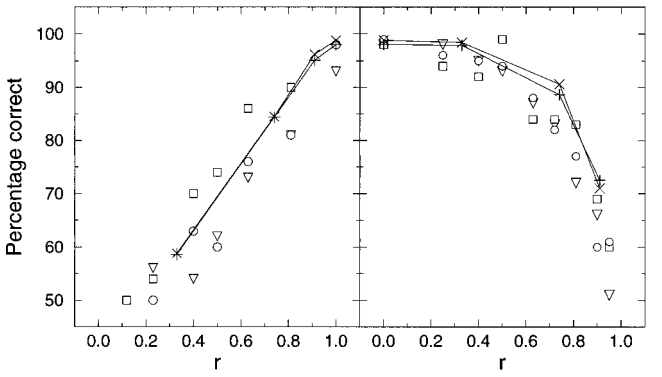

FIG. 11. Percentages of correct discrimination for several values of the envelope cross covariance. The two panels show data from Richards (1987) (open symbols) and model prediction based on the envelope cross correlation (+) and the envelope cross covariance (×). For the left and right panels the reference covariance was 0 and 1, respectively.

envelope cross covariance could be related unequivocally to the sample-to-sample variability of the envelope cross covariance. In order to show this, Richards transformed envelope cross covariances into Fisher's z scores and showed that the sample-to-sample distribution, of each stimulus set that was used, was normal with constant variance independent of the mean z score of that stimulus set. In addition, it was shown that the discriminability of two sets of stimuli in percentages correct was directly related to the difference in mean z scores of each set.

Richards used the ''three generator case'' (Licklider and Dzendolet, 1948) with Gaussian noises to generate stimuli with different correlation values. Because Gaussian noise was used in this experiment, the envelope cross correlation and the envelope cross covariance of stimuli were related linearly (cf. Sec. V). Therefore we can surmise that the experimental support that Richards found for the envelope cross covariance also holds for the envelope cross correlation. In order to verify this notion we tested the detection performance of a simple model based on either the envelope cross covariance or the envelope cross correlation. This may seem trivial because the envelope cross correlation and the envelope cross covariance are linearly related for the stimuli used by Richards. However, this linear relation only applies to the expected values of the correlation and the covariance. The sample-to-sample values are only approximately related linearly as is shown in Fig. 10. Here the open symbols show the relation between changes in correlation and covariance with respect to unity for three series of 100 stimuli generated in the same way as Richards did, while the opaque symbols show the expected values of changes in the correlation and the covariance. Since the open symbols are not on top of the solid line showing expected values, the sample-to-sample values are clearly not linearly related.

In our modeling, on each trial, a reference and a test stimulus were generated following Richards' specifications. More specifically, two stimuli were generated according to the ''three generator case'' with different degrees of envelope coherence by specifying the level ratio of the ''paired'' and the 'independent' bands (cf. Richards, 1987). Internal noise was modeled by adding two independent Gaussian noises to each of the noise bands. The internal noise had the same bandwidth as the stimulus noise bands and was added at a level of -8 dB with respect to the masker level. The decision variable that was used by the model was the envelope correlation between the two noise bands. On each trial, this variable was calculated for the two stimuli with different degrees of envelope coherence. Due to the internal noise and the variability in envelope correlation values for a given level ratio of ''paired'' and ''independent'' bands, discrimination is not perfect and usually percentages of correct discrimination of less than 100 are obtained. A total of 2500 pairs of stimuli were presented to the model for each condition and the resulting percentages of correct discriminations are shown in Fig. 11 (black symbols) together with the data measured by Richards (open symbols). The model was either based on the envelope cross correlation (+) or on the envelope cross covariance (×).

Independent of the type of envelope correlation, the performance of the model is similar to that of the subjects. Therefore, for the stimuli that she employed, Richards' conclusion in support of correlation cues applies to both types of envelope correlation discussed in the present paper.

Hall *et al.* (1988) studied CMR for multicomponent signals. In one of the conditions the masker consisted of two comodulated noise bands. The signal consisted of either one single sinusoid, added to the spectral center of one of the masker bands, or of two sinusoids each of which was added to one of the masker bands. Their analysis of the distribution of the envelope correlation was based on the cross covariance measure. They concluded that this measure was not a good descriptor of their data. On the other hand, they also analyzed their data with an Equalization and Cancellation type model (Buus, 1985) and found that it provided a much better description of their data. Interestingly, Green (1992)

showed that an EC-based model is equivalent to a detection model based on envelope correlation. Unfortunately, Green's derivations can be interpreted in two ways. They can either be interpreted to apply to the envelopes perse, or to the envelopes from which the dc components are subtracted (cf. Bernstein and Trahiotis, 1996). In the first case, the EC model (with envelopes as input) is equivalent to the envelope cross correlation. In the latter case, the EC model (with envelopes without dc components as input) is equivalent to the envelope cross covariance. Since Hall *et al.* (1988) worked with envelopes *with* dc components, their EC approach is equivalent to the envelope cross correlation. Thus the study of Hall *et al.* in fact shows that the two measures for envelope correlation give different results and that the envelope cross correlation is a better descriptor for their CMR thresholds.

Eddins and Wright (1994) investigated the detectability of a sinusoidal signal which was added in phase to one of two simultaneously presented sinusoidally amplitude modulated (SAM) tonal maskers. The sinusoidal signal had a center frequency which was equal to the center frequency of one of the SAM maskers. Thresholds were compared with the case that there was only one SAM masker. The data showed that thresholds for the case of two SAM maskers were lower than for one SAM masker. Based on this result, the authors rejected the involvement of envelope correlation in their CMR experiments. They argued that ''... for SAM-tonal maskers, the addition of a signal produces no change in the correlation among on-frequency and flanking-band maskers. The signal is simply an increase in the magnitude of the central component of the on-frequency masker, which produces a corresponding decrease in modulation depth. The sinusoidal envelope pattern, however, is unchanged. Thus an envelope correlation model would predict no CMR for SAM-tonal maskers, contrary to the present results.'' (Eddins and Wright, 1994, p. 3439). This statement of an unchanged envelope correlation is correct for the cross covariance [Eq. (6)], but it is incorrect for the the cross correlation [Eq. (5)]. For the stimuli Eddins and Wright used, the envelope cross *correlation* would change due to the addition of the signal and this could have supported the lower detection thresholds for the case that there are two SAM maskers instead of only one.

Without claiming here that the envelope cross correlation can be generally used to explain detection in CMR experiments, we want to draw attention to the fact that there is more support in favor of this cue than is generally acknowledged in the recent literature.

C. The effect of bandwidth on CMR

One of the strong arguments against the idea that the envelope correlation is an important cue in CMR experiments is the fact that the CMR decreases with increasing masker bandwidth. In a study by Moore and Emmerich (1990) the dependence on bandwidth was discussed for CMR and for its effect on the ability of subjects to discriminate two comodulated noise bands from two uncorrelated noise bands. In the discrimination condition, performance was best for the larger bandwidths, while CMR is largest for narrow bandwidths. These results were interpreted as suggesting that different mechanisms are involved in the two types of experimental conditions.

At this point in the discussion, one has to distinguish carefully between the *threshold value* in the comodulated condition and the *size* of the CMR effect, which is the difference between CMR threshold and reference threshold. This is of relevance because it has been long known (e.g., Bos and de Boer, 1966) that thresholds for sinusoids in a single band of noise with a subcritical bandwidth and with constant overall level increase considerably with decreasing bandwidth.

Our own analysis in the present paper has shown that, for sufficiently low SMRs the envelope correlation is only dependent on the signal-to-masker ratio of the stimulus. Thus if the envelope correlation is used as a cue, detection thresholds should not depend on bandwidth, as long as each noise band is confined to one critical band. However, some dependence on bandwidth may occur, because for stimuli of finite duration, the variability of envelope correlation values decreases with increasing bandwidth.

For the comodulated condition, we therefore expect that the signal-to-masker ratio in the masking release conditions are fairly independent of bandwidth. However, the amount of CMR may change as a function of bandwidth, due to changes in thresholds for the reference condition.

In order to examine CMR results from this point of view, data from three studies are combined in Table VII. All data are for conditions with a sinusoidal signal centered in one noise band and different numbers of comodulated flanking bands. Data are shown for reference conditions where there is no benefit from across frequency listening and for the comodulated condition. The bandwidth of all noise bands was equal and is given in the first column. The upper panel shows data from Eddins and Wright (1994) measured with five comodulated noise bands, which varied in center frequency from 1.5 to 3.5 kHz, and a signal frequency of 2.5 kHz. The middle panel shows data from Hall (1986), measured for a masker of 500 Hz and a flanking band of 350 Hz. The bottom panel are data from Schooneveldt and Moore (1987), measured for a masker of 2 kHz with varying flanking-band frequency. Average results are shown for flanking-band frequencies of 1, 1.4, 2.6, and 3 kHz. All data in Table VII are averages across subjects.

From the results shown in Table VII it is clear that signal-to-masker ratios for the comodulated conditions remain fairly constant with increasing bandwidth up to 100 Hz and that they are therefore consistent with the hypothesis that subjects are sensitive to changes in the envelope correlation. In contrast the reference data show a clear decrease with increasing bandwidth. This shows that the decrease in CMR with increasing bandwidth is due to the decrease of the reference thresholds, and not to an increase of the threshold in the comodulated condition. For bandwidths beyond 100 Hz, one can expect that, due to auditory filtering, the envelopes of the various masker bands start to become decorrelated. Since the middle panel shows low-frequency data, such a decorrelation is expected at even smaller bandwidths.

In contrast, the data of Moore and Emmerich (1990)

TABLE VII. Results of Eddins and Wright (1994) (upper data panel), Hall (1986) (middle data panel), and Schooneveldt and Moore (1987) (bottom data panel). The columns show masker bandwidth, signal thresholds, overall masker level, and the signal-to-masker ratio. Signal thresholds and signal-to-masker ratios are both given for the reference and the comodulated conditions. For Schooneveldt and Moore, data are taken from the monotic conditions shown in their Fig. 5 for the four largest flanking band versus signal-frequency separations.

	Signal threshold (dB)		Overall noise level (dB)	SMR (dB)	
Bandwidth (Hz)	Reference	Comodulated		Reference	Comodulated
10	63.5	52.5	60.0	3.5	−7.5
16	63.0	52.5	62.0	1.0	−9.5
20	65.0	54.0	63.0	2.0	−9.0
32	65.0	55.5	65.0	0.0	−9.5
50	67.0	58.0	67.0	0.0	−9.0
100	68.5	62.5	70.0	−1.5	−7.5
200	71.5	67.5	73.0	−2.0	−5.5
50	66.0	58.5	67.0	−1.0	−8.5
100	68.0	62.5	70.0	−2.0	−7.5
200	69.0	68.0	73.0	−4.0	−5.0
25	61.5	57.0	67.0	−6.5	−10.0
50	58.0	56.0	67.0	−9.0	−11.0
100	57.0	56.0	67.0	−10.0	−11.0

suggest that the discriminability of pairs of noise bands with coherent and incoherent envelopes is better for larger noise bandwidths. However, comparing the improvement in percentages correct discrimination going from 25-Hz to 100-Hz bandwidth we find only a 6% difference for high-frequency stimuli (on-frequency band 2500 Hz) and an 11% difference for low-frequency stimuli (on-frequency band 350 Hz).[5] These improvements do not seem to be large considering that the variability between subjects and of each individual data point is of the order of 10%. Taking this into account and considering that the change in CMR with bandwidth is due to changes in the reference thresholds, these data do not seem to provide sufficient support for making the strong claim that different detection mechanisms underly the two situations.

Because this question is of interest for understanding across-channel processes, at the end of our theoretical paper we propose some experiments that could shed light on this issue. It would be interesting to investigate within one experimental study whether thresholds that are found in CMR situations with a sinusoidal signal are in line with the jnds in envelope correlation with respect to fully correlated envelopes (note that this latter case is very similar to an experiment where the signal to be detected would be a noise with the same bandwidth and center frequency as the masker band). According to the derivations in Sec. II, the thresholds for both situations should be the same and the results should therefore support or weaken the hypothesis that changes in envelope correlation are the basis of the CMR.

Furthermore, one could measure psychometric functions for the discriminability of pairs of noises with different degrees of envelope correlation for several noise bandwidths in a way similar to that of Richards (1987). Applying the same data analysis as Richards did would give an idea about whether envelope correlation is a valid cue for the different noise bandwidths investigated. In addition, it would be possible to derive detection thresholds form the psychometric functions (by finding envelope correlation values with 70.7% correct responses and transforming these envelope correlation values to SMRs using Fig. 2). These thresholds should be in line with thresholds found in CMR experiments. The psychometric functions can also supply the percentages of correct discrimination of coherent and incoherent envelopes, which should be in line with the findings of Moore and Emmerich (1990). Thus such an experiment could show to what extent the study by Moore and Emmerich (1990) and various CMR studies are consistent with the assumption that detection in these cases is based on envelope correlation.

VII. SUMMARY

(1) The derivations in the previous sections show that for a given MoS*m* stimulus the values of the envelope cross correlation and the envelope cross covariance are generally not the same.

(2) Whereas the waveform correlation does not depend on the statistics of the masker and signal, the envelope cross correlation and envelope cross covariance are dependent on these statistics.

(3) Only for very small SMRs, the envelope cross correlation is nearly independent of masker and signal statistics and is approximately equal to the square root of the waveform correlation. The only exception is found for a multiplied-noise masker or signal for which the phase between masker and signal fine structure is fixed.

(4) The envelope cross covariance can also be related to the waveform correlation in a simple way, but in this case the envelope distribution of the masker has to be taken into account. This implies that for small SMRs, the envelope cross covariance is dependent not only on the SMR but also on the masker statistics.

(5) The data from Richards (1987) in support of the hypothesis that subjects use the envelope cross covariance for discriminating between noise bands with different de-

grees of envelope coherence are also consistent with the hypothesis that subjects use the envelope cross correlation.

(6) Although the data from several CMR studies are not in line with the assumption that subjects are sensitive to changes in the envelope cross covariance, they seem nevertheless to be consistent with an assumed sensitivity to envelope cross correlation.

(7) The dependence on masker bandwidth in CMR and of the percentages of correct discrimination between coherent and incoherent noise bands does not seem to provide sufficient support for assuming that different detection mechanisms are involved in the two types of experiments.

ACKNOWLEDGMENTS

We thank Dr. Andrew Oxenham and both reviewers for their very helpful comments on an earlier version of this manuscript.

APPENDIX A: APPROXIMATIONS FOR THE ENVELOPE CROSS CORRELATION

For small SMRs, a simple approximation can be found for the envelope cross correlation as given in Eq. (22). Since $\langle s^2\rangle \ll \langle m^2\rangle$, the probability of finding $s^2 \ll m^2$ is close to unity. For $s^2 \ll m^2$, the quantity in Eq. (20)

$$T_n \equiv \frac{m^{2n+1}s^{2n}}{(m^2+s^2)^{2n-1/2}} \tag{A1}$$

can be approximated in the following way:

$$T_0 = m\sqrt{m^2+s^2} \approx m^2 + \tfrac{1}{2}s^2, \tag{A2}$$

$$T_1 = \frac{m^3 s^2}{(m^2+s^2)^{3/2}} \approx s^2, \tag{A3}$$

and for $n>1$

$$T_n \approx \frac{s^{2n}}{m^{2n-2}} \approx \frac{s^{2n}}{m^{2n-2}+s^{2n-2}}. \tag{A4}$$

For the rare cases that $s^2 \gg m^2$ or $s^2 \approx m^2$, the approximations of Eqs. (A2)–(A4) are not valid. However, this has little effect on the expected values of T_n, because the approximations have a value close to s^2 in these cases. To assure this, the last approximation in Eq. (A4) is necessary. The error that is introduced by the approximation of T_0 and T_1 is at least of the same order as T_n for $n>1$. The terms T_n are approximated to indicate their magnitudes in order to assures that they are negligibly small.

Substituting the expected values of the approximations into Eq. (20), we can write:

$$\langle E_L E_R\rangle \approx \langle m^2\rangle + \frac{1}{2}\langle s^2\rangle - \frac{1}{4}\langle s^2\rangle - \frac{15}{64}\left\langle \frac{s^4}{m^2+s^2}\right\rangle + \cdots. \tag{A5}$$

Of the terms in Eq. (A5), only the first three are needed for a good approximation. For sufficiently small SMRs, all further terms have successive expected values that are negligible with respect to the preceding values. The normalization factor in Eq. (21) can be approximated by the first two terms of a Taylor series as

$$\sqrt{\langle E_L^2\rangle\langle E_R^2\rangle} \approx \langle m^2\rangle + \tfrac{1}{2}\langle s^2\rangle. \tag{A6}$$

By dividing Eqs. (A5) and (A6) and using Eqs. (3) and (4), an approximation for the envelope correlation is obtained:

$$\rho_{E_L E_R} \approx \frac{\langle M^2\rangle + \frac{1}{4}\langle S^2\rangle}{\langle M^2\rangle + \frac{1}{2}\langle S^2\rangle} \approx \frac{\langle M^2\rangle - \frac{1}{8}\langle S^2\rangle}{\langle M^2\rangle + \frac{1}{8}\langle S^2\rangle}. \tag{A7}$$

For the case that the SMR is very large, an approximation can be made for the asymptotic value of the envelope correlation. This approximation is based on the assumption that the probability of finding $s^2 \gg m^2$ is close to unity. The expected value within the summation of Eq. (20) (denoted with U_n) can be expressed as:

$$U_0 = \langle m\sqrt{m^2+s^2}\rangle = \left\langle ms\sqrt{1+\frac{m^2}{s^2}}\right\rangle \approx \langle ms\rangle = \langle m\rangle\langle s\rangle, \tag{A8}$$

and for $n>0$

$$U_n \approx \left\langle \frac{m^{2n+1}}{s^{2n-1}+m^{2n-1}}\right\rangle. \tag{A9}$$

Because $s^2 \gg m^2$ with a probability close to unity, we can expect that also $U_0 \gg U_n$ for each $n>0$. From the numerator of Eq. (22), only the first term has to be taken into account for a good approximation of the envelope correlation at large SMRs.

The denominator can be approximated as follows:

$$\langle m^2\rangle\sqrt{1+\frac{\langle s^2\rangle}{\langle m^2\rangle}} \approx \sqrt{\langle m^2\rangle\langle s^2\rangle}. \tag{A10}$$

By substituting Eqs. (A8) and (A10) into Eq. (22), an approximation for the envelope correlation is obtained:

$$\rho_{E_L E_R} \approx \frac{\langle m\rangle\langle s\rangle}{\sqrt{\langle m^2\rangle\langle s^2\rangle}}. \tag{A11}$$

APPENDIX B: APPROXIMATIONS FOR THE ENVELOPE CROSS COVARIANCE

We can derive an approximation for the envelope cross covariance for the case that $\langle m^2\rangle - \langle m\rangle^2 \gg \langle s^2\rangle$; the first two terms of Eq. (28) give a good approximation. The same line of reasoning can be followed here as was used for the cross correlation [cf. Eq. (22)]. We use the fact that

$$\langle\sqrt{m^2+s^2}\rangle = \langle m\rangle + \epsilon_1, \tag{B1}$$

with $\epsilon_1 \ll \langle m\rangle$ and ϵ_1 of the order $\langle s^2/(m+s)\rangle$. Furthermore, we denote the first term of the series in Eq. (28) as ϵ_2, and we know that ϵ_2 is of the order $\langle s^2/(m+s)\rangle$ and thus that $\epsilon_2 \ll \langle m\rangle$. This results in the following expression for the mean of the envelope:

$$\langle E_L\rangle = \langle m\rangle + \epsilon, \tag{B2}$$

with $\epsilon = \epsilon_1 + \epsilon_2$. Evaluating Eq. (20) while taking into account the first two terms of the series yields

$$\langle E_L E_R\rangle = \langle m^2\rangle + \tfrac{1}{4}\langle s^2\rangle + \epsilon_3, \tag{B3}$$

with $\epsilon_3 \ll \langle s^2\rangle \ll \langle m^2\rangle - \langle m\rangle^2$. Since, in addition, the terms ϵ_1 and ϵ_2 are both of the order $\langle s^2/(m+s)\rangle$, the cross covariance of the envelopes can be written as

$$r_{E_L E_R} = \frac{\langle m^2\rangle + \tfrac{1}{4}\langle s^2\rangle + \epsilon_3 - (\langle m\rangle + \epsilon)\langle m\rangle}{\sqrt{(\langle m^2\rangle + \langle s^2\rangle - \langle m\rangle^2 - 2\epsilon\langle m\rangle - \epsilon^2)(\langle m^2\rangle - \langle m\rangle^2)}}. \tag{B4}$$

Using the assumption that $\langle m^2\rangle - \langle m\rangle^2$ is much larger than $\langle s^2\rangle$ and ϵ, along with the fact that ϵ_3 is much smaller than $\langle s^2\rangle$ for small SMRs, we can write an approximation for the envelope cross covariance:

$$r_{E_L E_R} \approx \frac{\langle m^2\rangle - \langle m\rangle^2 + \tfrac{1}{4}\langle s^2\rangle + \epsilon_3 - \epsilon\langle m\rangle}{\langle m^2\rangle - \langle m\rangle^2 + \tfrac{1}{2}\langle s^2\rangle - \epsilon\langle m\rangle}$$

$$\approx \frac{\langle m^2\rangle - \langle m\rangle^2 - \tfrac{1}{4}\langle s^2\rangle}{\langle m^2\rangle - \langle m\rangle^2}. \tag{B5}$$

[1]One can see that the cases for which $|\cos\phi| = 1$ and simultaneously $|m| = |s|$ contributes little to the overall expected value by assuming that the expected value is only calculated for cases where $||m| - |s|| > \delta$. From Eq. (14) it can be seen that we can make δ arbitrarily small in order to make the effect of this assumption negligibly small. At the same time this assumption makes sure that the sum of Eq. (18) converges.

[2]Depending on the SMR, the number of terms needed for an accurate calculation of $\rho_{E_L E_R}$ varied. For very small or very large SMRs, only two terms were needed, while for SMRs around 0 dB up to 22 terms were needed. The calculation of terms was stopped whenever a term was a factor of 200 000 smaller than the average of all the previous terms.

[3]About a year before we derived Eq. (46), Bernstein (1995) suggested a very similar but empirical relation between the envelope cross correlation and the envelope cross covariance.

[4]Most of the ideas in the following section were first put forth in a manuscript by Kohlrausch and van de Par (1995). This manuscript was referred to in the recent article by Bernstein and Trahiotis (1996) as ''Kohlrausch and van de Par (1996).''

[5]For this condition the noise bandwidth of 100 Hz exceeds the width of one auditory filter and therefore one can question to what extent these experiments can be understood in terms of a simple envelope correlation model. Furthermore, at low frequencies, not only the envelope but also the fine structure of the stimulus is coded in the auditory-nerve activity. It is not obvious how envelope correlation models should be applied to such conditions.

Bernstein, L. R. (**1995**). Personal communication.

Bernstein, L. R., and Trahiotis, C. (**1992**). ''Discrimination of interaural envelope correlation and its relation to binaural unmasking at high frequencies,'' J. Acoust. Soc. Am. **91**, 306–316.

Bernstein, L. R., and Trahiotis, C. (**1996**). ''On the use of the normalized correlation as an index of interaural envelope correlation,'' J. Acoust. Soc. Am. **100**, 1754–1763.

Bos, C. E., and de Boer, E. (**1966**). ''Masking and discrimination,'' J. Acoust. Soc. Am. **39**, 708–715.

Buus, S. (**1985**). ''Release from masking caused by envelope fluctuations,'' J. Acoust. Soc. Am. **78**, 1958–1965.

Buus, S., Zhang, L., and Florentine, M. (**1996**). ''Stimulus-driven, time-varying weights for comodulation masking release,'' J. Acoust. Soc. Am. **99**, 2288–2297.

Cohen, M. F., and Schubert, E. D. (**1987**). ''Influence of place synchrony on detection of a sinusoid,'' J. Acoust. Soc. Am. **81**, 452–458.

Colburn, H. S. (**1977**). ''Theory of binaural interaction based on auditory-nerve data. II. Detection of tones in noise,'' J. Acoust. Soc. Am. **61**, 525–533.

Davenport, W. B., and Root, W. L. (**1958**). *An Introduction to the Theory of Random Signals and Noise* (McGraw-Hill, New York).

Durlach, N. I., Gabriel, K. J., Colburn, H. S., and Trahiotis, C. (**1986**). ''Interaural correlation discrimination: II. Relation to binaural unmasking,'' J. Acoust. Soc. Am. **79**, 1548–1557.

Eddins, D. A., and Wright, B. A. (**1994**). ''Comodulation masking release for single and multiple rates of envelope fluctuation,'' J. Acoust. Soc. Am. **96**, 3432–3442.

Fantini, D. A. (**1991**). ''The processing of envelope information in comodulation masking release (CMR) and envelope discrimination,'' J. Acoust. Soc. Am. **90**, 1876–1888.

Green, D. M. (**1992**). ''On the similarity of two theories of comodulation masking release,'' J. Acoust. Soc. Am. **91**, 1769.

Hall, J. W. (**1986**). ''Binaural frequency selectivity and CMR,'' in *Auditory Frequency Selectivity*, edited by B. C. J. Moore and R. D. Patterson (Plenum, New York).

Hall, J. W., Grose, J. H., and Haggard, M. P. (**1988**). ''Comodulation masking release for multicomponent signals,'' J. Acoust. Soc. Am. **83**, 677–686.

Kohlrausch, A., and van de Par, S. (**1995**). ''On the need for a clear definition of the term 'envelope correlation' in comodulation masking release,'' unpublished IPO manuscript No. 1068.

Licklider, J. C. R., and Dzendolet, E. (**1948**). ''Oscillographic scatterplots illustrating various degrees of interaural correlation,'' Science **107**, 121–124.

McFadden, D. (**1986**). ''Comodulation masking release: Effects of varying the level, duration, and time delay of the cue band,'' J. Acoust. Soc. Am. **80**, 1658–1667.

Moore, B. C. J., and Emmerich, D. S. (**1990**). ''Monaural envelope correlation perception, revisited: Effects of bandwidth, frequency separation, duration, and relative level of the noise bands,'' J. Acoust. Soc. Am. **87**, 2628–2633.

Moore, B. J. C., Hall, J. W., Grose, J. H., and Schooneveldt, G. P. (**1990**). ''Some factors affecting the magnitude of comodulation masking release,'' J. Acoust. Soc. Am. **88**, 1694–1702.

Råde, L., W. B., and Westergren, B. (**1990**). *Beta—Mathematics Handbook* (StudentLitteratur, Lund).

Richards, V. M. (**1987**). ''Monaural envelope correlation perception,'' J. Acoust. Soc. Am. **82**, 1621–1630.

Schooneveldt, G. P., and Moore, B. C. J. (**1987**). ''Comodulation masking release (CMR): Effects of signal frequency, flanking-band frequency, masker bandwidth, flanking-band level, and monotonic versus dichotic presentation of the flanking-band,'' J. Acoust. Soc. Am. **82**, 1944–1956.

van de Par, S., and Kohlrausch, A. (**1995**). ''Analytical expressions for the envelope correlation of certain narrow-band stimuli,'' J. Acoust. Soc. Am. **98**, 3157–3169.

van de Par, S., and Kohlrausch, A. (**1998**). ''Diotic and dichotic detection using multiplied-noise maskers,'' J. Acoust. Soc. Am. **103**, 2100–2110.

An adaptive noise canceller for hearing aids using two nearby microphones

Jeff Vanden Berghe
Lab. Exp. ORL, KULeuven, Kapucijnenvoer 33, B 3000 Leuven, Belgium and ESAT, KULeuven, Kardinaal Mercierlaan 94, B 3001 Leuven, Belgium

Jan Wouters
Lab. Exp. ORL, KULeuven, Kapucijnenvoer 33, B 3000 Leuven, Belgium

(Received 25 March 1997; accepted for publication 19 February 1998)

An adaptive noise cancellation scheme based on two-stage adaptive filtering as proposed by Van Compernolle [*Proceedings of the IEEE International Conference on Acoustics, Speech and Signal Processing* (IEEE, New York, 1990)] was tested for two identical directional microphones mounted in an endfire configuration within a single behind-the-ear (BTE) hearing aid. Speech intelligibility tests were carried out with two normal hearing subjects and three hearing aid users with moderate hearing losses, in a realistic test environment using open set words and sentences. A significant improvement, on average more than 5 dB, of speech reception threshold (SRT) in background noise was obtained. © *1998 Acoustical Society of America.* [S0001-4966(98)01606-3]

PACS numbers: 43.66.Ts, 43.60.Gk, 43.60.Lq [JWH]

INTRODUCTION

The interference of noises and undesirable sounds is very disturbing for speech recognition in everyday conditions, especially for hearing-impaired listeners. This is due to reduced hearing abilities that lead, for example, to increased masking effects of the target signal, speech (Moore, 1995).

A number of techniques based on single- and multi-microphone systems have already been applied to suppress unwanted background noise. Single microphone techniques generally perform poorly when the frequency spectra of the desired and the interfering sounds are similar, and when the spectrum of the interfering sound varies rapidly (Preves, 1994; Levitt *et al.*, 1993).

By using more than one microphone, sounds can be sampled spatially and the direction of arrival can be used for discriminating desired from undesired signals. In this way it is possible to suppress stationary and nonstationary noise sources independently of their spectra. An application for hearing aids requires a noise reduction approach with a microphone array that is small enough to fit into a behind-the-ear (BTE) device. As BTEs are limited in size and computing power, only directional microphones are currently used to reduce the effects of interfering noise sources. Compared to omnidirectional microphones, directional ones have shown improved attenuation of diffuse background noise by about 2.5 dB (Soede *et al.*, 1993b). In multi-microphone systems two major types of noise reduction strategies are used, strategies based on fixed beamforming and strategies based on adaptive processing schemes.

Beamforming with fixed arrays focuses on a target direction independently of the interfering signal. To obtain effective and at the same time stable directivity, the array lengths should be comparable to the wavelength of the signal. Improvements of speech intelligibility in noise have been obtained with microphone arrays of 10 and 14 cm (Soede *et al.*, 1993b; Kates and Weiss, 1996). However, this is not possible with array spans that can be integrated in a BTE hearing aid.

The second technique is adaptive noise cancellation, which tries to null out the interfering noise source(s). However, in comparison with fixed beamforming, it requires more computational power for signal processing. Although the potential of small arrays to reduce the effect of directional jammers has already been demonstrated (Peterson, 1989), most studies testing adaptive systems for hearing aids make use of microphone arrays which have dimensions that are larger than those of BTE hearing aids and/or which have unlimited computing power. Adaptive filtering schemes have been studied using microphone arrays with lengths down to about 7 cm (Greenberg and Zurek, 1992; Weiss, 1987; Kates and Weiss, 1996) and with binaural hearing aid systems (Peterson *et al.*, 1987; van Hoesel and Clark, 1995; Kompis and Dillier, 1994; DeBrunner and McKinney, 1995). The main disadvantage of small microphone arrays is that they cannot suppress directional noise sources at small angles compared to the desired signal source (Peterson, 1989). Large intermicrophone distances on the other hand, as for the binaural systems, have the disadvantage of spatially undersampling the high-frequency components of the signal (Greenberg and Zurek, 1992).

Here we report on the performance of a two-stage adaptive filtering strategy for noise suppression. It is implemented for a normal-sized BTE hearing aid equipped with two identical front-facing directional microphones, mounted in an endfire configuration. The intermicrophone distance is about 3 cm. We assume that the desired signal is speech and that it comes from the frontal direction. The strategy was evaluated both off-line using physical criteria (improvement in signal-to-noise ratio, SNR) and tested perceptually using a real-time implementation with both normal-hearing and moderately impaired listeners.

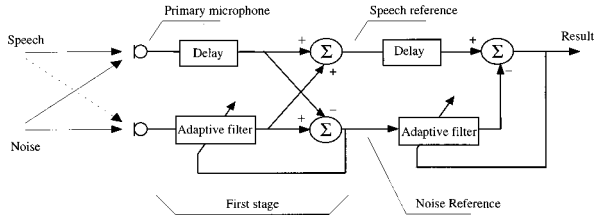

FIG. 1. Two-stage adaptive noise cancelling. Both microphone signals contain speech as well as noise. The first section of the system serves at improving the noise reference by eliminating speech, and may therefore only adapt when speech peak energy is dominant. The second section consists of an unconstrained ANC of which the coefficients are only allowed to adapt during absence of speech, as there is still a signal component in the reference channel, albeit much smaller.

I. STRATEGY DESCRIPTION

A disadvantage of head-sized arrays for enhancing the ratio of speech to background noise is that all microphones contain an important amount of both speech and noise. One cannot speak about a true noise reference as in the adaptive noise canceller (ANC) by Widrow and Stearns (1985). In the adaptive beamformer proposed by Griffiths and Jim (1982), a delay and subtract operation was used to eliminate the speech from the noise reference. However, this scheme can suffer from signal leakage into the reference channel even when adaptation is inhibited during speech (Van Compernolle, 1990a) due to reverberation and target misalignment which could lead to uncontrollable signal distortion. An adaptive filter can be used instead of the simple delay and subtract method to better model some of the room characteristics and so improve the noise signal estimate (Van Compernolle, 1990b). It has the advantage that it can adapt to slowly moving targets and head movements, does not need a fixed sampling rate, and is nearly independent of construction parameters or differences in microphone types. An illustration of the signal processing strategy is shown in Fig. 1. Both microphone signals contain speech as well as noise. The first section of the system serves at improving the noise reference by eliminating speech, and may therefore only adapt when speech peak energy is dominant. The output of the first adaptive filter should converge towards the delayed signal of the primary microphone as far as the speech component is concerned. In this way, preference is given in the first section to emphasizing the speech source over eliminating the noise signal. The second section consists of an unconstrained ANC of which the coefficients are only allowed to adapt during absence of speech, as there is still a signal component in the reference channel, albeit much smaller. The second adaptive filter models the difference between the noise reference and the noise portion of the delayed speech reference.

In order to adapt the filters during the appropriate intervals, a criterion is required to determine whether the desired signal is present or not. A real-time speech detector based on energy measurements of 10-ms nonoverlapping signal windows was implemented (Van Gerven and Xie, 1997). It calculates speech onset and offset thresholds as a function of the momentary noise statistics. Simulations were carried out with stationary and nonstationary noise sources. As long as the interfering signal does not exhibit the same dynamics as speech, this speech detection algorithm functions well down to about -5 dB SNR. A prerequisite for a real-time speech/noise discriminator is a minimal introduced time delay because the processed auditory signal should be reasonably well synchronized with visual information. The output of the system is delayed by about 16 ms, compared to the signal at the primary microphone, of which the frame-based speech detector uses 10 ms for time averaging and about 6 ms is taken by the adaptive filtering operation itself. This amount of delay is not expected to influence lip-reading performance, and can still be decreased if necessary.

II. OFF-LINE PHYSICAL EVALUATION

A. Methods

Physical evaluation of the system was performed with prerecorded signals using a two-microphone BTE in a moderately reverberant test room ($70\ m^3$, $T_{60}=450$ ms). The tests were carried out with hearing aid prototypes based on Philips M41-D Rainbow hearing aids equipped with a second directional microphone. The additional directional microphone was identical to the original one (Microtel model 61, cardioid with specified directivity index 5 dB, and specified forward–backward differences of 22, 16, and 12 dB at 0.5, 1, and 4 kHz, respectively) and mounted onto the earhook. The intermicrophone distance was 30 mm. With the hearing aid fitted to the right ear of a dummy head, the two microphones were on a horizontal line in an endfire configuration.

Speech and noise were presented with identical loudspeakers (Yamaha CBX-S3) at 1 m and at the same height as the center of the dummy head. The estimated direct to reverberant ratio was 7 dB at 1 m (Peutz, 1971). The speech source was at 0° azimuth. The azimuth angle of the noise source was varied, without changing the amplification (both sources at 70 dB SPL at 1 m). The long-term spectrum of the noise was matched to that of the speech. The sampling rate was 10.67 kHz, and the lengths of the first and second FIR filters were 6 and 50 coefficients, respectively. To allow for a noncausal response of the adaptive filters, a delay was introduced in both sections (three and six samples, respectively). The frontal microphone was chosen as the primary microphone because its SNR for a noise source at $+90°$ is slightly better.

B. Results

In Fig. 2 the improvement of the noise-to-signal ratio (NSR) in the noise reference, and the improvement of SNR in the speech reference, both with respect to SNR in the primary microphone, are shown. At the noise reference in Fig. 1, the first stage reduces the target speech by 8 dB,[1] and the noise by -3 to $+3$ dB depending on the noise source location. This improves the noise reference. After summation at the output of the first stage, the speech level is increased by about 5.5 dB. The noise also increases depending on the noise source angle as shown in Fig. 2. This does not lead to a large increase in SNR at the speech reference in Fig. 1, except for the peak around 130°. The resulting spatial re-

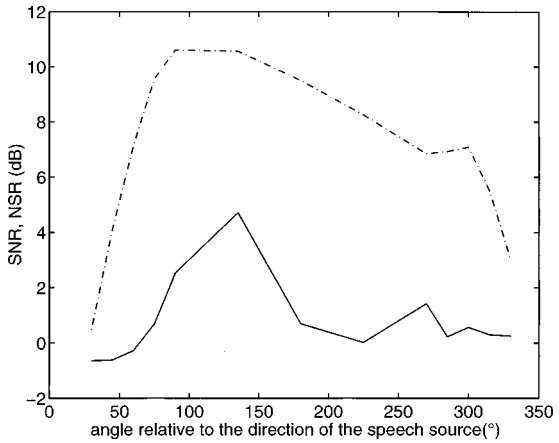

FIG. 2. Improvement of the noise-to-signal ratio (NSR) in the noise reference (··) and improvement of SNR in the speech reference (———), both with respect to SNR in the primary microphone, as a function of the noise source angle and measured on the basis of speech weighted noise.

sponse (for this specific setup of mannequin and speech source) shows a dip at about 130° due to destructive interference.

The SNR at the output of the system, for a SNR of 0 dB at the position of the head in absentia, was more than 6 dB for all noise angles from +45° to +315°, as shown in Fig. 3, e.g., for a noise source at 90° azimuth, noise suppression is in excess of 10 dB for frequencies above 700 Hz. Within a few dB, all noise source angles give rise to a flat transfer function magnitude[2] for speech between the signal of the speech at the output of the primary microphone and the output of the system. The two dashed lines in Fig. 3 show the contributions of the microphone (with head-shadow) and adaptive processing to the overall improved SNR. It can be noted from Fig. 3 that the directional characteristic of the microphones (head shadow included) and the asymmetric performance of the algorithm add up to a total SNR improvement of about 12 dB for a noise source in the hindmost hemisphere. This value is relative to the physical SNR at the center of the head in absentia. Due to head-shadow and microphone characteristics, the contribution of the direct component of a noise source at the rear or contralateral side is smaller and more complex to model by the second adaptive filter. These are the main factors contributing to the asymmetric performance of the algorithm.

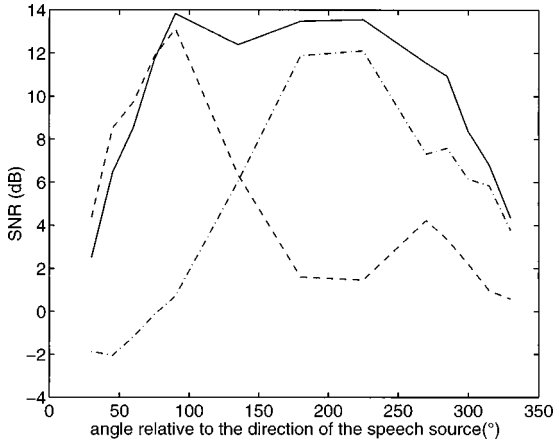

FIG. 3. The SNR at the output of the system (———), improvement due to adaptive processing (---), and SNR in the primary microphone (—·) as a function of the noise source angle when the SNR at the center of the head is 0 dB and measured on the basis of speech weighted noise.

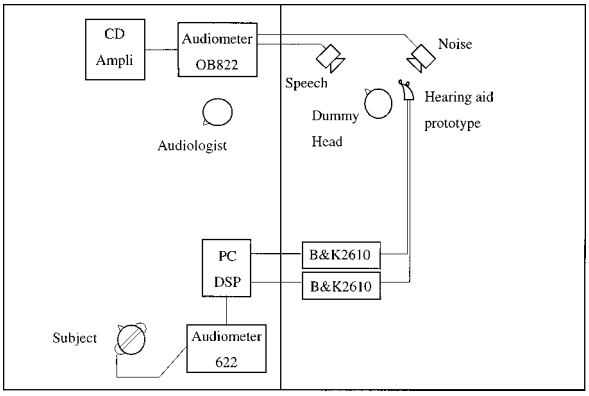

FIG. 4. Experimental setup for the perceptual evaluation of the ANC.

III. PERCEPTUAL EVALUATION

A. Methods

To allow perceptual evaluation, a real-time implementation of this two-stage adaptive filtering strategy was achieved on a portable PC-platform using a LSI C30 PC-board with a Texas Instruments TMS320C30 digital signal processor (DSP) and two channels of 16-bit analog-to-digital conversion (ADC) input and DAC output. The tests were carried out with the same hearing aid prototype as for the off-line evaluation.

The experimental setup is shown in Fig. 4. Two neighboring rooms were used for the experiments. The prototype hearing aid was positioned on a dummy head in the test room, which is an office-sized room used for prostheses fittings (about 25 m^3) with an average reverberation time of 0.35 s.

The signals of the two microphones were amplified using two B&K 2610 amplifiers and digitized at a sampling frequency of 10.67 kHz in the two input channels on the PC-board. After signal processing, which introduces a delay of 16 ms, the resulting signal was routed on one output channel of the PC-board. For further amplification a Madsen Midimate 622 audiometer was used (same settings for all conditions within-subject) after which the processed speech was presented monaurally to the subjects through headphones TDH39 with MX41/AR cushions.

Speech and noise were presented with identical loudspeakers (Kenwood LS34) at 1 m and at 0° and +90° (at the side of the hearing aid), respectively, relative to the position of the dummy head. The estimated direct to reverberant ratio was 4 dB at 1 m (Peutz, 1971). The presentation of the speech materials was carried out using the standard audiometric setup of SONY CDP991 CD player and MADSEN OB822 audiometer connected to the two loudspeakers in the test room.

The effect of this noise cancellation technique on the intelligibility of speech in noise was tested with two normal hearing subjects and three hearing aid users. The thresholds

TABLE I. Perceptual results of five subjects: the subject's initials, age in years, average of three pure tone thresholds at 0.5, 1, and 2 kHz in dB HL and the SRT value in quiet in dB SPL are shown in the first four columns. The measured SNR values in dB for the direct mode, for the unprocessed, and for the two-stage adaptively processed conditions are presented in columns 5–10 for sentence lists and two-syllable word lists. The effect in SNR (dB) of processing versus no processing is shown for both speech materials in the last two columns. Because of time constraints, subject KC was not able to complete all tests. Averaged over the hearing impaired and the normal hearing subjects, the SNR effect is -5.6 ± 1.0 dB for sentence speech material and -4.7 ± 1.8 dB for two-syllable word lists.

Subject	Age (y)	Average pure tone threshold (dB HL)	SRT in quiet (dB SPL)	SNR (dB)						Effect in SNR (dB) Processed–unprocessed	
				Direct		Unprocessed		Processed			
				Sent.	Words	Sent.	Words	Sent.	Words	Sent.	Words
IS	12	50	65	−2.4	−3.1	−2.8	−2.8	−7.1	−7.2	−4.3	−4.4
SS	25	55	75	−1.4	+1.4	+0.3	−0.4	−6.1	−4.0	−6.4	−3.6
IV	23	45	55	−2.0	−4.6	+1.2	−3.8	−4.0	−6.2	−5.2	−2.4
OP	24	0	18	−4.6	6.4	−2.9	−4.6	−9.4	−10.8	−6.5	−6.2
KC	24	0	23		−5.4		−6.0		−12.7		−6.7

of the two normal hearing subjects were not higher than 10 dB HL in the 250-Hz to 8-kHz frequency range. The three hearing impaired subjects were all regular hearing aid users monaurally fitted and with moderate pure sensorineural hearing loss (mean pure tone thresholds at 0.5, 1, and 2 kHz of about 50 dB HL). The ear of the hearing impaired subjects that is normally fitted with their regular hearing aid was tested.

Speech reception thresholds (SRT) for standard sentence and two-syllable word speech materials were measured in noise and speech-to-noise ratios in dB for 50% intelligibility were obtained. The SRTs were measured with the five subjects in three conditions: (1) unprocessed, (2) processed with the noise cancellation algorithm using two-stage adaptive filtering, and (3) direct monaural presentation of both the speech and noise via headphones. In the unprocessed mode the signal of the primary (frontal) microphone was routed to the output. In condition 2, the signals from both microphones were used as inputs to the noise cancellation algorithm and the output of the algorithm was presented monaurally to the subject via the headphones. The difference between conditions 3 and 1 is that condition 1 includes the microphone.

Speech-weighted noises were used that were adjusted to match the average spectrum of the respective speech materials (all lists combined). Both speech materials with their speech-weighted noise are available on CD.[3] An adaptive testing procedure was used to obtain the SRT. In the tests using the microphones the noise level measured at the center of the dummy head in absentia is kept constant at 70 dBA and the level of the speech materials is adjusted to extract the 50% speech recognition level, the SRT. The first sentence or word is increased in level until the subject correctly identifies it. If the word or sentence is identified correctly, the level is decreased upon the next presentation. If it is identified incorrectly, the level is increased (Plomp and Mimpen, 1979, and references therein). The step sizes were 2 and 3 dB for the sentences and the two-syllable words, respectively. The speech materials consist of 10 lists of 13 sentences each (Plomp and Mimpen, 1979) and 15 lists of 10 two-syllable words from the BLU list (Wouters *et al.*, 1994). The average SNR for the last 10 sentences of a list and 15 words of two BLU lists together is used to determine the SRT. The results are accurate within about 1 dB (Plomp and Mimpen, 1979), and are used for efficient determination of signal-to-noise ratios for the different processing schemes.

All SRTs were determined in a single session. To exclude eventual fatigue and/or training effects in the data, the order of the conditions were changed from subject to subject and within subject for the different measurements. The experimental design was such that most of the available speech material was used, that no subject was presented the same list twice, and that different speech lists per condition were used for each subject. With the available speech material three SRT measurements with sentences and two with BLU words were obtained per condition.

Software and hardware were developed to run the adaptive testing procedure automatically from a portable PC using an infrared transmission link to the CD player and an audiometer control.

B. Results

The results of these experiments are shown in Table I. The table lists in the first three columns each subject's initials, age, and average of three pure tone thresholds at 0.5, 1, and 2 kHz (dB HL), respectively. The fourth column lists each subject's SRT in quiet (dB SPL), obtained using standard clinical procedures. Columns 5–10 show individual SRTs in terms of SNR for both sentences and words for direct, unprocessed, and processed conditions, respectively. The SRT improvements, processed-unprocessed, for both sentences and words are shown in the last two columns. The SNR values shown are averages of the different lists presented. The standard deviations on the averaged SNR values are approximately 1 dB.

For all subjects, measurement of the SRT for the two-stage adaptive filtering strategy shows a much lower SNR when compared to the unprocessed condition. An analysis of variance indicates this difference to be highly significant ($p<0.0001$). The effect of processing versus no processing averaged over the hearing-impaired and the normal-hearing subjects is -5.6 ± 1.0 dB for sentence speech material and -4.7 ± 1.8 dB for two-syllable BLU word lists. Furthermore, the analysis of variance shows no significant difference for this effect between hearing-impaired and normal-hearing subjects ($p=0.11$).

The results obtained in the unprocessed mode are similar to the data obtained with direct monaural presentation through the headphone. The test does not indicate a significant difference ($p = 0.32$).

IV. DISCUSSION

Two-stage adaptive filtering, as described in this document, can provide appreciable enhancements of speech understanding in noise. Furthermore, this strategy is shown to be feasible for single BTE hearing aids equipped with two microphones. In this study we focused on a fully automatic system based on an existing BTE hearing aid. The application can be worked out for an aesthetically acceptable hearing aid. Although signal processing is carried out in a PC-hosted DSP processor in this study, the first DSP-based hearing aids have become available and will overcome this present limitation in the near future.

We should add that in critical listening situations (close to 50% intelligibility score) an increase of 1 dB in SNR corresponds to an increase of about 15% in speech intelligibility score (Plomp and Mimpen, 1979), and about 10% for the word speech material (Wouters *et al.*, 1994).

Behavior in the presence of multiple noise sources will depend on the location of the sources. If they are within the areas well attenuated by the joint microphone and head shadow characteristic, they will not adversely affect the performance of the system. However, if there is more than one source in the area not well attenuated, performance will degrade rapidly (see, e.g., Widrow and Stearns, 1985).

In these measurements no specific subject-dependent fitting of the noise reduction strategy nor hearing aid implementation were taken into account. This is not necessary for the subjects participating in this study, as recent studies have shown that the SRT value does not differ significantly for the majority of spectrum shapings for moderate hearing losses (van Buuren *et al.*, 1995).

An important objective of this strategy is to improve the noise reference in the first stage of the scheme (see Fig. 1). This allows an efficient noise suppression in the second stage with minimal speech distortion. As an adaptive filter is used in the first stage, the system can filter direct speech and some strong early reflections out of the noise reference. This means the system can be made less sensitive to reverberation than other adaptive systems if longer filters are used. In this study filter lengths of only 6 coefficients in the first stage and 50 coefficients in the second stage were used, and the experiments were carried out in moderately reverberant environments ($T_{60} = 450/350$ ms). In general, the effect of directivity (by fixed or adaptive beamforming) decreases as reverberation increases. This remains to be investigated further.

The system described is not expected to depend much on the exact construction geometry or alignment of the microphones, as compared to highly directional fixed beamformers (see Soede *et al.*, 1993a).

The speech detector in the present study is based on the signal from either microphone. Although the speech/noise discriminator is already efficient at a rather low SNR (> -5 dB), more complex speech detection schemes, exploiting the full configuration of the system, have to be investigated for an optimal application in different types of background noises. Use can be made of the signals of both microphones (e.g., Greenberg and Zurek, 1992; van Hoesel and Clark, 1995).

ACKNOWLEDGMENTS

We thank the two anonymous reviewers, A. van Wieringen, and L. Geurts for their comments on an earlier version of the manuscript. We also acknowledge D. Vandenzavel for help with the subject tests and D. Van Compernolle for valuable discussions. We would like to thank J. Leenen and B. Geerdink of Philips Hearing Instruments, Eindhoven, The Netherlands, for the construction of the hearing aid prototypes. This work is supported by the Fund for Scientific Research—Flanders (Belgium).

[1]All differences in energy (in dB) are measured on the basis of speech-weighted noise.

[2]The magnitude of the transfer function was calculated in the following manner: after a few seconds of convergence, adaptation was stopped and speech-weighted noise was presented separately via the loudspeaker that served as the source of the desired signal (0° azimuth) and via the noise source. The power spectral density, and the difference in energy between the signal in the primary microphone and the output of the system were calculated. From these data we calculated the magnitude of the estimated transfer function and the improvement in SNR for speech-weighted noise.

[3]The authors can supply information about where to purchase both CDs.

DeBrunner, V. E., and McKinney, E. D. (**1995**). ''A directional adaptive least-mean-square acoustic array for hearing aid enhancement,'' J. Acoust. Soc. Am. **98**, 437–444.

Greenberg, J. E., and Zurek, P. M. (**1992**). ''Evaluation of an adaptive beam-forming method for hearing aids,'' J. Acoust. Soc. Am. **91**, 1662–1676.

Griffiths, L. J., and Jim, C. W. (**1982**). ''An alternative approach to linearly constrained adaptive beamforming,'' IEEE Trans. Antennas Propag. **30**, 27–34.

Kates, J. M., and Weiss, M. R. (**1996**). ''A comparison of hearing-aid array-processing techniques,'' J. Acoust. Soc. Am. **99**, 3138–3148.

Kompis, M., and Dillier, N. (**1994**). ''Noise reduction for hearing aids: Combining directional microphones with an adaptive beamformer,'' J. Acoust. Soc. Am. **96**, 1910–1913.

Levitt, H., Bakke, M., Kates, J., Neuman, A., Schwander, T., and Weiss, M. (**1993**). ''Signal Processing for Hearing Impairment,'' Scand. Audiol. Suppl. **38**, 7–19.

Moore, B. C. J. (**1995**). *Perceptual Consequences of Cochlear Damage* (Oxford U.P., Oxford, UK).

Peterson, P. M. (**1989**). ''Adaptive Array Processing for Multiple Microphone Hearing Aids,'' Ph.D. thesis, MIT, Cambridge, MA.

Peterson, P. M., Durlach, N. I., Rabinowitz, W. M., and Zurek, P. M. (**1987**). ''Multimicrophone adaptive beamforming for interference reduction in hearing aids,'' J. Rehab. Res. Devel. **24**, 103–110.

Peutz, U. M. A. (**1971**). ''Articulation loss of consonants as a criterion for speech transmission in a room,'' J. Audio Eng. Soc. **19**, 915–919.

Plomp, R., and Mimpen, M. A. (**1979**). ''Improving the reliability of testing the speech reception threshold for sentences,'' Audiology **18**, 43–52.

Preves, D. A. (**1994**). ''Current and future applications of digital hearing aid technology,'' in *Understanding Digitally Programmable Hearing Aids*, edited by R. E. Sandlin (Allyn and Bacon, Boston), pp. 275–313.

Soede, W., Berkhout, A. J., and Bilsen, F. A. (**1993a**). ''Development of a directional hearing instrument based on array technology,'' J. Acoust. Soc. Am. **94**, 785–798.

Soede, W., Bilsen, F. A., and Berkhout, A. J. (**1993b**). ''Assessment of a directional microphone array for hearing-impaired listeners,'' J. Acoust. Soc. Am. **94**, 799–808.

van Buuren, R. A., Festen, J. M., and Plomp, R. (**1995**). ''Evaluation of a wide range of amplitude-frequency responses for the hearing impaired,'' J. Speech Hear. Res. **38**, 211–221.

Van Compernolle, D. (**1990a**). ''Hearing aids using binaural processing principles,'' Acta Oto-Laryngol. Suppl. **469**, 76–84.
Van Compernolle, D. (**1990b**). ''Switching Adaptive Filters for Enhancing Noisy and Reverberant Speech from Microphone Array Recordings,'' in *Proceedings of the IEEE International Conference on Acoustics, Speech and Signal Processing*, Albuquerque, April 1990 (IEEE, New York), pp. 833–836.
Van Gerven, S., and Xie, F. (**1997**). ''A Comparative Study of Speech Detection Methods,'' Proc. EUROSPEECH, Vol. III, Rodos, Greece, September 22–25 1997, pp. 1095–1098.
van Hoesel, R. J. M., and Clark, G. M. (**1995**). ''Evaluation of a portable two-microphone adaptive beamforming speech processor with cochlear implant patients,'' J. Acoust. Soc. Am. **97**, 2498–2503.
Weiss, M. (**1987**). ''Use of an adaptive noise canceler as an input preprocessor for a hearing aid,'' J. Rehab. Res. Devel. **24**, 93–102.
Widrow, B., and Stearns, S. (**1985**). *Adaptive Signal Processing* (Prentice–Hall, Englewood Cliffs, NJ).
Wouters, J., Damman, W., and Bosman, A. J. (**1994**). ''Vlaamse opname van woordenlijsten voor spraakaudiometrie,'' Logopedie **7**(6), 28–33.

Deformation analysis of the vocal folds from videostroboscopic image sequences of the larynx

Abdul Karim Saadah and Nikolas P. Galatsanos[a)]
Illinois Institute of Technology, Department of Electrical and Computer Engineering, Chicago, Illinois 60616

Diane Bless
Department of Communicative Disorders, Department of Surgery–Otolaryngology, University of Wisconsin–Madison, Madison, Wisconsin 53706

Carmen Ana Ramos
St. Michael's Hospital, Voice Disorders Clinic, Toronto, Ontario M5B 1W8, Canada

(Received 24 October 1997; accepted for publication 23 February 1998)

Videostroboscopy is an examination which yields a permanent record of the moving vocal folds. Thus, it allows the diagnosis of abnormalities which contribute to voice disorders. In this paper, in order to find and quantify the deformation of the vocal folds in videostroboscopic recordings, an active contours- (snakes) based approach is used to delineate the vocal folds in each frame of the videostroboscopic image sequence. After this delineation, a new elastic registration algorithm is used to register the vocal fold contours between adjacent frames of the video sequence. This algorithm is based on the regularization principle and is very effective when large deformations are present. A least-squares approach is used to fit an affine model to the displacement vectors found by elastic registration. The parameters of this model, rotation, translation, and deformation along two principle axes, quantify the deformation and allow the succinct characterization of the videostroboscopic recordings based on the deformations that occurred. Experiments are shown with synthetic and real videostroboscopic data that demonstrate the value of the proposed approach. [S0001-4966(98)01506-9]

PACS numbers: 43.70.Aj [AL]

INTRODUCTION

Videostroboscopy is a method for the clinical examination of the vibrational characteristics of the vocal folds.[1,2] The method provides a permanent image record of the moving vocal folds, and is thus used for diagnosis of vibrational abnormalities which contribute to voice disorders that cannot be detected by other clinical methods.[1,2] Since the vocal folds vibrate too fast to be recorded on video, stroboscopic flashes which are slightly ''off phase'' with the frequency of the vocal folds are used to yield an image sequence in which the vocal folds appear to move in ''slow motion.'' [1] It is of great interest to voice clinicians both for diagnostic and research purposes to measure and to quantify the deformation of the vocal folds during phonation.[2] Voice clinicians routinely inspect videostroboscopic recordings visually for diagnostic purposes. However, it is clear that the observer bias and the inability of humans to absorb and quantify the large amounts of information in video sequences compromise the effectiveness of this examination. The goal of the work in this paper is to measure and quantify the deformations that occur in videostroboscopic recordings of the vocal folds.

The need for this measurement and quantification stems from the simple fact that computers are much better than humans at sorting out information in large amounts of data. The unaided human observer, no matter how trained, cannot capture and quantify all the available information about the motion of the vocal folds that is available in a videostroboscopic image sequence. For example, it is impossible for the human observer to measure accurately quantities such as the direction of motion and the change of the area of the vocal fold opening. *Small changes* in these quantities that could indicate the initial stages of a disease or a trend during treatment could escape undetected from a human observer. In addition, it is widely known that during videostroboscopic examinations as performed today, where trained humans observe the vibratory pattern, the *bias* of the observer is a serious problem limiting the usefulness of this examination.[2] It is impossible just by visual inspection to classify always *objectively*, let alone quantify and measure, properties of the motion pattern of the vocal folds. Motivated by the above limitations of this examination, the objective of this work is to propose a system that will help ameliorate some of these difficulties.

The vocal folds are nonrigid objects. Nonrigid objects when in motion change shape over time. Finding the motion of nonrigid objects is a hard problem which has been studied in the past for a number of different medical imaging applications in mind (see, for example, Refs. 3–8 and the references within). There exist three main methodologies to find the motion of nonrigid objects. For the first, specific anatomical features of the object (tokens) are employed to find the motion from frame-to-frame. For the second, the mechanical properties of the underlying elastic body are modeled and laws of mechanics are used to describe the motion.

[a)]Electronic mail: npg@ece.iit.edu

For the third, no information about the shape or the mechanical properties of the underlying objects is used. Thus, the motion is determined using only a set of rules that describe the desired properties of the resulting motion field. Most of the approaches in the above-mentioned references are guided by the features of the application in mind and use a combination of these methodologies.

For this work the vocal folds are first detected using active contour models (snakes).[9] Then, the deformation of the vocal folds is found by elastically registering the contours of the vocal folds from frame-to-frame. The main characteristics of this elastic registration problem are the following: (1) There are no distinct features in the images that can be used as tokens to help track the motion from frame-to-frame. (2) The mechanical properties of the vocal folds are not yet very well understood, thus it is hard to write down equations that describe their motion. Therefore, the third methodology has to be used for finding nonrigid motion for this problem. (3) The registration algorithm which will be used must be able to accommodate large deformations that appear in the data due to the severe temporal subsampling that occurs in videostroboscopy.

Recently, combinatorial optimization algorithms have been employed to find the motion when only the third methodology is used. A method based on dynamic programming and autoregressive modeling was proposed in Ref. 3. This approach was modified and used successfully in Ref. 4 for the problem of motion estimation of skeletonized angiographic images. Another approach was also proposed in Ref. 5. Unlike the approach in Ref. 3, the approach in Ref. 5 is based entirely on dynamic programing. We found that the algorithm in Ref. 4 and our implementation of the algorithm in Ref. 5 experience difficulties when applied to contours that have been severely deformed. For this purpose we proposed a new elastic contour matching algorithm[10] that ameliorates the difficulties that we encountered when applying the algorithms in Refs. 4 and 5. The proposed algorithm is based on a cost function which is minimized using *simulated annealing*.[11] Simulated annealing is an optimization algorithm that is able to obtain near-optimal solutions for a wide variety of combinatorial optimization problems. The definition of the cost function is based on the principle of regularization (see, for example, Refs. 12 and 13), and thus trades off between two requirements: first, smoothness of the displacement vector field and, second, that the overall displacement is small.

The collection of all the vectors that describe the displacement of the contours of the vocal folds in a point-by-point manner from frame-to-frame is called the displacement vector field. Once the displacement vector field is found, the need to model it quantitatively arises. Although the displacement vector field captures the vocal field deformations, it does not provide a succinct description of them. Thus, a model that describes them is necessary. A simple model that is easy to compute and also captures the deformations of the vocal folds is an *affine transformation* model.[14] In this paper, a least squares procedure is developed to fit the affine transformation model to the displacement vector field between successive frames. The obtained affine transformation is then decomposed to a rotation and a deformation along two principle axes. The time evolution of the rotation and deformation parameters characterizes succinctly the deformation of the vocal folds in the videostroboscopic sequence.

It is well known that the vocal fold vibration consists of the inferior portion (in a coronal plane) of a vocal fold moving approximately 50 degrees out of phase with the superior portion. This vertical phase difference means that during part of the closing phase of a glottal cycle, the bottom part of the vocal folds are closer together than the top. Problems with adequate illumination make reliable visualization and measurement difficult for the motion of the inferior portion of the vocal fold. Consequently, for the purposes of this study measurements were limited to the *superior margin of the glottal surface* that could be easily visualized.

The rest of this paper is organized as follows. In Sec. I, we present the snakes implementation that we used to delineate the vocal folds in the videostroboscopic data. In Sec. II, we present the new elastic registration algorithm that was used for the registration of the vocal fold contours from frame-to-frame. In Sec. III, we present the modeling of the vocal fold deformations using the displacement vector field and the affine transformation model. In Sec. IV, we present our experimental results. Finally, in Sec. V, we present our conclusions from this work and our future research directions.

I. BOUNDARY DETECTION OF VOCAL FOLDS USING SNAKES

The delineation of the vocal folds can be viewed as the combination of two tasks: (1) finding the locations of abrupt intensity changes, edges, that signify the presence of the folds and (2) ordering the edges to form connected curves or edge linking. There is an enormous amount of research in edge detection and edge linking (see for example Refs. 15 and 16). The approaches that exist to handle these tasks can be classified into two broad categories: (1) *data-driven* approaches,[17] where an edge detector operates directly on image intensities. The problem with these approaches is that errors made in edge detection propagate to edge linking without any opportunity for correction. (2) *Model-driven* approaches,[18] where a parametric expression for the curve is assumed. The main advantage of this technique is that it is insensitive to noise and gaps in curves. However, the quantization of the image and the parameter space used influence the final outcome. Furthermore, this method does not use any information about the local structure of the image.

Active contour models (snakes) is a method that combines the advantages of both previous approaches.[19,20] The main difficulty in applying snakes to different problems is in selecting the initial positions for them. For our application, this initialization problem can be solved by user interaction in the first frame. For the following frames, the snake position found in the preceding frame can be used as the initial position for the current frame.

A snake is an energy-minimizing spline guided by external forces and is influenced by image forces that pull it towards features such as lines and edges. Snakes are active contour models which lock on to nearby edges localizing

them accurately. *Snakes* were originally proposed in Ref. 9 in which an energy functional was defined for the contour and the minimum energy contour was determined using variational calculus. A snake is represented by a vector $\mathbf{v}$ whose elements are functions of two spatial coordinates x and y, i.e., $v(i)=(x(i),y(i))$ are the locations on the snake and are called snake elements, or *snaxels*. A snake is *closed* if $\mathbf{v}$ forms a closed curve, otherwise it is *open*. The total snake energy, E_{snake}, consists of a sum of two energy terms:

$$A_{\text{snake}}(\mathbf{v})=\sum_{i=1}^{n} E_{\text{snake}}(i)$$

$$=\sum_{i=1}^{n} (\lambda E_{\text{int}}(i)+(1-\lambda)E_{\text{ext}}(i)), \tag{1}$$

where $E_{\text{int}}(i)$ and $E_{\text{ext}}(i)$ are the internal and external energies respectively, at snaxel $v(t)$. This definition of the energy function complies with the principle of regularization. According to this principle, fidelity to the data E_{ext} and prior knowledge E_{int} are combined to resolve the ambiguities of imperfect data in estimation problems (see, for example, Refs. 12 and 13). The parameter $\lambda\in[0,1]$ is the *regularization parameter* that determines the relative tradeoff between data fidelity and prior knowledge, which for this problem are captured by the terms E_{ext} and E_{int}, respectively.

We seek the optimum locations $v(i)$, $i=1,2,...,n$, that minimizes the snake energy in Eq. (1). The internal energy E_{int} imposes a model of smooth curves which restricts the solutions to the class of controlled continuity splines; the external energy E_{ext} causes the snake to attach itself to salient features in the image. The combined effect of this two-energy term yields a model that allows itself to deform in conformation to the nearest salient features. In general, E_{int} consists of a continuity term E_{cont} and a curvature term E_{curv}. The E_{cont} encourages snaxel to be evenly spaced and eliminates the tendency of shrinkage and expansion. The E_{curv} imposes the smoothness constraint on the snake. For the external energy, both the magnitude and direction of intensity gradient are used in the formulation of E_{ext}.

We use similar definitions as in Refs. 19 and 20; the energy functional thus yields the following $E_{\text{snake}}(i)$:

$$E_{\text{snake}}(i)=\lambda E_{\text{int}}(i)+(1-\lambda)E_{\text{ext}}(i)$$

$$=\lambda(\gamma E_{\text{cont}}(i)+(1-\gamma)E_{\text{curv}}(i))$$

$$+(1-\lambda)E_{\text{ext}}(i), \tag{2}$$

where $\lambda,\gamma\in[0,1]$.

The regularization parameter λ weights the importance of the internal and the external energy terms. For the values of $\lambda\gg(1-\lambda)$, the E_{int} is dominant. This restricts the snake to concur more with the *model-driven* approach, while for the values of $\lambda\ll(1-\lambda)$, the E_{ext} is dominant. This causes the snaxels to settle at locations of high-intensity gradient, causing the snake to behave like an edge-linking algorithm. This concurs more with the *data-driven* approach. In the continuum of $\lambda\in[0,1]$, the snake exhibits an intermediate behavior between the *model-driven* and *data-driven* approaches.

II. REGULARIZATION-BASED ELASTIC REGISTRATION OF THE VOCAL FOLDS

Once the vocal fold contours have been delineated, they have to be matched elastically from frame-to-frame. In elastic contour matching the two contours, say the smaller 1 and the larger 2, are matched/registered by finding the correspondence between points in contours 1 and 2. Assume that the vocal fold contours 1 and 2 in two successive frames are defined by points $(x_1(m),y_1(m))$ and $(x_2(k),y_2(k))$, for $m=1,2,...,L_1$ and $k=1,2,...,L_2$. Matching the two contours corresponds to finding the pair of indices $(m(i),k(i))$ for $i=1,2,...,L_2$, where L_2 is the larger contour, that describe a correspondence of points between the two contours. The pair of points $(m(i),k(i))$ defines the ith displacement vector, and the collection of all these points for $i=1,2,...,L_2$ vectors gives the displacement vector field. The displacement vector field describes the elastic deformation of the two contours.

An elastic contour registration method based on dynamic programming[21] and autoregressive modeling was proposed in Refs. 3 and 4. The cost function to be minimized using dynamic programing is chosen to be a function of the estimated (using autoregressive models) displacement vector and the actual displacement vector found. The advantage of this algorithm is that the complexity of the deformation does not affect the computational cost. However, the main limitations of this approach for our application are the following: First, it does not guarantee that all pixels of the smaller contour will correspond to points in the larger contour. This will affect the motion estimation in the next stages. Second, there is a possibility of crossovers between adjacent displacement vectors when severe shrinking/expansion is present.

Another algorithm that also matches deformed contours was proposed in Ref. 5. Unlike the approach in Refs. 3 and 4, this approach is based entirely on dynamic programing. However, instead of choosing as the cost function the distance between two points (size of the displacement vectors), the weighted sum of the difference between two successive displacement vectors and the size of the displacement vectors themselves is used. In order to keep the implementation cost at a reasonable level, dynamic programing is applied to a subgraph which is based on a neighborhood system which is defined around every point of the largest contour. The main drawback of this approach for our application is the choice of the cost function which makes this method unsuitable for matching contours which are different in size. This is exactly the case when severe shrinking/expansion is present from contour-to-contour. In other words, one-to-one matching leaves unmatched points when the two contours are not of equal sizes. Finally, this approach requires that both contours are described as an ordered list of points.

In this section, we present a original elastic contour matching algorithm[10] that alleviates the difficulties of the algorithms in Refs. 4 and 5 for our application. The proposed algorithm is based on a cost function that is minimized using *simulated annealing*.[11] The simulated annealing algorithm is

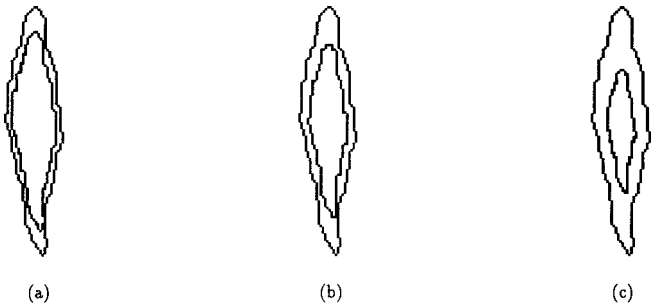

FIG. 1. The inner contour is obtained by deforming the outer contour using the matrix D in Eq. (18) and a rotation $\theta=0°$ [see Eq. (7)] for (a) $d=0.8$, (b) $d=0.7$, and (c) $d=0.5$.

a general optimization technique for solving combinatorial optimization problems. The algorithm is based on *randomization techniques*. However, it also incorporates a number of aspects related to *local search* techniques. In contrast to local search techniques, the simulated annealing algorithm finds high-quality solutions which do not strongly depend on the choice of the initial solution, i.e.,the algorithm is *effective* and *robust*. Furthermore, the simulated annealing algorithm can escape from local minima while it still exhibits the favorable features of local search algorithms, i.e., simplicity and general applicability. Due to the highly nonconvex nature of the function that is minimized, an optimization algorithm which is based on a random search would be appropriate for this problem. Simulated annealing is such an algorithm.

Finding the displacement vector field is an *ill-posed* problem and it is common in all ill-posed problems to impose simultaneously fidelity to the data and prior knowledge. In our case the former is accomplished by using the mean-square error and the latter the smoothness of the displacement vector field. This is the very well-known *regularization principle*.[12,13] A cost function based on the regularization principle is defined. This cost function is minimized with respect to the choice of the displacement vectors $(m(i),k(i))$ for $i=1,2,...,L_2$ and is of the form

$$C=(1-\lambda)\sum_{i=1}^{L_2}[(x_1(m(i))-x_2(k(i)))^2 + (y_1(m(i))-y_2(k(i)))^2]+\lambda\sum_{i=1}^{L_2}[|\phi(m(i),k(i)) - \phi(m(i-1),k(i-1))|]^2, \quad (3)$$

where the parameter $\Lambda\in[0,1]$ is the regularization parameter and $\phi(m(i),k(i))$ is the angle of the ith displacement vector which is defined by the points $m(i)$ and $k(i)$ of the contours 1 and 2, respectively. The first part of the function C captures the requirement that the total distance between points that are matched should be small. The second part of the function imposes the smoothness constraint to the displacement vector field by constraining adjacent motion vectors to have similar directions. The use of the regularization principle in the registration problem is especially helpful when the deformations are severe and the contours are not smooth. In this case, the data alone are not sufficient to provide a meaningful displacement vector field.

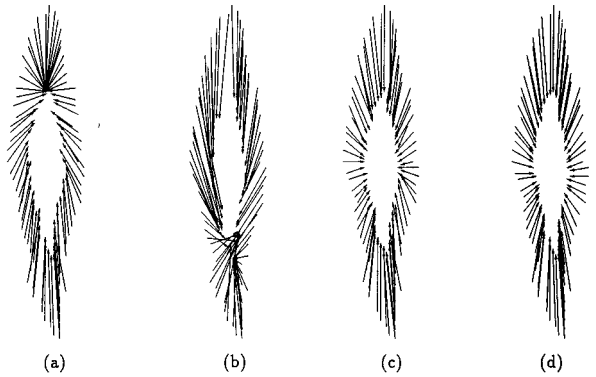

FIG. 2. The DVF registration for $d=0.5$ and $\theta=0°$ using the (a) algorithm in Ref. 7, (b) algorithm in Ref. 5, (c) proposed regularization based approach, and (d) true displacement vector field.

A. Simulated annealing

Simulated annealing has been applied in the past to a number of nonconvex combinatorial optimization problems in image processing (see, for example, Ref. 22). The name simulated annealing originates from the analogy with the physical annealing process of solids.

Simulated annealing associates a ''temperature,'' T, with a model and searches for the optimal configuration based on a defined energy by repeatedly trying to alter the state of the system. At each *iteration*, a transition is first generated and then either accepted or rejected. A rejected transition is regarded as a transition from the current state to itself. By appropriately selecting the probability of generating and accepting state j from state i, the simulated annealing algorithm can be shown to converge,[23] for any value of the temperature $T>0$, after a (possibly large) number of transitions. The temperature is then lowered repeatedly, and after enough iterations the system approaches equilibrium. This process is terminated using a stopping rule when the change of the expected cost is very small compared to the expected cost at T_0 (see, for example, Refs. 10 and 11).

A simulated annealing algorithm is completely defined upon specifying a cooling schedule. This cooling schedule consists of the initial temperature of the system T_0, a rule for determining the number of transitions at each temperature, a rule for determining the lowering of the temperature, and a termination criterion.

We used the rule for lowering the temperature described in Ref. 11; the temperature T_{k+1} is given by

TABLE I. The E_{MSE} for the three algorithms for the different deformations in Fig. 1.

		E_{MSE} for the algorithm		
d	θ	in Ref. 7	in Ref. 5	using SA
0.85	0°	2.67	3.62	1.42
0.8	0°	3.85	4.59	1.49
0.7	0°	6.14	11.49	1.53
0.5	0°	7.18	14.27	1.70

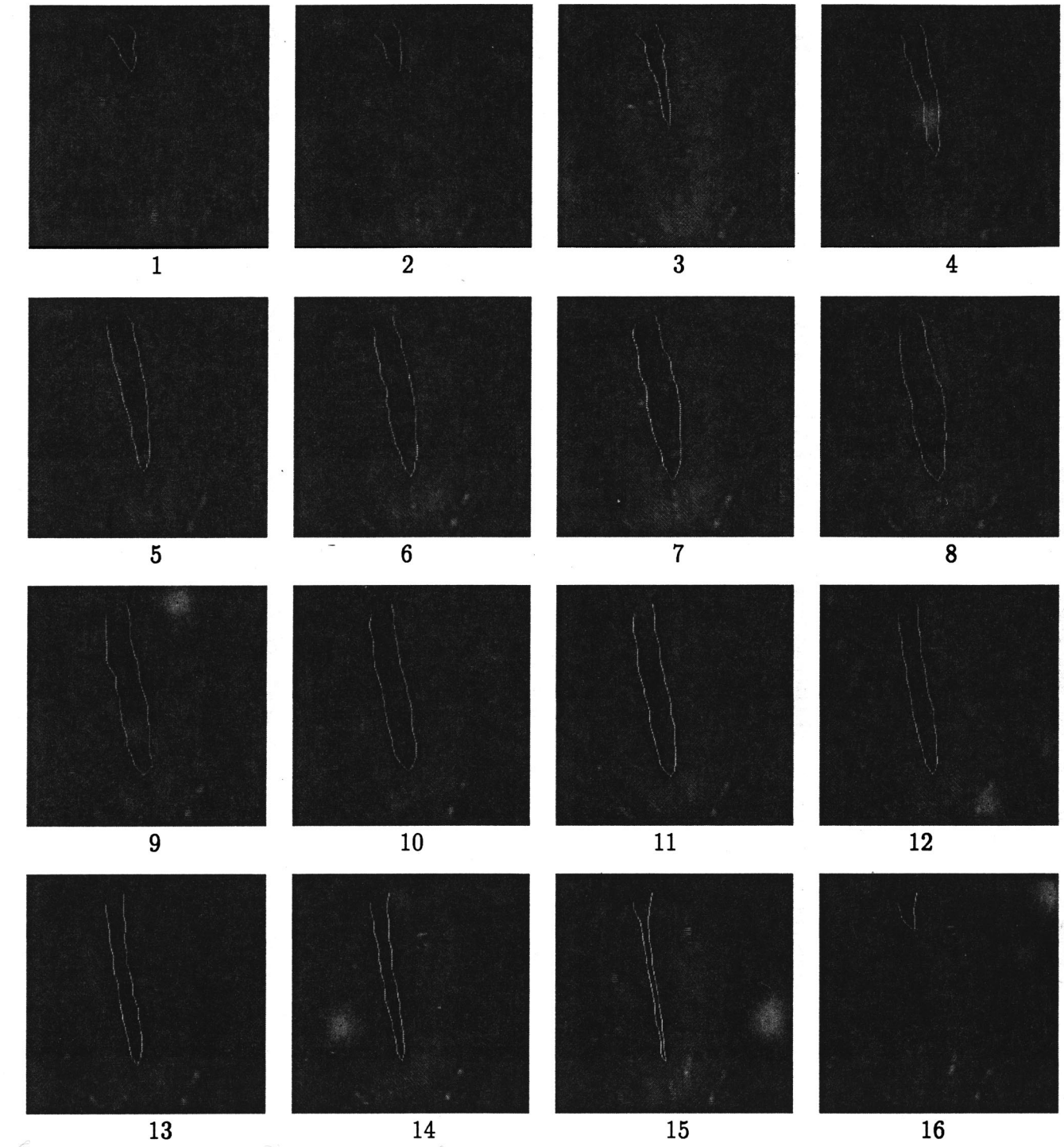

FIG. 3. The bright closed contours delineate the boundaries of the vocal folds in successive frames of a normal larynx run from top left to the bottom right.

$$T_{k+1}=\frac{T_k}{1+T_k \ln(1+\delta)/3\sigma_{T_k}}, \quad k=0,1,..., \tag{4}$$

where δ is a small positive number. Small δ values lead to small decrements of the temperature. Here σ_{T_h} is the standard deviation of the cost function at T_k where

$$\sigma_{T_k}=\left(\frac{1}{L}\sum_{i=1}^{L_{T_k}}(C_{T_k}(i)-\overline{C_{T_k}})^2\right)^{1/2}$$

and

$$\overline{C_{T_k}}=\frac{1}{L}\sum_{i=1}^{L_{T_k}} C_{T_k}(i),$$

$C_{T_k}(i)$ is the value of the cost function at state i when the temperature is T_k, and the bar denotes averaging over all values of the cost function $C_{T_k}(i)$, for $i=1,2,...,L_{T_k}$ generated at a given temperature T_k.

The algorithm terminates when, for some k, we have $\Delta\overline{C}_{T_k}$ is small compared to $\overline{C}_{T_0}$,[11] i.e.,

$$\frac{T_k}{\overline{C}_\infty}\left.\frac{\partial \overline{C}_T}{\partial T}\right|_{T=T_k} < \varepsilon_s, \tag{5}$$

where ε_s is some small positive number called the *stop parameter*, $\overline{C}_\infty$ is the expected cost at $T\to\infty$, and $\partial C_T/\partial T|_{T=T_k}$ is the partial derivative of the expected cost at $T=T_k$.

Let T_k denote the value of the temperature L_{T_k} denote the length of the Markov chain when the temperature, is T_k, and i_0 denote the initial state (configuration). Then, our registration algorithm can be described in pseudo code as follows:

begin
  INITALIZE(i_0, T_0)
  $k := 0$;
  $i := i_0$;
  repeat
    for $l := 1$ **to** L_{T_k} **do**
    begin
      GENERATE (new state j);
      if $C(j) \leqslant C(i)$ **then** $i := j$
      else
      if $\exp\left(\frac{C(i)-C(j)}{T_k}\right) >$ random$[0,1)$ **then** $i := j$
    end;
    $k := k+1$;
    CALCULATE (T_k) Eq.(4);
  until stop criterion Eq.(5)
end;

We used $L_{T_k} = L_1$ for $k = 1,2,\ldots$. The initial state i_0 is selected randomly. We start at an initial value of the temperature T_0 evaluated using the same approach as in Ref. 11. The **GENERATE** (new state j) picks at random at state i two adjacent points from the larger contour, which are the origins of two displacement vectors. Then the new state j is generated by exchanging the displacement vectors of the two points previously selected.

III. AFFINE TRANSFORM MODELING OF THE DEFORMATION

After elastic registration, the displacement vector field between adjacent frames of the vocal folds is available. The displacement vector field provides a better visualization of the deformation than the raw video recordings. However, the displacement vector field alone does not provide a *quantitative* description of the deformation. Therefore in this section we present the model that is used to quantify the deformation from the displacement vector field.

As explained previously the deformation at the location i between two successive frames, for example, 1 and 2, is represented as a vector which is given by two pairs of coordinates. This vector is called the displacement vector (DV).

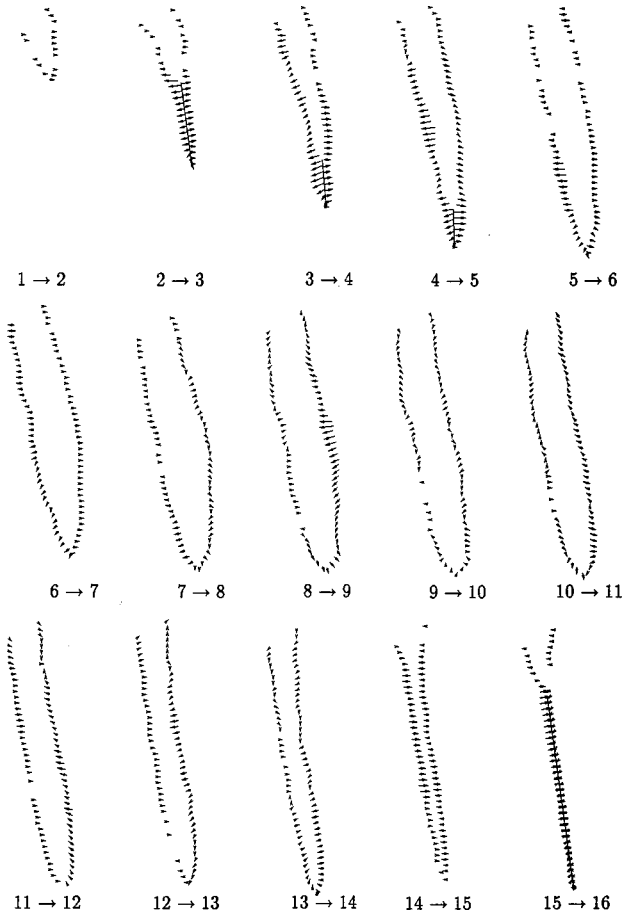

FIG. 4. The registration of the successive boundaries of the sequence of videostroboscopic images of a normal larynx using the proposed simulated annealing based approach runs from top left to the bottom right; the displacement vector fields are sampled and magnified.

Let $(x_1(i), y_1(i))$ and $(x_2(i), y_2(i))$ denote the origin and the endpoint of the DV at location i. Assuming that L such points are given, then the displacement vector field between frames 1 and 2 is given by the collection of all available displacement vectors. The displacement vector field is fully described by the set of points

$$(x_l(i), y_l(i)) \quad \text{for } l = 1,2 \quad \text{and } i = 1,2,\ldots,L.$$

A simple model for the displacement vector field that is very appropriate because it can capture the deformation during the motion of the vocal folds is based on the *affine*

TABLE II. The E_{pmse} of the affine transformation model based on prediction of the displacement vector field of the sequence with the polyps in Fig. 7.

Frames	E_{pmse}	Frames	E_{pmse}
1→2	0.68	2→3	1.70
3→4	0.94	4→5	0.76
5→6	1.10	6→7	1.25
7→8	1.20	8→9	0.84
9→10	1.37	10→11	0.25
11→12	0.36	12→13	0.14
13→14	0.22	14→15	1.26
15→16	0.72		

transformation.[14,24] This model is described by the following set of linear equations

$$\begin{bmatrix} x_2(i) \\ y_2(i) \end{bmatrix} \approx \begin{bmatrix} a_{11} & a_{12} \\ a_{21} & a_{22} \end{bmatrix} \begin{bmatrix} x_i(i) \\ y_1(i) \end{bmatrix} + \begin{bmatrix} T_x \\ T_y \end{bmatrix} \quad \text{for } i=1,2,...,L. \tag{6}$$

The $\approx$ sign is used because fitting an affine transformation model to more than three motion vectors is an overdetermined problem which has to be solved approximately. In what follows, we will elaborate on this point. The matrix A defined by the coefficients a_{11}, a_{12}, a_{21}, a_{22} describes *deformation* and *rotation*,[14] while T_x, T_y describe *translation* in the x and y directions, respectively. More specifically, the matrix A can be decomposed into the product of R and D,[25] where D is a symmetric positive definite matrix that represents deformation and R is an orthonormal matrix. More specifically,

$$A = \begin{bmatrix} a_{11} & a_{12} \\ a_{21} & a_{22} \end{bmatrix} = R \cdot D, \tag{7}$$

$$R = \begin{bmatrix} \cos\theta & -\sin\theta \\ \sin\theta & \cos\theta \end{bmatrix}, \quad \text{and} \quad D = \begin{bmatrix} a & c \\ c & b \end{bmatrix}.$$

Because of the symmetry of D we can also write

$$D = \begin{bmatrix} a & c \\ c & b \end{bmatrix} = \begin{bmatrix} \vec{\mathbf{e}}_1^T \\ \vec{\mathbf{e}}_2^T \end{bmatrix} \begin{bmatrix} \lambda_1 & 0 \\ 0 & \lambda_2 \end{bmatrix} [\vec{\mathbf{e}}_1, \quad \vec{\mathbf{e}}_2], \tag{8}$$

where λ_i, $\vec{\mathbf{e}}_i$, for $i=1,2$ are the eigenvalues and the corresponding orthogonal eigenvectors, respectively, of matrix D. To find D and R we observe that

$$A^TA = (RD)^T(RD) = D^TR^TRD. \tag{9}$$

However, since R is orthonormal matrix then

$$R^TR = I, \tag{10}$$

where I is the identity matrix. Therefore,

$$A^TA = D^TD. \tag{11}$$

However, since D is symmetric, there exists a unique decomposition of A^TA such that D is symmetric and positive definite.

Let λ_α^2, $\vec{\mathbf{e}}_\alpha$, for $\alpha=1,2$, be the eigenvalues and eigenvectors, respectively, of the symmetric matrix A^TA, i.e.,

$$A^TA = \lambda_1^2 \vec{\mathbf{e}}_1 \vec{\mathbf{e}}_1^T + \lambda_2^2 \vec{\mathbf{e}}_2 \vec{\mathbf{e}}_2^T. \tag{12}$$

Then

$$D = \lambda_1 \vec{\mathbf{e}}_1 \vec{\mathbf{e}}_1^T + \lambda_2 \vec{\mathbf{e}}_2 \vec{\mathbf{e}}_2^T. \tag{13}$$

Once D is estimated, R can be estimated uniquely as $R = AD^{-1}$. The eigenvectors of the D matrix give the perpendicular directions of the maximum and minimum deformation.[14] These directions are given by the angles

$$\phi_1 = \tan^{-1}\left(\frac{\mathbf{e}_1(y)}{\mathbf{e}_1(x)}\right) \quad \text{and} \quad \phi_2 = \tan^{-1}\left(\frac{\mathbf{e}_2(y)}{\mathbf{e}_2(x)}\right), \tag{14}$$

where $\mathbf{e}_j(x)$ and $\mathbf{e}_j(y)$ are the x and y components of the vector $\vec{\mathbf{e}}_j$. The corresponding eigenvalues give the changes of the magnitude of the deformation along these directions. Therefore, the affine transformation model of the displacement vector field provides a succinct description of the changes that occurred in the shapes of the contours.

The $\approx$ sign in Eq. (6) is used because, in general, it is impossible to find a unique set of (a_{11}, a_{12}, a_{21}, a_{22}, T_x, T_y) parameters that will satisfy Eq. (6) exactly for all $i=1,2,...,L$.

Thus, a set of such parameters is found that ''on the average'' is optimal for $i=1,2,...,L$. For this problem the *least-squares* approach is used.[26] According to this approach, a model is found which minimizes the sum of the squared error over the entire set of range data that is fitted with our model. Rearranging Eq. (6) for $i=1,2,...,L$ we can write the following system of linear equations $Bx=b$ with

$$B \begin{bmatrix} x_1(1) & y_1(1) & 0 & 0 & 1 & 0 \\ 0 & 0 & x_1(1) & y_1(1) & 0 & 1 \\ x_1(2) & y_1(2) & 0 & 0 & 1 & 0 \\ 0 & 0 & x_1(2) & y_1(2) & 0 & 1 \\ \vdots & \vdots & \vdots & \vdots & \vdots & \vdots \\ x_1(L) & y_1(L) & 0 & 0 & 1 & 0 \\ 0 & 0 & x_1(L) & y_1(L) & 0 & 1 \end{bmatrix}, \tag{15}$$

$$x = [a_{11}, \quad a_{12}, \quad a_{21}, \quad a_{22}, \quad T_{sx}, \quad T_y]^T, \tag{16}$$

$$b = [x_2(1), \quad y_2(1), \quad x_2(2), \quad y_2(2), .., \quad x_2(L), \quad y_2(L)]^T, \tag{17}$$

where B and b are a $2L\times 6$ matrix and $2L\times 1$ vector, respectively, of the data. Vector x is 6×1 and contains the parameters that are fitted to the data. For $L>6$ clearly this is an overdetermined system of equations so we resort to a least-squares solution.

Minimizing $\|Bx-b\|_2$, where $\|\cdot\|_2$ is the l_2-norm, gives the following equations,

$$B^TB\hat{x}_{LS} = B^Tb,$$

from which we can solve for $\hat{x}_{LS}$ and get the affine model parameters. The matrix B^TB is a 6×6 symmetric matrix given by

$$\begin{bmatrix} \sum_{i=1}^{L} x_1^2(i) & \sum_{i=1}^{L} x_1(i)y_1(i) & 0 & 0 & \sum_{i=1}^{L} x_1(i) & 0 \\ \sum_{i=1}^{L} x_1(i)y_1(i) & \sum_{i=1}^{L} y_1^2(i) & 0 & 0 & \sum_{i=1}^{L} y_1(i) & 0 \\ 0 & 0 & \sum_{i=1}^{L} x_1^2(i) & \sum_{i=1}^{L} x_1(i)y_1(i) & 0 & \sum_{i=1}^{L} (i) \\ 0 & 0 & \sum_{i=1}^{L} x_1(i)y_1(i) & \sum_{i=1}^{L} y_1^2(i) & 0 & \sum_{i=1}^{L} y_1(i) \\ \sum_{i=1}^{L} x_1(i) & \sum_{i=1}^{L} y_1(i) & 0 & 0 & L & 0 \\ 0 & 0 & \sum_{i=1}^{L} x_1(i) & \sum_{i=1}^{L} y_1(i) & 0 & L \end{bmatrix}.$$

Apart from the trivial straight line case where $y_1(i) = \alpha x_1(i)$ for $i=1,2,...,L$, where α is a constant, B^TB is positive definite and thus $(B^TB)^{-1}$ exists. Therefore, the computation of $\hat{x}_{LS}$ is easy.

IV. EXPERIMENTAL RESULTS

In this section we present two categories of experiments. In the first, the performance of the new simulated annealing-based elastic registration approach that we propose is com pared to previous elastic registration algorithms that are based on the same methodology. To the best of our knowledge two such algorithms exist; more specifically, the algorithms in Refs. 4 and 5. In the second,the proposed system (contour delineation, elastic registration, deformation modeling) is tested on videostroboscopic recordings of normal larynges, a larynx with a polyp, and a larynx with a cyst.

For the first category, experiments are presented to test the new registration algorithm on contours produced by synthetic deformations since in order to evaluate the algorithms' performances quantitatively, the true displacement vector field must be known. More specifically, the three registration algorithms from Refs. 4 and 5 and Sec. II were compared. For the algorithm in Ref. 4 the authors of that paper provided us with their code. The algorithm in Ref. 5 was modified to match all the points of the larger contour. For our modification, the algorithm was reapplied in the regions were points were left unmatched. All three algorithms were applied to contours that have been deformed in a controlled manner by an affine transformation, given by

$$D=\text{diag}\{d,d\} \quad d<1.0, \tag{18}$$

and a $\theta°$ rotation [see Eq. (7)]. This affine transformation when applied to the outer contour of Fig. 1 results in the deformed inner contours (see Fig. 1). Notice that D ''squeezes'' the initial contour in both the x and y directions.

For the simulated annealing that was used in our elastic registration algorithm,[10] we chose a cooling schedule defined by three parameters, i.e., the initial acceptance ratio χ_0, the δ parameter, and the stop parameter ε_s. In the previous, and all of the following, experiments we used $\chi_0=0.98$, $\delta = T_0/500$, and $\varepsilon_s=10^{-8}$. Choosing $\chi_0\approx 1$ sets the initial temperature T_0 of the system at very high value, while δ, which controls the decrease rate of the temperature in Eq. (4), is relatively small, and finally the stop parameter ε_s is chosen to be very small.

A mean square error metric, E_{MSE}, in pixels for the simulated elastic matching problem was used to objectively evaluate the results. Here E_{MSE} is defined by

$$E_{\text{MSE}}=1/N\sum_{i=1}^{N}[(x_2(i)-\hat{x}_2(k(i)))^2+(y_2(i)-\hat{y}_2(k(i)))^2], \tag{19}$$

where $(x_2(i),y_2(i))$ are the true positions computed from Eq. (6) and $(\hat{x}_2(k(i)),\hat{y}_2(k(i)))$ were found from the elastic matching of contours 1 and 2.

We applied the three algorithms for different deformations. Figure 1 shows some of these deformations of the outer contour. Applying the three algorithms for $d=0.5$ and $\theta=0°$ yields the displacement vector fields of Fig. 2. Registration errors of the first two algorithms can be seen where crossings of motion vectors occurred in Fig. 2(a) and (b). In Fig. 2(c) the resulting displacement vector field from the proposed approach is shown. Using the definition in Eq. (19) with $N=303$, the E_{MSE} for the three algorithm in Refs. 4 and 5 and for the proposed approach for different deformations are shown in Table I.

The previous experiments were run on a SUN/SPARC-10 workstation. For $d=0.5$ and $\theta=0°$ the processing time for the algorithm in Ref. 5 was 50 s, for the algorithm in Ref. 4 it was 55 s and for the proposed approach it took 390,870 iterations in 69 s. For the other experiments similar numbers in terms of times and iterations were observed. These simple experiments indicate that the proposed

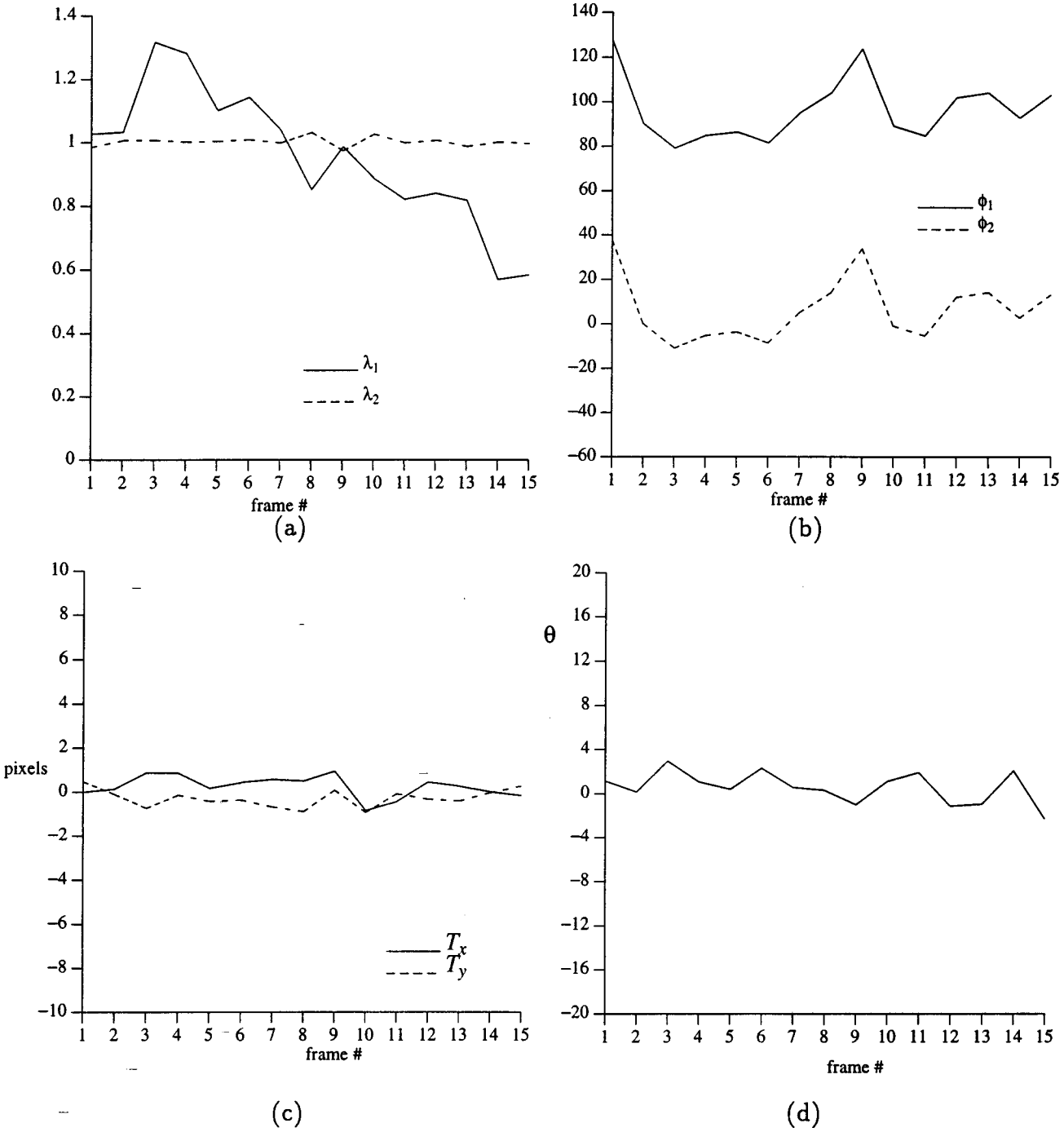

FIG. 5. The figures in (a), (b), (c), and (d) represent time evolution of the eigenvalues, principal directions of deformation, the translation along the x and y axes, and the rotation angle for the frames of the first normal larynx videostroboscopic image sequence, respectively. The units of the vertical axes in (b) and (d) are degrees.

approach has the ability to track better elastic contours during deformation and computationally it is not much more expensive.

In the second category, experiments are presented that test the proposed algorithms on real data of videostroboscopic image sequences of a normal and abnormal larynges. In the first experiment, we used a 16-frame videostroboscopic image sequence showing a complete vibrational cycle of normal vocal folds. All our real data was provided by the last two authors. In Fig. 3, the sequence is shown running from top left to bottom right starting from frame 1 and ending at frame 16. The bright contours delineate the boundaries of the vocal folds in the successive frames and were produced using the snake algorithm described in Sec. I. It can be seen that the positions and changes in the shape of the vocal folds are correctly extracted using the snakes. In locating the contours of the vocal folds we used a small number (30–40) of snaxels, then the complete boundary was obtained by applying cubic spline interpolation[27] to the snaxels at the right and the left side of the vocal folds separately. For our application we chose the value of $\gamma=0.5$ and the value of $\lambda=0.8$; this yields more of a model-driven solution and is

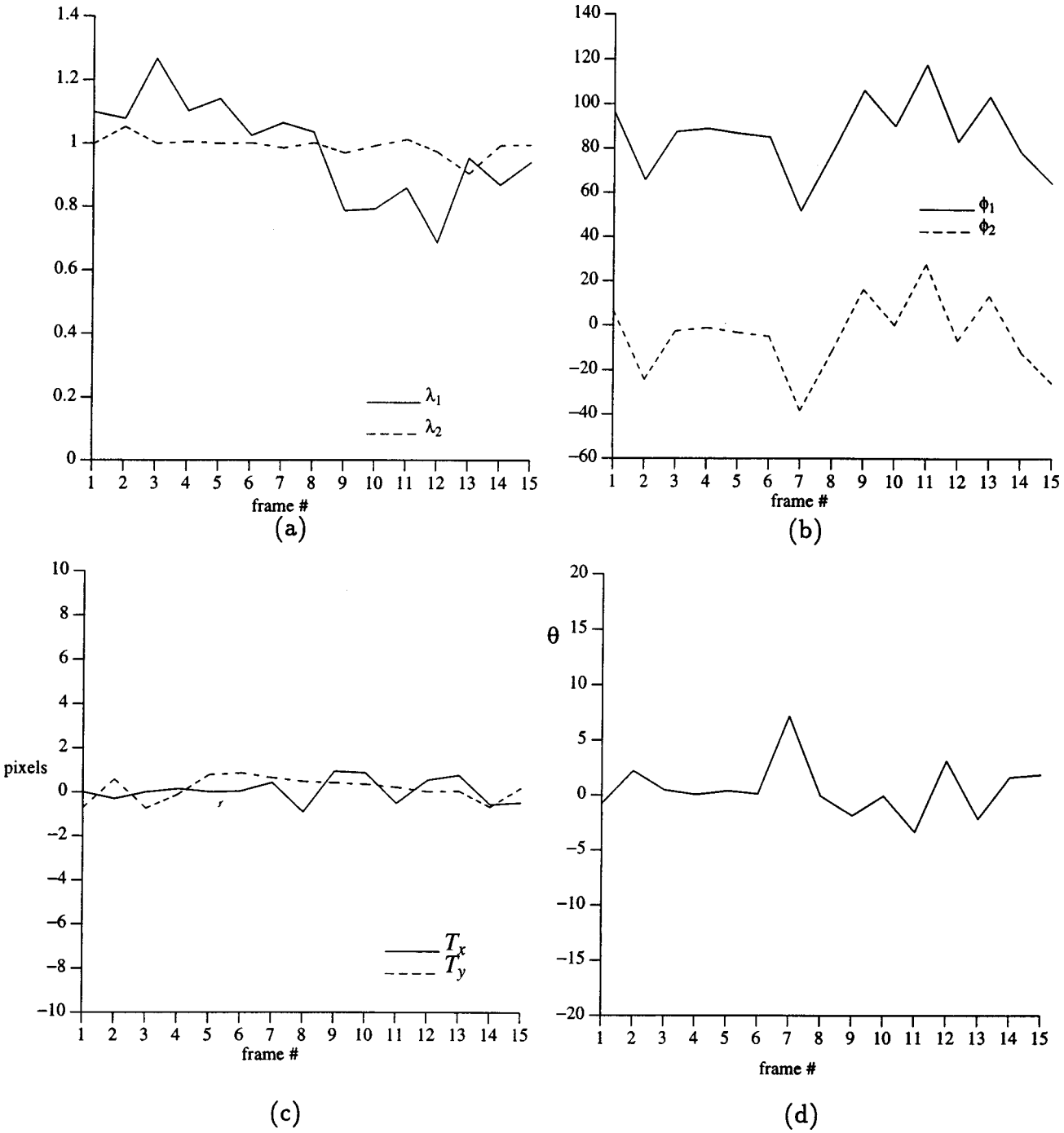

FIG. 6. The figures in (a), (b), (c), and (d) represent time evolution of the eigenvalues, principal directions of deformation, the translation along the x and y axes, and the rotation angle for the frames of the second normal larynx videostroboscopic image sequence, respectively. The units of the vertical axes in (b) and (d) are degrees.

robust to noise. The displacement vector fields of all contours for the successive frames are shown in Fig. 4. From this figure and in frames 7–10 it is observed that some points on the vocal fold contour move together while others move oppositely. This seems to happen only around the time of maximum opening and the ''turn-around'' toward closure.

Because of the frame rate limitations of videostroboscopy, as explained in the Introduction, the frames in an apparent videostroboscopic cycle originate from a number depending on the frequency of phonation. For example fundamental frequency of 140 Hz at 33 frames/s would sample every fourth cycle. Therefore, there are instances where the visible anterior closure of the vocal folds shows a large discrepancy, large lateral distances between adjacent frames, as seen for example in Fig. 4 (displacement vector fields of frames $2\rightarrow3$, $3\rightarrow4$, $4\rightarrow5$, and $15\rightarrow16$); therefore the line connecting the most anterior aspects of the openings between adjacent frames was used as the reference for reconstructing the glotal contour for the subsequent motion analysis.

This correction is based on the observation that the structural motion is medial–lateral (horizontal in the images)

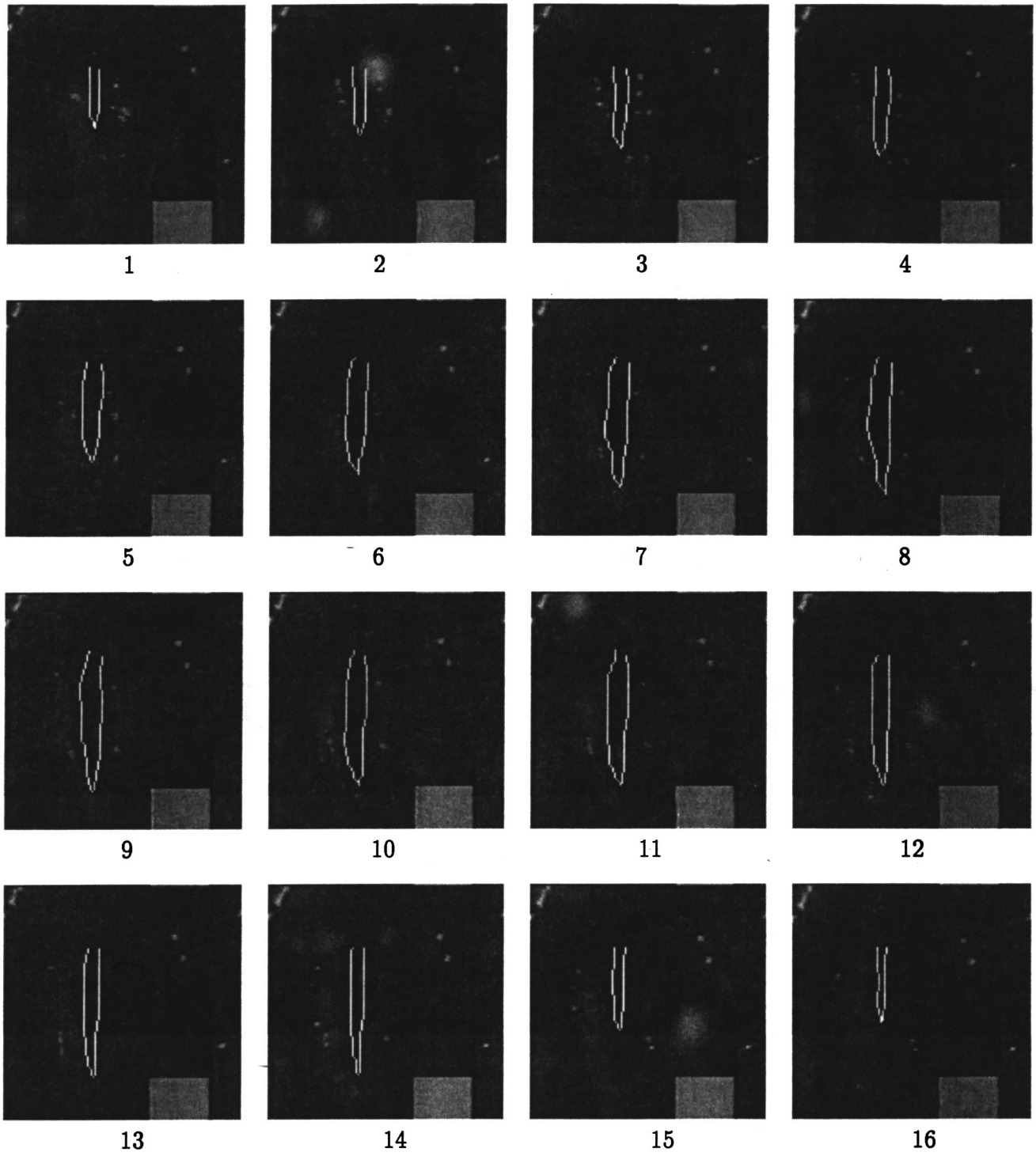

FIG. 7. The bright closed contours delineate the boundaries of the vocal folds in the successive frames of the first abnormal larynx sequence for a patient with polyps run from top left to the bottom right.

rather than anterior–posterior and is consistent with high-speed photography descriptions of the vocal folds vibratory patterns.[28,29] In order to have anterior–posterior motion there would need to be concomitant shortening at the ventricular folds and other visible structures which was not the case. Therefore, it is safe to assume in these images that all the missing motion was medial–lateral and that the line correction enhanced the motion interpretation analysis of the data. This is not to discount vertical movement. However, while the vertical position is continuously changing, over the one second representing a cycle the motion is negligible as evidenced by no change in the size of the true vocal folds or the position of the supraglotic structure.

In order to evaluate the performance of the affine transformation parameters in modeling the displacement vector and characterizing the deformation of the vocal folds, a pre-

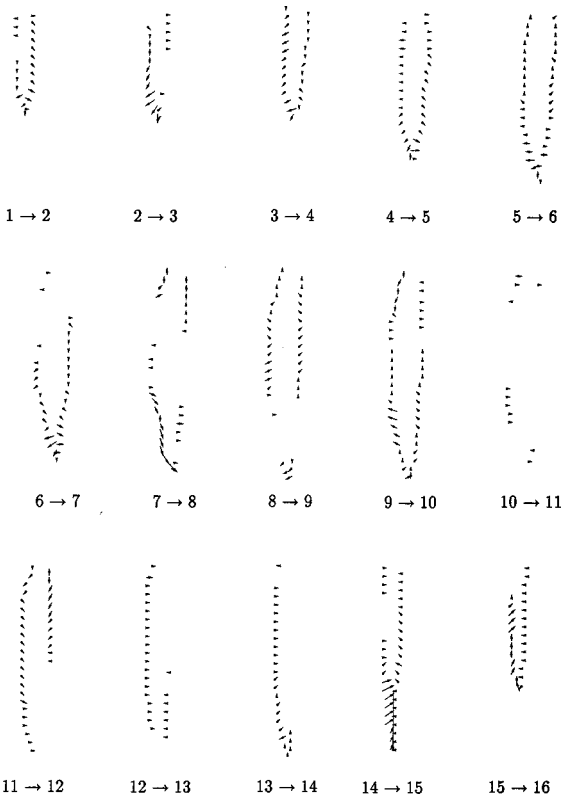

FIG. 8. The registration of the successive boundaries of the first abnormal larynx sequence of videostroboscopic images using the proposed SA-based approach runs from top left to the bottom right; the displacement vector fields are sampled and magnified.

diction mean-square-error metric was used. The E_{pmse} is defined by

$$E_{\text{pmse}} = 1/N \sum_{i=1}^{N} \|d(i) - \hat{d}(i)\|^2, \tag{20}$$

where N is the number of displacement vectors, $d(i) = (x_2(i) - x_1(i), y_2(i) - y_1(i))$ is the displacement vector found from the elastic registration of contours 1 and 2, and $\hat{d}(i) = (\widehat{x_2}(i) - x_1(i), \widehat{y_2}(i) - y_1(i))$ is the displacement vector predicted by

$$\begin{bmatrix} \widehat{x_2}(i) \\ \widehat{y_2}(i) \end{bmatrix} = \begin{bmatrix} a_{11} & a_{12} \\ a_{21} & a_{22} \end{bmatrix} \begin{bmatrix} x_1(i) \\ y_1(i) \end{bmatrix} + \begin{bmatrix} T_x \\ T_y \end{bmatrix} \quad \text{for } i = 1,2,...,N, \tag{21}$$

where $(a_{11}, a_{12}, a_{21}, a_{22}, T_x, T_y)$ are the affine transformation parameters obtained for this displacement vector field. Using the definition in Eq. (20), the E_{pmse} for the displacement vector fields in Fig. 8 is shown as an example in Table II for the larynx with a polyp. The values of the E_{pmse} are small, which indicates the ability of the affine transformation model to capture the deformation of the vocal folds. This sequence was chosen as an example to demonstrate the ability of the affine transformation model to capture the motion information even when it is irregular.

Figure 5(a) and (b) show the relative deformation and the directions of deformation, respectively, for the vocal folds from frame-to-frame. The relative deformation from frame-to-frame is given by the eigenvalues of matrix D, i.e., λ_1 and λ_2, while the corresponding directions of deformation are given by the angles ϕ_1 and ϕ_2. As seen, λ_2, which represents the relative deformation along the ϕ_2 direction, is close to one, i.e., $\lambda_2 \approx 1$. This implies that the deformation along the vertical direction x axis is very small. For this sequence, a larger deformation occurs along the horizontal direction (y axis), i.e., $\phi_1 \approx 90$. The time intervals for which $\lambda_1 > 1$ define the opening cycle of the vocal folds. From Fig. 5(a) we observe that the opening cycle lasts until frame 8, after which the vocal folds start the closing cycle ($\lambda_1 < 1$). Also from Fig. 5(a) we observe that the maximum relative opening movement takes place between frames 3 and 4 and the maximum relative closing movement takes place between frames 14 and 15. These observations cannot be made from the raw images in Fig. 3 or from the displacement vector field in Fig. 4. For this sequence, as shown in Fig. 5(c), the translational motion along the x and y directions is very small since it represents the small translational motion of the centroid of the vocal folds. By observing the images and the motion vectors, which are not shown in this paper due to space limitations, we concluded that the sudden change in the curves of the angles ϕ_1 and ϕ_2 in Fig. 5(b) around frames 8–10 is probably due to patient or camera motion.

Another 16-frame videostroboscopic image sequence of a normal larynx was analyzed and the deformations are shown in Fig. 6. From Fig. 6(a) and as in the previous sequence, the opening cycle ($\lambda_1 > 1$) lasts until frame 8, after which the vocal folds start the closing cycle ($\lambda_1 < 1$). Similar comments as for the previous sequence can be made here about the curves for ϕ_1 and ϕ_2.

In another experiment, we used 16 frames from a videostroboscopic image sequence of a patient with polyps.[2] In Fig. 7 the sequence is shown running from top left to bottom right. The bright contours delineate the boundaries of the vocal folds in the successive frames. Figure 8 shows the displacement vector fields between each two successive contours of the vocal folds using the new algorithm described in Sec. II. The translational and rotational components of the deformation are again very small [see Fig. 9(c) and (d)].

For this sequence also there is almost no deformation along the ϕ_2 direction for which $\lambda_2 \approx 1$ [see Fig. 9(a)]. From Fig. 9(a) we can again observe that the dominant deformation is along the ϕ_1 direction. From this figure we can also tell that the vocal folds kept the opening movement until frame 6 ($\lambda_1 > 1$), then an unexpected closing movement occurred between frames 7–9, then they opened between frames 9 and 10 and after that the closing cycle began.

In the last experiment, we used 20 frames from a videostroboscopic image sequence of a patient with a cyst.[2] The translational and rotational components of the deformation are again very small [see Fig. 10(c) and (d)]. From this figure we can also tell that the vocal folds kept the opening movement until frame 7 ($\lambda_1 > 1$), then an unexpected closing movement occurred between frames 8 and 9, then they continued to open until frame 11.

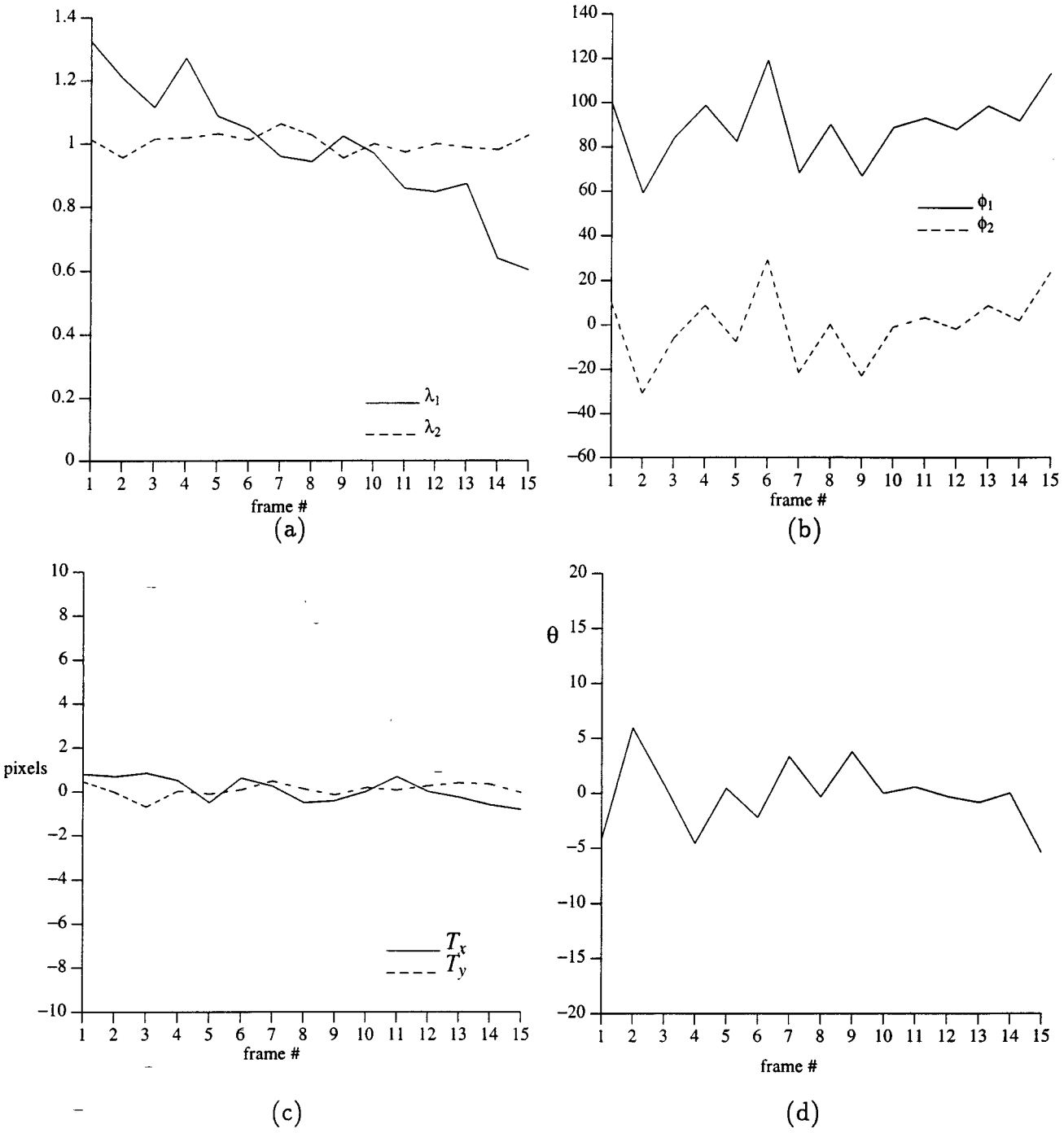

FIG. 9. The figures in (a), (b), (c), and (d) represent time evolution of the eigenvalues, principal directions of deformation, the translation along the x and y axes, and the rotation angle for the frames of the first abnormal larynx videostroboscopic image sequence, respectively. The units of the vertical axes in (b) and (d) are degrees.

V. CONCLUSIONS

In this paper the problem of modeling the deformations of the vocal folds from videostroboscopic recordings was addressed. For this purpose a system that delineates the contours of the vocal folds using snakes, elastically registers the contours using a new regularization-based algorithm, thus the displacement vector field between adjacent frames is obtained, and finally fits an affine transform model to the available displacement vector field was developed.

We found that the affine transformation describes well the deformations of the vocal folds. The proposed affine transformation model is quite general and can be applied in a number of different ways. For example, when the symmetry of the vocal fold motion is examined, then, two affine transformation models, one for the left and one for the right side of the vocal folds, should be used. In the experiments we show, we observed that many important features of the deformation of the vocal folds can be captured very effectively by the time evolution of only a few affine transform parameters of our model. The most significant parameter is λ_1,

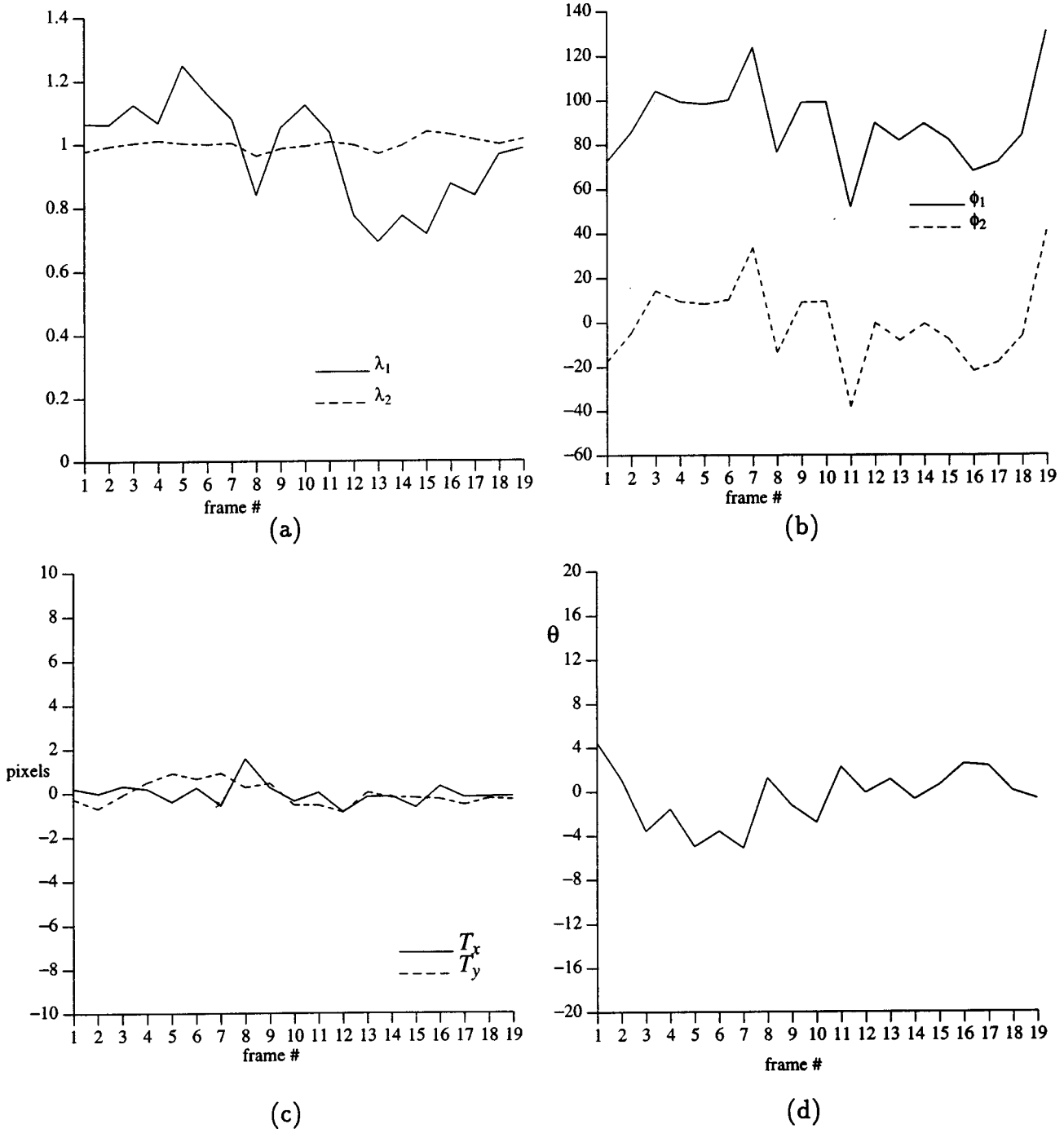

FIG. 10. The figures in (a), (b), (c), and (d) represent time evolution of the eigenvalues, principal directions of deformation, the translation along the x and y axes, and the rotation angle for the frames of the second abnormal larynx videostroboscopic image sequence, respectively. The units of the vertical axes in (b) and (d) are degrees.

which represents the deformation along the horizontal direction. However, there exist scenarios where the other parameters of the affine transformation might be significant. One such scenario is when global motion is present.

Although videostroboscopy is considered to be one of the most valuable clinical tools available for assessing vocal fold vibrations, it is not without problems. It produces an averaged signal and does not provide detail about any single cycle. It is based on assumptions that the vocal fold vibration is fairly regular, which frequently is not the case.

Recently a high-speed digital video system that has neither of these limitations has been used to investigate nonperiodic vibration characteristics of the vocal folds. With such systems recordings are made at 1000 frames/s or faster so that in contrast to recordings made at 30 frames/s, many video frames are captured during one true rather than one apparent glottal cycle, removing the periodicity limitation of stroboscopy.[30] However, the methods described in this paper could be applied to high-speed video images, thus providing more powerful interpretations of vocal fold vibrations.

ACKNOWLEDGMENTS

This work was supported by the Whitaker foundation. The authors of this paper are grateful to the authors of Ref. 4 for kindly providing them with the code for their registration algorithm and to the authors of Ref. 20 for providing them with a preprint of their paper.

[1] D. Bless, M. Hirano, and R. Feder, ''Videostroboscopic evaluation of the larynx,'' Ear Nose & Throat Journal **66**(7), 289–296 (1987).
[2] M. Hirano and D. Bless, *Videostroboscopic Examination of the Larynx* (Singular, San Diego, 1993).
[3] H. Maître and Y. Wu, ''Dynamic programming algorithm for elastic registration of distorted pictures based on autoregressive model,'' IEEE Trans. Acoust. Speech Signal Process. **37**(2), 288–297 (1989).
[4] B. Tom, S. N. Efstratiadis, and A. K. Katsaggelos, ''Motion estimation of skeletonized angiographic images using elastic registration,'' IEEE Trans. Med. Imaging **13**, 450–460 (1994).
[5] D. Geiger, A. Gupta, L. A. Costa, and J. A. Vlontzos, ''Dynamic programming for detecting, tracking, and matching deformable contours,'' IEEE Trans. Pattern. Anal. Mach. Intell. **17**(3), 294–302 (1995).
[6] J. S. Duncan, R. L. Owen, L. H. Staib, and P. Anandan, ''Measurement of non-rigid motion using contour shape descriptors,'' Int. J. Comput. Vis. **1**(4), 321-331 (1988).
[7] P. Shi, G. Robinson, R. T. Constable, A. Sinusas, and J. Duncan, ''A Model-based integrated approach to track myocardial deformation using displacement and velocity constraints,'' International Conference on Computer Vision (1995), pp. 687–692.
[8] C. Nastar and N. Ayache, ''Non-rigid motion analysis in medical images: a physically based approach,'' *13th International Conference, Information Processing in Medical Imaging* (1993), pp. 17–32.
[9] M. Kass, A. Witkin, and D. Terzopoulos, ''Snakes: active contour models,'' Proc. IEEE Conf. Comput. Vision Patt. Recogn., June 1991, pp. 318–324.
[10] A. K. Saadah, N. Galatsanos, and D. Bless, ''A new elastic registration algorithm for videostroboscopic images of the larynx,'' Proceedings of IASTED, International Conference Signal and Image Processing-SIP-95, Las Vegas, Nevada (1995), pp. 93–96.
[11] E. Aarts and J. Korst, *Simulated Annealing and Boltzman Machines* (Wiley, New York, 1990).
[12] N. P. Galatsanos and A. K. Katsaggelos, ''Methods for choosing the regularization parameter and estimating the noise variance in image restoration and their relation,'' IEEE Trans. Image Process. **1**(3), 322–336 (1992).
[13] D. Terzopoulos, ''Regularization of inverse visual problems involving discontinuities,'' IEEE Trans. Pattern. Anal. Mach. Intell. **8**(4), 413–424 (1986).
[14] E. A. Cemal, *Continuum Physics* (Academic, New York, 1976).
[15] J. Canny, ''A computational approach to edge detection,'' IEEE Trans. Pattern. Anal. Mach. Intell. **8**, 679–698 (1986).
[16] A. Martelli, ''Edge detection using heuristic search methods,'' Comput. Graph. Image Process. **1**, 169–182 (1972).
[17] D. Marr and H. K. Nishihara, ''Visual information processing: artificial intelligence and the sensorium of sight,'' Technology Reviews **81**(1), 2–23 (1978).
[18] R. O. Duda and P. E. Hart, ''Use of the Hough transformation to detect lines and curves in pictures,'' Commun. ACM **15**, 11–15 (1972).
[19] K. F. Lai and R. T. Chin, ''On regularization, formulation and initialization of the active contour models (Snakes),'' Asian Conference of Computer Vision (1993), pp. 542–545.
[20] K. F. Lai and R. T. Chin, ''On modeling, extraction, detection and classification of deformable contours from noisy images,'' Europe-China Workshop on Geometrical Modeling and Invariants for Computer Vision, Xi'an, China, pp. 27–29, April 1995.
[21] R. E. Bellman, *Applied Dynamic Programming* (Princeton U.P., Princeton, NJ, 1962).
[22] S. Geman and D. Geman, ''Stochastic relaxation, Gibbs distribution, and Bayesian restoration of images,'' IEEE Trans. Pattern. Anal. Mach. Intell. **6**(6), 721–741 (1984).
[23] N. Metropolis, A. Rosenbluth, M. Rosenbluth, A. Teller, and E. Teller, ''Equation of state calculations by fast computer machines,'' J. Chem. Phys. **21**, 1087–1092 (1953).
[24] P. A. van den Elsen, E J. D. Pol, and M. A. Viergever, ''Medical image matching—a review with classification,'' IEEE Eng. Med. Biol. Mag. **12**(1), 26–39 (1993).
[25] T. Y. Young and S. Gunasekaran, ''A regional approach to tracking 3D motion in an image sequence,'' in *Advances in Computer Vision and Image Processing*, edited by T. S. Huang (JAI, Greenwich, 1988), pp. 63–99.
[26] G. H. Golub and C. F. Van Loan, *Matrix Computations* (Johns Hopkins U.P., Baltimore, 1989).
[27] B. P. Flannery, W. H. Press, S. A. Teukolsky, and W. T. Vetterling, *Numerical Recipes in C* (Cambridge U.P., Cambridge, 1988).
[28] R. Timcke, H. vonLeden, and P. Moore, ''Laryngeal vibrations: II. Physiologic vibrations,'' Arch. Otolaryngol. **69**, 438–444 (1959).
[29] H. vonLeden, P. Moore, and R. Timcke, ''Laryngeal vibrations: III. The pathologic larynx. Archives of Otology **71**, 1232–1250 (1960).
[30] T. Wittenberg, M. Moser, M. Tigges, and U. Eysholds, ''Recording, processing and analysis of digital high-speed sequences in glottography,'' Mach. Vision Appl. **8**, 399–404 (1995).

Fundamental frequency during phonetically governed devoicing in normal young and aged speakers

Ben C. Watson
Department of Otolaryngology, New York Medical College, Valhalla, New York 10595

(Received 23 October 1997; accepted for publication 2 March 1998)

Age-related changes in the laryngeal system can be perceived as altered vocal pitch and increased pitch variability. However, reports vary as to the nature and extent of an age effect on fundamental frequency ($F0$) for analyses taken over long segments of connected speech. Analysis of $F0$ across a smaller time frame may be more informative. Young speakers show an increase in $F0$ associated with phonetically governed devoicing gestures that is likely mediated by increased vocal fold stiffness. Anatomic and neurophysiologic changes in the aged larynx may limit the role of increased vocal fold stiffness in the devoicing gesture. This study tests the hypothesis that aged speakers show a smaller increase in $F0$ in association with the devoicing gesture for production of an intervocalic voiceless obstruent than do young speakers. Normal young and aged speakers produced a short sentence containing an intervocalic voiceless obstruent. Measures of $F0$ were obtained for ten cycles before voice offset and ten cycles after voice onset. Young speakers showed a small increase in $F0$ during devoicing whereas aged speakers showed a decrease in $F0$ during devoicing. Aged speakers seem to rely more on vocal fold abduction rather than a combination of abduction and tensing to achieve devoicing.
[S0001-4966(98)04006-5]

PACS numbers: 43.70.Aj, 43.70.Fq [AL]

INTRODUCTION

Age-related changes in the laryngeal system are well documented. The hyaline cartilage framework becomes calcified and/or ossified (Chamberlain and Young, 1935; Hately *et al.*, 1965). Surfaces of the cricoarytenoid joints become thinner and more irregular (Kahane and Hammons, 1987). Changes occur in the synovial membrane surrounding the cricoarytenoid joint (Kahane and Hammons, 1987). Layers of the lamina propria undergo morphologic changes (Hirano *et al.*, 1983). Laryngeal muscles atrophy (Bach *et al.*, 1941). Degeneration of afferent and efferent nerves compromises the integration of sensory input from mucosal and articular receptors with motor output to intrinsic laryngeal muscles that is critical to coordinating the laryngeal system with the articulatory and respiratory systems (Weismer and Liss, 1991). Certain of these changes can be perceived in the aged as changes in pitch and in pitch variability during speech production (Ryan and Burk, 1974; Shipp *et al.*, 1992).

Fundamental frequency, the physical correlate of vocal pitch, can be characterized at several levels of temporal resolution during connected speech. Relatively long stretches of connected speech are analyzed to obtain measures of the mean and standard deviation of speaking $F0$ and of speaking $F0$ range. Syllable-length materials are analyzed to document control of $F0$ associated with the production of stress. Transitions between successive speech segments (specifically, between voiced and voiceless segments) are analyzed to document control of $F0$ associated with phonetic voicing distinctions.

Investigations of average speaking $F0$ report an inconsistent pattern in the expression of this feature in aged subjects. That is, studies report an increase (Mysak, 1959; Hollien and Shipp, 1972; Brown *et al.*, 1991; Shipp *et al.*, 1992), a decrease (Stoicheff, 1981; Benjamin, 1981; Morgan and Rastatter, 1986; Morris and Brown, 1988; Pegoraro-Krook, 1988; Brown *et al.*, 1989, 1991), or no difference (Charlip, 1968; Pegoraro-Krook, 1988; McGlone and Hollien, 1963; Ramig and Ringel, 1983; Biever and Bless, 1989; Bless *et al.*, 1993; Russell *et al.*, 1995) in average speaking $F0$ in aged compared to young speakers. Reports of variability in speaking $F0$ (measured as $F0$ range or standard deviation) are more consistent in showing an age effect expressed as decreased $F0$ range (Ptacek *et al.*, 1966; Morgan and Rastatter, 1986; Bless *et al.*, 1993) and increased $F0$ variability (Mysak, 1959; Stoicheff, 1981; Morris and Brown, 1988; Biever and Bless, 1989; Brown *et al.*, 1989; Morris and Brown, 1994). One study, however, reported a greater $F0$ range in aged speakers as compared to young speakers (Benjamin, 1981).

Two studies examined age effects on $F0$ associated with the production of stressed and unstressed syllables. Scukanec *et al.* (1992) reported greater intrasubject variability in $F0$ during both stressed and unstressed syllables in aged females relative to young females. The aged females also showed greater intersubject variability in $F0$ during the production of stressed syllables. Scukanec *et al.* (1996) examined $F0$, duration, and intensity (sound pressure level) characteristics of stressed syllables in young and aged females. Both groups significantly increased $F0$, duration, and intensity during the production of contrastive stress. The magnitude of increase in $F0$ was significantly higher for the aged subjects.

To summarize, studies of aged speakers reveal variability in the nature and extent of a chronological age effect on $F0$ for analyses conducted over relatively long segments of connected speech. Inconsistency among studies that examined relatively long segments of connected speech may arise,

in part, from differences in experimental task (for example, reading aloud versus extemporaneous speaking) and from effects of idiosyncratic speaking styles on $F0$. That is, connected speech tasks may not reveal important details of physiologic constraints on $F0$.

A measurement domain that is less likely to be influenced by idiosyncratic speaking styles is the phonetic segment. Therefore, physiologic constraints on the control of $F0$ during connected speech are more likely to be revealed at the segmental level; in particular, during transitions between adjacent voiced and voiceless segments. House and Fairbanks (1953) reported higher $F0$ for vowels that occur in voiceless contexts. Ohde (1984) reported that $F0$ decreases after voice onset following both voiceless and voiced stops.

Two studies report electromyographic (EMG) data from cricothyroid (CT), one of the intrinsic laryngeal muscles involved in regulating vocal fold tension, during the devoicing gesture. Löfqvist *et al.* (1989) focused their investigation primarily on $F0$ and CT during the postconsonantal vowel. However, their analysis window included the preceding vowel and the consonant. Löfqvist *et al.* (1989) report that average EMG activity for CT begins to increase during the preceding vowel and ''shortly before the corresponding audio envelope begins its rapid descent'' (p. 1317); that is, before the onset of vocal tract constriction. They also reported that $F0$ is high at the beginning of a vowel following a voiceless obstruent and decreases during the first several vocal cycles. Taken together, these findings implicate an increase in $F0$, mediated by CT activity, as one component of the phonetically governed devoicing gesture. Ludlow *et al.* (1991), however, did not observe increased CT activity in association with a phonetic devoicing gesture. Instead, they found CT activity associated with stress changes and, to some extent, as complimentary to thyroarytenoid activity for vocal fold adduction. Ludlow *et al.* (1991) did not report $F0$ data. Thus, empirical evidence for a CT-mediated increase in $F0$ as part of the devoicing gesture is inconclusive. Theoretically, Stevens' (1977) model of the laryngeal state for voiceless obstruents posits that the vocal folds are stiff and the arytenoids are in either an abducted (aspirated) or a neutral (unaspirated) position.

The goal of this study is to compare normal young and aged adult speakers with respect to cycle-to-cycle changes in $F0$ associated with production of an intervocalic, voiceless obstruent. As noted above, there is theoretical (Stevens, 1977) and limited empirical (Ohde, 1984; Löfqvist *et al.*, 1989) evidence that an increase in $F0$ is associated with phonetically governed devoicing and, further, that such increase is mediated by increased vocal fold stiffness.

Changes in the aged larynx may affect the role of transient increases in vocal fold stiffness in the devoicing gesture and this affect should be evident in patterns of change in $F0$ during the termination and initiation phases of vocal fold vibration adjacent to the voiceless obstruent. Morphologic changes in the layers of the lamina propria described by Hirano *et al.* (1983) (specifically, thickening of the superficial layer, decreased density, and atrophy of elastic fibers in the intermediate layer, and an increase in the size and density of collagenous fibers in the deep layer) increase the stiffness of the vocal fold cover. Atrophy of the vocalis muscle (Honjo and Isshiki, 1980; Hirano *et al.*, 1983) decreases the stiffness of the vocal fold body. Together, these anatomic changes may make it more difficult for aged speakers to produce transient increases in vocal fold tension. Neuromuscular changes associated with aging may also limit aged speakers ability to produce transient increases in vocal fold tension as part of the devoicing gesture. Rodeno *et al.* (1993) reported a decrease in the percentage of type 2 muscle fibers in intrinsic laryngeal muscle as a function of increased age. Porter *et al.* (1995) described reduced numbers of motor units and muscle fibers and reduced size of type 2 muscle fibers in aged skeletal muscle. These changes likely contribute to weakening and slowing the response time of muscles involved in changing vocal fold stiffness.

In light of the anatomic and neurophysiologic changes described above, the hypothesis under test is that aged speakers show a smaller increase in $F0$ in association with the devoicing gesture for production of an intervocalic, voiceless obstruent than do young speakers.

I. METHOD

Ten aged and ten young adult speakers provided informed consent to participate in this study. Each group included six females and four males. Mean age of the aged speakers was 74 yr (range: 68–85 yr). Mean age of the young speakers was 24 yr (range: 23–27 yr). All subjects reported no history of significant speech, language, hearing, neurologic, pulmonary, or voice disorder, and no history of alcoholism. One young speaker reported a 10-yr history of smoking two cigarettes/day. Two aged speakers reported a history of smoking (both have been nonsmokers for at least the past 12 yr). Aged speakers passed a hearing screening at 35 dB in at least one ear for octave frequencies from 0.5–4.0 kHz. All aged subjects were living independently and described themselves as being in good health.

Aged subjects were screened on three measures of cardiac function. Group mean resting heart rate was 78 bpm (range: 60–96). Group mean systolic blood pressure was 134 mmHg (range: 120–180). Group mean diastolic blood pressure was 75 mmHg (range: 55–92). The *WHO Expert Committee on Arterial Hypertension* set levels of systolic pressure <160 and/or diastolic pressure <95 as criteria for ruling out clinically significant arterial hypertension (DHEW publication, NIH 74-618). All of our aged subjects met these criteria (the aged subject whose systolic pressure was 180 mmHg had a diastolic pressure of 72 mm Hg).

Aged persons are at increased risk for affective and cognitive disorders that can affect motor performance (Hubbard, 1991). Consequently, aged subjects' cognitive and affective status were screened using the Mini-mental State Inventory (Folstein *et al.*, 1975) and Beck Depression Inventory (Beck, 1987), respectively. All aged speakers achieved a score of at least 23 on the Mini-Mental State inventory (group mean: 27; range: 23–30) and a score within normal limits (that is, score $\leqslant 9$) on the Beck Depression Inventory (group mean: 4.8; ranges 2–9). These scores indicate no clinically significant cognitive disorder or depression among these aged subjects. Young subjects were recruited from the student popu-

lation of New York Medical College and all reported being in good health and free of clinically significant cardiac disorder. Young speakers also scored within normal limits on the Beck Depression Inventory (group mean: 1.2; range: 0–9).

Subjects produced the sentence ''A new seed grows fast'' in a conversational manner. Vocal $F0$ was measured for the offset of /u/ and the onset of /i/ in ''new seed.'' Subjects were instructed to place primary stress on the word ''new'' as though answering the question, ''Does an old seed grow fast?'' The task was repeated until three acceptable tokens were recorded. A token was deemed acceptable if it was perceptually fluent, contained no misarticulations, conformed to the prescribed placement of primary stress, and was judged by the experimenter to be produced at a conversational pitch and loudness.

A miniature electret microphone was positioned approximately 4 cm in front of the lips at the oral midline. The acoustic signal was routed through a pre-amplifier, amplifier, digital lowpass filter ($f_{co}=5$ kHz) (SIU-200, Alamed Corp., Vega, TX), and to an analog-to-digital converter (10-kHz sampling rate; 12-bit resolution) (Data Translation, DT2821-FE) housed in a personal computer (Compaq Prosignia 486).

The digitized acoustic signal was displayed and analyzed using the Voice+ signal processing library (Alamed Corp., Vega, TX). A copy of the acoustic signal was digitally low-pass filtered at 350 Hz and downsampled to a sample rate of 5 kHz. Low-pass filtering reduced the amplitude of the vocal tract resonances to facilitate measurement of vocal $F0$. Downsampling expedited the filtering process. Ten vocal cycles in /u/ immediately before voice offset and ten vocal cycles in /i/ immediately after voice onset were extracted automatically from the low-pass-filtered signal using a mid-level-crossing criterion to define pitch period boundaries. Temporal resolution of boundary detection was enhanced by use of linear interpolation. The effective resolution for temporal measures was 0.1 ms.

Transition-related changes in $F0$ are superimposed upon a dynamic base-line $F0$ (intonation contour). Superposition of the transition upon the intonation contour may be problematic for analysis of aged speakers since they show greater variability than young speakers in base-line $F0$ across repeated productions of the same utterance, even when instructed to use a consistent stress pattern (Weismer and Fromm, 1983), and high intrasubject variability in $F0$ for stressed syllables (Scukanec *et al.*, 1992). High variability in base-line $F0$ could obscure a transition effect on $F0$ that is likely to be of a smaller magnitude. To minimize effects of intra- and intersubject variability in the intonation contour, $F0$ values were normalized within individual tokens by converting them to semitones relative to a reference cycle. Since the focus of the study was on $F0$ changes immediately adjacent to voice offset and onset, the vocal cycles furthest from these points were used as the referents for computation of semitone values. Semitone values were averaged across the three tokens for each of the ten vocal cycles preceding and following the /s/ for each subject.

Average semitone values were entered into two 2×10 repeated measures multivariate analyses of variance to investigate the significance of age (young versus old) and vocal cycle (1–10) separately for the preceding (/u/) and following (/i/) vowels. Age was entered as the between groups factor and vocal cycle was entered as the within groups factor.

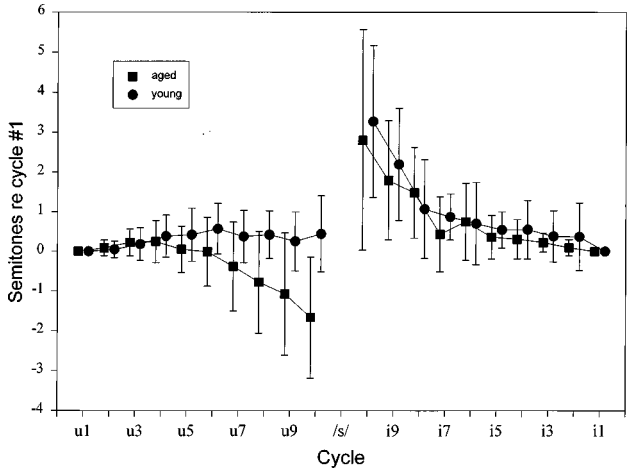

FIG. 1. Mean semitone values (±1 standard deviation) as a function of vocal cycle for aged (■) and young (●) speakers for the /u/ and /i/ vowels. Vocal cycles are numbered in ascending order from the referent cycles ($u1$ and $i1$).

II. RESULTS

Figure 1 shows mean semitone values ($\pm$ one standard deviation) as a function of vocal cycle for aged (■) and young (●) speakers for the /u/ and /i/ vowels. Young speakers show a small but consistent increase in $F0$ from cycle $u1$ to a peak of 0.56 semitones at cycle $u6$. Semitone values then decline to a value of 0.44 at cycle $u10$. The young speakers also show a decrease in $F0$ from a peak of 3.27 semitones at cycle $i10$ following the fricative. The greatest change in $F0$ (-2.73 semitones) occurs across cycles $i10$ through $i5$.

Aged speakers show a small increase in $F0$ to a peak of 0.24 semitones at cycle $u4$ and then a decrease in $F0$ to -1.66 semitones at cycle $u10$. Aged speakers show a decrease in $F0$ from a peak of 2.80 semitones at cycle $i10$ following the fricative. The greatest change in $F0$ (-2.44 semitones) occurs across cycles $i10$–$i5$. Aged speakers also show greater within-group variability in $F0$ than young speakers for most of the vocal cycles.

Multivariate, repeated measures ANOVA were conducted separately for the /u/ and /i/ vowels to investigate the significance of group and cycle effects. Analysis of semitone data for the /u/ vowel revealed significant group [$F(1,18)=5.36$, $p=0.0327$], cycle [$F(9,10)=3.53$, $p=0.0311$], and group by cycle interaction [$F(9,10)=3.8351$, $p=0.0238$] effects. Analysis of semitone data for the /i/ vowel revealed only a significant cycle effect [$F(9,10)=3.7989$, $p=0.0246$].

Post hoc between-group comparisons of semitone values for the /u/ vowel as a function of vocal cycle were conducted using the Tukey's test for unconfounded means (Linton and Gallo, 1975). This relatively conservative test requires calculation of a critical value that serves as the threshold for detection of the significance of between-group differences in

TABLE I. Group mean semitone values and between-group difference as a function of vocal cycle. Cycle $u10$ is the last cycle before the voiceless obstruent (/s/).

Vocal cycle	Aged speakers	Young speakers	Group difference
$u1$	0	0	0
$u2$	0.0872	0.4963	0.4091
$u3$	0.2245	0.1804	0.0441
$u4$	0.2472	0.3828	0.1356
$u5$	0.0487	0.4177	0.369
$u6$	−0.0093	0.5675	0.5768
$u7$	−0.3837	0.3730	0.7567
$u8$	−0.7793	0.4195	1.1988[a]
$u9$	−1.0773	0.2511	1.3284[a]
$u10$	−1.6649	0.4419	2.1068[a]

[a] $p=0.01$, critical value $=0.9221$.

mean scores; that is, mean differences greater than the critical value are statistically significant. The critical value for $p=0.01$ was 0.9221 for these data. Table I shows mean semitone values for each group and the group difference in semitones as a function of vocal cycle. Group difference values increase monotonically beginning at cycle $u4$ because of the decrease in semitone values for the aged speakers. Mean semitone values for the two groups are significantly different for cycles $u8-u10$.

It is possible that changes in transglottal pressure related to constriction of the vocal tract could account for $F0$ lowering in the aged speakers. An indirect test of this possibility is to compare $F0$ and root-mean-square (rms) amplitude values. A decrease in rms amplitude may be associated with increased oral constriction since intraoral pressure increases and, consequently, transglottal pressure decreases during the constriction gesture. If $F0$ lowering was secondary to a drop in transglottal pressure, as reflected in rms amplitude, then $F0$ lowering should be simultaneous with, or slightly lag, rms lowering. Figure 2 shows mean $F0$ (aged: ○; young: △) and rms (aged: ●; young: ▲) values for /u/ and /i/. Young speakers show evidence of $F0$ raising and rms lowering beginning at cycle $u1$. That is, there is an inverse relation between changes in $F0$ and rms amplitude for the young speakers. Aged speakers show a decrease in rms amplitude after cycle $u5$, and the major decrease in rms amplitude occurs after cycle $u7$. The decrease in $F0$ begins at cycle $u4$. We conclude, therefore, that aerodynamic factors likely do not contribute to $F0$ lowering for the aged speakers since the relation between changes in $F0$ and rms amplitude is not consistent with predicted effects of changes in transglottal pressure on $F0$.

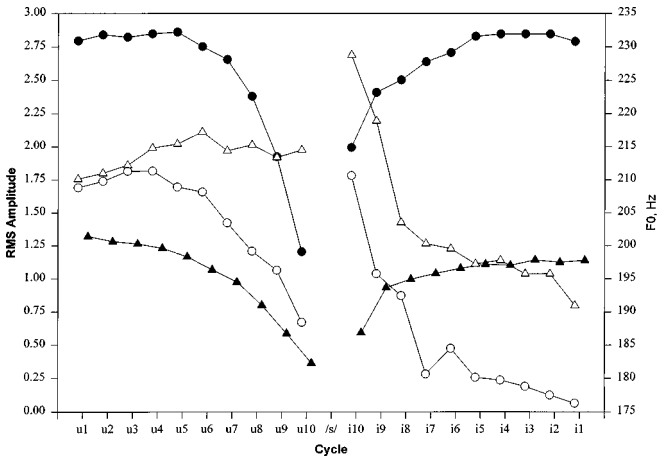

FIG. 2. Mean $F0$ (△) and rms amplitude (▲) for the young speakers and mean $F0$ (○) and rms amplitude (●) for the aged speakers for the /u/ and /i/ vowels.

III. DISCUSSION

The presence or absence of vocal fold vibration during the period of oral constriction underlies the phonetic voicing feature for fricative consonants. Whether or not vocal fold vibration will occur during the constriction is determined by vocal fold tension (Löfqvist *et al.*, 1989), transglottal airflow (Hirose and Niimi, 1987), and glottal configuration (abduction/adduction) (Yoshioka *et al.*, 1981; Stevens, 1991).

The following phenomena have been observed in young speakers in association with the cessation of vocal fold vibration for production of voiceless fricatives: (a) increased vocal tension as evidenced by an increase in $F0$ and in cricothyroid muscle activity that begins during the preceding vowel (Löfqvist *et al.*, 1989) [but, see Ludlow *et al.* (1991) for conflicting findings]; (b) peak and minimum airflow values that increase monotonically across vocal cycles immediately before the onset of frication (Löfqvist and McGowan, 1991; Löfqvist and McGowan, 1992); and (c) relatively wide glottal opening that occurs rapidly and begins before the onset of frication (Yoshioka *et al.*, 1981; Fukui and Hirose, 1983). In sum, the devoicing gesture can be characterized as a combination of vocal fold abduction and tensing. Löfqvist *et al.* (1989) suggest that increased vocal fold tension may supplement abduction to achieve devoicing. It is against this model that we will evaluate the findings of the present study.

We found significant between-group differences in normalized $F0$ values during the vowel preceding the voiceless fricative, but no group differences for these values during the vowel following the fricative. Young speakers showed a small increase in $F0$ across the first six cycles and a relatively flat $F0$ contour across the last four cycles before voice offset. They showed a decrease in $F0$ across the first five cycles following voice onset. Mean $F0$ at voice onset was higher than for any cycle before voice offset (see Fig. 2). This $F0$ pattern is consistent with an increase in vocal fold tension as part of the devoicing gesture. Löfqvist *et al.* (1989) did not report $F0$ data for vowels preceding voiceless obstruents. However, their EMG data reveal that CT activity begins to increase during the preceding vowel and reaches a peak near the release of the obstruent consonant. They estimate that the interval between the onset of CT activity and an increase in $F0$ is in the range of 20–80 ms. If CT activity begins during the preceding vowel, then the present observation of a small increase in $F0$ immediately before voice offset likely falls within the 20–80-ms window.

Aged speakers showed a small increase in $F0$ across the first four cycles and a decrease in $F0$ across the last six cycles before voice offset. They showed a decrease in $F0$ across the first five cycles following voice onset. Mean $F0$ at

voice onset was equal to the highest mean $F0$ value observed before voice offset (see Fig. 2). This pattern of change in $F0$ is not consistent with the use of increased vocal fold tension to achieve devoicing. Morphologic and neuromuscular changes described earlier may limit the ability of aged speakers to produce transient increases in vocal fold tension as part of the devoicing gesture. Recall that morphologic changes include thickening of the superficial layer, decreased density and atrophy of elastic fibers in the intermediate layer, an increase in the size and density of collagenous fibers in the deep layer (Hirano *et al.*, 1983), and atrophy of the vocalis muscle (Honjo and Isshiki, 1980; Hirano *et al.*, 1983). Neuromuscular changes associated with aging include a decrease in the percentage of type 2 muscle fibers in intrinsic laryngeal muscle (Rodeno *et al.*, 1993), reduced numbers of motor units and muscle fibers, and reduced size of type 2 muscle fibers (Porter *et al.*, 1995).

As a consequence of the morphologic and neuromuscular changes noted above, aged speakers may rely on vocal fold abduction as the primary mechanism for devoicing. If so, then vocal fold stiffness might have been relatively constant from cycle $u4$, the maximum $F0$ before voice offset, to cycle $i1$, the maximum $F0$ at voice onset. Further, if these aged subjects rely on abduction to achieve devoicing, and they begin abduction during the preceding vowel [as Fukui and Hirose (1983) suggest typically occurs], then the measured decrease in $F0$ associated with devoicing could be attributed to biomechanical factors associated with the abductory gesture, rather than to changes in vocal fold stiffness.

Several factors could contribute to $F0$ lowering secondary to a prolonged vocal fold abductory gesture. Effects of these factors can be described in the context of changes in vocal fold contact during the vibratory cycle. First, decreased vocal fold contact area during the vibratory cycle as the vocal folds abduct may reduce the magnitude of recoil forces that accelerate lateral displacement of the vocal folds. Reduction of this force may prolong the decontacting phase of the vibratory cycle. Second, failure to achieve contact along the length of the vocal folds means that there is no abrupt end (collision) to the contacting phase of the vibratory cycle. Consequently, the contacting phase of the cycle may increase in duration as the folds gradually decelerate to their maximum medial position. Increased duration of both the contacting and decontacting phases of the vibratory cycle will increase the cycle period (that is, decrease $F0$). Finally, as the folds abduct, the arytenoid cartilages slide outward, forward, and downward along the superior edge of the cricoid cartilage (Fink and Demarest, 1978). This action may shorten the vocal folds and, in the absence of increased CT activity, decrease $F0$.

In conclusion, data reported here fail to support the research hypothesis under test. Normal aged speakers did not show a smaller increase in $F0$ in association with the devoicing gesture than young speakers. In fact, finding a decrease in $F0$ for the aged speakers in this context leads to formulation of the new hypothesis that normal young and aged speakers use different strategies (abduction and tensing versus abduction alone) to achieve phonetically governed devoicing.

Bach, A., Lederer, F., and Dinolt, R. (**1941**). ''Senile changes in the laryngeal musculature,'' Arch. Otolaryngol. **34**, 47–56.

Beck, A. T. (**1987**). *The Beck Depression Inventory* (The Psychological Corp., San Antonio).

Benjamin, B. J. (**1981**). ''Frequency variability in the aged voice,'' J. Gerontol. **36**, 722–726.

Biever, D. M., and Bless, D. M. (**1989**). ''Vibratory characteristics of the vocal folds in young adult and geriatric women,'' J. Voice **3**, 120–131.

Bless, D., Glaze, L., Biever-Lowery, D., Campos, G., and Peppard, R. (**1993**). ''Stroboscopic, acoustic, aerodynamic and perceptual analysis of voice production in normal speaking adults,'' National Center for Voice and Speech, Status and Progress Report **4**, 121–134.

Brown, Jr., W. S., Morris, R. J., and Michel, J. F. (**1989**). ''Vocal jitter in young adult and aged female voices,'' J. Voice **3**, 113–119.

Brown, Jr., W. S., Morris, R. J., Hollien, H., and Howell, E. (**1991**). ''Speaking fundamental frequency characteristics as a function of age and professional singing,'' J. Voice **5**, 310–315.

Chamberlain, W., and Young, B. (**1935**). ''Ossification (so-called 'calcification') of normal laryngeal cartilages mistaken for foreign bodies,'' Am. J. Roentgenol. Radium Ther. **33**, 441–450.

Charlip, W. S. (**1968**). ''The aging female voice: Selected fundamental frequency characteristics and listener judgments,'' Doctoral thesis, Purdue University.

Fink, B. R., and Demarest, R. J. (**1978**). *Laryngeal Biomechanics* (Harvard U.P., Cambridge).

Folstein, M., Folstein, S., and McHugh, P. (**1975**). '' 'Mini-Mental State': a practical method for grading the cognitive state of patients for the clinician,'' J Psychol. Res. **12**, 189–198.

Fukui, N., and Hirose, H. (**1983**). ''Laryngeal adjustments in Danish voiceless obstruent production,'' Annu. Bull. RILP **17**, 61–71.

Hately, B., Evison, G., and Samuel, E. (**1965**). ''The pattern of ossification in the laryngeal cartilages: A radiological study,'' Br. J. Radiol. **38**, 585–591.

Hirano, M., Kurita, S., and Nakashima, T. (**1983**). ''Growth, development, and aging of human vocal folds,'' in *Vocal Physiology: Contemporary Research and Clinical Issues*, edited by D. M. Bless and J. H. Abbs (College Hill, San Diego), pp. 44–49.

Hirose, H., and Niimi, S. (**1987**). ''The relationship between glottal opening and the transglottal pressure differences during consonant production,'' in *Laryngeal Function in Phonation and Respiration*, edited by T. Baer, C. Sasaki, and K. Harris (College Hill, Boston), pp. 381–390.

Hollien, H., and Shipp, T. (**1972**). ''Speaking fundamental frequency and chronologic age in males,'' J. Speech Hear. Res. **15**, 155–159.

Honjo, I., and Isshiki, N. (**1980**). ''Laryngoscopic and voice characteristics of aged persons,'' Arch. Otolaryngol. **106**, 149–150.

House, A. S., and Fairbanks, G. (**1953**). ''The influence of consonant environment upon the secondary acoustical characteristics of vowels,'' J. Acoust. Soc. Am. **25**, 105–113.

Hubbard, R. W. (**1991**). ''Mental health and aging,'' in *Handbook of Geriatric Communication Disorders*, edited by D. N. Ripich (Pro Ed., Austin), pp. 205–226.

Kahane, J. C., and Hammons, J. (**1987**). ''Developmental changes in the articular cartilage of the human cricoarytenoid joint,'' in *Laryngeal Function in Phonation and Respiration*, edited by T. Baer, C. Sasaki, and K. Harris (College Hill, Boston), pp. 14–28.

Linton, M., and Gallo, Jr., P. S. (**1975**). *The Practical Statistician* (Brooks/Cole, Monterey).

Löfqvist, A., and McGowan, R. (**1991**). ''Voice source variations in running speech,'' in *Vocal Fold Physiology: Acoustic, Perceptual, and Physiological Aspects of Voice Mechanisms*, edited by J. Gauffin and B. Hammarberg (Singular, San Diego), pp. 113–120.

Löfqvist, A., and McGowan, R. (**1992**). ''Influence of consonantal environment on voice source aerodynamics,'' J. Phonetics **20**, 93–110.

Löfqvist, A., Baer, T., McGarr, N., and Seider Story, R. (**1989**). ''The cricothyroid muscle in voicing control,'' J. Acoust. Soc. Am. **85**, 1314–1321.

Ludlow, C. L., Sedory, S. E., and Fujita, M. (**1991**). ''Neurophysiological control of vocal fold adduction and abduction for phonation onset and offset during speech,'' in *Vocal Fold Physiology: Acoustic, Perceptual, and Physiological Aspects of Voice Mechanisms*, edited by J. Gauffin and B. Hammarberg (Singular, San Diego), pp. 197–205.

McGlone, R. E., and Hollien, H. (**1963**). ''Vocal pitch characteristics of aged women,'' J. Speech Hear. Res. **6**, 164–170.
Morgan, E. E., and Rastatter, M. (**1986**). ''Variability of voice fundamental frequency in elderly female speakers,'' Perceptual & Motor Skills **63**, 215–218.
Morris, R. J., and Brown, Jr., W. S. (**1988**). ''Age-related differences in *F*0 and pitch sigma among females,'' IASCP Bulletin **2**, 36–40.
Morris, R. J., and Brown, Jr., W. S. (**1994**). ''Age-related differences in speech variability among women,'' J. Comm. Dis. **27**, 49–64.
Mysak, E. D. (**1959**). ''Pitch and duration characteristics of older males,'' J. Speech Hear. Res. **2**, 46–54.
Ohde, R. (**1984**). ''Fundamental frequency as an acoustic correlate of stop consonant voicing,'' J. Acoust. Soc. Am. **75**, 224–230.
Pegoraro-Krook, M. I. (**1988**). ''Speaking fundamental frequency characteristis of normal Swedish subjects obtained by glottal frequency analysis,'' Folia Phoniatr. **40**, 82–90.
Porter, M. M., Vandervoort, A. A., and Lexell, J. (**1995**). ''Aging of human muscle: structure, function and adaptability,'' Scand. J. Med. Sci. Sports **5**, 129–142.
Ptacek, P., Sander, E. K., Maloney, W. H., and Jackson, C. C. R. (**1966**). ''Phonatory and related changes with advanced age,'' J. Speech Hear. Res. **9**, 353–360.
Ramig, L., and Ringel, R. (**1983**). ''Effects of Physiological Aging on Selected Acoustic Characteristics of Voice,'' J. Speech Hear. Res. **26**, 22–30.
Rodeno, M. T., Sanchez-Fernandez, J. M., and Rivera-Pomar, J. M. (**1993**). ''Histochemical and morphological ageing changes in human vocal cord muscles,'' Acta Otolaryngol. (Stockh.) **113**, 445–449.
Russel, A., Penny, L., and Pemberton, C. (**1995**). ''Speaking fundamental frequency changes over time in women: a longitudinal study,'' J. Speech Hear. Res. **38**, 101–109.
Ryan, W. J., and Burk, K. W. (**1974**). ''Perceptual and acoustic correlates of aging in the speech of males,'' J. Comm. Dis. **7**, 181–192.
Scukanec, G. P., Petrosino, L., and Colcord, R. D. (**1996**). ''Age-related differences in acoustical aspects of contrastive stress in women,'' Folia Phoniatr. Logop. **486**, 231–239.
Scukanec, G. P., Petrosino, L., and Rastatter, M. (**1992**). ''Fundamental frequency variability in elderly women during production of stressed and unstressed words,'' Perceptual & Motor Skills **74**, 1091–1095.
Shipp, T., Qi, Y., Huntley, R., and Hollien, H. (**1992**). ''Acoustic and temporal correlates of perceived age,'' J. Voice **6**, 211–216.
Stevens, K. (**1977**). ''Physics of laryngeal behavior and larynx modes,'' Phonetica **34**, 264–279.
Stevens, K. (**1991**). ''Vocal-fold vibration for obstruent consonants,'' in *Vocal Fold Physiology: Acoustic, Perceptual, and Physiological Aspects of Voice Mechanisms*, edited by J. Gauffin and B. Hammarberg (Singular, San Diego), pp. 29–36.
Stoicheff, M. L. (**1981**). ''Speaking fundamental frequency characteristics of nonsmoking female adults,'' J. Speech Hear. Res. **24**, 437–441.
Weismer, G., and Fromm, D. (**1983**). ''Acoustic analysis of geriatric utterances: segmental and nonsegmental characteristics that relate to laryngeal function,'' in *Vocal Fold Physiology: Contemporary Research and Clinical Issues*, edited by D. M. Bless and J. H. Abbs (College Hill, San Diego), pp. 317–332.
Weismer, G., and Liss, J. M. (**1991**). ''Speech motor control and aging,'' in *Handbook of Geriatric Communication Disorders*, edited by D. N. Ripich (Pro Ed., Austin), pp. 205–226.
Yoshioka, H., Löfqvist, A., and Hirose, H. (**1981**). ''Laryngeal adjustments in the production of consonant clusters and geminates in American English,'' J. Acoust. Soc. Am. **70**, 1615–1623.

Depolarizing the perceptual magnet effect

Andrew J. Lotto[a)]
Department of Psychology and Parmly Hearing Institute, Loyola University Chicago, 6525 N. Sheridan Road, Chicago, Illinois 60626

Keith R. Kluender and Lori L. Holt
Department of Psychology, University of Wisconsin—Madison, 1202 W. Johnson Street, Madison, Wisconsin 53706

(Received 1 October 1997; revised 6 February 1998; accepted 9 March 1998)

In recent years there has been a great deal of interest in demonstrations of the so-called ''Perceptual-Magnet Effect'' (PME). In these studies, AX-discrimination tasks purportedly reveal that discriminability of speech sounds from a single category varies with judged phonetic ''goodness'' of the sounds. However, one possible confound is that category membership is determined by identification of sounds in isolation, whereas, discrimination tasks include pairs of stimuli. In the first experiment of the current study, identifications and goodness judgments were obtained for vowels (/i/–/e/) presented in pairs. A substantial shift in phonetic identity was evidenced with changes in the context vowel. In a second experiment, listeners participated in an AX-discrimination task with the vowel pairs from the first experiment. Using the contextual identification functions from the first experiment, predictions of discriminability were calculated using the classic tenets of Categorical Perception. Obtained discriminability functions were well accounted for by predictions from identification. There was no additional unexplained variance that required the proposal of ''perceptual magnets.'' These results suggest that PME may be nothing more than further demonstration that general discriminability is greater for cross-category stimulus pairs than for within-category pairs.
[S0001-4966(98)05606-9]

PACS numbers: 43.71.An, 43.71.Es [WS]

INTRODUCTION

One of the more fruitful areas of speech research in the last decade has been the study of the internal structure of phonetic categories.[1] Instead of the traditional concentration on the ability of listeners to distinguish phonetically relevant contrasts, this research has focused on functional relations of speech sounds within a single phonetic distribution. As may be expected, it has been demonstrated that not all exemplars of a distribution identified by a single phoneme are considered to be equally good representatives of that phoneme (Grieser and Kuhl, 1989; Miller and Volaitis, 1989; Kuhl, 1991; Volaitis and Miller, 1992). More surprising are results suggesting that perceived ''category goodness'' influences the discriminability of exemplars. Relatively good exemplars appear to be harder to discriminate from neighboring tokens; whereas, relatively poor exemplars are easier to discriminate from neighboring tokens. Because the perceptual space appears to ''shrink'' around good members of a category, this finding has been termed the Perceptual-Magnet Effect (PME; see Kuhl, 1991, 1993; Kuhl *et al.*, 1992). Kuhl (1991) suggests that the prototype (judged as best representative) vowel acts as a magnet drawing in vowel exemplars and increasing similarity between the magnet and other members of the category.

A typical demonstration of PME is presented by Iverson and Kuhl (1995). In their first experiment, a series of vowels varying in first ($F1$) and second ($F2$) formant frequency were presented to adult listeners for phonetic identification and goodness judgments. This vowel series (Fig. 1) contained equal mel-spaced steps and was equivalent to the diagonal from the /i/ distributions utilized by Grieser and Kuhl (1989) and Kuhl (1991). Subjects identified each vowel, presented in isolation, as either /i/ or /e/. Vowels 1 through 9 (as labeled in Fig. 1) were each identified as /i/ over 50% of the time and were considered by Iverson and Kuhl to all be appropriate members of the phonetic category /i/. Subjects also judged the goodness of each vowel token as a representative of /i/. There was a clear gradient in the goodness judgments with those tokens with higher $F2$ and lower $F1$ frequencies being given higher average goodness ratings. Iverson and Kuhl designated vowel 5 as the prototype (**P**) vowel and vowel 9 as the nonprototype (**NP**). Of course, ''prototype'' is a label with some theoretical content as, for example, in the categorization work of Rosch (1975) and Posner and Keele (1968, 1970). Moreover, Kuhl (1992, 1993) has suggested that internal prototypes may play a key role in human speech-sound categorization. However, in this case, the ''prototype'' vowel refers simply to a relatively good exemplar and ''nonprototype'' refers to a poorer exemplar. In fact, **P** did not receive the highest goodness rating in this series, but was chosen because it had $F1$ and $F2$ values identical to the ''prototype'' used in earlier experiments by Kuhl (1991; Grieser and Kuhl, 1989). These $F1$ and $F2$ values were also, not coincidentally, the values reported by

a)Electronic mail: alotto@luc.edu

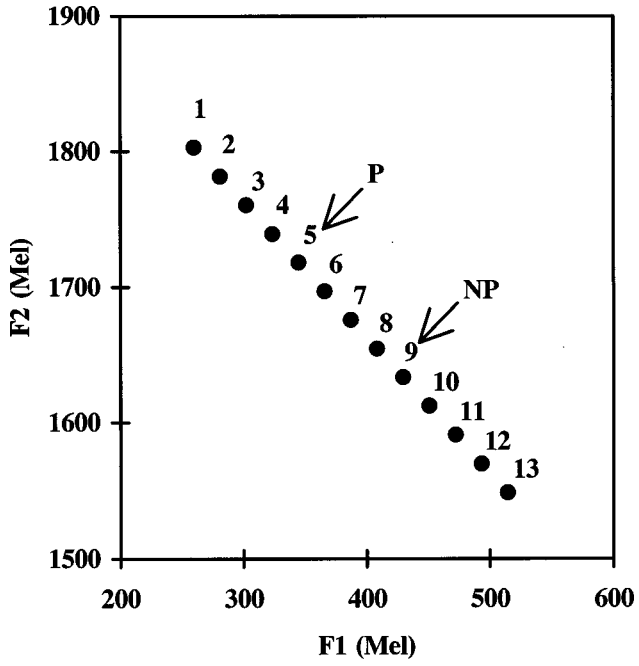

FIG. 1. Formant-frequency values in mel for stimuli used in Iverson and Kuhl (1995) and the present study. **P** is the ''prototype'' vowel and **NP** is the ''nonprototype'' as specified in Kuhl (1991). Vowels 1 and 13 are not used in the present design.

Peterson and Barney (1952) for the average production of /i/ by 33 adult male speakers.

In the second Iverson and Kuhl (1995) experiment, subjects participated in an AX (same/different) discrimination task. In one block of trials, subjects attempted to discriminate **P** from its six nearest neighbors (vowels 2, 3, 4, 6, 7, and 8) and, in another block, discriminated **NP** from its neighbors (vowels 6, 7, 8, 10, 11, and 12). Because the distance between vowels was presumably psychophysically equal (30 mels), one might predict that **P** and **NP** would be equally discriminable from their neighbors. However, the results of a signal-detection analysis (Macmillan and Creelman, 1991) indicated that subjects were better at distinguishing **NP** from surrounding vowels. Even when one disregards discriminations across the category boundary (i.e., **NP** vs vowels 10, 11, and 12), there still appears to be a relation between discriminability and category goodness. Discrimination scores (d') were lower for pairings of **P** with vowels that received higher goodness ratings (vowels 2, 3, and 4) than for pairings of **P** with poorer exemplars (vowels 6, 7, and 8). These intracategory discrimination differences define PME.

The fecundity of this effect in terms of research and theory is notable. Demonstrations of perceptual magnet effects have been described for several phonetic categories (e.g., Davis and Kuhl, 1994; Iverson *et al.*, 1994; Iverson and Kuhl, 1996); the effect has been elicited from infant listeners (Grieser and Kuhl, 1989; Kuhl *et al.*, 1992; Polka and Werker, 1994); it has been modeled by various computational ''neural network'' approaches (Guenther and Gjaja, 1996; Lacerda, 1998); and has served as the foundation of a developmental speech-perception theory (Kuhl, 1992, 1993).

Despite the comprehensive nature of this work, there have been some concerns raised about the demonstrations of PME. One of these concerns is that not all stimuli in these experiments are actually members of the same phonetic category. Lotto *et al.* (1996) reported data from an experiment in which phonetically naive adults were presented with the series from Iverson and Kuhl (1995) and were asked to identify the vowel as /i/, /æ/, /e/, /ɪ/, /ɛ/, /ʊ/, or ''none of the above.'' The vowel stimulus **NP** was identified as /i/ only 7.3% of the time. Similar results were obtained by Sussman and Lauckner-Morano (1995), who presented the entire /i/ distribution from Kuhl (1991) to phonetically-trained listeners for identification. The same **NP** vowel was identified as /i/ only 8% of the time. Thus it appears that infants and adults in the studies of Grieser and Kuhl (1989) and Kuhl (1991) were actually displaying better discrimination for *inter*-category pairings (more likely with **NP**) than for *intra*-category pairings (those containing **P**). This result would not be novel; increased discriminability of cross-boundary contrasts is one of the classical findings of speech perception as a defining feature of ''Categorical Perception'' (Liberman *et al.*, 1957; Stevens *et al.*, 1969; Pisoni, 1971; Wood, 1976).[2]

This concern about stimulus set is exacerbated by an aspect of the methodology used in the design of Iverson and Kuhl (1995) and which is typical of PME experiments. As described above, vowels were presented in isolation for identification and goodness rating, but were presented as pairs in the discrimination task. This is problematic because there is ample evidence that identification of vowels can be affected by the presence of contextual sounds (e.g., Fry *et al.*, 1962; Eimas, 1963; Nearey, 1989). In particular, Thompson and Hollien (1970) demonstrated that the identification of an ambiguous vowel can be shifted to /ɪ/ when preceded by a good exemplar of /ɛ/ and can be shifted to /ɛ/ when preceded by a good /ɪ/. If this applies to the Iverson and Kuhl (1995) experiment, then vowels identified as /i/ in isolation may be perceived as /e/ when presented in context during discrimination. This shift is more likely to happen for boundary stimuli. Therefore, **NP** may be perceived as /e/ when presented with vowels 6, 7, or 8 and as /i/ when presented with vowels 10, 11, or 12. Thus all of these discriminations would be between phonetic categories. This possibility makes the interpretation of the data from Grieser and Kuhl (1989), Kuhl (1991), Kuhl *et al.* (1992), and Iverson and Kuhl (1995) more problematic.

To analyze this possibility, experiments 1 and 2 in this paper are replications of the first two experiments of Iverson and Kuhl (1995) except that identification and goodness ratings (experiment 1) are elicited in the same contexts as are present in the AX-discrimination experiment. In fact, in the present identification and discrimination tasks, experimental design and stimulus presentation are exactly the same; only the response labels differ. Thus the identification responses will presumably be a good representation of the perceived phonetic identities of the vowels during the discrimination task. In this way, one is able to determine if these patterns of discriminability really hold for stimuli from a single category.

I. EXPERIMENT 1

The design of this experiment is nearly identical to the AX-discrimination task constructed by Iverson and Kuhl (1995). However, instead of responding to differences between stimuli, subjects identify or rate the category goodness of one member of the stimulus pair. If context affects the perceived identity and category goodness of a vowel, then one would expect differences between these data and those collected by Iverson and Kuhl (1995) for stimuli presented in isolation.

A. Methods

1. Subjects

Ten listeners participated in the identification task and twenty-one different listeners participated in the category-goodness rating task. All subjects were students at the University of Wisconsin-Madison and reported that they were native English speakers with normal hearing.

2. Stimuli

The stimuli were synthesized at a 10-kHz sampling rate with the cascade formant synthesizer described by Klatt (1980) using the parameter values from Iverson and Kuhl (1995). Each vowel was 435-ms long and had steady-state frequency values of 3010, 3300, and 3850 Hz for the third through fifth formants. Frequency values for $F1$ and $F2$ varied to produce a Euclidean distance of 30 mel between each vowel as shown in Fig. 1. $F1$-frequency varied from 197 to 429 Hz and $F2$-frequency varied from 1925 to 2489 Hz. The values for **P** were 270 and 2290 Hz for $F1$ and $F2$, respectively. For **NP** these values were 347 and 2102 Hz. For all vowels, $f0$ rose from 112 to 130 Hz over the first 100 ms and then declined to 92 Hz over the final 335 ms of the vowel.

All stimuli were matched in rms energy. Following D/A conversion (Ariel DSP-16), stimuli were low-pass filtered (Frequency Devices 677, cutoff frequency: 4.8 kHz) prior to being amplified (Stewart HDA4), and played over headphones (Beyer DT-100) at 75 dB SPL.

3. Procedure

In each experimental session, one to three subjects were tested concurrently in single-subject sound-attenuated booths (Suttle Equipment). There were four blocks of trials in a session. In two of the blocks, **P** (vowel 5) was paired with itself or with one of the neighboring stimuli (vowels 2, 3, 4, 6, 7, 8). In the other two blocks, **NP** (vowel 9) was paired with itself or with its neighbors (vowels 6, 7, 8, 10, 11, 12). In each block there were 30 *same* trials containing the standard (**P–P** or **NP–NP**), five *same* trials for each of the six neighbor stimuli (2–2, 3–3, 4–4, etc.) and 10 *different* trials for each of the comparison stimuli (e.g., P-2, P-3, 6-P, or NP-6, 10-NP, NP-8). In half of the *different* trials, **P** or **NP** were presented first in the pair. For one block each of the **P** and **NP** conditions, subjects either identified or gave a goodness rating for the first vowel in the pair; during the other block they identified or rated the second vowel. The order of presentation of the **P** and **NP** blocks and the order of instructions to label the first or second stimulus were counterbalanced across subjects.

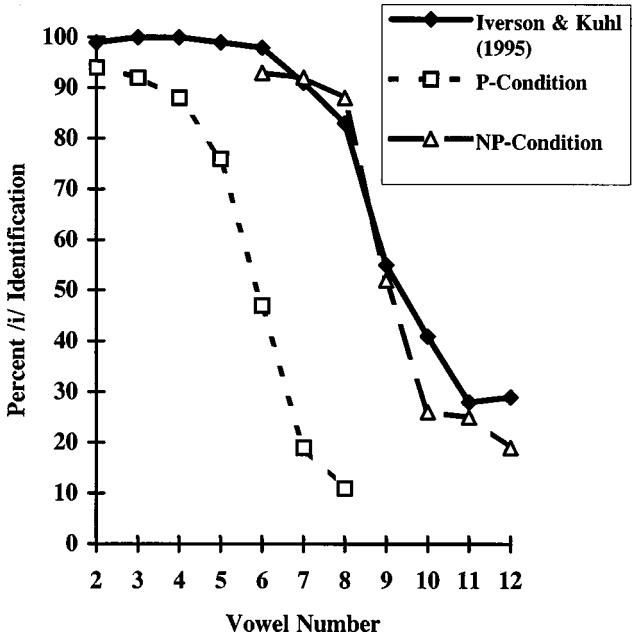

FIG. 2. Identification functions for stimuli presented in context of **P** and **NP**. For comparison, identification function of stimuli presented in isolation from Iverson and Kuhl (1995, numbers taken from their Fig. 2) are also presented.

On each trial, a randomly determined pair of stimuli were played with an ISI of 250 ms. Subjects in the identification task were instructed to label either the first or second stimulus as the vowel in ''he'' or as the vowel in ''hay'' by pressing an appropriately labeled button on a response box. Subjects in the goodness-rating task were asked to evaluate the ''goodness'' of the first or second vowel as an example of the vowel in ''he.'' These ratings were made by pressing one of seven buttons on a response box labeled from ''very good'' (7) to ''very poor'' (1). Stimulus pairs were presented about once every four seconds.

Prior to the four blocks of 120 stimuli, two short training blocks were presented. Subjects heard each of the 19 pair types (7 *same* pairs and 12 *different* pairs) but did not make any responses. This allowed subjects to become familiar with the range of the stimuli in context. Training and testing together lasted approximately 45 min.

B. Results and discussion

1. Identification task

Identification functions in the context of **P** and **NP** are presented in Fig. 2 along with the identification data from Iverson and Kuhl (1995) for stimuli presented in isolation. Identification percentage is collapsed across presentation order. For example, identifications of vowel 10 in the **NP** condition are averaged across five identifications of vowel 10 followed by **NP** and five identifications of vowel 10 preceded by **NP**. Data for **P** (vowel 5) and **NP** (vowel 9) are for identifications of repeated stimuli (e.g., identify **P** preceded by **P**).

TABLE I. Mean percent /i/ identifications and goodness ratings for vowels 6, 7, and 8 in **P** and **NP** contexts. These are the vowels which appear in both conditions. Matched-sample *t* tests comparing the differences between contexts are also displayed. *=significant for two-tailed test at alpha of 0.05.

Vowel	**P** condition identification	**NP** condition identification	*t* test df(9)	**P** goodness	**NP** goodness	*t* test df(20)
6	47%	93%	4.01*	4.13	5.41	3.66*
7	19%	92%	6.03*	2.92	5.26	6.28*
8	11%	88%	7.45*	2.40	4.66	6.57*

It is clear from Fig. 2 that identification of a vowel is affected considerably by context. Identification functions for the **P** condition differed substantially from the data reported by Iverson and Kuhl (1995) for stimuli presented in isolation. The shift in identifications with changes in context are similar to those presented in earlier demonstrations of vowel contrast (e.g., Fry *et al.*, 1962; Thompson and Hollien, 1970). Vowels presented with a relatively good exemplar of /i/ (**P** condition) were identified as /i/ less often than when presented in isolation. Of particular interest is the identification of vowel 6, 7, and 8, because these were presented in context of both **P** and **NP**. Table I presents the mean percentage of /i/ identification for each vowel in each context along with results of tests of the significance of the effects of context. All three vowels changed identity from /i/ (average /i/ identification=91%) in the **NP** condition to /e/ (average /i/ identification=25.67%) in the **P** condition.

Also of importance to demonstrations of PME is the perceived identity of **P** and **NP** themselves in the context of other vowels. Table II displays the mean percentage of /i/ identifications for **P** and **NP** in all contexts collapsed across presentation order. Context effected a change in perceived identity for both vowels. In the context of better /i/ representatives (vowels 6, 7, and 8), **NP** was perceived most often to be /e/ (average /i/ identification=27.33%). In the context of poor /i/ representatives (vowels 10, 11, and 12), **NP** was labeled more often as /i/ (average /i/ identification =66.67%). The percentage of /i/ identifications for **P** was also affected by context, but was above 50% for all contexts except for vowel 2 (48%).

TABLE II. Mean percent /i/ identification for **P** (vowel 5) and **NP** (vowel 9) in the context of their neighboring vowels. **P** was identified in the context of vowels 2 through 8 and **NP** was identified in the context of vowels 6 through 12.

Context vowel	**P** identification	**NP** identification
2	48	···
3	52	···
4	69	···
5	76	···
6	79	23
7	82	23
8	84	36
9	···	52
10	···	56
11	···	62
12	···	82

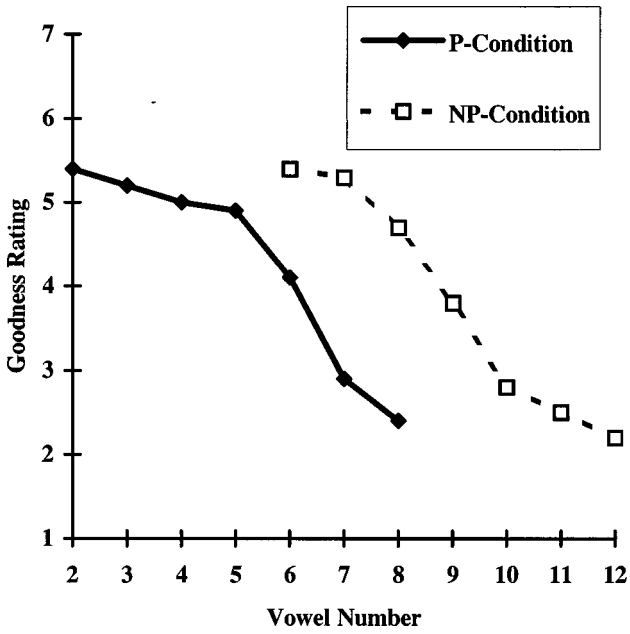

FIG. 3. Category goodness ratings for stimuli presented in context of **P** and **NP**. Scale goes from 7 (very good /i/) to 1 (very poor /i/).

2. Goodness judgments

One subject's data was omitted from the analysis because the subject only used one rating for all of the vowels in the experiment. Mean goodness judgments collapsed across the remaining 20 subjects' data are presented in Fig. 3 for both **P** and **NP** contexts. Perceived category goodness also appears to be highly dependent on vowel context. Again, vowels 6, 7, and 8 were rated in both contexts and significantly different ratings were obtained for the **P** and **NP** contexts (Table I). Vowels presented in the context of a relatively good /i/ exemplar (**P**) were judged to be poorer members of the category /i/ (mean rating of 2.7) than when those same vowels were presented with **NP**, a relatively poor exemplar (mean rating of 5.3).

This context sensitivity of perceived vowel identity and category goodness makes PME demonstrations (e.g., Grieser and Kuhl, 1989; Kuhl, 1991; Kuhl *et al.*, 1992; Iverson and Kuhl, 1995) difficult to interpret. For example, results from the second experiment of Iverson and Kuhl (1995) indicate that discriminability of **NP** from neighboring vowels is higher than discriminability of **P** from its neighbors. Complicating these results, the data from the current experiment suggest that all of the comparisons involving **NP** are *inter*-categorical and most of the comparisons with **P** are *intra*-categorical. When **NP** is paired with vowels 6, 7, or 8, **NP** is identified as /e/ (73% of the time) and the other vowel is perceived as /i/ (91% of the time). On the other hand, when **NP** is paired with the vowels 10, 11, or 12, **NP** is identified as /i/ (67% of the time) and the paired vowel is identified as /e/ (77% of the time; all of these numbers represent averages). That is, listeners are always asked to discriminate an /i/ token from an /e/ token during **NP** ''different'' trials. During blocks of **P** stimuli, discriminations are always made between two /i/ tokens, except when **P** is paired with vowel 2. If the results of the identification task of experiment 1 are reasonable estimates of perceived identity during the dis-

crimination task, then the obtained pattern of discrimination results can be described as follows: Discriminability of two vowels judged to be from different phonetic categories is higher than discriminability of two vowels judged to be from the same phonetic category. This pattern of results is exactly that described classically as Categorical Perception.

If, in fact, PME does reduce to a demonstration of phonetic Categorical Perception, then one can predict quantitatively the differences in discrimination scores between **NP** and **P** conditions. Past research on categorical perception of speech sounds has shown that discrimination can be fairly well modeled by assuming that discriminability of two speech sounds is solely a function of their perceived phonetic identities. That is, two sounds labeled as different phones can be discriminated; whereas, those labeled equivalently cannot be discriminated (e.g., Liberman *et al.*, 1957; Miyawaki *et al.*, 1975). Experiment 2 was designed to determine if this simple method (along with context effects on identification demonstrated in experiment 1) could account for PME.

II. EXPERIMENT 2

Experiment 2 is a nearly exact replication of the second experiment from Iverson and Kuhl (1995). Listeners were asked to discriminate the same vowels that were presented in experiment 1 in order to investigate the ability of identification percentages to account for the differences of discriminability in **P** and **NP** conditions. Discrimination data from Iverson and Kuhl (1995) were not used because there has been some suggestion that dialect differences and heterogeneous laboratory procedures may have been responsible for some of the past discrepancies in vowel identification (e.g., Sussman and Lauckner-Morano, 1995) and choice of ''best'' or ''prototypical'' vowel (e.g., Lively, 1993) with these very same stimuli. Thus listeners from the same subject pool were chosen for the two experiments in this paper. Besides this difference in subjects, the current experiment was designed to be as similar as possible to the discrimination experiment of Iverson and Kuhl (1995).

A. Methods

1. Subjects

Twenty-two University of Wisconsin undergraduate students participated in experiment 2. All reported normal hearing and had learned English as their first language. None of these subjects had participated in experiment 1. While using the same subjects for the identification and discrimination tasks may have made comparisons between the tasks more valid, different subjects were used for the discrimination task to make the results as comparable to previous PME studies as possible. Iverson and Kuhl (1995) used different subjects in their identification and discrimination tasks, and it was decided that giving subjects in the current experiment extra experience with the stimuli (in an identification task) would introduce an undesired confound.

2. Stimuli

Stimuli were identical to those used in experiment 1.

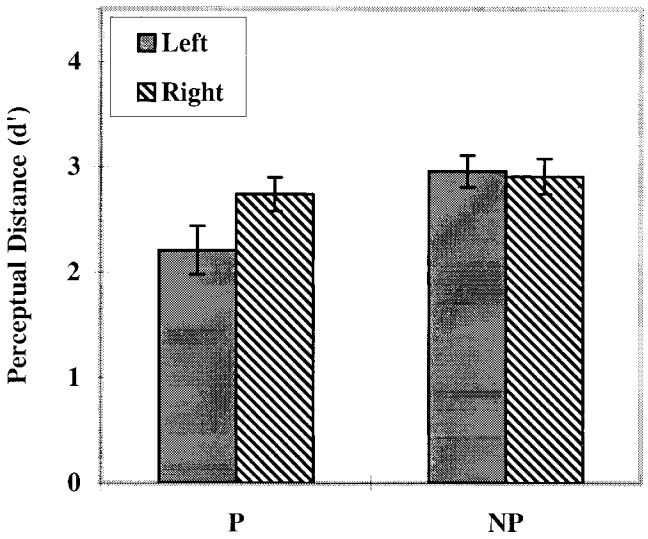

FIG. 4. Average d' scores for experiment 2 separated by standard (**P** or **NP**) and by position of compared stimulus with respect to standard (Left or Right).

3. Procedure

Stimulus presentation was similar to that used in experiment 1, except that there were now only two blocks of stimuli; a 240-trial block of **P** trials and a 240-trial block of **NP** trials. Each block consisted of 120 *same* trials (60 of **P** or **NP** and 10 of each neighboring stimulus) and 120 *different* trials, and order of block presentation was counterbalanced.

After presentation of a vowel pair, subjects pressed one of two labeled buttons to register whether the pair was ''same'' or ''different.'' This is slightly different from the response requested by Iverson and Kuhl (1995). Their subjects held down a key during vowel presentation and lifted the response key when they thought that they heard a different pair. This response technique was more similar to the go/no-go task used by Kuhl (1991) for monkeys and human infants.

Prior to each block of test trials, subjects participated in a short training block. These blocks consisted of 12 *same* trials and 12 *different* trials randomly ordered. Subjects received feedback of the correct button response during training. A block of training trials containing **P** stimuli were presented prior to the **P** testing block and a similar block of **NP** stimuli were presented prior to testing with **NP** stimuli. This is also slightly different from Iverson and Kuhl (1995). Their subjects received only one block of training (either **P** or **NP**) prior to testing.

B. Results and discussion

A bias-free measure of discriminability, d' (Macmillan and Creelman, 1991), was calculated for each vowel pairing for each subject. Average d' scores are presented in Fig. 4 and Table III. Statistical analyses of the obtained data replicated all qualitative results from Iverson and Kuhl (1995). Of greatest significance, the PME was apparent in the data. Paired-sample t-test revealed that listeners were significantly worse at discriminating stimuli from **P** than from **NP** $[t(21) = -3.40,\ p < 0.005]$. In addition, discrimination

TABLE III. Average perceptual distance (d') for each comparison in experiment 2. Each comparison stimulus is identified by a distance (in mel) and direction (left or right) of **P** or **NP**.

Stimulus location	30 mel	60 mel	90 mel
Left of **P**	1.19	2.24	3.20
Right of **P**	1.60	2.92	3.71
Left of **NP**	1.86	3.15	3.86
Right of **NP**	1.76	3.26	3.69

was significantly worse [$t(21)=3.3$, $p<0.005$] to the left of **P** than to the right of **P**. Iverson and Kuhl (1995) propose that this difference is indicative of PME without the confound of inter-categorical pairs, because vowels 2, 3, 4, 6, 7, and 8 were all labeled as /i/ over 80% of the time in their identification task. Results of experiment 1 raise doubts about the perceived identities of these vowels and it is possible that the difference in discriminations to the right and left of **P** also result from confounds with category membership. This possibility will be analyzed later in this report. For the boundary stimulus **NP**, there was no significant difference [$t(21)=0.31$, $p=0.76$] between discriminations from the right and left. Also, there was no significant difference [$t(21)=-1.31$, $p=0.21$] for discriminations of the shared vector (i.e., vowels 6, 7, and 8) in the **P** and **NP** conditions.

Another way of analyzing these discrimination data in light of the purported theoretical basis of PME is offered by Kuhl (1991). The *generalization score* is the percentage of misses on trials containing a nonidentical pair. That is, it is the percentage of ''same'' responses on trials with two different stimuli. If, in fact, prototypical members of a category act as perceptual magnets, then listeners should produce generalization errors more often when presented **P** and its neighbors than when presented **NP** and its neighbors. This is exactly the pattern of results obtained in the present discrimination task. The generalization score was significantly greater [$t(21)=3.20$, $p<0.005$] in the **P** condition (mean score=23.60) than in the **NP** condition (mean score =17.99). Additionally, generalization scores were significantly higher [$t(21)=6.24$, $p<0.0001$] for discriminations to the left side of **P** (mean score=30.53) than for discriminations to the right of **P** (mean score=16.67). This is also indicative of PME.

One concern with these results, however, is the possible confound of intercategorical discriminations. One way to examine this confound is to compare the observed generalization scores with scores that are predicted solely on the basis of a simple relation between perceived identity and discrimination. As pointed out by Liberman *et al.* (1957), if it is assumed that listeners can only discriminate speech sounds that differ in their phonemic label, then the percentage of misses should be comparable to the probability of a listener labeling the two (different) vowel sounds equivalently.[3] That is, listeners are presumed to be unable to discriminate speech sounds that they identify with the same phonemic label. For the present discrimination task, these computations will reveal the degree of difference in generalization score between **P** and **NP** conditions that arise solely from the differences in perceived identity that were demonstrated in experiment 1.

These predicted generalization scores for the two conditions will not include any variation due to ''phonetic goodness'' and will simply be based on phonemic identity. If the theory of perceptual magnets is correct, then the obtained generalization scores should be a result of *both* phonemic identity and phonetic goodness. Because, **P** is a ''better'' member of the category /i/, there should be higher obtained generalization scores for this condition above and beyond those predicted from mere phonemic identity. That is, if PME is due to a shrinking of the perceptual space around the prototype, then the differences between predicted generalization scores for **P** and **NP** conditions should be substantially less than the scores that were obtained. For these comparisons, it is the *differences* in the generalization scores and not the actual scores themselves that are important. Predictions of discriminability using this method understandably underestimate the discriminability of speech sounds (e.g., Miyawaki *et al.*, 1975). If one assumes that other bases for discrimination other than perceived identity (e.g., guessing, spectral difference) are equally potent for the **P** and **NP** conditions, then it is appropriate to compare the predicted differences and the observed differences.

Average percent /i/ and /e/ identifications from experiment 1 for vowels presented in context were used to estimate the probability of perceived identifications. Based solely on predicting discrimination from identification, the predicted generalization score is 44.40 for the **P** condition and 35.83 for the **NP** condition resulting in a predicted difference in generalization scores of 8.57. The obtained difference in generalization scores was 5.61. The difference predicted on the basis of identification functions from experiment 1 is actually larger than the obtained difference. This is opposite the prediction of PME theory. The prototype **P** is *more* discriminable from its neighbors as compared to **NP** than would be expected according to classic findings of Categorical Perception.

Iverson and Kuhl (1995) cite the comparison of discrimination to the left and right of **P** as a measure of PME that is less confounded by the effects of perceived identity. The predicted difference between generalization scores to the left (54.79) and to the right (33.97) of **P** is 20.82. The obtained difference was 13.86. Again, when one uses identifications percentages from a labeling task of vowels in context, the predicted difference in generalizations is *greater* than that actually obtained in a discrimination task. If category goodness plays any role in predicting discriminations it must be in a manner opposite to what has previously been suggested! Good representatives of a vowel category are equally or more discriminable than poorer representatives for within-category comparisons. Following application of timeworn models of Categorical Perception and classical findings of phonetic perception in context, PME theory makes the wrong predictions.

III. GENERAL DISCUSSION

Traditionally, discriminability of speech sounds has been considered solely a function of differences in acoustic structure and phonemic identity. In contrast, PME purportedly demonstrated that the interior structure of a single pho-

netic category was a determinant of discriminability. It is essential to this claim that the speech sounds being discriminated belong to the same phonetic category. Iverson and Kuhl (1995) used stimuli that were labeled in isolation as /i/ more than 50% of the time. However, perceived category membership and representativeness are substantially variable with changes in context. In experiment 1, vowels labeled as good exemplars of /i/ in the context of **NP** were labeled as /e/ when presented with **P**. These results are problematic for interpretations of PME for two reasons. First, if phonetic identity and category ''goodness'' are so pliable, then it becomes difficult to claim that they indicate the structure of stable mental representations of phonetic categories. The theoretical value of ''prototypical'' and ''nonprototypical'' vowels is questionable when their very phonetic identity can be so easily manipulated.

More troublesome for the theory of perceptual magnets is that these shifts in vowel identity are apt to create *inter*-categorical comparisons in a discrimination task. Because the effect of context is contrastive, pairs of vowels will tend to be labeled as different phonemes. This is much more likely to occur for poor exemplars of a category, such as in the **NP** condition, because the identity of these vowels is more ambiguous. It has long been known that cross-boundary discriminations are easier than within-category discriminations. Therefore, one would predict that poor exemplars of a category would be easier to discriminate than relatively good unambiguous exemplars. This is exactly the finding that has been come to be known as PME.

This is all in marked contrast to the generally accepted interpretation of PME as a demonstration of the shrinking of perceptual space around prototypical members of a phonetic category. The results of experiment 2 offer no evidence for a smaller perceptual space or greater similarity amongst good vowel exemplars. In fact, the obtained difference in discriminability of good versus poor tokens was smaller than predicted from identification functions. There is no evidence that the prototype (**P**) served as a ''perceptual magnet.'' Thus the results do not support the Natural Language Magnet model of phonetic category-acquisition (Kuhl, 1993) or various computational models which result in smaller response spaces around prototypical category members (e.g., Guenther and Gjaja, 1996; Lacerda, 1998).

This is not to say that phonetic-category structure is not an important indicator of processes involved in the perception of speech. In experiment 1, vowels that were judged to be good exemplars when presented in isolation were more effective at changing the identity of stimuli with which they were paired (see Fig. 2). This is similar to previous results demonstrating that some stimuli serve as more effective ''adapters'' in ''selective adaptation'' tasks (Miller *et al.*, 1983).

Questions remain as to the genesis and purpose of graded structures within phonetic categories. It is quite possible that categories come to mirror the statistical characteristics of experienced phonetic distributions. Kluender *et al.* (under review) have collected data from birds, humans and computational models responding to vowel distributions, and the data suggest that category structure is a result of the input distribution itself and its relation to other phonetic categories. It will be beneficial for speech scientists to continue investigating the structure of phonetic categories and their relation to natural speech perception. What is challenged by the present data, however, is whether a link between ''goodness'' judgments and discriminability is informative about the nature of categories. Once confounding effects are accounted for, putative differences in discriminability are neutralized and perceptual magnets are depolarized.

[1]The authors prefer the term ''functional equivalence class'' instead of ''category,'' because ''category'' has a long theoretical history and is used in several different ways that obscure important conceptual differences. However, for ease of reading and to facilitate comparison with other reports, the more familiar term will be used. In this report, ''category'' will be used to refer to a set of stimuli that are linguistically functionally equivalent for a particular perceiver and to the pattern of responses to those stimuli. That is, a category is defined by identification functions. The term is *not* meant to refer to mental representations of external sets of stimuli which may determine the identification responses, though this is a common use of the term.

[2]Both ''Categorical Perception'' and ''Perceptual-Magnet Effect'' are meant to refer to patterns of results which are obtained using experimental tasks. Both terms have also been used as descriptions of theoretical constructs which are the purported cause of these effects. The use of the terms should not imply that the authors are advocating either theoretical view.

[3]The assumption that discrimination is based solely on identification is quite different from the assumptions underlying signal-detection analysis. Thus predictions of d' scores using the Liberman *et al.* (1957) equations would be inappropriate.

Davis, K., and Kuhl, P. K. (**1994**). ''Tests of the perceptual magnet effect for American English /k/ and /g/,'' J. Acoust. Soc. Am. **95**, 2976.

Eimas, P. D. (**1963**). ''The relation between identification and discrimination along speech and nonspeech continua,'' Language and Speech **6**, 206–217.

Fry, D. B., Abramson, A. S., Eimas, P. D., and Liberman, A. M. (**1962**). ''The identification and discrimination of synthetic vowels,'' Language and Speech **5**, 171–189.

Grieser, D., and Kuhl, P. K. (**1989**). ''Categorization of speech by infants: Support for speech-sound prototypes,'' Develop. Psych. **25**, 577–588.

Guenther, F. H., and Gjaja, M. N. (**1996**). ''The perceptual magnet effect as an emergent property of neural map formation,'' J. Acoust. Soc. Am. **100**, 1111–1121.

Iverson, P., Diesch, E., Siebert, C., and Kuhl, P. K. (**1994**). ''Cross-language tests of the perceptual magnet effect for /r/ and /l/,'' J. Acoust. Soc. Am. **96**, 3228.

Iverson, P., and Kuhl, P. K. (**1995**). ''Mapping the perceptual magnet effect for speech using signal detection theory and multidimensional scaling,'' J. Acoust. Soc. Am. **97**, 553–562.

Iverson, P., and Kuhl, P. K. (**1996**). ''Influences of phonetic identification and category goodness on American listeners' perception of /r/ and /l/,'' J. Acoust. Soc. Am. **99**, 1130–1140.

Klatt, D. H. (**1980**). ''Software for a cascade/parallel formant synthesizer,'' J. Acoust. Soc. Am. **67**, 971–995.

Kluender, K. R., Lotto, A. J., Holt, L. L., and Bloedel, S. L. (under review). ''Role of experience for language-specific functional mappings of vowel sounds.''

Kuhl, P. K. (**1991**). ''Human adults and human infants show a 'perceptual magnet effect' for the prototypes of speech categories, monkeys do not,'' Percept. Psychophys. **50**, 93–107.

Kuhl, P. K. (**1992**). ''Infants' perception and representation of speech: Development of a new theory,'' in *Proceedings of the International Conference on Spoken Language Processing*, edited by J. J. Ohala, T. M. Nearey, B. L. Derwing, M. M. Hodge, and G. E. Wiebe (University of Alberta, Edmonton, Alberta), pp. 449–456.

Kuhl, P. K. (**1993**). ''Innate predispositions and the effects of experience in speech perception: The native language magnet theory,'' in *Development Neurocognition: Speech and Face Processing in the First Year of Life*, edited by B. de Boysson-Bardies, S. de Schonen, P. Jusczyk, P. McNeilage, and J. Morton (Kluwer Academic, Dordrecht, The Netherlands), pp. 259–274.

Kuhl, P. K., Williams, K. A., Lacerda, F., Stevens, K. N., and Lindblom, B. (**1992**). ''Linguistic experience alters phonetic perception in infants by 6 months of age,'' Science **255**, 606–608.
Lacerda, F. (**1998**). ''An exemplar-based account of emergent phonetic categories,'' J. Acoust. Soc. Am. **103**, 2980(A).
Liberman, A. M., Harris, K. S., Hoffman, H. S., and Griffith, B. C. (**1957**). ''The discrimination of speech sounds within and across phoneme boundaries,'' J. Exp. Psychol. **54**, 358–368.
Lively, S. E. (**1993**). ''An examination of the perceptual magnet effect,'' J. Acoust. Soc. Am. **93**, 2423.
Lotto, A. J., Kluender, K. R., and Holt, L. L. (**1996**). ''Effects of language experience on perceptual organization of vowel sounds,'' paper presented at the Fifth Conference of Laboratory Phonology, Northwestern University, July 6.
Macmillan, N. A., and Creelman, D. (**1991**). *Detection Theory: A User's Guide* (Cambridge U.P., New York).
Miller, J. L., Connine, C. M., Schermer, T. M., and Kluender, K. R. (**1983**). ''A possible auditory basis for internal structure of phonetic categories,'' J. Acoust. Soc. Am. **73**, 2124–2133.
Miller, J. L., and Volaitis, L. E. (**1989**). ''Effect of speaking rate on the perceptual structure of a phonetic category,'' Percept. Psychophys. **46**, 505–512.
Miyawaki, K., Strange, W., Verbrugge, R., Liberman, A. M., Jenkins, J. J., and Fujimura, O. (**1975**). ''An effect of linguistic experience: The discrimination of [r] and [l] by native speakers of Japanese and English,'' Percept. Psychophys. **18**, 331–340.
Nearey, T. M. (**1989**). ''Static, dynamic, and relational properties in vowel perception,'' J. Acoust. Soc. Am. **85**, 2088–2113.
Peterson, G. E., and Barney, H. L. (**1952**). ''Control methods used in the study of the vowels,'' J. Acoust. Soc. Am. **24**, 175–184.
Pisoni, D. B. (**1971**). ''On the nature of categorical perception of speech sounds,'' Doctoral thesis, University of Michigan.
Polka, L., and Werker, J. F. (**1994**). ''Developmental changes in perception of non-native vowel contrasts,'' J. Exp. Psychol. **20**, 421–435.
Posner, M. I., and Keele, S. W. (**1968**). ''On the genesis of abstract ideas,'' J. Exp. Psychol. **77**, 28–38.
Posner, M. I., and Keele, S. W. (**1970**). ''Retention of abstract ideas,'' J. Exp. Psychol. **83**, 304–308.
Rosch, E. H. (**1975**). ''Cognitive representations of semantic categories,'' J. Exp. Psychol. **3**, 193–233.
Stevens, K. N., Liberman, A. M., Studdert-Kennedy, M., and Ohman, S. E. G. (**1969**). ''Crosslanguage study of vowel perception,'' Language and Speech **12**, 1–23.
Sussman, J. E., and Lauckner-Morano, V. J. (**1995**). ''Further tests of the perceptual magnet effect in the perception of [i]: Identification and change/no-change discrimination,'' J. Acoust. Soc. Am. **97**, 539–552.
Thompson, C. L., and Hollien, H. (**1970**). ''Some contextual effects on the perception of synthetic vowels,'' Language and Speech **13**, 1–13.
Volaitis, L. E., and Miller, J. L. (**1992**). ''Phonetic prototypes: Influence of place of articulation and speaking rate on the internal structure of voicing categories,'' J. Acoust. Soc. Am. **92**, 723–735.
Wood, C. C. (**1976**). ''Discriminability, response bias, and phoneme categories in discrimination of voice onset time,'' J. Acoust. Soc. Am. **60**, 1381–1389.

Adapting to supernormal auditory localization cues. I. Bias and resolution

Barbara G. Shinn-Cunningham,[a] Nathaniel I. Durlach, and Richard M. Held
Massachusetts Institute of Technology, Cambridge, Massachusetts 02139

(Received 23 September 1996; revised 27 January 1998; accepted 2 March 1998)

Head-related transfer functions (HRTFs) were used to create spatialized stimuli for presentation through earphones. Subjects performed forced-choice, identification tests during which allowed response directions were indicated visually. In each experimental session, subjects were first presented with auditory stimuli in which the stimulus HRTFs corresponded to the allowed response directions. The correspondence between the HRTFs used to generate the stimuli and the directions was then changed so that response directions no longer corresponded to the HRTFs in the natural way. Feedback was used to train subjects as to which spatial cues corresponded to which of the allowed responses. Finally, the normal correspondence between direction and HRTFs was reinstated. This basic experimental paradigm was used to explore the effects of the type of feedback provided, the complexity of the simulated acoustic scene, the number of allowed response positions, and the magnitude of the HRTF transformation subjects had to learn. Data showed that (1) although subjects may not adapt completely to a new relationship between physical stimuli and direction, response bias decreases substantially with training, and (2) the ability to resolve different HRTFs depends both on the stimuli presented and on the state of adaptation of the subject. © *1998 Acoustical Society of America.* [S0001-4966(98)03306-2]

PACS numbers: 43.71.Hw, 43.72.Ew, 43.66.Qp [RHD]

INTRODUCTION

Many recent studies have investigated the utility of sophisticated auditory display techniques for presenting information to human operators. In particular, the maturation of auditory spatial display technologies over the last decade has enabled spatial auditory cues to be presented to operators involved in a variety of everyday tasks (e.g., see Durlach, 1991; Smith, 1991; McKinley and Ericson, 1992; Begault, 1993a, 1993b; Ericson, 1993; Begault and Pittman, 1994; Begault, 1995; Begault *et al.*, 1995; Shinn-Cunningham and Kulkarni, 1996). Most of these studies have examined the utility of presenting auditory spatial cues, rendered as realistically as is practical, compared to presenting the same information without such spatial cues.

A previous paper (Durlach *et al.*, 1993) pointed out that the normal human auditory system has relatively poor spatial resolution and that it should be possible to improve performance by synthesizing ''supernormal'' localization cues that are not constrained by the laws of physics which determine normal localization cues. More specifically, it should be possible to design localization cues that span a larger range of just-noticeable differences (jnd's) than do normal cues, and thereby allow listeners to improve their ability to resolve nearby spatial positions. A number of approaches for creating supernormal auditory localization cues were discussed, including simulating localization cues from a larger-than-normal head, remapping the relationship between normal localization cues (i.e., normal HRTFs) and the corresponding spatial directions to create regions of supernormal spatial acuity, increasing interaural differences [for instance, by raising the difference spectrum to a power greater than one, e.g., see Durlach and Pang (1986) and Van Veen and Jenison (1991)], and emphasizing cues that are thought to relate to the perception of source distance.

While such approaches should clearly improve subjects' ability to resolve sources in jnd-type experiments, the effects of such cue manipulation on resolution in other types of tasks (such as identification tasks in which a larger range of physical stimuli are presented) or on response bias are not well understood. In general, the apparent location of a source simulated with supernormal localization cues will be displaced from its desired location when a naive listener is first exposed to such cues. The degree to which such errors can be overcome with training is a measure of how well subjects ''adapt'' to the given sensorimotor spatial discrepancy.

Previous studies of sensorimotor adaptation have focused on how mean response affected by discrepancies between localization cues from one modality versus other modalities. However, no previous studies have examined the effect of adaptation on resolution, nor taken into account whether changes in mean response are significant relative to the variability in subject responses. In addition, most sensorimotor adaptation work is qualitative rather than quantitative, and thus is of limited use in trying to develop a quantitative description or model of adaptation. General background on adaptation can be found in Welch (1978) and Welch and Warren (1986).

The main goal of the current experiments was to determine the extent to which adaptation to supernormal localization cues is achievable. In addition, experimental conditions were designed to examine how a variety of experimental factors (which have previously been shown to affect different aspects of spatial perception) might affect how subjects adapt to such altered cues.

[a]Current address: Boston University, Department of Cognitive and Neural Systems, Room 311, 677 Beacon St., Boston, MA 02215. Electronic mail: shinn@cns.bu.edu

While previous studies provide few quantitative measures of adaptation, many such studies suggest that one of the most important factors affecting adaptation is the type of exposure to the rearranged spatial cues that the subjects receive. In particular, active motor tasks generally yield more complete adaptation than comparable experiments with passive exposure to the rearrangement (Freedman and Zacks, 1964; Pick and Hay, 1965). Two different types of feedback are investigated in the current study in order to determine how active motor involvement affects adaptation in our experimental paradigm.

Other studies of spatial perception have shown that the complexity of the visual or acoustic field can affect the perception of source motion. For example, if a single point light source is seen to move around a subject in an otherwise dark room, the subject perceives himself to be stationary and the source to be moving. However, if multiple lights move with a fixed angular velocity around a stationary subject, the subject perceives himself to be rotating within a fixed room (Lackner, personal communication). In our studies, results when subjects are presented with an acoustic field (two ongoing, stationary sources in addition to the target) are compared to results from an experiment in which only the target source is presented.

The degree to which different stimuli can be resolved is determined in part by the range of target stimuli presented in an experiment (Durlach and Braida, 1969). The effect of stimulus range on resolution is examined by comparing results in adaptation experiments using a stimulus range of 120 degrees compared to a range of 60 degrees.

Finally, the strength of the cue rearrangement is systematically varied in order to examine how the rate and degree of adaptation depend upon the quantitative strength of the change in acoustic localization cues and the overall range of cues presented.

In the current study, subjects were asked to adapt to supernormal remappings of auditory localization cues. In the experiments described, subjects are first tested with ''normal'' localization cues to yield baseline measures, then with the ''supernormal'' cues to examine how performance changes as subjects adapt. Finally, at the end of each experimental session, subjects are retested with the ''normal'' cues to look for any aftereffects in performance that may result from the training with the supernormal cues. Two quantitative measures were used to track how subject performance changed over the course of the experimental session. Bias (a measure of response error in units of standard deviation in subject response) was used to measure the degree to which subjects adapted to the supernormal cues. While bias is related to the error in mean response, the measures are not equivalent. In particular, since bias is measured in units of standard deviation, the absolute magnitude of response errors cannot be determined from bias results. As a metric, bias describes the magnitude of response errors relative to the variability in subject responses; thus, a decrease in bias could result either from a decrease in absolute error or an increase in variability. In the current study, bias is examined instead of mean response error in order to quantify the importance of errors relative to response variability. In particular, if response variability is large, the relative importance of a given magnitude error is much less than if response variability is small. The ability to resolve adjacent stimulus positions was measured in order to gain insight into whether better-than-normal resolution is achievable in a localization task using supernormal cues. Estimates of the standard psychophysical metric d' (again, a measure with units in standard deviation) were found for adjacent stimulus positions to summarize resolution.

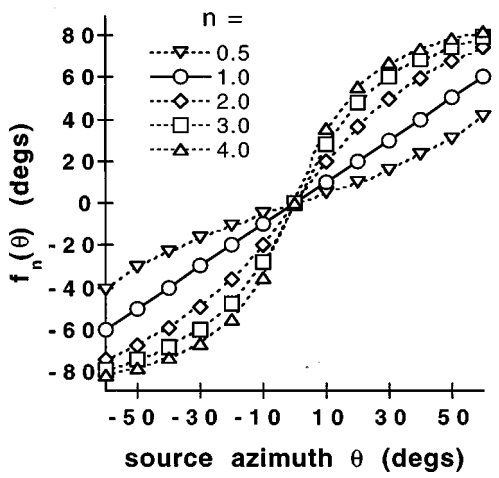

FIG. 1. Plot of the family of functions $f_n(\theta)$ used to transform auditory localization cues. With this transformation, a source from azimuth θ was synthesized using the HRTF that normally corresponded to the position $f_n(\theta)$.

I. SUPERNORMAL CUES

Supernormal localization cues were created in this study by remapping the relationship between source position and normal head-related transfer functions, or HRTFs. Normally, to simulate a source at azimuth θ and elevation ϕ, one simply uses the empirically measured HRTF for that direction, denoted in the frequency domain by $H(\omega,\theta,\phi)$, where ω denotes angular frequency. In the current study, the correspondence between HRTFs and azimuth values was remapped such that the HRTF used to simulate a source at position $[\theta,\phi]$ was given by

$$H'(\omega,\theta,\phi)=H(\omega,f_n(\theta),\phi). \tag{1}$$

In the current study, the family of mapping functions $f_n(\theta)$ used to transform azimuth cues is given by

$$f_n(\theta)=\frac{1}{2}\tan^{-1}\left[\frac{2n\,\sin(2\theta)}{1-n^2+(1+n^2)\cos(2\theta)}\right], \tag{2}$$

where the correct response azimuth is given by θ.[1] In other words, in the altered-cue situation, the HRTF associated with $[\theta,\phi]$ was equal to the HRTF normally associated with $[f_n(\theta),\phi]$. The parameter n in Eq. (2) corresponds to the slope of the transformation at $\theta=0$. With this function (shown in Fig. 1 for different values of n), the HRTFs used to generate stimuli are displaced laterally relative to the HRTFs normally used to present normal spatial sounds from those locations. The differences in localization cues for two positions in the frontal region are larger than normal with

this remapping, while two positions off to the side would give rise to more similar cues than are normally heard.[2] As a result, subjects were expected to show better-than-normal resolution in the front and reduced resolution on the side, creating an enhanced ''acoustic fovea'' toward the front in which supernormal auditory localization could occur. In addition to affecting resolution, however, this transformation was expected to cause a bias whereby sources were perceived farther off-center than were their ''correct'' locations. If the same family of transformations is used with $n<1$, the opposite would be true: sources heard in front of the listener would have smaller-than-normal differences in localization cues and sources off to the sides of the listener would have larger-than-normal differences. The experiments discussed in the current paper used values of $n=1$ (normal cues, or no transformation), 2, 3, and 4.[3] The main questions of the study concern the extent to which (1) bias could be eliminated by subjects over time such that subjects interpreted the new relationship between HRTF and spatial location accurately, and (2) resolution was enhanced in the ''acoustic fovea'' with the transformed cues.[4]

Generating supernormal cues by remapping which HRTF corresponds to which direction has the advantage that subjects should hear a compact source image for every possible source position, because all localization cues are consistent with a normal source from some position [the position $f_n(\theta)$]. In other words, ignoring intersubject differences, all localization cues at all frequencies are consistent with a normal sound source at $f_n(\theta)$; subjects do not have to learn to interpret unusual combinations of interaural time, interaural level, and spectral cues.

Ideally, individualized HRTFs would be used to guarantee a ''realistic'' and compact sound image; however, in the current study, a single, standard set of nonindividualized HRTFs was used for all subjects. In general, the use of nonindividualized HRTFs may lead to mislocalizations in elevation, front/back confusions, and nonexternalized source images, especially when head tracking is not employed (e.g., see Wenzel *et al.*, 1993). In the current experiments, the response locations were always restricted to be in the horizontal front hemifield and front/back and up/down confusions cannot occur. In addition, the current experiments did not depend upon the subjective externalization of sound sources, the location dimension of interest (azimuth) does not rely heavily on the portions of the HRTF that show greatest intersubject variability, and the gross manipulations of HRTFs that were being studied should have a large effect on perception of source azimuth compared to any relatively minor effects caused by individual differences in HRTFs. Similarly, since the main effect, that of radically altering the azimuthal position of a source, should not show any bias due to any consistent overall spectral cues, the HRTFs used to generate stimuli were not equalized for the headphones used in the study. As a result, subjectively, sources were not always externalized; however, the ability to adapt to the required mapping of source cues to source location was not adversely affected by these subjective impressions. Finally, it should be noted that the focus of the current study is the ability of subjects to extract and use location information, not on subjective impressions of realism or source externalization.

The described approach to generating supernormal localization cues has the disadvantage that better-than-normal resolution is not possible for all locations around a listener; for positions where $df_n\theta/d\theta<1$ (sources off to the side with $n>1$), the transformation actually results in subnormal localization cues. One approach to generating supernormal localization cues for all positions around a listener would be to use HRTFs from a larger-than-normal head [a practical method for approximating such HRTFs is discussed in Rabinowitz *et al.* (1993)]. However, even this approach has its drawbacks. In particular, with such an approach, localization cues are not consistent with any normal-cue source position. As a result, source images may be broad, diffuse, and difficult to localize. This problem may be particularly true for sources off to the side since the interaural differences caused by such sources would be outside the range of interaural differences normally experienced. In contrast, although supernormal localization cues are only present for a limited range of directions in the current experiments, the sounds should be spatially compact and easy to localize.

II. GENERAL METHODS

A. Subjects

Subjects were recruited through the student employment agency at MIT. They were 18–28 years in age and either MIT students or related family members. All subjects reported normal hearing and were able to perform the localization tests employed in the study without difficulty. Different subjects were used in each of the seven experiments performed. The number of subjects completing a given experiment was between 3 and 8 (see Table III).

B. Stimuli

In all experiments, the target to be localized consisted of a periodic train of clicks (with a repetition rate of 10 clicks/s) generated by a Krohn-Hite model 5300A function generator. A 500-ms-long rectangular envelope gated the click train off and on so that roughly 5 clicks were heard per stimulus in each localization trial (described in Sec. II E below). In training runs (also described below), the click train was heard continuously until the subject completed his response. In some experiments, background sources were heard in addition to the click-train target. These background sources came from commercially recorded audio tapes, and consisted of a book on tape (Auel, 1980) and classical music (Handel, 1985) played from a Sony TCW490 tape deck.

C. Equipment

An auditory virtual environment (VE) was used to ''spatialize'' the acoustic stimuli in our experiments. The auditory VE consisted of a Convolvotron processor using HRTFs from subject SDO [measured and reported by Wightman and Kistler (1989)], a commercial, electromagnetic head tracker, a controlling PC, and headphones. In any given experiment, either the Isotrak (from Polhemus) or the Bird (from Ascension Technologies) head-tracking system was employed (for

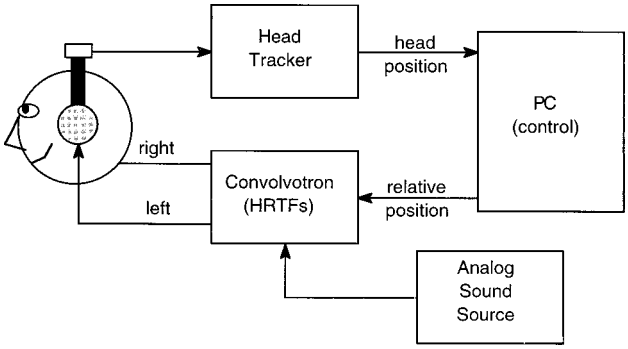

FIG. 2. Block diagram of the auditory virtual environment used to simulate acoustic sources.

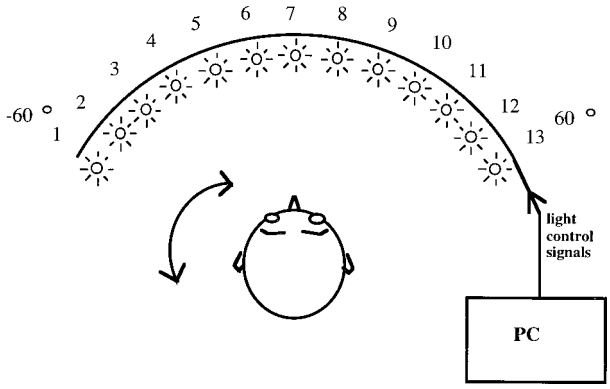

FIG. 3. Diagram of the visual display. Thirteen lights were positioned in front of the listener, spaced at 10-degree intervals ranging from −60 to +60 degree azimuth.

all practical purposes, the two systems are interchangeable in their performance characteristics). A 486-based PC controlled the Convolvotron and the head tracker. The Convolvotron took monaural input stimuli (which were amplified, antialiased signals from the sources described above) and created appropriate binaural signals to simulate the stimuli from azimuthal locations specified by the controlling PC. Figure 2 shows a block diagram of the auditory virtual environment.

In most experiments, the binaural signals generated by the Convolvotron were played out through Etymotic Research 3A insert earphones with Bilsom earmuffs worn over the earphones. The combination of insert earphones and commercial hearing protectors helped to block background sounds from the subject during experiments. Taken together, the insert earphones and Bilsom earmuffs reduced sounds reaching the subjects via direct paths by roughly 40–50 dB across all audible frequencies. Experiment T_1 was performed before the insert earphones were incorporated into the experimental setup, using TDH-30 circumaural earphones. In this experiment, background sounds were not attenuated well. However, as this caused little difference in the observed pattern of results, this difference is thought to be of little consequence.

A visual display, consisting of 13 lights on a 5-ft-diam arc (every 10 degrees from −60 to +60 degrees azimuth), was located in front of the subjects at eye level throughout the experiments. The lights, labeled 1–13 from left to right, corresponded to the possible locations of the click-train target presented in the experiments (see Fig. 3). This visual display was used to present visual, spatial feedback about the simulated auditory sources used in the experiments.

D. Test procedure

Each subject performed eight identical test sessions over a period of between two to six weeks. Each session lasted roughly 2 h, and consisted of multiple runs separated by two 5-min breaks. Two types of experimental runs were used: localization test runs and training runs, described in detail below. In the training experiments (T_1 and T_3), no feedback was given during localization test runs, but training runs were interspersed with the localization test runs. In the feedback experiments (F_3, F_{3mid}, F_2, F_{4a}, and F_{4b}), correct-answer feedback was given during localization test runs and no training runs were performed (i.e., the training consisted of giving feedback during the test runs).

1. Test runs

In each localization test run, subjects were presented with a target stimulus simulated as coming from 1 of the 13 possible locations marked by the visual display, chosen at random. Each of the possible locations was presented exactly twice in each run. For most experiments, all 13 positions were employed for a total of 26 trials per run; however, in experiment F_{3mid}, only the middle 7 positions (positions 4–10) were used for a total of 14 trials per run. During the presentation of the target stimulus, subjects had to remain facing straight ahead (within 3 degrees of 0 degrees azimuth). If the head tracker reported that the subject turned his head off-center during a trial, that trial was thrown out and an additional trial was added to the run. In the test runs, the subject entered a number (1–13) corresponding to his/her best guess as to the location of the stimulus by typing on a laptop computer keyboard following presentation of the target. In experiments using correct-answer feedback (experiments F_3, F_{3mid}, F_2, F_{4a}, and F_{4b}), the light at the correct location was lit for 500 ms after the subject responded. In these experiments, the correct-answer feedback was the only information subjects received about the supernormal transformation employed (since no training runs were performed by the subjects). In the remaining experiments, no feedback was given during a test run (information about the transformation was obtained from the training runs, described below). A new trial began 500 ms after the subject entered his response to the previous trial.

2. Training runs

In experiments in which no feedback was given during test runs (T_1 and T_3), training runs were interspersed with test runs. During training runs, both synthetic auditory and real visual light sources were simultaneously turned on from 1 of the 13 possible locations, chosen at random. Subjects were instructed to turn their heads to face each audiovisual target. Once they faced the target (turned their head to within 1 degree of the target location), the light/sound source was

TABLE I. Order of runs in experiments T_1 and T_3. Each run consisted either of training or testing (shown in column one). The type of localization cues presented is given in columns two (for normal cues) and three (for supernormal or altered cues).

Run type	Norm	Super
Test 1	**x**	
Train	*x*	
Test 2	**x**	
	break	
Test 3		**x**
Train		*x*
Test 4		**x**
Train		*x*
Test 5		**x**
Train		*x*
Test 6		**x**
	break	
Test 7		**x**
Train		*x*
Test 8	**x**	
Train	*x*	
Test 9	**x**	
Train	*x*	
Test 10	**x**	

turned off, a 500-ms pause occurred, and a new random location turned on. Training runs lasted 10 min each, with a variable number of trials (usually between 30 and 60 and determined by the speed with which subjects performed each trial) performed in each run. In training runs, exposure to the supernormal transformation entailed an active sensorimotor task (turning to face the audiovisual target). When this training method was employed, subjects never received feedback during the testing runs (and thus received no explicit feedback regarding any errors made during the testing portion of the experimental session).

3. Run order

In each session, auditory sources were first synthesized using ''normal'' HRTFs, then synthesized using the ''supernormal'' HRTF mapping, then synthesized with the normal HRTFs again. In the training experiments, a total of ten localization test runs were performed in each session: two normal-cue runs, five transformed-cue runs, and then three normal-cue runs. The training runs were performed in between test runs (see Table I). In the feedback experiments, 40 localization test runs were performed, one after another. In these experiments, 2 normal-cue tests were performed, followed by 30 supernormal tests, and then 8 normal-cue tests (see Table II). Two 5-min breaks were scheduled during each session for both types of experiments, as shown in the tables.

TABLE II. Order of runs in Experiments F_3, F_{3mid}, F_2, F_{4a}, and F_{4b}. Each test run used either normal cues or supernormal cues as shown in columns two and three.

Test runs	Norm	Super
1–2	*x*	
3–10		*x*
	break	
11–32		*x*
	break	
33–40	*x*	

4. Subject instructions

Subjects were informed before the start of the experiment that they would be hearing both ''normal'' and ''transformed'' sound sources, and that the apparent location of transformed sources might not correspond to the ''correct'' location. They were instructed to always try to localize the sound sources correctly. Prior to the experiment, subjects were given a list of the experimental runs, including information about when they would hear normal sounds and when they would hear transformed sounds. In addition, prior to any change of cues (from normal to supernormal or from supernormal back to normal), subjects were reminded that the sources were about to change, and that they should answer as accurately as they could for the current sources. Beyond being told that sources were ''transformed,'' subjects were given no information about how the apparent source location might differ from the correct answer.

E. Experimental conditions

As mentioned above, the various experiments undertaken in this study were designed to probe some parameters that might affect how quickly and completely subjects adapted to remapped localization cues. Table III summarizes the important differences between the experiments. The effect of the complexity of the simulated sound field is shown

TABLE III. Summary of experiments performed. The altered-cue transformation ''strength'' [defined in Eq. (2)] is given in the second column. The number of subjects who completed eight sessions is shown in column 3. The ''Exp type'' describes whether subjects were exposed to training runs or given correct-answer feedback in order to cause adaptation. The number of source positions used in the experiment is given in column 5, and the number of acoustic sources simulated in the experiment (target plus additional background sources) is given in column 6. The head tracker used in the experiments is shown in the final column.

Exp	*n*	Subs	Exp type	Pos	Sources	Tracker
T_1	3	4	training	13	1	Isotrak
T_3	3	8	training	13	3	Isotrak
F_3	3	5	feedback	13	3	Bird
F_{3mid}	3	4	feedback	7	3	Bird
F_2	2	4	feedback	13	1	Bird
F_{4a}	4	3	feedback	13	1	Bird
F_{4b}	4, 0.5	3	feedback	13	1	Bird

by comparing results from experiments T_1 and T_3. If a complex sound field allows subjects to extract more information about the cue transformation than does a sound field consisting of a single source, more complete adaptation might be found in experiment T_3 than in experiment T_1. Comparisons between results from experiments T_3 and F_3 contrast the effects of active sensorimotor training (experiment T_3) versus correct-answer, cognitive feedback (experiment F_3). Experiments F_3 and F_{3mid} address the question of how the number of stimuli presented affects adaptation and resolution. Different strength transformations were employed in order to gather data that could lead to the development of a quantitative model of the adaptation process (comparison of results from experiments F_3, F_2, F_{4a}, and F_{4b}). Finally, experiment F_{4b} was identical to experiment F_{4a} except that subjects were exposed to a transformation of strength $n=0.5$ after exposure to the supernormal transformation. This final experiment investigated whether exposure to an inverse transformation might allow subjects to readapt to normal localization cues more quickly than without explicit inverse training.

III. RESULTS AND DISCUSSION

Although many experiments on adaptation to transformed sensorimotor cues have shown that exposure on one day can affect performance on a subsequent day (e.g., see Welch and Warren, 1980), no such effects are seen in the current experiments. However, this may be due to the fact that there are too little data to show any significant effects. In any case, any differences from session to session were small relative to the differences within a session. Thus, all the data reported here were combined across the eight identical sessions performed by each subject. This resulted in 16 trials (2 trials from each of 8 sessions) for each position and run, for each subject.

A. Analysis

We were interested in estimating how large subject response errors were relative to the variability in subject responses and how well subjects could distinguish stimuli from each other. Two metrics were used to summarize these quantities: bias and resolution.

A maximum likelihood method was used to estimate bias and resolution from the confusion matrices (pattern of responses observed for every possible physical stimulus) for each subject and run (combining data across the eight experimental sessions). This approach assumed that each presentation of a physical stimulus gives rise to a random variable whose value falls along a unidimensional, internal decision axis (see Fig. 4). The mean of the random variable depends upon which physical stimulus is presented. On each trial, the subject decides how to respond based upon the value of the unidimensional decision variable; in particular, it is assumed that the decision axis is divided into N contiguous segments by $N-1$ thresholds (or criteria) in order to decide which of N possible stimuli was presented on that trial (for an N-alternative, forced-choice experiment). It was further assumed that the decision variable has a Gaussian distribution for all physical stimuli, and that the standard deviation of the

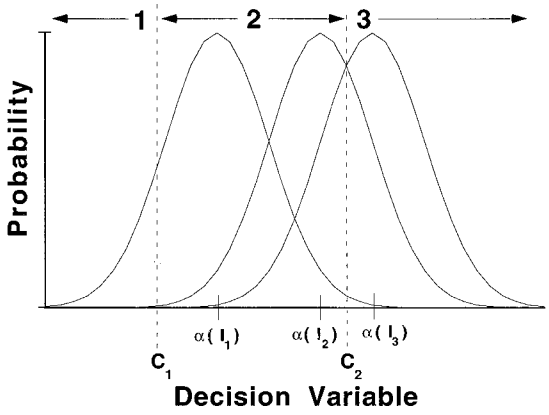

FIG. 4. Diagram of the assumed underlying decision space for a sample three-alternative, forced-choice experiment. The abscissa corresponds to the internal, unidimensional decision variable (which is assumed to relate monotonically to the azimuth of the physical location cues presented), and the ordinate shows the probability of hearing a given value of the decision variable. Shown are three Gaussian distributions with means $\alpha(I_1)$, $\alpha(I_2)$, and $\alpha(I_3)$, which result from the presentation of the three corresponding physical stimuli, I_1, I_2, and I_3. Note that it is assumed that the three distributions have equal standard deviation. The internal decision axis is broken into three contiguous regions by the placement of two criteria (labeled C_1 and C_2). On a given trial, the subject is assumed to respond that he heard stimulus i if the value of the internal decision variable falls into the ith contiguous region (see arrows at top of figure). As shown, C_2 is placed optimally, halfway between the means of the distributions for stimuli I_2 and I_3, resulting in a zero bias for C_2. Here C_1 is displaced from its optimal location, resulting in a nonzero bias for C_1. This placement of C_1 will cause the mean response to stimulus I_1 to be larger than 1, the ''correct'' answer. Resolution between stimuli I_1 and I_2 will be better than between stimuli I_2 and I_3, since the distance between $\alpha(I_1)$ and $\alpha(I_2)$ is larger than the distance between (I_2), and $\alpha(I_3)$.

Gaussian decision variable was independent of the physical stimulus presented in a run.[5] Finally, the mean of the Gaussian distribution was assumed to be monotonically related to the ''correct'' response of the physical stimulus presented on a given trial (specifically, the mean was assumed to vary monotonically with the azimuth of the HRTF used in a given trial). These assumptions are consistent with standard decision-theory models of psychophysical tasks. Since the hypothesized decision axis has arbitrary units, it can further be assumed without loss of generality that the standard deviation of the distribution is equal to one. Bias and resolution are given in units of standard deviation.

With these assumptions, the bias for each response depends on the placement of the $N-1$ criteria that divide the decision axis into N regions. If all stimuli are equally likely to be presented, subjects will maximize the probability of answering correctly by placing the nth criterion exactly halfway between the means of the distributions for the Nth and the $(N+1)$th stimuli (see Fig. 4).[6] If the means of the distributions corresponding to the different stimuli are equally spaced along the internal decision axis, then this optimal placement of the criteria will lead to mean responses which are roughly equal to the correct response.[7] Bias can then be defined as the difference between the optimal criteria placement and the actual criteria placement, measured in units of standard deviation. Errors in mean response arise when criteria are displaced from their optimal locations (i.e., when there is nonzero bias).

The ability to resolve adjacent positions depends only on the distance between the means of the corresponding distributions, measured in units of standard deviation in the distributions (the standard d' measure often used in psychophysical experiments). When the means of two physical stimuli are relatively close, subjects will be less able to resolve the stimuli from each other, independent of where criteria are placed. Similarly, when the means of two distributions are relatively far apart, subjects will rarely confuse the two stimuli (see Fig. 4).

In order to determine bias and resolution using this underlying model, the relative locations of the $N-1$ criteria and the means of the N decision-variable distributions (corresponding to the N physical stimuli) were estimated. These values were found using a gradient-descent algorithm which maximized the likelihood of obtaining the actual confusion matrix observed in a given run. Estimates were made for each subject and run (averaging all data across the eight experimental sessions). Bias was estimated by subtracting the estimated location of the Nth criterion from the average of the estimated means of the distributions corresponding to the Nth and $(N+1)$th stimuli (with the standard deviation in the underlying distributions assumed equal to one). Resolution was estimated by subtracting the estimated mean of the $(N+1)$th distribution from the estimated mean of the Nth distribution. This approach has previously been used to estimate resolution in intensity experiments (Lippmann *et al.*, 1976).

All subjects showed similar patterns of results for both bias and resolution. Thus, the results plotted below were found by averaging bias and resolution across all subjects in an experiment. While the basic patterns of results were identical across subjects, there were differences in the magnitudes of the effects; in general, these differences were due mainly to differences in the magnitude of the standard deviation in responses (i.e., some subjects showed greater response variability and consequently smaller overall bias and resolution than did other subjects).

In addition to the above-described maximum-likelihood estimates, simple estimates of bias and resolution were computed. With this approach, bias was determined simply by subtracting the mean response from the correct response for each position and normalizing the result by the experimental standard deviation in the response for that position.[8] Resolution was determined by finding the difference between means for adjacent stimuli, and normalizing by the geometric mean of the experimental standard deviations for those two positions. In general, this simple method gave results which were consistent with the more complex, maximum-likelihood method. However, the maximum-likelihood approach partially compensates for inaccuracies inherent with this simpler method. For instance, in both cases, there will be an edge effect in estimating bias. In particular, estimated bias tends to be positive for the leftmost position and negative for the rightmost position because subjects could not respond that a source was left of position 1 or right of position 13, even if a stimulus sounded far off to one side. With the simple method for estimating bias, bias is *always* less than or equal to zero for position 1, since the mean response must be greater than or equal to one. With the maximum-likelihood estimation, bias will *tend* to be less than zero for position 1 for the same reason, but the approach also takes into account the variability in subject responses in order to estimate bias. For this reason, the maximum-likelihood estimates are better at dealing with edge effects and consequently are more accurate. Only the maximum-likelihood estimates are presented here.

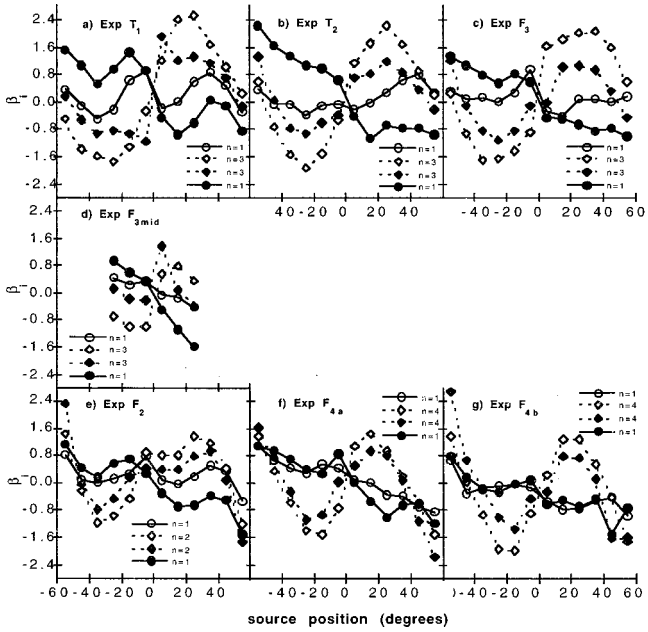

FIG. 5. Bias results for the seven experiments. In each panel, the average estimated bias is plotted as a function of correct source position (in degrees). For each panel, bias was estimated for each subject and run in the experiment and then averaged across all subjects in the experiment. Four runs are plotted in each panel: the first run in the experiment (open circles), the first run with the transformed cues (open diamonds), the final run with altered cues (filled diamonds), and the first normal-cue run following altered-cue exposure (filled circles). In each panel, the legend details the strength of the cue transformation employed in the normal- (n always equals 1) and altered-cue runs ($n=2$, 3, or 4).

B. Bias

The first test using normal cues was expected to show little systematic bias since the cues presented were consistent with everyday experience (at least within the limits of the simulation method). As such, they provided a baseline for performance. The first test with the transformed localization cues was expected to show a strong bias whereby source locations were heard farther off center than were their ''correct'' locations since the ''correct'' location was suddenly and arbitrarily changed. After training with the altered cues, bias was expected to decrease in magnitude for all positions. Finally, results from the first, posttraining, normal-cue test were expected to show either (1) a bias in the direction opposite that shown when the transformed cues were first presented (if changes in subject performance were unconscious, and therefore could not be immediately ''turned off'' by the listener following training) or (2) little bias (if subjects were capable of consciously interpreting cues as either normal or altered, as appropriate).

Figure 5 shows bias results as a function of source position for the seven experiments. Normal-cue runs are plotted

with circles and solid lines; altered-cue runs with diamonds and dashed lines. The open symbols represent runs prior to altered-cue training while filled symbols correspond to results from the tests following exposure to the altered cues. In all experiments, four runs are plotted: the initial run (which uses normal cues); run 3, the first run with altered cues; the final run with altered cues (run 7 in the training experiments, run 32 in the feedback experiments); and the first run with normal cues following altered-cue exposure (run 8 in the training experiments, run 33 in experiments F_3, F_{3mid}, F_2, and F_{4a}, and run 37 in experiment F_{4b}).

Independent of the exact training method employed, the range of source positions presented, the number of sources simulated in the acoustic field, and the strength of the cue transformation employed, bias results were similar. First of all, in all experiments, bias results are roughly left–right symmetrical, as expected. Since there is no reason to expect asymmetrical results, the degree of left–right symmetry in the results is one measure of variability in estimates of bias. Results from the first normal-cue run (open circles) showed some bias, although these errors were much smaller than those found in other runs. A strong bias occurred in the first test with transformed cues (open diamonds) in the direction predicted by the transformation and the aforementioned edge effect (subjects heard sources farther off-center than they were). Without these edge effects, one would expect bias to increase monotonically with the magnitude of the source azimuth. Results for the test using transformed cues after training (filled diamonds) showed a clear reduction in bias over the whole range of positions tested; however, this adaptation was not complete. In all experiments, the final bias when testing with altered cues is roughly one-third to half of the initial bias (compare filled to open diamonds). Finally, a negative aftereffect is seen in the results from the final normal-cue test following exposure (filled circles), indicating that performance was not controlled solely by conscious correction which could be easily ''turned off'' at will.

In general, the four runs plotted in Fig. 5 summarize the important aspects of performance across all runs. In particular, these runs show the starting and ending points for performance as subjects adapt to the transformation in localization cues. Intermediate runs, which are not shown in Fig. 5, show intermediate levels of performance changing from the initial to the final results shown in Fig. 5. It is important to note that the changes in performance (evidenced by differences between the open and filled symbols in Fig. 5) actually occurred rapidly during the course of the experiments and that performance had clearly stabilized by the end of the altered-cue test period in all seven experiments (performance was close to the final values within approximately two altered-cue runs in the training experiments and four altered-cue runs in the feedback experiments). The exact time course of these changes will be fully explored in a subsequent paper. However, because performance was stable by the last altered-cue run in all experiments, direct comparisons of the final results from the various experiments can be made, even across the training and feedback experiments, for which completely different training paradigms were investigated.

Differences between experiments appear to depend mainly on differences in the transformation employed. First, examine results from experiments T_1, T_3, and F_3 [panels (a), (b), and (c) in Fig. 5]. Results for these three experiments are roughly the same, despite the differences in the exposure method (experiment T_1 had only a single source on at all times, while experiment T_3 presented two continuous background sources in addition to the target source in order to give a more complete auditory scene; experiments T_1 and T_3 used active sensorimotor training, while correct-answer feedback was used in experiment F_3.) In these three experiments, the largest biases occur for positions at -30 and $+30$ degrees. Similar results are seen in experiment F_{3mid} [Fig. 5(d)], except that the largest biases occur for sources near -20 and $+20$ degrees, slightly closer to the center position than occurred with experiments T_1, T_3, and F_3. This result is consistent with the fact that a smaller range of positions was used in experiment F_{3mid}, so that the edge effects were significant for sources closer to the 0 degrees azimuth. In experiment F_2 [Fig. 5(e)], a less extreme transformation was employed. In this experiment, the largest biases occurred for source positions nearer to -40 and $+40$ degrees. Once again, this result can be explained on the basis of the transformation employed. In this experiment, smaller biases are expected for a given source position than occurred in experiments T_1, T_3, and F_3 because the transformation was less extreme. In addition, the edge effects described above should affect fewer positions, since fewer sources will be heard outside of the allowed response range in this experiment. Finally, results from experiments F_{4a} and F_{4b} [Fig. 5(f) and (g)] show a larger bias than the other experiments for the centermost source positions. The largest biases occur for sources near -20 and $+20$ degrees. For these experiments, the more extreme cue transformation resulted in more sources falling outside the normal range of source positions, so that a larger number of sources were affected by the edge effects. Any differences between the results for experiments F_{4a} (in which normal cues were presented in runs 33–40) and F_{4b} (in which a transformation of 0.5 was used in runs 33–36 and normal cues were presented in runs 37–40) should be evident by comparing the final, normal-cue run results (filled circles). However, any such differences are small relative to the variability seen in the results.

C. Resolution

In general, resolution was expected to be somewhat better in the center region than at the edges of the range of source positions in the first run using normal cues, since resolution is best straight ahead of the listener. Independent of the exact pattern of results, the first normal-cue test provides a baseline measure against which results from later tests could be compared. Given the remapping function shown in Fig. 1, results from the first test with altered cues were expected to show improved resolution (relative to the first, normal-cue test) in the center of the range and decreased resolution at the sides. Following training with the altered cues, resolution was expected to either (1) remain as it had been for the first altered-cue test (if resolution depended solely on the difference between the magnitudes of

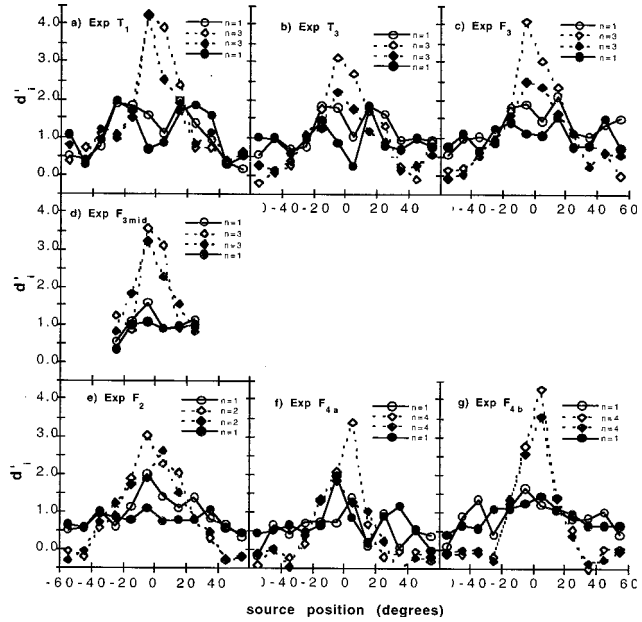

FIG. 6. Resolution results for the seven experiments. In each panel, the average estimated d' is plotted as a function of correct source position (in degrees). For each panel, resolution was estimated for each subject and run in the experiment and then averaged across all subjects in the experiment. Four runs are plotted in each panel: the first run in the experiment (open circles), the first run with the transformed cues (open diamonds), the final run with altered cues (filled diamonds), and the first normal-cue run following altered-cue exposure (filled circles). In each panel, the legend details the strength of the cue transformation employed in the normal- (n always equals 1) and altered-cue runs ($n=2$, 3, or 4).

the cues at adjacent positions) or (2) change with time (if performance depended upon high-level cognitive factors which were affected by training).

Resolution results for all seven experiments are shown in Fig. 6. The same four runs are plotted in this figure as were plotted in the bias results in Fig. 5. The initial test with normal cues is plotted with open circles and solid lines, the initial test with altered cues is plotted with open diamonds and dashed lines, the final test with altered cues is plotted with filled diamonds and dashed lines, and the first normal-cue test following altered-cue exposure is plotted with filled circles and solid lines.

As with bias, the basic patterns of results are the same across all experiments, and results are roughly left–right symmetric. Overall, resolution for normal cue runs showed a consistent pattern in which resolution appeared to be slightly *worse* for the center positions compared to positions just off center, rather than slightly better as was expected. This result may be due to positional dependencies on the accuracy of the simulation as well as true differences in resolution arising from perceptual issues. In any case, the results from the initial run using normal cues provides a baseline against which results from the other runs can be measured. As expected for the transformation employed, resolution on the first run using the transformed cues was enhanced for positions in the central region and degraded at the edges of the range compared to results from the initial run. Of particular interest are the results for the final, altered-cue test (filled diamonds): although resolution remains enhanced over that achieved with normal cues, there tends to be a decrease in resolution compared to results for the first test using the transformed cues, demonstrating that resolution does not depend solely on physical cues. A similar decrease can be seen when comparing the final normal-cue test (following training) with the initial, preexposure normal-cue test. There is a tendency for resolution to decrease with training, both for the normal-cue and for the altered-cue results.

Comparing results for experiments T_1, T_3, and F_3 [Fig. 6(a)–(c)], there is substantially more variability in the resolution results across these three experiments than was seen in the bias results. In particular, the increase in resolution with the first altered-cue run seen in experiment T_1 is larger than that seen in experiments T_3 and F_3. However, in all cases, the estimated value of d' is quite large. Generally speaking, when d' for two stimuli is larger than about 3.0, there are large changes in the amount of overlap of the distributions for relatively small changes in distance between the means of the distributions. As a result, estimates of d' are very sensitive to small changes in the pattern of responses when d' is relatively large. Thus, although the apparent differences between results for experiments T_1, T_3, and F_3 are pronounced, they arise in part from the numerical instability of estimating large values of d'. This numerical instability can also be seen in left–right asymmetries in many experiments for some of the large values of d' [e.g., examine the estimates of d' for the middle two positions in experiment T_1, particularly for the final test with altered cues (filled diamonds)]. Results from experiment F_{3mid} [Fig. 6(d)] are roughly consistent with results for experiments T_1, T_3, and F_3. The increase in resolution seen in experiment F_2 for the first test with altered cues is slightly smaller than was seen in the first four experiments, consistent with the fact that the transformation in experiment F_2 is less extreme than in the first four experiments. Finally, the increase in resolution in experiments F_{4a} and F_{4b} tends to be greater than in the other five experiments, all of which used a less extreme transformation. As with bias, there are no obvious differences in resolution results for experiments F_{4a} and F_{4b}, despite the fact that a transformation of 0.5 was used in runs 33–36 in experiment F_{4b}.

IV. CONCLUSIONS AND FUTURE WORK

The results demonstrate that subjects are able to learn remappings between acoustic cues and physical locations in the sense that they are able to reduce bias with training. However, subjects never completely overcome their systematic errors when responding to altered localization cues. Instead, over time, their errors grow smaller in magnitude, but retain the same pattern of results as is seen in their initial errors with altered cues (i.e., larger errors at the center of the range, smaller errors at the edges of the range). Since performance was stable by the final test with altered cues, it appears that subjects cannot adapt completely to the transformation employed in these experiments (shown in Fig. 1). This result is consistent with previous results investigating sensorimotor adaptation (Welch, 1986) which show that adaptation usually occurs, but is seldom complete; instead, systematic biases remain even after performance is stable (and additional exposure causes no further change in localization

performance). A negative after-effect was found for all experiments, implying that changes in performance were not based solely on conscious correction; instead, changes occurred gradually, with training. These gradual changes occurred both when subjects were first exposed to the altered cues (adaptation), and when subjects were returned to normal cues at the end of the experiments (recovery).

Unlike previous experiments investigating sensorimotor adaptation, our experiments imply that there is no qualitative difference in the final level of adaptation achieved when using training paradigms that involve subjects in active sensorimotor tasks (experiments T_1 and T_3) compared to the adaptation achieved in experiments in which simple correct-answer feedback is provided (experiments F_3, F_{3mid}, F_2, F_{4a}, and F_{4b}). In fact, the relative insensitivity of bias and resolution results to the various experimental conditions is somewhat surprising. Bias and resolution appeared to be insensitive to the complexity of the auditory scene, since results from experiments T_1 and T_3 are comparable. Even when subjects are explicitly trained to an inverse transformation in an attempt to allow their normal-cue test results to return to preexposure patterns more rapidly, no clear effect is seen (compare results for experiments F_{4a} and F_{4b}).

While changing exposure conditions causes little difference in results, changing the strength of the transformation (compare results for experiments F_3, F_2, F_{4a}, and F_{4b}) and/or the range of stimuli used (compare results for experiments F_3 and F_{3mid}) did cause differences in bias and resolution. In particular, the stronger the transformation, the larger the initial errors in performance (bias) and the larger the initial increase in resolution for center positions. Similarly, the bias in the final run with the altered cues (filled diamonds in Fig. 5) varies with transformation strength, with larger final errors tending to occur for experiments using more extreme transformations. While the absolute size of initial bias errors depended on the transformation employed, it appears that the decrease in bias with training is roughly proportional to the initial error. For all experiments, final bias was roughly one-third to one-half of the bias initially measured in the first altered-cue run. It should be noted that a reduction in bias may arise either from decreases in mean error or increases in response variability. Subsequent analysis (described in Shinn-Cunningham *et al.*, 1998) that examines mean response in detail shows that localization errors decrease with exposure to supernormal localization cues, and that this is the main reason that bias decreases over time. However, there is a small increase in the estimated internal decision noise as subjects adapt which contributes to the decrease in response bias.

Increasing the physical differences in the stimuli that correspond to the 13 possible responses allows subjects to achieve better-than-normal resolution. However, as subjects adapt to these changes, their ability to resolve adjacent stimuli appears to decrease. Previous investigations of the dependence of resolution on experimental conditions have shown that resolution depends on both the physical cues used in an experiment, and on the range of physical cues presented during an experiment. For instance, earlier models of resolution explain that resolution of two stimuli in a jnd task is better than resolution of the same two stimuli during a many-alternative, forced-choice task by positing that internal decision noise grows as the range of the physical stimuli increases (Durlach and Braida, 1969; Braida and Durlach, 1972, 1985). However, the current results show that resolution also depends upon the past history of exposure of the subject. If resolution depended only on the range and values of the physical stimuli, then resolution would be identical in the first and last runs using altered cues. In these two runs, an identical set of 13 physical stimuli are presented; however, resolution decreases over time.

One possibility is that the decrease in resolution arises because data are averaged over time periods during which the decision criteria shift significantly. If this were the case, estimates of the variability in the underlying probability densities would be too large and estimates of d' too small simply due to estimation errors. Thus, an apparent decrease in resolution might be due to changes in criteria placement during the final test with altered cues. However, this explanation is inconsistent with other aspects of the data. In particular, analysis in a companion paper (Shinn-Cunningham *et al.*, 1998) shows that the greatest changes in mean response occur at the beginning of the altered-cue exposure period, and that performance is stable well before the final test run with altered cues. In other words, shifts in response criteria may cause estimates of d' for the initial test with altered cues to be too small but will have little effect on the estimates of d' for the final test with altered cues.

An alternative explanation assumes that resolution depends upon the range of stimuli being attended to by the subject (not the range of the physical stimuli used in a run). Prior to adaptation, subjects expect positions to span 120 degrees (from -60 to $+60$ degrees), but during training, they hear acoustic cues covering a much larger range (see Fig. 1) and learn to attend to this broader range. Perhaps, over time, as subjects adapt to the change in cues, they begin to attend to a larger and larger range of physical stimuli. Earlier models of resolution performance may be extended to include specifications for how performance changes over time in an adaptation experiment by specifying how the effective mean response and the effective range depend upon training. A preliminary model of adaptation based on the model of intensity perception by Durlach and Braida (Durlach and Braida, 1969; Braida and Durlach, 1972, 1985) is currently under development.

ACKNOWLEDGMENTS

This work was mainly supported by AFOSR Grant Nos. 90-200, 93NL387, and 96NL145. Supplementary support was received from Navy Grant No. N61339-93-C-0047. Portions of this work were presented at the 124th (November 1992) and 127th (June 1994) meetings of the Acoustical Society of America. We are grateful to Lorraine Delhorne and John Crouch for their help with data collection.

[1]This family of transformations was chosen because it changes smoothly as a function of angular position, and maps the positions -90, 0, and 90 degrees to themselves for all values of n.

[2]For the family of transformations $f_n(\theta)$, the point at which the slope

$df_n(\theta)/d\theta$ equals one is given by $|\theta| = \frac{1}{2}\cos^{-1}((n^2-2n+1)/(n^2-1))$. Thus, the range of positions that have larger-than-normal changes in physical cues for a given azimuthal increment are $(-35,+35)$ degrees when $n=2$; $(-30,+30)$ degrees when $n=3$; and $(-27,+27)$ degrees when $n=4$.

[3]In Experiment F_{4b}, subjects were exposed to a transformation of strength $n=0.5$ after the normal ''supernormal'' exposure period in order to test whether such retraining might increase the speed with which their performance returned to preexposure patterns.

[4]In the current experiments, only azimuthal position was transformed to achieve better-than-normal resolution. In the future, we hope to perform similar experiments involving elevation and distance. Since the main cue for azimuthal position is interaural time delay (ITD; see, for example Wightman and Kistler, 1992), it is likely that similar adaptation results would obtain for experiments involving only ITD transformations.

[5]Since the standard deviation of the internal decision variable is assumed independent of the physical stimulus, nonuniform sensitivity to the physical variable of interest (i.e., azimuth) implies a nonlinear dependence of the decision-variable distribution mean on the physical stimulus. In particular, the means of the decision variable distributions for sources at 0 and 10 degrees (sources that are relatively easy to distinguish from one another) will be farther apart than will the means of the decision variable distributions for sources at 50 and 60 degrees (sources that are harder to distinguish from one another). This is consistent with other decision-theory models, for instance, see Durlach and Braida (1969).

[6]It is possible that subjects change the placement of criteria as a run progresses to reflect the fact that there is less uncertainty in which stimuli will be presented at the end of the run than at the start of the run. For instance, if the position directly in front of the listener is not presented until the last two trials of the run, in principal it is possible that the listener is aware that the last two trials are more likely to come from the center than anywhere else, and may shift his criteria to reflect this fact. In our analysis, we ignore any such effects. In practice, there were enough trials in each run that subjects did not keep track of how often each of the stimuli had been presented during the run.

[7]While this is true in general, mean response for sources at the edges of the response range will not have this property. For instance, in Fig. 4, the mean response to stimulus 3 will always be less than 3, since the left tail of the distribution for stimulus 3 falls into the ''2'' response range and there is no ''4'' response allowed to counterbalance the effect of these ''2'' responses on the mean response to stimulus 4.

[8]Note that, using this simple estimation method, bias values are calculated for each of the N stimulus values presented, not for the $N-1$ criteria. Assuming the same underlying stimulus distributions and Thurstonian decision model, the ith bias estimated in this manner reflects ''error'' in the placement of all the criteria in the vicinity of the mean of the distribution of the ith stimulus value, while the bias estimated by the maximum likelihood estimate reflects only the ''error'' in the placement of the ith criteria.

Auel, J. (**1980**). *Clan of the Cave Bear* (Crown, New York).

Begault, D. (**1993a**). ''Call sign intelligibility improvement using a spatial auditory display,'' Technical Report 104014, NASA Ames Research Center.

Begault, D. (**1993b**). ''Head-up auditory displays for traffic collision avoidance system advisories: A preliminary investigation,'' Hum. Factors **35**, 707–717.

Begault, D. R. (**1995**). ''Virtual acoustic displays for teleconferencing: Intelligibility advantage for telephone grade audio,'' 95th Convention of the Audio Engineering Society, 25–28 February 1995, Paris, France.

Begault, D., and Pittman, M. T. (**1994**). ''3-D audio versus head down TCAS displays,'' Technical Report 177636, NASA Ames Research Center.

Begault, D. R., Wenzel, E. M., Miller, J., and Shrum, R. (**1995**). ''Preliminary investigation of spatial audio cues for use during aircraft taxi under low visibility conditions,'' NASA Ames Research Center.

Braida, L. D., and Durlach, N. I. (**1972**). ''Intensity perception. II. Resolution in one-interval paradigms,'' J. Acoust. Soc. Am. **51**, 483–502.

Braida, L. D., and Durlach, N. I. (**1985**). ''Peripheral and central factors in intensity perception,'' in *Auditory Function: Neurobiological Bases of Hearing*, edited by G. M. Edelman, W. E. Gall, and W. M. Cowan (Wiley, New York), pp. 559–583.

Durlach, N. I. (**1991**). ''Auditory localization in teleoperator and virtual environment systems: ideas, issues, and problems,'' Perception **20**, 543–554.

Durlach, N. I., and Braida, L. D. (**1969**). ''Intensity perception. I. Preliminary theory of intensity resolution,'' J. Acoust. Soc. Am. **46**, 372–383.

Durlach, N. I., and Pang, X. D. (**1986**). ''Interaural magnification,'' J. Acoust. Soc. Am. **80**, 1849–1850.

Durlach, N. I., Shinn-Cunningham, B. G., and Held, R. (**1993**). ''Supernormal auditory localization. I. General background,'' Presence **2**, 89–103.

Ericson, M. A. (**1993**). ''A comparison of maskers on spatially separated competing messages,'' J. Acoust. Soc. Am. **93**, 2317.

Freedman, S. J., and Zacks, J. L. (**1964**). ''Effects of active and passive movement upon auditory function during prolonged atypical stimulation,'' Perceptual and Motor Skills **18**, 361–366.

Handel, G. F. (**1985**). ''Concerti a due Corni,'' recorded by the English Chamber Orchestra, Philips.

Lippmann, R. P., Braida, L. D., and Durlach, N. I. (**1976**). ''Intensity perception. V. Effect of payoff matrix on absolute identification,'' J. Acoust. Soc. Am. **59**, 129–134.

McKinley, R. L., and Ericson, M. A. (**1992**). ''Minimum audible angles for synthesized localization cues presented over headphones,'' J. Acoust. Soc. Am. **92**, 2297.

Pick, H. L., and Hay, J. C. (**1965**). ''A passive test of the Held reafference hypothesis,'' Perceptual and Motor Skills **20**, 1070–1072.

Rabinowitz, W. R., Maxwell, J., Shao, Y., and Wei, M. (**1993**). ''Sound localization cues for a magnified head: Implications from sound diffraction about a rigid sphere,'' Presence **2**, 125–129.

Shinn-Cunningham, B. G., and Kulkarni, A. (**1996**). ''Recent Developments in Virtual Auditory Space,'' in *The Generation and Applications of Virtual Auditory Space*, edited by S. Carlile (Landes, Austin, TX), pp. 185–243.

Shinn-Cunningham, B. G., Durlach, N. I., and Held, R. M. (**1998**). ''Adapting to supernormal auditory localization cues. II. Constraints on adaptation of mean response,'' J. Acoust. Soc. Am. **103**, 3667–3676.

Smith, S. (**1991**). ''An auditory display for exploratory visualization of multidimensional data,'' in *Workstations for Experiment*, edited by G. Grinstein and J. Encarnacao (Springer-Verlag, Berlin).

Van Veen, B. D., and Jenison, R. L. (**1991**). ''Auditory space expansion via linear filtering,'' J. Acoust. Soc. Am. **90**, 231–240.

Welch, R. (**1978**). *Perceptual Modification: Adapting to Altered Sensory Environments* (Academic, New York).

Welch, R. (**1986**). ''Adaptation of Space Perception,'' in *Handbook of Perception and Human Performance*, edited by K. R. Boff, L. Kaufman, and J. P. Thomas (Wiley, New York), Vol. I, pp. 24.1–24.45.

Welch, R., and Warren, D. H. (**1986**). ''Intersensory interactions,'' in *Handbook of Perception and Human Performance*, edited by K. R. Boff, L. Kaufman, and J. P. Thomas (Wiley, New York), Vol. I, pp. 25.1–25.36.

Welch, R. B., and Warren, D. H. (**1980**). ''Immediate perceptual response to intersensory discrepancy,'' Psychol. Bull. **88**, 638–667.

Wenzel, E. M., Arruda, M., Kistler, D. J., and Wightman, F. L. (**1993**). ''Localization using nonindividualized head-related transfer functions,'' J. Acoust. Soc. Am. **94**, 111–123.

Wightman, F. L., and Kistler, D. J. (**1989**). ''Headphone simulation of free-field listening. I. Stimulus synthesis,'' J. Acoust. Soc. Am. **85**, 858–867.

Wightman, F. L., and Kistler, D. J. (**1992**). ''The dominant role of low-frequency interaural time differences in sound localization,'' J. Acoust. Soc. Am. **91**, 1648–1661.

Adapting to supernormal auditory localization cues. II. Constraints on adaptation of mean response

Barbara G. Shinn-Cunningham,[a] Nathaniel I. Durlach, and Richard M. Held
Massachusetts Institute of Technology, Cambridge, Massachusetts 02139

(Received 23 September 1996; revised 27 January 1998; accepted 2 March 1998)

A series of experiments was performed in which subjects were trained to interpret auditory localization cues arising from locations different from their normal spatial positions. The exact pattern of mean response to these alterations (as a function of time) was examined in order to begin to develop a quantitative model of adaptation. Mean responses were roughly proportional to the normal position associated with the localization cues presented. As subjects adapted, the best-fit slope (relating mean response and normal position) changed roughly exponentially with time. The exponential rate and adaptation asymptote were found for each subject in each experiment, as well as the rate and asymptote of readaptation to normal cues. The rate of adaptation does not show any statistical dependence on experimental conditions; however, the asymptote of the best-fit slope varied with the strength of the transformation used in each experiment. This result is consistent with the hypothesis that subjects cannot adapt to a nonlinear transformation of auditory localization cues, but instead adapt to a linear approximation of the transformation. Over time, performance changes exponentially towards the best-fit linear approximation for the transformation used in a particular experiment, and the rate of this adaptation does not depend upon the transformation employed. [S0001-4966(98)03406-7]

PACS numbers: 43.71.Hw, 43.72.Ew, 43.66.Qp [RHD]

INTRODUCTION

A series of experiments described in detail in Shinn-Cunningham *et al.* (1998) examined how bias and resolution are affected when subjects are trained with ''supernormal'' localization cues. While the rationale behind the experiments, the experimental protocol, and the experimental conditions are described in detail in other papers (Durlach *et al.*, 1993; Shinn-Cunningham *et al.*, 1998), earlier results are summarized here for convenience. In the experiments, subjects were presented with auditory localization cues simulated over headphones using head-related transfer functions [HRTFs; for a review of these techniques, see Wenzel (1992)]. The goal of the work was to determine if subjects could adapt to learn a new correspondence between the localization cues of the physical HRTFs and the reported azimuthal position. To this end, subjects trained to identify the azimuthal location of an auditory source whose physical cues normally correspond to a different source position.

Normally, a source at azimuth θ and elevation ϕ is simulated by using the HRTF for that position. In these experiments, the HRTF used to simulate a source at position $[\theta,\phi]$, was equal to the HRTF normally corresponding to position $[f_n(\theta),\phi]$, where $f_n(\theta)$ is given by

$$f_n(\theta)=\frac{1}{2}\tan^{-1}\left[\frac{2n\,\sin(2\theta)}{1-n^2+(1+n^2)\,\cos(2\theta)}\right]. \quad (1)$$

The parameter n corresponds to the slope of the transformation at $\theta=0$. ''Normal'' localization cues are presented when $n=1$ [i.e., the function $f_n(\theta)$ is a straight line of slope one through the origin]. This mapping is shown in Fig. 1 for the values of n used in the experiments.

In order to determine whether subjects could adapt to the remapping of HRTF cues, they were repeatedly tested over the course of experimental sessions lasting roughly 2 h, first using the ''normal'' mapping ($n=1$) and then an altered mapping ($n>1$). At the end of the experimental session, testing with the ''normal'' mapping was repeated to look for aftereffects of the learned remapping.

Subjects were seated inside a 5-ft-radius arc of 13 light bulbs, spaced every 10 degrees in azimuth from -60 to $+60$ degrees, which were labeled (left to right) with the numbers 1–13. In each test run, a 500-ms-long wideband click train was simulated from each of the possible locations exactly twice, in random order. Subjects were asked to identify the source azimuth corresponding to the simulated source position while facing straight ahead.

In ''training'' experiments (experiments T_1 and T_3), subjects were not provided with any feedback during these test runs. Instead, they were expected to learn about the transformation of localization cues during training runs (interspersed with the test runs) in which synthetic auditory and real visual light sources were simultaneously turned on from one of the 13 possible locations, chosen at random. During these 10-min-long runs, subjects were instructed to turn their heads to face each audiovisual target. Once they faced the target, the light/sound source was turned off and a new random location turned on. In the training experiments, subjects performed two ''normal-cue'' test runs, five ''altered-cue'' test runs, followed by three ''normal-cue'' test runs.

Training was achieved in the ''feedback'' experiments (experiments F_3, F_{3mid}, F_2, F_{4a}, and F_{4b}) by turning on the

[a]Current address: Boston University, Department of Cognitive and Neural Systems, Room 311, 677 Beacon St., Boston, MA 02215, Electronic mail: shinn@cns.bu.edu

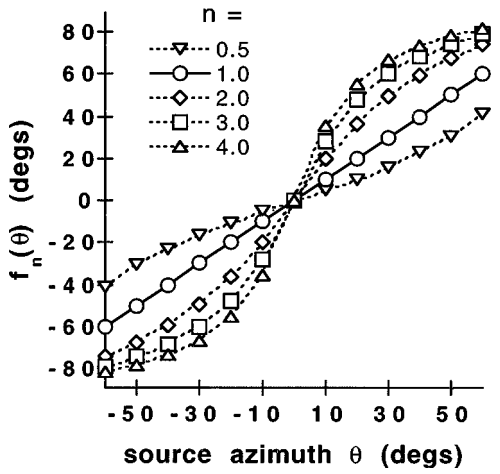

FIG. 1. Plot of the family of functions used to transform auditory localization cues. With this transformation, a source from azimuth θ was synthesized using the HRTF that normally corresponded to the position $f_n(\theta)$.

light at the ''correct'' location for 500 ms after a response in a test run. In these experiments, each subject performed 2 ''normal-cue'' runs, 30 ''altered-cue'' runs, followed by 8 posttraining runs. In all but one feedback experiment, the posttraining runs all used normal cues. In experiment F_{4b}, the eight posttraining runs consisted of four runs in which $n=0.5$ followed by four ''normal-cue'' runs.

The experimental conditions tested are summarized in Table I. In the previous analysis, bias and resolution were estimated at various points during the course of the experiment using a maximum likelihood estimation technique. In general, bias (a measure of the average error in response, normalized by the standard deviation in responses) grew smaller as subjects were exposed to the remapped cues, consistent with subjects learning the new mapping of physical cue to source location (Shinn-Cunningham *et al.*, 1998). However, errors remained, even after performance had stabilized. In addition, localization errors were not uniform, but varied with stimulus azimuth. The ability to resolve adjacent response locations showed an abrupt change when the remapping was introduced, as expected: resolution improved for stimuli which were physically more distinct than in the ''normal'' mapping (sources in the front region, as seen in Fig. 1) and decreased for stimuli which were more similar than normal (for $n>1$, this occurs for sources at the edges of the range). As subjects adapted to the remapped cues, however, their ability to resolve the *same* physical stimuli showed an overall decrease, indicating that subjects confused adjacent stimuli more often following training than prior to training. It was shown that the amount by which subject performance changed depended primarily on the strength of the transformation [i.e., the value of n in Eq. (1)] and the range/number of source positions presented (Shinn-Cunningham *et al.*, 1998). Conversely, results were largely independent of the complexity of the simulated auditory field. In addition, changes in bias and resolution after exposure to the altered cues were similar for both training and feedback experiments.

TABLE I. Summary of experiments performed. The altered-cue transformation ''strength'' [defined in Eq. (1)] is given in the second column. The ''Exp type'' describes whether subjects were exposed to training runs or given correct-answer feedback. The number of source positions used in the experiment is given in column 5, and the number of acoustic sources simulated in the experiment (target plus additional background sources) is given in column 6.

Experiment	n	Exp type	Position	Sources
T_1	3	training	13	1
T_3	3	training	13	3
F_3	3	feedback	13	3
F_{3mid}	3	feedback	7	3
F_2	2	feedback	13	1
F_{4a}	4	feedback	13	1
F_{4b}	4, 0.5	feedback	13	1

The current paper examines in greater detail how subjects' mean responses change over time when trained with supernormal localization cues. One goal of this analysis is to determine why subjects do not adapt completely to the supernormal cue remapping (i.e., why systematic biases remain in subject responses, even after subject performance has stabilized). In addition, the exact time course of changes in mean response is examined in order to help develop a quantitative model of adaptation (Shinn-Cunningham, 1998).

I. RESULTS

A. Mean response

Subject responses were averaged for each position within each run by combining results from the eight identical experimental sessions performed by each subject. Since each position was presented twice in each run of each session, the mean response for each position was the average of 16 responses. The resulting mean responses were then analyzed to see how mean response related to the physical cues presented to the subjects. An example of mean response for a typical subject (taken from experiment T_1) is shown in Fig. 2. In this figure, the mean response is shown as a function of the normal-cue location of the HRTFs [$f_n(\theta)$ in Eq. (1)]. Starting in Fig. 2(a) and examining the panels in counterclockwise order, the figure shows how mean response changes over the course of the experimental session for the same physical stimuli. In each panel, the correct responses when normal cues ($n=1$) are used are shown by the diagonal solid line. When transformed cues are used, correct responses are shown by the dashed curve [given by the inverse of the transformation function shown in Fig. 2(a)]. Note that in this figure, the HRTF locations presented to the subjects range from -60 to $+60$ degrees in panels (a)–(c) and from approximately -80 to $+80$ degrees in panels (d)–(f). In the lower panels, the range of HRTF positions is greater than the range of response positions (-60 to $+60$ degrees) because the HRTF locations are transformed by the supernormal-cue transformation; however, the feedback presented to the subjects trains them to interpret these physical cues as arising from positions ranging from -60 to $+60$ degrees (examine the dashed line in all panels).

Two important trends are seen in Fig. 2 that are evident for all subjects in all experiments. First, the training with the transformed cues does affect mean response as expected. For

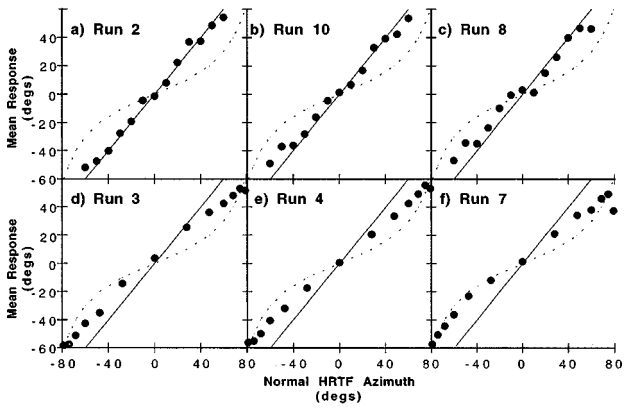

FIG. 2. Plot of mean response for one subject in one experiment as a function of the normal spatial position of the auditory localization stimuli used. In panels (a)–(c), localization cues were not transformed and normal spatial positions ranged from -60 to $+60$ degrees. In panels (d)–(f), transformed localization cues were presented, so that the normal spatial position of the cues ranged from -80 to $+80$ degrees. The order of the runs within the experiment is given by starting in panel (a) and moving counterclockwise to panel (b). The solid line shows the correct response for normal-cue runs. The dashed curve shows the correct response for altered-cue runs. In general, mean response was roughly a linear function of the normal spatial position of the stimuli, even in the altered-cue runs (runs 3, 4, and 7). Subject adaptation is exhibited by changes in the slope of the line relating mean response to normal spatial position over time.

the first two runs, which took place prior to any transformed-cue training, mean response is roughly equal to the correct response [compare the mean response, filled circles, to the correct response, solid line, for run 2 in of Fig. 2(a)]. Thus, for these runs, mean response is proportional to the normal-cue locations with a slope of one. As subjects are exposed to the transformed cues [runs shown in panels (d)–(f)], the mean responses change such that the error in mean response (difference between mean response, filled circles, and the correct response, dashed curve) decreases, even though it does not go to zero. When tested and trained with normal cues following exposure to the transformation [run 8 in panel (c) and 10 in panel (b)], the mean responses begin to change back towards their original pattern.

The second trend seen in the data is that mean response is roughly proportional to the location normally associated with the HRTFs used, even after subjects have been trained using the nonlinear transformation. This result is most obvious when examining Fig. 2(d)–(f). In these runs, correct responses (as defined by the training given subjects) are nonlinear as a function of the normal-cue source location (dashed lines); however, the mean response is roughly linear (with a y intercept of zero) for the transformed-cue test runs, even after 30 min of training with the transformed-cue transformation [cf. results from run 7 in Fig. 2(f)].

B. Test of best-fit hypotheses

The two trends discussed above are seen in the data from all subjects in all experiments. The second observation, that mean response is always proportional to the normal location of the physical HRTFs used, was explicitly tested for each subject in each experiment. Two hypotheses were used to fit mean response as a function of normal-cue source position. Under both hypotheses, a single parameter summarizes how perceived source position is related to the physical stimuli in a given run.

The first hypothesis, suggested by the data, was that in run r, the mean perceived position p of a source whose ''correct'' location is θ is given by

$$p(\theta,r)=k(r)f_n(\theta) \tag{2}$$

for stimulus $f_n(\theta)$, where the value of $f_n(\theta)$ is determined by the altered-cue transformation used in the experiment [see Eq. (1)]. Under this hypothesis, changes in subject performance are characterized by changes in the best-fit slope $k(r)$ with run r. This hypothesis assumes that subjects cannot adapt to the transformation completely; instead, the average perceived position of the source is constrained to be proportional to the normal-cue source position $f_n(\theta)$. In other words, rather than adapting fully to the given transformation, the subject adapts to a linear approximation to the transformation. For a naive subject, $k(r)$ should start near 1, indicating that the subject perceives localization cues normally. As the subject adapts, $k(r)$ should decrease, consistent with the subject altering his responses to reduce his mean localization error. However, some error between mean perceived position $p(\theta,r)$ and correct response θ will remain, since the imposed transformation $f_n(\theta)$ is nonlinear but subjects can only adapt to a linear transformation.

An alternative hypothesis is suggested by Eq. (3). In this hypothesis, it is assumed that the mean perceived position is given by

$$p(\theta,r)=f^{-1}_{m(r)}(\theta), \tag{3}$$

where $f_n^{-1}(\theta)$ is the inverse of the function $f_n(\theta)$ defined in Eq. (1) and $m(r)$ varies between 1 and n. The value $m(r)=1$ indicates that subjects perceive source locations in the normal manner. Conversely, the value $m(r)=n$ is consistent with subjects adapting completely to the supernormal transformation $f_n(\theta)$. Thus, this hypothesis assumes that any nonlinearity in mean response will take the form of the nonlinear transformation used to rearrange the acoustic cues. With this hypothesis, subjects achieve zero mean error for all source positions when $m=n$. Partial adaptation occurs when $1<m<n$.

For each subject, run, and experiment, the values of $k(r)$ and $m(r)$ that minimized the mean squared error between measured mean response and predicted mean response was calculated. For most stimuli, the predicted mean response was simply the value of $p(\theta,r)$ predicted from Eq. (2) or (3). However, since responses were constrained to fall between -60 to $+60$ degrees predicted responses were also constrained to fall within the closed interval $[-60,60]$ degrees. Any predictions falling outside this range of possible responses were set to equal the nearest extreme value [i.e., if the mean response calculated from Eq. (2) or (3) was equal to 65 degrees, the prediction used to calculate the mean-square error was 60 degrees].[1] The minimum mean square error (in degrees) for the two curve fits were then compared for each run and subject in each experiment.

Table II summarizes the results of these tests. In general, both approaches fit the data reasonably well. The average

TABLE II. Comparison of linear and nonlinear curve fitting of mean response. Column 1 gives the experiment number, columns 2 and 3 show the mean square error (in degrees) for linear and nonlinear curve fits, respectively. Column 4 shows the number of cases for which the linear curve fit yielded a better fit than did the nonlinear curve fit. Column 5 shows the total number of cases in each experiment. Column 6 shows the percentage of the cases in which the linear curve fit yielded better results. The final row shows average results across all experiments.

Experiment	mse linear	mse x form	Linear better	Total cases	Percent
T_1	1.3	1.5	33	40	82.5
T_3	1.7	1.7	41	80	51.3
F_3	1.0	1.4	182	200	91.0
F_{3mid}	0.7	0.8	104	160	65.0
F_2	1.5	1.6	109	160	68.1
F_{4a}	2.0	3.0	113	120	94.2
F_{4b}	1.7	2.6	113	120	94.2
overall	1.3	1.7	695	880	79.0

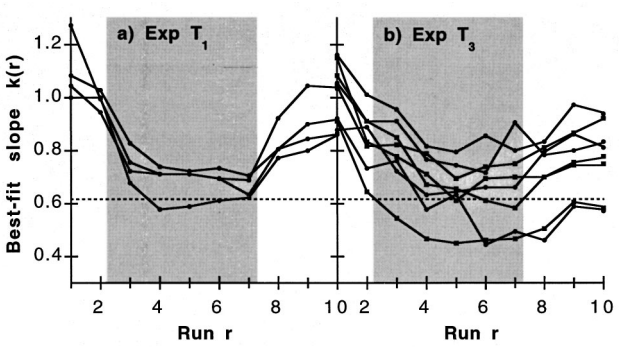

FIG. 3. Plot of best-fit slope $k(r)$ for each subject in experiments with active sensorimotor training. Best-fit slope for the transformation used in each experiment is shown by the horizontal dashed line in each panel. Normal-cue runs are plotted against a white background; altered-cue runs are plotted against a gray background.

mean square error in the predictions was 1.3 degrees using the linear curve fit and 1.7 degrees using the nonlinear curve fit. More importantly, however, in almost all of the conditions, the linear curve fit yielded a smaller mean square error than the nonlinear curve fit. Table II shows that the linear curve fit yielded a smaller mean square error than did the nonlinear curve fit in 695 of 880, or 79% of the cases. Both hypotheses will fit normal, unadapted responses equally well [i.e., $k(r)=m(r)=1$ yield identical predictions]. Thus, for runs in which the mean response is near the ''normal'' response (i.e., prior to exposure to the supernormal cues, and as subjects readapt to normal cues at the end of the experiment), there should be no clear advantage to using the linear

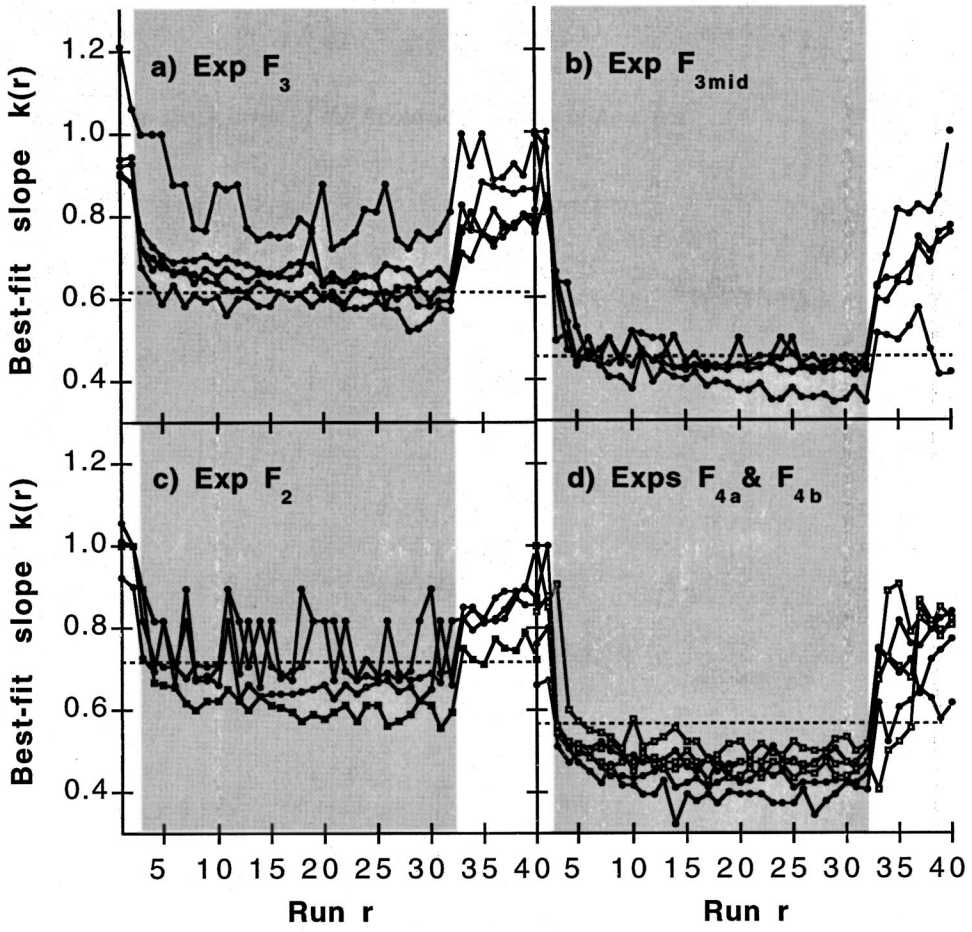

FIG. 4. Plot of best-fit slope $k(r)$ for each subject in experiments with correct-answer feedback. Best-fit slope for the transformation used in each experiment is shown by the horizontal dashed line in each panel. Normal-cue runs are plotted against a white background; altered-cue runs are plotted against a gray background. In panel (d), results are shown for both experiment F_{4a} (solid symbols) and experiment F_{4b} (open symbols), which were identical up through run 32. In experiment F_{4b}, an inverse transformation was used in runs 33–36.

curve fit compared to the nonlinear curve fit; thus, the superiority of the linear curve fit over the nonlinear curve fit is even more compelling.

Although it is possible that other nonlinear curve fits might yield even better fits than those found with the linear curve fit described in Eq. (2), it is unlikely that any other single-parameter curve fit would provide more insight into the pattern of subject responses. If there were any nonlinear trends in the mean response, they should arise from the nonlinear cue transformation employed in the experiment, a hypothesis tested explicitly in the comparison summarized in Table II.

C. Best-fit slope $k(r)$

These results demonstrate that the mean response for each subject at each point in time can be summarized by the best-fit slope $k(r)$ defined in Eq. (2). The fact that mean response is roughly proportional to the normal-cue position of the acoustic stimulus implies that subjects cannot completely adapt to a nonlinear cue transformation. Instead, subjects adapt to a linear approximation of the nonlinear transformation employed. Thus, for the type and length of training used in these experiments, some error will remain in their mean responses. Let k_{opt} denote the slope which will minimize the mean squared error in mean response for a given experiment. Given that mean perceived position is constrained by Eq. (2), this slope describes the most complete adaptation achievable for a given experiment. Thus, if subjects adapt as completely as possible, $k(r)$ should approach k_{opt} asymptotically over the course of the exposure period in the experiment. The value of k_{opt} will depend not only on the strength of the transformation employed, but also on the source positions used in the experiment.

Figure 3 plots $k(r)$ as a function of run r for each of the experiments in which active sensorimotor training runs were used in between test runs, while Fig. 4 plots $k(r)$ for the experiments in which correct-answer feedback was employed during each test run. In both figures, each panel shows the best-fit values of $k(r)$ for each subject with a solid line. The dashed horizontal line in each panel shows the best-fit slope k_{opt} for that experiment. Runs in which the altered cues were used are shown with a gray background, while normal-cue runs are shown against a white background.

The plots in Figs. 3 and 4 show that the parameter $k(r)$ changes with run number, consistent with subjects adapting to the supernormal cues over time. In all of the experiments, independent of the experimental conditions, the value of $k(r)$ approaches a value which is roughly equal to k_{opt}, the optimal slope for the given experiment. The change in $k(r)$ is quite rapid; most subjects have slopes near their final asymptotic value by the fifth run with altered cues. When subjects are tested with normal cues following the supernormal-cue exposure period, the value of $k(r)$ increases towards the ''normal-cue'' optimal value of 1.

While there is substantial intersubject variability in the absolute values of $k(r)$, all subjects showed a rapid change in $k(r)$ over the course of the experiment. In general, the asymptotic value of $k(r)$ is close to the best-fit slope of k_{opt}. In experiments T_1, T_3, and F_3, the same transformation ($n=3$) and range of positions (from -60 to $+60$ degrees) were presented, so that k_{opt} is equal to 0.6161 in all of these experiments. Looking at the results across all subjects in these three experiments, the final value of $k(r)$ tends to be equal to or greater than the optimal value of k_{opt}. However, there are subjects for whom the best-fit slope $k(r)$ was actually less than k_{opt} as well. Given the intersubject variability, the value k_{opt} is a good predictor for the asymptotic values of slope $k(r)$. In experiment F_{3mid}, k_{opt} is equal to 0.4565 ($n=3$, but only the middle seven response positions, from -30 to $+30$ degrees were presented), while in experiment F_2, k_{opt} is equal to 0.7142 ($n=2$, all 13 source positions used). In these experiments, the majority of the subjects adapt to values of $k(r)$ extremely close to k_{opt}. Finally, in experiments F_{4a} and F_{4b}, in which the transformation was strongest ($n=4$) and all 13 source locations were presented, on average, the asymptotic values of $k(r)$ tend to be smaller than the calculated value of $k_{opt}=0.5646$.

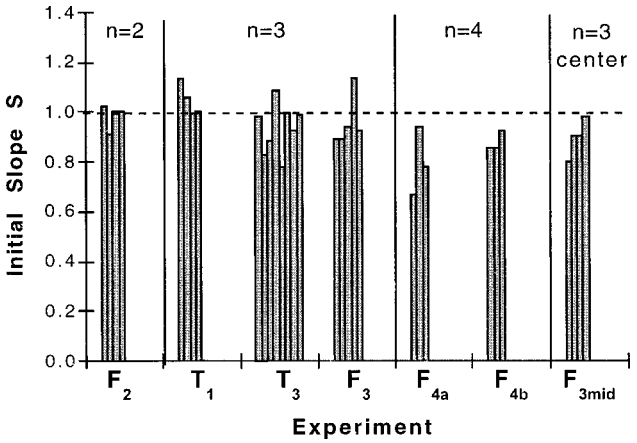

FIG. 5. Estimates of initial values of k prior to exposure to the supernormal (transformed) cues. Each bar represents the estimate of the initial slope for one subject. The horizontal dashed line shows the expected value of initial slope of 1.0.

In experiment F_{4b}, subjects were presented with a transformation of strength 0.5 for four runs (runs 33–36), then normal cues for the final four runs (runs 37–40). In order to examine the effect of this exposure period, slope estimates from runs 33–40 from experiment F_{4a} (which was identical to experiment F_{4b} except that normal cues were presented for runs 33–40) were compared with slope estimates for experiment F_{4b}. As can be seen in Fig. 4(d), results from the three subjects in experiment F_{4b} (small diamond symbols) were indistinguishable from results from the three subjects in experiment F_{4a} (small circle symbols), despite the training with the inverse transformation.

II. FITTING $k(r)$

The graphs shown in Figs. 3 and 4 imply that changes in mean localization performance can be summarized by $k(r)$, which appears to change exponentially towards an asymptotic value. In order to better quantify these results, the

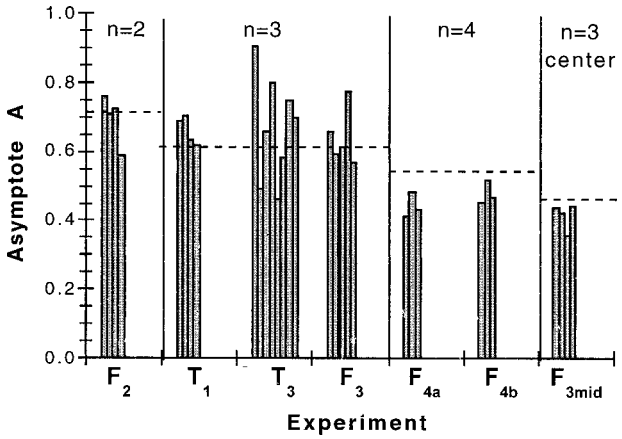

FIG. 6. Estimates of asymptotes of $k(r)$ during adaptation. The best-fit slopes (k_{opt}) for the transformations used in each experiment are shown by the horizontal dashed lines. Each bar represents the estimate of the asymptote for one subject.

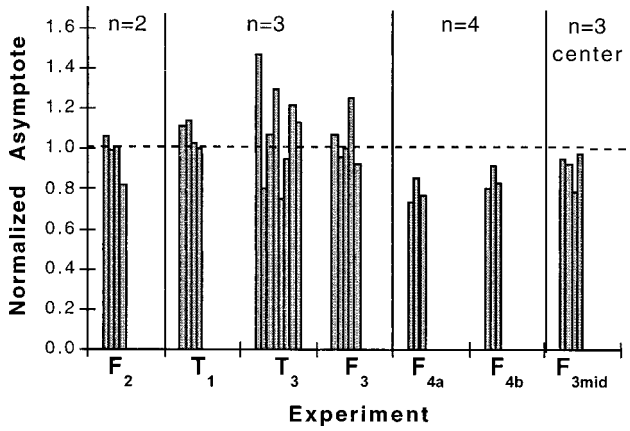

FIG. 7. Normalized asymptotes of $k(r)$. Each bar represents the estimate of the asymptote for one subject, normalized by the best-fit slope (k_{opt}) for that experiment. The dashed line is at 1.0, the normalized value of k_{opt} for all experiments.

values of $k(r)$ found for each subject were analyzed to determine more precisely how performance changed with time.

A. Initial, unadapted slope

The first quantity to be examined was the starting value of $k(r)$. Although some subjects may show a change in $k(r)$ between the first two runs in the experiment (both of which use ''normal'' localization cues), these changes are relatively small compared to the changes which occur as subjects adapt to the intentionally altered cues. Also, while many subjects in experiments T_1 and T_3 show a tendency for $k(2)$ to decrease from the initial value of $k(1)$, subjects in the subsequent experiments were equally likely to show an increase or a decrease in slope between runs 1 and 2. For this reason, estimates of the initial slope prior to training with the supernormal cues were found by averaging the values of $k(1)$ and $k(2)$ for each subject.

Figure 5 plots estimates of S, the initial slope prior to exposure to altered cues, for each subject in each experiment. In order to be consistent with later plots, the data are plotted in a bar graph in which subjects from each experiment are grouped together, and the experiments are ordered on the basis of k_{opt}, the best-fit slope for the transformation of cues used in that experiment.

The plot in Fig. 5 shows little systematic dependence of the initial slope on either experiment or on the transformation strength used in the experiment. This was explicitly tested with a one-way ANOVA, in which S showed no statistical dependence on experiment [$F(6,1)=2.86$, $p>0.005$]. Although there is no statistical dependence of S on experiment, there is obvious subject variability in the estimates of initial slope. Subjects in experiments F_{3mid}, F_{4a}, and F_{4b} tended to have a smaller initial slope than did subjects in other experiments; however, the initial slope values shown by the subjects in these two experiments is within the range of values shown by subjects in other experiments (e.g., note values in experiment T_3 or F_2). On average, across all experiments, the initial slope is 0.94, close to the expected slope of unity for subjects hearing normal cues, prior to exposure to altered cues.

B. Adaptation asymptote

For each subject in each experiment, the asymptote of $k(r)$ during the altered cue exposure was estimated from the values of $k(r)$ plotted in Figs. 3 and 4. For the training experiments (shown in Fig. 3), the asymptote was estimated as the value of $k(7)$, the value from the final, altered-cue run in the experiments. For the feedback experiments (shown in Fig. 4), the asymptote was estimated by averaging the values of $k(30)$, $k(31)$, and $k(32)$, the slopes from the last three runs using the altered cues.

Figure 6 shows estimates of the asymptotes (denoted by A) for each subject in each experiment. In the graph, the data are grouped according to the value of k_{opt}, the best-fit slope fitting the transformation used in that experiment. In each group, k_{opt} is shown by a dashed horizontal line. A one-way ANOVA showed that A has a clear statistical dependence on the experiment [$F(6,1)=6.46$, $p<0.005$].

In order to examine the extent to which the dependence of the asymptote A on experiment can be accounted for by differences in the best-fit slope k_{opt}, the estimates of asymptote were normalized by the best-fit slope and replotted in Fig. 7. Plotted in this way, the best-fit slope has a value of 1.0 for all experiments (shown by the dashed horizontal line). When normalized by the best-fit slope in the experiment, there is little clear systematic variation in the values of asymptote with experiments. Although the normalized asymptotes in experiments F_{3mid}, F_{4a}, and F_{4b} all have values less than 1.0, there are many subjects in the other four experiments for whom the normalized asymptotes is less than 1.0 as well. It is also interesting to note that S, the *initial* slope value, tends to be less in these three experiments than in the other four experiments (see Fig. 5). This difference may occur because the subjects in these experiments all tend to interpret the ''normal'' HRTFs [taken from subject SDO, Wightman and Kistler (1989)] as closer to straight ahead than the nominal position of the HRTF. In other words, normal intersubject variability in HRTFs may be responsible for the tendency of subjects in some experiments to have smaller-than-expected slopes. A second possibility is that this tendency is the result of training with supernormal cues.

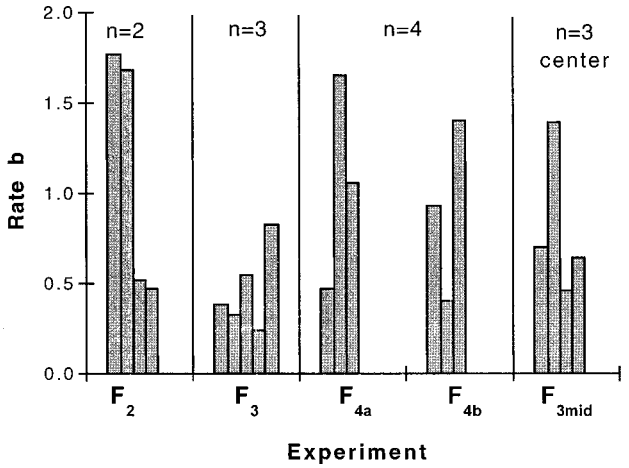

FIG. 8. Rate of adaptation b. Each bar represents the estimate of the exponential rate of adaptation (in units of run^{-1}) for one subject.

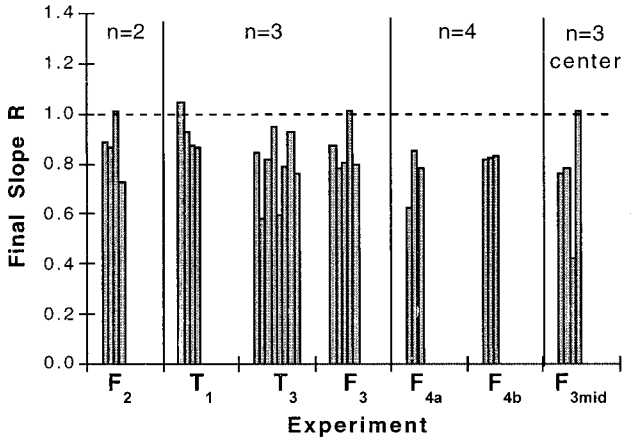

FIG. 9. Estimate of slope at end of experiment after retraining with normal cues. Each bar represents the final estimate of k at the end of the experiment for one subject. The solid error bar shows the initial estimate of slope for that subject (as shown in Fig. 4). The dashed line is at 1.0, the optimal slope for normal-cue runs.

The three experiments in question (in experiments F_{3mid}, F_{4a}, and F_{4b}) used supernormal transformations with the smallest values of k_{opt} and the greatest change in perception from normal. Thus, any supernormal training effects would be greatest in these experiments. Training effects can only explain the tendency for the initial slope S to be less than one if it is assumed that training carries over from session to session, a hypothesis that was not evident when examining the results across sessions. In any case, a one-way ANOVA failed to find any statistically significant differences between the values of normalized asymptote in the different experiments [$F(6,1)=2.28$, $p>0.005$], further implying that intersubject variability is the likely explanation for the smaller-than-average slope values in experiments F_{3mid}, F_{4a}, and F_{4b}. Thus, intersubject variability is the most parsimonious explanation for the tendency for both initial slope and normalized asymptote to be smaller in experiments F_{3mid}, F_{4a}, and F_{4b} than in other experiments. Since there is no statistically significant dependence of normalized asymptote on experiment, the statistical variability in absolute asymptote A can be accounted for (at least in part) by differences in the best-fit slope k_{opt}.

From examining Fig. 7, it is also clear that the best-fit slope in each experiment is a relatively good predictor for the asymptote. The value of the normalized asymptote is close to 1.0 for most experiments. The normalized asymptote averaged across all subjects in all seven experiments equals 0.99, further showing that the best-fit slope in each experiment is, on average, equal to the asymptotic value of $k(r)$.

C. Rate of adaptation

The rate at which adaptation occurs is quite rapid, as evidenced by the data shown in Figs. 3 and 4. This observation was further refined by assuming that the curves plotted in Fig. 4 changed exponentially (as a function of run) from their initial values S (found in Sec. II A) towards their asymptotic values A (found in Sec. II B) and estimating the decay value of the exponential. For each experiment, $k(r)$ was thus assumed to vary as

$$k(r)=A+(S-A)e^{-b(r-2)}, \tag{4}$$

where A is the asymptote, S is the initial slope, r is the run number, and b is the rate of adaptation (in units of run^{-1}). With this equation, the slope in the second run equals the initial value of S. As r increases, $k(r)$ approaches A asymptotically.

Estimates of the adaptation rate b were found for each subject in each experiment by finding the value of b which minimized the mean-square error between the estimate [given by Eq. (4)] and the actual values of $k(r)$ which are plotted in Fig. 4.[2] These estimates are shown in Fig. 8 for the feedback experiments.

It is clear from Fig. 8 that estimates of rate show great intersubject variability. Values range from roughly 0.3 to 1.8. No systematic dependence of rate on experiment or on transformation is evident in the data. A one-way ANOVA on b confirmed this observation, showing no statistical dependence of b on experiment [$F(4,1)=1.19$, $p>0.005$]. The average value of b (across the five experiments) equals 0.84 run^{-1}. In other words, on average, by the sixth altered-cue test run ($r=8$), the slope has changed by 99% of the total change expected after infinite training [from Eq. (4)].

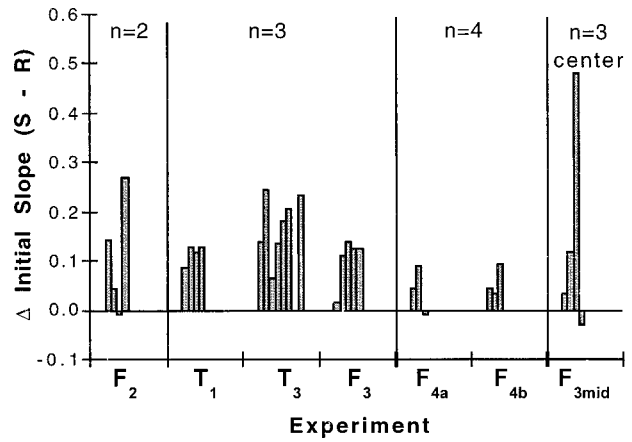

FIG. 10. Difference between initial and final slope (S-R). Each bar plots the difference between the initial slope estimate and the final slope estimate.

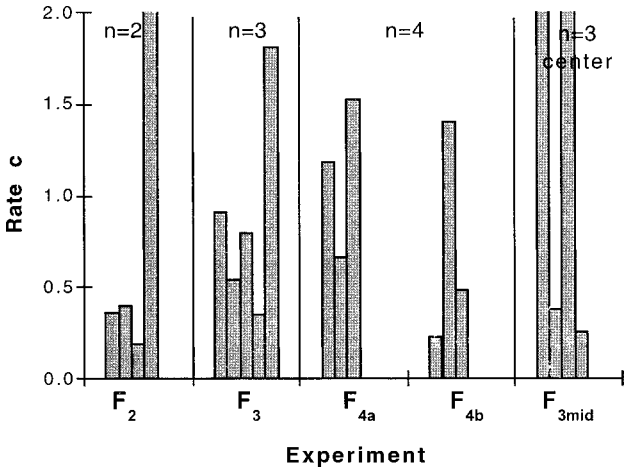

FIG. 11. Estimates of c, rate of adaptation back to normal cues. Each bar represents the estimate of the exponential rate of adaptation (in units of run^{-1}) for one subject.

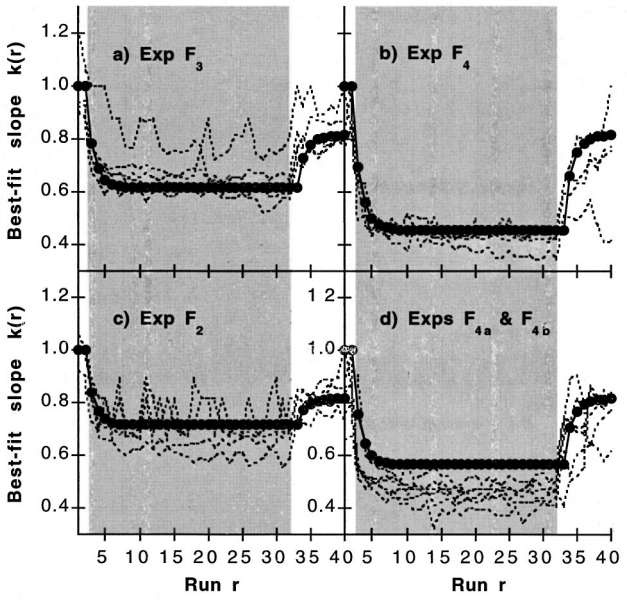

FIG. 12. Predictions of $k(r)$ for each experiment. Dashed lines replot individual subject data, while predictions are given by filled circles and solid lines.

D. Final slope

The final values of $k(r)$ were compared across all experiments to determine whether subject performance returned to normal by the end of the experiment (after retraining with normal cues). The final slope R was estimated as the value of $k(10)$ for the training experiments and $k(40)$ for the feedback experiments. These values are plotted in Fig. 9.

In general, values of the final slope are slightly less than one. In fact, the average value of R across all experiments equals 0.82, which is less than 0.94, the average value of starting slope S. This is shown explicitly in Fig. 10, which plots the difference between initial and final slope estimates for each subject. This difference is generally positive, indicating that subjects have not returned to normal performance after retraining with normal cues. Of most interest, there is no difference between the results of experiments F_{4a} and F_{4b}, despite the fact that subjects in experiment F_{4b} were trained with an inverse transformation for four runs prior to returning to normal cues. One-way ANOVAs showed that neither final slope R [$F(6,1)=0.4211$, $p>0.005$] nor the difference between initial and final slopes $(S\text{-}R)$ [$F(6,1)=0.711$, $p>0.005$] were statistically dependent on experiment. However, initial slope was statistically greater than final slope according to a paired t test [$t(56)=3.756$, $p<0.005$].

It is likely that with sufficient time, subjects would readapt back to their original state, and the values of R would approach the starting slope values of S. However, the rate of such a change must be very slow relative to the rate of adaptation to supernormal cues. After eight runs of altered cues, most subjects had neared their asymptotic levels of performance; when returning to normal cues, performance was significantly different from performance prior to exposure to the altered cues. While this difference is statistically significant, the practical impact of this difference is relatively small. For instance, by the end of the readaptation period, the average difference in the mean response for a source at 10 degrees azimuth is only 1.2 degrees, a change within the average standard deviation in response for a source at that location.

E. Rate of readaptation

Readaptation to normal cues takes place during runs 33–40 for the feedback experiments. Since the exposure to the inverse transformation in experiment F_{4b} had no discernible effect on the slope estimates shown in Fig. 4, all five of these experiments were treated identically in trying to quantify how performance changed back towards normal at the end of the experiment.

As with the adaptation period (runs 3–32), the slope k during the readaptation period was fit by an exponential curve given by

$$k(r)=R+(A-R)e^{-e(r-32)}, \tag{5}$$

where r is the run number. The final slope R was determined as described in Sec. II D, while the initial value (in run 32) was determined by the processing described in Sec. II B. Estimates of the rate c were found using the same algorithm described in Sec. II C.

Estimates of c are shown in Fig. 11. There is even more intersubject variability evident in these estimates than was seen in the estimates of b (see Fig. 8). In part, this is due to the fact that the estimates of c depend directly on the estimates of R. Estimates of R depend on only one value of $k(r)$ and are therefore noisier than are estimates of A, which were derived by averaging three values of $k(r)$. In addition, performance had clearly stabilized for all subjects by run 32 during the adaptation period, so that estimates of A will be relatively good predictors of the actual final asymptote. It is less evident that performance during the readaptation period had stabilized by the 40th run. If the actual rate of readaptation is relatively slow (and performance had not stabilized by the end of the experiment), then estimates of R will be less than the final asymptote, and estimates of rate will be larger than their actual values. In a number of cases, estimates of R are less than many other values of k in runs 33–39. When

this occurs, estimates of c will be extremely large. However, on the whole the estimates of c shown in Fig. 11 are roughly equivalent to the estimates of b shown in Fig. 8. The average value of b, the rate of adaptation, equaled 0.84 run^{-1}, while the average value of c, the rate of readaptation, equaled 0.94 run^{-1}. A paired t test found no statistical difference between b and c [$t(28)=0.44$, $p>0.005$]. In addition, ANOVA analysis showed that there was no statistical dependence of c on experiment [$F(4,1)=0.08$, $p>0.005$].

F. Predictions of $k(r)$

While there is large intersubject variability in all of the parameters determined in the previous sections, the average values of adaptation rate, starting and ending slope, and normalized asymptote appear to summarize results of all experiments.

Equations (4) and (5) were used to predict $k(r)$ for the feedback experiments by setting $S=1.0$, the optimal initial slope; $A=k_{\text{opt}}$, the optimal slope during the adaptation period; $R=0.82$, the average final slope across the five experiments; and b and c set equal to 0.84 (the average value of b across the five experiments). As such, the predictions should show how a typical, idealized subject adapts over time.

Figure 12 plots the predictions of $k(r)$ for each experiment (solid lines and filled circles). Individual subject data from each experiment (repeated from Fig. 4) is shown in the same figure (dashed lines) for direct comparison.

On average, the predicted curves are quite close to the average results for each experiment. While the predictions cannot capture the large intersubject variability in the data, the fit is quite reasonable. The predictions lie above the actual subject data for experiments F_{4a} and F_{4b}; however, for all other experiments, the predictions fall well within the range of results seen across subjects in the experiments. With only two free parameters (R, the final slope asymptote, and b, the rate of adaptation and readaptation), results from 31 subjects are well summarized.

III. DISCUSSION

Subjects adapt to changes in auditory localization cues; however, there are limits to the adaptation they exhibit. In the current experiments, auditory cues were transformed using a nonlinear transformation; however, subjects adapted to a linear approximation of the transformation. The final slope relating mean response to normal-cue position is roughly equal to the slope of the line which best approximates the transformation employed. This result implies that there may be limits on the plasticity of human subjects in interpreting auditory localization cues. In particular, subjects may be able to accommodate only linear transformations of cues, rather than being able to adapt to arbitrarily complex remappings.

An alternative explanation is that the nonlinearities in the remappings used in the current experiments are not sufficient to cause subjects to adapt to the exact shape of the transformation. Under this hypothesis, subjects may be capable of adapting to nonlinear cue transformations, but only if the nonlinearities in the cue remapping are extreme. If adapting to a simple approximation of the remapping removes most of the error in subject responses, then there may not be sufficient impetus for subjects to adapt to the more complex remapping.

If subjects cannot adapt to nonlinear transformations at all, there are fundamental implications about the way in which subjects interpret auditory localization cues. In addition, similar fundamental limitations may affect sensorimotor rearrangement in other sensory modalities [e.g., possible constraints on visual-motor rearrangement are discussed in Bedford (1989, 1993); recent experiments by Schloerb (1997) have shown that adaptation to interpupillary distance are consistent with this type of constraint as well]. It is interesting to note that subjects, on average, adapted to the best-fit linear approximation of the nonlinear cue transformations used in the current experiments (although some systematic errors in localization judgments, due to the nonlinearity of the employed transformations, remained). In most previous studies of auditory adaptation, subjects appeared to adapt only partially to sensory rearrangements (e.g., see Freedman and Wilson, 1967; Freedman and Gardos, 1965; Freedman and Stampfer, 1964a, 1964b; Freedman *et al.*, 1967; Freedman and Zacks, 1964; Held, 1955; Kalil and Freedman, 1967; Lackner, 1974; Mikaelian, 1974; Mikaelian and Russotti, 1972). This apparent failure to adapt completely may be the result of an inability to adapt perfectly to the type of transformation employed.

In any case, for the current experiments, the single value of the slope $k(r)$ (relating physical cue to mean response) summarizes the adaptive state of the subject during run r. Subject adaptation is exhibited by exponential changes in slope $k(r)$ from a ''normal'' value of 1.0 at the beginning of the experiment towards an asymptotic value roughly equal to the best-fit slope (assuming that mean response was constrained to be proportional to the normal location of the physical stimuli). At the end of the experiment, the slope changes back towards the nominal value of 1.0, but appears to asymptote to a level less than the normal value (or perhaps to change extremely slowly back toward the value of 1.0).

While there is large intersubject variability, a simple exponential model of the changes in $k(r)$ with run r was able to fit the data across all the experiments relatively well. In this model, subjects begin with $k=1$. As training proceeds, k changes exponentially towards the best-fit slope for the transformation used in the experiment with an estimated rate of 0.84 run^{-1}. At the end of the experiment, k changes exponentially toward an asymptotic value near 0.82 at roughly the same rate of 0.84 run^{-1}.[3] Two free parameters, the rate of adaptation (assumed equal to the rate of readaptation) and the final asymptote were used to fit data for five separate experiments.

ACKNOWLEDGMENTS

This work was mainly supported by AFOSR Grant Nos. 90-200, 93NL387, and 96NL145. Supplementary support was received from Navy Grant No. N61339-93-C-0047. Portions of this work were presented at the 127th (June, 1994) meeting of the Acoustical Society of America.

[1]This approach to dealing with the edges of the response range is not perfect. In particular, subjects will only have a mean response equal to the most extreme response if they *always* respond with that extreme value. In practice, subjects always show some variability in their responses, so that the mean response for all sources (even those whose actual mean perceived position is outside the range of responses) will never equal either of the most extreme response values. By setting the predictions exactly equal to the extreme response values, there will be a tendency for the least-square error fits to underestimate slope $k(r)$ and overestimate transformation strength $m(r)$. However, this method of processing the data is the most tractable, consistent method for estimating all response values.

[2]Rates were not found for subjects in experiments T_1 and T_3. In these experiments, rate will not be directly comparable to the rates for the remaining experiments due to differences in the experimental methods. In experiments T_1 and T_3, active sensorimotor training occurs between runs, while in experiments F_3, F_{3mid}, F_2, F_{4a}, and F_{4b} training (via correct answer feedback) occurs during each run. Thus, both the absolute time between runs and the amount of training occurring from run to run are not equivalent in the training experiments and the feedback experiments.

[3]An alternative fit to the data in the readaptation period could be made by assuming that performance asymptotes back towards one. With this assumption, the rate of readaptation would be an order of magnitude slower than the rate of adaptation.

Bedford, F. L. (**1989**). ''Constraints on learning new mappings between perceptual dimensions,'' J. Exp. Psychol. **15**, 232–248.

Bedford, F. L. (**1993**). ''Perceptual and cognitive spatial learning,'' J. Exp. Psychol. **19**, 7–530.

Durlach, N. I., Shinn-Cunningham, B. G., and Held, R. M. (**1993**). ''Supernormal auditory localization. I. General background,'' Presence **2**, 89–103.

Freedman, S. J., and Gardos, G. (**1965**). ''Compensation for auditory rearrangement and transfer to hand-eye coordination,'' unpublished manuscript.

Freedman, S. J., and Stampfer, K. (**1964a**). ''Changes in auditory localization with displaced ears,'' Paper presented at the Psychonomic Society, Niagara Falls, Ontario.

Freedman, S. J., and Stampfer, K. (**1964b**). ''The effects of displaced ears on auditory localization,'' AFOSR Technical Report 64-0938.

Freedman, S. F., and Wilson, L. (**1967**). ''Compensation for auditory rearrangement following exposure to auditory-tactile discordance,'' Perceptual and Motor Skills **25**, 961–966.

Freedman, S. J., and Zacks, J. L. (**1964**). ''Effects of active and passive movement upon auditory function during prolonged atypical stimulation,'' Perceptual and Motor Skills **18**, 361–366.

Freedman, S. J., Wilson, L., and Rekosh, J. H. (**1967**). ''Compensation for auditory rearrangement in hand-ear coordination,'' Perceptual and Motor Skills **24**, 1207–1210.

Held, R. M. (**1955**). ''Shifts in binaural localization after prolonged exposure to atypical combinations of stimuli,'' Am. J. Psychol. **68**, 526–548.

Kalil, R., and Freedman, S. J. (**1967**). ''Compensation for auditory rearrangement in the absence of observer movement,'' Perceptual and Motor Skills **24**, 475–478.

Lackner, J. R. (**1974**). ''Influence of visual rearrangement and visual motion on sound localization,'' Neuropsychologica **12**, 291–293.

Mikaelian, H. H. (**1974**). ''Adaptation to displaced hearing: a nonproprioceptive change,'' J. Exp. Psychol. **103**, 326–330.

Mikaelian, H. H., and Russotti, J. S. (**1972**). ''Lack of bilateral generalization of adaptation to auditory rearrangement,'' Technical Report 715, Naval Submarine Medical Research Laboratory.

Schloerb, D. (**1997**). ''Adaptation to perceived depth related to changes of the effect interpupillary distance in computer-graphic stereoscopic displays,'' Doctoral dissertation, Department of Mechanical Engineering, Massachusetts Institute of Technology, Cambridge, MA.

Shinn-Cunningham, B. G. (**1998**) ''Adapting to remapped auditory localization cues: A decision-theory model,'' Perception and Psychophysics (under review).

Shinn-Cunningham, B. G., Durlach, N. I., and Held, R. M. (**1998**). ''Adapting to supernormal auditory localization cues. I. Bias and resolution,'' J. Acoust. Soc. Am. **103**, 3656–3666.

Wenzel, E. M. (**1992**). ''Issues in the development of virtual acoustic displays,'' Presence **1**, 80–107.

Wightman, F. L., and Kistler, D. J. (**1989**). ''Headphone simulation of free-field listening. I. Stimulus synthesis,'' J. Acoust. Soc. Am. **85**, 858–867.

Complementarity and synergy in bimodal speech: Auditory, visual, and audio-visual identification of French oral vowels in noise

Jordi Robert-Ribes,[a] Jean-Luc Schwartz,[b] Tahar Lallouache,[b] and Pierre Escudier[b]
Institut de la Communication Parlée CNRS UPRESA 5009/INPG-U. Stendhal ICP, INPG, 46 Av. Félix-Viallet, 38031 Grenoble Cedex 1, France

(Received 31 July 1996; revised 7 January 1998; accepted 24 February 1998)

The efficacy of audio-visual interactions in speech perception comes from two kinds of factors. First, at the *information* level, there is some ''*complementarity*'' of audition and vision: It seems that some speech features, mainly concerned with manner of articulation, are best transmitted by the audio channel, while some other features, mostly describing place of articulation, are best transmitted by the video channel. Second, at the *information processing* level, there is some ''*synergy*'' between audition and vision: The audio-visual global identification scores in a number of different tasks involving acoustic noise are generally greater than both the auditory-alone and the visual-alone scores. However, these two properties have been generally demonstrated until now in rather global terms. In the present work, audio-visual interactions at the *feature* level are studied for French oral vowels which contrast three series, namely front unrounded, front rounded, and back rounded vowels. A set of experiments on the auditory, visual, and audio-visual identification of vowels embedded in various amounts of noise demonstrate that complementarity and synergy in bimodal speech appear to hold for a bundle of *individual* phonetic features describing place contrasts in oral vowels. At the information level (complementarity), in the audio channel the height feature is the most robust, backness the second most robust one, and rounding the least, while in the video channel rounding is better than height, and backness is almost invisible. At the information processing (synergy) level, transmitted information scores show that all individual features are better transmitted with the ear and the eye together than with each sensor individually. © *1998 Acoustical Society of America.* [S0001-4966(98)01806-2]

PACS numbers: 43.71.Ma, 43.71.Es, 43.71.Gv [WS]

INTRODUCTION

Understanding and modeling the sensor fusion problem in audio-visual speech perception and automatic recognition is becoming a major challenge for speech research, as demonstrated by the increasing number of publications, workshops, and specialized books (see, e.g., Stork and Hennecke, 1996; Campbell *et al.*, 1998). Bimodal interactions tell us a lot about the representation and processing of speech in the human brain, and technological or social spin-offs related to the identification of noisy (see Erber, 1975; MacLeod and Summerfield, 1987; Benoît *et al.*, 1994) or incomplete speech (see Grant *et al.*, 1985; Breeuwer and Plomp, 1986; for a review see Summerfield, 1985) are many.

A. Complementarity and synergy in bimodal speech

If we consider the dichotomy between information and information processing proposed by Massaro (1987, 1989), a fascinating characteristic of the bimodal nature of speech is its efficacy at both levels. Efficacy in *information content* is related to what is generally called the ''*complementarity*'' of audition and vision for speech perception. Indeed, it seems that some speech features, mainly concerned with manner of articulation, are best transmitted by the audio channel, while some other features, mostly describing place of articulation, are best transmitted by the video channel. For instance, the voicing feature (e.g., [p] vs [b]) is best transmitted acoustically and is almost invisible. On the other hand, the place contrast [b] vs [g] is highly visible but the auditory perception is easily disrupted by noise (Summerfield, 1987). This complementarity has been known as Vision-Place Audition-Mode (VPAM, see McGurk and MacDonald, 1976). The complementarity between vision and audition has been explained by the fact that the visible articulators are rather related to high frequencies in the acoustic spectrum, and therefore are more easily disrupted by acoustic noise (Miller and Nicely, 1955; Summerfield *et al.*, 1989).

Efficacy in *information processing* is related to a well-known property of the speech identification system, namely that the audio-visual global identification scores in a number of different tasks involving acoustic noise are generally greater than both the auditory-alone or the visual-alone scores (Erber, 1975; Benoît *et al.*, 1994): We call this property ''*synergy*'' of the auditory and visual channels.

However, these two properties have been demonstrated until now in rather global terms. In what concerns complementarity, it is conceived, as we have said previously, as a kind of vision-place auditory-mode complementarity, and a systematic description of the *compared* audibility and visibil-

[a]Also at CSIRO Mathematical and Information Sciences, Private Bag 17, North Ryde, NSW 2113, Australia, Electronic mail: jordi.robert-ribes@cmis.CSIRO.AU
[b]Electronic mail: (schwartz, lallouache, escudier)@icp.inpg.fr

ity of individual phonetic features is not available (except perhaps in the rather global portrait by Summerfield, 1987). In what concerns synergy, studies involving noisy or incomplete speech either deal with global identification scores at the sentence or word levels (see Erber, 1975; Benoît *et al.*, 1994), or with a single phonetic feature (see Breeuwer and Plomp, 1986, for a study of the voicing feature; Summerfield, 1979; Massaro and Cohen, 1983, for a study of the place contrast in voiced plosives; Cohen and Massaro, 1995, for a study of the [i]–[u] contrast) but it is not known if synergy holds for each separate feature when a *bundle* of features is involved simultaneously.

B. Audio-visual vowel perception

The present paper aims at studying the complementarity and synergy of bimodal speech at the feature level, for oral vowels. Curiously enough, while several studies have been concerned with the visual perception of vowels, there is no systematic work on the comparison of auditory and visual identification of noisy vowels. The following study addresses this point with French vowels. The French vowel system provides the opportunity to contrast three series, namely front unrounded, front rounded, and back rounded vowels. These three phonetic features have a number of acoustic/auditory and optic/visual correlates.

1. Acoustic-auditory correlates

In acoustic terms, it is well-known that the open–close dimension is mainly correlated with $F1$, while the front–back and rounded–unrounded dimensions are mainly correlated with $F2$ (see, e.g., Jakobson *et al.*, 1952), the [i] vs [y] contrast being specifically related to $F3$ (Schwartz *et al.*, 1993). In auditory terms, it is commonly accepted that the perceptual vowel space has two main dimensions, respectively correlated with $F1$ and $F2$ (Plomp, 1975) or possibly $F'2$ (Carlson *et al.*, 1975), $F3$ being a potential candidate for a third dimension, eventually linked to the $F2-F3$ distance (see, e.g., Lonchamp, 1981; Syrdal, 1985).

This description has two consequences. First, the open–close dimension, rather related to $F1$, is likely to be both better represented in auditory distances, because of the larger intensity of $F1$ in the vowel spectrum (Lindblom, 1986), and more resistant to noise, the more so since the critical-band effect results in increasing the masking power of white noise in the high-frequency domain (Zwicker and Feldtkeller, 1969). Second, the rounding and front–back dimensions are likely to be somehow merged in the auditory domain. This is clearly demonstrated in a study by Lisker and Rossi (1992). In this study, 22 French-speaking speech researchers had to determine the rounding category of 18 isolated vowels by sound alone, sight alone or both sound and sight. Their work show that the judgement by sound alone is quite difficult, particularly in the acoustic region between [y] and [u]. Unrounded vowels [ɯ] and [ɨ] are rather perceived as rounded, which confirms the difficulty to separate by the ear the rounding and front–back dimensions.

2. Optic-visual correlates

The geometry of lip contrasts has been extensively studied. Abry and Boë (1980, 1986) studied the geometrical correlates of the rounding contrast in French and showed the discriminating power of the so-called parameter A measuring the interolabial width (see data on other languages by Linker, 1982; Zerling, 1992; Van Son *et al.*, 1994). Benoît *et al.* (1992) provided a descriptive analysis of the labial geometry of French, taking into account the coarticulatory effects of vowels on consonants and vice versa. This led to the definition of a set of French ''visemes,'' showing that unrounded vowels have a roughly constant interolabial width (A), the interolabial height (B) being a good correlate of the open–close dimension, while for rounded vowels, interolabial width A was systematically lower than for their unrounded counterparts (which confirms the data by Abry and Boë) but A and B increase together from close to open vowels.

In perceptual terms, two studies on the visual identification of French vowels by normal subjects (Mourand-Dornier, 1980) and hearing-impaired subjects (Gentil, 1981) lead through multidimensional analysis to a two-dimensional perceptual space (Tseva, 1989) where [i], [a], and [y] are situated at the extremes of a roughly triangular pattern. The role of the basic front parameters, namely interolabial width (A), height (B), and area (S) has been demonstrated for the perception of English (Jackson *et al.*, 1976; Plant, 1980; Montgomery and Jackson, 1983) and French vowels (Cathiard, 1994), while profile parameters (lip protrusion) may reveal a surprising efficiency for the visual perception of rounding ([i] vs [y]) in French (Cathiard *et al.*, 1992). The previously mentioned study by Lisker and Rossi (1992) shows that the identification of rounding contrasts by the eye is much easier than by the ear, although not perfect in the region of large opening. All this shows that the open–close and rounding contrasts provide the basic dimensions of the visual vowel space, while the front–back contrast is almost invisible.

3. Audio-visual complementarity

The audio-visual complementarity in the perception of French vowels has been considered by Benoît *et al.* (1994). Their study dealt with /VCVCVz/ logatoms where V was one of [a i y] and C was one of [b v z ʒ ʁ l]. Their stimuli were presented auditorily alone at several noise levels (with signal-to-noise ratios ranging from 0 to -24 dB) or visually alone. The three vowels were chosen because they are the extrema of the labial movement in French. Their subjects had to identify the vowel and the consonant. The authors compared the identification of the three vowels independently of the consonant context. The auditory stimuli [a] were better identified than [i] which were better identified than [y]. On the other hand, the visual stimuli [y] were better identified than [a] which were better identified than [i]. Some complementarity between auditory and visual stimuli is thus found: The best vowel in the visual channel is the worst in the auditory channel. However, this work does not inform us on the identification of minimal pairs such as [i] vs [e] or [y] vs [u].

The research presented in this paper deals with a systematic study of the auditory, visual and audio-visual perception of French oral vowels embedded in various levels of acoustic white noise. In Sec. I we describe the acoustic and optic stimuli. In Sec. II, we report the results of the identification tests of these stimuli. The discussion in Sec. III enables us to determine if the efficacy of bimodal speech, both at the information (complementarity) and at the information processing (synergy) levels holds at the fine-grain level of individual phonetic features for vowels.

I. ACOUSTIC AND OPTIC STIMULI

A. Stimulus acquisition

Each of the 10 French oral vowels [i e ε y ø œ u o ɔ a] was pronounced 34 times in isolation by a single speaker in a single recording session. The vowel order was random. The speaker was asked to pronounce sustained vowels, so that the duration of each stimulus was at least 900 ms. The corpus was recorded with the ICP ''Video-Speech Workstation'' (Lallouache, 1990) which allows for the acquisition of synchronized sounds and images. The audio signal was sampled at 16 kHz, while the video signal consisted in 50 images per second. The speaker's lips were made up in blue, so that a chroma-key process directly connected to the RGB output of the camera could turn the lips to black. This procedure allows an easy automatic detection process of the inner and outer contours of the lips.

From each 900-ms stimulus, three 200-ms stimuli were extracted, respectively, 40 ms, 240 ms, and 440 ms after the stimulus beginning, automatically detected by the thresholding of acoustic energy. The reason for this procedure was to obtain a large corpus (specially for statistical analyses and automatic-recognition experiments) while keeping the recording charge at a reasonable level (the recording of a single utterance requires a special procedure for ensuring a perfect audio-visual synchronization, see Lallouache, 1990). A number of statistical analyses have been performed to verify that the three stimuli extracted from a single 900-ms utterance where indeed different: Their acoustic and optic variations within a 900-ms utterance are comparable to those of 200-ms stimuli extracted from different 900-ms utterances (Robert-Ribes, 1995).

Thus we obtained $3\times34=102$ ''realizations'' of each vowel, and we kept only the first 100 for further analyses, hence altogether 1000 200-ms audio-visual items, namely 100 per class with 10 vowel classes.

B. Acoustic stimuli

For each 200-ms acoustic occurrence, a spectrum was computed by FFT on the first 64 ms. The first three formants were extracted by LPC, and Fig. 1 shows that they provide classical patterns for French vowels. Then, noisy acoustic signals were obtained by adding various amounts of white gaussian noise on the temporal stimuli, with eight signal-to-noise ratios (SNR), namely, no noise, 24 dB, 12 dB, 6 dB, 0 dB, −6 dB, −12 dB, and −18 dB. For each stimulus, the SNR was defined as the ratio between the energy of the stimulus and the energy of the added white noise, which means that rms amplitudes of all stimuli were equalized prior to mixing with a given level of noise.

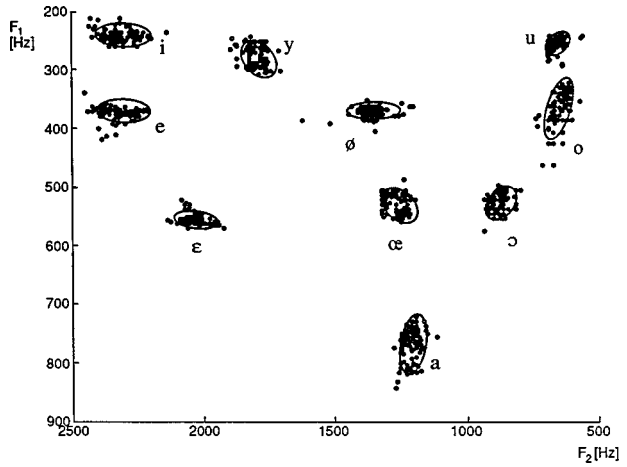

FIG. 1. Formant values of the 1000 acoustic spectra.

To have a rough idea of the degradation imposed by the acoustic noise on our stimuli, we performed a linear Principal Component Analysis (PCA) on a corpus grouping stimuli at four SNRs, namely, no noise, SNR=24, 12, and 0 dB. At the input of this analysis, each spectrum was characterized by the dB values in 20 1-Bark wide channels between 0 and 5 kHz, with Bark defined by the formula proposed by Schroeder *et al.* (1979), namely,

$$z(\text{Bark}) = 7\ \text{Arg sh}\left(\frac{F(\text{Hz})}{650}\right).$$

The principal axes of the PCA were determined on one-half of the total corpus, namely, 2000 20-D vectors (50 occurrences per class and SNR, balanced over the three positions of an occurrence within a 900-ms utterance; 10 classes and 4 SNRs). The first four axes explain 90% of the total variance. Figure 2 displays the representation of the stimuli in the second half of the corpus, in the first projection plane (made of the first two principal axes, which, respectively, account for 61% and 19% of the total variance) for increasing levels of noise. We observe a progressive shrinking of the vowel triangle, the open–close dimension being, as expected, the most robust in noise.

C. Optic stimuli

For each of the 1000 200-ms stimuli, the first video image was processed by the chroma-key system in order to produce faces with perfectly black lips, on which the system developed by Lallouache (1990) allowed us to extract three basic front geometric parameters, namely, interolabial width (A), height (B), and area (S). In Fig. 3 we display the geometric parameters in the A/B and S/B planes. Figure 3(a) confirms a classical pattern (see, e.g., Abry and Boë, 1986; Benoît *et al.*, 1992): we observe a clear separation between rounded and unrounded vowels mainly based on the A parameter, with a subdivision within each group based on height contrasts which are only partially ''visible.'' For rounded vowels, A and B covary, with two main subgroups

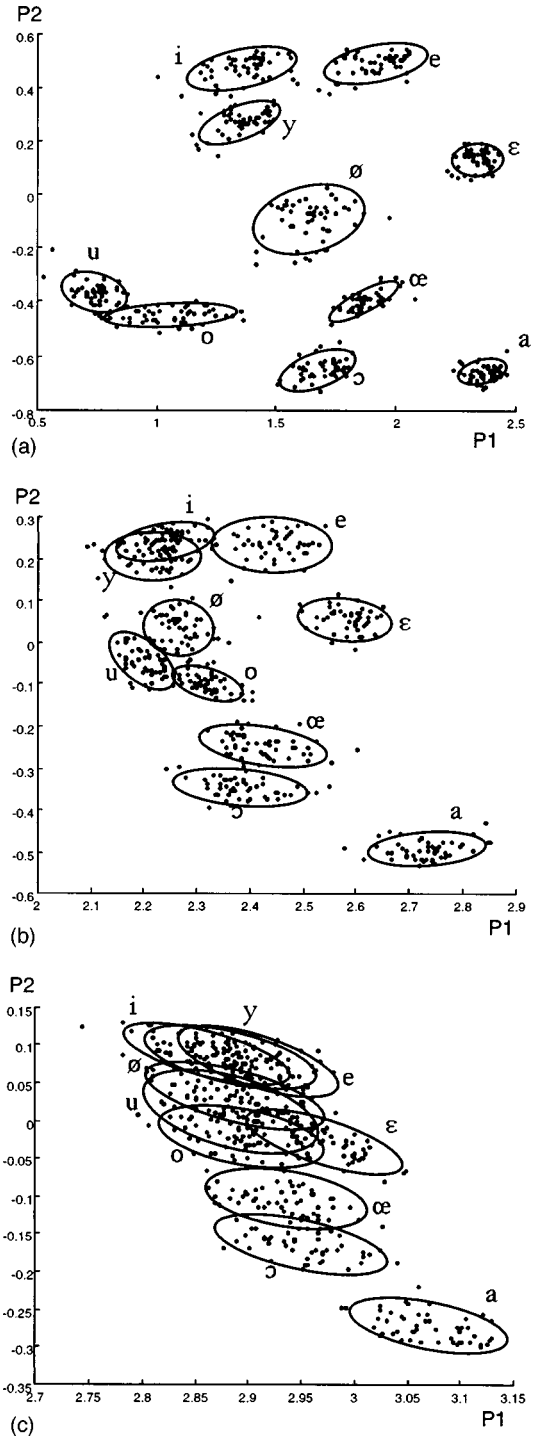

FIG. 2. Projection of the acoustic stimuli on the first projection plane, for various SNRs, namely, (a) no noise, (b) SNR=12 dB, (c) SNR=0 dB.

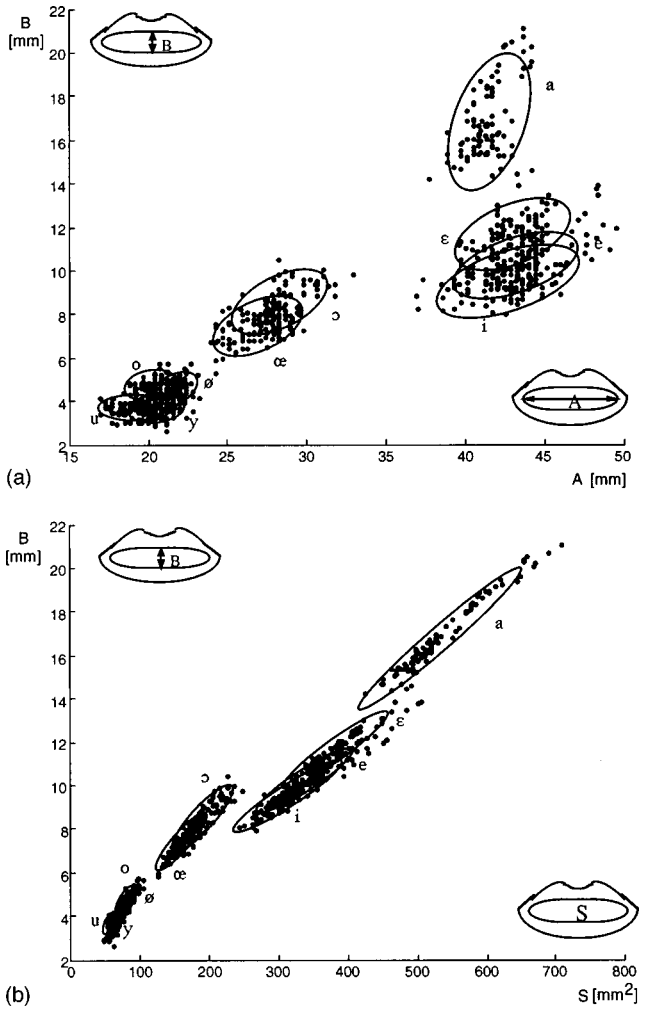

FIG. 3. Representation of the optic stimuli, respectively, (a) in the (A,B) and (b) in the (B,S) planes.

corresponding to mid–low vowels on one hand, high and mid–high vowels on the other. In both subgroups, front–back contrasts are almost invisible (and would be completely blurred by individual variability), which is not a surprise. For unrounded vowels, A is almost constant, and there is a separation between nonlow [i e ε] vowels with a ''spread'' pattern (large A, small B) and the low [a] with an ''open'' pattern (large A and B). Figure 3(b) shows that there is a large correlation between parameters B and S ($r=0.98$). Correlation is even larger if one considers separately rounded and unrounded vowels, with two different slopes corresponding to the two different sets of A values. At last, it is well-known that S is highly correlated to the A times B ($A\times B$) value (Abry and Boë, 1986; Benoît *et al.*, 1992), and we observe such a correlation ($r=0.999$) in our own data with the regression line: $S=0.76\cdot A\times B[\mathrm{mm}^2]$.

II. PERCEPTUAL DATA

We submitted our corpus to an identification experiment, in order to test the perception of vowel phonetic contrasts by ear, by eye, and by ear and eye, under various conditions of noise degradation.

A. Methods

1. Choice of the speech material

We did not test the mid–low versus mid–high contrast (e.g., [ε] vs [e]) since it raises, particularly in the context of isolated fixed-duration vowels, two series of problems. First, the phonemic status of this kind of contrast is questionable, because of phonotactic constraints in French (/ε œ ɔ/ generally exist in close syllables, and /e ø o/ in open syllables). Second, these contrasts, though basically spectral, may be accompanied by temporal co-variations between

longer mid–high and shorter mid–low vowels in production (Delattre, 1959, 1962), if not in perception (Gottfried and Beddor, 1988). Hence we decided to limit the perceptual test to seven vowels: [i e y ø u o a].

We used 10 occurrences for each vowel selected randomly among the 100 occurrences we had at our disposal. Each occurrence consisted in a 200-ms acoustic stimulus and a 5-images optic stimulus, with the first image synchronous with the first acoustic sample. Considering the rather small number of occurrences necessary for the experiment, we decided to select them in 10 different original 900-ms utterances, and always at the same position, that is the ''middle'' one. Hence, acoustic stimuli were extracted from 900-ms signals 240 ms after their beginning, with 10-ms sinusoidal ramps applied at the beginning and the end, to avoid transient clicks. They were superimposed with white acoustic noise at 7 signal-to-noise ratios (SNR), namely, no noise, 12 dB, 6 dB, 0 dB, −6 dB, −12 dB, −18 dB, with SNR being defined as in Sec. I B. Notice that the 24-dB value, cited in the acoustic study in Sec. I B, appeared in preliminary perceptual experiments to provide quite the same performances as the ''no-noise'' condition, hence it was discarded in the final experimental setup.

2. Subjects

Twenty-one French students (17 female and 4 male) without any particular knowledge on audio-visual speech completed the test. The average age was 21.5 years old (min=20, max=28). Their sight was correct or corrected (9/10 or more, in the Monnoyer scale) and an audiogram did not reveal any auditory problem (average loss-threshold higher than −10 dB, from 250 Hz to 8000 Hz). They received extra points for one of their courses for taking part in the experiment.

3. Experimental conditions

The test was comprized of three conditions, namely, audio-visual, visual-alone, and auditory-alone. It is classical to present these conditions according to a counterbalanced design. However, learning may increase quite significantly the scores from one presentation to another when visual speech is involved (Breeuwer and Plomp, 1986), and the effects of learning and experience may vary considerably with time and with individual subjects (see, e.g., Breeuwer and Plomp, 1986; Blamey *et al.*, 1989), which generally leads to very large variability in audio-visual performances (e.g., MacLeod and Summerfield, 1987). Hence, in order to decrease the variability of performances in the audio-visual condition, we decided to limit the role of learning by using a fixed order of presentation, namely audio-visual first, followed by visual and auditory. This choice may have a disadvantage by limiting the effect of learning in the audio-visual condition, and possibly enhancing it in the auditory and visual conditions. Thus we may reduce the advantage of bimodal perception on monomodal conditions. Hence, if our results demonstrate synergy (namely audio-visual scores higher than audio-alone or visual-alone scores), the effect will be slightly underrated by our design. However, the advantage is to keep the variance of audio-visual performances at a reasonably low value. Indeed, we will see in Sec. II C 3 that the inter-individual variance of audio-visual scores is not greater than the variance of auditory scores in our paradigm, which is often not the case in such experiments.

4. Procedure

The audio-visual and auditory-alone conditions were divided into seven sessions. Each session was prepared with noisy auditory stimuli of a given SNR, in the following order: no noise, 12 dB, 6 dB, 0 dB, −6 dB, −12 dB, and −18 dB. The visual-alone condition had only one session since there were no noisy stimuli. Each session was composed by 7 familiarization stimuli (not used for the results) and 70 test stimuli (7 vowels × 10 occurrences). The order of these 70 stimuli was random and different for each subject. Thus for each subject results were obtained from 490 audio-visual stimuli (70 stimuli per SNR, 7 SNRs), 70 visual stimuli, and 490 auditory stimuli. The screen was neutral gray after each stimulus and the subject's response launched the next stimulus. The end of each session was indicated by a message on screen; thus subjects could take a rest between sessions. The whole test for each subject lasted 1 h.

The task was to identify the vowel pronounced by the speaker. The answer was given by the keyboard on which the following labels appeared:

[a], [é], [i], [eu], [u], [o] and [ou].

It was thus a closed-choice task with orthographic labels.

B. Analysis tools

The raw data were confusion matrices for each subject, each condition, and each SNR, from which we derived two kinds of information.

1. Global identification scores

For each SNR we computed global identification scores in percentage corrected for guessing. Supposing all vowels equiprobable, this percentage was calculated using the following formula:

$$\text{Corrected score} = 100 \cdot \frac{\left| \frac{\text{correct responses}}{\text{total responses}} - \frac{1}{\text{number of vowels}} \right|}{1 - \frac{1}{\text{number of vowels}}}.$$

2. Transmitted information scores

Second, we computed the transmitted information for three individual phonetic features: rounding, height, and front–back contrast. This kind of procedure had first been employed by Miller and Nicely (1955) in their study of the robustness of various consonantal features in various kinds of acoustic degradations. In our case, the features are defined in Table I. Rounding and front–back contrasts have two lev-

TABLE I. The specification of phonetic features for each vowel class.

Vowel	Rounding	Backness	Height
i	−	−	+
e	−	−	−
y	+	−	+
ø	+	−	−
u	+	+	+
o	+	+	−
a	?	?	--

els while the height feature has three levels. We suppose that only the height feature is known for vowel [a]. Thus we use neither the stimuli nor the answers corresponding to [a] in the computation for the rounding and the front–back features.

The percentage of transmitted information is defined by (Ventsel, 1973, Chap. 18; Breeuwer and Plomp, 1986):

$$T = 100\,\frac{H(s,r)}{H(s)},$$

with $H(s,r)$ the transmitted information from stimuli (s) to answers (r), and $H(s)$ the existing information in the stimuli. These values are defined by

$$H(s,r) = -\sum_i \sum_j p(s_i,r_j)\log_2\left(\frac{p(s_i)p(r_j)}{p(s_i,r_j)}\right),$$

$$H(s) = -\sum_i p(s_i)\log_2(p(s_i)),$$

with $p(s_i)$ the probability of occurrence of feature s_i in the stimuli, $p(r_j)$ the probability of occurrence of feature r_j in the answers, and $p(s_i,r_j)$ the probability of shared occurrence of feature s_i in the stimuli and feature r_j in the answers. The probability $p(s_i)$ is known:

$$p(s_i) = n_{i.}/n.$$

The probabilities $p(r_j)$ and $p(s_i,r_j)$ are not known but can be estimated by:

$$p(r_j) = n_{.j}/n \quad \text{and} \quad p(s_i,r_j) = n_{ij}/n,$$

with $n_{i.}$ the number of occurrences of stimulus s_i, $n_{.j}$ the number of occurrences of answer r_j, n_{ij} the number of occurrences of stimulus s_i with answer r_j, and n the total number of stimuli. n and $n_{i.}$ values are fixed, $n_{.j}$ and n_{ij} values are provided by the confusion matrices.

C. Results

1. Auditory perception

The confusion matrices for the auditory stimuli averaged over all subjects are shown in Table II. Figure 4(a) shows the global identification scores as a function of SNR. Identification is almost perfect at SNR=12 dB, and quasi-zero at SNR=−18 dB. At this SNR value, although subjects loose all their discriminating ability, they have different response strategies: Most of them provide random responses, but a few others select a given category and use it as a systematic ''garbage'' response.

TABLE II. Confusion matrices averaged over all subjects in the audio conditions.

no added noise

Answer \ Stimulus	a	e	i	ø	y	o	u
a	209	1					
e	1	209					
i			210				
ø				210	2		
y					208		1
o						210	3
u							206

SNR = 12 dB

Answer \ Stimulus	a	e	i	ø	y	o	u
a	208						
e		210		3			
i			210				
ø	1			207			1
y					210		1
o						209	1
u	1					1	207

SNR = -6 dB

Answer \ Stimulus	a	e	i	ø	y	o	u
a	210						1
e		99	1	74	4	53	10
i		3	109	1	86	1	41
ø		83	5	105	6	74	15
y		6	75		91		36
o		17		26		80	12
u		2	20	4	23	2	95

SNR = 6 dB

Answer \ Stimulus	a	e	i	ø	y	o	u
a	210						
e		210		15			
i			204		1		
ø				195	3	5	2
y			6		206		2
o						202	4
u						3	202

SNR = -12 dB

Answer \ Stimulus	a	e	i	ø	y	o	u
a	126	18	23	13	26	10	29
e	12	47	18	51	21	59	31
i	22	21	80	14	65	13	48
ø	31	67	30	72	31	61	24
y	7	12	36	19	43	12	40
o	4	31	5	33	6	47	15
u	8	14	18	8	18	8	23

SNR = 0 dB

Answer \ Stimulus	a	e	i	ø	y	o	u
a	209						
e		196	1	55	4	3	
i		1	155		33		5
ø		13		132		22	10
y			51		163		10
o				23		184	9
u	1		3		10	1	176

SNR = -18 dB

Answer \ Stimulus	a	e	i	ø	y	o	u
a	30	15	16	22	24	16	16
e	48	55	55	51	49	57	54
i	38	45	47	43	45	43	42
ø	45	45	41	46	47	48	47
y	25	21	33	18	22	20	25
o	11	15	12	16	8	19	12
u	13	14	6	14	15	7	14

In general, the confusions are made amongst vowels with the same height, and the vowel [a] is remarkably robust in noise. Thus height perception seems to be more robust than the perception of roundness and backness. Rounding oppositions are the first to be lost ([i] vs [y]; [e] vs [ø]), followed by front–back ones. The transmitted information percentages for height, roundness and backness for the different signal-to-noise ratios are presented in Fig. 4(b). These data indicate that the height feature seems the most robust in noise, followed by the front–back one, the rounding contrast being the poorest. This is also true for each individual subject (see Robert-Ribes, 1995). Statistical analyses confirming this picture will be provided in Sec. III.

2. Visual perception

The confusion matrix for the visual stimuli averaged over all subjects is presented in Table III. The global identification score is 43%. Three perceptive groups are clearly recognised: [a], [e i], and [ø y o u]. Confusions inside each group are many but between groups they are almost nonexistent. The global identification score of these three groups is higher than 75%. Thus taking into account the classical definitions of viseme (Tseva, 1989; Walden *et al.*, 1977) we observe three visemes in our stimuli: ''open'' ([a]), ''spread'' ([e i]), and ''rounded'' ([ø y o u]). Notice that within each visemic group, the pattern of confusions is highly asymmetric, with a strong trend to perceive the spread [i e] group as [e], and the rounded [y ø u o] group as a front, generally nonhigh vowel, namely [ø]. The preference for nonhigh

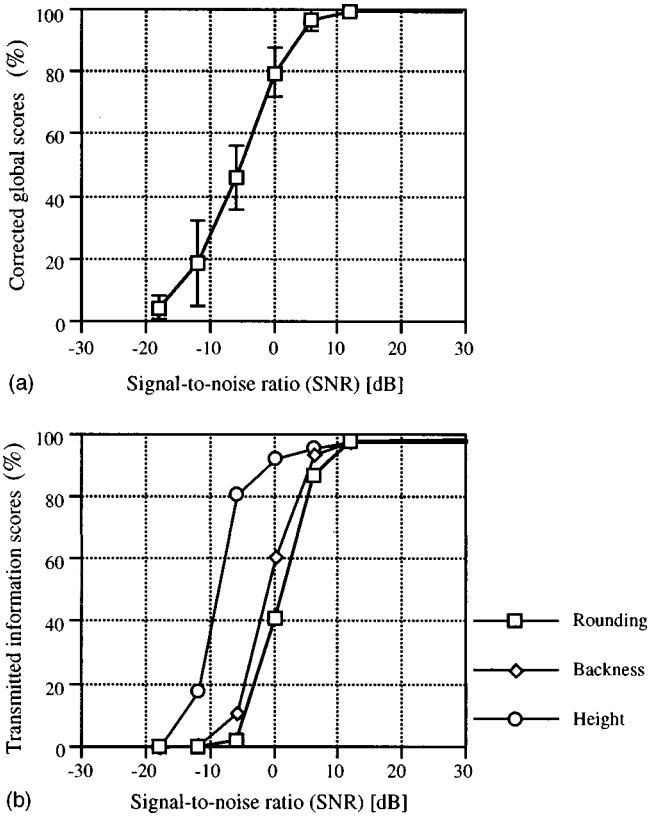

FIG. 4. (a) Global identification scores for auditory vowels (mean and standard deviation within the 21 subjects), and (b) transmitted information in the audio channel for each phonetic feature as a function of SNR.

vowels is probably due to the pronunciation of our stimuli in isolation, which is likely to lead to ''hyperarticulated'' speech (see Lindblom, 1990). Indeed, an examination of Fig. 3(a) shows that the *B*-values for [i] and [e] are around 10 mm, which is rather close to the typical value for a French [e] in various contexts according to the study by Benoît *et al.* (1992), and slightly larger than the typical value for [i]. In the rounded group, the preference for a ''front'' choice is probably rather arbitrary, although quite robust in our data—notice that the choice may be inverse in other studies (see Tseva, 1989)—and the (slight) preference for [ø] rather than [y] probably also comes from hyperarticulation, as the preference for [e] over [i].

The transmitted information percentages are 90% for the rounding feature, 42% for the height feature, and 9% for the backness feature. This trend is the same for each individual subject (Robert-Ribes, 1995).

TABLE III. Confusion matrix averaged over all subjects in the video condition.

	Stimulus						
Answer	a	e	i	ø	y	o	u
a	209						
e		150	140				
i		58	68	2	4	4	2
ø	1	2	2	107	82	76	95
y				64	100	23	73
o				12	3	91	10
u				25	21	16	30

TABLE IV. Confusion matrices averaged over all subjects in the audio-visual conditions.

no added noise

Answer \ Stimulus	a	e	i	ø	y	o	u
a	210						
e		208					
i		2	210				
ø				210			
y					210		
o						210	6
u							204

SNR = 12 dB

Answer \ Stimulus	a	e	i	ø	y	o	u
a	210						
e		210		8			
i			210				
ø				202			
y					210		2
o						210	5
u							203

SNR = -6 dB

Answer \ Stimulus	a	e	i	ø	y	o	u
a	209						
e		203	12	3	1	1	
i		6	196		4		
ø		1		169	12	89	26
y			2	4	165		53
o	1			34	1	118	12
u					27	2	119

SNR = 6 dB

Answer \ Stimulus	a	e	i	ø	y	o	u
a	210						
e		210		4			
i			210				
ø				206			1
y					210		5
o						210	7
u							197

SNR = -12 dB

Answer \ Stimulus	a	e	i	ø	y	o	u
a	209		1				
e		182	62	1	1	1	
i		26	146	1	5	1	3
ø	1	1		157	27	116	58
y			1	21	144	7	96
o		1		20	5	81	10
u				10	28	4	43

SNR = 0 dB

Answer \ Stimulus	a	e	i	ø	y	o	u
a	210						
e		207	5	1			
i			202		2		1
ø		3		193	2	8	4
y			3		197		8
o				14		201	8
u				2	9	1	189

SNR = -18 dB

Answer \ Stimulus	a	e	i	ø	y	o	u
a	207						
e	1	130	116	2	1	1	
i		79	92				1
ø	1	1		86	67	96	75
y			1	84	113	26	90
o				17	5	77	18
u	1		1	21	24	10	26

3. Audio-visual perception

The confusion matrices for the audio-visual stimuli averaged over all subjects are shown in Table IV. In Fig. 5(a) we display the global identification scores compared with those in the audio condition. The standard deviations plotted on this figure illustrate our preliminary comment in Sec. II A 3. Indeed, standard deviations are rather low, and their order of magnitude is similar to the standard deviation of auditory data.

The minimum percentage for the audio-visual stimuli is roughly equal to the percentage for the visual stimuli [41% in the audio-visual condition at SNR$=-18$ dB vs 43% in the visual condition, $\chi^2(1)=0.78$, $p=0.38$; difference not significant]. Hence the audio-visual performance is, at worst, equal to the visual one. Notice, too, that the confusion matrix for the audio-visual stimuli at -18 dB is quite similar to the one for the visual stimuli. This can indicate that at this noise level the audio-visual perception is completely dependent on the visual perception.

Vowel [a] is correctly perceived at all noise levels. Front vowels ([e i]) are correctly perceived for signal-to-noise levels equal or superior to 0 dB. Notice that rounded vowels are not confused with unrounded ones. Altogether, it is clear that the three visemes found in the visual data have an important role in audio-visual perception.

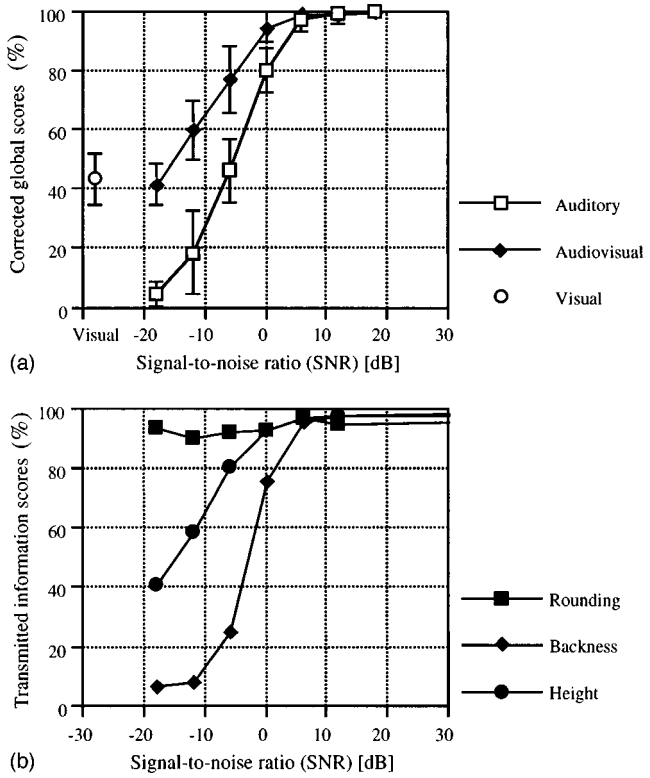

FIG. 5. (a) Global identification scores for audio-visual vowels (mean and standard deviation within the 21 subjects, compared with audio and visual scores), and (b) transmitted information in the audio-visual condition for each phonetic feature as a function of SNR.

The transmitted information percentages for height, roundness and backness for the different signal-to-noise ratios are presented in Fig. 5(b). The transmitted information for rounding is very good (higher than 90%) whatever the noise level. The transmitted information for backness is quickly degraded by noise and is lost at high noise levels (low SNR). The transmitted information for height is degraded with noise but it never decreases below the visually transmitted level. This pattern is the same for each individual subject (Robert-Ribes, 1995).

III. DISCUSSION

The compared auditory, visual, and audio-visual results in terms of global identification scores and transmitted information for the three features studied (rounding, height, and backness) will allow us to demonstrate how the complementarity and synergy of bimodal speech applies to individual features in the perception of oral vowels.

A. Complementarity

1. Analysis of the auditory data

The portrait of Fig. 4(b) indicates a clear hierarchy of the auditory robustness of individual phonetic features in acoustic white noise, namely:

$$\text{height}_A > \text{backness}_A > \text{rounding}_A . \quad (1)$$

To assess the statistical significance of this hierarchy, we performed a number of χ^2-tests on the proportion of correct identification of each feature at each SNR value. This was realized with two restrictions. First, we removed [a] from these statistical analyses. The reason is that this vowel has a very special status in the present work: It is not specified in relation to two of the three features, and it is far from all other concurrent vowels since we have eliminated the mid–low [ɛ œ ɔ] group from our experiment (see Sec. II A 1). By removing it, we wanted to test whether the robustness of the height feature is not only due to the strong robustness of [a], which is clearly the ''star'' at all SNR values above -12 dB in Table II. Second, although the transmitted information tool aims at extracting independent information from a given set of data, there is a risk to attribute to one feature a benefit coming from another one because of the partial interdependence of the rounding and front–back features in French: Indeed, the back vowels [u o] are always rounded, while the unrounded [i e] vowels are always front. Hence we restricted our analysis to the contrast [i e] vs [y ø] for rounding, [y ø] vs [u o] for front–back, and [i y u] vs [e ø o] for height. The results are displayed in Table V. For each SNR value where the identification is neither perfect nor random, that is between -12 dB and $+6$ dB, we assessed the difference between each pair of contrasts in terms of (1) differences in transmitted information, (2) χ^2 values for the difference in proportion of correct identification of each feature, and (3) level of statistical significance of the transmitted information difference with the following conventions: $p > 0.1$ means ''not significant'' (NS), $0.01 \leqslant p < 0.1$ means ''significant'' (*), $0.001 \leqslant p < 0.01$ means ''highly significant'' (**), and $p \leqslant 0.001$ means ''very highly significant'' (***).

The result is clear: The auditory hierarchy is statistically significant, even with the restrictions we have adopted. Indeed, even without [a], height is more robust than rounding at all tested SNRs and more robust than backness between -12 and 0 dB, while backness is more robust than rounding between -6 and 6 dB. In short, we can say that in acoustic white noise, [y ø] are closer to [i e] than to [u o], and more separated from each other than from their neighbors at the same height value.

The interpretation of this pattern in terms of spectral representations and distances is not completely clear. In Fig. 6, we present the results of a pattern recognition experiment in which we applied Gaussian classifiers to the 20-D acoustic spectra defined in Sec. I B. The experiment was performed with the ten vowel classes, including mid–low [ɛ œ ɔ], since there are no ''phonotactic'' constraints to apply to the recognizer. For each of the ten classes, the Gaussian classifier was characterized by its mean vector and covariance matrix, the parameters of which were tuned on a learning subcorpus comprising half the acoustic stimuli at four levels of noise, that is no noise, SNR = 24, 12, and 0 dB. The figure displays the recognition scores on the other half of the acoustic stimuli, degraded at various levels of noise from no noise to SNR = -18 dB. The results were analyzed with the same tools as the perceptual data, that is global recognition scores [Fig. 6(a)] and transmitted information for each phonetic feature [Fig. 6(b)]. The transmitted information scores were computed with the ten vowel classes and the same kind of grid as the one displayed in Table I, but with four height

TABLE V. Statistical assessment of the differences in transmitted information. For each tested condition (audio at +6 dB, audio at 0 dB, audio at −6 dB, audio at −12 dB, and video) and from left to right: transmitted information scores TI for each feature (H for height, B for backness, R for rounding), difference in transmitted information percentages between the first and the second member of each pair of features, corresponding $\chi^2(1)$ value, probability p to obtain this value in the null hypothesis, and level of significance of the transmitted information difference.

		Auditory channel				
	TI(%)	Pair	TI(1)−TI(2)(%)	$\chi^2(1)$	p	
SNR=+6 dB	TI(H)=92.4	H–B	0.03	0.10	0.75	NS
	TI(B)=92.4	B–R	9.5	5.30	0.02	*
	TI(R)=82.9	H–R	9.5	8.79	0.003	**
SNR=+0 dB	TI(H)=86.8	H–B	34.4	63.3	<0.001	***
	TI(B)=52.4	B–R	23.1	26.0	<0.001	***
	TI(R)=29.3	H–R	57.5	183.5	<0.001	***
SNR=−6 dB	TI(H)=69.3	H–B	57.3	217	<0.001	***
	TI(B)=12.0	B–R	11.2	24.3	<0.001	***
	TI(R)=0.8	H–R	68.5	441	<0.001	***
SNR=−12 dB	TI(H)=16.9	H–B	15.6	46.2	<0.001	***
	TI(B)=1.3	B–R	1.1	1.16	0.28	NS
	TI(R)=0.2	H–R	16.7	77.8	<0.001	***
		Visual channel				
	TI(%)	Pair	TI(1)−TI(2)(%)	$\chi^2(1)$	p	
	TI(H)=2.2	H–B	−3.0	0.81	0.37	NS
	TI(B)=5.2	B–R	−85.0	335	<0.001	***
	TI(R)=90.2	H–R	−88.0	404	<0.001	***

levels instead of three, that is high [i y u], mid–high [e ø o], mid–low [ɛ œ ɔ], and low [a].

First we notice that the global scores are degraded with noise in a way comparable with what happens for human subjects [Fig. 4(a)]. Looking at individual features confirms that height is the most robust feature in white noise, and a close examination of the confusion matrix (Table VI) shows that all height distinctions are well preserved up to large levels of noise. However, the front–back and rounding features have more or less the same robustness, with even a slight advantage for rounding, particularly at SNR=0 dB. This pattern was confirmed by another study based on Mahalanobis distances after a linear discriminant analysis (see Robert-Ribes, 1995). We also tested a number of spectral distances between utterances of pairs of vowel classes at each SNR, that is Plomp distance on the 20-D vectors (Plomp, 1970), and Itakura or Itakura-Saito distances (Itakura, 1975): They all confirm a pattern in which height is the winner (that is, produces the greatest distances within minimal pairs in noise), but rounding is slightly better or at least as robust as the front–back feature. The only representation in which the front rounded series is closer to the front unrounded than to the back rounded series is the formant space ($F1$,$F2$) or ($F1$,$F'2$) when formants are expressed in Bark. Indeed, typical $F'2$ values reach 16 Bark for [i], 13 Bark for [y], and 6 Bark for [u], or 15 Bark for [e], 12 Bark for [ø], and 6 Bark for [o] (Mantakas, 1989; Schwartz *et al.*, 1997b). It remains that, though a number of spectral distances have been shown to provide a good *global* match to perceptual distances in the vowel space (see, e.g., Plomp, 1970; Pols, 1975), our study of the shrinking of the perceptual vowel space in acoustic white noise reveals some unexpected limitations of these distances, that will have to be taken into account in the future.

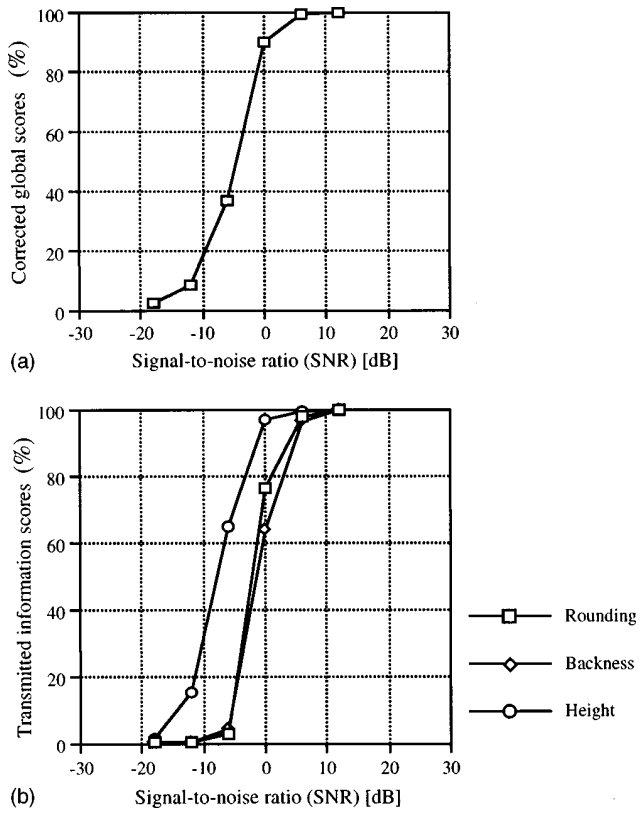

FIG. 6. Results of a recognition experiment performed on the acoustic stimuli of the corpus (see text): (a) Global identification scores, and (b) transmitted information scores for each phonetic feature as a function of SNR.

2. Analysis of the visual data

The hierarchy of transmitted information scores in the visual channel may be summarized by the hierarchy:

TABLE VI. Confusion matrices of the auditory speech recognition experiment.

no added noise — Stimulus

Answer	a	e	i	ø	y	o	u
a	209	1					
e	1	209					
i			210				
ø				210	2		
y					208		1
o						210	3
u							206

SNR = 12 dB — Stimulus

Answer	a	e	i	ø	y	o	u
a	208						
e		210		3			
i			210				
ø	1			207			1
y					210		1
o						209	1
u	1					1	207

SNR = -6 dB — Stimulus

Answer	a	e	i	ø	y	o	u
a	210						1
e		99	1	74	4	53	10
i		3	109	1	86	1	41
ø		83	5	105	6	74	15
y		6	75		91		36
o		17		26		80	12
u		2	20	4	23	2	95

SNR = 6 dB — Stimulus

Answer	a	e	i	ø	y	o	u
a	210						
e		210		15			
i			204		1		
ø				195	3	5	2
y			6		206		2
o						202	4
u						3	202

SNR = -12 dB — Stimulus

Answer	a	e	i	ø	y	o	u
a	126	18	23	13	26	10	29
e	12	47	18	51	21	59	31
i	22	21	80	14	65	13	48
ø	31	67	30	72	31	61	24
y	7	12	36	19	43	12	40
o	4	31	5	33	6	47	15
u	8	14	18	8	18	8	23

SNR = 0 dB — Stimulus

Answer	a	e	i	ø	y	o	u
a	209						
e		196	1	55	4	3	
i		1	155		33		5
ø		13		132		22	10
y			51		163		10
o				23		184	9
u	1		3		10	1	176

SNR = -18 dB — Stimulus

Answer	a	e	i	ø	y	o	u
a	30	15	16	22	24	16	16
e	48	55	55	51	49	57	54
i	38	45	47	43	45	43	42
ø	45	45	41	46	47	48	47
y	25	21	33	18	22	20	25
o	11	15	12	16	8	19	12
u	13	14	6	14	15	7	14

$$\text{rounding}_V > \text{height}_V > \text{backness}_V . \quad (2)$$

However, we display in the bottom of Table V the same kind of statistical analysis as for the auditory channel. It appears that the advantage of height over backness almost disappears when [a] is discarded. This confirms that the eye discriminates only three visemes, namely, open, spread, and rounded, which means a perfect discrimination of rounding, a discrimination of height limited to the contrast between the low [a] and all the other nonlow front unrounded vowels, and almost no discrimination at all of the front–back contrast. This whole pattern is perfectly in line with the geometrical data displayed in Fig. 3.

3. The audio-visual vowel space

From inequations (1) and (2) there emerges a kind of ''perceptual portrait'' of the audio-visual space, which confirms that there is indeed some complementarity of the auditory and visual channels at the feature level. This portrait may help us better understand two important characteristics of vowel systems in human languages. First, it provides a good basis for understanding why vowel inventories make larger use of the height dimension than of the two other ones (Lindblom, 1986) since height emerges as the ''best'' dimension in both sensory modalities. Second, it suggests that the visual input could play some part in the existence of a rounding contrast in the front region of vowel systems (e.g., [i] vs [y]). Indeed, this contrast happens in a significant proportion of languages (Schwartz *et al.*, 1997a), although in a region acoustically crowded. Our data summarized in inequation (1) confirm that the auditory basis is poor, while the visual input could probably help this contrast to ''survive'' in human communication (see Schwartz *et al.*, 1997b, for an introduction of other auditory arguments in this discussion).

B. Synergy

Our results clearly show that the synergy between the auditory and visual channels for the bimodal identification of noisy speech holds for vowels, both in global terms and feature by feature: The performance is always better with two channels than with only one, whatever it is. At the highest levels of noise, the performance is entirely based on vision, then for increasing SNR it efficiently combines the two channels to exhibit performances higher than the individual performances of both of them, and without noise perfect identification of all features is realized, mainly thanks to the auditory channel, plus vision for rounding.

This pattern is in fact very strong, and holds more or less perfectly for individual subjects. It raises a strong challenge for any model of bimodal speech recognition. There exist a variety of such models, which differ mainly in two aspects: (1) the architecture of the sensor fusion process, that is the level at which fusion occurs and the representation of the sensory inputs at this level; and (2) the nature of the fusion process, and the contextual variables on which it may depend (Schwartz *et al.*, 1998). We implemented various architectures and fusion processes and compared their performances in the recognition of this corpus, particularly in relation to the synergy criterion (Robert-Ribes *et al.*, 1996; Teissier *et al.*, submitted). This study demonstrated two major facts.

1. Consequences on the fusion architecture

First, all the architectures we tested display some synergy in global terms: The visual input somewhat increases the overall recognition score for speech in noise, as it is the case in all studies published in the literature. However, things are more complicated at the *feature* level. This is particularly the case of one model, the so-called ''Dominant Recoding'' model. This model was originally proposed in parallel by Summerfield (1987) from a theoretical point of view, and by Yuhas *et al.* (1990) in a neural network application to sensory integration in the bimodal recognition of noisy vowels. It consists of estimating from a visual speech input the most probable acoustic spectrum corresponding to the image (by neural nets in the Yuhas *et al.*'s study), then mixing the true acoustic spectrum with the estimated one, possibly with a variable weight indexed on the level of acoustic noise, and finally identifying the weighted spectrum thanks to any kind of pattern recognition device. It has been shown to produce good performance on American English vowels by Yuhas *et al.* However, we showed that though this model, as all the others, produces in the audio-visual condition a higher global recognition score in noise than in the audio-alone condition, the transmitted information score is significantly lower in the audio-visual recogniser than in the *visual* recognizer at large levels of noise for the *rounding* feature and lower in the audio-visual recognizer than in the

auditory recognizer at medium levels of noise for the *height* feature. The reason is that this model, which we called ''dominant recoding'' since it implicitly assumes that audition is ''dominant'' and vision must be recoded in the dominant modality (Schwartz *et al.*, 1998), precisely suffers from the fact that audition is *not* systematically dominant. In contrast, audition may be less useful than vision for certain tasks, such as the determination of the rounding feature, even without noise, as demonstrated in the study by Lisker and Rossi (1992) cited in the Introduction. Therefore, it is easy to predict a major problem for this model with a phonological system as the French oral vowel system with three independent features: The recoding of vision into audition should lead to project a set of visual patterns as [i], [y], [u] in which [i] is far from [y] and [y] is almost confounded with [u], toward a set of auditory patterns in which [i] is close to [y], and [u] is somewhat far apart. This would produce both a theoretical difficulty, namely, how to solve the problem of identical visual patterns with different acoustic spectra, e.g., [y] and [u], and a technical difficulty, namely, how to exploit the good separation between visual [i] and [y] if they are mapped onto close acoustic spectra. This results in a suboptimal use of the visual input for the identification of the rounding contrast at large levels of acoustic noise, and our recognition study shows that there is also a suboptimal use of the auditory input for the identification of the height feature at medium levels of acoustic noise.

2. Consequences on the fusion process

The second major conclusion of our recognition study is that a complete exploitation of the audio-visual synergy (that is, audio-visual scores higher than the audio or video scores at all SNRs and for all features) can be obtained in a given architecture only if the fusion process is guided by a contextual input which provides some estimate of the *reliability* of each sensor. Part of the explanation can be found on the example provided in Table VII, which gives the confusion matrices for one subject (subject HC) for the visual condition and the audio and audio-visual conditions at SNR$=-18$ dB.

The audio matrix shows that this subject, as all the others, has lost any discrimination ability at this SNR value: The corrected recognition score is 0. However, this subject does not realize a random choice between all responses, as do some other subjects in this condition. Rather, he chooses a ''garbage'' category, namely [ø], and uses this choice for most stimuli at -18 dB. In a fusion process directly exploiting the auditory and visual inputs with no control of the reliability of the audio sensor, this response would receive a somewhat stronger support than all its concurrents in the audio channel, which should bias the behavior of the subject in the audio-visual condition. But we see that this is not the case: The audio-visual confusion matrix is quite similar to the visual one, and there is no bias in favor of [ø]. This shows that subject HC ''knows'' that the auditory sensor is not reliable, and discards it from his final choice, although his choice in the auditory condition seems unambiguous. Reciprocally, other perceptual data indicate that ambiguous responses can be related to a high degree of confidence in a fusion process (see Schwartz *et al.*, 1998). In summary, *ambiguity* and *reliability* are likely to be two different properties of a sensor in a fusion process. In consequence, our recognition study shows that a given architecture cannot display a satisfactory synergy in the audio-visual condition if there is not a contextual input related to the SNR value in the audio channel.

TABLE VII. Confusion matrices for subject HC in the audio at -18 dB, video, and audio-visual at -18 dB conditions.

Visual

Answer \ Stimulus	a	e	i	ø	y	o	u
a	10						
e		3	6				
i		7	4				
ø				5	6	9	3
y				5	4		6
o						1	
u							1

Audio −18 dB

Answer \ Stimulus	a	e	i	ø	y	o	u
a	1		1		1	1	
e							
i		2		1			
ø	9	8	9	9	9	9	10
y							
o							
u							

AV −18 dB

Answer \ Stimulus	a	e	i	ø	y	o	u
a	10						
e			4				
i		10	6				
ø				5	3	2	4
y				2	3		1
o				2	1	7	4
u				1	3	1	1

SNR = 6 dB

Answer \ Stimulus	a	e	i	ø	y	o	u
a	210						
e		210		15			
i			204		1		
ø				195	3	5	2
y			6		206		2
o						202	4
u						3	202

SNR = -12 dB

Answer \ Stimulus	a	e	i	ø	y	o	u
a	126	18	23	13	26	10	29
e	12	47	18	51	21	59	31
i	22	21	80	14	65	13	48
ø	31	67	30	72	31	61	24
y	7	12	36	19	43	12	40
o	4	31	5	33	6	47	15
u	8	14	18	8	18	8	23

SNR = 0 dB

Answer \ Stimulus	a	e	i	ø	y	o	u
a	209						
e		196	1	55	4	3	
i		1	155		33		5
ø		13		132		22	10
y			51		163		10
o				23		184	9
u	1		3		10	1	176

SNR = -18 dB

Answer \ Stimulus	a	e	i	ø	y	o	u
a	30	15	16	22	24	16	16
e	48	55	55	51	49	57	54
i	38	45	47	43	45	43	42
ø	45	45	41	46	47	48	47
y	25	21	33	18	22	20	25
o	11	15	12	16	8	19	12
u	13	14	6	14	15	7	14

IV. CONCLUSION

The efficacy of bimodal speech, both at the information (complementarity) and information processing (synergy) levels therefore appears to hold for individual phonetic features, at least for French oral vowels spoken in isolation (see Benoît *et al.*, 1994, for data on coarticulated French vowels in various consonantal contexts). In the auditory channel, height is the most robust feature in acoustic white noise, followed by the front–back feature, rounding being the poorest, while the visual channel discriminates three visemes, with a perfect identification of rounding, a partial identification of height, the front–back feature being invisible. At last, at all SNRs, each feature is better perceived with the ear and the eye together than with the ear alone or with the eye alone. The ''double efficacy'' of bimodal speech constitutes a major challenge for future models of audio-visual speech perception and automatic recognition of speech in noise and adverse conditions.

ACKNOWLEDGMENTS

This work has been supported by an EEC ESPRIT-BR funding (6975, Speech-MAPS). It benefited from a number of useful comments from the editor Winifred Strange, and from Dominic Massaro and two anonymous reviewers. We also thank Christian Abry, Marie-Agnès Cathiard, Laurent Girin, and Pascal Teissier for help and discussions in the preparation and interpretation of these results.

Abry, C., and Boë, L. J. (**1980**). ''A la recherche de corrélats géométriques discriminants pour l'opposition d'arrondissement vocalique en français,'' in *Labialité et Phonétique*, edited by C. Abry, L. J. Boë, P. Corsi, R. Descout, M. Gentil, and P. Graillot (Publications de l'Université des Langues et Lettres de Grenoble, Grenoble), pp. 217–237.

Abry, C., and Boë, L. J. (**1986**). ''Laws for lips,'' Speech Commun. **5**, 97–104.

Benoît, Ch., Lallouache, T., Mohamadi, T., and Abry, Ch. (**1992**). ''A set of visual French visemes for visual speech synthesis,'' in *Talking Machines: Theories, Models and Designs*, edited by G. Bailly, C. Benoît, and T. R. Sawallis (Elsevier Science, Amsterdam), pp. 485–504.

Benoît, C., Mohamadi, T., and Kandel, S. D. (**1994**). ''Effects of phonetic context on audio-visual intelligibility of French,'' J. Speech Hear. Res. **37**, 1195–1203.

Blamey, P. J., Cowan, R. S. C., Alcantara, J. I., Whitford, L. A., and Clark, G. M. (**1989**). ''Speech perception using combinations of auditory, visual, and tactile information,'' Journal of Rehabilitation Research and Development **26**, 15–24.

Breeuwer, M., and Plomp, R. (**1986**). ''Speechreading supplemented with auditorily presented speech parameters,'' J. Acoust. Soc. Am. **79**, 481–499.

Campbell, R., Dodd, B., and Burnham, D., Eds. (**1998**). *Hearing by Eye, II. Perspectives and Directions in Research on Audiovisual Aspects of Language Processing* (Erlbaum/Psychology Press, Hillsdale, NJ).

Carlson, R., Fant, G., and Granström, B. (**1975**). ''Two-formant models, pitch and vowel perception,'' in *Auditory Analysis and Perception of Speech*, edited by G. Fant and M. A. Tatham (Academic, London), pp. 55–82.

Cathiard, M. A. (**1994**). ''La perception visuelle de l'anticipation des gestes vocaliques: Cohérence des événements audibles et visibles dans le flux de la parole,'' Doctoral Report, Cognitive Psychology, Université Pierre Mendès France, Grenoble.

Cathiard, M. A., Tiberghien, G., and Abry, C. (**1992**). ''Face and profile identification skills for lip-rounding,'' Bulletin de la Communication Parlée **2**, 43–58.

Cohen, M. M., and Massaro, D. W. (**1995**). ''Perceiving visual and auditory information in consonant-vowel and vowel syllables,'' in *Levels in Speech Communication: Relations and Interactions*, edited by C. Sorin, J. Mariani, H. Méloni, and J. Schoentgen (Elsevier Science, Amsterdam), pp. 25–37.

Delattre, P. (**1959**). ''Rapports entre la durée vocalique, le timbre et la structure syllabique en français,'' The French Review **23**, 547–552.

Delattre, P. (**1962**). ''Some factors of vowel duration and their cross-linguistic validity,'' J. Acoust. Soc. Am. **34**, 1141–1142.

Erber, N. P. (**1975**). ''Auditory-visual perception of speech,'' J. Speech Hear. Disorder **40**, 481–492.

Gentil, M. (**1981**). ''Etude de la perception de la parole: Lecture labiale et sosies labiaux,'' Technical report IBM, France.

Gottfried, T., and Beddor, P. S. (**1988**). ''Perception of temporal and spectral information in French vowels,'' Language and Speech **31**, 57–75.

Grant, K. W., Ardell, L. H., Kuhl, P. K., and Sparks, D. W. (**1985**). ''The contribution of fundamental frequency, amplitude envelope, and voicing duration cues to speechreading in normal-hearing subjects,'' J. Acoust. Soc. Am. **77**, 671–677.

Itakura, F. (**1975**). ''Minimum prediction residual principle applied to speech recognition,'' IEEE Trans. Acoust. Speech Signal Process. **23**, 67–72.

Jackson, P. L., Montgomery, A. A., and Binnie, C. A. (**1976**). ''Perceptual dimensions underlying vowel lipreading performance,'' J. Speech Hear. Res. **19**, 796–812.

Jakobson, R., Fant, G., and Halle, M. (**1952**). *Preliminaries to Speech Analysis* (MIT, Cambridge, MA).

Lallouache, M. T. (**1990**). ''Un poste 'visage-parole.' Acquisition et traitement de contours labiaux,'' Proceedings of the XVIII Journées d'Études sur la Parole, Montréal, pp. 282–286.

Lindblom, B. E. F. (**1986**). ''Phonetic universal in vowel systems,'' in *Experimental Phonology*, edited by J. J. Ohala (Academic, Orlando), pp. 13–44.

Lindblom, B. E. F. (**1990**). ''Explaining phonetic variations: a sketch of the H&H theory,'' in *Explanations for Languages Universals*, edited by B. Butterworth, B. Comrie, and Ö. Dahl (Mouton, New York), pp. 181–203.

Linker, W. (**1982**). ''Articulatory and acoustic correlates of labial activity in vowels: a cross-linguistic study,'' UCLA Working Papers on Phonetics **56**.

Lisker, L., and Rossi, M. (**1992**). ''Auditory and visual cueing of the [±rounded] feature of vowels,'' Language and Speech **35**, 391–417.

Lonchamp, F. (**1981**). ''Multidimensional vocalic perceptual space: how many dimensions?,'' J. Acoust. Soc. Am. **69**, S94.

MacLeod, A., and Summerfield, Q. (**1987**). ''Quantifying the contribution of vision to speech perception in noise,'' Br. J. Audiol. **21**, 131–141.

Mantakas, M. (**1989**). ''Application du second formant effectif F'2 à l'étude de l'opposition d'arrondissement des voyelles antérieures du français,'' Thèse de Docteur de l'INPG, Systèmes Electroniques.

Massaro, D. W. (**1987**). *Speech Perception by Ear and Eye: A Paradigm for Psychological Inquiry* (Erlbaum, London).

Massaro, D. W. (**1989**). ''Multiple book review of speech perception by ear and eye: A paradigm for psychological inquiry,'' Behav. Brain Sci. **12**, 741–794.

Massaro, D. W., and Cohen, M. M. (**1983**). ''Evaluation and integration of visual and auditory information in speech perception,'' J. Exp. Psychol.: Human Perception and Performance **9**, 753–771.

McGurk, H., and MacDonald, J. (**1976**). ''Hearing lips and seeing voices,'' Nature (London) **264**, 746–748.

Miller, G. A., and Nicely, P. E. (**1955**). ''An analysis of perceptual confusions among some English consonants,'' J. Acoust. Soc. Am. **27**, 338–358.

Montgomery, A. A., and Jackson, P. L. (**1983**). ''Physical characteristics of the lips underlying vowel lipreading performance,'' J. Acoust. Soc. Am. **73**, 2134–2144.

Mourand-Dornier (**1980**). ''Le rôle de la lecture labiale dans la reconnaissance de la parole,'' Doctoral Report, Medical Sciences, Université de Franche-Comté.

Plant, G. L. (**1980**). ''Visual identification of Australian vowels and diphthongs,'' Australian J. Audiol. **2**, 83–91.

Plomp, R. (**1970**). ''Timbre as a multidimensional attribute of complex tones'' in *Frequency Analysis and Periodicity Detection in Hearing*, edited by R. Plomp and G. F. Smoorenburg (Sijthoff, Leiden), pp. 397–414.

Plomp, R. (**1975**). ''Auditory Analysis and Timbre Perception,'' in *Auditory Analysis and Perception of Speech*, edited by G. Fant and M. A. Tatham (Academic, London), pp. 7–22.

Pols, L. C. W. (**1975**). ''Analysis and synthesis of speech using a broad-band spectral representation,'' in *Auditory Analysis and Perception of Speech*, edited by G. Fant and M. A. A. Tatham (Academic, London), pp. 23–36.

Robert-Ribes, J. (**1995**). ''Modèles d'intégration audiovisuelle de signaux linguistiques: De la perception humaine à la reconnaissance automatique des voyelles,'' Doctoral Report, Signal-Image-Parole, INPG.

Robert-Ribes, J., Piquemal, M., Schwartz, J. L., and Escudier, P. (**1996**). ''Exploiting sensor fusion architectures and stimuli complementarity in AV speech recognition,'' in *Speechreading by Man and Machine: Models, Systems and Applications*, edited by D. G. Stork and M. Hennecke, NATO ASI Series (Springer, Verlag, New York), pp. 193–210.

Schroeder, M. R., Atal, B. S., and Hall, J. L. (**1979**). ''Objective measure of certain speech signal degradations based on masking properties of human auditory perception,'' in *Frontiers of Speech Communication Research*, edited by B. Lindblom and S. Ohman (Academic, London), pp. 217–229.

Schwartz, J. L., Beautemps, D., Abry, C., and Escudier, P. (**1993**). ''Inter-individual and cross-linguistic strategies for the production of the [i] vs [y] contrast,'' J. Phon. **21**, 411–425.

Schwartz, J. L., Boë, L. J., Vallée, N., and Abry, C. (**1997a**). ''Major trends in vowel inventories,'' J. Phon. **25**, 233–253.

Schwartz, J. L., Boë, L. J., Vallée, N., and Abry, C. (**1997b**). ''The dispersion-focalization theory of vowel systems,'' J. Phon. **25**, 255–286.

Schwartz, J. L., Robert-Ribes, J., and Escudier, P. (**1998**). ''Ten years after Summerfield ... a taxinomy of models for AV fusion in speech perception,'' in *Hearing by Eye, II. Perspectives and Directions in Research on*

Audiovisual Aspects of Language Processing, edited by R. Campbell, B. Dodd, and D. Burnham (Erlbaum/Psychology Press, Hillsdale, NJ), pp. 85–108.

Stork, D. G., and Hennecke, M., Eds. (**1996**). *Speechreading by Man and Machine: Models, Systems and Applications* (NATO ASI Series, Springer-Verlag, New York).

Summerfield, Q. (**1979**). ''Use of visual information for phonetic perception,'' Phonetica **36**, 314–331.

Summerfield, Q. (**1985**). ''Speech-processing alternatives for electrical stimulation,'' in *Cochlear Implants*, edited by M. Merzenich and R. Schindler (Raven, New York), pp. 195–222.

Summerfield, Q. (**1987**). ''Some preliminaries to a comprehensive account of audio-visual speech perception,'' in *Hearing by Eye: The Psychology of Lipreading*, edited by B. Dodd and R. Campbell (Erlbaum, London), pp. 3–51.

Summerfield, Q., MacLeod, A., McGrath, M., and Brooke, M. (**1989**). ''Lips, teeth and the benefits of lipreading,'' in *Handbook of Research on Face Processing*, edited by A. W. Young and H. D. Ellis (Elsevier Science, North-Holland), pp. 223–233.

Syrdal, A. (**1985**). ''Aspects of a model of the auditory representation of American English vowels,'' Speech Commun. **4**, 121–135.

Teissier, P., Robert-Ribes, J., Schwartz, J. L., and Guérin-Dugué, A. (**submitted**). ''Comparing models for audio-visual fusion in a noisy-vowel recognition task,'' IEEE Trans. Speech Audio Process.

Tseva, A. (**1989**). ''L'arrondissement dans l'identification visuelle des voyelles du français,'' Bulletin du Laboratoire de la Communication Parlée **3**, 149–186.

VanSon, N., Huiskamp, T. M. I., Bosman, A. J., and Smoorenburg, G. F. (**1994**). ''Viseme classifications of Dutch consonants and vowels,'' J. Acoust. Soc. Am. **96**, 1341–1355.

Ventsel, H. (**1973**). *Théorie des probabilités* (MIR, Moscow).

Walden, B. E., Prosek, R. A., Montgomery, A. A., Scherr, C. K., and Jones, C. J. (**1977**). ''Effects of training on the visual recognition of consonants,'' J. Speech Hear. Res. **20**, 130–145.

Yuhas, B. P., Goldstein, M. H., Sejnowski, T. J., and Jenkins, R. E. (**1990**). ''Neural network models of sensory integration for improved vowel recognition,'' Proc. IEEE **78**, 1658–1668.

Zerling, J. P. (**1992**). ''Frontal lip shape for French and English vowels,'' J. Phon. **20**, 3–14.

Zwicker, E., and Feldtkeller, R. (**1969**). *Das Ohr als Nachrichtenempfänger* (S. Hirzel Verlag, Stuttgart).

Sinuous instability of a planar air jet: Propagation parameters and acoustic excitation

A. W. Nolle
Department of Physics, The University of Texas at Austin, Austin, Texas 78712

(Received 11 November 1997; revised 2 March 1998; accepted 4 March 1998)

The sinuous instability wave of a planar air jet is excited by localized acoustic flow across the nozzle. Phase velocity and the growth exponent are found from synchronous hot-wire measurements made beyond the excited region, where the profile is approximately sech-squared. In the observed range of scaled radian frequency, 0.02–1.33 (the stability limit), results agree with real-frequency (spatially growing) analysis but not with complex-frequency (temporally growing) analysis. The latter predicts smaller phase velocity at low frequencies and has been questioned in edgetone analysis. In further tests, the acoustic driving signal is made independent of downstream distance, as in an organ pipe. The jet deflection is then the sum of acoustic convection and of the instability wave, summing to zero at the nozzle, as proposed by Fletcher, Elder, and others. The instability-wave theory applies to linear behavior in the inviscid limit and therefore to a hypothetical nonspreading jet. The local velocity profile width must be considered in relating to a physical jet. In a flue organ pipe oscillating at equilibrium amplitude the stability-wave theory is not applicable near the lip, where the laminar flow assumed in the theory disappears and the jet deflection exceeds the range of linear behavior. Direct sound generation by the jet is investigated briefly. [S0001-4966(98)04706-7]

PACS numbers: 43.75.Np, 43.28.Py, 43.28.Ra [WJS]

LIST OF SYMBOLS

a_s	shear layer half-thickness
c_p	phase velocity of sinuous instability
b	half-thickness of jet, esp. as defined by (1)
k	(unscaled) wave number
J	velocity-squared integral across jet profile
$T=(U_0/b)t$	scaled time
U	local flow velocity in x direction, no modulation
U_0	central max. of U; also velocity difference across shear layer
U_p	additive constant (pedestal) in sech-squared profile fit
U_s	velocity of steady lateral stream
$\mathbf{v}$	cross-stream velocity perturbation
x	downstream distance
$-x_0$	virtual origin for jet spreading
y	distance from local jet center
y_0	instantaneous center of jet or shear layer
$X=(x/b)$	(Mattingly/Criminale) scaled x
$Y=(y/b)$	scaled y
$\alpha=\alpha_r+i\alpha_i$	(Mattingly/Criminale) scaled wave number, where real is $(U_0/c)\omega_r$ and imag. is $-\mu b$
$\beta=(\omega a_s/U_0)$	scaled frequency for shear layer
Ξ_a	acoustic displacement amplitude
ξ	local displacement of shear layer or of jet center
ξ_0	local fundamental-frequency amplitude of $y_0(t)$
μ	(unscaled) exponential growth factor
ν	kinematic viscosity
ρ	fluid density
θ	phase lag of fundamental component of jet or shear-layer displacement waveform, usually relative to value at $x=0$
ϕ	stream function
$\omega_r=(\omega b/U_0)$	scaled angular frequency

INTRODUCTION

A useful practical description of acoustically forced undulation of a planar jet (the sinuous jet instability) has developed in flute and organ pipe research; see for example Coltman (1992b) and Thwaites and Fletcher (1983), and citations in these references. Some essentials are: Jet oscillation (the sinuous instability wave) is initiated by the acoustic cross flow at the origin of the jet, i.e., the flue opening. The phase velocity of the jet deflection wave for many practical situations is somewhat less than half the central stream velocity. The phase of the jet deflection wave, extrapolated back to the flue through a region of initial anomalous behavior, coincides approximately with that of the acoustic particle acceleration (negative displacement).

Questions remain in spite of this general understanding of wave motion on the jet. Calculations of the temporal growth of the instability (Drazin and Howard, 1962, 1966), when inverted to describe spatial behavior, indicate that the phase velocity of the disturbance vanishes in the low-frequency limit, a prediction which has not been confirmed experimentally. Crighton (1982) found that the phase velocity as deduced from the temporal analysis is unsatisfactory

when used in edgetone theory. More recently Verge *et al.* (1994a) found in studying an experimental organ pipe that the spatial growth of the jet disturbance is better predicted by a direct spatial analysis (Mattingly and Criminale, 1971) than by the inverted temporal analysis. Therefore it has seemed desirable to make a systematic investigation of the sinuous instability on a free jet, to determine whether the phase velocity as well as the growth are properly described by the spatial rather than temporal analysis. The investigation also gives an opportunity to confirm the role of the acoustic displacement at the flue in driving the jet and to examine other aspects of the driven jet.

In these tests, the lateral displacement of the jet, caused by a controlled acoustic cross flow, is investigated for jet velocities in the experimentally convenient range of 6–20 m/s. This is less than the usual jet velocities of some 20–40 m/s in organ pipes, but is within the range found in edge tone experiments and in studies of recorders (Verge *et al.*, 1994a). The Reynolds number lies between 300 and 2000.

The experimental method allows localized upstream acoustical excitation of the jet, so that the instability wave can be observed farther downstream under free-jet conditions. The study includes these topics and results:

(1) The growth exponent (amplification) and the wave number of the free-jet instability wave are measured over a range of scaled frequency, and the results are shown to agree with spatial rather than temporal theoretical calculations.

(2) The contiguous sound field due to the oscillation of the free jet is explored.

(3) The deflection of the jet by a steady cross flow is shown to be quadratic in the cross velocity, as expected from momentum arguments, and thus distinct from the linear response of the instability-wave mechanism.

(4) For distributed acoustic excitation, as in an organ pipe, it is shown that the observable jet deflection wave is a superposition of the sinuous instability wave and the oppositely phased acoustic displacement, as suggested by earlier workers.

(5) For a jet with tophat velocity profile near the flue, the phases of the individual shear-layer displacements are shown in relation to the overall jet displacement oscillation.

(6) For the tophat jet, with distributed acoustic excitation, the acoustic pressure at the flue opening modulates the jet flux in approximate Bernoulli behavior, as reported by Verge *et al.* (1994b).

(7) An asymmetric flue structure distorts the velocity profile near the flue, but the instability-wave displacement at the flue is still in phase with the negative acoustic displacement.

Turbulence on the jet and incipient vortex formation are not issues here. For the small stream velocities in this study, effects of these complications are suppressed by signal-averaging and curve-fitting techniques which discriminate against chaotic behavior and extract results consistent with the laminar flow that is considered in the linear theory.

I. THEORETICAL BACKGROUND

The theoretical background concerns (a) the well-established profile and spreading of the stationary jet in the incompressible approximation, which will be described first, and (b) the oscillatory instability of the jet, in the inviscid and incompressible approximation. The results of (b) have appeared in two forms. One of the aims of this paper is to show experimentally which is appropriate.

Schlichting (1933) and Bickley (1937) showed theoretically that the flow from an infinitesimal slit, into a volume of fluid otherwise at rest, produces a spreading planar jet whose velocity profile evolves to the sech-squared form (henceforth designated sech^2). In the experiments of Andrade (1939) this behavior was observed in a jet issuing from a finite slit (excluding a short region immediately in front of the slit). To relate the theory to the experimental jet, Andrade replaced the streamwise distance from the slit used in the theory, x, with $x+x_0$, placing the equivalent infinitesimal slit at $x=-x_0$. Let y be the coordinate perpendicular to the flow. Andrade verified that the streamwise velocity profile at a particular x is (not in Andrade's notation)

$$U(Y)=U_0\ \mathrm{sech}^2(Y), \tag{1}$$

where $Y=y/b$, and $2b$ measures the width of the profile. Further, if the values of b and of U_0, the central maximum velocity, are temporarily taken as functions of x, the spreading of the jet is described by the increasing width,

$$b(x)=3.635(\nu^2/K)^{1/3}(x+x_0)^{2/3}, \tag{2}$$

where ν is the kinematic viscosity, and the decreasing maximum velocity,

$$U_0(x)=0.454(K^2/\nu)^{1/3}(x+x_0)^{-1/3}, \tag{3}$$

where K is the velocity-squared integral over the infinite range of y. Total momentum flux is conserved; thus $\rho[U_0(x)]^2b(x)$ is just a numerical factor times ρK, where ρ is the density, independent of x. Mass flux increases through entrainment of fluid surrounding the jet. It was suggested that either a tophat initial profile or a parabolic one evolves to the sech^2 form, not necessarily with the same x_0. No method is available for calculating x_0 from first principles.

The instability-wave analysis has been done only in the inviscid approximation, and therefore relates to a fictitious nonspreading jet, a restriction which must be considered in comparisons with experiment. The sinuous (waving) instability is mainly considered here, rather than the varicose instability to which the theory also applies.

Savic (1941) found a solution in closed form for the sinuous disturbance, but since it applied only in the limit of neutral stability, the comparison with experiment was unrealistic. Further work has involved numerical solution of the stability equation, which appears below following identification of the variables. Drazin and Howard (1962, 1966) treated a disturbance growing in time. This temporal solution does not directly apply to the present studies on spatial growth of instability waves, but proposals have been made for using it to describe spatial behavior [for example, Fletcher and Thwaites (1979)]. It will be shown that better agreement with experiment is obtained from the spatial analysis, which will now be described. This arises from the work of Michalke (1965), who treated an isolated shear layer at the edge of a thick tophat jet, and of Mattingly and Crimi-

nale (1965), who dealt with a complete sech^2 jet. Their notation will be used. Spatial analysis involves complex wave number and real frequency, the reverse of the approach in temporal analysis. The dimensionless (scaled) quantities to be used are $X=(x/b)$, $Y=(y/b)$, $T=(U_0/b)t$, and the frequency $\omega_r=(\omega b/U_0)$, which is 2π times a commonly used form of the Strouhal number S. ω is the ordinary radian frequency. The cross-stream velocity perturbation will be sought as

$$v(X,Y,T)=\mathrm{Re}\{\mathbf{v}(Y)\exp[i(\alpha X-\omega_r T)]\}, \tag{4}$$

where $\mathbf{v}(Y)$ is the complex Y-dependent form of the function. The complex wave number $\alpha=\alpha_r+i\alpha_i$ yields a complex propagation velocity $c=\omega_r/\alpha$. Comparison of Eq. (4) with the usual spatial dependence function in a traveling wave, $\exp(i\omega/c_p)x$, yields the real scaled phase velocity $c_p=(\omega_r/\alpha_r)$, which is the actual velocity divided by U_0. Describing amplitude growth as $\exp(\mu x)$ with real positive growth factor μ gives $\mu b=-\alpha_i$. Like Drazin and Howard, Mattingly and Criminale are concerned with the eigenvalues of the inviscid and incompresssible form of the Rayleigh stability equation,

$$[U(Y)-c][\mathbf{v}''(Y)-\alpha^2\mathbf{v}(Y)]-U''(Y)\mathbf{v}(Y)=0. \tag{5}$$

(As in Michalke's analysis, the stream function ϕ can also serve as the dependent quantity.) Double primes indicate second derivatives with respect to Y.

For a given $U(Y)$ and ω_r it is desired to find the complex α (the eigenvalue) and the associated eigenfunction $\mathbf{v}(Y)$ which has the appropriate asymptotic behavior and symmetry: $\mathbf{v}(Y)=\mathbf{v}(-Y)$, $\mathbf{v}'(0)=0$, with limiting behavior $\exp(\pm\alpha Y)$. The eigenvalues appear in a small graph in Mattingly and Criminale (1971). Because this does not show the behavior of α for $\omega_r \ll 1$, which is of special interest here, further eigenvalue calculations have been done for the present work. The results appear in Fig. 1, which includes the range considered by Mattingly and Criminale. The calculations are described, with numerical results, in the Appendix.

The results for $\omega_r \to 0$ are of special interest. The temporal analysis predicts that α_i, α_r, and c_p vanish in the limit (see Fig. 7 for this version of c_p). However, Michalke (1965) finds that for the shear-layer instability, α_r vanishes in such a way that c_p remains nonzero. For small ω_r, values of c_p from the present spatially formulated calculations exceed those from the temporal analysis, as is expected if the quantity does not vanish. An analytical argument would be required to confirm that the limit of c_p is nonzero.

Another product of the calculations from the Rayleigh equation is $\mathbf{v}'(Y)$, which may be shown through the stream function to be proportional to the streamwise perturbation $\mathbf{u}(Y)$ (the disturbance function). Figure 2 shows the magnitude of the disturbance function for several frequencies ω_r, with each plot arbitrarily adjusted to a maximum value of 1.0. If continued to negative Y, each plot would show odd symmetry, $\mathbf{u}(Y)=-\mathbf{u}(-Y)$. At the stability limit, $\omega_r=4/3$, the shape of $\mathbf{u}(Y)$ is that of $U'(Y)$, producing a local shift of the jet profile without change of shape. In the vicinity of $\omega_r=1.0$, however, $\mathbf{u}(Y)$ differs strongly from $U'(Y)$, indicating that the profile is distorted when displaced. For $\omega_r<0.5$ (which characterizes almost all the present measurements) the distortion has moved out to the skirts of the profile, so that the large central peak is expected to show little change of shape in small-amplitude oscillations (see the experimental illustration in Fig. 6). Associated with each of the notches in $\mathbf{u}(Y)$ in the vicinity of $\omega_r=1.0$ is a phase change somewhat less than π. With decreasing ω_r the phase change becomes larger, becoming a full phase reversal for $\omega_r \leqslant 0.25$.

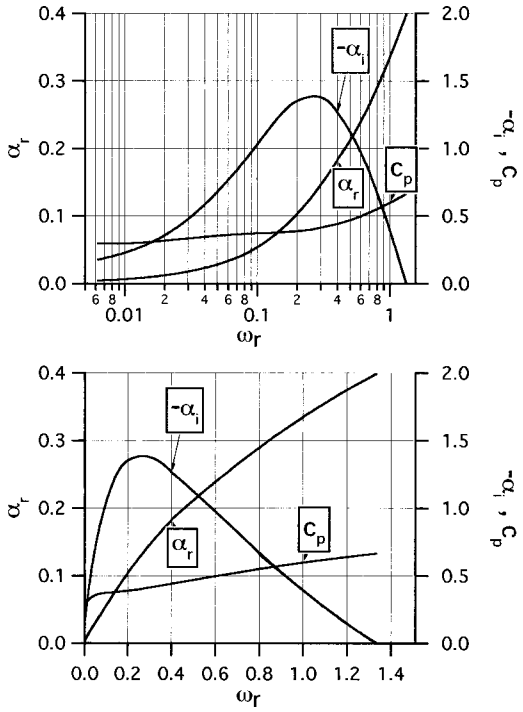

FIG. 1. Theoretical instability-wave propagation constants on linear and logarithmic frequency scales. Data from Table AI (App.).

In the present work it is useful to introduce a family of velocity profiles described by the *ad hoc* function

$$U(Y)=U_0\ \mathrm{sech}^2(Y^n). \tag{6}$$

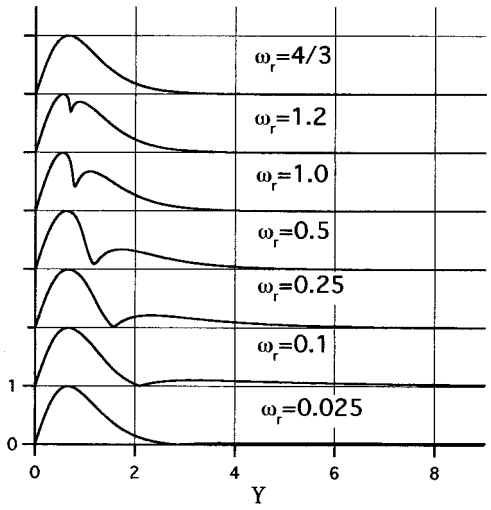

FIG. 2. Disturbance function magnitude (streamwise velocity perturbation) vs Y for various scaled frequencies. The maximum value of each plot has been arbitrarily set to unity.

TABLE I. Eigenvalues of Eq. (5) for flattened jet profiles given by Eq. (6).

n Flattening parameter	ω_r	α_r	α_i	c_p
1	0.1	0.269	−0.207	0.371
2	0.1	0.213	−0.206	0.469
3	0.1	0.199	−0.200	0.502
1	0.2	0.516	−0.270	0.387
2	0.2	0.401	−0.332	0.499
3	0.2	0.362	−0.323	0.552

The usual profile (1) is given by $n=1$. Each function has $U/U_0=\mathrm{sech}^2(1)$ at the reference distance $y=b$. Increasing n gives flatter profiles, which prove to be excellent fits to experimental data for tophat jets near the flue. (Figure 10 contains an illustration for $n=3$.) The sinuous-instability eigenvalues calculated for flattened profiles having $n=2$ and $n=3$, with $\omega_r=0.1$ and 0.2, are shown in Table I. The phase velocity c_p increases greatly with the onset of flattening. Again, this result applies to a hypothetical jet profile independent of x. Because the tophat profile exists only near an entrance slit, where the profile is evolving rapidly, accurate testing would be difficult.

The dynamical problem of the acoustical forcing of the instability wave at the flue has not been treated fully. Crighton (1992) formulated the problem for a tophat jet velocity profile, but in order to have a tractable case, represented the flue by semi-infinite parallel walls, which would in actuality produce a parabolic profile. The present investigation tests what will be called the flue boundary condition, which relates the phase and amplitude of the instability wave to the acoustic driving signal. The flue boundary condition appears to originate with Fletcher (1976). Basic to the boundary condition is the assumption of acoustic convection of the jet, that the instability wave exists as it would for a jet issuing into an undisturbed medium, but is referred to coordinates which follow the transverse acoustic displacement (Chanaud and Powell, 1962). The observable jet center-line displacement is a linear superposition of the acoustic particle displacement and that from the instability wave. The flue boundary condition asserts that at the flue opening the two displacements are opposite in phase, giving zero total displacement as required to maintain finite lateral acceleration. In essence this adopts the boundary condition for the edges of the opening and applies it to the jet center line. Without detailed analysis of jet forcing, the flue boundary condition predicts (1) the initial amplitude of the sinuous-instability wave equals the acoustic displacement amplitude in front of the flue, and (2) the initial phase of the instability wave is that of the negative acoustic displacement. Elder (1978, 1980) applied these conditions to the acoustic deflection of a single shear layer over a cavity. He showed experimentally that the lateral displacement of the layer following the downstream edge of a long plate is of the form

$$\xi=\Xi_a[1-\exp(\mu x)\exp(ikx)]\exp(-i\omega t), \tag{7}$$

where the acoustic amplitude Ξ_a is made real for convenience, and the edge at which the two oscillations are equal

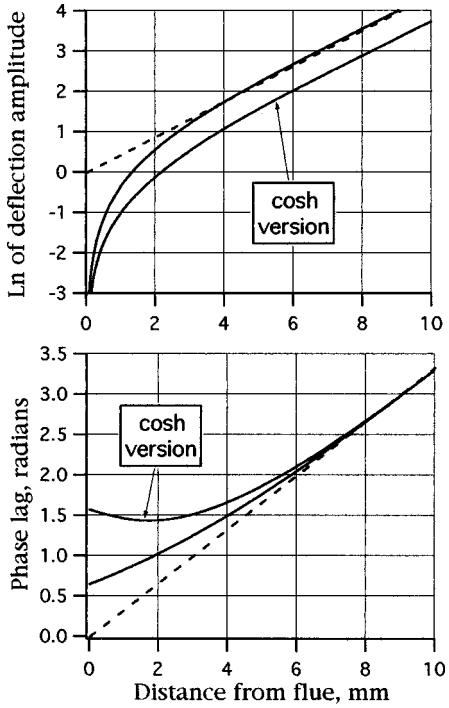

FIG. 3. Numerical example from Eq. (7), using $\mu=0.44$ and $k=0.33$ showing jet deflection phase and logarithmic amplitude curves approaching straight lines from the origin when $\mu x \gg 1$. Phase is referred to negative acoustic displacement.

is at $x=0$. Elder justified Eq. (7) through boundary conditions on the shear layer, regarding it as a manifestation of a Kutta condition at the edge. If ξ is redefined as displacement of a jet center line, Eq. (7) expresses Fletcher's 1976 flue boundary condition and has appeared in later work by Fletcher.

When μ is not too small, there is a downstream region where the jet is still laminar and where its displacement is dominated by the instability wave. Here, for given values μ and k, it is predicted from Eq. (7) that the plot of the jet-displacement phase is asymptotic to a straight line from the origin, and similarly the plot of logarithmic amplitude is asymptotic to a line which, at the slit, represents the acoustic displacement amplitude. This is illustrated in Fig. 3, a numerical example from (7). Generally, the phase difference at $x=0$ between the jet deflection curve and the straight line is $\tan^{-1}(k/\mu)$. While this discussion ignores the slow variation of μ and k because of jet spreading, it provides a useful view of the data. A similar extrapolation procedure was used by Fletcher and Thwaites (1979) to relate the flue boundary conditions to a frequency plot of jet deflection measurements by Coltman (1976), rather than to a spatial plot.

Figure 3 shows that in the entry region the superposition phenomenon flattens the phase curve. A further contribution to this flattening comes from the increased phase velocity associated with the flatter velocity profile that precedes the sech^2 region.

There has been some discussion as to whether the growth function in Eq. (7) should be $\cosh(\mu x)$ rather than $\exp(\mu x)$. With this modification (see curves marked ''cosh version'' in Fig. 3), the log amplitude curve extrapolates back to $-\ln(2)$ instead of zero at the flue, and the phase lag

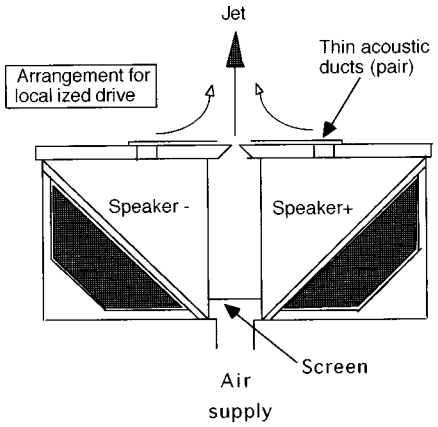

FIG. 4. Apparatus for localized acoustic excitation of jet. Slit length, perpendicular to diagram, is 38 mm; width ca. 1 mm is adjustable. Thin acoustic ducts of inside height 1.6 mm are excited from loudspeaker chambers, out of phase, to produce lateral acoustic flow with pressure null at slit. The hot-wire probe is moved by micrometer screws either across the jet or downstream.

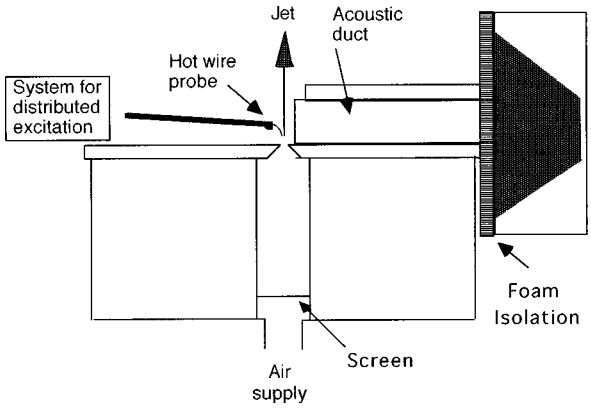

FIG. 5. Modification for distributed excitation. Single acoustic duct extends 19-mm downstream.

curve is bent upward, both changes incompatible with the presumed conditions at the flue. Fletcher (1976) proposed the cosh form. It implies a diminishing downstream-traveling wave component, permitted by the well-known Rayleigh temporal description of jet instability and symmetry arguments. Later the exponential form was adopted in Fletcher and Rossing (1991). Elder (1992) suggested differences in boundary conditions for a planar jet as compared to the shear layer and suggested a more general combination of downstream and upstream waves, as proposed by Cremer and Ising (1968). Crighton (1992, p. 389) cites proofs by Hardisty (1974) against the existence of an upstream-moving disturbance. The tests in the present study are not consistent with the cosh option. In Sec. X the behavior of an individual shear layer in a tophat jet is related to Eq. (7).

Elder showed that for small μ the displacement described by Eq. (7) near the origin (the flue) resembles a single propagating disturbance where k is replaced by $k/2$, preventing a straightforward measurement of the instability-wave propagation constants in this region.

The water-tank experiment of Chanaud and Powell (1962), which provided visualization of a planar jet emerging into a transversely oscillating body of like fluid, showed the convection of the waving jet by the acoustic motion, and also revealed some dynamical details—the jet deflection develops only beyond an initial boundary layer, and an ''embryo vortex'' develops periodically within the base of the jet.

Coltman (1992b) concluded from studies of an acoustically driven jet that the deflection at the flue has the phase of the negative acoustic displacement, as assumed in the present discussion, but that the frequency dependence of the magnitude of the deflection may relate the initial deflection to the acoustic pressure gradient. The latter conclusion does not appear firm, however, because the frequency dependence of the instability-wave growth exponent was not considered.

II. EXPERIMENTAL APPARATUS AND METHODS

The setup for localized excitation of the jet is shown in Fig. 4. The jet issues from a rectangular slit in a 140×285 mm plate of thickness 6.4 mm, shaped to provide a converging flue passage of interior angle 90°. The slit width was set to 0.5, 1.0, or 1.5 mm. This configuration provides approximately a tophat velocity profile. Machined parallel-sided jet inserts, 38 mm long in the flow direction, can be installed to produce a parabolic velocity profile. Air flow to the jet is supplied by an adjustable centrifugal blower followed by a settling tank. The pressure head between the screen and the flue opening is indicated by an electronic gauge and verified with a manometer. Immediately outside the opening, where there is an acoustic pressure node in the absence of the jet, the jet is subject to acoustic cross flow from ducts of height 1.6 mm. The hot-wire probe, with the wire parallel to the long slit dimension, can be moved either across the jet or in the stream direction by micrometer screws.

For velocity calibration, the hot wire is placed in the tophat jet, two widths downstream from the flue, with the acoustic ducts removed. Velocity is calculated by the Bernoulli relation, and voltage-to-velocity formulas prepared.

The modified apparatus shown in Fig. 5 gives distributed excitation of the jet by a single acoustic duct, in general, resemblance to jet drive by an organ pipe. In this case there is not an acoustic presure node at the flue exit. The acoustic duct extends 19-mm downstream, whereas measurements are not done beyond 13 mm.

III. EXPERIMENTAL PROCEDURES

At each chosen downstream distance, cross-jet hot-wire scans were made with steps of 0.1 or 0.05 mm. At each step, a synchronous digital waveform of eight periods duration was stored in a two-channel data acquisition device at a sampling rate of 16 times the acoustic frequency. The second channel sampled a reference signal having a consistent phase relation to the jet excitation, which was usually the loudspeaker driving voltage. Signal frequencies compatible with the sampling equipment were 900 Hz and submultiples. Synchronous sampling, although differing in detail, was also used by Elder (1978), Coltman (1992b), and others.

The following computer operations were done automatically for each point: (1) The eight-period sample was averaged to give a noise-reduced one-period waveform. (2) A zero-time reference (for example, 1.42 sample intervals after

the first point in the waveforms) was computed from the upward axis crossing of the fundamental Fourier component of the reference channel signal. (The resolution of the time reference found in this way is not limited by the sampling period.) (3) The voltage-to-velocity conversion was made. (4) The velocity waveform was resolved into harmonic components (usually eight) by Fourier analysis, and then reconstituted by Fourier synthesis as though the first digital sample had been taken at the zero reference time.

Each scan across the jet at N stations (typically from 25 to 75) produced a set of N 16-point waveforms with a consistent time reference, defining an array of 16 by N points. The array consists of point values of the time-dependent velocity profile $U(y,t)$. Ordinarily the array was processed into 16 experimental jet velocity profiles, each having N points and pertaining to one of the times 0, $T/16,\ldots,15T/16$, where T is the acoustic period. The profile center positions, best identified through a fitting function, indicate the jet deflection.

The fitting function that was used where the jet had evolved to the sech^2 shape was the following modification of Eq. (1):

$$U(y)=U_p+(U_0-U_p)\mathrm{sech}^2[(y-y_0)/b]. \tag{8}$$

Here b and U_0 again measure the velocity profile half-width and the central stream velocity, the jet displacement y_0 locates the center of the instantaneous profile, and U_p is a baseline shift or pedestal. The four parameters are evaluated by conventional numerical curve fitting. The velocity represented by the pedestal, the direction of which is not indicated by the hot wire, is due partly to fluid circulation toward the base of the jet, induced by entrainment. For an upstream profile (say, within a distance $10b$ from the flue), U_p has trivial time dependence. For the jet-displacement waveform, y_0 vs time, these procedures yield the phase lag of the fundamental-frequency component within 0.01 radian or better, and the amplitude x_0 of that component within limits well below 0.001 mm.

The following extension of Eq. (6) provides a good fitting function for the flattened profile found near the exit of the converging flue, where the shear layers are unmerged:

$$U(y)=U_p+(U_0-U_p)\mathrm{sech}^2\{[(y-y_0)/b]^n\}, \tag{9}$$

where $n=2$ or 3, according to the steepness of the bounding shear regions. An individual shear layer also can be fitted closely with the theoretically justified tanh profile (Michalke, 1965). In analogy to Eq. (8), the fitting function for this case is

$$U(y)=U_p+(U_0-U_p)\{1+\tanh[(y-y_0)/a_s]\}/2 \tag{10}$$

defining the experimental layer half-thickness a_s.

The data array also gives the local disturbance function (see Fig. 2 and discussion). For each of the N values of y, a Fourier series gives the local jet velocity as a function of time; dropping the constant term from each series leaves the local disturbance function. For small jet deflection amplitude, the fundamental-frequency Fourier component of the streamwise velocity oscillation at a given y is an approximate measure of the disturbance function. Further, when a symmetric jet executes a small displacement oscillation, at the center the magnitude of the disturbance function is zero and there is a phase change of π with respect to y.

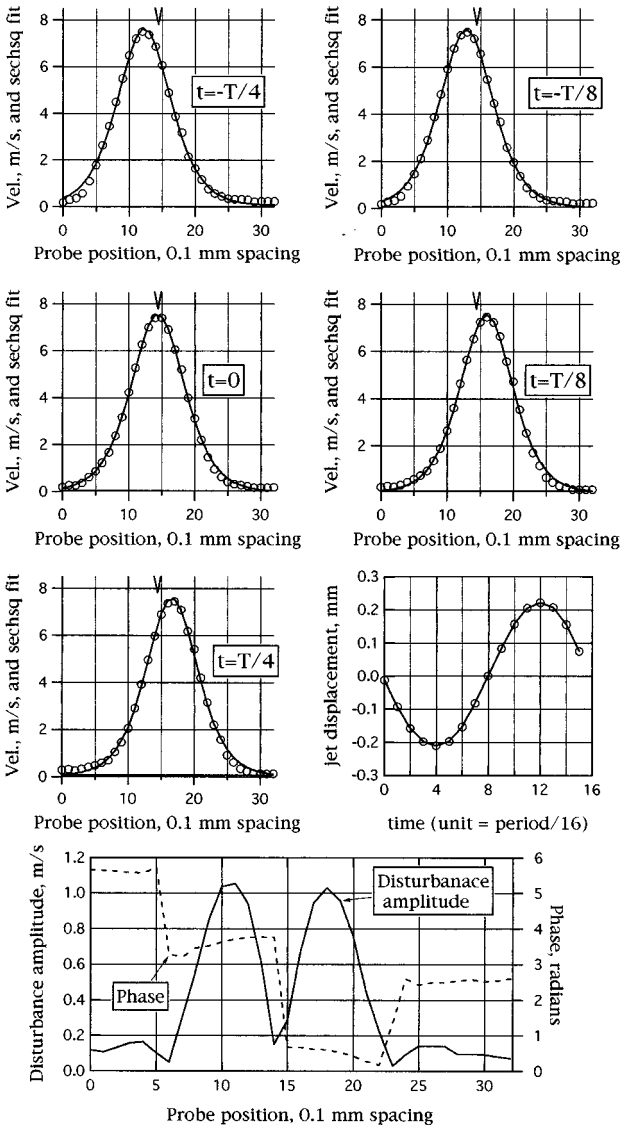

FIG. 6. Five instantaneous jet profiles, 100 Hz, with sech^2 fits. ''V'' shows average jet center position. Also, jet displacement versus time curve from 16 such profiles. At the bottom, amplitude and phase of local disturbance function, approximated as fundamental-freuquency component of time-varying velocity at each point (450 Hz). Measurements taken 8 diameters downstream; initially parabolic jet from 1-mm-wide flue, localized excitation.

The sample data in Fig. 6, for local excitation of a parabolic-profile jet from a 1-mm-wide flue, show some capabilities and limitations of the method. The observations were made at a downstream distance of eight times the full jet thickness, where the jet has approximately the sech^2 shape. Five instantaneous profiles are shown with fitted curves from Eq. (8). The full set of 16 profiles yields a smooth, well-defined displacement curve (y_0 vs time). However, the profile fits are not accurate in the skirts, partly because of a time-varying asymmetry, and partly because the disturbance function needed to maintain the sech^2 shape only occurs for $\omega_r=4/3$ (Sec. I). Therefore there is some ambiguity in the values of b and U_0; this is reduced when time averages of the quantities are used. Finally, Fig. 6 shows the

experimental approximation to the disturbance function. The minima flanking the central peaks were discussed in connection with Fig. 2.

The experimental local phase velocity of the jet-displacement wave is given by $\omega/(d\theta/dx)$, found from a sequence of local jet displacement waveforms;[1] similarly, the experimental growth factor μ is $d[\ln(\xi_0)]/dx$. An alternative approach, involving a two-channel quadrature lock-in detector at the hot-wire bridge output, was also used extensively. Here the computer converted one-second boxcar averages of the two analog outputs of the lock-in device to signal amplitude and phase, and kept track of the cumulative average phase difference and amplitude ratio as measurements were repeated alternately at two positions, usually 6- and 8-mm downstream. As remarked by Powell (1965), such x-direction probing within the stream can yield propagation constants in disagreement with profile displacement observations. The problem was avoided in the present work by performing the two-station measurements at a y position where the disturbance phase plot is flat, that is, where θ is nearly independent of y. The repetitive two-point procedure has the advantages that effects of drifts in temperature and jet velocity are reduced, and that the experimental frequency need not be related to the digital sampling rate. Experimental measurement of μ by this method requires correction for the change of the velocity profile with x. [That is, at each of the measuring positions the signal is proportional to the jet deflection times the zero-signal profile slope, $U'(y)$; the effect of differing slopes must be removed from the data.] The amplitude of the oscillatory hot-wire signal is proportional to the product of the jet displacement and the zero-signal slope.

A pair of probe microphones sampled the acoustic driving signal on both sides of the jet. In the apparatus of Fig. 4, the microphones communicated directly with the centers of the thin acoustic ducts. In the the case of Fig. 5, acoustic probe tubes of 0.75-mm i.d. terminated near the base plate, 7 mm either side of the flue. A linear modification of the waveform sampling procedure was used to process acoustic probe signals. The acoustic pressure difference from the probe pair was converted to a pressure gradient and used to calculate the nominal acoustic particle velocity and displacement at the flue, midway between the probes, there being no direct procedure to observe the acoustic flux in the presence of the jet flow. The acoustic pressure difference, which changes when the jet is turned on, was measured in the presence of the jet. With the setup in Fig. 5, activating the jet can cause an increase of more than 15% in the pressures at the probes, an effect which has been traced to the flow dependence of the acoustic impedance of the orifice (also see Sec. VIII). With an alternative long parallel-sided flue in place, this process is unimportant and the presence of the jet changes the acoustic pressure readings only on the order of 2% or less. This includes the contribution from the sound generated by the waving jet (see Sec. VI) and any contribution due to failure of the jet to be acoustically transparent. The latter is expected to be small for a jet of very small Mach number, and proves too small to evaluate is these experiments.

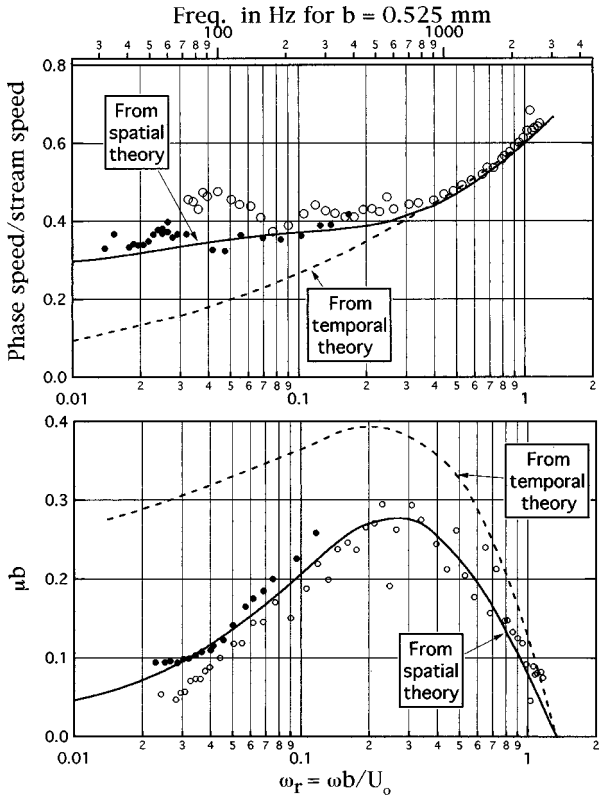

FIG. 7. (Bottom, a; top, b) Experimental jet-displacement phase velocity and growth data, with theoretical curves from spatially based calculations (Fig. 1), and temporally based calculations of Drazin and Howard (1966). Points ○: flue width 1 mm; ●: 0.5 mm. Localized excitation used.

IV. EXPERIMENTAL RESULTS: LOCAL EXCITATION

These are results from local jet excitation with the arrangement of Fig. 4. Figure 7 shows experimental values for the growth factor and the phase velocity of the sinuous instability. Most data were taken in the region 6–8 mm downstream (local U_0, 7.5 m/s) for an initially parabolic jet from a flue of 1-mm total width; some data taken 3 to 5 mm downstream, for a 0.5-mm-wide flue, are included. These conditions approximate a sech^2 jet nearly free of external excitation. Both of the methods described following Eq. (10) were used in measuring the propagation constants.

Measurements of the growth factor are in agreement with the spatially formulated calculation described in Sec. I and replotted in Fig. 7(a), but not with the temporally formulated calculation of Drazin and Howard (1966). (For this comparison, ω_r as used in Sec. I is identified with αc_r from Table I of Drazin and Howard, and μb with $\alpha c_i/c_r$. Their α is not the same as that used elsewhere in the present paper.)

Figure 7(b) shows the experimental sinuous-instability phase velocity c_p along with temporally based and spatially based theoretical curves. In the region $\omega_r > 0.5$ there is no significant disagreement between the spatial and temporal calculations, and experiment and theory agree. For much smaller values of ω_r the two calculations disagree strongly. The experimental data show no evidence for the low-frequency result from the temporal calculation, that c_p is proportional to ω_r, but are consistent with the larger values from the present calculations.

Certain local peaks in the experimental c_p are reproduc-

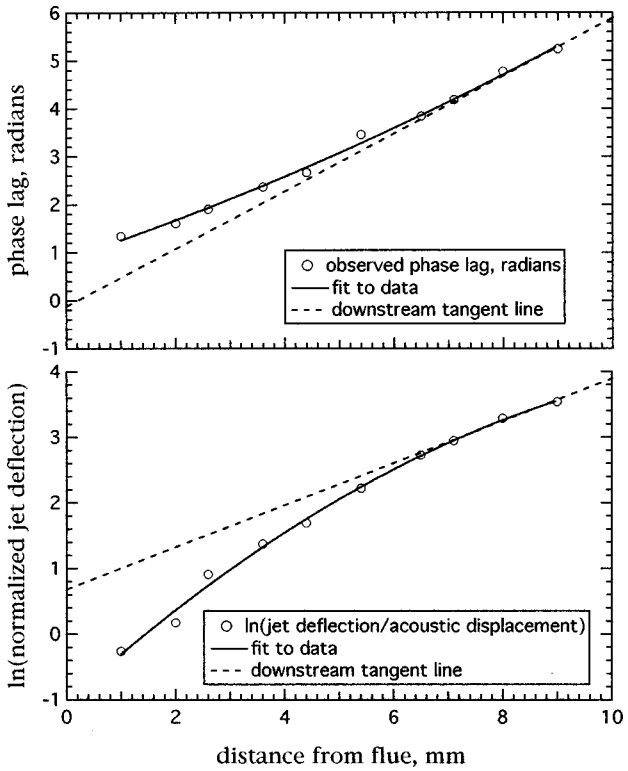

FIG. 8. Distributed excitation. Amplitude of fundamental-frequency component of jet deflection, and its phase lag in radians relative to the negative acoustic particle displacement, vs downstream distance. Jet with initial parabolic profile, 1-mm flue width, exit velocity 8.2 m/s. Straight lines extrapolate downstream slopes back to the origin as in Fig. 3.

ible, and appear to involve the acoustic signal produced by the jet itself, discussed in Sec. VI, which is of more importance for the thicker jet.

V. EXPERIMENTAL RESULTS: DISTRIBUTED EXCITATION

Figure 5 shows the experimental arrangement. Again the jet with initial parabolic profile (with $U_0=8.2$ m/s) is used, subject now to a cross-stream acoustic velocity nearly independent of x. Figure 8 shows experimental jet deflection amplitude and phase for 300 Hz ($\omega_r \approx 0.12$, rising slowly in the downstream direction). The broken line, in resemblance to Fig. 3, is approximately tangent to the farthest downstream part of the phase curve, and passes near the origin. (Because the phase and amplitude plots have some curvature everywhere, the fitted lines approximate tangents rather than asymptotes.) Since the parabolic jet has fully merged shear layers everywhere, general correspondence to the predictions for the sech^2 jet is expected; indeed, the slope of the broken line agrees with the phase velocity measurements in Fig. 7. The similar treatment of the logarithmic amplitude curve is less satisfactory; the slope of the broken line is 20% less than the theoretical value, and the implied amplitude at the origin is greater than the acoustic amplitude.

The jet setup used for Fig. 8 is well suited to showing the role of jet spreading. The increase of the semi-width b with x plotted in Fig. 9. The experimental points are well represented by the curve, which was calculated from Eq. (2) with $x_0=14.5$ mm the only adjustable parameter. From Eq.

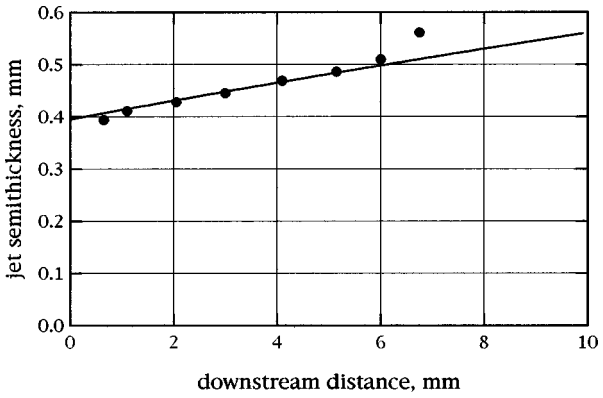

FIG. 9. Jet semithickness b vs distance from flue opening. Solid curve, calculated values from Eq. (2) with $x_0=14.5$ mm. Circles, experimental values.

(3) and the values of b, the calculated value of U_0, which varies as $b^{-0.5}$, falls by 12% from $x=0$ to $x=7$ mm. U_0 and b have contrary effects on the scaled phase velocity c_p, which rises by 2% (calculation through Table AI, the Appendix). The calculated decrease in the actual phase velocity is 10%, roughly just the result of the fall in U_0. Because of jet spreading, the linear phase curve fitted in Fig. 8 is only approximate; actually the plot should curve upward to reflect the behavior of the reciprocal phase velocity.

The next results are for the tophat velocity profile. Figure 10 shows the velocity profile and the apparent disturbance function (the cross-stream variation of the magnitude and phase of the time-varying part of the stream velocity), observed just one-half diameter from the flue. In contrast to the disturbance function in Fig. 6, the magnitude of the present function is not proportional to the absolute value of the slope of the profile. The explanation is that the local velocity variation now includes a large contribution from the acoustically induced time variation of U_0, discussed in Sec. VIII. An oversimplified simulation (not shown), in which a y-independent signal having the phase of the time-varying U_0 is added to the disturbance function expected for oscilla-

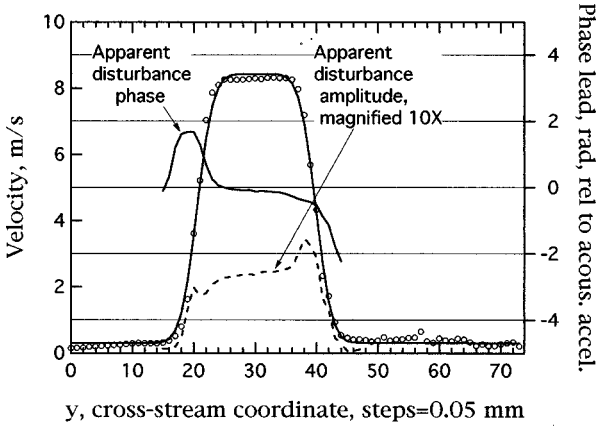

FIG. 10. Tophat jet, instantaneous velocity profile and fit from Eq. (6) with $n=3$; also cross-jet phase and amplitude profiles, called apparent disturbance functions because time dependence of stream velocity is due to modulation of stream flux as well as jet deflection. Observations 0.5-mm downstream from flue, of width 1 mm.

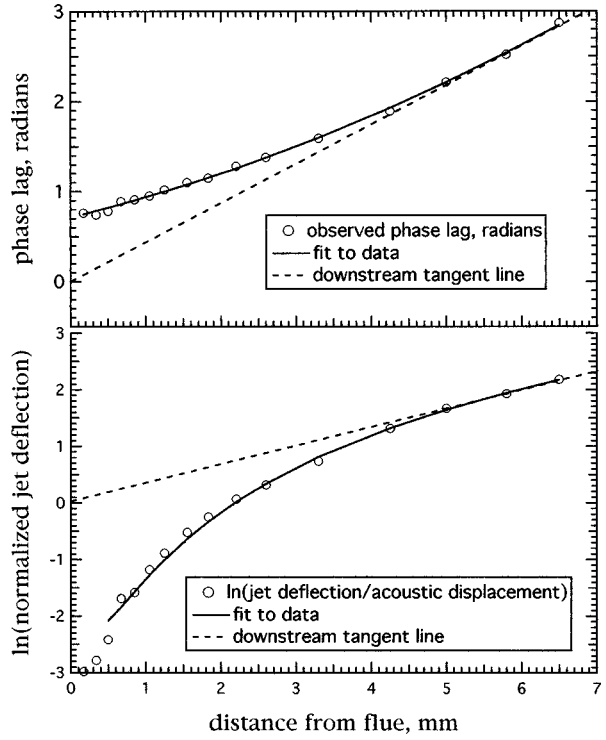

FIG. 11. Similar to Fig. 8, except that jet is from converging flue having 1 mm width, and initially has tophat profile.

tion of the jet with constant U_0, describes the apparent disturbance function well.

Again for the tophat jet with distributed acoustic drive, Fig. 11 shows that the linear back-extrapolation procedure works well, even though the transition from a tophat profile to an approximately sech^2 shape occupies the first 3 to 4 mm of travel. At the origin the downstream tangent lines behave as expected from Fig. 3. The slope of the line for logarithmic amplitude agrees with the theoretical value for μ, while the slope of the line for phase is some 20% less than expected from the calculations for the sech^2 jet (Table AI, the Appendix).

That the scheme of Fig. 3 gives near-quantitative results appears to be fortuitous. The presentation ignores the slow streamwise variation in the wave parameters associated with jet spreading. Further, there is not actually a single instability-wave phase just in front of the flue; Fig. 12 shows that the apparent overall jet deflection has a phase intermediate between the phases of the individual shear-layer positions, defined by the time dependence of y_0 in Eq. (8). From the results in Sec. I, after the shear layers merge to form a profile flatter than the sech^2 shape, the effective wave number $k(x)$ for the instability wave increases in the downstream direction by more than 20% as the jet profile evolves from tophat to sech^2 form (for example, from $n=2$ to $n=1$ in Table I) even without allowance for the decreasing U_0. To summarize, the linear extrapolation procedure suggests that $\int k(x)dx$ from the flue to a test point x_d far downstream is experimentally nearly equal to $x_d k(x_d)$, although $k(x)$ theoretically varies with x, and is not well defined near the flue.

An alternative approach to the jet behavior immediately

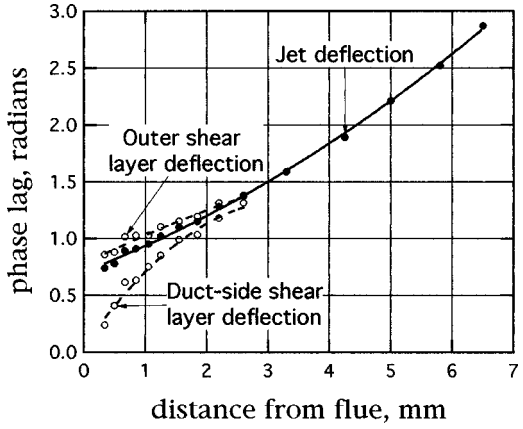

FIG. 12. Plots showing that, in the region of unmerged flow, the phase for deflection of the complete jet profile lies between the phases for deflection of the individual shear layers. Same system as for Fig. 11. Phase is relative to negative acoustic displacement.

in front of the flue is to analyze the oscillation of one of the unmerged shear layers, as in Sec. X.

VI. CONTIGUOUS SOUND FIELD

The wave motion on the jet is accompanied by oscillatory pressure changes within the jet and in the contiguous medium, including an audible signal in the vicinity of the apparatus. A particular reason for interest in the contiguous pressure is the inference that jet-generated sound contributes to the convection of the jet, as mentioned at the end of Sec. IV.

Figure 13 shows the result of a probe microphone scan perpendicular to the jet center plane, 6 mm from the opening. The setup of Fig. 4 is used, with the parallel-sided flue in place. Within the jet, the oscillating pressure is expected to be of fluid-dynamical origin. This pressure can be calculated in the limit of neutral stability ($\omega_r = 4/3$) from the analysis of the instability wave in the sech^2 jet given by Savic (1941); from this it is possible to show that the maximum value of the dynamic pressure is $0.51(\xi_0/b)\rho U_0^2$, where ξ_0 is the amplitude of jet oscillation. This accounts at least roughly for the internal pressure at the actual test frequencies; for

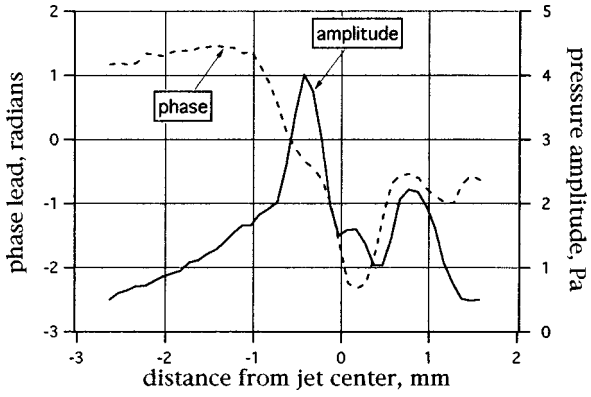

FIG. 13. Acoustic scan toward and through jet, 7.17 mm from opening of parallel flue. Local jet excitation, 300 Hz. Initial jet center velocity, 10.7 m/s. Amplitude and phase lead (radians) of fundamental-frequency pressure signal are shown. Zero phase is that of the local jet displacement (amplitude 0.19 mm), considered positive toward the left.

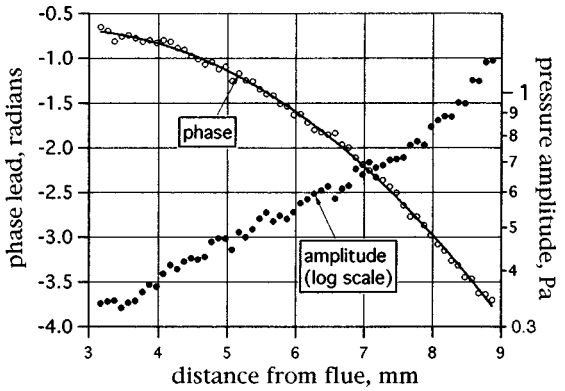

FIG. 14. Streamwise acoustical scan, on a path at -2.33 mm on the scale of Fig. 13. Initial jet-center velocity, 8.2 m/s. Local excitation, 300 Hz. Reference phase as for Fig. 13.

example, the observed pressure maximum in Fig. 13 is 70% of this value. (It is also several times that from the exciting ducts.)

The sharp kink in the amplitude curve of Fig. 13 at -0.7 mm on the abcissa scale marks the beginning of the contiguous pressure field. This can be regarded as an acoustic phenomenon, although in the near field explored here the compressibility of the medium is unimportant. More information, from a streamwise scan, is given in Fig. 14. The microphone probe is stepped along a path parallel to and 2.3 mm distant from the average midplane of the jet. The acoustic pressure amplitude is from 8 to 40 times that produced by the exciting ducts without the jet. The acoustic signal grows exponentially in the first 8 mm from the slit, but does not track the local jet displacement; its growth exponent is $0.18\,\mathrm{mm}^{-1}$, compared to $0.30\,\mathrm{mm}^{-1}$ for the jet deflection. Apparently stronger signals originating downstream modify the upstream readings. At other frequencies or other jet velocities, the growth exponent seen in the acoustical scan may be larger or smaller than that for the jet instability; similarly the rate of phase change with downstream distance may be larger or smaller than that for the jet wave. The acoustical signal at a given point represents the integrated contribution of the local acoustical sources corresponding to the jet displacement, plus the acoustical signal generated farther downstream (say farther than 12 diameters from the flue) where the shear layers roll up into vortices, themselves sound sources. A calculation taking all of this into account is not possible with present data, because the experimental methods do not reveal the vortex behavior, and also the dynamical equations for the jet assume an incompressible fluid, and therefore do not directly give acoustic results.

The jet-generated sound has a large phase difference between the two sides of the jet. This suggests that the jet is subject to a self-induced acoustic cross flow, in some resemblance to the stronger feedback process that would generate the edgetone if a downstream edge were present. The resulting small contribution to the driving signal at the flue opening has steady phase and amplitude for given apparatus settings and does not affect the measurement of the jet propagation constants. However, at the downstream measuring sites, where the jet is supposed to be free of external drive, the convection of the jet by self-induced sound causes errors in the stability-wave velocity and gain measurements, which can have either sign. This is apparently the source of the reproducible experimental irregularities in Fig. 7. A worst-case estimate of the the acoustic displacement due to the jet-induced signal is obtained by taking the pressure amplitude in Fig. 13, divided by distance from jet center, as an acoustic pressure gradient. This indicates an acoustic displacement that is comparable to the jet displacement, and therefore sufficient to affect measurements. In the present apparatus it is found that the self-induced acoustic displacement varies approximately as ω^{-1} times the jet displacement, so the difficulty occurs at the lower measurement frequencies. A much more rigorous analysis is needed.

VII. STEADY DEFLECTION

The deflection of the jet by a steady cross flow is a quadratic response, distinct from the low-frequency limit of the linear acoustic excitation considered above. In lieu of the rigorous fluid dynamical solution, this can be demonstrated by invoking momentum conservation. Consider an apparatus which differs from Fig. 5 in the respect that a wide, steady tophat jet of velocity U_s replaces the acoustic cross flow. The thin main jet has a tophat profile with velocity U_0 in the x direction. This simple model ignores the asymmetric distortion of the U_0 velocity profile; experimentally a rounded profile with a well-defined maximum is observed, and the jet deflection can be determined from velocity-profile curve fitting as before. Let $\xi(x)$ be now the steady deflection as a function of distance from the flue. In the streamwise interval 0 to x the composite jet acquires (per unit length in the z direction) momentum flux $\rho U_s^2 x$ in the y direction, which combines with the constant x-direction momentum flux $2\rho U_0^2 b$, where $2b$ is the jet thickness. At x, consideration of momentum components yields

$$\frac{d\xi}{dx}=\left(\frac{U_s}{U_0}\right)^2\frac{x}{2b}, \tag{11}$$

which is consistent with

$$\xi=(U_s/U_0)^2x^2/4b. \tag{12}$$

The actual deflection is expected to be somewhat less, as there is some escape of the lateral stream through the jet.

Experimental verification was obtained with a main jet having $U_0=10.5$ m/s, $b=0.5$ mm, and a side jet of thickness 7 mm, with $U_s\leqslant 4$ m/s. The deflection ξ was proportional to $(U_s x)^2$, as expected from Eq. (12). The observed jet deflection was 79% of the predicted value.

If it were supposed that Eq. (12) could be applied to a low-frequency oscillating cross flow, U_s would be written in terms of the acoustic displacement amplitude as Ξ_a/ω. For the conditions of the present experiments, the jet deflection then predicted by Eq. (12) would be several orders of magnitude less than the observed results. Also, in the present acoustic experiments there is no evidence of the square-law distortion in Eq. (12).

The static deflection process explains a phenomenon of flue organ pipes; if a pipe having an open end is adjusted so that the jet passes just inside of the upper lip, it fails to

oscillate, but if the end is then closed, oscillation occurs. Evidently the jet fluid in the stopped pipe returns through the pipe mouth as a low-velocity lateral flow which automatically deflects the jet to some equilibrium position about the lip, as required for organ pipe oscillation. Let F be the fraction of the jet flow that enters the pipe and returns through the mouth, and h the height of the mouth. The splitting of the jet at the lip gives

$$F = 1 - [\xi(h)/2b], \tag{13}$$

where for simplicity the initial jet thickness is used. In terms of the mouth flux and the jet flux,

$$F = hU_s/2bU_0. \tag{14}$$

From Eqs. (12) and (14),

$$\xi(h) = F^2 b. \tag{15}$$

The relevant solution of Eqs. (13) and (15) is $F = \sqrt{3} - 1 = 0.73$, independent of mouth height, jet thickness, and jet velocity in this simple model.

Through the mechanism described here, the mean jet position for a stopped pipe follows (through some physically realizable distance) as the lip is adjusted inward or outward. For an illustration see (Nolle, 1983, Figs. 4 and 6). There, oscillation occurred in an open pipe model, with cutup 6 mm, as the lip position was changed over a range of 2.9 mm. When a stopper was added, oscillation was observed as the lip position was varied over a remarkable range of 7.3 mm. In that reference, the static pressure inside the stopped pipe should be given as 1% of the supply pressure, rather than 10%.

VIII. TIME-VARYING JET FLUX AND WIDTH

In the distributed-excitation apparatus of Fig. 5, fitted with a sharply converging flue, acoustic pressure exists in front of the slit, in contrast to the arrangement in Fig. 4, which has a pressure null. Thus there can be a streamwise acoustic pressure difference in the flue. Its magnitude Δp_{ac}, which depends on the acoustic impedances of the opening and of the delivery channel (in the presence of the stream), was measured by microphone probes placed above and below the slit. The time-varying pressure difference causes the exit velocity to oscillate about its average value, U_0. This can cause losses in a flue pipe (Verge *et al.*, 1994b). The amplitude Δv_{ac} of the time-varying part of the velocity is expected to be somewhat less than the static Bernoulli value given by $(U_0 + \Delta v_{ac})/U_0 = [(P_0 + \Delta p_{ac})/P_0]^{1/2}$, where P_0 is the average head. Here the observed Δv_{ac} was some 60% of this static value. (The sharply converging flue has a flow-dependent acoustic impedance, causing the acoustic pressure readings due to the forcing signal to change when the jet is turned on. The alternative long parallel-sided flue, which has larger acoustic impedance, shows little of flow-velocity modulation or flow dependence of impedance.)

Experimentally, the time variation of the central jet velocity and that of the profile width are described by Fourier analysis of the time series for $U_0 - U_p$ and for b in Eq. (8). Alternatively, stream modulation can be described by Fourier analysis of the total jet flux. In either case, in the upstream region of nearly laminar flow the modulation components above the fundamental frequency are weak.

There was no clear indication of the varicose instability, which would have the following properties: (1) The time variation of $U_0 - U_p$ would have opposite phase to that of b. (2) For present conditions, in the region of the sech^2 profile, the phase velocity would be at least $0.8U_0$ (Mattingly and Criminale, 1971). (3) For such conditions, the gain exponent $-\alpha_i$ would be less than 20% of that for the sinuous instability. (4) The amplitude would be near zero at the slit, where the stream width is fixed. However, the time variation of flux at the flue is also expected to force jet width oscillation, not necessarily having the form of the varicose instability.

In the incompletely merged region, within some three diameters of the slit, the stream-width oscillation was in phase with the stream velocity oscillation, rather than out of phase. Farther downstream, in the sech^2 jet region, the phases of the stream-velocity and width oscillations differ, but erratic streamwise variation for the width oscillation suggests that a single mechanism is not dominant. The large phase velocity predicted for the varicose instability was not seen.

Also in the unmerged flow, the amplitude of the time-varying jet flux bears a constant ratio to the time-average flux, which increases with x by entrainment. Therefore the amplitude growth does not indicate varicose instability in this region. Farther downstream, in the sech^2 region, the amplitude change is no longer monotonic, but increasing flow noise makes it impracticable to separate out any varicose instability.

IX. RELATION TO ORGAN PIPE

The preceding work verifies the linearized jet stability theory under appropriate restrictions; the jet displacement does not exceed the half-width, b, and tests are confined to the region of laminar flow (say, within 8–10 diameters of the flue) where noise-reducing measurements give the regular velocity profiles expected from the theory.

These restrictions are not met in organ-pipe oscillation, except possibly in the early buildup. Coltman (1992b) has described some of the complications which arise in the closely related problem of the jet in a flute. In the neighborhood of the edge on which the jet impinges, the jet profile broadens and develops secondary maxima, the jet deflection does not have the phase expected from free-jet behavior, and the flux delivered to the resonator depends on the recent history of the jet deflection at the edge. Organ pipe oscillation will not be studied here in detail.

Coltman reported profile distortion at large amplitudes even in the absence of an edge. [Apparently related to this, Rockwell (1986), Chanaud and Powell (1962) and others found that eddies develop eventually along the jet even without an obstacle.] Saturation of momentum and mass flux into the resonator, when the displacement of the velocity profile at the lip is comparable to the profile width, is important in limiting the oscillation amplitude; Verge *et al.* (1994a) have shown that nonlinear acoustic loading at the mouth is also extremely important. Relating to the modification of the stream by the lip, it is known that the shear layers roll up into

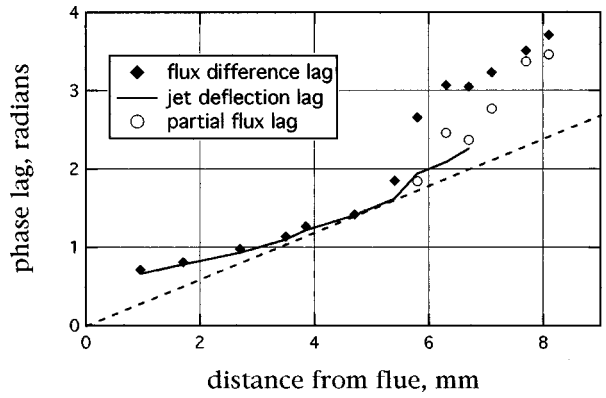

FIG. 15. Organ pipe simulation: Self-oscillation at 225 Hz of tophat jet, $U_0 = 10.5$ m/s, with stopped pipe. Solid curve: Phase lag of local jet deflection relative to negative acoustic displacement. Broken-line curve: Phase lag expected for sinuous jet instability, $c = 0.37U_0$ (compare construction in Fig. 3). Darkened markers: Phase lag of flux difference oscillation. Open circles: Phase lag of partial flux oscillation. (Definitions in text.)

eddies periodically at downstream obstacles such as the lip here or the wedge in edgetone systems. Near the obstacle, where the velocity distribution no longer resembles a free sech^2 jet, lateral flow may invalidate the techniques used here.

The experiment below shows the result of looking for the free-jet phase shift in equilibrium organ pipe oscillation. The jet apparatus was converted to a simulated organ pipe by installing a vertical closed-end resonator, of section 37 by 57 mm, in place of the horizontal acoustic duct shown in the apparatus of Fig. 5. The mouth height was 9 mm. The resonator length was adjusted to give oscillation at 225 Hz, with the entry stream velocity in front of the 1-mm flue opening 10.5 m/s.

The phase of the jet-displacement oscillation in the mouth is shown in Fig. 15, where the distance scale extends from flue to lip. The zero-phase reference is the fundamental-frequency acoustic pressure in the bottom part of the resonator; that is, a jet oscillation of zero phase would have maximum displacement toward the interior of the resonator at the time of maximum acoustic particle displacement toward the outside. The solid curve represents jet deflection data from the profile-fitting procedure described earlier.

The profile-fitting procedure fails within two millimeters of the lip, where the remaining semblance of an oscillating sech^2 profile disappears during portions of the cycle into a broad oscillating profile having about four times the width of the original jet, as shown in Fig. 16. To get around this difficulty, the waving jet was also analyzed with two versions of time-varying flux. The first version (darkened points in Fig. 15) shows the fundamental-frequency phase of the flux on the $+y$ (resonator) side of the mean flow center less the flux on the $-y$ side. This flux difference agrees with profile-fitting results where these are available, and has been identified by Coltman (1976) as the driving signal to the resonator. The second version is the partial flux, that which passes inside the resonator lip at a given time (open circles). The peak partial flux was about one-third of the total stream flux just below the lip. The broken line, which starts with zero phase at the flue, represents the theoretical phase velocity $c_p = 0.37U_0$ of the underlying instability wave for $\omega_r = 0.071$. For $x < 6$ mm the various measures of phase cluster about this line, but with the breakup of the sech^2 profile between 6 and 8 mm the flux phases acquire an extra lag of about one radian compared to this instability-wave prediction.

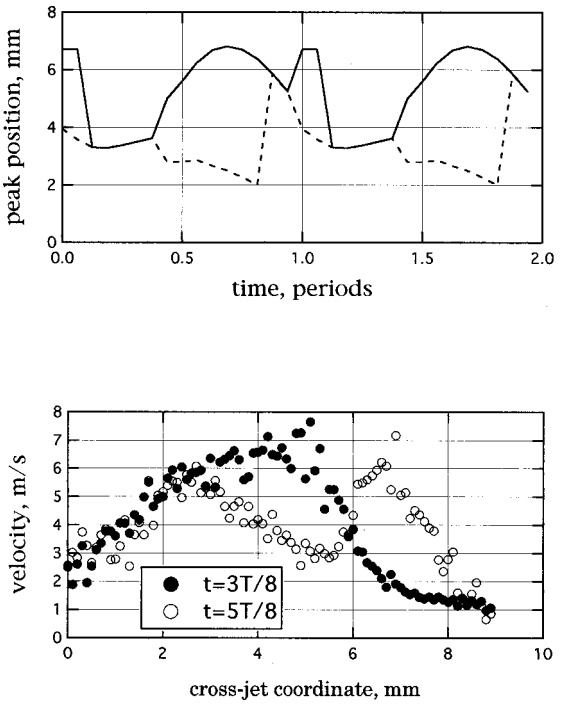

FIG. 16. Breakdown of free-jet displacement behavior near lip of oscillating pipe. Top: Solid and broken curves, jet profile peak locations, sometimes double, at downstream distance 8.1 mm (0.9 mm below lip). Bottom: Velocity profiles shown as experimental points for two time values, where $t = 0$ is time for most negative acoustic pressure in resonator. Flue center is at 4.75 mm and lip at 6.25 mm on position scales.

Figure 17 shows spatial growth of jet oscillation in terms of the amplitude of jet profile displacement and in terms of the time-varying flux difference. (The values from flux difference have been adjusted to track the other set near the flue.) As in Fig. 3 and Fig. 11, the broken straight line shows the amplitude of the underlying sinuous instability wave, starting with the same amplitude as the acoustic displacement. Its slope represents the theoretical μ (Sec. I). Its left

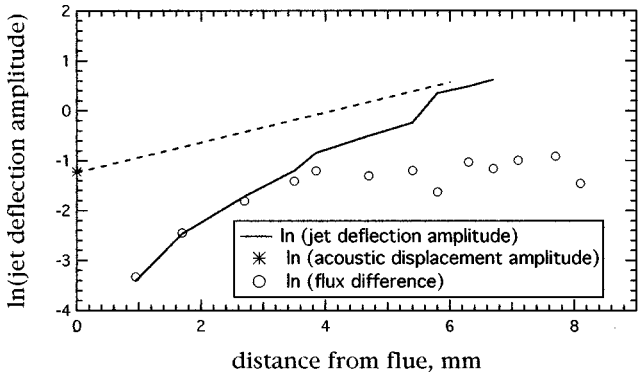

FIG. 17. Jet oscillation growth across mouth of oscillating pipe. Solid curve, ln of jet deflection amplitude in mm. Broken line, theoretical growth of instability wave, starting with the acoustic particle displacement amplitude. Circles, flux-difference amplitude, arbitrary units.

intercept corresponds to the acoustic displacement amplitude of 0.3 mm. The jet-displacement growth curve (solid) resembles that found without the resonator (Fig. 11), but the flux difference does not increase after some 4 mm of jet travel. This is the expected result of the jet deflection amplitude becoming greater than the stream width.

In equilibrium oscillation the overall gain of the instability wave is not expected to figure directly, provided that it exceeds a required minimum. The flux variations driving the pipe have approached a limiting amplitude, insensitive to gain. The acoustic level of oscillation, which sets the initial jet deflection amplitude, is simply that for which this flow input overcomes the losses. It is seen from Fig. 16 that most of the flux at the lip enters the pipe, as suggested by the approximate relation Eq. (15).

X. FURTHER TESTS IN ENTRY REGION

Further work is needed on the forced deflection of a jet with tophat velocity profile in the region immediately in front of the flue. Michalke (1965) cited experiments showing that each of the initially unmerged shear layers behaves like an isolated shear layer, for which he presented instability-wave calculations. In the low-frequency limit the phase velocity approaches U_0. However, the profile evolves within a few diameters to a flattened sech^2 shape, which theoretically can support whole-jet undulations having the much smaller phase velocities in Table I, and finally to the sech^2 shape for which the propagation constants are documented in Fig. 7. No attempt will be made here to resolve the motion at all distances into a combination of these modes, but a brief investigation will show that immediately in front of the flue the motion of one of the unmerged shear layers can be described by Eq. (7), in resemblance to the result of Elder (1978, 1980) for an isolated layer.

Equation (7) will be used to extract the shear-layer instability wave from the observed displacement of the layer. This serves to verify Eq. (7) and also allows Michalke's calculations to be tested in the entry region, near the zero-thickness limit. To avoid the complications of profile evolution, this test of Eq. (7) is based on the shear-layer deflection as a function of U_0, at a fixed small downstream distance x. The complex acoustic displacement is known.

For present purposes Eq. (7) takes the form

$$\xi_{\mathrm{rat}} = 1 - \exp(\mu x)\exp(ikx), \tag{16}$$

where ξ_{rat} is the complex ratio of the fundamental-frequency displacement of a shear layer (found by hyperbolic-tangent profile fitting) to the acoustic particle displacement. Experimental values of μ and k for a given x are found from the the real and imaginary parts of Eq. (16).

The theoretical values of the real and imaginary parts of the shear-layer propagation constant are tabulated by Michalke as $-\alpha_i$ and α_r, functions of a dimensionless frequency β that is analogous to ω_r in Eq. (4). The reference distance is twice the momentum thickness Θ_m, or equivalently for a hyperbolic tangent profile, a_s as defined in Eq. (10); thus $\beta = \omega a_s / U_0$. For $\beta \ll 1$ Michalke finds $-\alpha_i = \alpha_r = \beta$.

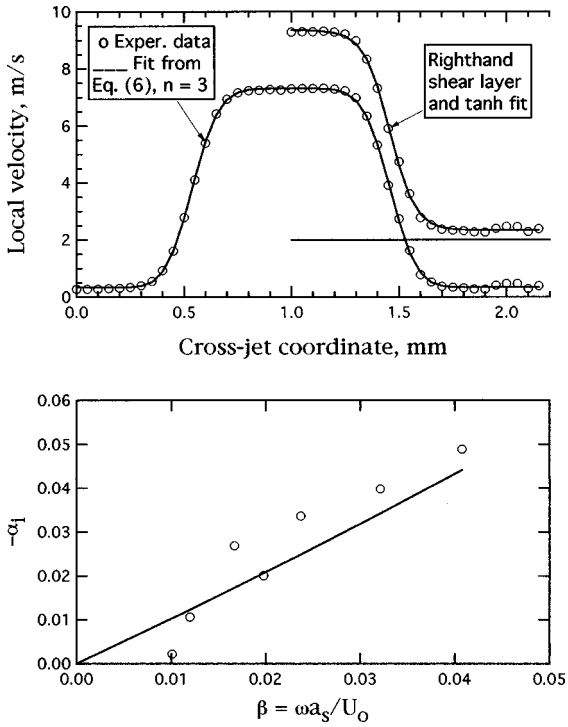

FIG. 18. Shear-layer test of tophat jet in entry region. Details in text. Top: An instantaneous jet profile, and tanh fit to shear layer nearest acoustic duct. Bottom: Measured gain exponent for shear-layer deflection versus dimensionless frequency parameter, which was varied by changing U_0. Solid line, Michalke's calculation.

With the setup of Fig. 5 the 1-mm driven jet, excited at 300 Hz, was investigated at the fixed downstream position $x = 0.41$ mm, for exit velocities between 6 and 15 m/s. The shear layer nearest the acoustic duct was observed. α_r and $-\alpha_i$ were found from Eq. (16) as described above. The top part of Fig. 18 shows an instantaneous profile and the fit by Eq. (10) to one of the shear layers, which yields a_s and U_0. The lower part of the figure shows the experimental $-\alpha_i$ vs β, and also Michalke's prediction. The rather scattered points show agreement between theory and experiment when the errors in obtaining the instability wave as a very small difference from Eq. (16) are considered. Also, the average of $-\alpha_i/\alpha_r$ (not plotted) is near unity as expected from Michalke for the low-frequency limit.

XI. ASYMMETRIC FLUE

To investigate changes in jet behavior when an asymmetric flue is used rather than the symmetric structures in the preceding work, the apparatus of Fig. 5 was modified by replacing the wedge-shaped metal plate forming the left-hand side of the flue opening with a square-cut one. The geometry of the opening then resembled that in a metal flue organ pipe with inverted languid; the flue opening was bounded on one side by a 6-mm-long flat surface, and on the other by a 45° wedge. Acoustic jet deflection was explored under the same conditions as for Fig. 11, except for the flue modification.

The following similarities with the results for the symmetric jet were found: (1) At a given downstream diatance, the phases of the shear-layer deflections and the overall jet

deflection remained in the same order as in Fig. 12. (2) A straight line extending the downstream phase delay plot back to the origin, like that shown in Fig. 11 for the symmetric jet, intercepted the left-hand axis at the same place. That is, for both the symmetric and asymmetric flue, the instability-wave displacement at the flue was in phase with the negative acoustic particle displacement.

The behavior of the asymmetric jet differed from that of the symmetric jet in these respects: (1) The velocity profile, even as far as 7 diameters downstream, remained somewhat flatter than the sech^2 shape. (2) The phase velocity of the instability wave, found from the slope of the tangent to the phase curve in the manner of Fig. 11, was $0.48U_0$ for the asymmetric flue as compared to $0.56U_0$ for the symmetric flue. (3) (Measurements taken 0.5 diameter from the flue.) The shear layer from the blunt-edge side of the flue was thicker by 10% than that from the sharp-edge side. (4) The flat central portion of the velocity profile near the flue, found in the symmetric case, was tilted in the asymmetric case, showing some 5% greater velocity on the sharp-edge side. (5) The periodic thickness variation in the outer shear layer (the one farther from the acoustic duct) lagged in phase by $\pi/2$ relative to that for the inner one, rather than approximately π as in the symmetric case. (6) Periodic steepening of the velocity profile, particularly on the sharp-edge side of the jet, suggested vortex formation.

These results came from a single asymmetric configuration. It would be desirable to extend the work to a flue where the flat-wall side is quite long. There would be some practical interest in finding further indications of the decrease in instability-wave phase velocity when the flue is asymmetric.

XII. SUMMARY AND DISCUSSION

The propagation of the sinuous instability in a planar jet, excited by localized acoustic flow across the flue opening, has been observed with noise-reducing techniques in a downstream region where the forcing signal is negligible, and where the velocity profile approximates the sech^2 shape. The results agree well with calculations based on the spatial evolution of the instability, as given by Mattingly and Criminale (1971) and additional calculations in the present work. The results are not well described by the conventional methods for converting calculations of temporal evolution of the instability to spatial evolution, although both the spatial and the temporal decriptions start with the Rayleigh stability equation. In particular, at low frequencies the temporal approach predicts phase velocity significantly less than that observed.

Again in the downstream region where the forcing signal is weak, a brief study was made of the pressure signal near the jet. The amplitude of this signal does not track the local jet displacement growth. This appears to confirm that this disturbance accompanying the forced jet oscillation is a contiguous acoustic signal, the observed amplitude at a given point being the integrated, acoustically propagated contribution from all regions along the stream.

In tests where the cross-stream acoustic forcing signal is independent of downstream distance, as would be found approximately in an organ pipe, the observed streamwise variation of the time-varying jet deflection is approximately explained as a superposition of acoustic convection of the jet and an instability wave which exactly cancels the acoustic particle displacement at the flue opening. This relationship has been suggested by several investigators. Near the flue, the combined effects yield an apparent phase velocity that can be of the order of twice the free-jet value for the sech-squared profile. An additional contribution to this phenomenon is found in further instability-wave calculations (Table I), which show that the phase velocity is increased by flattening of the jet profile relative to the sech-squared shape. Flattening is found in the region near the origin of the jet in the common situation where the stream is defined by edges having little streamwise length.

When the acoustical forcing signal is replaced by a steady cross flow, the jet deflection is quadratic in the cross-flow velocity, as expected from momentum considerations. The jet deflection in this case is thus not simply the zero-frequency limit of the linear acoustical forcing phenomenon. The jet deflection by a steady flow explains a phenomenon observed with stopped flue organ pipes, that return flow from the pipe causes an outward deflection of the jet so that the flow splits at the lip. A simplified model indicates that the fraction of the jet flux that passes inside the lip, to return through the whole mouth, is $\sqrt{3}-1$. This self-adjusting behavior of the jet in the stopped pipe reduces the need for adjustments of the airway and the lip. Wooden pipes, which are less easily adjusted than those of soft metal, are most often of this kind.

The small-signal free-jet instability wave which was studied here presumably can exist in an organ pipe from the flue to near the lip (the downstream edge) during some portion of the initial growth of oscillation, while the jet-displacement amplitude is smaller than the jet thickness. However, in an organ pipe excited at the normal steady-state level of oscillation, it has not been possible to detect either the small-signal phase velocity or the small-signal growth rate in the region near the lip. The major difficulties arise from nonlinearity due to the large jet-displacement amplitude and from extreme distortion of the velocity profile near the lip. Because of this profile distortion the usual concept of jet deflection fails. In an experiment reported here, the phase delay of the instability wave from the flue to a point some two jet thicknesses before the pipe lip is approximately that predicted for a sech^2 jet, but because of final profile distortion the time-dependent flux into the pipe has an additional lag of about 0.6 radian. The problems are similar to those found in experiments by Coltman (1992b). The accumulated experimental results show that for equilibrium amplitudes of oscillation in an organ pipe the oscillating jet flow at the lip is not a simply a time-delayed, broadened, and amplified version of that nearer the flue. That is, there is not a simple transfer function giving the downstream response of the jet in response to the acoustic excitation at the flue. The transfer-function concept permits plausible modeling of some features of both growing and steady-state pipe oscillation, for example in Fletcher (1976), McIntire *et al.* (1983), Nolle and Finch (1992), and Coltman (1992a). Nevertheless, for high-amplitude oscillation it has to be supplemented, at

the pipe lip, by phase-shift corrections and a modified, time-dependent velocity profile, both difficult to calculate.

The main body of results was obtained with symmetric flue openings. Further work with an asymmetric flue, such as that in a principal organ pipe, revealed distortion of the jet profile and changes in the relative phases of the initial displacements of the individual shear layers, but again showed the initial displacement in the the instability wave follows the negative acoustic displacement.

ACKNOWLEDGMENT

The author acknowledges a number of helpful discussions with professor Alan Powell.

APPENDIX: EIGENVALUE CALCULATIONS FOR THE STABILITY EQUATION

The eigenvalues of Eq. (5) were found by the procedure used by Michalke for the shear layer, where the dependent quantity is taken to be the complex stream function ϕ. Equation (5) is reduced to first degree by the substitution

$$\phi = \exp\left(\int \Phi \, dY \right) \tag{A1}$$

to become

$$\Phi' = \alpha^2 - \Phi^2 + U''/(U - \omega_r/\alpha), \tag{A2}$$

which has the same eigenvalues as Eq. (5). The independent variable range, $Y = -\infty$ to $Y = \infty$, is collapsed to the range $z = -1$ to $z = 1$ by the substitution

$$z = \tanh Y. \tag{A3}$$

Instead of $U = (1+z)/2$ in Eq. (A2), which was used by Michalke for the single shear layer, the sech^2 jet requires

$$U = 1 - z^2. \tag{A4}$$

TABLE AI. Eigenvalues of Eq. (5) for sech^2 profile.

ω_r	α_r	α_i	c_p
0.00625	0.0211	−0.0428	0.296
0.009	0.0305	−0.0428	0.295
0.0125	0.0414	−0.0536	0.302
0.018	0.0573	−0.0688	0.314
0.025	0.0765	−0.0860	0.327
0.036	0.1052	−0.1055	0.342
0.05	0.1415	−0.1361	0.353
0.072	0.1977	−0.1710	0.364
0.1	0.2692	−0.2068	0.371
0.14	0.3708	−0.2428	0.378
0.2	0.5163	−0.2704	0.387
0.25	0.6276	−0.2765	0.398
0.4	0.9085	−0.2533	0.440
0.5	1.0641	−0.2251	0.470
0.6	1.2033	−0.1946	0.499
0.8	1.4497	−0.1342	0.552
1.0	1.6688	−0.0786	0.599
1.2	1.8713	−0.0294	0.641
4/3	2.0000	0.0000	0.667

The present calculations from Eq. (A2) were made by integrating from $z = -1$ to $z = 0$. Following Michalke, the asymptotic solution was introduced by setting $\Phi(-1) = \alpha$. The value of $\Phi'(-1)$ was found from Eq. (A2) and the known $\Phi(-1)$ through a l'Hospital treatment for $z \to -1$. Following these transformations the goal in the eigenvalue search, which was previously that the eigenfunction have zero slope at the stream center, becomes $\Phi(0) = 0$. This approach was implemented with 16-digit calculations in 4000-element files, starting with $z = -0.999\,998\,34$ in lieu of -1. The step size started at 1.25×10^{-7}, becoming uniform after 200 points. A set of the resulting eigenvalues is shown in Table AI and Fig. 1.

The eigenfunction ϕ, which is proportional to $\mathbf{v}(Y)$, may be found from the eigenvalues by reversing the steps in Eqs. (A1)–(A3). A convenient choice of phase is that used by Mattingly and Criminale, where $\mathrm{Im}[\mathbf{v}'(0)] = 0$. The disturbance function is proportional to $\mathbf{v}'$.

The results for the profiles $n = 2$ and 3 in Table I were obtained by repeated numerical integrations of Eq. (5) to find the null of $\mathbf{v}'(0)$ in (α_r, α_i) space.

[1]The increment in θ is found from the phase difference of two temporal displacement waveforms, like the one in Fig. 6, for locations differing in x by much less than a wavelength. An alternative, basing the phase velocity on the distance between axis crossings of the waveform of jet displacement vs x at constant time, is less accurate, because of the variation of the phase velocity with x that is due to profile spreading.

Andrade, E. N. da C. (**1939**). ''The velocity distribution in a liquid-into-liquid jet, Part 2: The plane jet,'' Proc. Phys. Soc. London **51**, 784–793.

Bickley, W. (**1937**). ''The plane jet,'' Philos. Mag. **23**, 727–731.

Chanaud, R. C., and Powell, Alan (**1962**). ''Experiments concerning the sound-sensitive jet,'' J. Acoust. Soc. Am. **34**, 907–915.

Coltman, John W. (**1976**). ''Jet drive mechanism in edge tones and organ pipes,'' J. Acoust. Soc. Am. **60**, 725–733.

Coltman, John W. (**1992a**). ''Time-domain simulation of the flute,'' J. Acoust. Soc. Am. **92**, 69–73.

Coltman, John W. (**1992b**). ''Jet behavior in the flute,'' J. Acoust. Soc. Am. **92**, 74–83.

Cremer, L., and Ising, H. (**1968**). ''Die selbsterregten Schwingungen von Orgelpfeifen,'' Acustica **19**, 143–153.

Crighton, D. G. (**1992**). ''The jet edge-tone feedback cycle: Linear theory for the operating stages,'' J. Fluid Mech. **234**, 361–391.

Curle, N. (**1953**). ''The mechanics of edge-tones,'' Proc. R. Soc. London, Ser. A **216**, 412–424.

Drazin, P. G., and Howard, L. (**1962**). ''The instability to long waves of unbounded parallel inviscid flow,'' J. Fluid Mech. **14**, 257–284.

Drazin, P. G., and Howard, L. (**1966**). ''Hydrodynamic stability of parallel flow of inviscid fluid,'' *Advances Applied Mechanics* (Academic, New York), Vol. 9, pp. 1–89.

Elder, S. A. (**1978**). ''Self-excited depth-mode resonance for a wall-mounted cavity in turbulent flow,'' J. Acoust. Soc. Am. **64**, 877–890.

Elder, S. A. (**1980**). ''Forced oscillations of a separated shear layer with application to cavity flow-tone effects,'' J. Acoust. Soc. Am. **67**, 774–81.

Elder, S. A. (**1992**). ''The mechanism of sound production in organ pipes and cavity resonators,'' J. Acoust. Soc. Jpn. (E) **13**, 11–23.

Fletcher, N. H. (**1976**). ''Sound production by organ flue pipes,'' J. Acoust. Soc. Am. **60**, 926–936.

Fletcher, N. H., and Thwaites, S. (**1979**). ''Wave propagation on an acoustically perturbed jet,'' Acustica **42**, 323–334.

Fletcher, N. H., and Rossing, Th. D. (**1991**). *The Physics of Musical Instruments* (Springer-Verlag, New York), p. 432.

Hardisty, M. (**1974**). ''The effect of sound on vortex sheets,'' Ph.D. thesis, University of Dundee.

Mattingly, G. E., and Criminale, Jr., W. O. (**1971**). ''Disturbance characteristics in a plane jet,'' Phys. Fluids **14**, 2258–2264.

McIntire, M. E., Schumacher, R. T., and Woodhouse, J. (**1983**). ''On the oscillations of musical instruments,'' J. Acoust. Soc. Am. **74**, 1325–1345.
Michalke, A. (**1965**). ''On spatially growing disturbances in an inviscid shear layer,'' J. Fluid Mech. **23**, 521–544.
Nolle, A. W. (**1983**). ''Flue organ pipes: Adjustments affecting steady waveform,'' J. Acoust. Soc. Am. **73**, 1821–1832.
Nolle, A. W., and Finch, T. L. (**1992**). ''Starting transients of flue organ pipes in relation to pressure rise time,'' J. Acoust. Soc. Am. **91**, 2190–2202.
Powell, A. (**1965**). ''Aspects of edge tone experiment and theory,'' J. Acoust. Soc. Am. **37**, 535–536.
Rockwell, D. (**1986**). ''Vortex-edge interactions,'' in *Recent Advances in Aerodynamics (1983 symposium)*, edited by A. Krothapalli and C. A. Smith (Springer-Verlag, New York), pp. 181–203.
Savic, P. (**1941**). ''On acoustically effective vortex motion in gaseous jets,'' Philos. Mag. **32**, 245–252.
Schlichting, H. (**1933**). ''Laminare Strahlausbreitung,'' Z. Angew. Math. Mech. **13**, 260–263.
Thwaites, S., and Fletcher, N. H. (**1983**). ''Acoustic admittance of organ pipes,'' J. Acoust. Soc. Am. **74**, 400–408.
Verge, M. P., Caussé, R., Fabre, B., Hirschberg, A., Winands, A. P. J., and van Steenbergen, A. (**1994a**). ''Jet oscillations and jet drive in recorder-like instruments,'' Acta Acust. (China) **2**, 403–419.
Verge, M. P., Fabre, B., Mahu, W. E. A., Hirschberg, A., vanHassel, R. R., Wijnands, A. P. J., de Vries, J. J., and Hogendoorn, C. J. (**1994b**). ''Jet formation and jet velocity fluctuations in a flue organ pipe,'' J. Acoust. Soc. Am. **95**, 1119–1132.

Variables controlling contrast generation in a urinary bladder model

Emma Y. Hwang, J. Brian Fowlkes, and Paul L. Carson
University of Michigan Medical Center, Department of Radiology, Basic Radiological Sciences Division, Kresge III, R3315, Ann Arbor, Michigan 48109-0553

(Received 20 May 1997; revised 15 September 1997; accepted 5 March 1998)

An ultrasound system has been developed to generate microbubbles *in vivo* for use as ultrasound contrast agent. Possible applications include diagnosis of reflux in the urinary tract. In experiments designed to elucidate the contrast microbubble generation process, acoustic bursts (at 1.8 MHz, 125 ms) were propagated through a latex rubber balloon, modeled after a rabbit urinary bladder, containing fluids of various air and carbon dioxide saturations and concentrations of cavitation nuclei (0.198-μm-diam polystyrene particles). The peak rarefactional pressure threshold for contrast microbubble generation, as visualized with a diagnostic ultrasound system, decreased approximately a factor of 2 for increasing particle concentration from 10^8 to 10^{10} particles/cc, with the lowest threshold of 5.24 MPa. For samples with gas saturations below 50% and 10^{10} particles/cc, the average thresholds were at least twice as high as those of more saturated fluids (with mean threshold for saturated fluids of 6.45 MPa), and samples containing CO_2 had considerably lower thresholds than respective under-saturations in air. At a fixed pressure amplitude, echogenicity tended to increase with both increasing particle concentration and gas saturation; this was more favorable for samples containing CO_2. Even in a restricted-nuclei environment such as the urinary bladder, generation of vaporous cavitation should be possible; however, subsequently, abundant gas is needed to grow vaporous bubbles to persistent and imageable sizes, to assist in the diagnosis of urinary reflux. © *1998 Acoustical Society of America.* [S0001-4966(98)04406-3]

PACS numbers: 43.80.Vj, 43.80.Cs [FD]

INTRODUCTION

Injectable air-filled microbubbles (such as Albunex®) have been approved for use in cardiac ultrasound imaging. These bubbles, on the size order of 3 μm, are stabilized with an albumin shell that allows the bubble to persist in the circulatory system for several cardiac cycles. These air-filled microbubbles provide enhanced ultrasound signal (contrast) from the areas where the bubbles are present, due to the strong reflection (backscatter) of the transmitted ultrasound off the air interface of the microbubble. These shelled microbubbles are highly imageable by a diagnostic ultrasound system.

The question of whether imageable microbubbles can be produced in *in vivo* biological fluids such as blood or urine, instead of being injected, has been studied by several investigators in *in vitro* and *in vivo* animal experiments.[1–6] This transcutaneous generation of microbubbles occurs by acoustic cavitation of the fluid using focused high-intensity ultrasound. Generation of ultrasound contrast microbubbles directly in the urinary bladder would be advantageous for such diagnoses as urinary reflux (vesicoureteral reflux, VUR). This is a condition in which urine incorrectly flows from the bladder to the kidney due to defective valve function at one or both ureteralvesicular junctions, the connections between the ureters and the bladder. Presently urinary reflux is diagnosed using x-ray or radiolabeled contrast solution administered by uretheral catheterization. Use of a nonionizing imaging technology and the elimination of catheterization by transcutaneous ultrasonic contrast agent generation could considerably reduce the anxiety and complications associated with the diagnosis of urinary reflux.

In recent ultrasound studies, reflux was demonstrated by injection of ultrasound contrast agents.[7–12] Ivey *et al.* used color flow Doppler to visualize reflux of Albunex®, injected into the urinary bladder, progressing from the bladder through the ureters and into the collecting system of the kidney in a canine model where reflux was surgically induced. The reflux was also confirmed by the standard method of using x-ray contrast.[7] Atala *et al.* obtained similar results with a porcine model using sonicated albumin.[9]

In human studies, Hanbury *et al.* and Kessler and Altman diagnosed urinary reflux by agitating solutions to create microbubbles as contrast agents that were introduced into the urinary bladder by uretheral catherization.[10,11] Hanbury *et al.* used agitated saline and was able to detect higher grades (III and IV) of reflux with 100% sensitivity. Kessler and Altman injected agitated cystographic contrast agent (Cysto-Conray) into catheterized patients and visualized microbubbles in the kidney of refluxing patients. Even more promising was Darge *et al.*'s use of Levovist® ultrasound contrast agent for detection of grades I–III with sensitivity of 100% and specificity of 93%; all the sonographic scans were followed by standard x-ray voiding cystourethrography (VCUG).[12] The microbubbles were visualized in the ureters and/or renal pelvises for patients with VUR. These human studies, however, still required catherization of the patient. Matsumoto *et al.* were able to detect intraureteral reflux from the bladder and dual reverse urine flow in the ureter using color flow imaging.[13] This color flow method, though not using cath-

 0001-4966/98/103(6)/3706/11/$10.00

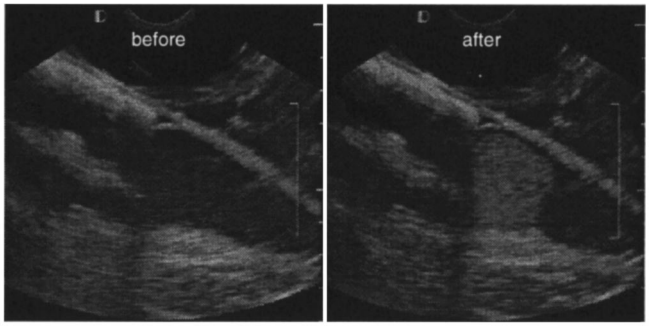

FIG. 1. *In vivo* transcutaneous contrast microbubble generation in a rabbit urinary bladder using a 125-ms, 8-MPa peak rarefactional pressure pulse, at 1.8 MHz.

eterization, is not known to be specific enough to distinguish between different grades of reflux.

In vivo studies were performed in canine urinary bladder in order to generate contrast agent without injection, using either 1.8- or 0.725-MHz ultrasound.[14] However, microbubbles were observed in only one of five canine experiments. The rarefactional pressure threshold for bubble generation was on the order of 6.6 MPa (an interpolated value assuming a linear frequency response of the calibrated hydrophone) for a 250-ms burst at 725 kHz. An imageable level of contrast microbubbles was maintained by repeated bursts, at a slightly subthreshold drive pressure, every 20 s after the initial cavitation event.[14] Similar rabbit experiments were also performed, and in seven of eight rabbits a significant amount of contrast microbubbles was produced in the urinary bladder. The average peak rarefactional pressure for contrast agent generation in rabbits was 8.9 ± 1.7 MPa for a 125-ms burst at 1.8 MHz.[15] The images in Fig. 1 show a case of successful transcutaneous generation of contrast microbubbles in a rabbit bladder at about 8 MPa. In these *in vivo* canine and rabbit experiments, no extrinsic cavitation nuclei were introduced into the animal urinary bladders.

The results of these preliminary *in vivo* experiments indicated a potential dependence of contrast microbubble generation on particulate concentration and gas saturation of the fluid. The difference in the particulate concentration of the canine and rabbit urine was qualitatively observed; the canine urine was typically clear, while the rabbit urine was characteristically turbid and cloudy in appearance. Solids were sometimes even visible in the rabbit bladder when the ultrasound scan was performed during experimentation. Gas analysis was not done on the canine subjects. For the rabbit subjects, gas analysis was performed and there was a correlation seen between the content of carbon dioxide in the urine and the threshold for imageable microbubble generation. This type of dependence was not seen for oxygen or for *p*H.[15]

Since urine is an aqueous fluid, reference will be made to studies of thresholds for acoustic cavitation in aqueous media without and with microparticles as cavitation nuclei. Holland and Apfel[16] measured deionized water (filtered to 0.2 μm) cavitation thresholds of 19.4, 23.5, and 24.3 atm for drive frequencies of 0.757, 0.989, and 2.3 MHz, respectively, with a 10-μs pulse duration and 1-kHz pulse repetition frequency (PRF). When 1-μm polystyrene spheres were added, at an approximate concentration of 3.35×10^8 spheres/cc, the thresholds for the same pulsing parameters dropped to 11.6, 11.3, and 13.0 atm for the respective frequencies, where thresholds were determined by using a passive cavitation detection system. Holland and Apfel also point out that a Blake threshold of 11.8 atm, which is on the same order of the cavitation threshold with the microparticles, can be computed from a 0.05-μm-radius bubble nuclei in water. This suggests that the crevices on the microspheres are nucleation sites for small cavitation bubbles.[16] Roy *et al.* showed using passive cavitation detection that water with a gas saturation of about 72% and particle concentration of 1.4×10^8 particles/cc (0.245 μm polystyrene microspheres) had a mean threshold of 7.9 bars for a 757-kHz transmitter with a 10-μs duration and 1-kHz PRF.[17]

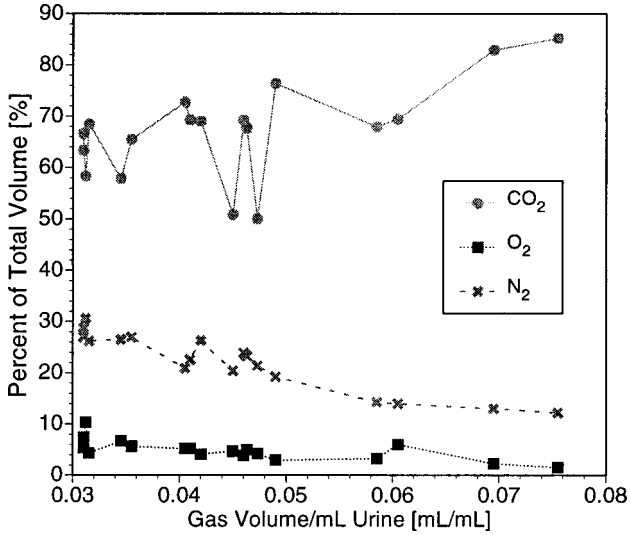

FIG. 2. Analysis of the dissolved gas composition of urine from a study[18] of 18 patients whose urine was collected over the course of a day. The major components extracted from the urine samples were carbon dioxide, nitrogen, and oxygen. The total volume of dissolved gases extracted per 1 cc of urine is shown on the abscissa. The percent of the three major gas components of the gas volume is plotted. The percent by volume of CO_2 appears to increase as the total gas volume in the urine increases. In contrast the percent by volume of O_2 and N_2 remains relatively constant or decreases as total gas volume increases.

To better delineate the factors for production of copious imageable cavitation bubbles for use as a contrast agent in the urinary system, aqueous experiments were performed in a simulated bladder. From the *in vivo* canine and rabbit experiments described above, it was observed that particle content and gas saturation might be key variables in bubble generation which could be manipulated experimentally. A French study[18] also showed that there is a greater amount of carbon dioxide dissolved in urine than of oxygen or nitrogen as measured by an extracted volume of all gases in a study of 18 human patients. As the volume of dissolved gases in urine increased, the percent of dissolved CO_2 in that volume increased, while the content of O_2 and N_2 tended to decrease (Fig. 2). Figure 3 also indicates that the urine is undersaturated by 29% of standard atmospheric pressure in total dissolved gas (the mean total gas pressure for all patients was 537 mmHg, compared to 760 mmHg for the hydrostatic pressure in the fluid or 754 mmHg for arterial blood[19]). This

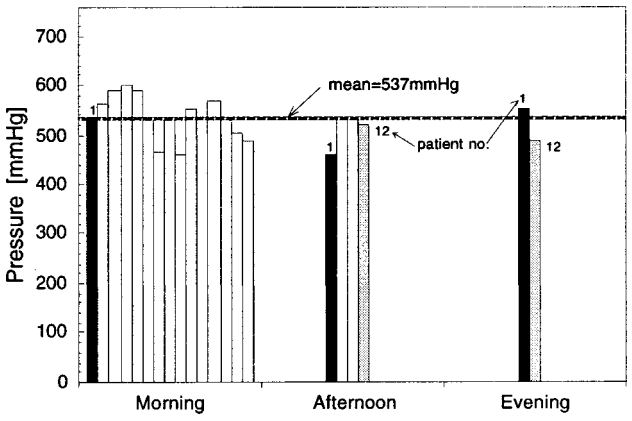

FIG. 3. Analysis of total gas pressure in urine from a study[18] of 18 human patients whose urine was collected over the course of a day. The total gas pressure is plotted for the morning, afternoon, and evening urine samples; only patient number 1 had urine samples for the three collection periods. The urine of all the patients is clearly under-saturated in gas, with an average pressure of 537 mmHg compared to 760 mmHg for the hydrostatic pressure in the fluid.

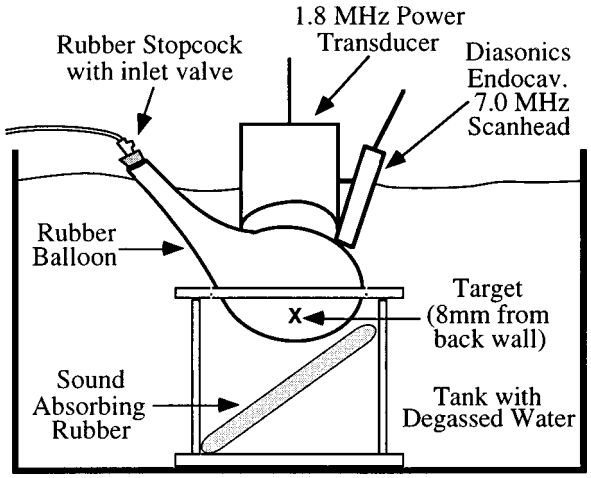

FIG. 4. Experimental apparatus used for contrast microbubble generation tests in a urinary bladder model. The balloon was filled with fluid of varying particle concentration and gas saturation. The coupled transducer assembly was identical to that used in previous *in vivo* rabbit experiments.

shortage of dissolved gas could prove to be an obstacle for initiating cavitation in human urine. Urine is actually under-saturated in oxygen by 65% and in nitrogen by 30% compared to arterial blood; and even though it is also under-saturated in CO_2 (38%), the large partial pressure of CO_2 (26 mmHg) yields an order of magnitude larger volume of CO_2 per unit volume of urine compared to the other gases due to the high solubility of CO_2 in aqueous solutions.

Therefore, the experiments presented here explore the dependence of microbubble generation in water on varying particulate concentration and gas content, in a test vessel modeled after an *in vivo* urinary bladder. This study will provide a better understanding of the possible manipulations necessary to transcutaneously generate imageable ultrasound contrast agent in *in vivo* biological fluids, for purposes such as diagnosing urinary reflux without ionizing agents or catheterization.

I. MATERIALS AND METHODS

Since the previous *in vivo* rabbit experiments were more successful at contrast microbubble generation in the urinary bladder, the experimental conditions and apparatus for the rabbit studies were simulated for these aqueous experiments, as shown in Fig. 4. A 1.8-MHz single-element spherically focused transducer (6.35-cm-diam aperture, 6.35-cm focal length, Etalon, Inc., Lebanon, IN), subsequently referred to as the power transducer, was coupled to a 7 MHz endocavitary diagnostic transducer (Diasonics VST, Diasonics Ultrasound, Milpitas, CA), referred to as the scanhead. Following the scheme outlined in a previous publication,[5] the transducers were coupled so that the focus of the power transducer was well within the field of view of the scanhead; this focal position was marked on the ultrasound scanner monitor for targeting purposes. The transducer assembly was then immersed in a large tank of degassed, filtered water.

A latex rubber balloon, measuring approximately 4.5 cm in diameter (the average size of a rabbit urinary bladder) was used as the exposure vessel for these microbubble generation studies. The exposure vessel was affixed in a Plexiglas holder to keep it immobilized during insonification (see Fig. 4). The holder was lined with sound-absorbing rubber (SOAB, BF Goodrich, Jacksonville, FL), and a slab of SOAB was placed beneath the balloon at an angle of 45 degrees in order to reduce standing wave conditions. During insonification, the focus of the power transducer was positioned 0.8 cm from the back wall of the exposure vessel, to simulate the exposure conditions for the *in vivo* rabbit experiments.

The opening of the balloon was capped with a rubber stopper in which a LuerLOK® tubing valve was inserted to control the flow of solution into and out of the balloon (see Fig. 4). The fluid to be exposed was prepared in large volume, and 50 cc of the solution was slowly injected into the balloon. The balloon was an appropriate size such that the 50 cc of fluid resulted in the distention of the balloon with little or no over-pressure; this was to simulate a full *in vivo* bladder.

The fluid parameters for testing the dependence of contrast agent generation on varying gas saturation and particle concentration are shown in Table I. The shaded boxes indicate the fluid conditions tested; those parameter combinations not tested are shown with a clear box. The three groups of experiments performed are highlighted by a shaded column or row, and were (1) air-saturated fluids with varying particle concentration, (2) samples with particle concentra-

TABLE I. Fluid parameters for varying particle concentrations and gas saturations tested in these experiments are indicated by the shaded boxe

		Particle Conditions			
		filtered DI water	*tap water*	*10^8 particles/cc*	*10^{10} particles/cc*
Gas Conditions	*air saturated*				
	air under-saturated				
	CO_2 saturated				
	CO_2 under-saturated				

tion of 10^{10}/cc at varying gas saturations, and (3) particle-free samples at varying gas saturations.

All tested fluids were prepared with deionized (DI) water, except for tap water samples, that was filtered to 0.2 μm and allowed to equilibrate to air saturation for at least 24 h before fluid preparation. The tap water was taken from a regular laboratory faucet and allowed to settle to air saturation before testing. To obtain different particle conditions, concentrated solutions of 0.198-μm-diam polystyrene particles (Cat. No. 5020A uniform latex polystyrene microspheres, Duke Scientific Corp., Palo Alto, CA) were added to the DI water.

These polystyrene particles were added to act as sites for nucleation of microbubbles. Normal urine sediments consist of small quantities of erythrocytes, leukocytes, and hyaline casts (protein material) and some crystalluria; these sediments can vary in size from 1 μm to several hundred micrometers.[20] It is possible that the crystalline sediment sometimes found in urine can act as cavitation nuclei. This was observed in the rabbit experiments where the turbidity of the urine is due to the presence of large amounts of phosphate crystals in the rabbit urine, and the generation of contrast microbubbles was more successful than in canines. The normal amount of solids excreted over a 24-h period is on average 70 g for an adult male human.[21]

The variations in air saturation in the samples was obtained by degassing the DI water to desired levels and then introducing the particles, if needed. Carbon-dioxide-saturated and under-saturated solutions were prepared by taking degassed water, with or without 10^{10} particles/cc, and bubbling medical grade carbon dioxide (98% pure) into the fluid at atmospheric pressure to a target gas saturation. After the bubbling process, the stock test fluid was allowed to equilibrate for at least 30 min before being injected into the exposure vessel (balloon). The saturation of the fluid with air or carbon dioxide was measured using a blood-gas analyzer (ABL300, Radiometer America, Inc., Westlake, OH).

For the power transducer, a 125-ms pulse at 1.8 MHz was used to attempt to initiate cavitation in the test vessel. This pulse parameter was chosen since it was identical to that used in the rabbit experiments, and yielded approximately the same number of acoustic cycles as used for microbubble generation in the *in vivo* canine urinary bladder studies mentioned previously; this was done so these experiments could be related to previous *in vivo* animal results.

The contrast agent generation threshold for this study is defined as the rarefactional pressure required to produce microbubbles imageable by a standard medical ultrasound scanner. The peak rarefactional pressure of the drive pulses was ramped from low (2.75 MPa or 203 W/cm$^2_{\mathrm{SPPA}}$) to threshold, or as high as the drive system would allow (14.6 MPa or 11, 440 W/cm$^2_{\mathrm{SPPA}}$). At each drive amplitude level, two bursts were applied with the bursts separated by about 20 s. If visible bubbles were not observed on the diagnostic scanner display, then the next pressure amplitude level was used. This ramping was continued until microbubble generation was observed or until the drive system limit was reached.

The same procedure for insonification of each sample volume was performed as closely as possible. Once the balloon was filled with the desired fluid, it was allowed to equilibrate, usually in a solution of the same gas content as the sample, for about 15 min. Just before the balloon was placed in the degassed tank, a small sample of the fluid inside the balloon was drawn and was injected into the blood-gas analyzer to record the gas content of the test fluid at time zero. When positioning the balloon in the tank, it was important to minimize the amount of time between targeting the test vessel and beginning the experiment so that the outgassing of the sample into the degassed tank water could be decreased. Video taping of the real-time scan from the diagnostic transducer was started at this point and continued for the duration of the test. The depth of focus, transmitted power, and B-mode gain for the scanner was fixed throughout the experiment so that the images could be compared. Beginning with the lowest pressure amplitude, the two 125-ms pulses separated by about 20 s were applied to the test fluid in the balloon. After waiting 1 min from the second pulse, the pressure applied was linearly stepped up; this sequence of increasing applied pressure was continued until an imageable bubble generation event occurred or drive limits were reached (as explained above). If microbubbles were observed, the drive voltage value (measured at the power transducer) was recorded. After the testing was complete on the sample, the balloon was taken out of the tank and final gas content measured with the blood-gas analyzer. The rest of the tested fluid was discarded and the balloon thoroughly rinsed with filtered DI water before a new test solution was injected.

The microbubble generation threshold voltage values were converted to rarefactional pressures using the data from the power transducer calibration at 1.8 MHz. This calibration was performed using a shock wave hydrophone with a disposable membrane (Sonic Industries, Hatboro, PA). A recently calibrated standard coplanar membrane hydrophone (Y-33-703 PVDF membrane, The Marconi Research Centre, Chelmsford, England) was used to reference calibrate the disposable hydrophone using low-amplitude acoustic waves at 1.8 MHz. Then the disposable membrane was employed to measure the field of the power transducer at high shock-wave intensities, which would have been detrimental for operation of the standard coplanar hydrophone.

The calibration relationship between the input drive voltage to the transducer and the resulting peak rarefactional pressure and spatial peak pulse average (SPPA) intensity at the power transducer focus is shown in Fig. 5. The polynomial fits in the plot and equations in the caption were used to interpolate pressure/intensities used in the experiments that were not performed in the points calibration. Therefore, the pressure and intensity values interpolated from this calibration take into account the nonlinear effects of high-intensity ultrasound in water (this is not merely a linear interpolation). Pressures stated throughout this manuscript are peak rarefactional, and intensity values stated are SPPA intensities, which were computed by numerical integration of the pressure waveforms following the method outlined in the AIUM standards.[22]

Echogenicity is a relative measure of the increase in contrast seen in the ultrasound image when an event such as

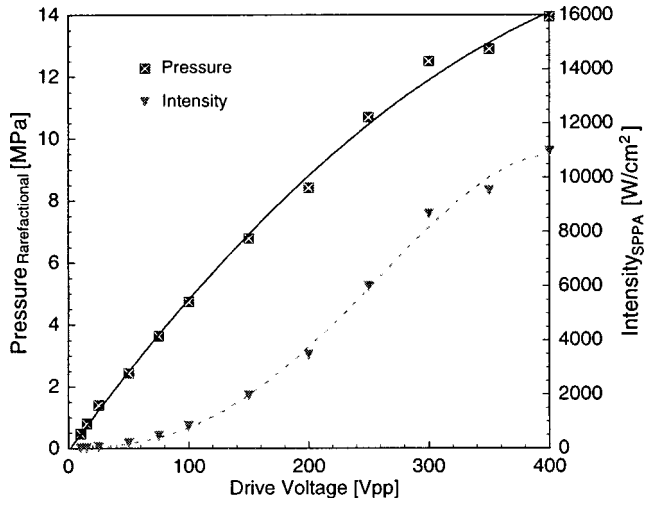

FIG. 5. Calibration of 1.8-MHz power transducer (Etalon 2) using a disposable hydrophone system referenced to a standard Marconi coplanar hydrophone. The resulting intensity and rarefactional pressure are plotted against the voltage applied to the power transducer. The data shown are fitted using the best polynomial fit; equations are $y=-4E-05\cdot x^2+0.0526\cdot x(R^2=0.9974)$ for rarefactional pressure and $y=-1E-06\cdot x^4+0.0005\cdot x^3+0.0295\cdot x^2+0.7972\cdot x(R^2=0.9968)$ for intensity. These fits were used to interpolate pressure and intensity values between calibration points.

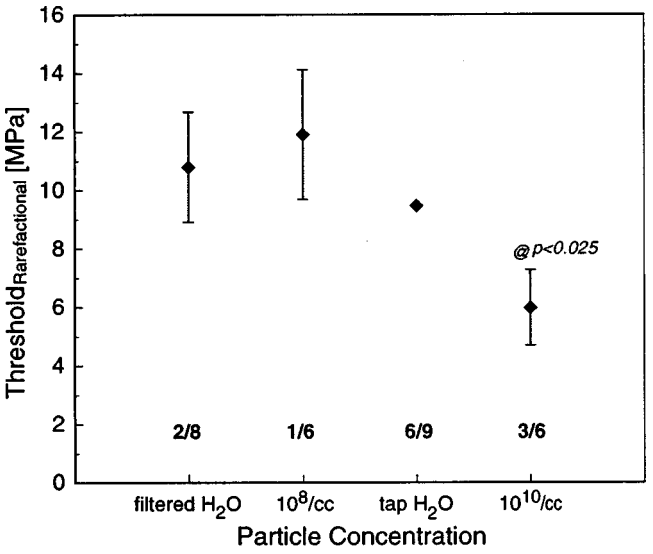

FIG. 6. Contrast microbubble generation thresholds (rarefactional pressures) for air-saturated water with varying particle conditions. The ratios shown next to the abscissa represent the frequency of occurrence at which microbubble generation was observed for the respective particle concentrations. Notice that at higher particle concentrations the threshold is lower and the error bars about the means, which denote one standard deviation, are smaller. The thresholds for the 10^{10} particles/cc samples are statistically different from thresholds in the three other conditions, with a p value of 0.025.

cavitation generates imageable bubbles, i.e., bubbles producing signal stronger than the background or previous image. A quantitative measure of echogenicity resulting from contrast microbubble generation was made for all the various particle and gas saturation samples insonified at the same pressure amplitude, 10.8 MPa (or 6184 W/cm^2). This constant pressure amplitude is above threshold for most samples and was chosen so that the samples could be compared. An estimate of the echogenicity was made by selecting a frame from the video recording of the highest apparent echogenicity; that is a frame where the highest contrast signal was seen from all the video frames within 20 s after each single burst from the power transducer. A background image before each insonification of the samples was also captured digitally.

The AVS image processing software (Advanced Visual Systems, Inc., Waltham, MA) was used to select spatially identical regions of interest (ROI) from each pair of background and high signal images. The ROI was selected well within the test vessel and excluded the balloon wall. The pixel values from the pre- and post-exposure ROIs were then log decompressed to obtain approximately linearized signal amplitude values. The signal amplitudes from the pre-exposure ROI were then subtracted pixel by pixel from the post-exposure ROI, and the resultant ROI pixel values were summed to give a quantitative measure of the approximate overall increase in the echogenicity that resulted from microbubble generation for a single burst. To determine the dependence of the varied fluid parameters on the resulting echogenicity, the echogenicity values for a parameter group (gas saturation or particle content) were normalized to the greatest echogenicity value in that group; for example, when computing echogenicity as a function of gas saturation, these echogenicity values were normalized to the largest computed absolute echogenicity value of all the samples where gas saturation was varied. The normalized echogenicity results were plotted on a dB scale.

Statistical analysis of the threshold and echogenicity data was performed using the software package JMP (version 3.2.1 for the Macintosh, SAS Institute, Inc., Cary, NC). For particle content experiments, the data was grouped by particle condition (four groups) for computing means and standard deviations. For gas saturation experiments, analysis was performed by grouping data by saturation less than or greater than 50% and by gas type (four groups). Group means were compared for statistically significant differences using paired Student's t testing.

II. RESULTS

A. Particle concentration experiment

The imageable microbubble generation threshold measurements in air-saturated fluids as a function of particle concentration, shown in Fig. 6, indicate that at 10^{10} particles/cc the threshold was statistically lower (p value of 0.025) than at lesser particle concentrations, with the lowest threshold being 5.2 MPa (934 W/cm^2). The mean threshold decreased by approximately a factor of 2 (or four times in intensity) for an increase in particle concentration of two orders of magnitude, from 10^8 to 10^{10} particles/cc. The error bars, on this and all subsequent plots, represent one standard deviation from the mean. The ratios shown for each particle condition indicate the frequency of occurrence of imageable bubbles at these pressures with repeated trials.

Similarly, there appears to be a general increase in the echogenicity at higher particle concentrations, as seen in Fig. 7, although the trend is arguably more gradual. The mean echogenicity of air-saturated fluids containing 10^{10}

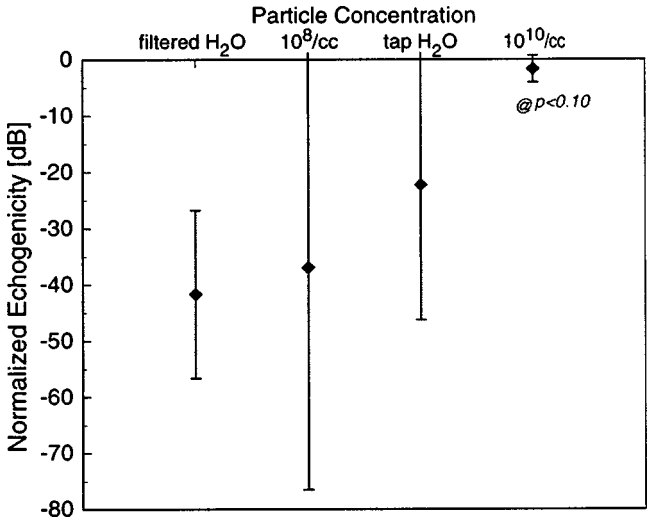

FIG. 7. Echogenicity as a measure of contrast generation for air-saturated water with varying particle concentrations, measured at a peak rarefactional pressure of 10.8 MPa. The error bars represent one standard deviation from the mean. The echogenicity for the 10^{10} particles/cc samples is only statistically different from the filtered DI water samples, with a p value of 0.10.

particles/cc was almost 20 dB higher than that with the lower 10^8 particles/cc concentration; however, the 10^{10} particles/cc samples are only statistically different from the filtered DI water samples with a p value of 0.10, and not different from the other sample conditions.

B. Gas saturation experiments

Figure 8 shows that at gas saturations above 50% and particle concentrations of 10^{10}/cc, the thresholds for contrast

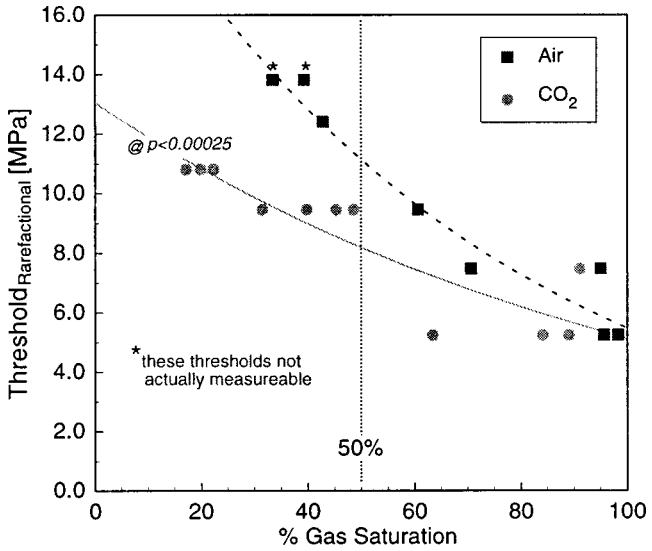

FIG. 8. Contrast generation thresholds (rarefactional pressures) for 10^{10} particles/cc water with varying air and carbon dioxide saturations. The asterisks next to the data points indicate that these values might be higher, but the limit of the power transducer drive system was reached. The fit lines are shown to emphasize the decreasing trends for the thresholds as gas saturation increases. The thresholds for samples containing CO_2 appear lower than for respective air samples, particularly at gas saturations below 50% (data points to the left of the vertical 50% line in the plot); for data left of the 50% line, the mean thresholds for CO_2 samples were statistically different from air samples, with a p value of 0.00025.

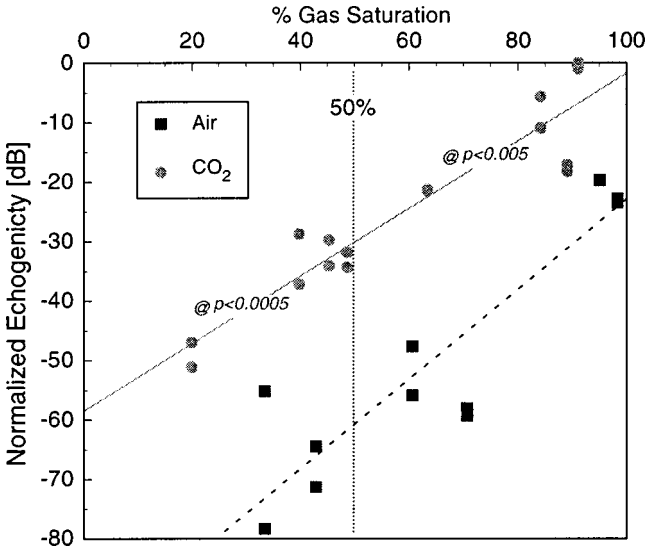

FIG. 9. Echogenicity as a measure of contrast microbubble generation for 10^{10} particles/cc water with varying air and carbon dioxide saturation, measured at a peak rarefactional pressure of 10.8 MPa. Echogenicity values were normalized to the highest computed value for absolute echogenicity from all the samples. The fit lines are shown to emphasize the increasing trend in echogenicity as gas saturation increases. All the echogenicities for the CO_2 samples are at least 20 dB, higher than respective air samples. For samples left of the 50% vertical line (less than 50% gas saturation), the mean echogenicity for CO_2 samples was statistically higher than air samples (p value of 0.0005); for data right of the 50% line, mean echogenicity for CO_2 samples was also greater with a p value of 0.005.

microbubble generation for both air and CO_2 samples were at the level seen in *in vivo* rabbit experiments or lower, with average thresholds of 6.5 ± 1.5 MPa (2040 ± 1460 W/cm^2). For aerated samples at saturations below 50%, though, some thresholds were very high, particularly for the least saturated samples (as indicated in Fig. 8 by the asterisk next to the data point), and were not actually determined due to the limits of the amplifier used to drive the power transducer. The important result to note is that the samples with CO_2 saturation below 50% have statistically lower thresholds, 10.0 ± 0.7 MPa (5276 ± 995 W/cm^2), than respective cases of air saturation (13.4 ± 0.8 MPa), with a p value of 0.00025. The fit lines are shown just to emphasize the trend of decreasing threshold as gas saturation increased.

Echogenicity, at a peak rarefactional pressure of 10.8 MPa with all samples having 10^{10} particles/cc, measured at the various gas saturations showed a distinct trend of increase in echogenicity as saturation increased, as plotted in Fig. 9. This was true both for air and CO_2 samples; however, the echogenicity for the CO_2 samples was significantly greater than seen in the air samples by at least 20 dB. The mean echogenicity for samples with CO_2 saturation less than 50% was statistically higher than those samples with less than 50% air saturation, with a p value of 0.0005; for samples greater than 50% saturation, the mean echogenicity for CO_2 samples was also higher with a p value of 0.005.

The thresholds and echogenicity for samples containing air or CO_2 at various gas saturation levels and without added particles were determined. However, these experiments showed much variability and inconsistency in the thresholds and echogenicity, which can be attributed to the lack of nu-

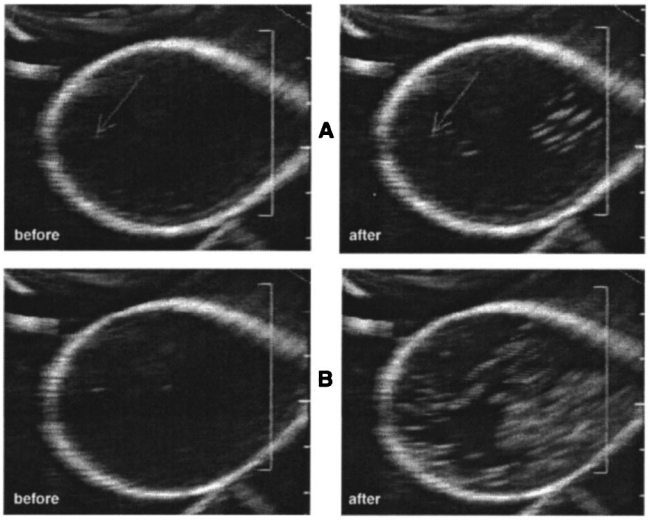

FIG. 10. Representative images of contrast microbubble generation in the urinary bladder model. All samples have particle concentration of 10^{10}/cc and gas saturation of about 100%. Image pair A is for a sample saturated with air, while B is a pair with CO_2 saturation. Each pair of images shows the results before and after a single 10.8-MPa pulse was delivered. Note the greater echogenicity in B after the pulse.

clei present to initiate cavitation. A summary of the results of samples with no added particles will be elaborated upon in the next section, where the effects of both variables, particle concentration and gas saturation, will be discussed.

C. Combined effects

Figure 10 are representative images for imageable microbubble generation in samples with particle concentration of 10^{10}/cc and with gas saturation of near 100%. The top pair of images (A) are typical results for a sample saturated with air, before and after the sample was exposed to one pulse at 10.8 MPa. The bottom pair of images (B) are for a sample saturated with CO_2, with the same amplitude pulse. Notice the greater amount of echogenicity resulting from samples with CO_2 (comparing A and B after-images) shown qualitatively in Fig. 10, but confirmed quantitatively in Fig. 9.

In contrast, Fig. 11 shows images from representative samples with no particles added and at a gas saturation of approximately 100%. The A image pair is for air and B images are for CO_2. Again, the echogenicity for the CO_2 sample is greater than for the air sample, but this amount is significantly less when compared to those samples with 10^{10} particles/cc (comparing respective images from Figs. 10 and 11); this will be quantitatively presented below.

Figures 12 and 13 show the combined effect of particle concentration and gas saturation on threshold for contrast microbubble generation and echogenicity, respectively. Each bar represents the average of the thresholds for samples with gas saturation above or below an arbitrarily selected value of 50%; the bars that have solid shading have gas saturation above 50%, where the hatched bars are saturations below 50%. The bars are also separated into those samples that have air or CO_2, where the dark shading is for air (horizontal hatching for under-saturated) and the lighter shading is for CO_2 (vertical hatching for under-saturated) samples.

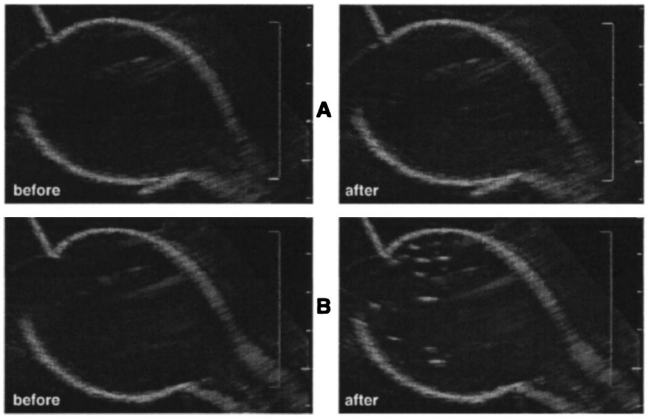

FIG. 11. Representative images of contrast microbubble generation in the urinary bladder model. These samples have no particles added and gas saturation of about 100%. Image pair A is for a sample saturated with air, while B is a pair with CO_2 saturation. Each pair of images shows the results before and after a single 10.8-MPa pulse was delivered. Note the decreased overall echogenicity of these samples compared to those images in Fig. 10.

The threshold plot (Fig. 12) shows that with plenty of cavitation nuclei (10^{10} particles/cc), the threshold decreases by about half with increased gas saturation whether the gas is air or CO_2 (referring to the set of four bars on the right side of the plot). However, the thresholds for samples containing air or CO_2 with saturation above 50% (comparing bars that have solid shading) are not statistically different from each other, with or without particles. However, when the saturation drops below 50%, the thresholds of the samples containing air or CO_2 are statistically different (comparing the adjacent pairs of hatched bars) with p values of 0.001, with CO_2 samples having lower thresholds whether particles are present or not. For under-saturated samples ($<50\%$), it

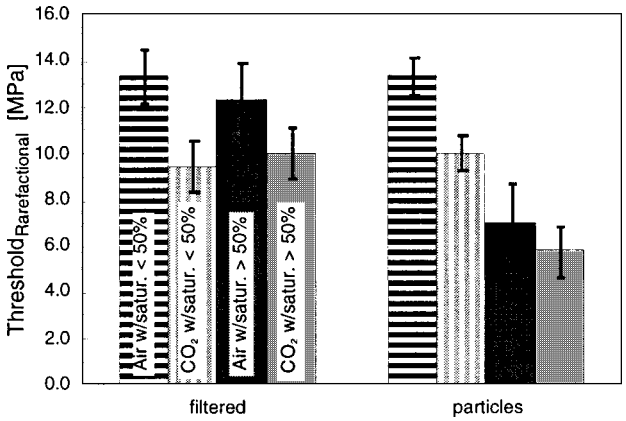

FIG. 12. Rarefactional pressure thresholds shown for all samples grouped such that each bar represents the average of the thresholds for samples with gas saturation above or below 50% and containing CO_2 or air, resulting in four groups. The samples are then grouped according to particle content; the filtered category is for no added particles and the particles classification is for samples with 10^{10} particles/cc. The error bars represent one standard deviation about the mean for each group of samples (each group has a varying number of samples, with n for each group equal to or greater than 3). There is a distinct trend of decreasing threshold with an increase in gas saturation when particles are present, whether for CO_2 or air samples. However, for filtered samples, the thresholds are consistently high. Note that for under-saturated samples (hatched bars), the thresholds are unchanged whether particles are added or not.

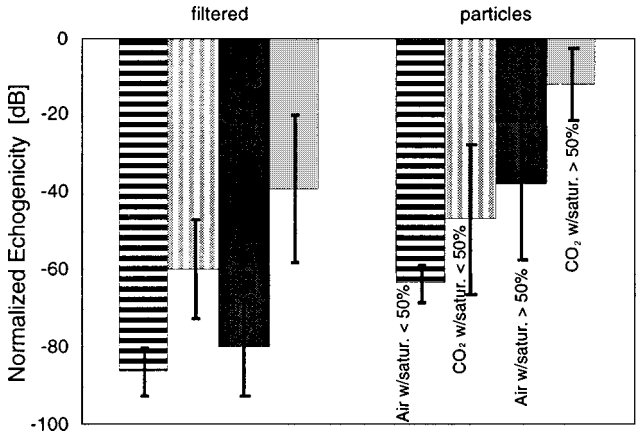

FIG. 13. Normalized echogenicity shown for all samples grouped as explained in the caption for Fig. 12. There is a distinct trend of increasing echogenicity with increase in gas saturation when particles are present, whether for CO_2 or air samples. Note that for samples containing CO_2, the mean echogenicity is higher by at least 20 dB than the respective group of air samples; this is particularly significant when looking at the filtered group of bars.

made no difference in the thresholds if there were added particles or not (comparing the same hatched-bars in the filtered and particles groups). As expected, though, the threshold for samples with particles is statistically lower than those without particles when there are sufficient amounts of gas (gas saturation greater than 50%; comparing the same solid bars for filtered and particles), also with p values of 0.001.

When there were plenty of cavitation nuclei, such as in the case of samples with 10^{10} particles/cc, there was a distinct trend of increasing echogenicity as gas saturation increased (shown in Fig. 13 on the right side of the plot, and referring again to Fig. 9). Note in particular that the effect of having CO_2 versus air improves the mean echogenicity; this significance can be seen for both the cases with particles and without, and in both gas saturation categories. However, the effect is only statistically significant for the case of filtered samples with saturation less than 50% with a p value of 0.001.

III. DISCUSSION

Human urine was not collected and used in these aqueous experiments for several reasons. Although human urine can readily be collected, the quality of the collection and the preservation of the physiological conditions during *in vitro* experimentation cannot be guaranteed with the current experimental setup. A rigid protocol must be developed to collect urine without introducing external contamination; this can be more difficult with collection of urine from female subjects. Also, once the urine has been emptied from the bladder the gas saturation, temperature, and pH can change significantly from normal, causing precipitation of additional solids if the sample is left standing. The collected urine properties would no longer be similar to that found in the *in vivo* bladder. Of course, water with particles is also not equivalent to urine in the bladder; however, these aqueous experiments were performed as a baseline to understand what parameters could be manipulated to increase the generation of imageable contrast microbubbles. For these manipulations, it was more reasonable to use water samples rather than trying to change parameters of excreted urine that would already have varying properties from one collection time to another that could not be easily controlled in *in vitro* experiments.

The threshold for imageable microbubble generation was determined by the operator's observation of the images from the diagnostic scan of the exposure process. A more objective method for determining the threshold can be developed by performing echogenicity calculations on all pulse amplitudes applied to a single sample. When the calculated echogenicities are plotted as a function of the drive voltage or applied pressure amplitude, then there theoretically should be a point where the echogenicity will increase rapidly from a baseline value to very high values at super-threshold pressures. A threshold value can then be objectively extrapolated from such a plot. This method of determining the threshold can be time consuming in the processing, which is a reason this was not done for these experiments. This method has been tested with data from rabbit experiments, with some success and some problems identified. However, in the future this threshold method can still be performed since each sample was video recorded throughout the exposure procedure.

A. Particle concentration experiment

Note that although the filtered, tap, and 10^8 particles/cc water samples had almost the same microbubble generation threshold (Fig. 6), the experiments in tap water more consistently resulted in imageable microbubbles, as evidenced by the absence of error bars, that denote one standard deviation about the average threshold. The higher consistency of bubble generation in tap water and the lower threshold for solutions with 10^{10} particles/cc, as shown in these results, perhaps are a consequence of the wider variety and/or number of cavitation nuclei present in these samples.

However, the consistency in the amount of echogenicity is greater for samples with concentration of 10^{10} particle/cc than the other particle concentrations, as indicated by the smaller standard deviation (Fig. 7). So although the tap water samples had consistent thresholds, they did not result in as consistent amounts of echogenicity. This is a direct consequence of the greater number of nuclei leading to more consistent cavitation and a lower threshold for microbubble generation as discussed above, especially since all echogenicities were measured at 10.8 MPa which was well above threshold in this air-saturated case. It is expected that, in the case of sufficient cavitation nuclei present and at air saturation, as the drive pressure increases above threshold there is a trend toward greater echogenicity due to the increasing number of nuclei cavitating and cascading to form more dense bubble clouds. The echogenicity will reach a limit, however, due to the finite amount of dissolved gas in the fluid.

The concentrations of 10^8 and 10^{10} particles/cc of 0.198-μm polystyrene microparticles were chosen based upon previous cavitation threshold studies in aqueous solutions.[16,17] Roy *et al.* showed by passive cavitation detection that a solution with a concentration of 1.4×10^8 particles/cc of 0.245-μm polystyrene microspheres had a cavitation threshold of about 0.8 MPa, with 10-μs bursts at 757 kHz

and 1-kHz PRF; here the threshold was determined when at least one event was observed while the amplitude was slowly ramped upward. The procedure by Roy *et al.* results in a large number of exposures per unit time compared to the requirement here for cavitation from at least one of only two bursts at a given amplitude. From review of Roy *et al.*, particle concentrations of 10^8 and 10^{10} were chosen as reasonable solutions for attempting to generate consistent cavitation microbubbles. Figure 6 shows that the threshold for imageable microbubble generation was found to be 11.9 ± 2.2 MPa for a filtered (to 0.2 μm) fluid with 10^8 particles/cc added particulates. This threshold for contrast microbubble generation is an order of magnitude higher than thresholds for cavitation stated by Roy *et al.* (8 bars) for similar fluid conditions; however, it must be kept in mind that the method of detection, exposure conditions, and the end product in the two cases are quite different. For the aim of generating contrast agents for diagnosis of urinary reflux, it is necessary to identify a threshold at which imageable, residual bubbles are obtained, preferably copious amounts of bubbles. So the threshold in this study was based upon detecting visible residual bubble generation with a diagnostic scanner, whereas Roy *et al.* used a passive acoustic backscatter detection technique that is possibly more sensitive to the onset of cavitation. Since imageable microbubble generation was more consistent (as seen in the error bars in Fig. 6) and occurred at a lower threshold with 10^{10} particles/cc, the higher concentration of particles was used for the subsequent studies of varying the gas content in the sample fluid.

B. Gas saturation experiments

With plenty of particles, it is evident that the imageable microbubble generation threshold is inversely proportional and echogenicity is proportional to gas content in the fluid (Figs. 8 and 9). In the presence of particle nuclei, microbubbles are released at a certain threshold and then must grow to an imageable size by rectified diffusion. With more gas available, more of these microbubbles can easily grow to large enough size to be imaged, which results in greater amounts of echogenicity.

From visual observation of all the samples, the microbubbles generated in samples with CO_2 resided longer in the fluid before dissolving or disappearing than those generated in air samples. Dwell time for clouds of contrast microbubbles in CO_2 samples was on the order of 10–20 s. The extended lifetime of the microbubbles seen in the presence of CO_2 could be the result of many factors, including differences in the size of gas bubbles generated during rectified diffusion and/or dissolution times based on the various gases dissolved in the fluid and contained in the bubble.

C. Combined effects

Given that the objective of potentially diagnosing urinary reflux with ultrasound requires generating copious amounts of imageable bubbles, then it may be necessary to operate well above the threshold for cavitation. This is the rationale for choosing to measure echogenicity at a high rarefactional pressure of 10.8 MPa (or 6184 W/cm^2) as a function of particle concentration and gas saturation. At this pressure all samples with particle concentration of 10^{10}/cc resulted in cavitation, except for the lowest air undersaturated fluids, as seen in Fig. 8. Recall also that 10^{10} particles/cc concentration was chosen as the fluid parameter for investigating the dependence of threshold and echogenicity on gas saturation (results in Figs. 8 and 9) because at air saturation the samples of 10^{10} particles/cc had lower thresholds and cavitation was more consistent than for 10^8 particles/cc samples (referring again to Fig. 6).

Since it is already known that human urine is considerably under-saturated in dissolved gas by 27% of standard atmospheric pressure[18] and is highly filtered by the kidneys, the results of the samples with saturation below 50% and with no added particles (filtered water samples represented by the hatched bars) are particularly interesting to review more closely. Although the thresholds for the samples with no particles added and gas saturation above 50% were high and not statistically different for different gases (Fig. 12, solid bars on left of plot), when contrast microbubbles were generated the filtered samples containing CO_2 had considerably greater echogenicity compared to the air samples (Fig. 13, solid bars on left of plot) with a p value of 0.001. For the samples above 50% saturation, the mean echogenicity for the samples with CO_2 is 40 dB, higher than the group of samples containing air. However, for samples with gas saturation below 50%, the effect of having CO_2 present was evident in both the decreased threshold and increased mean echogenicity; the threshold was statistically different from air samples with a p value of 0.005 and the mean echogenicity was more than 20 dB, greater than samples with air (means significantly different with a p value of 0.05). From these results, it could be expected that the presence of CO_2 would have a significant impact on bubble production and dwell time, as well as the threshold for initiating cavitation.

The decrease in threshold and increase in echogenicity with increasing particle concentration is evident as shown in these tests (Figs. 6, 7, 12, and 13). However, it may be difficult to apply these optimal changes in particle content and gas saturation to physiological experiments since the human body, through homeostasis, tries to correct any changes from normal. The particle concentration in canine urine was apparently lower than that in rabbit urine as indicated by the higher turbidity of the latter. This appears to correlate to the observation that contrast microbubble generation in the canine bladders was much more difficult than in rabbit bladders. Qualitatively, human urine would be more akin to canine urine in particle concentration, so it would be expected that cavitation would be similarly difficult in *in vivo* human bladders.

The chemical composition of urine is influenced by many daily factors such as physical activity, diet, fluid or drug intake, environment, etc. Crystals can be found in normal urine, and their type and quantity depends primarily on metabolic activity, diet, and urine concentration. In acidic urine the most frequently found crystals are of uric acid and calcium oxalate, and in alkaline urine several types of phosphate crystals may be present.[21] Albright and Harris have actually exploited this chemical phenomenon to safely pre-

cipitate phosphate crystals in human urinary bladder. The crystal formation was achieved by making the urine alkaline from the patient's ingestion of sodium bicarbonate and milk. The phosphate crystals were used as acoustic scatterers for characterizing the flow of urine in the urethra.[23] This method of increasing particulate content in the urine within physiological means can potentially be applied to humans in order to help lower the threshold for transcutaneous contrast agent generation. However, increased gas content would also be needed to lower the threshold and increase the echogenicity (referring to Figs. 10–13).

Chaigneau and LeMoan[18] showed that physiological urine varies in dissolved carbon dioxide content with change in volume, when other dissolved gases vary little or not at all (Fig. 2). There exist medical interventions that would allow shifting of the dissolved carbon dioxide content of the urine, as well as of blood.[24] These results show that the carbon-dioxide-saturated fluids had lower thresholds and greater echogenicity than similarly air-saturated samples (Figs. 8–13). Also, as the saturation of carbon dioxide increased the threshold tended to decrease (Fig. 8) and the echogenicity increased (Fig. 9) almost linearly. This manipulation of the gas saturation along with conditioning the particulate content in the urine could yield copious amounts of imageable and residual bubbles for performing a urinary reflux diagnosis.

IV. CLINICAL APPLICATION AND SIGNIFICANCE

Vesicoureteral reflux often spontaneously occurs in children with estimated incidence of 0.14% to 0.5% in neonates, 1% to 3% in children under 11 years of age, and 8% to 46% in siblings of a child with VUR.[25–27] If a bacterial infection exists in the bladder, then urinary reflux can lead to kidney infection. Furthermore, because of the ''leak'' in the bladder, the kidney can be exposed to high pressures, particularly at the time of micturation. Ultimately continued kidney infection or hypertension can result in acute renal dysfunction and/or failure.

The current ''gold standard'' diagnosis method for urinary reflux is VCUG. In this procedure the patient is catheterized via the urethra in order to devoid the bladder of urine and to fill the bladder with x-ray contrast. Since often the patient being evaluated is a young child, this procedure can be particularly uncomfortable and traumatic.

Darge *et al.* has already demonstrated in human clinical studies that a 10% by volume injection of shelled microbubbles via catheterization can diagnose VUR using B-mode ultrasound with high sensitivity and specificity, when compared to the gold standard VCUG.[12] Thus if these microbubbles can be generated *in vivo* transcutaneously at similar volumes, then this could eliminate the radiation exposure involved with VCUG and the trauma of catheterization experienced with VCUG and the Darge *et al.* method. The challenge in implementing this transcutaneous contrast agent generation method *in vivo* may be the need to manipulate the physiological urine properties, and, even when this manipulation is possible, large amounts of bubbles (at least 10% by volume) must be generated, grown, and collected in order for this method to have as high sensitivity and specificity as the Darge *et al.* diagnosis.

From the recent investigations of ultrasound as a method for diagnosing urinary reflux in humans,[10–13] there is strong indication that the proposed method of transcutaneous generation of contrast agent should be the next logical step in eliminating the invasiveness of the diagnosis of VUR. Ultimately, perhaps, this method can replace VCUG as the primary imaging technique or ''gold standard'' for VUR detection.

V. CONCLUSION

These simulated urinary bladder results follow the trend of what was qualitatively and quantitatively seen in the rabbit experiments, where higher particle content of the fluid and CO_2 saturation had a profound effect on the ease of cavitation and the generation of abundant imageable bubbles. However, since human urine will be more difficult to cavitate, manipulation of the urine should be focused on increasing dissolved gas content, and, perhaps most importantly, reasonable concentrations of CO_2 should be present in the urine to aid in the bubble production. Even in a restricted nuclei environment such as the bladder, generation of vaporous cavitation should be possible; however, plenty of gas is needed in order to grow the vaporous bubble into one of residual, imageable size.

Further work is needed to fully characterize how physiological urine should and can be manipulated in order to generate sufficient contrast agent within the urinary bladder. A method for measuring all the gas concentrations in the samples needs to be employed, so more than just O_2 and CO_2 saturations can be measured; particularly, the content of nitrogen in the samples should be determined to study if it has any direct effect on microbubble generation. *In vitro* tests should be performed on excised canine and rabbit bladders which will contain physiologically representative nuclei and gas content. Also, more *in vivo* canine experiments will be performed since the canine urinary system is more similar to humans. Applying the drug interventions and particle manipulations of the *in vivo* urine should be possible in the canine model. A potential technique might be to use a high-intensity short burst, of a few cycles, to initiate cavitation followed by a low-intensity growth and trapping pulse in order to sustain copious contrast microbubbles in the urinary bladder for aiding in the diagnosis of urinary reflux.

ACKNOWLEDGMENTS

This work was supported in part by USPHS Grant Nos. 5 R01 DK42290 (80%) and 1 R01 HL54201 (20%) from the National Institute of Diabetes and Digestive and Kidney Diseases and the National Heart, Lung and Blood Institute, respectively.

[1] J. B. Fowlkes, P. L. Carson, E. H. Chiang, and J. M. Rubin, ''Acoustic generation of bubbles in excised canine urinary bladders,'' J. Acoust. Soc. Am. **89**, 2740–2744 (1991).

[2] E. A. Gardner, J. B. Fowlkes, P. L. Carson, J. A. Ivey, and D. A. Ohl, ''Bubble generation in excised urinary bladders using an electrohydraulic lithotripter,'' in *Ultrasonics Symposium Proceedings*, edited by M. Levy and B. R. McAvoy (Institute for Electrical and Electronic Engineers, Piscataway, NJ, 1993), Cat.#93CH3301-9, pp. 905–908.

[3] D. R. Gross, D. L. Miller, and A. R. Williams, ''A search for ultrasonic

cavitation within the canine cardiovascular system,'' Ultrasound Med. Biol. **11**, 85–97 (1985).
[4] A. R. Williams, M. Delius, D. L. Miller, and W. Schwarze, ''Investigation of cavitation in flowing media by lithotripter shock waves both *in vitro* and *in vivo*,'' Ultrasound Med. Biol. **19**, 803–813 (1989).
[5] J. A. Ivey, E. A. Gardner, J. B. Fowlkes, J. M. Rubin, and P. L. Carson, ''Acoustic generation of intra-arterial contrast boluses,'' Ultrasound Med. Biol. **21**(6), 757–767 (1995).
[6] P. L. Carson, J. B. Fowlkes, E. A. Gardner, M. Taljanovic, and J. A. Ivey, ''Effects of Various Gases on Cavitation Thresholds Measured in Blood,'' J. Ultrasound Med. **14**(3), S12 (1995).
[7] J. A. Ivey, J. B. Fowlkes, E. A. Gardner, W. F. J. Feitz, D. A. Bloom, P. L. Carson, and J. M. Rubin, ''*In vivo* observation of urinary reflux using ultrasound contrast agents,'' Annual Meeting, Association of University Radiologists, Cincinnati, OH, May 19–23, 1993.
[8] J. H. Wible, M. D. Adams, P. F. Sherwin, J. K. Wojdyla, A. K. Parsons, A. Atala, J. B. Fowlkes, and L. Needleman, ''Noncardiac applications of Albunex®,'' Invest. Radiol. **29(Suppl. 2)**, S145–S148 (1994).
[9] A. Atala, J. H. Wible, J. C. Share, M. C. Carr, A. B. Retik, and J. Mandell, ''Sonography with sonicated albumin in the detection of vesicoureteral reflux,'' J. Urol. (Baltimore) **150**, 756–758 (1993).
[10] D. C. Hanbury, R. A. Coulden, P. Farman, and T. Sherwood, ''Ultrasound cystography in the diagnosis of vesicoureteric reflux,'' Br. J. Urol. **65(3)**, 250–253 (1990).
[11] R. M. Kessler and D. H. Altman, ''Real-time sonographic detection of vesicoureteral reflux in children,'' AJR, Am. J. Roentgenol. **138**, 1033–1036 (1982).
[12] K. Darge, J. Troeger, T. Duetting, C. Weber, R. Schlief, and W. K. Rohrschneider, ''Echo-enhanced Real-time Sonographic Detection of Vesicoureterorenal Reflux in children—Comparison with X-ray Voiding Cystourethrography,'' 1997 Scientific Program of the Radiological Society of North America, Radiology **205(P)**, 348 (1997).
[13] T. Matsumoto, K. Fukushima, H. Motoyama, E. Higuchi, and H. Kato, ''Colour-flow imaging for detection of vesicoureteral reflux,'' Lancet **347**, 757 (1996).
[14] J. B. Fowlkes, E. A. Gardner, P. L. Carson, and E. Y. Hwang, ''Generation of Ultrasound Contrast by Cavitation in the Urinary Bladder: Preliminary *In Vivo* Results,'' J. Ultrasound Med. **15**(3), S20–S21 (March 1996).
[15] E. Y. Hwang, J. B. Fowlkes, and P. L. Carson, ''Variables Controlling Ultrasound Contrast Generation in the Urinary Bladder: A Urinary Reflux Diagnosis,'' in *Proceedings of the 1997 IEEE Ultrasonics Symposium* (IEEE, New York), Cat. No. 97CH36118, Vol. 2, pp. 1185–1188.
[16] C. K. Holland and R. E. Apfel, ''Thresholds for transient cavitation produced by pulsed ultrasound in a controlled nuclei environment,'' J. Acoust. Soc. Am. **88**, 2059–2069 (1990).
[17] R. A. Roy, S. I. Madanshetty, and R. E. Apfel, ''An acoustic backscattering technique for the detection of transient cavitation produced by microsecond pulses of ultrasound,'' J. Acoust. Soc. Am. **87**, 2451–2458 (1990).
[18] M. M. Chaigneau and G. LeMoan, ''Biochemistry—On the composition of gas dissolved in human urine,'' CR Acad. Sci. (Paris), Ser. D **267(22)**, 1893–1895 (1968).
[19] T. C. Lloyd, Jr., ''Respiratory gas exchange and transport,'' in *Physiology*, edited by E. E. Selkurt (Little, Brown and Co., Boston, MA, 1971), 3rd ed., Chap. 20, pp. 453–470.
[20] G. Piccoli, D. Varese, and M. Rotunno, *Atlas of Urinary Sediments, Diagnosis and Clinical Correlations in Nephrology* (Raven, New York, 1984).
[21] *Hawk's Physiological Chemistry*, edited by B. L. Oser (McGraw–Hill, New York, 1965), Chap. 31, pp. 1197–1214.
[22] *Acoustic Output Measurement and Labeling Standard for Diagnostic Ultrasound* (American Institute of Ultrasound in Medicine, Rockville, MD, 1992).
[23] R. J. Albright and J. H. Harris, ''Diagnosis of Urethral Flow Parameters by Ultrasonic Backscatter,'' IEEE Trans. Biomed. Eng. **BME-22(1)**, 1–11 (1975).
[24] R. M. Portwood, D. W. Seldin, F. C. Rector, and R. Cade, ''The relation of urinary CO_2 tension in bicarbonate excretion,'' J. Clin. Invest. **38**(5), 770–776 (1959).
[25] T. Bergstrom, H. Larson, K. Lincoln, and J. Winberg, ''Studies of urinary tract infections in infancy and childhood. XII. Eighty consecutive patients with neonatal infection,'' J. Pediatr. (St. Louis) **80**(5), 858–866 (1972).
[26] J. Winberg, H. J. Andersen, T. Bergstrom, B. Jacobsson, H. Larson, and K. Lincoln, ''Epidemiology of symptomatic urinary tract infection in childhood,'' Acta Paediatr. Scand. **252**, S1–20 (1974).
[27] J. J. Mulcahy, P. P. Kelalis, G. B. Stickler, and E. C. Burke, ''Familial vesicoureteral reflux,'' J. Urol. (Baltimore) **104**(5), 762–764 (1970).

LETTERS TO THE EDITOR

This Letters section is for publishing (a) brief acoustical research or applied acoustical reports, (b) comments on articles or letters previously published in this Journal, and (c) a reply by the article author to criticism by the Letter author in (b). Extensive reports should be submitted as articles, not in a letter series. Letters are peer-reviewed on the same basis as articles, but usually require less review time before acceptance. Letters cannot exceed four printed pages (approximately 3000–4000 words) including figures, tables, references, and a required abstract of about 100 words.

Enhancement of the Q of a nonlinear acoustic resonator by active suppression of harmonics

Vitalyi E. Gusev,[a] Hélène Bailliet, Pierrick Lotton, Stéphane Job, and Michel Bruneau
Laboratoire d'Acoustique de l'Université du Maine UMR CNRS 6613, Av. O. Messiaen, 72085 Le Mans Cedex 9, France

(Received 10 June 1997; revised 19 December 1997; accepted 16 February 1998)

Finite-amplitude stationary acoustic waves in a closed resonator subjected to simultaneous excitation at fundamental frequency and its second harmonic are analyzed in the frame of the second-order nonlinear theory. The conditions when the dual-frequency excitation leads to a quality factor Q higher than in the case of a single-frequency excitation are derived. The Q enhancement can be explained in terms of active suppression of cascade processes of the generation of higher harmonics. The second harmonic generated in the resonator is compensated by the second harmonic radiated by the piston. Suppression of higher harmonics also can be explained as being due to effective down conversion of energy from the second harmonic to the fundamental wave in the nonlinear parametric process. © *1998 Acoustical Society of America.* [S0001-4966(98)06005-6]

PACS numbers: 43.25.Gf [MAB]

The renewed interest in finite-amplitude standing acoustic waves[1–3] is due to the current progress in the design of thermoacoustic engines.[3,4] It was observed in experiments[1] that acoustic waves developed in a thermoacoustic prime mover contain weak shock fronts. In experiments with a large thermoacoustic engine[2] the amplitude of the second harmonic of the fundamental frequency was measured to be one-third of the amplitude of the fundamental oscillations. Higher harmonics were successively smaller by about the same factor. From the point of view of the final goal of thermoacoustics (design of prime movers with high efficiency and refrigerators with high coefficient of performance[4]), it is very important to develop methods to suppress cascade processes. One of the reasons for this is the fact that energy transport to higher frequencies via the nonlinear acoustic interactions increases the rate of energy dissipation because sound absorption increases with frequency. Consequently, the quality factor Q of an acoustic resonator is reduced by the presence of nonlinear processes. Another reason is related to the fact that typical thermoacoustic engines are designed to operate optimally at a single (fundamental) frequency.[4] The interaction of the higher harmonics with the stacks, designed and positioned to work at the fundamental frequency, is less efficient.

A few opportunities for the suppression of acoustic spectrum broadening have already been tested in experiments with rigid wall resonators. In Ref. 2, frequency shift of the second mode of the resonator was achieved by putting specially constructed inserts near the velocity antinodes of the second mode. Thus the second harmonic of the fundamental frequency was no longer in resonance. The same effect was achieved by using anharmonic tubes composed of a few sections of different diameters.[3] In Ref. 5 it was proposed that the quality factor of a nonlinear acoustic resonator can be enhanced by introducing additional selective absorption of the second harmonic. This opportunity was later verified experimentally by using a selectively absorbing reflector in the resonator.[6] All of the abovementioned techniques diminish the accumulation of the second harmonic, which is the most important intermediate frequency in nonlinear processes. However, these methods themselves introduce additional losses via acoustical[6] or nonacoustical[3] mechanisms.

In this Letter theoretical analysis of the possibility to enhance the quality factor Q of an acoustic resonator by active suppression of the second harmonic is presented. The analytical solutions (exact in the frame of the second-order nonlinear theory) predict that additional launching in the resonator of the second harmonic (with an optimal phase relative to the fundamental wave) leads to the suppression of the cascade of harmonic generation and to Q enhancement.

Consistent with the second-order nonlinear theory, steady-state standing waves can be represented as a superposition of simple waves propagating in opposite directions[7,8,5]

[a]On leave from Moscow State University, 119899 Moscow, Russia.

$$v=v_+ + v_-, \quad \frac{\partial v_\pm}{\partial x} - \frac{\epsilon}{c_0^2} v_\pm \frac{\partial v_\pm}{\partial \tau_\pm} = 0, \qquad \tau_\pm = t \mp \frac{(x-L)}{c_0}, \tag{1}$$

which are slowly varying in space $v_\pm = \mu v_\pm(\mu x, \tau_\pm)$. Here v denotes particle velocity, c_0 is the adiabatic speed of sound, ϵ is the nonlinear acoustic parameter, and $\mu \ll 1$ is a small scaling parameter. The nonlinear waves of Eqs. (1) are assumed to not interact in the volume of the resonator; they are coupled only by the boundary conditions on the sound radiating piston at $x=0$ and on the rigid immobile reflector at $x=L$

$$v(x=0) = v_1 \sin \omega t + v_2 \sin(2\omega t + \varphi), \quad v(x=L) = 0. \tag{2}$$

It is explicitly stated in Eq. (2) that the vibrating piston radiates, in addition to fundamental frequency ω, its second harmonic 2ω (with a relative phase φ) v_1 and v_2 are the amplitudes of the piston velocity at ω and 2ω, respectively. It was demonstrated by different methods[7,5] that, in the vicinity of resonance, the problem governed by Eqs. (1) and (2) reduces to the analysis of acoustic wave excitation by quasi-synchronous (transonic) moving sources. In the present letter it is assumed that the resonator is precisely tuned to the first linear resonant angular frequency $\omega = \pi c_0 / L$ (half-wavelength resonator). Then, the profile of the traveling wave satisfies the equation.

$$-\frac{\epsilon}{c_0} v \frac{\partial v}{\partial t} = \frac{\omega}{2\pi} [v_1 \sin \omega t + v_2 \sin(2\omega t + \varphi)], \qquad v_+ = v(t=\tau_+), \quad v_- = -v(t=\tau_-). \tag{3}$$

This equation differs from one derived in Ref. 7 only by the additional second harmonic source in the right-hand side and is similar to the equation applied in Ref. 9 to the analysis of parametric amplification of subharmonics in closed tubes. It should be noted that in Eqs. (1) and (3) it is assumed that nonlinear acoustic effects, leading to shock front formation, play the dominant role in the saturation of the wave amplitude in the resonator (i.e., the ''nonlinear absorption'' of sound is the major source of energy losses).

It is suitable to rewrite Eq. (3) introducing nondimensional functions and variables $M = v/c_0$, $M_1 = v_1/c_0$, $M_2 = v_2/c_0$ (acoustic Mach numbers), and $\tau = \omega t$:

$$-\epsilon M \frac{\partial M}{\partial t} = \frac{1}{2\pi} [M_1 \sin \tau + M_2 \sin(2\tau + \varphi)] \equiv F(\tau, \varphi). \tag{4}$$

The formal mathematical solutions of Eq. (4) (phase trajectories[9–11]), from which the physical solution should be constructed, are

$$M = \pm \sqrt{\frac{2}{\pi\epsilon}} \sqrt{C + M_1 \cos^2\left(\frac{\tau}{2}\right) + \frac{M_2}{2} \cos^2\left(\tau + \frac{\varphi}{2}\right)} \equiv \pm \Phi(\tau, \varphi). \tag{5}$$

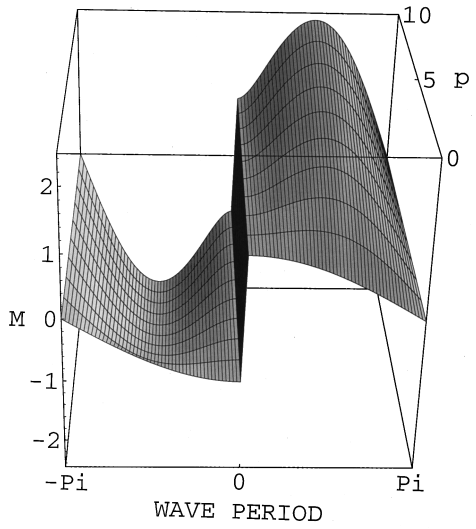

FIG. 1. Transformation of the profile of nonlinear acoustic wave propagating in the resonator with the increase of the amplitude of the actively launched second harmonic. Nondimensional parameter p is equal to the ratio of the amplitudes of the fundamental frequency and its second harmonic at the sound radiator.

The choice of the constant C in Eq. (5) provides an opportunity to make the absolute minimum of the function $\Phi(\tau,\phi)$ equal to zero. Then, in the moments of time corresponding to minimum of the function $\Phi(\tau,\phi)$ the wave profile continuously changes sign from $M>0$ to $M<0$ [i.e., switches from the trajectory $M=\Phi(\tau,\phi)$ to the trajectory $M=-\Phi(\tau,\phi)$]. The switching of wave polarity in the opposite direction [from $M=-\Phi(\tau,\phi)$ to $M=\Phi(\tau,\phi)$] takes place discontinuously at the weak shock fronts. Position $\tau=\tau_f$ of the shocks is derived from the condition that the velocity averaged over a wave period should be equal to zero [$\langle M \rangle \equiv (1/2\pi)\int_{-\pi}^{\pi} M d\tau = 0$]. The analysis demonstrates that the optimal phase of the radiated second harmonic for the Q enhancement is equal to π. In that case the description of a wave period ($-\pi \leqslant \tau \leqslant \pi$) takes the form

$$M = \sqrt{\frac{2M_1}{\pi\epsilon}} \operatorname{sign} \tau \cos\left(\frac{\tau}{2}\right) \sqrt{1 + 2\frac{M_2}{M_1} \sin^2\left(\frac{\tau}{2}\right)}. \tag{6}$$

It is evident from Eq. (6) that active pumping of the frequency 2ω with an appropriate phase ($\varphi=\pi$) does not change the amplitude of the shock front located at $\tau=\tau_f=0$. This means that energy dissipation is not changed. At the same time the energy accumulated in the wave grows. This behavior is illustrated in Fig. 1, which presents the evolution of the normalized wave profile ($M/\sqrt{2M_1/\pi\epsilon}$) with the increasing value of parameter $p \equiv M_2/M_1$. In the limiting case $p \gg 1$, the derived solution, Eq. (6), predicts the dominance of the fundamental frequency in the spectrum [$M(p \gg 1) \cong \sqrt{M_2/\pi\epsilon} \sin \tau$]. Fourier analysis of Eq. (6) demonstrates that, with the increase of amplitude of the second harmonic (actively launched in the resonator), the amplitude of oscillations at the fundamental frequency grows, while the amplitudes of all the harmonics decrease. For example, the dependence of the amplitudes of the fundamental wave $M^{(1)}$, the second harmonic $M^{(2)}$, and the third har-

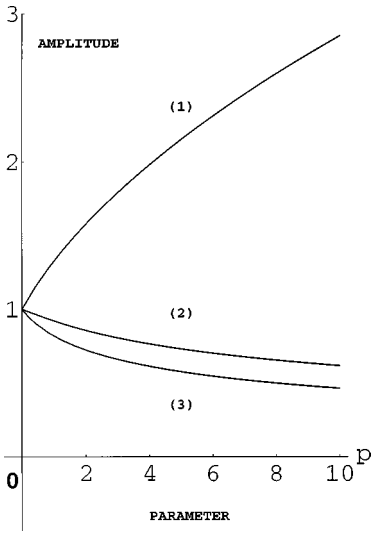

FIG. 2. Dependence of the normalized amplitudes of the oscillations at the fundamental frequency (1), at the second harmonic (2), and at the third harmonic (3) on the ratio p of the amplitudes of the fundamental wave and its second harmonic launched into the resonator by the sound source.

monic $M^{(3)}$ on the parameter p can be conveniently presented as

$$M^{(1)}(p)=\sqrt{\frac{2M_1}{\pi\epsilon}}\left(\frac{2}{\pi}\right)\left\{\frac{2p-1}{4p}+\frac{(2p+1)^2}{8\sqrt{2}p^{3/2}}\times\left[\frac{\pi}{2}+\arcsin\left(\frac{2p-1}{2p+1}\right)\right]\right\},$$

$$M^{(2)}(p)=[M^{(1)}(p)-M^{(1)}(0)]/p, \tag{7}$$

$$M^{(3)}(p)=M^{(2)}(p)+5[M^{(2)}(p)-M^{(2)}(0)]/4p.$$

The evolution of the wave spectrum with increasing parameter p described by Eq. (7) is illustrated in Fig. 2, where the amplitudes of spectral components are normalized to their values in the absence of additional pumping at 2ω $[M^{(1)}(0)=(8/3\pi)\sqrt{2M_1/\pi\epsilon}$, $M^{(2)}(0)/M^{(1)}(0)=2/5$, $M^{(3)}(0)/M^{(2)}(0)=9/14]$.

The quality factor of the resonator can be found as the ratio of the energy accumulated in the wave ($\propto\langle M^2\rangle$) to the work done by the piston during a period of oscillation ($\propto 4\pi\langle MF\rangle$). Here F is defined in Eq. (4). With the help of Eq. (6) it was derived that

$$Q_{\omega+2\omega}(p)=\frac{3}{8}\sqrt{\frac{\pi}{2\epsilon M_1}}\left(1+\frac{M_2}{2M_1}\right)\equiv\left(1+\frac{p}{2}\right)Q_\omega, \tag{8}$$

where $Q_{\omega+2\omega}$ is the quality factor of a nonlinear resonator in the presence of active launching of 2ω and $Q_\omega=Q_{\omega+2\omega}(0)$ is the Q of a half-wavelength resonator excited only at fundamental frequency. The latter was evaluated in Ref. 8. In accordance with Eq. (7) (see Fig. 2), the Q enhancement is due to active suppression harmonic generation. This is achieved by radiating from the boundary into the resonator the second harmonic with a phase shift π relative to the second harmonic generated in the bulk of the resonator due to nonlinearity of the medium.

It is interesting to note that another complementary physical explanation of the predicted Q enhancement is possible. The increase of the fundamental amplitude with the increasing parameter $p\equiv M_2/M_1$ can be viewed as its parametric amplification in the field of the second harmonic. In the case $M_1=0$, $M_2\neq 0$, $\varphi=\pi$, the profile of the nonlinear wave in the resonator in the time interval $-\pi\leqslant\tau\leqslant\pi$ is

$$M=\sqrt{\frac{M_2}{\pi\epsilon}}\,\mathrm{sign}\left(\tau+\frac{\pi}{2}\right)\mathrm{sign}\left(\tau-\frac{\pi}{2}\right)\cos\left(\tau-\frac{\pi}{2}\right). \tag{9}$$

The wave in Eq. (9) contains two shock fronts at $\tau=\tau_f=\pm\pi/2$ and does not contain the fundamental frequency or the odd harmonics. The Q for this wave excited by pumping at a single angular frequency 2ω is $Q_{2\omega}=(3/16)\sqrt{\pi/\epsilon M_2}$. In accordance with Ref. 9, additional launching in the resonator of a wave at fundamental frequency ω initiates the motion of the shocks and transformation of the profile in Eq. (9) into the profile in Eq. (6). This transformation leads to the increase of Q

$$Q_{\omega+2\omega}(p)=\frac{3}{8}\sqrt{\frac{\pi}{2\epsilon M_1}}\left(1+\frac{M_2}{2M_1}\right)\equiv\sqrt{2p}\left(1+\frac{p}{2}\right)Q_{2\omega}>Q_{2\omega} \tag{10}$$

only if the parameter p exceeds the critical value $p>p_{\mathrm{cr}}\approx 0.6$. The explanation for the possible Q enhancement is that the parametric process converts energy down in frequency, thus diminishing accumulation of energy in higher harmonics and, consequently, it diminishes nonlinear dissipation. It can be concluded from the derived formulas, Eqs. (8) and (10), that compared to a single-frequency pumping (at ω or at 2ω), the quality factor of a nonlinear resonator can be increased by combined pumping at ω and 2ω if the amplitudes of the radiated waves satisfy the critical condition $M_2\geqslant 0.6M_1$.

In conclusion, we would like to mention some advantages of active suppression of the second harmonic in comparison with passive methods.[2,5] One of them is the possibility to tune the system to the highest Q by changing the amplitude and phase of the pump at 2ω if the resonator is changed (for example, by installing stacks or as a result of temperature variation). Another advantage is the possibility to compensate/enhance the possible negative/positive influence of the second harmonic which is usually generated inside the radiator even in the case of a single-frequency electrical input. Additional research is required to know the usefulness of the excitation of a nonlinear resonator simultaneously at several frequencies (for example, at ω, 2ω, and 3ω) or what should be the spectrum of the periodic pump to achieve the highest Q.

ACKNOWLEDGMENTS

Support from D.G.A. through Contract No. 952597 A and in the form of a fellowship to one of the authors (V.E.G.) and a scholarship to another one (H.B.) is gratefully acknowledged.

[1] A. A. Atchley, H. E. Bass, and T. J. Hofler, ''Development of nonlinear waves in a thermoacoustic prime mover,'' in *Frontiers of Nonlinear Acoustics 12th ISNA*, edited M. F. Hamilton and D. T. Blackstock (Elsevier, New York, 1990), pp. 603–608.

[2] G. W. Swift, ''Analysis and performance of a large thermoacoustic engine,'' J. Acoust. Soc. Am. **92**, 1551–1563 (1992).

[3] D. F. Gaitan and A. A. Atchley, ''Finite amplitude standing waves in harmonic and anharmonic tubes,'' J. Acoust. Soc. Am. **93**, 2489–2495 (1993).

[4] G. W. Swift, ''Thermoacoustic engines,'' J. Acoust. Soc. Am. **84**, 1145–1180 (1988).

[5] V. E. Gusev, ''Frequency-selective action on nonlinear waves in an acoustic cavity,'' Moscow Univ. Phys. Bull. **39**, 29–34 (1984) [Vestnik Mosk. Univ. Fizika **39**, 33–36 (1984)].

[6] V. G. Andreev, V. E. Gusev, A. A. Karabutov, O. V. Rudenko, and O. A. Sapozhnikov, ''Enhancement of Q of a nonlinear acoustic resonator bymeans of a selectively absorbing mirror,'' Sov. Phys. Acoust. **31**, 162–163 (1985) [Akust. Zh. **31**, 275–276 (1985)].

[7] W. Chester, ''Resonant oscillations in closed tubes,'' J. Fluid Mech. **18**, 44–64 (1964).

[8] V. Kaner, O. Rudenko, and R. Khokhlov, ''Theory of nonlinear oscillations in acoustic resonators,'' Sov. Phys. Acoust. **23**, 432–437 (1977) [Akust. Zh. **23**, 756–765 (1977)].

[9] V. E. Gusev, ''Parametric amplification of acoustic waves in closed tubes,'' Sov. Phys. Acoust. **30**, 176–180 (1984) [Akust. Zh. **30**, 298–305 (1984)].

[10] V. E. Gusev, ''Buildup of forced oscillations in acoustic resonator,'' Sov. Phys. Acoust. **30**, 121–125 (1984) [Akust. Zh. **30**, 204–212 (1984)].

[11] V. E. Gusev and A. A. Karabutov, *Laser Optoacoustics* (American Institute of Physics, New York, 1993), Chap. 6.

Robust matched-field localization in uncertain ocean environments

Brian F. Harrison[a)]
Naval Undersea Warfare Center, Submarine Sonar Department, Newport, Rhode Island 02841

Richard J. Vaccaro and Donald W. Tufts
Department of Electrical Engineering, University of Rhode Island, Kingston, Rhode Island 02881

(Received 18 March 1996; accepted for publication 18 February 1998)

Matched-field source localization methods can be sensitive to environmental parameter mismatch. A statistically optimal approach to source localization in the presence of environmental uncertainty is the maximum *a posteriori* probability (MAP) estimator. Unfortunately, practical implementation of the MAP estimator results in a computationally intensive processor. In this paper, a localization technique is presented that is a computationally efficient approximation to the MAP estimator. A two-step search procedure is used to estimate source position. The first step utilizes an approximation to the MAP estimator which allows much of the computation to be computed efficiently off-line. This step also includes a computationally efficient range-depth smoothing which provides robustness to grid density. In step two, ambiguities arising from step one are resolved using a fine-grid search procedure over the source location parameters. Simulations using the NRL Workshop benchmark environment, which has seven uncertain environmental parameters, show the performance of the technique to be comparable to that of the MAP estimator while requiring only a fraction of the computations. © *1998 Acoustical Society of America.* [S0001-4966(98)06406-6]

PACS numbers: 43.60.Gk, 43.30.Wi [JLK]

INTRODUCTION

Matched-field processing (MFP) uses complex acoustic propagation models of the signals received at a sensor array for source localization.[1] These models include the parameters of the ocean environment. Examples of such parameters are the sound velocity profile, water depth, density, and bottom characteristics. Source localization involves comparing the sensor array outputs with models computed over a range of hypothesized source positions. The location parameters of the model producing the best match between the measured and modeled array outputs is the desired estimate of source location. However, precise knowledge of the environmental parameters is required in order to obtain accurate source location estimates. Small errors in the assumed environmental parameters can introduce large errors in the source location estimates, especially in the presence of noise.[2] This is a major difficulty which must be overcome in order to apply MFP to practical, real-world problems.

Previously we presented the replica-subspace weighted projection (RSWP) algorithm which was shown to provide robustness to a small number of uncertain environmental parameters.[3] A computationally efficient smoothing of the Bartlett surface over source range, source depth, and all uncertain environmental parameters was performed to initially identify the regions in range-depth space most likely to contain the true source location parameters. Next, a maximum-likelihood search was conducted over a fine grid of points in all regions exceeding a threshold level to estimate source location and all uncertain environmental parameters. The name replica-subspace weighted projection derives from the implementation of the smoothing. The replica vector in the Bartlett processor is replaced by a matrix whose columns are the weighted principal components of replica vectors spanning a region in parameter space. Thus, the data vector is projected onto a subspace generated by the weighted principal components, i.e., a replica subspace.

As the number of uncertain environmental parameters grows, techniques which require the joint estimation of source location and environmental parameters rapidly become computationally intensive. In this case, techniques which provide robustness without estimating the uncertain environmental parameters are desired. One such technique is the maximum *a posteriori* probability (MAP) estimator. It is a statistically optimal approach to source localization in the presence of environmental uncertainty. The MAP estimator treats the uncertain environmental parameters as random variables with assumed prior probability density functions and integrates over them in the process of estimating source location. A MAP estimator derived in the context of robust MFP was given in Refs. 4, and 5 and called the optimum uncertain field processor (OUFP). However, practical implementation of this MAP estimator results in a computationally intensive processor.

In this paper, we present a technique which is a computationally efficient approximation to the MAP estimator. A two-step estimation process is employed. The first step utilizes an approximation to the MAP estimator which allows much of the computation to be computed efficiently off-line and also incorporates a computationally efficient range-depth smoothing for robustness to grid density. In step two, a fine-grid search is performed over range-depth space in those regions from step one exceeding a threshold level.

[a)]Electronic mail: harrison@abacus-2.npt.nuwc.navy.mil

I. MU-RSWP: A ROBUST MATCHED-FIELD SOURCE LOCALIZATION ALGORITHM

A. Background

For a given set of environmental parameters, a frequency-domain representation of the signals received at an underwater acoustic array from a point source can be written in vector form as

$$\mathbf{y}(\omega_n) = s(\omega_n)\mathbf{a}(\omega_n, \boldsymbol{\Theta}, \boldsymbol{\Psi}) + \mathbf{n}(\omega_n), \tag{1}$$

where $\mathbf{y}(\omega_n)$ is the vector of the N-element array output at frequency ω_n, $s(\omega_n)$ is the nth Fourier coefficient of the source, and $\mathbf{n}(\omega_n)$ is the vector of noise at the array output at frequency ω_n. The vector $\mathbf{a}(\omega_n, \boldsymbol{\Theta}, \boldsymbol{\Psi})$, called a *replica vector*, is the acoustic transfer function between a source at location $\boldsymbol{\Theta} = [r_s, z_s]$ and the array and $\boldsymbol{\Psi}$ is the vector of environmental parameters.

The OUFP, a MAP estimator for matched-field localization, was derived in Ref. 4. If the replica vectors are normalized to have unit norm and the noise is assumed to be spatially white and uncorrelated, the OUFP can be written as[6]

$$\hat{\boldsymbol{\Theta}} = \arg\max_{\boldsymbol{\Theta}} \int_{\boldsymbol{\Psi}} \exp\left\{\frac{(\sigma_A^2/2)|\mathbf{a}^H(\boldsymbol{\Theta}, \boldsymbol{\Psi})\mathbf{y}|^2}{\sigma_A^2 + 1}\right\} \times p(\boldsymbol{\Psi})\, d\boldsymbol{\Psi}, \tag{2}$$

where σ_A^2 is the signal amplitude variance. Dependence on ω has been dropped, since we will be considering monochromatic signals. For numerical implementation of this estimator, we approximate the integral by a summation

$$\hat{\boldsymbol{\Theta}} = \arg\max_{\boldsymbol{\Theta}} \sum_{j=1}^{M} \exp\left\{\frac{(\sigma_A^2/2)|\mathbf{a}^H(\boldsymbol{\Theta}, \boldsymbol{\Psi}_j)\mathbf{y}|^2}{\sigma_A^2 + 1}\right\}, \tag{3}$$

where the $\boldsymbol{\Psi}_j$ are vectors of environmental parameters sampled from their probability distributions. Note that the argument of the exponential in (3) is the Bartlett processor computed at ω, $\boldsymbol{\Theta}$, and $\boldsymbol{\Psi}_j$ and scaled by a constant. The surface generated by the summation in (3) at a fixed frequency is essentially the exponentiation of Bartlett surfaces averaged over environment. This exponentiation produces a nonlinear mapping of the Bartlett surface points prior to averaging.

Computational efficiency can be achieved by applying a linear approximation to the exponential in (3) which results in

$$\hat{\boldsymbol{\Theta}} = \arg\max_{\boldsymbol{\Theta}} \mathbf{y}^H \mathbf{R}_e(\boldsymbol{\Theta})\mathbf{y}, \tag{4}$$

where

$$\mathbf{R}_e(\boldsymbol{\Theta}) = \sum_{j=1}^{M} \mathbf{a}(\boldsymbol{\Theta}, \boldsymbol{\Psi}_j)\mathbf{a}^H(\boldsymbol{\Theta}, \boldsymbol{\Psi}_j). \tag{5}$$

We have shown that $\mathbf{R}_e(\boldsymbol{\Theta})$ rank deficient implies that the linear approximation used in (4) is accurate.[6]

The advantage to using the approximate MAP estimator of (4) over the MAP estimator of (3) is that the computation of $\mathbf{R}_e(\boldsymbol{\Theta})$ can be done off-line before the processing of data. It has been our experience that the matrix $\mathbf{R}_e(\boldsymbol{\Theta})$ is usually well approximated by matrix of lower rank. Thus, the number of on-line inner products computed by (4) for each $\boldsymbol{\Theta}$ will equal at most N, where $N \ll M$. In contrast, (3) must compute M inner products over each point in $\boldsymbol{\Theta}$ space on-line. With moderate environmental uncertainty, M can assume values exceeding 51^7.[5] In Ref. 5, a Monte Carlo approach to computing (3) was proposed.

B. MU-RSWP step 1: Coarse search procedure

We have shown previously that range-depth smoothing can provide robustness to coarse grid spacing in $\boldsymbol{\Theta}$ space.[3] This computationally efficient smoothing technique will also be developed here for the approximate MAP estimator. Essentially, the range-depth search space is partitioned into equally spaced regions and all of the Bartlett inner products within the region are summed. Smoothing the approximate MAP processor over range and depth can be expressed as

$$\beta_{S\text{-MAP}}(\boldsymbol{\Theta}_C) = \sum_{k=1}^{P} \mathbf{y}^H \mathbf{R}_e(\boldsymbol{\Theta}_k)\mathbf{y}, \tag{6}$$

where P equals the number of possible combinations of the range-depth points in the region which is defined by the $\boldsymbol{\Theta}$ value at its center, $\boldsymbol{\Theta}_C$.

The matrix $\mathbf{R}_e(\boldsymbol{\Theta}_k)$ is formed from the set of replica vectors as in (5) where the $\boldsymbol{\Psi}_j$ consist of samples of the environmental parameters selected at random from their uncertainty intervals. Every point in a given uncertainty interval is equally likely to be selected. Given an array which sufficiently samples the mode functions, $\mathbf{R}_e(\boldsymbol{\Theta}_k)$ is approximately low rank for moderate environmental uncertainty. A low-rank approximation to $\mathbf{R}_e(\boldsymbol{\Theta})$ can be made by computing the eigen decomposition

$$\mathbf{R}_e(\boldsymbol{\Theta}_k) = \mathbf{U}_e(\boldsymbol{\Theta}_k)\boldsymbol{\Sigma}_e(\boldsymbol{\Theta}_k)\mathbf{U}_e^H(\boldsymbol{\Theta}_k), \tag{7}$$

and using the principal components of (7) to approximate $\mathbf{R}_e(\boldsymbol{\Theta}_k)$. The eigenvectors in $\mathbf{U}_e$ corresponding to the largest eigenvalues, denoted $\tilde{\mathbf{U}}_e$, are the principal components. The number of principal components used is the least number which satisfies

$$\frac{\|\mathbf{R}_e(\boldsymbol{\Theta}_k) - \tilde{\mathbf{U}}_e(\boldsymbol{\Theta}_k)\tilde{\boldsymbol{\Sigma}}_e(\boldsymbol{\Theta}_k)\tilde{\mathbf{U}}_e^H(\boldsymbol{\Theta}_k)\|^2}{\|\mathbf{R}_e(\boldsymbol{\Theta}_k)\|^2} < 0.01.$$

A related approach for computing an environmental perturbation constraint matrix to improve the minimum variance processor's sensitivity to environmental uncertainty can be found in Ref. 5.

We can rewrite (6) as the norm squared of a matrix-vector product by substituting in the low-rank approximation of $\mathbf{R}_e(\boldsymbol{\Theta}_k)$. This results in inner products between $\mathbf{y}$ and the principal components weighted by the square roots of their corresponding eigenvalues. However, the finite set of M environments used to generate $\mathbf{R}_e(\boldsymbol{\Theta}_k)$ leads to different relative weighting of the principal components by the eigenvalues for different sets of M environments. A very large number of environmental realizations would be required to achieve stability in the eigenvalues. To compensate for this

we can set the eigenvalues in $\tilde{\Sigma}_e(\Theta_k)$ equal to one and project $\mathbf{y}$ onto the unweighted principal components which gives

$$\beta_{S\text{-MAP}}(\Theta_C)=\sum_{k=1}^{P}\|\tilde{\mathbf{U}}_e^H(\Theta_k)\mathbf{y}\|^2. \tag{8}$$

Equation (8) is a smoothed version of the FASTMAP estimator derived in Ref. 6. Note that the number of on-line inner products computed by (8) for each Θ_k is equal to q, the number of principal components for $\mathbf{R}_e(\Theta_k)$, where $q \leqslant N \ll M$.

To efficiently implement the smoothing, we define $\mathbf{P}(\Theta_C)$ as a $N\times L(L\gg N)$ partitioned matrix of the principal components for a region,

$$\mathbf{P}(\Theta_C)=[\tilde{\mathbf{U}}_e(\Theta_1),\ldots,\tilde{\mathbf{U}}_e(\Theta_P)], \tag{9}$$

and using the fact that for a set of vectors $\mathbf{x}_l$, $l=1,...,K$,

$$\sum_{l=1}^{K}\|\mathbf{x}_l\|^2=\|[\mathbf{x}_1^T\cdots\mathbf{x}_K^T]^T\|^2, \tag{10}$$

Eq. (8) can be written as

$$\beta_{S\text{-MAP}}(\Theta_C)=\|\mathbf{P}^H(\Theta_C)\mathbf{y}\|^2. \tag{11}$$

Computational efficiency is achieved by using the eigen decomposition of $\mathbf{P}(\Theta_C)\mathbf{P}^H(\Theta_C)=\mathbf{U}_P\mathbf{\Sigma}_P^2\mathbf{U}_P^H$. Using a low-rank approximation to $\mathbf{P}(\Theta_C)$ and substituting the result into (11) gives

$$\beta_{\text{mu-rswp}}(\Theta_C)=\|\tilde{\Sigma}_P\tilde{\mathbf{U}}_P^H\mathbf{y}\|^2. \tag{12}$$

We will call this technique, which is a combination of the FASTMAP estimator with RSWP smoothing, *multiple uncertainty*-RSWP or MU-RSWP.

C. MU-RSWP step 2: Fine search procedure

The MU-RSWP method is an environmentally robust technique for locating the region in range-depth space which is most likely to contain the true source location parameters. A fine point search can then be conducted over that region to accurately estimate source range and depth. However, due to the underlying ambiguities of the Bartlett surface, the subspace region producing the largest magnitude in (12) may not always be the true region. To compensate for this, a threshold level is set and any subspace region whose magnitude in (12) exceeds this level is included in the fine search.

A reasonable fine search procedure would be to compute Bartlett surfaces for the environments parametrized by Ψ_j, $j=1,...,M$, over those regions exceeding the threshold level and sum them, forming an average over environment, i.e.,

$$\beta_{\text{Ave-Bart}}(\Theta)=\sum_{j=1}^{M}|\mathbf{a}^H(\Theta,\Psi_j)\mathbf{y}|^2, \tag{13}$$

where Θ only includes source locations within regions exceeding the threshold level. Here again, the value of Θ producing the largest amplitude in (13) may not always be the true source location due to the ambiguities of the Bartlett surfaces at each environment when the environmental parameters are not sampled very finely. Improved performance would result if the ratio of the peaks at approximate true environments to the peaks at incorrect environments could be increased. This increased discrimination can be accomplished by combining the Bartlett surfaces at each environment nonlinearly using an L_p norm for large p (e.g., $p>10$). Such norms accentuate large values and attenuate smaller values. Using an L_p norm in (13) yields

$$\beta_{L_p}(\Theta)=\left[\sum_{j=1}^{M}[|\mathbf{a}^H(\Theta,\Psi_j)\mathbf{y}|^2]^p\right]^{1/p}. \tag{14}$$

Equation (14) is the second step of the complete MU-RSWP algorithm.

II. SIMULATION RESULTS WITH A BENCHMARK ENVIRONMENT

A. Problem introduction

To assess the state of the art in MFP, a workshop was held in May 1993 at the Naval Research Laboratory where the participants tested their algorithms against a series of environmental scenarios.[7] The most complex of the environmental scenarios was called the *general mismatch* case or GENLMIS. It contained seven uncertain environmental parameters. The vertical sensor array in the water channel consisted of 20 elements spaced at 5 m apart with the shallowest element at 5-m depth. To illustrate the effectiveness of the MU-RSWP algorithm, we will test it against the GENLMIS case.

In calculating the $\mathbf{R}_e(\Theta)$ matrices, 100 random realizations of Ψ_j were selected from the intervals for each of the environmental parameters. The total range-depth search space, as given in the NRL Workshop, was 5000–10 000 m in range and 0–100 m in depth. Each smoothing region in range-depth space was selected to have a width of 80 m in range and 5 m in depth, resulting in a total of 1260 regions. In each region, there were five sample points across range and two sample points across depth. Guidance in selecting the size and number of sample points for each region is given in Ref. 3. For the fine search using (14), an L_{20} norm was used.

The array output vectors for the simulations were generated using the model of (1) where $s(\omega_n)$ and the elements of $\mathbf{n}(\omega_n)$ are independent complex Gaussian random variables of zero mean. The signal-to-noise ratio (SNR) is defined by $\sigma_s^2\|\mathbf{a}(\omega_n,\Theta,\Psi)\|^2/J\sigma_w^2$, where $J=20$ is number of sensors, σ_s^2 is the signal amplitude variance, and σ_w^2 is the noise variance.

The threshold level was set corresponding to a percentage of the peak of the surface produced by (12) for each trial. An empirically determined value of 95% of the surface maximum was used as the threshold level in all trials.

B. Monte Carlo trial performance

Simulation trials were run over a range of SNR from -10 to 40 dB with 100 trials at each SNR. In each of the 100 trials, a unique randomly selected environmental realization and source position were chosen. The environmental realization was selected from the uncertainty intervals of the envi-

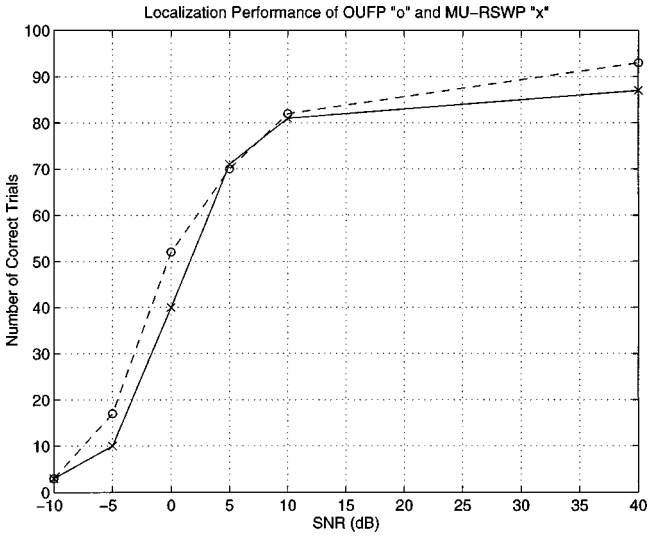

FIG. 1. Performance of MU-RSWP, and the OUFP for the NRL Benchmark environment.

ronmental parameters independent of the set of 100 environments used in processing and the source position was selected from a range interval of 5000–10 000 m and a depth interval of 0–100 m. Note that source position is allowed to lie **anywhere** in the range-depth interval, since the RSWP smoothing provides robustness to grid density. It is not restricted to lie on specific grid points as is the case with most of the MFP results reported in the literature.

A correct localization was defined as estimating the source location parameters to within a neighborhood of ± 200 m in range and ± 4 m in depth. An important consideration when comparing performance statistics reported for MFP algorithms is how a correct localization was defined in each case. Figure 1 shows the results of the trials along with the results reported for the OUFP in Ref. 5 for the identical scenario. The results for MU-RSWP closely match those of the OUFP. The tradeoff for the slight decrease in performance of MU-RSWP is the large decrease in computation required for MU-RSWP compared with that of the OUFP.

We will compare the computational requirements for both processors using this environmental scenario. A realistic grid spacing of 20 m in range and 2.5 m in depth was selected for the OUFP. This results in 500 grid points across range and 40 grid points across depth, for a total of 20 000 inner products per environmental realization. Using 100 random environmental realizations produces a total of 2 000 000 inner products to process a snapshot of array data.

For MU-RSWP, a total of 18 497 principal components were required. Thus, 18 497 inner products were computed for the coarse search procedure. In the fine search procedure, each region was gridded at four points across range and two points across depth. This resulted in a grid spacing of 20 m in range and 2.5 m in depth. From the simulations, an average of ten regions were included in the fine search procedure. Therefore, the number of inner products computed for the fine search per environmental realization was 80. Using 100 random environmental realizations results in a total of 8000 inner products for the fine search. The total number of inner products required to process a snapshot of data is then the sum of 8000 and 18 497 which equals 26 497. Comparing the totals for both methods, MU-RSWP provides a computational savings of approximately 75:1 over the OUFP.

Additional examples using MU-RSWP on experimental and simulated data, for broadband signals and short arrays as well, are given in Ref. 8.

III. CONCLUSIONS

This paper presented a matched-field source location estimator which was robust to environmental parameter uncertainty. The MU-RSWP algorithm is a two-step technique which is a computationally efficient approximation to the maximum *a posteriori* processor. Using the NRL Workshop benchmark environment, results were presented which demonstrate that the performance of MU-RSWP is comparable to that of the MAP processor, but at only a fraction of the computational load.

[1] H. P. Bucker, ''Use of calculated sound fields and matched-field detection to locate sound sources in shallow water,'' J. Acoust. Soc. Am. **59**, 368–373 (1976).
[2] D. F. Gingras, ''Methods for predicting the sensitivity of matched-field processors to mismatch,'' J. Acoust. Soc. Am. **86**, 1940–1949 (1989).
[3] B. F. Harrison, R. J. Vaccaro, and D. W. Tufts, ''Robust source localization in an acoustic waveguide,'' J. Acoust. Soc. Am. **100**, 384–391 (1996).
[4] A. M. Richardson and L. W. Nolte, ''*A posteriori* probability source localization in an uncertain sound speed, deep ocean environment,'' J. Acoust. Soc. Am. **89**, 2280–2284 (1991).
[5] J. A. Shorey, L. W. Nolte, and J. L. Krolik, ''Computationally efficient monte carlo estimation algorithms for matched field processing in uncertain ocean environments,'' J. Comput. Acoust. **2**, 285–314 (1994).
[6] B. F. Harrison, D. W. Tufts, and R. J. Vaccaro, ''Fast, approximate maximum *a posteriori* probability parameter estimation,'' IEEE Signal Process. Lett. **4**, 96–99 (1997).
[7] M. B. Porter and A. Tolstoy, ''The matched field processing benchmark problems,'' J. Comput. Acoust. **2**, 161–185 (1994).
[8] B. F. Harrison, ''Robust matched-field processing: A subspace approach,'' Ph.D. dissertation, University of Rhode Island, Kingston, RI, 1996.

A method for forward and inverse solutions of a three-dimensional model of the cochlea

Egbert de Boer[a)]
D2-226, Academic Medical Center, Meibergdreef 9, 1105 AZ Amsterdam, The Netherlands

(Received 18 April 1997; accepted for publication 11 March 1998)

In this Letter a method is described for computing the response of a linear three-dimensional classical model of the cochlea. The method can be applied when the geometry of the model lends itself to separation of variables, for instance, when the model has the shape of a homogeneous rectangular block or box. The method is an improvement over previously published computation methods, because it handles forward and retrograde traveling waves symmetrically, and it can be used for forward as well as inverse solutions. Furthermore, the method can be extended to a time-domain solution. © *1998 Acoustical Society of America.* [S0001-4966(98)06606-5]

PACS numbers: 43.64.Kc, 43.64.Bt [RDF]

INTRODUCTION

In principle, there are two strategies that can be followed in modeling the mechanism of cochlear functioning. In one, the structure and the parameters of the model are specified to the largest degree of precision and detail, and the model equations are solved by a laborious procedure (a recent example: Kolston and Ashmore, 1996). In the other strategy, geometry and structure of the model are simplified as much as possible (cf. de Boer, 1981, 1991, 1996) so that the fluid equations lead to separation of the variables, which allows the problem to be reduced to a not-too-complicated equation in terms of one variable (the longitudinal place coordinate, x). On modern PC-type computers, the solution for a linear model of this form can generally be obtained in a few seconds.

In the present report a solution method is described that belongs to the second category. We will restrict ourselves to linear models because it is felt that the response of the cochlea with low levels of stimulation (for instance, below 30 dB SPL) is very close to linear. The reader is referred to de Boer (1997a) to find to which extent *nonlinear* effects in the cochlea can be considered in terms of *linear* systems and models. The solution method to be treated here is based upon the same simple three-dimensional structure that was used in recent reports by the author (de Boer, 1995a,b, 1996). However, a new and potentially more useful method is given for the solution. The main advantage is that reflection problems are treated faithfully because all expressions are symmetrical in x (on a micro-scale, wave propagation is symmetrical in x). This implies that the method can be extrapolated to a time-domain solution in a straightforward way. Furthermore, problems associated with evoked oto-acoustical emissions can be handled with ease and confidence. The present report describes the basic theory and the solution methods for the forward as well as the inverse problem in the frequency domain.

[a)]Electronic mail: e.deboer@amc.uva.nl

I. THEORY

The model we are going to use has a rectangular cross section which is the same over the full length in the longitudinal (x-)direction. The basilar membrane (BM) occupies a fraction, ϵ, of the width of the channel, and that fraction is constant over the full length too (see Fig. 1 of de Boer, 1995a, or Fig. 5.1 of de Boer, 1996). The function $Q(k)$ plays the central part in the general theory of waves in this type of model (de Boer, 1991, Section 2.3; de Boer, 1996, Sections 5.1 to 5.3). This function describes the hydrodynamics of the fluid contained in the cochlear channels, the real variable k is the wave number (2π divided by the wavelength), $i\ \omega\ \rho\ Q(k)$ is the impedance the fluid in one channel presents to the BM when a single wave with wave number k and radian frequency ω travels in the fluid (ρ is the fluid density). This concept is only valid if the model's geometry is homogeneous and the fluid is ideal (i.e., incompressible, inviscid and linear). The function $Q(k)$ takes into account *three-dimensional* effects, i.e., the fact that the BM is moving over only a fraction of its width, that the fluid can move in three dimensions, and that long as well as short waves and the transition between these may be present. We quote the basic equation for a linear model (cf. de Boer, 1991, Eq. 2.3.f) that results from the analysis:

$$\frac{2\,i\omega\rho}{Z_{\mathrm{BM}}(x)}\int_{-\infty}^{\infty} Q(k)V_{\mathrm{BM}}(k)e^{-ikx}dk=-v_{\mathrm{BM}}(x). \qquad (1)$$

The meaning of the variables is as follows: x is the longitudinal coordinate along the BM, $Z_{\mathrm{BM}}(x)$ is the BM impedance, $v_{\mathrm{BM}}(x)$ is the velocity of the BM and $V_{\mathrm{BM}}(k)$ its Fourier transform (only real values of k are involved). In all variables and parameters the independent variable ω has been omitted for simplicity. For the derivation of Eq. (1) and the form of $Q(k)$ for the rectangular-block model we refer to de Boer (1981).

An alternative, more general, solution method is based on the concept of the Green's function (see for an early application Allen, 1977, and for a more recent one Mammano and Nobili, 1993). For the simple regular type of model geometry we are considering here, the Green's function is pro-

 0001-4966/98/103(6)/3725/4/$10.00

portional to the inverse Fourier transform $q(x)$ of $Q(k)$. Sondhi (1978) has studied the way to circumvent problems with the logarithmic singularity which $q(x)$ displays at $x=0$. Conversely, the function $Q(k)$ has a singularity at $k=\infty$, where it behaves as $(1/|k|)$—which is a nonanalytic function of k—to describe the character of short waves.

In de Boer and van Bienema (1982), the function $Q(k)$ for the three-dimensional model was approximated by the quotient of two polynomials in k, one of the second and one of the third degree in k, and a solution method for three-dimensional models was based on it. The same approximation has been used for the ''inverse solution'' described in de Boer (1995a,b). However, the so-obtained $Q(k)$ function is not symmetrical in k, it behaves in the right manner for $k\rightarrow+\infty$ but not for $k\rightarrow-\infty$; therefore, the way reflected waves are treated is unpredictable. Furthermore, the approximate $Q(k)$ function cannot be extended to a realizable spatial operator as would be needed for a time-domain solution. To improve upon these points, approximate $Q(k)$ by the *symmetrical* function

$$Q(k)=\frac{1}{h_{\text{eff}}k^2}\,\frac{1+a_2k^2h^2+a_4k^4h^4}{1+b_2k^2h^2+b_4k^4h^4}, \tag{2}$$

where h is the height of each of the cochlear channels, ϵ is the fraction of the width of the cochlear partition occupied by the (flexible) BM, and the ''effective height'' h_{eff} equals h/ε. That we have to go from the relatively simple third-order expression in de Boer and van Bienema (1982) to the sixth order in Eq. (2) is due to the problem of properly representing $Q(k)$ for large values of $|k|$ by a quotient of *even* polynomials in k. Appendix A gives numerical values for the coefficients a_2 to b_4 for various values of ϵ which produce a good approximation of the ''true'' $Q(k)$ function by Eq. (2). For example, in the case $\epsilon=0.3$ it is found that Eq. (2), with the coefficients filled in according to Appendix A, provides a satisfactory approximation to the ''true'' $Q(k)$ function for $|kh|<50$. In fact, larger values of $|kh|$ than 50 should not play a noticeable part in cochlear modeling. When a_4 and b_4 are zero, the approximation is good to $|kh|=10$.

II. FORWARD SOLUTION

Substitute Eq. (2) in the standard equation for a ''classical'' model [Eq. (1)]:

$$\frac{2i\omega\rho}{Z_{\text{BM}}(x)}\int_{-\infty}^{\infty}\frac{1}{h_{\text{eff}}k^2}\,\frac{1+a_2k^2h^2+a_4k^4h^4}{1+b_2k^2h^2+b_4k^4h^4}\times V_{\text{BM}}(k)\,e^{-ikx}\,dk=-v_{\text{BM}}(x). \tag{3}$$

Introduce the new variable $u(x)$ by defining its Fourier transform $U(k)$ in the following way:

$$\frac{1}{h_{\text{eff}}k^2}\,\frac{1}{1+b_2k^2h^2+b_4k^4h^4}\,V_{\text{BM}}(k)=U(k). \tag{4}$$

Because in the k domain each multiplication with $(-ik)$ is equivalent to differentiation with respect to x, the x domain counterparts $v_{\text{BM}}(x)$ and $u(x)$ are related by

$$v_{\text{BM}}(x)=h_{\text{eff}}\left[-\frac{d^2}{dx^2}+b_2h^2\frac{d^4}{dx^4}-b_4h^4\frac{d^6}{dx^6}\right]u(x). \tag{5}$$

When $u(x)$ is known, $v_{\text{BM}}(x)$ can be computed from Eq. (5). To solve for $u(x)$, substitute Eq. (5) in model Eq. (3):

$$\frac{2i\omega\rho}{h_{\text{eff}}Z_{\text{BM}}(x)}\int_{-\infty}^{\infty}(1+a_2k^2h^2+a_4k^4h^4)U(k)e^{-ikx}dk=\left[\frac{d^2}{dx^2}-b_2h^2\frac{d^4}{dx^4}+b_4h^4\frac{d^6}{dx^6}\right]u(x), \tag{6}$$

and reduce this relation to an equation in x:

$$\frac{2i\omega\rho}{h_{\text{eff}}Z_{\text{BM}}(x)}\left[1-a_2h^2\frac{d^2}{dx^2}+a_4h^4\frac{d^4}{dx^4}\right]u(x)=\left[\frac{d^2}{dx^2}-b_2h^2\frac{d^4}{dx^4}+b_4h^4\frac{d^6}{dx^6}\right]u(x). \tag{7}$$

Equation (7) is a differential equation of the sixth order in $u(x)$, and can be solved by standard methods. Appendix B defines the matrix elements for solving Eq. (7) digitally. Note that, when all coefficients (a_2 to b_4) are zero, Eq. (7) reduces to the standard long-wave equation with h_{eff} as the channel height. In that case, the *long-wave case*, the channel pressure $p(x)$ is proportional to $u(x)$:

$$p(x)=i\omega\rho u(x). \tag{8}$$

This relation can be used to formulate the boundary conditions at and near the stapes.

From the function $u(x)$ the BM velocity $v_{\text{BM}}(x)$ can be obtained by using Eq. (5). Or, alternatively, Eqs. (5) and (7) can be combined to express the BM velocity in terms of lower-order derivatives of $u(x)$:

$$v_{\text{BM}}(x)=\frac{-2i\omega\rho}{Z_{\text{BM}}(x)}\left[1-a_2h^2\frac{d^2}{dx^2}+a_4h^4\frac{d^4}{dx^4}\right]u(x). \tag{9}$$

III. INVERSE SOLUTION

The inverse solution can be obtained by direct substitution of $v_{\text{BM}}(x)$ into Eq. (1) and using the exact expression for $Q(k)$. There may arise problems with convergence for large values of $|kh|$, however. It is often better to use the approximation of Eq. (2). Then, $u(x)$ can be obtained directly by solving Eq. (5). The effective BM impedance $Z_{\text{BM}}(x)$ is found from:

$$Z_{\text{BM}}(x)=\frac{-2i\omega\rho}{v_{\text{BM}}(x)}\left[1-a_2h^2\frac{d^2}{dx^2}+a_4h^4\frac{d^4}{dx^4}\right]u(x), \tag{10}$$

which is a simple variation of Eq. (9).

IV. APPLICATION NOTES

It has been our general experience that the forward-computation method as described in this paper is very robust. In testing locally active models of the cochlea, and trying out variations of the parameters or introduction of irregularities, it is often found that the region of the response peak becomes the source of strong reflections. The solution method described in this paper can cope well with reflected waves. This stands in contrast to the de Boer–van Bienema (1982)

method which often fails in such cases (see, for instance, the resynthesis results in de Boer, 1995b). We may conclude that the method developed is a good and useful instrument for the further development of cochlear models, especially when it is required that the models be three-dimensional in nature and should include and properly represent retrograde waves or reflections.

On a tentative basis, we applied the method to locally active models like that of Neely and Kim (1986) and that of Geisler and Sang (1995). The model of Neely and Kim is a ''classical'' model in the sense that the reaction of the cochlear partition at location x is completely determined by the BM movement at the same location. The model of Geisler and Sang (1995) is not a ''classical'' model because the dynamics of the cochlear partition at location x is influenced by events taking place elsewhere. The response of that model is, however, identical to the response of a ''classical'' model when the two models have the same effective BM impedance (de Boer, 1997b). Both of these models have been conceived as long-wave models. We found that their parameters need to be modified considerably before these models produce an acceptable response in a three-dimensional setting. This is undoubtedly due to the fact that in the response-peak region, the waves in those models are not long waves but are closer to being short waves, and the parameters are clearly not right for these.

ACKNOWLEDGMENTS

The author is indebted to Dan Geisler (University of Wisconsin), Fred Nuttall (Oregon Health Sciences University) and Arnold Tubis (Purdue University) for fruitful discussions on the theme treated in this paper. This work has been executed as a continuation of project nr SLW 01.011 supported by the Netherlands Foundation for Scientific Research (NWO).

APPENDIX A: POLYNOMIAL COEFFICIENTS FOR EQ. (1)

Suitable polynomial coefficients for the three-dimensional model are

	Numerator		Denominator	
ϵ	a_2	a_4	b_2	b_4
0.1	0.9	5.0×10^{-3}	1.2×10^{-2}	8.0×10^{-6}
0.15	0.75	5.0×10^{-3}	2.0×10^{-2}	8.0×10^{-6}
0.2	0.85	6.0×10^{-3}	3.0×10^{-2}	1.0×10^{-5}
0.3	0.55	1.0×10^{-3}	1.0×10^{-2}	3.0×10^{-6}
0.4	0.4	1.0×10^{-3}	1.4×10^{-2}	3.0×10^{-6}
0.5	0.4	1.0×10^{-3}	1.6×10^{-2}	4.0×10^{-6}
0.6	0.4	1.0×10^{-3}	2.0×10^{-2}	5.0×10^{-6}
0.7	0.38	1.0×10^{-3}	2.5×10^{-2}	7.0×10^{-6}
0.8	0.35	1.0×10^{-3}	2.5×10^{-2}	8.0×10^{-6}
0.9	0.3	1.0×10^{-3}	2.5×10^{-2}	1.0×10^{-5}

APPENDIX B: FORWARD SOLUTION, MATRIX COMPOSITION

We consider the solution of Eq. (7) by way of discretization of the x axis. We have to express the second, fourth and sixth derivatives to an accuracy of the order $(\delta x)^7$, where δx is the length of one segment in the x direction. Consider the sequence y_i (with i an integer) as a function of x_i with $x_i = x_0 + i\,\delta x$; both sequences are samples of the continuous variables $y(x)$ and x. A Taylor's series expansion of y around its value $y_0 = y(x_0)$ can be made in the range from -3 to $+3$ of i, and leads to

$$\begin{aligned}
y_{-3} - y_0 &= -3D^{(1)} + 9D^{(2)} - 27D^{(3)} \\
&\quad + 81D^{(4)} - 243D^{(5)} + 729D^{(6)}, \\
y_{-2} - y_0 &= -2D^{(1)} + 4D^{(2)} - 8D^{(3)} + 16D^{(4)} \\
&\quad - 32D^{(5)} + 64D^{(6)}, \\
y_{-1} - y_0 &= -D^{(1)} + D^{(2)} - D^{(3)} + D^{(4)} \\
&\quad - D^{(5)} + D^{(6)}, \\
y_{+1} - y_0 &= +D^{(1)} + D^{(2)} + D^{(3)} + D^{(4)} \\
&\quad + D^{(5)} + D^{(6)}, \\
y_{+2} - y_0 &= +2D^{(1)} + 4D^{(2)} + 8D^{(3)} + 16D^{(4)} \\
&\quad + 32D^{(5)} + 64D^{(6)}, \\
y_{+3} - y_0 &= +3D^{(1)} + 9D^{(2)} + 27D^{(3)} \\
&\quad + 81D^{(4)} + 243D^{(5)} + 729D^{(6)},
\end{aligned} \tag{B1}$$

where the symbol $D^{(j)}$ denotes

$$D^{(j)} = \frac{(\delta x)^j}{j} \frac{d^j}{dx^j} y(x_0). \tag{B2}$$

Inversion of the coefficient matrix in (B1) (for instance, via MATLAB®) yields:

$$\begin{aligned}
D^{(2)} &= (4y_{-3} - 54y_{-2} + 540y_{-1} + 540y_{+1} \\
&\quad - 54y_{+2} + 4y_{+3} - 980y_0)/720, \\
D^{(4)} &= (-5y_{-3} + 60y_{-2} - 195y_{-1} - 195y_{+1} \\
&\quad + 60y_{+2} - 5y_{+3} + 280y_0)/720, \\
D^{(6)} &= (y_{-3} - 6y_{-2} + 15y_{-1} + 15y_{+1} \\
&\quad - 6y_{+2} + y_{+3} - 20y_0)/720.
\end{aligned} \tag{B3}$$

From Eqs. (B2) and (B3) the elements of the matrix to be used in solving Eq. (7) are easily found. Obviously, the matrix is a band matrix, with three elements on both sides of the main diagonal.

The equation set needs six boundary conditions, to be formulated in the matrix rows that are incomplete. For stimuli of not too low frequency, the conditions at the end of the model are easily formulated: the value of $u(x)$ as well as of its first and second derivative are set to zero. For stimuli that do not have their short-wave region near the stapes, the boundary condition at $x = 0$ can be formulated by using Eq. (8) to relate $u(x)$ to the stapes velocity. We further prescribe that $u(x)$ obeys the long-wave equation at the two next points.

Allen, J. B. (**1977**). ''Two-dimensional cochlear fluid model: New results,'' J. Acoust. Soc. Am. **61**, 110–119.

de Boer, E. (**1981**). ''Short waves in three-dimensional cochlea models: Solution for a 'block' model,'' Hearing Res. **4**, 53–77.

de Boer, E. (**1991**). ''Auditory physics. Physical principles in hearing theory. III,'' Phys. Rep. **203**, 127–229.
de Boer, E. (**1995a**). ''The ''inverse problem'' solved for a three-dimensional model of the cochlea. I. Analysis,'' J. Acoust. Soc. Am. **98**, 896–903.
de Boer, E. (**1995b**). ''The ''inverse problem'' solved for a three-dimensional model of the cochlea. II. Application to experimental data sets,'' J. Acoust. Soc. Am. **98**, 904–910.
de Boer, E. (**1996**). ''Mechanics of the cochlea: modeling efforts,'' in *The Cochlea*, edited by P. Dallos, A. N. Popper, and R. R. Fay (Springer-Verlag, New York), pp. 258–317.
de Boer, E. (**1997a**). ''Connecting frequency selectivity and nonlinearity for models of the cochlea,'' Aud. Neurosci. **3**, 377–388.
de Boer, E. (**1997b**). ''Classical and non-classical models of the cochlea,'' J. Acoust. Soc. Am. **101**, 2148–2150.
de Boer, E., and van Bienema, E. (**1982**). ''Solving cochlear mechanics problems with higher-order differential equations,'' J. Acoust. Soc. Am. **72**, 1427–1434.
Geisler, C. D., and Sang, C. (**1995**). ''A cochlear model using feed-forward outer-hair-cell forces,'' Hearing Res. **86**, 132–146.
Kolston, P. J., and Ashmore, J. F. (**1996**). ''Finite element micromechanical modeling of the cochlea in three dimensions,'' J. Acoust. Soc. Am. **99**, 455–467.
Mammano, F., and Nobili, R. (**1993**). ''Biophysics of the cochlea: Linear approximation,'' J. Acoust. Soc. Am. **93**, 3320–3332.
Neely, S. T., and Kim, D. O. (**1986**). ''A model for active elements in cochlear biomechanics,'' J. Acoust. Soc. Am. **79**, 1472–1480.
Sondhi, M. M. (**1978**). ''Method for computing motion in a two-dimensional model,'' J. Acoust. Soc. Am. **63**, 1468–1477.

Comments on "A method for forward and inverse solutions of a three-dimensional model of the cochlea" [J. Acoust. Soc. Am. 103, 3725 (1998)]

Hendrikus Duifhuis
Neurobiophysics Department, Center of Behavioral and Cognitive Neurosciences, University of Groningen, Nÿenborgh 4, 9747 AG Groningen, The Netherlands

(Received 14 January 1998; accepted for publication 11 March 1998)

This comment specifies reservations about the generalizability of de Boer's letter [J. Acoust. Soc. Am. **103**, 3725 (1998)] in which he claims that the real (nonlinear) cochlea can be analyzed using a straightforward extension of a common linear analysis. Two points are elaborated. Basically they regard physical aspects of boundary conditions at the cochlear partition and at the helicotrema. © *1998 Acoustical Society of America.* [S0001-4966(98)06706-X]

PACS numbers: 43.64.Kc, 43.64.Bt [RDF]

This comment specifies reservations about the generalizability of de Boer's proposal, where in passing his claim is that the real cochlea can be analyzed as a straightforward extension of linear analysis. It is clear that our knowledge about analysis of linear systems is formidable. But so is our lack of understanding essential nonlinear systems. This does not mean to imply that a linear approximation of the nonlinear structure is irrelevant, but it should imply caution, and analytical and/or computational checks.

Let me focus the attention on two (linear) points in the current letter, which is an extension of de Boer and van Bienema (1982). In my view the assertion that the wave number k describing the fluid hydrodynamics should be real (Sec. I) is incorrect. As far as I can follow the argument, referring back to de Boer (1981), it consists of the following steps. It starts with the assumption that the x, y, and z components in the fluid flow are separable. The next assumption is that the fluid flow at the base is in the longitudinal (x) direction (de Boer, 1981, Eq. 7–10). It seems that the conditions for separation are not fulfilled because the boundary conditions at the cochlear partition (or basilar membrane) differ from those at the walls, even though the membrane deflection may be negligible in a first approximation.

However, pressure gradients will be quite different from those at the walls. Hence, in three dimensions (3D), just as in one dimension (e.g., Kanis and de Boer, 1993, Eq. 2), the general solution to the eikonal equation in k is complex. The imaginary part physically accounts for loss of energy flow in the x direction, which is compensated for by an increased flow towards the partition (Duifhuis, 1988, Appendix). The effect that the energy flow entering the cochlea focuses on the partition near (before) the point of resonance, seems to be accepted by most cochlear modelers, including de Boer in most of his studies.

The assumption that the x, y, and z components are separable has been made before in several studies. The arguments for the y direction are quite convincing if one realizes that it implies a nonexisting symmetry. For x and z it seems to be a quite different matter. If the pressure $p(x,z)$ is separable in say $q(x)\cdot r(z)$, then the Fourier transform with respect to x would be $Q(k)r(z)$. If the Fourier transform (FT) is derived without the assumption of separation it turns out to be $Q(k;z=0)\cosh[k(h-z)]/\cosh[kh]$ (e.g., Siebert, 1974). I fail to see how the connection of k and z in the latter relation can be transformed analytically into the product relation required for the separation.

A second point that I want to stress is that the boundary condition at the helicotrema, viz., $p(L)=0$, is (bio)physically incorrect, even though it appears in quite a few models. In fact, several 3-D models assume $p(L,y,z)=0$, for all y and z. Sometimes this assumption is stated explicitly, sometimes implicitly, e.g., in certain cases of periodical continuation. (Bio)physically, the pressure profile of the slow wave (Lighthill, 1981; Duifhuis, 1988) will have a nonzero component at $x=L$. This component can cause significant effects in the time domain, but effects that may be missed altogether by a frequency domain analysis (see also Duifhuis and van den Raadt, 1997, p. 228).

In view of these issues, I considered de Boer's current analysis a straightforward expansion of his 1982 article, rather than an elucidating step toward a better understanding of cochlear mechanics.

de Boer, E. (**1981**). ''A method for forward and inverse solutions of a three-dimensional model of the cochlea,'' Hearing Res. **4**, 53–57.

de Boer, E., and van Bienema, E. (**1982**). ''Solving cochlear mechanic problems with higher order differential equations,'' J. Acoust. Soc. Am. **72**, 1427–1434.

Duifhuis, H. (**1988**). ''Cochlear macromechanics,'' in *Auditory Function*, edited by G. M. Edelman, W. E. Gall, and W. M. Cowan (Wiley, New York), pp. 189–211.

Duifhuis, H., and van den Raadt, M. P. M. G. (**1997**). ''Usefulness of the nonlinear residual response method,'' in *Diversity in Auditory Mechanics*, edited by E. R. Lewis, G. R. Long, R. F. Lyon, P. M. Narins, C. R. Steele, and E. Hecht-Poinar (World Scientific, Singapore), pp. 226–232.

Kanis, L. J., and de Boer, E. (**1993**). ''Self-suppression in a locally active nonlinear model of the cochlea: A quasilinear approach,'' J. Acoust. Soc. Am. **94**, 3199–3206.

Lighthill, J. (**1981**). ''Energy flow in the cochlea,'' J. Fluid Mech. **106**, 149–213.

Siebert, W. M. (**1974**). ''Ranke revisited—A simple short-wave cochlea model,'' J. Acoust. Soc. Am. **56**, 594–600.

Auditory saltation: A new measure for an old illusion

David I. Shore,[a] Susan E. Hall, and Raymond M. Klein
Department of Psychology, Dalhousie University, Halifax, Nova Scotia B3H 4J1, Canada

(Received 28 October 1997; accepted for publication 12 February 1998)

Auditory saltation is a mislocalization phenomenon in which click trains presented successively at two discrete spatial locations appear to originate from a smoothly varying series of source locations spanning the true source locations. The temporal parameters of this illusion are investigated with click stimuli delivered via headphones with the goal of establishing a portable test of the illusion. A simple rating scale was developed which required human participants to indicate the degree to which the perceived sound locations were heard as continuous (evenly distributed across space) versus discontinuous. Control conditions were devised to provide a baseline against which to compare the illusion. Auditory saltation is discussed in terms of perceptual grouping. © *1998 Acoustical Society of America.* [S0001-4966(98)05905-0]

PACS numbers: 43.66.Lj, 43.66.Mk, 43.66.Qp [JWH]

INTRODUCTION

Sensory saltation is a spatiotemporal illusion in which a stimulus occurring later in time affects the perception of one which occurs earlier. The basic phenomenon is a perceptual mislocalization of a brief stimulus when it is presented in close temporal proximity to a similar stimulus at a different location (Geldard, 1982; Geldard and Sherrick, 1986). The original observation involved a train of tactile vibrations in one location, followed by a second train in a different location (Geldard and Sherrick, 1972). Instead of feeling taps in only two locations, the participant reported feeling a train of taps spread evenly throughout the intervening space between the veridical locations. The degree of spreading was linearly related to the interval between the taps such that with interstimulus intervals (ISI) less than 20 ms, the first train of taps was felt at the second location. With ISIs greater than 250 ms, no illusion was observed. Since its original discovery the phenomenon has been observed in both the auditory (Bremer *et al.*, 1977) and visual modalities (Geldard, 1976; Lockhead *et al.*, 1980). The present experiment expands on a recent study of auditory saltation (Hari, 1995). This study is germane to our goals of developing a portable test because it made use of headphones instead of a free-field setup as was done in the past. As outlined below we expanded on this study in three ways. We devised an intuitive response method, included control stimuli against which the illusory trains could be compared, and tested stimuli whose interaural time difference (ITD) fell within the dynamic range of cortical neurons.

Auditory saltation warrants exploration for several reasons. First, it demonstrates a situation in which our perceptual system does not provide veridical information. Saltation is especially interesting because it represents an interaction between time and space. Second, there is recent evidence that dyslexic adults perceive the illusion over a much longer time span than normals (Hari and Kiesilä, 1996). If future testing proves this claim to be true, and extends to school-aged children, there is the possibility of using the strength of the illusion in a diagnostic fashion. Finally, since the illusion is experienced in all three spatial modalities, it can be used to investigate the degree to which spatiotemporal relations are represented in the brain in terms of modality specific maps of time and space, or, alternatively, in multi-modal maps.

Previous research using the auditory modality is sparse. There are several older reports which used free-field click stimuli (Bremer *et al.*, 1977; Geldard, 1976; Geldard and Sherrick, 1974, 1975). These helped to establish the phenomenon and some of the conditions which disrupt it. For example, making the pulses irregular eliminates the illusion (Bremer *et al.*, 1977). More recently, two studies have used clicks delivered via headphones and found a robust illusion (Hari, 1995; Hari and Kiesilä, 1996). These authors discovered that the illusion does not arise when clicks are delivered monaurally to the left and right ears alone, but requires the use of binaural click pairs delivered with a sub-millisecond ITD. Each binaural click thus composed is perceived as a single click that is lateralized to the side of the leading element of the pair. In Hari's studies, eight such binaural clicks (all with ITD of 800 μs) were presented per stimulus trial, four with left ear leading followed by four with right ear leading. The participant's task was to assign each of the eight clicks a unique location. At a long inter-click interval (ICI), participants perceived the first four clicks to the far left, and the next four clicks at the far right. As the ICI between the eight clicks was reduced, participants perceived the second through seventh clicks as originating in the intervening space. At the shortest ICIs, the perceived locations were evenly spaced between the two endpoints. This is a clear observation of the saltation illusion. In a simple control, monaural clicks were presented to the left and right ears with ICIs of 45 ms and 75 ms, and only a very slight tendency to mislocalize was observed at the shorter ICI.

The present experiment was designed to extend the previous study (Hari, 1995) in three distinct ways. First, a simple rating scale was developed. In order to localize each click in a stimulus train, as Hari's task demanded, the clicks must first be individuated. At short ICIs, the click train is perceived as a single moving entity having a buzzing quality.

[a]Electronic mail: David.Shore@dal.ca

 0001-4966/98/103(6)/3730/4/$10.00

It is difficult to count the constituent clicks, much less assign a location to each of them. We tested several adolescent children with this method and they reported the task to be very difficult. Whether the ability to individuate the constituent clicks is a functional correlate of the saltation illusion is an empirical question which we address in the discussion. Nevertheless, a response that requires click individuation confounds these two perceptual responses. For this reason, we developed a tool, described in Sec. I, which both simplifies the participant's task, and does not require click individuation in order to quantify the strength of the illusion.

The second extension to the previous work (Hari, 1995) was the inclusion of two control trains. The first, monaural train, replicated the partial control used by Hari (1995) but presented these stimuli at all ICIs used for the experimental trains. This functioned as a check of the participants' use of the rating scale, and as discussed below, led to some interesting observations. The second control train was composed of binaural clicks with ITDs that varied systematically from $+300$ μs to -300 μs in uniform steps within the stimulus train of eight clicks. We termed this train the varying interaural time difference train (VITD). ITD is a strong cue to stimulus location. Single binaural clicks having ITDs of these values are perceived to originate from roughly evenly spaced azimuthal locations ranging from about $+45°$ to $-45°$. This stimulus allowed us again to confirm that the rating scale was being used appropriately, and served as a comparison for the illusory displacement generated in the other conditions. While it is true that the changing ITDs in this stimulus were unaccompanied by intensity and spectral changes that would result from a truly displacing click source (in free field), the ITD cue alone is a strong cue to location and as such provides an adequate comparison.

Finally, we tested two ITDs. The binaural clicks used by Hari (1995) had an ITD outside the range which most neurons in the auditory cortex encode (Phillips and Brugge, 1985; Kelly and Phillips, 1991). That is, the responses of cortical neurons vary with increasing stimulus ITD up to about 500 μs. Further increases in stimulus ITD lead to no further changes in the response of these neurons. The perceived location of binaural clicks delivered through headphones becomes increasingly lateralized as ITD increases up to about 500 μs, at which point the percept tends to be of clicks originating from the leading ear. Beyond about 500 μs, the location remains at the leading ear, until at some ITD the binaural image is no longer fused and two clicks are heard. Within this range, where the click is perceived only from the leading ear, there is simply a perceptual ''suppression'' of the click at the lagging ear. This effect may be an analog to what has been called the ''precedence effect'' (Wallach *et al.*, 1949).

In the present study, we used binaural clicks with an 800-μs ITD, following Hari (1995), and in addition used binaural clicks having an ITD of 300 μs, which is well within the range coded by neurons in the auditory cortex. In this way, we wished to confirm that the illusion as experienced with headphones was not dependent on the use of the large 800-μs ITDs which might be expected to activate precedence effect mechanisms.

I. METHOD

A. Participants

Sixteen naive participants (nine males, seven females) who reported having normal hearing were recruited from the undergraduate participant pool at Dalhousie University. Each participant was given extra credit in one of the undergraduate courses at the university. One participant (assumed noncompliant) was excluded from analysis because she gave the same rating (discontinuous) for all conditions and all ICIs. Three additional participants were analyzed separately as discussed below. This left 12 participants for the main analysis.

B. Apparatus

A Macintosh 8500 computer running Hypercard was used to present the stimuli and collect responses using the mouse. Stimuli were presented over GenEXXA model HP-40 stereo headphones with an impedance of 100 ohms and a frequency response of 20–20 000 Hz. Stimuli were created using SoundEdit 16 version II.

C. Stimuli

Each click was generated from a 1-ms rectangular pulse to the transducer. Stimulus amplitudes (A-weighted dB sound pressure levels, i.e., dB *re:* 20 μPa) were measured using a Bruel & Kjaer type 2203 sound level meter equipped with type 4152 artificial ear and a type 4144 condenser microphone. Peak equivalent sound pressures varied with stimulus rate, from around 70 dB for clicks at 250- or 500-ms inter-click intervals, to 83 dB for click trains with 30-ms inter-click intervals.

There were two factors manipulated in this experiment: ICI [30, 45, 60, 75, 90, 120, 150, 250, and 500 ms] and stimulus type [Monaural, VITD, 800 μs, and 300 μs]. Monaural stimuli consisted of four single clicks presented to the left followed by four presented to the right. VITD stimuli consisted of binaural clicks with ITDs which varied from $+300$ μs to -300 μs in eight equal steps. The 800-μs and 300-μs stimuli consisted of four binaural clicks with the left ear leading followed by four binaural clicks with the right ear leading.

D. Procedure

Participants were first presented with a train of monaural clicks with an ICI of 60 ms. They were asked what they heard. Invariably, they said something akin to ''four clicks on the left followed by four clicks on the right.'' They were then shown the rating scale which had a step function at the top and told that stimuli like this which were heard separately on the left and right should be rated at this end of the scale. Next, participants were presented a VITD train with an ICI of 60 ms. Invariably, participants would report hearing a sound moving smoothly from the left to the right. We then showed them the bottom of the scale which had a smoothly sloped line and said that any series like this which appeared to move continuously from left to right should be rated at this end of the scale. The points inbetween were for stimuli

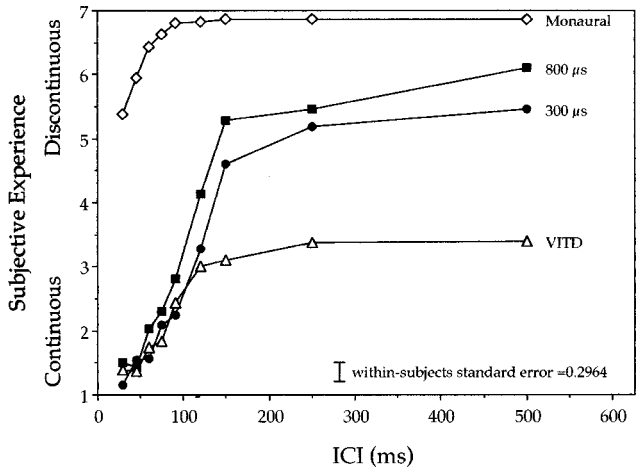

FIG. 1. Mean rating data from 12 participants presented across inter-click interval for the four conditions in this experiment. The within-subjects standard error bar shown in the bottom right corner was calculated using the highest order interaction term from the analysis of variance presented in the Results section.

which appeared to move part of the way and then jumped over some distance. Participants found this task easy to do. The participant used the mouse to indicate their response.

The participant then completed a practice block consisting of all 36 train types [9 ICIs×4 train types] presented in random order. The participant could listen to the trains as many times as desired before making a final rating. Both the final rating and the number of times listened were recorded. After completing the practice, the participant was asked if they had any questions or concerns. Finally, the participant was presented with five repetitions of the 36 trains in random order.

II. RESULTS

Mean response data for 12 participants are shown in Fig. 1. These data were submitted to a two factor repeated measures ANOVA. The two factors were ICI [30, 45, 60, 75, 90, 120, 150, 250, 500 ms] and train type [monaural, VITD, 300 μs, and 800 μs]. Both main effects were significant as was the interaction [ICI: $F(8,88)=66.28$, $MS_e=1.00$; train type: $F(3,33)=138.14$, $MS_e=2.61$; ICI×train type: $F(24,264)=11.84$, $MS_e=0.52$; all $p<0.001$].

The saltation illusion is reflected in the continuous ratings given to the two binaural train for ICIs less than about 120 ms. These ratings did not differ from the VITD controls indicating that participants perceived the saltation trains (300 μs and 800 μs) and the VITD trains similarly. With an ICI of 120 ms, participants reliably rated the 800-μs trains as more discontinuous than the VITD control trains [$t(264)=3.84$, $p<0.01$] while for the 300 μs their ratings did not differ from this control condition [$t(264)<1$]. With ICIs greater than this value, ratings for the two binaural trains were different from the VITD control [300 μs vs VITD: $F(1,264)=91.02$, $p<0.01$; 800 μs vs VITD: $F(1,264)=185.92$, $p<0.01$], and from each other [$F(1,264)=16.77$, $p<0.01$]. This indicates that participants reliably differentiated between the VITD trains and both of the saltation trains beyond an ICI of 150 ms.

Participants consistently rated the monaural control trains as discontinuous, with only a slight decline at the shortest ICIs. This trend was evident in the following pairwise comparisons made using a protected t-test. Ratings were more continuous for an ICI of 30 ms compared to an ICI of 60 ms [$t(264)=3.54$, $p<0.01$]. Further, ratings for an ICI of 45 ms were more continuous for an ICI of 75 ms [$t(264)=2.34$, $p<0.025$].

The option of multiple observations per sound was given to subjects to be sure that they were confident of their rating. There were no consistent trends in these data across ICI or stimulus type. Subjects opted for more exposures early in the experiment. By the second block (i.e., the first block of the experiment) few subjects listened to any sound more than twice. The modal number of observations was one. These data were not further analyzed. It should be noted that the illusion does not diminish with experience. From our informal experience, the perception seems to get stronger if anything.

As discussed in Sec. I, three participants were excluded from the main analysis just presented. These participants experienced the saltation illusion across the entire range of ICIs tested (i.e., they rated the two saltation trains (300 μs, and 800 μs) and the VITD trains identically). It is possible, although highly speculative, that these participants belong in the group labeled as dyslexic by Hari and Kiesilä (1996).

III. DISCUSSION

The main goals of this study were to develop a measure of the auditory saltation illusion which was easy and intuitive, and to replicate previous findings (Hari, 1995) with further temporal variations. As well, the inclusion of VITD trains and monaural controls at all ICIs allowed an assessment of the relative strength of the illusion. The results clearly showed that the saltation illusion is a robust phenomenon in the auditory modality. Ratings for the 300-μs and 800-μs stimuli were indistinguishable from those for the VITD stimuli at short ICIs, but diverged for ICIs greater than about 150 ms. Further, the ratings for the 300-μs trains were more similar to the VITD stimuli than those for the 800-μs trains. This was seen for ICIs of 120 ms and beyond. The monaural trains were consistently rated as coming from two discrete stationary sources.

It is clear that the rating scale we used replicated previous findings (Hari, 1995) and that those results generalize to click stimuli constructed with ITDs which are within the range coded by neurons in the auditory system. As such, we can be confident that the saltation illusion can be found using headphones. This provides an easy and portable methodology for the assessment of auditory saltation.

In comparing the 300-μs and 800-μs ITDs we found ratings of slightly greater continuity for the 300-μs stimuli across almost the entire range of ICIs. In other words, the saltation illusion was stronger for the 300-μs stimuli and extended to longer ICIs (120 ms for 300 μs, and less than this for 800 μs). This effect may be a result of the better localization associated with the stimuli within the dynamic range of cortical neurons. In general, these stimuli would be better localized in the sense that they would be discriminable

from other stimuli with similar ITDs. The longer ITDs lead to an almost total lateralization of the click, perhaps because of the precedence effect. A better localization could be responsible for the greater continuity ratings given to the short ITD stimuli because the perceptual system would have found it easier to assign relative locations to the illusory clicks in the intervening space. Note that the difference, while small, is consistent. In future work, it seems prudent to use an ITD which is within the dynamic range of neurons in the auditory system.

IV. PERCEPTUAL GROUPING: A POTENTIAL EXPLANATION FOR THE SALTATION ILLUSION

In trying to explain the saltation illusion, we were struck by the percept of the saltation trains. With short ICIs one perceives a blur of clicks as opposed to the eight individual clicks experienced at the longer ICIs. As the Gestalt psychologists noted, the perceptual system strives for the simplest interpretation of the complex stimuli present in the real world. A simple way to account for the mass of clicks perceived at the short ICIs is to group them and assume that a single sound source is moving smoothly through space and emitting these clicks as it moves. When the ICI is long, this interpretation begins to break down because each click can be identified and localized, and thus assigned its own source. As noted by Geldard (1982) for tactile saltation, as more taps are presented within a fixed time interval, a greater spatial extent can be covered. By squeezing more taps into the same extent, the task of individuation essentially becomes more difficult, and thus, a greater area can be accounted for by the same sound source. At present, this theory is highly speculative and further support needs to be gathered. This is similar to the distinction, in vision, between global and local processing (Navon, 1977), or the distinction, made by the Gestalt psychologists, between form and material (Klein and Barresi, 1985). A nice feature of this conjecture is that it accounts for the existence of the illusion in all three modalities.

One interesting observation, which is seemingly inconsistent with this model, is that saltation is not experienced for the monaural control stimuli. This observation may be related to the finding that in touch and vision, the saltation illusion does not cross the midline (Geldard, 1982). This finding is consistent with the present theory if we consider how these stimuli are represented in the auditory system. For the binaural stimuli, there exists a continuum between positive and negative ITDs which corresponds to the intervening space in which the illusory stimuli are perceived. For the monaural stimuli, there is no possible continuum from a left-only stimulus to a right-only stimulus. It is conceivable that the perceptual system re-interprets the representation of ITD to accommodate the illusory movement of the sound source. Such modification is not possible with stimulation to only one ear.

V. CONCLUSIONS

The present experiment demonstrated that the saltation illusion can be reliably found in the auditory modality, using headphones and an intuitive response method. This paves the way for testing outside the laboratory setting with younger children. The role of perceptual grouping is proposed as an organizing factor in the illusion.

ACKNOWLEDGMENTS

This project was supported by the Killam foundation by way of a post-doctoral fellowship to DIS and by the Natural Science and Engineering Research Council of Canada by way of a research grant to RMK. Dennis Phillips deserves a great deal of thanks for his expert technical advice and astute comments on previous drafts of this manuscript. We would also like to thank William C. Schmidt for comments on this manuscript and Bill Matheson for collecting the data. This paper has also been presented at the Psychonomics Society Meeting in Philadelphia, PA (November 1997).

Bremer, C. D., Pittenger, J. B., Warren, R., and Jenkins, J. J. (**1977**). ''An illusion of auditory saltation similar to the cutaneous ''rabbit,'' '' Am. J. Psychol. **90**, 645–654.

Farmer, M., and Klein, R. M. (**1995**). ''The evidence for a temporal processing deficit linked to dyslexia: A review,'' Psychonomic Bull. Rev. **2**, 460–493.

Geldard, F. A. (**1976**). ''The saltatory effect in vision,'' Sensory Processes **1**, 77–86.

Geldard, F. A. (**1982**). ''Saltation in somesthesis,'' Psychol. Bull. **92**, 136–175.

Geldard, F. A., and Sherrick, C. E. (**1972**). ''The cutaneous ''rabbit'': A perceptual illusion,'' Science **178**, 178–179.

Geldard, F. A., and Sherrick, C. E. (**1974**). ''Princeton cutaneous research project reports (No. 24),'' Princeton University.

Geldard, F. A., and Sherrick, C. E. (**1975**). ''Princeton cutaneous research project reports (No. 26),'' Princeton University.

Geldard, F. A., and Sherrick, C. E. (**1986**). ''Space, time and touch,'' Sci. Am. **255**, 90–95.

Hari, R. (**1995**). ''Illusory directional hearing in humans,'' Neurosci. Lett. **189**, 29–30.

Hari, R., and Kiesilä, P. (**1996**). ''Deficit of temporal auditory processing in dyslexic adults,'' Neurosci. Lett. **205**, 138–140.

Kelly, J. B., and Phillips, D. P. (**1991**). ''Coding of interaural time differences of transients in auditory cortex of *Rattus norvegicus*: Implications for the evolution of mammalian sound localization,'' Hearing Res. **55**, 39–44.

Klein, R. M., and Barresi, J. (**1985**). ''Perceptual salience of form versus material as a function of variations in spacing and number of elements,'' Percept. Psychophys. **37**, 440–446.

Lockhead, G. R., Johnson, R. C., and Gold, F. M. (**1980**). ''Saltation through the blind spot,'' Percept. Psychophys. **27**, 545–549.

Navon, D. (**1977**). ''Forest before trees: The precedence of global features in visual perception,'' Cogn. Psychol. **9**, 353–383.

Phillips, D. P., and Brugge, J. F. (**1985**). ''Progress in neurophysiology of sound localization,'' Annu. Rev. Psychol. **36**, 245–274.

Wallach, H., Newman, E. B., and Rosenzweig, R. (**1949**). ''The precedence effect in sound localization,'' Am. J. Psychol. **42**, 315–336.

Effect of climate upon organ tone

N. Thompson-Allen
Yale School of Music, Stoeckel Hall, 96 Wall Street, New Haven, Connecticut 06511

J. M. Harrison
Department of Psychology and Hearing Research Center, Boston University, 64 Cummington Street, Boston, Massachusetts 02215

(Received 7 July 1997; revised 2 March 1998; accepted 4 March 1998)

Woolsey Hall, Yale University, which houses the Newberry Memorial Organ is not climate controlled and some listeners have the impression that the tone of the organ varies with the seasons. The present work measured the overall SPL, and the SPL's of the harmonics of the C's of a number of flue and reed stops of the organ in August and March, 1996 to determine possible seasonal differences. The C's of flue and reed stops were recorded in the hall using a calibrated microphone and digital tape recorder system. The tapes were played into a computer, using Spectraplus 4 software, and the overall SPL levels of each C together with the SPL levels of the harmonics were extracted. The overall levels of 67 out of the 76 observations of the C's were 0.5–14 dB higher in August than in March, confirming the impression that the organ sounds louder in the summer. In 55 observations higher numbered harmonics that were present in August were absent in March. These findings are compatible with the impression that the organ sounds brighter in summer. © *1998 Acoustical Society of America.* [S0001-4966(98)05006-1]

PACS numbers: 43.75.Np [WJS]

INTRODUCTION

Many organs reside in buildings which do not have air conditioning during the summer, resulting in large humidity and temperature changes over the year. It is well known that changes in temperature change the pitch of sounding pipes. However, it is also reported by some organ builders (personal communications) that the temperature and humidity changes over the seasons also seem to change the loudness and brightness of the organ, in addition to altering the pitch. It is difficult to establish such tonal changes by simply listening because it requires an accurate memory of the sound in the summer, for example, in the middle of winter.

Woolsey Hall, Yale University, which houses the Newberry Memorial Organ, is not temperature or humidity controlled during the summer, and, from listening, it appears that the organ is louder and brighter in the summer. It was the purpose of the present work to measure the overall sound pressure level and the spectra of a number of flue and reed pipes of the organ under summer and winter conditions, to determine the possible presence and size of the putative seasonal changes.

I. METHOD

A. Apparatus

A 1-in. Bruel & Kjaer condenser microphone (4145) was mounted on a tripod set in front of seat #13 of the front row of the first balcony in Woolsey Hall. This is a prime listening location for the organ. The output of the microphone was fed to a low-pass filter (Khrone-Hite 3100-R), set to cut off frequencies above 15 kHz, and then to a digital tape recorder (DAT) (Sony DTC79, set to a 48-kHz sampling rate), both located at the organ console at the front of the stage. The microphone was 29.7 m from the front of the organ. A digital multimeter (Tektronix 502A) was connected in parallel with the input to the DAT recorder and set to show the dBC SPL. The recording level of the DAT was set to a fixed value throughout the recording sessions, and the whole system was calibrated using a Bruel and Kjaer pistonphone (4220).

The DAT records were analyzed using Spectraplus 4.0 (Pioneer Hill Software). The tapes were played into the computer and the spectra, and overall SPL levels of all the C's of four diapason stops and nine chorus reed stops were measured.

B. Procedure

Measurements were taken in March 1996 (Temp. 69.6 F, RH 32%) and August 1996 (Temp 87.6 F, RH 58%). The procedure in each recording session was the same. All the C's of each of the stops were recorded. For each note, the tape was started and allowed to record about 10 s of hall ambient noise; the note was then played for 10 s. At the termination of the note the tape was allowed to run for a further 12 s to show the reverberation time. Nine chorus reed stops and four Diapason stops were measured.

Changes in the overall SPL of each note between August and March were obtained by subtracting the SPL of the note in March from the SPL in August. The pressure level of each harmonic of each note was measured in August and March, and spectral differences were obtained by subtracting the level of each overtone in March from the level in August. Harmonics of less than 10 dB SPL and having frequencies greater than 10 kHz were not measured.

II. RESULTS

A. Overall SPL change

The difference in dB between August and March is shown for all the stops in Table I. Of the 76 differences

 0001-4966/98/103(6)/3734/3/$10.00

shown in the table, only six are negative, and three zero. That is, 67 of the notes had a 0.5–14 dB higher SPL in August than March. These data indicate that pressure level of the organ was higher in summer than winter, confirming the subjective impression that the organ sounds louder in Summer.

B. Spectral changes

The difference (dB) in level between the August and March spectral levels was obtained for each harmonic of each note. The results were essentially the same for all the stops, so the results for five typical stops are shown in Tables II, III, and IV. The extent to which the upper partials departed from being harmonics of the fundamental frequency was not investigated (Ando and Yamaguchi, 1993). However, the status of the upper partials described here is the same as those described as harmonic, for example, by Boner (1938), and Fletcher *et al.* (1964). That is, the frequencies of the partials appeared to be harmonically related within the limits of the measuring technic used.

The number of harmonics decreased from a maximum of 28 at the note C2 to two at the note C8. This decrease is the product of, one, the fact that the pipes generated a decreasing number of harmonics as the frequency increased, and two, an increasing number of harmonics fell below the threshold of hearing as the frequency of the note increased in agreement with other observations (Harrison and Thompson-Allen, 1998; Fletcher *et al.*, 1964; Boner, 1938; Lottermoser, 1940, 1950). Harrison and Richards (1941) reported up to 20 harmonics in 9 different trumpet pipes (all sounding C4). Both of these sets of data are in agreement with the present findings.

TABLE I. Overall pressure level difference (dB) between August and March.

	16 ft					
	C1	C2	C3	C4	C5	C6
16-ft Tromb (Gt)	7	4	4	7	5	5
16-ft Diap (Gt)	6	4	4	2	4	6

	8 ft					
	C2	C3	C4	C5	C6	C7
8-ft Trump (Sw)	5	6.5	1	8	1.5	1.5
8-ft Trump (Solo)	4	[a]	2	9	−2	2
8-ft Tuba (Solo)	3	3	2	8	1	−4
8-ft Tromba (Gt)	6	7	3	0.5	5	7.5
8-ft #1 Diap (Gt)	8	4.5	7	1	−9	2
8-ft #4 Diap (Gt)	1	0	0.5	5	9	0

	4 ft					
	C3	C4	C5	C6	C7	C8
4-ft Clarion (Gt)	7	0	4	−0.5	−2	3
4-ft Clarion (Sw)	3	9.5	3	6.5	1.5	[a]
4-ft Clarion (Solo)	1.5	5	10	2	1	1
4-ft Oct. Trom (Gt)	3	1	14	8	3.5	5.5
4-ft Prin (Gt)	2	2	4	1	−4	4

[a]Datum missing.

III. DISCUSSION

The sound reaching the microphone is the product of the sound produced by the organ pipes and the transfer characteristic of the hall at the listening site. Any tonal changes as a function of climate change may be the product of either changes in the organ, in the hall, or in both.

A. Variation of frequency with temperature

Because of the increase in the speed of sound with temperature, the frequency of an a 2-ft open flue pipe (middle C) would, theoretically, be approximately 6 Hz higher than 261.63 Hz (based on A4 440 Hz) in August than March. The frequency of all the other flue pipes would shift a corresponding amount. Thus the flue pipes of the organ will stay more or less in tune as temperature increases, but the pitch will become sharper.

The frequency of chorus reed pipes is less affected by temperature change, hence the flue pipes go sharp with respect to the reed pipes with increase in temperature. The organ is usually brought into tune at the higher temperature by sharpening the reeds using the tuning wires. Sharpening the reeds will reduce the size of the open area of the shallot, and possibly reduce the pressure level of the sound produced by the pipe. However, inspection of Table I indicates that there was no systematic difference in level between March and August for flue and reed pipes.

TABLE II. Changes in pressure level (dB) of spectra, August SPL–March SPL.

	Note C2				Note C3					
Stop	A	B	C		Stop	A	B	C	D	E
Over#	Diff	Diff	Diff			Diff	Diff	Diff	Diff	Diff
1	8	3	2		1	6	−3	4	1	
2	14	2	8		9	3	12	2	16	
3	5	−1	0		0	−2	4	4	7	
4	8	3	6		9	−4	8	1	−16	
5	7	14	−1		10	8	9	18	−2	
7	2	10	7		11	10	9	8	3	
8	7	4	−12		2	6	3	10	10	
9	5	3	14		13	−6	4	5	7	
10	5	5	6		−4	9	25	8	0	
11	13	5	16		0	7	4	9	12	
12	2	−3	4		13	9	1	8	14	
13	2	3	2		7	5	−5	−4	7	
14	18	12	5		5	[a]	5	3	2	
15	−8	5	2		[a]	9	17	0	2	
16	5	−3	−17		12	12	13	9	8	
17	3	−1	12		6		8	11	[b]	
18	−1	[a]	−2				5	1	[a]	
19	12	3	2				14	−9	[a]	
20	−7	−8	18				20	[a]	[a]	
21	11	−11	12				12	11		
22	−1	−1	[a]				11	−3		
23	[a]	[a]	[a]				[a]	[a]		
24	[a]	8	4				9	[a]		
25	[a]	9	[a]					[a]		
26	[a]	−1	[a]							
27			[a]							
28			[a]							

[a]March harmonics absent; Stops A, Gt 8-ft Trombone; B, Solo 8-ft Tuba; C, Sw 8-ft Trumpet; D, Gt Clarion; E, Gt Oct. Trom.
[b]Both harmonics absent.

TABLE III. Changes in pressure level (dB) of spectra, August SPL−March SPL.

Note C4						Note C5					
Stop Over#	A Diff	B Diff	C Diff	D Diff	E Diff	Stop	A Diff	B Diff	C Diff	D Diff	E Diff
1	0	9	−2	9	−7		7	15	12	0	16
2	2	−2	3	1	12		4	6	11	9	22
3	10	−3	9	−10	11		−8	2	−1	−6	16
4	0	−19	7	5	−4		7	7	10	−11	9
5	10	10	−11	8	14		16	9	26	9	16
6	6	10	2	6	11		10	6	11	12	[a]
7	9	5	1	−3	8		13	−4	4	25	1
8	15	5	12	15	14		[a]		20	[c]	
9	17	9	1	10	0		[a]			[c]	
10	4	−4	4	0	20					[c]	
11	15	[a]	18	[b]	[a]					[a]	
12	[a]		−8	[a]	[a]					[a]	
13	[a]		10	[b]	[a]					[a]	
14	[a]		[a]	[a]	[a]					[a]	
15	[a]		[a]		[a]						
16			[a]								

[a]March harmonics absent. See Table III for stop names.
[b]Both harmonics absent.
[c]August harmonics absent.

As an example of actual frequency changes over the seasons, the frequency of C4 of the #1 Diapason was measured in August and March. C4 was 5.39 Hz sharper in August than March, a little less than the theoretically estimated 6 Hz.

B. Reduced number of harmonics in winter

The most striking feature of Tables II, III, and IV is that many higher number harmonics were missing in March. There were 55 occasions when harmonics were present in August but absent in March (indicated by asterisks in Tables II, III, and IV). Typically, it was the higher numbered harmonics that were missing in March, confirming the impression that the organ sounds brighter in August than March. In only three cases (see Table III) were overtones present in March but absent in August.

The higher numbered harmonics have pressure levels between about 10 and 20 dB (SPL), and it is possible that they do not contribute to the sound of the note (Churcher, 1962). However, listening to recordings with either the lower numbered harmonics, or the higher numbered harmonics filtered out, showed that the higher numbered harmonics contributed to the sound of the note.

TABLE IV. Changes in pressure level (dB) of spectra, August SPL−March SPL.

Note C6						Note C7					
Stop Over#	A Diff	B Diff	C Diff	D Diff	E Diff	Stop	A Diff	B Diff	C Diff	D Diff	E Diff
1	1	−3	0	−28	9		8	0	1	−1	4
2	10	2	6	1	10		9	18	12	4	5
4	2	10	6	18	14		−2	[a]	[a]	[a]	9
5	12	11	16	5	[a]		15		[a]	[b]	[a]
6	10	[a]	[a]	[a]						[a]	[a]
7			11	5							
8				[a]							

Note C8

Stop Over#	D Diff	E Diff
1	8	13
2	−5	[a]

[a]March harmonics absent. See Table II for stop names.
[b]Both harmonics absent.

C. Woolsey Hall

The acoustics of Woolsey Hall have not been studied, so the extent to which the Hall contributes to the climatic changes in the sound of the organ is not known. The reverberation time of the empty Hall, 3.9 s (extrapolated to −60 dB) was measured in June 1996 using a wide-band noise.

ACKNOWLEDGMENTS

We thank Professor Thomas Murray, University Organist for permission to measure the Woolsey Hall organ. We also thank the Department of Psychology, and the Hearing Research Center, Biomedical Engineering, Boston University for support.

Ando, S., and Yamaguchi, K. (**1993**). ''Statistical study of spectral parameters in musical instrument tones,'' J. Acoust. Soc. Am. **94**, 37–45.

Boner, C. P. (**1938**). ''Acoustic spectra of organ pipes,'' J. Acoust. Soc. Am. **10**, 32–40.

Churcher, B. G. (**1962**). ''Calculation of loudness levels for musical sounds,'' J. Acoust. Soc. Am. **34**, 1634–1639.

Fletcher, H., Blackham, E. D., and Christensen, D. A. (**1963**). ''Quality of organ tones,'' J. Acoust. Soc. Am. **35**, 314–325.

Harrison, G. D., and Richards, E. (**1941**). ''Analysis of nine reeds by Dr. Boner,'' The American Organist **24**, 235–238.

Harrison, J. M., and Thompson-Allen, N. (**1998**). ''Steady state spectra of diapason class stops of the Newberry Memorial organ, Yale University,'' J. Acoust. Soc. Am. **103**, 626–629.

Lottermoser, V. (**1940**). ''Klangspektren einer Silbermannorgel,'' Akust. Zh. **5**, 324–330.

Lottermoser, V. (**1950**). ''Elektroakustische Messungen an beruhmten Barockorgeln Oberschwabens II. Klanganalytische Untersuchungen,'' Z. Naturforsch. A **5a**, 159–167.